ISSN 0915-6348

NATIONAL INSTITUTE FOR FUSION SCIENCE

Joint Conference of
17th International Toki Conference on
Physics of Flows and Turbulence in Plasmas and
16th International Stellarator/Heliotron Workshop 2007
Proceedins
Ceratopia Toki, Gifu, Japan, October 15-19, 2007

(Received - Dec. 5, 2007)

NIFS-PROC-69 Jan. 2008

**RESEARCH REPORT
NIFS-PROC Series**

TOKI, JAPAN

Joint Conference of

17th International Toki Conference on

Physics of Flows and Turbulence in Plasmas and

16th International Stellarator/Heliotron Workshop 2007

Proceedings

Ceratopia Toki, Gifu, Japan, October 15-19, 2007

International Advisory Committee

O. Motojima (Chair, Japan), C. Alejardre (Spain), B. Blackwell (Australia), J.H. Harris (USA), O. Kaneko (Japan), S. Imagawa (Japan), K. Kawahata (Japan), T. Klinger (Germany), A. Komori (Japan), L. Kovrizhnykh (Russia), J.F. Lyon (USA), T. Mutoh (Japan), N. Nakajima (Japan), N. Noda (Japan), N. Obysov (Russia), N. Ohyabu (Japan), J. Sanchez (Spain), M. Sato (Japan), S. Sudo (Japan), V.I. Tereshin (Ukraine), E.D. Volkov (Ukraine), F. Wagner (Germany), H. Yamada (Japan), M.C. Zarnstorff (USA)

International Program Committee

C. Hidalgo (Chair, Spain), B. Blackwell (Australia), V. Chechkin (Ukraine), J.H. Harris (USA), R. Kleiber (Germany), L. Kovrizhnykh (Russia), J. Sanchez (Spain), H. Yamada (Japan), M.C. Zarnstorff (USA)

Local Organizing Committee (National Institute for Fusion Science)

H. Yamada (Chair), T. Morisaki (Scientific Secretary), N. Ashikawa, H. Funaba, M. Goto, K. Hayashi, S. Ido, N. Iguchi, S. Ishiguro, N. Kano, M. Kobayashi, S. Masuzaki, J. Miyazawa, A. Morinaga, S. Morita, Y. Nagayama, S. Nakagawa, Y. Narushima, M. Nishiura, H. Okumura, B. J. Peterson, S. Sakakibara, R. Sakamoto, A. Shimizu, M. Shoji, H. Sugama, C. Suzuki, M. Tokitani, F. Tsutsumi, T. Watanabe, S. Yamada, S. Yoshimura

Preface

Joint Conference of
the 17th International Toki Conference and
the 16th International Stellarator/Heliotron Workshop

Carlos HIDALGO
CIEMAT, Madrid, Spain
Chairperson of International Program Committee

Hiroshi YAMADA
National Institute for Fusion Science, Toki, Japan
Chairperson of Local Organizing Committee

The Joint Conference of 16th International Stellarator/Heliotron Workshop (ISHW) and 17th International Toki Conference (ITC) was held in Toki (Japan) October 15-19 2007 and organized by the National Institute for Fusion Science (NIFS). More than 200 experts in stellarator/heliotron research from Australia, Austria, Belgium, Germany, Japan, Russia, Serbia, Spain, Ukraine and the United States of America gathered at the conference. The International Advisory committee chaired by O. Motojima, the International Program Committee (IPC) chaired by C. Hidalgo and the Local Organizing Committee (LOC) chaired by H. Yamada have played the leading role in the elaboration of the scientific programme of the joint conference. This series of Stellarator Workshops is organized biennially in the framework of the International Energy Agency (IEA) Implementing Agreement on the Stellarator Concept. NIFS has organized the ITC as an annual meeting for fusion related sciences since its establishment in 1989. The IPC arranged 2 plenary talks, 1 review talk, 2 tutorial talks, 23 invited talks in addition to 201 contributed presentations.

The driving force behind magnetically confined fusion research is the design of magnetic traps to confine high temperature plasmas of deuterium and tritium in reactor relevant conditions (i.e. to produce self-sustaining fusion reactions to release useful energy). Although next step magnetic confinement devices, such as ITER, will be based on the tokamak idea, it is not clear that a unique magnetic configuration will be the answer to the various possible applications of fusion energy and hence other magnetic confinement concepts should be explored. The stellarator is an alternative magnetic confinement concept, with the specific advantages of an intrinsically steady state magnetic field and disruption free operation. The 3D magnetic field geometry in stellarators needs an elaborate optimization to guarantee confinement properties which meet the basic requirements of a fusion reactor plasma. Development of stellarators as an alternative fusion reactor concept is a key issue confronting the stellarator community. This issue was addressed in the meeting by including special sessions on topics which are particularly relevant in the stellarator line as reactor concepts (e.g. divertor physics).

From the perspective of the basic understanding of systems far from thermal equilibrium, fusion plasma studies are a fully multi-disciplinary area of research. The joint ISHW/ ITC conference has emphasized the topical area of "*Flows and Turbulence*" which are seen widely in nature and are also becoming a high priority research area in magnetically confined plasmas.

Stellarators and tokamaks are complementary magnetic confinement concepts, but nevertheless share many common aspects. Thus, we should exploit synergies with the tokamak wherever meaningful. The International Stellarator/Heliotron Workshop benefited greatly from the presence of invited talks from the tokamak community, as in previous stellarator workshops.

The development of stellarator/heliotron working groups, including confinement database and profile database working groups, has been very a successful activity to fully promote international collaboration. Invited talks reporting on these key activities in the stellarator community were included in the programme. In addition, the workshop has been an adequate forum to trigger discussion on possible additional stellarator/heliotron working groups. This discussion has been fully welcomed and stimulated by the IEA Stellarator Executive Committee. Considering that a fusion reactor stellarator should operate at high beta with control of particle and energy exhaust, it was agreed to promote the development of a new stellarator/heliotron working group for further development of helical divertor concepts.

Slides of some oral presentations as well as the proceedings are available at http://itc.nifs.ac.jp/. Extended papers of major contributions will be also published in the special issue of Plasma and Fusion Research (http://www.jspf.or.jp/PFR/).

The next seventeenth International Stellarator Workshop will be held in Princeton, USA in 2009 and will be hosted by the Princeton Plasma Physics Laboratory.

Group photo

Contents

Plenary Talks

Review Talk

Tutorial Talks

Invited Talks

Oral Presentations

Poster Presentations 1

Poster Presentations 2

Plenary Talks

Proceedings of ITC/ISHW2007

Physics of Flows and Turbulence in Fusion Plasmas

Ulrich Stroth[1)]

[1)] *Institut für Plasmaforschung, Universität Stuttgart, 70569 Stuttgart, Germany*

(Received 2007 / Accepted 2007)

Results on flows and turbulent transport as obtained from stellarators, tokamaks and non-fusion devices are highlighted to discuss the complex interaction between them. Both neoclassical and turbulent transport processes are needed to cover the rich spectrum of experimental observations. The magnetic configuration plays an important role for both processes. Therefore, a better understanding of this important field could lead – after the first neoclassical optimisation of stellarators – to a second optimisation step which envisages improved control on turbulent transport.

Keywords: Plasma confinement, turbulence, rotation, zonal flows

DOI: 10.1585/pfr.1.001

1 Introduction

The interplay between flows and turbulence is a fascinating and rich topic of fusion research. Background flows aligned with the flux surfaces are a prerequisite for confinement of high-temperature plasmas. But even in globally stable plasmas, micro-instabilities lead to the development of turbulence. The interaction between flows and turbulence is twofold. Sheared flows can reduce turbulence and trigger the development of transport barriers while turbulence is able to power large scale zonal flows in a self-adjusting manner.

The physical description of flows and turbulence depends on details of the magnetic configuration used to confine the plasma: Magnetic curvature and trapped-particle drifts enter the calculation of growth rates and determine the character of turbulence. The topology of magnetic ripples not only defines the trapped-particle populations but also the parallel viscosity and hence the damping of the flows. Rational values of the rotational transform, magnetic islands and magnetic shear are further configurational elements with relevance for both flows and turbulent transport.

2 Physics of flows

In a simple magnetised torus, the physics of flows is relatively straightforward. The toroidal coordinate is identical with the symmetry axis and the plasma can flow freely parallel to the magnetic field $\mathbf{B}$. The poloidal plasma flow is decoupled from the poloidal one. It can only be generated by the diamagnetic and the $E\times B$ Drift. Even in a tokamak with ideal toroidal symmetry, due to the helical field lines the parallel flow is coupled to the poloidal one. The toroidal flow now is a superposition of a parallel flow and drifts due to the poloidal magnetic field component B_θ. Furthermore, due to the toroidal magnetic field ripple, poloidal flows are damped by a viscous force.

Equilibrium flows in toroidal geometry follow from the condition $\boldsymbol{\nabla} p = \mathbf{j}^{dia} \times \mathbf{B}$. As it can be seen in Fig. 1, diamagnetic flows have poloidal and toroidal components. Due to their mass, the ions are the relevant species for momentum studies. The toroidal component of the ion diamagnetic flow points into the same direction a plasma current has to flow in order to generate the rotational transform (call *co-direction*).

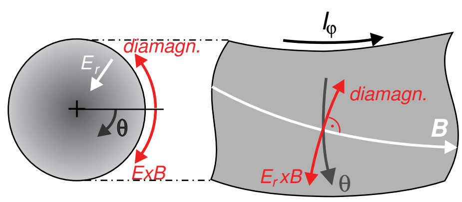

Fig. 1 Ion flows in toroidal geometry.

The poloidal flow u_θ is subject to a viscous force which, for qualitative studies, can be approximated by $F_\theta^{visc} \approx \sqrt{m}\hat{\mu}_\theta u_\theta$. The force depends on the mass m of the species and the parallel viscosity coefficient $\hat{\mu}_\theta$. The neoclassical transport can be understood as a radial drift $v_D = \mathbf{F}^{visc} \times \mathbf{B}/qB^2$ in response to the viscous force. Since the ion viscosity is higher, ion losses would be stronger than electron losses (assuming the same pressure gradient). This results in non-ambipolar radial transport and thus a negative radial electric field. This process goes on until the $E\times B$ drift, which slows down the poloidal ion flow and increases the electron flow, is strong enough to make the viscous forces on the two species equal and therefore transport ambipolar. What remains is a slow poloidal ion flow into the ion-diamagnetic direction, which has a small component into the toroidal co-direction. Even for a complex stellarator field as the one of W7-AS, the thus

author's e-mail: stroth@ipf.uni-stuttgart.de estimated ambipolar radial electric field

$$E_r^{amb} \approx \nabla_r p_i / en \tag{1}$$

agrees rather well with measurements and fully neoclassical calculations [1, 2].

Experiments on plasma rotation rely on measurements on impurities and not the mains ions. The impurity ion pressure p_I, their density n_I and flow velocity perpendicular to the magnetic field $u_{I\perp}$ have to be measured to allow for the calculation of the radial electric field according to the radial force balance for the impurity ions

$$\frac{E_r}{B} + u_{I\perp} - \frac{p_I'}{ZenB} = 0. \tag{2}$$

With expression (1) inserted for ambipolar electric field one finds

$$u_{I\perp} = -E_r/B + \partial_r p_I / Z_I e n_I. \tag{3}$$

E_r is set by the main ions. Since the pressure gradient of the impurities is in general smaller than the one of the main ions, the impurity-ion flow points into the $E \times B$ (ctr.) direction.

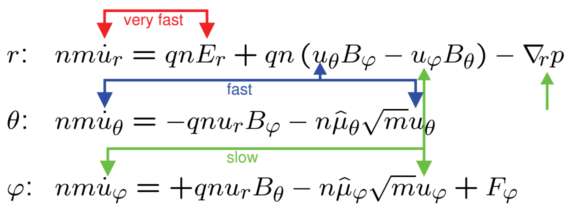

Fig. 2 Components of the ion-momentum equation.

The equilibrium flows can be modified by external and internal torques. As shown in Fig. 2, forces F_θ and F_φ act through the ion momentum equation on the ion flow. The ion and electron equations are coupled through the radial electric field. External momentum input can stem from neutral-beam injection (NBI), ion or electron-cyclotron-resonance heating (ICRH and ECRH). Momentum can also be redistributed internally by Reynolds stress. Locally this can be treated as a force. Furthermore, radial momentum transport is also a local source or sink of momentum, which can be represented by the forces in Fig. 2. The characteristic response time of flows to toroidal and poloidal forces are $\tau_\varphi = \hat{\mu}_\varphi/\sqrt{m} \gg \hat{\mu}_\theta/\sqrt{m} = \tau_\theta$. Since $\hat{\mu}_\varphi$ is small, the toroidal flows adjust rather slowly to equilibrium changes. Furthermore, due to their small mass electrons react much faster than ions. If the collisionality changes with time, the viscosities can also be modified leading to a distortion of the equilibrium and changes in flows and radial electric field. These changes happen on a fast time scale as far as the electron viscosity is concerned. Otherwise, the modifications in the flows should happen slower.

Modifications in the equilibrium act on the ambipolarity condition through the Lorentz force (indicated by arrows). Due to the fast reaction of the electrons, the reconstitution of ambipolarity through the radial component is a very fast process, too. Slow changes are also connected to the pressure gradient, which can only be modified on the confinement-time scales. A more direct manipulation of the radial electric field occurs if radial losses of fast electrons or ions are generated by e.g. ECRH or ICRH.

3 Toroidal flows

The recent interest in toroidal flows arises from their stabilising influence on MHD modes like the resistive wall modes in tokamaks [3]. In present day devices, toroidal plasma flows can readily be driven by NBI heating. In a fusion reactor, however, external momentum sources will be absent or insufficient. Hence, it is worthwhile to study the possibilities of an intrinsic generation of toroidal flows. In principle, there are two mechanisms which can drive core plasma rotation: a momentum inward pinch with the momentum source located at the plasma edge, and the toroidal component of the turbulent Reynolds stress. While the existence of a momentum pinch can be shown in transient phases of the plasma, the turbulent drive can only be assessed if all neoclassical effects are taken into account correctly. Alternatively, it can be attempted to measure the Reynolds stress directly.

In order to asses the importance of pinches or turbulent drives, the measured flow velocities have to be carefully compared to the neoclassical predictions addressed above. In Ohmically heated (OH) discharges on Alcator C-mod [4], the impurity ions flow into the direction opposite to the plasma current and the flow reverses sign with plasma current. The same is true for Ohmic plasmas in TCV [5]. The measured toroidal flow of C^{6+} in the core is into the ctr-direction, too. Little flow was observed close to the separatrix. These results agree with the expectations from neoclassical theory. The scaling of core flow velocity is $u_\varphi \sim T_i(0)/I_p$ [5]. The dependence on the central ion temperature can be understood in terms of the simple estimate of Eq. (1). Surprising is the spontaneous change in flow direction observed in TCV [6]: at a critical density, the flow changes from ctr to co-direction. This could be an effect of changing collisionality or due to the onset of a pinch or a turbulent drive.

On the DIII-D tokamak, a comparison of the rotation profiles with neoclassical theory has been carried out, too. Ohmic and ECRH H-mode discharges have been analysed [7]. In OH discharges, slow impurity core rotation was found. In the H-mode edge, where the impurity pressure gradient might become strong, the flow was stronger and co-directed. When ECRH was added leading to $T_e > T_i$, ctr-rotation became evident in the plasma core. The strong rotation coincided with the ECRH deposition profile. The comparison with neoclassical theory points to an additional toroidal torque.

Externally driven radial currents e.g. due to fast electron losses generated by ECRH must lead to a fast change in the ambipolar electric field. If electrons are lost, E_r becomes less negative and impurity rotation should become more co-directed. Ion losses, on the other hand, would lead to faster impurity rotation into the ctr-direction. A study of the effect of ion-ripple losses on toroidal rotation has been carried in JT-60U [8]. Although the plasma was heated with co-NBI, the impurity rotation at the plasma edge was into the ctr-direction. This is consistent with the the expected effect of ion losses due to the toroidal field ripple at the plasma edge. Consequently, a reduction of the magnetic ripple due to the insertion of ferritic steel tiles changed the edge rotation into the co-direction. Also in Alcator C-mod, a change of the toroidal rotation from ctr to co was observed, when ICRH was added onto Ohmic plasmas [9]. Although this behaviour is qualitatively consistent with neoclassical theory, a detailed analyses revealed that a momentum pinch is required to explain the data. Similar experiments carried out in ASDEX Upgrade, where ICRH was added to NBI discharges, yielded a reduction of the rotation velocity in both cases, with co and ctr-NBI. Here confinement changes were made responsible for the reduction in toroidal momentum [10].

If additional torques are applied due to NBI or wave momentum input parallel to the magnetic field, the ambipolar electric field is going to change on the slow time scale. The parallel flow contributes an additional flow component into the poloidal direction which now reads

$$u_\theta = (|u_{E\times B}| - |u_{dia}|)\cos\alpha \pm u_\parallel \sin\alpha \qquad (4)$$

Here α is the pitch angle of the field lines. If the arguments from above still apply and neglecting changes in the pressure profiles, the poloidal ion flow must remain unchanged. Consequently according to the discussion of Fig. 1, an external co-torque must lead to a reduction of the radial electric field, while a ctr-torque makes E_r more negative. The change happens slowly as plasma speeds up. The resulting electric field will be such that the flow mainly aligns with the direction of symmetry.

Here differences between stellarators and tokamaks can be expected. In an ideal tokamak the driven flow will align with the toroidal direction. Since the viscosity in this direction is small, neoclassical transport will not change substantially. In case of a stellarator, the resulting direction of rotation will depend on the specific magnetic configuration. In quasi-symmetric devices, strong flows can be driven without strongly increasing neoclassical transport. In the absence of symmetry, the momentum input will not drive the same rotation velocity and the influence on neoclassical transport will be more important.

In the CHS heliotron, the alignment of the flows with the direction of minimum ∇B was experimentally demonstrated [11]. In discharges with combined ECRH and NBI, an internal electron-transport barrier with positive radial electric field developed. The measured impurity flow pointed opposite to the direction NBI. It was shown that the net flow of the main ions is such that it aligns with the direction of minimum ∇B.

The presented survey shows that there exists no uniform picture of toroidal momentum transport yet . To disentangle neoclassical effects from turbulent ones is not simple. But it has to be done properly in order to conclude on spontaneous turbulent drives. Clearer than steady state analyses are transient transport experiments. They have already been successfully applied to particle transport, where an anomalous pinch has been observed in tokamak [12, 13] and stellarator experiments [14, 15]. Recently, a pinch has also been discovered in the momentum transport channel [16] and for the explanation, theoretical models related to symmetry breaking of turbulence [17] and a inwards drift due to the Coriolis force [18] have been put forward. If momentum is generated at the plasma edge, the pinch can transport it to the core. Hence the momentum pinch is one possible source of toroidal rotation for the plasma core. However, the momentum source needed for a complete model remains still unexplained.

Furthermore, there exists also first direct evidence for a turbulent drive of toroidal rotation. Measurement of the parallel Reynolds stress have been carried out in TJ-II [19]. Above a critical density, net energy transfer from turbulence to parallel flows has been found by means of probe measurements in the plasma edge.

4 Poloidal flows

Sheared poloidal flows are widely accepted to be beneficial for the reduction of turbulent transport. Of special interest are zonal flows, which are radially localised $E\times B$ flows with poloidal and toroidal mode numbers $m = n = 0$. Recent reviews of the vast experimental and theoretical work can be found in Refs. [20, 21, 22]. Still open are questions addressing the nature of the momentum sources, which can have neoclassical and turbulent elements, and the detailed mechanism of turbulence reduction. It is also well known, that the zonal flow couples to the Geodesic Acoustic Mode (GAM) [23], which appears at the characteristic frequency $f_{\text{GAM}} \sim c_s/R$. Hence, zonal flows mostly appear in the form of GAMs as it has been demonstrated in many devices using heavy-ion beam probes, beam emission spectroscopy and Doppler reflectometry (see Ref. [24] for a survey).

Zonal flows are also observed in fluid and gyro-fluid turbulence simulations. In the numerical models, the generation of zonal flows is clearly due to the turbulent Reynolds stress $\partial_r \langle \tilde{v}_\theta \tilde{v}_r \rangle$. Also in simulations they are oscillatory (GAMs) and radially localised. If interchange turbulence with radially elongated streamers is dominant, one can visually observe the decorrelation of the large turbulent structures [25]. Fluid simulations using the drift-Alfvén turbulence code DALF3 [26] have been carried out [27] to test analyses techniques for the study of the turbulent drive of zonal flows. The averaged poloidal flow from the simulations exhibited typical GAM structures. Using a cross-bispectrum technique, evidence for Reynolds-stress drive of the flows was found and correlation analyses also showed the reduction of turbulence in regions of maximum flow shear.

In the TJ-II heliac, the Reynolds stress has been measured directly with a probe array [28]. Gradients in the Reynolds stress were found in the vicinity of a shear layer. Also in linear devices, evidence for turbulent flow drive was found [29]. Poloidal rotation was observed in a plasma without net momentum input. The poloidal momentum balance was successfully checked using measured flow and Reynolds stress profiles. The generation of a zonal flow can also be interpreted as sign of an inverse turbulent cascade, which is expected to be active in magnetised plasmas. First direct evidence for the inverse cascade were was obtained from the TJ-K torsatron applying bispectral analyses methods on 2-dimensional probe data [30].

Hence there is ample evidence of the existence of poloidal flows and the importance of a turbulent drive.

5 Flows acting on turbulence

Zonal flows play a key role in the regulation of turbulent transport. Once generated through Reynolds stress, the flows can act back to reduce turbulence [20]. This interplay can be observed in turbulence simulations, but is rather difficult to be unambiguously demonstrated in experiment. Although the shear-decorrelation mechanism has been pointed out already in 1990 [31], there is still no clear experimental evidence on the reduction of the turbulent scales due to sheared flows.

Turbulent transport, which can be written as

$$\tilde{\Gamma} \sim |\tilde{n}| \left|\tilde{\phi}\right| \sin \delta_{n\phi}, \tag{5}$$

can be manipulated by different means. The density and potential fluctuation amplitudes $\tilde{n}$ and $\tilde{\phi}$ can be reduced. According to the mixing-length argument, this would be done by a reduction of the turbulent radial correlation length. On the other hand, a change in the cross phase $\delta_{n\phi}$ can influence transport, too. Which of the two effects is more important can sensitively depend on the dominant type of turbulence present in the plasma. While interchange turbulence is characterised by a cross phase of $\delta_{n\phi} \approx \pi/2$, the phase of drift-wave turbulence is close to zero. In the first case, a small change of $\delta_{n\phi}$ does not substantially alter transport while in the latter case small changes can already have strong influence on the its magnitude. Hence, in order to predict the role of shear flows in future devices, a knowledge of the expected dominant type of turbulence is of great importance. In Ion-Temperature-Gradient (ITG) or Trapped-Electron Modes (TEM), which both are of the interchange type, the characteristic streamer-like turbulent structures can efficiently be reduced by sheared flows while the effect of the cross phase might be negligible. This kind of turbulence is expected to be dominant in the core of tokamak plasmas. In the plasma edge of both stellarators and tokamaks, drift-wave turbulence might be more important. Drift waves do not show the radially elongated structures but they have small cross phases, hence the phase might be the key parameter to reduce transport at the plasma edge. Therefore related important questions are what is the character of turbulence in the core of stellarators and what is the dominant instability in the plasma edge of both stellarator and tokamak plasmas.

Already with the discovery of the H-mode in the ASDEX tokamak it was shown that the region of the transport barrier is related to reduced fluctuation amplitudes [32]. This has been confirmed in many different devices since where a edge transport barrier could be achieved. But sheared flows can also act on the cross phases as shown in biasing experiments on the small stellarator TJ-K, where drift waves have been shown to be the dominant instability [33, 34]. In this case no decorrelation of turbulent structures was detected. Confinement improvement happened rather due to cross-phase modifications [35].

Less is known about core transport in stellarators. In the core of larger tokamaks, ITG and TEM modes are likely to be dominant. This kind of turbulence can account for one major property of the temperature profiles, namely the profile resilience as, e.g. shown for the tokamak ASDEX Upgrade [36]. The fact that

$$\frac{1}{L_T} = \frac{\nabla T_e}{T_e} \approx \text{const.} \tag{6}$$

results in an offset-linear scaling of the electron heat flux vs. electron-temperature gradient as, e.g. shown for Tore Supra [37]. Although the electron temperature profiles in stellarators can become flat in the centre when ECRH is deposited off-axis, in the W7-AS stellarator there was also evidence for profile resilience when the central heating power was different from zero [38]. It should be stressed, that in a tokamak there is always residual Ohmic heating in the centre. Hence, similar concepts may also apply to stellarators plasmas and a quantitative comparison of the W7-AS results with tokamak models gave a quite good agreement, although the critical gradient in W7-AS is steeper [39].

If profile resilience is also present in stellarators, ITG and TEM turbulence may also be candidates to explain turbulent transport. Both instabilities are driven in the bad curvature regions of the plasma. Furthermore, to develop the TEM needs trapped particles in the region of bad curvature. Therefore, a optimisation of the magnetic configuration can also be carried out in view of a stabilisation of these modes. The W7-X stellarator has been optimised with respect to neoclassical properties. For neoclassical transport, the separation of curvature and trapped particles is also a criterium. In this respect, W7-X has also achieved some degree of optimisation against TEM turbulence.

First gyrokinetic simulations of TEM turbulence in W7-X geometry show [40] that the spatial distribution of local transport maxima reflects the fivefold symmetry of the magnetic configuration. The largest transport levels are found in regions where magnetic wells and bad curvature still overlap to some extent.

6 Summary and Conclusions

The paper intended to demonstrate the richness of the phenomena related to the interplay between flows and turbulence in toroidal plasmas and their importance for the development of future fusion devices. The importance arises from their ability to stabilise MHD modes and to reduce turbulent transport. Since future devices will not be equipped with sufficient means to drive strong flows, the spontaneous generation of flows is especially important.

The radial electric field, which is closely related to neoclassical transport, is the key player of the flow system. In plasmas without external momentum input, qualitative agreement with neoclassical expectations is found in many cases. But there also exist observations like the spontaneous flow reversal in TCV, that cannot readily be explained by neoclassical theory and need more sophisticated codes for interpretation. And there exists also clear evidence for momentum pinches which cannot be explained by standard neoclassical theory. The pinch can act as a momentum source in the plasma core, but a momentum source is still needed at the plasma edge. First evidence also exists that Reynolds stress can redistribute toroidal momentum to generate sheared toroidal flows.

Radially localised poloidal flows and their characteristics have been well documented in many experiments. There also exist strong indications for the importance of Reynolds-stress drive of these flows. Due to the toroidal field ripple, zonal flows also should interact with neoclassical transport. This aspect needs further attention and global turbulence simulations including neoclassical effects are desirable. There is also agreement that zonal flows have the ability to reduce turbulent transport. Details on the suppression mechanisms, however, are not yet fully understood and can be expected to depend on the type of the dominant instability.

The magnetic configuration enters in different aspects the flow-turbulence system. It sets the values of the different components of the parallel viscosity and therefore determines the amount of neoclassical transport for a given flow on the flux surface. In the same way the configuration determines the ability of the plasma to respond to torques and to develop zonal flows. On the other hand, curvature and trapped-particle populations are leading ingredients for driving turbulence. Both parameters are predefined by the magnetic configuration. A better understanding of the flow-turbulence system could therefore help to attempt an optimisation of the stellarator configuration with respect to both neoclassical and turbulent transport.

[1] H. Ehmler *et al.*, Nucl. Fusion **43**, L11 (2003).
[2] U. Stroth, in *Plasma Physics: Confinement, Transport and Collective Effects*, *Lect. Notes Phys.*, edited by A. Dinklage (Springer, Berlin, Heidelberg, 2005), Chap. 9, p. 213.
[3] E. J. Strait *et al.*, Phys. Rev. Lett. **74**, 2483 (1995).
[4] J. E. Rice, E. S. Marmar, F. Bombarda, and L. Qu, Nucl. Fusion **37**, 421 (1997).
[5] A. Scarabosio *et al.*, Plasma Phys. Controll. Fusion **48**, 663 (2006).
[6] A. Bortolon, B. P. Duval, A. Pochelon, and A. Scarabosio, Phys. Rev. Lett. **97**, 235003 (2006).
[7] J. S. deGrassie *et al.*, **11**, 4324 (2004).
[8] M. Yoshida *et al.*, Plasma Phys. Controll. Fusion **48**, 1673 (2006).
[9] J. E. Rice *et al.*, **45**, 251 (Nucl. Fusion).
[10] D. Nishijima *et al.*, Plasma Phys. Controll. Fusion **47**, 89 (2005).
[11] K. Ida *et al.*, Phys. Rev. Lett. **86**, 3040 (2001).
[12] D. R. Baker *et al.*, Nucl. Fusion **38**, 485 (1998).
[13] V. Mertens *et al.*, Plasma Phys. Controll. Fusion **32**, 965 (1990).
[14] U. Stroth *et al.*, Phys. Rev. Lett. **82**, 928 (1999).
[15] H. Nozato *et al.*, (2004).
[16] W. D. Lee *et al.*, Phys. Rev. Lett. **91**, 205003 (2003).
[17] Ö. D. Gürcan, P. H. Diamond, T. S. Hahm, and R. Singh, Phys. Rev. Lett. **14**, 042306 (2007).
[18] A. G. Peeters, C. Angioni, and D. Strintzi, Phys. Rev. Lett. **98**, 265003 (2007).
[19] B. Goncalves *et al.*, Phys. Rev. Lett. **96**, 145001 (2006).
[20] P. H. Diamond, S. Itoh, K. Itoh, and T. S. Hahm, Plasma Phys. Controll. Fusion **47**, R35 (2005).
[21] K. Itoh, S. Itoh, P. H. Diamond, and T. S. Hahm, .
[22] A. Fujisawa *et al.*, Phys. Rev. Lett. **98**, 165001 (2007).
[23] N. Winsor, J. L. Johnson, and J. M. Dawson, Phys. Fluids **11**, 2448 (1968).
[24] A. Fujisawa *et al.*, Plasma Phys. Controll. Fusion (2007).
[25] Z. Lin *et al.*, Nature **281**, 1835 (1998).
[26] B. Scott, Plasma Phys. Controll. Fusion **39**, 1635 (1997).
[27] M. Ramisch, U. Stroth, S. Niedner, and B. Scott, New J. Phys. **5**, 2012 (2003).
[28] C. Hidalgo *et al.*, Plasma Phys. Controll. Fusion **42**, A153 (2000).
[29] G. R. Tynan *et al.*, Plasma Phys. Controll. Fusion **48**, S51 (2006).
[30] P. Manz *et al.*, Plasma Phys. Controll. Fusion (2007), submitted.
[31] H. Biglari, P. H. Diamond, and P. W. Terry, Phys. Fluids **2**, 1 (1990).
[32] F. Wagner *et al.*, Phys. Rev. Lett. **49**, 1408 (1982).
[33] U. Stroth *et al.*, Phys. Plasmas **11**, 2558 (2004).
[34] N. Mahdizadeh *et al.*, Plasma Phys. Controll. Fusion **47**, 569 (2005).
[35] M. Ramisch *et al.*, Plasma Phys. Controll. Fusion **49**, 777 (2007).
[36] F. Ryter *et al.*, Phys. Rev. Lett. **86**, 5498 (2001).
[37] G. T. Hoang *et al.*, Phys. Rev. Lett. **87**, 125001 (2001).
[38] U. Stroth *et al.*, Phys. Scr. **51**, 655 (1995).
[39] F. Ryter *et al.*, Plasma Phys. Controll. Fusion **48**, B453 (2006).
[40] P. Xanthopoulos, F. Merz, T. Görler, and F. Jenko, Phys. Rev. Lett. **99**, 035001 (2007).

PL-02

Proceedings of ITC/ISHW2007

Competition and Synergy of Macro- and Micro-scale Physics – Status and Prospects of Macro-Micro Interlocked Simulation –

Kanya KUSANO, Shigenobu HIROSE, Tooru SUGIYAMA,
Akio KAWANO, Shinichiro SHIMA, Hiroki HASEGAWA, Yuji KAWAMURA

The Earth Simulator Center,
Japan Agency for Marine-Earth Science and Technology, Yokohama 236-0001, Japan

Multi-scale phenomena are now crucial issue in the wide range of research fields, not only plasma physics, but also chemistry, astrophysics, geo-science, bio-science and so on. For the last decade, aiming to understand the interaction between macro-scale and micro-scale dynamics, several new methodologies for numerical simulations have been quickly developed. Macro-Micro Interlocked (MMI) Simulation is one of such new simulation frame-works. The MMI simulation is performed by the two-way connection of different numerical models, which may handle macroscopic and microscopic dynamics, respectively. The application of the MMI simulation to different multi-scale phenomena, for instance, cloud formation, gas detonation, and plasma dynamics, is investigated. The results of all the applications demonstrates that the MMI simulation is a prospective methodology for multi-scale studies.

Keywords: multi-scale, simulation, plasma, cloud, detonation

1 Introduction

Multi-scale phenomena, in which the micro-scale elementary process and the macro-scale system dynamics mutually influences each other, are now a crucial issue in vastly different research fields, not only plasma physics, but also chemistry, astrophysics, geo-science, bio-science, material science, mechanical engineering, and so on. However, fundamental difficulty arises for the research of the multi-scale processes, because physical processes in different scales are governed by different physical laws, for instance, the molecular dynamics in micro-scale and the continuum dynamics in macro-scale.

Although computer simulation must be a powerful tool for the understanding and the predicting the complex nonlinear phenomena, the applicability of simulation cannot get rid of restriction of the scale, because computer simulation is usually formulated on the basis of the theoretical description like partial differential equations, which is valid only in some limited scale. Therefore, the applicability of each simulation model is also limited to the scale where the basic theory is valid.

To conquer this limitation, several new frameworks are proposed recently. So far, the multi-scale simulations have been developed by two different manners. The first is the extension of macroscopic simulation, in which the microscopic effects are included as phenomenological parameters, just like the anomalous resistivity caused by micro-scale turbulence in high-temperature plasmas and the bulk cloud parameterization in atmospheric global circulation model. However, since the phenomenological parameterization is not guaranteed to work well in unknown circumstances, the applicability of such a method must be restricted by given knowledge.

Another approach is the large-scale microscopic simulation, whereby the macroscopic phenomena are attempted to be built from the elementary block of micro-scale processes. The large-scale molecular dynamics (MD) simulation is the typical example of that. However, it is computationally so demanding. Since the scale which we can directly calculate with the MD model is limited to the order of micron meter, even using the world largest super-computer [4], we need the 10^{24} $(= 10^{6 \cdot 4})$ times faster computational capability than the current super computer. It would not be feasible at least in near future.

The limitation of the computational feasibility requires that a new type of software and mathematical frame-work should be developed to conquer the difficulty of multi-scale simulation. In fact, several new numerical models have been proposed recently for this purpose. One of the most promising concept is given by the interconnection of different numerical models. [1] developed a new way to make the interconnection between the finite-element, molecular dynamics and semi-empirical tight-binding

author's e-mail: kusano@jamstec.go.jp

representations, and demonstrated that the connection model, called MAAD (macroscopic, atomistic, ab initio dynamics), is effective as the methodology for the study of brittle crack propagation in silicon. On the other hand, [13] proposed the concept of heterogeneous multi-scale method (HMM) as a general methodology for multi-scale modeling. In the HMM, scale separation is exploited so that coarse-grained variables can be evolved on macroscopic spatial/temporal scales using data that are predicted based on the simulation of the microscopic process. Similar model was proposed also for meteorological simulation, which is called "super-parameterization," by [3] and [7]. Super-parameterization is performed by the mutual connection between atmospheric global circulation model (AGCM) and cloud system- resolving (CSR) model. In the super-parameterization, the CSR models are embedded inside each grid cell of AGCM, and the results of them are used for the cloud parameterization of AGCM.

Macro-Micro Interlocked (MMI) Simulation was proposed by [8] as a new methodology for the multi-scale simulation. The fundamental principle of the MMI simulation is in common with the heterogeneous multi-scale method (HMM) and the super-parameterization. The MMI simulation consists of the macro- and micro-simulation models, which are carried out simultaneously and interconnected to each other. The micro-model is performed under the environmental condition calculated by the macro-model, and the microscopic information is fed back to the macro-model [6]. Originally, the MMI simulation has been proposed as a computational algorithm suitable to the hardware of heterogeneous architecture, called MMI simulator, in which different types of architecture fitting respectively to the numerical models of macro- and micro-scales are interconnected. In particular, heterogeneous vector/scalar architecture is the most promising design of the MMI simulator, and we have developed several applications for that.

The objective of this paper is to present the brief review of the application study of the MMI simulation. In the following section, we will explain the principle and the typical results of each MMI simulations for cumulus cloud formation, gas detonation, and plasma dynamics. Finally, the prospects of the MMI simulation will be summarized in Sec.3.

2 Applications

2.1 Cloud Simulation

Although clouds play a crucial role in any meteorological phenomena like global warming, the numerical modeling of cloud is not well established yet. The reason of that is attributed to the fact that the formation of clouds and the development of precipitation are essentially governed by multiscale-multiphysics processes. The macro-scale processes such as the fluid motion of moist air associated with clouds is called "cloud dynamics", and the micro-scale processes such as the condensation and coalescence of water droplets are called "cloud microphysics". These two processes mutually affect each other.

Although the cloud dynamics simulation has been quickly developed with the achievement of large-scale fluid model, the first-principle simulation of cloud microphysics is still difficult. It is due to the fact that huge number of tiny droplets are involved in cloud processes. Therefore, some empirical approximation called 'bulk-parameterization' has been widely used for cloud modeling. However, the applicability of any empirical model is restricted as mentioned in Sec.1, and we cannot use it for the prediction of unknown phenomena like global warming.

Aiming to overcome this difficulty in the cloud modeling, we recently developed a novel simulation model of cloud microphysics, named Super-Droplet Method (SDM) [10], which is a particle-based cloud microphysics model. The *super-droplet* is defined as computational particle representing multiple real droplets, which have common properties, *e.g.* position, velocity, cloud condensation nuclear (CCN), and electric charge. The motion of each super-droplet is calculated by the equation of motion or by the assumption that each droplet immediately attains terminal velocity. The condensation and the evaporation of droplets can be directly calculated based on Köhler's theory using the properties of super-droplet and the state variable of atmospheric environment. The coalescence of droplets is handled by the stochastic manner just like the Direct Simulation Monte-Carlo (DSMC) method.

The cloud dynamics is simultaneously calculated with SDM using the non-hydrostatic model equations,

$$\rho\frac{D\vec{U}}{Dt} = -\nabla P - (\rho+\rho_w)\vec{g} + \lambda\nabla^2\vec{U}, \tag{1}$$

$$P = \rho R_d T, \tag{2}$$

$$\frac{D\theta}{Dt} = -\frac{L}{c_p\Pi}S_v + \kappa\nabla^2\theta, \tag{3}$$

$$\frac{D\rho}{Dt} = -\rho\nabla\cdot\rho, \tag{4}$$

$$\frac{Dq_v}{Dt} = S_v + \kappa\nabla^2 q_v, \tag{5}$$

where ρ is the density of moist air, ρ_w the density of liquid water, $\vec{U}$ the wind velocity, P the pressure, λ the viscosity, R_d the gas constant for dry air, T the temperature, θ the potential temperature, L the latent heat, q_v the mixing ratio of vapor, S_v the source of water vapor, and Π is the Exner function, respectively.

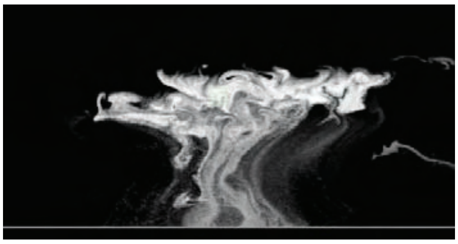

Fig. 1 The simulation results of cloud formation and precipitation using the super-droplet models. Horizontal line on the bottom indicates ground level, and gray-scale represents the cloud droplets.

The density of droplets

$$\rho_w(\vec{x},t) = \sum_i \xi_i m_i(t) w(\vec{x},\vec{x}_i),$$

and the conversion ratio between vapor and liquid

$$S_v(\vec{x},t) = -\frac{1}{\rho(\vec{x},t)} \frac{\partial \rho_w(\vec{x},t)}{\partial t},$$

are sent to the fluid model, and used in the source terms, where i is the index of super-droplet, ξ_i the multiplicity of super-droplet, m_i the mass of droplet, and w is the shape function of super droplet.

The algorithm of SDM, in which particles (droplets) and fluid (moist air) interact with each other, is basically same as particle-in-cell (PIC) plasma simulation, in which particles for electron and ions interact with electromagnetic fields assigned at cells. It is also similar to the plasma simulation that each super-droplet represents multiple number of real droplet.

In order to demonstrate the feasibility of SDM, it has been applied to the simulation of cloud formation and precipitation in maritime cumulus. The simulation system is given by 2-dimensional $x-z$ domain just for simplicity. The initial state consists of un-saturated stratified layer, which is slightly unstable only under 2km in altitude, and number of tiny droplets, which contain soluble substance as Cloud Condensation Nuclear (CCN), are uniformly distributed in the entire domain. As shown in Fig.1, the results indicate that the particle-continuum coupled model may work to simulate the whole process from cloud formation to precipitation without introducing any empirical parameterizations. The new model may provide a powerful tool for the study of cloud-related various problems, although the predictability of SDM should be evaluated more carefully.

2.2 Detonation Simulation

Combustion fluid dynamics is also the typical subject of multi-scale simulation, in which chemical reaction is mutually interacted with the macroscopic flow dynamics. In the conventional methods, the reaction is treated by the Arrhenius rate equation. However, the reaction rate of the equation must be derived from the distribution function assuming local thermal equilibrium (LTE). Although the LTE assumption could be satisfied in normal condition of fluids, when the local Knudsen number, which is defined as the ratio of mean free path to characteristic length scale, is larger than 0.01, the assumption of LTE may not be valid. In the case, the flow should be treated as rarefied gas and we have to solve the Boltzmann equation. Especially, detonation, which is sustained by shock wave driven by combustion wave, is the case, because the thickness of shock may be comparably thin as the mean free path. It implies that the Arrhenius rate equation may not be valid on the shock front.

So, we have developed a novel method for simulation of combustion by connecting a microscopic molecular model and a macroscopic continuum model, those are based on the Boltzmann equation and the Navier-Stokes equation, respectively. We adopted non-steady DSMC method for the molecular model, and the continuum model is carried out by the HLLC method.

Our detonation model is an extension of Hybrid Continuum-Atomistic Simulation, which has been developed by many authors [2, 14, 9]. The algorithm to connect the molecular model and the continuum model is summarized as follows: (1) Gradient of pressure is monitored during the simulation by the continuum model, and the molecular model is embedded in the region where the steepness exceed some threshold and the continuum model is failed. (2) Interlocking layers are laid around the outer-most region of the molecular domains, where particles are generated to let the distribution function be able to represent the macroscopic variables; density, velocity and pressure. Numerical flux on the outer-most boundary of the continuum domain is calculated from the particle motion.

Some result of the two-dimensional detonation simulation is shown in Fig.2. It represents the distribution of pressure on the detonation front. The domain between dotted lines corresponds to the region, where the particle-based model is adopted. The smooth connection between fluid and particle-based models indicates that the continuum-atomistic simulation is applicable also to the combustion process.

2.3 Plasma Simulation

Plasma inherently forms a multi-scale system, in which different characteristic scales related to electron and ions mutually interact. The key issue in multi-scale plasma processes is how macroscopic magneto-hydrodynamics (MHD) is related to microscopic particle kinetics. For instance, in magnetic reconnection

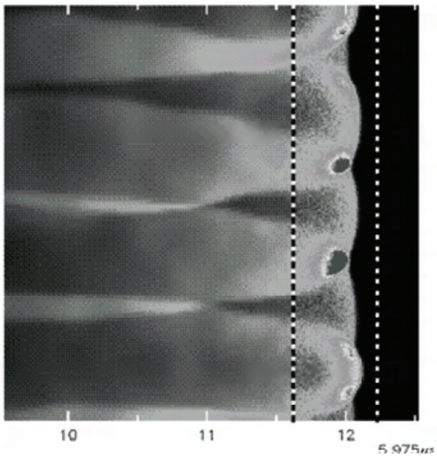

Fig. 2 The pressure distribution of the detonation simulation. The particle-based domain, which corresponds to the region bounded by dotted lines, tracks the detonation front.

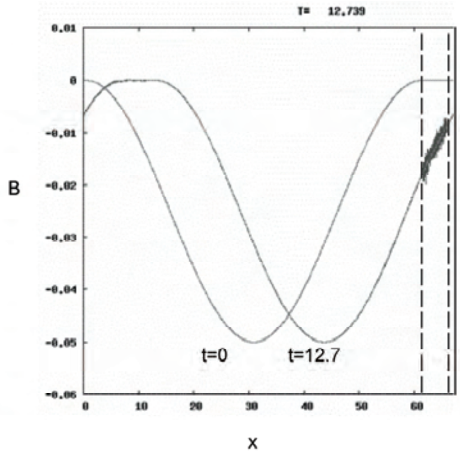

Fig. 3 Magnetic field distribution in the test simulation for Alfvén wave using the PIC-MHD interlocked model. The region between two dotted line corresponds to the part where PIC model is embedded.

that is responsible for explosive energy release in high-temperature plasmas, the kinetics might be important especially in the restricted diffusion region, which is formed when anti-parallel magnetic fluxes collide each other.

So, we have developed the new algorithm for such a multi-scale plasma dynamics. Our model is constituted by the connection of the particle-in-cell (PIC) model and the magnetohydrodynamic (MHD) model, the former of which is embedded in the MHD simulation domain[11]. This MHD-PIC interlocked model is resembled to the continuum-atomistic simulation, which was explained in the previous subsection. However, it should be mentioned that, in plasma simulation, several characteristics described by PIC model are negated in continuum (MHD) model, in contrast to the hydrodynamic simulations. So, in order to make the smooth interlocking between MHD and PIC models, we have to introduce some special filter, which passes only the MHD mode from the PIC domain to the MHD domain. The filtering process is actualized by the sophisticated sub-cycle procedure. Refer to [11] for the detail.

Figure 3c shows the magnetic wave form in the test-simulation for the one-dimensional Alfvén wave propagation. In this simulation, PIC model is embedded only in a small part of the simulation box, and we examined whether long wavelength Alfvén wave can smoothly propagate in the interlocked system of PIC and MHD. The figure shows that the wave form is scarcely affected by interlocking with the PIC model, as high-frequency modes appear in the PIC domain. It indicates that the particle-continuum connection model is applicable also to plasma simulations.

Recently, [12] applies the interlocked technique to connect different hybrid simulations for the study of particle acceleration on plasma collision-less shock. In that study, the conventional hybrid simulation, in which ions are calculated by particles, is used for the calculation of particle acceleration in shock and is connected to the energetic particle hybrid simulation, which calculates only high energy ions as particles and handles the thermal ion as fluid. Since the computational cost of the energetic particle hybrid model is much cheaper than the ion particle hybrid model, we can dramatically reduce the computational demand using the new interlocked plasma simulation, and it enables the macroscopic plasma simulation including kinetic effects.

3 summary

Three different applications for the MMI simulation are demonstrated. In any examples, the particle-continuum connection technique plays a crucial role. However, it is worthwhile to note that the particle-continuum connection in the cloud simulation is not based on the domain decomposition method, but the application of particle-in-cell technique, unlike the other two applications of plasma and detonation, because cloud is ubiquitous phenomena and we cannot restrict the cloud domain into a limited region. It is a new challenge to embed the cloud microphysics model into the atmospheric global circulation model.

Although the MMI technique is much effective for the multi-scale simulation, in which the micro-scale model is necessary in a limited region, the gap of time-scale between the macro-scale and micro-scale processes is still issue to be resolve, because the micro-scale model is usually time-consuming and it is difficult to calculate the two different models simultaneously. Several new technique to fulfill the time-scale gap is now proposed. For instance, equation-free method proposed by [5] tries to accelerate the time integration using extrapolation technique based on the micro-scale calculation.

The MMI simulation is now opening a new world of simulation science, because the new numerical model can cast off the restriction of theoretical description. The MMI simulation is applicable to vastly wide range of fields, and some common technique can be used for the model of even different phenomena. The particle-continuum connection and the particle-in-cell technique are applicable to the simulation of different processes. It demonstrates that the MMI simulation can also play an important role for inter-disciplinary communication.

Acknowledge: The study is the results of the research program of "Development of Multi-scale Coupled Simulation Algorithm" in the Earth Simulator Center. The works presented in this paper is partially supported by the Grant-in-Aid for Scientific Research from Japan Society for the Promotion of Science (Science Research (B) 19340180).

[1] F. F. Abraham, J. Q. Broughton, N. Bernstein and E. Kaxiras, Europhys. Lett. **44** 783-787 (1998).

[2] O. Aktas, N. R. Aluru, J. Comp. Phys. **178** 2 (2002) 342–372.

[3] W. W. Grabowskii, & P. K. Smolarkiewicz, Physica D **133** 171–178.

[4] K. Kadau, T. C. Germann, P. S. Lomdahl, Int. J. Modern Phys. C **12** (2006) 1755–1761.

[5] I. G. Kevrekidis, C. W. Gear, G. Hummer, Aiche J. **50** 7 (2004) 1346-1355.

[6] K. Kusano, S. Hirose, T. Sugiyama, S. Shima, A. Kawano, and H. Hasegawa, Computational Science–ICCS 2007, Lecture Notes in Computer Science (Springer Berlin / Heidelberg) (2007) pp.0302-9743 (Print) 1611-3349 (Online).

[7] D. Randall, M. Khairoutdinov, A. Arakawa, and W. Grabowski Bulletin of the American Meteorological Society **84**, 11, 1547–1564 (2003)

[8] T. Sato, Journal of Physics: Conference Series SciDAC 2005 Scientific Discovery through Advanced Computing, Vol.16, (2005) 310–316.

[9] T. E. Schwartzentruber, I. D. Boyd, J. Comp. Phys. **215** 2 (2006) 402-416.

[10] S. Shima, K. Kusano, A. Kawano, T. Sugiyama, and S. Kawahara, Super-Droplet Method for the simulation of Cloud and Precipitation; a Particle-Based Microphysics Model Coupled with Non-hydrostatic Model., to be submitted.

[11] T. Sugiyama, and K. Kusano, J. Comp. Phys. (in press).

[12] T. Sugiyama, and K. Kusano, submitted to ASP Conf. Ser.

[13] E. Weinan, B. Engquist, Z. Huang, Phys. Rev. B, **67** 092101-1–4 (2003)

[14] H. S. Wijesinghe, N. G. Hadjiconstantinou, Int. J. Multiscale Computational Engineering **2** 2 (2004) 189–202.

Review Talk

Proceedings of ITC/ISHW2007

Recent Development in the Operational Regime of Large Helical Device Toward a Steady-State Helical Fusion Reactor

Y. Takeiri, A. Komori, H. Yamada, K. Kawahata, T. Mutoh, N. Ohyabu, O. Kaneko, S. Imagawa, Y. Nagayama, K.Y. Watanabe, T. Shimozuma, K. Ida, R. Sakamoto, M. Kobayashi, A. Sagara, K. Nagaoka, M. Yoshinuma, S. Sakakibara, Y. Suzuki, M. Yokoyama, S. Sudo, O. Motojima, and LHD experimental Group

National Institute for Fusion Science, 322-6 Oroshi-cho, Toki 509-5292, Japan

(Received 29 October 2007 / Accepted 29 October 2007)

Recent progress of the plasma performance and the related physics understanding is overviewed in Large Helical Device. The volume-averaged beta value is increased with an increase in the NBI heating power, and reached 5.0% of the reactor-relevant value. In the high-β plasmas, the plasma aspect ratio should be controlled so that the Shafranov shift would be reduced mainly to suppress the transport degradation and the deterioration of NBI heating efficiency. The operational regime of the high-density plasma with internal diffusion barrier (IDB) has been extended, and the IDB, which was originally found by use of the local island divertor, has been realized in the helical divertor configuration. The central density was recorded as high as $1x10^{21}m^{-3}$, and the central pressure reached 130kPa. Based on these high-density plasmas with the IDB, a new ignition scenario has been proposed. This should be a specific scenario to the helical fusion reactor, in which the helical ripple transport would be mitigated. A low-energy positive-NBI system was newly installed for an increase in the direct ion heating power. As a result, the T_i exceeded 5.2keV at a density of $1.2x10^{19}m^{-3}$ in the hydrogen plasma. The T_i-increase tends to be accompanied by a large toroidal rotation velocity of the order of 50km/s in the core region. The plasma properties in the extended operational regime are discussed with regard to a perspective to the steady-state helical fusion reactor.

Keywords: Large Helical Device, MHD stability, Shafranov shift, internal diffusion barrier, ion transport, toroidal rotation, impurity hall, helical fusion reactor, neoclassical transport, anomalous transport, core electron-root confinement

1. Introduction

The Large Helical Device (LHD) is the world's largest superconducting helical device, which started its operation in 1998 [1-3]. The objective of LHD is to demonstrate high performance of net-current free heliotron plasmas relevant to the steady-state helical fusion reactor. During the nine years' operation, LHD has exploited novel operational regimes related to plasma confinement, MHD stability and steady-state operation, including plasma-wall interaction [4,5].

Recently, much progress of the plasma performance has been achieved together with the physics understanding, which was mainly brought by the upgrade of the heating systems. The volume-averaged β value is increased with an increase in the NB injection power, and reached 5% as a consequence of the enhancement of the negative-NBI power to 14MW. A low-energy positive-NBI system has been installed recently for an increase in the direct ion heating power, and, as a result, the T_i exceeded 5.2keV at a density of $1.2x10^{19}m^{-3}$ in a hydrogen plasma. The distinguished feature found in LHD is the formation of the internal diffusion barrier (IDB) [6], which is realized by combination of efficient pumping with the local island divertor (LID) [7] and core fuelling with repetitive pellet injection [8], and it is sustained by the high-power NBI heating. In a super-dense core (SDC) plasma with the IDB, the central density was recorded as high as $5x10^{20}m^{-3}$ [6]. The IDB has also been observed recently in the helical divertor (HD) configuration with a well-conditioned wall. Based on the SDC/IDB plasmas, a new ignition scenario has been proposed, and this should be a specific scenario to the helical fusion reactor, in which the helical ripple transport would be mitigated [9]. Inherent advantage to steady-state operation has been demonstrated with the improvement of the ICRF and ECH heating systems. A long-pulse plasma was sustained for 54min with ICRF and

author's e-mail: takeiri@nifs.ac.jp

ECH, and the input heating energy reached 1.6GJ [10].

One of the specific characteristics in LHD is the dependence of the plasma properties, such as confinement, transport, MHD stability, and divertor structure, on the magnetic axis position. In the inward-shifted configuration, the transport including the high-energy particle confinement is improved while the MHD stability is degraded due to the enhancement of the magnetic hill region, and the tendency is reversed in the outer-shifted configuration. The most significant achievement in the LHD research is the compatibility of the transport and the MHD stability, which is realized by the sophisticated optimization of the magnetic configuration including the magnetic axis position and the control of the Shafranov shift due to the plasma pressure [11].

In this overview, we present the recent development in the operational regime of the LHD experiments, highlighting mainly topics for the high-β, high-density with IDB, and the high-T_i, and the related physics understanding is discussed with a perspective of the steady-state helical fusion reactor.

2. Large Helical Device and Heating Systems

The Large Helical Device (LHD) employs a heliotron configuration, and consists of a pair of continuous helical coils, which has an l=2/m=10 poloidal/toroidal field period, and three pairs of poloidal coils [3]. These coils are all superconducting, and provide a wide variety of the magnetic configuration by controlling the current ratio of these coils. The magnetic axis position is changed with the poloidal coils, and ranges 3.5-4.1m in the major radius in the experiments. The averaged minor radius is about 0.6m at the maximum and the corresponding plasma volume is about 30m^3, and these are dependent on the magnetic configuration. The magnetic field strength on the axis is 3T at the maximum.

The LHD has the intrinsic helical divertor (HD), which is a sort of helically twisted double-null open divertor. Additionally, the LHD is equipped with a local island divertor (LID) system, which utilizes the m/n=1/1 magnetic island induced externally with the perturbation coils [7]. The LID facilitates the edge plasma control with highly efficient pumping capability.

The main heating system is a negative-ion-based neutral beam injection (negative-NBI) system, which consists of three tangential injectors with the nominal hydrogen-injection energy of 180keV [12,13]. The total injection power achieved is 14MW. A low-energy positive-NBI system, the injection direction of which is perpendicular to the magnetic axis, was operational in 2005, and 40keV-6MW injection has been achieved [14].

The electron cyclotron resonance heating (ECRH) system is equipped with 168GHz, 84GHz, and 82.7GHz gyrotrons, and the total injection power achieved is 2.1MW [15]. Using antenna systems with quasi-optical mirrors, each microwave is injected as a highly focused Gaussian beam, and the focused location can be changed at 3.5-3.9m of the major radius on the equatorial plane.

The ion cyclotron range of frequencies (ICRF) heating system facilitates the long-pulse operation, which is capable of a steady-state injection of 1MW with four antennas, while the achieved power is 2.9MW in a short pulse injection [16].

3. Properties of Reactor-Relevant High-β Plasmas

As described above, the LHD-plasma performance is strongly dependent on the magnetic axis position. Since the heliotron configuration has a weak magnetic shear in the core region and a magnetic hill toward the peripheral region, the linear theory indicates that the interchange mode is unstable in the inward-shifted configurations, in which the particle orbit and the transport are better. On the other hand, in the outward-shifted configurations, although the MHD mode is stable due to expansion of the magnetic well region, the particle orbit and the transport are degraded. Through the optimization of the magnetic axis position, it was found that the interchange mode in the core region is stabilized and the Mercier criterion does not prohibit the access to higher β, even in the inward-shifted configuration of R_{ax}^{vac}=3.6m by the spontaneous generation of a magnetic well due to the finite β effect [11].

However, as the β increases further, the Shafranov shift becomes larger. As a result, the transport is degraded

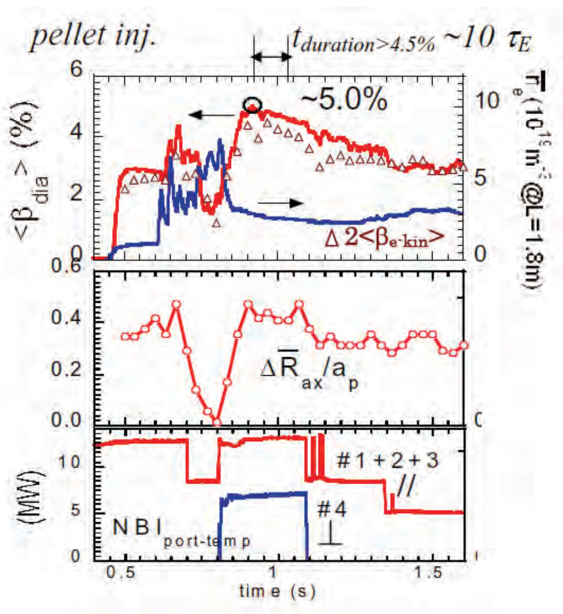

Fig.1 Waveforms in a high-β plasma of <β>=5.0% achieved with the repetitive pellet injection.

and the NBI heat deposition is deteriorated due to the enhancement of the orbit loss by the outward shift of the magnetic axis. Moreover, the large Shafranov shift lowers the MHD equilibrium beta limit. Then, the plasma aspect ratio, A_p, which can be controlled by changing the current ratio of the three layers of the helical coils, should be optimized [17]. A large A_p reduces the Shafranov shift, but an excessive increase in the A_p violates the MHD stability due to immoderate suppression of the spontaneous generation of the magnetic well. As a consequence of a series of experiments for the A_p optimization including the magnetic field strength, we have achieved 5% of the volume-averaged beta value, <β>, which is a reactor-relevant value, at A_p=6.6, B=0.425T, and preset R_{ax}^{vac}=3.6m with an increased NBI absorbed power of 11MW.

Figure 1 shows discharge waveforms in the high-β plasma of <β>=5.0% achieved with a pellet injection. The tangential NBI power is reduced in the repetitive pellet injection phase for effective penetration of the pellets. At that time, the Shafranov shift is rapidly reduced, and then the perpendicular NBI is injected together with the restoration of the tangential NBI immediately after the end of the pellet injection. Due to the reduction of the Shafranov shift, the perpendicularly injected beam effectively heats the plasma, and the <β> is rapidly increased, then reaching 5%. Although <β>=5% was transiently achieved due to the effective fueling by the pellet injection and the effective heating by the perpendicular NBI during the reduction of the Shafranov shift, no crucial MHD instability was observed in a period of 10 times the confinement time, during which the <β> was over 4.5%.

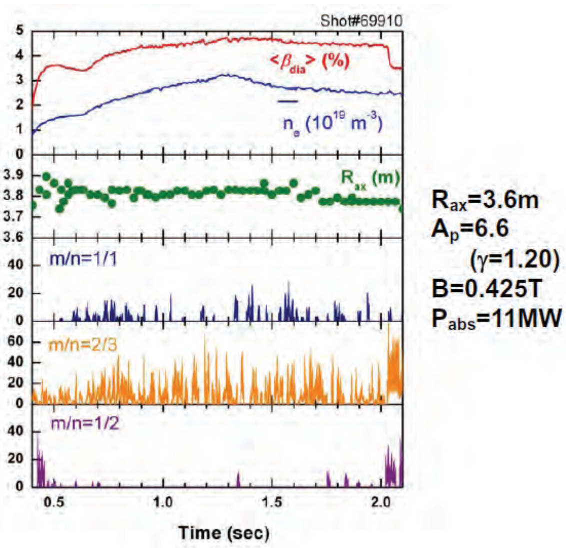

Fig.2 Waveforms in the stationary sustained high <β> plasma with only the gas puffing.

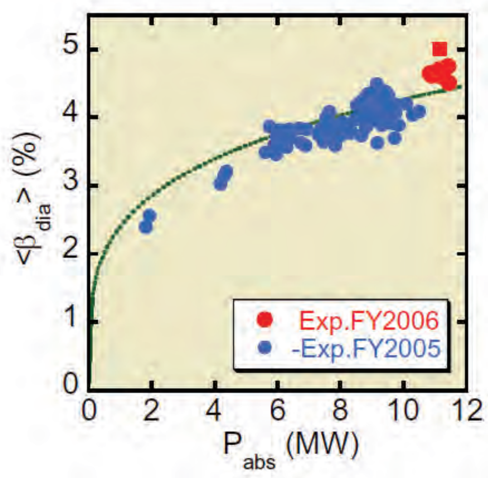

Fig.3 Volume-averaged beta value, <β>, as a function of the NBI-absorbed power.

With only the gas puffing, 4.8% of <β> was stationary sustained without any disruptive phenomena as shown in Fig. 2. The Shafranov shift normalized by the effective plasma minor radius is as large as around 40%, approaching the equilibrium beta limit of 50%. Although the MHD modes excited in the peripheral region with the magnetic hill are dominantly observed, they become stable spontaneously from the inner region to the outer region as the <β> increases. According to the linear MHD analysis, the Mercier criterion is not violated, and the observed peripheral MHD modes in the magnetic hill region is not crucial due to the strong magnetic shear there [18].

Even in the highest-β plasma, as described above, the MHD instabilities do not limit the achievable beta, but the heating power does. As shown in Fig. 3, the <β> is increased linearly to the 0.25 power of the NBI absorption power without saturation. The deduced absorbed power dependence of the <β> from the energy confinement scaling ISS95 is $P_{abs}^{0.4}$, and, thus, confinement degradation from the scaling law is suggested in the high <β> plasmas. The peripheral transport is enhanced with increasing the <β>. The dependence of the magnetic fluctuation resonated with the peripheral rational surfaces on the magnetic Reynolds number, S, suggests that the observed MHD modes are resistive interchange modes [19]. Thus, the resistive g-mode turbulence would cause the transport enhancement. Since the S is proportional to $B_t T_e^{3/2} n_e^{-1/2}$, the MHD mode amplitude is expected to be reduced for plasmas with higher temperature at higher magnetic field, relevant to the reactor-class plasma conditions. Another possible cause for the confinement degradation is the increase in the effective helical ripple due to the Shafranov shift [20]. The real-time control of the magnetic axis position during the discharge is planned, and that should resolve this issue. That should also be effective to enhancement of the heating power by the perpendicular NBI, and then the further increase in the <β> is expected.

4. Extension of Operational Regime in High-Density Plasmas with Internal Diffusion Barrier

Formation of the super-dense core (SDC) plasma with the internal diffusion barrier (IDB) is a distinguished feature in LHD, which has been never observed in tokamaks. The IDB is originally formed in the LID-controlled plasmas which are fueled directly in the core region by the repetitive pellet injection. The LID functions as a strong pumping, which realizes a low recycling condition through the particle control at the plasma edge. Even in the helical divertor (HD) configuration, intensive wall conditioning should lead to a pumping by the wall. In the outward-shifted configuration, localization of the neutrals is small, and the recycling is suppressed due to weaker plasma-wall interaction. We have realized the IDB formation in the HD configuration in the outward-shifted configuration with such a kind of well-conditioned wall.

Figure 4 shows typical waveforms of an SDC plasma with the IDB realized in the HD configuration. The preset vacuum-magnetic axis position, R_{ax}^{vac}, is 3.8m. During the repetitive pellet injection into the plasma heated with high-power NBI, the electron density is greatly increased and the central density exceeds $5\times10^{20}m^{-3}$. After the core

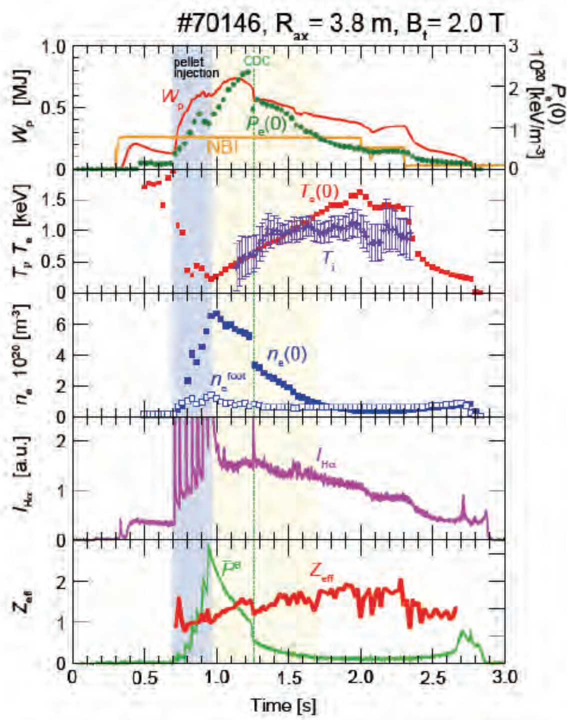

Fig.4 Typical waveforms of the SDC/IDB plasma formed in the HD configuration.

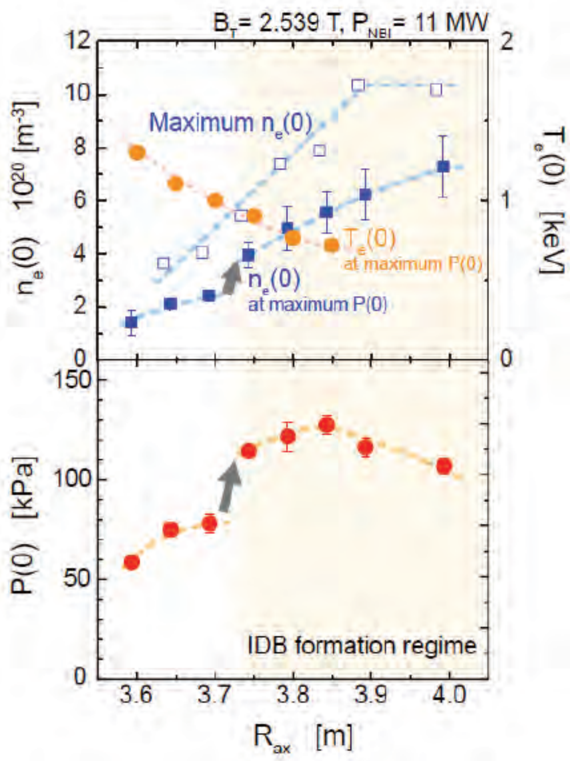

Fig.5 Maximum central density, $n_e(0)$, and pressure, P(0), as a function of the preset vacuum-magnetic axis position, R_{ax}^{vac}.

fueling with the pellet injection, the peripheral density is rapidly decreased in the density relaxation and temperature recovery phase, and, then, the SDC plasma with the IDB is formed. The central pressure continues to be still increased after the plasma stored energy turns to be decreased, and, occasionally, the core density collapse (CDC) occurs with an abrupt decrease in the central pressure as well as the central density. The impurity accumulation is not observed and the Z_{eff} is as low as around 1.5 during the discharge.

A series of the SDC/IDB experiments were performed in the HD configuration with a variation of the R_{ax}^{vac}, and the results are shown in Fig. 5. The formation of the IDB is definitely observed in the outward-shifted configuration at R_{ax}^{vac}>3.7m. The achieved central density, $n_e(0)$, is increased as the R_{ax}^{vac} is shifted more outward, and reaches $1\times10^{21}m^{-3}$ at R_{ax}^{vac}=3.9m, while the peripheral density is maintained low, independent of the R_{ax}^{vac}. The central pressure, P(0), jumps up at the IDB formation, and the maximum P(0) is 130kPa, exceeding an atmospheric pressure, at R_{ax}^{vac}=3.85m.

The IDB formation is closely correlated with the edge-region temperature, which is strongly affected by the neutral density there. An increase in the neutral pressure in the SOL region causes an increase in the edge density with enhanced recycling, leading to a decrease in the edge temperature. Then, the heating power is lost by enhanced

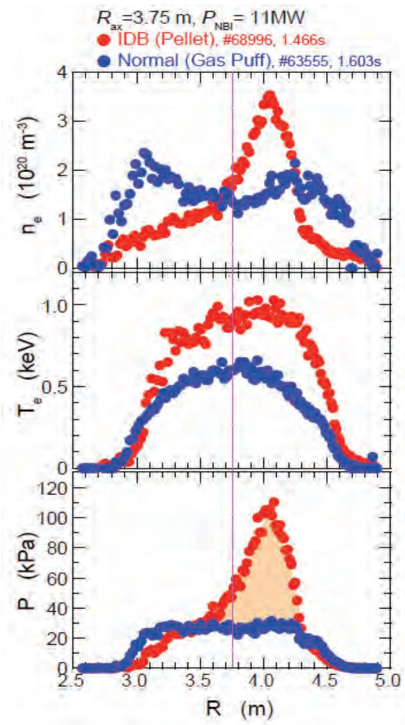

Fig.6 Comparison of the density, temperature, and pressure profiles of the SDC/IDB plasma with those of the gas-puffing plasma with no IDB. R_{ax}^{vac}=3.75m.

radiation in the low temperature region, resulting in the radiative collapse [21]. In the outward-shifted configuration, the recycling is suppressed compared with that in the inward-shifted configuration, and, thus, the low edge-density can be maintained by the wall-pumping effect without the LID. With a closed helical divertor system equipped with a strong pumping function, the stable IDB discharge would be realized even in the inward-shifted configurations.

Comparison of the pressure profile of the SDC/IDB plasma with that of the normal gas-puffing plasma at R_{ax}^{vac}=3.75m is shown in Fig. 6. The magnetic field strength on the axis and the NBI power are the same for both plasmas, and 2.539T and 11MW, respectively. Although the central density is about 2 times higher, the electron temperature is also higher in the SDC/IDB plasma. As a result, the central pressure is much higher with a steep pressure profile, indicating the confinement improvement in the SDC/IDB plasma. In the peripheral region, low density is maintained, leading to high T_e-gradient toward the core in the SDC/IDB plasma. On the other hand, since the peripheral density is high and the T_e-gradient region is narrow, the core T_e is low in the normal plasma. The central beta value, $\beta(0)$, reaches 4.5% even at the high confinement magnetic field, and a large Shafranov shift of about 0.3m is observed due to the high central pressure with a peaked profile. The achievable $\beta(0)$ is higher at lower confinement magnetic field, and 5.8% is observed at B_t=1.5T. The Shafranov shift is approaching to the equilibrium beta limit of 50% of the effective minor radius. The CDC event shown in Fig. 4 occurs when the Shafranov shift is so large that the shifted axis position would exceed R=4.0m. Vertically elongated modification by the ellipticity change of the magnetic surface is applied to suppress the Shafranov shift, and the CDC event is mitigated. The real-time control of the magnetic axis position by the dynamic control of the vertical field should be effective to improve the SDC/IDB plasma properties.

The achievable plasma stored energy of the SDC/IDB plasmas in outward-shifted configurations is linearly dependent on the plasma volume at the preset vacuum magnetic axis position, R_{ax}^{vac}, including the non-IDB plasmas in inward-shifted configurations. The plasma volume is smaller as the magnetic axis shifts more outward. Considering that the actual plasma volume is smaller due to the large Shafranov shift in the SDC/IDB plasmas, the plasma confinement is thought to be improved in the SDC/IDB plasmas.

Compared with the high-β plasma at the low magnetic field, the SDC/IDB plasma has a similar central beta, a steeper pressure gradient, and a larger Shafranov shift. The

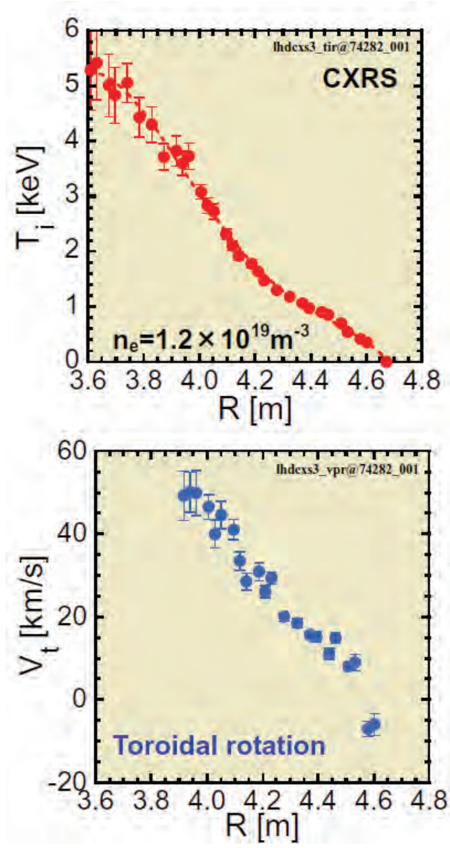

Fig.7 Profiles of the ion temperature and the toroidal rotation velocity in the high-T_i plasma.

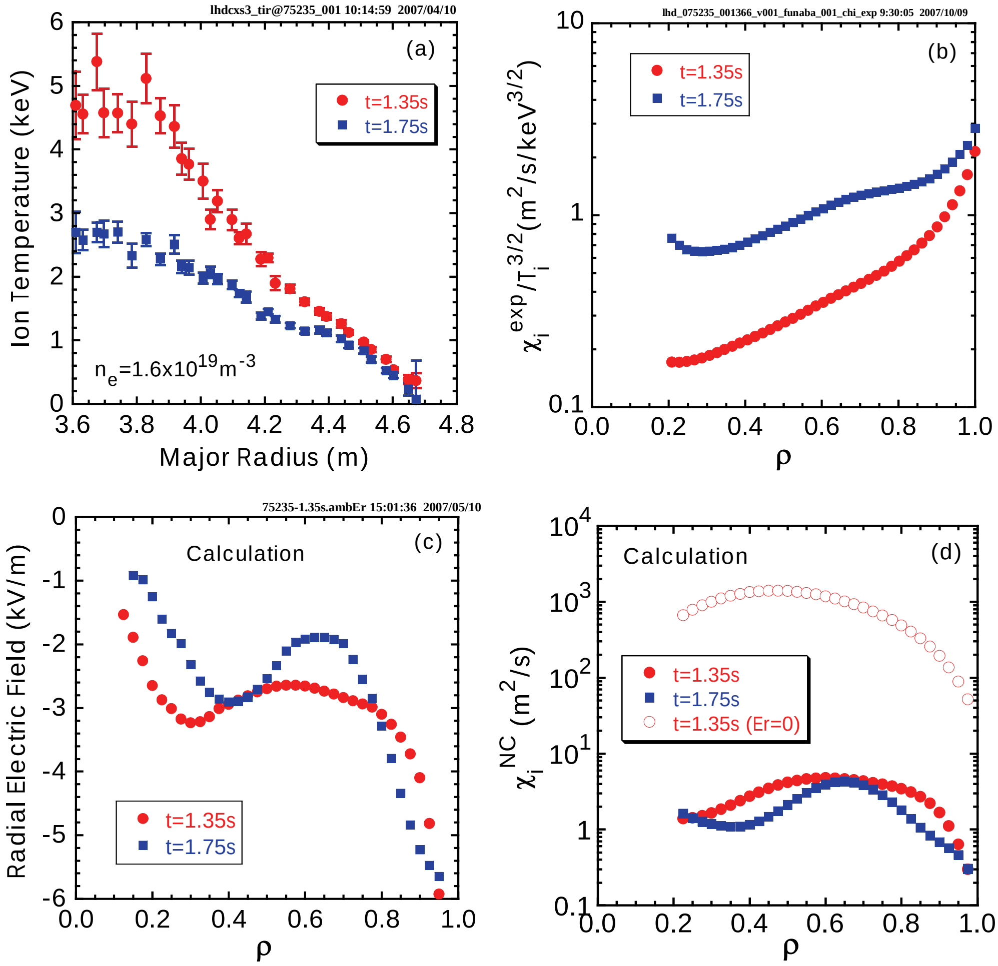

Fig.8 (a) T_i profiles, (b) ion thermal diffusivities divided by the gyro-Bohm factor, $\chi_i/T_i^{3/2}$, (c) radial electric field, E_r, obtained with the neoclassical ambipolar calculation, and (d) neoclassical ion thermal diffusivities, χ_i.

finite-β equilibrium in the SDC/IDB plasma at R_{ax}^{vac}=3.85m is investigated, using the HINT2 equilibrium code in which the nested magnetic surface is not assumed. The preliminary results show that due to the large Shafranov shift the magnetic surfaces are distorted in the peripheral region surrounding the IDB, and that inside the IDB the magnetic surfaces are clearly closed. Since the connection lengths of the magnetic field lines are much longer than the electron mean-free paths even in the region of the distorted magnetic surfaces, it is possible for the electron temperature profile to have a gradient. These analyses of the MHD equilibrium for the SDC/IDB plasmas should apply to the reactor-relevant high-β plasmas.

5. Increase in Ion Temperature and the Related Ion Transport

The high-energy NBI, which is the main heating device in LHD, dominantly heats electrons, and, thus, the high-Z discharge was utilized for the high-T_i experiments in LHD to increase effectively the ion heating power. As a result, the T_i was increased with an increase in the ion heating power, and reached 13.5keV at 0.3x10^{19}m^{-3} with Ar-gas puffing [22]. To apply this result to the hydrogen discharge, a low-energy NBI system with a radial injection, which dominantly heats ions, has been installed, and 40keV-6MW injection was achieved in the last experimental campaign [14,23]. This radially injected beam is also utilized for the T_i-profile measurement with the CXRS along a toroidal line of sight, which is better for the measurement in the central region than that along a poloidal line of sight [24].

With combination of the high-energy NBI and the low-energy NBI, 5.2keV of the ion temperature is obtained at 1.2x10^{19}m^{-3} as shown in Fig. 7. The density profile tends to be peaked by the low-energy NBI and to be flat or hollow by the high-energy NBI. The peaked density profile seems to be preferable for the T_i rise, suggesting a role of the fueling effect and/or the inward pinch effect with the low-energy NBI. Figure 7 also shows a profile of the toroidal rotation velocity, V_t. The toroidal rotation is enhanced in the same direction as the dominant direction of the tangential NB injectors. As shown in Fig. 7(b), large V_t of 50km/s and the V_t shear are observed in the core region accompanied by the T_i rise. That suggests a correlation between the ion transport improvement and the toroidal rotation.

Figure 8 shows the results of the transport analysis. The ion thermal diffusivities normalized by $T_i^{3/2}$ of the gyro-Bohm factor are shown in Fig. 8(b) for the plasmas in Fig. 8(a). It is found that the $\chi_i/T_i^{3/2}$ is much reduced in the T_i rise to 5keV. As shown in Fig. 8(c), the neoclassical ambipolar calculation shows negative E_r in the core region in association with the T_i rise [25], meaning that the T_i is increased in the neoclassical ion root. The calculated neoclassical χ_i is shown in Fig. 8(d). Without consideration of the E_r effect, the ripple transport is greatly enhanced by the T_i rise, and it is found that by the negative E_r the ripple transport is greatly reduced. As a result, the neoclassical χ_i is not so changed by the T_i rise. Considering that the experimental $\chi_i/T_i^{3/2}$ is much reduced, the experimental improvement of the ion confinement is due to the reduction of the anomalous transport in the ion root. The negative E_r is induced by the increased ion temperature, and a role of the negative E_r in the reduction of the anomalous transport should be investigated.

The CXRS intensity profile of the CVI emission shows that the carbon impurity profile becomes strongly hollowed as the T_i is increased. This "impurity hole" is clearly observed in the plasmas with the carbon pellet injection. After the carbon pellet injection, the T_i is increased in the density-decay phase, and the carbon density ratio is rapidly decreased to 0.2% at the plasma center while it is 10% at the edge. As a result, the T_i measurement in the core region becomes impossible. The outward flux of carbon is observed even at a negative carbon-density gradient. In the neoclassical theory, the outward flow of impurities is predicted in the electron root with positive E_r, and the impurity pump-out effect is observed in the ECRH plasmas. However, the "impurity hole" is observed in the ion-root plasma with negative E_r. The physics of the "impurity hole" in the high-T_i plasmas should be investigated as an inherent subject in the helical systems.

On the other hand, the T_i rise is observed also in the electron root. When the ECRH is superposed on the NBI-heated plasma, the T_i is increased accompanied by the formation of the electron-ITB with positive E_r [22]. The transport analysis indicates that both electron and ion transport is improved in the core region with the reduction of the anomalous transport. The toroidal rotation is driven in the co-direction by adding the ECRH, and the spontaneous toroidal rotation is suggested to be related to

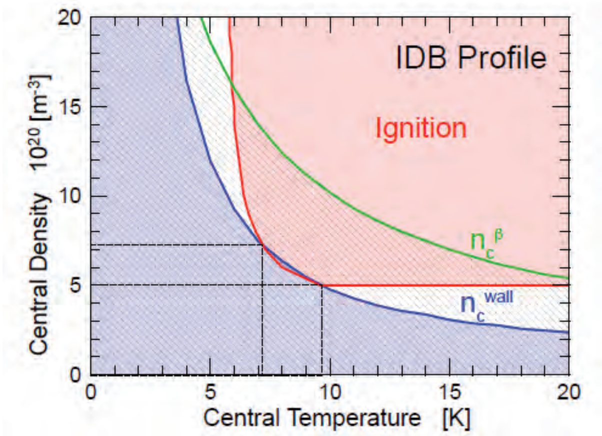

Fig.9 Operational regime for the high-density ignition based on the IDB profile in the helical reactor.

the transport improvement in the electron-root plasma [26]. Although the electron transport improvement is a common feature in the CERC (core electron-root confinement) plasmas [27], the ion transport improvement in the CERC suggests a possible approach to achieve the reactor-relevant high-temperature plasmas.

6. High-Density Ignition Scenario for a Helical Fusion Reactor

For the steady-state helical fusion reactor, a novel ignition approach based on the high-density SDC/IDB plasma is proposed. Figure 9 shows the operational regime for the self-ignition based on the high-density IDB profile in the helical reactor. In tokamaks, since high-density operation is limited by the current drive condition and the MHD stability, a high-temperature path at relatively low density is the possible ignition scenario. On the other hand, LHD is capable to achieve high-density plasmas above $5\text{x}10^{20}\text{m}^{-3}$ without any limitation, and, based on this high-density plasma, the required temperature for the ignition, then, should be reduced below 10keV. This scenario is advantageous to the helical devices which require no current drive. The operation at a relatively high collisionality mitigates the helical ripple transport, and the engineering demand derived from the high-temperature operation is reduced. In the peripheral region of the SDC/IDB plasma, a temperature gradient is established due to the low density there, and the core temperature high enough to realize the ignition is achieved by this temperature gradient. Maintaining the low density in the peripheral region is also desirable for avoiding the radiative collapse as well as suppression of the enhanced synclotron radiation. At present, an LHD-type fusion reactor is being designed based on this high-density ignition scenario [9].

7. Concluding Remarks

Recent extension of the operational regime in the LHD experiments is reviewed together with the progress of the physics understanding. By the sophisticated optimization of the magnetic field configuration with regard to the magnetic axis position and the plasma aspect ratio, the volume-averaged beta was increased to 5.0% with an increase in the NBI heating power. Even in this fusion-relevant high-β plasma, no crucial MHD instability is observed in the core region while the resistive interchange modes degrade the plasma confinement in the peripheral region. However, these MHD modes should be stabilized in reactor-relevant plasmas with higher temperature at higher magnetic field.

The SDC/IDB plasmas, which were originally observed in the LID configuration, were realized in the helical divertor configuration. The central density is increased as the preset vacuum-magnetic axis position is shifted outward, and reaches $1x10^{21}m^{-3}$ at R_{ax}^{vac}=3.9m. The central pressure exceeds an atmospheric pressure and reaches 130kPa. The core plasma confinement is improved while the particle transport in the peripheral plasma surrounding the IDB is degraded. This, in turn, realizes the low density with an electron temperature gradient in the peripheral region. The Shafranov shift due to the high central beta and the steep pressure gradient is approaching the equilibrium limit, leading to the core density collapse occasionally. The dynamic control of the magnetic axis position by the vertical field is required as well as in the high-β plasmas.

For an increase in the ion heating power, a low-energy NB injector was newly installed, and 40keV-6MW injection was achieved. The ion temperature is raised to 5.2keV at $1.2x10^{19}m^{-3}$ with the combined heating of the low-energy NBI and the high-energy NBI. The ion transport is improved with the reduction of the anomalous transport in the neoclassical ion root. An increase in the toroidal rotation is observed to be related to the ion-temperature rise. The impurity hall is recognized, in which the carbon impurity is drastically decreased in the core region with an increase in the T_i. The impurity pump-out effect in the ion root is attractive for the helical reactor because no impurity accumulation is expected in the high-T_i core plasma.

The SDC/IDB high-density plasma allows us to propose a high-density ignition scenario. In this ignition approach the temperature requirement is reduced below 10keV at a high-density above $5x10^{20}m^{-3}$, and the helical ripple transport is mitigated together with the reduction of the engineering demand caused by the high-temperature operation. Including this scenario, most of the LHD results presented here are relevant to the steady-state helical fusion reactor, and the upgrade of the LHD is now planned including the deuterium experiments for investigations of the high-performance plasmas, which should lead to a definite design of the LHD-type fusion reactor.

Acknowledgements

The authors greatly acknowledge all contributions from overseas and domestic collaborators for the progress of the LHD achievements. They are also grateful to the technical staff in the LHD for the excellent operation of the LHD and the heating systems.

References

[1] A. Iiyoshi, *et al.*, Fusion Technol. **17**, 169 (1990).
[2] A. Iiyoshi, *et al.*, Nucl. Fuion **39**, 1245 (1999).
[3] O. Motojima, *et al.*, Nucl. Fuion **40**, 599 (2000).
[4] A. Komori, *et al.*, Fusion Sci. Technol. **50**, 136 (2006).
[5] O. Motojima, *et al.*, Nucl. Fusion **47**, S668 (2007).
[6] N. Ohyabu, *et al.*, Phys. Rev. Lett. **97**, 055002 (2006).
[7] A. Komori, *et al.*, Nucl. Fusion **45**, 837 (2005).
[8] R. Sakamoto, *et al.*, Nucl. Fusion **46**, 884 (2006).
[9] A. Sagara, *et al.*, this conference.
[10] T. Mutoh, *et al.*, Nucl. Fusion **47**, 1250 (2007).
[11] H. Yamada, *et al.*, Plasma Phys. Control. Fusion **43**, A55 (2001).
[12] O. Kaneko, *et al.*, *Proc. 16th Int. Conf. on Fusion Energy 1996 (Montreal, 1996)* Vol. 3 (Vienna, IAEA) p. 539.
[13] Y. Takeiri, *et al.*, Nucl. Fusion **46**, S199 (2006).
[14] M. Osakabe, *et al.*, this conference.
[15] S. Kubo, *et al.*, Plasma Phys. Control. Fusion **47**, A81 (2005).
[16] T. Mutoh, *et al.*, Nucl. Fusion **43**, 738 (2003).
[17] K.Y. Watanabe, *et al.*, Nucl. Fusion **45**, 1247 (2005).
[18] S. Sakakibara, *et al.*, *Proc. 21st IAEA Conf. on Fusion Energy (Chengdu, 2006)*, IAEA-CN-149, EX/7-5 (2006).
[19] S. Sakakibara, *et al.*, Fusion Sci. Technol. **50**, 177 (2006).
[20] H. Yamada, *et al.*, Nucl. Fusion **45**, 1684 (2005).
[21] J. Miyazawa, *et al.*, Plasma Phys. Control. Fusion **48**, 325 (2006).
[22] Y. Takeiri, *et al.*, Nucl. Fusion **47**, 1078 (2007).
[23] K. Nagaoka, *et al.*, this conference.
[24] M. Yoshinuma, *et al.*, this conference.
[25] S. Matsuoka, *et al.*, this conference.
[26] Y. Takeiri, *et al.*, this conference.
[27] M. Yokoyama, *et al.*, Fusion Sci. Technol. **50**, 327 (2006).

Tutorial Talks

Proceedings of ITC/ISHW2007

Experimental Tests of Quasisymmetry in HSX

J.N. Talmadge, F.S.B. Anderson, D.T. Anderson, C. Deng, W. Guttenfelder, K.M. Likin, J. Lore, P.H. Probert, J.C. Schmitt, K. Zhai

HSX Plasma Laboratory, University of Wisconsin-Madison, USA

(Received)

This paper discusses the results from experiments in HSX testing the properties of a quasisymmetric stellarator. HSX is a quasihelical stellarator with minimal toroidal curvature and a high effective transform. The high effective transform was verified from passing particle orbits as well as from the magnitude of the Pfirsch-Schlüter and bootstrap currents. The passing particle orbit shift, the helical structure of the Pfirsch-Schlüter current and the direction of the bootstrap current were all consistent with minimal toroidal curvature. Good agreement was observed between data from plasma currents obtained by a set of magnetic pick-up coils and the results of the V3FIT code. Good confinement of trapped particles was observed with quasisymmetry. These particles may be responsible for a coherent global MHD mode that was detected during ECH at B = 0.5 T. It was found that the breaking of quasisymmetry increased the hollowness of the density profile and the damping of plasma flow while decreasing the core electron temperature, in good agreement with neoclassical models. At 0.5 T, anomalous transport appeared unaffected by the degree of quasisymmetry; more work is need to understand if this still holds at 1.0 T. The experimental energy confinement time and electron temperature profile could be reproduced reasonably well with a combination of neoclassical transport and a modified Weiland model for ITG/TEM turbulence.

Keywords: quasisymmetry, HSX, quasihelical symmetry, transport, effective transform, bootstrap current, Pfirsch-Schlüter current, turbulence

1. Introduction

The poor neoclassical transport in the low collisionality regime of conventional stellarators has spurred efforts to design stellarators which combine the good single particle confinement of the tokamak and the steady-state, disruption-free characteristics of stellarators. The paper by Mynick [1] summarizes various approaches by which neoclassical transport in stellarators might be improved. One such approach is the quasisymmetric stellarator, pioneered by Nührenberg and Zille [2] and by Garabedian [3]. A quasisymmetric stellarator is one in which the magnetic field spectrum is dominated by a single harmonic. Aside from the tokamak-like neoclassical transport, quasisymmetric stellarators possess a direction of symmetry in |B| and hence minimal parallel viscous damping in that direction. Such a property may be advantageous for improving anomalous transport.

The quasisymmetric approach to improving transport in stellarators is the thrust of the U.S. stellarator program. The Helically Symmetric Experiment (HSX) [4] is the first quasisymmetric stellarator in the world. The symmetry in this experiment is in the helical direction. The quasi-axisymmetric National Compact Stellarator Experiment (NCSX) [5], is symmetric in the toroidal direction and is currently under construction at PPPL. Finally, the proposed Quasi Poloidal Stellarator (QPS) [6] at ORNL has a direction of symmetry in the poloidal direction.

In Boozer coordinates, the magnitude of the magnetic field for a quasihelically symmetric (QHS) stellarator can be written as

$$B/B_0 = 1 - b_{nm}\cos(n\phi - m\theta) \quad (1)$$

where ϕ is the toroidal angle and θ is the poloidal angle. In a straight field-line coordinate system given by $\theta = \iota\phi$, where ι is the rotational transform, the magnetic field variation on the field line is given by

$$B/B_0 = 1 - b_{nm}\cos([n - m\iota]\phi) \quad (2)$$

This is similar to the variation along a field line in a tokamak with the substitution $\iota_{eff} = n - m\iota$ for the rotational transform. For HSX, with n = 4, m = 1 and $\iota \geq 1$, the effective transform ι_{eff} is about 3.

The combination of quasisymmetry and high effective transform in HSX results in small drifts of passing particles from a flux surface, small banana widths, small plasma currents, low neoclassical transport and low parallel viscous damping. On the other hand, the high curvature

author's e-mail:talmadge@wisc.edu

and small connection length in HSX may be responsible for somewhat larger anomalous transport. This paper discusses what recent experimental results from HSX can tell us about the properties of a quasisymmetric stellarator.

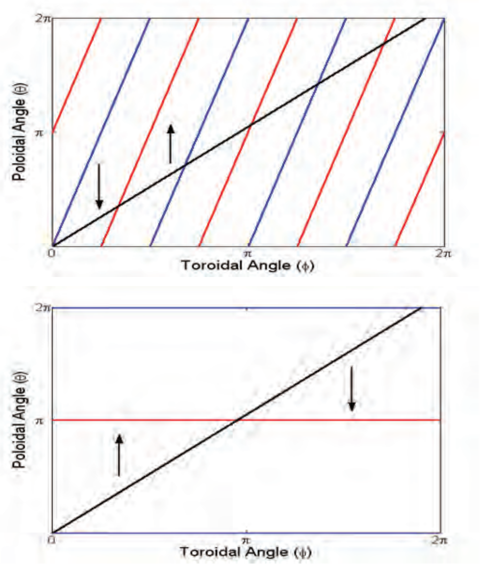

Fig.1 Contours of constant |B| for a quasihelically symmetric configuration (top) and for a tokamak (bottom). Also shown is a magnetic field line with a rotational transform of 1.06. The arrows point in the direction of increasing |B| in the poloidal direction. Red is the maximum field, blue is the minimum.

2. Drift Orbits

The leading $m \neq 0$ terms of the vacuum magnetic field spectrum in HSX were determined by measuring the orbit shift of passing electrons from a flux surface [7]. At low energies, the electrons injected with a filament stay close to the flux surface and were used to map the lab coordinate frame into Boozer coordinates using a neural network. At higher energies, the electrons deviate from the flux surface and measurement of this deviation at several toroidal locations yields the spectrum.

The direction of the shift of the electron from a magnetic surface is a verification of the lack of toroidal curvature in HSX. Figure 1 is a comparison of the contours of constant |B| in HSX and in a tokamak. Along a magnetic field line close to a toroidal angle of zero degrees, the direction of increasing B is oppositely directed in the two cases. Since the radial drift velocity in Boozer coordinates for a curl-free magnetic field is given by $B_0 r\, dr/dt = -(mv_{\parallel}^2/eB)\, dB/d\theta$, the radial drift from the home flux surface should be in the opposite direction for the two configurations. Figure 1 also illustrates the high effective transform that is characteristic of quasihelically symmetric stellarators. For the QHS configuration, as the magnetic field line rotates once around the magnetic axis poloidally, |B| undergoes just under 3 oscillations. For the corresponding tokamak with the same transform, there is 1 oscillation. Another way to look at it is to see that the gradient of |B| changes sign over a much smaller spatial scale in a QHS device than in a tokamak, resulting in smaller deviation from a flux surface.

Figure 2 shows the measured electron orbit in HSX after mapping to Boozer coordinates. The deviation of the orbit from a flux surface is due to the $n = 4, m = 1$ helical field on the right side of the experimental data and to the $n = 1, m = 1$ earth's field on the left. The earth's field is significant in this case because the experiment was done at a magnetic field of only 90 g; at higher fields the earth's field can be neglected. To the right of the data is a calculated orbit of the electron if it were in a tokamak (and neglecting the earth's field). Comparing the two figures it can be seen that indeed the orbit shift is outside the flux surface for the QHS case and inside the surface for the tokamak. Also, the orbit shift is smaller for the QHS case because of the higher effective transform.

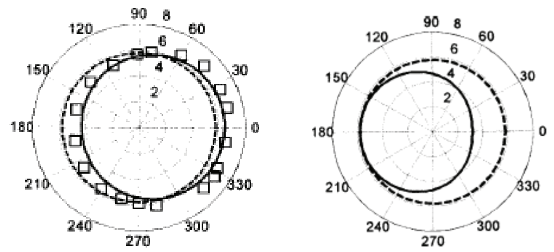

Fig. 2 Experimental data from HSX mapped into Boozer coordinates (left) and a calculation of the orbit of the same electron in a tokamak magnetic field (right).

2. Pfirsch-Schlüter and Bootstrap Currents

Because of the lack of toroidal curvature in HSX, the Pfirsch-Schlüter (PS) and bootstrap currents have some unique properties. For a quasihelically symmetric configuration, the PS current is given by Boozer [8],

$$J_{PS} = \frac{1}{B_0}\frac{dp}{d\psi}\frac{nI + mg}{n - m\iota}\delta_{nm}\cos(n\phi - m\theta) \qquad (3)$$

and the bootstrap current has the expression [9],

$$J_{BS} = 1.46\sqrt{b_{nm}}\,\frac{m}{n - m\iota}\frac{g}{B_0}\left[1.67(T_e + T_i)\frac{dn}{d\psi} + 0.47n\frac{dT_e}{d\psi} - 0.29n\frac{dT_i}{d\psi}\right] \qquad (4)$$

There are several things to notice about these expressions. For one thing, both currents are reduced by the same factor,

$n - m\iota$ which is the effective transform. Also, the Pfirsch-Schlüter current is helical so that from the beginning of the field period to the half-period the dipole currents reverse direction. Note that at $\phi = 0^0$ where the magnetic field in a QHS device is tokamak-like (that is, the high field side is on the inboard side), the PS current distribution is reversed from what it would be in a tokamak. From the equation this appears as a sign change between a $n = 4, m = 1$ and a $n = 0, m = 1$ configuration. Physically this effect occurs because of the reversal in the gradient of the magnetic field between a QHS and tokamak configuration, just like in the particle orbit. Note too, that the bootstrap current in a QHS device is in the opposite direction from that in a tokamak, resulting in a rotational transform that decreases as the pressure gradient increases. The transport however doesn't degrade with the decrease in the transform, because the effective transform actually increases slightly.

The reversal of the bootstrap current in a QHS device compared to a tokamak can be understood using the model developed by Shaing and Callen [10]. The top plot of Figure 3 shows how the parallel current flows in one direction for HSX so that when added to the diamagnetic current, the total current flows along the direction of symmetry. The bottom plot shows how this parallel current has to flow in the opposite direction along the field line so that the total current flows in the axial direction.

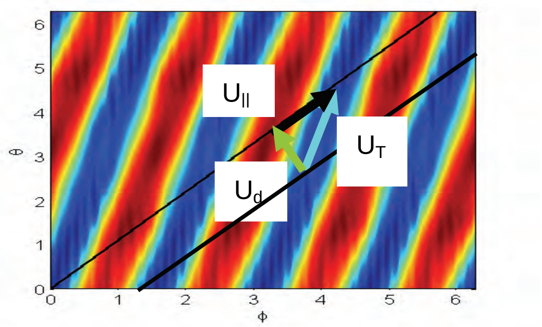

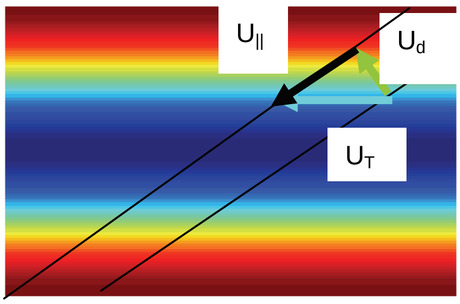

Fig. 3 Diamagnetic current (U_d), parallel bootstrap current ($U_{\|}$) and total current (U_T) in HSX (top) and a tokamak (bottom) illustrating that the bootstrap current flows in the opposite direction for the two configurations.

To measure the plasma current in HSX there is a Rogowski coil and a belt to which is attached a set of 16 3-axis magnetic coils. Both are mounted outside the vacuum chamber of HSX. To measure the signals due to the helical Pfirsch-Schlüter current, the belt containing the set of 16 triplets was first placed at the half-field period and subsequently at the one-sixth period location. Figure 4 is an illustration of the helical nature of the current and the approximate locations of the 16 triplets. The red and blue colors denote currents that are flowing in the opposite directions.

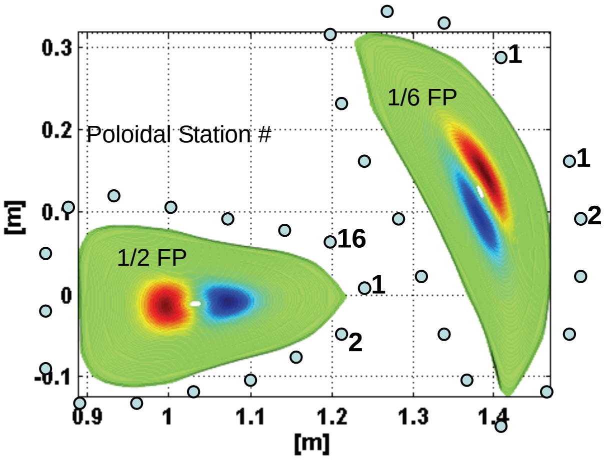

Fig. 4 Last closed magnetic surface and Pfirsch-Schlüter current contours at two toroidal locations where the 16 3-axis magnetic coils were located.

Figure 5 shows the polodial and radial magnetic fields due to the plasma current at a time, late in the discharge, just before the ECH is turned off. It can be seen from the figure that the radial magnetic field at the 1/2 field period is almost 180^0 degrees out of phase with the signals at the 1/6 field period location. This confirms that indeed the Pfirsch-Schlüter current in HSX is helical.

Another interesting feature of Figure 5 is that the polodial magnetic field is offset vertically indicating that there is a current flowing in the plasma in addition to the Pfirsch-Schlüter current. We have made estimates of the bootstrap current in HSX using the BOOTSJ code [11] using the data from the Thomson scattering array as input. However, since the magnetic diffusion time is generally greater than the ECH pulse length, the total current measured by the Rogowski coil has not reached a steady-state by the end of the discharge.

A comparison of the current calculated by BOOTSJ with the measured current when the ECH turns off as well as an extrapolated steady-state value of the total current is shown in Figure 6. The agreement is fairly good. In addition, the direction of the measured current is opposite from what it would be in a tokamak, as expected.

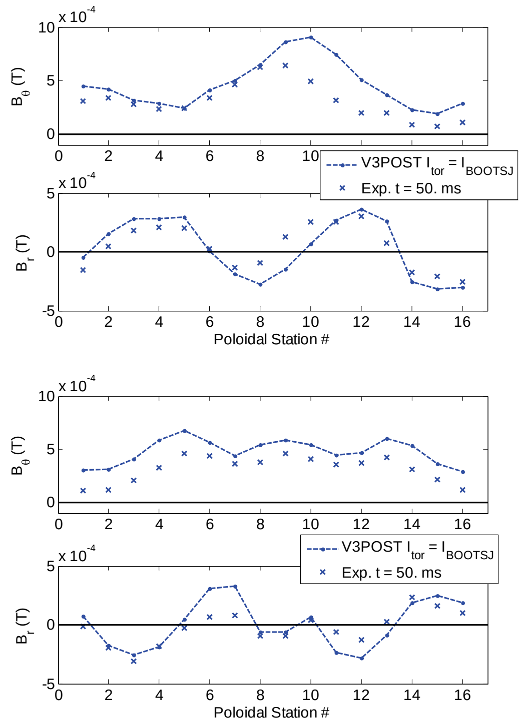

Fig. 5 Amplitude of magnetic field components (marked by 'x') in the polodial and radial directions at the 1/6 field period (top) and 1/2 field period (bottom) locations. Also shown are the calculated values using the V3FIT code (dashed line).

To model the signals detected by the 16 coil array, we use the V3FIT [12] code which takes as input the pressure and current profiles. When we include the current profile due to the bootstrap current in the V3FIT calculation, we obtain reasonably good agreement with the data that explains the vertical offset in the polodial magnetic field. The calculation however does not take into account the evolution of the bootstrap current which could alter the agreement between the V3FIT code and the data. This will be addressed in the future. More information is provided in the paper by Schmitt [13].

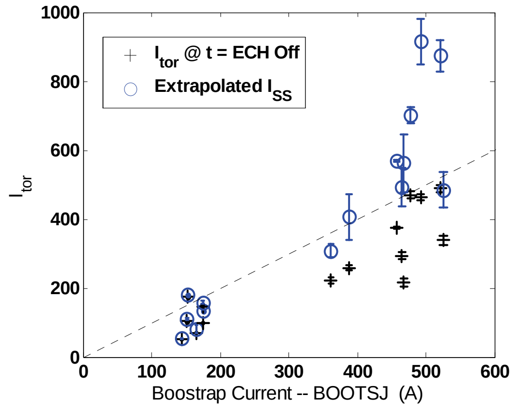

Fig. 6 Bootstrap current calculated by the BOOTSJ code compared with the measured current at the ECH turnoff (+) as well as an extrapolated value (circles) of the current based on its time evolution.

3. Magnetic Flexibility

One of the best ways to test quasisymmetry is to degrade the symmetry and see what the result is on the plasma. To accomplish this, HSX has a set of 48 auxiliary planar coils that are outside the modular coil set that produces the quasihelical field. Depending on the arrangement of the coil distribution in the auxiliary coils, it is possible to vary the magnetic field spectrum as well as the rotational transform, well depth, neoclassical transport, parallel viscous damping and MHD stability.

In particular, one configuration is termed 'Mirror' because it introduces spectral terms with (n,m) = (4,0) and (8,0). The effect of these extra spectral terms is to increase the effective ripple at r/a ~ 2/3 from 0.005 to 0.04. The increase in the effective ripple is even larger towards the plasma core. For this configuration, the plasma volume, rotational transform, magnetic axis and well depth vary little from the QHS configuration. There is another, earlier, configuration which we term the "old Mirror", which differs slightly from the "Mirror" in the current distribution of the auxiliary coils. The "old Mirror" had about a 1 cm magnetic axis shift between the QHS and "old Mirror" that made it difficult to obtain a Thomson scattering profile that included the plasma core. For the "Mirror" the shift is only about 1 mm. The first sets of experiments described below were done at a magnetic field of 0.5 T; further in the article we will discuss the 1.0 T data.

4. Trapped Particle Confinement

In the QHS configuration, calculations indicate that trapped particles should be very well confined. Similar calculations for the Mirror configurations show that the trapped particle confinement should be considerably degraded. We tested the trapped particle confinement by mounting a collector disk inside the vacuum chamber at the top and bottom of the confinement region and monitoring the floating potential [14].

Figure 7 shows the floating potential versus plasma density for the QHS and "old Mirror" configurations. With quasisymmetry, the floating potential of the plates in both the ion and electron drift directions show little change as the density is varied. However, with the quasisymmetry degraded, the floating potential becomes increasingly negative at lower density. This is only observed in the direction of the electron drift, as expected. For the plate in the ion drift direction, the floating potential is relatively unchanged.

Another indication of the improved confinement of trapped particles with quasisymmetry is the higher x-ray flux in this configuration [15]. The hard x-ray emission in HSX was analyzed using a CdZnTe detector that was housed outside the vacuum vessel in a lead box with a 0.8 mm pinhole and a 200 mm SS filter. Pulse height analysis was used to obtain the energy spectrum in a set of similar ECH discharges. Figure 8 shows the spectrum for QHS and 'old Mirror' at the same density of 2×10^{12} cm^{-3}. The high-energy tail for the QHS configuration is indicative of the improved confinement of the superthermal electrons that gives rise to the more efficient heating during the ECH.

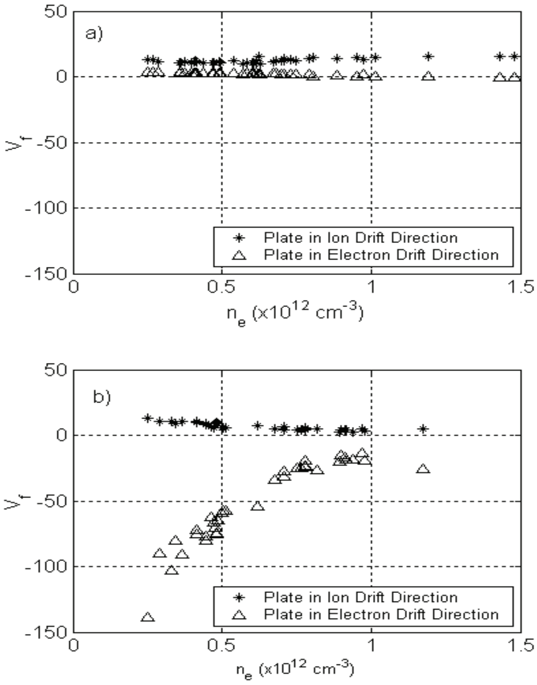

Fig. 7 Floating potential versus plasma density for the QHS configuration (top) and "old Mirror" configuration (bottom). Shown are the data for the plate in the ion (+) and electron (triangles) drift directions.

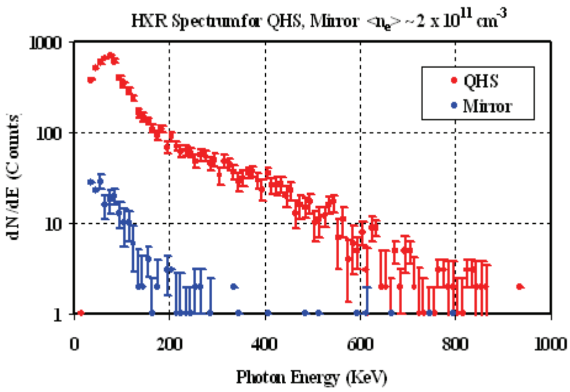

Fig. 8 X-ray spectrum for QHS and "old Mirror" configuration.

5. Fluctuations at B = 0.5 T

One distinguishing feature of the QHS configuration is the presence of a global coherent low-frequency mode that is observable from Langmuir probes, the interferometer, the radiometer as well as magnetic pick-up coils [16]. Indications from the interferometer, and more recently from a reflectometer, are that the mode is localized towards the plasma core. The estimated mode number is n = 1, m = 1. From probe measurements, the mode propagates in the electron diamagnetic direction. The mode frequency decreases with increasing density, in approximate agreement with an Alfvén mode. However, without a direct measurement of the electric field, it is difficult to determine the scaling in the laboratory frame of reference.

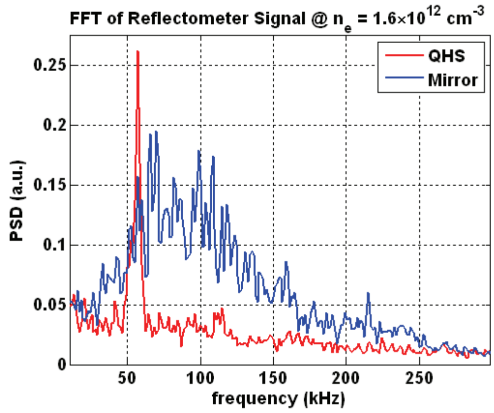

Fig. 9 Frequency spectrum of reflectometer signal for QHS and Mirror configurations at r/a ~ 0.4.

The striking feature of the mode is that it decreases in amplitude with increasing quasisymmetry degradation. Figure 9 shows a comparison of the frequency spectrum of density fluctuations measured by the reflectometer for the QHS and Mirror configurations [17]. The frequency of the reflectometer was tuned in this case to a spatial location of r/a ~ 0.4. In contrast to the broad turbulent spectrum for the Mirror configuration, the QHS spectrum is more quiescent, but with a large coherent mode at around 55 kHz. This mode is absent in the Mirror spectrum. Based on the measurements of an energetic tail population that is better confined in the QHS configuration, as discussed in the previous section, we infer that the coherent mode is most likely driven by nonthermal electrons. Future work will concentrate on whether the broader turbulent spectrum in the Mirror configuration might be due to the larger fraction of trapped particles for that configuration, close to the core.

6. Particle, Momentum and Heat Transport at B = 0.5 T

A number of experiments were performed to compare particle, momentum and heat transport between the QHS and the Mirror configurations. More details are given in the papers by Gerhardt [18] and Canik [19]. A common feature of the experiments is that the neoclassical reduction in transport could be observed by altering the magnetic field spectrum, in approximate agreement with a neoclassical model, but in each case there remained a large level of anomalous transport that didn't appear to change between the configurations.

Figure 10 shows the density profiles measured with a 10 channel Thomson scattering system. For the Mirror configuration, the profile is flat to hollow, which is typical of ECH discharges in many other stellarators. For the QHS configuration however, the profile is peaked. The experimental particle flux was inferred from a set of H_α

detectors and the DEGAS [20] code. Inside r/a ~ 0.3, the experimental particle flux in the Mirror was found to be close to the neoclassical flux driven by temperature gradients. This flux, termed the thermodiffusive flux, is reduced in the QHS configuration, accounting for the peaked density profile. In the outer regions of the plasma the experimental particle flux was found to be similar for the two configurations and, in both cases, much greater than the neoclassical level.

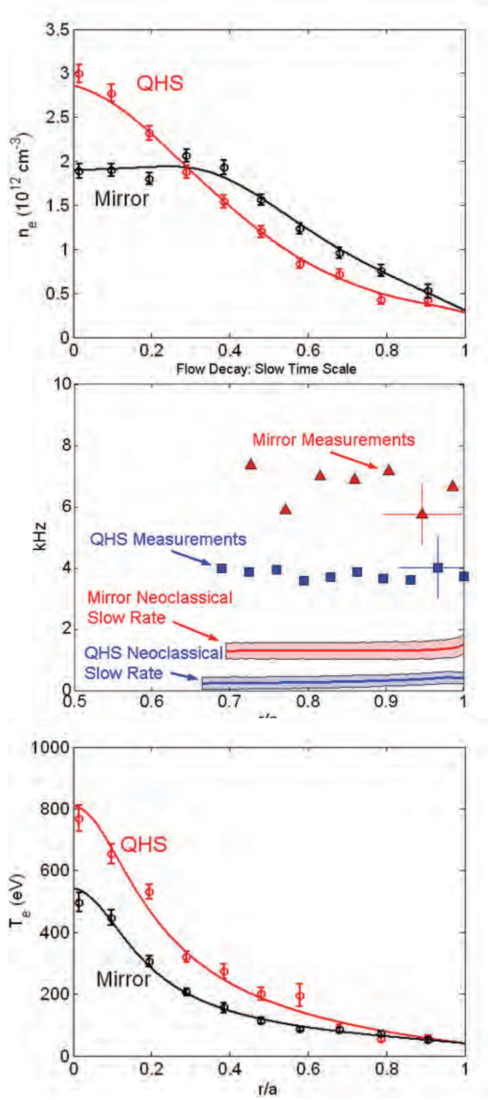

Fig. 10 Comparison of the density profile (top), flow decay rate (middle) and electron temperature profile (bottom) for QHS and Mirror configurations.

The middle figure of Figure 10 shows the results of a comparative experiment using a biased electrode to spin up the plasma in the two configurations. It was found that for the quasisymmetric configuration, the plasma flow, as measured by a Mach probe, increased more slowly and rose to a higher value than for the Mirror configuration. After the bias turn-off, the decay in the flow was faster for the nonsymmetric configuration. The results were compared to a neoclassical model which predicted two time scales for the plasma flow, a faster and a slower time scale. The difference in the measured damping rates is roughly the same as the difference in the slow neoclassical rates. However, for both configurations, there is an additional source of flow damping that is unaccounted for in the neoclassical model.

The final comparison to be made is of the electron thermal diffusivity. The bottom plot of Figure 10 shows the electron temperature profile for the two configurations with the same ECH input power. The central temperature is about 800 eV for the QHS configuration and 500 eV for the Mirror. The higher temperature for the quasisymmetric configuration is indicative of a lower neoclassical thermal conductivity.

A more rigorous comparison was made of the two configurations with the same temperature profile and similar density profiles, except for the core where thermodiffusion dominates for the Mirror. A comparison of the thermal conductivity for the two configurations is shown in Figure 11. At a r/a ~ 0.2 – 0.3, the electron thermal conductivity is around 2 m^2/s for QHS and around 4 m^2/s for Mirror. This difference is comparable to the difference in the neoclassical values. Towards the edge, where the neoclassical thermal conductivity is small, the two configurations have comparable transport.

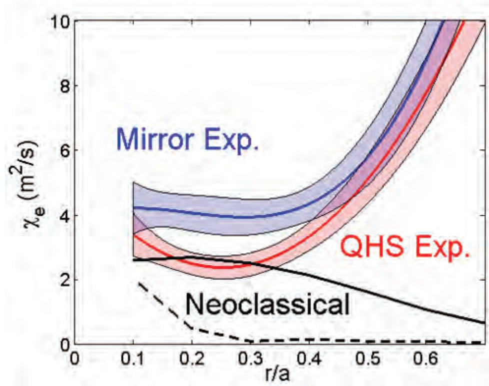

Fig. 11 Experimental and neoclassical thermal conductivities for the QHS and Mirror configurations.

7. Electron Thermal Conductivity at B = 1.0 T

For second harmonic extraordinary mode heating at 0.5 T, the transport analysis was complicated by the presence of a superthermal electron population. This prevented an estimate of the absorbed power from being obtained based on the decay of the diamagnetic loop. Rather, a fairly tedious process of estimating the absorbed power was employed based on the time evolution of the total integrated kinetic energy obtained from Thomson scattering measurements. For fundamental ordinary mode heating at 1.0 T however, the superthermal population was much reduced based on diamagnetic, ECE and x-ray measurements. This simplified the measurement of the absorbed power and the calculation of the thermal conductivity. Figure 12 shows that for 100 kW input power, electron temperatures up to 2.5 keV were obtained for the

QHS configuration, while around 1.5 keV was measured for the Mirror.

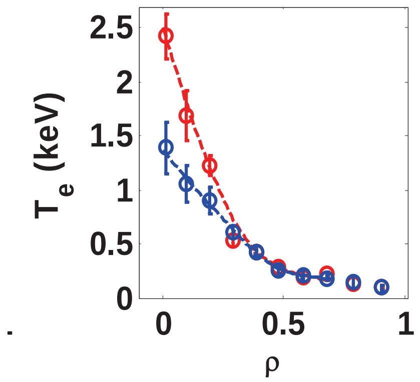

Fig. 12 Electron temperature profile for QHS (red) and Mirror (blue) with 100 kW input power.

The neoclassical and anomalous components of the total electron thermal conductivity were compared by matching as close as possible the temperature and density profiles. This required decreasing the QHS input power to 44 kW, while the Mirror input power stayed at 100 kW as in Figure 12. The experimental and neoclassical electron thermal conductivities for the QHS and Mirror configurations are shown in Figure 13. The large error bar for the Mirror case is because of the difficulty obtaining reproducible discharges. Still, roughly a factor of 3 reduction in the conductivity is observed at the plasma core due to the quasisymmetry. Further analysis is needed however at this point to understand how the anomalous transport compares between the two configurations. More details are given in the paper by Lore [21].

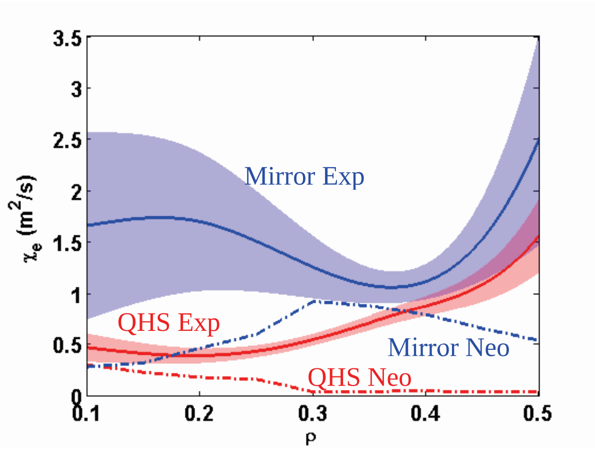

Fig. 13 Experimental and neoclassical electron thermal conductivities for QHS and Mirror.

8. Modeling Anomalous Transport in HSX

With ECH, the electron temperature in HSX is much higher than the ion temperature so that the dominant long wavelength instability is the trapped electron mode (TEM) Because of the quasisymmetry, the magnetic geometry in HSX looks similar to that in a tokamak with high effective transform. In a comparison of microinstabilities in different stellarator geometries, Rewoldt [22] found that HSX had a fairly high growth rate because of this short connection length and also because of the substantial bad curvature at the location of the trapped particles.

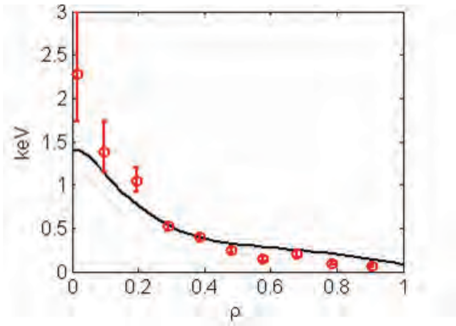

Fig. 14 Electron temperature profile from Thomson scattering (red circles) and model (black line).

To simulate anomalous transport in HSX, the Weiland ITG/TEM model [23], originally used to describe transport in tokamaks, was modified to approximate the local geometry in HSX. This required the substitution of the helical ripple in place of the toroidal ripple and a local curvature about 3 times that of a tokamak with the same major radius. The 3D gyrokinetic code GS2 [24] was then used to confirm that the linear growth rates using the modified Weiland model were accurate to within 30%. Details are given in the paper by Guttenfelder [25].

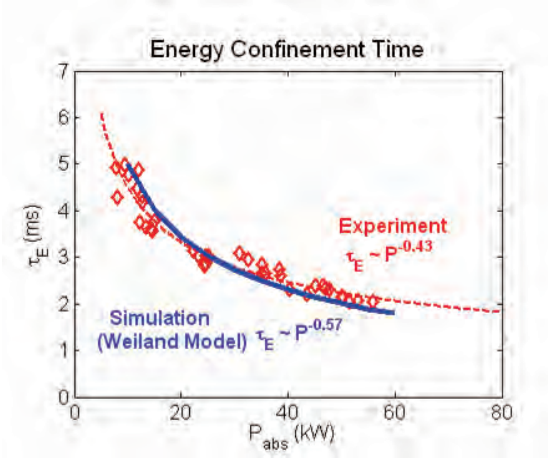

Fig. 15 Comparison of model dependence of confinement time (blue line) on absorbed power with experimental data (red diamonds).

The temperature profile in HSX was modeled by assuming a thermal conductivity consisting of the neoclassical term and the Weiland contribution. The power deposition profile is based on a calculation using a ray-tracing code and the total absorbed power comes from the decay of the diamagnetic loop signal. Figure 14 shows a comparison of the experimental data to the model calculation. Outside the region of r/a ~ 0.3, the agreement is quite good. Towards the core the agreement isn't as good, possibly because of the omission of non-linear effects or $E \times B$ shear suppression of turbulence. The predicted energy confinement times agree well with the experimental confinement times. The dependence of the experimental confinement time on the absorbed power is slightly weaker than the model prediction. This is shown in Figure 15.

9. Conclusions

This paper reviewed a number of different ways in which quasisymmetry was tested in HSX. A quasihelically symmetric configuration is noted for its lack of toroidal curvature and high effective transform. The high effective transform was observed in small deviation of a passing particle orbit from a magnetic surface as well as the small Pfirsch-Schlüter and bootstrap currents that were measured. The lack of toroidal curvature was noted by the drift of an electron to the inside of the flux surface, rather than to the outside if toroidal curvature dominated. Also, the helical Pfirsch-Schlüter current and the direction of the bootstrap current were also indication of a very small toroidal curvature. Measurements of the polodial and radial components of the magnetic field due to the plasma currents showed good agreement with the V3FIT code.

Another feature of the quasisymmetric configuration is the good confinement of energetic trapped particles as seen from collector plates and hard x-ray measurements. This good confinement may be responsible for an MHD instability which is observed to decrease in amplitude and then disappear as the degree of quasisymmetry breaking increases. First measurements of density fluctuations at the plasma core were obtained with a reflectometer and showed a quiescent background with a large coherent global mode for the QHS configuration, versus a broad spectrum of turbulent fluctuations without the coherent mode for the Mirror configuration.

With ECH at a magnetic field of 0.5 T, the results showed that the parallel momentum damping, particle thermodiffusion and electron thermal conductivity could all be decreased with quasisymmetry. The level of decrease roughly agreed with the calculated decrease in the neoclassical values, however a large anomalous component to particle, momentum and heat transport still remained. To date, there is no evidence in the data obtained at 0.5 T that the anomalous contribution differs substantially between the quasisymmetric and nonsymmetric configurations.

At a magnetic field of 1.0 T, central electron temperatures were up to 2.5 keV for the QHS configuration when 100 kW ECH was injected into the plasma. With the quasisymmetry degraded, the core temperature fell to 1.5 keV. Analysis of the transport for similar temperature and density profiles showed substantial reduction in the experimental thermal conductivity at the plasma core. Further analysis is needed before it can be understood whether the anomalous transport for the QHS case was different from that in the Mirror configuration.

Finally, while the short connection lengths in HSX are shown to be good for decreasing particle orbits, plasma currents and neoclassical transport, initial evidence seems to indicate that the combination of the short connection lengths and large curvature may be responsible for somewhat higher anomalous transport. Calculations of the temperature profile and energy confinement time based on a combination of neoclassical transport plus a modified Weiland model for anomalous transport, show reasonable agreement with the data. So far the model ignores zonal flows, $E \times B$ shear suppression of turbulence, nonlinear effects and the differences in the fraction of trapped particles between the quasisymmetric and nonsymmetric configurations. Future work will concentrate on understanding how the degree of quasisymmetry affects the radial electric field and plasma turbulence.

In summary then, initial experimental results indicate that the quasisymmetric configuration has fulfilled its promise of reducing neoclassical transport. More work is needed to resolve what effect the quasisymmetric configuration has on anomalous transport.

Acknowledgments

The authors wish to thank the V3FIT team for the use of their code and especially Steve Knowlton for invaluable assistance. This work was supported by the U.S. Department of Energy under Contract No. DE-FG02-93ER54222.

References

[1] H.E. Mynick, Phys. Plasmas **13**, 058102 (2006).
[2] Nuhrenberg and R. Zille, Phys. Lett. A **129**, 113 (1988).
[3] P. R. Garabedian, Phys. Plasmas **4**, 1617 (1997).
[4] F. S. B. Anderson *et al.*, Fusion Technol. **27**, 273 (1995).
[5] G. H. Neilson, M. C. Zarnstorff, J. F. Lyon and the NCSX Team, J. Plasma Fusion Res. **78**, 214 (2002).
[6] D. A. Spong, S. P. Hirshman, L. A. Berry *et al.*, Nucl. Fusion **41**, 711 (2001).
[7] J. N. Talmadge, V. Sakaguchi, F. S. B. Anderson, D. T. Anderson and A.F. Almagri, Phys. Plasmas **8**, 5165 (2001).
[8] A.H. Boozer, Phys. Fluids **24**, 1999 (1981).
[9] A.H. Boozer and H.J. Gardner, Phys. Fluids **B2**, 2408 (1990).
[10] K.C. Shaing and J.D. Callen, Phys. Fluids **26**, 3315 (1983).
[11] K.C. Shaing *et al*., Phys. Fuids **B4**, 148 (1989).
[12] S.P. Hirshman, E.A. Lazarus, J.D. Hanson, S.F. Knowlton, L.L. Lao, Phys. Plasmas **11**, 595 (2004).
[13] J.C. Schmitt, J.N. Talmadge, P.H. Probert, D.T. Anderson, *Proceedings of ITC/ISHW2007.*
[14] J.C. Canik, personal communication.
[15] A. Abdou, Ph. D. thesis, University of Wisconsin-Madison (2005).
[16] D.L. Brower, C. Deng *et al., Transport Task Force, 2005.*
[17] K. Likin *et al*., *Proceedings of ITC/ISHW2007*
[18] S.P. Gerhardt, J.N. Talmadge, D.T. Anderson, J.M. Canik, Phys. Plasmas **12**, 56116 (2005).
[19] J.M. Canik, D. T. Anderson, F. S. B. Anderson, C. Clark, K.

M. Likin,, J. N. Talmadge, and K. Zhai, Phys. Plasmas **14**, 056107 (2007).
[20] D. Heifetz *et al.*, J. Comput. Phys. **46**, 309 (1982).
[21] J. Lore *et al*., *Proceedings of ITC/ISHW2007*.
[22] G. Rewoldt, L.-P. Ku, W.M. Tang, Phys. Plasmas **12**, 102512 (2005).
[23] H. Nordman *et al*., Nucl. Fusion **30**, 983 (1990).
[24] M. Kotschenreuther *et al*., Comp. Phys. Comm. **88**, 128 (1995).
[25] W. Guttenfelder *et al.*, *Proceedings of ITC/ISHW2007*.

Proceedings of ITC/ISHW2007

Inter-linkage of transports and its bridging mechanism

Katsumi IDA

National Institute for Fusion Sciences, Toki, Gifu 509-5292, Japan

(Received / Accepted)

The physical mechanisms determining the diffusive and non-diffusive terms of particle, momentum and heat transport are described. The non-diffusive term in the particle transport, which causes inward pinch or outward flow is driven by the temperature gradient and the magnetic field curvature. The non-diffusive term in the momentum transport, which drives spontaneous toroidal rotation, is found to be sensitive to the sign of the electric field. In heat transport, there is no clear non-diffusive term observed. The temperature and temperature gradient dependences of the diffusive terms are discussed.

Keywords: Plasma Transport Inter-linkage

DOI: 10.1585/pfr.1.001

The existence of the non-diffusive term of transport has been recognized in particle transport (and impurity transport) as the Ware pinch by the toroidal electric field[1] or convection by ion temperature gradient driven turbulence[2] . The peaked profile of the electron density observed in the steady-state with gas puff fueling clearly shows the significant contribution of the non-diffusive inward particle flux, because the particle source is localized near the plasma periphery. The inward pinch observed in a stellarator where there is no toroidal electric field, suggests that turbulence driven convection can easily overcome the thermodiffusion[3]. The Non-diffusive term in the momentum transport was found experimentally[4] and it appears as an spontaneous toroidal rotation[5]. The significant contribution of the non-diffusive term to the transport shows a strong inter-linkage of the transport between particle, (poloidal and toroidal) momentum and (ion and electron) heat transport. In the plasmas with a transport barrier, where a strong gradient is produce, the inter-linkage of the transport becomes more significant. (A good example is a large spontaneous toroidal rotation at the internal transport barrier[6, 7]). This is because these non-diffusive terms are correlated to the gradients of other plasma parameters (ion temperature gradient for particle transport or potential gradient for momentum transport). Therefore these non-diffusive term are considered to be off-diagonal terms of the so-called transport matrix. Recent turbulence transport theory explores the physics bridging mechanism for the off-diagonal terms of the transport matrix[8]. For example, the theoretical model of symmetry breaking of turbulence by radial electric field shear[9] could explain the strong correlation between non-diffusive momentum flux and ion pressure gradients (and also radial electric field) observed in experiments. In this paper, non-diffusive terms of particle and momentum transport and diffusive terms of heat transport are discussed based on experiments in stellarators and tokamaks.

It is well known that the non-diffusive term has a significant contribution to the radial flux of particles and it causes the inward flux which is necessary to achieve a peaked density profile with a particle source localized near the plasma edge. Due to the role of spontaneous toroidal rotation in MHD stability, the non-diffusive term of momentum transport has become highlighted in recent momentum transport studies. On the other hand, the non-diffusive term of heat transport has not been clearly identified, although there were experimental results that suggest the heat pinch. Figure 1 shows the physics mechanism determining the diffusive term and non-diffusive terms of the radial flux of a particle, momentum and energy transport. There are various physics mechanisms contributing to the non-diffusive term in the particle transport. The inward pinch driven by the toroidal electric field is well known as the Ware pinch in tokamaks. However, the inward pinch observed in steady state plasmas in tokamaks and in stellarators can not be explained by the Ware pinch, because there is no toroidal electric field in these experiments. In stellarator plasmas, the thermodynamic force driven by the electron temperature gradient contributes to significant outward flux. This term has been confirmed experimentally in stellarators. It is well known that momentum and energy transport have convection terms due to the radial flux of particles. In general, these convective terms are relatively small. It is interesting that the radial electric field and the magnetic field curvature affects both the non-diffusive terms of particle transport and momentum transport, while the radial electric field and its shear affect both the diffusive

author's e-mail: xxxyyyzzz@u-plasma.ac.jp

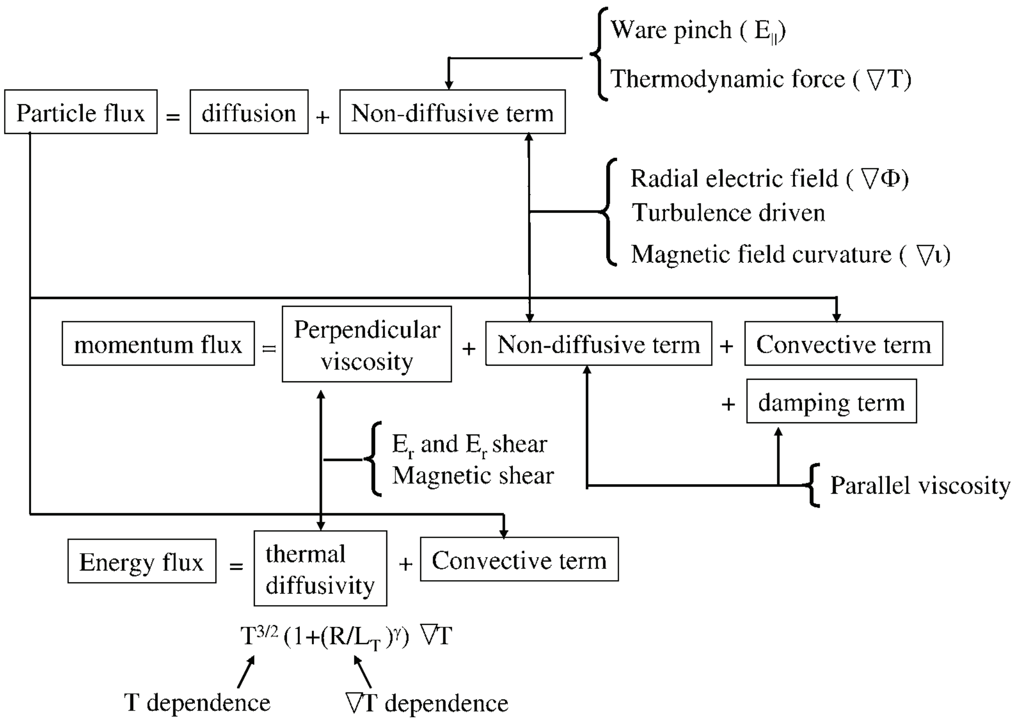

Fig. 1 Physics mechanism determining the diffusive term and non-diffusive terms of the radial flux of particle, momentum and energy transport.

term of momentum transport and energy transport. Therefore particle, momentum and heat transport are coupled to each other through these physics elements.

The diffusive term of particle transport has been derived from the time dependent transport analysis of a discharge with gas puff modulation. Figure 2 (a) shows the temperature dependence of the diffusion coefficient evaluated in LHD. The diffusion coefficient measured is larger than the prediction by neoclassical theory by one order of magnitude. Both in the core and edge, the diffusion coefficient has the electron temperature dependence of $\alpha \approx 1$, where $D \propto T_e^{\alpha}$, which is weaker than that of the neoclassical prediction ($\alpha \approx 2.6$). Figure 2(b) shows the relation between the normalized temperature and density gradients experimentally obtained in Wendelstein 7AS and LHD. Since both the density gradient and temperature gradient contribute to the outward flux, there should be an inward flux to sustain the steady state density profile where $\Gamma \approx 0$. The particle flux can be written as $\Gamma = -n_e(D_{11}\nabla n_e/ne_e + D_{12}\nabla T_e/Te - u)$. Where D_{11} and D_{12} are the on- and off-diagonal elements of the transport matrix and the velocity u is a convective contribution. The ratio of these coefficient derived from the slope of the data plotted in Fig2(a) are $D_{12}/D_{11} \approx 1.4$ and $u/D_{11} \approx -12.5\ \mathrm{m}^{-1}$, respectively. The significant contribution of the inward term of u/D_{11} overcomes the outward term of D_{12}/D_{11} of the non-diffusive term as well as the diffusive term and sustains the peaked density profile in steady state. Because various physics mechanisms contribute to the non-diffusive term of particle transport, it is still open to question which physics mechanisms become dominant. A more comprehensive understanding should be sought from the comparison of density profiles in stellarators (typically flat or hollow) with these in tokamaks (typically peaked).

Similar experiments have been done in steady state fully noninductive current plasmas in tokamaks to eliminate the contribution of the Ware pinch due to toroidal electric field to drive ohmic current. Figure 3 shows the relations between $\nabla n_e/n_e$, $\nabla T_e/T_e$ and $\nabla q/q$ in the Tore Supra tokamak. As seen in Fig.3(a) and Fig.3(b), there are two distinguished regions ($\rho < 0.3$ and $0.35 < \rho < 0.6$) that show different slopes. The direction of the thermodiffusion flux is found to change when moving from the outer to the inner plasma. The sign of the thermodiffusion pinch is determined by the slope. This experiment shows that thermo-diffusion can be inward ($\rho < 0.3$) or outward ($0.35 < \rho < 0.6$) depending on the plasma radius, where the unstable mode (ITG or ETG) is expected to be different because of the change in the ratio of $\nabla T_e/\nabla T_i$. In the region of $\rho = 0.35 - 0.6$, where the thermo-diffusion flux is outward, a physics mechanism driving the inward pinch is necessary in

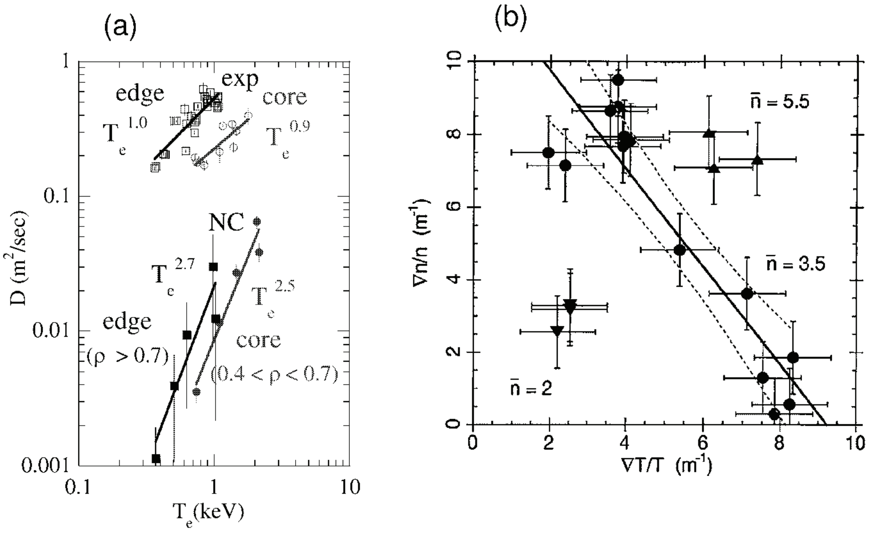

Fig. 2 (a) Temperature dependence of the diffusion coefficient in the core ($0.4 < \rho < 0.7$) and edge ($\rho > 0.7$) experimentally evaluated and neoclassically predicted in LHD[10] and (b) average density versus temperature gradient scale length estimated between r = 2 and 8 cm for three densities. For $\Gamma \approx 0$ it follows that $D_{12}/D_{11} \approx 1.4$ and $u/D_{11} \approx -12.5$ m^{-1} [3] and (b) the relation of normalized temperature and density gradient. The core and edge values are estimated from the average value in the core ($0.4 < \rho < 0.7$) and edge ($0.7 < \rho < 1.0$) at R_{ax} = 3.6m, B_t = 2.75, 2.8T.

order to sustain the sharp density gradient in steady state. A clear relation between $\nabla n_e/n_e$ and $\nabla q/q$ in Fig.3(c) strongly suggests that the magnetic field curvature drives the inward pinch. It is interesting that the sign of the magnetic field curvature driven flux in stellarators is opposite to that in tokamak and outward flux is expected. It is still open to question what the physics mechanism is causing the inward flux near the plasma edge in sterllarators, where there is no Ware pinch and both the thermo-diffusion flux and the flux driven by the magnetic field curvature are expected to be outward because of $\nabla T_e/T_e < 0$ and $\nabla q/q < 0$. Because the impurity has a higher ion charge, Z, impurity transport is more sensitive to the radial electric field than bulk particle transport. The positive radial electric field in the electron root tends to drive outward flux and suppress the accumulation of impurities and radiation collapse[15, 16]. It is a crucial issue to achieve poor impurity confinement (impurity exhaust) and good energy confinement, simultaneously. In stellarators, poor impurity confinement is observed in plasmas with good energy transport, for example the HDH mode in Wendelstein 7-AS[17] and the electron ITB and high ion temperature mode in LHD.

Since the damping of the plasma toroidal velocity owing to parallel viscosity is significant near the plasma periphery in stellarators[12], toroidal rotation near the plasma edge is determined by the radial electric field, while the core toroidal rotation is determined by the momentum from the tangential NBI. The momentum flux including the non-diffusive term due to the radial electric field can be expressed as $P_\phi = -mn(\mu_\perp \nabla V_\phi - \xi E_r/B_\theta)$[13]. In order to investigate the effect of the radial electric field on the toroidal rotation, a density scan is made near the threshold of the transition from the ion root (negative E_r) to electron root (positive E_r). In LHD, the transition from the ion root to the electron root takes place at the low density where the plasma is well into the collisionless regime $\mu_e^* < 0.1$, because of the non-ambipolar particle flux as predicted by neoclassical theory. As seen in Fig.4, the plasma rotates more in the counter direction (anti parallel to equivalent plasma current) for positive E_r, while it rotates more in the co direction for negative E_r. The relation between the toroidal rotation and the radial electric field is plotted in Fig4(c). This result shows that the positive radial electric field drives the toroidal rotation in the counter direction, where the toroidal rotation contributes to the negative radial electric field. It should be emphasized that the direction of the toroidal flow is anti-parallel to the direction of the $< E_r \times B_\theta >$ drift. This is in contrast to the spontaneous flow in a tokamak, where the direction of the toroidal flow is parallel to the direction of the $< E_r \times B_\theta >$ drift, because the toroidal viscosity is nearly zero due to the toroidal symmetry. The spontaneous toroidal flow becomes more significant in the plasma with an internal transport barrier, where large electric fields are observed. In CHS the sponta-

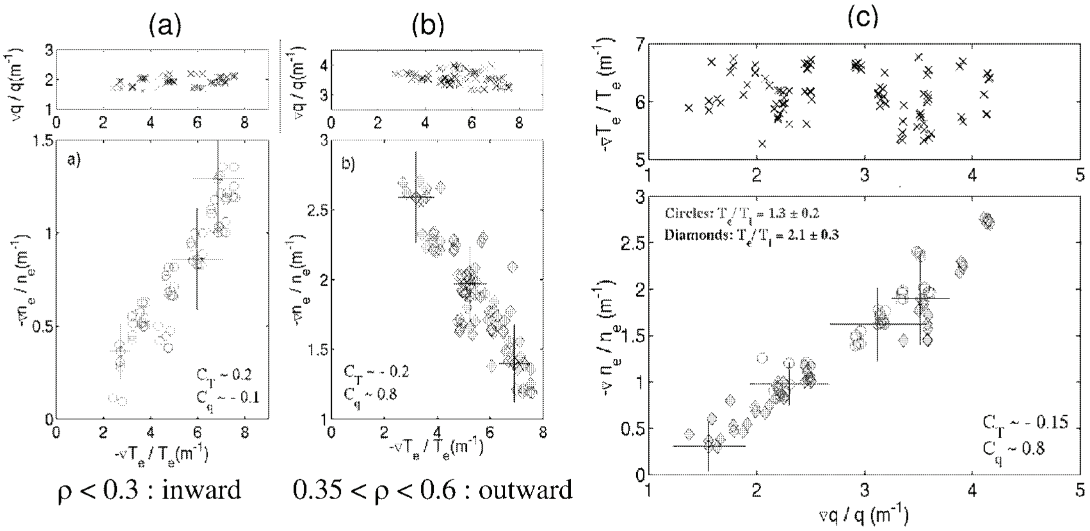

Fig. 3 $\nabla n_e/n_e$ $\nabla T_e/T_e$ from a set of seven discharges: (a) for $r/a \leq 0.3$, $T_e/T_i = 2 \pm 0.4$, $\nabla T_e/T_e = 3.8$-4.8; (b) for $0.35 \leq r/a \leq 0.6$, $T_e/T_i = 1.2 \pm 0.4$, $\nabla T_e/T_e = 0.7$-3.5. Corresponding variation of $\nabla q/q$ is displayed at the top. (c) $\nabla n_e/n_e$ versus $\nabla q/q$ within $0.3 \leq r/a \leq 0.6$ from a set of seven discharges, keeping $|\nabla T_e/T_e|$ at the values of $6m^{-1} \pm 10$ % and $\nabla T_e/T_e = 0.6 \pm 0.3$ [11].

neous toroidal flow overcomes the toroidal flow driven by co-NBI and the plasma rotates in the counter direction associated with the formation of a large positive E_r. In contrast, in JT-60U, the plasma rotates in the counter direction at the ITB region where a strong negative radial electric field is produced. The significant difference between tokamaks and heliotron devices is the relationship between the poloidal field direction and the direction of the dominant symmetry. The pitch angle of the dominant symmetry is even larger than that of the averaged poloidal field in a Heliotron device, while it is zero due to the toroidal symmetry in a tokamaks.

In a stellarator turbulence in the plasma as well as non-ambipolar flux can drive flows perpendicular ($E \times B$) and parallel (spontaneous toroidal flow) to the magnetic field though Reynolds stress. The experiments to investigate the turbulence driven $E \times B$ flow and the spontaneous toroidal flow have been done in the vicinity of the last closed flux surface (LCFS) in JET and in TJ-II. The radial-perpendicular component of the production term has been investigated in the LCFS vicinity in the JET tokamak as seen in Fig.5(a). Figure 5(b) shows the radial structure of the cross correlation between parallel and radial fluctuating velocities in the proximity of the LCFS in the TJ-II stellarator. The level of cross correlation $< vM_{||} >$ increases for plasma densities above the threshold value to generate $E \times B$ sheared flows. The appearance of gradients on $< vM_{||} >$ is due to both radial variations in the level of fluctuations and in the cross-phase coherence between fluctuating radial and parallel velocities. It has been found that the energy transfered from dc flows to turbulence, directly related to the momentum flux and the radial gradient in the perpendicular flow, can be both positive and negative in the proximity of sheared flows. Furthermore, the energy transfer rate is comparable with the mean flow of kinetic energy normalized to the correlation time of the turbulence, implying that this energy transfer is significant. These results show that turbulence can act as an energy sink and energy source for the mean flow near the shear layer.

There is no clear evidence of a non-diffusive term of the energy transport except for a few experiments in plasmas with ECH[21]. In most cases the diffusive term only can explain the energy transport observed in experiments. The diffusive term of the energy transport is evaluated as thermal diffusivity (the ratio of heat flux normalized by density to the temperature gradient). In general, the heat flux depends on the temperature and the temperature gradient and it is non-linear. Therefore the thermal diffusivity has a temperature dependence and also a temperature gradient dependence in the non-linear regime. Figure 6 shows the ∇T_e dependence of χ_e (obtained from the static analysis i.e. the power balance analysis) in JT-60U, Wendelstein 7-AS and LHD. In Fig.6, the thermal diffusivity is normalized by $T_e^{3/2}$, which is predicted by Gyro-Bohm transport, in order to eliminate the T_e dependence of χ_e and make the ∇T_e dependence clear. The ∇T_e is normalized by R/T_e, Because the ratio of the major radius to the scale length of the temperature is expected to give the threshold of turbulence in the critical temperature gradient transport model. As seen in Fig.6, there is no clear critical gra-

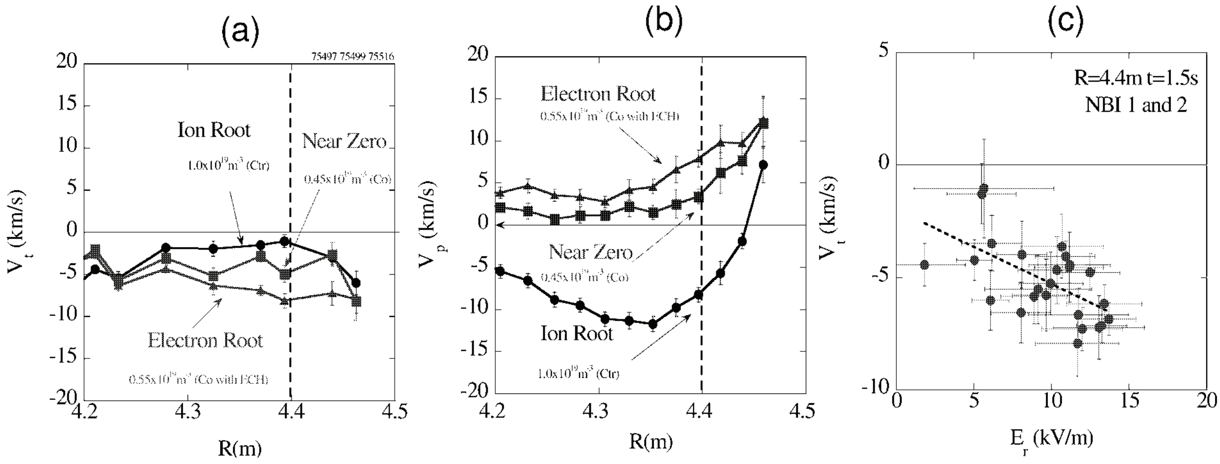

Fig. 4 Radial profiles of (a) toroidal and (b) poloidal rotation velocities and (c) relation between toroidal and poloidal rotation velocities in LHD.

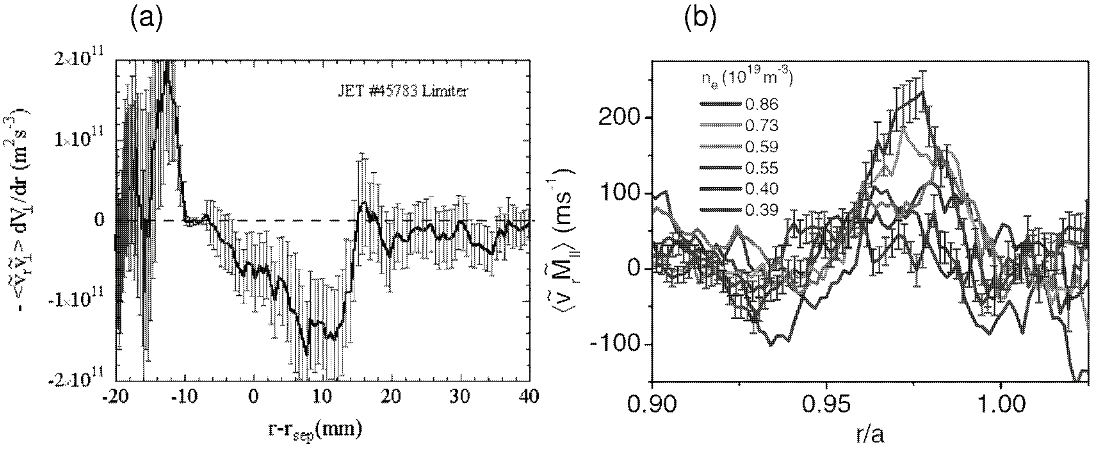

Fig. 5 Radial profile of the (a) radial-perpendicular Reynolds stress component in the plasma boundary region in the JET tokamak and the (b) radial-parallel Reynolds stress component in the TJ-II plasma boundary region at different plasma densities. Parallel velocity is quantified by the parallel Mach number [14, 18].

dient scale length observed in LHD, although the existence of a critical gradient scale length is suggested in Wendelstein 7-AS and JT-60U. The thermal diffusivity χ_e shows a Gyro-Bohm type T_e dependence when the temperature gradient is small enough, while it depends mostly on the scale length above a critical value of the temperature gradient. This implies that there is a strong nonlinear mechanism in transport. One of the candidates for the mechanism causing strong nonlinearity is non-linear flow damping of the zonal flow in a tokamak plasma. In the LHD heliotron, there is no critical value of the temperature gradient, because the transition from L-mode to an electron ITB take place at a lower temperature gradient[22]. The transition from L-mode to the electron ITB is due to the change in the temperature dependence of α from positive values ($\sim 3/2$ as predicted by gyro-Bohm scaling) to negative values ($\sim -3/2$), where α is defined as $Q/n_e \propto T_e^{\alpha}\nabla T_e$[23]. The temperature dependence tends to decrease (weak temperature dependence) as the electron density is increased. This change in the temperature dependence of the thermal diffusivity is consistent with the change in the power degradation of the energy confinement time. It should be noted that the L-mode scaling of the global energy confinement time expressed by $t_E \propto (n_e/P)^{3/5}$ is equivalent to the temperature dependence of the thermal diffusivity expressed by $\chi \propto T_e^{3/2}$. Therefore the weak temperature dependence ($\alpha = 1/2$) appears as a tendency of the saturation of the energy confinement time at higher density as $n_e^{1/3}$. The temperature dependence factor α becomes ~ 0.5 at lower temperatures below the critical value (in the more collisional regime[24]) or in the plasma with pellet injection[25]

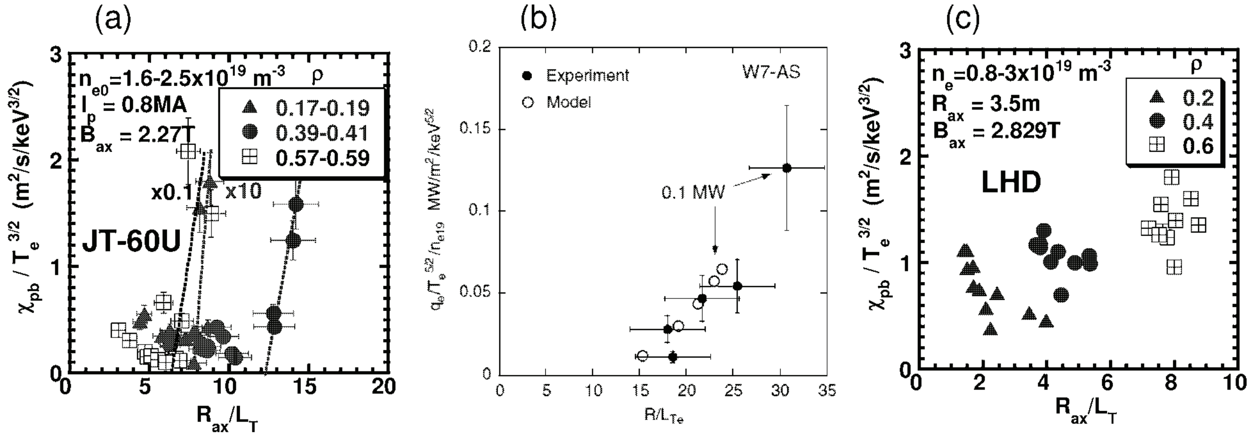

Fig. 6 ∇T_e and T_e dependence of χ_e at different normalized radii in (a)JT-60U, (b) Wendelstein 7AS and (c) LHD NBI plasmas. χ_e is normalized by the gyro-Bohm T_e dependence and ∇T_e is normalized by (R/T_e), where R is the major radius and $L_T = \nabla T_e/T_e$ in (a) and (c)[19, 20].

In summary, the non-diffusive term driven by the thermo-diffusion due to the temperature gradient is experimentally identified in stellarators and tokamaks. In stellarators, thermo-diffusion always drives outward flow, while that in tokamak drives inward or outward flow depending on the unstable mode of the turbulence. The inward pinch due to the magnetic field curvature is found in steady state fully non-inductive current plasmas in tokamaks. However, this does not explain the inward pinch observed in the heliotron plasma, where the non-diffusive term due to the magnetic field curvature is expected to be outward. In momentum transport, the significant contribution of the non-diffusive term is experimentally observed and is identified as spontaneous flow. The physics mechanisms driving the spontaneous flow, which is parallel to the magnetic field, are investigated. Both the mean flow perpendicular and parallel to the magnetic field are driven by turbulence as well as by non-ambipolar flux. The mean flow parallel to the magnetic field (spontaneous toroidal flow) is in the direction of the toroidal flow anti-parallel to the $< E_r \times B_\theta >$ drift, which is in contrast to the spontaneous flow in a tokamak, where the direction of the toroidal flow is parallel to the direction of the $< E_r \times B_\theta >$ drift. Finally the parameter dependence of the diffusive term of the energy transport is discussed. The thermal diffusivity shows a Gyro-Bohm type T_e dependence when the temperature gradient is small. When the temperature gradient exceeds the threshold of the scale length, the thermal diffusivity increases rapidly if the plasma stays in L-mode. The threshold of the scale length is observed in tokamaks and Wendelstein 7-AS plasmas, but not in the LHD plasma, where the transition from L-mode to the electron ITB mode take place before the threshold.

The author would like to thank Drs.K.Tanaka and M.Yoshinuma (NIFS) for fruitful discussions in organizing this paper. The author also would like to thank Drs.C.Hidalgo (CIMAT) and U.Stroth(Kiel Univ.), G.T.Hoang(CEA) for useful discussions on the interpretation of the experimental data in their devices.

[1] A. A. Ware, Phys. Rev. Lett. **25**, 15 (1970).
[2] P.W.Terry, Phys. Fluids B **1**, 1932 (1989).
[3] U.Stroth, et al., Phys. Rev. Lett. **82**, 928 (1999).
[4] K.Ida et al., Phys Rev Lett **74**, 1990 (1995).
[5] B. Coppi Nucl. Fusion **42**, 1 (2002).
[6] K.Ida et al., Phys Rev Lett **86** 3040 (2001).
[7] Y.Sakamoto et al., Nucl Fusion **41** 865 (2001).
[8] S.-I.Itoh Phys Fluids B **4** 796 (1992).
[9] O.D.Gurcan , P.H.Diamond, et al., Phys Plasmas **14**, 042306 (2007).
[10] K.Tanaka, et al., Nucl. Fusion, **46**, 110 (2006).
[11] G.T.Hoang, et al., Phys. Rev. Lett. **93**, 135003 (2004).
[12] K.Ida et al., Phys Rev Lett. **67** 58 (1991).
[13] K.Ida et al., Plasma Phys. Control. Fusion, **44**, 361 (2002)
[14] C.Hidalgo et. al., Plasma Phys. Control. Fusion, **48**, S169 (2006)
[15] Y.Nakamura, et. al., Nucl. Fusion **43** 219 (2003).
[16] K.Ida et al., Nucl. Fusion **45** 391 (2005).
[17] K. McCormick, et. al., Phys. Rev. Lett. **89**, 015001 (2002).
[18] B.Goncalves, et al., Phys. Rev. Lett. **96**, 145001 (2006).
[19] S.Inagaki, H.Takenaga, K.Ida, et. al., Nucl. Fusion **46**, 133 (2006).
[20] F.Ryter et. al., Plasma Phys. Control. Fusion, **48**, B453 (2006)
[21] T.C.Luce, et. Al., Phys. Rev. Lett. **68**, 52 (1992).
[22] K.Ida et. al., Phys Rev Lett **91** 085003 (2003).
[23] K.Ida et. al., Phys Plasmas **11** 2551 (2004).
[24] J. Miyazawa et al., Plasma Phys. Controlled Fusion **47** 801 (2005).
[25] K.Ida et. al., Phys Rev Lett **96** 1250063 (2006).

Invited Talks

Effect of rotational transform and magnetic shear on confinement of stellarators

E. Ascasíbar(1), D. López-Bruna(1), F. Castejón(1), V.I. Vargas(1), V. Tribaldos(1), H. Maassberg(2), C.D. Beidler(2) R. Brakel(2), A. Dinklage(2) J. Geiger(2), J.H. Harris(3,4), A. Kus(2) T. Mizuuchi(5), S. Murakami(5), S. Okamura(6), R. Preuss(2), F. Sano(5), U. Stroth(7), Y. Suzuki(6), J. Talmadge(8), K.Y. Watanabe(6), H. Yamada(6), M. Yokoyama(6)

(1) CIEMAT, Madrid, Spain
(2) Max-Planck-Institut für Plasmaphysik, EURATOM Association, Greifswald, Germany
(3) Oak Ridge National Laboratory, USA
(4) Australian National University, Canberra, Australia
(5) Kyoto University, Kyoto, Japan
(6) National Institute for Fusion Science,322-6 Oroshi-cho, Toki 509-5292, Japan
(7) Institut für Plasmaforschung, Universität Stuttgart, Germany
(8) University of Wisconsin, USA

ABSTRACT: This papers studies the effect of rotational transform and magnetic shear on the confinement of low shear stellarators.

Keywords: confinement, rotational transform, magnetic shear

1. Introduction

The fact that the confining field in stellarators is largely independent of the plasma itself provides an extraordinary freedom of design and is the reason behind the variety of configurations existing or under construction [1]. A significant degree of freedom is the capability of choosing different values and profiles of rotational transform, ι. Historically, two approaches have been followed to prevent the expected confinement deterioration due to the presence of low order resonances. The first one is to design machines with very flat $\iota -$profiles (extremely low magnetic shear, $\hat{s}$), trying to avoid resonances (for example, the Wendelstein family [2, 3], TJ-II [4], HSX [5], Heliotron-J [6]). W7-X, the large stellarator appearing in the horizon follows the low shear approach and its design has been optimized to have a weak dependence of ι on the plasma pressure. The second approach is to look for strongly varying $\iota -$profiles that do not avoid the resonances but force the islands to shrink and prevent them to overlap (for example, Heliotron-E [7], L2 [8], ATF [9], CHS [10], LHD [11]).

After those experiments rotational transform and magnetic shear remain as two important issues whose role must be considered in future designs of candidates for a stellarator reactor.

The extensive inter-machine 0-D global scaling studies performed to date do not yield a clear picture about the role of ι on confinement, as will be discussed later. Additional 1-D information contained in the temperature and density profiles should be considered as well. Local transport analysis can provide valuable information on the role played by the resonances and help in understanding the influence of rotational transform on confinement. This work points in this direction, within the framework of the International Stellarator/Heliotron Confinement DataBase (ISHCDB) under auspices of the IEA Implementing Agreement for Cooperation in the Development of the Stellarator Concept [12]. As a first step, it has been found convenient starting with a survey based only on low shear machines, which should help in deciding further steps where large shear devices must be included.

A summary of the results obtained so far on the influence of rotational transform value on global confinement is presented in section 2. The effect of low order resonances on confinement is discussed in section 3. The role of magnetic shear is presented in section 4.

2. Dependence of global confinement on the rotational transform value

Early tokamak studies predicted that high rotational transform values are favourable for confinement, with exponent 0.4 [13]. In stellarators, the W7-AS group was the first to publish experimental results on the confinement dependence on ι owing to the capability of their device to perform $\iota -$scans. They reported a general improvement (energy confinement time and electron heat diffusivity) at higher rotational transform values provided that distinct optimum confinement windows close to low order resonances (1/3 and 1/2) were chosen [14, 15].

ISS95, the first extensive stellarator study based on international collaboration compiled a database from the main devices at that time and deduced an intermachine scaling law, which predicted an improvement of global confinement with increasing ι [16]. However, the fact that an offset between the shear-less machines and the heliotron/torsatrons appeared in the unified scaling required the use of an "ad-hoc" parameter to arrive at a unified expression. This so-called "parameter s" accounted for the difference in confinement between stellarators with and without shear.

The individual results from the TJ-II flexible heliac showed again the beneficial effect of ι on the global energy confinement and supported the W7-AS finding in a wider ι range ($1.2 < \iota_{2/3} < 2.2$) [17].

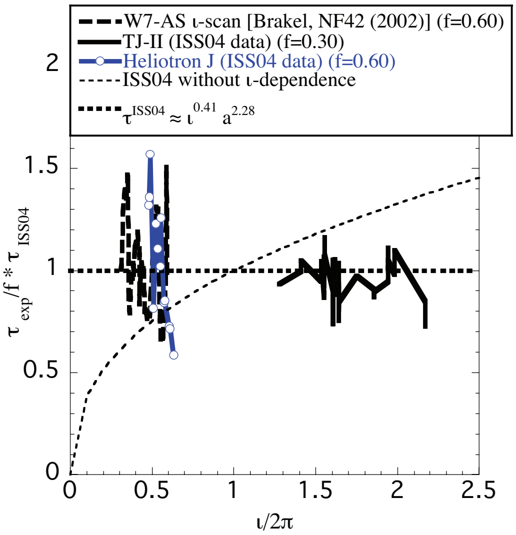

Fig. 1: Comparison of the dependence of renormalised confinement times on ι, for data subsets of W7-AS, TJ-II and Heliotron J.

For the ISS04 revision of ISS95, new devices entered the confinement database: LHD, TJ-II, Heliotron-J and HSX. Particularly important was the contribution from LHD, the largest device, which extended the parameter regime to substantially lower values of normalized collisionality and ion gyro radius, much closer to reactor regimes than those of the ISS95 devices [18]. Besides, W7-AS had discovered significant high confinement regimes with divertor operation. Thus, a new larger database was compiled including these new results. ISS04, the new scaling expression was derived from a restricted set from the full database. The dependence of global confinement on ι deduced from ISS04 is again positive, with exponent 0.4, in line with ISS95, but again a caveat questions this result. In ISS04, the use of the old "parameter s" is not sufficient to arrive at a unified scaling and a new empirical configuration-descriptive renormalization factor, f_{ren}, derived for each configuration subgroup, was used [19, 20]. This factor was related to specific properties of the helical field structure of each device; it appears to be correlated, for instance, with the corresponding effective helical ripple, plateau factor and elongation. Taking into account the corresponding configuration factors, the ι-dependence of different machines can be compared.

Fig. 1 shows, for example, the renormalized confinement times of data subsets from W7-AS, TJ-II and Heliotron-J [19, 21]. It can be seen that the intermachine comparison is consistent as regards the ι-dependence (the data clouds are positioned over the ISS04 horizontal line) but there is a saw-like fine structure within each data subset, which is a typical feature of low shear stellarators. It is related to the effect of low order rationals and influenced also by the reduction of plasma radius due to the appearance of natural islands at the boundary [16, 22]

The conclusion of this summary is that the search for physical mechanisms behind the configuration factors suggested by the ISS04 study requires a step beyond, considering detailed profile information as well as neoclassical and turbulent transport effects. Local transport analysis appears as an essential tool in this process to understand which are the plasma regions where the confinement is improved and to go deeper in the physics involved in the transport reduction.

3. Effect of low order resonances on confinement

Both low and high shear approaches face challenges regarding the effect of low order resonances. Examples are i) keeping the configuration free of resonances at high β in low shear devices or ii) maintaining the divertor capabilties in high shear machines. In any case, there are some open questions that need to be addressed:

-Is there a threshold for the magnetic shear over which low order resonances lose their detrimental character? Does this threshold depend on the value of the rotational transform itself?

-What is the effect of resonances when the shear is above this threshold?

-Is the sign of the shear important, or is only its magnitude what matters?

The logic behind this type of questions is clear: Provided that low order resonances do not deteriorate confinement anymore in the presence of enough (perhaps very low) magnetic shear then the design constraints of future stellarators might be relieved: a strict control of the magnetic shear (i.e. internal currents) would no longer be necessary and the available configuration space to optimize other physics aspects would expand.

In the process of answering the questions posed above (goal beyond this article) a first step would be to summarize some well-established results from low shear devices. In the following subsections we try to survey the major effects of the low order rationals on confinement and transport. In section 4 we put the emphasis on the effect of magnetic shear through its impact on the rationals.

3.1 Degraded confinement due to low order resonances at low β

As is well known, in the absence of magnetic shear, low order resonances placed in the confined region produce large magnetic islands, which cause confinement degradation. The stellarators of the Wendelstein line have documented this result extensively [23, 24, 14, 25].

In Heliotron J, a clear transient degradation of confinement was observed around ι_a = 0.59-0.62 for ECH+NBI plasmas ($<\beta>$ < 0.5%) with accompanying bursting coherent magnetic fluctuations with m~5/n=3. On the other hand, no obvious degradation of confinement was observed around ι_a = 0.49-0.51 despite the existence of the m~2/n=1 mode [26].

In conditions of high ECR heating power density and low plasma density (≈ 0.5-07 x 10^{19} m^{-3}) transient degraded confinement states -sometimes interspersed with phases of improved confinement- are observed in TJ-II in a variety of different experimental conditions, normally associated to the presence of low order rationals. The experimentally measured characteristics of the features associated to the observed transport events depend on the position of the resonance [27, 28, 29, 30].

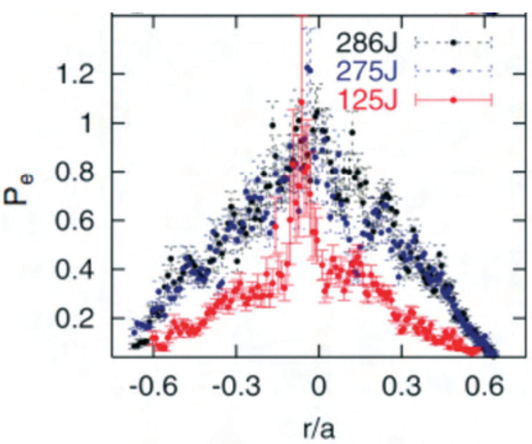

Fig. 2: Pressure profile (Thomson scattering) for three reproducible discharges with induced OH current. Black and blue profiles are measured at t=1125 ms. A clear flattening is found at t=1170 ms (red) (see Fig. 3).

An example of flattening of the pressure profile in TJ-II is shown in Fig. 2, where a Thomson Scattering profile measured in an ECH discharge with induced OH current to study magnetic shear effects is shown. The time evolution of the rotational transform can be estimated considering the measured net current as due only to the OH transformer and taking into account the evolving T_e profiles from the ECE diagnostic. As the plasma current density diffuses inwards due to the effect of (Spitzer) resistivity, it is found that the 3/2 ι-value disappears from the plasma at t ≈ 1170 ms with null shear. An effective χ_e is obtained simultaneously from power balance calculations. The results shown in Fig. 3 are a clear indication that the short transient with large χ_e (or small ∇T_e) around 1170 ms seen in the experimental data are a consequence of the ι = 3/2 resonance occupying a large fraction of the plasma core, thus causing a transient flattening of the T_e profile [31].

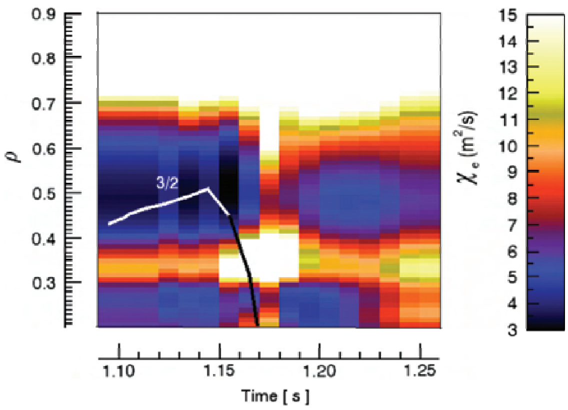

Fig. 3: Time evolution of the effective $\chi_e \approx 1/\nabla T_e$ profile obtained from ECE data for a TJ-II ECRH discharge with small induced OH current. The evolving ι –profile has its 3/2 value moving as shown by the black/white line.

Note that the presence of the 3/2 resonance (white/black line) does not really alter transport unless something in the rotational transform profile favours a singular effect of transient nature. Despite the approximated character of these calculations, the figure suggests that the transient of large diffusivity at t ≈ 1170 ms, coincident with the narrowed profiles shown in Fig. 2, is a consequence of the ι-profile having been forced by the OH current to flatten and occupy a portion of the plasma with very small shear. It is worthwhile noting that, after the clearly degraded transport at t ≈ 1170 ms due to the 3/2 resonance in no shear condition, the resonance disappears completely from the plasma due to the larger induced current. In spite of this, after the crash, the transport coefficient remains larger than before it. This behaviour is attributed to the fact that the shear continues decreasing in the external part of the plasma [32].

3.2 Improved electron transport in the vicinity of low order resonances

W7-AS results show that narrow optimum confinement windows with smaller transport are located close to (but no at) the low order resonances. The explanation given for this result is based on an empirical model, which assumes that transport is always enhanced at resonant surfaces and that this enhancement is reduced by magnetic shear [22]. This model invokes the rarefaction of high order resonances in the immediate vicinity of low order ones, which is expected to decrease the turbulent transport

There is abundant experimental evidence of the role of low order resonances as triggers for different improved transport events [28]. Transport barriers close to resonant surfaces have been found in tokamaks [33, 34]. Several stellarators like LHD and TJ-II have also found electron transport barriers close to rational surfaces located in the core region [35, 36] or in the plasma edge [37, 38]. In TJ-II low collisionality plasmas, when the 3/2 resonance is in the core, an increase of the positive radial electric field is measured, synchronized with the electron transport barrier formation [35, 39]. The phenomenon is similar to the improved heat confinement found in the neoclassical electron root feature in several stellarators, the so-called CERC [40]. Recent experiments in TJ-II, in low collisionality plasmas, have shown also for the first time an increase in the central ion temperature, simultaneous to the increase of electron temperature and triggered by the 4/2 resonant surface [41].

Heliotron J has reported experimental evidence of rotational transform windows for the high quality H-mode ($\tau^{exp}/ f\times\tau^{ISS04} > 1.5$) close to the low order rationals of the vacuum rotational transform at the last closed flux surface (LCFS). In these windows, Langmuir probe measurements show reduced fluctuation-induced transport in the plasma edge region. Simultaneously, a negative radial electric field E_r (or E_r -shear) forms near the LCFS at the transition. The power and density thresholds of the H-mode are observed to depend on the rational surface, but the systematic dependences between them are not fully understood at present [20]. It might have to do with the influence of the topology ("shape") of the magnetic surfaces on the poloidal viscous damping rate [42, 21].

3.3 Tracking the local lowering of χ_e due to low order rationals in TJ-II plasmas

In this section the results of local power balance analysis of a series of TJ-II discharges obtained in several magnetic configuration scans in TJ-II are presented [43]. The low order rationals included in this scans have poloidal mode number m in the range $2 < m \leq 6$.

In TJ-II, one possible way of scanning the rotational transform profile through the confined plasma consists of varying in small steps (down to 0.1 kA) the current through the helical coil, which is the one with strongest effect over the ι – value, and keeping the currents in the rest of coils essentially unchanged. This procedure, in a shot-to-shot basis, allows "sweeping" a certain low order rational through the confined plasma region in a very controlled way, in a close-to-vacuum shear condition.

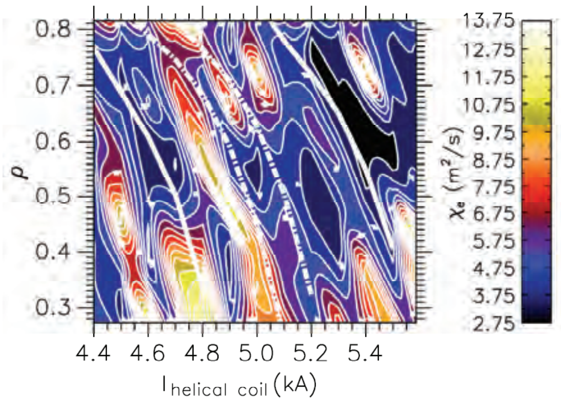

Fig. 4: Contour plot of the effective χ_e obtained from TS data for a set of 13 magnetic configurations labelled by their helical coil current. Each profile is an average over a few discharges with similar line density

The results for χ_e are shown in Fig. 4, in the form of a contour plot. The experimental data have been interpolated linearly along a rotated mesh aligned with the path of the ι = 8/5 in the range $0.6 < \rho < 0.8$ (see [46] for details). The white solid and dashed lines correspond to the path followed by the lowest order rationals of the vacuum-ι present in the scan (from left to right, ι = 8/5, 13/8, 18/11 and 5/3). The figure shows a pattern of "ridges" and "grooves" whose direction follows roughly the path of rationals along the minor radius as I_{hc} increases (i.e, as the rationals move inwards). Therefore, the power balance analysis suggests that low order rationals retain heat fluxes at their radial location. This is very likely for $\rho > 0.6$, where ι should be practically the vacuum one due to the small net plasma currents typically found in these experiments. At this respect, preliminary estimations of the bootstrap current [44] indicate that there should be a change of sign near half radius, according to which the net current would approach zero as one moves inwards in radius up to $\rho \approx 0.6$, making the vacuum ι to be even closer to the one with plasma. All these aspects require further study and a careful estimation of internal currents. However, taking as a hypothesis that the grooves are coincident with the low order rationals, the proximity of the grooves and the location of vacuum values of the low order rationals in Fig. 4 would be indicating that the bootstrap currents are indeed small in TJ-II ECH discharges.

4. The role of magnetic shear

There is a robust experimental evidence showing that the confinement degradation produced by the presence of low order rationals in the confined plasma is restored if enough magnetic shear is generated, no matter the origin of the current (pressure driven, inductive, EC driven) [24].

An example of W7-AS is shown in Fig. 5, which shows the effect of ι_a and plasma current (using the OH transformer) on the plasma energy content, for discharges with identical plasma radius and densities. The strong dependence on rotational transform of the energy content, at zero current, decreases as the current is raised and disappears at the highest current value.

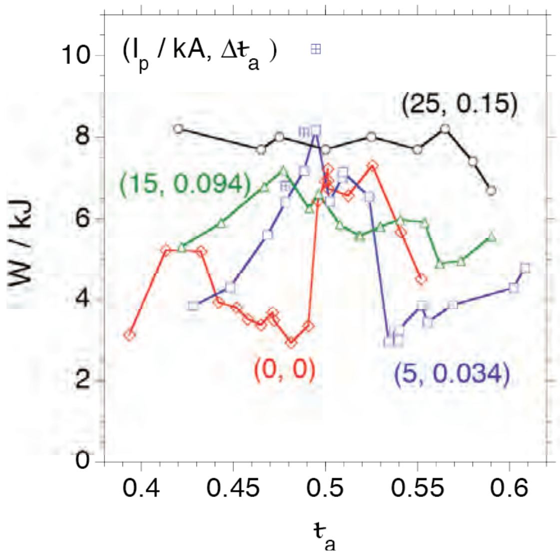

Fig. 5: Plasma energy content vs. ι_a for four values of induced OH current.

Local power balance analysis also provides clear evidence of restoration of degraded confinement via magnetic shear in W7-AS, as illustrated in Fig. 6. It shows degraded confinement in the no shear situation (0 kA). Increasing the shear with inductively driven current, reduces strongly the electron heat diffusivity in the gradient region. The discharges with I_p = 10 kA and 25 kA have ι = 1/2 in the plasma region without any significant local degradation of confinement. It is clear that confinement improves with shear independently of the sign.

Dedicated experiments in TJ-II have also allowed studying the influence of shear on confinement [32]. Figure 7 shows the effective thermal diffusivity obtained in ρ = 0.75 for a number of different ECRH discharges with similar density, in plasmas operated under ohmic induction. Negative induction drives the ι-values towards more negative and conversely. Positive induction cases do not reach high $\hat{s} > 0$ values because the largest plasma current (≈ 10 kA) does not allow for further variation of the rotational transform profile. The results indicate that the largest χ_e is found around zero shear. The confinement is clearly improved for negative shear. Positive shear seems also to reduce transport although the result is less clear due to the smaller explored range. These TJ-II results are in line with the W7-AS conclusion.

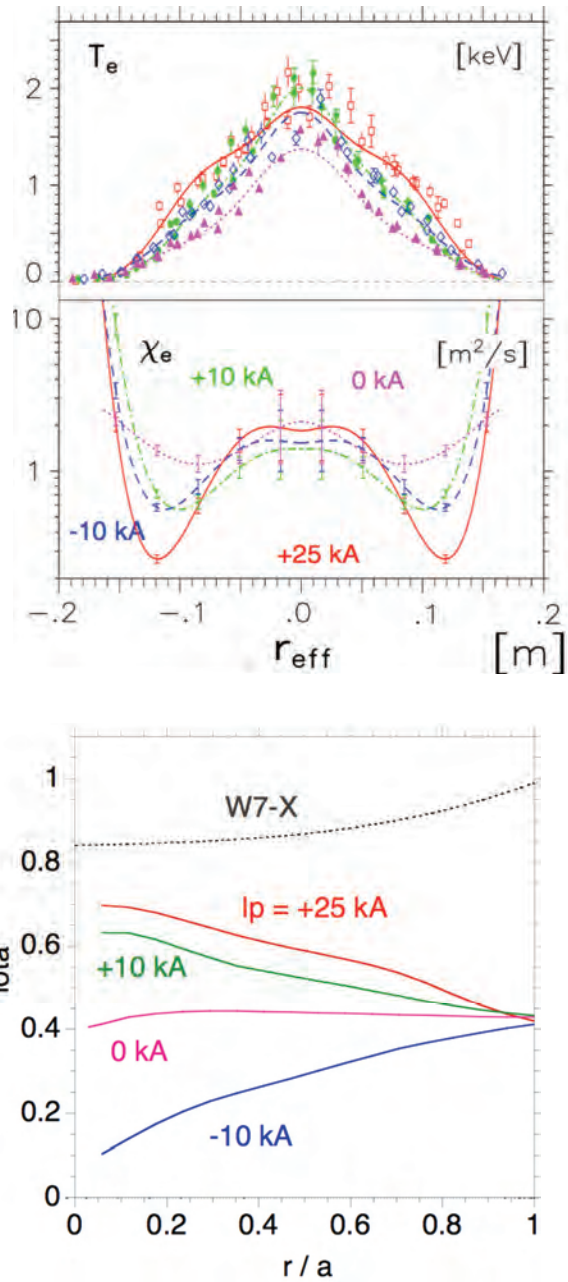

Fig. 6: T_e (upper box) and χ_e (middle box) profiles for discharges with ι_a = 0.42 and different values of plasma current. The corresponding ι-profiles are shown in the lower box.

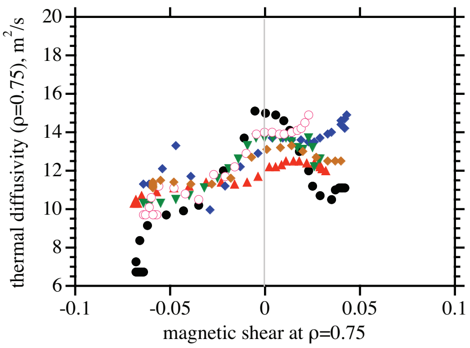

Fig.7: Thermal diffusivity at $\rho = 0.75$ vs. magnetic shear for several discharges with induced OH current.

5. Summary

- Keeping the configuration free of low order resonances in real experimental conditions is a difficult task for devices with low vacuum magnetic shear. The optimized design of Wendelstein 7-X will allow it to fully explore and characterize this scenario at high β. The fine-tuning capability of the available modern ECRH systems provides an additional tool, if needed, to compensate undesired internal currents by means of localised heating.

- Certain amount of shear allows the presence of even the lowest order rationals (1/2 in the W7-AS case) within the confinement region without degradation. Low shear values, $|\hat{s}| \approx 0.1$, are enough in TJ-II -which is the stellarator with highest ι- to observe the beneficial effect of the shear. Further comparisons between devices with different ι are needed in order to study whether there is a threshold value for the shear, which depends on the $\iota -$value.

-Narrow optimum confinement windows are found in W7-AS and Heliotron-J close to low order rational values. Provided a small amount of magnetic shear is present, the low order resonances are found to trigger a variety of improved transport events in TJ-II. Fine configuration scans in this machine have shown that low order rationals retain heat fluxes at their radial location.

-Both W7-AS and TJ-II results show that the beneficial effect of shear on confinement does not depend on the sign.

-Many of the results presented in this paper are based on local heat balance analysis. A word of warning concerning the ISHCDB must be considered seriously in this respect: W7-AS has shown that also the particle confinement can depend on ι and shear [45]. This fact could give rise to misleading conclusions if only the power balance is considered because quite different T_e profiles, indicating a degraded global τ_E, could have a negligible impact on the local χ_e. So, complete analysis of temperature and density profiles would be needed.

This work contributes to the International Stellarator/Heliotron Confinement DataBase (ISHCDB) under auspices of the IEA Implementing Agreement for Cooperation in the Development of the Stellarator Concept [12]

References

1 J. Sánchez et al., Plasma Phys. Contr. Fusion **47** B349 (2005)
2 H. Wobig, S. Rehker, Proc. 7th SOFT (Grenoble) (1972)
3 J. Sapper et al., Fusion Technol. **17** 62 (1990)
4 C. Alejaldre et al., Fusion Technol. **17** 131 (1990)
5 F. Anderson et al., Fusion Technol. **27** 273 (1995)
6 T. Obiki et al., Plasma Phys. Control Fusion **42** 1151 (2000)
7 K. Uo et al., Nucl. Fusion **24** 1551 (1984)
8 D.K. Akulina et al., Proc. 6th Int. Conf. on Plasma Phys. and Contr. Fusion (Berchtesgaden) **2** 115 (1976)
9 J. F. Lyon et al., Fusion Technol. **10** 179 (1986)
10 K. Nishimura et al., Fusion Technol. **17** 309 (1990)
11 A. Iiyoshi et al., Fusion Technol. **17** 169 (1990)
12 The ISHCDB is jointly hosted by NIFS and IPP at the sites http://iscdb.nifs.ac.jp/ and http://www.ipp.mpg.de/ISS
13 K. Lackner and N. Gottardi., Nucl. Fusion **30** 767 (1990)
14 H. Ringler et al., Plasma Phys. Control Fusion **32** 933 (1990)
15 R. Brakel et al., Proc. 20th EPS Conf. (Lisbon) 361 (1993)
16 U. Stroth et al., Nucl. Fusion **36** 1063 (1996)
17 E. Ascasíbar et al., Nucl. Fusion **45** 276 (2005)
18 H. Yamada et al., Fusion Sci. and Technol. **46** 82 (2004)
19 H. Yamada et al., Nucl. Fusion **45,** 1684 (2005)
20 A. Dinklage et al., Fusion Sci. and Technol. **51**, 1 (2007)
21 F. Sano et al., Nucl. Fusion **45** 1557 (2005)
22 R. Brakel and W7-AS Team, Nucl. Fusion **42** 903 (2002)
23 G. Grieger et al., Plasma Phys. Control Fusion **28** 43 (1986)
24 H. Renner et al., Plasma Phys. Contr. Fusion **31** 1579 (1989)
25 R. Brakel et al., Plasma Phys. Contr. Fusion **39** B273 (1997)
26 S. Yamamoto et al., Fusion Sci. Technol. **50** 92 (2007)
27 E. Ascasíbar et al., Plasma Phys. Contr. Fus. **44** B307 (2002)
28 F. Castejón et al., Plasma Phys. Contr. Fusion **47** B53 (2005)
29 T. Estrada et al., Plasma Phys. Contr. Fusion **44** 1615 (2002)
30 I. Garcia-Cortes et al., Nucl. Fusion **40** 1867 (2000)
31 J. Romero et al., Nucl. Fusion **43** 387 (2003)
32 D. López-Bruna et al, Ciemat Technical Report 1089 (2006)
33 N. Lopes-Cardozo et al., P. Phys. Cont. Fus. **39** B303 (1997)
34 R. Wolf, Plasma Phys. Control. Fusion **45** R1 (2003)
35 T. Estrada et al., Plasma Phys. Contr. Fusion **46** 277 (2004)
36 F. Castejón et al., Nucl. Fusion **44** 593 (2004)
37 C. Hidalgo et al., Plasma Phys. Contr. Fus. **43** A313 (2001)
38 N. Ohyabu et al., Phys. Rev. Lett. **84** 103 (2000)
39 T. Estrada et al., Plasma Phys. Contr. Fusion **47** 57 (2005)
40 M. Yokoyama et al., Fusion Sci. Technol. **50** 327 (2006)
41 T. Estrada et al., Nucl. Fusion **47** 305 (2007)
42 F. Sano et al., Fusion Sci. Technol. **46** 288 (2004)
43 V.I. Vargas et al., Nucl. Fusion **47** 1367 (2007)
44 V. Tribaldos et al., Proc. 30th EPS Conf. **27A** P-1.28 (2003)
45 O. Heinrich et al., Proc. 24th EPS Conf. (Berchtesgaden) 1593 (1997)

Proceedings of ITC/ISHW2007

Alfvén range instabilities in H-1: interpretation, mode structure, and relation to rational surfaces.

B. D. Blackwell [1),]D.G. Pretty [1], J. Howard [1)], D.R. Oliver [1)], F. Detering [1)], D. Byrne[1)], M. Hegland [3)], C.A. Nuhrenberg[4)], R.L. Dewar [2)], S.T.A. Kumar [1)], M. McGann[2)], M.J. Hole [2)] and J.H. Harris[5)]

1) Plasma Research Laboratory, and
2) Department of Theoretical Physics, Research School of Physical Sciences and Engineering, and
3) Mathematical Sciences Institute, all of the Australian National University, ACT 0200,AUSTRALIA.
4) Max-Planck-Institut fu¨r Plasmaphysik, IPP-Euratom Association, D-17489 Greifswald, Germany
5) Oak Ridge National Laboratory, Tn, USA.

email: boyd.blackwell@anu.edu.au

The H-1 flexible heliac (R/<a>=1/0.2m,[1]) is a 3 period stellarator which exhibits a range of shear from low negative values ("tokamak like") to moderate positive shear. Configuration scans in the range $1.1 < \iota_0 < 1.5$ have shown a detailed rotational transform dependence of plasma density and fluctuation spectra. Fluctuations are observed in the range 1-150kHz, on two arrays of magnetic probes and on a 2mm density interferometer. Detailed configuration studies have been performed on hydrogen/helium plasma at 0.5T ($<n_e>\sim 1\times 10^{18}$, $1.1 < \iota < 1.5$). Datamining[2] of the ~1GB data set has revealed several clusters of phenomena, a number of which exhibit Alfvénic frequency scaling with both ι and n_e, within a constant factor in frequency. Mode numbers are derived from poloidal and toroidal phase differences, and are typically n/m=4/3, 5/4 and 7/5, and consistent with ι. Observed frequencies are proportional to $\omega/V_A = k_{||} = (m/R_0)(\iota - n/m)$, and show clear "V" structures near rational surfaces ($\iota \sim n/m$). In addition to their intrinsic interest, in a low shear device such as H-1, these structures can provide accurate locations of resonant surfaces under plasma conditions, which are found to agree very well with recent magnetic field line mapping[3] at high magnetic field.

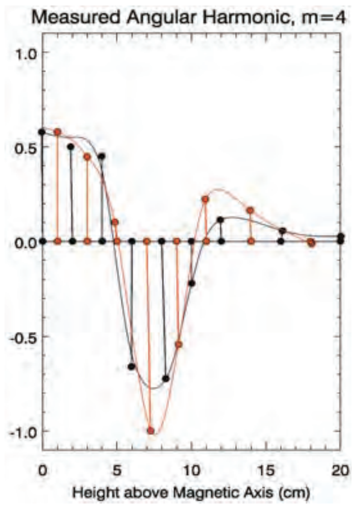

Fig. 1: Radial structure of oscillations in n_e (projections)

The radial structure of these modes has been unravelled (figure 1) from synchronously-detected line integral density scans across the plasma. This is compared with eigenmode structures computed by the CAS3D code. A significant fraction of clearly non-Alfvénic fluctuations indicate that other instabilities are present. Possible interpretations as interchange, sound or drift modes are discussed. These and other recent observations of Alfvén activity in various low and high temperature plasma, thermal and non-thermal suggests these phenomena may be more ubiquitous --and thus fundamental to toroidal confinement--- than previously thought.

[1] Hamberger S.M., Blackwell B.D., Sharp L.E. et al., *Fusion Technol.* **17**, 1990, p 123.
[2] B. D. Blackwell**,** D.G. Pretty et al., 21st IAEA Fus. Energy Conf., Chengdu, China, 2006
[3] S.T.A Kumar, B.D. Blackwell and J.H. Harris, Rev. Sci. Ins, **78** 013501-8 (2007)

Proceedings of ITC/ISHW2007

Stability and Variation of Plasma Parameters in the L-2M Stellarator by Exciting Induction Current in ECR Heated Plasma

Lev M. KOVRIZHNYKH, Diana K. AKULINA, German M. BATANOV, Mikhail S. BEREZHETSKII, Oleg I. FEDYANIN, Grigorii A. GLADKOV, Stanislav E. GREBENSHCHIKOV, Irina A. GRISHINA, Nikolaii K. KHARCHEV, Yurii V. KHOL’NOV, Aleksandr V. KNYAZEV, Leonid V. KOLIK, Aleksandr B. KUZNETSOV, Nataliya F. LARIONOVA, Aleksandr A. LETUNOV, Vladimir P. LOGVINENKO, Nikolaii I. MALYKH, Aleksei I. MESHCHERYAKOV, Yurii I. NECHAEV, Aleksandr E. PETROV, Anton A. PSHENICHNIKOV, Vyacheslav V. SAENKO, Karen A. SARKSYAN, Sergei V. SHCHEPETOV, Nina N. SKVORTSOVA, Ildar Yu. VAFIN, Dmitrii G. VASIL’KOV, Gennadii S. VORONOV, Elena V. VORONOVA

A.M. Prokhorov General Physics Institute, Russian Academy of Sciences, Moscow, 119991 Russia

Variation of parameters of ECR heated plasma was studied in the L-2M stellarator under conditions that the basic magnetic configuration was modified by exciting induction current. Experiments were carried out at ECRH power of ~200 kW (~1 MW m^{-3}) and average plasma density of ~$2\cdot10^{19}$ m^{-3}. The direction of the current was chosen such that the total rotational transform decreased, and its value was large enough (up to 17 kA) for rotational transform to change sign in the inner layers of the plasma column. Computer modeling predicts the formation of a multi-axis magnetic structure in the inner layers of the plasma column. Magnetic probe measurements show the presence of bursts in signals of Pfirsh-Schluter currents and variations of the spectrum and mode of MHD oscillations of the plasma column. The appearance of the n = 0 mode at currents above 10 kA is correlated to the appearance of the region where $\iota/2\pi = 0$. It is shown that, in the presence of the induction current, the electron temperature in the region $r/a \leq 0.6$ is lower by a factor of 1.3, whereas a characteristic jump in the temperature in the edge plasma remains; the density gradient at the plasma edge decreases. The behavior of turbulent density fluctuations was studied by using diagnostics of scattering of probing radiation. It is found that the probability density functions for increments of density fluctuations have heavier tails in the presence of a multi-axis structure. The spectral characteristics of turbulent fluctuations in the edge plasma and the poloidal plasma velocity were found to vary with radius. The experimental evidence suggests that the formation of the magnetic island structure in the core plasma leads to more intense transport in both core and edge plasma, but the change in transport is not catastrophic.

Keywords: stellarator, ECR heated plasma, plasma magnetic structure, omic current, MHD oscillations, plasma radial profiles, turbulence

1. Introduction

The straightforward method to study stability and confinement properties of stellarator magnetic configurations is the excitation of longitudinal (toroidal) currents.

Experiments with current were performed in the L-2 stellarator in the late 1970s, the results are presented in [1-3].

The present experiments in L-2M were carried out in the ECRH regime under conditions that an induced plasma current produced negative rotational transform with respect to the stellarator rotational transform. Calculations show that, at amplitudes of this “negative” current I/B > 0.25 A/G, the net rotational transform at the magnetic axis changes the sign in which case a flux surface with zero rotational transform should appear in the plasma. The higher the amplitude of induction current, the larger the radius of this flux surface. In toroidal geometry, such a magnetic configuration is topologically unstable. The transverse field of the current in the case $\iota/2\pi = 0$ is a perturbation resulting (even for $\beta = 0$) in a magnetic island with dimensions comparable to the minor radius of flux surfaces. In plasma with finite beta, such a magnetic configuration will be progressively modified

author’s e-mail: lmkov@fpl.gpi.ru

and may be transformed into a multi-axes magnetic structure.

Plasma equilibrium under conditions that zero rotational transform exists inside the plasma column was studied experimentally in Heliotron-E [4]. Experiments showed that the appearance of zero transform in the plasma was accompanied by strong MHD activity and relaxation oscillations. The observed processes were attributed to activity of the m = 1, n = 0 tearing mode (m and n are the poloidal and toroidal indices, respectively).

In [5], the problem on equilibrium in the presence of a flux surface with zero rotational transform was studied numerically for the LHD configuration. Three-dimensional calculations, performed for various values of β, showed a possibility of one or two islands with zero rotational transform. In experiments [6] performed in configuration where islands might be expected, no apparent effect on plasma confinement was observed. At the same time, MHD activity of the m = 0, n = 0 was observed in the experiment.

The objective of the present work is to study the effect of such phenomena on plasma confinement and stability in the L-2M stellarator.

2. Experimental conditions

Experiments for studying the effect of a negative induction current on plasma confinement and stability were carried out in the "standard" magnetic configuration of the L-2M stellarator (R = 100 cm, a = 11.5 cm), where the ratio of the amplitude of the main harmonic of helical field (l = 2) to the amplitude of toroidal field at the axis is equal to 0.228. In this case, the rotational transform is $\iota(0)/2\pi = 0.2$ at the axis at the magnetic axis and $\iota(a)/2\pi = 0.8$ at the last closed magnetic surface for the vacuum magnetic configuration. In [7], the dependence of the rotational transform $i/2\pi$ on the mean radius of the magnetic surface was calculated for various current values under the assumption that topology of the L-2M magnetic configuration is only slightly affected by the current. It was shown that, at negative currents I/B= 1 A/G, we have $\iota/2\pi<0$ for normalized radii $\rho = r/a \leq 0.65$. The induction current, excited using the ohmic heating transformer, was switched on simultaneously with the ECRH pulse. Electron cyclotron heating (2nd harmonic of gyrofrequency, X-mode) was performed using a gyrotron with power P = 200 kW, frequency f = 75 GHz, and pulse duration of 10-12 ms. A focused Gaussian beam of diameter ≈4 cm was injected in the equatorial plane. The magnetic field B_0 = 1.34 T corresponded to the position of cyclotron resonance at the magnetic axis, R = 100 cm. The plasma density varied in the range, the amplitudes of induction current varied in the range 3-17 kA.

3. Numerical simulation of the magnetic structure

To study the equilibrium of a plasma with a current, we used a mathematical procedure based on the combination of numerical codes [8, 9]. For modeling the effect of the current, we numerically solved the average problem of MHD equilibrium with free boundary for the averaged poloidal flux (a quasilinear elliptical differential equation in partial derivatives). The model current profile for calculations was taken in the form

$j = J_0(1 - r^2)^k$, with variable k.

The numerical calculation of the averaged problem of equilibrium with a current yields values of the poloidal flux on a grid of polar coordinates with the origin at the magnetic center of the averaged equilibrium configuration.

The structure of three-dimensional surfaces, affected by both the current and plasma pressure, was determined by solving the magnetic-line equation and by tracing the results on map. The maps were constructed for tree basic cross sections.

According to calculations, the zero rotational transform inside the plasma results in a complicated magnetic structure with islands. Island dimensions depend on radial profiles of current and plasma pressure, and also on vertical magnetic field controlling the plasma position. As an illustration, Fig. 1 shows the calculated flux surfaces for a plasma current of 7 kA with a radial current density profile $j_\alpha \sim (1-\rho^2)^2$. The structure with two magnetic axes contains magnetic islands occupying a good fraction of the cross-sectional area.

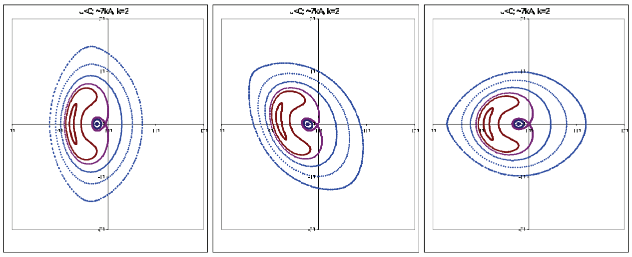

Fig. 1. Structure of flux surfaces in three cross sections of the L-2M stellarator in the presence of a "negative" induction current. The axis of the vacuum chamber is at R = 100 cm.

4. Time behavior of Pfirsh-Schluter currents, diamagnetic current and MHD oscillation during excitation of a negative induction current

Figure 2 shows the time behavior of the ECR heating power, induction current, derivative of equilibrium field determined by Pfirsch-Schluter currents (dPS/dt), average electron density (measured by a 2-mm interferometer over the central chord), and central electron temperature (measured from electron cyclotron emission at a frequency of 76 GHz). The quasi-steady state lasts from 50 to 60 ms. Characteristically, the dPS/dt signal in the regime with current shows sharp peaks of relaxation oscillations at ~1-ms intervals (Fig. 2c), which are absent in the currentless regime (Fig. 2d). It should be noted that such oscillations were always absent in the signal of diamagnetic flux derivative (dW/dt) in the regime with a negative current. The plateau current is also undisturbed. Hence, it may be concluded that the arising MHD perturbations are associated with Pfirsch-Schluter currents.

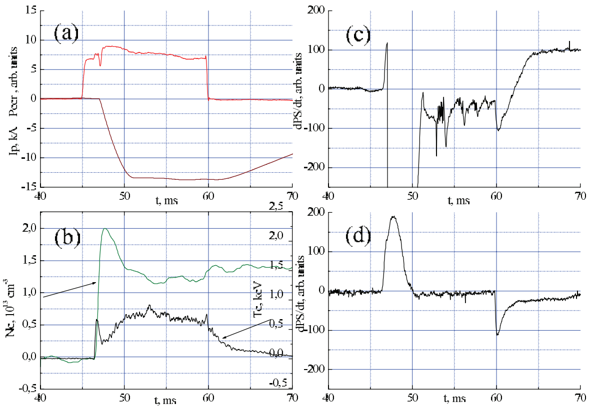

Fig. 2. Time behavior of signals in a discharge with a "negative" current: (a) gyrotron power P_{ecr} (red) and induction current I_p (brown), (b) average density N_e (green), central electron temperature T_e (ECE, 76 GHz) (black), (c) derivative of transversal magnetic flux dPS/dt (for current 13 kA), (d) derivative of transversal magnetic flux dPS/dt (without current).

To clear up the cause of perturbations in the Pfirsh-Schluter currents, we compared the data of this diagnostics with data of a set of Mirnov coils. The Mirnov coils were placed outside the vacuum chamber, in front of the quartz windows in order to reduce the shielding effect of the chamber, and were so oriented as to measure the poloidal component of the magnetic field.

Figure 3 shows the signals from Mirnov coils for different regimes. The signal amplitudes are of the same order for the regimes with and without current. Fourier spectra of the signals span the range 1-150 kHz. Analysis revealed a time correlation between the appearance of relaxation peaks in the dPS/dt signal and the appearance of a peak in the range 5-15 kHz in the spectrum.

Data of Mirnov coils showed that the mode composition of MHD perturbations changed in the regime with negative current, specifically, perturbations with toroidal index n = 0 were observed in the plasma. It should be noted that the perturbations in Pfirsh-Schluter currents and the n = 0 mode were observed when the magnitude of the negative current exceeded the threshold value of 10 kA.

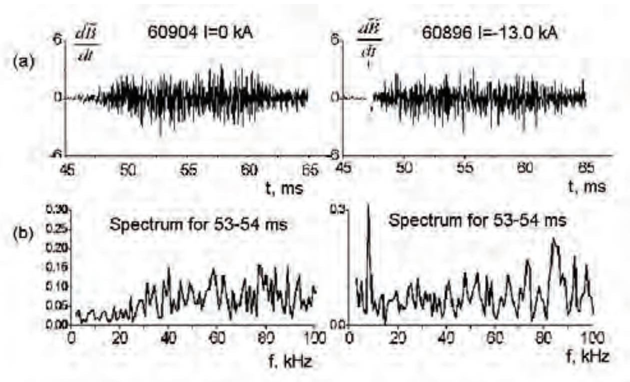

Fig. 3. Time evolution of magnetic field fluctuations:
(a) Mirnov coil signal, $d\tilde{B}/dt$.
(b) Fourier spectra of Mirnov coil signals.

5. Measurements of the radial electron temperature and density profiles

Figure 4 shows the radial electron temperature profile (on semi-log scale) in the ECRH regime in the absence of an induction current. The electron temperature was measured from the intensity of ECE at the second harmonic of the gyrofrequency in the central region (r/a≤0.6) and from intensity of impurity lines BIV (282.2 nm) and CIII (464.7nm) at the periphery (0.6≤r/a≤1.0). The half-with of the profile is estimated as (0.4-0.5) a. A characteristic feature of the temperature profile is the temperature jump near the last closed flux surface, within a region Δr/a ≤ 0.1. The temperature jump may be interpreted as a thermal barrier [10].

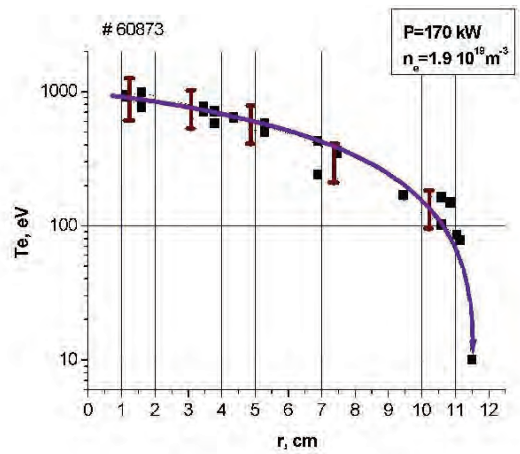

Fig. 4. Radial electron temperature profile in currentless plasma. ECRH power 170 kW, average density $1{,}9{\cdot}10^{13}$cm^{-3}.

Figure 5 compares the temperature profiles (ECE frequency spectra) averaged over 10 shots for the regimes without and with currents -(13-15) kA. The profile shape does not change in the regime with current, but the maximum temperature drops by a factor of ~1.3.

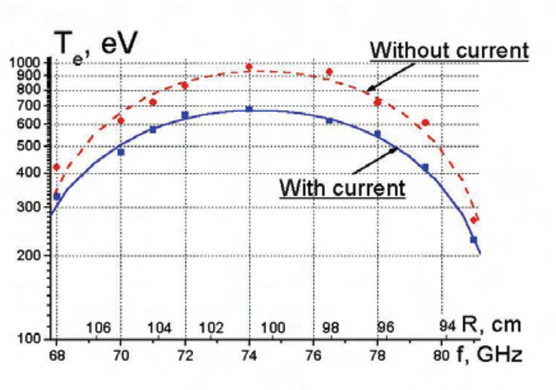

Fig. 5. Comparison of electron temperature profiles (ECE) in the core plasma for regimes without/with negative current 13-15 kA Average density without current $1{,}7\cdot10^{13}$cm^{-3}, with current $1{,}5\div1{,}7\cdot10^{13}$cm^{-3}

From spectral measurements of the BIV line (the ionization energy of B^{+3} ions is about 250 eV), it may be deduced that the characteristic form of the profile at the edge is retained. Thus, the intensity of this line drops very steeply on the interval R = 89-87 cm in the currentless regime, and so does it in the regime with current -(8-15) kA, but on the interval R = 88-86.5 cm (spectral measurements are made on the inside of the magnetic axis, R < 100 cm). The intensity distribution shifts by ~1 cm toward smaller R. This result is consistent with the expected shift of flux surfaces under the action of the transverse field produced by negative current. Therefore, it may be concluded that a temperature jump at the edge takes place.

Figure 6 shows the average density values measured by an HCN laser interferometer over 7 chords in the regimes with and without current of -13 kA. From Fig. 6a, it is seen that the density on central chords initially drops somewhat at the beginning of the ECRH pulse. After 52 ms, the radial density profile changes only slightly. Characteristically, the radial profile in the currentless plasma in L-2M is flat, with a sharp drop near the plasma boundary.

The electron density profile and its evolution change markedly in the presence of a negative induction current: the profile is less flattened as compared with the currentless plasma. A sharp drop in the density over all the central chords is observed at the beginning of the ECRH pulse, which indicates substantial losses of electrons from the core plasma. Besides, we observe substantial (up to 20%) irregular changes in the average density for all of the central chords, including in the ohmic phase of the discharge (after 60 ms).

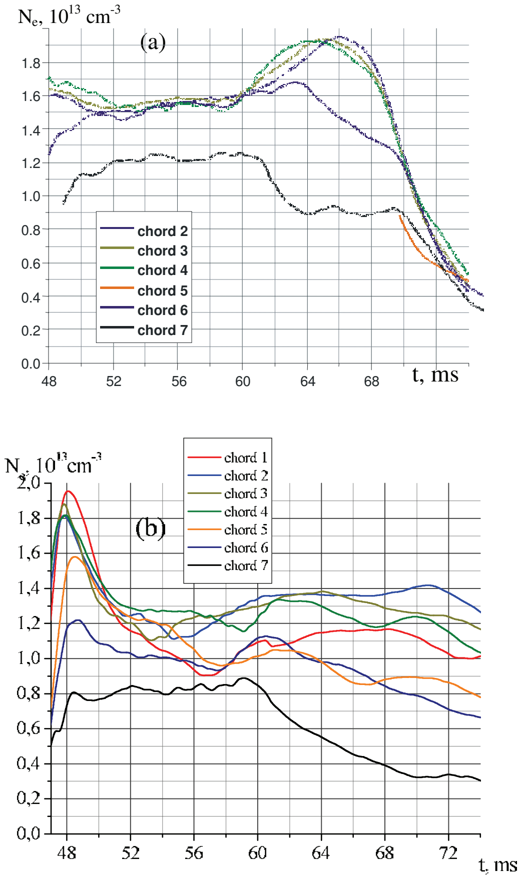

Fig. 6. Time evolution of average electron densities measured over 7 chords:
(a) currentless plasma,
(b) regime with current 13 kA.

Calculations of the flux surfaces in plasma with current (Fig. 1) show that the outer flux surfaces retain their structure. This allows us to compare the regimes with and without current by using data for the peripheral chord ("7"), normalized to the central-chord density. Estimates show that the density gradient near the boundary is 1/4 less in the regime with current.

Thus, according to interferometric measurements, the electron density profiles in the core plasma are less flattened, with smaller gradient near the plasma boundary in the regime with current.

6. Fourier spectra and statistical characteristics of turbulent plasma density fluctuations

To study turbulent plasma density fluctuations in the central region of the plasma column, we used scattered ordinary microwaves arising as a result of double refraction of the gyrotron radiation, produced and heated the plasma column (the radiation wavelength is 4 mm). In this method, the probing radiation passes through the central chord and allows measurements in the central regions. Fluctuations of the wave phase are averaged over the central chord, whereas geometric sizes of the beam and the detector ensure measurements of scattered radiation in the near wave zone.

Turbulent density fluctuations in the edge plasma were studied with the help of a Doppler reflectometer using the scattering of a low-power probing beam (wavelength from 8 to 9 mm) at total reflection of radiation incident obliquely on the plasma column (see, e.g., [11-13]). Geometry of this diagnostic allows measurements of scattered signals from density perturbations with wavelengths of 4-6 cm; the growth rate of these perturbations is three times smaller than for the ion drift-temperature mode.

Typical Fourier spectra of small-angle scattering are presented in Figs. 7. The Fourier spectra for regimes with and without current are essentially different. In the absence of current, we observe a continuous spectrum with feebly marked wide bands. In the regime with current, the spectral density is maximal in the low-frequency range 5-15 kHz decreases toward 50 kHz and there is wide band with a maximum at 100-150 kHz.

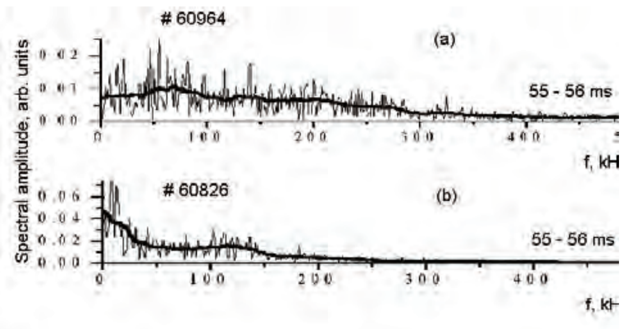

Fig. 7. Fourier spectra of small-angle scattering signals. Average density 1,4÷1,5·10^{13}cm^{-3}, ECRH power 200 kW.

The reflectometer measurements in the edge plasma were performed with probing frequencies of 30.9, 34.8, and 37.6 GHz, at angles of incidence of 4^0, 8^0, and 12^0 with respect to the normal to the plasma boundary. These frequencies correspond to the scattering regions with plasma densities $1.73\cdot10^{13}$, $1.48\cdot10^{13}$, and $1.17\cdot10^{13}$ cm^{-3} at the edge of the plasma column, 0.8≤r/a≤0.9. The reflectometer measured density fluctuations with poloidal wavenumber $k \approx 2$cm^{-1}.

Figure 8 compares Fourier spectra of the complex signals for regimes without and with current (-14 kA). The probing frequency is 30.9 GHz, the angle of incidence is 8^0. Gray lines are for a time resolution of 1.22 kHz; black lines are for a time resolution of 25.62 kHz. Both spectra are averaged over the time interval 819.2 µs. The spectral peak is shifted into the red region by ~250 kHz, which is a Doppler shift in frequency and corresponds to a poloidal velocity of ~~10^6 cm s^{-1}. The Fourier spectra for probing frequencies of 34.8 and 37.6 GHz are very similar in shape and shift value. From these results it may be inferred that the poloidal rotation velocity is uniform over the region with density from ~$1.7\cdot10^{13}$ to ~$1.1\cdot10^{13}$ cm^{-3}.

The excitation of the induction current causes changes in the scattered spectra, but these changes are different for different probing frequencies. For a frequency of 30.9 GHz, the spectrum becomes narrower and the Doppler shift decreases. For a frequency of 37.6 GHz, the Doppler shift increases, which corresponds to an increase by 50% in the poloidal velocity.

Thus, the excitation of the magnetic island structure in the core plasma affects the edge plasma. The Doppler shift of the spectrum varies with radius, which is evidence for the radial shear of the poloidal velocity.

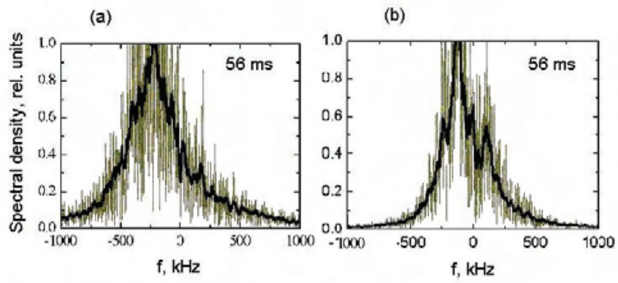

Fig. 8. Comparison of Fourier spectra of scattered signals for frequency 30.9 GHz of the Doppler reflectometer with a 5-kHz filter for regimes without (a) and with (b) negative current 14 kA. Average density 1,4÷1,5·10^{13}cm^{-3}, ECRH

The time behavior of the scattered signals and the form of their Fourier spectra reveal stochastic nature of plasma density fluctuations. Statistical analysis of signals of small-angle scattering showed that the probability density functions (PDFs) of signal increments are non-Gaussian and broaden out in the presence of a current. Similar effects were observed for the reflectometer signals measuring density fluctuations in the edge plasma.

Thus, the spectral-statistical characteristics of turbulent plasma turn out to be sensitive to changes in the magnetic field structure. It may be assumed that this is a manifestation of interrelation between turbulence and transport processes.

7. Conclusions

Experiments in the regime of simultaneous ECR and ohmic heating have been carried out in the L-2M stellarator for studying the effect of a negative induction current decreasing the rotational transform. The amplitudes of induction current were properly chosen to achieve zero rotational transform on some flux surface in the plasma column.

A numerical analysis of the magnetic structure demonstrated a possibility for multi-axis structure with magnetic islands whose dimensions reach one-half the plasma radius.

Characteristic oscillations in the Pfirsh-Schluter currents and changes in the mode composition of MHD perturbations (the excitation of MHD fluctuations with toroidal index n = 0) were observed at currents above 10 kA.

The excitation of the current leads to a decrease in the electron temperature in the core plasma to 0.7 of its value for currentless plasma, the temperature jump near the plasma boundary is retained. The radial density profile and its evolution change in the presence of the current: the density profiles in the core plasma are less flattened, the density gradient decreases near the boundary. A density by 1/3 of its initial value was observed at the initial stage of the discharge. These data constitute evidence of more intense heat transport processes in the core plasma and more intense particle transport in the edge plasma.

The excitation of the current involves changes in the characteristics of turbulent density fluctuations in the core plasma as well as in the edge plasma. The probability of large amplitudes in the PDF of increments of density fluctuations in the core plasma increases, resulting in wide deviations and the normal (Gaussian) law. The turbulent spectra and poloidal velocity in the edge plasma turn out to be nonuniform over a narrow plasma region $\Delta r/a \approx 0.1$, in contrast with the currentless plasma where the poloidal velocity is uniform. The PDFs become asymmetric, which is indicative of convection transport. From these results it may be concluded that MHD processes occurring in the core plasma influence turbulent fluctuations at the edge.

Thus, the formation of the multi-axis magnetic structure with islands in the L-2M magnetic configuration leads to more intense transport and changes turbulence characteristics, but the change in transport is not catastrophic.

This work was supported by the RF Presidential program for Support of Leading Scientific Schools (grant no. NSh-5382.2006.2).

References

[1] E.D. Andryukhina, M.S. Berezhetsky, M.A. Blokh et al., Plasma Phys. and Contr. Nucl. Fusion Res., IAEA, Vienna (1981),V.**1**, p.199.

[2] S.E. Grebenshchikov, L.M. Kovrizhnykh, B.I. Kornev et al., Sov. J. Plasma Phys. (1985), V. 11, p.299.

[3] S.E. Grebenshchikov, B.I. Kornev, I.S. Shpigel et al., Sov. J. Plasma Phys. (1982), V. 8, p.256.

[4] H. Zushi, O. Motojima, H. Kaneko, et al., J. Phys. Soc. Japan, 57 (1988) 3009.

[5] R. Kanno, K. Toi, K. Watanabe et al., Journal of Plasma and Fusion Reseach, 79 (2003), No9, 839.

[6] K. Toi, K.W. Watanabe, K. Narihara et al. Annanal Report of NIFS (2003-2004), 25.

[7] D.K. Akulina, G.A. Gladkov, S.E. Grebenshchikov et al. Plasma Phys. Rep. (2006), V. 32. p.461.

[8] D.Yu. Sychugov, S.V. Shchepetov, Sov. J. Plasma Phys. (1988), V. 14, p. 390.

[9] A.B. Kuznetsov, S.V. Shchepetov. Nucl. Fusion 36 (1996), 1095.

[10] G.S. Voronov, E.V. Voronova, D.K. Akulina et al. Plasma Phys. Control Fusion 42 (2006) A 303-308.

[11] V.A. Bulanin, S.V. Lebedev, L.S. Levin, V.S. Roitershtein, Plasma Phys. Rep. (2000), V. 26. p.813.

[12] M.Hirsch, E. Holzhauer. Plasma Phys. Control. Fusion, V46 (2004), p.593-609.

[13] G.D. Conway, J. Schirmer, S. Klenge et al., ibid V46 (2004), p.951-970.

Proceedings of ITC/ISHW2007

Properties of internal diffusion barrier in high density plasmas on Large Helical Device

Ryuichi SAKAMOTO[1)], Masahiro KOBAYASHI[1)], Junichi MIYAZAWA[1)], Satoshi OHDACHI[1)], Tomohiro MORISAKI[1)], Suguru MASUZAKI[1)], Ichihiro YAMADA[1)], Motoshi GOTO[1)], Katsumi IDA[1)], Shigeru MORITA[1)], Satoru SAKAKIBARA[1)], Kenji TANAKA[1)], Kazuo KAWAHATA[1)], Kiyomasa WATANABE[1)], Yasuhiro SUZUKI[1)], Hisamichi FUNABA[1)], Sadayoshi MURAKAMI[2)], Naoko ASHIKAWA[1)], Yoshio NAGAYAMA[1)], Yoshiro NARUSHIMA[1)], Byron J. PETERSON[1)], Mamoru SHOJI[1)], Chihiro SUZUKI[1)], Masayuki TOKITANI[1)], Shinji YOSHIMURA[1)], Nobuyoshi OHYABU[1)], Hiroshi YAMADA[1)], Akio KOMORI[1)], Osamu MOTOJIMA[1)] and LHD experimental group[1)]

[1)]*National Institute for Fusion Science, Japan*
[2)]*Kyoto University, Japan*

An experimental study is performed in order to extend the operational space of internal diffusion barrier (IDB) plasma, which was originally found in pellet fueled high density discharges with the local island divertor configuration, to an intrinsic helical divertor configuration in large helical device (LHD). It is revealed that the IDB can be reproducibly formed in intrinsic helical divertor configurations as in the local island divertor configuration. The IDB is efficiently formed by central pellet fueling in the outer shifted magnetic configuration ($R_{ax} > 3.7$ m). Attainable core plasma density becomes higher as the magnetic axis shifts outward. Maximum core density reaches 1×10^{21} m^{-3}. Central pressure exceeds 130 kPa, and therefore very large Shafranov shift ($\Delta/a_{\mathrm{eff}} \geq 1/2$) due to high central beta is observed even at high magnetic field ($B_t \sim 2.54$ T).

Keywords: stellarator, internal diffusion barrier, pellet fueling, divertor, magnetic configuration

1 Introduction

Confinement improvement is one of the most important issues of magnetic confined fusion plasma research. The internal diffusion barrier (IDB) which enables core plasma to access high-density/high-pressure regime has been found in multi pellets fueled high density discharges with an active pumped local island divertor (LID) configuration in large helical device (LHD) [1]. A high density core plasma with 5×10^{20} m^{-3} is maintained by the IDB located at $\rho = 0.5$ and the IDB plasma exhibit the highest fusion triple product on LHD, $n_0 T_0 \tau_E = 4.4 \times 10^{19}$ keV m^{-3}s.

The IDB is similar to pellet enhanced performance (PEP) mode, which is first found in JET[2] then in the other tokamaks [3, 4], on the point that both lead to strongly peaked pressure profile. On the other hand, unlike the tokamak PEP mode, there is no clear indication of increase in the temperature gradient and inward particle convection in IDB. Although the LID configuration has efficient pumping due to the localized installation, heat removal is problem for the same reason with the present LID design. Therefore, IDB formation in intrinsic helical divertor configuration which have larger heat receiving area than LID configuration is highly desired from a standpoint of compatibility with a fusion reactor.

An experimental study has been performed in order to explore the operational space of the IDB discharge with the intrinsic helical divertor configuration in LHD.

2 Experimental Set-up

LHD is a heliotron type full superconducting stellarator with a pair of continuously wound $M = 10$ helical coils and three pairs of poloidal coils. The plasma major radius at vacuum magnetic field is variable in the range of 3.5 m to 4.0 m, the averaged plasma minor radius is ~ 0.6 m and the magnetic field strength is ≤ 3 T[5]. A helical divertor is intrinsic divertor configuration in heliotron type device. The divertor has open structure with forced water-cooled carbon target plate and there is no pumping capacity except wall pumping. The heat receiving area is about 50 times larger than LID configuration and it arrow high heating power and long pulse experiments.

Three negative ion based high energy (up to 180 keV) neutral beam injector (NBI) are employed for plasma heating. Typical NBI heating power is 12 MW in total. Solid hydrogen ice pellets are launched from outboard side mid-plane by using 10 barrels *in-situ* pipe-gun pellet injector[6]. The typical pellet mass and velocity are

author's e-mail: sakamoto@LHD.nifs.ac.jp

1.5 – 2.0 × 10^{21} atoms per pellet and 1000-1200 m/s, respectively.

3 Internal Diffusion Barrier Formation in Helical Divertor Configuration

3.1 fueling

Typical plasma profiles of the gas-puff and pellet fueled discharges at the same magnetic configuration $R_{ax} = 3.75$ m in the same line integrated density $n_e l = 3 \times 10^{20}$ m^{-2} are shown in figure 1. The normalized minor radius ρ is expressed as flux coordinate, namely, $\rho = \sqrt{\Phi}$ where Φ is the toroidal flux function, which is normalized by the value of the last closed flux surface. The negative and positive ρ value indicate inboard and outboard side of the plasma, respectively. Since particle source is limited to peripheral for the gas-puff fueling, the density profile typically becomes flat or slightly hollow. In the case of the pellet fueling, the IDB which has a steep density gradient inside $\rho = 0.55$ is formed and the central density is remarkably increased while peripheral density is reduced. A noteworthy finding is that the electron temperature of the pellet fueled plasma is higher in spite of the fact that the central density is more than double. The plasma pressure profile calculated assuming the ion temperature profile is the same as measured electron temperature profile, show an obvious increase of the plasma energy density in the core region ($\rho < 0.55$).

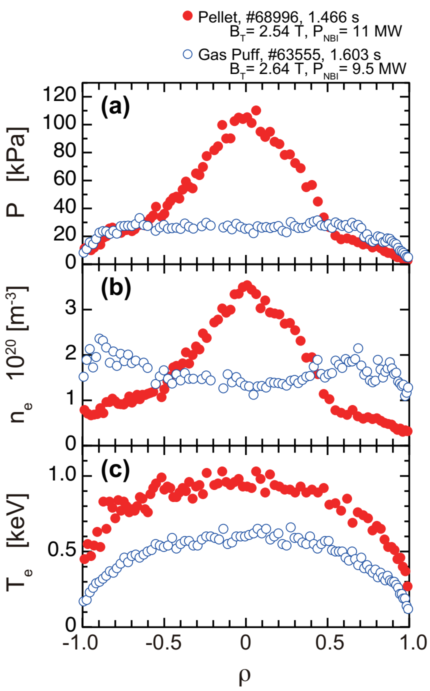

Fig. 1 Comparison of (a) Plasma pressure, (b) electron density and (c) electron temperature in the gas-puff (blue open circle) and pellet (red filled circle) fueled discharges at the same magnetic configuration $R_{ax} = 3.75$ m.

The attainable central pressure of the pellet fueled plasma is about four times larger than that of the gas-puff fueled plasma, even exceeding atmospheric pressure. The plasma β becomes high even though the magnetic field is high ($B_t > 2.54$ T) and thus the plasma profiles suffer very large Shafranov shift ($\Delta/a_{\rm eff} \sim 1/2$) .

3.2 pre-set magnetic axis

The global energy confinement time reaches a maximum in inward shifted magnetic configurations ($R_{ax} = 3.60 - 3.65$ m which give a maximum plasma volume) by employing pellet fueling[7]. The IDB, on the other hand, is easy to produce in outward shifted magnetic configurations ($R_{ax} > 3.7$ m). One characteristic difference between configurations is magneto-hydrodynamic stability properties, considered to be favorable as the magnetic axis shifts outward[8] because the region with magnetic well is wide, especially at finite β. It is also important that the poloidal distribution of a divertor flux changes with magnetic configurations[9]. The divertor flux tends to concentrate on the inboard side and this leads to a localized increase of neutral pressure due to recycling in the inward shifted magnetic configurations. This situation is estimated to cause a peripheral density rise which is incompatible with the core fueling. Contrary to this, the divertor flux tends to spread uniformly poloidally in the outward shifted magnetic configurations and this behavior leads to suppression of peripheral particle source. This situation is expected to compensate the lack of pumping capacity at helical divertor.

Figure 2 shows the temporal evolution of characteristic plasma parameters in several nine-pellet fueled discharges at magnetic axes $R_{ax} = 3.65$ m, 3.75 m and 3.85 m. Let timing of the final pellet injection be $t = 0$. In each cases, NB heating power and magnetic strength are 11 MW and 2.54 T, respectively. The IDB formation period is denoted by filled symbol. It is difficult to define onset and termination timing of the IDB regime because the IDB profile gradually changes in time. The IDB is temporarily defined by existence of a clear bend in the density profile. While the same number of pellets were injected, attainable central plasma density becomes higher as the magnetic axis shifts outward and the maximum central density at $R_{ax} = 3.85$ m is doubled compare to the density at $R_{ax} = 3.65$ m. At the same time, the central temperature follows quite a similar course after pellet injection although central density varies widely depending on magnetic configuration. As the result, higher central pressure is attainable in the outward shifted magnetic configurations where the IDB is formed. The point to observe is that there is a plateau of the pressure rise in the high density phase as shown by two-headed arrows in figure 2(a). The plateau begins to appear during the pellet injection phase, namely density increase phase, and continues until the excess density drops to the onset level. This phenomenon indicates

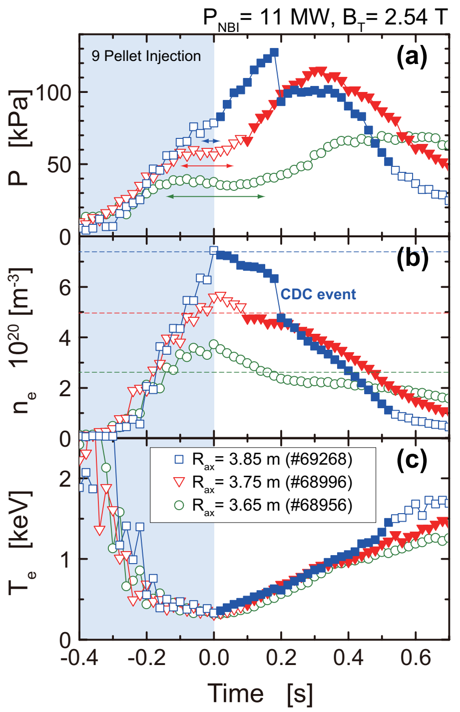

Fig. 2 The temporal evolution of (a) Plasma pressure, (b) electron density and (c) electron temperature in nine-pellets fueled discharges at magnetic axes R_{ax} = 3.65 m (green circle), 3.75 m (red triangle) and 3.85 m (blue square). The magnetic field strength and NB heating power are 2.54 T and 11 MW, respectively. Filled symbols denote the formation of IDB.

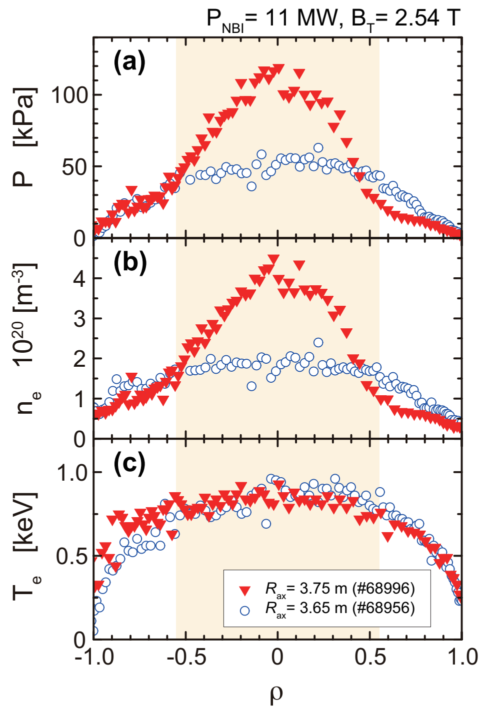

Fig. 3 Comparison of (a) Plasma pressure, (b) electron density and (c) electron temperature between R_{ax} = 3.65 m (blue open circle) and 3.75 m (red filled triangle) at the timing of $T_e(0)$ = 1 keV. The magnetic field strength and NB heating power are 2.54 T and 11 MW, respectively. Hatching denotes IDB formation region.

confinement degradation in high density regime. As the magnetic axis shifts outward, the onset density level increase as indicated by broken line in figure 2(b), namely 2.7×10^{20} m^{-3} at R_{ax} = 3.65 m and 5.0×10^{20} m^{-3} at R_{ax} = 3.75 m, and duration of the plateau becomes shorter. Finally the plateau of the pressure rise is hardly observed at R_{ax} = 3.85 m and the pressure is increase in a linear fashion during and after pellet injection. After that, the pressure and density decrease suddenly at t = 0.18 s, while any noticeable changes are not observed in the temperature. This unexpected event is referred to as core density collapse (CDC) and will be discussed later. It must be also noted that the final density levels out after the disappearance of the IDB. The final density becomes lower as the magnetic axis shifts outward, contrary to the IDB phase, and this observation supports a reduced recycling in the outward shift configurations.

Figure 3 shows a comparison of plasma profiles between R_{ax} = 3.65 m and 3.75 m at the timing of $T_e(0)$ = 1 keV. Density profiles of the two configurations are quite different even though the temperature profiles are identical. For R_{ax} = 3.65 m, the density profile has a parabolic shape. On the other hand, the IDB with steep density gradient is formed on the inside of ρ = 0.55 and central density reached to almost double in the case of R_{ax} = 3.75 m. Thus magnetic configuration is another factor of the IDB

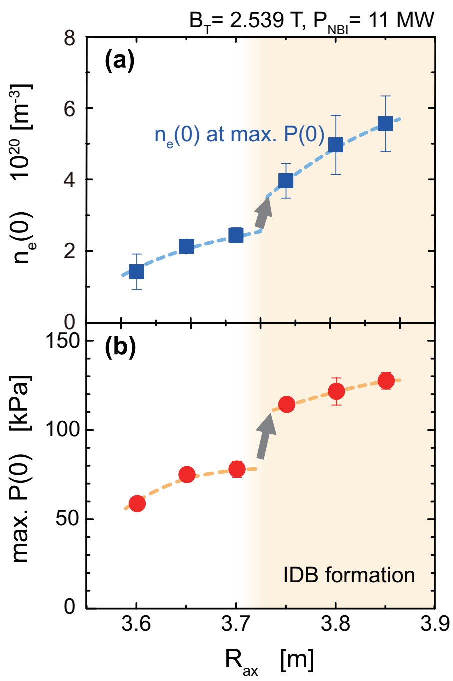

Fig. 4 Configuration dependence of (a) central electron density at the instant of maximum central pressure and (b)maximum central pressure. The magnetic field strength and NB heating power are 2.54 T and 11 MW, respectively.

formation in addition to pellet core fueling.

The magnetic axis dependence of the IDB plasmas is summarized in figure 4. Attainable central density becomes higher as the magnetic axis shifts outward and the central density exceeds 5×10^{20} m^{-3}. The point to observe is that there is a sharp increase in central density and pressure around R_{ax} = 3.7 m and central pressure reach its greatest value, ~ 130 kPa, at the neighborhood of R_{ax} = 3.85 m. The maximum central pressure is limited by the CDC event as shown in figure 2.

4 Properties of IDB Plasmas

4.1 particle transport

Figure 5 shows a change of IDB profiles from moment to moment. The IDB structure, which has localized sharp density gradient, namely box-like density profile, is observed at 1.2 s. Then density gradient is gradually decreases and spread into core region during density decay and temperature recover phase. Finally the IDB structure changes to linear profile at 1.6 s with keeping central pressure. During the profile change, a collisionality ν_b^*, which is normalized by a bounce frequency of banana particles, decrease monotonically in the plateau regime ($10 \geq \nu_b^* \geq 1$). This IDB structure change, from box-like profile to linear profile, is explained by lack of particle source inside IDB for the following particle transport analysis.

The particle transport coefficient of IDB plasma is calculated by using relationship between time evolution and gradient of density profiles after pellet injection. Figure

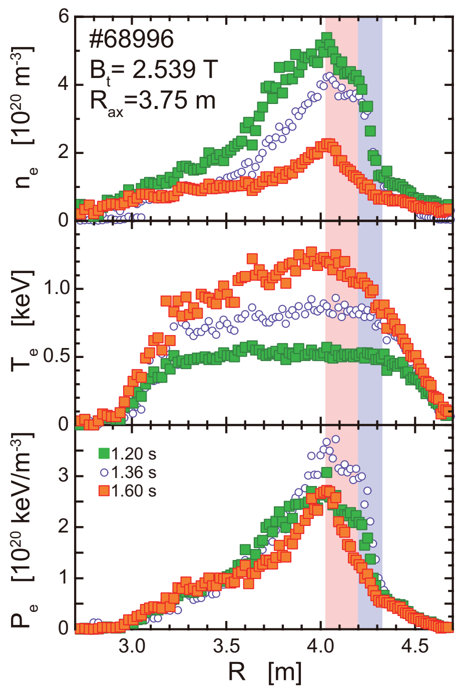

Fig. 5 Change of IDB structure.

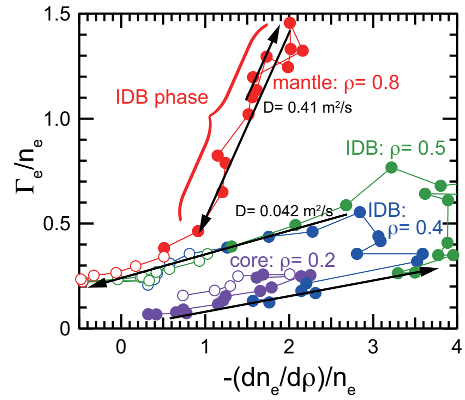

Fig. 6 Particle flux normalized by electron density as a function of density gradient after pellet injection in various minor radius. Filled symbols denote the period of IDB formation.

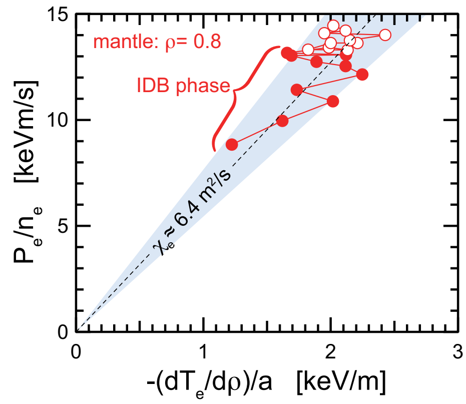

Fig. 7 Heat flux normalized by electron density as a function of temperature gradient after pellet injection in low density mantle (ρ = 0.8). Filled symbols denote the period of IDB formation.

6 shows relationship between normalized particle flux and normalized density gradient. Gradient and y-intercept of this plot indicate diffusivity (D_e) and convection velocity (v_e) according to the following relational expression.

$$\frac{\Gamma_e}{n_e} = -D_e \frac{1}{n_e}\frac{\partial n_e}{\partial \rho} + v_e,$$

where $\Gamma_e = -\frac{1}{A}\int \frac{\partial n_e}{\partial t} dV$ is particle flux assuming no particle source inside the flux surface. The filled symbols denote the period of IDB formation. Diffusivity of core region inside IDB ($\rho \geq 0.5$) is kept at low level as $D = 0.042$ m^3s even high density gradient and inward convection velocity can not be observed. Therefore IDB core can be described with diffusive nature and the profile change, box-like to linear, is explained by lack of particle source inside IDB. And also the core diffusivity is said to be not sensitive to collisionality in the range of plateau regime. On the other hand, the mantle plasma cannot keep the density gradient in high particle flux IDB phase, namely, mantle diffusivity deteriorates during IDB phase. Notable characteristics of the IDB plasma is that the thermal transport coeffi-

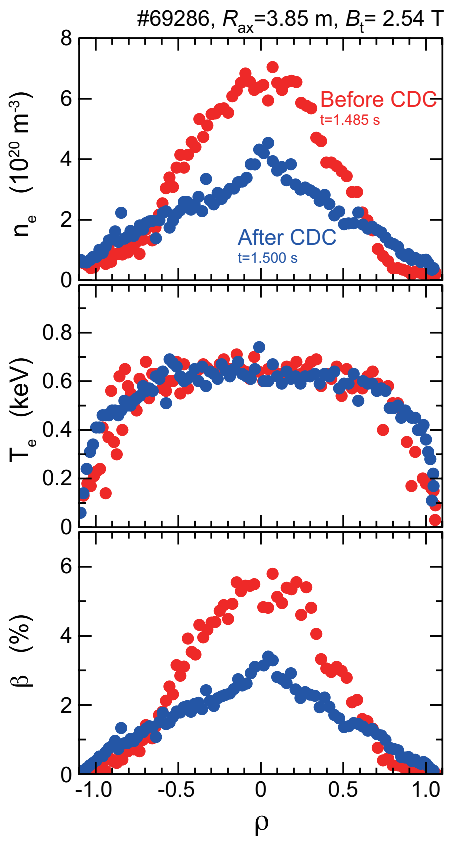

Fig. 8 Change of plasma profiles before and after CDC event.

cient, which is relationship between heat flux and temperature gradient remain unaffected by big change of the particle transport as shown in figure 7. These results lead to separation of confinement region between the IDB core (high density gradient) and low density mantle (high temperature gradient), and therefore high-density/high-pressure plasma is attained in the IDB discharge. The IDB core is formed by the deep pellet fueling and intrinsic good particle confinement property. The low density mantle have advantages to suppress radiation loss, and therefore density limit of IDB plasma is extremely extend to high-density regime. In addition, low density mantle secure temperature gradient for high-density/high-pressure core plasma.

4.2 core density collapse event

Figure 8 shows plasma profiles just before and after CDC event. In the CDC event, the high density core plasma is expelled on the sub millisecond time scale () without having any impact on the central temperature. CDC event is typically observed in the high performance discharges with IDB. The mechanism of the CDC is not yet elucidated, but it may be involved with MHD instability and/or equilibrium limit arising from very large Shafranov shift. Therefore, suppression of the Shafranov shift is potential solution to avoid CDC event. Pfirsch-Schlüter current control by a vertical elongation, namely ellipticity κ control, is a means of Shafranov shift suppression [10] in helical system.

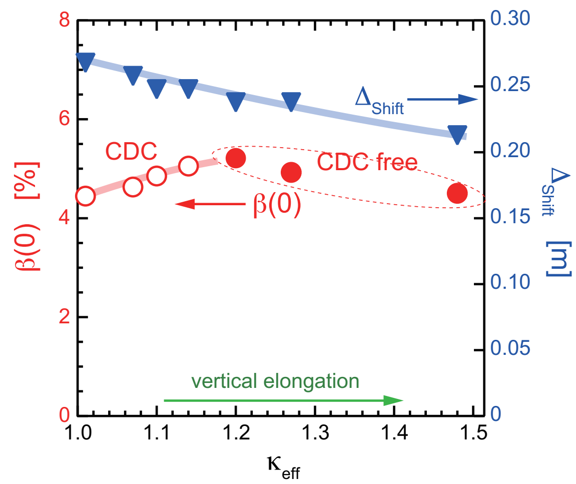

Fig. 9 Shafranov shift amount Δ_{shift} and central beta β_0 at the maximum central pressure as a function of the effective ellipticity κ_{eff}. The filled symbol in β_0 denote the occurrence of CDC event.

Figure 9 shows the Shafranov shift amount and central beta at the maximum central pressure as a function of the effective ellipticity κ_{eff}, which is defined by ratio of line densities between vertical elongated and horizontally elongated poloidal cross-section. As the κ_{eff} become large, amount of Shafranov shift monotonically get smaller. Attainable central pressure, which is restricted by CDC event, is become large until κ_{eff} = 1.2 and the attainable central pressure increase by 20 % compare to standard configuration κ_{eff} = 1.0. Extreme vertical elongation beyond κ_{eff} = 1.2 result in a degradation of central beta although the CDC event is not observed. Under the condition of $\kappa_{eff} \geq 1.2$, MHD instability which is different from CDC event is observed and confinement degradation is suggested.

4.3 impurity behavior

In helical system, neoclassical ambipolar diffusion predict ion root (negative radial electric field E_r) in high density regime and the negative E_r lead to impurity accumulation. In general, impurity behavior is one of the most concerned topics in high-density discharges, because radiation collapse due to loss of power balance tends to take place by less impurity contamination than a low density discharges. Contrary to theoretical prediction, significant indication of impurity accumulation is not observed by Z_{eff} and bolometric measurements although negative E_r in the IDB plasma is verified by a charge exchange recombination spectroscopy. Existence of impurity accumulation due to negative radial electric field has not been confirmed, nevertheless impurity contamination is not a significant problem in the IDB discharge. Divertor modeling study using EMC3-EIRENE code suggests impurity shielding potential in ergodic layer [11], namely, outward friction force by plasma flow dominate impurity behavior and impurity tend to be expelled from LCFS in high-density regime.

5 Conclusion

An experimental study is performed to explore the operational space of a high density plasmas due to the IDB which was originally found in pellet fueled high density discharges with the active pumped LID configuration in LHD. The IDB with steep density gradient has been produced at an intrinsic helical divertor configuration as in LID configuration by optimizing the pellet fueling and magnetic configuration. Core fueling by multiple pellet injection is essential for the IDB formation and the IDB easily appears in the outer shifted magnetic configuration ($R_{ax} > 3.7$ m). Confinement region is separated into low density mantle and high density core in IDB plasma. This lead to high-density/high-pressure core plasma. The central density reaches 1×10^{21} m^{-3} at $R_{\rm ax} \geq 3.9$ m and the central pressure has reached 1.3 times atmospheric pressure. Although negative $E_{\rm r}$ is verified, harmful impurity contamination has not been observed in IDB plasma. CDC event, which arise from very large Shavranov shift, restrict operational regime. Suppression of Shafranof shift with ellipticity control can mitigate CDC event and the central pressure increase by 20 % of standard configuration. Investigation of long-duration sustainability of the pellet fueled IDB is critically important from a perspective of extrapolation to fusion reactor scenario. Nonetheless, the IDB is an encouraging finding and it demonstrates the potential for alternative path to high-density/low-temperature fusion reactor in helical devices.

This work is supported by NIFS06ULPP521.

[1] N. Ohyabu *et al.*, Phys. Rev. Lett. **97**, 055002 (2006).
[2] JET Team, Plasma Phys. Control. Fusion **30**, 1467 (1988).
[3] Y. Takase *et al.*, Phys. Plasmas **4**, 1647 (1997).
[4] L.R. Baylor *et al.*, Phys. Plasmas **7**, 1878 (2000).
[5] O. Motojima *et al.*, Phys. Plasmas **6**, 1843 (1999).
[6] H. Yamada *et al.*, Fusion Eng. Des. **49-50**, 915 (2000).
[7] R. Sakamoto *et al.*, Nucl. Fusion **41**, 381 (2001).
[8] H. Yamada *et al.*, Plasma Phys. Controlled Fusion **43**, A55 (2001).
[9] S. Masuzaki *et al.*, Nucl. Fusion **42**, 750 (2001).
[10] T. Kobuchi *et al.*, Plasma Phys. Controlled Fusion **48**, 789 (2006).
[11] M. Kobayashi *et al.*, this conference , I-07 (2007).

Proceedings of ITC/ISHW2007

Comparative Divertor-Transport Study for W7-AS and LHD

Y. Feng[a)], M. Kobayashi [b)], N. Ashikawa [b)], L. Giannone [a)], P. Grigull [a)], K. Ida[b)], J. Kisslinger [a)], A. Komori [b)], R. König [a)], LHD experimental group [b)], S. Masuzaki [b)], K. McCormick [a)], J. Miyazawa [b)], T. Morisaki [b)], S. Morita [b)], O. Motojima [b)], Y. Nakamura [b)], K. Narihara [b)], N. Ohyabu [b)], B.J. Peterson [b)], F. Sardei [a)], K. Sato [b)], M. Shoji [b)], N. Tamura [b)], H. Thomsen [a)], M. Tokitani [b)], F. Wagner [a)], U. Wenzel [a)], H. Yamada [b)], I. Yamada [b)]

[a)] *Max-Planck-Institut für Plasmaphysik, Euratom Association, Germany*
[b)]*National Institute for Fusion Science, Toki, Japan*

Using the W7-AS island divertor and the helical divertor in LHD as examples, the paper presents a comparative divertor transport study, aiming at identifying the essential differences and similarities in divertor function between two typical helical devices of different size and divertor concept. Investigated are the impacts of specific field and divertor topologies on plasma, impurity and neutral transport. Topics addressed are neutral screening, impurity retention, thermal power removal via impurity line radiation, detachment and Marfes. Special attention is paid to the SOL screening effect on intrinsically-released impurities, as predicted by the EMC3/EIRENE code for both divertors. The conditions for realizing the impurity-screening regime in the SOL are analyzed and its role in achieving high-density plasmas in helical devices is assessed. Discussion is guided by EMC3/EIRENE simulations. Key physics issues are compared with experimental results.

Keywords: W7-AS, LHD, EMC3-EIRENE, Divertor, SOL transport, Impurity screening, Detachment

1. Inroduction

Unlike the standard poloidal-field divertor in tokamaks, divertor concepts presently investigated in stellarators are based on specific edge magnetic field structures intrinsically available in each device [1]. Typical examples are the island divertor for the advanced low-shear stellarators W7-AS [2] and W7-X [3], and the helical divertor for the high-shear, largest heliotron-type device LHD [4]. The former utilizes the divertor potential of inherent edge magnetic islands while the latter is based on a stochastic field resulting from island overlapping. In view of the large differences in field and divertor geometry among helical devices, it is interesting to see whether there exist certain common physics issues in terms of divertor transport or divertor functionality. Recently a collaboration work between IPP and NIFS was started for this purpose and the paper presents a comparative divertor transport study for the island divertor (ID) in W7-AS and the helical divertor (HD) in LHD. Discussion throughout this paper is guided by EMC3[5]-EIRENE[6] simulations. Topics addressed are particle flux enhancement, neutral screening, impurity retention, impurity radiation and detachment, as already extensively studied for the W7-AS ID (see e.g [7]). They are also the important basic elements of a divertor which need to be firstly investigated and understood especially for a divertor concept based on a complex 3D field structure like the ID in W7-AS and the HD in LHD. In particular, the paper is concentrated on understanding the elementary, global transport processes associated with the specific field topologies, aiming at forming a comparison basis for two typical helical devices of completely different divertor concept and geometry.

e-mail: feng@ipp.mpg.de

2. Divertor and field topology

W7-AS is a low-shear stellarator having a five-fold field symmetry. The low-shear in W7-AS favors large island formation as the radial size of the islands scales as $r_i \propto \sqrt{Rb_{mn}/n\iota'}$ where R is major radius, b_{mn} the resonant radial perturbation field normalized to the toroidal field, n the poloidal mode number and ι' the shear. Within the operational ι-range (0.3~0.7), a number of low-order islands of different poloidal mode numbers are available at the edge. The extensively-explored, so-called standard divertor configuration is based on the 5/9 island chain, which is shown in Figure 1. Two up/down symmetric divertor modules are installed at the elliptical plane of each field period, with five identical divertor module pairs covering the whole torus. The divertor plates are discontinuous due to technical reasons. Each

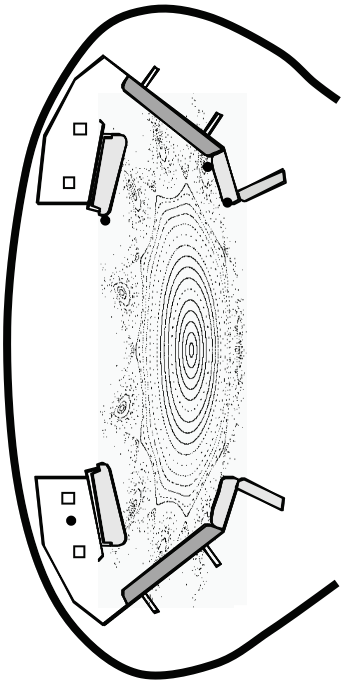

Fig.1 Standard W7-AS island divertor configuration: Nine islands are formed at the edge of the 5/9 configuration. A divertor module pair is up/down-symmetrically installed on the elliptical cross-section.

target plate toroidally extends over 18 degrees and poloidally cuts two islands in order to increase the deposition area. The baffles prevent the recycling neutrals from escaping from the divertor region towards the midplane where the magnetic islands are radially strongly compressed and optically thin for the recycling neutrals. The island size and the internal field-line pitch can be adjusted externally by ten control coils.

LHD is the largest heliotron-type device with 10 field periods. In contrast to W7-AS, LHD has a large shear, especially at the edge. The rotational transform in the edge region of the helical divertor configuration covers countless resonances which overlap each other, forming a stochastic layer of ~10 cm thickness. Unlike the single island chain in W7-AS, the stochastic SOL in LHD exhibits a complex field structure characterized by coexistence of remnant magnetic islands, stochastic fields and edge surface layers. Deep in the SOL, the moderate shear does not destroy the low-order islands completely, so that closed island surfaces still exist in limited regions around the O-points. Moving outwards, the shear increases quickly, leading to stronger island overlap. The remnant island cores become smaller and eventually disappear. In this case, the Chirikov parameter [8] should largely exceed unity and the field lines are then expected

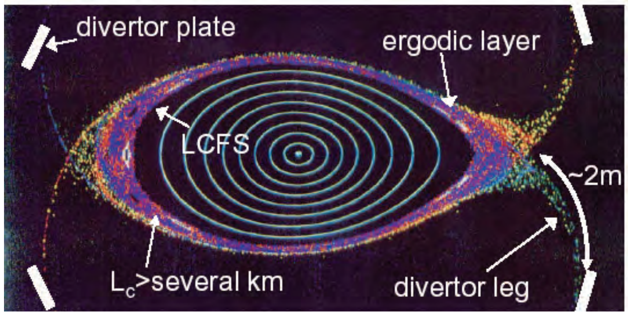

Fig. 2 Field and divertor geometry of the helical divertor in LHD.

to behave diffusively [9]. In reality, however, thin open surfaces have been identified to exist within the outer, strong island-overlapping region in LHD [4]. In the outermost region close to the wall, the increased poloidal field components of the two helical coils form a configuration similar to the double-null configuration in tokamaks, as shown in figure 2. Graphite targets cut the four divertor legs at the position just before their termination on the wall. The large poloidal component of the field along the divertor legs result in short connection lengths (~2 m on average) from the X-points to the targets [10]. Thus, the divertor legs are optically thin for the recycling neutrals, especially for the presently-open divertor structure.

2. Basic common transport features

Plasma transport in the island SOL of W7-AS can well be explained in terms of regular magnetic islands [7]. In order to clarify to what extent the plasma transport follows the complex field structure in LHD, EMC3/EIRENE simulations have been performed [10, 11]. In the following, we make a transport analysis based on figure 3, starting with the field topology shown in the lower picture. The 10/8 island chain has a quasi-closed island structure, which is clearly shown by the Poincare-plots. Starting from the 10/7 island chain, the field lines in the most region become irregular, with small island cores, however, remaining in the 10/7 and 10/6 island chains. Moving outwards, closed island cores vanish and Poincare-plots show a strong irregularity of the field lines, thus indicating that the field is highly stochastic. On the other hand, the underlying connection length contour plots show a strong field-line correlation even in the outer region without remnant island cores. The connection length contour reflects actually the basic field structure of low-order resonances. Indeed, all the low-order modes expected within the give ι-range can be identified. This strong field-line correlation contradicts obviously the diffusive behavior of field lines characterized by

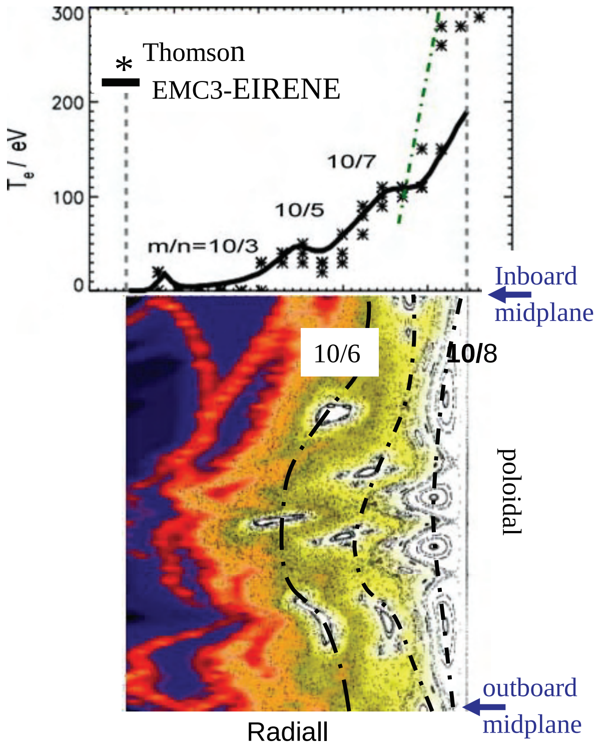

Fig.3 Comparison of Te-profiles between simulations and Thomson measurements (upper) and a radially-zoomed connection length contour with an overlying Poincare plot (lower) over half poloidal field period at a toroidal location as shown in figure 2. The three dot-dashed lines indicate the 10/6, 10/7 and 10/8 island chains which have remnant closed island cores.

ergodicity. The upper picture of figure 3 shows the calculated and measured (Thomson) T_e-profiles along the inboard midplane at a ϕ-position where the long axis of the elliptical plasma cross-section lies horizontally, as shown in figure 2. Both the code and Thomson results show clearly the impact of the low-order 10/7, 10/5 and 10/3 magnetic islands on electron energy transport. The 10/8, 10/6 and 10/4 mode structures have a poloidally-shifted phase distribution, with the X-points being on the midplane. This is reason why they are not reflected by the T_e-profiles. In addition, the code shows a strong correlation of parallel plasma flows with the island structure where positive and negative flows surround the O-points [11]. Even for the mode structures without a closed island core, flow channels residing on the island chains are still identifiable. Thus, it is to conclude that the plasma transport in the stochastic layer is governed by the low-order islands, although the relative importance of the stochastic effects can not yet be quantified.

Particle transport along field lines is governed by a classical convective process, with the parallel flow velocity being determined by momentum balance. Momentum transport in both W7-AS and LHD divertor configurations is characterized by friction between opposite flows in different parts of the magnetic islands which gives rise to significant momentum loss and thereby breaks up the pressure conservation along open field lines already under low-density, high-temperature conditions without intensive plasma-neutral interaction. This can be understood qualitatively by the following pressure balance equation:

$$p\left(1+M^2\right)=2p_{up}-mD\int\frac{nV_{\parallel}}{\Delta_{\perp}^2}dl \qquad (1)$$

where p is the total thermal pressure of ions and electrons, M the Mach number and the subscript *'up'* indicates upstream. The last term on the right side of eq. (1) represents the frictional momentum loss between opposite flows separated by a characteristic perpendicular distance of $\Delta_{\perp}$. D is the diffusivity. The integration is performed along field lines from upstream down to targets. This term is relevant for W7-AS and LHD because of the small $\Delta_{\perp}$ and the long integration (connection) length. In W7-AS, interaction between opposite flows happens in both poloidal and radial directions [7], while in LHD radial approach of counter-flows residing on neighboring island chains is the main reason for flow damping [10,11].

As a consequence, a high recycling regime as observed in tokamaks does not take place in the island/stochastic SOLs of W7-AS and LHD. Target Langmuir probes show, in consistence with H_a-signals, typically a roughly-linear dependence of ion saturation currents on the upstream (defined at the LCFS in the presented analysis) density up to a rollover point, as

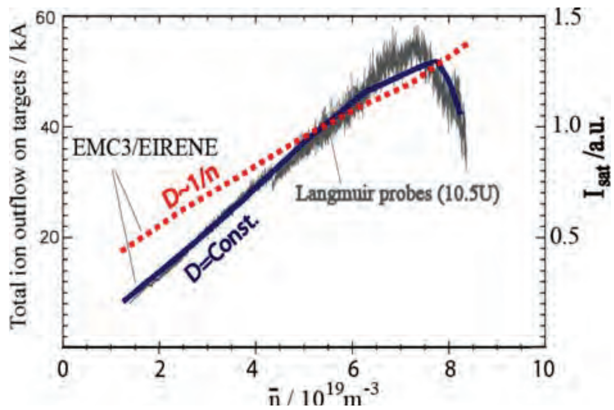

Fig. 4 Ion saturation currents increase linearly with plasma density. This linear-dependence can well be reproduced by the 3D code, independent on the D-ansatz.

shown in figure 4 for LHD. This linear behavior can be well reproduced by the EMC3/EIRENE code, insensitive to the selected D-ansatz. Nevertheless, the use of a constant D results in an ion flow slope matching better that of I_{sat} from the probes. Similar results are found in W7-AS, as shown in figure 5 where the calculated average downstream density n_{ed} is compared with those

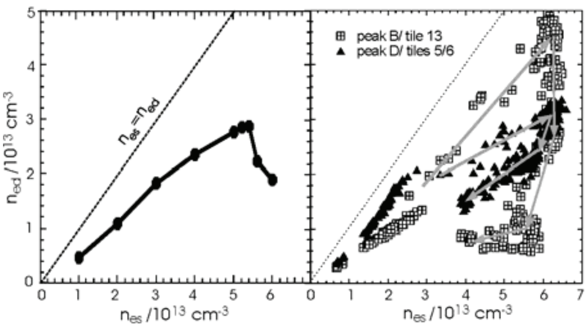

Fig.5 Absence of a high recycling regime in W7-AS, predicted by the EMC3 code (left) and confirmed by experiments (right).

from target probes of different peak locations. There is no evidence for a high recycling regime characterized by a strongly-nonlinear increase of n_{ed} with the upstream density n_{es}.

2. SOL screening effects on CX-neutrals and intrinsic impurities

Both the ID in W7-AS and the HD in LHD have an open divertor structure and the first wall is made of stainless steel. High-energetic CX-neutrals hitting the wall is a potential source producing impurities by mains of physical sputtering. An optically-thick

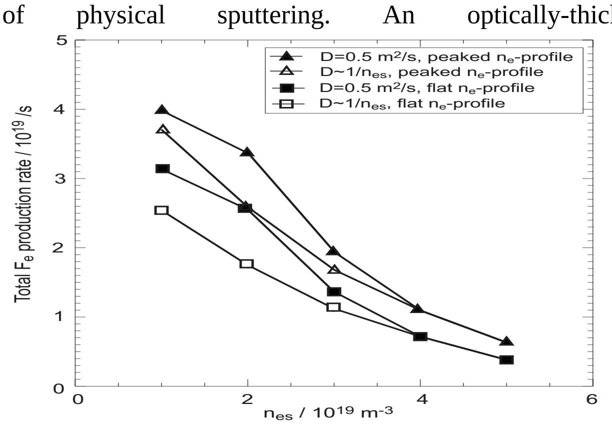

Fig.6 Sensitivities of high-energetic CX-neutrals to core profiles and cross-field transport coefficients as well as separatrix density, calculated by ECM3-EIRENE for W7-AS.

island/stochastic SOL can move the CX-neutrals to a lower energy band in the energy spectrum and thereby

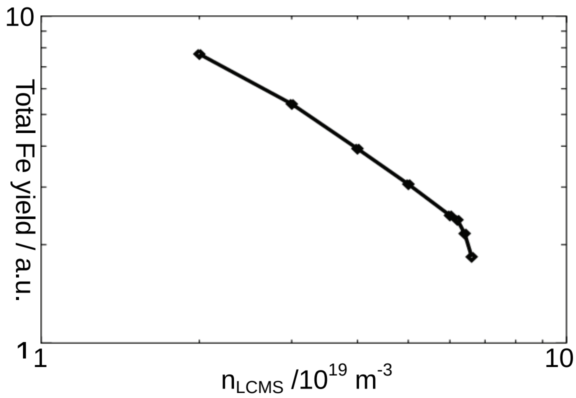

Fig.7 Calculated Fe-prodution rate as a function of n_{LCMS} in LHD.

reduce the sputtering-relevant neutral flux. For a given input power entering the SOL, the SOL temperature drops with increasing the SOL density, especially at the downstream of maximum population of the recycling neutrals. Figures 6 and 7 show respectively the total Fe yield sputtered by CX-neutrals for W7-AS and LHD. Because of the existing uncertainties in wall conditioning, the Fe yield shown here should be regarded as a physics quantity for measuring the sputtering-relevant, high-energetic CX-neutral flux, rather than an absolute iron production. For both W7-AS and LHD, the 3D code simulation results show that a dense, cold island/stochastic SOL can effectively reduce the high-energetic CX-neutral flux and thereby the related Fe sputtering yield.

3. SOL impurity transport and retention

Although, as shown in the previous section, a high-density SOL moderates the physical sputtering process of CX-neutrals on plasma-facing components, high-Z impurities like the wall-released Fe can, even with a reduced source, cause significant radiation loss if they reach the confinement core region, preventing plasma from a high density operation. EMC3/EIRENE code has predicted that, under enhanced recycling conditions, the edge islands in W7-AS have a retention effect on intrinsic impurities [12]. Similar retention effect has been also predicted for the stochastic layer in LHD. Using the intrinsic carbon as test impurities, figures 8 and 9 show how the carbon impurity density distribution changes from peaked to hollow profiles with increasing the SOL density. Parallel-force balance analysis based on the 3D simulations shows that the net force acting on impurities can be, with increasing the SOL density, changed from thermal-force dominating to friction dominating, leading to a reversal of the convective impurity flow from inwards- to outwards-directed [7, 12]. This is the reason for the carbon density profile change with the SOL density, as shown in figures 8 and 9 for W7-AS and LHD.

The reduction of the dominating ion thermal force under high SOL-density conditions are attributed to the significant contribution of the cross-field heat conduction to the energy transport in the island SOLs because of the small divertor-relevant field-line pitch in both W7-AS

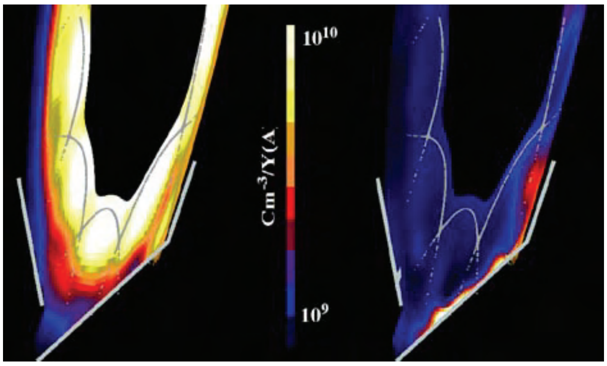

a) n_{es} = 1.5 x 10^{19} m^{-3} **b) n_{es} =5.0 x 10^{19}**

Fig. 8 Island retention effect on intrinsic impurities predicted for W7-AS.

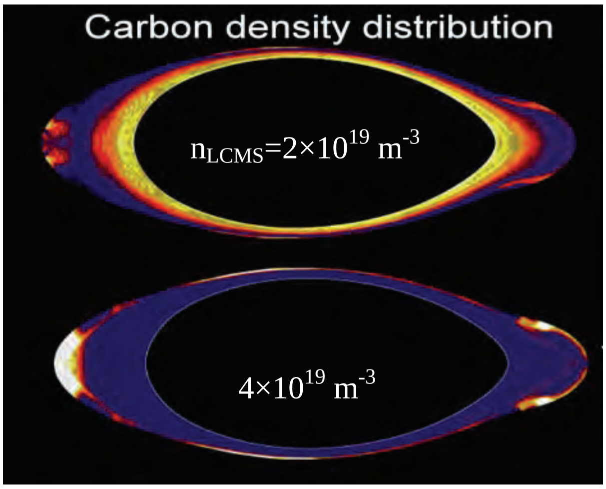

Fig. 9 Similar impurity retention effect predicted also for the stochastic layer of LHD.

and LHD. Because of the high sensitivity of the parallel heat conductivity to the ion temperature, it can be shown that, for a given input power, there exists a threshold SOL density above which the ion thermal force can be switched off and friction becomes dominating [7]. This is consistent with the experimental observations in both devices where Fe-radiation originating from core drops sharply once the plasma density is raised above a threshold density. It should be mentioned that here, a possible, still-unknown core transport mechanism setting in at high collisionallities to flush impurities could not yet be completely excluded.

A separation between core and SOL transports of intrinsic impurities has been recently realized experimentally in LHD by observing the relative changes in radiation intensity among different ionization stages of the intrinsic carbon impurities [13]. Carbon impurities of different ionization stages are populated in different depths of SOL and the radiation ratio between low and high ionization stages reflects the profile form of carbon density. Observed was a sharp decrease in the radiation ratio of high- to low-ionization stages at a SOL density roughly consistent with the code-predicted one, thus confirming the code prediction of SOL impurity retention.

4. Stability of detached plasmas

Detachment has been achieved in both devices at very high SOL densities. However, stabilizing a detached plasma turned out to be difficult. In W7-AS, stable detachment is always partial and restricted to large island and field-line pitch configurations. Configurations with small islands or field line pitch will drive detached plasmas immediately into an unstable stable, with an unstable, Marfe-like radiation inside the LCFS. In LHD, a stable partial detachment remains still a challenge and a quasi-stable complete detachment leads always to a strong degradation of the global energy confinement due to the location of a rotating radiation belt inside the LCFS. These experimental observations motivated detailed numerical studies in order to understand the underlying mechanisms driving instability. It is found numerically that the radiation distribution is highly sensitive to the

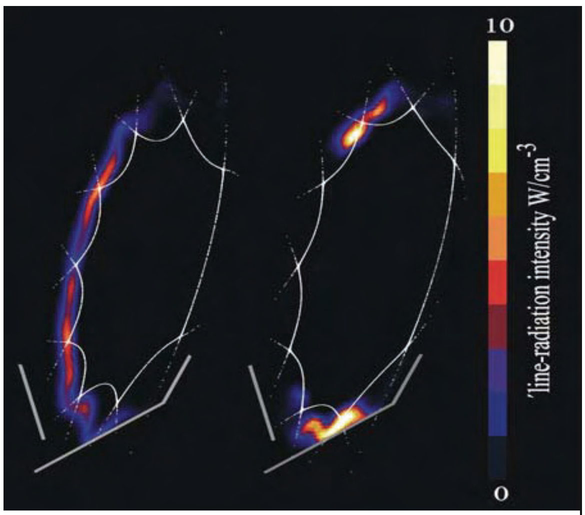

Fig. 10 Inboard side radiation (left) or divertor rediation (right), depending on the island geometry.

island geometry. For the island configurations in which stable detachment is established in W7-AS experiments, the 3D code shows a radiation belt formed on the inboard

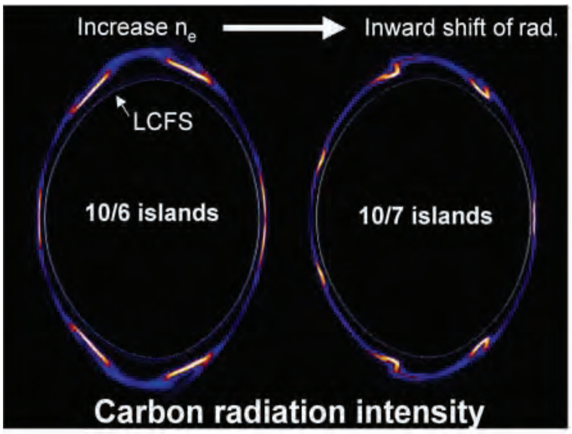

Fig. 11 Radiation prefers remnant island cores.

side (see figure 10). For small islands or field line pitch, radiation is located at the X-point in the recycling region, as shown in figure 10, leading to a strong reduction of the island neutral screening efficiency in comparison to the inboard side radiation case. A linear stability analysis shows that the loss of neutral screening could be the reason for the detachment instability observed in experiments [14]. For the stochastic layer in LHD, the 3D code predicts that remnant island cores attract radiation. Converged numerical solution is found when the radiation layer touches the 10/6 and 10/7 island chains which have small closed island cores, as shown in figure 11. Till to now, such radiation patterns could not yet be stabilized in LHD experiments. One of the possible reasons for the discrepancy, as for the divertor radiation pattern in W7-AS, is that the SOL power, which is fixed in simulations, should decrease in experiments due to the increased code density resulting from recycling neutrals after the detachment transition. The stability analysis made for W7-AS [14] should also be valid for the LHD case. More detailed analysis is left for further.

5. Conclusions

Low-order magnetic islands are the basic elements forming helical SOLs of the divertor configurations in both W7-AS and LHD. Although the large shear in LHD leads to overlapping of multi-island chains, the basic island structures of the low-order modes are not destroyed completely to allow really a diffusive approximation of field-line trajectories. EMC3-EIRENE simulations show that the SOL transport in both devices is governed by the low-order islands, which is supported by Thomson T_e-measurements in LHD. Counter plasma flows reside in different parts of the islands chains. Viscous transport due to spatial approach of the counter flows cause significant momentum loss of the streaming ions, being the reason for the absence of a high recycling regime in both devices. It is numerically shown that a dense, cold island SOL shifts the CX-neutrals to low energy range and reduces the physical sputtering yield on plasma facing components. Benefiting from geometric advantage of the small effective field-line pitch in the islands, the parallel ion heat conductive flux can be, under high density, low temperature conditions, strongly reduced by the perpendicular one, resulting in a strong reduction of the related thermal force. Conditions for achieving a purely friction-dominated impurity transport regime are predicted by the 3D code for both W7-AS and LHD. Consistent with the code predictions, both W7-AS and LHD experiments show a sharp drop in Fe radiation from core when plasma density exceeds a threshold value. The correlation and relevance of the observations to the predicted impurity retention effect of the SOL will be checked further by isolating the SOL transport from core effects. The strong reduction of high-Z impurity concentration in the core extends the plasma to rather high densities until detachment sets in due to intensive carbon radiation. Stable partial detachment can be established in W7-AS through careful choice of the island configuration, while in LHD it is not yet successful to stabilize the radiation layer outside the confinement region. 3D simulations suggest that loss of the SOL neutral screening efficiency after detachment transition prevents the radiation layer from being stopped in the SOL. More detailed analysis on this issue is under way.

References

[1] R. König *et al.*, *PPCF* **44**, 2365 (2002)
[2] P. Grigull *et al.*, *PPCF* **43**, A175 (2001)
[3] H. Renner *et al.*, *Nucl. Fusion* **40**, 1083 (2000)
[4] N. Ohyabu *et al.*, *Nucl. Fusion* **34**, 387 (1994)
[5] Y. Feng *et al.*, *J. Nucl. Mat.* **266-269**, 812 (1999)
[6] D. Reiter, *Fusion Sci. Technol.* **47**, 172-86 (2005)
[7] Y. Feng *et al.*, *Nucl. Fusion* **46**, 807 (2006)
[8] B. V. Chirikov B. V. , *Phys. Rep.* **52**, 265 (1960)
[9] M. N. Rosenbluth *et al.*, *Nucl. Fusion* **6**, 297 (1996)
[10] M. Kobayashi *et al.*, *J. Nucl. Mater.* **363-365**, 294 (2007)
[11] Y. Feng *et al.*, *"Fluid features of the stochastic layer transport in LHD"*, to be published in *Nucl. Fusion*, (2007)
[12] Y. Feng *et al.*, *32nd EPS*, vol **29C** (ECA), P1.012 (2005)
[13] M. Kobayashi *et al.*, *this conference*
[14] Y. Feng *et al.*, *Nucl. Fusion* **45**, 89 (2005)

Proceedings of ITC/ISHW2007

On impurity retention effect in the edge ergodic layer of LHD

Masahiro KOBAYASHI[1)], Yuehe FENG[2)], Sigeru MORITA[1)], Kuninori SATO[1)], Malay Bikas CHOWDHURI[3)], Suguru MASUZAKI[1)], Mamoru SHOJI[1)], Yukio NAKAMURA[1)], Masayuki TOKITANI[1)], Nobuyoshi OHYABU[1)], Motoshi GOTO[1)], Tomohiro MORISAKI[1)], Ichihiro YAMADA[1)], Kazumichi NARIHARA[1)], Naoko ASHIKAWA[1)], Hiroshi YAMADA[1)], Akio KOMORI[1)], Osamu MOTOJIMA[1)] and the LHD experimental group

[1)] *National Institute for Fusion Science, Toki 509-5292, Japan*
[2)] *Max-Planck-Institute fuer Plasmaphysik, Wendelsteinstrasse 1, D-17491 Greifswald, Germany*
[3)] *Graduate University for Advanced Studies, Toki 509-5292, Gifu, Japan*

The impurity transport characteristics in the ergodic layer of LHD is analyzed using the 3D edge transport code (EMC3-EIRENE), in comparison with the experimental data. The 3D modelling predicts the impurity retention (screening) in the ergodic layer at high density plasma. It is found that the edge surface layer plays an important role for the retention, where the friction force significantly dominates over the thermal force. The line intensity measurements of CIII to CVI shows consistent behaviour with the modelling, indicating the existence of impurity retention in the ergodic layer. The applicability of the model for high Z impurity is also discussed, where it is found that the experimental data is, at least, consistent with the results of edge transport modelling.

Keywords: ergodic layer, impurity transport, LHD

1 Introduction

Control of impurity transport in a fusion device is one of the most important issues, in order to avoid impurity contamination of core plasma, which leads to confinement degradation by radiative cooling, as well as reduction of fusion power due to fuel dilution [1]. The impurity that released at divertor plates or the first wall, reaches first the scrape-off layer (SOL), where they experience ionization and thereby transported as charged particles. The transport in the SOL then determines the influx of the impurity to the core region [2]. This paper focuses on the impurity transport in the edge region, especially the effect of stochastic magnetic field. It has been reported in Tore Supra experiments that there is an indication of plasma decontamination during the ergodic divertor configuration [3], and an interpretation for this phenomena was discussed using (1D) analytical model [4, 5], as an enhanced outflux of plasma by the stochastic field lines, that tends to exhaust impurity. Similar explanation was given also by D. Kh. Morozov et al. [6].

On the other hand, the Large Helical Device (LHD) in National Institute for Fusion Science, intrinsically has ergodic layer in the edge region. It is found that even with extremely high core density operation, where the negative radial electric field is formed, it is free from radiation collapse, suggesting no serious impurity contamination [7]. In this paper, we try to discuss impurity transport in the edge ergodic region of LHD using 3D numerical transport code that takes into account all relevant terms of impurity transport model as well as precise magnetic field configuration (i.e. braiding magnetic field). This enable us to directly compare the impurity transport model with experimental results and thus gives us clearer interpretation of the impurity transport process in the ergodic layer.

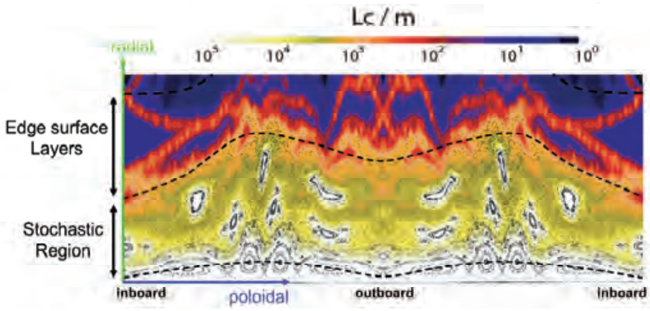

Fig. 1 Connection length (L_C) profile in ergodic layer of LHD, superposed with Poincare plot of field lines. L_C is resolved up to 100 km.

2 Magnetic field structure of ergodic layer in LHD

LHD is a heliotron type device with steady state magnetic field sustained by superconducting helical coils of l = 2. The major and averaged minor radii are 3.9 m and ~ 1.0 m, respectively [8]. The helical coils' winding creates magnetic field structure of 10 field periods in toroidal direction. The radial magnetic field coming from the helical coils with many different modes, produces magnetic islands at the edge region, and they overlap to create ergodic field structure there.

author's e-mail: kobayashi.masahiro@lhd.nifs.ac.jp

The connection length profile of the ergodic layer is plotted in Fig.1, together with Poincare map. In this paper, the ergodic layer is divided into three regions, following the terminology of ref.[8], which is defined based on the magnetic field topology that affects thereby the transport properties of plasma (impurity), as shown later. The region with m=8 magnetic islands are considered as confinement region because of the clear island structure and the long connection length (> 100 km). The stochastic region starts from m=7 islands, where they are overlapping with neighbouring islands and the separatrix is no longer clear. From the mode of m=4, it is called the edge surface layer, where short and long field lines are mixed. This structure is an unique feature of of heliotron divertor configuration, which is created by strong magnetic shear that stretches and bends the flux tubes, and thus mixes up the long and short flux tubes. The outside of the edge surface layer is divertor legs, which connects to divertor plate in several metes, which is, however, not shown in Fig.1.

3 Impurity transport analysis in the ergodic layer

The impurity transport analysis has been carried out by using the edge transport code EMC3 [9] - EIRENE [10], in order to take into account the magnetic field structure of the ergodic layer. The code solves the fluid equations of mass, momentum and energy as well as impurity in a realistic 3D geometry. The details of the model are described in ref.[9]. EIRENE solves a kinetic equation for neutral gas, which recycles at the divertor plates or first wall.

The impurity transport along the field lines is considered to be governed by the momentum equation,

$$m_z\frac{\partial V_{z\parallel}}{\partial t} = -\frac{1}{n_z}\frac{\partial T_i n_z}{\partial s} + m_z\frac{V_{i\parallel} - V_{z\parallel}}{\tau_s} + ZeE_\parallel + C_e\frac{\partial T_e}{\partial s} + C_i\frac{\partial T_i}{\partial s}, \tag{1}$$

where the subscript z and i denote the impurity with charge state Z and the bulk plasma ion, respectively. The s is the coordinate along magnetic field line and it is assumed that $T_z \approx T_i$. τ_s, $E_\parallel$ and $V_\parallel$ are the impurity-ion collision time, parallel electric field and parallel flow velocity, respectively. $C_i \approx 2.6Z^2$ and $C_e \approx 0.71Z^2$. The first term on the right hand side is pressure gradient force of impurity. The second term, friction force, and the third term, parallel electric field, are usually directed to the divertor, while the forth and fifth terms on the right hand side, electron and ion thermal force, are pulling impurity upstream because of the parallel temperature drop to the divertor plate. It is easily shown that the dominating terms in the equation are the ion thermal force and the friction force [11] [12]. In

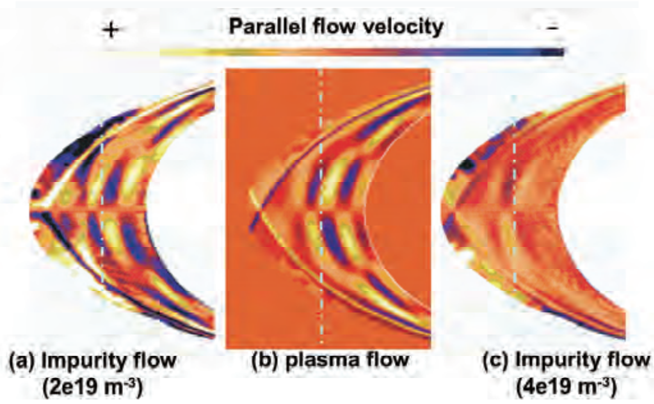

Fig. 2 (a) Parallel impurity flow velocity at $n_{LCFS} = 2\times10^{19}m^{-3}$, (b) parallel flow velocity of bulk plasma, (c) same as (a) but for $n_{LCFS} = 4\times10^{19}m^{-3}$. The yellow and blue indicate positive and negative flow in toroidal direction. The dashed lines are located at the same radial position for eye guide.

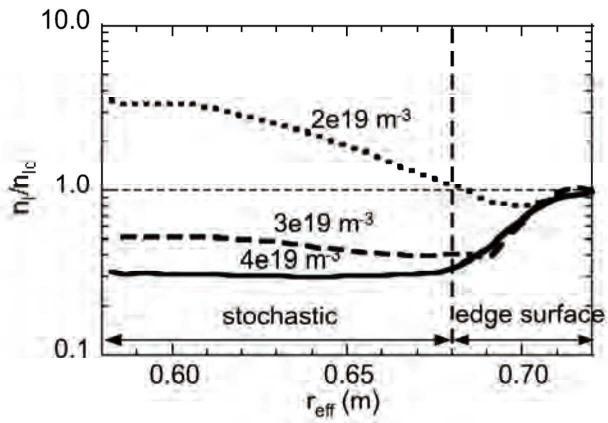

Fig. 3 Radial profiles of carbon density summed up over all charge states, for different density, $n_{LCFS} = 2, 3, 4\times 10^{19}m^{-3}$ normalized with the downstream density. r_{eff} is defined by cylindrical approximation of the volume enclosed by the radial surface of computational mesh.

force balance, eq.(1), therefore, reads,

$$V_{z\parallel} = V_{i\parallel} + C_i\frac{\tau_s}{m_z}\frac{\partial T_i}{\partial s} \tag{2}$$

Since $V_{i\parallel}$ flows towards divertor plate, while $\frac{\partial T_i}{\partial s}$ directs upstream, when the friction dominates over the thermal force, the impurity flows to the divertor. The ratio of the friction and the thermal force in eq.(1) is given by [13] [14],

$$\frac{friction force}{thermal force} \sim \frac{5/2 n_i T_i V_{i\parallel}}{\kappa_i^0 T_i^{2.5}\nabla_\parallel T_i} \propto \frac{n_i|M|}{T_i\nabla_\parallel T_i}, \tag{3}$$

with M being Mach number. The numerator represents convective energy flux while the denominator does conductive one.

Eq.(3) shows that as the plasma becomes dense and cold with substantial flow acceleration, the friction force dominates over the thermal force, resulting in impurity retention at the divertor. In the present analysis, carbon is selected as the impurity species, which is released at the divertor plate, with source rate being proportional to the divertor flux, and traced according to eq.(1), also in perpendicular to field lines as diffusive process. Plotted in Fig.2 are the parallel impurity flow velocity as well as the bulk plasma flow obtained by the 3D modelling, for different density with fixed input power, where the yellow and black colours mean flows in positive and negative toroidal directions, respectively. In this figure, it is clearly observed that at $n_{LCFS} = 2 \times 10^{19} m^{-3}$, the impurity flow direction is opposite to the bulk plasma flow, i.e. thermal force pushes the impurity upstream, while at $n_{LCFS} = 4 \times 10^{19} m^{-3}$ the direction of impurity flow becomes same phase as the bulk plasma flow due to the friction force. The resulting total impurity density (summed up over all charge states) profiles are plotted in Fig.3, in radial coordinate r_{eff} for the different plasma density. r_{eff} is defined by cylindrical approximation of the volume enclosed by the radial surface of computational mesh. At the low density, $n_{LCFS} = 2 \times 10^{19} m^{-3}$, the thermal force is so effective that the impurity is drawn to LCFS, and accumulates there. With increasing density, the upstream impurity density gradually decreases, and at $n_{LCFS} = 4 \times 10^{19} m^{-3}$, the impurity is driven towards divertor by the friction force, resulting in divertor retention as seen in Fig.3.

As the retention effect is switched on, the profile become flat in the stochastic region and lower than the downstream, where the density gradient is formed especially in the edge surface layer. The profile indicates that the friction force to push the impurity outward is effective only in the edge surface layer. Plotted in Fig.4 (c) is eq.(3), the ratio of friction and thermal force, as well as (a) electron temperature and density, (b) Mach number and ionization source of bulk plasma. In the edge surface layer, there appears substantial acceleration of Mach number, which is considered caused by the hydrogen ionization source there and also the particle sink due to the short connection length flux tubes that are embedded in-between the long ones. The temperature decreases towards the edge. These parameter change results in the significant increase of the friction-thermal force ratio in the edge surface layer, as observed in Fig.4 (c).

4 Comparison with experiments

Figure 5 (a) shows radial profiles of carbon density in different charge states at $n_{LCFS} = 4 \times 10^{19} m^{-3}$, where the impurity retention is effective as discussed above. For comparison, the profiles at $n_{LCFS} = 2 \times 10^{19} m^{-3}$ is plotted in Fig.5 (b), in which case the impurity accumulates around LCFS because of the dominant thermal force. Due to the large jump in the ionization potential between C^{+3} (=64.5 eV) and C^{+4} (=392 eV), there appears clear separation of

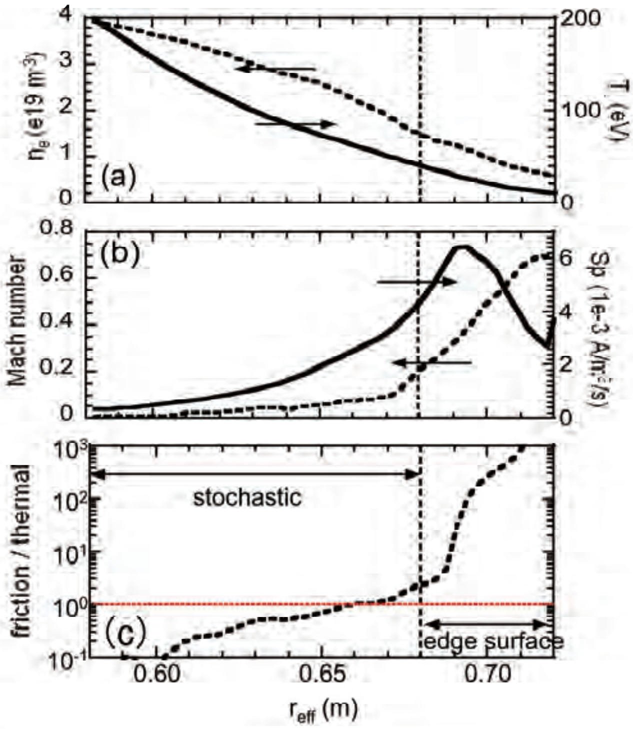

Fig. 4 Radial profiles of (a) n_e and T_i, (b) Mach number and ionization source, (c) eq.(3), as a function of r_{eff}, for $n_{LCFS} = 4 \times 10^{19} m^{-3}$.

the location of peak positions between the low and high charge states groups, i.e. lower charge states C^{+1}, C^{+2} and C^{+3} are mainly located at $r_{eff} > 0.67m$, while higher ones C^{+4}, C^{+5} and C^{+6} have peaks at $r_{eff} < 0.67m$. At $n_{LCFS} = 4 \times 10^{19} m^{-3}$, it is seen that the lower charge states increases due to the retention effect at the outer radius, at the same time the density of higher charge group near LCFS is suppressed. In the case of $n_{LCFS} = 2 \times 10^{19} m^{-3}$, on the other hand, the higher charge group increases significantly in the inner radius, with reduced lower charge group at outer radius. The difference of the profiles are reflected on the radiation intensity, which are shown in Fig.6 (a). The radiation from lower charge states, CII, CIII and CIV, increases monotonically with increasing bulk plasma density. This is due both to the increase of carbon yield, which is proportional to divertor flux, and to the retention effect. On the other hand, the radiation from higher charge states, CV and CVI, remains almost constant. This is mainly due to the reduction of the density caused by the retention at higher density, also partly because of the temperature change caused by density scan, where the CIV and CV are still sensitive to the temperature in the range of 100 to 200 eV. In order to illustrate the impact of friction exerted by bulk plasma flow, $V_{i\parallel}$ is set to be zero in eq.(1), keeping all other parameters unchanged. The results are plotted in Fig.6. In this case, because of no outward component of impurity flow, the absolute content of impurity increases, and thus the radiation intensity is relatively higher than Fig.6 (a). One should also note the quali-

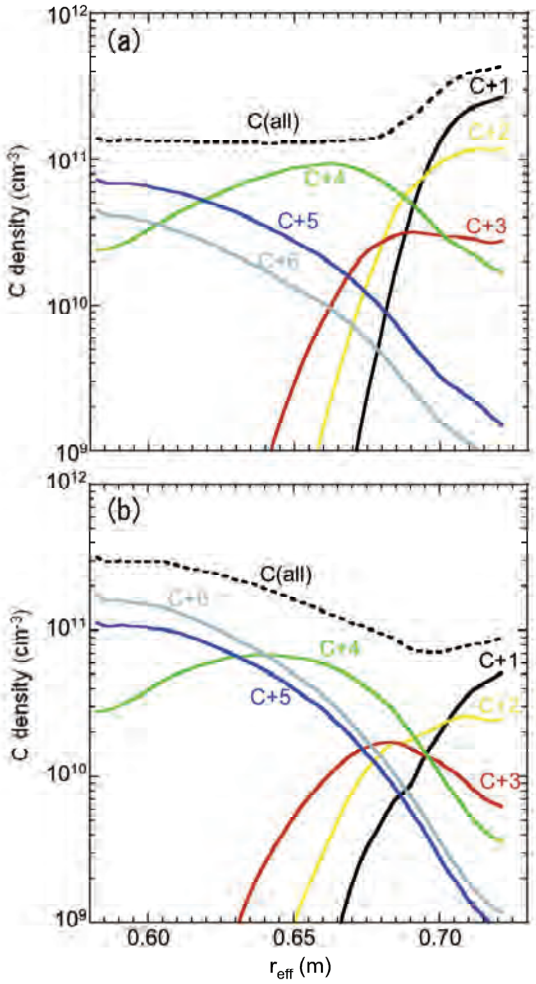

Fig. 5 Radial profiles of carbon density at different charge states, black : C^{+1}, yellow : C^{+2}, red: C^{+3}, green : C^{+4}, blue : C^{+5}, grey : C^{+6}, dashed lines : total density of carbon. (a) $n_{LCFS} = 4 \times 10^{19} m^{-3}$, (b) $n_{LCFS} = 2 \times 10^{19} m^{-3}$.

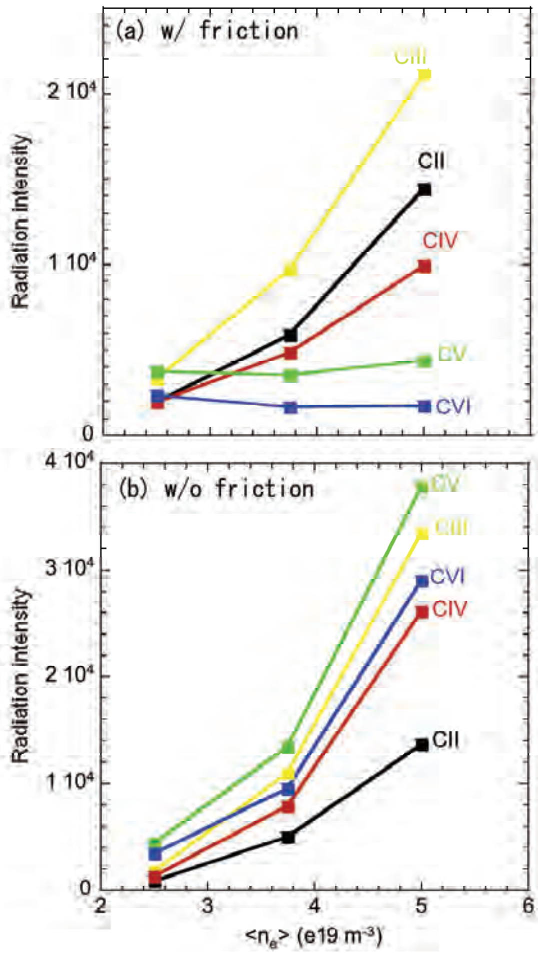

Fig. 6 (a) Radiation intensity from different charge states as a function of density. (b) Same as (a) but with $V_{i\parallel} = 0$ in impurity transport. black : CII, yellow : CIII, red : CIV, green : CV, blue : CVI.

tatively different behavior of CV and CVI, i.e. the radiation from higher charge states (CV and CVI) monotonically increases with increasing density. This is attributed to the large increase of C^{+4} and C^{+5} density at the inner radius of ergodic layer because of the lack of flushing effect by the bulk plasma flow.

The radiation intensity is measured in the experiments, using VUV monochromators and EUV spectrometer. It is found that the CII radiation is negligibly small in the experiments, while it has substantial intensity in the modelling. This is probably because in the modelling the divertor legs are neglected, which then allows the C^{+1} to reach the ergodic layer, while in experiments they are ionized much earlier downstream in the legs. The obtained line integrated intensity for different charge stages are plotted in Fig.7 as a function of density. In this plot, the sum of CIII (977 Å) & CIV (1548 Å) and CV (40.27 Å) & CVI (33.73 Å) are plotted rather than each. The radiation of individual charge states shows similar behavior as Fig.7. The CIII + CIV increases monotonically with increasing density, on the other hand the CV + CVI stays almost constant against density scan. These results are in qualitative agreement with the modelling with friction force, Fig.6 (a), and can be interpreted as a clear experimental evidence of impurity retention in the ergodic layer.

It should be noted that the effective impurity retention is also due to the geometrical advantage of the ergodic layer in LHD, where the edge surface layer surrounds the plasma in all poloidal and toroidal direction, and thus it can protect the plasma from the impurity neutrals coming from all direction, e.g. impurity released at the divertor plate by plasma flux or at the first wall by charge exchanged neutrals.

5 Implication for high Z impurity

From eq.(2), one sees that the balance between the first and second terms on the right hand side is independent of the charge Z, because $\tau_s \propto 1/Z^2$, which then cancels with the Z^2 at the numerator.

In order for the friction force to drive the impurity

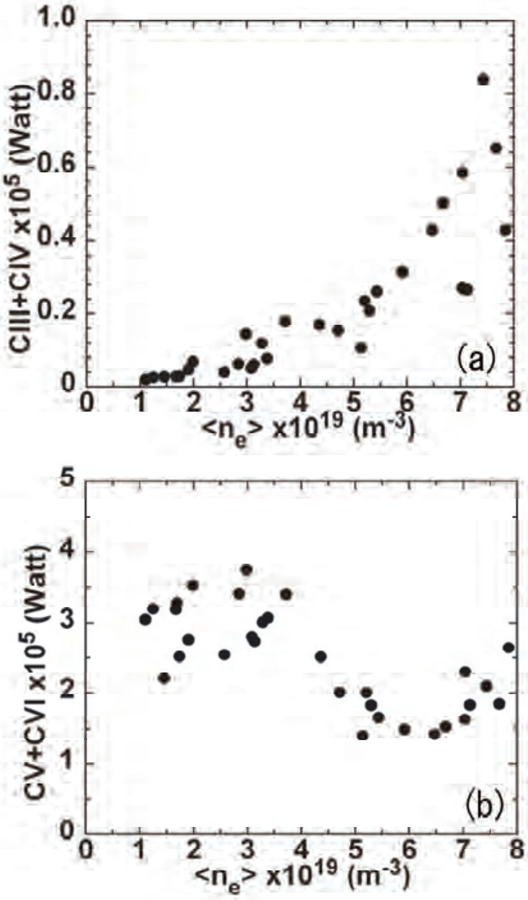

Fig. 7 Radiation intensity from different charge states as a function of density, measured by the VUV monochromators and EUV spectrometer. (a) CIII (977 Å) + CIV (1548 Å). (b) CV (40.27 Å) + CVI (33.73 Å).

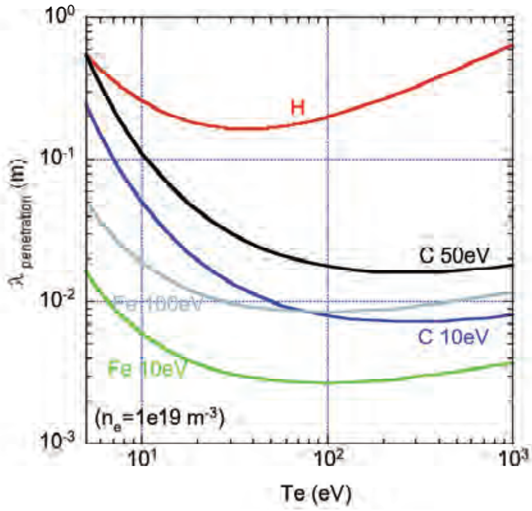

Fig. 8 Estimated neutral penetration length for hydrogen, carbon and iron, indicated with H, C and Fe, respectively.

to the downstream, the ionization location of impurity species, in the present case C^0, should be far downstream of that of the bulk plasma. The larger the separation between the source locations of impurity and bulk plasma is, the stronger the retention effect. Because of the lower ionization potential of carbon than that of hydrogen, this is usually the case unless the carbon is injected with very high energy. Figure 8 shows the estimated penetration length of neutral hydrogen, carbon and iron as a function of electron temperature. Due to the very low ionization potential of Fe^0, 7.9 eV, the penetration length of Fe is even shallower than carbon, indicating that the impurity retention model presented in section 3 could also apply.

Figure 9 shows the time trace of line radiation intensity of FeXX (132.85 Å) + FeXXIII (132.87 Å) measured by VUV spectrometer, for different plasma density, being normalized with n_e at the centre of plasma. From t = 1.0 s to 2.0 s, the plasma density and temperature was kept constant for each shot. The input power was fixed at ~ 8 MW. As the density increases, the normalized intensity decreases gradually, while the intensity at $n_{LCFS} = 3 \times 10^{19} m^{-3}$ shows strong increase in spite of the constant plasma parameters during flat top. The increase seems to continue further after t = 2 s, although the discharge was terminated just after 2 s. This increase indicates impurity accumulation at the core region. The similar behavior was observed in the low power discharge with ~ 1 MW [15]. Nevertheless, at the higher density of $n_{LCFS} = 4 \times 10^{19} m^{-3}$, the intensity is significantly suppressed and no such accumulation is observed. Compared to the low density case, the reduction is a factor of 5. With the increase of the density, the electron temperature at the centre of the plasma decreases from ~ 2 keV to ~ 1 keV, i.e. by a factor of 2, due to the fixed input power. However, taking into account the temperature dependence of the line intensity of FeXX (132.85 Å) + FeXXIII (132.87 Å), which is almost saturated around 1 to 2 keV, the reduction of the measured radiation (normalized by density) indicates reduction of Fe^{+19} and Fe^{+22} at the centre of plasma. Although in order to consistently analyze the transport of the high charge states of the iron we need to address the core impurity transport, the behavior is consistent with the prediction of the edge model in the section 3.

6 Summary

The impurity transport properties in the ergodic layer of LHD has been analyzed, using the edge transport code (EMC3-EIRENE) in comparison with experimental data. The 1D impurity transport model along field lines predicts the impurity retention (screening) when the plasma becomes dense and cold with substantial flow acceleration. This is demonstrated in the ergodic layer of LHD by the 3D numerical simulations. It is found that the edge surface layer plays an important role for the retention, where the ratio of friction force and the thermal force (eq.(3)) significantly increases due to the flow acceleration and the

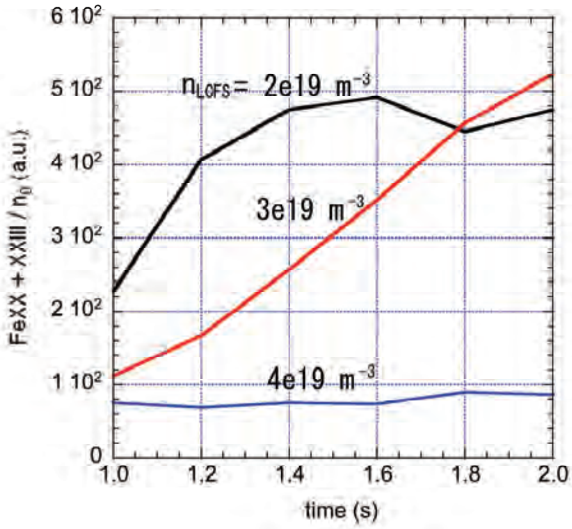

Fig. 9 Time traces of line intensity of FeXX (132.85 Å) + FeXXIII (132.87 Å) measured by VUV spectrometer for different density, at flat top discharge during t = 1 to 2 sec. The intensity is normalized with electron density at the centre of plasma.

temperature decrease. The carbon line radiation measurements is compared with the simulation results, where the good qualitative agreement is obtained with the modelling results with friction force, indicating the existence of impurity retention in the experiments. It should be noted that the retention effect is also due to the geometrical advantage of the magnetic field structure of ergodic layer in LHD, where the edge surface layer surrounds the plasma in all poloidal and toroidal directions. This structure efficiently stops the impurity originating from any locations, i.e. divertor or first wall.

Applicability of the model for the high Z impurity was discussed with respect to the charge dependence and the neutral impurity penetration distance. The brief estimation implies the mechanism could also apply for the high Z impurity. The behavior of measured line intensity of FeXX + FeXXIII against density change is consistent with the prediction of edge modelling. It is, however, necessary to address the core impurity transport properties in order to understand the behavior of high Z impurity, for which we still need further experimental as well as theoretical work.

Acknowledgements

The authors are grateful for the support for computational resource, AMD Opteron-InfiniBand Cluster Machine, by Grant-in-Aid for Science Research on Priority Areas (Area 465, No.18070005) from Ministry of Education, Culture, Sports, Science and Technology, Japan. The part of the computational work is also financially supported by the budget code NIFS07ULPP538. One of the authors, M.K., is grateful to N. Yamamoto for the fruitful discussion and the calculation for temperature dependence of line intensity of Fe.

[1] ITER Physics Basis Editors, Chapter 4, *"Power and particle control"*, Nucl. Fusion **47**, S203 (2007).
[2] P.C. Stangeby and J.D. Elder, Nucl. Fusion **35**, 1391 (1995).
[3] C. Breton et al., Nucl. Fusion **31**, 1774 (1991).
[4] M.Z. Tokar et al., Plasma Phys. Control. Fusion **39**, 569 (1997).
[5] M.Z. Tokar, Phys. Plasmas **6**, 2808 (1999).
[6] D.Kh. Morozov and J.J.E. Herrera, Phys. Plasmas **2**, 1540 (1995).
[7] H. Yamada et al., Plasma Phys. Control. Fusion **49**, B487 (2007).
[8] N. Ohyabu et al., Nucl. Fusion **34**, 387 (1994).
[9] Y. Feng et al., Contrib. Plasma Phys. **44**, 57 (2004).
[10] D. Reiter et al., Fusion Sci. Technol. **47**, 172 (2005).
[11] P.C. Stangeby, *The plasma boundary of magnetic fusion devices*, chap.6, (Institute of Plasma Publishing, 2000).
[12] Y. Feng et al., Nucl. Fusion **46**, 807 (2006).
[13] Yu. L. Igitkhanov, Contrib. Plasma Phys. **28**, 477 (1988).
[14] S. I. Krashenninikov et al., Nucl. Fusion **31**, 1455 (1991).
[15] Y. Nakamura et al., Nucl. Fusion **43**, 219 (2003).

Proceedings of ITC/ISHW2007

Gyrokinetic Studies of Ion Temperature Gradient Turbulence and Zonal Flows in Helical Systems

Hideo SUGAMA[1,2)], Tomo-Hiko WATANABE[1,2)], and Sergi FERRANDO-MARGALET[1)]

[1)] *National Institute for Fusion Science, Toki 509-5292, Japan*

[2)] *Graduate School for Advanced Studies (Sokendai), Toki 509-5292, Japan*

Gyrokinetic theory and simulation results are presented to investigate regulation of ion temperature gradient (ITG) turbulence due to $\mathbf{E}\times\mathbf{B}$ zonal flows in helical systems. In order to examine effects of changes in helical magnetic configuration on anomalous transport and zonal flows, magnetic field parameters representing the standard and inward-shifted configurations of the Large Helical Device (LHD) [O. Motojima, N. Ohyabu, A. Komori, *et al*., Nucl. Fusion **43**, 1674 (2003)] are used. The linear gyrokinetic analyses show that the largest growth rate of the linear ITG instability for the inward-shifted configuration is higher than that in the standard one while, for the former case, zonal flows generated by given sources decay more slowly because of lower radial drift velocities of helical-ripple-trapped particles than for the latter as theoretically predicted. It is shown from the gyrokinetic Vlasov simulation of the ITG turbulence that, in spite of the higher ITG-mode growth rate, the inward-shifted plasma takes a smaller average value of the ion thermal diffusivity in the steady turbulent state with a higher zonal-flow level. These results imply that neoclassical optimization contributes to reduction of the anomalous transport by enhancing the zonal-flow level and give a physical explanation for the confinement improvement observed in the LHD experiments with the inward plasma shift. When equilibrium radial electric fields produce poloidal $\mathbf{E}\times\mathbf{B}$ rotation of helically-trapped particles with reduced radial displacements, further enhancement of zonal flows and resultant transport reduction are theoretically expected.

Keywords: zonal flow, ITG turbulence, gyrokinetic simulation, helical system, LHD

1 Introduction

In fusion science, numerous theoretical and experimental works have been done on zonal flows which are now well known to play a critical role in regulation of turbulent transport in plasmas [1, 2]. Therefore, in order to improve plasma confinement in helical systems, where various geometrical configurations are explored [3, 4, 5, 6, 7], it is very important to elucidate effects of magnetic geometry on both microinstabilities and zonal flows. This work presents results from gyrokinetic theory and simulation to investigate regulation of ion temperature gradient (ITG) turbulence due to $\mathbf{E}\times\mathbf{B}$ zonal flows in helical systems.

It was shown in our previous papers [8, 9, 10, 11] that, in helical systems, zonal flows can be maintained for a longer time by reducing the radial drift velocities of particles trapped in helical ripples. This implies a possibility that helical configurations optimized for reducing the neoclassical transport can enhance zonal flows and accordingly lower the turbulent transport as well because the neoclassical particle and heat fluxes are also decreased by slowing down the radial drift of helical-ripple-trapped particles. In fact, it is observed in the Large Helical Device (LHD) [12] that not only neoclassical but also anomalous transport is reduced by the inward plasma shift [13] which decreases the radial particle drift but increases the unfavorable magnetic curvature to destabilize pressure-gradient-driven instabilities such as ITG modes. This reduction of anomalous transport by neoclassical optimization is a very attractive property of helical systems to recent researches on advanced concepts of helical devices [3, 4, 5, 6, 7]

It was shown by the ITG turbulence simulation in our previous work [10, 11], in which model helical fields for the standard and inward-shifted LHD configurations were used in the gyrokinetic Vlasov (GKV) code [14], that the turbulent ion thermal transport in the inward-shifted model, which has larger growth rates of the ITG stability, was considerably regulated by the zonal flows to a level comparable to the standard case although the thermal diffusivity χ_i for the inward-shifted case was slightly but still larger than for the standard case. However, in the recent GKV simulation with more accurate configuration models installed [15], we find that further stronger zonal-flow generation occurs and makes χ_i smaller for the inward-shifted configuration [16].

Recently, Mynick and Boozer [17] predicted by using the action-angle formalism that the collisionless residual zonal-flow level will be enhanced when the equilibrium radial electric field causes helical-ripple-trapped particles to follow closed poloidal orbits with small radial displacements. Here, our gyrokinetic theory of zonal-flow response is also extended to analytically derive detailed expressions for the effects of the equilibrium electric field on zonal flows in helical systems.

author's e-mail: sugama.hideo@LHD.nifs.ac.jp

2 Basic Equations

The nonlinear gyrokinetic equation for the perturbed ion gyrocenter distribution function $f_{i\mathbf{k}_\perp}$ with the wave number vector $\mathbf{k}_\perp$ perpendicular to the magnetic field $\mathbf{B}$ is written as

$$\begin{aligned}
&\left(\frac{\partial}{\partial t} + v_\parallel \mathbf{b}\cdot\nabla + i\omega_{Di}\right) f_{\mathbf{k}_\perp} \\
= \;& (-v_\parallel \mathbf{b}\cdot\nabla - i\omega_{Di} + i\omega_{*Ti})\left(F_0 J_0(k_\perp \rho)\frac{e\phi_{\mathbf{k}_\perp}}{T_i}\right) \\
&+\frac{c}{B}\sum_{\mathbf{k}'_\perp+\mathbf{k}''_\perp=\mathbf{k}_\perp}[\mathbf{b}\cdot(\mathbf{k}'_\perp\times\mathbf{k}''_\perp)]J_0(k'_\perp\rho)\phi_{\mathbf{k}'_\perp} f_{i\mathbf{k}''_\perp},
\end{aligned} \tag{1}$$

where F_0 is the local ion equilibrium distribution function that takes the Maxwellian form, $J_0(k_\perp\rho)$ is the zeroth-order Bessel function, $\rho = v_\perp/\Omega_i$ is the ion gyroradius, and $\Omega_i = eB/(m_i c)$ is the ion gyrofrequency. The two frequencies ω_{Di} and ω_{*i} are defined by $\omega_{Di} = \mathbf{k}_\perp\cdot\mathbf{v}_{Di}$ and by $\omega_{*Ti} = \omega_{*i}[1+\eta_i\{m_i v^2/2T_i - 3/2\}]$ respectively, where $\mathbf{v}_{Di} \equiv (c/eB)\mathbf{b}\times(e\nabla\Phi + \mu\nabla B + m_i v_\parallel^2 \mathbf{b}\cdot\nabla\mathbf{b})$ is the ion gyrocenter drift velocity, $\omega_{*i} \equiv \mathbf{k}_\perp\cdot(\mathbf{b}\times\nabla r)(cT_i/eB)(d\ln n_0/dr)$ is the ion diamagnetic frequency, and $\eta_i \equiv L_n/L_{Ti}$ is the ratio of the density gradient scale length $L_n \equiv -1/(d\ln n_0/dr)$ to the ion temperature gradient scale length $L_{Ti} \equiv -1/(d\ln T_i/dr)$. In Eq. (1), $f_{i\mathbf{k}_\perp}$ is regarded as a function of the kinetic energy $w \equiv \frac{1}{2}m_i v^2$, the magnetic moment $\mu \equiv m_i v_\perp^2/(2B)$, and the toroidal coordinates (r,θ,ζ), where r, θ, and ζ denote the flux surface label, the poloidal angle, and the toroidal angle, respectively. A closed system of equations to determine the perturbed ion distribution function $f_{i\mathbf{k}_\perp}$ and the electrostatic potential $\phi_{\mathbf{k}_\perp}$ in the ITG turbulence are given by Eq. (1) and the quasineutrality condition,

$$\int d^3v\, J_0 f_{i\mathbf{k}_\perp} - n_0\frac{e\phi_{\mathbf{k}_\perp}}{T_i}[1-\Gamma_0(b)] = n_0\frac{e}{T_e}\left(\phi_{\mathbf{k}_\perp} - \langle\phi_{\mathbf{k}_\perp}\rangle\right), \tag{2}$$

where $\langle\cdots\rangle$ represents the flux-surface average and $\Gamma_0(b)$ is defined by $\Gamma_0(b) \equiv I_0(b)e^{-b}$ with the zeroth-order modified Bessel function $I_0(b)$ and $b \equiv k_\perp^2 T_i/(m_i\Omega_i^2)$.

The magnetic field is written as $\mathbf{B} = \nabla\psi(r)\times\nabla(\theta - \zeta/q(r))$, where $2\pi\psi(r)$ is equal to the toroidal flux within the flux surface labeled r and $q(r)$ represents the safety factor. In the present work, the radial coordinate r is defined by $\psi = B_0 r^2/2$. Following Shaing and Hokin [18], we here consider helical systems with the magnetic field strength B written by

$$\begin{aligned}
B/B_0 &= 1 - \epsilon_{00}(r) - \epsilon_{10}(r)\cos\theta - \epsilon_{L0}(r)\cos(L\theta) \\
&\quad - \sum_{|n|\le n_{max}} \epsilon_h^{(n)}(r)\cos\{(L+n)\theta - M\zeta\} \\
&= 1 - \epsilon_{00}(r) - \epsilon_T(r,\theta) \\
&\quad - \epsilon_H(r,\theta)\cos\{L\theta - M\zeta + \chi_H(\theta)\},
\end{aligned} \tag{3}$$

Table 1 Parameters at the flux surface $r \simeq 0.6a$ in the standard and inward-shifted configurations.

	q	r/R_0	ϵ_t	ϵ_h/ϵ_t	ϵ_-/ϵ_t	ϵ_+/ϵ_t
standard	1.9	0.099	0.087	0.91	-0.28	0
inward	1.7	0.114	0.082	1.20	-0.74	-0.24
	s	$r\epsilon'_{00}/\epsilon_t$	$r\epsilon'_t/\epsilon_t$	$r\epsilon'_h/\epsilon_t$	$r\epsilon'_-/\epsilon_t$	$r\epsilon'_+/\epsilon_t$
standard	-0.85	0.22	1.02	1.96	-0.63	0
inward	-0.96	0.71	1.00	2.44	-0.36	-0.61

where

$$\begin{aligned}
\epsilon_T(r,\theta) &= \epsilon_{10}(r)\cos\theta + \epsilon_{L0}(r)\cos(L\theta), \\
\epsilon_H(r,\theta) &= \sqrt{C^2(r,\theta)+D^2(r,\theta)}, \\
\chi_H(r,\theta) &= \arctan[D(r,\theta)/C(r,\theta)], \\
C(r,\theta) &= \sum_{|n|\le n_{max}} \epsilon_h^{(n)}(r)\cos(n\theta), \\
D(r,\theta) &= \sum_{|n|\le n_{max}} \epsilon_h^{(n)}(r)\sin(n\theta),
\end{aligned} \tag{4}$$

and M (L) is the toroidal (main poloidal) period number of the helical field. In the present work, we use $L = 2$ and $M = 10$ to consider the LHD configurations. Here, we assume that $L/(qM) \ll 1$. Multiple-helicity effects can be included in the function $\epsilon_H(r,\theta)$. Hereafter, we put $\epsilon_{L0} = 0$, $n_{max} = 1$, and $\epsilon_{00} = 0$ (but $\epsilon'_{00} \equiv d\epsilon_{00}/dr \neq 0$) in Eq. (3) at the radial position r that we consider.

In order to model the standard and inward-shifted LHD configurations, we use numerical values shown in Table I for the safety factor q, the magnetic shear parameter $\hat{s}$, the inverse aspect ration r/R_0, the Fourier components of the field strength ($\epsilon_t \equiv \epsilon_{10}, \epsilon_h \equiv \epsilon_h^{(0)}, \epsilon_- \equiv \epsilon_h^{(-1)}, \epsilon_+ \equiv \epsilon_h^{(+1)}$), and their radial derivatives. The two sets of parameters in Table I for the standard and inward-shifted configurations are called S-B an I-B, respectively, in [15]. These parameters correspond to the flux surface at $r \simeq 0.6a$ (a : the plasma surface label) and they are taken from the vacuum magnetic field data, which describe the LHD configurations more accurately than the model field used in our previous study [10, 11]. The use of vacuum field data is justified because low beta plasmas are considered here.

3 Linear Analyses of ITG Modes and Zonal Flows

In this section, the linearized version of Eq. (1) and the quasineutrality condition given by Eq. (2) are numerically solved by using the GKV code in order to obtain the linear dispersion relation for the ITG instability and the zonal-flow response to the initial perturbation in the standard and inward-shifted configurations with the parameters shown in Table I.

3.1 Linear ITG instability

Figure 1 shows real frequencies and growth rates of the linear ITG instability as a function of the normalized poloidal wave number $k_\theta\rho_{ti}$ where $\rho_{ti} \equiv v_{ti}/\Omega_i$ is the ion thermal gyroradius. Here, $\eta_i \equiv L_n/L_{Ti} = 3$, $L_n/R_0 = 0.3$, $T_e/T_i = 1$, $\alpha \equiv \zeta - q\theta = 0$, and the parameters in Table I are used. The real frequencies and growth rates for the inward-shifted configuration take similar values to those for the standard configuration. Compared with the results in our previous work [10, 11], where simple model field parameters are used, the difference in the growth rates between the standard and inward-shifted configurations are reduced because of changes in values of q, $\hat{s}$ and magnetic curvature although the maximum growth rate for the latter case is still larger than for the former case.

3.2 Zonal-flow response

Collisionless time dependence of the zonal-flow potential, which has the wave number vector $\mathbf{k}_\perp = k_r\nabla r$ perpendicular to the flux surface, is analytically derived as [9]

$$\begin{aligned}
&\frac{e\phi_{\mathbf{k}_\perp}(t)}{T_i} \\
&= \mathcal{K}(t)\frac{e\phi_{\mathbf{k}_\perp}(0)}{T_i} + \frac{1}{n_0\langle k_\perp^2\rho_{ti}^2\rangle}\int_0^t dt'\ \mathcal{K}(t-t') \\
&\times\left\{1 - \frac{2}{\pi}\left\langle(2\epsilon_H)^{1/2}\left\{1 - g_{i1}(t-t',\theta)\right\}\right\rangle\right\}^{-1} \\
&\times\left\langle\int_{\kappa^2<1} d^3v\ e^{-ik_r\bar{v}_{dri}(t-t')}\ F_{i0}S_{i\mathbf{k}_\perp}(t')\right. \\
&\left. + \int_{\kappa^2>1} d^3v\ F_{i0}S_{i\mathbf{k}_\perp}(t')\left\{1 + ik_r\left(\Delta_r - \langle\Delta_r\rangle_{\rm po}\right)\right\}\right\rangle,
\end{aligned} \tag{5}$$

where $\mathcal{K}(t)$ is defined by

$$\mathcal{K}(t) = \mathcal{K}_{GAM}(t)[1 - \mathcal{K}_L(0)] + \mathcal{K}_L(t). \tag{6}$$

Here, $\mathcal{K}_{GAM}(t)$ and $\mathcal{K}_L(t)$ are written as

$$\mathcal{K}_{GAM}(t) = \cos(\omega_G t)\exp(\gamma t), \tag{7}$$

and

$$\mathcal{K}_L(t) \equiv \frac{1 - (2/\pi)\langle(2\epsilon_H)^{1/2}\{1 - g_{i1}(t,\theta)\}\rangle}{1 + G + \mathcal{E}(t)/\left(n_0\langle k_\perp^2\rho_{ti}^2\rangle\right)}, \tag{8}$$

respectively. Detailed definitions of variables in Eqs. (5)–(8) are found in [9]. In Eq. (7), the real frequency and damping rate of the geodesic acoustic mode (GAM) [19] are denoted by ω_G and $|\gamma| = -\gamma (> 0)$. Equation (6) represents that the GAM oscillations described by $\mathcal{K}_{GAM}(t)$ are superimposed around the averaged zonal-flow evolution expressed by $\mathcal{K}_L(t)$. We note that $\mathcal{K}(0) = 1$ and $\lim_{t\to+\infty}\mathcal{K}_{GAM}(t) = 0$. In Eq. (8), G represents the ratio of the neoclassical polarization due to toroidally trapped ions to the classical polarization while $\mathcal{E}(t)$ and $\{1-g_{i1}(t,\theta)\}$ are associated with the shielding caused by the radial drift of non-adiabatic helically trapped particles. We have $\mathcal{E} = 0$ and $g_{i1} = 1$ at $t = 0$ because helically trapped particles give no shielding before they begin radial drift. On the other hand, $\mathcal{E}$ approaches a finite value and $g_{i1} \simeq 0$ for $t \gg \tau_c = 1/(k_r v_{dr})$ where τ_c represents the characteristic time for the shielding due to helically-trapped particles to occur. The response kernel $\mathcal{K}_L(t)$ for the long-time behavior of the zonal-flow potential takes the constant limiting values,

$$\mathcal{K}_< \equiv \lim_{t/\tau_c\to+0}\mathcal{K}_L(t) = \frac{1}{1+G}, \tag{9}$$

and

$$\begin{aligned}
\mathcal{K}_> &\equiv \lim_{t/\tau_c\to+\infty}\mathcal{K}_L(t) \\
&= \langle k_\perp^2\rho_{ti}^2\rangle\left[1 - (2/\pi)\langle(2\epsilon_H)^{1/2}\rangle\right] \\
&\quad\times\left\{\langle k_\perp^2\rho_{ti}^2\rangle[1 - (3/\pi)\langle(2\epsilon_H)^{1/2}\rangle + G]\right. \\
&\quad\left. + (2/\pi)(1 + T_i/T_e)\langle(2\epsilon_H)^{1/2}\rangle\right\}^{-1}.
\end{aligned} \tag{10}$$

In Eq. (10), the term proportional to T_i/T_e is derived from taking account of the radial drift of helical-ripple-trapped electrons which cannot be described by the perturbed electron density model used in Eq. (2). Therefore, this term should be neglected when using Eq. (10) for comparison to numerical solutions of Eqs. (1) and (2).

Responses of the zonal-flow potential to the initial perturbation $\mathcal{K}(t) = \langle\phi_{\mathbf{k}_\perp}(t)\rangle/\langle\phi_{\mathbf{k}_\perp}(0)\rangle$ obtained by the linear gyrokinetic simulation for the standard and inward-shifted configurations are shown in Fig. 2, where the initial condition for the perturbed ion gyrocenter distribution function is given by $f_{i\mathbf{k}_\perp}(t = 0) = n_{\mathbf{k}_\perp}(t = 0)\exp(-m_i v^2/2T_i)$ with $n_{\mathbf{k}_\perp}(t = 0)$ determined from $\phi_{\mathbf{k}_\perp}(t = 0)$ through Eq. (2). Figure 2 also shows $\mathcal{K}_L(t)$ predicted by Eq. (8) for comparison to simulation results. We see that the change in the zonal-flow response $\mathcal{K}(t) = \langle\phi_{\mathbf{k}_\perp}(t)\rangle/\langle\phi_{\mathbf{k}_\perp}(0)\rangle$ between the standard and inward-shifted configurations are well described by $\mathcal{K}_L(t)$ except for the GAM oscillations. In order to measure the change in the zonal-flow response, we define the zonal-flow decay time as

$$\tau_{ZF} \equiv \int_0^{t_f}\langle\phi_{\mathbf{k}_\perp}(t)\rangle/\langle\phi_{\mathbf{k}_\perp}(0)\rangle, \tag{11}$$

where t_f represents the time at which the zonal flow reaches the final residual level and $t_f = 24R_0/v_{ti}$ is used in the present cases. Then, the simulation results give $\tau_{ZF} = 1.68\ R_0/v_{ti}$ for the inward-shifted case which is about 65% larger than $\tau_{ZF} = 1.02\ R_0/v_{ti}$ for the standard case. The increase in τ_{ZF} is attributed to the decrease in radial drift velocities of helical-ripple-trapped particles and the resultant delay in their shielding of the zonal-flow potential in the inward-shifted configuration. The improvement of the zonal-flow response due to the inward plasma shift was also found in our previous work [10, 11] using simpler configuration models although the degree of the improvement is more evident in the present study (see [15]).

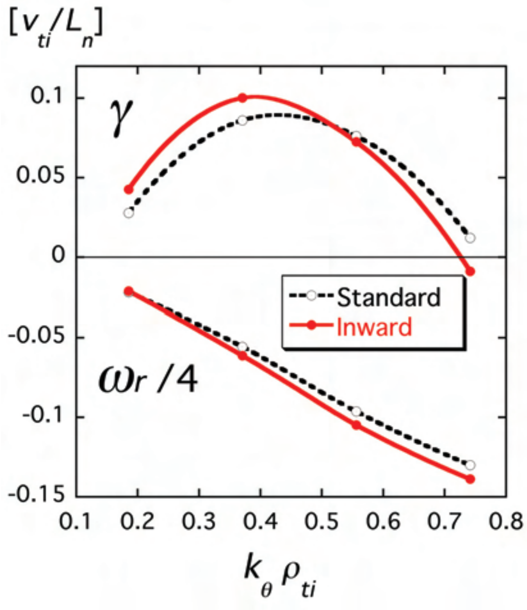

Fig. 1 Real frequencies and growth rates of the linear ITG instability as a function of the normalized poloidal wave number $k_\theta \rho_{ti}$ for the standard and inward-shifted configurations. Here, $\eta_i \equiv L_n/L_{Ti} = 3$, $L_n/R_0 = 0.3$, $T_e/T_i = 1$, $\alpha = 0$, and the parameters in Table I are used.

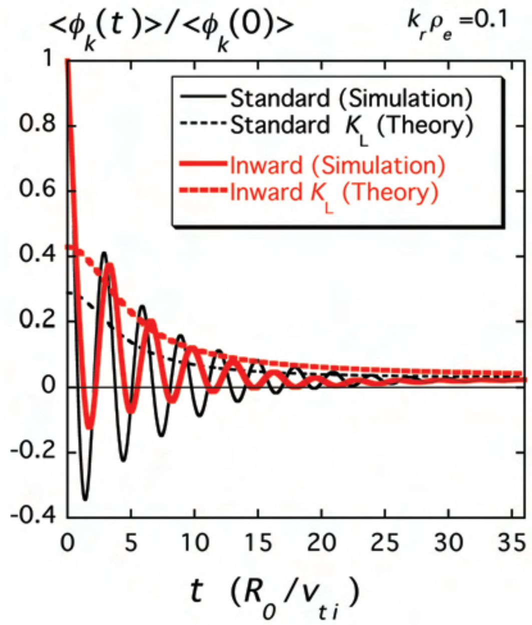

Fig. 2 Time evolution of the zonal-flow potential for the standard and inward-shifted configurations. Here, $k_r \rho_{ti} = 0.1$ is used. Solid curves are obtained from the linear gyrokinetic simulation. Dashed curves correspond to the long-time zonal-flow response kernel $K_L(t)$ in Eq. (8) which does not include the GAM oscillations.

4 Nonlinear Simulation of ITG Turbulence and Zonal Flows

This section presents nonlinear simulation results of the ITG turbulence and zonal flows obtained by solving Eqs. (1) and (2) with the GKV code (see also [16]). The GKV code employs the toroidal flux tube domain and we here use the same local plasma parameters ($\eta_i \equiv L_n/L_{Ti} = 3$, $L_n/R_0 = 0.3$, $T_e/T_i = 1$, and $\alpha = 0$) as in the linear calculations in Sec. 3.1. Figure 3 shows the turbulent ion thermal diffusivity χ_i as a function of time t obtained by the GKV simulation with the magnetic field data in Table I used for the standard and inward-shifted configurations. We see that, as expected from the results in Sec. 3.1, χ_i grows faster for the inward-shifted configuration in the early time stage ($t < 40L_n/v_{ti}$) than for the standard configuration and the peak value $\chi_i \simeq 3.8\rho_{ti}^2 v_{ti}/L_n$ for the former case is about 50% larger than the peak value $\chi_i \simeq 2.6\rho_{ti}^2 v_{ti}/L_n$ for the latter case. However, in later time ($t > 60L_n/v_{ti}$), the turbulent transport reaches statistically steady states and then the average ion thermal diffusivity $\chi_i \simeq 1.45\rho_{ti}^2 v_{ti}/L_n$ for the inward-shifted case is about 20% smaller than the average value $\chi_i \simeq 1.78\rho_{ti}^2 v_{ti}/L_n$ for the standard case. This reversal of the χ_i-value order results from a greater amount of zonal flows generated by turbulence in the inward-shifted plasma as seen below.

The GKV simulation shows that radially-elongated eddy structures (streamers) are first driven by the toroidal ITG instability although they are destroyed into small eddies by the self-generated $\mathbf{E} \times \mathbf{B}$ zonal flows in the later steady turbulent state [16]. The time-averaged spectrum of the zonal-flow potential ϕ_{k_x} is plotted in Fig. 4. It is found that the zonal-flow amplitude for $k_r \rho_{ti} \simeq 0.25$ in the inward-shifted configuration is about three times larger than that in the standard configuration. The stronger zonal-flow generation in the inward-shifted case is consistent with the larger zonal-flow decay time as mentioned in Sec. 3.2. A typical radial scale length of the zonal flows observed in the helical ITG simulations is shown to be shorter than those found in the tokamak ITG case for the Cyclone DIII-D base case parameters. Accordingly, the zonal-flow potential spectrum in the low k_r-region has relatively smaller amplitude than for the tokamak case. This tendency is also expected from the k_r-dependence of the zonal-flow response expressed in Eqs. (8) and (10).

5 Effects of Equilibrium Radial Electric Fields on Zonal Flows

So far, we have neglected effects of the equilibrium electrostatic potential $\Phi(r)$ which yields the radial electric field $\mathbf{E} = E_r \nabla r$ ($E_r = -d\Phi/dr$) and accordingly the $\mathbf{E} \times \mathbf{B}$ drift velocity $\mathbf{v}_E \equiv (c/B)E_r \nabla r \times \mathbf{b}$ in the direction tangential to the flux surface. Regarding the ITG modes, $\mathbf{v}_E$ will just give the Doppler shift $\mathbf{k}_\perp \cdot \mathbf{v}_E$ to the real frequencies without changing the growth rates. For the zonal-flow components with $\mathbf{k}_\perp = k_r \nabla r$, at first, the equilibrium electric field does not seem to influence the zonal-flow response

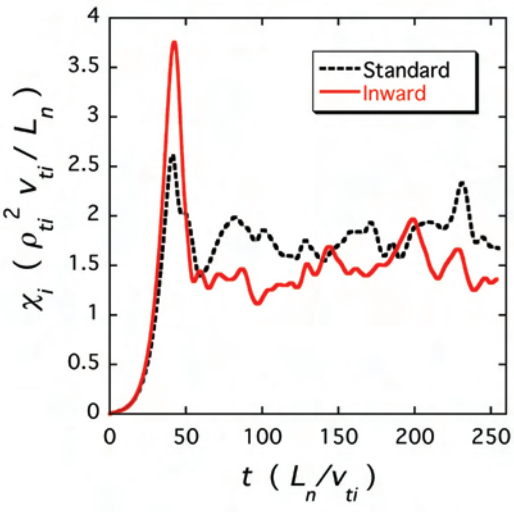

Fig. 3 Time evolution of the ion thermal diffusivity χ_i obtained by the ITG turbulence simulations for the standard and inward-shifted configurations.

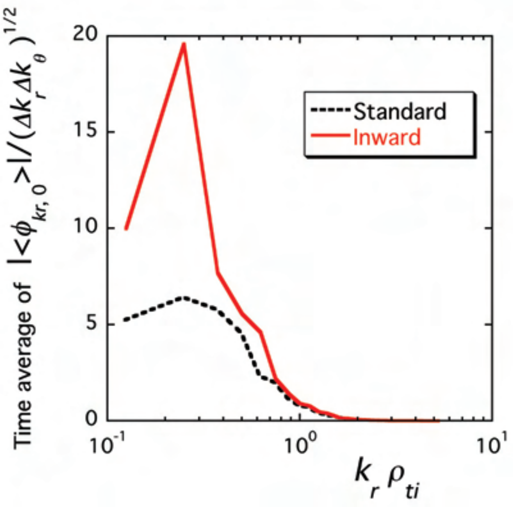

Fig. 4 Time-averaged radial-wave-number spectrum of the zonal-flow potential obtained by the ITG turbulence simulations for the standard and inward-shifted configurations. The time average is taken over $60 \le v_{ti}t/L_n \le 250$.

because $\mathbf{k}_\perp \cdot \mathbf{v}_E = 0$. However, when treating helical configurations, we find subtle points about the above argument with respect to the zonal-flow response. In the previous sections, we have used the ballooning representation and the local flux tube model, in which only the neighborhood of a single field line labeled by $\alpha \equiv \zeta - q(r)\theta$ is considered. For helical systems, the field line label α explicitly appears in the gyrokinetic equation in contrast to tokamak cases although we have so far regarded α as a fixed parameter based on the above-mentioned local model. But, even if the zonal-flow potential ϕ is independent of α, the explicit appearance of α in the magnetic drift terms of the gyrokinetic equation causes the perturbed gyrocenter distribution function δf to depend on α. Therefore, in helical configurations, we generally have $\mathbf{v}_E \cdot \nabla \delta f \neq 0$ so that the zonal-flow response can be affected by the existence of the equilibrium electric field.

Compared with passing and toroidally trapped particles, helical-ripple-trapped particles will have their orbits changed more greatly by the equilibrium radial electric field E_r. The radial displacements of helical-ripple-trapped particles are significantly reduced when the $\mathbf{E} \times \mathbf{B}$ drift due to E_r generates their rapid poloidal rotations as shown in Fig. 5. For such cases, neoclassical ripple transport is reduced and, in addition, higher zonal-flow responses are expected because the shielding of the zonal-flow potential by the helically-trapped particles is weakened. This scenario was first presented by Mynick and Boozer [17], who employed the action-angle formalism and pointed out the analogy between the mechanisms of zonal-flow shielding and neoclassical transport.

Taking account of the dependence of the perturbed distribution function on the field line label α, our formulation of zonal-flow response is extended to derive detailed expressions for the E_r effects on the zonal-flow response. We now assume the bounce centers of helically-trapped particles to draw poloidally-closed orbits with the poloidal angular velocity $\omega_\theta \equiv -cE_r/(rB_0)$. Furthermore, considering the helical configuration with the single-helicity component, for which $\epsilon_H = \epsilon_h$ is independent of θ, we find that, for $t \gg 1/\omega_\theta$, the shielding term $\mathcal{E}$ due to the helically-trapped particles in Eq. (8) is replaced with $\mathcal{E}_{Er}$ defined by

$$\mathcal{E}_{Er} = \frac{15}{8\pi}(2\epsilon_h)^{1/2}(k_r\rho_{ti})^2\left(\frac{\epsilon_t v_{ti}}{r\omega_\theta}\right)^2\left(1+\frac{T_e}{T_i}\right) \tag{12}$$

Using Eq. (12), the collisionless long-time limit of the zonal-flow response kernel, which represents the residual zonal flow level, is now given not by Eq. (10) but by

$$\mathcal{K}_{Er} = \frac{1}{1+G+\mathcal{E}_{Er}/(k_r\rho_{ti})^2} = \left[1+G+\frac{15}{8\pi}(2\epsilon_h)^{1/2}\left(\frac{\epsilon_t v_{ti}}{r\omega_\theta}\right)^2\left(1+\frac{T_e}{T_i}\right)\right]^{-1} \tag{13}$$

We see that, as E_r increases, $\mathcal{K}_{Er}$ increases and approaches the same value $1/(1+G)$ as in Eq. (9) because $\mathcal{E}_{Er}$ is inversely proportional to the square of E_r. It is noted that $\mathcal{E}_{Er}/k_r^2$ given from Eq. (12) corresponds to the product of the helically-trapped-particles' fraction ($\sim \epsilon_h^{1/2}$) and the square of the radial orbit width $\Delta_E (\propto 1/\omega_\theta \propto 1/E_r)$ of helically-trapped-particles' poloidal rotation (see Fig. 5), which agrees with Mynick and Boozer [17]. In helical configurations such as the inward-shifted LHD case, which are optimized for reduction of neoclassical transport, the enhancement of zonal-flow response due to E_r is expected to work more effectively than in others because the neoclassical optimization reduces radial displacements Δ_E of helically-trapped particles during their poloidal $\mathbf{E} \times \mathbf{B}$ rotation.

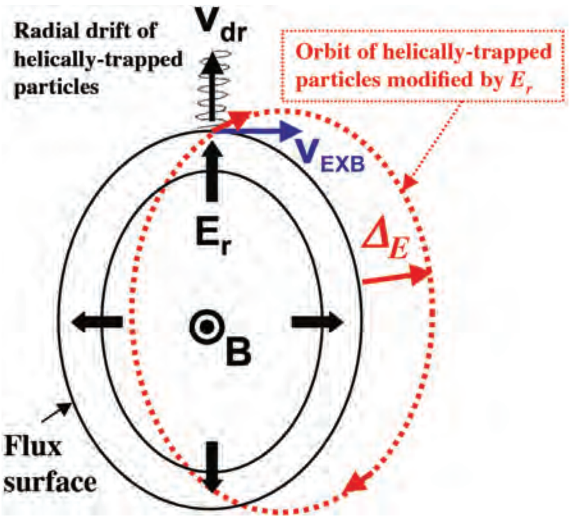

Fig. 5 Orbit of bounce-center motion of helical-ripple-trapped particles modified by the radial electric field E_r. Here, Δ_E represents the radial displacement of the orbit.

6 Conclusions

In the present work, effects of changes in helical magnetic configuration on anomalous transport and zonal flows are investigated based on gyrokinetic theory and simulation of ITG turbulence and zonal flows. In order to represent a specific flux surface ($r \simeq 0.6a$) in the standard and inward-shifted LHD configurations, magnetic parameters such as the Fourier components of the field strength, their radial derivatives, the safety factor, and the magnetic shear are used, which describe the configurations more accurately than our previous model parameters. We find from the linear analyses that the largest growth rate of the linear ITG instability for the inward-shifted configuration is slightly higher than that in the standard one while, for the former case, the zonal-flow response is more favorable to generation of low-frequency zonal flows because of lower radial drift velocities of helical-ripple-trapped particles than for the latter as theoretically predicted. The nonlinear gyrokinetic simulation shows that the turbulent ion thermal diffusivity χ_i for the inward-shifted plasma takes a higher peak value in the early time stage but a lower average value in the later steady turbulent state with stronger zonal-flow generation. Thus, it is confirmed that neoclassical optimization contributes to reduction of the anomalous transport by enhancing the zonal-flow level. This presents a physical mechanism to explain the confinement improvement observed in the LHD experiments with the inward plasma shift. Also, further enhancement of zonal flows and resultant transport reduction are theoretically expected when the equilibrium radial electric field E_r causes poloidal $\mathbf{E} \times \mathbf{B}$ rotation of helically-trapped particles with reduced radial displacements. Simulation studies on the E_r effects require global treatment in the direction parallel to the $\mathbf{E} \times \mathbf{B}$ drift velocity and remain as a future task.

Acknowledgments

This work is supported in part by the Japanese Ministry of Education, Culture, Sports, Science and Technology, Grant Nos. 16560727, 17360445, and 17·05373, and in part by the NIFS Collaborative Research Program, NIFS06KDAD006, NIFS06KNXN060 and NIFS06KTAT038. Numerical simulations were carried out with the use of the Earth Simulator under the support from the Japan Agency for Marine-Earth Science and Technology, and with the use of the Plasma Simulator and the LHD numerical analysis system at the National Institute for Fusion Science.

[1] P. H. Diamond, S.-I. Itoh, K. Itoh, and T. S. Hahm, Plasma Phys. Controlled Fusion **47**, R35 (2005).
[2] K. Itoh, S.-I. Itoh, P. H. Diamond, *et al.*, Phys. Plasmas **13**, 055502 (2006).
[3] M. Yokoyama, J. Plasma Fusion Res. **78**, 205 (2002).
[4] H. E. Mynick, Phys. Plasmas **13**, 058102 (2006).
[5] D. A. Spong, S. P. Hirshman, L. A. Berry, *et al.*, Nucl. Fusion **41**, 711 (2001).
[6] J. N. Talmadge, V. Sakaguchi, F. S. B. Anderson, *et al.*, Phys. Plasmas **9**, 5165 (2001).
[7] G. Grieger, W. Lotz, P. Merkel, *et al.*, Phys. Fluids B **4**, 2081 (1992).
[8] H. Sugama and T.-H. Watanabe, Phys. Rev. Lett. **94**, 115001 (2005).
[9] H. Sugama and T.-H. Watanabe, Phys. Plasmas **13**, 012501 (2006); H. Sugama and T.-H. Watanabe, *ibid.* **14**, 079902 (2007).
[10] T.-H. Watanabe and H. Sugama, 21th IAEA Fusion Energy Conference (Chengdu, China, 2006), EX/5-4.
[11] T.-H. Watanabe, H. Sugama, and S. Ferrando-Margalet, Nucl. Fusion **47**, 1383 (2007).
[12] O. Motojima, N. Ohyabu, A. Komori, *et.al.*, Nucl. Fusion **43**, 1674 (2003).
[13] H. Yamada, *et al.*, Plasma Phys. Controlled Fusion **43**, A55 (2001).
[14] T.-H. Watanabe and H. Sugama, Nucl. Fusion **46**, 24 (2006).
[15] S. Ferrando-Margalet, H. Sugama, and T.-H. Watanabe, "*Zonal flows and ion temperature gradient instabilities in multiple-helicity magnetic fields*", to be published in Phys. Plasmas.
[16] T.-H. Watanabe, H. Sugama, and S. Ferrando-Margalet, *Joint Conference of 17th International Toki Conference on Physics of Flows and Turbulence in Plasmas and 16th International Stellarator/Heliotron Workshop 2007* (Toki, Japan, 2007), P2-06.
[17] H. E. Mynick and A. H. Boozer, Phys. Plasmas **14**, 072507 (2007).
[18] K. C. Shaing and S. A. Hokin, Phys. Fluids **26**, 2136 (1983).
[19] N. Winsor, J. L. Johnson, and J. J. Dawson, Phys. Fluids **11**, 2248 (1968).

Proceedings of ITC/ISHW2007

Zonal flows in 3D toroidal systems

H. E. MYNICK[1)], and A. H. BOOZER[2)]

[1)]*Plasma Physics Laboratory, Princeton University, Princeton, NJ, USA*
[2)]*Dept. of Applied Physics & Mathematics, Columbia University, New York City, NY, USA*

(Received 12 October, 2007)

A range of techniques for mitigating stellarator neoclassical (nc) transport has been developed, and attention is now turning to also reducing the turbulent transport fluxes. As for tokamaks, zonal flows (ZFs) will be an important tool in achieving this, and understanding the effect of machine geometry on these is important. This paper discusses a theory of the shielding and time evolution of zonal flows in stellarators and tokamaks, which attains greater generality and conciseness by use of the action-angle formalism. The theory supports the earlier perspective that neoclassically-optimized devices should have less ZF damping, but it is pointed out that the further view, that this implies that optimized devices should therefore also have less turbulent transport, is overly simplistic, neglecting the additional configuration dependence of the nonlinear source which drives the ZFs.

Keywords: stellarators, zonal flows, transport, turbulence, action-angle variables

DOI: 10.1585/pfr.1.001

Since the 1980s, a range of techniques for mitigating stellarator neoclassical (nc) transport has been developed, and attention is now turning to also reducing the turbulent transport fluxes. As for tokamaks, an important tool for achieving this will be producing strong zonal flows (ZFs), which can act to suppress the turbulence producing the transport. It is thus of interest to understand how machine geometry will affect the strength of these flows, and their effectiveness in suppressing turbulent transport. This paper describes an analytic study of the shielding and time evolution of ZFs in stellarators and tokamaks,[1] discusses some of its implications, and its context in recent work on ZFs.

ZFs are primarily poloidal $E \times B$ flows due to a radially-varying electrostatic potential $\phi_z(r,t)$ driven by the nonlinearity in the kinetic equation. For present purposes, this is the Vlasov equation,

$$(\partial_t + \hat{H}_0)\delta f(\mathbf{z}, t) = -\hat{h} f_0 - \hat{h}\delta f, \tag{1}$$

with nonlinearity $-\hat{h}\delta f \equiv -\{\delta f, h\}$. Here, $\hat{b}a \equiv \{a, b\}$ is the Poisson bracket of $a(\mathbf{z})$ with $b(\mathbf{z})$ in the 6-dimensional phase space $\mathbf{z}$, and the Hamiltonian $H(\mathbf{z}, t) = H_0 + h$ and distribution function $f(\mathbf{z}, t) = f_0 + \delta f$ are divided into their unperturbed (subscript 0) and perturbed portions, with f_0 satisfying $\hat{H}_0 f_0 = 0$. Here we consider electrostatic perturbations only, $h(\mathbf{z}, t) = e\delta\phi(\mathbf{r}, t)$, where $\mathbf{r}(\mathbf{z})$ is the particle position. The dynamics of ZFs are determined by a self-consistent loop between ϕ_z and the potential fluctuations $\phi_\mathbf{k}$ of the turbulence. Via the nonlinearity in Eq.(1), the $\phi_\mathbf{k}$ produce a source $S \sim |\phi_\mathbf{k}|^2$ for ϕ_z, which in turn affects the growth and amplitudes of the $\phi_\mathbf{k}$.[2, 3, 4] The theory developed in Ref. [1] follows earlier work[5, 6, 7, 8] in primarily addressing the former of these 2 legs of the loop, taking the nonlinearity $-\hat{h}\delta f$ as a known source $S f_0$ and computing the resultant ϕ_z as a linear response problem, $k^2\phi_z = 4\pi\delta\rho^{xt}/\mathcal{D}$, where $\delta\rho^{xt}$ is the *ext*ernal charge-density perturbation driven by S, $\delta\rho^{xt} \sim \int dt S(t)$, and $\mathcal{D}$ is the dielectric function. Regarding the latter leg, the effect of machine geometry on S is relatively unexplored to date, but is an important issue in understanding the overall dynamics. This is discussed further later in this paper.

In Ref. [1] the action-angle (aa) formalism[9] was used to solve the kinetic equation without expansion of that equation in small parameters of radial excursions and timescale, resulting in more general expressions for the dielectric shielding, and extending results from earlier work.[5, 6, 7, 8, 10] From these expressions, it was found that for each mechanism of collisional transport, there is a corresponding shielding mechanism, of closely related form and scaling. Assuming the amplitude of the nonlinear source is unchanged, this correspondence supports the suggestion raised in earlier work[11, 6, 12, 10] that neoclassically-optimized stellarators will also have larger ZFs, and consequently lower turbulent transport. On a longer, diffusive timescale, ZF evolution was shown to be governed by a Langevin-like equation, with radial electric field $E_r(t)$ moving diffusively about roots E_a of the ambipolarity equation. The resultant probability distribution function is bounded, a balance between the turbulent fluctuations inducing diffusion and the neoclassical fluxes providing a restoring force toward $E_r = E_a$. A fuller exposition of the analytic theory is given in Ref. [1]. Here we recap the elements of that theory, and discuss some of its implications and related issues yet to be addressed.

Action-Angle formalism

In the aa formalism one parametrizes phase points $\mathbf{z}$ with the 3 invariant actions $\mathbf{J}$ of the unperturbed motion and their 3 conjugate angles $\boldsymbol{\theta}$, instead of the more directly physical particle position $\mathbf{r}$ and momentum $\mathbf{p}$. The unper-

author's e-mail: mynick@pppl.gov

turbed Hamiltonian is then independent of $\boldsymbol{\theta}$, $H_0 = H_0(\mathbf{J})$. The key feature of aa variables is that they make the description of particle motion very simple. Hamilton's equations are:

$$\begin{aligned} \dot{\boldsymbol{\theta}} &= \partial_{\mathbf{J}} H = \boldsymbol{\Omega}(\mathbf{J}) + \partial_{\mathbf{J}} h \simeq \boldsymbol{\Omega}(\mathbf{J}), & (2) \\ \dot{\mathbf{J}} &= -\partial_{\boldsymbol{\theta}} h = -i \sum_{\mathbf{l}} \mathbf{l} h_{\mathbf{l}}(\mathbf{J}, t) \exp(i\mathbf{l} \cdot \boldsymbol{\theta}), & (3) \end{aligned}$$

where $\partial_{\mathbf{J}}$ ($\partial_{\boldsymbol{\theta}}$) denotes a gradient in $\mathbf{J}$ (θ)-space, $\boldsymbol{\Omega}(\mathbf{J}) \equiv \partial_{\mathbf{J}} H_0$, and $\mathbf{l}$ is the 3-component vector index, specifying the harmonic of each component of $\boldsymbol{\theta}$ in the Fourier decomposition $h(\mathbf{z}) = \sum_{\mathbf{l}} h_{\mathbf{l}}(\mathbf{J}) \exp(i\mathbf{l} \cdot \boldsymbol{\theta})$.

Following Refs. [5, 6, 7] in replacing the nonlinear term $-\{\delta f, h\}$ with a specified source $S(\mathbf{z}, t) f_0$, and Laplace transforming in time and Fourier transforming in $\boldsymbol{\theta}$, one readily obtains a solution for δf, nonperturbative in the excursions made in a particle orbit,

$$\begin{aligned} \delta f_{\mathbf{l}}(\mathbf{J}, \omega) &= G_0[i\mathbf{l} \cdot \partial_{\mathbf{J}} f_0 h_{\mathbf{l}}(\mathbf{J}, \omega) + \\ &\quad \delta f_{\mathbf{l}}(\mathbf{J}, t = 0) + S_{\mathbf{l}}(\mathbf{J}, \omega) f_0], \quad (4) \end{aligned}$$

with propagator $G_0 \equiv (-i\omega + i\mathbf{l} \cdot \boldsymbol{\Omega} + \nu_f)^{-1}$, in which we include an effective damping rate ν_f, to later consider the effect of collisions. Inserting Eq.(4) into the expression for the charge density, (now showing species label s) $\delta\rho_s(\mathbf{x}) = \int d\mathbf{z} \rho(\mathbf{x}|\mathbf{z}) \delta f_s(\mathbf{z})$, where $\rho(\mathbf{x}|\mathbf{z}) \equiv e_s \delta(\mathbf{x} - \mathbf{r}(\mathbf{z}))$ is the charge density kernel and e_s is the species charge, one obtains 3 contributions, labelled A, B, and C, corresponding to the 3 terms on the right side of (4):

$$\begin{aligned} \delta\rho_{sA}(\mathbf{x}, \omega) &= \int d\mathbf{x}' K_s(\mathbf{x}, \mathbf{x}', \omega) \delta\phi(\mathbf{x}', \omega) \quad (5) \\ \delta\rho_{s,B+C}(\mathbf{x}, \omega) &= (2\pi)^3 \int d\mathbf{J} \sum_{\mathbf{l}} \rho_{\mathbf{l}}^*(\mathbf{x}|\mathbf{J}) G_0 \times \\ &\quad [\delta f_{s\mathbf{l}}(\mathbf{J}, t = 0) + S_{s\mathbf{l}}(\mathbf{J}, \omega) f_{s0}], (6) \end{aligned}$$

with response kernel[9]

$$\begin{aligned} K_s(\mathbf{x}, \mathbf{x}', \omega) &= K_s^{ad}(\mathbf{x}, \mathbf{x}') + (2\pi)^3 \int d\mathbf{J} \sum_{\mathbf{l}} \times \\ &\quad \rho_{\mathbf{l}}^*(\mathbf{x}|\mathbf{J}) \frac{\omega \partial_{H_0} f_{s0} + \mathbf{l} \cdot \partial_{\mathbf{J}})_{H_0} f_{s0}}{\mathbf{l} \cdot \boldsymbol{\Omega} - \omega - i\nu_f} \rho_{\mathbf{l}}(\mathbf{x}'|\mathbf{J}). \quad (7) \end{aligned}$$

$\delta\rho_{sA}$, proportional to h or $\delta\phi$, gives the self-consistent response of the plasma, with response kernel K_s. $\delta\rho_{sB}$, due to the initial conditions of δf, gives the transient ballistic response, and the third term, $\delta\rho_{sC}$, is due to the nonlinear drive. $K_s^{ad}(\mathbf{x}, \mathbf{x}') \equiv e_s \delta(\mathbf{x} - \mathbf{x}') \int d\mathbf{z} \rho(\mathbf{x}|\mathbf{z}) \partial_{H_0} f_{s0}$ is the (generalized) adiabatic term, reducing to the usual adiabatic term when f_0 is specialized to the local Maxwellian form

$$f_M(\mathbf{J}) \equiv \frac{n_0}{(2\pi M T)^{3/2}} \exp[-(H_0 - e\Phi_a)/T), \quad (8)$$

where density n_0, ambipolar radial potential Φ_a, and temperature T are functions of the drift-averaged minor radius $r_d(\mathbf{J})$, and M is the particle mass.

Specialization to Toroidal Geometry

The expressions given thus far are valid for any system where a complete set $\mathbf{J}$ of constants of the motion exists. We now specialize to toroidal geometries, including tokamaks and stellarators. We represent position in terms of flux coordinates $\mathbf{r} = (\psi, \theta, \zeta)$, where $2\pi\psi$ is the toroidal flux within a flux surface, and θ and ζ are the poloidal and toroidal azimuths. In terms of these, the magnetic field may be written $\mathbf{B} = \nabla\psi \times \nabla\theta + \nabla\zeta \times \nabla\psi_p = \nabla\psi \times \nabla\alpha_p$, with $2\pi\psi_p$ the poloidal flux, Clebsch angle $\alpha_p \equiv \theta - \iota\zeta$, constant along a field line, and $\iota \equiv q^{-1} \equiv d\psi_p/d\psi$ the rotational transform. α_p and momentum $(e/c)\psi$ form a canonically conjugate pair for motion perpendicular to the field line. It is also useful to define an average minor radius $r(\psi)$ by $\psi \equiv \bar{B}_0 r^2/2$, with $\bar{B}_0 \equiv \bar{B}(r = 0)$ the average magnetic field strength on axis. We consider toroidal systems with the nonaxisymmetric portion of magnetic field strength B dominated by a single helical phase $\eta_0 \equiv n_0\zeta - m_0\theta$,

$$B(\mathbf{x}) = \bar{B}(r)[1 - \epsilon_t(r)\cos\theta - \delta_h(\mathbf{x})\cos\eta_0], \quad (9)$$

but with ripple strength $\delta_h(\mathbf{x})$ allowed to vary slowly over a flux surface, with flux-surface average $\epsilon_h(r) \equiv \langle\delta_h\rangle$.

In such configurations, collisionless particle motion occurs on 3 disparate timescales, the gyro, transit/bounce, and perpendicular drift scales, denoted by subscripts g, b, and d. The characteristic gyro, bounce, and drift frequencies satisfy $\Omega_g \ll \Omega_b \ll \Omega_d$, and the corresponding radial excursions particles make on those scales are the gyroradius $\rho_g = v_\perp/\Omega_g$, the radial bounce excursion/banana width $\rho_b \simeq v_{Bt}/\Omega_b$, and the "superbanana width" excursion $\rho_d \simeq \sigma_h v_{Bt}/\Omega_d$. Here, $v_{Bt} = \epsilon_t \mu \bar{B}/(M\Omega_g r)$ is the grad-B drift amplitude, μ is the magnetic moment, and σ_h equals 1 for a ripple-trapped particle (in trapping state $\tau = h$), and 0 otherwise. Thus, passing or toroidally-trapped particles ($\tau = p$ and t, resp.) have $\rho_d = 0$.

The aa variables can be chosen so that motion on each timescale can be described by one of the 3 pairs (θ_i, J_i). A suitable choice is $\boldsymbol{\theta} = (\theta_g, \theta_b, \bar{\alpha}_p)$, $\mathbf{J} = (J_g, J_b, (e/c)\bar{\psi})$, with $J_g \equiv (Mc/e)\mu$ the gyroaction, θ_g the gyrophase, describing the fastest time scale of the motion, J_b the bounce action, θ_b its conjugate bounce phase, $\bar{\psi}$ the drift-orbit averaged value of ψ, and its conjugate phase $\bar{\alpha}_p$, the orbit-averaged Clebsch coordinate α_p, describing the slow, drift timescale. To make the periodicity of the drift angle 2π as for the other 2 phases, instead of $(\bar{\alpha}_p, (e/c)\bar{\psi})$ we use the closely related canonical pair $(\theta_d, J_d = (e/c)\bar{\psi}_d)$, with $\theta_d \equiv \bar{\alpha}_p/(1 - \iota q_{mn0})$, $\bar{\psi}_d \equiv \bar{\psi} - \bar{\psi}_p q_{mn0}$, where $q_{mn0} \equiv m_0/n_0$. For typical parameters, $\iota q_{mn0} \ll 1$, so that $(\theta_d \simeq \bar{\alpha}_p, \bar{\psi}_d \simeq \bar{\psi})$. Correspondingly one has the characteristic frequencies of motion $\boldsymbol{\Omega} \equiv (\Omega_g, \Omega_b, \Omega_d)$, and vector index $\mathbf{l} \equiv (l_g, l_b, l_d)$.

We adopt an eikonal form for the structure of any mode a,

$$\phi_a(\mathbf{x}) = \bar{\phi}_a(r) \exp i\eta_a(\mathbf{x}), \quad (10)$$

with wave phase $\eta_a(\mathbf{x}) \equiv [\int^r dr' k_r(r') + m\theta + n\zeta]$, and slowly-varying envelope $\bar{\phi}_a(r)$. Then using Eqs. (5,6,7), and (10) in the Poisson equation, one obtains the radially-local response equation[1]:

$$k^2\mathcal{D}(\mathbf{k},\omega)\frac{e_i\phi_a(r)}{T_i} = \sum_s \lambda_{si}^{-2}\sum_{\mathbf{l}}\langle G^*_{\mathbf{l}a}(\mathbf{J})\times \frac{i[\delta f_{s\mathbf{l}}(t=0)/f_{s0} + S_{s\mathbf{l}}(\omega)]}{(\omega - \mathbf{l}\cdot\mathbf{\Omega} + i\nu_{fs})}\rangle \qquad (11)$$

Here, $\lambda_{si}^2 \equiv T_i/(4\pi n_{s0}e_s e_i)$, $k^2 \equiv |\mathbf{k}|^2$, $\langle\ldots\rangle \equiv (2\pi)^{-2}\oint d\theta d\zeta \int d\mathbf{p}(f_0/n_0)\ldots$ is the flux surface and momentum-space average over the unperturbed distribution function f_0, $G_{\mathbf{l}a}(\mathbf{J}) \equiv (2\pi)^{-3}\oint d\boldsymbol{\theta}\exp(-i\mathbf{l}\cdot\boldsymbol{\theta})\exp i\delta\eta_a(\mathbf{z})$ the "orbit-averaging factor", a concise expression for the interaction of mode a with particles with actions $\mathbf{J}$, and $\delta\eta_a$ the portion of η_a oscillatory in $\boldsymbol{\theta}$ (so having zero $\boldsymbol{\theta}$–average). Dielectric function $\mathcal{D}$ is given by $\mathcal{D}(\mathbf{k},\omega) \equiv 1 + \sum_s \chi_s(\mathbf{k},\omega)$, with susceptibility $\chi_s(\mathbf{k},\omega) = (k\lambda_s)^{-2}g_s(\mathbf{k},\omega))$, and shielding function

$$g_s(\mathbf{k},\omega) = 1 - \sum_{\mathbf{l}}\langle|G_{\mathbf{l}a}(\mathbf{J})|^2\frac{\omega - \omega^f_{*s}}{\omega - \mathbf{l}\cdot\mathbf{\Omega} + i\nu_{fs}}\rangle. \quad (12)$$

Here, $\omega^f_* \equiv \omega_*[1 + \eta(u^2 - 3)/2]$, with $\omega_* \equiv -k_\alpha cT/(eBL_n)$ the diamagnetic drift frequency, $\eta \equiv d\ln T/d\ln n$, $u \equiv v/v_s$ the particle velocity, normalized to the thermal speed v_s, $k_\alpha \equiv l_d/r$, and $L_n^{-1} \equiv -\partial\ln n_0/\partial r$. The 1 in g_s comes from the adiabatic term K^{ad}_s in Eq.(7). The 2 terms on the right side of Eq.(11) arise from $\delta\rho_{s,B+C}$. This response equation is of the same form as that obtained in Refs. [5, 6], or of any linear response calculation. The differences lie in the form of the dielectric $\mathcal{D}$, and in the use of the aa form, which facilitates dealing with the range of timescales and of orbit-averaging effects in complex geometries in a general manner.

To evaluate the $G_\mathbf{l}$, we describe the radial motion by $r \simeq r_d + \delta r^{(d)}(\theta_d) + \delta r^{(b)}(\theta_b) + \delta r^{(g)}(\theta_g)$, where for each $i = g, b, d$, we make a harmonic approximation of the motion in that phase, $\delta r^{(i)}(\theta_i) \simeq \rho_i\cos\theta_i$. This is a very good approximation for gyromotion, and a good approximation for bounce motion not too near a trapping-state boundary. For simplicity, we assume that superbanana ($\tau = h$) particles do not detrap, but precess poloidally dominated by $E \times B$ poloidal drift, $\Omega_d \simeq \Omega_{dE}$, which is roughly constant on a given orbit, while drifting radially as $v_{Bt}\sin\theta$, as usual. This yields radial motion of the given harmonic form, with superbanana width $\rho_d = \sigma_h v_{Bt}/\Omega_{dE}$, as noted above. For completeness, one may also include in this description the finite banana widths ρ_{bh} of $\tau = h$ particles, which give rise to the helically–symmetric nc transport branch in straight stellarators[13], and a second type of superbanana width, the finite radial excursions ρ_{dt} made by $\tau = t$ particles on the drift timescale, which give rise to the "banana-drift" transport branch.[14, 15, 16] One then finds

$$G_{\mathbf{l}a}(\mathbf{J}) = J_{l_g}(z_g)J_{l_b}(z_b)J_{l_d}(z_d)e^{-i\xi_a}, \qquad (13)$$

with $z_{g,b,d} = k_r\rho_{g,b,d}$, and ξ_a a phase factor, whose value is irrelevant, since $G_\mathbf{l}$ enters only as $|G_\mathbf{l}|^2$.

For drift turbulence, which is driving the ZFs, one typically has $k^d_\perp\rho_{gi} \sim 0.3$, and frequencies $\omega_\mathbf{k} \sim \omega_*(k^d_\perp)$. For ZFs, one has much smaller k_r and frequencies ω_Z, down by an order of magnitude, perhaps by the "mesoscale" ratio, $k^Z_r/k^d_\perp \sim \sqrt{\rho_{gi}/a}$. Thus, for both species, one has the ordering $\omega_Z, \Omega_d \ll \Omega_b \ll \Omega_g$, and $z_g < z_b < 1$. For the moment we leave the relative sizes of ω_Z and Ω_d unspecified. Also, one may have $z_d \gtrsim 1$ for trapped particles, for ions and also, notably, for electrons, as noted by [6]. Thus, as opposed to tokamaks, in stellarators electrons can participate in orbit averaging, because their radial excursions on the drift timescale can be comparable with those of ions.

Because $\omega_Z \ll \Omega_{b,g}$, the sum over $\mathbf{l}$ in Eq.(12) is dominated by the terms with $l_{g,b} = 0$, an approximation strengthened for $z_{g,b} \ll 1$, for which the factors $J^2_{l_{g,b}}$ in $|G_\mathbf{l}|^2$ in Eq.(12) are negligible unless $l_{g,b} = 0$. These reduce the triple sum there to a single sum $\sum_{l_d}$. In that sum, if one has $\omega \gg \Omega_d$, then over the l_d–range $\Delta l_d \sim z_d$ over which $J^2_{l_d}$ in Eq.(12) is appreciable the integrand does not change greatly, so that one can perform the summation, using the identity $\sum_l J^2_l = 1$, which eliminates the $J^2_{l_d}$ factor, leaving only the factor $J^2_{l_g}J^2_{l_b}$. In the other limit $\omega \ll \Omega_d$, the sum is dominated by the $l_d = 0$ term, and the effect of $J^2_{l_d}$ survives. Thus, for $\omega \ll \Omega_d$, all of gyro-, bounce- and drift-averaging contribute. Neglecting ν_{fs}, Eq.(12) becomes

$$\begin{aligned} g_s(\mathbf{k},\omega) &\simeq 1 - \Lambda_{0b}(b_g, b_b),\ (\Omega_d \ll \omega), \qquad (14)\\ g_s(\mathbf{k},\omega) &\simeq 1 - \Lambda_{0d}(b_g, b_b, b_d),\ (\omega \ll \Omega_d), \end{aligned}$$

where $\Lambda_{0d}(b_g, b_b, b_d) \equiv \langle J^2_g J^2_b J^2_d\rangle$, $\Lambda_{0b}(b_g, b_b) \equiv \Lambda_{0d}(b_g, b_b, b_d = 0) \equiv \langle J^2_g J^2_b\rangle$, $J^2_{g,b,d} \equiv J^2_0(z_{g,b,d})$, $b_g \equiv k^2_r\rho^2_{gT}$, $b_b = b_g q^2/(F_t\epsilon_t^{1/2})$, and $b_d \equiv k^2_r\rho^2_{dT}$, with $\rho_{gT} \equiv v_T/\Omega_g$, v_T the species thermal velocity, $\rho_{dT} \equiv \rho_d(v = v_T) \propto v^2_T$, and F_t the fraction of toroidally-trapped particles.

The physics represented by Eqs.(14) is that if the the ZF drive in a stellarator has a time variation slow compared with Ω_d [*cf.* Eq.(14b)], $\tau = h$ particles have time to partially shield out ϕ_z by drifting along their collisionless superbanana orbits, an averaging mechanism not available to tokamaks. If the ZF drive varies rapidly compared with Ω_d [Eq.(14a)], this new mechanism for radial averaging is lost.

The functions Λ_{0b} and Λ_{0d} succinctly describe the additional contributions from finite b_b, corresponding to shielding due to the "bounce" contribution g^b to the shielding function computed in Refs. [5] and [6], and from finite b_d, corresponding to a "drift" contribution g^d to g, extending the result in Ref. [6]. Table 1 synopsizes some of the limiting cases covered by earlier work, extended in Ref. [1], of which Eqs.(14) here are Eqs.(15) in [1] noted in the table. One notes that most of the entries are for collisionless theory, $\nu_f = 0$. In the tokamak limit ($\epsilon_h, b_d \to 0$), $\Lambda_{0d}(b_g, b_b, b_d) \to \Lambda_{0b}(b_g, b_b)$, so that Eq.(14a) again holds. In the further cylindrical limit ($\epsilon_t \to 0$), b_b vanishes, and the Λ's in Eqs.(14) reduce to the more familiar $\Lambda_0(b_g) \equiv \Lambda_{0h}(b_g, b_h = 0) \equiv \langle J^2_g\rangle = I_0(b_g)e^{-b_g}$, with $I_0(b)$ the modi-

Parameter range	Ref.
$\nu_f = 0$:	
tokamak limit ($\epsilon_h, b_d = 0$), $\omega < \Omega_b$:	
$b_b < 1$	[5]
b_b arbitrary	[17]
stellarators ($\epsilon_h, b_d > 0$) :	
$b_d \to \infty, \omega < \Omega_d$	[6, 7]
$b_d < 1, \omega < \Omega_d$	[1](16b)
$b_d < 1, \Omega_d < \omega$	[1](16a)
b_d arbitrary, $\omega < \Omega_d$	[1](15b)
b_d arbitrary, $\Omega_d < \omega$	[1](15a)
$\nu_f > 0$:	
$\nu_h/\Omega_d > 1$	[8]
ν_h/Ω_d arbitrary	[1]

Table 1 Cases covered by the present theory

fied Bessel function of the first kind. For $b_g < 1$, one has $\Lambda_0(b_g) \simeq 1 - b_g$, and thus $g \simeq b_g$, the gyro- contribution g^g to g, corresponding to the classical (gyro) polarization current $J^{p,g}$.

Using the small-argument expansion $J_0(z) \simeq 1-(z/2)^2$ for z_d as well as $z_{g,b}$ in Λ_{0d}, Eqs.(14) reduce to [1]

$$\begin{aligned} g_s(\mathbf{k},\omega) &\simeq b_g + F_t c_b b_b,\ (\Omega_d \ll \omega), \qquad (15)\\ g_s(\mathbf{k},\omega) &\simeq b_g + F_t c_b b_b + F_h c_d b_d,\ (\omega \ll \Omega_d), \end{aligned}$$

where $F_h = (2/\pi)\sqrt{2\epsilon_h}$ is the fraction of particles with $\tau = h$, $c_d \simeq (15/2)$, and for a tokamak, one finds $c_b \simeq 10\sqrt{2}/(3\pi) \simeq 1.5$, in approximate agreement with the value in Ref. [5].

One notes that the drift contribution $g^d = F_h c_d b_d \simeq F_h(k_r\rho_d)^2$ in Eq.(15b) has a form analogous to the bounce and gyro contributions, differing from the scaling $g^d \simeq F_h$ found in Refs. [6, 7]. This is because in Refs. [6, 7], the term $\Omega_d\partial_{\theta_d}\delta f$ was neglected in their kinetic equation, thereby implicitly taking the limit $b_d \to \infty$ (see Table 1), also of physical interest. Taking that limit in Eq.(14b) also recovers that scaling.

As discussed in Ref. [1] and illustrated by Eqs.(15), there is a correspondence between the contributions g^j to the shielding function and the radial collisional (classical+nc) transport coefficients D^j: the gyromotion producing the classical polarization term g^g also gives rise to classical transport, the bounce motion producing g^b gives rise to axisymmetric nc transport, and the drift motion yielding g^d also produces the "superbanana" branch of transport, dominant in conventional stellarators. For each mechanism j, one may use the heuristic form $D^j \simeq F_j\nu_{fj}(\Delta r_j)^2$, with F_j the fraction of particles participating in that mechanism, Δr_j the radial step in the random walk process, and ν_{fj} the effective stepping frequency in that random walk. For example, for the $1/\nu$ superbanana regime, one has $F_j \to F_h \simeq \epsilon_h^{1/2}$, $\Delta r_j \to v_{Bt}/\nu_h$, and $\nu_{fj} \to \nu_h \simeq \nu/\epsilon_h$. And for the shielding contributions g^j, one has the approximate form $g^j \simeq F_j(k_r\Delta r_j)^2$, exemplified by Eqs.(15). Hence, $g^{j'}/g^j \simeq (D^{j'}/D^j)(\nu_{fj}/\nu_{fj'})$. Thus, for $j \to g$ and $j' \to b$, one expects the gyro- contribution g^g in Eqs.(15) to be smaller than the bounce contribution g^b, because classical diffusion D^g is subdominant to banana diffusion D^b. Similarly, for $j \to b$, $j' \to d$, one expects the bounce contribution g^b to dominate g^d in Eq.(15b) as long as superbanana transport D^d is subdominant to D^b. For NCSX, for example, evaluations have shown[18] that, at a self-consistent radial ambipolar field E_a, NCSX should have D^d down from D^b by about an order of magnitude. Correspondingly, one expects that the ripple contribution g^d to ZF damping should be small compared with the tokamak contribution g^b.

It has been argued[11, 6, 12, 10] that neoclassically-optimized stellarators should also have lower turbulent transport, due to less damping of ZFs. The basic idea of most nc optimization techniques has been to reduce ripple transport (D^d) by reducing either F_h, or by reducing superbanana width $\rho_d \simeq v_{Bt}/\Omega_d$.[19] One notes from the resemblance of D^d to g^d, characterized by the argument $\frac{1}{2}\langle z_d^2\rangle \simeq F_h k_r^2 \rho_{dT}^2$, that the present theory supports this argument.

However, as noted in the introduction, the shielding of ZFs from a given source, which most analytic ZF studies to date (including the present one) address, is only 1 of the 2 legs of the feedback loop in ZF dynamics. That work demonstrates that neoclassically-optimized stellarators will also tend to have lower damping of ZFs. However, in general, different configurations will have differing levels of drive for instabilities, and thus differing strengths of the ZF source S. Thus, recent gyrokinetic simulations[10] comparing configurations modeling LHD in its (A)standard and (B)inward-shifted operation, reported that the ZFs increased (by about 50%) in going from A to B, as might be expected from the better nc-optimization of case B. However, because case B also has much stronger (about 60%) ITG growth rates, the turbulent flux in that case is *increased* (by about 16%) over that in case A, in contrast with the experimentally–observed reduction[11] in turbulent transport. Very recent further simulations[20] of this same comparison, but with more realistic equilibrium profiles, have brought the numerical transport trends more into accord with experimental observations. Thus, it appears that the now commonly-cited correlation between nc and turbulent optimization is too simple, and a more refined understanding of this relationship must come from also accounting for the effects of machine geometry on the source strength.

Longer-time ZF evolution

As discussed in Ref. [1], the effects on ZFs from the g^j (describing dielectric shielding) and the D^j (describing radial collisional fluxes) come together in the time evolution equation for the flux-surface averaged radial electric field $E_r \equiv \langle\nabla r \cdot \mathbf{E}\rangle$, obtained from the surface average of

Ampere's law, plus an expression for the surface-averaged radial current J_r,

$$\begin{aligned} \partial_t E_r &= -4\pi J_r, \qquad (16)\\ J_r &= (4\pi)^{-1}\chi\partial_t E_r + \sigma(E_r - E_a) + F_S/B. \end{aligned}$$

The first term in J_r, proportional to the time derivative of E_r, represents the polarization current J^p, with χ containing the dielectric shielding contributions. The second term represents the nonambipolar radial current due to nc transport, from a first-order expansion in $E \equiv (E_r - E_a) = -\langle\nabla r \cdot \nabla\phi_z\rangle$ of the nc radial current $\sum e_s\Gamma_s(E_r)$, where $E_a = -\langle\nabla r \cdot \nabla\Phi_a\rangle$ is the ambipolar value at which the ion and electron particle fluxes are equal. F_S is the force, coming from the source S in Eq.(1), exerted by the turbulence within a magnetic surface normal to the magnetic field, which acts as a source driving E_r. Using Eq.(16b) in (16a) yields a Langevin-like equation, which in the ω domain may be written

$$-i\omega E(\omega) + \gamma_E E(\omega) = c_S(\omega), \qquad (17)$$

where $\gamma_E(\omega) \equiv 4\pi\sigma/\mathcal{D}(\omega)$, $c_S(\omega) \equiv -4\pi F_S/B\mathcal{D}(\omega)$, and $\mathcal{D}(\omega) \equiv 1 + \chi(\omega)$ as before. γ_E, absent in a tokamak, provides the restoring force toward the point $E_r = E_a$ of ambipolarity. If $\mathcal{D}(\omega)$ is ω-independent, then γ_E is as well, and in the time domain Eq.(17) reduces to a standard Langevin equation for E,

$$\partial_t E(t) + \gamma_E E(t) = c_S(t). \qquad (18)$$

The source c_S that drives the ZFs is approximated as random. Thus, ensemble averaging (18), one has

$$\partial_t\langle E\rangle_p = -\gamma_E\langle E\rangle_p, \qquad (19)$$

where $\langle ...\rangle_p \equiv \int dE...p(E,t)$ is the ensemble average with probability distribution function (pdf) $p(E,t)$. It satisfies

$$\partial_t p = \partial_E(D_E\partial_E p + \gamma_E Ep), \qquad (20)$$

with $D_E \equiv \int_0^\infty d\tau\langle c_S(t)c_S(t-\tau)\rangle_p$ the diffusion coefficient in E-space. From this follows Eq.(19), and

$$\partial_t\frac{1}{2}\langle E^2\rangle_p = D_E - \gamma_E\langle E^2\rangle_p. \qquad (21)$$

One notes from this the balance between diffusion and the restoration toward $E_r = E_a$. In steady-state, Eqs.(20) and (21) yield $p(E) = p_0\exp(-\gamma_E E^2/2D_E)$, and $\langle E^2\rangle_p = D_E/\gamma_E$. Since $\gamma_E \sim \mathcal{D}^{-1}$ and $D_E \sim \mathcal{D}^{-2}$, one has $\langle E^2\rangle_p \sim \mathcal{D}^{-1}$. Thus, assuming the turbulent forces F_S driving the ZFs are unaffected, the larger $\mathcal{D}$ implied at low-ω by the drift-polarization shielding would reduce γ_E, but reduce the diffusion D_E even more, resulting in a smaller ZF amplitude $\langle E^2\rangle_p^{1/2}$.

Discussion

In the tokamak limit $\sigma, \gamma_E \rightarrow 0$, Eq.(18) or (21) predicts an unbounded diffusion. Then other restoring mechanisms, such as those given in the model Eq.(19) of Ref. [5], become important, and would provide an analogous bounded statistical evolution of E_r, though for that model equation the time-average value of E_r would shift from the stellarator value E_a to 0. The more robust ambipolar field E_a in a stellarator provides a turbulence-suppression mechanism additional to, enhancing or diminishing that of, the ZFs themselves. For example, internal transport barriers induced by jumps in $E_a(r)$ from the ion to the electron root[21, 22, 23] (which enhances the shear in E_r and resultant flow-shear) have been observed on W7AS[24], LHD[25], and on CHS[26]. Better understanding how the ambipolar and ZF-induced flow shear act together presents an additional issue, and potential opportunity, for stellarators.

The theory from Ref. [1], as for earlier work[5, 6, 7, 8] which it extends, treats one leg of the self-consistent ZF loop, the time evolution of zonal flows, given a specified turbulent source S. The relationship between the transport coefficients D^j and shielding function contributions g^j established by that theory indicates that neoclassically-optimized stellarators should have less ZF damping, and thus supports the earlier view[11, 6, 12, 10] that neoclassically-optimized stellarators should also have lower turbulent transport. However, as noted here, the assumption that S remains fixed from one configuration to another is unwarranted, and further study of the dependence of S on configuration is clearly indicated. In fact, the recent results[10, 20] from LHD simulations indicate that this widely-held view is too simplistic, and that a fuller perspective will include additional variables beyond only the degree of a configuration's neoclassical optimization.

Understanding the configuration-dependence of S is of course complicated, possibly the reason most analytic work has focussed mainly on the first leg of the ZF loop. Theoretical progress here can be aided greatly by analysis of further numerical simulations designed to elucidate this relationship.

[1] H.E. Mynick, A.H. Boozer, *Phys. Plasmas* **14** 072507 (2007).

[2] P.H. Diamond, Y.-B. Kim, *Phys.Fluids*-B **3**, 1626 (1991).

[3] H. Biglari, P.H. Diamond, P.W. Terry, *Phys.Fluids*-B **2**, 1 (1990).

[4] L. Chen, Z. Lin, R.B. White, *Phys. Plasmas* **7**, 3129 (2000).

[5] M.N. Rosenbluth, F.L. Hinton, *Phys. Rev. Letters* **80**, 724 (1998).

[6] H. Sugama, T.H. Watanabe, *Phys. Rev. Letters* **94**, 115001 (2005).

[7] H. Sugama, T.H. Watanabe, *Phys. Plasmas* **13**, 012501 (2006).

[8] K.C. Shaing, *Phys. Plasmas* **13**, 052505 (2006).

[9] A.N. Kaufman, *Phys. Fluids* **15**, 1063 (1972).

[10] T.-H. Watanabe, H. Sugama, S. Ferrando-Margalet, *Nucl. Fusion* **47**, 1383 (2007).

[11] H. Yamada, J.H. Harris, A.Dinklage, E. Ascasibar, F.Sano, S.Okamura, U.Stroth, A.Kus, J.Talmadge, S.Murakami, M.Yokoyama, C.Beidler, V.Tribaldos, K.Y.Watanabe, *Proc. 31st EPS Conference on Plasma Physics*, London, June

29-July 2, 2004 (European Physical Society, Pepip-Lancy, 2004), P5-9.

[12] K.C. Shaing, *Physics of Plasmas* **12**, 082508 (2005).

[13] A. Pytte, A.H. Boozer, *Phys. Fluids* **24**, 88 (1981).

[14] A.H. Boozer, *Phys. Fluids* **23**, 2283 (1980).

[15] R. J. Goldston, R. B. White and A. H. Boozer, *Phys.Rev. Lett.* **47**, 647 (1981).

[16] R. Linsker, A.H. Boozer, *Phys. Fluids* **25**, 143 (1982).

[17] Y. Xiao, P.J. Catto, *Phys. Plasmas* **13**, 102311 (2006).

[18] D.R. Mikkelsen, H. Maassberg, M.C. Zarnstorff, C.D. Beidler, *et al.*, *Fusion Science and Technology* **51** 166-180 (2007).

[19] H.E. Mynick, *Phys. Plasmas* **13**, 058102 (2006).

[20] H. Sugama, T.-H. Watanabe, S. Ferrando-Margalet, (this meeting, paper I-08).

[21] H.E. Mynick,W.N.G. Hitchon, *Nucl. Fusion* **23**, 1053 (1983).

[22] K.C.Shaing, *Phys. Fluids* **27**, 1567 (1984).

[23] D.E.Hastings, W.A. Houlberg, K.C.Shaing, *Nucl. Fusion* **25**, 445 (1985).

[24] U Stroth, K Itoh, S-I Itoh, H. Hartfuss, H. Laqua, the ECRH team, & the W7-AS team, *Phys. Rev. Letters*, **86**, 5910 (2001).

[25] K. Ida, T. Shimozuma, H. Funaba, *et al.*, *Phys. Rev. Letters* **91**, 085003 (2003).

[26] T. Minami, A. Fujisawa, H. Iguchi, *et al.*, *Nucl. Fusion* **44**, 342 (2004).

Proceedings of ITC/ISHW2007

Global Simulations of Turbulence and Dynamos in Differentially Rotating Astrophysical Plasmas

R. Matsumoto, M. Tanaka, M. Machida[a]

Department of Physics, Graduate School of Science, Chiba University, 1-33 Yayoi-cho, Inage-ku Chiba 263-8522, Japan

[a]National Astronomical Observatory, 2-21-1 Osawa, Mitaka, Tokyo 181-8588, Japan

matumoto@astro.s.chiba-u.ac.jp

We present the results of global three-dimensional resistive magnetohydrodynamic (MHD) simulations of astrophysical plasmas rotating around a gravitating object. When the initial magnetic field is weak (i.e., $\beta = P_{\rm gas}/P_{\rm mag} \gg 1$), differential rotation enables the growth of the magneto-rotational instability (MRI) , which amplifies azimuthal magnetic fields and generates MHD turbulence in the disk. Angular momentum transport due to the Maxwell stress of the turbulent magnetic field leads to the infall of the disk plasma. The gravitational energy of the plasma released during this infall is believed to be the energy source of accretion powered objects such as black hole candidates.

We found that the direction of equatorial mean azimuthal magnetic field reverses with time scale about 10 rotation period at the characteristic radius of the disk. Formation of the bisymmetric magnetic fields and the buoyant rise of the magnetic flux from the disk to the disk corona enables the amplification and reversal of azimuthal magnetic field in the disk. The appearance of global mean azimuthal magnetic field with net azimuthal flux in the disk elevates the saturation level of magnetic energy. The quasi-periodic reversal of azimuthal magnetic field is similar to the 11 year cycle of the reversal of the polarity of solar magnetic fields.

When we adopt the gravitational potential of our galaxy, numerical results indicate that the mean azimuthal magnetic field is amplified up to μG. The interval of the reversal of the azimuthal magnetic field is about 1Gyr at 5kpc from the galactic center. The mean magnetic fields are mainly azimuthal in the outer disk but vertical component becomes important near the galactic center, consistent with the observations of our galactic center.

In black hole accretion disks, sawtooth-like oscillations of magnetic energy appears when the accreting matter forms an inner torus near the black hole. In such tori, the magnetic energy approaches $\beta \sim 1$ and is released by magnetic reconnection. Such dynamo-driven quasi-periodic activities can explain low-frequency(1-10Hz) quasi-periodic oscillations (QPO) observed in galactic black hole candidates. We found that during the growth of the magnetic field, the accretion disk deforms itself into a crescent shape. Such non-axisymmetric structure can excite higher frequency oscillations in the disk.

Proceedings of ITC/ISHW2007

Suppression of turbulence by mean flows in two-dimensional fluids

Michael SHATS[1)], Hua XIA[1)], Horst PUNZMANN[1)] and Gregory FALKOVICH[2)]

[1)]*Australian National University, Canberra ACT 0200, Australia*
[2)]*Weizmann Institute of Science, Rehovot 76100, Israel*

(Received 15 October 2007)

A review of recent experimental studies of turbulence suppression by mean flows in quasi-two-dimensional fluids is presented. Large-scale mean flows develop during spectral condensation of 2D turbulence as a result of the inverse energy cascade in spatially bounded flow. The spectral energy which is accumulated at the largest scale supports the mean flow which in turn affects turbulence. We show that such a flow can reduce the energy flux in the inverse energy cascade range *via* shearing and sweeping of the turbulent eddies. The former mechanism is more efficient at larger scales, while the latter acts on the smaller scales. Similar suppression of turbulence has been found in the presence of externally imposed flows. Turbulent (inverse energy) cascade is reduced in the presence of imposed flow, but still supports Kolmogorov-Kraichnan $k^{-5/3}$ power law spectrum in the energy range.

Keywords: two-dimensional fluids, turbulence, mean flow, shear decorrelation, inverse energy cascade

DOI: 10.1585/pfr.1.001

1 Introduction

The idea of turbulence suppression in the presence of a background sheared flow has its origin in the physics of magnetically confined plasma. It was proposed in 1990 [1, 2] as a simple hydrodynamic model aimed at explaining turbulence reduction near transport barriers which form in plasma in the so-called high (H) confinement regime [3]. Since then this concept has received wide recognition in the plasma literature (e.g. [4, 5, 6, 7]). The model of the shear suppression is supported by substantial indirect experimental evidence, namely, the correlation between the onset of the strong sheared flows in plasma and the reduction in the turbulent transport during transitions to improved confinement.

The main mechanism of the shear suppression is as follows. When a turbulent eddy is placed in a stable laminar flow whose velocity varies in the direction perpendicular to the flow direction, it becomes stretched and distorted. The shear suppression can be viewed as the reduction in the eddy's lifetime. It occurs when the inverse shearing rate $\tau_s \approx \omega_s^{-1}$ becomes shorter than the eddy turnover time, or its lifetime, τ_e whatever is shorter, providing that the interaction time between turbulence and flow is longer than other time scales. A reduction in the spectral power in the presence of a shear flow is due to the shortened correlation time of eddies. Dimensional scaling analysis which takes into account turbulent diffusion, shows that this shortened correlation time τ_e^s is related to the shear straining time τ_s and the eddy turnover time τ_e as [8]: $\tau_e^s = \tau_e^{1/3}\tau_s^{2/3}$. The theory of the shear suppression is considered an extension of the rapid distortion theory into the nonlinear regime [8].

author's e-mail: Michael.Shats@anu.edu.au

Despite its wide recognition in plasma physics, and attempts to extend its application to other fields (see e.g. [9]), this hydrodynamic phenomenon is not a familiar one in fluids [10]. This fact has triggered arguments both against [11] and in favor [12] of the shear turbulence suppression mechanism, casting a shadow on its existence in plasma.

Results reviewed in this paper represent the first experimental evidence of the turbulence suppression by mean flows in quasi-two-dimensional fluids. First we describe the experimental setup and methods of the turbulent flow detection. Suppresion of turbulence is studied (a) during spectral condensation of the spatially bounded flow, and (b) in the presence of externally imposed mean flow.

2 Experimental setup and results

In the experiments reported here, turbulent flow is generated in stratified thin layers of electrolyte (NaCl water solutions of different concentrations, heavier solution at the bottom, total thickness of 6 mm). This setup is similar to those used in [13] and [14]. Turbulence is generated by forcing 576 $J \times B$-driven vortices (24×24) in a cell. Spatially varying, vertically directed (normal to the fluid layers) magnetic field B is produced by a 24×24 matrix of permanent magnets placed under the bottom of the fluid cell (300×300 mm^2) in a checkerboard fashion (10 mm between the centers of magnetic dipoles). The schematic of the experimental setup is shown in Fig. 1. Solid Perspex square boundaries of various sizes are inserted to generate spectral condensate. Two carbon electrodes on the either side of the cell are connected to the power supply. An electric current in the electrolyte can be either modulated, for example, by driving positive and negative current pulses

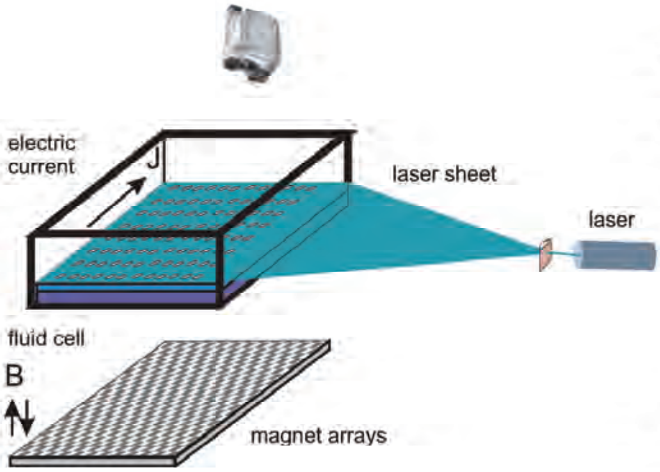

Fig. 1 Schematic of experimental setup.

having random-in-time polarity and the pulse lengths, or it can be DC. Since we are mostly interested in the development of strong coherent condensate flows, a DC mode is chosen in these experiments. Constant forcing is found to be the most efficient in supporting coherent monopole condensate. This agrees with findings of numerical simulations of the generation of large coherent structures in 2D turbulence [15]. The $J \times B$ forcing is chosen such that there is no ripple on the free surface, which would violate quasi-two-dimensionality of the flow.

To visualize the flow, imaging particles (polyamid, 50 μm diameter, specific gravity of 1.03) are suspended in the top layer of the fluid and are illuminated using thin (1 mm) laser sheet aligned parallel to the free surface of the fluid. Laser light scattered by particles is filmed from above, using video camera at 25 frames per second. Cross-correlation based particle image velocimetry technique is used to obtain the velocity fields from the sequence of the video frames.

First we discuss the generation of the spectral condensate. It is well known that the evolution of spectra in 3D flows leads to the transfer of the spectral energy $E(k)$, towards smaller scales (larger k), a forward energy cascade, until it reaches the dissipation scale determined by the viscosity. Spectral regions of the turbulence forcing (k_f) and of the dissipation range (k_d) do not generally coincide. The spectral range between them is called the inertial range. Viscous processes determine the energy dissipation rate ϵ in the system. Kolmogorov assumed that (a) the statistical properties of turbulence in the inertial range ($k << k_d$) are determined only by k and ϵ, and (b) that ϵ is the universal constant of a given flow in time and in space. Dimensional considerations have led to the famous Kolmogorov law for the spectral energy: $E(k) = C\epsilon^{2/3}k^{-5/3}$. In 2D flows, in addition to the energy conservation, enstrophy, or the volume integral of the squared vorticity $\Omega = 1/2\int \omega^2 dV$ (where $\omega = \nabla \times V$ is the vorticity and V is velocity) is also conserved [16]. The existence of this second invariant of the flow modifies the spectral transfer, which is determined by both the energy and the enstrophy ϵ_ω dissipation rates, and leads to the onset of two inertial ranges. If energy and enstrophy are injected into the system at k_f, then energy in 2D flow cascades towards larger scales, or lower $k < k_f$ (inverse energy cascade range), while the enstrophy is transferred towards higher $k > k_f$ (forward enstrophy cascade). The former is described by the Kolmogorov law,

$$E(k) = C_k\epsilon^{2/3}k^{-5/3}, \tag{1}$$

(though the energy is transferred in the opposite direction to that in the 3D turbulence), while the latter is described by

$$E(k) = C_\omega\epsilon_\omega^{2/3}k^{-3}, \tag{2}$$

The maximum of the energy spectrum thus lies in the low-k range at k_E, and in the absence of the energy dissipation at large scales k_E can not be constant in time. In the presence of damping for large scales, for example via linear damping μ, the scale corresponding to the maximum of the spectrum, stabilizes at

$$k_E \approx \left(\frac{\mu^3}{\epsilon}\right)^{1/2}. \tag{3}$$

If the system size is larger than this dissipation scale $\lambda_E = \pi/k_E$, one should observe the stationary energy spectrum showing two inertial ranges corresponding to the inverse energy cascade ($\propto k^{-5/3}$) and the direct enstrophy cascade ($\propto k^{-3}$). If however dissipative scale is smaller than the system size, $\lambda_E < L$, spectral energy is accumulated at the largest scale. Such a process, in which energy piles up in the largest scale k_c, has been predicted by Kraichnan in 1967 who also noted the similarity between the condensation of the turbulent energy and the Bose-Einstein condensation of the 2D quantum gas [17].

A self-generated coherent flow can develop spontaneously during spectral condensation of the bounded 2D turbulence [17]. In a large domain, inverse cascade proceeds up to the integral scale λ_E. When λ_E is larger than the size of the boundary L, energy accumulates at the box scale and self-generation of a large vortex occurs. This phenomenon has been confirmed in numerical simulations [18, 19, 20, 21] and has been observed in experiments [22, 13, 14]. For given μ and ϵ, the easiest way to achieve spectral condensation is to reduce the size of the boundary to satisfy $\lambda_E \geq L$. In the described experiments, square boundaries of different sizes of $L = 90 \div 120$ mm were used. The spectral condensation leads to the onset of the self-generated mean flow, which interacts with the background turbulence.

First we consider the effect of the self-generated flow on the bounded ($L = 110$ mm) turbulence [23]. The time evolution of the total kinetic energy of the 2D turbulent flow is shown in Fig. 2(a). The inverse energy cascade leads to the development of larger eddies and to the growth

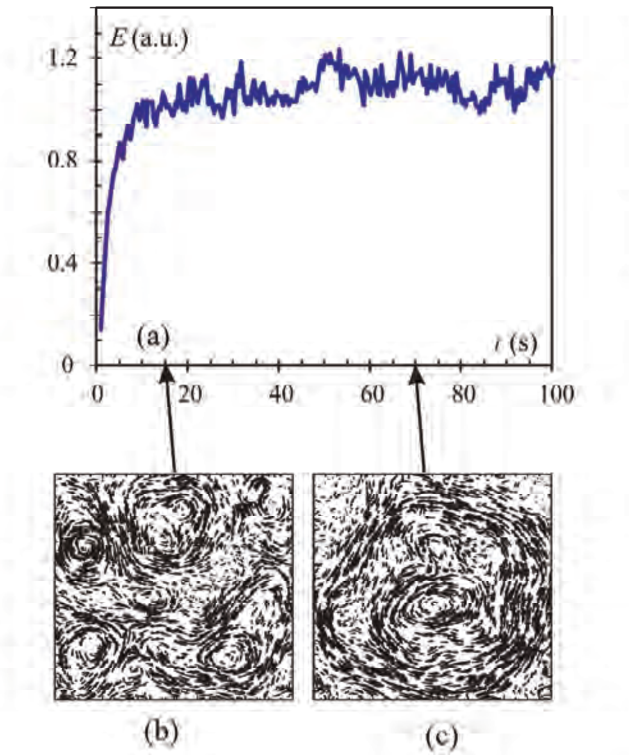

Fig. 2 Time evolution of the total kinetic energy (a) and instantaneous velocity fields at $t = 13$ s (b), and $t = 71$ s (c).

of the kinetic energy of the system. By about 10 s the kinetic energy reaches 80% of its maximum value. By this time several large-scale coherent vortices develop in the flow, as seen in Fig. 2(b). These vortices persist for 4-5 turnover times (about 10 s) before they start merging. After this transient stage, large vortices merge to form a single coherent vortex, which then persists in a steady state, Fig. 2(c). This stable vortex imposes mean flow which affects 2D turbulence.

We compare the turbulence spectra during the transient stage, at $t = (9-17)$ s, and after the single vortex formation, at $t = (61-79)$ s. The analysis time in the transient stage is limited to 8 s during which the flow is quasi-steady. The wave number spectra are averaged over $N = 200$ realizations (400 in the steady condensate regime) of the "instantaneous" velocity fields (computed every 40 ms using two consecutive video frames):

$$E_{tot}(k) = 1/N \sum_{n=1}^{N} F(V)F^*(V), \qquad (4)$$

where F denotes Fourier transform and F^* is its complex conjugate. This is a total spectrum which includes both mean and fluctuating velocity. Before the large vortex formation, this spectrum shows a power-law scaling of $E(k) \propto k^{-3}$ both above and below the forcing wave number $k_f = 350\ m^{-1}$, Fig. 3(a). Such a scaling, which was already observed in the experiments in the spectral condensate regime [14] and in numerical simulations [24, 25, 26, 21], apparently contradicts the $E(k) \propto k^{-5/3}$ spectrum expected for

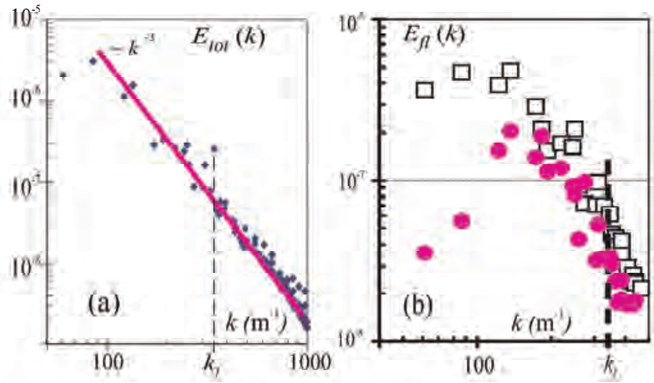

Fig. 3 Spectrum of the total spectral energy of the flow at $t =$ (9-17)s (a). Spectra of the turbulent velocity fluctuations before, $t =$ (9-17)s (open squares) and after the formation of a single large vortex, $t =$ (61-79)s (solid circles) (b).

the inverse energy cascade inertial range [17]. It was suggested in [21] that a k^{-3} power law is due to the presence of large-scale persistent vortices rather than due to the turbulent cascade. To eliminate this effect, we subtract from the instantaneous velocity the mean $\langle V \rangle = 1/N \sum_{n=1}^{N} V(x,y)$ obtained by averaging over N instantaneous fields $V(x,y)$. The resulting spectra,

$$E_{fl}(k) = 1/N \sum_{n=1}^{N} F(V - \langle V \rangle)F^*(V - \langle V \rangle), \qquad (5)$$

computed for two time intervals, before and after the generation of the single vortex, are shown in Fig. 3(b). Such subtraction, proposed in [21], leads to a spectrum less steep than k^{-3}, somewhat close to $k^{-5/3}$.

After the formation of the single vortex, turbulence levels are significantly reduced for the wave numbers in the range of $k < 160\ m^{-1}$. The explanation of this will be given below. The level of turbulent fluctuations changes less between $k \approx 160\ m^{-1}$ and the injection scale, $k_f \approx 350\ m^{-1}$. That interval is too short to distinguish between $E_{fl}(k) \propto \epsilon^{2/3}k^{-5/3}$ and $E_{fl}(k) \propto \epsilon/\tau_s k$ that one may expect assuming that the scale-independent energy transfer is of order of the shear time τ_s. One can see that in the forward cascade range ($k \geq k_f$) fluctuations are also reduced. This reduction at small k is significant (up to a factor of ten) and reproducible.

Now we turn to the experiment in which a large-scale mean flow was externally imposed on the quasi-2D turbulence [23]. The flow is generated using large permanent magnet, as illustrated in Fig. 4. In this case the boundary box exceeds the integral scale ($L \approx 300$ mm). We refer to this configuration as to "unbounded" turbulence.

A large magnet ($40 \times 40\,\mathrm{mm}^2$) placed 2 mm above the free surface imposes a large-scale vortex flow, which slowly decays (for approximately 60 seconds) after the magnet is removed. Instantaneous velocity fields before and after the generation of this mean flow are shown in Figs. 5(a,b). Energy spectra shown in Figs. 5(c) are com-

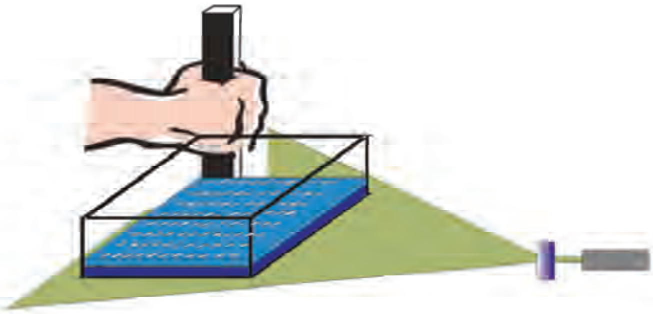

Fig. 4 Schematic of the generation of external mean flow

puted after subtracting the mean flow, using Eq. 5. Both with and without the large vortex, spectra are close to the $k^{-5/3}$ scaling. The mean flow reduces the spectral power of the turbulent fluctuations everywhere within the inverse cascade range by a factor of 8.

3 Analysis and discussion

In the presence of the self-generated large vortex the observed reduction in the spectral power of turbulent eddies is consistent with the mechanism of the shear turbulence suppression. We estimate the shear suppression criterion $s = \omega_s \tau_e > 1$ as follows. The turnover time of an eddy of the scale l is

$$\tau_e \approx \frac{l}{\langle|\delta V(l)|\rangle} = \frac{l}{S_1(l)}, \tag{6}$$

that is estimated from the mean velocity difference across scale l,

$$\delta V(l) = V(r_0 + l) - V(r_0). \tag{7}$$

The angular brackets denote averaging over all possible positions r_0 within the boundary box (or within the computation box in the "unbounded" case), and $S_1 = \langle \delta V \rangle$ is the first-order structure function averaged over N velocity fields.

To estimate the shearing rate of the large-scale mean flows, both self-generated [Fig. 2(c)] and externally forced [Fig. 5(b)], the polar coordinate system with its origin in the center of the vortex is used. The azimuthal component of the velocity V_θ dominates the flow after the vortex is formed. Its radial distribution is shown in Figs. 6(a,c). In the case of the self-generated flow radial coordinates $r = 0$ and $r = 0.05$ m correspond to the vortex center and to the square boundary respectively. In the case of externally driven flow $r = 0.09$ m corresponds to the size of the imaged area of "unbounded" turbulent flow. It is seen that the amplitude of velocity of the externally forced flow is a factor of two higher than in the self-organized case. The shearing rate is determined as follows:

$$\omega_s = l\frac{d\Omega}{dr}, \tag{8}$$

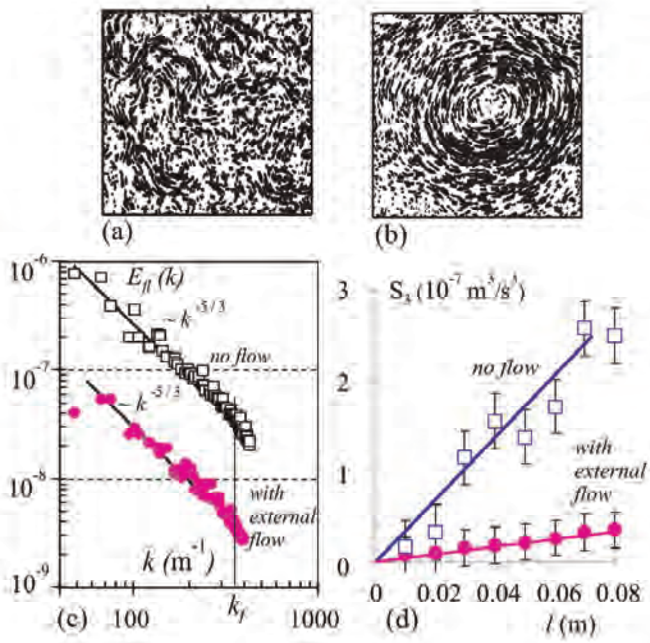

Fig. 5 Instantaneous velocity fields of "unbounded" turbulence (a) and in the presence of externally generated large scale azimuthal flow. Spectra of turbulence are computed with mean flow subtracted: before the large flow is imposed (open squares) and in the presence of the mean flow (solid circles). Third-order structure functions without (open squares) and with (solid circles) externally imposed mean flow (d).

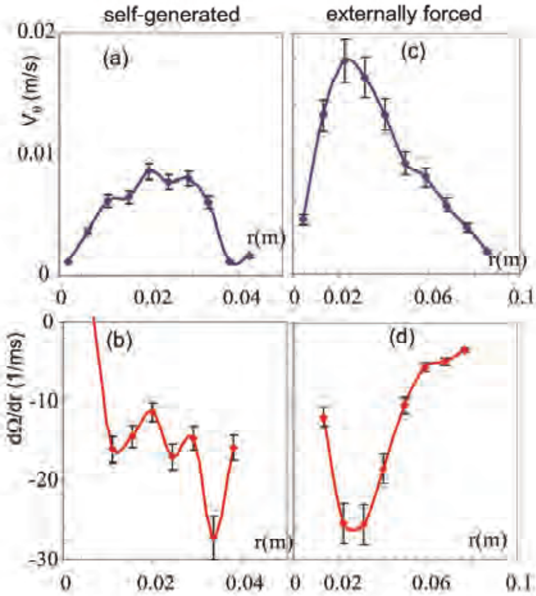

Fig. 6 Mean azimuthal velocity of the flow after the large-scale vortex generation (a,c) and the derivative of its angular velocity (b,d) during spectral condensation of the bounded turbulence (a,b), and in the case of externally forced "unbounded" flow (c,d).

where l is the radial extent of the eddy. The derivative of the radially localized angular velocity $\Omega = V_\theta/r$ is determined as

$$\frac{d\Omega}{dr} = \frac{1}{r}\frac{dV_\theta}{dr} - \frac{V_\theta}{r^2}, \tag{9}$$

which is zero for the solid-body mean flow rotation and nonzero for the sheared flow. Figs. 6(b,d) show $d\Omega/dr$ for the self-generated and externally driven shear flows. Since both ω_s and τ_e grow with l, the shear affects larger scales first.

For the case of the self-generated flow $d\Omega/dr \approx 15$ $(ms)^{-1}$, $S_1 \approx 8\times10^{-3}$ m/s, and the shearing parameter $s \approx 2\times10^3 l^2$. The criterion for the shear suppression, $s > 1$, is satisfied for the scales $l > 0.022$ m. This gives an estimate of the affected wave number range $k = \pi/l \le 145$ m^{-1}, which is in agreement with the observation of the turbulence suppression in the wave number range of $k \le 160$ m^{-1} seen in Fig. 3(b).

For the externally forced mean flow $d\Omega/dr \approx 22$ $(ms)^{-1}$, $S_1 \approx 2\times10^{-3}$ m/s, and the shearing parameter $s \approx 1.1\times10^4 l^2$. The suppression criterion is satisfied for the scales $l > 0.0095$ m, which extends very close to the forcing scale $l_f \approx 9$ mm ($k_f = 350m^{-1}$). Again, this is in agreement with our observation that the spectral energy is reduced everywhere within the inverse energy cascade inertial range, Fig. 5(c).

The externally driven flow must be strong enough to affect the energy flux through the $k < k_f$ inertial range. To test this we computed the third-order structure function $S_3(l) =< \delta V(l)^3 >$ to estimate the energy flux ϵ from the Kolmogorov law.

$$S_3(l) = -\frac{3}{2}\epsilon l. \tag{10}$$

Similarly to S_1, the third-order structure function S_3 is computed by averaging over the boundary box and then by averaging S_3 in time over 100 subsequent velocity fields. It should be noted that $\delta V(l)$ represents here the longitudinal velocity increment, $\delta V_\parallel(l)$, defined in Kolmogorov's theory [16]. Also, S_3 is computed allowing positive and negative values of the velocity increments $\delta V_\parallel(l)$. Such computations require very large statistical averaging to obtain converged results. We obtained satisfactory convergence for the steady-state "unbounded" turbulence and for the turbulence in the presence of the slowly decaying externally driven flow. The result is illustrated in Fig. 5(d). Both before and after the mean flow is imposed, S_3 is a linear function of the scale l. As a result, the energy flux $\epsilon = -(2/3)S_3/l$ is constant to within 15% for all scales in the energy inertial range. This flux ϵ is reduced in the presence of the flow by one order of magnitude compared to the case without the flow.

The reduction in the energy flux can be attributed to two phenomena in this case. First, it is the shearing of the forcing scale vortices discussed above. However, the force-connected vortices (with $k \approx k_f$) must be more resistant to shearing than the inertial scale eddies at $k < k_f$. Second, the force-fed vortices are *swept* by the mean flow relative to the magnets, which must also reduce the energy input. This effect is schematically illustrated in Fig. 7.

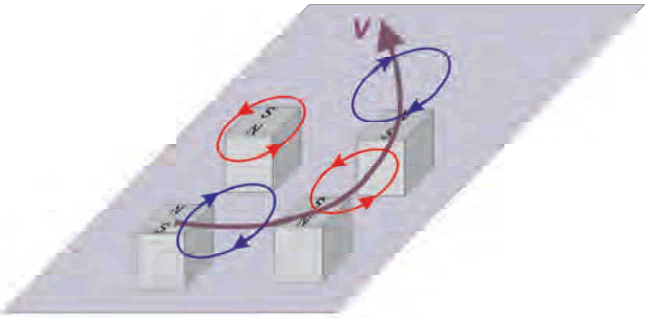

Fig. 7 Schematic illustration of the effect of sweeping of the forcing scale vortices by mean flow relative to the magnets

One can define a dimensionless sweeping parameter $sw = \omega_{sw}\tau_e$, where the sweeping rate is given by $\omega_{sw} = V_\theta/l$. Since

$$sw = \frac{V_\theta}{l}\frac{l}{S_1} \sim V_\theta(\epsilon l)^{-1/3}, \tag{11}$$

sweeping acts more efficiently on the smaller scales (while shearing is more effective on larger scales). At the forcing scale l_f, this parameter is $sw \approx 0.75$ for the self-generated flow and it is $sw \approx 7$ with externally forced mean flow. Thus the sweeping can be responsible for the reduction in the energy flux through the inverse cascade range in the presence of an externally-induced flow. The dominant role of sweeping in this case is also supported by the fact that the spectrum of the inverse cascade remains $k^{-5/3}$, just shifted down as shown in Fig. 5(c). Such modifications to the spectrum are also consistent with a ten-fold decrease in the energy flux ϵ, since $E(k) = C_k\epsilon^{2/3}k^{-5/3}$.

Let us stress the qualitative difference between Fig. 3(b) (strong decrease at small k) and Fig. 5(c) (uniform decrease for all k) which shows that there are two mechanisms of suppression. Sweeping may also be responsible for the reduction in the enstrophy flux through the forward cascade ($k > k_f$) in the presence of the self-generated flow [see Fig. 3(b)]. In this case, we could not obtain statistically converged computations of S_3 during spectral condensation to compare ϵ before and after the formation of the large vortex.

4 Conclusions

We have shown in [23] that turbulence is quasi-2D flow is significantly reduced in the presence of a large coherent vortex. In the case of a self-generated vortex, larger scales are affected more than the smaller ones. This qualitatively agrees with the description of the shear turbulence suppression mechanism as a reduction in the eddy life-time [1]. In the presence of externally imposed flow two effects may be responsible for the observed strong reduction in the turbulence level. The vortex sweeping by the mean flow seems to play an important role here. In this case the shape of the spectrum is not modified but the (inverse) spectral energy flux is substantially reduced.

It should be noted that three conditions needed for the shear turbulence suppression in fluids discussed in [10] are satisfied in our experiment. The shear flow must be stable in a sense that the time during which turbulence remains in the region of flow shear should exceed both the eddy life-time τ_e and the shear straining time τ_s. The shear flow is stable in our experiment. Due to the dominant flow in the azimuthal direction after the monopole formation, turbulence stays in the region of shear, $\rho = (0.2 - 0.9)$, Fig. 6. Finally, the 2D dynamics of the flow is imposed on the system by the stratification of thin fluid layers.

The mechanism of the shear suppression in plasma is often described as the loss of coherence by a turbulent eddy and a breakup into two eddies of the smaller scale (e.g. [9]). One would expect in this case an increase in the spectral power of eddies of intemediate scales. We have not found any evidence in support of the eddy breakup. Observations in 2D fluids are more consistent with the idea of reduction in the turnover time of the larger scale eddies [8]. In this case the inverse energy cascade is arrested at the scales affected by the shear flow, which presumably leads to the reduction in the spectral energy, similar to that seen in Fig. 3(b).

[1] H. Biglari, P.H. Diamond and P.W. Terry, *Phys. Fluids B* **2** (1990) 1.
[2] K.C. Shaing, E.J. Crume and W.A. Houlberg, *Phys. Fluids B* **2** (1990) 1492.
[3] F. Wagner et al. *Phys. Rev. Lett.* **49** (1982) 1408.
[4] T.S. Hahm and K.H. Burrell, *Phys. Plasmas* **2** (1995) 1648.
[5] T.S. Hahm, *Phys. Plasmas* **4** (1997) 4074.
[6] K.H. Burrell, *Phys. Plasmas* **6** (1999) 4418.
[7] K.H. Burrell, *Phys. Plasmas* **4** (1997) 1499.
[8] P.W. Terry, *Rev. Mod. Phys.* **72** (2000) 109.
[9] E.-J. Kim, *Astron. and Astrophysics* **441** (2005) 763.
[10] P.W. Terry, *Phys. Plasmas* **7** (2000) 1653.
[11] D.C. Montgomery, *Phys. Plasmas* **7** (2000) 4785.
[12] P.W. Terry, *Phys. Plasmas* **7** (2000) 4787.
[13] J. Paret and P. Tabeling, *Phys.Fluids* **10** (1998) 3126.
[14] M.G. Shats, H. Xia, H. Punzmann, *Phys. Rev. E* **71** (2005) 046409.
[15] N.N. Kukharkin, *J. Sci. Comp.* **10** (1995) 409.
[16] U. Frisch, *Turbulence: The Legacy of A. N. Kolmogorov* (Cambridge University Press, Cambridge,1995).
[17] R.H. Kraichnan, *Phys. Fluids* **10** (1967) 1417.
[18] M. Hossain, W. H. Matthaeu, D. Montgomery, *J. Plasma Phys.* **30** (1983) 479.
[19] L. M. Smith, V. Yakhot, *Phys. Rev. Lett.* **71** (1993) 352.
[20] D. Molenaar, H.J.H. Clercx and G.J.F. van Heijst, *Physica D* **196** (2004) 329.
[21] M.Chertkov, C. Connaughton, I. Kolokolov and V. Lebedev, *Phys. Rev. Lett.* **99** 084501 (2007).
[22] J. Sommeria, *J. Fluid Mech.* **170** (1986) 139.
[23] M.G. Shats, H. Xia, H. Punzmann and G. Falkovich *Phys. Rev. Lett.* **99** 164502 (2007).
[24] V. Borue, *Phys. Rev. Lett.* **72** (1994) 1475.
[25] L.M. Smith and F. Waleffe, *Phys. Fluids* **11** (1999) 1608.
[26] C. V. Tran and J. C. Bowman, *Phys. Rev. E* **69** (2004) 036303.

Proceedings of ITC/ISHW2007

Transport Dynamics and Multi-Scale Coupling of Turbulence

S. Inagaki[1)], N. Tamura[2)], Y. Nagashima[1)], T. Tokuzawaa[2)], T. Yamada[1)], K. Ida[2)], T. Maruta[3)], S. Kubo[2)], K. Terasaka[3)], T. Shimozuma[2)], Y. Nagayama[2)], K. Kawahata[2)], A. Komori[2)], S. Shinohara[3)], A. Fujisawa[2)], M. Yagi[1)], Y. Kawai[1)], S.-I. Itoh[1)], K. Itoh[2)] and the LHD experimental group

[1)]*RIAM, Kyushu University, 6-1 Kasuga-Koen, Kasuga 816-8580, Japan*
[2)]*National Institute for Fusion Science,322-6 Oroshi-cho, Toki 509-5292, Japan*
[3)]*IGSES, Kyushu University, 6-1 Kasuga-Koen, Kasuga 816-8580, Japan*

Correlation between electron heat flux and electron temperature gradient is obtained in cold pulse experiments. Evidence for a long distance correlation is found in plasma, where the nonlocal temperature rise is observed. Multi-scale coupling of density fluctuation is analysed by using envelope method. Existence of the low frequency ($\leq$ 2 kHz) modulator of the density fluctuation is suggested in a nonlocal plasma.

Keywords: dynamics, nonlocal, correlation, fluctuation, LHD

1 Introduction

Turbulence transport is higher than the neoclassical level in the edge to intermediate region in helical devices (heliotron, stellarators, heliac and others) as well as in tokamaks. The turbulence causes not only quantitative features of transport but also qualitative ones. Transport dynamics reveals such qualitative features of transport. Various transient transport phenomena observed in helical plasmas indicate complexities of turbulent transport. Recent theoretical works on drift wave turbulence show drift waves are strongly coupled with micro-scale, meso-scale and macro-scale waves. These non-linear couplings form turbulent structures, which have strong influences on transport. Thus, the dynamics and the multi-scale coupling of drift waves are now the most important issues to be clarified in transport studies. A comprehensive understanding of transport dynamics through first principle turbulence models is strongly required for achieving predictive capability of turbulence transport.

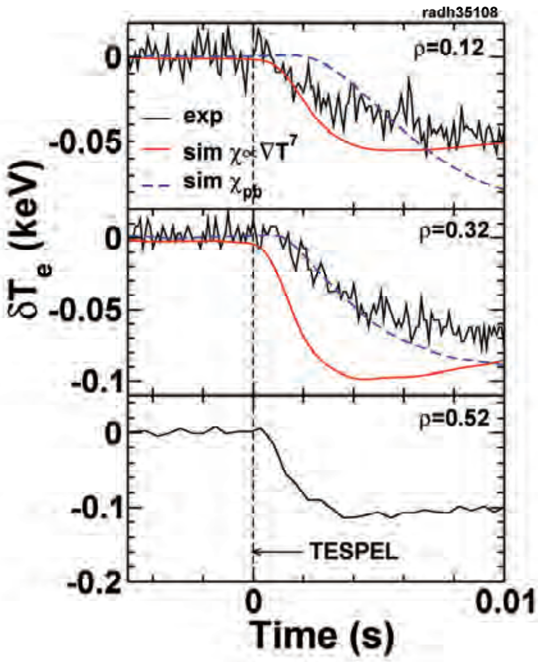

Fig. 1 Time evolution of δT_e at three different normalized radii. The simulation results based on models of $\chi = \chi_{pb}$ and $\chi_e \propto \nabla T_e^{\alpha}, \alpha = 7$ are also shown.

2 Nonlocal Transport in LHD

Some local transport models based on temperature-gradient-driven turbulence indicate that the heat transport is non-linear and thus the electron heat diffusivity, χ_e, has a dependence on electron temperature, T_e, and/or electron temperate gradient, ∇T_e [1]. To study the non-linearity of heat transport, transient transport analysis is recognized as a very powerful tool because it can yield $\partial q_e/\partial \nabla T_e$ and $\partial q_e/\partial T_e$, here q_e is the electron heat flux [2]. The transient experiments (inducing cold and/or heat pulses) have been performed and many non-linear transport models have been proposed and tested[3]. However, fast propagation of a temperature perturbation were observed, for example, the ballistic propagation observed in TJ-II[4], the heat pulse propagation caused by L-H transition [5] and heating power switching [6]. If χ_e has a dependence like $\chi_e \propto \nabla T_e^{\alpha}$, $\alpha \sim 50$ is required to explain these transient responses. Fast cold pulse propagation is also observed in the Large Helical Device (LHD) [7]. Figure 1 shows typical time evolution of a cold pulse induced by a tracer encapsulated solid pellet (TESPEL) injection in the low density (1×10^{19}m^{-3}) NBI plasma on LHD (a major radius at the magnetic axis of R_{ax} = 3.5/3.6 m, an averaged minor radius of a = 0.6 m and a magnetic field at axis of up to 2.83T) [8]. The simulation results based on models of $\chi = \chi_{pb}$ and $\chi_e \propto \nabla T_e^{\alpha}$ are also shown, here χ_{pb} is a heat diffusivity determined from the power balance analysis in

author's e-mail: inagaki@riam.kyushu-u.ac.jp

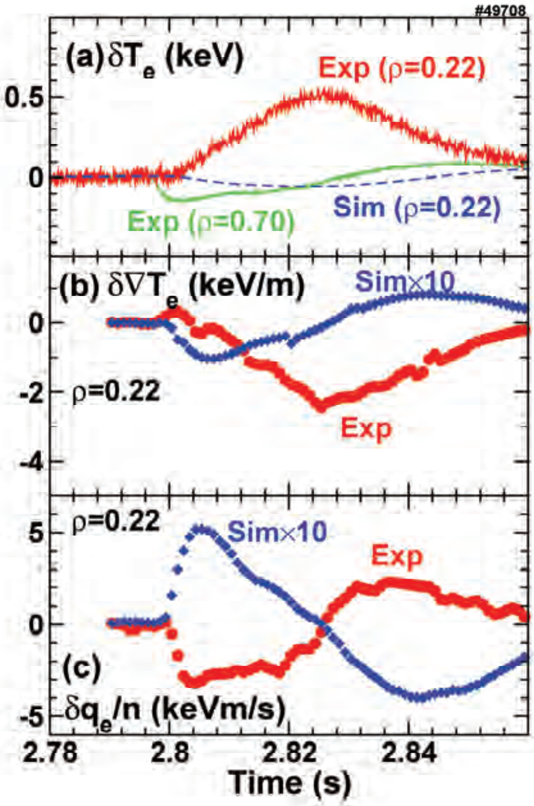

Fig. 2 Time evolution of (a) δT_e at two different normalized radii, (b) $\delta\nabla T_e$ at $\rho = 0.22$ and (c) δq_e at $\rho = 0.22$. Simulation result based on the power balance χ model are also shown. Simulated results are much smaller than experimental observations, and thus, simulation results are multiplied by ten in this figure.

stationary state [9]. In simulation, the electron temperature perturbation, δT_e, is calculated from the perturbation equation written as

$$\frac{3}{2} n_e \frac{\partial \delta T_e}{\partial t} = -\nabla \cdot \delta q_e. \tag{1}$$

The core T_e begins to decrease before the diffusive transport effect (calculated by χ_{pb}) reaches this region. To explain this prompt response of the core T_e by the non-linearity of χ_e, a strong ∇T_e dependence of χ_e ($\alpha = 7$) is required. On the other hand, $\alpha = 1 - 3/2$ is required to explain the stationary transport property both in tokamaks and helical devices [9]. A new perspective to turbulence transport (i.e. non-locality) has been introduced to explain this discrepancy.

In addition, the response to edge cold pulses often have reversed polarity, with the core T_e increasing in response to edge cooling in many tokamaks and LHD [10, 11, 12, 13, 14]. A significant core T_e rise has been observed by TESPEL injection in LHD as shown in Fig. 2 (for more details see [13]). Typical parameters in this experiment are as following: line averaged density $1 - 2 \times 10^{19}\mathrm{m}^{-3}$, central electron temperature up to 1.5 keV, central ion temperature of 1-2 keV, plasma β value of 0.1%, absorbed ECH power of 0.8 MW, deposited neutral beam power of 2 MW. Characteristic time and spacial scales are ion Larmor radius $\rho_i \sim 1$ mm, $c/\omega_p \sim 2$ mm, typical spatial scale of meso-scale structure $\sqrt{a\rho_i} \sim 30$ mm, $a/c_s \sim 1\mu s$, global energy confinement time of 50 ms, meso-scale time $\sqrt{(a/\rho_i)(a/c_s)} \sim 30\mu s$, where ω_p is the plasma frequency, c is the speed of light and c_s is the ion sound velocity. The relationship between heat flux and temperature gradient is essential to understand heat transport. Thus, time evolutions of the core ∇T_e perturbation and the heat flux perturbation (normalized by density) are also shown in Fig. 2. Multi-channel heterodyne radiometer is used to track the small T_e perturbations at different normalized radii [15]. The absolute error of ∇T_e determined by the absolute calibration of ECE is 20% and the relative errors of the ∇T_e determined by the noise levels of ECE is only 1%. The electron heat flux perturbation can be determined from the perturbation equation written as and it can be written as,

$$\delta q_e(\rho, t) = -\frac{1}{S(\rho)} \int_0^V \frac{3}{2} n_e \frac{\partial \delta T_e(\rho, t)}{\partial t} dV, \tag{2}$$

where S is the surface area of the closed flux surface, V is the volume. The power balance simulation indicates small changes in the temperature gradient and heat flux in the core region and they are quite different from experimental observations. In addition, the local transport assumption can not explain the sign of change in the heat flux. In spite of the smooth change in the temperature gradient, abrupt reductions in the heat flux (heat flux jump) are observed after several ms from the TESPEL injection.

To determine the nonlocal correlation between the heat flux and the temperature gradient, two-point cross-correlations between the core and the edge are calculated. The cross-correlation is defined as $C_{f,g}(\rho_{\mathrm{ref}}, \rho, \tau) = \langle f(\rho_{\mathrm{ref}}, t) g(\rho, t+\tau)\rangle / \sqrt{\langle f^2(\rho_{\mathrm{ref}}, t)\rangle\langle g^2(\rho, t)\rangle}$, here $\langle\rangle$ means temporal average, defined as $\langle h(t)\rangle = (T)^{-1} \int_0^T h(t)dt$. Figure 3 indicates time evolution of cross correlations, $C_{\delta q_e/n_e, -\delta\nabla T_e}(\rho_{\delta q_e/n_e}, \rho_{\delta\nabla T_e}, \tau)$, between core to core (local: $\rho_{\delta q_e/n_e} = 0.19$, $\rho_{\delta\nabla T_e} = 0.19$), core to edge (non-local: $\rho_{\delta q_e/n_e} = 0.19$, $\rho_{\delta\nabla T_e} = 0.58$), edge to core (non-local: $\rho_{\delta q_e/n_e} = 0.58$, $\rho_{\delta\nabla T_e} = 0.19$) and edge to edge (local: $\rho_{\delta q_e/n_e} = 0.58$, $\rho_{\delta\nabla T_e} = 0.58$). In the paradigm for local transport, a strong correlation between $q_e(\rho)$ and $\nabla T_e(\rho)$ is trivial and the relation of $\delta q_e = -n_e\chi_{pb}\nabla\delta T_e$ is indeed satisfied in a simulation. On the other hand, experimental result indicates that core ($\rho = 0.19$) heat flux is strongly coupled with edge ($\rho = 0.58$) temperature gradient for a short time lag, and therefore, a presence of the long distance/non-local correlation between heat flux and temperature gradient is clarified. The strong negative non-local correlation is reduced with a increase in the time lag. The correlation time, which is defined as peak width of time lag at half height, is 8 ms. This time is much longer than a/c_s and $\sqrt{(a/\rho_i)(a/c_s)}$. The local core to core correlation indicates a gradual reduction similar to that predicted by local transport when $\tau \geq 15$ ms. Subsequently, the non-local correlation is dominant over the local correlation. The edge

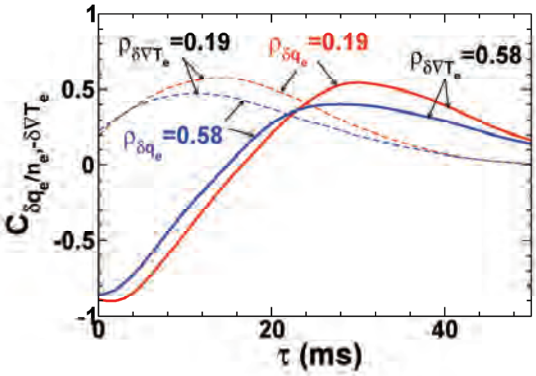

Fig. 3 Time evolution of cross correlations between core to core ($\rho_{\delta q_e/n_e}$ = 0.19, $\rho_{\delta\nabla T_e}$ = 0.19), core to edge ($\rho_{\delta q_e/n_e}$ = 0.19, $\rho_{\delta\nabla T_e}$ = 0.58), edge to core ($\rho_{\delta q_e/n_e}$ = 0.58, $\rho_{\delta\nabla T_e}$ = 0.19) and edge to edge ($\rho_{\delta q_e/n_e}$ = 0.58, $\rho_{\delta\nabla T_e}$ = 0.58).

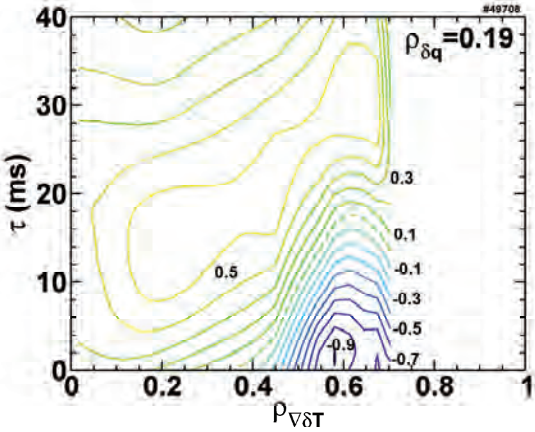

Fig. 4 Contour map of cross correlation between δq_e at $\rho = 0.19$ and $\delta\nabla T_r$ at different normalized radii.

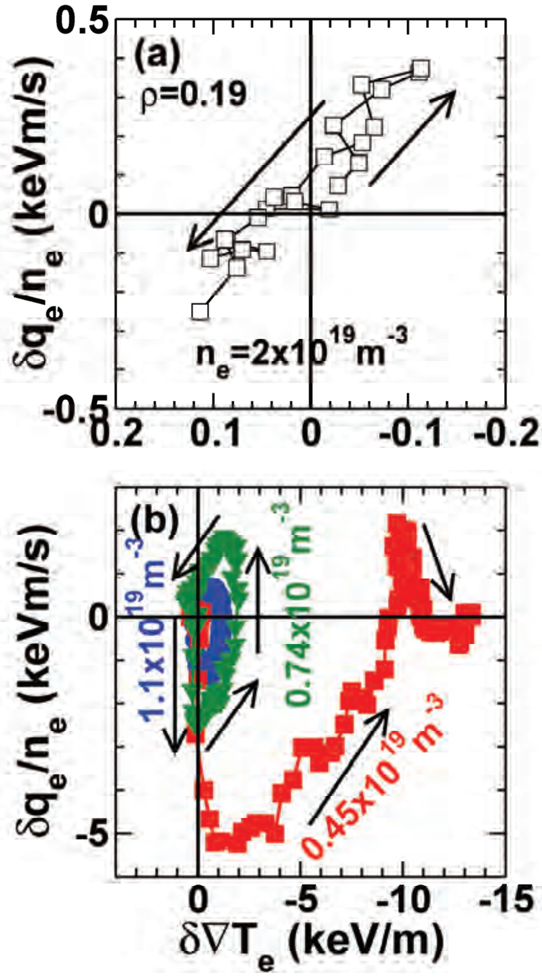

Fig. 5 Flux-gradient Lissajous diagrams at $\rho = 0.19$ in (a) the local transport condition (density is above critical value) and (b) the nonlocal condition (density is below critical value). The arrows denote the direction of variation.

heat flux is not coupled with core temperature gradient. The local edge to edge correlation indicates strong negative coupling, i.e. a decrease in the flux with an increase in the gradient (negative heat diffusivity). The negative heat diffusivity is often observed in the transition phase. Some sort of transition, thus, may take place in the nonlocal T_e rise phenomena.

To demonstrate a presence of the long distance correlation in turbulent transport, the cross correlations between the core heat flux and the temperature gradient at different normalized radii is shown in fig. 4. This diagram indicates the temperature gradient at $\rho = 0.54-0.61$ has strong negative correlation (≤ -0.8) with the core heat flux. The obtained correlation length ($0.6a$) is obviously larger than the so-called meso-scales and thus the global scales. A presence of the long distance/nonlocal correlation between heat flux and temperature gradient is clarified.

The nonlocal T_e rise takes place in the low-n_e and high-T_e (low collisionality) regime in LHD just as TFTR scaling predicts.[13, 14, 11]. The critical density for nonlocal T_e rise is $1.5 \times 10^{19}\mathrm{m}^{-3}$ in LHD. This value is 2-3 times larger than that for eITB formation ($0.6 \times 10^{19}\mathrm{m}^{-3}$).

The relations between the heat flux and the temperature gradient are determined both above and below the critical condition and shown in fig. 5. The heat transport above the critical condition is considered to be dominated by local processes. As shown in Fig. 5(a), the obtained data lie on the straight line. In other words, local heat flux is proportional to local temperature gradient. On the other hand, Lissajous diagrams (Fig. 5(b)) reveal hysteresis in heat flux versus temperature gradient. After the TESPEL injection, the heat flux changes abruptly and discontinuously. This flux jump is not accompanied by a change in the local temperature gradient, therefore transport is non-diffusive and non-local. The area of the hysteresis loop increases with a decrease in the density. The density is close to the critical value for the eITB formation, the nonlocal T_e rise triggers the eITB formation.

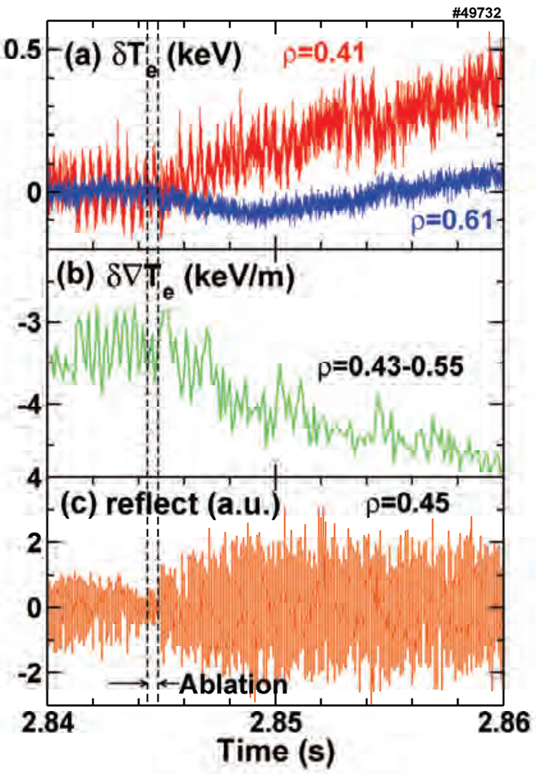

Fig. 6 Time evolution of (a) δT_e at $\rho = 0.41$ and 0.61, (b) averaged temperature gradient in the region of $\rho = 0.43 - 0.55$ and (c) X-mode reflectmetry signal at $\rho = 0.45$.

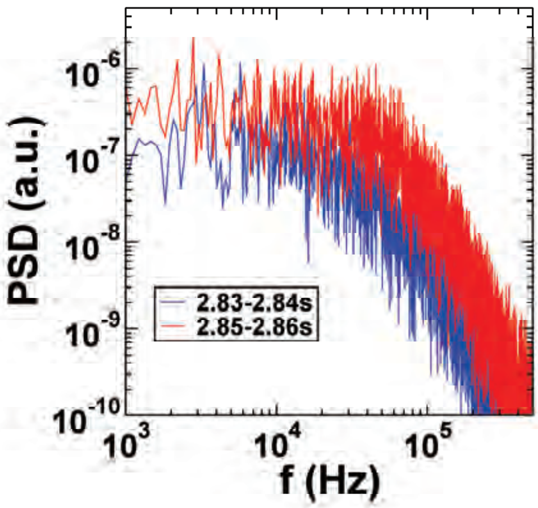

Fig. 7 Change of power spectral density of reflectmetry signal at $\rho = 0.45$. Note the high pass filter ($\geq$ 1 kHz) is applied to the reflectmetry signal.

3 Envelope Analysis

The nonlocal mechanism in plasma considered to be implicated in a structure, which is generated by interactions of turbulence over long distances. Models assuming the existence of the fluctuations with long radial correlation length on the order of the minor radius has successfully explained several features of nonlocal transport dynamics [16]. However, the experimental observation for the structures with a long correlation length has not been observed. For further study of nonlocal transport, experimental observations of spatiotemporal structure of turbulence is essential. Langmuir probe diagnostics are most suitable to fulfill a high temporal and spatial resolution measurement of fluctuations. The low temperature plasma, therefore, is very useful to study structures in turbulent plasma. The drift wave turbulence is successfully excited in the LMD-U plasmas [17]. The LMD-U has a linear magnetic configuration. In other words, geometrical effects due to configuration can be simplified. Thus, thermodynamical and statistical features of plasma turbulence will be emphasized in the turbulent structure formation. Thereby, results obtained in LMD-U experiments have a commonality beyond configuration differences. The many analysis tools are developed and tested in LMD-U. The non-linear coupling of fluctuation is identified by using bi-spectral analysis. Envelope analysis is also one of new tools.

In toroidal plasmas, the most common methods to measure fluctuations are those for density fluctuations such as conventional reflectometry. However, it is difficult to detect a certain type of fluctuation (e.g. zonal flows) by simply using the density fluctuation diagnostics due to the low level of density fluctuation component. Recent progress in the fluctuation diagnostics (e.g. HIBP[18]) has clarified non-linear coupling of drift wave turbulence and structures. For example, the turbulent density fluctuations are modulated by the zonal flows through the parametric modulational instability[19]. Thus, density fluctuations have some information about structures which can modulate them [20]. The multi-channel reflectmetry, thereby, has a capability to measure a correlation length of structure. Two channel X-mode reflectmetry was worked on the low density plasma in LHD. Figure 6 shows typical time evolution of a refrectmetry signal during the nonlocal T_e rise. After a TESPEL injection, T_e at $\rho = 0.61$ drops and T_e at $\rho = 0.41$ rises, hence, temperature gradient begins to increase. The refrectmetry signal ($\geq$ 10kHz) at $\rho = 0.45$ increases after TESPEL injection as shown in Fig. 7. This enhancement of density fluctuation may be driven by an increase in pressure gradient at $\rho = 0.45$. In order to deduce the existence of modulator, the envelope analysis is applied. Figure 8 shows an example of signal envelope and power spectrum densities of the envelope. An envelope is calculated from a high-pass filtered signal ($\leq$100kHz) by using of Hilbert transform. The refrectmetry signal data in stationary state before TESPEL injection are used to make ensemble averaging for reduction of statistical error. It is found that the envelope is modulated. The power spectrum density at $\rho = 0.45$ appears an existence of the modulator in the low frequency region ($\leq$2kHz). The geodesic acoustic mode (GAM) frequency is higher (~10kHz) than that of the modulator, and thus GAM is ruled out as a candidate of the modulator. There is no significant MHD mode

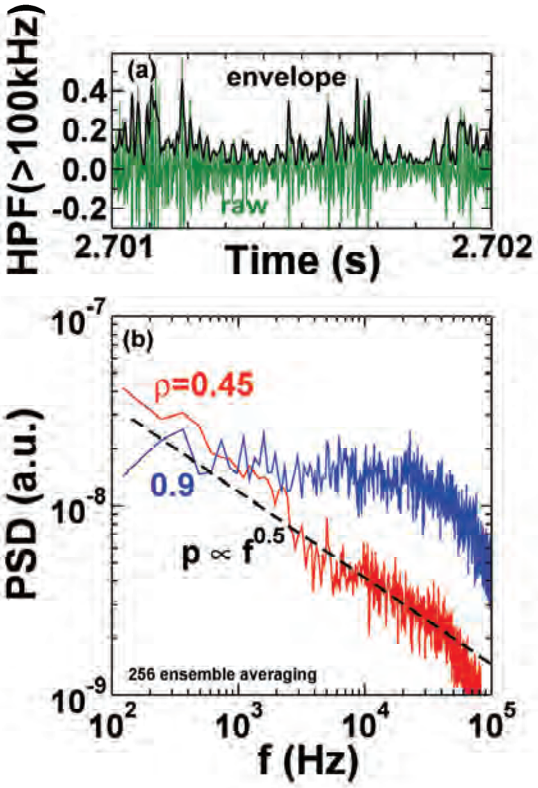

Fig. 8 (a) Time evolution of high-pass filtered signal (≤100kHz) at ρ = 0.45 and its envelope. (b) Power spectrum density of envelopes at two different normalized radii.

observed with the magnetic measurement system. In theoretical works, fluctuation of the long wave length mode excited from background micro fluctuation is predicted as the candidate[21]. On the other hand, there is no clear modulator in the power spectrum density at ρ = 0.9 and no strong coherence between envelopes at ρ = 0.45 and ρ = 0.9. The core heat flux is correlated to the edge temperature gradient around ρ = 0.6, thus, reflectmetry around ρ = 0.6 is required to discuss the correlation length of a observed modulator. The multi-channel reflectmetry and coherence and bi-spectral analysis will be the object of future work.

4 Summary

In summary, we investigate the dynamical structure of LHD cold pulse experiments providing experimental evidence for the presence of nonlocal coupling. We have found that 1) a correlation structure which have, indeed, the global spatiotemporal scales exists in turbulent plasma, 2) existence of turbulent density fluctuation modulators with low frequency.

Acknowledgments

We thank Professor O. Motojima for his continuous encouragements. We are grateful to the technical group for their excellent support. This work is partly supported by a grant-in-aid for Specially-Promoted research (16002005) and by the collaboration programs of NIFS (NIFS07KOAP017).

References

[1] F. Ryter *et al*, Phys. Rev. Lett. **86** (2001) 5498
[2] N. J. Lopes Cardozo, Plasma Phys. Control. Fusion **37** (1995) 799
[3] S. Inagaki *et al*, Nucl. Fusion **46** (2006) 133
[4] B. P. van Milligen *et al*, Nucl. Fusion **42** (2002) 787
[5] V. V. Parail *et al*, Nucl. Fusion **37** (1997) 481
[6] U. Stroth *et al*, Plasma Phys. Control. Fusion **38** (1996) 1087
[7] O. Motojima *et al*, Nucl. Fusion **43** (2003) 1674
[8] S. Sudo *et al*, Plasma Phys. Control. Fusion **44** (2002) 129
[9] H. Yamada *et al*, Nucl. Fusion **43** (2003) 749
[10] K. W. Gentle *et al*, Phys. Rev. Lett. **74** (1995) 3620
[11] M. W. Kissick *et al*, Nucl. Fusion **38** (1998) 821
[12] P. Mantica *et al*, Phys. Rev. Lett. **82** (1999) 5048
[13] S. Inagaki *et al*, Plasma Phys. Control. Fusion **48** (2006) A251
[14] N. Tamura *et al*, Nucl. Fusion **47** (2007) 449
[15] K. Kawahata *et al*, Rev. Sci. Instrum. **74** (2003) 1449
[16] T. Iwasaki *et al*, J. Phys. Soc. Japan **68** (1999) 478
[17] K. Terasaka *et al*, Plasma Fusion Res. **2** (2007) 031
[18] A. Fujisawa *et al*, Phys. Rev. Lett. **93** (2004) 165002
[19] K. Itoh P. H. Diamond, S.-I. Itoh and T. S. Hahm, Plasma Phys. Control. Fusion **47** (2005) R5
[20] Y. Nagashima *et al*, Plasma Phys. Control. Fusion **49** (2007) 1611
[21] S.-I. Itoh and K. Itoh, Plasma Phys. Control. Fusion **43** (2001) 1055

Confinement study on the reactor relevant high beta LHD plasmas

K.Y. Watanabe, S. Sakakibara, H. Funaba, S. Ohdachi, K.Tanaka, I. Yamada, L. Garcia[a], Y. Narushima, C. Michel, H. Yamada, Y. Suzuki, N. Nakajima, K. Narihara, T.Tokuzawa, K. Kawahata and LHD experimental group

National Institute for Fusion Science,322-6 Oroshi-cho, Toki 509-5292, Japan

[a]Univ. Carlos III, Avda. de la Universidad, 3028911 Leganes, Madrid, Spain

By improving the heating efficiency of the perpendicular NB injection due to the suppress the Shafranov shift by the pellet injection and the NBI power modulation, in addition to the increment of the parallel NBI power, we had the 5% beta plasma, and we had the 4.8% beta plasma in quasi-steady state with only gas-puffing and parallel NB injection. According to an analysis of the resistive g-mode by using 3 dimensional resistive MHD analyzing code for a typical high beta discharge with 4% beta and 10^6 magnetic Reynolds number, the radial mode width normalized by a plasma minor radius is ~5%. This fact supports that we have never observed disruptive phenomena in the LHD high beta discharges because the predicted MHD instabilities are located at peripheral surfaces with the high magnetic shear and their radial mode structure is quite narrow. According to the transport properties in the high beta discharges, the gradual degradation of the local transport with beta comparing with GB (Gyro-Bohm) model is observed. An anomalous transport model based on a GMT (G-Mode Turbulence) model is fairly consistent with the beta dependence of the experimental thermal transport. However, for a fusion reactor with LHD like configuration, the anomalous transport based on the GMT is still important, but it would not be strong obstacle for the production of the high performance plasmas because the magnetic Reynolds number in a reactor is much less by 300~400 times than that in the present LHD high beta discharges.

Keywords: Heliotron, LHD, high beta, MHD stability, Local transport, g-mode turbulence

1. Introduction

A heliotron device is a helical type toroidal magnetic plasma confinement system and a probable candidate as thermonuclear fusion reactor under steady-state operation because it can confine plasma with only external coils and install a well-defined divertor configuration. For an economical fusion reactor, achievement and sustainment of high beta plasma with <β>=5% is necessary. Then, the <β>=5% is a targeted value in the LHD projects from the design phase [1]. It has been considered to have a disadvantage with respect to pressure driven magneto-hydrodynamics (MHD) instabilities because the magnetic hill region exists. In order to predict the behavior of reactor plasma, we have made big effort aimed at achieving <β>=5% by increasing the heating capabilities and optimizing the operational conditions like the configurations, the heating efficiency of NBI and so on. The achieved beta value is increasing yearly as shown in Fig.1. Recently By improving the heating efficiency of the perpendicular NB injection due to the suppress the Shafranov shift by the pellet injection and the NBI power modulation, in addition to the increment of the parallel NBI power, we had the 5% beta plasma, and we had the 4.8% beta plasma in quasi-steady state with only gas-puffing and parallel NB injection. In both cases, we have not observed the disruptive phenomena.

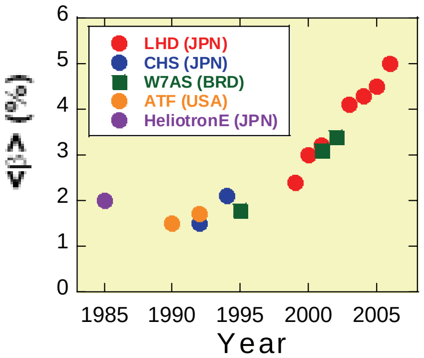

Fig.1 The yearly progress of the achieved beta value in helical devices

In this paper, we make comparative analyses between the observed beta gradient and the prediction of ideal MHD instabilities, and between the experimental thermal conductivity and the prediction based on some theoretical models, such as the Gyro-Reduced-Bohm (GRB) and the resistive g-Mode Turbulence (GMT) in the LHD with different magnetic hill configuration (plasma aspect ratio).

2. Achievement of reactor relevant high beta plasma

author's e-mail: journal@jspf.or.jp

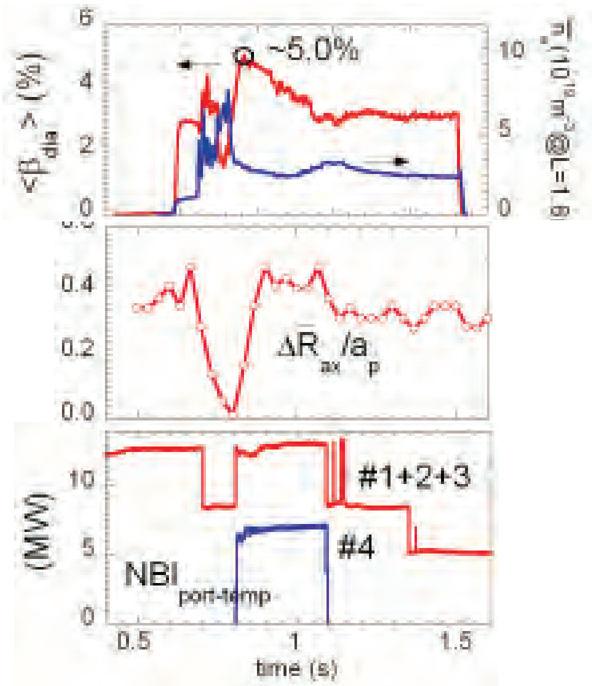

Fig.2 The waveform of the $<\beta_{dia}>$=5.0% plasma. (a) the averaged beta value and the line averaged electron density. (b) the normalized magnetic axis shift. (c) the port-through NBI power.

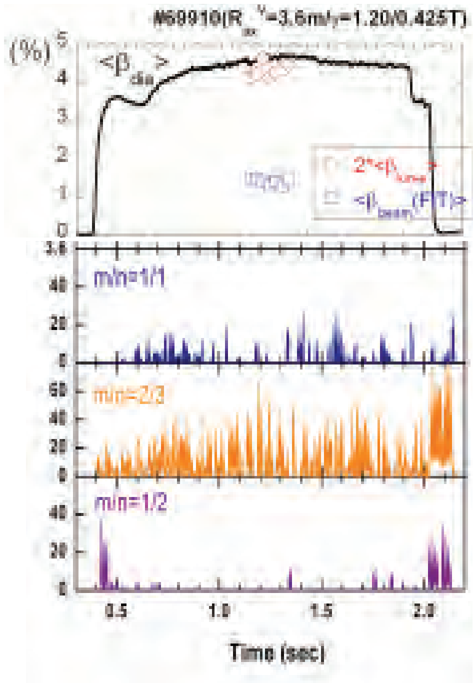

Fig.3 The waveform of the $<\beta_{dia}>$=4.8% plasma. (a) the averaged beta value and the beam component. (b)-(d) the mode amplitude of the magnetic fluctuations.

At first, we briefly mention the progress of the extension of the operational high beta regime up to the experimental campaign before last [2-4]. The heating efficiency of the NB and the MHD stability are the very important key parameters to extend the operational high beta regime. In early high beta operation in LHD, the plasma was heated only with the tangentially injected neutral beam (NB). Because the tangential radius of the NB is located at ~3.65m, the maximum of the heating efficiency is located around R_{ax}=3.6m. As well known, the magnetic axis shifts torus-outwardly as the beta increases. In order to keep the magnetic axis ~3.6m in the high beta regime, the vacuum magnetic (pre-set) configurations with the much torus-inward shifted magnetic axis and/or the high aspect plasma ratio are favorable. On the contrary, the both configurations with the more torus-inward shifted pre-set magnetic axis and the higher aspect plasma ratio are more unfavorable for the property of MHD stability. After optimizing the magnetic axis position and the plasma aspect ratio, we found the R_{ax}=3.6m and A_p=6.6 configuration the most optimum for the high beta operation, and we obtained a $<\beta_{dia}>$=4.5% plasma in F.Y.2005 [4].

In last experimental campaign in F.Y.2006, we finely study the heating efficiency of perpendicular NBI in the high beta discharges to use it more effectively for the extension of the operational high beta regime than ever before. According to a calculation, the heating efficiency of perpendicular NBI is much more sensitive to the magnetic axis position of the configurations than that of the tangential NBI. It suddenly decreases as the magnetic axis shift torus- outwardly because most of the ionized NB is trapped helically. Up to last experimental campaign, the contribution of the perpendicular NBI to the beta value was very small in the high beta discharges where the large magnetic axis shift was observed. In the high beta and low-density discharges, the beam component of the pressure is fairly large [2]. Then, it is expected that, just after the pellet injection, the beam pressure suddenly decreases, and that the magnetic axis shift decreases. Moreover, the reduction of the NBI power leads to the reduction of the magnetic axis shift due to beta. In order to control the magnetic axis position before perpendicular NB injection, we apply the pellet injection and a short break down of the tangential NBI. Due to the suppress the Shafranov shift by the pellet injection and the NBI power modulation and the addition to the perpendicular NBI power, we transiently had the 5.0% beta plasma, where plasma with more than 90% of maximum $<\beta_{dia}>$, $<\beta_{dia}>_{max}$, is maintained for a short time, ~10τ_E. Here $<\beta_{dia}>$ is the volume averaged beta value [2] and τ_E is the energy confinement time based on the diamagnetic measurement. Figure 2 shows the waveform of the $<\beta_{dia}>$=5.0% plasma. In Fig.2(a), the averaged beta value and the line averaged electron density are shown, the normalized magnetic axis shift in Fig.2(b), and the port-through NBI power in Fig.2(c), where #1+2+3 corresponds to the sum of the tangentially NB injected power and #4 to the perpendicularly NB injected power. The pellets are injected during t=0.6-0.8s. Before the pellets inject, the normalized shift of the magnetic axis exceeded 40%. During pellet injections and a NBI line break down for 0.1s, the shift of the magnetic axis approaches to zero. The perpendicular NB injection starts just after all pellet injections. After the last pellet injection, the electron density suddenly decreases and the beta value increases and reaches the maximum value of the beta, when the shift of the magnetic axis is more than 40% of the minor radius. After the beta maximum it decreases gradually. It should be noted that according to the comparison the discharges with and without perpendicular NBI, the contribution of the perpendicular NBI to the beta value is ~10% of the total beta value.

Figure 3 shows the waveform of the $<\beta_{dia}>$=4.8% plasma, which corresponds to the maximum beta value without pellet injection and the perpendicular NBI. The extension of the beta range is mainly due to the increment of the tangential NBI power comparing with the experimental campaign before last. In Fig.3(a), the averaged beta value and the beam component of the stored energy are shown, the magnetic fluctuations in Fig.3(b)-(d). The high beta plasma with $<\beta_{dia}> > 0.9\mathrm{x}<\beta_{dia}>_{max}$ is maintained for more than 80 times of τ_E (in quasi-steady). And the MHD activities corresponding to the peripheral rational surfaces are observed and its levels are not so large. The above properties are almost same with those in the

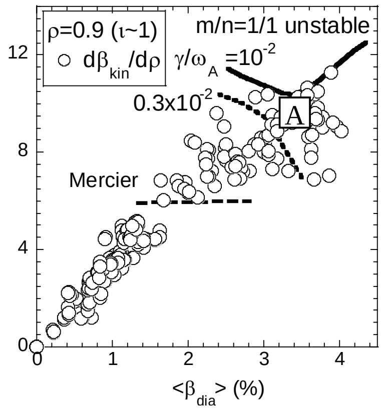

Fig.4 The peripheral beta gradients as the function of $<\beta_{dia}>$ in A_p=6.2 configuration. The contours of the growth rate of the low-n ideal MHD unstable modes are over plotted.

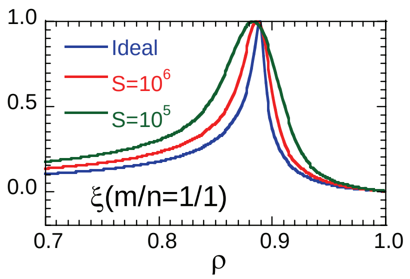

Fig.5 The radial mode structure of the global mode (m/n=1/1) for the plasma of 'A' in Fig.4 taking the resistivity into account by FAR3D. .

$<\beta_{dia}>$=4.5% plasma [2-4].

3. Effect of global MHD mode on high beta confinement

According to the analysis of the MHD equilibrium properties in the high beta configuration, the stability in the core region is improved as the beta increases. On the contrary, the stability in the peripheral region becomes worse as the beta increases. This characteristics is consistent with the fact shown in the previous section that only the MHD activities corresponding to the peripheral rational surfaces are observed in the LHD high beta plasmas. In this section, the effect of the global MHD mode resonating with the peripheral surface like m/n=1/1 (m and n are the poloidal and toroidal mode numbers, respectively) on the confinement is studied.

Figure 4 shows the thermal beta gradients at the m/n=1/1 rational surface (ρ~0.9) as faction of $<\beta_{dia}>$ in the A_p=6.2 configuration, where the achieved $<\beta_{dia}>_{max}$ is

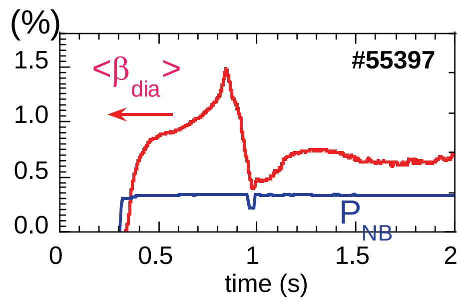

Fig.6 The evolution of the beta value and the NBI port-through power in A_p=8.3 configuration.

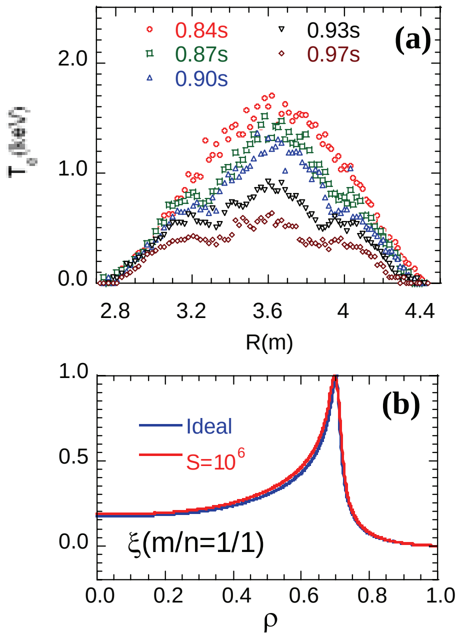

Fig.7 (a) The evolution of the electron temperature in collapse. (b) The radial mode structure of the global mode (m/n=1/1) at the just before collapse calculated by FAR3D. .

4.1% [2]. In Fig.4, the contours of the growth rate of the low-n ideal MHD unstable modes by terpsichore code [5] are superposed. It should be noted that the gradients are estimated as the averaged value for $\Delta\rho$=0.1. Around Mercier unstable region, the gradients slightly changes, but the strong reduction of the gradients are not observed in the region where the ideal global mode is predicted unstable. According to the analysis of the dependence the amplitude of magnetic fluctuation on the magnetic Reynolds number, S around $<\beta_{dia}>$~3%, it scales $S^{-0.69}$ [3]. This fact supports that the observed magnetic fluctuation in the high beta plasmas is due to the resistive interchange instability (g-mode) because the mode width estimated by a simple model, $w \sim \sqrt{\tilde{b}_\theta / B_t}$, is consistent with the theoretically predicted linear mode width of the g-mode. Figure 5 shows the mode structure of the g-mode calculated by FAR3D code [6] for the plasma presented by the ‘A’ in Fig.4. For the plasma consistent with the experimental S, ~10^6, the mode width is expected narrow, ~5% of the plasma minor radius. This fact supports that we have never observed disruptive phenomena in the LHD high beta discharges because the predicted MHD instabilities are located at peripheral surfaces with the high magnetic shear and their radial mode structure is quite narrow. It is noticed that, in the LHD high beta plasmas, the mode width of the resistive mode is a little bit larger than that of the ideal mode.

In order to confirm the above statement, we study the comparative analysis between the theoretical predicted mode structure and the electron temperature profile in the high aspect configuration, A_p=8.3, which is expected the much more unstable than the A_p=6.2 due the low magnetic shear and the high magnetic hill, there the achieved $<\beta_{dia}>_{max}$ is 2.6% and the collapse phenomena are observed shown in Fig.6, where the beta drops suddenly at t~0.85s. Figure 7(a) shows the evolution of the electron temperature profiles just before collapse and after it. The electron temperature at the core region significantly decreases due to the collapse. Figure 7(b) shows the linear mode structure predicted by FAR3D code. In this case the mode width is more than 10% of the minor radius and the amplitude of the mode at center is fairly large, which is much larger than that in Fig.5. It supports that the radial mode width is the very important key parameter against the apparent effect of the global MHD instabilities on the plasma confinement like the collapse. The identification of the threshold value should be investigated more.

4. Transport properties of high beta plasmas

As shown in Fig.4, the strong reduction of the beta gradients is not observed in the high beta plasma. However, a gradual degradation of global confinement performance is observed as the beta value increases as shown in ref.[2]. Here we focus the study of the peripheral transport property because it affects a large effect on the global confinement. Figure 8 shows the dependence of the normalized thermal conductivity, χ_{eff}/χ_{GB}, by the GB (Gyro-Bohm) model in the peripheral region on the beta value for the A_p=6.2 configuration. It should be noted that the GB model has the similar property of ISS95 confinement scaling [7], and it is proportional to β^0. In the low beta regime, the χ_{eff}/χ_{GB} is insensitive to the beta value. In the high beta regime, χ_{eff}/χ_{GB} looks proportional to β^1 [8].

As the transport model proportional to β^1, the MHD driven turbulence model is known. Here as a MHD driven turbulence model, we introduce an anomalous transport model based on the resistive interchange turbulence (g-mode turbulence, GMT) proposed by Careras et al. [9]. The thermal conductivity of the GMT model are written as the following,

$$\chi_{GMTe} \propto G_{GMTe}\ \beta^1\ \nu_*^{0.67}\ \rho_*^{0.33}\chi_B .$$

Here G_{GMTe} is defined as a geometric factor, which increases with the bad curvature and decreases the magnetic shear, and χ_B is the thermal conductivity of Bohm model. In heliotron devices as LHD, the g-mode is always unstable due to the magnetic hill in the peripheral region.

In order to study the GMT on the confinement properties in high beta LHD plasmas, we analyze the confinement property in 2 configurations with different magnetic hill height, and compare with the experimental data the local transport analysis for the 2 configurations with the different magnetic hill height. Figure 9 shows the thermal conductivities normalized by the GMT model, χ_{GMTe}, as a function of $<\beta_{dia}>$. Here we focus on the peripheral region, ρ=0.9. (a) and (b) in Fig.9 correspond to the A_p=6.2 and 8.3 configurations, respectively. The amplitude of the bad curvature in A_p=8.3 is larger than that in A_p=6.2, that is, G_{GMTe} is larger by twice. In Fig.9(a), χ_{eff}/χ_{GMTe} in the beta range of $<\beta_{dia}>$ < 1% is quit large, which occurs because there the effect of the GMT is quite small. In the beta range of $<\beta_{dia}>$ >1%, the

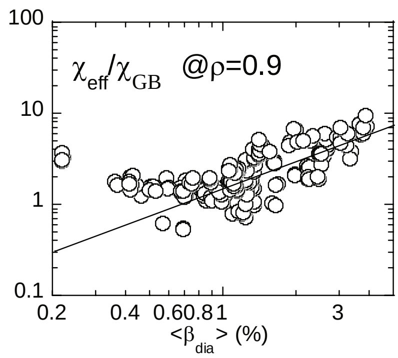

Fig.8 The normalized thermal conductivities at ρ =0.9 on the beta value in the A_p=6.2 configurations. χ_{GB} denotes the gyro-Bohm model.

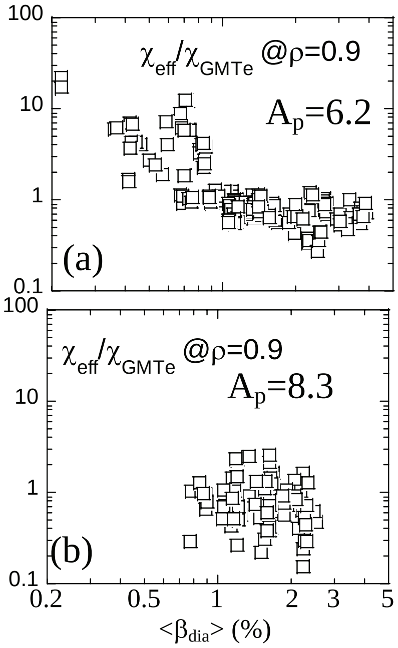

Fig.9 The normalized thermal conductivities at ρ =0.9 on the beta value. (a) and (b) correspond to the A_p=6.2 and 8.3 configurations, respectively. χ_{GMTe} denotes a g-mode turbulence model.

beta dependence of the χ_{eff} looks consistent with the GMT model. As shown in Fig.9(b), the beta dependence of the χ_{eff} looks also consistent with the GMT model in the higher magnetic hill configuration though the dispersion of χ_{eff}/χ_{GMTe} is fairly large. It should be noted that at the same $<\beta_{dia}>$ (~2%), the χ_{eff} in A_p =8.3 is larger by 6~7 times than that in A_p=6.2, and that the magnetic Reynolds number, S ($\sim\beta^{0.5}\nu_*^{-1}\rho_*^{-2}$), in A_p=8.3 is smaller by ~10 times than that in A_p=6.2. The above facts support the probability that the peripheral thermal transport in the reactor relevant high beta plasma in LHD is governed by the g-mode turbulence.

According to the analysis of the beta dependence of the density fluctuation with relatively long wavelength, le>30mm for the A_p =6.2 configuration, the amplitude of the fluctuation is quite small in the low beta regime with $<\beta_{dia}> < 1\%$ and it suddenly increases with beta value in the beta range of $<\beta_{dia}> >1\%$. This behavior looks synchronized with Fig.8. And according to ref.[10], the probable poloidal mode number of the turbulence is ~10, which is consistent with the observation of the density fluctuation. This result would be another collateral evidence for the effect of the g-mode turbulence on the LHD high beta plasma.

Next we consider the effect of the g-mode turbulence on the confinement in reactor relevant plasmas. Figure 10 shows a contour of the thermal conductivity based on the GMT model in S-R_0dβ/dr space. The thermal conductivity becomes large with the decrease of S and increase of R_0dβ/dr. Especially in high beta range, decrease of S leads to significant increase of the thermal conductivity. In Fig.10, the operation rage of S-R_0dβ/dr

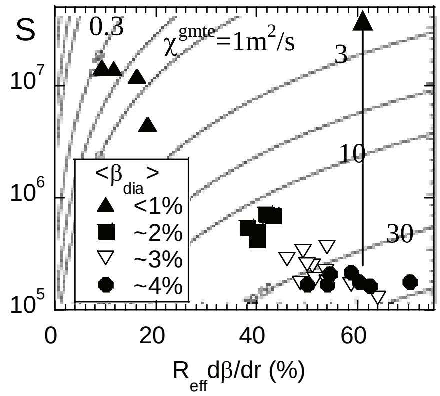

Fig.10 The predicted thermal conductivity by a t model in S-dβ/dρ diagram with the experimental data.

for the data of Fig.9(a) is also shown in Fig.10. In LHD, the decreasing the operational magnetic field strength extends the operational beta range. Then in LHD high beta operation, S is small, which leads to the prediction of large thermal conductivity. Here we shall consider a Fusion reactor. Its geometrical factor on the GMT model, such as magnetic shear and magnetic curvature, and the normalized beta gradient are almost same with those in present LHD high beta operations. On the other hand, the magnetic Reynolds number would be much larger by 300~400 times than that in the present LHD high beta operations because the magnetic field strength would be larger by around 10 times and the device size would be larger by ~3 times than the present LHD [11]. When S is 300~400 times larger comparing with present LHD high beta operation, the predicted thermal conductivity would be ~1m^2/s. For a fusion reactor with LHD like configuration, the anomalous transport based on the GMT is still important, but it would not be strong obstacle for the production of the high performance plasmas.

5. Summary

By improving the heating efficiency of the perpendicular NB injection due to the suppress the Shafranov shift by the pellet injection and the NBI power modulation, in addition to the increment of the parallel NBI power, we had the 5% beta plasma, and we had the 4.8% beta plasma in quasi-steady state with only gas-puffing and parallel NB injection, where the duration time with $<\beta_{dia}>/<\beta_{max}>$ > 90% is longer than 100τ_E.

The characteristics of the high beta plasmas with β~5% is as the followings;

1. As MHD activities of global modes, only the modes resonated with peripheral rational surfaces are observed.
2. The apparent pressure-flattening region is not observed according to the electron pressure profile measurements.
3. According to linear global MHD stability analyses

taking resistivity effect into account, the global mode resonated with peripheral rational surfaces is predicted unstable, but its radial mode width is ~5% of the plasma minor radius.

From results of the comparative analyses between achieved pressure gradients and linear MHD numerical analyses for the high beta and the high aspect configurations, it is supported that the radial mode width is the very important key parameter against the apparent effect of the global MHD instabilities on the plasma confinement like the collapse.

From the comparative analyses between experimentally obtained thermal conductivities and some theoretically predictions in high beta plasmas, there is possibility that a theoretical model based on g-mode turbulence (GMT) explains the beta dependence of the peripheral thermal conductivity in high beta plasmas. This fact is supported by the similar analyses against other configuration and the beta dependence of the observed density fluctuation amplitude with relatively long wavelength.

For a fusion reactor with LHD like configuration, the anomalous transport based on the GMT is still important, but it would not be strong obstacle for the production of the high performance plasmas. Because the anomalous transport based on the GMT strongly depends on the S value, and the S value of a reactor is much larger by 300~400 times than that in the present LHD high beta discharges.

Acknowledgments

We special thank the LHD technical staff for their great effort of LHD operation and maintenance. We are grateful to Dr. A.Cooper for permitting use of the terpsichore code, to Drs. S.P.Hirshman and P.Merkel for the VMEC code, to late Prof. T.Hayashi for the HINT code and to Dr. Y.Nakamura for KMAG and KSPDIAG codes. We acknowledge continuous encouragement by Prof. O.Motojima. This work is supported by NIFS under Contract No. NIFS06ULHH519.

References

[1] A.Iiyoshi et al., Fusion Technol. 17 (1990) 169.
[2] K.Y.Watanabe et al., Nucl. Fusion, 45, 1247-1254 (2005).
[3] S.Sakaibara et al., Fusion Sci. Technol., 50, 177 (2006).
[4] S.Sakaibara et al., in Fusion Energy 2006 (Proc. 21th Int. Conf. Chengdu, 2006) (Vienna: IAEA) CD-ROM file EX/7-5 and http://www-pub.iaea.org /MTCD/Meetings/FEC2006/ex_7-5.pdf
[5] W.A.Cooper, Plasma Phys. Control. Fusion, 34, 1011 (1992).
[6] L.Garcia, in Proc. of the 25th EPS Int. Conf., (Prague, 1998) 22A, Part II (1998) 1757.
[7] U.Stroth et al., Nucl. Fusion, 36, 1063- (1996).
[8] H.Funaba et al., Fusin Sci. Technol., **51** (2007) 129.
[9] B.A.Carreras and P.H.Diamond, Phys. Fluids B, 1, 1011 (1989).
[10] B.A.Carreras et al., Phys. Fluids 30, 1388 (1987).
[11] K.Yamzaki et al., in Proc.16th IAEA Fusion Energy Conf., Montreal, IAEA-CN-64/G1-5.

Proceedings of ITC/ISHW2007

SIESTA: an Scalable Island Equilibrium Solver for Toroidal Applications*

R. Sanchez, S.P. Hirshman and V.E. Lynch

Fusion Energy Division

Oak Ridge National Laboratory

Oak Ridge, TN 37831, U.S.A.

The construction and development of a new ideal MHD 3D-equilibrium solver, capable of dealing with magnetic islands and stochastic regions in a fast, accurate and scalable manner will be described. The SIESTA code will complement other existent 3D MHD island solvers and is particularly suited for applications that require not only accuracy but speed of evaluation as well, such as experimental 3D equilibrium reconstruction or stellarator design. SIESTA will also be useful to calculate MHD equilibria at very high spatial resolutions, such as those that might be required for the investigation of NTMs at ITER-relevant temperature and resistivity conditions. SIESTA is based on a preconditioned, iterative algorithm that takes advantage of a pre-existent VMEC solution to provide both a background coordinate system that guarantees a compact representation as well as a good initial guess for the iterative procedure. Details of the algorithm implementation, its performance on some simple test problems and initial steps towards its porting to a massively parallel environment will be discussed.

* Research supported by US-DOE under contract No. DE-AC05-00OR22725.

Proceedings of ITC/ISHW2007

Physics Mechanisms of Toroidal Rotation Profile and Properties of Momentum Transport in JT-60U

M. Yoshida, Y. Kamada, H. Takenaga, Y. Sakamoto, H. Urano,
N. Oyama, G. Matsunaga, and the JT-60 Team

Japan Atomic Energy Agency, 801-1, Mukoyama, Naka 311-0193, Japan

The roles of the elements determining the toroidal rotation velocity (V_t) profile, i.e. the momentum transport, the external momentum input, and the intrinsic rotation are found by the transient momentum transport analysis. The perturbation techniques enable us to evaluate the momentum diffusivity (χ_ϕ) and the convection velocity (V_{conv}), and to calculate V_t profiles driven by external torque input by neutral beams (NBs). The measured V_t profiles at low heating power are almost reproduced by χ_ϕ and V_{conv}. At higher heating power, the CTR directed (anti-parallel to the plasma current, I_p) intrinsic rotation, which is locally determined by the local pressure gradient is observed in the core region. This rotation increases with increasing the pressure gradient in CO and CTR rotating L-mode plasmas. Concerning the momentum transport, χ_ϕ increases with increasing heating power, and decreases with increasing I_p. In the H-mode plasmas, χ_ϕ is smaller than that in the L-mode under similar experimental conditions. It is found that χ_ϕ separated from non-diffusive term increases with increasing the heat diffusivity (χ_i), and $-V_{conv}$ increases with increasing χ_ϕ in H-mode plasmas.

Keywords: toroidal rotation velocity, intrinsic rotation, momentum transport, L-mode, H-mode.

1. Introduction

The Burning plasma is the self-regulating system, where the pressure, rotation, and current profiles are strongly linked to each other [1]. The JT-60 project has addressed major physics issues towards the understanding and the operation of the burning steady-state plasmas, and promoted an integrated research project focusing on the rotation. In many present-day tokamak experiments, the toroidal rotation velocity (V_t) is driven by external momentum input from neutral beam (NB) injection. However, in future burning plasma experiments, the external momentum input from the auxiliary heating is expected to be small. Intrinsic toroidal plasma rotations generated by the plasma itself have recently become the subject of intense interest and investigation in the magnetically confined tokamak plasma research, since such an intrinsic rotation could dominate the total plasma rotation in future devices [2]. Therefore, the critical importance of understanding the physical mechanisms determining the V_t profile including the intrinsic rotation, and controlling V_t profile has been increasingly recognized for next step devices.

It is now widely recognized that the rotation and its radial shear play essential roles in determining magnetohydrodynamic stability at a high plasma pressure, such as the stabilization of the resistive-wall mode [3, 4], and in the suppression of turbulence leading to enhanced confinement, such as the transport barrier formation [5, 6]. However, the mechanism determining rotation profile is not understood well. Because the V_t profiles are determined by various mechanisms. The worldwide progress in understanding the physics of momentum transport and rotation has been made experimentally [7-12] and theoretically [13-15]. As for the elements determining the V_t, characteristics of momentum transport which consists of diffusive (the toroidal momentum diffusivity, χ_ϕ) and non-diffusive (the convection velocity, V_{conv}) terms [7, 12], the external momentum input and the intrinsic rotation [8-11] have been reported individually. However, the understanding of rotation mechanisms with integrating all of the terms (the momentum transport, the external momentum input and the intrinsic rotation) remains an open issue despite its urgency towards the next step devices. This is due mainly to an experimental difficulty in evaluating the diffusive term of the momentum transport, the non-diffusive term of that and the intrinsic rotation separately.

In order to address this issue, we have applied the perturbation techniques developed in our recent works [7,

author's e-mail: journal@jspf.or.jp

12], which enable us to evaluate χ_ϕ and V_{conv} separately. As a novel momentum source, fast ion losses due to the toroidal field ripple, which locally induce a toroidal rotation in the direction antiparallel to the plasma current, i.e. the counter (CTR) direction in the peripheral region through the formation of an inward electric field have been used [7]. This momentum source is found by a beam perturbation experiment and orbit following Monte Carlo (OFMC) code [16]. The effects of the ripple loss of fast ions on the toroidal rotation are also investigated by using data with and without ferritic steel tiles (FSTs) [16]. The characteristics of the χ_ϕ and the V_{conv}, and the correlations between χ_ϕ, V_{conv} and χ_i are investigated by I_p and heating power scans in L- and H-mode plasmas. We have separately identified the roles of the momentum transport and the intrinsic rotation on V_t profiles in the CO (in the direction to the plasma current, I_p), and CTR rotating L-mode plasmas. In this paper, negative sign of V_t designates CTR-directed rotation and positive sign of V_t CO-directed rotation, and the momentum balance equation is solved using a cylindrical model for toroidal momentum with flux surface averaged parameters.

2. Neutral beams in JT-60U

In JT-60U [17], NBs of various injection geometries are installed. They consist of; two tangential beams directing the same direction as that of the plasma current (CO-NBs), two tangential beams directing opposite to the plasma current (CTR-NBs) and seven near perpendicular beams as shown in Fig. 1(a). The injection angle of tangential beams is 36 degree and that of near-perpendicular neutral beam (PERP-NB) is 75 degree with respect to the magnetic axis. The deuterium beam acceleration energy is about 85 keV, and the input power per injected unit is about 2 MW. The plasma rotation in the toroidal direction is varied using a combination of these NBs. In addition such a direction, one of each tangential beams in the same direction is almost on-axis deposition and the other is off-axis deposition, four of PERP-NBs are almost on-axis deposition and the others are off-axis deposition as shown in Fig. 1(b).

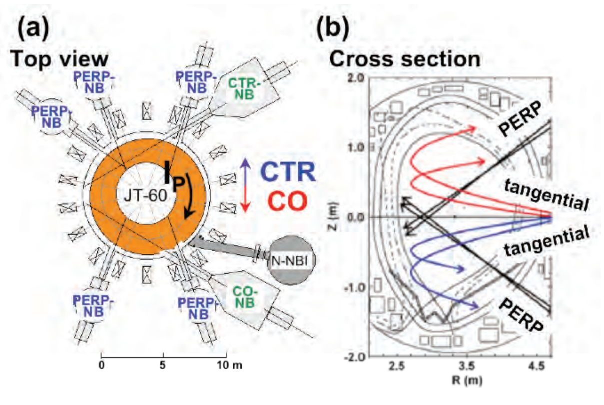

Fig.1 (a) Neutral beam (NB) system on JT-60U (b) A poloidal cross-section with NB trajectories.

3. Driving source of CTR rotation

In JT-60U, CTR rotation is observed with PERP-NB injections in the case with large ripple loss condition. In this section, the effects of the ripple loss of fast ions and the location of the driving source of CTR rotation are investigated in an L-mode plasma.

The relation between V_t in the peripheral region (r/a~0.9) and the ripple loss power is investigated by NB power and the toroidal field ripple (with and without FSTs) scans, as shown in Fig. 2(a). In this data set, I_P, the toroidal magnetic field (B_T), the plasma volume (Vol.), and the line averaged electron density ($\bar{n}_e$) are kept almost constant (I_p=1.15 MA, B_T=2.6 T, the safety factor at 95% flux surface, q_{95}~4.1, Vol.~65 m^3, $\bar{n}_e \sim 1.5-2\times10^{19}\,\mathrm{m}^{-3}$). Each arrow indicates the change in V_t by installing FSTs under the condition of almost same absorbed power (solid arrow: P_{ABS}~1.4-1.8 MW, dotted arrow: P_{ABS}~2.8-3 MW). As shown in Fig. 2(a), it is recognized that the systematic dependence of CTR rotation on the ripple loss of fast ions can be obtained by using data with and without FSTs.

In order to confirm the location of the driving source of CTR rotation, beam perturbation techniques [7] are

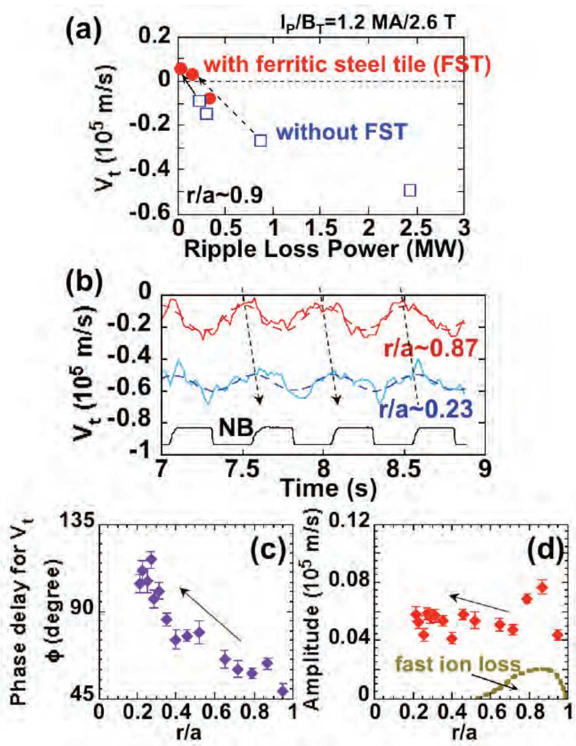

Fig.2 (a) V_t dependence on the ripple loss power. (b) Response of V_t to modulated beams. Profiles of (c) phase delay, (d) modulated amplitude, fast ion loss.

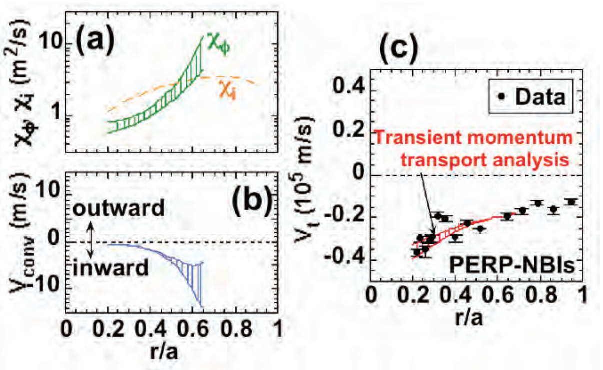

Fig.3 Profiles of (a) the toroidal momentum diffusivity (χ_ϕ), (d) the convection velocity (V_{conv}), and (c) V_t from calculation and measurements.

applied in an L-mode plasma. In this experiment, the plasma with low I_P (I_P=0.87 MA, B_T=3.8 T, q_{95}=8.2) and large volume (Vol.=72 m^3) was selected in order to enhance ripple losses. In order that the central region is free from direct external momentum input, off-axis PERP-NBs (the injected power P_{IN}=3.9 MW) are injected with a square wave modulation at 2 Hz into the discharge. As mentioned above, the injection angle of PERP-NBs is 75 degree with respect to the magnetic axis. For the purely PERP-NB injections (i.e. with no external momentum input), one unit of CO PERP-NB and that of CTR PERP-NB are injected simultaneously. Figure 2(b) shows the waveforms of modulated V_t at r/a=0.87 and 0.23 (solid lines), and the total injected power. Each trace is fitted to a sinusoidal function at the modulation frequency (dotted lines). The radial profiles of the phase delay ϕ and of the amplitude of the modulated part of the toroidal rotation velocity V_{t0} are shown in Figs. 2(c) and 2(d), respectively. The phase delay is taken from the start of NB injection. Using OFMC code [16], the profile of the prompt fast ion loss is also shown in Fig. 2(d). Large amplitude and small phase delay are recognized in the peripheral region (0.7<r/a<0.9), and this region agrees with the location at which fast ion losses take place. Therefore, we conclude the fast ion losses due to the toroidal field ripple induce CTR rotation in the edge region.

4. Evaluation of momentum transport coefficients

The toroidal momentum balance equations are written as

$$m_i \frac{\partial n_i V_t}{\partial t} = -\nabla \cdot M + S, \quad (1)$$

$$M = -m_i \chi_\phi \frac{\partial n_i V_t}{\partial r} + m_i V_{conv} n_i V_t, \quad (2)$$

where m_i, n_i, M and S are the ion mass, the ion density, the toroidal momentum flux and the toroidal momentum source, respectively [7, 12]. In this paper, ions are defined as the main (deuterium) and impurity ions, assuming that the toroidal rotation velocity of the main ions is same as that of the carbon impurity ions, which is measured by the charge exchange recombination spectroscopy [18]. We can express the modulated n_iV_t assuming $n_i^c \tilde{V}_t >> \tilde{n}_i V_t^c$, $\tilde{n}_i \tilde{V}_t$ as follows (the validity of this assumption in this experiment is shown later),

$$\tilde{V}_t(r,t) = V_{t0}(r) sin(\omega t - \phi(r)), \quad (3)$$

From equations (1)-(3), the time-independent solution of χ_ϕ and V_{conv} can be obtained [12].

Figures 3(a) and 3(b) show χ_ϕ and V_{conv} as evaluated from above mentioned modulation analysis (i.e. ϕ and V_{t0} profiles in Figs. 2(c) and 2(d)) assuming that the momentum source in the core region (0.2<r/a<0.65) is negligible (the momentum flux due to the modulated PERP-NBs, M on the left-hand side of equation (2) is one order of magnitude smaller than $-m_i\chi_\phi \partial n_i V_t/\partial r$ and $m_i V_{conv} n_i V_t$ at r/a~0.6). These transport coefficients in the region r/a>0.7 are not evaluated, because the driving source of CTR rotation is localized near the peripheral region as shown in Fig. 2(d).

The solid lines in Fig. 3(c) show V_t profiles calculated from equations (1) and (2) using transport coefficients in Figs. 3(a) and 3(b) with the boundary condition at r/a~0.65. Experimental data is also shown with solid circles. As shown in Fig. 3(c), V_t profile in the core region can be reproduced by momentum transport considering χ_ϕ and V_{conv}.

In Fig. 3(c), we compared the measured V_t profile to calculation from equations (1) and (2) using transport coefficients for a PERP-NBs injected L-mode plasma. We also treat the plasmas in which the external momentum source is injected, in order to investigate whether the toroidal rotation in the core region is dominated by the momentum transport with the coefficients. Experimental data (solid circles) in L-mode plasmas with one unit of CO tangential NB (I_P=1.2 MA, B_T=3.8 T, β_N=0.39, q_{95}=5.7 and $\bar{n}_e$=1.2x10^{19} m^{-3}) and that of CTR tangential NB (I_P=0.87 MA, B_T=3.8 T,

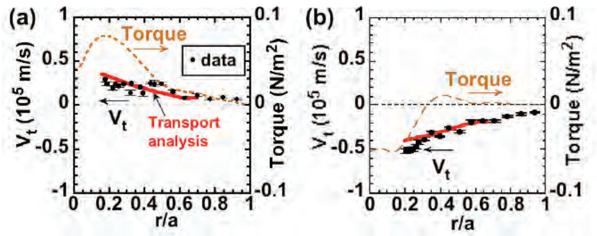

Fig.4 Data (solid circles) and reproduced V_t profile (solid lines) (a) with CO-NBI, (b) with CTR-NBI.

β_N=0.34, q_{95}=8.2 and $\bar{n}_e$=1.6x10^{19} m^{-3}) are shown in Figs. 4(a) and 4(b), respectively. In both plasmas, one unit of PERP-NB is injected for the CXRS measurements [18]. Toroidal momentum source (torque) density profiles (dashed line) are also shown. The solid lines show V_t profiles evaluated by the above-mentioned equations (1) and (2). In the both cases, the toroidal rotation profiles almost agree with calculations. The toroidal rotation profiles in the presence and absence of external torque have been explained by the momentum transport in the core region.

5. Characteristics of χ_ϕ and V_{conv}

Parameter dependences of the momentum transport coefficients (i.e. χ_ϕ and V_{conv}) evaluated above-mentioned method are shown in this section. Experiments have been carried out to investigate the momentum transport as the heating power is varied under otherwise similar conditions. As shown below, the degradation of momentum confinement with increasing heating power is observed similar to thermal confinement: the absorbed power range varied over the range 2.4 MW<P_{ABS}<10.7 MW. Over the entire power range, L-mode phase was maintained due to the high power threshold at the high B_T=3.8 T. The operation regimes in L-mode plasmas are β_N=0.39-1, $_{pol}$*=0.03-0.05 and ν*=0.07-0.14. Here, β_N is the normalized β, $_{pol}$* is the ion poloidal Larmor radius normalized to the minor radius, and ν* is the effective electron collision frequency normalized to the bounce frequency. As noted above, these L-mode plasmas satisfy L-mode scaling in JT-60U [19]. Other plasma parameters for this series of discharges were I_p=1.5 MA, q_{95}=4.2, δ=0.3 and Vol.=74 m^3. The profiles of χ_ϕ and V_{conv} during this heating power scan are shown in Figs. 5(a) and 5(b), respectively. The momentum diffusivity χ_ϕ increases systematically with increasing the heating power, and the shape of χ_ϕ is nearly identical. Non-diffusive inward flux exists and has maximum value at r/a~0.6. The dependences of χ_ϕ and V_{conv} at r/a=0.6 on absorbed power are shown in Fig. 5(c). The momentum diffusivity at r/a=0.6 roughly scaled linearly with heating power in this data set. The data in H-mode phase is also plotted in Fig. 5(c). The momentum diffusivity in the H-mode is smaller than in L-mode by factor of 2-3.

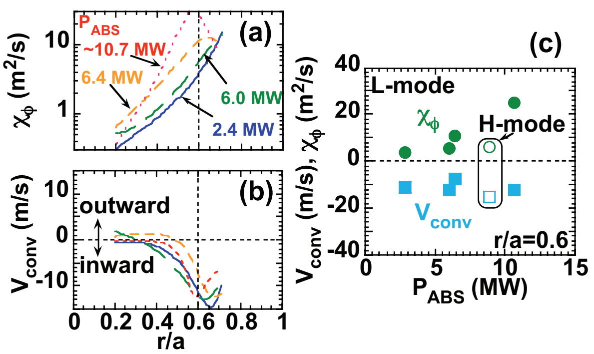

Fig.5 Profiles of (a) χ_ϕ and (b) V_{conv} during a heating power scan in L-mode plasmas. (c) Dependence of χ_ϕ and V_{conv} at r/a=0.6 on absorbed power.

6. Relation between χ_ϕ, χ_i and V_{conv}

In this section, the relations between χ_ϕ, χ_i, V_{conv} in H-mode plasmas are denoted by I_p and P_{ABS} scans.

After separating the diffusive and convective terms, the relation between χ_ϕ and χ_i is found for the fast time. Figures 6(a)-6(c) illustrate the radial profiles of χ_ϕ, V_{conv}, χ_i in a I_p scan, where B_T also varies so that q_{95}~4.3 is same value (I_p/B_T=1.2/2.8, 1.5/3.8, 1.8/4 MA/T). For these plasma discharges, two units of CO tangential NB and PERP-NBs are injected with P_{ABS}=7.2-8.9 MW. Other plasma parameters for this series of discharges were δ=0.35 and $\bar{n}_e$=2.0-2.5x10^{19} m^{-3}. The momentum diffusivity χ_ϕ decreases with increasing I_p over the whole radius. Also V_{conv} and χ_i decrease with increasing I_p. The dependences of the $1/\chi_\phi$ and $1/\chi_i$ at r/a=0.6 and the energy confinement time τ_E on I_p are also shown in Fig. 6(d). These coefficients are almost proportional to I_p, and the coefficients are similar value ($1/\chi_\phi$~0.12 I_p, $1/\chi_i$~0.14 I_p, τ_E~0.15 I_p).

The comparison of χ_ϕ and χ_i in the I_p scan is shown in Figs. 7(a) and 7(b). Figure 7(a) is the data from the profile data (0.25<r/a<0.6) shown in Figs. 6(a), and 6(b). The relation at fixed radius (r/a=0.5, 0.6) is shown in Fig. 7(b). A similar data set during the heating power scan is shown in Figs. 7(c) and 7(d), where two units of CO tangential NBs and PERP-NBs are injected at constant

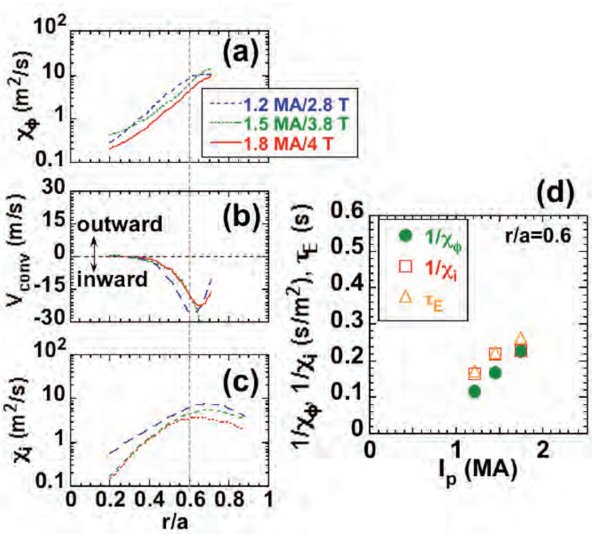

Fig 6 Profiles of (a) χ_ϕ, (b) V_{conv} and (c) χ_i during an I_p scan in H-mode plasmas. (c) Dependence of $1/\chi_\phi$ and $1/\chi_i$ at r/a=0.6 and τ_E on I_p.

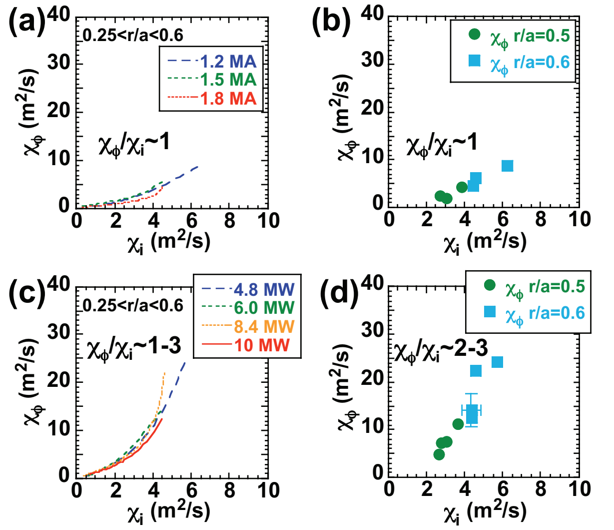

Fig.7 Relation of χ_ϕ and χ_i (a), (b) during the I_p scan, and (c), (d) during the heating power scan in H-mode plasmas. (a), (c) are the data from the profile, (b), (d) are the data at r/a=0.5, 0.6.

I_p=1.2 MA. Other plasma parameters for this series of discharges were δ=0.34 and $\bar{n}_e$=1.8-2.2x10^{19} m^{-3}. One can see that χ_ϕ increases with increasing χ_i. This tendency is observed over a wide range of radii for each discharge. In the case of the conventional steady-state analyses without considering V_{conv}, the evaluated χ_ϕ tended to be much smaller than χ_i. However, in this study, χ_ϕ is close to χ_i by analyzing both the diffusive and convective terms. This means that the momentum diffusivity is also anomalous in a similar level with the heat diffusivity.

We have also found the correlation between V_{conv}

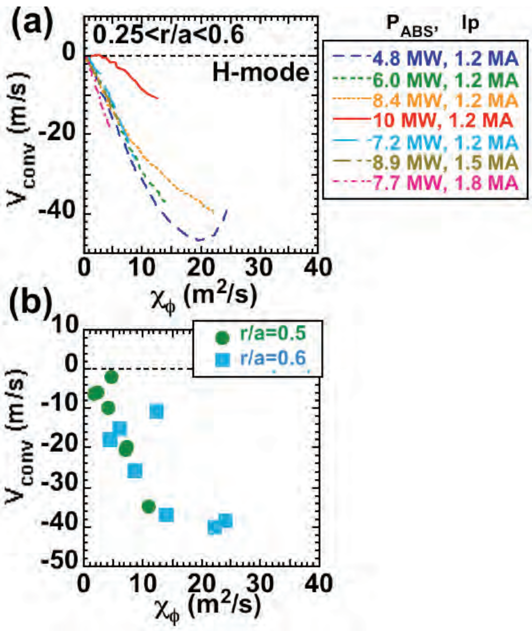

Fig.8 Correlation between V_{conv} and χ_ϕ (a) from the profile data for each discharge, and (b) at r/a=0.5, 0.6 in H-mode plasmas.

and χ_ϕ for the first time. Figures 8(a) and 8(b) show the correlation between -V_{conv} and χ_ϕ from the profile data in the region 0.25<r/a<0.6, and from the data at fixed radius (r/a=0.5, 0.6). The inward convection velocity (-V_{conv}) increases with increasing χ_ϕ over a wide range of radii for each discharge and at fixed radius in P_{ABS} and I_p scans. This finding of the correlation between χ_ϕ and V_{conv} can contribute to the understanding of the anomalous momentum transport.

7. Intrinsic rotation

In section 4, the V_t profiles in the case with and without external momentum input can be almost reproduced by momentum transport calculations with χ_ϕ and V_{conv}. However, not all measured V_t can be explained with the momentum transport model including χ_ϕ and V_{conv}, the boundary condition of V_t, and the external momentum input by NBs. In this section, the characteristics of the V_t profiles, which cannot be explained with the momentum transport model, are investigated.

Figure 9(a) shows the radial profile of the measured V_t (open circles) in the case with a higher heating power P_{ABS}=11 MW L-mode plasma. The solid line in Fig. 9(a) shows the calculated V_t from the momentum transport equations using χ_ϕ and V_{conv} with the boundary condition (setting the measured V_t equal to the calculated one at r/a~0.65) [7]. Although the measured V_t agrees with the calculation in the region 0.45<*r/a*<0.65, the measured V_t deviates from the calculated one in the CTR-direction in the core region 0.2<*r/a*<0.45. These results mean that the measured V_t cannot be explained with the momentum transport model including momentum transport

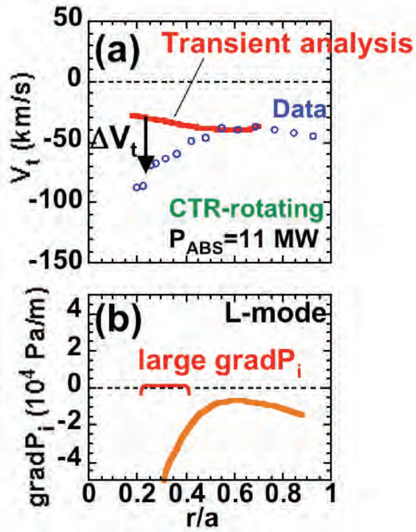

Fig.9 (a) Profiles of the measured V_t (open circles) and the calculated one (solid line), (b) and $gradP_i$ in the case of higher P_{ABS}=11 MW L-mode plasma.

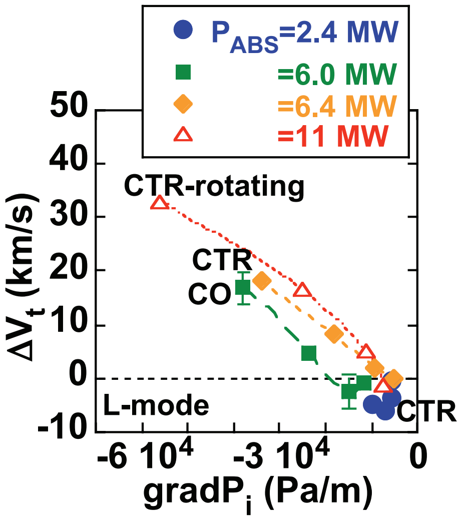

Fig.10 -ΔV_t is plotted against the $gradP_i$ in a heating power scan for L-mode (I_p=1.5 MA, B_T=3.8 T).

coefficients, the boundary condition of V_t, and the external momentum input by NBs. In such plasma, the large pressure gradient ($gradP_i$) is observed in the core region (0.2<r/a<0.45) as shown in Fig. 9(b).

In order to investigate the relation between the increase of CTR rotation and the $gradP_i$, the difference between the measured V_t and the calculated one, i.e. $\Delta V_t = V_t(measurement) - V_t(calculation) = intrinsic\ rotation$ in the region 0.3<r/a<0.6 is plotted against the $gradP_i$ in the heating power scan in Fig. 10. The symbols denote ΔV_t at r/a=0.3, 0.4, 0.5 and 0.6. In these plasmas, the larger values of $gradP_i$ are obtained in the core region. As shown in Fig. 10, ΔV_t in L-mode plasmas grows with increasing $gradP_i$ in all cases. This tendency is almost the same, even the direction of the V_t is different (CO- and CTR-rotating plasmas), over a wide range of χ_ϕ which varies by about one order of magnitude radially (χ_ϕ~1-30 m^2/s) and by about a factor of three (χ_ϕ~1-3 m^2/s) (in the heating power scan) at fixed radius (r/a~0.4). These results indicate $gradP_i$ affects the intrinsic rotation even in L-mode plasmas, and the local $gradP_i$ affects the local value of the intrinsic rotation. This good correlation between the local intrinsic rotation velocity and the local $gradP_i$ indicates that the $gradP_i$ appears to cause the value of the local intrinsic rotation velocity. The proper evaluation of the momentum coefficients enables us to evaluate the intrinsic rotation.

8. Summary

The elements determining the V_t profile have been identified, and the roles of these elements on V_t profile are also found. The fast ion losses due to the toroidal field ripple induce CTR rotation in the edge region. As a novel momentum source, this edge localized momentum source has been used for the transient momentum transport analysis. The χ_ϕ and V_{conv} have been separately evaluated using the transient momentum transport analysis. We have found that χ_ϕ, which separated from the convective term increases with increasing χ_i. The -V_{conv} increases with increasing χ_ϕ over a wide range in radii. At low plasma pressure, the steady V_t profiles with CO and CTR-NBIs can be almost reproduced by calculations with χ_ϕ and V_{conv}. On the other hand, At higher plasma pressure, the intrinsic rotation (ΔV_t) increases with increasing gradP$_i$ in CO-, CTR-rotating L-mode plasmas. The results indicate that the local gradP$_i$ appears to cause the local value of intrinsic rotation.

References

[1] Y. Kamada, Plasma Phys. Control. Fusion **42**, A65 (2000).

[2] Special issue on Progress in the ITER Physics Basis [Nucl. Fusion **47**, S18 (2007)].

[3] M. Takechi *et al.*, Phys. Rev. Lett. **98**, 055002 (2007).

[4] H. Reimerdes *et al.*, Phys. Rev. Lett. **98**, 055001 (2007).

[5] Y. Sakamoto *et al.*, Nucl. Fusion **41**, 865 (2001).

[6] E. J. Synakowski *et al.*, Nucl. Fusion **39**, 1733 (1993).

[7] M. Yoshida *et al.*, Plasma Phys. Control. Fusion **48**, 1673 (2006).

[8] W.D. Lee *et al.*, Phys. Rev. Lett. **91**, 205003 (2003).

[9] J. E. Rice *et al.*, in *Proceedings of the 21st IAEA Fusion Energy Conference,* (IAEA, China, 2006) EX/P3-12.

[10] A. Bortolon *et al.*, Phys. Rev. Lett. **97**, 235003 (2006).

[11] K. Ida *et al.*, J. Phys. Soc. Jap. **67**, 4089 (1998).

[12] M. Yoshida *et al.*, Nucl. Fusion **47**, 856 (2007).

[13] O. D Gurcan, P. H. Diamond, T. S. Hahm, *et al.*, Phys. Plasmas **14**, 042306 (2007).

[14] T. S Hahm, P. H. Diamond, O. D Gurcan and G. Rewoldt, Phys. Plasmas **14**, 072302 (2007).

[15] B. Coppi, Nucl. Fusion **42**, 1 (2002).

[16] K. Shinohara *et al.*, Plasma Fusion Res. **1**, 007 (2006).

[17] S. Ide and the JT-60 Team, Nucl. Fusion **45**, S48 (2005).

[18] Y. Koide *et al.*, Phys. Rev. Lett. **72**, 3662 (1994).

[19] H. Shirai *et al.*, in Plasma Physics and Controlled Nuclear Fusion Research 1994 (*Proc. 15th Int. Conf. Seville, 1994*), Vol. 1, p. 355, IAEA, Vienna (1995).

Proceedings of ITC/ISHW2007

Theory of Stellarators and Tokamaks in Three Dimensions

Paul R. Garabedian

Courant Institute of Mathematical Sciences, New York University
New York, New York 10012 USA

The NSTAB computer code applies the MHD variational principle to calculate equilibrium and stability of toroidal plasmas in three dimensions. Differential equations are solved in a conservation form that describes force balance correctly across islands that are treated as discontinuities. The method has been applied to stellarators, including LHD, and tokamak configurations such as DIII-D and ITER. Sometimes the solution of the equations turns out not to be unique, and there may exist bifurcated equilibria that are nonlinearly stable when theory predicts linear instability. With appropriate pressure profiles, the LHD plasma is found to be stable at $\beta = 0.045$, which correlates with recent experiments. Hence reactor values of pressure can be confined stably in a stellarator configuration with robust flux surfaces. A similar analysis shows that tokamak configurations like ITER do not remain axially symmetric at finite β, for they develop helical islands, which may manifest themselves experimentally as neoclassical tearing modes (NTMs) and edge localized modes (ELMs). These results motivate a continuing search for improved stellarator configurations which (a) employ relatively simple coils to generate good flux surfaces even at low aspect ratios typical of a tokamak; (b) retain the favorable high β equilibrium and stability characteristics demonstrated in LHD; and (c) promise reduced transport by virtue of quasiaxial symmetry.

1. Computational Science of Magnetic Fusion

For a long time it has been recognized that fusion of hydrogen to form helium is what powers the sun and the stars. Now a community of scientists believes that a similar process releasing energetic neutrons can be exploited to construct nuclear reactors that might eliminate global warming by fossil fuels. A very hot plasma of deuterium and tritium is to be confined in toroidal geometry by a strong magnetic field that separates the ionized gas from material walls. The most successful fusion experiments have been axially symmetric tokamaks with net toroidal current induced in the plasma itself to produce a poloidal field required for equilibrium. The stellarator is a more stable configuration with the external field generated by a system of complicated coils in three dimensions. Modern methods of computational science enable physicists to perform parameter studies necessary to design practical configurations for experiments to establish the feasibility of this concept of magnetic fusion.

Three-dimensional computer codes have been written to study equilibrium, stability and transport of plasmas in toroidal geometry for magnetic fusion. Advanced numerical methods have been employed to solve systems of differential equations that model these configurations. Despite the simplicity of some of the models, good correlation has been obtained with observations from experiments. We shall discuss comparisons with the Large Helical Device built and operated in Japan and the International Thermonuclear Experimental Reactor planned for construction in France by a consortium of countries. Afterwards we shall propose an alternate device, the Modular Helias-like Heliac 2, a stellarator that seems to perform better according to the predictions of a mathematical theory which we have developed.

2. Equations

The Maxwell stress tensor enables one to put the differential equations describing force balance in the conservation form

$$\nabla \cdot \Big[\mathbf{BB} - (B^2/2 + p)\mathbf{I}\Big] = 0, \nabla \cdot \mathbf{B} = 0.$$

Comparable finite difference equations, summed over a test volume, telescope down to a correct statement of force balance over the boundary. This way we capture discontinuities in solutions

$$\mathbf{B} = \nabla s \times \nabla \theta = \nabla \phi + \zeta \nabla s$$

of the MHD variational principle

$$\delta \int\int\int (B^2/2 - p(s))\, dV = 0$$

for a plasma with separatrix defined by the Fourier series

$$r + iz = e^{iu} \sum \Delta_{mn}\, e^{-imu+inv} .$$

Islands occur where the spectrum B_{mn} defined by

$$\frac{1}{B^2} = \sum B_{mn}(s) \cos\left[m\theta - (n - \iota m)\phi\right]$$

activates small denominators of the parallel current

$$\frac{\mathbf{J}\cdot\mathbf{B}}{p'B^2} = \sum \frac{mB_{mn}(s)}{n - \iota m} \cos\left[m\theta - (n - \iota m)\phi\right].$$

As an example, consider the RFP model problem

$$(\Psi_x^2)_x = \eta \Psi_{xxx} \quad , \quad \Psi = 1 - |x| .$$

References

1. R. Alexander and P. Garabedian, Choice of coils for a fusion reactor, Proc. Natl. Acad. Sci. USA **104** (2007) 12250-12252.

2. F. Bauer, O. Betancourt and P. Garabedian, *Magnetohydrodynamic Equilibrium and Stability of Stellarators*, Springer-Verlag, New York, 1984.

3. F. Bauer, P. Garabedian, D. Korn and A. Jameson, *Supercritical Wing Sections II*, Springer-Verlag, New York, 1975.

4. D. Brennan, R. La Haye, A. Turnbull, M. Chu, T. Jensen, L. Lao, S. Kruger and D. Schnack, A mechanism for tearing onset near ideal stability boundaries, Phys. Plasmas **10** (2003) 1643-1652.

5. P. Garabedian and L. Ku, Reactors with stellarator stability and tokamak transport, Fusion Sci. Technol. **47** (2005) 400-405.

6. P. Garabedian and M. Taylor, Tokamak transport driven by quasineutrality and helical asymmetry, Nucl. Fusion **32** (1992) 265-270.

7. S. Hirshman and O. Betancourt, Preconditioned descent algorithm for rapid calculations of magnetohydrodynamic equilibria, J. Comp. Phys. **96** (1991) 99-109.

8. A. Komori and H. Yamada, Overview of the Large Helical Device, Plasma Phys. Control. Fusion **42** (2000) 1165-1177.

9. J. Nuehrenberg and R. Zille, Quasi-helically symmetric toroidal stellarators, Physics Letters **129A** (1988) 113-116.

10. M. Taylor, A high performance spectral code for nonlinear MHD stability, J. Comp. Phys. **110** (1994) 407-418.

Figures

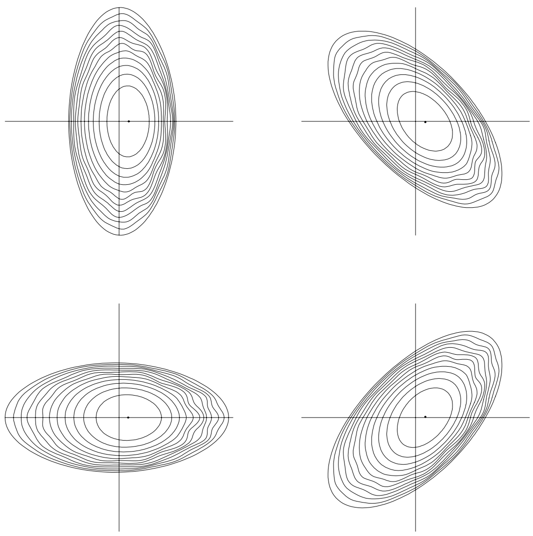

Figure 1: Poincaré sections of the flux surfaces of a bifurcated, nonlinearly stable LHD equilibrium at $\beta = 0.048$. The ripple in the flux surfaces on the right suggests that ballooning modes appear in the solution, but a reliable prediction of the β limit cannot be made without more information about the experiment. The existence of several solutions of the ideal MHD equilibrium equations is considered to be evidence of linear instability.

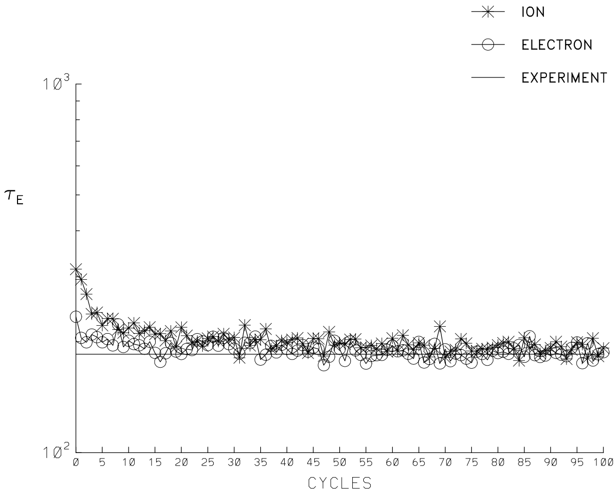

Figure 2: Cycles of a calculation of the energy confinement time τ_E in milliseconds for an NBI shot of the LHD experiment using a quasineutrality algorithm to adjust the electric potential Φ. Oscillations of Φ along the magnetic lines model anomalous transport, so there is good agreement with the observed value. Results from the LHD experiment have served to validate the numerical simulations of equilibrium, stability and transport that are provided by runs of the NSTAB and TRAN computer codes. The TRAN code models thermal transport by performing a random walk among complicated orbits of the ions or electrons, which are found from Runge-Kutta solutions of a system of ordinary differential equations for guiding centers. The results depend primarily on the magnetic spectrum of the plasma, which is obtained from runs of the NSTAB code.

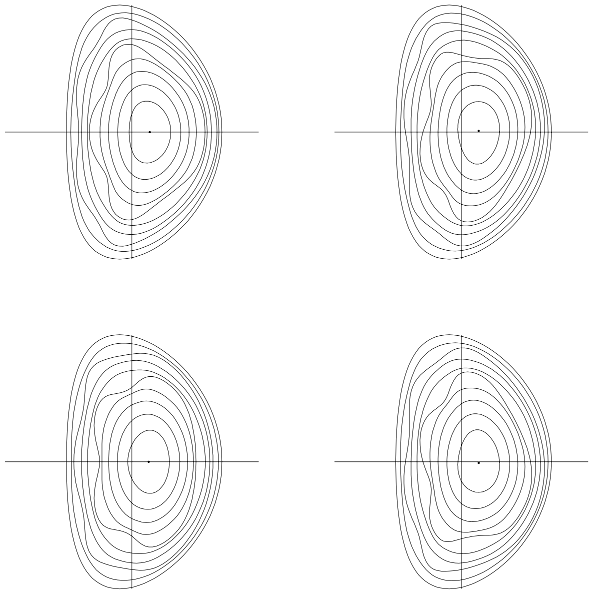

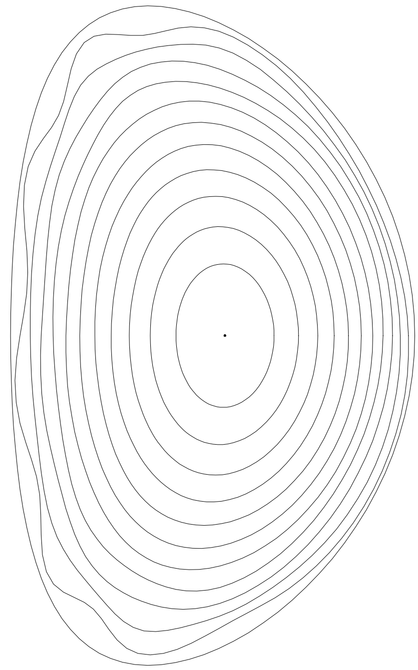

Figure 3: Four Poincaré sections of the magnetic surfaces over one out of three artificial field periods of a bifurcated, nonlinearly stable ITER equilibrium at $\beta = 0.03$ with $0.9 > \iota > 0.4$. The ripple in the flux surfaces suggests that there may be NTMs and ELMs in this three-dimensional solution of an axially symmetric problem. Extensive studies of numerical examples produce ample evidence that bifurcated equilibria can be expected to appear in most tokamak problems, so provision should be made for that. Convergent runs of the NSTAB code can capture islands whose widths are smaller than the radial mesh size and compute bifurcated equilibria in examples where there is marginal linear instability, but global nonlinear stability, of the ideal MHD model.

Figure 4: Poincaré section of the flux surfaces of a bifurcated ITER equilibrium at $\beta = 0.027$ with net current bringing the rotational transform into the interval $0.93 > \iota > 0.37$. There are helical islands in this three-dimensional solution of an axially symmetric MHD problem, which may model ELMs. A forcing term was used early in the run to trigger a mode that appears as a discontinuity in the three-dimensional solution. This double precision calculation converges to the level of round off error, showing that the discrete problem has been solved. Islands are captured numerically by finite difference equations in a conservation form that works despite the nested surface hypothesis present in our mathematical formulation of the problem. The results are plausible on the long time scale of a magnetic fusion reactor.

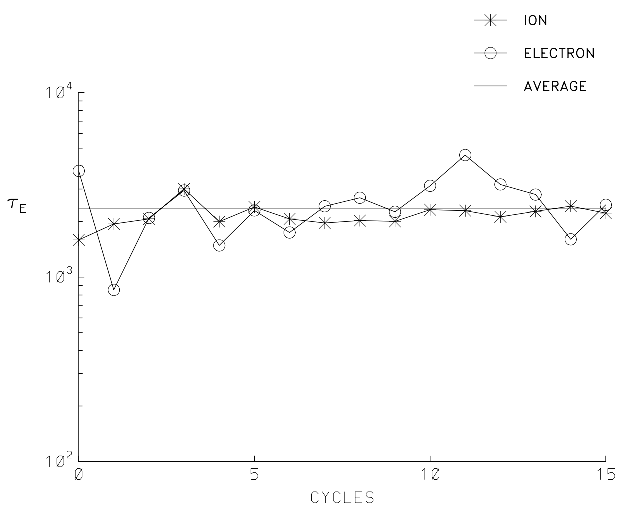

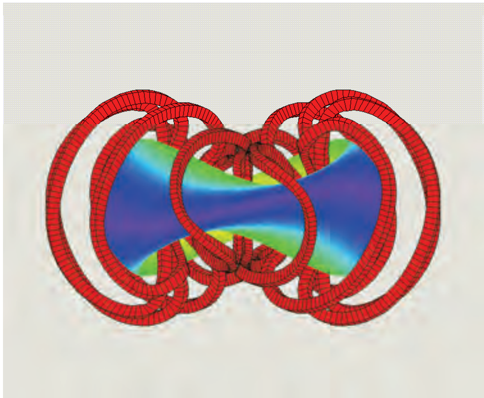

Figure 5: Cycles of a calculation of the energy confinement time τ_E in milliseconds for the ITER tokamak using a quasineutrality algorithm to adjust the electric potential Φ. The three-dimensional effect of ripple associated with a system of just twelve toroidal coils has been introduced to drive the radial electric field and cause the plasma to spin. It is not clear that two-dimensional models describe transport in tokamaks adequately. The energy confinement time is calculated from an empirical relationship with the particle confinement time. Without three-dimensional terms we have not been able to reconcile discrepancies between the ion and the electron confinement times that are computed by the Monte Carlo method in tokamaks.

Figure 6: In magnetic fusion, hot deuterium and tritium ions are combined to form helium and release neutrons intended to provide a commercial source of energy. The color map of the hydrogen plasma shown in the figure displays a symmetry property that enhances confinement. Twelve only moderately twisted coils generate a magnetic field designed to keep the plasma in stable equilibrium separated from material walls. The side view of this compact stellarator shows that there is ample space between the coils for NBI heating. Our hope is that a judiciously optimized QAS stellarator may overcome the troubles with poor transport and low ion temperature in conventional stellarators, and with poor stability and ELMs crashes in tokamaks.

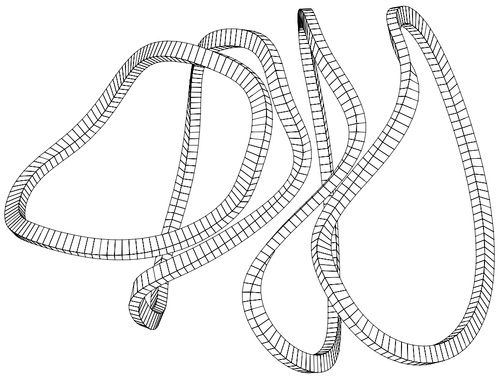

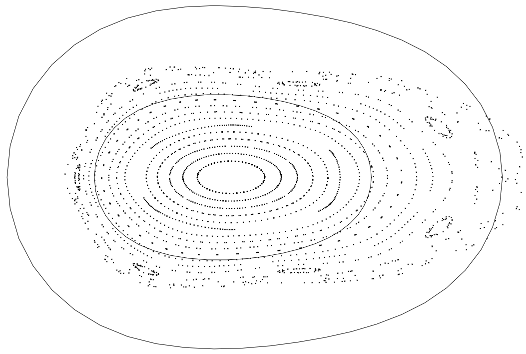

Figure 7: Four out of twelve modular coils of the MHH2 stellarator in a vacuum magnetic field given by the Biot-Savart law. The coils at the sides of the diagram are located at corners over the full torus, so the distances between all the coils can be estimated from the figure. Judicious filtering of the Fourier series used to calculate filaments specifying the geometry of the configuration defines shapes that are not excessively twisted. Parameters have been adjusted to provide ample space around each coil, and the aspect ratio of the plasma is 2.5. The spacing is adequate for superconducting coils in a reactor with major radius 7 m or 8 m, but there is difficulty fitting the coils together inside a small experiment at high magnetic field. Through rigid motions, four copies of the quadrant of coils shown in the plot can be combined to give an accurate picture over the full torus.

Figure 8: Cross section of a line tracing calculation for a QAS stellarator displaying curves that define the control surface for the coils and the shape of the plasma, together with magnetic lines computed at $\beta = 0$. The flux surfaces and islands outside the separatrix show that the magnetic field is well organized for a divertor. This works because smooth coils were found to provide the external field confining the plasma. It is essential to choose the coils both so that the stellarator can be constructed without too much difficulty and so that the flux surfaces remain robust when realistic changes are made in physical parameters. The formulas we apply to represent the plasma surface and the shape of the coils are motivated by a knowledge of conformal mapping and Runge's theorem in the theory of analytic functions of a complex variable.

Proceedings of ITC/ISHW2007

ECCD Experiments in Heliotron J, TJ-II, CHS and LHD

K. Nagasaki[a)], G. Motojima[b)], A. Fernández[c)], Á. Cappa[c)], J. M. Fontdecaba[c)], Y. Yoshimura[d)], T. Notake[d)], S. Kubo[d)], T. Shimozuma[d)], H. Igami[d)], K. Ida[d)], M. Yoshinuma[d)], T. Kobuchi[d)], Heliotron J Team[a) b)], TJ-II Team[c)], CHS Team[d)] and LHD Team[d)]

a) Institute of Advanced Energy, Kyoto University, Gokasho, Uji, Kyoto, Japan

b) Graduate School of Energy Science, Kyoto University, Gokasho, Uji, Kyoto Japan

c) Laboratorio Nacional de Fusión, EURATOM-CIEMAT, Madrid, Spain

d) National Institute for Fusion Science, Oroshi-cho, Toki, Gifu, Japan

Electron cyclotron current drive (ECCD) experiments have been made in stellarator/heliotron (S/H) devices such as Heliotron J, TJ-II, CHS and LHD. The experimental results show that ECCD can be controlled by the power injection angle, absorption position and magnetic field structure. The current drive efficiency is similar, $\gamma = n_e I_{EC} R/P_{EC}$=8-16×10^{16} A/Wm^2, $\zeta=32.7 n_e I_{EC} R/P_W T_e$ =0.03-0.05. The reversal of driven current direction is observed depending on the magnetic field ripple structure, indicating that the amplitude and direction of EC current is determined by the balance between the Fisch-Boozer effect and the Ohkawa effect, and that the Ohkawa effect is strong in S/H devices compared with tokamaks. Control of net toroidal current by using ECCD is demonstrated; net zero current state is attained by cancelling the bootstrap current.

Keywords: electron cyclotron current drive, stellarator, heliotron, Heliotron J, TJ-II, CHS, LHD, current drive efficiency, Fisch-Boozer effect, Ohkawa effect

1. Introduction

Non-inductive current has an important role on the realization of high performance plasmas and the sustainment of steady state plasmas in toroidal fusion devices. In S/H systems, no Ohmic current is required for equilibrium since the confinement magnetic field is generated by external coils. However, it is known that finite plasma pressure drives bootstrap current as well as in tokamaks, which modifies rotational transform profile, resulting that the equilibrium and stability is affected. For example, the bootstrap current increases the rotational transform in LHD, moving the rational surface of $\iota/2\pi=1$ to low shear region, giving rise to the confinement degradation due to the formation of magnetic island [1].

Electron cyclotron current drive (ECCD) is recognized as a useful scheme for stabilizing MHD instabilities and analyzing heat and particle transport [2][3]. For example, in large tokamaks such as JT-60U, neoclassical tearing mode has been stabilized by localized ECCD, leading to the improvement of normalized beta [4]. In S/H systems, on the other hand, the ECCD is expected to avoid dangerous rational surface by cancelling the bootstrap current particularly in low shear S/H devices. From the viewpoint of diagnostics, the S/H systems have the advantage of precise measurement of the EC current. The estimate of EC current is not so simple in tokamaks since a large amount of Ohmic current flows, and the effects of toroidal electric field and plasma resistivity have to be taken into account. In the S/H systems, we are able to measure the EC current with the accuracy of the order of less than 1 kA by using a conventional Rogowskii coil because of no Ohmic current.

A systematic research on ECCD in S/H systems was performed experimentally and theoretically in W7-AS for the first time [5] [6]. Several results such as the dependence on injection angle and electron density and the effect of trapped particles were discussed. Recently international collaboration research on ECCD has been conducted in Heliotron J (Kyoto Univ.) [7], TJ-II (CIEMAT) [8], CHS (NIFS) [9][10] and LHD (NIFS) [11] in order to understand the ECCD physics and to investigate the applicability of ECCD to the control of plasma equilibrium and stability. This paper summarizes these recent experimental results on ECCD. The comparison of experimental results from these four devices will give us common understanding of the current drive physics.

This paper is organized as follows. The experimental set up including the ECH/ECCD system is described in Sec. 2. The experimental results, especially the dependence on injection angle, electron density and magnetic field structure are shown in Sec. 3. The trapped

author's e-mail: nagasaki@iae.kyoto-u.ac.jp

particle effect generated by the magnetic field ripple is discussed, which strongly affects the current drive efficiency. Summary is given in Sec. 4.

2. Experimental Setup

Heliotron J, TJ-II, CHS and LHD are S/H fusion devices, which have the device parameters of major radius, R=1.2 m, minor radius, a=0.1-0.2 m, magnetic field, B=1.5 T (Heliotron J), R =1.5 m, a =0.1-0.2 m, B =1.0 T (TJ-II), R =1.0 m, a =0.2 m, B =1.9 T (CHS), and R =3.75 m, a =0.6 m, B =2.8 T (LHD). The plasma parameters discussed in this paper ranges as n_e=0.2-1.5×10^{19} m^{-3}, T_e=0.3-2 keV and T_i=0.1-2 keV. The plasmas are produced and heated by ECH only, and the upper density limit is determined by second harmonic X-mode cut-off, n_e^c = 1.75×10^{19} m^{-3} for 53.2 GHz (TJ-II and CHS), n_e^c = 3.0×10^{19} m^{-3} for 70GHz (Heliotron J), n_e^c = 4.4-×10^{19} m^{-3} for 84 GHz (LHD) and n_e^c = 17.5×10^{19} m^{-3} for 168 GHz (LHD),

The magnetic field structure is different among four devices since the field spectrum is different. Figure 1 illustrates the magnetic field profiles along the magnetic axis. Heliotron J has a capability of controlling the coil current independently, making it possible to change the magnetic ripple structure at the launching position. The magnetic field has a structure from local maximum (ripple top structure) to local minimum (ripple bottom structure) at the ECH power deposition. In TJ-II, the EC power is injected near the local minimum position. In CHS and LHD, the magnetic field ripple is small along the magnetic axis at the magnetic axis location of R=0.95 m and R=3.75 m, respectively, and the ripple structure appears when the magnetic axis is shifted by vertical coils.

The ECH/ECCD system is routinely used for plasma production and heating in S/H systems. Since the S/H system has 3-D magnetic field structure, wide injection angle range and precise polarization control are required to change the absorption profile and parallel refractive index. Recent progress on high power millimeter wave technology gives us focused Gaussian beam injection system with injection angle and polarization well controlled. Table 1 shows the main features of ECH/ECCD system in Heliotron J, TJ-II, CHS and LHD (see the references for details). The focused Gaussian beam is injected with a wide range of both toroidal and poloidal injection angle by using a steering mirror, which enables us to have enough oblique launch angle for large refractive index. In Heliotron J, a focused Gaussian beam is launched from the corner section (the toroidal angle, φ=0 deg) for $N_{||}$ scan, and non-focused Gaussian beam is launched from the straight section (φ=45 deg) for the other scans. In TJ-II, two unit 53.2 GHz ECH/ECCD

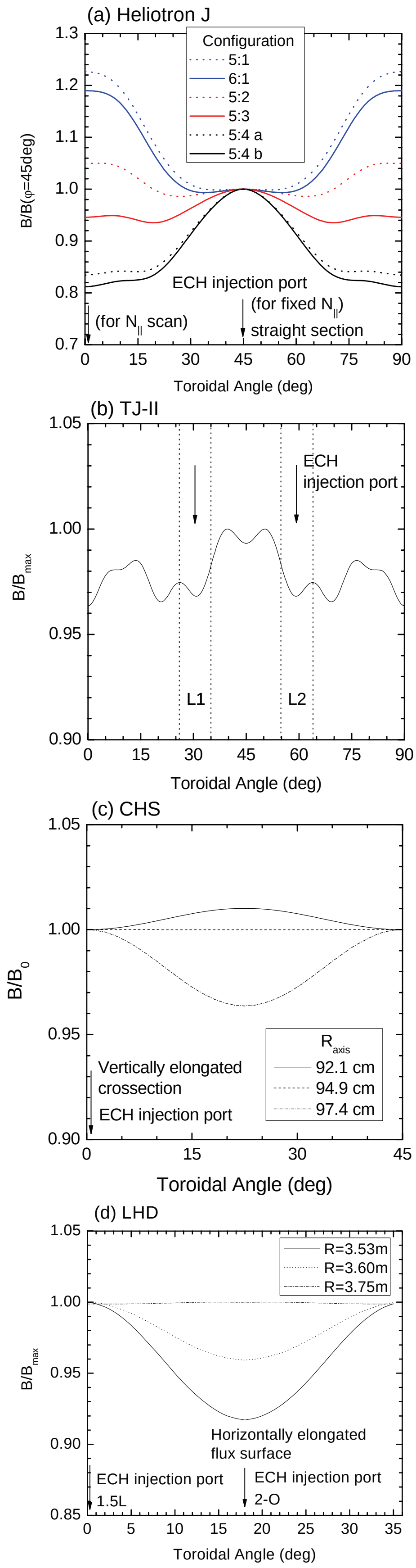

Fig. 1 Magnetic field profile along magnetic axis in (a) Heliotron J, (b) TJ-II, (c) CHS and (d) LHD.

systems are used, in which a steering mirror is installed in each injection system. The injection position is symmetric with respect to the toroidal angle, leading that the EC current can be widely controlled by scanning the injection angle with different $N_{\|}$. In CHS, the EC beam is injected from the top of torus, and the refractive index is 0.16 in vacuum at the magnetic axis of R=0.95 m for the toroidal angle of 7 deg. In LHD, the toroidal angle is 8.3 deg at vertical port (1.5L port), 9.9 deg at horizontal port for co-injection, and it is -5.9 deg at vertical port, -9.9 deg for counter-injection.

	Heliotron J	TJ-II	CHS	LHD
Frequency	70GHz	53.2GHz	53.2GHz	84GHz
Maximum injection power	0.4MW	0.3MWx2	0.3MW	1.3MW
Maximum pulse length	0.2sec	0.5sec	0.1sec	3sec
Injection mode	Focused/ nonfocused Gaussian	Focused Gaussian	Focused Gaussian	Focused Gaussian
Injection angle	Controllable/ fixed	Controllable	Controllable	Controllable
Polarization	Controllable	Controllable	Controllable	Controllable
Injection mode	2nd X	2nd X	2nd X	1st O/2nd X
Reference	[12]	[13]	[14]	[15]

Table 1 Heating systems for ECCD experiment in Heliotron J, TJ-II, CHS and LHD

3. Experimental Results

Plasmas are produced and heated by the second harmonic X-mode ECH. A rough estimation of development time of total toroidal current is given by L_p/R_p where L_p and R_p are the plasma inductance and resistance. L_p/R_p is estimated from 0.1 to a few sec by assuming neoclassical conductivity. The measured toroidal current is continued to increase during discharge at low densities so that the current is somewhat underestimated in the low-density regime. Finite current may modify the rotational transform, affecting global confinement. However, neither strong confinement degradation nor MHD instabilities were observed in the experiment reported here. Details of ECCD experiment in each device are described in Refs. [7-11]

As predicted from the ECCD theory, the amplitude and driven direction depends on the parallel refractive index, $N_{\|}$. Figure 2 shows the dependence of the toroidal angle on the EC injection angle. It can be seen that I_p increases with increasing $N_{\|}$, and saturates at a certain $N_{\|}$. ECCD is a main contribution to the total current since the bootstrap current is small due to the low pressure at n_e = 0.5×10^{19} m^{-3}. The flow direction is the one expected from the Fisch-Boozer effect opposite to $\mathbf{N}_{\|}$ [16]. The same tendency is observed in LHD when the injection angle is changed from the clockwise to counter-clockwise direction. The EC current amplitude is the same order, a few kA, up to now in all the devices, although the magnetic field structure is different. As discussed later, the toroidal direction of EC current strongly depends on

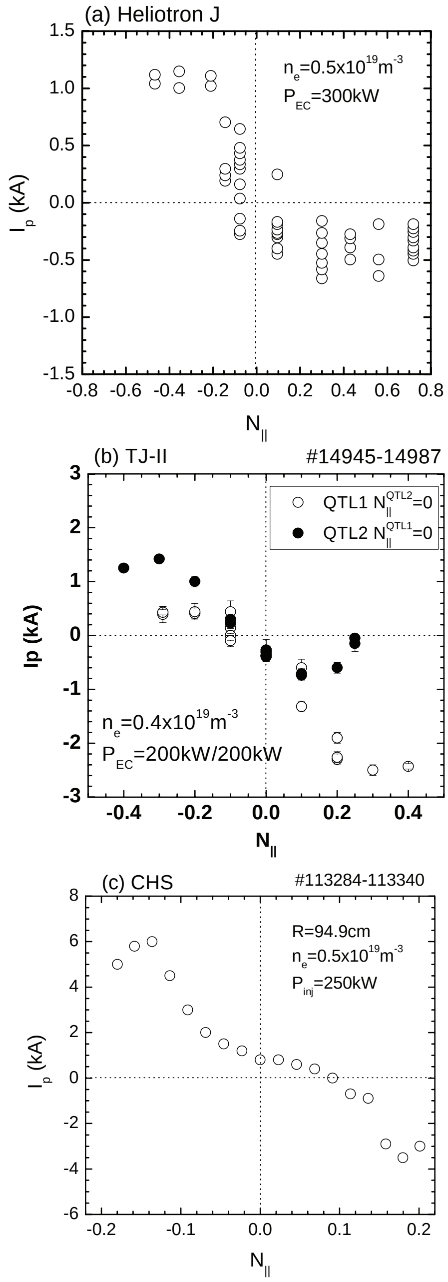

Fig.2 Dependence of toroidal current on EC injection angle. The magnetic axis in CHS is 94.9cm.

the magnetic ripple structure. Under the condition for toroidal injection scan, the Fisch-Boozer effect may be stronger than the Ohkawa effect. In the injection angle scan with the magnetic field fixed, the electron cyclotron resonance is Doppler-shifted due to finite $N_{\parallel}$, resulting that the decrease in electron temperature and/or the change in ripple structure possibly affects the EC current. The $N_{\parallel}$ dependence considering the Doppler shift effect is left for future.

The measured non-inductive current in ECH plasmas is composed of bootstrap current and EC current. The exclusion of bootstrap current is required for accurate estimation of the EC current. One method is to estimate the bootstrap current by EC beam launch in the direction normal to the magnetic field where the bootstrap current should be dominant. Another way is to use their different dependence on the magnetic field direction. The bootstrap current, which is proportional to $\mathbf{B}\times\nabla B$ drift, changes the flowing direction when reversing the magnetic field, while that of the EC current associated with the B strength does not change its flowing direction. Magnetic field reversal experiments have been conducted in Heliotron J in order to separate the EC current from the bootstrap current. We confirmed that the global plasma parameters such as stored energy and Te did not change when reversing the magnetic field direction. Figure 3 shows the density dependence of estimated bootstrap current and EC current in Heliotron J. The bootstrap current increases with increasing plasma density, and saturate at $n_e > 1.0\times10^{19}$ m^{-3}. This amplitude of bootstrap current agrees with a neoclassical prediction [17]. The bootstrap current is less than 0.5 kA at low density, which is smaller than the EC current, so that the toroidal current is mainly driven by ECCD.

In Heliotron J, the magnetic field ripple structure at power deposition position can be widely changed by controlling current in each coil. As illustrated in Fig. 1, the power deposition varies from the ripple top to the ripple bottom mainly by changing the bumpiness component in field spectrum with the magnetic field strength fixed. Figure 4 shows the density dependence of EC current for three field configurations. Here the contribution of bootstrap current is eliminated by the field reversal experiment. The maximum EC current of 4.6 kA is attained at the ripple top heating (the ratio of the magnetic field at the straight section to that at the corner section, h=1.06). The EC current flows in the opposite direction at the ripple bottom heating (h=0.82), and its amplitude is one-third as low as the ripple top heating.

One reason for current reversal is that velocity space effects are responsible for the ECCD. The Fisch-Boozer effect considers the perpendicular excursion in the velocity of a group of electrons with positive $v_{\parallel}$.

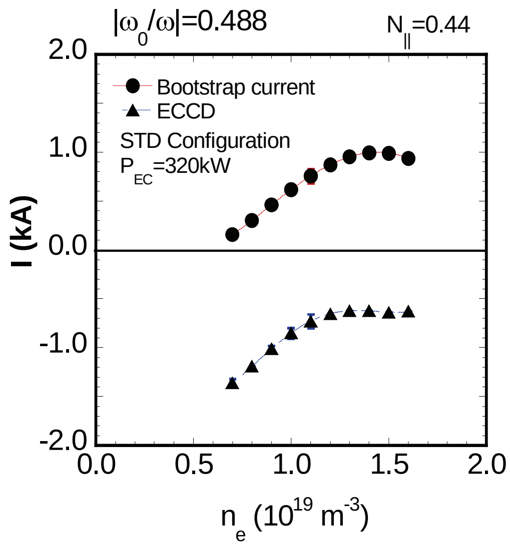

Fig.3 Separation of bootstrap current and EC current in Heliotron J.

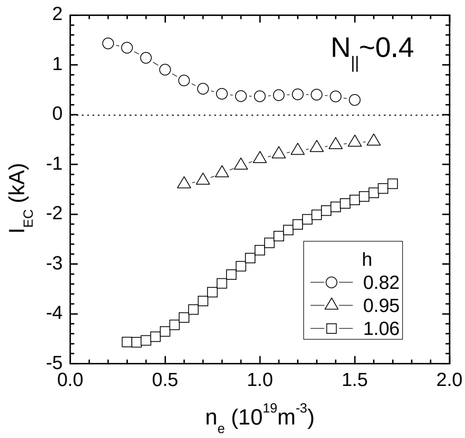

Fig.4 Density dependence of EC current in Heliotron J. The circle, triangle and square symbols denote the EC current at the ripple bottom (h=0.82), flat (h=0.95) and ripple top (h=1.06) heating, respectively.

Acceleration of these electrons causes an excess of electrons with counter-clockwise $v_{\parallel}$, resulting in a current in the clockwise toroidal direction. On the other hand, the Ohkawa effect drives current in the opposite direction to the Fisch-Boozer current [18]. Asymmetry in $v_{\parallel}$ is lost due to the bounce in the magnetic ripple, and a deficit in velocity space generates an electrical current in the counter-clockwise toroidal direction. In the high bumpiness configuration, the electrons are accelerated in the valley of the ripple, and they tend to become trapped, thus enhancing the Ohkawa effect. These qualitative predictions are consistent with the experimentally measured ECCD direction. The transition from the Fisch-Boozer current drive to the Ohkawa current has been demonstrated also in Ref. [5]. These suggest that the Ohkawa effect has comparable strength to the Fisch-Boozer effect in S/H systems, and the ECCD

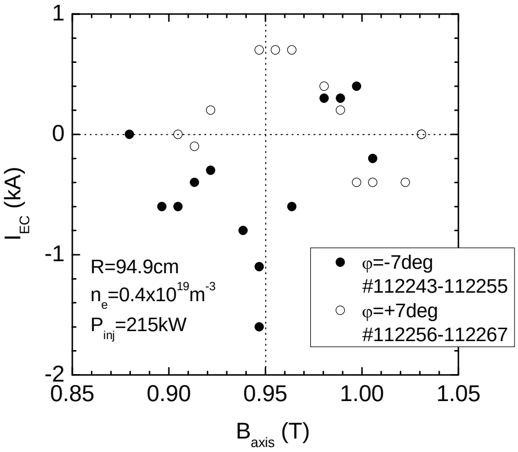

Fig.5 EC current as a function of magnetic field strength in CHS

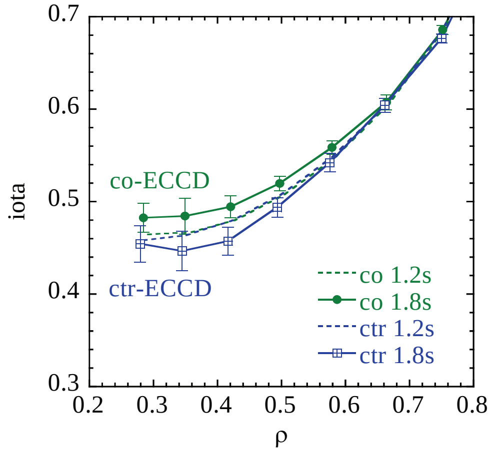

Fig. 6 Measurement of rotational transform by MSE diagnostic in LHD.

direction is determined by the difference between them.

The experimental results on magnetic field scan in CHS are shown in Fig. 5. The injection angle is +7 deg and -7 deg, and the magnetic axis is fixed; R_{axis}=94.9 cm. The Doppler shift of cyclotron resonance is estimated as $(\omega\text{-}2\omega_{ce})/\ \omega\ \sim 1\ \%$ for T_e=1 keV and $N_{\|}$=0.16, meaning that the Doppler shift effect is weak. The EC current is largest when the resonance is located at magnetic axis. The flowing direction is consistent with the Fisch-Boozer effect. The reduction in current drive efficiency at off-axis ECCD is observed also in Heliotron J. This may be because the electron temperature is decreased and/or the ripple effect is large.

In low shear devices, even a small amount of current strongly affects rotational transform profile. According to HINT2 code simulation results on a Heliotron J configuration, a localized current of -5 kA changes the central rotational transform from 0.56 to 0.18, generating high magnetic shear at the core region. The rotational transform profile has been measured by an MSE diagnostic in LHD. Figure 6 shows the measurement results for co-ECCD, no ECCD and ctr-ECCD. The co-ECCD increases the central rotational transform, vice versa. This tendency qualitatively agrees with the direction of poloidal magnetic field generated by the measured EC current. The quantitative comparison with measured current will be done in the future experiment.

The ratio of driven current to injection power, I_{EC}/P_{EC}, and the figure of merit,

$$\gamma = \frac{n_e I_{EC} R}{P_{EC}} \qquad (1)$$

are conventionally used for the estimation of ECCD efficiency. The drawback of these functions is that they have dimension, and they do not reflect the *Te* dependence. A figure of merit describing dimensionless ECCD efficiency including the *Te* dependence is proposed in the following form [3]

$$\varsigma = \frac{e^3}{\varepsilon_0^2}\frac{n_e I_{EC} R}{P_{EC} T_e} = 32.7\frac{n_e I_{EC} R}{P_{EC} T_e} \qquad (2)$$

where parameters have a unit of n_e in 10^{20} m^{-3}, I_{EC} in A, R in m, P_{EC} in W, and T_e in keV. This dimensionless figure of merit includes important parameters such as n_e and T_e. If ζ changes under the same plasma conditions, it means that ζ reflects the effect of electron thermal velocity and trapping. Table 2 summarizes the ECCD efficiency on Heliotron J, TJ-II and CHS. No result from LHD is included since it is not estimated yet due to short ECH pulse length compared to the current evolution time. It should be noted that these efficiencies are typical values ever obtained, not optimized ones. Although the magnetic field structure is different among the devices, the EC current amount is a few kA in all the devices, and the ECCD efficiency is similar within a factor of 2. Rather low efficiency compared to tokamaks may be due to the strong Ohkawa effect enhanced by the magnetic ripple. The ray tracing calculation code is under development, which would clarify the role of trapped electrons by comparing between experiment and theory.

	Heliotron J	TJ-II	CHS
Maximum I_{EC}	4.6 kA	2 kA	6 kA
$\eta = I_{EC}/P_{EC}$	14 A/kW	10-15 A/kW	35 A/kW
$\gamma = n_e I_{EC} R/P_{EC}$	~ 8x10^{16} A/Wm^2	~ 9x10^{16} A/Wm^2	~16x10^{16} A/Wm^2
$\zeta = 32.7 n_{20} I_A R_m / P_W T_{keV}$	~0.05	~0.03	~0.04

Table 2 ECCD efficiency in Heliotron J, TJ-II and CHS.

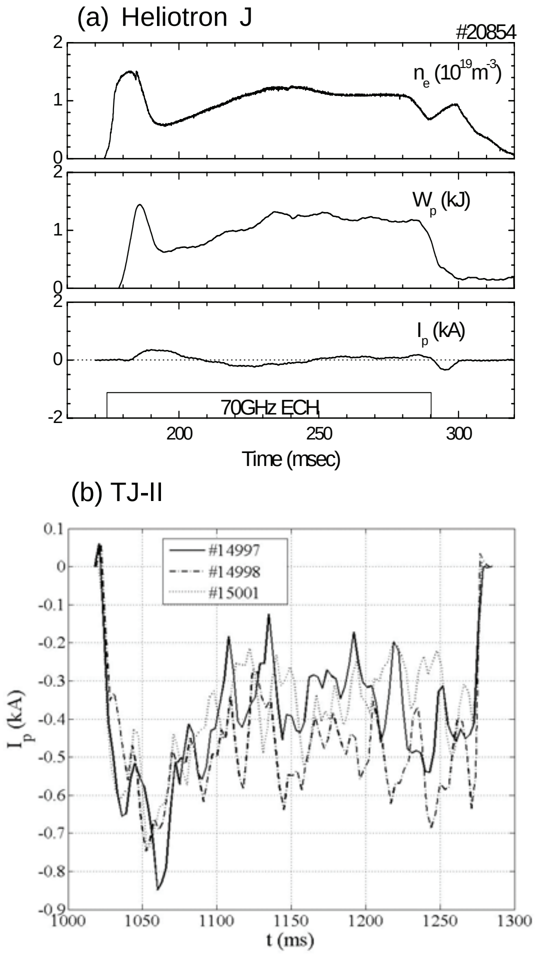

Fig.7 Demonstration of control of toroidal current, (a) zero toroidal current state in Heliotron J, (b) cancellation of EC current using two unit ECH systems in TJ-II

While the ECCD efficiency is not so high, the EC current is comparable to the bootstrap current, meaning that we are able to control the total toroidal current. Zero net current state has been demonstrated in Heliotron J as shown in Fig. 7. The total current is suppressed below 0.4 kA during the discharge by compensating the bootstrap current of 1.5 kA with ECCD. Such a state has also been demonstrated in CHS. In TJ-II, the EC current driven by each launcher is cancelled and the low current of I_{BS}=-0.5 kA is kept. The multi ECCD systems are useful for extending the current control range.

4. Conclusion

The ECCD experiment has been performed in Heliotron J, TJ-II, CHS and LHD. The driven current is affected by plasma and field parameters such as $N_{||}$, collisionality, resonance position and magnetic field structure. The injection angle scan experiment indicates that the control ability for EC current is high. The estimated driven current and its efficiency are similar. The maximum current ever observed is 6 kA, and the ECCD efficiency is $\gamma = n_e I_{EC} R/P_{EC}$=8-16×$10^{16}$ A/Wm^2, $\zeta = 32.7 n_e I_{EC} R/P_{EC} T_e$=0.03-0.05. In S/H systems, the magnetic ripple structure strongly affects the ECCD. The direction of EC current is reversed in Heliotron J when the power is deposited at the ripple bottom position, indicating that the electron trapping is a key factor to determine the EC current.

The EC current is comparable to the bootstrap current, and the ECCD has a potential to control the rotational transform profiles. The control of net current has been successfully demonstrated by compensating the bootstrap current with the EC current. Since the bootstrap current profile should be different from the EC current profile, we will need to extend the controllability of rotational transform profile connected to the suppression of MHD instabilities.

Acknowledgements

The authors are grateful to the Heliotron J, TJ-II, CHS and LHD staff for conducting the experiments. This work was partly supported by NIFS/NINS under the NIFS Collaborative Research Program (NIFS04KUHL005) and under a project sponsored by the Formation of International Network for Scientific Collaborations.

References

[1] Y. Narushima, J. Plasma and Fusion Research **1**, 004 (2006)

[2] V. Erckmann and U. Gasparino, Plasma Phys. Control. Fusion **36**, 1869 (1994),

[3] R. Prater, Phys. Plasmas **11**, 2349 (2004)

[4] K. Nagasaki, et al., 45 Nucl. Fusion **45**, 1608 (2005)

[5] V. Erckmann, et al., Fusion Eng. Design **53**, 365 (2001)

[6] H. Maaßberg, et al., Plasma Phys. Control. Fusion 47 (2005) 1137-1163

[7] G. Motojima, et al., Nucl. Fusion **47**, 1045 (2007)

[8] A. Fernández, et al., to be published in Fus. Sci. Technol.

[9] Y. Yoshimura et al., Journal of the Korean Physical Society, Vol. 49, December 2006, pp. S197-S200

[10] Y. Yoshimura, et al., to be published in Fusion Sci. Technol.

[11] T. Notake, et al., this workshop

[12] H. Shidara, et al., Fusion Sci. Technol. 45 (2004) 41

[13] A. Fernández, et al., Int. J. Infrared adn Millimeter Waves 22 (2001) 649

[14] Y. Yoshimura et al., J. Phys. Soc. Jpn., Vol.75, (2006) 114501

[15] T. Shimozuma et al. Fusio Sci Tech. **50**, 403 (2006)

[16] N. J. Fisch and A. Boozer, Phys. Rev. Lett. 45 (1980) 720

[17] G. Motojima, et al., Fusion Sci. Technol. **51**, 122 (2007)

[18] T. Ohkawa, General Atomics Report GA-A13847 (1976)

Proceedings of ITC/ISHW2007

Comparison of Impurity Transport in Different Magnetic Configurations

Kieran J. McCarthy[a], R. Burhenn[b], K. Ida[c], H. Maassberg[b], Y. Nakamura[c], N. Tamura[c]

[a] *Laboratorio Nacional de Fusión, Asociación EURATOM-CIEMAT, E-28040 Madrid, Spain*
[b] *Max-Planck-Institut für Plasmaphysik, EURATOM Association, D-17491 Greifswald, Germany*
[c] *National Institute for Fusion Science, 322-6 Oroshi-cho, Toki-shi, Gifu-ken 509-5292, Japan*

The goal of achieving steady state operation in stellarators brings into perspective the outstanding question of successful management of impurities, in particular, the avoidance of core impurity accumulation during improved energy confinement modes, with the resultant degradation of plasma energy due to radiation losses. Now, the dependence of impurity transport on plasma parameters has been systematically investigated during recent decades (LHD, W7-AS, TJ-II), in particular with regard to the influence of density and heating power on confinement. While certain global trends have been found in the different devices other behaviours are machine specific.

Here, after summarising the techniques for studying transport, we review transport observations under various stellarator plasma conditions in order to make comparisons, we draw attention to differing results for injected metallic and intrinsic impurities (core and edge), we identify those parameters that drive accumulation and discuss how observations compare with model predictions. Finally, in the light of results from LHD and W7-AS, we consider recent features such as the introduction of divertor modules in W7-AS that has allowed access to a high-density H-mode regime where radiation profiles reach a steady state, or the onset purification of LHD plasmas at higher density.

Keywords: Impurities, confinement, accumulation, transport,

1. Introduction

Impurities are an intrinsic component in fusion plasmas. Indeed, impurities are acceptable at low concentrations where they can be considered as being beneficial. For instance, impurities can provide a controlled manner to achieve radiative cooling at the plasma edge or their study, using spectroscopy, can provide essential information about the plasma edge or core. However, as we move towards advanced stellarators it has become imperative to avoid core impurity accumulation, in particular when operating in improved energy confinement modes, where accumulation (of high-Z impurities) can give rise to an overbalance of equilibrium between radiation losses and heating power with a resultant degradation of plasma energy and discharge termination.

The study of transport behaviour of intrinsic impurity ions in fusion plasmas is a long-standing field of research. Research on impurity accumulation and control remains a key issue in fusion research and is an indispensable part of ongoing investigations. In tokamaks, the appearance of, for example, edge-localized modes (ELMs) (which also exist in stellarators but difficult to control) or sawtooth crashes, which originally are confinement-degrading phenomena, can be employed to clear out impurities. However, stellarators are free of externally induced currents and, consequently cannot utilize current-connected phenomena such as sawtoothing for impurity reduction. Moreover, owing to the existence of a magnetic topology that is quite different to that of tokamaks, additional transport regimes in the long-mean-free-path regime (lmfp) exist in stellarators[1] that might also affect impurity transport in the plateau or Pfirsch-Schlueter regime (*e.g.* the influence on temperature screening).

The continued study of impurity transport in stellarators is therefore fundamental, in particular, as the database in this area is smaller and less detailed than for tokamaks. A key question is to what extent observed impurity behaviour can be described by theoretical models developed for axisymmetric devices that nowadays have been adapted for stellarators, in particular, for the highly-collisional Pfirsch-Schlueter regime, where the difference between tokamak and stellarator is

author's e-mail: journal@jspf.or.jp

assumed to be small. If good agreement with the theoretical model can be found, then the observed transport features are well understood and conclusions can be drawn with respect to further improvements and extrapolations. However, in the case of disagreement with theory, then this might point either to the domination of turbulent transport or the disregard of stellarator-specific transport contributions in the transport model. In this case, further interpretation becomes difficult and predictions have to be substituted by measurements. Depending on the collisionality regime of the impurities, the implementation of such non-axisymmetric effects self-consistently with the background plasma is an ambitious task and is not yet available for analysis.

In this paper, after a brief summary of theory and experimental techniques used for transport studies, we review transport observations under various stellarator plasma conditions in different stellarator devices in order to make comparisons, we then identify parameters that drive accumulation. We also consider recent features such as the introduction of divertor modules in W7-AS that has allowed access to a high-density H-mode regime where radiation profiles reach a steady state, or the onset purification of LHD plasmas at higher density, that may provide possible doorways to achieving improved management of impurities in long pulsed discharges. Finally, compare similarities and differences from the different configuration and we review database needs.

2. Background

At this point, it is useful to recall that the impurity influx into the plasma from the chamber walls, or other sources, is governed by transport at the open magnetic field and by retention whilst impurity transport inside the closed magnetic surface is governed by diffusive and convective terms. Indeed, impurity flux can be written simply in terms of diffusive and convective parts as

$$\Gamma = D \cdot \nabla n + v \cdot n \quad .$$

Here the convective part, v, is a strong function of ion temperature and density gradients, which for analysis purposes are often afflicted by certain errors depending on the profile quality, as well as by the collisionality regime of the background plasma. The diffusive part, D, may be considered less susceptible to error and better for comparisons.

Now, when the impurity ions are mostly in the highly collisional (Pfirsch-Schluter) regime it would be expected that the impurity transport in stellarators would be sufficiently decoupled from the magnetic topology so as to be similar to tokamaks. However, as stated before, the convective flux and its sign are determined by density and temperature gradients as well as the collisionality regime of the background plasma. For tokamaks with the background plasma in the banana regime, this convective flux can be outward directed and helps to flush out impurities (“temperature screening”). In stellarators, however, additional collisionality regimes for the background gas appear in the *lmfp* region (ν-, $1/\nu$-, $\nu^{0.5}$-regime) due to the 3-dimensional magnetic topology[2]. Unlike tokamaks, they are expected to lead to inward directed convective impurity fluxes (accumulation) also in the Pfirsch-Schlueter collisionality regime for impurities. This would have important consequences for stellarators with respect to impurity radiation losses. Therefore, a comparison of experimental data with transport code predictions is a useful approach to elucidate the possible role of any neglected stellarator-specific aspects.

In order to study impurity transport several tools are available. On the experimental side, the monitoring of soft x-rays, from highly ionized high-Z impurities in the plasma core, or broadband radiation (using bolometers), is a common means of following impurity evolution. Moreover active tools are also available. These include laser blow-off, where a focused laser beam ablates a small amount of tracer material (typically a non-intrinsic metallic element) off a substrate, pellet injection where a micro-ball of material is accelerated to 100’s m s^{-1} along a pipe-gun[3], and gas oscillation. The tracer material released enters and traverses the plasma and the temporal behaviour of the different ionization states of the tracer ions in the plasma is monitored by spectrometers with central lines-of-sight. Thus, the impurity confinement time, τ_{imp}, a global transport quantity, is derived from the temporal decay of the radiation emitted by the highest states. In order to extract local transport quantities across the plasma minor radius from such data, iterative procedures based on transport codes are employed. Similarly, the evolution of an intrinsic impurity can be evaluated by following the radiation emitted by highly ionized states and a model to reconstruct a steady-state solution of the charge-state distribution for the plasma with given density and temperature profiles. It should be noted here, that whilst the transport of intrinsic impurities is governed by transport both in the core and in the edge, impurity screening effects play no role in determining the transport of impurities injected using laser blow-off.

2. Experimental Impurity Transport

In this section we review results from a number of impurity transport experiments carried out for a range of plasma conditions in different stellarator machines. In most cases a short summary of the experiment is given and the most important results or findings are highlighted.

2.I W7-AS

Electron cyclotron radiation (ECR)-heated plasmas with a limiter configuration in W7-AS revealed a strong dependence of impurity confinement time on several plasma parameters, *i.e.*, on minor radius a_p, heating power P_{ECRH}, and plasma density n_e ($\tau_{Al} \sim a_p^{2.4}\ n_e^{1.2}\ B^{0.3}\ /\ P_{ECRH}^{0.8}$)[4]. See Fig. 1. Note: similar scalings were found for energy confinement and for particles[5]. The most important impact of this scaling on impurity transport with respect to consequences on machine performance is the unfavourable density dependence: at high densities (*e.g.*, $7\text{x}10^{19}\ \text{m}^{-3}$), the confinement time reached values close to 1s or more. Stationary radiation levels could usually be sustained at low density without problems. However, beyond a central density of ~$5\text{x}10^{19}\ \text{m}^{-3}$, the intrinsic impurity radiation, as well as the Z_{eff}, started to rise continuously throughout the pulse length (see Fig. x, where all signals within the shaded region belong to discharges with densities $>5\text{x}10^{19}\ \text{m}^{-3}$). Thence, depending on the impurity flux level from the walls, this led to a degradation of plasma energy by excessive radiation losses.

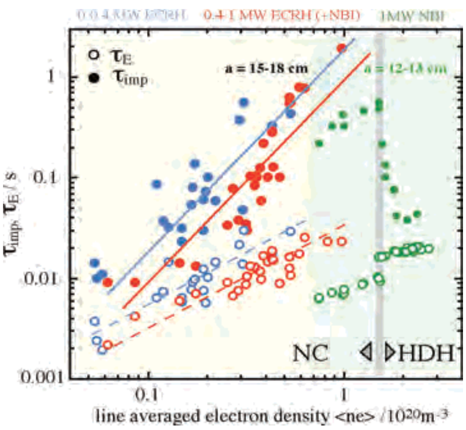

Fig.1. Energy and impurity confinement times vs. electron density for NC limiter ECRH plasmas (pink shaded region) and NBI plasmas (green shaded region) including the HDH transition during divertor operation. The gap between ECRH and NBI plasmas in the overlapping region is due to differences in the chosen plasma size.

These findings gave rise to several important questions. For instance, whether this effect was a consequence of changes in transport – as would be indicated by the long confinement times – or was the result of temporally increasing impurity sources from the wall (*e.g.* heating up of inboard tiles). This was investigated in an experiment using a constant fluorine gas puff (CHF_3) applied throughout the pulse duration of a high-density discharge (Ref. 6) to simulate a stationary impurity source. The fluorine radiation in the plasma core rose continuously until the end of the pulse, this indicating an accumulation of fluorine in the core plasma. This supported the idea of a change of impurity transport being responsible for the impurity accumulation at high density – rather than growing impurity source rates as a consequence of the heating up of inboard tiles.

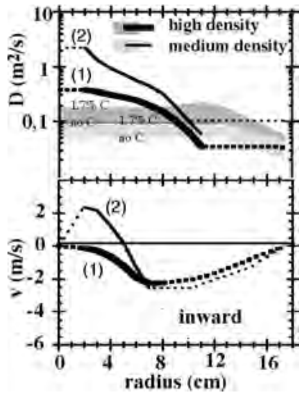

Fig.2. Transport coefficients for high ($7\text{x}10^{19}\text{m}^{-3}$ (1)) and low density ($3.5\text{x}10^{19}\text{m}^{-3}$ (2)) ECRH plasmas and model predictions (shaded area).

Another puzzling factor is the nearly missing dependence of the impurity confinement time on magnetic field strength B (i.e. ~$B^{0.3\ (+/-0.2)}$). In order to elucidate two nearly identical plasmas with 1.25 and 2.5 T central magnetic field strengths were compared (Ref 6). It was revealed that the local impurity diffusion coefficient, *D*, in the plasma core was significantly higher (x 3 or 4) in the case of 1.25 T for radial positions with comparable densities. However, the inward convection *v* was also increased, so that, overall, the global impurity confinement time did not change. Although it is unclear whether this was a general characteristic, in the Pfirsch-Schluter regime, *v* may be directly related to *D* via some terms containing gradients in the background density and temperature profiles so the simultaneous increase of both transport coefficients may not contradict theory and may explain the unchanged confinement time.

It was also found that there was no electron temperature dependence. Furthermore, using laser blow-off into plasmas with different absolute densities, but very similar density profile shapes, it was found that the confinement time was not radial electric field dependent. This was further confirmed when comparing electric fields, as measured by charge-exchange, for different electron densities.

Now from a study comparing the intrinsic impurity radiation evolution in ECRH plasmas with different densities it was found that the different time behaviors of the intrinsic impurities could be explained by changes in transport alone[7]. For this, local transport coefficients were compared for a medium ($3.5\ \text{x}\ 10^{19}\ \text{m}^{-3}$) and a high ($7\ \text{x}\ 10^{19}\ \text{m}^{-3}$) central density discharge[7]. See Fig. 2. From analysis, it was seen that the centrally peaked *D* reduced by a factor ~2 to 3 at high density whilst *v*'s were similar except in the centre where the differences with respect to the large diffusion coefficients were considered of minor importance for overall confinement. It is interesting to remark here, that similarly peak *D* profiles and density tendency were observed in the TJ-II, albeit at lower densities[8]. This brings up the question as to whether the peaked profiles in both devices are connected with ECRH deposition. This is a point for further investigation. Now, returning to W7-AS, model predictions (shaded areas) with different background impurity concentration assumptions suggests that the fast onset of a stationary radiation level can be well described by high-diffusive transport whilst the increase of radiation at high density was compatible with lower diffusion coefficients, in particular at the edge, where low diffusion coefficients govern the time constant for transport. Moreover, reduced impurity fluxes caused a longer time scale for achieving stationary conditions within the discharge duration (it was predicted that stationarity could be achieved after ~1.7 s in the high density case)[9]. This is noteworthy as it implies that stationary radiation levels depend on impurity sources, i.e., small impurity sources may be acceptable for high-density plasmas. In such a case, wall conditioning comes to play an important role in accumulation prevention.

The scaling law also shows a degradation of impurity confinement with increased heating power. This was manifested by shorter decay times and by enhanced *D*'s, when laser blow-off was performed into plasmas with similar central densities, magnetic field strength and edge rotation transform but different injected ECRH power[9]. The difference in *D* was considered to be an indication for enhancement of turbulent transport at increased heating power in agreement with the observed power degradation of energy confinement. In contrast, the differences in *v* were relatively small. A degradation of impurity confinement with ECRH power ($\tau \sim P^{-3}$) was found also in the TJ-II[10]. Indeed, it turned out to be stronger than the one observed in the global energy confinement ($P^{-0.6}$). Again, the manifestation of similar tendencies in different stellarator devices may be an indication of common underlying physics for impurity transport.

The investigation of impurity transport at densities higher than the ECRH cut-off frequency in W7-AS (1.2×10^{20} m^{-3}) was restricted to neutral beam injection (NBI) heated plasmas. These were also characterized by long impurity confinement times, low diffusion coefficients and high inward convection. However, the previously observed density dependence on confinement, as well as the absolute values of transport coefficients, were not compatible with and often fell below neoclassical (and Pfirsch-Schlueter) predictions of the transport model for axisymmetric devices. Indeed, differences in transport between H-mode and normal confinement-mode (NC) plasmas were difficult to extract because at higher densities where the H-mode usually appeared, the impurity confinement time of the NC plasma was already large.

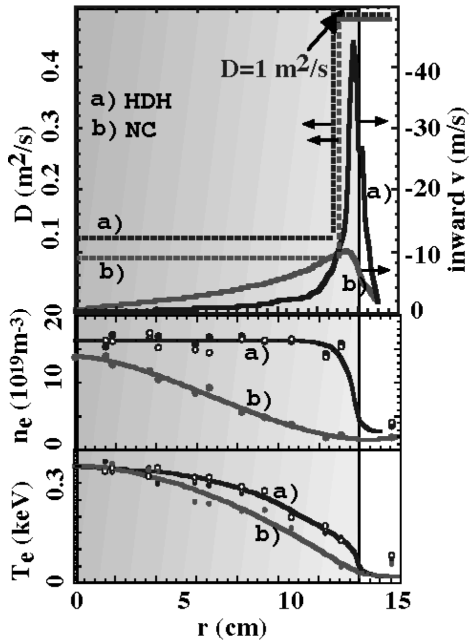

Fig.3. Top: transport coefficients for an HDH (a) and an NC (b) plasma with 1 MW NBI heating power. The shaded region is the confinement region of the plasma with separatrix around 14cm. bottom: density and temperature profiles of HDH and NC plasmas.

Finally, when operation with new island divertor modules began densities up to 4 x 10^{20} m^{-3} were achieved[11]. Moreover, it was found that beyond a certain power dependent threshold density (1.5 to 2.1×10^{20} m^{-3}), the unfavourable density scaling of impurity confinement in the NC regime changed suddenly. See Fig. 1. Within a narrow density interval, the plasma entered the High density H-mode regime where the impurity confinement time dropped by more than a magnitude to values comparable to the energy confinement time, which simultaneously increased by nearly a factor of 2[12,13]. As a result, quasi-stationary operation at densities up to 4×10^{20} m^{-3} was possible.

The drop in impurity confinement in HDH was in agreement with the observed reduction of inward convection in the core (this being related to the flattening of the density profile) but is in contradiction to the strong inward convection at the plasma edge. Note; the temperature profile is very similar in both cases. Comparison with the H*-mode, with nearly similar profiles to HDH but a large impurity confinement time, indicates the importance of edge transport. Now, in order to compensate for this large inward convection at the plasma edge, a high edge diffusion pedestal is needed to achieve the short confinement times observed in HDH. See Fig. 3. This would highlight more the importance of the plasma edge for impurity transport.

2.II LHD

Impurity transport in the LHD device has been ongoing for several years. Indeed, both intrinsic and injected impurity transport has been studied in constant density and density ramp-up long pulse discharges (up to several 10's) heated by NBI[14,15]. One of the most notable findings has been the observation of intrinsic metallic accumulation in a narrow density window ($<n_{e}>$ ~1 to $3x10^{19}$ m^{-3}) in hydrogen discharges. This was observed both for constant density and density ramp-up situations. In a constant density experiment, where the plasma density was kept almost constant at $2.9x10^{19}$ m^{-3}, this core accumulation (the main metallic impurity being iron) manifested itself by an increase of central radiation power (the edge radiation power remaining almost constant) with a long timescale[15]. The increase in central radiation gave rise to a significant decrease in the central electron temperature. However, there was no radiation collapse of the plasma. In another experiment, with a slow density ramp-up, a dramatic alteration of impurity behaviour was observed. In the first instance, the central radiation increased rapidly with density. See Fig. 4. Then, as the density was increased further, the central radiation began to reduce steadily. From analysis of the evolution of the central radiation power and highly-ionised iron line emission evolutions using the one-dimensional impurity transport code (MIST)[16] an impurity accumulation window was deduced. Here, the central iron density increased steadily when $<n_e>$ was above $\sim 10^{19}$ m^{-3}, reaching a peak at about $<n_e>$ ~2.7 x 10^{19} m^{-3}. When the plasma density increased beyond this density turning point the central iron

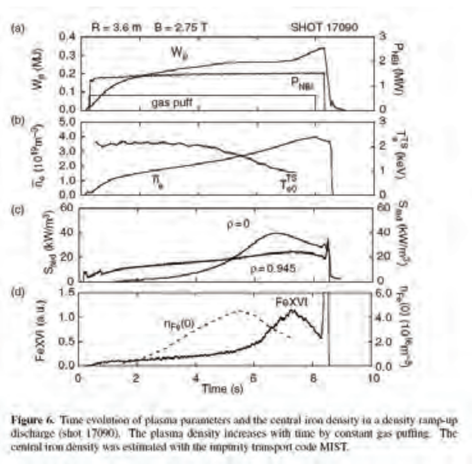

Fig. 4. Time evolution of LHD plasma parameters and central iron density in a density ramp-up discharge.

density fell off, this being interpreted as impurity clear- or flush-out processes. In another similar study, it was also found that accumulation could be avoided in this accumulation window by performing a fast density ramp-up. It was then found that metallic impurities would not accumulate as they passed through the accumulation window before accumulation could occur.

In order to further understand this impurity behaviour, radial electric field profiles, E_r, derived from poloidal rotation velocity measurements made using charge exchange spectroscopy of neon, were also considered[17]. It was found that E_r near the plasma edge changed from positive (electron root) to negative (ion root) as density increased, the transition occurring near the density where the accumulation window begins (10^{19} m^{-3} with T_i ~2 keV). Indeed in LHD where the density profile is flat in the core and the temperature profile is almost parabolic for discharges maintained with gas puffing, it was determined that the impurity flux is determined by the convection velocity for the metallic impurities. In the region of high temperature and low density, high-Z accumulation was avoided due to this positive E_r. towards the edge. In the high density and low temperature region (high collisionality), accumulation was not seen, this being attributed to the dominant contribution of the temperature gradient in the PS regime (temperature screening effect). Here, the qualitative behaviour of neon penetration into the plasma core could be accounted for by a large convection contribution due to the radial electric filed, this being explained from neoclassical impurity transport for the v^{-1} regime for a nonaxisymmetric which predicted a large convective component proportional to E_r. On the whole, the qualitative features were considered consistent with neoclassical impurity transport. However, the inward impurity flux (accumulation) is not found in a simple analysis with neoclassical theory, even when including an expression for axisymmetric torus plasmas.

Pellet injection experiments using titanium have also been perform for a range of constant density plasmas[18]. At low density, the titanium exited the plasma and there was no accumulation. Furthermore, the associated Ti emission decay time, which is closely connected to impurity confinement time, could be explained by the diffusion component only in an impurity transport analysis. At higher density, an abrupt increase in the Ti emission decay was observed right across the accumulation window region implying long confinement. Indeed, it is not unrealistic to consider that the impurity confinement time could continue to increase when above the accumulation window density region. Moreover, if the τ and E_r were to continue to rise at high density, then the purification window would mean that there is a decrease of impurity influx but still long confinement times. If so then this may be similar to HDH on W7-AS.

3. Similarities and Differences

In summary, there are indications for anomalous/ turbulent transport at low and medium densities in all machines and a tendency to approach neoclassics at high density. In addition, it has been indicated that there is an improvement of impurity core confinement with increasing density. Moreover, it is important to determine if impurity screening mechanisms at high density are similar or not in W7-AS and LHD. Indeed, many features are qualitatively consistent with traditional neoclassics but not quantitatively consistent with traditional neoclassics. Finally there is a need to implement non-axisymmetric neoclassical theory in order to achieve a better understanding of the underlying physics.

4. Database

For an impurity transport database, new data, or the systematic reviewing and cataloguing of existing data, are required in order to improve scaling laws for the different machines. For instance, this might include the influence on τ_{imp} of magnetic field strength, density, temperature, iota, heating power and type, radial electric field. Furthermore, diffusion and convective coefficients at 2 or more radial points would also be needed in order to evaluate the contribution of local transport. Furthermore, such data would help to achieve a better understanding of the physics of impurity transport and aid comparison. Also, in order to attain a basis for better understanding it will be necessary to consider stellarator specific features in neoclassical models, for instance, 3-D magnetic topology, gradB-drift, *etc*. Finally, a crucial point for future predictions will be to determine when can impurity transport be described by a neoclassical model and when is it anomalous or turbulent.

Acknowledgements

This work contributes to the International Stellarator Profile Database under the auspices of the IEA Implementing Agreement for Cooperation in the Development of the Stellarator Concept. The authors acknowledge the contributions of the W7-AS, LHD and TJ-II teams to this work.

References

[1] A.A Galeev and R.Z. Sagdeev, Reviews of Plasma Physics, Vol. 7, M.A. Leontovich, Ed. Consultants Bureau, New York (1979).
[2] H. Maassberg et al., Plasma Phys. Control. Fusion 41, 1135 (1999).
[3] S. Sudo et al., Plasma Phys. Control. Fusion 44, 129 (2002).
[4] R. Burhenn et al., Proc. 22nd Conf. Controlled Fusion and Plasma Physics, Bournemouth, United Kingdom, 1995, Europhysics Conference Abstracts, Vol. 19C, Part III, p. 145, European Physical Society-
[5] U. Stroth et al., Nucl. Fusion 36, 8 (1996).
[6] R. Burhenn et al., Proc. 27th Conf. Controlled Fusion and Plasma Physics, Budapest, Hungary, 2000, Europhysics Conference Abstracts, Vol. 24B, Part 3.041, European Physical Society.
[7] R. Burhenn et al., Proc. 24th Conf. Controlled Fusion and Plasma Physics, Berchdesgaden, Germany, 1997, Europhysics Conference Abstracts, Vol. 21A, Part IV, p.1609, European Physical Society.
[8] B. Zurro et al., Rev. Sci. Instrum. 75, 10 (2004)
[9] R. Burhenn et al. Fusion Sci. Tech. 46, 115 (2004).
[10] C. Hidalfo et al., Nucl. Fusion 45, S266 (2005).
[11] P. Grigull et al., Fusion Eng. Design 66-68, 49 (2003).
[12] K. McCormick et al., Phys. Rev. Lett. 89,015001-1 (2002).
[13] R.R. Jaenicke et al., Plasma Phys. Control. Fusion 44B, 193 (2002).
[14] Y. Nakamura et al. Nucl. Fusion 43, 219 (2003).
[15] Y. Nakamura et al., Plasma Phys. Control. Fusion 44, 2121 (2002).
[16] R.A. Hulse, Nucl. Tech./Fusion 3, 259 (1983).
[17] K. Ida et al., Rev. Sci. Instrum. 71, 2360 (2001).
[18] N. Tamura et al., Plasma Phys. Control. Fusion 45, 27 (2003).

Proceedings of ITC/ISHW2007

Zonal Flows and Fields Generated by Turbulence in CHS

A. Fujisawa, K. Itoh, A. Shimizu, H. Nakano, S. Ohshima, K. Matsuoka, S. Okamuara, CHS-group

National Institute for Fusion Science, Oroshi-cho, Toki, Japan 509-5292

The paper reports two major progresses made in heavy ion beam probe (HIBP) measurements carried out in CHS. One is to prove the nonlinear couplings between zonal flows and turbulence by using the modern nonlinear data analyzing techniques. The other is the identification of zonal magnetic field, generated by the turbulence, utilizing the potential ability of the HIBP. The measurements of magnetic field fluctuations successfully provide the fluctuation spectrum, and the first experimental evidence of the turbulence dynamo, which is a long-standing historical candidate for the geomagnetism and analogous phenomena, that the turbulence generates a structured magnetic field.

Keywords: zonal flows, turbulence, zonal magnetic field, heavy ion beam probe, nonlinear interaction, mesoscale structure, dynamo, wavelet bicoherence analysis

1. Inroduction

Turbulence is a ubiquitous phenomenon observed in the universe. It has been recognized that the turbulence is not the process of randomization, but also the one to produce a structure. For example, it is well known that the Rossby wave turbulence should generate the Jovian belt or zonal flows [1], and that turbulence should be the cause for the geomagnetic (dipole) field. In 1970s, it was pointed out that the drift wave turbulence should obey the same equation as the Rossby wave turbulence [2], therefore, it is expected that the zonal flows should exist in toroidal plasmas.

In the research of magnetic confinement, recently, the importance of the zonal flows has been recognized since the saturation level of drift wave turbulence, which governs the transport processes, should be determined by the interaction between zonal flows and drift waves [3]. After the evidence to hint the zonal flows and their roles in transports was presented in theoretical and simulation works [4-6], the existence of zonal flows was experimentally proven in a number of devices [7-19] (for review [20]).

After the identification of the zonal flows [4], the CHS experiments have made a great progress in the physics of zonal flows and turbulence. The investigation has been made on the interaction or nonlinear coupling between zonal flows and turbulence [21-24]. Besides, we have developed a potential ability of the heavy ion beam probe (HIBP), which means the direct measurement of magnetic field fluctuations of plasma interior from the horizontal secondary beam movement, and successfully obtained a spectrum of magnetic field fluctuations in CHS plasmas [25].

The paper presents the direct quantitative evidence to show the coupling between zonal flows and turbulence with an advanced analysis technique, the wavelet bicoherence, and presents the existence of zonal magnetic field, as well as zonal flows, with recently developed technique of the magnetic field fluctuation measurement with HIBP. The discovery of the zonal magnetic field should be the first evidence to show that the turbulence really generates the structured magnetic field, which is associated with a historical physics problem, i.e., dynamo problem.

2. Experimental Set-up

CHS is a toroidal helical device of which the major and averaged minor radii are R=1 m and a=0.2 m, respectively. The device is equipped with two HIBPs to measure plasma potential in different toroidal sections apart by 90 degree. Each HIBP has three channels to observe the adjacent spatial points of the plasma. The local electric field can be directly measured by making a difference between potentials of neighboring two channels.

It has been known for HIBPs, in addition to the electrostatic potential, that a vector potential component can be measured from the beam movement on the detector; particularly in an axisymmetric magnetic configuration, a formula is derived to relate the movement to the toroidal component of the vector potential [26]. In a real geometry, the fluctuation of a magnetic field component, or derivative of vector potential, can be directly measured by taking the

e-mail: fujisawa@nifs.ac.jp

difference between the beam movements on the detectors from the neighboring ionization points. The details of the method are described in ref. [25].

3. Coupling between Zonal Flows and Turbulence

The target plasmas for the experiments introduced below are produced with electron cyclotron resonance heating of ~200 kW. The magnetic field strength of the discharges is B=0.88 T, and the density is kept constant approximately at n_e~ $5x10^{12}cm^{-3}$. The HIBP measurement is performed at ρ~0.35, where the amplitude of zonal flow tends to be large, which gives a better condition to investigate the interaction between zonal flows and turbulence.

In this discharge condition, electron and ion temperatures T_e~ 0.5 keV, T_i~0.1 keV, (i.e., in collisionless regime), ion Larmor radius ρ_i~0.1 cm, time scale of micro-instabilities $\omega^*/2\pi R$~50 kHz with $k_{perp}\,\rho_i$~0.3 and energy confinement time τ_E~2 ms (or characteristic frequency of global confinement τ_E^{-1}~0.1 kHz), where k_{perp} is the wavenumber and ω^* is the drift frequency defined as $k_{perp}T_e/eBL_n$ with L_n being a characteristic length of density gradient. Here the pressure-gradient-driven microinstabilities are associated with electromagnetic field fluctuations.

The fundamental statistical properties of electric field fluctuation are obtained from the traditional analysis using the Fast Fourier Transformation (FFT). Figure 1 shows the spectrum of electric field fluctuation at ρ~0.35, with coherence between electric field fluctuations at two toroidal positions. The spectrum can be divided into four ranges, i) a lower frequency range less than f<~ 1.5 kHz with a quite high coherence of ~0.7, ii) an inertia range of f<10 kHz, iii) the range of 10<f<30 kHz with a sharp peak, and iv) the background turbulence range with a broad-band peak around ~50 kHz. The fluctuation in f~2 kHz to show a long-distance correlation is regarded as the zonal flow. Besides the sharp peak at 19 kHz, there can be seen the other two peaks (at least) at 38 and 57 kHz. These three modes have a long-distance characteristic, since the coherence between the potential fluctuation and that of electric field at the other toroidal position gives a quite high value for three peaks (>0.5). Therefore, the peaks are conjectured as the GAMs. The detailed analysis of the coherent modes is available in ref. [18].

The intermittent characteristics of fluctuation can be extracted using a wavelet analysis. Figure 2a shows an example of the evolution of the zonal flow Z(t) and the wavelet power spectrum of electric field fluctuation W(f,t) at ρ~0.35. The used wavelet analysis [27] has the natural correspondence with the traditional Fourier transformation. The zonal flow component is filtered out from electric field fluctuation using a numerical low-pas filter (see details in ref. [7]). Note that the positive value means the ion diamagnetic direction. The zonal flow amplitude (the blue dashed line) shows a slow change in confinement time scale.

Figure 2b shows three plots of normalized fluctuation power as a function of the normalized zonal

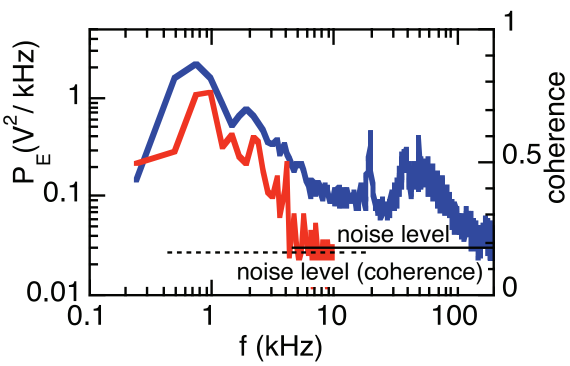

Fig. 1 A spectrum of electric field fluctuation. The measurement is carried out at ρ~ 0.35 (solid line). The coherence between electric field fluctuations at two toroidal locations (dashed line). The coherence is plotted in the low frequency range where the result is above the noise level (in ref. [22])

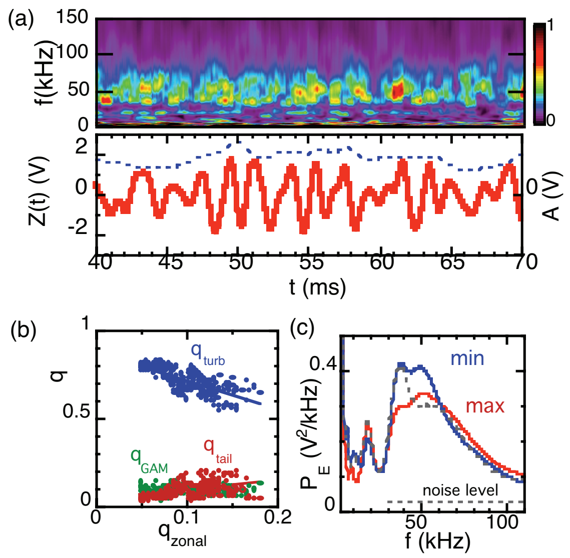

Fig. 2 (a) Evolutions of wavelet spectrum of electric field fluctuations as a function of frequency, and evolution of zonal flow with low-pass filtered. The unit of the color bar is in V^2/kHz. (b) Fluctuation power fractions in three frequency regimes as a function of zonal flow power fraction. (c) Conditional averaged spectra of wavelet power in the local maxima and minima of the zonal flow. The grey dashed line represents the conditional averaged spectrum when |Z(t)|~ 0 (in ref. [22])

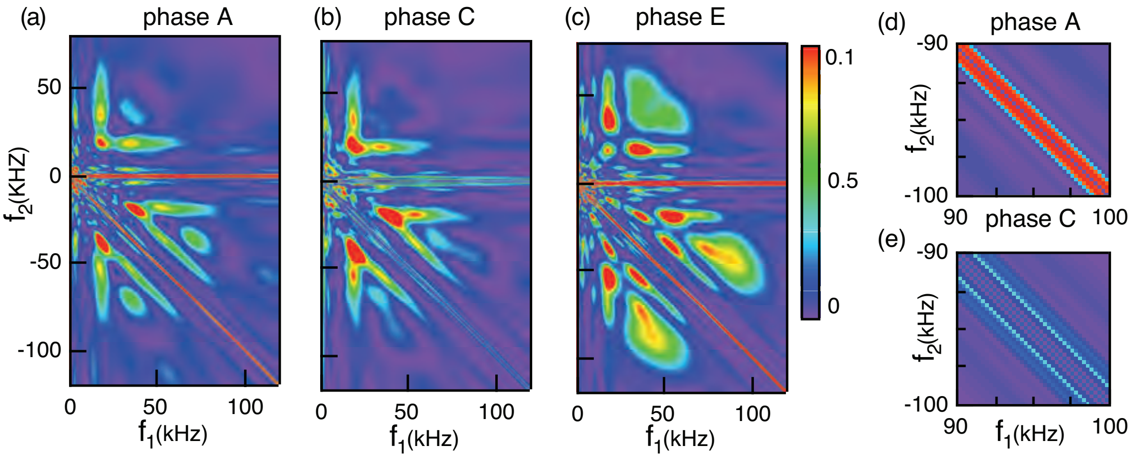

Fig. 3 Diagrams of wavelet squared bicoherence for three phases of zonal flow. The zonal flow is divided into five phases in its magnitude as is shown in Fig. 2a for the conditional integral of the wavelet bicoherence. (a) Bicohrence diagram of the phase A (maximum), (b) that of the phase C (zero) and (c) that of the phase E (minimum). (d) An expanded view of the diagram for the phase A, and (e) another for the phase C [in ref. [23]].

flow power, q_{zonal}(=q(0.25,1.5 kHz)). The regression analysis shows that the turbulence power q_{turb}(30,200) should be strongly dependent on the zonal flow power as q_{turb}~0.9-1.6 q_{zonal} with their correlation coefficient being γ=0.74, while no significant relation γ=-0.01 is found for the fluctuation power of the coherent mode q_{GAM}(10,30). On the other hand, the fluctuation neighboring to the zonal flow shows a positive correlation (γ=0.49), and follows the zonal flow concomitantly like a tail as q_{tail}(1.5,10)~0.63 q_{zonal}. Accordingly, the zonal flow power fraction increases as the turbulence power fraction decreases [22].

In comparison between zonal flow and the wavelet fluctuation powers (Fig. 2a), the colored pattern seems to be synchronous with the tide of the zonal flow. The phase dependency can be examined by taking the conditional averages of the wavelet spectra for the phase of zonal flow. Figure 2c shows the conditional averaged wavelet spectra for the maxima and minima of the zonal flow. It is obvious that the fluctuation power around ~ 50 kHz shows an increase (an decrease) around a local minimum (a maximum) of the zonal flow. In addition, the FFT analysis indicates that the modulation frequency of W(f,t) all over the frequencies should coincide with the zonal flow frequency. The result suggests that the fluctuation characteristics should be varied with the phase of zonal flow, as well as with its amplitude [22].

The wavelet bicoherence analysis [27] could be useful in order to reveal the *hidden* linkage between the zonal flow and fluctuations. The analysis is extended to adopt a conditional average in consideration for the

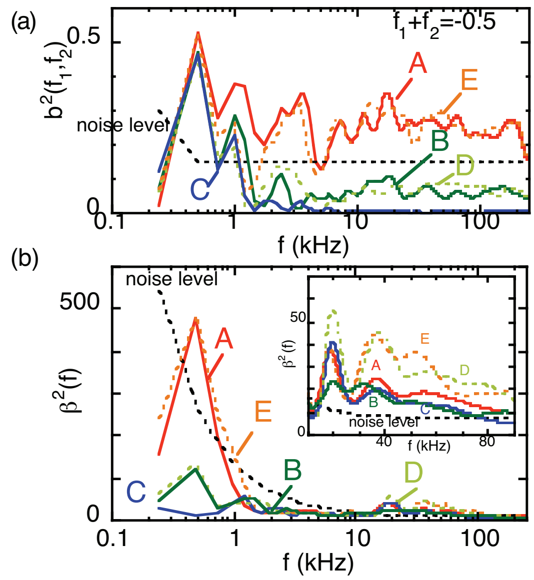

Fig. 4 (a) The squared bicoherece along the line of f_1+f_2=-0.5 kHz for the five phases of the zonal flow. (b) Summed squared bicoherence for the five phases of the zonal flow. The grean and red solid (dashed) lines represent the zonal flow phases of A and B (E and D)), respectively. The blue solid line indicates the phase C. The inset is an expanded view of the frequency range from 10 kHz to 90 kHz (in ref. [23]).

dependency of the fluctuations on the zonal flow phase [23]. The conditional bicoherence is evaluated on the electric field fluctuation for five phases of the zonal flow (see Fig. 2b); A) Z(τ)>0.8 V, B) 0.8> Z(τ)>0.25 V, C)0.25> Z(τ)>-0.25 V, D) -0.25> Z(τ)>-0.8 V, and E) Z(τ)<-0.8 V. The number of used ensembles is approximately the same as ~20000 for every case.

Figure 3 shows three bicoherence diagrams for the phases, A, C and E. The results indicate clear changes in the coupling between waves according to the phase of the zonal flow. The most important feature is that the couplings become stronger along the lines of f_1+f_2~0.5, -0.5 kHz at the phases A (maximum) or E (minimum). The expanded views of a region (90<|f|<100 kHz) clearly demonstrate that the couplings on the lines of f_1+f_2~0.5 and -0.5 kHz becomes stronger in the phase A. Figure 4a shows the squared bicoherence as a function of $f_1$along the line of f_1+f_2=-0.5 kHz for every phase of the zonal flow. Obviously, the coupling becomes stronger in the range of f>~2 kHz as the absolute value of the zonal flow |Z(t)| increases. However, the coupling of the lower frequency of f<~2 kHz is rather high and almost the same for every phase.

As a consequence of degraded independency of ensembles in lower frequency, the statistical noise level of the wavelet bicoherence analysis is usually evaluated according to ref. [27]. The noise level is regarded as, however, a statistically sufficient condition to show the significance of couplings, since the phase of the zonal flow lying in the frequency around f_3~0.5 kHz is conditioned for the evaluation. This finding supports the image that the waves with adjacent frequencies interacts collectively with each other to produce the zonal flow through the processes of such as the modulational instabilities.

The results confirm that the coupling becomes stronger when the zonal flow increases in the absolute value. In two phases, A and E, the level of the summed bicoherence in the frequency range of the zonal flow (f<~1 kHz) is significantly large to surpass the maximum noise level, or a statistically sufficient condition for the existence of the coupling. As for the couplings between turbulent waves, as is shown in the inset of Fig. 4b, the total bicoherence in the range of f>~30 kHz is larger as the zonal flow is in the opposite direction to the bulk flow. The couplings between turbulent waves are varied with the sign of the zonal flow to cause the modulation of the turbulence power spectrum (Fig. 2c). The corresponding increase in the bicoherence can be seen particularly in the regions around (f_1,f_2)~(50,-80) kHz, and (f_1,f_2)~ (80,-50) kHz in the bicoherence diagram of the phase E (Fig. 3c).

4. Identification of Zonal Magnetic Field

As is similar to the previous case, the target plasma is also produced with electron cyclotron resonance heating of ~200 kW, to avoid a large-scale plasma motion caused by magnetohydrodynamic (MHD) instabilities that interfere with the generation of magnetic fields in the meso-scale range. The plasma parameters in the experiment are; magnetic field strength B = 0.88 T and density n_e~5x10^{12} cm^{-3}. The normalized plasma pressure, β-value, is ~0.2%.

Collisionless (or electron) and collisional skin depths are estimated as 2.4 mm and 12 mm at 0.5 kHz, respectively. The magnetic Prandtl number is evaluated as μν/η~10^2 using the experimental viscosity of ν ~χ~ 10

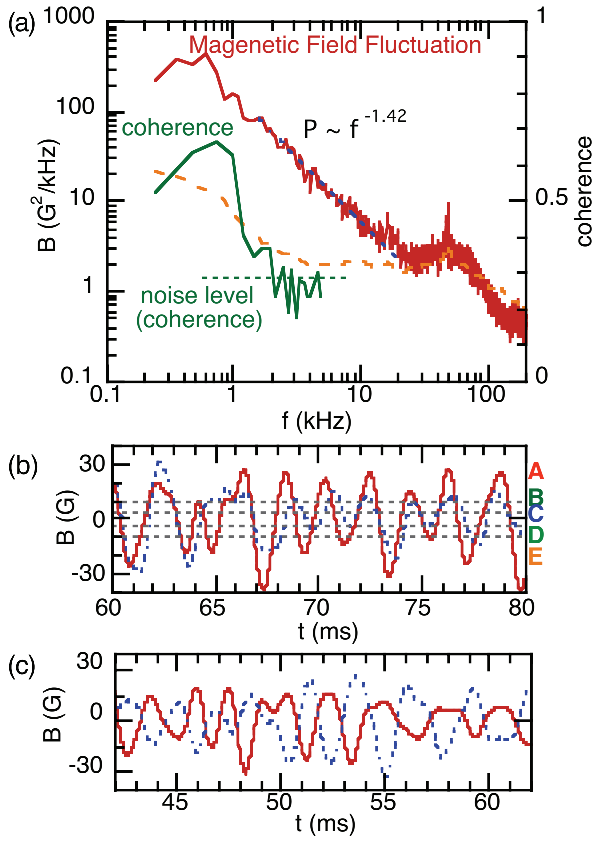

Fig. 5 Magnetic field fluctuation spectrum and existence of mean field. (a) Power spectrum (poloidal component), and coherence between the magnetic field at two toroidal locations. The fluctuation less than ~1 kHz shows a quite high coherence, which means generation of global magnetic field of azimuthal symmetry. The spectrum is calculated for the stationary period of ~50 ms for the discharge duration of ~100ms with frequency resolution of 0.24 kHz and the Nyquist frequency of 250 kHz. (b) The waveforms of zonal fields at the same radial but different toroidal locations. The positive sign means the direction of vacuum field direction. (c) The other waveforms of zonal fields at the different positions in both toroidal and radial directions. The difference in radial direction is 1 cm (in ref. [25])

m^2/s and resistivity of $\eta \sim 10^{-7}$ Ωm, where χ represents the thermal diffusivity evaluated as the global average from the confinement time.

The measurement was done at the radial position of r_{obs}=12+-.5 cm, where the signal-to-noise ratio is maximal for the HIBP measurement. In this measurement, it is known from a trajectory calculation that the horizontal beam movement reflects the poloidal magnetic field. A spectrum of the magnetic field fluctuation is shown in Fig. 4, with coherence between two toroidal locations. In the low frequency range, the contamination is sufficiently small, while the electric field contamination may be dominant around ~50 kHz and above. The coherence of the frequency lower than 1 kHz is quite high (~0.7), which is an average of ~70 temporal windows from identical shots; a higher coherence value is obtained in an appropriate period of a single shot. This means that the probing beams are coherently swung by the magnetic field at two toroidal positions. It is unambiguously demonstrated that a mean magnetic field fluctuation with long-distance correlation does exist.

The magnetic field fluctuations in that frequency range are visualized using a low-pass filter [7,22]. Figures 5b and 5c demonstrate two examples of evolution of the magnetic field fluctuation in the frequency range (0.3 -1 kHz). The zonal field amplitude is evaluated to be ~ 30 G at maximum. The accuracy of the absolute magnetic field value is about 50% owing to uncertainty in the absolute measurement of beam location, although the relative motion of the beam is more precisely measured with accuracy of ~0.1%. The in-phase movement of two beams on the same magnetic flux surface (Fig. 5b) suggests that the fluctuation is symmetric or homogeneous around the magnetic axis under the assumption of poloidal symmetry. In contrast, the other waveforms in anti-phase behavior (Fig. 5c), when the position is different in radial direction by 1 cm from the other, suggests that the fluctuation should have a finite radial structure.

A constant phase relation between the signals from two different radial positions, as is shown in Figs 5b and 5c, allows us to estimate the spatio-temporal characteristics of the mean zonal field in the radial direction by calculating the correlation function of low pass-filtered magnetic field fluctuations with spatio-temporal separation of $\Delta r = r' - r$ and $\Delta t = t' - t$. Figure 6a shows the cross-correlation obtained by altering an observed position r', shot by shot with fixing the other at r (=12 cm). Figure 6b illustrates the spatial structure of three times at Δt = 0, 1 and 2 ms. These correlation diagrams show a quasi-sinusoidal structure in the radial direction with a characteristic radial wavelength of $\lambda_r \sim 1$ cm, while memory of the structure is lost in ~ 2 ms. These observations in Figs. 5 and 6 show, therefore, the existence of the mean magnetic field with radially zonal structure symmetric around the magnetic axis. This magnetic field resistively damps away, if there is no driving source, on a time scale of $\tau_R = \mu_0 \eta^{-1} k_{r}^{-2} \sim 50$ μs. It cannot be sustained by the external circuit through inductive coupling, because the direction changes with radius. It therefore must be sustained by the internal plasma dynamics.

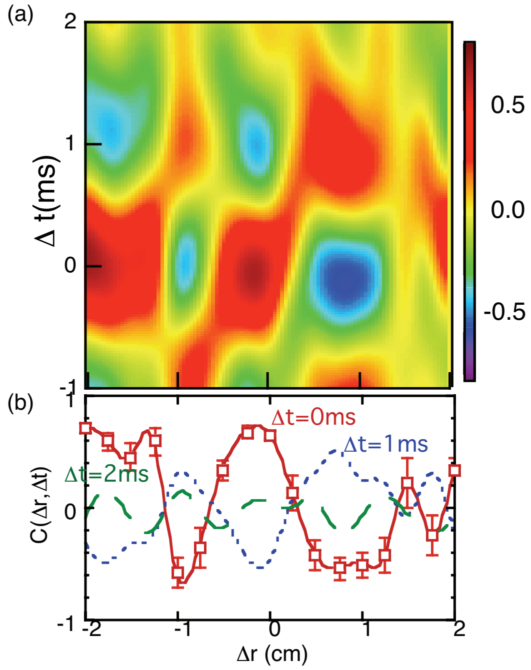

Fig. 6 Radial structure of zonal field. (a) Correlation function of space and time, C(Δr, Δt), around the radial position of r=12 cm. (b) Correlation functions with three different time delays; Δt=0,1 and 2 ms. These correlation diagrams show radial structure of zonal field, which has a quasi-sinusoidal radial structure with a characteristic radial wavelength (~1cm) in mesoscale. On the other hand, the temporal correlation indicates that the memory of the mesoscale structure fades away with oscillation in ~2 ms (in ref. [25])

The wavelet bicoherence analysis is applied, as is similar to the case of zonal flow, to quantify the nonlinear coupling strength between the zonal magnetic field and turbulence. The results showed the intermittent coupling between the zonal field and the background turbulence [25]. In this analysis, the contamination of electric field fluctuation in the turbulence regime may disturb the absolute quantification of the coupling between the zonal field and the pure magnetic field turbulence. In the previous measurement [7], the electrostatic mode conjectured as Geodesic Acoustic Mode (GAM) was clearly identified as a sharp peak at ~ 20 kHz in the electric field spectrum. However, the corresponding peak is completely absent in the magnetic field spectrum. This means that the electric field contamination can be much smaller than the level of the upper boundary shown in Fig. 5. The degree of the contamination could be evaluated more precisely in a future analysis with taking into account the detailed fluctuation properties.

Finally, the presented observations verify the existence of zonal magnetic field, as well as zonal flow, generated from the turbulence, probably through modulational instabilities. From the analogy to the zonal flows in the Jupiter, future observations might find zonal magnetic field structure in a rotating star. A residual macroscopic field could be expected even in the average over the whole zonal structure, in an inhomogenous background. In addition, the zonal field could serve as a *seed* leading to global instabilities to cause a macroscopic field or dynamo. Therefore, the discovery could be a step toward general understanding the dynamo problem, stimulating a question if the mesoscopic zonal field can be developed into macroscopic structure.

5. Summary

In summary, we have shown two recent findings for turbulence and mesoscale structure, *i.e.,* zonal flow and zonal field. The first one is the direct measurement on electric field fluctuation combined with the wavelet bicoherence analysis, which succeeds to find an intermittent coupling structure between fluctuations, *e.g.,* the zonal flow and turbulence, turbulence and turbulence and so on. The most important finding is that the nonlinear coupling between turbulence changes according to the phase of the zonal flow. The couplings of fluctuations and turbulence to the zonal flow turn visible in the maximum or minimum phases of the zonal flows.

Finally, the presented observations verify the existence of zonal magnetic field, as well as zonal flow, generated from the turbulence, probably through modulational instabilities. A residual macroscopic field could be expected even in the average over the whole zonal structure, in an inhomogenous background. In addition, the zonal field could serve as a *seed* leading to global instabilities to cause a neoclassical tearing mode in toroidal plasmas, or macroscopic field or dynamo in the universe. Therefore, the discovery could be a step toward general understanding the dynamo problem, stimulating a question if the mesoscopic zonal field can be developed into macroscopic structure.

Acknowledgments

The author thanks Profs. S. Okamura, K. Matsuoka and the members of CHS experimental group for their cooperation in the experiments, Profs K. Itoh, S-I. Itoh, O. Motojima for their continuous supports. This work is partly supported by the Grant-in-Aids for Specially-Promoted Research (16002005) and Scientific Research (18360447).

References

[1] G. P. Williams, J. Atom. Sci. **35** 1399 (1978).
[2] A. Hasegawa, C. G. Maclennman, Y. Kodama, Phys. Fluids **22** 2122 (1979).
[3] P. H. Diamond, K. Itoh, S-I. Itoh, T. S. Hahm, Plasma Phys. Control. Fusion **47** R35 (2005).
[4] A. Hasegawa, M. Wakatani, Phys. Rev. Lett. **59** 1581 (1987).
[5] M. N. Rosenbluth, F. L. Hinton, Phys. Rev. Lett. **80** 724 (1998).
[6] A. M. Dimits, G. Bateman, M. A. Beer et al., Phys. Plasmas **7** 969 (2000).
[7] A. Fujisawa et al., Phys. Rev. Lett. **93** 165002 (2004).
[8] G. R. Tynan, C Holland, J H Yu, A James, D Nishijima, M Shimada and N Taheri, Plasma Phys. Control. Fusion **48** S51 (2006).
[9] G. S. Xu, B. N. Wan, M. Song, J. Li, Phys. Rev. Lett. **91** 125001 (2003).
[10] D. K. Gupta, R. J. Fonck, G. R. McKee, D. J. Schlossberg, M. W. Shafer, Phys. Rev. Lett. **97** 125002 (2006).
[11] M. Jakubowskim, R. J. Fonck, G. R. McKee, Phys. Rev. Lett. **89** 265003 (2002).
[12] M. G. Shats et al., Phys. Rev. Lett. **88** 45001 (2002).
[13] Y. Hamada et al , Nucl. Fusion **45** 81 (2005).
[14] T. Ido et al., Nucl. Fusion **46** 512 (2006).
[15] G. R. Mckee et al., Plasma Phys. Control. Fusion **45** A477 (2003).
[16] G. D. Conway et al., Plasma Phys. Control. Fusion **47** 1165 (2005).
[17] P. M. Schoch et al., Rev. Sci. Instrum. **74** 1846 (2003).
[18] A. Fujisawa et al., Plasma Phys. Control. Fusion **48** S31 (2006).
[19] A. Kramer-Flecken, S. Soldatov, H. R. Koslowski, O. Zimmermann, TEXTOR team, Phys. Rev. Lett. **97** 045006 (2006).
[20] A. Fujisawa et al., Nucl. Fusion **47** S718 (2007).
[21] A. Fujisawa et al., Plasma Phys. Control. Fusion **48** S205 (2006).
[22] A. Fujisawa et al., J. Phys. Soc. Jpn. **76** 033501 (2007).
[23] A. Fujisawa et al., Plasma Phys. Control. Fusion **49** 211 (2007).
[24] A. Fujisawa, A. Shimizu, H. Nakano, S. Ohshima, Plasma Phys. Control. Fusion **49** 845 (2007).
[25] A. Fujisawa et al., Phys. Rev. Lett. **98** 165001 (2007).
[26] T. P. Crowley, P. M. Schoch, J. W. Heard, R. L. Hickok, X. Y. Yang, Nucl. Fusion **32** 1295 (1992).
[27] B. Ph. Van Milligen, C. Hidalgo, E. Sanchez, Phys. Rev. Lett. **74** 395 (1995).

Proceedings of ITC/ISHW2007

Impact of lithium-coated walls on plasma performance in the TJ-II stellarator

F.L. Tabarés, I. García-Cortés, D. Tafalla, J.A. Ferreira, M.A Ochando, R. Balbín, F. Medina and the TJ-II Team.

Laboratorio Nacional de Fusión. CIEMAT. Avenida Complutense 22, 28040 Madrid, Spain

e-mail: tabares@ciemat.es

The TJ-II stellarator has been operated under several first wall conditions until now: full metallic scenario, full boronized walls and, in the last campaign, lithium coating. Particularly conspicuous has been the change in recycling associated to the different wall conditions, but also in impurity content. Lithium coating, tested for the first time in a stellarator, has proven a very effective method for particle control in TJ-II. Changes in the shot by shot fuelling characteristics as well as in the total particle inventory compatible with good density control have been recorded after the Li deposition. Thus, a factor of 4 increase in the fuelling rate at constant density compared with the B-coated walls was recorded, and even a higher value was estimated for the allowed H inventory in the puffing-controlled ECRH discharges. These changes were also mirrored in the radiation and edge radial profiles, with increased electron temperatures. This led to enhanced interaction with the poloidal graphite limiters, which had a deleterious effect on plasma performance. The lower instantaneous recycling also worked for the density control under NBI heating scenarios. Record values of plasma energy content were measured at densities up to $4.5.10^{13}$ cm^{-3} under Li-coated wall conditions.

Keywords: plasma-wall interaction, density control, low Z components, wall coatings, low recycling, lithiumization, TJ-II stellarator.

author's e-mail: journal@jspf.or.jp

1. Introduction

Plasma wall interaction issues are paramount in achieving fusion plasmas with high purity, controlled density and high confinement. Even when the selection of plasma facing components, such as limiter and divertor target materials, is made based on their ability to withstand the very high particle and power fluxes characteristics of present fusion plasmas, the interaction with the first wall, reached by charge exchange neutrals, photons and some more or less tenuous plasma, is considered to contribute to the plasma impurity content as much as the PFCs do. Therefore, a growing concern about proper conditioning of the total inner wall of the fusion device has been taking place in the last decades. Compared to tokamaks, stellarator plasmas show distinct features in their interaction with the surrounding materials. On the good side, the lack of disruptions and type I ELMs make them more reliable for reactor operation. So it is the lack of MHD-driven density limit. However, due to their significantly higher aspect ratio, they offer a less favorable area to volume ratio and also, a worse screening of recycled neutrals. This last parameter has obvious implications in divertor design and, in general, in density control by external sources. Although some specific divertor concepts have been developed for stellarator with reasonable success for impurity and particle control, no specific coating strategies for the first wall exist. However, the application of those concepts with good performance in tokamaks, such as boronization or Ti gettering, has also improved machine operation in the stellarator community. It must be said here that, due to the systematically higher complexity in the vacuum vessel topography of stellarators, homogeneous coatings are harder to produce, in particular if line of sight deposition (i.e. Ti gettering) is sought. In the present work, the implementation of a system for the full coating of the inner walls of a stellarator with lithium (the TJ-II Heliac) is described for the first time. Compared to other low Z coating elements such as Be, C and B, lithium is a very attractive element due to its very low radiation power, strong H retention (leading to the formation of the very stable hydride, LiH) and strong O getter activity and excellent results have been achieved recently in tokamaks [1]

The structure of the paper is as follows: first, the inner wall conditioning history of the device is summarized. Then, results achieved in terms of particle control by the use of Li walls are presented. The performance of plasma parameters associated to the change in wall conditions is then addressed. Finally, the prospects for improvement and possible extension to other stellarators are described.

author's e-mail: journal@jspf.or.jp

2. Wall conditioning of the TJ-II stellarator

The TJ-II stellarator has been operated under diverse first wall conditions since its beginning [2]. Under ECR plasma generation and heating, density control is hampered by the combination of low cut-off density and the large surface/volume ratio of the vacuum vessel respect to the plasma. However, different origins of the problem were identified depending on wall conditioning and plasma facing materials. For the initial scenario, a full metal machine, desorption of high recycling He from the walls, which was implanted during overnight GD conditioning, either by the plasma or by direct interaction with the microwave beams was the main responsible. The systematic use of a short Ar GD period led to a significant improvement of the control. Under boronized walls and graphite limiters (low Z scenario), the improvement in plasma purity and the low recycling conditions at the beginning of the operation (shortly after the depletion of H from the film by He GD) provided a higher tolerance of the plasma to the external fuelling. Two complications, however, were found under boronized walls. First, the gradual loading of the C/B film by hydrogen deteriorates the good recycling characteristics in a relatively short period. After a total implantation dose corresponding to the maximum uptake of the film of~1.10^{17}cm^{-2}, was achieved, spontaneous density rise drove the discharge to cut-off density, even in the absence of external puffing. The application of a few dry discharges was required for recovery, but this was only transiently obtained. A second factor in play was the presence of the Enhanced Particle Confinement (EPC) mode, characterized by a sudden increase of particle confinement at a critical density in the order of $0.6.10^{13}$ cm^{-3} [3] This mode, whose presence seems correlated with edge collisionality and the development of a velocity shear layer at the edge [4], was found to strongly depend on fuelling pulse shape and amplitude [5] and, its development can be eventually suppressed by proper tailoring of the gas puffing.

In the 2007 campaign, a low recycling, low Z wall has been tested. For that purpose, an *in situ* lithium coating technique was developed. It is based on evaporation under vacuum from four ovens, symmetrically spaced and oriented tangentially to the plane of the corresponding flanges in the equatorial plane of the vacuum vessel, filled with 1g of metallic Li each. A set of metallic resistances (Thermocoax) and thermocouples (K type, two per oven) are operated at pre-programmed temperatures of 500-600 ºC by a central, PID-based power supply. Effusion from the ovens creates an atomic beam aiming at the remote region opposed to the corresponding flange. Under HV operation, the mean free path of the Li atoms is long enough to produce a thin layer at the vessel walls located midway between adjacent ovens. The deposition pattern, directly visible in the groove protecting the central coils, matches the line of-sight flight of the Li atoms. .Alternatively, effusion under a He atmosphere was tried to enhance lateral diffusion of the beam, hence providing a more homogeneous coating of the walls in areas closer to the ovens. A pressure of 10^{-5} mbar was chosen, based on the experimentally determined mean free path for the He-Li system at this pressure, $\lambda\sim$ 70 cm and the characteristic length of the vacuum vessel, V/S ~ 20 cm (assuming pure cylindrical geometry). In order to extend the lifetime of the Li coating, and due to the very high reactivity of this species with background gases (water, O_2, N_2, CO…) a ~50 nm boron layer was deposited prior to the evaporation by conventional GD of an o-carborane/He mixture. The B coating was depleted of H by a pure He GD after its deposition. Also, He GD was applied every day on the Li layer in order to remove hydrogen from the areas not fully covered by the coating. A total of 12 g of Li were evaporated for the ~650 discharges performed in this period.

3. Particle control on Li walls

Compared to former operation on boronized walls, the control of plasma density by external puffing was very much upgraded upon lithiumization of TJ-II. Not only the required puffing levels were significantly higher for the same density, but also no sign of saturation was observed after a full day of ECRH operation. Of particular relevance on machine performance is the recovery of pumping walls characteristics after shots with densities above cut-off. Typically, one or two purges (dry discharges) were required in B scenarios. However, no such a need was found upon lithiumization, the wall memory effect being basically washed out. In order to quantitatively understand this effect, the particle balance in a shot to shot basis was evaluated from the injected hydrogen, and the desorbed one after the plasmas, the latter being measured by an absolutely calibrated mass spectrometer. In figure 1 the results for a typical operation day under both types of wall conditions are displayed. Two main differences between B and Li walls are clearly seen from the figure. First, the required particle injection for a give density is systematically higher in the Li case. Second, while the B wall shows saturation at total retained inventory of H< 5.10^{20} (which, for the nominal saturation level of B films,

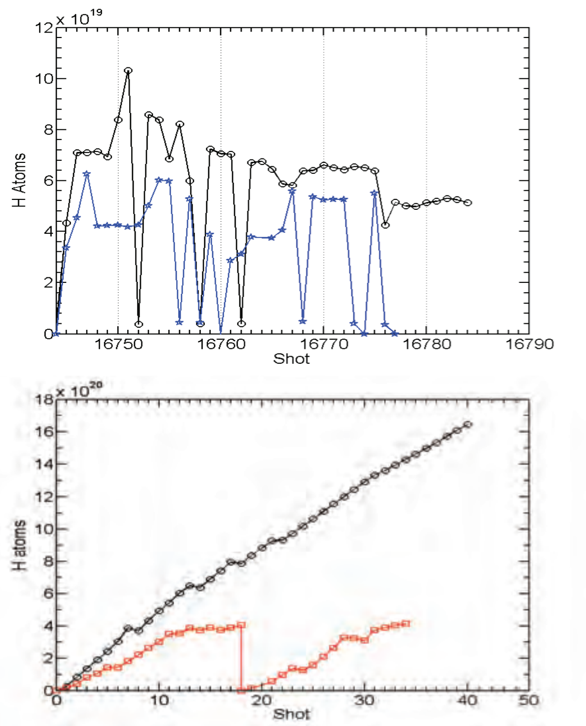

Fig.1. Particle balance under B and Li wall conditions. Top: integrated particle injected per pulse. Bottom. Cumulative retention of H in the walls. Black, Li. Blue and red, B.

implies an effective interaction area of less than 1 m^2) no sign of such saturation is seen for values up to 4 times higher in the Li case.

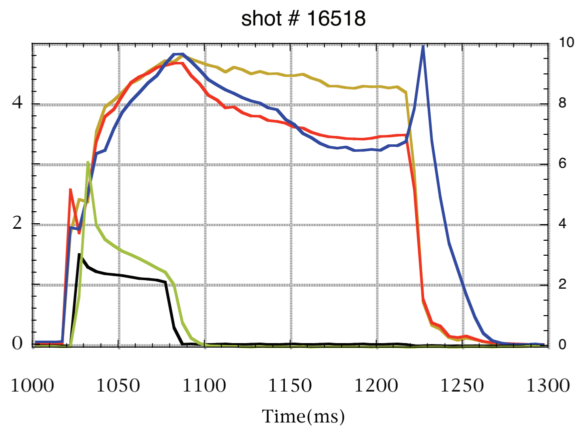

Fig.2. Time response of electron density (blue) and Ha fluxes to the wall (red and brown) to a short gas puff (green Ha and black manometer)

The dynamic behavior of plasma particles during the discharge is shown in figure 2 for a characteristic shot. First, gas puffing is injected for density built up. Then it is abruptly interrupted and the evolution of cord density and Hα emission are recorded. For pure H plasmas, a simple equation of the form

$$dN/dt= f.\ Qin-N/(\tau p/1-R) \qquad (1)$$

can be applied. Here, Qin stands for the puffing rate (e⁻/s), τp is the particle confinement time, f is the fueling efficiency and R the recycling coefficient. Application of eq.1 to the data of fig. 2 yields a f value near unity and an effective confinement time, τp/1-R, of ~30 ms. Assuming no major changes in particle confinement respect to the boron and metal cases (see below), a value of ~0.65 is obtained for R. This value, although lower than that deduced under boronized walls, is significantly higher than expected for a fully absorbing wall and may reflect the limited extension of the wall coverage by the Li coating achieved.

Another important factor contributing to density control by external puffing in the absence of discontinuities in the confinement characteristics, as that introduced by the transition to the EPC mode. In figure 3, the dependence of line average density with particle flows to the wall (Hα signal) is shown for Li wall operation. The location of the EPC transition for the B and metal cases is also shown. For constant recycling conditions and negligible contribution of impurities to Ne, the linearity displayed in the figure obviously implies that no change in the particle confinement characteristics of the plasma is taking place during the scan. This is also confirmed through the ion energy confinement analysis shown in section 5.

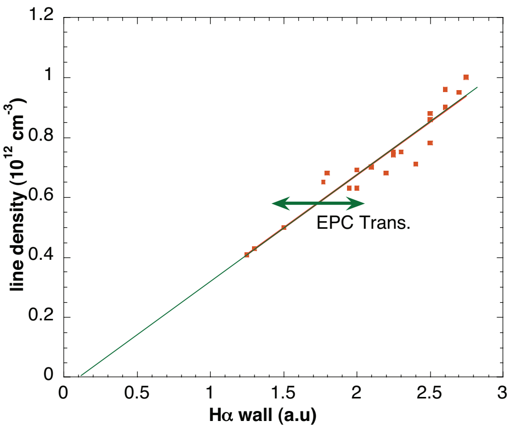

Fig.3. Line average density vs. flux to the walls for Li wall conditions. Line is a linear regression to the data

4. Impurity behavior and plasma parameters

Clean plasmas are routinely obtained in TJ-II ECR heated plasmas under low Z scenarios, largely due to the strong oxygen gettering effect of the B coatings and the use of graphite limiters [6] Although the Li coatings were not aimed at improving this situation, a significant effect has been observed in that last campaign. So, carbon emission was seen to decrease during the operation day. Figure 3 shows the shot by shot evolution of some relevant signals, normalized to the line average density. As seen, after an initial spike in all impurity monitors, associated to the very first shots after Li deposition, a systematic decrease takes place upon plasma operation. Of special relevance is the strong decay of the bolometer signal, closely related to the suppression of carbon impurities from the plasma. The strong reduction of carbon source in the presence of Li is a well documented effect which has been associated to the decrease of physical and chemical sputtering of carbon by its coating with Li [7]. The second day of operation is preceded by 30 min of He GD. The impurity levels are seen to rise again, but they soon recover to their low levels, the Li signal reaching levels

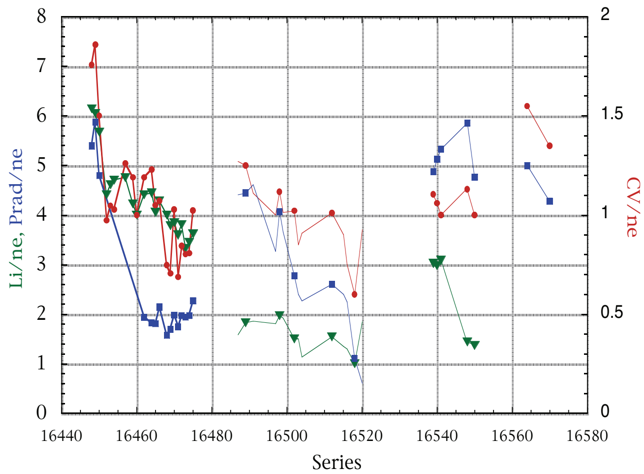

Fig. 4. Shot to shot evolution of some impurity signals normalized to the line density. Circles (left) CV, triangles LiI, squares, Bolometer

even lower than before. Since its measurement is local, the erosion of the initial layer at the observation window, with subsequent spreading over other areas of the vessel, could account for this effect. This will also account for the concomitant decrease of impurity radiation, not to be expected if simple removal of the beneficial effect was taking place. After discharge 16540, systematic higher contamination of the plasma is seen. This is associated to the insertion of the graphite limiters one cm into the separatrix during several shots. The interaction of the limiters with the plasmas was seen to be stronger under Li walls than in the B case, as monitored trough the increase in total radiation and CV signal upon their insertion up to 2 cm. This is apparent contradiction with the effect just described, and it was ascribed to the higher edge temperature in Li-wall plasmas. A profile of edge parameters, as deduced from the supersonic He beam diagnostic, is displayed in figure 4. Although electron densities are similar to those found under boronized walls, electron temperatures are higher by a factor between 1.5 and 2, tentatively ascribed to changes in dominant impurity and edge power balance rather than to changes in confinement. Since physical sputtering of carbon has been proposed as the main contamination mechanism in TJ-II ECRH plasmas [8], these changes are in line with the observed increase.

Impurity radiation profiles are also seen to evolve upon changing the wall material. Even when total radiation levels are somehow lower in the Li case (clean discharges), the analysis of SXR emission profiles suggests central values of Zeff higher for the Li case. The important issue of impurity accumulation in central heated plasmas, however, deserves a more rigorous analysis of the observed changes and it is out of the scope of this work.

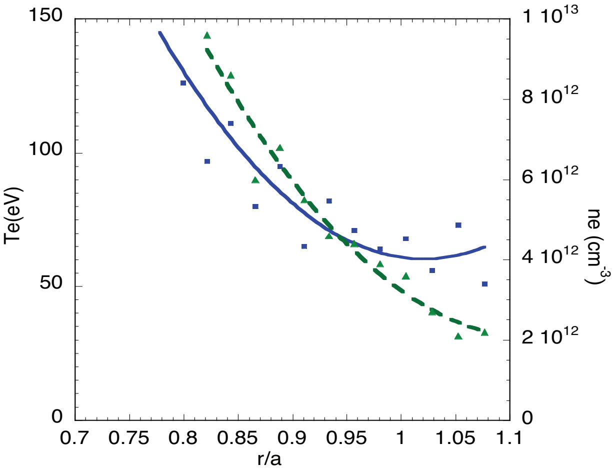

Fig. 5. Edge parameters under Li-wall conditions

Although no major changes in density profiles is seen by the Thompson Scattering diagnostic, it is worth mentioning that cut-off line densities are a 10% higher than in the B counterpart, and a more detailed characterization of the profiles is presently underway. Ion energy balance and confinement has been analyzed through a simple 0-dimensional model for the metal and boron cases in previous campaigns [9]. In its volume average notation, for an ECRH plasma it can express in the form

$$\nu_{i\text{-}e}.\Delta T_{i\text{-}e}.ne\text{-}\ (Ti/\tau_i+K_{cx}n_0Ti).ni=0 \qquad (2)$$

where electron-ion collision frequency, ion energy confinement time and CX losses are integrated in the steady-state balance. Volume averaged electron temperatures are used for Te. Previous estimate of CX losses allow for neglecting this channel in eq. 2 under ECRH conditions in TJ-II, which allows for the evaluation of the characteristic τ_i value by simple plotting the terms of the equation, as displayed in figure 6. Two important remarks must be made from the behavior displayed in the figure. First, a very similar slope, directly giving a first-order estimate of the τ_i value of ~5 ms, in agreement with particle confinement times above mentioned, is found in the three cases. Secondly, the discontinuity observed at collisional frequencies of 10 s^{-1}, corresponding to the transition to the EPC mode is missing in the Li case, thus

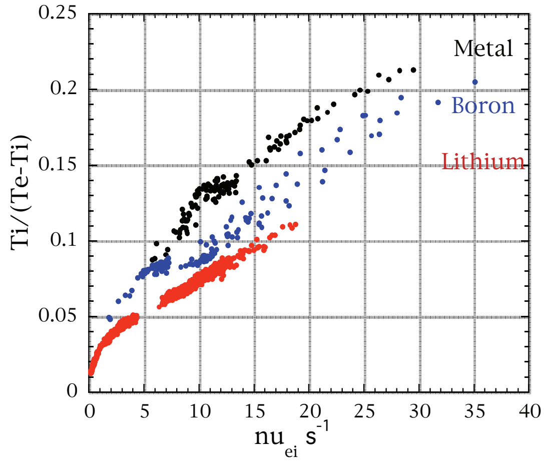

Fig. 6. Ion energy balance analysis for three wall scenarios.

confirming the results found through the fueling analysis of figure 3. Thus, although central electron temperatures were found to be higher under Li walls, which can be initially ascribed to the higher performance of the ECRH system in the last campaign, no changes in the ion channel are observed as the wall material is changed, at least at electron-ion collisionalities high enough to disregard CX losses.

5. NBI plasmas

High beta operation is one of the major goals of the TJ-II program. Therefore, extensive NBI heating must be coupled to the plasma and efforts in this direction have been made in the last years. It was early found, however, that proper density control was extremely challenging under additional heating, partly due to the extra fuelling term introduced by the beams and their interaction with the vessel walls. In the absence of divertor configurations, a low recycling wall can be of great help in preventing plasma collapse by excess density under finite heating power. Although at present, the discharge duration under NBI heating is still dominated by this problem, important changes have been detected in the evolution of the NBI plasma parameters. In figure 7, a comparison of these parameters under boron and lithium walls is shown. Central electron temperature, edge and central radiations and line average densities are shown in both cases. The

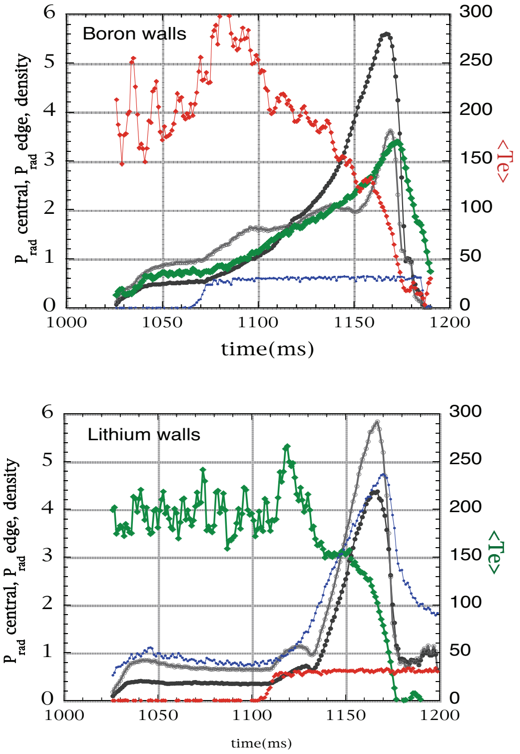

Fig.7. Plasma emissivity (W.cm^{-3}, central and edge lines), line density (10^{13} cm^{-3}) and central electron temperature during the injection of a 500kW neutral beam during the time indicated by the squared pulse.

time of injection is shown by a squared pulse. Although central emissivites are similar at the collapse, a higher line density (4.6 vs. 3.4) is reached in the Li case. Interestingly, edge emissivities are significantly lower in the Li case. Furthermore, the ratio of central to edge radiation behaves in a significantly different way in both cases. According to the running models for radiation collapse in stellarators [10] and the different shape of the cooling rates for the dominant impurities at the edge, the results here presented suggest the presence of radiative instability as candidate for the B case, while a pure thermal collapse would be limiting the plasma density in the lithium wall scenario, with obvious implications in the future upgrading of the NBI power in TJ-II.

6. Conclusions

The TJ-II has been operated under lithiated wall conditions, the first time that this technique has ever been applied to a stellarator. Very encouraging results in terms of density control and impurity level have been obtained; even when only partial coverage was achieved. The strong improvement in density control is not only due to lower recycling of the walls but also to the inhibition of the transition to the EPC mode by the higher puffing levels required. NBI heating has been possible for record densities of 4.5 10^{13} cm^{-3}, its limit possibly due to a pure thermal collapse under the limited NBI power available at present. New techniques for improvement of film homogeneity and careful control of limiter conditions are foreseen in order to improve the results.

References

[1] G. Mazzitelli el al. Proc. 34th EPS Conference Warsaw (2007) to appear in Plasma Phys. Control Fusion and ref. therein

[2] F.L. Tabarés, D, Tafalla et al. J.Nucl. Mater **266-269**,1273 (1999) Also, D. Tafalla and F.L. Tabarés, ibid. **290-293** 1195 (2001)

[3] F.L. Tabarés et al. Plasma Phys. Control. Fusion. **43**, 1023(2001)

[4] L. Guimarais et al. These Proceedings

[5] F.L. Tabarés et al. Proc. 28th EPS Conference on Plasma Physics and Controlled Fusion, Funchal, Madeira (2001)

[6] D.Tafalla and F.L. Tabarés. Vacuum **67**, 393 (2002)

[7] S. Kato et al. J. Nucl. Mater 266-269, 411 (1999)

[8] I. Garcia Cortés, F.L. Tabarés et al. J. Nucl. Mater 337-339, 441 (2005)

[9] R. Balbin, F.L. Tabarés et al Proc. 14th Stell Workshop Greifswald (2003)

[10] M.A. Ochando, F. Castejon and A.P. Navarro. Nucl. Fusion **37**, 225 (1997)

Proceedings of ITC/ISHW2007

Transport Modeling for W7-X on the Basis of W7-AS Experimental Results

C.D. Beidler, J. Geiger, H. Maaßberg, N.B. Marushchenko, Yu. Turkin, W7-AS Team

Max-Planck Institut für Plasmaphysik
IPP-EURATOM Association, Greifswald Germany

October 12, 2007

Exploratory simulations of plasma confinement in the Wendelstein 7-X (W7-X) stellarator are presented, concentrating on scenarios which simultaneously achieve high temperature and high β (normalized plasma pressure) at the full magnetic field of $B = 2.5$ T. Efficient 1-D transport and ray-tracing codes are combined to provide an approximately self-consistent description of the heating and current drive (ECCD) to be expected from up to 10 MW of electron cyclotron resonance heating (ECRH) in W7-X. Best performance is exhibited in high density ($n = 1.8 \times 10^{20}$ m^{-3}) simulations heated at the second harmonic of the ordinary mode, although control of the magnetic topology at the plasma edge — needed to insure functioning of the island divertor — becomes problematic due to the imbalance of the bootstrap current and ECCD.

Keywords: Wendelstein 7-X, neoclassical transport, bootstrap current, electron cyclotron current drive.

The design specifications of the Wendelstein 7-X (W7-X) stellarator were chosen so as to enable this device to demonstrate the reactor potential of the advanced stellarator concept. The ultimate goal of the experimental program is thus to heat, confine and exhaust plasmas with reactor-relevant β and collisionality values under steady-state conditions. This goal must be viewed in its entirety, and it is therefore mandatory to avoid the common experimental expedient of breaking it up into a number of self-exclusive portions (e.g. performing "high-β" experiments at small values of the magnetic field or "low-collisionality" experiments by reducing the density). Currently, there exists no single numerical tool capable of simulating all aspects of such a multifaceted problem but exploratory investigations have been carried out to determine the expected range of W7-X plasma parameters assuming electron cyclotron resonance heating (ECRH) and the prospects for magnetic configuration control using the accompanying current drive (ECCD). The results of these investigations are the subject of this paper.

The basis for these investigations is provided by the theoretical interpretation of experimental results from the W7-AS device, which operated in Garching, Germany, from 1988 until 2002. Three observations are of principal importance for the simulations carried out here:

(1) With the exception of the low-temperature edge region, high-performance W7-AS discharges (with central densities $n(0) > 5 \times 10^{19}$ m^{-3} and central ion and electron temperatures $T^{i,e}(0) > 1$ keV) were described well by the predictions of stellarator neoclassical theory. This was true for all quantities of interest including the radial particle fluxes, energy fluxes and ambipolar electric field [1] as well as the bootstrap current [2, 3]. For the radial losses, this may be attributed to the strong temperature dependence of the neoclassical transport coefficients in the so-called $1/\nu$ regime, which scale

$$\propto \frac{\epsilon_{eff}^{3/2} T^{7/2}}{n B_0^2 R_0^2}$$

where ϵ_{eff} is the effective helical ripple (a measure of how well a stellarator's magnetic field confines trapped particles), B_0 is the magnitude of the magnetic field and R_0 is the major radius of the torus. For W7-AS, a device with moderate values of ϵ_{eff}, this led to neoclassical energy diffusivities $\chi > 1$ m^2/s when $T > 1.5$ keV at $n = 10^{20}$ m^{-3}. Although W7-X was optimized to have much smaller values of ϵ_{eff}, the temperature dependence of this scaling remains unchanged and justifies the continued relevance of neoclassical theory for describing high-temperature bulk plasmas in W7-X.

(2) The low-temperature periphery of W7-AS discharges exhibited anomalously large radial transport, considerably in excess of neoclassical expectations. Assuming this anomalous transport to be purely diffusive, a data set of experimental profiles for ECRH discharges was used to solve the local energy balance in the gradient region and to determine the dependence of the energy diffusivity on local plasma parameters using linear regression; results found that χ was inversely proportional to density and independent of temperature [4]. This result is noteworthy as the density scaling is identical to that of $1/\nu$ transport so that a simple "combination" of these anomalous and neoclassical results would predict a global energy confinement time obeying $\tau_E \propto n$ (assuming n is varied while holding its profile shape constant). Experimental results for such a density scan are shown in Fig. 1 for two different W7-AS

author's e-mail: crb@ipp.mpg.de

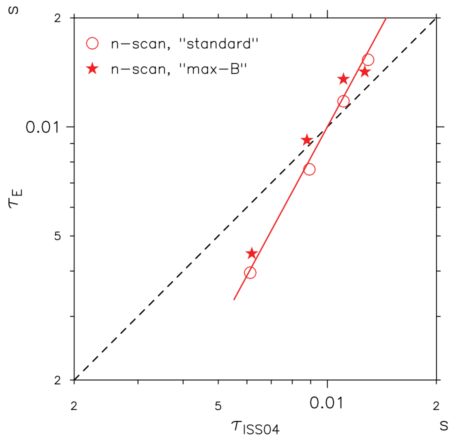

Fig. 1 Energy confinement times for 1.2 MW ECRH discharges in two W7-AS configurations for different central densities compared to the expectations of ISS04. A linear scaling of τ_E with n is shown by the red line.

magnetic configurations heated by 1.2 MW ECRH. A linear scaling of τ_E with density is indicated by the red line and describes the results considerably better than the $n^{0.54}$ dependence of the International Stellarator Scaling ISS04 [5] which is shown by the dashed line for comparison.

(3) A linear description of ECCD using the adjoint approach with a Spitzer function modified to account for trapped-particle effects provided an excellent description of electron cyclotron current drive experiments in W7-AS at densities of 6×10^{19} m^{-3} and larger [3]. As a consequence, high-density ECRH simulations in W7-X can accurately model both power deposition and ECCD using the ray-tracing technique without the need to resort to lengthy solutions of the Fokker-Planck equation.

At the moment, simulations are restricted to a handful of fixed W7-X equilibria which are calculated using VMEC [6] for specified pressure profiles. Modifications of the equilibrium caused by internal current densities (due to ECCD and the bootstrap current) or changes in the pressure profile are not accounted for. For each equilibrium the mono-energetic neoclassical transport coefficients are determined using the Drift Kinetic Equation Solver (DKES) [7] for the relevant range of electric field, E_r, and collisionality values on several magnetic flux surfaces (typically entailing more than 3000 individual DKES calculations); routines are also provided for interpolation of intermediate values in this three-dimensional space and to perform the energy convolutions necessary to calculate the neoclassical transport matrix. With the specification of a model for the anomalous energy diffusivity (based on W7-AS results, $\chi_{an} = 10^{19} n^{-1}$ m^2/s is taken here) one has sufficient information to solve a system of four coupled diffusion equations for the radial profiles of T^e, T^i, E_r and the toroidal plasma current using a 1-D transport code [8]; the density profile is held fixed for these simulations so that a model for the anomalous particle diffusion coefficient is not required. Heating of the plasma by ECRH and calculations of the associated ECCD are simulated with the ray-tracing code TRAVIS [9]. Through direct coupling with the transport code, temperature effects on the ECRH deposition and the current-drive efficiency are fully accounted for. Radiation losses have been ignored for these simulations and impurities are only accounted for insofar as an effective charge number $Z_{eff} = 1.5$ is assumed to exist throughout the plasma.

The ECRH system of W7-X will consist of ten 1 MW gyrotrons, designed for thirty minutes of continuous wave operation at a frequency of 140 GHz (resonant at B = 2.5 T) [10]. Operation at the second harmonic of the extraordinary mode (X2) offers an extremely flexible means of heating the plasma due to its excellent first-pass absorption, allowing a wide choice of launch angles and thus the ability to vary the ECCD over a broad range of values in both the co- and counter-directions (by convention, current in the co-direction increases the rotational transform, ι, and decreases it when flowing in the counter-direction). A limitation is the X2 density cut-off which occurs at $n^e = 1.2 \times 10^{20}$ m^{-3}, roughly a factor of two less than possible if operation is switched to the second harmonic of the ordinary mode (O2). Unfortunately, first-pass absorption of O2 ECRH is relatively poor for the projected plasma temperatures in W7-X, forcing the adoption of a multi-pass absorption scheme with a fixed launching geometry to conform to the placement of mirrors and reflecting surfaces within the vacuum vessel. This launching geometry has been chosen to provide equal ECCD in the co- and counter-directions so that full-power operation implies doing without any net driven current. This drawback is not as serious as it might seem, however, since the current-drive efficiency falls rapidly with increasing density, regardless.

High-density O2 operation in W7-X is potentially of critical importance for optimum divertor performance in the device. Preliminary simulations with the 3-D edge package EMC3/EIRENE [11] have shown that pumping of neutral gas in the W7-X divertor geometry becomes efficient at edge densities of at least 3×10^{19} m^{-3} [12]; a similar value of the edge density was found to provide the impurity screening effect observed experimentally in W7-AS HDH-discharges. Ratios of central to edge density in W7-AS were seldom less than five making it appear questionable whether such high edge densities can be reached in W7-X with X2 ECRH. Heating with O2 was not attempted in W7-AS but is the most attractive option for high-density operation in the early W7-X campaigns as neutral-beam-injection heating will be limited to ten-second pulses during this time.

The requirement of sufficient ECCD to balance the bootstrap current is also a consequence of the divertor concept chosen for W7-X. This makes use of the naturally occurring magnetic islands with $\iota = 5/m$ at the plasma edge (configurations with m = 4, 5 or 6 may be realized with

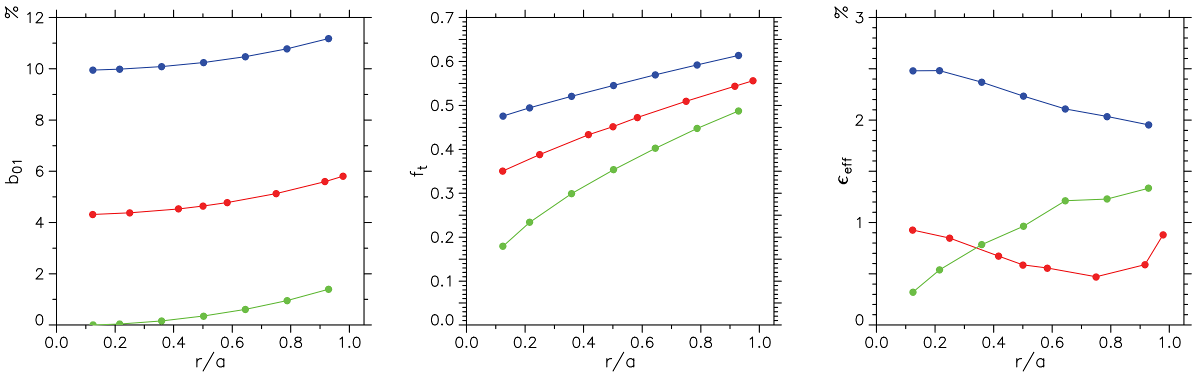

Fig. 2 Radial profiles of the toroidal mirror harmonic (left), the fraction of trapped particles (center) and the effective helical ripple (right) for the W7-X high-mirror (blue), standard (red) and low-mirror (green) configurations.

the W7-X coil system) to guide the outflowing plasma into prepared divertor regions where recycling and exhaust is to take place. For this "island divertor" concept to be effective the magnetic topology of the edge region must be maintained throughout the discharge, which is equivalent to preserving the original value of the rotational transform at the edge. This is possible to sufficient accuracy for net plasma currents of the order ±10 kA.

Simulation Results

The simulations presented here were performed for three different W7-X configurations with the currents in the modular coils chosen to either increase or decrease the magnitude of the toroidal mirror term in B relative to a standard case. (Having the designation b_{01} in the poloidal-, toroidal-angle Fourier decomposition of B, the toroidal mirror is also commonly referred to as the "bumpiness" of the magnetic field strength.) Radial profiles of relevant quantities for the vacuum fields are plotted in Fig. 2. The high-mirror configuration (blue curves) has the largest fraction of trapped particles (f_t) at all radii which generally helps to reduce the bootstrap current while the low-mirror configuration (green curves) provides the opposite extreme. With regard to confinement, however, the standard configuration (red curves) has the smallest values of ϵ_{eff} over most of the plasma radius and these values are further reduced by finite-β effects, especially near the plasma axis. With its much larger ϵ_{eff}, the high-mirror configuration can be expected to have the poorest confinement of these three. The fraction of trapped particles is also of relevance to the current-drive efficiency with small values of f_t most conducive for maximizing ECCD. It will be noted that the simultaneous goals of minimum bootstrap current, maximum confinement and maximum ECCD are contradictory and that the simulations are therefore also a means to search for the best compromise.

A first set of simulations was carried out to determine whether compensation of the bootstrap current by ECCD is possible in all W7-X configurations assuming X2 heating at a density value close to cut-off. The bootstrap current flows in the co-direction in these simulations so that the launch angles of the ECRH system were chosen to maximize counter-ECCD. For significant counter-current near the axis the rotational transform goes to zero in the vicinity, implying a loss of confinement in this region. Indeed, for similar discharges in W7-AS, this loss of confinement was clearly indicated by flat temperature profiles throughout the $\iota \approx 0$ portion of the plasma [3]. Such an effect is not accounted for in the present simulations as self-consistent alterations to the equilibrium are not attempted (the original equilibrium with $\iota(0) > 5/6$ is maintained during the simulation). To avoid this difficulty, off-axis heating was also considered; an example of the results for the $<\beta>= 2\%$ equilibrium of the W7-X standard configuration with 10 MW ECRH is presented in Fig. 3. The shift of the ECCD current density away from the plasma axis (green curve labeled J_{cd} in the lower center) conforms closely to the deposition profile (lower left). The total driven current in this simulation, $I_{ECCD} = -88$ kA, is more than sufficient to compensate the bootstrap current of $I_{bs} = 75$ kA as evinced by the slight reduction of the edge rotational transform relative to the current-free VMEC equilibrium value (compare black and green ι curves on the lower right). The significant reduction of the rotational transform over a large portion of the plasma is the price one pays for using ECCD to compensate the bootstrap current (due to the inherent mismatch of the current-density profiles); nevertheless, ι remains well above zero for off-axis deposition. The simulation results yield $<\beta>= 2.70\%$, in reasonably good agreement with the assumed equilibrium.

The impact which the magnetic configuration has on the results can be illustrated by considering a similar off-axis X2 simulation for the high-mirror W7-X. As shown in Fig. 4, the bootstrap current density assumes small values over the entire plasma radius due to the approximate cancellation of the ion and electron contributions. The negative J^e_{bs} is due to the lower temperatures reached in this

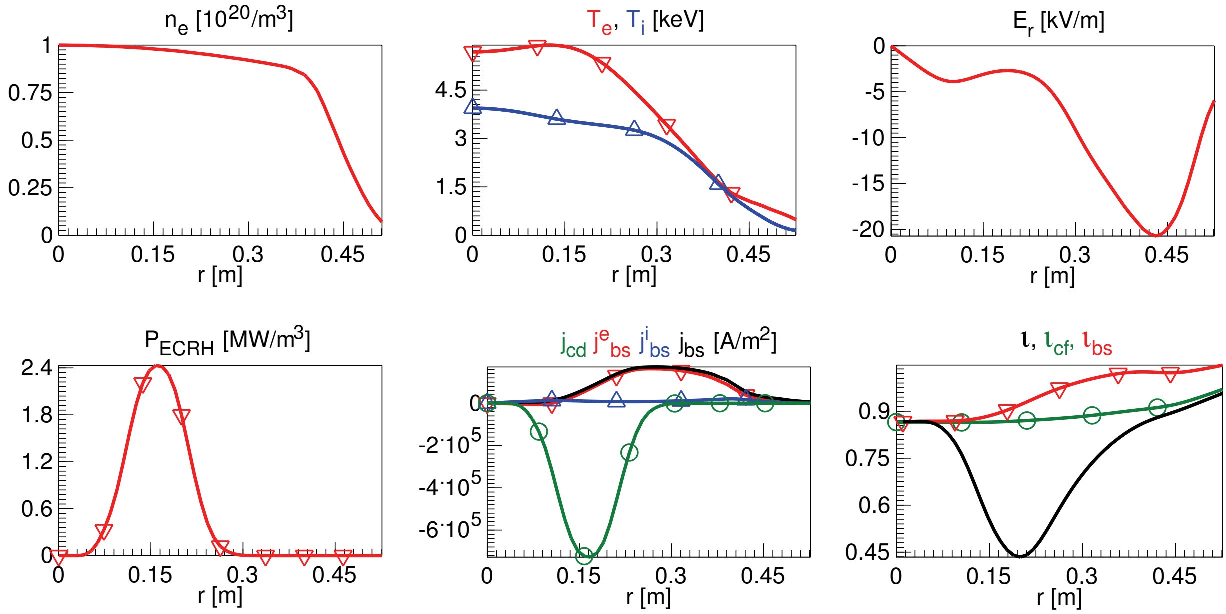

Fig. 3 Simulation results for 10 MW off-axis X2 ECRH in the $<\beta>= 2\%$ standard configuration. Density, temperature and radial electric field profiles are plotted in the upper row; power deposition, current densities and rotational transform are given in the lower row. In the temperature plot, T^e is shown in red, T^i in blue. In the current density plot, J_{cd} is given in green, J^e_{bs} in red, J^i_{bs} in blue and the total bootstrap current density in black. In the rotational transform plot, the current-free (VMEC equilibrium) ι is shown in green, the alteration of this profile due to the bootstrap current appear in red and the rotational transform profile accounting for all currents is given in black.

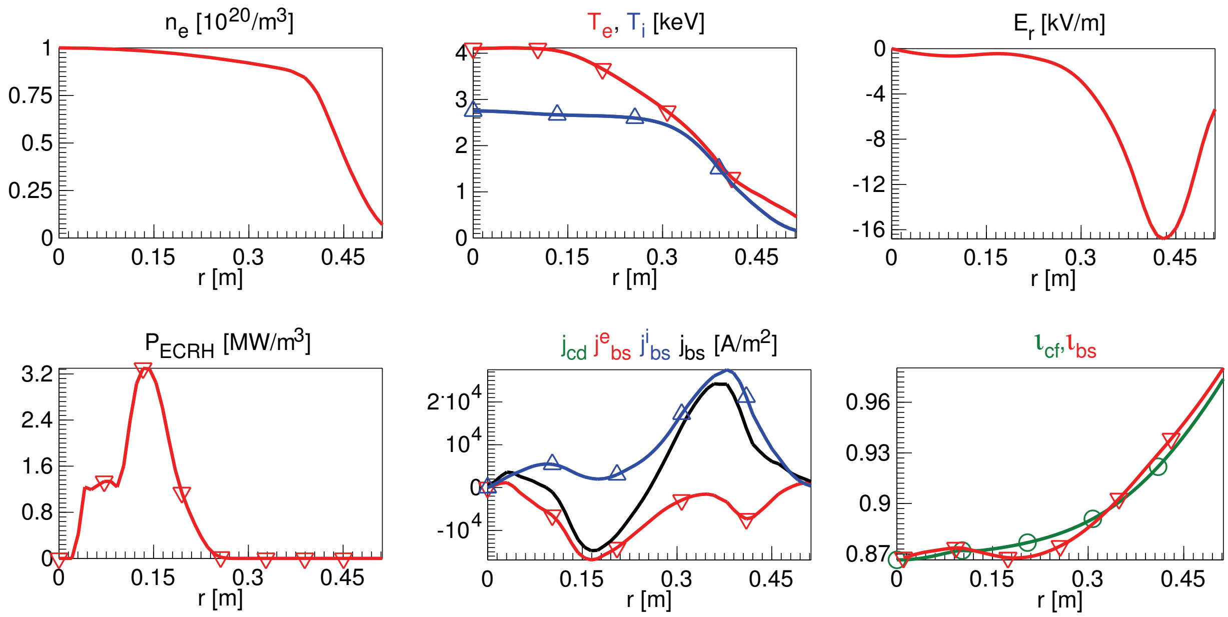

Fig. 4 As in Fig. 3 for 10 MW off-axis X2 ECRH in the vacuum high-mirror configuration.

simulation, shifting the collisionality to higher values where the helical components of the magnetic field are predominant and can reverse the sign of the bootstrap current coefficients. I_{ECCD} as large as -48 kA can be achieved in the high-mirror configuration but is not required for this simulation as the residual bootstrap current is only I_{bs} = 6 kA, which has little effect on the rotational transform profile (red curve on the lower right). The poorer confinement also reduces the normalized plasma pressure to $<\beta>= 2.40\%$.

A summary of the X2 results is provided in Fig. 5 which depicts the values of I_{bs}, I_{ECCD} and the plasma stored energy, W, for on-axis and off-axis heating simulations as a function of the axis value of b_{01} for the equilibrium. From largest to smallest value of b_{01}, these equilibria are for the high-mirror vacuum, standard vacuum, standard $<\beta>= 2\%$, standard $<\beta>= 4\%$ and low-mirror vacuum configurations. The toroidal mirror is reduced by increasing plasma pressure; as already noted, this is expected to improve confinement in the standard configuration which is indeed verified by the increase in W. At the same time, however, both I_{bs} and I_{ECCD} are significantly increased. Also as expected, confinement is poorest in the high-mirror configuration. The stored energy is nearly independent of the deposition profile so that off-axis heating must be favored due to its more benign effects on the rotational transform profile.

For O2 operation current drive can only be realized by doing without a portion of the ECRH power. To maximize the counter-ECCD, the five gyrotrons which would provide co-ECCD are therefore not utilized, limiting the heating power to 5 MW. Additionally, O2 absorption is a strong function of the electron temperature so that O2 ECRH is only possible when a high-T^e "target" plasma is already in existence before O2 heating is begun. This is the basis for the series of simulations which are summarized in Fig. 6, which were performed in the $<\beta>= 2\%$ standard configuration. Here X2 heating is assumed at low to moderate densities but with the identical launching geometry necessary for O2 operation; as in the previous X2 simulations, I_{ECCD} exceeds I_{bs} at all densities with their sum ≈ -12 kA at $n = 10^{20}$ m^{-3} (note that $-I_{ECCD}$ has been plotted in the figure). For O2 operation at this density, however, the ECCD is considerably reduced with its magnitude falling below that of the bootstrap current which is only slightly affected through the differing ECRH deposition profiles of X2 and O2. At higher densities, the "gap" between the two currents closes but is probably initially too great to expect an adequate degree of configuration control during a simple density ramp.

For scenarios where ECCD compensation of the bootstrap current is not possible, there remains the option of factoring the resulting change in the edge value of the rotational transform into the experimental plans. For example, a vacuum magnetic configuration could be chosen with an

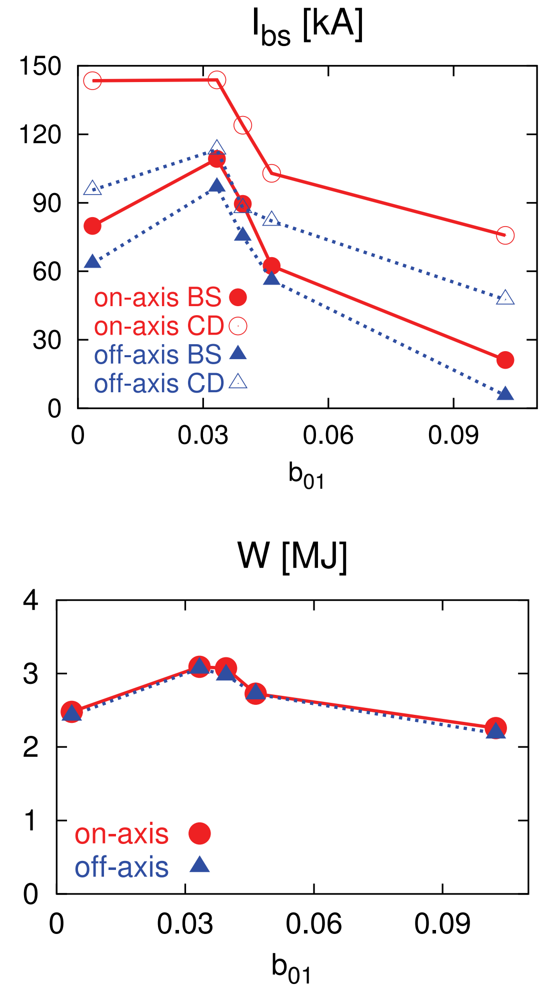

Fig. 5 Values of the bootstrap current and ECRH driven current (top) and plasma stored energy (bottom) as functions of the axis value of the toroidal mirror for X2 simulations with on-axis and off-axis deposition.

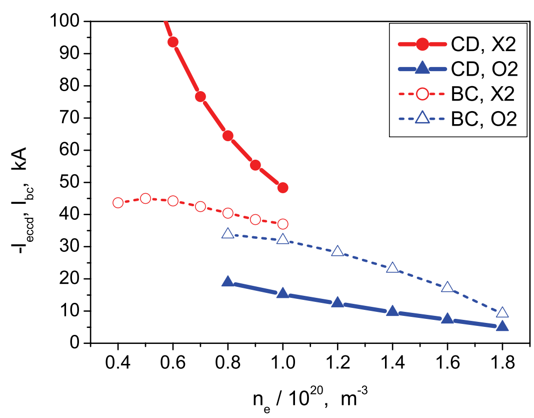

Fig. 6 Values of the bootstrap current and ECRH driven current for 5 MW ECRH simulations in the $<\beta>= 2\%$ standard configuration. The X2 simulations were performed with the O2 launching geometry.

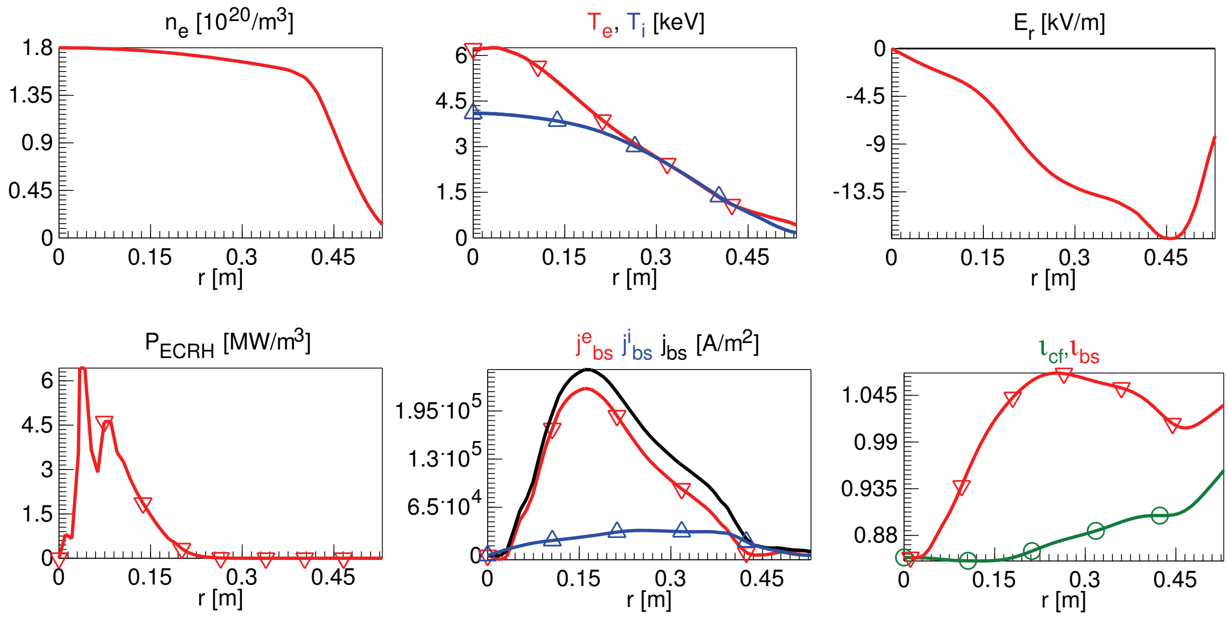

Fig. 7 As in Figure 3 for 10 MW on-axis O2 ECRH in the $<\beta>= 4\%$ standard configuration.

edge ι reduced by an amount which is then to be provided by the net current of the planned discharge. Such a scenario poses additional complications since one must provide co-ECCD at the initial stage to provide the "missing" bootstrap current and be able to adjust the ECCD during later stages according to the changes in I_{bs}. This is plausible using X2 heating and offers the only opportunity for subsequently continuing with the discharge, transferring the full 10 MW of ECRH into the O2 mode. At the moment, such simulations are beyond the capabilities of the approach used here, but it is possible to determine the magnitude of the bootstrap current in the steady-state portion of such a discharge. Results for 10 MW on-axis O2 ECRH assuming a central density of 1.8×10^{20} m^{-3} are given in Fig. 7 for the $<\beta>= 4\%$ standard configuration. The total bootstrap current of 82 kA determined for this simulation and its rather peaked current density profile lead to the alteration of the ι profile shown in red on the lower right. It is expected that a more monotonic profile of ι can be realized by shifting the deposition off axis, although this is likely to result in a modest deterioration of the 97.5% three-pass absorption for the O2 heating in this simulation and in the $<\beta>= 4.13\%$ value which on-axis deposition makes possible.

From the preceding discussion it is clear that time-dependent discharge scenarios will be high on the priority list of future tasks. Near-term plans also include determining free-boundary VMEC equilibria with the pressure profiles and internal current densities calculated here so as to enable modeling of the magnetic field topology in the (assumed) vacuum region outside the last-closed-flux-surface. This will enable one to reach a considerably more detailed verdict concerning the compatibility of edge topology with the island divertor than was possible in the present work where only the edge value of ι was considered.

[1] J. Baldzuhn, M. Kick, H. Maaßberg and the W7-AS Team, Plasma Phys. Control. Fusion **40**, 967 (1998).
[2] V. Erckmann, U. Gasparino and H. Maaßberg, Plasma Phys. Control. Fusion **34**, 1917 (1992).
[3] H. Maaßberg *et al.*, Plasma Phys. Control. Fusion **47**, 1137 (2005).
[4] H. Ringler *et al.*, Plasma Phys. Control. Fusion **32**, 933 (1990).
[5] H. Yamada *et al.*, Nucl. Fusion **45**, 1684 (2005).
[6] S.P. Hirshman, W.I. van Rij and P. Merkel, Comput. Phys. Comm. **43**, 143 (1986).
[7] W.I. van Rij and S.P. Hirshman, Phys. Fluids B **1**, 563 (1989).
[8] Yu. Turkin, H. Maaßberg, C.D. Beidler, J. Geiger and N.B. Marushchenko, Fusion Sci. Technol. **50**, 387 (2006).
[9] N.B. Marushchenko *et al.*, Plasma Fusion Res. **2**, S1000 (2007).
[10] V. Erckmann *et al.*, Fusion Sci. Technol. **52**, 291 (2007).
[11] Y. Feng *et al.*, Contrib. Plasma Phys. **44**, 57 (2004).
[12] D. Sharma, Y. Feng, F. Sardei and D. Reiter, Nucl. Fusion **45**, 825 (2005).

Proceedings of ITC/ISHW2007

Design Integration toward Optimization of LHD-type Fusion Reactor FFHR

A. Sagara, O. Mitarai[a], S. Iamagawa, Y. Kozaki, T. Watanabe, T. Tanaka, N. Yanagi, K. Takahata, H. Tamura, H. Chikaraishi, S. Yamada, T. Mito, A. Shishkin[b], Y. Igitkhanov[c], H. Igami, T. Morisaki, M. Kobayashi, R. Sakamoto, O. Motojima and FFHR design group

National Institute for Fusion Science, Toki, Gifu 509-5292, Japan

[a]Kyushyu Tokai University, 9-1-1 Toroku, Kumamoto 862-8652, Japan

[b]Kharkov Institute of Physics and Technology, Kharkov-108, Ukraine

[c]Max-Planck-Institut fur Plasmaphysik, IPP-EURATOM Ass., Greifswald, Germany

(Received / Accepted)

Recent activities on optimizing the base design of LHD-type helical reactor FFHR2m1 is presented. Three candidates to secure the blanket space are proposed in the direction of reactor size optimization without deteriorating α-heating efficiency and with taking cost analyses into account. For this direction the key engineering aspects are investigated; on 3D blanket designs, it is shown that the peaking factor of neutron wall loading is 1.2 to 1.3 and the blanket cover rate over 90% is possible by proposing Discrete Pumping with Semi-closed Shield (DPSS) concept. Helical blanket shaping along divertor field lines is a next big issue. On large superconducting magnet system under the maximum nuclear heating of 200W/m^3, CICC and alternative conductor designs are proposed with a robust design of cryogenic support posts. On access to ignited plasmas, new methods are proposed, in which a long rise-up time over 300 s reduces the heating power to 30 MW and a new proportional-integration-derivative (PID) control of the fueling can handle the thermally unstable plasma at high density operations.

Keywords: helical reactor, blanket, COE, nuclear heating, superconducting magnet, ignition

1. Introduction

On the basis of physics and engineering results established in the LHD project [1], conceptual designs of the LHD-type helical reactor FFHR have made continuous progress from 1991 [2-5], aiming at making clear the key issues required for the core plasma physics and the power plant engineering, by introducing innovative concepts expected to be available in this coming decades. Those design activities have led many R&D works with international collaborations in broad research areas [6].

Due to inherent current-less plasma and intrinsic diverter configuration, helical reactors have attractive advantages, such as steady operation and no dangerous current disruption. In particular, in the LHD-type reactor design, the coil pitch parameter γ of continuous helical winding can be adjusted beneficially to reduce the magnetic hoop force (Force Free Helical Reactor: FFHR) while expanding the blanket space, where $\gamma=(ma_c)/(lR_c)$ with a coil major radius R_c, a coil minor radius a_c, a pole number l, and a pitch number m.

As a key feature of helical reactors, the blanket space directly couples to the helical coils configuration as well as the core plasma performances under physics and engineering key constrains. Therefore, as the second step after concept definition of the initial FFHR1 (l=3) design [2], optimization studies have begun on the reactor size, based on the LHD-type (l=2, m=10) compact design FFHR2 (γ=1.15, R_c=10 m) [3]and modified FFHR2m1 (γ=1.15 and outer shifted plasma axis, R_c=14 m) and FFHR2m2 (inward shifted plasma axis, R_c=17 m) [4].

This paper presents recent activities on optimizing FFHR2m1 as a base design to make clear key issues, mainly focusing on blanket space, neutronics performance, large superconducting magnet system, and plasma operation.

sagara.akio@LHD.nifs.ac.jp

Table 1. Design parameters of helical reactor

Design parameters			LHD	FFHR2	FFHR2m1	FFHR2m2
Polarity	l		2	2	2	2
Field periods	m		10	10	10	10
Coil pitch parameter	γ		1.25	1.15	1.15	1.25
Coil major Radius	R_c	m	3.9	10	14.0	17.3
Coil minor radius	a_c	m	0.98	2.3	3.22	4.33
Plasma major radius	R_p	m	3.75	10	14.0	16.0
Plasma radius	a_p	m	0.61	1.24	1.73	2.80
Plasma volume	Vp	m^3	30	303	827	2471
Blanket space	Δ	m	0.12	0.7	1.1	1.15
Magnetic field	B_0	T	4	10	6.18	4.43
Max. field on coils	B_{max}	T	9.2	14.8	13.3	13.0
Coil current density	j	MA/m^2	53	25	26.6	32.8
Magnetic energy		GJ	1.64	147	133	118
Fusion power	P_F	GW		1	1.9	3
Neutron wall load	Γ_n	MW/m^2		1.5	1.5	1.3
External heating power	P_{ext}	MW		70	80	100
α heating efficiency	η_α			0.7	0.9	0.9
Density lim.improvement				1	1.5	1.5
H factor of ISS95				2.40	1.92	1.76
Effective ion charge	Z_{eff}			1.40	1.34	1.35
Electron density	$n_e(0)$	10^19 m^{-3}		27.4	26.7	19.0
Temperature	$T_i(0)$	keV		21	15.8	16.1
Plasma beta	$\langle\beta\rangle$	%		1.6	3.0	4.1
Plasma conduction loss	P_L	MW			290	463
Diverter heat load	Γ_{div}	MW/m^2			1.6	2.3
Total capital cost		G$(2003)		4.6	5.6	6.9
COE		mill/kWh		155	106	87

2. Candidates to secure the blanket space

The design parameters of FFHR2 are listed in Table 1, which newly includes the recent results of cost evaluation based on the ITER (2003) design [7]. Figure 1 shows the 3D view of the FFHR2m1. In this base design, one of the main issues is the structural compatibility between blanket and divertor configurations. In particular, the blanket space at the inboard side is still insufficient due to the interference between the first walls and the ergodic layers surrounding the last closed flux surface. To overcome this problem, helical x-point divertor (HXD) has been proposed to remove the interference [8]. In this concept, very effective screening of recycling neutrals with 99% ionization is expected according to 3D simulations [9].

From the point of view of a-heating efficiency over 0.95, the importance of the ergodic layers has been found by collisionless orbits simulation of 3.52MeV alpha particles as shown in Fig.2 [10]. Therefore, three alternatives without adopting HXD are considered. One is to reduce the shielding thickness only at the inboard side. Fig. 3 shows that the WC can reduce about 0.2 m in the shield thickness in comparison to the standard FFHR design with B_4C and JLF-1 [11]. The second is to improve the symmetry of magnetic surfaces around the magnetic axis, without shifting the magnetic axis inward, by increasing the current density at the inboard side of the helical coils while decreasing at the outboard side. Modulation of the current density can be practically obtained by splitting the helical coils [12, 13]. The third is to increase the reactor size. In this case, as shown in Fig.4, it is expected that there is an optimum size around R_c of

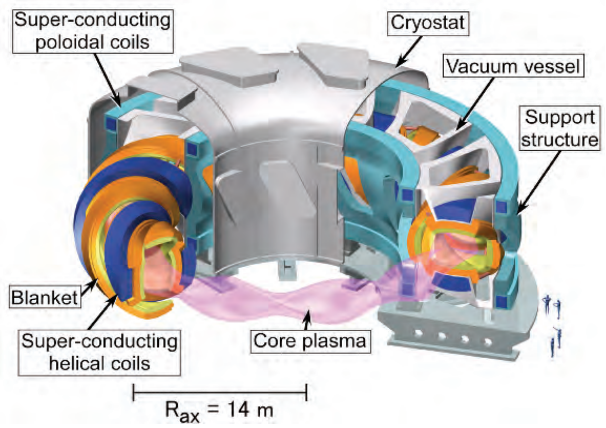

Fig.1. The 3D illustration of the FFHR2m1.

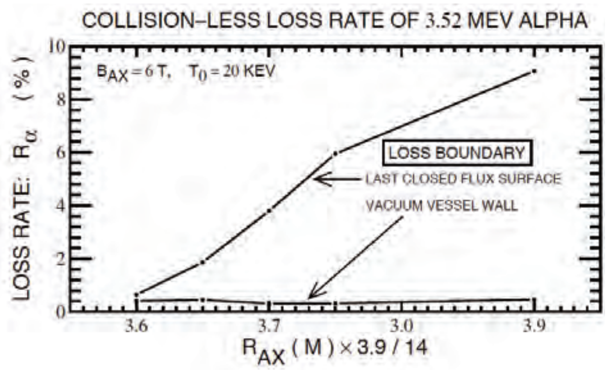

Fig.2 The loss rate of alpha particle in the FFHR2m1, where the two cases on loss boundary are shown as a function of the position of the magnetic axis R_{ax}.

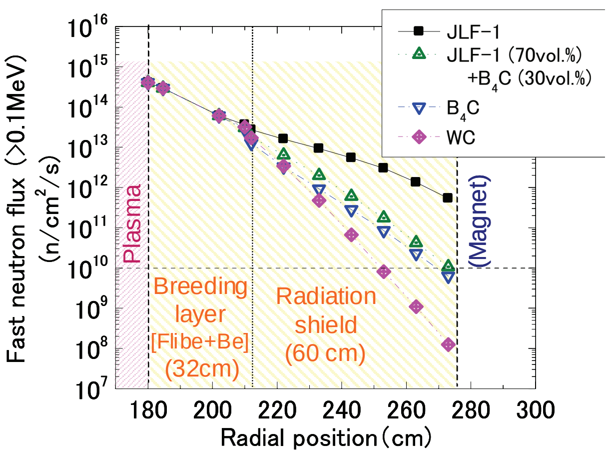

Fig.3 Distributions of first neutron flux (> 0.1 MeV) in the standard FFHR blanket, depending on materials composition of the radiation shield.

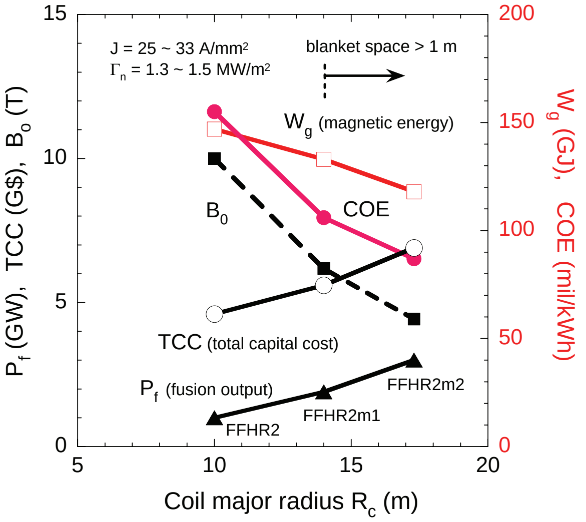

Fig. 4 R_c dependences of the fusion output P_f, the total capital cost (TCC), magnetic field B_0 at the plasma center, cost of electricity (COE) and magnetic energy W_g under almost same conditions on neutron wall loading □ and current density J on helical coils.

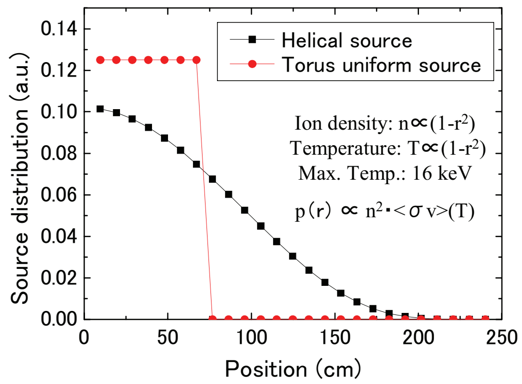

Fig. 5 Neutron source distributions used for neutronics calculations in the FFHR2m1.

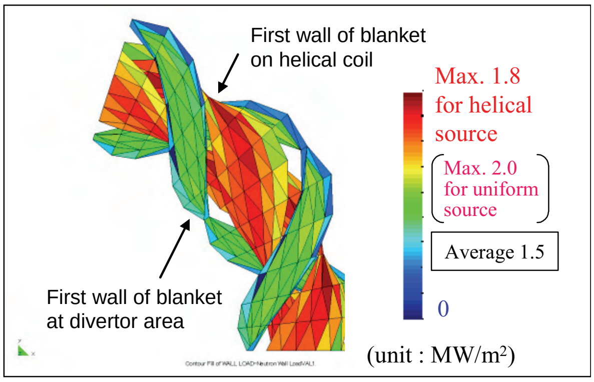

Fig.6 The 3D top view of calculated neutron wall loading distributions. (72° of the torus)

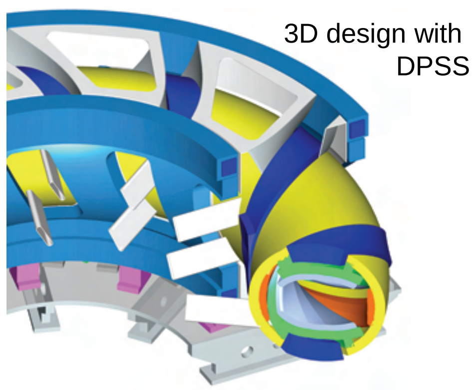

Fig.7 Discrete Pumping with Semi-closed Shield (DPSS) concept, where the helical divertor duct is almost closed with partly opened at only the discrete pumping ports.

15m by taking into account the cost of electricity (COE), the total capital cost, and engineering feasibility on large scaled magnets. More detailed and integrated optimization, by selecting or mixing those three candidates, is one of key next issues.

3. Progress and issues on 3D blanket designs

In the direction of optimizing neutronics performances, the 3D distribution of neutron wall loading is basically important. Using the recently developed 3D neutronics calculation system for non-axisymmetric helical systems as LHD [14], two cases of neutron sources have been compared as shown in Fig.5: one is a centralized torus uniform source which represents a peaked plasma profile, the other is a helical source which comes from a typical parabolic distributions of plasma density and temperature in the elliptic cross section with the long and short radii of 2.4 m and 1.8 m, respectively. Under the averaged neutron wall loading of 1.5 MW/m^2, the maximum loading for the uniform and helical source to be 2 MW/m^2 and 1.8 MW/m^2, respectively, at the first wall of blankets on the helical coils as shown in Fig.6 [14]. Therefore the peaking factor is estimated to be 1.2 to 1.3.

The FFHR blanket designs have been improved to obtain the total TBR over 1.05 for the standard design of Flibe+Be/JLF-1 and long-life design of Spectral-shifter and Tritium Breeding (STB) blanket [4, 14] by enhancement of the blanket cover rate to 80%. More increase of the cover rate over 90% will be effectively possible by a new proposal of Discrete Pumping with Semi-closed Shield (DPSS) concept as shown in Fig.7, where the helical divertor duct is almost closed with partly opened at only

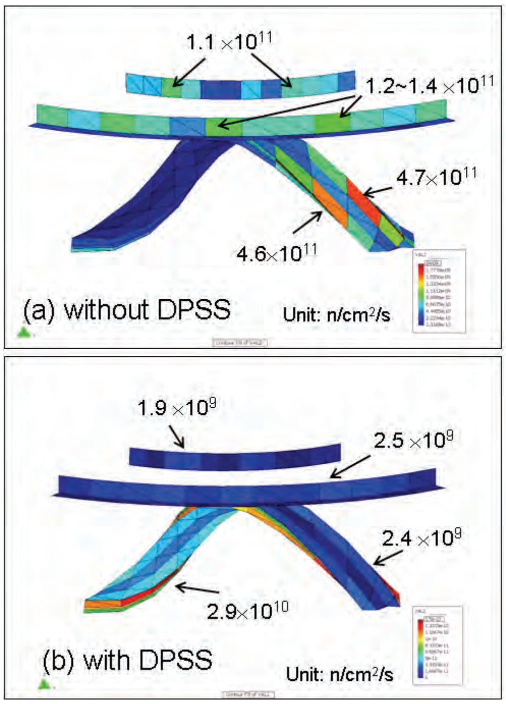

Fig.8 The first neutron fluxes at the poloidal and helical coils (a) without and (b) with the DPSS, where the flux at the rear side of helical coils is high in (a) and one order reduced in (b).

the discrete pumping ports. This DPSS is very important not only to increase the total TBR over 1.2 but also to reduce the radiation effects on magnets. In fact, as shown in Fig.8, the first neutron fluxes at the poloidal coils just out side the divertor duct and at the side of the helical coils are successfully reduced to the acceptable level lower than 1E22 n/m^2 in 40 years. The total nuclear heating is also reduced from 250kW to 40kW, which means the cryogenics power to be about 12MW and acceptable level below 1% of the fusion output.

When the HXD is not adopted as mentioned in the previous section, the blanket design in divertor area should be largely modified, because the intrinsic divertor null point deeply intersects the blanket [8]. Figure 9 shows the tentatively modified design, where the radial position of the divertor area blanket is moved outward. In this case the location of poloidal coils should be also moved in the minor radial direction, resulting in about 11 % increase of the magnetic energy [15]. It is noted in Fig.9 that re-adjustment of helical blanket shaping should be a next big issue by taking into account the blanket space, distribution of wall loading and divertor field lines.

4. Base design of large superconducting magnet system

The base design for the FFHR2m1 superconducting

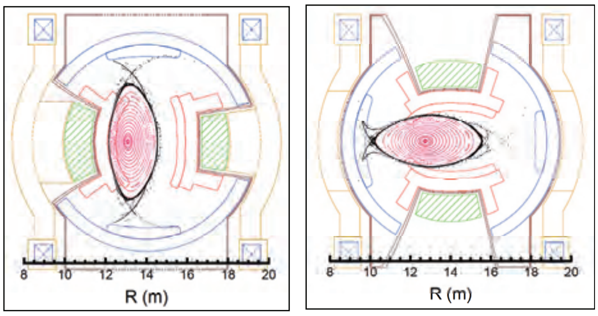

Fig.9 The tentatively modified design to avoid intersection of divertor null points with blankets, where an inward shifted plasma configuration at γ=1.15 is selected as a reference case for optimization.

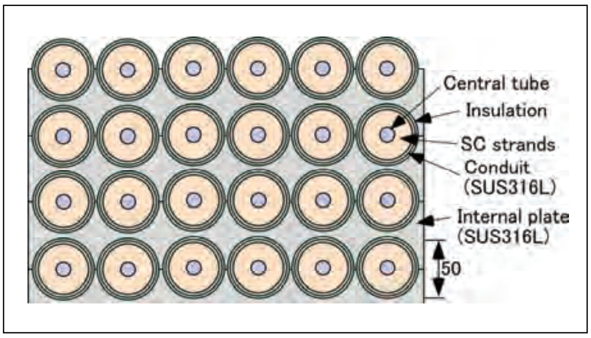

Fig. 10 Concept of helical winding with CIC conductors of current 90 kA with Nb_3Al strands, where the maximum length of a cooling path is about 500 m.

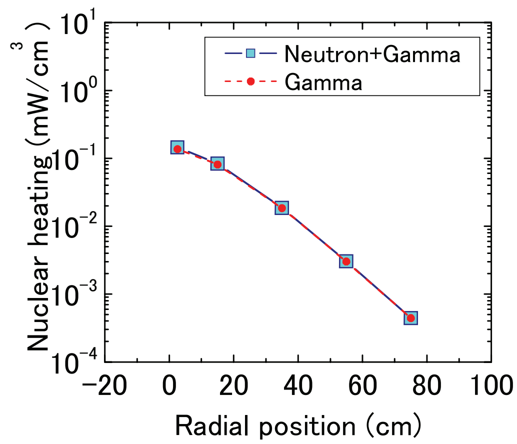

Fig.11 The nuclear heating distribution calculated on the uniformed torus model of FFHR helical coils shown in Fig.10.

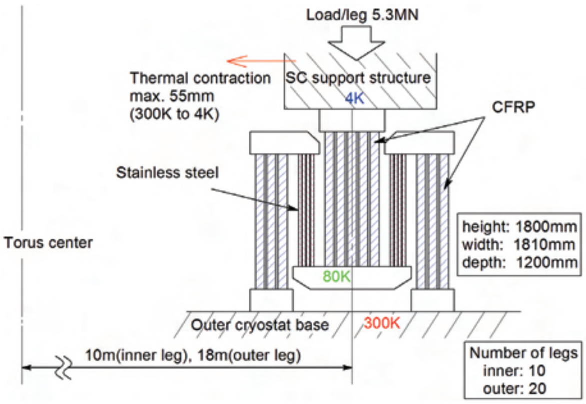

Fig.12 The present design of cryogenic support posts for the FFHR2m1, adopting the same type of the LHD support post.

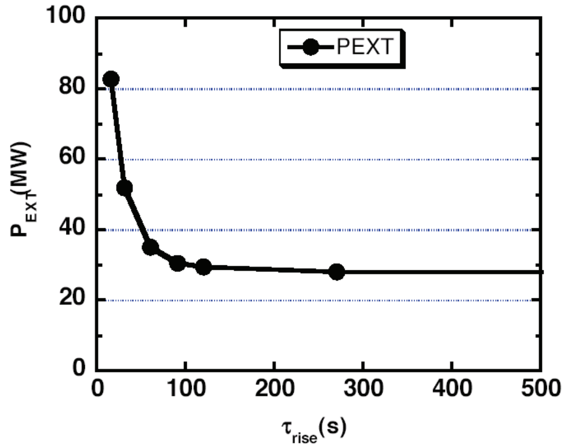

Fig.13 The maximum feedback controlled heating powers to reach self-ignition for various fusion power rise-up times in FFHR2m1.

magnet system has been preliminary proposed [16] on the engineering base of ITER-TF coils as a conventional option. Figure 10 shows the cross sectional structure of continuous helical coil, where the magnet-motive force of helical coils is about 50 MA and the cable-in conduit conductors (CICC) of current 90 kA with Nb_3Al strands are wound in the grooves of the internal plates. In this concept, react and wind method is preferred to use conventional insulator and to prevent huge thermal stress. The maximum length of a cooling path is about 500 m that is determined by the pressure drop for the required mass flow against the nuclear heat of 1000 W/m^3. This value has a 5 times margin of the maximum nuclear heating calculated on the FFHR helical coils as shown in Fig.11, in which the gamma-ray heating is dominant and the maximum is about 200 W/m^3.

Advanced concepts for the FFHR magnet system is of importance as alternative candidates. "Indirect cooling" is promising, because it solves the issue of the pressure drop. The preliminary design using Nb_3Sn has been proposed for the FFHR helical coils, where a conventional quench protection circuit using an external resistor is employed by dividing the coil into several subdivisions [17].

The total weight of the coils and the supporting structure exceeds 16,000 tons. This weight is supported by cryogenic support posts which are set on a base plate of a cryostat vessel. Fig.12 shows the present design of the post [18] adopting the same type of the LHD support post, which is a folded multi plates consisted of Carbon Fiber Reinforcement Plastic (CFRP) and stainless steel plates. The FEM analyses indicate that the LHD-type support post is also valid for the large sized device such as FFHR in mechanical and thermal points of view. The modal and dynamic response analysis using typical earthquake vibrations are the next issue for design optimization.

5. New proposals on access to ignited plasmas

Minimization of the external heating power to access self-ignition is advantageous to increase the reactor design flexibility and to reduce the capital and operating costs of the plasma heating device in a helical reactor. While the fusion power rise-up time in a tokamak depends on the OH transformer flux or the current drive capability, any fusion power rise-up time can be employed in a helical reactor, because the confinement field is generated by the external helical coils. It has been recently found that a lower density limit margin reduces the external heating power, and over 300 s of the fusion power rise-up time can reduce the heating power from such as 100 MW to minimized 30 MW in FFHR2m1 as shown in Fig.13 [19].

A new and simple control method of the unstable operating point in FFHR2m1 is proposed for the ignited operation with high-density plasma [20]. Proportional-integration-derivative (PID) control of the fueling has been used to obtain the desired fusion power with the fusion power error of $e(P_f)=(P_{fo}-P_f)$ in the stable operating point. It has been discovered that in the unstable regime the error of the fusion power with an opposite sign of $e(P_f)= - (P_{fo}-P_f)$ can stabilize the unstable operating point. Around the unstable operating point, excess fusion power supplies fueling and then increases the density and decreases the temperature. Less fusion power in the sub-ignited regime reduces the fueling, decreases the density, and increases the temperature. The operating point approaches the final unstable operating point as oscillation is damped away.

6. Summary

Recent activities on optimizing the base design of LHD-type helical reactor FFHR2m1 is presented. Three candidates to secure the blanket space are proposed in the direction of reactor size optimization without deteriorating a-heating efficiency and with taking cost analyses into account. For this direction the key engineering aspects are investigated.

On 3D blanket designs, it is shown that the peaking factor of neutron wall loading is 1.2 to 1.3 and the blanket cover rate over 90% is possible by proposing Discrete Pumping with Semi-closed Shield (DPSS) concept. Helical blanket shaping along divertor field lines is a next big issue.

On large superconducting magnet system under the maximum nuclear heating of $200W/m^3$, CICC designs of 500 m cooling path and 90 kA with Nb_3Al strands and alternative Indirect cooling Nb_3Sn conductor designs are proposed with the LHD-type robust design of cryogenic support posts. The modal and dynamic response analyses are the next issue for design optimization.

On access to ignited plasmas, using the advantage of current-less plasma, new methods are proposed, which are a long rise-up time over 300 s to reduce the heating power to 30 MW and a new proportional-integration-derivative (PID) control of the fueling to handle the thermally unstable plasma at high density operations.

Acknowledgments

This work has been performed under the research programs of NIFS (code ULAA116).

References

[1] O. Motojima et al., to appear in Nuclear Fusion.

[2] A. Sagara, O. Motojima, K.Watanabe et al., Blanket and Divertor Design for Force Free Helical Reactor (FFHR), Fusion Eng. and Design, 29 (1995) pp.51-56.

[3] A. Sagara, K.Y.Watanabe, K.Yamazaki et al., LHD-Type Compact Herical Reactors, in Proceeding of the 17th Int. Conf. on Fusion Energy (1998, Yokohama), IAEA, Vienna

[4] A. Sagara, S. Imagawa, O. Mitarai et al., Improved structure and long-life blanket concepts for heliotron reactors, Nuclear Fusion, 45 (2005) pp.258-263.

[5] A. Sagara, O. Mitarai, S. Imagawa et al., Conceptual design activities and key issues on LHD-type reactor FFHR, Fusion Eng. and Design, 81 (2006) pp.2703-2721.

[6] A. Sagara, T. Tanaka, T. Muroga et al., Innovative Liquid Breeder Blanket Design Activities in Japan, Fusion Sci. and Tech., 47 (2005) pp.524-529.

[7] Y. Kozaki, S. Imagawa, A. Sagara, Design Windows Analysis based on a Cost Model of Helical Reactor (HeliCos), NIFS annual repo. 2006-2007

[8] T. Morisaki, S. Imagawa, A. Sagara, O. Motojima, Numerical study of magnetic field configuration for FFHR from a viewpoint of divertor and edge field structure, Fusion Eng. and Design 81 (2006) 2749–2754.

[9] M. Kobayashi, N. Ohyabu, T. Mutoh et al., Edge Transport Control with The Local Island Divertor and Recent Progress in LHD, The 17th ANS Topical Meeting on the Technology of Fusion Energy (TOFE), Albuquerque, NM, 2006.

[10] T. Watanabe, A. Sagara, Alpha Particle Loss Fraction in the FFHR, NIFS annual repo. 2006-2007.

[11] L. El-Guebaly, R. Raffray, S. Malang, et al., Benefits of Radial Build Minimization and Requirements Imposed on ARIES Compact Stellarator Design, Fusion Science and Technology 47 (2005) 432-439.

[12] N. Yanagai, K. Nishimura, A. Sagara, Design of Split-Type Helical Coils for FFHR-2S, NIFS annual repo. 2006-2007.

[13] K. Nishimura, M. Fujiwara, J. Phys. Soc. Japan 64 (1995) 1164.

[14] T. Tanaka, A. Sagara, T. Muroga, M. Youssef, Neutronics Investigation of Advanced Self-Cooled Liquid Blanket Systems in Helical Reactor, presented at 21st IAEA Fusion Energy Conf., 2006, Chengdu, China.

[15] S. Imagawa, A. Sagara, Y. Kozaki, Structural Design of Magnet Systems for LHD-type Reactor FFHR2m, in this conference.

[16] S. Imagawa, A. Sagara, Y. Kozaki, Conceptual Design of SC Magnets of a Helical Reactor with CIC Conductors, NIFS annual repo. 2006-2007.

[17] K. Takahata, T. Mito, H. Tamura, S. Imagawa, A. Sagara, Conceptual design of an indirect-cooled superconducting magnet for the LHD-type fusion reactor FFHR, SOFT2006.

[18] H. Tamura, A. Sagara, Conceptual Design of Support Post for FFHR Cryogenic Components, NIFS annual repo. 2006-2007.

[19] O. Mitarai, A.Sagara, H.Chikaraishi et al., Minimization of the External Heating Power by Long Fusion Power Rise-up Time for Self-ignition Access in the Helical Reactor FFHR2m, presented at 21st IAEA Fusion Energy Conf., 2006, Chengdu, China.

[20] O. Mitarai, A. Sagara, N. Ohyabu, et al., New Control Method of the Unstable Operating Point in the FFHR Helical Reactor, Plasma and Fusion Research, Rapid Communications, 2, 021 (2007) .

Proceedings of ITC/ISHW2007

Evolutionary development of an ignited toroidal fusion reactor

M. Zarnstorff, J. H. Harris[a], D. T. Anderson, S. Knowlton[c], J. F. Lyon[a]

Princeton Plasma Physics Laboratory, USA
Oak Ridge National Laboratory[a], USA
University of Wisconsin[b], USA
Auburn University[c]

e-mail: zarnstor@pppl.gov

The tokamak, with its axisymmetric field configuration and induced plasma current, has been the primary vehicle for studying the physics of toroidal plasma confinement, and can be used effectively to explore burning fusion plasmas. The stellarator has traditionally been seen as a contrasting alternative to the tokamak, substituting external non-symmetric helical fields for the plasma current to form nested magnetic surfaces.

However, as we move forward towards a reactor in which a high-pressure plasma must be stably sustained for weeks or more, the tokamak configuration is evolving. The axially symmetric tokamak develops unstable, non-symmetric helical perturbations whose suppression requires the imposition of multiple helical control fields and/or carefully programmed local heating. Continuous, toroidally asymmetric sources of current drive and momentum input are required to maintain the plasma in an enhanced confinement regime: the steady-state power required for these can exceed that used initially to raise the plasma to fusion temperatures. All these maintenance schemes require active feedback control.

Recent advances in toroidal physics understanding and computation techniques allow these essential sustainment functions to be carried out using a carefully shaped 3-D stellarator field in place of the numerous active schemes. The rotational transform required to make magnetic surfaces together with the shaping required to maintain plasma stability come directly from the structure of the DC magnetic field itself. Additional rotational transform required for high-beta confinement comes from the self-consistent bootstrap current. The sheared flows required for improved confinement come from the ambipolar electric field, which arises naturally in suitably tailored 3-D configurations. The losses of heat and fusion alphas arising from particle orbits in the 3-D field can be reduced to low values by optimization that minimizes the departure from symmetry in a chosen direction. The ARIES collaboration has developed a 1 GWe compact stellarator fusion reactor embodiment based on these concepts (ARIES-CS). The design fits within the size envelope of typical tokamak reactor designs, with R/a = 4.5, and yields a comparable cost-of-electricity.

Key questions about the physics features and engineering challenges of these compact stellarators require experimental assessment. Therefore, the US stellarator program has embarked on a series of experiments involving university-scale and national laboratory devices. These include three quasi-symmetric configurations, the Helically Symmetric Experiment (HSX, Univ. Wisconsin, operating), the National Compact Stellarator Experiment (NCSX , PPPL, under construction) and the Quasi-Poloidal System (ORNL, under design). These experiments explore the physics properties of quasi-symmetric configurations. An additional university device, the Compact Toroidal Hybrid (Auburn Univ., operating) is being used for studies of the diagnosis, stability, and control of current carrying stellarator plasmas.

Oral Presentations

Proceedings of ITC/ISHW2007

Stability of Current-Driven Discharges in the Compact Toroidal Hybrid Helical Experiment

S. F. Knowlton, G. J. Hartwell, J. D. Hanson, J. Peterson, J. Shields, B. A. Stevenson

Physics Department, Auburn University, Auburn, Alabama, 36849-5311

knowlton@physics.auburn.edu

With stellarators now attaining significant values of volume-averaged β, issues of equilibrium and stability associated with pressure-driven currents are of renewed interest to understanding helical plasmas. Moreover, advanced compact stellarators such as NCSX [1] may operate in a hybrid configuration with driven current before high-β plasmas are achieved. Exploratory experiments to understand stability and disruption avoidance in current-driven helical plasmas are underway on the Compact Toroidal Hybrid (CTH) device. Also in progress is the testing of the new V3FIT procedure of 3-D equilibrium reconstruction [2], primarily with magnetic diagnostics.

CTH is a five field period torsatron with additional toroidal field and poloidal field coils for control of the vacuum rotational transform and shear. The magnetic field is $B_0 \leq 0.7$ T, with the edge vacuum rotational transform variable in the range $0.1 < \iota/2\pi < 0.5$. Ohmic plasma currents of $I_p \leq 40$ kA are induced in target plasmas generated by 12 kW ECRH at the fundamental resonance of 18 GHz. The duration of the ohmic phase of the discharge is up to 100 msec.

During the plasma current rise, instabilities and hesitations in the rate of current increase correlated with low-order rational values of the net edge rotational transform are observed. These values are independent of applied vacuum rotational transform. At edge rotational transform values of 1/3 or 1/2, the current often undergoes repetitive relaxations in which the current rise is arrested, and the value of the total current drops by about 3%. Major disruptions associated with these instabilities, or any others, have not been found to occur. Efforts to operate with an edge transform above a value of ½ are ongoing.

To verify the magnetic configuration and also determine an improved coil model for use in the equilibrium reconstruction process, vacuum field mapping measurements are compared with predictions from the original coil design. Measurement of the magnetic axis in different field periods for a variety of coil current settings are incorporated into an SVD optimization procedure to arrive at a modified winding law for the helical coil consistent with the physical constraints of the helical winding form.

This work is supported by US DOE Grant DE-FG02-00ER54610

[1] G. H. Neilson, A. H. Reiman, M. C. Zarnstorff, A. Brooks et al., Phys. Plasmas **7**, 1911 (2000)

[2] S. P. Hirshman, E. A. Lazarus, J. D. Hanson, S. F. Knowlton, and L. Lao, Phys. Plasmas, **11** 595 (2004)

Proceedings of ITC/ISHW2007

Studies of Configuration Control Effects on Dynamic Behavior of Heliotron J Plasmas

Tohru Mizuuchi, Shinji Kobayashi, Satoshi Yamamoto[a], Hiroyuki Okada, Kazunobu Nagasaki, Gen Motojima[b], Shinya Watanabe[b], Hajime Arimoto[b], Kensuke Murai[b], Fumiyori Hamagami[b], Daisuke Katayama[b], Hironori Matsuoka[b], Akino Nakajima[b], Hiroshi Takahashi[b], Hiroyuki Yasuda[b], Kiyofumi Mukai[b], Akiyuki Matsuyama[b], Yusuke Kowada[b], Katsuyuki Hosaka[b], Shiori Mihara[b], Nobuhiro Nishino[c], Takashi Minami[d], Yousuke Nakashima[e], Yasuhiro Suzuki[d], Sadayoshi Murakami[f], Kiyomasa Watanabe[d], Masayuki Yokoyama[d], Yuji Nakamura[b], Kiyoshi Hanatani, Katsumi Kondo[b], Shoichi Okamura[d], Fumimichi Sano

Institute of Advanced Energy, Kyoto University, Gokasho, Uji 611-0011, Japan
[a]Kyoto University Pioneering research Unit for Next Generation, Gokasho, Uji 611-0011, Japan
[b]Graduate School of Energy Science, Kyoto University, Gokasho, Uji, 611-0011, Japan
[c]Graduate School of Engineering, Hiroshima University, Higashi-Hiroshima 739-8527, Japan
[d]National Institute for Fusion Science, 322-6 Oroshi-cho, Toki 509-5292, Japan
[e]Plasma Research Center, University of Tsukuba, Tsukuba, Ibaraki 305-8577, Japan
[f]Graduate school of Engineering, Kyoto university, Kyoto 606-8501, Japan

(Received day month year / Accepted day month year)

The transition to an improved confinement mode in NBI-only plasma is investigated in Heliotron J, focusing on the onset condition of the transition. The transition, identified by a drop in the Hα intensity and an increase in the stored energy, the line-averaged electron density, has been observed in the Co-injection case. The experiment shows (1) the delay time between the NBI turned-on and the drop of the Hα intensity decreases with the power, and (2) the transition occurs at a certain toroidal current (bootstrap current and NBCD current). The critical current depends on the vacuum rotational transform. The free-boundary equilibrium calculation predicts that the rotational transform and the shape of the magnetic surface, especially in the outer region, can be modified asymmetrically to the current direction.

Keywords: Heliotron J, rotational transform, effect of non-inductive plasma current, transition of confinement mode, NBI plasma

1. Introduction

Heliotron J [1, 2] is a low-magnetic-shear device with an L/M = 1/4 helical coil (R_0 = 1.2 m, $B_0 \leq 1.5$ T) based on the helical-axis heliotron concept [3], where the bumpiness, ε_b, is introduced as a new control knob of field configuration in addition to the other major field harmonics, helicity and toroidicity. One of the major objectives of Heliotron J project is to examine the effects of the new field parameters on the plasma performance and to experimentally explore this advanced concept. The configuration control studies are essential parts of the Heliotron J experiment.

The study of ε_b-control effects on the bulk plasma confinement and behavior of fast-ions were initially performed for ECH plasmas selecting three different ε_b configurations with the same rotational transform at the last closed flux surface (LCFS), $\iota(a)/2\pi$ in the vacuum condition (i.e. no plasma effects) [4, 5]. As for the ε_b-effect on the fast-ion behavior, which was examined by superimposing an NBI or ICRF pulse on ECH target plasmas, the higher ε_b configuration is preferable for the confinement of low- and high-pitch angle fast-ions. These observations are qualitatively consistent with the drift optimization viewpoint. On the other hand, as for the global energy confinement, the dependence is not so simple and we have tried to understand the observations based on the discussion of the effective ripple modulation amplitude, ε_{eff}. The preliminary analysis suggests that the lower ε_{eff} configuration seems to be preferable for the global confinement for ECH-only plasma These experiments have expanded to NBI-only plasmas [6], where the difference of τ_E^{exp} in high- and medium-ε_b configurations is not clear compare to that for ECH-only plasma. These observations suggest the possibility of different ε_b-dependence of the global energy confinement time between ECH-only and NBI-only plasmas.

On the other hand, as experimentally demonstrated

author's e-mail: mizuuchi@iae.kyoto-u.ac.jp

in W7-AS [7] and Heliotron J [8], the value of the edge rotational transform ι(a)/2π is essential for the good plasma confinement in a low magnetic-shear device, including L-H transition and MHD activities. The effects of rational surfaces in the core region have been studied in many tokamaks and helical devices from the viewpoint of MHD activities. Recently the effects of low-order rational surfaces have been discussed from the viewpoint of the appearance of external/internal transport barriers or enhanced confinement modes in helical devices [9, 10]. In addition, the edge rotational transform is also closely related with the field topology for so-called a "built-in" divertor in heliotron/stellarator systems.

The initial study of rotational transform effects on the global confinement in Heliotron J were performed by for ECH-only plasma [11]. Since the transition to the improved confinement mode (H-mode) was discovered in Heliotron J, the accessibility condition to the transition has been experimentally investigated for different configurations labeled by the vacuum edge rotational transform $\iota(a)/2\pi|_{vac}$ [8]. ECH- and ECH+NBI experiments indicate the existence of $\iota(a)/2\pi|_{vac}$-windows for the high quality H-mode ($\tau_E^{exp}/(f\times\tau^{ISS04}) > 1.5$) close to the low-mode rational numbers of $\iota(a)/2\pi|_{vac}$. Here, τ^{ISS04} and f are the global energy confinement time by the international (inter-machine) stellarator scaling and a new configuration-descriptive re-normalization factor driven for each configuration subgroup of the experimental database, respectively [12, 13]. Figure 1 shows such $\iota(a)/2\pi|_{vac}$-dependence for ECH+NBI plasmas [8]. The

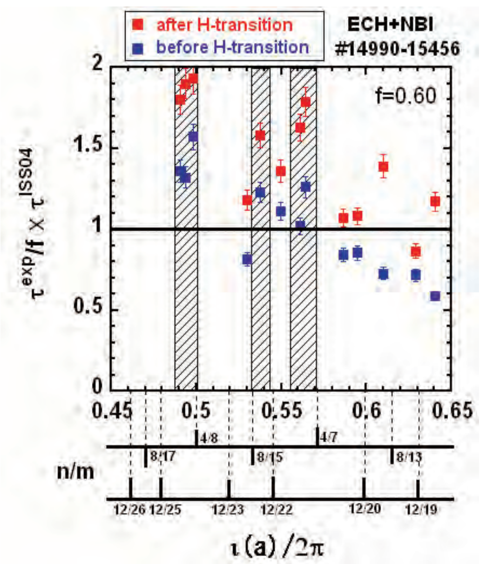

Fig. 1 Configuration effect on the normalized global energy confinement time of for ECH+NBI plasma. Each configuration is labeled by $\iota(a)/2\pi|_{vac}$. The window for the high quality H-mode (hatching zone) is observed close to the low-mode rational numbers of $\iota(a)/2\pi|_{vac}$ [8].

power and density thresholds of the H-mode are observed to depend on the configuration (i.e. $\iota(a)/2\pi|_{vac}$), but the systematic dependences between them are not fully understood. It might have to consider the influence of the topology ("shape") of the magnetic surfaces on the poloidal viscous damping rate, which influences the formation of the radial electric field through the plasma poloidal rotation [14]. The poloidal viscous damping rate depends also on the existence of the rational surface [15].

Even for non-Ohmic heating plasmas in a helical device, non-inductive plasma current can be driven by the pressure-gradient (bootstrap current), ECCD and NBCD. The modification of ι(r)/2π due to such non-inductive plasma current can create new rational surfaces in the core region. In the edge region, the change of the rotational transform can modify the divertor plasma distribution in a low-shear device. In the Heliotron J experiments, it is experimentally confirmed that the bootstrap current and ECCD can be controlled by the bumpiness tailoring [16]. A tangential NBI system [17] can also control the direction and intensity of NBCD current by selecting the beam lines and by controlling the injection power. Experimentally, the effects of the plasma current and its radial profile on the edge field topology and divertor plasma distribution have been investigated in Heliotron J from viewpoints of divertor control and balk plasma confinement [18]. An experimental detection of the rotational transform modification during a discharge has been tried in Heliotron J by using the sensitivity of MHD activities on the rational surfaces [19].

This paper reports recent experimental investigation into the effects of the non-inductive plasma current (or resultant modification of ι(r)/2π) on the onset of the

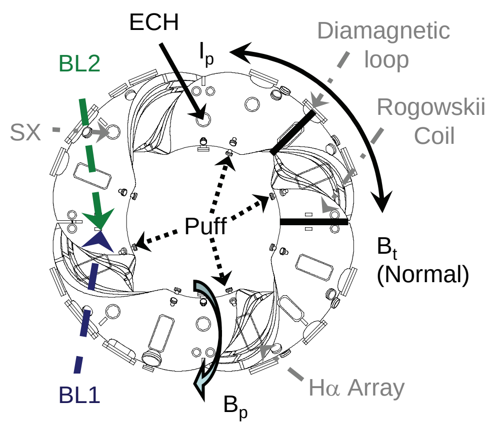

Fig.2 Top view of the Heliotron J device. In the case of the "normal" operation, the direction of the magnetic field is clockwise, where the toroidal current flowing in the counter-clockwise direction enhances the poloidal magnetic field strength. ("additive current")

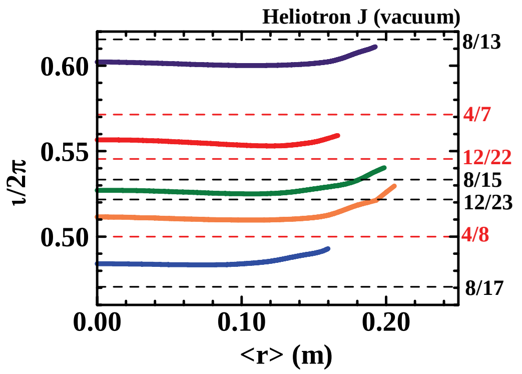

Fig. 3 Radial profile of the vacuum rotational transform for several configuration. The horizontal dashed lines indicate some low-mode rationals.

transition event.

2. Experimental setup

The details of the Heliotron J device is described in [1, 2]. Figure 2 schematically shows the top view of Heliotron J with the main heating and diagnostic systems. The initial plasma is produced by the 70GHz second harmonic X-mode ECH system launched from a top port located at the straight section of Heliotron J. The hydrogen neutral beam (30 keV, 0.7 MW/beam-line) is injected using two tangential beam-lines facing each other (BL1 and BL2). Selecting one of the beam-line or changing the direction of the confinement field, Co- or CTR-injection is performed. The working gas is hydrogen or deuterium.

The configuration of the confinement field is controlled using the five types of the external coils, the helical coil, two individual sets of the toroidal coils (TA and TB) and two sets of the vertical coils (AV and IV). The major part of the field configuration is determined by the helical and toroidal coil currents. The bumpiness is mainly controlled by changing the coil current ratio of TA and TB coils, I_{TA} and I_{TB}, respectively. Trimming of other coil currents, it is possible to control ε_b within tolerable change in the other major Fourier components of the confinement field (helicity and toroidicity), $\iota(a)/2\pi|_{vac}$, the plasma volume and the major radius [4]. On the other hand, $\iota(r)/2\pi|_{vac}$ can be controlled by mainly changing the current ratio of the helical coil to the toroidal coils. Here, it is possible to minimize the change of the bumpiness by keeping the current ratio of I_{TA}:I_{TB} to be constant. Some examples of radial profile of the rotational transform in the vacuum condition are shown in Fig. 3. The ε_b at ρ = 2/3 and $\iota(a)/2\pi|_{vac}$ for the standard (STD) configuration of Heliotron J are ≈ 0.06 (I_{TA}:I_{TB} = 5:2) and ≈ 0.56, respectively.

3. Numerical study of plasma current effects on the field configuration

A free-boundary equilibrium calculation is useful to obtain a prospect of the deformation of the configuration by plasma pressure and/or current, and to understand the experimental observations.

Figures 4 and 5 show an example of such calculation obtained by using HINT2 [20] for the STD configuration. Here, we assume rather peaked plasma pressure- and current-profiles: $\beta(s) = \beta_0\times(1-s)^2$ with β_0 = 0.5%, $j_p(s) = j_0\times(1-s)^2$, where s denotes toroidal flux corresponding to the square of the normalized minor radius (= ρ^2). In Fig. 4, "vacuum" means no plasma condition (i.e. β = 0 %, the

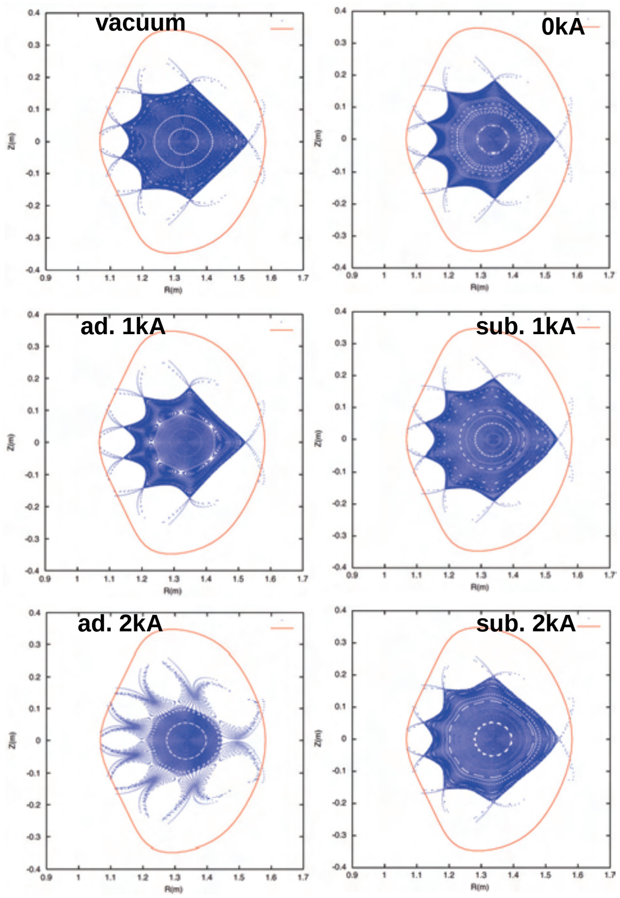

Fig.4. Effects of plasma pressure and current on the configuration.

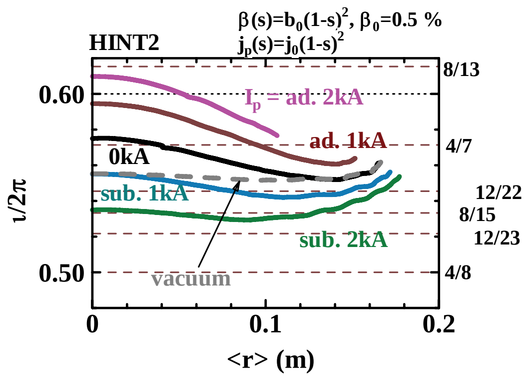

Fig.5. Effects of plasma pressure and current on the rotational transform.

net current I_p = 0 kA). The case of “additive current” direction (i.e. the current increases $\iota/2\pi|_{vac}$) is indicated as “ad. *kA” and the opposite case is “sub. *kA” in the figure. Figure 5 shows the effects on the rotational transform obtained by the same calculations for Fig. 4. As shown in Figs. 4 and 5, the plasma current can modify not only the rotational transform but also the “shape” of the last closed flux surface. Moreover, as discussed in [18], even for the same net-current value, the difference in current profile j(s) has important effects on the modification. It should be noted that the effects are not symmetry to the net current direction. The effect of the plasma pressure can be somewhat compensated by the subtractive current. Moreover, the “proximity” to the rational number, 4/7 for the STD configuration, is important since the low-mode resonance has an important role on the field topology,. The vacuum rotational transform at the edge is about 0.56 (i.e. less than the rational number 4/7) in the standard configuration, $\iota(a)/2\pi$ become close to the rational by the additive current, but the subtractive current increase the distance from the resonance condition.

4. Transition in NBI-only plasma

In this study, we focus on the NBI-only plasmas to simplify the situation and to take advantage of current controllability of NBCD in the density region higher than the empirical critical (lower-limit) density for the transition [8].

Figure 6 shows an example of the time traces for the stored energy, line-averaged density and Hα intensity from an NBI-only plasma in the STD configuration, where the direction of the confinement field is the normal direction and the working gas is hydrogen. The plasma initiation was performed by using a short pulse (~ 6ms) of the 70GHz 2X ECH microwaves. After that, the plasma was heated and sustained by Co-NBI (BL2, P_{inj} ~ 0.46 MW/28kV). Here, “Co-”means the NBCD current increases the vacuum rotational transform (“additive” current). At t ~ 206 ms, a sudden drop of Hα intensity and increases of the stored energy and line-averaged density were observed, indicating the onset of transition to an improved confinement mode. The changes in the radial profile of SX-intensity and the ion saturation current in the scrape-off region (not shown) indicate that this phenomenon is an edge relating event. The Hα intensity was rapidly increased from ~ 220 ms, and finally the back transition occurred followed by the decrease of the stored energy. It is interesting to note that there is some time delay between the start of NBI and the drop of the Hα intensity. This delay time is longer than the “build-up time” of NBI-only plasma (~16 ms (from t ~186 to t ~102 ms) in this particular shot).

As shown in the previous section, the toroidal current and plasma pressure (<β> ~ 0.2 % in this shot) can modify the rotational transform profile and the shape of LCFS.

4.1. Differences between Co- and CRT-NBI

The Co- and CTR-NBI plasmas are compared in the same vacuum configuration with $\iota(a)/2\pi|_{vac} \approx 0.54$ [21], where a natural resonance of m/n = 15/8 exists at $\rho \approx 0.87$ in vacuum. Figure 7 shows the time traces of some plasma parameters for CO- and CTR-NBI plasmas. In this experiment, only the beam-line of BL1 was injected into D^+ plasma initiated by ECH. By changing the field direction, Co- and CTR-injections were examined. The port-through NB powers (P_{inj}) are 0.58 and 0.56 MW for Co- and CTR-injection cases, respectively. Although the evaluation of the absorption efficiency of CTR-injection NBI is an on-going task, the stored energy and the line-averaged density for the both discharges have similar

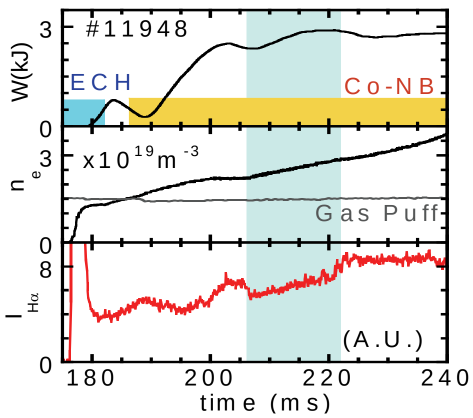

Fig.6. Typical example of NBI-only plasma showing the transition. Time trace of the stored energy (top), the line-averaged density (middle) and the intensity of Hα (bottom) are plotted.

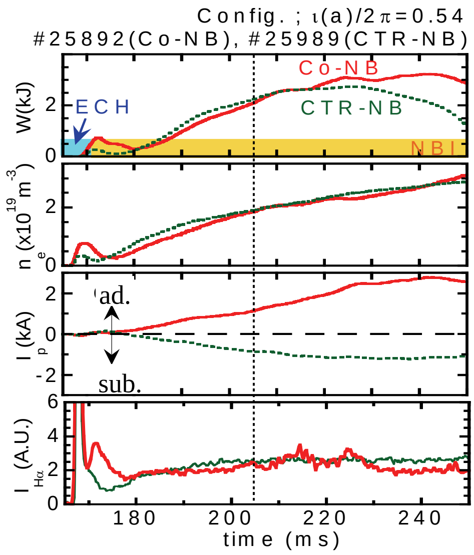

Fig.7. Comparison of Co- (red) and CTR-NBI (green) plasmas in the same vacuum configuration.

values, respectively, at least for the time interval of 200 ms < t < 220 ms. The direction of the plasma current is consistent with the expectation from the NBCD scenario but the intensity is not the same for the both discharges. Since the bootstrap current I_{BS} always flows to the additive direction in this configuration, NBCD current in the CTR-NBI case is somewhat compensated by I_{BS}. This cancellation effect usually becomes large in higher density (or stored energy) range since I_{BS} is an increasing function of the pressure gradient.

As shown in Fig. 7, the decrease in the Hα intensity and increase in the growth rate of the stored energy are observed in the Co-NBI case, but no clear change in Ha intensity or change in the "growth rate" of the stored energy were observed in the CTR-NBI case. In other configurations with different $\iota(a)/2\pi|_{vac}$ or the bumpiness, the transition event has not been observed for CTR NBI-only plasma in the range of P_{inj} ~ 0.25-0.6 MW.

In the Co-NBI case, the changes in Hα and the stored energy were observed at three timing (t ~ 204, 214 and 225 ms), indicating repetitive L-H-L sequences in this discharge. In next subsection, we will discuss the delay time between the start of NBI and the onset timing of the transition (determined by the drop of Hα intensity), we focus on the first event since for later event it is not so easy to control the density by gas-puffing.

4.2. Heating power dependence of the delay time

The delay time between the start of NBI and the drop of the Hα intensity was investigated by changing the heating power for two vacuum configurations with ε_b = 0.06 (medium ε_b) and 0.15 (high ε_b), where $\iota(a)/2\pi|_{vac}$ was set at almost the same value of 0.56. The experiment was performed under the reversed field direction with the beam-line BL1 (Co-injection for this field direction). Since the density was controlled in the range of $1.5–2.0\times10^{19}$ m^{-3} in this experiment, the absorption efficiency of NBI is considered to be almost the same (~ 30%) for the both configurations. This density range is higher than the empirical critical (lower-limit) density for the transition obtained from the previous experiments. The similar NBI-only plasma experiment was also performed for the vacuum configuration with ε_b = 0.01 (low ε_b) and $\iota(a)/2\pi|_{vac} \approx 0.56$. However no clear transition event was observed for the low-ε_b configuration even in the same experimental conditions of the injection power and the plasma density. It should be noted that for ECH+NBI plasmas, the transition was rather easily observed in the previous experiment although the improvement factor was low compared to that for the medium-ε_b case [4].

Figure 8(a) shows the delay time Δt as a function of P_{inj} for the high- and medium-ε_b configurations. The delay time for each configuration is almost the same value and depends on the injected power; Δt ~ 20 ms at P_{inj} ~ 0.6 MW,

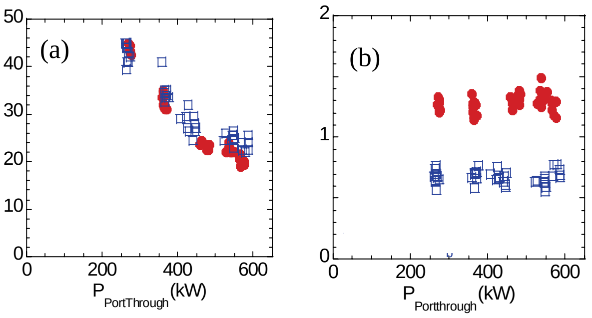

Fig.8. Power dependences of the delay time (a) and the plasma current at the onset timing of the transition (b) for high (red) and medium (blue) bumpiness configuration.

and it elongates to Δt ~ 40 ms at ~ 0.3 MW.

From the viewpoint of the configuration effect on the transition, it is interesting to check the value of the plasma current at the onset timing of the transition event since the plasma current modifies the field configuration as shown in Section 3. Figure 8(b) shows the toroidal current at the onset timing as a function of P_{inj}. It is clearly shown that the transition happens when the toroidal current reaches a critical I_p value which depends on the configuration; 0.7±0.1kA for the medium-ε_b 1.3±0.2kA for the high-ε_b configurations, respectively.

4.3. Configuration effects on the critical current

The effects of the plasma current on the field configuration should depend on the vacuum rotational transform. In order to investigate the effect of $\iota(a)/2\pi|_{vac}$ on the critical current discussed in the previous subsection, the $\iota(a)/2\pi|_{vac}$-scan experiment was performed for NBI-only plasma by changing the coil current ratio of the helical coil to the toroidal coils with the fixed $I_{TA}:I_{TB}$ ratio. ($I_{TA}:I_{TB}$ = 5:2, medium-ε_b). Figure 9 shows the toroidal current at the onset timing as a function of

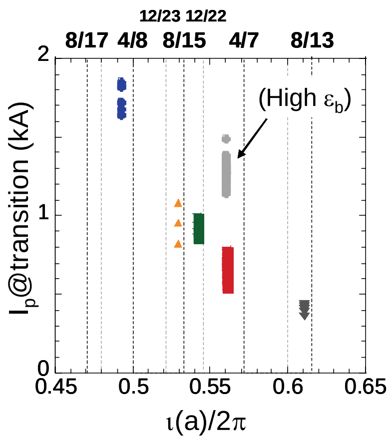

Fig.9. $\iota(a)/2\pi|_{vac}$-dependence of the critical toroidal current for the transition in NBI-only plasmas. Major low-mode rational numbers are also indicated.

$\iota(a)/2\pi|_{vac}$. The density and NBI power range are the same as that for Fig. 8 in this experiment, and the data from Fig. 8(b) for the high-ε_b case is also plotted as a reference. Although we tried Co- and CTR-injection experiments in the same configurations, no transition has been observed in the CTR-injection NBI-only plasmas under the present experimental conditions and selected $\iota(a)/2\pi|_{vac}$-values. Therefore, the plots in Fig. 9 are all additive current data. As shown in the figure, the critical current exists for all configurations and its value systematically decreases as increase of $\iota(a)/2\pi|_{vac}$.

5. Discussions

Under the present experimental condition (P_{inj} and magnetic configuration), no transition has been observed in the CTR-injection NBI-only plasmas. The P_{inj}-scan experiment shows the power dependence of the delay time after the NBI turned-on to the onset of the transition. This might indicate that the effective heating power P_{heat} was too low for the CTR-injection to make the transition. However, it is natural to consider that P_{heat} is not so different between Co- and CTR-cases since almost the same stored energy as that in Co- NBI plasma was obtained in the CTR-NBI plasma (Fig. 7).

In this study, we found out the existence of the critical current for the onset of the transition. In the CTR-injection case, since the current direction of NBCD is opposite to that of the bootstrap current, the total current becomes lower than that in Co- injection case and the current profile would be different. The free-boundary equilibrium calculation predicts that the rotational transform and the shape of the magnetic surface can be modified asymmetrically to the current direction (Fig. 4). As shown in Fig. 9, the examined values of $\iota(a)/2\pi|_{vac}$ in this study were located at smaller side of the nearest low-mode rational number. Therefore, roughly speaking, the additive current increase the edge rotational transform and approach to the low-mode rational number, but the subtractive current has the opposite effect. It is not easy to directly explain the $\iota(a)/2\pi|_{vac}$–dependence of the critical current by this simple idea, but the rational near the plasma edge would have some important effect on the transition event. Similar power dependence of delay time for ETB event is reported [22] in a high shear device, CHS. Here the delay time decreases as getting close $\iota(a)/2\pi|_{vac}$ to 1.

6. Summary

The transition to an improved confinement mode in NBI-only plasma is investigated in Heliotron J, focusing on the onset condition of the transition. In this study, we found out the existence of the critical current for the onset of the transition in NBI-only plasma. This critical current depends on the vacuum field configuration, $\iota(a)/2\pi|_{vac}$ and the bumpiness, but is independent of P_{inj}.

As for the H-mode in tokamaks, the effects of plasma rotation are discussed. We should take care of the effect of different momentum input direction from Co- and CTR-NBI. In order to obtain the toroidal/poloidal rotation velocity, we are preparing the diagnostic system of the charge exchange recombination spectroscopy.

Acknowledgments

The authors are grateful to the Heliotron J supporting group for their excellent arrangement of the experiments. They would also like to acknowledge Profs. T. Fukuda, T. Isobe, T. Mutoh, C. Suzuki, Y. Takeiri, N. Tamura, E. Ascasibar, B. Blackwell, C. Hidalgo, Q. Yang, B. Zurro for valuable discussions. This work is performed with the support and under the auspices of the Collaboration Program of the Laboratory for Complex Energy Processes, IAE, Kyoto University and Kyoto University 21st century COE Program “Establishment of COE on Sustainable Energy System”, the NIFS Collaborative Research Program (NIFS04KUHL001-005, NIFS05KUHL007, NIFS06KUHL007, NIFS06KUHL 009-010, NIFS06KUHL011, NIFS06KUHL 014-015) as well as and the Formation of International Network for Scientific Collaborations..

References

[1] F. Sano, et al., J. Plasma Fusion Res. **Ser.3**, 26 (2000) 26.
[2] T. Obiki, et al., Nucl. Fusion **41**, 833 (2001).
[3] M. Wakatani, et al., Nucl. Fusion **40**, 569 (2000).
[4] T. Mizuuchi, et al. Fusion Sci. Tech. **50**, 352 (2006).
[5] H. Okada, et al., Fusion Sci. Tech. **50**, 287 (2006).
[6] S. Kobayashi, et al., in the 2nd Joint Meeting of US-Jpn WS and Kyoto Univ. 21st COE Sympo. on "New approach in Plasma Confine. Exp. in Helical Systems", (Auburn, 2006).
[7] Wagner F, et al., 19th IAEA Fusion Energy Conference (Lyon, France, 2002) (Vienna: IAEA), OV2-4
[8] Sano F, et al., Nucl. Fusion **45**, 1557 (2005).
[9] F. Castejon, et al., Nucl. Fusion **44**, 593 (2004).
[10] K. Ida, et al., Nucl. Fusion **44**, 290 (2004).
[11] T. Obiki, et al., J. Plasma Fusion Res. **Ser.3**, 288 (2002).
[12] H. Yamada et al., Nucl. Fusion **45,** 1684 (2005).
[13] A. Dinklage et al., Fusion Sci. Tech. **51**, 1 (2007)
[14] F. Sano et al., Fusion Sci. Tech. **46**, 288 (2004)
[15] M. Hirsh, et al., Plasma Phys. Control. Fusion **42**, A231 (2000).
[16] G. Motojima, et al., Nucl. Fusion **46**, (2007).
[17] S. Kobayashi, et al., 20th IAEA Fusion Conf. (Vilamoura, Portugal, 2004) (Vienna: IAEA), EX/P4-41
[18] T. Mizuuchi, et al., Nucl. Fusion **47**, 395 (2007).
[19] G. Motojima, et al., P2-046 in this conference.
[20] Y. Suzuki, et al., Nucl. Fusion **46**, L19 (2006).
[21] S. Kobayashi, et al., in the 11th IAEA Tech. Meeting on H-mode Phys. Transport Barriers (Tsukuba, 2007).
[22] S. Okamura, et al., Nucl. Fusion **45**, 863 (2005).

Proceedings of ITC/ISHW2007

Experimental studies and modelling of edge shear flow development in the TJ-II stellarator

M.A. Pedrosa[(1)], B.A. Carreras[(1)], C. Silva[(2)], C. Hidalgo[(1)], J.A. Alonso[(1)], L. García[(3)], I. Calvo[(1)], J.L. de Pablos[(1)], R.O. Orozco[(1)], D. Carralero[(1)] and the TJ-II team

[(1)] EURATOM-CIEMAT, Spain, [(2)] EURATOM-IST, Portugal, [(3)] Universidad Carlos III, Spain

The universality of the characteristics of sheared flows points to a general ingredient to explain the damping/driving mechanisms responsible for the development of these flows in the plasma boundary region of fusion devices. Experiments in the TJ-II stellarator showing that the generation of spontaneous sheared flows at the plasma edge requires a minimum plasma density or density gradient, open a unique possibility to characterize the dynamics of sheared flow development in fusion plasmas.

The effective viscosity at the plasma edge can be deduced by the decay rate of the perpendicular flow measurement once the driving force is removed. In TJ-II changes in the plasma rotation and turbulence have been studied when an electric field is externally applied. Measurements of the decay time suggest an increase in decay times above the threshold gradient value to trigger the emergence of shear flow (i.e. once edge perpendicular sheared flows are fully developed).

The emergence of the plasma edge sheared flow as a function of plasma density can be explained using a simple second order phase transition model. This simple model reproduces many of the features of the TJ-II experimental data and captures the qualitative features of the transition near the critical point.

Keywords: Turbulence, sheared flows, plasma edge, biasing, stellarators.

1. Introduction

The importance of the ExB shear in flows as a stabilizing mechanism to control plasma fluctuations in magnetically confined plasmas has been widely established. In fact, both H-mode and core transport barriers are related to a large increase in the ExB sheared flow [1, 2, 3]. Clarifying the driving/damping mechanisms of sheared flow remains a key issue for the development of fusion. Both neoclassical (e.g. ion orbit losses [4]) and anomalous mechanisms (i.e. anomalous stringer spin-up [5] and Reynolds stress [6, 7]) have been considered as candidates to explain the generation of sheared flows. Atomic physics via charge-exchange momentum losses [8, 9], parallel viscosity (magnetic pumping) [10] and turbulent viscosity are considered as candidates to explain perpendicular flow damping physics.

The role of neoclassical mechanisms to explain poloidal flows is an open issue in the fusion community. The result of the experiments carried out in TJ-II stellarator can help to understand and quantify the importance of anomalous versus neoclassical mechanisms on the damping physics of radial electric fields and flows in fusion plasmas.

author's e-mail: angeles.pedrosal@ciemat.es

2. Experimental set-up

Experiments were carried out in Electron Cyclotron Resonance Heated plasmas ($P_{ECRH} \leq$ 400 kW, B_T = 1 T, R = 1.5 m, $\langle a \rangle \leq$ 0.22 m, $\iota(a)/2\pi \approx$ 1.5 – 1.9) obtained in the TJ-II stellarator. The plasma density was modified in the range (0.35 – 1) x 10^{19} m^{-3}. Different edge plasma parameters were characterized using two multi-Langmuir probe systems, installed on similar fast reciprocating drives (approximately 1 m/s) [11], that allows obtaining radial profiles simultaneously in a single shot, in two toroidal locations approximately 180º apart in high (HFS) and low (LFS) field sides of TJ-II.

A Carbon composite mushroom-shaped electrode (12 mm high with a diameter of 25 mm) was installed on another fast reciprocating drive similar to the one used with probes. The electrode was inserted typically 2 cm inside the last-closed flux surface (LCFS) and biased positively (200-300 V) with respect to one of the two poloidal limiters located in the scrape-off layer region

(SOL) (about 0.5 cm beyond the LCFS). Measured electrode currents were in the range of 30-50 A [12].

3. Development of sheared flows

It has been previously shown that the development of the sheared flows at the plasma edge of the TJ-II requires a critical value of the plasma density or density gradient [13, 14] that depends on the plasma magnetic configuration [15].

Radial profiles of plasma edge are strongly modified as plasma density increases: Gradient of the ion saturation current (i.e. local density) increases and floating potential becomes more negative at the plasma edge [13, 14]. Consistent with the changes in the floating potential, above a threshold density value the perpendicular phase velocity reverses sign at the plasma edge from positive to negative values due to the development of the natural shear layer, with a shearing rate about 10^5 s^{-1} of the order of the inverse of the correlation time of fluctuations ($dv_\theta/dr \approx 1/\tau \approx 10^5$ s^{-1}) [16]. Figure 1 shows the perpendicular flows and the fluctuations of the perpendicular electric field (i.e. the turbulent radial velocity) deduced from measurements at the plasma edge of the TJ-II (r/a≈0.9, where a is the averaged minor radius of the plasma). Measurements have been obtained simultaneously in two toroidal locations and changing density from shot to shot. The levels of turbulent transport and fluctuations increase as density increases up to the critical value for which sheared flow is developed. For densities above the threshold fluctuations and turbulent transport slightly decrease although edge gradients become steeper. Edge sheared flows are developed at the same threshold density in the two toroidal positions [17].

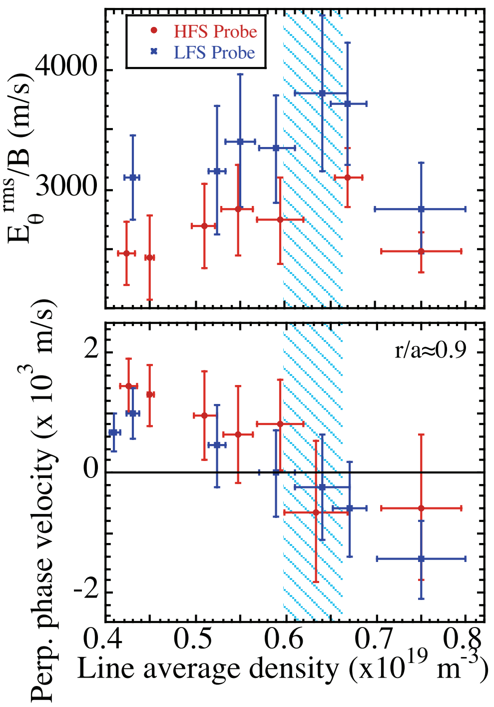

Fig. 1 Perpendicular flows and fluctuations of the perpendicular electric field measured for different plasma densities at the TJ-II plasma edge (r/a≈0.9).

Sheared flows have been also developed in TJ-II using an electrode that externally imposed a radial electric field at the plasma edge. The modifications in the plasma properties induced by electrode biasing depend on several parameters such as the biasing voltage, the electrode location and the plasma density. The latter is very important on TJ-II as the edge parameters and global plasma confinement depend strongly on it. The response of the plasma to bias is, therefore, different at densities below and above the threshold value to trigger the spontaneous development of ExB sheared flows [12].

The results of the TJ-II biasing experiments presented in this paper correspond to positive applied bias in the plasma edge of TJ-II. The changes observed in the edge profiles, edge electric fields and fluctuation levels show evidence of biasing induced improved confinement as was observed in previous limiter biasing experiments in TJ-II [18]. The floating potential profile is strongly modified by the electrode bias in the region $r/a < 0.9$, leading to the formation of a strong positive radial electric field (up to 10 kV/m) and as a consequence the perpendicular phase velocity is also modified.

As in the spontaneous development of the shear [19], two different time scales arise in the relaxation of externally induced electric fields in TJ-II: a slow time scale, in the range of the particle confinement time (tens of milliseconds) that evolves with plasma density, and a fast time scale in the range of few turbulence correlation times (10 – 100 μs). The fast time evolution of floating potential signals (V_{fl}), when biasing is switched off, can be fitted to an exponential function using the expression

$$V_{fl}(t) = V_{max}\exp(-t/\tau) + V_{min} \qquad (1)$$

from which the exponential relaxation time τ is deduced. This fitting procedure has been done for floating potential signals measured at different densities and at different radial and toroidal locations. Experimental results show that the characteristic time decay obtained for the fast decay is in the range of 10 - 100 μs for different values of mean plasma density (in the range 0.4 – 1 x 10^{19} m^{-3}). Figure 2a shows the two time evolution scales of the floating potential signal measured inside the LCFS (r/a ≈ 0.77) in TJ-II together with the evolution of plasma density with biasing and in Fig 2b the fast decay scale is shown together with the fitting.

Figure 3 shows the behaviour of the fitting of the fast relaxation time at the TJ-II plasma edge (0.75<r/a<0.92) after switch-off the biasing as a function of the average ion saturation current, measured when switching off the biasing and normalized to its value at the critical point (i.e. when shear flow develops). Results suggest an increase in decay times above the critical value of the control parameter (i.e. once edge perpendicular sheared flows are fully developed).

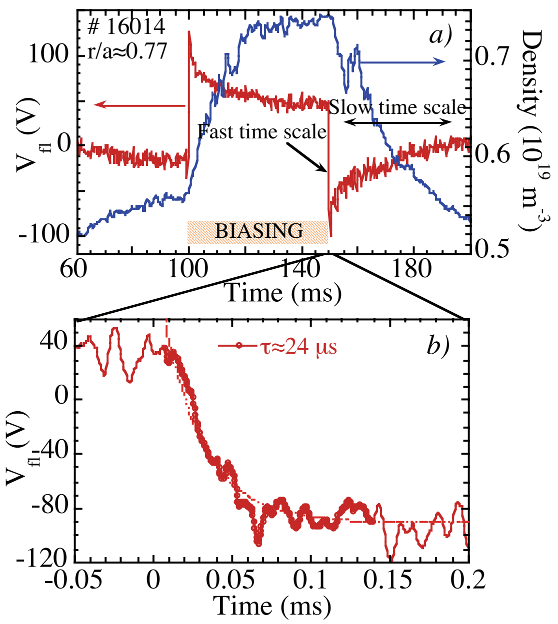

Fig 2 a) Time scales of the floating potential measured at r/a≈0.8 and plasma density evolution with biasing. b) Fast decay of the floating potential at the bias switch off (time =0).

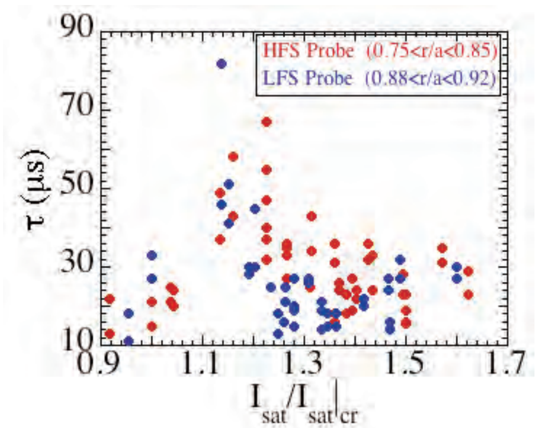

Fig. 3 Relaxation time measured at the TJ-II plasma edge in both probes, as a function of normalized ion saturation current measured after switch off the biasing.

These time decays have been compared with the ones obtained in similar experiments in other devices with different characteristics [19] being the values in the same range (tens of μs) in all of them. As a consequence and in spite of another mechanisms (i.e. magnetic pumping, charge exchange) turbulence can be considered as an important element in the physics of flows and electric fields. Turbulent damping mechanisms are likely to apply for short time scales, in the order of few turbulence correlation times (typically $\tau_c \approx 10$ μs), this being consistent with experimental time decay findings.

4. Model coupling shear flow and turbulence

A simple model to explain the generation of the sheared electric field has been used [20, 21]. This model, as the pressure increases, predicts two successive transitions. The first one is a second-order transition controlled by the poloidal shear flow that leads to a reduction of the turbulence level. The second, that describes the H-mode, is a first-order transition controlled by the pressure gradient that leads to the suppression of turbulence. The first transition model (the second-order one), that has the characteristic properties of the emergence of the sheared flow layer, has been used to compare the theoretical predictions with the experimental results of the formation of the sheared flow layer in TJ-II. In order to do that, we normalize all the physical magnitudes to their values at the critical point so we can write the solutions of the model in terms of measurable quantities [22].

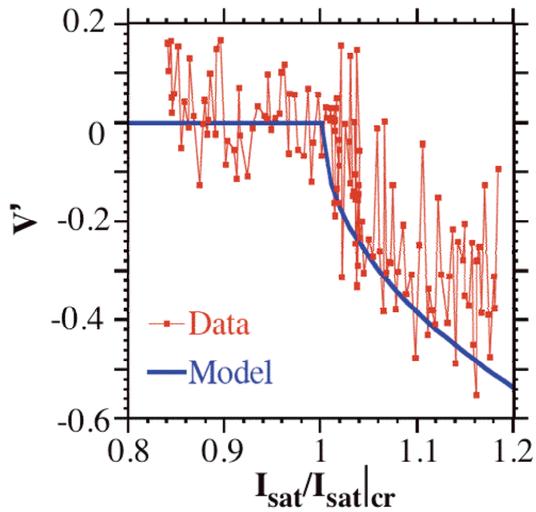

Fig. 4 Comparison between the velocity shear obtained by the model and from the experimental data.

Comparisons between the model and experimental data show that in spite of the simplicity of the model, it captures the qualitative features of the transition near the critical point as can be seen in Fig 4, that shows a comparison between the velocity shear obtained by the model and the deduced from the experimental data as a function of the control parameter defined in the previous section. Note that the model has no free parameters once the position of the critical point is determined. Results from plasmas with more complicated density evolutions than a simple ramp are also in good agreement with experiments [22].

Apart from the problem of interpreting the decay rate in terms of viscosity, an effective viscosity at the plasma edge can be determined by measuring the decay rate of the perpendicular flow once the driving force has been removed. The properties of the damping rate of the flow in TJ-II have been investigated in the framework of a model based in the previously described with an external drive added: the applied bias. Fig 5 shows the short time scale decay after switching off the bias potential deduced by the model showing an increase of the decay time close to the critical point as has been observed experimentally (Fig 3). The exponential decay of the flow is also reproduced, giving the model a qualitative description of the behaviour of the decay time obtained experimentally.

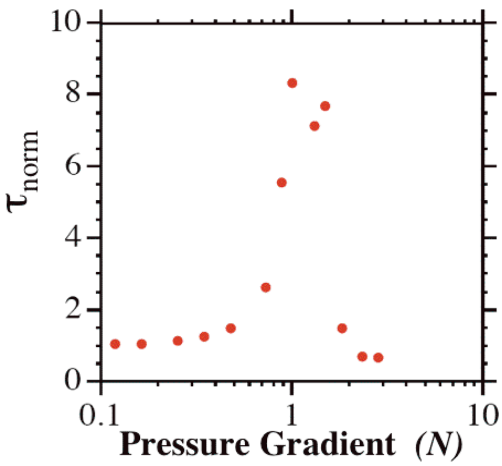

Fig. 5 Decay time obtained by the model as a function of the local average ion saturation current normalized at the corresponding critical point (development of shear flow).

5. Summary and conclusions

The generation of the shear layer depends in TJ-II on the plasma density gradient, being necessary a threshold value for its development. These sheared flows appear to be organized near marginal stability with fluctuations in TJ-II. The universality of this property is easily understood assuming that edge sheared flows are controlled by turbulence. These results can shed light in the understanding of the physics responsible for the generation of critical sheared flows, pointing to the important role of turbulence as a driving mechanism.

Two time scales have been found for edge plasma potential decay measured in the TJ-II edge plasma region when electrode applied potential is turned off. The fast scale decay times are in the range of few turbulence correlation times, suggesting the important effect of anomalous (turbulent) mechanisms in the damping rate of sheared flows in the plasma boundary of fusion devices. In the slow time scale (comparable to the particle confinement time) plasma potential modifications are linked to the evolution of the plasma density.

Measurements of the fast decay time suggest an increase in decay times above the threshold gradient value to trigger the emergence of shear flow (i.e. once edge perpendicular sheared flows are fully developed).

The emergence of the plasma edge shear flow as a function of the plasma density can be explained using a second-order phase transition model that reproduces many of the features of the TJ-II experimental data and of the transition near the critical point. The properties of the damping rate of the flow in TJ-II have also been described by means of the model adding a driving force.

[1] P. W. Terry, Reviews of Modern Physics, **72,** 109 (2000).
[2] K. Burrel, Phys. Plasmas **6** (1999) 4418
[3] B.A. Carreras, IEEE Trans. Plasma Sci. **25** (1997) 1281
[4] K.C. Shaing and E.C. Crume, Phys. Rev. Lett. **63** (1989) 2369.
[5] A.B. Hassam and T.M. Antonsen, Phys. Plasmas **1** (1994) 337.
[6] P.H. Diamond and Y.B. Kim, Phys. Fluids **3** (1991) 1626.
[7] B.A. Carreras, V.E. Lynch and L. García, Phys. Fluids B **3** (1991) 1438.
[8] P. Monier-Garbet, K.H. Burrel, et al., Nuclear Fusion **37** (1997) 403.
[9] M.A. Mahdavi, N. Brooks, et al., J. Nuclear Mater **176&177** (1990) 32.
[10] S.P. Hirsman, Nuclear Fusion **18** (1987) 917.
[11] M.A. Pedrosa, et al., Rev. Sci. Instrum. **70** (1999) 415.
[12] C. Silva et al., Czech. J. Phys. **55** (2005) 1589.
[13] C. Hidalgo et al., Phys. Rev. E, **70** (2004) 067402.
[14] M.A. Pedrosa et al., Plasma Phys. Control. Fusion **47** (2005) 777.
[15] M.A. Pedrosa, C. Hidalgo, et al., Czech. J. Phys. **55** (2005) 1579
[16] C. Hidalgo, M.A. Pedrosa and B. Gonçalves, New J. Phys. 4 (2002) 51.1
17 M.A. Pedrosa et al.,Procceedings 16th Stell. Workshop (2007)
[18] C. Hidalgo, M.A. Pedrosa et al., Plasma Phys. Control. Fusion **46** (2004) 287
[19] M. A. Pedrosa, B.A. Carreras et al. Plasma Phys. Control. Fusion To be published
[20] P. H. Diamond, Y. M. Liang, B. A. Carreras, and P. W. Terry, Phys. Rev. Lett. **72**, 2565 (1994).
[21] B. A. Carreras, D. E. Newman, P. H. Diamond, and Y.-M. Liang, Phys. Plasmas **1**, 4014 (1994).
[22] B.A. Carreras, L. García et al., Phys. Plasmas **13** (2006) 122509

Proceedings of ITC/ISHW2007

Overview of Edge Turbulence and Zonal Flow Studies on TEXTOR

Y. Xu[1], A. Krämer-Flecken[2], D. Reiser[2], M. Vergote[1], S. Jachmich[1], M. Van Schoor[1], M. W. Jakubowski[3], M. Lehnen[2], Y. Liang[2], M. Mitri[2], S. Soldatov[2], B. Unterberg[2], D. Reiter[2], U. Samm[2], R. R. Weynants[1] and the TEXTOR team

** Partners in the Trilateral Euregio Cluster (TEC):*

*[1] Laboratory for Plasma Physics, Ecole Royale Militaire/Koninklijke Militaire School, Euratom-Belgian State Association, Avenue de la Renaissance 30, B-1000 Brussels, Belgium**

*[2] Institute für Energieforschung-Plasmaphysik, Forschungszentrum Jülich, Association Euratom, D-52425 Juelich, Germany**

[3] Max-Planck-Institut für Plasmaphysik, IPP-EURATOM Association, Greifswald, Germany

In the TEXTOR tokamak, the edge turbulence properties and turbulence-associated zonal flows have been systematically investigated both experimentally and theoretically. The experimental results include the investigation of self-organized criticality (SOC) behavior, the intermittent blob transport and the geodesic acoustic mode (GAM) zonal flows. During the Dynamic Ergodic Divertor (DED) operation in TEXTOR, the impact of an ergodized plasma boundary on edge turbulence, turbulent transport and the fluctuation propagation has also been studied in detail. The results show substantial influence by the DED on edge turbulence. The theoretical simulations for TEXTOR parameters show characteristic features of the GAM flows and strong reduction of the blob transport by the DED at the plasma periphery. Moreover, the modelling reveals the importance of the Reynolds stress in driving mean (or zonal) flows at the plasma edge in the ohmic discharge phase in TEXTOR.

Keywords: Tokamak, edge turbulence, self-organized criticality, blob transport, zonal flows, Dynamic Ergodic Divertor, Reynolds stress.

1. Inroduction

In the TEXTOR tokamak, the edge turbulence properties and turbulence-associated zonal flows have been systematically investigated experimentally by fast reciprocating Langmuir probe and correlation reflectometry measurements, and theoretically by three-dimensional (3D) non-linear electromagnetic drift-turbulence simulations. The role of the Reynolds-stress in driving mean plasma flows has also been studied by fluid modelling. In this paper, an overview of the recent work is given.

2. Experimental results

First, we report on some fundamental features of the edge turbulence observed on TEXTOR. These include: (i) the self-organized criticality (SOC) behavior and self-similar characters in the fluctuation data [1]; (ii) the turbulence intermittency and blob transport in the plasma boundary [2]; (iii) identification of geodesic acoustic mode (GAM) zonal flows in density and velocity fluctuations by poloidal correlation reflectometry [3].

(i) For the SOC studies, we have measured both the potential and density fluctuations by the Langmuir probes and analyzed the data using various methods [1]. The results show a lot of characteristics associated with the SOC dynamics, including similar frequency spectra to the "running sandpile" modelling and f^{-1} dependence in the spectrum as an indication of avalanche overlapping, a slowly decaying long tail in the autocorrelation function, a long-range radial propagation of avalanche-like events in the edge plasma region, and values of Hurst parameters larger than 0.5 at all detected radial locations, as shown in Fig. 1(a).

(ii) The intermittent convective transport has also been investigated by Langmuir probes in the plasma edge and in the scrape-off layer (SOL) [2]. It has been observed that the probability distribution function (PDF) of the density fluctuations are positively skewed, while a Gaussian shape is recorded for the negative values [see Fig. 1(b)]. The deviation of the signals from Gaussian statistics increases from the plasma edge to the SOL. Conditional averaging reveals that in the SOL the wave form of blobs is asymmetric in time and the blobs move radially outwards at velocities of 0.5~1 km/s. The large bursts ($\geq$ 2.5×rms) account for ~ 40% of the total transport. Statistics of the waiting-time indicate that the PDF of the time interval follows a Poisson-distribution for small duration events and changes into a power-law form for larger ones. Moreover, the turbulence intermittency shows self-similar characters in the fluctuation data.

E-mail: y.xu@fz-juelich.de

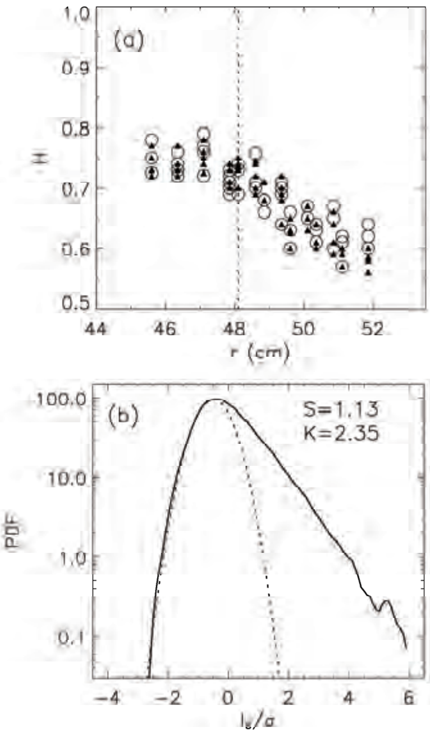

Fig. 1 (a) The radial dependence of Hurst exponent (H) estimated by rescaled range (open circles) and structure function (solid triangles) analysis of potential fluctuations. The dotted line marks the limiter position [1]. (b) Semi-log plot of the PDF of the density ($\propto I_s$) fluctuations normalized by the standard deviation, measured in the SOL. The S and K denote skewness and kurtosis. The dotted line is the best Gaussian fit [2].

(iii) In TEXTOR, the GAMs have been measured by an *O*-mode correlation reflectometer system [3]. Figure 2 shows the amplitude, cross phase ϕ, and coherence spectrum of density fluctuations measured by the top antenna array. The GAMs appears around 17 kHz for the reflection layer detected. The $\partial\phi/\partial f \cong 0$ at the GAM frequency implies a poloidal homogenous structure of the GAM zonal flows. The frequency dependence of the GAMs on the acoustic speed has been verified under different discharge conditions. The poloidal asymmetric (m=1) feature of density fluctuations of GAMs has also been identified by the cross-correlation of the top and midplane antennas. The influence of the GAMs on the ambient turbulence level has been observed from the modulation of the GAM flows on the fluctuation amplitudes of ambient turbulence. More recently, the direct evidence of the GAMs on the poloidal velocity fluctuations has been observed.

Secondly, we investigated the influence of DED (Dynamic Ergodic Divertor) on edge turbulence. During

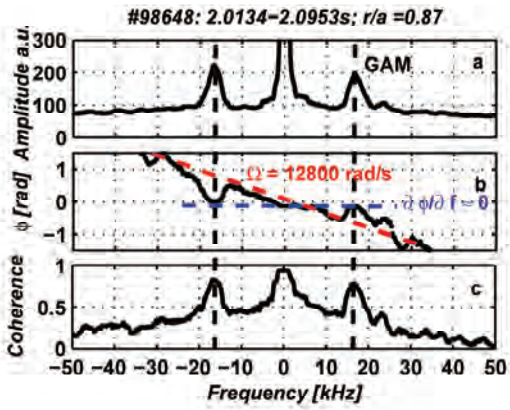

Fig. 2 Spectra of (a) amplitude, (b) cross-phase and (c) coherence of density fluctuations measured by the top antenna array of a correlation reflectometer [3].

the DED operation in TEXTOR, the magnetic perturbation creates a chaotic behavior of the field lines at the plasma boundary, including an ergodic zone with long and a laminar zone with short connection lengths, respectively [4]. The impact of the static DED (dc DED current) on edge equilibrium profiles, turbulence properties, turbulent transport, plasma rotations, Reynolds stress profiles and the blob transport has been investigated in detail [5]. Common features have been found among different DED configurations (m/n =12/4, 6/2 and 3/1). At the plasma edge, the density and temperature profiles are steepened *or* flattened by the DED, depending on discharge conditions [5, 6]. During the DED, a typical behavior is the increase of the floating potential in the perturbation area, leading to a reversal of the radial electric filed E_r from the negative to positive in most of the laminar and the ergodic zone, as can be seen in Fig. 3(a). A possible interpretation is that during DED the electrons mover faster than massive ions along the field line to the wall so that a positive E_r must be brought about to restore the ambipolarity [7]. The influence of the DED on turbulence mainly occurs in the ergodic region. With DED, the fluctuation amplitudes in potential and poloidal electric field fluctuations are largely reduced, whereas for density fluctuations the modification is small. In the DED phase, it has been generally observed that the local turbulent flux reverses direction from radially outwards to inwards in the ergodic area, as illustrated in Fig. 3(b). Meanwhile, the turbulence itself is profoundly modified by energy re-distribution in frequency spectra, suppression of large-scale structures and reduction of the radial and poloidal correlation lengths at all frequencies [7]. With DED, the poloidal propagation of fluctuations changes direction from the electron diamagnetic drift to ion drift direction in the perturbation region, consistent with the observed reversal of the $E_r \times B$ flow [5, 8]. Moreover, in the plasma boundary the size of the blobs and the blob transport are significantly reduced by the DED [9]. In the ohmic discharge phase before the DED the Reynolds stress displays a radial gradient at the plasma edge while during DED the profile is suppressed, suggesting a rearrangement by the DED on the flow momentum profile [7, 10].

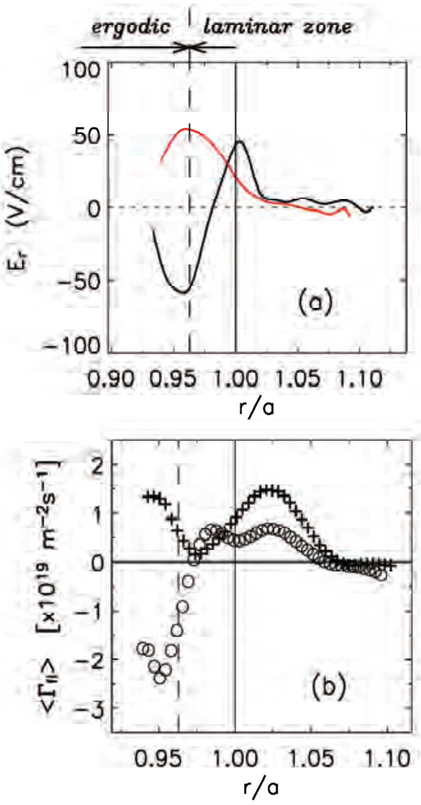

Fig. 3 (a) The radial dependence of radial electric field E_r measured by fast reciprocating probes before (black curve) and during (red curve) a static 6/2 DED [5]. (b) The radial dependence of fluctuation-induced flux, $<\Gamma_{//}>$, measured by fast reciprocating probes before (crosses) and during (circles) a static 6/2 DED [5]. The vertical solid line denotes the limiter position. The dashed line separates the ergodic (left side) and laminar (right side) zones.

3. Theoretical modelling and simulations

For the study of the impact of the resonant magnetic perturbation fields on turbulence, three-dimensional numerical simulations of drift fluid turbulence for 4 fields (potential, density, magnetic potential and parallel ion velocity) have been performed [11, 12]. The simulations show a lot of results consistent with the experimental observations in TEXTOR-DED, for instance, the suppression of blob amplitudes by magnetic perturbation at the plasma boundary, as shown in Fig. 4. The simulations also show characteristic features of the GAM flows before the DED and the suppression of GAMs at the resonances during the DED.

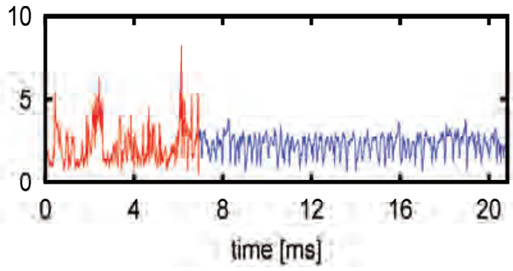

Fig. 4 Time trace of density fluctuations simulated before (red color) and during (blue color) the magnetic perturbation in the SOL. The blob amplitudes are suppressed by the magnetic perturbation.

In addition, starting from renewed 2D Hasegawa-Wakatani equations to explore the poloidally geometrical dependence of the Reynolds stress (*RS*), another fluid modeling (with flux-surface averaging in toroidal geometry) reveals the importance of the Reynolds stress in driving mean (or zonal) flows at the plasma edge in the absence of magnetic perturbation [13, 14]. To illustrate the role of *RS* in driving the mean poloidal flow and therefore the development of edge radial electric field E_r, the modeled E_r without *RS* (dotted blue line) and with *RS*

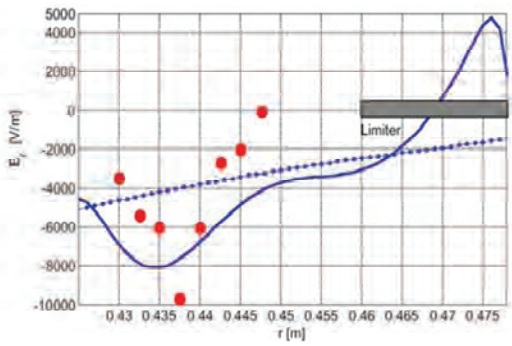

Fig. 5 Comparison of the simulated E_r (dotted blue curve without RS contribution and solid curve with RS contribution) and the experimentally measured one (red points).

(solid blue line) are depicted in Fig. 5 in comparison with the experimentally measured one (red points). It can be seen that with the contribution of *RS*, the solid blue curve is much closer to the measured E_r in the plasma edge.

4. Conclusions

In this paper, the recent experimental and theoretical work on the study of the edge turbulence and zonal flows on TEXTOR tokamak has been briefly summarized. The experimental observation of the basic features of edge turbulence, like SOC behavior, blob transport and GAM zonal flows, and the influence of the DED on turbulence properties have been presented. The simulation results show a lot of characteristics of turbulence, in agreement with the experimental observations.

References

[1] Y. Xu, *et al.*, Phys. Plasmas **11**, 5413 (2004).
[2] Y. Xu, *et al.*, Plasma Phys. Control. Fusion **47**, 1841 (2005).
[3] A. Krämer-Flecken, *et al.*, Phys. Rev. Lett. **97**, 045006 (2006).
[4] K. H. Finken, *et al.*, Fusion Eng. Des. **37**, 335 (1997).
[5] Y. Xu, *et al.*, Phys. Rev. Lett. **97**, 165003 (2006).
[6] O. Schmitz, *et al.*, to be published in Nucl. Fusion.
[7] Y. Xu, *et al.*, Nucl. Fusion (2007, in press).
[8] A. Krämer-Flecken, *et al.*, Nucl. Fusion **46**, S730 (2006).
[9] Y. Xu, *et al.*, the 34th EPS conference, Warsaw, 2007.
[10] Y. Xu, *et al.*, Journal of Nucl. Mater. **363-365**, 718 (2007).
[11] D. Reiser and B. Scott, Phys. Plasmas **12**, 122308 (2005).
[12] D. Reiser, Phys. Plasmas **14**, 082314 (2007).
[13] M. Vergote, *et al.*, Plasma Phys. Control. Fusion **48**, S75 (2006).
[14] M. Vergote, PhD thesis, Univ. Gent, 2007.

Proceedings of ITC/ISHW2007

Searching for a flux-expansion divertor in TJ-II

Francisco Castejón[1,2], Antonio López-Fraguas[1], Alfonso Tarancón[2,3] and José L. Velasco[2,3]

[1]*Laboratorio Nacional de Fusión-Asociación Euratom/Ciemat, Madrid 28040, Spain*
[2]*Instituto de Biocomputación y Física de Sistemas Complejos, Universidad de Zaragoza, Zaragoza 50009, Spain*
[3]*Departamento de Física Teórica, Universidad de Zaragoza, Zaragoza 50009, Spain*

October 11, 2007

In this work, we explore the possibility of having a flux-expansion divertor in TJ-II. A 3D map of the particle flux has been obtained for two different plasma regimes using the code ISDEP, which follows the ion guiding-centre trajectories. In TJ-II, one must consider the particle trajectories rather than the field lines due to the fact that common ion orbits can separate from the field lines, and moreover the plasma electric field and the collisionality must be considered. We have chosen a configuration that presents flux expansion at given toroidal positions. We have estimated the heat and particle fluxes and checked that it is possible to reduce them strongly by intersecting the trajectories at a given zone of the space. Future studies, maybe including the creation of an ergodic zone, will determine the strategy for intercepting such trajectories.

Keywords: flux expansion, divertor, ion kinetic transport, Montecarlo code.

1 Introduction and motivation.

The quest for the stellarator reactor needs a robust divertor concept to guarantee low plasma-wall interaction and power exhaust [1]. A good divertor concept should reduce the particle and heat fluxes on its divertor. Additionally, the path of the recycled neutrals that will enter the plasma must be large in the real space, and the plasma profiles should ideally present a steep pressure gradient in the edge. These facts ensure that they cannot go beyond the plasma edge. The tokamak divertor, based on locating one or two X points inside the vacuum chamber, has been demonstrated as a good solution in such devices. It has been recently suggested that this kind of effects can also be reached in tokamaks locating the X point outside the vacuum chamber (see [2] and references therein). This transforms the divertor configuration into a limiter configuration with flux expansion.

The divertor programme in stellarators needs to consider a wider range of concepts due to the diverse possible configurations. To start with, LHD presents the helical divertor concept. It is based in a natural ergodic zone of its magnetic configuration that rotates with the same law as the helical coils of the device [3].

The island-based divertor is a promising concept, as has been demonstrated in W7-AS [4], where excellent results have been obtained. This concept is suitable for devices like W7-X, which has a fixed robust magnetic configuration. For this concept to work, it is necessary that the island positions and widths do not change substantially during plasma operation. The same can be said about the helical divertor: its topology must remain unchanged during plasma operation. This fact makes island and helical divertors not appropriated for devices that rely their configuration on the bootstrap current, like QPS or NCSX, or for devices that present high flexibility in their rotational transform values, like TJ-II. For these cases, the flux expansion concept [5] could be a good candidate for the divertor. This concept is based on intercepting the particle and energy fluxes with plates in an ergodic area of the plasma where the magnetic lines are well separated, so that the power flux onto the plates is small enough and the resulting neutrals and impurities can be pumped. The large flux expansion should also guarantee that the neutrals entering the plasma have to perform a large path, thus diminishing the probability that they go deep inside the device core.

TJ-II presents specific plasma-wall interaction issues. Due to its magnetic configuration, the groove is the preferred zone for the escaping particles to strike. Since the groove is physically close to the centre of the device, one should try to diminish such flux by intersecting the particle trajectories far from that position.

We have found several magnetic configurations that are suitable for such a divertor concept, since they have plasma zones where the density of magnetic surfaces is especially low. The point is to look for a position in which the efficiency of the divertor is maximum (i.e. intersects a large fraction of the flux) and to try to make compatible this requirement with a low enough heat flux on the plates.

No natural ergodic zones appear outside the last closed flux surface in TJ-II. Therefore, a second phase of this work may imply the creation of such ergodic zone by introducing extra coils that create a resonant magnetic field.

author's e-mail: francisco.castejon@ciemat.es

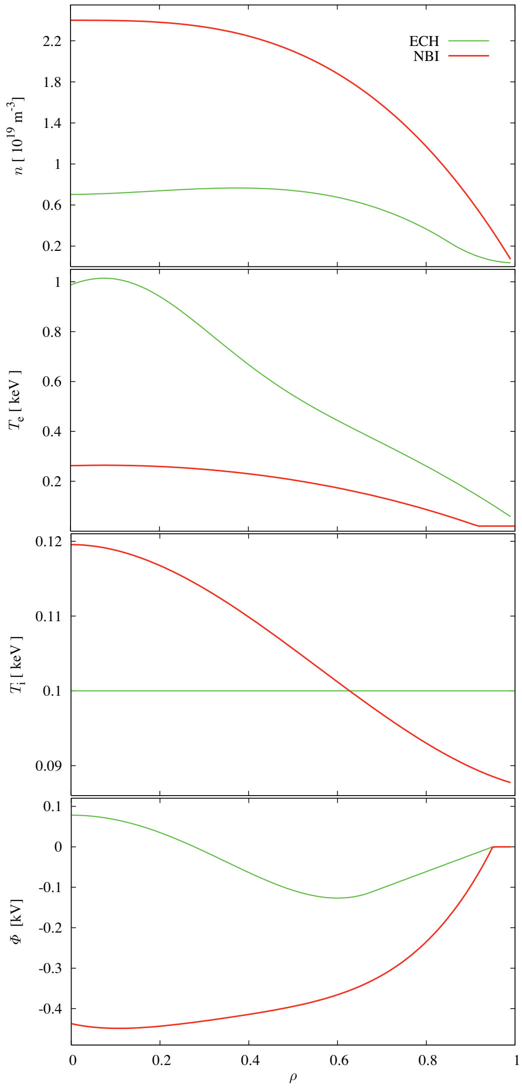

Fig. 1 Radial plasma profiles in the two regimes.

2 ISDEP code and the chosen plasma conditions.

Previous calculations performed to explore the flux expansion concept divertor in NCSX [5] followed magnetic field line trajectories, including a diffusion coefficient of about 1 ms^{-2}, of the order of the one experimentally measured. This approach happens to be valid for devices where the particle trajectories do not separate very much from the field lines. This is not fulfilled in TJ-II [6], and the particle trajectories must be followed to estimate the fluxes.
ISDEP (Integrator of Stochastic Differential Equations in Plasmas) [7], is a Montecarlo code that follows ion guiding-centre trajectories considering a given electrostatic potential profile and ion-ion as well as ion-electron Coulomb collisions [8]. This code has been used in the present work to study the ion collisional flux properties in the chosen magnetic configuration and various plasma regimes. The plasma parameters used in our simulations are taken from experimental measurements: the density and electron temperature are obtained from Thomson-Scattering measurements [9], the ion temperature from the CX-NPA diagnostic [10], and the electrostatic potential comes from HIBP measurements [11].
Obviously, the quantitative results will depend on plasma characteristics, namely the collisionality and the electrostatic potential. Nevertheless, we expect our results on the divertor effect to hold in a range of plasma parameters. In order to check this, two characteristic (and very different) plasma regimes have been chosen in this work. The plasma parameters are shown in Fig. 1 as a function of the effective radius ρ: a low density, low collisionality ECRH plasma, which presents a positive electric field in the core, according to the electron root [12], and an NBI plasma, with high density and low electron temperature. The electrostatic potential is negative in this case, which will have strong consequences on the ion confinement.

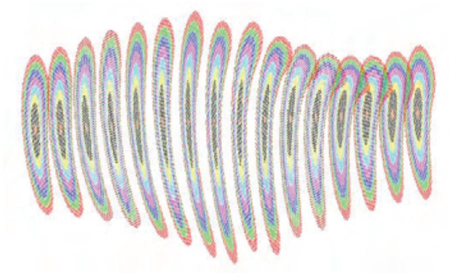

Fig. 2 Plasma toroidal sections. The surfaces in the ends lay in $\phi=0$ (left) and $\phi=\frac{\pi}{2}$ (right).

3 The chosen configuration.

One of the main properties of TJ-II heliac is its flexibility. By changing the currents that circulate by the two coils of the central conductor, it is possible to change the plasma size and shape as well as the rotational transform (TJ-II is an almost shearless device).
After studying several magnetic configurations, we have chosen the 100_68_91 (the numbers stand for the currents that circulate by the coils), which presents a large flux expansion in given toroidal positions. The average minor radius is $a=0.2$ m and the rotational transform in the edge is 1.825. In this magnetic configuration, similarly to the majority of TJ-II ones, a large fraction of the particle fluxes strike the groove, as will be shown in Section 4. Therefore, the neutrals coming from the wall appear very close to the plasma bulk. Hence, the main goal of this divertor should be to diminish as much as possible the fluxes that are directed to the groove. Fig. 2 shows several Poincaré maps of the field lines of the chosen configuration (the sections have been rotated for a better comparison). It is possible to appreciate that the maximum flux expansion happens for a toroidal angle around $\phi = \frac{\pi}{4}$ (and of course also around

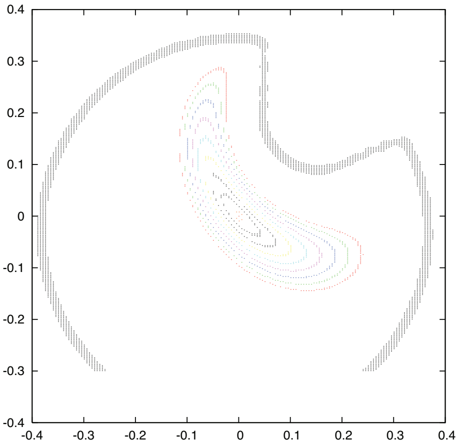

Fig. 3 Plasma coronas at $\phi \approx \frac{\pi}{6}$ and sketch of the wall of the vacuum chamber.

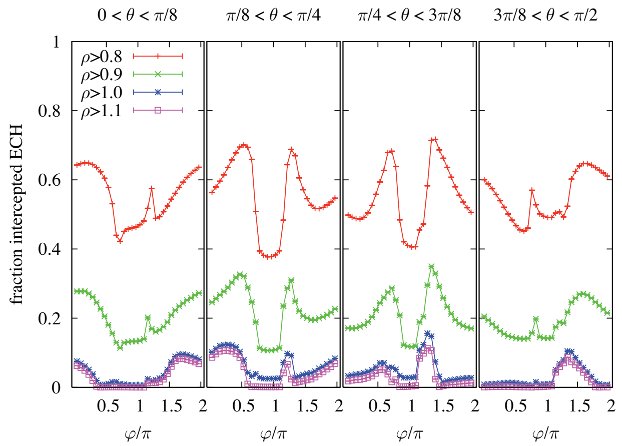

Fig. 4 Proportion of ions intersected as a function of the angular position of the plate for the ECH plasma.

$\phi = \frac{3\pi}{4}$, $5\pi/4$ and $\frac{7\pi}{4}$). Fortunately, the zone with large flux expansion lays on a wide range around these angles. This gives us quite a lot freedom in our optimizing task. Fig. 3 shows a particular toroidal section, together with a sketch of the wall of the vacuum chamber. The distance from the magnetic axis to the groove is about 12 cm, and only a thin sheet separates the edge and the plasma bulk. If the plasma-wall interaction can be concentrated at the zone where the flux expansion is maximum, the particle flux onto the groove will be strongly reduced. The amount of neutrals that enter the plasma bulk will also decrease.

4 Design and results.

In order to search for the optimal position of the plates, we have performed a map of the ion flux on several magnetic surfaces and at different toroidal and poloidal angles. Since TJ-II is a four-field-period device, we will center our discussion in one of the periods, but will consider all of them in calculation. We have accomplished this task defining our plates as the locus of points such that:

$$\rho > \rho_0, \; \frac{2\pi}{N_\phi} i < \phi < \frac{2\pi}{N_\phi}(i+1), \; \frac{2\pi}{N_\theta} j < \theta < \frac{2\pi}{N_\theta}(j+1). \quad (1)$$

By setting $N_\phi = 4$ (four ϕ intervals in each period) and $N_\theta = 32$, we have 128 plates defined. An sketch of one ensemble of them will be shown in Fig. 6. We follow a number of trajectories and study the individual effect of each plate on the particle flux. More precisely, in Fig. 4 we show, for the ECH plasma, the fraction of the trajectories that would be intercepted by each plate in the case where this plate were the only one in our device. Note that the contributions of two plates cannot be directly added, since they may partly shadow each other. The structures in Fig. 4 suggest the positions where a plate can be more effective. We will be interested in plates in the outer region of the plasma, where $\rho > 1.0$, for an acceptable interaction with the hot plasma. In such radial positions, $\theta \approx \frac{3\pi}{2}$ for

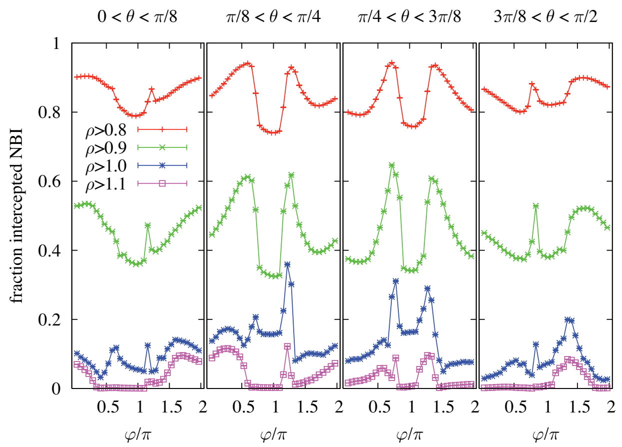

Fig. 5 Same as Fig. 4 for the NBI plasma.

$\frac{\pi}{4} < \phi < \frac{3\pi}{8}$ and $\frac{3\pi}{8} < \phi < \frac{\pi}{2}$ looks promising, since 10% of particles would be intercepted by each of them. Considering the mirror images of these plates in the other three periods (altough, as we know, their contributions do not simply add up), one could expect to concentrate a great proportion of the plasma-wall interaction in these plates. Note that our choice is not the optimal intercepting particles, but it is the best that makes it far from the groove.

Fig. 5 shows the same quantity for the case of the NBI plasma. Here, the radial electric field clearly improves the confinement. One of the consequences is that each ion has more probability of being intercepted by each plate, since it performs more toroidal turns around TJ-II. Our former proposal of divertor configuration still seems one of the best possible. These are good news, since one would desire a divertor design valid for a wide range of plasma parameters. Looking at both figures, our first tentative design will be plates located at $\rho > 1.0$, $\frac{11\pi}{8} < \theta < \frac{23\pi}{16}$ along all the toroidal angle. This configuration is sketched in Fig. 6.

In the ECH case, our plates intercept about half the particles in the plasma. This includes ions that end their trajectories in the groove of and ions that do not. The original

Fig. 6 Tentative design of plates. The $0.9 < \rho < 1.0$ surfaces are plotted in black, and the plates in red.

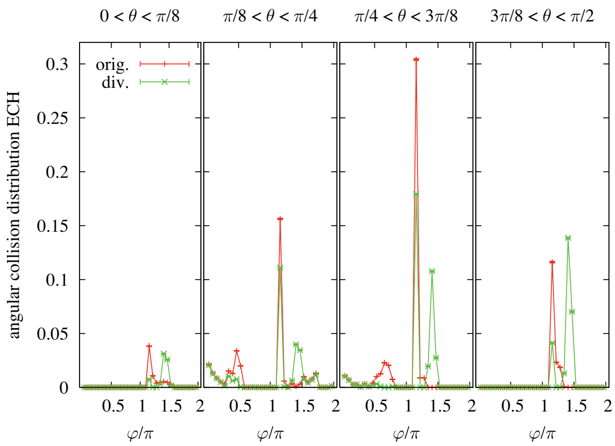

Fig. 7 Angular distribution of the collisions with the vacuum chamber and the plates for the ECH plasma with and without divertor.

and the modified angular distribution of trajectory ends are shown in Fig. 7. The high original peaks correspond to collisions with the groove, which in usual operation represent around 60% of the collisions with the vaccum chamber. The effect of our plates is to diminish this quantity to be around 35%, about half the proportion existing before. New peaks appear, corresponding to the location of our plates. This means that we have concentrated a great part of the plasma-wall interaction on the divertor plates. In the case of the NBI plasma, see Fig. 8, the same effect still exists, although a bit weaker. The proportion of the total trajectories that are intercepted is about 63%. Nevertheless, from about 50% of ions colliding with the groove, one reduces it to about 35%.

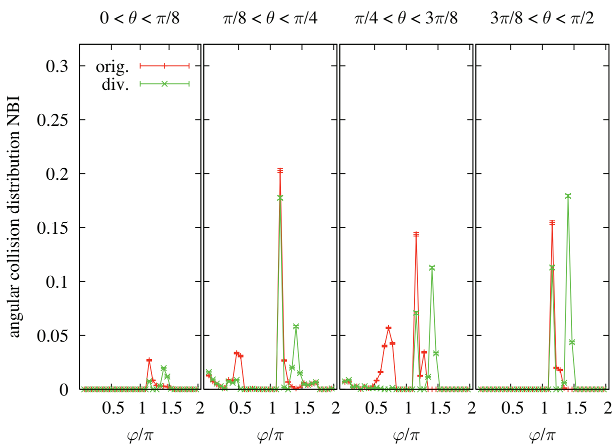

Fig. 8 Same as Fig. 7 for the NBI plasma.

5 Conclusions and future work.

We have found a promising configuration for having a flux expansion divertor, since the particle collisional flux maps are characterised by presenting strong poloidal asymmetries, showing a high value in the poloidal position corresponding to one of the extremes of the "bean".

This magnetic configuration has the property that the flux expansion is maximum in a region where the main part of the particle flux that goes onto the groove passes through. Therefore, one may minimize at the same time the flux onto the groove and onto the plates. Due to the TJ-II configuration characteristics, this effect is especially beneficial because we move the main plasma wall interaction to a zone much farther from the plasma bulk.

The beneficial effect of the divertor is larger in the NBI regime despite of the fact that this case presents a smaller mean free path, because the structure of electrostatic potential ensure that a large fraction of particles is intercepted.

The next step of this work is to optimize the design of the divertor plates in order that the interrupted particle flux on the groove is maximum. It may be also necessary to create an ergodic zone in order to minimize the particle and heat flux on the plates. Before assessing the feasibility of this construction, new flux calculations with the ergodic zone are mandatory. For this last phase of calculation, the effect of turbulence on particle trajectories must be included in order to have more refined calculations, especially in high-beta plasmas. Once the flux on the divertor plate is estimated, including the field ergodization effect, and before starting the engineering assessment of the coils and the divertor plates, it will be necessary to calculate the outgasing coming from the plate. A 2D neutral transport code is available and will be applied to this case. Experiments are also foreseen in TJ-II to benchmark all these theoretical results.

[1] R. König *et al.*, Plasma Phys. Control. Fusion **44**, 2365 (2002).
[2] P. H. Rebut, Plasma Phys. Control. Fusion **48**, B1 (2006).
[3] N. Ohyabu *et al.*, Nucl. Fusion **34** (1994).
[4] Y. Feng *et al.*, Nucl. Fusion **46**, 807 (2006) .
[5] R. Maingi, Magnetic Field Line Tracing Calculations for Conceptual PFC Design in NCSX, and possibilities for a divertor design collaboration. 33th EPS Conference on Plasma Phys. Control. Fusion. Roma, 2006.
[6] F. Castejón *et al.*, Fusion Sci. and Tech. **50**, 412 (2006).
[7] F. Castejón *et al.*, Plasma Phys. Control. Fusion **49**, 753 (2007).
[8] A. Boozer and G. Kuo-Petravic, Plasma Phys. **24**, 851 (1981).
[9] J. Herranz *et al.*, Phys. Rev. Lett. **85**, 4715 (2000).
[10] R. Balbín *et al.*, Fusion Sci. Technol. **46**, 271 (2004).
[11] Melnikov *et al.*, Fusion Sci. Technol. **46**, 299 (2004).
[12] M. Yokohama *et al.*, Nucl. Fusion **47**, 1213 (2007).

Nonlinear competition between zonal flows and geodesic acoustic modes

K. Itoh[1], S.-I. Itoh[2], M. Yagi[2] , S. Toda[1], A. Fujisawa[1], N. Kasuya[1], A. Fukuyama[3]

[1]National Institute for Fusion Science, Toki 509-5292, Japan
[2]Research Institute for Applied Mechanics, Kyushu University, Kasuga 816-8580, Japan
[3]Department of Nuclear Engineering, Kyoto University, Kyoto, 606-8501, Japan

It has been known that the zonal flows (ZFs) and geodesic acoustic modes (GAMs) are destabilized by microscopic fluctuations in the range of drift wave frequencies [1]. The rates, at which ZFs and GAMs are driven by background microscopic turbulence, have been derived [1,2]. The nonlinear saturation of the Reynolds stress, when the ZFs have finite amplitude, was also derived [3]. That is, when the induced flow has finite amplitude, the drift wave spectrum is deformed so that the energy input from turbulence to the flow is suppressed. This result was derived by renormalizing the higher order kinetic of quasiparticle response. Under the presence of ZFs and GAMs, the deformation of drift wave spectrum causes the modification of the driving rates of ZFs and GAMs. Thus, the nonlinear competition between ZFs and GAMs occurs. The turbulent transport is strongly affected by the inclusion of zonal flows. Thus, the competition between ZFs and GAMs must be taken into account, in order to analyze the turbulent transport in toroidal plasmas.

In order to study the competition between the ZFs and GAMs, the effect of the return flow along the magnetic field line must be taken into account. The coupling of the poloidal flow to the parallel flow enhances the effective inertia of plasma [4]. For ZFs, one has an enhancement factor for the effective inertia $1+2q^2$ (in the plateau regime). The back interaction of the ZFs and GAMs on drift wave turbulence closes the set of coupled equations, which determines the level of turbulence and turbulent transport. The self-consistent solution of the microscopic fluctuations, ZFs and GAMs is obtained. The competition between ZFs and GAMs is summarized in the parameter space of the damping rates.

[1] P H Diamond, S.-I. Itoh, K. Itoh, T. S. Hahm: Plasma Phys. Control. Fusion **47** (2005) R35
[2] K. Itoh, K. Hallatschek, S.-I. Itoh: Plasma Phys. Control. Fusion **47** (2005) 451
[3] K. Itoh, et al.: Phys. Plasmas **12** (2005) 062303
[4] K. Itoh and S.-I. Itoh: Plasma Phys. Control. Fusion **38** (1996) 1

This work was partly supported by Grants-in-Aid for Specially-Promoted Research (16002005) and for Scientific Research (19360418).

Proceedings of ITC/ISHW2007

Modeling of Anomalous Transport in ECRH Plasmas at HSX

W. Guttenfelder[1], D.T. Anderson[1], J.M. Canik[1], K.M. Likin[1], J. Lore[1], J.N. Talmadge[1], W. Dorland[2], M. Barnes[2]

[1] *University of Wisconsin, Madison, USA*

[2] *University of Maryland, USA*

The gyrokinetic code GS2 has been used to calculate the linear growth rates of the underlying micro-instabilities presumably responsible for the anomalous transport in HSX. With ECRH heating ($T_e >> T_i$), the dominant long-wavelength instability is the trapped electron mode (TEM). To test whether available TEM transport models can reproduce the transport in HSX, the Weiland ITG/TEM transport model is used, in addition to calculations of neoclassical transport, to predict plasma profiles in HSX. To approximate the 3D geometry of HSX in the Weiland model, the necessary input geometry information is taken from the region in HSX where the fastest growing modes are spatially localized in the 3D GS2 calculations. Specifically, the local curvature/∇B scale lengths (~R/3) and helical ripple (ε_H) are used in place of the axisymmetric values (R and ε_T = r/R, respectively). With these approximations, the TEM linear growth rates predicted by the Weiland model agree quantitatively (within 30%) with those predicted by the 3D GS2 calculations for HSX experimental parameters. Predicted density and temperature profiles using the above transport estimates are in reasonable quantitative agreement with a number of experimental profiles in the QHS configuration. The predicted confinement times are within ~10% of the experimental confinement times.

Keywords: turbulent transport model, quasi-linear transport, 3D gyrokinetic stability, trapped electron mode

1. Introduction

It has become routine to optimize stellarators using neoclassical theory [1]. It is hoped that in the future, stellarators may also be optimized to reduce anomalous transport, thought to be caused by plasma turbulence. Indeed, there is evidence in LHD that anomalous transport is reduced when neoclassical transport is reduced [2]. While significant advances have been made in the predictive capability for turbulent transport in tokamaks [3], relatively little work has been performed for 3D toroidal configurations such as stellarators.

Turbulent transport in tokamaks (caused by drift waves) has been modeled through the use of quasi-linear transport estimates that have been scaled to match non-linear simulations [4-6]. Suppression of turbulent transport via equilibrium E×B shear has also been included to successfully model H-mode pedestals and internal transport barriers [7]. These two features appear to provide the dominant scaling in predicting turbulent transport (via drift waves) in tokamak plasma.

Measured turbulence characteristics [8] and energy confinement time scaling [9] are quite similar in tokamaks and stellarators. Furthermore, recent non-linear simulations [10,11] have demonstrated that predicted turbulence characteristics in stellarator geometries display similarity to those predicted in tokamaks. However, because of the 3D shaping, stellarator non-linear simulations require increased resolution to treat the non-symmetric geometry and various classes of trapped particles, and are therefore more computationally expensive.

Given the similarity in turbulence and energy confinement between stellarators and tokamaks, a logical first step in performing predictive transport modeling for present stellarator experiments is to follow the same framework as used for tokamak predictions. Following this reasoning, this paper will present predictions of density and temperature profiles in the HSX stellarator using a tokamak transport model. To justify the use of this model for the 3D geometry in HSX, comparisons will be made between linear growth rates predicted by the tokamak model, and those calculated using a 3D gyrokinetic code that uses the HSX equilibrium.

2. 3D Gyrokinetic Microstability Calculations

The initial value gyrokinetic code GS2 [12] has been previously used to calculate linear micro-stability in a stellarator configuration [13]. To perform these

author's e-mail: guttenfe@cae.wisc.edu

calculations, 3D equilibrium are calculated using VMEC [14,15], which are then transformed into Boozer coordinates using TERPSICHORE [16]. GS2 uses a ballooning representation, and the necessary geometry coefficients along a field line are calculated using VVBAL [17]. Since stellarators in general have multiple ripples in |B| along a field line, care must be taken in creating a grid that captures these additional non-symmetric ripples. Multiple grids have been created for the quasihelically symmetric (QHS) configuration of HSX with varying number of grid points to determine how well these additional ripples must be resolved to reach a converged solution. For the calculations shown in this paper, 400 grid points (over a range of $\theta = \pm 4\pi$) were sufficient. Typically 16 energy and ~30 pitch angle grid points were needed for the calculations to converge. To verify accuracy, a few cases were benchmarked against the independent linear gyrokinetic FULL code for the HSX geometry [18]. The GS2 calculations were performed on the NERSC IBM SP3 supercomputers using up to 256 processors, requiring a few minutes per run.

The linear stability calculations were performed on a field line where the magnetic axis undergoes the largest excursion to the outboard side, and hence has the strongest bad curvature drive. Figure 1 (top) shows eigenfunctions calculated for the QHS configuration for multiple poloidal wavenumbers ($k_\theta \rho_s$ = 0.3-0.8), at a normalized minor

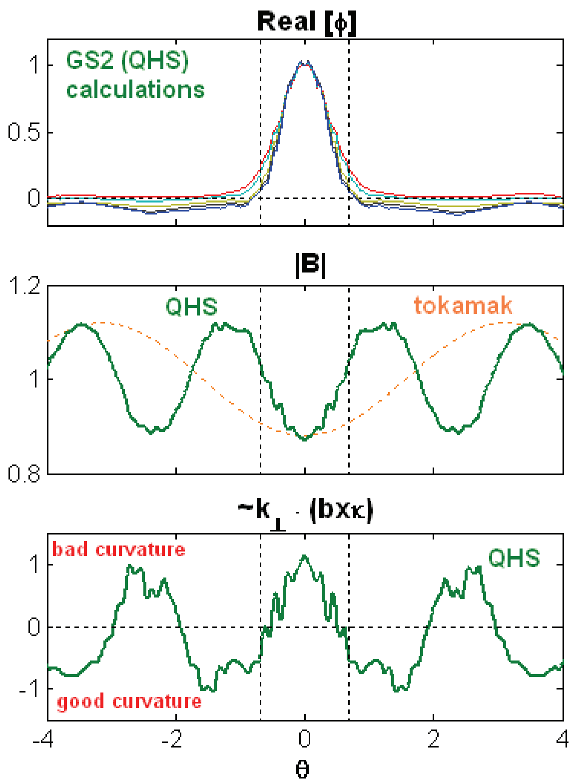

Fig.1 Normalized eigenfunctions (top), |B| (center), and curvature drift (bottom) for GS2 calculations in HSX.

radius of ρ = 0.86, for experimentally relevant parameters (a/L_{Ti} = 0, T_e/T_i = 2, $a/L_n = a/L_{Te}$ = 3, υ = 0). For these conditions, the instability is the collisionless trapped electron mode (CTEM), with a mode frequency propagating in the electron diamagnetic drift direction. Also shown in Fig. 1 are |B| along a field line (middle) and the term proportional to the curvature drift (bottom). The eigenfunctions for these unstable TEMs are strongly localized in the low field, bad curvature region of the device, where the trapped particles exist. The structure of these instabilities is very similar to that observed in tokamaks, due to the quasisymmetric field.

3. 1D Predictive Transport Modeling

To model the anomalous particle and electron heat transport in HSX [19], the Weiland model [4] is utilized. The Weiland model is a toroidal fluid model for the ion temperature gradient (ITG) and TEM instabilities. It is a linearized set of equations that provides both linear stability predictions, and quasi-linear transport estimates of particle, and ion and electron heat transport. These transport estimates have been checked against a limited number of non-linear simulations [4,20] with good results. The Weiland ITG/TEM model forms the core of the Multi-Mode Model [21] used for numerous tokamak calculations.

As input, the Weiland model requires density and temperature gradient scale lengths (L_n, L_{Te}, L_{Ti}), temperature ratio (T_e/T_i), wavenumber ($k_\theta \rho_s$), trapped particle fraction (f_t), and a $\nabla B/\kappa$ scale length (L_B) to approximate the toroidal drift terms. In a tokamak, the trapped particle fraction is simply found using the toroidal ripple, $\varepsilon_T = r/R$, $f_t = \sqrt{2\varepsilon_T/(1+\varepsilon_T)}$, and the $\nabla B/\kappa$ scale length is the major radius, $L_B = R$.

To use the axisymmetric Weiland model for HSX, two approximations must be made to account for the local 3D geometry. These assumptions are based on the 3D gyrokinetic calculations discussed in Sec. 2. Since the unstable eigenmodes are strongly localized in the low field, bad curvature region (Fig. 1), the trapped particle fraction and $\nabla B/\kappa$ scale length are taken from this localized region of HSX. Because of the quasihelical symmetry, the trapped particle fraction is calculated using the dominant helical ripple ($\varepsilon_H = 0.14 \cdot r/a = 1.4 \cdot r/R$). In this location, where the axis undergoes an excursion to the outboard side, the local curvature is roughly three times larger than that of a tokamak with the same major radius. Therefore, the $\nabla B/\kappa$ scale length is reduced by a factor of three, $L_B = R/3$.

The Weiland model has been used with the above approximations to calculate the linear stability of HSX plasmas. Growth rates have also been calculated for the same input parameters using the 3D GS2 code for the QHS equilibrium. A comparison of growth rates is shown in Fig.

2 for a scan over density and electron temperature gradient, with the other parameters the same as in Fig. 1. As seen in the top two plots, the growth rates from the Weiland model are close in magnitude to the 3D GS2 calculations. For the range of gradients indicative of experiment (highlighted red lines) the agreement is better than 30%. If the local HSX geometry approximations are not used, the Weiland model underpredicts the growth rates by about a factor of two (Fig. 2, bottom).

In order to predict density and temperature profiles, 1-D flux surface averaged transport equations for electron density and temperature are solved numerically (Eqs. 1).

$$\frac{\partial}{\partial t}n+\frac{1}{V'}\frac{\partial}{\partial \rho}V'\left(-D\frac{\partial n}{\partial \rho}\left\langle|\nabla\rho|^2\right\rangle+V^{(n)}n\left\langle|\nabla\rho|\right\rangle\right)=\sum S(\rho) \tag{1a}$$

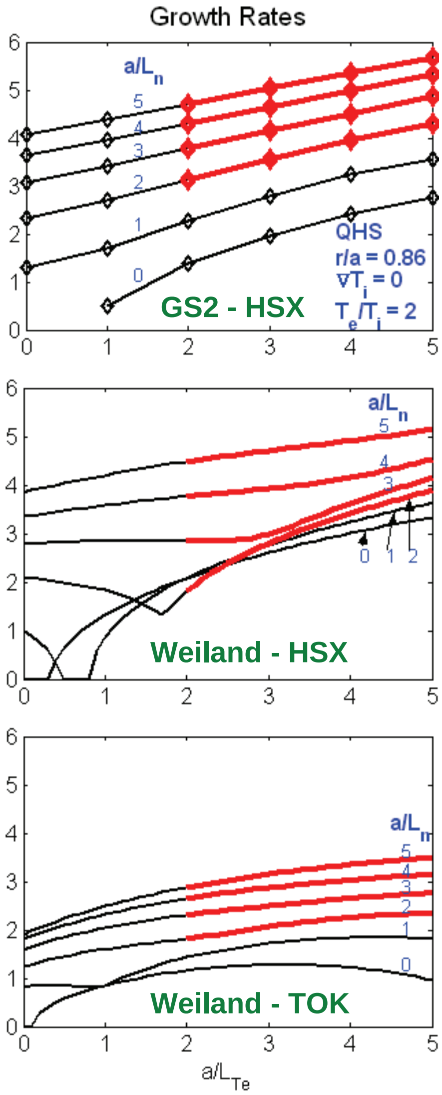

Fig.2 Growth rates (10^5 s^{-1}) calculated in HSX using 3D GS2 (top), the Weiland model with geometry approximations (center), and the Weiland model without geometry approximations (bottom). The highlighted lines represent typical experimental gradients.

$$\frac{3}{2}n\frac{\partial}{\partial t}T+\frac{1}{V'}\frac{\partial}{\partial \rho}V'\left(-n\chi\frac{\partial T}{\partial \rho}\left\langle|\nabla\rho|^2\right\rangle+V^{(nT)}nT\left\langle|\nabla\rho|\right\rangle\right)=\sum\frac{1}{e}P(\rho) \tag{1b}$$

A multi-mode model approach is used, summing transport from the Weiland model (with geometry approximations), neoclassical transport (calculated using DKES [22,23]), and a small transport contribution from a resistive ballooning mode model, as used in [21]. For the neoclassical and Weiland model, the transport components are represented by both diffusive (D,χ) and convective ($V^{(n)}$, $V^{(nT)}$) components. The ECRH power deposition profile is calculated using a ray-tracing code, and the total absorbed power is determined from the time response of the diamagnetic flux loop during ECRH turn off. The particle source rate profile used is based on 3D neutral gas calculations [19]. The total magnitude is adjusted to minimize the difference in predicted and measured densities, but is usually within a factor of two of the neutral gas calculations that have been scaled to match absolutely calibrated H_α measurements.

Using the above sources and transport models, Eqs. 1 are integrated to steady state. Figure 3 shows a comparison of predicted and measured electron density and temperature profiles (using Thomson scattering) for B=1.0T QHS plasmas for two different injected powers (P_{inj} = 44 & 100 kW, O1 ECRH). The density profiles agree very well across the entire minor radius. The temperature profiles agree outside a normalized minor radius of ρ = 0.3, but the model underpredicts the core temperature. For four different injected powers (including two cases not shown here), the rms deviation of the simulated and experimental density profile

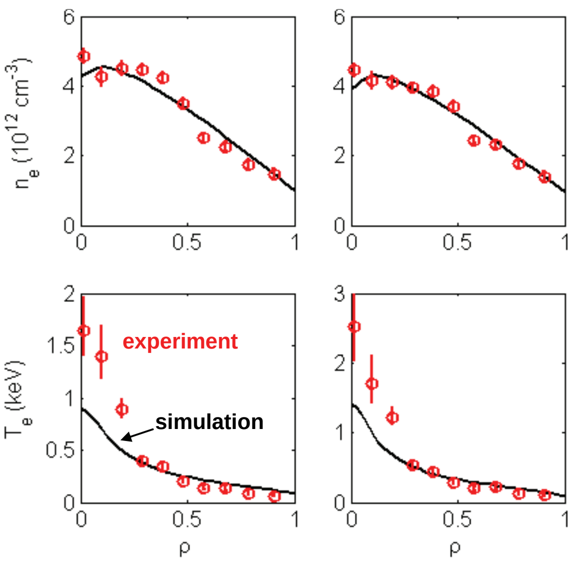

Fig.3 Predicted and measured electron density (top) and temperature (bottom) profiles for the QHS configuration for P_{inj} = 44 kW (left) and 100 kW (right).

($\sqrt{\sum\left(n^{sim}(\rho_j)-n_j^{exp}\right)^2}\Big/\sqrt{\sum\left(n_j^{exp}\right)^2}$, following ref. 3) is 9%. The rms deviation for T_e is considerably higher (40%).

The discrepancy of the core T_e profiles is due to a large χ_e from the Weiland TEM between ρ = 0.2-0.3, and a large neoclassical χ_e as the magnetic axis is approached. It is of interest to note that in the region between ρ = 0.2-0.3, the radial electric field predicted from the neoclassical ambipolarity constraint varies rapidly due to a change from the ion root to the electron root as the hot core is approached. In this region, estimated E×B shear rates [24] are larger than the linear TEM growth rates predicted from the transport modeling. This may indicate that E×B shear suppression could be important for determining the appropriate anomalous transport contribution.

Although the central T_e is not predicted with accuracy, the simulated energy confinement times agree within 10% of the experimental confinement times. Figure 4 shows the kinetic electron energy confinement times measured experimentally (red) and predicted by the simulations (blue) for four injected powers (26, 44, 70, 100 kW). The predicted confinement times scale like $\sim P^{-0.57}$, similar to empirical scaling laws [9] and to that expected from gyroBohm transport. Also shown are the energy confinement times determined from the diamagnetic measurements for similar line-averaged densities (black). These confinement times have a slightly weaker scaling with absorbed power, $\sim P^{-0.42}$.

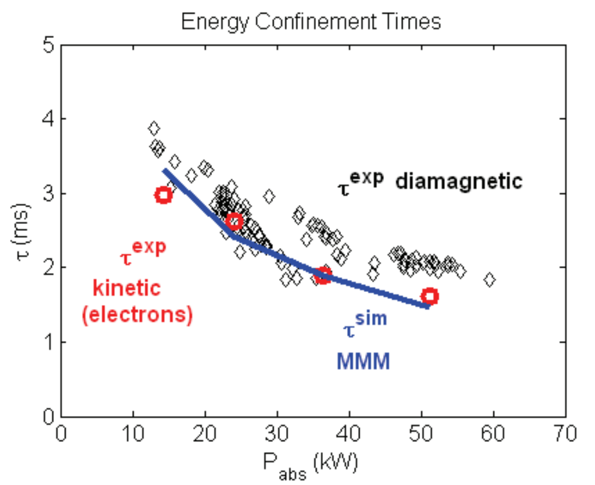

Fig.4 Predicted (blue) and experimental (red) kinetic energy confinement times. Also shown are confinement times from diamagnetic measurements only (black).

4. Conclusions

The Weiland ITG/TEM anomalous transport model has been used to predict transport in the HSX stellarator. By using approximations to represent the local geometry in HSX, the Weiland model predicts linear growth rates that agree within 30% of those calculated using the 3D gyrokinetic code GS2. Although non-linear effects or E×B shear suppression have not been included, the linear scaling should be captured reasonably well by this approximation. Predicted density profiles and energy confinement times (using the Weiland model plus appropriate neoclassical calculations) agree within 10% of experimentally measured values. Root mean square deviations in the electron temperature profile are larger (40%) due to a systematic underprediction of the core T_e.

References

[1] H.E. Mynick, Phys. Plasmas **13**, 058102 (2006).
[2] H. Yamada et al., Nucl. Fusion **41**, 901 (2001).
[3] ITER Physics Basis, Ch. 2 Nucl. Fusion **39**, 2175 (1999).
[4] H. Nordman et al., Nucl. Fusion **30**, 983 (1990).
[5] M. Kotschenreuther et al., Phys. Plasmas **2**, 2381 (1995).
[6] R.E. Waltz et al., Phys. Plasmas **4**, 2482 (1997).
[7] J.E. Kinsey et al., Phys. Plasmas **12**, 052503 (2005).
[8] A.J. Wooton et al., Plasma Phys. Contr. Fusion **34**, 2023 (1992).
[9] U. Stroth et al., Nucl. Fusion **36**, 1063 (1996).
[10] P. Xanthopoulos et al., Phys. Rev. Lett. **99**, 035002 (2007).
[11] T.-H. Watanabe et al., Nucl. Fusion **47**, 1383 (2007).
[12] M. Kotschenreuther et al,. Comp. Phys. Comm. **88**, 128 (1995).
[13] E.A. Belli et al., Bull. Am. Phys. Soc. **46**, No. 8, 232 (2001).
[14] S.P. Hirshman & D.K. Lee, Comp. Phys. Comm. **39**, 161 (1986).
[15] S.P. Hirshman et al., J. Comp. Phys. **87**, 396 (1990).
[16] D.V. Anderson et al., Int. J. Supercomp. Appl. **4**, 34 (1990).
[17] W.A. Cooper, Plasma Phys. Contr. Fusion **34**, 1011 (1992).
[18] G. Rewoldt et al., Phys. Plasmas **12**, 102512 (2005).
[19] J.M. Canik et al., Phys. Rev. Lett. **98**, 085002 (2007).
[20] A. Dimits et al., Phys. Plasmas **7**, 969 (2000).
[21] G. Bateman et al., Phys. Plasmas **5**, 1793 (1998).
[22] S.P. Hirshman et al., Phys. Fluids **29**, 2951 (1986).
[23] W.I. van Rij & S.P. Hirshman, Phys. Fluids **B** 1, 563 (1989).
[24] T.S. Hahm, Phys. Plasmas **4**, 4074 (1997).

Proceedings of ITC/ISHW2007

Bispectral analysis of harmonic oscillations measured using beam emission spectroscopy and magnetic probes in CHS

T. Oishi, S. Kado[a], M. Yoshinuma, K. Ida, T. Akiyama, T. Minami,
K. Nagaoka, A. Shimizu, S. Okamura, and CHS group

National Institute for Fusion Science, 322-6 Oroshi-cho, Toki 509-5292, Japan

[a]High Temperature Plasma Center, The University of Tokyo, 5-1-5 Kashiwanoha, Kashiwa, Chiba 277-8568, Japan

The coherent MHD oscillation which has the fundamental frequency of several kilohertz and its higher harmonics (harmonic oscillation: HO) has been observed in the compact helical system (CHS). HO consists of two pairs of harmonic series. One locates in the core region near ι = 0.5 rational surface, the other locates in the edge region near ι = 1.0 rational surface. In the present study, bispectral analysis is applied to the fluctuation data having HO measured using beam emission spectroscopy (BES) and magnetic probes. It has revealed that fundamental mode of HO in both the magnetic fluctuation and core density fluctuation have phase correlation with the harmonics including fundamental oscillation, while HO in edge density fluctuation does not have such phase correlation. Mode numbers of HOs are same between harmonic components having difference frequencies. It suggests that the generation of harmonics can not be interpreted simply as the mode coupling, even though bicoherence value is significant. The bicoherence value and relative amplitude of higher harmonics correlate with each other, which suggests that bicoherence means the degree of distortion of the signals.

Keywords: bispectral analysis, bicoherence, fluctuation, magnetohydrodynamics, edge harmonic oscillation, compact helical system, beam emission spectroscopy, edge transport barrier

1. Inroduction

Fluctuations of plasma parameters have been recognized to correlate with the properties of plasma confinement. Characteristics of the fluctuations includes the amplitude and level, frequency and wavenumber spectrum, spatial structure represented by radial locality or poloidal/toroidal mode number *m/n*, and so on. In addition to these characteristics, recently, attention has been paid to the nonlinear characteristics such as the correlation between spectral components having different frequencies. In order to investigate the nonlinear characteristics of the fluctuations, bispectal analysis is consider to be useful [1]. The bispectral analysis has been applied to several tokamaks [2], helicals [3] and other types of plasma confinement devices to investigate the interaction among turbulence, magnetohydrodynamic (MHD) oscillations, and zonal flows [4-6].

Recently, a coherent MHD mode which consists of the fundamental frequency of several kilohertz and its higher harmonic (harmonic oscillation: HO) [7,8] has been observed in the edge transport barrier (ETB) discharges of the compact helical system (CHS), which is a low-aspect-ratio, middle-sized heliotron (major radius = 1.0 m, minor radius = 0.2 m, toroidal period number = 8, polarity = 2) [7,9-13]. The characteristics of the oscillation have been investigated in the viewpoint of the comparison with edge harmonic oscillation (EHO) [14-17], which is recognized to have a role enhancing the particle transport in the quiescent H-mode of tokamaks. Fluctuation measurement using the beam emission spectroscopy (BES) [18,19] and magnetic probe (MP) array [20] have revealed that HO in CHS consists of two pairs of harmonic series located in different radial position. One locates in the core region of normalized minor radius ρ = 0.4~0.5 near ι = 0.5 rational surface (denoted as “HO (core))”, the other locates in the edge region of ρ = 0.9~1.0 near ι = 1.0 rational surface (denoted as “HO (edge)). All harmonic components of both HO (core) and HO (edge) have same mode numbers, namely, *m/n* = -2/1 for HO (core) and *m/n* = -1/1 for HO (edge), even though the frequency of *p*th harmonic is *p* times larger than that of 1st harmonic for both HO (core) and HO (edge), where *p* is positive integer [21].

In the present study, bispectral analysis is applied to the fluctuation data having HO measured using BES and MP in order to investigate the correlation between the harmonic components.

2. Experimental Setup

BES has been developed in CHS to simultaneously measure both local density fluctuations and gradients. The BES method detects emissions from the collisionally

author’s e-mail: oishi@nifs.ac.jp

excited neutral beam atoms (denoted as "beam emission") [22]. The spatial channels used in BES consist of 16 optical fibers with an object lense. In the present experiment, H_α emission from the neutral hydrogen atomic beam for heating in the intersection of the beam line and the sightline for each fiber channel was measured as the beam emission. One can select the arrangement of the fibers in the radial or poloidal direction to measure each structure of the fluctuations.

Magnetic probe array was also used to measure both the poloidal and toroidal structures of the magnetic fluctuations. The poloidal magnetic probe array consists of sixteen probes covering the poloidal angle $\Delta\theta$ = 235.5 deg. We define the absolute poloidal coordinate as θ = 0 deg. and 180 deg. at the midplane outside and inside torus, respectively [23]. Five toroidal magnetic probes covering the toroidal angle $\Delta\phi = \pi$ were located at every $\pi/4$ section at the major radius R = 1.2 m.

3. Data Analysis Method

When the wave having the frequency f is phase correlated with the spectral components with the frequencies of f_1 and f_2 satisfying the summation rule $f = f_1 \pm f_2$, we can use the bicoherence value as an indicater of phase correlation of these three waves [1]. Bicoherence $b^2(f_1, f_2)$ for the waves having the frequency f, f_1 and f_2 is defined as

$$b^2(f_1, f_2) = \frac{|< X(f_1) X(f_2) X^*(f) >|^2}{<|X(f_1)X(f_2)|^2><|X(f)|^2>} \qquad (1)$$

where $X(f)$ is the Fourier transform of the time trace $x(t)$ and < > means ensemble averaging.

Wave-wave coupling, namely which is the wave having the frequency f is generated by the coupling between the waves having the frequencies f_1 and f_2, is the representative case of which the bicoherence value becomes significant. However, the wave-wave coupling is not necessary the only mechanism responsible of the phase correlation revealed by bicoherence analysis. Summation rule about both frequency $f = f_1 \pm f_2$ and wavenumber $k = k_1 \pm k_2$ must be obeyed to generate the another wave by wave-wave coupling.

4. Experimental Results

Figure 1 shows Typical experimental conditions and temporal evolution of plasma parameters for a discharge in which the harmonic oscillation appears: (a) heating condition, (b) H_α intensity, (c) magnetic fluctuation, and (d) frequency spectrum of magnetic fluctuation. Plasma was initiated by electron cyclotron heating and was further heated by two neutral beam injection (NBI) systems. Additional gas was puffed as a means to increase density. The standard magnetic field configuration of CHS was applied, in which the vacuum magnetic axis position R_{ax} was 92.1 cm from the torus center, the toroidal magnetic field strength at the magnetic axis B_{ax} was 0.95 T, and the magnitude of the quadrupole field B_q denoting the degree of cancellation of the intrinsic quadrupole component formed by the helical coils was -50 %. In the cases in which the heating power exceeds a certain threshold, ETB characterized by a sudden drop in the H_α intensity signal as shown in Fig. 1(b) is formed. It has been found that the line-averaged density, the edge density gradient, and the stored energy begin to increase at the ETB transition [7,9-13]. In the latter half of the phase having ETB, HO which consists of a 1st harmonic with the frequency of 4.0 kHz and a 2nd harmonic appears in the magnetic fluctuation as shown in Fig. 1(c) and (d). It is known that this oscillation is identical to HO (core) [21].

We applied the bispectral analysis to the fluctuation data having harmonic oscillation measured using the magnetic probes and BES. Figure 2 shows the bicoherence plane of (a) magnetic fluctuation, (b) core (ρ = 0.42) density fluctuation, and (c) edge (ρ = 0.95) density fluctuation. $b^2(f_1, f_2)$ of both the magnetic fluctuation and core density fluctuation have a clear peak having the frequencies (f_1, f_2) = (4.0 kHz, 4.0 kHz). This indicates the 1st component of HO (core) having the frequency 4.0 kHz is phase correlated with both the 1st component itself and the 2nd component having the frequency 8.0 kHz = $f_1 + f_2$, where $f_1 = f_2$ = 4.0 kHz. On the other hand, $b^2(f_1, f_2)$ edge density fluctuation does not have such a peak, even

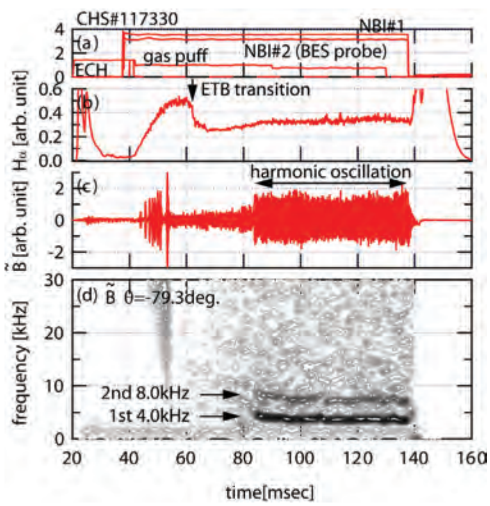

Fig.1 Typical experimental conditions and temporal evolution of plasma parameters for a discharge in which HO appears: (a) heating condition, (b) H_α intensity, (c) magnetic fluctuation, and (d) frequency spectrum of magnetic fluctuation.

though HO (edge) observed in BES signal consists of the 1st frequency of 4.0 kHz and its 2nd harmonic. It indicates that phase correlation between harmonic components seems to be different between HO (core) and HO (edge).

We have found that $b^2(f_1, f_2)$ which indicates the phase correlation between harmonic components has a poloidal asymmetry. Figure 3 shows the frequency spectrum of magnetic fluctuation having up to 3rd harmonic of HO. The 1st, 2nd, and 3rd frequency f(1st), f(2nd), and f(3rd) is 3.0 kHz, 6.5 kHz, and 10.0 kHz, respectively. The bicoherence planes of magnetic fluctuations (a) outside torus and (b) inside torus are shown in Fig. 4. $b^2(f_1, f_2)$ outside torus has peaks with (f_1, f_2) = (f(1st), f(1st)), (f(2nd), f(1st)), (f(3rd), f(1st)), (f(2nd), f(2nd)) and so on which indicates the phase correlation between each harmonic component. On the other hand, $b^2(f_1, f_2)$ inside torus also has peaks located at similar frequencies as those outside torus, however the values are small. Figure 5 shows (a) $b^2(f_1, f_2)$ at (f_1, f_2) = (f(1st), f(1st)) and (f(2nd), f(1st)) and (b) amplitudes of the 2nd (f(2nd) = f(1st) + f(1st)) and 3rd (f(3rd) = f(2nd) + f(1st)) harmonic of HO divided by that of the 1st harmonic with respect to poloidal angles. One can see that relative amplitudes of higher harmonics decrease with decreasing corresponding $b^2(f_1, f_2)$ in the poloidal direction.

We should pay attention to the physical interpretation of the result of the bispectral analysis. In the present study, $b^2(f_1, f_2)$ has peaks at f(1st) + f(1st) = f(2nd) and f(2nd) + f(1st) = f(3rd). However, the poloidal/toroidal mode number m/n does not satisfy the summation rule, namely, they show m(1st) = m(2nd) = m(3rd) = -2, n(1st) = n(2nd) = n(3rd) = 1 [23]. Therefore, generation of harmonics can not be interpreted simply as the mode coupling. $b^2(f_1, f_2)$ can be regarded as the degree of "distortion" of the signals in our case, because the poloidal asymmetry of $b^2(f_1, f_2)$ and relative amplitude of higher harmonics indicates that they have a positive correlation. Mechanism to distort signals has not been clarified yet, which remains as a future study.

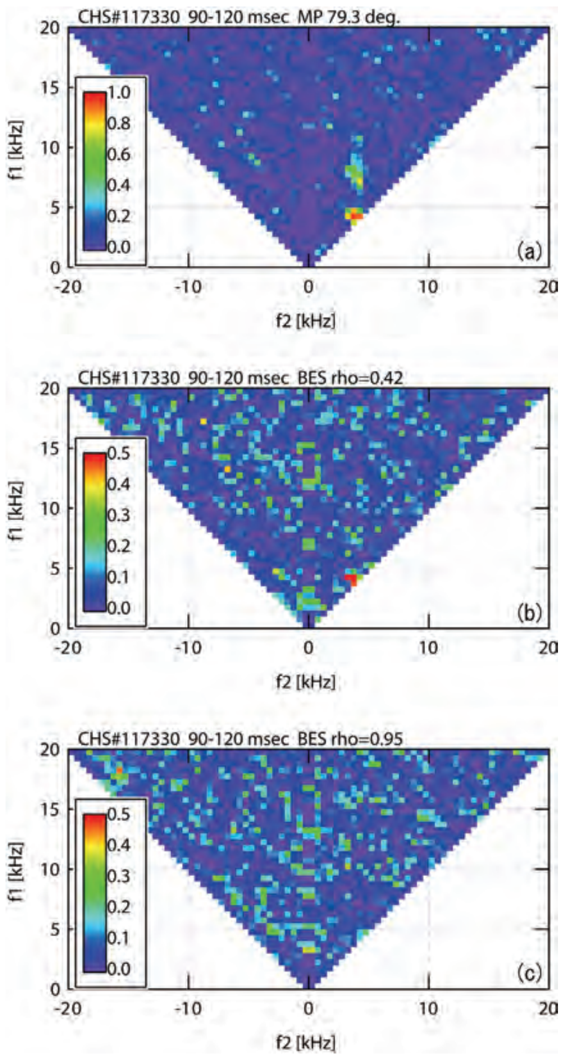

Fig.2 Bicoherence plane of (a) magnetic fluctuation, (b) core (ρ = 0.42) density fluctuation, and (c) edge (ρ = 0.95) density fluctuation. $b^2(f_1, f_2)$ of both the magnetic fluctuation and core density fluctuation have a clear peak having the frequencies (f_1, f_2) = (4.0 kHz, 4.0 kHz), while that of edge density fluctuation does not have such a peak.

5. Summary

HO having the fundamental frequency of 3~5 kHz and its higher harmonics has been observed in CHS. It consists of two pairs of harmonic series. One locates in core region near ι = 0.5 rational surface, the other locates in edge region near ι = 1.0 rational surface.

We applied the bispectral analysis to the fluctuation data having HO measured using BES and MP. It revealed that fundamental mode of HO in both the magnetic fluctuation and core density fluctuation have phase correlation with the harmonics including fundamental oscillation, while HO in edge density fluctuation does not have such phase correlation.

Generation of harmonics can not be interpreted simply as the mode coupling, even though bicoherence

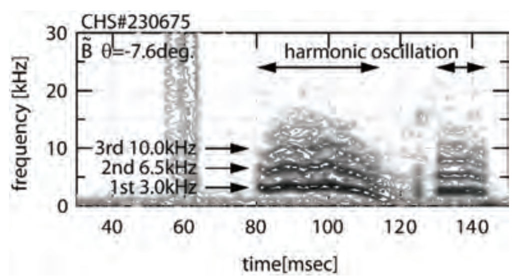

Fig.3 Frequency spectrum of magnetic fluctuation having up to 3rd harmonic of HO.

value $b^2(f_1, f_2)$ is significant, because mode numbers of HOs are same between harmonic components having difference frequencies. Correlation between $b^2(f_1, f_2)$ and relative amplitude of higher harmonics suggests that $b^2(f_1, f_2)$ means the degree of distortion of the signals.

The reason why the signals are distorted and all harmonic components have same mode numbers should be investigated in the future.

Acknowledgement

The work was supported in part by the National Institute for Fusion Science Collaborative Research Program (NIFS02KZPD003) directed by the second author.

References

[1] Y. C. Kim and E. J. Powers, Phys. Fluids **21**, p. 1452 (1978).

[2] Ch. P. Rits *et al.*, Phys. Fluids **B 1**, p. 153 (1989).

[3] C. Hidalgo *et al.*, Phys. Rev. Lett. **71**, p. 3127 (1993).

[4] S. Sesnic *et al.*, Nucl. Fusion **34**, p. 1365 (1994).

[5] D. Raju *et al.*, Plasma Phys. Control. Fusion **45**, p. 369 (2003).

[6] Y. Nagashima *et al.*, Phys. Rev. Lett. **95**, 095002 (2005).

[7] T. Oishi *et al.*, Nucl. Fusion **46**, 317 (2006).

[8] T. Oishi *et al.*, Phys. Plasmas **13**, 104504 (2006)

[9] S. Okamura *et al.*, J. Plasma Fusion Res. **79**, 977 (2003).

[10] S. Okamura *et al.*, Plasma Phys. Controlled Fusion **46**, A113 (2004).

[11] T. Minami *et al.*, Plasma Fusion Res. **1**, 032 (2006)

[12] T. Akiyama *et al.*, Plasma Phys. Control. Fusion, **48**, 1683 (2006)

[13] M. Takeuchi *et al.*, Plasma Phys. Control. Fusion, **48**, A277 (2006)

[14] C. M. Greenfield *et al.*, Phys. Rev. Lett. **86**, 4544 (2001).

[15] W. Suttrop *et al.*, Plasma Phys. Controlled Fusion **45**, 1399 (2003).

[16] W. Suttrop *et al.*, Plasma Phys. Controlled Fusion **45**, 1399 (2003).

[17] W. Suttrop *et al.*, Nucl. Fusion **45**, 721 (2005).

[18] T. Oishi *et al.*, Rev. Sci. Instrum. **75**, 4118 (2004).

[19] T. Oishi *et al.*, J. Plasma Fusion Res. SERIES **6**, 449 (2004).

[20] S. Sakakibara *et al.*, Jap. J. Appl. Phys. **63**, 4406 (1994)

[21] T. Oishi *et al.*, Plasma Fusion Res. **2**, S1097 (2007).

[22] R. J. Fonck *et al.*, Rev. Sci. Instrum. **61**, 3487 (1990).

[23] S. Kado *et al.*, J. Nucl. Mat. **363-365**, p. 522 (2007)

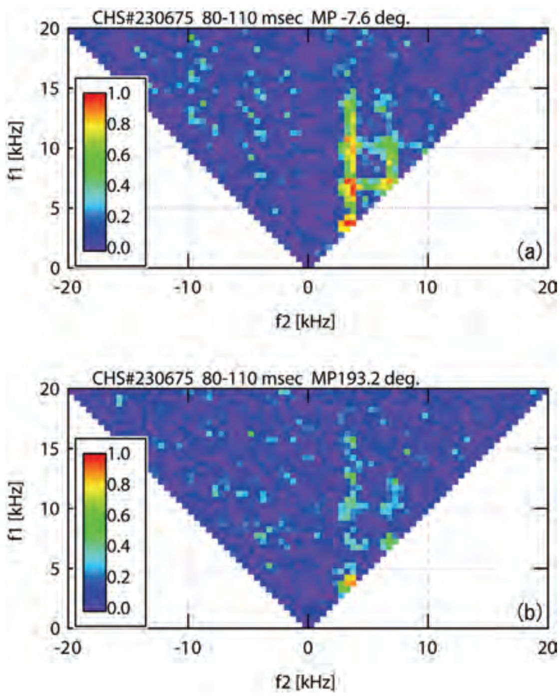

Fig.4 Bicoherence plane of magnetic fluctuations (a) outside torus and (b) inside torus having frequencies of HO f(1st) = 3.0 kHz, f (2nd) = 6.5 kHz, and f (3rd) = 10.0 kHz. $b^2(f_1, f_2)$ outside torus has peaks with (f_1, f_2) = (f(1st), f(1st)), (f(2nd), f(1st)), (f(3rd), f(1st)), (f(2nd), f(2nd)) and so on which indicates the phase correlation between each harmonic component. $b^2(f_1, f_2)$ inside torus has peaks located at similar frequencies as those outside torus, however the values are small.

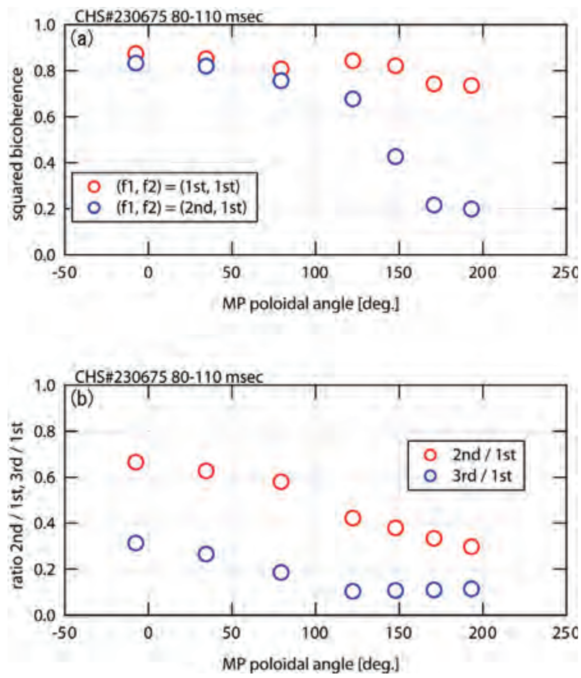

Fig.5 (a) $b^2(f_1, f_2)$ at (f_1, f_2) = (f(1st), f(1st)) and (f(2nd), f(1st)), (b) amplitudes of the 2nd (f(2nd) = f(1st) + f(1st)) and 3rd (f(3rd) = f(2nd) + f(1st)) harmonic of HO devided by that of the 1st harmonic with respect to poloidal angles. Relative amplitudes of harmonics decrease with decreasing corresponding $b^2(f_1, f_2)$ in the poloidal direction.

Proceedings of ITC/ISHW2007

Effects of Superimposed Parallel and Perpendicular Flow Velocity Shears on Drift-Wave Instabilities in Magnetized Plasmas

Toshiro KANEKO, Shuichi TAMURA and Rikizo HATAKEYAMA

Department of Electronic Engineering, Tohoku University, Sendai 980-8579, Japan

Plasma flow velocity shears parallel and perpendicular to magnetic field lines are independently controlled and superimposed using a modified plasma-synthesis method with concentrically three-segmented electron and ion emitters. The fluctuation amplitude of the drift wave which has an azimuthal mode number $m = 3$ is observed to increase with increasing the parallel shear strength in the absence of the perpendicular shear. When the perpendicular shear is superimposed on the parallel shear, the drift wave of $m = 3$ is found to change into that of $m = 2$. Furthermore, the parallel shear strength required for the excitation of the drift wave becomes large with a decrease in the azimuthal mode number. Based on these results, the superposition of the parallel and perpendicular shears can affect the characteristics of the drift wave through the variation of the azimuthal mode number.

Keywords: plasma flow velocity shear, drift wave, azimuthal mode number, plasma-synthesis method

1 Introduction

Plasma flows and their velocity shears in magnetized plasmas have attracted much attention not only in fusion oriented plasmas but also in space plasmas, because the ion flow velocity shear parallel to the magnetic field lines has been reported to enhance the ion-acoustic [1, 2], ion-cyclotron [3, 4], and drift-wave [5, 6] instabilities, while the perpendicular flow velocity shear has been confirmed to regulate not only the drift-wave but also ion-cyclotron instabilities independent of the sign of the shear [7]. In order to clarify the mechanisms of excitation and suppression of these instabilities in the real situation of the fusion and space plasmas, it is necessary to realize the controlled superposition of the parallel and perpendicular flow shears in magnetized plasmas.

Thus, the aim of the present work is to independently control and superimpose the parallel and perpendicular flow shears in the basic plasma device with concentrically three-segmented electron and ion emitters [8], and to carry out laboratory experiments on the drift-wave instability excited and suppressed by the superimposed flow shears in collisionless magnetized plasmas.

2 Experimental Setup

Experiments are performed in the Q_T-Upgrade machine of Tohoku University. We attempt to modify a plasma-synthesis method with an electron (e^-) emitter using a 10-cm-diameter tungsten (W) plate and a potassium ion (K^+) emitter using another W plate, which are oppositely located at the machine ends as shown in Fig. 1. The collisionless plasma is produced when the surface-ionized potassium ions and the thermionic electrons are generated by the spatially separated ion and electron emitters, respectively, and are synthesized in the region between these emitters. A negatively biased stainless (SUS) grid, the voltage of which is typically $V_g = -60$ V, is installed at a distance of 10 cm from the ion emitter surface. Since the grid reflects the electrons flowing from the electron emitter side, the electron velocity distribution function parallel to the magnetic fields are considered to become Maxwellian.

Both the emitters are concentrically segmented into three sections with the outer diameters of 2 cm (first electrode), 5.2 cm (second electrode), and 10 cm (third electrode), each of which is electrically isolated. When each section of the electron emitter is individually biased, the radially-different plasma potential, or radial electric field is expected to be generated even in the fully-ionized collisionless plasma. This electric field causes the E×B flows and flow shears perpendicular to the magnetic-field lines. Voltages applied to the electrodes set in order from the center to the outside are defined as $V_{ee1}, V_{ee2}, V_{ee3}$, respectively. On the other hand, the parallel K^+ flow with radially different energy, i.e., the parallel K^+ flow shear, is generated when each section of the segmented ion emitter is individually biased ($V_{ie1}, V_{ie2}, V_{ie3}$) at a positive value above the plasma potential that is determined by the bias voltage of the electron emitter. Therefore, these

author's e-mail: kaneko@ecei.tohoku.ac.jp

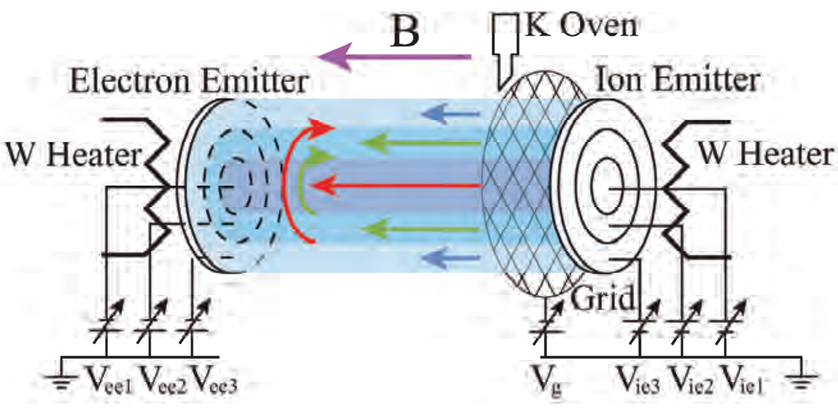

Fig. 1 Schematic of experimental setup.

parallel and perpendicular K^+ flow velocity shears can be superimposed by controlling the bias voltage of the ion and electron emitters independently. Here, V_{ee3} and V_{ie3} are always kept at 0 V. A small radially movable Langmuir probe and an electrostatic energy analyzer are used to measure radial profiles of plasma parameters and ion energy distribution functions parallel to the magnetic fields, respectively. Under our conditions, the plasma density is 10^9 cm^{-3}, the electron temperature is 0.2 eV, and the ion temperature is almost the same as the electron temperature. A background gas pressure is less than 10^{-6} Torr.

3 Experimental Results

At first, we demonstrate the independent control of the parallel and perpendicular K^+ flow velocity shears and the superposition of these shears. Figure 2 shows the plasma potential ϕ (closed circles) and the K^+ flow energy E_{K^+} (open circles) at the radial center r = 0 cm of the plasma column as functions of V_{ie1} and/or V_{ee1}, where V_{ie2} and V_{ee2} are fixed at 5.0 V and −2.0 V, respectively. When V_{ie1} is changed at constant $V_{ee1} = -2.2$ V [Fig. 2(a)], the K^+ flow energy is found to increase in proportion to V_{ie1}, while the plasma potential is almost constant at $\phi = -5.5$ V. Since the K^+ flow energy and the plasma potential in the second electrode region are confirmed to have constant values of 7 eV and −5.5 V, respectively, only the parallel flow velocity shear can be generated in the boundary region between the first and second electrodes by changing V_{ie1}.

When V_{ie1} and V_{ee1} are simultaneously changed keeping the bias-voltage difference $V_{ie1} - V_{ee1}$ constant [Fig. 2(b)], on the other hand, the K^+ flow energy does not change, while the plasma potential is found to increase in proportion to V_{ee1}. This result denotes that the parallel shear does not change as far as $V_{ie1} - V_{ee1}$ is constant, and the radial plasma potential difference, i.e., the perpendicular flow velocity shear can be con-

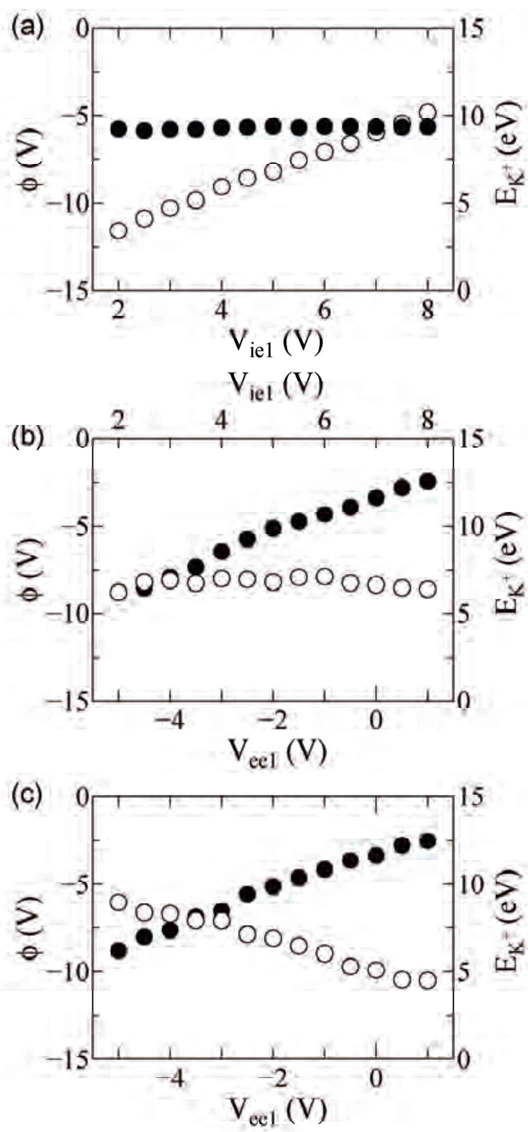

Fig. 2 Plasma potential ϕ (closed circles) and K^+ flow energy E_{K^+} (open circles) as functions of (a) V_{ie1}, (b) V_{ie1} and V_{ee1}, and (c) V_{ee1}. $r = 0$ cm, $V_{ie2} = 5.0$ V, $V_{ee2} = -2.0$ V.

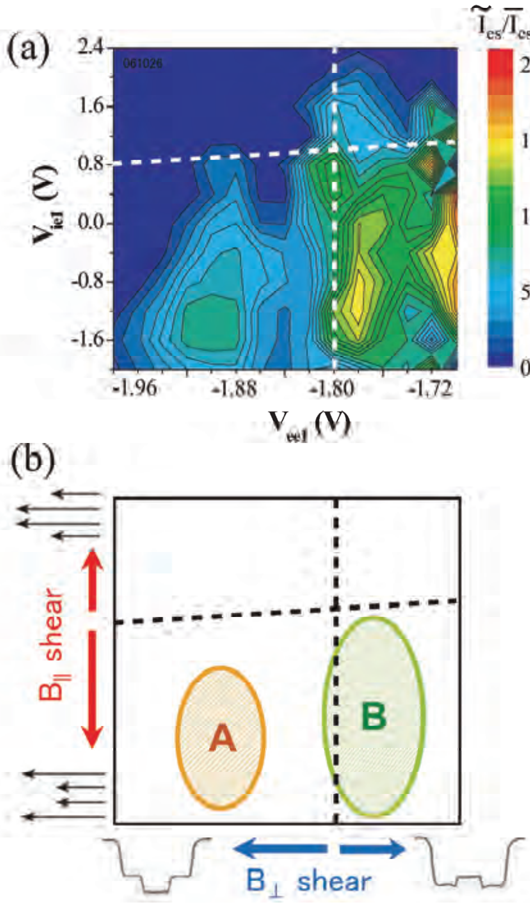

Fig. 3 Contour views of normalized fluctuation amplitudes as functions of V_{ie1} and V_{ee1}. r = 1.5 cm. $V_{ie2} = 1.0$ V, $V_{ee2} = -2.0$ V.

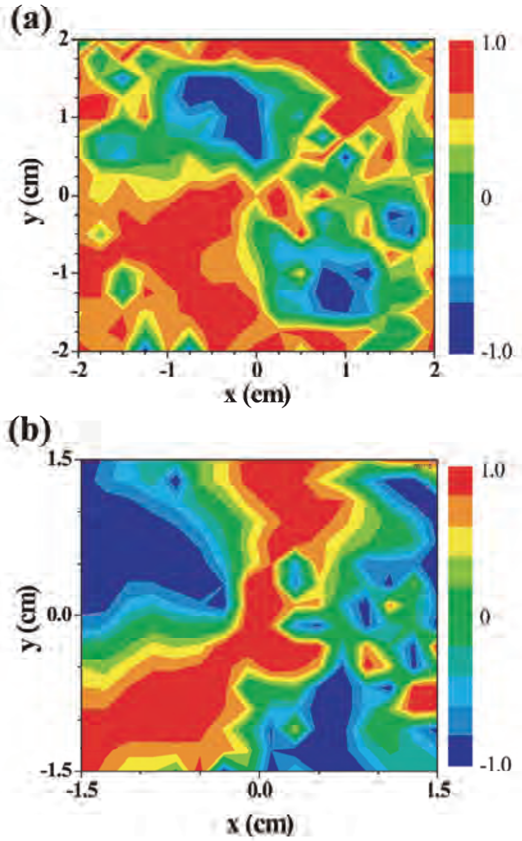

Fig. 4 2-dimensional profile of fluctuation phase θ which is plotted as $\sin\theta$ for (a) fluctuation A ($V_{ee1} \simeq -1.90$ V) and (b) fluctuation B ($V_{ee1} \simeq -1.78$ V). $V_{ie1} = -1.0$ V, $V_{ie2} = 1.0$ V, $V_{ee2} = -2.0$ V.

trolled by the bias voltages of the electron emitter. Since the parallel and perpendicular shears are now able to be controlled independently, we attempt to superimpose these shears.

Figure 2(c) presents the plasma potential and the K^+ flow energy as a function of V_{ee1} at constant $V_{ie1} = 5$ V. In this case, the plasma potential is directly changed by V_{ee1}, and the K^+ flow energy is also changed by V_{ee1}, because the bias-voltage difference $V_{ie1} - V_{ee1}$ decreases with an increase in V_{ee1} for the fixed V_{ie1}. Based on these results, the superposition of the parallel and perpendicular flow velocity shears is realized by controlling the V_{ie1} and V_{ee1} simultaneously. These parallel and perpendicular shears are found to give rise to several types of low-frequency instabilities. Here, we concentrate on the drift-wave instability which is excited in the density gradient region around $r = 1.0 \sim 1.5$ cm.

Figure 3(a) shows a contour view of normalized fluctuation amplitudes $\tilde{I}_{es}/\bar{I}_{es}$ obtained from frequency spectra of an electron saturation current I_{es} of the probe as functions of V_{ie1} and V_{ee1} for $V_{ie2} = 1.0$ V and $V_{ee2} = -2.0$ V. Schematic model of the parallel and perpendicular shears introduction is shown in Fig. 3(b), where black arrows described at ordinate axis mean the parallel ion flow velocity and solid curves described at abscissa axis mean the radial potential profiles, which are controlled by V_{ie1} and V_{ee1}, respectively, corresponding to the variation of the parallel and perpendicular flow velocity shears. Here, horizontal and vertical dotted lines in Fig. 3 denote the situations in the absence of the parallel and perpendicular shears, respectively, which are confirmed by the actual measurements of the ion flow energy and the space potential.

In the case that the perpendicular shear is not generated at $V_{ee1} = -1.8$ V, the fluctuation amplitude of the drift-wave instability is observed to increase with increasing the parallel shear strength by changing V_{ie1} to the negative value from 1.0 V, but the instability is found to be gradually stabilized when the shear strength exceeds the critical value. The destabilizing and stabilizing mechanisms are well explained by a plasma kinetic theory including the effect of radial density gradient [5]. When the perpendicular shear is superimposed on the parallel shear, the drift wave excited by the parallel shear is found to be suppressed by the perpendicular shear independently of the sign of the perpendicular shear. Furthermore, we can observe two characteristic fluctuation peaks depending on the perpendicular shear strength as presented in the contour views [Fig. 3(a)], which are defined as fluctuations A and B as described in the schematic model [Fig. 3(b)].

To readily identify the azimuthal component of each fluctuation's wavevector, we measure 2-dimensional (x, y) profiles of fluctuation phase in the plasma-column cross section. The phase is measured with reference to a spatially fixed Langmuir probe located at an axial distance of 26 cm from the 2-dimensionally translatable probe. Figure 4 presents the 2-dimensional phase profiles for (a) fluctuation A and (b) fluctuation B. Since the phase difference θ between the 2-dimensional probe and the reference probe is plotted as $\sin\theta$, red (1.0) and blue (-1.0) indicate the phase of $+\pi/2$ and $-\pi/2$, respectively, relative to the reference probe. Green corresponds to zero and π relative phase. In the case of the small perpendicular shear strength, i.e., fluctuation B [Fig. 4(b)], the azimuthal mode is found to be $m = 3$. On the other hand, in the presence of the relatively large perpendicular shear, i.e., fluctuation A [Fig. 4(a)], the azimuthal mode changes into $m = 2$. The perpendicular shear can modify the azimuthal mode number depending on its strength.

For these two kinds of drift waves, we measure the dependence of fluctuation amplitudes on the parallel shear strength, which are obtained from Fig. 3(a). As a result, with an increase in the parallel shear strength, it is found that $m = 3$ mode ($V_{ee1} \simeq -1.78$ V) first excited and $m = 2$ mode ($V_{ee1} \simeq -1.90$ V) needs strong parallel shear strength to excite the mode. These phenomena can be explained by the theoretical calculation that the growth rate of the parallel-shear excited drift wave sensitively depends on the azimuthal wave number, i.e., mode number [6]. Therefore, the superposition of the parallel and perpendicular shears can affect the characteristics of the drift wave through the variation of the azimuthal mode number.

4 Conclusions

The independent control of parallel and perpendicular flow velocity shears in magnetized plasmas is realized using a modified plasma-synthesis method with segmented plasma sources. The ion flow velocity shear parallel to the magnetic-field lines is observed to destabilize the drift-wave instability depending on the strength of the parallel shear. On the other hand, when the perpendicular shear is superimposed on the parallel shear, the drift wave of $m = 3$ is found to change into that of $m = 2$, and the instability is suppressed for strong perpendicular shears. The superposition of these shears can affect the characteristics of the drift wave through the variation of the azimuthal mode number.

Acknowledgments

The authors are indebted to H. Ishida for his technical assistance. We also express our gratitude to Professor M. Koepke and Dr. G. Ganguli for their useful comments and discussion. This work was supported by a Grant-in-Aid for Scientific Research from the Ministry of Education, Culture, Sports, Science and Technology, Japan.

References

[1] E. Agrimson, N. D'Angelo, and R.L. Merlino, Phys. Rev. Lett. **86**, 5282 (2001).

[2] C. Teodorescu, E. W. Reynolds, and M. E. Koepke, Phys. Rev. Lett. **88**, 185003 (2002).

[3] C. Teodorescu, E.W. Reynolds, and M.E. Koepke, Phys. Rev. Lett. **89**, 105001 (2002).

[4] E. Agrimson, S.-H. Kim, N. D'Angelo, and R. L. Merlino, Phys. Plasmas **10**, 3850 (2003).

[5] T. Kaneko, H. Tsunoyama, and R. Hatakeyama, Phys. Rev. Lett. **90**, 125001 (2003).

[6] T. Kaneko, E.W. Reynolds, R. Hatakeyama, and M.E. Koepke, Phys. Plasmas **12**, 102106 (2005).

[7] R. Hatakeyama and T. Kaneko, Phys. Scripta **T107**, 200 (2004).

[8] T. Kaneko, Y. Odaka, E. Tada, and R. Hatakeyama, Rev. Sci. Instrum. **73**, 4218 (2002).

Proceedings of ITC/ISHW2007

Strong Shear Formation by Poloidal Chain of Magnetic Islands

Vasyl .I. Maslov[1], Franco Porcelli[2]

[1]*NSC Kharkov Institute of Physics and Technology, Kharkov 61108, Ukraine*

[2]*Politecnico di Torino, Turin, Italy*

(Received day month year / Accepted day month year should be centered 10-point type)

We estimate the electron angular velocity shear $\partial_r \omega_{\theta o}$ which can be formed due to plasma heating near the low order rational surface with poloidal chain of magnetic islands (MIs). We suppose that the electrons are heated sufficiently that they propagate without collisions around torus. Then the plasma electrons start to miss the MIs during their radial shift. This provides ion volume charge in some region of MIs. Then the essential shear is formed. The time of shear formation is small. The conditions on MI width are derived, at which it leads to strong shear. It is shown that even narrow MIs can lead to shear. Shear can damp instabilities with growth rate smaller than ion cyclotron frequency.

The spatial structures of some convective cells have been described. We derive inverse dependences of radial width of excited vortices on $\partial_r \omega_{\theta o}$ and on $\partial_r n_{0e}$. Amplitude of the electron radial oscillations is smaller for larger $\partial_r \omega_{\theta o}$ and $\partial_r n_{0e}$. These dependences promote abrupt plasma density profile and internal transport barrier.

Keywords: internal transport barrier, shear, magnetic island, vortex, rational surface, radial electrical field

1. Introduction

Now ITB formation is widely investigated (see [1-3]). Earlier the effect is considered, that shear of the electron angle velocity $\partial_r \omega_{\theta o}$ damps anomalous transport, separating the coherent ordered motion owing the relative movement of layers. ITB is formed for under-threshold shear. We consider one more effect of anomalous transport suppression in plasma, located in crossed magnetic $\vec{H}_0$ and electrical $\vec{E}_{0r}$ fields. Namely, the shape of vortices is described. The exact nonlinear eq., connecting the electron vorticity and density, is derived in vector view without any approximations. We derive inverse dependences of radial width of some excited vortices on the shear $\partial_r \omega_{\theta o}$ in crossed fields and on degree of steepness of the plasma density profile $\partial_r n_{0e}$. These dependences promote abrupt plasma density profile and ITB formation. The amplitude of the vortex saturation is inversely proportional to the shear. It also promotes ITB formation, suppressing the transport especially in the case of small magnetic shear. It is determined by that small magnetic shear leads to large spatial interval Δ between rational surfaces [4]. If radial correlation length of excited perturbations becomes less than Δ the radial transport could be suppressed. The convective-diffusion equation, describing transport of plasma particles in the field of lattice of overlapped vortices, is derived.

Formation [5, 6] and role (see [4, 7, 8]) of MIs in nuclear fusion plasma are investigated now intensively. In particular, their effect on ITB formation is very important. It is shown that due to sufficient plasma electron heating near the rational surface with the poloidal chain of MIs, that they become to propagate approximately without collisions around torus, electrons start to miss MIs and in consent with [7] the essential shear is formed. The time of shear formation is derived and shown to be small.

The conditions on MI width are derived, at which it leads to essential shear formation. The condition on MI width is known, at which it does not lead to anomalous transport on trapped particles. For that the island should be narrow. It is shown that even narrow island can lead to essential shear. One can note that several poloidal chain of islands are better for ITB formation as in [7].

It is shown that this shear can damp instabilities with growth rate γ smaller than ion cyclotron frequency $\gamma < \omega_{ci}$.

There are some effects, connected with shear. At strong anomalous transport, when it is determined by a streamer, formed by single wide vortex, which one

author's e-mail: vmaslov@kipt.kharkov.ua

overlaps all inhomogeneous area, the shear mince vortices. It leads to intermediate ITB formation. But in this case some anomalous transport remains after ITB formation [1]. At not strong anomalous transport, determined by lattice of vortices, the shear can spatially separate vortices. In this case the strong ITB is formed.

2. Spatial structure of vortical convective cells

Let us describe some chain on azimuth θ of the vortices in the plasma, located in crossed $\vec{H}_0$ and $\vec{E}_{r0}$ fields. Neglecting nonstationary and nonlinear on electric potential ϕ of vortices members, from electron motion eq. one can obtain at small $\delta r \equiv r - r_v$ deviations r from radial position of vortices r_v, eq., describing oscillatory dynamics of electrons in the field of the perturbation

$$(\delta r)^2 + 4\left(e\phi - \delta p_e / n_e(r_v)\right) \Big/ r_v m_e \omega_{ce}(r_v) \partial_r \omega_{\theta o}\Big|_{r=r_v} = C \,. \quad (1)$$

$$\omega_{\theta o} \equiv V_{\theta o}(r)/r$$

$$\vec{V}_{\theta 0} = -e\left[\vec{e}_z, \vec{E}_{ro}\right] \Big/ m_e \omega_{ce} - \left[\vec{e}_z, \vec{\nabla} p_{0e}\right] \Big/ n_e m_e \omega_{ce} \,,$$

δp_e is the electron density perturbation. (1) describes the radial electron oscillations $\delta r \equiv r - r_v$ through dependences of $\phi(\theta, r)$ and electron density perturbations $\delta n_e(\theta, r)$ on θ and r. Let us connect $e\phi - \delta p_e / n_e(r_v)$ with characteristic of electron vortical movement $\alpha \equiv \vec{e}_z \mathrm{rot} \vec{V}_e$. From electron eq. of motion we derive

$$\alpha / V_{thi} \rho_{ci} = e\Delta\varphi / T_e - \Delta n_e / n_e \quad (2)$$

For vortex with dimension ρ_{ci} we have $\alpha < \omega_{ci}$ and $e\varphi/T_e - \delta n_e / n_e \approx \alpha / \omega_{ci}$. One can see that the amplitude of the radial oscillations of the electrons for the given amplitudes of the electrical potential and density perturbation is smaller for larger shear $\partial_r \omega_{\theta o}$. The latter helps the ITB formation.

In crossed fields the vortices can be with phase velocity $V_{ph} \approx V_{\theta 0}$, as well as slow vortices $V_{ph} << V_{\theta 0}$, for example of Rossby kind. Let us derive the spatial structure of slow vortex. For this purpose one can derive similar to [9] without any approaches general nonlinear vectorial equation, describing vortical electron dynamics

$$d_t\left(\frac{\vec{\alpha} - \vec{\omega}_{ce}}{n_e}\right) = \frac{1}{n_e}\left(\left(\vec{\alpha} - \vec{\omega}_{ce}\right)\vec{\nabla}\right)\vec{V} \quad (3)$$

$\vec{\alpha} = \left[\vec{\nabla} \times \vec{V}\right]$, $d_t \equiv \partial_t + \left(\vec{V}\vec{\nabla}\right)$. From it one can obtain eq., describing the vortex of the small amplitude. Hence we derive for perturbation of electron trajectory in the field of the vortex

$$\delta r(\theta, r) = -\frac{1}{\omega_{ceo} \partial_r \left(n_{oe}/\omega_{ce}\right)} \delta n_e(\theta, r) \,. \quad (4)$$

From here one can see that at the same amplitude of plasma density perturbation δn_e the vortex is narrower in radial direction for larger $\partial_r\left(n_{oe}/\omega_{ce}\right)$, i.e. for more abrupt plasma density profile. The latter helps ITB formation.

The vortex is excited up to the amplitude, at which the layers, trapped by it, during excitation time γ^{-1} are shifted relative to each other due to shear on the angle not larger $2\pi/\ell_\theta$, i.e. $\delta r_v \left(\ell_\theta / 2\pi\right) \partial_r \omega_{\theta 0}\Big|_{r=r_v} \le \gamma$. Here ℓ_θ is the azimuth wave number of excited vortices. From this expression we derive

$$\left|e\phi_o - \delta p_{e0}/n_e(r_v)\right| = \left(\gamma\pi/\ell_\theta\right)^2 r_v m_e \omega_{ce} \Big/ 2\left|\partial_r \omega_{\theta o}\right|_{r=r_v}\Big| \quad (5)$$

The amplitude of the vortex saturation is inversely proportional to $\partial_r \omega_{\theta 0}$. The decrease of level of fluctuations at ITB formation has been observed in [3]. It promotes ITB formation.

3. Convective – diffusion equation

Let us consider the finite amplitudes, when frequency Ω_r of the electron oscillations, forming the vortex, in its field becomes larger than the growth rate γ of the excitation $\Omega_r > \gamma$. Then in vicinity of the vortex borders the jumps on electron density profile $n_e(r)$ are formed. Hence, on these n_e jumps new cells with the greatest growth rates are excited. It results in ordering of convective cells. Therefore at achievement of the large amplitudes the instability is developed for ordering of cells similar investigated in [10]. Inside borders of a vortex ordered convective movement of the electrons occurs. However, they are influenced by environmental vortex fields and fluctuations. Also it is important that amplitudes of vortexes are not stationary. Instead of average $n_{oe}(t,r)$, which does not take into account correlations, we use four densities of the electrons $n_{ke}(t,r)$ average on small-scale oscillations: $n_{1e}(t,r)$ ($n_{2e}(t,r)$) is the average density of the electrons, located in region 1 in depth of a cell on $r>r_v$ (in region 2 in depth of a cell on $r<r_v$); $n_{3e}(t,r)$ ($n_{4e}(t,r)$) is the average density of the electrons, placed in region 3 near border of a cell on $r>r_v$ (in region 4 near border of a cell on $r<r_v$). The importance of use of different $n_{ke}(t,r)$ is also determined by that angular speeds of electron rotation inside a cell are different in dependence on distance from its axis. Also in central area of the convective cell the following processes are still realized: plateau formation on $n_e(r)$ due to difference of angular speeds of electron rotations; due to jump formation on $n_e(r)$ at the certain moments of time in the regions 1 and 2 there is an accelerated diffusion and an exchange by electrons between regions 1 and 3 (factor α), and also between regions 2 and 4. α is the factor of mixing also due to influence of fluctuations, growth of amplitudes, differences of characteristic times of the electrons.

But at ordering the adjacent cells form integrated border. The particle in space between individual cell border and integrated border move in radial direction from cell to cell for the distance $\min\{\ell_{cor}, \delta r_v \tau_{cor} \Omega_r / \pi\}$. ℓ_{cor}, τ_{cor} are the correlation length and time of vortical convective cell turbulence.

From the above we have approximately

$$n_1(t+\tau, r) = (1-\alpha) n_2(t, r) + \alpha\beta n_3(t, r)$$

$$n_2(t+\tau, r) = (1-\alpha) n_1(t, r) + \alpha\beta n_4(t, r) \quad (6)$$

author's e-mail: vmaslov@kipt.kharkov.ua

$$n_3(t+\tau, r) = \alpha n_1(t, r) + \beta(1-\alpha) n_3(t, r-\delta r_v) + $$
$$+ 0.5(1-\beta)[n_3 + n_4]$$

$$n_4(t+\tau, r) = \alpha n_2(t, r) + \beta(1-\alpha) n_4(t, r+\delta r_v) + $$
$$+ 0.5(1-\beta)[n_3 + n_4]$$

β is the factor of the convective exchange of cells by particles. The value of β is determined by ratio of the area with convective electron dynamics, located between individual cell borders and integrated borders to all area, located between individual cell borders and integrated borders of adjacent cells. From these equations, entering $\bar{n} = (n_3 + n_4)/2$, $\delta n = n_3 - n_4$, $\bar{N} = (n_1 + n_2)/2$, $\delta N = n_1 - n_2$, we derive

$$\tau\partial_t \bar{n} = \alpha(\bar{N} - \beta\bar{n}) - (\beta/2)(1-\alpha)\delta r_v \partial_r \delta n$$
$$\tau\partial_t \delta n + [1 - \beta(1-\alpha)]\delta n = \alpha\delta N - 2\beta(1-\alpha)\delta r_v \partial_r \bar{n} \qquad (7)$$
$$\tau\partial_t \bar{N} = \alpha(\beta\bar{n} - \bar{N}), \quad \tau\partial_t \delta N + (2-\alpha)\delta N = \alpha\beta\delta n$$

One can see that introduction $\bar{n}$ is similar to average $n_{oe}(t,r)$ but with taking into account correlations. From these equations we have similar to [10] the following convective – diffusion equation

$$\tau^2\partial_t^2 \delta n + \tau\partial_t[(1-\beta(1-\alpha))\delta n - \alpha\delta N] =$$
$$= -2\beta(1-\alpha)\delta r_v \partial_r \left[\alpha(\bar{N} - \beta\bar{n}) - \frac{\beta}{2}(1-\alpha)\delta r_v \partial_r \delta n\right] \qquad (8)$$

As β is proportional to $(\delta r_v - \Delta)/\delta r_v$ then at $\delta r_v < \Delta$ we have $\beta = 0$ and there is no convective radial transport because convective cell exchange by particles disappears.

4. Shear formation by magnetic islands

Let us consider the shear formation near the poloidal chain of narrow magnetic islands. The electrical field E_{r0} is approximately equal to zero on the axis of a plasma column. It receives maximum value inside a plasma column at $r = r_m$. We suppose, that on a some interval $0 < r < r_m$ (r_0-δR<r<r_0+Δr+δR around chain of MIs, located in r=r_0+Δr/2 with radial width Δr, r_o is the lower border of island) on radius r the electrical field E_{r0} in the case of shear absence is proportional to $E_{r0} \propto r$. Then on this interval it is possible to present

$$E_{r0} = -2\pi e N_0 r, \ 0 < r < r_m, \ N_0 \equiv n_e - n_i. \qquad (9)$$

It means, that there is no shear $\omega_{\theta 0} \neq \omega_{\theta 0}(r)$. One can take into account effect of oscillations on electron transport by effective collision frequency ν_{ef} in diffusion coefficient $D_\perp \propto (\nu_e + \nu_{ef})$. ν_e is the electron collision frequency

On the plasma cross-section $0 < r < R$ several chains of magnetic islands can exist [7]. But we for the simple case consider influence of one poloidal chain of islands on shear formation. We consider low order rational magnetic surface, because important property of this surface is appeared, when plasma is heated sufficiently that its electrons perform several rotation around toroidal surface during free pass time. The shear formation at

$$2\pi r_{tor}\nu_e < V_{the} \qquad (10)$$

[7] is considered near this surface. V_{the} is the electron thermal velocity, moving near this surface. According to [4, 7] we consider local plasma heating near this surface. The local heating leads to important effect: inequality (10) becomes to be satisfied more easier.

If condition (10) is satisfied the electrons starts to miss the island. The part of the electrons, located in the island, escapes its, up to reaching E_r to zero inside it, except for the layer of width

$$\delta r_{sep} \approx 2\pi n r_{tor}\sqrt{D_\perp / D_\parallel} \approx \rho_{ce}\sqrt{(\nu_e + \nu_{ef\perp}) / (\nu_e + \nu_{ef\parallel})}$$

near r=r_0. $D_\perp$, $D_\parallel$ are the transversal and longitudinal diffusion coefficients, $\nu_{ef\perp}$ and $\nu_{ef\parallel}$ are the transversal and longitudinal effective collision frequencies. When part of the electrons escapes the magnetic island, in the region of the island the plasma ion volume charge n_i are not compensated by electrons on δn. δn can be determined from observed in experiment condition, that in the island $E_{r0} \approx 0$ is approximately established.

Let us consider shear formation near chain more in detail. In the case (10) the electron transport through MIs changes from slow collisional to quick one. Electrons miss MI. Though the radial size of MI is small the quick electron transport leads to appearance of strong uncompensated ion volume charge in MI and to the strong shear $\partial_r \omega_{\theta o}$.

That in the region of the magnetic island the uncompensated ion volume charge appears it is necessary that its width Δr should be larger $\Delta r > \rho_{ce}$ in comparison with the electron cyclotron radius.

Let us consider radial electron dynamics in small neighborhood of the chain of islands. The electrons move in radial direction in crossed $\vec{E} \times \vec{H}$ fields with velocity $V_{0r} = -(eE_{or} + \partial_r p_{0e}/n_e)(\nu_{ef} + \nu_e)/m_e\omega_{ce}^2$. When electron reaches with V_{0r} island from the side of small r, it propagates collisionally through island in the case $2\pi r_{tor}\nu_e >> V_{the}^{(hot)}$. But in the case $2\pi r_{tor}\nu_e << V_{the}^{(hot)}$ electron without collision quickly, during the time $2\pi r_{tor}/V_{the}^{(hot)}$ get on the second boundary of the island. After that electron again slow propagates with velocity V_{0r} in the direction of large r.

Thus at $2\pi r_{tor}\nu_e < V_{the}^{(hot)}$ near the island the shear is formed. Using approximation of poloidal chain of narrow MIs as a azimuth symmetrical narrow layer we have for the radial electric field distribution

$$E_{r0} \approx -2\pi e \begin{cases} N_a r, \ 0 \le r \le r_0 \\ N_a r_0^2/r - \delta n(r - r_0^2/r), \ r_0 \le r \le r_0 + \delta r_{sep} \\ 0, \ r \ge r_0 + \delta r_{sep} \end{cases} \qquad (11)$$

If the field is small $E_{r0} \approx 0$ at $r = r_0 + \delta r_{sep}$, we have $N_a \approx 2\delta n \delta r_{sep}/r_0$. One can see that the density of uncompensated plasma ion volume charge is relative large in the island $r_0 >> \Delta r$ if $E_r \approx 0$ at $r = r_0 + \delta r_{sep}$.

author's e-mail: vmaslov@kipt.kharkov.ua

One can use estimation $N_a \approx 4n_0(e\Delta\varphi/T_i)(r_{di}/L)^2$. L is the width of the region with essential E_r , $\Delta\varphi$ is the potential on L. One can conclude that the island can be narrow for essential shear formation

$$(e\Delta\varphi/T_i)(r^2_{di}/L\delta r_{sep})<1 . \qquad (12)$$

This inequality means that in real island the small ion volume charge uncompensation $\delta n << n_0$ is sufficient for essential shear formation.

Let us calculate shear of the electric field and normalize it on the electric field $E_r = -2\pi eN_0 r$ in shear absence $S \equiv \left(E_r\big|_{no\ TB}\right)^{-1} r^2\partial_r(E_r/r)$. If $E_r\big|_{r=r_0+\delta r_{sep}} \approx 0$ we have

$$S = \begin{cases} (N_a/N_0)(r_0^2/r^2)(2 + r_0/\delta r_{sep}), & r_0 \le r \le r_0 + \delta r_{sep} \\ 0, & r \ge r_0 + \delta r_{sep} \end{cases} \qquad (13)$$

The shear is large for region of narrow magnetic islands $r_0 >> \Delta r > \delta r_{sep}$

$$S \approx (N_a/N_0)(r_0/\delta r_{sep}), \quad r_0 \le r \le r_0 + \delta r_{sep}. \quad |S| >> 1 \qquad (14)$$

Really, in experiment [7] the decrease of correlation of plasma density fluctuations were observed.

Let us consider the shear of $\omega_{\theta 0} = V_{\theta 0}/r$

$$V_{\theta 0} = (m_e\omega_{He})^{-1}(-eE_{r0} - \partial_r p_{0e}/n_{0e}), \qquad (15)$$

as for ITB formation this shear $\partial_r\omega_{\theta 0}$ is more important. We determine the angular velocity shear

$$S_\omega \equiv \left(\omega_{\theta 0}\big|_{no\ TB}\right)^{-1} r\partial_r\omega_{\theta 0}, \quad \omega_{\theta 0}\big|_{no\ TB} = (\omega_{pe}^2/\omega_{He})(N_0/2n_0)$$

Then we derive

$$S_\omega = -\begin{cases} (N_a/N_0)(r_0^2/r^2)(2 + r_0/\delta r_{sep}), & r_0 \le r \le r_0 + \delta r_{sep} \\ 0, & r \ge r_0 + \delta r_{sep} \end{cases}$$

Absolute value of the relative angular velocity shear is of order of $S_\omega = -(N_a/N_0) r_0/\delta r_{sep}$. But absolute shear can be increased. In several experiments the strong localization of the region with $V_{0\theta} \ne 0$ has been observed. As in experiments the radial width Δr_{sh} of area $V_{0\theta} \ne 0$ localization $\Delta r_{sh} = 1\text{cm}$ is observed, the shear $(\partial_r V_{0\theta})_{apr}$ can be increased in existing nuclear fusion installations in comparison with smooth case $(\partial_r V_{0\theta})_{smooth} \approx V_{0\theta}/R$ almost in 100 times $(\partial_r V_{0\theta})_{apr} \approx V_{0\theta}/\Delta r_{sh} \approx (\partial_r V_{0\theta})_{smooth} R/\Delta r_{sh}$.

The shear is formed during

$$\tau_{TB} \approx (\nu_{ef} + \nu_e)^{-1}(\omega_{ce}^2/2\omega_{pe}^2)(r_0/\Delta r) \qquad (16)$$

the short time for not very narrow MI.

Narrow islands, though provide a fast electron transport through island dimension Δr , strong suppress transport in broad their neighborhood. Really in experiment [4] $\Delta r << R$.

In the island, placed on rational surface with numbers n, m the uncompensated ion volume charge has appeared at $(\Delta r)^2/D_\perp > (2\pi n r_{tor})^2/D_\parallel$. r_{tor} is the toroidal radius. Hence the island should be wider

$$\max\{\rho_{ce}, 2\pi n r_{tor}\sqrt{D_\perp/D_\parallel}\} < \Delta r . \qquad (17)$$

$D_\perp/D_\parallel = (\nu_{ei} + \nu_{ef\perp})(\nu_{ei} + \nu_{ef\parallel})/\omega_{ce}^2$ <<1. But for ITB formation the island should be narrow [11]

$$\Delta r << R .$$

Let during free pass time the electron has time to make q rotations around the torus. Then

$$\max\{\rho_{ce}, (n\rho_{ce}/q)\sqrt{(1+\nu_{ef\perp}/\nu_{ei})(1+\nu_{ef\parallel}/\nu_{ei})}\} < \Delta r . \qquad (18)$$

From obtained expressions and from condition [1-3]

$$L\partial_r\omega_{\theta 0} > \gamma \qquad (19)$$

using

$$\Delta\varphi \approx 2\pi eN_a L^2 \qquad (20)$$

one can show

$$(\Delta\varphi e/T_i)(\rho_{ci}^2/L\delta r_{sep}) > \gamma/\omega_{ci} \qquad (21)$$

that shear can damp low-frequency instabilities with growth rate $\gamma < \omega_{ci}$.

5. Conclusions

It is shown that the amplitude of the radial electron oscillations is smaller or the vortex is narrower in radial direction for larger shear $\partial_r\omega_{\theta o}$ and for more abrupt plasma density profile in nuclear fusion plasma. The latter helps ITB formation. The amplitude of the vortex saturation is inversely proportional to $\partial_r\omega_{\theta o}$. It also promotes ITB formation. The convective-diffusion equation for electron transport has been derived.

It is shown that the value of the shear can be large. The shear is formed in consent with [7] due to plasma heating near the low order rational surface with poloidal chain of narrow magnetic islands. The plasma is heated up to such electron temperature that the electrons become to propagate approximately without collisions around torus. Small part of electrons leaves the island and the shear is formed. The time of shear formation is small. The conditions on island width is derived, at which it leads to shear formation. Even narrow island can lead to shear formation. The condition on island width is known, at which it does not lead to anomalous transport. This shear can damp instabilities with growth rate smaller than ion cyclotron frequency $\gamma < \omega_{ci}$.

References

1. J.W. Connor et al. Nucl. Fusion **44**, R1 (2004).
2. R.C.Wolf. Plasma Phys. Contr. Fus. **45**, R1 (2003).
3. A. Fujisawa. Plasma Phys. Contr. Fus. **45**, R1 (2003).
4. T. Shimozuma et al. Nucl. Fusion **45,** 1396 (2005).
5. F. Porcelli et al. Phys. Scr. **T107**, 153 (2004).
6. M Ottaviani et al. Plasma Phys. Contr. Fus. **46**, B201 (2004).
7. E.D.Volkov et al. Czech. J. Phys. **53**, 887 (2003).
8. K. Ida et al. Phys. Rev. Lett. **88**, 015002 (2002).
9. M.V. Nezlin, G.P. Chernikov. Plasma Phys. Rep. **21**, 975 (1995).
10. A.S. Bakai. Lett. ZhEThPh. **28**, 10 (1978).
11. B.B. Kadomzev, O.P. Poguze. Plasma Theory Questions /editor M.A. Leontovich. V. 5. M.: Atomizdat, 1967.

author's e-mail: vmaslov@kipt.kharkov.ua

Proceedings of ITC/ISHW2007

Ion Heating Experiments Using Perpendicular Neutral Beam Injection in the Large Helical Device

K. Nagaoka, M. Yokoyama, Y. Takeiri, K. Ida, M. Yoshinuma, S. Matsuoka[1)], H. Funaba, S. Morita, T. Mutoh, T. Seki, K. Ikeda, M. Osakabe, K. Tsumori, Y. Oka, O. Kaneko, and the LHD Experimental Group

National Institute for Fusion Science,322-6 Oroshi-cho, Toki 509-5292, Japan

[1)]Dep. Nuclear Engineering, Kyoto Univ., Kyoto 606-8501, Japan

(Received day month year / Accepted day month year should be centered 10-point type)

Perpendicular neutral beam (P-NB) injector was installed in the large helical device (LHD), and utilized for high-power ion heating and measurement of ion temperature profile by charge exchange spectroscopy. The ion heating experiments have a significant progress using P-NB, and the high-ion-temperature of 5.2keV was achieved at plasma center. The peaked profile of ion temperature with steep gradient of ion temperature was observed. The enhancement of toroidal flow was observed with the ion temperature rise in the core region. The transport analysis shows the improvement of anomalous transport in the core region, when the high ion temperature is realized.

Keywords: perpendicular NBI, ion heating, charge exchange spectroscopy, beam fueling, toroidal rotation, ion thermal transport

1. Introduction

Ion temperature is one of the most important parameters to realize burning plasmas in magnetically confined fusion plasmas.

Before 9th experimental campaigns of the large helical device (LHD), ion heating experiments were performed by tangential neutral beam (NB) injection. There are three beam lines of negative-ion-based NB with very high beam energy of 180keV, and total port-through beam power was beyond 13MW. However, such high energy beam over the critical energy (E_c~120keV for plasmas with T_e~4keV) mainly heats electrons, thus ion heating power was relatively low. In order to increase the net ion-heating power, the ion heating experiments were performed in the high-Z discharge, and the high-ion temperature of T_i=13keV was realized [1-2], showing high potential high-temperature plasma confinement in helical devices.

For ion heating experiment in low Z plasmas, low energy and high current NB was required, and perpendicular NB (P-NB) with low beam energy of 40keV and port-through power of 3MW was installed and started the beam injection in 9th experiment campaign of LHD, and the power was upgraded to 6MW at 10th experimental campaign [3]. The NB has a high ion-heating efficiency of 80% for plasmas with T_e=4keV, and the ion heating power was significantly increased in LHD.

The P-NB can be utilized for profile measurements of ion temperature by charge exchange spectroscopy (CXS) [4], thus ion heat transport can be experimentally estimated. Moreover, the P-NB has a high particle fueling rate due to the high beam current of 150A, and is also utilized for particle fueling and control of density profile. In this paper, recent results of high-ion-temperature experiment using P-NB in LHD are presented, and the density profile dependence of ion temperature, ion transport property, toroidal flow associated with high-ion-temperature are discussed.

2. Experimental

The LHD is a world-largest helical device with major radius of 3.9m and averaged minor plasma radius of 0.6m. The toroidal and poloidal periods are n=10 and m=2, respectively. The plasmas are heated by electron cyclotron resonance heating (ECH) of 2MW, ion cyclotron heating (ICH) of 2MW and three tangential negative-ion-based NBIs with total port-through power of 14MW. A perpendicular NBI with low energy of 40keV was installed in 5-O port of LHD in 2005. Four positive ion sources were mounted on the beam line and the total port-through power is 6MW. Two power supply systems (#4A and #4B) can independently control the beam operation such as pulse timing, beam energy, beam duration and so on. The nominal pulse duration is 10 sec, and the beam species is hydrogen. The beam injection with total port-through

author's e-mail: nagaoka@LHD.nifs.ac,jp

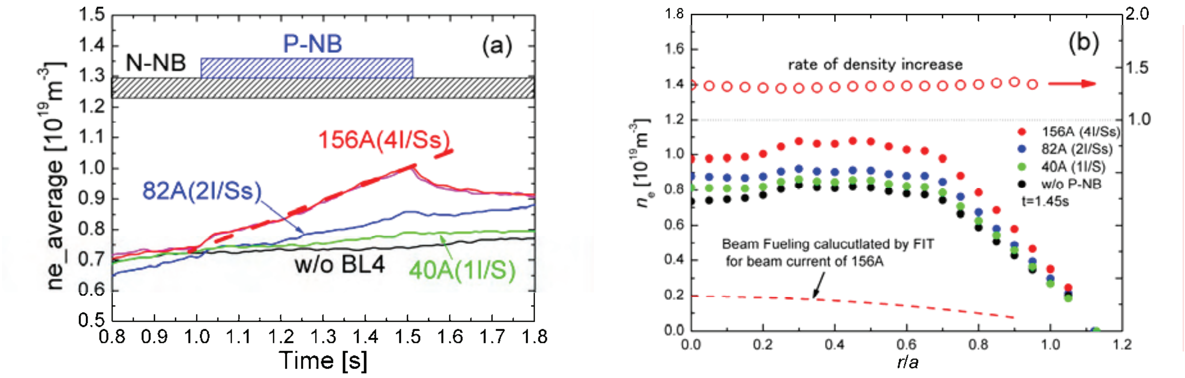

Fig. 1. (a) The response of line averaged electron density with P-NB injections. (b) The density profiles with P-NB injection of 0A, 40A, 82A and 156A. The profile of density increase is shown in upper region. The beam fueling rate calculated by FIT code is also shown in the bottom region, which is consistent with the observed density increase.

power of 7MW was achieved in 10th experimental campaign.

Two systems of active CXS were installed for the P-NB as a probe beam. One is toroidal system having toroidal line of sights and can measure profiles of ion temperature and toroidal rotation of the plasmas. The other is poloidal system having poloidal line of sights and can measure profiles of ion temperature and poloidal rotation of the plasmas. The P-NB is modulated (100msec ON and 100msec OFF) for CXS measurement to acquire the background signal.

3. Results and Discussions

A low beam energy and high current beam has a large particle fueling rate. In order to investigate beam fueling, the beam current of P-NB was performed by changing the number of operating ion source with the same gas condition. The electron density increases with the beam current, which is shown in Fig. 1(a) and the increase rate of $3x10^{16}m^{-3}s^{-1}A^{-1}$ or $2.3x10^{20}s^{-1}MW^{-1}$ was obtained. The change of the density profile and the profile of density increase rate are shown in Fig. 1(b). The density increase rate has a flat profile. The deposition profile is considered to be broad profile because of low density of the target plasma. The beam deposition calculated by FIT code, which is also shown in Fig. 1(b), is consistent with the experimental results.

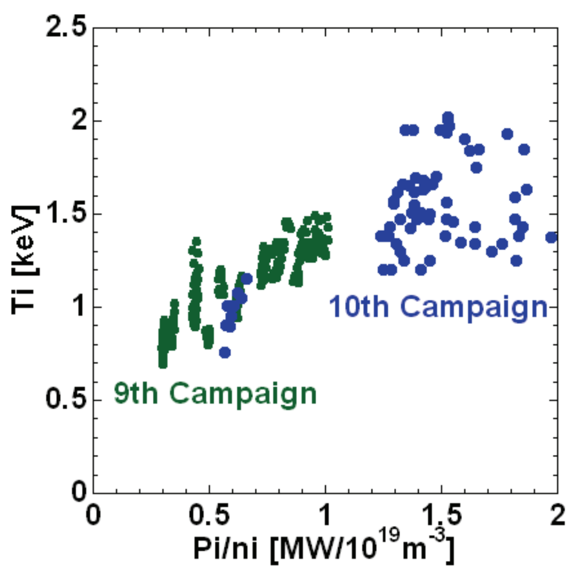

Fig. 2. The ion temperature as a function of ion heating power.

The P-NB power dependence of ion temperature was investigated in the plasmas heated by only P-NB. The maximum ion temperatures of each discharge are plotted in Fig. 2 as a function of ion heating power normalized by the ion density. In this figure, it is clearly seen that the ion temperature increases with ion heating power. It is also experimentally confirmed that the ion temperature increases with P-NB power in the other heating condition such as full power heating with tangential NBs.

The high ion temperature experiments using P-NB were performed and central ion temperature of 5.2keV was realized with the central electron density of $1.2x10^{19}m^{-3}$, which is shown in Fig. 3. The high ion temperature regime was extended toward high density plasmas, and the central ion temperature of 3keV was achieved with the central electron density of $3.2x10^{19}m^{-3}$. The central electron temperature is lower than ion temperature in low density region, indicating the strong ion heating. The electron and ion temperatures are almost same in high density region. This is considered to be attributable to short equi-partition time. These high ion temperature were realized in the

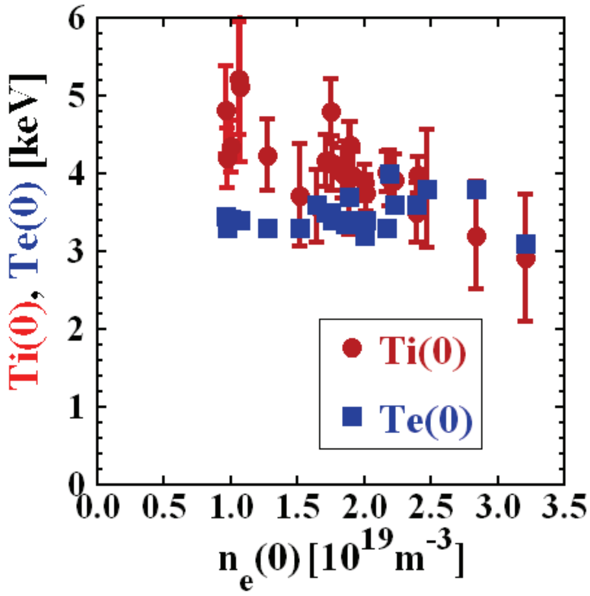

Fig. 3. The central ion temperature as a function of central electron density. The central electron temperature at the time with maximum ion temperature is also shown.

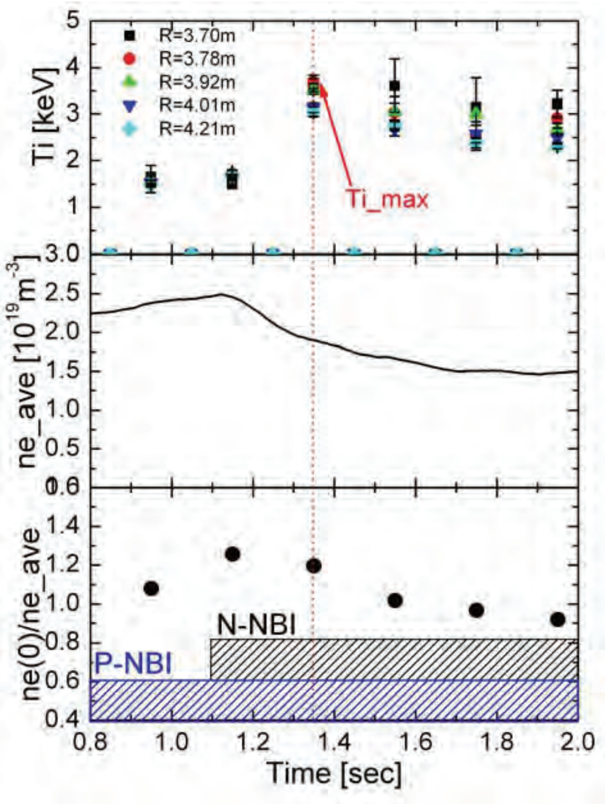

Fig. 4. The ion temperature (upper), line averaged electron density (middle) and a peaking factor (bottom) given by the central density normalized by the line averaged density are shown, respectively.

density decay phase after superimpose of tangential NBI on the P-NB heated plasmas. The time trace of ion temperature, line averaged electron density and the central density divided by line averaged density as a density peaking factor are shown in Fig. 4. After superimpose of tangential NBs heating (t=1.1sec), the electron density decreases, and the ion temperature increase and reaches the maximum values at t=1.35sec. Then the ion temperature starts to decrease gradually while the electron density continues to decrease. The peaking factor increases in the P-NB heating phase and decreases after superimpose of tangential NBs. This is a general tendency in LHD plasmas; the density profile becomes peaked one in P-NB heating plasmas and flat or hollow one in tangential NBs. The peaking factor of the electron density keeps still high value when ion temperature reaches the maximum, while the electron density decreases quickly. Therefore, it seems that the peaking factor of electron density is important for ion temperature rise and the peaked density profile is preferable to realization of high ion temperature.

Figure 5(a) shows the profiles of ion temperature at P-NB phase (t=0.95sec), maximum ion temperature phase (t=1.35sec) and after the decrease of ion temperature (t=1.75sec). The ion temperature has a peaked profile and a steep gradient is formed when ion temperature becomes high. The electron temperature is 4keV at the center and is almost same at R>4.2m when t=1.35sec. The large toroidal flow with velocity of 60km/sec was generated in the core region, when the high ion temperature was realized, which is shown in Fig. 5(b). The flow direction is consistent with that of tangential NB injection. These observations indicate strong correlation between ion transport and toroidal rotation. The poloidal rotation in core region can not be observed when ion temperature becomes high, because the carbon impurity has a strong hollow profile associated with ion temperature rise. This “impurity hole” also shows strong correlation with ion temperature rise. The outward flow of carbon impurity against a negative gradient of carbon density was also observed. The large error bars of ion temperature in core region with t=1.35sec in Fig 5(a) are attributable to formation of impurity hole. The neoclassical calculation shows negative radial electric field (ion root), while the impurity pumping-out can be expected by electron root in neoclassical theory. Therefore the understanding of impurity hole formation in the neoclassical ion root is a new subject related to the high-ion temperature experiments.

The neoclassical ion thermal diffusivity does not change significantly in core region [5], which is shown in Fig. 5(c), while ion temperature increases more than twice. In such a low collisional regime, the neoclassical ion flux without electric field strongly depends on ion temperature as $T_i^{7/2}$.

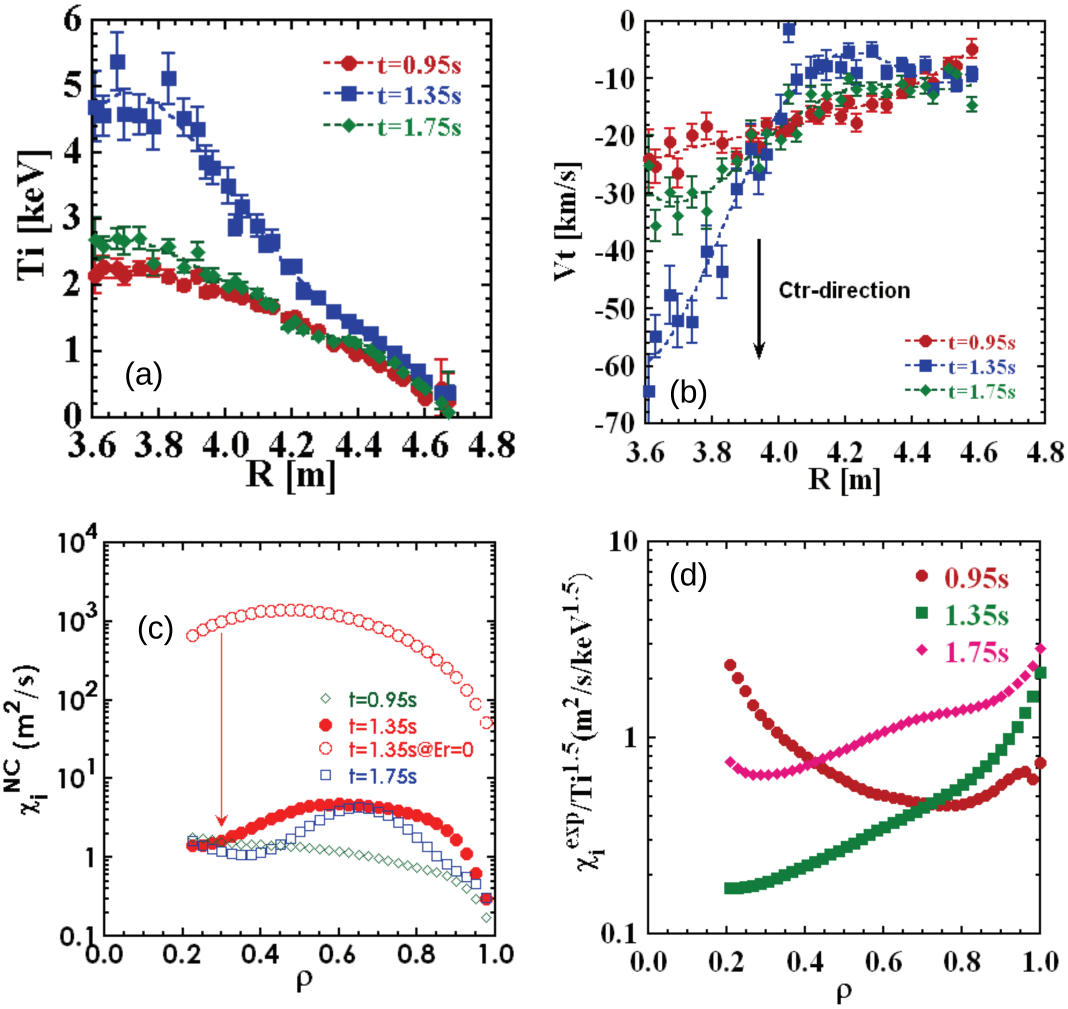

Fig. 5. (a) The profiles of ion temperature of the plasma heated by only P-NB (*t*=0.95sec), just after superimpose of N-NB (*t*=1.35sec) and mainly heated by N-NB (*t*=1.75sec). (b) The toroidal rotation profile at the same time with (a). (c) The neoclassical ion-thermal diffusivity w/ and w/o neoclassical ambipolar radial electric field. (d) The ion thermal diffusivity obtained by power balance analysis.

The degradation of ion transport is considered to be significantly suppressed by negative radial electric field. The neoclassical electron diffusivity also remains unchanged in high ion temperature phase. The ion thermal diffusivity normalized by gyro-Bohm factor, which is estimated by power balance analysis, is shown in Fig 5(d), and the significant reduction of thermal diffusivity was clearly observed in core region, when ion temperature increases. Therefore, it is considered that the reduction of anomalous transport occurs when ion temperature increases.

3. Conclusion

The installation of P-NB injection was significantly progressed high ion temperature experiments on LHD; one is upgrade of ion heating power, and the other is profile measurements of ion temperature, toroidal and poloidal flow, impurity density. The high ion temperature over 5keV was achieved and extended toward high density plasmas. The large toroidal flow and impurity hole were observed in core region associated with ion temperature rise. The negative radial electric field (neoclassical ion root) significantly suppresses the degradation of ion thermal diffusivity, and reduction of anomalous transport was observed in core region. These results are still preliminary and not fully understood yet. The systematic experimental study and neoclassical viscosity analysis are in progress.

References

[1] Y. Takeiri, *et al.*, Nucl. Fusion **47**, 1078 (2007).

[2] S. Morita *et al.*, 19th IAEA Fusion Energy Conference, Lyon, 2002, EX/P2-18.

[3] M. Osakabe, *et al.*, this conference.

[4] M. Yoshinuma, *et al.*, this conference.

[5] S. Matsuoka, *et al.*, this conference.

Proceedings of ITC/ISHW2007

Observation of Toroidal Flow on LHD

Mikirou Yoshinuma, Katsumi Ida, Masayuki Yokoyama, Kenichi Nagaoka, Masaki Osakabe and the LHD Experimental Group

National Institute for Fusion Science,322-6 Oroshi-cho, Toki, 502-5292, Japan

In order to investigate the formation of toroidal flow in helical systems, both NBI driven flow and spontaneous toroidal flow are observed in the Large Helical Device (LHD). The toroidal flow driven by NBI is dominant in the plasma core while the contribution of the NBI driven toroidal flow is small near the plasma edge. The spontaneous toroidal flow changes its direction from co to counter when the radial electric field is changed from negative to positive at the plasma edge. The direction of the spontaneous toroidal flow due to the radial electric field near the plasma edge is observed to be opposite to that in the plasma core where the helical ripple is small.

Keywords: Toroidal Flow, Spontaneous Flow, Charge Exchange Spectroscopy

1. Introduction

The transport in the plasma is considered to be sensitive to the profile of flow velocity. A moderate shear of poloidal flow can suppress the turbulence and reduce the transport. On the other hand, it has been pointed out that the toroidal flow contributes the stabilization of resistive wall mode in tokamaks [1]. Therefore the spontaneous toroidal flow becomes important in the next fusion device such as ITER, where the toroidal flow velocity driven by external momentum is expected to be not enough to stabilize the MHD mode. The mechanism of driving the spontaneous toroidal flow has a great interest in the momentum transport physics and has been investigated in tokamaks experimentally and theoretically [2-8].

Besides the toroidal flow driven by the external momentum input of neutral beam injected tangentially, there is the spontaneous toroidal flow driven by the coupling of ExB force and viscosity tensor. Stress tensor re-directs some fraction of diamagnetic and ExB flows into parallel flows. The radial electric field can be controlled by changing the collisionality as predicted by neoclassical transport in the helical system. The radial electric field at the plasma edge changes its sign from negative to positive by reducing the electron density in the NBI plasma, while the radial electric field in the plasma core becomes positive by applying the center focused ECH to NBI plasma in LHD. There are three NBI tangentially injected; one is injected in CW direction and the other two are injected in CCW direction. The various combinations of these three beams give the scan of momentum input to the plasma in the wide range. Both the toroidal and poloidal rotation velocities are measured with the charge exchange spectroscopy using the charge exchange line of fully ionized carbon. In this paper, we will report the observations of both the NBI driven toroidal flow and spontaneous toroidal flow in helical plasma.

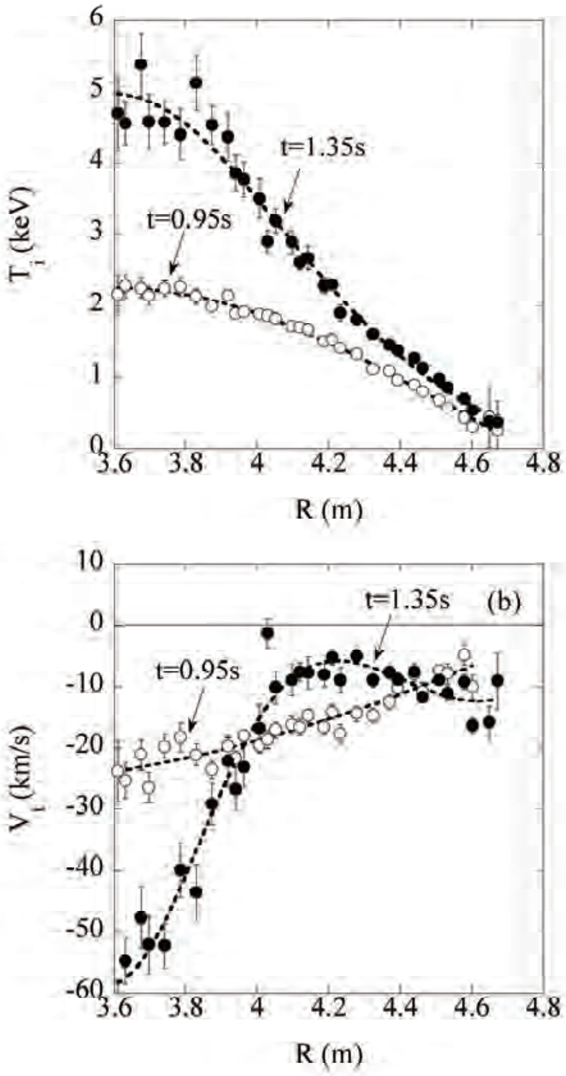

Fig.1 Radial profiles of (a) ion temperature and (b) toroidal flow velocity before (open circle) and after (close circle) the injection of tangential neutral beams in the plasma with R_{ax}=3.6m, B=2.85T and γ=1.254.

author's e-mail: yoshinuma@nifs.ac.jp

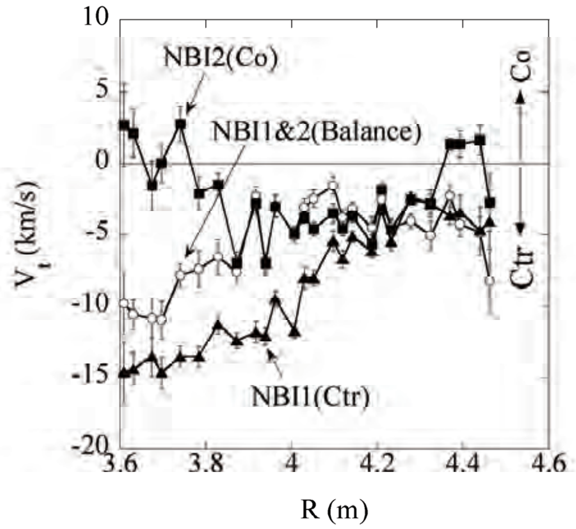

Fig.2 Radial profiles of toroidal flow velocity in the plasma with R_{ax}=3.6m, B=1.5T and γ=1.174. The tangential NBI is selected for co-injection (square), counter-injection (triangle), and balanced injection (circle).

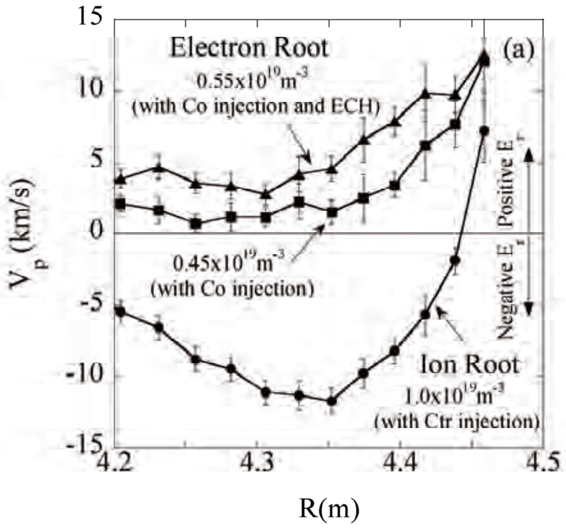

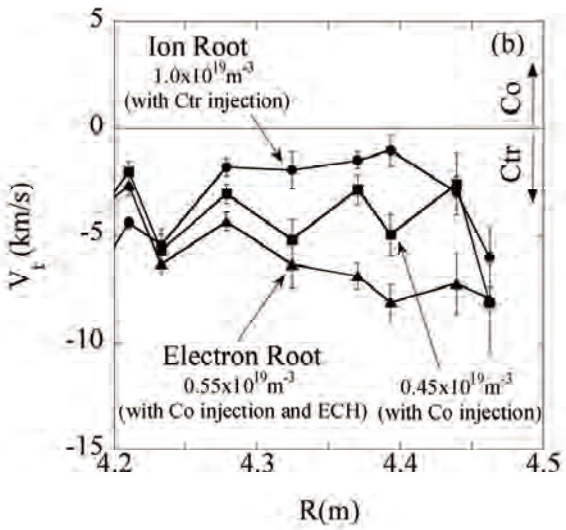

Fig.3 Radial profiles of (a) poloidal rotation velocity and (b) toroidal rotation velocity near the plasma edge in the case of electron root (triangle and square) and ion root (circle), in the plasma with R_{ax}=3.6m, B=1.5T and γ=1.174.

2. Lines of Sight of CXS on LHD

The charge exchange spectroscopy (CXS) has been widely used to measure the profiles of ion temperature, toroidal flow velocity, and impurity in neutral beam injected plasmas. In LHD, charge exchange line of the fully ionized carbon is used for the CXS measurement. The extreme hollow profile of carbon impurity is observed associated with the peaking of the ion temperature profile in LHD. Because of the finite beam width comparable to the half of the plasma minor radius, the integration effect along the line of sight can be a serious problem in the poloidal view when the carbon density profile become hollow. Therefore the CXS measurements with the toroidal view are applied to measure the ion temperature more accurately in the plasma with peaked ion temperature where the carbon density profile tends to be hollow. Figure 1 shows the example of the CXS measurement with toroidal line of sight in the plasma with the magnetic axis R_{ax} of 3.6m, magnetic field strength B of 2.75T, pitch parameter γ of 1.254 and counter dominant neutral beam injection. The central ion temperature achieved to 4.5keV after the injected of three tangential neutral beams. The increase of the ion temperature gradient and strong toroidal flow near the magnetic axis in the direction parallel to the momentum input of NBI are observed. The spontaneous toroidal flow in the opposite direction to NBI is observed at the mid minor radius (R=4.2m) where the ion temperature gradient becomes steep. Thus, the combination of NBI driven flow near the plasma core and the spontaneous flow at mid minor radius produces the interesting radial profile of toroidal flow.

3. NBI driven Toroidal Flow

Figure 2 shows the radial profiles of the toroidal flow velocity in the plasma with co-injected (parallel to the equivalent toroidal plasma current), counter-injected (anti-parallel to the equivalent toroidal plasma current), and balance-injected of tangential NBI. The toroidal flows in the counter-direction are observed whole the major radius in the plasma with balance-injected NBI shows the existence of spontaneous component. The toroidal flow

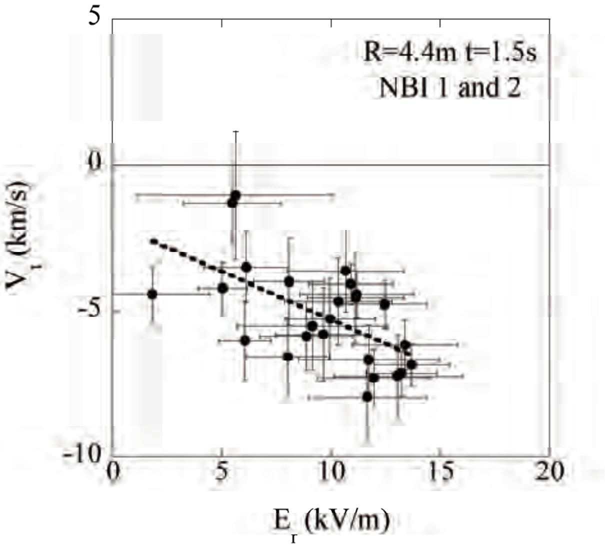

Fig.4 Dependence of toroidal rotation velocity on radial electric field at R=4.4m in the plasma with R_{ax}=3.6 m , B=1.5T and γ=1.174.

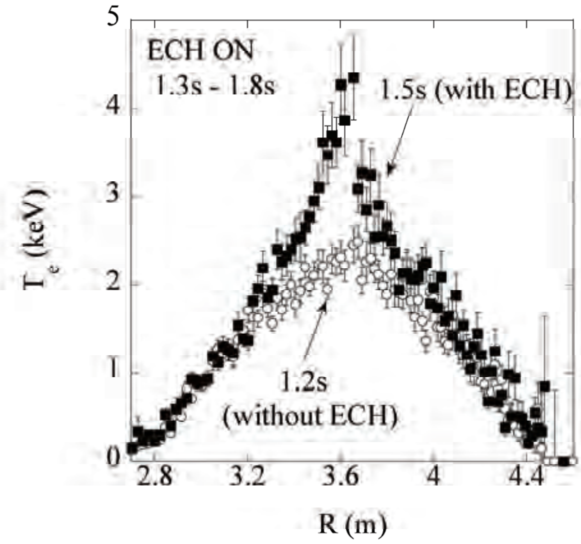

Fig.5 Radial profile of electron temperature with (square) and without (circle) ECH in the plasma with R_{ax}=3.6m, B=1.5T and γ=1.174.

near the magnetic axis depends on the direction of NBI, while no significant change of toroidal flow is observed near the plasma edge. It is suggested that the NBI driven toroidal flow is small at the plasma edge, because of the strong helical ripple and small deposition of the NBI power. Therefore the effect of the radial electric filed on the spontaneous flow becomes more visible at the edge.

4. Spontaneous Toroidal Flow at the Edge

Figure 3 shows profiles of poloidal flow and toroidal flow near the plasma edge where the effect of the radial electric filed on the spontaneous flow is large. The poloidal flow, which has a dominant contribution to the radial electric field, is changed from negative value to positive value by decreasing the plasma density and by increasing the heating power. The magnitude of the toroidal flow velocity in the counter direction increases when the sign of the poloidal flow velocity changes from negative value ($E_r < 0$: the ion root) to positive value ($E_r > 0$: the electron root). Figure 4 shows the relation between the toroidal flow velocity and on the radial electric field at the plasma edge (R=4.4m). The counter flow (negative) increases when the radial electric field becomes more positive. Theses results are consistent with the experiment in CHS, where the spontaneous toroidal flow in the counter direction appears associated with the transition from the ion root with small negative E_r to the electron root with large positive E_r [9]. It should be noted that the direction of the spontaneous toroidal flow is anti-parallel to the direction of $\langle E_r x B_\theta \rangle$ drift. The spontaneous toroidal rotation flows in the direction reducing the radial electric field rather. This is

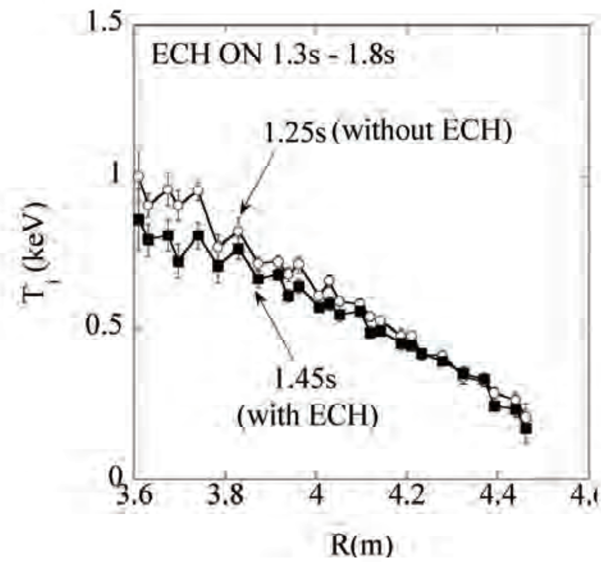

Fig.6 Radial profile of ion temperature with (square) and without (circle) ECH in the plasma with R_{ax}=3.6m, B=1.5T and γ=1.174.

because the viscosity tensor re-directs some fraction of ExB flows into the direction of minimum gradient of magnetic field strength. The direction of the parallel flows re-directed by the viscosity in helical plasma is opposite to that in tokamaks because the pitch angle of minimum gradient B is larger than the pitch angle of magnetic field averaged in magnetic flux surface in helical plasma, while the pitch angle of minimum gradient B is zero in tokamaks.

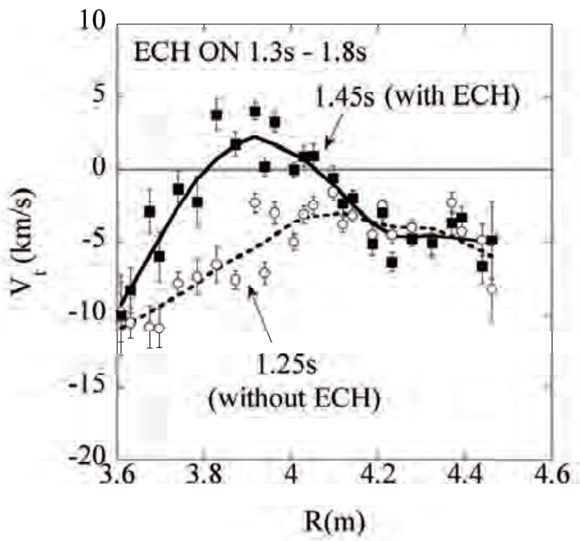

Fig.7 Radial profile of toroidal rotation velocity with (square) and without (circle) ECH in the plasma with R_{ax}=3.6m, B=1.5T and γ=1.174.

5. Spontaneous Toroidal Flow in the Core

The improvement of electron heat transport near the magnetic axis (electron ITB) is observed in various helical systems by applying the center focused ECH to the low density plasma [10-13]. When the transition to the electron ITB takes place, the positive radial electric field is formed in the plasma core. The spontaneous toroidal flow driven by the ExB flow associated with the electron ITB is observed in the plasma core. The tangential NBI is balanced to make the NBI driven toroidal flow to be minimized small in the plasma core. The profiles of the electron temperature, the ion temperature and the toroidal flow velocity in the plasma with and without the ECH are shown in Fig 5, Fig. 6 and Fig.7, respectively. The electron ITB profile is observed in the electron temperature profile during the ECH pulse (t=1.3–1.8 sec) while no significant change in the ion temperature profile is observed. Associated with the transition to electron ITB, which is characterized by the peaked electron temperature, a large positive radial electric field appears in the plasma core [10] as predicted by neoclassical theory. The toroidal flow in the co-direction during the ECH is clearly observed. This result shows that the positive electric field drives the toroidal flow in the co-direction in the plasma core where the modulation of the magnetic field due to helical ripple is smaller than that due to toroidal effect ($\varepsilon_h < \varepsilon_t$). The direction of the spontaneous toroidal flow near the magnetic axis is parallel to the direction of $\langle E_r x B_\theta \rangle$ drift, which is in contrast to the spontaneous toroidal flow anti-parallel to the direction of $\langle E_r x B_\theta \rangle$ drift near the plasma edge as shown in Fig.3 and Fig.4.

In tokamak, the spontaneous toroidal rotation in the counter direction is observed in the plasma with negative E_r as reported in JFT-2M [3]. The spontaneous toroidal rotation becomes most significant in the ITB region where the strong negative E_r appears [14]. The direction of the spontaneous toroidal rotation in tokamaks is parallel to the direction of $\langle E_r x B_\theta \rangle$ drift.

6. Summary

Radial profiles of the plasma flow velocity both in the toroidal direction and poroidal direction are measured with the charge exchange spectroscopy using the charge exchange line of fully ionized carbon. Toroidal flow parallel to the momentum input of NBI is observed to be localized in the core region of the plasma. The relations between the spontaneous toroidal flow and radial electric field are investigated and the positive radial electric field drives spontaneous rotation in the counter direction near the plasma edge and in the co direction near the magnetic axis. This observation shows the spontaneous rotation near the magnetic axis is opposite to that near the plasma edge. The difference in the direction of spontaneous flow between core and edge is considered to be due to the difference in the ratio of the toroidal effect to the helical ripple. In LHD, the spontaneous toroidal flow re-directed ExB flow by the viscosity tensor in the core region is parallel to that observed in tokamaks, while the spontaneous toroidal flow near the plasma edge is anti-parallel to that in tokamak.

We would like to thank technical staff for their effort to support the experiment in LHD. This work is partly supported by a Grant-in-aid for Scientific research (18206094) of MEXT Japan. This work is also partly supported by NIFS05LUBB510.

References

[1] D. J. Ward, A.Bondeson, Phys.Plasmas **2**, 1570 (1995).
[2] K. Nagashima et al., Nucl. Fusion **34**, 449 (1994).
[3] K.Ida et al., Phys. Rev. Lett. **74**, 1990 (1995).
[4] J.E.Rice et al., Nucl. Fusion **38**, 75 (1998).
[5] K.Ida et al., J.Phys.Soc.Jpn. **67** 4089 (1998).
[6] M.Yoshida et al., Plasma Phys.Control.Fusion **48**, 1673 (2006).
[7] B.Coppi, Nucl. Fusion **42**, 1 (2002).
[8] O.D.Gurcan, P.H.Diamond et al., Phys.Plasmas **14**, 042306 (2007).
[9] K. Ida et al., Phys. Rev. Lett **86**, 3040 (2001).
[10] K.Ida et al., Phys. Rev. Lett. **91**, 085003 (2003).
[11] T.Shimozuma et al., Plasma Phys.Control.Fusion. **45**, 1183 (2003).
[12] Y.Takeiri et al., Phys. Plasma. **10**, 1788 (2003).
[13] K.Ida et al., Phys. Plasma, **11**, 2551 (2004).
[14] Y.Sakamoto et al., Nucl Fusion **41** (2001) 865.

Proceedings of ITC/ISHW2007

Status of the NCSX Project

G. H. Neilson[1], J. L. Anderson[1], A. Brooks[1], T. Brown[1], M. Cole[2], J. Chrzanowski[1], L. Dudek[1], H. M. Fan[1], P. Fogarty[2], G. Gettelfinger[1], P. Goranson[2], P Heitzenroeder[1], M. Kalish[1], G. Labik[1], J. Lyon[2], B. Nelson[2], S. Raftopoulos[1], B. Stratton[1], R. Strykowsky[1], M. Viola[1], M. Williams[1], D. Williamson[2], and M. Zarnstorff[1]

[1]*Princeton Plasma Physics Laboratory, Princeton, NJ 08543, U.S.A.*
[2]*Oak Ridge National Laboratory, Oak Ridge, TN 37831, U.S.A.*

hneilson@pppl.gov

The National Compact Stellarator Experiment (NCSX) is being constructed at the Princeton Plasma Physics Laboratory (PPPL) in partnership with the Oak Ridge National Laboratory (ORNL). Its mission is to develop the physics understanding of the compact stellarator and evaluate its potential for future fusion energy systems. The NCSX has major radius 1.4 m, aspect ratio 4.4, 3 field periods, and a quasi-axisymmetric magnetic field. The device will provide the plasma configuration flexibility and the heating and diagnostic access needed to test physics predictions. The design features eighteen modular coils of three different shapes, and toroidal field, poloidal field, and trim coils for flexibility

Component production has advanced substantially since the first contracts were placed in 2004. Manufacture of the vacuum vessel was completed in 2006. Installation of heating / cooling tubes and magnetic diagnostics on the vessel surface is nearly complete. All eighteen modular coil winding forms have been delivered and twelve modular coils have been fabricated. A contract for the (planar) toroidal field coils was placed in 2006 and those coils are now in production. Preparations for assembly of modular coils into three-coil modules are under way. Plans for completing the construction, included an updated schedule, will be presented.

Poster Presentations 1

Proceedings of ITC/ISHW2007

Impact of Dynamic Ergodic Divertor on Plasma Rotation in the Small Tokamak HYBTOK-II

Y. Hasebe, M. Okamoto, S. Kajita[a] , N. Ohno[b] , S. Takamura[c]

Graduate School of Engineering, Nagoya University, Furo-cho, Nagoya 464-8603, Japan

[a]Japan Atomic Energy Agency, 801-1, Mukoyama, Naka 311-0193, Japan

[b]EcoTopia Science Institute, Nagoya University, Furo-cho, Nagoya 464-8603, Japan

[c]Department of Electronics, Aichi Institute of Technology, Yakusa-cho, Toyota 470-0392, Japan

(Received day month year / Accepted day month year should be centered 10-point type)

Plasma rotation or its shear is important on the formation of transport barrier. It is thought that the rotating helical magnetic field generated by Dynamic Ergodic Divertor (DED) could generate a rotational torque in tokamak plasmas and control rotation profiles as a result. In order to measure the plasma rotations and to investigate the effect of DED on them, we developed a passive spectroscopic measurement system for the small tokamak HYBTOK-II to measure plasma rotations. A spontaneous toroidal plasma rotation in co-current direction and the poloidal plasma rotation in electron diamagnetic drift direction have been observed without DED. Considerable changes of the plasma flow have been obtained with DED to show some reduction of toroidal and poloidal rotation velocity near the resonant magnetic surface. The modification of plasma rotation velocity was found to couple to the change of the radial electric field.

Keywords: plasma rotation, dynamic ergodic divertor, passive spectroscopy, radial electric field, HYBTOK-II

1. Introduction

To achieve high performance in magnetically confined plasmas, control of plasma rotations and their profiles play important roles on forming and sustaining transport barrier through the modification of radial electric field [1,2]. In burning plasma, it is not easy to control plasma properties by external current drive or auxiliary heating (i.e. controlling current and temperature profiles) due to large bootstrap current and self-α heating. However, in present devices, neutral beam injection is useful to control the plasma rotations as an external momentum source.

Dynamic ergodic divertor (DED), which has been developed to control energy and/or particle transport at the edge region, is believed to generate rotational torque on plasmas. Modulation of particle and/or energy transport in DED comes from the magnetic field structure caused by magnetic islands induced by externally-applying Rotating Helical magnetic perturbation Field (RHF) [3-7]. Mechanism of controlling of plasma rotation by use of DED relates to the Lorentz torque due to interaction between shielding current produced by the rotating perturbation field in plasmas and perturbation field itself [7]. The torque is expected to be large when the relative angular frequency between plasma and RHF in DED is large. However, the high frequency RHF in the plasma becomes weak due to the shielding effect of the vacuum vessel because the helical coils are wound outside of the vacuum vessel. On the other hand, lower frequency RHF can penetrate much deeper inside of plasma. Therefore, in the present paper, we focus on the lower frequency RHF (~ several kHz) case to investigate the effect of stochastic magnetic field formed inside the separatrix in this paper.

In order to study the effect of DED on plasma rotation in the small tokamak HYBTOK-II, an optical measurement system, which may observe the inner plasma region, has been developed with the working gas of helium.

2. Experimental Setup

The experiments have been performed on the small tokamak HYBTOK-II (the major radius R_0 = 40 cm, the plasma minor radius $a \approx 10$ cm, the limiter radius a_w = 11 cm). In the machine operation, the main plasma parameters were as follows: the plasma current I_p = 5 kA, the toroidal magnetic field B_t = 0.28 T, and the pulse duration time is 10 ms. The HYBTOK-II is equipped with DED coils, which consist of two sets of coils that are wound on the out-vessel locally in the toroidal direction. The RHF with

author's e-mail: y-hasebe@ees.nagoya-u.ac.jp

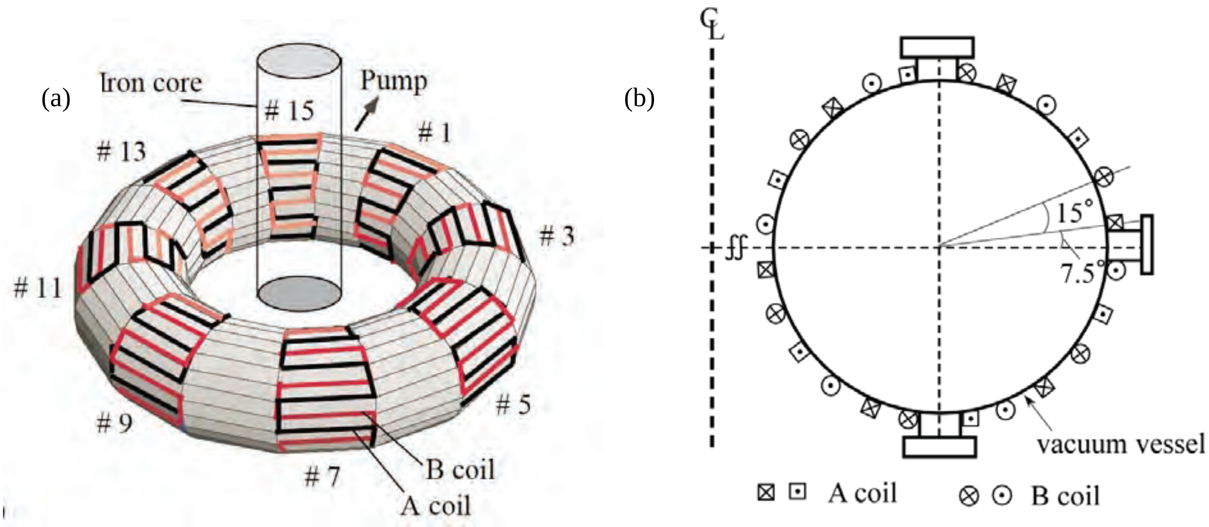

Fig. 1 Arrangement of the DED coils (a) bird's eye view (b) on poloidal cross section [5].

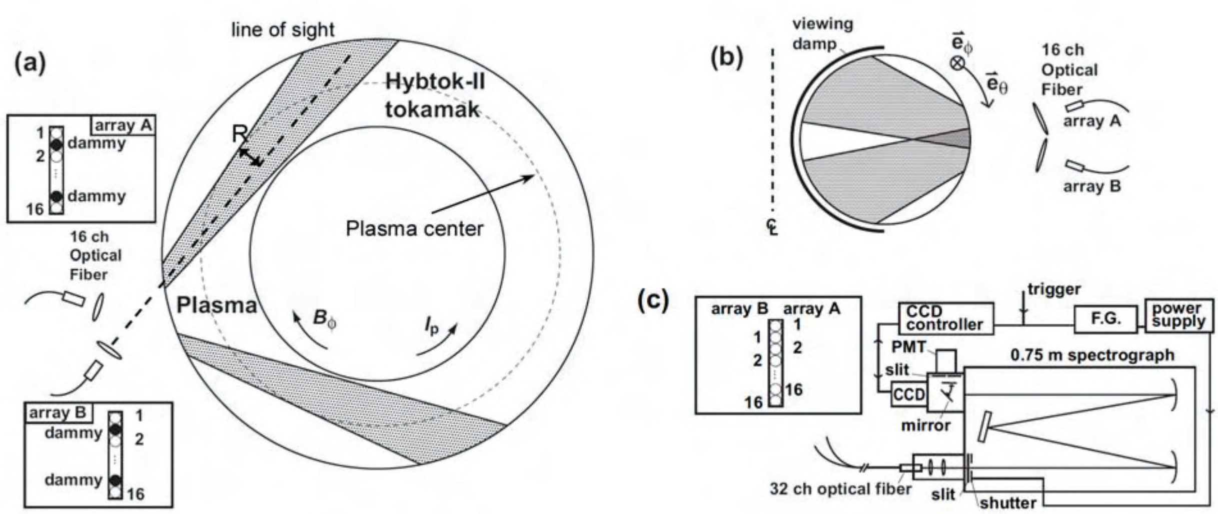

Fig. 2 Optical arrangements for (a) toroidal and (b) poloidal flow velocity measurements.
(c) Spectrometer, detection device and synchronized system with external trigger.

the poloidal and toroidal mode numbers of m/n = 6/1 resonates with magnetic rotational transform at q = 6 magnetic surface (Fig. 1) [5]. These two sets of coils are powered independently by insulated gated bipolar transistor inverter power supply with a phase difference of ± 90°. We can control the poloidal rotation direction of RHF by changing the phase difference between two coils. RHF's rotation frequency of 3 kHz was selected. Duration of the RHF was 10 msec.

The optical measurement system consists of bifurcated 32 ch (16 ch×2) optical fiber arrays, focusing lens (103 mm focal length in a toroidal direction, 34.5 mm in a poloidal direction), Czerny-Turner spectrometer (1800 gr/mm grating, 1.0 m focal length and 0.01 nm resolution) and 1024×256 pixels CCD detector (Fig. 2). By changing the position of the fiber arrays using by movable stages, the distance between the line of sight and the plasma center, r, can be varied from r = 0-100 mm. The flow velocity, V, is given by $V = c\cdot \Delta\lambda/\lambda$, where c is the speed of light, $\Delta\lambda$ the Doppler shift and λ the central wavelength of the observed spectrum. The shifted value $\Delta\lambda$ was estimated by $\Delta\lambda = (\lambda_{blue} - \lambda_{red})/2$ in this system, where λ_{blue} and λ_{red} are the central wavelength of the spectrum observed from the upstream, and downstream of the plasma flow, respectively. Thus, one branch of bifurcated arrays faces upstream-side and another looks forwards the downstream-side as shown in Fig. 2. In this experiments, singly ionized helium emission (n = 3 – 4, λ = 468.54 – 468.59 nm) was employed for the flow measurements. The spectrum was fitted with multi-Gaussian functions considering the fine

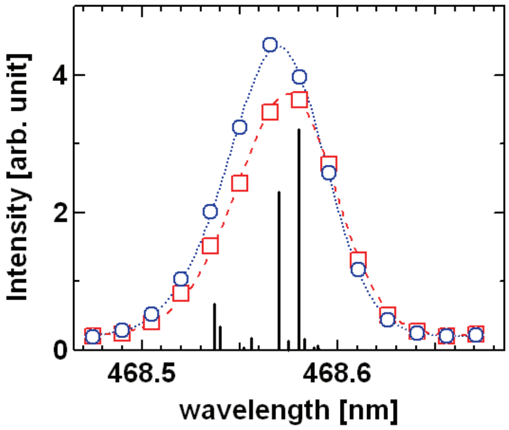

Fig.3 Observed spectra at both upstream- (open circle) and downstream-side (open square), with fitted curves.

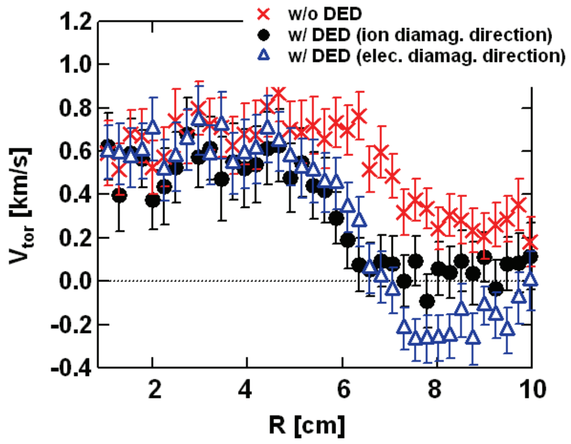

Fig. 4 Toroidal rotation velocity profile without (cross) and with DED in the direction of ion diamagnetic drift (closed circle) and in that of electron (triangle).

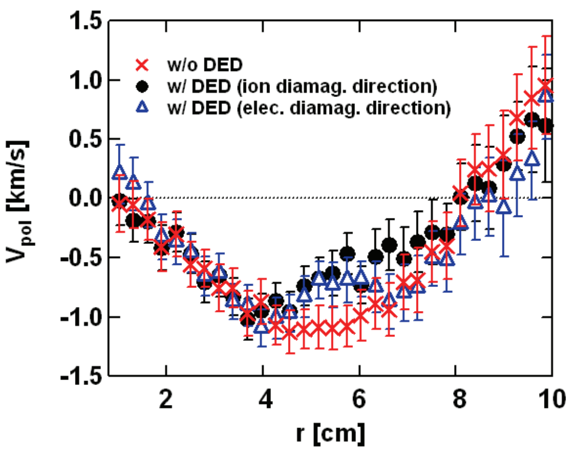

Fig.5 Poloidal rotation velocity profile. The markers of each cases are same as Fig. 4.

structure of the transition [9].

A triple probe which is accessible up to the center of plasma column is installed to measure the electron temperature T_e, the electron density n_e and the floating potential V_f. The Plasma potential V_p is estimated by using the relation $V_p = V_f + 3T_e$.

3. Results and Discussion

In the measurements, pure helium plasma was employed to improve S/N ratio by obtaining the strong He II emission. Typical electron density and electron temperature are $n_e \sim 6 \times 10^{18}$ m^{-3} and $T_e \sim 30$ eV, respectively. At first, we briefly present the fundamental spectral measurements obtained from the passive spectroscopy. Figure 3 shows the spectra observed both at the upstream-side and at the downstream-side with the relative strength of the fine structure multiplet. The observed spectra are fitted by multi-Gaussian functions. The ion temperature obtained from the Doppler width with considering an instrumental width and the fine structure is about 5 eV, and it is found that there is no clear radial positional dependence. The toroidal plasma rotation velocity profiles are shown in Fig. 4 as a function a distance R between a line of sight and the center of the plasma column, which lies on 1 cm inside that of the vacuum vessel, as shown in Fig. 2(a). It is noted that the velocity does not shows the local value because of the limitation of the passive spectroscopy owing to line integration. Thus, only the averaged value over the line of sight is available at the moment, especially for the toroidal direction. A spontaneous plasma rotation in the co-current direction has been observed. The maximum velocity is about 0.8 km/s. By applying RHF with 150 A of the maximum coil current, a reduction of plasma rotation is clearly observed around R = – 4 cm in both RHF rotation directions. Figure 5 shows poloidal plasma rotation velocities without and with 3 kHz DED. "r" in horizontal axis means distance between the line of sight and the plasma center. Without DED, the direction of plasma rotation is the same as that of the electron diamagnetic drift from r = – 2 to r = – 8 cm. With DED case, plasma rotation is damped around r = – 4 cm. Radial electric field E_r derived by the plasma potential profile is shown in Fig. 6 for both without and with DED cases. $E_r \times B$ drift direction matches the poloidal rotation, and reduction of E_r at inside r ~ 7.5 cm agrees with the reduction of the poloidal rotation. The variations of the plasma rotations by DED were found to be coupled with radial electric field.

In the low frequency case (3 kHz DED), the changes in rotation due to DED was observed at the same location

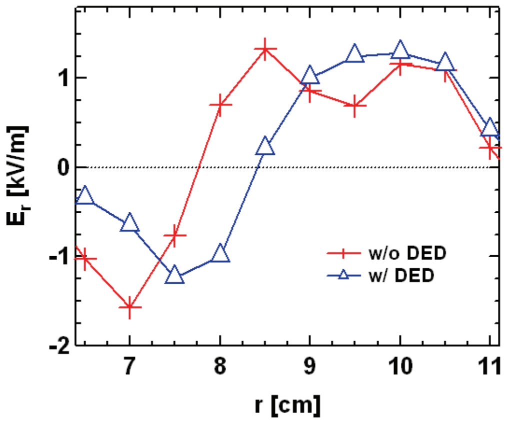

Fig. 6 Radial electric field evaluated by using the triple probe. Negative E_r means inward field.

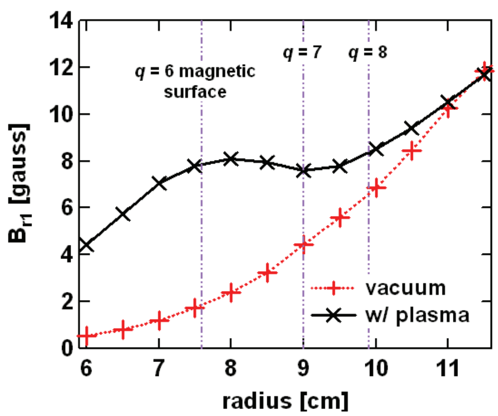

Fig. 7 Perturbation component of radial magnetic field The locations of rational surface of q = 6, 7, 8 are also shown.

for both toroidal and poloidal rotations. Perturbation component of radial magnetic field B_{r1} was measured by using a radially movable magnetic probe and is shown in Fig. 7. The B_{r1} in vacuum decreases with distance from the coil placed on out-vessel. However, B_{r1} in the plasma was amplified compared with that in vacuum near resonance surface (r ≈ 7.6 cm). This can be contributed to the re-distribution of plasma current due to the growth of the magnetic island structure [6,7]. It is thought that poloidal rotation damping was caused by the enhancement of poloidal parallel viscosity due to the island formation. In steady-state plasma, the radial component of equation of motion for ion fluid in the toroidal coordinates is as follows:

$$E_r = (1/eZ_i n_i)(\partial P_i/\partial r) - V_\theta B_\phi + V_\phi B_\theta \,. \qquad (1)$$

Here, eZ_i, n_i and P_i are the electrical charge, the number density and pressure of the ion, respectively. V and B are the flow velocity and the magnetic field, respectively. The changes of E_r estimated from eq. (1) using the results of the rotation measurements are in agreement with the experimental results, qualitatively. On the other hand, the toroidal rotation decrease seems to be caused by friction increase due to variation of magnetic structure at the edge region or friction with neutral helium which exists more near the edge region. Thus, it could be said that changes of the rotations originate in the magnetic island structure, and consequently the E_r changes, in these cases.

4. Conclusion

A modification of plasma rotation properties with DED is reported. The plasma flow was measured by the optical emission spectroscopy developed in HYBTOK-II. Doppler shift of He II line obtained from the system is large enough to estimate the rotation velocity and its direction in pure helium discharge. The spontaneous toroidal plasma rotation in the co-current direction and the poloidal rotation in the electron diamagnetic drift direction were observed without DED. By applying a low frequency RHF (~ 3 kHz), both the toroidal and the poloidal rotations decreased. It is likely that they are caused by magnetic island formation. Modification of Radial electric field was also observed.

In future, it is necessary to generate plasma with higher electron temperature in order to study an influence of shielding current in the plasma. As a modification of radial electric field due to enhancement of electron transport in the stochastic region are observed on the TEXTOR [10], there is also need to consider these effects.

References

[1] K. Ida, Phys. Fluid B **4**, 2552 (1992).
[2] Y. Sakamoto *et al*., Nucl. Fusion **41**, 865 (2001).
[3] S. Takamura, H. Yamada and T. Okuda, Nucl. Fusion **28**, 183 (1988).
[4] M. Kobayashi, H. Kojima, K. Zhai and S. Takamura, Phys. Plasmas **7**, 3288 (2000).
[5] S. Takamura, Y. Kikuchi, Y. Uesugi and M. Kobayashi, Nucl. Fusion **43**, 393 (2003).
[6] M. Kobayashi et al., Nucl. Fusion **40**, 181 (2000).
[7] Y. Kikuchi *et al*., J. Nucl. Mater. 313-316, 1272 (2003).
[8] Y. Kikuchi *et al.*, Plasma Phys. Control. Fusion **49**, A135 (2007).
[9] S. Kado and T. Shikama, J. Plasma Fusion Res. **79**, 841 (2001).
[10] K. H. Finken et al., Phys. Rev. Lett. **94**, 015003 (2005).

Proceedings of ITC/ISHW2007

Geodesic Acoustic Mode with the Existence of a Poloidal Shock Structure

Naohiro KASUYA and Kimitaka ITOH

National Institute for Fusion Science, 322-6 Oroshi-cho, Toki 509-5292, Japan

In H-mode plasmas, two-dimensionally steep structures of the potential and density are formed, when a large poloidal flow exists, and its formation mechanism has been studied for quantitative understanding of the particle transport in the H-mode transport barriers. Extension of the previous two-dimensional model is carried out to investigate parallel flow dynamics, when potential and density distributions do not satisfy the Boltzmann relation. The extended model includes the generation mechanism of a poloidal shock structure and a geodesic acoustic mode, and their competitive formation can be studied.

Keywords: poloidal shock structure, geodesic acoustic mode, H mode, poloidal asymmetry, structural formation

1. Introduction

A variety of structures are formed in the toroidal plasmas, and their formation mechanism is one of the keys to understand the transport phenomena. The typical example appears in the high-confinement mode (H mode) [1]. The steep radial electric field plays an important role for turbulent suppression in H-mode transport barriers [2]. In addition, a poloidally steep structure can be formed, associated with a large poloidal flow. Theories have predicted that the poloidal shock can appear in H-mode plasmas [3,4]. The poloidal shock structure is a steady density or potential jump in the poloidal direction, resulting from the plasma compressibility and the inhomogeneity of the magnetic field by the toroidicity, and is important, because it induces radial particle fluxes to accelerate the density pedestal formation on the L/H transition [5]. Some experiments have indicated the existence of poloidal asymmetry [6,7]. Therefore, it is important to understand the formation mechanism of H-modes by analyzing the two-dimensional (2-D) electric field structure.

We have extended the one-dimensional (1-D) model in tokamak H modes to give 2-D structures, taking into consideration of coupling between different magnetic surfaces by shear viscosity, and obtained 2-D potential and density structures in edge transport barriers [5]. Our evaluation clarifies the non-negligibility of the particle transport arising from poloidal asymmetry, and the self-consistent mechanism of the density pedestal formation on the L/H transition [8].

In this paper, extensions of the previous 2-D model are carried out to investigate two effects on the structural formation, i.e., the deviation from the Boltzmann relation and the parallel flow dynamics. The distribution of the potential and density different from the Boltzmann relation contributes to induce a particle pinch [8], and the parallel flow dynamics is important to obtain the flow pattern, which contributes to the structural formation [2]. These extensions enable to analyze the geodesic acoustic mode (GAM) [9], which is the oscillatory zonal flow, caused by compressibility of the E × B flow in the presence of the geodesic magnetic curvature [10]. The zonal flow nonlinearly interacts with turbulence and determines the transport level. Therefore, many experimental observations have been made to clarify the role of the zonal flow in plasma confinements [11]. Both the poloidal shock and the geodesic acoustic mode induce density asymmetry in the magnetic flux surface, so their competition must be examined to deepen our understanding of the transport barrier physics.

The paper is organized as follows. The derivation of the model equations is described in Sec. 2. In Sec. 3, the extreme cases with a large and small poloidal flow are shown to deduce the formation mechanism of the poloidal shock and the GAM. The summary is presented in Sec. 4.

2. Set of Model Equations

For analyzing the potential, the density and the flow velocity, a set of fluid equations consists of the momentum conservation equation, the continuity equation of the density, the charge conservation equation, and the Ohm's law:

$$m_{\mathrm{i}} n \frac{d}{dt}\vec{V}_{\mathrm{i}} = \vec{J}\times\vec{B} - \vec{\nabla}\left(p_{\mathrm{i}} + p_{\mathrm{e}}\right) - \vec{\nabla}\cdot\vec{\pi}_{\mathrm{i}}, \qquad (1)$$

$$\frac{\partial n}{\partial t} + \vec{\nabla}\cdot\left(n\vec{V}_{\mathrm{i}}\right) = 0, \qquad (2)$$

$$\vec{\nabla}\cdot\vec{J} = 0, \qquad (3)$$

$$\vec{E} + \vec{V}\times\vec{B} = 0, \qquad (4)$$

where m_{i} is the ion mass, $\vec{V}$ is the flow velocity, $\vec{J}$ is the current, p is the pressure, $\vec{\pi}$ is the viscosity. We assume density $n = n_{\mathrm{i}} = n_{\mathrm{e}}$ for simplicity, where n_{i} and n_{e} are the ion and electron density, respectively. We consider a large aspect ratio tokamak with a circular cross-section and the coordinates (r, θ, ϕ) are used (r: radius, θ: poloidal angle, ϕ:

author's e-mail: kasuya@nifs.ac.jp

toroidal angle). The magnetic field is taken to be

$$\vec{B}=\frac{1}{1+\varepsilon\cos\theta}\begin{pmatrix}0\\ B_{\mathrm{p}0}(r)\\ B_{\phi 0}\end{pmatrix}, \tag{5}$$

where ε is the inverse aspect ration. Using Eq. (4), the flow velocity can be written to be

$$\vec{V}=\vec{V}_{//}+\frac{\vec{E}\times\vec{B}}{B^2}=\begin{pmatrix}-\dfrac{1}{rB}\dfrac{\partial\Phi}{\partial\theta}\\ \dfrac{KB_{\mathrm{p}}}{n}\\ \dfrac{KB_{\phi}}{n}-\dfrac{1}{B_{\mathrm{p}}}\dfrac{\partial\Phi}{\partial r}\end{pmatrix}, \tag{6}$$

where

$$K\equiv nV_{\mathrm{p}}/B_{\mathrm{p}}\,, \tag{7}$$

and Φ is the potential. Using Eq. (6), Eq. (2), the poloidal and parallel component of Eq. (1) are given to be

$$\frac{\partial n}{\partial t}-\frac{\partial}{\partial r}\left(\frac{n}{rB}\frac{\partial\Phi}{\partial\theta}\right)+\frac{1}{r}\frac{\partial}{\partial\theta}\left(KB_{\mathrm{p}}\right)=0\,, \tag{8}$$

$$\begin{aligned}&B_{\mathrm{p}}^{2}\frac{\partial}{\partial t}\left(\frac{K}{n}\right)-\frac{n}{KrB}\frac{\partial\Phi}{\partial\theta}\frac{\partial}{\partial r}\left[\frac{1}{2}\left(\frac{KB_{\mathrm{p}}}{n}\right)^2\right]+\frac{B_{\mathrm{p}}}{r}\frac{\partial}{\partial\theta}\left[\frac{1}{2}\left(\frac{KB_{\mathrm{p}}}{n}\right)^2\right]\\&=\frac{1}{m_{\mathrm{i}}}\frac{JB_{\mathrm{p}}B_{\phi}}{n}-\frac{1}{m_i}\frac{B_{\mathrm{p}}}{r}\frac{\partial}{\partial\theta}\left(\frac{\bar{p}_e}{\bar{n}}\ln n+\frac{5\bar{p}_i}{2\bar{n}^{5/3}}n^{2/3}\right)\\&-\frac{1}{m_{\mathrm{i}}}\left(\frac{\vec{B}_{\mathrm{p}}\cdot\vec{\nabla}\cdot\vec{\pi}_{\mathrm{i}}}{n}\right)_{\mathrm{bulk}}-\frac{1}{m_{\mathrm{i}}}\left(\frac{\vec{B}_{\mathrm{p}}\cdot\vec{\nabla}\cdot\vec{\pi}_{\mathrm{i}}}{n}\right)_{\mathrm{shear}},\end{aligned} \tag{9}$$

$$\begin{aligned}&B^2\frac{\partial}{\partial t}\left(\frac{K}{n}\right)-\frac{B_{\phi}}{B_{\mathrm{p}}}\frac{\partial}{\partial t}\frac{\partial\Phi}{\partial r}-\frac{n}{KrB}\frac{\partial\Phi}{\partial\theta}\frac{\partial}{\partial r}\left[\frac{1}{2}\left(\frac{KB}{n}\right)^2\right]\\&+\frac{B_{\mathrm{p}}}{r}\frac{\partial}{\partial\theta}\left[\frac{1}{2}\left(\frac{KB}{n}\right)^2\right]+\frac{B_{\phi}}{rB}\frac{\partial\Phi}{\partial\theta}\frac{\partial}{\partial r}\left[\frac{B}{B_{\mathrm{p}}B_{\phi}}\frac{\partial\Phi}{\partial r}\right]\\&-\frac{KB_{\mathrm{p}}B_{\phi}}{nr}\frac{\partial}{\partial\theta}\left[\frac{B}{B_{\mathrm{p}}B_{\phi}}\frac{\partial\Phi}{\partial r}\right]\\&=-\frac{B_{\mathrm{p}}}{m_{\mathrm{i}}r}\frac{\partial}{\partial\theta}\left(\frac{\bar{p}_e}{\bar{n}}\ln n+\frac{5}{2}\frac{\bar{p}_i}{\bar{n}^{5/3}}n^{2/3}\right)\\&-\frac{1}{m_{\mathrm{i}}n}\left(\vec{B}\cdot\vec{\nabla}\cdot\vec{\pi}_{\mathrm{i}}\right)_{\mathrm{bulk}}-\frac{1}{m_{\mathrm{i}}n}\left(\vec{B}\cdot\vec{\nabla}\cdot\vec{\pi}_{\mathrm{i}}\right)_{\mathrm{shear}}\,,\end{aligned} \tag{10}$$

respectively. Isothermal electrons and adiabatic ions are assumed. The viscosity of ions $\vec{\pi}_{\mathrm{i}}$ is divided into two terms: the bulk viscosity given by a neoclassical process [12], and shear viscosity given by an anomalous process [2]. The forms of viscosity terms are represented in Ref. [13].

The 2-D structures of the potential, the density and the flow velocity are obtained. These variables are divided into the average part and the perturbation part: $f = f_0(r) + f_1(r, \theta)$, where f represents each quantity. The variable K is replaced by M_{p}, which corresponds to the poloidal Mach number and defined as

$$M_{\mathrm{p}}\equiv\frac{KB_0}{\bar{n}\mathrm{v}_{\mathrm{ti}}C_{\mathrm{r}}}\,. \tag{11}$$

where $\mathrm{v}_{\mathrm{ti}}=\sqrt{2T_{\mathrm{i}}/m_{\mathrm{i}}}$, $C_{\mathrm{r}}^{\,2}=5/6+T_{\mathrm{e}}/(2T_{\mathrm{i}})$, T_{i} and T_{e} is the ion and electron temperature, respectively. Here, the shock ordering, which is the perturbations to be $O(\varepsilon^{1/2})$, is adopted. In the case in which $M_{\mathrm{p}}\sim 1$, the steep structure in the poloidal direction is formed, and the perturbations become larger than $O(\varepsilon)$. The set of equations for obtaining $M_{\mathrm{p}0}$, $M_{\mathrm{p}1}$, Φ_1, n_1 is derived from Eqs. (8-10), assuming $V_{\mathrm{r}}/V_{\mathrm{p}} << 1$, which is satisfied, even if a strong poloidal shock exists:

$$\frac{\partial\chi}{\partial\tau}=M_{\mathrm{p}0}\varepsilon\sin\theta-\frac{\partial M_{\mathrm{p}1}}{\partial\theta}\,, \tag{12}$$

$$\begin{aligned}&\frac{B_{\mathrm{p}0}^{\,3}\mathrm{v}_{\mathrm{ti}}^{\,2}C_r^{\,2}}{B_0^{\,2}r}\frac{\partial M_{\mathrm{p}0}}{\partial\tau}=\frac{1}{m_{\mathrm{i}}}\left\langle\frac{JB_{\mathrm{p}}B_{\phi}}{n}\right\rangle\\&-\frac{1}{m_{\mathrm{i}}}\left\langle\frac{\vec{B}_{\mathrm{p}}\cdot\vec{\nabla}\cdot\vec{\pi}_{\mathrm{i}}}{n}\right\rangle_{\mathrm{bulk}}-\frac{1}{m_{\mathrm{i}}}\left\langle\frac{\vec{B}_{\mathrm{p}}\cdot\vec{\nabla}\cdot\vec{\pi}_{\mathrm{i}}}{n}\right\rangle_{\mathrm{shear}},\end{aligned} \tag{13}$$

$$\begin{aligned}\frac{\partial E_1}{\partial\tau}&=-\hat{\mu}r^2\frac{B_0}{B_{\mathrm{p}0}}\frac{\partial^2}{\partial r^2}\left\{M_{\mathrm{p}0}\left[\exp(-\chi)-1\right]\right\}\\&+\frac{2}{3}D\exp(-\chi)\frac{\partial^2\chi}{\partial\theta^2}\\&+\left(1-M_{\mathrm{p}0}^{\,2}\right)\frac{\partial\chi}{\partial\theta}+2A\frac{\partial\chi^2}{\partial\theta}\\&-\varepsilon\left\{D-\hat{\mu}\frac{B_0}{B_{\mathrm{p}0}}\left[2r^2\frac{\partial^2M_{\mathrm{p}0}}{\partial r^2}+4r\frac{\partial M_{\mathrm{p}0}}{\partial r}-2M_{\mathrm{p}0}\right]\right\}\\&\times\cos\theta+2\varepsilon M_{\mathrm{p}0}^{\,2}\sin\theta\\&-\left(\chi-\frac{\chi^2}{2}+2\varepsilon\cos\theta\right)\frac{\partial M_{\mathrm{p}0}}{\partial\tau}\\&+\frac{\partial M_{\mathrm{p}1}}{\partial\tau}-M_{\mathrm{p}0}\exp(-\chi)\frac{\partial\chi}{\partial\tau}\,,\end{aligned} \tag{14}$$

$$\begin{aligned}\frac{\partial M_{\mathrm{p}1}}{\partial\tau}&=M_{\mathrm{p}0}\frac{\partial\chi}{\partial\tau}+\chi\frac{\partial M_{\mathrm{p}0}}{\partial\tau}\\&-\frac{B_0}{B_{\mathrm{p}0}}\frac{1}{\mathrm{v}_{\mathrm{ti}}C_{\mathrm{r}}}\frac{\partial}{\partial\theta}\Big(M_{\mathrm{p}1}-M_{\mathrm{p}0}\varepsilon\cos\theta-\chi M_{\mathrm{p}0}\\&\qquad-\chi M_{\mathrm{p}1}+\frac{\chi^2}{2}M_{\mathrm{p}0}\Big)\\&-\frac{B_0}{B_{\mathrm{p}0}}\frac{1}{\mathrm{v}_{\mathrm{ti}}C_{\mathrm{r}}}\varepsilon\cos\theta\frac{\partial}{\partial\theta}\left(M_{\mathrm{p}1}-M_{\mathrm{p}0}\varepsilon\cos\theta-\chi M_{\mathrm{p}0}\right)\\&-\frac{B_0^{\,2}}{B_{\mathrm{p}0}^{\,2}}\left[\frac{\partial}{\partial\theta}\left(\chi+\frac{5}{18}\frac{1}{C_r^{\,2}}\chi^2\right)+\varepsilon\cos\theta\frac{\partial\chi}{\partial\theta}\right]\\&+\frac{B_0^{\,2}r}{B_{\mathrm{p}0}^{\,3}\mathrm{v}_{\mathrm{ti}}^{\,2}C_{\mathrm{r}}^{\,2}}\frac{1}{m_{\mathrm{i}}}\\&\times\left[\frac{JB_{\mathrm{p}}B_{\phi}}{n}-\left(\frac{\vec{B}_{\mathrm{p}}\cdot\vec{\nabla}\cdot\vec{\pi}_{\mathrm{i}}}{n}\right)_{\mathrm{bulk}}-\left(\frac{\vec{B}_{\mathrm{p}}\cdot\vec{\nabla}\cdot\vec{\pi}_{\mathrm{i}}}{n}\right)_{\mathrm{shear}}\right],\end{aligned} \tag{15}$$

where

$$\chi=\ln\left(n/\bar{n}\right), \tag{16}$$

$$E_1=\frac{1}{B_{\mathrm{p}0}\mathrm{v}_{\mathrm{ti}}C_{\mathrm{r}}}\frac{\partial\Phi_1}{\partial r}\,, \tag{17}$$

$$D=\frac{4\sqrt{\pi}}{3}\frac{I_{\mathrm{ps}}K_0B_0}{\bar{n}\mathrm{v}_{\mathrm{ti}}C_{\mathrm{r}}^{\,2}}\,, \tag{18}$$

$$A = \frac{M_{p0}{}^2}{2} + \frac{5}{36}\frac{1}{C_r{}^2}, \tag{19}$$

$\hat{\mu}$ is the shear viscosity coefficient, and the form of I_{ps} is represented in Eq. (10) of Ref. [4], and depends on M_p and the collision frequency [14]. The variables n_1 and Φ_1 are replaced by χ and E_1 in this set, respectively. Time t is normalized as $\tau = t/t_p$, where

$$t_p = \frac{B_0 r}{B_{p0} v_{ti} C_r}. \tag{20}$$

Eqs. (13) and (14) are the flux surface average and the 2nd order of Eq. (9), respectively. Current J is obtained from Eq. (3), which includes polarization current $\varepsilon_0 \varepsilon_\perp \partial E_r / \partial t$, and external components as driven by an electrode, orbit losses, etc. [15], where ε_0 is the vacuum susceptibility, and $\varepsilon_\perp$ is the perpendicular dielectric constant of a toroidal plasma, which depends on the flow pattern and is of the order of $c^2 / v_A{}^2$, where v_A is the Alfvén velocity [2].

3. Formation Mechanisms of Poloidal Asymmetry

A set of model equations consists of Eqs. (12-15). This extended model includes the generation mechanism of the poloidal shock structure and the GAM. Some simplified cases are described to depict the fundamental mechanisms in this section.

3.1. Poloidal Shock Structure

The key mechanism for poloidal shock formation is in the momentum conservation Eq. (1). With the existence of the large poloidal flow, nonlinear effects in the convective derivative and the density gradient generate the poloidal shock structure by coupling with toroidicity. Assumption of Boltzmann relation

$$n = \bar{n} \exp \frac{e\Phi_1}{T_i} \tag{21}$$

and strong toroidal flow damping

$$V_\phi = 0, \tag{22}$$

which makes M_p to be proportional to the radial electric field, give a simplified set of equations. Equation (14) is given to be

$$\begin{aligned} M_{p0} \exp(-\chi) \frac{\partial \chi}{\partial \tau} = & -\hat{\mu} r^2 \frac{B_0}{B_{p0}} \frac{\partial^2}{\partial r^2} \{ M_{p0} [\exp(-\chi) - 1] \} \\ & + \frac{2}{3} D \exp(-\chi) \frac{\partial^2 \chi}{\partial \theta^2} + \left(1 - M_{p0}{}^2\right) \frac{\partial \chi}{\partial \theta} + 2A \frac{\partial \chi^2}{\partial \theta} \\ & - \left(\chi - \frac{\chi^2}{2} + 2\varepsilon \cos\theta \right) \frac{\partial M_{p0}}{\partial \tau} \\ & - \varepsilon \left\{ D - \hat{\mu} \frac{B_0}{B_{p0}} \left[2r^2 \frac{\partial^2 M_{p0}}{\partial r^2} + 4r \frac{\partial M_{p0}}{\partial r} - 2M_{p0} \right] \right\} \cos\theta \\ & + 2\varepsilon M_{p0}{}^2 \sin\theta \end{aligned} \tag{23}$$

In this case, an iterative process can be taken to obtain the solution, i.e., time evolution of the 2-D structure is calculated from Eq. (23) by substituting M_{p0} obtained by Eq. (13). Then, using Boltzmann relation (21), the potential profile is obtained.

Figure 1 shows the example of the 2-D structure (the detail of the simulation parameters is presented in Ref. [8]). With a prescribed inhomogeneous density profile as shown in Fig. 1 (a), normal and enhanced radial electric field branches are taken in the small and large gradient regions (near the boundary $r - a$ = -5, 0 [cm], where $r = a$ is the position of the

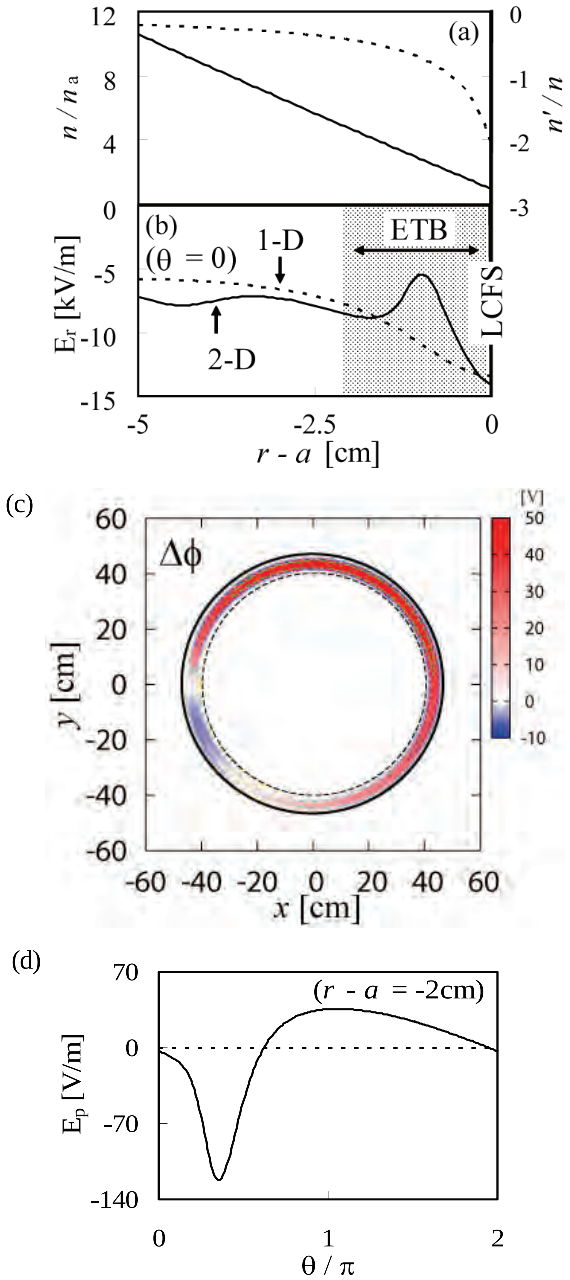

Fig.1 (a) Radial profiles of the density (n) normalized by the density at the edge $r = a$ (n_a) (solid line), and the reciprocal of the density scale length (dashed line). (b) Radial profiles of the radial electric field at $\theta = 0$ (Solutions of the 1-D and 2-D model), and (c) 2-D structure of the potential perturbation. (d) Poloidal profile of the poloidal electric field at $r - a$ = -2 [cm] in spontaneous H mode.

last closed flux surface), respectively, and a critical layer is formed between these regions (at r - a ~ -1 [cm]). The steep gradient of the radial electric field is formed in this layer. The radial electric field profiles in the radial direction are shown in Fig. 1 (b) by solving the 1-D and 2-D model. The 2-D structure of the potential perturbation is shown in Fig. 1 (c). There exists a poloidal structure, and Fig. 1 (d) shows the poloidal electric field profile. The poloidal shock structure exists at $\theta \sim 0.2\pi$ - 0.5π in this case.

3.2. Geodesic Acoustic Mode

The GAM exists in the toroidal plasmas by coupling between the (m, n) = (0, 0) electrostatic potential and (1, 0) sideband density perturbation, where m and n are the poloidal and toroidal mode number, respectively [10]. Taking the ordering that perturbations have $O(\varepsilon)$ with a small poloidal flow, Eq. (12), flux surface average of Eqs. (13) + (14) and Eq. (15) with $\hat{\mu} = 0$ are give to be

$$\frac{\partial \chi}{\partial \tau} = M_{\mathrm{p0}} \varepsilon \sin\theta - \frac{\partial M_{\mathrm{p1}}}{\partial \theta}, \tag{24}$$

$$\frac{\partial M_{\mathrm{p0}}}{\partial \tau} = -\frac{B_0^{\ 2}}{B_{\mathrm{p0}}^{\ 2}} \left\langle \varepsilon \cos\theta \frac{\partial \chi}{\partial \theta} \right\rangle, \tag{25}$$

$$\frac{\partial M_{\mathrm{p1}}}{\partial \tau} = -\frac{\partial \chi}{\partial \theta}, \tag{26}$$

respectively. This set of equations describes the GAM oscillation. If the density perturbation has a $\sin\theta$ dependency

$$\chi = \chi_{\mathrm{r}}(r,t) \sin\theta, \tag{27}$$

Eqs. (24-26) gives the dispersion relation

$$\Omega^2 - \frac{\varepsilon^2}{2} \frac{B_0^{\ 2}}{B_{\mathrm{p0}}^{\ 2}} - k_\theta^{\ 2} = 0, \tag{28}$$

where Ω is the oscillation frequency and k_θ is the wave number in the poloidal direction. The time is normalized by t_{p} shown in Eq (20), and the frequency in real unit is given to be

$$\omega = \frac{C_{\mathrm{r}}}{\sqrt{2}} \frac{\mathrm{v}_{\mathrm{ti}}}{R} \left(1 + \frac{2k_\theta^{\ 2}}{q^2} \right), \tag{29}$$

where q is the safety factor.

4. Summary

The extended set of fluid equations, which consists of the momentum conservation equation, the continuity equation of the density, the charge conservation equation, and the Ohm's law, is derived to obtain 2-D structures of the potential, the density and the flow velocity in H-mode transport barriers. This model includes the generation mechanism of the poloidal shock structure and the GAM, and their competitive formation can be studied. The derivation is the first step to analyze the multi-dimensionality of transport in the toroidal plasmas, which gives quantitative understandings of the transport barrier physics.

Acknowledgement

Authors acknowledge discussions with Prof. S.-I. Itoh, Prof. M. Yagi, Prof. A. Fukuyama and Prof. Y. Takase. This work is partly supported by the Grant-in-Aid for Specially-Promoted Research (16002005) and for Scientific Research (19360418) of MEXT, by Research Fellowships of the Japan Society for the Promotion of Science for Young Scientists, and by the collaboration programs of NIFS (NIFS06KDAD005, NIFS07KOAP017) and of RIAM of Kyushu University.

References

[1] F. Wagner *et al*., Phys. Rev. Lett. **49**, 1408 (1982).
[2] K. Itoh, S.-I. Itoh and A. Fukuyama, *Transport and Structural Formation in Plasmas* (IOPP, Bristol, 1999).
[3] T. Taniuti, H. Moriguchi, Y. Ishii, K. Watanabe and M. Wakatani, J. Phys. Soc. Jpn. **61**, 568 (1992).
[4] K. C. Shaing, R. D. Hazeltine and H. Sanuki, Phys. Fluids B **4**, 404 (1992).
[5] N. Kasuya and K. Itoh, Phys. Rev. Lett. **94**, 195002 (2005).
[6] A. Mohri and M. Fujiwara, Nucl. Fusion **14**, 67 (1974).
[7] R. J. Taylor, P. Pribyl, G. R. Tynan and B. C. Wells, in *Proc. of 15th International Conference on Plasma Physics and Controlled Nuclear Fusion Research, Seville, 1994* (IAEA, Vienna, 1995) Vol. 2, p. 127.
[8] N. Kasuya and K. Itoh, submitted to Nucl. Fusion (2006).
[9] N. Winsor, J. L. Johnson and J. M. Dawson, Phys. Fluids **11**, 2448 (1968).
[10] For a review, e.g. P. H. Diamond, S.-I. Itoh, K. Itoh and T. S. Hahm, Plasma Phys. Control. Fusion **47**, R35 (2005).
[11] For a review, e.g. A. Fujisawa et al., Nucl. Fusion **47**, S718 (2007).
[12] K. C. Shaing, E. C. Crume and W. A. Houlberg, Phys. Fluids B **2**, 1492 (1990).
[13] N. Kasuya and K. Itoh, J. Plasma Fusion Res. **81**, 553 (2005).
[14] N. Kasuya and K. Itoh, Phys. Plasmas **12**, 090905 (2005).
[15] N. Kasuya, K. Itoh and Y. Takase, Nucl. Fusion **43**, 244 (2003).

Proceedings of ITC/ISHW2007

A Comparison of Intermittency in Neutral Fluids and Magnetically Confined Plasmas

Milan RAJKOVIĆ[1)], Miloš ŠKORIĆ[2)] and Mitsuo KONO[3)]

[1)] *Institute of Nuclear Sciences Vinča, Belgrade, Serbia*
[2)] *National Institute for Fusion Science, Toki* 509 – 5292, *Japan,*
[3)] *Chuo University, Hachioji, Tokyo, Japan*

Intermittency in the scrape-off layer (SOL) region of magnetically confined plasma and velocity intermittency of helium gas are compared from the aspect of global and local multifractal properties. The analysis reveals subtle differences in the global aspect between turbulent fluctuations of confined plasmas and neutral fluid as well as differences among magnetically confined devices themselves especially with respect to energy cascade mechanisms in the corresponding systems. Analysis of local multifractal characteristics reveals even more pronounced differences.

Keywords: turbulence, plasma edge turbulence, intermittency, multifractal

1 Introduction

Velocity field statistics are an essential tool and the major source of information in neutral fluid turbulence. The theory of local velocity field structure of incompressible hydrodynamic turbulence, introduced by Kolmogorov in 1941 and usually denoted as K41, is based on the assumptions of homogeneity, isotropy, and the existence of an inertial range. The inertial range in the kinetic energy spectrum is a range in wave number, $k\tilde{}1/l$ where l is the separation length between two points (eddie size), which is located between typical large scales and small dissipative scales and is therefore independent of external drive or output dissipation. The spectrum in the inertial range does not depend on viscosity and is characterized by the power law dependence of the form $E(k) = C_K \langle\epsilon\rangle^{-2/3} k^{-5/3}$, where C_K is the Kolmogorov constant and $\langle\epsilon\rangle$ is the average rate of energy dissipation per unit mass.

The influence of the external magnetic field on turbulent flow of an incompressible fluid leads to much more complicated behavior which modifies turbulent motions. Even more dramatic effects are observed in the case of compressible fluids. Hence, significant differences exist between turbulent flows of neutral fluids and confined plasma. In particular, nonlinearities in plasma turbulence are more numerous having different spectral cascade directions in addition to the $E \times B$ nonlinearity, leading to more complex fluctuating characteristics. One of the most important differences is that time and space measurements lead to different information on the structure of turbulence [1]. Driving mechanisms and damping characteristics are reflected in the temporal aspect of fluctuations while measurements at different spatial locations provide information on spatial structures for various scale lengths. For the case of neutral fluids, time records of turbulent velocity at a single spatial location obtained with the use of a hot-wire or laser Doppler anemometer, are usually interpreted via Taylor's frozen flow hypotheses, as one-dimensional spatial cuts through the flow. However, this approach that generates information about temporal measurements from spatial ones and vice versa, is not applicable in the case of plasma turbulence. Specifically, turbulence in the case of neutral fluids is generated at a certain spatial position and carried by the flow past the probe location so that recordings at different times at a fixed location are equivalent to simultaneous recordings at different spatial locations along the flow. However, in plasma turbulence due to specific nature of nonlinearities, turbulence is created and damped at the same spatial position where measurements are taken so that spatial and temporal informations are interwoven. For the same reason the inertial range [2], may exist only locally in space or in time, and the extent of this range changes along the temporal scale as well as along space, for example along poloidal direction.

In this study we present differences between these two types of turbulences from the aspect of their global and local multifractal properties. In particular we are interested in the intermittency phenomenon in the two cases, and in the case of confined plasma we study the intermittency in the scrape-off layer (SOL) and also compare three different confinement regimes, the L-mode, dithering H-mode and the H-mode. The quantity of interest in the case of neutral fluid turbulence is one-component fluid velocity while in the plasma case it is the ion saturation current fluctuations of recipro-

author's e-mail: milanr@vin.bg.ac.yu

cating Langmuir probe installed at the edge of magnetic confinement devices. We study intermittency properties of the MAST spherical tokamak (L-mode, dithering H-mode and H-mode) and the Tore Supra tokamak with limiter configuration (L-mode). Intermittency of liquid helium recorded in a specially designed cryogenic apparatus [3], is considered in the case of neutral fluid turbulence. The specific design of the apparatus enabled access to a wide range of Reynolds numbers at constant geometry.

The important issue in the multifractal spectra analysis of intermittent plasma turbulence is the choice of relevant measure. In neutral fluid turbulence, in addition to velocity, enstrophy and energy dissipation represent quantities of particular interest although they cannot be constructed in their entirety from a single point velocity time-series. To overcome the difficulty surrogate dissipation

$$\epsilon_{surr}(x) = C\nu \left(\frac{\partial v_x}{\partial x}\right)^2, \tag{1}$$

where C is a constant, sometimes taken equal to 15 is usually used . Using Taylor's frozen flow hypothesis which is naturally justified in neutral fluid turbulence, expression (1) becomes

$$\epsilon_{surr}(t) \sim \nu \left(\frac{\partial v_x}{\partial t}\right)^2. \tag{2}$$

In the plasma case, based on the arguments explained in detail in [4], we devise two measures yielding identical multifractal spectra

$$\epsilon = c \cdot \frac{\left(\left|n\frac{dn}{dt}\right| - \left\langle\left|n\frac{dn}{dt}\right|\right\rangle\right)^2}{\left\langle\left(\left|n\frac{dn}{dt}\right| - \left\langle\left|n\frac{dn}{dt}\right|\right\rangle\right)^2\right\rangle}, \tag{3}$$

and

$$\epsilon = c \cdot \frac{\left(\left(n\frac{dn}{dt}\right)^2 - \left\langle\left(n\frac{dn}{dt}\right)^2\right\rangle\right)^2}{\left\langle\left(\left(n\frac{dn}{dt}\right)^2 - \left\langle\left(n\frac{dn}{dt}\right)^2\right\rangle\right)^2\right\rangle}, \tag{4}$$

where c is a constant.

2 Large Deviation Spectra

The datasets analyzed here consist of measurements of the ion saturation current (I_{SAT}) performed by the moveable Langmuir probe located at the outboard midplane on MAST device [5], at a sampling rate of 1 MHz. Discharge 6861 is high density L-mode plasma and 9031 represents a dithering H-mode with heating power close to the threshold for L-H transition with intermittent high frequency edge localized modes (ELMs), while 5738 is an H-mode with ELMs

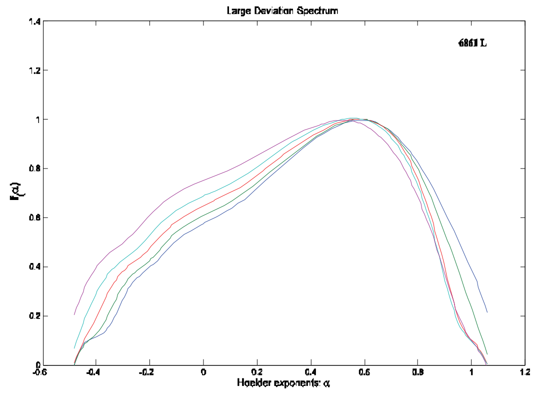

Fig. 1 Fig. 1 LDS of 6861 L-mode of the MAST device

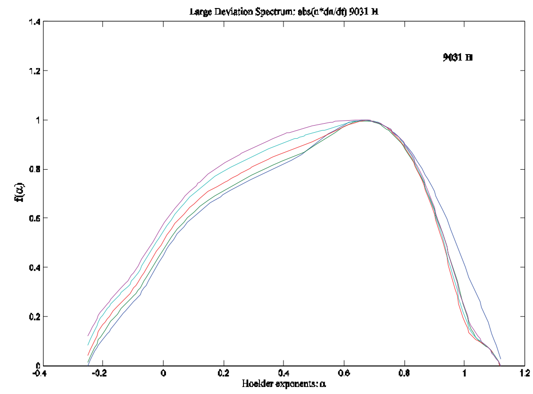

Fig. 2 Fig. 2 LDS of 9031 L-mode of the MAST device

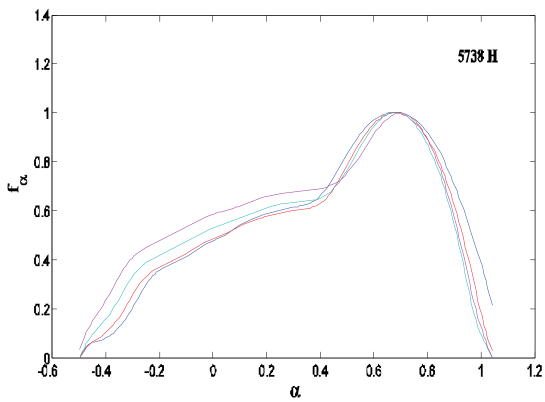

Fig. 3 LDS of the H-mode of the MAST device

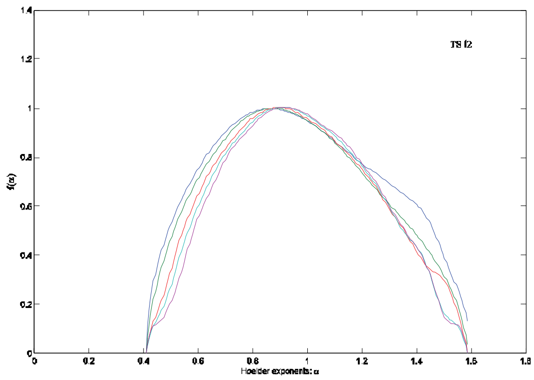

Fig. 4 LDS of the L-mode of Torre Supra.

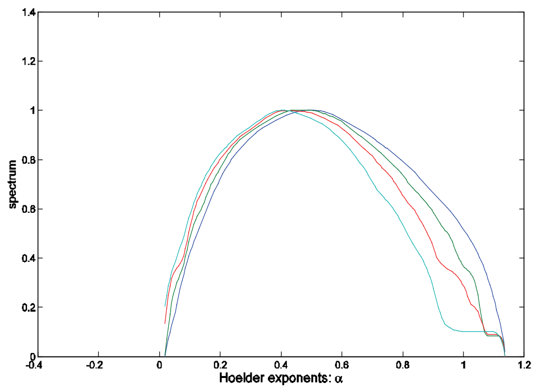

Fig. 5 LDS for the neutral fluid turbulence, Re=328.

at 400 Hz. The corresponding Large Deviation Spectra (LDS) are presented in Figs. 1, 2 and 3. LDS [6] reveal differences between each confinement regime as well as between the two devices. The most striking feature of the MAST spectra (Figs. 1,2 and 3) is their departure from a pure bell-shape and concavity and is a good example where LDS provide more information than Legendre spectra, which are strictly concave although they may be asymmetrical. Their shape reflects existence of several multiplicative laws underlying the cascade processes so that there is a lumping of measures whose supports are disjoint. It is evident that the L-mode of MAST has more complex multifractal structure in the sense that there are more α-values at which the irregularity of the spectrum occurs (i.e. more phase changes) than in the case of L/H-mode or H-mode of MAST. The most striking feature in the Tore Supra L-mode spectra is nonexistence or very mild lumping of measures with no superposition of measures. In Fig. 5 we show the LDS for the case of neutral fluid turbulence.The LDS reveal multifractal similarity of neutral fluid turbulence and the Tore Supra L-mode, while a striking difference with respect to the MAST turbulence.

3 Local Turbulence properties

Local properties of turbulence are modeled with fractal Brownian motion [7]. Since fBm is a self-similar process it provides unique parameter values for H and σ in the restricted temporal domain in which turbulent signal is self-similar (the Hurst exponent H determines the correlation distance for the increments of the process and the quantity σ^2 quantifies the absolute level of correlations). For this purpose a range of frequencies over which the power law

$$P_{B_H} \propto \sigma^2 \, |\omega|^{-(2H+1)} \, . \tag{5}$$

pertains is detected and then the parameters from the same expression are evaluated. Wavelet scale spectra are used for this purpose because they provide time-scale decomposition that is compliant with power law processes, independent of their stationarity. Parameters of the power-law model, σ and H are functions of time and model is applied only over a subset of scales known as the inertial range. Usually multifractal data, besides variations in σ and H, show variations in the inertial range itself.

The main steps in estimation of local turbulence properties are the following:

1. Partitioning of data into segments of equal temporal extent within which turbulent signal is approximately stationary. A special filtering procedure is devised in order to remove dependence of the estimated parameters on segmentation.

2. Wavelet decomposition of the data and evaluation of the scale spectra within each segment.

3. Determination of the inertial range of the scale spectra and evaluation of the power law parameters based on the fBm model. The turbulent data corresponding to the inertial range are assumed to be statistically well represented by fractal Brownian motion. Local turbulence parameters σ and H are therefore determined from the scale spectra corresponding to the inertial range. The extent of the inertial range varies from segment to segment and is rarely equal to the segment size. Since inertial range exists over specific scales (or equivalently over corresponding time range) evaluated parameters have local character.

In Figs.6 and 7 we present temporal variations of the Hurst exponent for the MAST L-mode and the L-mode of Tore Supra. The same quantities are presented in Fig. 8 for the case of neutral fluid turbulence.

A brief comparison of Figs. 6, 7 and 8 shows that there are considerable differences in values of the local Hurst exponent and variance at unit lag for the two magnetic confinement devices and for the neutral fluid

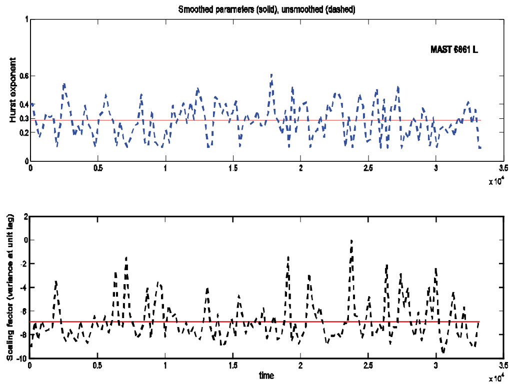

Fig. 6 Parameters of the fBm model, Hurst exponent and the variance at unit lag for the L-mode in MAST. Note random variations of each parameter reflecting multifractal character of the plasma density fluctuations.

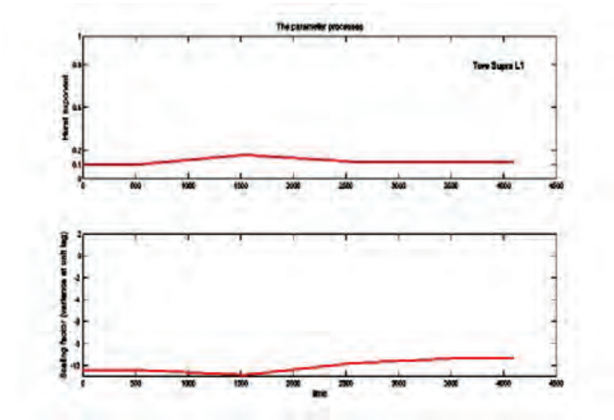

Fig. 7 Parameters of the fBm model, Hurst exponent and the variance at unit lag for the L-mode of Torre Supra. Note very small variations of both quantity.

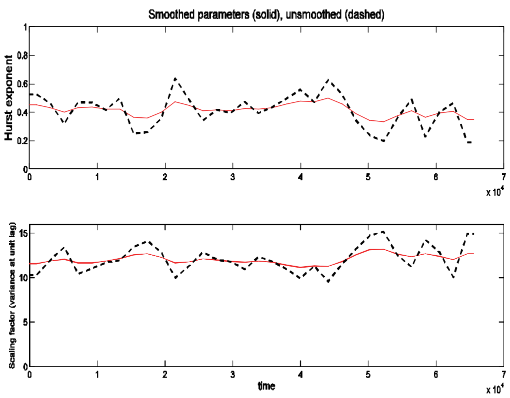

Fig. 8 Parameters of the fBm model, Hurst exponent and the variance at unit lag for the neutral fluid case, Re=328.

turbulence. Namely, these local fractal quantities exhibit purely stochastic variation for the case of MAST L-mode while for the case of the L-mode of Tore Supra these variations are very small and deterministic-like. On the other hand stochastic variations are evident in the case of neutral fluid turbulence indicating its multifractal character, however the values of H and σ are very much different in two cases (and in all cases presented here). Hence, in spite of similarity of large-deviation spectra for the L-mode of Tore Supra and the neutral fluid turbulence, their local (multi)fractal characteristics are very different. Briefly summarizing the multifractal features of each type of turbulence, several characteristics are immediately evident:

1. Large deviation spectra reveal considerable differences between different regimes and different devices of magnetically confined plasma. These disparities indicate different cascade mechanisms of energy transfer among coherent structures.

2. Local features of turbulence in all cases exhibit unique variability and range of values with the possibility of multifractional behavior (not purely multifractal) in certain devices instead of the multifractal properties which dominate both the magnetically confined plasma turbulence and neutral fluid turbulence.

3. Neutral fluid turbulence has very well defined inertial range which is well captured in the wavelet scale spectra irrespective of the segmentation of the turbulent signal. On the other hand scale spectra reveal that in the plasma case inertial ranges are hard to detect and to a large extent depend on the segmentation of the signal. These properties pertain to all regimes in spite of particular features of each. Moreover the extent of inertial ranges is different for all cases considered.

[1] B. Carreras, V.E. Lynch, D.E. Newman, R. Balbin, J. Bleuel, M.A. Pedrosa, M. Endler, B. van Milligen, E. Sánchez and C. Hidalgo, Phys. of Plasmas, 7 (2000) 3278-3287.

[2] U. Frisch, *Turbulence, the Legacy of A. N. Kolmogorov,* Cambridge University Press, Cambridge, 1995.

[3] B. Chabaud, A. Naert, J. Peinke, F. Chillà, B. Castaing and B. Hébral, Phys. Rev. Lett. 73 (1994) 3227-3230.

[4] M. Rajković, M. Skorić, K. SØlna and G. Antar, Nucl. Fusion 47 (2007) 1-13.

[5] B. D. Dudson, R. O. Dendy, A. Kirk, H. Meyer and G. F. Councel, Plasma Phys. Control Fusion 47 (2005) 885-901.

[6] R. H. Riedi, J. Math. Anal. Appl. 189 (1995) 462-490.

[7] K. SØlna and G. Papanicolaou, Wavelet Based Estimation of Local Kolmogorov Turbulence in *Theory and Applications of Long-range Dependence*, Editors P. Doukhan, G. Oppenmeim and M. S. Taqqu, Birkhäuser Boston, 2002, pp 473-506.

Proceedings of ITC/ISHW2007

Geodesic acoustic modes in multi-ion system

Makoto Sasaki[1)], Kimitaka Itoh[2)], Akira Ejiri[3)] and Yuichi Takase[3)]

[1)] *Graduate School of Science, The University of Tokyo, Tokyo, 113-0033, Japan*
[2)] *National Institute for Fusion Science, Toki 509-5292, Japan*
[3)] *Graduate School of Frontier Sciences, The University of Tokyo, Kashiwa, 277-8561, Japan*

The eigenmodes of geodesic acoustic modes (GAMs) in the multi-ion sysytem are investigated. The high-frequency branch of the eigenfrequency decreases due to the increase of effective ion mass. The low-frequency branch (ion sound wave (ISW)) of the damping rate bemoces small. The ratio between the damping rate of GAM and ISW is found to become order unity at $q \sim 3$ (q is the safety factor).

Keywords: geodesic acoustic modes, ion sound wave, multi-ion system, impurity, eigenmode

DOI: 10.1585/pfr.1.001

1 Introduction

Recently, the self-organizing meso-scale structure has attracted much attention. In particular, zonal flows (ZFs) is thought to reduce the anomalous transport driven by turbulence [1]. In toroidal plasma, geodesic acoustic modes (GAMs) exist [2], which are oscillatory modes. The study of GAMs is also essential for plasma research, because GAMs and ZFs share the energy from turbulence. The radial eigenmode of GAM is investigated [3, 4, 5]. In addision, the new diagnostic method, GAM spectroscopy is proposed [6]. This method enables to detect the effective ion mass, which is equal to abundance ratio of ions by detecting radial eigenmode of GAM. It is relevant to investigate whether the method of GAM spectroscopy provides information of impurities. Therefore, the GAMs eigenmodes in multi-ion system is very important.

In this study, the GAMs eigenfrequencies in the collisionless plasma with multiple ion species is investigated. The plasma is assumed to have circular cross section and high aspect ratio. The analytical expression for eigenfrequency of GAM is derived. In addition, the lower-frequency branch, which is the ion sound wave (ISW), is also analyzed. As a result, GAM eigenfrequency is found to become small due to the increase of the effective ion mass. The damping rate of GAM eigenmode becomes small around $q \sim 3$ (q is the safety factor). The analytical expression of low-frequency branch is obtained, which is the extension of [7]. The damping rate of ISW is found to become small in multi-ion system to such a degree that the ratio between the damping rate of ISW and GAM becomes order of unity. This result indicates that the ISW can be detected experimentaly, in the case that the energy is injected from the turbulence to this branch as well as GAM. The general formula of this study is explained in section2, GAM eigenmode is in section3, ISW eigenmode is in section4, and summary is given in section5.

author's e-mail: sasaki@fusion.k.u.tokyo.ac.jp

2 General formula

The model is explained in this section. The magnetic field is assumed to be written as

$$\boldsymbol{B} = \frac{B_0}{1+\epsilon\cos\theta}\left(\boldsymbol{e}_\zeta + \frac{\epsilon}{q}\boldsymbol{e}_\theta\right), \tag{1}$$

where $\boldsymbol{e}_\theta,\ \boldsymbol{e}_\zeta$ are poloidal and toroidal directions respectively. $\epsilon,\ q$ are the inverse aspect ratio and the safety factor. The basic equation, Gyrokinetic equation and quasi-neutral condition can be wriiten as

$$\begin{aligned}\left\{\frac{\partial}{\partial t} \right. &+ \left. v_\parallel \boldsymbol{b}\cdot\nabla + i\boldsymbol{k}_\perp\cdot\boldsymbol{v}_{dr}\right\}\delta f_{k_\perp}^{(j)} = -\left\{ v_\parallel \boldsymbol{b}\cdot\nabla \right. \\ &+ \left. i\boldsymbol{k}_\perp\cdot\boldsymbol{v}_{dr}\right\}\left(F_0^{(j)} J_0(k_\perp\rho)\frac{e\phi_{k_\perp}}{T}\right), \end{aligned} \tag{2}$$

$$\begin{aligned}\sum_j Z_j \int dv^3 \delta f_{k_\perp}^{(j)} &- \sum_j Z_j n_j \left(1-\Gamma_0(k^2\rho_j^2/2)\right) \\ \times\frac{e\phi_{k_\perp}}{T_i} &= \frac{n_e}{T_e}\left(\phi_{k_\perp} - <\phi_{k_\perp}>\right), \end{aligned} \tag{3}$$

where $\delta f_{k_\perp}^{(j)},\ \phi_{k_\perp}$ are the response of distribution of jth ion and ZF potential, resectively. Z_j, n_j, n_e, T_i, T_e are jth ion charge, density, ion temperature, electron density, and electron temperature. The blaket $<>$ represents the average over the magnetic surface. $F_0^{(j)}$ is Maxwell distribution, which is written as $F_0^{(j)} = n_j/\pi^{3/2}\exp\left(-\hat{v}_j^2\right)$. $\hat{v}_j$ is the velocity normalized by jth ion thermal velocity. The thermal velocity can be written as $\hat{v}_j = \sqrt{T_i/m_j}$. m_j is jth ion mass. Here, $\delta f_{k_\perp}^{(j)},\ \phi_{k_\perp}$ are expanded by Foureir series as

$$\delta f_{k_\perp}^{(j)} = \sum_{m=-\infty}^{\infty} e^{im\theta - i\omega t}\delta f_m^{(j)}(\omega) \tag{4}$$

$$\phi_{k_\perp} = \sum_{m=-\infty}^{\infty} e^{im\theta - i\omega t}\hat{\phi}_m(\omega). \tag{5}$$

Using Eqs. (2), (3), the response of ion to ZFs potential is obtained as [8]

$$
\begin{aligned}
i\hat{\omega}\delta f_0^{(j)} &= \frac{1}{2}J_0\left(s\frac{\hat{v}_{\perp j}}{q}\right)k\hat{u}_j(\delta f_{-1}^{(j)} - \delta f_1^{(j)} \\
+ \quad & \hat{\phi}_{-1} - \hat{\phi}_1), \qquad (6) \\
\delta f_m^{(j)} &= \sum_{l,l'} J_0(s\hat{v}_{\perp j}/q)F_0\frac{\hat{v_{\parallel j}}(m-l)}{\omega - \hat{v_{\parallel j}}(m-l)}i^{l'-l} \\
& J_l(k\delta_1)J_{l'}(k\delta_1)\phi_{m-l-l'}., \qquad (7)
\end{aligned}
$$

where s_j is the finite orbit width, which is defined by $s_j = kv_jq/\Omega_j$. $\delta_j = -s_j\left(\hat{v}_{\parallel j} + \hat{v}_{\perp j}^2/2\hat{v}_{\parallel j}\right)$ represents the Doppler shift due to toroidal effect. $\hat{\omega}_j = \omega R_0 q/v_j$ is the normalized frequency. Here, the poloidal harmonics are truncated, and the poloidal modes $m = 0, \pm 1$ are kept. The ion response can be written as

$$
\begin{aligned}
i\hat{\omega}\delta f_0^{(j)} &= n_j\left(C_{00}^{(j)}\hat{\phi}_0 + C_{01}^{(j)}\hat{\phi}_1\right) \qquad (8) \\
\delta f_1^{(j)} &= n_j\left(C_{10}^{(j)}\hat{\phi}_0 + C_{11}^{(j)}\hat{\phi}_1\right). \qquad (9)
\end{aligned}
$$

C_{ij} is the coefficient which is the function of velocity. Combining Eqs. (8), (9) with the quasi-neutral condition Eq. (3), the dispersion relation is given by

$$
\begin{aligned}
\Delta \quad = \quad & \left\{\sum_j \frac{Z_j n_j}{n_e} i \frac{s_j^2}{2}\left[\frac{\hat{\omega}_j}{q^2} + \frac{1}{2}\right.\right. \\
\times \quad & \left.\left.\left\{\frac{3}{2}\hat{\omega}_j + \hat{\omega}_j^3 + \left(\frac{1}{2} + \hat{\omega}_j^2 + \hat{\omega}_j^4\right)Z(\hat{\omega}_j)\right\}\right]\right\} \\
\times \quad & \left\{\frac{1}{\tau_e} - \sum_j \frac{Z_j n_j}{n_e}(1 + \hat{\omega}_j Z(\hat{\omega}_j))\right\} \\
- \quad & \sum_j \frac{Z_j n_j}{n_e} s_j \left\{\hat{\omega}_j^2 + \left(\frac{1}{2}\hat{\omega}_j + \hat{\omega}_j^3\right)Z(\hat{\omega}_j)\right\} \\
\times \quad & \sum_j \frac{Z_j n_j}{n_e} i \frac{s_j}{2}\left\{\hat{\omega}_j + \left(\hat{\omega}_j^2 + \frac{1}{2}\right)Z(\hat{\omega}_j)\right\} \\
= 0. & \qquad (10)
\end{aligned}
$$

3 GAM eigenmode

The high-frequency branch, standard GAM is the solution derived under the assumption $\hat{\omega} >> 1$. In this case, the plasma dispresion function $Z(\hat{\omega})$ can be expanded as

$$
Z(\hat{\omega}) \approx -\left(\frac{1}{\hat{\omega}} + \frac{1}{2\hat{\omega}^3} + \frac{3}{4\hat{\omega}^5}\right) + i\sqrt{\pi}e^{-\hat{\omega}^2}. \quad (11)
$$

The dispersion relation Eq.(10) can be expanded explicitly as

$$
\begin{aligned}
\Delta \quad = \quad & A\hat{\omega} - (B + \delta B)\frac{1}{\hat{\omega}} - \frac{C}{\hat{\omega}^3} \\
+ \quad & i\left(De^{-\hat{\omega}^2} + Ee^{-\hat{\omega}^2/4}\right), \qquad (12)
\end{aligned}
$$

where $A,\ B,\ \delta B,\ C,\ D,\ E$ can be written as

$$
\begin{aligned}
A \quad &= \frac{1}{2q^2\tau_e}\sum_j \frac{Z_j n_j}{n_e}\left(\frac{Z_{main}}{Z_j\zeta_j}\right)^2\frac{1}{\zeta_j} \qquad (13) \\
B \quad &= \frac{7}{8\tau_e}\sum_j \frac{Z_j n_j}{n_e}\left(\frac{Z_{main}}{Z_j\zeta_j}\right)^2\zeta_j \\
+ \quad & \frac{1}{2}\sum_{j,j'}\frac{Z_j n_j}{n_e}\frac{Z_{main}}{Z_j\zeta_j}\frac{Z_j' n_j'}{n_e}\frac{Z_{main}}{Z_j'\zeta_j'}\zeta_j' \qquad (14) \\
\delta B \quad &= \frac{1}{4q^2}\sum_{j,j'}\frac{Z_j n_j}{n_e}\left(\frac{Z_{main}}{Z_j\zeta_j}\right)^2\frac{1}{\zeta_j} \\
\times \quad & \frac{Z_j' n_j'}{n_e}\frac{Z_{main}}{Z_j'\zeta_j'}\zeta_j'^2 \qquad (15) \\
C \quad &= \frac{23}{16\tau_e}\sum_j \frac{Z_j n_j}{n_e}\left(\frac{Z_{main}}{Z_j\zeta_j}\right)^2\zeta_j^3 \\
- \quad & \frac{7}{16}\sum_{j,j'}\frac{Z_j n_j}{n_e}\left(\frac{Z_{main}}{Z_j\zeta_j}\right)^2\zeta\frac{Z_j' n_j'}{n_e}\zeta_j'^2 \\
+ \quad & \frac{1}{2}\sum_{j,j'}\frac{Z_j n_j}{n_e}\frac{Z_{main}}{Z_j\zeta_j}\frac{Z_j' n_j'}{n_e}\frac{Z_{main}}{Z_j'\zeta_j'} \\
\times \quad & \left(\zeta_j'^3 + \zeta_j^2\zeta_j'\right) \qquad (16) \\
D \quad &= \sqrt{\pi}\frac{Z_{main}n_{main}}{n_e}\frac{1}{2\tau_e}\hat{\omega}^4 + \left\{\frac{1}{2} - \frac{\tau_e}{4}\right. \\
& \sum_j \frac{Z_j n_j}{n_e}\zeta_j^2 + \frac{\tau_e}{2}\frac{Z_j n_j}{n_e}\frac{Z_{main}}{Z_j\zeta_j} \\
& \left. + \frac{\tau_e}{2}\frac{Z_j n_j}{n_e}\frac{Z_{main}}{Z_j}\right\}\hat{\omega_G}^2 \qquad (17) \\
E \quad &= \sqrt{\pi}\frac{Z_{main}n_{main}}{n_e}\frac{1}{2\tau_e}\frac{\hat{\omega}^6}{1024} \qquad (18) \\
\zeta_j \quad &= \sqrt{\frac{m_{main}}{m_j}\tau_j}, \qquad (19)
\end{aligned}
$$

where ζ_j is the thermal velocity ratio, τ_j is the j ion temperature normalized by main ion temperature $\tau_j = T_j/T_{main}$. $m_{main}, Z_{main}, n_{main}$ are the mass, the charge and the density of main ion. The solution of this dispersion relation can be obtained as

$$
\begin{aligned}
\omega_G \quad &= \quad \frac{v_T}{R_0 q}\frac{B}{A}\left\{1 + \left(\frac{B\delta B}{A^2} + \frac{C}{A}\right)\frac{B}{A}\right\} \qquad (20) \\
\gamma_G \quad &\approx \quad -\sqrt{\pi}\frac{Z_{main}n_{main}}{n_e}q\frac{v_T}{R_0}\left\{\sum_j \frac{Z_j n_j}{n_e}\left(\frac{Z_{main}}{Z_j\zeta_j}\right)^2\right. \\
\times \quad & \left.\frac{1}{\zeta_j}\right\}^{-1}\left[\left\{\frac{\hat{\omega_G}^4}{2} + \left\{\frac{1}{2} - \frac{\tau_e}{4}\sum_j \frac{Z_j n_j}{n_e}\zeta_j^2\right.\right.\right. \\
+ \quad & \left.\frac{\tau_e}{2}\frac{Z_j n_j}{n_e}\frac{Z_{main}}{Z_j\zeta_j} + \frac{\tau_e}{2}\frac{Z_j n_j}{n_e}\frac{Z_{main}}{Z_j}\right\} \\
\times \quad & \left.\left.\hat{\omega_G}^2\right\}e^{-\hat{\omega_G}^2} + s^2\frac{\hat{\omega_G}^6}{1024}e^{-\hat{\omega_G}^2/4}\right]. \qquad (21)
\end{aligned}
$$

The real eigenfrequency ω_G agrees with the result of [8, 9] in the limit of single-ion $\sum_j Z_j n_j \rightarrow n_{main}$. In the limit of $\sum_j Z_j n_j \rightarrow Z_1 n_1$, which is impurity limit, ω_G becomes

$$\omega_G \rightarrow \zeta \omega_{G0} \left(1 + \frac{\zeta}{Z_1} \frac{\alpha}{q^2}\right), \qquad (22)$$

where $\omega_{G0} = v_T/R_0\sqrt{7/4+\tau_e}, \alpha = (23+16\tau_e+4\tau_e^2)/(7+4\tau_e)^2$. Approximately, the frequency of leading order becomes ζ times small as compared with that for hydrogen plasma. Higher order term, which is $1/q^2$ order term becomes ζ/Z_1 times small. In short, the effect of mass on the real eigenfrequency is more significant than the the effect of charge. The result of the real eigenfrequency in two-ion system is shown in Fig. 1. The behavior of the damping rate is shown in Fig. 2 in the case of $Z_{eff} = 4$. The damping rate in multi-ion system is found to be larger. This is because the effect of the Landau damping becomes large due to the decrease of $\hat{\omega}_G$. Especially, the dampng rate becomes smaller around $q \sim 3,\ 4$, because the $m = \pm 2$ coupling becomes effective.

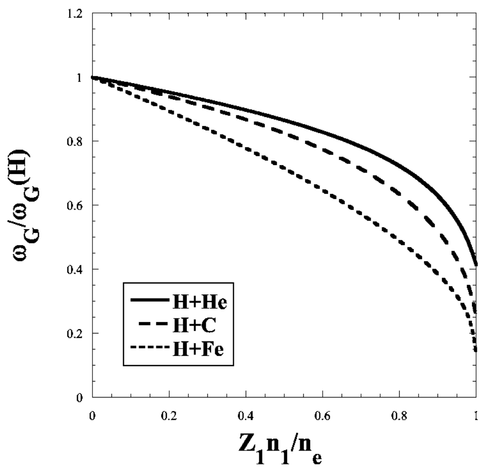

Fig. 1 The multi-ion effect on the GAM real frequency.

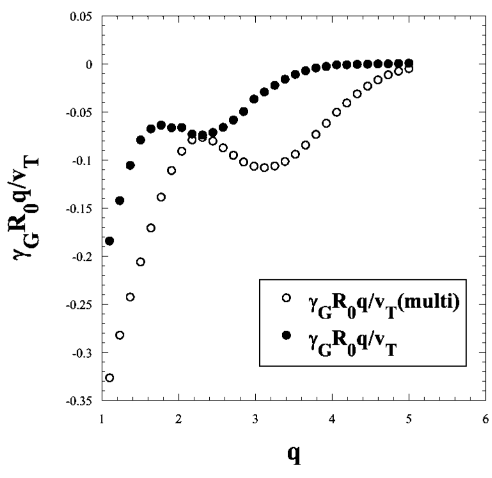

Fig. 2 The multi-ion effect on the GAM damping rate. Ions consist of hydrogen and carbon. $Z_eff = 4$.

4 ISW eigenmode

The low-frequency branch, ISW, has the real frequency which has a resonant frequency with heavier ions. The solution is derived under the assumption $\hat{\omega} << 1$. In the case of single-ion system, the plasma dispersion function $Z(\hat{\omega})$ can be expanded as

$$Z(\hat{\omega}) \approx -2\hat{\omega} + \frac{4}{3}\hat{\omega}^3 - \frac{8}{15}\hat{\omega}^5 + i\sqrt{\pi}e^{-\hat{\omega}^2}. \qquad (23)$$

However, in multi-ion system, the argument of Z-function is $\hat{\omega}/\zeta_j$. The coefficient ζ_j is less than unity. Therefore, it is difficult to estimate the analytical representation of eigenfrequency in multi-ion system. Here, the eigenmode in single-ion system is investigated. The dispersion relation is written as

$$\Delta = a\hat{\omega} + b\hat{\omega}^3 + i\left(c + d\hat{\omega}^2\right) \qquad (24)$$

Coefficients a to d can be written as

$$a = \left(\frac{1}{2} + \frac{1}{q^2}\right)\left(\frac{1}{\tau_e} + 1\right) - \frac{\pi}{4} \qquad (25)$$

$$b = \frac{-2}{q^2} - \frac{1}{3\tau_e} + \frac{\pi}{2} \qquad (26)$$

$$c = \frac{\sqrt{\pi}}{2\tau_e} \qquad (27)$$

$$d = \sqrt{\pi}\left(\frac{1}{q^2} + \frac{1}{\tau_e} - \frac{1}{2}\right). \qquad (28)$$

The solution of $\Delta = 0$ is obtained by following procedure. In this case, due to $\omega_{isw} \sim \gamma_{isw}$, ω is replaced by $\omega = \omega_r + i\gamma$. Eq.(24) can be expressed as

$$\begin{aligned}\Delta &= \hat{\omega}_r\left\{a + b\left(\hat{\omega}_r^2 - 3\hat{\omega}_r\hat{\gamma}^2\right) - 2d\hat{\gamma}\right\} + i\left\{a\hat{\gamma}\right.\\ &+ \left. b\left(3\hat{\omega}_r^2\hat{\gamma} - \hat{\gamma}^3\right) + c + d(\hat{\omega}_r^2 - \hat{\gamma}^2)\right\} \qquad (29)\end{aligned}$$

The obvious solution for $\omega_r = 0$ is

$$\omega \sim 0 \qquad (30)$$

$$\gamma = \frac{1}{2}\frac{v_T}{R_0 q}\left(\frac{a}{d} - \sqrt{\frac{a^2}{d^2} + \frac{4c}{d}}\right). \qquad (31)$$

This solution is the extension of [7] for finite τ_e. The solution for the dispersion relation Eq.(24) whose frequency is finite (ISW) is difficult to obtain in an analytic expansion to this order. To get the analytical expression, it needs to be expanded in higher order terms. The solution of ISW is obtained by Eq.(10) numerically. The compasion between the eigenfrequency of multi-ion system and single-ion system is shown in Fig.3. The damping rate in multi-ion system becomes much smaller than that in single-ion system. This attributes the fact that the Landau damping becomes smaller due to the decrease of real frequency. Discontinuity in the calculated damping rate arises the fact that we chose the minimum damping rate solution among many solutions. The ratio of damping rates of ISW and GAM is found to become the order of unity. This result indicates that ISW can be observed experimentally.

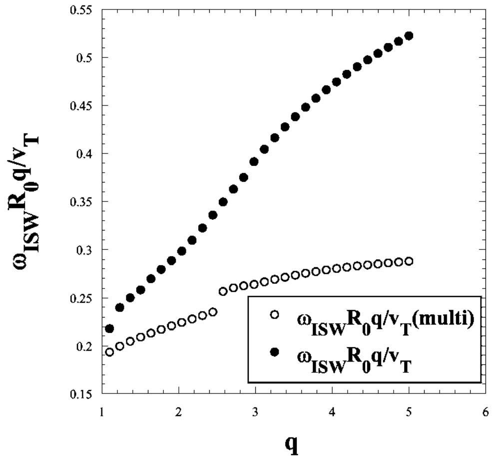

Fig. 3 The comparison between the real frequency of ISW in multi-ion (hydrogen and carbon. $Z_eff = 4$) and single-ion.

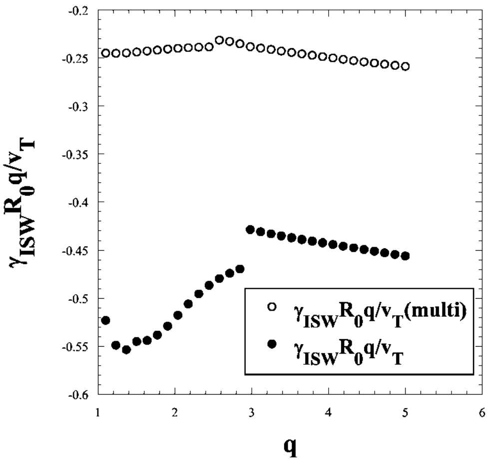

Fig. 4 The comparison between the damping rate of ISW in multi-ion and single-ion.

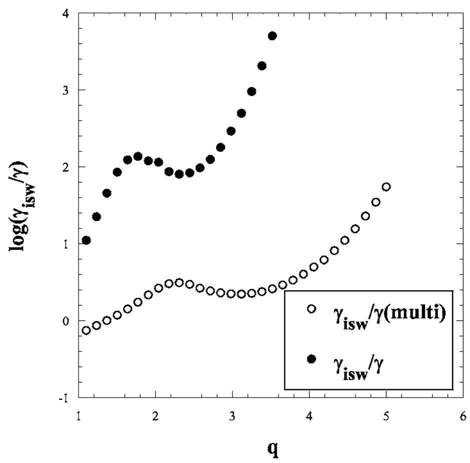

Fig. 5 The ratio between the damping rate of ISW and GAM.

5 Summary

The GAMs eigenmode in multi-ion system is investigated in the collisionless limit. The plasma is assumed to have circular cross section, and high aspect ratio. The high-frequency branch, standard GAM, is analyzed. The analytic expression for eigenfrequency is obtained. With the increase in effective ion mass, GAM frequency decreases. The mass dependence is more significant than the charge dependence. These results are essential for GAM spectroscopy. The damping rate of standard GAM becomes smaller than single-ion system. This influences the energy partition between ZFs and GAMs. In addition, the low-frequency branch, ISW, is analyzed. The damping rate in multi-ion system becomes small, and their damping rates become comparable. Thus, if the turbulent energy is injected to this brach, this mode can be observed in experiment.

6 Acknowledgment

This work was supported by JSPF Grant-in-Aid for Scientific Research 16106013 and NIFS Collaborative Research Program NIFS07KOAR008.

[1] P. H. Diamond, S.-I. Itoh, K. Itoh, and T. S. Hahm, Plasma Phys. Control. Fusion, **47**, R35 (2005).

[2] N.Winsor, J.L.Johnson, J.J.Dawson, Phys.Fluids **11**, 2248 (1968)

[3] T. Ido, Y. Miura, K. Hoshino, K. Kamiya, Y. Hamada, A. Nishizawa, Y. Kausumi, H. Ogawa, Y. Nagashima, K.S hinohara, Y. Kusama, and JFT-2M group, Nucl. Fusion **46**, 512 (2006).

[4] K. Itoh, S.-I. Itoh, P. H. Diamond, A. Fujisawa, M. Yagi, T. Watari, Y. Nagashima, and A. Fukuyama, Plasma Fusion Res. **1**, 037 (2006).

[5] M. Sasaki, K. Itoh, A. Ejiri, Y. Takase, Contribution to Plasma Phys in press

[6] S-I. Itoh1, K. Itoh, M. Sasaki, A. Fujisawa, T. Ido, Y. Nagashima, Plasma Phys. Control. Fusion **49** L7-L10 (2007)

[7] Zhe. Gao, K. Itoh, H. Sanuki, J. Q. Dong, Phys of Plasma **13** 100702 (2006)

[8] H. Sugama, and T.-H. Watanabe, J. Plasma. Phys. **72**, 825 (2006).

[9] M. Sasaki, K. Itoh, A. Ejiri, Y. Takase, submitted to Plasma Fusion Res.

Proceedings of ITC/ISHW2007

Generation of supersonic and super-Alfvénic flow by using ICRF heating and a magnetic nozzle

Akira Ando[1], Tatsuya Hagiwara[1], Toshihiro Komagome[1], Kunihiko Hattori[2], Masaaki Inutake[3]

[1]*Graduate School of Engineering, Tohoku University, Aoba-yama 6-6-05, Sendai, 980-8579, Japan*
[2]*Nippon Institute of Technology, Saitama, 345-8501 Japan.*
[3]*Research Institute of Electrical Communication, Tohoku University, Sendai, 980-8577, Japan*

(Received / Accepted)

Fast-flowing plasmas in supersonic and super-Alfvénic regime are generated in combined experiments of ion cyclotron resonance heating (ICRH) and acceleration in a magnetic nozzle. During radio-frequency (RF) wave excitation in a fast-flowing plasma produced by a magnet-plasma-dynamic arcjet (MPDA), strong ion cyclotron heating is clearly observed. Thermal energy in the heated plasma is converted into flow energy in a diverging magnetic nozzle, where the magnetic moment μ is nearly kept at constant. Plasma flow energy can be controlled by changing the input RF power and/or modifying the magnetic nozzle configuration. In a strongly diverging magnetic nozzle, an Alfvén Mach number as well as an ion acoustic Mach number attains to more than unity, that is, supersonic and super-Alfvénic plasma flow is realized.

Keywords: supersonic plasma flow, super-Alfvenic plasma flow, ion cyclotron heating, magnetic nozzle, advanced plasma thruster

1. Introduction

Recently, the production and control of fast-flowing plasma are of growing significance for clarifying various MHD phenomena observed in space and fusion plasmas, for developing advanced electric propulsion systems and for applying in various industrial researches.

In cosmic plasmas, astrophysical jet from a fast rotating star is one of the most interesting phenomena [1]. Helical structure is often observed in the jet, and the physical mechanism of the jet formation is still under investigation. In fusion plasmas such as in multiple mirror [2]. and toroidal devices [3, 4], dynamics of a fast-flowing plasma in magnetic fields are important from the view point of stabilizing and improving the plasma confinement.

As for future space exploration projects, an electric propulsion system is one of the inevitable technologies to be urgently developed. In an advanced space propulsion system for a manned interplanetary space flight, not only a high power density plasma thruster generating higher thrust, but also a thruster which has capability of varying a specific impulse are requisite to improve propellant utilization and thrust performance.

A magneto-plasma-dynamic arcjet (MPDA) is one of the plasma sources which can generate high density plasma with high exhaust plasma velocity. It is utilized not only as one of the representative devices for electric propulsion systems but also as a supersonic plasma flow source.

Recently, intensive researches to develop an advanced space thruster named as Variable Specific Impulse Magnetoplasma Rocket (VASIMR) have been performed for the purpose of manned Mars exploration. The thruster can control a ratio of specific impulse to thrust at constant power. The exhausting plasma flow can be controlled by a combined system of the ion cyclotron heating and the magnetic nozzle [5]. A flowing plasma is heated by ion cyclotron range of frequency (ICRF) heating and thermal energy of the heated plasma is converted to flow energy in a magnetic nozzle.

We have demonstrated for the first time both the ion cyclotron resonance heating and the acceleration of ions in a magnetic nozzle [6]. Plasma flow was produced by an MPDA installed in the HITOP (HIgh density Tohoku Plasma) device in Tohoku University. Strong ion heating was observed and the conversion of thermal energy to flow energy in a magnetic nozzle was confirmed. This technology can be applied for production and control of fast-flowing plasma in various applications.

In this paper we report experimental studies of a fast-flowing plasma heated by ICRH and accelerated by a diverging magnetic nozzle in the HITOP device, Tohoku University. We also obtained a fast-flowing plasma in supersonic and super-Alfvénic regime at the end of a strongly diverging magnetic nozzle.

author's e-mail: akira@ecei.tohoku.ac.jp

2. Experimental setup

Experiments were performed in the HITOP device in Tohoku University [7,8]. Schematic view is shown in Fig.1. The diameter of a cylindrical vacuum chamber is 0.8m, and length is 3.3m. An external magnetic field can be produced up to 0.1T with magnetic coils surrounding around the vacuum chamber. An MPDA is installed at one end port of the HITOP, which consists of coaxial pair of electrodes. A rod cathode is made of tungsten (10mm in diameter), and an annular anode is made of molybdenum (30mm in diameter). A quasi-steady plasma was formed during 1ms by a high power MPDA with helium as a working gas. The plasma was heated by RF waves launched by a right-handed helically-wound antenna set at Z=0.6m downstream of the MPDA. RF frequency f_{RF} can be varied from 0.2MHz to 0.5MHz with a RF power P_{RF} up to 20kW.

Diamagnetic coil is set at Z=2.3m to measure the plasma thermal energy. Electrostatic energy analyzers (EEAs) are set at Z=2.33m and Z=3.13m to measure ion energy distribution and ion temperature $T_{i\perp}$ and $T_{i//}$. Here, the suffix $\perp$ and // indicate perpendicular and parallel components to the axial magnetic field, respectively.

In the region far downstream of the MPDA, we evaluated ion acoustic Mach number M_i by a Mach probe. The Mach probe has two plane surfaces, one of which faced the flow upstream while the other faced downstream. The ion Mach number could be derived as a function of the ratio of two ion saturation current densities, J_{up} and J_{down}, The relationship between M_i and J_{up}/J_{down} was calibrated with the spectroscopic measurements [9,10]

3. Experimental results

3-1. Combined experiments of ICRH and a magnetic nozzle

Experiments were performed with both a magnetic-beach and a diverging nozzle magnetic field configurations. In Fig.1 the magnetic field configuration is also shown with a constant B_U (=0.1T) at the antenna position, a variable B_D (corresponding to ion cyclotron resonance condition) at the diamagnetic coil position, and a variable B_N (corresponding to the EEA position of downstream region).

Figure 2 shows the typical waveforms of the discharge current I_d of the MPDA and the diamagnetic coil signal $W_\perp$. When radio-frequency (RF) waves were launched by a helically-wound antenna in a plasma passing through a magnetic beach configuration, strong increase of plasma thermal energy was observed, as shown in Fig.2 (b). We have confirmed that the strong increase of $W_\perp$ occurred when the magnetic field B_D was slightly lower than that of the ion cyclotron resonance condition, ω / ω_{ci} = 1. This shift was caused by the Doppler effect. Here, ω and ω_{ci} are the angular frequency of excited RF wave and ion cyclotron motion, respectively, and ω_{ci} is expressed as $\omega_{ci} = eB/m_i$ with electron charge e and ion mass m_i.

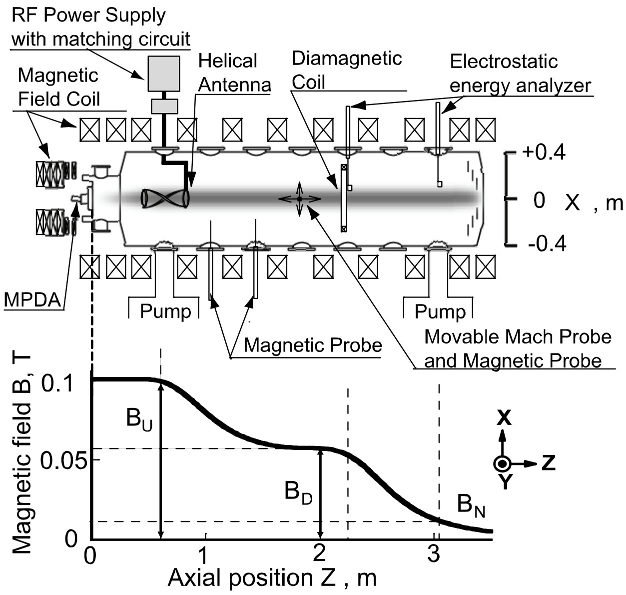

Fig.1 Schematic of the HITOP device. Magnetic field with magnetic beach and diverging nozzle configuration is also shown.

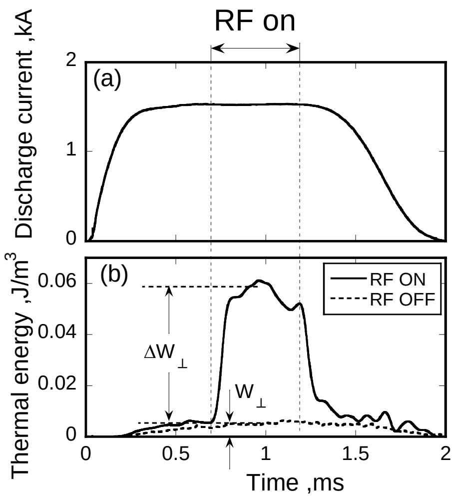

Fig.2 Time evolutions of (a) I_d and (b) $W_\perp$. He plasma. f_{RF}=0.24MHz.

The plasma thermal energy was converted to flow energy in a diverging magnetic nozzle. We measured ion temperatures by the EEAs in three types of magnetic nozzle configurations. Figure 3 shows typical EEA signals obtained before and after the nozzle with B_D (Z=2.33m) = 57.5mT and B_N (Z=3.13m) = 6.9mT. Strong increase of ion temperature, especially in the perpendicular direction was occurred before the magnetic

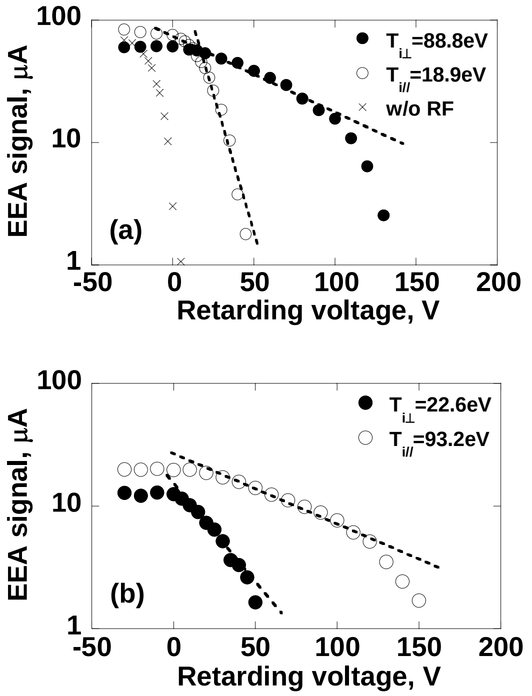

Fig. 3 Electrostatic energy analyzer signals measured at (a) Z=2.33m and (b) Z=3.13m. He plasma. P_{RF}=19kW, f_{RF}=0.24MHz, n_e=1.0×10^{17}m^{-3}, B_D=57.5mT, and B_N=6.9mT.

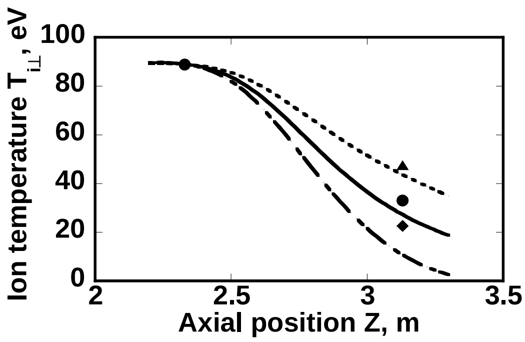

Fig. 4 Axial profile of $T_{i\perp}$ in the three magnetic nozzle configurations. Lines are calculated ones assuming μ=const. Closed triangles : B_N=28.1mT, closed circles : B_N=17.2mT, closed diamonds : B_N=6.9mT.

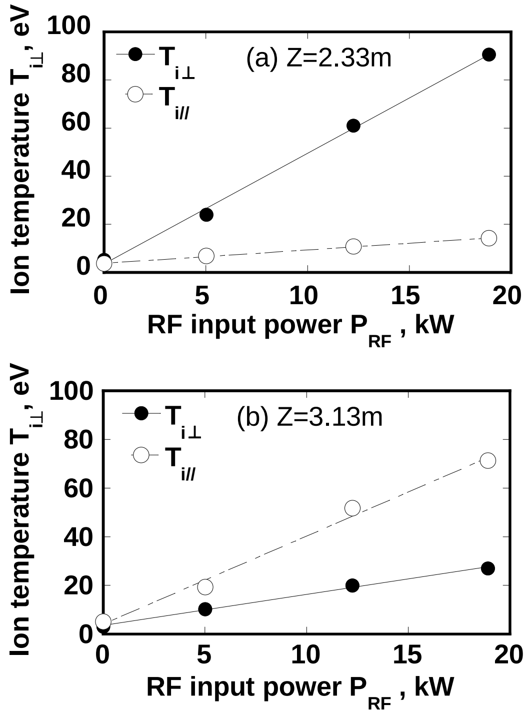

Fig. 5 Dependence of $T_{i\perp}$ (closed circles) and $T_{i//}$ (open circles) on RF input power measured at (a) Z=2.33m and (b) Z=3.13m. f_{RF}=0.24MHz, n_e=1.0×10^{17}m^{-3}, B_D=57.5mT, and B_N=17.2mT.

nozzle. $T_{i\perp}$ increased from 5eV to 89eV with the RF input power of 19kW.

The EEA signal decreased above the retarding voltage of 100V as shown in Fig.3 (a). The Larmor radius of helium ions becomes 5cm with $T_{i\perp}$ = 100eV and B = 57.5mT, which almost equals to the plasma radius. The highly-heated ions expanded to outer region and the signal measured at the center position decreased above the retarding voltage of 100V.

By passing through the diverging magnetic nozzle, increase of $T_{i//}$ and decrease of $T_{i\perp}$ were clearly observed in the analyzer signals shown in Fig.3 (b). This energy conversion was occurred due to the conservation law of the magnetic moment, μ (=$W_\perp/B$).

Figure 4 shows an axial profiles of measured $T_{i\perp}$ in the three magnetic fields. Profiles of $T_{i\perp}$ calculated by assuming μ =const. are also shown in the figure. It is confirmed that $T_{i\perp}$ varied so as to keep the magnetic moment constant but some discrepancy was observed in larger gradient of the magnetic field. It should be caused by a particle motion along a weak magnetic field.

We also measured axial profile of plasma potential V_s by an electrostatic Langmuir probe and an emissive probe. When RF wave was excited and ion heating was occurred, the potential decreased along the field line and axial electric field was formed. The electric field appeared in a magnetic nozzle accelerates ions to the downstream direction. The ion velocity distribution in parallel direction to the magnetic field was determined by the energy conversion from the increased thermal energy and the acceleration by the electric field. The formation of the electric field is probably due to the ambipolar electric field, but further study is necessary to understand this phenomena.

The ion acoustic Mach number M_i is one of the important parameters of an accelerated flow, which is defined as the following equation

$$M_{\mathrm{i}} = \frac{U_{\mathrm{z}}}{C_{\mathrm{s}}} = \frac{U_{\mathrm{z}}}{\sqrt{k_{\mathrm{B}}\left(\gamma_{\mathrm{e}}T_{\mathrm{e}} + \gamma_{\mathrm{i}}T_{\mathrm{i}}\right)/m_{\mathrm{i}}}} \tag{1}$$

Here, C_s is the ion acoustic wave velocity, U_z is ion flow velocity, k_B is the Boltzmann constant, m_i is the ion mass, and γ_i and γ_e are the specific heat ratios of the ions and electrons, respectively. The square of M_i is related with the ratio of flow energy to thermal energy of the flowing plasma. At the end of the magnetic nozzle region, this ratio attained to more than 4, which corresponds to $M_i > 2$, that is supersonic plasma flow was formed.

The parallel energy of exhausting plasma can be changed by controlling the input RF power P_{RF}. Figure 5 shows dependences of $T_{i\perp}$ and $T_{i//}$ on P_{RF} measured at Z=2.33m (before the magnetic nozzle) and Z=3.13m (after the magnetic nozzle). As shown in Fig.5 (a), $T_{i\perp}$ increased linearly with the increase of P_{RF}, whereas $T_{i//}$ slightly increased with P_{RF} in the ion heating region (Z=2.33m). After the energy conversion in the magnetic nozzle, $T_{i//}$ strongly increased linearly with the increase of P_{RF} as shown in Fig.5 (b).

These experimental data clearly show that parallel energy of exhausting plasma, thus also the ion Mach number of the plasma flow, can be controlled by changing the input RF power and/or modifying the magnetic nozzle configuration.

3-2. Supersonic and super-Alfvénic plasma flow in a strongly diverging magnetic nozzle

In order to realize super-Alfvénic flow, plasma flow should exceed the Alfvén velocity V_A. The Alfvén Mach number M_A is defined as the following equation.

$$M_{\mathrm{i}} = \frac{U_{\mathrm{z}}}{V_A} = \frac{U_{\mathrm{z}}}{B_z/\sqrt{\mu_0 n_i m_{\mathrm{i}}}} \tag{2}$$

Here, V_A is the Alfvén velocity, μ_0 is permeability, n_i is the ion density.

We have measured ion Mach number by a Mach probe and ion density by Langmuir probe and obtained axial profiles of M_i and M_A in the diverging magnetic field as shown in Fig.6. Here, no ICRF heating was applied. As is shown in the figure, both of M_i and M_A attained to more than unity, that is, supersonic and super-Alfvénic plasma flow was realized in a laboratory plasma. Further experiments should be necessary with the combination of ICRF heating.

Acknowledgments

This work was supported in part by Grant-in-Aid for Scientific Researches from Japan Society for the Promotion of Science, and under the auspices of the NIFS Collaborative Research Program (NIFS07KKMB001 and NIFS06KUGM018).

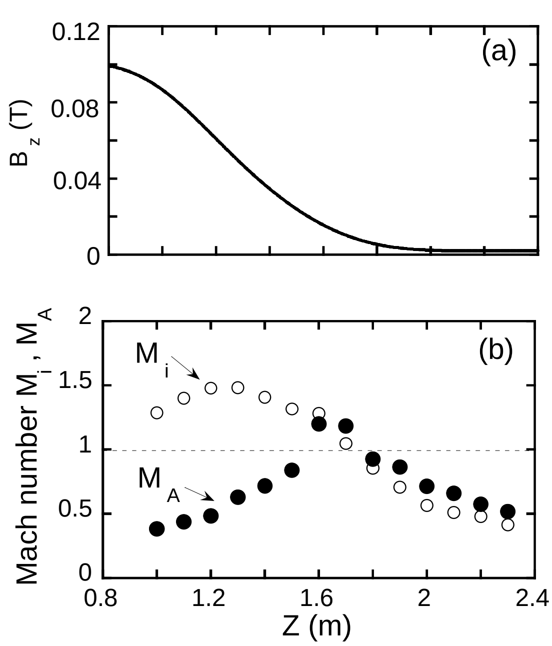

Fig. 6 Axial profile of (a) magnetic field and (b) ion Mach number M_i and Alfvén Mach number M_A in the diverging magnetic nozzle configurations.

References

[1] D.L. Meier, S. Koide,Y. Uchida, Science, **291**, 84 (2001) ; M. Nakamura, Y. Uchida, S. Hirose, New Astronomy, **6**, 61 (2001).

[2] V.V. Mirnov and A.J. Lichtenberg, *Rev. of Plasma Physics* (Consultant Bureau, New York-London, 1996), Vol.19, p.53.

[3] L.C. Steinhauer and A. Ishida, Phys. Rev. Lett., **79**, 3423 (1997).

[4] S.M. Mahajan and Z. Yoshida, Phys. Rev. Lett., **81**, 4863 (1998).

[5] F.R.ChangDiaz, et.al., Proc. of 36th Joint Propulsion Conf., (Huntsville, 2000), **AIAA-2000-3756**, pp.1-8.

[6] A.Ando, et.al., Phys. Plasmas. **13**, 057103 (2006).

[7] M. Inutake, et al., Trans. of Fusion Technology, **43**, 118 (2002).

[8] M. Inutake, et al., Plasma Phys. Control. Fusion, **49**, A121 (2007).

[9] A.Ando, et al., Thin Solid Films, **506-507C**, 601 (2006).

[10] A.Ando, et al., Contrib. to Plasma Physics, **46**, 335 (2006).

Proceedings of ITC/ISHW2007

Investigation of plasma turbulence in strongly sheared $E \times B$ flows using multi-probe arrays

M. RAMISCH[1)], F. GREINER[2)], N. MAHDIZADEH[1)], K. RAHBARNIA[1)] and U. STROTH[1)]

[1)] *Institut für Plasmaforschung, University Stuttgart, 70569 Stuttgart, Germany*

[2)] *Institut für Experimentelle und Angewandte Physik, University Kiel, 24098 Kiel, Germany*

Poloidal $E \times B$ shear flows can act on turbulent transport through the shear decorrelation mechanism, which can reduce the radial size of turbulent structures [1] or change the phase relation between density and potential fluctuations [2]. In this contribution, the influence of sheared $E \times B$ flows on the microscopic structure of turbulence is investigated in the toroidally confined plasma of the torsatron TJ-K. Multi-probe arrays are used to detect turbulent structures and study the dynamics perpendicular to the magnetic field. Sheared poloidal $E \times B$ flows are generated by plasma biasing. It turns out that at strong flow shear, the fluctuations are dominated by large-scale coherent structures with increased correlation and poloidal wave lengths. Constant particle flux is realised at steeper gradients due to modifications of the cross-phase, which relates the large-scale structures to inward transport.

Keywords: drift-wave turbulence, shear flows, turbulence suppression, biasing, probe array, torsatron TJ-K.

1 Introduction

The understanding of the formation of transport barriers during transitions from low-confinement (L-mode) to high-confinement (H-mode) regimes is one of the key objectives in fusion research. Poloidal $E \times B$ shear flows are widely accepted as a trigger mechanism of transport barriers in the edge of fusion plasmas [3]. This has been confirmed in experiments with spontaneously excited transport barriers [2] and such triggered by external plasma biasing [4]. Strong $E \times B$ flows can act on turbulent transport through the shear decorrelation mechanism [1], which can reduce the radial size of turbulent structures or change the phase relation between density and potential fluctuations [2].

For interchange and ion-temperature-gradient driven turbulence it was found that a transport reduction by sheared flows is mostly due to a reduction of the fluctuation amplitudes [5]. Other analytical studies suggested, however, that strong shear flows predominantly influence the cross-phase leading to reduced or in case of collisional drift-waves even locally inward directed transport [6]. In fact, strong cross-phase modifications have already been observed during spontaneous [7] as well as externally induced L-H transitions [8].

In this work, the influence of strong $E \times B$ shear flows on the microscopic structure of turbulence is investigated in high detail using multi-probe arrays inside the confinement region of a toroidal plasma. The experiments are carried out on the low-temperature plasma of the torsatron TJ-K, which is dimensionally similar to fusion edge plasmas [9]. $E \times B$ flows are generated by biasing an internal flux surface.

author's e-mail: ramisch@ipf.uni-stuttgart.de

2 Experimental setup

The torsatron TJ-K [10] toroidally confines a low-temperature plasma, which is dimensionally similar to fusion edge plasmas [9]. The major and the minor plasma radius is $R_0 = 0.6$ m and $a = 0.1$ m, respectively. The confining magnetic field has a rotational transform of about $1/3$ with low magnetic shear. TJ-K can be operated with nominal magnetic field strengths in the range $B = 70$–100 mT when electron-cyclotron-resonance heating (ECRH) at 2.45 GHz is used for plasma generation. In the present experiment, the working gas was hydrogen at a neutral gas pressure of $p_0 = 4 \times 10^{-5}$ mbar, a heating power of $P_{\mathrm{ECRH}} = 1.8$ kW and a magnetic field strength of $B = 72$ mT. For these parameters, the typical electron temperature and maximum density is $T_e \approx 7$ eV and $n \approx 2 \times 10^{17}$ m^{-3}, respectively. The ions are cold ($T_i < 1$ eV).

In order to generate the appropriate $E \times B$ flow, an electrode consisting of a closed stainless steel wire in the shape of the poloidal cross-section of an inner flux surface was used. The wire had a diameter of 3 mm. It was biased positively with respect to the grounded vacuum vessel via a single lead, which was insulated by a ceramics tube. A grounded electrode will be referred to as unbiased. The electrode was introduced from a top port at a toroidal angle of $\phi = 50°$, where the flux surfaces are elliptical. Equilibrium-profile and fluctuation measurements have been carried out at two outer ports at $\phi = 270°$ or $330°$ and $\phi = 90°$, respectively. At the positions of the outer ports, the flux-surface cross-sections are triangular. In Fig. 1, the mapping of the electrode onto such a position is shown.

For the measurements of turbulent structures in the density fluctuations, two diagnostics consisting of 64

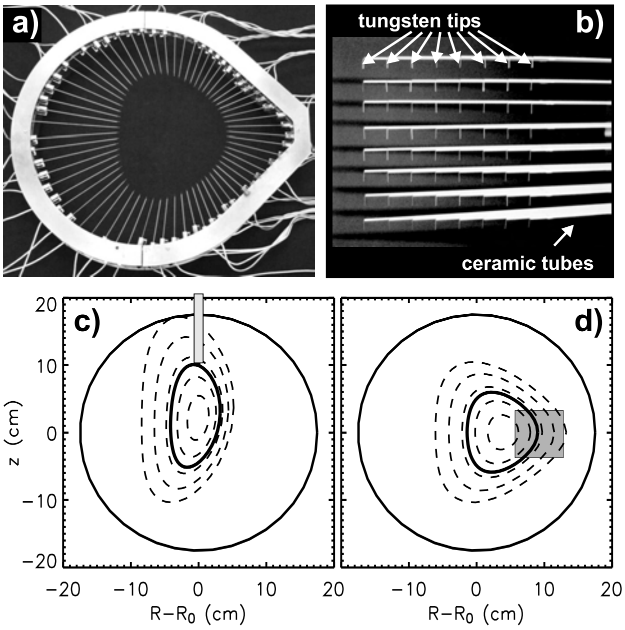

Fig. 1 Photo of the poloidal 64-tip probe array (a) and the 8×8 probe matrix (b). Position of the electrode inside the separatrix (c) and mapping onto the probe section (d). The shaded area depicts the region covered by the probe matrix.

Langmuir probes were used. The first diagnostics is set up on a two-dimensional grid of 8×8 points in the poloidal cross-section on the low-field side and centered at the biased surface as shown in Fig. 1. The spatial resolution is 1 cm in vertical and horizontal direction. At all 64 positions, the fluctuations in the ion-saturation current were simultaneously acquired with 16 bit accuracy at a rate of 1 MHz within a time interval of 1 s. Cross-correlation analyses carried out on these data reveal the spatio-temporal evolution of turbulent density structures. The cross-correlation between each probe of the matrix at a position (R_i, z_j) and one reference probe as a function of a time lag Δt is calculated according to

$$C_{i,j}(\Delta t) = \int \frac{\widetilde{n}_{\rm ref}(t)}{\sigma_{\rm ref}} \frac{\widetilde{n}_{i,j}(t+\Delta t)}{\sigma_{i,j}}\, {\rm d}t, \tag{1}$$

where each signal is normalised to its respective rms value σ. In Ref. [11], the probe array and the analysis technique is introduced in more detail. In order to resolve the poloidal structure of turbulence, the matrix has been replaced by a poloidal probe array. The probes are poloidally arranged on a complete circumference of a flux surface near the biased one with a poloidal resolution of 7 mm. Both the poloidal and the two-dimensional probe array are shown in Fig. 1.

3 Perpendicular dynamics without strong $E \times B$ flow

In TJ-K, the turbulence drive is governed by drift waves. Evidence for drift-wave signatures in the spectral cross-phase between density and potential fluctuations and for the parallel structure in toroidal geometry is provided in Ref. [9] and [12], respectively.

In order to investigate the dynamics perpendicular to the magnetic field, turbulent structures are used as tracers of the background flow. Therefor, cross-correlation analyses according to Eq. (1) are carried out on density fluctuations measured with the matrix. For consecutive time lags Δt, the result is shown in Fig. 2. Quasi-coherent structures

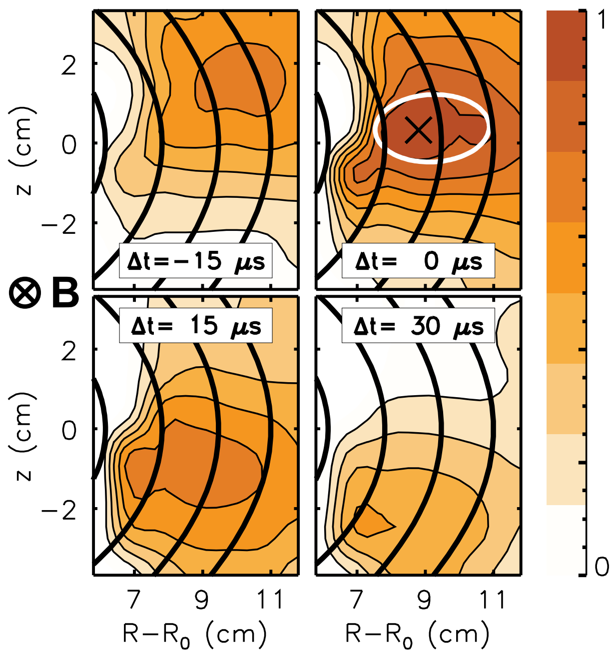

Fig. 2 Contour plots of cross-correlations between matrix probes with the reference probe located at (×). The ellipse at $\Delta t = 0$ approximates the structure size at 87 % correlation.

are observed, which propagate clockwise with a speed of about 800 ms^{-1}. The direction corresponds to the direction of the electron-diamagnetic drift $U_{\rm dia}$. Since the radial electric field is weak, the poloidal $E \times B$ flow velocity is negligible compared to $U_{\rm dia}$. Hence, the propagation is in agreement with expectations from the linear drift-wave dispersion relation [13]

$$\omega \approx U_{\rm dia} k_\perp / (1 + k_\perp^2 \rho_s^2), \tag{2}$$

where $k_\perp$ is the perpendicular wavenumber and $\rho_s = \sqrt{T_e M_i}/eB$ the drift-scale with T_e the electron temperature, M_i the ion mass and B the magnetic field strength. For the discharge presented in Fig. 2, the normalised wavenumber $k_\perp \rho_s$ is about 0.26 [14]. Therefore, the propagation velocity directly reflects the electron-diamagnetic drift velocity within a deviation of 6 %. In Fig. 2, the approximate structure size at 87 % correlation at $\Delta t = 0$ is indicated by an ellipse and will be used below for comparison with the case, where strong flow shear is present.

4 Influence of shear flows on the perpendicular dynamics

In order to generate a strong $E \times B$ shear flow, the electrode was biased to 100 V. In Fig. 3, the effect on the potential profile is shown. The potential inside the biased surface is

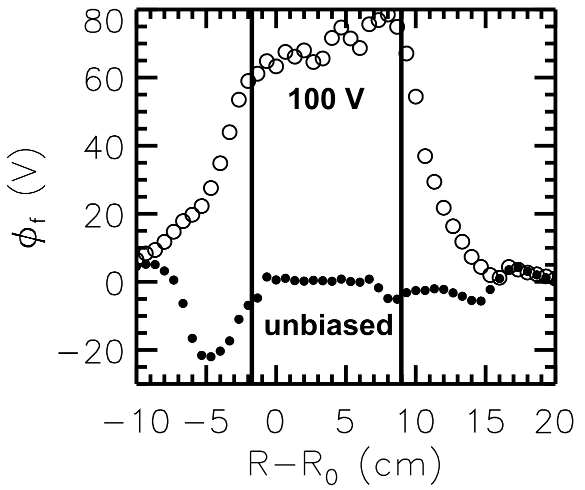

Fig. 3 Radial profile of the floating potential for the unbiased (•) and the biased case (∘). Vertical lines mark the position of the biased flux surface.

strongly increased leading to enhanced radial electric fields outside. The potential drops by about 80 V over a distance of 7 cm. The resulting radial electric field of 1100 Vm^{-1} corresponds to a poloidal $E \times B$ velocity of $U_{E\times B} = 16$ kms^{-1}. The shearing rate of the generated flow with values between 100 and 400 kHz in almost the entire radial range becomes larger than the decorrelation rate of about 50 kHz in the unbiased case. At the same time, the density gradient is steepened by a factor of five [15].

In the biased state, turbulent structures have been measured with the probe matrix and detected by cross-correlation analyses. The result is shown in Fig. 4. In comparison with the unbiased state (see Fig. 2), the propagation points into the opposite direction, i.e., in the direction of the $E \times B$ drift. The propagation speed is increased by a factor of 15 from 0.8 to about 12 kms^{-1}. This can be understood directly by taking into account the changes in the equilibrium profiles. For the unbiased case, the potential profile in Fig. 3 does not show steep gradients, which would lead to substantial radial electric fields and, thus, poloidal $E \times B$ rotation. The propagation of the structures is governed by the electron-diamagnetic drift velocity. During biasing, the density gradient and, therefore, $U_{\rm dia}$ increased by a factor of five to 4 kms^{-1} ($k_\perp \rho_s$ reduces

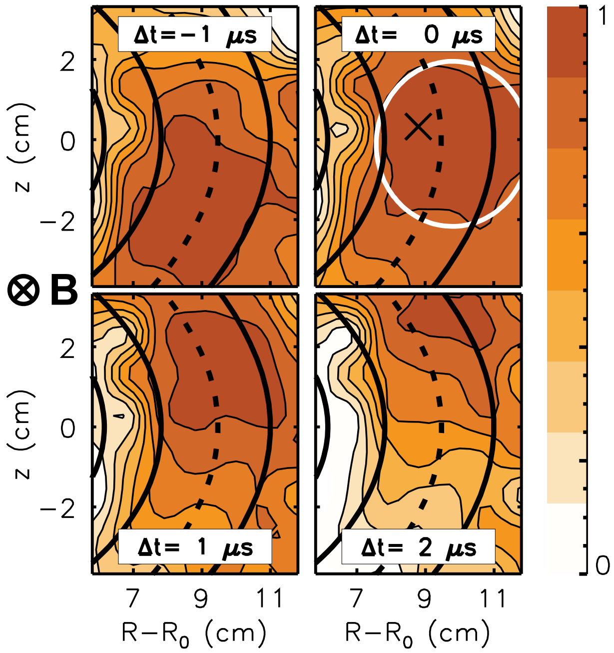

Fig. 4 Contour plots of cross-correlations between matrix probes with the reference probe in the same representation as in Fig. 2 (but note the different time windows in both cases). Here, the dashed line marks the biased flux surface.

to 0.2, see below). But now, $U_{E\times B} = 16$ kms^{-1} dominates the poloidal flow resulting in a poloidal propagation speed of 12 kms^{-1}.

Strong flow shear as in the biased case with shearing rates larger than the turbulence decorrelation rate in the absence of shear is expected to reduce the radial correlation length of turbulent structures [1]. However, instead of a reduction an increase in the structure size is observed, when figures 2 and 4 are compared. The structure becomes more circular and essentially exceeds the matrix dimensions.

5 Poloidal mode structure under strong shear

For a proper statement on the change in the mode structure, the comparative biasing studies have been repeated with the poloidal probe array. Density fluctuations have been recorded under the same conditions and cross-correlation analyses have been carried out on the data. The mode structure as a function of the poloidal coordinate Δs with respect to the reference probe is represented by the cross-correlation function at $\Delta t = 0$. The calculation was done with all 64 probes one by one taken as reference probe. Then the 64 correlation functions have been averaged. For the unbiased and biased case, the result is shown in Fig. 5. It can be seen that the poloidal mode structure changes from $m = 4$ to $m = 3$ during biasing. With a safety factor of about $q \approx 3$, this corresponds to a single helical

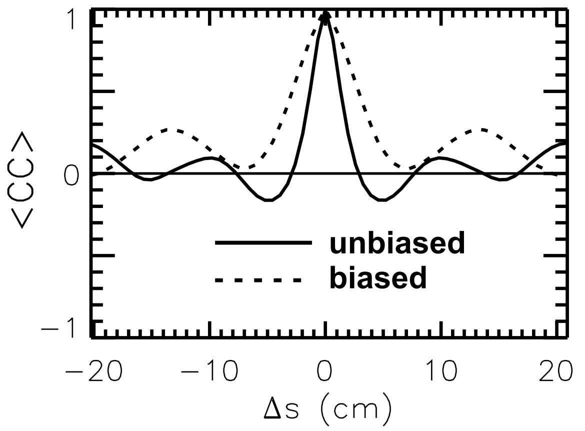

Fig. 5 Average spatial poloidal mode structure in the unbiased (solid) and the biased case (dashed line). The mode structure changes from $m = 4$ to $m = 3$ during biasing.

structure.

During biasing, the local value of ρ_s at the centre position of the structure stays constant, while the poloidal wavelength increases by a factor of 4/3, which reduces $k_\perp\rho_s$ from 0.26 to about 0.2. Hence, the contribution of the diamagnetic drift to the total propagation velocity of the large-scale structure is still consistent with the linear dispersion relation of drift waves given by Eq. (2).

In the unbiased case, $m = 3$ with $U_{\text{dia}} = 800\,\text{ms}^{-1}$ corresponds to a frequency of about 5 kHz. An increase of the poloidal rotation by a factor of 15 would lead to a shift of this mode to about 75 kHz. In fact, the large-scale structure is related to a dominant peak at 72 kHz in the power spectrum. Modes $m \geq 4$ were found to be suppressed. The $m = 3$ mode was shown to be related to local turbulent inward transport due to a modification of the cross-phase between density and potential fluctuations [15]. The total particle flux, thus, remains unchanged compared to the unbiased case, i.e., the same flux is realised at steeper density gradients, which implies an improvement of the particle confinement.

In H-mode fusion plasmas, reduced radial correlation lengths were found in the shear layer [16]. However, the results presented here rather point to the importance of the phase relation between density and potential fluctuations for confinement improvement. Significant cross-phase modifications have been predicted for systems with a quasi-coherent fluctuation spectrum [6] under the influence of very strong shear like in the present case and such modifications have also been found during H-mode discharges in several devices (see, e.g., Refs. [7, 8, 17]).

6 Summary

The influence of strong $E \times B$ shear flows on the microscopic structure of drift-wave turbulence has been investigated by means of multi-probe arrays. Turbulent density structures were detected with an 8×8-probe array perpendicular to the magnetic field inside the confinement region of the torsatron TJ-K. The poloidal mode structure was measured with a 64-tip poloidal probe array. The $E \times B$ flow was generated by biasing an internal flux surface. This way, a poloidal $E \times B$ flow with a velocity of about $16\,\text{kms}^{-1}$ and a shearing rate larger than 100 kHz with a maximum value of about 400 kHz has been achieved. At the same time, the density gradient steepened by a factor of 5. In both the unbiased and biased case, the propagation of turbulent structures, which were used as tracers of the background flow, was due to poloidal $E \times B$ and electron-diamagnetic drift velocities in agreement with the linear drift-wave dispersion relation. During biasing, the turbulence suppression criterion [1] was well fulfilled in almost the entire radial range. However, the fluctuations were found to be dominated by large-scale structures. The characteristic poloidal mode structure changed from $m = 4$ to $m = 3$. Hence, it has been demonstrated that strong shear can change the spatial structure of drift-wave turbulence in toroidal geometry in favour of coherent structures with larger correlation lengths. In Ref. [15], these structures were shown to be associated with local turbulent inward transport due to modifications in the phase relation between density and potential fluctuations.

References

[1] H. Biglari, P. H. Diamond, and P. W. Terry, Phys. Fluids, B **2**, 1 (1990).
[2] K. H. Burrell, Phys. Plasmas **4**, 1499 (1997).
[3] K. Itoh and I. Sanae-I, Plasma Phys. Controll. Fusion **38**, 1 (1996).
[4] R. J. Taylor *et al.*, Phys. Rev. Lett. **63**, 2365 (1989).
[5] E.-J. Kim, P. H. Diamond, and T. S. Hahm, Phys. Plasmas **11**, 4554 (2004).
[6] P. W. Terry, D. E. Newman, and A. S. Ware, Phys. Plasmas **10**, 1066 (2003).
[7] R. A. Moyer *et al.*, Phys. Plasmas **2**, 2397 (1995).
[8] J. A. Boedo *et al.*, Phys. Rev. Lett. **84**, 2630 (2000).
[9] U. Stroth *et al.*, Phys. Plasmas **11**, 2558 (2004).
[10] N. Krause *et al.*, Rev. Sci. Instrum. **73**, 3474 (2002).
[11] M. Ramisch *et al.*, Phys. Plasmas **12**, 032504 (2005).
[12] N. Mahdizadeh *et al.*, Plasma Phys. Controll. Fusion **49**, 1005 (2007).
[13] M. Wakatani and A. Hasegawa, Phys. Fluids **27**, 611 (1984).
[14] M. Ramisch, E. Häberle, N. Mahdizadeh, and U. Stroth, submitted to Plasma Sources Sci. Technol. (2007).
[15] M. Ramisch *et al.*, Plasma Phys. Controll. Fusion **49**, 777 (2007).
[16] J. Schirmer *et al.*, Plasma Phys. Controll. Fusion **49**, 1019 (2007).
[17] M. G. Shats *et al.*, Phys. Rev. Lett. **84**, 6042 (2000).

Proceedings of ITC/ISHW2007

Cascade process of two-dimensional turbulence observed in magnetized pure electron plasmas

Yosuke KAWAI[1)], Yasuhito KIWAMOTO[1)], Yukihiro SOGA[1)*] and Jun AOKI[1)*]

[1)] *Graduate School of Human and Environmental Studies, Kyoto University, Yoshida Nihonmatsu-cho, Sakyo-ku, Kyoto 606-8501, Japan*

(15 October 2007)

Elementary dynamics of two-dimensional (2D) turbulence are examined experimentally by extensive analyses of fine-scale structures in the density distribution of a magnetized pure electron plasma. We observe the relaxation process of the electron plasma involving stochastic mergers of vortex patches generated by the instability in terms of a spatial pattern of vorticity, and compare with the theoretical picture of the 2D turbulence described in the wave-number (k) space. In the merging process among vortex patches, the energy spectrum shows a algebraic dependence of $k^{-\alpha}$ above the k_{inj} corresponding to the size of the first generated patches. The energy and enstrophy tranfer rate show the characteristic features of the cascade process predicted by the theory, i.e., in the fine-length scale of $k > k_{inj}$ the enstrophy cascades upward at a constant transfer rate, and in the region $k < k_{inj}$ the energy transfers down to lower k. Through time-averaging the evolution of the spectra, we derive the spectrum in the stationary turbulence sustained by the successive input of vortices due to the instability. The resultant spectrum is qualitatively consistent with the 2D turbulence theory, but also shows the discrepancies that the power index of the energy spectrum is larger than the theoretical prediction of $\alpha = 3$ and that the enstrophy transfer rate is almost zero around $k \approx k_{inj}$ reflecting the effect of coherent vortices.

Keywords: non-neutral plasmas, two-dimensional turbulence, vortex dynamics, spectral analysis, enstrophy cascade

DOI:

Macroscopic dynamics of pure electron plasmas transverse to a strong magnetic field are equivalent to the two-dimensional (2D) Euler fluid within the guiding-center approximation, and the electron density $n(x, y)$ and the potential distribution $\phi(x, y)$ are proportional to the vorticity $\zeta(x, y)$ and the stream function $\psi(x, y)$, respectively [1, 2]. Taking advantage of this equivalence, magnetized pure electron plasmas have been employed extensively for detailed examinations of many aspects of 2D vortical dynamics, that constitute the elementary processes of 2D turbulence, such as the advection, merger, filamentation of vortices [2–4]

Vortex patches are spontaneously generated in the nonlinear stage of the diocotron instability from the ring-shaped electron density with a strong radial shear of the azimuthal flow [1, 5]. Free relaxations of the unstable system include stochastic dynamics of vortex patches. Time-resolved spectral analyses have been carried out along the relaxation of the turbulent states, focusing on the particle transport [6]. In this paper, we extend these examinations further to explore fundamental properties of 2D turbulence of the vorticity distribution in terms of the transport of the energy and enstrophy in the wave-number (k) space.

*Present address: Department of Physics, Graduate School of Science, Osaka University, 1-1 Machikaneyama, Toyonaka, Osaka 560-0043, Japan

author's e-mail: kwaiyosuke@h01a0395.mbox.media.kyoto-u.ac.jp

Theoretical picture of 2D turbulence have been conjectured by Kraichnan [7] and Batchelor [8]. Both of them proposed that in the isotropic and homogeneous 2D turbulence, the enstrophy injected at the length-scale of l_{inj} ($\propto 1/k_{inj}$) cascades at a constant transfer-rate of η down to a scale of dissipation l_d ($\propto 1/k_d$) and dissipates by viscosity. This cascade picture of 2D turbulence leads to an energy spectrum characterized by the power-law $E(k) \propto k^{-3}$ in the inertial range of $k_{inj} \leq k \leq k_d$ in the wave-number space.

The cascade process of the enstrophy has been investigated experimentally by using thin layers of electrolytes [9, 10] and soap films [11], and k^{-3} scaling has been observed. However, in these experiments, it is difficult to resolve the fine vortical structures extending to the dissipative range, and therefore there remains some uncertainties in comparing the vortex dynamics observed in the real space with the theoretical picture of 2D turbulence described in the spectral space.

In the experimental investigation with pure electron plasmas, the vorticity distribution can be observed directly in terms of the electron density distribution $n(x, y)$ down to the dissipative scale at a high signal-to-noise ratio. With this advantage, in this paper, we examine the cascade process of the free-decaying 2D turbulence extensively in wide length scales. Moreover, by considering this phenomena as an elementary process of forced 2D turbulence, we

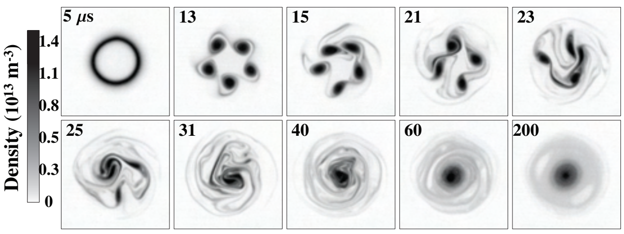

Fig. 1 Images of the time evolution of the density distribution. The darkness is proportional to the density. The time of observation (in μs) is indicated at the upper left corner.

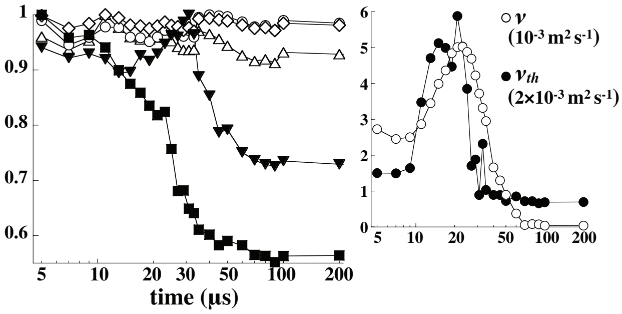

Fig. 2 The time evolution of energy E (○), total electron number N (◊), angular momentum L (△), enstrophy Z_2 (■) and palinstrophy P (▼). Inset: The time evolution of the viscosity coefficients estimated experimentally (○) and calculated from Eq. (62) in Ref. [16] (●).

derive the spectrum in the stationary state through time-averaging the evolution of spectra and compare with the Kraichnan-Batchelor theory.

The experiment is carried out by containing a pure electron plasma in a Malmberg-trap with a uniform magnetic field (B_0 = 0.048 T) and a square-well potential. After the plasma is formed into a ring-shaped profile, the density distribution at a specific time in the relaxation process is observed by damping the electrons onto the conducting phosphor screen and recording the luminosity distribution with a 512 × 512 pixel CCD camera providing the spatial resolution of 0.1 mm/pix. This destructive diagnostic requires a high reproducibility of the initial profiles, because the relaxation process of the turbulence triggered by the instability is stochastic in nature. Therefore in this experiment, in addition to technically minimizing shot-by-shot variations in the initial profiles, an ensemble-average is applied over typically 5 shots of data for each time of the observation in examining the time evolution of physical quantities characterizing the turbulence. The details of the experimental configuration and method are reported in Refs. [4, 6, 12, 13].

The time evolution of the observed density distribution is shown in Fig. 1. The ring profile is produced at 5 μs, and distorted by the diocotron instability within a few μs. The deformed distribution grows on the fastest growing diocotron mode and eventually 5 high-density vortex patches are generated at 13 μs. After the formation of the first vortex patches, the number of patches decreases successively through intermittent mergers among the patches. This stochastic process is accompanied by the generation of filamentary structures in the low density part of the population that extend the length-scales to finer regions. The outward transport of the filamentary structures is accompanied by the inward transport of the high-density patches as observed at 31 μs. The concentrated patches rotating with the period of 10 μs expel filaments from the central region, and finally form a bell-shaped core distribution that is surrounded by a low density halo with striations (t = 200 μs).

Turbulent states are characterized by areal integrals of the vorticity ($\propto n(x, y)$). Figure 2 plots some of the integrals calculated from the measured density distribution $n(r, \theta)$ as a function of time. Each integral is normalized to unity. The integrals include the electrostatic energy (fluid kinetic energy) $E = 1/2 \int d^2\mathbf{r} n\,(-e\phi)$, the total electron number (total circulation) $N = \int d^2\mathbf{r}n$, the angular momentum (angular impulse) $L = \int d^2\mathbf{r}nr^2$, the enstrophy $Z_2 = 1/2 \int d^2\mathbf{r}n^2$ and the palinstrophy $P = 1/2 \int d^2\mathbf{r}\, |\nabla n|^2$. The palinstrophy is a measure of the fine-scale structures in the turbulence [8, 9, 14].

Throughout the whole process, E, N and L do not show any systematic change except 5 % variations probably attributable to the shot-by-shot fluctuations in the generation process of the unstable initial distributions. Therefore the three integrals may be considered to be invariant. In contrast, Z_2 and P show unambiguous systematic changes. The enstrophy Z_2 undergoes a substantial decaying through the merging processes, and finally goes down to 40 % of the initial value. The palinstrophy P shows a rapid increase while mergers among the vortex patches are active. It is maximized at 31 μs when the filamentary structures are conspicuous in the region outside the high-density core as shown in Fig. 1. After the maximization, P drops steeply concomitantly with the reduction of the decreasing rate of the enstrophy, suggesting the manifestation of dissipative effects in finer length-scales.

In order to estimate the degree of enstrophy dissipation in this experiment, we introduce a Newtonian viscosity into the 2D Euler equation as a correction, i.e., $Dn/Dt = \nu\nabla^2 n$, where ν is the kinematic viscosity. (Note that n is propotional to the vorticity.) This equation leads to the relation of the decreasing rate of the enstrophy to the viscosity and palinstrophy as follows [8, 9, 14]:

$$\frac{DZ_2}{Dt} = -2\nu P \tag{1}$$

By introducing the experimental values of Z_2 and P into Eq. (1), the effective viscosity ν is evaluated and plotted as a function of time in Fig. 2. ν is maximized at time $t \approx 23$ μs when the density configuration changes drastically from separated vortex patches to a single-peaked distribution.

The collisional transport of a magnetized pure electron plasma in the 2D regime [15] has been studied analytically, in which the viscosity coefficient is predicted as Eq. (62) in Ref. [16]. By introducing the parameters of the present experiment to the proposed formula, we estimate the viscosity coefficient ν_{th} and plot the results in Fig. 2. Though the present study is not under quasi-stationary states as assumed in the theory, the experimental evaluation agrees within a factor of 2 with ν_{th}. This agreement may suggest that the stochastic motions of individual particles under fluctuating fields play a important role in the dissipation process of vortex dynamics in fine scales.

To compare the experimental results to the theoretical picture of 2D turbulence, we calculate the energy spectrum in k space from the measured density distribution. The energy spectrum $E(k)$ is determined from the Fourier transform of the density distribution $n(\mathbf{k}) = \int d^2\mathbf{r}e^{-i\mathbf{k}\cdot\mathbf{r}}n(\mathbf{r})$ as

$$E(k) = \frac{1}{2}\left(\frac{e}{\varepsilon_0 B_0}\right)^2 \int_0^{2\pi} kd\varphi \frac{|n(\mathbf{k})|^2}{k^2}, \quad (2)$$

where φ is the azimuthal angle of $\mathbf{k}$. The time evolution of $E(k)$ thus obtained is shown in Fig. 3. In the initial distribution at 5 μs, the energy spectrum shows oscillatory structures due to the concentration of the energy at the ring radius. When the ring distribution is torn into the vortex patches at 13 μs, the spectrum has a local maximum around the wave number $k = k_{inj} \approx 500$ consistent with the size of the first vortex patches. Along with the subsequent mergers between patches ($t = 13 \sim 31$ μs), the location of the spectral maximum shifts progressively down to lower wave numbers, and the dip around $k \equiv k_{core} \approx 300$ which corresponds to the core size in the final state is filled.

In length-scales smaller than the width of the vortex patches $k > k_{inj}$, the energy spectrum broadens upward and the $E(k)$ exhibits a power-law dependence of $\propto k^{-\alpha}$. The slope of the spectrum in the interval $700 \leq k \leq 5000$ is drawn in Fig. 3. Throughout the merging processes, the power index α remains around 5, apparently larger than the theoretically predicted value of 3 [8]. The upper limit in the wave-number space $k = k_d$ to which $E(k)$ shows a power-law scaling reaches its maximum value of ≈ 8300 at 31 μs when the palinstrophy is maximized. This scale-length (≈ 0.38 mm) is consistent with the thickness of the filamentary structure at the end of spiral arms displayed in Fig. 1.

In the slow relaxation process toward the asymptotic state after the merger ($t = 40 \sim 200$ μs), the energy concentrates at k_{core} and decreases steeply beyond $k \approx 1000$. The power index in the high wave-number region $1000 \leq k \leq 5000$ decreases slowly from ≈ 5 toward 3.5. The power-law spectrum at high k represents fine structures remaining in the halo region surrounding the high density core.

The rate of upward energy transfer $\varepsilon(k)$ through k is evaluated from the time-resolved energy spectrum in Fig. 3 as

$$\varepsilon(k) = -\int_0^k dk\ \frac{\partial E(k)}{\partial t}. \quad (3)$$

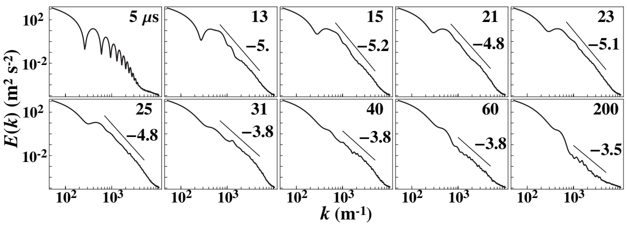

Fig. 3 The time evolution of the energy spectrum calculated from the measured $n(\mathbf{r})$. Numbers at the upper-left corner stand for the time of the observation.

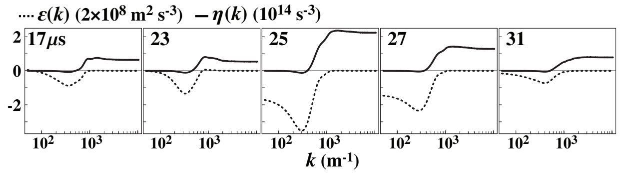

Fig. 4 The time evolution of the upward transfer rates of the energy $\varepsilon(k)$ (dashed line) and enstrophy $\eta(k)$ (solid line) through k.

The enstrophy transfer rate $\eta(k)$ is evaluated similarly from the enstrophy spectrum $Z(k) = k^2E(k)$. The time evolution of $\varepsilon(k)$ and $\eta(k)$ during the period in which $E(k)$ follows the power-law is shown in Fig. 4. The observation of $\varepsilon(k)$ indicates that the energy is transfered downward and the rate of transfers is maximum around k_{core} at each time. In contrast, the enstrophy is transferred upward in the wave-number space with $k \geq k_{inj}$. In particular, over the wide range of $k \geq 1500$, $\eta(k)$ is almost constant as assumed in the theoretical picture of 2D turbulence. Both in the energy and in the enstrophy, the transfer rates are maximized at $t \approx 25$ μs when the density configuration changes drastically.

The observation that $\eta(k)$ decreases to zero at $k < 2k_{inj}$ from a constant value at $k > 3k_{inj}$ corresponds to the observed vortex dynamics in Fig. 1, i.e., the vortex patch retain its shape for a long time with high vorticities (enstrophy) and the filamentation of the structure dominates in the outside region of the patches.

The time-resolved data presented above include details of free-decaying 2D turbulence whose enstrophy is fed at $k = k_{inj}$ corresponding to the first generation of vortex patches and that is left in an isolated state. Here we try to construct the energy spectrum in a stationary state that is maintained by continuous energy input at $k = k_{inj}$ due to the instability and by the continuous dissipation at $k \gg k_{inj}$ by using the above data as an elementary process constituting a stationary turbulence. If the interaction among the structures appearing in different stages of the free-decaying turbulence is negligible, the time-averaged spectra, $\bar{E}(k)$, $\bar{\varepsilon}(k)$ and $\bar{\eta}(k)$, may approximately represent the characteristic features of the stationary turbulence. The results of the time-weighted average of the observed data are summarized in Fig. 5.

The constructed spectra exhibit characteristics close to the fundamental features of stationary 2D turbulence:

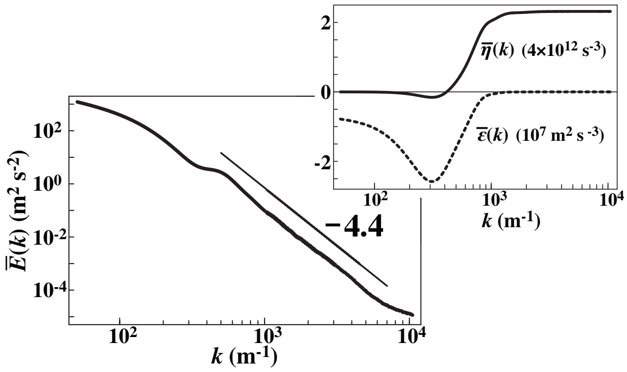

Fig. 5 The energy spectrum $\bar{E}(k)$ time-averaged in the interval $t = 13 \sim 200\ \mu$s. Inset shows the time-averaged transfer rates of the energy $\bar{\varepsilon}(k)$ (dash line) and enstrophy $\bar{\eta}(k)$ (solid line).

The enstrophy is transfered upward at a constant rate above $k \approx 3k_{inj}$. With this transfer rate, the dissipative wave number is estimated at $k_d \approx 7200$ from the expression $l_d \approx \eta^{-1/6}\nu^{1/2}$ proposed in Ref. [8]. Figure 5 also shows that $\bar{E}(k)$ depends algebraically on k in a wide range of the wave-number space $k_{inj} \leq k \leq k_d$. In contrast to $\bar{\eta}(k)$, it is confirmed that in the region $k < 3k_{inj}$, the energy flux $\bar{\varepsilon}(k)$ proceeds toward small wave-numbers and is maximized around k_{core} corresponding to the size of the core distribution in the asymptotic state.

Through the region $k \geq 3k_{inj}$ where the enstrophy transfer rate is constant, the energy transfer rate is observed to be zero. This observation supports the theoretical expectations that the spectral dynamics at high wave-numbers of the 2D turbulence are governed by the enstrophy cascade process [7]. On the other hand, in the region $k < k_{inj}$, the observation that $\bar{\eta}(k) \sim 0$ and $\bar{\varepsilon}(k) < 0$ indicates that the dynamics in the energy spectra obey the inverse cascade process. The observed non-uniformity of $\bar{\varepsilon}(k)$ is understood in terms of the absence of a dissipation mechanism at large length-scales in the strongly magnetized pure electron plasma.

In the intermediate region $k_{inj} \leq k < 3k_{inj}$, neither $\bar{\varepsilon}(k)$ nor $\bar{\eta}(k)$ is zero, indicating that the transfer exists in the k space of both the energy and enstrophy. The local non-uniformity of $\bar{\varepsilon}(k)$ and $\bar{\eta}(k)$ in this region suggests the break-down of the ubiqitous cascade model. This observation is closely related to the persisting presence of coherent vortices that capture a large amount of enstrophy and inhibit the cascade as observed by numerical simulations [17, 18]. This is probably the reason why the power index of the observed energy spectrum $\bar{E}(k)$ in the inertial range of $k_{inj} \leq k \leq k_d$ is $\alpha = 4.4$ and larger than the theoretical prediction of $\alpha = 3$ [7].

In this paper, we have examined the vortex dynamics of 2D turbulence in a magnetized pure electron plasma over a wide range of length-scales extending from the injection scale down to the dissipative scale, and compared the experimental results to existing theories of 2D turbulence. In the stage characterized by the successive mergers between vortex patches starting from the unstable initial density profile, the observed density distribution exhibits turbulent characteristics. While the energy is transfered downward, the enstrophy undergoes an upward transport starting from the injection wave number k_{inj}. In finer length-scales with $k \geq 3k_{inj}$, the transfer rate of the enstrophy is observed to be constant, and the energy spectrum shows a power-law scaling $E(k) \propto k^{-\alpha}$ in a broad inertial range with α ranging from 5.2 to 3.5. The discrepancy from the theoretically-expected value of $\alpha = 3$ is attributed to the inhibition of the cascade process reflecting the effect of the long persistence of high-vorticity patches.

The author thanks Professor K. Itoh of NIFS for enlightening discussions. This research was supported by the Grant-in-Aid for Scientific Research (B) 17340173 of JSPS and partly by the collaborative program of NIFS.

[1] R. H. Levy, Phys. Fluids **8**, 1288 (1965).
[2] C. F. Driscoll and K. S. Fine, Phys. Fluids B **2**, 1359 (1990).
[3] T. B. Mitchell and C. F. Driscoll, Phys. Fluids **8**, 1828 (1996).
[4] Y. Kiwamoto, K. Ito, A. Sanpei and A. Mohri, Phys. Rev. Lett. **85**, 3173 (2000).
[5] A. J. Peurrung and J. Fajans, Phys. Fluids A **5**, 493 (1993).
[6] Y. Kawai, Y. Kiwamoto, K. Ito, A. Sanpei, Y. Soga, J. Aoki and K. Itoh, J. Phys. Soc. Jpn. **75**, 104502 (2006).
[7] R. H. Kraichnan, Phys. Fluids **10**, 1417 (1967).
[8] G. K. Batchelor, Phys. Fluids **12** (Suppl.II), 233 (1969).
[9] P. Tabeling, Physics Reports **362**, 1 (2002).
[10] J. Paret, M. C. Jullien, P. Tabeling, Phys. Rev. Lett. **83**, 3418 (1999).
[11] M. A. Rutgers, Phys. Rev. Lett. **81**, 2244 (1998).
[12] K. Ito, Y. Kiwamoto and A. Sanpei, Jpn. J. Appl. Phys. **40**, 2558 (2001).
[13] J. Aoki, Y. Kiwamoto, Y. Soga and A. Sanpei, Jpn. J. Appl. Phys. **43**, 7267 (2004).
[14] U. Frisch, *TURBULENCE* (Cambridge University Press, Cambridge, 1995).
[15] C. F. Driscoll, F. Anderegg, D. H. E. Dubin, D.-Z. Jin, J. M. Kriesel, E. M. Hollmann and T. M. O'Neil, Phys. Plasmas. **9**, 1905 (2002).
[16] D. H. E. Dubin and T. M. O'Neil, Phys. Plasmas. **5**, 1305 (1998).
[17] J. C. McWilliams, J. Fluid Mech. **146**, 21 (1984).
[18] P. Santangelo, R. Benzi and B. Legras, Phys. Fluids A **1**, 1027 (1989).

Proceedings of ITC/ISHW2007

Neutral Flow Measurement Using a Tunable Diode Laser

Kohei OGIWARA[1)], Shuzo ETOH[1)], Mitsutoshi ARAMAKI[2)], Shinji YOSHIMURA[3)] and Masayoshi Y. TANAKA[1)]

[1)]*Kyushu University, Fukuoka 816-8580, Japan*
[2)]*Nagoya University, Aichi 464-8603, Japan*
[3)]*National Institute for Fusion Science, Gifu 509-5292, Japan*

A vortex with anti-$\mathbf{E}\times\mathbf{B}$ flow has been observed in an argon cylindrical plasma. It is considered that the anti-$\mathbf{E}\times\mathbf{B}$ flow is generated by interaction between the background neutral flow and the ion fluid. To confirm the new mechanism of vortex formation, we have developed the high resolution laser induced fluorescence (LIF) spectroscopy system for measuring the neutral flow. The wavelength resolution of this LIF system is 14 fm, which corresponds to a velocity of 6 m/sec. The high wavelength resolution is attained by using a tunable external cavity diode laser (ECDL), whose spectral width is typically 5 fm. Preliminary results on neutral flow velocity measurements using newly developed LIF system are presented.

Keywords: anti-$\mathbf{E}\times\mathbf{B}$, neutral flow, Laser Induced Fluorescence, diode laser

1. Introduction

In understanding dynamical behavior of plasma, the effect of neutrals on the motion of ion fluid is usually neglected (collisionless). Even when it is considered, the contribution of neutrals is included as a small dissipation term, which slightly modifies the motion of ion fluid. In these circumstances, large-scale flow structure in a plasma is primarily determined by $\mathbf{E}\times\mathbf{B}$ drift [1, 2]. In a case of cylindrical geometry with axial magnetic field, azimuthal rotation takes place due to the radial electric field, forming a vortical flow structure.

Recently, it is experimentally found that there exists a class of vortices [3], which rotate to the opposite direction of $\mathbf{E}\times\mathbf{B}$ drift (referred to as anti-$\mathbf{E}\times\mathbf{B}$ vortex). One typical example is tripolar vortex, and is shown in Fig. 1. This result suggests that there is a force acting on ion fluid and it does exceed the electric field. The problem is then the generation mechanism of this force.

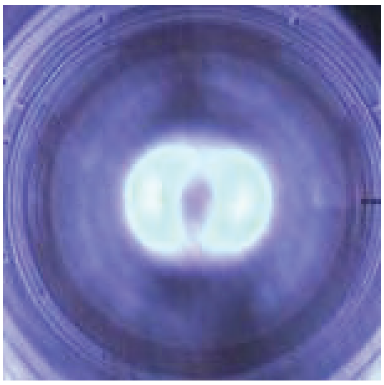

Fig. 1 CCD image of tripolar vortex. Three vortices, center and two satellites, respectively rotate to the anti-$\mathbf{E}\times\mathbf{B}$ direction.

author's e-mail: ogiwara@aees.kyushu-u.ac.jp

The anti-$\mathbf{E}\times\mathbf{B}$ vortices are considered to be driven by the strong interaction between neutrals and ions [3, 4]. As shown in later section, anti-$\mathbf{E}\times\mathbf{B}$ vortices always accompany deep density depletion in the background neutrals (see Fig. 2) [5]. In the case of monopolar vortex, steep gradient of the neutral density causes a flow of the neutrals, which directs to the center of vortex. When the momentum of neutral flow (inward) is transported to the ions through charge exchange collisions, an inward force arises, and the anti-$\mathbf{E}\times\mathbf{B}$ drift occurs when this force exceeds the electric field (outward). To understand the effect of neutrals on the behavior of ion dynamics, visualization of neutral flow field is of primary importance. However, method for measuring neutral flow velocity with high accuracy has not been established yet. The reason is that flow velocity of neutrals is expected to be two-order slower than ion flow velocity, and consequently high resolution laser induced fluorescence (LIF) Doppler spectroscopy system is needed.

We have been developing a high precision LIF system using a tunable external cavity diode laser. A narrow bandwidth laser is essential for high resolution measurement of the neutral velocity distribution function and Doppler shift [6, 7]. The system is capable of determining Doppler shift of about 9 MHz (14 fm), which corresponds to a velocity of about 6 m/sec. In this paper, a newly developed LIF system is described as well as the preliminary results on neutral flow velocity measurement.

2. Measurement of Neutral Flow

The experiments have been performed in the high density plasma experiment (HYPER-I) device at National Institute for Fusion Science, (Fig. 3). The vacuum vessel is 0.3 m in diameter and 2 m in axial length. Plasmas are generated and sustained by electron cyclotron resonance

P1-009

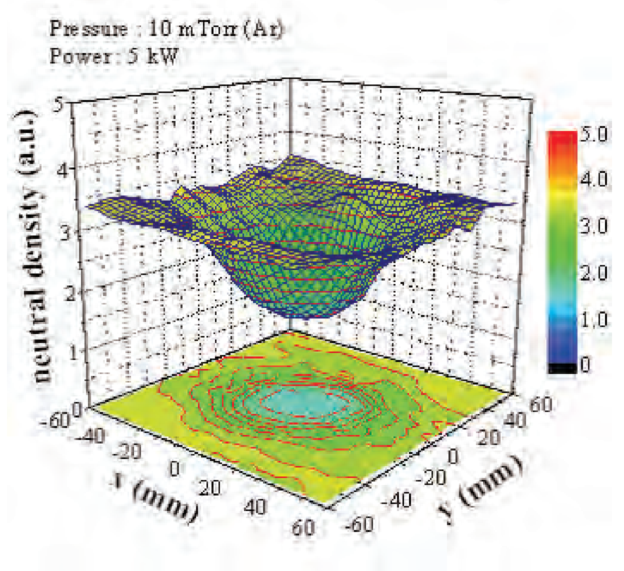

Fig. 2 Density profile of background neutrals in the region of a monopolar vortex. This is obtained from emissions with 480.6 nm ($\propto n_p^2$), and 420.1 nm ($\propto n_p n_n$).

(ECR) heating of argon with the pressure of 10 mTorr. The frequency of microwave is 2.45 GHz, and the input power (Pw) is changed from 40 W (low power operation) to 5 kW (high power operation). The LIF system (laser and collection optics) has been first developed with the plasma in low power operations, in which the LIF signal is easy to observe. The anti-**E** × **B** vortex appears in the high power operations.

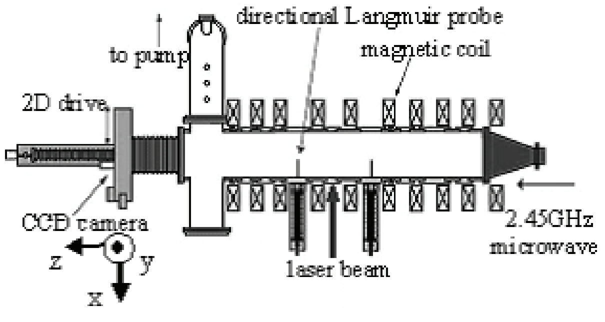

Fig. 3 HYPER-I (High Density Plasma Experiment) device. A laser beam is introduced along x axis.

The schematic diagram of LIF spectroscopy system is shown in Fig. 4. A tunable diode laser (external cavity diode laser), whose bandwidth is 5 fm (3 MHz) and output power is 15 mW, is tuned at a wavelength 696.7352 nm (430281.8 GHz) and is introduced into the plasma. Metastable argon atoms are excited to an upper energy level ($3s^2 3p^5 (^2P^o_{3/2}) 4s \rightarrow 3s^2 3p^5 (^2P^o_{1/2}) 4p$), and then deexcited by $3s^2 3p^5 (^2P^o_{1/2}) 4p \rightarrow 3s^2 3p^5 (^2P^o_{1/2}) 4s$ transition, emitting fluorescence photons of 826.6794 nm (362646.6 GHz). A photomultiplier tube (PMT) with collection optics is installed on the top viewing port of the vacuum vessel, and receives the fluorescence light collected by a lens. The laser beam is modulated by an optical modulator, and the PMT signal is detected by a lock-in amplifier to improve the signal to noise (S/N) ratio. The focal length of the collecting lens is 250 mm, and the effective diameter of the lens is 45 mm. The solid angle of collection optics is 0.012 sr (the latest version of the collection optics is 0.065 sr).

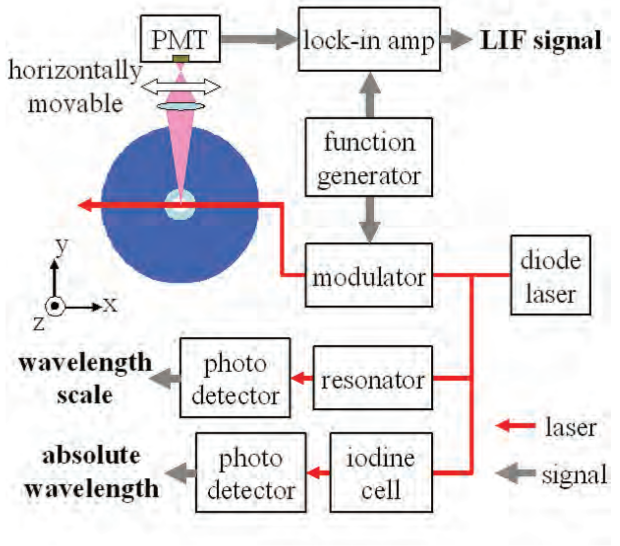

Fig. 4 Schematic diagram of LIF spectroscopy system.

The laser beam is split into two parts, and the sub beam is fed into two optional units; one consists of Fabry Perot resonator, which functions as a wavelength scale, and the other is an iodine gas cell, which gives absolute wavelength reference (Fig. 5). The free spectral range of the resonator is 476 fm, and the absorption lines of iodine located at 696.7428 nm and 696.7337 nm (430277.1 GHz, 430282.7 GHz, respectively) are used as the wavelength references [8].

Sweeping the laser wavelength (16 pm), we have obtained the LIF spectrum, which is proportional to the neutral distribution function. Moving the collection optics along the horizontal axis, the distribution functions at radially different positions can be obtained. The flow velocity of neutrals is determined by the Doppler shift of distribution functions.

3. Experimental Results

To confirm the existence of metastable atoms, we carried out absorption spectroscopy experiment. The maximum absorption was 34 % in the low power operation (P_w = 40 W), while 8 % in the high power operation (P_w = 5 kW). This result means that the number of metastable atoms decreases in the high power operation due to collisional deexcitation process.

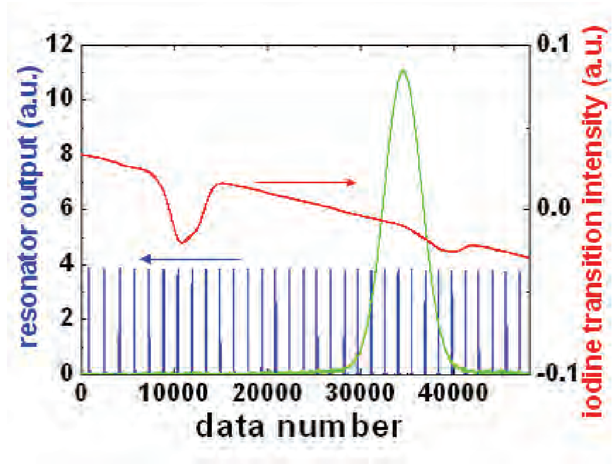

Fig. 5 Wavelength calibration sub-system is composed of resonator and iodine gas cell. A left vally of the iodine transition spectrum is used for calibration. Wavelength of the absorption line is 696.7428 nm.

After confirming the presence of metastable atoms, we measured the LIF spectrum at P_w = 40 W, which is shown in Fig. 6. The observed spectrum is quite well fit by a Gaussian distribution, and the temperature of metastables is 0.034 eV. Measuring the LIF spectra and determining the Doppler shift at different points along the horizontal axis, we have obtained the radial flow velocity profile. An inward flow with the maximum velocity 12 m/sec has been observed.

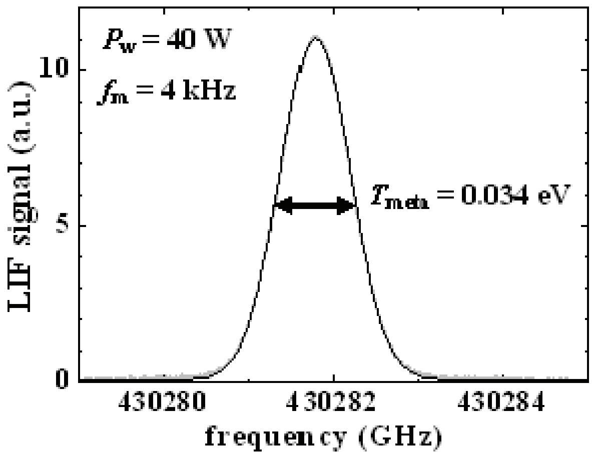

Fig. 6 LIF spectrum for a low power case (P_w = 40 W, f_m = 4 kHz). The neutral velocity distribution function is in well agreement with a Gaussian distribution.

In the high power operations, the level of background light at 825 nm ($\Delta\lambda$ = 10 nm) increases by 20 times higher than the low power case (see Fig. 7), which causes further reduction in S/N ratio in addition to the decrease in metastable atoms. The LIF spectrum obtained with the same LIF system as in the low power case gives unphysical result. This means that S/N ratio is not sufficient for this case. The reasons for the result are already mentioned above, i.e., depletion of metastable atoms and increase of background light.

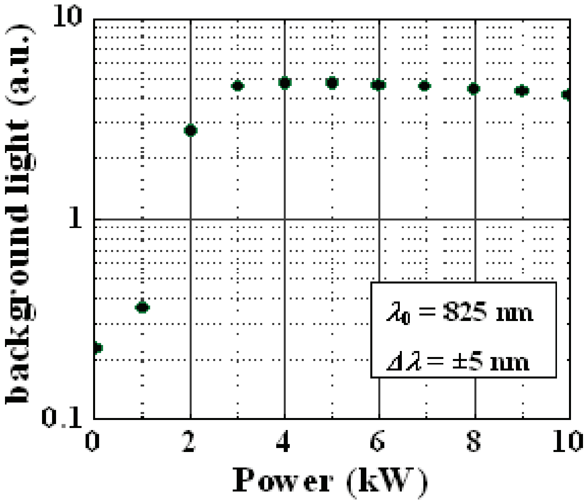

Fig. 7 Background light with wavelength 825 ± 5 nm, emitted from plasma, as a function of input microwave power.

In order to overcome the reduction of S/N ratio, we have improved the collection optics so as to receive more LIF signal. The solid angle is increased to 0.065 sr, and the modulation frequency f_m is raised up to 100 kHz. As shown in Fig. 8, the output signal which originates from the background light decreases with increasing the modulation frequency, and becomes minimum in the frequency range between f_m = 70 kHz and 600 kHz.

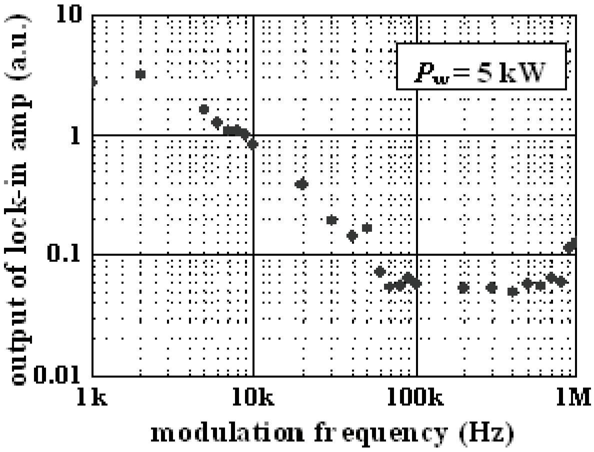

Fig. 8 Plasma background light detected by a lock-in amplifier. Detected background light is reduced logarighmically till f_m = 70 kHz.

When the modulation frequency of lock-in amplifier is set at 100 kHz, several ten times of increase in S/N ratio is expected compared with that of 4 kHz modulation. We have modified the LIF spectroscopy system by introducing an electro-optical modulator, and carried out high frequency lock-in detection. The result is shown in Fig. 9. As seen in the figure, the expected LIF spectrum is clearly recovered. The temperature of metastables in this case is 0.11 eV.

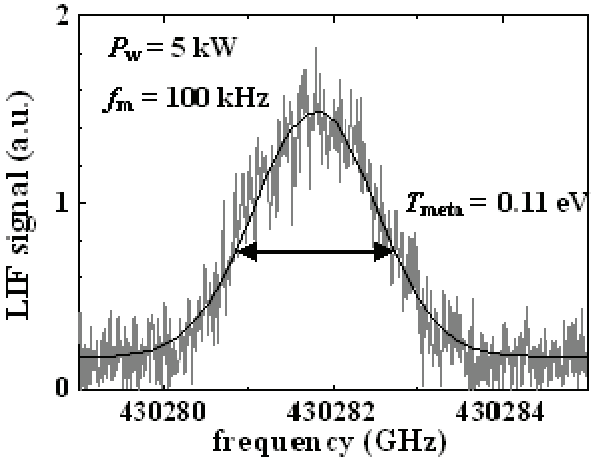

Fig. 9 LIF spectrum for a high power case. (P_w = 5 kW, f_m = 100 kHz). By increasing modulation frequency f_m, LIF spectrum comes to be observable. A smooth solid line is a Gaussian fits to the experimental data.

Measuring the distribution functions of neutrals at different points on the horizontal axis, we have found that there exists an inward flow with the maximum velocity 70 m/sec. The distribution functions except for that of vortex core are slightly asymmetric. This result suggests that the distribution function of the neutrals consists of slow bulk and fast component, which respectively comes from the wall and is produced through charge exchange process with fast ions. In the present experiments, the spatial resolution (radial) of collection optics is 5 mm in order to collect a lot of LIF photons. Further improvement in spatial resolution is needed for detailed experiments on this problem, which is left for future work.

4. Conclusion

A high resolution LIF spectroscopy system for neutral flow velocity measurements is described. The preliminary experiments show that this system is capable of measuring slow velocity field of 10 m/sec. To extend this performance into velocities of the order of m/sec, there remain a few problems to be solved. Wavelength stabilization (long term and short term) is the most important. The present limit of wavelength resolution is close to the stability limit of the laser system (ECDL). By introducing an additional external feedback circuit, the stability problem will be overcome.

The improvement of S/N ratio is still left for future work. It will be raised to a certain extent by increasing the laser power because the LIF signal does not saturate at the present power level (15 mW).

In addition to radial flow velocity, azimuthal flow velocity measurement is of interest from the viewpoint of ion-neutral interaction. The distribution function consists of neutrals from the wall and those from the ions through charge exchange collisions, the latter of which constitute fast rotating component. Therefore, measuring the azimuthal distribution will give us important information of the degree of ion-neutral interaction.

Our system can be applied to ion flow velocity measurements with an appropriate ECDL, which is tuned to a certain energy level of ion. Comparison of the ion flow velocity profiles obtained by LIF spectroscopy and that with a directional Langmuir probe [9] provides a systematic and *in-situ* calibration of probes (directional probe or Mach probe), which is still under discussion in case of supersonic regime.

[1] M. Makino T. Kamimura and T. Taniuti, J. Phys. Soc. Jpn. **50**, 980 (1981).
[2] H. L. Pecseli, J. J. Rasmussen, H. Sugai and K. Thomsen, Plasma Phys. Controlled Fusion **26**, 1021(1984).
[3] A. Okamoto, K. Hara, K. Nagaoka, S. Yoshimura, J. Vranješ, M. Kono and M. Y. Tanaka, Phys. Plasmas 10, 2211 (2003).
[4] J. Vranješ, A. Okamoto, S. Yoshimura, M. Kono and M. Y. Tanaka, Phys. Rev. Lett. **89**, 265002 (2002).
[5] A. Tomida, Master Thesis, Graduate School of Science, Nagoya University, 2006.
[6] N. Sadeghi, M. van de Grift, D. Vender, G. M. W. Kroesen and F. J. de Hoog, Appl. Phys. Lett. **70**, 835 (1997).
[7] R. Engeln, S. Mazouffre, P. Vankan, D. C. Schram and N. Sadeghi, Plasma Sources Sci. Technol. **10**, 595 (2001).
[8] G. D. Severn, Xu Wang, E. Ko and N. Hershkowitz, Phys. Rev. Lett. **90**, 145001 (2003).
[9] K. Nagaoka, A. Okamoto, S. Yoshimura and M. Y. Tanaka, J. Phys. Soc. Jpn. **70**, 131 (2001).

Proceedings of ITC/ISHW2007

Scaling Laws of Intermittent Plasma Turbulence in Edge of Fusion Devices

V.P. Budaev[1,2], S. Masuzaki[2], T. Morisaki[2], N. Ohno[3], N. Asakura[4] , S.Takamura[5] , H. Yamada[2], A. Komori[2]

[1] *Nuclear Fusion Institute, RRC Kurchatov Institute, 123182, Kurchatov Sq.1, Moscow, Russia*
[2] *National Institute for Fusion Science, Oroshi 322-6, Toki, Gifu 509-5292, Japan*
[3] *Eco Topia Science Institute, Nagoya University, Nagoya 464-8603, Japan*
[4] *JAEA, Naka Fusion Research Establishment Naka-machi, Naka-gun, Ibaraki-ken, Japan.*
[5] *Faculty of Engineering, Aichi Institute of Technology , 1247 Yachigusa, Yagusa-cho, Toyota, Japan*

(Received day month year / Accepted day month year)

The high-order structure functions have been analyzed to characterize the edge plasma intermittency in fusion devices. The scaling properties of edge turbulence have shown a strong deviation from a prediction of the Kolmogorov's K41 model. The turbulent fluctuations demonstrate a generalized scale invariance and log-Poisson statistics.

Keywords: edge plasma turbulence, intermittency, log-Poisson model, extended self-similarity, multifractal statistics

1. Inroduction

Incompressible hydrodynamic turbulence is described by Kolmogorov theory [1] (K41) which considers a hierarchical energy cascade and the energy scaling E(k) $\sim k^{-5/3}$. At large Reynolds numbers Re>1, statistical quasi-equilibrium of fluctuations is established in the process of energy transfer from large turbulent eddies towards the smaller ones in the inertial range l ($\eta \ll l \ll L$, where L is the largest eddy/ structure scale, η - dissipation Kolmogorov's scale). Investigation of self-similar turbulence properties resulted in multiplicative hierarchical cascade models [2]: the log-normal model K62, the β-model, and most favorable the log-Poisson model [3, 4]. To quantify whether boundary conditions influence the statistical properties in turbulence it was proposed multifractal formalism (see [2]). Intermittency leads to a local breaking of the turbulence homogeneity, when 'active' regions coexist with quasi-laminar ones. The intermittent fluctuations demonstrate non-Gaussian statistics, self-similarity and multifractality. The intermittency is observed in turbulent hydrodynamic fluids [3] and in turbulent magnetized plasmas (see e.g [5]).

The spectrum of magnetohydrodynamic (MHD) turbulence was first addressed by Iroshnikov and Kraichnan (IK) who considered the turbulent energy cascade affected by a magnetic field (see [6,7]). The IK model yields $E(k) \sim k^{-3/2}$ resulted from Alfven decorrelation effect. The validity of the two phenomenologies (K41 and IK) in MHD turbulence and plasma confined in fusion devices is still under a discussion. Numerical and experimental data indicate that in MHD turbulence the energy transfer occurs predominantly in the field-perpendicular direction [6]. This raises a question whether anisotropy is crucial for the energy cascade, and whether it changes the spectrum of turbulence. The two-dimensional direct numerical simulations (DNS) support the IK picture, while three-dimensional simulations and recent analytical results suggest K41 energy spectra (see [6]). A phenomenology of "intermediate" turbulence by Goldreich and Sridhar [7] (GS95) postulates a balance between K41 and IK energy cascades and accounts for the local anisotropy induced by a magnetic field. The GS95 assumes one-dimension filaments as the most dissipative structures, the same as in hydrodynamic turbulence. Other MHD turbulence models assume the singular structure shape of a current sheet [6,7].

There are numerous experimental observations of the magnetized plasma turbulence that share a lot of features of neutral fluid turbulence including many scales, the cascades, strong mixing, non-linear scalings and so on. Despite equations described neutral fluids and plasmas are different they have the same type of scale invariance (dilatation symmetry, namely, $x \to \lambda x$, $t \to \lambda^{1-h} t$, $\upsilon \to \lambda^{h} \upsilon$). This common dilatation symmetry is responsible for a common scaling property.

Most favorable log-Poisson model of intermittent turbulence consider anisotropic stochastic cascade and the generalized self-similarity implying the long-range correlations, which drive an anomalous transport, e.g. superdiffusion. An experimental analysis of the statistical moments in the frame of the log-Poisson model suggests a description of the transport processes in the real turbulent

author's e-mail: budaev@mail.ru

plasmas. Despite the large amount of experimental data that has been obtained in fusion devices, our understanding of the turbulence and diffusive transport process in magnetized plasmas is still rather limited. In this work we focus on the scale invariance property and scaling laws of the edge plasma turbulence in fusion devices and test analytical fits.

2. Experimental data

We analyze Langmuir probe signals of ion saturation current I_{sat} that is essentially plasma density. On Large Helical Device [9] I_{sat} was measured by 16 graphite dome-type electrodes (diameter of 1 mm separated by 6 mm) embedded in the divertor plate and by reciprocating probe. On JT-60U tokamak measurements (L-mode) in the SOL has been done by reciprocating Mach probes [10] installed at the low field side (LFS) mid-plane and just below the X-point .On T-10 tokamak [5] (R/r= 1.5 m / 0.4 m, I_p=200÷220 kA, B=2.2÷2.4 T) Langmuir probe (tungsten tips of 0.5 mm in a diameter and 3 mm in a length) I_{sat} was measured at SOL in a steady state of repetitive ohmic discharges with no MHD activity. In the linear divertor plasma simulator NAGDIS-II (n_e~ 10^{20} m^{-3} , T_e~ 1–3 eV , B= 0.25 T) attached and detached plasmas were investigated [11,5]. All signals are digitized with sampling rate 0.5 MHz in JT-60U and LHD and 1 MHz in other devices, the sample number 10^5 - 10^6. Signals have the intermittent behaviour typically observed in edge of fusion devices [5]. Power spectra exhibit a complicated frequency dependence without a trivial power-law behavior [5].

3. Generalized scale invariance

The classical approach [12] for an exploration of statistical features is an analysis of statistical moments (structure functions) $S_q(\tau)= \langle|X(t+\tau)-X(t)|^q\rangle$, where $\langle\ldots\rangle$- means an ensemble average of the time-dependent signal X(t). The structure function technique is equivalent to the detailed investigation of the probability distribution function of the turbulent fluctuation. The Kolmogorov theory K41 of isotropic turbulence infers Gaussian statistics for fluctuations. It predicts the structure function scaling $S_q(\tau)\sim\tau^{\zeta(q)}$, $\zeta(q)=q/3$, in the inertial range. Experimental investigations of the developed hydrodynamic turbulence demonstrate a departure of the high-order structure function scalings (q > 3) from the Kolmogorov K41 prediction due to the intermittency. The experimental structure functions typically shows a power law only over a limited (inertial) range $\eta << l << L$ (of ~10 μs in fig.1). Whereas the generalized self-similarity is registered in a broadened range extended to the dissipation scales [13,2]. A generalized scale invariance (extended self-similarity - ESS) was proposed in [13], and then considered in the log-Poisson model of turbulence [3,4]. Hidden statistical symmetries of the Navier-Stockes equations, hierarchy of moments, multifractality are behind the property of the ESS. The ESS infers a scaling $S_q(l)\sim S_3(l)^{\zeta(q)/\zeta(3)}$ for the extended range $l \geq 5\eta$. All data from fusion devices, that we analyzed, demonstrate such ESS property(linear behavior in fig.2) over the time scales ~1

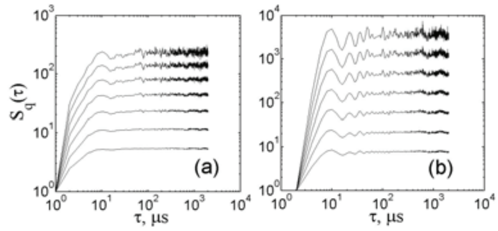

Fig.1. The structure functions $S_q(\tau)$ of high orders (q=2÷8 from bottom to top) vs. time scale τ. (a) LHD divertor probe #10 (b) LFS SOL JT-60U,shot#44421

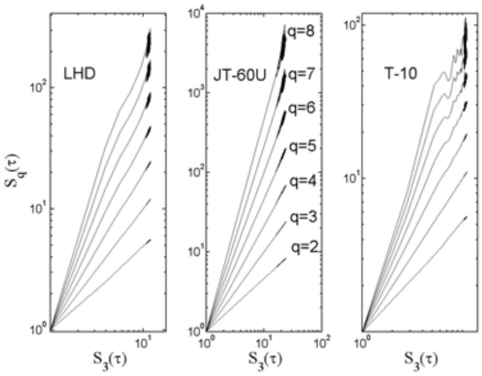

Fig.2. ESS plot of the structure function $S_q(\tau)$ of high orders (q=2÷8 from bottom to top) from the third-order one. (a) LHD divertor probe, (b) LFS SOL JT-60U,distance from separatrix 42mm (c) SOL T-10

msec substantially longer than an inertial range in fig.1. The ESS corresponds to the considering of the scaling in a turbulent cascade not with respect to the usual distance, but with respect to an effective scale defined by the third order moment of the velocity field.

4. **The log-Poisson model of the turbulence**

The scaling of the third-order moment can be deduced analytically ($\zeta(3)$ =1), therefore scaling of $\zeta(q)/\zeta(3)$ can be analyzed in experiments to improve the precision of the scaling estimation, especially at moderate Reynolds numbers assessed in experiments. It allows to obtain more accurate values of $\zeta(q)$ by using a property of the ESS plotting S_q as a function of S_3, fig. 2. We treat experimental scalings in the frame of log-Poisson turbulence model [4] predicted a scaling:

$$\zeta(\boldsymbol{q}) = (1-\Delta)\frac{\boldsymbol{q}}{3} + \frac{\Delta}{1-\beta}\left[1-\beta^{\frac{q}{3}}\right] \qquad (1).$$

It is based on the hypotheses of a “hidden symmetry” and a hierarchical structure of the moments of the energy dissipation. The logarithm of energy dissipation obeys the Poisson statistics (so-called the log-Poisson statistics) characterized by special scale-covariance properties. A hidden symmetry can be interpreted as a generalized scale covariance and β is a characteristic of the intermittency of the energy dissipation ($\beta=1$ for non-intermittent fully developed turbulence). The quantity ε_l^{∞} (associated with the most intermittent dissipative structures) has a divergent scaling $\varepsilon_l^{\infty} \sim l^{-\Delta}$, as $l \to 0$, where Δ is a parameter depending on the dimension of the dissipative structure. In an isotropic 3D turbulence $\Delta = \beta = 2/3$ which is obtained if the most dissipative structures are filaments. The ESS property is involved in the log-Poisson model. We use the wavelet transform modulus maxima method (WTMM) [5] to estimate $\zeta(q)$ from experimental signals. In fig.3, the

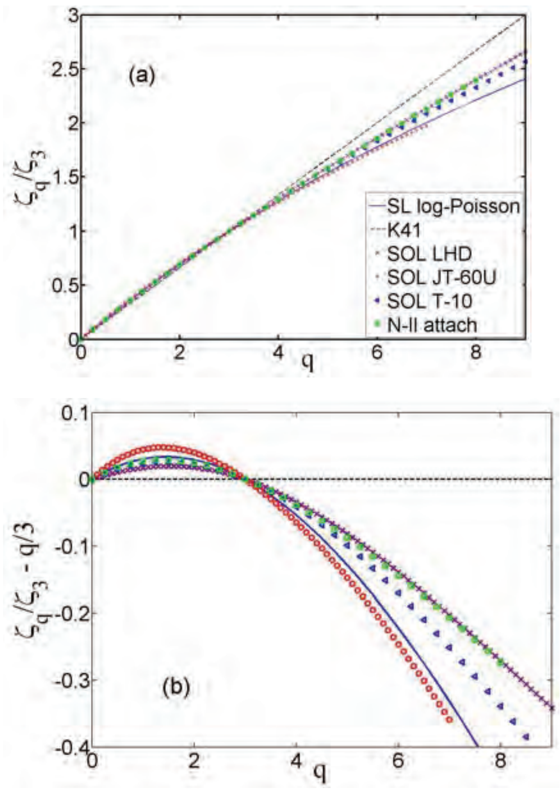

Fig.3. (a) Structure function scaling vs. order q. Kolmogorov K41 (a dashed line) and log-Poisson (a solid line, β=Δ=2/3) models and (b) the same for a departure of the scaling from the K41.

scalings $\zeta(q)/\zeta(3)$ are shown in the same plot with the scalings predicted by the K41 and the log-Poisson models. The scalings are anomalously deviated from the K41 scaling, fig.3b. Each experimental scaling could be fitted by (1) with adjusted parameters Δ and β. A solving of non-linear least-squares problem of fitting to (1) gives indexes in the range $\Delta = 0.15 \div 0.8$, $\beta = 0.25 \div 0.7$. Some signals have non-intermittent behaviour ($\beta=1$). The observed range of Δ (between 1/3 and 2/3) can be interpreted [14] that the most intermittent dissipative structures are one-dimensional filament structures in these cases. Such dissipative structures have most likely not a trivial geometrical topology but a fractal one.

The log-Poisson model of 3D turbulence was modified in MHD case to account for the IK phenomenology [7]. To test IK model we plot in fig.4 a deviation of relative exponents $\zeta(q)/\zeta(4)$ from IK scaling q/4. The scaling of data in the vicinity of X-point in JT-60U is close to the IK indicating strong MHD turbulence property. The data from SOL are deviated strongly from IK scaling (see [6]). At the same time they are not fitted by the scaling for MHD log-Poisson model (see definition in [7]). It can be interpreted that IK phenomenology (two-dimension strong anisotropy) is not available for a treatment of the SOL plasma turbulence.

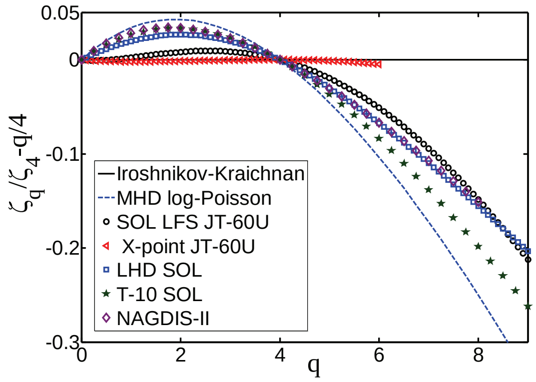

Fig.4. Deviation of scaling from Iroshnikov-Kraichnan scaling q/4 (solid line). MHD IK log-Poisson scaling (dashed line). Scaling in the vicinity of X-point JT-60U is close to IK.

5. Transport scaling laws

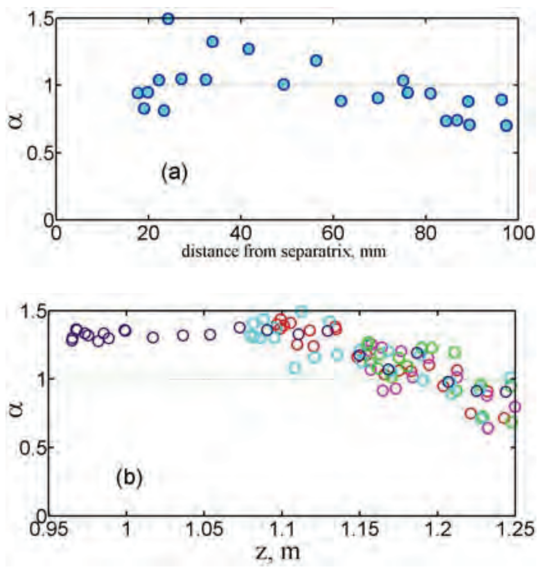

Fig.5 Diffusion scaling index (a) JT-60U LFS SOL (shot# 44421) (b) SOL LHD high β shots vs. vertical coordinate z, B=0.425 T

The statistical description of transport processes in fusion plasmas is an alternative approach to the traditional characterization of a transport based on the computation of effective transport diffusion coefficients.

The log-Poisson model could be used to estimate a transport scaling based on the self-similarity indexes β and Δ (1) that responsible for percolation effect in the turbulence. In a simplified approach [14], the diffusion scaling depends on the structure function scaling as $D \propto \tau^{K(-1)}$, the exponent $K(q)$ relates with the scaling of the high-order structure function $\zeta(q)$ as $K(q)=q-\zeta(3q)$. A displacement of particles across a magnetic field with time τ is scaled as $\langle\delta x^2\rangle \propto D\tau \propto \tau^{\alpha}$ with an exponent $\alpha \propto 1+K(-1)$. This index was estimated from experimental

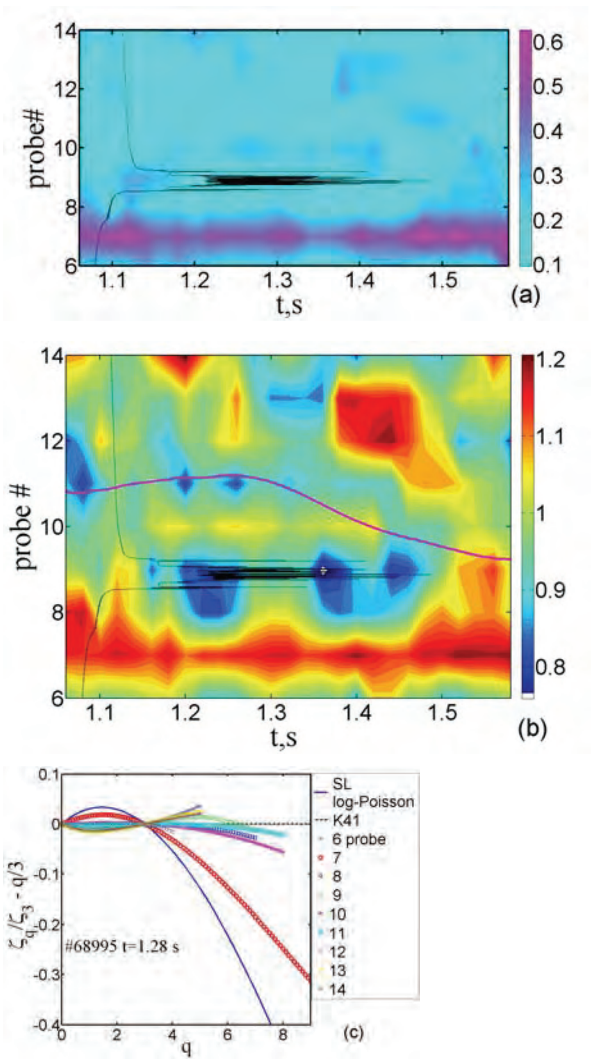

Fig.6 LHD divertor probes data, shot #68995 with SDC.
(a) Multifractality level, (b) Diffusion scaling index α,
(c) Structure function scalings, deviation from K41, cf. fig3a.
Magnetic connection length Lc (logarithm of magnitude,a.u.)
in black line, and plasma storage energy evolution (magenta)

scalings. It varies with a radius in JT-60U SOL (fig.5) indicating superdiffusion process (α>1) at radial distance 20-50 mm where the direction of the parallel SOL flow changes upward to downward [10]. In LHD the natural island layers overlap and the stochastic field structure (a natural helical divertor) appears between the LCFS and the residual X-point. The magnetic field line with large connection length L_c reaches the ergodic layer surrounding the core plasma region. L_c varies from less than a few meters to over a few kilometers (see black line in fig.6a,b). Ion particle flux to the divertor plates [9] and multifractality level (deviation from Gaussian statistics, see a definition in [5]) follows the deposition profile of the magnetic field lines, fig.6a. The probe connected to the field line with a large L_c has a large ion particle flux. In LHD, an increasing of α>1 was observed in domains that are characterized by short connection length (probe # 7 in fig.6b). Scalings illustrate specific behaviour of #7 probe location compare with others that are closer to K41 scaling, fig.6c. This property is kept even at discharge evolution at super-dense core (SDC).

In conclusion, the statistical properties of the intermittent turbulence show a striking empirical similarity in the SOL plasma region of fusion devices. Scalings of the structure functions strongly deviate from the Kolmogorov's K41 theory prediction. The anomalous behavior of scaling is similar in the SOL plasma of helical device, tokamaks, and linear machine. Experimental scalings are close to the log-Poisson model. One-dimension filament structures are likely the most intermittent dissipative structures. The similar behavior of the scalings has been observed in the edge of fusion devices with different magnetic topology and heating. It supports a view that the edge plasma turbulence displays universality. By using self-similarity indexes, transport scaling indexes are estimated from percolation property of the turbulence with non-trivial self-similarity. The results of our study improve our understanding of intermittent turbulence in the edge of fusion devices.

Acknowledgements. This work was supported by the NIFS budged NIFS06ULPP511, JT-60U budged,the Rosatom RF

References

[1]A.N.Kolmogorov,Dokl. Akad.Nauk SSSR 30, 299 (1941) (Proc. R. Soc. London, Ser. A 434, 9 (1991)).

[2]U.Frish, Turbulence:The Legacy of A N Kolmogorov (Cambridge : Cambridge University, 1995).

[3] Z.S. She and E. Leveque, Phys. Rev. Let. 72, 336 (1994).

[4] B. Dubrulle, Phys. Rev. Lett. 73, 959 (1994).

[5] V.P. Budaev et al , Nucl. Fus 46, S181 (2006).

[6] W. Müller and D. Biskamp, Phys.Rev. Let. 84 475 (2000).

[7] H.Politano and A.Pouquet Phys. Rev. E 52, 636 1995

[8] P.Goldreich and S.Sridhar, Astrophys.J.438 763 1995

[9] S.Masuzaki et al, Nucl. Fusion 42, 750 (2002).

[10] Asakura et al Nucl. Fusion 44 503 (2004)

[11] N.Ohno et al , Nucl. Fusion 41, 1055 (2001).

[12] A. S. Monin and A. M. Yaglom, Statistical Fluid Mechanics (MIT Press, Cambridge, MA, 1975.

[13] R. Benzi et al., Phys.Rev.E 48,R29 (1993).

[14] V.P. Budaev et al Contrib. Plasma Phys (to be published)

Proceedings of ITC/ISHW2007

Instability of Thin-Walled Annular Beam in Dielectric-Loaded Cylindrical Waveguide

S. Tamura, M. Yamakawa, Y. Takashima and K. Ogura

Graduate School of Science and Technology, Niigata University, 950-2181, Japan

(Received 15 October 2007 / Accepted 3 August 2007)

Cherenkov and slow cyclotron instabilities driven by an axially injected electron beam in cylindrical waveguide are studied by using a new version of self-consistent liner theory considering three dimensional beam perturbations. There are three models of beam instability analysis, which are based on solid beam, infinitesimally thin annular beam, and thin-walled annular beam. Among these models, a model properly representing the often used actual annular electron beams is thin-walled annular beam. We develop a numerical code for a cylindrical waveguide with a thin-walled annular beam having a finite thickness. Our theory is valid for any beam velocity. We present eigen modes with plasma and beam. And instabilities driven by thin-walled annular beam in dielectric-loaded waveguide are examined.

Keywords: Thin-walled annular beam, low-frequency surface wave mode, high-frequency surface wave mode, Cherenkov instability, slow cyclotron instability

1. Introduction

The backward wave oscillator (BWO) or traveling wave tube (TWT) is one of the high power microwave sources and can be driven by an axially injected electron beam without initial perpendicular velocity. For relatively low power in some 10 kW level or less, Pierce type cathodes are commonly used and beam shape is approximated by a solid beam. In many high power experiments, cold cathodes are used and the shape of electron beam is a thin-walled annulus. A new version of self-consistent field theory considering three-dimensional beam perturbations are developed based on a solid beam [1-2]. For infinitesimally thin annular beam, the boundary is modulated due to the transverse modulation of annular surface. Analyses of infinitesimally thin annular beam need to be based on a different theory from thin-walled annular and solid beam. A pioneering work can be seen in Ref. [3]. Recently, instabilities of eigen mode due to the surface modulation are analyzed in Ref. [4], presenting a self-consistent field theory considering the moving surface modulation.

In this work, we develop a numerical code for a cylindrical waveguide with a thin-walled annular beam. Note that the annular beam thickness is finite. The boundary condition at the beam surface is different from the infinitesimally thin annular beam. Solid beam and thin-walled annular beam are based on the same boundary condition, but the number of boundary is different. Thin-walled annular beam has outside and inside surface, and solid beam has only outside surface. Our numerical codes are valid for any beam velocity v. We present the eigen modes for waveguide with plasma (v=0) and beam (v>0) modes.

The organization of this proceeding is as follows. In Sec. 2, we describe numerical method of thin-walled annular beam and solid beam. In Sec. 3, dispersion carves of thin-walled annular plasma and solid plasma are examined. In Sec. 4, we examine Cherenkov and slow cyclotron instabilities driven by thin-walled annular beam in dielectric-loaded waveguide. Discussion and conclusion of this paper are given in Sec. 5.

2. Numerical method

For slow-wave devices, the periodically corrugated slow-wave structure (SWS) is used [5, 6]. However, analyses of these devices are very complex. Therefore, we analyzed basic electromagnetic characteristics of cylindrical waveguide with straight wall. We consider a dielectric-loaded waveguide (Fig.1). The wall radius R_w=1.445 cm, dielectric radius R_d=0.85 cm. In the case of plasma (v=0), relative permittivity of dielectric ε_r=1.0. For analyzing beam interactions, ε_r=4.0. We used this model to examine basic characteristics of the electromagnetic wave and the beam interaction. For thin-walled annular beam, average beam radius R_a=0.75 cm, and beam thickness Δ_p=0.1 cm. For solid beam, beam outside radius R_b=0.8 cm.

author's e-mail: f06e072j@mail.cc.niigata-u.ac.jp

A guiding magnetic field $\mathbf{B_0}$ is applied uniformly in axial direction. An electron beam is propagating along the guiding magnetic field. The temporal and spatial phase factor of all perturbed quantities is assumed to be $\exp[i(k_z z+m\theta-\omega t)]$. Here, m is the azimuthal mode number and k_z is the axial wave number.

In the system with magnetized plasma or beam such as Fig.2, electromagnetic modes are the hybrid mode of transverse magnetic (TM) and transverse electric (TE) mode. Two letters of EH and HE is used, to designate the hybrid mode. In this paper, TM is dominant in EH mode and TE is dominant in HE mode.

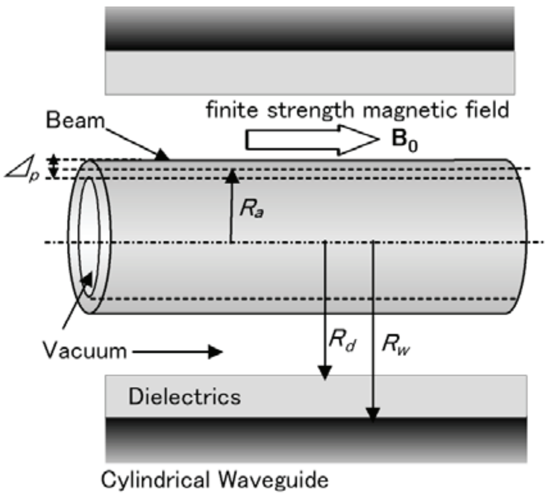

Fig.1 Model of thin-walled annular beam analysis.

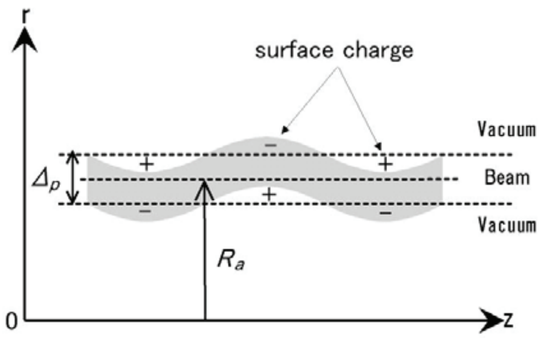

Fig. 2 Beam surface of thin-walled annular beam.

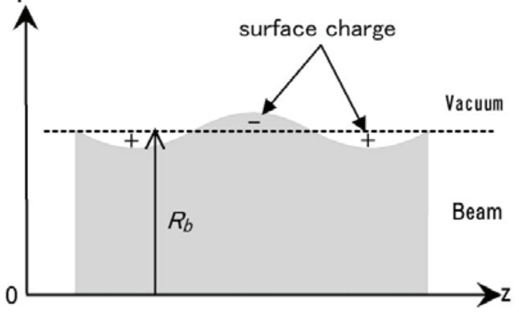

Fig. 3 Beam surface of solid beam.

An electron beam surface is modulated as beam is propagating. For thin-walled annular beam and solid beam, the transverse moderation appears as the surface electric charge at the fixed boundary as shown in Figs.2 and 3. Solid beam has one surface. Thin-walled annular beam has another surface inside beam because there is a vacuum region inside the beam.

3. Dispersion curves of plasma

We present results of thin-walled annular plasma and solid plasma analyses (v=0). Here ω_p and Ω are plasma frequency and cyclotron frequency. In this section, $\omega_p=3\times10^{10}$ rad/s. Figure 4 shows the dispersion curves of thin-walled annular plasma and Fig. 5 shows the dispersion curves of solid plasma in the absence of magnetic field. Axisymmetric electromagnetic modes are the TM_{0n} and TE_{0n} mode. Here, n is any positive integer. Dispersion curves of thin-walled annular plasma shows two surface waves due to the inner and outer surface space charges: high- and low-frequency surface wave modes. Solid plasma has only one surface wave mode due to the outer surface space charge.

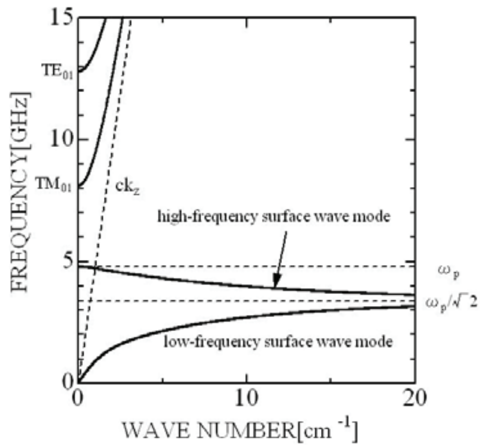

Fig. 4 Dispersion curves of thin-walled annular plasma in absence of magnetic field.

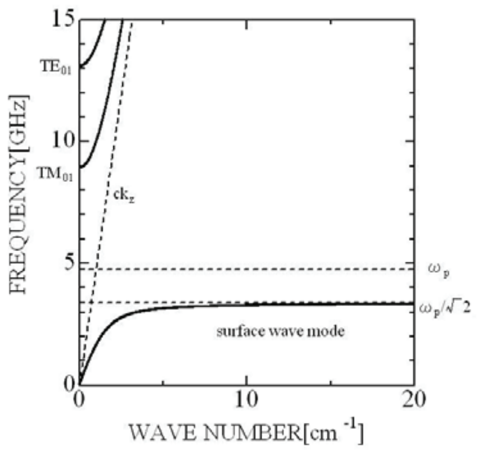

Fig. 5 Dispersion curves of solid plasma in absence of magnetic field.

The high-frequency surface wave mode is attributed to the inner boundary of thin-walled annular plasma (Fig.2). The low-frequency surface wave mode is attributed to the outer surface of annulus and corresponds to the surface wave mode of solid plasma. Their frequency is zero at k_z=0, increases with increasing k_z, and approaches an asymptotic limit as $k_z \to \infty$. This limit is $\omega_p/\sqrt{2}$. The frequency of high-frequency surface wave mode for the annulus is ω_p at k_z=0, decrease with increasing k_z, and approach an asymptotic limit as $k_z \to \infty$. This limit is also $\omega_p/\sqrt{2}$.

Te dispersion curves for the thin-walled annular and solid plasma are respectively shown in Figs. 6 and 7 at B_0=0.1 T ($\omega_p > \Omega$) and in Figs. 8 and 9 at B_0=0.2 T ($\Omega > \omega_p$). With the finite strength magnetic fields, electromagnetic modes are the hybrid mode of TM and TE modes: axisymmetric EH_{0n} and HE_{0n} modes in the figures. And cyclotron modes are appeared in addition to the space charge modes. For both of thin-walled annular and solid plasma, the frequencies of cyclotron mode are between the upper hybrid frequency $\omega_h=(\Omega^2+\omega_p^2)^{1/2}$ and Ω or ω_p, whichever is larger.

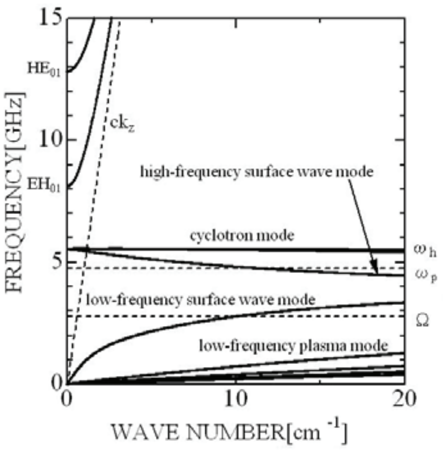

Fig. 6 Dispersion curves of thin-walled annular plasma with B_0=0.1T.

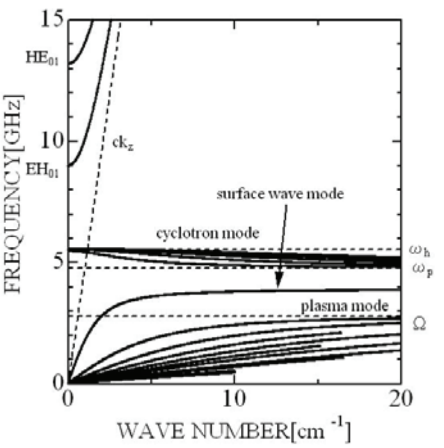

Fig. 7 Dispersion curves of solid plasma with B_0=0.1T.

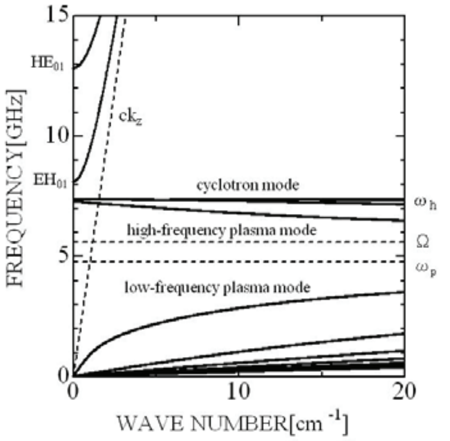

Fig. 8 Dispersion curves of thin-walled annular plasma with B_0=0.2 T.

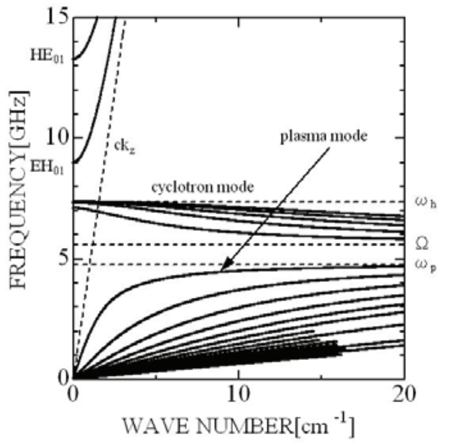

Fig. 9 Dispersion curves of solid plasma with B_0=0.2 T.

As for the space charge modes, surface wave modes exist as in the case of B_0=0 if $\Omega < \omega_p$. With increasing k_z, the frequencies of low-frequency surface wave mode and surface wave mode of solid plasma are increased and approach an asymptotic limit as $k_z \to \infty$. The limit is between ω_p and $\omega_p/\sqrt{2}$. The frequency of high-frequency surface wave mode is decreased with increasing k_z, and has the same asymptotic value as the low-frequency mode in the limit of $k_z \to \infty$

The presence of magnetic field yield plasma modes due to the volume space charge perturbation, those are denoted as plasma modes in Figs.6-9 [2]. The low-frequency plasma mode of thin-walled annular plasma and the solid plasma mode have frequencies that are zero at k_z=0, increase with increasing k_z, and approach an asymptotic limit as $k_z \to \infty$. This limit is ω_p or Ω whichever is smaller. The annular plasma has high-frequency plasma mode. Its frequency approaches an asymptotic limit between ω_h and Ω, as $k_z \to \infty$ with $\Omega > \omega_p$.

5. Instabilities driven by thin-walled annular beam

In this section, we examine instabilities driven by beam (v>0). Figure 10 shows the dispersion curves for a thin-walled annular beam with the energy 660 keV, beam current 2.3 kA and B_0=0.8 T. For an electron beam propagating along the direction of an axial magnetic field, there exist four beam modes. They are the fast and slow space charge modes and the fast and slow cyclotron modes. Slow space charge mode and slow cyclotron mode couple with both of EH_{01} and HE_{01} mode, resulting in the Cherenkov and slow cyclotron instabilities. Instabilities for EH_{01} mode are predominating, compared with those for HE_{01}mode.

Figure 11 shows the dependence of the temporal growth rate on beam thickness Δ_p. The beam outer radius is fixed to 0.8 cm, and beam inner radius has been changed with a fixed line charge density. The growth rate of Cherenkov instability increases by decreasing Δ_p.

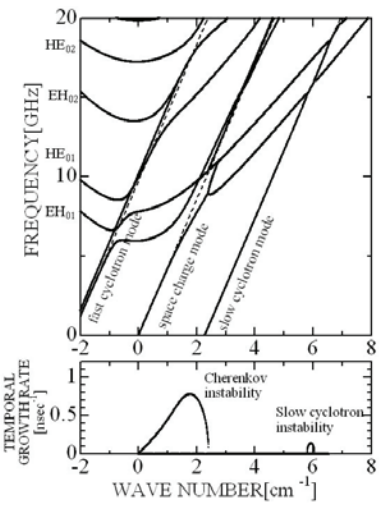

Fig. 10 Dispersion curves of thin-walled annular beam in dielectric-loaded waveguide with beam energy 660 keV, beam current 2.3 kA and B_0=0.8 T.

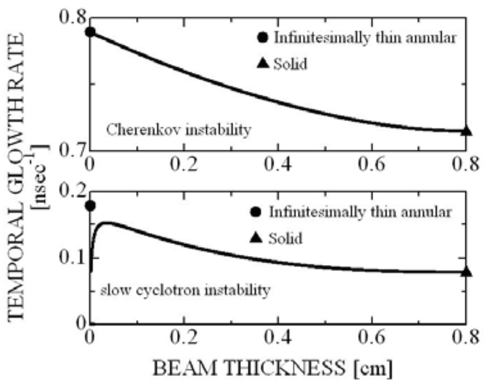

Fig. 11 The dependence of the temporal growth rate on beam thickness.

The growth rate of slow cyclotron instability also increases by decreasing the beam thickness. But, in the region of Δ_p < 0.035 cm, the growth rate decreases.

In the limit that the beam inner radius is zero, the growth rate of Cherenkov and slow cyclotron instabilities of thin-walled annular beam approaches the growth rate of solid beam, ▲ in Fig.11. In the other limit that $\Delta_p \rightarrow 0$, the corresponding growth rates are those of an infinitesimally thin annular beam model with Δ_p=0 [2] and are depicted by ● in Fig.11. Two models based on finite and zero Δ_p give almost the same results for the Cherenkov instability. For slow cyclotron instability, the growth rates are different between two models. This might be caused by the difference of annulus structure: one has an internal structure between the inner and outer surface and the other is just a sheet without any internal structure.

5. Conclusion

We develop a numerical code for a cylindrical waveguide with a thin-walled annular beam considering three-dimensional beam perturbations, which is valid for any beam velocity v. Electromagnetic modes are the hybrid mode of TM and TE mode. Cyclotron and space charge modes corresponding to the solid case exist. Note that, for space charge modes, surface wave modes exist in addition to the volume wave mode if $\Omega < \omega_p$. As characteristic modes of annular case, the high-frequency space charge modes appear due to the inner surface. A thin-walled annular beam drives slow cyclotron as well as Cherenkov instability. The Cherenkov instability increases by decreasing Δ_p to zero. The slow cyclotron instability increases by decreasing Δ_p, reaches the maximum at a certain value of Δ_p and decreases in the limit of $\Delta_p \rightarrow 0$.

Acknowledgments

This work was partially supported by a Grant-in-Aid for Scientific Research from the Ministry of Education, Science, Sports and Culture of Japan, and partially performed under the Collaborative Research Program between NIFS and University of Tsukuba in cooperation with Japanese universities.

References

[1] O. Watanabe, *et al.*, Phys. Rev. E. **63**, 056503 (2001).
[2] K. Ogura *et al.*, Jpn. J. Appl. Phys. **42**, 7095 (2003).
[3] J. R. Pierce, *Traveling-Wave Tube* (Van Nostrand, Toronto, 1950).
[4] K. Ogura, *et al.*, J. Plasma Phys. **72**, 905 (2006).
[5] H. Yamazaki, *et al.*, IEEJ Trans. FM, **125**, 739(2005).
[6] Y. Kiuchi, *et al.*, Trans. Fusion Sci. Tech. **51**, 331(2007).

Proceedings of ITC/ISHW2007

Spatiotemporal Behavior of Drift Waves in LMD-U

Takuma YAMADA[1)], Sanae -I. ITOH[1)], Kenichiro TERASAKA[2)], Naohiro KASUYA[3)], Yoshihiko NAGASHIMA[1)], Shunjiro SHINOHARA[2)], Takashi MARUTA[2)], Masatoshi YAGI[1)], Shigeru INAGAKI[1)], Yoshinobu KAWAI[1)], Akihide FUJISAWA[3)] and Kimitaka ITOH[3)]

[1)] *Research Institute for Applied Mechanics, Kyushu University, Kasuga 816-8580, Japan*

[2)] *Interdisciplinary Graduate School of Engineering Sciences, Kyushu University, Kasuga 816-8580, Japan*

[3)] *National Institute for Fusion Science, Toki 509-5292, Japan*

In the LMD-U linear magnetized plasma, fluctuation measurements with multi-channel poloidal Langmuir probe arrays have been performed. The mean poloidal mode number of the fluctuation and its spread suggest the existence of broadband fluctuation, which is considered to be produced by nonlinear couplings. The broadband fluctuation develops into high poloidal mode number and high frequency region, which do not satisfy the linear dispersion relation of drift wave modes. The broadband fluctuation revealed small correlation time and poloidal length than the fluctuation peaks. Poloidal mode decomposed axial coherence was measured with two poloidal probe arrays. The axial coherence was strong both for the broadband fluctuation and fluctuation peaks.

Keywords: linear plasma, multi-probe, drift wave, turbulence, nonlinear coupling

1 Introduction

Recently, there has been an advance in the study of nonlinear interaction between drift wave turbulence and meso-scale structures such as zonal flows and streamers [1, 2]), and experiments in linear plasma devices have been in progress [3–10]. In these studies, complex wave patterns in poloidal direction have been observed (see also reports from toroidal plasma experiments, e.g., [11–14]). These advancements highlight the need to measure fluctuations at multiple spatial positions simultaneously. Fluctuation measurements using poloidal multi-probe arrays have been performed in linear plasmas and torus plasmas [3, 4, 6, 15].

In the LMD-U linear magnetized plasma [16], multi-point measurements of the ion saturation current and floating potential fluctuations using poloidal Langmuir probe arrays have been in progress. Drift wave modes driven by steep radial density gradient were identified, and a drift wave turbulence regime was achieved [17]. The poloidal mode numbers and frequencies of the drift wave modes were compared with the calculated linear dispersion relation of drift wave [18], and they were in a good agreement. Moreover, in a drift wave turbulence regime, quasi-modes and broadband components that do not satisfy the dispersion relation were found and suggested that they were produced by nonlinear couplings of parent modes [19]. In this article, we report the details about the broadband components found in the drift wave turbulence regime.

2 Poloidal Probe Arrays

We have performed a quasi-two-dimensional measurement of the ion saturation current fluctuation of the LMD-U linear plasma [16]. The schematic view of the LMD-U device is shown in Fig. 1. A linear magnetized plasma is created by an rf (the frequency of 7 MHz and the power of 3 kW) antenna in a quartz tube (the axial length of 0.4 m and the inner diameter of 0.095 m) with argon gas filled in. The plasma is guided along straight magnetic field created by magnetic coils surrounding the vacuum vessel to form a column shape. The axial length and inner diameter of the vacuum vessel are 3.74 m and 0.445 m, respectively.

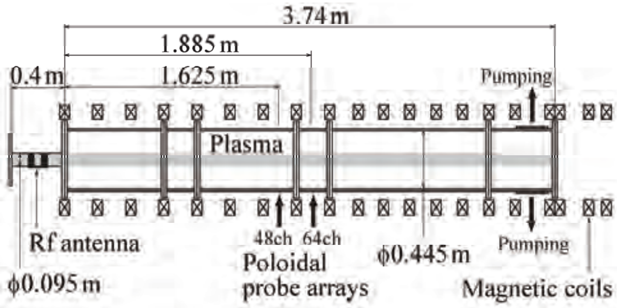

Fig. 1 Schematic view of the LMD-U linear plasma device, and the positions of the polodial probe arrays (64-channel and 48-channel).

There are two poloidal Langmuir probe arrays installed on LMD-U. A 64-channel poloidal probe array is installed at the axial position of 1.885 m and a 48-channel poloidal probe array is installed at 1.625 m. The tungsten probe tips of the 64-channel probe array are fixed at the measuring radius of 40 mm (the probe tips are 3.9 mm apart), and the position of the whole probe array is adjustable two-dimensionally in the plasma cross section. Therefore, the precise poloidal mode number of the fluctuation is available by this probe array [20]. The 48-channel probe array consists of 16 probe units, which are mov-

author's e-mail: takuma@riam.kyushu-u.ac.jp

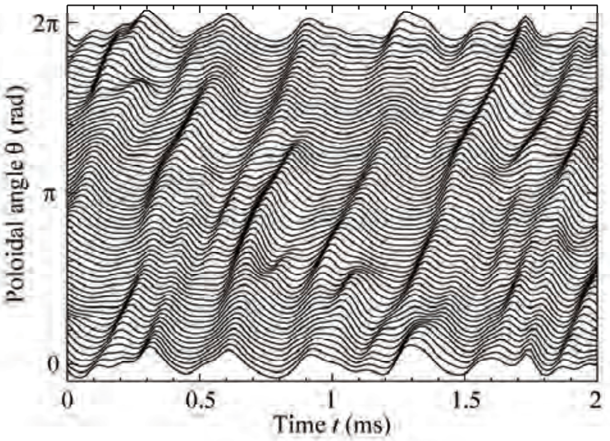

Fig. 2 Spatiotemporal behavior of the ion saturation current $I(\theta, t)$ measured with the 64-channel poloidal probe array.

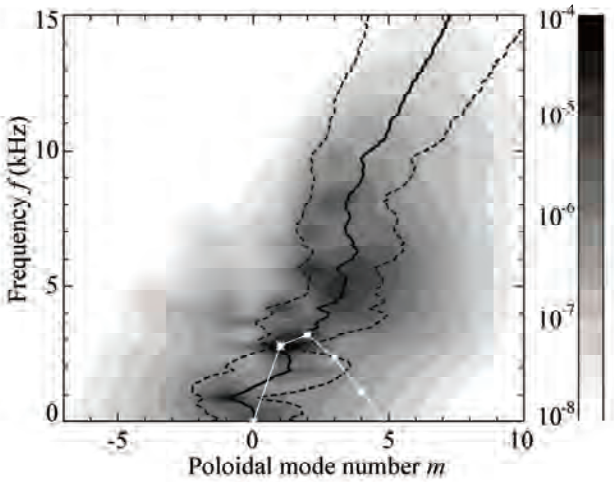

Fig. 3 Contour plot of the power spectrum $S(m, f)$ (arb. unit) over plotted with the calculated linear dispersion relation of drift waves (white asterisks). The solid black line shows the mean poloidal mode number, and the broken black lines show its spread.

able in the radial direction. Each probe unit has 3 tungsten probe tips. The probe tips line up to equal distance when the measuring radius is set to 40 mm (the probe tips are 5.2 mm apart). This probe array can measure the poloidal wave number and radial profile of the plasma fluctuation [17]. By these two poloidal probe arrays, the details of the broadband fluctuation and fluctuation peaks such as poloidal mode numbers, poloidal correlation lengths and poloidal mode decomposed axial correlations are measurable.

3 Spectral Analysis

The spatiotemporal behavior of the ion saturation current fluctuation varies by changing parameters from periodical coherent wave structure to turbulence regime, which consists of many fluctuation components with different poloidal mode numbers and frequencies [4]. In LMD-U, increasing the magnetic field (over 0.04 T) and decreasing the filled argon pressure (under 0.4 Pa) make the plasma into turbulence regime by affecting the density gradient and collision with neutrals [16]. Figure 2 shows the spatiotemporal behavior of the ion saturation current $I(\theta, t)$, where θ is the poloidal angle and t is the time, in the turbulence regime measured with the 64-channel probe array. The magnetic field was 0.09 T and the argon pressure was 0.27 Pa. The increasing direction of the poloidal angle θ corresponds to the electron diamagnetic direction. The spatiotemporal waveform consists of a number of fluctuation components. The main fluctuation is the flow in the electron diamagnetic direction with the frequency of about 3 kHz.

The spatiotemporal waveform in the turbulence regime can be decomposed into the poloidal mode number and frequency spaces by spectral analysis. By two-dimensional Fourier transformation (poloidal angle θ to poloidal mode number m, and time t to frequency f), $I(\theta, t)$ is transformed to $\hat{I}(m, f)$. Figure 3 shows the power spectrum $S(m, f) = \langle |\hat{I}(m, f)|^2 \rangle / df$, where df is the frequency resolution and is 0.1 kHz in this case. The power spectrum $S(m, f)$ was an ensemble of 300 time windows with 10 ms ($= df^{-1}$) span each. One of the advantages of poloidal multi-point detection to single point measurement is that the poloidal flow direction can be determined. When the frequency is set to $f \geq 0$, the fluctuations with positive poloidal mode numbers flow in the electron diamagnetic direction and that with negative poloidal mode numbers flow in the ion diamagnetic direction.

The white asterisks in Fig. 3 show the calculated linear dispersion relation of drift waves with a uniform rotation by dc radial electric field assumed. The fluctuation peaks at $(m, f) = (1, 2.8\,\text{kHz})$ and $(2, 3.2\,\text{kHz})$ satisfy the dispersion relation, and they are considered to be drift wave modes. The peak at $(m, f) = (-1, 0.9\,\text{kHz})$ is a flute wave-like mode in the ion diamagnetic direction. Other fluctuation peaks such as $(m, f) = (2, 5.6\,\text{kHz})$ and $(3, 4.7\,\text{kHz})$ do not satisfy the dispersion relation, and they are quasi-modes. The solid and broken lines in Fig. 3 show the frequency dependences of the mean poloidal mode number and its spread, respectively. They are defined by

$$\langle m(f) \rangle = \sum_m m S(m, f) \Big/ \sum_m S(m, f), \quad (1)$$

$$\Delta m(f)^2 = \frac{\sum_m [m - \langle m(f) \rangle]^2 S(m, f)}{\sum_m S(m, f)}. \quad (2)$$

The mean poloidal mode number traces the strong fluctuation peaks, and the spread decreases in the existence of the strong peaks. In the high frequency region with no remarkable fluctuation peaks ($f > 10\,\text{kHz}$), the mean poloidal

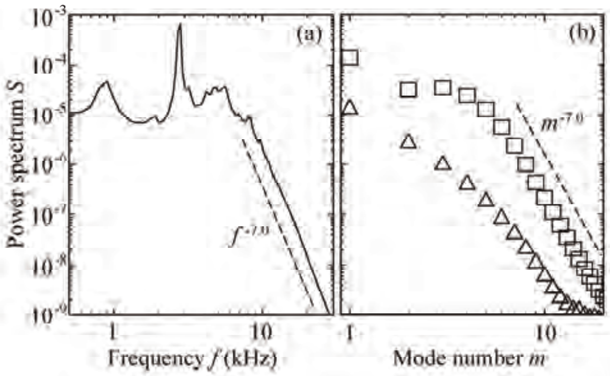

Fig. 4 One-dimensional power spectra (a) $S(f)$, (b) $S(m)$ (squares) and $S(-m)$ (triangles) (arb. unit). Dashed lines show the relationship $S \propto f^{-7.0}$ and $S \propto m^{-7.0}$.

mode number increases with the relationship $\langle m \rangle \propto f$ and the spread is an increasing function of f. These facts imply the existence of broadband components. The quasi-mode peaks and broadband components appear nearly on the line $\langle m \rangle \propto f$, and they are away from the linear dispersion relation curve of the drift wave. This is because nonlinear couplings between the parent modes force to excite quasi-mode peaks and broadband components in the position away from the dispersion relation. Thus, energy cascade to high m and high f region is expected [19].

Figure 4 shows the logarithmic plots of power spectra $S(f)$ and $S(m)$ calculated by integrating $S(m, f)$ with m and f, respectively. Both spectra have relations $S(f) \propto f^{-7.0}$ and $S(m) \propto m^{-7.0}$ in broadband regions ($f > 10$ kHz or $m > 5$). It is interesting that the decay laws are the same in the frequency and poloidal mode number spaces. It is also interesting that the power law of $S(m)$ is nearly equal to that led from the previous work (i.e., $S(m)^{0.5} \propto m^{-3.6}$ [3]). Although different experimental conditions induce individual eigen functions, the power laws in broadband regions become almost the same.

4 Broadband Fluctuation

Figure 5 shows the auto-correlation functions of the ion saturation current fluctuation in the frequency ranges of full-range and $f > 10$ kHz. Owing to the main fluctuation peaks, the auto-correlation time of the frequency of full-range is long (about the order of 10 ms). On the other hand, the auto-correlation time of the frequency of $f > 10$ kHz, which is in the broadband fluctuation region, is short (about the order of 1 ms). It means that the broadband fluctuation has a short time life than the main fluctuation peaks. Many short time fluctuations with various frequencies accumulate to form a broadband fluctuation.

Correlation length (poloidal angle) was calculated from the 64-channel data. Coherence coh of two time data

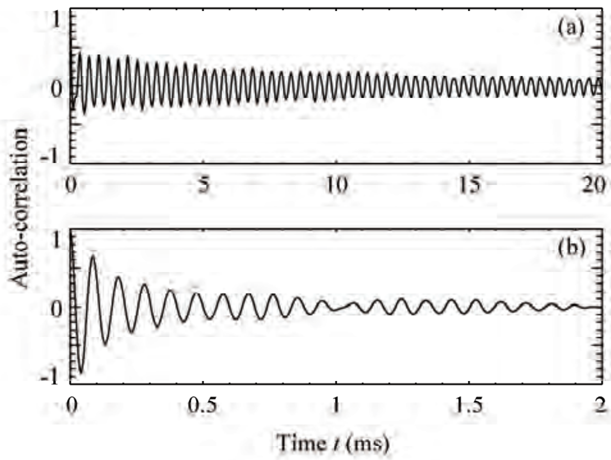

Fig. 5 Auto-correlation functions of the ion saturation current fluctuation in the frequency ranges of (a) full-range and (b) broadband region ($f > 10$ kHz).

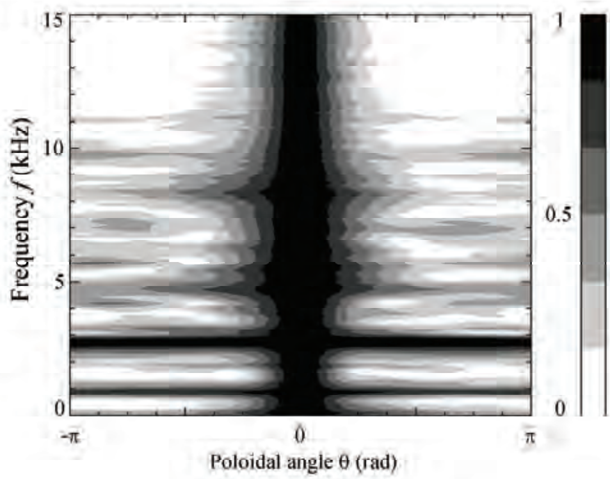

Fig. 6 Frequency dependence of the coherence in the poloidal angle space. Correlation length is long for fluctuation peaks and short for broadband fluctuation.

I_x and I_y is defined by

$$coh^2(f) = \frac{|S_{xy}(f)|^2}{S_{xx}(f)S_{yy}(f)}, \tag{3}$$

where $S_{xy} = \langle \hat{I}_x \hat{I}_y^* \rangle / df$. Correlation length is the distance where the coherences become e^{-1}. Figure 6 shows the frequency dependence of the coherence in the poloidal angle space. The coherence between different poloidal channels of the 64-channel probe array was calculated to produce Fig. 6. The correlation length in the poloidal direction is long for fluctuation peaks such as 0.9 kHz and 2.8 kHz, and is small (under $\pi/4$) for broadband fluctuation. The correlation length gradually decreases as the frequency becomes high. From this result, strong fluctuation peaks are produced globally in the poloidal direction, while broadband fluctuation is produced locally in the poloidal direction.

One of the features of our experiment is that two poloidal probe arrays are used for fluctuation measure-

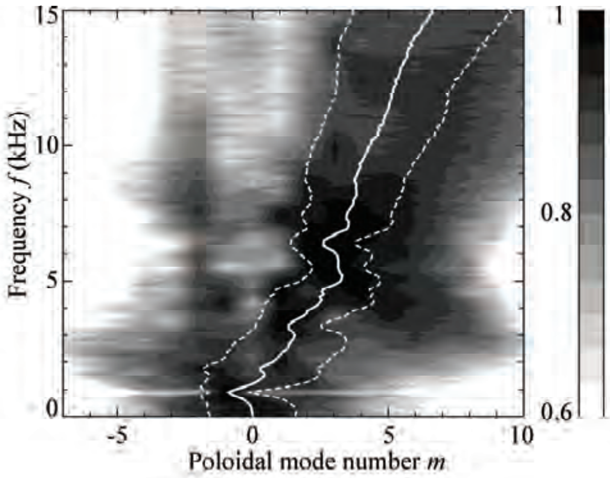

Fig. 7 Poloidal mode number decomposed axial coherence between the two poloidal probe arrays. The coherence is strong not only for fluctuation peaks but also for broadband fluctuation. The solid white line shows the mean poloidal mode number, and the broken white lines show its spread.

ments and so that quasi-two-dimensional measurement is available. By setting all of the measuring radii of the 48-channel probe array tips to 40 mm, poloidal analyses of the plasma column in separate of 0.26 m in the axial direction are performed. The 64-channel probe array can measure the poloidal mode number of $|m| \leq 32$, and the 48-channel probe array can measure $|m| \leq 24$. Although the two probe arrays have different numbers of probes, and many of the channels measure at different poloidal angles, the fluctuations of the poloidal mode number in the region $|m| \leq 24$ can be compared, and the poloidal mode number decomposed axial correlations can be calculated. Figure 7 shows the coherence between the two poloidal probe arrays in the poloidal mode number–frequency space. Compared with Fig. 3, it can be said that the coherence is strong not only for the fluctuation peaks such as drift wave modes, but also for broadband fluctuation even the spectral power is small. This fact suggests quasi-two-dimensional characteristics of the magnetized plasma turbulence

5 Summary

In summary, we have performed a measurement of drift wave turbulence in the LMD-U linear magnetized plasma by use of poloidal probe arrays. The obtained two-dimensional power spectrum $S(m, f)$ showed the excitation of drift wave modes and cascade to quasi-mode peaks and broadband components ($\langle m \rangle \propto f$ and $S \propto f^{-7.0}, m^{-7.0}$), which do not satisfy the linear dispersion relation of drift wave modes. The correlation time of the broadband fluctuation was shorter than that of the fluctuation peaks. The correlation length in the poloidal direction was short (under $\pi/4$) for broadband fluctuation, which suggests that this fluctuation is produced locally in the poloidal direction. Poloidal mode number decomposed axial coherence between the two poloidal probe arrays was calculated and showed that the broadband fluctuation and fluctuation peaks had strong axial coherences.

Acknowledgments

This work was supported by Grant-in-Aid for Specially-Promoted Research of MEXT (16002005) (Itoh Project), by Grant-in-Aid for Young Scientists (B) of JSPS (19760597), and by the collaboration programs of NIFS (NIFS07KOAP017) and of RIAM, Kyushu University.

[1] P.H. Diamond *et al.*, Plasma Phys. Control. Fusion **47**, R35 (2005).
[2] A. Yoshizawa, S.-I. Itoh and K. Itoh, *Plasma and Fluid Turbulence, Theory and Modelling* (Institute of Physics Publishing, Bristol and Philadelphia, 2003).
[3] A. Latten, T. Klinger and A. Piel, Rev. Sci. Instrum. **66**, 3254 (1995).
[4] T. Klinger *et al.*, Phys. Rev. Lett. **79**, 3913 (1997).
[5] M. Kono and M.Y. Tanaka, Phys. Rev. Lett. **84**, 4369 (2000).
[6] C. Schröder *et al.*, Phys. Rev. Lett. **86**, 5711 (2001).
[7] T. Kaneko, H. Tsunoyama and R. Hatakeyama, Phys. Rev. Lett. **90**, 125001 (2003).
[8] V. Sokolov and A.K. Sen, Phys. Rev. Lett. **92**, 165002 (2004).
[9] M.J. Burin *et al.*, Phys. Plasmas **12**, 052320 (2005).
[10] G.R. Tynan *et al.*, Plasma Phys. Control. Fusion **48**, S51 (2006).
[11] C. Lechte, S. Niedner and U. Stroth, New J. Phys. **4**, 34 (2002).
[12] Y. Nagashima *et al.*, Phys. Rev. Lett. **95**, 095002 (2005).
[13] Y. Hamada *et al.*, Phys. Rev. Lett. **96**, 115003 (2006).
[14] F.M. Poli *et al.*, Phys. Plasmas **13**, 102104 (2006).
[15] U. Stroth *et al.*, Phys. Plasmas **11**, 2558 (2004).
[16] S. Shinohara *et al.*, *Proc. 28th Int. Conf. on Phenomena in Ionized Gases* (Institute of Plasma Physics AS CR, Prague, 2007), 1P04-08.
[17] K. Terasaka *et al.*, Plasma Fusion Res. **2**, 031 (2007).
[18] N. Kasuya *et al.*, J. Phys. Soc. Jpn. **76**, 044501 (2007).
[19] T. Yamada *et al.*, submitted to Plasma Fusion Res.
[20] T. Yamada *et al.*, submitted to Rev. Sci. Instrum.

Proceedings of ITC/ISHW2007

Confinement and dynamics of electron-rich plasmas in the Columbia Non-neutral Torus

T. Sunn Pedersen, J. W. Berkery, A. H. Boozer, Q. R. Marksteiner, M. S. Hahn, P. W. Brenner, B. Durand de Gevigney, J. P. Kremer, R. G. Lefrancois, H. Himura[a]

Department of Applied Physics and Applied Mathematics, Columbia University, New York, NY 10025, USA

[a]*Kyoto Institute of Technology, Department of Electronics, Matsugasaki, Kyoto, Japan*

tsp22@columbia.edu

The Columbia Non-neutral Torus (CNT) is a compact, two-period stellarator created from four circular coils, dedicated to the study of non-neutral and electron-positron plasmas on magnetic surfaces [1]. First results included the confirmation that pure electron plasmas can be confined stably in a stellarator, that confinement times of up to 20 msec can be achieved, and that confinement is limited by the perturbing presence of internal rods [2], as well as by electron-neutral collisions [3]. In the absence of perturbing rods, and at neutral pressures of 2×10^{-10} Torr, we expect a confinement time exceeding 1 second. Despite these rather long confinement times, the electron-neutral limited confinement time is much smaller than expected from neoclassical predictions, and is on the order of the electron-neutral collision time. The electron orbits in CNT are now being investigated numerically.
At neutral pressures $< 10^{-7}$ Torr and magnetic field strengths $B > 0.02$ T, the plasmas are rather quiescent and well confined. At higher neutral pressures (and consequently, higher ion fraction), and lower B-field strengths, oscillations [4] and confinement jumps are seen. The oscillations that are observed are generally periodic or near-periodic with frequencies in the $10 - 50$ kHz range, and result from an interaction between the ion and electron fluids. These oscillations decrease the confinement somewhat. The confinement jumps are sudden and occur at specific values of the emission current of electrons from the emitting filament that sustains the plasma. The confinement change can be as large as a factor of two, and shows hysteretic behavior. A copper mesh boundary, conforming to the shape of the last closed flux surface, is being installed in CNT, and will be used to impose an electrostatic boundary condition that conforms to the magnetic surface shape, minimizing electrostatic potential variations on the outer magnetic surfaces. An increase in confinement is expected with this new boundary. The electrostatic boundary will also be used to diagnose the plasma from the outside. Combined with the now operational retractable emitter, this will allow studies of electron plasmas unperturbed by internal material objects. The absence of internal objects should also improve confinement and is necessary for future experiments with electron-positron plasmas.

[1] T. Sunn Pedersen et al., Phys. Plasmas **13** (2006) 012502
[2] J. P. Kremer et al., Phys. Rev. Letters **97** (2006) 095003
[3] J. W. Berkery et al., Phys. Plasmas **14** (2007) 062503
[4] Q. R. Marksteiner et al., submitted to Phys. Rev. Letters (2007)

Proceedings of ITC/ISHW2007

Viscosity Estimation Utilizing Flow Velocity Field Measurements in a Rotating Magnetized Plasma

Shinji YOSHIMURA[1)] and Masayoshi Y. TANAKA[2)]

[1)] *National Institute for Fusion Science, 322-6 Oroshi-cho, Toki 509-5292, Japan*

[2)]*Kyushu University, 6-1 Kasuga-koen, Kasuga 816-8580, Japan*

The importance of viscosity in determining plasma flow structures has been widely recognized. In laboratory plasmas, however, viscosity measurements have been seldom performed so far. In this paper we present and discuss an estimation method of effective plasma kinematic viscosity utilizing flow velocity field measurements. Imposing steady and axisymmetric conditions, we derive the expression for radial flow velocity from the azimuthal component of the ion fluid equation. The expression contains kinematic viscosity, vorticity of azimuthal rotation and its derivative, collision frequency, azimuthal flow velocity and ion cyclotron frequency. Therefore all quantities except the viscosity are given provided that the flow field can be measured. We applied this method to a rotating magnetized argon plasma produced by the Hyper-I device. The flow velocity field measurements were carried out using a directional Langmuir probe installed in a tilting motor drive unit. The inward ion flow in radial direction, which is not driven in collisionless inviscid plasmas, was clearly observed. As a result, we found the anomalous viscosity, the value of which is two orders of magnitude larger than the classical one.

Keywords: viscosity, flow, vorticity, fluid equation, directional Langmuir probe, Hyper-I device

1. Introduction

In various fields of plasma research such as fusion plasmas, space and astrophysical plasmas and laboratory plasmas, the importance of plasma flow has been widely recognized and many studies on plasma flow related phenomena have been performed extensively. In some cases, viscosity plays a crucial role in determining plasma flow structures. In torus plasmas, for example, poloidal plasma flow driven by the radial electric field produces toroidal plasma flow through the effect of viscosity. Anomalous viscosity has been found experimentally both in helical devices and tokamaks [1]. In addition, strong viscosity, the value of which is up to 10^8 times larger than predicted by classical collision theory, has been observed in magnetized pure-electron plasmas [2]. In spite of its importance, little attention has been paid to the viscosity of laboratory plasmas so far.

In a laboratory plasma, however, spontaneous formation of a stationary vortex with a density hole around the central axis, which is referred to as plasma hole [3-5], has been observed, where the viscosity has an essential role. The flow velocity field associated with the plasma hole exhibits a monopole sink vortex, and the vorticity distribution is identified as Burgers vortex [6], which is intrinsic in viscous fluids. Scale length of the Burgers vortex is determined by the kinematic viscosity and the inward convergent flow. The viscosity estimated from the size of the vortex is found to be up to four orders of magnitude larger than the classical value. Therefore we can conclude that the anomalous viscosity does occur in laboratory plasmas and its measurement is necessary for the deeper understanding of flow structure formation.

In this paper, we present and discuss an experimental estimation method using flow velocity field measurements and apply it to a rotating magnetized argon plasma as an example.

2. Radial flow of ion fluid with finite viscosity

The equation of motion of ion fluid with finite viscosity in an external constant magnetic field $\mathbf{B_0} = (0, 0, B_0)$ is written as

$$\frac{\partial \boldsymbol{\upsilon}}{\partial t} + (\boldsymbol{\upsilon}\cdot\nabla)\boldsymbol{\upsilon} = \frac{e}{M}\left[-\nabla\phi + \boldsymbol{\upsilon}\times\mathbf{B}_0\right] - \frac{1}{Mn}\nabla p + \nu\nabla^2\boldsymbol{\upsilon} + \frac{1}{3}\nu\nabla(\nabla\cdot\boldsymbol{\upsilon}) - \nu_c\boldsymbol{\upsilon} \qquad (1)$$

, where $\boldsymbol{\upsilon} = (\upsilon_r, \upsilon_\theta, \upsilon_z)$ is the ion flow velocity, n the ion density, M the ion mass, e the elementary charge, ϕ the plasma potential, p the pressure, ν the kinematic viscosity, and ν_c the collision frequency. Here we neglect the second viscosity. If the fluid may be regarded as incompressible, the term which contains $\nabla\cdot\boldsymbol{\upsilon}$ is vanished, and the equation becomes considerably

author's e-mail: yoshimura.shinji@LHD.nifs.ac.jp

simpler. In cylindrical polar coordinates $r, \theta, z,$ the azimuthal component of the fluid equation is given as follows [7].

$$\frac{\partial \upsilon_\theta}{\partial t} + (\boldsymbol{\upsilon}\cdot\nabla)\upsilon_\theta + \frac{\upsilon_r \upsilon_\theta}{r} = \frac{e}{M}\left[-\frac{1}{r}\frac{\partial \phi}{\partial \theta} - \upsilon_r B_0\right]$$
$$-\frac{1}{Mn}\frac{1}{r}\frac{\partial p}{\partial \theta} + \nu\left[\Delta \upsilon_\theta + \frac{2}{r^2}\frac{\partial \upsilon_r}{\partial \theta} - \frac{\upsilon_\theta}{r^2}\right] - \nu_c \upsilon_\theta. \quad (2)$$

Imposing the steady ($d/dt \to 0$) and axisymmetric ($d/d\theta \to 0,\ d/dz \to 0$) condition into eq. (2), we have

$$\upsilon_r\left[\frac{\partial \upsilon_\theta}{\partial r} + \frac{\upsilon_\theta}{r}\right] = -\upsilon_r \Omega_\mathrm{i} + \nu\left[\frac{\partial^2 \upsilon_\theta}{\partial r^2} + \frac{1}{r}\frac{\partial \upsilon_\theta}{\partial r} - \frac{\upsilon_\theta}{r^2}\right] - \nu_c \upsilon_\theta \quad (3)$$

, where Ω_i is the ion cyclotron frequency. Note that the terms in the square bracket on the left and on the right are equivalent to the vorticity $\omega = (\nabla \times \boldsymbol{\upsilon})_z = (1/r)(\partial/\partial r)(r\upsilon_\theta)$ and its derivative, respectively. Finally, we have considerably simple expression for radial flow velocity as

$$\upsilon_r = \frac{\nu(\partial\omega/\partial r) - \nu_c \upsilon_\theta}{\omega + \Omega_\mathrm{i}}. \quad (4)$$

It is obvious from eq. (4) that the radial flow is not driven in collisionless inviscid plasmas, which have axial symmetry. In other words, the existence of radial flow indicates the nonnegligible effect of finite viscosity and/or collisions. Eq. (4) contains kinematic viscosity, vorticity of azimuthal rotation and its derivative, collision frequency, azimuthal flow velocity and ion cyclotron frequency. Since all quantities except the viscosity are given when the flow field can be measured, we can estimate the magnitude of viscosity from eq. (4).

3. Experimental setup

The experiments were performed in the high density plasma experiment (Hyper-I) device [8] at National Institute for Fusion Science. The Hyper-I is a cylindrical plasma device (30 cm in diameter and 200 cm in length) with ten magnetic coils (Fig. 1). Plasmas are produced by electron cyclotron resonance (ECR) heating with a microwave of frequency 2.45 GHz. The magnetic field configuration is a so-called magnetic beach structure (1.2 kG at z=10 cm (measured from the microwave injection window), 875 G (ECR point) at z=130 cm). In the present experiment, the microwave input power was 7 kW and the operation pressure of an argon gas was 1.3×10^{-4} Torr. A Langmuir probe was used to measure the electron temperature and the electron density, typical values of which are 13 eV and $1\times10^{11}\ \mathrm{cm}^{-3}$, respectively.

The ion flow velocity measurements were carried out with a directional Langmuir probe (DLP) [9]. The DLP collects a directed ion flux through a small opening made on the side of insulator body. The Mach number of the flow velocity component at a certain angle θ is given by the difference between upstream ($I(\theta)$) and downstream ion currents ($I(\theta+\pi)$) as follows:

$$\frac{\upsilon(\theta)}{C_\mathrm{s}} = K\frac{I(\theta+\pi) - I(\theta)}{I(\theta+\pi) + I(\theta)} \quad (5)$$

, where K is the calibration constant of the order of unity. We set $K = 1.9$ in the present experiments, which was justified by comparing the flow velocity measured with the DLP to the $\mathbf{E}\times\mathbf{B}$ drift velocity determined from the potential measurement with an emissive probe.

The DLP was installed in a tilting motor drive unit, which can vary the insertion angle up to ± 23 degrees. The schematic of the DLP measurement system is shown in fig. 2. Scanning simply in a straight line passing through the cross-sectional center of the device twice with collecting azimuthally-opposed DLP currents, we can obtain the continuous $\upsilon_\theta(r)$ profile. On the other hand, several steps are needed to measure $\upsilon_r(r)$ profile. At first, the insertion angle of the DLP is varied by tilting mechanism of the motor drive unit. Then the DLP position is set to the tangent point of the circumference of a circle of which radius is r_0 and the center is identical to the device center. By measuring radially-opposed DLP current, we have one data point of $\upsilon_r(r = r_0)$. Repeating this operation with changing insertion angles, discrete data set of $\upsilon_r(r)$ can be obtained.

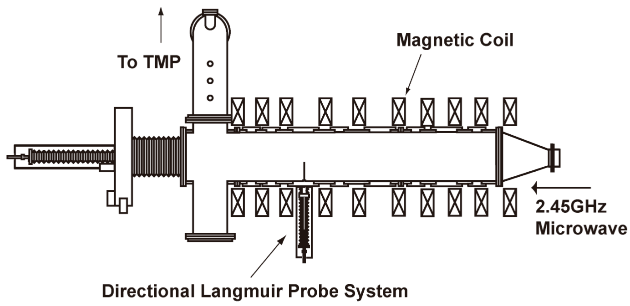

Fig. 1. Schematic of the Hyper-I device.

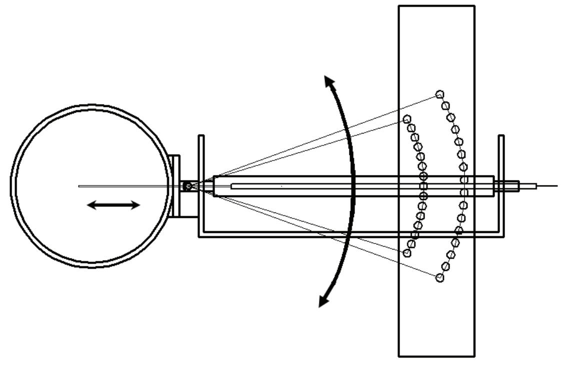

Fig. 2. Schematic of the DLP measurement system.

4. Results and Discussions

To demonstrate the validity of the viscosity estimation method proposed in Sec. 2, a plasma which exhibits a good axial symmetry is needed. Density and space potential profiles of the argon plasma we studied in the present experiments are shown in fig. 3(a) and (b), respectively. It is confirmed that both profiles, which are hollow in the centers, show good symmetry. The electron temperature is 13 eV, which is approximately constant over the experimental region.

The hollow potential profile shows that an inward electric field exists in this plasma, which drives counterclockwise $\mathbf{E}\times\mathbf{B}$ rotation. Figure 4 shows the azimuthal flow velocity profiles, where the open circles connected with solid lines indicate the velocities obtained by the DLP and the filled circles denote the $\mathbf{E}\times\mathbf{B}$ velocities calculated from the potential profile. Both velocities, which are normalized to the ion sound speed Cs, show quite a good agreement, where the calibration factor *K* in the eq. (5) is set to 1.9. The azimuthal flow profile shows an axial symmetry. Rigid like rotation is found around the central axis, and the maximum Mach number is $\upsilon_\theta / Cs \sim 0.4$.

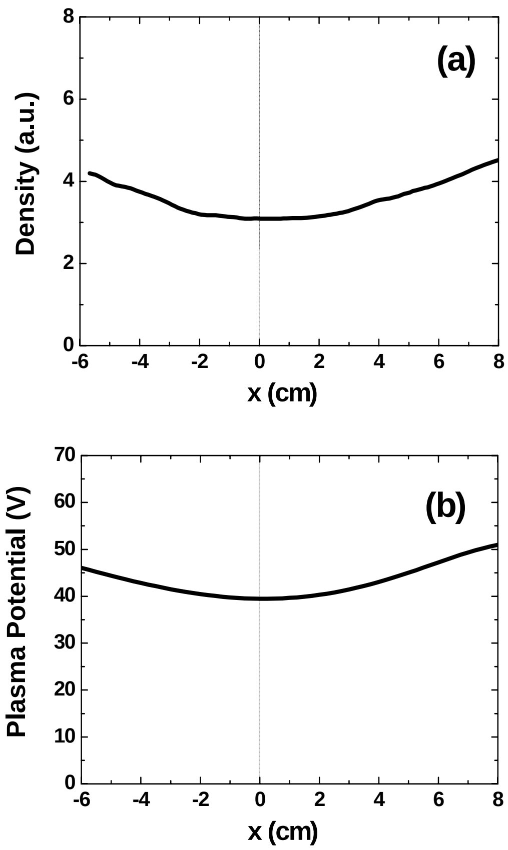

Fig. 3. (a) Density (ion saturation current) profile measured by Langmuir probe. (b) Plasma potential profile measured by emissive probe.

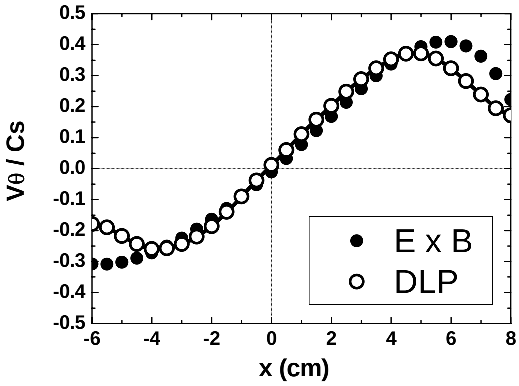

Fig. 4. Comparison between the azimuthal velocity measured with the DLP (open circle) and the E×B drift velocity determined from the potential profile (filled circle).

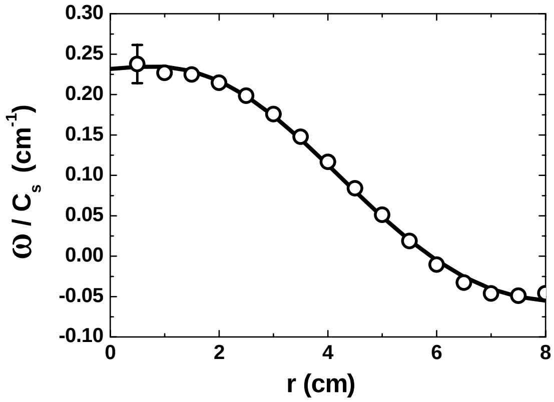

Fig. 5. Profile of the z-component of vorticity.

Once the azimuthal flow velocity profile is obtained, the vorticity profile can be easily calculated when the axisymmetric condition is satisfied. The vorticity profile is shown in fig. 5, where open circles, which denote the experimental data, are depicted with fitted curve (solid line). When we evaluate the radial flow velocity, the derivative of this fitted curve is substituted to eq. (4).

The ion cyclotron frequency is determined by the magnetic field strength (900 G) and the ion mass (40 u), so that we have $\Omega_i = 2.16\times10^5\ \mathrm{s}^{-1}$. Adopting the charge exchange with neutrals as the dominant collisional process, the collision frequency is given $\nu_c \sim 3\times10^3\ \mathrm{s}^{-1}$, where the cross section of the charge exchange collision for low energy argon is given by Sheldon [10]. Now we have all quantities except the kinematic viscosity on the right of eq. (4).

Figure 6 shows the comparison between the radial flow velocity measured with the DLP system (open circle) and the eq. (4) (solid curve, where anomalous kinematic viscosity $\nu = 2\times10^5\ \mathrm{cm^2/s}$ is assumed). In this figure, the inward flow, which implies the finite

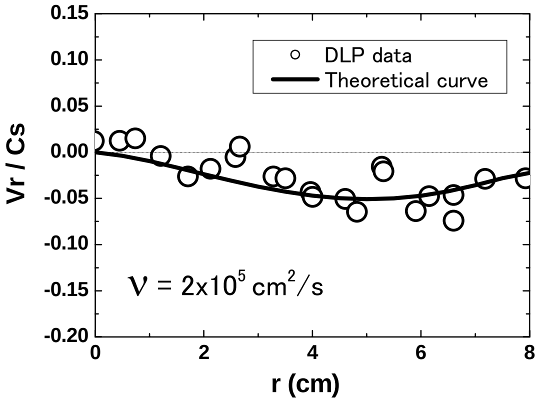

Fig. 6. Comparison between the radial flow velocity measured by the DLP (open circle) and theoretical curve given by eq. (4) with anomalous kinematic viscosity.

viscosity, is evident.

If the plasma may be regarded as inviscid, the radial flow velocity can be estimated as

$$\upsilon_r / C_s \sim (\nu_c / \omega + \Omega_i) \times (\upsilon_\theta / C_s) \sim 0.002.$$

This radial flow speed is considerably small and cannot explain the present experimental result. In contrast, the solid curve in fig. 6 well agrees with the DLP data and shows similar tendency. Note that the kinematic viscosity predicted by classical theory is $\nu_{cl} \sim 3\times10^3$ cm^2/s. The value of the viscosity we used in fitting curve is two orders of magnitude larger than the classical one, and therefore we can conclude that the anomalous viscosity was found in a laboratory magnetized plasma.

To make the presented estimation method more powerful, an accurate absolute velocity measurement system is required. Since there is an ambiguity in determining absolute velocity using the DLP or Mach probes, we are now preparing laser induced fluorescence (LIF) Doppler measurements for velocity field determination [11]. Detailed study of viscosity effects on flow structure formation utilizing LIF measurements will form our future work.

Acknowledgments

This work was partially supported by Japan Society for the Promotion of Science, Grant-in-Aid for Young Scientists (B) (No. 19740348) and by the National Institute for Fusion Science, a budgetary Grant-in-Aid NIFS07 ULPP103.

References

[1] K. Ida, Plasma Phys. Control. Fusion **40**, 1429 (1998).
[2] J. M. Kriesel and C. F. Driscoll, Phys. Rev. Lett. **87**, 135003 (2001).
[3] K. Nagaoka *et al*., Phys. Rev. Lett. **89**, 075001 (2002).
[4] S. Yoshimura *et al*., J. Plasma Fusion Res. Ser. **6**, 610 (2004).
[5] M. Y. Tanaka *et al*., IEEE Trans. Plasma Sci. **33**, 454 (2005).
[6] J. M. Burgers, Adv. Appl. Mech. **1**, 171 (1948), Sec. XV.
[7] The equation for ordinary viscous fluid (without collision term) is described in detail; L. D. Landau and E. M. Lifshitz, *Fluid Mechanics 2nd edition*, (Butterworth-Heinemann, Oxford, 1987), Chap. II.
[8] M. Y. Tanaka *et al*., Rev. Sci. Instrum. **69**, 980 (1998).
[9] K. Nagaoka *et al*., J. Phys. Soc. Jpn. **70**, 131 (2001).
[10] J. W. Sheldon, Phys. Rev. Lett. **8**, 64 (1962).
[11] A. Okamoto *et al*., J. Plasma Fusion Res. 80, 1003 (2004).

Spatial Distribution of Toroidal Flow in a Field-Reversed Configuration

T. Asai[1)], T. Matsuzawa[1)], N. Yamamoto[1)], K. Sakuraba[1)], T. Kiguchi[1)], K. Kishi[1)], T. Takahashi[1)], S. Hiromori[1)], T. Ikeyama[1)], Y. Nogi[1)] and T. Takahashi[2)]

[1)] *College of Science and Technology, Nihon University, 1-8 Kanda-Surugadai, Tokyo 101-8308, Japan*

[2)] *Dept. of Electronic Engineering, Gunma University,1-5-1 Tenjin-cho, Kiryu 376-8515, Japan*

A radial profile of toroidal flow in a field-reversed configuration plasma has been measured with a newly built ion Doppler spectroscopy system with a line-spectrum of impurity carbon (CV: 227.2nm). With this system, radial profile of toroidal flow was observed preliminary on the theta-pinch FRC plsma. The toroidal flow inside the separatrix starts to spin-up just after the formation and the flow velocity is gradually increased. The velocity is comparable with an ion diamagnetic velocity at 25μs from the formation. However, the flow velocity out side the separatrix keeps small value or settled. It indicates the existence of flow shear in vicinity of the separatrix. The observed results were also compared with a numerical calculation by newly proposed toroidal spin-up mechanism which employs direct conversion of the kinetic angular momentum from the magnetic flux [T. Takahashi, *et al.*, Plasma Fusion Res. **2** (2007) 008]. The calculated results are consistent with the presented experimental results.

Keywords: field-reversed configuration, n = 2 mode rotational Instability, toroidal flow, flow shear, toroidal spin-up

1. Inroduction

Rotational instability with toroidal mode number n = 2 is the only destructive instability in a field-reversed configuration (FRC) plasma. Also, the toroidal velocity shear potentially has a stabilization effect on an interchange instability with highr toroidal mode numbers $n \geq 3$. Therefore, investigation of mechanism of toroidal spin-up and its spatial structure are longstanding problems in the FRC research to improve confinement and stability property. The toroidal plasma current just after formation is primarily carried by electrons, while ions are approximately at rest [1]. The ions, however, gradually gain angular momentum in the direction with the ion diamagnetic before the onset of the n = 2 deformation due to rotational instability. The mechanism of toroidal spin-up has been discussed theoretically with several possible mechanisms of selective loss of ions [2-4], end-shorting [5-8], and both [9]. However, only a few experimental investigations have been performed so far.

In this work, radial velocity profile of toroidal flow in a FRC plasma has been measured with a newly built ion Doppler spectroscopy (IDS) system in detail. From the ion Doppler shift measurement of impurity ions, radial profile of toroidal flow and its time evolution are observed preliminary on the theta-pinch FRC plasma.

The experimental observation will also be compared with the newly proposed toroidal spin-up mechanism, which employs direct conversion of the kinetic angular momentum from the magnetic flux [10].

author's e-mail: asai@phys.cst.nihon-u.ac.jp

2. Experimental Apparatus and Diagnostic

Figure 1 shows a schematic view of experimental apparatus and diagnostic. The FRC plasma is formed by a negative-biased theta-pinch method in the Nihon University Compact Torus Experiment (NUCTE) –III device.

The device has a 1.5m one-turn solenoidal theta-pinch coil. It consists a center confinement coil with a diameter of 0.34m and a length of 1.0m and a mirror coil with a diameter of 0.30m and a length of 0.25m at the both end. A ratio of the passive mirror is about 1.22. A slow bank with 5kV-1980μF and a first bank with 32kV-67.5μF are connected with the theta pinch coil through a collector plate. The coil produces a bias field up to 0.064T with a rising time of 90ms and a

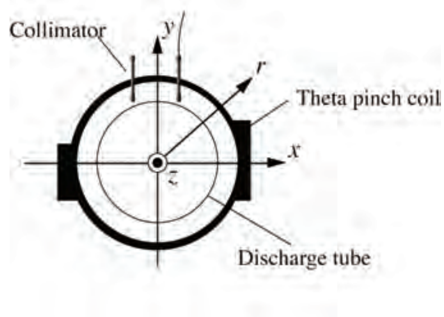

Fig.1 Toroidal section of NUCTE-III device and arrangement of collimators for IDS.

confinement field up to 0.6T with a rising time of 4ms and a decay time of 120μs. The transparent fused silica discharge tube with a diameter of 0.256m and a length of 2.0m is evacuated to about 1.5×10^{-4} Pa using a turbo molecular pump. A 10mTorr of deuterium gas is filled and pre-ionized by a *z*-discharge method.

An axial separatrix profile ($r_s(z)$) is observed by an excluded flux measurement. An averaged electron density ($\bar{n}_e$) is estimated by a line integrated electron density, which is measured by a quadrature 3.39μm He-Ne laser interferometer on the midplane (z = 0). A total plasma temperature ($T_t = T_i + T_e$: sum of a ion and electron temperature), is calculated from a radial pressure and an axial force balances,

$$T_t = (1 - 0.5(r_s/r_w)^2)B_e^2/2\mu_0\bar{n}_e\,. \qquad (1)$$

A poloidal flux and its time evolution can also be estimated by the equation,

$$\phi_p = 0.32\pi r_s(0)^2 B_e/r_w \qquad (2)$$

which is given by the assumption of a rigid rotor profile equilibrium model.

The IDS system consists of a collector with f = 100 convex-plane lens, a quartz optical fiber tube with 5m of length, a Czerny-Turner grating monochrometer, and a 16 channels photo-multiplier tube (PMT). Dispersed light is magnified by a cylindrical lens with a diameter of 5 mm and detected on the PMT. An impurity line intensity of CV (227.1nm) emitted from the FRC plasma is collected by the collector and transferred to the IDS system through the optical fiber tube. Wavelength resolution and sensitivity between channels are calibrated by Hg line spectrum of 254 nm. The optical resolution per channel is about 0.05 nm in the system. From the obtained shift and broadening of the line spectrum, ion temperature and ion flow velocity. To confirm a motion of the FRC plasma and reproducibility of FRC formation, a visible light multi-channel optical detector is arrayed in the *x*-direction at the same toroidal cross section with the IDS.

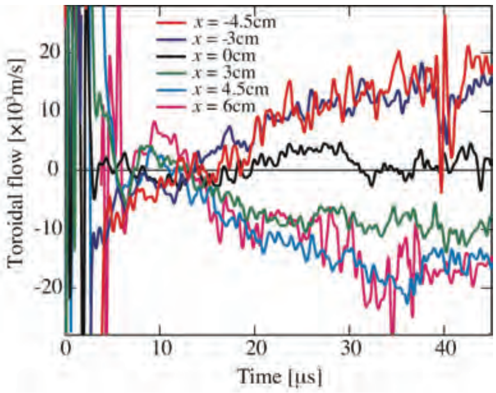

Fig.2 Time evolution of toroidal flow velocity measured by the IDS measurement.

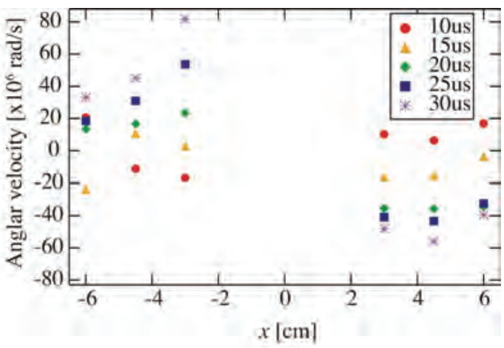

Fig. 3 Time evolution of radial profile of toroidal angular velocity.

3. Experimental Results

Typical FRC plasma parameters of this experiment at equilibrium phase (t = 20 μs) are $\bar{n}_e$: 2×10^{21} m^{-3}, T_t: 190 eV, $r_s(0)$: 0.06 m, Trapped poloidal flux: 0.5 mWb, particle confinement time: 80 μs and decay time of poloidal flux: 100 μs.

Figure 2 shows the time evolution of the toroidal flow velocity at the midplane along the chords (x = - 4.5, -3, 0, 3, 4.5 and 6 cm) measured by the IDS system. The rotation velocity already has a finite value just after formation period of field-reversal phase. The velocity of CV ion is increased gradually during the equilibrium phase. The rotation velocity at 20 μs is approximately 10 km/s at x = ±4.5 cm. The measured velocity and direction are corresponded to the ion diamagnetic drift. Flow velocity on the chord at x = 0 is almost at rest during the discharge.

The time evolution of radial profile of toroidal flow is shown in Fig.3. The radial profile of toroidal velocity is almost flat in the very early phase of FRC discharge pulse. However, the rotation velocity outside of the separatrix is not accelerated compared to the rotation inside of the separatrix. It indicates the existence of velocity shear near the separtrix. The stability effect of this observed shear on higher toroidal mode number of interchange instability could be a reason why the higher mode of toroidal deformation predicted in the theoretical works has never been observed in the FRC experiments. In Table 1, the results of these toroidal flow measurements are summarized.

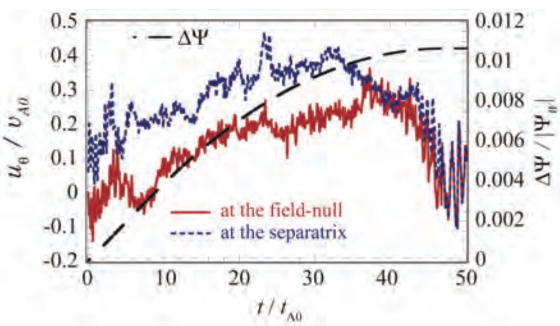

Fig. 4 Time evolution of the flux decay and numerically calculated troidal flow velocity.

Table 1 Summary of experimental results

Position	Rotation direction	Radial profile
Inside of Separatrix	Diamagnetic	Uniform (like rigid body)
Outside of Separatrix	No rotation	-

Table 2 Summary of past theoretical predictions

Mechanism	Plasma rotation	Ion flow (inside)	Ion flow (outside)
Particle loss	Diamagnetic	Diamagnetic	Paramagnetic
End-shorting	Diamagnetic	Diamagnetic	Diamagnetic

4. Discussion

The past proposed theoretical predictions are summarized in Table 2. The presented experimental results show faster spin-up of the plasma column inside the separatrix. Also directions of the toroidal flow are same with ion diamagnetic direction. It is not consistent with past theoretical prediction of toroidal ion spin-up shown in Table 2. Recently, some of the authors have proposed new mechanism of toroidal spin-up [10]. In the scenario, flux decay is directly converted toroidal momentum of ions. Under the assumtion of axisymmetry and canonical momentum conservation, every ion gains angular momentum in the ion diamagnetic direction when the polodial flux decays. While the flux is decreasing, change of ion trajectory type, *i.e.* figure-8 shape trajectory changes into betatron one results in increment of the toridal angular momentum. Inductive electric field by the poloidal flux decay is also a possible cause of the rotation.

To compare the experimental result with the new theory, particle simulation has been performed taking into account of these possible sources of ion spin-up for the plasma parameter in the presented experiment. Figure 4 indicates the calculated time evolution of the flux decay and the toroidal flow velocity. The time, the toloidal flow velocity and the decay flux are normalized by Alfven time

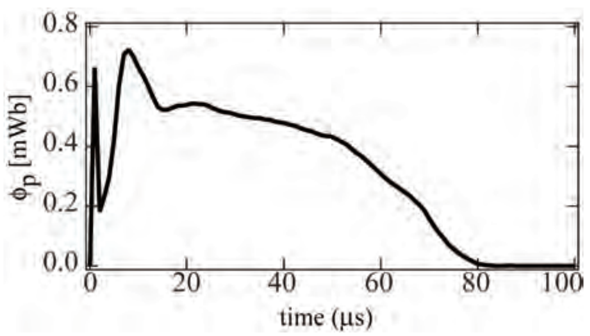

Fig. 5 Time evolution of the poloidal flux estimated under the assumption of rigid rotor profile model.

t_{A0}, Alfven velocity v_{A0} and the magnetic flux at coil wall Ψ_W, respectively. In this calculation, toroidal flow velocity is shown as a function of the amount of change in the poloidal flux $\Delta\Psi$. In this experiment, Alfven velocity and Alfven time are about 140 km/s and 1.2 μs. Figure 5 shows the time evolution of the poloidal flux which is obtained experimentally on the NUCTE-III FRC. In Fig. 3, the decayed flux can be estimated about 0.31mWb. Also decayed flux in the experiment is about 0.12mWb for 40μs of equilibrium phase. The normalized toroidal flow velocities in the experiment and the calculation at 35 t_{A0} are 0.15 v_{A0} and 0.25 v_{A0}, respectively. The calculation is consistent with the presented experiment results. It will be expanded to discuss the radial profile of flow.

5. Summary

Investigation of the toroidal flow profile and its time evolution has been started with both methods of experiments and numerical approach. Experimentally observed flow profile is not consistent with past theoretical predictions. Then the experimental results are compared with the newly proposed theory and it is shown that the calculated result agrees with the experimental result. Detailed flow profile measurements and confirmation of the new theory will be continued.

This work was partially supported by a Grant-in-Aid for Science Research from the Ministry of Education, Culture, Sports, Science and Technology of Japan (MEXT), a Nihon University Research Grant, and NIFS collaborative Research Program (NIFS06KDBD003) and (NIFS06KKMP003).

References

[1] M. Tuszewski, Nucl. Fusion **28** (1988) 2033.
[2] W. M. Manheimer and J. M. Finn, Phys. Fluids **24** (1981) 1865.
[3] D. S. Harned and D. W. Hewett, Nucl. Fusion **24** (1984) 201
[4] M.-Y. Hsiao and G. H. Miley, Phys. Fluids **26** (1985) 1440.
[5] K. S. Thomas, Phys. Rev. Lett. **23** (1969) 746.
[6] A. Kadish, Phys. Fluids **19** (1976) 141.
[7] L. C. Steinhauer, Phys. Fluids **24** (1981) 328.
[8] L. C. Steinhauer, Phys. Plasmas **9** (2002) 3851.
[9] M. Tuszewski, G. A. Barnes, R. E. Chrien, et al., Phys. Fluids **31** (1988) 946.
[10] T. Takahashi, H. Yamaura, F. P. Iizima et al., Plas. Fus. Res. **2** (2007) 008.

Proceedings of ITC/ISHW2007

Modification of transport due to low order rationals of the rotational transform in ECH plasmas of the TJ-II Heliac

D. López-Bruna, T. Estrada, F. Medina, J. Herranz, V. I. Vargas, A. Baciero, E. Ascasíbar, J. A. Romero, F. Castejón

Laboratorio Nacional de Fusión, Avda. Complutense 22, 28040 Madrid, Spain

daniel.lopezbruna@ciemat.es

One of the two main research lines in the TJ-II Heliac project consists of exploring features related to the magnetic configuration. Actually, the TJ-II can produce plasmas in a wide range of rotational transform ι values (at very low magnetic shear), mostly above $\iota/2\pi = 3/2$. From past experiments we infer that (i) the magnetic shear correlates locally with transport in the density gradient region [1]; and (ii) above a threshold shear that is compatible with zero within errors, the lowest order rationals are locally coincident with lower electron heat diffusivities [2]. The former experiments were performed in boronized wall. Now, in a first campaign with Lithium wall-conditioning, we have done a new scan on rotational transform moving a non-natural low order rational (7/4) through different radial positions to perform new transport analysis. In these experiments the magnetic shear remains unchanged and very small except in the core region of the plasma. The experimental profiles are constructed from several diagnostics: Electron Cyclotron Emission (T_e), Thomson Scattering (T_e, n_e), reflectometry, interferometry and soft X-ray bolometry (n_e). The results confirm the main observations from our first experiments. In addition, care has been taken to characterize the plasma density profiles so particle transport has been attempted as well. By comparison with the vacuum profiles of the rotational transform, an estimate of the bootstrap current density profile that would explain the results is presented. These results are aimed at understanding the effect of magnetic configuration singularities in the transport propoerties of currentless magnetically confined plasmas. New experiments are planned to study magnetic shear effects.

[1] D. López-Bruna and the TJ-II Team, *Overview of TJ-II experiments*, AIP Conf. Proc., Subseries: Plasma Physics, Vol. 875, 357-362 (2005).
[2] V. I. Vargas *et al.*, Submitted to Nucl. Fusion (2007).

Effects of Coulomb Collisions on the Toroidal Spin-up of a Field-Reversed Configuration

Toshiki Takahashi, Hidefumi Yamaura, Yoshiomi Kondoh, Tomohiko Asai[a], and Tsutomu Takahashi[a]

Department of Electronic Engineering, Gunma University, Gunma 376-8515, Japan

[a]College of Science and Technology, Nihon University, Tokyo 101-8308, Japan

A direct conversion process from the magnetic flux to the kinetic angular momentum of plasma ions is a possible mechanism of a toroidal spin-up of a field-reversed configuration (FRC) [T. Takahashi *et al.*, Plasma Fusion Res. **2**, 008 (2007)]. For quantitative discussion, the toroidal rotation velocity of a FRC plasma which is resistively decaying is calculated numerically. The ion-ion pitch-angle scattering is reproduced by a Monte Carlo method. The obtained toroidal rotation velocity at the field-null is found to increase linearly up to $0.3v_{\mathrm{A0}}$, where v_{A0} is the Alfvén velocity defined by the external magnetic field and the ion density at the field-null just after the formation. The result is reasonable in a view of a time evolution of the toroidal flow velocity by the Doppler shift measurement at the Nihon University compact torus experiment-III device. It is found that a classical particle loss has an insignificant effect on the spin-up of a FRC.

Keywords: field-reversed configuration, toroidal spin-up, n=2 rotational instability, pitch-angle scattering, end loss, classical diffusion

1. Inroduction

The rotational instability with the toroidal mode number n=2 of a field-reversed configuration (FRC) plasma is a global instability that is most often observed experimentally [1-5]. The FRC current just after formation is primarily carried by electrons, while ions are approximately at rest [6]. The ions, however, gradually gain angular momentum in the ion diamagnetic direction before the onset of the n=2 rotational instability. Rotation of the FRC plasma has been often explained by selective loss of ions [7-9], end-shorting [10-13], or both [14]. Recent computer simulation shows that a resistive decay of the internal flux cause selective loss of ions and resultant spin-up of the FRC plasma [15, 16]. The work is valuable in that contribution of the flux decay to the spin-up of a FRC is firstly proposed. However, is a selective loss of ions necessary to explain toroidal spin-up of a FRC plasma?

Recently, we have proposed an another possible spin-up mechanism, which is direct conversion from the magnetic flux to the kinetic angular momentum [17]. Comparison between experiment and calculation with a simple model will show validity of our explanation.

Suppose a FRC plasma is axisymmetric. This assumption is valid until the rotational instability is triggered. In a collisionless plasma, the canonical angular momentum $P_\theta = mv_\theta r + q\psi(r,z)$ of every particle is conserved, where m, q are the mass and charge, respectively, v_θ is the toroidal velocity component, and $\psi(r,z)$ is the poloidal flux function. If the poloidal flux decays due to resistivity and toroidal axisymmetry still holds, then

$$m\Delta(v_\theta r) = -q\Delta\psi \ . \qquad (1)$$

Equation (1) shows that when the poloidal flux decays, every ion gains angular momentum in the ion diamagnetic direction. Generally, the separatrix radius decreases during the decay phase. If the guiding center r is also decreased, the toroidal velocity v_θ is further increased.

Another explanation for FRC plasma rotation can be given from a viewpoint of particle trajectories; it is not essentially different from discussion above. In a FRC plasma, small-gyroradius drift orbits, figure-8 orbits, and betatron orbits are three possible types of trajectories [18, 19]. In contrast to the betatron particles, the small-gyroradius drift particles and the figure-8 particles have smaller angular momentum. If the poloidal flux decays, the figure-8 particles can change abruptly to the betatron particles due to the increase of the Larmor radius. The transition of trajectory type results in the increment of the toroidal angular momentum.

The inductive electric field is also a possible cause of toroidal spin-up. The betatron particles move around the field-null. The toroidal electric field always accelerates the betatron ions in the ion diamagnetic direction. Here, the radial $\mathbf{E}\times\mathbf{B}$ drift motion contributes to the betatron oscillation, and therefore the guiding center is fixed at the

author's e-mail:t-tak@el.gunma-u.ac.jp

equilibrium position at which the centrifugal force of the betatron motion and the Lorentz force are balanced.

Coulomb collisions of ions, however, break conservation of P_θ. The conversion process given above may not work in this case. In the present paper, effects of the ion-ion pitch-angle scattering on the spin-up of a FRC plasma are investigated. We assume that the plasma ions are fully thermalized, and therefore the slowing-down collisions are neglected here.

2. Calculation Model

To investigate the time evolution of toroidal flow velocity of a FRC plasma, plasma ions are traced numerically. The fields are resistively decaying, and they are modeled as the poloidal flux decay given by

$$\frac{\partial \psi}{\partial t} = -r\eta J_\theta . \qquad (2)$$

Here, the electric resistivity η equals $f_A \eta_{cl}$, where f_A is the anomaly factor and η_{cl} is the classical resistivity. The flux lifetime is controlled by the parameter f_A. By integrating Eq. (2) by means of the Runge-Kutta method, the flux function ψ at a calculation point is found. The electromagnetic fields are then written by the obtained ψ as

$$\mathbf{B} = \nabla \times \mathbf{A} = \nabla \times \left(\frac{\psi}{r} \mathbf{e}_\theta \right),$$

$$\mathbf{J} = \frac{1}{\mu_0} \nabla \times \mathbf{B}, \quad \mathbf{E} = \eta \mathbf{J} . \qquad (3)$$

For a detailed calculation, we often use $\mathbf{E} = \eta\mathbf{J} - \mathbf{u}_e \times \mathbf{B} - \nabla p_e / (en_e)$. When ions are at rest and $\mathbf{J} \times \mathbf{B} = \nabla p_e + \nabla p_i$ is satisfied, then $\mathbf{E} \approx \eta\mathbf{J} + \nabla p_i / (en_e)$. The azimuthal electric drift due to the ion pressure gradient is in paramagnetic direction. Therefore, it is impossible to explain ion spin-up by the electric drift due to the ion pressure gradient. The electric field due to both the Lorentz force acting on electrons and the electron pressure gradient is neglected in calculating orbits of ions. Initially, ions are loaded in the r-z plane uniformly. The ion as a super-particle is weighted by the non-shifted Maxwellian distribution, and therefore the ions are initially at rest. The ion temperature is set to be uniform inside the separatrix, and it decreases with the flux function exponentially in open field region. The initial electron density is calculated to satisfy the Grad-Shafranov equation. The equation of motion is solved for ions in $\mathbf{B}$ and $\mathbf{E}$ fields given by Eq. (3), and the ion density and toroidal flow velocity are obtained by a particle in cell method at each calculation time step.

The ion-ion pitch-angle scattering is reproduced by a Monte Carlo method [20]. The pitch-angle is calculated as

$$\lambda_n = \lambda_o (1 - \nu_d \tau) \pm \left[(1 - \lambda_o^2) \nu_d \tau \right]^{1/2},$$

$$\lambda = \frac{v_{//}}{v} = \cos\theta_p , \quad -1 \le \cos\theta_p \le 1 . \qquad (4)$$

Here, ν_d is the deflection collision frequency and τ is the time interval of random number generation. The subscripts n and o mean new and old variables. We choose either sign equally by the uniform random number at the sign $\pm$.

Calculation results are compared with the experiment data measured on the NUCTE (Nihon University Compact Torus Experiment)-III device. Typical experiment parameters of the NUCTE-III device are the external magnetic field B_{ex}=0.4 T, the coil radius $r_c = 0.17$ m, and the typical plasma parameters are the separatrix radius $r_s = 0.05$ m, the separatrix length $\ell_s = 0.40$ m, the ion temperature $T_i \approx 100$ eV, the electron temperature $T_e \approx 100$ eV and the density at the field-null $n_0 = 2.0 \times 10^{21}$ m^{-3}. A measured flux Φ at the field-null is shown in Fig. 1, where the flux Φ is equal to $2\pi\psi$. Gradual decrease of the flux can be seen after completion of FRC formation at about 8 μs. Decrement of the flux reaches 0.32 mWb by 50 μs, which corresponds to $35t_{A0}$ after formation, where $t_{A0} \equiv r_c / v_{A0}$ and $v_{A0} \equiv B_{ex} / \sqrt{\mu_0 m_i n_0}$. When f_A is 10, decrement of the calculated flux for $35t_{A0}$ is estimated by $\Delta\Phi = 2\pi(\Delta\psi) \approx 2\pi(0.01|\psi_w|) \approx 0.31$ mWb ; it is comparable to the NUCTE-III experiment. Therefore, orbits of ions are calculated at f_A of 10, and then the resultant toroidal flow velocity is compared with the NUCTE-III experiment.

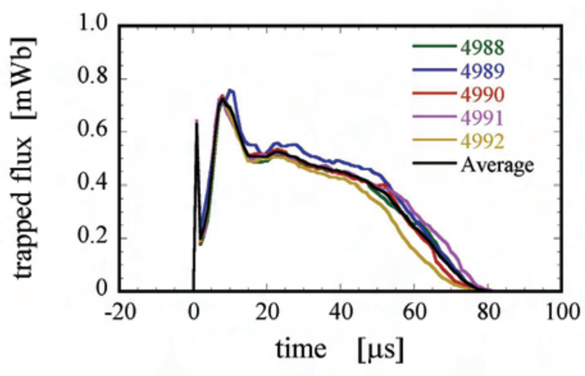

Fig. 1 The time evolution of the maximum poloidal flux measured at the NUCTE-III device.

3. Results and Discussion

To study an effect of flux decay on toroidal spin-up of a FRC plasma, orbits of ions are calculated for the presence of and absence of flux decay. The calculated time evolution of the toroidal flow velocity normalized by v_{A0} is shown in Fig. 2, where flux decay is present for Fig. 2(a) and is absent for Fig. 2(b). Here, the flow velocities at the separatrix (the solid line) and at the field-null o-point (the dotted line) are presented separately. Gradual increases are found at both the separatrix and o-point in Fig. 2(a), whereas no increase can be seen in Fig. 2(b). By the time of $35t_{A0}$, the FRC plasma is found to rotate with the toroidal velocity up to $0.35v_{A0}$ at the separatrix and up to $0.25v_{A0}$ at the o-point.

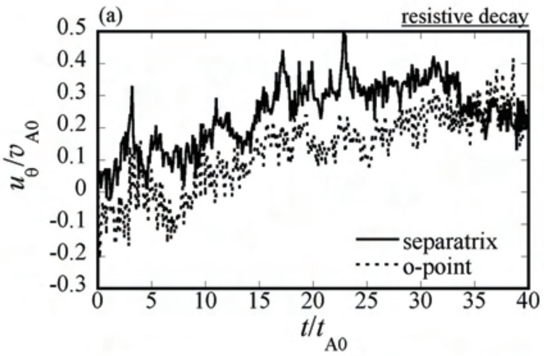

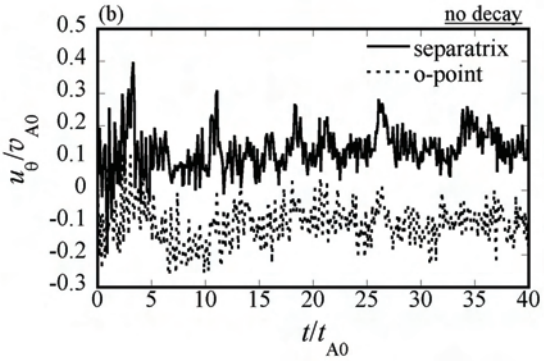

Fig. 2 The toroidal flow velocity evolution at the separatrix (the solid line) and at the field-null o-point (the dotted line). (a) The poloidal flux decays due to resistivity. (b) The flux decay is absent.

For comparison, the toroidal velocity measured by the Doppler shift of the impurity line $C^{4+}$is shown in Fig. 3. The measured velocity can be read as the average along the line of sight, whose distance of closest approach from the geometric axis is 4.5 cm; it locates initially between the separatrix and o-point. As with Fig. 2(a), an almost linear increase is found by the experimental result. Therefore, a qualitative agreement can be observed between experimental and computational results of the toroidal rotation velocity. Because $v_{A0} = 138$ km/s , the velocity of 20 km/s corresponds to about $0.15v_{A0}$ .A toroidal flow can be observed even for the absence of flux decay as shown in Fig. 2(b), although ions are assumed to obey the non-shifted Maxwellian distribution. The ion diamagnetic drift and absence of the radial and axial electric field may play a role of the rotation velocity in Fig. 2(b).

Comparison of the time evolution of toroidal flow velocity at the separatrix between the presence of and absence of end-loss ions are made as shown in Fig. 4. The axial direction of motion is reversed at the axial end of the calculation region for the case w/o end loss. Therefore, in this case no ions suffer from the end loss. Calculation of orbit stops for the case with end loss, when ions pass through the axial end. It is found that there is little difference between two cases, because near the separatrix few thermal ions are lost by $35t_{A0}$ even in the decaying plasma. Therefore, it appears the effect of the ion loss on spin-up of FRC plasma is negligible.

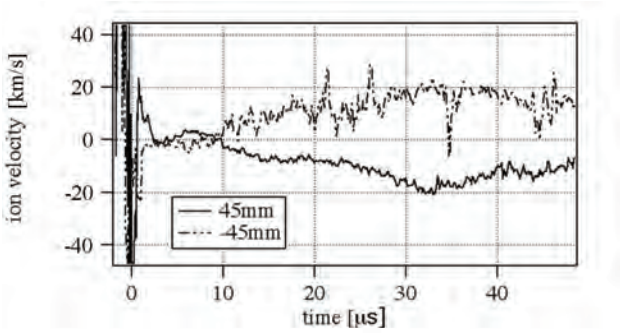

Fig. 3 The time evolution of toroidal velocity measured by the Doppler shift of a spectral line of impurity carbon at NUCTE-III device in Nihon University.

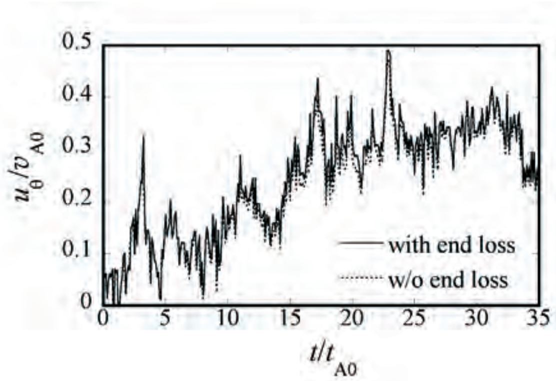

Fig. 4 Comparison of the time evolution of toroidal flow velocity at the separatrix between the presence of and absence of end-loss ions. The axial direction of motion is reversed at the axial end of the calculation region for the case w/o end loss (the dotted line). Calculation of orbit stops for the case with end loss (the solid line), when ions pass through the axial end.

When the ion-ion pitch-angle scattering is considered, the particle loss fraction gradually increases with time due to the classical transport process. The particle loss may enhance the spin-up of a FRC plasma, we compare the rotation velocity between the collisional case and the collisionless case. The time evolution of the particle loss fraction that is the ratio of the number of end-loss ions to the number of all ions inside the confinement region is shown in Fig. 5. Although the flux decays, it is found that ions are lost only before $20t_{A0}$ for the collisionless case. About 10 % difference between the collisionless and collisional case is observed until $35t_{A0}$, and it may cause a significant difference in the toroidal rotation velocity.

Comparison of the toroidal velocity between the collisionless and collisional case is shown in Fig. 6.

Higher fluctuation level is found for the collisionless case, and reduction of its level for the collisional case is due to the viscosity. Except time fluctuation, however, insignificant difference is observed. Therefore, the particle loss by the classical transport process is not be responsible for the spin-up of a FRC plasma.

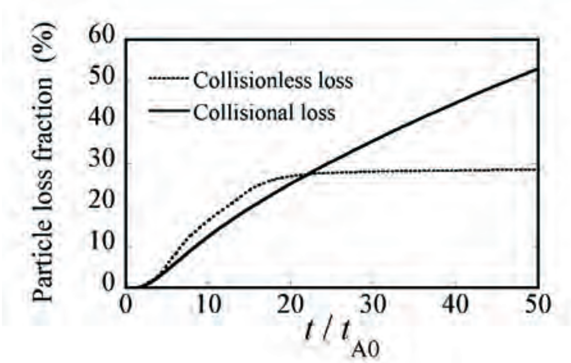

Fig. 5 The time evolution of the particle loss fraction. The ion-ion pitch angle scattering is taken into account for the solid line and is not taken into account for the dotted line.

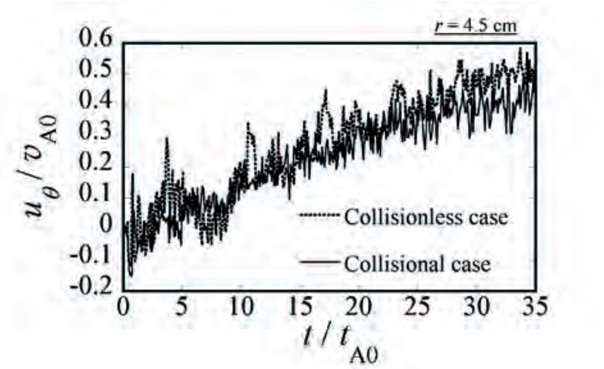

Fig. 6 The time evolution of the toroidal rotation velocity at the radial position of 4.5 cm. The solid and dotted lines are drawn as Fig. 5.

4. Summary

It has been shown that a FRC plasma can spin up without any loss of ions because of the direct conversion process from the poloidal flux to the kinetic angular momentum of ions. Abrupt change of the type of ion trajectory, such as the betatron, figure-8 and small-gyroradius drift orbits, is possible cause of spin-up of a FRC plasma. The rotation velocity is calculated, and the results are found to be in qualitative agreement with the experiment at the NUCTE-III device.

In this paper, Coulomb collisions that break conservation of the canonical angular momentum have also been considered. If collisionality increases, the loss of flux is not always converted to the angular momentum. Insignificant difference of the toroidal velocity, however, is found between the collisional and collisionless case. Therefore, the conversion process still plays an important role of the spin-up of a FRC plasma. The particle loss due to classical transport has been found to have a small effect on the spin-up process. Though the toroidal flow affects the electromagnetic fields and the ion motion, this effect is neglected in the present letter and is left as a subject for future study.

Acknowledgement

This work is supported under the auspices of the NIFS Collaborative Research Program (NIFS05KNXN033, NIFS06KDBD003 and NIFS06KKMP003).

References

[1] M. Tuszewski, D. P. Taggart, R. E. Chrien, D. J. Rej, R. E. Siemon, and B. L. Wright, Phys. Fluids B **3**, 2856 (1991).
[2] S. Sugimoto, T. Niina, and S. Goto, J. Appl. Phys. **66**, 5228 (1989).
[3] D. J. Rej, D. P. Taggart, M. H. Baron, R. E. Chrien, R. J. Gribble, M. Tuszewski, W. J. Waganaar, and B. L. Wright, Phys. Fluids B **4**, 1909 (1992).
[4] J. T. Slough and A. L. Hoffman, Phys. Fluids B **5**, 4366 (1993).
[5] T. Asai, T. Takahashi, T. Kiguchi, Y. Matsuzawa, and Y. Nogi, Phys. Plasmas **13**, 072508 (2006).
[6] M. Tuszewski, Nucl. Fusion **28**, 2033 (1988).
[7] W. M. Manheimer and J. M. Finn, Phys. Fluids **24**, 1865 (1981).
[8] D. S. Harned and D. W. Hewett, Nucl. Fusion **24**, 201 (1984).
[9] M.-Y. Hsiao and G. H. Miley, Phys. Fluids **28**, 1440 (1985).
[10] K. S. Thomas, Phys. Rev. Lett. **23**, 746 (1969).
[11] A. Kadish, Phys. Fluids **19**, 141 (1976).
[12] L. C. Steinhauer, Phys. Fluids **24**, 328 (1981).
[13] L. C. Steinhauer, Phys. Plasmas **9**, 3851 (2002).
[14] M. Tuszewski, G. A. Barnes, R. E. Chrien, W. N. Hugrass, D. J. Rey, R. E. Siemon, and B. Wright, Phys. Fluids **31**, 946 (1988).
[15] E. V. Belova, R. C. Davidson, H. Ji, and M. Yamada, Phys. Plasmas **11**, 2523 (2004).
[16] E. V. Belova, R. C. Davidson, H. Ji, M. Yamada, C. D. Cothran, M. R. Brown, and M. J. Schaffer, Nucl. Fusion **46**, 162 (2006).
[17] T. Takahashi, H. Yamaura, F. P. Iizima, Y. Kondoh, T. Asai, T. Takahashi, Y. Matsuzawa, T. Okano, Y. Hirano, N. Mizuguchi, Y. Tomita, and S. Inagaki, Plasma Fusion Res. **2**, 008 (2007).
[18] J. M. Finn and R. N. Sudan, Nucl. Fusion **22**, 1443 (1982).
[19] Y. Hayakawa, T. Takahashi, and Y. Kondoh, Nucl. Fusion **42**, 1075 (2002).
[20] A. H. Boozer and G. K.-Petravic, Phys. Fluids **24**, 851 (1981).

Observation of Helical Structure with a Fast Camera in a Low-Aspect Ratio RFP "RELAX"

T. Onchi, N.Nishino[1)], R.Ikezoe, A.Sanpei, H.Himura, S.Masamune

Kyoto Institute of Technology, Matsugasaki, Sakyo-ku, Kyoto 606-8585, Japan
[1)] Hiroshima University , Kagamiyama HigashiHiroshima 739-8527, Japan

onchi5t@nuclear.dj.kit.ac.jp

A fast camera has provided the appearance of a clear simple helical structure in the visible light emission region for the first time in the RFP configuration. The observed structure is consistent with magnetic field structures deduced from magnetic measurements with the help of equilibrium reconstruction. The observed simple structure may be an indication of the simple MHD mode dynamics of low-aspect ratio RFP configuration.

Keywords: Reversed Field Pinch, Low-Aspect ratio, Fast Camera, Helical structure

1. Introduction

The reversed field pinch (RFP) is one of the toroidal magnetic confinement systems for compact, high-beta plasmas for nuclear fusion reactor. The RFP configuration is formed and sustained as a result of nonlinear MHD phenomena such as MHD relaxation and RFP dynamo. Recent progress in the RFP research has revealed the importance of resistive tearing modes in improving the RFP confinement. One of the solutions to the confinement problems is the (quasi-) single helicity ((Q)SH) RFP state[1], in which a large helical magnetic island dominates over a significant area of a plasma minor cross section.

A low-aspect ratio (A) RFP configuration is expected to have an advantage of simpler magnetic mode dynamics because mode rational surfaces are less densely spaced, which may allow us to expect easier access to the QSH RFP state than in conventional medium-A RFP. Furthermore, it has also been pointed out that the QSH configuration might be self-sustained by the laminar dynamo mechanism, which does not accompany magnetic chaos. With the aim to explore the possibility of active control of transition to the QSH state, an RFP machine RELAX (REversed field pinch of Low Aspect ratio eXperiment)[2] has been constructed which has the aspect ratio of 2 (R/a=0.51m/0.25m).

Recently it has become possible to use a fast camera for the study on plasma instability and turbulent structures in many magnetic confinement devices[3-5]. We have installed a fast camera in RELAX for the first time in the RFP configuration to study the plasma dynamics. Time evolution of the visible light image of the RFP plasma has been observed over ~60% of the minor cross sectional area through a tangential port in RELAX.

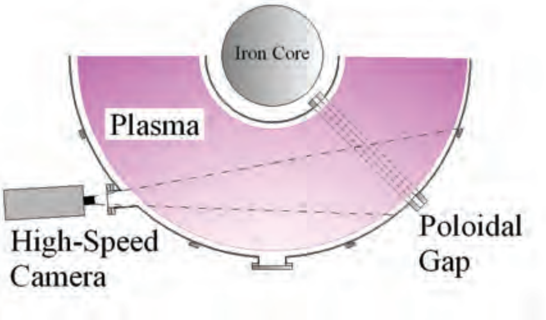

Fig.1 Experimental setup of the installation of a fast camera in RELAX from a tangential port.

2. Experimental arrangement and characteristics of RELAX RFP plasmas

Figure 1 shows the experimental setup in the present fast camera experiment. The fast camera is set to observe the RELAX plasma through a tangential port. The camera takes 80,000 images per second at the maximum rate with pixel size of 96×80. Typical discharge regime of RELAX RFP plasmas are as follows: plasma current Ip from 40 to 70 kA, discharge resistance Vl/Ip estimated at the current maximum decreasing with Ip from 4 mΩ to 1.5 mΩ, and Since discharge duration of the RELAX plasma is about 2 ms, we have observed time evolution of the tangential image of the visible light emission from the start to the end of low-aspect ratio RFP plasmas.

Figure 2 shows typical waveforms of a round-topped RELAX discharge. The plasma current grows to 60 kA in about 0.5 ms, with formation of RFP configuration at

author's e-mail: onchi5t@nuclear.dj.kit.ac.jp

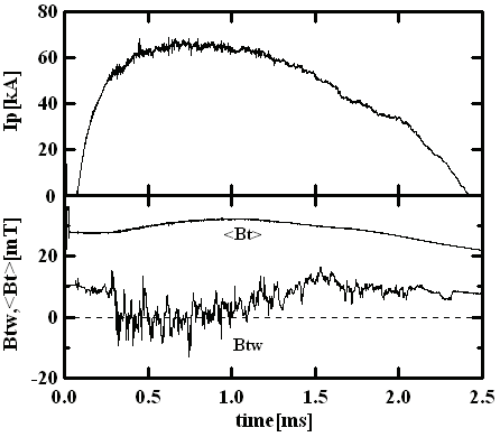

Fig.2 The typical discharge waveforms round-topped RFP discharge in RELAX. Ip is the plasma current, edge toroidal magnetic field Btw and average of torodal magnetic field <Bt>.

0.3ms into the discharge. The plasma current maintains the value higher than 60 kA for 1 ms, followed by a gradual decay after the loss of field reversal at 1.2ms. Thus, in round-topped discharges, the RFP configuration can be sustained for 1 ms followed by the so-called Ultra-Low Q (ULQ) configuration with decaying current. The total duration of this round-topped RFP discharge is about 2 ms. A single-chord soft-X ray diagnostics with absorbing method using two polyethylene filters has provided line-averaged electron temperature higher than 50eV, exceeding the radiation barrier for a hydrogen plasma at least in the core region.

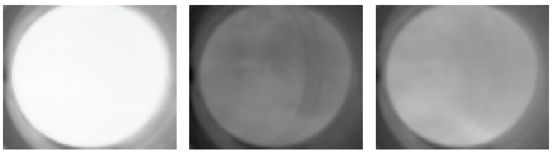

(a)t=100μs (b)t=500μs (c)t=1ms

Fig.3 Some typical fast camera images in "RELAX" plasma, corresponding to shot of Fig.2.

3. Observation of helical structures in the visible light image

First, we will describe typical evolution of the fast camera images in this type of round-topped discharges. As shown in Fig.3(a), strong visible light emission due to Hα line radiation is observed over the minor cross section in the early phase of a discharge, 0.1ms into the discharge in the case of Fig.3(a). This strong Hα emission is the indication of ionization phase of a discharge. As the plasma current Ip grows, the RFP configuration is set up at 0.3 ms, and sustained for about 1 ms with Ip of 50-60 kA. The visible light emission decreases as the current rises, as shown in Fig.3(b) at 0.5ms into the discharge. During the RFP sustainment phase, intensity of the emission is too weak to identify any characteristic structures. In the round-topped discharge, it happens at 1-1.2 ms into the discharge that the toroidal field reversal is lost with a smooth transition of the magnetic field configuration from RFP to non-reversed low-q discharge, so called ultra-low q (ULQ) regime. The emission increases again at the incidence of transition, as shown in Fig.3(c) 1.0 ms into the discharge. The increased emission is probably an indication of enhanced influx of hydrogen particles at the configuration transition phase. In round-topped RFP discharges, we can identify the characteristic structure in the visible light emission most evidently in the ULQ discharge regime, and the observed structure in the emission shows good correlation with magnetic fluctuation behavior. .

Figure 4 shows time evolution of the emission images for 50μs before and after the appearance of simple helix structure in the emission image. The time evolution shows that transition from three or two helices structure in Fig.4(a) and (b) to a simple single helix structure at 1.4125 ms in Fig.4(c), followed by a gradual fading away of the helices. It has been shown that the simple helix structure agrees well with simulated helix tube on the m=1/n=4 mode rational surface which was reconstructed using the modified MSTFIT code. This is simple helical structure in the emission image may indicate that the density and temperature of electrons have the similar structure, because it is unlikely that residual neutral particles distribute with such kind of helical structure.

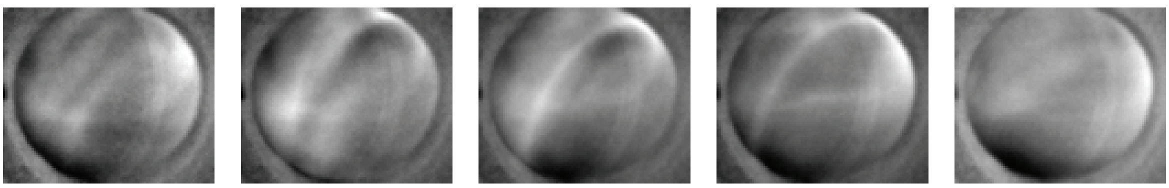

(a)t=1.38750ms (b) t=1.4000ms (c) t=1.4125ms (d) t=1.4250ms (e) t=1.4375ms

Fig.4. Time evolution of the fast camera images during 50 μs before and after the transition to simple helical structure at (c). These data correspond to the same shot as in Fig.2.

P1-018

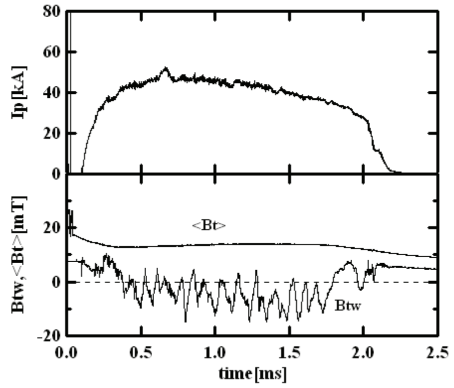

Fig.5 The waveforms of Ip, Btw and <Bt> in "RELAX" RFP plasma, which are different from Fig.2.

This helical structure in the emission image has some correlation with magnetic fluctuations as discussed in [6].

Next, we will describe typical evolution of the fast camera images in flat-topped RFP discharges with plasma current of 40-50 kA, as shown in Fig.5. In this type of discharges, the RFP configuration is sustained for 1.5-2.0 ms, almost to the end of discharge. Typical evolution of visible light images throughout a discharge is similar to that in round-topped discharge. The main difference is that we can identify characteristic helical structures in the fast camera images in the RFP sustainment phase. The magnetic mode behavior shows that m=1/n=4 mode grows after ~1.4ms, becoming dominant mode towards the end of discharge.

Figure 6 shows time evolution of the fast camera images from 1.650ms to 1.775ms. The set of pictures indicates that there are some helical structures observable in the images throughout the period of 0.1 ms. The helical structures are, however, not so simple as in the case shown in Fig.4. Figure 7 shows the toroidal mode spectrum of m=1 modes ,

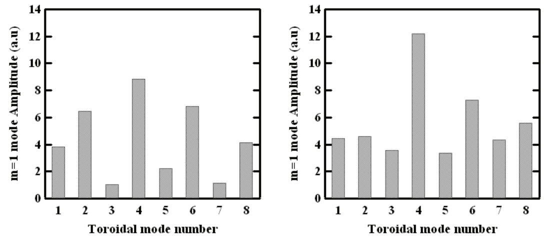

(a) t=1.6750ms (b) t=1.7000ms

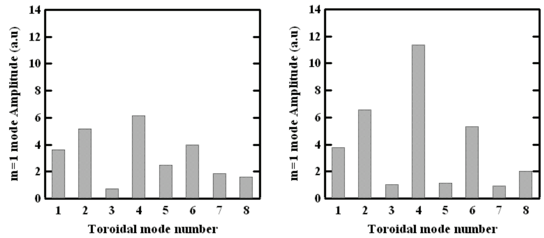

(c) t=1.7375ms (d) t=1.7625ms

Fig.7 Comparison of some toroidal mode spectrum. (a),(b),(c) and (d) are correspond to Fig.7(c),(e),(h) and (j).

indicating that m=1/n=4 mode is dominant throughout the duration of 0.1 ms, with some secondary resonant modes. Comparing these two figures, we can identify that the number of dominant helicities in the fast camera pictures agrees with the number of dominant and secondary modes throughout this period of 0.1 ms. Equilibrium reconstruction in order to deduce the q profile to identify the radial locations of mode rational surfaces both the dominant and secondary modes has been in progress to compare the observed helical structures with magnetic field structures inside the plasma.

We can also identify toroidal rotation of the helical structures in the opposite direction to the toroidal plasma current. Detailed comparison of the toroidal rotation of the

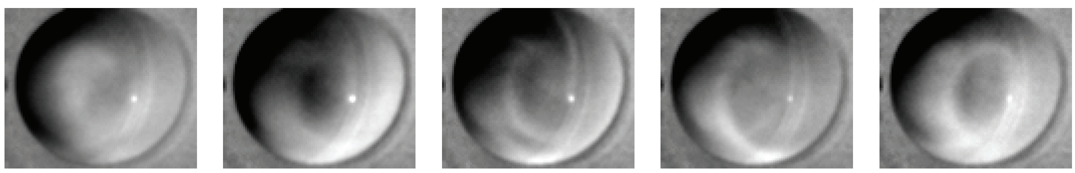

(a)t=1.6500ms (b) t=1.6625ms (c) t=1.6750ms (d) t=1.6875ms (e) t=1.7000ms

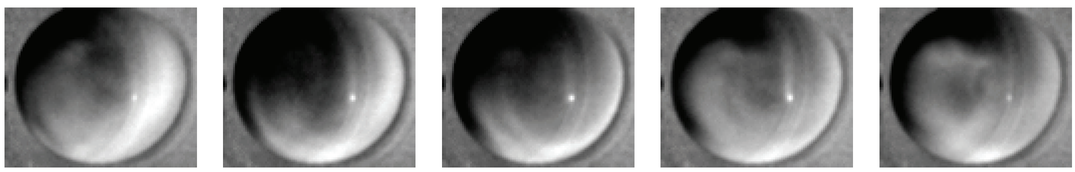

(f) t=1.7125ms (g) t=1.7250ms (h) t=1.7375ms (i) t=1.7500ms (j) t=1.7625ms

Fig.6 Time evolution of the fast camera images, corresponding to the same shot as in Fig.6. Time zone is 1.650~1.775ms.

m=1 modes are also in progress.

4. Conclusion

There have been observed several types of helical structures in the fast camera images in low-A RFP plasmas in RELAX. This is the first observation of helical structures in the visible light images in the RFP plasma. Such structures are an indication of the similar structure of both the density and temperature of electrons because it is not likely that the residual or enhanced neutral particles have such kind of structure. The remaining issue is the reason for the formation of such kind of helical structures in the visible light emission. It may be closely related to the magnetic island issues in low-A RFP configurations, so we need to implement the soft-X ray imaging diagnostics.

References

[1] D. F. Escande *et al*, Phys. Rev. Lett. **85**, 1662 (2000).
[2] S. Masamune et al., Trans. Fusion Science and Technology, **51**, 197 (2007).
[3] N. Nishino et al., J. Plasma Fusion Res. **78**, 1278 (2002).
[4] N. Nishino et al., J. Plasma Fusion Res. **80**, 175 (2004).
[5] N. Nishino et al., Plasma Fusion Res. **1**, 035 (2006).
[6] T.Onchi et al., submitted to PFR.

Fast imaging of edge plasma instabilities in the TJ-II stellarator and JET tokamak.

J.A. Alonso, P. Andrew[1], E. de la Cal, P. Carvalho[2], D. Carralero, H. Fernandes[2], T. Happel, C. Hidalgo, G. Kocsis[3], A. Manzanares, B.Ph. van Milligen, A. Murari[4], A. Neto[2], J.L. de Pablos, M.A. Pedrosa, G. Petravich[3], L. Rios, C. Silva[2], H. Thomsen[4] and S.J. Zweben[5].

Asociación EURATOM-CIEMAT, Av. Complutense 22, 28020 Madrid – Spain

[1]*EURATOM-UKAEA Association, Culham Science Center, Abingdom – UK*

[2]*Associação EURATOM-IST, Av. Rovisco Pais, 1049-001 Lisbon – Portugal*

[3]*EURATOM-HAS Association, KFKI-RMKI, H-1525 Budapest-114 – Hungary*

[4]*Max-Planck IPP, Boltzmannstrasse 2D-85748 Garching – Germany*

[5]*Princeton Plasma Physics Laboratory, Princeton, NJ, USA*

High speed visible imaging has become a popular diagnostic in magnetic confinement fusion devices in the last years. Fast commercial cameras provide a time resolution of up to 4 us with image sizes of few tenths of pixels per side. The relatively cold (1-100 eV) plasma edge mainly emits radiation in the visible range and can thus be diagnosed by means of these fast cameras. This work is a summary of the results of high speed visible imaging obtained in the TJ-II stellarator and JET tokamak.

In the TJ-II stellarator the visible radiation is locally increased around the poloidal limiter. The tangential view of the edge region in the vicinity of the limiter revealed the presence of spatially coherent turbulent structures or eddies. We studied the geometrical properties of these structures in plasma regimes with and without edge shear layer [1]. The presence of a shear layer was seen to increase the elongation of turbulent eddies and to reduce the scatter in the direction of the structures' main axis, suggesting that the shear flow in the edge of TJ-II stretches and orders the eddies.

In the JET tokamak a wide-angle view endoscope provides a half torus perspective. This allows the study of large scale instabilities. ELMs and disruptions have been observed at high frame rates (30-210 kfps) for the first time in JET [2]. Ultra high speed recordings of the divertor region in ELMy plasmas provided an estimation of the effective ELM radial velocity. These and other edge plasma observations like wall material sputtering and MARFEs will be presented.

[1] J.A. Alonso *et al*., Plasma Phys. Control. Fus. **48** B465 (2006)

[2] J.A. Alonso *et al*., 34th EPS conference, Warsaw 2007, P1.124

Proceedings of ITC/ISHW2007

Measurement of peripheral plasma turbulence using a fast camera in Heliotron J

N. Nishino, T. Mizuuchi[1], S. Kobayashi[1], K. Nagasaki[1], H. Okada[1], F. Sano[1], S. Yamamoto[2], and K. Kondo[3]

Graduate School of Engineering, Hiroshima University

1) Institute of Advanced Energy, Kyoto University

2) Kyoto University Pioneering Research Unit for Next Generation

3) Graduate School of Energy Science, Kyoto University

(Received 15 Oct. 2007 / Accepted)

Keywords: turbulence, peripheral plasma, L-H transition, H-mode, Heliotron J, fast camera

1. Introduction

Study of peripheral turbulence is very important issue for fusion research due to the relationship to the energy confinement and H-mode physics. Fast cameras have been installed in Heliotron J [1] to get information on the peripheral plasma turbulence since several years ago. In our previous work, using a combination method of a fast camera (Ultima-SE, Photron) and a small movable carbon target, a structure of a low frequency (5-6kHz) edge plasma oscillation in high electron density ECH discharges was observed just after the L-H transition [2]. Also a combination of a fast camera (FX-K4, NAC image technology), movable probe and directional gas puff technique gave us important information that the spatial profile of turbulent burst in the edge plasma were observed as a filamentary structure in the L-mode [3-5]. Each burst of the ion saturation current was corresponding to that the filamentary structure hit the probe simultaneously.

Recently the turbulent structures during the L-mode and H-mode were observed by the latter camera with/without directional gas puff [6]. It was clear that the spatial structure of peripheral turbulence during the L-mode was different with that of the H-mode. Relative wide structure along the magnetic field was observed in the H-mode however, narrower structure along the magnetic field was observed in the L-mode. Moreover, these filamentary structures were sometimes disappeared in the H-mode.

In this paper the obtained results included in the latest results of Heliotron J plasmas by the fast camera are reported.

nishino@hiroshima-u.ac.jp

2. Experimental Setup

The tangential port was provided with the fast camera to measure peripheral plasma behavior easily. Fig.1 shows the tangential port position (green) and horizontal port position (blue) for the fast camera. These measurements could not be done simultaneously because of the same fast camera (FX-K4, NAC image technology).

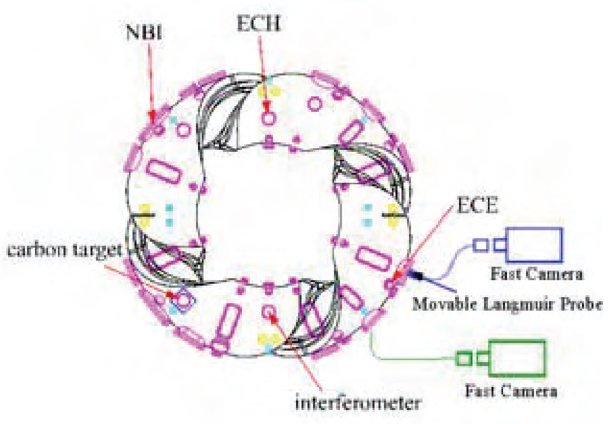

Fig.1. Location of tangential view for the fast camera in Heliotron J

Fig. 2 shows the tangential view of the fast camera. This view is the initial phase of Heliotron J plasma discharge. The first bright string in the images became thicker and darker, and the equilibrium state was obtained.

Unfortunately the adjustment of the up-down direction in the image was not completed this time, however, it was clear to see the port and its position. In the image the grids were each fiber of the coherent bundle fiber.

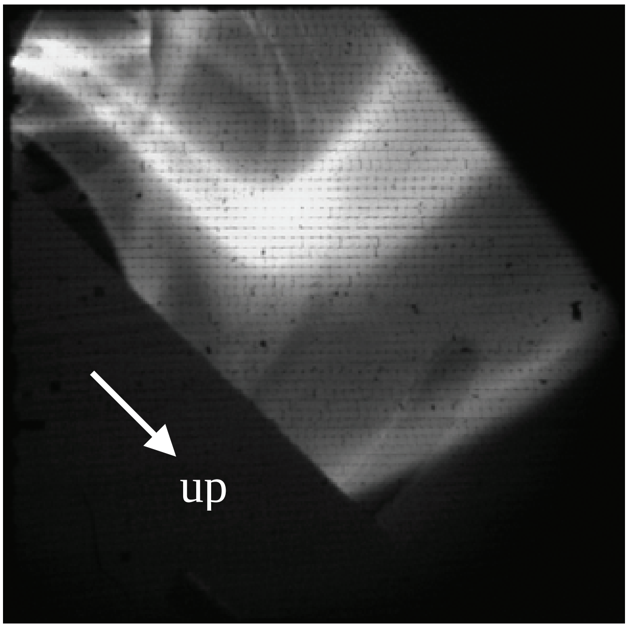

Fig.2 Tangential view from the fast camera
A part of the original image (448x368pixels, 10000FPS)

3. Results and discussion

In high density ECH discharge of STD configuration (-86%, -87%, –88%, -89% of the magnetic field strength) the abrupt drop of Dα signal were observed and the H-mode plasmas were obtained. In these shots the reproducibility was very good. Typical waveform of H-mode shot is shown in Fig.3. Fig.4 shows the ion saturation current of the movable probe of the same shot. The power spectra of this ion saturation current show the low frequency fluctuation were suppressed during H-mode (not shown here).

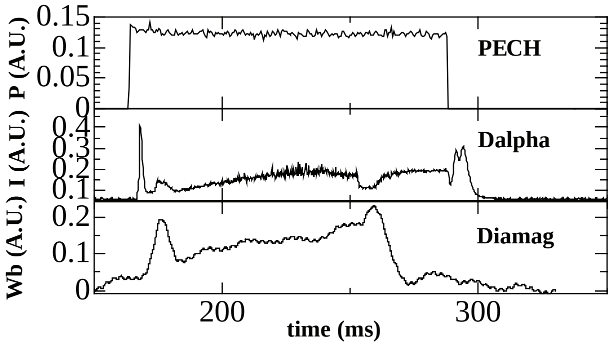

Fig.3 Typical waveform of H-mode in ECH discharge

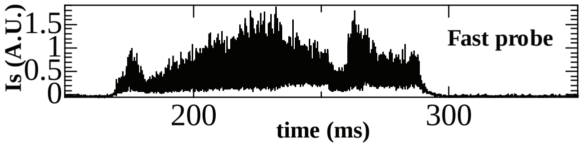

Fig.4 Ion saturation current signal

From the tangential view images the plasma rotation was observed clearly, moreover, it was observed that plasma rotated counterclockwise in the images during the L-mode and stopped to rotate during the L-H transition, at last plasma rotated clockwise in the images during the H-mode. The magnetic field direction and the camera viewing direction were counterclockwise from the horizontal plan (see Fig.1) in these shots. Therefore, if plasma would rotate by E_rxB drift, E_r should be positive in the L-mode and E_r should be negative in the H-mode in Heliotron J plasmas. These results were consistent with the past results on the H-mode in Heliotron J [7]. The low frequency of 8.75kHz signal was relative strong during L-mode in the power spectra of the camera pixel data and no strong peak was obtained during H-mode. To evaluate rotation effect with two-dimension this low frequency fluctuation was chosen to see how behaves during the L- and H-modes.

Fig.5 shows two-dimensional phase images using time-dependent FFT analysis from the original camera images. The column of the left shows images during the L-mode, the center shows images during the L-H transition, and the right shows images during the H-mode. The time progresses downward where time difference between each frame is 25μs at each column.

The frequency of each frame was 8.75kHz and the fast camera operated with 40000 frames per second (FPS). We used 32 frames for time-dependent FFT. The color is corresponding to the phase $-\pi$ to π. The same color region has the same phase. Therefore, these images show the propagation phenomena and/or wave at the selected frequency.

The rotation speed of 3000m/s was roughly estimated in the images during H-mode and it was about half during L-mode. Therefore, according to this rough estimation from the images Er is -2kV/m during the H-mode, and Er is +1kV/m during the L-mode. The magnetic field is about 1.5T. These results were consistent with Ref[7].

Transition period of the L-H transition was also deduced in the images. The number of the camera frames that rotation stopped is only one at 40000 frames per second. That shows the transition period in Heliotron J plasma is below than 50μs, because to get the light emission the shutter was open in these shots.

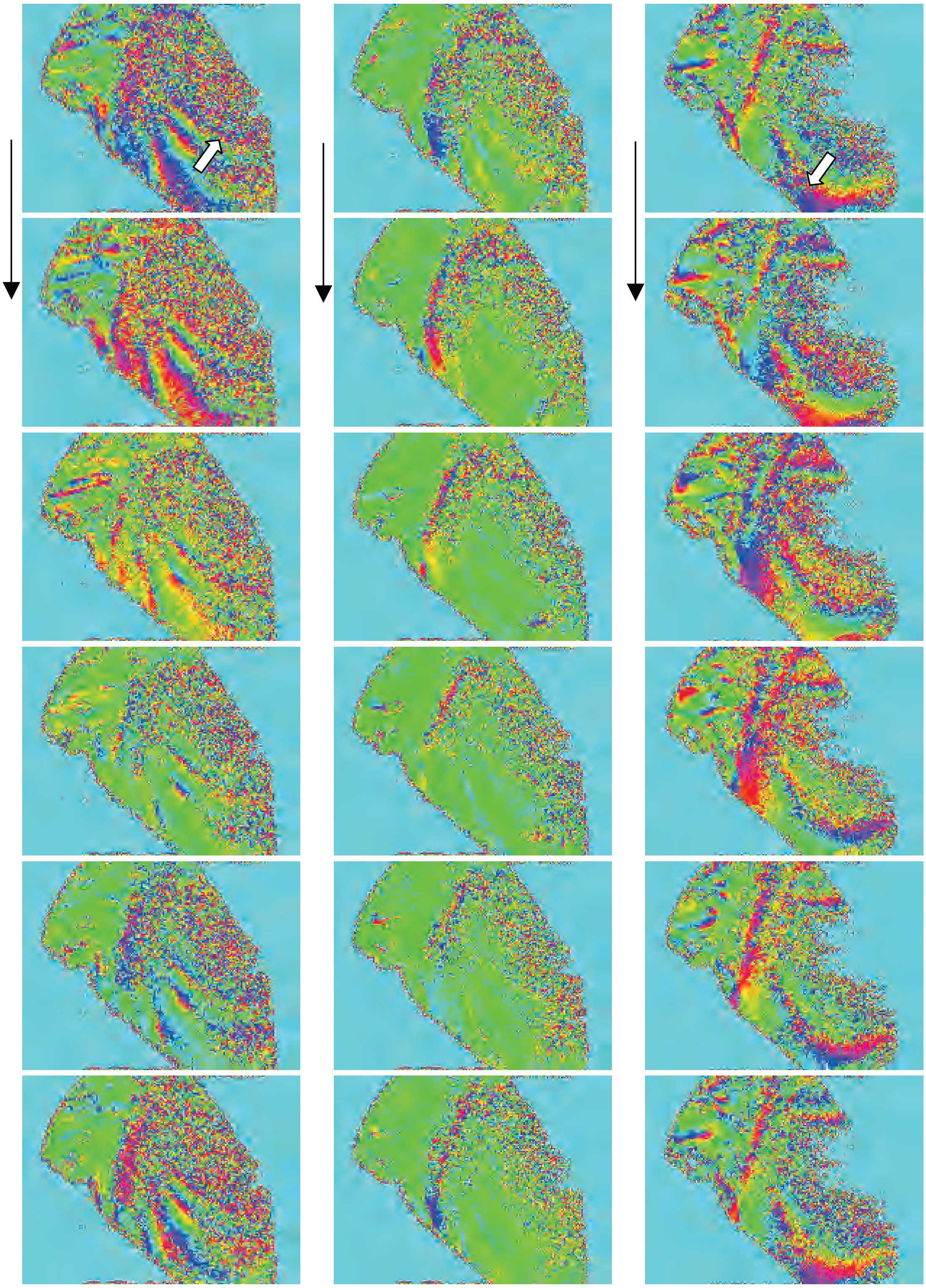

L-mode L-H transition H-mode

Fig. 5 Phase images during the L-mode, the L-H transition, and the H-mode
Time progresses downward, and time difference between each frame is 25μs.

4. Conclusion

Using fast camera peripheral plasma turbulence was measured successfully. In particular, it was observed that the direction of plasma rotation was changed due to H-mode. Moreover, the transition period was estimated by fast camera images because the plasma stopped to rotate during the transition.

The fast camera usage for two-dimensional plasma diagnostics is started recently in Heliotron J and we believe this method will be very hopeful to get the image of the plasma parameters in the future.

References

[1] T. Obiki, T. Mizuuchi, K. Nagasaki, et al., Nucl. Fusion **41** 883 (2001).

[2] N. Nishino, K. Takahashi, H. Kawazome, et al., J. Nucl. Mater. **337** 1073 (2005).

[3] N. Nishino, T. Mizuuchi, K.Kondo, et al., J. Nucl. Matter. **363-365** 628 (2007)

[4] T. Mizuuchi, et al., J. Nucl. Matter. **337-339** 332 (2005)

[5] T. Mizuuchi, W. L. Ang, Y. Nishioka, et al., J. Nucl. Matter. **313-316** 947 (2005)

[6] N. Nishino, T. Mizuuchi, et al., to be published in JFPR.

[7] F. Sano, T. Mizuuchi, K.Kondo, et al., Nucl. Fusion **45** 1557 (2005)

Proceedings of ITC/ISHW2007

Activation Analysis for LHD Experiments with Deuterium Gases

Kiyohiko Nishimura, Hirokuni Yamanishi and Akio Komori
National Institute for Fusion Science, 322-6 Oroshi-cho, Toki 509-5292, Japan

Identification of radionuclides and evaluation of dose rate level have been carried out on the structural materials of the Large Helical Device and the Experimental Hall. The neutron fluence was calculated using two-dimensional transport code DOT-3.5. Energies of neutron sources are 2.45 MeV (D-D reaction) and 14 MeV (D-T reaction). Generations of radionuclides were calculated using CINAC code. Radionuclides of ^{93m}Nb, ^{63}Ni and ^{60}Co for helical coils, ^{55}Fe and ^{60}Co for stainless steel, ^{55}Fe, ^{60}Co and ^{93m}Nb for poloidal coils, ^{40}K and ^{55}Fe for floor concrete were dominant after a series of experiments with deuterium gases. Evaluation of dose rate level for the structural materials and air were calculated taking account a present experimental schedule.

Keywords: Large Helical Device, deuterium operation, Superconducting coils, radioactivity, dose rates, DOT-3.5 code, CINAC code, cobalt 60

1. Introduction

In fusion devices such as JT-60U, TFTR and JET neutron production generated by deuterium-deuterium reactions is increased accompany with the increase in fusion power and the devices are subsequently activated. As a result, maintenance and repair works during off-operational periods become difficult because an access around and/or into a vacuum vessel is so limited from a health physics point of view. A safety analysis is also a major concern of experiments with deuterium gases in the Large Helical Device (LHD) [1-4] and a design of DEMO reactors with high neutron yield operations.

Several calculations concerning induced activities for the tokamak devices have been reported. In these tokamaks, varied structural materials are used so that characteristics of radioactivity differ with each device. For this reason, it is clear that information of inherent property of activation on LHD is essential to an understanding of the dose rate around the device in maintenance works.

The radiation protection concepts of the LHD was carried out at the building design phase [5] and revised at the building construction phase [6]. The neutron fluence was calculated using two-dimensional transport code DOT-3.5 [7]. Generations of radionuclides caused by 2.45 MeV (D-D reaction) and 14 MeV (D-T reaction) were calculated using CINAC code [8].

In this paper, identification of radionuclides and evaluation of the dose rate on the LHD are described.

2. Large Helical Device

LHD is the largest superconducting heliotron type device with l=2/m=10 continuous helical coils and three pairs of poloidal coils. The major and minor radii of the plasma are 3.5-3.9 m and 0.6-0.65 m, respectively. Schematic figure of LHD are shown in Fig. 1. The maximum magnetic field strength is about 3 T at the magnetic axis.

The LHD project is aimed at exploring the feasibility of helical plasmas for fusion applications. In particular, to demonstrate the steady-state currentless plasmas confined in the helical fields generated by super-conducting coils.

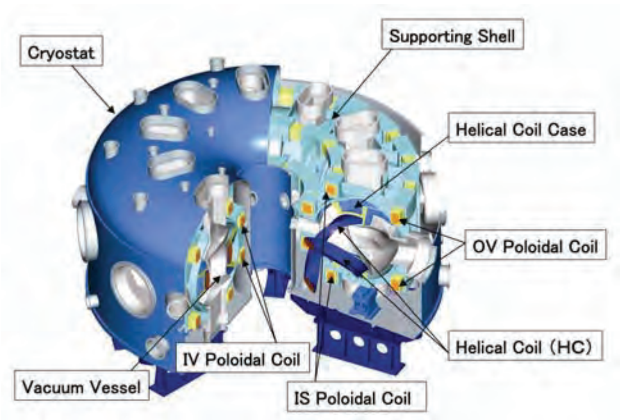

Fig. 1. Schematic figure of LHD.

author's e-mail: nisimura@LHD.nifs.ac.jp

3. Calculation

Standard numbers and energies of neutron sources using calculations are shown in Table 1. One shot is 10 seconds pulse and 1000 shots are operated in a year.

Table 1. Parameters of neutron

Energy (MeV)	Number (1/shot)
2.45	2.4×10^{17}
14.0	4.3×10^{15}

The most of 2.45MeV neutrons (D-D neutron) are generated by D plasma and D^0 beam reaction, which is called TCT effect. The14.0 MeV neutrons (D-T neutron) are generated by the reaction of deuterium with tritium (1.01 MeV) through D-D reaction. The number of D-D thermonuclear reaction is 1 – 3 % of that of TCT effect.

The neutron fluence data and the distribution of γ-ray were calculated using two-dimensional transport code DOT-3.5 by means of the FUSION-40 nuclear data set [9]. Generations of radionuclides were calculated using CINAC code. Effects of chain disintegration were taking account in this code. Since the LHD has three-dimensional structure, it is difficult to model this geometry on a two-dimensional configuration. Two models (a horizontal port model and a vertical port model) with R-Z geometry were used in these calculations. Figure 2 shows cross sections of these two models near the LHD. Calculated area was divided into twelve regions; plasma, helical coil, helical coil case, supporting shell, IV poloidal coil, IS poloidal coil, OV poloidal coil, cryostat, vacuum vessel, wall and ceiling concrete, floor concrete and air. LHD experimental hall has 45m x 75m of floor area and 40m of height. Thickness of walls and floor concrete is 2m and thickness of ceiling concrete is 1.3m. In R-Z model calculation, R of 2.5m and Z of 40m were assumed.

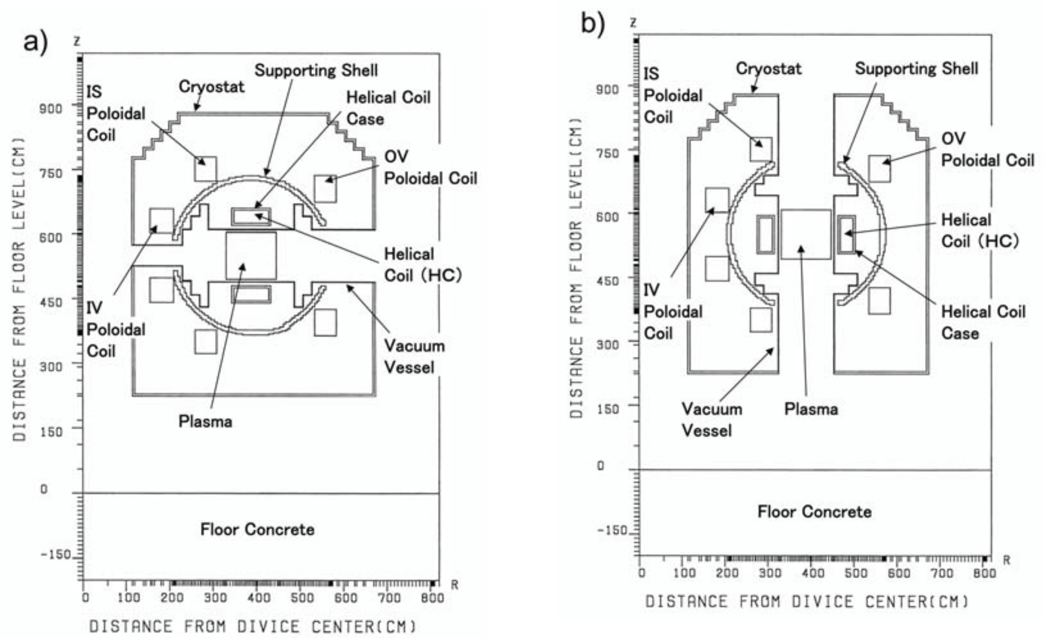

Fig. 2. Cross sections of models.
a) vertical port model, b) horizontal port model.

4. Results

Detail analysis was carried out to identify the radionuclides, which give the contribution to the γ-ray dose rate, and to calculate time evolution of the dose rate after a stop of D-D experiments.

Figures 3 and 4 show results of specific radionuclide activities as a function of time after 1 shot pulse. Two figures show averaged activities of the cryostat (SS-316) and the floor concrete. In the cryostat, ^{56}Mn (half-life of 2.6h) generated by a reaction of ^{55}Mn(n,γ) is dominant by the time of one day. After disappearance of ^{56}Mn, ^{51}Cr (27.7d) becomes dominant. After that, ^{60}Co (5.27y) generated by a reaction of ^{59}Co(n,γ) becomes dominant. In floor concrete, many radionuclides with short half-life are dominant by the time of one day. After disappearance of these shot life time nuclides, ^{24}Na (15.0h) generated by a reaction of ^{23}Na(n,γ) becomes dominant for a week. After that, ^{40}K (1.28×10^9y) becomes dominant. Most of the ^{40}K are nuclides naturally existing in a concrete.

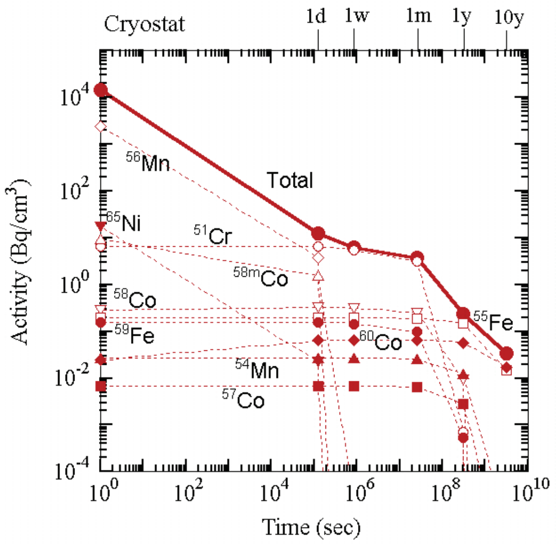

Fig. 3. Specific activity in the Cryostat (SS316) after 1 shot.

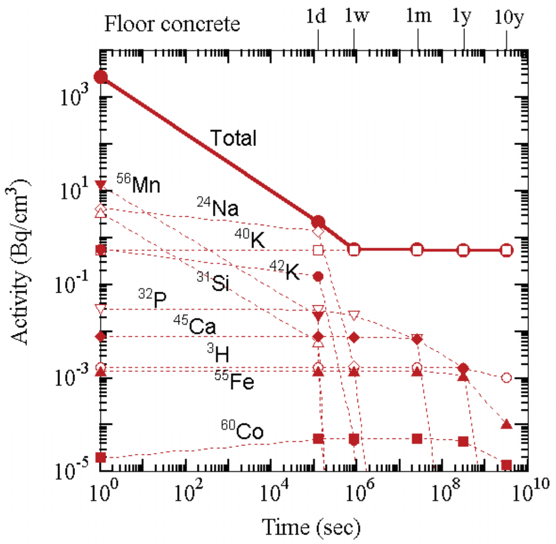

Fig. 4. Specific activity in the floor concrete after 1 shot.

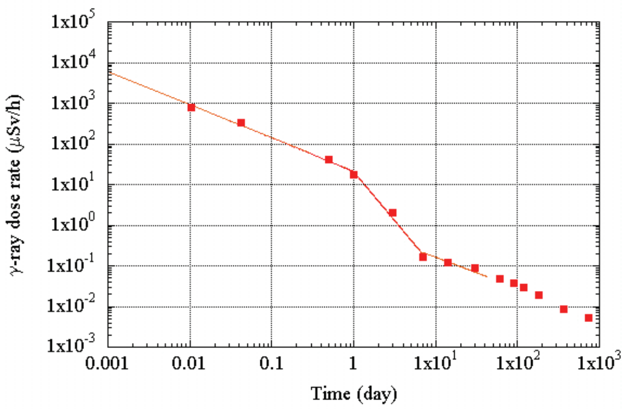

Fig. 5. Time evolution of total γ-ray dose rate after 3 seconds pulse.

To estimate the γ-ray dose rate around the vacuum vessel, total dose by all structural materials was calculated at the front of L-port of LHD. Figure 5 shows this result.

In this calculation, actual experimental plan were used; 3 seconds pulse in each 15 minutes, 30 shots in a day, 4 days in a week, 3 weeks experiment and 3 weeks intermission. Using this curve, time evolution of γ-ray dose rate during experimental series was calculated by summing up contributions of each shot. Figure 6 shows a result of one experimental series. During three days in weekend, the γ-ray dose rate decreases one order. This level of 10μSv/h is lower than the limitation for worker (20mSv/y) who works for 2000 hours per year.

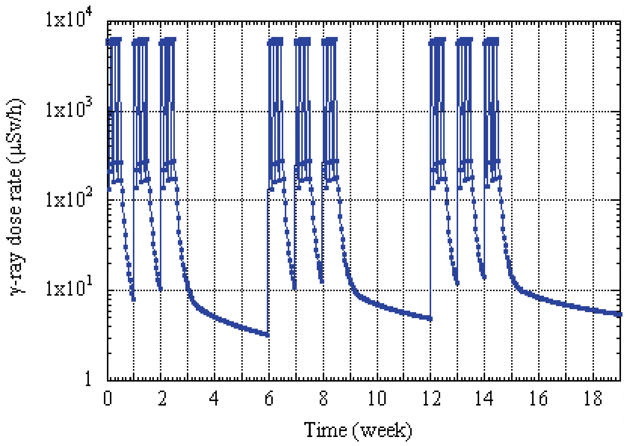

Fig. 6. Time evolution of γ-ray dose rate during experimental series.

Table 2-1. Activities of typical radionuclides on stainless steel structures 1.

Activities of typical radionuclides on stainless-steel 1.

after 1000 shots
horizontal port model

Volume (cm^3)	
VV	6.08E+06
HC Case	5.88E+06

radio-nuclides	Vacuum Vessel		HC Case	
	after 1year (Bq/cc)	after 10years (Bq/cc)	after 1year (Bq/cc)	after 10years (Bq/cc)
Be-10	3.97E-09	3.97E-09	1.88E-09	1.88E-09
C-14	1.27E-02	1.26E-02	1.83E-02	1.82E-02
Si-32	9.28E-11	9.20E-11		
P-32	4.39E-07	9.20E-11	5.23E-07	
P-33	2.93E-06			
S-35	1.29E-04			
Cr-51	1.08E-02		5.63E-03	
Mn-53	1.25E-05	1.25E-05	6.26E-06	6.26E-06
Mn-54	2.39E+02	1.62E-01	1.34E+02	9.08E-02
Fe-55	4.21E+02	4.12E+01	5.57E+02	5.46E+01
Fe-59	1.01E+00		2.17E+00	
Fe-60	7.31E-10	7.31E-10	3.46E-10	3.46E-10
Co-56	2.01E-03		9.52E-04	
Co-57	5.49E+01	1.25E-02	2.69E+01	6.12E-03
Co-58	2.44E+02	2.89E-12	1.38E+02	1.77E-12
Co-60	8.80E+01	2.70E+01	2.34E+02	7.16E+01
Ni-59	2.26E-02	2.26E-02	5.58E-02	5.58E-02
Ni-63	1.54E+00	1.45E+00	5.79E+00	5.44E+00
Zr-93	2.69E-08	2.69E-08	1.40E-08	1.40E-08
Zr-95	4.42E-03		2.27E-03	
Nb-95m	4.22E-05		2.16E-05	
Nb-94	1.21E-05	1.21E-05	6.16E-06	6.16E-06
Nb-95	1.11E-02		5.72E-03	
Nb-93m	4.23E-05	3.39E-04	2.17E-05	1.74E-04
Mo-93	9.45E-04	9.43E-04	4.86E-04	4.85E-04
Tc-99	1.47E-03	1.47E-03	2.55E-03	2.55E-03

Table 2-2. Activities of typical radionuclides on stainless steel structures 2.

Activities of typical radionuclides on stainless-steel 2.

after 1000 shots
horizontal port model

Volume (cm^3)	
SS	2.33E+07
Cryostat	2.71E+07

radio-nuclides	Supporting Shell after 1year (Bq/cc)	Supporting Shell after 10years (Bq/cc)	Cryostat after 1year (Bq/cc)	Cryostat after 10years (Bq/cc)
Be-10	5.53E-10	5.53E-10	1.25E-10	1.25E-10
C-14	5.95E-03	5.95E-03	4.46E-03	4.46E-03
Si-32			5.16E-12	5.11E-12
P-32	1.95E-07		1.53E-07	5.11E-12
P-33			3.68E-07	
S-35			1.85E-04	
Cr-51	1.61E-03		3.41E-04	
Mn-53	1.76E-06	1.76E-06	3.66E-07	3.66E-07
Mn-54	4.25E+01	2.87E-02	8.73E+00	5.91E-03
Fe-55	2.02E+02	1.98E+01	1.17E+02	1.15E+01
Fe-59	8.92E-01		4.62E-01	
Fe-60	1.00E-10	1.00E-10	1.43E-11	1.43E-11
Co-56	2.75E-04		3.93E-05	
Co-57	7.93E+00	1.80E-03	1.15E+00	2.63E-04
Co-58	4.78E+01	5.59E-13	6.92E+00	8.22E-14
Co-60	7.20E+01	2.21E+01	5.01E+01	1.53E+01
Ni-59	1.52E-02	1.52E-02	9.64E-03	9.64E-03
Ni-63	9.90E-01	9.30E-01	1.00E+00	9.43E-01
Zr-93	4.04E-09	4.04E-09		
Zr-95	6.44E-04			
Nb-95m	6.14E-06			
Nb-94	1.75E-06	1.75E-06		
Nb-95	1.63E-03			
Nb-93m	6.19E-06	4.97E-05		
Mo-93	1.38E-04	1.38E-04		
Tc-99	1.31E-03	1.31E-03		

Table 3. Activities of specific radionuclides on concrete structures.

Activities of typical radionuclides on concrete

after 1000 shots

Volume (cm^3)	
Floor	1.75E+09
Wall & Ceiling	1.34E+10

radio-nuclides	Wall & Ceiling Concrete (Horizontal port model) after 1year (Bq/cc)	Wall & Ceiling Concrete (Horizontal port model) after 10years (Bq/cc)	Floor Concrete (Vertical port model) after 1year (Bq/cc)	Floor Concrete (Vertical port model) after 10years (Bq/cc)
Be-10	8.08E-13	8.08E-13	3.76E-12	3.76E-12
C-14	2.16E-05	2.15E-05	8.18E-05	8.17E-05
Na-22	3.91E-05	3.56E-06	1.84E-04	1.68E-05
Al-26	2.58E-10	2.58E-10	1.22E-09	1.22E-09
Si-32	6.05E-13	6.00E-13	2.84E-12	2.81E-12
P-32	7.63E-10	5.99E-13	3.64E-09	2.81E-12
P-33	3.78E-08		1.88E-07	
S-35	1.36E-03		5.08E-03	2.80E-14
Cl-36	1.37E-07	1.37E-07	5.35E-07	5.35E-07
Ar-37	6.78E-04		3.28E-03	
Ar-39	2.57E-04	2.51E-04	1.25E-03	1.22E-03
K-40	8.58E-01	8.58E-01	8.58E-01	8.58E-01
Ca-41	1.67E-04	1.67E-04	6.24E-04	6.24E-04
Ca-45	3.68E-01	3.70E-07	1.37E+00	1.38E-06
Cr-51	2.12E-08		9.87E-08	
Mn-53	2.03E-11	2.03E-10	9.54E-11	9.54E-11
Mn-54	4.24E-04	2.87E-07	2.03E-03	1.37E-06
Fe-55	2.24E-01	2.19E-02	8.38E-01	8.21E-02
Fe-59	6.41E-04		2.45E-03	

Tables 2, 3 show results of the typical radionuclide densities on the stainless steel (SS-316) structures and concretes.

Two kinds of data, one-year interval and ten years interval after 1000 shots operation, were shown. In these tables, data less than 1.0×10^{-14} (Bq/cc) were omitted. Since neutron flux through the big vertical port gives strong contribution to the floor concrete, result of the vertical port model is shown for floor concrete. Others are results of the horizontal port model.

From one to ten years after 1000 shots operation, main radionuclides contributed to the γ-ray dose are ^{55}Fe (half-life of 2.73 y) and ^{60}Co (5.27 y) for structures of stainless steel, and ^{40}K (1.28×10^9 y) and ^{55}Fe for concretes. However, almost of ^{40}K are natural nuclides existing in concrete.

5. Conclusions

In this paper, the 2-D neutron transport code DOT-3.5 and the induced radioactivity calculation code CINAC were employed to identify the radionuclides and to evaluate the dose rate during and after experimental series in LHD. Detailed analysis of activation properties and the dose rate for individual structural materials of LHD were carried out. Major results are as follows:

(1) In the SS-316 materials, dominant radionuclides just after shots are ^{56}Mn. Finally ^{60}Co becomes dominant.

(2) In concrete, dominant radionuclides just after shots are ^{24}Na. Although ^{40}K becomes dominant finally, it is almost natural nuclides.

(3) γ-ray dose rate decreases one order during weekend interval. This level of 10μSv/h is lower than the limitation for worker (20mSv/y) who works for 2000 hours per year.

References

[1] A. Iiyoshi, M. Fujiwara, O. Motojima, N. Ohyabu and K. Yamazaki, Fusion Technology **17**, 169 (1990).

[2] O. Motojima, K. Akaishi, M. Asao, K. Fujii *et al*., in Plasma Phys. and Contr. Nucl. Fus. Res 1990 (Proc. 13th Int. Conf. Washington DC, 1990), Vol.**3**, IAEA, Vienna, 513 (1990).

[3] A. Iiyoshi, A. Komori, A. Ejiri, M. Emoto *et al*., Nucl. Fusion **39**, 1245 (1999).

[4] M. Fujiwara, H. Yamada, A. Ejiri, M. Emoto *et al*., Nucl. Fusion **39**, 1659 (1999).

[5] H. Handa, K. Hayashi, Y. Ogawa, Y. Sakuma, H. Obayashi et al., Fusion Eng. Des. **17** 335 (1991).

[6] H. Handa, K. Hayashi, H. Yamanishi, Y. Sakuma, H. Kaneko et al, Fusion Eng. Des. **28** 515(1995).

[7] W.A. Rhoades, F.R. Mynatt, Tech. Memo. ORNL/TM-4280, Oak Ridge National Laboratory, Oak Ridge, TN, 1973.

[8] Fukumoto, J. Nucl. Sci. Technol., **23**, 97 (1986).

[9] K. Maki, K. Kosako, Y. Seki, H. Kawasaki, Rep. JAERI-M 91-072, Japan Atomic Energy Research Institute, June 1991.

Proceedings of ITC/ISHW2007

Transport Studies in HSX at 1 Tesla

J. Lore, F.S.B Anderson, J.M. Canik, W. Guttenfelder, K.M. Likin, J.N. Talmadge, K.Zhai

HSX Plasma Laboratory, University of Wisconsin

Initial results at B=1.0T at HSX demonstrate a reduction in particle and heat transport due to quasisymmetry, supporting the results of B=0.5T operations. Electron temperature and density profiles from Thomson scattering for several injected powers show a factor of 2-2.5 increase in the core temperature and a more peaked density profile for the quasi-helically symmetric configuration (QHS) as compared to the configuration where the symmetry is spoiled (Mirror). In a case where the temperature profiles are matched (requiring 2.3 times the injected power in Mirror) the core electron thermal diffusivity has been measured to be reduced by a factor of 3. The particle transport was analyzed using the neutral gas transport code DEGAS to obtain the source rate. These results indicate that for a given temperature gradient the particle flux, which is dominated by thermodiffusion, is smaller in QHS. Additional work is required on neoclassical calculations before conclusions on the effect of quasisymmetry on anomalous transport can be made.

Keywords: Neoclassical transport, quasisymmetry, DKES, DEGAS, HSX, Thermal transport

1. Introduction

The Helically Symmetric Experiment (HSX) is a mid-sized stellarator at the University of Wisconsin. The magnetic field of HSX can be varied from a quasi-helically symmetric configuration (QHS) to a configuration with the symmetry intentionally degraded by a set of toroidal field coils (Mirror). Aside from the magnetic spectrum, other properties such as the rotational transform, plasma volume and well depth are very similar. The change in the magnetic spectrum can be quantified by the effective ripple, which is increased in the core from 0.007 in QHS to 0.05 in Mirror with the largest change occurring in the core of the plasma. In this paper the effect of spoiling the symmetry on particle and electron heat transport will be discussed.

2. 0.5 Tesla Operation

A transport analysis at B=0.5T demonstrated that both the particle and electron heat transport were reduced in the QHS configuration [1]. For the same injected power the density profiles were peaked in QHS and hollow in Mirror due to a reduction in the thermodiffusive particle flux. It was also shown that 2.3 times the injected power is required in Mirror to match the temperature profiles between the configurations, and that for this matched case the electron thermal diffusivity is reduced in the core for the QHS configuration. The reduction in the core diffusivity was comparable to the calculated difference in the neoclassical diffusivities.

The transport analysis at B=0.5T was complicated by the presence of a suprathermal electron population driven by the 2nd harmonic X-Mode electron cyclotron heating. This suprathermal tail was observed by measurements from several diagnostics including the ECE system, hard X-ray detectors and a diamagnetic loop. Due to the contamination of the diamagnetic loop signal, the absorbed power was measured using many discharges while varying the Thomson scattering firing time around the ECH turnoff time. This limitation meant that very few configurations could be studied at B=0.5T.

3. 1.0 Tesla Operation

HSX has recently began regular operation at B=1.0T. At the higher field strength fundamental frequency O-Mode heating is used greatly reducing the drive of a suprathernal population. Fundamental frequency heating also allows for operation at higher densities, increasing the damping on a tail population. Measurements from the ECE system and the diamagnetic loop indicate that the suprathermal contamination has been greatly suppressed at B=1.0T allowing for a transport analysis to be performed at several injected powers in both QHS and Mirror.

4. Profiles from Thomson Scattering

A ten channel Thomson scattering system installed on HSX has been used to measure the electron density and temperature profiles in the QHS and Mirror configurations for four injected powers: 26, 44, 70 and 100kW.

The profiles shown in Figure 1 clearly show that for each injected power the central electron temperatures are 2-2.5 times greater in the QHS configuration. Also, for each injected power above 26kW the density profiles are more peaked for QHS. The greatest differences in the profiles are seen in the core, where the change in effective ripple is the largest and neoclassical transport is significant (see Section 7). These profiles indicate that transport properties change between the two configurations and that

author's e-mail: jlore@wisc.edu

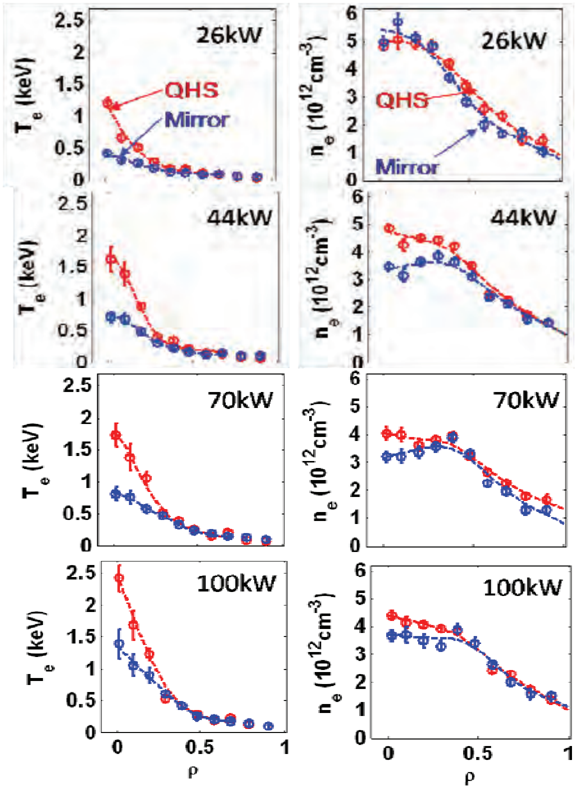

Fig.1 QHS and Mirror electron temperature (left) and density (right) profiles for several injected powers.

both particle and electron thermal transport are improved in the QHS configuration.

Due to the differences in the temperature gradients, the profiles cannot be exactly matched between the configurations. To minimize the difference in the profiles over the whole minor radius 2.3 times the injected power (1.8 times the absorbed power) is needed in the Mirror configuration, again demonstrating the improvement in electron thermal transport (Figure 2).

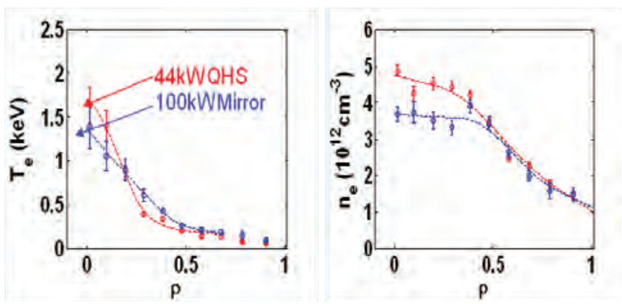

Fig.2 Profiles demonstrating that 2.3 times the injected power is required in Mirror to minimize the difference in the temperature profiles.

5. Electron Thermal Transport

To quantify the change in thermal transport seen in Figure 2 the electron thermal diffusivities were calculated. An expression for the diffusivity can be obtained by taking the flux surface average of the energy continuity equation (1).

$$\frac{d}{dt}\left(\frac{3}{2}n_e T_e\right) = -\nabla\cdot\mathbf{q} + p_{in} - p_{out} \qquad (1)$$

Where p_{in} and p_{out} are generic power sources and sinks. Assuming that the heat flux is purely diffusive, the effective electron thermal diffusivity can be written as seen in (2).

$$\chi_e = \frac{-\int_0^{\rho} V'(p_{in}-p_{out})d\rho'}{n_e\left\langle V'\frac{\partial T_e}{\partial\rho}|\nabla\rho|^2\right\rangle} \qquad (2)$$

Where $V'=dV/d\rho$ and $\nabla\rho$ account for the deviation of the geometry from a straight cylinder.

For the following calculations the power sinks such as radiation and ionization losses were ignored. These losses are small compared to the total injected power for HSX plasmas and were found to be similar between the configurations at B=0.5T [2].

A ray-tracing code is used to calculate the power deposition profiles based on the local temperature and density from the Thomson scattering profiles. The power deposition profiles are volume integrated and scaled to match the absorbed power calculated at ECH turnoff from the diamagnetic loop.

Figure 3 shows the effective thermal diffusivities for the profiles in Figure 2. The diffusivity in the core has been reduced by a factor of three due to quasi-symmetry.

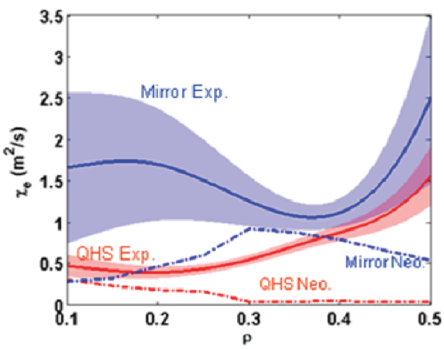

Fig.3 Experimental and neoclassical effective thermal diffusivities for the QHS and Mirror profiles in Figure 2.

6. Particle Transport

The density profiles seen in Figure 1 indicate that the particle transport changes in the core of the plasma between the two configurations. At B=0.5T it was found that the thermodiffusive component of the particle flux was reduced in the QHS configuration. At B=1.0T neoclassical calculations show that the thermodiffusive component is the dominant particle flux drive in both configurations (Figure 4).

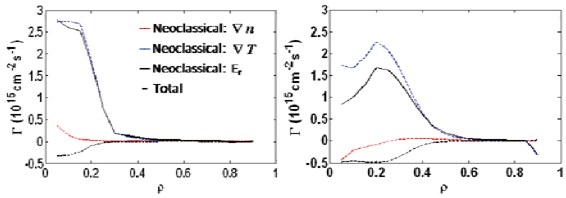

Fig.4 Components of the neoclassical particle flux for QHS (left) and Mirror (right). In each configuration the dominant component is thermodiffusion.

To calculate the experimental particle flux the particle source rate is required. To obtain the source rate the neutral transport code DEGAS was used [3]. DEGAS is a 3D Monte Carlo code that can calculate several quantities including, significantly, the H_α emission. The code is run for each set of Thomson scattering profiles on a fully 3D computational grid representing the HSX vacuum vessel. The results of the code are coupled to experiment using a suite of absolutely calibrated H_α detectors located on the machine.

For each set of profiles DEGAS is run for two cases. One of the cases is for the main fuelling source, a puff valve located on the vessel wall. DEGAS calculates the H_α emission to be localized toroidally for this case, and the results are then scaled to match the measured H_α emission from a poloidal array located at the puff valve. The other case is for a recycling source, located at the locations where the magnetic field lines just outside the separatrix intersect the vessel. The results from this case are scaled to match the measured emission from a toroidal array of detectors. The scaled results of the two cases are then added to obtain the total source rate.

The particle flux can be calculated by taking the flux surface average of the particle continuity equation (3) ins steady state yielding (4).

$$\frac{\partial n}{\partial t} + \nabla \cdot \Gamma = S \qquad (3)$$

$$\Gamma = \frac{1}{\langle \nabla \rho \rangle V'} \int_0^\rho V' S(\rho') d\rho' \qquad (4)$$

The dependence of the particle flux on the temperature gradient is plotted at ρ=0.3 in Figure 5. Figure 5 shows that for a given temperature gradient the particle flux is lower in the QHS configuration.

7. Neoclassical Calculations

The neoclassical particle and thermal transport were calculated using the DKES code to find the monoenergetic diffusion coefficients [4][5]. At each radial location the monoenergetic diffusion coefficients are numerically integrated over a Maxwellian by using a fit form to the DKES results to yield the neoclassical transport coefficient matrix. The particle and heat fluxes can then be calculated for a given radial electric field. The radial electric field is then determined by the ambipolarity constraint.

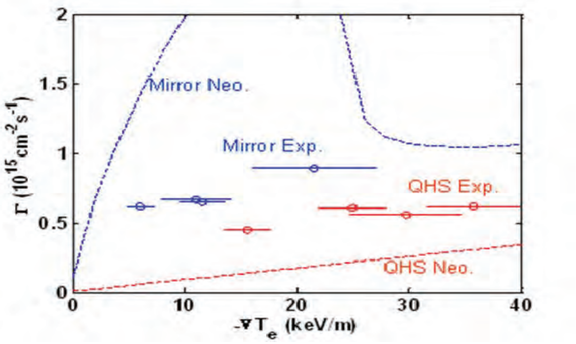

Fig.5 Dependence of the experimental and neoclassical particle flux on temperature gradient.

The neoclassical electron thermal diffusivity profiles for the temperature and density profiles in Figure 2 can be seen in Figure 3. The diffusivity is reduced in the core region due to the strong positive radial electric fields which greatly reduce the ion flux. Figure 3 shows that unlike at B=0.5T, the reduction in the neoclassical transport is not enough to account for the reduction in the experimental transport. This could indicate a reduction in anomalous transport due to quasi-symmetry, however further work on the neoclassical calculations is required as will be explained below.

In Figure 5 the neoclassical calculations also show that for a given temperature gradient the particle flux is expected to be smaller in the QHS configuration. However, the large difference in the neoclassical values is not seen in the experimental results.

As mentioned above, several additional effects and corrections can be applied to the neoclassical calculations, two of which will be briefly described here. The monoenergetic diffusion coefficients calculated by DKES were fit to an analytic form to allow a fast numerical integration over a Maxwellian. The analytic form however did not account for the effect of the poloidal resonance of the radial electric field on the ion flux. To correct for this the analytic form was modified to include this effect. This effect will in the future be more accurately accounted for by performing a very fine DKES scan and directly interpolating the results instead of fitting to an analytic form.

The above method has been applied to many stellarators[6], however DKES only considers pitch angle scattering which results in a collision operator that is not momentum conserving. Due to the symmetric nature of HSX the effect of momentum conservation may be important, as in a tokamak. To address this, the PENTA code [7], which uses a momentum conserving collision operator will be run and compared to the results obtained using DKES and ambipolarity.

8. Conclusion

Initial results at B=1.0T demonstrate a reduction in particle and electron thermal transport due to quasi-symmetry. Profiles from Thomson scattering clearly show an improvement in electron thermal transport, with 2.3 times the injected power required to match the electron temperature profiles. A large (factor of three) reduction in the core electron thermal diffusivity has also been measured. A particle transport analysis indicates that for a given temperature gradient the particle flux is reduced in the QHS configuration. Finally, neoclassical calculations suggest a reduction in anomalous transport in the QHS configuration, but further work is required to confirm this.

References

[1] J.M. Canik *et al*., Phys. Rev. Letters **98**, 085002 (2007).
[2] J.M. Canik, Ph.D. Thesis, University of Wisconsin, Madison, 2007.
[3] D. Heifetz *et al*., J. Comp. Phys. **46**, 309 (1982).
[4] S.P. Hirshman *et al*., Phys. Fluids **29**, 2951 (1986).
[5] W.I. van Rij and S.P. Hirshman, Phys. Fluids B **1**, 563 (1989).
[6] C.D. Beidler *et al*., Proceedings of the 14^{th} ISW, Greifswald, Germany, Sept. 29-Oct. 1, 2003.
[7] D.A. Spong, Phys. Plasmas **12**, 056114 (2005).

Design Study on Plasma-Loaded Cyclotron Resonance Maser Utilizing TPD-II Machine in NIFS

Kazuo MINAMI and Masaharu SUGITO[a)]

Tokyo Denki University, Chiyoda-Ku, Tokyo, 101-8457 Japan
[a] National Institute for Fusion Science, 322-6 Oroshi-cho Toki 509-5292 Japan
(Received 30, October 2007/ Accepted)

Design study of an experiment for plasma-loaded cyclotron resonance maser (CRM) utilizing TPD-II Machine at NIFS, Japan is described. We derive and analyze numerically an exact linear dispersion relation of radiation from a large orbit electron beam, and found that the relation includes two principles of cyclotron emission with oscillation frequencies above and below the relativistic electron cyclotron frequency. The former is conventional CRM instability, and the latter is named Cherenkov instability in the azimuthal direction (CIAD). In this study, the existence of CIAD is tried to verify experimentally. For plasma density $n > 1.5 \times 10^{11}$ cm^{-3}, the CRM instability may be suppressed and the CIAD may take turn.

Keywords: Cavity, Cherenkov instability in azimuthal direction, cyclotron resonance maser, fast wave, gyrotron, negative absorption, microwave, slow wave, TPD-II, wiggler.

1. Introduction

The principle of gyrotrons, high-power millimeter microwave sources indispensable for fusion research, is believed cyclotron resonance maser (CRM) instability [1-4]. The CRM was verified in an experiment in which negative absorption was observed for $\omega > \tilde{\Omega}$ [2]. Here, ω and $\tilde{\Omega} = eB_0/\gamma_0 m$ are, respectively, oscillation angular frequency and relativistic electron cyclotron frequency.

However, all the existing linear dispersion relations of CRM instability [3, 4] include unphysical (numerical) modes unstable at infinite values of axial wavenumber k_z in slow wave region, $\omega / k_z < c$, that can never be observed experimentally. To overcome the difficulty, we derive and analyze numerically exact linear dispersion relations of CRM for a large orbit (LO, hereafter) electron beam, for the first time in the history of the CRM research [5-7]. The conventional unphysical modes are replaced by stable modes near the fast cyclotron mode. Here, LO means that all the electrons have an identical location of guiding center on the center axis of waveguide.

Our exact dispersion relations [5-7] include two principles of cyclotron emission with oscillation frequencies above and below the branch of relativistic fast electron cyclotron wave $\omega = \tilde{\Omega} + V_z k_z$. The former is well-known CRM instability $(\omega > \tilde{\Omega})$, and the latter $(\omega < \tilde{\Omega})$ is named Cherenkov instability in the azimuthal direction (CIAD). The reason why the CIAD has not been included in the existing dispersion relations is that the boundary conditions with inevitable finite Larmor radius effect at beam-vacuum interface were not analyzed correctly.

It should be emphasized, however, that the CIAD we found remains only a proposal of possible cause of cyclotron emission, until its physical existence is verified experimentally. To verify the CIAD, we try to extend the CRM experiment in vacuum made by Hirshfield and Wachtel [2] to a plasma environment.

We design and fabricate a plasma-loaded CRM in the TPD-II Machine at National Institute for Fusion Science (NIFS), Japan, utilizing as beam source. With increase in density of plasma in TPD-II, the CRM instability may be suppressed and the CIAD may take turn. In other words, frequency of negative absorption observed in vacuum [2] may change from above to below $\tilde{\Omega}$ with increase in the beam density in the cavity such that $n > 1.5 \times 10^{11}$ cm^{-3}.

2. Theoretical Study on CRM Instability and CIAD

The CRM instability [1, 2] has been believed to be caused by the faster branch $\omega > \tilde{\Omega} + V_z k_z$ of the fast cyclotron wave $\omega = \tilde{\Omega} + V_z k_z$. It must be emphasized, however, that all the existing linear dispersion relations [3, 4] of the CRM instability include unphysical branches unstable at infinite values of axial wavenumber k_z. Gyrotron researchers have trusted that the growth rate near $k_z = 0$ was still CRM instability. The fact is as follows: Their physical explanation [3, Fig. 1] of CRM instability was correct, but their relation [3, Eq. 1] of CRM was entirely incorrect. Both of them have nothing to do with each other. In order to understand CRM instability physically, one must take into account the logical presence of CIAD that is unavoidable in general whenever a high density beam has a boundary.

We consider a circular waveguide of radius r_{cav} including concentric LO infinitely thin thickness beam. If the beam is neutralized by cold ions, no radial motion of the gyrating electrons is allowed, and they must stay on the original LO circle at any moment. The derivation of our exact dispersion relation for infinitely thin thickness annular beam is described in [5]. Somewhat surprisingly, infinitely thin annular beam does not exhibit CRM instability, but CIAD is obtained. On the other hand, when all the non-relativistic terms in the surface current density are dropped, without legitimacy through approximation $c \to 0$, to exclude the nonrelativistic effect, we obtain the relation identical to conventional linear dispersion relations of CRM obtained by Sprangle and Drobot [3, Eq. 1], and by Chu and Hirshfield [4, Eq. 8] that include unphysical branches in the limit of wavenumber $k_z \to \pm\infty$. These classical relations were still understood to be correct, because the obtained branch of CRM instability with $\omega > \tilde{\Omega}$ at k_z=0 [3, Fig. 1] was qualitatively identical to the experimental fact $\omega > \tilde{\Omega}$ [2, Fig. 2(a)]. However, this superficial coincidence cannot justify to ignore the presence of unphysical branches in their dispersion relations. The unphysical branches are the evidence of inadequate derivation of the linear dispersion relations of CRM. Such unphysical instabilities flat for k_z are observed often in numerical analyses, but have never been observed experimentally. A correct dispersion relation that includes both CIAD and CRM instability is obtained, when one analyzes a finite-thickness LO annular beam that allows radial displacement of the electrons. Our exact dispersion relations [5, 7] are exceptions that have overcome the difficulty in a particular case of LO electron beams for the first time in physics of gyrotrons.

3. Design Study of Plasma-Loaded CRM in TPD-II Machine

For experimental verification of the CIAD, a design and fabrication of plasma-loaded CRM have been conducted. Schematic view of the TPD-II Machine and our constructed apparatus are shown in Fig. 1. In (a), total view of the apparatus is depicted. Plasma is produced by DC helium gas discharge between a hot cathode and grounded anode in TPD-II at the right-side.

(a)

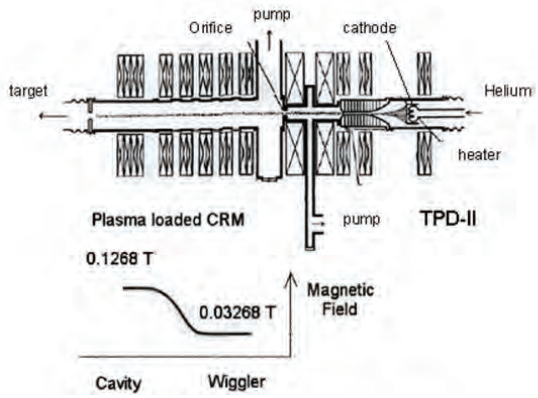

(b)

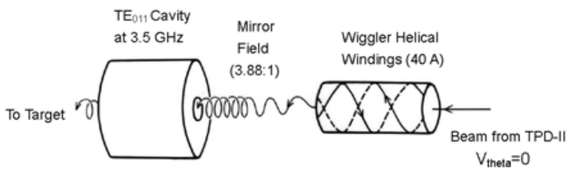

(c)

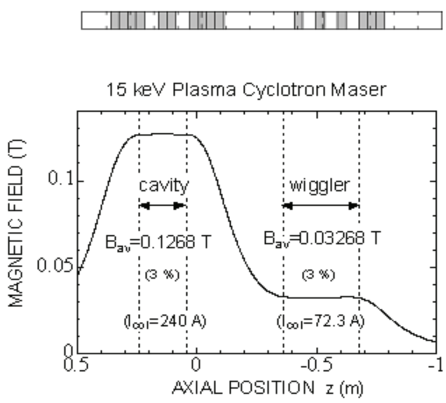

Fig. 1 Plasma-loaded CRM installed inside the TPD-II Machine, NIFS, Japan. (a) Total view. (b) Principle of plasma-loaded CRM. (c) Distribution of axial magnetic field in the wiggler and the cavity. Bar code shows the location of 16 coils.

Plasma is emitted from a small orifice in the anode into left-side plasma container in solenoid coils where the plasma-loaded CRM is located. This portion is evacuated by high speed pumps to

-

remove neutral gases for attaining fully ionized plasma. The plasma column has high density up to 10^{14} cm^{-3}, temperature of a few eV and beam diameter 10 mm.

To detect negative absorption caused by CRM instability or CIAD, a large number of gyrations of the beam inside the cavity are required. The principle of the plasma-loaded CRM is schematically shown in Fig. 1(b). It consists roughly of two different portions: (i) A pair of helical windings called wiggler in this paper for creating transverse velocity in the beam at the right-hand side, and (ii) the TE_{011} mode cylindrical cavity at the left-hand side. The latter is connected to microwave circuits for detecting negative absorption of incident low power microwave near 3.45 GHz. An electron beam from TPD-II Machine is incident from the right-hand side. The beam, however, has no azimuthal velocity component, namely $V_\theta \simeq 0$.

In order to create a large V_θ for gyrations, the beam is introduced on the axis of the wiggler that produces a helical circularly polarized static magnetic field b_t of the order of 10^{-3} (T) near the axis. Here, b_t can be quite small, because it does not give any energy to the beam. In Fig. 1(c), calculated distribution of axial magnetic field on the axis of the plasma-loaded CRM is shown.

If the pitch length λ_w of the right-hand circularly polarized DC magnetic field b_t generated by the wiggler is equal to axial pitch length $2\pi V_z/\tilde{\Omega}$, the electrons are accelerated in azimuthal direction secularly by the Lorentz force $-e\vec{v}_z \times \vec{b}_t$ at the expense of their axial velocity. The designed wiggler is a pair of four turn bifilar conductors with pitch length $\lambda_w = 8.0$ cm, radius $a = 1.775$ cm and total length $L = 32$ cm. The pitch factor $\alpha = V_\theta / V_z \simeq 0.65$ will be obtained at the exit of the wiggler.

The obtained α can be increased further, by transmitting the beam before the incidence on the cavity through the mirror field shown in Fig. 1(c) from B_s=0.03268 T at the wiggler to another axial field B_0=0.1268 T at the cylindrical cavity. The mirror ratio is B_0/B_s=3.88, and α =1.28 will be obtained that enables many gyrations in the cavity.

In Fig. 2, expected electron properties through wiggler and mirror magnetic field are demonstrated by trajectory tracking in order to show an example that helical field b_t enhances perpendicular pitch $\alpha = V_\theta / V_z$. In (a) and (b), the profiles of axial and perpendicular magnetic fields, B_z, B_r and B_θ on the axis, are calculated. In (b), B_r and B_θ with and without b_t=0.0008 T (I_{tot}=40 A) are depicted. In (c), an example of radial position of electron trajectories is followed from z=-1.1 to 0.3 m for both cases b_t=0.0008 T and b_t=0. In (d), changes in perpendicular pitch $\alpha = V_\theta / V_z$ are depicted for both b_t. It is clearly shown in (c) and (d) that the presence of wiggler magnetic field b_t=0.0008 T enhances significantly the spiral motion.

The frequency of incident microwave on the fabricated cylindrical stainless-steel cavity works at TE_{011} mode near 3.5 GHz. Inner diameter of the TE_{011} cavity is 0.1083 m, and the length is varied from 0.17 to 0.21 m by the adjustable shorting disk. Figure 3 shows the calculated curves of positive and negative absorptions as a function of axial magnetic field B_0. The frequency of incident microwave is adjusted at the resonance in empty cavity to observe the minimum $|R_{\max}|^2$. The vertical axis $|R|^2$ is assumed to be proportional to attenuation constant α for round-trip of microwave in the cavity as [1, 2]:

$$\alpha = \frac{\pi G}{Q_e}\left(1 + \frac{2py}{1+y^2}\right), y = \frac{\omega - \omega_1}{2B_1},$$

where ω_1, B_1 and p are given numerical constants to fit the positive and negative absorptions. In Fig. 3, coupling factor s=0.15 and other parameters shown in the figure are assumed. Negative absorption (in fact, decreased positive absorption) arises for $|p|>1$ [1]. The resonant curve of the CRM instability for p=1.5 is depicted by solid curve, whereas the case of the CIAD for p=-1.5 is shown by dashed curve. Negative absorption of the CRM instability and the CIAD could be observed, respectively, for $\omega > \tilde{\Omega}$ and $\omega < \tilde{\Omega}$ as shown in Fig. 3. In other words, the CRM and the CIAD are expected for low-field and high-field sides of $\omega = \tilde{\Omega}$ that corresponds to the axial magnetic field $B_0 = 0.3106$ T for our 15 keV beam.

According as beam current increases, the region of the negative absorption is expected to move from left-hand side (solid curve) to right-hand side (dashed curve) of $B_0 = 0.1306$ T. Or, probably we may observe both negative absorptions at the same time for the incidence of high density beam such as $n > 1.5\times 10^{11}$ cm^{-3}, where $n = 1.5\times 10^{11}$ cm^{-3} corresponds to $\omega = \tilde{\Omega} = \omega_b$.

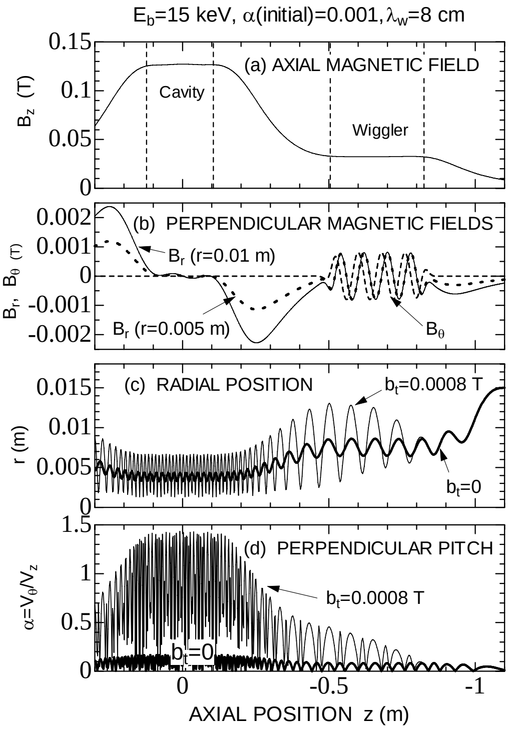

Fig. 2 Electron beam properties obtained by trajectory tracking. Helical field b_t enhances significantly perpendicular pitch $\alpha = V_\theta / V_z$.

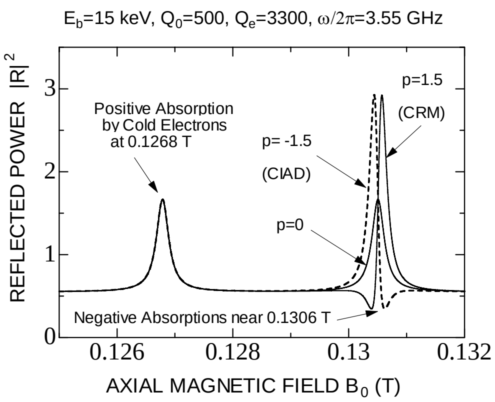

Fig. 3 Curves of absorption expected for CRM (solid curve) and CIAD (dashed curve).

The physical meaning of $|p| > 1.0$ for negative absorption is physically analogous to $N(V_\theta / c)^2 > 1$ that many gyrations in the cavity are required for detecting the resonant curves correctly, where $N \gg 1$ is number of gyrations in the cavity.

Diagram of constructed microwave interferometer including the TE_{011} plasma cavity is shown in Fig. 4. In near future, the measurements of negative absorption caused by the CRM instability and the CIAD will be conducted.

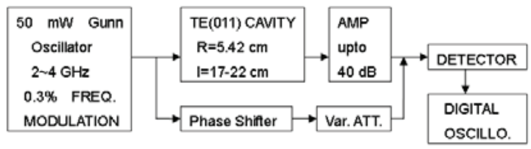

Fig. 4 Constructed microwave interferometer circuits including fabricated TE_{011} mode cylindrical two-port cavity with resonant frequency near 3.45 GHz.

4. Discussion and Conclusion

Currently, it may not be a fashionable subject of research to discuss which oscillation frequency $\omega > \tilde{\Omega}$ or $\omega < \tilde{\Omega}$ is observed in real gyrotrons. This is partly because ω is almost a fixed quantity given by the sizes of a cavity. Moreover, the distinction between $\omega > \tilde{\Omega}$ and $\omega < \tilde{\Omega}$ is practically difficult from experimental point of view, because $\tilde{\Omega}$ is a quantity spatially non-uniform, whereas ω can be measured very precisely. The difference between ω and $\tilde{\Omega}$ can be observed, only when a device to fit the particular purpose of distinction between CRM and CIAD were carefully designed [2].

The CIAD and the CRM instability are probably coexisting mechanisms of cyclotron emission from various gyro-devices incliding the gyrotrons. The CRM instability ($\omega > \tilde{\Omega}$) may not be the exclusive principle of gyrotron oscillation, because there has been no experimental verification to be $\omega > \tilde{\Omega}$ in gyrotrons. It is quite important to distinguish between $\omega > \tilde{\Omega}$ and $\omega < \tilde{\Omega}$ in cyclotron emissions in plasma physics and in gyrotron research, since physical reasons are different. It should be emphasized that, sometimes, physics requires a stringent accuracy for better understandings, even though such accuracy may not be required from engineering point of view.

The gyrotron community over the world is partly spoiled by the defect of unphysical solutions [3,4]. We regret that fundamental understandings of physics of gyrotrons are not very firm yet, although there exist huge amount of research reports for technical and hardware developments. For decades, many of students in universities over the world are left to study the incorrect theory of CRM.

Our constrained gyration model and the resultant CIAD [5] remains only a proposal at this moment, until the physical existence is verified experimentally. It is the purpose of our experimental program to verify a physical cause of cyclotron emission that has not been known up to date. In our plasma-loaded CRM, negative absorption due to the CRM instability may be suppressed in high-density beam such as $\omega_b^2 \gg \tilde{\Omega}^2$, namely density $n > 1.5 \times 10^{11}$ cm^{-3}, and the CIAD may take turn. In this experimental program, we try to observe the new principle of cyclotron emission different from the CRM instability. The present experimental study contributes to a deeper understanding and a widened future prospect in gyrotron research.

This work is carried out in a collaborative research program NIFS04KQHH002, under the supervision of Professor Kuninori Sato, NIFS, Japan.

[1] J. Schneider, Phys. Rev. Lett. **2**, 504 (1959).
[2] J. L. Hirshfield and J. M. Wachtel, Phys. Rev. Lett. **12**, 533 (1964).
[3] P. Sprangle, and A. T. Drobot, IEEE Trans. MTT **25**, 528 (1977).
[4] K. R. Chu and J. L. Hirshfield, Phys. Fluids **21**, 461 (1978).
[5] Y. Choyal, T. Watanabe and K. Minami, IEEE Trans Plasma Sci. **32**, 1298 (2004).
[6] K. Minami, Y. Choyal, and T. Watanabe, J. Plasma Phys. **73**, 523 (2007).
[7] K. Minami, Research Report-NIFS No. **880** (August 2007).

P1-024

Proceedings of ITC/ISHW2007

The experimental effect of encouraging transparent-cathode in relativistic magnetron with "ETIGO-IV"

Hoshiyuki Yamazaki and Weihua Jiang

Extreme Energy-Density Research Institute

Nagaoka University of Technology, Nagaoka, Niigata 940-2188, Japan

The Magnetron is one of the efficiency high-power microwave source, although the energy conversion efficiency decreases with pulsed-power relativistic electron beam. We study the capability to increase energy conversion efficiency of Relativistic Magnetron by using Transparent Cathode. The Transparent-Cathode consists of independent cathode strips. Each cathode strip caused azimuthal magnetic field, and the radial drift velocity of electrons are accelerated more than that of electron emitted from general cathode. It can make abbreviating start-up times. We study the relativistic Magnetron with “ETIGO IV” that is 400kV class repetitive pulsed-power generator. This pulse length is longer considering pulsed-power. In this work, we appear the effect of Transparent cathode compared with traditional cathode. The start-up time of magnetron with Transparent cathode is shorter than that with traditional cathode. The peak power and oscillation efficiency are unconfirmed. We feel strongly that Transparent cathode is encouraging method.

Keywords: high-power Microwaves, relativistic Magnetron, Transparent cathode, combined efficiency, rapid start-up, long pulse

1. Introduction

The Magnetrons are one of the most efficiency microwave source, so these are studied by for many years. Magnetrons come into use for radar, electrical power transmission, microwave oven and etc. The features of magnetron are high oscillation efficiency and comparatively low demand for external magnetic field [1-2]. And this means reduction of the device scale and weight are expected. And these are comparative excellence efficiency in the region of hi-power microwaves, although the operation frequency regions are within the lower microwave region by comparison other high-frequency generator (e.g. gyrotron). In general the efficiency of high-power microwaves is determined by momentary output energy and momentary input energy measured at the time which is fixed the same time at the peak oscillation. In these years, we consider the total efficiency: total input energy and total output energy at least [1]. I.e. enhanced combined efficiency is requested. Some recipes become a candidate to enhance magnetron oscillation efficiency: magnetic priming and cathode priming and anode priming [3-5], among them the Transparent-Cathode is concise and hopeful procedure [6-7]. The Transparent-Cathode consists of independent cathode strips, as against the conventional cathode which consists of a solid columnar cathode. Figure 1 (a) shows the model of Transparent Cathode. Each cathode strip caused azimuthal magnetic field, and the radial drift velocity of electrons are accelerated more than that of electron emitted from general cathode shown in Fig.1 (b). Additionally azimuthal electric field penetrates the cathode strips. The crossed field devices like Magnetron generate from the interaction between azimuthal electric motion and electromagnetic wave. So Transparent Cathode causes electrons rapid spreading, which means rapid start-up, and the penetrating electric field potentiates more efficiency interaction. Additionally the shorter start-up increases the interaction term in pulsed electron beam, and can enhance the combined efficiency.

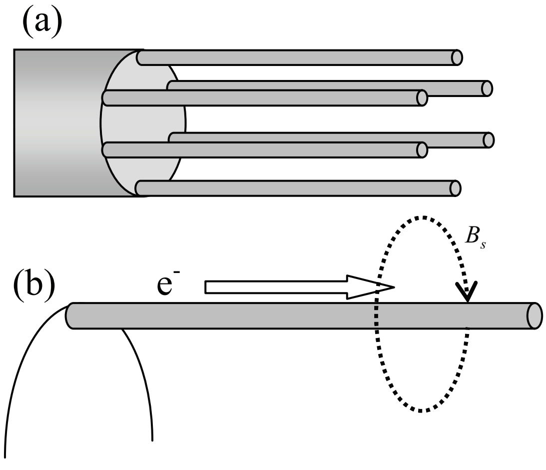

Fig. 1 The models of Transparent cathode
(a)The transparent cathode consists of independent cathode strips. (b)The magnetic effect of transparent cathode near the strip

author's e-mail: yamazaki@etigo.nagaokaut.ac.jp

It's hope that shorter start-up times and improve operation efficiency.

We aspire for the enhanced combined efficiency by amelioration of Magnetrons structure. We approach the enhanced efficiency through the way abbreviating the start-up time. In this work, we study the effect of Transparent cathode mainly for rapid start-up. The experimental setups are fed by ETIGO IV that is 400kV class repetitive pulsed-power generator.

2. The schematic of Magnetron and Transparent Cathode

The cross section diagram of Magnetron shows in Figure 2. The magnetron comprises the cylindrical anode enclosing coaxial cylindrical cathode. The broken lines within the conventional cylindrical cathode line, show the Transparent cathode. The anode has the spaces as resonator vans. The electrons are emitted by the central cathode are subjected axial magnetic field $\boldsymbol{B}_z$ and drift by Lorentz force. The drifting electrons interact in the space between the two electrodes with the characteristic mode from the structure of resonator vans. In the case of Magnetron with Transparent Cathode, the current flowing each cathode strips cause azimuthal magnetic field $\boldsymbol{B}_s$.

$$B_s = \frac{\mu_0 I}{2\pi r_s}$$

And the radial drift velocity of electrons v_e are shown

$$v_e = \frac{E_0 B_z}{B_z^2 + B_s^2}$$

The electrons are accelerated more than that of electron emitted from traditional cathode. So Transparent Cathode causes electrons rapid spreading, and rapid start-up.

The characteristic dimensions are designed from type A6 Magnetron, which has studied for relativistic magnetrons [3]. The parameter of A6 magnetron is the radius of cathode r_c=15.8 mm, radius of anode r_a=21.1 mm, the gap of resonator vanes on the side of anode $\psi = 20°$, and the depth of resonator vans r_v=41.1 mm. The number of resonator vans is M=6. The external radius of transparent cathode is same to the radius of conventional magnetron cathode r_c. And the number of strips is same to that of resonator vans M. This number is reported developed by numerical simulations [6-8].

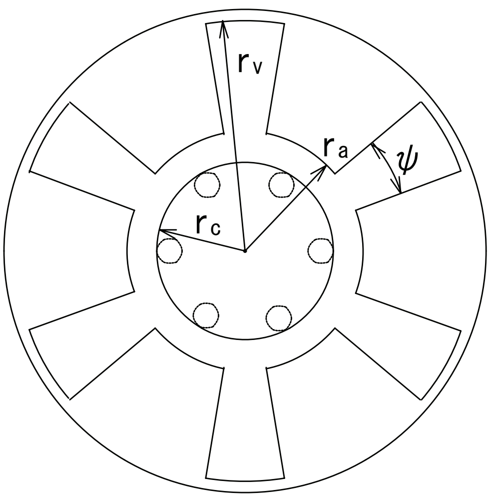

Fig. 2 The schematic of magnetron

3. Experimental Setup

Figure 3 shows the features of Magnetron operations region. These lines show the Hull cutoff and Buneman-Hartree resonance conditions [9] for A6 Magnetron. The power source is repetitive pulsed-power generator called "ETIGO IV" [10], which is capable of delivering, to a matched load, an output pulse of 400 kV in voltage, 13 kA in current, and 130 ns in pulse width, at the repetition rate of 1 Hz. The circle dots and full line are point out Hull criterion. In general, the Hartree voltage is less than the Hall cutoff voltage magnetic insulation. Other dots and lines show Hartree voltage for several oscillation modes. We assume the main operation modes are fundamental π-mode (2.34GHz) or high order 2π-mode (4.6GHz). The Hartree voltage is corresponds to the breakdown voltage of magnetron in the presence of a rotating perturbation field. The Hartree voltage causes the perturbation facilitates the motion of electrons across the cathode-anode gap. The potential energy of the electron efficiently interacts with and provides the electromagnetic wave. On this device, A6 relativistic magnetron requires external magnetic field about 0.5 T to 1.0 T.

The experimental setup consists of stainless steel (SUS304) vacuum chamber encrusted by external magnets. The external magnets architected at Helmholtz coil. These magnets form constant axial magnetic field covering the Magnetron resonator. It can be controlled by outer power source and can form maximal 1.0 T magnetic filed. Anode blocks made from aluminum, and cathode

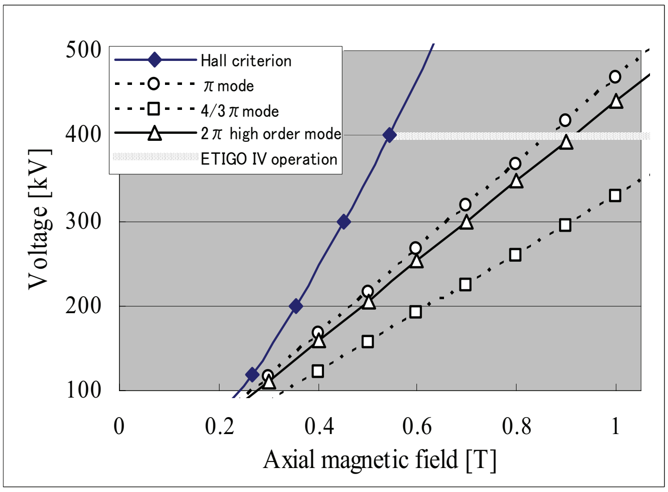

Fig. 3 The features of Magnetron operations region

made from carbon graphite. Graphite as cathode has the advantage of forming good filed emission characteristics and small excitation delays [11] and having resistance to discharge more than aluminum. The axial length of body is 125 mm, which is decided by the wave length of the operation electromagnetic wave 2.34 GHz, and avert discharge from converging electric filed. The stick of Transparent cathode made from graphite shapes like rounded trapezium by manufactural problem. Graphite is breakable.

4. Experimental result

Our magnetrons ware run at constant diode input power, which is maximum voltage not to discharge. Figure 4 shows the voltage and current characteristics of our magnetron as a function of external axial magnetic field $\boldsymbol{B}_z$. Full dots show voltage values as a function of magnetic field, and hollow dots show current values as a function of magnetic field. The diamond dots indicate measured value with traditional cathode, and the triangle dots indicate measured value with transparent cathode. The voltage rises slightly and the current falls fairly monotonically, results which are typical of conventional magnetrons [3]. The transparent cathode shows high resistance than traditional cathode. And in the lower magnetic filed the voltage falls andante, so current not increase rapidly near the Hall cutoff magnetic field. On the other hand, the current with transparent cathode increase by the plasma forming might happen at the high magnetic field. This is caused by pulse time increase as high impedance. Figure 5 shows diode voltage, diode current and microwave pulse from oscilloscope. The waveforms from the magnetron with transparent cathode draw full lines, and the waveforms from the magnetron with traditional cathode draw dashed lines. And heavy lines indicate diode voltage, normal lines indicate diode current. The top lines shows output microwave pulses measured at the point, which distance 2.5 m from output window on central axis. The operation regions are assumed about S-band to C-band: mainly 2 GHz to 5 GHz, we use horn antenna admitting nearly S-band: it assuring calibration coverage 2.45 GHz to 4.6 GHz. The microwave pulse lengths of the magnetron with "ETIGO

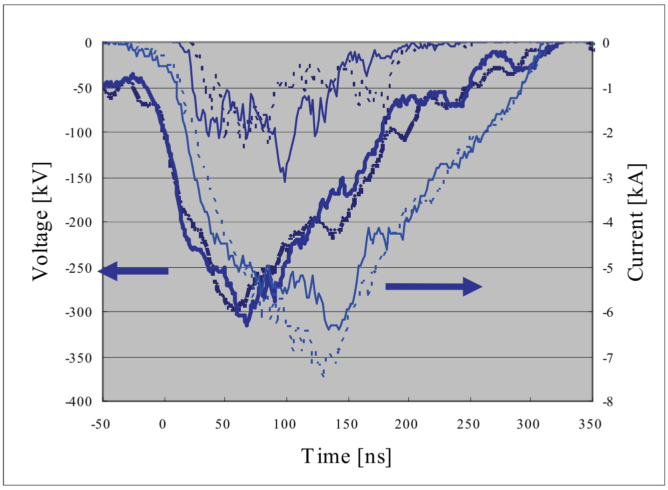

Fig.5 Voltage, current and microwave pulse shapes at 0.76 T. The full lines show the operation with transparent cathode. The dashed lines show the operation with traditional cathode. The heavy lines indicate diode voltage. The normal lines indicate diode current. The top lines indicate microwave pulse shapes.

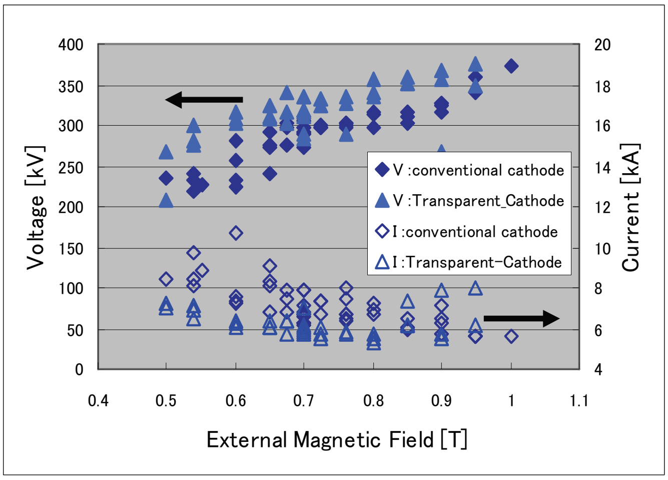

Fig.4 The voltage-current characteristics of the magnetron as a function of magnetic field. The diamond dots denote measured values with traditional cathode. The triangle dots denote measured values with Transparent Cathode.

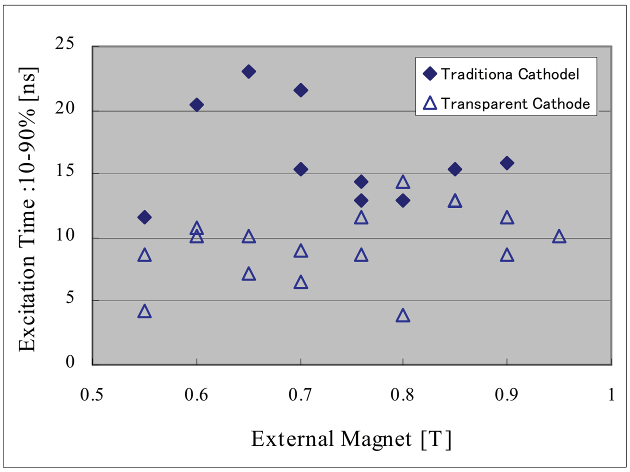

Fig.6 The Excitation time until first peak: 10% to 90% time. The diamond dots denote the time with traditional cathode. The triangle dots denote the time with Transparent Cathode.

IV" are more than 100 ns. And the pulse width (half to half) of voltage and current are respectively about 150 ns and 160 ns. These times go way beyond the time requiring static state magnetron operation. Our experimental setups may research steady oscillation region for relativistic magnetron operation, although the power source is pulsed power device. The peak voltage is less than rated capacity, because the plasma sheath is formed at circumferential cathode, which can not be analyzed at particle in cell simulation. The current with transparent cathode instantaneously increases, as the plasma and electron sheath forming decrease diode impedance. This problem stands out in proportion as increasing external magnetic field, as the electrons are constrained strongly and electron sheath thicken. These problems will come to a settlement by re-designing cathode. It would increase diode voltage and stabilize pulse forms and enhanced pulse width that the cathode is re-designed considering the plasma sheath. The comparing the output microwave form of Transparent cathode to that of traditional cathode, the start-up times are rapidly on an average. The peak value itself is determined by mode stability, which is dependent on situation of electron emission. The oscillation modes are approximate shown in Fig.3, and the diode voltage fluctuates. So the oscillation mode fluctuates too as affairs stand. The excitation time until first peak: 10% to 90% time are shown in Figure 6. The diamond dots denote the time with traditional cathode. The triangle dots denote the time with Transparent Cathode. The oscillation mode turn as external magnetic filed, consequently the start-up time turn as external magnetic field. On the average, the start-up times of oscillation with Transparent cathode are rapidly than that with traditional cathode. Whereas the rapid start-up bind the oscillation mode when the voltage is rising. This mode is not most efficient resonance mode not infrequently. The peak power and enhanced efficiency need high accuracy mode control.

5. Summary and Discussion

The transparent cathode makes high impedance diode at the same external diameter cathode. Especially in the lower magnetic filed nearly Hull cutoff the magnetron with transparent cathode is stabilized. The relativistic magnetron with Transparent cathode may rapid start-up than that with traditional cathode. Our experimental setups may research on over to steady oscillation region for relativistic magnetron operation, using the pulsed power source. By the calibration and assortment of output microwave will discover the occasional oscillation modes, the momentary maximum output powers, total output powers, conventional (momentary) efficiency and total efficiency too.

References

[1] J. Benford and J. Swegle, "*High-Power Microwaves*(Artech House, Norwood, MA, 1992)

[2] S.H. Gold and G.S. Nusinovich, Rev. Sci. Instrum. **68**, 11, pp.3945-3974 (1997)

[3] A. Palevsky and G. Bekefi, Phys. Fluids. **22**, 5, pp.986-996 (1979)

[4] R.W. Lemke, T.C. Genoni and T.A. Spencer, Phys. Plasmas **6**, 2, pp.603-613 (1999)

[5] V. Bogdam, C. Jones, R.M. Gilgenbach, Y.Y. Lau, J.W. Luginsland, B.W. Hoff, M.White, N.M. Jordan, P. Pengvanich, Y. Hidaka and H.L. Bosman, IEEE Trans. plasma **33**, 1, pp.94-102 (2005)

[6] Michael C. Jones, V. Bogdom Neculaes, William M. White, Y.Y. Lau, Ronald M. Gilgenbach, John W. Luginsland, P. Pengvanich, N. M. Jordan, Y. Hidaka and Herman L. Bosman, IEEE transactions on electron devices **52**, pp.858-863 (2005)

[7] M. Fuks, A. Andreev, H. Bosman, S.Prasad, and E.Schamiloglu, Department of Electrical & Computer Engineering, University of New Mexico, USA (2006)

[8] M.C. Jones, V.B.Neculaes, Y.Y. Lau, R..M. Gilgenbach, W.M. White, B.W. Hoff and N.M. Jordan, Appl. Phys. Lett. **87**, 08151 (2005)

[9] R.V. Lovelace, T.F.T. Young, Phys. Fluids **28**, pp.2450-2452 (1985)

[10] A. Tokuchi, N. Ninomiya, W. Jiang and K. Yatsui, IEEE Trans. Plasma sci. **30,** 5, pp.1637-1641 (2002)

[11] R.K. Parker, R.E. Anderson, and C.V. Duncan, J. Appl. Phys. **45**, 2463 (1974)

Effects of H-mode transition on plasma flow characteristics in the helical divertor of the Uragan-3M torsatron

CHECHKIN Viktor V., GRIGOR'EVA Lyudmila I., SOROKOVOY Yegor L., SOROKOVOY Eduard L., BELETSKII Aleksej A., SLAVNYJ Aleksandr S., LAVRENOVICH Yurij S., VOLKOV Yevgenij D., BURCHENKO Pavel Ya., TSYBENKO Sergej A., LOZIN Aleksej V., KULAGA Anatolij Ye., KURILO Dmitrij V., MIRONOV Yurij K., ROMANOV Vladislav S.

Institute of Plasma Physics, National Science Center
"Kharkov Institute of Physics and Technology", Kharkov 61108, Ukraine

In the l=3/m=9 Uragan-3M (U-3M) torsatron with an open helical divertor and RF produced and heated plasmas, effects of H-mode transition on (i) diverted plasma flow (DPF) magnitude in the spacings between the helical coils and (ii) fast ion escape into DPF are studied by using arrays of plane Langmuir probes and electrostatic ion energy analyzers. Data have been obtained on how the amount and energy of lost ions change with transition in several field periods. A strong toroidal nonuniformity in ion loss has been observed. The island structure of the real U-3M magnetic configuration and the locality of RF power injection into the plasma are considered as possible reasons for such nonuniformity.

Key words: torsatron, divertor, H-mode, fast ions, ion loss, island structure

1. Introduction

In the Uragan-3M (U-3M) torsatron (Fig. 1,2) with an open natural helical divertor the plasma is RF produced and heated (multi-mode Alfven resonance: $\omega \lesssim \omega_{ci}(0)$). With this, a two-temperature ion energy distribution arises with a tail of suprathermal ions (Fig. 3) [1]. The faster ions (higher-temperature and suprathermal ones) can undergo the neoclassical transport $1/\nu$.

One more U-3M feature is a spontaneous transition to an H-like mode (Fig. 4) where an edge $E_r \times B$ velocity shear occurs (or is enhanced), resulting in suppression of turbulence and turbulence-induced anomalous transport. It is supposed [2], that the fast ion orbit loss is responsible for $E_r \times B$ shear formation [3]. Also, the specific for stellarators drift-orbit transport flux driven by helically trapped ions [4] can contribute to this process.

We study effects of H-transition on (i) diverted plasma flow (DPF) magnitude in the spacings between the helical coils and (ii) fast ion escape into DPF. Data have been obtained on how the amount and energy of lost ions change with transition in several field periods. A strong toroidal nonuniformity in ion loss has been observed. The island structure of the real U-3M magnetic configuration and the locality of RF power injection into the plasma are considered as possible reasons for such nonuniformity.

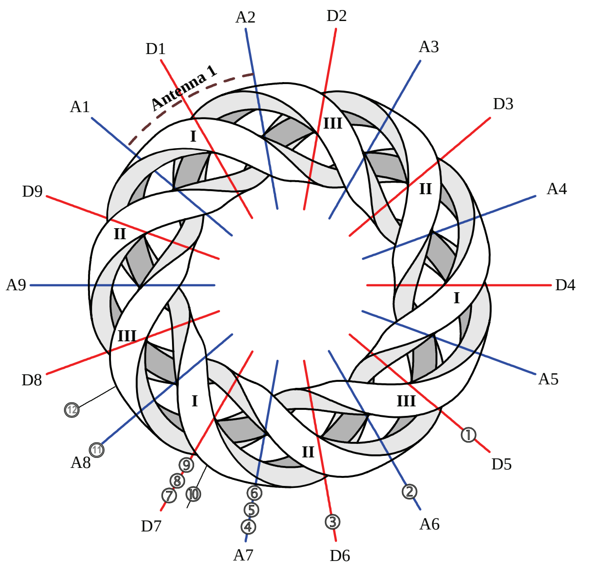

Fig. 1. *Helical coils I, II, III; indicated are symmetric poloidal cross-sections A and D in all field periods 1-9 (A1, D1, A2, D2,..., A9, D9).*
1 – array of electrostatic ion energy analyzers (IEAs) in the top spacing D5 (D5 top)
2 – IEAs in A6 top
3 – IEAs in D6 top
4,5,6 – divertor electric probe arrays in A7 (see Fig. 2)
7,8,9 – divertor electric probe arrays in D7 (see Fig. 2)
10 – IEAs near D7 top
11 – IEAs in A8 top
12 – CXN energy analyzer detecting neutrals from the spacing between A8 top and D8 top

2. Experimental conditions

Main parameters of U-3M:

$l = 3$, $m = 9$, $R = 1$ m; $\bar{a} \approx 0.12$ m

$\iota(\bar{a}) \approx 0.3$; $B_\phi = 0.72$ T

$P_{RF} \lesssim 0.2$ MW, $\bar{n}_e \sim 10^{18}$ m^{-3}

$T_e(0) \sim 500$ eV

author's e-mail:chechkin@ipp.kharkov.ua

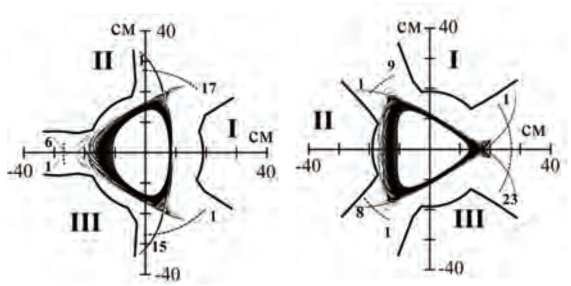

Fig. 2. *Disposition of divertor electric probe arrays in the poloidal cross-sections A7 (left) and D7 (right).*

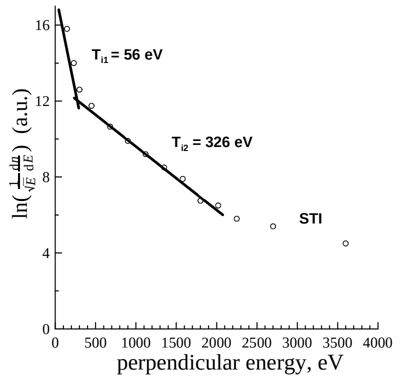

Fig. 3. *CXN energy spectrum corresponds to two-temperature ion energy distribution + supratermal tail.*

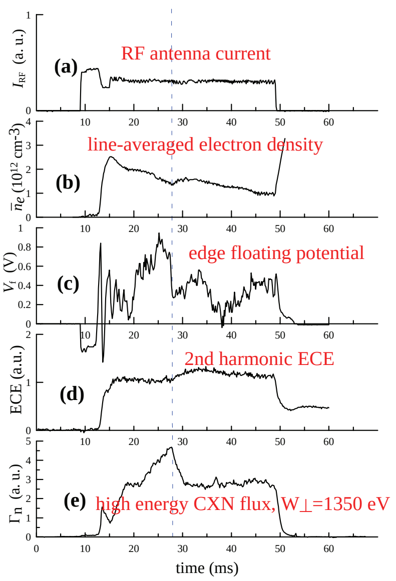

Fig. 4. *Some indications of H-mode transition*

3. H-mode-induced DPF changes (field period 7)

The H-transition results in substantial changes in the DPF magnitude estimated as maximum ion saturation current I_s in the corresponding spacing between the helical coils (Fig. 5).

<u>In A7</u> (Fig. 5, left column) I_s decreases in all spacings while $\bar{n}_e$ increases, evidencing a reduction of particle loss in this poloidal cross-section. The vertical DPF asymmetry decreases with transition: its degree is $\alpha \approx 3$ before transition and drops to $\alpha \approx 2$ after transition. This means that the fast ion outflow is also reduced [5,6] as a part of the total particle loss reduction.

<u>In D7</u> (Fig. 5, right column) DPF increases on the ion ∇B drift side (top spacing, (b)) and outboard spacing over the midplane (d)), while it decreases in the bottom spacing (c) and in the outboard spacing under the midplane (e), i.e., on the electron drift side.

The DPF vertical asymmetry in D7 increases after the transition: from $\alpha \approx 5$ to $\alpha \approx 9$ for the top and bottom spacings and from $\alpha \approx 3$ to $\alpha \approx 4$ for the top and bottom legs in the outboard spacing. This indicates a rise of fast ion loss in this cross-section after the transition [5, 6].

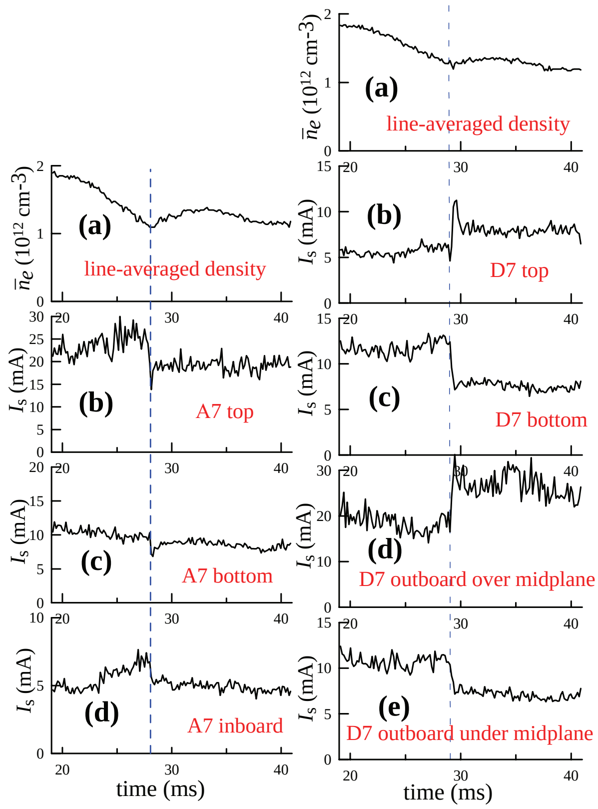

Fig. 5. *H-transition-induced changes in DPF magnitude in cross-sections A7 (left column) and D7 (right column)*

4 . Energies of ions outflowing to DPF

<u>Cross-section A8, top spacing.</u>

It follows from Fig. 6 that the fast ion loss roughly follows fast ion content in the confinement volume (represented by Γ_n) and seems not to rise with transition.

The same is in A6 top.

The energy of ions escaping to DPF on the ion ∇B drift side in A8 top (Fig. 7) and A6 top do not change with transition and are minimum compared with D5 top, D6 top, D7 top (see below).

<u>Cross-section D5, top spacing</u>

Similar to A8 (and A6), the fast ion loss in D5 top roughly follows Γ_n and seems not to increase with transition (Fig. 8). The energies of ions escaping to DPF on the ion ∇B drift side considerably exceed those in A8

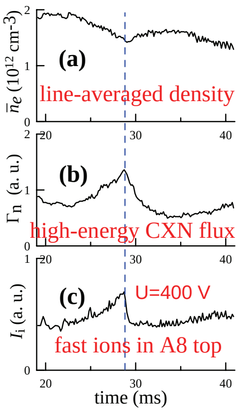

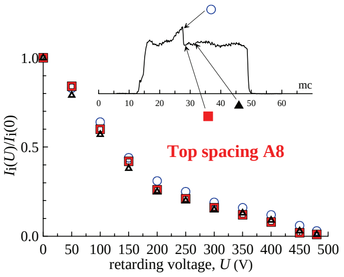

↑ ***Fig. 7.*** *Normalized ion current $I_i(U)/I_i(0)$ to the collector of IEA versus retarding voltage U in the top spacing A8.*

↑ ***Fig. 6.*** *Time evolution of density $\bar{n}_e$ (a), high energy CXN flux Γ_n (b) and fast ion flow outflowing to DPF I_i (c) in the vicinity of H-transition in A8 top.*

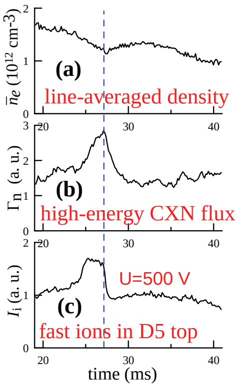

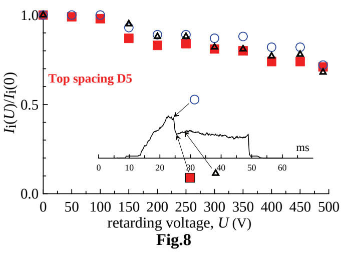

↑***Fig. 9.*** *Same as in Fig. 7 for the top spacing D5.*

↑ ***Fig. 8.*** *Same as in Fig. 6 for the top spacing D5*

(and A6) but also do not change with transition (Fig.9).

The same is in the top spacing D6.

<u>Top spacing in a cross-section close to D7 ($\Delta\phi = 5^0$).</u>

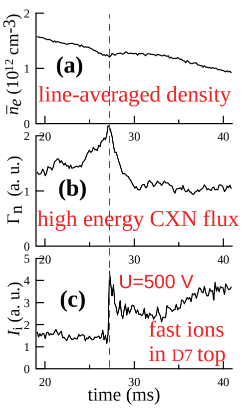

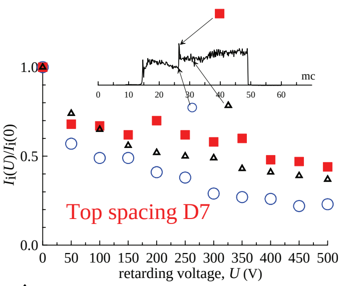

↑

Fig. 11. *Same as in Fig.7 for the top spacing of a cross-section close to D7.*

↑ ***Fig. 10.*** *Same as in Fig. 6 for the top spacing of a cross-section close to D7.*

Opposite to D5 top (Fig. 8) and D6 top, in the vicinity of D7 top the fast ion loss *increases* with transition (Fig. 10c) synchronously with a *decrease* of fast ion content in the confinement volume (Fig. 10b).

Also opposite to D5 top and D6 top, the energies of escaping ions on the ion ∇*B* drift side increase with transition (Fig. 11).

<u>Effects of magnetic field reversal</u>

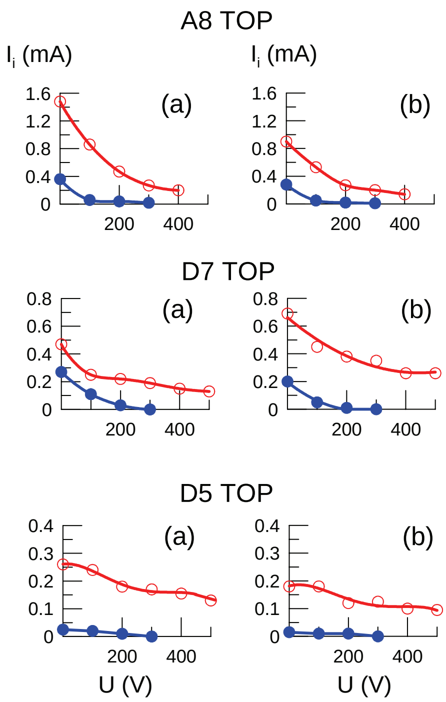

← Fig. 12.

○ – positive field (ion ∇B drift upward);
● - negative field

(a) – before transition;
(b) – after transition

The I_i versus *U* plots measured at opposite directions of the magnetic field demonstrate that the fast ion loss dominates on the ion ∇*B* drift side, being at least partially a real reason for the observed DPF vertical asymmetry in a heliotron/torsatron device like U-3M [5,6].

6. Summaries and discussions

The DPF characteristics such as flow magnitude, its vertical asymmetry, energy of ions in DPF are distinct by a considerable toroidal nonuniformity both in the initial state (i.e, before transition) and by the character of changes induced by H-transition. Juxtaposing the data on time behavior of $\bar{n}_e$, Γ_n, DPF magnitude (current I_s) and current I_i of fast ions in DPF, we note the following.

1. In all spacings A7 the transition entails a DPF reduction. Taking the $\bar{n}_e$ and ECE increase into account, this should be associated with a total particle loss reduction in the vicinity of A7. In a similar manner the fast ion component in DPF drops in A6 and A8 on the ion ∇*B* drift side. At the same time, the fast ion content represented by Γ_n decreases in the confinement volume too. Therefore, strictly speaking, we can only presume that the transition does not result in a fast ion loss increase in the vicinity of A6 and A8.

The energies of ions outflowing to DPF in A6 and A8 do not change with transition. A valuable contribution of fast ion loss to DPF vertical asymmetry obviously follows from comparison of $I_i(U)$ plots measured in the top spacings of A6 and A8 at opposite magnetic field directions.

2. Similar to A6 and A8: (i) the transition induces a DPF reduction in D5 and D6 on the ion ∇B drift side. This is consistent with the Γ_n reduction and allows one to presume fast ion loss not to increase with transition; (ii) the energies of ions outflowing to DPF do not increase in D5 and D6, but they are considerably higher than in A6 and A8 both in the initial state and after the transition; (iii) the $I_i(U)$ plots in the top spacings of D5 and D6 when measured at opposite directions of the magnetic field evidence a substantial contribution of fast ion loss to the DPF up-down asymmetry.

3. The H-transition-induced reduction of Γ_n indicates a rise of fast ion loss. Among all poloidal cross-sections having been explored, only in D7 on the ion drift side the H-transition-induced *increase* of DPF and of fast ion outflow occurs synchronously with the Γ_n *decrease*. Hence, toroidal segments can in principle arise in U-3M where fast ion loss increases with H-mode transition, this being one more manifestation of a strong toroidal non-uniformity of some plasma properties in U-3M.

The data available are not sufficient to clear up distinctly the factors responsible for the non-uniformities observed. Only some general considerations seem to be possible at present.

1. It has been observed experimentally [7] and confirmed numerically [8] that an island structure is inherent to the real magnetic configuration of the U-3M torsatron, that includes two main chains of magnetic islands at $\iota = 1/4$, each of them rotating poloidally when going round the torus and thus causing a difference between magnetic configurations in the same poloidal cross-sections belonging to different field periods. As is mentioned in [8], the real magnetic system of U-3M has actually only one field period instead of 9 ones in the ideal system, and we should not expect an exact reproducibility of all plasma characteristics from period to period.

2. Helically (locally!) trapped ions should be highly sensitive by their loss to the magnetic distortions in the field period where they are trapped. The $1/\nu$ transport (effective ripple $\varepsilon_{eff}^{3/2}$) significantly increases near the islands [8]. Therefore an enhanced escape of fast ions into separate components of DPF is possible in principle (D5 top, D6 top).

3. In U-3M the ion orbit loss [3] and the drift-ion-orbit flux [4] are expected to be possible mechanisms driving the polodal velocity $E_r \times B$ to bifurcation with formation of gradients high enough to suppress the edge turbulence and turbulence-induced anomalous transport. The island-caused nonuniformity in fast ion loss distribution over the U-3M torus can presumably result in a nonuniformity in formation of edge plasma layers and in appearance of zones where the E_r profile is not favourable for fast ion confinement. Possibly, this could explain the occurrence of zones of enhanced fast ion loss after the transition (in particular, in the vicinity of D7 top).

4. The non-uniformity in toroidal distribution of some DPF characteristics could also originate from the local character of RF power injection into the U-3M plasma (RF antenna disposition in one field period only, RF power injection through only one spacing between the helical coils, embracing of the plasma by the antenna only under one pair of the helical coils) and RF power deposition at the plasma edge. In these conditions we cannot exclude a nonuniformity in fast particle generation both along the torus and over the minor azimuth.

References

[1] E.D. Volkov *et al.*, Proc.14th IAEA Conf. (Wurzburg 1992), Vol. 2, IAEA, Vienna, 679 (1993).
[2] V.V. Chechkin *et al.*, Plasma Phys. Control. Fusion **48** A241 (2006).
[3] K.S. Shaing, E.C. Crume, Phys. Rev. Lett. **63** 2369.
[4] K.S. Shaing, Phys. Rev. Lett. **76** 4364 (1996).
[5] V.V. Chechkin *et al.*, Nucl. Fusion **42** 192 (2002).
[6] V.V. Chechkin *et al.*, Nucl. Fusion **43** 1175 (2003).
[7] G.G. Lesnyakov *et al.*, *Nucl. Fusion* **32** 2157 (1992).
[8] V.N. Kalyuzhnyj, V.V. Nemov, *Fusion Science and Technology* **46** 248 (2004).

Proceedings of ITC/ISHW2007

Time Evolution of Spatial Structure of Radial Electric Field in Tohoku University Heliac

H. Aoyama, S. Kitajima, M. Sasao, A. Okamoto, T. Kobuchi, Y. Tanaka, H. Utoh, H. Umetsu, K. Ishii, H. Takahashi[a]

Department of Quantum Science and Energy Engineering, Tohoku University, Sendai 980-8579, Japan

[a]National Institute for Fusion Science, 322-6 Oroshi-cho, Toki 509-5292, Japan

Radial electric field is closely related with the confinement of plasma. In Tohoku University Heliac (TU-Heliac), the electrode biasing experiments were carried out to control the radial electric field actively by ramping up/down the electrode current. An emissive probe array consisting of three filaments was designed as new measurement equipment. With this probe, time evolutions of the spatial structure of the radial electric field were measured in the biasing experiments. There was the tendency for the radial electric field to extend from the inner region to the outer region while the electrode current was ramping up. In the plasma inner region, the radial electric field was maintained the longer time compared with the outer region while the electrode current was ramping down. The radial electric field, poloidal flow of plasma and fluctuation level of the ion saturation current changed appreciably in the period when the electrode voltage showed nonlinearity against the electrode current. Therefore, the plasma nonlinearity period was the transition region to the improved mode.

Keywords: radial electric field, emissive probe, electrode biasing experiment, LH transition, fluctuation

1. Introduction

The neoclassical theory describes that the ion viscosity has a local maximal value against the poloidal rotation velocity [1]. The rapid increase of the poloidal rotation arises when the driving force in the poloidal direction exceeds a critical value. At that moment, it is considered that the plasma transits into the improved mode. One of the characteristics of the transition into the improved mode is sudden growth of the radial electric field [2]. Therefore, it is important to investigate the time evolution of the spatial structure of the radial electric field to comprehend the detailed transition mechanism. The radial electric field can be controlled actively by the electrode biasing experiments. In fact, the electrode biasing experiments have been done in various devices [3, 4]. In addition, the shear of the radial electric field plays an important role in the improvement of the plasma confinement with suppression of fluctuation level [5, 6].

In TU-Heliac, the electrode biasing experiments using a hot cathode made of LaB_6 have been carried out to control the transition into the improved mode [7, 8]. We tried the forward/reverse transition experiments by ramping up/down the electrode current. In those experiments, the negative plasma resistance and the hysteresis between the radial electric field and the stored energy were observed in the transition region [9]. The nonlinear change of the electrode voltage against the electrode current is one of the characteristics of the transition. To understand the behavior of the radial electric field in the transition region, it is important to measure the time evolution of the spatial structure of the radial electric field around the period when the electrode voltage shows nonlinearity against the electrode current. For this purpose, we developed the emissive probe array to define the radial electric field. Using this probe, we measured the distributions of the radial electric field and compared them with the results of a mach probe and the fluctuation level of the ion saturation current.

2. Experimental Setup

TU-Heliac is a small heliac device with three sets of magnetic field coils. Top view of TU-Heliac is shown in Fig. 1. The size of this device is as follows: major radius R = 0.48 m, and average plasma radius a ~ 0.07 m. In electrode biasing experiments, the target plasma was He plasma produced by alternative ohmic heating with f = 18.8 kHz, P ~ 35 kW and the discharge time was 10 ms. Electron temperature T_e, electron density n_e, floating potential V_f and their fluctuation level were measured by the triple probe placed at toroidal angle $\phi = 0$ °.

The hot cathode made of LaB_6 was used as an electrode in the electrode biasing experiments. The hot cathode was a cylindrical shape with a length of 17 mm and a diameter of 10 mm. This cathode was inserted into

author's e-mail: hiroshi.aoyama@ppl2.qse.tohoku.ac.jp

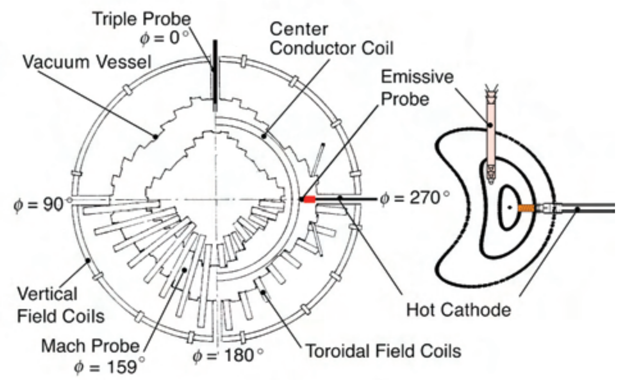

Fig. 1 Top view of TU-Heliac and cross section of magnetic surface at $\phi = 270°$.

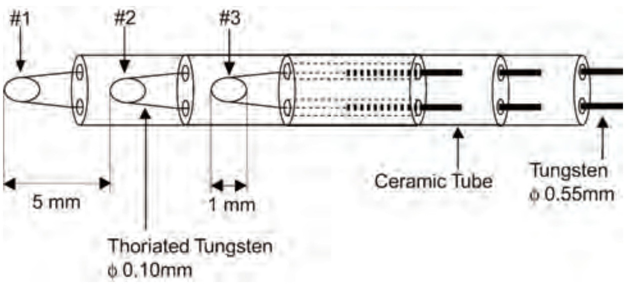

Fig. 2 Schematic of the emissive probe array

the plasma horizontally at $\phi = 270°$. In the electrode biasing experiments, the electrode was negatively biased against the vacuum vessel by a current control power supply.

The plasma poloidal flow relates closely to the radial electric field E_r. The mach probe was used to compare the E_r with the plasma poloidal flow. It was inserted vertically into the plasma from the upper port at $\phi = 159°$.

We designed the emissive probe array shown in Fig. 2. It had three filaments made of 1% thoriated tungsten (Th-W) with a diameter of 0.1 mm. Th-W is very useful material to emit the electron at low temperature compared with pure tungsten. The intervals of each filament were 5 mm. The Th-W wires were 30 mm in length and bent into a circle with a diameter of 1 mm. The both ends of the wires were connected with the tungsten wires with a diameter of 0.55 mm in a doubly drilled ceramic tube. This probe was inserted vertically into the plasma from the upper port at $\phi = 270°$. The all filaments were set facing toward the magnetic axis. This setting was adopted not to intersect the plasma flow and the magnetic field line. When the filaments are heated, they start to emit electrons and the floating potential measured by the emissive probe shifts to the plasma space potential V_s. The advantage of emissive probe is the direct measurement of the V_s compared with other Langmuir probe methods. In this experiment, the electron density was $n_e \sim 10^{12}$ cm^{-3}, the filaments were heated to 2000 K or less by the heating current about 2 A to 2.5 A, and the floating potential was almost saturated in this condition. This probe is able to measure the V_s in three points at the same time. Therefore, the coincident measurements of the E_r at three points can be carried out.

3. Experimental Results

Figure 3 shows the typical time evolution of the electrode voltage V_E and the current I_E. The I_E was controlled such that (a) the I_E was ramped up to -4 A for 6 ms starting from 4 ms or (b) the I_E was maintained at -4 A at first, and was ramped down to 0 A for 6 ms. In these experiments, the hot cathode was located at $\rho = 0.18 \sim 0.62$, where ρ is the normalized minor radius defined by $\rho = \langle r \rangle / a$, $\langle r \rangle$ is the average radius of the flux surface. The V_E shows nonlinearity against the I_E in the period surrounded by broken lines.

The radial profiles of the V_s measured by the #1 filament in the emissive probe array are shown in Fig. 4. The each profile was obtained from the results of 18 discharges. The broken lines in Fig. 4 are corresponding to that drawn in Fig. 3, and the solid line indicates the start time of ramping up/down. As can be seen in Fig. 4 (a), the V_s became deeper negatively, starting from the

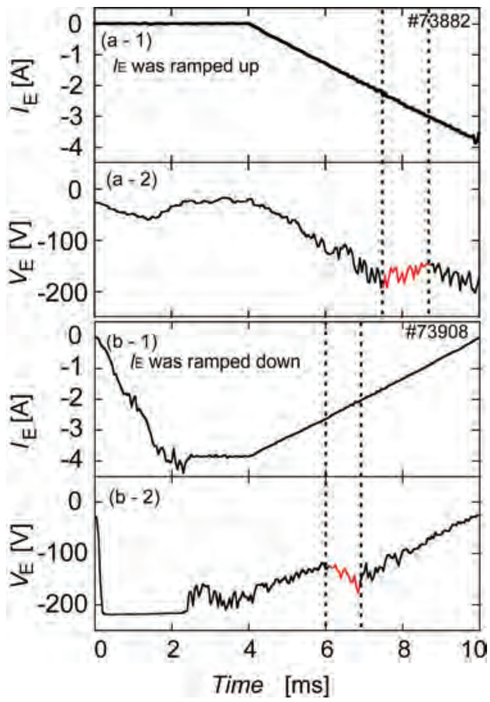

Fig. 3 Typical time evolution of V_E and I_E; (a) in the discharge of the I_E was ramped up, (b) in the discharge of the I_E was ramped down.

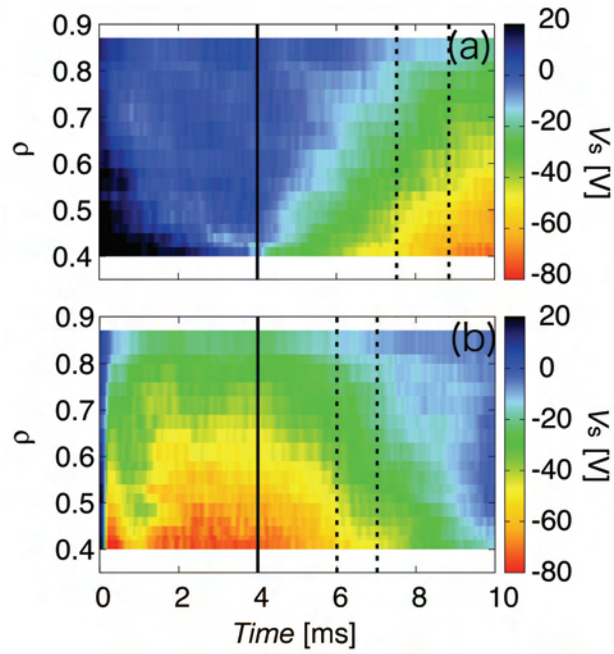

Fig. 4 The plasma space potential V_s measured with the emissive probe array in the discharge of (a) I_E ramped up and (b) I_E ramped down.

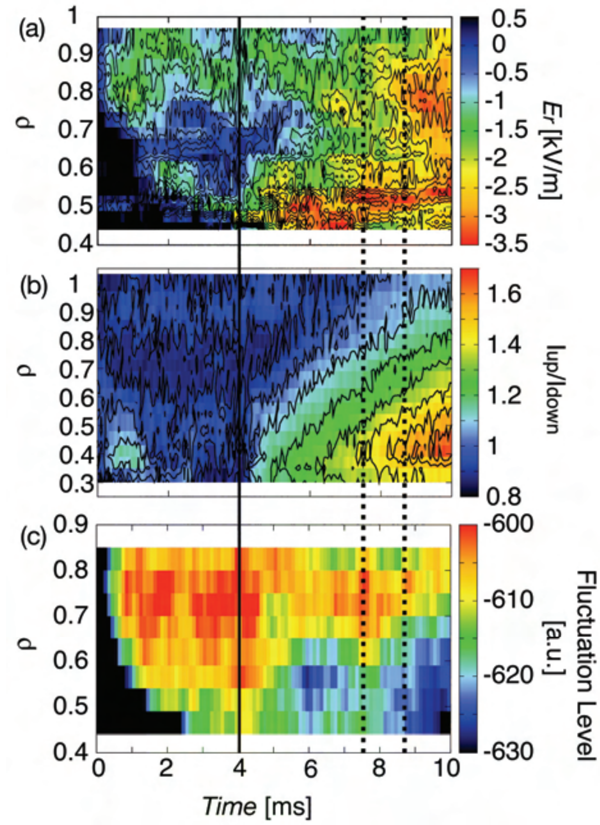

Fig. 5 The time evolution of the spatial structure of (a) the E_r, (b) the current ratio of the mach probe, (c) the fluctuation level of ion saturation current. All of them show the data in the discharges of the I_E ramped up. Solid line indicates the start time of ramping up. Broken lines are indicator of nonlinear period.

plasma inner region when the I_E was ramped up. In Fig.4 (b), when the I_E was ramped down, the V_s changed into shallow level from the plasma outer region. The similar results were also obtained with the other two filaments #2 and #3. The V_s near the magnetic axis ($\rho < 0.35$) could not be measured with the emissive probe array, because the probe scanned the plasma along the code that was off-center to the magnetic axis.

Figure 5 shows the time evolution of the spatial structure of (a) the E_r, (b) the current ratio of the mach probe and (c) the fluctuation level of the ion saturation current in the discharges of I_E ramped up, which is corresponding to Fig.3 (a). The E_r was calculated from the differential of the V_s measured with filaments of #1 and #3. In Fig. 5 (b), I_{up} and I_{down} indicate the ion saturation currents, which flowed into pins at upstream side and downstream side. It can be considered that the current ratio of the mach probe shows the plasma flow, which has a close connection to the E_r. Moreover, the suppression of fluctuation level also relates to the E_r and its shear. In this experiment, the fluctuation level was the integral of power spectrum from 0 to 100 kHz. As can be seen in Fig. 5 (a), the strong E_r arose in the plasma inner region, and diffused to the plasma outer region. Figure 5 (b) indicates the poloidal plasma flow in the electron diamagnetic direction, which is the same direction as the ***E***x***B*** poloidal flow. The high-speed flow spread from inside to outside. Figure 5 (c) shows that the fluctuation level was suppressed after the second broken line ($t > 8.7$ ms), especially in the inner region ($\rho < 0.65$). In the region of $\rho < 0.7$ and $t > 8$ ms, the region where the strong E_r was formed was corresponding to the high current ratio region of the mach probe and the low fluctuation region. In the period surrounded by broken line in Fig. 5, the E_r and the current ratio were significantly increased. And after the second broken line, both of them were saturated at higher values. On the contrary, the fluctuation level changed gradually in this period and was suppressed remarkably after this period.

The results in the discharges of the I_E ramped down are shown in Fig. 6. In the plasma inner region the strong E_r was maintained the longer time compared to the outer region. The plasma flow gradually weakened from the plasma outer region. The fluctuation level was compressed at the low level during $2 < t < 6$ ms. This period was corresponding to that with the strong E_r and the large current ratio shown in Fig. 6 (a) and (b). This

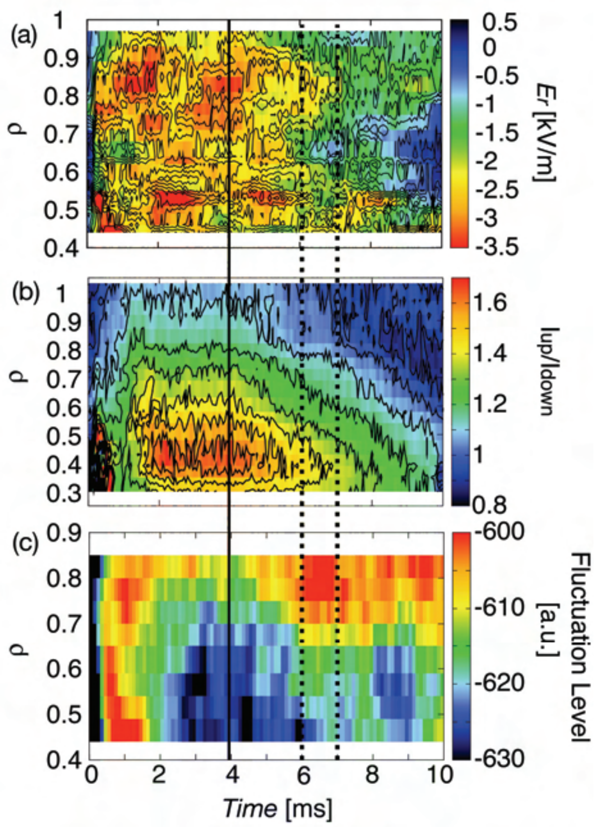

Fig. 6 The time evolution of the spatial structure of (a) the E_r, (b) current ratio of the mach probe, (c) the fluctuation level of the ion saturation current. All of them show the data in the discharge of the I_E ramped down. Solid line indicates the start time of ramping up. Broken lines are indicator of nonlinear period.

indicates that the E_r suppressed the fluctuation level. In the period surrounded by broken lines, the E_r decreased appreciably, and the fluctuation level had the maximum value in the plasma outer region. Although the current ratio did not change greatly in the outer region, the large change was seen in the inner region ($\rho < 0.6$). After the second broken line ($t > 8$ ms), the E_r became strong again and the fluctuation level became lower. It is suggested that the E_r was connected with the suppression of the fluctuation.

In both of the discharges of the I_E ramped up and down (shown in Fig. 5 and Fig. 6), the E_r was sustained at high level although the current ratio was very small in the part of outer region.

The strong E_r, the high-speed flow and the suppression of the fluctuation were observed at the period of $t > 8.7$ ms in Fig. 5 and $t < 6$ ms in Fig.6. These results suggested characteristics of the improved mode. Therefore the plasma nonlinearity region surrounded by broken lines was the transition region to the improved mode.

4. Summary

It was demonstrated that the emissive probe array had enough capability to measure the time evolution of the spatial structure of the plasma space potential in the electrode bias experiments in TU-Heliac. The estimation of the spatial profile of the radial electric field from the results of the plasma space potential was carried out. It was confirmed that the strong radial electric field spread from the inner region to the outer region in the discharge of the I_E ramped up, and was maintained for the longer time in the inner region in the discharge of the I_E ramped down. The characteristic region of the spatial and time profile of the radial electric field was corresponding to those of the current ratio of the mach probe and the fluctuation level of the ion saturation current, although the radial electric field had weak correspondence to the plasma poloidal flow at the part of the plasma outer region.

The E_r, the flow and the fluctuation level changed appreciably in the period when the bias electrode voltage shows nonlinearity against the bias electrode current. Therefore the plasma nonlinearity region was the transition region to the improved mode.

Acknowledgement

This work was supported by a Grant-in-Aid from the Ministry of Education, Science and Culture of Japan (No. 17360439).

References

[1] K. C. Shaing, Phys. Rev. Lett. **76**, 4364 (1996).
[2] K. H. Burrell *et al.*, Plasma Pys. Control. Fusion **31**, 1649 (1989).
[3] R. J. Taylor *et al.*, Phys. Rev. Lett. **63**, 2365 (1989).
[4] E. Y. Wang *et al.*, Nucl. Fusion **35**, 467 (1995).
[5] H. Bigrali *et al.*, Phys. Fluids B **2**, 1 (1990).
[6] R. J. Groebner *et al.*, Phys. Rev. Lett. **64**, 3015 (1990).
[7] S. Kitajima *et al.*, Nucl. Fusion **46**, 200 (2006).
[8] S. Inagaki *et al.*, Japan. J. Appl. Phys. **36** 3697 (1997).
[9] H. Takahashi *et al.*, Plasma Pys. Control. Fusion **48**, 39 (2006).

Proceedings of ITC/ISHW2007

Effects of Rotating Magnetic Islands Driven by External Perturbation Fields in TU-Heliac

S. Kitajima, H. Umetsu, M. Sasao, A. Okamoto, T. Kobuchi, Y. Tanaka, H. Utoh, H. Aoyama, K. Iwazaki, S. Inagaki[a], M. Takayama[b], A. Komori[c], K. Nishimura[c], Y. Suzuki[c], M. Yokoyama[c], H. Takahashi[c]

Department of Quantum Science and Energy Engineering, Tohoku University, Sendai 980-8579, Japan

[a] *Research Institute for Applied Mechanics Kyushu University, 6-1 Kasuga-kouen, Kasuga, Fukuoka 816-8580, Japan*

[b] *Akita Prefectural University, Honjyo, Akita 015-0055, Japan*

[c] *National Institute for Fusion Science, 322-6 Oroshi-cho, Toki 509-5292, Japan*

New method of rotating the magnetic islands by the external perturbation fields was proposed. The perturbation fields were produced by 4 pairs of cusp field coil, in which the alternating currents flowed and the currents had the $\pi/2$ phase shift. The phase shifter for the coil currents was designed and constructed. The phase difference in the floating potential signals measured by the two Langmuir probes confirmed that the rotation of the magnetic islands in the counterclockwise direction (c/c) direction. The clockwise (c/w) rotation was also observed in the plasma biased by the hot cathode electrode. These experimental results suggest the ability of the plasma poloidal rotation driven by rotating islands.

Keywords: stellarator, heliac, magnetic islands, poloidal rotation, perturbation field, electrode bias

1. Inroduction

Study of magnetic island effects on the transport in helical devices is important, because it leads to the advanced control method for a plasma periphery in a fusion reactor. For the research on island effects on confinement modes, the Tohoku University Heliac (TU-Heliac) has advantages that (1) the position of a rational surface is changeable by selecting the ratio of coil currents, (2) the island formation can be controlled by external perturbation field coils, (3) a radial electric field and particle transport can be controlled by the electrode biasing. In TU-Heliac the improved mode transition has been triggered by electrode biasing using a hot cathode made of LaB_6. The driving force $\boldsymbol{J} \times \boldsymbol{B}$ for a plasma poloidal rotation was externally controlled and the poloidal viscosity was successfully estimated from the external driving force [1-3]. In recent experiments the ion viscosity in the biased plasma with islands was roughly estimated. It suggested that the ion viscosity increased according to the increase of the magnetic island width [4]. Therefore it is expected that plasma poloidal rotation will be driven by the poloidal rotation of the island. The purposes of this experiment are, to propose the new method of rotating islands by the external perturbation fields, to survey the ability of the plasma poloidal rotation driven by rotating islands and, to study the rotating island effects on confinement modes in TU-Heliac.

sumio.kitajima@qse.tohoku.ac.jp

2. Experimental Setup

2.1. TU-Heliac

The TU-Heliac is a 4-period heliac (major radius, 0.48 m; average plasma radius, 0.07 m). The heliac configurations were produced by three sets of magnetic

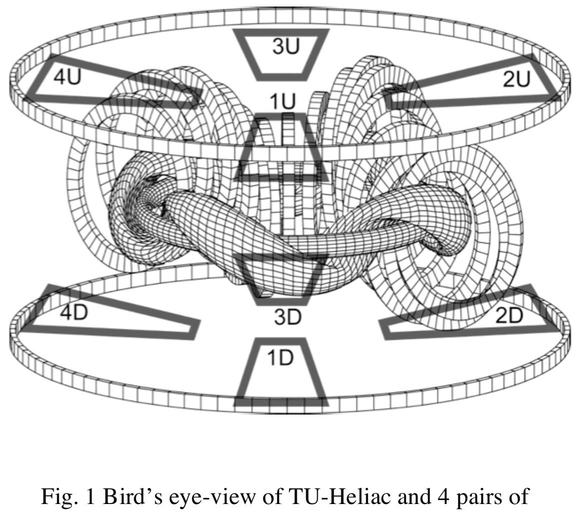

Fig. 1 Bird's eye-view of TU-Heliac and 4 pairs of upper and lower external perturbation field coils. 4 pairs of coils were divided into two groups (the first group consists of 1U1D and 3U3D, the second group of 2U2D and 4U4D).

field coils: 32 toroidal field coils, a center conductor coil, and one pair of vertical field coils as shown in Fig. 1. Three capacitor banks consisting of two-stage pulse forming networks separately supplied coil currents of 10 ms flat top [5]. The target plasma for external perturbation fields was He plasma produced by low frequency joule heating (f = 18.8 kHz, P_{out} ~ 35 kW). The joule heating power was supplied to one pair of poloidal coils wound outside the toroidal coils [6]. The vacuum vessel was filled with fueling neutral He gas and sealed from the evacuation system before every discharge. The electron density and temperature measured by a Langmuir probe (triple probe) were ~ 6 x 10^{17} m^{-3} and ~ 20 eV at the magnetic axis and the magnetic field strength at the axis was 0.3 T.

2.2. External Perturbation Coils

In TU-Heliac we selected the current ratio to locate a rational flux surface (n/m = 5/3) in the plasma periphery. The efficient configuration of perturbation coils for generating islands (m = 3) has been searched. We decided 4 pairs of upper and lower external perturbation field coils, which located at the toroidal angle ϕ = 0°, 90°, 180° and 270°, and generated cusp field at each toroidal angle as shown in Fig. 1. We explored the possibility of the poloidal rotation of islands by changing the phase of the each perturbation coil current. We tried the method that, dividing perturbation coils into two groups (the first group consists of 1U1D and 3U3D, the second group of 2U2D and 4U4D), changing perturbation current separately, one

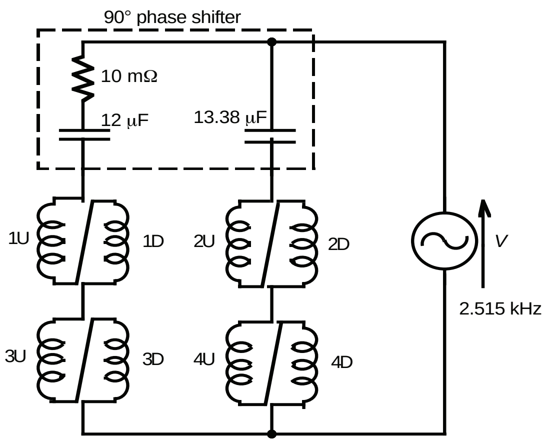

Fig.2 Schematic circuit for the external perturbation coils.

group's current was $I_{ex} = I_0\sin(\omega t)$ and other was $I_{ex} = I_0\sin(\omega t - \pi/2)$. Each coil produces an alternating cusp field with the frequency ω. The result of magnetic surface calculations suggested that islands rotate to poloidal direction with the poloidal velocity of $\langle r\rangle\omega/m$. Here, $\langle r\rangle$ is the average radius of the rational flux surface (n/m = 5/3) and m is the mode number of magnetic islands. The poloidal rotation velocity can be changeable by the frequency ω. Furthermore we can select the poloidal rotation direction (clockwise c/w or counterclockwise direction c/c) by changing the polarity of the phase shift. Here the c/c direction means the ion diamagnetic direction.

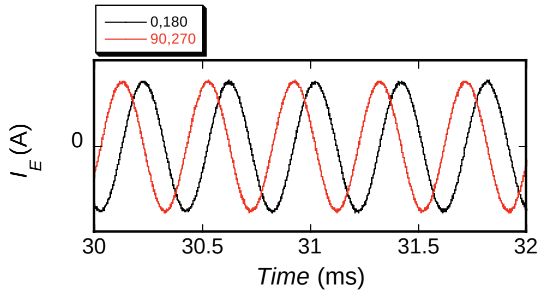

Fig. 3 Perturbation coil currents measured by the Rogowsky coils. Two group coil currents have π/2 phase shift and same values.

In the experiment we adopted the phase shifter shown in Fig. 2, which consisted of precisely tuned capacitors and resister. The perturbation field coil current was 1.2 kAT and the frequency was 2.515 kHz. The current and the frequency were selected to perform the preliminary experiments and we have the plan of increase in current and frequency. Figure 3 shows the perturbation coil currents measured by the Rogowsky coils. We can see that two group coil currents have π/2 phase shift and same values.

Figure 4 shows the magnetic surfaces with m = 3 magnetic islands which were produced by the external perturbation fields. The m = 3 magnetic islands rotated by

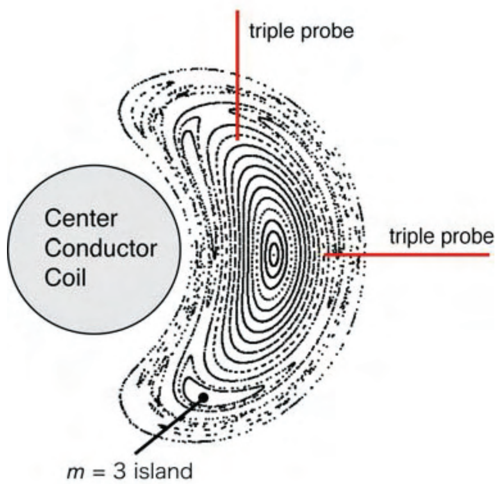

Fig. 4 Cross section of magnetic surfaces with m = 3 magnetic island. Two Langmuir probes on the magnetic surface at the positions which were separated about a half of the poloidal length of the island.

the alternating perturbation fields.

3. Phase shift in Probe Measurements

To check experimentally the effect of the external perturbation field, we measured the floating potential by a Langmuir probe (high speed triple probe [7, 8]), which was inserted from the low field side at the toroidal angle $\phi = 0°$. In Fig. 5 it is clear that the floating potential signal has the frequency component of the perturbation fields (lower trace) and the phase shift to the external perturbation coil current (upper trace). Then we measured the radial profile of the FFT power spectrum in the floating potential signals. Figure 6 shows the relation between the power spectrum of the floating potential and the radial position of the Langmuir probe. Figure 6 clearly shows that the frequency of the perturbation field coil current (f = 2.515 kHz) was excited around the m = 3 magnetic island.

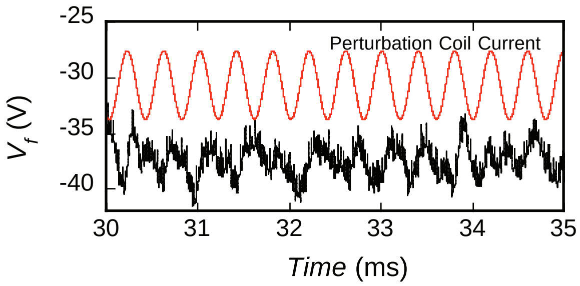

Fig. 5 External perturbation coil current and the floating potential measured by a Langmuir probe (high speed triple probe).

In order to confirm the rotation of magnetic islands we set two Langmuir probes on the magnetic surface at the positions which were separated about a half of the poloidal length of the island. These probes were set at the same meridian plane at the toroidal angle $\phi = 0°$ as shown in Fig. 4. We measured the phase shift in the frequency of the perturbation fields (f = 2.515 kHz) between two probe signals. Figure 7 shows the difference of the phase between the floating potential signals at the three radial points. The open symbols and closed symbols denote the c/w and c/c directions of the rotating islands which were expected by the calculations. We can confirm that at the inside the m = 3 islands the phase difference was about π in the c/c direction case, which was consistent with the calculation results and suggested the rotation at the inside of the island (R = 102 mm), and corresponded to the poloidal rotation velocity of ~ 0.2 km/s. These experimental results suggest the ability of the plasma poloidal rotation driven by rotating islands. However in the c/w case the phase difference had the small positive values, which were inconsistent with the calculation, because it should be -π. In these experiments the target plasma had the weak positive radial electric fields (E_r ~ 2 kV/m), thus the bulk plasma rotated in the c/c direction by the $\boldsymbol{E} \times \boldsymbol{B}$ rotation. Therefore we can explain that there are some restrictions on the rotation of the islands in the direction which is opposite to the natural direction of the bulk plasma rotation (c/c direction).

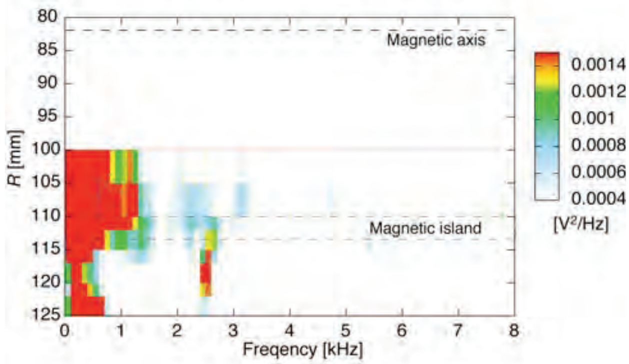

Fig. 6 Relation between the FFT power spectrum of floating potential and the radial position of the Langmuir probe.

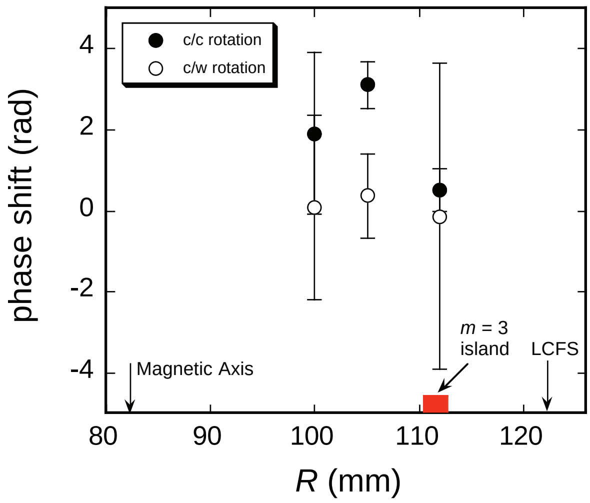

Fig. 7 Difference of the phase between the floating potential signals at the three radial points. The open symbols and closed symbols denote the c/w and c/c directions of the rotating islands which are expected by the calculations.

In TU-Heliac we can bias the potential to the plasma by the hot cathode electrode made of LaB_6. We can control the negative radial electric field externally by the electrode biasing. The hot cathode (diameter, 10 mm; length, 17 mm) was inserted horizontally into the plasma from the low magnetic field side at a toroidal angle ϕ = 270°. The m = 3 islands were formed at the outside of the hot cathode. The direction of the $\boldsymbol{E}$ x $\boldsymbol{B}$ rotation was the c/w direction, thus we can decelerate the natural c/c plasma rotation. Here $\boldsymbol{E}$ is the radial electric field made from the biasing. We tried to apply the external perturbation fields to rotate the islands in the biased plasma. Figure 8 shows the relation between the differences of the phase in two floating potential signals and the electrode current used for the plasma biasing. The increase in the electrode current means the increase in the c/w plasma rotation velocity. We showed again the results without the electrode biasing (I_E = 0 A) shown in Fig. 7. Before the application of the external perturbation fields we tried to measure the velocity of the

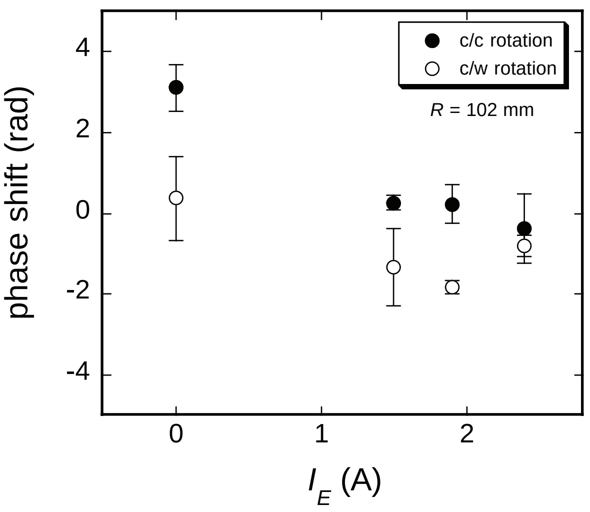

Fig. 8 Relation between the differences of the phase in two floating potential signals and the electrode current. The increase in the electrode current means the increase in the velocity of the c/w bulk plasma rotation.

plasma poloidal rotation by the phase velocity of high frequency fluctuations in floating potential [2, 9]. From this results the plasma poloidal rotation disappeared in the case which the electrode current was about 2 A. In Fig. 8 we can see that in the c/w island rotation case the phase difference had about -2 rad at I_E = 2 A, which was consistent with the calculations and suggested the rotation of the magnetic island, although in the c/c island rotation cases the phase difference decreased compared with the experimental results in Fig. 7. This suggested that the bulk plasma rotation by the biasing was overdriven.

4. Summary

We proposed the method to rotate the magnetic islands by the external perturbation fields which were produced with 4 pairs of cusp field. The alternating currents for the perturbation coils have the $\pi/2$ phase shift. We designed and constructed the phase shifter for the coil currents and we measured the phase difference in the floating potential signals by two Langmuir probes, which confirmed that the rotation at the inside of the magnetic islands in the c/c direction. Furthermore the c/w rotation was also observed in the plasma biased by the hot cathode electrode. These experimental results suggest the ability of the plasma poloidal rotation driven by rotating islands, though the island rotation was affected by the rotation of the target plasma. We can expect the higher poloidal rotation velocity by increasing in the frequency of the perturbation coil current.

Acknowledgment

This work was supported by a Grant-in-Aid from the Ministry of Education, Science and Culture of Japan (No. 17360439).

References

[1] S. Inagaki *et al.*, Jpn. J. Appl. Phys. **36**, 3697 (1997).
[2] S. Kitajima *et al.*, Nucl. Fusion **46**, 200 (2006).
[3] H. Takahashi *et al.*, Plasma Phys. Control. Fusion **48**, 39 (2006).
[4] S. Kitajima *et al.*, Fusion Sci. Technol. **50**, 201 (2006).
[5] S. Kitajima *et al.*, Jpn. J. Appl. Phys. **30**, 2606 (1991).
[6] S. Kitajima *et al.*, J. Plasma Fusion Res. **4**, 391 (2001).
[7] Y. Tanaka *et al.*, Plasma Fusion Res., **2**, S1019 (2007).
[8] Y. Tanaka *et al.*, Plasma Phys. Control. Fusion, **48**, A285 (2006).
[9] Y. Tanaka *et al.*, Trans. Fusion Sci. Tech., **51**, 265 (2007).

Proceedings of ITC/ISHW2007

Transitions to improved core electron heat confinement in TJ-II plasmas

T. Estrada, F. Medina, E. Ascasíbar, R. Balbín, F. Castejón, C. Hidalgo, D. López-Bruna and S. Petrov[a]

Laboratorio Nacional de Fusión, EURATOM-CIEMAT, 28040 Madrid, Spain

[a] A.F. Ioffe Physical Technical Institute, St. Petersburg, Russia

Transitions to improved core electron heat confinement are triggered by low order rational magnetic surfaces in TJ-II ECH plasmas. Transitions triggered by the rational surface n=4/m=2 show an increase in the ion temperature synchronized with the increase in the electron temperature. SXR measurements demonstrate that, under certain circumstances, the rational surface positioned inside the plasma core region precedes and provides a trigger for the transition.

Keywords: Stellarator, Improved Heat Confinement, Rational Magnetic Surfaces

1. Introduction

In stellarator devices, transitions to improved core electron heat confinement are established in conditions of high ECH power density and are characterized by peaked electron temperature profiles and large positive radial electric field in the core plasma region [1-7]. These transitions, called CERC (Core Electron Root Confinement [8]), have been observed in CHS, LHD, W7-AS and TJ-II. TJ-II experiments show that transitions to CERC can be triggered by positioning a low order rational surface at the plasma core region [6,7]. The rational surface contributes to the outward electron flux that creates a locally strong positive radial electric field. This can be explained taking into account that the diffusion coefficient in ergodic layers or magnetic islands depends on the parallel velocity of the species; consequently the presence of the island will enhance the electron flux more than the ion flux, modifying the equilibrium ambipolar radial electric field [7]. In this way, for constant P_{ECH} the transitions are achievable at higher plasma densities when low order resonances are present, reducing the ECH power per particle (P_{ECH}/n_e) threshold. Experiments performed in LHD also indicate that the magnetic island linked to the rational surface n=1/m=2 contributes to the CERC formation reducing the power threshold [9].

The characteristics of CERC triggered by the n=3/m=2 rational surface in TJ-II plasmas are already described in [6,10]. In this work we report on experiments performed to study the transitions triggered by the rational surface n=4/m=2.

2. Experimental results

CERC triggered by the n=4/m=2 rational has been recently studied in TJ-II ECH plasmas [11]. Firstly, it is important to mention that ECH discharges performed in magnetic configurations having the “natural” 4/2 resonance surface in the ι-profile in vacuum show a degraded confinement and often an unstable evolution. The reason may be the large island width due to both, the low order of the “natural” 4/2 resonance and the low magnetic shear of TJ-II. However, at the plasma edge where the magnetic shear is not that low - the vacuum magnetic shear at the plasma edge and in the bulk are $s \approx -0.1$ and -0.02, respectively -, an increase of the sheared ExB flow is measured linked to the 4/2 rational [12]. As it will be shown, the rational 4/2 positioned in the plasma core region can have a favourable effect on the confinement provided a moderate magnetic shear is established. CERC triggered by the 4/2 rational are obtained in a magnetic configuration with vacuum rotational transform above two by inducing a small amount of negative OH current. This negative current reduces ι mainly in the inner plasma region, crossing the rational 4/2 with increased negative magnetic shear. CERC triggered by the 4/2 rational produces an increase in the electron temperature at the plasma centre of about 20% at relatively high line densities: 0.7-0.9 10^{19} m^{-3}. Comparatively, the increase in the central T_e in CERC triggered by the 3/2 rational is

author’s e-mail: teresa.estrada@ciemat.es

less pronounced - close to 10-15% - at similar densities: 0.7-0.8 $10^{19}\,m^{-3}$.

Figure 1 shows an example of CERC triggered by the 4/2 rational in a discharge in which the plasma current gradually increases due to OH induction. In this example the barrier is formed at about t = 1100 ms and it is spontaneously lost and recovered. At the CERC formation, synchronized with the change in the T_e, we observe an increase in the ion temperature measured by CX-NPA diagnostic [13] and a reduction in the H_α signals. As CERC is lost, ECE traces show a heat pulse propagating radially outwards. The ι-profile evolution is calculated with the ASTRA system [14] considering that the main contribution to the current profile is the induced OH current and imposing the measured net plasma current evolution as boundary condition. We use Spitzer resistivity corrected by the fraction of passing particles [15].

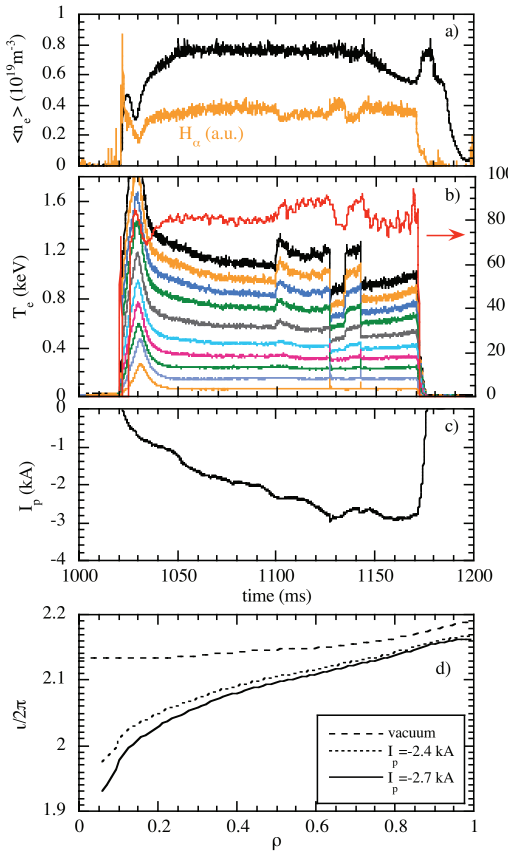

Figure 1: The time evolution of (a) line-averaged density and H_α signal, (b) T_e at different radial positions and T_i measured along a central plasma chord, and (c) I_p. (d) ι_profile in vacuum and with I_p=-2.4 and -2.7 kA.

The plasma potential measured using the HIBP diagnostic increases in the central plasma region. However, accurate measurements of plasma potential profiles have not been achieved in this magnetic configuration so far, what has precluded the characterization of the radial electric field rise.

For the first time an increase in T_i synchronized with the increase in T_e has been observed during CERC formation (see figure 1.b). The change in T_i is relatively modest (about 10-15 %), but it had not been previously observed either in TJ-II or in the other helical devices [8]. Outer plasma chords have been scanned with the CX-NPA diagnostic in a series of reproducible discharges; changes in T_i synchronized with T_e are still visible but lay within the error bars of the CX-NPA diagnostic. In figure 2 we have represented T_i vs. the central T_e of the discharge shown in figure 1. It can be seen that the change in T_e (1 & 3) precedes the change in T_i (2 & 4) during both, CERC formation (1 & 2) and disappearance (3 & 4), being the delay of about 2-3 ms (on the order of the energy confinement time of similar TJ-II ECH plasmas [16]). Simulations of ion orbits using the code ISDEP (Integrator of Stochastic Differential Equations for Plasmas) [17] show that the typical time of reaction of ion population agrees with the experimental value.

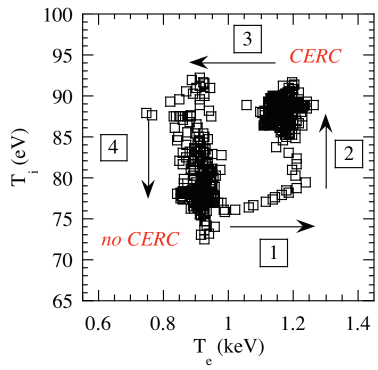

Figure 2: Ion temperature vs. central electron temperature of the discharge shown in fig 1.

From power balance calculations we find that the collisional electron-ion power transfer is about 10 kW and it remains almost unchanged as the CERC develops. Besides, a simple dimensional analysis calculation shows that a small T_i increment (as the one observed in the experiments) can easily come from electron-ion collisional heat transfer, as long as the ion confinement improves when the electron confinement does. The ion collisional transport before and during CERC has been calculated using the code ISDEP. These simulations show that there is an improvement in the ion confinement related to the increase of positive radial electric field that tend to reduce the ion orbit size [18].

In these experiments, the magnetic island associated to the rational surface 4/2 is detected by SXR tomography diagnostic [19] as a flattening in the SXR profiles with an m=2 structure. This m=2 structure is poloidally fixed indicating that the magnetic island does not rotate. These measurements allow us to identify when the magnetic island linked to the rational surface 4/2 enters the central plasma region. Experimentally we observed that in plasmas heated with 420 kW of ECH (each gyrotron supplying 210 kW), the rational surface enters the plasma, unambiguously, prior to the CERC onset.

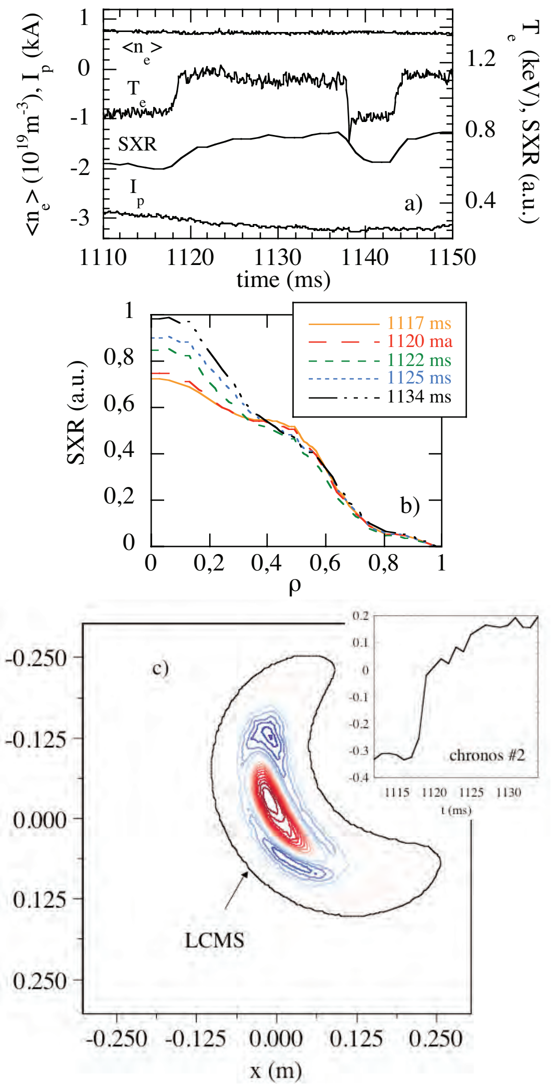

Figure 3: (a) Line density, T_e and SXR at the plasma centre, and I_p during CERC formation. (b) Evolution of the SXR profile; (c) second *topos* and *chronos* (inset plot) eigenmodes obtained by the SVD analysis of the SXR tomography reconstructions (in blue/red, negative/positive *topos* values).

An example is illustrated in figure 3. This figure shows: line-density, central T_e, central SXR and I_p (3.a), and the evolution of the SXR profile (3.b).

Additional information on the spatiotemporal behaviour of the SXR emission can be obtained applying the SVD (singular-value decomposition) technique [20] to the SXR data. The SVD technique is a bi-orthogonal decomposition that expands the signals into a set of spatial and temporal eigenmodes (called *topos* and *chronos*, respectively). We have applied this method to the tomography reconstructed SXR profiles obtained during the CERC transition. The first *topos/chronos* pair represents the averaged SXR profile and the second pair is characteristic of a 2-dim profile change. The second *topos* and *chronos* are shown in figures 3.c. For reference, the last closed magnetic surface (LCMS) of the vacuum configuration is also shown in figure 3.c. A clear m=2 poloidal structure is seen in the second *topos* that gives place to a peaked profile at the CERC transition.

Experimentally it is observed that the time interval between the recognition of the island by SXR and the CERC onset can vary from some tens to few milliseconds. So far we have not found an explanation for this rather large range of time interval values, but it could be related to slight changes in the ι- profile shape and/or in the central plasma density that imply changes in the ECH heating power density.

We have performed another set of experiments with lower ECH total power (335 kW) but injected mainly by one of the gyrotrons: only 85 kW are supplied by gyrotron 1 while 250 kW are supplied by gyrotron 2. An example is displayed in figure 4. This figure shows the time evolution of line-density, T_e and SXR at the plasma centre, and I_p (figure 4.a); and the evolution of the SXR profile (figure 4.b). In these discharges there is not evidence of island formation before the transition. Apparently, both the rational surface entering the plasma core and the CERC onset take place all at once. At the transition, there is a fast drop of the SXR emission at the plasma centre (SXR profiles turn out to be flat) and then the SXR profiles grow to be highly peaked (comparable to those shown in figure 3.b) with signatures of m=2 island structure.

In the later set of experiments it is likely that the high local ECH power (due to the 250 kW gyrotron), heating the rational surface when entering the plasma core, produces a momentary extra outward electron flux from the plasma centre. The corresponding transient in radial current would then create the strong positive radial electric field that triggers the transition to CERC. On the other hand, in the former set of experiments (figures 3), we observe that the magnetic island develops surrounding the central plasma region, where the ECH power is deposited, and afterwards triggers the CERC transition. Similarly, experiments performed at LHD [9] have shown that the 1/2 magnetic island contributes to the CERC formation reducing the power threshold, and that the electron transport is focussed at the X-point of the 1/2 magnetic island. These results put forward the relation between the characteristics of the electron transport at the magnetic island and the CERC transition mechanism: the electron transport, in this case eased by the island X-point region, may affect the ambipolarity condition and modify the radial electric field.

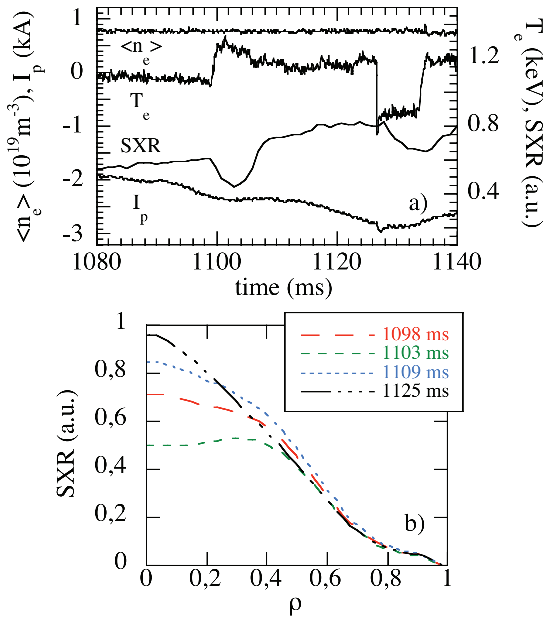

Figure 4: (a) Time evolution of line density, T_e and SXR at the plasma centre and I_p during CERC formation. (b) Evolution of the SXR profile.

As it has been already commented, the main difference between the two sets of experiments is the ECH power arrangement: while the power supplied by each gyrotron is equal in the first set of experiments (210 & 210 kW), it is very different in the second set (250 & 85 kW). This implies differences in the local ECH power density but it could also give rise to changes in the ι-profile shape due to, though small, unbalanced ECCD. Further experiments changing the power of each gyrotron separately will help to clarify this point.

3. Conclusions

CERC transitions triggered by the rational surface n/m=4/2 show an increase in the ion temperature synchronized with the increase in the electron temperature. The change in T_i is relatively modest (about 10-15 %) but it had not been previously observed in CERC transitions. The change in T_i can be the consequence of an improvement in the ion confinement related to the increase in the radial electric field [18]. SXR tomography provides a tool to identify the presence of the magnetic island linked to the rational surface 4/2. These experiments show that, under some circumstances, the island precedes and provides a trigger for CERC formation.

[1] A. Fujisawa *et al.*, Phys. Rev. Lett. **82** (1999) 2669

[2] U. Stroth *et al*, Phys. Rev. Lett. **86** (2001) 5910

[3] H. Maassberg *et al.*, Phys. Plasmas **7** (2000) 295

[4] K. Ida *et al.,* Phys. Rev. Lett. **91**, 085003 (2003).

[5] F. Castejón *et al.,* Nuclear Fusion **42** (2002) 271

[6] T. Estrada *et al.*, Plasma Phys. Control. Fusion **46** (2004) 277

[7] F. Castejón *et al.,* Nuclear Fusion **44** (2004) 593

[8] M. Yokoyama *et al.*, Fusion Science and Technology **50** (2006) 327

[9] K. Ida *et al.*, Phys. Plasmas **11** (2004) 2551

[10] T. Estrada *et al.*, Plasma Phys. Control. Fusion **47** (2005) L57

[11] T. Estrada *et al.*, Nuclear Fusion **47** (2007) 305

[12] C. Hidalgo *et al.,* New Journal of Physics **4** (2002) 51

[13] J. M. Fontdecaba *et al.*, Fusion Science and Technology **46** (2004) 271

[14] G.V. Pereverzev *et al.,* Max-Planck-Institut für Plasma Physik, Rep. IPP 5/98, Garching (2002)

[15] D. López-Bruna *et al.*, CIEMAT Technical Report 1089 ISSN 1135-9420, Madrid (2006)

[16] E. Ascasíbar *et al.*, Nuclear Fusion **45** (2005) 276

[17] F. Castejón *et al.*, Plasma Phys. Control. Fusion **49** (2007) 753

[18] F. Castejón *et al.*, 34th EPS Conference on Plasma Physics, Warsaw, Poland (2007)

[19] F. Medina *et al.*, Rev. Sci. Intrum. **70** (1999) 642

[20] M Anton *et al.,* Plasma Phys. Control. Fusion **38** (1996) 1849

P1-030

Density Control by Second Harmonic X Mode ECRH in LHD

Shin KUBO[1),]Takashi SHIMOZUMA[1)], Kenji TANAKA[1)], Teruo SAITO[1)], Yoshinori TATEMATSU[1)], Yasuo YOSHIMURA[1)], Hiroe IGAMI[1)], Takashi NOTAKE[1)], Shigeru INAGAKI[3)], Naoki TAMURA[1)] and LHD Experimental Group[1)]

[1)]*National Institute for Fusion Science, Toki 509-5292, Japan*
[2)]*Research Center for Development of FIR Region, Fukui Univ.,*
[3)]*Research Institute of Applied Mechanics, Kyushu Univ., Kasuga 816, Japan*

(Received 26 October 2007)

Density clamping or pump out phenomena are observed both in tokamaks and helical systems during high power heating, in particular electron cyclotron resonance heating. If the change of the particle flux and resultant electric field can be localized by the local heating of ECRH, it can be a powerful nob for the control of the particle as well as the heat transport. High power density local second harmonic X (X2) mode ECRH is applied to NBI target plasma at ripple top and bottom resonance conditions so as to keep the identical power deposition profile for both cases to distinguish the ECRH induced flux and enhanced diffusion due to the electron temperature rise. Experimental results indicates that the ECRH induced flux can explain the difference of the density clamping between ripple and bottom heating.

Keywords: ECRH, density pump out, density control, direct loss, radial electric field

1 Introduction

Density clamping or pump out is the common phenomena in tokamaks and helical systems during high power density heating, in particular electron cyclotron resonance heating. These phenomena are discussed in terms of the enhanced electron diffusion induced by the perpendicular acceleration in velocity space and the resultant electric field [1] [2] [3]. It is also pointed out that the change in the electron temperature profile can enhance radial flux due to a non zero off-diagonal term in the transport matrix which can be appreciable by the excitation of turbulent instabilities like trapped electron modes[4]. If the change of the particle flux and the resultant electric field can be localized by the local heating of ECRH, it can be a powerful nob for the control of the particle as well as the heat transport. In order to distinguish the effect of enhanced electron flux directly driven by the ECRH or enhanced diffusion due to the change in the electron temperature or off-diagonal transport matrix, series of experiments are performed. High power density local second harmonic X (X2) mode ECRH is applied to NBI target plasma at ripple top or bottom resonance for the different ripple conditions. The difference in the transient behavior of density profile is observed between top and bottom heating, or high and low ripple configurations. X2 mode is selected because the perpendicular acceleration is more enhanced in X2 than in fundamental O mdoe (O1) mode. The role and the mechanism of ECRH induced particle flux in the particle and heat transport is discussed based on these phenomena. Such degradation of particle confinement is also observed in a tangential negative ion neutral beam (N-NB) heated plasma in LHD for low density discharges, where the electron heating is dominant but heating in parallel to the magnetic field. Such observations also support the enhancement of the off-diagonal transport term. In order to distinguish both effects, series of experiments are performd. High power density second harmonic local ECRH is applied on the ripple top or bottom resonance position where the width of the loss cone is wider for bottom than that for top, but expected power deposition profile is identical to each other in LHD.

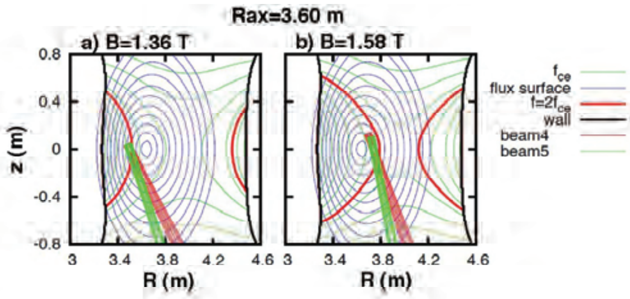

Fig. 1 Vertically elongated cross section of Mod-B, flux surfaces, second harmonic resonance layers and ECRH beams for ripple a) top and b) bottom heating geometries, for $R_{ax} = 3.60m$.

2 Experimental results

2.1 Ripple top and bottom heating condition

In order to enhance the difference in the electron flux by ECRH, the heating positions and magnetic field strength

author's e-mail: kubo@LHD.nifs.ac.jp

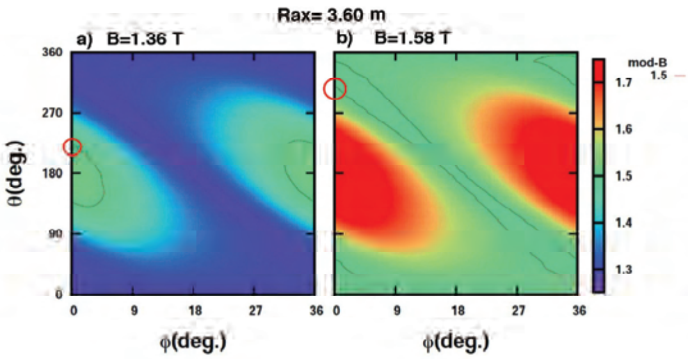

Fig. 2 Mod-B contour on toroidal poloidal plane on $\rho = 0.3$ of $R_{ax} = 3.60m$ configuration for ripple a) top and b) bottom heating geometries. Thin blue lines indicate the second harmonic resonance position for 84 GHz, and red circle indicates deposition region.

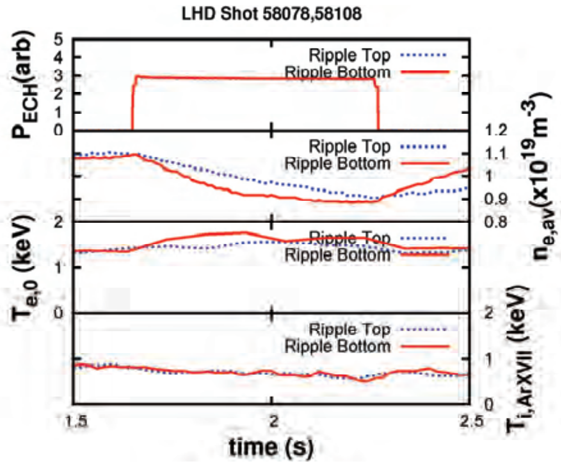

Fig. 3 Temporal evolutions of line averaged density, central electron and ion temperature for ripple top (dotted lines) and bottom (thick lines) ECRH on NB heated discharge.

are selected so that the toroidal ripple top and bottom are heated but keeping the identical normalized radial position on the same vertically elongated cross section. The magnetic field strength and ECRH injection angles are adjusted to meet the second harmonic resonance condition (1.5 T for 84 GHz) at desired position as shown in Figs. 1 and 2. Figure 1 are shown the vertically elongated cross section of LHD with the Gaussian beams from bottom for the magnetic field strength of a) 1.36 T and b) 1.58 T for the R_{ax} = 3.60 m configuration. The second harmonic resonance layer is also shown in thick red lines. Strong interactions are expected at the cross section between the injected beam and the resonance. The power deposition profiles estimated from the multi-raytracing code are confirmed to be identical and sharp at normalized minor radius, ρ=0.3, for both cases. Relative power deposition region on the expanded ρ=0.3 flux surface are shown by red circles in Fig. 2 for both magnetic field cases. Here, the strength of the total magnetic field (Mod-B) is expressed in color scale on the plane of toroidal and poloidal angle at ρ=0.3 flux surface for a) ripple top and b) bottom heating condition. Typical time evolutions of the plasma discharge are shown in Fig. 3. Ripple top and bottom second harmonic heating under the condition shown in Figs. 1 and 2 superposed on the base NBI plasma. A set of discharge is selected for the initial density is almost the same. Time response of the averaged density clearly differs in the case of ripple bottom heating case from that of bottom case. For both cases, the temperature responds rapidly within the time of 0.05 sec.

In order to confirm the ECRH clamping effect due to the ripple and bottom heating, similar experiments are performed for the smaller ripple condition. Here, the configuration R_{ax} = 3.75 m is chosen as a reference. In Figs. 4 and 5 are shown the injection condition and Mod B structure in relation to the heating region. As is seen from Fig. 2 and 5, the ripple ratio is 0.15 and 0.1 for the case of R_{ax} = 3.60 and 3.75 m, respectively. Typical discharge waveforms are shown in Fig. 6 for ripple top and bottom cases. The

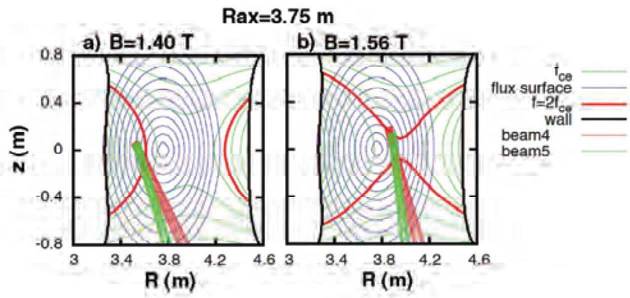

Fig. 4 Vertically elongated cross section of Mod-B, flux surfaces, second harmonic resonance layers and ECRH beams for ripple a) top and b) bottom heating geometries. for $R_{ax} = 3.75m$.

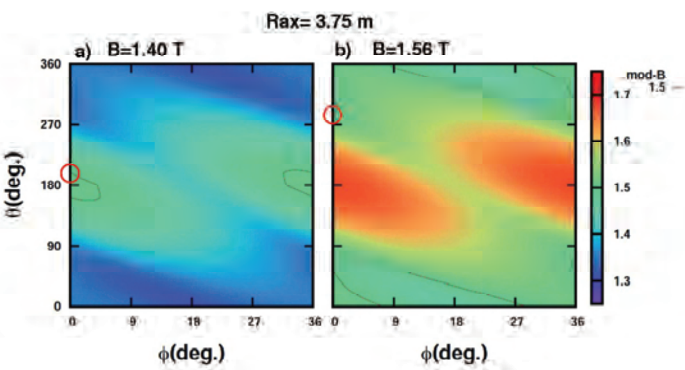

Fig. 5 Mod-B contour on toroidal poloidal plane on $\rho = 0.3$ of R_{ax}=3.75 m configuration for ripple a) top and b) bottom heating geometries. Red line indicates the resonance position.

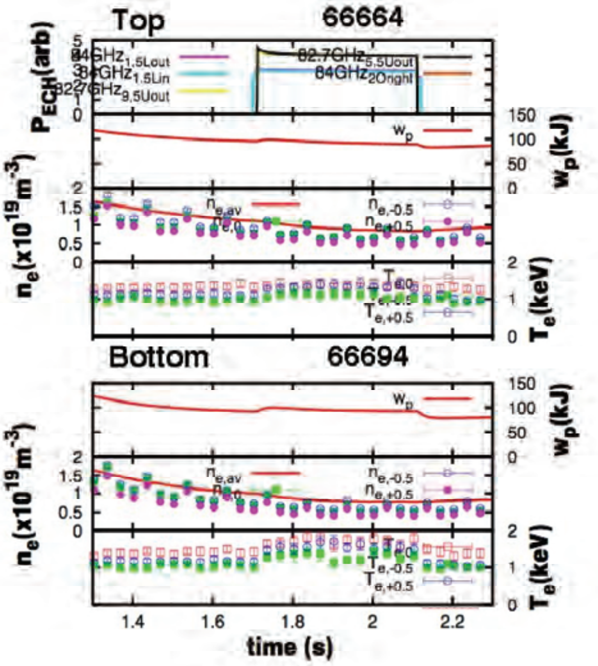

Fig. 6 Temporal evolutions of line averaged density, central electron and ion temperature for a) ripple top and b) bottom ECRH on NB heated discharge.

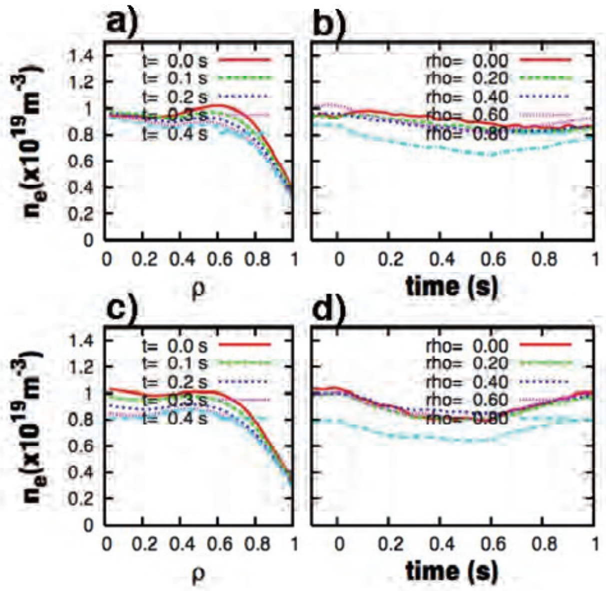

Fig. 7 Density profile at several time slices after ECH injection [a) and c)]. Time evolutions of the density at several spatial points b), and d) for ripple top [a) and b)] and bottom [c)and d)] heating cases.

increases in the electron temperature and stored energy in both cases are clear, but the clamping effect is week for both cases. The difference of clamping effect for both cases needs to be analyzed more in detail, but it is clear from the comparison with R_{ax}=3.60 m configuration that the density clamping is strongly related to the magnetic ripple rate at the heating region, implying that the ECRH related physics plays an important role in the clamping phenomena.

2.2 Detailed comparison of electron temperature and density profile for R_{ax} = 3.60 m configuration

In Fig. 3 are shown the time evolutions of the density, central electron and ion temperature in response to the ECRH on NB heated plasma for ripple top and bottom resonance heating conditions. In both cases, density decrease is observed by applying ECRH, but the time behavior of the decrease in the density clearly changes as the heating position. The line averaged density decreases faster in ripple bottom heating case than in top one. The decrease rate saturates in the time constant of 200 ms for the bottom heating case, while that for the top heating case keeps constant during the ECRH injection of 500 ms. Electron temperature increases within 100 ms and keeps almost constant during the injection for both cases. The profile changes of density reconstructed from a multi-chord FIR interferometer are shown in Fig.7. It should be noted that the density drops at $\rho > 0.4$ but central part does not affected by the ECRH injection for top heating case, while that drops almost whole region for bottom heating case. The change of the electron temperature profile at several timing during the ECRH phase and the temporal evolutions at several radial positions are shown in Fig. 8. The temperature increase of the central region for the case of ripple bottom due to the ECRH is larger as compared with the ripple top case. In both cases, the profile change occurs in less than 100 ms and kept almost constant after 100 ms from the ECRH injection. This means that the change in the density profile evolutions after 100 ms of ECRH injection are attributed to the diagonal term and direct flux due to the ECRH in the electron diffusion.

3 Discussion

Neglecting the source and sink term other than that due to ECRH, diffusion equation can be written by electron density $n_e(r,t)$and temperature profiles $T_e(r,t)$ as

$$\begin{aligned}\Gamma_e(r,t) = \quad & D_{e,n}(r,t)\frac{\partial n_e(r,t)}{\partial r} \\ & +D_{e,T}(r,t)\frac{\partial T_e(r,t)}{\partial r} \\ & +\Gamma_{ECH}(r,t).\end{aligned} \tag{1}$$

Here, $D_{e,n}(r,t)$ denotes the normal electron diffusion coefficient, while $D_{e,T}(r,t)$ does an off-diagonal element due to electron temperature gradient. Then, the diffusion equation is expressed with this electron flux $\Gamma_e(r,t)$ as

$$\frac{\partial n_e(r,t)}{\partial t} = -\frac{\partial}{r\partial r}\left(r\Gamma_e(r,t)\right). \tag{2}$$

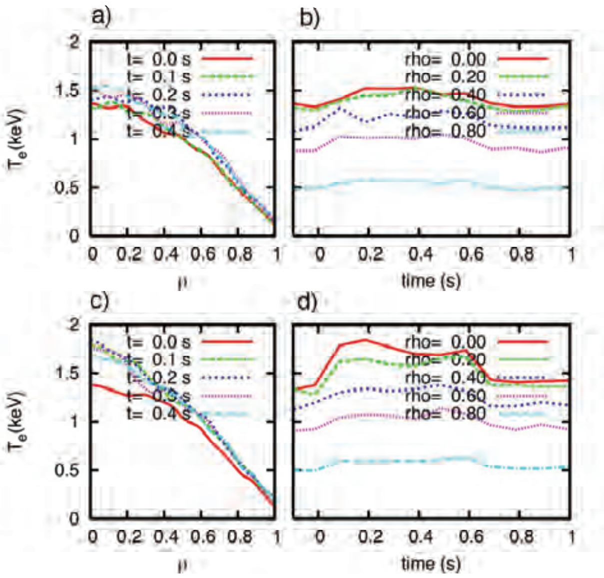

Fig. 8 Temperature profile at several time slices after ECH injection [a) and c)]. Time evolutions of the density at several spatial points b), and d) for ripple top [a) and b)] and bottom [c)and d)] heating cases.

Integrating over radius of Eq. (2) gives

$$\Gamma_e(r,t) = -\frac{1}{r}\int_0^r r' \frac{\partial n_e(r',t)}{\partial t}\mathrm{d}r'. \tag{3}$$

Thus total electron flux can be deduced from Eq. (3) by the experimentally observed quantity $n_e(r',t)$. In Fig.9 are shown the change in the particle flux deduced from Eq. (3) for the ripple a) top and b) bottom cases. Fast increase of the flux at $\rho > 0.3$ is clear in the ripple bottom heating case than that in the top case. The density gradient profile changes are also shown in Figs.9 c) and d) for comparison. As is expected from Eq. (1), the correlations between a) and c) or b) and d) indicate the effect of normal diffusion coefficient, but there seems no clear correlation between them. Second term in Eq. (1) describes the off-diagonal

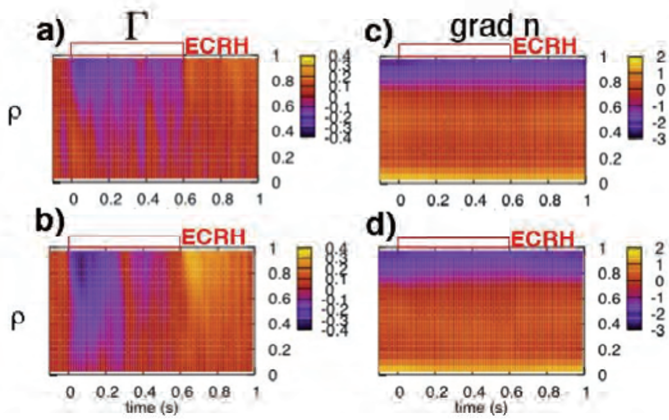

Fig. 9 Particle flux deduced from Eq. (3) for ripple a) top and b) bottom cases. c) and d) show a temporal change in the density gradient for each case.

term from the temperature gradient. As is described above, the temperature profile change occurs only at the beginning 100 ms after ECRH injection for both cases. So the correlation between the deduced flux and the temperature gradient should also be weak. These results indicate that the change in the deduced particle flux for the ripple top and bottom cases are directly driven by ECRH, although the dynamical dependence of the diffusion coefficient on the temperature and its gradient, off-diagonal term and the effect of the radial electric field should be considered more carefully.

4 Conclusion

By applying ripple top and bottom second harmonic ECRH, the density clamping phenomena are investigated. From the comparison of the density clamping between different ripple cases (R_{ax}=3.60 and 3.75 m), ECRH physics that is perpendicular acceleration of the electron, is shown to play an important role in the clamping phenomena. This indicates that the ECRH can be one of a nobs to control the local density. The difference in the temporal behavior of the electron density can be explained qualitatively by the direct electron flux by ECRH due to the enhanced ripple loss. The effect of the formation of radial electric field might have mitigated the degradation. Experimental and theoretical investigations of the effect of radial electric field are left for future work.

5 Acknowledgement

The authors would like to express their thanks to the continuous efforts of technical staff of ECRH and LHD to perform the experiments. This work is mainly performed under budget code NIFS05ULRR501-3.

[1] K. Ito *et al.*, J. Phys. Soc. Japan **58**, 482 (1989).
[2] H. Sanuki *et al.*, Phys. Fluids, **B2**, 2155 (1990).
[3] H. Idei *et al.*, Fusion Engineering and Design **26**, 167 (1995).
[4] C. Angioni *et al.*, Nuclear Fusion **44**, 167 (2004).

Proceedings of ITC/ISHW2007

Results of the stellarator optimization with respect to the neoclassical $1/\nu$ transport*

Bernhard SEIWALD[1)], Sergei V. KASILOV[1,2)], Viktor V. NEMOV[1,2)], Winfried KERNBICHLER[1)], Victor TRIBALDOS[3)], Thomas SUNN PEDERSEN[4)], Victor N. KALYUZHNYI[2)]

[1)]*Association EURATOM-ÖAW, Institut für Theoretische Physik - Computational Physics, TU Graz, Petersgasse 16, A–8010 Graz, Austria*

[2)]*Institute of Plasma Physics, National Science Center "Kharkov Institute of Physics and Technology", Akademicheskaya Str. 1, 61108 Kharkov, Ukraine*

[3)]*Asociación Euratom-CIEMAT, Madrid, Spain*

[4)]*Columbia University, Department of Applied Physics and Applied Mathematics, New York, New York 10027, USA*

Powerful tools have been developed in the last years for the design of new stellarator devices. This codes are usually working in magnetic coordinates. Tasks addressed by these codes are minimization of neoclassical transport, maximizing equilibrium and stability properties, etc. However, optimizing existing stellarators is time consuming because costly coordinate transformations are involved. A procedure working in real space coordinates for maximizing the plasma energy content, based on reducing the most unfavorable $1/\nu$ neoclassical transport, has been presented in [1]. This tool, named SORSSA, was developed especially for optimizing existing stellarator devices which are not fully optimized with respect to neoclassical transport. Some results for the stellarators Uragan 2M, U-2M, TJ-II and the Columbia Nonneutral Torus, CNT, are presented.

Keywords: Neoclassical Transport, Optimization, Stellarator

1 Introduction

One of the main disadvantages of non-axisymmetric confinement devices is their unfavorable, $1/\nu$, temperature scaling in the long mean free path collisionality (lmfp) regime, $\propto T^{7/2}$. The ∇B drift associated with their three-dimensional asymmetries leads to rapid losses of trapped particles. Therefore, improving stellarator transport starts, precisely, by optimizing the configurations against this disadvantageous $1/\nu$ lmfp regime [2].

2 Energy confinement

The scheme behind SORSSA analyzes the neoclassical $1/\nu$ transport properties of a magnetic field configuration. The measure of the neoclassical transport is the effective ripple $\epsilon_{\rm eff}$ [3]. For good confinement $\epsilon_{\rm eff}$ should be small. The effective ripple can be used to compute the total stored energy in the plasma volume, which is the figure of merit. The heat conductivity equation is solved under the premise that the neoclassical transport is the dominant transport mechanism. Assuming that the temperature profile is defined by the heat conductivity equation

$$\frac{1}{r}\frac{d}{dr}r\kappa_\perp\frac{dT}{dr} + Q(r) = 0\,, \qquad (1)$$

with the boundary conditions $T(a) = 0$ and $\lim_{r\to 0}\left(r\frac{dT}{dr}\right) = 0$, where a is the boundary of the plasma. The heat conductivity is proportional to $\epsilon_{\rm eff}^{3/2}T^{7/2}$ and computation of $\epsilon_{\rm eff}^{3/2}$ for sets of computed magnetic surfaces is an essential part of the optimization procedure. Integrating Eq. (1) leads to the normalized stored energy [4, 5]

$$\hat{W} = \int_0^a \mathrm{d}r\, r\,\hat{n}(r)\left(\int_r^a \frac{dr'}{r'\,\epsilon_{\rm eff}^{3/2}(r')}\right)^{2/9}\,. \qquad (2)$$

where $\hat{n} = n/n_0$ is the normalized particle density profile and a denotes the plasma radius. The integration variable is the effective radius of the flux surfaces. It is convenient to define the re-normalized stored energy W_n as

$$W_n = \hat{W}/\hat{W}_S\,, \qquad (3)$$

with $\hat{W}$ the normalized stored energy defined in Eq. (2) and $\hat{W}_S$ the normalized stored energy of the standard configuration.

The effective ripple $\epsilon_{\rm eff}^{3/2}$, which is part of the $1/\nu$ neoclassical transport coefficients and contains the characteristic features of the magnetic field geometry, is given by (see [3])

$$\epsilon_{\rm eff}^{3/2} \;=\; \frac{\pi R^2}{8\sqrt{2}}\lim_{L_s\to\infty}\left(\int_0^{L_s}\frac{\mathrm{d}s}{B}\right)\left(\int_0^{L_s}\frac{\mathrm{d}s}{B}|\nabla\psi|\right)^{-2}$$

*This work, supported by the European Communities under the contract of Association between EURATOM and the Austrian Academy of Sciences, was carried out within the framework of the European Fusion Development Agreement. The views and opinions expressed herein do not necessarily reflect those of the European Commission. Additional funding is provided by the Austrian Science Foundation, FWF, under contract number P16797-N08.

author's e-mail: seiwald@itp.tugraz.at

$$\cdot \int_{B_{\min}^{(\mathrm{abs})}/B_0}^{B_{\max}^{(\mathrm{abs})}/B_0} \mathrm{d}b' \sum_{j=1}^{j_{\max}} \frac{\hat{H}_j^2}{\hat{I}_j} . \qquad (4)$$

with

$$\hat{H}_j = \frac{1}{b'} \int_{s_j^{(\min)}}^{s_j^{(\max)}} \frac{\mathrm{d}s}{B} \sqrt{b' - \frac{B}{B_0}} \left(4\frac{B_0}{B} - \frac{1}{b'} \right) |\nabla\psi| k_G \qquad (5)$$

$$\hat{I}_j = \int_{s_j^{(\min)}}^{s_j^{(\max)}} \frac{\mathrm{d}s}{B} \sqrt{1 - \frac{B}{B_0 b'}} , \qquad (6)$$

and $b' = v^2/J_\perp B_0$. The geodesic curvature of the magnetic field line is given as $k_G = (\mathbf{h} \times (\mathbf{h} \cdot \nabla)\mathbf{h}) \cdot \nabla\psi/|\nabla\psi|$ with the unit vector $\mathbf{h} = \mathbf{B}/B$. Equation (4) is computed by integration over the magnetic field line, s, over a sufficiently large interval $0 - L_s$, and by integration over the perpendicular adiabatic invariant of trapped particles, $J_\perp$. Here, $B_{min}^{(abs)}$ and $B_{max}^{(abs)}$ are the minimum and maximum values of B within the interval $[0, L_s]$. The quantities $s_j^{(min)}$ and $s_j^{(max)}$ within the sum over j in (4) - (6) correspond to the turning points of trapped particles. This integration takes into account all kinds of trapped particles, such as those trapped within one magnetic field ripple as well as particles trapped within several magnetic field ripples.

The total stored energy, defined in Eq. (2), depends on ϵ_{eff} and on the plasma volume. A decrease of ϵ_{eff} at a fixed plasma volume increases the stored energy as well as an increase of the plasma volume at a fixed value of ϵ_{eff}. As the plasma volume and ϵ_{eff} are not independent in a stellarator, the optimum stored energy will not necessarily coincide with the largest attainable volume or at the lowest possible value of ϵ_{eff}.

3 Application

The total stored energy, defined in Eq. (2), has been used as figure of merit for optimizing the stellarators U-2M, TJ-II and CNT.

The U-2M device [6] is an $l = 2$ torsatron. An additional toroidal magnetic field is produced by a system of 16 toroidal field coils (TF coils) which are uniformly distributed in angle along the major circumference (four coils in each field period). The mean current in such a coil, I_{TFC}, is expressed in units of the helical winding current. For the standard configuration this current is $I_{TFC} = 5/12$, according Ref. [6]. In this case the parameter $k_\varphi = B_{th}/(B_{th} + B_{tt})$ is $k_\varphi = 0.375$ where B_{th} and B_{tt} are the toroidal components of the magnetic field produced by the helical winding and TF coils, respectively.

The vertical field coil (VF coil) system plays an important role in achieving the magnetic configuration of the torsatron. The total vertical magnetic field, $B_\perp$, is produced by the VF coils and the vertical magnetic field of the helical

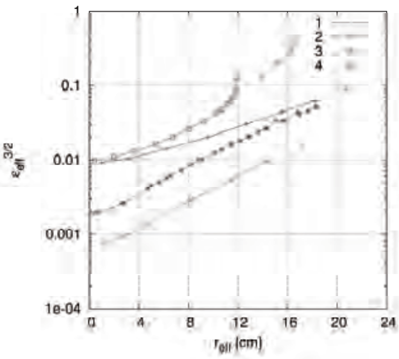

Fig. 1 Parameters $\epsilon_{\mathrm{eff}}^{3/2}$ as functions of r_{eff} for $k_\varphi = 0.31$ and various f_{VFC}; 1: $f_{VFC} = 1$, $\Delta I = 0$; 2: $f_{VFC} = 1.166$ ($B_\perp/B_0 = 0$), $\Delta I = 0$; 3: $f_{VFC} = 1$, $\Delta I = 0.06$; 4 (standard configuration): $k_\varphi = 0.375$, $f_{VFC} = 1$, $\Delta I = 0$. (taken from [1])

winding. The desired vertical field is obtained by adjusting the current in the VF coils. In the computations the VF coil system variant [7] is used which allows to suppress significantly the island structure of the magnetic surfaces.

Three control parameters are appropriate for the optimization. These parameters are related to the currents in the helical winding and in TF as well as VF coils:

(i) I_{TFC}, the mean current of TF coils, in units of helical winding current. It is directly connected to the above mentioned parameter k_φ (used in Refs. [6, 8]) by the ratio $k_\varphi = 1/(1 + 4I_{TFC})$ as it follows from the k_φ definition.

(ii) ΔI, which is introduced in view of the results of Ref. [8]. The currents in the TF coils are presented further in a form $I_{TFC} \pm \Delta I$ with a plus sign for the inner two coils in each field period and with a minus sign for the outer two coils (ΔI is also expressed in units of the helical winding current).

(iii) f_{VFC}, a multiplying factor for the currents in the VF coils. This factor is connected to an additional vertical magnetic field. It enters linearly into the expression for the magnetic field of the VF coils in a way that for k_φ=0.375 it results in $B_\perp/B_0 = 2.5\%$ for $f_{VFC} = 1$, $B_\perp/B_0 = 0$ for $f_{VFC} = 1.166$ and $B_\perp/B_0$ =-2.5% for $f_{VFC} = 1.332$. Here, $B_\perp$ is the resulting vertical magnetic field and B_0 is the mean toroidal magnetic field.

Here we focus on results for the studies of the total stored energy for a decreased parameter k_φ. Decreasing k_φ may reduce the helical ripple, may lead to an improvement of the stored energy in the $1/\nu$ transport regime and a reduction of the magnetic island structure produced by current-feeds and detachable joints of the helical winding.

In Fig. 1 results for $\epsilon_{\mathrm{eff}}^{3/2}$ corresponding to $k_\varphi \approx 0.31$ for $f_{VFC} = 1$ and 1.166 are presented. The latter value corresponds to a full compensation of the mean vertical magnetic field of the helical winding. Besides, curve 3 shows the results corresponding to $\Delta I \neq 0$ ($f_{VFC} = 1$, $k_\varphi \approx 0.31$). For comparison, the results for the standard configuration ($f_{VFC} = 1$, $\Delta I = 0$) are shown.

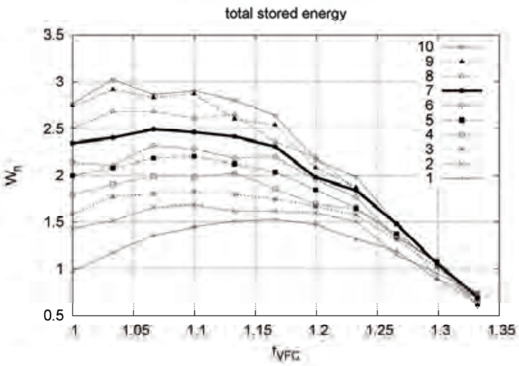

Fig. 2 Re-normalized stored energy (see Eqs. (2) and (3)) for various f_{VFC} ($B_\perp/B_0$) and I_{TFC} (k_φ) with taking into account limitations by the chamber; 1: I_{TFC} = 0.41667 (k_φ = 0.375); 2: I_{TFC} = 0.43928 (k_φ = 0.33627); 3: I_{TFC} = 0.4619 (k_φ = 0.3512); 4: I_{TFC} = 0.4845 (k_φ = 0.3404); 5: I_{TFC} = 0.5071 (k_φ = 0.3302); 6: I_{TFC} = 0.5298 (k_φ = 0.3206); 7: I_{TFC} = 0.55555 (k_φ = 0.3103); 8: I_{TFC} = 0.5976 (k_φ = 0.2949); 9: I_{TFC} = 0.62024 (k_φ = 0.2873); 10: I_{TFC} = 0.6429 (k_φ = 0.28). (taken from [1])

It can be seen in Fig. 2 that with decreasing k_φ the stored energy increases and the maxima in the stored energy correspond to some optimum values of f_{VFC} ($B_\perp$). For $k_\varphi \approx 0.31$ (thick line in Fig. 2) it follows that the maximum in the stored energy is approximately $2.5/1.5 \approx 1.65$ times higher than the corresponding maximum for $k_\varphi = 0.375$. The results corresponding to $I_{TFC} = 5/9$ ($k_\varphi \approx 0.31$) are of special interest because it follows from Ref. [11] that for $k_\varphi \approx 0.31$ the magnetic configuration of U-2M is less sensitive to the influence of current-feeds and detachable joints of the helical winding. It has been shown that in this case for the major part of the configuration the rotational transform stays within the range $1/3 < \iota < 1/2$ and big magnetic islands are absent.

The medium size heliac TJ-II ($R = 1.5$ m, $a < 0.2$ m) has four field periods [9] and consists of 32 helically displaced toroidal coils, one central helical coil wrapped around the central circular coil and two vertical field coils. The free parameters for the "common" TJ-II operation are (1) the toroidal coil current, (2) the current for the helical winding, (3) the current for the central circular coil and (4) the current for vertical field coils. For a run of the optimizer these parameters have been varied within the range of ±20% of the corresponding values for the standard configuration, which is within the technical constraints. Within the frame of optimization several configurations with enhanced stored energy compared to the standard configuration could be found. The re-normalized stored energy, defined in Eq. (3) is shown in Fig. 3. It can be seen, that the energy of the best configuration is about 1.45 times as high as the the energy of the standard configuration.

The radial dependency of $\epsilon_{\rm eff}$ on the effective radius is presented in Fig. 4. It can be seen that the effective ripple

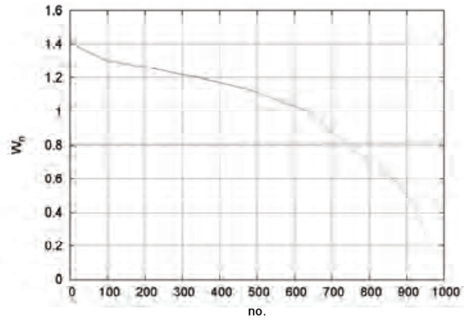

Fig. 3 The re-normalized stored energy (see Eqs. (2) and (3)) for the computed TJ-II configurations (taken from [4]).

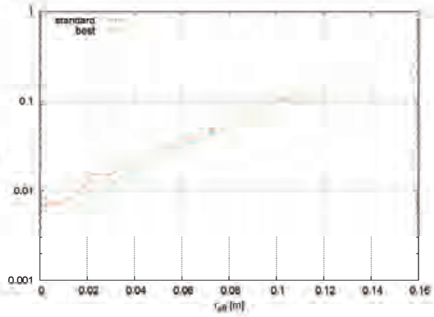

Fig. 4 Effective ripple $\epsilon_{\rm eff}^{3/2}$ vs. effective radius $r_{\rm eff}$ for TJ-II standard configuration and the best configuration(taken from [4]).

of the best configuration is slightly smaller compared to the standard configuration. Furthermore, the plasma radius of the best configuration (a ≈ 15 cm) is markedly increased compared to the standard configuration (a ≈ 11 cm).

The CNT was designed as a simple and compact stellarator with only two pairs of circular, planar coils [10]. These are one pair of interlocking (IL) coils inside the vacuum vessel and another pair of coils, the poloidal field (PF) coils, outside the vacuum vessel. The achieved design goals have been the error field resilience, a large flux surface volume relative to the experimental footprint and that it should be easy to build the experiment. However, minimizing the neoclassical transport was not a design goal. The two free parameters for the optimization are the current of the poloidal field coils (I_{PF}) and the angle between the interlocking coils, called tilt angle. The current for the interlocking coils is fixed at 170 kA which is the design current (see [10]). The two dimensional grid spanned by the PF coil current and the tilt angle has been scanned to get a good knowledge how the re-normalized stored energy W_n depends on the two free parameters. Two different values of the coil separation, which is the vertical distance between the centers of the two IL coils, have been used. One scan was done for the nominal value with 63 cm. The other scan was done for a IL coil separation of of 62.6 cm, because for 64 deg tilt angle the edges of the two IL coils would touch each other if they were at the 63 cm coil sep-

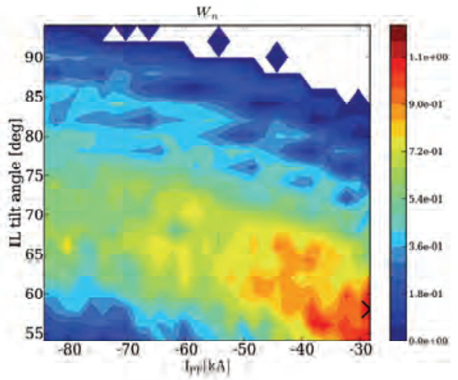

(a)

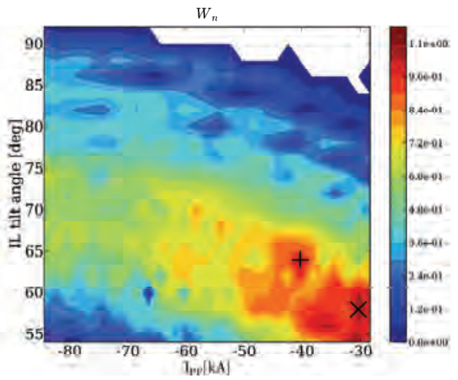

(b)

Fig. 5 The re-normalized stored energy for CNT (see Eqs. (2) and (3)) for 63 cm coil separation (a) and 62.6 cm coil separation (b) (taken from [5]). The standard configuration is marked with "+" and the best configuration of each scan is marked with "×".

aration. The results of these scans are presented in Fig. 5. From these plots can be seen, that W_n is increasing when approaching the area where the PF coil current is -30 kA and the tilt angle is 58 deg. Configurations where the tilt angle is about 90 deg and the PF coil current is in the range of -60 to -30 kA consist mainly of islands and stochastic zones.

The best configuration with a coil separation of 63 cm (referred as "best 630") exhibits an energy which is enhanced by 17% compared to the standard configuration. The energy of the best configuration with 62.6 cm coil separation (referred as "best 626") is about 1.1 times the energy of the standard configuration. The standard configuration exhibits the lowest values of $\epsilon_{\rm eff}$ of the three considered configurations. The plasma radius for the standard configuration is slightly smaller compared to the plasma radii of the two other configurations. The positive volume effect is stronger than the negative effect of an increased $\epsilon_{\rm eff}$ so that the stored energy is higher for the best configurations compared to the stored energy of the standard configuration.

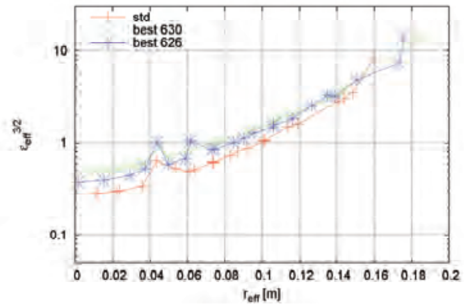

Fig. 6 Effective ripple $\epsilon_{\rm eff}^{3/2}$ vs. effective radius $r_{\rm eff}$ for the standard configuration and the best configurations for the two considered coil separations (taken from [5]).

4 Conclusion

A scheme for optimizing stellarators in real space with respect to the total stored energy based on neoclassical transport, has been developed and implemented numerically in the code SORSSA. Applying SORSSA to the fusion devices U-2M, TJ-II and CNT, it could be shown that, with a proper choice of the free parameters, configurations with enhanced total stored energy compared to well known standard configurations could be achieved.

[1] B. Seiwald, V. N. Kalyuzhnyj, S. V. Kasilov, W. Kernbichler, and V. V. Nemov. *Fusion Science and Technology*, 50(3):447–456, 2006.

[2] G. Grieger, W. Lotz, P. Merkel, J. Nührenberg, et al., *Phys. Fluids B*, 4(7):2081–2091, 1992.

[3] V. V. Nemov, S. V. Kasilov, W. Kernbichler, and M. F. Heyn, *Phys. Plasmas*, 6(12):4622–4632, 1999.

[4] B. Seiwald, S. V. Kasilov, W. Kernbichler, V. N. Kalyuzhnyj, V. V. Nemov, V. Tribaldos, and J. A. Jiménez, *J. Comput. Phys.*, 2007. submitted.

[5] B. Seiwald, V. V. Nemov, T. Sunn Pedersen, and W. Kernbichler, *Plasma Phys. Control. Fusion*, 2007. submitted.

[6] O. S. Pavlichenko, *Plasma Phys. Control. Fusion*, 35:B223–B230, 1993.

[7] V. E. Bykov, E. D. Volkov, A. V. Georgievskij, et al., In *Plasma Physics and Controlled Nuclear Fusion Research 1988 (Proc. of 12th Int. Conf., Nice, 1988)*, volume 2, pages 403–410, 1989.

[8] C. D. Beidler, N. T. Besedin, V. E. Bykov, et al., In *Plasma physics and controlled nuclear fusion research 1990. V. 2 . Proceedings of the thirteenth international conference. Vienna (Austria). Washington, D.C., 1 – 6 Oct 1990.*, pages 663 – 675. IAEA, 1991.

[9] C. Alejaldre, J. J. A. Gozalo, J. Botija Perez, et al., *Fusion Technol.*, 17:131–139, 1990.

[10] T. Sunn Pedersen, A.H. Boozer, J. P. Kremer, R. G. Lefrancois, W. T. Reiersen, F. Dahlgren, and N. Pomphrey, *Fusion Science and Technology*, 46:200, 2004.

[11] G. G. Lesnyakov, D. D. Pogozhev, et al., in 23rd EPS Conference on Controlled Fusion and Plasma Physics, 24-28 June 1996, Bogolyubov Institute for Theoretical Physics, Kiev, Ukraine, (European Physical Society, 1996), Vol.20 C, Part II, p.547 (Report b025).

Proceedings of ITC/ISHW2007

Electron Thermal Energy Transport Research Based on Dynamical Relationship between Heat Flux and Temperature Gradient

Takashi NOTAKE[1)], Shigeru INAGAKI[2)], Naoki TAMURA[3)], Shin KUBO[3)], Takashi SHIMOZUMA[3)], Kenji TANAKA[3)], Takeshi FUKUDA[4)], Teruo SAITO[1)] and Yoshinori TATEMATSU[1)]

[1)] *Research Center for Development of Far-Infrared Region, University of Fukui, Fukui 910-8507, Japan*

[2)] *Research Institute for Applied Mechanics, Kyushu University, Fukuoka, 816-8580, Japan*

[3)] *National Institute for Fusion Science, Toki, 509-5292, Japan*

[4)] *Graduate school of Engineering, Osaka University, Osaka, 560-0043, Japan*

In the nuclear fusion plasmas, both of thermal energy and particle transports governed by turbulent flow are anomalously enhanced more than neoclassical levels. Thus, to clarify a relationship between the turbulent flow and the anomalous transports has been the most worthwhile work.

There are experimental results that the turbulent flow induces various phenomena on transport processes such as non-linearity, transition, hysteresis, multi-branches and non-locality. We are approaching these complicated problems by analyzing not conventional power balance but these phenomena directly. They are recognized as dynamical trajectories in the flux and gradient space and must be a clue to comprehend a physical mechanism of arcane anomalous transport. Especially, to elucidate the mechanism for electron thermal energy transport is critical in the fusion plasma researches because the burning plasmas will be sustained by alpha-particle heating.

In large helical device, the dynamical relationships between electron thermal energy fluxes and electron temperature gradients are investigated by using modulated electron cyclotron resonance heating and modern electron cyclotron emission diagnostic systems. Some trajectories such as hysteresis loop or line segments with steep slope which represent non-linear property are observed in the experiment.

Keywords: Electron thermal transport, Transient response, Dynamic transport, Plasma turbulence, Gyrotron Electron cyclotron resonance heating, Electron cyclotron emission, Large Helical Device

1. Introduction

Anomalousness for thermal energy and particle transports triggered by turbulent flow in the high temperature nuclear fusion plasmas has been one of the most controversial issues. Especially, to grasp a physical mechanism of electron heat energy transport will be critical in nuclear fusion plasma researches because the burning plasmas will be sustained by alpha-particle heating which lead to electron heating.

The plasma transport was investigated mainly based on a global scalar quantity so-called the energy confinement time. However, it is nothing but a volume-averaged value of the effective transport coefficient $ÿ_e^{p:b:}$ weighted at plasma peripheral regions. Here, the effective means including not only pure diffusion term but also convection and off-diagonal ones. The $ÿ_e^{p:b:}$ can be deduced by solving the power balance equation, but the $ÿ_e^{p:b:}$ give us no dense information about complicated characteristic of the transport phenomena because the flux is not simply proportional to gradient anymore in the nuclear fusion plasmas. Therefore such analysis based on power balance equation is not suitable for clarifying the mechanism of complex anomalous transport.

2. Transport analysis

By using transport matrix, the electron thermal flux is related with thermodynamic driving forces as follow [1].

$$Q_e = à\, n_e ÿ_e\, r\, T_e + Q_{off}$$

Here, the $Q_e; n_e; T_e$ are the electron thermal flux, electron density and electron temperature respectively. And the Q_{off} is the term having dependences on some gradients except for $r\,T_e$ and may well include even convection term. A thermal diffusive coefficient derived from the power balance is equivalent to

$$ÿ_e^{p:b:} = ÿ_e\, à\, \frac{1}{n_e r T_e} Q_{off}.$$

This quantity is different from the y_e. Contrastively, a

author's e-mail: notake@fir.fukui-u.ac.jp

thermal diffusive coefficient derived from the transient response is given as

$$\chi_e^{h.p.} = \chi_e - \frac{1}{n_e \nabla \delta T_e}\left(\frac{\partial Q_{eff}}{\partial \nabla n_e}\nabla \delta n_e + \frac{\partial Q_{eff}}{\partial \nabla T_i}\nabla \delta T_i + \cdots\right),$$

Where δT_e; δn_e and δT_i represent the perturbation components of the electron temperature, electron density and ion temperature respectively. When these perturbations except for the electron temperature are negligible, $\chi_e^{h.p.}$ accord with a thermal diagonal element χ_e of transport matrix. In this manner, $\chi_e^{p.b.}$ and $\chi_e^{h.p.}$ are another physical quantities.

The discussion mentioned above still based on the linear theory for thermal diffusion. In the nuclear fusion plasmas, it has been demonstrated that the χ_e itself depends on ∇T_e and T_e[2-5]. In the case of the χ_e has dependence like $\chi_e \,/\, (\nabla T_e)^{\alpha}$, the ratio of $\chi_e^{h.p.}$ to $\chi_e^{p.b.}$ called the stiffness factor becomes as follow.

$$\chi_e^{h.p.}/\chi_e^{p.b.} = \alpha + 1$$

According to many experimental contributions all over the world, it has been reported that the $\chi_e^{h.p.}$ is larger than $\chi_e^{p.b.}$. This fact implies that drastic enhancement of electron thermal flux is accompanied with increment of electron temperature gradient.

The foregoing non-linearity on the transports is caused by the turbulent flow. Therefore, to grasp the relation between them has been the high-priority issue and it has been observed that the turbulent flow induces various patterns in the transport processes such as non-linearity, non-locality, multi-states, transition, hysteresis and so on [6-7]. The anomalous transport phenomena will be discriminated and described by apprehending these patterns. Therefore, to investigate the dynamical relationship between electron energy flux and electron temperature gradient directly over the wide plasma parameter regions must be essential. Also, experimental results analyzed with this scheme will give us a more natural comparison with sophisticated transport simulations considering microscopic instabilities such as TEM, ETG and ITG.

3. Flux-gradient technique

The electron thermal flux can be evaluated from the electron energy conservation under the approximation of cylindrical geometry as below.

$$Q_e = \frac{1}{r}\int_0^r r\,dr\left(P_e - \frac{\partial}{\partial t}\left(\frac{3}{2}n_e T_e\right)\right)$$

It is no necessity to introduce magnetic-coordinate system if the aspect ratio of the plasma confinement device is large. The P_e indicates effective input power to electrons per unit volume and should include the electron-ion energy equipartition and radiative transfer in a precise sense. But a contribution from the ECRH is only considered here for simplification. Modulated electron cyclotron resonance heating (MECH) can be used as perturbation source of the electron temperature [8] and which is measured with 32-channel ECE radiometer with high spatial and temporal resolutions. This sophisticated ECE system makes possible dynamical transport research that excludes the use of any transport models and gives us the radial electron energy flux as a function of the electron temperature gradient. The electron density is measured with FIR-interferometer and subtle density fluctuation during modulated ECRH can be neglected because the amplitude of the fluctuation much less than that of electron temperature. A merit of the flux-gradient technique is that the heat fluxes are deduced from integrals which are robust to errors of the integrands [9].

4. Experimental setup and results

To investigate the effect of electron thermal transport on the electron temperature gradient, productions of target plasmas with different electron temperature gradients are attempted. In LHD, ECRH system consists of five 84GHz range gyrotrons and three 168GHz ones [10]. One of 168 GHz gyrotrons is used as modulation source and the target plasmas are sustained by only ECRH using residual gyrotrons. Fig.1 shows all ECRH deposition profiles estimated from ray-tracing calculations. The solid line shows the case of the almost power is deposited within the ρ=0.4. The open circles show the case of certain power is deposited more outward to suppress the electron temperature gradient.

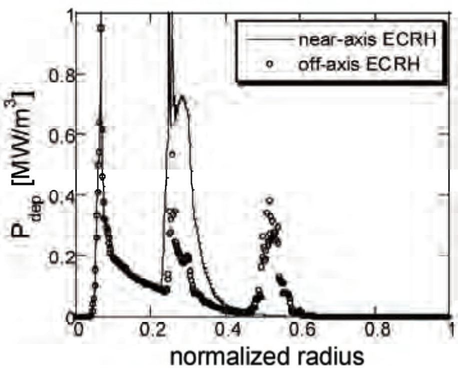

Fig.1. ECRH power deposition profiles in the experiment.

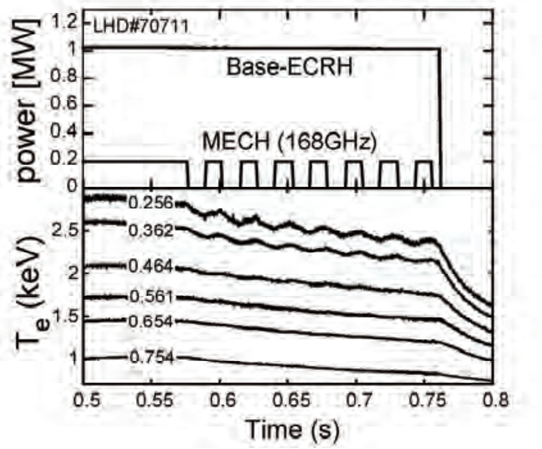

Fig.2 Temporal evolutions of injected ECRH power and electron temperature profiles measured with ECE. For clarity, not all of the 32 channels are shown.

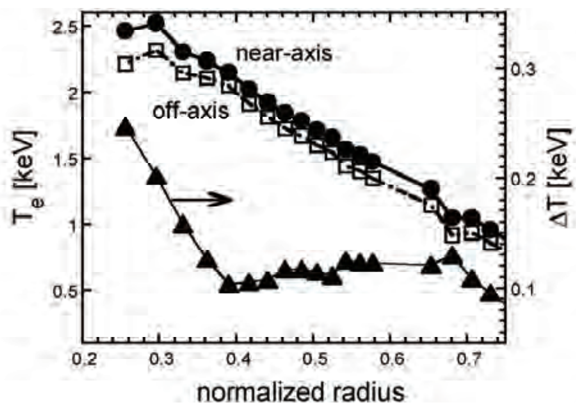

Fig.3. Electron temperature profiles of target plasmas and the difference of them at 0.57 s. The gradient have some differences from ρ=0.25 to ρ=0.4.

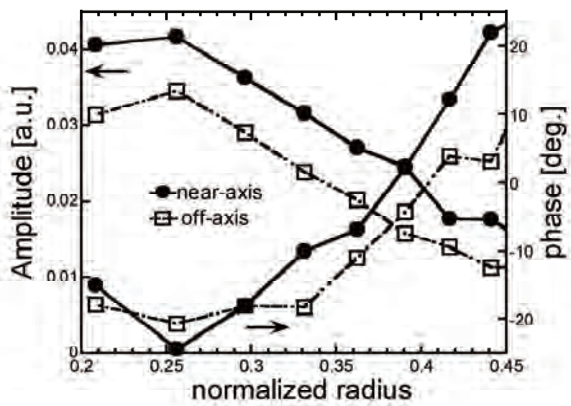

Fig.4. Amplitude and phase profiles deduced from the FFT. The extremal values appeared at the ρ=0.25.

Total injection power of ECRH is more than 1MW and the electron density is about 0.5×10^{19} m^{-3} at the experiment. The power deposition of the MECH as the heat pulse source is located at ρ=0.25 in both cases and the MECH is superposed to the target plasmas from 0.557 sec. to 0.756 sec. as shown in Fig.2. The power was modulated by handling anode voltage, so the power was almost 100% modulated.

Fig.3 shows the realized electron temperature profiles for two target plasmas at 0.57 sec. which is a timing before MECH was injected. And the triangles represent the temperature difference of them. These target plasmas have slight difference of electron temperature gradients from ρ=0.25 to ρ=0.4. In addition, amplitude and phase profiles of heat perturbation are analyzed at Fig.4. It is found that the peak of the amplitude and bottom of the phase profiles are located at the ρ=0.25 where the MECH power is deposited. The heat pulse propagates toward both sides as a center on there. According to the conventional linear theory, the solution of the heat diffusion equation under the slab geometry is given as follows with the modulation frequency ω_{mod}.

$$\delta T_e(x,t) = \delta T_{e0} \exp\left[i\omega_{mod} t - r\sqrt{3\omega_{mod}/4\chi_e}\,(1+i) \right]$$

The amplitude of the temperature perturbation generally decreases exponentially, while the time delay increase linearly with the distance from the power deposition region. The modulation frequency of ECRH should be well higher than the inverse of the characteristic time of transport. But the amplitude will be poor when the modulation frequency is set too high. In the experiment, modulation frequency is set to 50 Hz. The smaller χ_e which means better confinement give the slower heat pulse propagation. The $\chi_e^{h.p.}$ can be estimated from only phase distribution as follows.

$$\partial\varphi/\partial r = -\sqrt{(3/4)\,\omega_{mod}/\chi_e^{h.p.}}\ .$$

However, judging from the phase distribution around ρ=0.25 shown in Fig.4, the electron thermal transport in the plasma with more gradual gradient become more extensive. So the experimental result markedly didn't obey the linear theory based on the diffusive concept. There are strong non-linearity and/or any other effects. In this way, the heat transport coefficient χ_e has no crucial meaning any longer in the high temperature nuclear fusion plasmas. We had better to discuss the relationship between the electron thermal flux and electron temperature gradient genuinely without intervention of the χ_e.

In order to investigate the dynamical behaviors, ECE data are used to obtain temporal electron energy flux and they are spatially differentiated to derive the gradients at each normalized radius. Time is a parameter to describe the dynamical trajectories in the flux-gradient space. Fig.5 shows the experimentally obtained trajectories during a cycle of MECH for two target plasmas with different electron temperature gradients. The figures (a) and (b) correspond to near-axis ECRH and off-axis ECRH cases respectively. The vertical axis indicates themal flux per electron and the horizontal line is electron temperature gradient. The diagonal line showing $\chi_e^{p.b.}=10$ is also plotted as a mere indicator. The results show complicated relationships far from the expected ones based on diffusive features.

In the peripheral regions near the ρ=0.7, rough line segments with distinctly steep slopes are observed which suggest the strong stiffness, $\chi_e^{h.p.}=\chi_e^{p.b.}$ ÿ 1. And this slope may imply the critical gradient. In the intermediate region such as ρ=0.36, 0.46 and 0.56, multivalues like hysteresis loop appeared. This result signifies that transport is not uniquely decided to the flux and gradient. In the inward region near the magnetic axis, the modulation of both heat flux and gradient becomes very small and there are non-negligible measurement errors of ECE system. Hence, the results are less definitive and not shown here. The investigation of the dynamics in the plasma core regions where the appearances of more interesting results are expected is left as future works. Also, extending experimental plasma parameter regions will give us more effective information in order to grasp transport mechanism.

5. Summary

In this paper, we showed the initial results of dynamical electron thermal transport research by using MECH in high temperature LHD plasmas. Strong non-linearity is observed and the in-depth discussions have been possible by the dynamical research although they were impossible by the conventional power balance analysis. By applying this investigation in wider plasma parameter ranges, more comprehensive understanding to electron thermal transport in nuclear fusion plasmas will be expected.

Acknowledgment

I gratefully acknowledge fruitful discussions with Prof. Tetsuo Watari of NIFS. This work was supported by the NIFS under the Grant Number of NIFS06ULRR501,502 and 503.

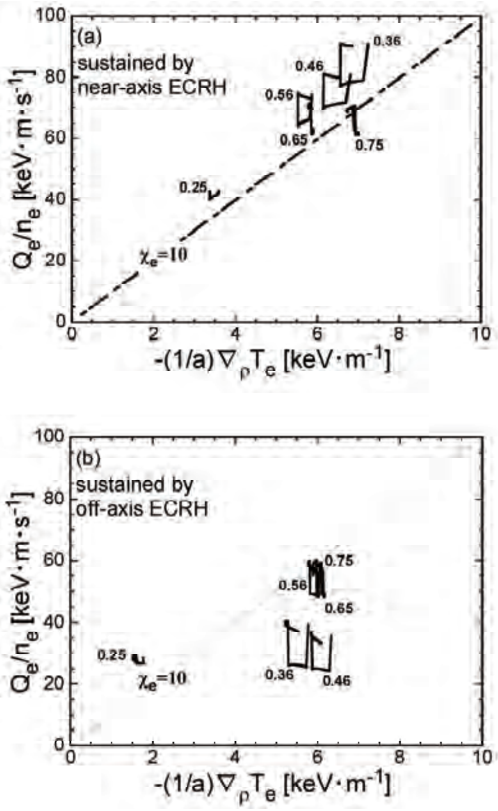

Fig.5. Dynamical relationship between electron thermal fluxes and electron temperature gradients at each normalized radius for (a) near-axis ECRH target plasma and (b) off-axis ECRH target plasma.

References

1). N.J.Lopes Cardozo, Plasma Physics and Controlled Fusion, vol.**37** (1995), pp799-852
2). U.Stroth, L.Giannone, et.al., plasma Physics and Controlled Fusion. Vol.**38** (1996), pp.611-618
3). A.Jacchia, et.al., Physics of Fluids, B3**(11)** (1991)
4). K.W.Gentle, M.E.Austin and P.E.Phillips, Physical Review letters, vol.**87**, 125001 (2001)
5). S.Inagaki, et.al., Nuclear Fusion, vol.**46** (2006)p.133
6). S.Inagaki, N.Tamura, et.al., Plasma Physics and Controlled Fusion, vol.**48** (2006).pp251-257
7). K.Ida, S.Inagaki, R.Sakamoto, et.al., Physical Review Letters, vol.**96**, 125006 (2006)
8). V.Erckmann and U.Gasparino, Plasma Phys. Control. Fusion, vol.**36**, 1869(1994)
9). K.W.Gentle, M.E.Austin, J.C.DeBoo, T.C.Luce and C.C.Petty, Physics of Plasmas, vol.**13** (2006).
10). T.Notake, S.Ito, S.Kubo, T.Shimozuma, et.al., Transaction of Fusion Science Tecnology, **51**(2007)

Study of neoclassical transport of LHD plasmas applying the DCOM/NNW neoclassical transport database

Arimitsu Wakasa, Sadayoshi Murakami[a)] and Shun-ichi Oikawa

Graduate School of Engineering, Hokkaido University, Sapporo 060-8628, Japan

[a)] *Department of Nuclear Engineering, Kyoto University, Kyoto 606-8501, Japan*

wakasa@fusion.qe.eng.hokudai.ac.jp

Abstract

A neoclassical transport database, DCOM/NNW, is developed including the configuration changes due to finite beta effect in LHD. The mono-energetic diffusion coefficients are evaluated based on the Monte Carlo method by DCOM code and the mono-energetic diffusion coefficient database is constructed using a neural network technique. Input parameters for the database are the collision frequency, the radial electric field, the minor radius and the plasma beta. The DCOM/NNW database is applied to finite beta plasma, and the neoclassical transport coefficients and the ambipolar radial electric field are evaluated in LHD.

Keywords:

LHD, neoclassical transport, neural network, Monte Carlo method

1. Introduction

In helical systems, neoclassical transport is one of the important issues for sustaining high-temperature plasma. In particular, in the long-mean-free-path (LMFP) regime, the neoclassical transport coefficient increases as collision frequency decreases ($1/\nu$ regime), and neoclassical transport plays an important role as well as anomalous transport by plasma turbulence.

Many studies have been carried out to evaluate the neoclassical transport coefficient analytically and numerically in helical systems. Among the studies, the Drift Kinetic Equation Solver (DKES)[1, 2] code has been commonly used for experimental data analyses[3, 4] and theoretical predictions.[5] However, in the LMFP regime, especially with finite beta, a large number of Fourier modes of the magnetic field must be used for distribution function and a convergence problem occurs.

On the other hand, the neoclassical transport coefficient has also been evaluated using the Monte Carlo method directly following particle orbits, where the mono-energetic diffusion coefficients are estimated by the radial diffusion of test particles.[6-8] This method has a good property in the LMFP regime except for its long calculation time. Thus, we have developed a Monte Carlo simulation code, the Diffusion Coefficient Calculator by Monte Carlo Method (DCOM) code,[9] which is optimized in performance in the vector computer.

To evaluate the neoclassical diffusion coefficient of thermal plasma, we must take energy convolution into account. Therefore, it is necessary to interpolate discrete data using the DCOM. In a non-axisymmetric system, the diffusion coefficient shows complex behavior and strongly depends on collision frequency and radial electric field (e.g., $1/\nu$, $\sqrt{\nu}$ and ν regimes). The interpolation based on a traditional analytical theory has a problem with connected regions between two regimes.

The neural network (NNW)[10], which has a strong nonlinearity and high fitting abilities for nonlinear phenomena, is applied in the study of fusion plasma and used in constructing the NNW database for neoclassical transport in TJ-II plasma.[11] Therefore, the NNW method is applied to the fitting of the diffusion coefficient of LHD, which shows a complex behavior in several collisional regimes, i.e., ν, $\sqrt{\nu}$, $1/\nu$, plateau, and P-S regimes. A multilayer perceptron NNW with only one hidden layer, generally known as MLP1, is used. The neoclassical transport database, DCOM/NNW[12], has been constructed with input parameters *r/a*, ν^*, and G and D^* can be obtained as an output of the NNW, where ν^* is the normalized collision frequency, G is the normlized radial electric field and D^* is the normalized diffusion coefficient respectively. We have constructed six database each of six LHD configurations with different values of the magnetic axis shift in the major radius direction between R_{axis} = 3.45 m and R_{axis} = 3.90 m.

At construction of this database, we assumed only vacuum plasma and have not taken into account finite beta plasma. However, a relatively large Shafranov shift occurs in finite beta LHD plasmas and the magnetic field configuration becomes complex leading to rapid increase of the number of Fourier modes in Boozer coordinates.

In order to analyze transport of experimental plasma with finite beta, we have to take account into finite beta. Therefore, we apply effect of finite beta to the neoclassical database, DCOM/NNW. We evaluate the neoclassical transport coefficients and the ambipolar radial electric field using improved DCOM/NNW..

2. Construction of neoclassical transport database including finite beta effect

The Fourier spectrum of the magnetic field $B_{m,n}$ in the Boozer coordinate as functions of normalized minor radius r/a in the R_{axis} = 3.75 m configuration with β_0 = 0% and β_0 = 3% is shown in Fig.1. Here, $B_{0,0}$ is the amplitude of the (0, 0) component of magnetic field strength at the magnetic axis, where (m, n) represents the Fourier component of magnetic field with the poloidal number, m, and the troidal number, n. It is shown taht the dominant magnetic field components in LHD with β_0=0% plasma are (2,10) and (1,0); (2,10) corresponds to the main helical mode and (1,0) is the toroidicity. Figure 1(b) shows that the amplitude of (2,10) and (1,0) component decrease and a lot of other components increase by the effect of beta value, especially in the edge plasma, and the magnetic field configuration becomes complex.

In this study, we calculate a mono-energetic diffusion coefficient, D, by DCOM code. Using DCOM code, we can calculate the diffusion coefficient without convergence problem even if we assume a lot of Fourier modes of the magnetic field. We use 50 Fourier modes to evaluate the magnetic field in this research. To obtain mono-energetic diffusion coefficients, we assume the electron energy of 1.0×10^{-3} eV. The magnetic field is set to 3T at the magnetic axis. The test particles are monitored for several collision times until the diffusion coefficient is converged. Figure 2 shows the normalized diffusion coefficient D^* at r/a = 0.5 in R_{axis} = 3.75m calculated using the DCOM code as a function of the normalized collision frequency ν^* without radial electric field. Here, we normalize the collision frequency by $\upsilon\iota/R$, and the diffusion coefficient by the tokamak plateau value in the mono-energetic case, D_P, as $D_P = (\pi/16)(\upsilon^3/\iota R_{axis}\omega_c^2)$, where υ, ι and ω_c are

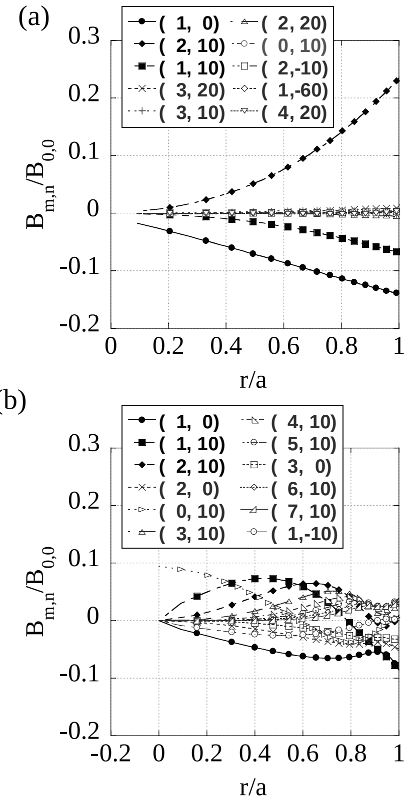

Fig. 1. Amplitude of dominant $B_{m,n}$ component normalized by B0,0 (r/a) as function of normalized minor radius r/a with (a) β_0=0% and (b) β_0=3%.

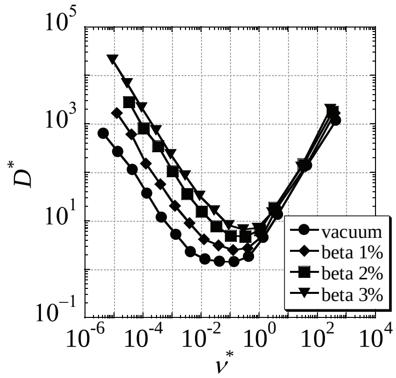

Fig. 2. Normalized monoenergetic diffusion coefficients as function of normalized collision frequency without radial electric field at r/a = 0.5 in R_{axis} = 3.75m.

the minor radius, the velocity of test particles, the rotational transform and cyclotron frequency of test particle, respectively. It is found that the normalized diffusion coefficients rise rapidly as the central plasma beta values increases from 0% to 3%.

In Fig. 3, the diffusion coefficient at r/a =0.5 are shown as function of β_0 in each regime. We can see that the diffusion coefficients are increased exponentially with β_0 in $1/\nu$ regime. It is found that the plateau values are also increased by the beta value. On the other hand, in the P-S regime, the diffusion coefficients are almost independent with the value of β_0.Thus, it is necessary to take into account the effect of the beta value in order to accurately evaluate transport in high temperature plasma, in which the collision frequency is in the $1/\nu$ or the plateau regime.

We add the beta values to the inputs of DCOM/NNW which is the neoclassical transport database.. We consider two LHD configurations, R_{axis} =3.60m and R_{axis} =3.75m. We adjust the weights of NNW using the computational results of DCOM, which are called training data. As beta value, we calculate the diffusion coefficient with β_0=0%, β_0=1%, β_0=2% and β_0 = 3% for training data. In this research, we totally used 2688 training data for R_{axis} = 3.75m configuration using the DCOM with various collision frequencies, radial electric fields, minor radius and beta values. Also, 1777 training data are used for R_{axis} = 3.60m configuration.

The accuracy of the NNW depends on the number of hidden units. The error between training data and outputs of NNW decrease as the number of hidden unit increases. However, if we increase the number of hidden unit too much, overlearning occurs, which gives poor prediction for a new parameter data although the error is very small.

In Fig.4, it is shown that the sum of relative error as function of the number of hidden unit of NNW. In this research, we assume the number of hidden unit is set to 15 and mean relative error is about 12.3 %.

We can obtain D^* by using the improved NNW database for arbitrary ν^*, G, r/a and newly, β_0. Figure 5 shows contour plot of D^*, obtained by the newly NNW, at r/a = 0.5, G = 0.0 in R_{axis} = 3.75m. The horizontal axis indicate ν^* and the vertical axis is β_0. We can found that D^*dose not depend on the beta value in P-S regime. And D^* is increased in $1/\nu$ and plateau regime as β_0 increases. It is also seen that the plateau regime has narrowed

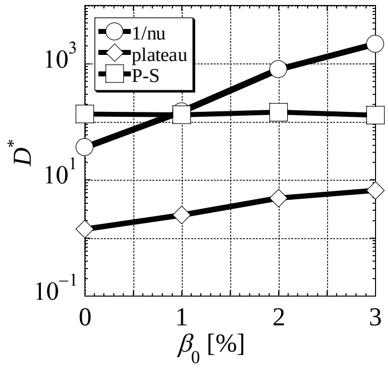

Fig. 3. Normalized diffusion coefficient as function of beta value, β_0, without radial electric field at r/a =0.5 in R_{axis} = 3.75m.

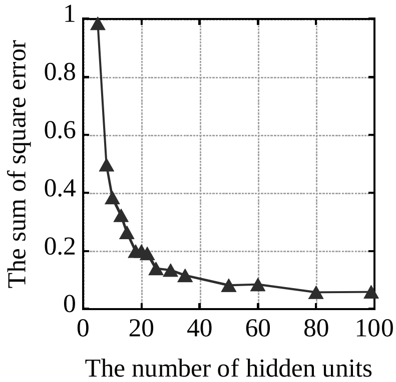

Fig. 4. The sum of relative error as function of number of hidden units of NNW.

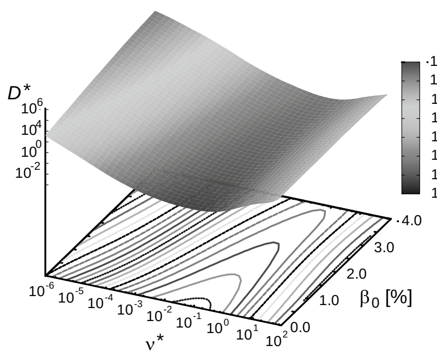

Fig. 5. The normalized monoenergetic diffusion coefficients, D^* as a function $D^*(\nu^*, G, r/a, \beta_0)$ in R_{axis} = 3.75m, where G and r/a are constant (G=0.0 and r/a = 0.5), which are outputs of DCOM/NNW.

as β_0 increases.

3. Neoclassical transport analysis

Next, we study the neoclassical transport by DCOM/NNW including the finite beta effect. In this analysis, we consider hydrogen plasma and R_{axis}= 3.75m. The assumed temperature and density profiles of electrons and ions are shown in Fig .6, and the magnetic field is B=1.5T (#48584, t = 1.48sec).

Figure 7(a) shows the ambipolar radial electric field as a function of r/a. There is only one root (ion root) with β_0= 0.0% and β_0=0.72%. We obtain similer profiles of the electric fields in both cases. However, it is found that the diffusion coefficient, D_1, with b0=0.0% and with 0.72% are greatly different as shown in Fig. 7(b). In the case of β_0=0.72%, D_1 increases to about three times that of β_0 = 0.0%. The heat conductivity, D_3, also increases with an increase of β_0. In the case of β_0=0.72%, D_3 increases to about four times that of β_0 = 0.0%.

This results show that the inclusion of finite beta effect is necessary for the accurate evaluation of neoclassical transport..

3. Summary

We have extended the neoclassical transport database, DCOM/NNW, to include the effect of configuration changes due to the finite beta effect. In the finite beta plasma, the magnetic field becomes complex and the number of necessary Fourier mode increases. Using extended DCOM/NNW we can estimate neoclassical transport more accurately than that using the previous DCOM/NNW.

We have investigated the neoclassical transport and evaluate the ambipolar radial electric field in LHD using DCOM/NNW.

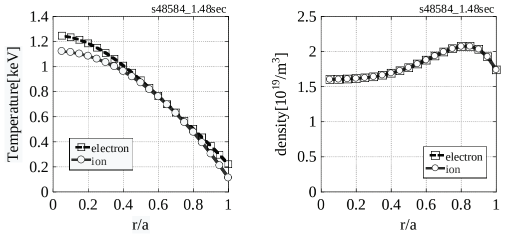

Fig. 6. Plasma temperature and particle density (#48584, t = 1.48sec, β_0 = 0.72%).

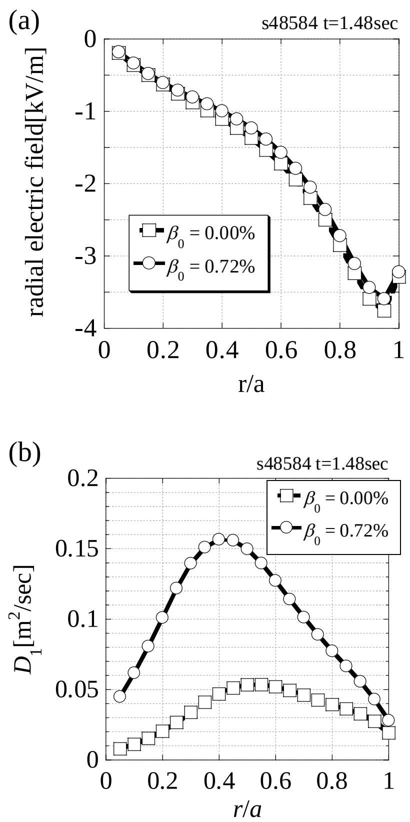

Fig. 7. (a) Radial electric field and (b) Diffusion coefficient as function of r/a with β_0 =0.0% and 0.72%.

Reference

[1] S. P. Hirshman, K. C. Shaing, W. I. van Rij, C. O. Beasley, Jr., and E. C. Crume, Jr.: Phys. Fluids **29** (1986) 2951.
[2] W. I. Van Rij and S. P. Hirshman: Phys. Fluids B **1** (1989) 563.
[3] H. Maassberg, R. Burhenn, U. Gasparino, G. Ku¨hner, H. Ringler, and K. S. Dyabilin: Phys. Fluids B **5** (1993) 3627.
[4] H. Maassberg, et al.W. Lotz, and J. Nu¨hrenberg: Phys. Fluids B **5** (1993) 3728.
[5] R. Kanno, N. Nakajima, H. Sugama, M. Okamoto, and Y. Ogawa: Nucl. Fusion **37** (1997) 1463
[6] A. H. Boozer and G. Kuo-Petravic: Phys. Fluids **24** (1981) 851.
[7] W. Lotz and J. Nu¨hrenberg: Phys. Fluids **31** (1988) 2984.
[8] C. D. Beidler and W. N. G. Hitchon: Plasma Phys. Control. Fusion **36** (1994) 317.
[9] A. Wakasa, S. Murakami et al.: J. Plasma Fusion Res. SERIES 4 (2001) 408
[10] C. M. Bishop: Rev. Sci. Instrum. **65** (1994) 1803.
[11] V. Tribaldos: Phys. Plasma **8** (2001) 1229.
[12] A. Wakasa, S. Murakami *et al.*: Jpn. J. Appl. Phys. **46** (2007) 1157.

Proceedings of ITC/ISHW2007

Improvement of Ion Confinement in Core Electron-Root Confinement (CERC) Plasmas in Large Helical Device

Y. Takeiri, M. Yokoyama, K. Nagaoka, K. Ida, S. Kubo, T. Shimozuma, H. Funaba, M. Osakabe, K. Ikeda, K. Tsumori, Y. Oka, M. Yoshinuma, S. Morita, M. Goto, K. Narihara, I. Yamada, K. Tanaka, O. Kaneko, A. Komori, and LHD Experimental Group

National Institute for Fusion Science,322-6 Oroshi-cho, Toki 509-5292, Japan

(Received 2 November / Accepted 2 November)

An increase in the ion temperature has been observed in the high-energy NBI-heated plasmas with superposition of the centrally focused ECRH in Large Helical Device. The T_i rise is accompanied by the formation of the electron-ITB. The transport analysis shows that the ion transport as well as the electron transport is improved with the reduction of the anomalous transport. The neoclassical ambipolar flux calculation shows the positive radial-electric field (E_r) in the region of the T_i rise, and the E_r should suppress the great enhancement of the ripple transport due to the T_i-rise. These analyses indicate the ion transport improvement in the core electron-root confinement (CERC) plasmas. The toroidal rotation is driven in the co-direction by adding the ECRH, and the toroidal rotation velocity is increased with the T_i rise. A correlation between the T_i rise and the toroidal rotation is suggested.

Keywords: core electron-root confinement, neoclassical transport, anomalous transport, radial electric field, ion transport, toroidal rotation, electron-ITB

1. Introduction

The helical devices have non-axisymmetric magnetic field configuration, which induces neoclassical ripple transport. The neoclassical ion and electron fluxes are strongly dependent on the radial electric field (E_r), the value of which is determined by the ambipolarity condition of these fluxes. The E_r also has a great influence on the plasma properties related to both the ripple transport and the anomalous transport. In major middle-sized helical devices such as CHS, W7-AS, and TJ-II, the improvement of the electron transport is commonly observed in the core electron-root confinement (CERC) plasmas [1,2], in which large positive E_r is observed in the core region. The CERC plasmas are obtained when the central electrons are strongly heated with the ECRH (electron cyclotron resonance heating), and they are also observed in Large Helical Device (LHD) [3-5]. In the CERC plasmas, the electron internal transport barrier (electron-ITB) with a steep gradient on the T_e profile is formed in the core region, and the core electron transport is improved in the neoclassical electron root with the positive E_r [1,2,6]. As a result, high T_e is achieved in the CERC plasmas.

The confinement improvement in the neoclassical electron root is specific to the helical system, and the ion transport should also be improved in the CERC plasmas in the theoretical prediction. We have observed a T_i rise in the NBI (neutral beam injection) plasma by applying the centrally focused ECRH in LHD, in which the T_e profile shows the electron-ITB formation. It is thought that the T_i rise is ascribed to the ion transport improvement in the CERC plasma. The transport analysis and the comparison with the neoclassical calculation are carried out, and the results are discussed. In the following, the plasma properties of the CERC plasmas, which are realized by applying the ECRH to the NBI plasmas, are presented with a view of the ion confinement improvement.

2. NBI and ECRH Systems

The Large Helical Device (LHD) is the world's largest superconducting helical device [7], and it is equipped with NBI and ECRH systems for the plasma heating. The NBI system consists of three high-energy negative-ion-based NB injectors [8,9] and a low-energy positive-ion-based NB injector [10]. The arrangement of the NBI systems is illustrated in Fig. 1. The injection direction of the negative-NBI is tangential while that of the positive-NBI is perpendicular to the magnetic axis. The injection energy of the negative-NBI is as high as 180keV and the plasma electrons are dominantly heated. The total injection power achieved is 14MW in the negative-NBI. To

author's e-mail: takeiri@nifs.ac.jp

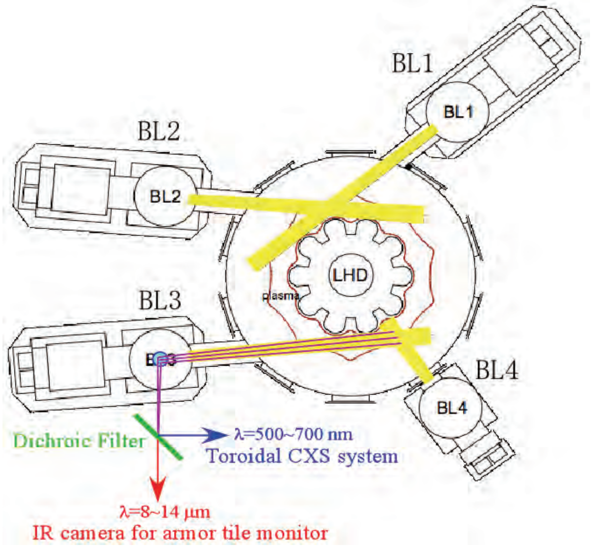

Fig.1 Arrangement of three high-energy tangential NB injectors (BL1, BL2 and BL3) and a low-energy perpendicular NB injector (BL4). A toroidal line of sight from the BL3 injection port for the CXS system, which utilizes the BL4 beam, is also indicated.

increase the ion heating power effectively with the negative-NBI, high-Z discharges are utilized for the high-T_i experiments with Ar/Ne gas puffing [11]. As a result, the T_i is increased with an increase in the ion heating power, and reached 13.5keV [12]. For efficient ion heating in the hydrogen plasmas, the positive-NBI has been recently constructed with the injection energy of 40keV, which dominantly heats the plasma ions, and 6MW of the injection power was achieved [10]. The positive-NBI is also utilized for the T_i-profile measurement with the CXS (charge-exchange spectroscopy) along a toroidal line of sight [13,14], which is better for the measurement in the central region than that along a poloidal line of sight. With this arrangement, the toroidal rotation is also measured.

The ECRH system employs 168GHz, 84GHz and 82.7GHz gyrotrons [15]. Each microwave is injected as a highly focused Gaussian beam using the vertical and horizontal antenna systems with quasi-optical mirrors. The beam-waist radius at the focal point is 15-30mm. The focused location can be changed at 3.5-3.9m of the major radius on the equatorial plane. The total injection power achieved is 2.1MW. In the experiments, the second-harmonic heating with 84GHz and 82.7GHz microwaves is utilized at around 1.5T of the magnetic field strength on the axis.

3. Ion Temperature Rise in the CERC plasmas

The core electron-root confinement (CERC) is a specific feature commonly observed in helical systems, and

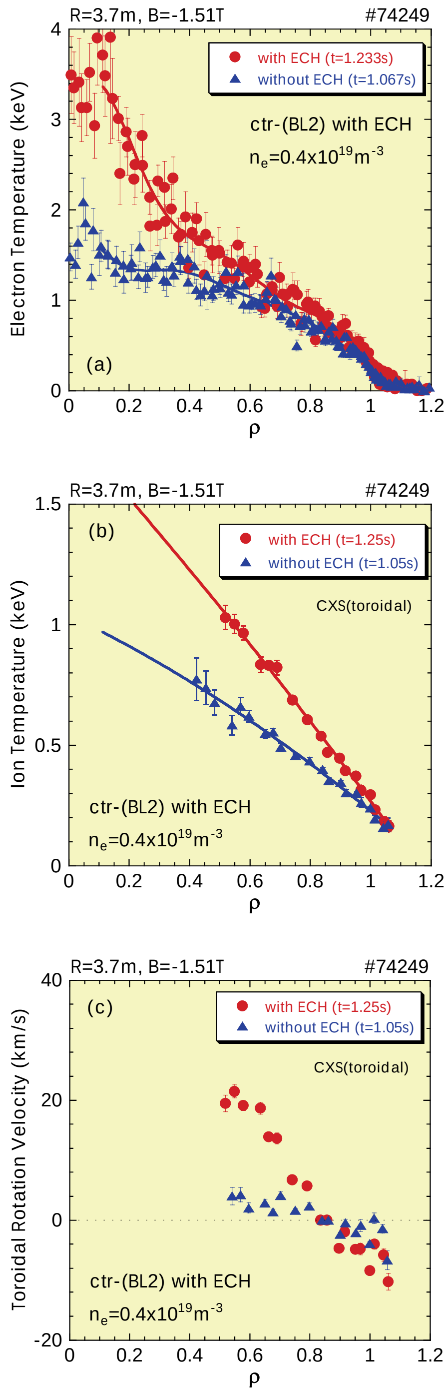

Fig.2 (a) Electron temperature profiles, (b) ion temperature profiles, and (c) toroidal rotation velocity profiles, for plasmas heated with the counter-NBI (BL2) and the perpendicular-NBI (BL4) with and without the ECRH superposition.

no counterpart in tokamaks. In LHD, by adding the centrally focused ECRH to the NBI plasma, a strongly peaked T_e profile is observed in the core region. Such a kind of the electron-ITB (internal transport barrier) formation indicates the improvement of the electron confinement, and the reduction of the electron thermal diffusivities is recognized together with positive radial electric field (E_r). This means that the improvement of the electron transport in the core region occurs in the neoclassical electron root. The ion transport is also expected to be improved in the electron root, and the ECRH was applied to the plasma heated by the negative-NBI and the positive-NBI.

Figures 2(a) and (b) show the electron and ion temperature profiles with and without the ECRH superposition, respectively. The electron density is $0.4\text{x}10^{19}\text{m}^{-3}$ and the target plasma is sustained by the counter-NBI (BL2) and the perpendicular-NBI (BL4). The applied ECH power is 0.68MW and is focused at around ρ=0.15. By adding the ECRH the T_e profile indicates a steep gradient inside ρ=0.4, which shows the improvement of the electron confinement in the electron root. The T_i is also increased in association with the T_e rise, as shown in Fig. 2(b). The ion temperature is measured with the charge exchange emission of CVI, and the carbon impurity profile in the core region is strongly hollowed due to the impurity pump-out effect when the ECRH is applied. As a result, the central T_i profile is not measured. Although it is unknown how much the central T_i is increased by the ECRH superposition, the T_i rise is observed in the mid-radius region. It seems that the T_i-rise location is different from the T_e-rise location.

The toroidal rotation is also measured with the CXS in the tangential line of sight. Figure 2(c) shows the toroidal rotation velocity, V_t, for the plasmas with and without adding ECRH. It is found that the toroidal rotation is driven in the co-direction at the T_i-rise location by adding the ECRH. The increase in the toroidal rotation seems to be correlated with the T_i rise, and the spontaneous toroidal rotation due to the ECRH applying is suggested to cause the confinement improvement.

The transport analysis based on the power balance was carried out for the plasmas with and without the ECRH applying shown in Fig. 2. Since there is no T_i data in the central region, the T_i profiles are parabolically fitted using the measured data, as shown in Fig. 2(b). Thus, the ion transport in the central region is not discussed here. As for the electron transport, since the heat exchange between the electrons and the ions is almost neglected in such a low-density plasma, the electron thermal diffusivity is obtained in the whole region. Figures 3(a) and (b) show the thermal diffusivities for the electrons and ions normalized by the gyro-Bohm factor of $T_e^{3/2}$ and $T_i^{3/2}$, respectively. The $\chi_e/T_e^{3/2}$ and the $\chi_i/T_i^{3/2}$ are regarded as a measure of the degree of the anomalous transport. As shown in Fig. 3, by adding the ECRH the thermal diffusivity normalized by the gyro-Bohm factor for the ions is reduced in the region of ρ>0.5 while that for the electrons is not changed in the

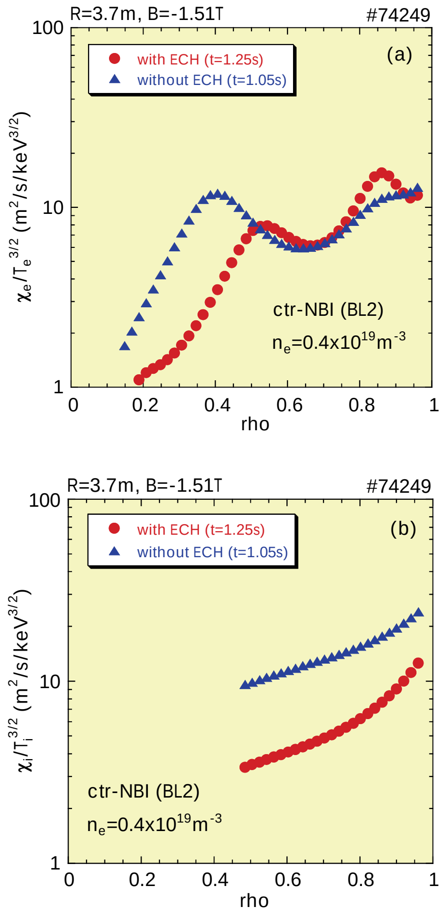

Fig.3 Profiles of (a) the electron thermal diffusivities normalized by $T_e^{3/2}$, $\chi_e/T_e^{3/2}$, and (b) the ion thermal diffusivities normalized by $T_i^{3/2}$, $\chi_i/T_i^{3/2}$, for NBI plasmas with and without the ECRH superposition shown in Fig. 2.

same region. In the central region of ρ<0.5, the $\chi_e/T_e^{3/2}$ is reduced by adding the ECRH although the change of the ion transport in the central region is unknown. These results suggest that the location of the transport improvement by adding the ECRH is different between the electrons and ions.

The neoclassical calculation was also carried out for the plasmas shown in Fig. 2. The used code is the GSRAKE code, and the calculated ambipolar E_r is shown in Fig. 4(a). Positive E_r is found at around ρ=0.6, which corresponds to the T_i-rise location. The value of the positive E_r is not so large, and the obtained electron root is a single solution. The calculated ion thermal diffusivities, χ_i, including the E_r effect, are shown in Fig. 4(b), and it is found that the neoclassical χ_i is not increased with the T_i rise. The ripple transport is greatly enhanced without the E_r, and the positive-E_r effect suppresses the enhancement of

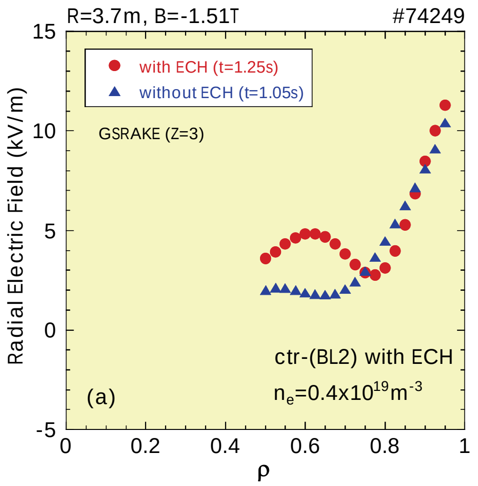

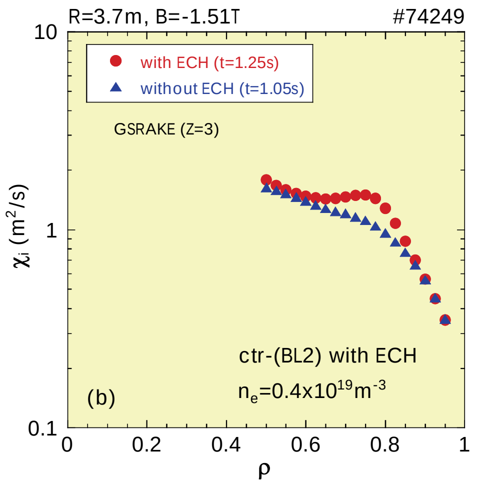

Fig.4 Results of the neoclassical calculation using the GSRAKE code for plasmas with and without the ECRH superposition shown in Fig. 2. (a) Radial electric-field profiles, and (b) ion thermal-diffusivity profiles.

the ripple transport due to the T_i rise. Considering that the neoclassical χ_i is not so changed by the ECRH applying, the T_i-rise is thought to be ascribed to the reduction of the anomalous transport.

4. Summary

An increase in the ion temperature has been observed in the NBI-heated plasmas with the superposition of the centrally focused ECRH in LHD. The target plasma is produced with high-energy NBI, and low-energy NBI is also utilized for the ion heating and the T_i-profile measurement with CXS. By adding the ECRH to the NBI plasma, an increase in T_e is observed with a steep T_e-gradient. That indicates the formation of the electron-ITB, in which the improvement of the electron transport is recognized in the CERC (core electron-root confinement). Therefore, it is thought that the T_i-increase is observed in the CERC conditions. The location of the T_i rise seems to be different from that of the T_e rise. The transport analysis shows that the ion transport improvement is ascribed to the reduction of the anomalous transport. The neoclassical ambipolar calculation shows that the E_r is positive at the location of the T_i-rise. This suggests that the ion confinement is improved in the CERC plasma. Considering that the neoclassical ion thermal diffusivity is not so changed, the experimental ion transport is dominated by the anomalous transport. The toroidal rotation is measured with the CXS in a toroidal line of sight, and a correlation is recognized between the toroidal rotation and the T_i-rise by adding the ECRH.

The improvement of the ion transport in the CERC is a possible scenario for increasing the ion temperature in the helical system, and this is experimentally demonstrated in LHD.

Acknowledgements

The authors are grateful to the technical staff in the LHD for the excellent operation of the LHD and the NBI and ECRH systems. This work has been supported by the NIFS under NIFS07ULBB501.

References

[1] M. Yokoyama, *et al.*, Fusion Sci. Technol. **50**, 327 (2006).
[2] M. Yokoyama, *et al.*, Nucl. Fusion **47**, 1213 (2007).
[3] Y. Takeiri, *et al.*, Phys. Plasmas **10**, 1788 (2003).
[4] T. Shimozuma, *et al.*, Plasma Phys. Control. Fusion **45**, 1183 (2003).
[5] K. Ida, *et al.*, Phy. Rev. Lett. **91**, 085003 (2003).
[6] Y. Takeiri, *et al.*, Fusion Sci. Technol. **46**, 106 (2004).
[7] O. Motojima, *et al.*, Nucl. Fusion **47**, S668 (2007).
[8] O. Kaneko, *et al.*, *Proc. 16th Int. Conf. on Fusion Energy 1996 (Montreal, 1996)* Vol. 3 (Vienna, IAEA) p. 539.
[9] Y. Takeiri, *et al.*, Nucl. Fusion **46**, S199 (2006).
[10] M. Osakabe, *et al.*, this conference.
[11] Y. Takeiri, *et al.*, Nucl. Fusion **45**, 565 (2005).
[12] Y. Takeiri, *et al.*, Nucl. Fusion **47**, 1078 (2007).
[13] K. Nagaoka, *et al.*, this conference.
[14] M. Yoshinuma, *et al.*, this conference.
[15] S. Kubo, *et al.*, Plasma Phys. Control. Fusion **47**, A81 (2005).

Proceedings of ITC/ISHW2007

Summary of H-mode studies in Compact Helical System

S. Okamura, T. Minami, T. Akiyama, A. Fujisawa, K. Ida, H. Iguchi, R. Ikeda, M. Isobe, S. Kado[a], K. Matsuo[b], K. Matsuoka, K. Nagaoka, K. Nakamura, H. Nakano, S. Nishimura, T. Oishi, S. Ohshima, A. Shimizu, C. Suzuki, C. Takahashi, M. Takeuchi, K. Toi, N. Tomita[c], S. Tsuji-Iio[c], Y. Yoshimura, M. Yoshinuma and CHS group

National Institute for Fusion Science, 322-6 Oroshi-cho, Toki 509-5292, Japan
[a] High Temperature Plasma Center, The University of Tokyo, Chiba 277-8568, Japan
[b] Fukuoka Institute of Technology, Fukuoka 811-0295, Japan
[c] Research Laboratory for Nuclear Reactors, Tokyo Institute of Technology, Tokyo, Japan

okamura@nifs.ac.jp

In about five years in the last phase of CHS experiment, H-mode physics was intensively studied. As well as a clear signal drop in the Hα emission, quick changes in the local densities gave reliable evidences of the bifurcation phenomena in the particle confinement in the plasma edge (edge transport barrier: ETB). Full diagnostics installed on CHS showed variations of profile information for the confinement improvement. In addition to the basic profile measurements of electron density and temperature by Thomson scattering, ion temperature and rotation measurements by the charge exchange spectroscopy showed the enhancement of the electric field during the H-mode, and the beam emission spectroscopy (BES) gave high speed measurements of local density variation which became available only at the last phase of CHS experiment. New diagnostics for the density fluctuation (BES, microwave scattering and phase contrast method of YAG laser) became also available in the last phase of CHS experiment. They observed clear suppression of the density fluctuations at the time of H-mode transition. Flexible controllability of the experimental conditions in CHS (heating power, density, magnetic field strength and configuration control) made it possible to study physical condition for the H-mode transition more carefully. High density H-mode operation combined with the reheat mode was an example of the successful extension of the improved confinement operation of CHS plasmas. This paper will summarize whole results of H-mode studies obtained in CHS experiment and try to evaluate the benefits of H-mode in CHS plasmas.

Proceedings of ITC/ISHW2007

The neoclassical plasma viscosity analyses relevant to high-ion-temperature plasmas in the Large Helical Device (LHD)

M.Yokoyama, O.Yamagishi, K.Ida, M.Yoshinuma, Y.Takeiri, S.Morita, H.Funaba, K.Nagaoka, O. Kaneko, and the LHD Experimental Group

National Institute for Fusion Science, 322-6 Oroshi, Toki 509-5292, Japan

High ion-temperature (T_i) hydrogen plasmas, about 5 keV at the density range of 1.2-1.6x10^{19}m^{-3}, have been successfully realized in the LHD. The toroidal-view charge exchange recombination spectroscopy (CXRS) has observed the fast toroidal rotation velocity (V_t) with a several 10 km/s at the core region in these high-T_i hydrogen plasmas. Previously, high-T_i (more than 10 keV) plasmas have also been obtained in high-Z (like Ar, Ne) plasmas in LHD, in which several 10 km/s of toroidal rotation at the core region was also observed. Although, the impact of fats toroidal rotation on confinement improvement of ions is still unclear, consideration how the toroidal viscosity can be lowered at the core region in the LHD to maintain the faster toroidal rotation would be an important research issue. For this purpose, neoclassical transport code, DKES, has been begun to be applied to high-T_i LHD discharges. The present status of this application and a possible future direction is reported.

Keywords: LHD, high-T_i plasmas, toroidal rotation, neoclassical viscosity and flow, DKES

1. Introduction

The high-energy (~150-180 keV) neutral beam injection (NBI) with mainly electron heating has realized high ion temperature (T_i) as much as 13.5 keV in low-density (in the range of several 10^{18}m^{-3}) high-Z (Ar) plasmas as a proof-of-principle experiment [1] by effectively increasing the ion heating power (per an ion). Recent installation and the power increase (~6 MW) of lower-energy (~40 keV) NBI increases the ion heating, which has resulted in the recent achievement of more than 5 keV in hydrogen plasmas (with a line average density of about 1.2×10^{19}m^{-3}) in LHD as shown in Fig. 1 [2]. This perpendicular injected beam is also utilized for the T_i-profile measurement with the charge exchange recombination spectroscopy (CXRS) with the toroidal line of sight. This toroidal line of sight enhances the measurement capability for the central region (even for the case of a hollow profile of carbon content used for measurement) compared to that with a poloidal line of sight [2].

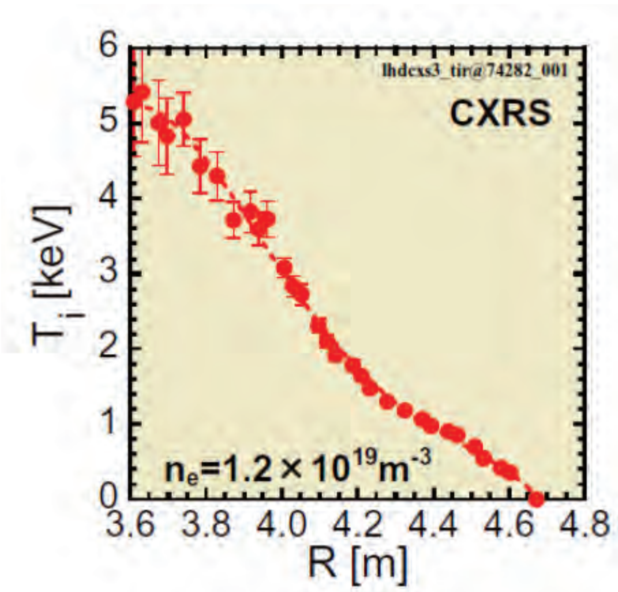

Fig.1 Ti profile in a high-Ti discharge measured by CXRS with a toroidal line of sight.

2. Toroidal rotation in high-T_i plasmas in LHD

The CXRS measurement has revealed that the toroidal rotation velocity (V_t) increases at the core region accompanied by the increase of T_i there as shown in Fig. 2(a) [the same shot and timing as that of Fig.1]. Since this plasma is heated by the 2-Co and 1-Counter (Ctr) NBI (in a configuration with the magnetic field reversed) with a perpendicular injection, the toroidal rotation direct in the Co-direction (positive value in Fig. 2(a)). We have also performed experiments in a configuration with the magnetic field un-reversed. In such a case, 3 parallel beam lines provide 1-Co and 2-Ctr. About 5 keV-T_i was

corresponding author's e-mail: yokoyama@LHD.nifs.ac.jp

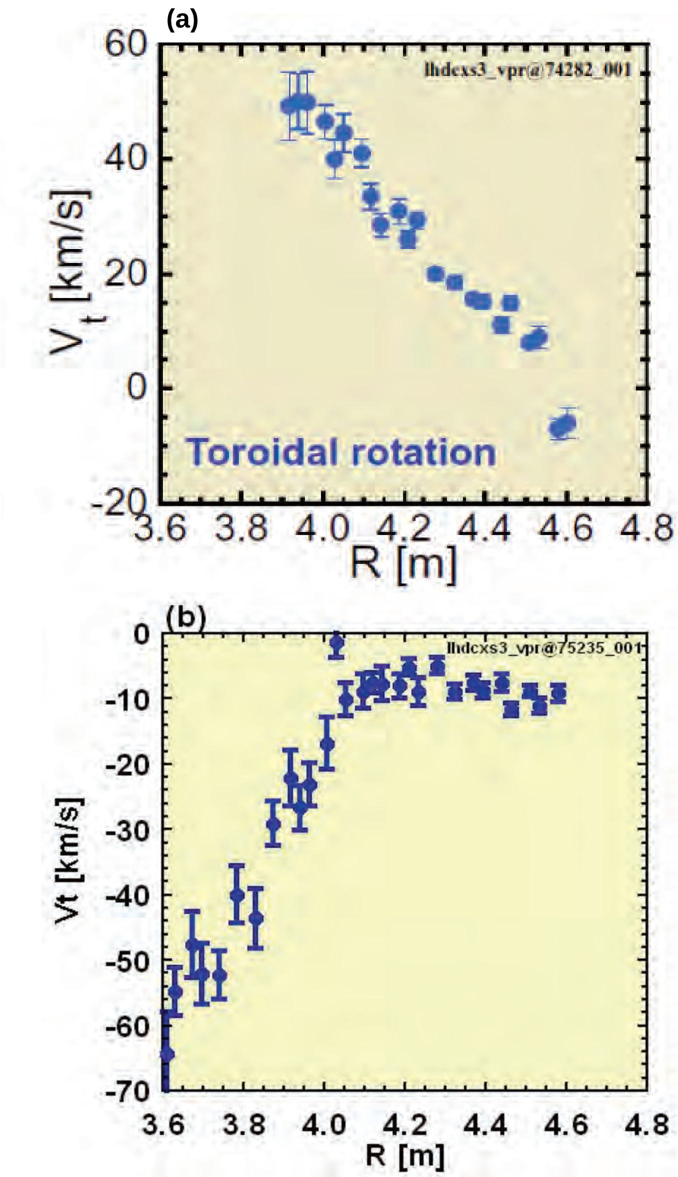

Fig.2 Toroidal rotation velocity profile in a high-Ti discharge measured by CXRS with a toroidal line of sight.

also obtained in such an experiment, where V_t directs in the Ctr-direction as shown in Fig. 2(b). These V_t are in the range of several tens of km/s at the core region. It should be also noted here that such a fast toroidal rotation at the core region was also observed in high-Z high-T_i discharges, which was measured by the Doppler shift of the X-ray line as in Ref. [4,5].

The impact of fast toroidal rotation on realizing high-T_i plasmas is uncertain. However, it is the experimental observation that these high-T_i discharges (regardless the ion species) in the LHD have been realized accompanied by such a fast toroidal rotation at the core region. Of course, large (mainly toroidal) momentum input exists from 3 parallel beam lines for these plasmas, which is the source of a fast toroidal rotation. Thus, it is meaningful to consider how the toroidal viscosity can be lowered at the core region in the LHD, to maintain the fast toroidal rotation with less damping.

2. Application of DKES code for high-T_i discharges in LHD

The neoclassical transport coefficients can be evaluated from the solution of the drift kinetic equation. The Drift Kinetic Equation Solver (DKES) [6] can solve the linearized DKE and provide mono-energy neoclassical transport coefficients in 3D magnetic configurations, without approximations connecting collisionality regimes. The mono-energy transport coefficients can be evaluated at given ν/v and E_r/v, where ν is the energy-dependent collision frequency, E_r is the radial electric field and v the thermal velocity. Since the evaluation of the ambipolar E_r is a key element of the analysis, the module interpolating the mono-energy transport coefficients on parameters ν/v and E_r/v has been added to the DKES code [7], so that ambipolar radial electric field can be determined by balancing the electron and ion particle fluxes depending on E_r.

DKES code, Sugama-Nishimura's method [8] included, has been applied to analyze high-T_i discharges in LHD such as shown in Fig. 1. Before injecting 3 parallel NBI, core T_i is about 1.5 keV at the same discharge. Calculations for these two cases (one is a case of $T_i(0)$~1.5 keV and the other is one with $T_i(0)$~5.2 keV) have been performed, and the evaluated ambipolar E_r is compared with those by GSRAKE code [9], as shown in Fig. 3. The parameters used for DKES calculations are as follows; (mpol, ntor, mpolb, ntorb, lalpha)=(16,12,6,2,100), where notations indicate poloidal and toroidal mode numbers for perturbed distributions function and magnetic field expression and Legendre polynomials, in order. For a case of lower $T_i(0)$, DKES and GSRAKE results are fairly close each other. The convergence of DKES calculations with the mini-max variational principle employed is rather well satisfied. On the other hand, for a case of higher $T_i(0)$, the difference between two codes becomes apparent especially toward the core region with higher T_i. It is also noted that the range of mini-max variation shown by "error bars" becomes larger there, indicating that the convergence becomes poorer at lower collisionality.

To examine the convergence properties, above mentioned parameters for DKES calculations are varied for the calculation at ρ~0.37 of "74282-1.15s". Figure 4 shows the parameter dependence of evaluated ambipolar E_r for several conditions with varied parameters written in the figure. It is noted that "the condition 1" corresponds to the result shown in Fig. 3. It seems that

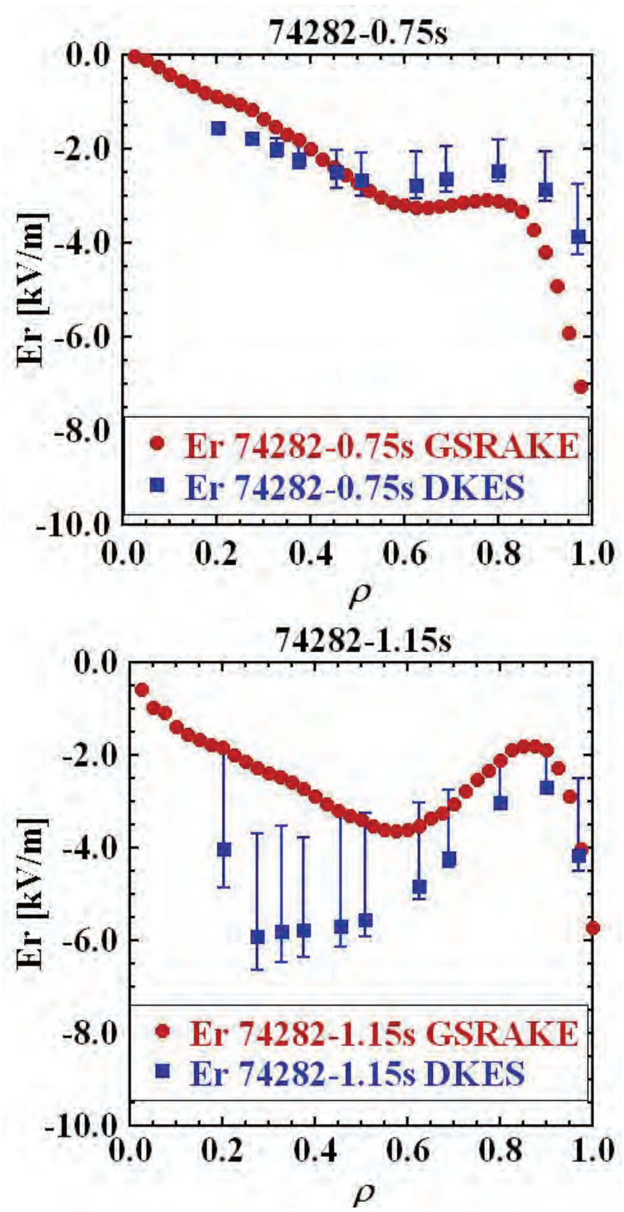

Fig. 3 Ambipolar E_r evaluated by DKES (blue) and GSRAKE (red) for cases with Ti(0)~1.5 keV (upper) and 5.2 keV (lower). (see the parameters used for DKES calculations in the text).

the averaged values (circles) tend to become gradually less negative according to the increase of mode numbers for perturbed distribution function (condition 3 to 4) with reduction of mini-max variation. The increase of mode numbers for magnetic field seems to increase the min-max variation (condition 1 to 2 and 3) with fixed mode numbers for perturbed distribution function, which indicates that the further increase of mode numbers of perturbed distribution function is required for larger mode numbers for magnetic field.

The difference of evaluated ambipolar E_r between

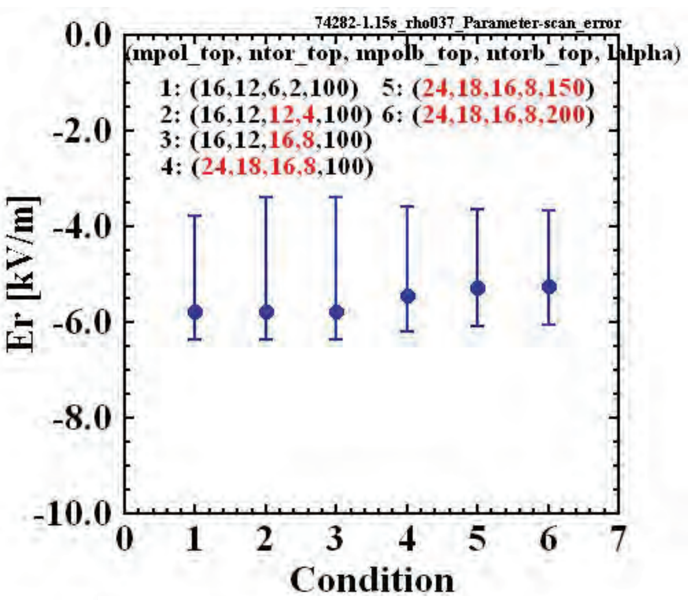

Fig. 4 Ambipolar Er evaluated at ρ~0.37 for "74282-1.15s" with varied parameters used for DKES calculations. The parameters are listed in figure according to the condition number.

DKES and GSRAKE are still large even for the largest parameters used for DKES calculations (condition 6). Detailed comparison between results from both codes and additional information provided by other neoclassical transport code (such as DCOM [10]) will be performed soon. It would be necessary to further increase the mode numbers used for DKES calculations when we consider the application to low collisional plasmas like high-T_i discharges in LHD. It has been already confirmed that DKES and GSRAKE predict almost similar values of ambipolar E_r each other [8] in collisional plasma like IDB/SDC (Internal Diffusion Barrier/Super Dense Core) in LHD [11].

The further investigation will be extensively performed so that DKES can be properly and practically applied for neoclassical transport analyses of high-T_i discharges in LHD. This will allow us to apply DKES code for analyses of further high-T_i and even reactor-relevant situations.

4. Conclusion and discussion

The fast toroidal rotation has been commonly observed in high-T_i (high Z and low Z (hydrogen), regardless the ion species) plasmas in LHD in circumstances of high power NBI heating.

DKES code has been attempted to apply for the viscosity and flow analyses for such plasmas. However, unfortunately, the difficulty for treating low collisional regime (high-T_i region) has been encountered so far so that relevant analyses have yet been performed. Extensive investigation how to resolve this difficulty will be performed so that DKES can be practically and properly applied for neoclassical transport analyses of high-T_i discharges in LHD.

At last, an "intuitive" consideration for plasma rotation is drawn. It is experimentally confirmed that the toroidal rotation is enhanced towards the core region in high-T_i discharges. It has been predicted by ambipolar E_r analysis and also experimentally demonstrated (as measured by CXRS with poloidal line of sight [12]) that the poloidal rotation is usually enhanced towards the plasma edge (either in ion-root and electron-root regime) [13]. This combination of radial variations of toroidal and poloidal rotation can provide a macroscopic shear of plasma rotation, which may be helpful to reduce radial transport. This feature is unique in L=2 (where L is the poloidal polarity of helical coils) heliotron–type configuration where the helicity of magnetic field increase towards the edge and the toroidicity becomes larger than helicity at the very core region. We will perform the analyses to make this "hypothesis" more evident.

Acknowledgements

Authors deeply acknowledge Dr. S.P.Hirshman for his kindness on providing recent version of the DKES code for application to the LHD experiment. Fruitful discussions with Prof. H.Sugama are also appreciated. This work has been supported by the grant-in-aid from the MEXT to one of the authors (MY) and also by the collaboration programs of NIFS (NIFS07KLDD011).

References

[1] Y.Takeiri et al., Nucl. Fusion **47** (2007) 1078.
[2] K.Nagaoka et al., in this conference, and M.Yokoyama et al., to be presented in the 49th APS-DPP Annual meeting, Nov. 2007.
[3] M.Yoshinuma et al., in this conference.
[4] S.Morita et al., 13th Stellarator Workshop, Proceeding-OIV1, http://wwwrsphysse.anu.edu.au/admin/stellarator/proceedings.html
[5] Y.Takeiri et al., Nucl. Fusion **45** (2005) 565.
[6] S.P.Hirshman et al., Phys. Fluids **9** (1986) 2951.
[7] H.Sugama and S.Nishimura, Phys. Plasmas **9** (2002) 4637.
[8] O.Yamagishi et al., to appear in the Annual Report of NIFS (2007).
[9] C.D.Beidler et al., Plasma Phys. Control. Fusion **37** (1995) 463.
[10] S.Murakami et al., Nucl. Fusion **42** (2002) L19.
[11] N.Ohyabu et al., Phys. Rev. Lett. **97** (2006) 055002.
[12] K. Ida *et al.*, Rev. Sci. Instrum. **71**, 2360 (2000).
[13] K.Ida et al., Nucl. Fusion **45** (2005) 391.

Proceedings of ITC/ISHW2007 P1-037

Status of the International Stellarator/Heliotron Profile Database

The ISHPDB Collaboration
A. Dinklage[a,*], E. Ascasibar[b], C.D. Beidler[a], R. Brakel[a], R. Burhenn[a], F. Castejon[b], T. Estrada[b], H. Funaba[c], Y. Feng[a], J. Geiger[a], J.H. Harris[d,e], C. Hidalgo[b], K. Ida[c], M. Kobayashi[c], R. König[a], G. Kühner[a], A. Kus[a], D. Lopez Bruna[b], H. Maaßberg[a], K. McCarthy[b], D. Mikkelsen[f], T. Mizuuchi[g], N. Nakajima[c], R. Preuss[a], S. Sakakibara[c], F. Sano[g], F. Sardei[b], U. Stroth[h], Y. Suzuki[c], J. Talmadge[i], H. Thomsen[a], Yu. A. Turkin [a], B. Ph. Van Milligen[b], K.Y. Watanabe[c], A. Weller[a], A. Werner[a], R. Wolf[a], H. Yamada[c], M. Yokoyama[c]

[a] *Max-Planck-Institut für Plasmaphysik, EURATOM Association, Greifswald, Germany*
[b] *Laboratorio Nacional de Fusión, Asociación Euratom/CIEMAT, Madrid, Spain*
[c] *National Institute for Fusion Science,322-6 Oroshi-cho, Toki 509-5292, Japan*
[d] *Oak Ridge National Laboratory, USA*
[e] *Australian National University, Canberra, Australia*
[f] *Princeton Plasma Physics Laboratory, Princeton, USA*
[g] *Kyoto University, Kyoto, Japan*
[h] *Institut für Plasmaforschung, Universität Stuttgart, Germany*
[i] *University of Wisconsin, USA*

The International Stellarator/Heliotron Profile Database (ISHPDB) is a community effort aiming at a concise documentation of experimental data and modeling of stellarator reactor relevant issues. ISHPDB extends the global stellarator confinement database ISCDB. ISHPDB is jointly hosted by IPP and NIFS [1]. The effort is structured by physics topics led by the acknowledged experts in their respective fields. A first inter-machine study of 1-d data as part of ISHPDB was given in [2] proving the concept of ISHPDB to result in significant progress. More extended inter-machine studies on high-β physics, impurity transport, edge physics, aspects of neoclassical transport and configuration dependencies will be given at this conference. This contribution focuses on a survey of the ISHPDB topical structure. The resulting requirements for physics oriented documentation will be summarized. A physics motivated quality assurance of the database will be discussed. A proposal for the implementation of an ISHPDB database schema compliant with existing tokamak databases and its interfaces will be introduced.

Keywords: International Stellarator/Heliotron Profile Database, Confinement, Transport

1. From 0d to 1d: transport assessment in 3-d devices towards reactor capabilities.

A concise documentation of stellarator/heliotron device operation is necessary for system assessment aiming at viable stellarator/heliotron reactor concepts. Consequently, joint databases for global confinement time τ_E in 3d devices were initiated as a joint effort of the stellarator/heliotron community. The International Stellarator/Heliotron Confinement Database (ISHPDB) is intended to continue this activity and to serve as a common documentation for physics investigations in 3d magnetic confinement fusion devices.

The first joint energy confinement scaling study for 3d devices led to the ISS95 scaling [3] which was largely confirmed with a broader and more extended data-set in the ISS04 study [4]. A particular result of the latter study was the identification of the impact of the magnetic configuration.

In view of possible reactor assessments, the studies of the global (0d) scaling for τ_E showed a couple of open issues. In particular, the validity of scaling laws with respect to extrapolation was discussed by means of physical model assessments. Applied on global data, model comparison techniques indicated differences in the basic transport mechanisms between low and high-β data [5]. A detailed assessment of the impact of plasma β on transport, however, was hindered by a lack of local transport analyses and needs to be pursued. High confinement regimes were assessed in places [6], but a systematic investigation of the differences in transport in the different options for device operation was only recently started for the core electron confinement [7]. In this conference, this philosophy is

corresponding author's e-mail: dinklage@ipp.mpg.de

extended to more detailed studies on the impact of the rotational transform and the shear [8] on confinement extending the 0d view by inclusion of profile information.

All recent global confinement studies [4-6] led to the conclusion that more detailed insight is required to perform a target-oriented assessment of performance measures in 3d devices. Nonetheless, global confinement data represent a relevant part of a full documentation form a basis for any comparative study.

This paper is a technical report summarizing the content and some infrastructure considerations of ISHPDB. This report summarizes also aspects from working group meetings with the intention to communicate these points to the community in order to discuss and possibly revise the concepts developed so far.

2. General strategy: physics issues towards a stellarator/heliotron fusion reactor

The status of ISPHDB is premature. For the moment being, files are collected and have to be stored in a common, reliable infrastructure allowing general access to the data. Nonetheless, the general structure is to be developed driven by the necessity from potential reactor assessments: issues resulting from this perspective define the necessities for a reasonable documentation and pragmatic approaches should be directed towards the goal of a common database for reactor assessments.

A common 1d profile database for stellarators and heliotron can be regarded as a documentation standard for performance studies. However, experience in respective tokamak databases [8] showed that documentation standards might vary from device to device, e.g. due to diagnostics availability. Moreover, different supplementary information is required for different issues, e.g. mode activity which is relevant to high-β discharges, but is less documented for quiescent H-modes.

Therefore, the requirement analysis for any documentation activity should start at relevant physics issues. Table 1 summarizes the high priority topics for inter-machine studies which were identified along community-open, dedicated workshops [9, 10].

The topic high performance operation is intended to study H-mode physics and further optimum confinement regimes in stellarators/heliotrons. Differently, the studies in high-β physics are much more advanced; a report will be given at this conference [11]. Similarly, comparative edge physics and divertor operation studies for LHD and W7-AS are underway [12]. A survey on the documentation of impurity transport studies will be given at this workshop as well [13]. CERC studies even serve as first input for the specific database [14]. Finally, confinement studies are intended to continue the global confinement documentation; an overlap to the previous topics is enforced to assure the continuation of the International Stellarator Confinement Database.

Physics Topics of ISHPDB
High Performance Operation
High β physics in 3-d devices
Edge physics and divertor operation
Impurity transport
Core electron root confinement (CERC)
Confinement studies

Tab.1 Summary of physics topics in addressed in the International Stellarator/Heliotron Profile Database ISHPDB.

Although the topic list in Tab. 1 is open for revisions, the issues represent stellarator/heliotron specific subjects whose documentation requirements may differ from topic to topic or which might be different to requirements for tokamak databases. A more detailed revision of requirements will be provided in the next section and a resulting proposal for a database structure will be given below. For the moment being, the actual database development is planned to be performed in parallel to the physics studies.

In a first step, the database is a collection of human readable files. As a general guideline, the documentation is the done by scientific papers along with a delivery of all supplementary material to ISHPDB.

Along with the consideration of physics requirements, ISPHDB has to take care for the assurance of quality measures in the database. The definition of quality standards is a community exercise which has still to be done. An agreed procedure must incorporate general standards but also specific points with respect to the physics issue. In a first step, the definition of deliveries needs to be worked out.

3. Functional and technical requirements

In general, the content of ISHPDB covers typical fusion data. ISHPDB starts mandatory from the 0d dataset as used for ISCDB. Furthermore, a link to additional information describes more background which refers to the dataset like magnetic configuration specifications, descriptive documents explaining specifics of the discharge under consideration etc.. A more specific guideline on this point needs to be worked out.

Beyond 0d data, time traces of the documented discharges are part of the discharge documentation. Here, the energy content, applied heating, mean density, loop voltage, temperature signals (ECE, soft-X), mode activity (Mirnov coils) and H_α emission are valuable signals in general.

Space dependent data for electron density, electron and ion temperature, the radial electric field form finally the profile database. Moreover, measurements for Z_{eff} and further supplementary data necessary for transport analyses should be provided.

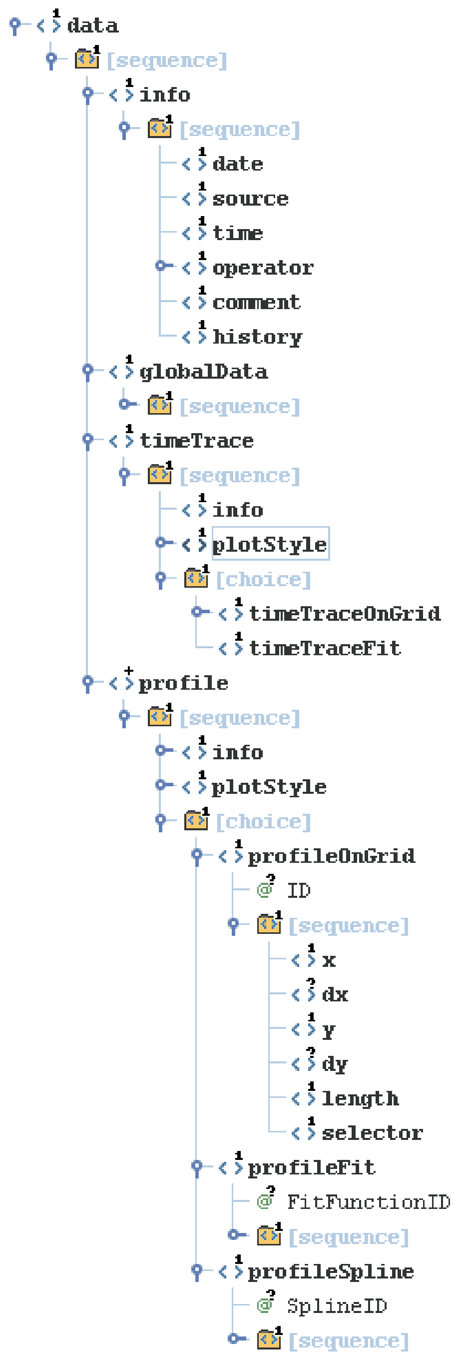

Fig.1 ISHPDB XML schema .

In addition to the data, the magnetic configurations used for mapping the data onto a common grid in flux surface coordinates should be provided. Edge physics data should be stored in real space coordinates.

All experimental data should be provided with their error. The squared standard deviation is used for weighting the data in fitting procedures. The used fit functions are to be chosen from a catalogue of standardized parametric functions [1] or by non-parametric fits.

Consequently, the database should be capable not only to store data with error bars but also parameters describing functional dependencies, e.g. to store also predictive results or outcome of interpretative transport analyses.

In an advanced version of the database, versioning is an essential feature to allow iterative evaluation steps. This is also important for the assessment of model assumptions, e.g. different mappings. Consequently, changes in different versions should be tracked. Search capabilities with respect to numerical, cardinal (e.g. $5*10^{19}$ m^{-3} < n_e < $2*10^{20}$ m^{-3}) and ordinal criteria (e.g. ECRH vs. NBI heating) should be possible as well as physics criteria (e.g. high-β discharges).

Technical requirements referring to the deployment of the database will be specified after exploring the first specific datasets to be included in a database. At present, both the National Institute for Fusion Science (Toki, Japan) and the Max-Planck-Institut für Plasmaphysik (Greifswald, Germany) offer to host the resources publicly and to develop web based interfaces to allow the community access the stored data.

4. A tentative database schema

Fig. 1 shows a tree structure representing a proposal for the ISHPDB data structure. For the description XML schema [15] was used. With the XML schema definition, which was chosen for convenience, all data files can be checked for consistency automatically. Moreover, there are a number of computing tools available to generate automated codes and interfaces to application programming.

As a general approach, data descriptive data fields form the header of the entries (e.g. data, source etc.). Then the three data categories form the data entries (globalData, timeTrace, profile). For profiles, choices between data on a grid, parametric functions and non-parametric functions are allowed. The specific entries are due to data presently available and are adjusted to match with the ITER profile database [16].

The schema works with experimental profile data from CERC studies as well as data from predictive calculations for W7-X.

A first exercise to create working interfaces is the adaptation of the ITER profile database interface definition employed for TASK analyses on LHD [14].

5. Summary and Outlook

ISHPDB aims at an extension of the stellarator/heliotron confinement database ISCDB with particular emphasis on reactor relevant issues. Starting from physics studies focused on stellarator specific topics, a requirement analysis both for data base structures and data handling procedures has been performed and will be extended along with practical experience.

A first case study was performed leading to an inter-machine comparison of core electron root confinement [7]. In this workshop, seven contributions were submitted as a result from the ISHPDB collaboration covering inter-machine studies on the impact of rotational transform and shear [8], extensions of the existing database with respect to high beta operation [11], intermachine studies of impurity transport [13] and comparisons of plasma edge physics in divertor operation [12]. Therefore, it can be concluded that ISHPDB is a living community exercise addressing relevant topics for the stellarator/heliotron community. A series of working group meetings was implemented and is agreed to be continued to follow the topics and general issues (see also [14]); since fall 2006 two meetings were held, a continuation is foreseen. The meetings are open to the community and a permanent revision of topics addressed is part of the database discussion.

The next specific technical step is the provision of the submitted data through a web interface allowing a general access to the data. An important task for the near future is the general agreement on quality assurance measures, i.e. the definition which data are to be provided and to define quality standards for the delivered data. This exercise is reasonably done with the data from this workshop.

For the moment being, responsible officers at the National Institute for Fusion Science (Toki, Japan) and Max-Planck-Institut für Plasmaphysik (Greifswald, Germany) are identified for receiving data and for processing data files [17]. These contact persons can be asked for any further details.

This work contributes to the International Stellarator Profile DataBase (ISHPDB) under auspices of the IEA Implementing Agreement for Cooperation in the Development of the Stellarator Concept (1992).

References

[1] http://www.ipp.mpg.de/ISHPDB and http://ishpdb.nifs.ac.jp
[2] M. Yokoyama et al., Fusion Sci. Technol. **50**, 395 (2006).
[3] U. Stroth et al., Nucl. Fusion **36**, 1063 (1996).
[4] H. Yamada et al., Nucl. Fusion **45**, 1684 (2005).
[5] A. Dinklage et al, Nucl. Fusion **47**, 1265 (2007).
[6] A. Dinklage et al, Fusion Sci. Technol. **51**, 1 (2007).
[7] M. Yokoyama, Nucl. Fusion **47**, 1213 (2007).
[8] E. Ascasibar et al., this conference, paper I-01
[9] http://p-grp.nucleng.kyoto-u.ac.jp/ktscwgm2006/
[10] http://www.ipp.mpg.de/ISS/CWGM2007/cwgm.html
[11] A. Weller et al., this conference, paper P1-039
[12] Y. Feng et al., this conference, paper I-06
[13] K. McCarthy et al., this conference, paper I-18
[14] H. Funaba et al, this conference, paper P-040
[15] http://www.w3.org/XML/Schema
[16] The ITER 1D Modelling Working Group, Nucl. Fusion **40**, 1955 (2000).
[17] Please send data files in copy to funaba@lhd.nifs.ac.jp and dinklage@ipp.mpg.de (subject ISHPDB).

Proceedings of ITC/ISHW2007

Effect of Ellipticity on Thermal Transport in ECH Plasmas on LHD

H.Yamada, M.Yokoyama, S.Murakami[a], K.Y.Watanabe, H.Funaba,
Y.Narushima, S.Sakakibara, T.Morisaki, Y.Nagayama,
S.Kubo, T.Shimozuma, K.Tanaka, T.Tokuzawa, I.Yamada and LHD Experimental Group

National Institute for Fusion Science, 322-6 Oroshi-cho, Toki 509-5292, Japan

a Dept. of Nucl. Engr., Kyoto Univ., Yoshida-honmachi, Sakyo, Kyoto 606-8501, Japan

Effect of ellipticity on thermal transport has been investigated for ECH plasmas in LHD. Ellipticity κ is scanned from 0.8 to 1.4 by controlling quadrupole magnetic field. Experimental data of energy confinement time align with the scaling for all configurations, however, there exist systematic offsets. Performance $\tau_E^{exp}/\tau_E^{ISS04}$ is summarized as 0.94±0.02 for κ=0.8, 1.41±0.07 for κ=1.0, and 0.91±0.03 for κ=1.4. Local transport analysis based on power balance indicates that plasma transport is predominated by anomalous transport. However, the observed anomaly shows correlation with the change of an effective helical ripple ε_{eff}. Physical background of this correlation, the dependence on the poloidal viscous damping rate C_p is discussed. The present experimental comparison suggests a negative evidence for relevance of C_p.

Keywords: Thermal transport, Configuration effect, Neoclassical transport, Anomalous transport, Net-current free plasmas, Ellipticity

1. Inroduction

Exploration of the effect of magnetic configuration on confinement is prerequisite for optimization of a helical system. Extensive efforts in experiments as well as theories have been done. Geometrical optimization for the neoclassical transport has been demonstrated in NBI plasmas on LHD and the anomalous transport has been suppressed as well in the neoclassical optimized configuration [1]. In these configuration studies, the position of the magnetic axis is the key control parameter [2].

International collaboration for the stellarator/heliotron confinement database has progressed [3-6] and a comprehensive comparative study has suggested that net-current free plasmas have robust and similar dependence on magnetic field, density and heating power [3-5]. Gyro-Bohm nature explains experimental trend in a variety of devices quite well, like in the ISS04 scaling [5];

$$\tau_E^{ISS04} = 0.134 a^{2.28} R^{0.64} P^{-0.61} \bar{n}_e^{0.54} B^{0.84} \iota_{2/3}^{0.41}$$
$$\propto \tau_{Bohm} \rho^{*-0.79} \beta^{-0.19} \nu_b^{*0.00} \iota_{2/3}^{1.06} \varepsilon^{-0.07}$$

Together with confirmation of this commonality, existence of systematic offsets between different configurations/devices has been pointed out. These device/configuration dependent offsets have been quantified by comparisons of subsets which reflect characteristic configurations, however, physical background of this quantity has not been clarified yet. The measure of the offsets correlates with the effective helical ripple ε_{eff} which is characterized by the neoclassical helical ripple transport in the collisionless 1/ν regime [5]. It should be noted that the transport in experiments itself is significantly larger than the neoclassical transport. Since the anomalous transport is predominate, a physical picture of neoclassical transport is not directly applicable to explain experimental observation. Therefore these observations postulates a working hypothesis that neoclassical optimization can suppress anomalous transport.

Large flexibility of the coil system of LHD enables us configuration scan other than the position of the magnetic axis, i.e., plasma elongation. Although the plasma elongation scan for NBI heated plasmas have been already reported [1], ECH plasmas which are located in the collisionless regime have not been studied yet.

2. Experimental Set-up

Plasma elongation has been controlled by the quadrupole field and scanned in the range between κ=0.8 and 1.4 (see Fig.1). Here elongation is defined by the toroidal averaged value since the elliptic surface rotates along the toroidal angle. The position of the magnetic axis R_{ax} is fixed at 3.6m. The magnetic field is fixed at 1.5 T, which provides centrally well focused deposition of ECH with 84GHz. The plasma volume, in other words, the plasma minor radius is kept the same by the control of the effective aspect ratio of helical coil. A helical coil consists of 3 blocks with independent power supplies, which can change the effective current center of the helical coil. Although the Shafranov shift and resultant change in rotational transport is sensitive to ellipticity [7], finite-β effect is not significant in the present study since the β is

author's e-mail: hyamada@LHD.nifs.ac.jp

limited to 0.3% in ECH plasmas.

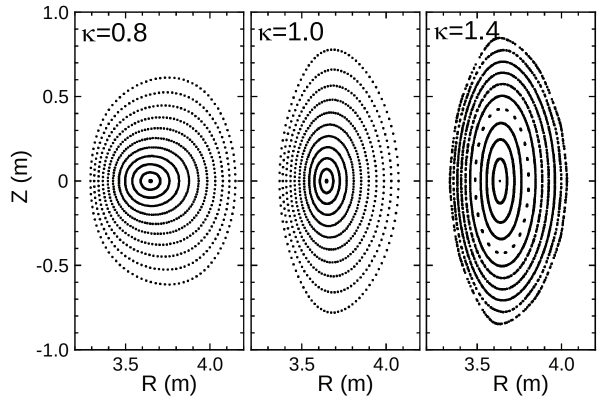

Fig.1 Magnetic flux surfaces for elongation scan. Cross-section at vertical elongated position where the helical coils are located on the equatorial plane.

In this study, the poloidal viscous damping rate is explored as a potential key parameter to bridge the neoclassical optimization and suppression of anomalous transport. Generally speaking, zonal flows are generated efficiently in the configuration with low poloidal viscosity and then suppression of anomalous transport is anticipated in such a configuration. The poloidal viscous damping rate C_p [8] is plotted with ε_{eff} for R_{ax} in Fig.2. Since C_p is affected by a toroidal curvature as ε_{eff}, C_p and ε_{eff} has a clear correlation. Indeed, in the standard ellipticity κ=1.0, both quantities have the same trend for R_{ax} and become the minimum in the vicinity of R_{ax}~3.6m where high performance can be obtained in the experiment.

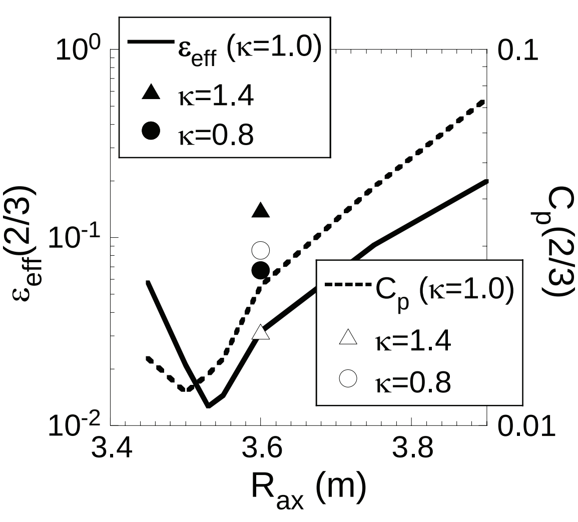

Fig.2 Dependence of effective helical ripple ε_{eff} and poloidal viscous damping rate C_p on the position of the magnetic axis. Elongation scans are plotted by triangles and circles at R_{ax}=3.6m.

Therefore which parameter; ε_{eff} or C_p is more essential in transport cannot be distinguished. However, plasma elongation can separate these two effects. As seen in Fig.2, a vertically elongated configuration (κ=1.4) has larger ε_{eff} than the standard configuration (κ=1.0) while it has smaller C_p.

3. Experimental Results

Two dimensionally similar discharges with different elongation have been compared to clarify the elongation effect on heat transport. The line averaged density is controlled at $1\times10^{19}\mathrm{m}^{-3}$ and electron temperature is also controlled to be the same in two case with κ=0.8 and 1.0 (see Fig.3). Heating power is also controlled to realize the same electron temperature (see Fig.4)

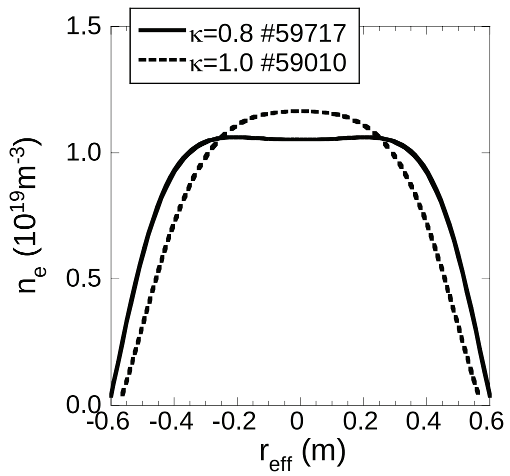

Fig.3 Electron density profiles in discharges with different elongation.

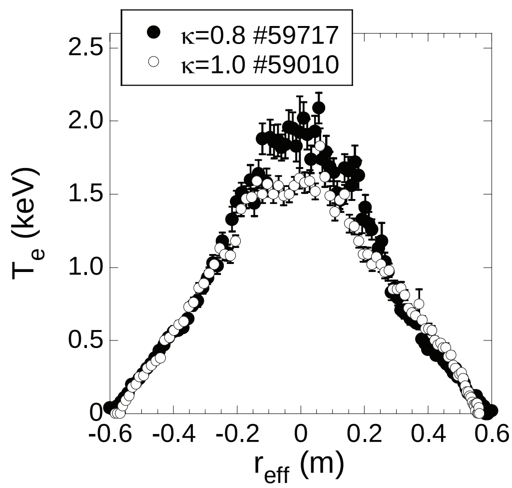

Fig.4 Electron temperature profiles in discharges with different elongation.

Here it should be noted that the investigated plasmas lie in 1/ν regime and that they do not enter so deeply in collisionless regime that electric field effect on neoclassical transport is not significant. Since the case with κ=1 shows the better confinement, the heating power is 0.93 MW for κ=0.8 and 0.35 MW for κ=1. The plasma parameters except for the elongation are similar to each other, therefore, representative non dimensional physical parameters such as normalized gyro-radius ρ*, collisionality ν*, and beta are also similar to each other.

Figure 5 shows the ratio of the electron heat diffusivity of these two cases. Since the plasma parameters of these two cases are the same, the deviation of this ratio from 1 can be attributed to the remained difference, i.e., elongation. Corresponding to the global confinement nature, local heat diffusivity in the experiment shown in a solid curve indicates enhancement of heat transport in the case with κ=0.8 by a factor of 2 to 3. A dotted line is the prediction from neoclassical theory. These two curves are close to each other, which suggest the neoclassical transport may make the difference in heat transport. However, this is not the case. Figure 6 shows the heat diffusivity profile. The fat solid curve is the experimental value in the case with κ=0.8 and the dotted fat curve is the corresponding neoclassical prediction. The experimental value is significantly larger than the neoclassical value, which indicates heat transport is anomalous even for the case with κ=0.8. Therefore, this is another example that configuration effect on anomalous transport is correlated or accidentally happens to coincide with nature of neoclassical transport [5].

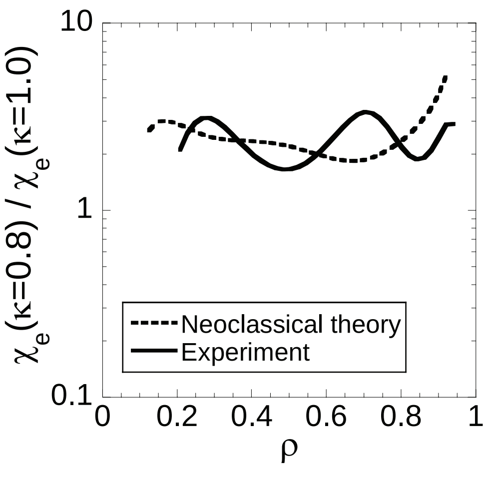

Fig.5 Ratio of heat diffusivity of two discharges with different elongation

Figure 7 shows the comparison of experimental energy confinement time with the prediction from the ISS04 scaling for plasmas with different ellipticity as shown in Fig.1. Energy confinement times have the maximum performance at κ=1 and degrades in both prolate (κ>1) and oblate (κ<1) directions. These trends agree with the observation in NBI heated plasmas [2].

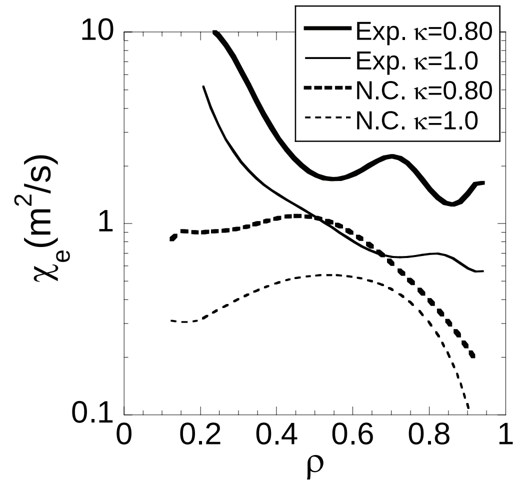

Fig.6 Experimental and neoclassical heat diffusivity.

Experimental data align with the scaling for all configurations. Each performance $\tau_E^{exp}/\tau_E^{ISS04}$ is summarized as 0.94±0.02 for κ=0.8, 1.41±0.07 for κ=1.0, and 0.91±0.03 for κ=1.4. If the C_p is more relevant parameter, the confinement should become the maximum at κ=1.4. However, the experiments indicate that the confinement is the best at κ=1.0 and declined by the both prolate (κ=1.4) and oblate (κ=0.8) modifications. The present experimental comparison suggests a negative evidence for relevance of Cp.

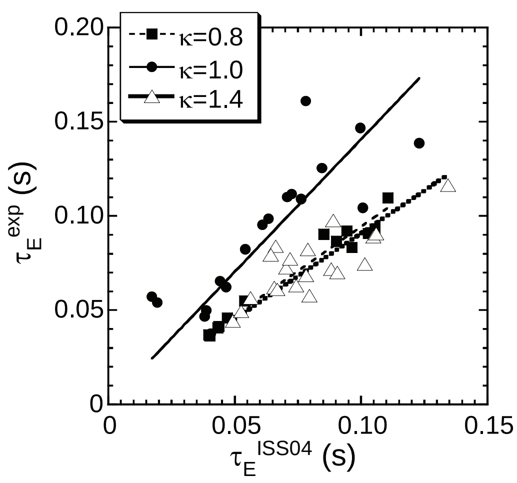

Fig.7 Comparison of experimental energy confinement time with prediction from the ISS04 scaling

4. Conclusions

Effect of ellipticity on thermal transport has been investigated for ECH plasmas in LHD. Ellipticity κ is scanned from 0.8 to 1.4 by controlling quadrupole magnetic field. Experimental data of energy confinement time align with the scaling for all configurations, however, there exist systematic offsets. Performance $\tau_E^{exp}/\tau_E^{ISS04}$ is summarized as 0.94±0.02 for κ=0.8, 1.41±0.07 for κ=1.0, and 0.91±0.03 for κ=1.4. Local transport analysis based on power balance indicates that plasma transport is predominated by anomalous transport. However, the observed anomaly shows correlation with the change of an effective helical ripple ε_{eff}. Since ε_{eff} should not be directly linked with anomalous transport model, clarification of configuration dependent parameter to bridge anomalous transport and ε_{eff} is required for establishment of optimization scenario of magnetic configuration. In this study, the poloidal viscous damping rate is explored as a potential key parameter. Generally speaking, zonal flows are generated efficiently in the configuration with low poloidal viscosity and then suppression of anomalous transport is anticipated in such a configuration. Since the poloidal viscous damping rate C_p is affected by a toroidal curvature as ε_{eff} describes, C_p and ε_{eff} generally have a correlation. Indeed, the inward shift of the magnetic axis realizes suppression of both C_p and ε_{eff} simultaneously. However, plasma elongation can separate these two effects. Here elongation is defined by the toroidal averaged value. A vertically elongated configuration (κ=1.4) has larger ε_{eff} than the standard configuration (κ=1.0) while it has smaller C_p. The experimental results indicate that the confinement is the best at κ=1.0 and declined by the both prolate (κ=1.4) and oblate (κ=0.8) modifications. The present experimental comparison suggests a negative evidence for relevance of C_p.

References

[1] H.Yamada et al., Plasma Phys. Control. Fusion **43**, A55 (2001)
[2] H.Yamada et al., Nucl Fusion **41**, 901 (2001)
[3] U.Stroth et al., Nucl .Fusion **36**, 1063 (1996)
[4] H.Yamada et al., Fusion Sci. Tech. **46**, 82 (2004)
[5] H.Yamada et al., Nucl. Fusion **45**, 1684 (2005)
[6] A.Dinklage et al., Nucl. Fusion **47**, 1265 (2007)
[7] T. Kobuchi et al., Plasma Phys. Control. Fusion **48** (2006) 789.
[8] C.D.Beidler et al. Plasma Phys. Control. Fusion **36**, 317 (1994)

Proceedings of ITC/ISHW2007

Extensions of the International Stellarator Database by High-β Data from W7-AS and LHD

A. Weller[1,*], K.Y. Watanabe[2], S. Sakakibara[2], A. Dinklage[1], H. Funaba[2], J. Geiger[1], J.H. Harris[3], R. Preuss[1], Y. Suzuki[2], A. Werner[1], H. Yamada[2], M.C. Zarnstorff[4], W7-AS Team[1], LHD Experimental Group[2]

[1]*Max-Planck-Institut für Plasmaphysik, IPP-Euratom Assoc., D-17491 Greifswald, Germany*
[2]*National Institute for Fusion Science, Toki, Gifu 509-5292, Japan*
[3]Oak *Ridge National Laboratory, Oak Ridge, TN 37831, USA*
[4]*Princeton Plasma Physics Laboratory, Princeton, NJ 08543, USA*

(Received 15 October 2007)

The ISS04 scaling of the energy confinement in stellarators/helical systems has been derived from selected data of the International Stellarator/Heliotron Confinement Database (ISHCDB), taking only few high-β data into account. Therefore, the basis for extrapolations to the reactor regime is insufficient. In the last years, regimes with reactor relevant beta became accessible in the Large Helical Device (LHD) and the W7-AS Stellarator. The high-β confinement regime is close to operational boundaries determined by degradation of the equilibrium surfaces, by stability limits of pressure driven MHD modes and by available heating power. This may lead to limits of the confinement and to modifications of scaling laws due to changes of the underlying physics. Therefore, an effort is made to establish and to extend the high-β data subset in the ISHCDB. The data are compared with existing scaling laws and predicted operational limits. The magnetic configuration has a significant impact on the confinement. In particular, a deterioration of the confinement with increasing beta is found in LHD which can partially be attributed to changes of the configuration. In order to identify the most important physical effects additional parameters are required to characterize the local transport and the predicted and experimental MHD properties.

Keywords: Stellarator, Helical System, Confinement, Transport, High Beta, Confinement Database, Beta Limit, Magnetic Configuration

1. Introduction

The ultimate goal of the international stellarator program is to provide a basis for a economically attractive fusion energy source. The prospects of the manifold of different configurations and approaches has to be assessed by inter-machine comparisons of the achieved global plasma parameters and local transport properties. Likewise, the collection of reference data from existing machines will allow to evaluate the benefit of configuration optimization as anticipated in the new W7-X [1] and NCSX [2] devices being presently under construction. Scalings of the global confinement have been established based on the analysis of different low-β ECRH (electron cyclotron resonance heating) and NBI (neutral beam injection) scenarios investigated in several stellarators and helical devices [3]. An extended ISHCDB database (including a first high-β dataset from W7-AS) resulted in the proposal of a new unified scaling of the confinement time in stellarators based on empirical renormalization factors depending on the configuration or device [4]. In order to get a more detailed understanding of the energy transport in stellarators and helical devices the international database effort is presently extended by the so-called International Stellarator/Heliotron Profile Database (ISHPDB) [5]. This activity attempts the documentation and analysis of 1-d data for various topics including local energy and particle transport. With regard to high-β physics, first studies of the effect of the magnetic configuration on the local transport in LHD high-β discharges have been made [6]. In addition, the definition of an appropriate set of configuration and plasma parameters is required to characterize the dependence and impact of ideal and resistive MHD modes on the magnetic configuration [7].

A compilation of high-β results in LHD and W7-AS including comparisons among each other as well as to tokamak results can be found in refs. [8], [9], [10], [11]. Until 2006/2007 further significant progress has been achieved in LHD reaching volume averaged values of $\langle\beta\rangle \approx 5\%$ [12]. These new data are particulary important to include in the ISHCDB/ISHPDB, since they bridge the

corresponding author's e-mail: arthur.weller@ipp.mpg.de

gap to the reactor relevant β-vales. Key issues concern the β-dependence of the confinement and the physical mechanisms determining the stationary level of $\langle\beta\rangle$.

The use of the database for inter-machine comparisons depends crucially on a clear definition of a set of key parameters and on standardized analysis procedures. However, in the high-β regime some parameters are not easily accessible, and their definition has to be reconsidered. Most importantly, the identification of the plasma boundary and hence the determination of the effective plasma radius requires a more sophisticated analysis, since the plasma edge region of high-β plasmas is usually characterized by stochastic field layers where a significant pressure gradient is still maintained [13], [14], [15]. For practical reasons, the measured pressure profiles are fitted by equilibria based on the assumption of nested flux surfaces as calculated with the VMEC code [16]. In LHD, the flux contour which contains 99 % of the measured kinetic plasma energy has turned out to be the most appropriate measure of the plasma edge location.

In W7-AS high-β discharges are effectively limited by the divertor structures, and therefore the plasma boundary is identified by the intersection of flux surfaces with the divertor. This is achieved by using the STELLOPT code [17] which is based on VMEC and iterates for equilibria consistent with the measured diamagnetic energy and kinetic data [18]. The pressure induced shift of the plasma axis can be compensated by an approprate vertical field so that plasmas with the maximal possible plasma volume were usually established.

In this paper, the main focus is to characterize and compare different sets of high-β data from LHD and W7-AS and to discuss their implementation in the ISHCDB. Some preliminary results on the scaling of the global confinement will be presented. In particular, the W7-AS high-β dataset is used to identify differences in the confinement compared to low-β plasmas by a probabilistic model comparison approach [19], [20]. Finally, some remarks about possible extensions towards MHD related data will be made.

2. W7-AS High Beta Data

A first database consisting of about 200 entries was compiled in 2003 [8] based on cases for which dedicated VMEC or STELLOPT calculations were made for different reasons. Standard parabolic pressure profiles were used in the VMEC calculations and (small) net-currents were modelled with a standard current profile. In single cases it could be shown that the experimental pressure profiles were close to parabolic apart near the plasma edge. The equilibria were calculated in such a way as to reproduce the measured diamagnetic energy and the

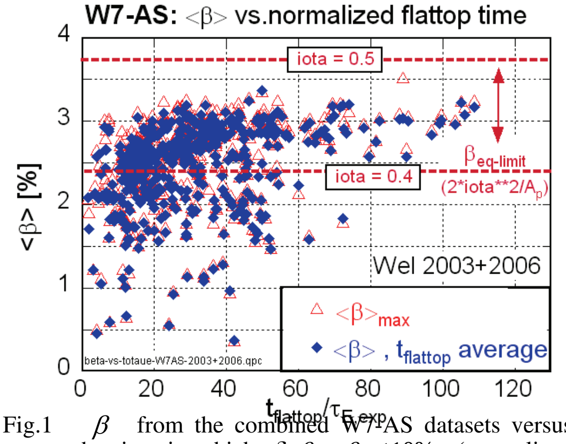

Fig.1 $\langle\beta\rangle$ from the combined W7-AS datasets versus the time in which $\delta\langle\beta\rangle/\langle\beta\rangle \le 10\%$, (normalized to $\tau_{E,\mathrm{exp.}}$).

plasma boundary just in contact with the divertor trough. Most of the configuration parameters (effective plasma radius, axis position, values of the rotational transform, volume averaged magnetic field, etc. as well as plasma data such as $\langle\beta\rangle$ were taken from the VMEC calculation. A second compilation was made in 2006 using a systematic W7-AS database search that was constrained to find all high-beta cases without significant toroidal plasma current. In a second step, only discharges were selected, which showed a quasi-stationary behaviour (for $\Delta t \gg \tau_E$). Using one or more time points per discharge during quasi-stationary periods almost 400 entries in this dataset were generated. The data cover a variety of different configurations with the majority of cases close to the optimum confinement at $\iota \approx 1/2$ (rotational transform). The achieved β-values in W7-AS taken from a combination of the 2 datasets are shown in fig. 1 plotted versus the time of the quasi-stationary period (normalized to the confinement time). The dashed horizontal lines indicate an equilibrium limit based on a simple model for a critical Shafranov shift for 2 particular configurations. Whereas in low-iota configurations the maximum achieved beta is clearly limited by equilibrium effects, the maximum

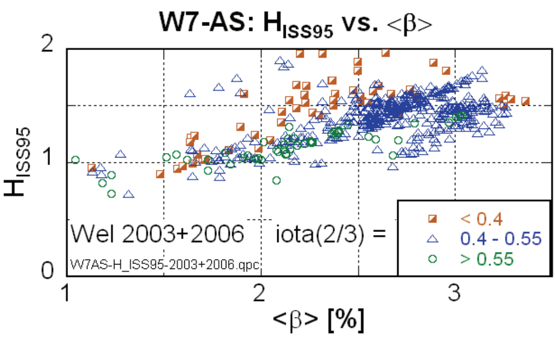

Fig.2 Energy confinement times normalized to ISS95 (combined W7-AS datasets). The data refer to different configurations. The renormalization factor according to [4] for these data is $f_{ren} = 0.86 \pm 0.18$.

beta at higher iota is mainly determined by the available heating power. The corresponding energy confinement times normalized to the ISS95 [3] scaling values are given in fig. 2 as a function of $\langle\beta\rangle$. Although a detailed equlibrium analysis [15] revealed a deteroration of the local transport in the outer plasma region with increasing beta due to the expansion of the stochastic layer, no such evidence is found in these global confinement data.

3. LHD High Beta Data

The first comprehensive survey of high-β data from the 7th and 8th experimental campaign [10] using a similar constrained database search was revised and extended up to the 10th campaign (2007) during the present study. Three datasets corresponding to 3 different configurations (3 helical coil current ratio parameters $\gamma = 1.25$, 1.22 and 1.20 corresponding to aspect ratios of $A_p = 5.7$, 6.1 and 6.5 at axis position $R_{ax} = 3.6\ \mathrm{m}$) with altogether about 1500 entries are compiled at the maximum of the diamagnetic energy within each discharge. All parameters refer to the vacuum configurations. Since the rotational transform in LHD scales as $A_p \sim \iota\!\!-$, the Shafranov shift is $\Delta/a \sim 1/A_p$, and hence is reduced in the $\gamma = 1.20$ configuration. This is a key to maximize the achievable beta. The $\langle\beta\rangle$ values achieved in the optimum configuration which are evaluated using parameters of the vacuum configurations are taken from the LHD database and are shown in fig. 3 in a similar form as the W7-AS data. The simple estimate of the equilibrium limit shows that the maximum beta values may already be affected by equilibrium limit effects (Note that for W7-AS the value has been doubled due to the configuration optimization [8]). Detailed investigations with the HINT code [14] show very extended regions of field line stochastization.

For the evaluation of the confinement scaling laws, the vacuum boundary was used, which is close to the 99% pressure contour at high beta. In contrast, VMEC gives much lower values for the plasma radius which is not consistent with the experimental data. However, the values for iota and the plasma position are derived from the available VMEC calculations.

Two more detailed datasets for studies of the local transport behaviour and its dependence on the magnetic configuration ($\gamma = 1.25$ and 1.22 with $R_{ax} = 3.6\ \mathrm{m}$) have been compiled (about 450 entries) by the LHD team [6][21]. These data have been added in a preliminary way to the existing ISHCDB dataset. In Fig. 4, $\tau_{E,\mathrm{exp.}}$ is plotted in comparison with the ISS95 scaling values. The two datasets are highlighted in red together with the two survey datasets of W7-AS (blue) on the background data (grey) from all the existing low-beta ISHCDB data. A closer inspection of the LHD data (fig. 5) reveals a progressive degradation of the confinement towards high beta, which has been found already earlier.

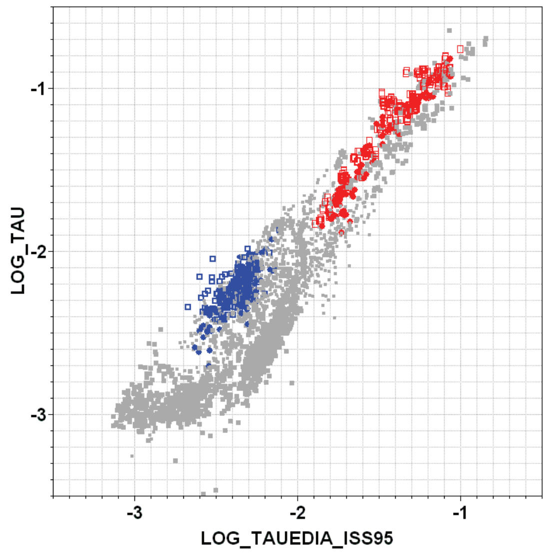

Fig.4 Logarithmic plot of $\tau_{E,\mathrm{exp.}}$ against the ISS95 scaling values. The data highlighted in blue represent the two W7-AS high-β survey datasets. In red, the two high-β datasets of LHD used for transport studies are shown (ISHCDB preliminary).

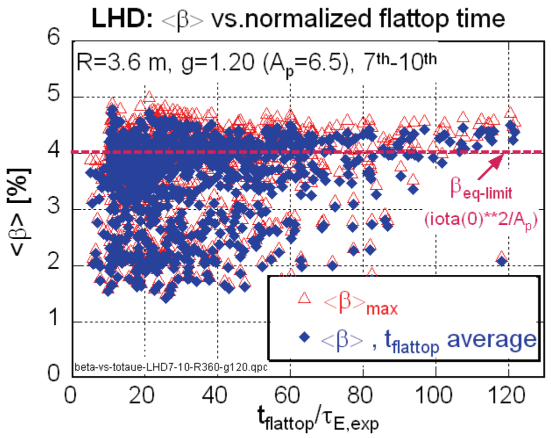

Fig.3 $\langle\beta\rangle$ from the new LHD survey dataset with $R_{ax} = 3.6\ \mathrm{m}$, $\gamma = 1.20$ versus the time in which $\delta\langle\beta\rangle/\langle\beta\rangle \le 10\%$, (normalized to $\tau_{E,\mathrm{exp.}}$).

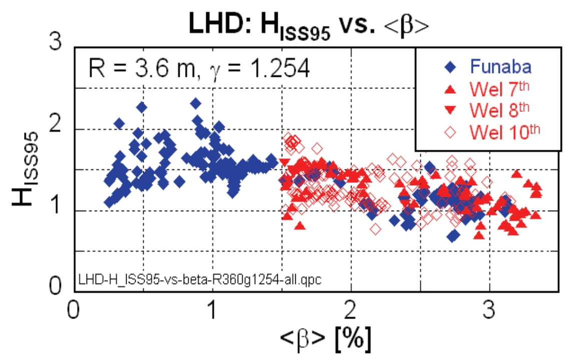

Fig.5 Energy confinement times normalized to ISS95 ($R_{ax} = 3.6\ \mathrm{m}$, $\gamma = 1.25$, comparison of different LHD datasets). A deterioration of the confinement is indicated towards high-β.

4. Discussion and Conclusions

The inclusion of high beta data from W7-AS and LHD in the ISHCDB data base provides an important test for the validity of existing scaling laws in the high-β regime and can lead to more reliable extrapolations to the reactor regime. In order to achieve this goal, results of local transport analyses have to be supplemented in the frame of the ISHPDB activity. This is currently in progress based on selected configurations in LHD [6][22].

In addition, the quality of extrapolations from the parameter space covered by the present database will be enhanced if the observed dependencies of the data (confinement times or local diffusivities) on the control parameters are consistent with basic physics models. For this purpose a Bayesian model comparison method was applied to W7-AS low-β and high-β global confinement data [19][20]. The significance of the results depends crucially on the quality of the data and the knowledge of their errors. According to the invariance principle of basic plasma model equations the scaling parameters are subject to constraints depending on the model used [23]. Models that ignore any finite-β effects were found to fit the low-β data best, whereas finite-β models gave the best agreement with the high-β data. Therefore, it is concluded that the global confinement depends on beta in this range. Since the

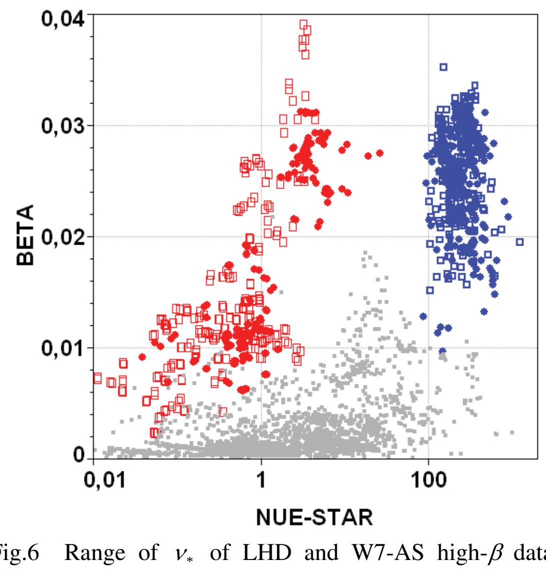

Fig.6 Range of ν_* of LHD and W7-AS high-β data. The data highlighted in blue represent the two W7-AS survey datasets. In red, the two datasets of LHD used for transport studies are shown (ISHCDB preliminary).

W7-AS high-β data are clustered in a high-collisionality region well separated from the LHD data (fig. 6), a similar model comparison analysis for LHD is required to confirm the results from W7-AS. This will be very important in order to assess the role of the collisionality as well. In LHD, a clear dependence of the confinement time (normalized to ISS95) was found in the high collisionality regime. Moreover, this survey indicates that LHD data even allow for a detailled assessment of the transition from low- to high-β regimes.

The high-β regimes in W7-AS and LHD are characterized by a parameter space which is close to operational limits depending on the configuration and on plasma parameters. In order to clarify the role of the configuration dependent beta limits imposed by equilibrium and stability effects, MHD related data including configuration parameters, data characterizing the MHD mode activity, data on local pressure profiles and results of numerical equilibrium and stability calculations are foreseen to include in the ISHPD in a next step, in addition to data required for local transport studies.

This work contributes to the International Stellarator Profile DataBase (ISHPDB) under auspices of the IEA Implementing Agreement for Cooperation in the Development of the Stellarator Concept. The first author (A. W.) would like to acknowledge his invitation by NIFS as Foreign Research Staff (Guest Professor).

References

[1] G. Grieger, et al. *J. Plasma Fusion Res.* **SERIES 1** 53-56 (1998)
[2] M. C. Zarnstorff, et al. *Plasma Phys. Control. Fusion* **43** A237–A249 (2001)
[3] U. Stroth, et al. *Nuclear Fusion* **36**(8) 1063-1077 (1996)
[4] H. Yamada, et al. *Nucl. Fusion* **45**(12) 1684–1693 (2005)
[5] A. Dinklage, et al. *Proc. of ITC/ISHW2007, Toki, Japan* P1-037 (2007)
[6] H. Funaba, et al. *submitted to Plasma and Fusion Research* (2006)
[7] S. Sakakibara, et al. *Fusion Sci. Technol.* **50**(2) 177-185 (2006)
[8] A. Weller, et al. *Plasma Phys. Control. Fusion* **45** (12A) A285-A308 (2003)
[9] K. Y. Watanabe, et al. *Fusion Sci. Technol.* **46**(1) 24-33 (2004)
[10] A. Weller, et al. *Fusion Sci. Technol.* **50** 158-170 (2006)
[11] H. Yamada, et al. *Fusion Sci. Technol.* **46** 82-90 (2004)
[12] O. Motojima, et al. *Nucl. Fusion* **47** S668-S676 (2007)
[13] K. Y. Watanabe, et al. *Plasma Phys. Control. Fusion* **49** 605-618 (2007)
[14] Y. Suzuki, et al. *Nucl. Fusion* **46** L19–L24 (2006)
[15] A. Reiman, et al. *Nucl. Fusion* **47**(7) 572-578 (2007)
[16] S. P. Hirshman, et al. *Comp. Phys. Commun.* **43**(1) 143-155 (1986)
[17] D. A. Spong, et al. **41**(6) 711-716 (2001)
[18] M. C. Zarnstorff, et al. *32nd EPS Conference on Plasma Phys., Tarragona, Spain*, **ECA Vol.29C** P1.062 (2005)
[19] R. Preuss, et al. *submitted to Phys. Rev. Lett.* (2007)
[20] A. Dinklage, et al. *Nucl. Fusion* **47** 1265-1273 (2007)
[21] K. Y. Watanabe, et al. personal communication (2007)
[22] H. Funaba, et al. *Proc. of ITC/ISHW2007, Toki, Japan* P1-040 (2007)
[23] J. W. Connor *Plasma Phys. Control. Fusion* **30**(6) 619-650 (1988)

Proceedings of ITC/ISHW2007

Data Structure for LHD Plasmas in the International Stellarator/Heliotron Profile Database

Hisamichi FUNABA[1)], Andreas DINKLAGE[2)], Hiroshi YAMADA[1)], Masayuki YOKOYAMA[1)], Kiyomasa WATANABE[1)], Kazumichi NARIHARA[1)], Ichihiro YAMADA[1)], Kenji TANAKA[1)], Tokihiko TOKUZAWA[1)], Sadayoshi MURAKAMI[3)], Masaki OSAKABE[1)], Kazuo KAWAHATA[1)] and the LHD Experimental Group[1)]

[1)] *National Institute for Fusion Science, Toki, Japan*
[2)] *Max-Planck-Institut für Plasmaphysik, EURATOM-Association, Greifswald, Germany*
[3)] *Department of Nuclear Engineering, Kyoto University, Kyoto, Japan*

The 2D-UFILEs are created from the experimental data of the Large Helical Device for the International Stellarator/Heliotron Priofle Database (ISHPDB). The data which were already published will be collected and opened to public on some WWW servers. The directory structure for the WWW server of ISHPDB is designed.

Keywords: stellarator, heliotron, profile database, UFILE, core electron-root confinement

1. Introduction

The International Stellarator/Heliotron Profile Database (ISHPDB) activity has been started as the extension of the International Stellarator/Heliotron Confinement Database (ISHCDB) [1] . This activity is intended to compare various physical phenomena which may be commonly observed among several stellarator/heliotron devices, such as the Large Helical Device (LHD), W7-AS, TJ-II, Heliotron J, CHS, HSX, H-1 and so on. For example, with respect to the features of CERC (Core Electron-Root Confinement) in helical plasmas are investigated in ref. [2]. The data which will be included in the ISHPDB database should be limited as the already published data in principle. In the case of LHD, the data for CERC were published in ref. [3].

The database will be developed in the following two steps: (1) collection and open to public of data files in the text format on the WWW servers for ISHCDB (http://iscdb.nifs.ac.jp/ on NIFS site). (2) detailed database which has ability of search and so on [4]. In this paper, the outline of the step 1 is introduced. The format and actual contents of the profile database are described in section 2. In Section 3, the structure of the directories is shown. A summary is provided in Section 4.

2. The format and contents of the profile database

At first, collection of text files has been started for ISHPDB. As for the data format of the LHD data, the UFILE format, which is adopted in the ITER profile database [5] is chosen. The data from the profile database will be used as the input file for transport codes. This UFILE format is also adopted for the input data form for the integrated simulation system for helical plasmas [6] which is an extension of the 1-dimensional transport code TASK (Transport Analyzing System for tokamaK) [7] to helical plasmas.

The profile data, such as the electron temperature, T_e, the ion temperature, T_i, the electron density, n_e, the radiation loss, P_{rad} and so on are derived based on the experimentally measured data. The profiles which are evaluated by some codes are also included such as the deposition power of NBI (Neutral Beam Injector) to electrons, P^e_{NBI}, and ions, P^i_{NBI}, the density of fast ions, n_{fast}, the particle source from NBI, S^e_{NBI}, the absorbed power of ECH (Electron Cyclotron Resonance Heating), P_{ECH}, and so on.

Figure 1 shows an example 2D-UFILE, which includes a profile of T_e data. This example is taken from the database of the CERC plasmas. The informations of the device, date, the independent variable labels, the dependent variable label and the number of data are written in the first 9 lines. The data of the 51 positions of the normalized average minor radius, ρ, are shown at the top of the data section. In this file, the T_e data at one timing of t = 2.003 sec. are shown. This timing information follows to the ρ data. The last 11 lines of the data section represent the T_e data. The comment lines are located at the last position.

The normalized average minor radius, $\rho = (\Phi/\Phi_a)^{1/2}$, ($\Phi$: toroidal magnetic flux) is derived from a magnetic flux surface data, which is selected based on the symmetry of the electron temperature profile. The name of the selected magnetic flux surface file is registered in the comment section of the UFILE. In this case, the file 'lhd-r375q100b016a2020.flx' was chosen. Many magnetic flux surface files were prepared in advance by using VMEC [8] or HINT2 [9] codes. The most suitable data is selected

author's e-mail: funaba@lhd.nifs.ac.jp

```
 032940 LHD 2                    ;-SHOT # TOK DIMENSIONS- 15-OCT-07
 18/01/02                        ;-SHOT DATE-  UFILES ASCII FILE SYSTEM
  0                              ;-NUMBER OF ASSOCIATED SCALAR QUANTITIES-
RHO                              ;-INDEPENDENT VARIABLE LABEL: X-
TIME                  SEC        ;-INDEPENDENT VARIABLE LABEL: Y-
TE                               ;-DEPENDENT VARIABLE LABEL-
2                                ;-PROC CODE- 0:RAW 1:AVG 2:SM 3:AVG+SM
        51                       ;-# OF X PTS-
         1                       ;-# OF Y PTS- X,Y,F(X,Y) DATA FOLLOW
 0.00000e+000  2.00000e-002  4.00000e-002  6.00000e-002  8.00000e-002
 1.00000e-001  1.20000e-001  1.40000e-001  1.60000e-001  1.80000e-001
 2.00000e-001  2.20000e-001  2.40000e-001  2.60000e-001  2.80000e-001
 3.00000e-001  3.20000e-001  3.40000e-001  3.60000e-001  3.80000e-001
 4.00000e-001  4.20000e-001  4.40000e-001  4.60000e-001  4.80000e-001
 5.00000e-001  5.20000e-001  5.40000e-001  5.60000e-001  5.80000e-001
 6.00000e-001  6.20000e-001  6.40000e-001  6.60000e-001  6.80000e-001
 7.00000e-001  7.20000e-001  7.40000e-001  7.60000e-001  7.80000e-001
 8.00000e-001  8.20000e-001  8.40000e-001  8.60000e-001  8.80000e-001
 9.00000e-001  9.20000e-001  9.40000e-001  9.60000e-001  9.80000e-001
 1.00000e+000
 2.00300e+000
 3.55164e+003  3.52288e+003  3.44586e+003  3.33319e+003  3.19583e+003
 3.04315e+003  2.88295e+003  2.72161e+003  2.56415e+003  2.41435e+003
 2.27484e+003  2.14731e+003  2.03256e+003  1.93069e+003  1.84120e+003
 1.76318e+003  1.69537e+003  1.63634e+003  1.58457e+003  1.53853e+003
 1.49679e+003  1.45807e+003  1.42130e+003  1.38562e+003  1.35042e+003
 1.31532e+003  1.28016e+003  1.24495e+003  1.20986e+003  1.17512e+003
 1.14099e+003  1.10771e+003  1.07542e+003  1.04414e+003  1.01373e+003
 9.83830e+002  9.53927e+002  9.23343e+002  8.91265e+002  8.56828e+002
 8.19197e+002  7.77667e+002  7.31799e+002  6.81488e+002  6.27042e+002
 5.69235e+002  5.09313e+002  4.48866e+002  3.89494e+002  3.32426e+002
 2.77660e+002
;----END-OF-DATA-----------------COMMENTS:-----------
  modeled profile based on YAG TS data
  type of fitting function :
  flx file name : lhd-r375q100b016a2020.flx
```

Fig. 1 An example of 2D-UFILE of T_e.

among them based on the T_e profile. The T_e profile are derived by fitting the experimental data by using a certain function.

The data file of 2D-UFILE is named like 'lhd_032940_002003_2d.dat', where the discharge number and the timing informations are included. When the 2D-UFILE contains the time evolution data, it becomes 'lhd_032940_2d.dat'.

The profiles of P^e_{NBI} and P^i_{NBI} are calculated by a three-dimensional Monte Carlo simulation code [10]. Figure 2 shows an example of the UFILE for P^e_{NBI}. QNBIE means the NBI heating power to electrons. This data is calculated by a set of codes of HFREYA, MCNBI and FIT. The comment 'PNBI = PFIT' means that the calculation result is used for the total amount of the NBI deposition power, which Z_{eff} largely affects.

The standard set of variables of 2D-UFILE includes some geometry informations, such as the normalized average minor radius, ρ, the geometric major radius, R, the geometric minor radius, r, the volume, V, the magnetic field strength, B, the elongation of the magnetic surface, κ, the geometric quantities, $\langle|\nabla\rho|\rangle$ and $\langle|\nabla\rho|^2\rangle$, and so on. It is important to make clear definition of them especially for the high β plasmas on LHD. In order to construct the database which includes data from several different devices, they should be commonly defined or at least their definition should be clearly documented when the data are registered.

More informations are needed to be included in the ISPDB server with respect to developing the database, such as the change of diagnostic analysis (calibration, abel conversion process, ...), the conversion from the real coordinate to ρ, revision of the equilibrium data, selection of the equilibrium data and so on. The assumptions which are used in deriving the profiles should be obviously described. For example, another assumption for the NBI power deposition of $P^{dep}_{NBI} = P^{dep}_{NBI\ FIT} \times P^{dep}_{NBI\ exp} / P^{birth}_{NBI\ FIT}$ is also used.

```
****************************************
  036159 LHD 2                   ;-SHOT # TOK DIMENSIONS- 11-JUL-07
  10/10/02                       ;-SHOT DATE-  UFILES ASCII FILE SYSTEM
   0                             ;-NUMBER OF ASSOCIATED SCALAR QUANTITIES-
 RHO                             ;-INDEPENDENT VARIABLE LABEL: X-
 TIME                 SEC        ;-INDEPENDENT VARIABLE LABEL: Y-
 QNBIE                           ;-DEPENDENT VARIABLE LABEL-
 2                               ;-PROC CODE- 0:RAW 1:AVG 2:SM 3:AVG+SM
        29                       ;-# OF X PTS-
         1                       ;-# OF Y PTS- X,Y,F(X,Y) DATA FOLLOW
  1.72400e-002  5.17200e-002  8.62100e-002  1.20700e-001  1.55200e-001
  1.89700e-001  2.24100e-001  2.58600e-001  2.93100e-001  3.27600e-001
  3.62100e-001  3.96600e-001  4.31000e-001  4.65500e-001  5.00000e-001
  5.34500e-001  5.69000e-001  6.03400e-001  6.37900e-001  6.72400e-001
  7.06900e-001  7.41400e-001  7.75900e-001  8.10300e-001  8.44800e-001
  8.79300e-001  9.13800e-001  9.48300e-001  9.82800e-001
  2.01000e+000
  1.00598e+005  1.18998e+005  1.41986e+005  1.46595e+005  1.56466e+005
  1.80822e+005  1.85729e+005  1.71238e+005  1.79137e+005  1.70279e+005
  1.59298e+005  1.66738e+005  1.58404e+005  1.50115e+005  1.36035e+005
  1.30726e+005  1.24899e+005  1.22783e+005  1.19995e+005  1.15461e+005
  1.07934e+005  1.06885e+005  1.06432e+005  1.06354e+005  1.02053e+005
  1.03616e+005  1.04584e+005  6.44148e+004  2.29218e+004
;----END-OF-DATA-----------------COMMENTS:-----------
  code : HFREYA, MCNBI, FIT
  PNBI = PFIT
****************************************
```

Fig. 2 An example of 2D-UFILE of P^e_{NBI}.

3. Structure of the directories

In this section, the directory structure for ISHPDB which is planned in order to open to public on a WWW server is described. Figure 3 shows an example of the directory structure for ISHPDB. Four directories are contained in the directory with the device name, e.g. 'LHD'. The contents of each directory are as follows.

(1) The 'data' directory includes the UFILEs of 2D, 1D, 0D. The time development of the data and the general information of the discharge should also be included. This directory is divided into the directories with the shot number.

(2) The 'config' directory includes the magnetic flux surface data for the mapping.

(3) The 'topics' directory includes the list of shot numbers and timings for each topics. This list will have the name like 'lhd_cerc_2006.lst' *etc.*

(4) The 'analysis' directory will contain the results of transport analysis and so on.

4. Summary

Making of the profile data of LHD for ISHPDB has been started. The 0D- and 2D-UFILEs from the LHD data are created for the registration of the ISHPDB. The definitions and assumptions in making these files are expressed in the comment lines. In order to construct the database which includes data from several different devices, the in-

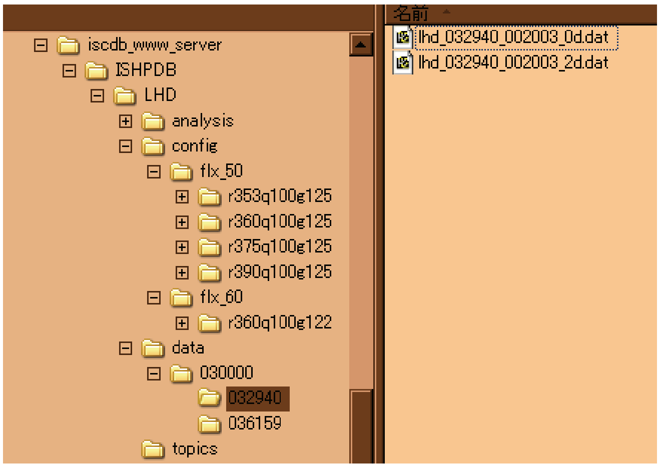

Fig. 3　Structure of directories for ISHPDB.

formations (especially the geometry informations) should be commonly defined or at least their definition should be clearly documented when the data are registered. The directory structure for the WWW server of ISHPDB is also designed.

[1] A. Dinklage, *et.al.*, Nucl. Fusion, (to be published).
[2] M. Yokoyama, *et.al.*, Fusion Sci. and Tech. **50**, 327 (2006).
[3] K. Ida, *et.al.*, Phys. Rev. Lett. **91**, 085003 (2003).
[4] A. Dinklage, *et al.*, this conference.
[5] The ITER 1D Modelling Working Group, Nucl. Fusion, **40**, 1955 (2000).
[6] Yuji Nakamura, *et al.*, Fusion Sci. and Tech., **50**, 457 (2006).
[7] A. Fukuyama, *et al.*, Proc. of 20th IAEA Fusion Energy Conf., IAEA-CSP-25/TH/P2-3, (Vilamoura, 2004).
[8] S.P. Hirshman, *et al.*, Phys. Fluids, **26**, 3553 (1983).
[9] K. Harafuji, *et al.*, J. Comput. Phys., **81**, 169 (1989).
[10] S. Murakami *et al.*, Trans. Fusion Technol.,**27**, 256 (1995).

Stability analysis of Wendelstein 7-X configurations with increased mirror ratio

Joachim Geiger

Max-Planck-Institut für Plasmaphysik, IPP-EURATOM Association, Greifswald, Germany

Wendelstein 7-X has been optimized with respect to equilibrium, stability and neoclassical transport properties. The resulting coil system offers a large variety of configurations. The paper summarizes the interchange stability characteristics of the reference configurations and extends them towards configurations with very large toroidal mirror fields. Two classes of configurations are found. In the first one stabilizing properties of shear and magnetic well of the vacuum configurations are decreased, with the effect that extreme cases are found to be Mercier-unstable for all investigated β-values less than 6% with no indication of stabilization by the finite-β magnetic well formation. The second class exhibits a strong additional suppression of the parallel current densities, a factor 3 larger than the reference configurations.

Keywords: stellarator, equilibrium, stability, Wendelstein 7-X, configuration variation

1. Introduction

The magnetic coil system of Wendelstein 7-X is the result of an optimization procedure concerned with the physics properties of a magnetic configuration important for a fusion reactor, such as equilibrium, stability, neoclassical transport and α-particle confinement [1]. The optimization led to the HELIcal-axis-Advanced-Stellarator configuration (HELIAS) with 5 field periods with reduced equilibrium and bootstrap currents. The good α-particle confinement requested a toroidal field mirror of 10% to be present in the configuration which was also beneficial for a further reduction of the bootstrap current. The mirror ratio is defined as $(B(\varphi=0^o)-B(\varphi=36^o))/(B(\varphi=0^o)-B(\varphi=36^o))$, where $\varphi=0^o$ is the bean-shaped plane in the corners where the toroidal curvature is largest. To avoid major resonances a rather flat profile of the rotational transform ι with a central value above 5/6 and below 1 at the boundary was chosen. A vacuum magnetic well of 1% together with the finite shear in the outer half of the plasma provides stability up to <β>-values of 5%. For experimental realization, the configuration was cast in a set of 10 modular coils per period for the optimized configuration. To increase the experimental flexibility and to explore the configuration space around the optimization point, the coil currents in the modular coil system can be adjusted independently. Thus, the toroidal field mirror can be varied to influence the size, location and behavior of the trapped particle population. An additional set of 4 planar coils per period, which are slightly inclined, provide the possibility to adjust the rotational transform and the plasma position. A number of reference cases have been proposed already at the beginning of the project [2], with slight modifications later [3], to show the fundamental flexibility in the value of the rotational transform (low-ι (5/6), standard (5/5), high-ι (5/4)) and its shear (low-shear), the toroidal mirror term (high- (10%) and low-mirror (0%) compared to standard (5%)), the plasma position (in- and outward shifted) and the plasma volume (limiter). Note, that the optimization point in this set is the high-mirror configuration. The standard configuration got its name because it is created by the modular coil system only, with all coils carrying the same current. However, up to now there was no systematic investigation of the large configuration space offered by the W7-X coil system. Only limited work has been done for an ι-variation of the high-mirror case with respect to stability [4], or for neoclassical transport in a more general way for optimized HELIAS-type configurations [5].

This paper starts a broader investigation of the configuration space by investigating the stability behavior of configurations with very large toroidal mirror field. In the beginning the important vacuum field properties of the reference cases are summarized and the implications for interchange stability are shown. Based on these results, the region of the configuration space defined by very large mirror ratios (ca. 20%) is explored with respect to ideal and resistive interchange stability. If not otherwise stated, the pressure profiles used are linear in the normalized toroidal flux s ($p \sim (1-s)$). The free-boundary 3D-equilibria were calculated with VMEC2000 [6]. For the analysis of the local interchange stability, the JMC-code was used [7].

2. Reference cases

The reference cases can be viewed as basic variations of the standard configuration in three directions of the

E-mail: joachim.geiger@ipp.mpg.de

configuration space: ι, mirror-ratio and plasma position. The low-shear and the limiter case can be interpreted as configurations resulting from combinations of these 3 basic variations. Except for the high- and low-ι cases, all reference cases are located at a boundary-ι value just below the 5/5-resonance. Figs 1 and 2 show shear and vacuum magnetic well depth for the different configurations since these are important quantities in the local interchange stability criteria. It can be seen that the shear increases and the mag-

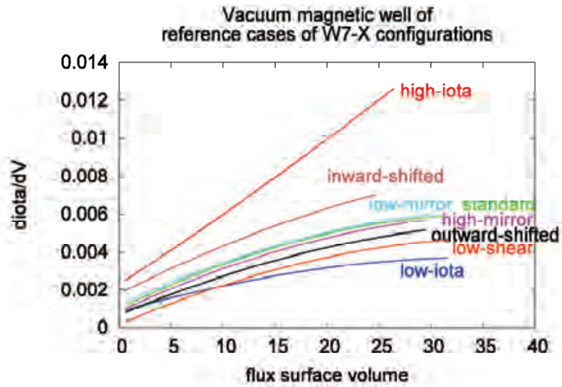

Fig. 1: Shear variation of reference cases.

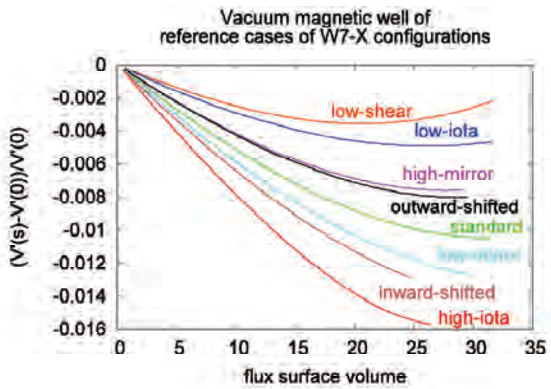

Fig.2: Vacuum magnetic well for reference cases.

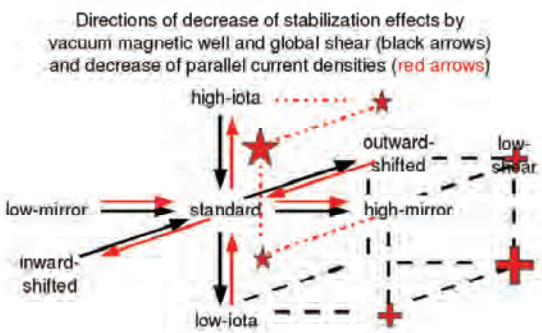

Fig.3: Summary of vacuum configuration changes on shear and magnetic well (black arrows), and on parallel current densities suppression (red arrows). Interesting regions are marked with symbols (stars/crosses).

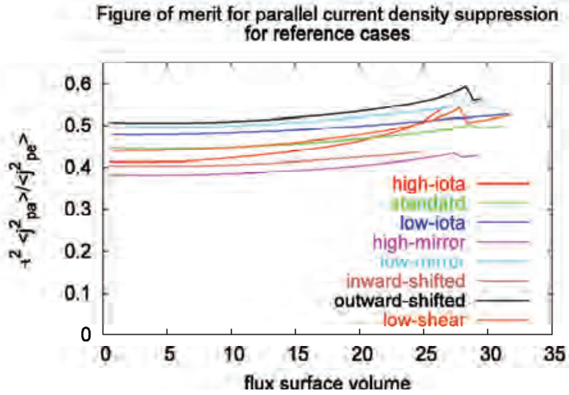

Fig.4: Parallel current density suppression for reference cases. A classical stellarator has the value 2.

netic well deepens with ι, with inward-shifting and with a lower mirror-ratio. Note, that with respect to inward/outward shifting the effect on the magnetic well is opposite to the situation in LHD where outward shifting deepens the magnetic well. For the reference cases, the mirror ratio affects the shear only slightly, but it affects the vacuum magnetic well depth in a way similar to inward/outward shifting. The joint effect can be seen when looking at the profiles of the low-shear configuration which is an outward-shifted configuration with an increased mirror field. This is summarized in Fig.3, where by following the arrows one moves towards configurations less stabilized by shear or vacuum magnetic well.

An analysis with respect to the ideal and resistive interchange criteria show that all configurations except the low-shear configuration are Mercier stable at all investigated <β>-values (up to 5-6%). The finite shear at outer radii stabilizes the ideal interchange modes in the cases where the derivative of V' is marginal or positive at these radii, e.g. low-ι and high-mirror cases. These show the development of a resistive interchange unstable region at the boundary for already low <β>-values (below 1%).

Another figure of merit to assess the configuration properties is the ratio of the average of the square of parallel to perpendicular current density (see [7] for its definition). Since the parallel current density is inversely proportional to ι, the dependency can be removed by multiplying the ratio by ι^2. For a classical stellarator this figure of merit can be estimated to have the value 2. The suppression of the parallel current density by optimization is then obvious by a reduction of the value. Fig. 4 shows that the values for the reference cases are reduced by roughly a factor of 4. Note, that within the reference cases, the ratio falls with increasing ι and mirror-ratio and also with inward-shifting. The latter gives rise to a different behavior than the one observed for shear and vacuum magnetic well.

E-mail: joachim.geiger@ipp.mpg.de

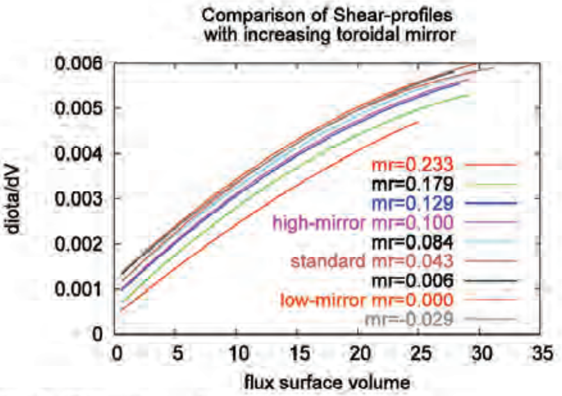

Fig.5: Shear for mirror ratio scan. Reference cases are indicated with names.

3. Cases with very large toroidal mirror

In a first step the mirror ratio was scanned from slightly inverted (ca -3%) to values twice as large as that of the high-mirror reference case (ca 23%) without using the planar coils, thus keeping the boundary value of the rotational transform roughly at 5/5. To perform the scan, the two coil currents around the triangular plane (φ=36^o) were varied simultaneously while the others were kept constant. The reference cases which vary the toroidal mirror are included in the scan for comparison. The tendency seen with mirror-ratio in the reference cases is obvious: with increasing mirror-ratio, the shear is slightly reduced (Fig.5) and the vacuum magnetic well becomes less stabilizing, so that for the largest mirror ratio considered here, a significant vacuum magnetic hill region exists in the outer half of the configuration (Fig.6). The parallel current densities show a significant suppression with increasing mirror ratio (Fig. 7). For the highest mirror-case (ca 23%), the suppression is almost a factor of 2 larger compared to the high-mirror reference case. The interchange stability behavior is dominated by the reduction of the stabilizing shear and vacuum magnetic well. With increasing mirror ratio the configurations become susceptible to interchange modes in the outer half where, as noted, for the highest mirror ratio a vacuum magnetic hill situation develops. For the latter case, ideal stability is still maintained at very low β-values due to the finite shear, but the outer half becomes unstable to ideal interchange already at moderate $\langle\beta\rangle$-values of 1%.

In a next step a variation around the configuration

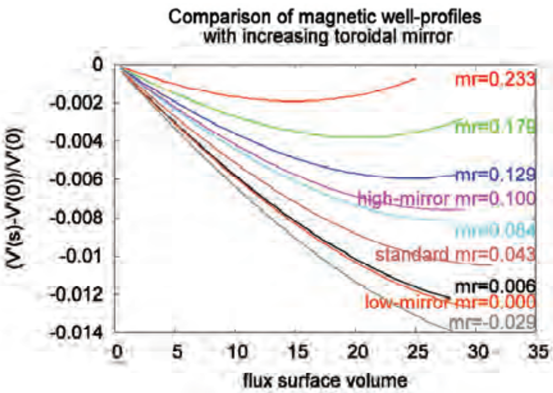

Fig.6: Vacuum magnetic well in mirror scan. Reference cases are indicated with names.

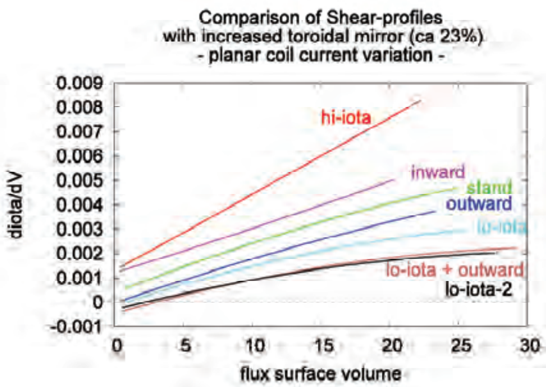

Fig.8: Shear variation with planar coil currents.

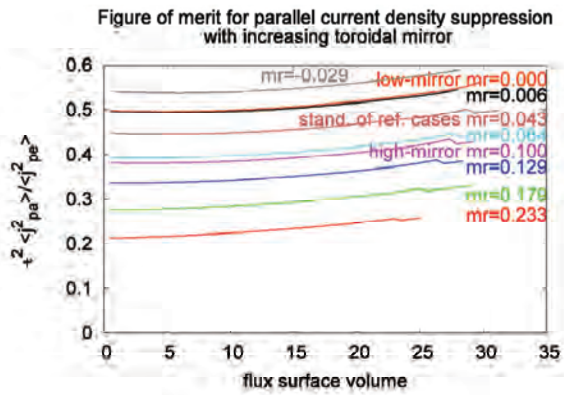

Fig.7: Parallel current density suppression with mirror ratio. Reference cases are indicated with names.

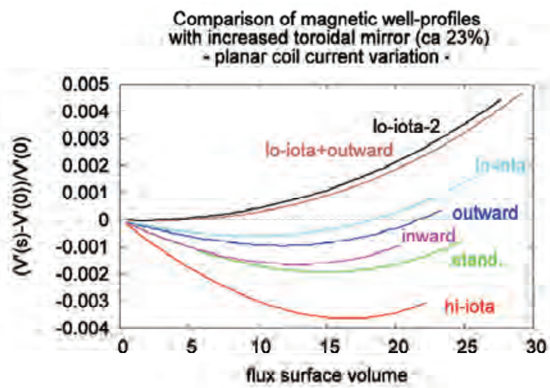

Fig.9: Variation of vacuum magnetic well with planar coil currents.

E-mail: joachim.geiger@ipp.mpg.de

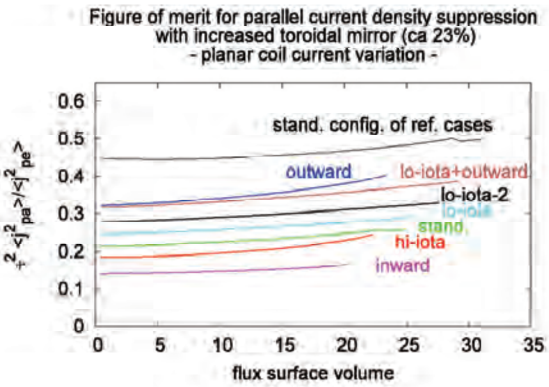

Fig. 10: Parallel current density suppression with planar coil current variation.

with the largest mirror (23%) was performed using the additional planar coils, to investigate the effect of varying ɫ and the plasma position. The effects seen in Figs 8-10 can be explained from the tendencies discussed previously. The names used for descriptive purposes refer to the center point for the variation, i.e. the case with a mirror ratio of 23%. From the variation two classes of interesting configurations emerge. The most unstable configurations result from going to low ɫ (lo-iota is around 5/6 and lo-iota-2 is below 5/6) possibly in combination with outward-shifting. In this case, a vacuum magnetic hill region with low shear extends over the entire plasma volume. These configurations are Mercier-unstable from the very beginning with no indication of stabilization with higher β-values. The other class shows a strong suppression of the parallel current density and arises when shifting inward or when going to high-ɫ. In these configurations, the shear increases and the vacuum magnetic well deepens. The parallel current density is suppressed by an additional factor of 3 compared to the standard configuration of the reference cases. Although these configurations are stable for very low β-values, they develop a Mercier-unstable region at the outer half of the plasma volume which grows as β increases. Not surprisingly, the strong reduction of the parallel current densities leads to very stiff configurations, i.e. very small changes in the ɫ-profile and the plasma position (Shafranov-shift) with increasing β.

4. Summary and discussion

The configuration space of W7-X is explored for configurations with very large toroidal mirror ratios. The properties of these configurations are the extensions of the properties already found in the reference cases. The exploration led to two configuration classes with large mirror field displaying interesting equilibrium and stability properties.

First, combining low-ɫ and outward-shifting with large mirror creates configurations with very low shear and a vacuum magnetic hill over the entire plasma cross-section. These configurations are unstable to interchange modes for all β-values. This offers the possibility to investigate the importance of interchange stability in a low-shear device which is expected to behave differently than in large shear devices like LHD. Second, the high-ɫ, inward-shifted branch of the very large mirror cases reveals configurations with a strong suppression of the parallel current densities. These configurations are less unstable than their low-ɫ, outward-shifted counterparts. However, they are also unstable from medium <β>-values onward. Nevertheless, the strong reduction of the parallel current densities leads to rather stiffer configurations with respect to finite-β induced equilibrium changes like the Shafranov-shift.

In a next step, it is planned to extend the analysis to neoclassical transport properties. Due to the large toroidal mirror, particle and energy transport will not be improved with respect to the standard case. However, it is known that the bootstrap current reduces with increasing mirror and may change sign [5]. With respect to neoclassical transport it might be interesting to explore the low or even inverted mirror region of the configuration space in search of configurations being closer to quasi-helical symmetry than the low-mirror configuration.

References

[1] W. Lotz, J. Nuehrenberg and C. Schwab, *13th Int. Conf. Plasma Physics Control. Nucl. Fus. Res.*, Washington, 1990 (Int. Atomic Energy Agency, vienna, 1991), Vol. 2, p.603

[2] J. Kisslinger et al., *Proc. 16th Symp. On Fusion Technology*, London 1990 (North Holland Publ., Amsterdam, 1991), Vol.2, 1520-1524

[3] T. Andreeva, IPP-Report, IPP III/270 (2002)

[4] C. Nuehrenberg, Phys. Plasmas **3**, 2401 (1996)

[5] H. Maassberg, W. Lotz and J. Nuehrenberg, Phys. Fluids B **5**, 3728-3736 (1993)

[6] S. Hirshman, W. van Rij and P. Merkel, Comput. Phys. Comm. **43**, 143-155 (1986)

[7] J. Nuehrenberg and R. Zille, in *Theory of Fusion Plasmas Varenna 1987* (Editrice Compositori, Bologna, 1988), Vol. EUR 11336 EN, p.3

E-mail: joachim.geiger@ipp.mpg.de

Motion of the plasmoid in helical plasmas

Ryuichi ISHIZAKI[1)] and Noriyoshi NAKAJIMA[1)]

[1)]*National Institute for Fusion Science, Toki 509-5292, Japan*

In order to clarify the difference on the motion of a plasmoid created by a pellet injection between tokamak and helical plasmas, the MHD simulation including ablation processes has been carried out. In a straight helical plasma, the plasmoid drifts to the lower field side in several Alfvén transit times, similarly to tokamak. However, it is found that the drift direction is subsequently reversed in the case that an initial location of the plasmoid is the higher field side than one at the magnetic axis. This fact might be one of the reasons why there is the difference on the motion of the plasmoid between tokamak and helical plasmas.

Keywords: Pellet, Ablation, Drift, Tire tube force, CIP

1 Introduction

Injecting small pellets of frozen hydrogen into torus plasmas is a proven method of fueling [1]. The physical processes are divided into the following micro and macro stages. The micro stage is the ablation of mass at the pellet surface due to the high temperature bulk plasma which the pellet encounters. The neutral gas produced by the ablation is rapidly heated by electrons and ionized to form a high density and low temperature plasma, namely a plasmoid. The macro stage is the redistribution of the plasmoid by free streaming along the magnetic field lines and by MHD processes which cause mass flow across flux surfaces. The micro stage is well-understood by an analytic method [2] and numerical simulation [3]. The drift motion of the plasmoid is investigated in the macro stage [4]. Since the plasmoid drifts to the lower field side, the pellet fueling to make the plasmoid approach the core plasma has succeeded by injecting the pellet from the high field side in tokamak. On the other hand, such a good performance has not been obtained yet in the planar axis heliotron; Large Helical Device (LHD) experiments, even if a pellet has been injected from the high field side [5]. The purpose of the study is to clarify the difference on the motion of the plasmoid between tokamak and helical plasmas.

In order to investigate the motion of the plasmoid, the three dimensional MHD code including the ablation processes has been developed by extending the pellet ablation code (CAP) [3]. It is found through the comparison between simulation results and an analytical consideration that the drift motion to the lower field side in tokamak is induced by a tire tube force due to the extremely large pressure of the plasmoid and a $1/R$ force due to the magnetic pressure gradient and curvature in the major radius direction [6]. It is also found that the plasmoid dose not drift when the perturbation of the plasmoid is small. In the study, the motion of the plasmoid is investigated in straight helical plasmas in the cases that the plasmoids are located at lower and higher field sides than one at the magnetic axis. In the former case, the plasmoid drifts to the lower field side, namely to the outside. In the latter case, it drifts to the lower field side, namely to the inside at first. Subsequently, the drift direction of it is reversed, namely a part of the plasmoid dirfts to the higher field side. This fact might be one of the reasons why the motion of the plasmoid dose not depend on the location of the pellet injection so much in LHD experiments.

author's e-mail: ishizaki@nifs.ac.jp

2 Basic Equations

Since the plasmoid is such a large perturbation that the linear theory can not be applied, a nonlinear simulation is required to clarify the behavior of the plasmoid. The drift motion is considered to be a MHD behavior because the drift speed obtained from experimental data [1] is about $0.01 \sim 1.0 v_A$, where v_A is an Alfvén velocity. Thus, the three dimensional MHD code including the ablation processes has been developed by extending the pellet ablation code (CAP) [3]. The equations used in code are:

$$\frac{d\rho}{dt} = -\rho \nabla \cdot \mathbf{u}, \quad (1a)$$

$$\rho \frac{d\mathbf{u}}{dt} = -\frac{\beta}{2} \nabla p + (\nabla \times \mathbf{B}) \times \mathbf{B}, \quad (1b)$$

$$\frac{dp}{dt} = -\gamma p \nabla \cdot \mathbf{u} + H, \quad (1c)$$

$$\frac{\partial \mathbf{B}}{\partial t} = \nabla \times (\mathbf{u} \times \mathbf{B}) \quad (1d)$$

All variables are normalized by ones at the magnetic axis, ρ_0, p_0, B_0 and v_A, where $v_A = B_0/\sqrt{\mu_0 \rho_0}$. γ and $\beta = 2\mu_0 p_0 / B_0^2$ are the ratio of the specific heats and plasma beta, respectively. Heat source H is given by:

$$H = \frac{dq_+}{dl} + \frac{dq_-}{dl}, \quad (2)$$

where $q_\pm$ is the heat flux model dependent on electron density and temperature in the bulk plasma and the plas-

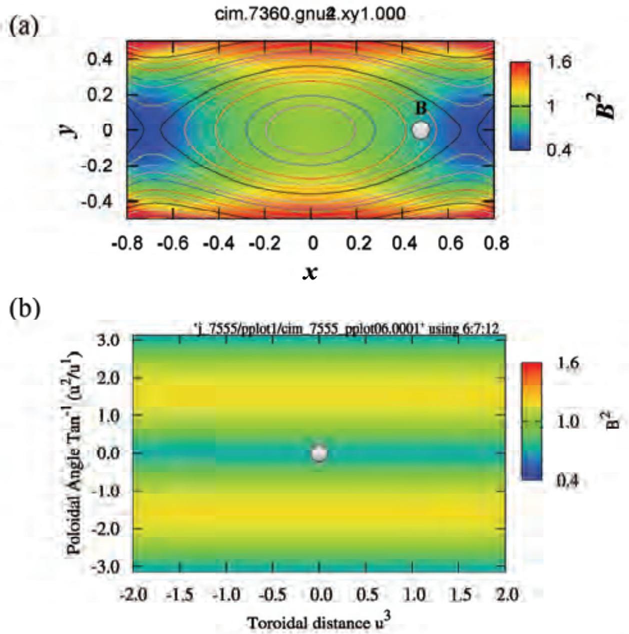

Fig. 1 Initial location of the plasmoid at lower field side than one at the magnetic axis in (a) the poloidal cross section at $u^3 = 0$ and (b) the flux surface through the center of the plasmoid in straight helical plasma. The initial location is denoted by circle. The colors show the contours of the magnetic pressures. The lines in (a) show the flux surfaces.

moid density. l is the distance along the field line. The subscript + (−) refers to the right (left)-going electrons. Then, the heat source can be calculated on each field line. Assuming Maxwellian electrons incident to the plasmoid, a kinetic treatment using a collisional stopping power formula leads to the heat flux model, $q_\pm$ [3] which is used in construction of one of the ablation models [2]. The rotational helical coordinate system (u^1, u^2, u^3) is used in which the poloidal cross section (u^1-u^2 plane) rotates along the straight toroidal direction (u^3) with same pitch as the external helical coils [7]. The Cubic Interpolated Pseudoparticle (CIP) method is used in the code as a numerical scheme [8].

3 Plasmoid simulations in straight helical

When a plasmoid is heated in tokamak plasmas, it is expanding along the magnetic field and simultaneously drifts to the lower field side due to a tire tube force and a $1/R$ force induced by the magnetic field with curvature [6]. In the study, the motion of the plasmoid is investigated in the straight helical plasma that consists of a uniform pressure and a vacuum magnetic field with $l = 2$ configuration. Figures 1(a) and (b) show the poloidal cross section (u^1-u^2 plane) at $u^3 = 0$ and the flux surface (u^3-θ plane) through the center of an initial plasmoid, respectively, where θ

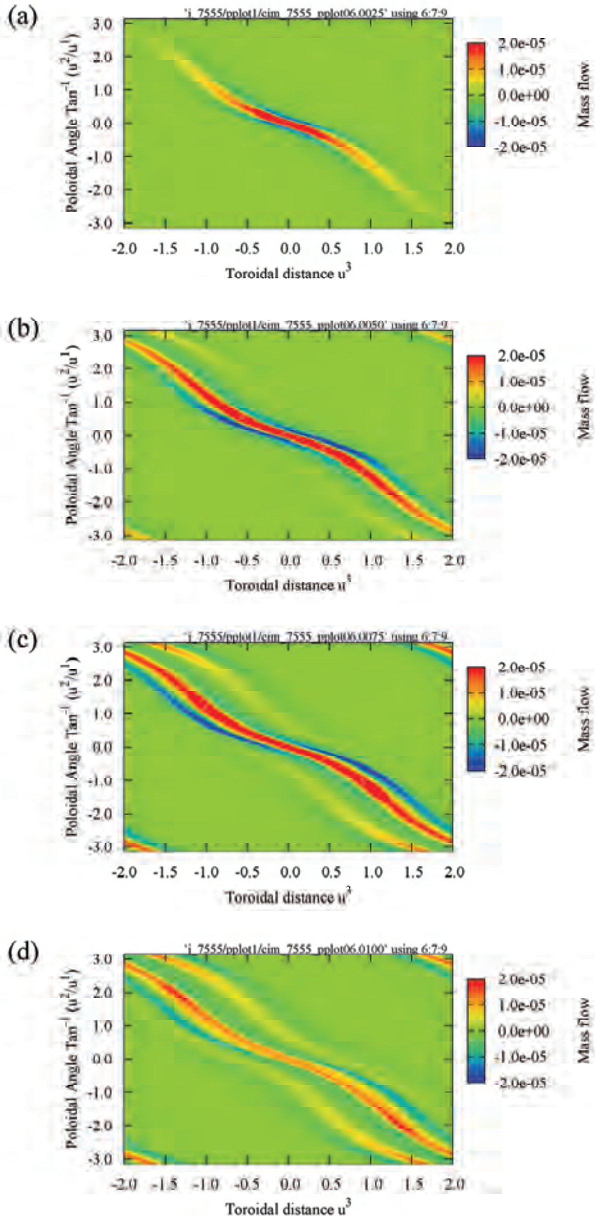

Fig. 2 Contours of the mass flow through the flux surface where the initial plasmoid is located. (a), (b), (c) and (d) are corresponding to t = 2.5, 5.0, 7.5, 10.0 τ_A, respectively.

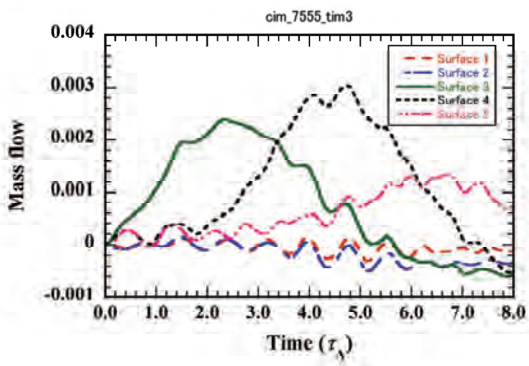

Fig. 3 Temporal evolution of mass flow integrated on the flux surfaces 1, 2, 3, 4 and 5 which are located from the magnetic axis to the outside. The initial plasmoid is located on the flux surface 3.

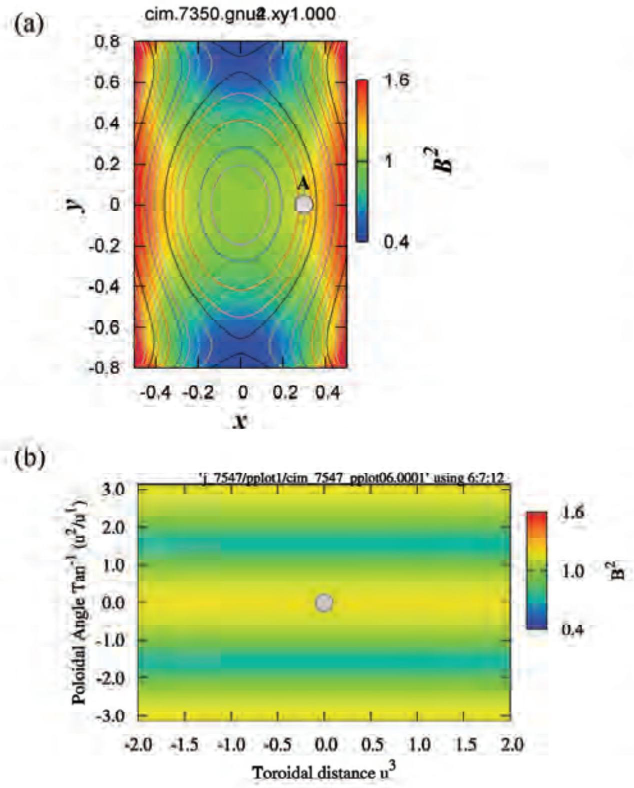

Fig. 4 Initial location of the plasmoid at higher field side one at the magnetic axis in (a) the poloidal cross section at $u^3 = 0$ and (b) the flux surface through the center of the plasmoid in straight helical plasma. The initial location is denoted by circle. The colors show the contours of the magnetic pressures. The lines in (a) show the flux surfaces.

is the poloidal angle defined by $\theta = \mathrm{Tan}^{-1}(u^2/u^1)$. The boundaries at $u^1 = \pm 0.8$ and $u^2 = \pm 0.5$ are assumed to be the perfect conductors in Fig. 1(a). The ones at $u^3 = \pm 2.0$ are the periodic conditions in Fig. 1(b). The colors show the contours of the magnetic pressures which is uniform in u^3-direction because the helical coordinate system is used. The lines show flux surfaces in Fig. 1(a). Initial location of the plasmoid is denoted by circle, namely it is located in the lowest field side in the flux surface. The peak values of density and temperature of the plasmoid are 100 times density and 1/100 times temperature of the bulk plasma, respectively. The plasmoid, whose half width is 0.03, encounters the electrons with fixed temperature 2 keV and density 10^{20} m^{-3}. Figure 2 shows the contours of the mass flow through the flux surface in which the initial plasmoid is located. A negative flow means one toward the magnetic axis. Figures 2(a), (b), (c) and (d) are the results at $t = 2.5, 5.0, 7.5, 10.0$ τ_A, respectively. When the plasmoid is heated, the pressure of it increases. It is found in Fig. 2 that the plasmoid quickly expands along the magnetic field and simultaneously drifts to the outside, namely the lower field side. The fact is due to a tire tube force and a $1/R$ force induced by the magnetic field with curvature similarly to the tokamak. Figure 3 shows the temporal evolution of the mass flow integrated on the flux surfaces 1, 2, 3, 4 and 5 which are located from the magnetic axis to the outside. The initial plasmoid is located on the flux surface 3. The mass flow in the surface 3 increases at first. Subsequently, it decreases after it reaches a peak value and one in the surface 4 increases because the plasmoid drifts the outside. One in the surface 5 increases after one in the surface 4 decreases. It is found that the plasmoid integrated on the flux surface also drift to the outside.

The case that the plasmoid is located at the highest field side on the flux surface is considered. Figures 4(a) and (b) show the poloidal cross section at $u^3 = 0$ and the flux surface through the center of an initial plasmoid, respectively, similarly to Figs. 1(a) and (b). The conditions except the initial location of the plamoid are same as Fig. 1. Figures 5(a), (b), (c) and (d) show the contour of the mass flow on the flux surface at $t = 2.5, 5.0, 7.5, 10.0$ μs, respectively. It is found that the plasmoid quickly expands along the magnetic field and simultaneously drifts to the inside, namely the lower field side as shown in Figs. 5(a) and (b). The mass flow at $\theta = \pm\pi/2$ becomes positive as shown in Fig. 5(c) because the direction to the lower field side becomes the one to the outside. Subsequently, the mass flow at $\theta = 0$ becomes positive as shown in Fig. 5(d), namely the plasmoid drifts to the outside. In other words, it drifts to the higher field side. Figure 6 shows the temporal evolution of the mass flow integrated on the flux surfaces 1, 2, 3, 4 and 5 which are located from the magnetic axis to the outside. The initial plasmoid is located on the flux surface 3. The mass flow in the surface 3 becomes negative at first. One in the surface 2 also becomes negative because the plasmoid drifts to the magnetic axis. Subsequently, the mass flow is reversed at $\theta = \pm\pi/2$ as shown in Fig. 5(c). In addition, it is also reversed at $\theta = 0$ as shown in Fig. 5(d). The integrated mass flow is thus reversed and becomes positive. This fact might be one of the reasons why the motion of the plasmoid dose not depend on the location of the pellet injection so much in LHD experiments.

4 Summary and Discussion

It is verified by simulations using the CAP code that the plasmoid with a high pressure induced by heat flux drifts to the lower field side in spite of the initial location in an early stage for several Alfvén transit times in a straight helical plasma. Such the drift is due to a tire tube force coming from a extremely large pressure of the plasmoid and $1/R$ force of magnetic curvature similarly to tokamak. However, it is found that the drift direction is reversed in the case that an initial location of the plasmoid is the higher field side than one at the magnetic axis. This fact might be one of the reasons why there is the difference on the motion of the plasmoid between tokamak and LHD experiments. The detail analysis will be needed to clarify the physics.

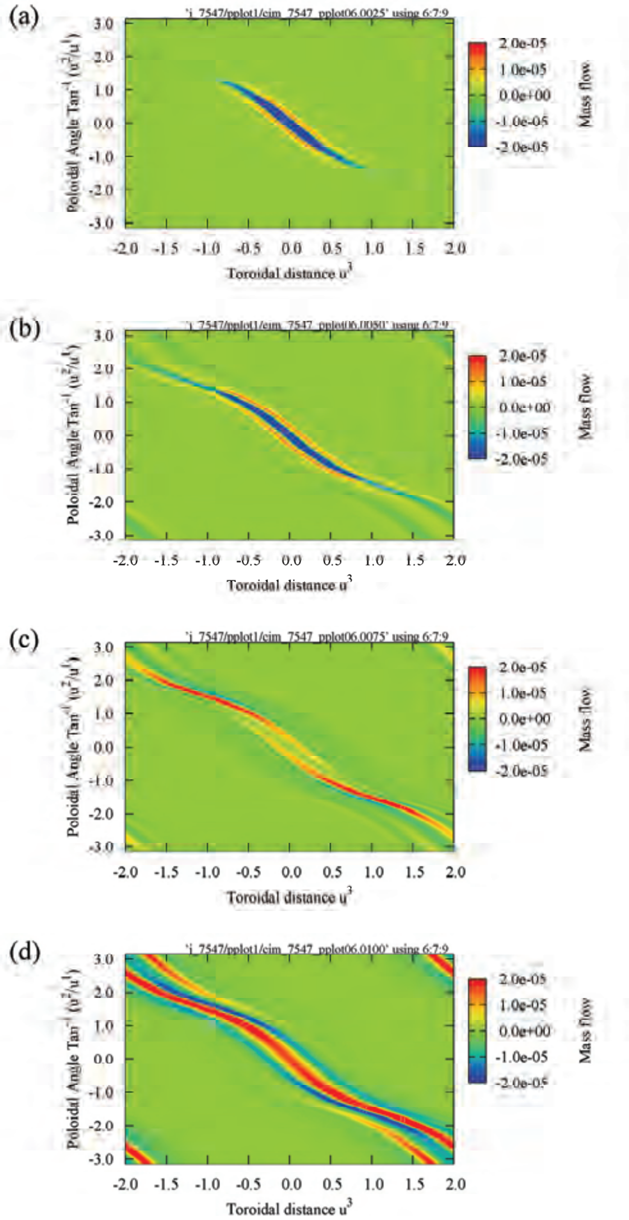

Fig. 5 Contours of the mass flow through the flux surface where the initial plasmoid is located. (a), (b), (c) and (d) are corresponding to t = 2.5, 5.0, 7.5, 10.0 τ_A, respectively.

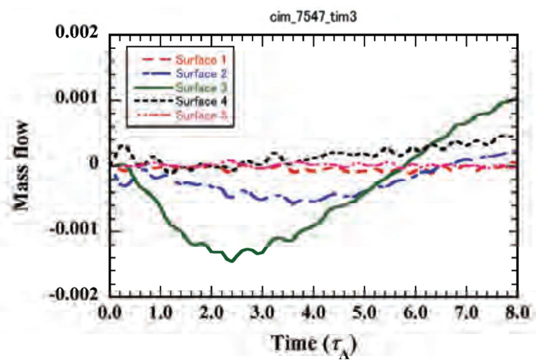

Fig. 6 Temporal evolution of mass flow integrated on the flux surfaces 1, 2, 3, 4 and 5 which are located from the magnetic axis to the outside. The initial plasmoid is located on the flux surface 3.

In addition, the simulation will be carried out in LHD configuration in order to seek the ways obtaining good performance on fueling.

[1] Y. W. Muller et al. Nucl. Fusion, **42**, 301 (2002).
[2] P. B. Parks and M. N. Rosenbluth. Phys. Plasmas, **5**, 1380 (1998).
[3] R. Ishizaki et al. Phys. Plasmas, **11**, 4064 (2004).
[4] P. B. Parks et al. Phys. Rev. Lett., **94**, 125002 (2005).
[5] R. Sakamoto et al. *in proceedings of 29th EPS conference on Plasma Phys. and Control. Fusion.*
[6] R. Ishizaki et al. IAEA-CN-149/TH/P3-6 (2006).
[7] K. Harafuji et al. J. Comp. Phys., **81**, 169 (1989).
[8] H. Takewaki et al. J. Comput. Phys., **61**, 261 (1985).

P1-043

Proceedings of ITC/ISHW2007

Numerical Study of Resistive Magnetohydrodynamic Mode Structures in Typical Plasmas of the Large Helical Device

Yutaka MATSUMOTO[1)], Kiyomasa WATANABE[2)] and Luis GARCIA[3)]

[1)]Graduate School of Engineering, Hokkaido University, Sapporo 060-8628, Japan
[2)]National Institute for Fusion Science, Toki 509-5292, Japan
[3)]Universidad Carlos III, Madrid, Spain

(Received 10 January 2006 / Accepted 24 January 2006)

We study the resistive instabilities typically observed in the Large Helical Device (LHD) in order to systematically investigate the effects of the resistive magnetohydrodynamics (MHD) instabilities on the plasma confinement. The resistive instabilities with the low toroidal mode number are investigated by using the three-dimensional linear resistive MHD code FAR3D. It is confirmed that both the growth rate and the mode width obey the theoretical formula of the gravitational interchange mode independent of the toroidal mode number. The range of the magnetic Reynolds number, in which the growth rate and/or the mode width obey the theoretical formula, is clarified. It is found that the growth rate is proportional to the mode width when beta is constant.

Keywords: resistive MHD, LHD, FAR3D

DOI: 10.1585/pfr.1.001

1 Introduction

It is important to understand the magnetohydrodynamic (MHD) equilibrium and stability properties for the realization of the nuclear fusion reactor. In a helical device, such as the Large Helical Device (LHD)[1] in Japan, the complex three-dimensional (3D) MHD study is needed for the successful operation. The MHD instability modes typically observed in the LHD experiments are summarized as follows. Some modes, of which the dependence property on the magnetic Reynolds number is similar to the resistive gravitational interchange mode[2], are obtained in the peripheral region of the high beta plasma with the strong magnetic shear. Others are frequently monitored in the core region of the high aspect ratio plasma with the relatively weak magnetic shear.

It is the purpose of this study to systematically investigate the effects of the resistive MHD instability on the plasma confinement in the LHD. Consequently, the typical MHD instability modes are numerically analyzed by using the 3D resistive MHD code FAR3D[3]. We especially focus on the mode width, i.e., the resistive layer thickness and systematically investigate the relationships between mode width (W), beta ($\langle\beta\rangle$), growth rate (γ) and magnetic Reynolds number (S).

In this paper, the resistive MHD instability modes in the high beta plasma with the strong magnetic shear are described. The outline of the FAR3D code and the numerical conditions are given in Section 2. The results of the calculations are summarized in Section 3. Section 4 is devoted to a brief summary.

author's e-mail: shopon@qe.eng.hokudai.ac.jp

2 Numerical Model

As mentioned in the preceding section, the FAR3D code is a 3D resistive MHD code[3]. In this code, a set of resistive MHD equations is time-advanced in the Boozer coordinates[4]. And the perturbed quantities are expanded in Fourier series in the generalized poloidal and toroidal angles by using the poloidal mode number (n) and the toroidal mode number (m). FAR3D appears in different forms depending on the approximation and the treatment for the MHD equations. We adopt one of the some versions of FAR3D, in which the reduced equations[3]:

$$\frac{\partial\psi}{\partial t} = \nabla_{\mathrm{p}}\Phi + \eta B_{\zeta}^{\mathrm{eq}} J_{\zeta}, \tag{1}$$

$$\begin{aligned}\frac{\partial U}{\partial t} &= -\boldsymbol{v}\cdot\nabla U \\ &+ S^2\left\{\frac{\beta_0}{2\epsilon^2}\left(\frac{1}{\rho}\frac{\partial\sqrt{g}}{\partial\theta}\frac{\partial p}{\partial\rho} - \frac{\partial\sqrt{g}}{\partial\rho}\frac{1}{\rho}\frac{\partial p}{\partial\theta}\right)\right. \\ &+ \left.\nabla_{\mathrm{p}}J^{\zeta} - \frac{1}{\rho}\frac{\partial}{\partial\rho}\left(\rho J_{\mathrm{eq}}^{\zeta}\right)\frac{1}{\rho}\frac{\partial\psi}{\partial\theta}\frac{1}{\rho}\frac{\partial J_{\mathrm{eq}}^{\zeta}}{\partial\theta}\frac{\partial\psi}{\partial\rho}\right\},\end{aligned} \tag{2}$$

and

$$\frac{\partial p}{\partial t} = -\boldsymbol{v}\cdot\nabla p + \frac{\mathrm{d}p_{\mathrm{eq}}}{\mathrm{d}\rho}\frac{\partial\Phi}{\partial\theta}, \tag{3}$$

are linearly calculated, where the velocity and the magnetic field are described as $\boldsymbol{v} = \sqrt{g}\nabla\zeta\times\nabla\Phi$ and $\boldsymbol{B} = R_0\nabla\zeta\times\nabla\Psi$, respectively.

The used MHD equilibria, i.e., the high beta plasma with the strong magnetic shear, is generated by using the 3D equilibrium code VMEC[5]. The equilibrium is described by using 1,000 radial grid points, and 20 helical

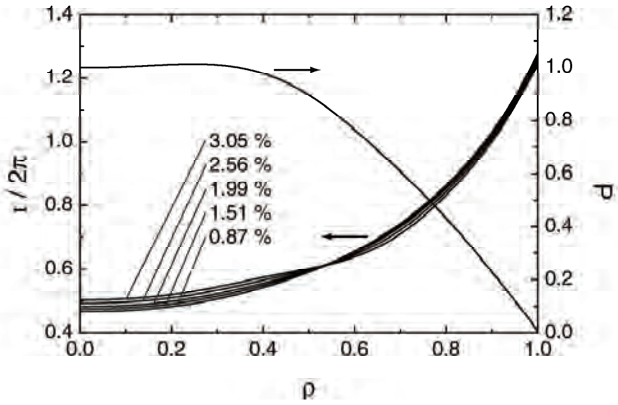

Fig. 1 Radial profiles of $\iota/2\pi$ and P in the equilibrium using in this study.

($n \neq 0$) and 3 toroidal ($n = 0$) Fourier modes. Figure 1 shows the rotational transform ($\iota/2\pi$) and the pressure (P) of the used equilibrium, in which the volume-averaged beta ($\langle\beta\rangle$) are 0.87, 1.51, 1.99 2.56, and 3.05 %, respectively.

In this paper, the resistive instabilities with the low toroidal mode numbers ($n = 1, 2, 3$) are described. It is seen from Fig. 1 that there are the rational surfaces of $m/n = 1/1, 2/1, 2/2, 3/2, 4/2, 3/3, 4/3, 5/3, 6/3$.

As mentioned in Section 1, we pay attention to the mode width, i.e., the resistive layer thickness. The mode width (W) is defined as the region that the growing speed of the instability to the radial direction (V_ρ) is larger than 70 % of the peak value. It is noted that $\partial\xi/\partial t = V_\rho$, where ξ is the perturbation to the radial direction. A example of the radial profiles of V_ρ, i.e., the mode structure, is shown in Fig.2.

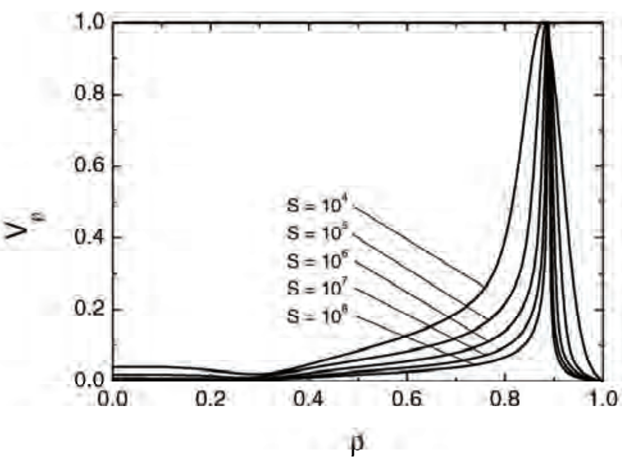

Fig. 2 Radial profiles of V_ρ of $m/n = 1/1$ modes in the case of $\langle\beta\rangle = 1.99$ %.

3 Results

3.1 $n = 1$ mode

In the cases of $\langle\beta\rangle \leq 1.51$ %, both $m/n = 1/1$ and $2/1$ modes are unstable and their peak values of V_ρs are almost the same. When the calculation without the $m/n = 2/1$ mode is done to determine the primary unstable mode, γ remains the same as the results of the calculations including the $m/n = 2/1$ mode. Both $m/n = 1/1$ and $2/1$ modes also appear in the cases of $\langle\beta\rangle \geq 1.99$ %. In these cases, the peak value of V_ρ of $m/n = 1/1$ mode is larger than that of $m/n = 2/1$ mode and γ remains the same as the results of the calculation without $m/n = 2/1$ mode. Therefore, the $m/n = 1/1$ mode is the primary unstable mode. There exist the rational surfaces of $m/n = 1/1$ around $\rho \simeq 0.89$.

The relationships between S and γ are shown in Fig. 3, and the relationships between S and W are shown in Fig. 4. It can be seen from Figs. 3 and 4 that both γ and W are proportional to $S^{-1/3}$. This dependency is similar to the resis-

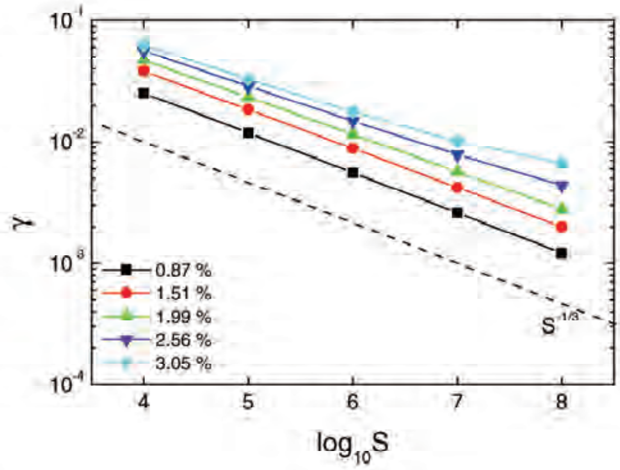

Fig. 3 Relationships between S and γ in the case of $m/n = 1/1$ mode.

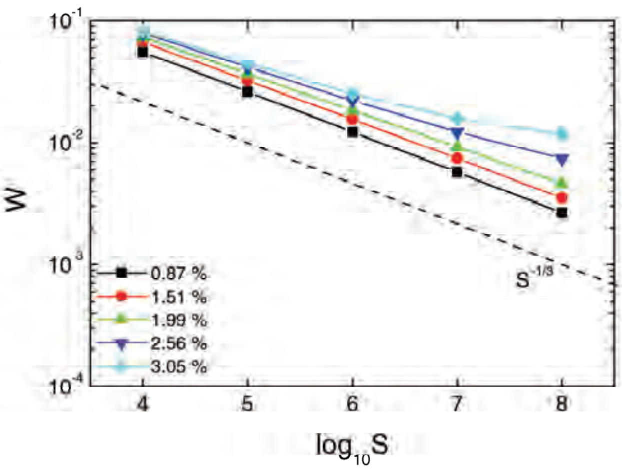

Fig. 4 Relationships between S and W in the case of $m/n = 1/1$ mode.

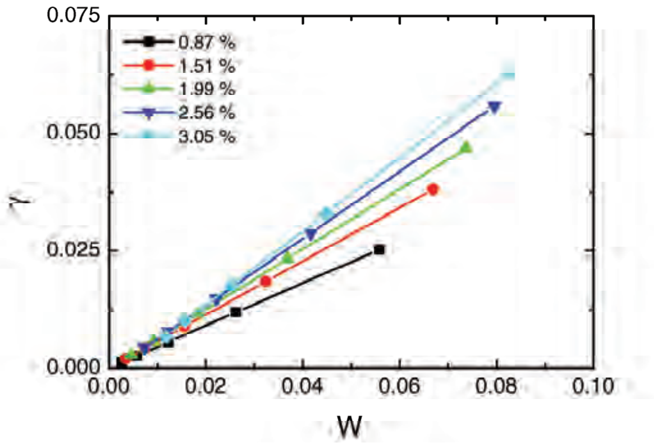

Fig. 5 Relationships between W and γ in the case of $m/n = 1/1$ mode.

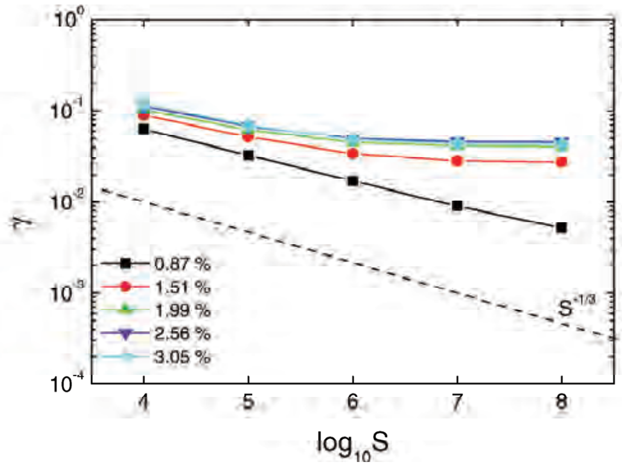

Fig. 6 Relationships between S and γ in the case of $m/n = 3/2$ mode.

tive gravitational interchange mode[2]. Such dependency of γ and W on S, however, becomes small when $\langle\beta\rangle = 3.05$ % and $\log_{10} S > 6$.

Figure 5 shows the relationships between W and γ. In each $\langle\beta\rangle$ cases, γ is proportional to W. The slopes become steep with $\langle\beta\rangle$ increasing.

3.2 $n = 2$ mode

In the case of $n = 2$, only the $m/n = 3/2$ mode is observed as the unstable mode. The rational surfaces of $m/n = 3/2$ exist around $\rho \simeq 0.63$.

The relationships between S and γ are shown in Fig. 6, and the relationships between S and W are shown in Fig. 7. Both γ and W are proportional to $S^{-1/3}$ in the case of $\langle\beta\rangle =$ 0.87 %. When $\langle\beta\rangle \geq 1.51$ % and $\log_{10} S > 5$, however, γ and W are almost independent of S. Both γ and W of the $m/n = 3/2$ mode hardly increase with $\langle\beta\rangle$ in the cases of $\langle\beta\rangle \geq 1.99$ % γ of the $m/n = 3/2$ mode as well as γ of the $m/n = 1/1$ mode is proportional to W. The slopes also become steep with the increase of $\langle\beta\rangle$ (Fig. 8).

Compared these results of the $m/n = 3/2$ mode with those of the $m/n = 1/1$ mode, γ of the $m/n = 3/2$ mode is larger than that of the $m/n = 1/1$ mode. On the other hand, W of the $m/n = 3/2$ mode is slightly smaller than that in the $m/n = 1/1$ mode. The range of S, in which γ and W $\propto S^{-1/3}$, in $n = 2$ case is narrower than that in $n = 1$ case. In the cases of $\langle\beta\rangle \geq 2.56$ %, the dependency of γ and W on $\langle\beta\rangle$ in $n = 2$ case is smaller than that in $n = 1$.

3.3 $n = 3$ mode

In the case of $\langle\beta\rangle = 0.87$ %, only the $m/n = 5/3$ mode is unstable. The $m/n = 4/3$ unstable mode, however, appears in the calculations without the $m/n = 5/3$ mode. In this case, γ is larger than that in the calculation including the $m/n = 5/3$ mode. Although both $m/n = 4/3$ and $m/n = 5/3$ modes are unstable in the $\langle\beta\rangle = 1.51$ %

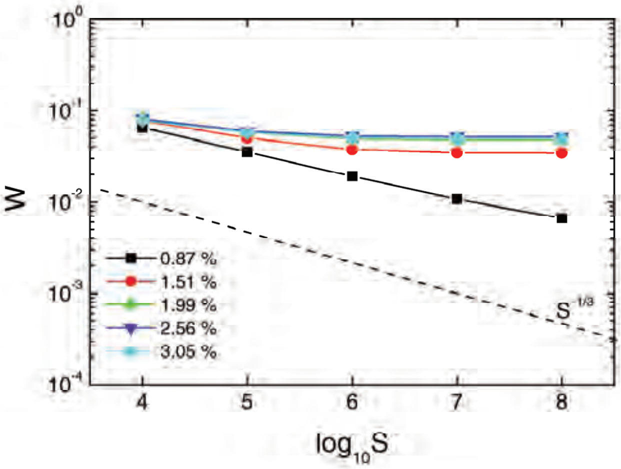

Fig. 7 Relationships between S and W in the case of $m/n = 3/2$ mode.

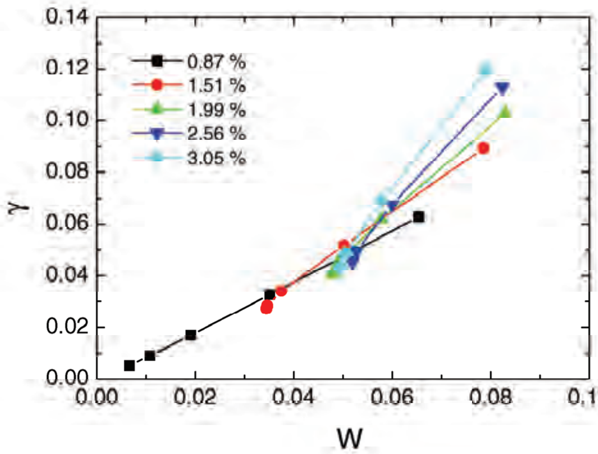

Fig. 8 Relationships between W and γ in the case of $m/n = 3/2$ mode.

case, V_ρ of the $m/n = 5/3$ mode is larger than that of the $m/n = 4/3$ mode. In the calculations without $m/n = 5/3$ mode, however, the $m/n = 4/3$ mode becomes unstable and its γ is larger than that in the calculation including the $m/n = 5/3$ mode. When $\langle\beta\rangle \geq 1.99$ %, both $m/n = 4/3$ and $m/n = 5/3$ modes are unstable. However, V_ρ of the $m/n = 4/3$ mode is larger than that of the $m/n = 5/3$ mode. These results indicate that $m/n = 4/3$ mode is the primary unstable mode. There are the rational surfaces of $m/n = 4/3$ around $\rho \simeq 0.72$.

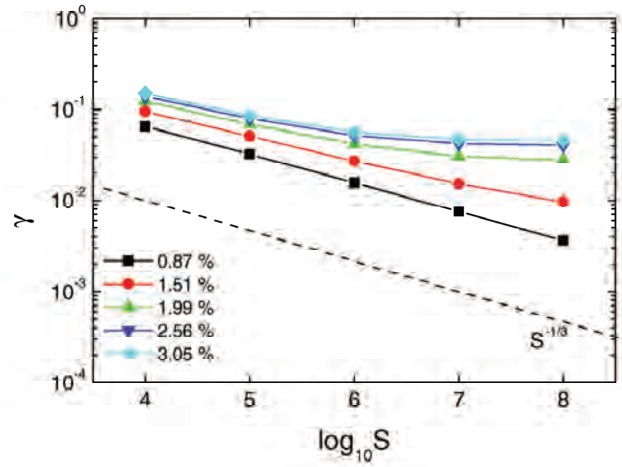

Fig. 9 Relationships between S and γ in the case of $m/n = 4/3$ mode.

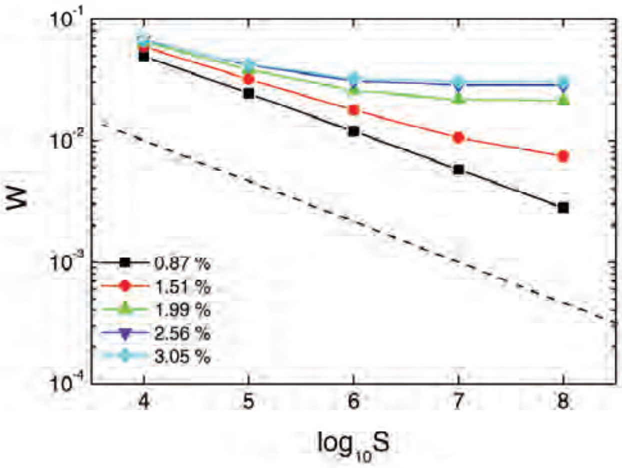

Fig. 10 Relationships between S and W in the case of $m/n = 4/3$ mode.

The relationships between S and γ are shown in Fig. 9, and the relationships between S and W are shown in Fig. 10. γ is proportional to $S^{-1/3}$ when $\langle\beta\rangle \leq 1.51$ %. On the other hand, W is proportional to $S^{-1/3}$ only if $\langle\beta\rangle = 0.87$ %. In high beta and $\log_{10} S > 6$ cases, the dependency of γ and W on S become small. Such changes of the dependency of W occur in lower beta cases than those of γ. The dependencies of γ and W of the $m/n = 4/3$ mode on $\langle\beta\rangle$ is as small as that of the $m/n = 3/2$ mode in the

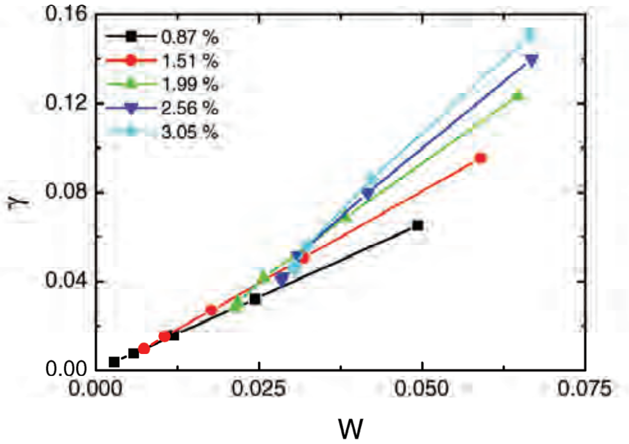

Fig. 11 Relationships between W and γ in the case of $m/n = 4/3$ mode.

case of $\langle\beta\rangle \geq 2.56$ %. As shown in Fig. 11, γ of the $m/n = 4/3$ mode is also proportional to W and the slopes become steep with the increase of $\langle\beta\rangle$.

Compared these results of $n = 1$, $n = 2$ and $n = 3$ modes, γ of $n = 3$ mode is the largest in three n cases. On the contrary, W of $n = 3$ mode is the smallest. The range of S, in which γ and $W \propto S^{-1/3}$, in $n = 3$ case is narrower than that in $n = 2$ case.

4 Summary

In this paper, the low n resistive instability modes in the typical LHD high beta plasma with the strong magnetic shear are analyzed by using the FAR3D code.

It is found that the primary unstable modes are $m/n = 1/1$, $3/2$, $4/3$. The rational surfaces of these modes exist in the plasma periphery ($\rho > 0.6$). It is confirmed that both γ and W obey the theoretical formula of the gravitational interchange mode($\propto S^{-1/3}$) independent of n. Their dependencies on S become small when $\langle\beta\rangle$ and/or S are high. The range of S, in which γ and/or W are proportional to $S^{-1/3}$, becomes narrow as n decreasing. When $\langle\beta\rangle$ = const., γ is proportional to W. The slope becomes steep with $\langle\beta\rangle$ increasing.

In near future, the resistive instabilities of $n > 4$ will be studied. In addition, the resistive instabilities in the different equilibrium of the LHD will also be investigated.

This work was supported by the collaborative research program of NIFS (NIFS06KLHH302).

[1] A. Iiyoshi *et al.*, Nucl. Fusion **39**, 1245 (1999).

[2] H. P. Furth, J. Killeen, M. N. Rosenbluth, Phys. Fluids **6**, 459 (1963).

[3] L. Garcia, *Proc. 25th EPS Conf. on Controlled Fusion and Plasma Physics* (Prague, 1998), VOL. 22A, PartII, p. 1757.

[4] A. H. Boozer, Phys. Fluids **23**, 904 (1980).

[5] S. P. Hirshman, Phys. Fluids **26**, 3553 (1983).

Proceedings of ITC/ISHW2007

Resistive MHD stability studies for LHD configurations

Luis GARCIA[1)], Jacobo VARELA[1)] and Kiyomasa WATANABE[2)]

[1)]*Universidad Carlos III, 28911 Leganés, Madrid, Spain*

[2)]*National Institute for Fusion Science, Toki, Gifu 509-5292, Japan*

October 15, 2007

A set of reduced equations is derived without making any assumption on the number of field periods. The equilibrium used in the equations is the exact three-dimensional equilibrium without any average in the toroidal angle. Using this set of equations, we study the ideal and resistive MHD properties of different LHD configurations. The linear results are compared with the ones obtained from the full MHD equations in the pressure-convection limit. The agreement is very good.

Keywords: Resistive MHD, LHD, Reduced equations

1 Introduction

Pressure-driven instabilities are a key feature in stellarator stability, since no net toroidal current flows in the plasma, avoiding the appearance of current-driven instabilities. Modes with high poloidal wavenumber m are usually studied using the ballooning formalism, which reduces the stability problem to finding the eigenvalue of a system of differential equations to be solved along the magnetic lines. The stellarator expansion can be applied to study the stability of modes with low toroidal wavenumber n whose variation along filed lines is slow compared with the variation of the stellarator terms. A reduced set of equations expressed in terms of the equilibrium flux coordinates was derived for those modes [1]. They are formally the same as the reduced set of MHD equations for a tokamak.

The calculation of global modes using the full three-dimensional equilibrium has been based on formulations of the ideal MHD energy principle in magnetic coordinates [2, 3]. However, these formulations cannot include the effect of resistivity and are not suitable for nonlinear calculations. In order to be able of studying the nonlinear evolution, we developed a numerical code (FAR3D), which solves the full set of resistive MHD equations [4].

2 Reduced Equations

For high-aspect ratio configurations with moderate β-values (of the order of the inverse aspect ratio), we can apply the method employed in Ref. [1] for the derivation of the reduced set of equations without averaging in the toroidal angle. In this way, we get a reduced set of equations using the exact three-dimensional equilibrium. In this formulation, we include linear helical couplings between mode components, which were not included in the formulation developed in Ref. [1].

The main assumptions for the derivation of the set of reduced equations are high aspect ratio, medium β (of the order of the inverse aspect ratio ε), small variation of the fields, and small resistivity. With these assumptions, we can write the velocity and perturbation of the magnetic field as

$$\mathbf{v} = \sqrt{g} R_0 \nabla\zeta \times \nabla\Phi, \quad \mathbf{B} = R_0 \nabla\zeta \times \nabla\psi, \tag{1}$$

where ζ is the toroidal angle, Φ is a stream function proportional to the electrostatic potential, and ψ is the perturbation of the poloidal flux.

The equations, in dimensionless form, are

$$\frac{\partial \psi}{\partial t} = \nabla_{\|}\Phi + \frac{\eta}{S} B_{\zeta}^{eq} J_{\zeta} \tag{2}$$

$$\frac{\partial U}{\partial t} = -\mathbf{v}\cdot\nabla U + \frac{\beta_0}{2\varepsilon^2}\left(\frac{1}{\rho}\frac{\partial\sqrt{g}}{\partial\theta}\frac{\partial p}{\partial\rho} - \frac{\partial\sqrt{g}}{\partial\rho}\frac{1}{\rho}\frac{\partial p}{\partial\theta}\right) + \nabla_{\|}J^{\zeta} - \frac{1}{\rho}\frac{\partial}{\partial\rho}\left(\rho J_{eq}^{\zeta}\right)\frac{1}{\rho}\frac{\partial\psi}{\partial\theta} + \frac{1}{\rho}\frac{\partial J_{eq}^{\zeta}}{\partial\theta}\frac{\partial\psi}{\partial\rho} \tag{3}$$

$$\frac{\partial p}{\partial t} = -\mathbf{v}\cdot\nabla p + \frac{dp_{eq}}{d\rho}\frac{1}{\rho}\frac{\partial\Phi}{\partial\theta} \tag{4}$$

Here, $U = \sqrt{g}\left[\nabla\times\left(\rho_m\sqrt{g}\mathbf{v}\right)\right]^{\zeta}$, where ρ_m is the mass density. All lengths are normalized to a generalized minor radius a; the resistivity to η_0 (its value at the magnetic axis); the time to the poloidal Alfvén time $\tau_{hp} = R_0(\mu_0\rho_m)^{1/2}/B_0$; the magnetic field to B_0 (the averaged value at the magnetic axis); and the pressure to its equilibrium value at he magnetic axis. The Lundquist number S is the ratio of the resistive time $\tau_R = a^2\mu_0/\eta_0$ to the poloidal Alfvén time.

Equilibrium flux coordinates (ρ, θ, ζ) are used. Here, ρ is a generalized radial coordinate proportional to the square root of the toroidal flux function, and normalized to one at the edge. The flux coordinates used in the code are those described by Boozer [5], and $\sqrt{g}$ is the Jacobian of the coordinates transformation. The code uses finite differences

author's e-mail: lgarcia@fis.uc3m.es

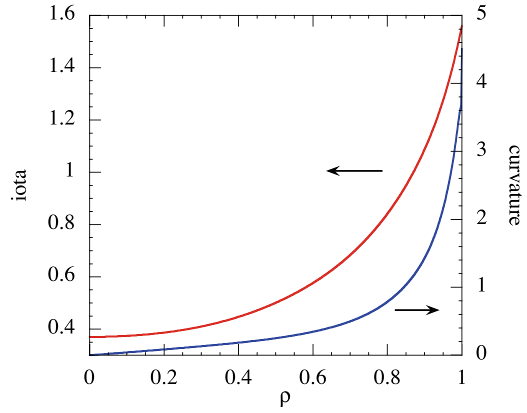

Fig. 1 Equilibrium profiles of the rotational transform and curvature for $\beta_0 = 2 \times 10^{-3}$. The LHD configuration is described in the text.

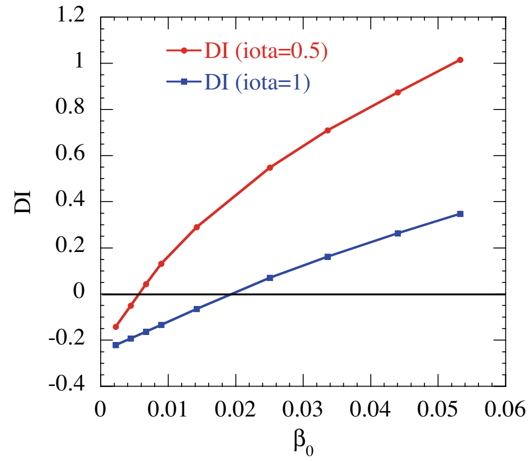

Fig. 2 Values of the ideal Mercier criterion vs. β_0 for the same LHD configuration as in Fig. 1 at the radial position of the $\iota = 1/2$ and $\iota = 1$ rational surfaces.

in the radial direction and Fourier expansions in the two angular variables. The numerical scheme if semi-implicit in the linear terms. The nonlinear version uses a two semi-steps method to ensure $(\Delta t)^2$ accuracy.

3 Linear Results

The method is especially suitable for the study of LHD configurations since they verify the assumptions, and the dominant equilibrium modes are $(m = 1, n = 0)$, and $(m = 2, n = 10)$. We start by studying the linear stability properties of a sequence of zero net-current fixed boundary equilibria with parameters $R_{ax} = 3.6$ m, $B_q = 100\%$, $\gamma = 1.25$, and a pressure profile $p \sim 1 - \rho^2$. The profiles of the rotational transform and curvature for the case with $\beta_0 = 2 \times 10^{-3}$ are shown in Fig. 1. The rotational transform profile changes very slightly for the scan in β. The value of the ideal Mercier stability criterion DI [6] as a function of β_0 at the position of the $\iota = 1/2$ and $\iota = 1$ rational surfaces is shown in Fig. 2. From the Mercier criterion we expect that ideal modes localized at $\iota = 1/2$ are stable for $\beta_0 < 6 \times 10^{-3}$, and those localized at $\iota = 1$ are stable for $\beta_0 < 0.02$. The results of the linear growth rate and the width of the dominant Fourier component $(m = 2, n = 1)$ of the $n = 1$ mode are shown in Fig. 3 for the ideal case and the case with $S = 10^7$. In these calculations, we include equilibrium components with $n = 0, 10, 20$, and, consequently, dynamic components with $n = 1, 9, 11, 19, 21$. The mode is ideally stable for $\beta_0 < 8 \times 10^{-3}$, a value close to the one given by the Mercier criterion. The resistive and ideal modes are very localized for β_0-values below 0.01, and they are very similar for β_0-values above 0.01.

The effect of the toroidal and helical couplings can be seen in Fig. 4, where the dominant component of the $n = 1$ family is shown for three different linear calculations: When only one dynamical component is included (Cylinder), when only components with $n = 1$ are included (Toroidal), and when components with $n = 1, 9, 11$ are included (Helical). The equilibrium parameters of this configuration are $R_{ax} = 3.6$ m, $B_q = 100\%$, $\gamma = 1.25$, $I_p < 0$, and correspond to an experimental discharge with localized oscillations at the $(m = 2, n = 1)$ rational surface [7]. The Lundquist number S is 8×10^7, and the growth rate increases by more than a factor of 2 from the cylindrical to the full calculation. The dominant radial magnetic field components are shown in Fig. 5. The importance of the helical couplings for the magnetic terms is clear from the Figure.

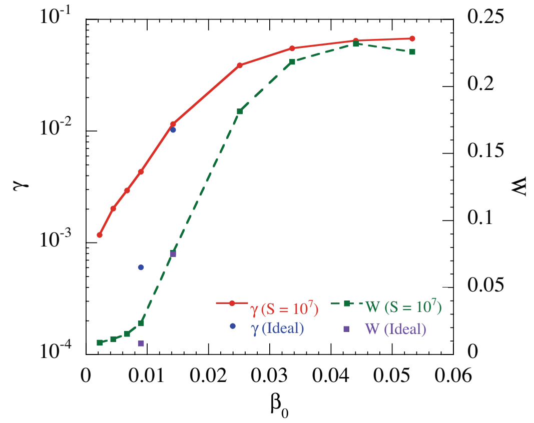

Fig. 3 Ideal and resistive $(S = 10^7)$ linear growth rate of the $n = 1$ mode vs. β_0 for the same LHD configuration as in Fig. 1. The width of the dominant $(m = 2, n = 1)$ Fourier component is also represented

4 Nonlinear Results

We have followed the nonlinear evolution in the cylindrical and toroidal limit. The value of S in these calculations is reduced in such a way that the linear growth rate and

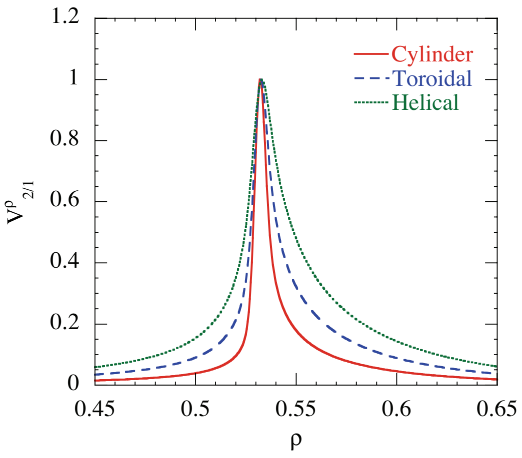

Fig. 4 Comparison of the dominant component of linear eigenfunctions with no couplings, with toroidal couplings, and with toroidal and helical couplings. The LHD configuration is described in the text.

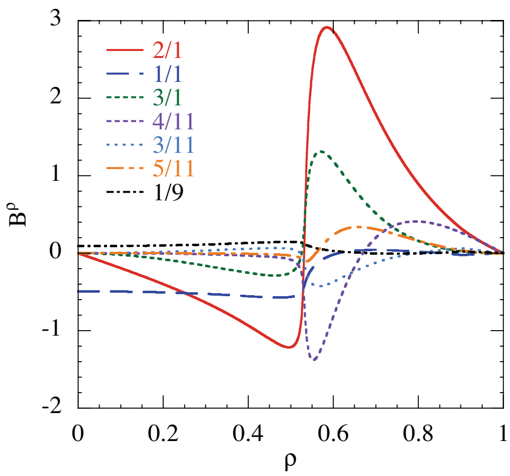

Fig. 5 Dominant radial magnetic field components for the case of Fig. 4 with all the couplings included.

width of the dominant component are similar to those of the linear calculation including helical couplings. The calculation for the cylindrical limit is single-helicity, that is, only components with $m/n = 2$ are included. As can be seen in Fig. 6, the nonlinear evolution for the cylindrical case leads to saturation with bursting activity. The pressure profile flattens around the $\iota = 1/2$ rational surface. For the toroidal limit, the components with the same n are linearly coupled. The saturation level increases with respect to the single-helicity case, and the profile of the root mean squared value of the radial velocity widens with respect to the linear eigenfunction, as can be seen in Fig. 7. In both calculations, the $(m = 2, n = 1)$ component dominates the spectrum. The calculation of the nonlinear evolution including linear helical couplings is under way.

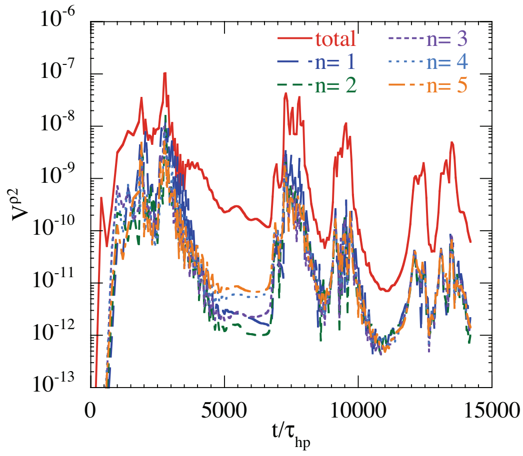

Fig. 6 Nonlinear evolution of the integral of the mean squared value of V^ρ for the case of Fig. 4.

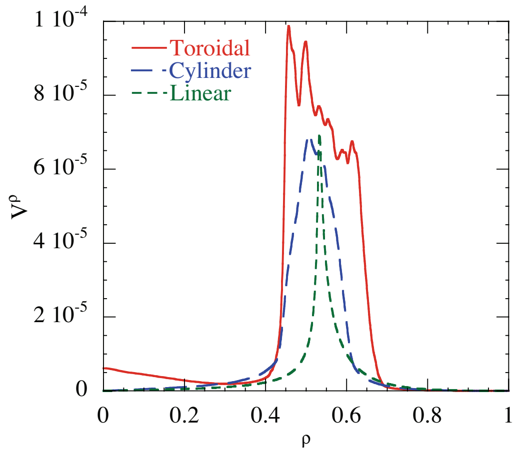

Fig. 7 Comparison of the time-averaged root mean squared value of V^ρ during the stationary phase for the nonlinear cylindrical and toroidal cases. The linear eigenfunction is also plotted.

5 Pressure-convection Limit

The natural generalization of the set of reduced equations would be to write the velocity and magnetic field as

$$\mathbf{v} = \sqrt{g}\left[R_0\nabla\zeta\times\nabla\Phi + \nabla\theta\times\nabla(\rho\Lambda)\right], \tag{5}$$

$$\mathbf{B} = R_0\nabla\zeta\times\nabla\psi + \nabla\theta\times\nabla(\rho\chi), \tag{6}$$

where Φ and Λ are velocity stream-functions, and ψ and χ, the perturbations of the poloidal and toroidal flux, respectively. In this formulation, the incompressibility condition is approximate (higher order in the reduced equations), $\nabla\cdot\left(\mathbf{v}/\sqrt{g}\right) = 0$. It corresponds to the pressure-convection limit of Ref. [4]. To ascertain the validity of the reduced set of equations for LHD, we have compared the results of linear calculations with those obtained using the full MHD equations in the pressure convection limit. The results practically do not change, and are consistent with the

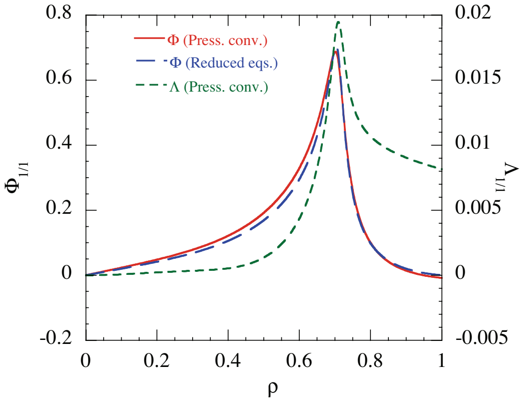

Fig. 8 Comparison of the dominant Fourier component of the stream-function Φ obtained from the reduced and pressure convection limit equations. The stream-function Λ is also plotted using a different scale. The corresponding LHD configuration is described in the text.

approximations made. This is illustrated in Fig. 8 where we have plotted the dominant component ($m = 1, n = 1$) obtained from both calculations for a configuration with aspect ratio 8.3 and $\gamma = 1.13$.

6 Summary

We have derived a set of reduced equations without any assumption on the number of field periods. For the calculation of the linear growth rates and nonlinear evolution, we use Boozer coordinates. The linear results agree very well with the ones obtained from the full MHD equations in the pressure-convection limit. We have studied the nonlinear evolution of the fluctuations in the cylindrical (single-helicity) and toroidal (only $n = 0$ equilibrium modes) limits. The saturated level widens with respect to the linear eigenfunction. The calculation of the nonlinear evolution including linear helical couplings is under way.

One of the authors (L.G.) thanks the staff at NIFS for their support during his stay when part of this work was done.

[1] L. Garcia, et al., Phys. Fluids B **2**, 2162 (1990).
[2] D.V. Anderson, et al., *Proceedings of Joint Varenna-Lausanne International Workshop on Theory of Fusion Plasmas* (Compositori, Bologna, 1988) p. 93.
[3] C. Schwab, Phys. Fluids B **5**, 3195 (1993).
[4] L. Garcia, *Proceedings of the 25th EPS International Conference, Prague, 1998*, VOL. 22A, Part II, p. 1757.
[5] A.H. Boozer, Phys. Fluids **25**, 520 (1982).
[6] C. Mercier, Nucl. Fusion **1**, 47 (1960).
[7] A. Isayama, et al., Plasma Phys. Control. Fusion **48**, L45 (2006).

Proceedings of ITC/ISHW2007

Mercier Stability Improvement in Nonlinear Development of LHD Plasma

Katsuji ICHIGUCHI[1)] and Benjamin A. CARRERAS[2)]

[1)]*National Institute for Fusion Science, 322-6 Oroshi-cho, Toki 509-5292, Japan*
[2)]*BACV Solutions Inc., 110 Mohawk, Oak Ridge, Tennessee 37831, USA*

(Received / Accepted)

Improvement of linear stability due to the nonlinear saturation of interchange modes in the increase of the beta value is studied for the inward-shifted LHD plasma. For this study, a multi-scale numerical scheme is utilized. In this scheme, the beta value is increased by adding small pressure increment to the background pressure. We focus on the dependence of the Mercier stability on the profiles of the pressure increment. It is obtained that the pressure profile approaches to the marginally stable profile when fixed profiles are employed for the pressure increment.

Keywords: MHD, LHD, multi-scale simulation, Mercier criterion, interchange mode, self-organization

1. Introduction

In the LHD experiments, good confinement of the plasma has been observed in the magnetic configuration with the vacuum magnetic axis located $R_{ax} = 3.6$m[1]. However, linear ideal interchange modes or Mercier modes were predicted to be unstable in this configuration. In order to investigate the stabilizing mechanism of the modes, we developed a nonlinear MHD code, NORM, based on the reduced MHD equations[2, 3]. In such investigation, it is crucial to follow the continuous change of the pressure profile in the increase of the beta value. For this purpose, we have also developed a multi-scale simulation scheme[4] by utilizing the NORM code and the VMEC code[5]. This scheme treats both the equilibrium change in the long time scale and the nonlinear dynamics of the instability in the short time scale simultaneously.

In the multi-scale scheme, the beta value is increased by adding a small increment of pressure to the background pressure obtained as the results of the nonlinear dynamics. In this case, there is a freedom in the determination of the profile of the pressure increment. One choice for the profile is to use the shape similar to the background pressure profile obtained by the nonlinear evolution. In the original study[4], we applied this pressure increment to the inward shifted configuration of LHD. We found a self-organization of the pressure profile which indicated a stable path to high beta regime.

On the other hand, the profiles of the heat deposition and the particle supply in experiments are usually fixed in the increase of beta. In order to take this situation into account, we consider to use a fixed profile for the increment of the pressure in the present study. We employ two types of increment profile and compare the results with that of the similar increment profile. Particularly, we focus on how the Mercier stability is improved by the self-organization of the pressure profile due to the nonlinear saturation of the interchange mode.

2. Multi-scale scheme with fixed pressure increment

The multi-scale scheme used in the present analysis is explained in Ref.[4] precisely. Here we start from a brief review of the multi-scale scheme, and then, explain the choice of the pressure increment profile and the conditions in the calculation.

The scheme consists of iterative calculations of nonlinear dynamics of the perturbations by the NORM code and three-dimensional equilibrium by the VMEC code. In this case, we divide the whole calculation time into short time intervals. At $t = t^i$, the beginning of an interval, we calculate new equilibrium quantities at the higher beta value with the VMEC code as the values of $t = t^{i+1}$, the beginning of the next interval. In order to keep a smooth continuity of the perturbation, we also divide the interval between t^i and t^{i+1} into some sub-intervals and employ a linear interpolation of the equilibrium quantities by using the equilibrium quantities of $t = t^i$ and t^{i+1}. Then, the nonlinear dynamics is calculated for each sub-interval with the interpolated equilibrium quantities with the NORM code.

When we calculate the equilibrium with the VMEC code, we incorporate the pressure deformation due to the nonlinear dynamics into the pressure profile. At $t = t^i$, the total pressure is obtained as

$$P^i_{tot} = \langle P \rangle^i + \sum_{m \neq 0 \text{ or } n \neq 0} \tilde{P}_{mn}, \qquad (1)$$

where the tilde means a perturbed quantity and m and n are the poloidal and the toroidal mode numbers. Here $\langle P \rangle^i$ denotes the average pressure which is given by

$$\langle P \rangle^i = P^i_{eq} + \tilde{P}^i_{00}. \qquad (2)$$

author's e-mail: ichiguch@nifs.ac.jp

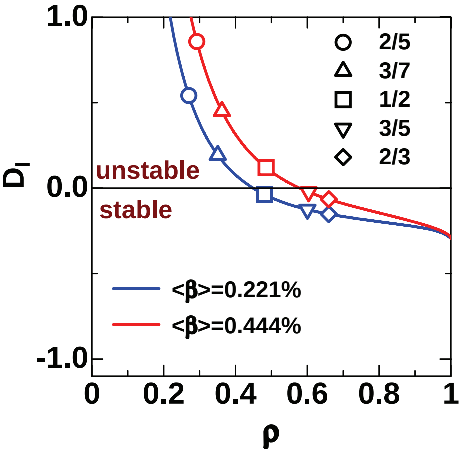

Fig. 1 Profiles of D_I of the equilibrium for the pressure profile of $P_{eq} = P_0(1-\rho^2)(1-\rho^8)$ in the inward-shifted LHD plasma. Each symbol shows the value of D_I at the position of the resonant surface.

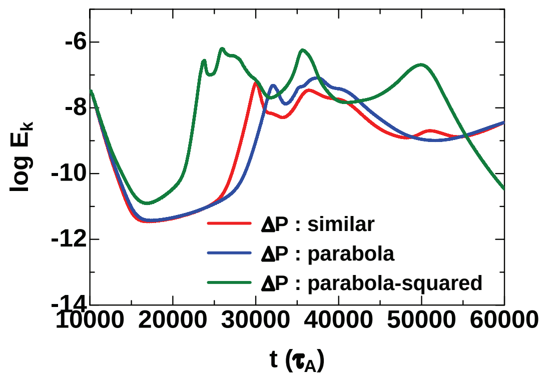

Fig. 2 Time evolution of kinetic energy for each case of the pressure increment.

The average pressure includes the effect of the nonlinear dynamics through $\tilde{P}^i_{00}$. We calculate P^{i+1}_{eq} by using $\langle P\rangle^i$ as

$$P^{i+1}_{eq} = \langle P\rangle^i + \Delta P^{i+1}. \tag{3}$$

Here ΔP^{i+1} denotes the increment of the pressure, which gives the increase of beta. In the original study[4], we employed a similar increment profile given by

$$\Delta P^{i+1} = \langle P\rangle^i \frac{\beta^{i+1} - \beta^i}{\beta^i}. \tag{4}$$

In the present study, we also consider two kinds of fixed profile for the increment given by

$$\Delta P^{i+1} = P_I(1-\rho^2)(1-\rho^8) \tag{5}$$

and

$$\Delta P^{i+1} = P_I(1-\rho^2)^2, \tag{6}$$

where ρ denotes the square-root of normalized toroidal magnetic flux. The factor P_I is adjusted so as to give a given beta increment. Hereafter, we call the increments given by (4)-(6) ‘similar increment’, ‘parabolic increment’ and ‘parabola-squared increment’, respectively.

We apply the scheme to the LHD plasma for the three types of pressure increment under following numerical conditions. We choose the configuration with the vacuum magnetic axis located at $R_{ax} = 3.6$m. We assume the resistivity of $S = 10^6$, where S is the magnetic Reynolds number. We examine the evolution for $0.221\% \le \langle\beta\rangle \le 0.498\%$. One time interval is $2500\tau_A$, where τ_A is Alfvén time. We increase the beta value by $\Delta\langle\beta\rangle = 0.0138\%$ every time interval. In the equilibrium calculation with the VMEC code, we use the free boundary condition and the no net-current condition. The time interval is divided into 10 sub-intervals for the linear interpolation.

To give the initial state, we start from the equilibrium for $P_{eq} = P_0(1-\rho^2)(1-\rho^8)$ at $\langle\beta\rangle = 0.221\%$. As is shown in Fig.1, the core region of $\rho \le 0.44$ of this equilibrium is Mercier unstable. The absolute value of D_I[6] decreases in the ρ direction. We follow the nonlinear evolution of the interchange mode for this equilibrium and obtain a saturation at $t = 10000\tau_A$. We employ the saturated state as the initial state of the multi-scale calculation and set $t = 10000\tau_A$ as the initial time. Then, the beta value reaches $\langle\beta\rangle = 0.498\%$ at $t = 60000\tau_A$.

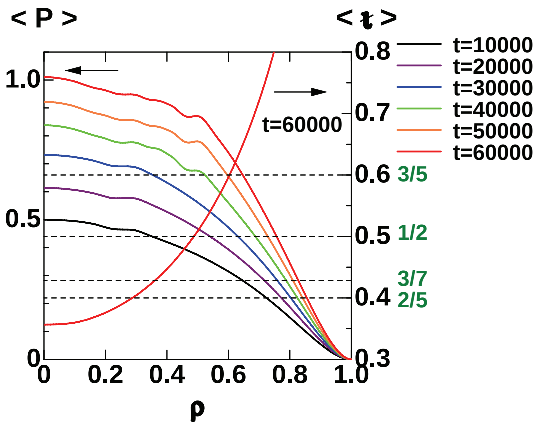

Fig. 3 Time evolution of average pressure in the case of the parabolic increment.

3. Self-organization of pressure profile

We follow the evolution of the plasma for the three types of increment profile and compare the resultant pressure profile. Figure 2 shows the time evolution of the total kinetic energy for the three pressure increments. It is common that the kinetic energy varies smoothly compared with the time scale of sub-interval. This feature indicates the multi-scale approach works well also in the fixed increment cases. The evolution of the parabolic increment case is close to that of the similar increment case, while the evolution in the parabola-squared increment case is a little more active.

Figure 3 shows the time evolution of the average pressure in the case of the parabolic increment. As in the case of the similar increment case[4], weak excitation and mild

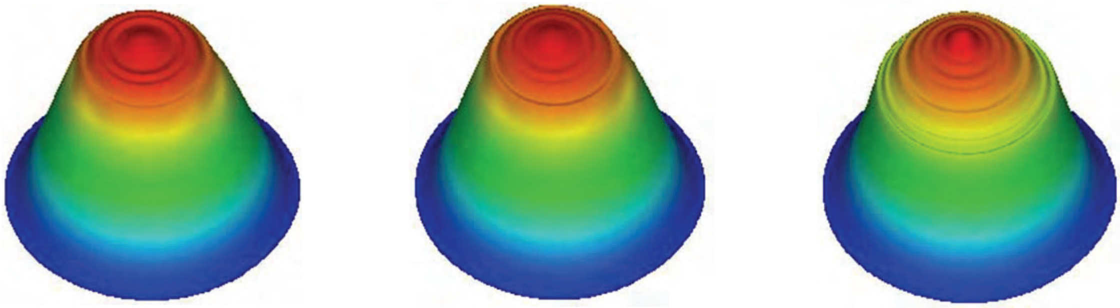

Fig. 4 Bird's-eye view of total pressure at t=60000τ_A for similar increment (left), parabolic increment (center) and parabola-squared increment (right).

saturation of the interchange modes occur. The saturation generates locally flat structure at the resonant surfaces in the average pressure profile. Since the Mercier quantity D_I is a decreasing function of ρ as shown in Fig.1, the flat region is generated from inward to outward of the plasma as the beta increases. Similar tendency is observed in the parabola-squared increment case.

Figure 4 shows the bird's-eye view of the total pressure at the final time of $t = 60000\tau_A$. The deformation of the total pressure is almost θ independent for all increment cases. This implies that almost all of the resonant interchange modes are saturated in a low level without any significant excitation. In other words, in each increment profile, the total plasma pressure evolves so that fluctuations are suppressed in the increase of beta.

Remarkable difference between the three increment profiles is seen in the average pressure profile at the final state. Figure 5 shows the profile of the average pressure at $t = 60000\tau_A$. In the similar increment case, a global flat structure is generated in the core region of $\rho < 0.4$. In the parabolic increment case, the gradient of the pressure is recovered in the core region. In the parabola-squared increment case, the gradient becomes larger. These differences are attributed to the gradient of the increment profile. In any case of the increment, the pressure profile is flattened in the core region once at low beta because (m,n)=(5,2) and (7,3) modes are saturated in the region. In the similar increment case, the average pressure is increased so that the shape should be maintained. Therefore, the local flat structure generated at low beta is kept even at high beta.

On the other hand, in the fixed increment cases, the gradient of the increment profile is always added to the total pressure. Therefore, the local flat structure of the average pressure tends to be smoothed out. Furthermore, the resonant mode can be excited again at the flattened region when the local pressure gradient enhanced by the increment exceeds a critical value. Since the driving force of the mode should be quite weak, it saturates immediately to generate a narrower flat region in the average pressure profile. Thus, the local pressure gradient approaches to the critical value through this process. The critical value can be measured in terms of D_I as explained in the next section.

In the parabolic increment case, the increment profile is the same as the equilibrium profile used in the initial state generation. Therefore, this process is limited in the core region. On the other hand, the more steep gradient is added in the parabola-squared increment case. The region of the process extends to the outer region including the surfaces resonant with the (5,3) and the (3,2) modes.

4. Mercier stability improvement

The global feature of the D_I profile is common in all cases of the increment. Figure 1 (red line) shows the D_I profile for the equilibrium with the pressure profile of $P_{eq} = P_0(1-\rho^2)(1-\rho^8)$ at $\langle\beta\rangle = 0.444\%$. In this case, the wide region of $\rho \leq 0.60$ is Mercier unstable. On the other hand, D_I has negative values around the resonant surfaces as shown in Fig.6, which shows the D_I profiles at $t = 60000\tau_A$ ($\langle\beta\rangle = 0.498\%$) for the three cases of the pressure increment. This comparison shows that the nonlinear saturation of the interchange mode stabilizes itself through the local pressure flattening.

The difference in the structure of the pressure profile is reflected to the precise structure of D_I profile. In the similar increment case, the improved values of D_I are -1.05, -0.49 and -0.21 at resonant surfaces with $\iota = 2/5$, 3/7 and 1/2. There is a tendency that the absolute value is a decreasing function of ρ_s, where ρ_s is the position of the resonant surfaces. This tendency is related to the Mercier stability at the initial equilibrium. The profile of D_I at $\langle\beta\rangle = 0.221\%$ implies that the driving force of the interchange mode is also the decreasing function of ρ. Therefore, the local deformation at inner resonant surface is larger than that at outer surface. Since such structure is almost maintained during the beta increase, the resonant surface is more stabilized beyond the marginal stability.

On the contrary, the absolute value of D_I is limited in the level of -0.32 in the parabolic increment case. In this case, even once the pressure profile is locally flattened, the enhancement of the gradient of the pressure degrades the Mercier stability. Therefore, the value of D_I approaches to a marginal value in the increase of beta. This tendency is the same as in the case of the parabola-squared increment. In this case, the local improvement is observed also

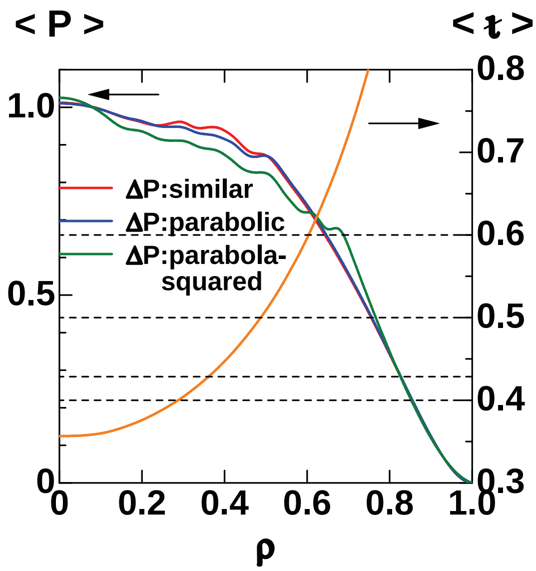

Fig. 5 Average pressure profiles at $t = 60000\tau_A$.

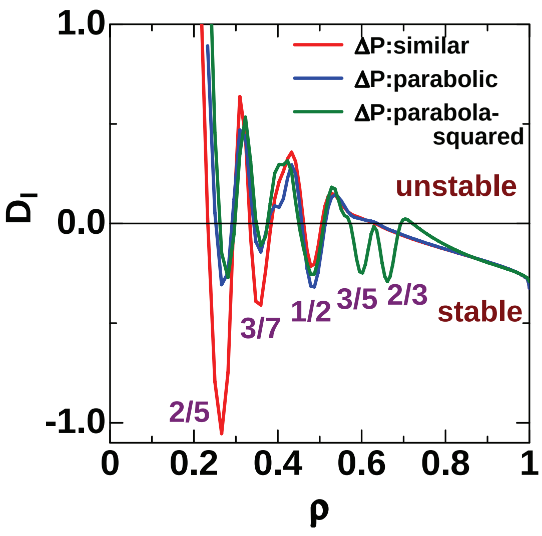

Fig. 6 Profiles of D_I at $t = 60000\tau_A$.

around the surfaces of $\iota = 3/5$ and 2/3. Including these surfaces, the absolute value of D_I is limited in the level of -0.29. The enhancement of the pressure gradient brought by the parabola-squared increment is larger than that by the parabolic increment case. Nevertheless, the maximum value of D_I is in the similar level of $D_I \sim -0.3$. This result indicates that this value of D_I corresponds to the marginal pressure gradient independent of the increment profile, if a fixed increment profile is employed. It can be concluded that the local pressure gradient is determined in the increase of beta so that D_I at the resonant surface should achieve to the marginal value.

5. Conclusions

The local improvement of the Mercier stability in the nonlinear evolution of the interchange mode is studied in the inward-shifted LHD plasma. The beta increase effect is incorporated by employing the multi-scale numerical scheme. The plasma is Mercier unstable in a wide region if there is no deformation of the pressure profile. However, the nonlinear saturation of the interchange mode locally improves the Mercier stability around the resonant surface through the generation of the local flat structure in the pressure profile.

The absolute value of D_I in the stabilized region depends on the pressure increment profile. If we use the similar increment profile, the absolute value of negative D_I becomes much larger in the vicinity of the axis than that in the outer region. This is attributed to that the locally flat structure in the pressure profile is maintained in the beta increase. On the other hand, if we use a parabolic increment profile, the reduction of the pressure gradient is compensated by the increment pressure. Therefore, the absolute values of D_I at all resonant surfaces are in a small level. In the case of the parabola-squared increment profile, the improvement of the Mercier stability extends to the outer rational surfaces. Even in this case, the absolute values of D_I are also limited in a small level including the outer rational surfaces. The level is almost the same as that in the parabolic increment case. These results indicates that the enhancement and the reduction of the pressure gradient is balanced so as to give a critical pressure gradient. The former is due to adding the increment pressure and the latter is due to the nonlinear saturation of the mode. In other words, in the case of the fixed profile of the pressure increment, the plasma is self-organized so that the pressure profile approaches to the marginally stable profile at the resonant surfaces with respect to the Mercier stability.

As a future plan, we consider to include an effect of the equilibrium diffusion. In this case, we can expect that the positive D_I values in the regions between the resonant surfaces also approach to marginal value.

Acknowledgments

This work is supported by NIFS cooperation programs NIFS07KLDD012 and NIFS07KNXN092. and also partly supported by the Grant-in-Aid for Scientific Research (C) 17560736 of the Japan Society for the Promotion of Science.

References

[1] K. Y. Watanabe, et al., Proc. of this conference, I-13 (2007).
[2] K. Ichiguchi, et al., Nucl. Fusion **43**, 1101-1109 (2003).
[3] K. Ichiguchi, et al., Fusion Science and Technology **46**, 34-43 (2004).
[4] K. Ichiguchi B. A. Carreras, J. Plasma Phys. **72** (2006) 1117-1121.
[5] Hirshman, S. P., et al., Comput. Phys. Commun. **43**, 143-155 (1986).
[6] A. H. Glasser, J. M. Greene, J. L. Johnson, Phys. Fluids **18**, 875-888 (1975).

Proceedings of ITC/ISHW2007

Growth of eigenmodes with moderate mode numbers in nonlinear MHD simulation of LHD

Hideaki MIURA[1)] and Noriyoshi NAKAJIMA[1)]

[1)]*National Institute for Fusion Science, Toki 509-5292, Japan*

(Received 15 October 2007)

Direct numerical simulations of compressible, nonlinear magnetohydrodynamic equations in the fully three-dimensional geometry of the large helical device are carried out to study the linear and nonlinear growth of the pressure-driven instability. Two parameter sets are adopted in the simulation study. One parameter set provides small dissipative coefficients so that the simulation results can be compared to the ideal linear stability analysis. By the use of this parameter set, the growth rates in the linear stage of our simulation coincides with the ideal linear growth rates. Another parameter set is provided to study nonlinear evolutions. Excitations of flows parallel to the magnetic field, its role to the nonlinear saturations are studied.

Keywords: direct numerical simulation, MHD instability

DOI: 10.1585/pfr.1.001

1 Introduction

In researches of magnetic confinement devices such as the Large Helical Device (LHD), Magnetohydrodynamics (MHD) instability is one of the key issues to understand plasma behaviors in the devices. Aiming to clarify the physics of the MHD activities observed in the LHD experiments[1], many linear analysis and nonlinear simulations have been carried out [2, 3, 4, 5, 6]. Because of the short wave instability nature of the the pressure driven instability, small scales must be sufficiently resolved in a numerical computation. In the numerical study of an instability, the linear growth rate is an important index. In linear analysis of an ideal MHD system, high mode behaviors can be well predicted. However, in numerical simulations, non-ideal (dissipative) MHD equations are studied because the dissipation is indispensable to avoid numerical instability. Since the resolution available in a numerical simulation are restricted, the dissipative coefficients in simulations are often far larger than the values expected to compare numerical results to experimental results. Typically, the adoption of the large coefficients brings about unfavorable damping of high modes.

In our recent work on nonlinear MHD simulations of LHD by the use of the MHD In Non-Orthogonal System (MINOS) code[3], the growth rate of the lowest mode coincides well with the linear ones obtained by the CAS3D code.[4] However, the growth rates of moderate and high modes in the simulation are apparently suppressed by the viscosity and the coincidence is lost as the mode number becomes larger. In this paper, the number of the grid points of our simulations is increased to study the moderate modes behaviors. Numerical simulations are carried out for the equilibrium magnetic field with the vacuum magnetic axis position 3.6m and the pressure profile $p(\psi) = (1 - \psi^2)$ where the ψ is the toroidal magnetic flux. Growth of the moderate mode numbers, generation of toroidal flows and nonlinear saturations of the instability are discussed. In this articles, two parameter sets are adopted: (A) the isotropic heat conductivity $\kappa = 1 \times 10^{-6}$ (that is, the parallel heat conductivity $\kappa_{//}$ and the perpendicular heat conductivity $\kappa_{\perp}$ is identical), the resistivity $\eta = 1 \times 10^{-6}$, the viscosity $\mu = 1 \times 10^{-6}$, and (B) $\kappa_{//} = 1 \times 10^{-2}$, $\kappa_{\perp} = 1 \times 10^{-6}$, $\eta = 1 \times 10^{-6}$, $\mu = 1 \times 10^{-4}$. These parameters are already normalized by some typical quantities (see Ref.[5]) and hence the reciprocal of the dissipative number can be considered as some similarity parameters such as the Reynolds number $Re = 1/\mu$ and the Lundquist number $S = 1/\eta$. The number of grid points are 193×193 on a poloidal cross-section and 640 in the toroidal direction. The number of grid points is doubled in the two directions of a poloidal cross-section compared to our earlier works.[5, 6] The parameter set (A) provides a high Reynolds number and the behaviors of the solutions may be easily compared to an ideal linear analysis. Though the simulation with this parameter set cannot be completed because the numerical resolution (number of grid points) is not sufficient for such a high Reynolds number flow, it serves to study linear stages. The parameter set (B) provides the moderate Reynolds number and nonlinear saturation within the numerical resolution, although the linear stage is influenced by the dissipative coefficients μ and $\kappa_{//}$. Thus we first study the former case, parameter set (A) so that the linear growth are clearly seen. Then the nonlinear growth is studied for the parameter set (B).

author's e-mail: miura.hideaki@nifs.ac.jp

2 Comparison to linear ideal analysis

Here we study the growth of Fourier amplitudes of the velocity vector. The velocity vector field V is decomposed into the normal ($V_{\nabla\psi}$), the parallel (V_b) and the binormal components ($V_{\nabla\psi\times b}$) Then each of the three vector components are decomposed into the Fourier modes m and n on the Boozer coordinate. By the use of the Fourier coefficient $V_{\alpha,mn}(\psi)$, the power spectrum $A_{\alpha,n} = \sum_m \int^{\psi} V_{i,mn}^2 d\psi$ is defined.[5] In Fig.1(a), the time evolution of the volume-integrated amplitudes of the three vector components of the velocity vector field are shown for the parameter set (A). Hereafter, the abscissa t is normalized by the toroidal Alfven time τ_A whenever a time series is plotted. In Fig.1(b), the time evolutions of $A_{\alpha,n}$ are shown. Here we recall that a single Fourier mode on the Boozer coordinate is not the linear eigen-function of the MHD equations by itself. A linear eigen-function consists of multiple Fourier modes, as are shown by Nakajima[8]. However, as is shown in the reference, the toroidal coupling in the LHD is so weak that the poloidal Fourier wavenumber n can be approximately recognized as a good quantum number. Based on this understanding, we see only the n-wavenumber dependence of the Fourier amplitude growth by summing m over all wavenumbers. Fig.1(c) is the magnification of the linear stage of this simulation. Observe in Figs.1(b) and (c) that some of the Fourier amplitudes achieve exponential growth while some show further acceleration. Because of the high Reynolds number $1/\mu = 10^6$, the computation is terminated in the midst of the growth. However, observations of the growth of the energy faster than an exponential growth in Figs.1(a) and (b) reveal that the final time 55 is already in the nonlinear stage of the evolution. We also find that the growth of the parallel energy coincides with those of the other two components only in short period at $40 < t < 45$, or rather faster than them. As is commented in the above, the final period of this simulation is influenced by nonlinear coupling in the MHD equations. Deviations of the parallel energy growth from the other two components should be attributed to the nonlinear growth. Based on studies of the growth of separate m/n Fourier modes (figures of which are omitted here), the linear growth is considered in between $t \simeq 30$ and $t \simeq 40$.

In Fig.2, the growth rates obtained in this simulation are compared to the ideal linear analysis. The CAS3D3[?] computation provides estimates of the growth rates. The growth rates for $n \leq 4$ in the simulation shows reasonable coincidence to the CAS3D computation. Compared to our previous work[5], the number of grid points are doubled into the two directions of a poloidal cross-section. Although the parameters are the same as the ones in the previous work, the artificial dissipations due to the truncation is drastically decreased thanks to the high resolution properties of the compact scheme.[10] Nonetheless, we still have to recognize that the moderate Fourier modes $n > 7$ is under the influence of the dissipative coefficients. We also note that $\mu = 1 \times 10^{-6}$ is the minimum value which makes sense as a *physical* viscosity for the current numerical resolution. Although we could reduce the viscosity below 1×10^{-6}, the growth of unstable modes becomes rather insensitive to the change of μ, suggesting that the numerical viscosity associated with the truncation errors become gradually dominant.

3 Nonlinear evolution

Next, the nonlinear evolutions of the instability is studied by the simulation with the parameter set (B). In Fig.3, the time evolution of the volume-integrated amplitudes of the three vector components of the velocity vector field are shown. The growth rate of the parallel flow component is the same as the other two component, making a difference to the observation in Fig.Fig:Run553total. It shows that the three components obey to the same kind of the instability. Among the three components of the velocity vector, the parallel component becomes dominant finally even though it is initially much smaller than the other two components.

Fourier amplitudes for some toroidal Fourier modes n of (a) the normal, (b) the binormal and (c) the parallel components of the velocity vector are shown in Figs.4(a)-(c), respectively. In Figs.4(a) and (b), Fourier amplitudes associated with the odd toroidal numbers $n = 1, 3, 5, 7, 9$, and 11 grows the fastest. The growth of the Fourier modes are mostly contributed by the Fourier mode set m/n associated with the $\iota/2\pi = 0.5$ rational surface. Growth rates of these Fourier modes are almost identical. Although the separation between odd and even wavenumbers are not clarified yet, the exponential growth of the even toroidal numbers are considered as a consequence of nonlinear couplings of the odd wavenumbers rather than their own linear instability, since the growth rates of these even numbers are as large as the twice of the growth rates of the odd numbers. Among the four dissipative coefficients, the parallel heat conductivity κ is considered as the most influencing one. For example, once the unstable Fourier modes which are resonant to the $\iota/2\pi = 0.5$ rational surface grow, the pressure distribution is modified because of the large $\kappa_{//}$. Since eigen-functions of low n modes cover wide are across the flux surfaces, the $\kappa_{//}$ effect can also modify the pressure profile in wide area. In Fig.4(c) the time evolutions of the Fourier amplitudes of the parallel velocity component are shown. In comparison to Figs.4(a) and (b) in which the toroidal modes $n = 1$, 3 and 5 have almost the same amplitudes, it is clearly seen that the $n = 1$ Fourier mode achieves the largest amplitude. Furthermore, there is no clear distinction between even and odd mode numbers.

In Fig.5, the pressure isosurfaces and contours on a poloidal cross-sections are shown at $t = 110\tau_A$ (upper) and $150\tau_A$ (lower). At $t \simeq 110\tau_A$, many of the Fourier modes are saturated or going to be saturated. The contour lines on the poloidal cross-section in Fig.5(a) exhibits clear mushroom-like structures. The mushroom-like structures have been repeatedly reported in our earlier works.[4, 5, 6] While the structures in the earliest work consist mainly of $m/n = 2/1$ Fourier modes, the structure in this article consist of many more Fourier modes which are resonant to the $\iota/2\pi = 0.5$ surface. The overlapping of the resonant modes provides quite large pressure deformation. Consequently, the contour plots of the pressure (and therefore the Poincare plots of the magnetic field lines, which are not shown here, too) become quite chaotic after the nonlinear saturations. However, at $t = 150\tau_A$, the pressure contour associate with the outermost closed surface is not deformed very much through the linear and nonlinear evolution, suggesting that the confinement is not critically damaged in spite of the strong instability. Furthermore, contour lines tend to form the concentric profiles again, showing a possibility of organizing relatively well confined state again.

4 Concluding Remarks

Direct numerical simulation study is conducted to study linear and nonlinear evolution of the instability in LHD. A simulation with relatively small dissipative coefficients shows good coincidence of the linear growth rates with the ideal analysis. In nonlinear simulations, the parallel flow becomes dominant after the nonlinear saturation. It is noteworthy that the parallel flow tends to grow much larger than the other two components of the velocity vector in the simulation with smaller dissipative coefficients than in the one with larger coefficients. It suggests that the parallel flow dominance is much stronger in simulations with very small dissipative coefficients. The numerical simulations in this work was carried out on NEC SX-7 "Plasma Simulator" in National Institute for Fusion Science under the NIFS program NIFS06KTA033.

[1] K. Watanabe et al., Nucl. Fusion **45**, 1247 (2005).
[2] H. Miura et al., Phys. Plasmas **8**, 4870 (2001)
[3] K. Ichiguchi et al., Nucl. Fusion **43** 1101 (2003).
[4] H. Miura et al., IAEA-CSP-25/CD/TH/2-3 (2004).
[5] H. Miura et al., AIP Conference Proceedings **871** (2006).
[6] H. Miura et al., Fusion Science and Technology **51**, 8 (2007).
[7] C.Nührenberg, Phys. Plasmas **6** 137 (1999).
[8] N. Nakajima, *Phys. Plasmas* **3** 4556 (1996).
[9] C. Nührenberg, *Phys. Plasmas*, **6** 137 (1999).
[10] S.K. Lele, *J. Compu. Phys.* **103** 16 (1992).

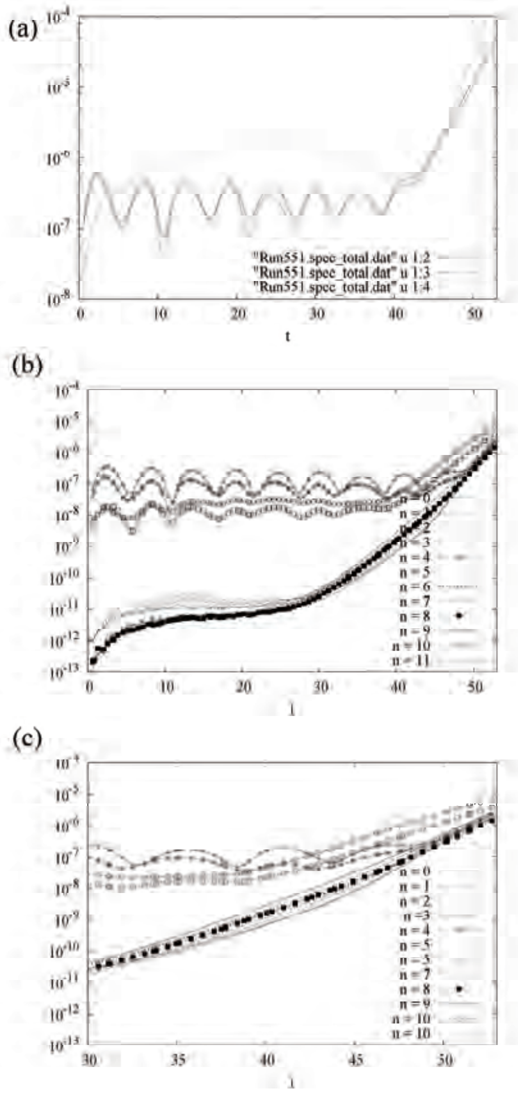

Fig. 1 Time evolutions of (1)the volume-integrated energy of the three components of the velocity vector. (b)the Fourier amplitudes of the normal velocity component $A_{\nabla\phi,n}$, and (c) an magnification of (b), in the parameter set (A) simulation.

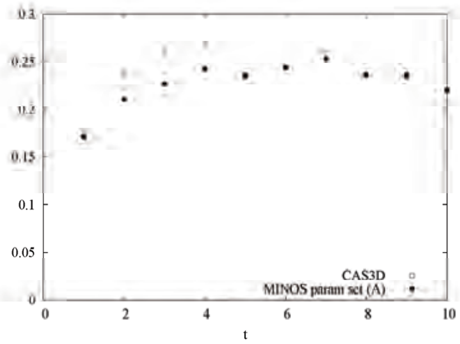

Fig. 2 Comparison of the growth rates of the Fourier amplitudes in the parameter set (A) simulation to those of the CAS3D computations.

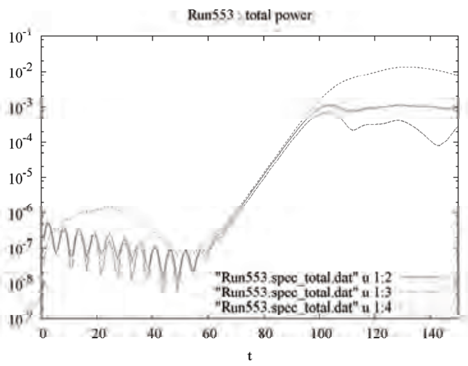

Fig. 3 Time evolutions of the Fourier amplitudes of the normal velocity component in the parameter set (B) simulation.

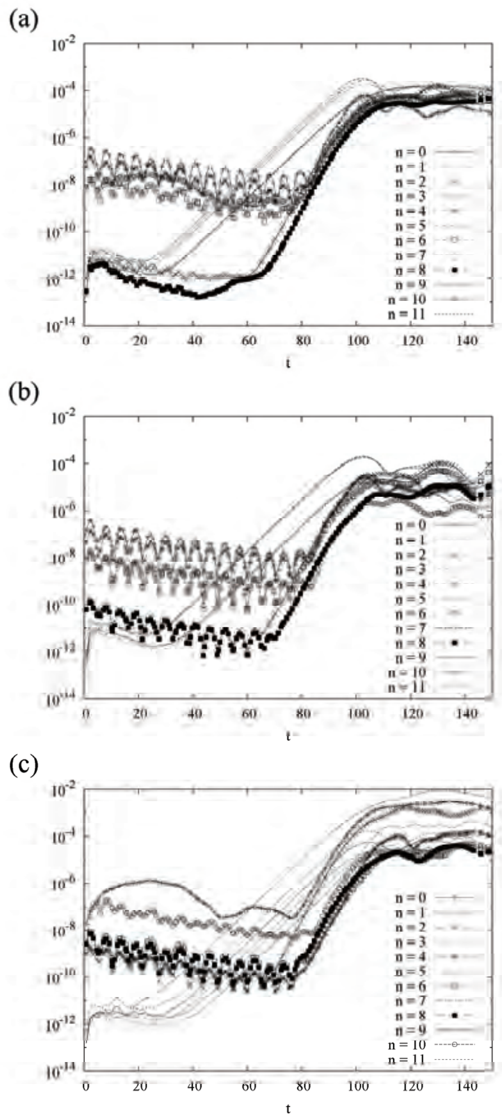

Fig. 4 Time evolutions of the Fourier amplitudes of (a)the normal, (b) the binormal and (c) the parallel velocity components in the parameter set (B) simulation.

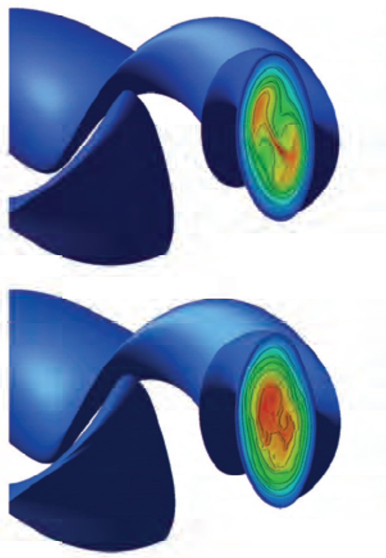

Fig. 5 Isosurfaces and contours of the pressure on a vertically-elongated poloidal cross-sections at $t = 110\tau_A$ (upper) and $150\tau_A$ (lower). At the midst of the two times, the contour lines of the pressure are much more chaotic. After the destruction of the closed contour lines, concentric profiles of the pressure tend to be recovered.

Proceedings of ITC/ISHW2007

MHD activity in TJ-II

R. Jiménez-Gómez[1], E. Ascasíbar[1], S. Yamamoto[2], G. Motojima[3], K. Nagaoka[4], M. Ochando[1], J. A. Jíménez[1], T. Estrada[1], T. Happel[1], A. V. Melnikov[5], M. A, Pedrosa[1], C. Hidalgo[1], A. Alonso[1], A. Fernández[1], M. Liniers[1].

1. *Laboratorio Nacional de Fusión, Asociación EURATOM-CIEMAT, E-28040 Madrid, Spain*
2. *Kyoto University Pioneering Research Unit,Gokasho Uji, 611-0011, Japan*
3. *Graduate School of Energy Science, Kyoto University, Gokasho Uji, 611-0011, Japan*
4. *National Institute for Fusion Science Oroshi-cho, Toki, 509-5292, Japan*
5. *Russian Research Centre "Kurchatov Institute", Nuclear Fusion Institute, 123182 Moscow, Russia.*

Abstract: Magnetic fluctuations have been studied in the TJ-II stellarator. MHD events have been analysed for ECRH heated pressure driven modes and NBI Alfvén Eigenmodes.

Keywords: MHD, Alfvén, GAE, chirping, confinement.

1. Introduction

TJ-II is a four period heliac-type stellarator with magnetic field, B = 1 T, major radius, R=1.5 m, and averaged minor radius, $<a> \leq 0.22$ m. TJ-II has low magnetic shear, and its rotational transform can be varied in a wide range ($0.9 \leq \iota/2\pi(0) \leq 2.2$). These characteristics allow controlling the presence of low order rationals in the rotational transform profile and, consequently, facilitate the identification and characterization of magneto hydrodynamic (MHD) instabilities. The plasma current is tipically ~1 kA, except for ECCD and Ohmic current induced discharges, where it can reach ~10kA.

Electron Cyclotron Heating (ECH) plasmas are produced with two gyrotrons with ~200 kW each, with frequency f = 53.2 GHz. The ECH power deposition profile can be focused at different plasma radius by moving the last mirror in the two quasi-optical transmission lines. The ECH cut-off condition imposes a maximum density of $n_e = 1.75 \times 10^{19}$ m^{-3}. Electron and ion temperatures are in the range 1-1.5 keV and 100-150 eV, respectively. The frequency range of the MHD activity observed in ECH plasmas is, typically, 10-80 kHz.

The experimental setup and data processing to study MHD instabilities in TJ-II has been recently improved. Fig. 1 shows the arrangement of the Mirnov coil array (25 coils) for measuring the poloidal component of the magnetic field. It has been extended to cover poloidally all the space available and now it spans $3\pi/2$ rad. The spatial structure (m-number) of the coherent modes detected are analyzed using different methods: SVD techniques [1], Lomb periodogram [2] and cross-checking against simulations.

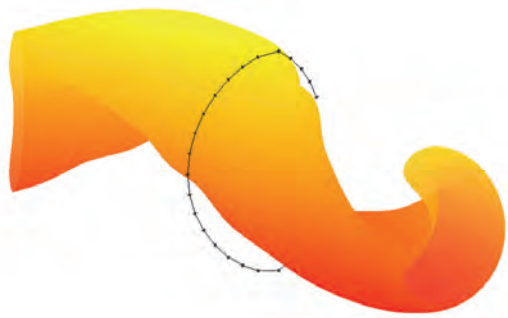

Fig.1: Schematic view of one period of the TJ-II plasma, showing the arrangement of the poloidal Mirnov array located in the period centre, $\phi = 45°$

Comparison of the magnetic fluctuation measurements with the results from other diagnostics with spatial resolution (reflectometer, bolometers) allow in some cases the radial localization of MHD events

2. Low frequency ECRH modes

The characteristics of low frequency MHD instabilities observed in TJ-II, mainly in ECRH discharges, have been found to depend on the magnetic configuration (low order rationals present in the iota profile), heating power, plasma density and plasma current [3].

In this section we are going to describe three magnetic configuration-related MHD events producing coherent mode activity.

Fig. 2 shows the rotational transform profiles of several

author's e-mail: rj.jimenez@ciemat.es

TJ-II configurations. The main low order resonances (3/2, 8/5 and 5/3) present in the confinement region are drawn.

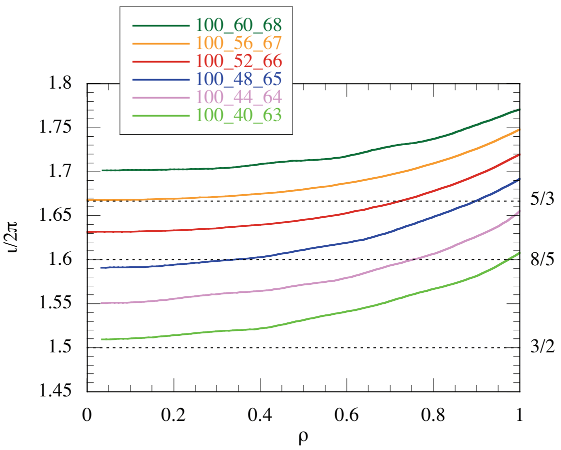

Fig. 2. Vacuum rotational transform profiles for several TJ-II magnetic configurations.

Fig.3 shows spectrograms of a Mirnov coil and a bolometer chord in the discharge #15817, with configuration 100_44_64 (see Fig. 2). A clear coherent mode with poloidal m number=5 at 20 kHz can be seen.

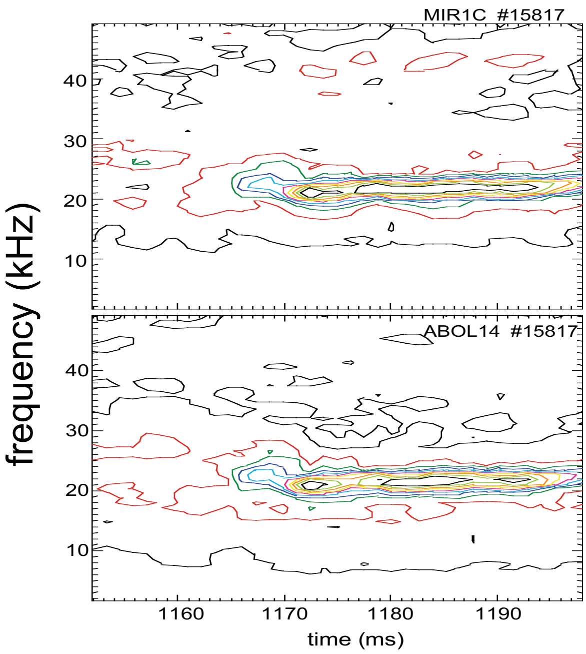

Fig. 3: Spectrograms a Mirnov coil (up) and a bolometer chord (down).

The m-number of the coherent mode deduced from the Mirnov coil array is 5. Fig. 4 shows the difference between two bolometer tomographic reconstructions corresponding to the maximum and the minimum of the oscillation. The measured plasma current in this discharge is negative, Ip ≈ -1 kA so it is expected to pull down from the iota profile in the central region. Thus, the MHD event could be interpreted as a periodical lose of emission in the inner region $0 < \rho < 0.3$ produced when the 3/2 resonance enters in the plasma central region. An outward flux is produced until it reaches $\rho \approx 0.7$ (which, as seen in Fig. 2, is the estimated position of rational surface 8/5), where it is retained.

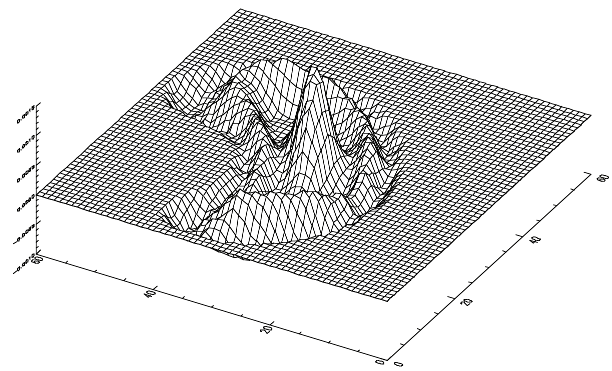

Fig 4: 3D plot showing the difference between radiation tomographic reconstructions corresponding to consecutives maximum and minimum of the coherent mode observed in #15817

Reflectometer signals also detect the mode rotation in this case and provide independently its radial localisation. The mode amplitude peaks at $\rho \approx 0.7$-0.8.

Figure 5 displays a Mirnov coil spectrogram and the time evolution of the plasma emissivity for the shot #15807 (configuration 100_40_63 with electrode biasing). It shows a transient phenomenon, which affects nearly all the plasma column.

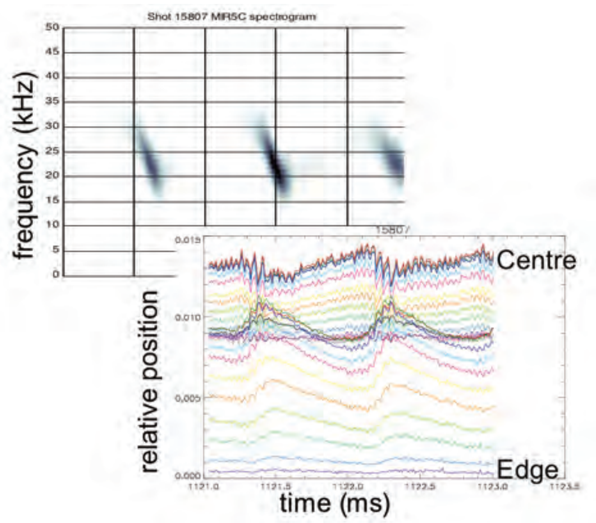

Fig. 5: Coil spectrogram (up) and time evolution of plasma emissivity (down) for shot #15807. Periodic bursts of MHD activity correlate with peaks of radiation from the centre (top) to the edge (bottom)

As the mode frequency chirps down, the plasma radiation shows an abrupt perturbation. In this occasion, the poloidal mode number of the fast magnetic periodic burst has been found to be m=5, probably related to the presence of 8/5 in the edge region. The reflectometer also detects the mode but no precise information on localization can be extracted. This transient phenomenon could be interpreted in terms of interaction between low order resonant surfaces, playing also a role the radiation of impurities (electrode).

The third example is a remarkable phenomenon, illustrated by the magnetic coil spectrogram (#11376) in Fig.6, which is found in NBI plasmas, for the standard configuration 100_44_64.

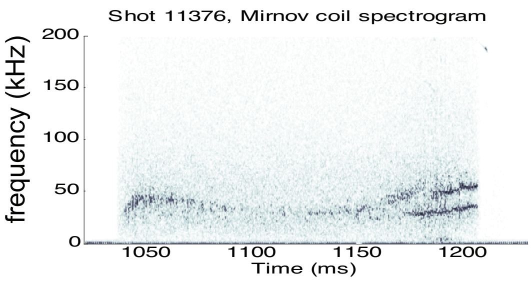

Fig. 6: Magnetic coil spectrogram showing a coherent mode that splits into two branches

As density increases during the NB injection, the typical low frequency MHD mode splits in two branches. Mode number reconstruction gives the same poloidal structure m=5 for both modes, moving in electron diamagnetic drift direction with poloidal angular velocities of about ~$0.6 \cdot 10^5$ rad/s. Both branches continue until the shot termination.

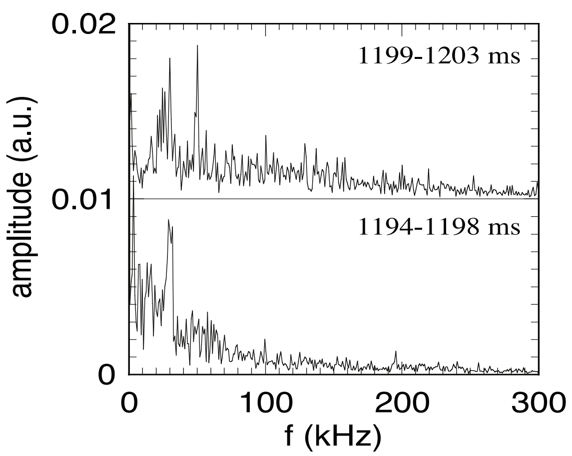

Fig. 7: Reflectometer spectra measured at two consecutive time windows in the shot #11364. Mode splitting is detected in the second one (upper box)

Fig. 7 shows that the reflectometer is able to detect the mode splitting in a similar discharge (# 11364): only one rotating mode is detected in the time window 1194-1198 ms; later, two modes are measured in 1199-1203 ms. The radial position of the mode is fixed at $\rho \approx 0.7$ and do not change in the time interval of mode splitting. There is yet no clear explanation of the phenomenon but it seems that two ingredients are needed: the presence of a low order resonance close to the edge (8/5 in this case) and NBI heating.

3. Global Alfvén modes

In NBI heated plasmas (with beam energy $v_{beam} \approx 30$ kV), high frequency coherent modes (150 - 300 kHz) are found in several magnetic configuration with a clear dependence of the frequency on plasma density and fuelling gas ($f \sim 1/n^{1/2}$, $f \sim 1/m_i^{1/2}$) which qualifies them as Global Alfven Eigenmodes (GAEs)[3]. The typical Alfven velocities found in TJ-II are $v_A \approx 5 \times 10^3$ Km/s. Fig. 8 (up) shows in a (β-v_A/v_{beam}) diagram all the configurations where GAEs have been observed. Fig. 8 (down) shows a typical example of GAE measured in TJ-II.

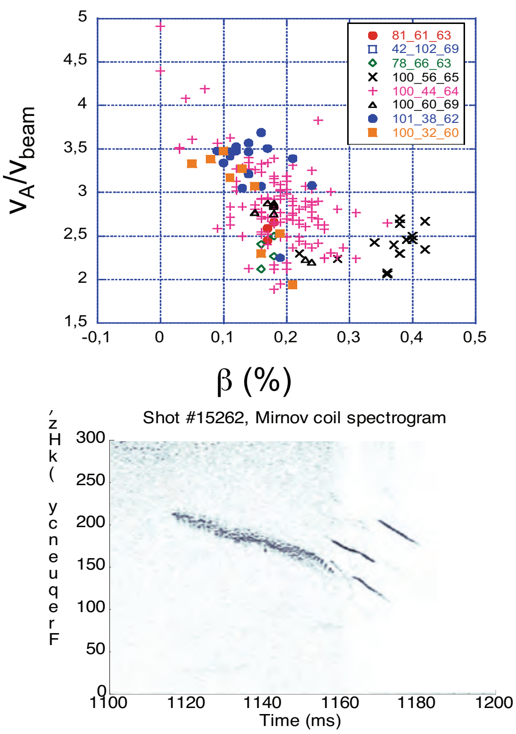

Fig 8.: Up: v_A/v_{beam} ratio versus β value. Down, typical Alfven activity in shot #15262, standard configuration, where three branches of m=4,2,6 appear.

Chirping Alfvén Modes

The Alfvén activity measured in TJ-II depends strongly on the way in which the plasma target is heated with ECRH. NBI shots whose target plasma is off-axis ECR heated show an interesting phenomenon not observed in on-axis ECRH plasmas. Chirping Alfvén -type modes are detected in the Mirnov signals as long as electron temperature at the $\rho \approx 0.6$ region remains above certain threshold that is $T_e \approx 0.2$ keV. Fig. 9 and 10 illustrate this finding. The reason of this threshold is related to the fact that off-axis ECRH in these discharges is deposited at $\rho \approx 0.4$. The electron temperature profile gets broader until it reaches the cut-off value in that region and then it drops. The frequency chirping observed can be upwards, downwards or both (see Fig. 11), with $\Delta f \sim 10\%$.

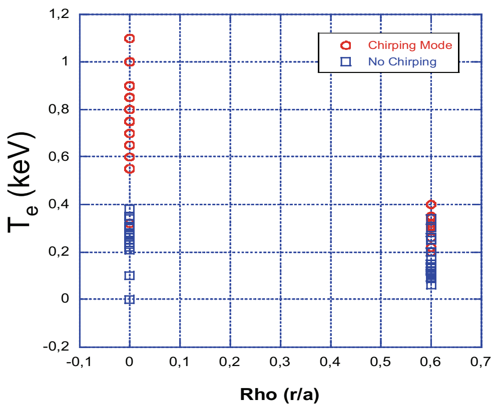

Fig.9: As density peaks and the electron temperature at $\rho \approx 0.6$ drops below ~0.2 keV, chirping modes disappear.

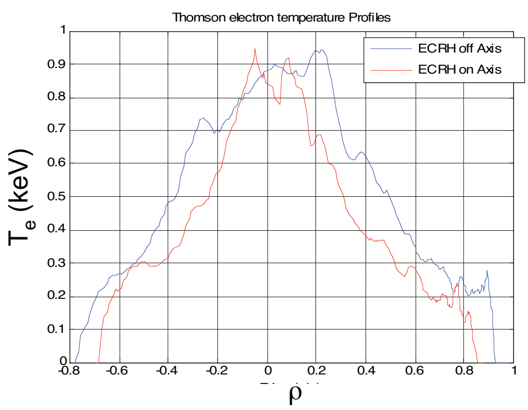

Fig. 10: Electron temperature profiles for discharges heated with on-axis (red) and off (blue) ECRH

These MHD burst do not correlate with Hα, bolometers or fast ion detector; no ion losses are detected. Chirping GAE phenomena have been studied before in stellarators and tokamaks [4, 5]. In particular, the 'Angelfish' frequency structure shown in fig. 10 [5], has been explained by Berk, et al [6] as a non-linear 'hole and clump' creation in the phase space.

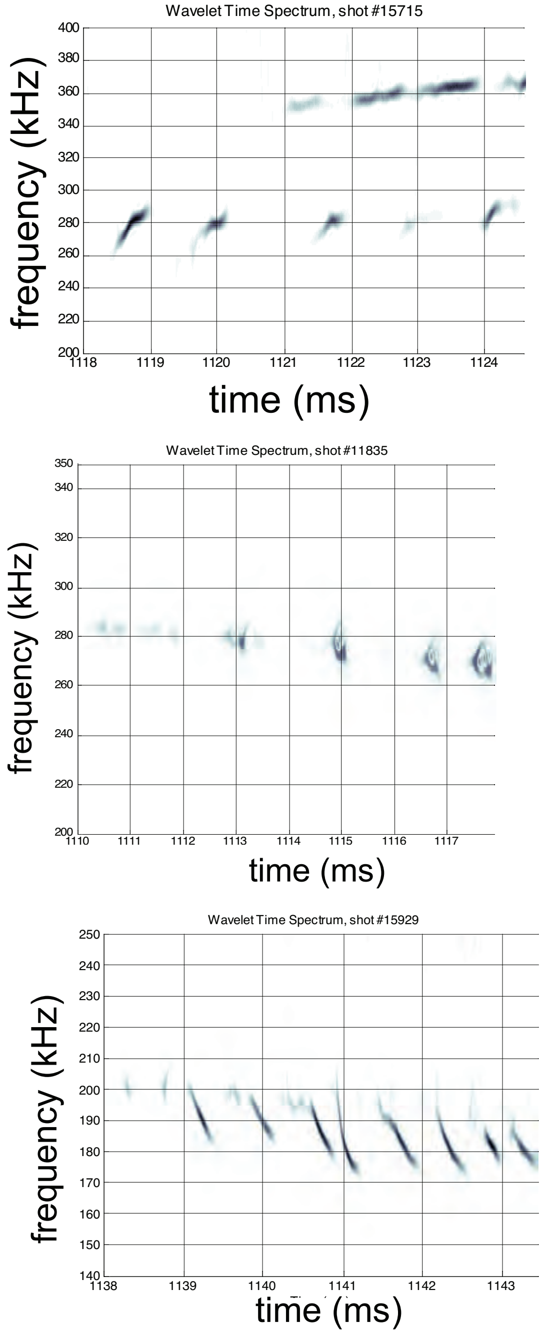

Fig. 11: Upwards, downwards and Angelfish bursting modes in TJ-II NBI discharges.

References

[1] M. Anton et al., Proc. 24th EPS Conf. **21A** 1645 (1997)

[2] S. Zegenhagen et al., Plasma Phys. Control. Fus. **48** 1333 (2006)

[3] R. Jiménez-Gómez et al., Fusion Sci. Technol., **51**, 20 (2007)

[4] A. Weller et al., 30th EPS Conf. 2003

[5] Fredrikson et al. Physics of Plasmas **13**, 056109 (2006)

[6] H. L. Berk et al, Phys. Lett. A **A234**,213 (1997)

Proceedings of ITC/ISHW2007

Analysis of MHD stability in high-β plasmas in LHD

Noriyoshi NAKAJIMA[1)], Satoru SAKAKIBARA[1)], Kiyomasa WATANABE[1)], Stuart HADOSON[2)], and Cris HEGNA[3)]

[1)]*National Institute for Fusion Science, 322-6 Oroshi-cho, Toki 509-5292, Japan*
[2)]*Princeton Plasma Physics Laboratory, PO Box 451, Princeton, NJ 08543, USA*
[3)]*Department of Engineering University of Wisconsin-Madison, WI 53706, USA*

()

Up to now, theoretically idealized MHD equilibria reflecting experimental conditions have been used in order to examine the ideal MHD stability. This approach has been useful from the aspect of investing general properties of the ideal MHD stability. Since the properties of a three dimensional MHD equilibirium with large Shafranov shift significantly change by the pressure profile, the current profile, and the boundary condition, however, ideal MHD stability analysis based on theoretically idealized MHD equilibria is considered not to be enough to investigate the proper MHD atbility of experimentally obtained MHD equilibria. Indeed, it is shown that ideal MHD stability based on the realistic reconstructed MHD equilibrium with fine structures is different from that based on the theoretically idealized MHD equilibrium. Especially, it is firstly reported that high-n ballooning modes are destabilized in the magnetic well region with tokamak-like magnetic shear.

Keywords: high-n ballooning modes, LHD

DOI: 10.1585/pfr.1.001

1 Introduction

In three-dimensional configurations, the confinement region is surrounded by the stochastic magnetic field lines related to magnetic islands or separatrix, leading to the fact that the plasma-vacuum boundary is not so definite compared with tokamaks that the various modulations of the plasma-vacuum boundary will be induced around the stochastic region by synergetic effects between a transport around the stochastic region and a large Shafranov shift of the whole plasma or a large Pfirsch-Schluter current, in especially high-β operations.

To examine such modulation effects of the plasma boundary on MHD instabilities, high-β plasmas allowing a large Shafranov shift or a large Pfirsch-Schluter current are considered in the inward-shifted LHD configurations with the vacuum magnetic axis R_{ax} of 3.6 m, so that it has been found that the free boundary motion of MHD equilibrium or the whole plasma outward-shift due to a large Pfirsch-Schluter current has significant stabilizing effects on ideal MHD instabilities, leading to partially resolving the discrepancy on MHD stability between experimental results and theoretical analyses [1].

Although experimental aspects on the boundary, the pressure profile, and the current condition are included in the equilibria used in Ref.[1], such equilibria are still theoretically idealized judging from the experimental point of view [2]. Thus, it is needed to use equilibria which are more relevant to the experimental conditions, in order to more clarify MHD stability in planar axis Heliotron configuration with a large Shafranov shift like LHD. The purpose of the present research is to clarify MHD stability especially in IDB-SDC plasma or high-β plasma of LHD by comparing between theoretically idealized MHD equilibria and experimentally reconstructed MHD equilibria. For such a purpose, especially, high-n ballooning local mode stability analysis is performed, because such local mode analysis does not need whole information of MHD equilibrium. The precise information of MHD equilibrium near the plasma periphery is not needed, once the core MHD equilibrium is consistently reconstructed to experimental conditions. This research might lead to more deeper understanding of MHD equilibrium and stability in the planar axis Heliotron configuration with a large Shafranov shift like LHD.

author's e-mail: nakajima.noriyoshi@nifs.ac.jp

2 in theoretically idealized MHD equilibria

In order to clarify dependence of the stability properties of the ideal high-n ballooning on MHD equilibrium, firstly, high-n ballooning stability analyses are performed for theoretically idealized MHD equilibria in the inward-shifted vacuum configuration with R_{ax} = 3.75 m.

2.1 in currentless MHD equilibria with peaked pressure profile

The properties of currentless MHD equilibria with a peaked pressure profile; $P(s) = P_0(1^s)^2$, under the fixed boundary condition are shown in Fig.1, where s is the normalized toroidal flux. As β increases by using P_0, tokamak-like magnetic shear is created near the magnetic axis. Although the magnetic hill still remains near the plasma periphery, the Mercier stability in the magnetic hill region is improved as β increases. Boundary between magnetic well and hill exists in helical-like maggnetic shear region. The corresponding normalized growth rates of high-n ballooning modes are shown in Fig.2. High-n ballooning modes are destabilized in the peripheral magnetic hill region with helical-like magnetic shear. As β increases, properties of the high-n ballooning modes change from helical-like ones with strong magnetic field line dependence to tokamak-like ones with weak magnetic field line dependence. Helical-like high-n ballooning modes become unstable only near the magnetic field line with $\alpha = \zeta - q\theta = 0$ where the local magnetic curvature is baddest. On the other hand, tokamak-like high-n ballooning modes become unstable independent of the magnetic field line, even in the magnetic field line with $\alpha = \pi/M$ (M is the toroidal field period of the MHD equilibrium) where the local magnetic curvature is locally good.

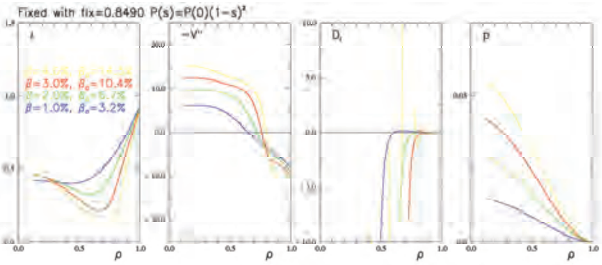

Fig. 1 β-dependences of the rotational transform , magnetic well and hill $-V''$, and Mercier criterion D_I with pressure profile P in currentless MHD equilibria with the peaked pressure profile under the fixed boundary condition.

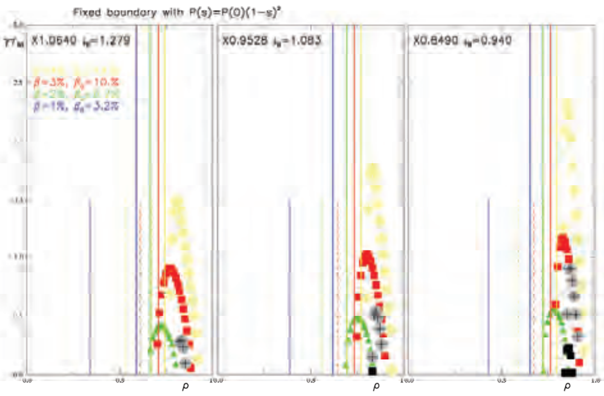

Fig. 2 β-dependence of the normalized growth rates $\gamma\tau_{A0}$ for three different plasma volumes. The most right column corresponds to 1

In order to investigate effects of the boundary condition, the MHD equilibria are created under the free boundary condition. In Fig.3, the properties of currentless MHD equilibria under the free boundary condition is shown. Although the β-dependences of the magnetic shear, magnetic well, and Mercier stability in free boundary equilibria are qualitatively similar to those in fixed boundary equilibria, change of iota in free boundary equilibrium is more significant than that in fixed boundary equilibrium, and formation of magnetic islands is suggested in shearless region judging from the spikes of D_I. The spike comes from the divergence of the Pfirsch-Sch"ulter current indicating existence of the magnetic island. The corresponding normalized growth rates of high-n ballooning modes are shown in Fig.4. Most significant differences between fixed boundary equilibria and free boundary equilibria are that helical-like ballooning modes destabilized in the magnetic hill region with helical-like magnetic shear extend to the magnetic well region with tokamak-like magnetic shear. Since ballooning formalism breaks near shearless region, the global mode analysis migh be needed for precise stability.

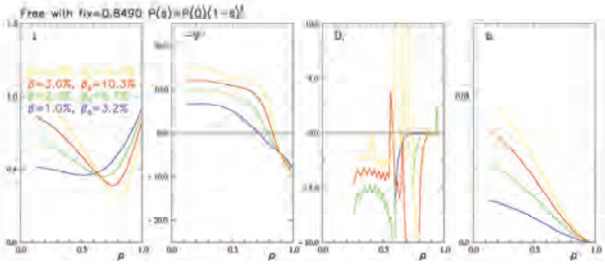

Fig. 3 β-dependences of the rotational transform , magnetic well and hill $-V''$, and Mercier criterion D_I with pressure profile P in currentless MHD equilibria with the peaked pressure profile under the free boundary condition.

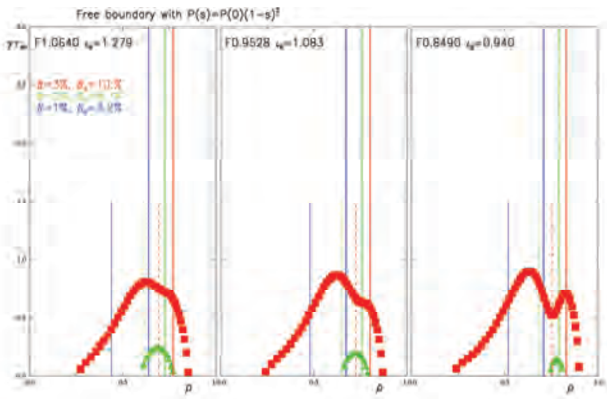

Fig. 4 β-dependence of the normalized growth rates $\gamma\tau_{A0}$ for three different plasma volumes. The most right column corresponds to 3

2.2 in currentless MHD equilibria with broad pressure profile

In order to investigate effects of the pressure profile, the currentless MHD equilibria are made with a broad pressure profile; $P(s) = P_0(1 - s^2)^5$. In Fig.5, the properties of the currentless MHD equilibrium with the broad pressure profile under the fixed boundary is shown. The steep pressure gradient near the plasma periphery coming from the broad pressure prifile makes magnetic hill region narrow.

The corresponding normalized growth rates are indicated in Fig.6. As well as the MHD equilibria with peaked pressure profile, high-n ballooning modes are destabilized in the peripheral magnetic hill region with helical-like magnetic shear. As β increases, properties of the high-n ballooning modes change from helical-like ones with strong magnetic field line dependence to tokamak-like ones with weak magnetic field line dependence.

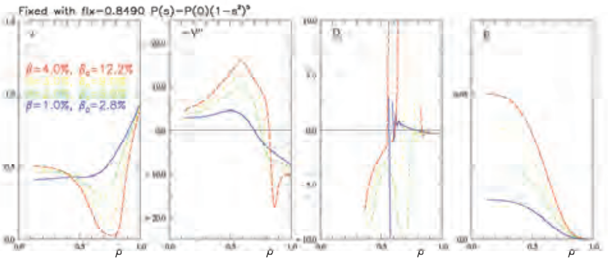

Fig. 5 β-dependences of the rotational transform , magnetic well and hill $-V''$, and Mercier criterion D_I with pressure profile P in currentless MHD equilibria with the broad pressure profile under the fixed boundary condition.

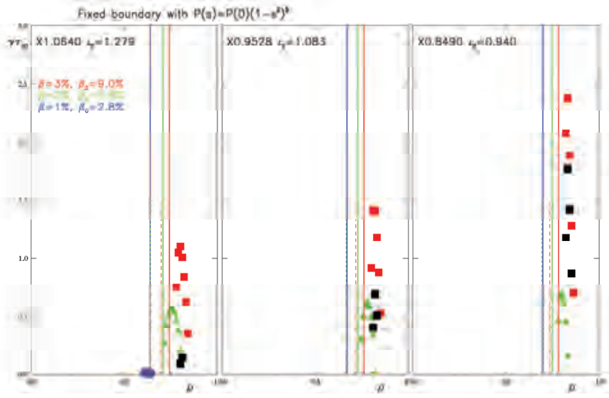

Fig. 6 β-dependence of the normalized growth rates $\gamma\tau_{A0}$ for three different plasma volumes. The most right column corresponds to 5

The effects of the free boundary are shown in Figs.7 and 8 for currentless MHD equilibria with a broad pressure profile. The differences between fixed boundary and free boundary are same as the case of currentless MHD equilibria with peaked pressure profile.

3 in reconstructed MHD equilibria

In this section, the stability of high-n ballooning modes is investigated in the reconstructed MHD equilibria.

The Fig.9 denotes the properties of both the reconstructed MHD equilibrium and the variations corresponding to IDB-SDC plasma in the standard configuraion with R_{ax} = 3.75m. The corresponding normalized growth rates are shown in Fig.10. The behaviors of all quantities of equilibrium and stability are similar to those in the theoretically idealized MHD equilibria.

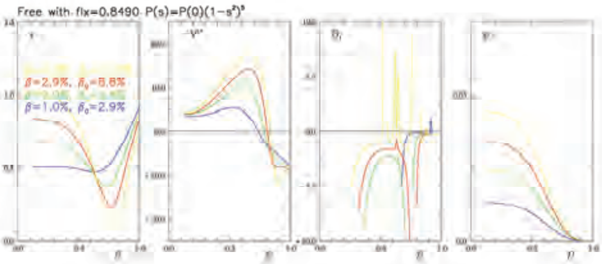

Fig. 7 β-dependences of the rotational transform , magnetic well and hill $-V''$, and Mercier criterion D_I with pressure profile P in currentless MHD equilibria with the broad pressure profile under the free boundary condition.

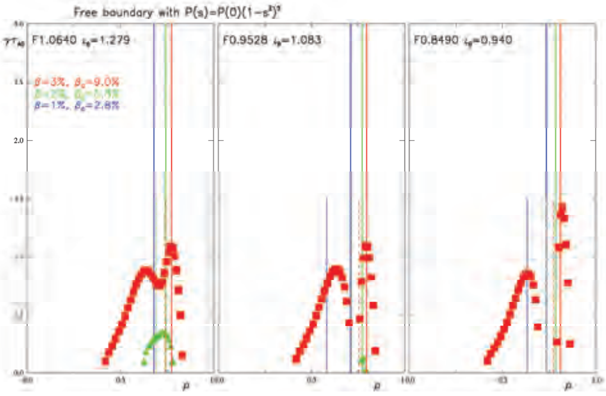

Fig. 8 β-dependence of the normalized growth rates $\gamma\tau_{A0}$ for three different plasma volumes. The most right column corresponds to 7

The properties of the reconstructed MHD equilibrium corresponding to IDB-SDC plasma in the outward-shifted vacuum configuraion with R_{ax} = 3.85m are denoted in the upper row of Fig.11. The corresponding normalized growth rate is shown in the left column of Fig.??. The most significant feature of stability of the high-n ballooning modes is that helical-like ballooning modes appear in the both magnetic hill region with helical-like magnetic shear and magnetic well region with tokamak-like magnetic shear. Moreover, high-n ballooning modes in the magnetic well region with tokamak-like magnetic shear are more tokamak-like ballooning modes than those in the magnetic hill region with helical-like magnetic shear, because the magnetic field lines where the mode is unstable are wider in the magnetic well region with tokamak-like magnetic shear than in the magnetic hill region with helical-like magnetic shear. As is understood from the pressure profile shown in upper row of Fig.11, the reconstructed pressure profile has fine structures, namely, slight stair-case like structures. Although those fine structures are not so significant, it is considered that such fine structure changes the stability criterion of the high-n ballooning modes through the balance between stabilization effect due to the local magnetic shear and destabilization effect due to the local magnetic curvature. High-n ballooning modes in the magnetic well region with tokamak-like shear might

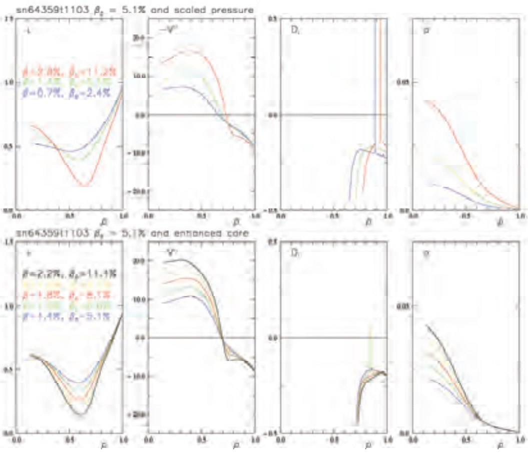

Fig. 9 β-dependences of the rotational transform , magnetic well and hill $-V''$, and Mercier criterion D_I with pressure profile P in reconstracted MHD equilibria and the variations in the stabdard vacuum configuration with $R_{ax} = 3.75$. The upper (lower) row includes the β-variations of whole (core) region.

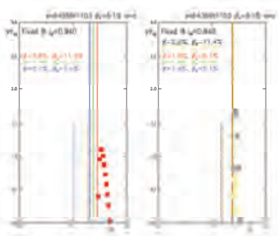

Fig. 10 β-dependence of the normalized growth rates $\gamma\tau_{A0}$ for three different plasma volumes. The left (right) column includes the β-variations of whole (core) region.

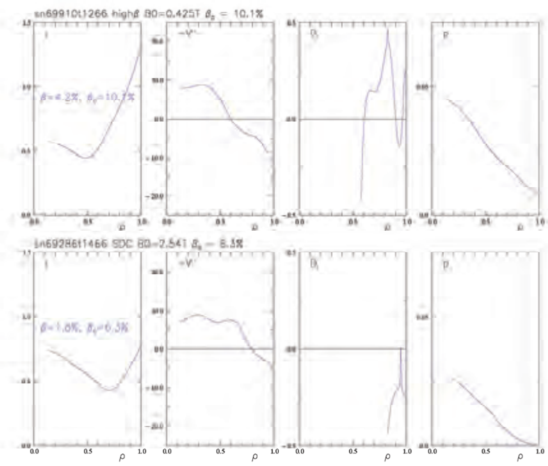

Fig. 11 β-dependences of the rotational transform , magnetic well and hill $-V''$, and Mercier criterion D_I with pressure profile P in reconstracted MHD equilibria. The upper (lower) row corresponds to the reconstructed equilibrium in the outward-shifted (inward-shifted) vacuum configuration with R_{ax} = 3.85 (3.60) m.

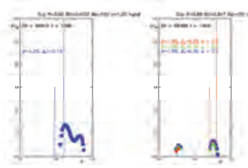

Fig. 12 β-dependence of the normalized growth rates $\gamma\tau_{A0}$. The left (right) column corresponds to the reconstructed equilibrium in the outward-shifted (inward-shifted) vacuum configuration with R_{ax} = 3.85 (3.60) m.

lead to core density collapse experimentally reported.

The properties of the reconstructed MHD equilibrium corresponding to high-β plasma in the inward-shifted vacuum configuraion with R_{ax} = 3.60m are denoted in the lower row of Fig.11. The corresponding normalized growth rate is shown in the right column of Fig.??. As well as the above case of IDB-SDC, fine structures of the pressure profile makes the significant change in the Mercier criterion, leading to the non-monotonic change in the normalized growth rate as os shown in the right column of Fig.??.

4 Summary

Up to now, theoretically idealized MHD equilibria reflecting experimental conditions have been used in order to examine the ideal MHD stability. This approach has been useful from the aspect of investing general properties of the ideal MHD stability. As is well know, however, the properties of a three dimensional MHD equilibirium with large Shafranov shift significantly change by the pressure profile, the current profile, and the boundary condition. Indeed, high-n ballooning stability is completely different between equilibria under fixed boundary and those under free boundary. Although free boundary equilibria are more stable than fixed boundary ones in the inward-shifted vacuum configuration with R_{ax} = 3.60m, free boundary equilibria are more unstable than fixed boundary ones in the standard vacuum configuration with R_{ax} = 3.75m. Moreover, it is shown that ideal MHD stability based on the realistic reconstructed MHD equilibrium with fine structures is different from that based on the theoretically idealized MHD equilibrium. Especially, it is firstly shown that high-n ballooning modes are destabilized in the magnetic well region with tokamak-like magnetic shear, which means that high-n ballooning stability is quite sensitive to MHD equilibrium. Stability analyses based on idealized MHD equilibria might not be enough to interpret experimental results on MHD stability. More extensive stability analyses based on reconstructed MHD equilibria will be needed.

[1] N. Nakajima, et al., Nucl. Fusion **46** (2006) pp.177-199.
[2] K.Y. Watanabe, et al., Plasma Phys. Control. Fusion, **49** (2007) pp.605-618.

Proceedings of ITC/ISHW2007

Configuration Dependence of Pressure Driven Modes in Heliotron Plasmas

S. Sakakibara, K.Y. Watanabe, H. Yamada, S. Ohdachi, Y. Suzuki, H. Funaba, Y. Narushima, F. Watanabe, K. Toi, K. Ida, I. Yamada, K. Narihara, K. Tanaka, T. Tokuzawa and LHD Experimental Group

National Institute for Fusion Science,322-6 Oroshi-cho, Toki 509-5292, Japan

This article describes experimental results on finding the onset parameters of the low-*m* MHD modes and the parameter dependence of the amplitude in the Large Helical Device. The control of peripheral pressure gradients with the gas-puff modulation technique was done in the plasmas with different magnetic Reynolds number *S*. The m/n = 1/1 mode excited in the periphery appeared when the pressure gradient on the resonance exceeded the critical value. The critical pressure gradient for the mode-onset is almost the same even in different S plasmas. Also it was found that the mode was enhanced clearly with the decrease in *S* under the condition with the same pressure gradient and magnetic configurations. These results contribute to verify the validity of the linear MHD stability.

Keywords: Large Helical Device, Heliotron Configuration, MHD Instability, Interchange Mode, Magnetic Reynolds Number

1. Introduction

An understanding of characteristics of pressure driven modes is one of the major issues for high-beta plasma production in magnetic confinement systems. Experimental characterization of ideal/resistive interchange instability has been required for clarifying the validity of theoretical prediction on linear stability boundary, which contributes the extension of free degree of configuration optimization in stellarators and heliotrons. In Large Helical Device (LHD), experimental studies on ideal and resistive instabilities by making a use of wide free degree of magnetic configurations are possible, and we have investigated them focusing on the effect of MHD activity on the plasma profile and confinement [1-4]. The experimental results suggest that MHD activities near ideal stability boundary affect the plasma profile and sometimes lead to the minor collapse, whereas they never grow as large as that causing the disruption in tokamaks [5]. It has been predicted that the resistive modes are unstable even in the low-beta plasmas and enhanced with beta value, while the growth of the mode is stopped immediately and the effect on the confinements seems to be weak in the beta range of 5 % [6].

The findings of the onset and saturation level of the mode are suitable for characterization of the instability. We have proceeded to construct the database on the above parameters of magnetic fluctuations observed in several machines in order to find the common understanding of MHD activity in stellarators and heliotrons [7]. Regarding the saturation level of the mode, the amplitude has clear dependence of the magnetic Reynolds number *S*, and the dependence is close to that of the linear growth rate of the resistive interchange mode [5]. This tendency can be seen in different machines with different *S* plasmas [1]. On the other hand, we made the experiments for controlling edge pressure gradient using movable limiter in order to find the onset of the mode [8]. The peripheral modes disappeared one after another when the limiter was inserted, and we found the *S* and D_R at the onset of each mode, where D_R is the index of the stability boundary of the resistive interchange mode. The results were consistent within a factor of two with theoretical prediction [8].

Here we report the experimental results of pressure gradient control using the gas-puff modulation technique in order to clarify the effects of pressure gradient and *S* on the onset of MHD mode. The active control of the pressure gradient is useful to find the onset-parameters because the peripheral MHD modes appear in the beginning of discharge, which means difficulty in identifying the mode-onset in the quasi-steady-state plasmas. The edge pressure (and the pressure gradient) was changed by the increase and decrease in gas-fueling in the different *S* plasmas. Here we focus on the behavior of the m/n = 1/1 mode which is excited in the periphery with magnetic hill.

2. Experimental Condition

The LHD is the heliotron device with a pair of continuous helical coils and three pairs of poloidal coils and all of coils are superconductive. The magnetic axis position R_{ax} can be changed from 3.4 to 4.1 m by controlling poloidal coil currents, whereas plasma aspect

author's e-mail: sakakibara.satoru@lhd.nifs.ac.jp

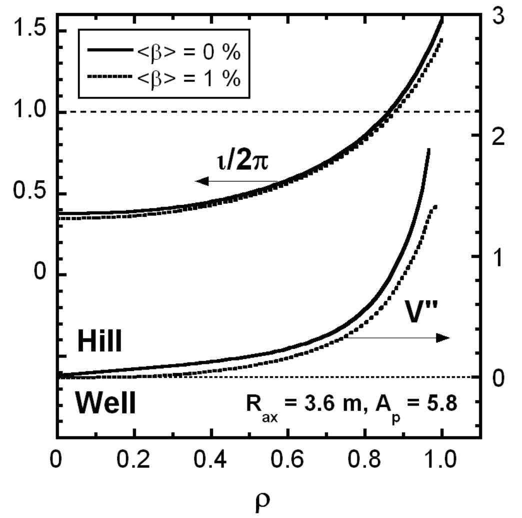

Fig.1 Rotational transform and V" profiles at the configuration with R_{ax} = 3.6 m and A_p = 5.8.

ratio A_p can be selected from 5.8 to 8.3. The configuration with R_{ax} of 3.6 m and A_p = 5.8 was applied for this experiments, which is the standard configuration in LHD. The toroidal magnetic field B_t was set at 1, 1.5 and 2 T for changing *S*.

Figure 1 shows the typical profiles of rotational transform and *V*" in the plasmas with $<\beta>$ = 0 and 1 %, respectively, where V denotes the volume encircled by the magnetic surface. The positive and negative V" regimes correspond to the magnetic hill and well, respectively. These profiles are calculated by 3D MHD equilibrium code VMEC under the currentless condition. The pressure profile was assumed as $P_0(1-\rho^2)(1-\rho^8)$, which is close to an actual profile in the low-beta plasma. The rotational transform profile slightly changes due to finite-beta effects, while the location of the $\iota/2\pi$ = 1 resonant surface at which *m*/*n* = 1/1 mode is excited almost remains at around ρ of 0.9. The *V*" decreases with the beta value due to the outward shift of the magnetic axis, whereas there is still magnetic hill, especially, in the periphery. The D_R at the $\iota/2\pi$ = 1 resonance increases with the beta value and the pressure gradient, and approaches 0.1 when the $<\beta>$ is around 1 %. Ideal interchange mode in the periphery is stable in this experiment.

Electron density is controlled by Hydrogen gas-puff. Electron temperature and density profiles were measured with Thomson scattering system and FIR interferometer, respectively. For identifying characteristics of MHD modes, 22 magnetic probes were applied mainly.

3. Gas Puff Modulation Experiments

Figure 2 shows the example discharge with modulating H_2 gas-fueling in the configuration with B_t = 1.5 T. The co- and counter neutral beams (NB) were applied here and the each input power is 1.3 and 2.5 MW, respectively. The NB's were injected from 0.3 s, and co-NB was turned off at 2.02 s. The gas-puff was applied from 0.7 s and started to decrease at 0.9 s, and then line-averaged electron density $\bar{n}_e$ and the volume averaged beta value $<\beta_{dia}>$ started to increase and oscillated between 0.8 % and 1 %. The central electron temperature T_{e0} is about 2 keV at 0.9 s and decreased stepwise when the $\bar{n}_e$ increased. The magnetic fluctuation with up to 50 kHz was enhanced with the increase in $\bar{n}_e$. The several MHD modes such as *m*/*n* = 1/1, 2/3, 3/4, 4/5 and 4/6 were observed as shown in the bottom figure, where *m* and *n* are poloidal and toroidal mode numbers, respectively. These modes nominally rotated in the electron-diamagnetic direction and are expected to be located in the periphery as predicted from Fig.1, if they are resonant modes. While the *m*/*n* = 1/1 mode appeared when the $\bar{n}_e$ and $<\beta_{dia}>$ were increased, it disappeared with the decreases in the $\bar{n}_e$ and $<\beta_{dia}>$. The frequencies of other modes were oscillated with $\bar{n}_e$ and T_e, which is predicted to be due to the change of the rotation of the bulk plasma with gas-puff modulation. The modes except for *m*/*n* = 1/1 one were continuously observed. The plasma current I_p decreasing the rotational transform gradually increases with time and reached about 15 kA at the end of the discharge. The current is mainly driven by NB because of unbalanced injection of NB. The central rotational transform is decreased to 0.03 when the I_p is

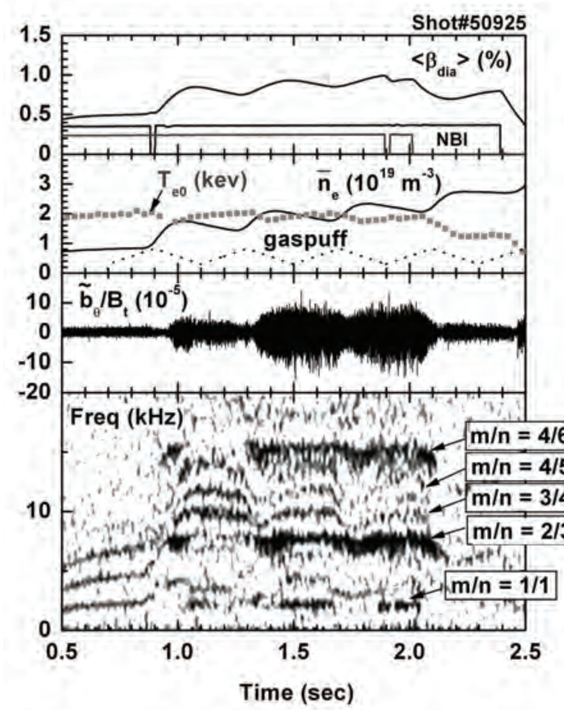

Fig.2 MHD activities in the Discharge with modulating gas-fueling in the configuration with R_{ax} = 3.6 m and B_t = 1.5 T.

15kA and has the parabolic profile, which hardly affects the stability property in the periphery.

The gas puff modulation experiments were done in the different B_t configuration in order to change the S. Figure 3 shows the temporal changes of S, the beta gradient $d\beta/dr$ at the $\iota/2\pi = 1$ resonance and the $m/n = 1/1$ mode in the configurations with 2, 1.5 and 1 T. The perturbations of the S and $d\beta/dr$ due to the gas modulation in the B_t = 2 T case is relatively smaller than the other cases because the modulation speed is relatively high compared with the fig.3 (b) and (c) cases. The $<\beta_{dia}>$ was set to 0.8 ~ 1.3 % at any configurations. The $d\beta/dr$ was increased and decreased with the increase and decrease in gas-fueling. The $m/n = 1/1$ mode appeared at around when the $d\beta/dr$ exceeded 3~ 4 %/m at Bt = 2 and 1.5 T cases, whereas the mode was continuously observed appear above the critical value of the $d\beta/dr$ as shown in Fig.3 (c). The onset seems to strongly depend on the $d\beta/dr$ rather than S. On the other hand, the mode was enhanced with the decrease in S rather than the increase and the decrease of $d\beta/dr$. The changes of the amplitude of the mode were summarized in Fig.4. The data in the steady state plasmas of 12 discharges was applied here. The amplitude of the mode was increased with the decrease in S at the constant $d\beta/dr$. This tendency is consistent with the previous study on high-beta plasma [5].

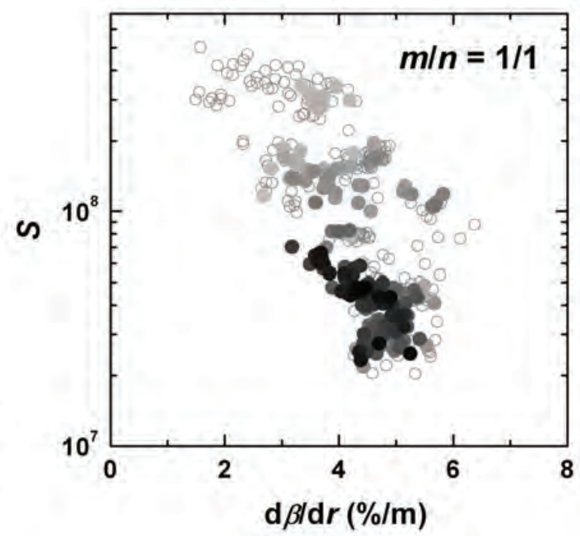

Fig.4 The amplitude of the $m/n = 1/1$ mode in the S and $d\beta/dr$ diagram. The open circle denotes no observation of the $m/n = 1/1$ mode, and the closed circle corresponds to the root mean square of the amplitude of the mode during 10 ms. The change of the color of the closed circle from gray to black corresponds to $b_\theta/B_t = 1 \times 10^{-6}$ to 3×10^{-5}.

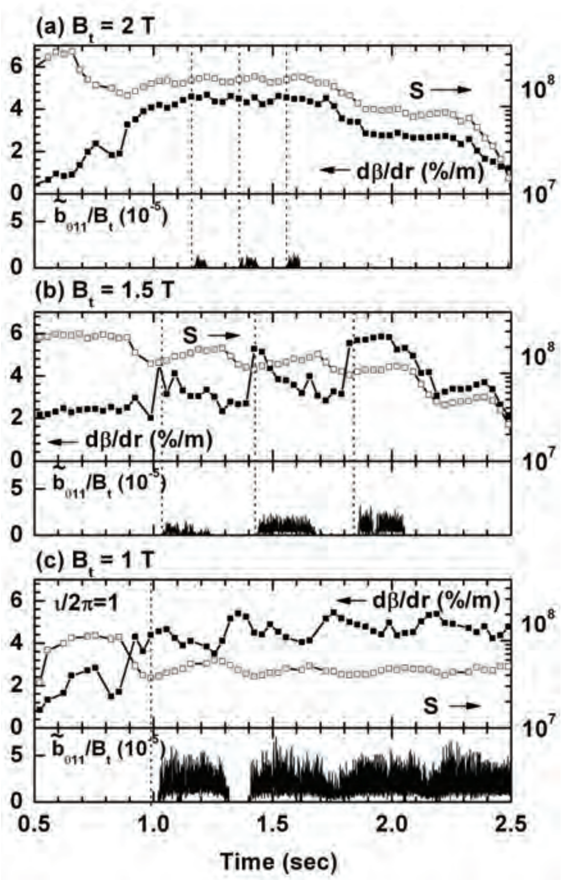

Fig.3 Temporal changes of magnetic Reynolds number, beta gradient at the $\iota/2\pi = 1$ magnetic surface and m/n = 1/1 mode in the configuration with (a) 2 T, (b) 1.5 T and (c) 1 T.

4. Discussion and Summary

The relationship between the mode property and the parameters related with the resistive interchange mode, the beta gradient and magnetic Reynolds number, has been investigated in the low-beta plasmas through the experiments with gas puff modulation. The plasmas were situated in ideal-stable and resistive-unstable regimes. According to the linear theory on the resistive interchange mode, the growth rate increases with D_R with the beta gradient as the driving term, and with the reduction of the magnetic Reynolds number [9]. Therefore, we speculate that the stability boundary which corresponds to 'mode-onset' has the same dependence. Regarding the amplitude of the mode, it strongly depends on the magnetic Reynolds number, and the mode was stabilized in the high-S region even under the condition that the beta gradient is constant as shown in Fig.4. The mode onset seems to depend on the beta gradient rather than magnetic Reynolds number, however, the analyses in the wider range of the beta gradient are required for clarifying the relation with their dependences For example, the regime with lower beta gradient and lower magnetic Reynolds number should be investigated.

The significance of the linear stability boundary, especially, of the resistive interchange mode, should be clarified experimentally because the mode is predicted to be unstable even in the low-beta plasma of the heliotron configuration despite several low-order resonances are located in the most unstable region. It has been found experimentally that their modes have the weak effect on the profile and the global confinement in the present beta range with up to 5%. However, there is the possibility that the island overlap due to their modes affect the property of the plasma confinement and the magnetic topology in the higher beta range. Therefore, the experiments for the identification of the mode-onset are important to verify the validity of the stability prediction.

Acknowledgements

This work is supported by NIFS under contract No.NIFS05ULHH517.

[1] S. Sakakibara *et al*., Nucl. Fusion **41**, 1177 (2001).
[2] S. Sakakibara *et al*., Plasma Phys. Control. Fusion **44**, A217 (2002).
[3] K.Y. Watanabe *et al*., Nucl. Fusion **45**, 1247 (2005).
[4] S. Sakakibara *et al*., Plasma Fusion Res. 1, 003 (2006).
[5] S. Sakakibara *et al*., Fusion Science and Technol. **50**, 177 (2006).
[6] K.Y. Watanabe *et al*., this conference.
[7] A. Weller *et al*., this conference.
[8] S. Sakakibara *et al*., Plasma Fusion Res. 1, 049 (2006).
[9] K. Ichiguchi *et al*., Nucl. Fusion **29**, 2093 (1989).

Proceedings of ITC/ISHW2007

Stability of Super Dense Core Plasmas in LHD

J. H. Harris[1], R. Sanchez[1], D. J. Spong[1], N. Ohyabu[2] , K. Watanabe[2], J-A. Jimenez[1]

[1]*Fusion Energy Division, Oak Ridge National Laboratory, USA*

[2]*National institute of Fusion Science, Toki, Japan*

[3]*CIEMAT, Madrid, Spain*

Author affiliations should be centered 10-point italic type

(Received 16 October 2007)

Recent experiments [1] using pellet injection into reduced-recycling discharges in the Large Helical Device have yielded Super Dense Core (SDC) plasmas with very peaked density profiles, high central density ~ 4.5 × 10^{20} m^{-3}, and improved confinement. We have examined ideal MHD stability of these SDC configurations the using the 3-D COBRA stability code [2]. These calculations show that the core region inside the zero-shear radius has direct access to second stability, i.e., the stability margin increases with β. Outside the zero-shear radius, the plasma becomes unstable to ballooning modes at average β ~3-4%. Of course, resistive versions of the modes are expected to appear at lower β. These MHD effects may play a role in improving core confinement, and may also provide a useful mechanism to constrain the plasma pressure in the outer plasma region and thus help maintain the favourable SDC state. Experiments like this in LHD and other stellarators such as the TJ-II heliac could also help elucidate the nature of ballooning modes in three-dimensional confinement systems.

Keywords: stellarator, heliotron, magnetohydrodynamic stability, ballooning modes, high-beta

1. Inroduction

Magnetohydrodynamic ballooning modes have long been thought to set the upper limit of normalized pressure $\beta = 2\mu_0 p/B^2$ in stellarator plasmas. As yet, however, their existence has not been confirmed experimentally, even in parameter ranges where they were expected, such as recent experiments in the Large Helical Device (LHD) in which values of β of nearly 5% were obtained [1]. It is therefore of great interest to look for specific experimental conditions in which the excitation and observation of ballooning modes might be possible.

Experiments [2] using pellet injection into reduced-recycling discharges in the Large Helical Device have yielded Super Dense Core (SDC) plasmas with very peaked density profiles, high central density > 5 × 10^{20} m^{-3}, improved confinement, and values of β in the range of 1-2%. Figure 1 shows sample profiles of density and pressure for one these plasmas taken from Reference 1. These plasmas have good confinement, and exhibit an internal diffusion barrier, whose mechanism is under study [3]. Since the maximum density in stellarators is limited only by input power, operation at very high densities > 1 × 10^{22} m^{-3} may make alternative reactor scenarios with low temperatures accessible.

author's e-mail: harrisjh@ornl.gov

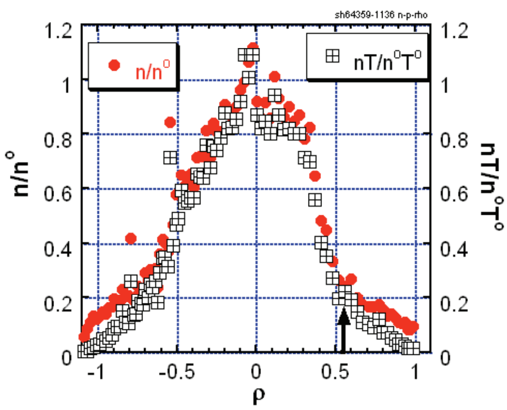

Fig. 1.Sample density and pressure profiles for an SDC plasma in LHD.

2. Stability calculations

We have examined the ideal MHD ballooning stability of these LHD SDC configurations the using the 3-D COBRA stability code [3], with a model pressure profile that approximates that seen in the experiment. Figure 2 shows the radio profiles (against normalized minor radius) of rotational transform (ι = 1/q, where q is the safety factor) and specific volume V′ = ∫ dl/B, where the integral is along field lines, and $V'' < 0$ corresponds to a magnetic well. The equilibria show very strong outward Shafranov shifts, a non monotonic ι profile in which the core region has tokamak-like shear ($\iota' < 0$) and a pronounced magnetic well, and surrounded by an edge or "mantle" region with stellarator-like shear ($\iota' > 0$) and a magnetic well.

COBRA calculations of ballooning growth rates (plotted in inverse Alfven times in Fig 2 show that the core region inside the zero-shear radius has direct access to second stability, i.e., the stability margin increases with β. Outside the zero-shear radius, the plasma becomes unstable to ballooning modes at average β ~3-4%. Studies of the eigenfunctions show that the modes are localized in the region of bad curvature in each field period. Radially, the inner edge of the region of ballooning instability is inside the magnetic well, a further indication of the mode's ballooning (as opposed to interchange) character. Of course, resistive analogues of the modes are expected to appear at the lower β values accessed in the experiments so far.

These MHD effects may play a role in improving core confinement, and may also provide a useful mechanism to constrain the plasma pressure in the outer plasma region and thus help maintain the favourable SDC state. Ongoing studies on LHD of radially resolved transport are expected to shed some light on this in the future.

Experience with tokamaks (TFTR) suggests that ballooning modes will be difficult to observe on external magnetic coils because of their short coherence length, so that internal diagnostics like local ECE emission will have to be used. So far, magnetic fluctuation measurements in high-beta LHD plasmas show only low mode number resistive interchanges that appear and then disappear as the plasma pressure is raised.

The non-monotonic rotational transform profile calculated for these equilibria is not surprising, but still merits experimental confirmation; the most convincing measurement would be a motional Stark broadening measurement of the poloidal magnetic field, a technique

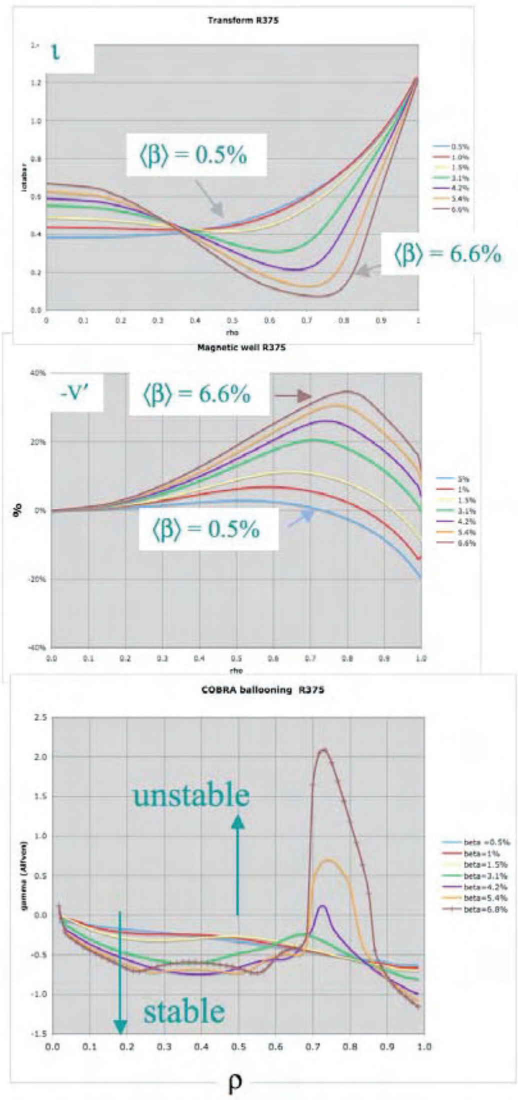

Fig. 2. Radial profiles of finite-beta rotational transform, specific volume, and ballooning growth rate for model sequence of LHD SDC equilibria.

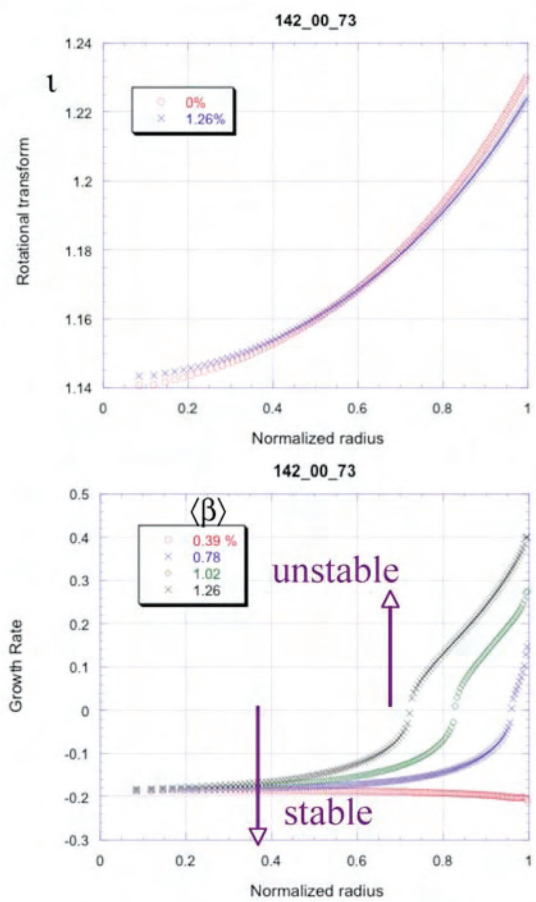

Fig. 3 Radial profiles of rotational transform and ballooning growth rate for TJ-II.

which is widely used in tokamaks, but needs to be imported to stellarators.

Similar computational studies have been carried out for the TJ-II heliac [4]. Figure 3 shows profiles of rotational transform and ballooning growth rate for a broad pressure profile $p = p_0(1\text{-}\rho^2)$ and several different values of β. Ballooning modes appear in the outer region for modest values of volume-averaged $\beta < 1\%$, which should become accessible with the 1-2 MW of neutral beam power (from injectors originally used at ORNL) expected to become available on TJ-II within the next year. Joint experiments by TJ-II and ORNL staff in 2007 have already succeeded in obtaining simultaneous operation of both injectors with a total injected power of just under 1 MW. These trials will continue when TJ-II re-commences operation in October, 2007.

3. Acknowledgements

Research supported by the US Department of Energy under Contract DE-/AC05-00OR22725 with UT-Battelle, LLC, MEXT-Japan, and by the Spanish Ministry of Science and Technology under project FTN2003-08337-C04-0.2.

[1] H. Yamada, invited paper, this conference.
[2] N. Ohyabu et al, Phys. Rev. Lett. **97,** 055002 (2006).
[3] R. Sanchez et al, Comp. Phys. Comm **141**, 55 (2001).
[4] E Ascasíbar et alPlasma Phys. Control. Fusion **44,** B307 (2002).

Proceedings of ITC/ISHW2007

MHD instabilities with sharply peaked pressure profile after ice-pellets injection in the Large Helical Device

Satoshi OHDACHI[1)], Kazuo TOI[1)], Satoru SAKAKIBARA[1)], Kiyomasa WATANABE[1)], Yoshiro NARUSHIMA[1)], Fumitake WATANABE[2)], Ryuichi SAKAMOTO[1)], Junichi MIYAZAWA[1)], Ichihiro YAMADA[1)], Kazumichi NARIHARA[1)], Kenji TANAKA[1)], Tokihiko TOKUZAWA[1)], Kazuo KAWAHATA[1)] and the LHD Experimental Group[1)]

[1)]*National Institute of Fusion Science, Oroshi-cho Toki-shi 509-5292, Japan*
[2)]*Department of Energy Engineering and Science, Nagoya Univ., Nagoya 464-8603, Japan*

The effect of peaked pressure profiles on the MHD behavior of the Heliotron type plasma is investigated. The pressure profile is more peaked with the ice-pellet injections than with normal gas-puffing. The degree of the peaking depends on the vacuum magnetic axis position. In inward-shifted plasma, where the interchange modes are unstable in the core region, larger levels of the MHD fluctuations are observed. Sawtooth-like relaxation events, which terminate the peaking, are also observed when the pressure gradient exceeds a threshold value. Existence of these MHD instabilities may explain the fact that we do not obtain internal density barrier discharge with inward shifted configurations.

Keywords: LHD, MHD instabilities, pellet, relaxation

1 Introduction

In the Large Helical Device (LHD), the highest volume-averaged beta are obtained in so-called inward-shifted configuration (the radius of the vacuum magnetic axis, $R_{axis} \sim$ 3.6 m) because this configuration is favorable for particle confinement and heating efficiency. However, they are unfavorable as MHD stability is concerned. Therefore, it has been believed that MHD stabilities are not important for normal operation in LHD; the pressure driven instabilities are saturated at a certain level and they do not deteriorate the confinement of the plasma seriously. Then, the next fundamental question is that in which experimental condition do MHD activities affect the confinement. We have observed several MHD related phenomena having impact on the confinement of the plasmas. They do restrict the operational regime of the LHD considerably. One is the configuration with low magnetic shear. When the magnetic shear is reduced at ι = 1 surface, an m/n = 1/1 structure evolves and results in a minor collapse phenomena [3]. Another examples is that when the neutral beam injection is switched from the co-direction to counter direction, the magnetic shear at the ι = 1/2 rational surface is reduced and m=2 MHD oscillations with large amplitude are observed [4].

The other experimental condition where the MHD instabilities affect the operational regime is the peaked pressure profile whose gradient is much larger than the Mercier–stable condition. When ice-pellets are injected into the plasma sequentially, the pressure profile is getting peaked after the last pellet. Several MHD related event have been observed in this experimental regime where the Mercier condition is profoundly violated [5]. The acievable pressure gradient in this type of discharges depends on the vacuum magnetic axis position (See, Fig. 1). When the R_{axis} is larger than 3.75m, a fairly high central beta value β_0 is realized. This kind of plasma is called as 'the internal diffusion barrier (IDB) plasma' or 'the super dense core (SDC) plasma' [1, 2]. In this paper we investigate the effect of the pressure driven modes with a pressure gradient exceeds the stability limit, which depends on the location of the vacuum magnetic axis.

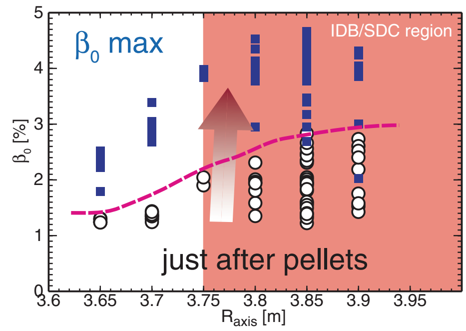

Fig. 1 Increase of the β_0 as a function of the vacuum magnetic axis R_{axis}.

2 Experiments

Typical time evolution of high-density plasma with pellet injection is shown in Fig. 2. After the last injection, a peaked density profile and a flat electron temperature profile are made (Fig. 3(a)). While the density is slowly de-

author's e-mail: ohdachi@nifs.ac.jp

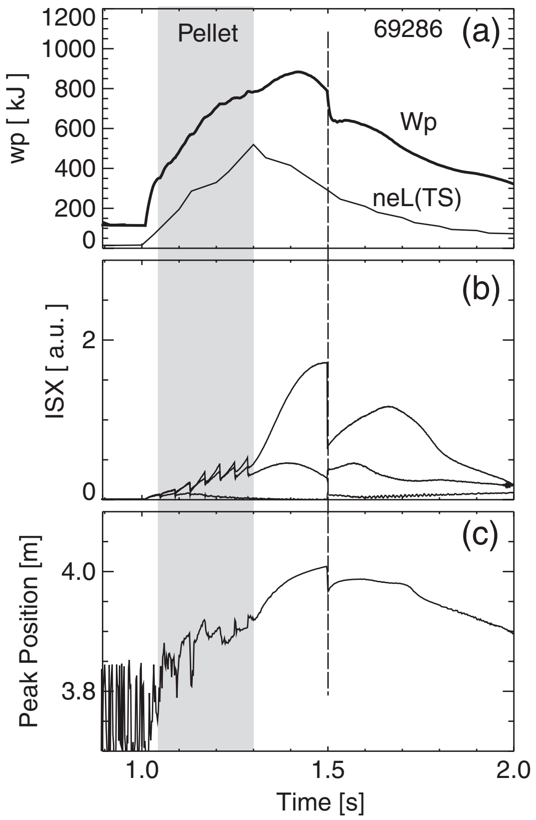

Fig. 2 Time evolution of the plasma parameters with pellet injection. The stored energy w_p and the line integrated electron density (a), soft X-ray radiation intensity(b) and the magnetic axis position estimated by the soft X-ray radiation profile (c) are shown. Vacuum magnetic axis in this discharge is 3.85m.

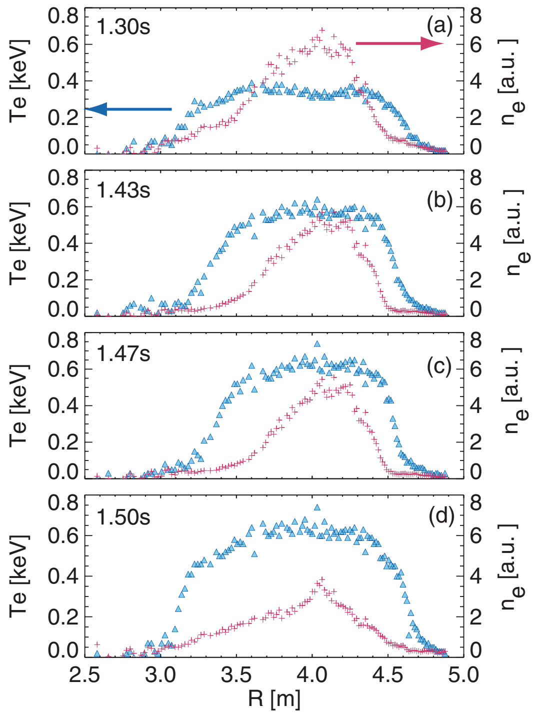

Fig. 3 The electron temperature and the electron density profile of #69286 after the pellet injection.

creased, the electron temperature increases and its profile is peaked. The recovery of the electron temperature is faster than the decrease in density. The pressure profile is thereby peaked. After the maximum of the stored energy, peaking of the profile still continues, which can be seen from the position of the magnetic axis estimated from the soft X-ray emission profile (Fig. 2(c)).

This peaking of the pressure is terminated at 1.5s by the so-called core density collapse (CDC) event (dashed line in Fig. 2). The plasma density at the center is decreased within 1 ms and the core plasma is redistributed to outer region, as is shown in Fig. 3(c)-(d).

In contrast to the case of the outward-shifted plasma, sawtooth-like activities are often observed inward-shifted plasmas. Time evolution of the discharges with R_{axis} = 3.65m and 3.75m are shown in Fig. 4. At the timing of the shaded stripes in Fig. 4, small relaxation events can be seen in the soft X-ray radiation (ISX). The waveforms are similar to those in the sawtooth phenomena observed on Tokamaks. The location of the inversion radius tells us that this instabilities are related to the $\iota = 1/2$ rational surface. Mode numbers of the precursor oscillations (m=2), which are rarely observed, support this.

Though the effect of these events on the confinement is small, the increase of the central beta (estimated by the magnetic axis position) is saturated by the sawtooth-like events; the events affect the peaking speed of the pressure profile. This is one example where MHD instabilities do affect the pressure profile.

3 Discussion

The evolution of the β_0 as a function on the magnetic axis position R_0 is shown in Fig. 5. The thick curves show the Mercier stability criterion, $D_I = 0$, estimated at the $\iota = 1/2$ rational surface. The area right side of the lines is stable region; when the magnetic axis is shifter outward the magnetic well depth is deeper. Three lines are corresponding to different pressure profiles; assumed pressure profile is $p(\rho) = p_0(1-\rho^2)(1-\rho^8)$ (dashed line), $p(\rho) = p_0(1-\rho^4)(1-\rho^8)$ (dotted line) and $p(\rho) = p_0(1-\rho^2)^2$ (solid line), respectively. The symbols in Fig. 5 show the time evolution of the central beta in the recovery phase after pellet injection.

Inward shifted plasmas ($R_{axis} < 3.75m$) are always Mercier–unstable at $\iota = 1/2$ in the recovery phase after the pellet injection. Sawtooth-like repeated relaxation events are destabilized as the pressure gradient increases. The corresponding area is shown in the shaded ellipse in Fig. 5. There exists a threshold value of the pressure gradient for the appearance of the instabilities. It is estimated as ($d\beta/d\rho \sim 1\%$) [5].

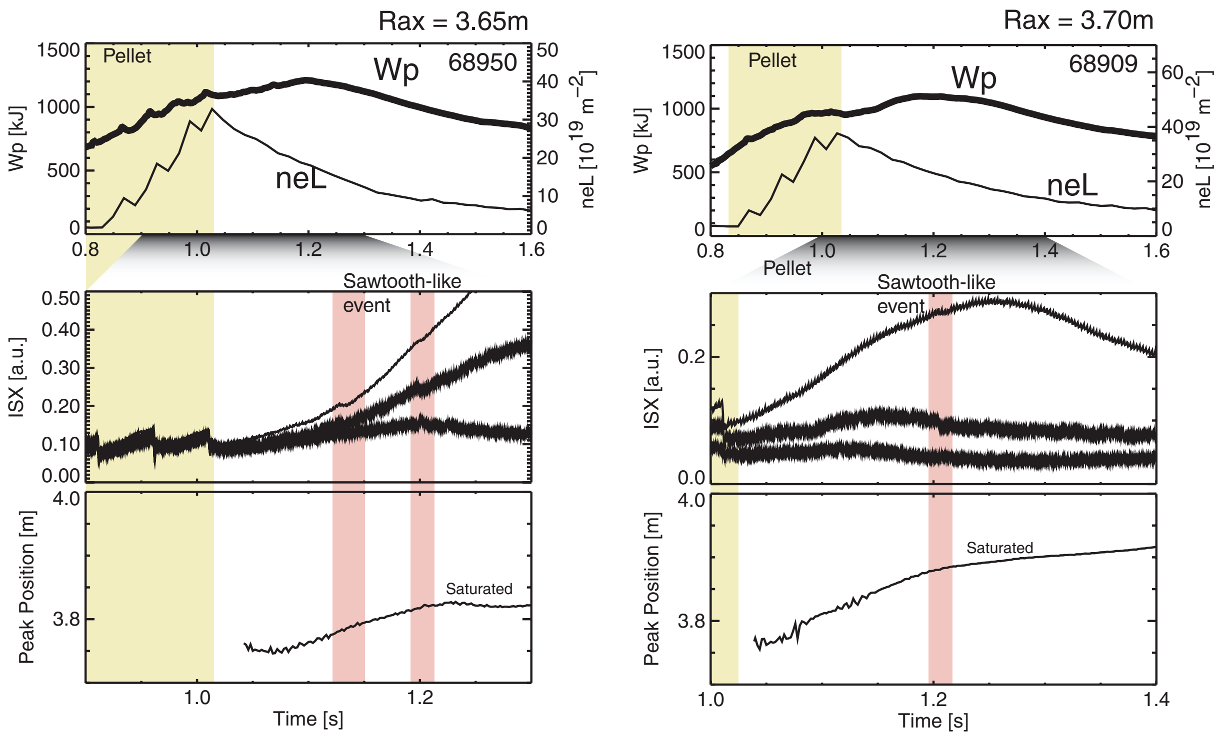

Fig. 4 Time evolution of the plasma parameters with sawtooth-like relaxation. Stored energy Wp and line-integrated density and the soft X-ray radiation and the magnetic axis position are shown together.

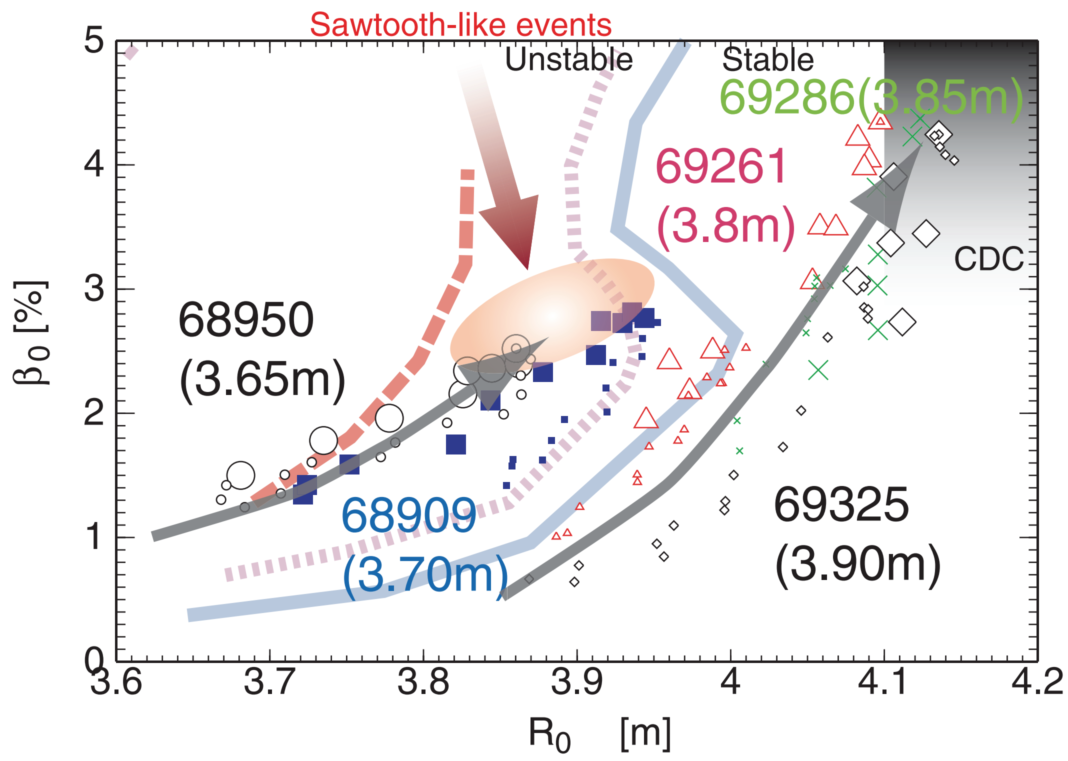

Fig. 5 Central beta value β_0 as a function of the magnetic axis position is shown. Thick lines show the stability boundary of Mercier mode. Three lines are corresponding to different pressure profiles; assumed pressure profile is $p(\rho) = p_0(1-\rho^2)(1-\rho^8)$, $p(\rho) = p_0(1-\rho^4)(1-\rho^8)$ and $p(\rho) = p_0(1-\rho^2)^2$, respectively. Open circle (R_{axis} = 3.65m), closed square (R_{axis} = 3.70m), open triangle (R_{axis} = 3.8m), cross (R_{axis} = 3.85m) and open diamond (R_{axis} = 3.9m) show the time evolution of the parameters after the pellet injection. Larger (smaller) symbols correspond to the period when the pressure profile is being increased (decreased).

Notice that the traces of 69286 ($R_{axis} = 3.85m$) or 69325 ($R_{axis} = 3.90m$) avoid the MHD unstable region in Fig. 5. In outward-shifted configurations ($R_{axis} > 3.75m$), Mercier stable condition for the core MHD mode is always satisfied that way. Achievable beta values are then higher than with inward-shifted configuration. However, as is already shown in Fig. 2, when the magnetic axis is shifted too large and exceeds a certain value (e.g. 4.1m), the CDC events are triggered and the further increase of the β_0 is terminated. Detailed mechanism of the CDC has not been clarified so far. However, there is a evidence that the magnetic axis position is a key parameter for the CDC event; when the Shafranov shift is reduced by the vertical elongation of the plasma, the achievable central beta is increased up to 7%[6]. Therefore, the fact the highest central beta can be obtained with $R_{axis} = 3.85m$ (Fig. 1) can be understood by the following way. Outward shifted plasma (e.g. $R_{axis} = 3.85m$) is free from core MHD instabilities and there is much space for the Shafranov shift until the CDC limit in configurations with $R_{axis} = 3.80, 3.85m$.

In addition to the sawtooth-like instabilities, broadband MHD fluctuations are enhanced in inward-shifted plasmas. The spectra of the magnetic fluctuation with different vacuum magnetic axis position are shown in Fig. 6. Coherent MHD fluctuations related to the rational surfaces located in the edge region (e.g. m/n = 1/1) make the small peaks in the spectra. It is clear that the fluctuation levels theemselves are larger when the vacuum magnetic axis is shifted inward (MHD unstable). The peaking speed of the central beta after pellet is slower in the inward-shifted plasma (See, Fig. 7). The anomalous transport due to the enhanced magnetic fluctuation can be a candidate for this.

In summary, the plasma performance with a peaked pressure profile with pellet injections is investigated. In MHD unstable inward-shifted plasmas, larger levels of the MHD fluctuations and sawtooth-like instabilities that affect the plasma confinement are activated. Whereas the outward-shifted plasma, larger central beta was obtained with smaller MHD fluctuations. Increased transport due to the larger MHD fluctuations and/or the sawtooth-like relaxation events might explain the fact that we do not obtain IDB/SDC plasma in inward-shifted configurations.

[1] N. Ohyabe, et. al., Phys. Rev. Lett., **97**, 055002 (2006)
[2] T. Morisaki, et. al., Phys. Plasma, **14**, 056113 (2007)
[3] S. Sakakibara, et. al, Fusion Engineering and Design **50**, 177 (2006)
[4] S. Isayama, S. Inagaki, et. al., Plasma Phys. Control. Fusion, **4**, L44 (2006)
[5] S. Ohdachi, et. al, in Proc. 21th IAEA Fusion Energy Conference, Chengdu, China, 16-21 October 2006, EX/P8-15
[6] J. Miyazawa, Abrupt Flushing of the High-Density Core in Internal Diffusion Barrier Plasmas and its Suppression by Plasma Shape Control in LHD, this conference. to be submitted to the Plasma Fusion Research

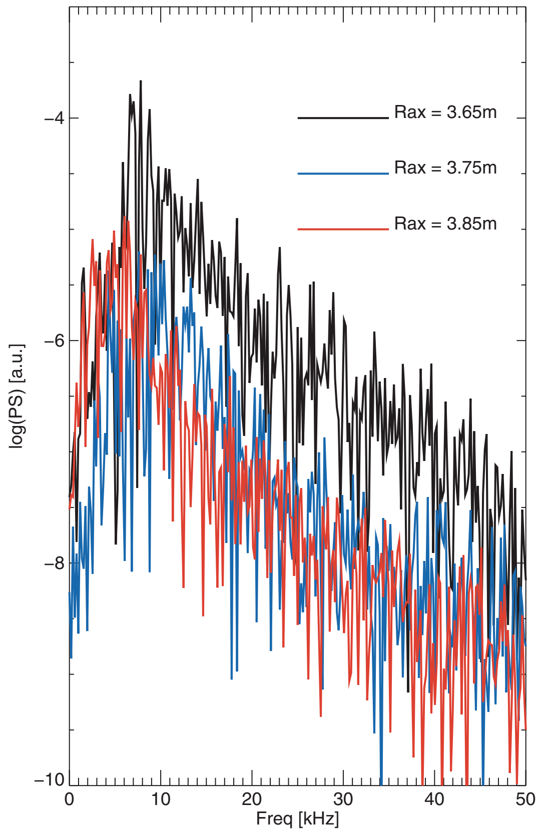

Fig. 6 Spectra of the magnetic fluctuations with different magnetic axis. The spectra are calculated when the stored energy take its maximum value.

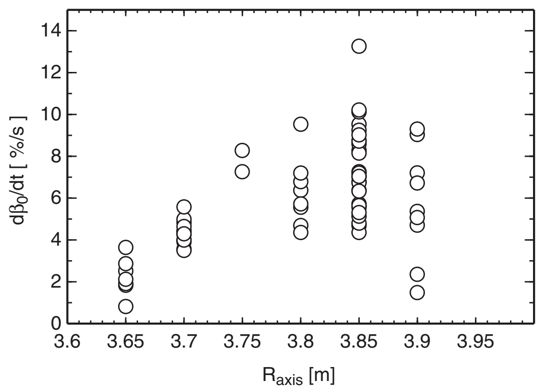

Fig. 7 The rate of the recovery speed of the central beta.

Proceedings of ITC/ISHW2007

Nonlinear simulation of collapse phenomenon in helical plasma with large pressure gradient

Naoki MIZUGUCHI[1,2], Yasuhiro SUZUKI[1] and Nobuyoshi OHYABU[1,2]

[1] *National Institute for Fusion Science, Toki 509-5292, Japan*

[2] *The Graduate University for Advanced Studies (SOKENDAI), Toki 509-5292, Japan*

Nonlinear magneto-hydrodynamics (MHD) simulations are executed for a helical plasma with large pressure gradient to investigate the collapsing event that is induced by the MHD instabilities. The simulation results show that the ballooning-like instabilities with intermediate spatial scale induce both the disordering of the structures in the barrier region and the drop of the central pressure. It has been revealed that the core pressure fall is related to the disordering of the magnetic field structure. The simulation results are compared qualitatively with the experimental observations of the collapse events in the super dense core state of the Large Helical Device (LHD). Compared with our previous simulation studies for the similar situations in the spherical tokamak (ST) plasma, the results for the helical cases show milder collapse than those in the ST case.

Keywords: magneto-hydrodynamics, collapse, helical system, simulation, super dense core

1 Introduction

In recent experiments in the Large Helical Device (LHD), high performance confinement with a super-dense core (SDC) inside the internal diffusion barrier (IDB) has been achieved by using the pellet injection scheme[1]. On the re-heating stage in such a discharge, where the plasma beta gradually increases after ceasing the pelletinjection, an abrupt flushing of the central density occurs in some cases. Such a collapse phenomenon, which is named "core density collapse (CDC)"[2, 3], should be avoided since it often limits the density increase. Although the physical mechanism of CDCs remains unclear up to the present, several models based on the magneto-hydrodynamic (MHD) instability or the equilibrium limit have been proposed. To reveal the mechanism of CDC is one of the key issues for further development of the confinement toward the high-density branch.

This article reports a first attempt to carry out a nonlinear MHD simulation in helical plasma with large pressure gradient, which corresponds to the IDB-SDC state of LHD. The result obtained by the simulation would provide us with basic understandings for the collapse phenomena, including the CDC, from the point of view of MHD.

2 Simulation model

We solve the time development of the standard set of the compressive, resistive, nonlinear MHD equations,

$$\frac{\partial \rho}{\partial t} = -\nabla \cdot (\rho \mathbf{v}), \tag{1}$$

$$\frac{\partial}{\partial t}(\rho \mathbf{v}) = -\nabla \cdot (\rho \mathbf{v}\mathbf{v}) - \nabla p + \mathbf{j} \times \mathbf{B} + \mu\left(\nabla^2 \mathbf{v} + \frac{1}{3}\nabla(\nabla \cdot \mathbf{v})\right), \tag{2}$$

$$\frac{\partial \mathbf{B}}{\partial t} = -\nabla \times \mathbf{E}, \tag{3}$$

$$\frac{\partial p}{\partial t} = -\nabla \cdot (p\mathbf{v}) - (\gamma - 1)(p\nabla \cdot \mathbf{v} + \eta \mathbf{j}^2), \tag{4}$$

in a full-toroidal three-dimensional geometry. The variables, ρ, $\mathbf{v}$, $\mathbf{B}$, and p represent the mass density, the fluid velocity, the magnetic field, and the pressure, respectively. The current density $\mathbf{j}$ and the electric field $\mathbf{E}$ are calculated from Maxwell's equations,

$$\mathbf{j} = \nabla \times \mathbf{B}, \tag{5}$$

$$\mathbf{E} = -\mathbf{v} \times \mathbf{B} + \eta \mathbf{j}. \tag{6}$$

In (1)-(4), the dissipation terms are included as the resistivity η and the viscosity μ. These terms are assumed to be uniform constants for simplicity. The Ohmic heating term is evaluated in the evolution of the pressure p, whereas the viscous heating is ignored for simplicity. All the spatial derivatives are expressed numerically by using the fourth-order central-difference scheme. The time integration is solved by using the fourth-order Runge-Kutta method.

To follow the geometry of the helical devices with continuously-wound magnetic coils, we adopt the helical-toroidal coordinate system which is used in the HINT code[4]. This coordinate system (u^1, u^2, u^3) uses a rectangular grid (u^1, u^2) in the poloidal cross section and a toroidal grid (u^3) with geometrically regular intervals. By using the poloidal angle θ, toroidal angle ϕ, and the minor radius r, (u^1, u^2, u^3) is described as[4]

$$u^1 = r\cos(\theta - h\phi), \tag{7}$$

$$u^2 = r\sin(\theta - h\phi), \tag{8}$$

$$u^3 = -\phi, \tag{9}$$

where the number of helical period h is 10/2 to follow the LHD configuration. The boundary condition of the com-

author's e-mail: mizu@nifs.ac.jp

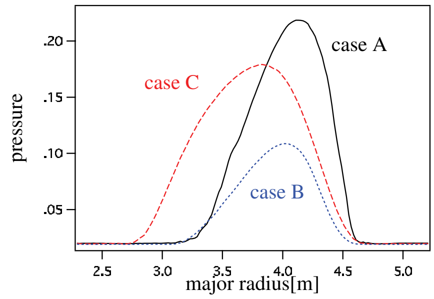

Fig. 1 Radial pressure profiles of the initial equilibria for the case A, B, and C on the horizontally elongated cross section.

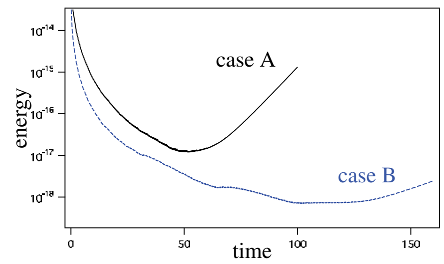

Fig. 2 Time development of kinetic energy for the linear simulation.

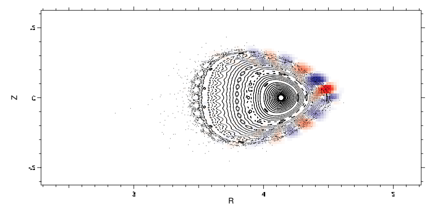

Fig. 3 Poloidal mode structure of the perturbations in the pressure on the horizontally elongated cross section.

putation for the u^1 and the u^2 directions is the perfect conductor condition, and that for the u^3 direction assumes the periodicity 2π. The number of the numerical grid points is $(N_1, N_2, N_3) = (62, 146, 500)$.

The initial condition for the simulation is given by the numerical solution of the HINT code which models an average experimental configuration of LHD[5]. The simulation geometry includes the region out of the separatrix. To treat such an external region continuously from the inside of the separatrix, we artificially add low uniform component in pressure initially.

The simulation starts by adding tiny random perturbations in the velocity component of the initial equilibrium. Thus, the spontaneous time development of the MHD system is solved by using vector-parallel calculation on a supercomputer.

3 Simulation result

The MHD equations (1)-(4) are solved in a dimensionless form by normalizing all the variables with characteristic values, such as 1[m] for the spatial scale, 1[T] for the magnetic field. Uniform density $\rho = 1$ is given for the initial condition for simplicity. The uniform constant for the dissipation coefficient $\eta = 10^{-4}$ and $\mu = 10^{-3}$ are used throughout this article. The unit of time, i. e., the Alfvèn transit time τ_A corresponds to the order of $\sim \mu$sec for the standard parameters of LHD experiment. For the main results described in this article, the initial equilibrium which roughly models the IDB-SDC state of LHD just before the CDC events is used. Its pressure profile is shown in Fig.1 (case A). The maximum and the volume averaged beta value are $\beta_0 = 6.6\%$ and $<\beta>= 1.8\%$, respectively. Compared with the standard high-beta discharges of LHD experiments (case C), the pressure gradient in the barrier region is markedly large due to the large Shafranov shift.

Figure 2 shows the time evolution of the kinetic energy in solving the linearized system of (1)-(6). One can see a linear growth of the instability at $t > 50$ for case A. In Fig.2, the trace for the case which uses a lower beta equilibrium with $\beta_0 = 2.5\%$ (case B) is also plotted for reference. One can see that the growth rate for case A is much larger than that for case B. Also, the resistivity scans show the independence of the growth rate on the resistivity, which proves the modes to be ideal ones. These modes have intermediate poloidal mode numbers $m \sim 10$. The poloidal mode structures, shown in Fig.3, clearly exhibit the ballooning nature in that the fluctuations are localized in the outer region.

The nonlinear long-term evolution of the energy and the maximum pressure is shown in Fig.4. One can see that the growth and saturation of the energy repeats three times before reaching a relaxed state. The growth shown in Fig.2 corresponds to the first one ($t < 100\tau_A$). During this relaxation process, the plasma changes its shape gradually. The temporal changes in the radial and the poloidal pressure profile are shown in Fig.5 and Fig.6, respectively. Since the primarily induced instability is localized in the outer region of the torus, as described above, the crash of the structures is first seen in the barrier region (see Fig.6(b)). The plasma

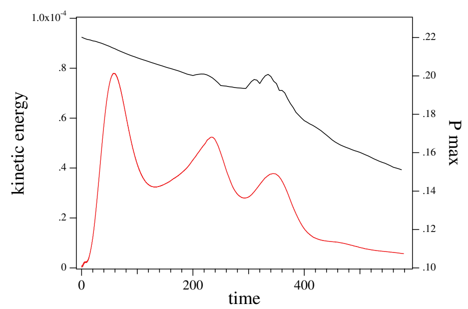

Fig. 4 Time evolution of the total kinetic energy and the maximum pressure.

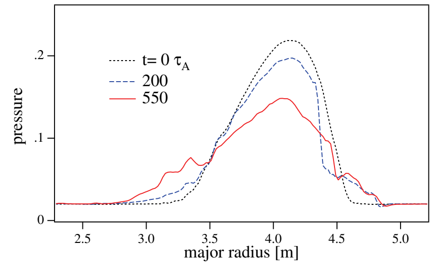

Fig. 5 Temporal change of the radial pressure profile on the horizontally elongated cross section.

surface is deformed, reflecting the linear eigenmode structures in the outer region, and the magnetic field structure in the inner region, as shown in Fig.3. Part of plasma is lost due to the disturbance. The resultant pressure gradient in the barrier region becomes steeper than in the initial state (see Fig.5 at $t = 200\tau_A$). It should be noted that the mode structures of the instability are located only in the barrier region, whereas the central pressure gradually decreases, as the lost plasma forms a pedestal pressure in the edge region, as shown in Fig.5 toward $t = 550\tau_A$ and Fig.6(b)-(d). If one see the time development of the maximum pressure at the core as shown in Fig.4, there is an abrupt change in the trace after $t = 300\tau_A$. The rapid fall in the core pressure might be related to the change in the magnetic field structure. Figure 7 shows the time development of the magnetic field structure which is expressed by the puncture plot of the field lines. The field line trace is executed by using a sixth-order Runge-Kutta method together with a fourth-order interpolation of the magnetic field. The magnetic surface structure is clearly formed entirely from the core to the edge region initially (see Fig.7(a)). Such a nested-surface structure is sound during the early stage of the relaxation process, although the edge structure is markedly deformed, as shown in Fig.7(b). At time $t = 300\tau_A$ (see Fig.7(c)), the magnetic surface structure abruptly diminishes throughout the whole poloidal plane. Finally, the structure reappears in the core region as shown in Fig.7(d). At the moment shown in Fig.7(c), the plasma in the core region at high pressure is linked to the external low-pressure region with an identical field line. Under this situation, the plasma outward flows due to the pressure imbalances along the field lines, which might cause the rapid fall of the core pressure, can be induced.

The system reaches a relaxed state within $\sim 600\tau_A$ in this result. The resultant pressure profile becomes a broader one because of the decrease in the core, and the spread in the edge, as shown in Fig.5 at $t = 550\tau_A$.

4 Discussion

The simulation result described in Sec.3 can be compared qualitatively with the experimental observations on the

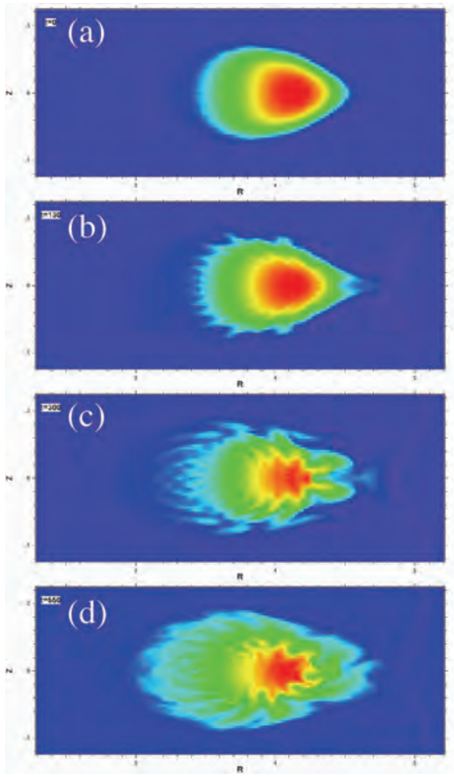

Fig. 6 Temporal change of the pressure profile. The iso-contour maps of the pressure on the horizontally elongated cross section are drawn. The time equals to (a)0, (b)130, (c)300, and (d)550 τ_A.

CDC event in LHD. The time scale of the whole simulation process roughly agrees with that of the crash phase of CDCs. There remains some several questions for the mechanism of occurrence of CDCs. The simulation results might provide us with interpretation for them. Firstly, the reason why the core density decreases is a basic question for CDCs. The fact that only the density decreases, keeping the core temperature unchanged, implies that the collapse is governed not by the conductive processes, but by the convective ones. In our simulation result, the core plasma is extracted convectively through the transiently disordered or reconnected field lines as shown in Fig.7. This convective loss mechanism is valid even if there is no significant unstable mode in the core region. The possibility of the coexistence of the instability in the barrier region and the significant drop in the core pressure is also comparable with another question why the edge fluctuation is observed just before the density collapse in the experiment. The simulation result gives a reasonable scenario for it. More detailed comparison would need systematic scans for the edge stability problem both in the simulation and experiment in future.

Now we compare the simulation result with the previous simulation which studies the nonlinear dynamics of ST plasma on an ELM crash[6]. Although both the simulations are initiated by the ballooning mode instability, and

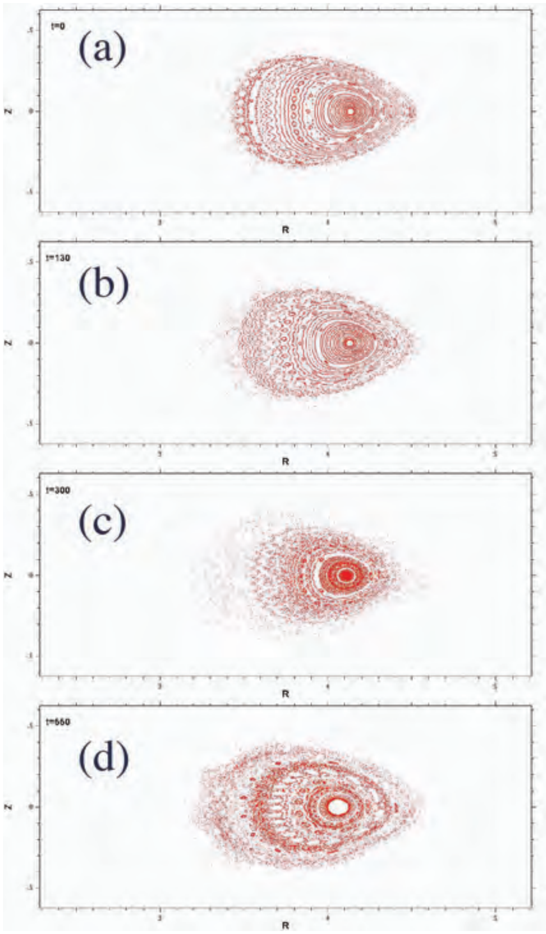

Fig. 7 Temporal change of the magnetic field. The puncture plots of the magnetic field lines on the horizontally elongated cross section are plotted. The time equals to (a)0, (b)130, (c)300, and (d)550 τ_A.

have several points in common, there is also qualitative difference between them. To compare both simulations would help us understand the key properties of the process. In Ref.[6], the crash process of the pressure profile is divided in two stages. The edge region is perturbed in the former stage, whereas the core pressure falls in the latter one, as is also observed in our simulation. However, for the ST case, the core collapse is caused by a secondary induced internal low-*n* instability, where *n* is the toroidal mode number, in contrast to the direct parallel loss in the helical case described in Sec.3. No prominent secondary low-*n* structure can be observed in the helical case simulation, as shown in Fig.8. The resultant temporal change of the core pressure profile shows milder activity for the helical case than for the ST case. The large internal plasma current of the ST would make difference in the core instability from the helical system, because the induced internal mode is a current driven one.

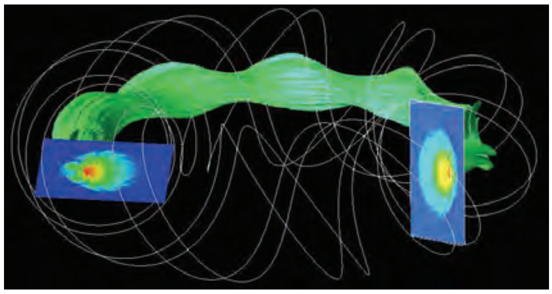

Fig. 8 Three-dimensional structure of plasma pressure at $t = 365\tau_A$. The iso-contour of the pressure together with an iso-pressure surface are drawn.

5 Summary

We have executed MHD simulations and revealed the nonlinear dynamics of the ballooning mode in helical systems with large pressure gradient. The simulation result has shown a physical mechanism that the pressure collapse in the barrier region is followed by the convective loss from the core region through the disturbance of the magnetic field. The simulation is qualitatively comparable with the experimental observations of the CDC events in LHD. Although the simulation result shows a closed scenario initiated by the ballooning instability, it is necessary to carry out the systematic stability analyses under the experimental situation before discussing the cause of the CDC in future.

The authors would like to thank Drs. S. Ohdachi, J. Miyazawa, R. Sakamoto, Y. Narushima, K. Itoh, K. Ichiguchi, Y. Todo, H. Miura, and N. Nakajima for fruitful discussion. This work is performed with the support and under the auspices of the NIFS Collaborative Research Program (NIFS07KNXN097).

[1] N. Ohyabu, T. Morisaki, S. Masuzaki, *et al.*, Phys. Rev. Lett. **97** 55002 (2006).
[2] R. Sakamoto, *et al.*, this conference.
[3] J. Miyazawa, *et al.*, this conference.
[4] K. Hatafuji, T. Hayashi, and T. Sato, J. Comp. Phys. **81** 169 (1989).
[5] Y. Suzuki, N. Nakajima, K. Watanabe, *et al.*, Nucl. Fusion **46** L19 (2006).
[6] N. Mizuguchi, R. Khan, N. Nakajima, and T. Hayashi, Nucl. Fusion **47** 579 (2007).

Proceedings of ITC/ISHW2007

3-D ideal MHD stability of super dense core plasma in LHD

Y. Narushima, K.Y. Watanabe, R. Sakamoto, Y. Suzuki, S. Sakakibara, S. Ohdachi,
H. Yamada and LHD experimental group
W.A. Cooper[a]

National Institute for Fusion Science, 322-6 Oroshi-cho, Toki 509-5292, Japan
[a] Centre de Recherches en Physique des Plasmas,
Association Euratom / Confederation Suisse, EPFL, 1015 Lausanne, Switzerland

The characteristics of confinement properties and magnetohydrodynamics (MHD) stabilities of the super dense core (SDC) plasmas are intensively studied in the Large Helical Device (LHD) experiment. The SDC plasmas are produced in the configuration with outward shifted magnetic axis and rapid fueling into the core region by pellet injection. The SDC plasmas have high electron pressure due to the large electron density (n_e~10^{21}[m^{-3}]) in the core region which induces a large Shafranov shift (Δ/a_{eff}>0.5). It is useful to apply the production method of the SDC plasmas for obtaining high-beta plasmas with high pressure in the core region. In this study, the characteristics of the ideal MHD instabilities of the SDC plasmas are analyzed by using the 3-D ideal MHD code TERPSICHORE. The calculated equilibrium of the typical SDC plasma with the central beta of β_0 = 5[%] solved as the result of the HINT/HINT2 codes shows that a deep magnetic well depth appears around the core region due to the large Shafranov shift. The Mercier criterion (D_I) shows that the plasma is stable all over the plasma region and consequently the low-n interchange modes do not appear. Although the typical SDC plasma is stable to the interchange mode, it is worthwhile to investigate the other pressure profiles and the magnetic field configurations to know the role of the MHD instabilities on the experimentally obtained SDC plasmas. In the experiment, the SDC plasmas cannot be produced in the configuration with inward shifted magnetic axis. Such configuration tends to be MHD unstable, in which the core resonant interchange modes become unstable in case of relatively low-beta plasma with finite pressure gradient in the core region. We will investigate how the MHD instabilities affect the production of the SDC plasma with steep pressure gradient in the core region in the configuration with inward shifted magnetic axis.

Keywords: Large Helical Device, MHD, Internal Diffusion Barrier,

1. Introduction

The characteristics of confinement properties and magnetohydrodynamics (MHD) stabilities of the super dense core (SDC) plasmas are intensively studied in the Large Helical Device (LHD) experiment [1]. Figure1 shows the attainable central beta β_0 against to the position of the magnetic axis R_{ax}. The SDC plasmas are produced in the outward-shifted configuration R_{ax} > 3.75[m]. On the other hand, in the inward-shifted configuration R_{ax} < 3.70[m], SDC plasmas are not obtained. The steep pressure gradient maintains at the core region for R_{ax} = 3.75m case whereas the gradual gradient appears in the inward-shifted configuration of R_{ax} = 3.6m as shown in Fig.2. We focus on stabilities of magnetohydrodynamics (MHD) of SDC plasmas in this study. MHD stabilities can be categorized into the ideal mode and resistive mode. Each mode, furthermore, can be classified into the low-n

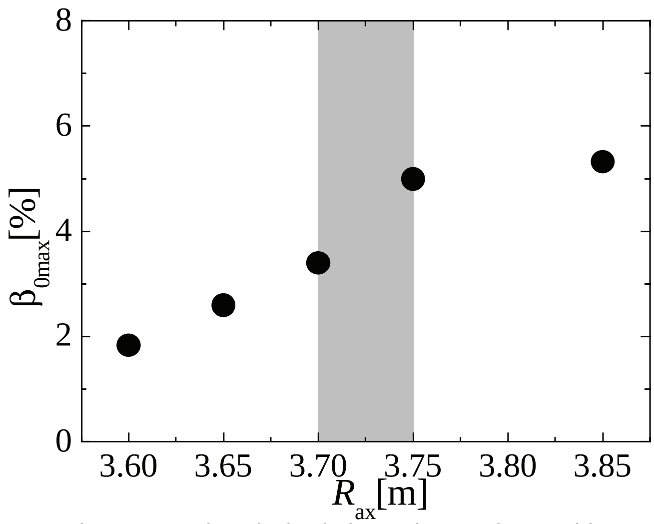

Fig.1 Magnetic axis (R_{ax}) dependence of central beta (β_0). Threshold is seen at between R_{ax} = 3.7m and 3.75m. The β_0 seems to be suppressed in inward shifted configuration (R_{ax} < 3.7).

author's e-mail:narusima@LHD.nifs.ac.jp

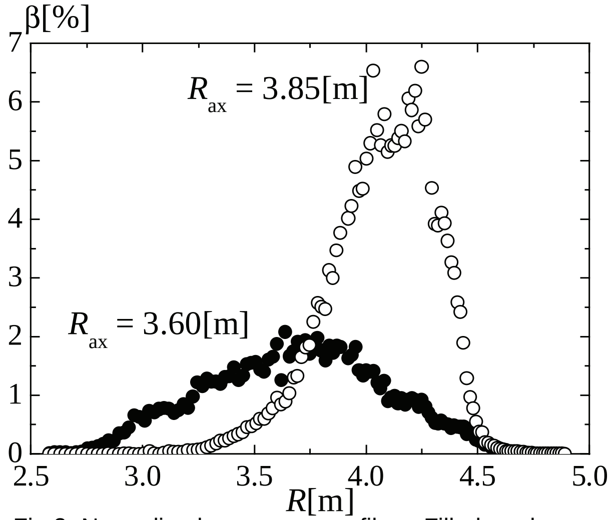

Fig.2 Normalized pressure profiles. Filled and open circles indicate the case of R_{ax} = 3.60[m] and 3.85[m] respectively. The steep gradient is seen in R_{ax} = 3.85[m].

(global) mode and high-*n* (local) mode. Here, *n* means the toroidal Fourier mode number. In this study, we have investigated about low-*n* ideal mode, high-*n* ideal mode, and resistive high-*n* mode. The latter mode relates to the plasma transport. The analyses of low-*n* ideal mode are carried out by using 3-D ideal MHD stability code TERPSICHORE [2]. The Mercier index shows the stability of ideal high-*n* mode. The resistive high-*n* mode is examined from local parameters of specific volume, Reynolds number and pressure gradient. The equilibria analyzed here are solved as the result of the HINT/HINT2 codes [3,4].

This paper is organized as follows. Characteristics of MHD stability of experimentally obtained plasmas are described in the following section. In section 3, equilibria with modeled pressure profiles are analyzed to orient the

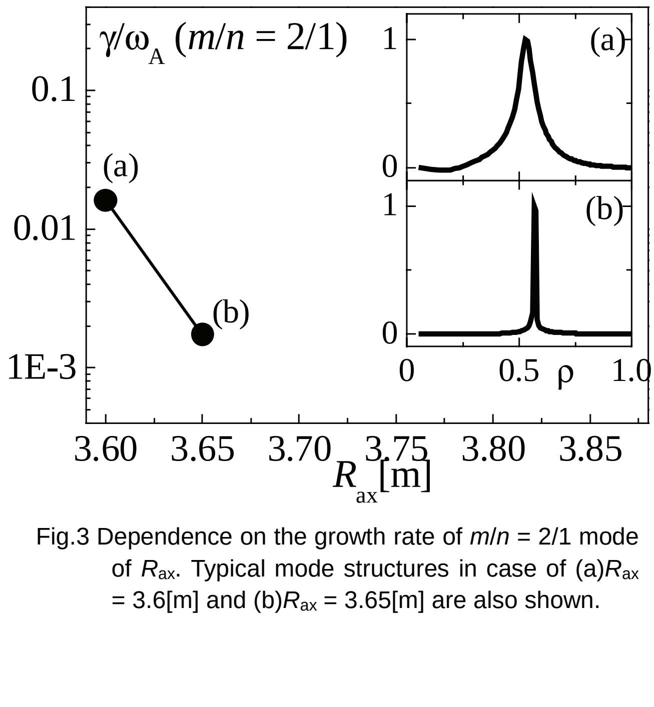

Fig.3 Dependence on the growth rate of *m*/*n* = 2/1 mode of R_{ax}. Typical mode structures in case of (a)R_{ax} = 3.6[m] and (b)R_{ax} = 3.65[m] are also shown.

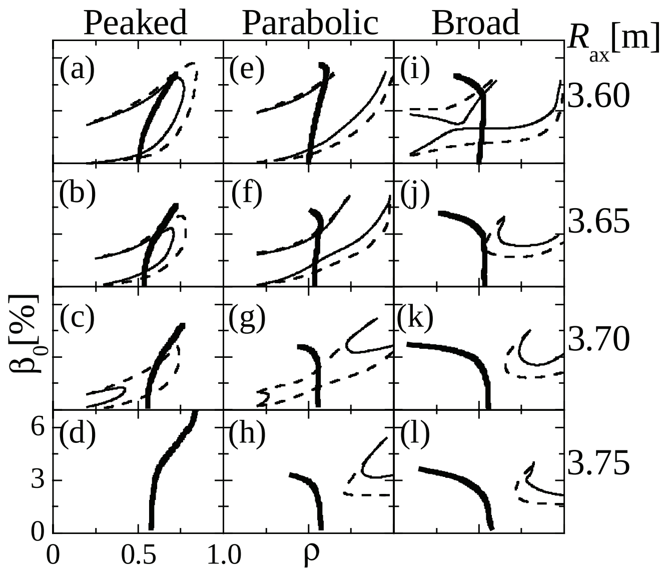

Fig.4 Contour lines of Mercier index and the position of $\iota/2\pi$ = 1/2 surface in ρ - β_0 space. Dashed and solid thin lines indicate D_I = 0 and 0.2 respectively. Bold solid lines correspond to the position of $\iota/2\pi$ = 1/2.

experimental results. Finally, we will discuss and summarize in section 4.

2. Characteristics of MHD stability of experimentally obtained plasmas

Experimentally obtained SDC plasmas have a steep pressure gradient in the core region which corresponds to around the position of the rotational transform $\iota/2\pi$ = 1/2. We focus on, therefore, the *m*/*n* = 2/1 mode as a low-*n* ideal MHD mode. Here, *m* means the poloidal Fourier mode number. The analyses of low-*n* ideal mode are carried out by using 3-D ideal MHD stability code TERPSICHORE. The relationship between the growth rate and R_{ax} is shown in Fig.3. In case of R_{ax} = 3.6[m], the *m*/*n* = 2/1 mode is unstable with the growth rate γ/ω_A = 1.62x10^{-2} and the wide mode structure appeasers as shown in Fig.3(a). In case of R_{ax} = 3.65[m], the growth rate is 1.74x10^{-3} and the width of the structure is narrower than that in case of R_{ax} = 3.6m. It is reported that the growth rate of γ/ω_A = 10^{-2} is defined as the stability boundary [5]. It can be, therefore, considered that the ideal low-*n* (*m*/*n* = 2/1) interchange mode is stable except for the configuration with R_{ax} = 3.6[m].

3. MHD stability of analytical equilibrium

Equilibria with modeled pressure profiles are analyzed to orient the experimental results. Here, three kinds of pressure profiles of parabolic ($\beta = \beta_0(1 - \rho^2)(1 - \rho^8)$), peaked ($\beta = \beta_0(1 - \rho^2)^2$), and broad ($\beta = \beta_0(1 - \rho^4)(1 - \rho^8)$) are adopted. The contour lines of Mercier index D_I are shown in Fig. 4 where dashed and solid thin lines

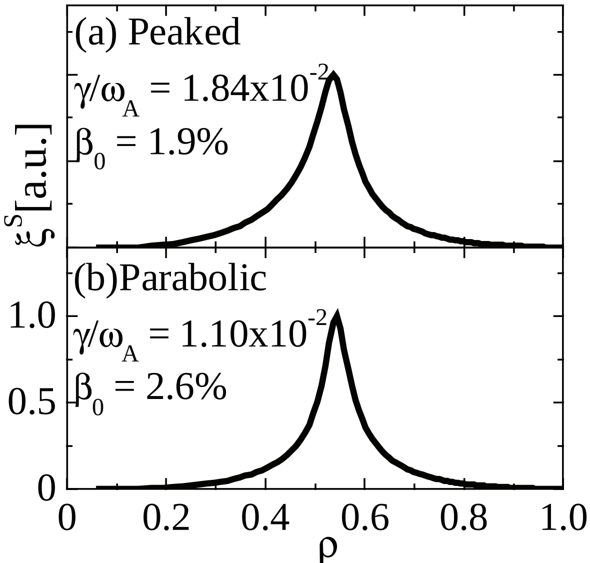

Fig.5 Typical structure of ξ^s of m/n = 2/1 mode. (a) Peaked pressure profile (b) Parabolic pressure profile.

indicate D_I = 0 and 0.2 respectively. Bold solid lines correspond to the position of $\iota/2\pi = 1/2$. In equilibria with R_{ax} = 3.60[m] (Fig.4(a)(e)(i)), Mercier unstable regions dominate the ρ - β_0 space. Mercier unstable region generally narrows with increasing R_{ax}. In particular, the equilibrium with peaked profile in R_{ax} = 3.75[m] is Mercier stable all over the region (Fig.4(d)).

In order to investigate the global ideal mode, we have analyzed the stability of m/n = 2/1 mode which mainly resonates at core region. The low-n ideal mode tends to be unstable when the resonant surface obviously enters the Mercier unstable region. The ideal low-n interchange mode is destabilized (as above mentioned, growth rate becomes $\gamma/\omega_A > 10^{-2}$) in R_{ax} = 3.60[m] with peaked and parabolic profiles, in which the mode structures are shown in Fig.5. In each cases, (peaked (Fig.5 (a)) and parabolic Fig.5 (b)), the growth rate is γ/ω_A = 1.84x10^{-2} and 1.10x 10^{-2} respectively. The shape of mode structure is similar to each other, in which the full width at half maximum, Δρ, is Δρ ~ 0.1 and the position of the peak corresponds to around ρ = 0.54. In the other equilibria (R_{ax} >3.6[m]), the low-n mode (m/n = 2/1) does not appear.

The orientation of experimental results from the viewpoint of ideal MHD instability is shown in Fig.6. The left figure (Fig.6 (a)) shows the global ideal MHD unstable region by solid lines and the right one (Fig.6 (b)) indicates the unstable region of the local MHD mode. The experimental results of central beta β_0 are superimposed. The experimentally obtained plasmas generally locate far from the MHD unstable (m/n = 2/1 mode) region as shown in Fig.6 (a). Some of experimental results (R_{ax} = 3.6[m] and 3.65[m]), on the

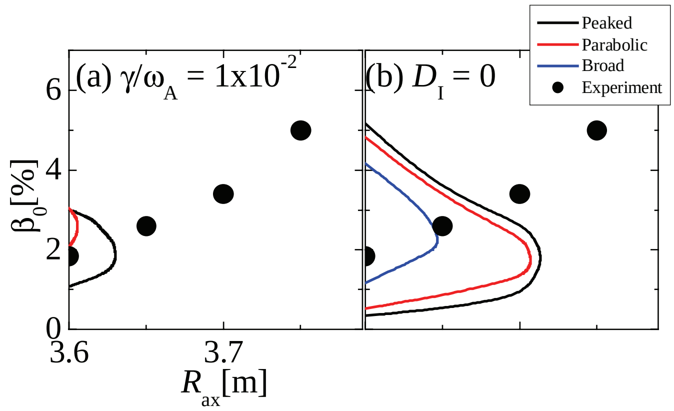

Fig.6 Ideal MHD unstable region of (a) global mode and (b) local mode. Black, red and blue solid line indicates pressure profile of peaked, parabolic and broad respectively. Closed circles shows experimental result of central beta.

other hand, enter the Mercier unstable region as shown in Fig.6(b). These results suggest that the ideal global mode does not affect the beta (gradient) in outward-shifted configuration. High-n ideal mode might influence the MHD characteristics because the unstable region of high-n ideal mode covers the region where the experimental data exists.

4. Discussion and summary

The ideal MHD stability of SDC plasma is investigated. The results show that the SDC plasmas are stable against to the ideal MHD mode. In order to investigate the other MHD stability, we will discuss the possibility of the resistive mode here. The resistive MHD instability is well correlated with the transport via the resistive pressure gradient driven turbulence. The coefficient of the particle diffusion D is defined by the magnetic curvature (κ_n), Reynolds number (S) and pressure gradient ($d\beta/d\rho$) as follows [6-7].

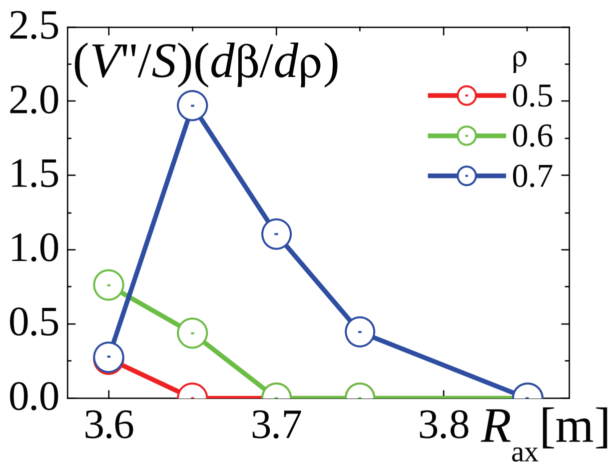

Fig.7 Qualitative behavior of diffusion by resistive pressure gradient driven turbulence.

$$D \propto \frac{\kappa_n}{S}\frac{d\beta}{d\rho} \qquad (1)$$

The qualitative behavior of the diffusion against to the R_{ax} is shown in Fig.7. The deferential of specific volume V'' is used here instead of κ_n to estimate the coefficient of the particle diffusion. The plot at $\rho = 0.7$ of R_{ax} = 3.6[m] indicates the small value, which comes from the local flatting of the pressure gradient. Figure 7 shows that the diffusion by the resistive pressure gradient driven turbulence generally continuously decreases with the R_{ax}. The diffusion at $\rho = 0.5$ and 0.6, in particular, goes to zero around R_{ax} = 3.7[m] where the threshold is seen as shown in Fig.1. In other word, diffusion tends to become large in the inward-shifted configuration. Further analyses about resistive mode are required.

Acknowledgement

This study was supported by a Grant-in-Aid for Scientific Research (A)(No.17206094) from the Ministry of Education, Culture, Sports, Science and Technology of Japan. This work was supported by NIFS under Contract No.NIFS07ULPP535.

References

[1] N. Ohyabu *et al* Phys. Rev. Lett. **97**,055002(2006)
[2] W.A. Cooper Plasma Phys. Control. Fusion **34**, 1011 (1992)
[3] K. Harafuji *et al* J. Comput. Phys. **81** 169 (1989)
[4] Y. Suzuki *et al* Nucl. Fusion **46** L19 (2006)
[5] K. Y. Watanabe *et al* Fusion Sci. Technol. **46** 24 (2004)
[6] B.A. Carreras et al. Phys. Fluids **30**,1388(1987)
[7] B.A. Carreras et al. Phys. Fluids B1,1011(1989)

Proceedings of ITC/ISHW2007

Non-ideal MHD ballooning modes in three-dimensional configurations

T. Rafiq, C. C. Hegna and J. D. Callen

University of Wisconsin, Madison, Wisconsin 53706-1609

A linear stability theory of non-ideal MHD ballooning modes is investigated using a two fluid model for arbitrary three-dimensional electron-ion plasmas. Resistive-inertia ballooning mode (RIBM) eigenvalues and eigenfunctions are calculated for a variety of equilibria including axisymmetric shifted circular geometry ($s-\alpha$ model) and configurations of interest to the Helically Symmetric Stellarator (HSX). For parameters of interest to HSX, characteristic growth rates exceed the electron collision frequency. In this regime, electron inertia effects dominate plasma resistivity and produce an instability whose growth rate scales with the electromagnetic skin depth. Attempts to generalize previous analytic calculations [1] of RBM stability using a two scale analysis on $s-\alpha$ equilibria to more general 3-D equilibria will be addressed.

Keywords: Drift, Resistive-inertia, Ballooning, Stellarator, HSX

Unstable resistive ballooning modes (RBM) may play an important role in producing edge plasma fluctuations and anomalous transport in tokamaks and stellarators. In this work, the stability criterion for non-ideal MHD ballooning modes is derived for arbitrary three-dimensionally ideal MHD stable electron-ion plasmas. In the presence of non-ideal effects, ballooning instabilities can be produced at plasma β levels below the critical β for ideal ballooning stability. Electron inertia, diamagnetic effects, parallel ion dynamics, transverse particle diffusion and perpendicular viscous stress terms are included in the calculations. Temperature perturbations and equilibrium temperature gradients are ignored for simplicity. For parameters of interest to the Helically Symmetric Experiment (HSX), characteristic growth rates exceed the electron collision frequency. In this regime, electron inertia effects can dominate plasma resistivity and produce an instability whose growth rate scales with the electromagnetic skin depth.

In this work, a unified theory of RBM and inertial ballooning modes is developed where both the effects of ideal MHD free energy (as measured by the asymptotic matching parameter Δ') and geodesic curvature drives in the non-ideal layer are included in the dispersion relation. This theory may explain the $k_y \leq 1/cm$ fluctuations and the anomalous plasma transport observed in HSX near $r/a = 0.7$ where $T_e = 100eV$. Resistive-inertia ballooning mode (RIBM) eigenvalues and eigenfunctions are numerically calculated for a variety of equilibria including axisymmetric shifted circular geometry ($s-\alpha$ model) and configurations of interest to the HSX.

The organization of this paper is as follows. In section I, linearized ballooning equations are derived from Ohm's law, vorticity, continuity and parallel momentum equations. In section II, RIMHD modes are numerically calculated for $\hat{s}-\alpha$ equilibria and for quasihelically symmetric stellarator (QHS) equilibria in the electrostatic limit. The results for QHS are compared and contrasted with a magnetic configuration that spoils the helical symmetry by adding mirror terms to the magnetic spectrum. In section III, the shear Alfvén and drift acoustic equations in general 3-D geometry are presented in Hamada coordinates using a multiple length scale analysis. Section IV is devoted to study of these equations using a multiple length scale expansion technique and derivation of the dispersion relation. In section V, we summarize the results.

author's e-mail: rafiq@engr.wisc.edu

I. Drift ballooning equations

The reduced Braginskii fluid equations for a four-field model of drift resistive ballooning modes are used. The equations for generalized Ohm's law, vorticity, electron continuity and total parallel momentum can take the following linearized form in an $\omega \sim \omega_s \sim \omega_{*j} \sim \omega_\eta$ ordering

$$\left(\omega - \omega_{*en} + \omega H + ic^2 k_\perp^2 \eta_\parallel / 4\pi\right)\widehat{\Psi} = c_s k_\parallel \left(\widehat{\Phi} - \widehat{n}\right), \tag{1}$$

$$\omega k_\perp^2 \rho_i^2 \left(\widehat{n} + \tau\widehat{\Phi}\right) = \omega_\kappa \widehat{n} - i\mu_\perp k_\perp^4 \rho_i^2 \left(\widehat{n} + \tau\widehat{\Phi}\right) + \frac{\tau v_A^2}{c_s} k_\parallel \left(k_\perp^2 \rho_i^2 \widehat{\Psi}\right), \tag{2}$$

$$\omega\widehat{n} - \omega_{*en}\widehat{\Phi} = \omega_{\kappa e}\left(\widehat{\Phi} - \widehat{n}\right) + c_s k_\parallel \widehat{v}_\parallel + \frac{i\eta_\perp c^2 k_\perp^2}{4\pi}\frac{c_s^2}{v_A^2}\widehat{n} - \frac{\tau v_A^2}{c_s} k_\parallel \left(k_\perp^2 \rho_i^2 \widehat{\Psi}\right), \tag{3}$$

$$(\omega + \omega_{\kappa i})\widehat{v}_\parallel + \omega_{*en}\widehat{\Psi} = c_s k_\parallel \widehat{n} - 4i\mu_\perp k_\perp^2 \widehat{v}_\parallel. \tag{4}$$

where $H = k_\perp^2 \delta_e^2$, $\delta_e^2 = c^2/\omega_{pe}^2$, is the electromagnetic skin depth, $\omega_{pe}^2 = 4\pi n e^2/m_e$, is the electron plasma frequency, $\mu_\perp = 0.3\nu_i \rho_i^2$, is the classical perpendicular viscosity, $\rho_i = v_{ti}/\omega_{ci}$, is the ion Larmor radius, $v_{ti} = \sqrt{T_i/m_i}$, is the ion thermal velocity, $\omega_{ci} = eB/m_i c$, is the ion cyclotron frequency, $\tau = T_e/T_i$, is the electron to ion temperature ratio, $v_A^2 = B^2/4\pi n m_i$, is the Alfvén speed, $\eta_\parallel$ and $\eta_\perp$ are the longitudinal and transverse Spitzer resistivities. $\widehat{\Psi} = ec_s\widetilde{A}_\parallel/cT_e$, $\widehat{\Phi} = e\widetilde{\phi}/T_e$, $\widehat{v}_\parallel = \widetilde{v}_\parallel/c_s$,

$\widehat{n} = \widetilde{n}/n$, are the dimensionless perturbed parallel component of vector potential, electrostatic potential, parallel ion flow and density, respectively. Also $\omega_\kappa = \omega_{\kappa i} + \omega_{\kappa e}$, where $\omega_{\kappa j} = \left(2cT_j/eB\right)\mathbf{k}\cdot\widehat{e}_\parallel \times \kappa$, $c_s = (T_e + T_i/m_i)^{1/2}$, $\omega_{*en} = -\left(cT_e/eB\right)\mathbf{k}\cdot\widehat{e}_\parallel \times \nabla \ln n$, are the curvature drift frequency, sound speed and the diamagnetic drift frequency.

The resistive-inertia MHD incompressible ballooning equation for high frequency ($|\omega| \gg \omega_{*e}, \omega_{ke}$) long wavelength ($k_\theta^2\rho_i^2 \ll 1$)limit can be written as follows:

$$\omega_A^2\frac{d}{d\theta}\left(\frac{\widehat{k_\perp^2}}{\omega + (\omega c^2k_\theta^2/\omega_{pe}^2 + i\omega_\eta)\widehat{k_\perp^2}}\frac{d\widehat{\Phi}}{d\theta}\right)+(\omega\widehat{k_\perp^2}+\frac{\tau'\omega_{\kappa e}\omega_{*e}}{\omega k_\theta^2\rho_s^2})\widehat{\Phi} = 0,\quad(5)$$

where $\omega_A = v_A/qR$, is the Alfvén frequency, q is the safety factor and R is the major radius, $\epsilon_n = L_n/R$, with $L_n = (d_r \ln n)^{-1}$, is the density gradient scale length, $k_\parallel = -i(1/qR)d/d\theta$, $k_\perp = \left(n_\phi q/r\right)\widehat{k}_\perp(\theta)$. $\omega_\eta = \left(c^2\eta_\parallel/4\pi\right)\left(n_\phi q/r\right)^2$, is the resistive frequency and $\tau' = 1 + 1/\tau$. Note that in Eq. (5) the electron inertia term, $\omega c^2k_\theta^2/\omega_{pe}^2$ is present. The incompressible ideal MHD (IMHD) ballooning equation can be retained by neglecting electron inertia and resistivity.

II. Numerical results

Equation (5) is solved numerically using a standard root finding algorithm for axisymmetric shifted-circle equilibrium (in Figures 1 and 2) and for three dimensional equilibria of relevance to HSX (Figure 3). For all cases, the parameters used are relevant to HSX edge plasmas, as indicated in the caption of Fig.1.

Figure 1 shows the normalized growth rate (γ/ω_A) as a function of the normalized pressure gradient (the ballooning parameter α). In this scan, tokamak-like global magnetic shear $\hat{s} = 0.1$ is chosen to show the ideal MHD unstable region. HSX has reverse shear and ideal MHD instabilities for which the mode amplitude does not vary along the field line (i.e., $k_\parallel$=0) are stable for the parameters studied. The electron inertia and resistivity induce an instability in the ideal MHD stable regimes. The modes are purely growing $\omega_r = 0$. The electron inertia modes ($\eta = 0$) are found to be more important than the resistive modes due to their existence in the first ideal stability region for HSX relevant parameters. Note that these modes persist in the ideal MHD second stable regime. Both the electron inertia and resistive instabilities are characterized by broad eigenfunctions in the ballooning space as shown in Fig. 2. Moreover, the qualitative nature of the eigenfunctions is insensitive to whether electron inertia is present.

Equation (5) is solved numerically in the electrostatic limit using three dimensional equilibria for a quasi-helically symmetric (QHS) stellarator and a configuration whose symmetry is spoiled (Mirror) by the presence of magnetic mirror contributions to the magnetic spectrum.

Figure 3 is a plot of the growth rate γ, normalized to the R/c_s as a function of $(k_\perp\rho)^2$. We perform this calculation for the field line that intersects the location $\theta_0 = 0$,

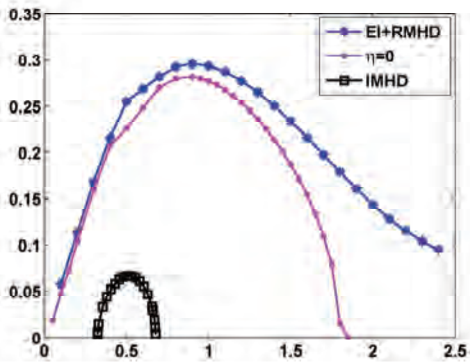

Fig. 1 The normalized growth rate (γ/ω_A) as a function of α for $\hat{s} = 0.1$, $k_\theta\rho = 0.3$, $\hat{\nu} = 0.023$, and $\beta = 0.0002$.

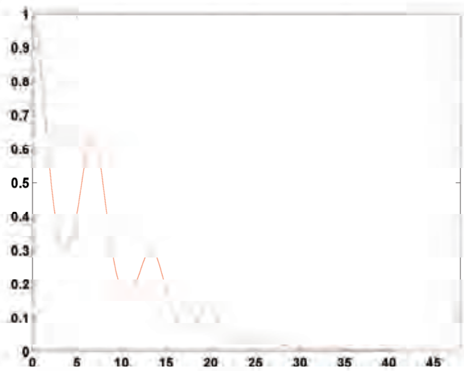

Fig. 2 Eigenfunction of RIBM as a function of θ for $\alpha = 0.3$. The other parameters are the same as used in figure 1.

$\zeta_0 = 0$ on the normalized magnetic surface $s = 0.8980$. This point is thought to be the most unstable choice since the local shear is small, the local value of the geodesic curvature is zero and the destabilizing influence of the normal curvature is strongest. The highly resistive ($\delta = 0$, $\nu \neq 0$) growth rate in QHS is compared with the growth rate in the Mirror case. In both configurations the magnitude of the linear growth rates are found to be comparable, crudely indicating the same level of anomalous flux. The common stability properties are due to a similar structure of the curvature and the local magnetic shear.

III. Shear-Alfvén and Drift acoustic equation in 3-D geometry

The general solution of Eqs. (1)-(4) can be written as a coupled system of a two second order differential equations, the shear-Alfvén equation and the drift-acoustic equation:

$$\frac{d}{dy}\left[\frac{(\omega-\omega_{ne})K^2 dU/dy}{B^2(\omega-\omega_{ne}+(\omega\delta_\theta^2+i\eta^*)a^2K^2)}\right]+\frac{8\pi p'\left(\kappa_v+q'y\kappa_\varphi\right)}{\chi^4}$$
$$\times(U+V) = -\frac{K^2}{\chi^2 v_A^2}\left(\omega+i\mu_\perp a^2K^2\right)\left[(\omega-\omega_{ni})U-(1+\tau)\omega_{ni}V\right].\quad(6)$$

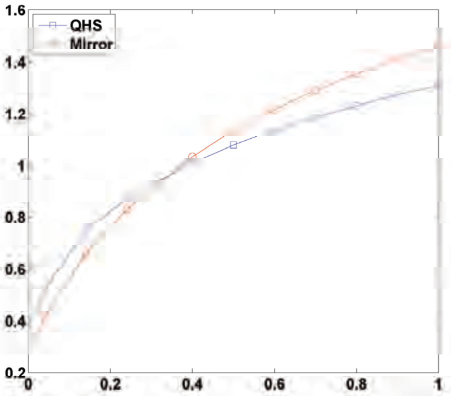

Fig. 3 Normalized growth rate ($R\gamma/C_s$) of the resistive-inertia ballooning modes in the electrostatic limit as a function of $(k_\perp\rho)^2$ for QHS and Mirror cases for $s = 0.8980$, $\tau = 1$, $Rv/2c_s = 0.42$, $\epsilon_n = 0.07$ and $\theta_0 = 0$, $\zeta_0 = 0$ field line.

and

$$\frac{d}{dy}\left(\frac{\chi'^2}{B^2}\frac{dV}{dy}\right)+\frac{(\omega-\omega_{ne})\left(\omega+4i\mu_\perp a^2K^2\right)}{c_s^2}V=$$
$$\Bigg[-\frac{\left(\omega+4i\mu_\perp a^2K^2\right)}{c_s^2}\left(2L_{nv}\left(\kappa_v+q'y\kappa_\varphi\right)+\frac{\tau\omega a^2K^2\rho_i^2}{\omega_{ne}}\right)$$
$$+\frac{\left(\omega\delta_e^2+i\eta^*\right)\left(\omega+i\mu_\perp a^2K^2\right)}{\omega-\omega_{ne}}\frac{a^2K^2}{v_A^2}\Bigg]\left[(\omega-\omega_{ni})U-(1+\tau)\omega_{ni}V\right]$$
$$+\left[\left(\frac{\omega\delta_e^2+i\eta^*}{\omega-\omega_{ne}}\right)\frac{8\pi a^2p'\left(\kappa_v+q'y\kappa_\varphi\right)}{\chi'^2}-\frac{\eta_\perp}{\eta_\parallel}\frac{i\eta^*\left(\omega+4i\mu_\perp a^2K^2\right)a^2K^2}{v_A^2}\right]$$
$$\times(U+V)+\frac{\chi'^2}{B^2}\frac{d}{dy}\ln\left(\omega+4i\mu_\perp a^2k_\perp^2\right)$$
$$\times\left[\frac{\left(\omega\delta_e^2+i\eta^*\right)a^2K^2}{\omega-\omega_{*e}+(\omega\delta_e^2+i\eta^*)a^2K^2}\frac{dU}{dy}+\frac{dV}{dy}\right], \tag{7}$$

where $K^2=|\nabla\varphi|^2-2q'y\nabla\varphi\cdot\nabla v+q'^2y^2|\nabla v|^2$, $a=\partial S/\partial\varphi$, is the "mode number" that describes the component of the **k** vector that is perpendicular to the magnetic field and lies within the magnetic surface, $\kappa_v = \kappa\cdot\nabla\theta\times\nabla\varphi$, $\kappa_\varphi = \kappa\cdot\nabla v\times\nabla\theta = (-\chi'/2p')\mathbf{B}\cdot\nabla\sigma$, is the geodesic curvature and $\sigma = \mathbf{j}\cdot\mathbf{B}/B^2$. The coordinate y is defined as labeling points along the magnetic field and as such $\mathbf{B}\cdot\nabla = \chi'(d/dy)$. Dot over quantities indicate derivatives with respect to the volume.

IV. Analysis of Resistive Ballooning Mode equations

We can make analytic progress to understand the structure of non-ideal MHD ballooning modes by using a multiple scale analysis. Our calculation generalizes the work of Hastie et al [1] to three-dimensional equilibria. A small parameter ϵ can be defined that accounts for the disparate timescales associated with current diffusion and the Alfvén time.

$$\epsilon=\left(\frac{\omega_\eta}{\omega_A}\right)^{1/3}\ll 1, \tag{8}$$

In the following, somewhat general ordering is used

$$\omega\sim\omega_s\sim\omega_{nj}\sim\epsilon\omega_A \tag{9}$$

and viscosity is comparable to resistivity, $\omega_\mu = \epsilon^3\omega_A$. Equations (6,7) can be solved using a two variable expansion procedure. We take y and $z = \epsilon y$ as two different length scales and make the ansatz

$$U(y)=U_0(y,z)+\epsilon U_1(y,z)+\epsilon^2U_2(y,z)+.... \tag{10}$$

$$U_i(y+N,z)=U_i(y,z),\quad i=0,1,2,... \tag{11}$$

The function U is periodic in y with period N whereas the variable z accounts for the long envelope of the eigenfunction along the magnetic field line. For $|y|\sim 1$ an ideal MHD region can be identified where resistivity, electron inertia and viscosity can be neglected. The Shear Alfvén equations in the zeroth order in ϵ can be written as

$$\frac{d}{dy}\left[\frac{K^2}{B^2}\frac{dU_0}{dy}\right]+\frac{4\pi}{\chi'^4}\left(2p'\kappa_v-q'\chi'^2y\frac{d\sigma}{dy}\right)U_0=0. \tag{12}$$

At large $|y|$, the solution of the Shear Alfvén equation yields the following asymptotic solution

$$U=a_1|y|^s+a_2|y|^{-1-s},\quad |y|\to\infty, \tag{13}$$

where

$$s=-\frac{1}{2}+\left[\frac{1}{4}+H^2-H-D_R\right]^{1/2}. \tag{14}$$

The quantities H and D_R are dependent upon the equilibrium and are defined as [3]

$$H=\frac{A^2\langle B^2/|\widehat{\nabla v}|^2\rangle}{q'\chi'^2}\left[\frac{\langle\sigma B^2\rangle}{\langle B^2\rangle}-\frac{\langle\sigma B^2/|\widehat{\nabla v}|^2\rangle}{\langle B^2/|\widehat{\nabla v}|^2\rangle}\right], \tag{15}$$

$$D_R=F+E+H^2. \tag{16}$$

$$F=\frac{A^2\langle B^2/|\widehat{\nabla v}|^2\rangle}{q'^2\chi'^4}\left[\langle\frac{B^2\sigma^2}{|\widehat{\nabla v}|^2}\rangle-\frac{\langle\sigma B^2/|\widehat{\nabla v}|^2\rangle^2}{\langle B^2/|\widehat{\nabla v}|^2\rangle}+p'^2\langle\frac{1}{B^2}\rangle\right], \tag{17}$$

$$E=\frac{A\langle B^2/|\widehat{\nabla v}|^2\rangle}{q'^2\chi'^4}\left[I'\Psi''-J\chi''-q'\chi'^2\frac{\langle\sigma B^2\rangle}{\langle B^2\rangle}\right] \tag{18}$$

For this analysis, thus, ideal stability is assumed; the Mercier stability criterion is satisfied

$$-D_I=\frac{1}{4}-(E+F+H)=\frac{1}{4}+H^2-H-D_R\geqq 0. \tag{19}$$

In the outer region solution along field lines ($|y|\gtrsim\epsilon^{-1}$), resistivity, inertia and viscosity must be taken into account.

P1-054

We solve Eq. (6) order by order. At second order a solubility condition for U_2 is derived that yields a differential equation for U_0 that depends upon integrals of U_1 and V_1

$$\left\langle \frac{\partial}{\partial z}\frac{q'^2 z^2\left|\widehat{\nabla} v\right|^2}{B^2 A_3}\frac{\partial U_1}{\partial y}\right\rangle = -\left\langle \frac{\partial}{\partial z}\frac{q'^2 z^2\left|\widehat{\nabla} v\right|^2}{B^2 A_3}\frac{\partial U_0}{\partial z}\right\rangle$$

$$-q'^2 z^2(\widehat{\omega}-\widehat{\omega}_{ni})U_0\left\langle\frac{\left|\widehat{\nabla} v\right|^2}{B^2}\left(\widehat{\omega}+i\widehat{\mu}q'^2 z^2\left|\widehat{\nabla} v\right|^2\right)\right\rangle$$

$$-\frac{A_1 q' z U_0}{\chi^2}\left[\langle 2p'\kappa_v\rangle - q' z\chi^2\left(\left\langle\frac{\partial\sigma}{\partial z}\right\rangle - \left\langle\left(\frac{\partial U_1}{\partial y}+\frac{\partial V_1}{\partial y}\right)\sigma\right\rangle\right)\right], \quad (20)$$

where $A_3 = 1 + q'^2 z^2\widehat{\omega}_{IR}\left|\widehat{\nabla} v\right|^2$. One special limit that can be pursued analytically is the electrostatic limit. In this case, $q'^2 z^2\widehat{\omega}_{IR}\left|\widehat{\nabla} v\right|^2 \gg 1$, and $V_1 = 0$.

$$\frac{d^2U_0}{dz^2} + W_1\left[\langle 2p'\kappa_v\rangle + q'\chi^2\left(\langle\sigma\rangle - \frac{\langle\sigma B^2\rangle}{\langle B^2\rangle}\right)\right]U_0$$

$$= -W_2\left[\langle\sigma^2 B^2\rangle - \frac{\langle\sigma B^2\rangle^2}{\langle B^2\rangle} - W_3\left\langle\frac{\left|\widehat{\nabla} v\right|^2}{B^2}\right\rangle\right]z^2U_0, \quad (21)$$

where

$$W_1 = \left(\frac{A}{\chi^4}\right)\widehat{\omega}_{IR}\langle B^2\rangle,\quad W_2 = \frac{q'^2\chi^4}{\langle B^2\rangle}W_1^2,\quad W_3 = \widehat{\omega}(\widehat{\omega}-\widehat{\omega}_{ni})\frac{q'^2\langle B^2\rangle}{W_2},$$

and

$$A = 4\pi(\overline{a}/q)^2\quad \widehat{\omega}_{IR} = \frac{\widehat{\omega}\delta^2/\epsilon^2 + i}{\widehat{\omega}-\widehat{\omega}_{ne}},\quad \widehat{\omega} = \frac{\omega}{\epsilon\omega_A},\quad \widehat{\nabla} = \frac{\overline{a}}{q}\nabla.$$

The condition for existence of a solution is $2p'\langle\kappa_v\rangle + q'^2\chi^2\left(\langle\sigma\rangle - \langle\sigma B^2\rangle/\langle B^2\rangle\right) > 0$. The solutions (21) give the following eigenvalue expression

$$\omega(\omega-\omega_{ne})(\omega-\omega_{ni}) = -\frac{\omega_A^2\left(\omega\delta^2+i\omega_\eta\right)}{\left\langle\left|\widehat{\nabla} v\right|^2/B^2\right\rangle}\left(\frac{4\pi(\overline{a}/q)^2}{\chi^2}\right)^2\left[\langle\sigma^2B^2\rangle\right.$$

$$\left.-\frac{\langle\sigma B^2\rangle^2}{\langle B^2\rangle} + \frac{\langle B^2\rangle}{\left(q'^2\chi^4(2n+1)^2\right)}\times\left\{\langle 2p'\kappa_v\rangle + q'\chi^2\left(\langle\sigma\rangle - \frac{\langle\sigma B^2\rangle}{\langle B^2\rangle}\right)\right\}^2\right], \quad (22)$$

Solutions to the the above equation lead to an infinite sequence of modes with growth rate scaling as for the resistive ballooning mode, $\gamma \sim \omega_\eta^{1/3}$ or for the electron inertia ballooning mode $\gamma \sim \delta$.

In the limit $\omega \gg \omega_s$, $V_0 = V_1 = 0$, sound wave propagation is neglected and the visco-resistive-inertia ballooning mode equation can be found

$$\frac{\partial}{\partial X}\frac{X^2}{1+X^2}\frac{\partial U_0}{\partial X} + \frac{H(1-H)}{(1+X^2)^2}U_0 - \frac{H(1+H)X^2}{(1+X^2)^2}U_0$$

$$+D_R U_0 - Q_1 U_0 X^2 - Q_2 U_0 X^4 = 0, \quad (23)$$

In the limit of zero viscosity ($\omega_\mu = 0$), $Q_2 = 0$ in Eq. (23), and the drift resistive ballooning equation is recovered. This equation has the same form as the resistive MHD case covered in Ref. [2] except for the diamagnetic corrections evident in the coefficient Q_1 (defined in Eq.(25) below). A valid solution can be constructed in the ideal and resistive region by matching the ideal solution for $|y| \longrightarrow \infty$ to the resistive solution for $|X| \longrightarrow 0$. We obtain the general dispersion relation, $\Delta = \Delta'$, where Δ' can be calculated by using the conventional definition as the ratio of coefficients of the large and small solutions of the asymptotic form of the ideal solution, which in this case defined as $\Delta' \equiv a_2/a_1$, and

$$\Delta \equiv \frac{4y_0^{1+2s}Q^{(5-2s)/4}}{Q_1-(1+s-H)^2}\frac{\Gamma[1/2+s]}{\Gamma[-1/2-s]} \times\frac{\Gamma\left[(1/4)\left(Q_1^{1/2}+3-2s-D_{R/}Q_1^{1/2}\right)\right]}{\Gamma\left[(1/4)\left(Q_1^{1/2}+1+2s-D_{R/}Q_1^{1/2}\right)\right]}, \quad (24)$$

where

$$Q_1 = \frac{\omega(\omega-\omega_{ni})(\omega-\omega_{ne})}{Q_0},\quad Q_0 = \frac{q'^2\langle B^2\rangle\omega_A^2\left(\omega\delta^2+i\omega_\eta\right)}{AN_1M}, \quad (25)$$

$$X^2 = \frac{Z^2}{y_0^2 Q_1},\quad y_0^2 = \frac{\omega_A^2}{AM\omega(\omega-\omega_{ni})},$$

$$M = \left\langle\frac{B^2}{\left|\widehat{\nabla} v\right|^2}\right\rangle\left[\left\langle\left|\widehat{\nabla} v\right|^2/B^2\right\rangle + \frac{1}{p'^2}\left\{\langle\sigma^2B^2\rangle - \frac{\langle\sigma B^2\rangle^2}{\langle B^2\rangle}\right\}\right]$$

and Γ is the gamma function. For the special case when $D_R > 0$, we also reproduce the stability criterion derived in Ref. [2] with electron inertia and diamagnetic corrections:

$$\omega(\omega-\omega_{ne})(\omega-\omega_{ni}) = -\frac{\omega_A^2\left(\omega\delta^2+i\omega_\eta\right)}{AN_1M}q'^2\langle B^2\rangle$$

$$\times\left[\left\{\left(\frac{1}{2}+s+2n\right)^2 + D_R\right\}^{1/2} - \left(\frac{1}{2}+s+2n\right)\right]^2. \quad (26)$$

V. Summary

A unified theory of resistive and electron inertia ballooning modes (RIBM) has been developed. The RIBM is characterized by broad eigenfunctions in ballooning space. In the absence of drift effects, the modes are purely growing and persist in regimes where ideal MHD ballooning modes are stable. For parameters of interest to HSX, electron inertia effects are more important than plasma resistivity; electron inertia modes are the most unstable and have growth rates that scale with the electron skin depth, $\gamma \sim \delta$. The magnitude of the linear growth rates are not sensitive to the magnetic configuration in HSX plasmas. This would indicate a comparable level of anomalous transport in QHS and mirror configurations; this is consistent with observations in the HSX edge region.

Acknowledgments

This research was supported by the U.S. DoE under Grant Nos. DE-FG02-99E54546 and DE-FG02-86ER53218.

[1] R. H. Hastie, J. J. Ramos and F. Porcelli, Phys. Plasmas **10**, 4405 (2003).

[2] D. Correa-Restrepo, Z. Naturforsch. A **37**, 848 (1982).

[3] A. H. Glasser, J. M. Greene and J. L. Johnson, Phys. of Fluids **18**, 875 (1975).

Proceedings of ITC/ISHW2007

Analysis of the Alpha Particle Orbits in the High Beta Plasma of the Large Helical Device

Ryousuke SEKI[1)], Yutaka MATSUMOTO[1)], Yasuhiro SUZUKI[2)], Kiyomasa WATANABE[2)], and Masafumi ITAGAKI[1)]

[1)]*Graduate School of Engineering, Hokkaido University, Sapporo 060-8628, Japan*
[2)]*National Institute for Fusion Science, Toki 509-5292, Japan*

We investigate the orbits of the 3.5 MeV alpha particles in the high beta plasma of the Large Helical Device (LHD), in which $B = 6$ T is assumed. For this purpose, we trace the 100 keV proton in the case of $B = 1$ T, the Larmor radius of which is almost the same as the Larmor radius of the alpha particle, by numerically solving the guiding-center equations. As a result, the particle orbit characteristics in the high beta plasma of the LHD are shown in detail. We point out the importance to appropriately trace the re-entering particles in the analyses of the orbits of the high-energy particles, such as the alpha particles, in the high beta plasma. It is found that the lifetime of the alpha particles depends on the lifetime of the chaotic orbit particles almost all of which is lost. The chaotic orbit particles are lost before they heat fuels because the lifetime of the chaotic orbit particles is much shorter than the alpha-electron relaxation time.

Keywords: alpha particle, particle orbit, high beta, re-entering particle, LHD,

1 Introduction

The volume-averaged beta-value $\langle\beta\rangle$ have reached up to 5 % in the recent experiments of the Large Helical Device (LHD)[1]. In a Deuterium (D)-Tritium (T) fusion reactor, alpha particles move in the plasma the beta-value of which is more than 5 %. It is one of the important issues for the realization of a fusion reactor to investigate the confinement of the alpha particles heating the D-T fuels. The magnetic field strength in a future fusion reactor is assumed $B \simeq 6$ T. The Larmor radius of the 3.5 MeV alpha particle in the case of $B = 6$ T is almost the same as that of the 100 keV proton in the case of $B = 1$ T. Therefore, we trace the 100 keV proton in the high beta plasma of the LHD with $B_{\rm ax} = 1$ T to investigate the alpha particle orbits.

In the high beta plasmas of the LHD, the magnetic configurations changes from the vacuum magnetic field to the followings. The flux surfaces shift to the direction of the major radius due to the Shafranov shift caused by the finite beta effect. Additionally, the volume inside the last closed flux surface (LCFS) in the high beta plasma becomes small since the flux surfaces in the periphery of the high beta plasma are destroyed[2]. In these cases, the number of the re-entering particles[3, 4, 5], which repeatedly pass into and out of the LCFS, could be larger than that in the vacuum magnetic field. Thus, the re-entering particles might play important roles for the plasma heating. But, the re-entering particles have been regarded as the loss particles in the conventional studies on the orbits of the high-energy particles in the high beta plasma of the LHD[6]. We appropriately trace the re-entering particles in the high beta plasma of the LHD.

The numerical model and the initial conditions are given in Section 2. The results of the calculations are summarized in Section 3. Section 4 is devoted to a summary.

2 Numerical Model

In order to trace the particles, we use the equilibrium magnetic field ($B_{\rm ax} = 1$ T, $\langle\beta\rangle = 2.7$ % and $R_{\rm ax} \simeq 3.9$ m) calculated by using the three-dimensional magnetohydrodynamic (MHD) equilibrium code, HINT[7, 8], in which the existence of the nested flux surfaces are not assumed.

We trace the particles by numerically solving the guiding-center equations in the collisionless case. In order to trace the re-entering particles appropriately, the particle loss boundary must set on the vacuum vessel wall, i.e., the particles reaching the vacuum vessel wall are regarded as the loss particles. Therefore, the rotating helical coordinate system[9] is adopted. We use the 6th-order Runge-Kutta formulas[10] and the three-dimensional higher order spline function[11] to accurately trace the complicated orbits of the particles in the plasma periphery.

The initial conditions are determined as follows. As mentioned in the preceding section, the traced particle is a proton and its initial energy is assumed to be 100 keV. The starting points of protons are set on the horizontally elongated poloidal plane as

$$R = 2.65 + 0.05n_{\rm R}\ (n_{\rm R} = 0, 1, \cdots, 45)\ \text{m}$$
$$Z = 0\ \text{m}$$

author's e-mail: seki@fusion.qe.eng.hokudai.ac.jp

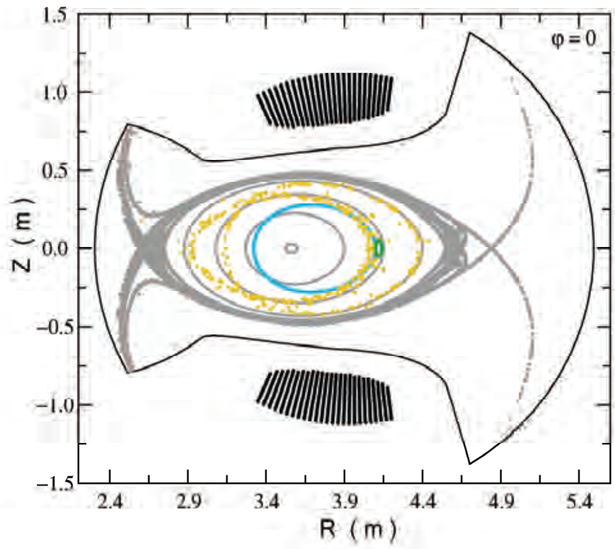

Fig. 1 Poincarè plots of the particles on the horizontally elongated poloidal plane. Typical orbits of the passing (blue), the chaotic orbit (green), and the banana orbit particles (yellow) are shown. These particles are traced from R = 4.1 m, Z = 0 m in the vacuum magnetic field. The magnetic field lines (gray) are also shown.

$$\phi = 0, \qquad (1)$$

where (R, Z, ϕ) are the cylindrical coordinates; R is the major radius, ϕ the toroidal angle. The initial pitch angles (χ_0) are varied from 0.05π to 0.95π with a step size of 0.05π. The protons with such initial conditions are traced for a period of 30 ms.

3 Results

Based on the results of the particle orbits tracing, we classify the particles into the four groups: passing particles, banana orbit particles, chaotic orbit particles[12], and prompt loss particles. Figure 1 is the Poincarè plot of the particles on the horizontally elongated poloidal plane. This shows the typical orbits of these four groups in the vacuum magnetic field, in which B_{ax} = 1 T. Both the passing (blue) and the banana orbit particles (green) make the closed drift surfaces. The chaotic orbit particles (yellow) repeatedly transit between the localized orbit and the blocked orbit[13], and make no closed drift surface. Since the prompt loss particles are lost without any poloidal rotations, we cannot make the Poincarè plots of the prompt loss particles. Based on this classification, the orbits of the alpha particles in the high beta plasma of the LHD are studied.

3.1 Orbit characteristics

Figure 2 shows the particle classifications in the case of B_{ax} = 1 T, $\langle\beta\rangle$ = 2.7 % on the space of the starting points versus the initial pitch angles. Horizontal axis is the major

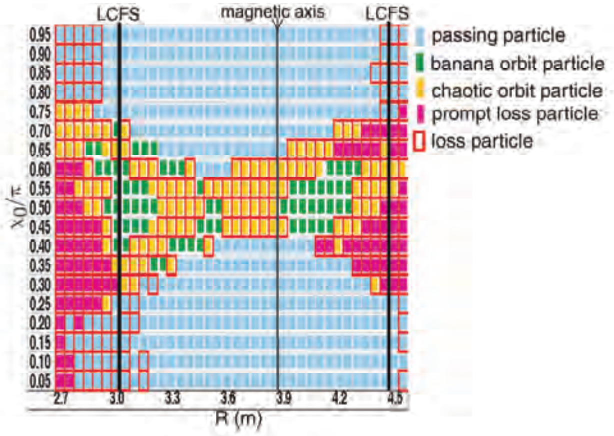

Fig. 2 Particle classifications on the space of the starting points versus the initial pitch angles. Horizontal axis is R of the starting points. Vertical axis denotes the initial pitch angles (χ_0) divided by π. The red squares show the loss particles.

radius of the starting points set on the line of Z = 0 m on the horizontally elongated poloidal plane. Vertical axis denotes the initial pitch angles divided by π. The positions of the magnetic axis and the LCFS on the line of Z = 0 m on the horizontally elongated poloidal plane are also shown. The red squares denote the loss particles, i.e., the particles reaching the vacuum vessel wall within 30 ms.

Almost all the particles with $\chi_0 \simeq 0.5\pi$ are the banana and the chaotic orbit particles. Especially in the particles traced from near magnetic axis, most of the particles with $\chi_0 \simeq 0.5\pi$ are the chaotic orbit particle. Almost all the chaotic orbit particles are lost within 30 ms. The range of the initial pitch angles, with which the particles are the passing particles, are maximum near R = 3.6 m. As the starting points are close to the LCFS, the such range of the initial pitch angles becomes narrow. There are no prompt loss particles traced from 3.05 m $\leq R \leq$ 4.0 m. Almost all the starting points of the prompt loss particles exist outside the LCFS. Some particles with $\chi_0 \simeq 0.35\pi$ or $\chi_0 \simeq 0.7\pi$ are also the prompt loss particles.

3.2 Re-entering particle

In order to investigate the effects of the re-entering partices on the confinement of the alpha particle, we evaluate the loss particle ratio. Figure 3 shows the loss particle ratio averaged over pitch angles[12] at each starting points after tracing particles for 30 ms. The black line is the loss particle ratio in the case of re-entering particles appropriately traced. The red line represents the loss particle ratio in the case of the re-entering particles regarded as the loss particles. This case is the same as the conventional study, in which the particle loss boundary is set on the LCFS. The positions of the magnetic axis and the LCFS on the line of Z = 0 m on the horizontally elongated poloidal plane are

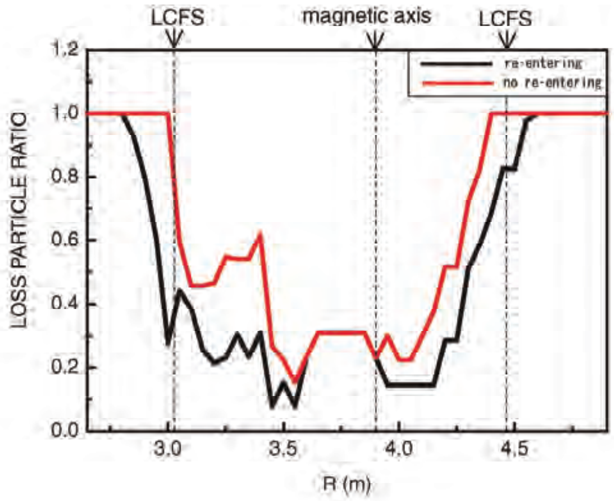

Fig. 3 Loss particle ratio after 30 ms particle tracing. The black line is the loss particle ratio in the case of re-entering particles appropriately traced and the red line the loss particle ratio in the case of the re-entering particles regarded as the loss particles. Horizontal axis is R of the starting points. Vertical axis denotes the loss particle ratio averaged over the pitch angles at each starting points. The positions of the magnetic axis and the LCFS are also shown.

also shown.

The significant difference between the black and the red lines can be seen from Fig. 3. This result implies that many re-entering particles exist in the high beta plasma. Especially, the difference between the black and the red lines is remarkable in the particles traced from $R \simeq 3.3$ m. This means that there exist many re-entering particles in the particles traced from $R \simeq 3.3$ m.

The loss particle ratio are overestimated in the case of the re-entering particles regarded as the loss particles. Thus, it is important to appropriately trace the re-entering particles in the analyses of the orbits of the high-energy particles, such as the alpha particles, in the high beta plasma.

3.3 Confinement of alpha particle

We investigate the confinement of the alpha particles generated by the D-T fusion reaction. As mentioned above, the Larmor radius of the 3.5 MeV alpha particle in the case of $B = 6$ T is almost the same as that of the 100 keV proton in the case of $B = 1$ T. The results of the 100 keV proton in the case of $B = 1$ T could be regarded as that of the 3.5 MeV alpha particle in the case of $B = 6$ T.

The birth points of the alpha particles produced by the D-T fusion reaction depend on the plasma pressure profile. The number of alpha particles is large in the region of the high plasma pressure, namely, the plasma core. Thus, we focus on the particles traced from the plasma core (3.3 m $\leq R \leq$ 4.2 m). It is seen from Fig. 2 that the prompt loss particles hardly exist in the particles traced from 3.3 m $\leq R \leq$ 4.2 m. Both the passing and the banana orbit particles are confined in the vacuum vessel wall for 30 ms. On the other hand, almost all of the chaotic orbit particles is lost. Therefore, the lifetime of the alpha particles is determined by the lifetime of the chaotic orbit particles.

The lifetime of the chaotic orbit particles is estimated as $\sim 10^{-3}$ s in the present study. In order to compare this lifetime with the collision times, we assume the D-T plasma with the ion temperature $T_i = 10$ keV, the ion density $n_i = 10^{21}$ m^{-3}, the electron temperature $T_e = 10$ keV, and the electron density $n_e = 10^{21}$ m^{-3}. In such plasma, the alpha-ion deflection time $\tau^{d}_{\alpha-i} \simeq 0.9$ s and the alpha-electron relaxation time $\tau^{r}_{\alpha-e} \simeq 1.6 \times 10^{-2}$ s. The lifetime of the chaotic orbit particles is much shorter than these collision times. Therefore, the chaotic orbit particles are lost before they heat fuels. In addition, the passing and the banana orbit particles confined in our calculations become the chaotic orbit particles by the pitch angle scattering during many toroidal and/or poloidal rotations. Thus, the passing and the banana orbit particles could not sufficiently heat the fuels by the Coulomb collision.

We have analyzed the orbit of the alpha particle in the current LHD (the major radius $R_0 = 3.9$ m, the averaged plasma minor radius $a_p \simeq 0.64$ m[14]). But, the size of the helical reactor, which satisfies the ignition condition, is assumed as $R_0 = 10$ m and $a_p = 2$ m[15]. In such a helical reactor, the region, in which the chaotic orbit particles can move, becomes large. Therefore, the chaotic orbit particle lost in the present study could be confined for a long time enough to heat the fuels.

Instead of the plasma heating by the Coulomb collision, the plasma heating called the alpha-channeling is proposed[16]. In the alpha-channeling, the fuels are heated by the wave in the plasma, which the alpha particle amplifies during the time scale shorter than collision times. If the alpha-channeling is used, the alpha particles could heat the fuels independent of the lifetimes of the alpha particles.

4 Summary

We have investigated the orbits of the 3.5 MeV alpha particles in the high beta plasma of the LHD, in which $B = 6$ T. For this purpose, we have traced the 100 keV proton in the case of $B = 1$ T, the Larmor radius of which is almost the same as the Larmor radius of the alpha particle, by numerically solving the guiding-center equations. The following information has been obtained.

- The passing particles play a large part in the particles traced from the plasma core. On the other hand, most of the particles with $\chi_0 \simeq 0.5\pi$ are the chaotic orbit particles. They are lost within 30 ms.
- It is important to appropriately trace the re-entering particles in the analyses of the orbits of the high-

energy particles, such as the alpha particles, in the high beta plasma.

- The lifetime of the alpha particles depends on the lifetime of the chaotic orbit particles almost all of which is lost.
- The chaotic orbit alpha particles are lost before they heat fuels because the lifetime of the chaotic orbit alpha particles is much shorter than the alpha-electron relaxation time.
- In the future helical reactor, the chaotic orbit alpha particle lost in the present study could be confined for a long time enough to heat the fuels because the size of the future helical reactor will be larger than that of the LHD.
- Through the alpha-channeling, the alpha particles could heat the fuels independent of the lifetimes of the alpha particles.

In the near future, the alpha particles in the higher beta plasma ($\langle\beta\rangle > 5$ %) will be studied. We will investigate the alpha particle orbit by numerically solving the equation of motion because the Larmor radius of the alpha particle is large.

This work is suported by the collaborative research program of NIFS (NIFS06KLHH302).

[1] http://www.nifs.ac.jp.
[2] T. Hayashi *et al.*, Contrib. Plasma Phys. **42**, 2-4, 309 (2002).
[3] R. H. Fowler, R. N. Morris, J. A. Rome and K. Hanatani: Nucl. Fusion. **30** 997 (1990).
[4] K. Hanatani and F. -P. Penningsfeld, Nucl. Fusion. **32** 1769 (1990).
[5] T. Watanabe, A. Ishida and T. hatori, Kakuyugo Kenkyu **68** 298 (1992).
[6] S. Murakami, J. Plasma Fusion Res., **80** 725 (2004).
[7] T. Hayashi, Theory of Fusion Plasmas, EUR 12149 EN 11 (1989).
[8] K. Harafuji, T. Hayashi and T. Sato, J. Comput. Phys. **81** 169 (1989).
[9] T. Watanabe and H. Akao, J. Plasma Fusion. Res. **73** 186 (1997).
[10] D. Sarafyan, J. Math, Anal and Appl. **40** 436 (1972).
[11] T. Watanabe, Trans. Jpn. Soc. Ind. Appl. Mat. **1** 101 (1991)[in Japanese].
[12] Y. Matsumoto, T. Nagaura, S. Oikawa and T. Watanabe, Jpn. J. Appl. Phys., **43** 332 (2004).
[13] A. Gibson and J. B. Taylor, Phys. Fulids **10** 2653 (1967).
[14] A. Iiyosi et al., Nucl. Fusion **39**, 1245 (1999).
[15] O. Mitarai and S. Sudo, Fusion Technol., **27** 377 (1995).
[16] N. J. Fisch *et al.*, *Proc. 16th IAEA Conf. Fusion energy*, montreal (1996) A2-3.

Proceedings of ITC/ISHW2007

Effect of symmetry-breaking on ballooning modes in quasi-symmetric stellarators

A. S. Ware,[1] E. Mondloch,[1] R. Sanchez[2], D. A. Spong[2]

[1] *University of Montana, Missoula MT 59812, USA*
[2] *Oak Ridge National Laboratory, Oak Ridge TN, USA*

andrew.ware@umontana.edu

Global ballooning stability is examined in three quasi-symmetric stellarators: the Quasi-Poloidal Stellarator (QPS), the Helically-Symmetric Experiment (HSX), and the National Compact Stellarator Experiment (NCSX). A focus of this work is the impact of symmetry-breaking on ballooning stability. In the ray tracing method, global ballooning mode stability is calculated by following rays in the eigenvalue space determined by the results of local, infinite-n ballooning theory. The eigenvalue is a function of the flux coordinate q (the safety factor), the field line label α, and the ballooning parameter, θ_k. For HSX and QPS configurations, the impact of breaking the symmetry (or degrading the quasi-symmetry) on ballooning modes is examined. For the HSX configuration, three cases are examined: the standard quasi-helically symmetric case, a mirror case, and a hill case. The mirror and hill cases represent degraded symmetry configurations for the HSX experiment. The weak global shear in HSX results in modes which only weakly depend on the ballooning parameter. For QPS, the standard quasi-poloidally symmetric case and a degraded symmetry case are examined. In all of the non-axisymmetric cases studied, the unstable modes are localized in the field-line label, α.

Acknowledgement Work supported by U.S. Department of Energy under Grant DE-FG02-03ER54699 at the University of Montana and Contract DE-AC05-00OR22725 at ORNL with UT-Battelle, LLC.

Proceedings of ITC/ISHW2007

Simulation of Angle and Energy Resolved Fluxes of Escaping Neutral Particles from Fusion Plasmas with Anisotropic Ion Distributions

E.A.Veshchev[1], P.R. Goncharov[1], T. Ozaki[1], S. Sudo[1] and LHD Experimental Group[1]

1) National Institute forFfusion Science, Toki, Gifu 509-5292, Japan

Multidirectional diagnostics employing high resolution atomic energy spectrometers [1,2] are being used to study the ion component heating mechanisms and fast ion confinement in helical plasmas. Since the natural atomic flux source is not localized in contrast to pellet charge exchange [3,4] or diagnostic neutral beam methods [5], the correct interpretation of such measurements in a complex toroidally asymmetric geometry requires a careful numerical modeling of the neutral flux formation and the knowledge of the charge exchange target distributions, relevant cross-sections and the magnetic surface structure. The measured neutral flux calculation scheme for LHD geometry was given in [6] and the influence of the geometry effect on the interpretation of measured data was shown. In the current work angular dependence of fast ion distribution function is taken into account. Experimental signals for all 20 channels of the Angular-Resolved Multi-Sightline Neutral Particle Analyzer (ARMS-NPA) were simulated for different cases of fast ion distribution functions. Calculation results are shown for heating-induced fast ion distribution tails obtained from Fokker-Planck modeling. The behavior of calculated and experimental ion spectra from NBI is discussed.

Keywords: neutral particles, fast ions, angle resolved measurements, fast particle flux simulation, ion distribution, angular distribution, energy resolved measurements, distribution function, diagnostic, analyzer.

1. Introduction

Multi-directional neutral particle analyzer beside high resolution energy spectra of fast particles can provide the information about their angular distribution during scan of plasma column in tangential direction. Vertical scan of plasma column by multi-directional diagnostic can provide information about the radial distribution of fast particles. Such measurements are required for the understanding of the fast ions behavior in plasma, for checking of the fast particle loss-cone presence, for studying if the heating mechanisms, etc. Such information is important for the fast particle confinement and ignition of the future fusion reactor. For this purpose the novel ARMS-NPA has been developed [1] which can measure plasma in vertical and tangential directions. As the magnetic field geometry of LHD has a very complex 3D structure, simulation of the experimental signal of the flux of fast particles is required with taking into account the attenuation of fast particles on the way to the detector due to the charge-exchange, and the influence path length of the particle along every scanning chord in order to understand how does geometry of measurements influences in the angular fast particle distribution. The difference in the geometry of measurements can be clearly seen on the illustration of the vertical cross-section plane of every detector sightline on Fig.1. Detector 1 corresponds to the most tangential direction and detector 20 is the direction close to the perpendicular one. The sheaf of sightlines was adjusted in such a way that all the channels to observe as closer as possible to the central region of plasma.

author's e-mail:veshchev.evgeny@lhd.nifs.ac.jp

2. The Calculation Scheme.

The escaping neutral flux formulation has been made in [6] for passive diagnostics and the atomic flax can be written as:

$$\Gamma(E,\vartheta)=e^{\int_{\rho_{\min}}^{1}\frac{Q^{-}(\rho')d\rho'}{\lambda_{mfp}(E,\rho')}}\frac{\Omega S_a}{4\pi}\int_{\rho_{\min}}^{1} g\left(E,\vartheta,\rho\right)\times$$
$$\times\left[Q^{+}(\rho)e^{-\int_{\rho_{\min}}^{\rho}\frac{Q^{+}(\rho')d\rho'}{\lambda_{mfp}(E,\rho')}}-Q^{-}(\rho)e^{-\int_{\rho_{\min}}^{\rho}\frac{Q^{-}(\rho')d\rho'}{\lambda_{mfp}(E,\rho')}}\right]d\rho$$

where $Q^{+}(\rho)=dX/d\rho>0$ and $Q^{-}(\rho)=dX/d\rho<0$ on the two intervals between $\rho=1$ and $\rho=\rho_{\min}$.

In order to check the geometry influence simulation of experimental signal was made for the isotropic Maxwellian plasma ion energy probability density uld be

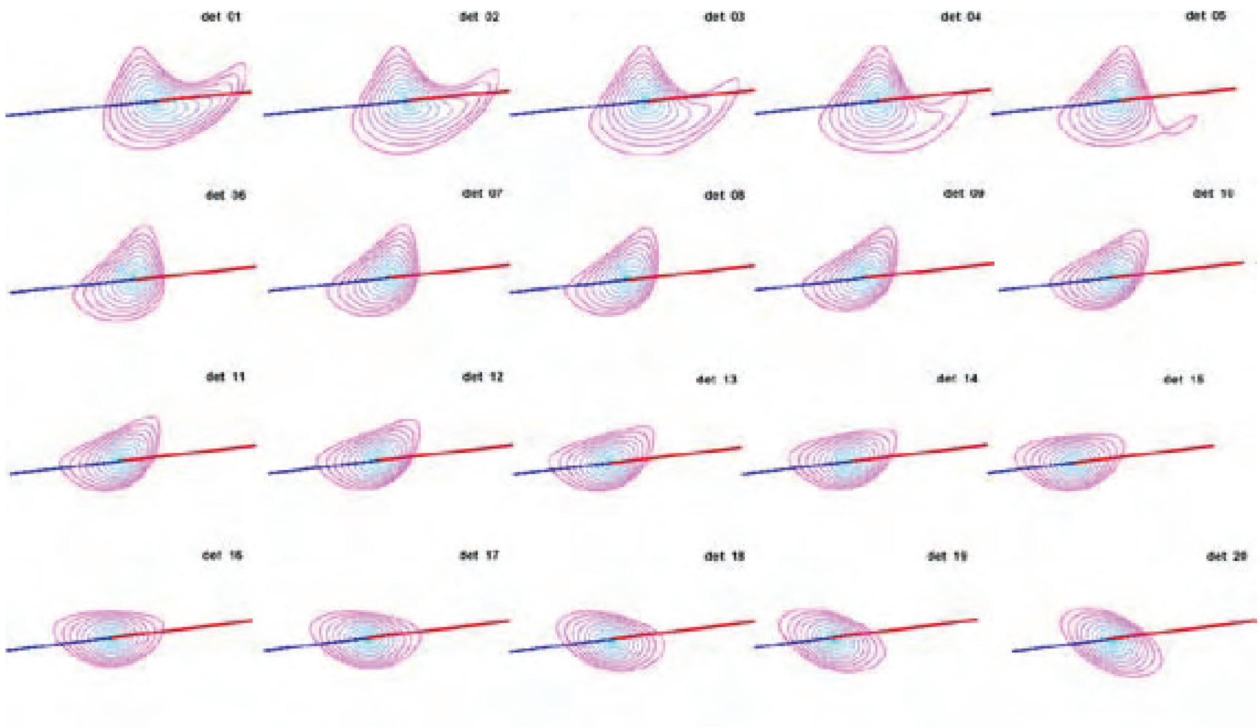

Fig.1 Vertical cross-section plane of every ARMS-NPA sightline. Red color of the line correspond to the scanned part of plasma close to the LHD center. Blue color is the part of sightline close to the detector. Detector 1 corresponds to the most tangential direction and detector 20 is the direction close to the perpendicular one.

function:

$$f_i^{(M)}(E,\rho)=\frac{2\sqrt{E}}{\pi^{1/2}T_i^{3/2}(\rho)}\exp\left(-E/T_i(\rho)\right)$$

It has already been shown that the geometry effect may influence on the fast particles spectra [6] but not as significantly as in experiment. That could be due to the not significant difference of the compared magnetic configurations Rax = 3.6m and Rax = 3.53m. Thus the new calculations were made for much more different magnetic axis configurations (Rax = 3.6m and Rax = 3.9m) for all 20 sightlines. The results of simulation can be seen on the Fig.2. Both cases demonstrate angular anisotropy due to the geometry influence and in both cases fast particle population is reduced in perpendicular region.

3. Experimental Results

Angular resolved measurements were made for both magnetic axis configuration (Rax = 3.6m and Rax = 3.9m). Angular resolved spectra plotted on Fig.3 Both cases demonstrate angular anisotropy and both cases demonstrate the reduceing of fas particle population in perpendicular direction. In order to understand if such a behavior of fast particle spectra is due to the geometry effect, it must be subtracted from experimental data. The geometry of measurements influences only on the relative values of fast particles but not on the shape of spectra, thus for the geometry effect subtraction it will be enough to divide experimental spectra along every sightline by relative values obtained from calculation results.

Angular resolved spectra plotted Fig.4 represent experimental data of angular distribution of fast particles after the geometry effect subtracting for Rax = 3.6 m and R_{ax} = 3.9 m correspondingly. Both cases still demonstrate angular anisotropy. Fast particle population in Rax = 3.6m configuration measured along four perpendicular sightlines are plotted on Fig.5 and demonstrate reducing of spectra. The case of R_{ax} = 3.9 m in addition to the reducing of the fast particle flux in perpendicular direction (Fig.103) still demonstrate the drop of fast particle population in the region of the 8th channel. Such a behavior can be due to the presence of the loss-cone region.

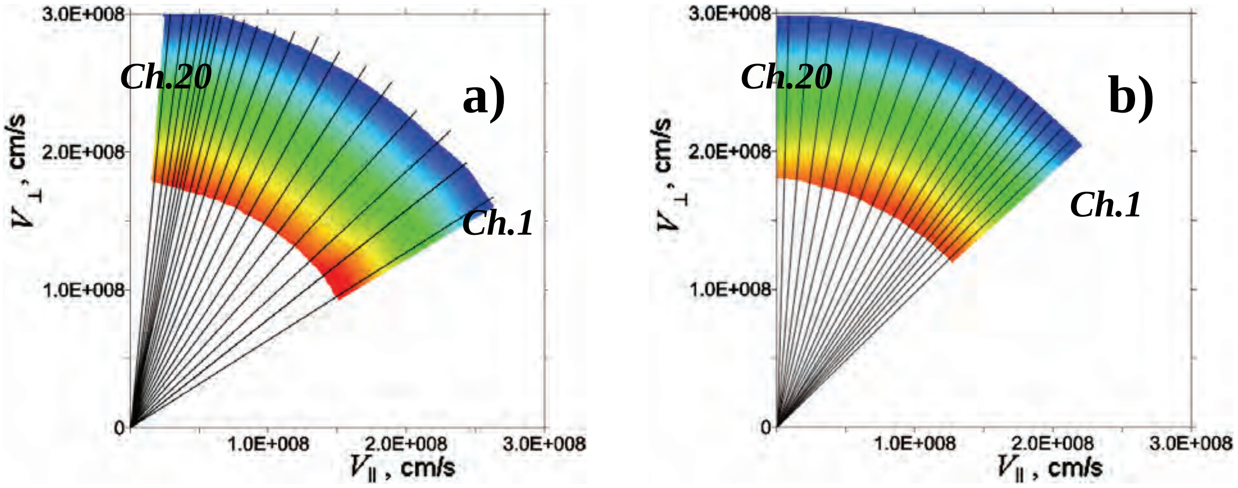

Fig.2 Calculated angular resolved spectra of fast particles a) for Rax = 3.6 m magnetic axis position and b) for Rax = 3.9 m magnetic axis position.

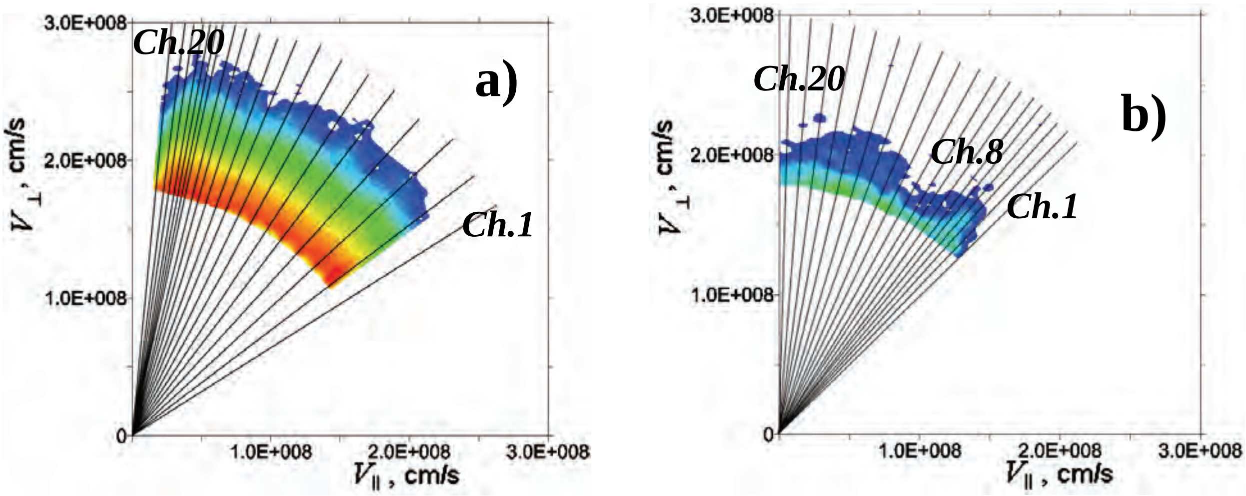

Fig.3 Experimental results of angular distribution of fast particles a) for Rax = 3.6 m magnetic axis position and b) for Rax = 3.9 m magnetic axis position.

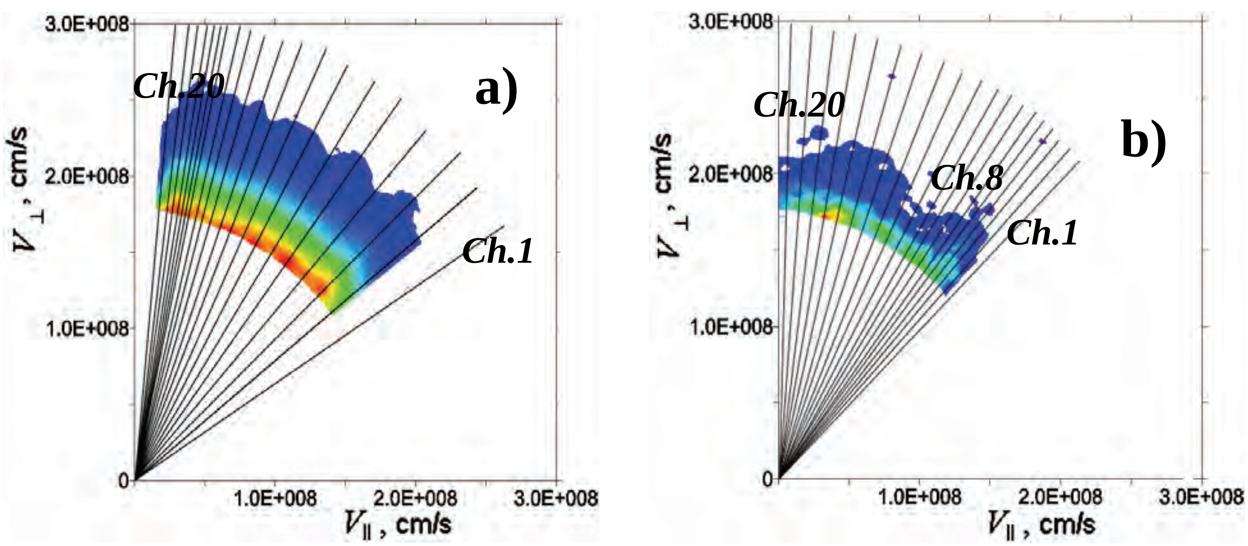

Fig.4 Experimental data of angular distribution of fast particles after the geometry effect subtracting a) for Rax = 3.6magnetic axis position and b) for Rax = 3.9 m magnetic axis position.

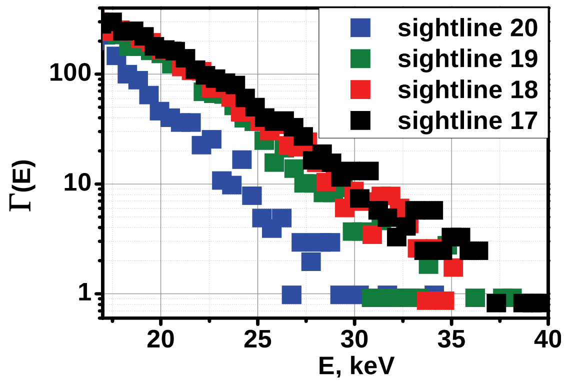

Fig.5 Fast particle spectra for four of the sightlines close to perpendicular direction (sightline 20 is the most perpendicular one) during perpendicularly-injecting NBI4 operation the case of Rax = 3.6 m B_T = 2.75T magnetic field after the geometry effect subtracting.

References

[1] E.A. Veshchev, T.Ozaki, *et al.*, Rev. Sci. Instrum., **77**, 10F129-1 (2006).

[2] J.F.Lyon, P.R.Goncharov, *et.al.* Rev. Sci. Instr., **74**, 1873.

[3] P.R. Goncharov, T.Ozaki, *et al.*, Rev. Sci. Instrum., **77**, 10F119-1 (2006).

[4] P.R.Goncharov, T.Saida, *et.al.*, Rev. Sci. Instr., **74**, 1869

[5] H. Matsushita and K.Ida *et al.*, Rev. Sci. Instrum., **75**, 3607 (2004).

[6] E.A. Veshchev, P.R.Goncharov, *et al.*, Rev. Sci. Instrum., **77**, 10F116-1 (2006).

Proceedings of ITC/ISHW2007

Damage evolution and particle retention in metals bombarded by neutral helium particles at the first wall positions in LHD

M. Tokitani, N. Yoshida [a], Y. Ohtawa [b], K. Tokunaga [a], T. Fujiwara [a], M. Miyamoto [c], N. Ashikawa, S. Masuzaki, M. Shoji, M. Kobayashi, A. Sagara, N. Noda, H. Yamada, A. Komori, LHD experimental group, S. Nagata [d], B. Tsuchiya [d]

National Institute for Fusion Science, 322-6, Toki, Gifu 509-5292, Japan
[a] *Research Institute for Applied Mechanics, Kyushu University, Kasuga, Fukuoka 816-8580, Japan*
[b] *Interdisciplinary Graduate School of Engineering Sciences, Kyusyu University, Kasuga, Fukuoka 816-8580, Japan*
[c] *Department of Material Science, Shimane University, Matsue, Shimane 690-8504, Japan*
[d] Institute for Materials Research, Tohoku University, Sendai, Miyagi 980-8577, Japan

(Received day month year / Accepted day month year should be centered 10-point type)

Specimens of W, Mo and stainless steel were inserted into the first wall equivalent position by using movable material probe system in LHD, and then, exposed to the several sequential helium discharges. After the exposure, very dense helium bubbles and dislocation loops were confirmed in all specimens from transmission electron microscopy (TEM) observation. It means that the energy of incidence helium particles is sufficiently higher than that of the minimum energy for creating the knock-on damage (E_{min}) in all specimens (e.g. W; E_{min}=0.53keV). Majority of such incidence helium particles to the specimens are energetic neutrals created by charge-exchange (CX) collisions [1]. It is known that helium atoms once injected into metals cause more intensive radiation damages than hydrogen atoms, because they have a strong interaction with lattice defects such as vacancies or dislocation loops. Understanding of the effects of charge exchanged helium particles (CX-helium) to the first wall is important for not only the elucidation of materials degradation but also realization of the high performance plasma operations in future fusion devices.

Keywords: Large Helical Device (LHD), Helium, Charge-exchanged neutrals, Microscopic damage, Transmission Electron Microscopy (TEM)

1. Introduction

The first wall materials of fusion reactors will suffer heavy bombardment of helium particles generated by D-T fusion reaction. Majority of such incidence helium particles are energetic neutrals (CX-neutrals) created by charge-exchange collisions [1]. Helium injection into metals causes serious radiation damages. Strong irradiation effects of helium have been observed in many kinds of metals such as tungsten, molybdenum and stainless steel [2-6].

The Large Helical Device (LHD) is the largest heliotron-type device with super conducting magnetic coils [7]. The first wall panels and divertor plates are made of stainless steel and isotropic graphite, respectively. Stainless steel is the major material in LHD and the graphite area is only about 5 % of the total plasma facing area. It was reported that for helium plasma discharge experiments in the LHD, about half of the inlet helium was trapped in the wall, even after a long helium glow discharge cleaning. Therefore, understanding of the effects of charge exchanged helium (CX-helium) atoms to the first wall is important for not only the elucidation of materials degradation but also the plasma operations. In the case of steady state operations, behavior of incidence CX-helium atoms to the first wall is much important.

In the present study, microscopic damages in metals generated by CX-helium bombardment were studied, and then, incident flux and energy of CX-helium were evaluated.

Furthermore, to investigate the effect of bombardment of CX-helium on optical reflectivity of Mo mirror, change of optical reflectivity was measured by means of spectrophotometer. Mo is one of the potential candidate of first mirror for plasma diagnosis in future fusion devices [8]. Effects of the hydrogen isotope irradiation on optical properties have been studied extensively [9-11] but not much for the helium irradiation. However, our fundamental study on helium irradiation effects on Mo mirror indicated that radiation damages by helium atoms cause serious degradation of optical reflectivity [12].

author's e-mail:tokitani.masayuki@LHD.nifs.ac.jp

2. Experimental procedures

2.1. Material irradiation experiments in LHD

Specimens of Mo and stainless steels mounted on the probe head were placed at the first wall equivalent position by using movable material probe system which installed in LHD, and then, exposed to the NBI + ICRF heated helium discharges. This material probe system makes possible to select desirable plasma discharges and irradiation position by using shutter and vertical movement mechanism. Fig. 1 shows a schematic view of the experimental set up in this study.

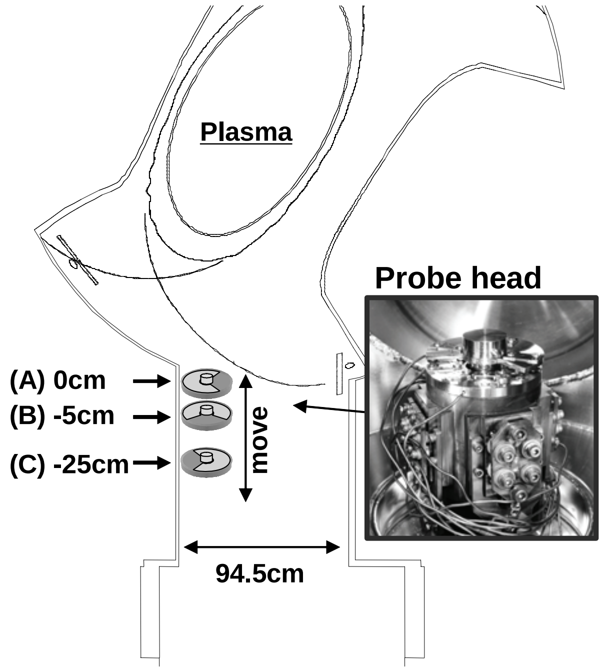

Fig. 1 Schematic view of the experimental set up on movable material probe system in LHD.

Total discharge time at each irradiation position which is identified by the distance measured from the first wall equivalent position and typical plasma parameters summarized in Table 1. For convenience these positions are denoted as (A), (B) and (C). (B) and (C) are the positions in 4.5L port as illustrated in Fig. 1. The temperature of the probe head during exposure was monitored by the thermocouples placed just beneath the specimens. It stayed almost constant near room temperature.

2.2. Material analysis

After the exposure, microscopic damage of the specimens was observed by means of transmission electron microscopy (TEM) and then, incidence flux and energy of CX-helium atoms were estimated by comparing with the in-situ TEM observation results under helium ion-beam irradiation experimental results [13].

Optical reflectivity of Mo mirror before and after the exposure was measured with a spectrophotometer (JASCO, V-670) for the wave length between 190 and 2500 nm.

3. Results and discussions

3.1. Evaluation of microscopic damage by TEM observation

Fig. 2 shows TEM images of (a)-Mo and (b)-stainless steel exposed to the NBI+ICRF heated helium discharges for the case of (A), (C) and (A)+(B)+(C). (A)+(B)+(C) means the specimen exposed at all positions. The upper series of micrographs of (a) and (b) are bright field images with large deviation parameter *s*. White dot images are helium bubbles. The lower series of (a) and (b) are dark field images with small deviation parameter *s*, which fits for observation of defects with strong lattice distortion such as dislocation loops and helium platelets. Defects with a strong white image, mainly dislocation loops. Although total irradiation time was only 349 s~1138 s, considerably large amounts of helium bubbles of about 1 to 2 nm and dislocation loops of about ~20 nm were formed in both specimen and all cases. Evolution of the microscopic damage was already saturated at the case of both (A) and (C). Thus, since the creation rate of defects in all specimens was very high, unfortunately, the difference of the damage rate could not identify as a function of irradiation time and position. This means that the damage is caused by CX-helium atoms which are not affected by magnetic field, and their energy and flux are sufficiently higher to create these defects. In general, radiation induced secondary defects are formed as aggregates of point defects produced by knock-on processes. Since the threshold energies of helium for displacement damage in Mo and stainless steel are about

	Distance from first wall position	Total discharge time	Ion temp. T_i (keV) (Plasma core)	Electron density ($x10^{19}m^{-3}$)
(A)	0 cm	408 s	0.5~2.0	0.25~3.6
(B)	-5 cm	349 s	0.2~2.0	0.25~2.25
(C)	-25 cm	352 s	0.5~2.0	0.25~3.6
(A)+(B)+(C)		1138 s	0.1~2.5	0.23~3.85

Table 1 Total discharge time at each irradiation distance from the first wall position as illustrated in Fig. 1 and typical plasma parameters. 0 cm corresponds to the first wall equivalent position. (Direction of -25 cm is farthest from plasma)

0.23 keV and 0.10 keV, respectively. The size and density of defects between (A) and (C) were very similar in both specimens. It is indicates that the flux of CX-helium atom does not decrease much even in the port.

3.2. Estimation of the flux and energy of CX-helium atoms

It was tried to estimate the flux and energy of CX-helium atoms to the first walls by comparing with systematic in-situ helium ion irradiation experiments [13]. The microstructural evolution of stainless steel at room temperature under irradiation with 2 keV-He^+ ions is shown in Fig. 3. Some of the images are re-produced data from Ref. [13]. The upper series of micrographs are bright field images with large deviation parameter *s*. The lower series are dark field images with small deviation parameter *s*. When Fig. 3 compared with Fig. 2-(b), size and density of helium bubbles and dislocation loops of the all cases of Fig. 2-(b) is corresponds to 2~5×10^{21} He/m^2. Therefore, the estimated flux and incidence energy is 2×10^{18}~1×10^{19} He/m^2s and about 1~2 keV, respectively. As mentioned above, majority of such incidence helium particles are energetic neutrals. This estimation is relatively rough. However, it is important

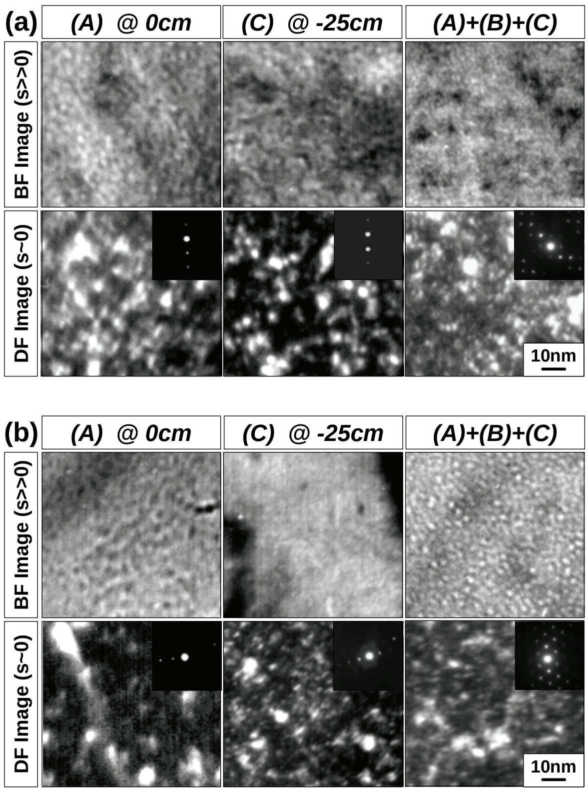

Fig. 2 TEM images of (a)-Mo and (b)-stainless steel specimens after exposed to ICRF heated helium discharges, BF images at large deviation parameter *s* (upper series). White dot contrast in DF images shows dislocation loops (lower series).

for elucidation of the CX-particle load to first walls. Also

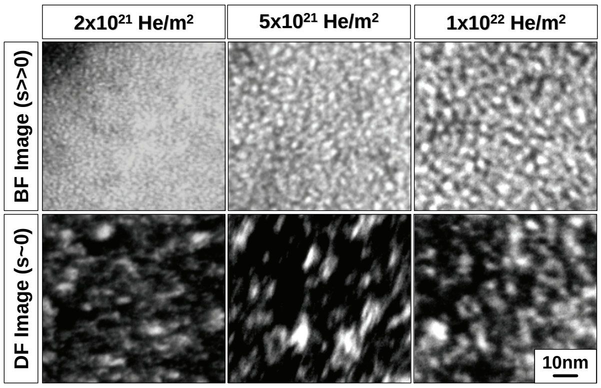

Fig.3 Microstructural evolution in stainless steel during helium ion irradiation (~1×10^{22} He/m^2) at room temperature with energies of 2 keV. BF images at large deviation parameter *s* (upper series). White dot contrast in DF images shows dislocation loops (lower series).

the case of only NBI heated helium discharges, very similar damages were confirmed after exposed to only ~100 s discharges in Mo and stainless steels specimens (not shown here). In the case of 2 keV-He^+, it was reported that at a dose level of lower than ~10^{20} He/m^2s, injected helium atoms are trapped by vacancy-helium complex and helium bubbles and finally filled with them. Above this dose level, additional trapping of helium atoms by helium bubbles become difficult [13].

Three-dimensional simulation of CX-neutral flux to the plasma facing components (whole torus wall ~300 m^2) during hydrogen discharge case in LHD as a function of line averaged electron density is under going now by using EMC3-EIRENE code (The calculation in helium discharge case is also under going). It is expected that more detailed analysis will be performed by comparing simulation results with experimental results.

3.3. Change of optical reflectivity

Fig. 4 shows the optical reflectivity of Mo specimen after exposed to NBI+ICRF heated helium discharges. This spectrum is from the specimen exposed to all position, (A)+(B)+(C) in table 1.

Reflectivity of virgin specimen was also plotted. It is clear that reduction of reflectivity has already occurred at the exposure time of only 1138 s. In particular, reduction of reflectivity about 500 nm or less is remarkable. Referring to our previous study [12], it is considered that reduction of optical reflectivity is due to the multiple scattering of light by the dense helium bubbles in the sub-surface region. In comparison with hydrogen irradiation, remarkable degradation of the optical reflectivity induced by hydrogen ions irradiation with similar energy occurs at the fluence above 10^{25}ions/m^2 [9]. We should note that effect of helium bombardment is three orders of magnitude higher than that of hydrogen bombardment. This result is important for the design and operation of plasma diagnostics using first mirror.

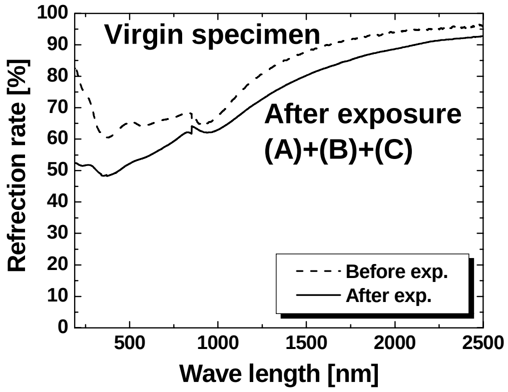

Fig.4 Optical reflectivity of Mo specimen after exposed to ICRF heated helium discharges. Solid line shows (A)+(B)+(C) in table 1. Dashed line shows virgin specimen.

4. Summary

Microscopic damages in metals bombarded by CX-helium atoms in LHD were observed by TEM, and the incident flux and energy of CX-helium particles to the first wall was discussed by comparing the microscopic damage properties with in-situ helium ion-beam irradiation experiment in laboratory. Dislocation loops and dense fine helium bubbles were formed in Mo and stainless steel specimens exposed only 349 s~1138 s to helium plasma discharges. It is considered that they are formed mainly by the bombardment of CX- helium atoms. The estimated flux and incident energy from size and density of the defects is the order of 2×10^{18}~1×10^{19} He/m^{2}s, and about 1~2keV, respectively.

Optical reflectivity of Mo specimen after exposed to NBI+ICRF heated helium discharges was measured by spectrophotometer. Reduction of reflectivity has already occurred at the exposure time of only 1138s. It is consider that reduction of optical reflectivity is due to the multiple scattering of light by the dense helium bubbles in the sub-surface region.

Generation of such high flux and high energy CX-helium atoms is serious problem for not only the deterioration of the first wall materials but also plasma diagnosis using metallic mirrors. In addition, phenomena in plasma confinement devices such as synergistic effects of helium bombardment and re-deposition will be investigated.

References

[1] R.J. Goldston, P.H. Rutherford, 1996 Introduction to Plasma Phys. p156
[2] H. Iwakiri et al., J. Nucl. Mater. 283-287 (2000) 1134
[3] N. Yoshida Y. Hirooka et a., J. Nucl. Mater. 258-263
[4] K. Ono et al., J. Nucl. Mater. 283-287 (2000) 210
[5] D. Nishijima et al., J. Nucl. Mater. 313-316 (2003) 97
[6] D. Nishijima et al., J. Nucl. Mater. 337-339 (2005) 927
[7] O. Motojima et al., 2003 Nucl. Fusion 43 1674
[8] A.E. Costley et al., Fusion Eng. Des. 55 (2001) 331
[9] V.S. Voitsenya et al., J. Nucl. Mater. 258-263 (1998) 1919
[10] V.S. Voitsenya et al., J. Nucl. Mater. 290-293 (2001) 336
[11] T. Sugie et al., J. Nucl. Mater. 329-333 (2004) 1481
[12] A. Ebihara et al., J. Nucl. Mater. 363-365 (2007) 1195
[13] M. Tokitani et al., J. Nucl. Mater. 329–333 (2004) 761

The boundary physics program plan for the initial research phase of the National Compact Stellarator Experiment

R. Maingi[a], M.C. Zarnstorff[b], D.N. Hill[c], T. Kaiser[c], J.F. Lyon[a], G.H. Neilson[b]

[a] Oak Ridge National Laboratory

[b] Princeton Plasma Physics Laboratory

[c] Lawrence Livermore National Laboratory

The National Compact Stellarator Experiment (NCSX) is a three-field period compact stellarator presently in the construction phase at Princeton, NJ. The design parameters of the device are major radius R=1.4m, average minor radius $\langle a \rangle = 0.32$m, $1.2 <$ toroidal field (B_t) < 1.7 T, and auxiliary heating power up to 12 MW. The NCSX average aspect ratio $\langle R/a \rangle$ of 4.4 lies well below present stellarator experiments and designs, allowing investigation of high β physics. Also the NCSX design choice for a quasi-axisymmetric configuration introduces the prospect of achieving tokamak-like transport. In this paper, we report on the planned research themes in the boundary physics areas during early NCSX research operations.

Broadly speaking, the present plan is envisioned to consist of two parts: one for scrape-off layer (SOL) characterization in preparation for installation of full plasma-facing components (PFCs), and access to enhanced confinement regimes with edge transport barriers. In the first area, three main topics are envisioned: 1) dependence of heat and particle flux profiles at PFCs on discharge configuration, 2) power accountability studies, and 3) edge and SOL width studies. Data from this set of experiments will be used to compare with field line tracing calculations for preliminary design of the PFCs[1-3]. In the second area, research will be focused around the conditions needed to access enhanced confinement regimes, including implementation of necessary wall conditioning procedures. Execution of the research plan will be enabled with a staged set of boundary diagnostics.

* Research sponsored by U.S. Dept. of Energy under contracts DE-AC05-00OR22725, W-7405-ENG-48, and DE-AC02-76CH03073.

1 T. B. Kaiser, et. al., *Bull. Am. Phys. Soc.* **49** (2004) 313.

2 R. Maingi, et. al., *Proc. 33rd EPS Conference on Plasma Physics and Contr. Fusion, Roma, Italy, June 19-23, 2006* (2006) Paper 5.116.

3 T. B. Kaiser, et. al., *Bull. Am. Phys. Soc.* **51** (2006) 39.

Proceedings of ITC/ISHW2007

Material science from the view point of energy flowing

M. Sato[a], M. Tanaka[a], S. Takayama[a], A. Matsubara[b], N. Nishi[c]

[a]*National Institute for Fusion Science,322-6 Oroshi-cho, Toki 509-5292, Japan*
[b]*Chubu University faculty y of Engineering,kasugai Aichi,487-850,1 Japan*
[c]*Institute for Molecular Science, Okazaki,Aichi,444,8585, Japan*

e-mail address satomoto@lhd.nifs.ac.jp

The microwave energy has been applied for plasma, especially to the ECRH. Recently, it has been cleared that microwave can also transmit into many materials, if it consisted of powders, such as very dense dust plasma. The powder metals are the typical examples. The microwave can transmit the energy into the molecule or crystalline of the materials almost at the speed of light and creates the non-thermal energy distributions in them.

The crystalline of the ferromagnetic powders deformed by the irradiation of high frequency magnetic filed of microwave in a few seconds to continuous Nano-domains consisting of small magnets with 5~15 Nano meters. While the Nano-domains could not obtain by the microwave electric field, as it transferred kinetic energy through the collisions by plasma with higher energy electrons and ions. It is clear that the microwave magnetic field supplied the energy directly to the electron structures of the materials; especially it couples with electron spin motions. Such a direct energy pass from the electromagnetic field to the electrons is usual in the plasma physics, especially in RF heating, but it is not an idea familiar to the materialist.

Here, we would propose a new physical aspect combining with plasma and material sciences on the bases of energy flows that creates and governs the non-equilibrium reactions by electromagnetic wave energy. It has " microscopic scale" in the molecules or crystals and it proceeds reactions in the time shorter than the relaxation time to thermally equilibrium. Practically, it is Nano to large molecules or crystalline in the size and Femto ~ Pico seconds in time. It covers wide range of science and scientist including, plasma, fluid dynamics, materials, femto-lasers and bio-medicals.

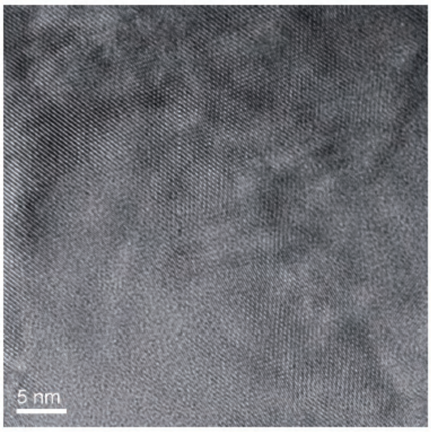

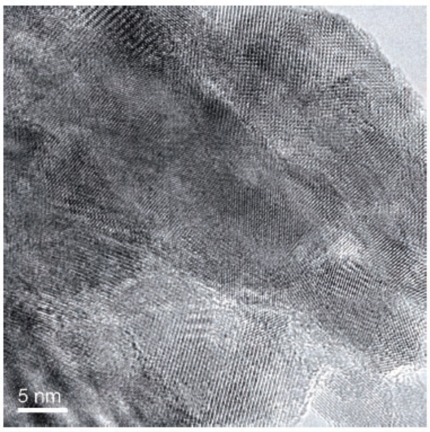

Left: In electric field of microwave
Keep the crystal structure

Right: In Magnetic field of microwave
deformed to continuous Nano-domains

Proceedings of ITC/ISHW2007

Microwave Frequency Effect for Reduction of Magnetite

A S. Takayama, G. Link[a], S. Sano[b], A. Matsubara [c], M. Sato, M. Thumm[a]
National Institute for Fusion Science,322-6 Oroshi-cho, Toki 509-5292, Japan
[a] *Forschungszentrum Karlsruhe GmbH, IHM, P.O.Box 3640, Karlsruhe 76021, Germany*
[b] *Advanced Industrial Science and Technology,2266-98,Anagahora,Shimoshidami, Moriyama-ku, Nagoya 463-8560, Japan*
[c] *Chubu University 1200, Matsumoto-cho, Kasugai-shi, Aichi 487-8501, Japan*
takayama.sadatsugu@nifs.ac.jp

(Received day month year / Accepted day month year should be centered 10-point type)

This paper describes experimental investigations on pig iron production by use of microwave heating. In order to explore possible effects of the microwave frequency identical mixtures of magnetite and carbon powder were processed in different microwave systems, operating at 2.45 GHz and 30 GHz, respectively. High quality pig iron was obtained in the 30 GHz mm-wave system in air. However, at 2.45 GHz FeO was produced mainly at similar conditions. This result might suggest that the chemical reduction of magnetite is more efficient with higher microwave frequencies.

Keywords: microwave processing, millimeter-wave processing, magnetite, pig iron,

1. Inroduction

Microwave technology is not only a substitute for conventional heating, but it resides in the new domain of materials science, namely, microscopic and strong thermal non-equilibrium systems [1]. The application of microwaves in the iron industry may be characterized by a high potential for an essential reduction of carbon dioxide emission. Iron ore refinement by means of blast furnaces was realized with the same basic furnace structure based on the same principle for two centuries. We have conducted a series of experiments to prove effectiveness of rapid and high purity refinement under low temperature and oxygen-containing environment by means of microwave application, and achieved highly positive results.

Nagata and coworkers of the Tokyo Institute of Technology have been working on the development of unique ultra high purity iron refinement technology based on an ancient Japanese iron refinement method called "Tatara" [2]. Their findings during microwave sintering of powder metals led to the idea that rapid refinement of iron should be possible by application of 2.45 GHz microwaves instead of relying on burning of carbon for heat production. Joint experiments at the National Institute on Fusion Science (NIFS) and Forschungszentrum Karlsruhe (FZK) proved that high purity iron (1% carbon concentration) with less than 1/10 of impurities as compared to irons that the modern blast furnaces can produce. More over it reduced the carbon consumption to 2/3.

In order to investigate the effect of microwave frequency, samples of magnetite powder mixed with carbon powder were processed in different microwave systems. The following paper discusses recent experimental results obtained by millimeter-wave (mm-wave) processing and processing in a 2.45 GHz microwave system.

2. Experimental Setup of theMM-wave Process

For mm-wave experiments, the applicator of a compact 30 GHz gyrotron system was used as shown in Figure 1(a) [3]. The mm-wave power generated by a so called gyrotron oscillator can be controlled from 0 - 15 kW. This power is launched via a quasi-optical transmission line through a vacuum-sealed boron nitride window into the hexagonal applicator which is characterized by a very homogeneous field distribution. The samples used were mixed powder of magnetite and carbon. The weight ratio of magnetite and carbon in the power mixture was 89 to 11 weight%. According to the corresponding chemical equation this should allow to produce pig iron including 2 weight% of carbon. Such type of powder samples were filled into an alumina crucible surrounded by thermal insulation (see Fig. 1(b)). The temperature was measured by two S-type thermocouples, one sticking in the center of the powder sample, another near the crucible wall. The heating process was controlled along a preset temperature-time program with a heating rate of 70 °C/min using the temperature signal of the thermocouple placed near the sample surface.

author's e-mail: journal@jspf.or.jp

Fig.1 (a) 30GHz gyrotron system (top),
(b) Experimental setup of the mm-wave (bottom)

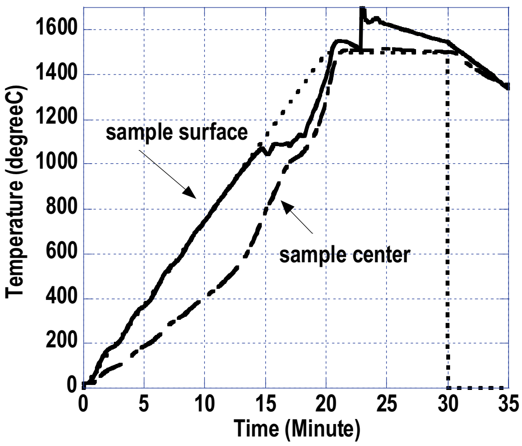

Fig.2 The measured temperatures of a mm-wave process.

Fig.3 Pig iron from the 30GHz mm-waves process.

Figure 2 shows the process temperatures measured during mm-wave heating of a powder sample of about 80 g mixed magnetite and carbon. It can be seen that during the initial step of heating that means during the first 15 minutes, the temperature measured at the sample surface was higher than the temperature measured within the sample volume. However thereafter, at a temperature of about 1100 °C the absorption behavior of the powder is changing dramatically. According to the Iron-Carbon phase diagram this temperature is close to the point where liquefaction of iron with 2% carbon content starts. That means microwave power is consumed by the melting process and heating of the material stagnates. Due to this melting process a strong rearrangement of the processed material happens, leading to changes in the thermocouple positions as well. Finally, when the material is completed molten, the thermal conductivity of the material increased. Thus the measured temperatures converge to each other. Figure 3 shows a picture of the obtained pure pig iron. EDX analysis along the cross section revealed a carbon content of 1 weight%. No oxygen could be detected.

3. Experimental Setup for CM-wave Process

The multimode test furnace at the National institute for Fusion Science shown in Figure 4 was employed for the present study at 2.45 GHz. According to the concepts developed in Germany in order to improve the homogeneity of the electromagnetic field, the applicator shape is hexagonal [4]. The furnace with 0.92 m^3 in volume is equipped with five magnetrons. The microwave power of a single magnetron is 2.5 kW. Two mode stirrers scatter the standing wave. The samples used had the same weight ratio of magnetite and carbon power as for the mm-wave process. The powder samples were filled into an alumina crucible surrounded by thermal insulation (see Figure 4) similar to the setup used for the mm-wave process. The temperature was measured by an IR pyrometer. The heating process was controlled along a preset temperature-time program with a heating rate of 70 °C/min using the temperature signal of the IR pyrometer measured at the top of the sample surface. In addition, the multi-point emission spectroscopic diagnostic was conducted through the viewing port on the furnace.

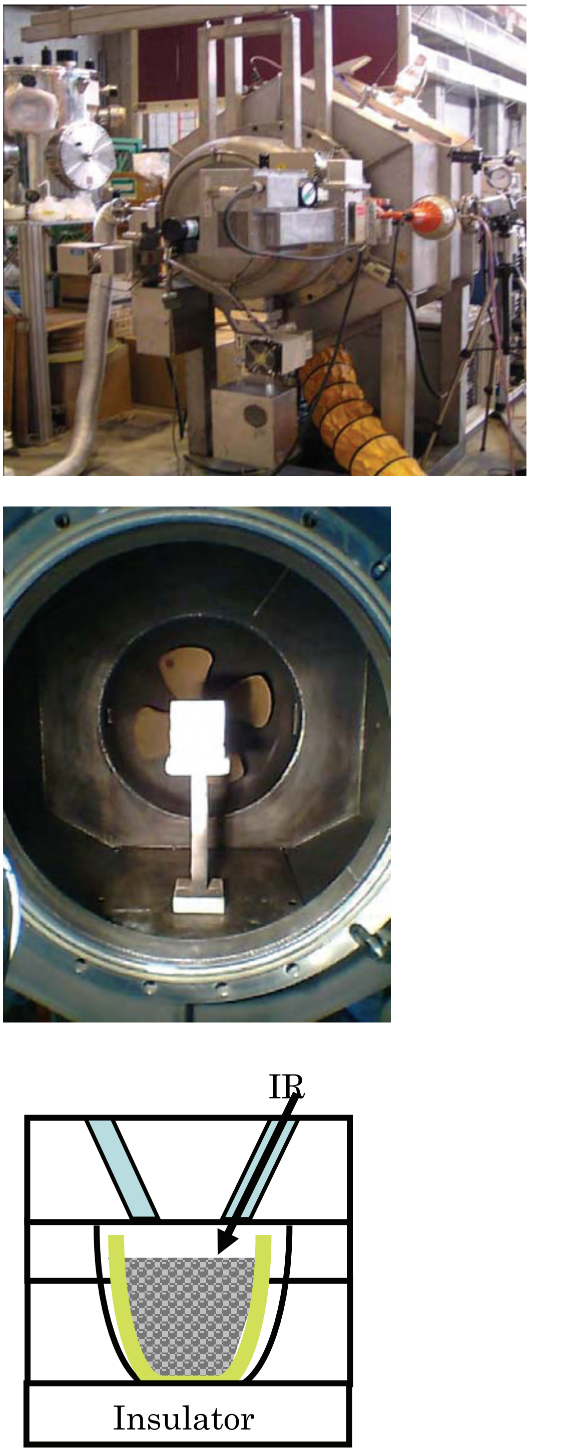

Fig.4. (a) 2.45GHz magnetron system (top), (b) Experimental setup of cm-wave process (middle), (c) Sketch of experimental setup (bottom).

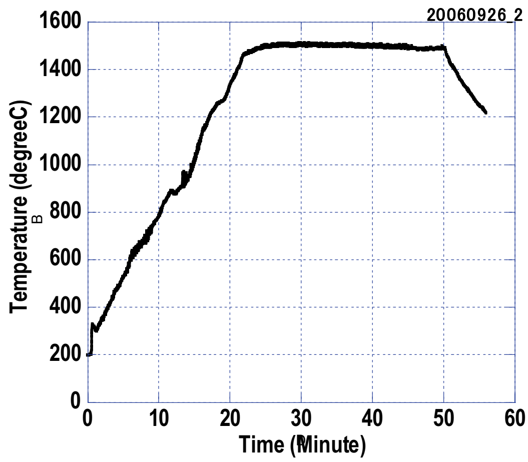

Fig.5 The measured temperatures of a cm-wave process.

Fig.6 Sample after 2.45GHz processing.

Figure 5 shows the process temperatures measured during cm-wave heating of a powder sample of mixed magnetite and carbon. After 15 minutes from start, strong radiation appeared due the ignition of a plasma at the sample surface [5]. The spectral intensity of the continuous spectrum is at least three orders of magnitude larger than that of black body emission for the temperature range of 860 °C – 1070 °C measured by the multi-point emission spectroscopic diagnostic conducted through the viewing port on the furnace. The pattern of the continuous spectrum is partly similar to a continuum of the emission light radiated by the free-band electron transition.

The origin for the continuous emission spectrum will be discussed. One candidate is a solid state fluorescence called cathodoluminescence induced by impingement of a plasma electron onto the sample surface of magnetite;

this results in the excitation of electrons from the valence band into the conduction band, and deexcitation with the broadband emission.

Figure 6, shows a picture of the material obtained by this process. The mainpart of the material was FeO as detected by XRD analysis.

4. CONCLUSIONS

High quality pig iron could be made from powder samples of mixed magnetite and carbon by 30 GHz mm-waves heating in air. However, in case of heating by 2.45 GHz at similar conditions, mainly FeO was produced. Therefore, we expect that there is frequency dependence in the reduction reaction.

ACKNOWLEDGEMENTS

This work was supported in part by KAKENHI (Grant-in-Aid for Scientific Research on Priority Areas) (1807004) of MEXT (Ministry of Education, Culture, Sports, Science and Technology).

References

[1] R. Roy, R. Peelamedu, L. Hutt, J. Cheng, D.Agrawal, “Definitive experimental evidence for microwave effects: radical new effects of separated E and H fields”, Mat. Res. Innovation **6**: 128-140, 2002.

[2] K. Nagata, R. Kojima, T. Murakami, M. Susa, H. Fukuyama, “Mechanisms of Pig-iron Making from Magnetic Ore Pellets Containing Coal at Low Temperature”, ISIJ International **41**: 1316-1323, 2001.

[3] G. Link et al., “Sintering of advanced ceramics using a 30-GHz, 10-kW, cw industrial gyrotron”; IEEE Transactions on Plasma Science, 27 (2): 547-554, 1999.

[4] Feher L., Link G., DE-PS 19633245C1 (27.11.1997); Feher L.; Nuss V.; Seitz T.; Flach A. DE-PS 10329411 (31.1.2005).

[5] A. Matsubara, et al., submitted to Proc.11th International Conference on Microwave and High Frequency Heating, (3-6 Sep 2007, Oradea, Romania).

P1-063

Microwave heating of materials: From polar liquid to metal oxides

Motohiko Tanaka, Motoyasu Sato, M.Suzuki, and M.Yamashiro

Coordination Research Center, National Institute for Fusion Science
322-6 Oroshi-cho, Toki 509-5292, Japan

Email: mtanaka@nifs.ac.jp

Energy efficient and environment-friendly heating and processing of materials have been made possible with the use of microwaves. Some materials are heated by absorbing the electric field energy of microwaves, and others by their magnetic field energy [1]. In series of our studies under the MEXT Tokutei Ryoiki Project [2], we are investigating the heating mechanisms of water (polar liquid) [3] and metallic oxide powders (solid). We have shown theoretically using molecular dynamics simulations that the heating mechanism certainly depends on materials: water is heated by electric field and metallic oxides by magnetic field. For the study of the former process, an explicit water model (Fig.1) is used, which has proven that water heating is due to rotational excitation of water molecules and irreversible energy transfer to translational energy by molecular collisions (Fig.2); crystal ice is not heated because of a strong hydrogen-bonded network. The latter heating can be explained by interactions between the microwave magnetic field and electronic spins of metallic atoms.

References:

[1] Peelamedu,R.D., Fleming,M., Agrawal, D.K., and Roy,R., Preparation of titanium nitride: Microwave-induced carbothermal reaction of titanium dioxide, *Journal of American Ceramic Society*, 85 (2002) 117.

[2] "Science and Technology of Microwave-Induced, Thermally Non-Equilibrium Reaction Fields", Grant-in-Aid for Special Research Area from the Japan Ministry of Education, Science and Culture (FY2006-2010); http://phonon.nifs.ac.jp/

[3] M.Tanaka and M.Sato, Microwave heating of water, ice and saline solution: Molecular dynamics study, *Journal of Chemical Physics* 126 (2007) 034509.

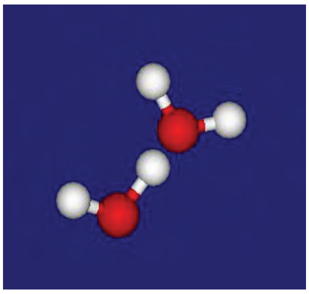

Fig.1 The simulation model of water molecules adopted in our molecular dynamics study. Adjacent molecules are virtually chained by strong hydrogen bonds between hydrogen and oxygen atoms, under which molecules interact with the microwave electric field.

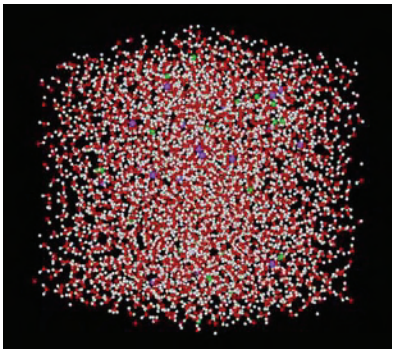

Fig.2 Bird's-eye view of microwave heated water containing $(14)^3$ water molecules of Fig.1. Na and Cl salt ions are also contained. In salt water, Joule heating of salt ions is predominant over ordinary dipole heating of water. Because of applied microwave and finite temperature, the ordered structure of ice is almost lost in a mesoscopic scale (> 10 Angstroms) [3].

Proceedings of ITC/ISHW2007

Investigation of effective cleaning method using ion cyclotron conditioning in LHD

Naoko ASHIKAWA, Kenji SAITO, Testuo SEKI, Akio SAGARA,
Masayuki TOKITANI, Yoshihisa OHTAWA[1)], Masaki NISHIURA,
Suguru MASUZAKI, Kiyohiko NISHUMURA, Ryuhei KUMAZAWA,
Hiroshi KASAHARA, Takashi MUTOH, Naoaki YOSHIDA[1)]
and the LHD experimental group

National Institute for Fusion Science, Toki 509-5292, Japan
[1)]Research Institute for Applied Mechanics, Kyushu University, Kasuga 816-8580, Japan

The ion cyclotron conditioning (ICC) is one of the conditioning methods to reduce impurities and to remove tritium from the plasma facing components. Advantages of ICC are to be operated under strong magnetic field for fully torus area and can be operated with high pumping efficiency. In particular, ICC in helical devices can be operated using the same magnetic configuration for of main plasma and a shot by shot operation is easy. The advantages of ICC in LHD are the durability of long-term operation and the flexibility of input power with pulse phases. Using material probe system, effective cleaning area by ICRF conditioning is estimated. On the plasma facing area of material holder, a lot of helium babble is observed by transmission electron microscope (TEM), but the gap area have no damage. It is suggested effective particles come to the wall straight and a clearing for shadow area is difficult.

Keywords: LHD, Wall conditioning, RF plasma, PWI, T inventory

1. Inroduction

The ion cyclotron conditioning (ICC) is one of the conditioning methods to remove tritium from the wall [1,2]. The operation of experimental devices for fusion plasma with superconducting coils needs long time duration for increasing and decreasing the magnetic fields. As typical wall conditioning methods, a DC-glow discharge cleaning is operated such as JT-60U and LHD [3,4] during non-magnetic field. In future, the superconducting reactors, which still will be operated over long discharge duration and will deuterium/tritium mixtures. Therefore, for future devices, a wall conditioning method in magnetic field will be required in general.

As a general wall conditioning method to remove impurities and retention gases, two type scenarios are planed in the international thermonuclear experimental reactor (ITER), one is an initial conditioning before main experimental campaigns and second one is a day by day conditioning during campaign. During experimental campaign, a magnetic field will be kept in ITER, and then the ICC method during magnetic field is important. As other reason, tritium retention is one of serious problem in ITER and the ICC is considered as a tritium removal method from the first wall and divertor target.

In the large helical device (LHD) [5], is provided with a superconducting coil as confinement magnetic field and DC-glow discharge cleaning are used in most case to operation the wall conditioning [4]. As other wall conditioning method, boronization and titanium gettering are operated a few times during experimental campaign.

Ion cyclotron range of frequency (ICRF) heating devices is developed for a high power and long pulse discharge plasma heating in LHD [6,7]. Using same ICRF antenna sets, ICC was operated in 2005 and a successful operation was done as an initial operation [8].

From experiences in LHD and AUG, effective cleaning areas by ICC are considered smaller than by glow discharge. But this RF plasma wall interaction is not investigated yet. In this paper, effective cleaning area by ICRF conditioning was estimated using damages on material probes for different area.

2. Experimental setup

For the ICC operation, one of the ion cyclotron ranges of frequency was choosing and this frequency is

author's e-mail:ashikawa@lhd.nifs.ac.jp

the second harmonic heating for helium. This is a heating method which takes advantage of finite Larmor radius effect and a heating efficiency at f = 38.47 MHz is about 40%. As a confined magnetic field, a magnetic field, B_t,=2.75T, and a magnetic axis, R_{ax}=3.6m were used. Hydrogen and helium partial pressure were measured by quadruple mass spectrometry (QMS) with a sampling time of 1 sec. As plasma facing components the first wall consists of stainless steel 304 and a divertor is made of carbon. A RF input phase of 3 sec and interval phase of 2 sec are used and it is determined by a stored duration time of data acquisition system. An input power and a helium pressure were scanning, but stable discharge was kept during ICC operation.

3. Material probe experiment in ICC

During ICC in FY2006, stainless steel samples on hexahedron block holder is installed using the movable sample stage system at 4.5L port and this stage level was set at just first wall as shown in Fig.1.

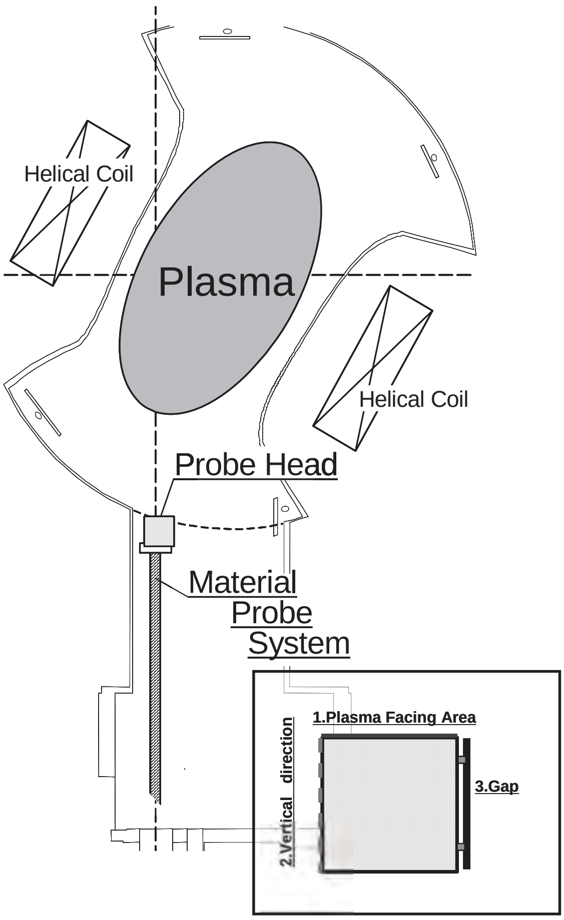

Fig.1 material probe system and sample holder.

Sample holder has three kinds of facing on this block as following 1) plasma facing area, 2) Vertical direction for plasma facing area and 3) Gap area. Samples installed on holder directory on plasma facing and vertical direction, and vertical area facing in-vessel component. The gap area is demonstrated between tiles and thin plate is connected to base holder with slit of 1.5mm. Samples installed on holder, and then samples are not exposed to plasma directory.

This sample holder kept during ICC plasma and integrated exposure time is about 4000 s. Stainless steel samples is analyzed by transmission electron microscope (TEM) and these bright field images are shown in Figs.2. From comparison number of damages due to helium babbles on different position, only plasma facing area as shown in Fig.2(a) has large number of damages. For a sample on the gap at position 3 in Fig.1, damage is not observed by TEM analysis. From helium babbles are produced by an interaction between RF helium plasma and target samples, large number of damages are estimated as strong interaction in this experiment. These results are suggested effective CX particles come to the wall straightly and a cleaning for shadow area will be difficult.

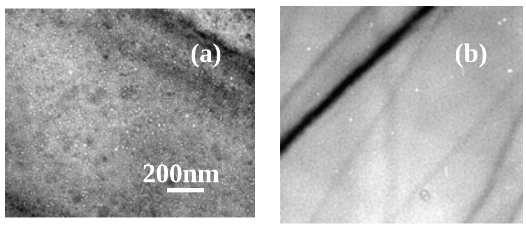

Fig.2 Bright field images by TEM, (a) on plasma facing are and (b) vertical area.

4. Particle flux from RF conditioning plasma

Using Natural Diamond Detector (NDD) [11] Charge exchange neutral particle is measured as shown in Fig.3. This NDD is installed at 4.5 lower side near the port and CX neutral particles by ICRF plasma can be detected on this poloidal cross-section. Using NDD data at shot # 70540, particle flux is estimated. Detected particle thought out of slit of 2mm and this integrated time is about 1.8 s. At shot #70840, using detected counts of full energy spectrum by NDD as shown in Fig.3 and area of detector, particle flux of charge exchange neutral is calculated about $1.6x10^5$~$3.2x10^5$ [$s^{-1}cm^{-2}$]. At this experiment, a particle flux can measured only RF input of frequency of 38.47 MHz, and it is to need changing an integrating time of time frequency for other frequency and low power case.

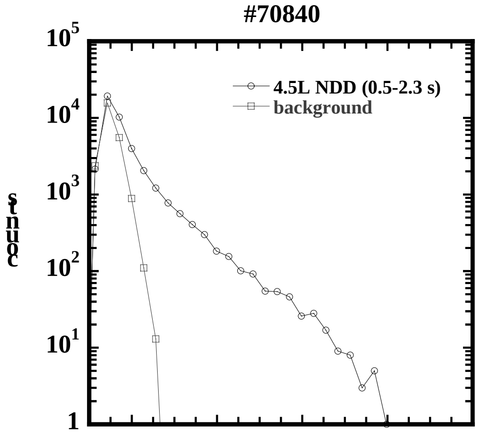

Fig.3 Energy spectrum of Natural Diamond Detector

5. Summary

Using material probe system, effective cleaning area by ICRF conditioning is estimated. From three kinds of area, number of helium bubble on samples is different. On the plasma facing area of material holder, a lot of helium babble is observed by transmission electron microscope (TEM), but the gap area have no damage. These results are suggested effective particles come to the wall straight and a clearing for shadow area is difficult. During ICC, particle flux is measured about $1.6x10^5$~$3.2x10^5$ [$s^{-1}cm^{-2}$] at port area.

In future works, using this estimated cleaning area comparison of removal efficiency of tritium by different method is important.

Acknowledgements

This work was supported by the NIFS budget NIFS06ULPP515, the JSPS-CAS Core University Program in the field of“Plasma and Nuclear Fusion”and the Joint Research System of Research Institute for Applied Mechanics, Kyushu University. This work was undertaken by IEA/ITPA joint experiment of DSOL-8 “ICRF conditioning”.

References

[1] A. Lyssoivan, D.A. Hartmann, et al., JNM **337-339** (2005) 456-460.
[2] E de la Cal and E. Gauthier, Plasma Phys. Control. Fusion **47** (2005) 197-218.
[3] T. Nakano, S. Higashijima, et al., JNM **313-316** (2003) 149-152.
[4] K. Nishimura, N. Ashikawa et al., JNM **337-339** (2005) 431-435.
[5] O. Motojima, N. Ohyabu, et al., Nucl. Fusion **43** (2003) 1674-1683
[6] K. Saito, R. Kumazawa, T et al., JNM **337-339** (2005) 145-153.
[7] T. Mutoh, R. Kumazawa, et al., Nucl. Fusion **43** (2003) 738-743.
[8] N.Ashikawa ,S. Masuzaki et al., FED **81** (2006) 2831-2836.
[9] K. Osakabe, T. Yamamoto, et al., Review of Scientific Instruments **72** (2001) 788.
[10] E. Gauthier, E. de la Cal, et al., JNM **241-243** (1997) 553-558.
[11] M. Isobe, M. Sasao, et al., RSI **72** Issue 1 (2001) 611-614.

Proceedings of ITC/ISHW2007

H/He ratio as a function of wall conditioning and plasma facing material during past 9 years in LHD

Shigeru MORITA, Motoshi GOTO, Suguru MASUZAKI, Naoko ASHIKAWA and LHD exp. group

National Institute for Fusion Science, Toki 509-5292, Gifu, Japan

(Received 15 October 2007 / Accepted 15 October 2007)

A simple method for monitoring the wall conditioning is presented for analysis on the flux ratio of hydrogen to helium ions, which is determined from intensity ratio of Hα (6563Å) to HeI (5876Å) visible spectral lines. The density and temperature dependences of the emissions, which are calculated with collisional-radiative model, can be mostly deleted by taking into account the ratio. The H/He ion flux ratio in LHD has been thus calculated from toroidally integrated Hα and HeI signals. All discharges during past 9 years since the LHD experiment was started have been analyzed. As a result, the effect of the discharge cleaning as wall conditioning, especially H_2 and He glow discharges, on LHD experiments becomes clearly visible. The history of the wall conditioning in LHD is presented with the analysis of the H/He ion flux ratio and results are discussed as a function of wall conditioning method and plasma facing materials.

Keywords: Hα, HeI, H/He ratio, wall conditioning, plasma facing material, visible spectroscopy, LHD

1. Introduction

Wall conditioning in fusion devices is one of important experimental techniques in order to improve the plasma performance. The edge temperature rise based on the reduction of the particle recycling is the main purpose of the wall conditioning. In LHD the wall conditioning becomes more important because the baking temperature of the plasma facing components is limited to 95° due to a narrow space between the superconducting helical coils and the vacuum vessel. In LHD, therefore, a variety of the wall conditioning techniques such as Ti gettering, low magnetic field ECR discharge, boronization and H_2, He and Ne glow discharges have been attempted until now and the He glow discharge has been finally selected as the main method. Although the He glow discharge was very effective to remove the hydrogen from the wall and divertor plates, a large amount of He was unexpectedly appeared as the influx in the H_2 discharge. It becomes then important to study the status of the plasma facing components after glow discharge cleaning.

Toroidal distributions of Hα and HeI visible emissions have been measured in LHD to monitor the uniformity of the hydrogen and helium influxes. In order to determine their influxes the edge n_e and T_e profiles are always required for the analysis in addition to the absolute values of the Hα and HeI emissions. However, it is really difficult to check all discharges in shot-by-shot basis. Therefore, a new method with more simple technique was required to monitor the status of the wall conditioning.

The Hα/HeI intensity ratio was then adopted for the purpose. The discharge conditions over past 9 years have been analyzed using ion flux ratio of hydrogen to helium evaluated from the Hα/HeI ratio. In this paper the history of the LHD discharge condition is reported as a function of the wall conditioning method and plasma facing component in addition to the description of the H/He ion flux ratio measurement technique.

2. Flux ratio calculation of H^+/He^+

The emission rates of the Hα and HeI lines are generally functions of T_e and n_e, and then the population of excited levels in neutral hydrogen and helium is calculated using a collisional-radiative model [1]. We need the ionization events per photon for calculating the hydrogen and helium influxes in addition to the emission intensity. Here, the ionization events per photon give the conversion rate from the emission to the ion flux. Result for the Hα ($2p^2P$-$3d^2D$: 6563Å) is shown in Fig.1 as a function of electron density. In the figure the calculation is done for four different electron temperatures as a parameter. The radial profile of the Hα emission has been measured in LHD. It is then confirmed that the electron temperature at the location where the Hα line is emitted generally ranges in

author's e-mail: morita@nifs.ac.jp

10-100eV except for the recombining phase after turning off the heating devices. Seeing Fig.1 it is understood that the temperature dependence of the ionization events per photon is really weak in the 10-100eV range. However, the density dependence becomes considerably large, especially at higher densities greater than $1\text{x}10^{13}\text{cm}^{-3}$, whereas the ionization events per photons for Hα have been frequently used to be constant [2].

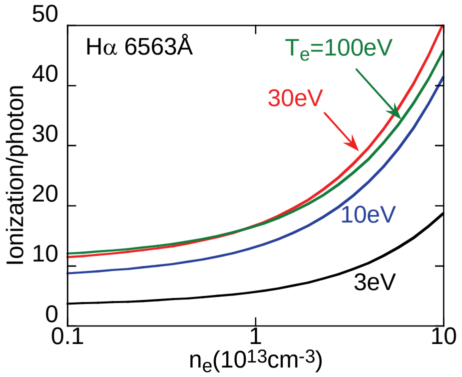

Fig.1 Ionization events per photon for Hα emission as a function of electron density. Calculation is done for four different electron temperatures.

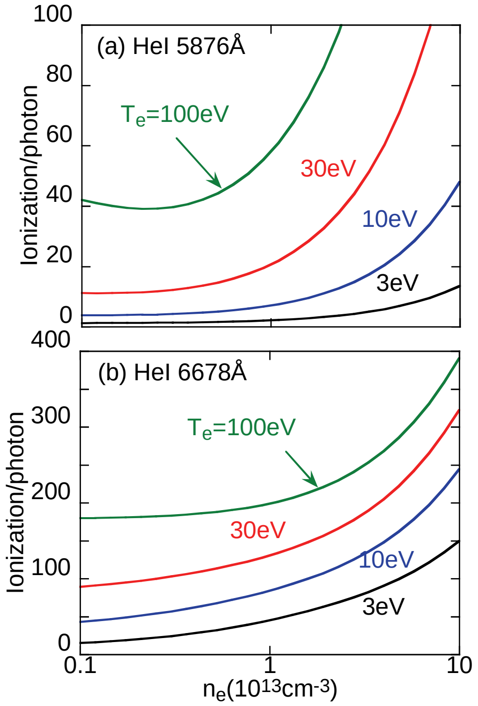

Fig.2 Ionization events per photon for HeI emissions of (a) 5876Å and (b) 6678Å as a function of electron density. Calculation is done for four different electron temperatures.

Results calculated for two neutral helium transitions of $2p^3P\text{-}3d^3D$ (5876Å) and $2p^1P\text{-}3d^1D$ (6678Å) are shown in Figs.2 (a) and (b). The ionization events per photon of HeI 5876Å have a large density and temperature dependences compared to HeI 6678Å. In particular it is emphasized exceeding the density of $1\text{x}10^{13}\text{cm}^{-3}$.

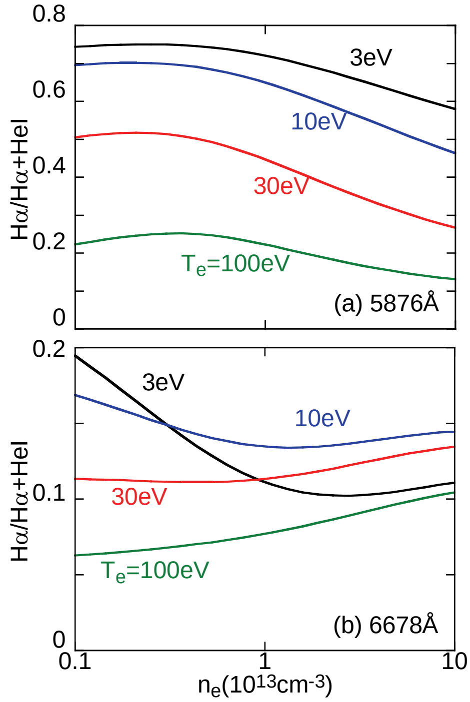

Fig.3 Ratio of hydrogen ion flux to total ion flux as a function of electron density; (a) HeI 5876Å and (b) HeI 6678Å. Calculation is done for four different electron temperatures.

The ratio of hydrogen ion flux to the total ion flux (≡sum of the hydrogen and helium ion fluxes) is shown in Figs.3 (a) and (b) for HeI5876Å and 6678Å, respectively. The calculation is done at the same photon number for both of the Hα and HeI. It is understood that the edge parameter dependence can be considerably reduced when the ratio of Hα to HeI emissions is taken into account. Especially, the disappearance of the parameter dependence tends to be favorable to the HeI 6678Å case. The low T_e of 3eV as seen in the figure is not realistic in normal LHD discharges except for the recombining phase. Thus, the analysis on the ratio can be practically done without consideration of the edge parameters.

The triplet transition (HeI 5876Å) of neutral helium is really strong compared to other singlet transitions like HeI 6678Å. The intensity of HeI 5876Å is always 5-10 times stronger than other lines in LHD. However, the ratio of hydrogen ion flux to total ion flux has a little large density and temperature dependences compared to HeI 6678Å case. Taking into account only the ratio itself, the use of HeI 6678Å is of course better than

5876Å. In the wavelength range near 6678Å, however, other weak emission lines exist in addition to the Hα emission. The HeI 5878Å is used in the present measurement in order to increase S/N ratio of the signal.

3. Measurement of Hα/HeI ratio

The Hα and HeI emissions have been measured using a combination of optical fibers, an interference filter and photomultiplier tubes. Ten optical fibers installed on each toroidal section, which correspond to m=10 toroidal pitch number in LHD, are set on the interference filter with focusing lenses. Since a large interference filter with diameter of 10cm is used, the transmission rate of the line is a little different for each fiber due to the spatially nonuniform transmission rate. Typical transmission rates of the filters for Hα and HeI are shown in Figs.4 (a) and (b), respectively.

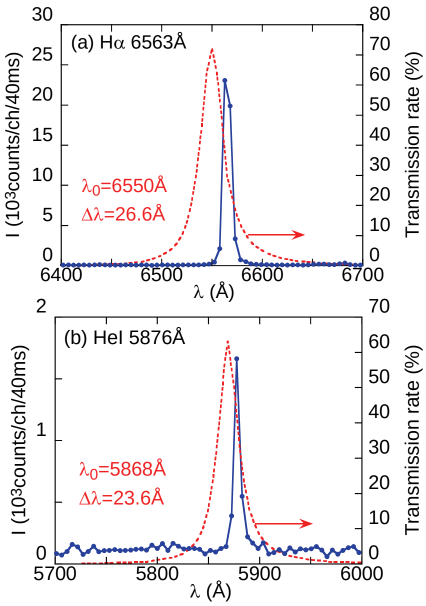

Fig.4 Transmission rates of interference filters and line spectra for (a) Hα and (b) HeI.

The full width at half maximum (FWHM) of the filter is Δλ=26.6Å at Hα 6653Å and Δλ=23.6Å at HeI 5876Å. It is difficult to adjust all the signals to the central position of the filter response because of its nonuniformity. However, the signals keep the transmission rate of, at least, 30-50% against the primary line intensity from the optical fiber.

On the other hand, the present system becomes unavailable to extremely high-density operation with H_2 pellet injection and Ne-seeded discharges. In case of the H_2 pellet injection the increase in the background continuum level mainly formed by the visible bremsstrahlung emission is really large, since the density is enough high and the temperature is considerably low like 0.3-1.0keV. Then, the output signal from the HeI filter involves a large amount of the continuum signal whereas the HeI signal intensity is not changed.

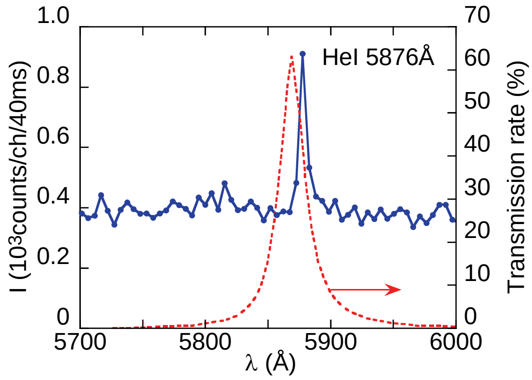

Fig.5 HeI 5876Å spectrum during H_2 pellet injection. Dashed line indicates filter response curve.

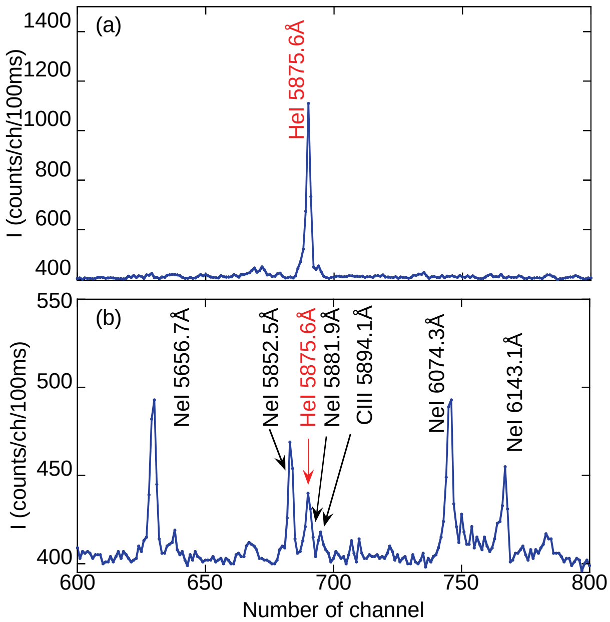

Fig.6 Visible spectra near HeI 5876Å from (a) without and (b) with Ne-seeded discharges.

In case of the Ne-seeded discharges many lines appear near the HeI 5876Å. The Ne-seeded discharges have been sometimes used in LHD for the diagnostic purpose, the increase in temperatures and resultant NBI-driven toroidal current. It is impossible to measure the HeI line using only the interference filter method.

The H/He flux ratio (accurately ion flux ratio of H^+/H^++He^+) is thus obtained by integrating 10 emission intensity signals from toroidal array observing the Hα and HeI lines.

3. H/He ratio during past 9 years in LHD

The H/He flux ratio has been analyzed in almost all discharges from the 2nd cycle (1998) to the 10th cycle (2006). Typical results are shown in Figs.7 (a), (b), (c) and (d) for the 2nd, 3rd, 4th and 7th cycles. The different wall conditionings were attempted during these 9 years;

- 2nd: daily He glow (stainless steel divertor)
- 3rd: daily H_2 or He glow (carbon divertor)
- 4-5th: daily He glow (carbon divertor)
- 6-7th: H_2 (He) glow before H_2 (He) experiment
- 8-10th: He glow only when necessary

The 2nd cycle (1998) had no carbon divertor plates and the discharges were operated with stainless steel wall. In addition, the H_2 and He discharges were repeated alternately. As a result, most of discharges were dominated by He. Before the 3rd cycle (1999) carbon divertor plates were installed on the vacuum wall. Both of the H_2 and He glow discharges were tried after experiments. In contrast to this only He glow discharges were done in the 4th cycle (2000). The difference is clearly visible in the two figures (see Figs.7 (b) and (c)). After He glow discharges any pure H_2 discharge can not be performed, although the He ion flux decreases according to accumulation of H_2 discharges. The additional He flux is mainly released from the carbon divertor plates. In the 7th cycle (2003) the H/He flux ratio was drastically changed as seen in Fig.7 (d). The working gas used in the glow discharge was selected according to the fueling gas in the next day's experiment. Since in the 7th cycle the He experiment was not done so frequently, almost pure H_2 operation became then possible in the H_2 gas fueled discharges.

Recent LHD operation (8th-10th cycles) excellently maintains good H_2 discharges with less He flux. On the contrary the maintenance of the He discharge becomes difficult by the enhanced hydrogen flux, since the number of NBI beam lines (at present NBI#1-#4) increases with further enhancement of hydrogen flux. Then, the increase in the H/He flux ratio is frequently appeared even in the He fueled discharge. It is shown in Fig.8 obtained from the 10th cycle (2006).

Finally, it is summarized that the present diagnostic method using the ratio of Hα to HeI can give useful information on the status of wall conditioning.

Acknowledgements

The authors would like to thank all the members of LHD experimental group. This work was carried out under the LHD project financial support (NIFS06ULPP527).

References

[1] M.Goto et al., Phys. Plasmas **9**, 4316 (2002).
[2] K.J.Behringer, J.Nucl.Matter. **145-147**, 145 (1987).

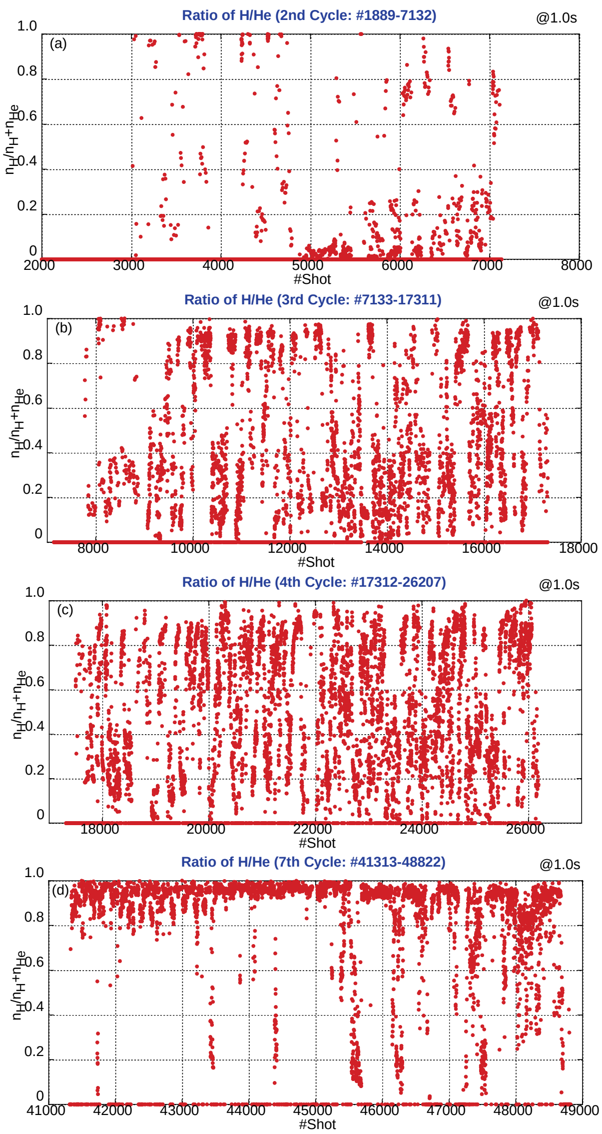

Fig.7 H/He flux ratio in the (a) 2nd, (b) 3rd, (c) 4th and (d) 7th experimental cycles. Repetitive H_2 pellet operation is very few in these cycles.

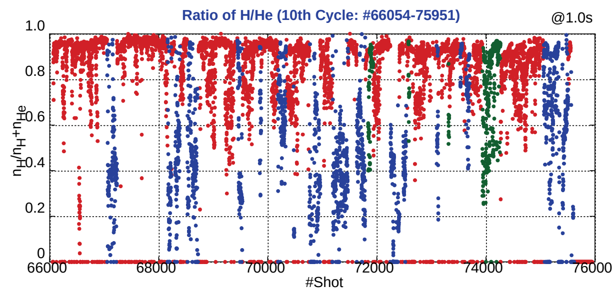

Fig.8 H/He flux ratio in the 10th cycle (2006) with H_2 discharges including H_2 pellet (red), He discharges (blue) and Ne-seeded discharges (green).

Abrupt Intense Radiation from Divertor Plates of the Large Helical Device

K. Narihara, I. Yamada, T. Minami and H. Hayashi

National Institute for Fusion Science, Toki 509-5292, Japan

This paper examines the phenomenon of abrupt intense radiation (AIR) from a graphite divortor plate measured by the DC-coupled Thomson scattering detectors on LHD. A time-integrated spectrum of this AIR resembles to a black body (BB) radiation mixed with plasma light line-radiation. We estimate the BB-radiation temperature from the ratios among signals from a five-color-channel polychromator. The BB-radiation temperature T_B, thus obtained, abruptly rises up to ~2000K and after some duration rapidly decays usually after a small drop in NBI power. Time evolution of BB radiation intensity calculated with this T_B well reproduces the observed signals. The experimental data are compared with 1D thermal transport simulations in graphite plate taking account of the nonlinear diffusivity. With the conventional thermal conduction model, including non-linear thermal diffusivity, the observed rapid T_B rise cannot be reproduced. Correlations between the size of AIR and various plasma/operational parameters are presented.

Keywords: Thomson scattering diagnostic, LHD, divertor plate

1. Introduction

Background radiation has degrading effects on Thomson scattering (TS) diagnostics [1]: it drops S/N ratio and sometimes introduces large systematic errors into the obtained data. In an extreme case the electron temperature (*Te*) and density (*ne*) profiles collapse as shown later. Even if the size of collapse is small, without quantitative data on the radiation intensity, the confidence on the obtained *Te* and *ne* profiles is low. In order to solve this problem to some extent, we installed 1040-channel scanning ADC so that the DC levels of the avalanche photo-diodes used for detecting the scattered light can be monitored. With this background light monitoring, we found that an abrupt intense radiation (AIR) often appears around divortor plates and invalidates TS data greatly. Intending to suppress or reduce the AIR, we examine this phenomenon.

2. Description of AIR

Figure 1(A) shows a *Te* and *ne* profiles with large collapse. The collapsed region coincides roughly with the scattering region that has a divortor plate in background scope of the light collection optics. The DC-coupled outputs (*DC_APD*) from light detectors 'seeing' this region exceed greatly 0.6V, which is upper limit for linearity for pulse response, thus invalidating the obtained data. (For DC response, linearity is preserved up to ~4 V.) It should be noted that the focal points of the light collection optics are on the laser beam, and hence the spatial distribution of *DC_APD*, Fig 1. (B), is not a real distribution but a convolution of it. Figure 2 shows

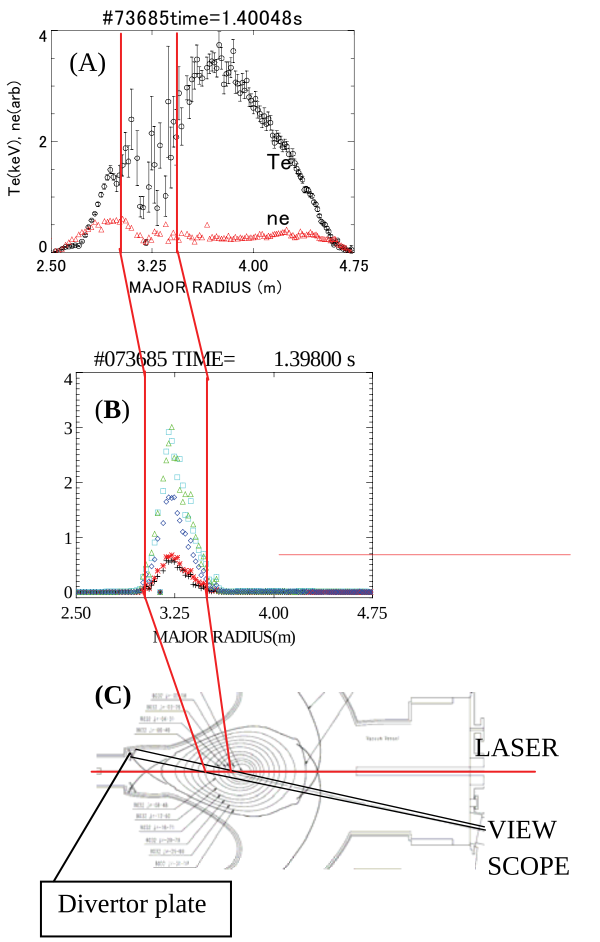

Fig. 1. (A) Collapsed Te and ne profiles. (B) Distribution of DC-outputs of APDs. (C) Thomson scattering configuration [2].

author's e-mail:narihara@nifs.ac.jp

the time evolutions of the 5-color-channel *DC_APD* signals from the polychromator#32 together with relevant plasma parameters. We can see that *DC_APD* starts to grow after additional NBI start its operation. It is hard to find a signal that well correlates with the startup of AIR.

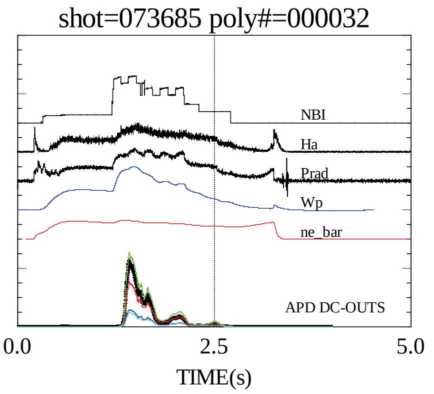

Fig. 2. Time evolutions of DC_APD together with the cord-averaged plasma density ne_bar, the diamagnetic energy Wp, the bolometer signal Prad, H-alpha, and total NBI power.

There seems to be a tendency, however, that an AIR sometimes appears at the time when the diamagnetic signal *Wp* approaches its peak. From the energy-flow equation: $P_{heat}= dW/dt + P_{out} + P_{rad}$, where P_{heat} is heating power, P_{out} is the wall loading power carried by particles and P_{rad} is radiation loss from plasma, the above statement leads us to an assumption that the AIR appears when P_{out} becomes large. This assumption is further supported by facts that there is a lower threshold in NBI power for AIR to occur and that the higher P_{rad} often reduces the size of AIR. Figure 3 (A) shows a time-integrated spectrum of the AIR appeared on the same shot as in Fig. 2 measured by a fiber-multi-channel spectrometer. The 3073K black body radiation spectrum from a standard lamp measured by the same spectrometer is shown in Fig. 3(B) for a reference. The spectrum of the AIR resembles well black body radiation.

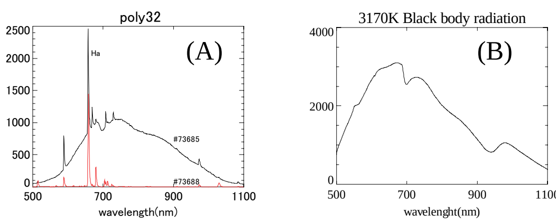

Fig. 3. (A) Time integrated multi-channel-spectrum of the light from the fiber connected to poly32 with/without AIR. (B) A 3170K BB radiation spectrum measured by the same spectrometer.

Assuming the black body radiation, we can estimate effective temperature of the AIR using the currently used polychromators, the spectrum of which is shown in Fig.4 (A) together with the BB radiation of various temperatures. The ratios F5/F1, F4/F1, F3/F1, F2/F1 as a function of T_B are shown in Fig. 4(B). The T_B that best fits to the observed signals as a function of time is shown in Fig. 5(A). The upper- and –lower limits of the error bars are given by the roots of the equation $H(T_B)=2*\min(H(T_B))$, where H is the residual square sum of the fitting. In the calculation, we set $T_B=0$ for signal < 10mV, to avoid large irregularities in T_B for small signals. Using this T_B-evolution, we can calculate the time evolution of signals as shown in Fig. 5(B), which surprisingly well reproduces the observed signals, Fig. 5(C) after signals reach their peaks. Here we assume that the BB emitting area is held constant. Although the BB assumption seems to approximately explain the observation, there is a difficulty in the startup phase: The T_B grows in a few ms, which is too rapidly to be realistic.

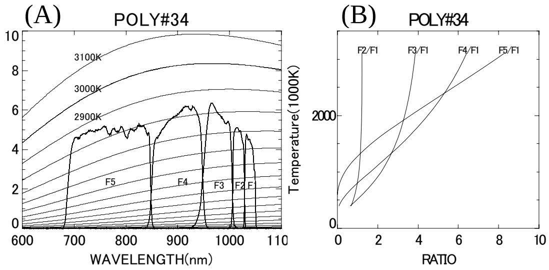

Fig. 4. (A) Responsivities of 5-color- polychromator #34 and BB radiation spectra of various temperatures. (B) Signal ratios among the five outputs vs. temperature.

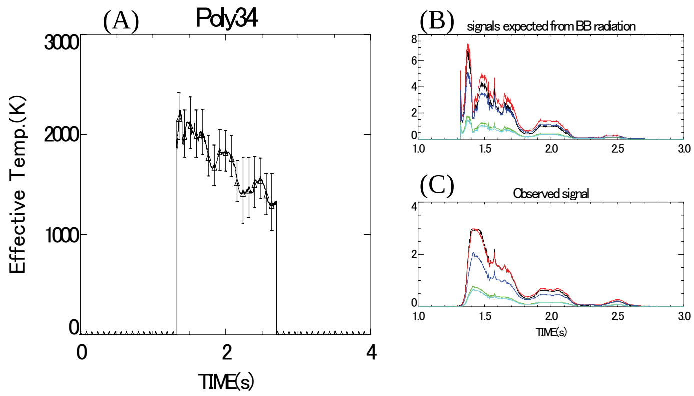

Fig. 5. (A) Deduced temperature evolution. (B). Calculated signal sizes from BB radiation of temperature shown left. (C): The observed signal size. Both waveforms are similar in shape.

3. 1D simulation

In order to examine the above fast rise of T_B, we consider 1D heat conduction model described below. One side of a graphite (x=0) is exposed to a heat flux q and emits BB-radiation σTs^4, where Ts is the surface temperature, and other end surface (x=15mm) is kept at a constant temperature $T(15)$=300K. We assume the heat is deposited in the surface layer of thickness τ. The heat diffusivity decreases rapidly as temperature rises as shown in Fig.6(B) [3], the non-linearity of which is expected to accelerate the temperature rise. An example of the numerical solution of the heat conduction equation

$$\frac{\partial T}{\partial t} = \alpha(T)\frac{\partial^2 T}{\partial x^2},$$

with boundary conditions

$$c\rho\tau\frac{\partial T_s}{\partial t} = q - \sigma T_s^{\ 4} + k\frac{\partial T_s}{\partial x}$$

and

$$T(15,t) = 300,$$

where c is heat capacity, ρ density, τ the thickness of heat deposition, σ Stefan-Boltzmann coefficient, k the heat conductivity, is shown in Fig. 6(A). We can see that as *q* increases the rise time becomes faster and the attainable temperature is higher. Within the above conventional model of heat conduction, we cannot reproduce the observed behavior of *Ts*. An exotic model such as bubbles or a crack formation beneath the heated surface, which switches off the heat conduction, may reproduce the observation. With this fast rise problem, we now hesitate to conclude the AIR is BB radiation. Further diagnostics such as IR camera will help us draw a conclusion.

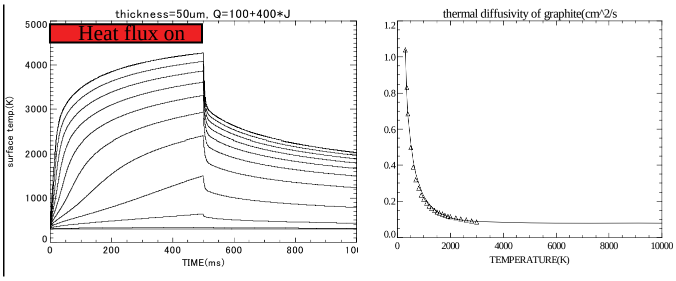

Fig. 6. Right: thermal heat diffusivity of graphite, which is highly non-linear function of temperature. Left: Examples of surface temperature evolutions for various heat flux. Heat deposition layer thickness is 50 μm. The top curve is Ts for q=3.7 kW/cm^2: From the top, q decreases by 400W/cm^2 from curve to curve.

4. Statistics

In order to get clues to the question what the AIR really is, we took statistics of the size of the AIR as a function of various operation/plasma parameters. Figure 7 shows the *DC_APD* distribution as a function of the major radius. The larger *DC_APD* appear in the range 3.6m≦ Rax ≦3.75m. Although the shot numbers on bins are largely different, they are large enough, except extremely inwards shifted cases, to show the general tendency. This tendency may be explained by fact that the particle/heat flux to inner-divertors is smaller for the outwards shifted configurations. Figure 8 shows *DC_APD* as a function of magnetic field intensity on the axis. There is a clear tendency that at higher magnetic fields, AIR is larger. This suggests that a stronger magnetic field may focus plasma flow more effectively to the divertor plate. Figure 9, bolometer signal vs. the size of AIR, indicates they anti-correlate. This seems to support our assumption that AIR is caused by heat flux to the divertor plate:

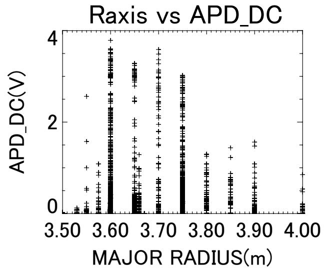

Fig. 7. Major radius vs. AIR size.

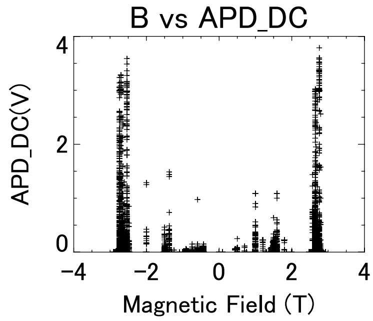

Fig. 8. Magnetic field intensity on the axis vs. AIR size.

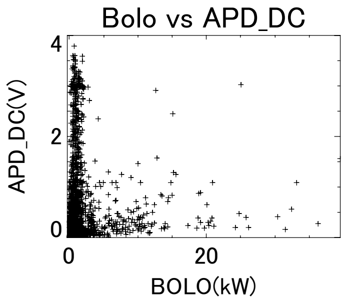

Fig. 9. Bolometer signal vs. AIR size.

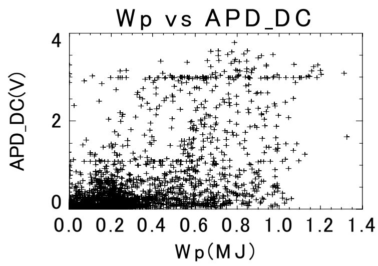

Fig. 10. Wp vs. AIR size.

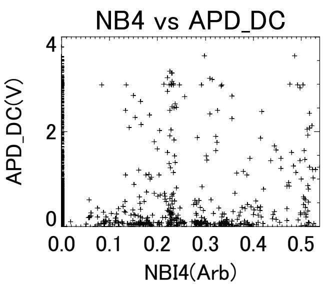

Fig. 11. NB4 injection power vs. AIR size.

higher radiation power lessens the wall-loading power, provided that the total loss power is held constant. Figure 10, *Wp* vs. AIR size relation, shows no correlation between them.

NB4 is injected in the radial direction, whereas the other NB, NB1, NB2 and NB3, are injected in tangential directions. It is expected that appreciably amount of the radially injected NB is promptly lost and hit divertor plate. In this respect, it is curious to investigate the correlation between NB4 power and AIR size. Figure 11 gives this. No correlation can be seen.

If the AIR is plasma light generated around the graphite divertor plate, it will accompany appreciable signal on the CIII-line-monitor installed on 1-O-port. Figure12, CIII vs. AIR size relation, however, reveals no positive correlation.

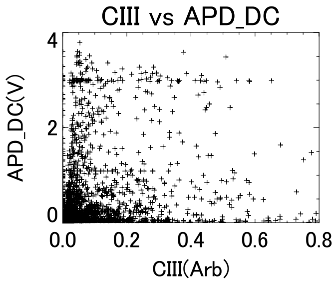

Fig. 12. CIII radiation vs. AIR size.

Figure 13 shows the distribution of *DC_APD* as a function of line averaged plasma density. There seems a high occurrence region in the lower density, but its significance is not yet clear.

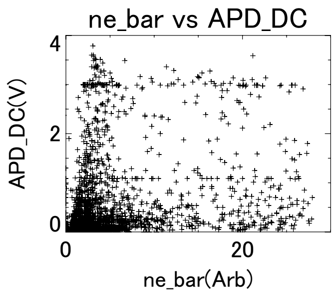

Fig. 13. ne_bar vs. AIR size.

5. Discussions and summary

The AIR poses a serious problem to the Thomson scattering diagnostic, but it seems that it has no appreciable adverse effect on the core plasma confinement. If the AIR is only black body radiation from the heated graphite plate, it is quite natural. On the other hand, if the AIR is radiation from plasma created on the surface of the divortor plate, there may be carbon impurity influx to the core plasma. But, up to now, no such indication has been observed. Even if the AIR is plasma radiation, the existence of the so-called stochastic region will shield the impurity influx efficiently.

We have not yet obtained a definite conclusion what the AIR really is. Probably, it is black body radiation from the heated divertor plate. But its very rapid rise makes us to hesitate to take this simple view. We are planning to replace the divertor plate with a new one with much higher heat conductance.

References

[1] K.Narihara, et al., *in ITC-16 proceedings, (2006).*
[2] K.Narihara, et al., Rev. Sci. Instrum. 72, 1122(2001).
[3] Thermo-physical properties of matter, Volume 10. Thermal Diffusivity, IFI/Plenum, New York-Washington 1970.

P1-068

Optimization of a closed divertor configuration for three dimensionally complicated magnetic structure in the LHD plasma periphery

M. Shoji, M. Kobayashi, S. Masuzaki, A. Iwamae[a], T. Watanabe, H. Yamada, A. Komori and LHD experimental groups

National Institute for Fusion Science, 322-6 Oroshi-cho, Toki 509-5292, Japan

[a]Department of Engineering Physics and Mechanics, Graduate School of Engineering, Kyoto

(Received day month year / Accepted day month year should be centered 10-point type)

The distribution of the strike points in an optimized closed divertor configuration with additional baffle plates installed in the toroidal ends of closed divertor components near lower and upper ports is calculated by tracing magnetic field lines from the last closed flux surface in various magnetic configurations (R_{ax}=3.50~3.90m). The calculation shows that the ratio of the number of the strike points on the baffle plates is maximum for R_{ax}=3.60m, showing that the plates are effective in this magnetic configuration. Neutral particle transport is investigated by a fully three-dimensional code EIRENE with a one-dimensional plasma fluid analysis on divertor legs, where the plasma parameter profiles on the legs are obtained by iterative calculation including interaction between the plasma and neutral particles. It shows that the baffle plates are ineffective for enhancing the pressure of neutral hydrogen molecules in the inboard side of the tours. The plates locally raise the pressure of molecular hydrogen near the baffle plates to more than 0.2 Pa which is enough to efficient particle control using the vacuum pumping systems installed near the baffle plates. The simulation proposes one possible candidate of optimized closed divertor configuration for three-dimensionally complicated magnetic structure in the LHD plasma periphery.

Keywords: plasma edge transport, neutral particle transport, EIRENE, closed divertor, plasma fluid analysis, strike points, baffle plate

1. Introduction

Control of the plasma density and neutral particles in the LHD plasma periphery is experimentally found to be essential for achieving super dense core (SDC) plasmas and sustaining long pulse discharges [1]. In the phase II experimental campaign, a closed divertor configuration with vacuum pumping systems is planned for efficient particle control. Magnetic components produced by two super-conducting coils (helical coils and poloidal coils) form three-dimensionally complicated magnetic field line structure in the plasma periphery. For this reason, we started optimization of the closed divertor configuration using a fully three-dimensional neutral particle transport code EIRENE with a one-dimensional plasma fluid analysis on divertor legs [2].

Previous neutral particle transport analysis in various magnetic configurations strongly suggests that installation of closed divertor components, which consist of baffle plates, a dome structure and slanted divertor plates which are installed along the space between two helical coils in the inboard side of the torus, is reasonable for efficient particle control, because the density of neutral particles is relatively high in the inboard side and the closed divertor components can keep the accessibility from outer ports for plasma heating and diagnostic systems. The calculations by the simulation are in good agreement with the measurements of polarization resolved H_α spectra and the vertical profiles of the line integrated H_α intensity [3]. The simulation predicts that the density of neutral hydrogen molecules in the inboard side for the closed divertor configuration rises by more than one order of magnitude compared to that in the present opened divertor case, which seems to be marginally acceptable for efficient particle control by the vacuum pumping systems.

Installation of additional baffle plates at the toroidal ends of the close divertor components near lower/upper ports can effectively contribute to further enhancement of the density of neutral particles in the inboard side. This is because the plates can confine neutral particles in the inboard side, and the plates change the position of the strike points (particle sources) from the lower/upper side to

author's e-mail: shoji@LHD.nifs.ac.jp

the inboard side.

This paper proposes one possible candidate of the optimized closed divertor configuration with the additional baffle plates. The effect of the baffle plates on particle control in the LHD plasma periphery is investigated by magnetic field line tracing and by using the neutral particle transport code with the one-dimensional plasma fluid analysis on the divertor legs.

2. Calculations of the Distribution of Strike Points

For designing of the optimized closed divertor configuration, the three-dimensional distribution of the particle source is an essential parameter for analyzing the spatial profile of the neutral particle density. The distribution of the source rate can be qualitatively estimated by that of the strike points on the divertor plates (made of carbon), which is experimentally supported by the measurements with the thermo-couples embedded in the divertor plates, Langmuir probes and H_α emission detectors. The strike point distribution is significantly changed by the radial position of the magnetic axis R_{ax}. We calculated the distribution of the strike points by tracing magnetic field lines from the last closed flux surface (LCFS) in a three-dimensional model including the geometry of the closed divertor [2]. Figure 1 (a) illustrates the closed divertor configuration and the calculations of the distribution of the strike points in various magnetic configurations (R_{ax}=3.60~3.90m). The purpose of the closed divertor is enhancement of the neutral particle density (molecular hydrogen) in the inboard side, which contributes efficient particle control by vacuum pumping systems installed in inner ports. The closed divertor components consist of a dome structure, baffle plates and slanted divertor plates. Neutral particles released from the divertor plates are led to the back side of the dome structure due to the reflection effect by the baffle plates locating between the main plasma and divertor region.

Figure 1 (b) gives the distribution of the strike points in the case with the additional baffle plates installed at the both toroidal ends of the closed divertor components. The additional plates change the distribution of the strike points originating from the one of the divertor legs near the lower/upper ports, which contributes to concentration of the strike points in the inboard side of the torus. The magnetic field lines on another divertor leg directly connect to the divertor plates located in the inboard side. The additional plates are expected to be effective for enhancement of the neutral pressure in the inboard side. Figure 2 shows the ratio of the number of the strike points on the additional baffle plates on the total number of the strike points in various magnetic configurations, which indicates that the ratio is maximum (more than 0.6) for

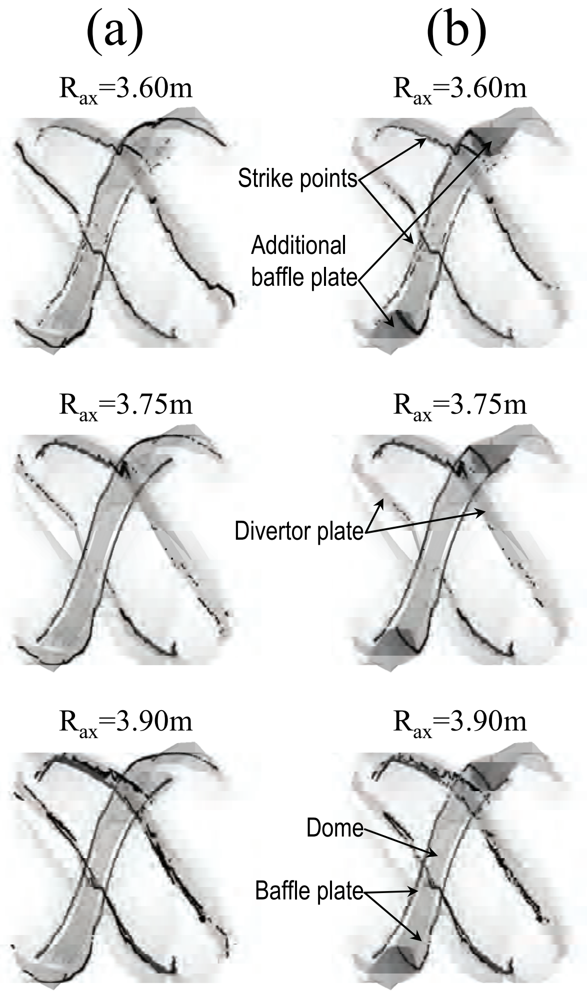

Fig.1 Three-dimensional distribution of the strike points (black dots) in the closed divertor configuration without (a) and with (b) additional baffle plates in various magnetic configurations (R_{ax}=3.60~3.90m).

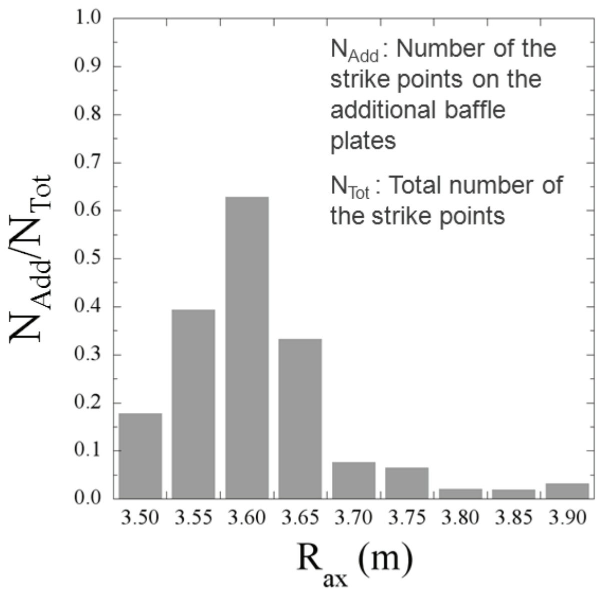

Fig.2 The ratio of the number of the strike points on additional baffle plates on the total number of the strike points in various magnetic configurations.

R_{ax}=3.60m. It means that the additional baffle plates are effective in this magnetic configuration which is the typical experimental condition for achieving high temperature and high confinement plasmas in LHD.

3. Neutral Particle Transport Simulation with a One-dimensional Plasma Fluid Analysis

EMC3-EIRENE code is widely used for detailed analysis of the plasma and neutral particle transport in the peripheral plasma in helical/stellarator and tokamak devices [4]. This sophisticated analysis by the fully three-dimensional plasma fluid code coupled with the neutral particle transport code is ideal but too time consuming. Furthermore, the code does not include the divertor legs due to some technical reasons. In order to overcome these restrictions, we extend the calculation domain so as to include the divertor legs with an assumption that the plasma parameter profiles inside the ergodic layer are fixed during the iteration process between the plasma and neutral particle transport. Following three differential equations for plasma density, momentum and energy are solved along the magnetic field lines on the divertor legs by using the Runge-Kutta method from the upstream of the divertor legs (in the proximity of X-points in the ergodic layer) to divertor plates [5],

$$\frac{d(nv_{//})}{ds} = S_p , \qquad (1)$$

$$\frac{d}{ds}(2nT + mnv_{//}^2) = -mv_{//} < \sigma v >_{cx} nn_0 , \qquad (2)$$

$$\frac{d}{ds}(5nTv_{//} - \kappa_{//}^0 T^{2.5} \frac{dT}{ds}) = Q_{loss} , \qquad (3)$$

where, S_p, $<\sigma v>_{cx}$, n_0, Q_{loss} are the particle source, the rate coefficient of charge exchange, the neutral density and the energy loss via ionization, respectively.

The connection length of the magnetic field line on divertor legs is very short (less than several meters), where the one dimensional plasma fluid analysis is applicable, because the plasma transport transverse to the magnetic field lines is negligible [6]. Iterative calculation of the plasma parameter profiles on the divertor legs coupled with neutral particle profiles (hydrogen atoms and molecules) gives a converged solution under the following two boundary conditions within a reasonable computation time:

1. The plasma flow velocity ($v_{//}$) at the surface of the divertor plates is fixed to be a sound speed c_s for satisfying the Bohm criterion,
2. Three invariants (density, momentum and energy) at the upstream of the divertor legs are fixed to be the calculations by the EMC3-EIRENE code in the case of P_{input}=8 MW, n_e^{LCFS}~4×10^{19} cm^{-3}, Γ_{total}=3.6×10^4 A.

Conversion of the one-dimensional plasma parameter profiles along the magnetic field lines on the divertor legs to that in the three-dimensional grid model in the EIRENE code is based on the procedure in a track-length estimator [7]. The parameters in a grid are calculated from the total path length of magnetic field lines in the grid, the parameter profile along the magnetic field line and the grid volume.

4. Calculations of the Density Profile of Neutral Particles in the Optimized Closed Divertor Configuration

Figure 3 shows four poloidal cross sections of the calculated density profile of neutral hydrogen molecules for the conventional closed divertor configuration (without the additional baffle plates) in the case of R_{ax}=3.60m, showing that enhancement of neutral density in the inboard side of the torus (ϕ=18°). In this calculation, the absolute neutral density is strongly dependent on the particle reflection ratio of the divertor plates. We determined the reflection ratio (R_{div}) to be 0.3 so as to lead the neutral pressure of the molecular hydrogen in the inboard side of the torus to be about 0.001 Pa for the present opened divertor configuration. This neutral pressure roughly agrees with measurements with a fast ion gauge during typical plasma discharges in this magnetic configuration [8].

The simple particle balance analysis during fueling pellet injection indicates that the neutral pressure of hydrogen molecules in the order of 0.1 Pa is favorable for efficient particle control and pumping. The calculation by the neutral particle transport simulation indicates that the pressure in the inboard side is expected to be about 0.022 Pa (n_{H2}~5×10^{12} cm^{-3}) in the conventional closed divertor configuration, which seems to be marginally acceptable for particle control in the plasma periphery. Further enhancement of the pressure of neutral particles is strongly desired for improving particle pumping efficiency in the closed divertor configuration.

We newly introduce additional baffle plates (made of carbon) into the three-dimensional grid model for the neutral particle transport simulation in LHD plasmas. We can introduce arbitrary shaped plates into the grid model by using the function of an 'additional surface' in EIRENE code. The additional plates are defined by some points (more than two) of Cartesian coordinate in the grid model [9]. The released particles from the additional plates are assumed to be neutral hydrogen molecules with the energy of the room temperature (300K), and the direction of the released molecules is normal to the plates. The quantity and profile of released hydrogen molecules are determined from the particle reflection ratio, the angle between the magnetic field lines and the baffle plates, and the calculated plasma flux which position is determined by averaging the coordinate of the strike points on the baffle plates (point neutral sources are assumed). In the closed divertor components, the quantity, profile and species of released neutral particles are determined by the code with TRIM particle reflection data base [9].

Figure 4 gives the four poloidal cross sections of the density profile of neutral hydrogen molecules for the optimized closed divertor configuration (with the additional baffle plates). It indicates that the pressure of neutral hydrogen molecules in the inboard side of the tours is about 0.021 Pa (n_{H2}~5.0×10^{12} cm^{-3}) which is not significantly different from that in the conventional closed divertor. While the additional baffle plates are found to be ineffective in enhancing the neutral pressure in the inboard side, the calculation shows that the molecular hydrogen density is locally high on the dome structure near the both baffle plates as shown in the toroidal angle ϕ=8 and 28°. The neutral pressure reaches to more than 0.2 Pa which is

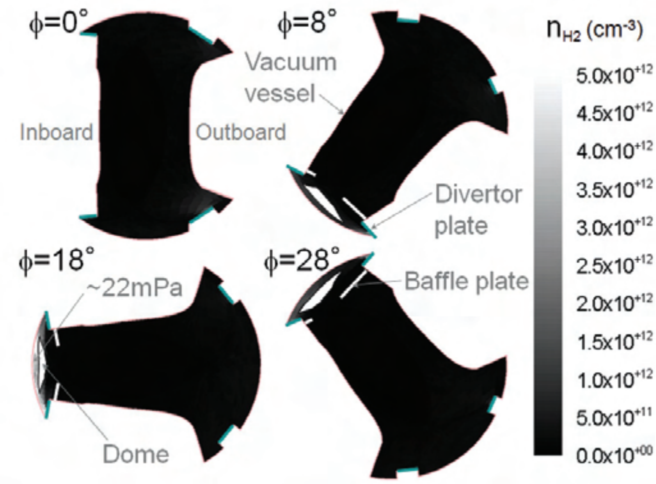

Fig.3 Four poloidal cross-sections of the calculated density profile of neutral hydrogen molecules for the conventional closed divertor configuration (without additional baffle plates).

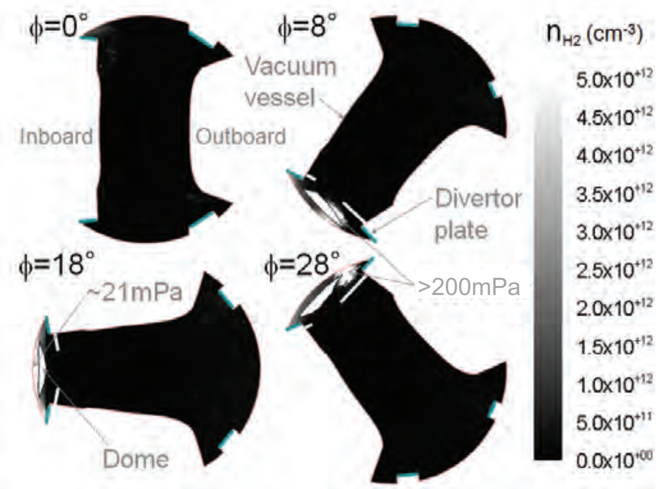

Fig.4 Four poloidal cross-sections of the calculated density profile of neutral hydrogen molecules for the optimized closed divertor configuration with additional baffle plates near lower/upper ports.

sufficient for efficient particle control. The neutral particle transport simulation strongly suggests that installation of the additional baffle plates at the toroidal ends of the closed divertor components with vacuum pumping systems installed in the dome structure near the baffle plates is quite effective for particle control and pumping in the LHD plasma periphery.

5. Summary

For finding an optimized closed divertor configuration, the effect of the additional baffle plates installed in the both toroidal ends of the closed divertor components near lower /upper ports is investigated.

Magnetic field line tracing from the last closed flux surface shows that the additional baffle plates change the position of the strike points from the lower/upper side to the inboard side. The ratio of the number of the strike points on the additional plates on the total number of the strike points in various magnetic configurations indicates that the baffle plates is effective in the case of R_{ax}=3.60m.

The neutral particle transport simulation with the one-dimensional plasma fluid analysis on the divertor legs shows that the additional baffle plates is ineffective in enhancement of the density of neutral particle (hydrogen molecules) in the inboard side of the torus. The baffle plates can locally raise the molecular hydrogen density near the additional baffle plates, where the molecular density is sufficient for efficient particle control.

The investigation by the neutral particle transport simulation proposes one possible candidate of an optimized closed divertor configuration in which the additional baffle plates are installed in the toroidal ends of the closed divertor components with vacuum pumping systems located in the dome structure near the baffle plates. The fully three-dimensional neutral particle transport simulation is successfully applied to finding an optimized closed divertor configuration for complicated magnetic structure in the LHD plasma periphery

References

[1] N. Ohyabu *et al.*, Phys. Rev. Lett. **97**, 055002 (2006).
[2] M. Shoji *et al.*, Contrib. Plasma Physics (to be published).
[3] A. Iwamae *et al.*, Phys. Plasmas **12**, 042501 (2005).
[4] Y. Feng *et al.*, Plasma Phys. Control. Fusion **44**, 611 (2002).
[5] P.C. Stangeby, *The plasma boundary of magnetic fusion devices* (Institute of Physics Publishing, Bristol and Philadelphia, 2000) p.423.
[6] T. Morisaki *et al.*, J. Nucl. Mater. **313-316**, 548 (2003).
[7] J. Spanier *et al.*, *Monte Carlo Principles and Neutron Transport Problem* (Addison-Wesley Pub., Reading Mass, 1969) p.66.
[8] M. Kobayashi *et al.*, J. Nucl. Mater. **350**, 40 (2006).
[9] D. Reiter, Technical Report Jul-1947, KFA Juelich, Germany (1984).

Proceedings of ITC/ISHW2007

Tracer impurity transport inside an IDB plasma of LHD

Naoki TAMURA, Kuninori SATO, Pavel R GONCHAROV, Hisamichi FUNABA, Yuri L IGITKHANOV, Shigeru SUDO, Ichihiro YAMADA, Kazumichi NARIHARA, Kenji TANAKA, Clive MICHAEL, Kazuo KAWAHATA, Shinji YOSHIMURA, Byron J PETERSON, Ryuichi SAKAMOTO, Masahiro KOBAYASHI, Hiroshi YAMADA, Nobuyoshi OYABU, Akio KOMORI and LHD Experimental Group

National Institute for Fusion Science, Toki 509-5292, Japan

Recently, in LHD, extremely high-density region accompanied with an Internal Diffusion Barrier (IDB) has been established by optimizing a pellet fueling and a magnetic configuration. In order to understand impurity transport inside the IDB plasma of LHD, a tracer-encapsulated solid pellet (TESPEL), which can deposit a tracer impurity locally inside the plasma, injection into the IDB plasma has been performed. In this experiment, titanium (Ti) particles are loaded into the TESPEL as a tracer. The local deposition of the Ti tracer impurity inside the IDB is successfully achieved with the help of the TESPEL technique, which is confirmed by an optical measurement. Considering temporal change in both electron density and electron temperature, temporal behavior of line emissions from the Ti tracer impurity ions measured by a vacuum ultra violet spectrometer indicates the Ti tracer impurity ions seems to be accumulated inside the IDB.

Keywords: impurity transport, TESPEL, local tracer deposition, ultrahigh density, internal diffusion barrier

1. Introduction

Understanding and control of impurity transport in magnetically confined plasmas is still an important issue for achieving a practical fusion reactor, since impurities can significantly influence the reactor performance through such effects as radiative losses, radiative instabilities, fuel dilution and so on. Especially when an “impurity accumulation” takes place in the core plasma, these problems become more acute. Thus impurity transport study has been performed diligently in many tokamaks and stellarators/heliotrons so far [1-6].

In Large Helical Device (LHD) [7], ultrahigh density region (the maximum density in the region is up to 1 x 10^{21} m^{-3}) accompanied with an Internal Diffusion Barrier (IDB) has been established by optimizing a pellet fueling and a magnetic configuration [8, 9]. One of the important points to be clarified for the IDB plasmas is whether the IDB causes an impurity accumulation or not. So far, the performance degradation of the IDB plasmas due to the impurity accumulation has not been observed despite the existence of a negative radial electric field. In LHD, a tracer-encapsulated solid pellet (TESPEL) [5, 10], which allow us to obtain a three-dimensionally localized deposition of the tracer impurity inside the plasma, has been utilized for impurity transport study. When a low-level transport such as an internal transport barrier for impurity is established inside the plasma, the TESPEL technique has a great advantage in the study of the transport inside and in the vicinity of that region, since it takes longer for an intrinsic impurity influx from the plasma facing components to arrive at there.

So TESPEL injection has been tried to investigate impurity transport inside the IDB plasma.

2. Experimental setup

The LHD with a heliotron type magnetic configuration is the world’s largest helical device and has superconducting l/m = 2/10 helical coils and 3 pairs of superconducting poloidal coils. In this experiment, the position of a magnetic axis R_{ax} is 3.85 m and the magnetic field strength at the axis is 2.571 T. The plasma was started up by an electron cyclotron heating and heated additionally by a tangential neutral beam injection (NBI). And then the ultrahigh core electron density accompanied with the IDB is obtained by a multiple solid hydrogen pellet injection [11], in which the size of the pellet and the time interval of injection are optimized. In order to introduce a tracer impurity inside the IDB, a TESPEL is utilized. As a tracer impurity, titanium (Ti) particles, the total amount of which is approximately 2 x 10^{17} particles, are loaded into the TESPEL. The TESPEL injector is installed on the equatorial plane at Port 3-O of LHD and the TESPEL is injected from the outboard side of the LHD plasma. A detailed radial profile of electron density n_e and electron temperature T_e is measured with a Thomson scattering system. Total radiated power P_{rad} is measured by a wide

author’s e-mail: ntamura@LHD.nifs.ac.jp

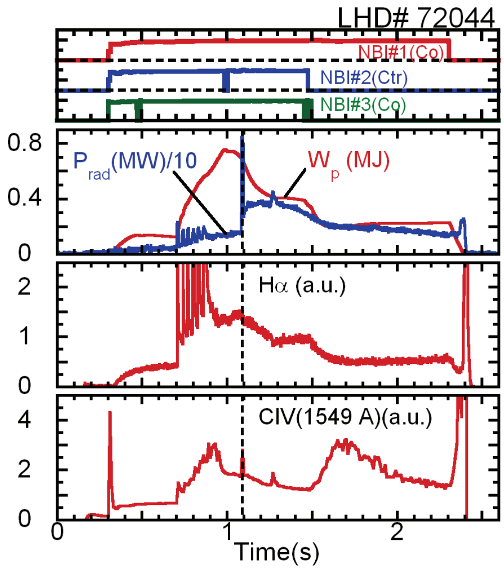

Fig. 1 Typical waveforms of the IDB plasma with TESPEL injection. A vertical dashed line denotes the TESPEL injection time, $t \sim 1.09$ s.

angle metal foil bolometer, which is installed at the same port (Port 3-O) as the TESPEL injector and plasma radiation light is done by absolute extreme ultra violet silicon photodiode (AXUVD) arrays, which are installed at Port 3.5U and 4-O on a semi-tangential cross-section in LHD [12]. The temporal behavior of the emissions in a vacuum ultra violet (VUV) domain from the Ti tracer ions is measured by a Schwob-Fraenkel soft x-ray multi-channel spectrometer (SOXMOS, typical exposure time ~ 50 ms).

3. Tracer Impurity Injection into IDB Plasma

Figure 1 shows typical waveforms of the IDB plasma with the TESPEL injection. In this discharge, as can be clearly seen in the Hα signal, the multiple solid hydrogen pellet injection is performed from $t = 0.71$ s to $t = 0.86$ s and then the ultrahigh density region with the IDB is established. And then The TESPEL is injected at $t \sim 1.09$ s. At this time there is a very sharp peak in the P_{rad}. This is because the wide angle bolometer, which is installed at the same port as the TESPEL injector, can also observe the emissions from the TESPEL ablation cloud. After this sharp peak, the P_{rad} is higher than that during the period from the end of the multiple pellet injection through until the time of the TESPEL injection (the period of the IDB plasma without the Ti tracer impurity) and remains at the higher level for about 300 ms. And then the P_{rad} is gradually decreased, which is started before NBIs (#2 and #3) are turned off. At about $t = 1.3$ s, a small peak can be seen in the signals of the P_{rad} and the C IV. This has no relationship to the TESPEL injection. This might be because carbon flakes fell into the plasma.

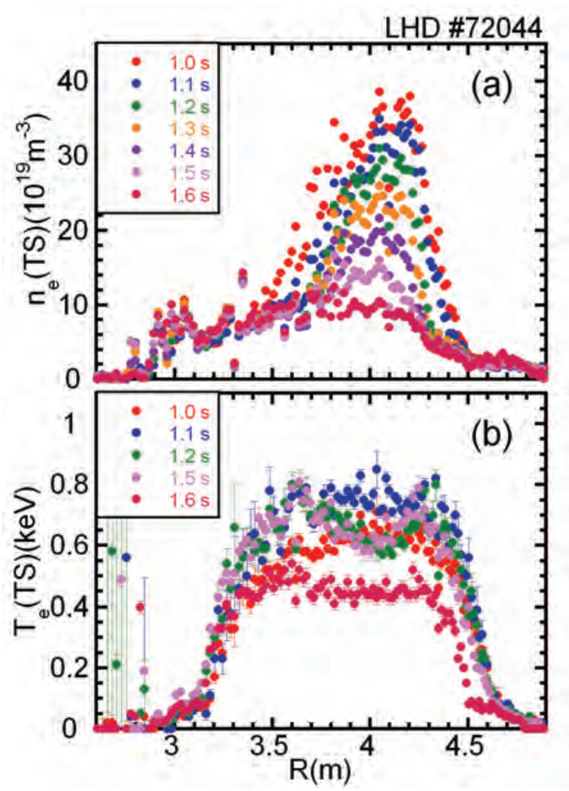

Fig. 2 Radial profile of (a) electron density n_e and (b) electron temperature T_e measured by the Thomson scattering system. TESPEL is injected at $t \sim 1.09$ s.

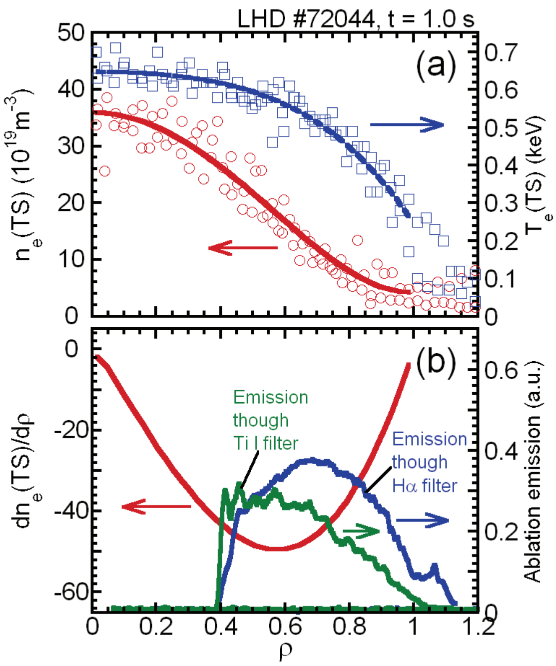

Fig. 3 (a) Electron density and electron temperature measured by the Thomson scattering system at $t = 1.0$ s before the TESPEL injection as a function of normalized averaged minor radius and (b) electron density gradient and TESPEL ablation emissions as a function of the normalized averaged minor radius. Ti-tracer would be deposited between $\rho = 0.4$ and $\rho = 0.5$.

Figure 2 shows radial profiles of n_e and T_e during the period from t = 1.0 s to t = 1.6 s. The ultrahigh density region fades gradually during this period and vanished completely at t = 1.6 s. The TESPEL injection, which is done at t ~ 1.09 s, seems to have little impact on the IDB. After the TESPEL injection (from t = 1.2 s), the T_e profile becomes the hollow profile, which remains until t = 1.5 s. This could be ascribed to the accumulation of the Ti tracer impurity inside the IDB.

Figure 3 (a) shows n_e and T_e at t = 1.0 s before the TESPEL injection as a function of the normalized averaged minor radius. To project the *R*-coordinate on the ρ-coordinate, the three-dimensional free boundary MHD equilibrium code VMEC is used. As seen in Fig. 3(a), the ultrahigh density region can be seen in a wide region of the plasma (The value of n_e with over 1.0 x 10^{20} m^{-3} is seen inside ρ ~ 0.75.) As can be seen in Fig. 3(b), the TESPEL penetrates deeply inside the IDB plasma and consequently the Ti tracer is deposited between ρ = 0.4 and ρ = 0.5. Thus the deposition of Ti tracer impurity inside the IDB is successfully achieved.

4. Temporal behavior of tracer impurity deposited inside the IDB

Figure 4(a) shows temporal evolutions of sight-line-integrated signals of AXUVD arrays, which are not equipped with any optical filters. Just after the TESPEL injection, the signals of the all channel in both arrays are increased drastically. Shortly thereafter the signals of the all channels except the channel 13 are decreased gradually (the signal of the channel 13 in both arrays is increased more and sustained.). Considering the geometry of line-of-sight of AXUVD arrays as shown in fig. 4(b), the profile of plasma radiation light become extremely peaky after the TESPEL injection. Moreover, taking the gradual decrease in n_e and no change in T_e during the period from t = 1.2 s to t = 1.5 s into account, the signals of AXUVD arrays suggests that the Ti tracer impurity is accumulated inside the IDB. Figure 5 shows temporal behavior of VUV emissions (Ti XV (O-like), 11.50 nm and Ti XI (Mg-like), 8.772 nm) from the Ti tracer ions measured with the SOXMOS. Just after the TESPEL injection, Both VUV emissions are increased rapidly and then are decreased gradually. When two NBIs (#2 and #3) are turned off at t = 1.5 s, the Ti XV intensity is drastically decreased, but Ti XI is not. Taking the gradual change in n_e and no change in T_e during the period from t = 1.2 s and t = 1.5 s into account, the experimental results obtained by the VUV spectrometer again suggest that the Ti tracer impurity deposited inside the ultrahigh core density region is accumulated.

In order to estimate quantitatively impurity transport inside the ultrahigh core density region, impurity

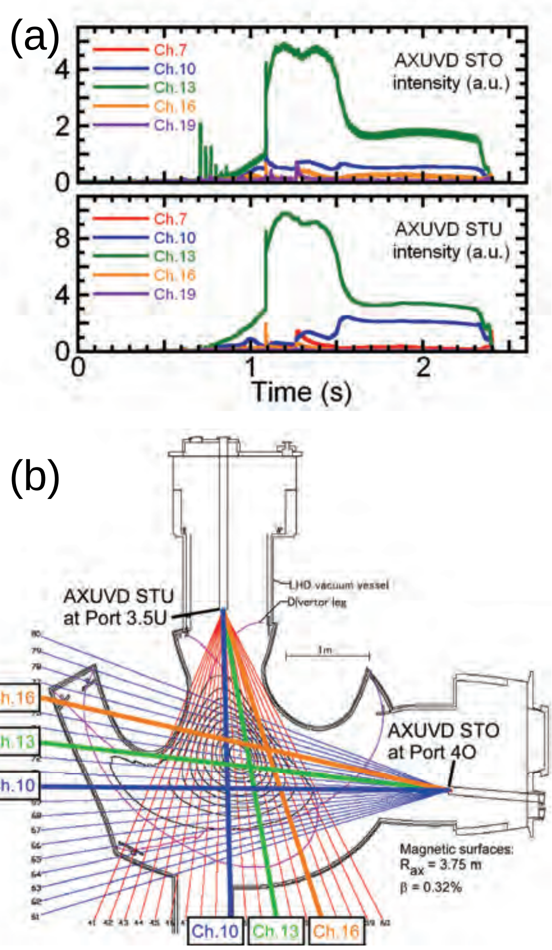

Fig. 4 (a) Temporal evolutions of AXUVD arrays' signals. TESPEL injection time is t ~ 1.09 s. (b) Line-of-sight of corresponding AXUVD arrays. Displayed magnetic surface is just an example.

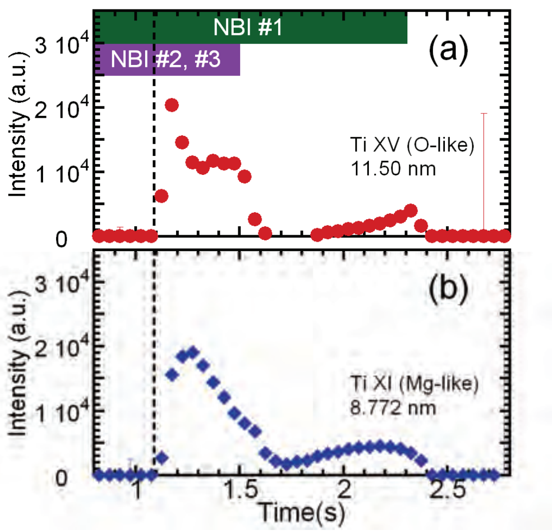

Fig. 5 Temporal evolutions of (a) Ti XV (O-like, 11.50 nm) and (b) Ti XI (Mg-like, 8.772 nm) measured with a VUV spectrometer. NBI #2 and #3 turned off at t = 1.5 s and NBI #1 turned off at t = 2.3 s.

transport analysis, taking temporal change in n_e and T_e into account, will be performed with 1-D transport code, such as MIST and Strahl. Further TESPEL injection experiments will be performed to obtain the tracer deposition inside and outside the IDB, allowing us to know qualitatively the effect of IDB on impurity transport.

5. Concluding remarks

Recently, in LHD, the ultrahigh core electron density accompanied with the internal diffusion barrier has been obtained. In order to investigate impurity transport inside the IDB, Ti tracer impurity injection into the ultrahigh core density region was tried by means of TESPEL. The local deposition of the Ti tracer impurity in the ultrahigh core density region is successfully achieved. Temporal behavior of the line emissions from the Ti tracer impurity ion has been clearly observed with the VUV spectrometer. Taking temporal change in both n_e and T_e into account, the Ti tracer impurity ions seems to be accumulated inside the IDB.

Acknowledgement

The authors acknowledge all of the technical staff of NIFS for their excellent support. They also would like to thank Prof. O. Motojima (Director of NIFS) for his continuous encouragement. This work is partly supported by a Grant-in-Aid for Scientific Research (B) (No. 19340179) from Japan Society for the Promotion of Science, a Grant-in-Aid for Young Scientists (B) (No. 19740349) from MEXT Japan and a budgetary Grant-in-Aid No. NIFS07ULHH510 and NIFS07ULHH524 of the National Institute for Fusion Science.

References

[1] R. Guirlet *et al.*, Nucl. Fusion **48**, B63 (2006).
[2] D. Stutman et al., Phys. Plasma **10**, 4387 (2003).
[3] K. Ida *et al.*, Plasma Phys. Control. Fusion **45**, 1931 (2003).
[4] Y. Nakamura *et al.*, Nucl. Fusion **43**, 219 (2003).
[5] N. Tamura *et al.*, Plasma Phys. Control. Fusion **45**, 27 (2003).
[6] H. Nozato et al., Phys. Plasmas **13**, 092502 (2006).
[7] O. Motojima *et al.*, Phys. Plasmas **6**, 1843 (1999).
[8] H. Yamada *et al.*, 34th EPS Conf. on Plasma Physics (Warsaw, Poland) (2007) I4.004.
[9] R. Sakamoto *et al*, this conference.
[10] S. Sudo *et al.*, Plasma Phys. Control. Fusion **44**, 129 (2002).
[11] H. Yamada *et al.*, Fusion Eng. Des. **49-50**, 915 (2000).
[12] B. J. Peterson *et al.*, Plasma Phys. Control. Fusion **45**, 1167 (2003)

Proceedings of ITC/ISHW2007

The DED at TEXTOR: transport and topological properties of a helical divertor

M. Lehnen[1)], S. Abdullaev[1)], S. Brezinsek[1)], M. Clever[1)], J.W. Coenen[1)], K.H. Finken[1)], M. von Hellermann[2)], M.W. Jakubowski[3)], D. Reiter[1)], U. Samm[1)], D. Schega[1)], O. Schmitz[1)], H. Stoschus[1)], B. Unterberg[1)] and the TEXTOR team

[1)] *Institut für Plasmaphysik, Forschungszentrum Jülich GmbH, EURATOM Association, Trilateral Euregio Cluster, D-52425 Jülich, Germany*
[2)] *FOM-Institute for Plasma Physics Rijnhuizen, Association EURATOM-FOM. Trilateral Euregio Cluster, The Netherlands, www.rijnh.nl*
[3)] *Max-Planck-Institut für Plasmaphysik, IPP-EURATOM Association, Teilinstitut Greifswald, Wendelsteinstr. 1, 17491 Greifswald, Germany*

The topological and transport properties in the edge plasma of the dynamic ergodic divertor is studied to clarify the functionality of this type of helical divertor. The heat and particle fluxes at the DED target plates were measured with Langmuir probes. Peak fluxes are found where field lines end, which penetrate deep into the plasma. The comparison of the measured target profiles to the magnetic topology shows, that heat and particles are mainly transported to the target plates via flux tubes of short connection length. About 65% of the fluxes are found in areas, where field lines with a connection length of 1-2 poloidal turns connect to the target. Analysis of the source distribution shows, that about 40% of the ion sources lie inside the downstream area of the divertor. The high fraction of convective heat flux prevents from establishing high recycling in the divertor for the pulse type discussed here.

Keywords: TEXTOR, stochastic plasmas, divertor

Introduction

The aim of this paper is to quantify the particle and power exhaust capabilities of the dynamic ergodic divertor (DED) at TEXTOR. The DED is a helical type of divertor with an open structure, comparable to the ergodic divertor in ToreSupra [1] . Such a divertor has topological similarities to helical or island divertors in heliotrons [2] or stellarators [3]. The ergodic divertor, existing of 16 helical coils at the HFS of TEXTOR, generates a resonant magnetic perturbation which focuses the particle and heat flux onto divertor target plates. In contrast to a poloidal divertor with a clear boundary between scrape-off layer and confined plasma, the above mentioned divertor types have a region with magnetic islands in the edge layer. By island overlap, this area turns (partly) into an ergodic layer.

Topology

The magnetic topology of the DED is determined by the position of the resonant surfaces (surfaces with low rational safety factor) and the base mode of the divertor coil current distribution [4]. Three base modes can be chosen with poloidal/toroidal mode numbers of $m/n = 3/1, 6/2$ and $12/4$. The spectrum of the $m/n = 6/2$ perturbation field is given in figure 1. Depending on the base mode, 2, 4 or 8 helical strike zones appear on the divertor target. An example of the target footprint for $m/n = 6/2$ is

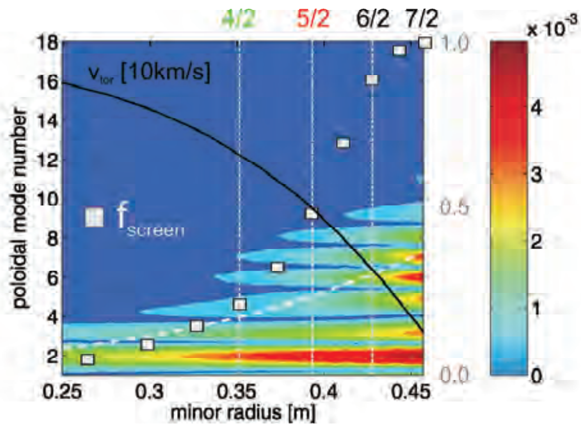

Fig. 1 *Spectrum of the perturbation field B_{m2} [T] for $m/n = 6/2$. The white dashed line indicates the position of the resonances. The gray rectangles give the screening factor for a typical edge rotation.*

given in figure 2. The colors indicate the penetration depth of the field lines. Peak particle and heat fluxes are found where field lines of long connection length hit the target. This is caused by the deep penetration of these field lines up to the last closed flux surface (LCFS). Flux tubes of one poloidal turn length are positioned further away from the LCFS [5, 6, 7]. They are filled by diffusion and can take a substantial part of the particle and heat to the target. The target structure is sensitive to the plasma equilibrium,

author's e-mail: m.lehnen@fz-juelich.de

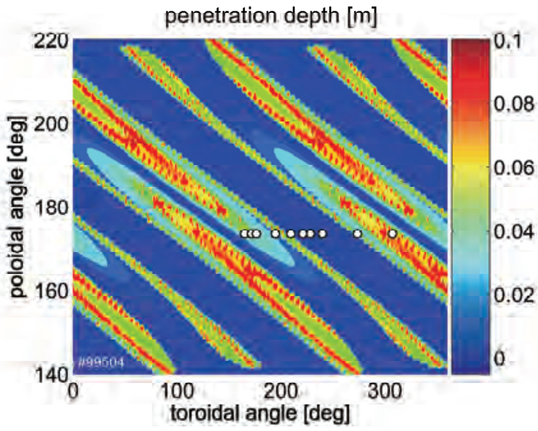

Fig. 2 *Map of the penetration depth of field lines starting on the DED target. The white circles indicate the position of the target Langmuir probes.*

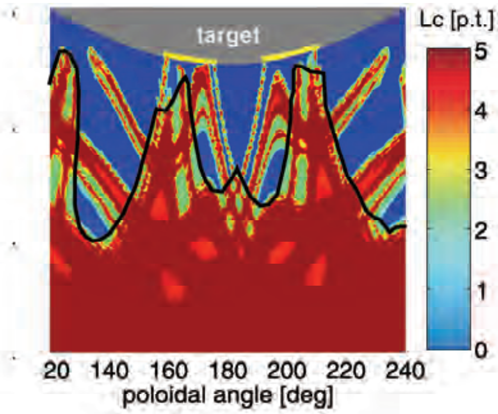

Fig. 3 *Connection length of the field lines passing the poloidal plane in front of the target at ϕ = 180°. The strike lines are indicated in yellow. The black line indicates the boundary of the downstream area.*

e.g. edge safety factor, plasma beta and plasma position. Moreover, plasma rotation can lead to screening currents, reducing the perturbation at the resonances [8, 9]. An example for a screening factor is indicated in figure 1; the toroidal rotation increases from about 1 km/s at the LCFS up to 10 km/s in the plasma center. The screening is relatively weak at the very edge, because of low plasma rotation and low temperature. Towards the plasma center, the screening increases. Thus the magnetic topology calculated usually for the vacuum case is valid for the outermost resonance layers. However, further inside, the size of the islands shrinks with higher plasma rotation and the width of the ergodic area is affected. In the following we concentrate on a pulse with $m/n = 6/2$, $q_a = 3.6$, $\beta \approx 0.45$ and the horizontal position off-center by $2-5$ cm towards the HFS to ensure particle recycling only at the divertor target plates.

A poloidal cut through the magnetic structure at ϕ = 180° is given in figure 3 for full perturbation field. This plot shows the connection length of the field lines from target to target as a function of poloidal angle and radius. A strong intermixture between field line bundles of long and short connection length exists. The particles and heat are guided to the target along complex structures of about 15 cm width in poloidal direction, when touching the target. It is remarkable, that the wetted area is mainly defined by the topology rather than by transport properties (c.f. [10]). The field line bundles with short connection length of less than 5 poloidal turns constitute the so called laminar area of about 7 cm width in this example. The link between last closed flux surface (LCFS) and this laminar region is the ergodic area of about 4 cm width.

Target Loads

Figure 4 shows the particle and heat flux at the target measured by Langmuir probes which are indicated in figure 2. A full profile is achieved by sweeping the strike point by ±22.5° in toroidal direction. This is possible with a coil current of 3.75 kA, which is half of the nominal coil current. The discharge had a total heating power of 1.1 MW and a radiated power of 0.5 MW, thus the power entering the edge layer P_{edge} is about 0.6 MW. The wetted area is, for the case shown here, A = 2.4m^2. The radial decay of heat and particle flux is mapped on the poloidal coordinate on the target with an expansion of about 2. From the probe measurements, we get an average parallel heat flux of about 20MWm^{-2} in the strike point, which is consistent with a perpendicular heat flux of $P_{edge}/A \approx$ 0.3MWm^{-2}, taking into account an average pitch angle of about 0.8° at the target. Because of the very shallow angle, slight misalignment of the target tiles leads to a non-regular distribution of the heat along the strike points in toroidal direction as seen by the infra-red camera [11]. However, the probes stick out by 2 mm (dome probe with r = 2 mm) and are therefore less sensitive to flux shadowing.

Additionally to the fluxes, the connection length L_c and also the penetration depth Δr of the field lines is indicated in figure 4. The calculation was done by field line mapping. To fit the target profiles best, a slight deviation from the experimental settings had to be chosen: a 5 kA higher plasma current (less than 2% higher than the measured current) and a 6° shift in toroidal direction. With this, the best fit of the strike point separation and toroidal position is achieved. Such adaptations are justified, taking into account the measurement errors on the discharge parameter and the uncertainties in the safety factor profile assumed for the field line mapping. Additionally, the probe has a radial extent of 2 mm, giving an uncertainty in toroidal direction of about 10 cm.

The area with L_c < 1 poloidal turn (p.t.) is equivalent to the private flux region. In this area almost no flux is reaching the divertor. About 65% of the particle and heat flux is transported to the target plates via flux tubes with 1 or 2 poloidal turns (L_c = 40 – 80 m). The magnitude of the

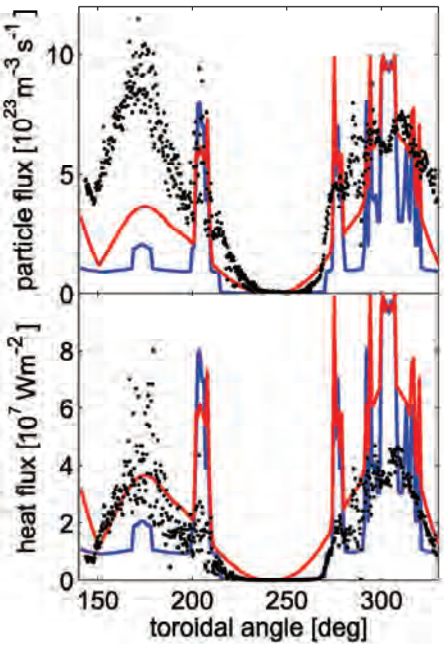

Fig. 4 *Particle flux on the target along the toroidal direction. The red curve gives the field line penetration depth in [10^{-2}m] (right axis) and the blue curve the connection length from target to target in poloidal turns (right axis).*

heat and particle flux depends on the penetration depth of the field lines with peak fluxes at field lines with deep radial penetration (c.f. [12, 13]). Those field lines are closest to the LCFS. The thickness of the perturbed edge layer and thus the maximum Δr is about 11 cm. The field lines with short connection length penetrate about 4 cm towards the LCFS. Only after many poloidal turns the field lines reach the innermost ergodised island chain and are thus close to the LCFS. However, the peak flux at the target for these field lines is not larger than that of the laminar field lines.

The information of the field line penetration in addition to the toroidal profiles of the fluxes can be used to reconstruct radial profiles of parallel heat and particle flux. The increase of the fluxes with Δr is shown in figure 5. Flux in the private flux region (L_c < 8m) is indicated in blue, flux in the laminar field line bundles with L_c = 40 – 80m are given in red and green are the data points for L_c > 2p.t.. From these profiles, e-folding lengths can be estimated. For this analysis the toroidal range with $\phi < 250°$ was chosen, because of the large fraction of short flux tubes. The e-folding lengths in the PFR is small, because of the short connection length: $\lambda_\Gamma = 3.5 \pm 0.4$ mm and $\lambda_q = 2.4 \pm 0.2$ mm for particle and heat flux. In the laminar flux bundles, these values are significant higher: $\lambda_\Gamma = (28 \pm 4)$ mm and $\lambda_q = (16 \pm 2)$ mm. The ratio between the e-folding lengths of PFR and flux tubes corresponds to the ratio of the connection lengths. Furthermore, the e-folding length of the electron density and temperature can be estimated to be $\lambda_T = 38 \pm 18$ mm and $\lambda_n = 45 \pm 23$ mm. Exploiting the relation between λ_n/λ_T and χ/D [14],

$$\frac{\gamma_e}{1 - f_{conv}} = \left(1 + \frac{\lambda_n}{\lambda_T}\right)\left(\frac{5}{2} + \frac{\chi}{D}\frac{\lambda_n}{\lambda_T}\right), \qquad (1)$$

we can estimate the fraction of convective heat flux f_{conv} to be about 0.6 (assuming $\chi/D = 3$).

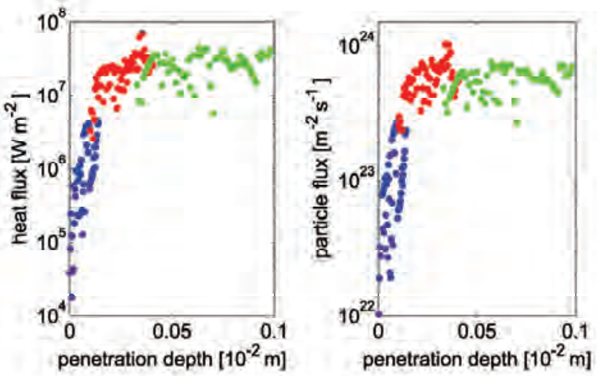

Fig. 5 *Particle and heat flux as function of the radial field line penetration.*

Particle Recycling

The DED is an open divertor and the recycling neutrals can penetrate deep into the edge plasma by by-passing the high temperature and high density areas. However, in comparison to the helical divertor in an heliotron device like LHD [2], the divertor legs are broad and their radial extent is much smaller. Important for a high recycling divertor and for impurity screening is the closure of the divertor by localised recycling in the divertor chamber. The transition from divertor chamber to ergodic area in the DED can not be attributed to a distinct radial position. This can be seen from figure 3, giving the connection length of field lines in front of the DED target at a toroidal angle of 180°. One finds a complex mixture of different types of field lines. Field lines with long connection length can come close to the target plates, but connect to these only after they passed again several times the divertor coils (red areas). Thus, neutrals can penetrate into these flux bundles at an upstream position. The downstream area of the divertor comprises all field lines connecting within less than one poloidal turn to the target. This definition is equivalent to that of a poloidal divertor. This downstream area is indicated by the black line in figure 3.

The radial extent of the downstream area in the 6/2 base mode is at maximum 7 cm and varies, depending on the DED current and the edge safety factor. Local divertor recycling is established, when all the particle sources are located in the downstream region. A parameter reflecting the divertor recycling fraction is the ration between downstream sources Q_{down} and total source Q_{tot}, which equals the incoming flux, if no wall retention is assumed. In the experiment, Q_{down} is measured as the H_{alpha} line emission integrated over the downstream area and Q_{tot} is the total emission in front of the target. The distribution of the H_α

emission is shown in figure 6, together with a contour plot of the shortest connection length to the target. Field lines, which have to pass the divertor target again before they end on the target plates, belong to the upstream area. Sources in these field lines contribute to convective flux to the divertor.

The ratio between downstream D^+ sources and total D^+ source strength, Q_{down}/Q_{tot}, reaches values of up to 50% [15]. The fraction of the sources in the downstream area of the flux tubes with 1 – 2 p.t. is about 25%. Assuming that $Q_{tot} = \Gamma_{tot}$, we get for these flux tubes $Q^{1,2}_{down}/\Gamma^{1,2} = 0.4$. Thus about 60% of the heat flux is transported convectively to the target in these flux tubes. Keeping in mind, that these are rough estimates, we find a good agreement with the above estimate from the e-folding lengths.

The accessibility of a high recycling regime can be assessed by including the convective heat flux into the two-point model:

$$q_{\parallel} = -\kappa_0 T^{5/2}\frac{\partial T}{\partial x} + (\frac{1}{2}mv_{\parallel}^2 + 5eT)\Gamma_{\parallel}\,. \qquad (2)$$

Neglecting the kinetic term and assuming that

$$\frac{\partial}{\partial x}\Gamma_{\parallel} = f_{conv}\frac{\Gamma_0}{L_c}\,, \qquad (3)$$

the heat flux equation $\partial q_{\parallel}/\partial x = q_{\parallel,t}/L_c$ can be solved. Figure 7 shows the temperature drop towards the target as function of the particle flux to the target. For the conditions of the pulse type discussed here (f_{conv} = 0.6 and $q_{peak} = 30\text{MWm}^{-2}$), no temperature gradient can build up. Would a high recycling DED for this configuration be possible? Because of the density limit, the particle flux can not exceed $10^{24}\text{m}^{-2}\text{s}^{-1}$ significantly. Thus the access to high recycling needs a reduction of convective heat flux as well as a reduction of the power entering the edge layer. The latter could be achieved for example by higher radiation through impurity seeding. The absence of a high recycling regime has also be found in the helical divertor and in the island divertor. In the former case, because of the same reasons found for the DED, too high convective fluxes [16], and in the latter case, because of the significant role of the cross field transport inside the island [17].

Conclusions

The heat and particle fluxes at the DED target plates were measured with Langmuir probes. Peak fluxes are found where field lines end, which penetrate deep into the plasma. The comparison of the measured target profiles to the magnetic topology shows, that heat and particles are mainly transported to the target plates via flux tubes of short connection length. About 65% of the fluxes are found in areas, where field lines with a connection length of 1-2 poloidal turns connect to the target. Analysis of the source distribution shows, that about 40% of the ion sources lie inside the downstream area of the divertor. The high fraction of convective heat flux prevents from establishing high recycling in the divertor for the pulse type discussed here.

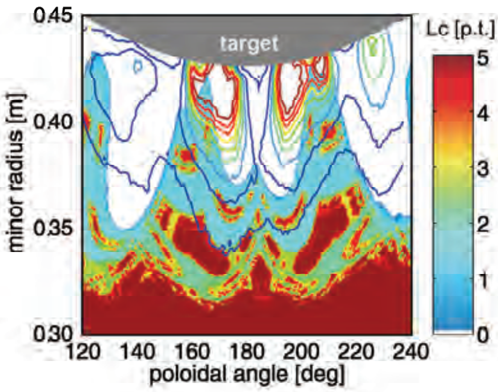

Fig. 6 *Magnetic structure in front of the DED target: shortest connection length to the divertor target. The contour lines indicate the intensity of the* H_α *radiation.*

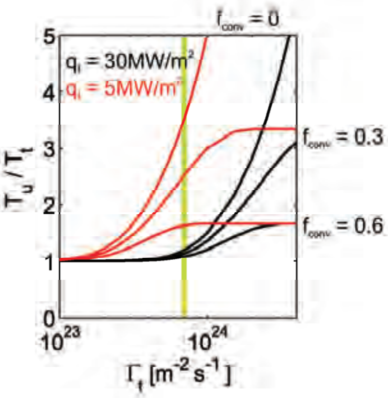

Fig. 7 *Temperature ratio between target und upstream position as function of the target particle flux. The green line indicates the peak particle flux for pulse #99504.*

[1] Ph. Ghendrih et al, Nucl. Fusion **42** (2002) 1221.
[2] T. Morisaki et al., J. Nucl. Mater. **337-339** (2005) 154
[3] R. König et al., Plasma Phys. Control. Fusion **44** (2002) 2365
[4] K.H. Finken et al., The structure of magnetic field in the TEXTOR-DED, Schriften des Forschungszentrum Jülich, Energy Technology **45**, ISSN 1433-5522 (2005)
[5] Th. Eich, D. Reiser and K.H. Finken, J. Nucl. Mater. **290-293** (2001) 849
[6] M. Lehnen et al. , Plasma Phys. Control. Fusion **47** (2005) B237
[7] O. Schmitz et al., J. Nucl. Mater. **363-365** (2007) 680
[8] A. Cole and R. Fitzpatrick, Phys. Plasmas **13** (2006) 032503
[9] Parail V. et al. Proc. 21st Int. Conf. Fusion Energy 2006 (Chengdu) (Vienna: IAEA) CD-ROM TP/P8-5
[10] S. Masuzaki et al., Nucl. Fusion **42** (2002) 750
[11] M.W. Jakubowski et al., J. Nucl. Mater. **337-339** (2004) 176
[12] M.W. Jakubowski et al., Plasma Phys. Control. Fusion **49** (2007) S109
[13] F. Nguyen et al., Nucl. Fusion **37** (1997) 743
[14] M. Lehnen et al., Nucl. Fusion 43 (2003) 168178
[15] M. Lehnen et al., J. Nucl. Mater. **363-365** (2007) 377
[16] M. Kobayashi et al., J. Nucl. Mater. **363-365** (2007) 294
[17] Y. Feng et al., Nucl. Fusion **46** (2006) 807

Proceedings of ITC/ISHW2007

Effect of plasma parameters on H alpha emission and its spectrum

Hiroto MATSUURA[1)], Shinichiro KADO[2)], Yosuke KUWAHARA[3)], Shin NISHIMURA[4)], Chihiro SUZUKI[4)], and Shoichi OKAMURA[4)]

[1)]*Osaka Prefecture University, Osaka 599-8531, Japan*
[2)]*The University of Tokyo, Chiba 277-8568, Japan*
[3)]*The University of Tokyo, Tokyo 113-8656, Japan*
[4)]*National Institute for Fusion Science, Gifu 509-5292, Japan*

Neutral particle behavior and H alpha emission spectrum are simulated with Monte Carlo code DEGAS. Plasma density in divertor simulator Material and Plasma(MAP)-II is lower than divertor plasma of the torus confinement plasma such as Compact Helical System (CHS). So whereas hydrogen molecular dissociation is important in H alpha emission in MAP-II, electron impact excitation of hydrogen atoms is dominant in CHS.

Keywords: DEGAS, CHS, MAP-II, H-alpha spectra,molecular dissociation

1 Introduction

Development of heat flux reduction method on divertor plate is an important issue for the future fusion reactor design. One of most promising scenario is to establish so-called detached plasma, whose electron temperature is kept below 1[eV] by powerful gas puffing. In this situation, neutral particles are expected to experience not only transport but also atomic/molecular process such as dissociation, ionization, and so on. This neutral behavior can be monitored with H alpha emission spectrum and simulated with Monte Carlo code such as DEGAS[1]. H alpha line emission results from radiative decay of exited hydrogen atoms from the principal quantum state $n = 3$ to $n = 2$, and it is widely used as a monitoring tool of neutral hydrogen behavior. The line intensity is the measure of density of H($n = 3$) and its wavelength spectra reflects the velocity distribution of hydrogen atoms.

According to previous DEGAS simulation study for the divertor simulator Material and Plasma(MAP)–II, dissociation of hydrogen molecules was found to play important rolls in H alpha emission.[2] This is because plasma density is not so large in MAP–II and hydrogen molecules can penetrate deeply into plasma. On the other hand, in the edge region of Compact Helical System (CHS), H alpha emission from atomic hydrogen is dominant.[3] Contribution from molecular hydrogen is limited only around the last closed flux surface (LCFS), where n_{H_2} is still large.

In this work, we compare the DEGAS results, especially on H alpha emission spectrum, for both devices. Dominant physical process which determine neutral hydrogen behavior will be made clear with it. Comparison with spectroscopic measurement data is also now under way.

author's e-mail: matsu@me.osakafu-u.ac.jp

In section 2, we explain device parameter and simulation model geometry of CHS and MAP-II briefly. In section 3, we present some simulation results on H alpha emission profile to be compared with experimental data. Section 4 shows contribution of various pathways generating H($n = 3$) to H alpha spectrum. Section 5 is the summary.

2 Model geometry

2.1 CHS device

CHS is a heliotron/torsatron device with major radius of 1 [m] and minor radius of 0.2 [m]. The pole number of the helical field coil is $\ell = 2$ and toroidal periodic number is $m = 8$. Profiles of plasma density and temperature are measured with YAG Thomson scattering. The Li-beam probe is also used to edge plasma measurement [4].

In order to study with DEGAS, core plasma and "vacuum" region is divided into 45 zones poloidally and into 13 zones radially. Nine radial zones are determined by using KMAGN code [5]. Other four zones are interpolated between the chamber wall and the Last Closed Flux Surface (LCFS). Toroidally 48 cross sections are selected to construct the 3 dimensional mesh. The schematic diagrams of thus produced mesh geometry have already been given in [6]. There isn't any sink of neutral particles in this model, so we chase neutral particle flights until they are ionized in core plasma.

2.2 MAP-II device

MAP–II is a dual-chamber linear divertor simulator.[7] Steady state plasma is produced by PIG arc discharge, passed through "source chamber " and terminated at target plate in "target chamber ". By turning off the differen-

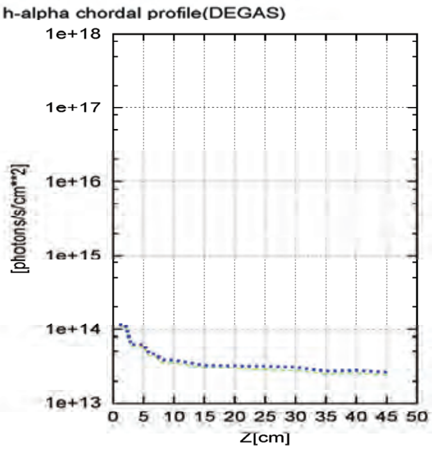

Fig. 1 H alpha chordal integrals for attached plasma in MAP-II. Target plate exists at $Z = 0$[cm] and the plasma inlet is $Z = 50$[cm].

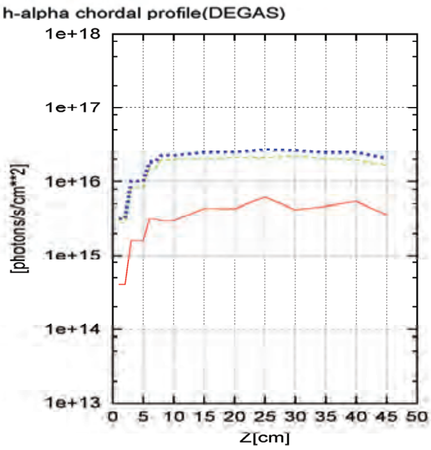

Fig. 2 H alpha chordal integrals for detached plasma in MAP-II. (Red:contribution from Hydrogen atoms, Green: contribution from Hydrogen molecules.)

tial pumping of the source chamber, electron temperature at target chamber entrance decrease. ((For example, 15 $\rightarrow$ 3 [eV].) Then plasma entering target plate becomes detached gradually with the increase of target chamber neutral pressure.

The target chamber of MAP-II is modeled with a simple cylinder of 50 [cm] diameter and 50 [cm] length, which is divided to 30 mesh radially and 20 mesh axially.[2] Since radius plasma column is very small (3 ~ 5[cm]) compared with that of the chamber (25[cm]), radial separation of mesh varies with radial position. Particle sinks are a plasma inlet from the source chamber and the pumping duct.

3 H alpha chordal integrals

MAP–II has a large view port on the side wall of the target chamber and spectroscopic measurement is done with the sight line which look plasma column radially. We set 17 sight lines along plasma column (that is z–axis) and integrate H alpha emission density along each sight line. One example is shown in Fig. 1. Plasma parameter used here is those for attached condition and assumed to be constant along z–axis. Peak density and temperature are $n_e = 2.5 \times 10^{11}$[cm^{-3}] and $T_e = 15$[eV]. H alpha signal is expected to have the maximum near target plate ($Z = 0$[cm]), since neutral density has peak there due to recycling.

On the other hand, in detached case (Fig. 2), plasma density and temperature decay toward the target plate. (Peak values at the upflow boundary are $n_e = 1.2 \times 10^{12}$[cm^{-3}] and $T_e = 3.5$[eV] .) H alpha intensity increases due to large hydrogen molecular density. (About 100 times larger than in Fig. 1.) But, near the target plate, plasma density are much smaller and H alpha emission is also small.

In both cases of MAP–II plasma , hydrogen atom contribution (red line) is negligible compared with molecules (green line). Even in the detached case, so called recombining zone can not be observed, since plasma density is still small and volume recombination has much less contribution to particle source compared with recycling and gas puff.

We also calculate H alpha chordal integrals for CHS visible light array along major radius (R) direction. About 30 optical fibers are set on vertical elongated cross section through an large vertical port.[8] Unfortunately, our 3D mesh model ignores this port. Obtained H alpha profile (not shown here) is rather flat in R-direction, whereas experimental data shows clear peak near inside vacuum chamber wall. There might exist leakage of neutrals toward the viewing port. This problem is left for future work.

4 H alpha spectrum

Since there is many pathways to generate H($n = 3$), many groups of H($n = 3$) with different density and characteristic energy exist. DEGAS ver.63 used here considers 10 pathways. [9]

Figure 3 shows three dominant contribution in H alpha spectra calculated with DEGAS for detached case of MAP–II (same condition as Fig. 1). Detector is located at $Z = 25$[cm] Narrow peak written with black line is the contribution of H($n = 3$) directly produced in dissociation of hydrogen molecules ($e + H_2 \rightarrow H(n = 3) + H^+ + 2e$, called as H2DE in DEGAS code). Two broad profiles come from the contribution of hydrogen molecular ions. (H2+DE: cyan line, H2+DI: yellow line) In DEGAS simulation, hydrogen molecular ions are produced by electron impact ionization of hydrogen molecules and assumed to be lost immediately by H2+DE($e + H_2^+ \rightarrow H + H(n = 3)$) or H2+DI($e + H_2^+ \rightarrow H(n = 3) + H^+ + e$). In order to im-

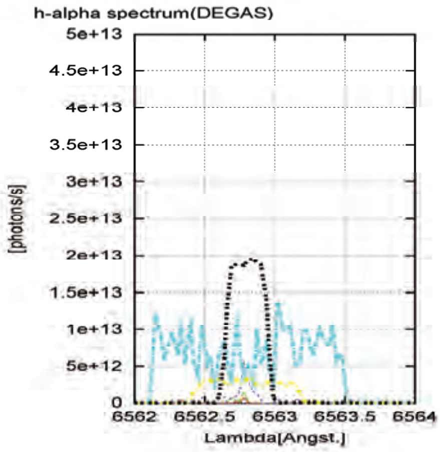

Fig. 3 H alpha spectrum for attached plasma in MAP-II. (Black:H2DE, Cyan:H2+DE, Yellow:H2+DI)

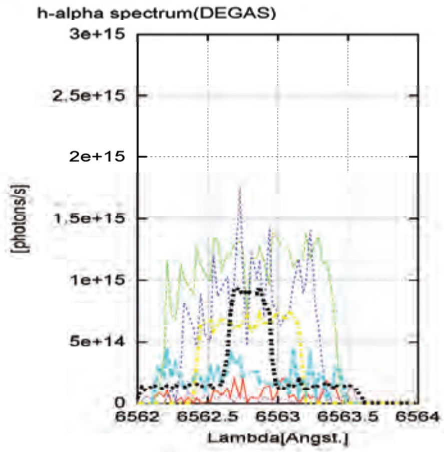

Fig. 5 H alpha spectrum for CHS inner sight at R_{det} = 85 [cm].(Black:H2DE, Green:H2+DI, Blue:H2DS)

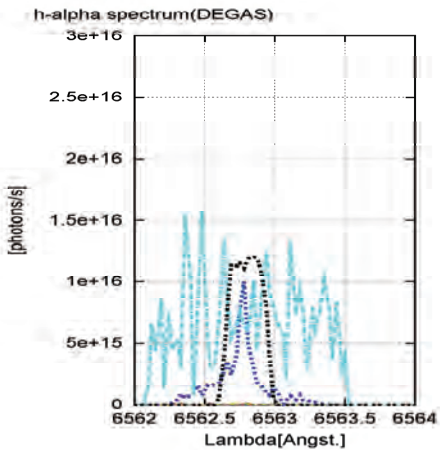

Fig. 4 H alpha spectrum for detached plasma in MAP-II. (Black:H2DE, Cyan:H2+DE, Blue:H2DS)

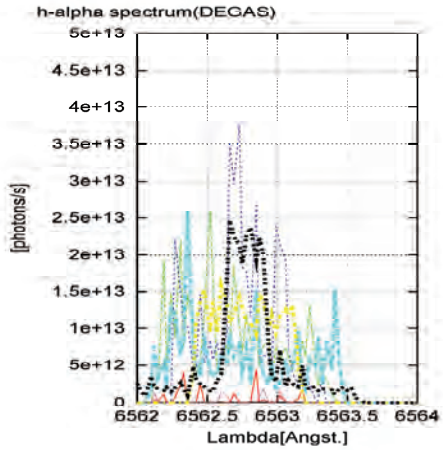

Fig. 6 H alpha spectrum for CHS outer sight at R_{det} = 100 [cm].

prove statistical accuracy of these H_2^+ contribution, more test particle flights is necessary in the simulation.

In detached case (Fig.4), the contribution of H2+DI disappears. Electron temperature is lower than attached case, so high energy electron which can react as H2+DI seems to decrease. On the other hand, electron density becomes larger and more H(n = 1) produced in H2DS($e + H_2 \rightarrow 2H + e$, blue line in the figure) could be excited to n = 3 with electron impact. In DEGAS, this excitation probability is calculated with collisional-radiative(CR) model and contribution of hydrogen atoms produced in ground state to H alpha emission spectra is also considered.

H alpha spectra in CHS is also calculated. In the so-called standard configuration, where magnetic axis exists at R_{ax} = 92.1[cm], plasma boundary is limited by inner wall of vertically elongated toroidal cross sections ($\phi = 0, 45, \ldots, 315$ [deg.]). So we set 8 neutral particle sources, since CHS helical coils have toroidal periodicity of m = 8. The total intensity of sources is estimated from particle confinement time (τ_p) data. CHS has two NBI beam lines and they could become high energy neutral source. But in present simulation, we consider only recycling at the chamber wall as the neutral source.

Fig.5 shows the spectra detected at R_{det} = 85.0[cm] sight. Compared with Fig.3, there are two new pathways which have large contribution here. One (green line in the figure) is H2+DI($e + H_2^+ \rightarrow H + H^+ + e$), which is not observed in the spectra for MAP–II plasma. Another (blue line) is H2DS, which is observed in the detached MAP–II case (Fig.4). These pathways produce hydrogen atoms in grand state. Since CHS edge plasma has higher density ($\sim 10^{13}$[cm^{-3}]) compared with MAP–II, these atoms are easily excited to $n = 3$ with electron impact and contribute H alpha emission.

Neutral density is very localized around recycling sources in the standard configuration. So H alpha signal of outer sight detectors decreases due to neutral density reduction. Hydrogen molecular density decays by about factor 100 in the poloidal direction in this vertically elongated cross section.[6] Fig.6 shows the data for

R_{det} = 100.0[cm]. Contribution reduction of pathways with H_2^+ (H2+DE and H2+DI) is larger than those with H_2. This can be explained by reduction of H_2^+ production.

There exists another fast pathway to produce hydrogen atom ($H_2 + H_2^+ \rightarrow H + H_3^+$) which is not included in present DEGAS code.[9] Produced atoms with this pathway stay at ground level, since H_2 has lower energy than electrons. So in order to contribute to H alpha emission, electron impact excitation will be necessary. We expect that H_3^+ formation is not so important for MAP–II low density plasma. But for CHS plasma, this may become important. H_3^+ behavior and contribution to H alpha spectra is left for future improvement of simulation code.

5 Summary

Obtained results in this paper are summarized like the following.

- CHS 3D mesh model and MAP–II 2D mesh model are constructed and their DEGAS simulation results are compared.
- H alpha signal becomes the maximum near target plate for MAP–II attached plasma, since neutral density has also peak there. For detached plasma, however, H alpha signal there becomes minimum due to electron density reduction.
- There is some discrepancy between experiment in CHS and DEGAS simulation on H alpha chordal integrals. Two possible reason (geometrical effect of viewing port and contribution of H_3^+ formation process) must be examined in future work.
- There exist a few dominant pathways to produce excited H atoms which depends on plasma temperature and density. Not only the electron impact dissociation but also the dissociative recombination of the molecular ions can contribute the H alpha emission spectra profile.
- H alpha emission detected in MAP–II is expect to be come from excited hydrogen atoms directly produced through dissociation of H_2 and H_2^+. Quantum level of produced Hydrogen atom must be consider more carefully.
- In standard configuration (limiter) of CHS, neutral particles is very localized around recycling source. Since plasma density is higher, ground state hydrogen atoms also contribute H alpha emission spectra.

In order to compare simulation results and experimental observation quantitatively, more detail modeling of neutral source and study on other configuration will be needed. These are left for the future work.

Acknowledgements

One of Authors (H.M.) acknowledges Dr. M.Shoji of National Institute for Fusion Science and Dr. Y.Nakashima of Tsukuba University for their advice on DEGAS simulation.

[1] D. Heifetz et al., J. Comp. Phys. **46**, 309 (1982).
[2] H. Matsuura et al., to be published in Contr. Plasma Phys. **47** (2007).
[3] H.Matsuura et al., J. Plasma Fusion Res. SERIES **7**, 106 (2006).
[4] K. Nakamura et al., J. Nucl. Matter. **313-316**, 725 (2003).
[5] Y. Nakamura et al., J.Plasma Fusion Res. **69**, 41 (1993).
[6] H.Matsuura et al.: J. Nucl. Mater. **363-365**, 806 (2007).
[7] S. Kado et al.: J. Plasma Fusion Res. **81**, 810 (2005).
[8] S.Nishimura et al.: Phys. plasma **7**, 437 (2000).
[9] D.P.Stotler et al.: Phys. Plasma **3**, 4084 (1996).

Proceedings of ITC/ISHW2007

Hydrogen Adsorption of Back Side of Graphene

Atsushi ITO[1)], Arimichi TAKAYAMA[2)] and Hiroaki NAKAMURA[2)]

[1)] *Department of Physics, Graduate School of Science, Nagoya University, Furo–cho, Chikusa–ku, Nagoya 464–8602, Japan.*

[2)] *National Institute for Fusion Science, Oroshi–cho 322–6, Toki 509–5292, Japan.*

(Received 15 October 2007 / Accepted ** ** 2007)

We studied the interaction between a single hydrogen atom and a single graphene using classical molecular dynamics simulation with modified Brenner REBO potential. Three interactions, which are adsorption, reflection, penetration, were observed. Overhang structure appears and creates an adsorption site on the backside of the graphene. It is considered that backside adsorption occurs under the two conditions that an incident hydrogen atom should have incident energy which is larger than the potential barrier of a hexagonal hole of the graphene and that after the hydrogen atom passes through the graphene, it does not keep its kinetic energy to be trapped by the adsorption site. The conditions explained that as the incident energy increased, the incident point of the backside adsorption shifted to the periphery of a hexagonal hole of the graphene in the simulation. Moreover, when a hexagonal hole of the graphene was expanded by the hydrogen atom incidence to the periphery of the hexagonal hole, its potential barrier was reduced.

Keywords: Chemical sputtering, Hydrogen, Graphene, Graphite, Adsorption

DOI: ****/pfr.****

1 Introduction

In the context of research into nuclear fusion, the plasma surface interaction (PSI) problem has been studied [1–5]. A portion of the plasma confined in an experimental device falls onto a divertor wall, which is shielded by graphite or carbon fiber composite tiles. The incident hydrogen plasma erodes these carbon tiles in a process called chemical sputtering. The erosion produces hydrocarbon molecules, such as CH_x and C_2H_x, which affect the plasma confinement.

To solve the PSI problem, the mechanism of the graphite erosion has been researched using molecular dynamics (MD) simulation [6–9]. Previously, we investigated the PSI of graphite surface which consists of 8 graphene sheets using the modified Brenner reactive empirical bond order (REBO) potential [10]. Subsequently, the isotope dependence of incident hydrogen atoms is investigated [11]. These simulations achieve steady state of the graphite erosion, the incident energy linear dependence of total carbon yield accords with experimental results [12, 13].

The MD simulation of graphite surface showed that if incident energy was 5 eV, almost of all incident hydrogen atoms were adsorbed by the graphite surface, while if the incident energy was 15 eV, most incident hydrogen atoms were reflected. This adsorption and reflection can be explained by the MD simulation of the elemental processes which is the chemical reaction between a single hydrogen atom and a single graphene [14–16]. This MD simulation indicates also that in a certain incident energy, the hydrogen atom can be adsorbed to the backside of the graphene. On the other hand, the other MD simulation for graphene erosion due to hydrogen atom gas implied that para–overhang configuration which has hydrogen atoms onto both side of the graphene is created and its C–C bond is easy broken [17]. Therefore, we consider that if the incident energy which brings about the backside adsorption is selected, the MD simulation of graphite surface shows a different dynamics.

Here, we attach weight to not only the macroscopic simulation of graphite surface but also understanding a elemental mechanism and dynamics. We, therefore, investigate the backside adsorption of the interaction between a single hydrogen atom and a single graphene in the present paper. We describe the simulation model and method in §2. In §3, we present and discuss the simulation results. This paper concludes with a §4.

2 Simulation Method

A graphene [18] consists of 160 carbon atoms measuring 2.13 nm × 1.97 nm, and is placed at the center of simulation box parallel to x–y plane. The simulation box in the x– and y–directions measures 2.13 nm × 1.97 nm with periodic boundary condition. In the z–direction, we do not prepare the boundary of the simulation box and the initial coordinate of the center of mass of the graphene is $z = 0$ Å. The initial graphene temperature is set to 0 K. The carbon atoms of the graphene are relaxed initially and compose

author's e-mail: ito.atsushi@nifs.ac.jp, nakamura.hiroaki@nifs.ac.jp, takayama@nifs.ac.jp

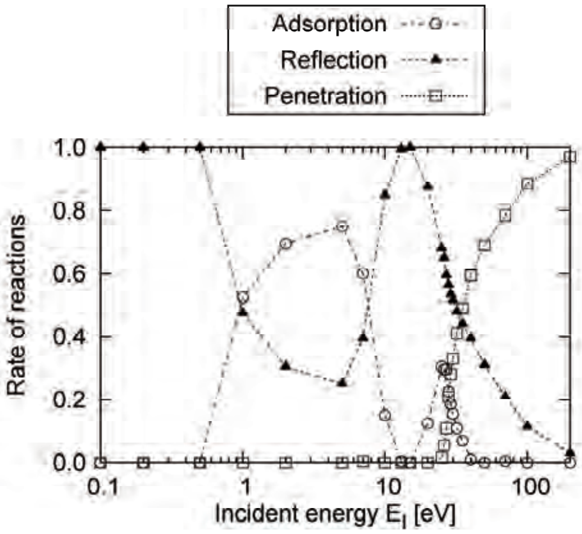

Fig. 1 The incident energy dependence of the rates of adsorption, reflection and penetration where the graphene temperature is 0 K. Dash–dotted line with open circle, long–dashed line with filled triangle, and short–dashed line with square denote the rates of adsorption, reflection and penetration, respectively.

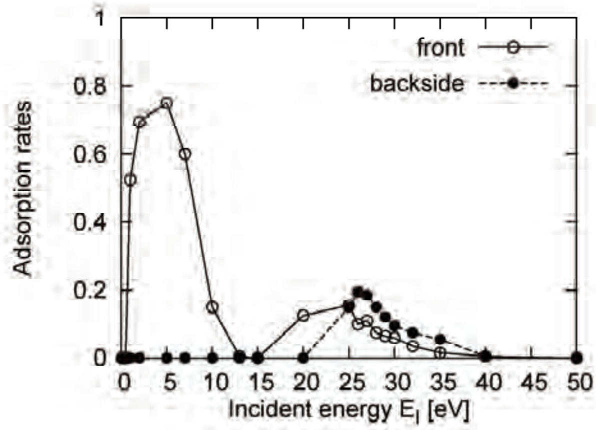

Fig. 2 The incident energy dependence of the rates of the front and backside adsorption where the graphene temperature is 0 K.

completely flat graphene structure. A hydrogen atom is injected from $z = 4$ Å parallel to the x–y plane, that is, normal incidence to the graphene surface. Incident position in the x– and y– directions are determined under a uniformed distribution function. The incident energy E_I decides an initial momentum vector $(0, 0, p_0)$ as follows:

$$p_0 = \sqrt{2mE_\mathrm{I}}, \tag{1}$$

where and m is the mass of the hydrogen atom.

We performed our MD simulation under NVE conditions, where the number of atoms, volume, and total energy are conserved. The simulation time was developed using second order symplectic integration [19]. The chemical interaction was represented by the modified Brenner REBO potential [15,20]:

$$U \equiv \sum_{i,j>i}\left[V^{\mathrm{R}}_{[ij]}(r_{ij}) - \bar{b}_{ij}(\{r\},\{\theta^{\mathrm{B}}\},\{\theta^{\mathrm{DH}}\})V^{\mathrm{A}}_{[ij]}(r_{ij})\right], \tag{2}$$

where r_{ij} is the distance between the i–th and j–th atoms. The functions $V^{\mathrm{R}}_{[ij]}$ and $V^{\mathrm{A}}_{[ij]}$ represent repulsion and attraction, respectively. The function $\bar{b}_{ij}$ generates multi–body force. To conserve the accuracy of the calculation, the time step was 5×10^{-18} s.

We note the condition to judge the type of reaction, which corresponds to the condition to finish the simulation. While the incident hydrogen atom interacts with one carbon atom, we count a trapped time. When the hydrogen atom leaves the carbon atom or starts interaction with the other carbon atom, the trapped time is cleared. When the trapped time reaches 0.1 ps (20000 time steps), the simulation is finished and this reaction is regarded as adsorption. Moreover, if the relative position from the nearest carbon atom to the hydrogen atom in the z–coordinate is positive, the reaction is front adsorption, while if the relative position in the z–coordinate is negative, the reaction is backside adsorption. When the hydrogen atom leaves the nearest carbon atom, we begin counting a escaping time. If the hydrogen atom interacts a carbon atom again, we clear the escaping time and restart counting the trapped time. When the escaping time reaches 0.05 ps (10000 time steps), the simulation is finished. And, if the escaping hydrogen atom has positive momentum in the z–coordinate, this reaction is reflection, while it has negative momentum, the reaction is penetration.

We repeated the above simulation 200 times for each incident energy, where the incident position in the x– and y– directions are every time changed randomly under the uniformed distribution function. Since we counted the types of the reactions, we obtained the rates of the reactions. Of course, the sum of the rates of the adsorption, reflection and penetration is always 1.

3 Results and Discussion

The simulations were executed for incident energy of 0.1 eV to 200 eV. The three interactions, which are adsorption, reflection, penetration, were observed. Figure 1 shows that the rates of the three interactions depend on the incident energy. Especially, the rate of adsorption has two peaks. Next, Fig. 2 shows the rates of the front and backside adsorption. Although the front adsorption occurs around the both adsorption peaks, the backside adsorption occurs around the high incident energy adsorption peak only. In the process of front adsorption, the nearest carbon atom which is connected to the incident hydrogen atom by a covalent bond is pulled out from flat surface of the graphene. This is called a overhang structure and creates an adsorption site for a hydrogen atom [14, 15]. In the backside ad-

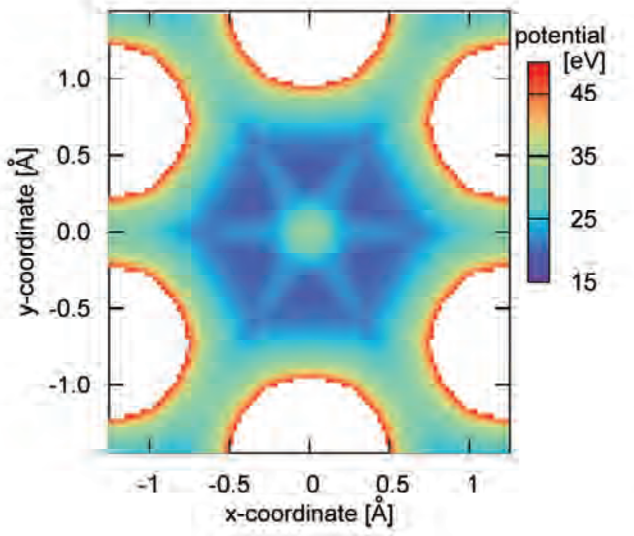

Fig. 3 The potential barrier of a hexagonal hole of the graphene. The mapped value is potential energy when the hydrogen atom is located in the plane of $z = 0$ Å.

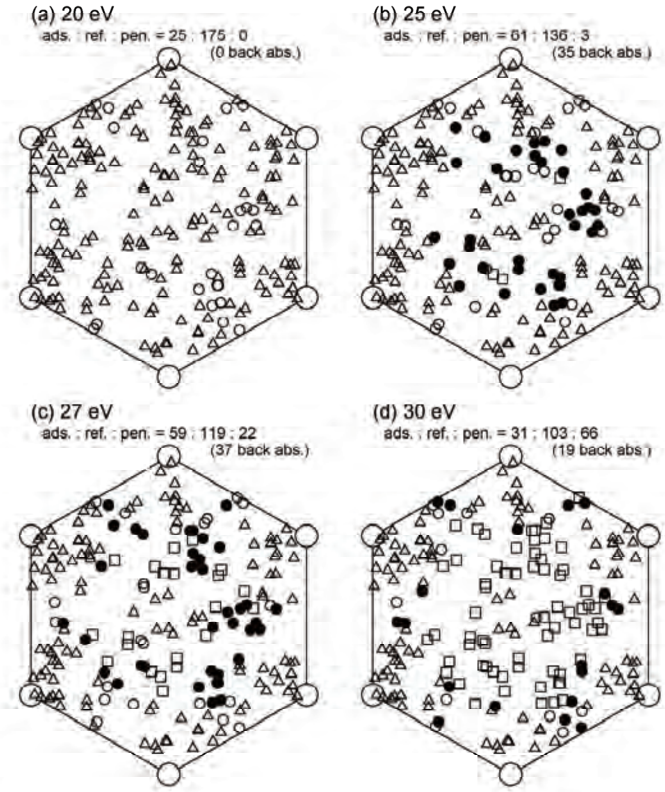

Fig. 4 Incident points v.s. the types of its interactions. Circles indicate incident points which bring about hydrogen atom adsorption where the opaque circles correspond to backside adsorption. Triangles and squares are reflection and penetration, respectively. Big six circles and six line represent six carbon atoms and six covalent bonds composing a hexagonal hole of the graphene.

sorption also, the overhang structure appears. That is, an adsorption site is created in the backside of graphene after the incident hydrogen atom goes through the graphene.

The incident energy dependence of the rates of interactions Fig. 1 is understood using energetics, which relates π–electron on the graphene surface, structure transformation to the overhang structure and the potential barrier of a hexagonal hole of the graphene [15]. In the present paper, we discuss the backside adsorption. We consider that the backside adsorption needs the following two conditions. One is that to go through the graphene, the incident hydrogen atom should have the incident energy which is larger than the potential barrier of a hexagonal hole of the graphene. The other is that after the hydrogen atom passes through the graphene, it is trapped by the adsorption site due to the overhang structure. Namely, to occur the backside adsorption, the kinetic energy of the hydrogen atom is diffused to carbon atoms of the graphene and must not remain. Concerning the first condition, the potential barrier of a hexagonal hole of the graphene, where the hydrogen atom is located at $z = 0$ Å, is shown by Fig. 3. The center of this figure corresponds to the center of a hexagonal hole of the graphene. The six white regions indicate higher potential barrier of more than 50 eV because carbon atoms exist there. The point of minimum potential barrier is not the center of a hexagonal hole of graphene and appears between the locations of carbon atoms and the center of a hexagonal hole of the graphene. Figure 4 shows incident points and the types of their interactions. It is understood and consistent with the potential barrier of a hexagonal hole of the graphene Fig. 3 that the backside adsorption occurs around the points of minimum potential barrier and does not occur around the center of a hexagonal hole of the graphene. As the incident energy increases, the incident points for the backside adsorption shift from the points of minimum potential barrier to the periphery of a hexagonal hole of the graphene which is over the covalent bonds between carbon atoms. This phenomenon is explained as follows. In the incident energy of 20 eV, because all incidences become the front adsorption or reflection, the hydrogen atom does not have enough incident energy to go over the potential barrier of a hexagonal hole of the graphene. In the incident energy of 25 eV, because the incident energy is higher than but close to the minimum potential barrier, only the hydrogen atoms which are injected around the points of the minimum potential barrier go through the hexagonal hole of the graphene and are trapped by adsorption site of the backside of the graphene. When the incident energy increases (27 and 30 eV), the region in which the potential barrier of a hexagonal hole of the graphene is lower than the incident energy extends. Therefore, the backside adsorption occurs in the periphery of a hexagonal hole of the graphene. However, the backside adsorption around the potential minimum point changes into penetration because the hydrogen atom leaves the kinetic energy enough to escape out of the adsorption site after it passed through a hexagonal hole of the graphene. More important thing is that while the backside adsorption happens in the periphery of a hexagonal hole of the graphene, it does not happen in the center of a hole of the graphene in spite of same potential barrier. It is demonstrated by the trajectory of atoms in the MD simulation that when the hydrogen atom is injected into the periphery of a hexagonal hole of the graphene, near two carbon atoms move and the hexagonal hole of the graphene is expanded. The expansion of the hexagonal hole of the graphene seems to reduce the potential barrier of the hexagonal hole of the graphene because the distance between hydrogen atom and the near carbon atoms become larger. On the other hand, if the hydrogen atom is injected to the center of a hexagonal hole of the graphene, it must push six carbon atoms to expand the hexagonal hole of the graphene. It is considered that at the incident energy of 30 eV, even if the hydrogen atom can move two carbon atoms, it cannot move six carbon atoms because of their larger mass. Consequently, the backside adsorption and penetration hardly occur in the center of a hexagonal hole of the graphene.

4 Summary

We study the interaction between a single hydrogen atom and a single graphene using classical molecular dynamics simulation with modified Brenner REBO potential. The three interactions, which are adsorption, reflection, penetration, were observed. Especially, in the present paper, we discuss the backside adsorption. As well as the front adsorption, the overhang structure appears in the backside of the graphene and creates the adsorption site. It is considered that the backside adsorption occurs under the two conditions that the incident hydrogen atoms should have the incident energy which is larger than the potential barrier of a hexagonal hole of the graphene and that after the hydrogen atom passes through the graphene, it does not keep its kinetic energy to be trapped by the adsorption site. The hydrogen atom in the incident energy of 25 eV brings about the backside adsorption only around the points of the minimum potential barrier, which is not the center of a hexagonal hole of the graphene and is the region between the center of a hexagonal hole and the locations of carbon atoms. When the incident energy increases, the incident points for the backside adsorption shift to the periphery of a hexagonal hole of the graphene. In addition, the backside adsorption around the potential minimum point change into penetration because the hydrogen atom leaves enough kinetic energy to escape from the adsorption site after it passed through a hexagonal hole of the graphene. Moreover, when a hexagonal hole of the graphene is expanded by the hydrogen atom incidence to the periphery of the hexagonal hole, its potential barrier is reduced. However, even if the hydrogen atom can move two carbon atoms in the incidence to the periphery of the hexagonal hole, it cannot move six carbon atoms in the incidence to the center of the hexagonal hole. Therefore, the backside adsorption and penetration hardly occur in the center of a hexagonal hole of the graphene.

References

[1] T. Nakano, H. Kubo, S. Higashijima, N. Asakura, H. Takenaga, T. Sugie, K. Itami, Nucl. Fusion **42**, 689 (2004).

[2] J. Roth, J. Nucl. Mater. **266–269**, 51 (1999).

[3] J. Roth, R. Preuss, W. Bohmeyer, S. Brezinsek, A. Cambe, E. Casarotto, R. Doerner, E. Gauthier, G. Federici, S. Higashijima, J. Hogan, A. Kallenbach, A. Kirschner, H. Kubo, J. M. Layet, T. Nakano, V. Philipps, A. Pospieszczyk, R. Pugno, R. Ruggieri, B. Schweer, G. Sergienko, M. Stamp, Nucl. Fusion **44**, L21 (2004).

[4] B. V. Mech, A. A. Haasz, J. W. Davis, J. Nucl. Mater. **241–243**, 1147 (1997).

[5] A. Sagara, S. Masuzaki, T. Morisaki, S. Morita, H. Funaba, M. Goto, Y. Takamura, K. Nishimura, N. Noda, M. Shoji, H. Suzuki, A. Takayama, A. Komori, N. Ohyabu, O. Motojima, K. Morita, K. Ohya, J. P. Sharpe, LHD experimental group, J. Nucl. Mater. **313–316**, 1 (2003).

[6] E. Salonen, K. Nordlund, J. Tarus, T. Ahlgren, J. Keinonen, C. H. Wu, Phys. Rev. **B 60**, R14005 (1999).

[7] E. Salonen, K. Nordlund, J. Keinonen, C. H. Wu, Phys. Rev. **B 63**, 195415 (2001).

[8] D. A. Alman, D. N. Ruzic, J. Nucl. Mater. **313–316**, 182 (2003).

[9] J. Marian, L. A. Zepeda–Ruiz, G. H. Gilmer, E. M. Bringaand, T. Rognlien, Phys. Scr. **T 124**, 65 (2006).

[10] H. Nakamura, A. Ito, Mol. Sim. **33**, 121 (2007).

[11] A.Ito and H. Nakamura, to be published in Thin Solid Films.

[12] B. V. Mech, A. A. Haasz and J. W. Davis, J. Nucl. Mater. **255**, 153 (1998).

[13] C. Garcia and J. Roth, J. Nucl. Mater. **196–198**, 573 (1992).

[14] A. Ito, H. Nakamura, J. Plasma Phys. **72**, 805 (2006).

[15] A. Ito, H. Nakamura, A. Takayama, submitted, (preprint:NIFS-872).

[16] H. Nakamura, A. Takayama, A. Ito, submitted, (preprint:NIFS-875).

[17] A. Ito, H. Nakamura, submitted.

[18] H. –P. Boehm, R. Setton, E. Syumpp, Pure & Appl. Chem. **66**, 1893 (1994).

[19] M. Suzuki, J. Math. Phys. **26**, 601 (1985).

[20] D. W. Brenner, O. A. Shenderova, J. A. Harrison, S. J. Stuart, B. Ni, S. B. Sinnott, J. Phys.: Condens. Matter **14**, 783 (2002).

Comparison of charge transfer in proton collisions with methane and silane for simulations of divertor impurities and technological plasmas

L. Pichl, S. Fukata[a], D. Kato[b], H.-P. Liebermann[c], Robert. J. Buenker[c], M. Kimura[a]
International Christian University, Osawa 3-10-2, Mitaka, Tokyo 181-8585, Japan
[a]Faculty of Sciences, Kyushu University, 6-10-1 Hakozaki, Fukuoka 812-8581, Japan
[b]Cooperative Research Center, National Institute for Fusion Science, Toki 509-5292, Japan
[c]Theoretische Chemie, Bergische Universitaet Wuppertal, Gaussstrasse 20, Wuppertal,42119 Germany

lukas@icu.ac.jp

Silane and methane are useful gasses for diagnostics of impurity deposition and implantation, as recently reported in case of the scrape off layer of inner divertor [1]. Hydrocarbons including methane naturally occur when graphite is used as plasma facing material; silane is used not only for fusion plasma diagnostics, but silane plasmas are also of key interest in the semiconductor industry. The data need for accurate charge transfer cross sections in proton collisions with both molecules has been stated in the series of Juelich reports by Janev and Reiter [2], who provide semi-empirical formulas for charge transfer in collisions of proton with CH_4,

$$\sigma_{CX} = \frac{9.96}{\sqrt{E} + 85E^{2.5}} + \frac{30.2}{E^{0.015} + 9.0\times10^{-6}E^{1.2} + 2.19\times10^{-18}E^{3.8} + 4.47\times10^{-22}E^{4.4}} (10^{-16}cm^2)$$

and for charge transfer in collisions of proton with SiH_4,

$$\sigma_{CX} = \frac{3.93}{\sqrt{E} + 445E^{2.3}} + \frac{46.2}{E^{0.094} + 9.0\times10^{-6}E^{1.2} + 2.845\times10^{-18}E^{3.8} + 5.81\times10^{-22}E^{4.4}} (10^{-16}cm^2)$$

respectively (energy E is given in units of eV).

Here we compare the above formulas with previous cross sections results on methane [3] and new results on silane, based on multi-reference single- and double-excitation configuration interaction (MRD-CI) calculation of electronic structure of collision intermediates, and molecular orbital close coupling calculation (MOCC) of electron capture dynamics. Figure 1 shows the electron capture cross section for H^+/SiH_4 collision.

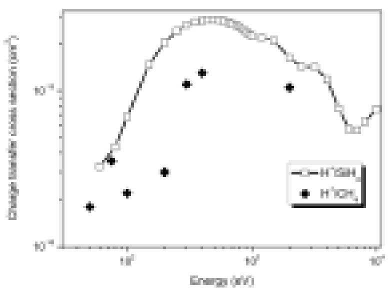

Fig. 1: Cross sections for proton-impact charge transfer

Implications for plasma impurity simulations and energy balance in low-temperature regions on the wall of fusion reactors will also be discussed at the conference.

[1] J. Likonen, S. Lehto, J. P. Coad, et al., "*Studies of impurity deposition/implantation in JET divertor tiles using SIMS and ion beam techniques*", Fusion Engineering and Design **66** (2003) 219-224.
[2] R. Janev and D. Reiter, Institut fur Plasmaphysik, Forschungszentrum Juelich, Juel-Report 3966 and Juel-Report 4038, 2002.
[3] M. Kimura, Y. Li, G. Hirsch, and R. J. Buenker, Physical Review A 52, 1197-1204 (1995).

Proceedings of ITC/ISHW2007

Use of a High Resolution Overview Spectrometer for the Visible Range in the TEXTOR Boundary Plasma

Sebastijan Brezinsek, Albrecht Pospieszczyk, Gennadij Sergienko, Phillipe Mertens, Ulrich Samm

Institut für Energieforschung - Plasmaphysik, Forschungszentrum Jülich GmbH
EURATOM-Association, Trilateral Euregio Cluster, D-52425 Jülich, Germany

October 22, 2007

Passive spectroscopy is a standard diagnostic to observe the boundary layer of fusion plasmas. This visible spectroscopy is focused on the measurement of the deuterium recycling flux as well as on the monitoring of impurity fluxes like e.g. O, He... or W, C... which result from erosion of plasma-facing components. Moreover, the ro-vibrational analysis of molecular transitions provide information about the molecular break-up in the plasma. Spectrometer for the plasma boundary have to fulfil high demands with respect to the spectral, spatial and time resolution, to the observable wavelength range, to the sensitivity and dynamic range of the detector to observe and analyse simultaneously the emission of atomic and molecular species present in the observed region. We present an overview spectrometer system which is able a) to measure at once strong atomic lines (e.g. D_α) and weak molecular bands (e.g. C_2 Swan-band), b) to resolve narrow molecular lines (e.g. D_2 Fulcher-α band) and allow their ro-vibrational analysis, and c) to provide information about the spatial distribution in the plasma boundary. A full characterisation of the custom-made system in cross-dispersion arrangement with respect to resolving power, simultaneous wavelength coverage, sensitivity etc. is done. Spectra examples ("footprints") taken from an injection of C_3H_4 into TEXTOR are presented.

Keywords: Plasma-Wall Interaction, Cross-Dispersion Spectrometer, Plasma Boundary Spectroscopy, Fulcher-α band Spectroscopy, Hydrocarbon Break-Up Mechanism

1 Introduction

Present-day fusion devices use graphite and/or tungsten as a plasma-facing material (PFM) at the locations of highest particle flux such as the divertor target plates. Complex processes such as physical and, in the case of graphite, chemical sputtering take place at the surface. Material erosion and subsequent deposition leads to the formation of surface layers, which can -in the presence of two or more PFMs- contain complex mixed materials. A limited number of *in situ* diagnostics is currently available to identify and monitor the different species which are released from these PFMs under particle bombardment.
Passive spectroscopy in the visible range is a standard diagnostic to monitor the fluxes of carbon-containing species (C, CD...), which are released from the surface or build during the molecular break-up [1], other fusion-plasma related impurities (W, O...) as well as the fluxes of recycled fuel particles (D, D_2...). To observe and analyse the emission of these species simultaneously from a given observation volume, a spectrometer system has to fulfil high demands with respect to the spectral, spatial and time resolution, to the observable wavelength range, to the sensitivity and dynamic range of the detector. An optimised system should be able a) to measure at once strong atomic lines (e.g. D_α) and weak molecular bands (e.g. C_2 Swan-band), b) to resolve narrow molecular lines (e.g. D_2 Fulcher-α band) and allow their ro-vibrational analysis, and c) to provide information about the spatial distribution.
We present and characterise a spectrometer in cross-dispersion arrangement which can be applied as good compromise and which fulfils most of the needs apart from the spatial distribution from a single measurement. Experiments with injection of C_3H_4 were carried out in TEXTOR and spectra of the break-up products such as CH and C_2 were recorded simultaneously to demonstrate the potential of the device. Moreover the D_2 Fulcher-α was observed during local D_2 injection and ro-vibrationally analysed.

2 The cross-dispersion spectrometer – principle function, set-up and technical data

Conventional spectrometers, e.g. in Czerny-Turner arrangement, are equipped with only *one* dispersive element: grating or prism. Single dispersion systems are restricted

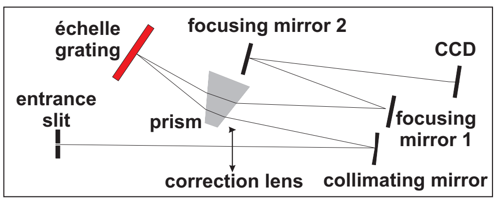

Fig. 1 Schematic view of the spectrometer set-up.

author's e-mail: s.brezinsek@fz-juelich.de

in the simultaneously covered wavelength span to a few nanometres at a typical resolving power $R = \lambda/\Delta\lambda$ of 20,000 which is mandatory for a ro-vibrational analysis of molecular transitions. The most prominent D_2 transition in fusion boundary plasmas - the Fulcher-α band - is spread over a wide spectral range (600 nm - 645 nm), thus, several discharges are necessary to record the full spectrum which is needed for spectral analysis.

In contrast, the custom-made spectrometer presented here (MI, model: Mechelle 7500 special; schematic set-up in fig. 1) consists of *two* dispersive elements: prism and grating. The system covers a spectral range of more than 300 nm without gap with the requested high spectral resolution. The wide span is achieved though the combined use of (i) a highly dispersive échelle grating (ruling: 31.6 grooves/mm, size 10.0 cm × 3.0 cm, blaze angle 63.5°) for wavelength dispersion in horizontal direction and (ii) an order sorter, a highly dispersive prism (BAF50 glass, reference angle 36°), which separates the orders in vertical direction. The prism is used twice in the optical path (fig. 1) to ensure complete order separation with compact prism size.

Fig. 2a shows the observable spectral orders m projected on the CCD array, starting from *m=153* at the bottom (blue spectral range) to *m=79* on the top (red spectral range), as well as the used spectral range in each order which is applied for the spectrum reconstruction. The centre wavelength in each order, positioned at the blaze angle of the grating, is determined by the order constant $m \times \lambda[\mu\text{m}]$ which amounts to 56.783 for this system. The overlap of different orders is determined by the condition $\frac{m=x+0.5}{56.783} = \lambda_{min}^{m=x} = \lambda_{max}^{m=x+1}$ while five additional pixels on each side are used for averaging. Fig. 2b shows the contribution of each order to the *standard range* between 372 nm *(m=152)* and 680 nm *(m=84)*. The 92th order is in the next figures marked in red as guide for the eye. The spectrum in each order is spread across several pixels in vertical direction. Thus, a summation over 5 to 7 pixels is made to increase the sensitivity of the system and provides a so-called spectral channel. Additionally, the spectrum reconstruction [2] takes into account the non-equidistant separation of the channels, which are more compressed in the lower orders, as well as their curvature in the higher orders.

Fig. 2c depicts the linear dispersion as a function of the wavelength in the standard range. Although the dispersion varies over the full range, the resulting resolving power, which was measured by applying the Rayleigh criterium to pairs of D_2 lines, is within 15% almost constant at 20,000 when the apparatus function is considered. The latter was estimated by the line width of Hg lines, in particular of Hg*I* at 529 nm to be below 3.1 channel (FWHM) as shown in the Gaussian fit in fig. 2d.

Further technical data of the Mechelle are: aperture value $f/7$, focal length $f_L = 190$ mm, entrance slit 25 μm×75 μm with SMA905 connector for fibre coupling. Light is coupled to the system by means of 600 m quartz fibre. A 16

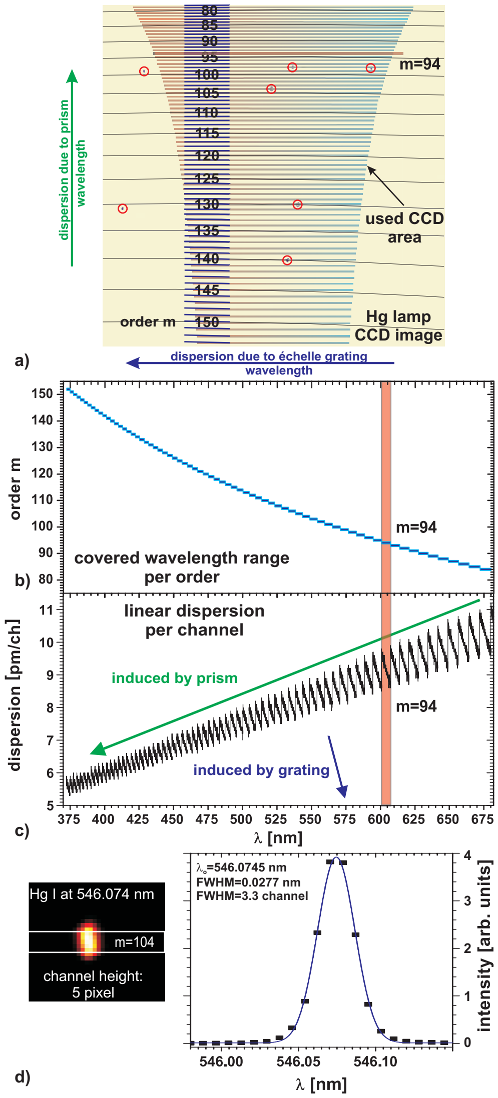

Fig. 2 Spectrum reconstruction: a) 2D image of a Hg line spectrum. The spectral range per order applied for the complete spectrum reconstruction is given by the envelope. b) Distribution of the wavelength coverage per order. c) The linear dispersion over the full spectral range. d) A Hg I line is used to approximate the apparatus function.

bit camera (Andor, model: DV434) with a Peltier-cooled back-illuminated CCD array, 1024×1024 pixels and 13 μm ×13 μm each pixel, is used as detector. The CCD has a broadband coating optimised for the visible range and provides a quantum efficiency of more than 90% at 500 nm and −60° C cooling temperature. The read-out time for the full frame amounts to one second at the maximum read-out frequency of 1 MHz.

3 Spectral and radiometric calibration

The spectral calibration is performed with the aid of a Hg lamp. The position of seven Hg*I* lines, marked in fig. 2a, is compared with theoretically calculated positions. The deviation between calculated and measured position is minimised in a least-square fit procedure. The overall position precision lies within two spectral channels and shows almost no drift under controlled temperature conditions. An

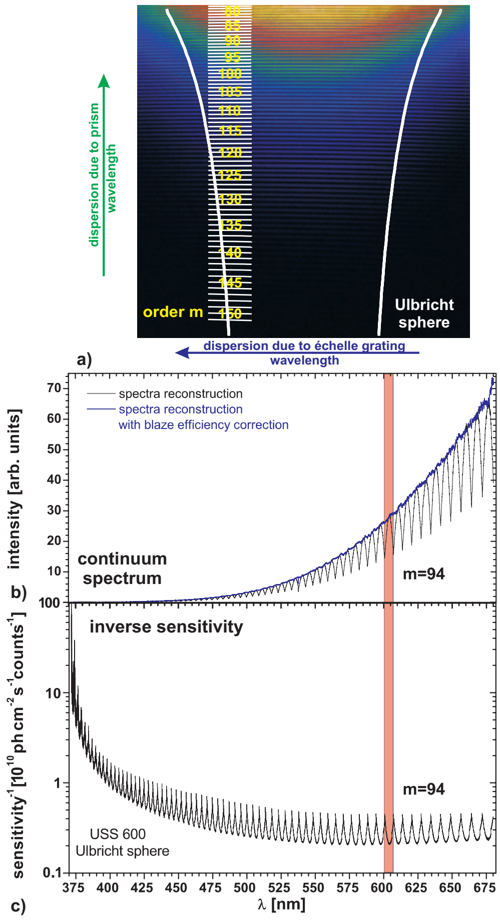

Fig. 3 Radiometric calibration of the cross-dispersion spectrometer. a) 2d image of the system during exposure by a continuum light source. b) Complete reconstructed spectrum of the continuum spectrum. Intensity drops caused by the blaze angle dependence of the grating are considered in the calibration by a correction function. c) The spectral response of the system for the full wavelength span.

Ulbricht sphere is used to calibrate the spectrometer system radiometrically. Fig. 3a shows a false-colour 2D image taken from the continuum source; the resulting reconstructed spectrum is depicted in fig. 3b. The spectrum is a convolution of the light source continuum and the sensitivity response of the detection system. Both image and spectrum show a non-uniformity of the measured radiation within each order. The reduction of the sensitivity of about 40% between the centre and the edges is caused by the blaze angle dependence of the grating. A correction function is introduced to compensate these strong sensitivity drops in the spectrum. The cross-talk between adjacent orders is measured to be below 10^{-3}, and any impact on the calibration can be neglected for the standard range.

The bare inverse sensitivity curve for the standard range is depicted in fig. 3c. The spectrometer system, which is optimised for the visible emission range according to the choice of prism, grating and CCD coating, shows an almost constant spectral response above 450 nm. However, the sensitivity drops significantly between 450 nm and 380 nm, which is largely caused by the reduction of the CCD quantum efficiency of about 50%, and by the decrease of the glass transmission from 95% to 55% due to 25 mm absorption length in the prism.

4 Spectra examples: hydrocarbon and deuterium molecules

A series of experiments with the injection of different hydrocarbon species (CH_4, C_3H_4 *etc.*) in similar plasmas has been started in TEXTOR. The aim of the experiments is a) to check if the injected stable hydrocarbon leaves a ”footprint” e.g. with regard to its appearance, intensity ratio, ro-vibrational population of the break-up products C_2, CH, CH^+ *etc.*, and b) to determine the inverse photon efficiencies and branching ratios which relate the photon flux of the break-up products to the particle flux of injected species. An example of a ”footprint” spectrum is depicted in fig. 4a. Spectra of the band heads of the most important transitions, CH Gerö-band and C_2 Swan-band, are enlarged. A ro-vibrational analysis and comparison with spectra of other injected species is outside the scope of this contribution, but can be found in detail in [3].

The deuterium spectrum of the Fulcher-band transition ($3p\ ^3\Pi_u \rightarrow 2s\ ^3\Sigma_g^+$) is depicted in fig. 4b. The main diagonal vibrational transitions ($v = v'$) up to $v = 5$ are indicated. The first main diagonal transition with $v = v' = 0$ is enlarged shown and the strongest Q lines (Q1-Q9) are marked. The rotational population of the excited state could be fitted according to a Boltzmann distribution with a rotational population temperature T_{rot} of about 1000 K which is in line with previous observations [4]. A more detailed analysis of the Fulcher-α band according to the methods described in [4] is topic of a forthcoming paper which will deal with the interpretation of the deuterium recycling flux and the molecular break-up [5] at the target plates of the helical divertor in TEXTOR [6].

5 Conclusion and outlook

The cross-dispersion spectrometer presented here is a good compromise to study spectroscopically the plasma boundary of fusion devices in the visible range, i.e the fuel recycling and the impurity sources. The system covers at once the spectral emission range between 372 nm and 680 nm with an almost constant resolving power of R=20000 over the full range. The dynamic range of 16 bit ensures the possibility of the simultaneous observation of atomic and molecular lines. The recommended integration time for the fibre-coupled system depends on the signal strength (extrinsic vs. intrinsic), but lays in the second range to ensure and optimised use of the dynamic range. Synergetic effects can be achieved when – like in TEXTOR – the system is embedded in a set of spectroscopic systems which complement one another [5]. The Mechelle provides the high

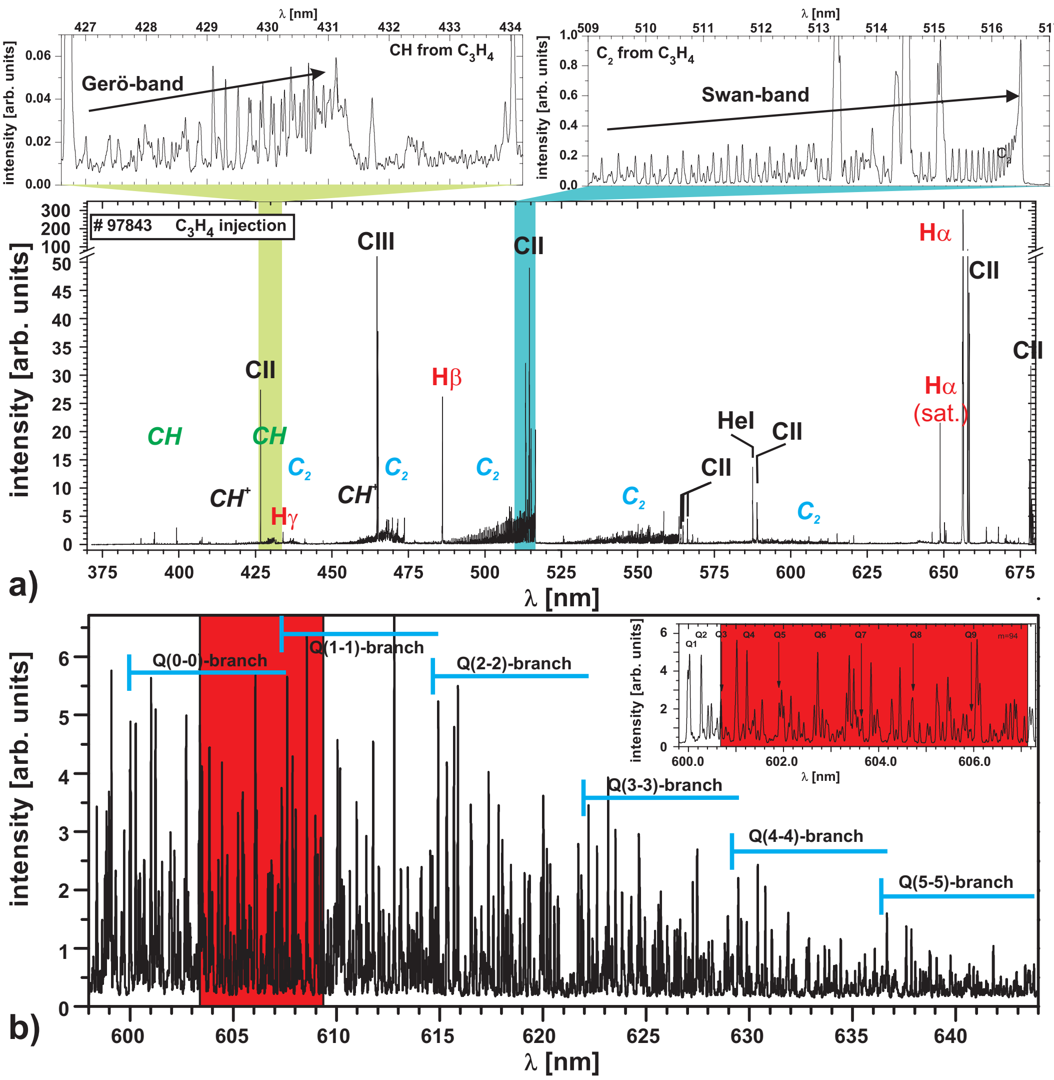

Fig. 4 a) C_3H_4 injection into the TEXTOR edge plasma through a gas injection module. The emission spectrum in the range between 372 nm and 680 nm recorded gap-free with the cross-dispersion spectrometer during the break-up of the injected hydrocarbon. The most important observable optical transitions of atomic and molecular break-up products are indicated. The CH Gerö band and the C_2 Swan band are highlighted and enlarged in separate figures on top of the "footprint" spectrum to demonstrate the good spectral resolution of the molecular bands. The integration time of the system was set to two seconds to ensure the complete coverage of the C_3H_4 injection pulse. b) The complete D_2 Fulcher-α band and the Q-lines of the first main diagonal transition. The spectral range in red indicates the coverage of the observation in the 94*th* order which is also highlighted in a separate box.

spectral resolution, the large wavelength coverage, and the high dynamic range, whereas the other systems with interference filters like photomultipliers or 2D CCD cameras provide the needed time and spatial resolution.

Experiments at TEXTOR provide "footprints" of the injected hydrocarbons C_3H_4 and information of D_2 molecules in the hot edge plasma. The appearance, the destruction path, the flux, the ratio, and the ro-vibrational population of the different species can now be studied in more detail within a single discharge.

Systems of the next generation of cross-dispersion spectrometers in prism /grating arrangement and equipped with prism, made of low absorption material with high dispersion, are currently developed to ensure a larger sensitivity in the spectral region below 450 nm. Such an optimised system will be used for the observation of the new first wall and boundary layer at JET after installation of the new ITER-like wall with W and Be as plasma-facing material. The installation of an Echelle cross-dispersion spectrometer system is a also panned for the observation of the boundary layer in W7-X.

References

[1] S. Brezinsek et al., Physica Scripta **T111**, 42 (2004).
[2] P. Lindblom, Anal. Chim. Acta **380**, 353 (1999).
[3] S. Brezinsek et al., J. Nuclear Materials **313-316**, 967 (2003).
[4] S. Brezinsek et al.,J. Nuclear Materials **363-365**, 1119 (2007).
[5] S. Brezinsek et al., Plasma Phys. Control. Fusion **47**, 615 (2005)
[6] M. Lehnen et al., this conference

Proceedings of ITC/ISHW2007

Emergence of ionization balance plasma in confinement region with the complete divertor detachment

Motoshi GOTO, Shigeru MORITA

National Institute for Fusion Science, Toki 509-5292, Japan

October 29, 2007

A spectroscopic measurement is made for the plasma in the rotating radiation belt accompanying the complete divertor detachment which is recently realized in the Large Helical Device (LHD) [J. Miyazawa, et al., Nucl. Fusion **46**, 532 (2006)]. The Balmer series lines of neutral hydrogen are clearly observed. The population distribution over the exited levels is determined from the Balmer series line intensities and is compared with the result of the collisional-radiative model calculation to determine the electron temperature T_e and density n_e. No reasonable pair of T_e and n_e is found when either the ionizing plasma or the recombining plasma is assumed. A good fitting is obtained under an assumption of the ionization balance plasma with $T_e = 1.8\,\mathrm{eV}$ and $n_e = 2 \times 10^{20}\,\mathrm{m}^{-3}$. The mechanism to sustain such a low temperature plasma inside the high temperature confinement region is unclear.

Keywords: radiation belt, spectroscopy, ionization balance plasma, Stark broadening

1 Introduction

In the study of magnetic confined fusion plasma the reduction of heat flux onto the divertor plate is an important issue. A possible solution of this problem is to induce the detached plasma in the divertor region through intentional radiation loss. For this purpose the impurity gas puffing has been attempted in various devices [1–5].

In the Large Helical Device (LHD) the complete detachment of the divertor plasma has been obtained with strong gas puff of hydrogen into the divertor region. A salient feature of the obtained plasma in LHD is that it is accompanied by emergence of a luminous radiation belt in the boundary region which has a helical structure and surrounds the core plasma. Furthermore, the radiation belt looks poloidally rotate with a frequency of, for example, 15 Hz.

Though the conditions of the discharge to obtain such a detached plasma have been investigated in detail [6], the plasma state in the radiation belt itself is still unclear. Our interest is the plasma state in the strong radiation region and its relevance to the occurrence of plasma detachment. This paper introduces our attempt to determine the plasma state and parameters, such as the electron temperature T_e and the electron density n_e, in the radiation belt from the measured spectra in the visible wavelength range.

2 Experiment

LHD is a heliotron type fusion experimental device of magnetic confinement. It forms a steady-state structure of magnetic field with a set of super-conducting coils. The plasma has an elliptical poloidal cross section and it rotates with a toroidal period number of five. The major and averaged minor radii of the last closed flux surface are 3.5 m–4.2 m and 0.6 m, respectively.

We use an optical fiber having the diameter of 100 μm to observe the light emitted from the plasma. One end of the optical fiber is placed at the observation port, and the field of view of the optical fiber is collimated with a lens so as to have a cylindrical shape with the diameter of roughly 30 mm in the plasma. The optical axis passes through the plasma center as shown in Fig. 1. The other end of the optical fiber is located at the entrance of a spectrometer. The spectrometer has a focal length of 50 cm and is equipped with three gratings of 100, 1800, and 3600 grooves mm^{-1}, respectively. The spectrum is recorded with a CCD (charge coupled device) detector. The maximum sampling rate is 200 spectra s^{-1}. The sensitivity of the whole observation system has been absolutely calibrated with a tungsten lamp.

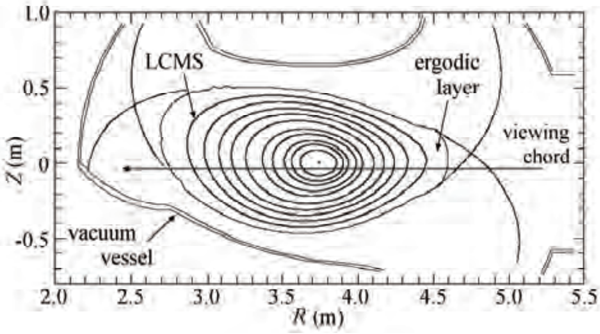

Fig. 1 Cross section of the vacuum vessel and the plasma for our observation. The major radius of the vacuum vessel center is 3.9 m. The plasma is observed with a single line-of-sight shown with the arrow.

author's e-mail: goto@nifs.ac.jp

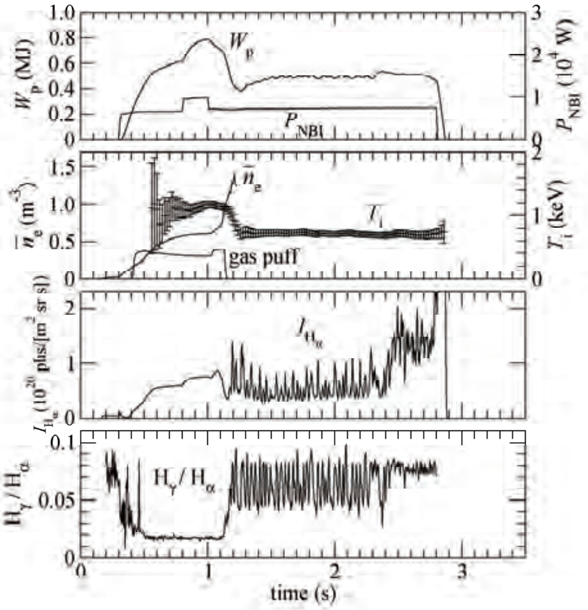

Fig. 2 Temporal development of the discharge for the present analysis. The measurement of the line-averaged electron density, $\bar{n}_e$ with the interferometer is limited until t = 1.2 s due to the fringe jump problem. The ion temperature, T_i, is determined from the Doppler width of a helium-like argon ion line.

Figure 2 shows the temporal behavior of a discharge for which the complete detachment has been obtained. The present experiment employs the magnetic configuration of R_{ax} = 3.65 m and B_{ax} = 2.712 T, where R_{ax} and B_{ax} are the magnetic axis radius and the magnetic field strength on the magnetic axis, respectively.

The plasma is sustained with three neutral beams (~ 7 MW). The line-averaged electron density $\bar{n}_e$, which is measured with the interferometer, is feedback-controlled with the gas puffing rate until t = 1 s. At t = 1 s a short pulse massive gas puff (~ 0.1 s and ~ 200 Pa m^3 s^1) is given and $\bar{n}_e$ suddenly increases. The $\bar{n}_e$ measurement is unavailable after t = 1.2 s due to fringe jump problem.

After such an abrupt change in $\bar{n}_e$, the stored energy W_p and the central ion temperature T_i, which is determined from the Doppler broadening of the heliumlike argon resonance line, are kept almost constant. During this stationary time period the particle flux onto the divertor plate, which is measured with Langmuir probes, is found decreased and the plasma detachment is suggested [7]. Simultaneously, the measurement with an absolute extreme ultra violet photodiode (AXUVD) camera [8] suggests the emergence of a rotating radiation belt [7].

Spectra of the emitted light from the plasma are measured with the 100 grooves mm^{-1} grating out of three. The wavelength range of 300 nm to 700 nm is simultaneously observed. Each emission line is fitted with a Gaussian function and the corresponding intensity is derived as the area of the line profile. The temporal variations of the Balmer α (656.3 nm) line intensity and the intensity ratio of the Balmer γ (434.0 nm) to α lines are shown in Fig. 2.

It is readily noticed that the Balmer α line intensity oscillates with a frequency of approximately 30 Hz which is twice the frequency of the radiation belt rotation derived from the AXUVD measurement. This is understandable because in a cycle of the radiation belt rotation the line intensity should take the maximum twice when the radiation region crosses the line-of-sight at the near side and the far side of the plasma edge. The ratio of the Balmer γ and Balmer α lines is also found oscillating with the same frequency. This result suggests that the plasma states inside and outside the radiation belt are considerably different.

3 Collisional-radiative model

We use the collisional-radiative (CR) model code [10] for the analysis of the obtained spectra. The CR model is based on the rate equations concerning the excited level populations. The time derivative of the population of a level p, $n(p)$, is expressed as

$$\frac{\mathrm{d}}{\mathrm{d}t}n(p) = \Gamma_{\mathrm{in}}(p) - \Gamma_{\mathrm{out}}(p), \tag{1}$$

where $\Gamma_{\mathrm{in}}(p)$ and $\Gamma_{\mathrm{out}}(p)$ stand for the population flows into the level p and out of the level p, respectively. These population flows are explicitly written with various elementary atomic processes as

$$\begin{aligned}\Gamma_{\mathrm{in}}(p) &= \sum_{q>p} A(q,p)n(q) + \sum_{q<p} C(q,p)n_e n(q) \\ &\quad + \sum_{q>p} F(q,p)n_e n(q) + \beta(p)n_e n_i + \alpha(p)n_e^2 n_i \\ &= \sum_{q<p} C(q,p)n_e n(q) \\ &\quad + \sum_{q>p} \{F(q,p)n_e + A(q,p)\}\, n(q) \\ &\quad + \{\beta(p) + \alpha(p)n_e\}\, n_e n_i,\end{aligned} \tag{2}$$

and

$$\begin{aligned}\Gamma_{\mathrm{out}}(p) &= S(p)n_e n(p) + \sum_{q>p} C(p,q)n_e n(p) \\ &\quad + \sum_{q<p} F(p,q)n_e n(p) + \sum_{q<p} A(p,q)n(p) \\ &= \left[S(p)n_e + \sum_{q>p} C(p,q)n_e \right. \\ &\quad \left. + \sum_{q<p} \{F(p,q)n_e + A(p,q)\} \right] n(p),\end{aligned} \tag{3}$$

respectively, where $S(p)$, $\alpha(p)$, and $\beta(p)$ are the rate coefficients for the electron impact ionization, three-body recombination, and radiative recombination, respectively, and $C(p,q)$ and $F(p,q)$ are the excitation and deexcitation rate coefficients, respectively, due to electron impacts from level p to level q. The expression $\sum_{q>p}$ means that the summation is conducted over the excited levels located higher than p.

The relaxation time of the excited level populations is generally so short that the left-hand-side of Eq. (1) is assumed to be zero except for the ground state and the ion. In this case, a collection of Eq. (1) for the all excited levels is regarded as a set of coupled linear equations which is solved readily. As the solution of the coupled equations $n(p)$ is found to be expressed as a linear combination of two terms which are proportional to the ground state density $n(1)$ and ion density n_i, respectively, like

$$n(p) = R_0(p)n_e n_i + R_1(p)n_e n(1), \tag{4}$$

where the first and the second terms are called the recombining plasma component and the ionizing plasma component, respectively, and $R_0(p)$ and $R_1(p)$, which are functions of T_e and n_e, are called the population coefficients.

Equation (1) for the ground state atom and ion can be rewritten in the form as

$$\frac{d}{dt}n(1) = -\frac{d}{dt}n_i = -S_{CR}n_e n(1) + \alpha_{CR}n_e n_i, \tag{5}$$

where S_{CR} and α_{CR} are composed from the obtained population coefficients and correspond to the effective ionization and recombination rate coefficients, respectively.

4 Results

Figure 3 shows the spectrum when the Balmer α line intensity takes maximum during the oscillation phase. This

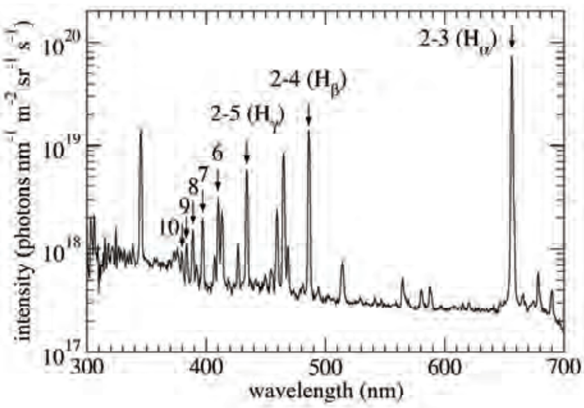

Fig. 3 Spectrum at the intensity maximum averaged between t = 1.2 s and 2.2 s.

result is the average of the spectra at the intensity maximums between t = 1.2 s and 2.2 s.

Since the observation system is absolutely calibrated, the signals from the detector can be translated into the emitted photon number. Each Balmer series line is fitted with a Gaussian profile and the line intensity $I(p,q)$ [photons s^{-1} m^{-2}], where p and q stand for the principal quantum number of the upper and lower levels, respectively, is determined.

From the viewpoint of atomic processes, the line intensity $I(p,q)$ is understood as

$$I(p,q) = N(p)A(p,q), \tag{6}$$

where $N(p)$ is the line-integrated population density of level p, and $A(p,q)$ is the spontaneous transition probability. We adopt $A(p,q)$ values of the NIST database [9] and derive $N(p)$ from Eq. (6). In Fig. 4 $N(p)$ normalized by their statistical weight $g(p)$ is plotted with the solid squares as a function of the ionization potential of the level p. In

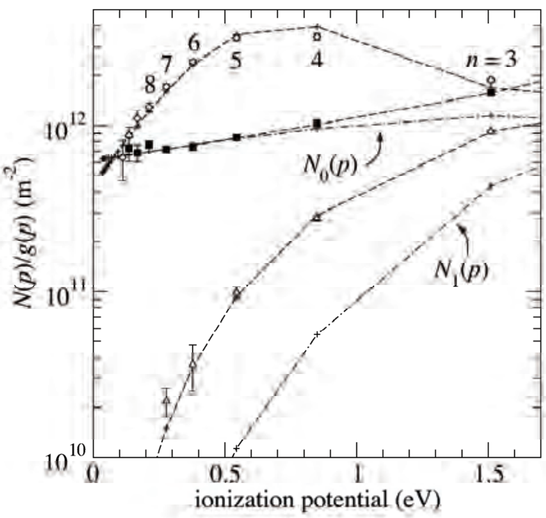

Fig. 4 Population distributions for different three plasma states in the discharge; the solid squares, open circles, and open triangles are obtained for the intensity maximum in the oscillation phase, before the detachment, and in the plasma terminating phase, respectively. Fitting results with the CR model are also shown with the dashed lines. The dotted-dashed lines, which are labeled as $N_0(p)$ and $N_1(p)$ are respectively the recombining plasma component and the ionizing plasma component in the total population $N(p)$ of the ionization balance plasma for the intensity maximum case.

Fig. 4 the results derived for other two different timings are also shown.

We attempt fittings of the all population distributions in Fig. 4 with Eq. (4) by adjusting T_e and n_e. The open triangles in Fig. 4 are taken in the time period from t = 0.6 s to 0.7 s. The population rapidly decreases with the increasing principal quantum number. This behavior is a typical characteristic of the ionizing plasma, for which each level population is dominated by the second term in Eq. (4). Since the dependence of the population distribution on the electron temperature and density is generally weak, it is difficult to uniquely determine those parameters from the obtained population distribution. The dashed line is, for example, the calculation result with T_e = 30 eV and $n_e = 8\times10^{18}$ m^{-3} which is normalized to the measurement.

The open diamonds in Fig. 4 are the result at $t = 2.85$ s in the plasma decay phase after the NBI heating is terminated. The result exhibits a typical characteristic of the recombining plasma; the populations of highly excited levels are relatively large. Roughly speaking, the slope of the highly excited level populations corresponds to T_e and the level having the maximum population to n_e. We fit the result with the first term in Eq. (4) and the parameters of $T_e = 0.2$ eV and $n_e = 1.3 \times 10^{19}$ m^{-3} are obtained. The fitting result is shown with the dashed line in Fig. 4.

The solid squares in Fig. 4 show a different distribution profile from those in the former two cases. No reasonable combination of T_e and n_e is found for the present case when either the pure ionizing plasma or recombining plasma is assumed. Instead, we attempt a fitting under the assumption of the ionization balance plasma. When the ionization rate and the recombination rate are balanced, namely, Eq. (5) is zero, the plasma is defined to be in the ionization balance. The ratio of n_i to $n(1)$ is expressed as

$$\frac{n_i}{n(1)} = \frac{\alpha_{CR}}{S_{CR}}, \tag{7}$$

and Eq. (4) is rewritten as

$$n(p) = \left\{ R_0(p) + R_1(p)\frac{S_{CR}}{\alpha_{CR}} \right\} n_e n_i. \tag{8}$$

The measured population distribution is well fitted with $T_e = 1.8$ eV and $n_e = 2 \times 10^{20}$ m^{-3}. The fitting result normalized to the measurement is shown with the dashed line in Fig. 4. The dotted-dashed lines labeled as $N_0(p)$ and $N_1(p)$ correspond to the first and second terms in Eq. (4). Equation (8) is evaluated with these parameters and $n(3)/g(3) = 7.3 \times 10^{12}$ m^{-3} is obtained. On the other hand, the line-integrated population $N(3)/g(3)$ is determined to be 1.6×10^{12} m^{-2} in the measurement. The normalization factor between these quantities, $\ell = 0.22$ m, corresponds to the thickness of the radiation belt. This result is consistent with that of the AXUVD measurement.

It is surprising that the strong radiation area having such a low electron temperature is located inside the last closed flux surface (LCFS), while the central T_i line is kept at approximately 800 eV. No reasonable explanation has been found to understand the fact that such an extremely low temperature plasma steadily exists in the confinement region of a high temperature plasma.

5 Discussion

The electron temperature and density are determined mainly from the population distribution over the $n = 3$ to $n = 6$ levels, and the points corresponding to $n = 7$ and higher levels apparently deviate from the expected values as seen in Fig. 4. Since the wavelength resolution to measure their corresponding emission lines is insufficient, the uncertainty of the obtained line intensity is large. In order to make clear this uncertainness, a measurement with higher wavelength resolution has been attempted for a similar discharge. The spectrum measured with the same spectrometer but with a grating of 1800 grooves/mm is shown in Fig. 5. The synthetic spectrum with the same plasma pa-

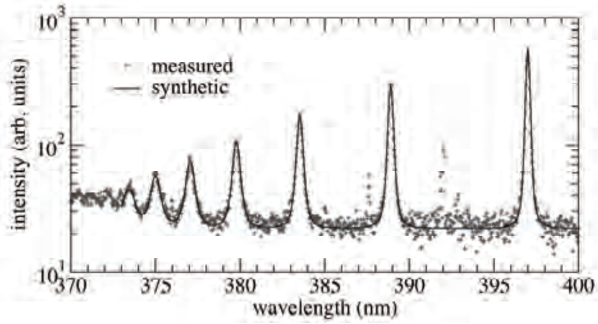

Fig. 5 Spectrum at the intensity maximum with a high wavelength resolution measurement. The solid line is a synthetic spectrum calculated with $T_e = 1.8$ eV and $n_e = 2 \times 10^{20}$ m^{-3} and normalized to the measurement. The Stark broadening and the instrumental width are taken into account for each line profile.

rameters as derived in the analysis above, i.e., $T_e = 1.8$ eV and $n_e = 2 \times 10^{20}$ m^{-3}, is also shown in the same figure. Here, the Stark broadening for individual line profiles is calculated with the numerical calculation data [11]. The agreement is satisfactory in both the intensity distribution and line profiles, and the plasma parameters derived here are verified.

Acknowledgments

The authors are grateful to the LHD experimental group for the helpful support. This study has been made in part under a financial support by the LHD project (NIFS07ULPP527).

[1] J. Neuhauser, M. Alexander, G. Becker, et al., Plasma Phys. Control. Fusion **37**, A37 (1995).
[2] C. S. Pitcher and P. C. Stangeby, Plasma Phys. Control. Fusion **39**, 779 (1997).
[3] A. Loarte, R. D. Monk, J. R. Martín-Solís, et al., Nucl. Fusion **38**, 331 (1998).
[4] N. Asakura, S. Sakurai, H. Tamai, et al., J. Nucl. Mater. **290–293**, 825 (2001).
[5] U. Wenzel, K. McCormick, N. Ramasubramanian, et al., Nucl. Fusion **44**, 1130 (2004).
[6] J. Miyazawa, S. Masuzaki, R. Sakamoto, et al., Nucl. Fusion **46**, 532 (2006).
[7] S. Masuzaki, R. Sakamoto, J. Miyazawa, et al., J. Plasma Fusion Res. **81**, 649 (2005).
[8] B. J. Peterson, A. Yu. Kostrioukov, N. Ashikawa, et al., Plasma Phys. Control. Fusion **45**, 1167 (2003).
[9] NIST Atomic Spectra Database http://physics.nist.gov/PhysRefData/ASD/index.html)
[10] T. Fujimoto, S. Miyachi, and K. Sawada, Nucl. Fusion **28**, 1255 (1988).
[11] C. Stehlé and R. Hutcheon, Astron. Astrophys. Suppl. Ser. **140**, 93 (1999).

Proceedings of ITC/ISHW2007

Behavior of CIII to CVI emissions during recombining phase of LHD plasmas

Malay Bikas Chowdhuri, Shigeru Morita[a] and Motoshi Goto[a]

Department of Fusion Science, Graduate University for Advanced Studies,

Toki 509-5292, Gifu, Japan

[a] National Institute for Fusion Science, Toki 509-5292, Gifu, Japan

(Received 15 October 2007 / Accepted 15 October 2007)

Carbon emissions of CIII-CVI during recombining phase of the Large Helical Device (LHD) plasma are studied to understand their behaviors. For the purpose four resonance transitions of CIII (977Å: $2s^2\ ^1S$-$2s2p\ ^1P$), CIV (1550Å: $2s\ ^2S$-$2p\ ^2P$), CV (40.27Å: $1s^2\ ^1S$-$1s2p\ ^1P$) and CVI (33.73Å: $1s\ ^2S$-$2p\ ^2P$) are observed using absolutely calibrated VUV monochromators and EUV spectrometers. One dimensional impurity transport code has been used to calculate the spectral emissivity under the consideration of measured n_e and T_e profiles. The temporal evolution of line emissions have been calculated and compared with the measured data. The comparison shows that the carbon density is 3% to n_e. However, the discrepancy between the calculated and measured values has been noticed in CIII and CIV. It has been argued that three dimensional structures of CIII and CIV emissions are likely to be the reason for this difference, which is based on the presence of relatively high-density and high-temperature plasmas in edge ergodic layer in LHD. It is also found that the CVI emission during recombining phase increases with n_e whereas it is nearly constant during steady state phase suggesting the disappearance of the edge particle screening effect.

Keywords: impurity, carbon, intensity computation, recombining phase.

1. Introduction

For the study of the impurity behavior in high temperature plasmas impurity densities in each charge state are usually analyzed using spectral absolute intensities measured from spectroscopic diagnostics in combination with a one-dimensional impurity transport code [1]. It evaluates radial profiles of charge state and emissivity based on measured electron density and temperature profiles. In general the impurity transport studies have been done during the steady-state phase of discharges using either of intrinsic or extrinsic impurity particles [2-5]. When the impurity time behavior is analyzed at the transient phase, especially the plasma termination phase, the time duration is very short in the case of tokamaks because of the abrupt disruption after the current termination. Even if the toroidal current is controlled for the smooth termination of the plasma, the magnetic field topology and resultant magnetic surface structure change so much as a function of time. In stellarator cases, on the other hand, the magnetic field for the confinement is externally supplied and maintains steadily even during the transient phase of the discharges. The temporal evolution of impurity emissions from such plasmas can be easily computed under the presence of steady magnetic surface.

In the Large Helical Device (LHD) the helical magnetic field for the plasma confinement produced by superconducting magnetic coils makes possible the steady state operation. The analysis is of course possible on the transient period at initial and final phases of the discharges. In such period the temporal variation of electron and ion densities is mainly governed by atomic ionization and recombination processes instead of the particle transport [6]. Therefore, the absolute intensities of edge spectral lines emitted from fueling gas and impurities can be basically converted to respective ion densities even if the edge temperature and density profiles are not measured in detailed. In this paper temporal behavior of edge carbon emissions is studied during the recombining phase of LHD discharges and the carbon density measurement is attempted with analysis of the carbon emissions as a function of n_e.

2. Experimental Setup

The experiment has been conducted with inwardly shifted configuration of R_{ax}=3.6m and B_t= 2.75T. A discharge is initiated by electron cyclotron heating (ECH)

author's e-mail: chowdhuri.malayl@nifs.ac.jp

and the plasma is sustained by three negative-ion-based neutral bean injection (NBI) devices. Several spectroscopic diagnostics covering visible to X-ray wavelength ranges have been installed to monitor and study the impurity behaviour of LHD discharges. In the present study emissions from different ionization stages of carbon have been measured using two extreme ultra violet (EUV) spectrometers [7, 8] and two vacuum ultra violet (VUV) monochromators [9]. Two absolutely calibrated EUV spectrometers cover 10–130Å (EUV_Short) and 50–500Å (EUV_Long) wavelength range, respectively. Back-illuminated VUV sensitive charge couple device (CCD) detectors are mounted with two EUV spectrometers and operated in full binning mode. Data from the CCD have been acquired in every 5 ms. Four resonance transitions of CIII (977Å, $2s^2\ ^1S$-$2s2p\ ^1P$), CIV (1548Å, $2s\ ^2S$-$2p\ ^2P$), CV (40.27Å, $1s^2\ ^1S$-$1s2p\ ^1P$) and CVI (33.73Å, $1s\ ^2S$-$2p\ ^2P$) are mainly monitored for this study. The CV and CVI emissions are measured using the EUV_Short spectrometer with a spectral resolution of ~0.10Å at 40Å. The resonance transitions from Li- and Be-like carbon ions are observed using two 20cm normal incidence VUV monochromators equipped with an electron multiplier tube detector. The signal is acquired with time interval of 100μs. The two VUV monochromators were absolutely calibrated using the carbon emissions by comparing the raw signals with the absolutely calibrated EUV_Long spectrometer for 50–500Å. Two experimental intensity ratios of $2s^2$-$2s3p$ (386.4Å) to $2s^2$-$2s2p$ (977Å) transitions from CIII and of 2s-3p (312.4Å) to 2s-2p (1550Å) transitions from CIV were adopted for the calibration. Electron temperature and density profiles measured with Thomson diagnostics and line-integrated electron density measured with FIR diagnostics are used for the present analysis.

3. Description of Calculation

Analysis on temporal behaviors of carbon emissions in different ionization stages are based on the calculation of the line-integrated emissivity using one-dimensional impurity transport code [1]. The time behavior of the impurity density profile is calculated by the following equation with the ionization balance of an impurity ion;

$$\frac{\partial n_q}{\partial t} = -\frac{1}{r}\frac{\partial}{\partial r}\left(r\Gamma_q\right) + \alpha_{q-1}n_{q-1}n_e + \beta_{q+1}n_{q+1}n_e - \left(\alpha_q + \beta_q\right)n_q n_e \qquad (1)$$

where n_q and Γ_q are the ion density and particle flux of qth charge state, respectively. The parameters of α and β represent the ionization and recombination rate coefficients, respectively. The empirical transport model [10], of which the validity was confirmed in LHD, using the diffusion coefficient D and convective velocity V is given by;

$$\Gamma_q = -D_q(r)\frac{\partial n_q}{\partial r} + V_q(r)n_q \qquad (2)$$

$$\text{and}\quad V_q(r) = -V(a)\frac{r}{a}. \qquad (3)$$

Here, a, D_q and V_q are the plasma radius, diffusion coefficient and convective velocity, respectively.

After the charge state calculation the emissivity and brightness profiles of emission line was evaluated. The emissivity of transition from level j to i, ε(i,j), is expressed by the relation of $\varepsilon(i, j) = N_q(j)A(i, j)$, where A(i, j) is the transition probability and $N_q(j)$ is the density of the level j in charge state q. The emissivity is calculated from the level-population in the upper level. The level-population is generally determined by the collisional and radiative processes among several quantum levels [11]. However, the coronal model is assumed in the present case for the simplicity. This assumption really gives a good agreement with the C-R model calculation, at least, for the H- and He-like systems. Therefore, the relation can be written as $E(i,j) = N_q(j)A(i, j) = n_q n_e Q(i, j)$, where Q(i, j) is the excitation rate coefficient for the transition of i to j. The excitation rate coefficient for individual line has been taken from calculated results by Itikawa et al. [12].

4. Results and Discussions

A typical waveform of NBI discharge used in the present impurity study is shown in Fig.1. The time evolution of carbon emissions has been analyzed at the recombining phase from 2.45s to the end of the plasma termination, where the T_e quickly decreases due to the absence of the heating source while the n_e stays constant. The central electron temperature $T_e(0)$ measured by Thomson scattering diagnostic was available until t=2.620s. The CV and CVI emissions, on the other hand, dropped to zero at 2.628s, and the CIII and CIV emissions disappeared 15ms later because of their low ionization energies (I.E.) (CIII: 50eV, CIV: 68eV, CV: 367eV and CVI: 475eV). Extrapolation of the measured T_e was therefore necessary to calculate the emissivity of the carbon emissions in different ionization stages. The T_e was calculated from magnetic energy and line-integrated electron density $\langle n_e \rangle$. The measured and extrapolated $T_e(0)$ and plasma radius r_b at horizontally elongated plasma cross section are plotted in Fig.2. The $T_e(0)$ and the plasma radius gradually decrease, and after t=2.550s the $T_e(0)$ begins to drop quickly. The CIII and CIV emissions also start to increase rapidly at t=2.550s.

Temporal evolution of carbon emissions during the recombining phase has been calculated using one-dimensional impurity transport code. The calculation has been done on the averaged magnetic surface by

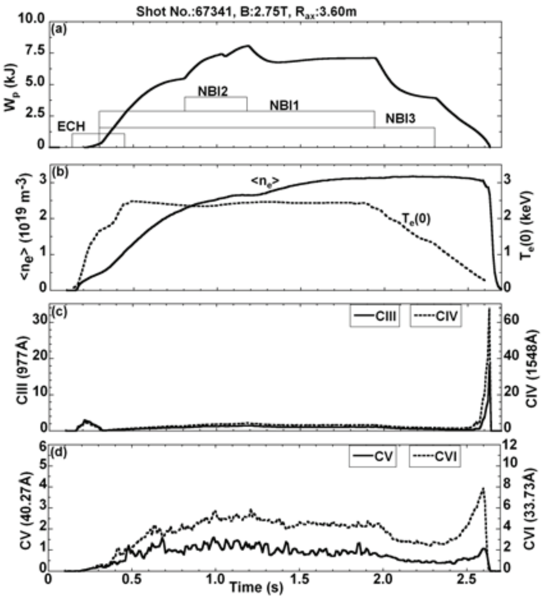

Fig.1 Typical discharge for the present analysis; (a) plasma stored energy and heating pulses, (b) line-averaged electron density (solid line) and central electron temperature (dashed line), (c) CIII (solid line) and CIV (dashed line) emissions and (d) CV (solid line) and CVI (dashed line) emissions. All carbon emissions have unit of 10^{14} photons.cm^{-2}.sr^{-1}.s^{-1}. Data between t=2.45s to 2.65s are used for analysis.

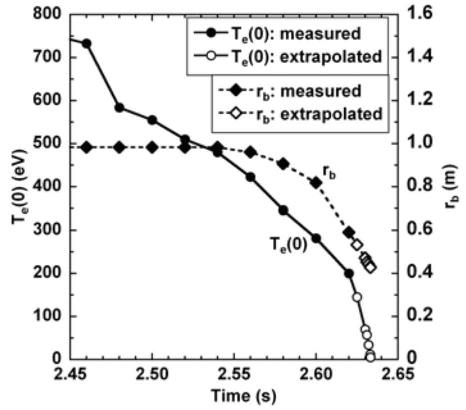

Fig.2 Time behaviors of central electron temperature ($T_e(0)$: circles) and horizontal plasma radius (rb: diamonds) at horizontally elongated plasma cross section during recombining phase. Closed circles and diamonds means measured values, and open circles and diamonds mean extrapolated values.

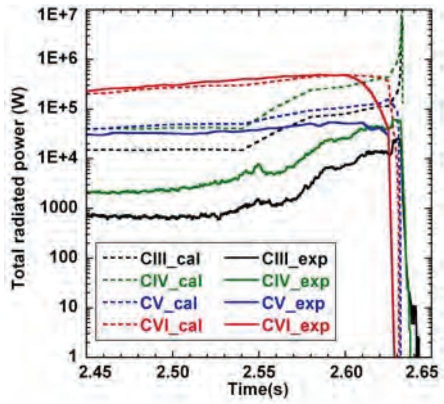

Fig.3 Calculated and experimental total radiation power of CIII to CVI. Dash and solid lines indicate calculated and experimental data.

replacing the elliptical shape of LHD plasmas with the circular shape. In this study the diffusion coefficient D_q is considered as an independent of q and r, and the inward convection velocity V_q is as a function of r. Here, the maximum value of V_q is given as V(a) at average plasma radius a (see Eq.3). The values of D_q and V(a) are taken to be 0.2m^{2}s^{-1} and 1.0ms^{-1} for the diffusion coefficient and inward convective velocity, respectively.

Figure 3 illustrates the total radiation power emitted from Be-like CIII to H-like CVI, which are obtained by integrating the whole plasma surface of LHD. The experimental and calculated results are indicated with solid and dashed lines, respectively. In the calculation 3% carbon density is assumed to the electron density. All the carbon radiations gradually increase after turning off the heating power as the T_e decreases. At first the CVI emissions reach the peak value at 2.60s where the $T_e(0)$ is 280eV. This is in good agreement with the calculation. Then, the CV and CVI radiations quickly decrease and become zero immediately at 2.625s. At this moment the $T_e(0)$ drops less than 150eV. The calculation of CV and CVI radiations also drop at 2.630s. Since the exposure time of CCD detector is 5ms in the present experiment, the difference between the measurement and calculation may originate in the uncertainty of the time window.

On the other hand, dynamic range of the CIII and CIV emissions is really large compared to the CV and CVI cases. The voltage applied to the SEM is always adjusted to monitor the main discharges, not the plasma termination phase. Then, the signals of CIII and CIV are always saturated at the plasma termination phase as seen during t=2.628-2.632s in the figure. The calculation of CIII and CV radiations reach the peak value at 2.632s when the $T_e(0)$ becomes 12eV. The calculation after 2.633s is, however, impossible in practice, because of the extremely low electron temperature. In the discharge very low temperature plasma is maintained until t=2.645s as apparently seen in the CIII temporal behavior.

During steady-state phase of discharges the carbon emissions are basically located inside the narrow shell at plasma edge. In LHD the CIII and CIV generally exist in

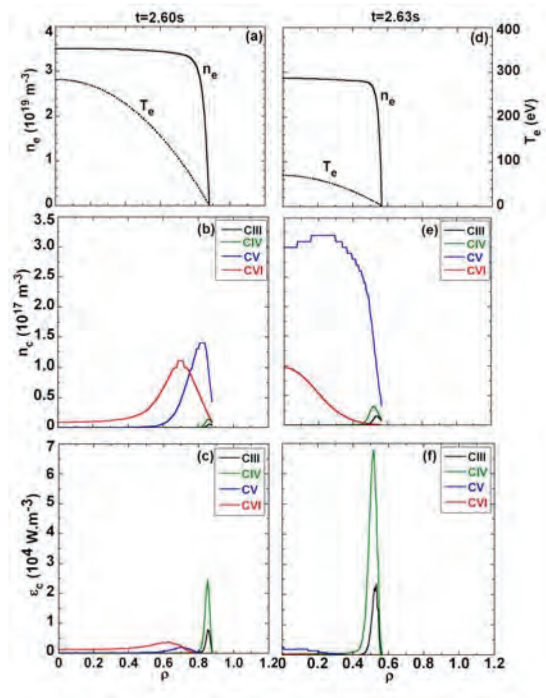

Fig.4 Radial profiles of n_e and T_e ((a) and ((d)), densities ((b) and (e)) and emissivities ((c) and (f)) of CIII to CVI taken at two different time frames of 2.60s (a, b and c) and 2.63s (d, e and f). Abscissa means normalized radius, ρ.

the ergodic layer [13] surrounding the main plasma and the CV and CVI exist near the last closed flux surface (LCFS). During recombining phase the width of the emission shells is broaden as the T_e decreases, and moves inside because of the reducing plasma size, as shown in Fig.2. Calculated results on the radial profiles of carbon densities and emissivities are shown in Fig.4. Figure 4 (a)-(c) and (d)-(f) are the radial profiles at t=2.60s and 2.63s in Fig.3, respectively. The CVI emission takes the maximum value at 2.60s and the CV and CVI entirely disappear at 2.63s. Fig. 4(a) and (c) are the measured n_e and T_e profiles used in the calculation. The CIII and CIV are always located at the plasma edge in these time frames with sharp peaks.

On the other hand, the CV and CVI emission profiles are quite different. At t=2.60s the shell widths of the CV and CVI densities become wider (see Fig.4 (b)), and resultant emission profiles also become much wider (see Fig.4 (c)). Especially the tendency is remarkable to the CVI emission profile, because the excitation coefficient of CVI quickly drops at T_e<200eV. This effect can be seen in the difference at the peak positions of CVI density and emissivity profiles (ρ=0.67 and 0.63). At t=2.63s the CV and CVI emissions entirely disappear as seen in Fig.4(f), whereas the CV and CVI densities increase at the plasma center (see Fig.4(e)). The excitation rate coefficient of

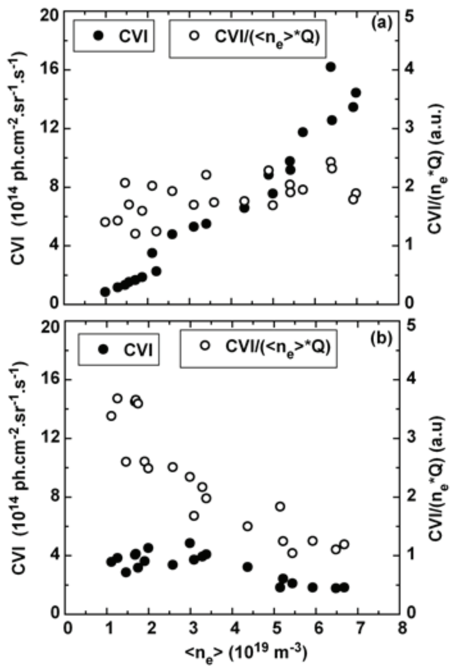

Fig.5 CVI intensity (closed circles) and CVI/(n_e*Q) (open circles) plotted against line-averaged electron density <n_e> for (a) recombining and (b) steady state phases. Value of Q means excitation rate coefficient of CVI.

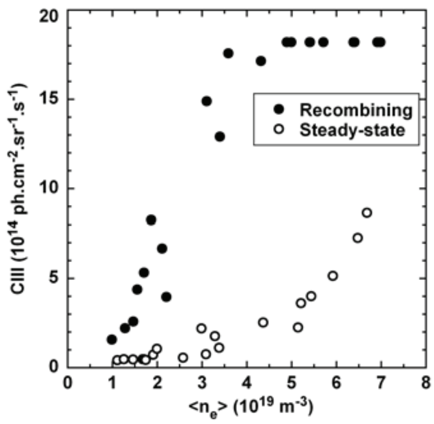

Fig.6 CIII intensity against line-averaged electron density <n_e> for recombining (closed circles) and steady state phases (open circles).

CVI at Fig.4(f) (T_e(0)=70eV) decreases 30 times compared to Fig.4(c) case (6×10^{-17}m^3.s^{-1} at T_e(0)=280eV).

Calculation of the total radiation power from the CV and CVI shows the good agreement with the experiment under assumption of 3% carbon density. However, the CIII and CIV results are ten times larger than the experimental values. The reason is not fully clear at present. At least it is known that the emission distribution from low ionized ions and neutral atoms is toroidally and poloidally inhomogeneous because of the presence of the ergodic layer. Indeed, recent studies indicate that the emissions from CIII and CIV have the asymmetric features reflecting the field line structure of the ergodic layer [14]. Especially, the vertical profile of CIV exhibits four peaks. The four peaks are formed at the inboard side near the X-point in addition to the top and bottom edge peaks at the horizontally elongated plasma cross section. It is reported that the particle recycling is enhanced at the inboard side [15]. It is also observed that the inhomogeneous poloidal distribution of neutral emissions arises mainly from inhomogeneity in the neutral particle density, not from the nonuniformity of the electron temperature and density [16]. This is likely to be one of the reasons for the difference.

Finally the CVI emission is examined for several discharges at the peak value during the recombining phase, where the plasma begins to shrink and the size becomes a little smaller than the LCFS. The CVI emission during steady-state phase is also studied for the comparison. Intensities of CVI are plotted against $\langle n_e \rangle$, as shown in Fig. 5(a) and Fig. 5(b) for the recombining and steady state phases, respectively. CVI intensities normalized to the electron density $\langle n_e \rangle$ and excitation rate coefficient, Q, (CVI/(n_e*Q), which means the carbon density of CVI), are also plotted in the figures. The excitation rate coefficient is calculated against the electron temperature at the LCFS for steady state phase and at the central electron temperature for recombining phase. This choice is reasonably correct since the CVI emission location is estimated from the CV radial profile. The difference between two phases is very clear. The CVI intensities from recombining phase increase with $\langle n_e \rangle$ but those from steady-state phase decrease with $\langle n_e \rangle$. Thus, we find a clear difference in the carbon density behavior with $\langle n_e \rangle$. That is to say, the CVI density is nearly constant with $\langle n_e \rangle$ for recombining phase, but it definitely decreases with $\langle n_e \rangle$ for steady state phase. On the other hand, the CIII intensities, which suggest the carbon influx for the ionizing plasma like during steady state phase, increase with $\langle n_e \rangle$ for both phases, as shown in Fig.6. The CIII intensities for recombining phase are saturated at densities greater than 5×10^{19} m^{-3}. The reduction of the CVI density for steady state phase may suggest the impurity screening effect. Increasing the density in the ergodic layer, the friction force becomes large, which leads to the impurity screening. In case of the recombining phase the understanding of carbon emissions is not really simple, because the CIII emissions do not indicate simply the influx. In addition, the origin of the carbon source is very unclear since the plasma shrinks and is completely detached from the divertor plates and vacuum wall. We need further investigation on the study of carbon behavior during the recombining phase.

4. Summary

Temporal evolution of carbon emission during the recombining phase of the discharges has been studied through the calculation of spectral emissitvity using 1-d transport code. From the calculation of CV and CVI radiation it indicates that carbon density is 3% of electron density, n_e. The discrepancy between computed and experimental CIII and CIV radiation has been found. Although the reason behind this is not fully clear it is argued that the three dimensional structure of CIII and CIV emissions might be responsible for the differences along with localized sources of carbon. Comparison of CVI emissions during steady state and recombining phase reveal its different dependence with n_e. From this observation it is also suggested that impurity screening effect increases with n_e during the steady state phase and it disappears during the recombining phase of the discharges.

Acknowledgements

The authors would like to thank the members of LHD experimental group for their technical support. This work was carried out partly under the LHD project financial support (NIFS06ULPP527).

[1] T. Amano, J. Mizuno and T. kako, Int. Rep. IIPJ-616, Institute for Plasma Physics, Nagoya University (1982).
[2] J. C. Moreno and E. S. Marmar Phys. Rev. E **31**, 3291 (1985).
[3] H. Chen et al., Plasma Phys. Control. Fusion **43**, 1 (2001).
[4] H. Nozato, S. Morita, M. Goto et al., Phys. Plasmas **11**, 1920 (2004).
[5] R. Burhenn et al., Fusion Sci. Tech. **46**, 115 (2004).
[6] M. Goto, S. Morita et al., Phys. Plasmas **10**, 1402 (2003).
[7] M. B. Chowdhuri, S. Morita, M. Goto et al., submitted to Applied Optics.
[8] M. B. Chowdhuri, S. Morita, M. Goto et al., Rev. Sci. Instrum. **78**, 023501(2007).
[9] S. Morita, M. Goto et al., Physica Script **T91**, 48 (2001).
[10] S. Morita, M. Goto et al., Plasma Sci. Tech. **8**, 55 (2006).
[11] M. Goto, J. Quant. Spect. Rad. Trans. **76**, 331 (2003).
[12] Y. Itikawa et al., Atomic Data and Nuclear Data Tables, **33**, 149 (1985).
[13] S. Morita, T. Morosaki, M. Goto et al., Nucl. Fusion **47**, 1033 (2007).
[14] R. Katai, S. Morita, M. Goto et al., Rev. Sci. Instrum. **77**, 10F307 (2006).
[15] M. Goto and S. Morita. Phys. Rev. E **65**, 026401 (2002).
[16] H. Yamazaki, M. Goto, S. Morita et al., submitted to PFR.

Proceedings of ITC/ISHW2007

Excitation of Stable Alfvén Eigenmodes by Application of Alternating Magnetic Field Perturbations in the Compact Helical System

T. Ito[a], K. Toi[a,b], G. Matsunaga[c], M. Isobe[b], K. Nagaoka[b], and CHS Group[b]

[a] *Department of Energy Engineering and Science, Nagoya University, Furo-cho, Chikusa-ku, Nagoya City, Aichi 464-8601, Japan*

[b] *National Institute for Fusion Science,322-6 Oroshi-cho, Toki 509-5292, Japan*

[c] *Japan Atomic Energy Agency, 801-1 Mukouyama, Naka, Ibaraki 311-0193, Japan*

ito.takafumi@lhd.nifs.ac.jp

In the Compact Helical System (CHS), alternating magnetic perturbations were applied to NBI heated plasmas by using two electrodes inserted near the plasma edge by 180 degree away toroidally, to excite stable Alfven eigenmodes and measure the damping rate. The frequency dependence of the transfer function defined by the ratio of a magnetic probe signal for an electrode current signal shows the presence of a few resonant peaks which would be related to stable Alfvén eigenmodes(AEs) excited. Each observed resonance frequency fo agrees well with the frequency of each corresponding toroidicity induced Alfvén eigenmode of which gap is located in peripheral plasma region, where fast ion drive of AEs would be sufficiently small. The derived damping rates γ are very large, i.e., $\gamma/(2\pi f_0)\sim 10\%$.

1. Introduction

In a D-T fusion plasma, one of the most dangerous MHD modes driven by energetic particle is the toroidicity-induced Alfvén eigenmodes (TAEs)[1]. In this situation, the first wall and various plasma facing components may be seriously damaged by energetic alpha particles lost by TAEs. It is important to assess the stability of energetic-ion driven MHD modes such as TAEs experimentally and compare the theoretical predictions. The stability of TAE is determined by competition between the linear growth rate and various damping rates. The linear growth rate will be expressed as[2],

$$\frac{\gamma}{\omega_0} \approx \frac{9}{4}\left[\beta_\alpha\left(\frac{\omega_{*\alpha}}{\omega_0}-1/2\right)F\left(\frac{\upsilon_A}{\upsilon_\alpha}\right)\right] \qquad (1)$$

Here, the quantities $\omega_{*\alpha}$, β_α, v_A, F and v_α are respectively the diamagnetic drift frequency of an energetic ion, the toroidal beta value of energetic ions, Alfven velocity, the fraction of resonant energetic particles with shear Alfven wave and energetic ion velocity. On the other hand, there are several important damping mechanisms: Landau damping by bulk electron and beam ions, continuum damping, radiative damping and so on. However, the theoretical prediction of these damping rates would include large uncertainty depending on theoretical models because of lack of precise information of eigenfunction of TAE, shear Alfven spectrum and so on. Accordingly, it is necessary to establish the most reliable theoretical model of the damping rates in a future burning plasma through comparison between various theoretical results and experimentally measured ones.

A powerful method to measure the damping rate was developed in the JET tokamak[3] and then has been applied to the Alcator C-Mod tokamak[4]. This method is based on a response analysis of a plasma for applied magnetic perturbations generated by a set of loop antennas arranged in the toroidal direction of a torus. In this method, the frequency of applied fields is swept to search resonance points related to TAE frequencies. Excitation of stable TAEs by application of magnetic perturbations was also attempted in the Compact

Helical System (CHS) where a couple of electrodes inserted into the plasma boundary were adopted to generate magnetic perturbations purely perpendicular to the toroidal magnetic field line [5]. This experiment was carried out in low temperature plasmas produced at the toroidal field less than 0.1T by using 2.45 GHz electron cyclotron waves, where no energetic ions were present. Recently, this method was also applied to a plasma heated by neutral beam injection(NBI). This paper describes the experimental results.

2. Experimental setup

Alternating voltage of about 75V was applied to a couple of electrodes inserted into a plasma edge region to produce alternating magnetic perturbations. The detailed structure and arrangement are shown in ref. 5. The driving frequency fext was swept up to 500 kHz to include the expected TAE frequency[6]. The maximum current of each antenna is ~5A, and the maximum amplitude of the perturbation field is estimated to be ~5x10^{-6}T at the magnetic axis position of 0.921m. These electrodes are placed by 180 degrees away in the toroidal direction to specify the toroidal mode numbers of applied perturbation fields. In this experiment, the polarity of two electrode currents were adjusted to be the same. This is called "even" mode operation. The so-called "general" mode operation was also tried by energizing only a single electrode. The dominant toroidal mode numbers of applied perturbation field are n=0, ±2, ±4, ... (n=0, ±1, ±2, ...) for "even" ("general") mode operation by using double (single) electrode. The electrode current and the applied voltage are monitored at the vacuum feedthrough. The magnitude of applied voltage to an antenna and a time-dependent sweeping pattern of fext are created by a function generator controlled with PC in the control room of CHS. The sweeping pattern of signal is amplified by a high-speed bipolar power supply. Typically, the frequency was swept from 1kHz to 300kHz in 100 ms. The response of a plasma for applied magnetic perturbations was obtained with the magnetic probes arranged in poloidal and toroidal directions. The toroidal array of magnetic probes consists of the five probes and is used to determine the toroidal mode number of the response. The poloidal mode number was determined by a poloidal array with 12 probes.

3. Experimental results

A typical discharge waveform of an NBI heated plasma in this experiment is shown in Fig.1. In this shot, the line-averaged electron density rises from 1.0x10^{19} m^{-3} to 4.6x10^{19} m^{-3} by gas puffing, as shown in Fig.1(b). The toroidal current and the volume-averaged toroidal beta value reach about 3kA and 0.25%, respectively, as shown in Figs.1(c) and

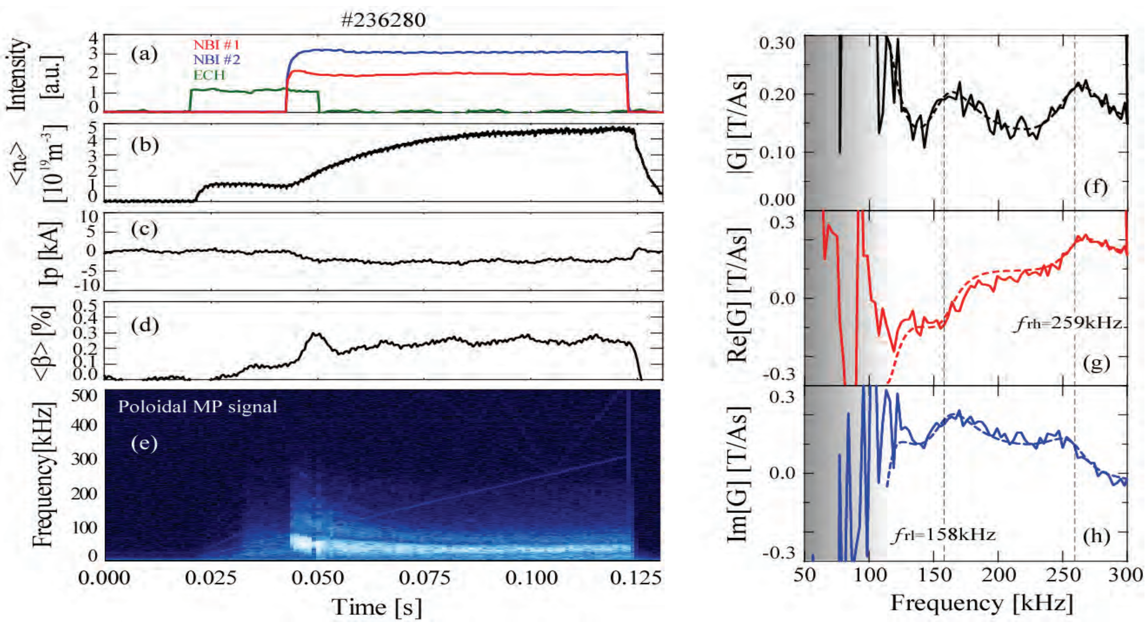

Fig.1. A typical discharge of the AE excitation experiment by using the double electrode(#236280). Time evolution of the power of external heat sources(a), line-averaged electron density(b), net toroidal current(c), volume averaged beta(d), the spectrogam of a magnetic probe signal(e). The absolute value of the transfer function (f), its real part(g) and imaginary part(h) as a function the driving frequency f_{ext} .

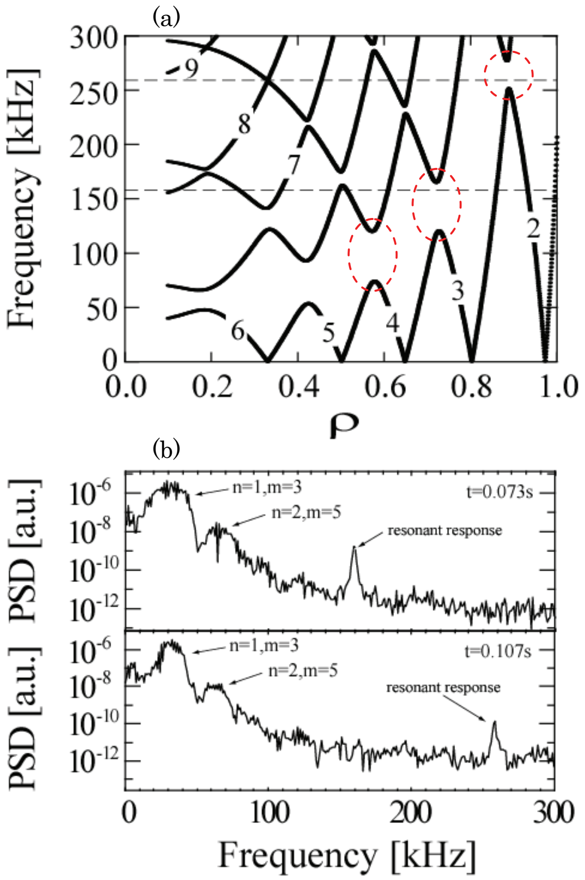

Fig.2(a). The n=2 shear Alfvén spectra calculated for two dimensional approximation of the actual CHS magnetic configuration (a). The dashed and the dot-dashed horizontal lines indicate the observed resonance frequencies of *fo*=158kHz and 259kHz, respectively. (b) The power spectra of magnetic fluctuations in the time windows of t=0.071s to t= 0.075 s and t=0.105s to t=0.109s. The modes in the lower frequency range less than 100 kHz are the energetic ion driven TAE and EPM. The broad spectral peaks of these modes are caused by rapid frequency sweeping.

(d). In Fig.1(e), the spectrogram of a magnetic probe signal is shown. In this figure, strong MHD activities driven by energetic ions are observed together with a weak perturbation signal induced by the electrode current. In this shot, two electrodes were driven with the same polarity, that is, “even” mode operation.

Figure 1(f), 1(g) and 1(h) show respectively the absolute value. the real part and imaginary part of the transfer function as a function of the driving frequency f_{ext}, of which transfer function was derived from the ratio of the magnetic probe signal for the electrode current. Two resonance peaks have been observed in the transfer function. The resonance frequency f_o and the normalized damping rate $\gamma/(2\pi f_o)$ were evaluated by fitting of the transfer function with that of a general viscous damping system . The transfer function of such system is expressed as [7]:

$$G(\omega) = \frac{B(\omega)}{A(\omega)} = \sum_{r=1}^{N}\left\{\frac{R_r}{i(\omega+\Omega_r)+\gamma_r} + \frac{R_r^{*}}{i(\omega-\Omega_r)+\gamma_r}\right\} \tag{2}$$

Here, Ω_r, γ_r, R_r, and R_r^* are respectively the angular eigenfrequency, damping rate, residue and its conjugate term at r-th resonance. The output signal $B(\omega)$ corresponds to the magnetic probe signal and the input signal $A(\omega)$ corresponds to the electrode current.

The part of $G(\omega)$ less than 120 kHz will be affected by the energetic ion driven instabilities. Accordingly, the fitting was carried out over the frequency range from 120 kHz to 300 kHz on the assumption that four resonances exist. The lowest peak corresponds to the peak of energetic ion driven TAE, which should be ignored. Moreover, the highest resonance much larger than 300 kHz was also obtained by this fitting, but was also ignored because of a virtual resonance. The second and third resonance frequencies f_{o2} and f_{o3} derived from the fitting are 158kHz and 259kHz, respectively. The corresponding damping rates are $\gamma/(2\pi f_{o2})$=6% and $\gamma/(2\pi f_{o3})$=12.5%, respectively. These damping rates are considerably larger than those obtained in JET experiments.

The toroidal and poloidal mode numbers for these resonant components were attempted to determine using the magnetic probe arrays. However, the mode numbers for these resonant fluctuations induced by the applied perturbations were not derived because of irregular phase relations among magnetic probes. The reason is not clarified yet, but may be due to the presence of bi-directional perturbations along the toroidal line of force. Here, the lowest and non-zero toroidal mode was assumed to be n=2 for these oscillations excited by the applied magnetic perturbations. An n=2 shear Alfven spectra calculated with two dimensional approximation of the CHS configuration is shown in Fig.2(a), where a hydrogen plasma with fully ionized carbon impurity was taken into account to be the effective charge of Z_{eff}=3. The frequencies of excited resonant magnetic perturbations agree well with the gap frequencies in the plasma peripheral region. That is, the mode of f=158kHz will correspond to the n=2 TAE due to m=3 and m=4 coupling, and that of f=258 kHz the n=2 TAE due to m=2 and m=3 coupling. In this shot, two types of energetic ion driven modes were observed in the lower frequency range less than 100 kHz, as seen from Fig.1(f) and Fig.2(b). In contrast to the excited modes by applied field perturbations, the mode numbers of them were clearly determined to be m~5/n=2 for the mode of f=65 kHz and m~3/n=1 for the mode of f=30 kHz. The former agrees very well with the n=2 TAE due to m=5 and m=6 coupling. The latter mode with n=1 is thought to be energetic particle mode (EPM) because the frequency is well below the expected minimum gap frequency. From this comparison, the above-mentioned resonant modes driven by electrodes are thought to be stable TAE near the plasma peripheral region where the fast ion drive will be too small to destabilize. So far, it is not clear whether or not the TAE resides more interior region was excited by applied magnetic perturbations. More larger magnetic perturbations will be necessary for the excitation of stable TAEs in more interior region.

4. Summary

An active diagnostic method for measuring the damping rate of Alfven eigenmodes by using external magnetic perturbations induced by a couple of electrodes has been developed in CHS. The single or double electrode inserted into a plasma edge was successfully applied to NBI heated plasmas. Several resonant responses are clearly observed at both of the single and double electrode operations. Some resonant peaks observed in the transfer function agree well with those of the low n TAEs of which gap locate near the plasma edge. The identification of the toroidal mode number of the excited stable TAEs is difficult in most of cases, which may be caused by simultaneous excitation of bi-directional waves and/or several modes having different toroidal mode number. Measured damping rates of excited TAEs are fairly large in the range of about 10% for the eigen-angularfrequency. Excitation of stable AEs by application of magnetic perturbations is being tried in the Large Helical Device (LHD).

References

[1] A. Fasoli *et al* (2007) Nucl. Fusion **47** S264
[2] E. J. Strait *et al* (1997) Fucl. Fusion **33** 1849
[3] A. Fasoli *et al* (1995) Phys. Rev. Lett. **75** 645.
[4] J. A. Snipes *et al* (2004) Plasma Phys. Control. Fusion **46** 611.
[5] G. Matsunaga *et al* (2005) Phys. Rev. Lett. **94** 225005.
[6] G. Matsunaga et al (2001) Rev. Sci. Instrum. **72** 402
[7] A. Nagamatsu (1993) Introduction to Modal Analysis, Corona publishing CO., LTD(in Japanese)

Proceedings of ITC/ISHW2007

A systematic study of impurity ion poloidal rotation and temperature profiles using CXRS in the TJ-II stellarator

J. M.Carmona, K. J. McCarthy, V. Tribaldos, M. Ochando and TJ-II Team

Laboratorio Nacional de Fusión, EURATOM-CIEMAT, E-28040 Madrid, Spain

A detailed analysis of the calibration methods for the new CXRS-DNBI diagnostic system and a systematic study of impurity profiles measured under different plasma conditions have been carried out in TJ-II and presented here. Ion temperatures profiles tend to be flat in the measured region, showing correlation between ECRH power, averaged electron densities and the Ti value. Transition of poloidal velocities from ion to electron diamagnetic direction when increasing the line averaged electron density ($<n_e>$) was confirmed, agreeing with previous works. As line averaged density was considered to be the driver-parameter of this transition, shots with the same electron density and different ECRH power were compared to highlight other contributions as T_e. A change in ion temperature and poloidal rotation direction is found when comparing these shots, suggesting that the plasma collision frequency ($\sim n_e T_e^{-3/2}$) tends to control the dynamics in TJ-II, giving a clearer description of the trigger mechanism. First experimental evidence in TJ-II that the shear point for impurity velocities moves outwards when increasing n_e, is also presented.

Keywords: Charge exchange spectroscopy, temperature profiles, poloidal rotation

1. Introduction

Spatially resolved measures of ion temperature and poloidal rotation are important for the understanding of plasma dynamics. For this reason, an active charge-exchange recombination spectroscopy (CXRS) diagnostic, based around a diagnostic neutral beam injector (DNBI) and a bidirectional (two vertical opposing views) multi-channel spectroscopic system [1, 2], has been set-up on the TJ-II, a four-period [3], low magnetic shear, stellarator. It provides 5 ms long pulses, up to two per discharge, of neutral hydrogen accelerated to 30 keV with equivalent current of 3.3 equ. A. The bidirectional diagnostic is designed to measure Doppler shifts and widths of the C VI line at λ = 529.06 nm in up to 3 arrays of 12 channels with ~1 cm spatial resolution across the plasma minor radius. The light dispersion element is a Holospec spectrograph with three 100 μm curved entrance slits (these are curved to compensate for its short focal length) and a transmission grating sandwiched between two BK7 prisms. It provides a focal-plane dispersion of ~1.15 nm/mm at 529 nm. Moreover, a narrow bandpass filter (2.0±0.5 nm at full-width at half-maximum FWHM) centred on 529 nm prevents spectral overlapping from the multiple fibre arrays at the image plane. The set-up includes a high-efficiency back-illuminated CCD camera and fast mechanical shutter (=4.5 ms time window). With on-chip binning, multiple spectra can be collected during discharges (=300 ms). Finally, fibre alignment was performed by illuminating each fibre bundle with a bright light source and observing, through an unused viewport, the orientation and location of the resultant bright spots with respect to markings on the inside of the opposing vacuum flange. In this way, the sightlines through plasmas can be determined using a cross-sectional machine drawing and magnetic configuration maps. Hence, when compared with the neutral beam geometry the normalized radius, r/a, corresponding to each beam/line-of-sight interaction volume is found. Finally, for the magnetic configuration used in this study, 100-44-64, the viewing system covered the plasma minor radius from r/a= 0.3 to 0.85.

author's e-mail: jm.carmona@ciemat.es

2. Experimental details

2.1. Diagnostic set-up

The TJ-II is a four field period heliac type stellarator ($B(0)$ = 1.2 T, R = 1.5 m, $<a>$ = 0.22 m) designed to explore a wide rotational transform range (0.9 = $\iota(0)/2\pi$ = 2.2) in low, negative shear configurations ($\Delta\iota/\iota$ < 6%). The experiments reported here were carried out in electron cyclotron resonance heated (ECRH) plasmas (P_{ECRH}= 300 – 500 kW, 53.2 GHz, 2nd harmonic, X-mode polarization, $t_{discharge}$ = 250 ms) with hydrogen as the working gas [3] and lithium coated walls (previously boronized). No auxiliary NBI heating was provided. As a result, central electron densities and temperatures up to ~10^{19} m^{-3} and ~1.5 keV respectively were achieved. The strong reduction in impurities concentration (i.e. carbon) due to the wall-coating results in reduced impurity photon fluxes thereby requiring efficient detection procedures. Nevertheless, the use of a high-throughput spectrograph and an efficient CCD detector made the goal of measuring in such conditions possible.

2.2. Instrument calibration

Special attention has been given to wavelength calibration and instrumental function determination. Calibration for each individual fibre was done in order to detect small variations in the alignment of the fibres and in the FWHM of spectral lines. Spectra were captured between discharges using a retractile pencil-type Neon lamp positioned between the lens and fibre bundle head.

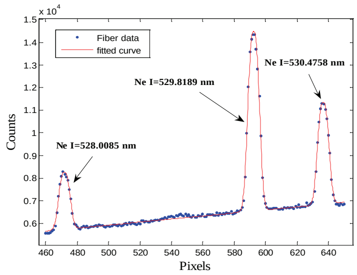

Fig.1 Ne I lines used for calibration (close to 529 nm)

Wavelength calibration was performed using a second order (polynomial) fit to the three nearby Ne I spectral lines (figure-1). As spectra are recorded simultaneously for all fibres, fine corrections can be made for any nonlinear dispersion present in the spectrometer or displacement errors in the entrance slits. Next, the instrument function was determined from the same spectra using a Gaussian function fitting. It was found to be ~7.6 pixels (~1.14 Å) and ~6.3 pixels (~0.95 Å) for the mid fibres of the upper and lower arrays respectively (figure-1 in [2]) and to vary along the fibre array.

Figure-2a illustrates the variation in FWHM along the lower array. Such a variation is inherent to the set-up of this instrument [4]. Part of it may also be due to inaccuracies when manufacturing the slits (a similar behaviour is observed for the upper array).

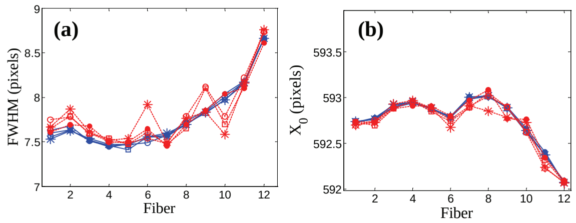

Fig.2 Variation of (a) instrumental FWHM (b) on fibre position along the middle fibres for robust (red) and non-robust (blue) methods. The symbols represent different frames.

It should be noted that the neon lines fits were made using a non-linear least squares method based on trust-region algorithms. For this, comparisons between different fitting methods were made (*i.e.* robust and non-robust). See figure-2a (FWHM) and figure-2b (central position). In general, robust algorithms are considered preferable to non-robust ones, as the former are less sensitive to outlier points (points numerically distant from the rest that can lead to misleading fits). However, here it was found that robust fits show significant fibre-to-fibre variations for both FWHMs (figure-2a) and line centres whilst non-robust fits (figure-2b) are more stable. Indeed, in certain situations robust methods may be preferable, *e.g.* for single Gaussian fits, but they prove to be weak when multiple Gaussian fits are performed. Hence, the non-robust method was chosen as the fitting method.

2.3. Active and passive signal treatment

CXRS is widely employed to obtain spatially resolved measurements, although it presents several challenges. For instance, contributions to measured signals from ionized impurities (called the *cold component* or *passive* signal) must be removed since it is a non localized emission. Also plasma conditions should remain constant along a discharge, or discharges should be reproducible (shot to shot technique), so that the active signal can be obtained by subtraction, i.e. (A+P)-(P) =A. See figure-3. For the data presented here, both techniques were employed.

2.4. Data Analysis

Once the instrumental and calibration functions have been obtained for each fibre using the neon lamp, fits to the line of interest (i.e. C VI @ 529.06 nm) can be made so that Doppler shifts and widths can be estimated together with errors. Ion temperatures and velocities are deduced from the usual relations:

$$T_i = 1.68 \cdot 10^8 \, A \left(\frac{\Delta\lambda_{fwhm}^2 - \Delta\lambda_{instrum}^2}{\lambda_0^2} \right)$$
$$v = \left(\frac{\lambda - \lambda_0}{\lambda_0} \right) c \qquad (1)$$

where A is the mass of the ion [amu], $\Delta\lambda_{\mathrm{fwhm}}$ the measured full width at half maximum (FWHM), $\Delta\lambda_{\mathrm{instrum}}$ the instrument FWHM, λ and λ_0 are the measured and the unshifted central wavelength of line under consideration respectively and *c* the speed of light. For this work, a wavelength of λ_0=529.06 nm is taken as reference value in equation (1) (the line centre depends weakly on plasma conditions).

2.4.1. Fine structure corrections to C VI data

A clear asymmetry was observed about measured spectra line data. This was interpreted as arising from fine structures in the transitions in this hydrogen-like ion [5, 6]. Indeed, there are up to 13 possible lines with different intensities depending on plasma conditions. Such fine structure give rise to the tail observed on the short wavelength side that results in apparent line broadening, and hence overestimated ion temperatures.

Thus, in order to correct for this a multi-Gaussian fit, using relative intensity ratios between fine structure components, was employed here. Finally, after careful analysis and consideration, contamination by a nearby O VI line was excluded as there is a strong oxygen reduction due to the boron and lithium coated walls.

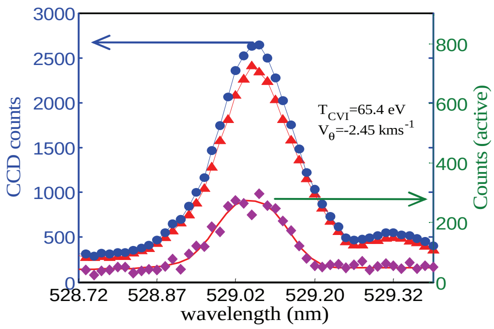

Fig.3 Spectra of subsequent CCD frame at r/a=0.55, showing CX with C^{+6}. Diamonds, triangles and dots are active, passive and active+passive signals respectively. A fit to the active CVI line is also shown.

3. CXRS profiles and discussion

For the study undertaken, hydrogen plasmas with lithium coated walls were made, lasting =250 ms, with line averaged electron densities between 0.4 x 10^{19} m^{-3} and 0.9 x 10^{19} m^{-3} heated only with ECRH. In order to separate active from active plus passive C VI signals only discharges with almost constant electron density and temperature were used.

3.1. Measurements of ion temperature and poloidal rotation profiles

First CXRS profiles of measured ion temperatures for two discharges with 395 kW of ECRH but different line averaged electron densities (n_e) are shown in figure-4. In these plots, the measured C^{6+} impurity temperature is found to be higher for the discharge with lower n_e. Previous studies carried out in the TJ-I tokamak for C^{4+} ions [7] and in the TJ-II for several different ions (C^{4+} and Fe^{15+}, etc…) [8] using passive spectroscopy, reported a similar behaviour. Then, the anomalous temperatures were attributed to non-thermal velocity contributions.

It is apparent from figure-4 that ion temperature profiles are relatively flat and begin to drop for r/a=0.7. Temperature values are measured between 50 and 150 eV, in accordance with the weak collisional coupling for these densities.

For the same shots, poloidal rotation profiles are shown in figure-5. A clear transition from ion to electron diamagnetic direction can be seen.

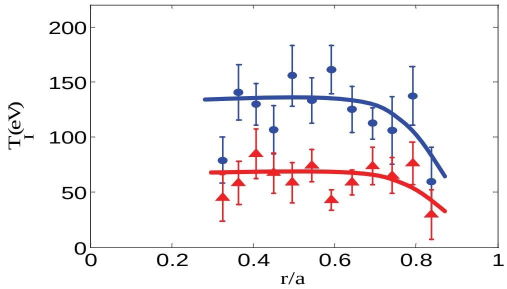

Fig.4. Ion temperature profiles obtained for two discharges with P_{ecrh}=395 kW and line averaged densities n_e=0.42 x 10^{19} m^{-3} (dots) and n_e=0.90 x 10^{19} m^{-3} (triangles) as a function of normalized plasma radius. Lines are plotted to aid the reader.

For lower line-averaged electron densities (<n_e>), C^{6+} ions appear to rotate poloidally in the ion diamagnetic direction whereas at higher values this changes towards the electron diamagnetic direction.

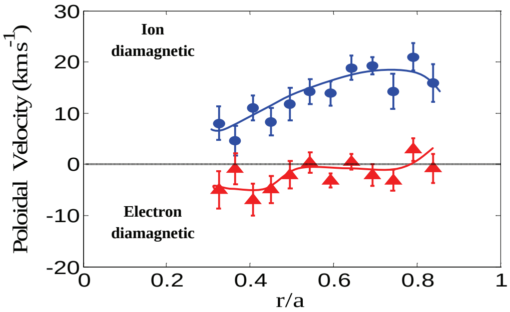

Fig.5. Poloidal rotation profiles of C^{6+} for shots included in figure 4. Lines are plotted to aid the reader.

An in depth analysis of this change in rotation has been performed from a detailed density scan with CXRS diagnostic. This is supported below.

3.2. Density scan

A density scan (from 0.4 to 0.92 x 10^{19} m^{-3}) for 395 kW of ECRH has been made and the poloidal velocities measured are presented. See figure-6. The impurity poloidal velocities show a change of direction as the line averaged electron density is increased, from ion to electron diamagnetic direction (transition from electron to ion root). Such behaviour was also reported in the TJ-II for passive measurements of CV ion temperatures previously [9] thereby providing us with confidence of these CXRS measurements.

Note that, the transition point (i.e. where the poloidal velocity~0) moves towards the edge (from r/a~0.4/0.55 to r/a~0.7/0.8) as <n_e> increases from ~0.57 to ~0.77 x 10^{19} m^{-3}.

This is the first experimental evidence for C^{6+} that the shear point of impurity ion rotation moves outwards in TJ-II with increasing electron density.

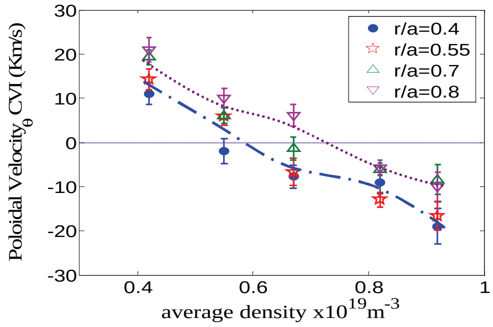

Fig.6. Change on C^{+6} poloidal velocity from ion to electron diamagnetic direction while increasing line averaged electron density. This is plotted for different normalized plasma radii r/a. Lines are plotted to aid the reader.

3.3. Profiles under different P_{ECRH}

Ion temperatures and poloidal rotation profiles are compared for different ECRH conditions. A comparison between shots with a fixed $<n_e>$ and P_{ECRH} of 400 kW and 500 kW are presented. See figure-7 and figure-8.

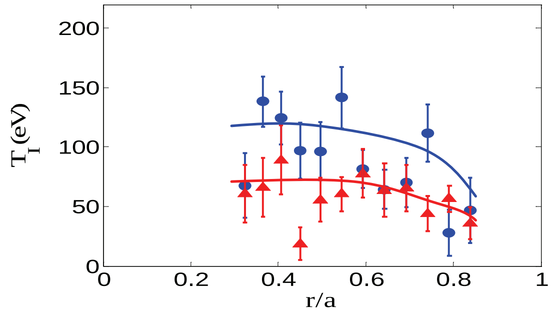

Fig.7. C^{6+} temperature profiles for 400 kW (dots) and 500 kW (triangles) of P_{ECRH} and the same line averaged density $<n_e>$=0.6 x 10^{19} m^{-3}, showing lower temperatures for higher P_{ECRH}.

In these figures, lower temperatures are found for higher P_{ECRH} at fixed $<n_e>$. The better coupling between electrons and ions for lower P_{ECRH} (lower T_e) and the decreasing impurity confinement times [10] are expected to cause the increase in temperature in these plasmas ECRH.

A simple power balance equation can help to explain the measured profiles. This is given by

$$\frac{dT_b}{dt} = \nu_E^{b/e}(T_e - T_b) - \frac{T_b}{\tau_E^b} \qquad (2)$$

where $\nu_E^{b/e} \sim n_e T_e^{-3/2}$. Better coupling (higher collision frequency $\nu_E^{b/e}$) between ion and electron species (increasing n_e or decreasing T_e) give rise to an increase of ion temperature. With fixed $<n_e>$ and varying T_e (power scan), or vice versa (density scan) ion temperatures can be expected to vary, i.e. increasing when (a) T_e decreases (fixed $<n_e>$) or (b) $<n_e>$ increases (fixed T_e).

From this, the impurity rotation profile in the region accessible, is seen to shift to the electron diamagnetic direction as the injected P_{ECRH} is increased.

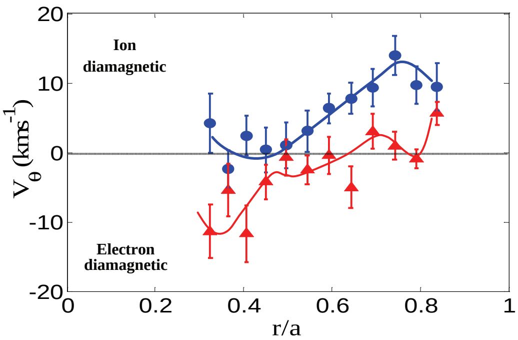

Fig.8. C^{6+} rotation profiles for 400 kW (dots) and 500 kW (triangles) of P_{ECRH} and line-averaged electron density $<n_e>$=0.60 x10^{19} m^{-3}.

4. Summary

A systematic study on the calibration system had been carried out to characterize system capabilities and determine the best data-analysis procedure. Ion temperature and poloidal rotation profiles were measured under different plasma conditions. As seen from experiments, the change from ion to electron diamagnetic direction and ion temperatures depends on $<n_e>$ and T_e, suggesting that the control-parameter is the plasma collision frequency $\nu_E^{b/e} \sim n_e T_e^{-3/2}$. Experimental evidence of displacement with electron density of the shear point for C^{6+} in ECR heated plasmas is reported for the first time in TJ-II.

References

[1] K.J. McCarthy *et al.*, Rev. Sci. Instrum. 75 (2004) 3499
[2] J.M. Carmona *et al.*, Rev. Sci. Instrum. 77 (2006) 10F107
[3] E. Ascasíbar *et al.*, Fusion Eng. Des. 56-57, (2001) 145
[4] R. E. Bell *et al.*, Rev. Sci. Instrum. 75 (2004) 4158
[5] R. J. Fonck, Phys. Rev. A 29, (1984) 3288.
[6] K. Ida *et al.*, Rev. Sci. Instrum. 71 (2000) 2360.
[7] B. Zurro *et al.*, Phys. Rev. Lett., 69 (1992) 2919
[8] K. J. McCarthy *et al.*, Europhys. Lett. 63 (2003) 49-55
[9] B. Zurro *et al.*, Fusion Sci. Technol. 50 (2006) 419-427
[10] R. Burhenn *et al.*, Fusion Sci. Technol. 46 (2006) 115

Proceedings of ITC/ISHW2007

Flux Surface Mapping in LHD

Tomohiro MORISAKI, Mamoru SHOJI, Suguru MASUZAKI, Satoru SAKAKIBARA,
Hiroshi YAMADA, Akio KOMORI, Osamu MOTOJIMA
and the LHD experimental group

National Institute for Fusion Science, Toki, Gifu 509-5292 Japan

Magnetic flux surface measurements have been carried out in the Large Helical Device (LHD) in the standard magnetic field configuration with toroidal magnetic field strength up to 2.75 T. Electron beam launched with a small electron gun moving across the flux surfaces was detected with a fluorescent screen or a probe array. Nested surfaces could clearly be visualized with both methods. Even the open ergodic region was also detected. In the experiment an unfavorable m/n = 1/1 magnetic island was found to exist near the last closed flux surface (LCFS), where m and n are poloidal and toroidal mode numbers, respectively. It was found that the source of the error field, in the low magnetic field strength of 0.0875 T, is terrestrial magnetism. On the other hand, in the standard magnetic field strength of 2.75 T, the main source of the error field is though to be ferromagnetic materials near the LHD. It was also found that such magnetic islands can be eliminated or reduced applying the correction field with some perturbation coils.

Keywords: flux surface mapping, magnetic island, ergodic layer

1. Introduction

Unlike tokamaks, helical devices, e.g. heliotron, stellarator, torsatron, do not need a plasma current to form the magnetic flux surfaces for the plasma confinement. These devices can thoroughly achieve the confinement configuration only by their external coils. This means that the magnetic flux surfaces exist in vacuum without any plasma current, thus one can easily identify or measure them, visualizing each surface with a proper instrument installed in the vacuum vessel. Several experiments to map the flux surfaces have been performed in major helical devices with various techniques [1-8]. The Large Helical Device (LHD) is a superconducting heliotron [9], which is by far a favorable device for the flux surface mapping experiment because the standard high magnetic field (~ 3 T) can be maintained in steady state during the mapping experiment.

In this paper, results of the flux surface mapping experiment on LHD are presented. The measurements have been performed in two different methods since the very early phase of the LHD experiment in 1998. In section 2, experimental apparatus and geometry are shown. After describing the experimental results in section 3, discussion is given in section 4. Finally summary is given in section 5.

2. Experimental Apparatus

The principle of the experiment is simple and clear. The electron beam launched on a flux surface from a small electron gun (e-gun) traces a magnetic field line. Projecting the positions on the poloidal plane, where the electron beam passes through, the flux surface is visualized. To identify the piercing points on the poloidal plane, two methods were employed in the experiment.

2.1 Electron Gun

In order to launch the electron beam, a small electron gun (e-gun) was utilized. For two different methods, i.e. fluorescent screen and probe array, two

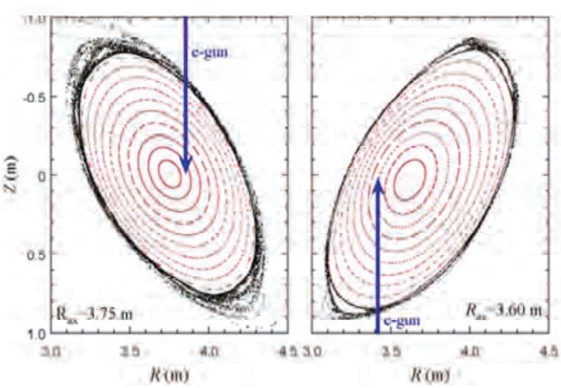

Fig. 1 Position of the e-gun scanning in the poloidal plane in the case of (a) fluorescent screen and (b) probe array methods. The e-gun can be inserted up to ρ = ~ 0.1 with the fluorescent screen method.

author's e-mail: morisaki@nifs.ac.jp

distinct ports to install the e-gun were utilized, as shown in Fig. 1. Moving radailly in the poloidal plane, the e-gun can reach as far as $\rho = \sim 0.1$ for the fluorescent screen method and ~ 0.3 for the probe array method, where ρ is a normalized minor radius. One can trace different flux surfaces by changing the radial position of the e-gun. For the precise alignment of the electron beam with a magnetic field line, the direction of the e-gun can also be changed, rotating on the supporting rod, since the magnetic shear is very high in the heliotron configuration.

The e-gun itself consists of a lanthanum hexaboride (LaB_6) cathode and a tantalum plate with a 3 mm diameter hole to extract electrons. The cathode is heated up to 1400 K and negatively biased at ~ 150 V to the ground (vacuum vessel). Although no mechanism to collimate or focus electron beams is equipped with, practical beam width (FWHM) is about 10 mm at B_t = 2.75 T, where B_t is the toroidal magnetic field strength.

2.2 Fluorescent Screen and Probe Array

In order to identify the positions where the electron beam passes through a poloidal plane, a fluorescent screen or a scanning probe array was employed.

The screen is made of 70 - 80 % transparent mesh coated with fluorescent powder P15 (ZnO: Zn). The electron beam glows on the screen mesh, circling along the torus for many times. The images on the screen in the poloidal plane are captured with a CCD detector viewing from the tangential port. Changing the radial position of the e-gun, the captured images of each flux surface are superimposed on one picture. Though this method is very simple and straight forward, it is restricted to the configuration between screen and CCD to be seen each other through the viewing window.

If one cannot obtain such a configuration mentioned above, there is another way to detect the electron beam. We introduced an 89 channel vertical probe array to measure the electron current on a flux surface. By scanning it in the horizontal direction, two-dimensional information which consists of 89 horizontal chords on the poloidal plane can be obtained. With this method, no viewing port is necessary, thus we do not have to mind about the geometrical problem. The diameter of each probe chip is 7.8 mm and the distance between adjacent chips is 9 mm. Since the orbit drift of the electron beam with 150 eV is negligibly small compared to the beam width, the spatial resolution of the system is consequently about 10 mm.

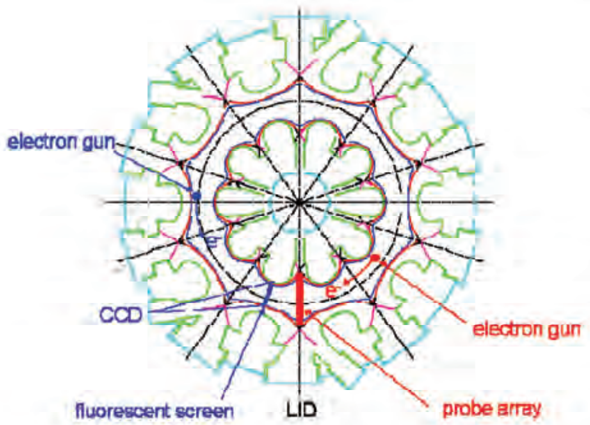

Fig. 2 Geometrical setup of flux surface mapping. Electron beam is launched in the clockwise direction for the probe array and the counterclockwise direction for the fluorescent screen.

2.3 Geometry

The geometrical setup of e-gun, fluorescent screen and probe array is shown in Fig. 2. The fluorescent screen of 2 m high and 1 m wide was installed in the toroidal position where the flux surfaces are vertically elongated. The CCD detector views the screen from the tangential port though the window, as shown in Fig. 2. Although the screen fully covers the poloidal plane of the flux surfaces, the CCD could not perfectly see the whole area of the flux surfaces because of the structure in the vacuum vessel blocking the CCD's view.

On the other hand, the probe array was located at the position where the flux surfaces are horizontally elongated and the Local Island Divertor (LID) [10] head is inserted from outboard side of the torus. Actually the probe head is mounted on the LID head, and travels horizontally with it more than 2 m with the translation mechanism of LID. Thus the 0.8 m high and 2 m wide scanning area covers more than 90 % of the flux surfaces.

3. Experimental Results

Flux surface mapping experiments have been performed three times since the beginning of the LHD experiment in 1998. The magnetic configurations of R_{ax} = 3.60 m, 3.75 m and 3.85 m were chosen for the measurement, where R_{ax} is the magnetic axis position. The B_t was set at B_t = 0.0875 T, 0.25 T and 2.75 T. Note that B_t = 2.75 T is used for the ordinary plasma experiment.

The vacuum vessel was evacuated less than 3×10^{-4} Pa in order to avoid the plasma production along the electron beam. Under this experimental condition, the mean free path of the electron is about 2500 m (100 toroidal turns).

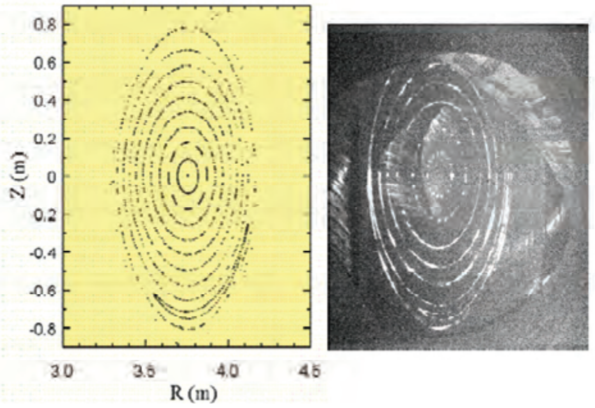

Fig. 3 Flux surfaces (a) calculated with field line tracing code and (b) mapped on the fluorescent screen.

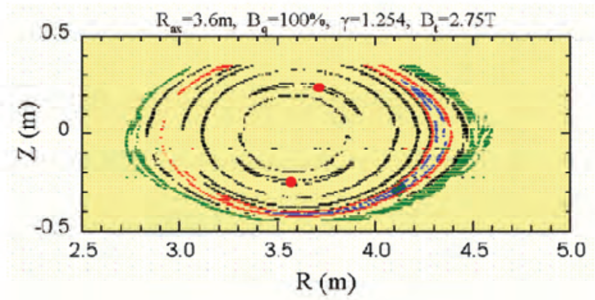

Fig. 4 Flux surfaces measured with 89 ch probe array. Red and blue closed circles are the O-points of $m/n = 2/1$ and 1/1 magnetic islands, respectively. Separatrix of the 1/1 island is depicted with red line and the ergodic region is colored in green.

3.1 Fluorescent Screen Method

Experimental result of flux surface mapping on the fluorescent screen method is presented in Fig. 3 (b), together with the calculation result with the field line tracing code, as shown in Fig. 3 (a). This experiment was carried out in the standard but low magnetic field configuration, i.e. R_{ax} (average) = 3.75 m and B_t = 0.0875 T. For this result presented in Fig. 3 (b), the position of the e-gun was changed six times and then six pictures were superimposed. It can clearly be seen that the experimental and numerical results agree well. The measured magnetic axis position which was derived by finding the center of each flux surface was found to be at R = 3.77 m where the calculated local magnetic axis position is R = 3.76 m. It can be said that the difference between them is within the error bar of experimental conditions.

It can be seen, unfortunately, that a relatively large magnetic island of which poloidal/toroidal mode numbers are m/n = 1/1. Such a magnetic island is often attributed to the error field caused, for example, by the ferromagnetic materials near the machine or misalignment of the coils. However, in this experiment, the B_t was so low as 0.085 T that it is necessary to take the geomagnetic effect into consideration. In the calculation shown in Fig. 3 (a), the local geomagnetic effect (using published data at Inuyama city near Toki) is taken into account. It is found that the m/n = 1/1 island clearly appears by introducing the terrestrial magnetism in the calculation, and the calculated width and the phase of the magnetic island agree well to the experimental result, as shown in Fig. 3. The cause of the magnetic island will be discussed later again.

3.2 Probe Array Method

Recently the flux surface mapping with an e-gun and a fluorescent screen was performed. As shown in Fig. 4, clear and precise results at the horizontally elongated cross section were obtained with this method. In this experiment, the standard magnetic configuration and magnetic field strength for the usual experiment were employed, i.e. R_{ax} = 3.60 m and B_t = 2.75 T. Outside of the nested closed surfaces depicted in black, it can be seen that complicated ergodic region colored in green spreads out. Such a fine structure has not been observed with the fluorescent screen method.

In spite of high magnetic field of B_t = 2.75 T, the m/n = 1/1 and 2/1 magnetic islands were still observed, as shown in Fig. 4. It is though that these 1/1 and 2/1 islands are toroidally coupled each other. Moving the e-gun precisely, nested closed surfaces within the islands were also detected. Finding one smaller flux surface after another in the island, we could finally reach the smallest magnetic surface at the center of the island, i.e. at the magnetic axis of the island. This is what is called an O-point of the island. In Fig. 4, the O-points of 1/1 and 2/1 island are emphasized by drawing the final smallest flux surface with larger symbols. Concerning the phase of the island (poloidal angle of O-points), it is consistent with that observed in the previous experiment with fluorescent screen, which is described in section 3.1. Thus the island phase calculated with the geomagnetic effect almost agrees to that obtained in the experiment presented in this section. However the relatively large island width shown in Fig. 4 cannot be explained simply by the geomagnetic effect, since B_t is far stronger than terrestrial magnetism. Detailed discussion is presented in the next section.

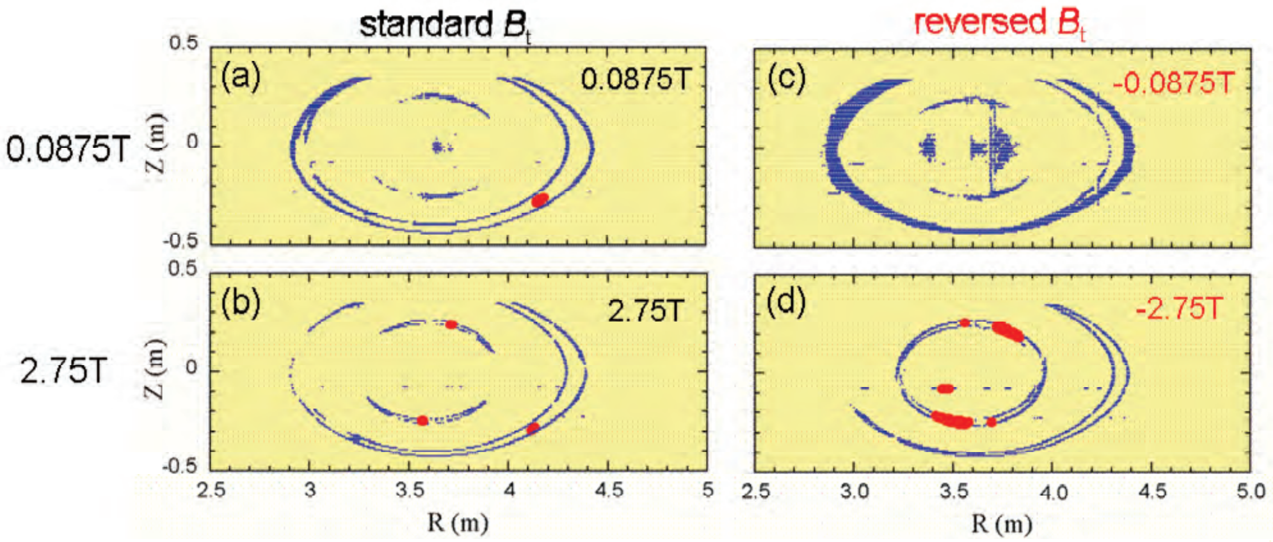

Fig. 5 Variation in magnetic island property under four experimental conditions, i.e. high (2.75 T) and low (0.0875 T) magnetic field strengths, and those reversals. The O-points of each island are emphasized with large red symbols.

4. Discussion

Further investigation for the magnetic islands observed in the flux surface mapping was carried out to find the source of the error field. In order to see the B_t dependence on the island properties, its phase and width were compared between B_t = 0.0875 T and 2.75 T. The direction of B_t was also reversed in each magnetic field strength. Summary of the experiments is presented in Fig. 5. The m/n = 1/1 and 2/1 islands measured with a probe array under four experimental conditions are shown.

Comparing Fig. 5 (a) and (c), it is found that the 1/1 and related 2/1 islands at low B_t are due to weak and steady perturbation, e.g. terrestrial magnetism. This is because, in reversed B_t (Fig.5 (c)), the island phase is also reversed, which suggests the direction of the error field never changes, according to the environmental field.

With increase in B_t, the island width surely decreases, however the decreasing rate is very small, as is seen between Fig. 5 (a) and (b), or between (c) and (d). If the source of the error field were purely from terrestrial magnetism, the island width decreased drastically, because B_t increased more than 30 times between two. This experimental result suggests the existence of another source of the error field, which increases with B_t. Comparing Fig. 5 (b) and (d), another important information can also be seen, namely the island phase never changes, even if B_t is reversed. This means that the direction of the error field changes with B_t direction. Thus we can conclude that there must be another source of the error field in addition to the terrestrial magnetism.

One of the candidates of the error field which has the characteristics mentioned above is the unsaturated ferromagnetic materials near the machine, e.g. magnetic shield for the neutral beam injector and/or diagnostics, deteriorated stainless steel by welding, etc. Fortunately it was also confirmed that these magnetic islands can be eliminated or reduced by using small correction coils.

5. Summary

Flux surface mapping with electron beam and fluorescent screen or probe array was successfully carried out in LHD. It was confirmed that the nested closed surfaces are formed in the standard LHD configuration. The m/n = 1/1 and 2/1 islands were found to exist, but can be eliminated or reduced with small correction coils.

Acknowledgement

This study was partially funded by the Grant Aid for Scientific Research from MEXT of Japanese government.

References

[1] R. M. Sinclair et al., Rev. Sci. Instrum. **41**, 1552 (1970).
[2] G. J. Hartwell *et al.*, Rev. Sci. Instrum. **59**, 460 (1988).
[3] H. Yamada *et al.*, Rev. Sci. Instrum. **61**, 686 (1990).
[4] G. G. Lesnyakov *et al.*, Nucl. Fusion **32**, 2157 (1992).
[5] R. Jaenicke *et al.*, Nucl. Fusion **33**, 687 (1993).
[6] M. G. Shats *et al.*, Nucl. Fusion **34**, 1653 (1994).
[7] H. Lin *et al.*, Rev. Sci. Instrum. **66**, 464 (1995).
[8] M. Otte *et al.*, *Proc. 29th EPS* (ECA, vol.26B, 2002) p-5.036.
[9] O. Motojima *et al.*, Phys. Plasmas **6**, 1843 (1999).
[10] T. Morisaki *et al.*, Phys. Plasmas **14**, 056113 (2007).

Proceedings of ITC/ISHW2007

Development of Microwave Imaging Reflectometer at NIFS

Y. Nagayama[1)], S. Yamaguchi[1)], Z. B. Shi[2)], Y. Kogi[3)], A. Mase[3)], S. Sugito[1)], N. Ohyabu[1)]

[1)]*National Institute for Fusion Science, Toki 509-5292, Japan*

[2)]*The Graduate University for Advanced Studies, Toki 509-5292, Japan*

[3)]*KASTEC, Kyushu University, Kasuga 816-8580, Japan*

(Received 15 October 2007 / Accepted 15 October 2007)

The Microwave Imaging Reflectometer (MIR) is under development at NIFS. The first MIR system is installed in Large Helical Device (LHD). The optics of this system is made of Aluminum mirrors and Plexiglas plates. In this system, the primary mirror is remotely controlled to optimize the reflection power. The illumination wave is generated by 3 IMPATT oscillators, and the local oscillator (LO) is a Gunn oscillator. This system uses wide band-pass filters. The second MIR system is installed in TPE-RX, which is a large RFP. The optics of this system is made of Aluminum mirrors, Teflon lenses and Plexiglas plates in order to reduce size. In this system the frequencies are so stabilized that noise can be reduced by using narrow band filters. The 4x4 2-D mixer array and phase detection system have been also developed.

Keywords: microwave, imaging, reflectometry, MIR, LHD, turbulence, fluctuation, diagnostics

1. Introduction

It is considered that plasma confinement in a fusion devise is governed by turbulence and instabilities, which often appear in the electron density fluctuations. The microwave reflectometry is a sensitive measurement of turbulent density fluctuations because it uses reflection of the microwave by the plasma with cut-off density [1]. The density fluctuation causes the amplitude modulation and the phase modulation in the reflected beam. Recently the Microwave Imaging Reflectometer (MIR) has been intensively developed because MIR may provide the 2D/3D image of density fluctuation to reveal the physics of turbulence [2]. The short wave fluctuation diverge the reflected wave. MIR takes advantage of large aperture optics to form an image of the reflecting layer onto an array of detectors located at the image plane, enabling localized sampling of small plasma areas.

Issues in the development of MIR are as follows: (1) improvement of sensitivity or the signal to noise ratio; (2) improvement of number of channels in the 2D detector array; (3) reducing the cost. The MIR is under development at National Institute for Fusion Science (NIFS) by collaborating with Kyushu University [3]. The first MIR system has been installed in the Large Helical Device (LHD) [3,4]. The second MIR system has been installed in TPE-RX, which is a large RFP device at National Institute of Advanced Industrial Science and Technology (AIST) [5]. This paper will present how to solve the above issues at NIFS.

author's e-mail: nagayama.yoshio@nifs.ac.jp

2. MIR System in LHD

Figure 1 shows a schematic diagram of the MIR system in LHD. The illumination wave (RF) is generated by 3 high power (0.5 W) IMPATT oscillators, whose frequencies are 53, 66 and 69 GHz, respectively. These oscillators used to be installed 5 m far from LHD. However, the operation of the IMPATT oscillators was interfered by the leakage of the magnetic field. Actually, the output power of the IMPATT oscillators reduces as the magnetic field increases, and finally no output power are observed. After enclosing in 5 mm thick soft-iron shield case, the power was dropped by 30 %. Therefore the microwave sources are installed 15 m far from LHD and the microwave is transferred using oversized rectangular waveguides (X-band, WR-90) and 90 degree H bends. By using optical system, the illumination wave radiated from a horn antenna (WR-15) is formed to a parallel beam with a diameter of 20 cm at the reflection layer in the plasma. The illumination wave is reflected by the three cutoff layers, which are determined by the local density and the magnetic field in the case of X-mode reflection.

The primary imaging mirror (M_1) is installed in the LHD vacuum vessel. This is an elliptic concave mirror with the size of 43x50 cm and the focal length of 106.5 cm. The distance between the mirror M_1 and plasma is 210 cm. The mirror M_1 is remotely manipulated by the use of ultrasonic motors (USMs). Since the LHD plasma is

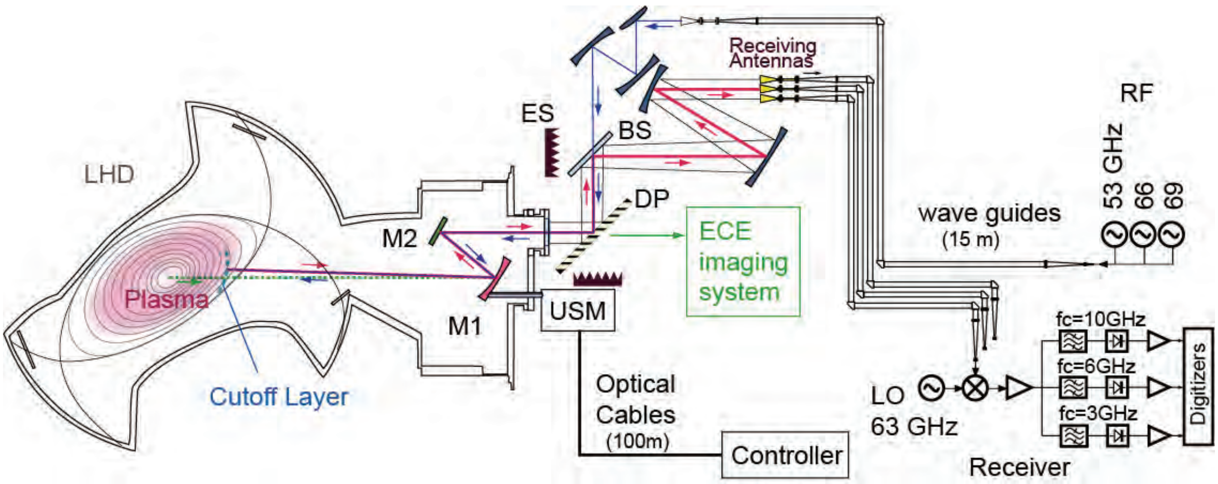

Fig. 1 Schematic view of MIR system in LHD. M1: Adjustable concave mirror, M2: Plane mirror, DP: Dichroic plate (70GHz), BS: Plexiglass beam splitter, US: Ultrasonic motor, ES: ECCOSORB CV3.

twisted, toroidal and poloidal angles of the main mirror should be controlled within 1 degree in order to obtain reflection from plasma [4].

The reflected wave is accumulated by the primary imaging mirror. ECE and the reflected wave are separated by a dichroic plate (DP), which is a high pass filter with a sharp cut-off frequency of 70 GHz. This dichroic plate is an 8 mm thick aluminum alloy plate with many circular holes. The diameter of each hole is 2.5 mm and they are separated by 2.8 mm. The hole has the angle of 45 degree to the plate so that ECE wave more than 70 GHz efficiently passes through the dichroic plate.

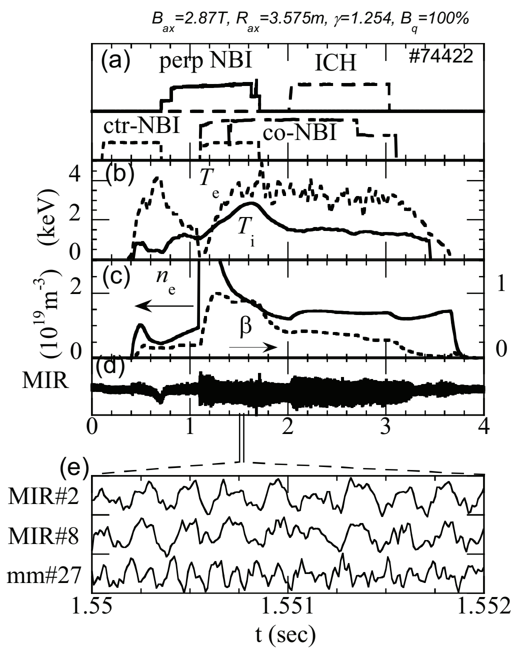

Fig. 2 (a) Heating, (b) temperatures, (c) electron density and beta, (d) MIR signal in slow scale, (e) MIR and magnetic probe signals in fast time scale in LHD.

The reflected beam and the illumination beam are separated by the beam splitter (BS), which is a 3 mm thick Plexiglas plate. The reflected illumination beam by BS and the transmitting illumination beam through DP are absorbed by microwave absorbing forms (ECCOSORB CV-3) in order to reduce background noise. Because of microwave absorbers and beam separation, the leakage of the illumination wave to the receiver is significantly reduced, so that the background level in the signal is drastically reduced.

The plasma image is formed on the front end of receiving horn antenna (WR-15) array by the mirror optics. The pair of antennas is separated by 8.4 cm in the poloidal direction, and another pair by 10.7 cm in the toroidal direction on the cutoff layer. Received reflection wave is transmitted to the heterodyne receiver with oversized waveguides (X-band). In the heterodyne receiver, reflected wave is mixed with the wave from local oscillator (LO) with the frequency of 63 GHz to make intermediate frequency (IF) signals. IF signals selected by band-pass-filters with the bandwidth of 10% of the central frequency are amplified by modular RF amplifiers. Finally they are rectified by Schottky barrier diodes, amplified by DC amplifiers and digitized by PXI digitizer modules.

Figure 2 shows an example of MIR signals in LHD. Clear MIR signals are obtained after adjusting the main mirror. Using this system, novel MHD modes are observed in the case of low density, as shown in Fig.2(e).

3. MIR System in TPE-RX

The second generation of MIR system has been developed for TPE-RX. Main features of the second generation are as follows: (1) narrow IF bandwidth; (2) 2D receiver array; (3) phase detection. Figure 3 shows the schematic view of the MIR system in TPE-RX. In this MIR system a Gunn oscillator generates the RF wave with frequencies of 20 GHz (ω). IMPATT oscillator is not used because its output has many modes with slightly different frequencies.

The primary mirror (M_1), which is an elliptic concave mirror with the size of 40x43 cm, makes the RF beam. The illumination beam designed as its diameter is 9 cm at the window and 10 cm in plasma. As the diameter of the quartz window of the TPE-RX viewing port is 10 cm, the illumination wave can pass through the window. This window size is similar to the open mouse (10.5x8.7 cm) of the 20 dB standard gain horn antenna for 20 GHz (WR-42). Since the magnetic field is very low in TPE-RX, the

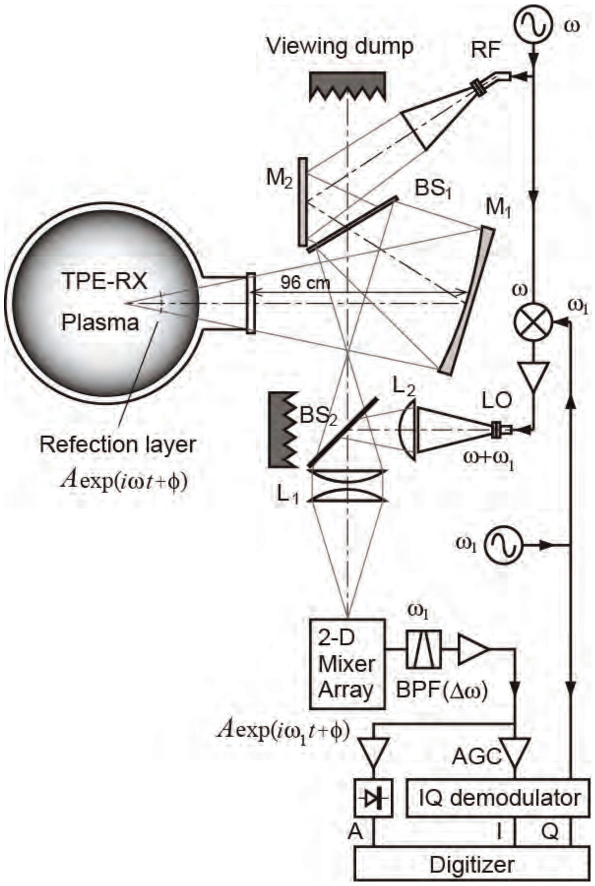

Fig. 3 Schematic view of MIR system in TPE-RX.

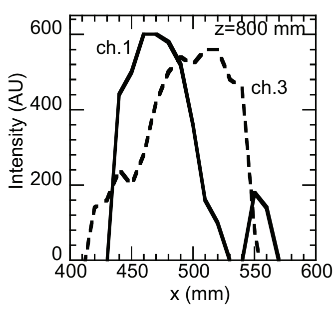

Fig. 4 Test beam profile at the plasma.

illumination wave is in the O-mode, of which cutoff frequency is the plasma frequency. The reflected wave is collected by M_1 and is separated from the illumination beam by the first beam splitter (BS_1). The LO wave and the reflected wave is mixed with the second beam splitter (BS_2). These beam splitters are made of 3 mm thick Plexiglas plate. RF wave reflected by BS_1 and LO wave passing through BS_2 are absorbed by foam absorber (ECCOSORB CV-3) in order to reduce background noise. An image of reflection layer is made onto the 2-D mixer array by the Teflon lens (L_1). As a test, the emission from the position of detector is measured at the position that is 80 cm far from the frame. This position is 133 cm far from the primary mirror M_1, and is 38 cm far from the window of the viewing port. This position corresponds to the position with the minor radius of 30 cm inside the plasma. Fig. 3 shows the resolution at the plasma is 8 cm. The channels 1 and 3 are separated by 4.5 cm at the detector position, and they are separated by 5 cm at the plasma position.

In the 2-D mixer array, four mixer elements are set on a circuit board with a distance of 12 mm, and 4 circuit boards are stacked with a distance of 15 mm. Each element consists of a planer Yagi-Uda antenna, a balun, a beam lead type Schottky barrier diode (SBD) and an IF amplifier. In this system, the balun is improved from the original planer Yagi-Uda antenna system [6]. On the design of antenna system, a computer code for electro-magnetic field (Microwave Office) is employed. Our Yagi-Uda antenna has 3 guiding elements, a pair of dipole and a reflector element. The IF amplifier consists of SAW filters (Murata SAFCC110MCA1T00) and RF amplifiers (RF Micro Devices RF3396). Also the mixer element has two voltage regulators (On Semiconductor MC78LC40NTR) for the power supply of amplifier and the DC bias of SBD. The signal output is a MMCX straight PCB jack connector (HUBER-SUHNER 82_MMCX-S50-0-2/111_KE). The circuit board is a thin Teflon circuit board (Nippon Pillar Packing NPC-F220A(18/18)) with a thickness of 0.18 mm. The circuit is made by the micro strip line technology. The shield box that contains 2-D mixer array has 16 signal output with SMA connector. The MMCX and SMA are connected with a coaxial cable inside the shield box.

The LO wave ($\omega+\omega_1$) is made by mixing the RF wave and the 110 MHz (ω_1) at an up-converter (Hittite HMC523). The lens L_1 and lens L_2 makes a spot of LO wave with the diameter of 10 cm on the 2-D mixer array. By mixing the reflected wave with the frequency of ω and the LO wave, the 2D mixer makes IF signal the frequency of ω_1. Since the IF frequency ω_1 is well stabilized, the noise can be significantly reduced by amplifying with band pass filter (BPF) with a narrow bandwidth (4 MHz).

The reflective wave contains the amplitude A and the phase ϕ, as, $A\exp(i\omega t+\phi)$, where the amplitude A and the phase ϕ is generated by a density fluctuation in the plasma. The phase ϕ is important because it indicates the vibration motion of the reflection layer. The IF signal also contains the amplitude and the phase, as, $A\exp(i\omega_1 t+\phi)$. The amplitude is obtained by rectifying the IF signal with MMIC (Analog Devices AD8362). The phase is obtained by comparing the differential wave (ω_1) and the signal wave with the IQ demodulator (Analog Devices AD8348). I and Q signals correspond to cosϕ and sinϕ, respectively.

Figure 5(a) shows plasma parameters of high Θ RFP plasma in TPE-RX. Here, I_p is the toroidal plasma current, and n_e is the line averaged electron density. F and Θ are the toroidal and poloidal fields normalized by the average toroidal field at the plasma boundary, defined as $F=B_t(a)/\langle B_t\rangle$, and $\Theta=B_p(a)/\langle B_t\rangle$, respectively. Example of MIR signals from this plasma is shown in Fig. 5(a,b). Fig. 5(c) shows MIR channel numbers at the detector position schematically. Here p and t denote the poloidal and the toroidal directions, respectively. Since the imaging optics makes up-side down image, the p direction corresponds to the positive sign in the plasma and the t direction corresponds to the clockwise direction in the top view. As waveforms are similar to other channels, the 2D receiver works well.

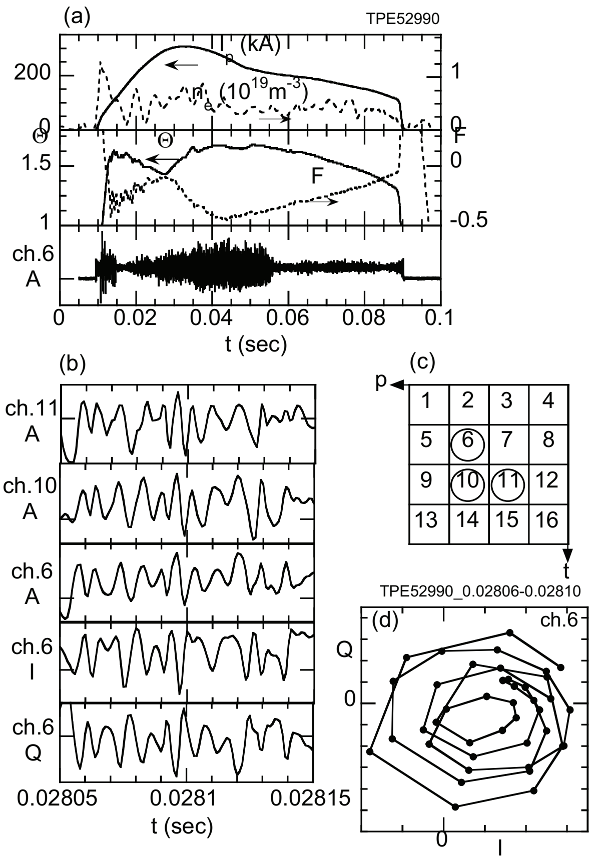

Fig. 5 (a) Plasma parameters and MIR signal in high Θ operation in TPE-RX. (b) Signals of the 2D mixer array of MIR in fast time scale. (c) Schematic view of the 2D mixer array. (d) Lissajous' curve of I-Q signals

Fig. 5(c) also shows I-Q signals of channel 6 of the 2D receiver. Fig. 5(d) shows Lissajous' curve of I-Q signals of channel 6 between t=28.06 and 28.10 msec. If I and Q signals are proportional to cosϕ and sinϕ, respectively, the Lissajous' curve should be circle. In this case, we can find amplitude of I and Q signals are about two times different. May be I and Q signals represent phase because the trajectory is rotating. So this trajectory indicates that the reflection layer moves back and forth. Closed circle indicates a data point, which is taken every 1 μs. At the point (I, Q)=(0.3, 0.2), which corresponds to t=0.028078 sec, the direction of trajectory is turned over. This indicates that the reflection layer motion is turned over at this time.

4. Conclusion

In conclusion, MIR is under development at NIFS. MIR is expected as a new imaging diagnostics of turbulences and instabilities in plasmas. The first generation of MIR has been installed in LHD. This system uses imaging optics and waveguide antenna array as a detector. The second generation of MIR has been installed in TPE-RX. In this system, the differential frequency between the reflected wave and the LO wave is so stabilized that sensitive measurement becomes possible. So, the 2D imaging detector array with planar Yagi-Uda antenna works well. Also preliminary operation of phase detection system has been successful. This result is very encouraging in the development of MIR.

Acknowledgements

This works is supported by National Institute for Fusion Science (No. NIFS07ULPP525) and by National Institute of Natural Sciences (No. NIFS07KEIN0021).

References

[1] E. Mazzucato, Rev. Sci. Instrum. **69**, 2201(1998).
[2] H. Park, et al., Rev. Sci. Instrum. **74**, 4239 (2003).
[3] S. Yamaguchi, et al., Rev. Sci. Instrum. **77**, 10E930 (2006).
[4] S. Yamaguchi, et al., "Microwave Imaging Reflectometry in LHD", accepted for publication in PFR.
[5] Y. Yagi et al., Nucl. Fusion **45**, 138 (2005)
[6] W. R. Deal, et al., IEEE Trans. Microwave Theory Tech. **48**, 910 (2000).

Proceedings of ITC/ISHW2007

Analysis of Density Fluctuation Data Measured by Microwave Imaging Reflectometry

Z. B. Shi[1)], Y. Nagayama[2)], S. Yamaguchi[2)], Y. Hamada[2)]
[1)] *The Graduate University for Advanced Studies, Toki 509-5292, Japan*
[2)] *National Institute for Fusion Science, Toki 509-5292, Japan*
(Received 13 July, 2007 / Accepted 3 August, 2007)

The density fluctuation in the Large Helical Device (LHD) plasma has been investigated by using the microwave imaging reflectometry (MIR) system. The statistical properties of the fluctuation spectral on MIR signals are quantified by using the time-frequency analysis with ensemble averaging technique. Statistical analyses by using cross correlation spectrum and coherence spectrum reveals characteristics of MHD modes, such as mode numbers, during high power NBI heating.

Keywords: density fluctuation, Microwave Imaging Reflectometry, ensemble average

1. Introduction

Turbulence and instabilities has been considered to correlate with the properties of confinement, so that the spatial structure of the fluctuation continues to be the basic issue in the fluctuation study. The microwave imaging Reflectometry (MIR) has been applied to LHD [1]. The MIR is expected to be one of the most powerful diagnostics to investigate instabilities in plasmas, since it enables 2D/3D local measurement of density fluctuations [1-4]. This technology is based upon the reflection of microwave at the density-dependent cutoff layer, and the fluctuating phase of the reflected wave is dominated by the density fluctuation close to the cutoff layer. In fact, the reflecting signal has rich physical phenomena, which include the plasma turbulence and MHD instabilities.

Fluctuation signals often submerge in the strong background noises such as electronic noise and thermal noise, especially when the reflection surface is in the core plasma region. After the onset of the turbulence the spectrum becomes broad, and the intermittently burst of the large-scale turbulence eddy may cause the distortion of the spectrum. Therefore, it is hard to see something from the oscillation even in the frequency domain.

Many digital noise reduction methods have been developed in previous studies [5-7]. These methods use the statistical feature of the random noises that is its power spectral density is similar in any frequency band. The expected error rate of the ensemble average decreases monotonically as a function of the number of the data sets in the ensemble average. Therefore, the statistical analysis of a fluctuating quantity over a long period of time may be useful to pickup fluctuating signals.

E-mail: shi.zhongbing@nifs.ac.jp

This work presents the methods to quantify the statistical properties of the fluctuation spectra based on MIR signals. The analysis methods and the effects of ensemble average on the noise reduction in the spectrum are presented in section 2 and 3. In section 4, some example of our analysis will be applied to MIR data in LHD. Significant results are as follows: three types of the modes and turbulence are observed by using the ensemble technique; the mode numbers are obtained by the cross correlation technique. The turbulence shows an ion drift characteristic during high power NBI heating.

2. Spectral analysis methods

Fourier analysis is the most broadly used signal processing technique. In digital signal processing, we often face the necessity to separate the weak signals from a serious noise contaminated time series. The oscillation looks not very useful in many situations. However, if the time series is transformed into the frequency domain, the frequency spectrum will show the fluctuation power, frequency and primary phase. The Fourier transformation is given by

$$X(f) = \int_{-\infty}^{+\infty} w(t)x(t)e^{-j2\pi ft}dt \qquad (1)$$

where x(t) is the time series, $w(t)$ is the window function which is used to reduce the leakage of the sideband. Here, hanning window is used. In general the spectrum of density fluctuation changes with time, the short time FFT analysis is used to show the time evolution of the spectrum.

The cross-power spectral analysis is used to identify the two time series which have the similar spectral properties. The cross-power spectrum between two time series x(t) and y(t) is defined as

$$G_{xy}(f) = Y(f)X(f)^* \qquad (2)$$

here * denotes the complex conjugate. $X(f)$ and $Y(f)$ is the discrete Fourier transforms of the time series $x(t)$ and $y(t)$, respectively. The auto-power spectrum is the same as taking the Fourier transform when use two identical time series, but the phase information is lost. The phase shift between two time series is:

$$\phi_{xy}(f) = \tan^{-1}\left\{\frac{\mathrm{Im}\left[G_{xy}(f)\right]}{\mathrm{Re}\left[G_{xy}(f)\right]}\right\} \qquad (3)$$

In order to obtain the phase shift whose value corresponds to a high correlation in the frequency domain, the coherence spectrum is introduced and it is defined by the cross-power spectrum normalized by the total power, as

$$\gamma_{xy}(f) = \frac{|< G_{xy}(f) >|}{\sqrt{< G_{xx}(f) >< G_{yy}(f) >}} \qquad (4)$$

where < > denotes ensemble average. The coherency is bounded between 0 and 1, and high value corresponds to high correlation, zero represents completely uncorrelated. The statistical confident level of coherence spectrum is determined by the number of the independent time series in the ensemble ($1/\sqrt{N}$).

The phase-frequency spectrum has a prominent advantage to show the dispersion relations of the MHD mode and turbulence with a distinct phase shift and propagation direction in a two dimensional figure. It can be obtained by two-point cross-correlation method.

$$S(\phi, f) = \left\langle |G_{xy}(f)|\,\delta\left(\phi_{xy}(f) - \phi\right)\right\rangle \qquad (5)$$

In the calculation the delta function is replaced by a rectangular window, and the width of the window is dependent on the number of the discrete sections in the value range of $\phi_{xy}(f)$. From phase shift, we can obtain the mode speed and the mode number by estimating the distance between two detecting points.

3. Ensemble averages

In many situations the signal from plasma is strongly contaminated by random noise. Sometimes its amplitude in the frequency domain is higher than the signal that we are interested in, causing difficult to get the useful information. Fortunately, by using the ensemble averaging technique in the frequency domain, the amplitude of the random jumps becomes an average power level in all frequency range and the peaks of the noise can be removed. The averaging has less influence on the mode whose amplitude doesn't change in the ensemble time. To show how the effect of the noise on signal in the frequency spectrum, a program with a test parameter composed of a sinusoid and a random function is developed. By changing the amplitude ratio of the random noise to signal (N/S), the ratio of the power spectra between the noise and the signal can be obtained. Figure 1 shows the ratio of the FFT amplitudes as a function of N/S. Here, the red star denotes the ratio of the amplitude spectra without ensemble and the black diamond is with ensemble. The ratio of FFT amplitudes changes as a linear function of N/S. The discriminating rate of the N/S is defined as it in the amplitude spectrum has decreased 1/e. With the ensemble technique the N/S increase to about 25, while it is only about 10 without ensemble. Therefore, the ensemble technique is an effective way to reduce noise. It requires the lifetime of the mode should be longer than the time window of FFT. If not, the signal might be distorted by averaging and new analysis method which has both high time and high frequency ability should be used, for example wavelet transforms [8-9].

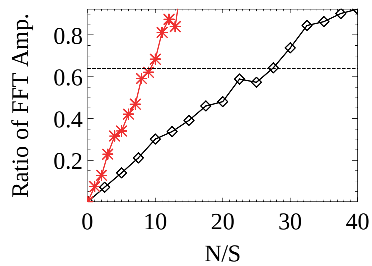

Fig. 1 The effects of the noise to signal (N/S) on the power spectrum. (Red star: without ensemble, Black diamond: with ensemble, dotted line: $1-e^{-1}$)

4. Analysis of MIR signals in LHD

At present MIR system on LHD has three antennas with 8.4cm spacing in toroidal and poloidal direction, and three probe beams with frequencies of 53, 66 and 69GHz in either O-mode or X-mode to illuminate the plasma [1]. The fluctuation signals are measured by the heterodyne receivers with the sampling frequency of 1 MHz. In this paper, we will present an analysis of one shot (75414) with the toroidal magnetic field of 1.5 T and the major radius of 3.6 m, heated by the co-injected NBI with the power of 2.5 MW and counter-injected NBI with the power of 1 MW between t=0.3 and 2.3 s, and the ECH with the total power of 1.2 MW is injected between t=1.4 and 2.0 s. X-mode is used for this shot. Therefore, the cutoff layer is determined by both the toroidal filed and the electron density. The electron density is obtained by the Thomson scattering with calibrating to the microwave interferometer. The normalized radius of the cutoff layer is about 0.1-0.3 during NBI heating.

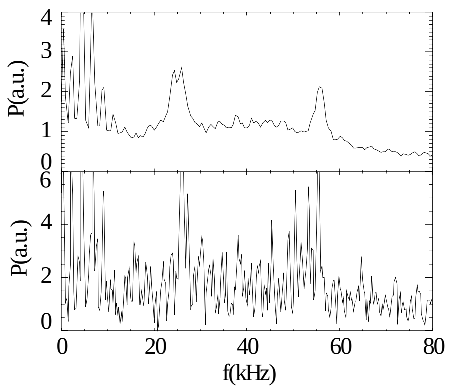

Fig. 2 Power spectrum at 1.6s (top: with ensemble averaging, 50 data sections with the time scale of 2ms each are used. bottom: without averaging and 4ms window is used.)

To extract the fluctuation information, FFT analysis with ensemble averaging technique is used. Figure 2 shows the power spectrum with/without ensemble averaging at 1.6 s. Without ensemble averaging, the MHD modes are concealed in the strong background fluctuation, leading to difficult to decide the mode frequency. With the ensemble averaging, the MHD modes clearly appear and the turbulence exhibits a broad spectrum with high coherency. Figure 3(a) shows the time-frequency spectrum. Three types of fluctuation appear in the MIR signals.

In the low frequency range, the density fluctuation has a fundamental frequency of 2.3 kHz and its higher harmonics. The frequency of this low frequency mode is much lower than that of the Alfvén eigen modes, and about 3 times higher than the electron diamagnetic frequency. It appears when turning on the NBI power and disappears after turning off the NBI power. It seems as if the onset of this mode depends strongly on the power of neutral beam. For the tangentially NBI heating, it is not easy to destabilize the fishbone instability. Indeed, the typical fluctuation of fishbone instability was not observed in magnetic probe signal. Therefore this mode is not the fishbone instability.

At *t*=0.9 s a mid-frequency mode (~23 kHz) appears when the plasma temperature increase to flat top. When turning on the ECH power, this frequency increases to 26 kHz and it disappears after turning off the ECH power. The frequency of this mode is close to the toroidal precession frequency of the resonant trapped fast ions [10].

When turning on the ECH power, a high frequency mode (~55 kHz) appears. This is in the range of Alfvén frequency. The mode frequency increases with time and it is up to 70 kHz at *t*=2.2 s. At *t*=2.0 s the turning-off of the ECH power causes no obviously effect on this mode. That means this mode may be related to the energetic ion mode but it is induced by the energetic electrons.

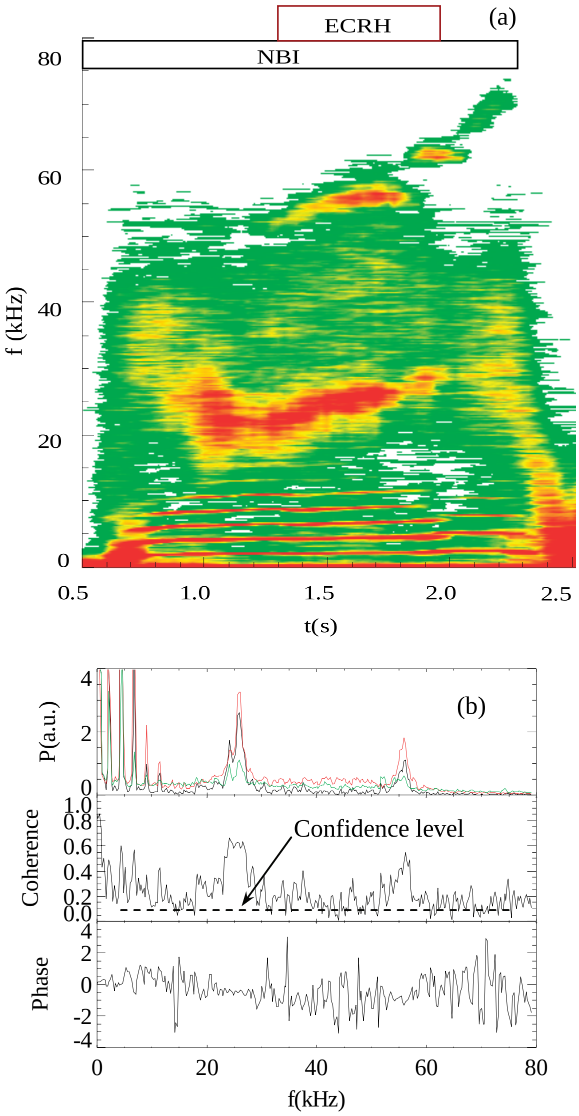

Fig. 3 (a) Time-frequency plot of FFT spectrum, (b) Cross-power spectrum (black: cross-spectrum, red and green: auto-spectrum), coherence and phase shift in the poloidal direction at t=1.6s.

When these modes appear, the cross-power spectrum is peaked and coherence become high, and the phase shift shows less jumps, as shown in figure 3(b). When calculating the cross-power and coherence spectra, FFT is done at every 200 data sections with the time period of 4 ms each. The overlap between the neighboring sections is the half of the time window. Before calculating the spectrum, the mean value and the linear trend have been removed from every time series.

Figure 4 shows the contour plot of the phase-frequency spectrum in the toroidal and poloidal direction at t=1.55 s. The high light color corresponds to the large amplitude. When the mode appears, it shows a wide spectral profile vs. the phase shift, maybe, this is because of the strong effects of the turbulence which may cause the distorted distribution of the spectrum. However, the exact phase shift can be obtained from the statistical profile of the phase spectrum. It should be the same as the phase shift in Fig. 3(b). The fluctuation is dominated by the frequency lower than 70 kHz and the turbulence propagates along the ion drift direction. The mode number of the 26 kHz is m=2/n=6, and the mode number of 56 kHz is m/n=4/7. The errors of mode numbers are about ± 1.

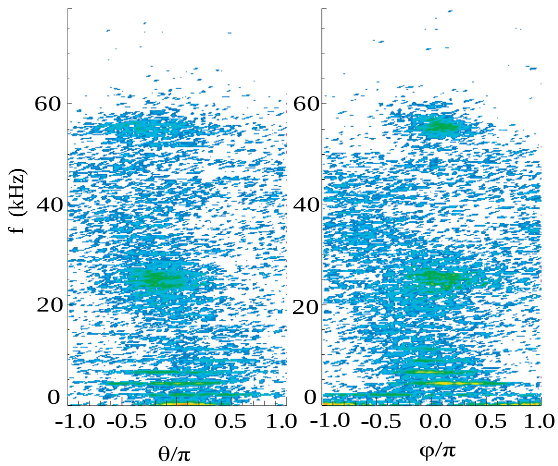

Fig. 4 The phase-frequency spectra in poloidal (left) and toroidal (right) directions at t=1.55s.

5. Summary

In summary, the analysis of plasma density fluctuation on LHD has been carried out based on MIR signals. The ensemble technique has been developed to reduce the noise effect in the spectrum analysis. This technique improves accuracy better than single data set when obtaining the statistical property of the fluctuation. Novel MHD modes and turbulence are observed during high power NBI heating. The mode numbers are obtained by the cross correlation technique. The turbulence shows an ion drift characteristic during high power NBI and ECH heating.

Acknowledgments:

This work is supported by National Institute of Natural Sciences (NIFS07KEIN0021) and by National Institute for Fusion Science (NIFS07ULPP525).

Reference:

[1] S. Yamaguchi, et al., Rev. Sci. Instrum. **77**, 10E930 (2006).

[2] R. Sabot, et al., Plasma Phys. Control. Fusion. **48**, B421 (2006)

[3] H. Park, et al., Rev. Sci. Instrum. **74**, 4239 (2003).

[4] E. Mazzucato, Rev. Sci. Instrum. **69**, 2201(1998).

[5] E. B. Hooper, Plasma Physics, **13,** 1 (1971)

[6] Ch. P. Ritz, et al., Rev. Sci. Instrum. **59**, 1739 (1988).

[7] G. S. Xu, et al., Physics of Plasmas. **13**, 102509 (2006)

[8] A. Grinsted, J. C. Moore, and S. Jevrejeva, Nonlinear Processes in Geophysics **11**,561(2004)

[9] V. P. Budaev, I. M. Pankratov, S. Takamura, etal., Nucl. Fusion **46**, S175 (2006)

[10] T. Kass, H. S. Bosch, F. Hoenen, et al., Nucl. Fusion **38**, 807 (1998)

Proceedings of ITC/ISHW2007

Observation of Novel Instability by using Microwave Imaging Reflectometry in LHD

S. Yamaguchi[1], Y. Nagayama[1], Z.B. Shi[2], Y. Kogi[3], and A. Mase[3]

[1] *National Institute for Fusion Science, Toki 509-5292, Japan*

[2] *Graduate University for Advanced Studies, Miura 240-0193, Japan*

[3] *Art Science and Technology Center for Cooperative Research, Kyushu Univ., Kasuga 816-8580, Japan*

(Received 15 October 2007 / Accepted day 15 October 2007)

A new magnetohydrodynamic (MHD) mode with equally separated higher harmonics has been observed in the Large Helical Device (LHD). The MHD mode appears as the density and magnetic fluctuations in the case of perpendicular ion heating. The poloidal and toroidal mode numbers are $m = 3$ / $n = 4$ respectively, and the fundamental frequency is 1 ~ 10 kHz, which looks depending on the ion temperature. The density fluctuation is radially localized in the edge region where the rotational transform is nearly $\iota = 4/3$. The feature of the newly observed mode is different from the interchange mode which is frequently observed in LHD.

Keywords: MIR, microwave, imaging, reflectometry, LHD

1. Introduction

The heliotron configuration is one of the promising candidates of the thermonuclear fusion reactor since the plasma is confined in the steady-state without hazardous disruption by using external superconducting coils and a full helical diverter. The Large Helical Device (LHD) is a superconducting heliotron device with the poloidal period number of L = 2, the toroidal period number of M = 10, the major radius of R_{ax} = 3.5 ~ 4.1 m and the averaged minor radius of 0.6 m [1]. The considerable experiment and theoretical efforts have been devoted to the study of instabilities in helical plasmas, however, the present understanding are still not satisfactory.

The recent advance in the microwave technology provides a new generation of the imaging diagnostics in magnetically confined plasma [2-5]. The microwave imaging diagnostics has a potential to obtain 2-D/3-D images of the turbulences and the instabilities with good time and spatial resolutions [6-8]. It brings understanding of the basic physics of the turbulence and the plasma confinement. The microwave imaging reflectometry (MIR) utilizes the radar technique for the measurement of the electron density profiles and its fluctuations by probing the density-dependent cutoff layer in the plasma. The MIR system is under development in the National Institute for Fusion Science, and it can observe the electron density fluctuation with good sensitivity in LHD [9]. In this paper we will present a newly observed magnetohydrodynamic (MHD) mode, which appears during perpendicular ion heating of neutral beam injection (NBI) or ion cyclotron resonance frequency (ICRF). This mode is accompanied with the equally separated higher harmonics. The experimental setup of the MIR system is described in Section 2, and the newly observed MHD mode is described in Section 3, followed by the conclusion in Section 4.

2. MIR System

Figure 1 shows the schematic view of the MIR system in LHD. The MIR system illuminates the LHD plasma by using the probe wave with frequencies of 53, 66 and 69 GHz in X-mode, and the probe beam is parallel with the diameter of 20 cm. The illumination wave is reflected by the three cutoff layers, which are determined by the local density and the magnetic field. The density fluctuation causes the amplitude modulation and the phase modulation in the reflected beam. The reflected wave is diverged in the case of the density fluctuation with short wavelength. An optical system focuses the reflected wave on the receiver in order to reproduce the microwave image of the fluctuation. The primary imaging mirror with the diameter of 45 cm is installed inside the LHD vacuum vessel. The distance between the mirror and the plasma is about 210 cm. The receiver contains three horn antennas

author's e-mail: yamaguchi.soichiro@LHD.nifs.ac.jp

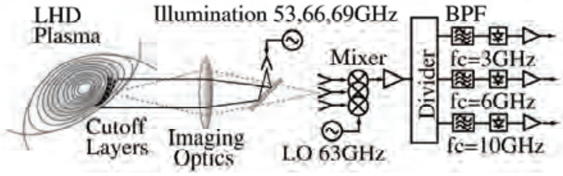

Fig.1 Schematic of the Microwave Imaging Reflectometry (MIR) in LHD.

to detect the microwave image. A pair of receiving antennas is separated by 8.4 cm in the poloidal direction, and another pair by 10.7 cm in the toroidal direction on the cutoff layer. The fluctuation signal is measured by the heterodyne receiver with the sampling time of 1 μsec. The fluctuation signal of the reflected wave represents the density fluctuation on the cutoff layer in the plasma.

3. Observation

A typical example of this MHD mode is shown in figure 2. The LHD configuration is as follows: R_{ax} = 3.575 m, a = 0.6 m, B_t = 2.870 T, γ = 1.254 and B_q = 100 %. The plasma is basically heated by the co-injected NBI with the power of 8.6 MW and the counter-injected NBI with the power of 3.8 MW. Figure 2 shows time evolutions of the heating power, the beta (β) measured by the diamagnetic diagnostics, the line averaged electron density n_e, the central electron temperature T_e, the central ion temperature T_{i0} and the MIR signal. Figure 2(e) shows the MIR and the magnetic signals showing the mode, which look semi-sinusoidal oscillation.

Figure 3 shows the time evolution of the FFT power spectrum of the MIR signal and the magnetic probe signal. When the plasma is heated by NBI in the co, counter and perpendicular directions, the target mode appears at t = 1.45 sec with the sharp spectrum in the FFT power spectrum of the MIR signals. This mode is accompanied with the equally separated several higher harmonics. The same mode appears in the FFT power spectrum of the magnetic fluctuations, however, another mode also appears with the broad spectrum at t = 1.3 sec. Right after turning off the perpendicular injected NBI with the power of 3.2 MW at t = 1.7 sec, the frequency of the target mode starts dropping, and it looks depending on the ion temperature. Right after turning on the ICRF heating with the power of 1.7 MW, the mode with equally separated several harmonics appears again. So, the perpendicular ion heating looks playing an important role to destabilize this mode. However, the present mode is sometimes observed during only the tangential NBI heating in the case of low density and high temperature plasma.

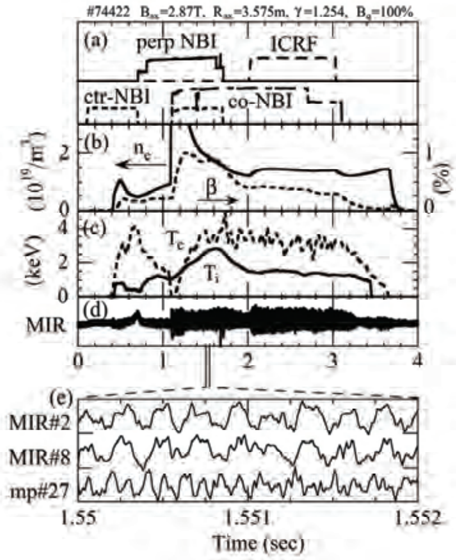

Fig.2 Typical discharge with a newly observed MHD mode. (a) The heating power; (b) the diamagnetic beta (dotted line) and the line averaged electron density (solid line); (c) the central electron temperature (dotted line) and the central ion temperature (solid line); (d) the MIR signal; (e) the MIR signal and the magnetic probe signal in a fast time scale.

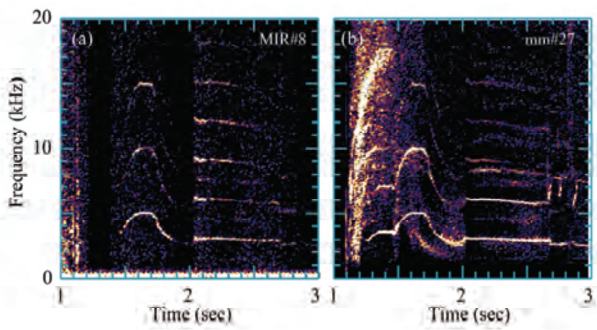

Fig.3 FFT Power spectrum of (a) the MIR and (b) the magnetic probe signal.

The mode numbers is estimated from MIR signals since the magnetic probe signal is not strong enough to identify the mode numbers in the case of low beta. MIR ch.2 and MIR ch.8, which detect the frequency of 63 GHz, are poloidally separated with the distance of about 84 mm at R = 4.55 m. It corresponds to the poloidal angle of θ = 4.9 degrees. The phase difference in the fundamental mode can be obtained from the cross power spectrum of these channels. At t = 1.55 sec, the phase difference δθ is about 15 degrees. So the poloidal mode number is m = 3, and the error is about 1. The mode number of higher

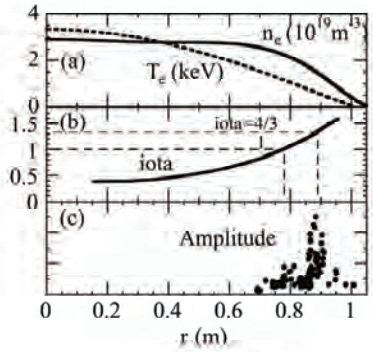

Fig.4 Radial profiles of (a) the electron density (n_e) and temperature (Te) at t = 1.6 sec, (b) the rotational transform, and (c) the amplitude of the fundamental mode of the density fluctuation.

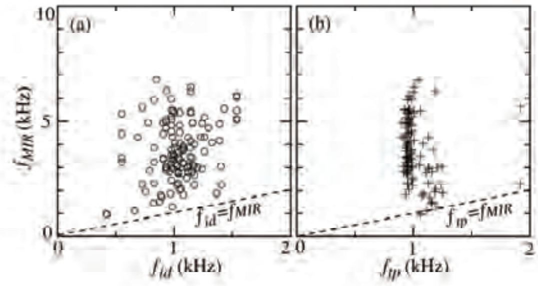

Fig.5 (a) Comparison of the fundamental frequency f_{MIR} vs. the ion diamagnetic frequency f_{id}; (b) f_{MIR} vs. the toroidal precession frequency f_{pr} in tokamak.

harmonics is proportional to the frequency.

Figure 4(a) shows the radial profile of the electron temperature and the electron density at t = 1.6 sec. These are measured with the YAG laser Thomson scattering with 200 spatial channels [10, 11]. By fitting to the 8th order polynomials, smooth T_e and n_e profiles are obtained. The absolute value of the electron density is calibrated by using the 2 mm wave 2-color interferometer [12], of which viewing line has the same configuration of the laser beam of the Thomson scattering in the different port. The radial density profile has the flat top shape and the steep gradient in the peripheral region of the plasma in this case. The cut-off layer for the probe wave in X-mode is obtained from this density profile and the calculated magnetic field in vacuum. Figure 4(b) shows the radial profile of the rotational transform ι. Figure 4(c) shows the amplitude of the fundamental mode between t = 1.5 sec and 1.7 sec. These are obtained from 9 discharges of similar operational conditions with slightly different densities. The mode amplitude is localized near r ~ 0.9 m where the rotational transform ι is about 4/3, as shown in Figure 4(c). Here, r is the minor radius in the horizontal port section, defined as $r = R - R_0$ and $R_0 = 3.575$ m in this case. The profile width of the mode amplitude is about 3 cm. At t = 1.6 sec the mode amplitude is large on the intermediate cutoff layer of 66 GHz (r = 0.88 m). However, it is quite weak on the slightly outer layer of 69 GHz (r = 0.85 m) and it disappears on the inner layer of 53 GHz (r = 0.98 m). Therefore, the mode is well localized in the radial direction.

The mode presented in this paper is different from known MHD instabilities in LHD. Usual MHD modes observed in LHD are the ideal and the resistive interchange modes [13, 14]. The edge region of LHD plasma is theoretically stable for the ideal interchange mode due to the high shear [15]. As shown in Figure 3, the resistive interchange mode appears in the magnetic fluctuations after the pellet injection at t = 1.06 sec. The frequency of the resistive interchange mode increases from t = 1.1 sec and decreases from t = 1.5 sec. The frequency range of the resistive interchange mode is similar to the target mode. However, features (spectrum and localization) are different. The present mode has sharp spectrum and is localized in narrow space, while the observed resistive interchange mode has a broader spectrum and is not very localized in the radial direction. Actually it spreads more than 12 cm in the MIR measurement. Usual beam driven MHD instabilities are Alfven eigen modes, and some of them have been observed in LHD [16]. The frequency of TAE mode is more than 100 kHz, and that of GAE mode is the order of 50 kHz. Those frequencies are much higher than that of the present mode.

The frequency characteristic of the target mode is similar to the fishbone oscillations in tokamaks [17]. In the case of tokamak there are two models for explaining the mechanism of the fishbone mode with high frequency branch and low frequency branch. In the high frequency branch the trapped energetic ion destabilizes the mode with the toroidal precession frequency f_{pr}. In the low frequency branch, the energetic ion destabilizes the mode with frequency close to the thermal ion diamagnetic frequency f_{id}. Those frequencies are calculated using the formula for tokamaks [17], as follows:

$$f_{pr} = \frac{E}{2\pi M r R \omega_0}, \quad f_{id} = \frac{\nabla p_i}{2\pi e B r R n}$$

where f_{pr} is the toroidal precession frequency of the resonant trapped fast ions, and f_{id} is the finite diamagnetic frequency evaluated at the safety factor q = 1 surface.

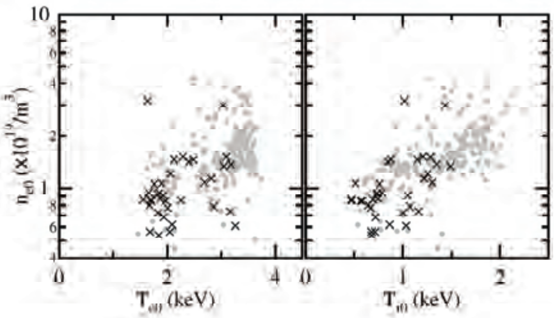

Fig.6 The parameter regions of (a) n_{e0} vs. T_{e0}, (b) n_{e0} vs. T_{i0}, where the mode appears (O) or disappears (X).

Here, E denotes the energy of the ions, $\omega_0 = eB/M$ the gyro frequency and M the mass of the particles, ∇p_i denotes the ion pressure gradient of the plasma bulk and n the plasma density.

In Figure 6, these frequencies are compared with the fundamental frequency of the mode. Here, the f_{id} is calculated by using the density profile and the ion temperature profile, which is measured by the charge exchange spectroscopy. The fundamental frequency is about $f_{MIR} = 1 \sim 7$ kHz, which is several times higher than the ion diamagnetic frequency of $f_{id} = 0.5 \sim 1.6$ kHz. The perpendicular NBI injects the beams with energy of 40 keV, therefore, the toroidal precession frequency around the $\iota = 1$ surface is about $f_{pr} = 1$ kHz. The toroidal precession frequency does not depend on the bulk ion temperature, while the mode frequency increases as T_{i0} increases in the experiment. The fundamental frequency is slightly higher than f_{id} and f_{pr}, however, the clear correlation between the target mode and the low frequency branch of the fishbone mode has not been found yet.

Figure 6 shows the parameter regions of n_{e0} vs. T_{e0} and n_{e0} vs. T_{i0}, where the target mode appears in LHD. In tokamaks, the plasma parameter of the fishbone activity is in the region of high n_e and high T_e [17]. The target mode appears in the cases of high temperature or low density, and is also different from fishbone instability in tokamak. The mode sometimes appears or not with similar plasma parameters. The neutral particle analyzer (NPA) [18, 19] and other diagnostics of LHD suggest that the appearance of the target mode might depend on both the vertical components of the fast ion and the pressure gradient at the resonance surface. The details will be presented soon.

4. Summary

In conclusion, we have observed the new MHD mode with the sharp spectrum and the equally separated higher harmonics by using the MIR in LHD. This is the $m = 3$ / $n = 4$ mode that is localized in the narrow layer with the width of 3 cm near the $\iota = 4/3$ surface in the edge region. The mode frequency is much less than that of known Alfven eigen modes, and is similar to the ion diamagnetic frequency. However, we have not obtained a clear evidence of the fishbone instability yet.

Acknowledgement

Technical assistance from S. Sugito and Y. Ito in Department of Engineering and Technical Services of NIFS is gratefully acknowledged. This work is supported by the budgets of the National Institute for Fusion Science (ULPP525), and by the National Institute of Natural Sciences (KEIN0021).

References

[1] O. Motojima et al., Nuclear Fusion, **45**, S255 (2005).
[2] C. Laviron et al., Plasma Phys. Control. Fusion. **38**, 905 (1996).
[3] E. Mazzucato, Nuclear Fusion, **41**, 203 (2001).
[4] E. Mazzucato, Plasma Phys. Control. Fusion, **46**, 1271 (2004)
[5] T. Munsat et al., Rev. Sci. Instrum. **74**, 1426 (2003).
[6] H. Park et al., Rev. Sci. Instrum. **74**, 4239 (2003)
[7] H. Park et al., Phys. Rev. Lett. **96**, 195003 (2006).
[8] A. Mase et al., Rev. Sci. Instrum. **74**, 1445 (2003).
[9] S. Yamaguchi et al., Rev. Sci. Instrum. **77**, 10E930 (2006).
[10] K. Narihara, Rev. Sci. Instrum. **72**, 1122 (2001).
[11] I. Yamada, et al., Rev. Sci. Instrum. **72**, 1126 (2001).
[12] K. Kawahata, et al., Rev. Sci. Instrum. **70**, 695 (1999).
[13] S. Sakakibara, et al., Nuclear Fusion, **41**, 1177 (2001).
[14] S. Sakakibara et al., Plasma Fusion Res. **1**, 003 (2006).
[15] M. Wakatani, *Stellarator and Heliotron Devices*, (Oxford University Press, New York, 1998).
[16] K. Toi, et al., Nucl. Fusion, **44**, 217 (2004).
[17] T. Kass et al., Nucl. Fusion, **38**, 807 (1998).
[18] T. Ozaki, et al., Rev. Sci. Instrum. **77**, 10E917 (2006).
[19] E. A. Veshchev, et al., Rev. Sci. Instrum. **77**, 10F116 (2006).

P1-083

Consideration of Density Fluctuation Measurement using Heavy Ion Beam Probe on Large Helical Device

Haruhisa NAKANO[1)], Takeshi IDO[1)], Akihiro SHIMIZU[1)], Masaki NISHIURA[1)], Shinji KATO[1)], Shinsuke OHSHIMA[1)], Akimitsu NISHIZAWA[2)], Yasuji HAMADA[1)], and LHD group[1)]

[1)]*National Institute for Fusion Science, Toki 509-5292, Japan*

[2)]*Tono Geoscience Center, Japan Atomic Energy Agency, Toki, 509-5102, Japan*

Heavy ion beam probe (HIBP) can measure density, potential, magnetic field and their fluctuations, simultaneously, in high temperature magnetic confinement plasma. However it is well-known that local density fluctuation is measured with difficulty due to a path integral effect. Ionization cross-sections of HIBP beam particles affects a detected beam current, which informs density. The ionization cross-sections due to not only electron impact but also proton impact are important for MeV-range beam. Take into account the proton ionization, the path integral effect becomes twice larger than that only due to electron impact. And the path integral effect can decrease by less than half, when phase difference between proton and net electron fluctuations is finite.

Keywords: heavy Ion beam probe, fluctuation measurement, path integral effect, proton impact ionization

1 Introduction

A fluctuation transport closely relates magnetic plasma confinement performance. This transport is represented fluctuations of density, temperature, and electric and magnetic fields. To measure them is one of the most important study in the magnetic plasma confinement. Heavy ion beam probe (HIBP) is one of powerful diagnostics which can measure density, potential, magnetic field, and their fluctuations, simultaneously. However, density, magnetic field and their fluctuations cannot be measured locally due to the path integral effects. Measured fluctuation amplitudes are simulated in previous paper [1, 2], and local density fluctuation amplitude is accomplished to be reconstructed under a specific condition [3].

A HIBP system on a large confinement device needs a few MeV order beam energy, like HIBP system on Large Helical Device (LHD) [4]. This HIBP system makes a difference from previous HIBP systems which have a few hundreds keV in beam energy. In the case of MeV order HIBP, beam particles ionize by mainly not only electron impact but also proton impact [5]. In this paper, we discuss influences of proton impact ionization on density fluctuation measurement, and simulate the path integral effect in this measurement on some conditions.

2 Brief description of density fluctuation measurements of HIBP

HIBP system consists of an accelerator, energy analyzer, and beam sweepers. In principle, a singly charged heavy ion beam (Rb^+, Cs^+ and Au^+, etc), called primary beam, is injected into a plasma. In the plasma, the beam ions are ionized to doubly (or higher) charged ions through the collisions with plasma particles. The doubly charged ions, called secondary beam, come out from the plasma, and are detected with the energy analyzer.

author's e-mail: nakano@nifs.ac.jp

The detected beam current I_d, which has density informations, is expressed in the following form:

$$I_d = I_0 l_{sv}(r_*)\left\{n_e(r_*)S_e^{12} + n_{H^+}(r_*)S_{H^+}^{12}\right\} \times \exp\left[\left\{-\sum_{i=1,2}\int\left(n_e(r)S_e^i + n_{H^+}(r)S_{H^+}^i\right)\mathrm{d}l_i\right\}\right] \quad (1)$$

where r_* is an ionization position, I_0 is an initial primary beam current, l_{sv} is a sample volume length, n_e and n_{H^+} are electron and proton density, respectively. The terms $S_\alpha^{12} = \langle\sigma_\alpha^{12}v_{the}\rangle_M/v_b$ and $S_\alpha^i = \langle\sigma_\alpha^i v_{the}\rangle_M/v_b$, where $\alpha = (\mathrm{e}, \mathrm{H}^+)$, and σ_e and σ_{H^+} are ionization cross-sections of electron and proton impacts, respectively. The terms v_{the} and v_{thi} are electron and proton thermal velocity, respectively. And v_b is beam particle velocity. Superscript 12 of σ_α means ionization from single charged ion to double charged ion, and superscripts 1 and 2 of σ_α express ionization from single and double charged ions to higher charged ions, respectively. Subscript M of bracket represents a Maxwellian average. And $\mathrm{d}l_1$ and $\mathrm{d}l_2$ are length elements of primary and secondary beam orbits, respectively. The term $l_{sv}(r_*)\left\{n_e(r_*)S_e^{12} + n_{H^+}(r_*)S_{H^+}^{12}\right\}$ and exponential term are brightness and attenuation of detected beam current, respectively.

By taking variations and square of Eq. (1), the instantaneous normalized measured fluctuation power is represented as

$$\left(\frac{\tilde{I}_d(r_*)}{I_d(r_*)}\right)^2 = T_0 - S_C + A_C \quad (2)$$

with expression of

$$\begin{aligned}
T_0 &= \frac{\left(\widetilde{n}_{\rm e}(r_*)S_{\rm e}^{12}+\widetilde{n}_{\rm H^+}(r_*)S_{\rm H^+}^{12}\right)^2}{\left(n_{\rm e}(r_*)S_{\rm e}^{12}+n_{\rm H^+}(r_*)S_{\rm H^+}^{12}\right)^2},\\
S_{\rm C} &= \frac{2\left(\widetilde{n}_{\rm e}(r_*)S_{\rm e}^{12}+\widetilde{n}_{\rm H^+}(r_*)S_{\rm H^+}^{12}\right)}{n_{\rm e}(r_*)S_{\rm e}^{12}+n_{\rm H^+}(r_*)S_{\rm H^+}^{12}}\\
&\quad\times\sum_{i=1,2}\left(\int\widetilde{n}_{\rm e}(r_i)S_{\rm e}^{i}{\rm d}l_i+\int\widetilde{n}_{\rm H^+}(r_i)S_{\rm H^+}^{i}{\rm d}l_i\right),\\
A_{\rm C} &= \left[\sum_{i=1,2}\left(\int\widetilde{n}_{\rm e}(r_i)S_{\rm e}^{i}{\rm d}l_i+\int\widetilde{n}_{\rm e}(r_i)S_{\rm H^+}^{i}{\rm d}l_i\right)\right]^2,
\end{aligned}\tag{3}$$

where a tilde expresses fluctuation.

The term $\widetilde{n}_\alpha$ are statistical variables, hence we will consider an ensemble of fluctuations $\widetilde{n}_\alpha$ with $\langle\widetilde{n}_\alpha\rangle_{\rm E}=0$, where $\langle\rangle_{\rm E}$ means an ensemble average. If $n_{\rm e}=n_{\rm H^+}$ and $\widetilde{n}_{\rm e}=\widetilde{n}_{\rm H^+}$, by taking ensemble average of Eq. (2), we obtain

$$\langle\widetilde{\eta}^2(r_*)\rangle_{\rm E}=\langle T_0\rangle_{\rm E}-\langle S_{\rm C}\rangle_{\rm E}+\langle A_{\rm C}\rangle_{\rm E}\tag{4}$$

with the expression on a condition of $S_\alpha^{12}\equiv S_\alpha^1$ of

$$\begin{aligned}
\langle T_0\rangle_{\rm E} &= \langle\widetilde{\xi}^2(x_*)\rangle_{\rm E}\\
\langle S_{\rm C}\rangle_{\rm E} &= 2\sum_{i=1,2}\int\langle\widetilde{\xi}(x_*)\widetilde{\xi}(x_i)\rangle_{\rm E}\hat{S}^i w_i(x_i){\rm d}x_i\\
\langle A_{\rm C}\rangle_{\rm E} &= \sum_{i=1,2}\sum_{j=1,2}\iint\langle\widetilde{\xi}(x_i)\widetilde{\xi}(y_j)\rangle_{\rm E}\hat{S}^i\hat{S}^j w_i(x_i)w_j(y_j){\rm d}x_i{\rm d}y_j
\end{aligned}\tag{5}$$

where the normalized fluctuations $\widetilde{\eta}(r)=\widetilde{I}_{\rm d}(r)/I_{\rm d}(r)$ and $\widetilde{\xi}(r)=\widetilde{n}_{\rm e}(r)/n_{\rm e}(r)$. The normalized ionization rate $\hat{S}=n_{\rm e}S_\alpha^i a$ which depends on beam energy, electron and proton temperature, and density, where $S_\alpha^i=S_{\rm e}^i+S_{\rm H^+}^i$. The term a is minor radius. And the weight in the integral $w_i(x_i)=\partial\hat{l}_i(x_i)/\partial x_i$, where $\hat{l}_i=l_i/a$. The ensemble average of two fluctuation is represented as

$$\langle\widetilde{\xi}(x)\widetilde{\xi}(y)\rangle=|\widetilde{\xi}(x)||\widetilde{\xi}(y)|\gamma(x,y)\Psi(x,y),\tag{6}$$

where $\gamma(x,y)$ and $\Psi(x,y)$ are coherence and phase between fluctuations at points x and y, respectively. Equation (4) and (5) are the same formula as those of previous HIBP system which has a few hundreds keV beam energy and beam particles are mainly ionized by electron impact [1], thus the ionization rate in Eq. (5) is only raised by proton impact ionization.

There are two kinds of path integral effects; screening effect $S_{\rm C}$ and accumulation effect $A_{\rm C}$ [3]. The term $\langle S_{\rm C}\rangle_{\rm E}$ has negative sign in Eq. (4), and is a local path integral effect which screens the local fluctuation. The other way, $\langle A_{\rm C}\rangle_{\rm E}$ has positive sign in Eq. (4), and is a long range path integral effect which is the same as well-known type effect in other line integral diagnostics.

3 Simulation of Measured Fluctuation

The measured fluctuation is simulated with linear beam orbit shown in Fig. 1 as the same as previous paper

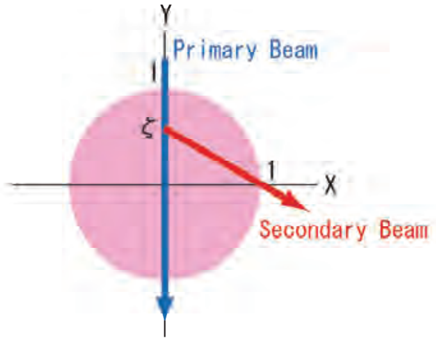

Fig. 1 Beam orbit model.

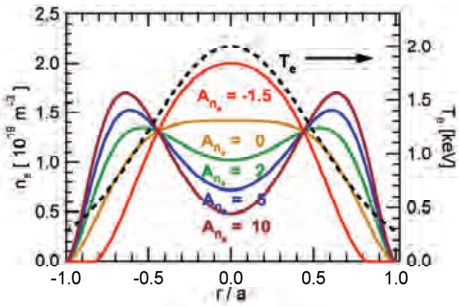

Fig. 2 Profiles of electron density (solid lines) and temperature (dashed line). A_{n_e} is hollow factor in Eq. (10). A case of $A_{n_e}=0$ expressed Eq. (8)

[1]. Using parameter s and t, the primary and secondary beam orbit are described as

$$\vec{\hat{l}}_1(s)=(0,-s+1),\quad\vec{\hat{l}}_2=(t,-\zeta t+\zeta)\tag{7}$$

The corresponding weight factors are $w_1=1$, $w_2=\sqrt{1+\zeta^2}$. In the calculation, minor radius a is assumed 600 mm, and profiles of density and electron temperature $T_{\rm e}$ are assumed as

$$n_{\rm e}=n_{\rm e,0}(1+\rho^4)^2\tag{8}$$

$$T_{\rm e}=T_{\rm e,0}\exp\left[-\frac{1}{2}\left(\frac{\rho}{0.5}\right)^2\right],\tag{9}$$

where $n_{\rm e,0}$ is calculated as the line averaged density is kept to be $1\times10^{19}\ {\rm m}^{-3}$, $T_{\rm e,0}=2$keV (Fig. 2), and $\rho=|r/a|$. The primary and secondary beam are selected Au^+ and Au^{2+}, respectively. Ionization cross-sections of electron and proton impacts are calculated using Lot'z empirical formula and results in Ref. [5], respectively. Electron temperature contribution to the path integral effect is assumed to be ignored.

First, we will examine dependence on a position of fluctuation peak and coherence. The local fluctuation profile is assumed $0.1\exp[-0.5(\rho-\rho_0)^2/0.2^2]$, and three patterns; $\rho_0=0.0$, 0.5 and 0.9, are simulated. The coherence γ is assumed $\gamma(x,y)=\exp(-|x-y|^2/\hat{l}_{\rm C}^2)$, where $\hat{l}_{\rm C}=l_{\rm C}/a$ is a normalized correlation length expressed with correlation length $l_{\rm C}$. And using delta function $\delta(x,y)$, the phase difference Ψ is assumed $\Psi(x,y)=\cos\delta(x,y)=1$. The beam

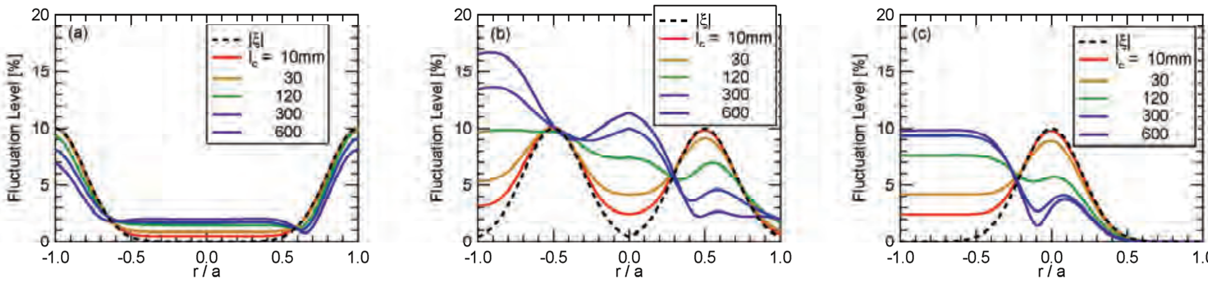

Fig. 3 Dependence of path integral effect on fluctuation peak position and coherence. Coherence is assumed $\gamma(x,y) = \exp(-|x-y|^2/\hat{l}_C^2)$, where $\hat{l}_C = l_C/a$ is the local correlation length. No phase difference is assumed; $\Psi(x,y) = 1$. Radial profile of the local density fluctuation and the measured fluctuation are indicated dashed and solid lines, respectively. (a) Edge (pattern A), (b) half of minor radius (pattern B), and (c) center (pattern C) peaks local density fluctuation profiles.

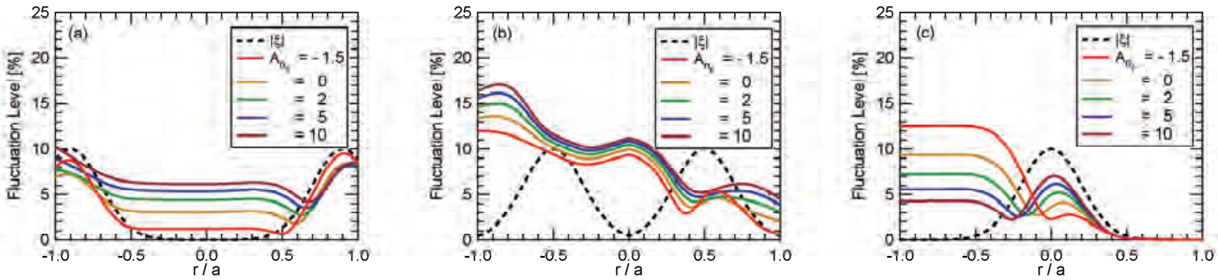

Fig. 4 Dependence of the path integral effect on density profile. The correlation length is 300mm, and other parameters are the same as Fig. 3 except density profile (Fig. 2). Radial profile of the local density fluctuation and the measured fluctuation are indicated dashed and solid lines, respectively.

energy is assumed to be 1.5 MeV. Figure 3 shows three profile patterns of local fluctuation $\tilde{\xi}$ with several correlation lengths; l_C = 10mm, 30mm, 120mm, 300mm and 600mm. The short and long correlation lengths are the cases of drift wave turbulence and MHD fluctuation, respectively. The primary beam is injected from right hand side in Fig. 3.

In all three cases, as correlation length becomes shorter, profile distortions of the measured fluctuation amplitudes from original local fluctuation amplitudes become smaller. The measured fluctuation profiles mostly correspond to the local fluctuation profiles in the cases of l_C = 10mm in upstream of the original peak. In pattern A, the measured fluctuation amplitude in the area of upstream ($r/a < 0.6$) remains finite amplitude ~ 2% in the case of l_C = 600mm due to the path integral effects of the plasma edge fluctuation (10%). The accumulating effect is larger than the screening effect in this area; $S_C/A_C < 1$. On the other hand, in pattern C, the peak of measured fluctuation amplitude reduces and shifts to upstream as l_C becomes large. The reduction of the measured fluctuation amplitude is calculated less than half of the original local fluctuation amplitude in the case of l_C = 600mm, and represents that the screening effect is larger than accumulating effect; $S_C/A_C > 1$. An amount of the local maximum shift is $r/a = 0.1$ in the case of l_C = 600mm. The shift arises as a result of which the accumulating effect along primary beam orbit is larger than that along the secondary beam orbit. In pattern B, a upstream peak of the measured fluctuation is reduced and shifts as the same as pattern A. An apparent peak, which can be larger amplitude than the original peak, can appear near the center. This is generated as the result of the screening effects around two original peaks and the accumulating effect originated from upstream peak of the local fluctuation. The qualitative property of the measured fluctuation profiles is the same as HIBP system considered only electron impact ionization [1], this is because model equations, Eq. (4) and (5), are the same formulae. However, the path integral effect considered electron and proton ionization can be twice larger than that considered only electron ionization in these case.

The dependence of measured fluctuation amplitude on density profile is simulated. Hollow and parabolic density profile are supposed for center heating of ECRH and NBI plasma, respectively. Here, Eq. (8) is instead of

$$n_e(\rho) = n_{e,0}\left(1+\rho^4\right)^2\left(1-A_{n_e}\rho^2\right). \qquad (10)$$

where A_{n_e} is hollow factor. Hollow depth becomes deep as hollow factor increases (Fig. 2). Figure 4 shows amplitude profiles of the measured fluctuations calculated for several hollow factors; $A_{n_e} = -1.5, 0, 2, 5$ and 10. The correlation length is assumed 300mm and other parameters are the same as Fig. 3 except density profiles. If density is calculated negative, density replaces sufficiently small positive value.

The measured fluctuation profiles change as density profile, even though in the same line average density (Fig. 4). In pattern A, contaminations of the measured fluctuation amplitudes in center region due to edge fluctuation amplitudes become large as the hollow factor increases. This is because the density around local fluctuation peak is relatively higher, then the path integral effect become large. For the same reason, in pattern C, distortions of measured fluctuation profiles become small as hollow factor increases. In pattern B, the distortion is medium between pattern A and C, and variation of the distortion is small for hollow factor. In the three case, although the amounts of the distortions are different, a tendency of distortion of measured fluctuation profile is the same as the simulation of Fig. 3.

4 Discussion

In a case of low frequency range fluctuation, like MHD fluctuation, net electron fluctuation is the same phase as proton fluctuation. However, in the case of higher frequency range fluctuation or the plasma including impurities, the net electron fluctuation cannot be the same phase as proton fluctuation.

We consider the two cases that net electron fluctuations are in-phase and anti-phase to ion fluctuations, as a extreme case. Assuming infinitesimal correlation in a homogeneous plasma, $\gamma(x,y) = \delta(x,y)$ and $dx_i dy_i = \delta(x_i - y_i)dx_i dy_i$. In the case of the net electron and proton fluctuation are in-phase, the ensemble averaged Eq. (4) is deformed, $\overline{\eta}^2 = \overline{\xi}^2\left[\overline{T}_0 - \overline{S}_C + \overline{A}_C\right]$, where $\overline{T}_0 = 1$, $\overline{S}_C = 2\sqrt{2\pi}\overline{l}_C\overline{n}_e\sum_{i=1,2}\left\{S'^i_{ei} + S'^i_{Loss}\right\}$ and $\overline{A}_C = \sqrt{2\pi}\overline{l}_C\overline{n}_e^2\sum_{i=1,2}\left\{(S'^i_{ei})^2 + (S'^i_{Loss})^2\right\}\hat{L}_i$. Overline expresses constant in the homogeneous plasma. The terms $\hat{L}_1$ and $\hat{L}_2$ are normalized lengths of primary and secondary beam, respectively. A path integral coefficient $\overline{\Phi}$ is defined as $\overline{\Phi} \equiv (\overline{S}_C + \overline{A}_C)/\overline{T}_0$, and furthermore, a distortion coefficient $\overline{D}_{ist}$ is defined as $\overline{D}_{ist} \equiv (-\overline{S}_C + \overline{A}_C)/\overline{T}_0$. The distortion ratio indicates the measured fluctuation distorts the local fluctuation. In the case of anti-phase on the same assumptions, the ensemble averaged Eq. (4) is deformed, $\overline{\eta}^2 = \overline{\xi}^2\left[\overline{T'}_0 - \overline{S'}_C + \overline{A'}_C\right]$, where $\overline{T'}_0 = \left(S^{12}_{ei}/S^{12}\right)^2 + \left(S^{12}_{Loss}/S^{12}\right)^2$, $\overline{S'}_C = 2\sqrt{2\pi}\overline{l}_C\overline{n}_e\sum_{i=1,2}\left\{(S'^i_{ei})^2 + (S'^i_{Loss})^2\right\}/S^{12}$ and $\overline{A'}_C = \sqrt{2\pi}\overline{l}_C\overline{n}_e^2\sum_{i=1,2}\left\{(S'^i_{ei})^2 + (S'^i_{Loss})^2\right\}\hat{L}_i$. A path integral coefficient in the case of anti-phase $\overline{\Phi'}$ is defined as $\overline{\Phi'} \equiv (\overline{S'}_C + \overline{A'}_C)/\overline{T'}_0$.

Figure 5 (a) shows D_{ist} with $\hat{L}_1 = \hat{L}_2 = 1$ and $l_C = 120$mm. The distortion coefficient $D_{ist} = 0$ means that the measured fluctuation amplitude can be the same as the local fluctuation amplitude, as a result of the screening and accumulating effects. Positive or negative D_{ist} represent that the measured fluctuation amplitude can increase or decrease from the local fluctuation amplitude. In the case of $n_e = 1\times10^{19}\mathrm{m}^{-3}$ and $T_e = 2$keV, the distortion ratio is negative ($D_{ist} = -0.8$), which is consistent with the measured fluctuation amplitude reduced at center in the case Fig. 3 (c). The ratio $\overline{\Phi'}/\overline{\Phi}$ shown in Fig. 5 (b) increases as the density increase, and is 0.2 at $n_e = 1\times10^{19}\mathrm{m}^{-3}$ and $T_e = 2$keV. This means that the path integral effect in the case of the anti-phase is 20 % of that in the case of in-phase. Hence, the case of anti-phase is more local measurement than that of in-phase.

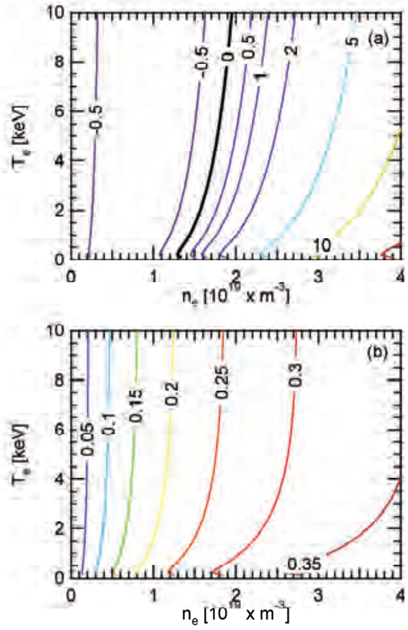

Fig. 5 (a) Contours of the distortion coefficient $\overline{D}_{ist}$ with l_C = 120mm and (b) the ratio of the path integral coefficients $\overline{\Phi'}/\overline{\Phi}$

5 Summary

The path integral effect on the density fluctuation measurement by use of MeV-range HIBP system is estimated. When net electron and proton fluctuations are in in-phase, the equation of the measured fluctuation is the same formula as a few keV-range HIBP system. And, the path integral effect of MeV-range HIBP system is much larger due to the proton ionization. If the net electron and proton fluctuations are in anti-phase, the fluctuation can be measure more locally.

[1] A. Fujisawa, H. Iguchi, S. Lee, and Y. Hamada, Rev. Sci. Instrum. **68**, 3393 (1997).

[2] A. Shimizu, A. Fujisawa, S. Ohshima, and H. Nakano, Rev. Sci. Instrum. **76**, 043504 (2005).

[3] H. Nakano, *et al.* Rev. Sci. Instrum. **78**, 063502 (2007).

[4] T. Ido, *et al*, Rev. Sci. Instrum. **77**, 10F523 (2006).

[5] M. Nishiura, *et al.* J. Plasma Fusion Research (2007) *in press*.

Proceedings of ITC/ISHW2007

Beam-plasma interaction in high temperature plasmas for a heavy ion beam probe diagnostics

M. Nishiura, T. Ido, A. Shimizu, V. P. Shevelko[a], R. K. Janev[b], T. Kato, S. Kato, H. Nakano, Y. Hamada, and LHD Experimental Group

National Institute for Fusion Science, National Institutes of Natural Sciences, 322-6 Oroshi, Toki, Gifu, 509-5292 Japan

[a] P.N.Lebedev Physical Institute, Leninskii prospect 53,119991 Moscow, Russia

[b] Macedonian Academy of Sciences and Arts, P.O.Box 428, 1000 Skopje, Macedonia

Heavy ion-beam probe (HIBP) is a powerful diagnostics tool to measure plasma potential and density fluctuation at a local position. These parameters are important to study the plasma transport and improvement of plasma confinements. It is essential to increase the signal-to-noise ratio of detected signals at an energy analyzer for recent high density operations at the Large Helical device (LHD). For this purpose, possible options are considered to increase the current density of heavy ion beams, as well as the optimization of the beam transport line and the improvement of beam detection efficiency.

The gold negative ion source in LHD-HIBP has made progress in Au^- beam current up to ~ 20 μA, and is being developed currently. Au^- beam is accelerated and is converted to Au^+ beam with the energy of ~ 6 MeV in the tandem accelerator. The MeV Au^+ beam is injected into plasmas. The Au^{2+} beam ionized in plasmas is detected by the energy analyzer.

Our curiosity is the possible diagnostics range under high density of ~ 10^{20} m^{-3} and high temperature plasmas of ~ a few ten keV in the LHD-HIBP system. In the previous paper [1], we pointed out the importance of electron loss processes, the electron- beam ion collision ionization and the proton-beam ion collision ionization in high temperature plasmas.

As a next step, the density and temperature profile is taken into account in the beam-attenuation calculations with the influence of atomic and molecular collision processes on the beam trajectories. These calculations are compared with experimental data. Moreover, the primary beam monitor on the first wall surface of LHD, which detects the injected Au^+ beams, is improved. The design of the primary beam monitor will be presented.

[1] M. Nishiura et al., J. Plasma and Fusion Res. (2007) in Press.

Proceedings of ITC/ISHW2007

The development of potential measurements with 6 MeV Heavy Ion Beam Probe on LHD

A. Shimizu, T. Ido, M. Nishiura, H. Nakano, S. Ohshima, I. Yamada, K. Narihara, T. Akiyama, T. Tokuzawa, K. Tanaka, K. Kawahata, H. Igama, Y. Yoshimura, T. Shimozuma, S. Kubo, K. Nagaoka, K. Ikeda, M. Osakabe, K. Tsumori, Y. Takeiri, O. Kaneko, S. Morita, M. Goto, M. Yokoyama, S. Kato, M. Yokota, K. Tsukada, H. Ogawa, T. Inoue, A. Nishizawa[1)], Y. Hamada and LHD Group

National Institute for Fusion Science, Oroshi-cho, Toki, Gifu,509-5292, Japan

1)Tono Geoscience Center, Japan Atomic Energy Agency, Izumi-cho, Toki, Gifu,509-5102, Japan

(15th Oct. 2007)

In order to measure the potential in Large Helical Device (LHD), 6 MeV heavy ion beam probe (HIBP) has been developed. The temporal evolvements of potential in the central region of plasmas, which were produced by neutral beam injection (NBI) and additionally heated by electron cyclotron heating (ECH), were measured with our HIBP system. The line averaged density of these shots were about $1 \sim 5 \times 10^{18}$ m^{-3}. At the time of ECH was applied, a rapid change of potential to positive direction was observed. In this ECH phase, negative pulses were observed in the potential signal, which were very similar to "pulsation" that was firstly found in Compact Helical System (CHS), however, the time constant of these pulses were larger than in the case of CHS. In the NBI phase, the fluctuation was observed with HIBP, of which frequency was correlated with potential of equilibrium. It is considered that this frequency was influenced by $E \times B$ drift.

Keywords: Heavy Ion Beam Probe, Large Helical Device, helical system, plasma potential, electric field, Internal Transport Barrier

1. Inroduction

In helical magnetic configurations, fluxes are not intrinsically ambipolar and the radial electric field is produced [1, 2]. In the neoclassical theory, the constraint that the ion and electron fluxes be equal determines the radial electric field. The theory gives two roots, so called "ion root" and "electron root". By the strong core heating by ECH, the internal transport barrier (ITB) / the core electron-root confinement (CERC) [3], which is an improved confinement mode, has been realized in various helical devices [4-7]. The study of radial electric field and transport of ITB has been continued in these machines. In order to investigate the physics of ITB in detail, we have been developing heavy ion beam probe (HIBP) system in large helical device (LHD) [8, 9].

By using HIBP, the potential in the inside of high temperature plasma can be measured with good spatial and temporal resolutions, without any disturbances to plasma. Moreover, density fluctuation can be measured simultaneously with potential fluctuation. Therefore flux caused by electrostatic fluctuation can be estimated experimentally. In this article, we will report the present status of HIBP system and recent results of potential measurements in LHD.

2. Heavy Ion Beam Probe System in LHD

Heavy ion beam probe diagnostics is based on the energy conservation low. A beam of single charged heavy ion is injected to plasma and the beam of doubly charged ion arises by the collision with plasma. The energy of the beam of doubly charged ion coming from plasma is measured in the outside. The change of energy between singly charged ion and doubly charged ion corresponds to potential at the ionized point. In order to inject heavy ion beam to the center of LHD plasma, the acceleration energy of 6 MeV is needed for the probing beam of Au^+ when toroidal magnetic field strength is 3 T. In our HIBP system, to reduce the required voltage of accelerator, we use a tandem accelerator and decrease the required voltage to be half (3 MV). In order to use tandem accelerator, negative gold ions (Au^-) are needed. Au^- ions are produced by an ion source of sputtering type. Detail of our negative ion source system is shown in Ref. [10]. The Au^- extracted from this ion source is pre-accelerated up to 50 keV. It is injected to tandem accelerator and accelerated by the voltage of 3 MV. In

author's e-mail: akihiro@nifs.ac.jp

the gas cell located at the center of the accelerator, Au^- ion is stripped two electrons, and changed to positive gold ion (Au^+). Au^+ is re-accelerated by the voltage of 3 MV, so the 6 MeV Au^+ beam is obtained. This beam is guided to plasma through several components: a charge separator, the 4.8 m cylindrical deflector, the 7.8 degree deflector. At the incident port, the beam incident angle can be changed by octapole deflector, by which the observation point is controlled. Injected Au^+ is stripped an electron by the collision with plasma, and Au^{2+} beam is produced. Here, we call the former the primary beam, and the latter the secondary beam. At the exit port of chamber, the ejection angle of the secondary beam is controlled by another octapole deflector to direct the beam to the energy analyzer. We have 3 slit holes at the entrance of this analyzer, so the potential of neighboring 3 points in plasma can be measured. For the energy analyzer, we apply the tandem energy analyzer [11] to suppress the required voltage and costs. For detecting beam, high gain detector, micro channel plates (MCPs) are used, by which a very small amount of secondary beam current, order of a few pA, can be detected. Detail of our HIBP system is shown in Ref. [8,9].

3. Potential measurements of internal transport barrier

As described above, strong core heating with electron cyclotron heating (ECH) produces an improved confinement region, ITB, which is related to an electron root. Temporal evolution of density and heating, when ITB was observed in LHD, are shown in Fig. 1 (a). The plasma was produced by neutral beam injection (NBI) heating, and ECH was applied at the time of 1 sec. In the figure, two shots which had different density are shown. The configuration of LHD is characterized by the strength of toroidal magnetic field, B_t, the major radius of magnetic axis, R_{ax}, the pitch parameter γ, and the quadrupole magnetic field B_q. In this experiment, these parameters were as follows: B_t = 1.5 T, R_{ax} = 3.6 m, γ = 1.254, B_q = 100 %. The acceleration energy of beam was 1.5 MeV. Temporal evolutions of potential at the center of plasma measured with HIBP are shown in Fig. 1 (b). At the beginning of discharge, the potential was negative. When the additional ECH was applied, the abrupt increase of potential was observed. It is considered that this positive potential was generated by the creation of ITB in the central region. Temperature profiles with Thomson scattering diagnostics before and during ECH are shown in Fig. 1 (c), low density case, and (d), high density case. High temperature region in the core was due to the creation of ITB. The increase of temperature in the low density case was larger than in the high density case. The ratio of temperature increase between high density case and low density case coincides with the ratio of potential increase between these two cases.

4. Fast temporal change of potential

When the ITB appears and multiple states of electron and ion root are allowed, the bifurcation phenomenon can be seen and the fast change of potential is observed. When plasma parameters satisfied some condition, the negative pulses were observed in the potential. In Fig. 2, the observed signal measured with HIBP is shown. This signal is very similar to the pulsation which was firstly found in Compact Helical System (CHS) [12]. The pulse was repeated about a few ms. The typical time constant of the pulse was 90 μs at the potential drop phase and 500 μs at the returning phase as shown in Fig 3. These are

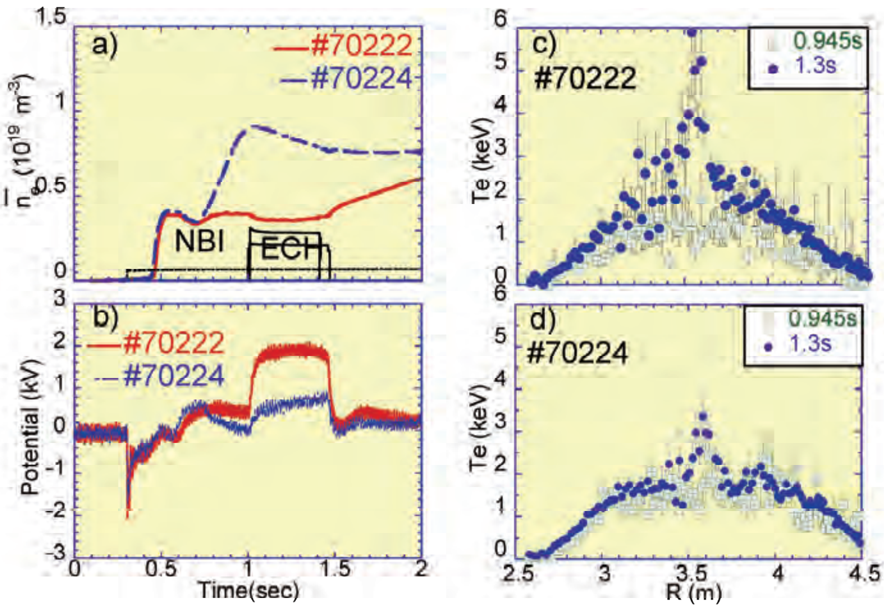

Fig.1 (a) Temporal evolutions of line averaged density and heating. (b) Temporal evolutions of potential measured with HIBP. (c) Temperature profiles of low density case (#70222), and (d), high density case (#70224).

larger than in CHS. This time constant is determined by the neoclassical theory, we will compare this experimental result with the theoretical prediction in a future.

The plasma parameters, in which the ITB and negative pulses were observed, are compared with the neoclassical theory as shown in Fig. 4. In the theoretical estimation, the electron and ion temperature profiles are assumed as $T_{i,e}(0)$ ($1 - \rho^2$). And density profile is assumed as $n_e(0)$ ($1 - \rho^8$). Here, ρ is a normalized minor radius. From the neoclassical theoretical prediction, T_i - T_e space is separated to three regions, in which ion root, electron root and multiple roots are expected. In the figure, boundary lines of these domains are shown. Points show the experimental data, when negative pulses were observed with ITB, no negative pulses with ITB, and no ITB was observed (NBI phase、L-mode). In NBI phase, the parameters exist in the ion root region. The pulses were observed in the region of the multiple roots. As shown in Ref. [12], the pulses are considered to occur in the region of multiple roots, so the experimental results in LHD are consistent with the neoclassical theory.

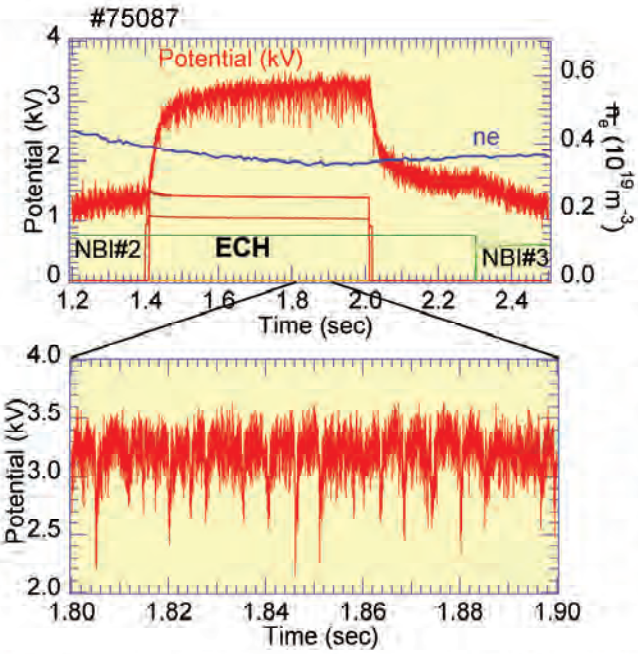

Fig.2 Negative pulses were observed in potential signal measured with HIBP.

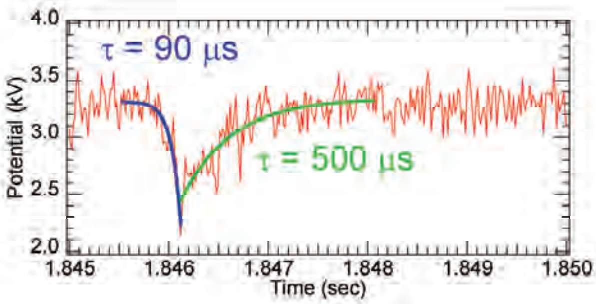

Fig.3 .Time constant of potential change is shown.

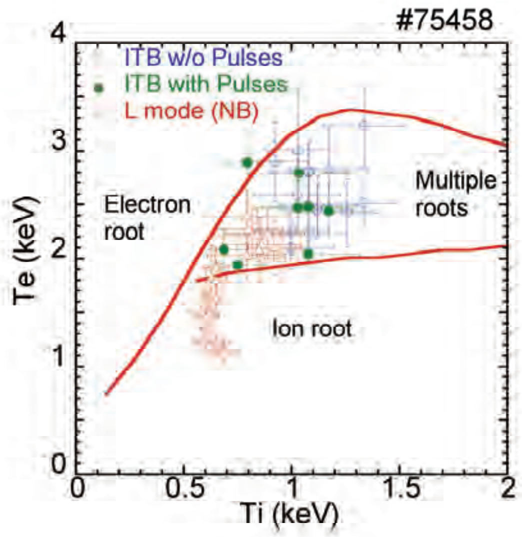

Fig.4 Electron temperature T_e and ion temperature T_i are compared with the neoclassical theory. Boundary lines separate T_i - T_e space to three domains, electron root, ion root, and multiple roots. Negative pulses in potential were observed in the region of multiple roots.

4. Fluctuation measurements with HIBP

HIBP has a good temporal/spatial resolution in the measurements, so if large S/N ratio is realized, the physics related to various fluctuations, such as MHD instability and micro instability, can be studied with this tool. With HIBP, the measured fluctuation of potential is local one, so interpretation is easy. However the density fluctuation measured with HIBP includes an effect of fluctuation on the beam path as well as at the observed point, due to so called "path integral effect". This effect in LHD is considered in Ref [13] in detail, so we do not discuss about it here.

In Fig. 5 (a), the temporal evolution of potential fluctuation spectrum measured with HIBP in LHD is shown. The vertical axis shows frequency and the color in the image shows power density of potential fluctuation. The fluctuation, of which frequency was changed temporally, can be seen in this figure. In Fig. 5 (b), the wave forms of line averaged density and heating are shown. The frequency of fluctuation has a weak correlation with density, however it is not clear. The frequency correlates more strongly with potential rather than density. In Fig. 5 (c), the temporal evolution of frequency, at which the fluctuation power density has maximum, is shown. The measured potential in the central region of plasma is also shown. The temporal changes of these signals are very similar except the slight time delay in the change of frequency at 0.75 sec. It seems that the rotation of $E \times B$ drift makes an effect on the frequency of fluctuation. The slight difference seen in Fig. 5 (c) may occur from the difference between the potential and electric field. In order to make clearer this effect, we need to measure a radial electric field, namely radial profile of potential. However, the profile could not obtain with a reliable accuracy because of the problem of diagnostics. The temporal character of current amplifier was also slow in this experiment. The improvement of the amplifier and the improved measurements of profile will be done in a near future.

5. Summary

In LHD, heavy ion beam probe system has been continued to develop. The temporal evolution of potential, when ITB was created by ECH, was measured with our system. The rapid increase of potential was observed in ECH phase. The fast negative pulses were observed in potential signal in ECH phase. It was very similar to pulsation, which was firstly found in CHS. The plasma parameter region, in which these pulses were observed, coincides with the region where multiple roots are predicted from the neoclassical theory. The fluctuation of potential, of which frequency changed temporally, was observed. This frequency was considered to correlate with $E \times B$ flow.

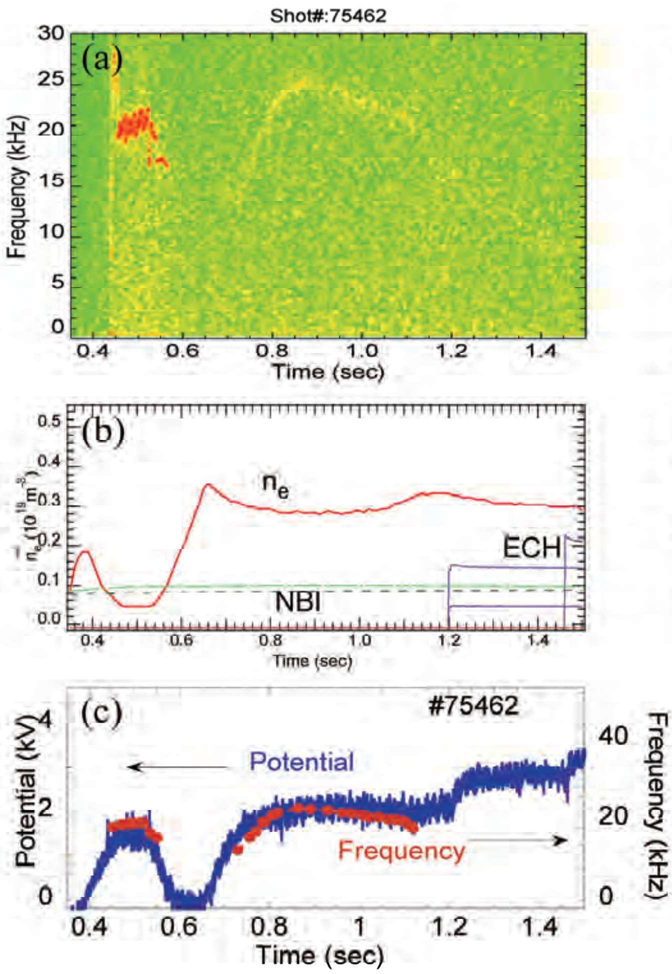

Fig.5 (a) Temporal evolution of spectrum of potential fluctuation measured with HIBP. (b) Line averaged density and heating. (c) Temporal evolution of potential and frequency where fluctuation power density has maximum.

Acknowledgements

This work was supported by NIFS under contract No. NIFS07ULBB505, 514, 515. The authors with to thank scientific and technical staff of LHD and CHS.

References

[1] L. M. Kovrizhnykh, Nuclear Fusion **24**, 851 (1984).
[2] D. E. Hastings, W. A. Houlberg, K. C. Shaing, Nuclear Fusion **25**, 445 (1985).
[3] M. Yokoyama, H. Maasberg, K. Ida, C. D. Beidler, *et al.*, "Core Electron-Root Confinement (CERC) in Helical Plasmas", IAEA, 2006.
[4] Maasberg *et al.*, Phys. Plasmas 7, 295 (2000).
[5] T. Shimozuma, S. Kubo, H. Idei, *et al.*, Nuclear Fusion **45**, 1396 (2005).
[6] T. Estrada, A. Lonso, *et al.*, Plasma Phys. Control. Fusion **47**, L57 (2005).
[7] A. Fujisawa, *et al.*, Phys. Plasmas 7, 4152 (2000).
[8] T. Ido, *et al.*, Rev. Sci. Instruments **77**, 10F523 (2006).
[9] A. Shimizu, *et al.*, Plasma Fusion Res. SERIES to be published (2007).
[10] M. Nishiura, T. Ido, A. Shimizu, *et al.*, "Beam plasma interaction in high temperature plasmas for a heavy ion beam probe diagnostics" in this conference.
[11] Y. Hamada, *et al.*, Rev. Sci. Instruments **68**, 2020 (1997).
[12] A. Fujisawa, *et al.*, Phys. Rev. Lett. **81**, 2256 (1998).
[13] H. Nakano, T. Ido, A. Shimizu, M. Nishiura, *et al.*, "Consideration of density fluctuation measurement using Heavy Ion Beam Probe on Large Helical Device" in this conference.

Proceedings of ITC/ISHW2007

Search for very-high-β MHD stable quasi-isodynamic configurations

V.R. Bovshuk[1)], W.A. Cooper[3)], M.I. Mikhailov[1)], J. Nührenberg[2)], and V.D. Shafranov[1)]

[1)]*NFI, Kurchatov Institute, Russia*
[2)]*IPP, EURATOM Association, Germany*
[3)]*CRPP, EURATOM Association, EPFL, Switzerland*

(Received October 12, 2007/ Accepted ?)

Quasi-isodynamic configurations offer the possibility of very good energetic particle confinement. They seem to offer the possibility of achieving very high plasma β, too.

Keywords: Plasma and Fusion Research, Stellarators, Quasi-isodynamicity, MHD stability, Very high plasma β

1 Introduction

Quasi-isodynamic [1] (*qi*) configurations have been previously found by computational optimization with high stability β limit, good neoclassical confinement properties and excellent fast particle collisionless confinement for configurations with poloidally closed contours of the strength of the magnetic field B [2,3]. It was shown analytically [3] that the secondary parallel current density in *qi* configurations remains contained within each plasma field period, namely, between the cross-sections with maximal magnetic field strength B. In the *qi* configurations considered earlier, the divergence of the current density perpendicular to the magnetic field lines changes sign only once along the magnetic field within one field period. From this it follows that the parallel current density cannot change sign along the magnetic field within one period. Thus, because of the vanishing net parallel current, the parallel current density exhibits a dipole component which impairs MHD stability at very high β in the *qi* situation considered here for configurations with shallow magnetic well in the associated vacuum magnetic field. The search for possible ways to diminish this current density in quasi-isodynamic configurations was the subject of [4].

For this search a two-staged approach had been taken. In a model investigation it was clarified that quasi-isodynamicity is compatible with vanishing dipole current density in a more elaborate structure of the topography of B exploiting the possibility of detailed toroidal design of B in 3d configurations; then a configurational investigation established a geometry realizing the essential features of this model and is seen in Fig. 1, Fig. 3 (left) and Fig. 4 (left).

In this work it is investigated whether MHD-stable equilibria of this type of configuration exist.

2 Current result at $\langle\beta\rangle \approx 0.2$

The configuration of Figs. 1 and 4 (left) had been obtained at zero β. It exhibits a significant magnetic hill so that one of the essential ingredients of its optimization towards high β has been the transition to a vacuum field magnetic well as a prerequisit for MHD stability. As seen from Fig. 1, the starting point of the optimization is characterized by a roughly hexagonal plasma shape, i.e. by as little curvature as compatible with the straight sections encompassing the maxima of B. Since a magnetic well necessitates plasma curvature and higher order poloidal shaping (triangularity, indentation, ...), it is plausible that the local plasma column curvature had to increase. This is seen in Fig. 2, but most clearly in Fig. 9 (while not prominent in Fig. 10). The subsequent achievement of high β is accompanied by two characteristic features. As in the initial condition, the Fourier components (in magnetic coordinates) of B and the volume element $\sqrt{g}$ corresponding to axisymmetric curvature are very small, simulating an aspect ratio of several hundred, see Fig. 5. Also, since the strong poloidal as well as toroidal shaping, see Fig. 4 (right), drives higher order Fourier components of $\sqrt{g}$, the optimization needed to exploit (and strictly observe) a window in rotational transform value, here chosen to be $\frac{6}{7} < \iota < \frac{6}{6}$. While introducing curvature is necessary for stability, see Fig. 6, ballooning instability will limit it. Preliminary evaluation of ballooning instability considering the local ballooning equation for symmetric ballooning at the four symmetry points of the field period and flux surface label $s \approx 0.3$ shows the abscence of strong-ballooning instability, see Fig. 7. This analysis needs to be completed following the procedure used in [3], in particular because of the gap in marginal β found there between local and non-local ballooning analysis. Some features observed in earlier stable configurations are prominent in the configuration obtained here, too: the triangular shape of the flux-surface cross-sections at the

author's e-mail: mikhail@nfi.kiae.ru

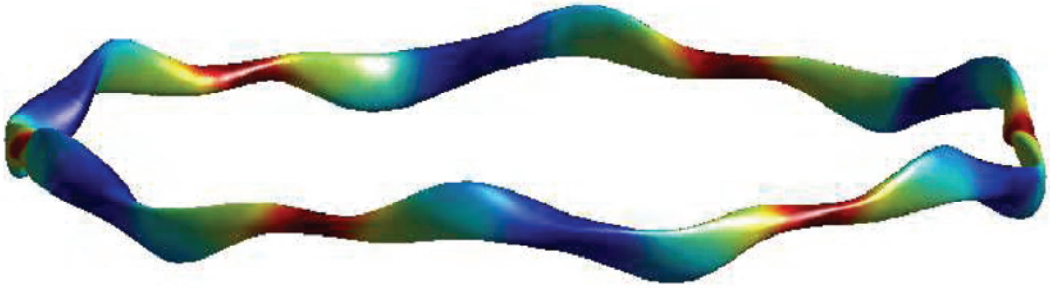

Fig. 1 Boundary magnetic surface showing the magnetic topography of [4].

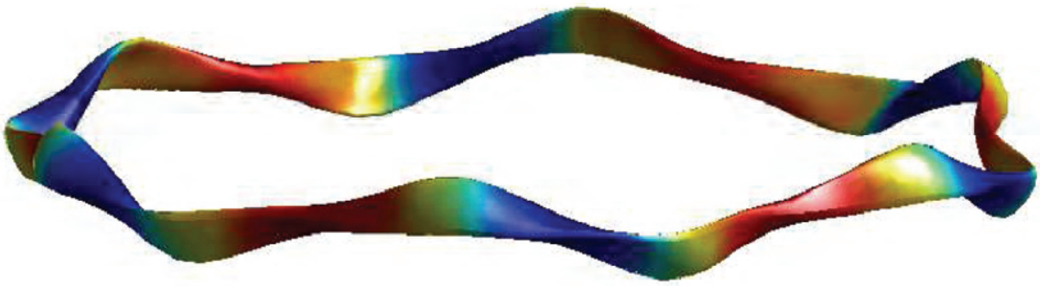

Fig. 2 Boundary magnetic surface showing the magnetic topography of the stable configuration.

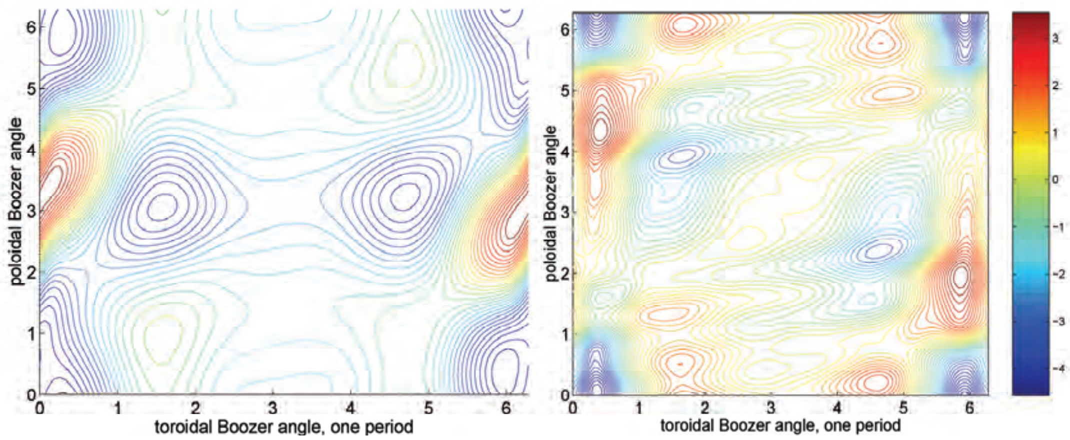

Fig. 3 *Left: the structure of the parallel current density ($j_{\parallel}/B$) of the configuration of Fig. 1 showing $j_{\parallel 1,0} = 0$; Right: the structure of the parallel current density ($j_{\parallel}/B$) of the configuration of Fig. 2.*

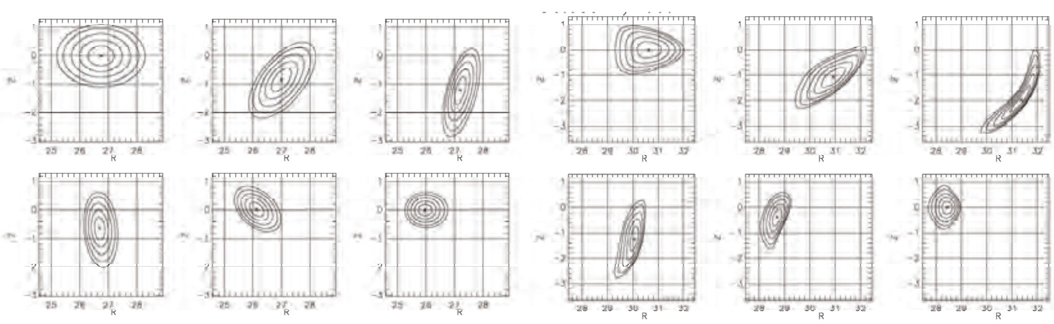

Fig. 4 *Cross sections of magnetic surfaces of the configurations in Figs. 1 and 2 along half a period beginning with the minimum of B and ending at the maximum of B.*

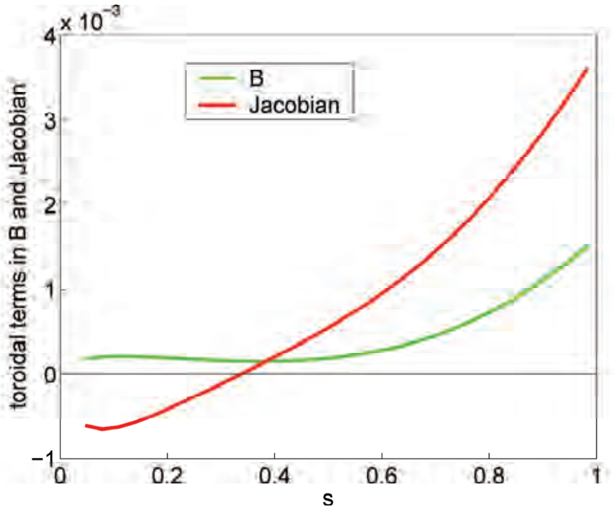

Fig. 5 Fourier coefficients of B and $\sqrt{g}$ in magnetic coordinates corresponding to toroidal curvature.

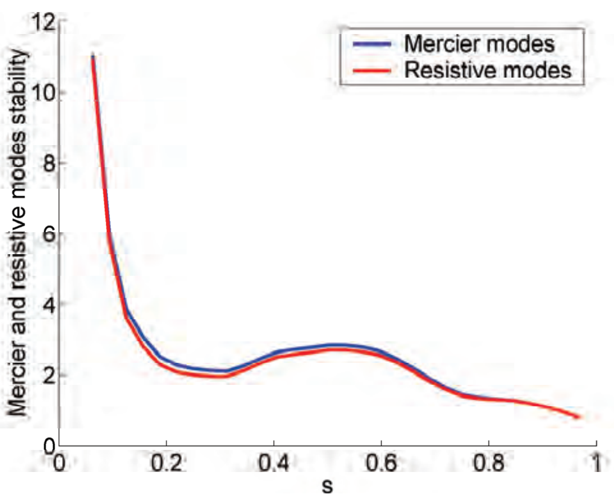

Fig. 6 Mercier and resistive-interchange stability.

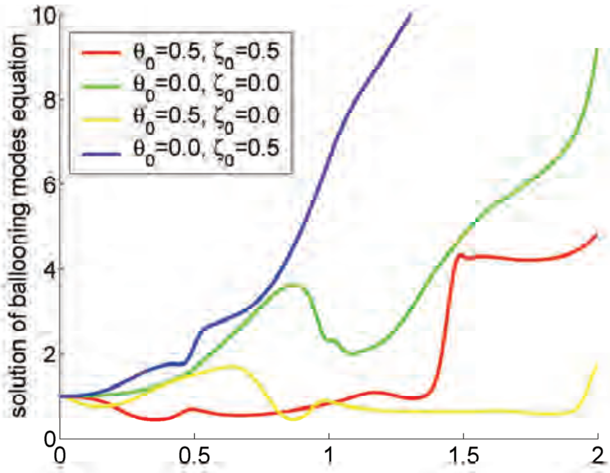

Fig. 7 Solutions of the ballooning equation along fieldlines covering two periods and passing through the four symmetry points on the flux surface at $s = 0.3$.

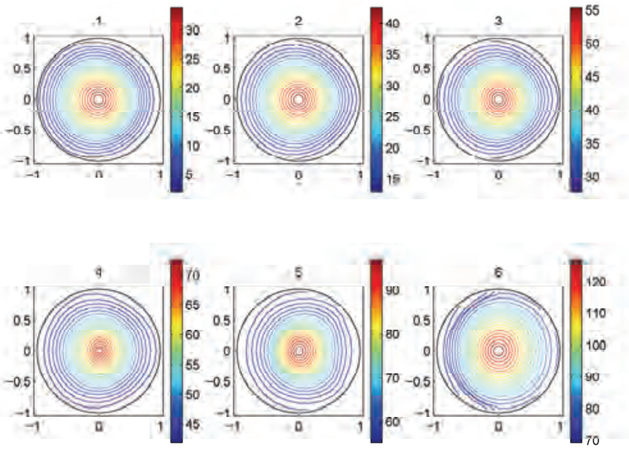

Fig. 8 Structure of $\mathcal{J}$ in the configuration obtained for different values of B, B_{ref}, at which trapped particles are reflected; 1 - near the minimum of B, 6 - near the maximum of B.

minimum of B and indentation in the range of strongest curvature. It remains to be investigated whether the higher-order poloidal and toroidal shaping found, e.g. the quadrangularity at the maximum of B and in Fig. 4 (right), is really necessary to achieve MHD stability.

The neoclassical physics properties have not in detail been part of this high-β optimization; they should be benign in view of the contours of the second adiabatic invariant, see Fig. 8 (right), but their detailed investigation and, eventually, optimization remains to be done in order to complete this case study of a very-high-β configuration.

3 Summary

In the context of quasi-isodynamic stellarators with poloidally closed contours of the magnetic field strength it is investigated whether very-high-β MHD-stable equilibria exist. With a previously introduced new structure of a period as a starting point equilibria are found which are Mercier, resistive-interchange and strong balooning (symmetric) stable at $\langle\beta\rangle \approx 0.2$. Further work will concern further MHD-stability analysis and the details of the neoclassical physics properties of this type of configuration.

4 Acknowledgment

Part of the computations of this work has been performed on the NIFS LHD Numerical Analysis Computer SX-8.

[1] S. Gori, W. Lotz, and J. Nührenberg, *Proc. Joint Varenna-Lausanne Int. Workshop on Theory of Fusion Plasmas* (Bologna: Editrice Compositori, 1996) p. 335.
[2] M.I. Mikhailov et al, Nucl. Fusion **42**, L23 (2002).
[3] A.A. Subbotin et al, Nucl. Fusion **46**, 921 (2006).
[4] V.R. Bovshuk et al, *34th EPS Conf. on Plasma Phys. and Control. Fusion*, P4.103.

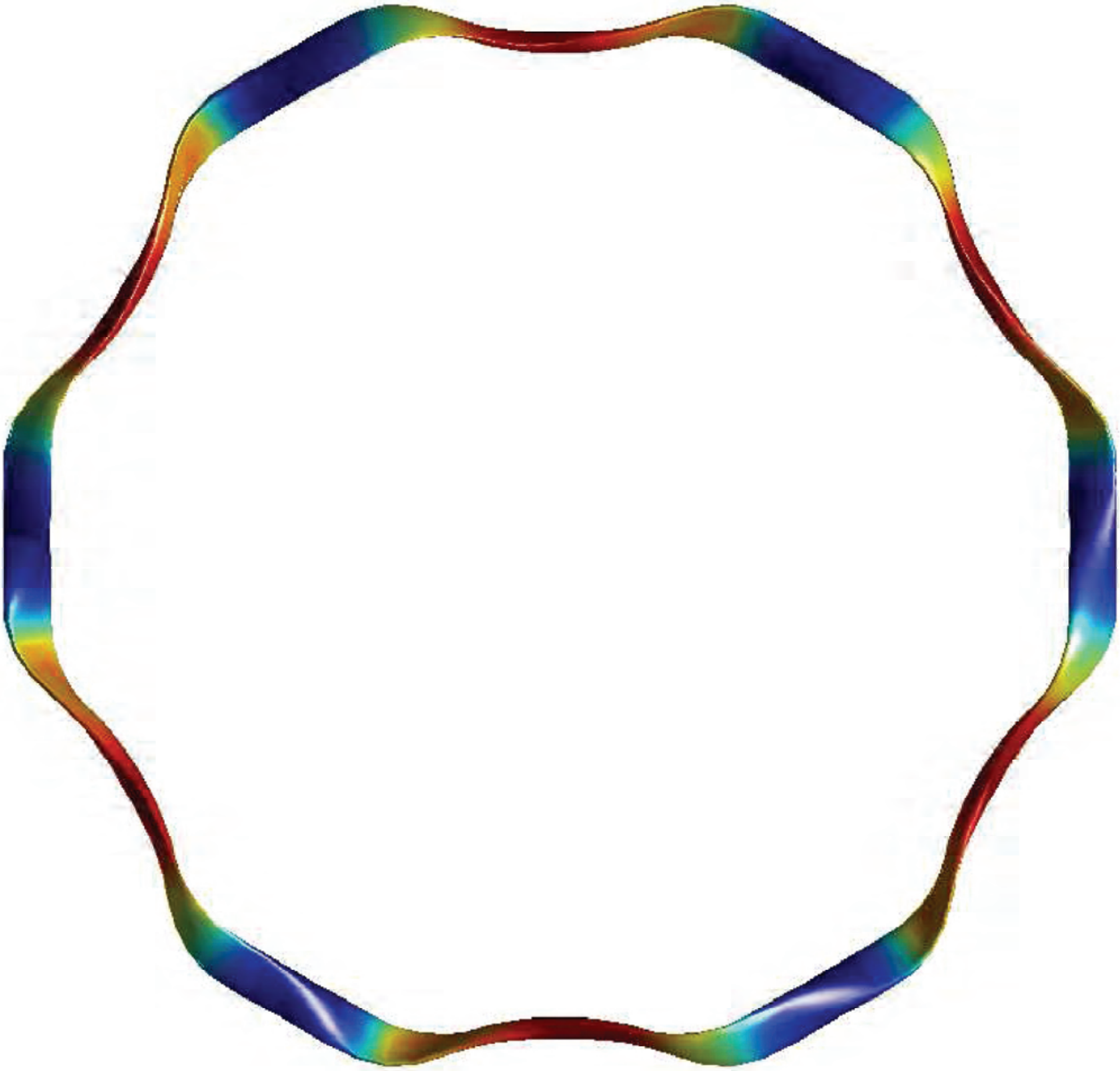

Fig. 9 Top view of the configuration shown in Fig. 2.

Fig. 10 Equatorial view of the configuration shown in Fig. 2.

Proceedings of ITC/ISHW2007

Abrupt flushing of the high-density core in internal diffusion barrier plasmas and its suppression by plasma shape control in LHD

J. Miyazawa, R. Sakamoto, S. Ohdachi, M. Kobayashi, S. Masuzaki, T. Morisaki, S. Sakakibara, M. Goto, S. Morita, I. Yamada, K. Narihara, H. Funaba, K. Tanaka, C. Michael, Y. Suzuki, K.Y. Watanabe, N. Ohyabu, H. Yamada, A. Komori, O. Motojima, and LHD experimental group

National Institute for Fusion Science, 322-6 Oroshi, Toki, Gifu 509-5292, Japan

(Received day month year / Accepted day month year should be centered 10-point type)

A super-dense core of the order of 10^{20} m^{-3} is formed inside the internal diffusion barrier (IDB) during the reheat phase of the central pressure after pellet injection in LHD. Large Shafranov shift of the plasma center is observed in IDB plasmas and it reaches roughly 50 % of the plasma minor radius. In some cases, abrupt flushing of the central density takes place and this event is called as "core density collapse (CDC)". CDC must be suppressed since it inhibits further increase of the central pressure. CDC is always accompanied by large Shafranov shift of the plasma center exceeding a critical position. Theoretically, it is predicted that vertical elongation of the plasma shape ($\kappa > 1$) is effective to mitigate the Shafranov shift and the κ is controllable with the quadrupole magnetic field, B_Q. According to this prediction, B_Q scan experiment has been performed in LHD. Shafranov shift is indeed mitigated by increasing κ. As a result, CDC is suppressed and high central β values reaching ~ 7 % have been achieved in vertically elongated plasmas.

Keywords: heliotron, pellet injection, SDC, Shafranov shift, beta limit, equilibrium, elongation.

1. Introduction

In toroidal plasmas, the vertical component of dipole magnetic field induced by the Pfirsh-Shlüter (PS) current, B_z^{PS}, causes the shift of magnetic axis from R_0 to $R_0 + \Delta$. This is called the Shafranov shift. Since the PS current is proportional to the pressure gradient, Δ is determined by the central plasma beta, β_0 [1]. Large Shafranov shift, reaching a half of the plasma minor radius, a, for example, causes destruction of magnetic surfaces that leads to loss of confinement. From this point of view, it is expected that there will be an equilibrium beta limit at $\Delta \sim 0.5\ a$ [2]. Mitigation of Shafranov shift is therefore an important issue to achieve high β_0.

A discovery of internal diffusion barrier (IDB) plasmas in LHD [3] makes it possible to realize the high central plasma pressure reaching 1.3 atm [4,5]. IDB plasmas are produced by hydrogen ice pellet injection and characterized by a strongly peaked density profile with relatively low density in the edge region, which is called "mantle". The low mantle density enables deeper penetration of heating beams reaching the plasma center. As long as the central heating power is kept constant, the central pressure increases with the density, following the preferable density dependence in the global confinement scalings, such as ISS95 and ISS04 [6]. IDB plasmas are also characterized by large Shafranov shift due to the high β_0. Recently, an unexpected phenomenon has been found in IDB plasmas. This takes place when the Shafranov shift of the plasma center exceeds a critical position. Then, the density in the core region is flushed out to the mantle region within < 1 ms [7], while the temperature profile scarcely changes. We call this event as "core density collapse (CDC)" [4,5]. CDC must be suppressed since it inhibits further increase of the central pressure and the fusion triple product. Since CDC is always accompanied by large Shafranov shift, its mitigation might affect CDC.

At least three methods are effective for Shafranov shift mitigation, *i.e.* 1) plasma position control with a vertical magnetic field that compensates B_z^{PS}, 2) increase of the rotational transform, $\iota\!\!\!- = \iota / (2\pi)$ (note that the PS current and B_z^{PS} is inversely proportional to $\iota\!\!\!-$ and as a result, $\Delta \propto B_z^{PS} / \iota\!\!\!- \propto 1 / \iota\!\!\!-^2$), and 3) vertical elongation of the plasma shape. The first method is straightforward and will be effective only if it is applied with feedback control. Use of a strong vertical field from the beginning of a discharge is not preferable, because the initial magnetic configuration should be strongly inward shifted and MHD instabilities are expected to be unstable in such configurations [8]. Unfortunately, feedback control of the

author's e-mail: miyazawa@LHD.nifs.ac.jp

vertical field is not equipped on LHD, to date, although it is under discussion as a future program (available magnetic field strength is expected to be low). As for the second method, this indeed works as reported in [9]. In LHD, $\iota\!\!\!-$ is controllable by changing the magnetic configuration, and especially, $\iota\!\!\!-$ increases with the aspect ratio of the torus. However, the magnetic field strength available in high aspect ratio configurations is limited to ~ 1 T, for instance. Therefore, the third method of vertical elongation is the only possible solution applicable at the maximum magnetic field strength of ~ 3 T.

In this study, experimental results of the elongation scan and its impact on CDC are reported.

2. Plasma shape control by the quadrupole field

In toroidal plasmas, the PS current is induced to cancel the charge separation due to the variation in the magnetic field strength, ΔB, on flux surfaces, which is proportional to $1/R$. Therefore, vertical elongation, which reduces the characteristic length of the torus in the major radius direction, ΔR, is also effective to reduce the $\Delta B \propto \Delta R$ and thus the PS current. The magnetic surfaces in heliotron plasmas with l = 2 as in LHD can be approximated by rotating ellipse, *i.e.* a horizontally elongated ellipse and a vertically elongated ellipse appear alternately as the toroidal angle changes. The plasma elongation, κ, is defined as a toroidally averaged ratio of the minor radius in the vertical direction to that in the major radius direction of the last closed flux surface (LCFS). In LHD, we measure two kinds of line-density, $nL_{\rm FIR}$ and $nL_{\rm MMW}$, passing through the "major axes" of vertically and horizontally elongated ellipses, by a far-infrared (FIR) interferometer and a millimeter wave (MMW) interferometer, respectively. Here, we define an effective elongation $\kappa_{\rm eff} \equiv nL_{\rm FIR} / nL_{\rm MMW}$. Note that these line densities include the information outside the LCFS (called ergodic region), and therefore $\kappa_{\rm eff}$ is merely an approximation of κ.

Both in helical plasmas and tokamaks, κ is controlled by the quadrupole magnetic field, $B_{\rm Q}$. In the standard configurations of LHD, the quadrupole component generated by two helical coils is 100 % cancelled by the quadrupole field generated by poloidal coils and therefore κ = 1. Hereinafter, the $B_{\rm Q}$ that results in κ = 1 is called "$B_{\rm Q}$ = 100 %". When $B_{\rm Q}$ is decreased to < 100 %, the κ becomes larger than 1, *i.e.* the plasma is vertically elongated. The relation between $B_{\rm Q}$ and experimentally measured $\kappa_{\rm eff}$ in low beta plasmas at $R_{\rm ax}$ = 3.75 and 3.85 m is shown in Fig. 1. The elongation of the LCFS estimated from the vacuum magnetic data for $R_{\rm ax}$ = 3.60 m is also shown in Fig. 1 (the point at $B_{\rm Q}$ = 150 % is measured). Even though $\kappa_{\rm eff}$ includes the information of the ergodic region, it well approximates the elongation of LCFS.

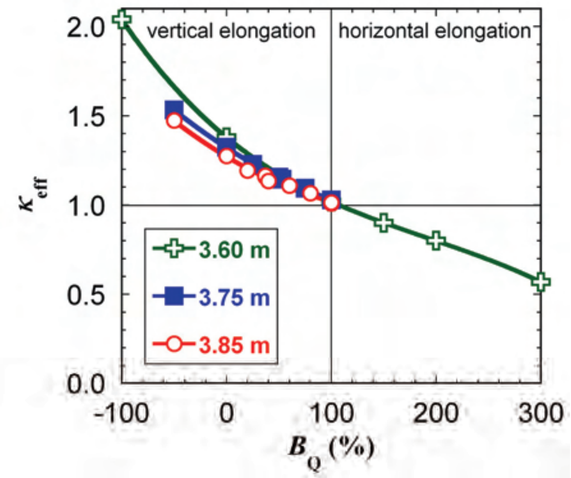

Fig. 1 Relation between the quadrupole magnetic field, $B_{\rm Q}$, and the effective plasma elongation, $\kappa_{\rm eff}$, in low beta plasmas of $R_{\rm ax}$ = 3.75 m (filled squares) and 3.85 m (circles). The LCFS elongation estimated from the vacuum magnetic data for $R_{\rm ax}$ = 3.60 m, except the point at $B_{\rm Q}$ = 150 % that is measured $\kappa_{\rm eff}$, is also shown (white crosses).

3. Core density collapse event

A super-dense core of the order of 10^{20} m^{-3} is formed inside the IDB during the reheat phase of the central pressure after pellet injection in LHD [3, 4]. Waveforms in a typical IDB discharge are shown in Fig. 2. Large Shafranov shift of the plasma center measured on a horizontally elongated slice, $R_0^{\rm h}$, is observed during the reheat phase (t = 0.95 – 1.12 s) and it reaches roughly 50 % of the plasma minor radius. In some cases, abrupt flushing of the central density is observed (t ~ 1.13 s in Fig. 2). This is what we call CDC. The CDC event finishes within < 1 ms, according to the fast soft X-ray measurement (not shown) [7]. At CDC, the Shafranov shift $R_0 + \Delta$ exceeds ~ 4.1 m on a horizontally elongated slice (this value is insensitive to the magnetic configuration, at least for R_0 = 3.75 – 3.90 m).

Radial profiles of the plasma pressure (beta) before and after CDC are shown in Fig. 2, which are taken from the same discharge shown in Fig. 1. The plasma center shifts outward (from left to right in Fig. 1), as the central beta increases from ~ 4.5 % (t = 1.0 s) to ~ 5.5 % (t = 1.1 s). At the same time, the inboard side plasma edge also shifts outward (see also $R_{90}^{\rm in}$ in Fig. 1 (c), which denote the inboard side radial position of $\beta = 0.1\ \beta_0$). Just after CDC (t = 1.134 s), both the plasma center and the inboard side edge moves inward, and the pressure profile changes from strongly peaked to approximately parabolic. It should be noted that the temperature profile is hardly affected by CDC. This is the reason why we call this

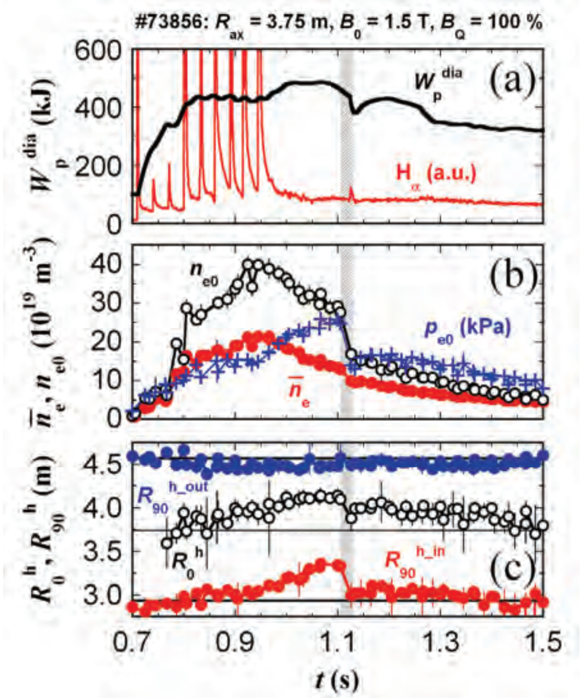

Fig. 2 Typical waveforms in an IDB discharge, where (a) the diamagnetic stored energy, W_p^{dia}, and the H_α intensity, (b) the central electron density, n_{e0}, the central electron pressure, p_{e0}, and the line-averaged electron density, (c) positions of the plasma center, R_0^h, and the inboard (outboard) side plasma edge, $R_{90}^{h\_in}$ ($R_{90}^{h\_out}$), where $\beta = 0.1\ \beta_0$, on a horizontally elongated slice, are shown from top to bottom. CDC takes place at t ~ 1.13 s (shaded).

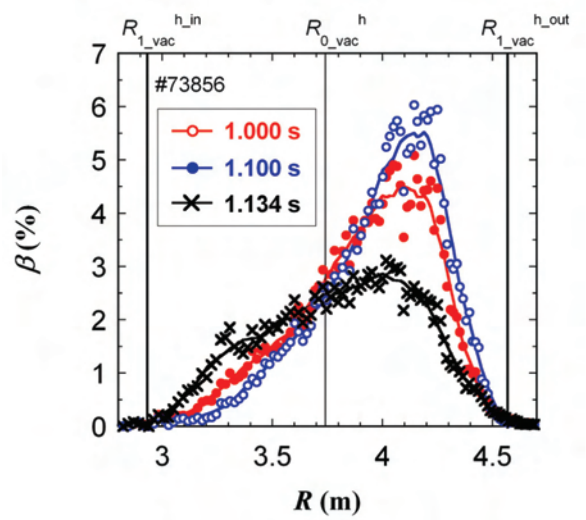

Fig. 3 Temporal change of the plasma beta profile (measured on a horizontally elongated slice), in the discharge shown in Fig. 1. Vertical lines denote radial positions of the inboard (outboard) side LCFS, $R_{1\_vac}^{h\_in}$ ($R_{1\_vac}^{h\_out}$), and the magnetic axis, $R_{0\_vac}^{h}$, in vacuum.

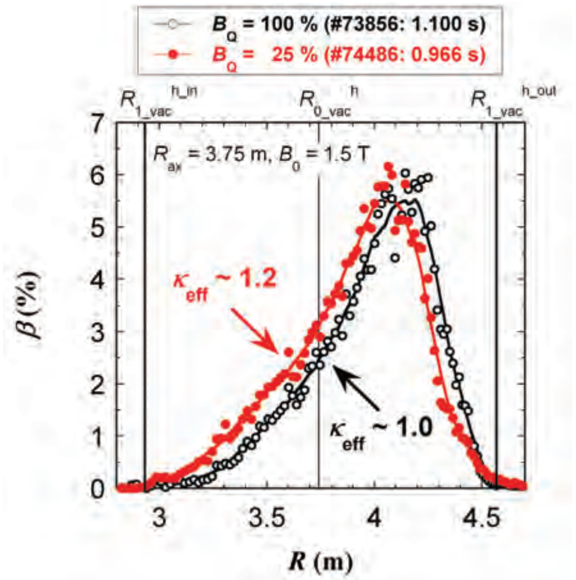

Fig. 4 Comparison of the plasma beta profiles (measured on a horizontally elongated slice), in two discharges with B_Q = 100 % (κ_{eff} ~ 1.0) and B_Q = 25 % (κ_{eff} ~ 1.2). Vertical lines denote radial positions of the inboard (outboard) side LCFS, $R_{1\_vac}^{h\_in}$ ($R_{1\_vac}^{h\_out}$), and the magnetic axis, $R_{0\_vac}^{h}$, in vacuum.

"density collapse".

CDC must be suppressed since it inhibits further increase of the central pressure and the fusion triple product. Since CDC is always accompanied by large Shafranov shift, it is expected that CDC can be suppressed if the Shafranov sift is mitigated. This working hypothesis has been examined by the elongation scan experiment described below.

4. CDC suppression by vertical elongation

As was explained in section 2, the plasma elongation is controlled by the quadrupole field, B_Q. Vertical elongation with B_Q < 100 % that results in κ_{eff} > 1 (see Fig. 1) will mitigate the PS current and thus the Shafranov shift. In Fig. 4, compared are the radial beta profiles in discharges with B_Q = 100 % (κ_{eff} ~ 1.0), which is identical to that shown in Fig. 3 (t = 1.1 s), and B_Q = 25 % (κ_{eff} ~ 1.2). Even though β_0 of ~ 5.5 % is similar for both cases, the Shafranov shift of the plasma center is smaller in the case of B_Q = 25 %.

Since the Shafranov shift is a function of β_0, the impact of vertical elongation on Shafranov shift mitigation is clearly observed when it is plotted against β_0, as in Fig. 5. The difference between B_Q = 100 % and 25 % is clearly seen at high β_0 of over 3 %, while it is small in low β_0 cases. Compared at β_0 ~ 5.5 %, R_0^h reaches ~ 4.15 m and CDC takes place in the case of B_Q = 100 %, while R_0^h is

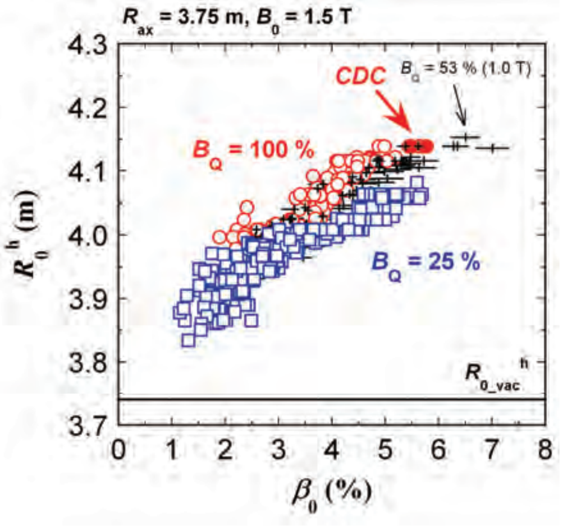

Fig. 5 The radial position of the plasma center position on a horizontally elongated slice, R_0^{h}, versus the central plasma beta, β_0. The magnetic field strength, B_0, is 1.5 T in the cases of B_Q = 100 % and 25 %, denoted by circles and squares, and B_0 = 1.0 T in the case of B_Q = 53 % ("+" with horizontal error bars). Filled circles denote the data just before CDC.

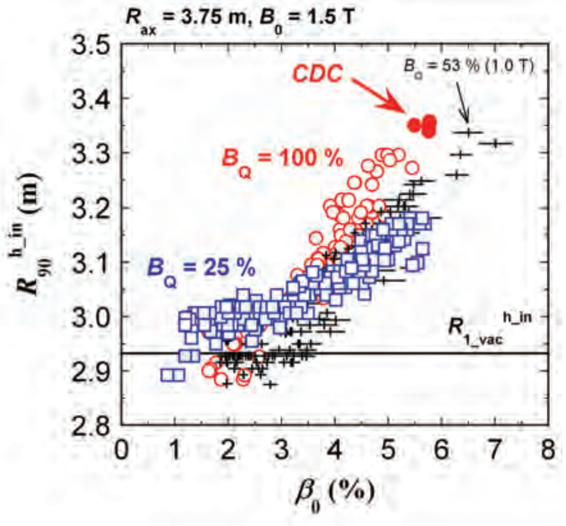

Fig. 6 The radial position of the inboard side plasma edge on a horizontally elongated slice, $R_{90}^{h\_in}$, where $\beta = 0.1\ \beta_0$, versus the central plasma beta, β_0. The magnetic field strength, B_0, is 1.5 T in the cases of B_Q = 100 % and 25 %, denoted by circles and squares, and B_0 = 1.0 T in the case of B_Q = 53 % ("+" with horizontal error bars). Filled circles denote the data just before CDC.

below 4.1 m and no CDC is observed in the case of B_Q = 25 %. Also shown in Fig. 5 is the data obtained in an intermediate case of B_Q = 53 %, where B_0 is decreased to 1.0 T to achieve higher β_0 under a limited heating power condition of ~ 10 MW. In this case, R_0^{h} is ~ 4.1 m at β_0 ~ 5 % and reaches ~ 4.15 m at β_0 > 6 %. The highest β_0 of ~ 7 % is achieved without CDC in this configuration.

The influence of vertical elongation is also recognized for the inboard side plasma edge position, R_{90}^{in}, as is shown in Fig. 6. CDC takes place when R_{90}^{in} reaches ~ 3.35 m at β_0 ~ 5.5 % in the case of B_Q = 100 %. In small B_Q cases, R_{90}^{in} remains less than 3.35 m even with high β_0 of > 6 %. It is expected that CDC will also take place in vertically elongated plasmas as in the case of B_Q = 100 %, but at higher β_0. It remains, however, for future study to explore the higher β_0 regime of > 7 %.

5. Discussion

It has been shown that plasma elongation is effective for Shafranov shift mitigation. No CDC is observed as long as the shift of the plasma center (or, the inboard side plasma edge) is kept apart from a critical position. In this sense, CDC seems to be related to the equilibrium limit. On the other hand, it is widely believed that the equilibrium limit will appear as a "soft limit" at which no fast event like CDC is expected. There still is a possibility that CDC is a phenomenon resulted from an unknown instability. This instability, if it really exists, should have a characteristic that it is stabilized in vertically elongated configurations. Because high β_0 reaching ~ 7 %, which is higher than those observed at CDC, is achieved in vertically elongated plasmas without CDC. It should be also noted that in vertically elongated plasmas, the pressure gradient, which might be a source of this instability, is similar to, or even larger than, those at CDC.

Acknowledgement

The authors are grateful to the LHD operation group for their support. This work is supported by NIFS07ULPP517.

References

[1] For example, V. D. Pustovitov, *Reviews of Plasma Physics* ***21*** (Consultants Bureau, New York, 2000) p. 1 – 201.
[2] A. Weller *et al.*, Plasma Phys. Control. Fusion **45**, A285 (2003).
[3] N. Ohyabu *et al.*, Phys. Rev. Lett. **97**, 055002 (2006).
[4] H. Yamada *et al.*, *34th European Physical Society Conferences on Plasma Physics 2007 (Warsaw, Poland)*, I4.004 (submitted to Plasma Phys. Control. Fusion).
[5] R. Sakamoto *et al.*, submitted to Plasma Fusion Res.
[6] H. Yamada *et al.*, Nucl. Fusion **45**, 1684 (2005).
[7] S. Ohdachi *et al.*, this conference, P1-051.
[8] O. Kaneko *et al.*, Phys. Plasmas **9**, 2020 (2002).
[9] O. Motojima *et al.*, Nucl. Fusion **45**, S255 (2005).

Proceedings of ITC/ISHW2007

Reactor System Analysis and Pellet Injection Simulation in Helical and Tokamak Reactors

Y. Higashiyama, K. Yamazaki, J. Garcia[a], H. Arimoto, T. Shoji

Nagoya University, Furo-cho, Chikusaku, Nagoya 464-8603, Japan

[a]*Universitat Polite `cnica de Catalunya (UPC), Barcelona, Spain*

In the future fusion reactor, the plasma density peaking is important for the increase in the fusion power gain and for the achievement of confinement improvement mode. The density control and the internal transport barrier (ITB) formation due to the pellet injection has been simulated in tokamak and helical reactors using the toroidal transport linkage code TOTAL. Firstly, the pellet injection simulation is carried out including the neutral gas shielding model and the mass relocation model in the TOTAL code, and the effectiveness of the high field side (HFS) pellet injection is clarified. Secondly, the ITB simulation with the pellet injection is carried out with the confinement improvement model based on the ExB shear effects, and it is found that the deep pellet penetration is helpful for the ITB formation as well as the plasma core fuelling in the reversed shear tokamk reactor, but the deep pellet penetration is not effective in the helical reactor.

Keywords: Transport simulation, Internal transport barrier, Pellet injection, Tokamak reactor, Helical reactor

1. Intoduction

The total fusion reactor power strongly depends on the radial profile of plasma temperature and density, and the density control is important to optimize reactor operation. To control plasma density and pressure profiles, the pellet injection is considered as a prospective technique. The pellet injection is used for the plasma core fuelling, and it brings a peaked density profile, so that the fusion power gain is increased. In JET and other tokamak experiments, it was shown that the density profile modifications disagree with pellet ablation theory [1] that assumes the pellet particles remain on the magnetic field lines where they are ionized [2]. The pellet penetration depth measured by the pellet light emission agreed well with the pellet ablation theory. This suggested that a fast outward major-radius drift may occur during the pellet ablation and toroidal symmetrization processes. To test this hypothesis the experiment of the high-field side (HFS) pellet injection has done in ASDEX-Upgrade, and it was shown that the fuelling efficiency and the penetration depth of pellets are improved [3]. The similar results are observed in DIII-D [4] and other tokamak experiments, and the HFS pellet injection is expected to be an effective technique of plasma core fuelling in future tokamak reactors.

The transport simulation studies have been carried out focusing on the ITB formation in tokamak and helical plasmas. When the ITB is formed in the plasma, it brings good confinement and rather peaked pressure profile, so that the operation scenarios with the ITB in tokamas are expected as enhanced performance modes such as high β_p mode [5], reversed shear mode [6], and pellet enhanced performance mode (PEP) [7,8]. In helical systems the ITB model based on Bohm and GyroBohm-like transport with ExB shear flow effects has already been compared with the LHD experimental ITB [9] and this model is inspired from the JET mixed-model [10]. This model is introduced into the toroidal transport linkage TOTAL code [11, 12], and is applied to the 1-dimensional (1-D) ITB formation simulation of both 3-D equilibrium helical and 2-D equilibrium tokamk plasmas.

Both the pellet injection and the ITB formation have big influence on the density profile and the fusion power output, so that we consider about operation scenario with ITB formation by pellet injection density control in helical and tokamak reactor plasmas by using the TOTAL code. Section 2 will describe the details of the transport models and the HFS pellet injection model included in the TOTAL code, and simulation results will be shown in section 3. The conclusion will be given in section 4.

2. TOTAL code

2.1. Transport model description

The Bohm and GyroBohm mixed transport model with the ExB shear flow effect has already been compared with the helical and tokamak experimental ITBs [9, 10]. The most widely accepted explanation for the ITB formation relies on the suppression of ITG

y-higashiyama@ees.nagoya-u.ac.jp

turbulence due to ExB shear flow. The suppression of the turbulence might occur when the ExB flow shearing rate ω_{ExB} exceeds the ITG linear growth rate γ_{ITG} . The shearing rate ω_{ExB} is defined as [13,14]

$$\omega_{E\times B} = \left(\frac{\Delta\psi_0}{\Delta\phi_0}\right)\left|\frac{\partial^2\Phi_0(\psi)}{\partial\psi^2}\right| \cong \left|\frac{RB_\theta}{B_\phi}\frac{\partial}{\partial r}\left(\frac{E_r}{RB_\theta}\right)\right|, \tag{1}$$

where $\Delta\psi_0$ and $\Delta\phi_0$ are the correlation lengths of the ambient turbulence in the radial and toroidal direction, and Φ_0, E_r , B_θ and B_ϕ are the equilibrium electrostatic potential, the radial electric field, the poloidal and toroidal magnetic field, respectively. In tokamaks, the radial electric field E_r is not easily measured directly, so that E_r can be calculated from the plasma radial force balance equation under the assumption that the poloidal velocities can be expressed according to the neoclassical theory [15, 16]. However in this paper, E_r is described simply as

$$\frac{dE_r}{dr} \cong -\frac{1}{en_i^2}\frac{dn_i}{dr}\frac{dp_i}{dr}, \tag{2}$$

in the H-mode condition [17], where n_i and p_i are ion density and ion pressure, respectively. The ITG growth rate γ_{ITG} is defined as [18]

$$\gamma_{ITG} = \frac{(\eta_i - 2/3)^{1/2}|s|c_i}{qR}, \tag{3}$$

where $\eta_i = L_n/L_T$, $c_i = \sqrt{T_i/m_i}$, and s is the magnetic shear defined as

$$s = \frac{r}{q}\left(\frac{dq}{dr}\right). \tag{4}$$

Most theoretical studies based on the ExB shear stabilization adopt a thermal diffusion coefficient χ in the form

$$\chi_{e,i} = \chi_{neoclassical} + \chi_{anomalous}, \tag{5}$$

$$\chi_{anomalous} = \alpha_1 \times \chi_{Gyrobohm} + \alpha_2 \times \chi_{Bohm} \times F\left(\omega_{E\times B}/\gamma_{ITG}\right), \tag{6}$$

where

$$F\left(\omega_{E\times B}/\gamma_{ITG}\right) = \frac{1}{1+\left(\omega_{E\times B}/\gamma_{ITG}\right)^2}. \tag{7}$$

The coefficient $\chi_{neoclassical}$ is the neoclassical part of thermal diffusion coefficient, and $\chi_{anomalous}$ is the anomalous part described as the Bohm and GyroBohm mixed transport model [9, 10]. And particle diffusion coefficient D is assumed as $D=\chi_{e,i}/C_{ano}$, in this paper $C_{ano}=3$ (tokamak) and 1 (helical).

2.2. HFS pellet injection

The high-field-side (HFS) pellet injection is described as two processes which are the pellet ablation and the mass relocation. We simulate the HFS injection with the pellet penetration model combined with the ablation model and the mass relocation model. There are a few models which satisfactorily describe the pellet ablation and give similar results [19]. So, we use here the most popular one: the neutral gas shielding (NGS) model [1]. The mass relocation width from ablation point with the plasmoid drift in the major-radius direction ΔR is described as [20]

$$\Delta R = -0.5q\beta B_t B_p^{-1}(1+qL_e/a)^{-1} \times a^{-2}r_0^2\delta n(n+\langle\delta n\rangle)^{-1}. \tag{8}$$

3. Simulation results

3.1. Demonstration of HFS pellet injection

The reactor machine parameters used in this paper were those of typical designs optimized using the reactor design system code PEC (Physics- Engineering- Cost) [12]. These parameters are derived from two 1GW electric power fusion reactor designs; high-field high-beta compact tokamak reactor TR-1 (major radius R=5.2m, magnetic field B=7.1T) and high-beta helical system HR-1 (R=12.1m, B=4.6T).

Typical results of the HFS pellet injection simulation in tokamak reactor are shown in figure 1. The pellet ablation densities are shown for the different pellet injection velocity. Here, the radial parabolic temperature and flat density profiles are assumed as $T(x)=T_0(1-x^2)^3$, $n(x)=n_0(1-x^2)^{0.5}$ with T_0=30kev and $\langle n\rangle=10^{20}m^{-3}$. This figure shows that the HFS injection could provide rather deep fuelling in the reactor-grade tokamak plasma, and the further increase in the injection velocity improves the central fuelling. For assumed temperature and density

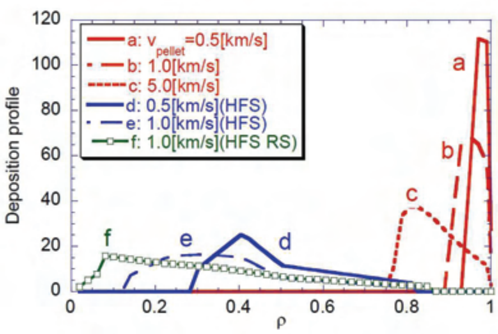

Figure 1. Model prediction for the HFS pellet injection in tokamak reactor. Ablation profiles are shown by a, b and c, and HFS injection simulation results are given by d, e, and f depending on the pellet injection velocities. The profiles d and e are in the normal shear case, and f is in the reversed shear case.

profiles, the HFS injection with the pellet velocity of 1 km/s could provide the density increase at the normalized radius r/a~0.1. Moreover, it shows that the reversed shear mode improves the central fuelling for the HFS injection based on the mass relocation model of equation (8).

3.2. ITB simulation with pellet injection

In the previous subsection, we show that the pellet injection could provide deep fuelling in tokamak reactor by the HFS injection. So that we consider about operation scenario with ITB formation in deep (by HFS injection) and shallow (by medium field side injection) penetration depth cases in the reversed shear ITB plasmas.

The figure 2 shows the operation scenarios of the tokamak reactor (reversed shear mode) in deep penetration case by HFS pellet injection. Alpha particle power and density are feedback-controlled by the adjustment of both heating power and fuelling. In this scenario, ITB is formed at 15 sec and plasma is ignited at 100 sec. The figure 3 shows the comparisons with radial profiles at steady state (time=200 sec) in deep (same as figure 2) and shallow cases. We can see that there are clear differences between both cases. In the deep penetration case shown in the left-hand of the figure 3, the ITB is formed at ρ~0.4, but in the shallow case in the right-hand figure the ITB is not formed.

This reason is shown in the bottom two figures in figure 3. In this simulation, the ITB formation is determined by two parameters, ω_{ExB} and γ_{ITG}. In both cases, γ_{ITG} is reduced at ρ~0.4 where the magnetic shear s~0. The suppression occurs when ω_{ExB} exceeds γ_{ITG}, so the ITB tends to be formed at low γ_{ITG} position. However, in the shallow penetration case the rate ω_{ExB} is small at ρ~0.4, because the gradient of radial electric field dE_r/dr is small depending on the term dn_i/dr in equation (2). The transient density profile and the relevant clear ITB formation depend on the pellet penetration depth. The deeper pellet penetration brings the larger gradient of E_r and the larger shearing rate ω_{ExB} at the position of small γ_{ITG}, so that the ITB is formed there. We can say that the deep pellet penetration plays an important role in the ITB formation, and the HFS pellet injection is a quite effective technique for the confinement improvement as well as the core density fuelling in the reversed shear tokamak reactor.

Figure 4 shows the results of the ITB simulation in the helical reactor. It is compared with deep and shallow pellet penetration depth cases (same in tokamak). In this simulation, different from tokamak case, the deep penetration case corresponds to the high speed pellet injection and not to the HFS injection, because the effectiveness of HFS injection has not been observed so far in helical system [21]. This might be because the field connection length between the high filed side and the low filed side is quite short in comparison with tokamak case. In the helical reactor, the radial electric filed is determined from the ambipolarity condition of helical ripple-induced neoclassical flux, and the large gradient of radial electric filed appears at the position of pellet penetration 'toe point' (after this, we call this large electric field gradient the 'sharp valley'). The electric field is influenced by the pellet penetration depth through

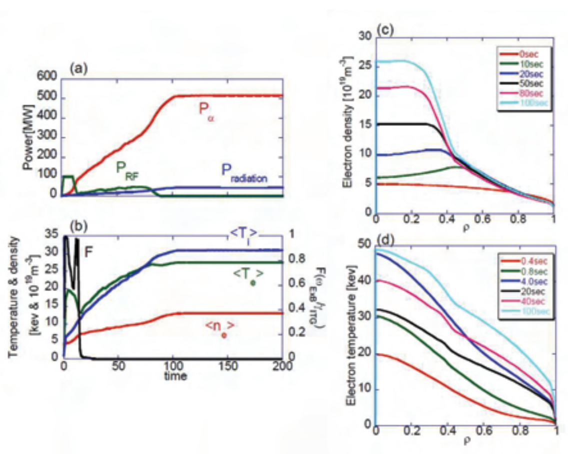

Figure 2. Figure (a) and (b) show the operation scenarios of the TR-1 (reversed shear) with HFS pellet injection. The improvement factor $F(\omega_{ExB}/\gamma_{ITG})$ which is defined in the equation (7) is the value at ρ=0.4. Figure (c) and (d) show the time evolution of the electron density and temperature radial profiles.

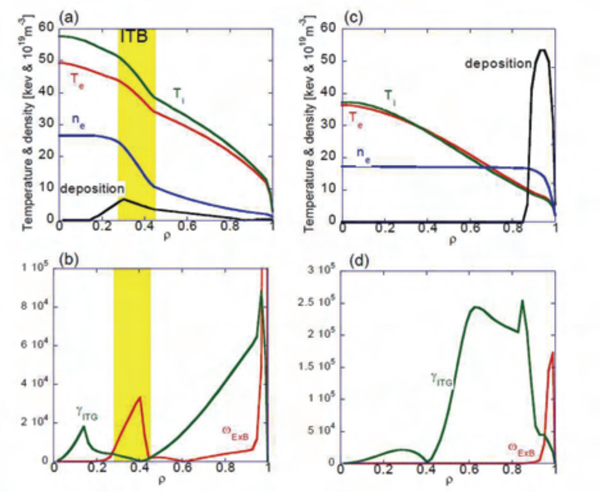

Figure 3. ITB simulation results with pellet injection in the reversed shear tokamak reactor. Left figures denote deep pellet penetration case (by HFS), and right figures are shallow penetration case (by the medium field side injection). The upper figures (a) and (c) show ion and electron temperatures, electron density, and pellet deposition profiles, and the lower figures (b) and (d) show ω_{ExB} and γ_{ITG} profiles.

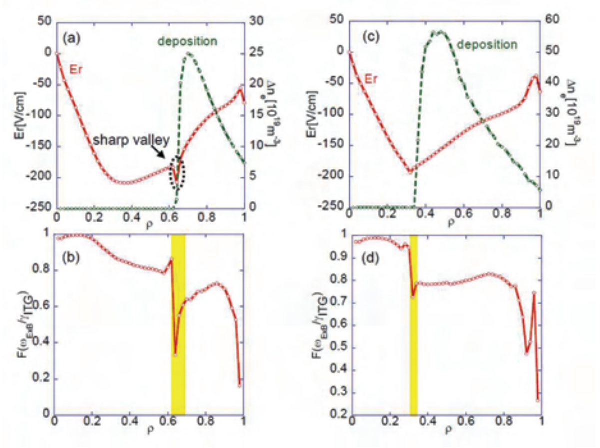

Figure 4. ITB simulation results with pellet injection in helical reactor. The left-hand figure corresponds to the shallow penetration case (pellet size = 4mm, injection velocity = 1.0 km/s), and the right-hand figure is the deep penetration case (pellet size = 6mm, injection velocity = 5.0 km/s). The upper figures (a),(c) show radial electric field and pellet deposition profiles, and the lower figures (b),(d) shows the improvement factor F($\omega_{ExB}/\gamma_{ITG}$) which is defined in the equation (7).

the density profile, which is similar to the tokamak case. But it is not same as in the tokamak that the ITB is formed in the both deep and shallow cases. The 'sharp valley' can be formed at the 'toe point' of the pellet penetration as shown in figure 4. In the deeper penetration case the sharp valley tends to be smaller, and the shearing rate ω_{ExB} becomes smaller, therefore the reduction in the anomalous transport becomes weaker. These results show that the deeper pellet penetration is not needed for the ITB formation in the helical reactor.

4. Conclusion

We investigated the relationship between the ITB formation and the pellet injection in tokamk and helical reactors. The high field side (HFS) pellet injection in the tokamak reactor was analyzed and its effectiveness was clarified. In the tokamak reactor with reversed shear profile, it was shown that the pellet penetration depth plays an important role in the ITB formation, and the HFS injection would be an effective technique for the confinement improvement as well as the plasma core fuelling. In the helical reactor, we showed that the deep pellet penetration is not needed for the ITB formation because the position of ITB is determined by the ambipolar radial electric field 'sharp valley' and the pellet penetration 'toe point', and the deeper penetration does not help the strong reduction in anomalous plasma transport.

References

[1] Parks P B and Turnbull R J 1978 *Phys. Fluids* **21** 1735

[2] Bayler L R *et al* 1992 *Nucl. Fusion* **32** 2177

[3] Lang P T *et al* 1997 *Phys. Rev. Lett.* **79** 1478

[4] Bayler L R *et al* 1998 *Fusion Technol.* **34** 425

[5] Ishida S *et al* 1993 Proc. *14th Int. Conf. Plasma Physics Controlled Nuclear Fusion Research (W¨urzburg,1992)* vol 1 (Vienna: IAEA) p 219

[6] Kimura H *et al* 1996 *Phys. Plasmas* **3** 1943

[7] JET Team (presented by Schmidt G L) 1989 *Proc. 12th Int. Conf. Plasma Physics and Controlled Nuclear Fusion Research (Nice, 1988)* vol 1 (Vienna: IAEA) p 215

[8] Tubbing B *et al* 1991 *Nucl. Fusion* **31** 839

[9] Garcia J, Yamazaki K, Dies J and Izquierdo J 2006 *Phys. Rev. Lett*. **96** 105007

[10] Tala T *et al* 2001 *Plasma Phys. Control. Fusion* **43** 507

[11] Yamazaki K and Amano T 1992 *Nucl. Fusion* **32** 633.

[12] Yamazaki K *et al* 2006 *Fusion Engineering and Design* **81** 2743

[13] Hahm T S and Burrell K H 1995 *Phys. Plasmas* **2** 1648

[14] Zhou P, Horton W and Sugama H 1999 *Phys. Plasmas* **6** 2503

[15] Ernst D R *et al* 2000 *Phys. Plasmas* **7,** 615

[16] Kim Y B, Diamond P H and Groebner R J 1991 *Phys. Fluids* B 3 2050

[17] Hinton F L and Staebler G M 1993 *Phys. Fluids* B 5 1281

[18] Esposito B et al 2003 Plasma Phys. Control. Fusion **45** 933

[19] Baylor L R *et al* 1997 *Nucl. Fusion* **37** 445

[20] Polevoi A R and Shimada M 2001 *Plasma Phys. Control. Fusion* **43**1525

[21] Sakamoto R *et al* 2002 *Plasma Phys. Control. Fusion* 26B, P-1.074

Proceedings of ITC/ISHW2007

Compact Stellarator Path to DEMO

J. F. Lyon for the U.S. stellarator community

Oak Ridge National Laboratory, Fusion Energy Division, Oak Ridge TN, USA

lyonjf@ornl.gov

The US fusion program is considering what new facilities are needed in addition to ITER and existing facilities to prepare the way to a DEMO reactor. The broad issues are familiar: sustainment of an ignited/high-Q plasma in steady state, avoidance of disruptions and large variations in power flux to the wall, adequate confinement of thermal plasma and alpha-particles, control of a burning plasma, particle and power handling (divertors), etc. Stellarators have key reactor advantages: steady-state high-plasma-density operation without external current drive or disruptions, stability without a close conducting wall or active feedback systems, and low recirculating power. While stellarators are at present less developed than tokamaks because of the higher parameters obtained in large tokamaks, D-T operation in TFTR and JET, and the decision to proceed with ITER, stellarators do present an attractive alternate path to a DEMO reactor.

Compact stellarators, with moderate plasma aspect ratios, good confinement, and high-beta potential lead to the smaller-size reactors that are favored by the US utility industry. The ARIES group, which had previously analyzed different tokamaks, an ST, an RFP and a modular stellarator (SPPS) as reactors, has recently examined compact stellarators. The ARIES-CS study established that compact stellarators can be economically competitive with tokamaks as reactors, but face serious issues with divertors, as do other toroidal concepts.

The favorable physics properties of compact stellarators follow from their quasi-symmetric magnetic geometry, analogous to the axisymmetry of $|\mathbf{B}|$ in tokamaks and RFPs. Basic physics properties depend only on $|\mathbf{B}|$ in the Boozer coordinate system in which magnetic flux surfaces are concentric, axisymmetric tori. This fundamental property allows mapping of physics properties from tokamaks to analogous stellarators. The different types of quasi-symmetry (helical, toroidal and poloidal) manifest themselves in the magnitude, direction, and variation of flow and flow shear, and instability thresholds for trapped particle modes. Initial results from HSX, a helically symmetric stellarator, are in general agreement with expectations for quasi-symmetry, and demonstrate its effectiveness.

Many of the issues that need to be resolved before committing to a compact stellarator DEMO can be answered using the results of the large tokamaks and stellarator experiments already in operation (LHD, TJ-II, Heliotron J, HSX, CTH), under construction (W 7-X, NCSX) or in development (QPS). The compact stellarator route to a DEMO can also incorporate results from ITER D-T experiments and fusion materials, technology and component development programs. However, a large next-generation stellarator experiment will be needed to address some physics issues: size scaling and confinement scaling at DEMO-relevant density, temperature, and beta; the burning plasma issues of adequate fast-ion (alpha-particle) confinement, robustness to Alfven instabilities, and helium ash removal; and operation with a strongly radiative divertor. Technology issues include simplification of the 3-D coil, structure, and divertor fabrication, the use of rapid prototyping as in the aerospace industry, and reliable costing techniques.

Proceedings of ITC/ISHW2007

Analysis of the ARIES-CS Compact Stellarator Power Plant

J. F. Lyon, L-P. Ku[a], L. El-Guebaly[b], L. Bromberg[c], L. M. Waganer[d], M. C. Zarnstorff[a]
and the ARIES Team

Oak Ridge National Laboratory, PO Box 2008, MS-6169, Oak Ridge TN 37831-6169, USA
[a] Princeton Plasma Physics Laboratory, PO Box 451, Princeton, NJ 08543-0451, USA
[b] University of Wisconsin, 1500 Engineering Drive, Madison, WI 53706-1687, USA
[c] Massachusetts Inst. of Technology, 167 Albany St., Cambridge, MA 02139, USA
[d] The Boeing Company, PO Box 516, St. Louis, MO 63166, USA

lyonjf@ornl.gov

The US ARIES group has analyzed different magnetic configurations as potential fusion power plants: different tokamaks, an ST, an RFP and a modular stellarator (SPPS). The latest ARIES study examined compact stellarators, which combine the best features of high-current tokamaks (moderate plasma aspect ratios, good confinement, and high plasma beta $\langle\beta\rangle$) with those of large-aspect-ratio currentless stellarators (steady-state high-plasma-density operation without external current drive or disruptions, stability without a close conducting wall or active feedback systems, and low recirculating power in a fusion power plant).

A stellarator systems/optimization code was used to optimize the ARIES-CS power plant parameters for minimum cost of electricity (CoE) and beta subject to a large number of variable physics, engineering, and in-vessel component constraints. The most important factors determining the size and composition of the fusion power core were the allowable neutron power flux to the wall, the distance needed between the edge of the plasma and the magnetic field coils for the intervening components and gaps, and adequate tritium breeding. The magnetic field and coil parameters were determined by plasma performance and coil pack constraints. The previous ARIES costing approach and algorithms were updated with revised material and component costs.

An NCSX-based compact-stellarator plasma and coil configuration and a LiPb/FS/He blanket and shield concept were used for the reference ARIES-CS power plant with R = 7.75 m, B = 5.7 T, β = 6.4% and a projected CoE = 78 mills/kWhr (in 2004 \$). A number of physics assumptions (density and temperature profiles, impurity radiation levels, confinement enhancement, β limits, alpha-particle energy losses, etc.) affected the plasma parameters, but had little effect on the size and cost of the fusion power core. Other parameters (maximum field at the coils, component cost penalties, different blanket and shield approaches, alternative plasma and coil configurations, etc.) had a larger impact. In particular, the use of an advanced LiPb/SiC blanket and shield concept like that adopted in the ARIES-AT tokamak power plant study could reduce the CoE by approximately 17 mills/kWhr.

Optimization was not just a matter of low plasma aspect ratio. More important was having a low plasma-coil-distance aspect ratio and a coil geometry that allowed a tapered blanket/shield concept that can satisfy the breeding requirement. Although the MHH2 plasma and coil configuration has a plasma aspect ratio 58% of the ARIES-CS configuration and a smaller plasma-coil-distance aspect ratio, the inability to use a tapered blanket/shield concept drove the size and CoE for an MHH2 power plant higher than that for even an SNS-based power plant where the plasma aspect ratio was a factor of 2.26 higher and the plasma-coil-distance aspect ratio was higher. Comparisons were also made with some earlier ARIES power plant studies.

Proceedings of ITC/ISHW2007

High-temperature superconducting coil option for the fusion reactor FFHR and development of indirectly-cooled HTS conductors

Gourab Bansal, Nagato Yanagi[a], Tsutomu Hemmi[b], Kazuya Takahata[a], Toshiyuki Mito[a], Akio Sagara[a]

The Graduate University for Advanced Studies, Toki, Gifu 509-5292, Japan

[a] National Institute for Fusion Science, Toki, Gifu 509-5292, Japan

[b] Japan Atomic Energy Agency, 801-1, Mukoyama, Naka 311-0193, Japan

Large current-capacity high-temperature superconducting (HTS) conductors using YBCO wires are being considered as an option for the fusion energy reactor FFHR [1, 2]. Typical required current for such conductors in FFHR is 100 kA at about 13 T magnetic field. The operating temperature for HTS magnets in FFHR is about 20 K with conduction cooling using an indirect cooling method. Since the specific heats of the materials at 20 K are significantly higher as compared with 4.2 K, which is the typical operating temperature of low temperature superconducting (LTS) magnets, the HTS magnets are operated much more stably and reliably against any mechanical or electromagnetic disturbances, which is one of the biggest advantages over LTS magnets. Another advantage is the reduction in required refrigeration power as the HTS magnets are operated at the elevated temperatures. Or, using HTS conductors, it is also considered to be viable to assemble the continuous helical coils in segments with a number of joints for conductors, as we can allow additional heat generation utilizing the surplus refrigeration power [3]. Two options of aluminum-alloy and SUS jacketed HTS conductors have been considered. The maximum strain in the winding has been estimated to be less than 0.3%, which is less than the critical strain of ~0.5% for YBCO conductors. As the first step towards the HTS conductor developments, a 10 kA-class conductor has been fabricated using Bi-2223/Ag tapes, by simply stacking and soldering them inside a copper sheath. The critical currents of the conductor have been measured at 4.2 K and at elevated temperatures up to 30 K. The stability margin experiments have also been done. The HTS conductor was found to be highly stable. In near future, the YBCO coated-conductors are planned to be used for next HTS conductor sample, and the stability and quench characteristics will be compared with those obtained for the present one.

Keywords: LHD, FFHR, fusion reactor, HTS, YBCO, BSCCO, superconductor, stability.

1. Introduction

Force free helical reactor (FFHR) is a LHD-type fusion energy reactor, which is being designed at National Institute for Fusion Science (NIFS) in the framework of inter-university collaborative research. Several designs of FFHR-series reactors have been proposed [4]. Among them, a state-of-the-art design FFHR2m1 has plasma major radius of 14 m, toroidal field of 6.2T, maximum field at the conductor 13 T, and fusion power of 1.9 GW. FFHR2m1 consists of one pair of helical coils and two pairs of poloidal field coils. Already well-developed low temperature superconductors (LTS) are being considered for the helical and poloidal coils of FFHR2m1. However, recently, the high temperature superconductor (HTS) technology has improved significantly and has shown good prospects for future applications. Considering this fact, the HTS has emerged as a competitive candidate for the helical coils of FFHR. The present study is focused on the HTS conductor design for the helical coils of FFHR. High temperature superconductors are being considered for high field magnets in fusion reactors due to their better performances in high magnetic field and elevated temperature operations [5] – [15]. In a fusion reactor, the HTS magnets can be operated at ~20 K or higher and therefore reduces the operational cost compared to conventional LTS magnets, which are used at ~4 K. Secondly, due to the increased specific heat of the HTS conductors at elevated temperatures, they become less prone to quench and therefore more safer operations of a fusion reactor are possible, which is perhaps the most desirable requirement from the magnets. The HTS magnets can be cooled by conduction cooling methods and therefore can avoid the complicated networks of pipings, generally necessary for force flow cooled LTS conductor magnets. The indirect cooling method has been proposed for aluminum-alloy jacketed Nb_3Sn conductor for FFHR helical coils [16]. The same indirect cooling technique can be easily adopted for HTS conductor coils as well. The increased thermal conductivity of the metals at elevated temperatures helps in quickly removing the

author's e-mail: bansal@nifs.ac.jp

heat generated in the conductor due to the AC losses, mechanical disturbances, nuclear heating and other sources.

2. HTS Conductor Design

Second generation coated conductors, such as YBCO and GdBCO, are the promising candidates for future demo fusion reactors as they sustain high critical currents at high magnetic fields. A cross-section of the proposed 100 kA-class HTS conductor for FFHR2m1 helical coils is shown in Fig. 1. This conductor uses YBCO or GdBCO tapes along with copper tapes inside a thick jacket of aluminum-alloy or SUS. The dimensions of the conductor have been chosen the same with its LTS counterpart proposed in [16]. The critical current of the HTS tape is considered as 100 A/mm-width at 13 T and 25 K, which is expected to be developed soon. The copper to superconductor ratio in HTS conductor is 7.0 and the critical current of the conductor is 128 kA at 13 T, 25 K.

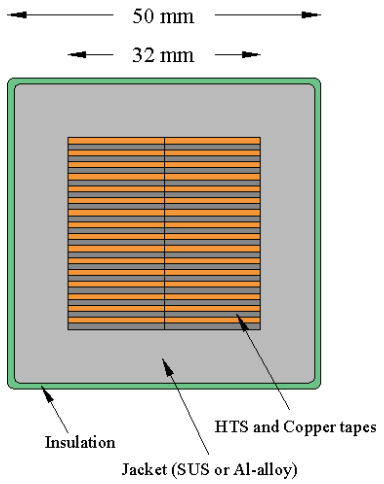

Fig.1 Cross-section of proposed HTS conductor for the helical coils of FFHR2m1.

Fig. 2 shows the rectangular cross-section of the helical coil (1.8 m wide and 0.9 m high). The helical coil consists of 12 layers with 36 turns in each layer. Inside the winding, four 75 mm thick cooling panels with embedded cooling channels are installed. The winding is cooled by conduction due to the flowing coolant through the cooling channels of the panels. The expected steady state nuclear heat load on the superconducting coil in FFHR is 100 W/m^3 [16,17], which should be removed by the coolant effectively. The temperature increase of the conductor, ΔT_{max}, can be estimated by one dimensional heat conduction equation.

$$\Delta T_{\max} = \frac{Ql^2}{2\lambda_e} \qquad (1)$$

where Q is the heat load, l is the distance, λ_e is the effective thermal conductivity. In Fig. 2, the maximum distance between heated zone and coolant, l, is 0.1 m. If the conductor temperature is allowed to be increased by 1 K due to the nuclear heating of 100 W/m^3, the required effective thermal conductivity is 0.5 W/m-K.

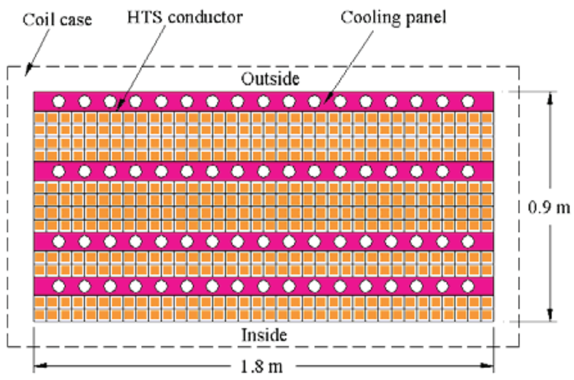

Fig.2 Cross-section of helical coil of FFHR2m1.

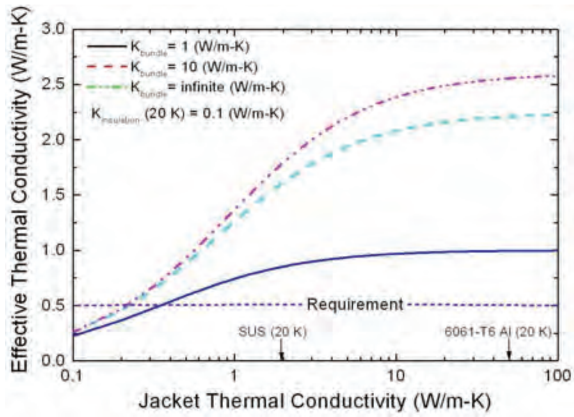

Fig.3 Effective thermal conductivity in the cross-sectional direction of the winding as a function of the jacket and HTS bundle thermal conductivities.

Fig. 3 shows the calculated effective thermal conductivity considering different materials over a length of 0.1 m in winding cross-section. The insulation thickness is taken as 1 mm and its thermal conductivity is 0.1 W/m-K at 20 K. The effective thermal conductivity is calculated by varying the jacket and HTS and copper tapes bundle thermal conductivities. In the worst case, when HTS and copper tapes bundle thermal conductivity is considered to be 1 W/m-K and HTS conductor jacket is SUS, the effective thermal conductivity comes out to be ~0.85 W/m-K at 20 K. This value is still higher than required effective thermal conductivity of 0.5 W/m-K, which suggests that SUS can also be used in HTS conductors, which was not possible for LTS counterpart proposed in [16]. Aluminum-alloy jacket provides higher effective thermal conductivity of ~1 W/m-K at 20 K and therefore is a better option as far as the heat removal is considered.

3. Stress and strain in the coil

The helical coils of FFHR will experience large electromagnetic forces and therefore the stresses and strain will be developed in the coil. Stresses and strain in the coil have been estimated by considering the coil as an infinite solenoid and only the radial forces are taken in account [16,18]. The average radius of curvature of helical coil is 5.5 m and therefore the same radius of curvature is considered for infinite solenoid model. The cross-section of the solenoid model is also the same as that of helical coil shown in Fig. 2. The calculated stresses and strain are shown in Fig. 4 for both the options of aluminum-alloy jacketed and SUS jacketed HTS conductors. The radial stress at inner radius and outer radius of the winding are taken to be zero as the boundary conditions. The maximum hoop stress in the SUS cooling panel and aluminum-alloy jacket are 510 MPa and 210 MPa respectively. The maximum hoop stress in SUS structure is 370 MPa when HTS conductor jacket is SUS. The stresses are always less than the yield strengths of the materials at 20 K and therefore safe under large electromagnetic forces in helical coils of FFHR. The strain is always less than 0.3%, which is less than the critical strain of ~0.5% for YBCO. Fig. 4 suggests that SUS jacketed HTS conductor is a better choice from stress and strain point of view.

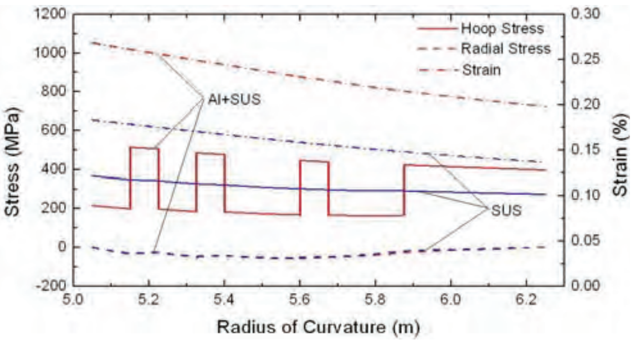

Fig.4 Hoop stress, radial stress, and strain in the helical coil of FFHR2m1. Both options of aluminum-alloy jacketed and SUS jacketed HTS conductor are shown.

4. Quench detection and protection

Due to the increased specific heat of the materials at elevated temperatures, the thermal diffusivity becomes smaller and therefore the quench propagation also becomes slower. Hence, the voltage development in HTS conductors at elevated temperatures is very slow and therefore the quench detection becomes difficult. This is one of the biggest problems in HTS conductors. Fig. 5 shows the voltage across the conductor as a function of conductor length at different temperatures and 100 kA current. At 45K, the conductor length is about 6 m to observe a voltage of 100 mV whereas it is about 2.5 m at 50 K. The required length further reduces with increased temperature. Fig. 6 shows the final hot-spot temperature with different jacket materials in adiabatic condition. The coil current is 100 kA at 25 K and the stored magnetic energy is dumped into an external resistor with a time constant of 20 s after the quench detection.

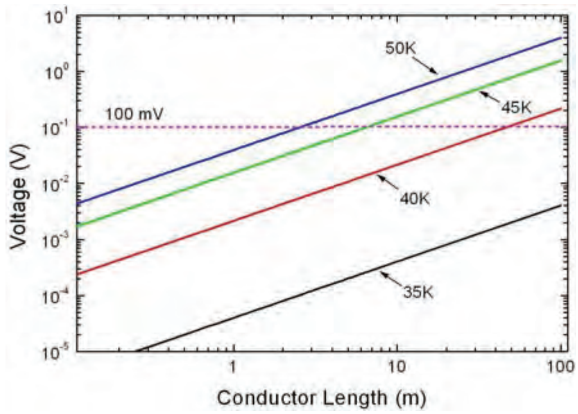

Fig.5 Voltage development as a function of conductor length at different temperatures and 100 kA current.

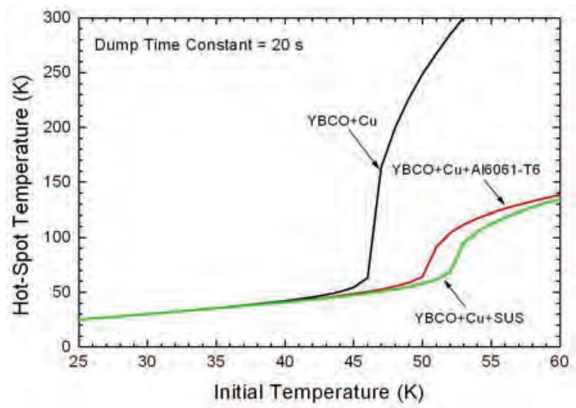

Fig.6 Final hot-spot temperature as a function of initial hot-spot temperature (just before the dumping) and jacket materials.

Fig. 6 suggests that SUS jacket for HTS conductor allows higher initial hot-spot temperature (for a condition of final hot-spot temperature less than 150 K) before dumping. This means that less conductor length is required to develop larger voltage as shown in Fig. 5, and therefore quench can be detected rather quickly and easily with SUS jacketed HTS conductor.

5. Proposal of segmented helical coils

It may not be easy to realize a continuous winding of the huge helical coils in FFHR, therefore, the segmented helical coils might be a viable choice to wind the helical coils with a number of joints between the segments. This idea was first proposed by Hashijume et al. [3]. Due to the elevated temperature operation of HTS coils, the surplus refrigeration power can be used to take away the heat generated by the joints between the helical coil segments. Since, the HTS conductor has large temperature margin, the temperature rise of few Kelvin due to the joints may not be a big concern for the stability of the coils. Fig. 7 shows the maximum temperature rise of the conductor as a function of heating density calculated by equation 1. Both the options of SUS jacketed and aluminum-alloy jacketed conductor have been considered. If a temperature rise of 5K of the conductor is acceptable, the heat density of about 990 W/m^3 on the winding can be allowed. This means a joint resistance of about 3 nΩ is acceptable as the number of joints between the conductors in one helical coil, made by 10 segments, is 4320.

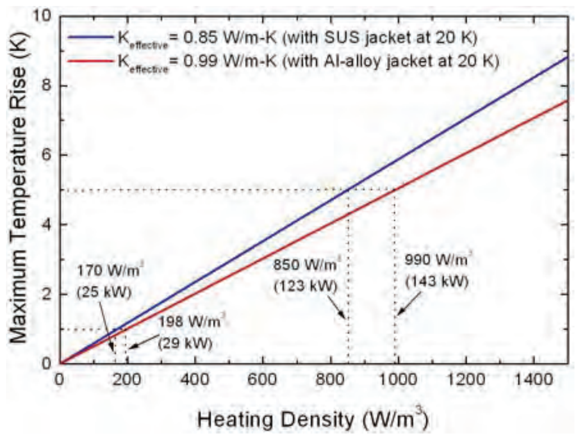

Fig.7 Maximum temperature rise of the conductor as a function of continuous heating density on the helical coil winding.

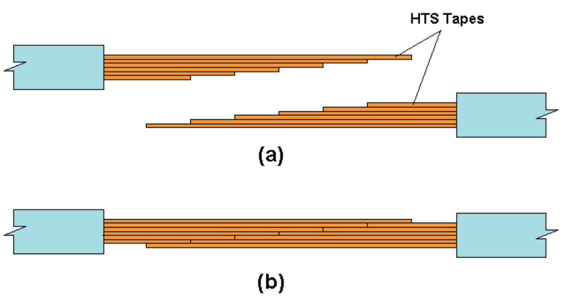

Fig.8 (a) HTS tapes cut in step like structure (b) overlap joint between two HTS conductors.

The joint between the conductors might be the mechanical joint proposed by Hashijume et al. in [3] or simple soldered lap joint. A soldered joint configuration with few numbers of HTS tapes is shown in Fig. 8. The HTS tapes are cut in step like structure and then overlapped and joined YBCO side with YBCO side.

6. Development of 10 kA-class HTS conductor

As the first step towards the development of large current capacity HTS conductor, we have developed a 10 kA-class HTS conductor using Bi2223/Ag HTS tapes. The critical current of one Bi2223/Ag tape is 140 A at 77K and self field. The HTS tapes were soldered inside a copper sheath of outer dimension of 12 mm × 7.5 mm. The HTS tapes were simply stacked and soldered. One HTS conductor consists of 34 HTS tapes and no copper tape. Thin stainless steel heaters were attached on the surface of

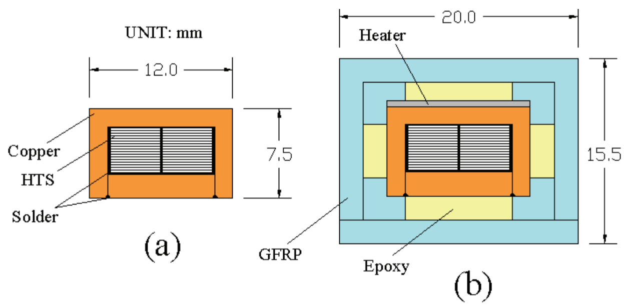

Fig.9 (a) Cross-section of 10 kA-class HTS conductor, (b) GFRP insulated HTS conductor configuration (to realize conduction cooling) in experiments.

the conductor to elevate the conductor temperature up to 30 K for the critical current and stability measurements at elevated temperatures. Then the conductor was insulated using epoxy and GFRP sheets to isolate it with liquid

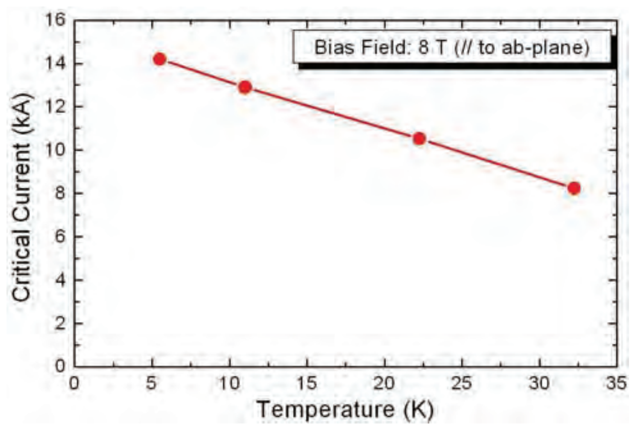

Fig.10 Measured critical currents of HTS conductor at different temperatures.

helium in the cryostat. During the experiments, the conductor was cooled by conduction through the ends. A cross-section of the HTS conductor is shown in Fig. 9. The epoxy and GFRP insulated conductor configuration (to realized conduction cooling in the experiments) is also shown.

Fig. 10 shows the measured critical current of the conductor at 4.2 K and elevated temperatures up to 30 K under a bias field of 8 T parallel to ab-plane of the HTS tapes. The critical currents are measured with 1μV/cm criterion. During the critical current measurements at 4.2K, it was not possible to maintain the conductor temperature exactly at 4.2 K due to the heating by flux flow resistance in the HTS conductor. At 1 μV/cm (criterion for critical current), the conductor temperature was about 5.5 K, which is reported in Fig. 10. The similar temperature rise was observed at elevated temperature measurements at 10K, 20K, and 30K as well. Fig. 10 suggests that the critical current of HTS conductor shows a linear dependence on temperature.

The stability of the HTS conductor was also measured using thin film heaters attached on the surface of the conductor. The conductor was found to be very stable and could not be quenched even with very high energy input of 30 J/cm^3 at 20 K and 10 kA conductor current (~90% of the critical current) under a bias field of 8 T. With 30 J/cm^3 energy input, the temperature of the conductor increased up to 34 K, which was more than the current sharing temperature of 31 K. But the conductor temperature goes down quickly due to the thermal conduction towards the ends of the sample and therefore no thermal runaway was observed. The typical stability margin for a LTS cable-in-conduit conductor (CICC) is 300 – 500 mJ/cm^3 at ~4 K and 30% – 50% of the critical current in the conductor. Hence, one can say that HTS conductors are highly stable compared to their LTS counterparts and therefore can provide much safer operation of the fusion machines. The details of the experimental set-up and results of the 10 kA-class HTS conductor can be found elsewhere [19].

7. Summary

The feasibility study of HTS conductor option for LHD-type helical fusion energy reactor FFHR has started. The preliminary design of the HTS conductor has been proposed, which seems to be suitable for FFHR helical coils. Quench detection and stress calculations suggest that SUS should be adopted as a jacket material for the conductor. On the other hand, aluminum-alloy might be a better choice from winding point of view being a softer material compared to SUS. Segmented helical coil with mechanical or soldered joints might be a viable choice due to the large temperature margin of the HTS conductor and available surplus refrigeration power, which is a big advantage in HTS conductors over their LTS counterparts. A 10 kA-class HTS conductor with Bi2223/Ag HTS tapes has been successfully fabricated and tested at 4.2 K and elevated temperatures up to 30 K. More studies e.g. error fields due to the shielding currents, current distribution in the conductor, and AC losses are planned to be done on the HTS conductors. The development and testing of a 10 kA-class conductor using YBCO tapes is also planned in near future.

References

[1] A. Sagara et al., Fusion Eng. Design **81, 2703** (2006).
[2] T. Hemmi et al., to be published in NIFS Annual Report (2007).
[3] H. Hashizume et al., J. Plasma Fusion Res. SERIES **5, 532** (2001).
[4] A. Sagara et al., Nucl. Fusion **45, 258** (2005).
[5] J. R. Hull, Jour. Nucl. Materials **191-194, 520** (1992).
[6] T. Ando et al., presented at SOFE 2005.
[7] F. Dahlgren et al., Fus. Eng. Design **80, 139** (2006).
[8] T. Isono et al., Fus. Eng. Design **81, 1257** (2006).
[9] G. Janeschitz et al., Fus. Eng. Design **81, 2661** (2006).
[10] P. Komarek, Fus. Eng. Design **81, 2287** (2006).
[11] W.H. Fietz et al., Fus. Eng. Design **75-79, 105** (2005).
[12] L. Bromberg et al., Fus. Eng. Design **54, 167** (2001).
[13] T. Ando et al., IEEE Trans. Appl. Supercond. **14, 1481** (2004).
[14] T. Isono et al., IEEE Trans. Appl. Supercond. **13, 1512** (2003).
[15] W Goldacker et al., J. Phys. Conf. Ser. **43, 901** (2006).
[16] K. Takahata et al., to be published in Fus. Eng. Design (2007), doi: 10.1016/j.fusengdes.2007.04.050.
[17] A. Sagara et al., Fus. Eng. Design **81, 1299** (2006).
[18] M. N. Wilson, Superconducting Magents, (Clarendon Press, Oxford, 1983) p. 41.
[19] G. Bansal et al., submitted to IEEE Trans. Appl. Supercond., August (2007).

P1-092

Conceptual Design of Magnets with CIC Conductors for LHD-type Reactors FFHR2m.

S. Imagawa, A. Sagara, and Y. Kozaki

National Institute for Fusion Science, 322-6 Oroshi, Toki, GIFU 509-5292, Japan

LHD-type reactors have attractive features for fusion power plants, such as no need for current drive, a wide space between the helical coils for the maintenance of in-vessel components. One disadvantage was considered a necessarily large major radius to attain the self-ignition condition or to secure a sufficient space for blankets. According to recent reactor studies based on the experimental results in LHD, the major radius of plasma is set to 14 to 17 m with the central toroidal field of 6 to 4 T. The magnetic stored energy is estimated at 120 to 130 GJ. Both the major radius and the magnetic energy are about three times as large as ITER. We intend to summarize requirements for superconducting magnets of the LHD-type reactors and to propose a conceptual design of the magnets with cable-in-conduit (CIC) conductors based on the technology for ITER.

Keywords: cable-in-conduit conductor, fusion reactor, helical coil, LHD, superconducting magnet.

1. Introduction

Superconducting magnets for fusion reactors need high mechanical strength, high reliability, and low costs as well as sufficient current densities in the high field. Cable-in-conduit (CIC) conductors have been developed for large pulse coils, and they are adopted for all magnets of ITER [1-3]. Major features of the CIC conductors are a large current up to 100 kA, high strength with thick conduits, small AC losses, and high cryogenic stability. One disadvantage is that they need circulation pumps for forced-flow cooling. The maximum length of a cooling path is about 500 m that is determined by the pressure drop for the required mass flow against the nuclear heating The CIC conductor will not be the best for magnets of a helical reactor that is operated with a constant current. However, technology related to CIC conductors will be strongly improved through the construction of ITER, especially in a cost and in the winding technique. Then, we study the helical winding with CIC conductors on the engineering base of ITER as a conventional option.

2. Magnet Systems of LHD-type Reactor

A magnet system of an LHD-type reactor consists of a pair of continuous helical coils and more than one pair of poloidal coils [4]. The position of the poloidal coils is determined by the dipole magnetic field, the quadruple magnetic field, the stray field, the position of ports, and so on. At least one set of poloidal coils is necessary to adjust the major radius of the plasma, the quadruple field, and the stray field. In this case, the magnetic field around the machine center is fairly high, and the magnetic stored energy is large. Two pairs of poloidal coils are appropriate, because they can reduce the total weight of supporting structures with reduction of the magnetic stored energy. Also, the position of plasma axis can be controlled without increase of the stray field. The position of the coils is not determined uniquely with the restrictions as above because of the rest of the degrees of freedom. The coil position can be adjusted to attain the space for the blanket, the mechanical support, and ports. In this study, we adopt two additional restrictions that $a_{IV}=a_{OV}$ and $Z_{IV}=Z_{OV}$, where a is the distance from the major radius circle of the helical coil, and Z is the height, as shown in Fig. 1.

The lead angle of the helical coil is defined as the pitch parameter $\gamma = (ma_c)/(lR_c)$, where l, m, R_c, and a_c are the pole number, the pitch number, the coil major radius, and the coil minor radius, respectively. Figure 2 shows the normalized stored energy of the LHD-type reactors with two sets of poloidal coils. Since the poloidal coils cancel the vertical field by the helical coils, the stored energy is the larger with the longer distance of the poloidal coils. Furthermore, it is the larger with the higher γ because the toroidal field area increases.

The coil current density, j, is very important for the design of superconducting magnets. Although the high density is useful to enlarge the space for blankets and for the maintenance, it is restricted by cryogenic stability, mechanical strength, and the maximum field. Considering the space for the structural materials inside the winding, j

author's e-mail: imagawa1@LHD.nifs.ac.jp

is set approximately 25 A/mm^2 in this study. The highest magnetic field is also important for the superconducting magnets. It depends mainly on the ratio of height of the helical coil to the minor-radius [5]. The highest magnetic field is set less than 13.5 T that is the same as the highest field of the ITER-CS coils.

The necessary magnetic field and size can be determined by the scaling low for the plasma confinement and the necessary space for blankets. The scaling law of ISS04 [6] for the energy confinement time is adopted in this study. At first, we have studied the necessary size under the condition of the enhancement factor of energy confinement of 1.12 to the ISS04 scaling. Since LHD has attained the factor of 0.93, the required further improvement is 1.2 that will be achieved in the near future. Table 1 shows examples of the design parameters of LHD-type reactors, FFHR2m2, under the conditions: the parabolic distribution of both the plasma density and temperature, the minimum space for blankets of 1.1 m, the helical coil current density of 27.5 A/mm^2, helium ash ratio of 3%, oxygen impurities ratio of 0.5%, and alpha particle heating ratio of 90%. The plasma density was set to just the density limit of the Sudo scaling [7]. The central temperature was adjusted to make the average β, the ratio of plasma pressure to the central magnetic pressure, at 5%. The plasma shape is assumed to be similar as that of LHD at the inward shift mode, in which the best plasma confinement has been achieved.

In the conditions as above, the smallest major radius is determined mainly by the space for blankets than the highest magnetic field. The plasma major radius around 15 m is necessary for a reactor similar to LHD. Since the high-density operations elongate the energy confinement time of the ISS04 scaling, the enhancement factor is less with the higher β operation in which the larger fusion power is produced.

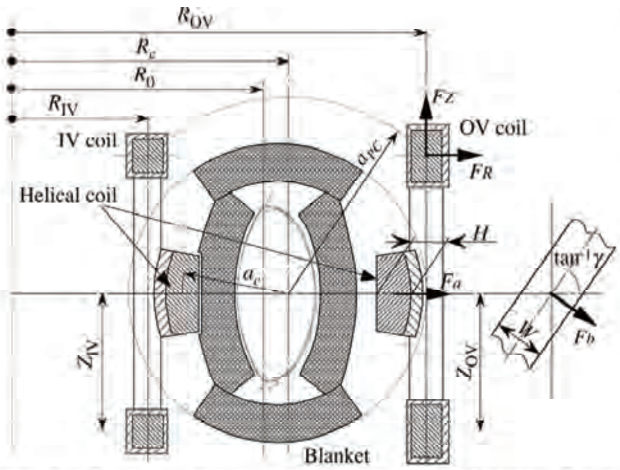

Fig. 1. Magnets and supporting structures of LHD-type fusion reactor.

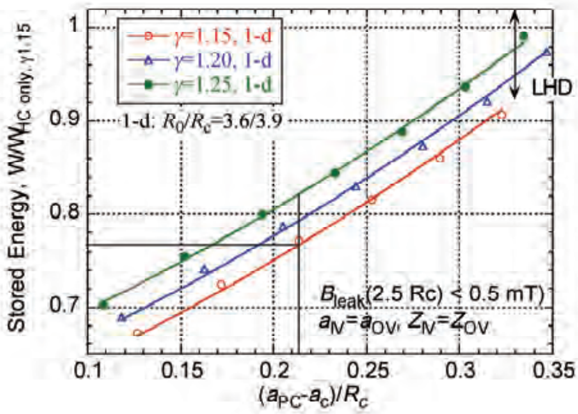

Fig. 2. Stored energy of magnets of LHD-type reactors with two pairs of poloidal coils under the condition of the same height and the same minimum distance from the helical coil in the poloidal cross-section.

Table 1. Case study of LHD-type reactors FFHR2m2-j27.5.

	γ1.15	γ1.2	γ1.25
Polarity / Field periods, l/m	2/10	2/10	2/10
Coil pitch parameter, γ	1.15	1.20	1.25
Coil major radius, R_c (m)	15.68	16.52	17.53
Coil minor radius, a_c (m)	3.61	3.97	4.38
Coil center line length (m)	150	162	176
Plasma major radius, R_0 (m)	14.47	15.25	16.18
Plasma minor radius, a_p (m)	1.75	2.24	2.83
Plasma volume, V_p (m^3)	877	1516	2559
Central magnetic field, B_0 (T)	5.53	4.95	4.49
Max. field on coils, B_{max} (T)	12.1	12.1	12.2
Coil current, I (MA)	40.0	37.7	36.3
Coil current density, j (A/mm^2)	27.5	27.5	27.5
Blanket space, Δ_d (m)	1.1	1.1	1.1
Magnetic energy, W (GJ)	128	124	125
Density, $n_e(0)$ (10^{19} m^{-3})	34.9	26.3	20.5
Ion temperature, $T_i(0)$ (keV)	16.9	17.9	18.9
Average beta, $\langle\beta\rangle$	5	5	5
Fusion power, P_F (GW)	3.9	4.2	4.8
Energy confinement time, τ_E (s)	1.33	1.65	2.01
Enhancement factor to ISS04	1.12	1.12	1.12

3. Helical Coil with CIC Conductors

Main specifications of helical coils for an LHD-type reactor, FFHR2m are as follows: the magnet-motive force of about 40 MA, the magnetic energy of 120 to 130 GJ, a coil center line of 150 to 175 m, and average coil current density of 25 to 30 A/mm^2. Design criteria for CIC conductors based on the ITER magnets are summarized in Table 2. Since the length of the coil center line of the helical coil is five times as long as the TF coil, some ideas are necessary in addition to adopting a large current of almost 100 kA. Parallel winding is a practical solution to shorten the cooling length within about 500 m.

Two types of mechanical structure are known for CIC conductors. One is a thick conduit type, in which rectangular conductors are simply wound with being wrapped by insulating tapes. Fairly high stress is induced in the insulators by summed up forces. The other is an internal plate type, in which the conductor is wound in the grooves of the internal plate. The stress in the insulation is reduced. Besides, the force for winding is relatively small because of thin conduits. Its disadvantage is complicated manufacturing process of the internal plates. However, its technology will be improved through the construction of ITER-TF coils. Internal plates with grooves are suite for parallel winding, because CIC conductors are just put in the grooves as shown in Fig.3. In this concept, react and wind method is preferred to use conventional insulator and to prevent huge thermal stress. Nb_3Al is a candidate for the superconducting strands of the conductor because of its good tolerance against mechanical strain. A method of "react and wind" can be adopted by managing strain during winding within about 0.5%.

The magnetic field in the helical coil is the highest in the first layer, and it is lower in the higher layers. Therefore, the average current density of the superconducting strands can be increased by grading the conductors in the case of layer winding. Non-copper current density of Nb_3Sn is given as [8],

$$j_c = 1/(1/j_{c1} + 1/j_{c0}) \tag{1}$$

$$j_{c0} = j_0\left(1-(T/T_{c0})^2\right) \tag{2}$$

$$j_{c1} = C_0\left(1-(T/T_{c0})^2\right)^2 B^{-0.5}(1-B/B_{c2})^2 \tag{3}$$

$$B_{c2} = B_{c20}\left(1-(T/T_{c0})^2\right)(1-T/3T_{c0}) \tag{4}$$

$$B_{c20} = B_{c20m}\left(1-a\varepsilon^{1.7}\right) \tag{5}$$

$$T_{c0} = T_{c0m}\left(1-a\varepsilon^{1.7}\right)^{0.333} \tag{6}$$

where j, T, B, and ε are the current density, the temperature, the magnetic field, and the strain, respectively. For ITER conductor j_0=33.51 kA/mm^2, T_{c0m}=18 K, B_{c20m}=28 T, a=1250 for tensile, 900 for compressive, and C_0=1150 [3]. Table 3 shows the non-copper current density of the strands for the various magnetic field at 7 K with the strain of -0.5%. In the case of B_{max} of 12 T, the average current density can be increased by 60% by adopting four grades of conductors.

The typical design parameters of the helical coil are listed in Table 4, compared with the ITER-TF coils. By adopting large conductors of about 90 kA and the parallel winding of five-in-hand, the length of a cooling path is within 530 m including the case of γ=1.25 in Table 1. By increasing the number of quench protection circuits, the maximum discharge voltage can be managed less than 10 kV in spite of the larger inductance and the shorter discharge time constant than ITER-TF coils. Consequently, the helical winding is expected to be realized with small extension of the technology for ITER.

Table 2. Design criteria for CIC conductors based on ITER.

Items	Design criteria	ITER-TF
Max. cooling length (m)	< 550	390
Current (kA)	< 100	68
Maximum field (T)	< 13	11.8
Non-Cu current density (A/mm^2)	< 300	273
Coil current density (A/mm^2)	< 30	20.3
SC material for HC	Nb_3Al (*1)	Nb_3Sn

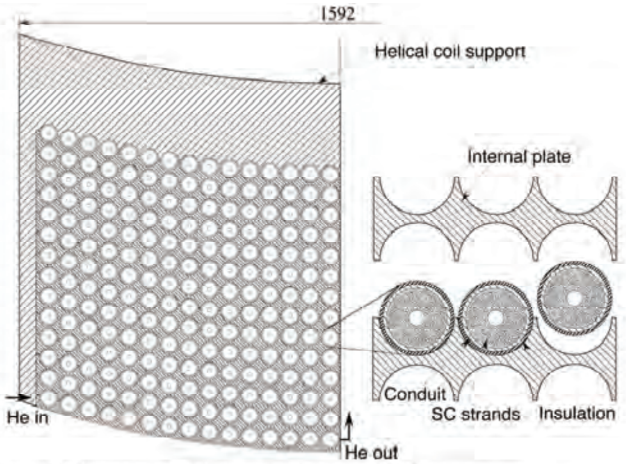

Fig. 3. Concept of helical winding with CIC conductors.

Table 3. Increase of non-copper current densities of SC strands of helical coil conductors by grading.

B_{max} (T)	J_c at B_{max} (A/mm^2)	Av. J_c by grading (A/mm^2) 3 grades	4 grades	5 grades
11.0	361	514	534	543
11.5	304	449	468	477
12.0	254	391	409	417
12.5	209	338	355	363
13.0	170	290	306	314

Table 4. Specification of helical coil with CIC conductors.

	HC_γ1.15	HC_γ1.20	ITER-TF
Maximum field (T)	12.1	12.1	11.8
Magnetic energy (GJ)	128	124	41
Number of coils	2	2	18
Turn number per coil	30*14	30*14	134
Conductor current (kA)	95.2	89.8	68.0
Length of a cooling path (m)	450	486	390
Number of parallel winding	5	5	1
Current density (A/mm^2)	27.5	27.5	20.3
Cu ratio of strand (–)	1	1	1
Non-Cu current density (A/mm^2)	400	400	273.4
Ratio of Cu strands in area (–)	0.452	0.452	0.360
Central tube diameter (mm)	12.0	12.0	8.0
Void fraction (–)	0.34	0.34	0.34
Cable outer diameter (mm)	43.5	42.3	40.2
Conduit outer diameter (mm)	46.7	45.5	43.4
Total length of conductor (km)	126	136	82.2
Total weight of SC strands (ton)	481	490	351
Total weight of Cu strands (ton)	442	450	206
Cu current density (A/mm^2)	151	151	128.7
Discharge time constant (s)	12	12	15
Inductance (H)	28.2	30.6	17.7
Number of coil blocks	35	35	9
Max. voltage (kV)	6.4	6.6	8.9

A winding method is a critical issue for the helical coil. In the case of LHD, a special winding machine was developed. The conductors from a rotating bobbin were plastically formed into the helical shape by the shaping head near the winding guide. This method will not be compatible with the "react and wind" method, because the allowable strain is in the range of 0.5% for Nb_3Al strands. A candidate of winding method is as follows:

(1) Conductors are heated for reaction of Nb_3Al on a bobbin the circumference of which is same as the length of one pitch of the helical coil.

(2) The conductors are transferred to a reel of a winding machine. The reel revolves through the helical coil as shown in Fig. 4.

(3) The conductors are pulled aside by a set of winding guides and wound in grooves of the inner plate with being wrapped with glass tapes.

(4) After winding the whole turns in a layer, the next inner plate are assembled.

The torsion strain $r\theta$ in winding is given as

$$r\theta = \frac{r \cdot tan^{-1}\eta}{2\pi a_c/4} \qquad (7)$$

where r and η are the radius of the conductor and the lead angle of the helical coil. In the case of FFHR2m2 in Table 1, the strain is estimated at about 0.3%. Since the effect of the torsion strain on the properties of superconducting strands is not known, the feasibility study is needed.

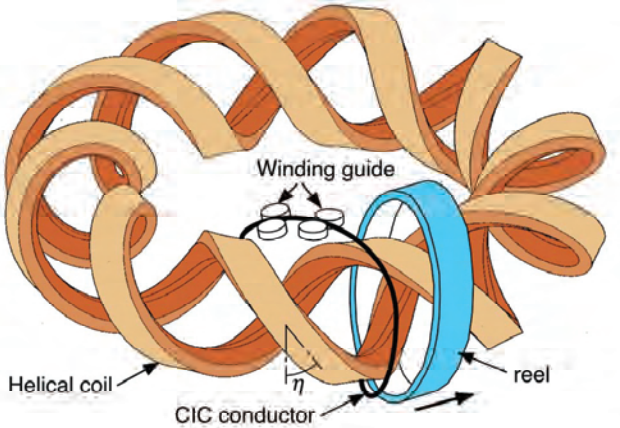

Fig. 4. Concept to wind a helical coil with CIC conductors.

4. Poloidal Coil with CIC Conductors

The poloidal coils of LHD-type reactors are circular, same as the poloidal field coils of ITER. The typical design parameters of the poloidal coil of the FFHR2m2 are listed in Table 5, compared with the largest poloidal field coil of ITER, PF3 coil. Since the radius of the larger coil, OV coil, is almost twice as large as the ITER-PF3 coil, parallel winding is also necessary. Although the coil current is huge, the highest magnetic field can be lowered than 7 T by decreasing the coil current density. Therefore, NbTi strands can be adopted, and these coils are expected to be realized with the same technology for ITER.

Table 5. Specification of poloidal coil with CIC conductors for FFHR2m2_γ1.20_j27.5.

	OV coil	IV coil	ITER-PF3
Radius of coils (m)	21.5	11.5	11.97
Number of coils	2	2	1
Coil current per coil, I (MA)	19.6	12.1	8.46
Current density (A/mm^2)	15.3	16.8	15.26
Maximum field (T)	6.6	6.3	4
Turn number per coil	14*28	10*20	11.75*16
Conductor current (kA)	50.1	60.4	45
Length of a cooling path (m)	473	361	441.9
Number of parallel winding	4	2	2
Cu ratio of strand (–)	2	2	1
Non-Cu current density (A/mm^2)	200	200	230
Ratio of Cu strands in area (–)	0	0	0.24
Central tube diameter (mm)	12.0	12.0	12.0
Void fraction (–)	0.34	0.34	0.34
Cable outer diameter (mm)	40.1	43.7	34.5
Conduit height*width (mm)	55.1*55.1	58*58	52.3*52.3
Total length of conductor (km)	106	28.9	14.1
Total weight of SC strands (ton)	653	215	41.4
Total weight of conductor (ton)	2140	641	258

5. Summary

CIC conductors can be adopted for large helical windings by adopting layer winding and parallel winding method. Since "react & wind" method is preferred for large magnets, Nb_3Al is a candidate for the helical coil conductor because of its good tolerance against mechanical strain. It is necessary to demonstrate the feasibility of its winding method. In addition, structural analyses of the winding area are needed in order to confirm the mechanical feasibility of the helical coil with the high current density of 25 to 30 A/mm^2. This conceptual design is expected to be a conventional option that can be realized by small extension from the ITER technology.

References

[1] ITER Final Design Report, Magnet Superconducting Design Criteria, IAEA, Vienna, 2001.

[2] N. Mitchell *et al.*, Fusion Eng. Des. **66-68**, 971 (2003).

[3] A. Ulbricht *et al.*, Fusion Eng. Des. **73**, 189 (2005).

[4] A. Sagara *et al.*, Nuclear Fusion **45**, 258 (2005).

[5] S. Imagawa and A. Sagara, Plasma Science & Technology **7**, 2626 (2005).

[6] H. Yamada *et al.*, Nuclear Fusion **45**, 1684 (2005).

[7] S. Sudo *et al.*, Nuclear Fusion **30**, 11 (1990).

[8] J. G. Weisend II, *Handbook of cryogenic engineering* (Taylor & Francis. 1998) p. 326.

Proceedings of ITC/ISHW2007

Internal Energy Dump for Superconducting Magnet Protection of the LHD-Type Fusion Reactor FFHR

Kazuya Takahata, Toshiyuki Mito, Hitoshi Tamura, Shinsaku Imagawa, and Akio Sagara

National Institute for Fusion Science, 322-6 Oroshi-cho, Toki 509-5292, Japan

The superconducting magnet systems of LHD-type reactors have large magnetic energies of over 100 GJ. When a quench occurs, this magnetic energy must be absorbed quickly with a resistor. A conventional energy dump with an external resistor generates a high terminal voltage, which may cause a serious dielectric breakdown. This paper presents the internal energy dump concept for quench protection of the LHD-type reactor FFHR**.** In an internal energy dump, a shorted secondary circuit acts as a heater and induces a normal transition of the whole coil. Most of the magnetic energy can be absorbed inside the coil while the temperature of the coil rises. In the case of the FFHR, the temperature rises up to 200 K. We designed and analyzed a secondary circuit using a copper winding. The designed circuit can reduce the terminal voltage by a factor of ten and induce a normal transition of the adjacent superconductor within 1 s. The results show that the internal energy dump concept is appropriate for design of superconducting magnets for fusion reactors.

Keywords: fusion reactor, heliotron reactor, large helical device, superconducting magnet, quench protection, magnetic energy, internal energy dump

1. Inroduction

Heliotron power reactors have competitive advantages for steady-state operation due to the fact that they employ currentless plasma. These advantages have been demonstrated by the Large Helical Device (LHD) with a superconducting magnet system since the start of experiments in 1998 [1]. Engineering and physics results from studies of the LHD confirm that LHD-type heliotron reactors are well suited for steady-state power plants. Based on the outputs from the LHD, we have performed design studies of LHD-type demonstration reactors (the FFHR series). The detailed design of the blanket, operating scenario, superconducting magnet, coil-supporting structure and maintenance procedures has been published previously [2, 3]. In the design studies, we applied realistic technologies that are expected to be developed in the near future.

Heliotron power reactors also have an important advantage in the superconducting magnet design. Superconductors do not generate heat loss due to a changing magnetic field, known as ac loss. Therefore, large cooling capability is not required, in contrast to Tokamak reactors. We therefore propose an indirect cooling method, which is commonly used in accelerator magnets, as an alternative to pool cooling and forced-flow cooling [4, 5]. The use of indirect cooling allows a simple coil structure to be used.

An important issue for the design of superconducting magnets is the dumping of magnetic energy when a quench occurs. A heliotron reactor magnet consists of continuous windings with large diameter. Therefore, the magnet has large magnetic energy of over 100 GJ. Because an unexpected quench may cause burn-out of a superconductor, a protection system must be developed to reduce the coil current rapidly and to dump the magnetic energy. The conventional protection system has an external resistor near a power supply, which absorbs most of the magnetic energy. This method is called the external energy dump. When employing an external energy dump in large magnets, there are two important engineering issues. First, high voltages over 10 kV are applied across a coil, which may cause a dielectric breakdown. Second, the external resistor must have a large mass of heat-absorbing material. When using water as heat-absorbing material, a large amount of water must be heated and evaporated. To absorb a magnetic energy of 100 GJ, 40,000 kg of water is required.

To resolve the issues of the external energy dump, we have investigated an internal energy dump concept [6, 7]. In this concept, the magnetic energy is absorbed into the coil using the normal resistance of the superconductor. When a quench occurs, an embedded heater induces the normal transition of the whole of the superconductor. A

author's e-mail: takahata@LHD.nifs.ac.jp

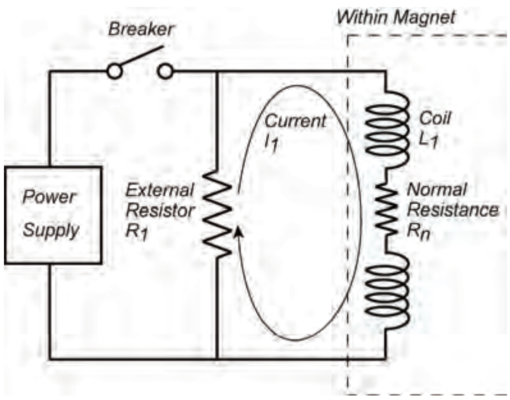

Fig. 1 Quench protection circuit with an external resistor.

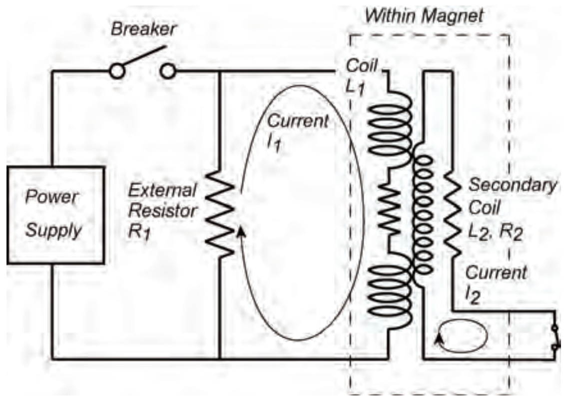

Fig. 2 Quench protection circuit with a secondary circuit.

conventional resistive heater needs a power supply, and hence we employ a shorted secondary circuit as a heater. The current of the secondary circuit is induced by the decay of the coil current. The secondary circuit, therefore, does not need a power supply. In this paper, we demonstrate the applicability of the internal energy dump as a protection system for the FFHR. The design of the secondary circuit is presented and its performance is investigated.

2. Comparison between External and Internal Energy Dumps

Figure 1 shows a typical quench protection system with an external resistor. When a quench is detected, the breaker is opened. The current then shifts from the power supply to the external resistor. The resistance of the resistor R_1 is usually much higher than that of the superconductor in the normal state R_n. The coil current I_1 decays with a time constant τ of L_1/R_1 while the resistor absorbs the magnetic energy. The maximum terminal voltage is I_0R_1, where I_0 is the initial current. The maximum voltage V_m can be rewritten as:

$$V_m = \frac{2E}{I_0\tau} \tag{1}$$

where E is the stored magnetic energy of the coil. The maximum voltage is proportional to the energy. Note that the coil current must be increased to reduce the voltage. For the FFHR with the coil current of 100 kA, the decay time constant should be less than 18 s to avoid burn-out of the superconductor [5]. The maximum terminal voltage then reaches 60 kV, which is much higher than the designed voltage for typical superconducting magnets. To reduce the voltage, the coil must be divided into several subdivisions.

In an internal energy dump, the resistance R_n is higher than R_1 because the whole of the superconductor become normal. Therefore, the decay time constant is assumed to be L_1/R_n. The maximum terminal voltage can be reduced because R_1 can be determined independently of the quench protection. Therefore, the coil current can potentially be reduced. In addition, the external resistor does not require a large amount of heat-absorbing material as most of the heat is absorbed by the coil itself.

3. Temperature Rise of the FFHR Magnet during an Internal Energy Dump

The internal energy dump causes a uniform temperature rise of the whole coil. Here we investigate whether the magnetic energy can be absorbed into the coil. The balance equation between the magnetic energy E and the heat capacity of the coil can be written as:

$$E = \sum_i V_i \int_{T_0}^{T_m} C_i(T)\,dT \tag{2}$$

where i is the material number, V_i is the volume of each material, and $C_i(T)$ is the specific heat per unit volume. T_0 and T_m are the initial and maximum temperatures. We applied this equation to the helical coil of the reactor design FFHR2m1. The coil structure is presented in detail in a previous paper [5]. The materials include superconductors, insulators, and cooling panels. The maximum temperature T_m was calculated to be 210 K for a magnetic energy of one helical coil of 66 GJ, which is within acceptable levels, indicating that the internal energy dump can be successfully applied.

4. Quench Protection with a Secondary Circuit

Figure 2 shows a quench protection circuit with a secondary circuit. The secondary circuit is a normal coil that is closely coupled to the superconducting coil. When the current of the superconducting coil starts to decay as the breaker is opened, the current shifts from the superconducting circuit to the secondary circuit. The

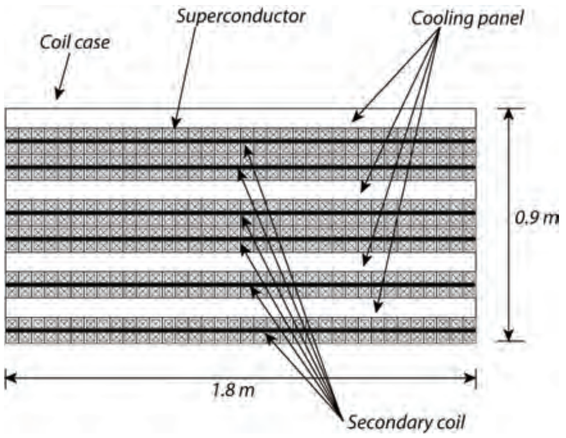

Fig. 3 Cross-sectional structure of the helical coil and arrangement of the secondary coils.

normal secondary circuit then heats the adjacent superconductor by Joule heating. Finally, the secondary circuit causes the whole of the superconducting coil to become normal. This process is referred to as quench back [6, 7]. This concept can induce a normal region more reliably than a resistive heater. The switch in the secondary circuit is closed only during a quench. A current shift during an excitation of the magnet is inhibited by opening the switch.

5. Quench Protection Circuit for the FFHR

Figure 3 shows the structure of the helical coil of the FFHR and the arrangement of the secondary coil [5]. The superconductor is wound by a layer winding method (36 turns/layer, 12 layers). Four cooling panels with cooling channels are embedded in the coil. The superconductor is cooled indirectly by the cooling panels. The secondary coils consist of copper wires and are arranged between sets of two superconductor layers. There are thus six layers of secondary coil. We determine the thickness of each layer to be 0.5 mm.

The shift of current from the primary circuit I_1 to the secondary circuit I_2 can be obtained by the following circuit equations:

$$\begin{aligned} L_1 \frac{dI_1}{dt} + M \frac{dI_2}{dt} + I_1(R_1 + R_n) = 0 \\ L_2 \frac{dI_2}{dt} + M \frac{dI_1}{dt} + I_2 R_2 = 0 \end{aligned} \quad (3)$$

where L_2 is the inductance of the secondary circuit, M is the mutual inductance between the two circuits, and R_2 is the resistance of the secondary coil. Note that the resistance of the normal zone R_n and the resistance of the secondary coil R_2 depend on temperature. The temperature rise of the superconducting coil can be estimated from the heat balance equation:

$$C_1(T)\frac{dT}{dt} = \lambda \rho_1(T) J_1^{\,2}(T) \quad (4)$$

where C_1 is the average specific heat per unit volume in the coil, λ is the ratio of coil volume to copper volume, ρ_1 is the resistivity of copper, and J_1 is the overall current density. In addition, the temperature of the secondary coil can be obtained by

$$C_2(T)\frac{dT}{dt} = \rho_2(T) J_2^{\,2}(T) \quad (5)$$

where C_2 is the specific heat per unit volume of copper, ρ_2 is the resistivity of copper, and J_2 is the current density. Even though the heat transfer between the superconducting and secondary coils is neglected, the calculations can be the first step in investigating the performance of the secondary circuit.

By solving Eqs. (3) and (5), we find that the temperature rise is independent of the turn number of the secondary coil if the thickness of the coil is fixed. Therefore, the cross-section of the wire and the turn number need not be considered further. The self inductance of the secondary coil also affects the temperature rise, which increases with increasing inductance. The inductance must then be adjusted to half the inductance of an ideal close winding to avoid a burn-out of the secondary coil itself. This adjustment of inductance is technically possible using a non-inductive winding method.

A key issue for this protection method is whether we can increase the initial decay time constant of the superconducting coil (L_1/R_1) and reduce the maximum terminal voltage (I_0R_1). We analyzed quench protection for a time constant of 200 s, about ten times larger than the maximum time constant for external energy dump protection of 18 s. Figure 4 shows the calculations of the current shift and the temperature rise of the secondary coil before quench back. In this calculation, the resistance of the superconducting coil R_n is zero. The currents are normalized by the initial current of the superconducting coil and the turn number. The results show that the temperature of the secondary coil increases to about 35 K within 1 s. This temperature rise can certainly induce a normal transition of an adjacent superconductor because the critical temperature in a magnetic field of 13 T is about 10 K in the case of a Nb_3Sn superconductor.

We next analyzed the temperature rise of the coils after quench back. Figure 5 shows the calculations of the current shift and the temperature rise. The quench back is assumed to occur with a time delay of 1 s from the start of the energy dump. After the quench back, the resistance R_n is calculated using the normal resistance of the whole superconducting coil. The current of the superconducting

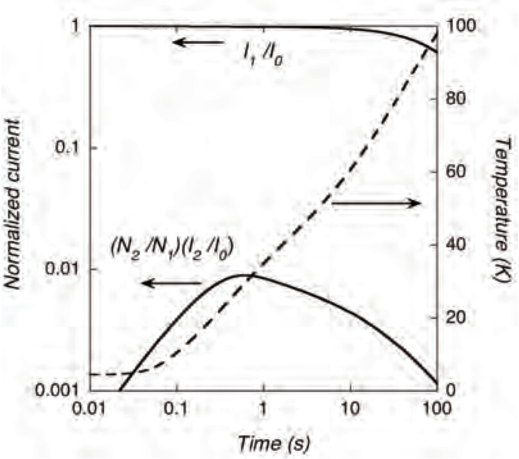

Fig. 4 Current shift (solid lines) and temperature rise (broken line) of the secondary coil before quench back. The currents are normalized by the initial current of the superconducting coil I_0 and the turn numbers. N_1 and N_2 are the turn numbers of the superconducting and the secondary coils, respectively.

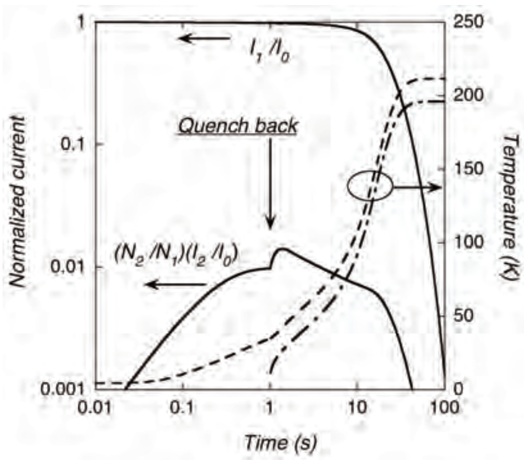

Fig. 5 Current shift (solid lines) and temperature rise of the superconducting and secondary coils during the energy dump. Quench back occurs with a time delay of 1 s. The dashed and the broken lines represent the temperatures of the superconducting and secondary coils.

coil decays rapidly with increasing temperature because the resistance of the coil increases with increasing temperature. The maximum temperatures of both the superconducting and secondary coils are about 200 K. The results demonstrate that the designed circuit can protect the coil safely even though the initial decay time constant increases by a factor of ten. The circuit also reduces the terminal voltage.

6. Conclusions

An internal energy dump concept has been demonstrated by applying it to the LHD-type fusion reactor FFHR. The analysis confirmed that the coil of the FFHR can be protected from a quench using an internal energy dump. The magnetic energy can be absorbed into the superconducting coil while the coil temperature increases to about 200 K. Quench back, which is necessary for the internal energy dump, can be induced using a shorted secondary coil consisting of copper wires. The maximum terminal voltage can be reduced by a factor of ten compared with the conventional external energy dump. The results demonstrate that the internal energy dump can be a key technology for large superconducting magnets for fusion reactors.

Acknowledgements

This work was funded by MEXT of the Japanese government under grant no. NIFS07ULAA107 and by the Japan Society for the Promotion of Science, Grant-in-Aid for Scientific Research (C) no. 18560793.

References

[1] O. Motojima *et al.*, Fusion Eng. Des. **81**, 2277 (2006).
[2] A. Sagara *et al.*, Nucl. Fusion **45**, 258 (2005).
[3] A. Sagara *et al.*, Fusion Eng. Des. **81**, 2703 (2006).
[4] T. Mito *et al.*, Fusion Eng. Des. **81**, 2389 (2006).
[5] K. Takahata et al, Fusion Eng. Des. (2007), doi:10.1016/j.fusengdes.2007.04.050
[6] M.A. Green, Cryogenics **24**, 3 (1984).
[7] M.A. Green, Cryogenics **24**, 659 (1984).

Proceedings of ITC/ISHW2007

Design and Optimization of Support Post for Cryogenic Components in the FFHR

Hitoshi TAMURA, Akio SAGARA and Shinsaku IMAGAWA
National Institute for Fusion Science, 322-6 Oroshi-cho, Toki 509-5292, Japan

FFHR is a design of a steady state fusion reactor which has been studied to demonstrate LHD-type fusion power plant. The weight and the deformation of the cryogenic components are sustained by support posts. A folded multi plate type post which was adopted in the LHD could be used for the FFHR. The dimensions of the post were decided according to buckling load estimation against a gravitational load. Using this fundamental design, a flexibility and stress distribution of the post were calculated by using FEM analysis. The flexibility against a radial displacement was 24kN/mm and the maximum stress was 159MPa for CFRP plate and 390MPa for stainless steel plate, respectively. These were under allowable level for the materials. The heat loads were also calculated and 10.5kW to 80K and 0.34kW to 4K were obtained and the result showed that the head load to 4K was almost 1/20 compare with the post which was all made of stainless steel. The natural frequency was analyzed to estimate safeness against external load such as an earthquake. Those results showed that the LHD-type support post was practical for the FFHR in mechanical and thermal points of view.

Keywords: FFHR, fusion reactor, superconducting coil, cryogenic component, support post, modal analysis

1. Introduction

FFHR is a concept design of a steady state fusion reactor which has been studied to demonstrate LHD-type fusion power plant [1-3]. Fig. 1 shows the schematic draw of the cryogenic components in the FFHR. Total weight of superconducting coils and supporting structure exceeds 16,000 tons. Since the cryogenic components can be mainly made of stainless steel, the thermal contraction between room temperature and the cryogenic temperature is about 0.3%. For example, the maximum displacement caused by the thermal contraction is almost 55mm at 18m in radial position from the center of the device where the outer poloidal field coils are set. The weight and the deformation are sustained by support posts which are set on a base plate of a cryostat vessel whose temperature is room temperature. The support post must have following functions; support the weight of the cryogenic components, reduce heat leak to lower temperature side, absorb the thermal contraction, maintain a cyclic deformation, give a safe warranty against an external load such as an earthquake.

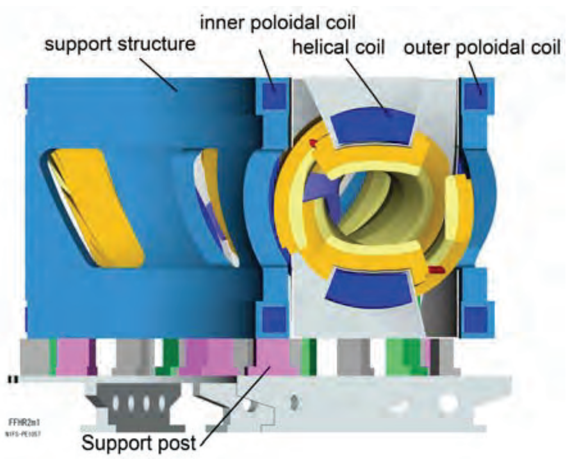

Fig. 1 Schematic draw of the cryogenic components in the FFHR.

author's e-mail:tamura@nifs.ac.jp

The Large Helical Device (LHD) has 3.9m of major radius and 850 tons of cold mass. The LHD adopted a “folded multi plates” type post [4,5]. The post consisted of carbon reinforced plastic (CFRP) and stainless steel (SS) plates. The SS plates were cooled down to 80K to be a thermal anchor region and the plates were connected to the CFRP plates through the thick SS blocks. To minimize a heat leak to low temperature side, the FRP plates were used between room temperature and the thermal anchor region, and the thermal anchor region to the cryogenic temperature. The maximum thermal contraction at the post position was 13mm and the post absorbed the contraction by its flexibility against the radial direction of the components. The CFRP was chosen since it has much larger compressive strength than another low heat conductive materials such as glass fiber reinforced plastic. This type of post can be also valid for the support post of the FFHR. A conceptual design and specification of the folded multi plate type post is introduced and stress distribution under several kind of operational situation are shown in this paper. The deformation mode and natural frequency of the cryogenic components including the post are also calculated and safeness against an earthquake is discussed.

2. Basic geometry of the folded multi plates

The cryogenic components which are cooled down to cryogenic temperature are superconducting helical coils, superconducting poloidal coils, and the coil supporting structure. Total weight of the cryogenic components in FFHR has been estimated 16,000ton so far. Considering a symmetrical and homogeneous distribution of the gravitational load, number of the posts were decided 30; 20 posts were located under the outer poloidal coil and other 10 posts were set under the inner poloidal coil. The span of each outer and inner post was 5.7m and 6.2m, respectively. The CFRP plates in the folded multi plate type post are subjected to a compressive load while the SS plates are subjected to a tensile load. The geometrical dimensions of the CFRP plates were decided according to buckling load estimation against a gravitational load with bent long column model. The buckling load in this model can be describes as follows.

$$P_k = \frac{\pi^2 EI}{4L^2}, \qquad I = \frac{bh^3}{12}, \tag{1}$$

where, E is Young's module of the longitudinal direction, I is the flexural rigidity, b is the width, h is the thickness, and L is the length of the plate. We defined that the safety factor against the buckling load was over 5 times larger than the nominal weight; (16,000ton)/(30posts)*(safety factor 5)=2667tons. The cross sectional dimensions of the CFRP plate were assumed 1200mm in width and 80mm in thickness considering a setting space. Fig. 2 shows the buckling load against plate length with the parameters of the number of the plate. Since the post must have flexibility, longer plate was desirable but an increase of number of the plate makes the size and weight bigger. 1.2m of the length was chosen and 5 plates and 3 plates were adopted for the center column and outer column, respectively. For the stainless steel plate, 1.2m in width, 30mm in thickness, 1.0m in length, and 3 plates for both side were chosen considering the tensile load and the strength of SS material. Fig. 3 shows the setting up of the support post and its dimension. The weight of a post itself was 10 tons in this case.

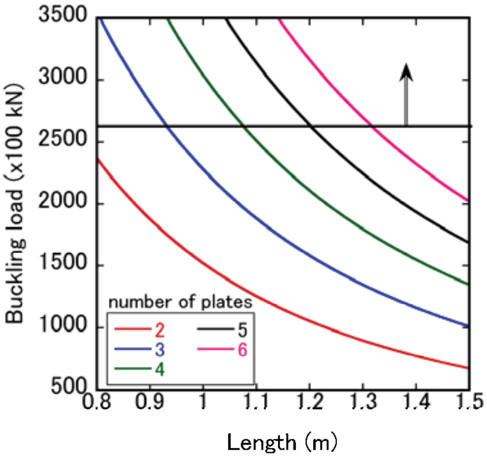

Fig. 2 Buckling load of the CFRP plate with the cross section 1200mm x 80mm using the bent long column model.

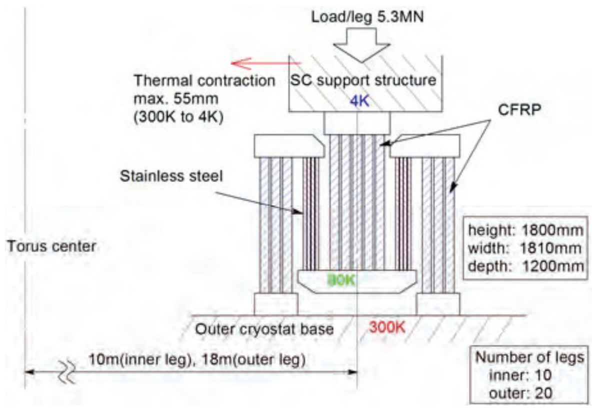

Fig. 3 Schematic draw of the support post for the FFHR.

3. FEM analysis

Using the basic geometrical design of the folded multi plates, a flexibility and stress distribution of the post were calculated by using FEM analysis. The FE model of the support post was prepared by using 3D beam element for a rigidity estimation and 3D shell element for a stress distribution analysis. A thermal condition was also investigated by 3D shell model. The entire 3D model included cryogenic components. Since the cryogenic components were rigid enough compared with support post, we prepared a simple torus shaped structure having not only the same weight of the components but also the same geometrical location of the center of gravity. This torus shaped structure was set on 30 support posts. The natural frequency of this structure was calculated by using this model. Physical properties of the stainless steel used in the analysis were from data base software [6]. The property of the CFRP material was an experimental data of the support post of LHD measured by a manufacture. ANSYS was used for calculation.

3.1 Static analysis

The flexibility against a radial direction was 22.9kN/mm and the maximum stress when 55mm of forced displacement was subjected to the top of the post was 155MPa for CFRP plate and 544MPa for stainless steel plate, respectively. These were under allowable level for the materials and they could be reduced by setting the post to the deforming direction in advance. For example, if the post bent 27.5mm to the outward direction and then the cryogenic components were set on the post, the final position of the top of the post could be 27.5mm bent to the inward direction since the thermal contraction of the cryogenic components forcibly acted the post. The stress level caused by the thermal contraction could be reduced to almost the half by this philosophy. The circumferential direction was more than 10 times as rigid as the radial direction.

The heat loads calculated by using the same model were 10.5kW to 80K and 0.34kW to 4K were obtained and the result showed that the head load to 4K was almost 1/20 compare with the post which was all made of stainless steel. On the other side, heat load to 80K was about a half of the all SS made post.

Here we introduced three operating situations and calculated the stress distribution for each case.

(1) Gravity only

This situation simulated a normal condition before cooling down. The top of the post was bent 27.5mm to the outward and no thermal contraction. In this case, the maximum von Mises stress appeared in CFRP plates and SS plates were 147MPa and 340MPa, respectively. The contour expression of the stress distributions are shown in fig. 4.

(2) Gravity + cool down + 0.2G of transverse acceleration.

This situation simulated 0.2G of transverse seismic load is subjected to the device while the cryogenic components are cooled down to 4K. The maximum von Mises stress appeared in CFRP plates and SS plates were both increased and the values were 159MPa and 390MPa, respectively as shown in fig. 5.

(3) Gravity + cool down + 1.0G of transverse acceleration.

In case of 1.0G of transverse acceleration was subjected, the maximum von Mises stress in CFRP plates was 429MPa and 881MPa in the SS plates.

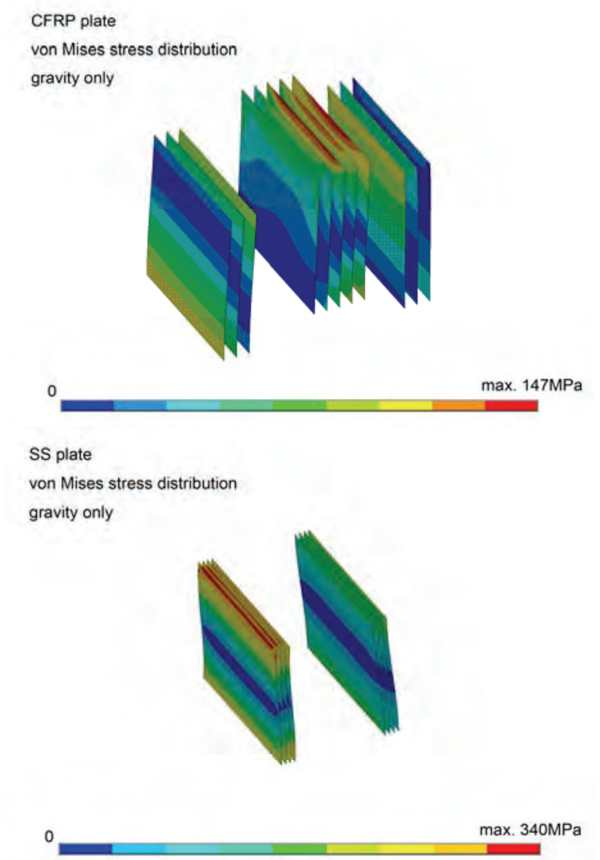

Fig. 4 The distribution of von Mises stress in the CFRP plates (above) and the SS plates (bottom) when the gravity load was only subjected.

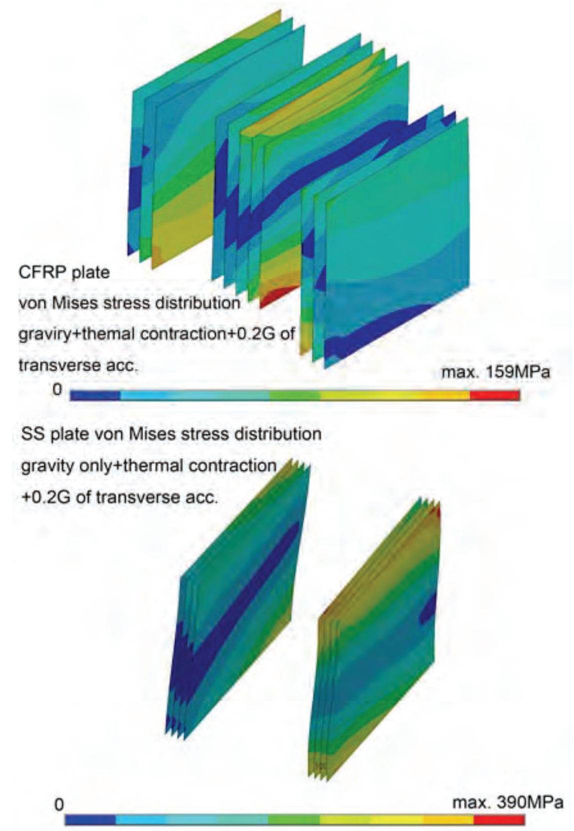

Fig. 5 The distribution of von Mises stress in the CFRP plates (above) and the SS plates (bottom) when the gravity and 0.2G of transverse acceleration were subjected together with the thermal contraction.

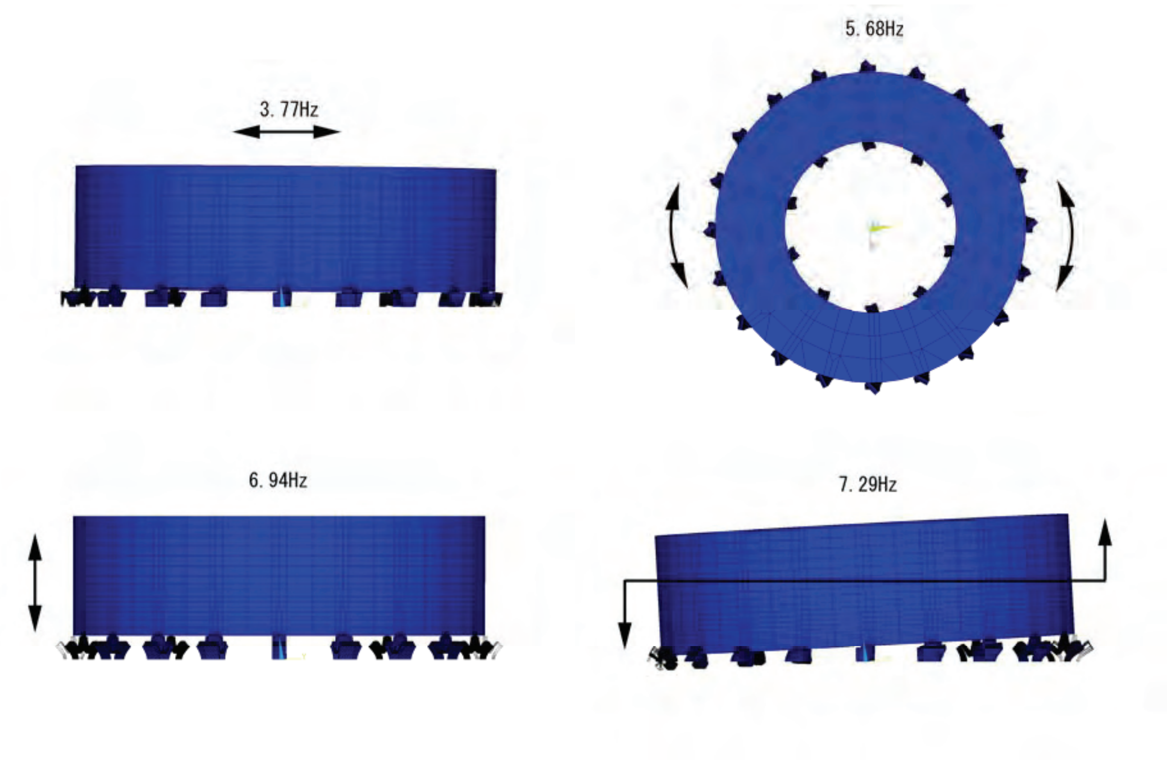

Fig. 6 Results of modal analysis. Natural vibrations mode and their frequency.

3.2 Modal analysis

The natural frequencies of the structure were in a range of 3Hz and 8Hz. Fig. 6 shows the first four modes of natural vibrations and their frequencies. The first mode was a horizontal vibration and the second one was rotational deformation on its axis. The third and fourth modes were concerning with an up-down movement. The higher natural frequencies exceeded 15Hz and the deformation modes were mainly in the cryogenic components.

4. Discussion

The safeness of the structure against an earthquake depends on a frequency and a magnitude of a seismic acceleration. Since a typical earthquake has the range of 0.5Hz to 20 Hz frequency, a structure which has a natural frequency near this range may resonate. From a response spectrum analysis of the typical earthquake such as El Centro, TAFT, etc, the response acceleration of this range would be 1.0 to 1.5G. The analytic result of 1.0G of transverse acceleration load seems that this case is a limit of transverse load since the maximum von Mises stress was slightly larger than permissible stress. This transverse load limit could be a criterion for a design of the building.

5. Conclusions

The “folded multi plates” support post was designed for the FFHR and obtained following conclusions.

The flexibility against a radial deformation was 24kN/mm. The circumferential direction was more than 10 times as rigid as the radial direction.

The total heat load to 4K was estimated not to exceed 340W. It was almost 1/20 value compare with the post which was all made of stainless steel.

The maximum von Mises stress was 159MPa for CFRP plate and 390MPa for stainless steel plate, respectively when 0.2G of transverse acceleration was subjected to the components under cooled down situation. Those stress level were allowable value.

Several natural frequencies of the structure closed to the frequencies in a seismic vibration. To keep the safeness of the device, the acceleration subjected to the structure should not be exceeded 1.0G from the results of static analysis.

Acknowledgement

This work was supported by National Institute for Fusion Science (07ULAA117).

References

[1] O. Motojima et al. Fusion Eng. Des. **81** 2277 (2006).
[2] Sagara A et al. Fusion Eng. Des. **81** 2703 (2006).
[3] Sagara A et al. Nucl. Fusion **45** 258 (2005).
[4] H. Tamura et al. Fusion Technology 1996 1019 (1996).
[5] H. Tamura et al. Adv. in Cryogenic Eng. **45** 753 (2000).
[6] Cryocomp software, Eckels Engineering and Cryodata Inc. (1997).

P1-095

Design studies on split-type helical coils for FFHR-2S

Nagato Yanagi, Kiyohiko Nishimura, Akio Sagara, Osamu Motojima

National Institute for Fusion Science, 322-6 Oroshi-cho, Tok, Gifu 509-5292, Japan

Configuration optimization is being carried out for the LHD-type fusion energy reactor FFHR. One of the present issues is to find a sufficient clearance between the ergodic layers of the magnetic field lines and the blankets so that direct loss of alpha particles is minimized and the heat flux on the first wall is reduced. It has been newly found that by having the combination of splitting the helical coils in the poloidal cross-section and adopting a small pitch parameter for the winding law of the helical coils, a large gap is clearly obtained. Here, splitting of the helical coils means that they have higher current density at the inboard side of the torus and lower at the outboard side, which contributes in enhancing the helical symmetry. A small value of the pitch parameter such as 1 is adopted in the configuration named FFHR-2S, and the plasma volume is almost the same as that with the original design of FFHR-2m1 that has the pitch parameter of 1.15. Various physical parameters of the vacuum magnetic surfaces are investigated with the new configuration, such as the rotational transform, specific volume and the drift orbits of helically trapped particles.

Keywords: FFHR, LHD, heliotron, split-type helical coils, forbidden zone, ergodic layers, blanket space, configuration optimization

1. Introduction

Based on the successful progress of fusion relevant plasma experiments performed for 10 years in the Large Helical Device (LHD) [1], the conceptual design studies on the LHD-type fusion energy reactor (FFHR) are being conducted both on physics and engineering issues, and the recent design activities are summarized in [2]. For FFHR, a heliotron magnetic configuration similar to that of LHD will be employed so that the confined plasma is current free and the steady-state operation is realized. Though the further optimization of the configuration is still being carried out, the basic parameters give the toroidal magnetic field of 6 T with a major radius in the range 14-18 m in order to generate 3 GW fusion power. By having the machine size approximately four times bigger than that of LHD, the stored magnetic energy of the superconducting coil system is in the range 120-150 GJ.

In these studies, the coil pitch parameter, γ, defined by $(m/l)(a_c/R_c)$ for continuous helical coils (having the toroidal pitch number m, poloidal pole number l, average minor radius a_c and major radius R_c), has been chosen to be lower than 1.25 adopted for the present LHD. This choice is made for the purpose of reducing the electromagnetic hoop-force on the helical coils while ensuring larger blanket space between the core plasma and the helical coils [3]. The latest standard configuration, named FFHR-2m1, has γ = 1.15 with m = 10, l = 2, a_c = 3.22 m and R_c = 14 m.

The vacuum magnetic surfaces of FFHR-2m1 is shown in Fig. 1(a). One of the most difficult issues with this configuration is found in the still observed interferences between the ergodic layers of the magnetic field lines and the blankets (thickness: ~1.1 m) especially at the inboard side of the torus. In order to reduce the heat flux on the blankets, the concept of "helical x-point divertor (HXD)" was proposed [4]. However, this choice gives a high heat flux on the limiter-like structures, and moreover, a recent study shows that the confinement of alpha particles is deteriorated. Since the alpha particles are lost finally along the magnetic field lines in the ergodic regions, the loss rate is substantially reduced if the ergodic layers are not cut by metallic materials.

In this connection, we are seeking for another approach of ensuring much clearer blanket space by modifying the coil configuration while keeping the major radius below 16-17 m. As was found in the previous study [5], the symmetry of magnetic surfaces around the magnetic axis is significantly improved, without shifting the magnetic axis inward, by increasing the current density at the inboard side of the helical coils while decreasing at the outboard side. Modulation of the current density can be practically realized by splitting the helical coils in the poloidal cross-section. Using this feature by splitting the helical coils, we found a new configuration that assures sufficient clearance between the ergodic layers and the blankets. For the new configuration, various physics properties of the magnetic field are investigated and the initial results of the parameter surveys are introduced in this paper.

author's e-mail: yanagi@LHD.nifs.ac.jp

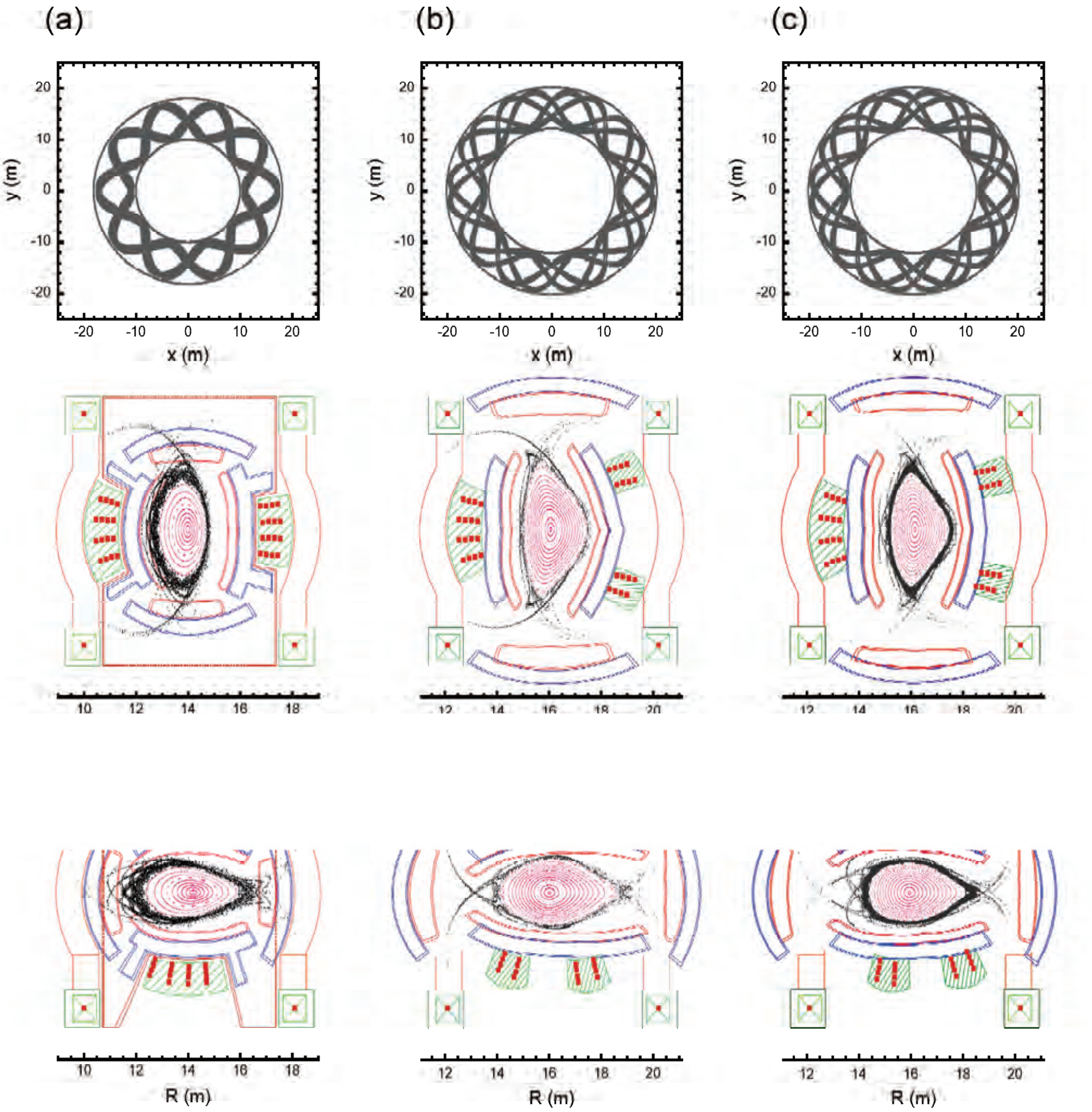

Fig.1 Plan views of the coils and magnetic surfaces at two cross-sections for (a) FFHR-2m1, (b) FFHR-2S (γ = 1.0, α = +0.1) and (c) FFHR-2S (γ = 1.0, α = -0.1). The coil currents are assumed by 16 filaments in one helical coil. For splitting a helical coil, the half portion of the coil is assumed by 8 filaments.

2. Vacuum magnetic surfaces of FFHR-2S and their properties

Using the remarkable properties of improving the helical symmetry by splitting the helical coils in the poloidal cross-sections, new magnetic configurations were surveyed. However, it was found that the ergodic layers could not be easily removed from the blanket area at the inboard side by simply splitting the helical coils while maintaining the original pitch parameter of γ = 1.15. In order to overcome this difficulty, we newly found that a drastically larger gap is obtained by reducing the pitch parameter to be as low as γ = 1.0 together with splitting of the helical coils. Figure 1(b) and (c) show examples of the vacuum magnetic surfaces with γ = 1.0 configurations. Two examples are shown with the pitch modulation parameter α of +0.1 and –0.1. The major radius is 16.1 m for both cases by keeping the minor radius of the helical coils to be 3.22 m, the same as that for FFHR-2m1. As is

P1-095

seen in these figures, the outermost ergodic layers are clearly displaced from the blankets. Here, the shapes and the positions of the blankets are adjusted in these figures in order to avoid any interference.

Here we should note that such a low pitch parameter of γ = 1.0 has never been examined so far, as it has been well known that one is already in the so-called forbidden-zone for generating magnetic surfaces with a l = 2 heliotron configuration [6]. We understand that the low pitch parameter is effective for making the ergodic layers compact, while the splitting of helical coils ensure larger closed magnetic surfaces. Figure 2 shows the distance between the helical coils and the ergodic layers. The magnetic configuration of FFHR-2m1 has an interference with the blankets unless it is with a much larger major radius. For FFHR-2S, much wider space is assured with a smaller major radius. Here it is assumed that the distance between the helical coils and vacuum vessel is constant at 110 mm, which is the same as that for LHD.

The basic physical quantities of the vacuum magnetic surfaces are evaluated, such as the rotational transform and specific volume as a function of the average minor radius. The radial variation of the rotational transform is shown in Fig. 3(a). Even with the lower pitch parameter, a larger plasma minor radius is expected for FFHR-2S. At the same time, a larger shear of the rotational transform is expected, which is good for MHD stability. On the contrary, the specific volume shows that a magnetic hill is formed all over the magnetic surfaces. It is expected that magnetic well is introduced by the plasma beta and this should be calculated in our future study. It should also be stressed, on the other hand, that by having a smaller pitch parameter, the helical coils experience less electromagnetic forces, which is one of the fundamental benefits of the FFHR concept [3].

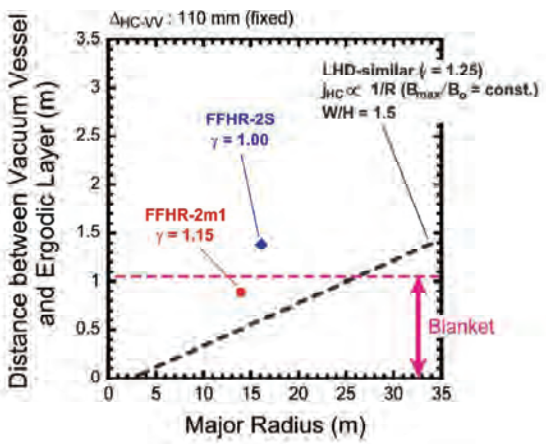

Fig.2 Distance between the vacuum vessel and the ergodic layers of magnetic field lines for FFHR-2m1 and FFHR-2s.

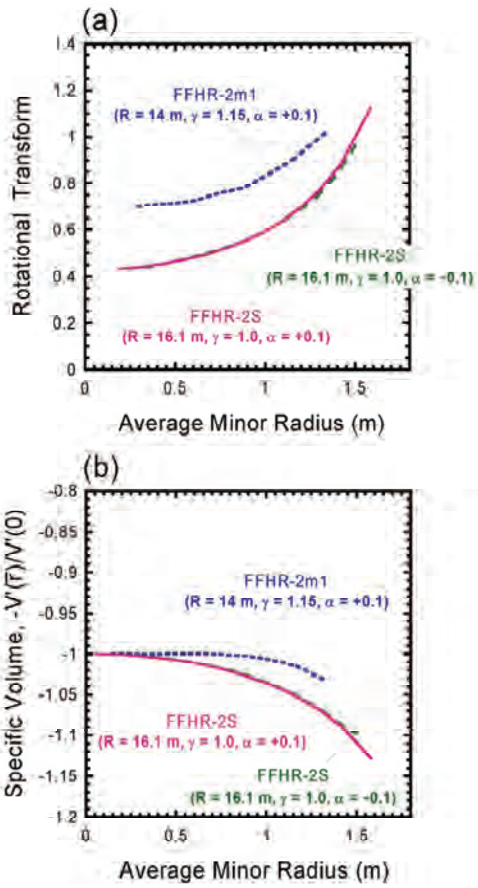

Fig.3 (a) Rotational transform and (b) specific volume for FFHR-2m1 and FFHR-2S with α = +0.1 and −0.1 as a function of the average minor radius.

3. Drift orbits of helically trapped particles

One of the important properties of magnetic configuration for helical devices is the particle orbits especially in terms of the direct loss of particles trapped in helical mirrors. Another advantage of the new configuration of FFHR-2S is found with its particle orbits for the pitch modulation parameter α of −0.1. A comparison of the orbits of perpendicularly injected deuterons is given for FFHR-2m1 and FFHR-2S in Fig. 4. As is always observed for conventional heliotron configurations such as LHD, the drift orbits of the helically trapped particles are shifted inward compared to the magnetic surfaces (with the magnetic axis at the center of the helical coils) as is seen in Fig. 4(a) for FFHR-2m1. The drift orbits for FFHR-2S has a similar tendency for the particles starting from the core region, however, the confinement of particles are better up to the plasma periphery, as is seen in Fig. 4(b).

In order to clarify the difference about particle orbits, the helical ripples are compared for the two configurations. Figure 5 shows the variation of the magnetic field strength along magnetic field lines. Compared to FFHR-2m1, the helical ripples in FFHR-2S are mitigating the toroidal ripples, which lead to the better confinement of helically trapped particles. Figure 6 shows the variation of the amplitude of the helical ripples as a function of the minor radius. The helical ripple of FFHR-2S is almost the same as that for FFHR-2m1 near the magnetic axis, however, it remains less than half at a larger minor radius. The small helical ripple should contribute in a better confinement of plasma not only in terms of neoclassical transport but also of anomalous one.

4. Conclusions

A new magnetic configuration for the LHD-type fusion energy reactor FFHR is examined by splitting the helical coils in the poloidal cross-section. It was found that by employing a low pitch parameter of $\gamma = 1.0$, a large clearance is obtained between the ergodic layers and blankets. This configuration with a negative pitch modulation parameter of $\alpha = -0.1$ has good properties for the drift orbits of helically trapped particles. The optimization of the coil configuration is being carried out also from the engineering viewpoint.

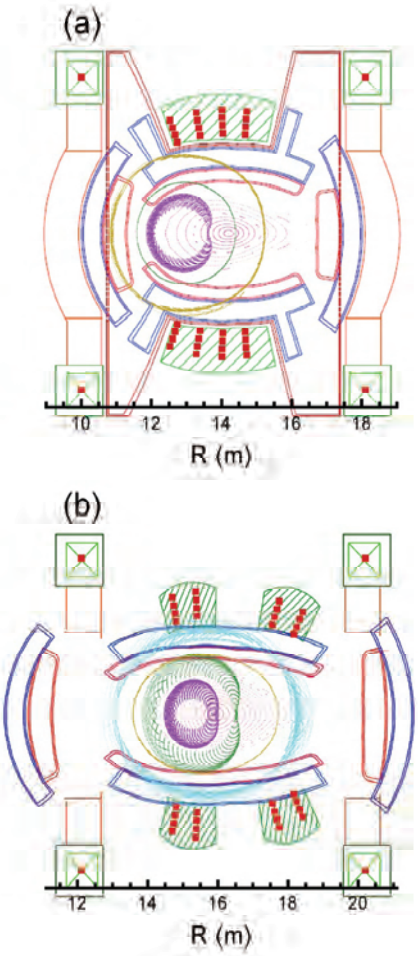

Fig.4 Drift orbits of deuterons for (a) FFHR-2m1 and (b) FFHR-2S. Deuterons with 500 keV energy are injected with a pitch angle of 90 degrees at various locations on the magnetic surfaces.

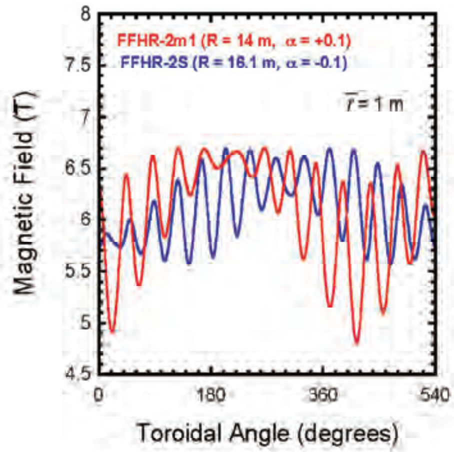

Fig.5 Variation of the magnetic field strength along the field lines for FFHR-2m1 and FFHR-2S ($\alpha = -0.1$) on the magnetic surfaces having the average minor radius of 1 m for both cases.

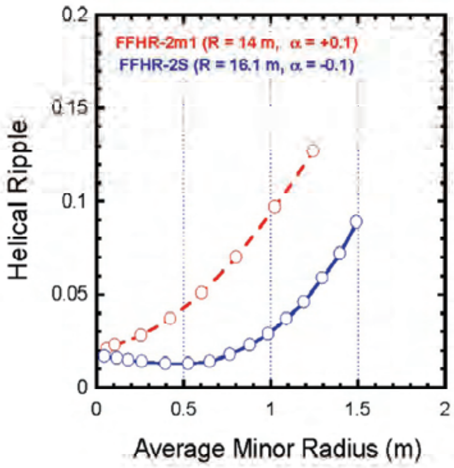

Fig.6 Variation of helical ripples as a function of the average minor radius for FFHR-2m1 and FFHR-2S ($\alpha = -0.1$).

Acknowlegments

The authors are grateful to many other staff in the FFHR design group for valuable discussion and support.

References

[1] O. Motojima et al., Fusion Eng. Des. **81** 2277 (2006).
[2] A. Sagara et al., Fusion Eng. Des. **81** 2703 (2006).
[3] S. Imagawa, et al., Journal of Plasma and Fusion Research SERIES, Vol. 5 (2002) pp.537-540.
[4] T. Morisaki et al., Fusion Eng. Des. **81** 2749 (2006).
[5] K. Nishimura and M. Fujiwara, J. Phys. Soc. Japan **64** 1164 (1995).
[6] K. Uo, Nuclear Fusion **13** 661 (1973).

P1-099

EMC3-EIRENE implementation on NCSX and first applications

F. Sardei [1], A. Brooks [2], Y. Feng [1], F. Herrnegger [1], T. Kaiser [3], J. Kisslinger [1], R. Maingi [4], D. Monticello [2], M.C. Zarnstorff [2]

[1] *Max-Planck-Institut für Plasmaphysik, Euratom Association, Greifswald/Garching, Germany*
[2] *Princeton Plasma Physics Laboratory, Princeton, USA*
[3] *Lawrence Livermore National Laboratory, Livermore, USA*
[4] *Oak Ridge National Laboratory, Oak Ridge, USA*

The paper presents the status of the implementation of the EMC3-EIRENE code on NCSX. Particular attention is devoted to the construction of the 3D plasma computational grid in the SOL, which consists of a 2D radial-poloidal system of finite flux tubes extending half a field period. In a first application, the code simulates the energy transport for electrons and ions in a typical SOL configuration bounded by model target plates. The distribution of connection lengths defined by the plates and the resulting temperature profiles are shown and discussed.

Keywords: stellarator, NCSX, divertor, transport, 3D modeling, EMC3-EIRENE code

1. Introduction

In helical devices, SOL plasmas and recycling are intrinsically three-dimensional due to non-axisymmetric magnetic fields and toroidally inhomogeneous divertor plates. Additional complexity arises from a large variety of magnetic topologies encountered in configurations with different magnetic shear and complex magnetic structures ranging from small or large island chains to even coexisting slightly or strongly ergodic regions. For such open topologies standard magnetic coordinates do not exist. The approach used by the EMC3 code [1,2] is a Monte Carlo (MC) technique optimized for highly anisotropic 3D fluid transport processes in open magnetic topologies of arbitrary complexity. The parallel and cross-field transport dynamics of mass, momentum and energy are simulated by advancing MC "particles" along and across field lines through local orthogonal steps. Up to now, the EMC3 code, coupled self-consistently to the EIRENE code [3] for neutral transport, has been applied to W7-AS, W7-X, LHD, TEXTOR-DED and ITER start-up.

Presently, the NCSX magnetic boundary region [4,5] is being implemented in the code to start the investigation of the SOL transport properties for different configurations on the way to a first divertor design. A major step of this implementation is the construction of a 3D field-aligned grid extending toroidally half a field period and covering the radial SOL region of interest. At the boundary of the periodicity domain, field-line coordinates are transformed reversibly to the next domain by applying the RFLM technique [6]. This technique avoids both a numerical cross-field diffusion of the fast parallel transport and a radial accumulation of interpolation errors, which are critical issues especially in the high temperature region close to the LCFS.

2. NCSX boundary configuration

NCSX is a quasi-axisymmetric compact stellarator with three field periods, major radius of 1.4 m and aspect ratio of 4.4 [7]. The plasma configuration chosen for the present first application

francesco.sardei@ipp.mpg.de

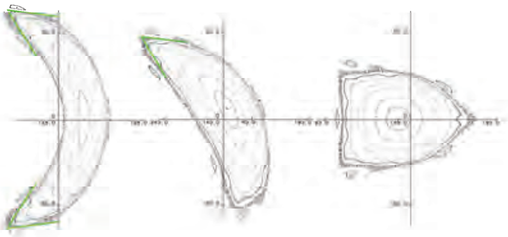

Fig. 1 NCSX configuration over half a field period (ϕ = 0°,30°,60°) with model target plates extending 1/4 of a field period at stellarator-symmetric positions.

(Fig. 1) has β = 4.1% and ι = 0.65 at the plasma edge (Fig. 2). The last closed flux surface (LCFS) is surrounded by a narrow weakly ergodic zone followed by an island chain at ι = 3/5 (Fig. 1). Outside this resonance strong radial field-line excursions to the wall indicate the end of the plasma region.

In a first approximation, four model target plates per field period are placed close to the LCFS at stellarator-symmetric positions. They are located at the tips of the bean-shaped cross section, which have the largest flux expansion (Fig. 1), and extend

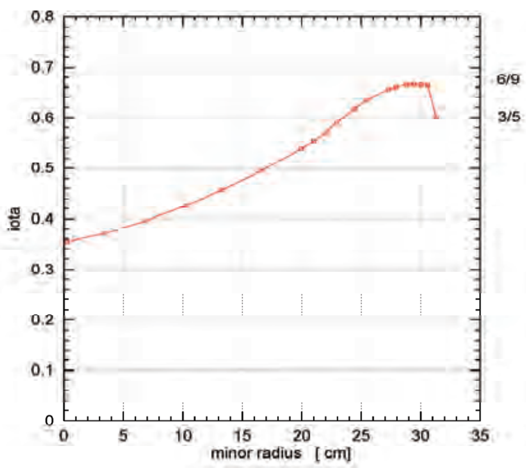

Fig. 2 ι profile for the configuration shown in Fig. 1.

1/4 of a field period starting at the bean-shaped symmetry plane (Fig. 1). The plates cut the LCFS at several toroidal positions, defining a limiter SOL with a highly inhomogeneous distribution of connection lengths (Fig. 3). Within a radial distance of about 3 cm from the LCFS, connection lengths L_c = 15-20 m, i.e. 5-7 field periods, dominate the SOL. The two relatively large up/down symmetric zones with $L_c \approx$ 3 m ≈ one field period in the upper and

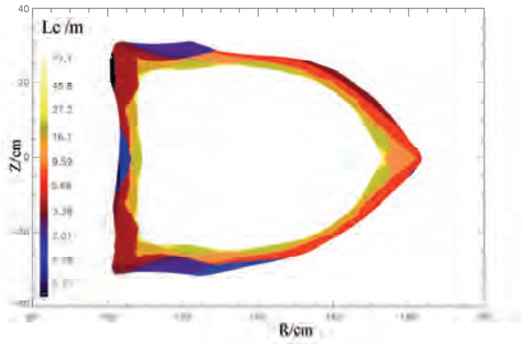

Fig. 3 Distribution of connection lengths as defined by the target plates shown in Fig. 1.

lower inboard corners of the ϕ = 60° symmetry plane (Fig. 3) are due to a local inward protrusion of the inboard plates into the core at toroidal angles of ϕ = 20°-25°. Deviations from up/down symmetry in the outermost short-L_c regions of the distribution are due to technical reasons and can be ignored.

3. Grid construction

In this section we shortly describe the structure of a typical 3D computational grid used by the EMC3-EIRENE code for stellarator-symmetric configurations and the basic steps of its construction. An extension to non-symmetric configurations is straightforward. Precomputed field lines are started from a fine 2D up/down symmetric grid of nested contours (Fig. 4) in the symmetry plane where the plates are located (bean-shaped plane of Fig. 1). The up/down symmetry of the grid is advisable because it allows a reduction of the computational domain to half a field period by a flux-coordinate representation of the boundary conditions and prevents an accumulation of radial interpolation errors [6]. The field lines are integrated numerically with high accuracy over half a field period and stored at fine-spaced toroidal intervals. The resulting two-parametric set of finite flux tubes covering the radial-poloidal region of interest contains all relevant information about the field structure including islands and ergodic regions. The radial and poloidal grid lines defining the cross-sections of the flux tubes become increasingly distorted in toroidal direction due to field shear. For high-shear devices, a strong distorsion may require a splitting of the flux-tube domain in two or more toroidal subdomains [6]. However, the distorsion does not affect the accuracy of the transport, as the flux-tube geometry does not enter the MC procedure, which is

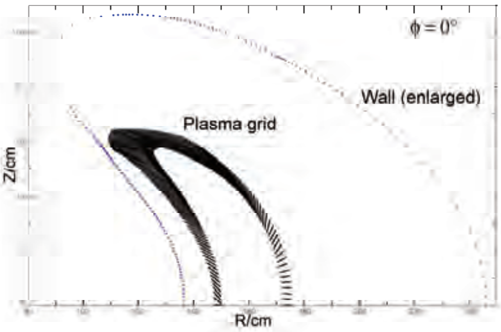

Fig. 4 Up/down symmetric cross-section of the computational grid at the starting plane. The wall (enlarged) is the radial boundary of the grid.

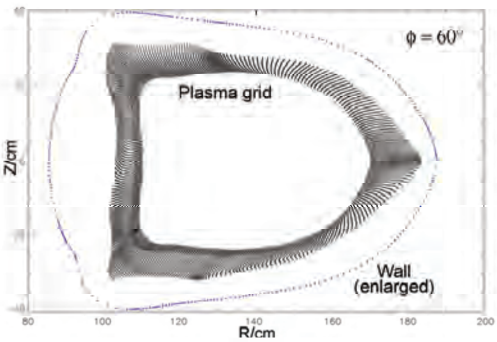

Fig. 5 Non-up/down symmetric cross section of the computational grid resulting from mapping of the starting grid (Fig. 4) over half a field period. The wall (enlarged) is the radial boundary of the grid.

based on local orthogonal displacements. In case of NCSX, the distortion is moderate and a single toroidal flux-tube domain is sufficient. However, the grid must be sufficiently fine to resolve small length scales of the plasma parameters especially near the target plates and to provide sufficient accuracy in the field-line interpolation.

The finite flux-tube SOL domain is bounded radially inwards by two flux surfaces close to the LCFS and outwards by a non-flux surface ("last surface") enclosing the relevant SOL plasma region (Figs. 4,5).

The two innermost flux surfaces are needed to correctly apply poloidal-dependent flux boundary conditions for the radial fluxes. They must be very close to each other and well defined, i.e. sufficiently sharp to form continuous, up/down symmetric toroidal surfaces in both planes of symmetry.

The "last surface" is the outer boundary of the finite flux-tube system defining the plasma computational domain. Together with the innermost flux surfaces, it should enclose a sufficiently large volume to completely cover the expected radial extension of the plasma SOL. If target plates are present, like in NCSX, the plasma SOL is bounded by the shadows of target plates catching most of the outflowing plasma. In the absence of target plates, like in LHD, the plasma SOL is bounded by flux tubes "hot-wired" to the wall, i.e. leading to wall contact within very short connection lengths. To a good starting approximation, the last surface could be identified with the radial boundary contour of a fine Poincaré distribution of particle orbits traced along field lines with cross-field diffusion. This could be the first step towards an optimization of the last surface, which eventually requires an iterative procedure based on the full plasma transport.

The space between the innermost and outermost surfaces is filled with nested surfaces obtained by radial interpolation between the bounding surfaces at the starting plane (Fig. 4).

In the present NCSX grid approximation, the last surface was obtained by adding a small toroidal field, thereby smoothing and shifting outwards the LCFS, and then radially extrapolating the basic island-free geometry of the edge configuration.

Since the 3D grid reflects the basic island-free topology of the boundary, it is not sensitive to small variations of rotational transform, ergodicity and edge island structures. Therefore, the same or a slightly modified grid may be used for different configurations.

Obviously, the 3D table of stored magnetic field used to integrate the field lines must fully cover the 3D plasma region. This requirement should be strictly controlled by the field-line tracing code to avoid errors which may be hardly detectable after the grid construction. Furthermore, both the table and flux-tube grids should be sufficiently fine to resolve magnetic flux conservation within a few %. This is an essential requirement not only for the intrinsic quality of the flux-tube system but also for the correct description of the parallel transport.

The wall represents the outer radial boundary of the 3D computational grid. No magnetic field is needed in the space between the wall and the plasma grid domain, this region being only populated by neutrals. Both the wall and the plasma facing components (target plates and baffles) are defined by their cross sections at $\phi =$ const planes.

Overlapping of grid cells arising from strong radial/poloidal distorsions, which may occur in the whole computational grid up to the wall, must be avoided. Within the plasma grid it is sufficient to check for flux-tube overlapping at the boundary of the toroidal domain, whereas in the space between the plasma grid and the wall surface, overlapping needs to be checked at any toroidal position, as the poloidal distributions of the wall grid points are not magnetically interconnected in toroidal direction.

4. First EMC3 application

In the first test application of the EMC3 code to NCSX, only the 3D energy transport for electrons and ions were simulated, whereas the plasma density was kept fixed at n_e = 10^{19} m^{-3} throughout the computational domain. A power of P_{SOL} = 1.2 MW entering the SOL was equally distributed between ions and electrons, and the anomalous cross-field heat diffusivities were set to $\chi_e = \chi_i = 3$ m^2/s. These numbers have to be considered only as an example, which does not reflect realistic NCSX parameter values, as the subject of the present study is the code implementation, not an edge physics study. As expected from the L_c contour plot (Fig. 3), the relevant radial energy transport takes place in a narrow radial zone dominated by L_c = 15-20 m. The corresponding collisionality $\nu_e^* = L_c/\lambda_{ee}$ = 1-2 < 10 indicates that the SOL transport is in the sheath-limited convection regime with no significant

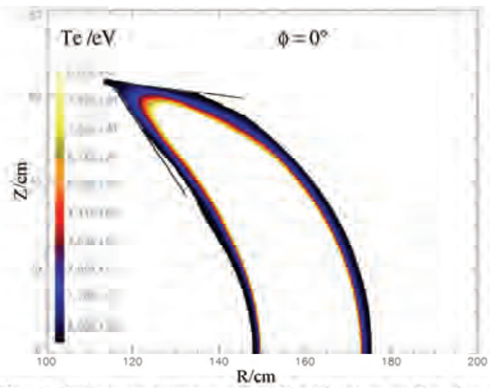

Fig. 6 Electron temperature distribution at the $\phi = 0°$ symmetry plane.

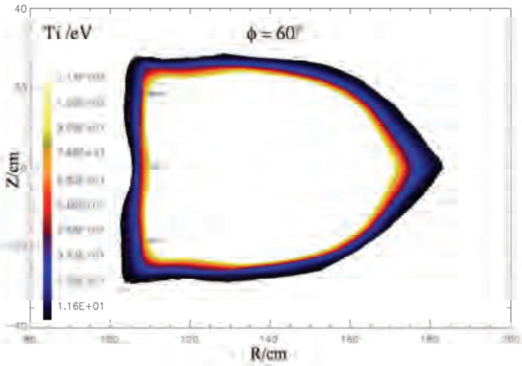

Fig. 7 Electron temperature distribution at the ϕ = 60° symmetry plane.

parallel temperature gradients [8]. The resulting temperature decay length (Figs. 6,7) is proportional to $\sqrt{L_c}$ and is estimated as $\lambda_T = \sqrt{2\chi_\perp \tau_{e//}}$ = 1-1.5 cm. A local energy sink in the two up/down symmetric SOL regions with $L_c \approx 3$ m (Fig. 3) is visible in Fig. 7 by comparing the radial T_e profiles at these two positions with that at the inboard midplane, which is governed by larger λ_T. The spatial distribution of T_i is similar as that of T_e, with T_i being about 10% higher throughout the SOL.

5. Next steps

Major technical steps still to be done towards a realistic description of the SOL transport in NCSX with the EMC3-EIRENE code are:

- improvement of the target-plate geometry
- improvement of the outermost plasma grid surface
- grid refinement near the plates
- activation of the full transport-equation system (particle, momentum, energy)
- activation of the self-consistent neutral gas transport
- tests of numeric convergence

Then, dedicated transport studies aiming, for example, at exploring the divertor potential of NCSX, could be started. Major tasks towards this goal would include

- characterizing the basic plasma transport properties for different 3D SOL configurations
- estimating the heat and particle deposition profiles on the target plates for different configurations and plate geometries
- optimizing the target-plate and baffle design with/without inboard plates with respect to wall protection, configuration flexibility, homogeneous load, neutral compression
- exploring the role of ergodicity and low-order edge islands for a divertor concept
- estimating the impurity retention capability in the SOL
- checking the sensitivity of the transport to low-

order resonances and ergodicity.

References

[1] Y. Feng, F. Sardei, J. Kisslinger, J. Nucl. Mater. **266-269,** 812 (1999)

[2] Y. Feng, F. Sardei, J. Kisslinger, P. Grigull, K. McCormick and D. Reiter, Contrib. Plasma Phys. **44** 1-3, 57 (2004)

[3] D. Reiter, M. Baelmans, and P. Boerner, Fusion Sci. Technol. **47**, 172 (2005)

[4] R. Maingi, et. al., Proc. of 33rd EPS on Plasma Physics and Controlled Fusion, Roma, Italy, June 19-23 (2006) paper P5.116

[5] T. Kaiser, et. al., Bull. Am. Phys. Soc. **51,** 39 (2006)

[6] Y. Feng, F. Sardei and J. Kisslinger, Phys. Plasmas **12,** 052505 (2005)

[7] M.C. Zarnstorff, et. al., Plasma Phys. Contr. Fusion **43,** A237 (2001)

[8] P.C Stangeby, The Plasma Boundary of Magnetic Fusion Devices, Plasma Physics Series, IoP 2000

Poster Presentations 2

Proceedings of ITC/ISHW2007

Derivation of jump conditions in multiphase incompressible flows with singular forces

Caesar O. Harahap[1)] and Hideaki Miura[2)]

The Graduate University for Advanced Studies (SOKENDAI), Toki 509-5292, Japan
[2)]National Institute for Fusion Science, Toki 509-5292, Japan

(Received 15 October 2007)

With the aim to numerically solve problems of plasma dynamics consisting of multiple phases and/or different governing equations, an immersed interface technique is extended to solve a system with mass density and viscosity jumps. The jump conditions for velocity, pressure and their derivatives (sets of coupled equations) are derived.

Keywords: dicontinuities, singular forces, jump conditions, immersed interface method

DOI: 10.1585/pfr.1.001

1 Introduction

Clarifying key physics of complex behaviors of a hot plasma in a magnetic confinement device such as the Large Helical Device (LHD) is essential for understanding experimental results. For this purpose, various kinds of simulation studies such as magnetohydrodynamics (MHD), two-fluid equations, Vlasov and gyrokinetic simulations have been conducted. (See, for example, Refs.[1, 2, 3]) The MHD simulation class is the simplest among them in the sense that the system of equations consists of a relatively few number of equations, and the number of dimensions of the independent variable space is only three. Nevertheless, there still remain many difficulties mimicking the device geometry in detail and taking various experimental and engineering parts into account. One of those difficulties is in connecting the hot plasma region and the vacuum region, which is complicated because the governing equations of these regions can be different from each other.

In MHD simulations, the vacuum region is often described by the MHD equations with very low pressure and/or mass density, or simply omitted from the simulation by imposing the boundary condition on the outermost magnetic surface. For the purpose of studying the effects of plasma deformations around the hot plasma boundary or to study peripheral regions and hot plasma core simultaneously, the former approach is preferable. In the former simulations, very large resistivity and/or viscosity are imposed to the low pressure region. However, jumps of physical variables such as mass density, pressure, and temperature often causes numerical oscillations. Although such oscillations may be avoided by adopting some numerical techniques such as the Godunov, TVD or CIP scheme, the computation becomes complex and the numerical accuracy can become ambiguous.

Recently, a class of numerical technique called the Immersed Interface Method (IIM) is developed to simulate the motion of a neutral fluid separated into two regions by a moving surface exerting forces. (See Xu and Wang [5] and references therein.) The IIM is a variant of the immersed boundary method, which was originally developed by Peskin[6] to simulate blood flows and has become one of the most powerful tool to solve fluid flows with material boundaries. The basic ideas of the IIM are (1)to utilize the generalized Taylor expansion[4] and (2)to derive the jump conditions required in (1). A schematic figure is shown in Fig.1. In a computational box, we have a material surface S. The dashed lines are some typical grid lines. Utilizing the generalized Taylor expansion, derivatives of a physical quantity $u(x)$ can be approximated in a manner similar to the standard finite difference method, provided that the jump conditions for $u(x)$ and its derivatives on the material surface[1] are already derived. Then the motion of the fluids is marched by standard techniques such as the Runge-Kutta-Scheme and the motion of the discontinuous surface can be tracked by a Lagrangean technique.

2 Jump conditions

While IIM is an excelent technique, at present its application is limited to the incompressible Navier-Stokes equation (for neutral fluids). One important step to make the technique applicable to fusion plasma simulations is to derive jump conditions for various physical quantities (including magnetic field and current density) in the case where the viscosity and the mass density are dicontinuous accross a surface. In this article, we present the jump conditions for velocity, pressure, and their derivatives in such a case. For simplicity, we restrict ourselves to the three-dimensional incompressible Navier-Stokes (NS)

[1]Note that the words *material surface* mean a flow does not go across it. The surface is not necessariry a wall but can be, for example, a fluid surface with surface tension.

author's e-mail: harahap.caesar@LHD.nifs.ac.jp

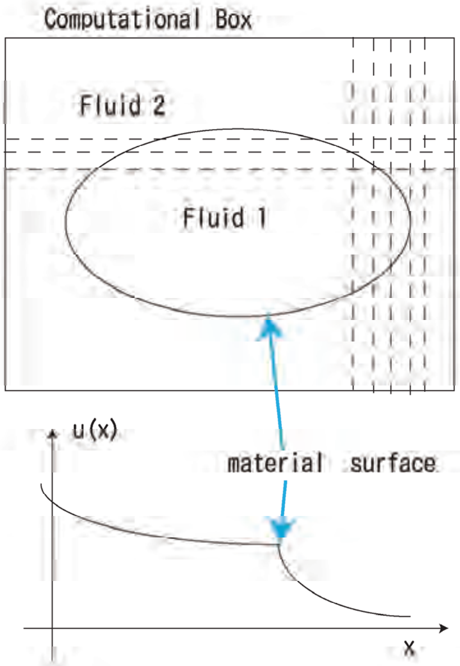

Fig. 1 A schematic view of two fluids separated by a material surface.

equations:

$$
\begin{aligned}
\rho\left(\frac{\partial u^i}{\partial t}+u^j\frac{\partial u^i}{\partial x_j}\right) &= -\frac{\partial p}{\partial x^i}+\frac{\partial}{\partial x^i}\left\{\mu\left(\frac{\partial u^i}{\partial x^j}+\frac{\partial u^j}{\partial x^i}\right)\right\} \\
&\quad +F^i, \qquad (1)\\
\frac{\partial u^i}{\partial x^i} &= 0, \qquad (2)\\
F^i &= \int_S f^i\left(\alpha^1,\alpha^2,t\right) \\
&\quad\times\ \delta\left(\boldsymbol{x}-\boldsymbol{X}\left(\alpha^1,\alpha^2,t\right)\right)d\alpha^1 d\alpha 2, \\
&\qquad (3)\\
\frac{\partial X^i\left(\alpha^1,\alpha^2,t\right)}{\partial t} &= u^i\left(\boldsymbol{X}\left(\alpha^1,\alpha^2,t\right),t\right), \qquad (4)
\end{aligned}
$$

where (α^1,α^2) are Lagrangian parameters of points on the surface at a reference time, f^i is a Lagrangian force density (due to surface tension, for example), $\delta\left(\boldsymbol{x}-\boldsymbol{X}\left(\alpha^1,\alpha^2,t\right)\right)$ is a three dimensional delta function, and $\boldsymbol{X}\left(\alpha^1,\alpha^2,t\right)$ are Cartesian coordinates of the surface points. (See Fig.2). Taking the divergence of the momentum equation, a Poisson equation for pressure is obtained.

$$
\begin{aligned}
\frac{\partial^2 p}{\partial x^i\partial x^i} &= \frac{\partial F^i}{\partial x^i}+2\frac{\partial^2}{\partial x^i\partial x^j}\left(\mu\frac{\partial u^i}{\partial x^j}\right) \\
&\quad -\frac{\partial}{\partial x^i}\left\{\rho\left(\frac{\partial u^i}{\partial t}+u^j\frac{\partial u^i}{\partial x_j}\right)\right\}. \qquad (5)
\end{aligned}
$$

Differentiating $\boldsymbol{X}$ we obtain two tangent vectors along the coordinate lines of the surface.

$$
\boldsymbol{\tau}_i = \frac{\partial \boldsymbol{X}}{\partial \alpha^i} \qquad (i=1,2). \qquad (6)
$$

The three components of the tangential vectors $\boldsymbol{\tau}_i$ in the Cartesian coordinates are denoted by $(\tau_i^1,\tau_i^2,\tau_i^3)$. The unit

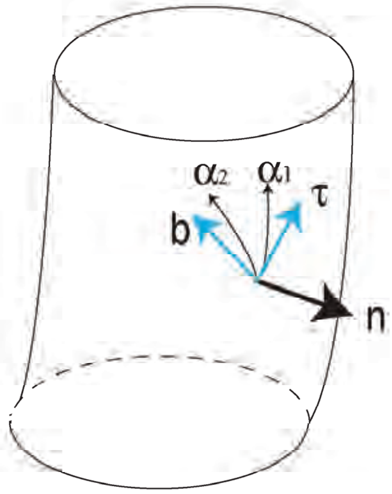

Fig. 2 Coordinate lines α^1, α^2 which cover the material surface and the tangential, normal and binormal unit vectors.

vector $\boldsymbol{n}$ normal to the surface (in Fig.1, pointing towards fluid 2) is given by

$$
\begin{aligned}
\boldsymbol{n} &= \frac{1}{J}(\boldsymbol{\tau}_1\times\boldsymbol{\tau}_2), \qquad (7)\\
J &= |\boldsymbol{\tau}_1\times\boldsymbol{\tau}_2|. \qquad (8)
\end{aligned}
$$

We also introduce three mutually orthogonal unit vectors as $\boldsymbol{\tau}=\boldsymbol{\tau}_1/|\boldsymbol{\tau}_1|$, $\boldsymbol{n}$, $\boldsymbol{b}=\boldsymbol{n}\times\boldsymbol{\tau}$.

We assume that fluid 1 and fluid 2 have constant but different mass densities and viscosities. To show the jump conditions, we define some symbols here. A jump of a physical quantity accross the two phases is denoted by [.] where

$$
\begin{aligned}
[.]\left(\boldsymbol{X}(\alpha^1,\alpha^2,t),t\right) &= (.)^+\left(\boldsymbol{X}(\alpha^1,\alpha^2,t),t\right) \\
&\quad -(.)^-\left(\boldsymbol{X}(\alpha^1,\alpha^2,t),t\right).(9)
\end{aligned}
$$

The superscript $^+(^-)$ denotes the side towards which $\boldsymbol{n}$ points, while $^-$ denotes the other side.

The jump conditions are derived as follows. First, we formulate some basic jump coditions following the work by Xu and Wang[4]. No slip condition on the dicontinuous surface S leads to

$$
\left[u^i\right] = 0. \qquad (10)
$$

and the acceleration jump condition

$$
\left[\frac{\partial u^i}{\partial t}\right]+u^j\left[\frac{\partial u^i}{\partial x^j}\right]=0, \qquad (11)
$$

Extensions from the works by Xu and Wang[4, 5] appear in the jump conditions associated with the viscosity and the mass density. The jump condition for the viscous stress tensor in eq.(1) is given by

$$
\begin{aligned}
\left[\mu\left(\frac{\partial u^i}{\partial x^j}+\frac{\partial u^j}{\partial x^i}\right)\right]n^j &= -\frac{f^i}{J}+\left(\frac{f^k n_k}{J}-2\,[\mu]\,\frac{\partial u^k}{\partial \tau}\tau_k\right.\\
&\quad \left. -2\,[\mu]\,\frac{\partial u^k}{\partial b}b^k\right)n^i \qquad (12)
\end{aligned}
$$

The pressure jump condition is given by

$$[p] = \frac{f^i n_i}{J} - 2[\mu]\frac{\partial u^k}{\partial \tau}\tau_k - 2[\mu]\frac{\partial u^k}{\partial b}b^k, \qquad (13)$$

in which the jump of the viscosity is included. The jump condition for the pressure normal derivative

$$\begin{aligned}\left[\frac{\partial p}{\partial x_i}\right]n^i &= \frac{1}{J}\left[\frac{\partial \widetilde{f^1}}{\partial \alpha^1} + \frac{\partial \widetilde{f^2}}{\partial \alpha^2}\right] \\ &+2[\mu]\left(\frac{\partial^2 u^i}{\partial \tau^2}n^i + \frac{\partial^2 u^i}{\partial b^2}n^i + \frac{\partial u^i}{\partial \tau}\frac{\partial n_i}{\partial \tau} + \frac{\partial u^i}{\partial b}\frac{\partial n_i}{\partial b}\right) \\ &- \left(\left[\rho\frac{\partial u^i}{\partial t}\right] + u^j\left[\rho\frac{\partial u^i}{\partial x_j}\right]\right)n^i. \qquad (14)\end{aligned}$$

contains both the viscosity jump and the mass density jump, making the formulation much more complicated than those in Refs.[4, 5].

After some manipulations, we have a set of coupled equations for the jump conditions as

$$\begin{pmatrix} \tau_1^1 & \tau_1^2 & \tau_1^3 & 0 & 0 & 0 & 0 & 0 & 0 \\ \tau_2^1 & \tau_2^2 & \tau_2^3 & 0 & 0 & 0 & 0 & 0 & 0 \\ 2n^1 & n^2 & n^3 & n^2 & 0 & 0 & n^3 & 0 & 0 \\ 0 & 0 & 0 & \tau_1^1 & \tau_2^1 & \tau_3^1 & 0 & 0 & 0 \\ 0 & 0 & 0 & \tau_1^2 & \tau_2^2 & \tau_3^2 & 0 & 0 & 0 \\ 0 & n^1 & 0 & n^1 & 2n^2 & n^3 & 0 & n^3 & 0 \\ 0 & 0 & 0 & 0 & 0 & 0 & \tau_1^1 & \tau_2^1 & \tau_3^1 \\ 0 & 0 & 0 & 0 & 0 & 0 & \tau_1^2 & \tau_2^2 & \tau_3^2 \\ 0 & 0 & n^1 & 0 & 0 & n^2 & n^1 & n^2 & 2n^3 \end{pmatrix} \cdot \begin{pmatrix} \left[\mu\frac{\partial u^1}{\partial x^1}\right] \\ \left[\mu\frac{\partial u^1}{\partial x^2}\right] \\ \left[\mu\frac{\partial u^1}{\partial x^3}\right] \\ \left[\mu\frac{\partial u^2}{\partial x^1}\right] \\ \left[\mu\frac{\partial u^2}{\partial x^2}\right] \\ \left[\mu\frac{\partial u^2}{\partial x^3}\right] \\ \left[\mu\frac{\partial u^3}{\partial x^1}\right] \\ \left[\mu\frac{\partial u^3}{\partial x^2}\right] \\ \left[\mu\frac{\partial u^3}{\partial x^3}\right] \end{pmatrix}$$

$$= \begin{pmatrix} [\mu]\frac{\partial u^1}{\partial \alpha^1} \\ [\mu]\frac{\partial u^1}{\partial \alpha^2} \\ r_u^1 \\ [\mu]\frac{\partial u^2}{\partial \alpha^1} \\ [\mu]\frac{\partial u^2}{\partial \alpha^2} \\ r_u^2 \\ [\mu]\frac{\partial u^3}{\partial \alpha^1} \\ [\mu]\frac{\partial u^3}{\partial \alpha^2} \\ r_u^3 \end{pmatrix}, \qquad (15)$$

and

$$\begin{pmatrix} \tau_1^1 & \tau_2^1 & \tau_3^1 \\ \tau_1^2 & \tau_2^2 & \tau_3^2 \\ n^1 & n^2 & n^3 \end{pmatrix}\begin{pmatrix} \left[\frac{\partial p}{\partial x^1}\right] \\ \left[\frac{\partial p}{\partial x^2}\right] \\ \left[\frac{\partial p}{\partial x^3}\right] \end{pmatrix} = \begin{pmatrix} \frac{\partial r_p}{\partial \alpha^1} \\ \frac{\partial r_p}{\partial \alpha^2} \\ r_{pn} \end{pmatrix}, \qquad (16)$$

where

$$R_p = \frac{f^i n_i}{J} - 2[\mu]\frac{\partial u^k}{\partial \tau}\tau_k - 2[\mu]\frac{\partial u^k}{\partial b}b^k, \qquad (17)$$

$$r_u^i = -\frac{f^i}{J} + R_p n^i, \qquad (18)$$

$$\begin{aligned} r_{pn} &= \frac{1}{J}\left[\frac{\partial \widetilde{f^1}}{\partial \alpha^1} + \frac{\partial \widetilde{f^2}}{\partial \alpha^2}\right] \\ &+2[\mu]\left(\frac{\partial^2 u^i}{\partial \tau^2}n^i + \frac{\partial^2 u^i}{\partial b^2}n^i + \frac{\partial u^i}{\partial \tau}\frac{\partial n_i}{\partial \tau} + \frac{\partial u^i}{\partial b}\frac{\partial n_i}{\partial b}\right) \\ &- \left(\left[\rho\frac{\partial u^i}{\partial t}\right] + u^j\left[\rho\frac{\partial u^i}{\partial x_j}\right]\right)n^i. \qquad (19)\end{aligned}$$

One way to utilize eqs.(15) and (16) is by giving the source terms in the right-hand-side by some appropriate interpolations or combinations of extrapolations from the two sides of each phases, forming a closed system of equations. Then the jump conditions can be obtained by inverting coefficient matrices in eqs.(15) and (16), enabling us to discretize the NS equations by the IIM method, and solve problems of multiphase flows with singular forces.

Jump conditions for $\left[\mu\partial^2 u^i/\partial x^j \partial x^k\right]$ are given as follows.

$$\begin{aligned}\begin{pmatrix} C_{11} & C_{12} & C_{13} \\ C_{21} & C_{22} & C_{23} \\ C_{31} & C_{32} & C_{33} \end{pmatrix}\begin{pmatrix} X_1 \\ X_2 \\ X_3 \end{pmatrix} &= [\mu]\begin{pmatrix} A_1 \\ A_2 \\ A_3 \end{pmatrix} \\ &- \begin{pmatrix} B_{11} & B_{12} & B_{13} \\ B_{21} & B_{22} & B_{23} \\ B_{31} & B_{32} & B_{33} \end{pmatrix}\begin{pmatrix} D_1 \\ D_2 \\ D_3 \end{pmatrix} + \begin{pmatrix} E_1 \\ E_2 \\ E_3 \end{pmatrix} \qquad (20)\end{aligned}$$

Since the expressions of the block matrices are lengthy, here we show only the first line of the expression:

$$X_1 = \begin{pmatrix} \left[\mu\frac{\partial^2 u^1}{\partial x^1 \partial x^1}\right] \\ \left[\mu\frac{\partial^2 u^1}{\partial x^1 \partial x^2}\right] \\ \left[\mu\frac{\partial^2 u^1}{\partial x^1 \partial x^3}\right] \\ \left[\mu\frac{\partial^2 u^1}{\partial x^2 \partial x^2}\right] \\ \left[\mu\frac{\partial^2 u^1}{\partial x^2 \partial x^3}\right] \\ \left[\mu\frac{\partial^2 u^1}{\partial x^3 \partial x^3}\right] \end{pmatrix}, \qquad (21)$$

$$C_{11} = \begin{pmatrix} 2\left(\tau_1^1\right)^2 & 2\tau_1^1\tau_1^2 & 2\tau_1^1\tau_1^3 & 2\left(\tau_1^2\right)^2 & 2\tau_1^2\tau_1^3 & 2\left(\tau_1^3\right)^2 \\ 2\tau_1^1\tau_2^1 & \tau_1^1\tau_2^2 + \tau_1^2\tau_2^1 & \tau_1^1\tau_2^3 + \tau_1^3\tau_2^1 & 2\tau_1^2\tau_2^2 & \tau_1^2\tau_2^3 + \tau_1^3\tau 2^2 & 2\tau_1^3\tau_2^3 \\ 2\left(\tau_2^1\right)^2 & 2\tau_2^1\tau_2^2 & 2\tau_2^1\tau_2^3 & 2\left(\tau_2^2\right)^2 & 2\tau_2^2\tau_2^3 & 2\left(\tau_2^3\right)^2 \\ 3n^1\tau_1^1 & 2n^1\tau_1^2 + n^2\tau_1^1 & 2n^1\tau_1^3 + n^3\tau_1^1 & 2n^2\tau_1^2 & n^2\tau_1^3 + n^3\tau_1^2 & 2n^3\tau_1^3 \\ 3n^1\tau_2^1 & 2n^1\tau_2^2 + n^2\tau_2^1 & 2n^1\tau_2^3 + n^3\tau_2^1 & 2n^2\tau_2^2 & n^2\tau_2^3 + n^3\tau_2^2 & 2n^3\tau_2^3 \\ 1 & 0 & 0 & 1 & 0 & 1 \end{pmatrix} \qquad (22)$$

$$C_{12} = \begin{pmatrix} 0 & 0 & 0 & 0 & 0 & 0 \\ 0 & 0 & 0 & 0 & 0 & 0 \\ 0 & 0 & 0 & 0 & 0 & 0 \\ n^2\tau_1^1 & n^2\tau_1^2 & n^2\tau_1^3 & 0 & 0 & 0 \\ n^2\tau_2^1 & n^2\tau_2^2 & n^2\tau_2^3 & 0 & 0 & 0 \\ 0 & 0 & 0 & 0 & 0 & 0 \end{pmatrix}, \qquad (23)$$

$$C_{13} = \begin{pmatrix} 0 & 0 & 0 & 0 & 0 & 0 \\ 0 & 0 & 0 & 0 & 0 & 0 \\ 0 & 0 & 0 & 0 & 0 & 0 \\ n^3\tau_1^1 & n^3\tau_1^2 & n^3\tau_1^3 & 0 & 0 & 0 \\ n^3\tau_2^1 & n^3\tau_2^2 & n^3\tau_2^3 & 0 & 0 & 0 \\ 0 & 0 & 0 & 0 & 0 & 0 \end{pmatrix}, \qquad (24)$$

P2-001

$$A_1 = \begin{pmatrix} \frac{\partial^2 u^1}{\partial\alpha^1\partial\alpha^1} \\ \frac{\partial^2 u^1}{\partial\alpha^1\partial\alpha^2} \\ \frac{\partial^2 u^1}{\partial\alpha^2\partial\alpha^2} \\ 0 \\ 0 \\ 0 \end{pmatrix}, \tag{25}$$

$$D_1 = \begin{pmatrix} \left[\mu\frac{\partial u^1}{\partial x^1}\right] \\ \left[\mu\frac{\partial u^1}{\partial x^2}\right] \\ \left[\mu\frac{\partial u^1}{\partial x^3}\right] \\ 0 \\ 0 \\ 0 \end{pmatrix}, \tag{26}$$

$$B_{11} = \begin{pmatrix} \frac{\partial\tau_1^1}{\partial\alpha^1} & \frac{\partial\tau_1^2}{\partial\alpha^1} & \frac{\partial\tau_1^3}{\partial\alpha^1} & 0 & 0 & 0 \\ \frac{\partial\tau_1^1}{\partial\alpha^2} & \frac{\partial\tau_1^2}{\partial\alpha^2} & \frac{\partial\tau_1^3}{\partial\alpha^2} & 0 & 0 & 0 \\ \frac{\partial\tau_2^1}{\partial\alpha^2} & \frac{\partial\tau_2^2}{\partial\alpha^2} & \frac{\partial\tau_2^3}{\partial\alpha^2} & 0 & 0 & 0 \\ 2\frac{\partial n^1}{\partial\alpha^1} & \frac{\partial n^2}{\partial\alpha^1} & \frac{\partial n^3}{\partial\alpha^1} & 0 & 0 & 0 \\ 2\frac{\partial n^1}{\partial\alpha^2} & \frac{\partial n^2}{\partial\alpha^2} & \frac{\partial n^3}{\partial\alpha^2} & 0 & 0 & 0 \\ 0 & 0 & 0 & 0 & 0 & 0 \end{pmatrix}, \tag{27}$$

$$B_{12} = \begin{pmatrix} 0 & 0 & 0 & 0 & 0 & 0 \\ 0 & 0 & 0 & 0 & 0 & 0 \\ 0 & 0 & 0 & 0 & 0 & 0 \\ \frac{\partial n^2}{\partial\alpha^1} & 0 & 0 & 0 & 0 & 0 \\ \frac{\partial n^2}{\partial\alpha^2} & 0 & 0 & 0 & 0 & 0 \\ 0 & 0 & 0 & 0 & 0 & 0 \end{pmatrix}, \tag{28}$$

$$B_{13} = \begin{pmatrix} 0 & 0 & 0 & 0 & 0 & 0 \\ 0 & 0 & 0 & 0 & 0 & 0 \\ 0 & 0 & 0 & 0 & 0 & 0 \\ \frac{\partial n^3}{\partial\alpha^1} & 0 & 0 & 0 & 0 & 0 \\ \frac{\partial n^3}{\partial\alpha^2} & 0 & 0 & 0 & 0 & 0 \\ 0 & 0 & 0 & 0 & 0 & 0 \end{pmatrix}. \tag{29}$$

$$E_i = \begin{pmatrix} 0 \\ 0 \\ 0 \\ \frac{\partial r_u^i}{\partial\alpha^1} \\ \frac{\partial r_u^i}{\partial\alpha^2} \\ E_i^6 \end{pmatrix}, \tag{30}$$

$$\begin{aligned} E_i^6 &= \left[\frac{\partial p}{\partial x^i}\right] + \left[\rho\frac{\partial u^i}{\partial t}\right] + u^1\left[\rho\frac{\partial u^i}{\partial x^1}\right] \\ &+u^2\left[\rho\frac{\partial u^i}{\partial x^2}\right] + u^3\left[\rho\frac{\partial u^i}{\partial x^3}\right]. \end{aligned} \tag{31}$$

The other block matrices are also derived easily. The jump conditions for $\left[\frac{\partial^2 p}{\partial x^j\partial x^k}\right]$ are given in similar expressions.

3 Concluding Remarks

We derived the jump conditions in multiphase Navier-Stokes flows with singular forces, the phases having different mass densities and viscosities. Numerical computations utilizing these formulations will be shown in our future work. To make the IIM method applicable to MHD simulations or other fluid models of fusion plasmas, jump conditions for many variables and coupled combinations of the variables must be formulated.

[1] H. Miura et al., J. Plasma Physics **72**, 1095 (2006).
[2] H. Miura et al., Fusion Science and Technology **51**, 8 (2007).
[3] T.-H. Watanabe et al., Nucl. Fusion **47**, 1383 (2007).
[4] S. Xu and Z. Jane Wang, SIAM J. Sci. Comput. **27**, 1948 (2006).
[5] S. Xu and Z. Jane Wang, Comput. Methods Appl. Mech. (2007), doj:10.10.16/j.cma.2007.06.012.
[6] C.S. Peskin, J. Comput. Phys. **25**, 220 (1977).

Proceedings of ITC/ISHW2007

Spectrum properties of Hall MHD turbulence

Dan HORI[1)], Hideaki MIURA[1)]

[1)]*National Institute for Fusion Science, Toki 509-5292, Japan*

(Received 15 October 2007;)

Aiming to understand roles of the two fluid effect on plasma dynamics, direct numerical simulations of Hall MHD turbulence are carried out. A comparison between the numerical results of the Hall MHD turbulence to those of one-fluid MHD turbulence reveal that Hall term modifies small scale properties of MHD turbulence.

Keywords: MHD turbulence, Two fluid effect, Hall term, Energy spectrum, Vortex structure

DOI: 10.1585/pfr.1.001

1 Introduction

In recent years, roles of two fluid effects have attracted attention in fusion plasmas [1, 2], as well as astrophysical plasmas [3, 4]. A two-fluid model contains various physical effects [5], and therefore exhibits rich phenomena. It may be sometimes expected that the two-fluid effects contribute to transfer the energy from larger scales to lower scales and enhance the dissipation. However, so far as the authors recognize, the two-fluid effects on the energy transfer among scales has not been studied sufficiently. One subject in which the energy transfer among the scales are well formulated and studied should be the isotropic turbulence of a neutral, incompressible fluid, as are seen in enormous number of works after the famous Kolmogorov's theory (see Ref. [6] and references therein) and MHD turbulence [7]. In studies of turbulence, the energy transfer among the scales are studied in the context of the Fourier energy spectrum and the energy transfer functions. Even in the long history of studies of isotropic turbulence, there remain some aspects of the energy transfer, such as the localness/non-localness, remains imperfect understandings. Compared to these preceding subjects, roles of the two-fluid effect in turbulence (whether it is fully developed or not) are not studied very well.

For studies of two-fluid effects among scales, a simpler model is more preferable so that the effects are distinguished easily from the other effects. Hall magnetohydrodynamics (Hall MHD) provides a minimal model which expresses two-fluid effects:

$$\frac{\partial \boldsymbol{u}}{\partial t} = -(\boldsymbol{u}\cdot\nabla)\boldsymbol{u} - \nabla p + \boldsymbol{j}\times\boldsymbol{B} + \mu\nabla^2\boldsymbol{u}. \quad (1)$$

$$\frac{\partial \boldsymbol{B}}{\partial t} = \nabla\times[(\boldsymbol{u}-\epsilon\boldsymbol{j})\times\boldsymbol{B}] + \eta\nabla^2\boldsymbol{B}, \quad (2)$$

where $\boldsymbol{B}$ is the magnetic field (normalized by a representative value B_0, $\boldsymbol{j}$ $(=\nabla\times\boldsymbol{B})$ is the current (normalized by B_0/L_0; L_0 is the characteristic length), $\boldsymbol{u}$ is the velocity (normalized by the Alfvén speed $V_A = B_0/\sqrt{\mu_0 n_i M_i}$; μ_0 is the permeability of vacuum, M_i is the ion mass and n_i is the ion number density, which is assumed to be constant for simplicity), ν is the viscosity and η is the resistivity (normalized by $V_A L_0$), and p is the pressure (normalized by B_0^2/μ_0). The scale parameter $\varepsilon = l_i/L_0$ is called Hall parameter, where $l_i = \sqrt{M_i/\mu_0 n_i e^2}$ (e is an elementary charge) is the ion skin depth.

A excellent tool to study the energy spectrum is the shell model proposed by Yamada and Ohkitani [8] for a neutral fluid turbulence. The shell model approach mimics the dynamics of the basic equations as sparse and artificial Fourier mode couplings. Although detailed dynamics of the original equations are abandoned, it achieves very high Reynolds number, which direct numerical simulation (DNS) can not achieve even by the most powerful supercomputer of the recent years. Recently, one of the authors (D.H.) have developed a new shell model for Hall MHD, and performed numerical simulations both the Hall MHD case ($\varepsilon \neq 0$) and the single fluid MHD case ($\varepsilon = 0$). [9, 10] The shell model computations predict a modification of the energy spectrum by the Hall effects, suggesting the energy transfer from the large scales to small scales.

Based on these understandings, we conduct numerical studies of Hall MHD turbulence by means of the DNS of both MHD and Hall MHD equations in order to study the effects of Hall term on the energy transfer in isotropic turbulence. We first review the computational results of the shell model for MHD and Hall MHD turbulence very briefly. Then, some basic views in the two kinds of turbulence are studied. Summary appears in the final section.

2 Shell Model Computation Review

Here we review some numerical results reported in Refs. [9, 10] so that the background of our computational work is well understood. Refer to the references for the details of the model and the scaling of the energy spectra obtained by the computations.

The energy spectra for (a) the single fluid MHD (hereafter we simply refer to MHD) and (b) Hall MHD (for $\varepsilon = 10^{-2}$) are shown in Fig. 1. As is observed in Fig. 1,

author's e-mail: hori.dan@nifs.ac.jp

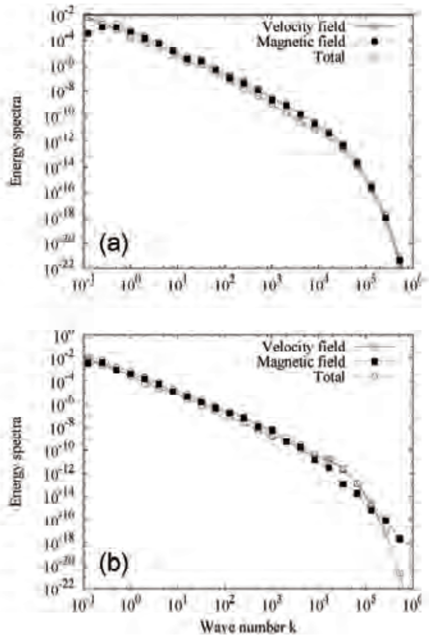

Fig. 1 Energy spectra obtained from the simulation of shell model. The MHD case is shown in the upper panel (a) and The Hall MHD case is done in the lower panel (b).

the scaling exponents of the magnetic field is significantly modified in very high wavenumbers. In the case of the MHD, the magnetic field spectrum is damped in the dissipation region in the same form as the velocity energy spectrum. However, in the Hall MHD spectrum, the magnetic field indicates $-7/3$ power-law in the small scale region. These contrast may reflect the contribution of the Hall term to the energy transfer in the wave number space.

3 Direct numerical simulation of MHD and Hall MHD turbulence

DNSs of the decaying MHD and Hall MHD turbulence are carried out for the $(2\pi)^3$ triple-periodic geometry. Spatial derivatives are approximated by the pseudo-spectrum method and the variables are marched into the time direction by the Runge-Kutta-Gill scheme. The aliasing error is removed by the 2/3-truncation method. The number of the grid points are $N^3 = 256^3$, so that the maximum wavenumber available in this simulation work is $k_{max} = 84$. In the case of Hall MHD case, Hall parameter is $\varepsilon = 1 \times 10^{-1}$. The dissipative coefficients are $\nu = \eta = 1 \times 10^{-2}$. Both the MHD and Hall MHD turbulence simulations start from the same initial conditions in which the velocity and magnetic fields have the energy spectrum roughly proportional to $k^2 exp(-(k/k_0)^2)$ (here $k_0 = 2$) and random phases. No external force is imposed so that the total energy of the velocity and the magnetic fields decays monotonically to time.

In DNS studies of fully developed turbulence, turbulent field is often characterized by the vorticity rather than the velocity field. It is partially because the vorticity field ω is invariant to the Galilean transform and partially because the vorticity field represents small scale structures much more than the velocity field . For the same reason, the current density $\boldsymbol{j}$ is considered to be more suitable for studying the small scale properties than the magnetic field.

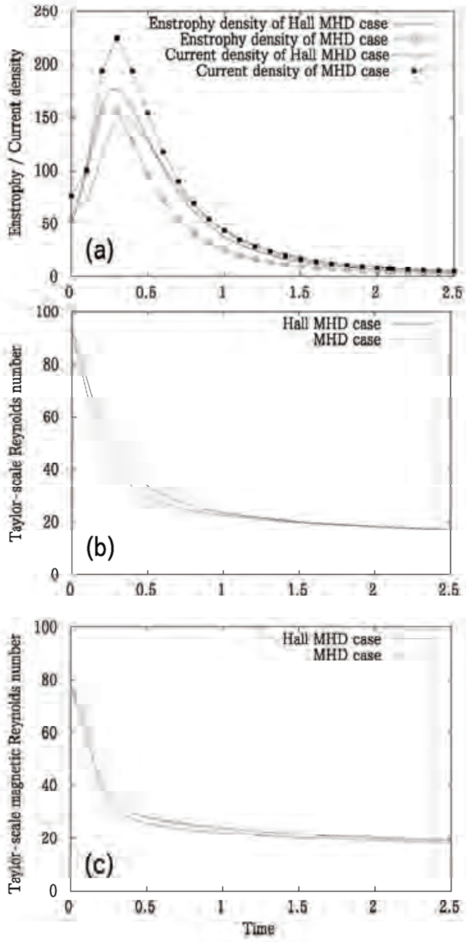

Fig. 2 Time series of the enstrophy density and the current density averaged over the computational volume is shown in the upper panel (a). Taylor scale Reynolds number Re_λ is shown in the middle panel (b), and Taylor scale magnetic Reynolds number is done in the lower panel (c).

In Fig. 2(a), time series of the enstrophy density $\langle|\omega|^2/2\rangle$ and the current density $\langle|j|^2/2\rangle$ are shown for the two kinds of turbulence, where $\langle\cdot\rangle$ denotes the volume average. A comparison on the enstrophy evolution shows that the enstrophy density is larger in the Hall MHD turbulence than in the MHD turbulence with the same ν and η. We also observe that the total current is larger in the MHD turbulence than in the Hall MHD turbulence. Another good index of fully developed turbulence is the Reynolds number Re_λ based on the Taylor micro-scale [6]. In Figs. 2(b) and (c), we see the time evolution of Re_λ and its counter part for the magnetic field, Re^b_λ for the two kinds of turbulence. We find in both Fig. 2(b) and (c) that the Hall MHD turbulence have larger micro-scale Reynolds numbers Re_λ

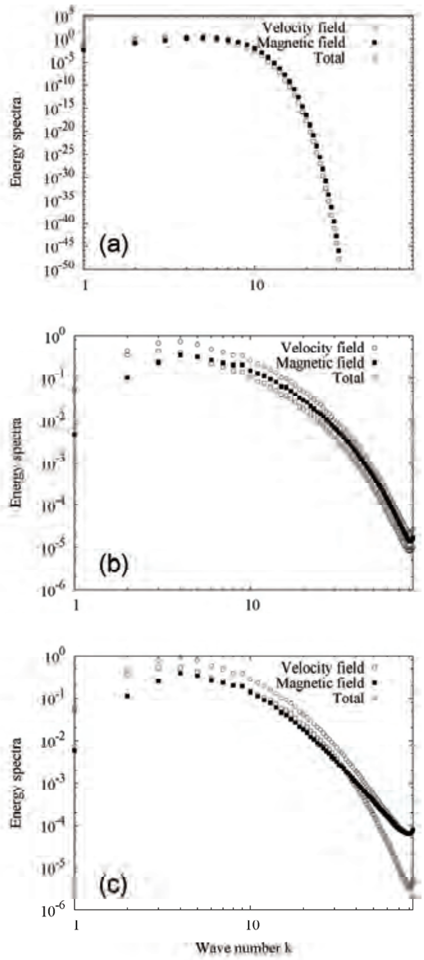

Fig. 3 Energy spectra in DNS of MHD and Hall MHD turbulence. The initial state is shown in the upper panel (a), the energy spectra of the MHD is done in the middle panel (b), and the energy spectra of the Hall MHD is done in the lower panel (c).

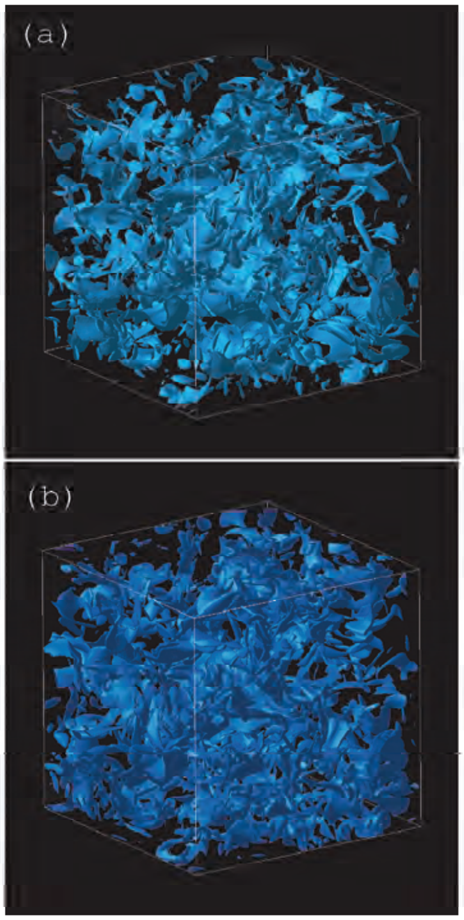

Fig. 4 Isosurfaces of the enstrophy density in (a) MHD and (b) Hall MHD turbulence.

and Re^b_λ than the MHD turbulence, although the difference between the two kinds of turbulence is smaller in (c) than in (b). These observations suggest that the small scales in the velocity (or the vorticity) field is more excited in the Hall MHD turbulence than in the MHD turbulence.

In Fig. 3(a) the energy spectra of the velocity and the magnetic field vectors at the initial time are shown. Since the energy is conserved as the total form $\boldsymbol{u}^2 + \boldsymbol{B}^2$ rather than the kinetic and magnetic energies separately in the ideal limit, we need to study not only the individual spectra u_k^2 and b_k^2 but also the total spectrum $u_k^2 + b_k^2$ as well. Figs. 3(b) and (c) are the plots of the energy spectra of the MHD and Hall MHD turbulence, respectively. By comparing Figs. 3(b) and (c), clear differences between the two kinds of turbulence are seen. The magnetic energy spectrum, denoted by the filled boxes, at the middle (near-peak) wavenumber region is larger in Fig. 3(b) than in Fig. 3(c), while it is opposite in the high wavenumber region. It explains the observations in Fig. 2 that the total current is larger in the MHD turbulence because of the dominance in the middle wavenumber region. In the middle wavenumber region (say, $10 < k < 30$), $b_k^2 > u_k^2$ in the MHD turbulence while $b_k^2 < u_k^2$ in the Hall MHD turbulence. In the highest wavenumber region $k > 40$, the difference between the MHD and Hall MHD turbulence becomes the clearest. The decay of b_k^2 obeys to rather a power-law than the exponential decay. It is similar to the earlier numerical results shown in Fig. 1 and considered to be the direct influence of the Hall term. The high wavenumber region of the velocity energy spectrum in the Hall MHD turbulence decays more rapidly than that in the MHD turbulence, as if compensating the slow decay of the magnetic spectrum b_k^2. The total spectrum $u_k^2 + b_k^2$ of the Hall MHD turbulence has also weaker amplitudes in the $10 \le k \le 50$ wavenumber region than that of the MHD turbulence, but becomes larger in the higher region $k > 50$.

In Figs. 4, isosurfaces of the enstrophy density of the MHD (a) and the Hall MHD turbulence (b) are shown. In Figs. 5, isosurfaces of the current density of the MHD (a) and the Hall MHD turbulence (b) are shown. The thresholds of the isosurfaces of the enstrophy density (current density) are the same between the MHD and the Hall MHD turbulence in Figs. 4 (Figs. 5), the volumes covered by the isosurfaces are clearly different between the two kinds of

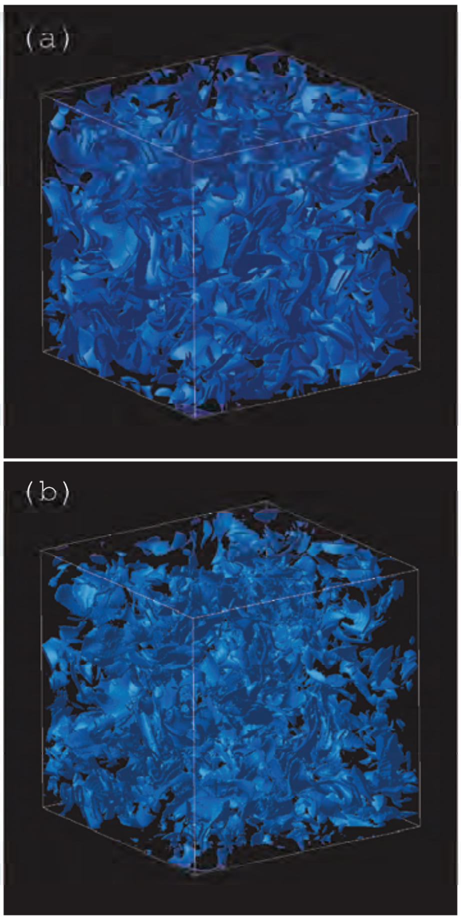

Fig. 5 Isosurfaces of the current density in (a) MHD and (b) Hall MHD turbulence.

turbulence.

4 Summary

We performed the direct numerical simulation of the both Hall MHD and MHD turbulence to study the role of the two fluid effect. Various data show clear difference between the MHD and the Hall MHD turbulence. Time series of the enstrophy, the current, and the Taylor scale Reynolds numbers show that small scale motions of the Hall MHD turbulence is more excited than those of the MHD turbulence. In the small scale, the energy spectra of the magnetic field in the Hall MHD turbulence is observed to be power-law decay, while that of the MHD turbulence is to be exponential decay.

[1] K. Itoh, K. Hallatschek, and et. al., Phys. Plasmas **12**, 062303 (2005).
[2] S. M. Mahajan and Z. Yoshida, Phys. Plasmas **7**, 635 (2000).
[3] S. Balbus and C. Terquem, Astrophys. J. **552**, 235 (2001).
[4] J. Shiraishi, S. Ohsaki, and et. al., **12**, 092901 (2005).
[5] R.D. Hazeltine, J.D. Meiss, *Plasma Confinement*, Addison-Wesley, 1992.
[6] W.D. McComb, *The Physics of Fluid Turbulence*, Oxford University Press, 1990.
[7] D. Biskamp, *Magnetohydrodynamic Turbulence*, Cambridge University Press, 2003.
[8] M. Yamada, K. Ohkitani., J. Phys. Soc. Jpn. **56**, 4210 (1987).
[9] D. Hori, M. Furukawa, and et. al., J. Plasma Fusion Res. **81**, 141 (2005).
[10] D. Hori, M. Furukawa, and et. al., J. Plasma Phys. **72**, 965 (2006).

Proceedings of ITC/ISHW2007

On rapid rotation in stellarators

Per HELANDER

Max-Planck-Institut für Plasmaphysik, 17491 Greifswald, Germany

The conditions under which rapid plasma rotation may occur in a three-dimentional magnetic field, such as that of a stellarator, are investigated. Rotation velocities comparable to the ion thermal speed are found to be attainable only in magnetic fields which are approximately isometric. In an isometric magnetic field the dependence of the magnetic field strength B on the arc length l along the field is the same for all field lines on each flux surface ψ. Only in fields where the departure from exact isometry, $B = B(\psi, l)$, is of the order of the ion gyroradius divided by the macroscopic length scale are rotation speeds comparable to the ion thermal speed possible. Moreover, it is shown that the rotation must be in the direction of the vector $\nabla\psi \times \nabla B$.

Keywords: plasma rotation, kinetic MHD, drift kinetic equation

1 Introduction

It is well known in tokamak research that the plasma tends to rotate faster in the toroidal direction than in the poloidal direction, particularly when there is strong neutral-beam injection. It is also well known that magnetic field ripples damp toroidal rotation. Theoretically, it is expected that an axisymmetric plasma should be free to rotate in the toroidal direction, but that the poloidal rotation should be damped. To be more precise, if the gyroradius ρ is small compared with the macroscopic scale length L, so that $\delta = \rho/L \ll 1$, then the toroidal rotation can be comparable to the ion thermal speed $v_T = (2T_i/m_i)^{1/2}$, but the poloidal rotation velocity is of order δv_T. This result follows from the drift-kinetic equation, and will be rederived below. The purpose of the present paper is to clarify under what conditions rapid rotation ($V \sim v_T$) is possible if the magnetic field is not axisymmetric.

We find that rapid rotation can only occur in a certain class of magnetic fields, namely, in fields that are approximately "isometric". The definition of an isometric magnetic field is that the field strength depends on the arc length l along $\mathbf{B}$ in the same way for all field lines on the same flux surface [1]. Thus in an isometric field $B = B(\psi, l)$, where ψ is a flux-surface label. Interestingly, such fields have attracted attention because of their favourable confinement properties. They are an important subclass of "omnigenous" magnetic fields, which are fields where the time-averaged cross-field drift vanishes for all particle orbits [2, 3]. Quasi-axisymmetric [4] and quasi-helically symmetric [5, 6] fields are examples of isometric fields, but isometry is a weaker condition than quasisymmetry. We also find that the the rotation velocity vector must point in the direction $\nabla\psi \times \nabla B$, so that the streamlines coincide with lines of constant magnetic field strength. These contraints follow from the drift kinetic equation in the limit of zero gyroradius (so-called kinetic MHD), and are therefore independent of the cross-field transport collisionality. A somewhat different version of this calculation is being published in Physics of Plasmas (October 2007).

author's e-mail: xxxyyyzzz@u-plasma.ac.jp

2 Expansion of the kinetic equation

First of all, it is important to choose the correct plasma model from which to proceed. Plasma equilibrium is usually described by ideal MHD, which is however not sufficient for our present purposes. Ideal MHD neglects transport altogether, both within and across flux surfaces, and therefore permits arbitrary toroidal and poloidal rotation as well as temperature variation within flux surfaces. In reality, parallel transport is many orders of magnitude larger than perpendicular transport, which implies that flux surfaces must be approximately isothermal and also constrains plasma rotation. These features are incorporated in so-called *kinetic MHD*, which follows from the terogyroradius limit of the ion kinetic equation

$$\frac{\partial f}{\partial t} + (\mathbf{V}+\mathbf{v})\cdot\nabla f + \frac{e}{m}\left(\mathbf{E}' + \mathbf{v}\times\mathbf{B} - \frac{\partial \mathbf{V}}{\partial t}\right.$$

$$\left. -(\mathbf{V}+\mathbf{v})\cdot\nabla\mathbf{V}\right)\cdot\frac{\partial f}{\partial \mathbf{v}} = C(f) + S, \qquad (0)$$

where $\mathbf{v} = \mathbf{u} - \mathbf{V}(\mathbf{r}, t)$ is the velocity vector measured relative to velocity field $\mathbf{V}$, $\mathbf{E}' = \mathbf{E} + \mathbf{V}\times\mathbf{B}$ the electric field in the moving frame, e and m the ion charge and mass, respectively, C the collision operator and

S represents any sources present in the plasma. Although $\mathbf{V}$ is in principle arbitrary, we shall choose it to be equal to the lowest-order mean ion velocity. As in MHD, the electic field is ordered to be so large that the $E \times B$ velocity is comparable to the thermal speed, $E \sim v_T B$, while the collsion frequency is taken to be comparable to the transit frequency, v_T/L, in order to allow for all conventional collisionality regimes. The dependent variables $f = f_0 + f_1 + \ldots$, $\mathbf{E} = \mathbf{E}_0 + \mathbf{E}_1 + \ldots$ and, unconventionally, also the magnetic field $\mathbf{B} = \mathbf{B}_0 + \mathbf{B}_1 + \ldots$ are expanded in the smallness of $\delta = v_T/\Omega L \ll 1$, where $\Omega = eB/m$. In order to study equilibrium (rather than the approach to it), the time derivatives of zeroth-order quantities are assumed to be small, $\partial f_0/\partial t \ll (v_T/L) f_0$, whilst higher-order quantities may vary more rapidly (to allow for turbulence, for instance). The electric field is thus electrostatic in lowest order, $\mathbf{E}_0 = -\nabla\Phi_0$.

The largest terms in Eq. (2) are of order Ωf, and the others of order $\delta\Omega f = v_T f/L$ or smaller. In lowest order, then, our kinetic equation becomes simply

$$\frac{e}{m}\left(\mathbf{E}_0' + \mathbf{v} \times \mathbf{B}_0\right) \cdot \frac{\partial f_0}{\partial \mathbf{v}} = 0,$$

and can only hold for all $\mathbf{v}$ if

$$(\mathbf{v} \times \mathbf{B_0}) \cdot \frac{\partial f_0}{\partial \mathbf{v}} = 0, \tag{1}$$

and $\mathbf{E}_0' = 0$, so that

$$\mathbf{V}_\perp = \mathbf{V} - \mathbf{V} \cdot \mathbf{bb} = \frac{\mathbf{B_0} \times \nabla\Phi_0}{B_0^2} \tag{2}$$

and $\mathbf{b} \cdot \nabla\Phi_0 = 0$, where $\mathbf{b} = \mathbf{B}_0/B_0$. We shall assume that the magnetic field at least approximately (i.e., in lowest order) possesses flux surfaces, so that $\Phi_0 = \Phi_0(\psi, t)$.

A drift kinetic equation can now be derived in the conventional way [7, 8, 9, 10] by writing

$$\mathbf{v} = v_\parallel \mathbf{b} + v_\perp(\mathbf{e}_1 \cos\vartheta + \mathbf{e}_2 \sin\vartheta),$$

where $\mathbf{e}_1$, $\mathbf{e}_2$ are unit vectors with $\mathbf{e}_1 \times \mathbf{e}_2 = \mathbf{b}$, and averaging over the gyro-angle ϑ. Equation (1) first implies that f_0 is independent of gyro-angle, $\partial f_0/\partial\vartheta = 0$, and Eq. (2) becomes

$$\Omega\frac{\partial f}{\partial \vartheta} = \frac{\partial f}{\partial t} + \Lambda(f) + \frac{e}{m}(\mathbf{v}\times\mathbf{B}_1)\cdot\frac{\partial f}{\partial \mathbf{v}} = C(f) + S(3)$$

where

$$\Lambda(f) = (\mathbf{v} + \mathbf{V}) \cdot \left[\nabla f + \nabla\mathbf{b} \cdot \mathbf{v}\left(\frac{\partial f}{\partial v_\parallel} - \frac{v_\parallel}{v_\perp}\frac{\partial f}{\partial v_\perp}\right)\right.$$

$$\left. + (\cos\vartheta\nabla\mathbf{e}_2 - \sin\vartheta\nabla\mathbf{e}_1) \cdot \frac{\mathbf{v}}{v_\perp}\frac{\partial f}{\partial\vartheta}\right]$$

$$+ \left[\frac{e\mathbf{E}_1'}{m} - \frac{\partial \mathbf{V}}{\partial t} - (\mathbf{V} + \mathbf{v}) \cdot \nabla\mathbf{V}\right]$$

$$\cdot \left(\mathbf{b}\frac{\partial f}{\partial v_\parallel} + \frac{\mathbf{v}_\perp}{v_\perp}\frac{\partial f}{\partial v_\perp} + \frac{\mathbf{b} \times \mathbf{v}}{v_\perp^2}\frac{\partial f}{\partial \vartheta}\right). \tag{4}$$

Taking the ϑ-average gives the desired drift kinetic equation

$$\bar{\Lambda}(f_0) = C(f_0) + S, \tag{5}$$

where

$$\bar{\Lambda}(f_0) = (\mathbf{V} + v_\parallel\mathbf{b}) \cdot \nabla f_0 + \frac{e\tilde{E}_\parallel}{m}\frac{\partial f_0}{\partial v_\parallel}$$

$$+ \frac{v_\perp^2}{2}(\nabla \cdot \mathbf{b})\left(\frac{\partial f_0}{\partial v_\parallel} - \frac{v_\parallel}{v_\perp}\frac{\partial f_0}{\partial v_\perp}\right)$$

$$-(\mathbf{V} + v_\parallel\mathbf{b}) \cdot \nabla\mathbf{V} \cdot \mathbf{b}\frac{\partial f_0}{\partial v_\parallel}$$

$$+ \frac{v_\perp}{2}(\mathbf{b} \cdot \nabla\mathbf{V} \cdot \mathbf{b} - \nabla \cdot \mathbf{V})\frac{\partial f_0}{\partial v_\perp},$$

with $\tilde{E}_\parallel = \mathbf{b} \cdot \mathbf{E}_1' = \mathbf{b} \cdot (\mathbf{E}_1 + \mathbf{V} \times \mathbf{B}_1)$. This equation, and its derivation, agrees with that derived in Ref. [9] except for the addition of the term containing $\mathbf{B}_1$. It looks simpler if one of the independent variables is chosen to be the magnetic moment measured in the moving frame, and then agrees with Refs. [7, 10].

3 Constraints on the flow velocity

In equilibrium, the source term balances transport losses and is therefore also relatively small, usually of order δ or δ^2. The solutions to the resulting equilibrium equation (5),

$$\bar{\Lambda}(f_0) = C(f_0) \tag{6}$$

are found from a familiar H-theorem argument. Multiplying the equation by $\ln f_0$, integrating over velocity space, and taking a flux surfaces average gives

$$\left\langle \int \ln f_0 C(f_0)\, 2\pi v_\perp dv_\perp dv_\parallel \right\rangle = 0, \tag{7}$$

and it follows that f_0 must be a Maxwellian, whose density n and temperature T may vary over each flux surface. Substituting this Maxwellian into Eq. (6) gives the equation $\bar{\Lambda}(f_0) = 0$, or

$$(\mathbf{V} + v_\parallel\mathbf{b}) \cdot \left[\nabla \ln n + \left(\frac{mv^2}{2T} - \frac{3}{2}\right)\nabla \ln T\right]$$

$$-\frac{e\tilde{E}_\parallel v_\parallel}{T} + \frac{mv_\parallel}{T}(\mathbf{V} + v_\parallel\mathbf{b}) \cdot \nabla\mathbf{V} \cdot \mathbf{b}$$

$$-\frac{mv_\perp^2}{2T}(\mathbf{b} \cdot \nabla\mathbf{V} \cdot \mathbf{b} - \nabla \cdot \mathbf{V}) = 0,$$

which can only be satisfied if the following relations are satisfied [9, 10]:

$$\mathbf{b} \cdot \nabla \ln n - \frac{e\tilde{E}_\parallel}{T} + \frac{m}{T}\mathbf{V} \cdot \nabla\mathbf{V} \cdot \mathbf{b} = 0,$$

$$\mathbf{b}\cdot\nabla T = 0,$$

$$\mathbf{V}\cdot\nabla\left(\ln n - \frac{3}{2}\ln T\right) = 0,$$

$$\nabla\cdot(n\mathbf{V}) = 0,$$

$$\mathbf{b}\cdot\nabla\mathbf{V}\cdot\mathbf{b} - \frac{1}{3}\nabla\cdot\mathbf{V} = 0.$$

These equations imply

$$\mathbf{V}\cdot\nabla\ln n = \nabla\cdot\mathbf{V} = \mathbf{b}\cdot\nabla\mathbf{V}\cdot\mathbf{b} = 0. \tag{8}$$

We now recall Eq. (2) and note that

$$0 = \nabla\times(\mathbf{V}\times\mathbf{B}_0) = \mathbf{B}_0\cdot\nabla\mathbf{V} - \mathbf{V}\cdot\nabla\mathbf{B}_0,$$

which combined with Eq. (8) leads to

$$\mathbf{V}\cdot\nabla\mathbf{B}_0\cdot\mathbf{B}_0 = 0.$$

Since $(\nabla\mathbf{B}_0)\cdot\mathbf{B}_0 = B_0\nabla B_0$ we thus conclude that

$$\mathbf{V}\cdot\nabla B_0 = 0.$$

In other words, the streamlines of the flow are given by the intersection between flux surfaces and surfaces of constant B_0. This means that the velocity field can be written as

$$\mathbf{V}(\mathbf{r}) = g(\mathbf{r})\nabla\psi\times\nabla B_0$$

for some function $g(\mathbf{r})$ of the spatial coordinates $\mathbf{r}$. The parallel component of the flow is thus

$$V_\parallel\mathbf{b} = g(\mathbf{r})\nabla\psi\times\nabla B_0 - \frac{d\Phi_0}{d\psi}\frac{\mathbf{b}\times\nabla\psi}{B_0}.$$

Taking the scalar product of this equation with $\mathbf{b}\times\nabla\psi$ gives an expression for g,

$$g\mathbf{b}\cdot\nabla B_0 + \frac{1}{B_0}\frac{d\Phi_0}{d\psi} = 0,$$

and thus enables us to write down an explicit expression for the lowest-order flow velocity,

$$\mathbf{V} = -\frac{d\Phi_0}{d\psi}\frac{\nabla\psi\times\nabla B_0}{\mathbf{B}_0\cdot\nabla B_0}. \tag{9}$$

If $\mathbf{B}_0$ is written in Clebsch coordinates, $\mathbf{B}_0 = \nabla\psi\times\nabla\alpha$, then $\mathbf{V}$ becomes

$$\mathbf{V} = \frac{\nabla\Phi_0\times\nabla B_0}{(\nabla\psi\times\nabla B_0)\cdot\nabla\alpha}.$$

The requirement (8) that this flow field should be incompressible now implies a constraint on the spatial variation of the magnetic field strength,

$$(\nabla\psi\times\nabla B_0)\cdot\nabla(\mathbf{B}_0\cdot\nabla B_0) = 0. \tag{10}$$

If B_0 is expressed in coordinates (ψ,α,l), where l is the arc length along $\mathbf{B}_0$ then it follows from Eq. (10) that

$$(\nabla\psi\times\nabla B_0)\cdot\nabla\dot{B}_0 = 0,$$

where $\dot{B}_0 = \partial B_0/\partial l$. Hence

$$\frac{\partial B_0}{\partial\alpha}\frac{\partial\dot{B}_0}{\partial l} - \frac{\partial B_0}{\partial l}\frac{\partial\dot{B}_0}{\partial\alpha} = 0, \tag{11}$$

and it follows that $\dot{B}_0$ must be expressible as a function of ψ and B_0, i.e., $\dot{B}_0 = \dot{B}_0(\psi, B_0)$, at least locally. This implies, in turn, that B_0 is isometric. To see this formally, we note that Eq. (11) can be written as

$$\frac{\partial\ln\dot{B}_0}{\partial l} = \frac{\partial}{\partial l}\ln\left(\frac{\partial B_0}{\partial\alpha}\right),$$

and integrated once, to yield

$$\frac{\partial B_0}{\partial l} = F(\psi,\alpha)\frac{\partial B_0}{\partial\alpha},$$

with F an arbitrary function. The general solution is

$$B_0 = B_0(\psi, l'),$$

where $l' = l - l_0(\psi,\alpha)$ is an arc length coordinate whose origin l_0 is related to F by $F\partial l_0/\partial\alpha = -1$. We conclude that rotation at a speed comparable to the thermal speed is only possible if the magnetic field is isometric in lowest order. The converse is also true: the flow field (9) satisfies the conditions (8) if B_0 is isometric, and our theorem can thus be stated in the following way. *The lowest-order drift kinetic equation admits solutions where the mean flow velocity is comparable to the thermal speed if, and only if, the magnetic field is approximately isometric.*

Another way of stating this result is that a sufficiently large radial electric field is only possible if the magnetic field is isometric. "Sufficiently large" in this context refers to fields that are strong enough to produce flow velocities comparable to v_T (sonic rotation), and it is worth noting that this may occur for fields that are in fact much smaller than $E \sim v_T B$ (though formally of this order, in the sense of the gyroradius ordering assumed). The result (9) can be written as

$$\frac{\mathbf{V}}{E/B_0} = \frac{\mathbf{n}\times\nabla B_0}{\mathbf{b}\cdot\nabla B_0}, \tag{12}$$

where $\mathbf{n} = \nabla\psi/|\nabla\psi|$ is the unit vector normal to the flux surfaces and $E = -\mathbf{n}\cdot\nabla\Phi_0$ is the electric field. The point is that the right-hand side of (12) can be relatively large (but not infinite in an isometric field), in which case the parallel component of the velocity (9) is significantly larger than the perpendicular one. In tokamaks, for instance, $|\mathbf{n}\times\nabla B_0|/(\mathbf{b}\cdot\nabla B_0) \sim q/\epsilon \gg 1$, where q is the safety factor and ϵ the inverse aspect ratio. As is well known, sonic rotation thus occurs already for radial electric fields of order $E \sim \epsilon v_T B/q$. In a stellarator, a similar estimate tends to hold approximately, but the details depend of course on the specific magnetic configuration. Importantly, sonic rotation can occur at roughly the same electric field as when the poloidal $E\times B$ drift cancels the poloidal component of $v_\parallel$ for a thermal ion. This "resonance" condition is thought to strongly affect the neoclassical transport [11].

It is interesting to note that Eq. (9) implies a simple expression for the neoclassical polarisation current. When combined with the momentum equation

$$\rho \frac{d\mathbf{V}}{dt} = \mathbf{j} \times \mathbf{B} - \nabla \cdot \mathbf{P},$$

where $\mathbf{P}$ is the pressure tensor, it yields the perpendicular current as

$$\mathbf{j}_\perp - \frac{\mathbf{B} \times (\nabla \cdot \mathbf{P})}{B^2} = \frac{\rho \mathbf{B}}{B^2} \times \frac{d\mathbf{V}}{dt} \simeq -\frac{\rho}{B^2} \frac{\partial \nabla \Phi}{\partial t},$$

where the last, approximate, equality refers to low speeds, $\partial \mathbf{V}/\partial t \gg \mathbf{V} \cdot \nabla \mathbf{V}$.

The result that the eletric field cannot be large unless the magnetic field is isometric suggests a paradox in the low-density limit, since any electric field strength is possible in vacuum. The resolution lies in our ordering of the collision frequency, $\nu_i \sim v_T/L$. This is the standard neoclassical ordering, and is usually followed by a subsidiary ordering where the collision frequency is taken to be smaller or larger than the transit frequency, but usually not as small as $\nu \sim \delta v_T/L$. At extremely low densities, this latter case must be allowed, in which case the lowest-order drift kinetic equation becomes $\bar{\Lambda}(f_0) = 0$ and does not constrain f_0 to be Maxwellian or B_0 to be isometric.

4 Conclusions

It is well established that plasma rotation tends to have a beneficial influence on plasma confinement. Therefore it is of interest to establish under which conditions rotation is allowed to occur. We have considered this question for general three-dimensional magnetic confinement systems, and found that sonic rotation is only possible in isometric magnetic fields, and can only occur in the direction of constant magnetic field strength. In the special case of a tokamak, plasma rotation must therefore be purely toroidal in lowest order, as is well known both theoretically and experimentally. (Although the poloidal rotation in experiments has been reported to exceed its neoclassical prediction, it is still far smaller than the toroidal rotation [12, 13].)

In stellarators, the radial electric field and rotation velocity are set by the condition of ambipolar cross-field transport, and is usually fairly slow in experiments, $V \ll v_T$. It is often the case that neoclassical transport dominates, and the magnitude and direction of the rotation then depend on the collisionality and heating channel. What we have shown in this paper is that rapid rotation can only occur in isometric magnetic fields and only in the direction $\nabla\psi \times \nabla B$. These constraints are approximate, in the sense that they only need to be satisfied to lowest order in gyroradius, but are independent of the cross-field transport. They therefore hold in all (conventional) collisionality regimes, and also in the presence of gyro-kinetic turbulence.

Acknowledgment

It is a pleasure to acknoledge useful discussions with C. Beidler, P. Catto, H. Maaßberg, J. Nührenberg, and Yu. Turkin.

[1] A.A. Skovoroda and V.D. Shafranov, Plasma Phys. Rep. **21**, 886 (1995).
[2] L.S. Hall and B. McNamara, Phys. Fluids **18**, 552 (1975).
[3] J.R. Cary and S. Shasharina, Phys. Plasmas **4**, 3323 (1997).
[4] J. Nührenberg, W. Lotz, S. Gori, in *Theory of Fusion Plasmas* (Editrice Compositori, Bologna, 1994), p. 3.
[5] J. Nührenberg and R. Zille, Phys. Lett. A **129**, 113 (1988).
[6] A.H. Boozer, Plasma Phys. Contr. Fusion **37**, A103 (1995).
[7] R.D. Hazeltine and A.A. Ware, Plasma Phys. Contr. Fusion **20**, 673 (1978).
[8] I.B. Bernstein and P.J. Catto, Phys. Fluids **28**, 1342 (1985).
[9] F.L. Hinton and S.K. Wong, Phys. Fluids **28**, 3082 (1985).
[10] R. Hazeltine and F.L. Hinton, Phys. Plasmas **12**, 102506 (2005).
[11] H. Maaßberg, R. Burhenn, U. Gasparino, G. Khner, H. Ringler, and K.S. Dyabilin Phys. Fluids B **5**, 3627 (1993).
[12] K. Crombé, Y. Andrew, M. Brix, C. Giroud, S. Hacquin, N. C. Hawkes, A. Murari, Phys. Rev. Lett. **95**, 155003 (2005).
[13] W.M. Solomon, K.H. Burrell, R. Andre, L.R. Baylor, R. Budny, P. Gohil, R.J. Groebner, C.T. Holcomb, W.A. Houlberg, and M.R. Wade, Phys. Plasmas **13**, 056116 (2006).

Proceedings of ITC/ISHW2007

Formation of Sweet-Parker-like electron dissipation region in a driven open system

Bin Li[1)], Ritoku Horiuchi[1,2)] and Hiroaki Ohtani[1,2)]

[1)]*The Graduate University for Advanced Studies,322-6 Oroshi-cho, Toki 509-5292, Japan*

[2)]*National Institute for Fusion Science,322-6 Oroshi-cho, Toki 509-5292, Japan*

October 4, 2007

Nonlinear development of collisionless driven reconnection is investigated by making use of the electromagnetic particle simulation code "PASMO" developed for an open system which is subject to an external driving source. The electric field at the reconnection point increases and approaches the external driving field as time goes on. After the formation of x-shaped field structure around the reconnection point, the length of the electron dissipation region continues to increase for a short time. Finally, it stops to grow and relaxes to a steady state when the ratio of the width to length is a constant. Thus, Sweet-Parker-like electron dissipation region is formed in a steady state, while the reconnection rate is controlled by the driving electric field.

Keywords: driven reconnection, collisionless, Sweet-Parker-like, steady state, electrons dissipation region

1 Introduction

Magnetic reconnection occurs in a wide variety of plasma systems, such as collision-dominated plasmas in the solar convection zone, weakly collisional plasmas in the solar corona, and collisionless plasmas in the Earth's magnetosphere, plasma experiments such as tokamak and reversed field pinch[1, 2]. During magnetic reconnection, most of magnetic energy is effectively transformed into plasma energy.

The structure of dissipation region, where reversed magnetic field lines are dissipated and reconnected, has not been understood well for a long time. Recently experimental results [3] of Magnetic Reconnection Experiment (MRX) and observations from WIND satellite [4] shed new light on this research direction. Their results have implied that the dissipation region has a Sweet-Parker like spatial geometry: a long and narrow current layer extends along the downstream direction.

Unfortunately, Sweet-Parker model is simply based on classical collisional resistivity assumption and cannot explain time scale of fast energy release in solar flare. Thus, it is necessary to investigate what mechanism is responsible for breaking the frozen-in flux constraint in the dissipation region. In a series of previous two dimensional simulations, dissipation mechanisms are generally thought to be provided by microscale collisionless kinetic effects, i.e., the inertia effect [5, 6] and the thermal effect [7, 8] based on the non-gyrotropic meandering motion. It is implied that the evolution of collisionless reconnection is controlled by the particle kinetic effects in two dimensions.

In this paper, we will pay attention to investigating steady state of fast magnetic reconnection in a driven case based on the three dimensional particle-in-cell (PIC) code "PASMO" [9, 10]. It is found that in our simulation around the X-line, an electron dissipation region is formed and extended to the downstream. In a steady state, it has a rectangular shape current layer, which is a typical prediction of the Sweet-Parker model.

The outline of the paper is as following; first we describe the simulation model, and second introduce the structure of the electron dissipation region and finally discuss the simulation results.

2 Simulation model

The simulation is carried out by using three dimensional PIC simulation code "PASMO", 2D version of which has been successfully used in previous investigations[7, 11, 12, 13, 14, 15].

Physical quantities at the boundary of z axis is ($z = \pm z_b$) are assumed to be periodic, upstream and downstream boundaries are set at those of y axis ($y = \pm y_b$) and x axis ($x = \pm x_b$), respectively.

At upstream boundary, plasmas satisfy the frozen-in condition. By adopting an external electric field $E_z(x,t)$ at $y = \pm y_b$ along z-axis, ions and electrons are driven into the simulation domain at the same drift velocity. The driving electric field is relatively larger within the input window size x_d around $x = 0$ during the Alfvén time $\tau_A = y_b/V_A$, where V_A is the initial average Alfvén velocity. Therefore, plasmas have larger speed within the size of the input window so as to make the convergent plasma flow into the center of simulation domain where magnetic reconnection will occur first. The driving field will approach a uniform profile with a constant value along the upstream boundary. Magnetic fields can change spatially and temporally according as the driving electric field evolves.

author's e-mail: li.bin@nifs.ac.jp

At the downstream boundary $x = \pm x_b$, plasmas number density is controlled by both the charge neutrality condition and the condition of the net number flux, which is associated with the fluid velocity in the vicinity of the boundary [14]. Thus, the plasma can freely flow in or out, the total number of particles may vary with time in this open system. The field quantities E_x,E_y and $\partial_x E_z$ are continuous at downstream boundaries. The other components of the electromagnetic field can be obtained by solving the Maxwell equations at the boundary.

One-dimensional Harris sheet equilibrium is adopted as an initial condition, where magnetic field and plasma pressure are given by $B_x(y) = B_0 \tanh(y/y_h)$ and $P(y) = B_0^2 \big/ 8\pi \cdot sech^2(y/y_h)$ with the scale height y_h. As a consequence of initially reversed magnetic field configuration, a neutral sheet appears at the center of y axis ($y = 0$). The Lorentz force pushes plasmas toward neutral line, while plasma pressure makes plasmas move away from it. Thus the initial equilibrium is maintained by two forces counterbalance. The distribution of particles is a shifted Maxwellian with a uniform temperature $T_{i0} = T_{e0}$. We set the particle mass ratio $m_i/m_e = 100$, the ratio of plasma frequency to the electron cyclotron frequency $\omega_{pe0} \big/ \omega_{ce0} = 2$, the strength of the inflow velocity $E_0/B_0 = -0.04$, and the ratio of input window size to inflow direction length $x_d = 1.5$ in our numerical simulations.

3 Electron dissipation region

In our simulation model, reconnection rate equals to the electric field at the X-line[7, 9, 10, 11, 12, 13, 14, 15]. When system relaxes to a steady state, both electric field E_z in the system and reconnection rate should equal to the external driving electric filed. After reconnection process begins, the electric field at X-line increases and equals to the driving field after $t\omega_{ce} = 750$. The difference between electric fields at the X-line and upstream boundary is shown in Fig.1. However, the electric field along the downstream direction does not reach uniform profile until $t\omega_{ce} \approx 1110$,as shown in Fig.2. After then, the electric field becomes equal to the driving field everywhere in the system, and thus the system relaxes to the steady state.

Fig.3 shows spatial profile of electrons current density at $t\omega_{ce} = 900$. The electron current density evolves gradually in a long and narrow rectangular region at the center of current layer. Thus, electron current sheet is formed in a narrow and long shape, which is the typical result predicted in the Sweet-Parker model. The current density increases from upstream boundary to the X-line in the inflow direction and magnetic field B_x gradient also increases. To understand the structure of the current sheet, let us consider three spatial scales: electrons meandering motion scale l_{me}, skin depth $d_e = c \big/ \omega_{pe}$, and half width of the sharp peak in the current density profile. The electron meandering scale is defined by the distance which satisfies the condition $\rho_e(y)/y = 1$ [5, 6], where $\rho_e(y)$ is the local electron Larmor radius. The half width of the current density sharp peak is defined by the half width at 80% maximum value of the current density. In Fig.4, time evolution of three spatial scales defined above are plotted, where they are normalized by Debye length and are measured along the vertical line through the X-line. The half width of the sharp peak value is close to the electrons meandering motion scale and has similar tendency in time evolution. This result implies that electrons dynamics control the current sheet formation around the X-line and thus a Sweet-Parker-like electrons dissipation region is generated.

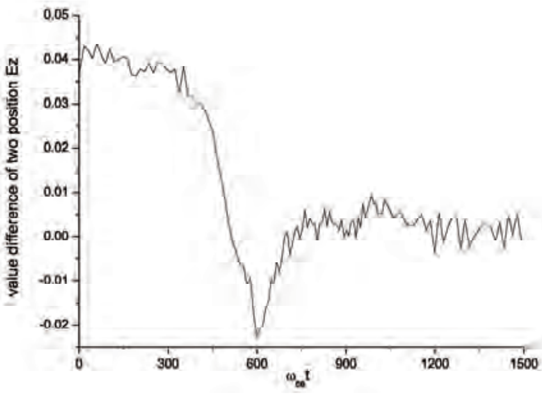

Fig. 1 Difference of electric fields at X-line and upstream boundary as a function of time.

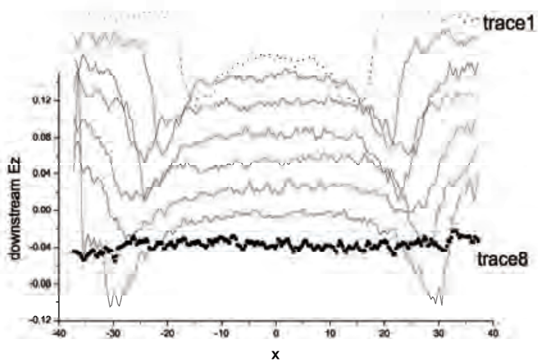

Fig. 2 Spatial profile of electric field E_z along the outflow direction at eight consecutive time periods, where trace 1 denotes the profile at $t\omega_{ce} = 662$, trace 8 at $t\omega_{ce} = 1148$. The reference level of each line is shifted vertically to avoid overlapping of lines.

In a kinetic regime non-ideal effects becomes significant through microscopic physical processes and macroscopic frozen-in condition is not satisfied [8, 12, 13, 14, 15]. Ion spatial scale in which non-ideal effects becomes significant for ions are larger than that for electrons. In other words, wider ion dissipation region is formed in the current sheet compared with electron dissipation re-

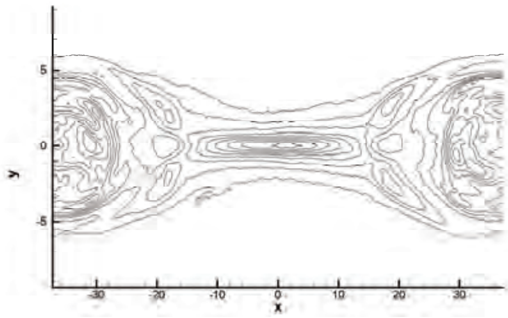

Fig. 3 Spatial profile of electrons current density at $t\omega_{ce} = 900$.

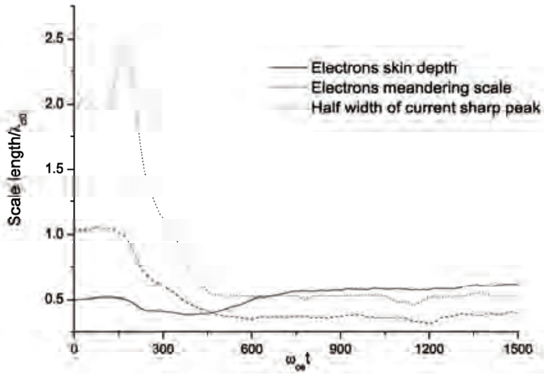

Fig. 4 Time evolution of three spatial scales; electron skin depth, electron meandering scale, and half width of current density peak.

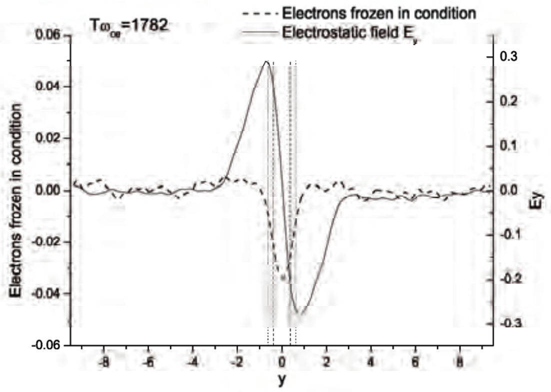

Fig. 5 Spatial profiles of electron frozen-in condition $(E + v_e \times B)_z$ and electrostatic field E_z along the inflow direction. Positions of electron skin depth and meandering scale are indicated by vertical dotted lines and dashed lines, respectively.

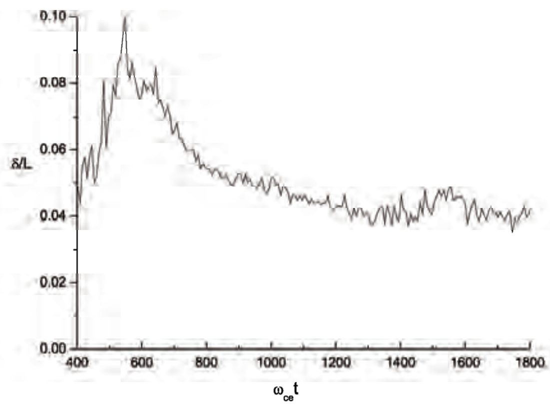

Fig. 6 Time evolution of the ratio of electron dissipation region width to its length.

gion. Figure 5 demonstrates the spatial profiles of electron frozen-in condition $(E + v_e \times B)_z$ and the electric field E_y. Because electrons remains magnetized while ions are not magnetized in the ion dissipation region, the driving field pushes mainly electrons inward and creates electron rich region inside the electron dissipation region. The in-plane electrostatic field is generated due to the charge separation in the kinetic regime and is largest at edge of electrons dissipation region, as shown in Fig. 5. The violation of electron frozen-in condition starts at electrons skin depth and becomes significant below the electron meandering scale

In the steady state, spatial configuration of magnetic field does not change with time and thus the width of electron dissipation region is expected to be a constant too, which is defined by the electrons skin depth. After reconnection rate becomes a constant ($t\omega_{ce} = 750$), the skin depth also becomes constant. Based on the electrons mass conversation let us define the length of the electrons dissipation region by the distance from the X-line to the position where electrons outflow speed is maximum. The ratio of these two scales, $r = d_e/l_e$, can be used to evaluate the structure of electrons dissipation region. In Fig.6, time variation of this ratio is plotted. Although the reconnection rate, electrons skin depth and its meandering motion scale already becomes constant(see in Figs.1 and 4), the curve still gradually decreases after that. The length of electrons dissipation region increases until $t\omega_{ce} \approx 1100$ and then the ratio becomes constant finally. This result corresponds the fact that the electric field in the downstream reaches a constant profile at $t\omega_{ce} \approx 1100$ (see Fig.2).

4 Summary

We have found that a Sweet-Parker-like electron dissipation region is formed during the process of magnetic reconnection. Its width is determined by electron skin depth while its length is defined by the distance from X-line to the position where electron outflow speed has maximum value. The electron dissipation region is mainly controlled by microscopic electron dynamics.

It should be mentioned that there is the delay in the period when inflow and outflow regions relax to the steady state. The length of electrons dissipation region and downstream electric field E_z still evolve in a while after reconnection rate at the X-line already become equal to diving electric field. The length of electron dissipation region is determined by using the position where electron outflow speed has maximum value. This means that the electron outflow speed starts to decrease as soon as they move into the ion dissipation region, and it gradually approaches the ion outflow speed. The simulation result also indicates that the ratio of the width of the electron dissipation region to its length is approximately given by $\frac{1}{2}(m_e/m_i)^{1/2}$. Thus, the relaxation of electron outflow speed may be determined by the cooperative action of both ion and electron dynamics. The details about this will be discussed in a future paper.

[1] D. Biskamp, *Energy Conversion and Particle Acceleration in the Solar Corona* (Springer Berlin/Heidelberg, Germany, 2003) p.109.

[2] E.Priest and T.Forbes, *Magnetic reconnection* (Cambridge University Press, Cambridge, UK, 2000) p.322.

[3] Hantao Ji, Masaaki Yamada, Scott Hsu, and Russell Kulsrud, Phys. Rev. Lett. **80**, 3256 (1998).

[4] M. Oieroset, T. D. Phan, M. Fujimoto, R. P. Lin and R. P. Lepping, Nature. **412**, 414 (2001).

[5] M. Ottaviani and F. Porcelli, Phys. Rev. Lett. **71**, 3802 (1993).

[6] Biskamp, E. Schwarz, and J. F. Drake, Phys. Rev. Lett. **75**, 3850 (1995).

[7] R.Horiuchi and T.Sato, Phys. Plasmas. **1**, 3587 (1994).

[8] M.Hesse,K.Schindler,J,Bim, and M.Kuznetsova, Phys. Plasmas. **6**, 1781 (1999).

[9] H. Ohtani, R. Horiuchi and A. Ishizawa, J. plasma phys. **72**, 929 (2006).

[10] R. Horiuchi, H. Ohtani and A. Ishizawa, J. plasma phys. **72**, 953 (2006)

[11] R.Horiuchi and T.Sato, Phys. Plasmas. **4**, 277 (1997).

[12] A.Ishizawa, R. Horiuchi, and H. Ohtani, Phys. Plasmas. **11**, 3579 (2004).

[13] W. Pei, R. Horiuchi and T. Sato, Phys. Plasmas. **8**, 3251 (2001).

[14] A. Ishizawa and R. Horiuchi, Phys. Rev. Lett. **95**, 45003 (2005).

[15] W. Pei, R. Horiuchi and T. Sato, Phys. Plasmas. **8**, 3251 (2001).

Proceedings of ITC/ISHW2007

Critical transition model of edge shear flow formation

Luis GARCIA[1)], José M. DELGADO[1)], Benjamin A. CARRERAS[2)], Iván CALVO[3)], M. Angeles PEDROSA[3)] and Carlos HIDALGO[3)]

[1)]*Universidad Carlos III, 28911 Leganés, Madrid, Spain*
[2)]*BACV Solutions Inc., Oak Ridge, TN 37830, USA*
[3)]*Asociación EURATOM-CIEMAT, 28040 Madrid, Spain*

October 15, 2007

Recently, the experimental results for the emergence of the plasma shear flow layer in TJ-II have been explained as a second-order phase transition like process by using a simple model of envelope equations for the fluctuation level, the averaged poloidal velocity shear, and the pressure gradient [Phys. Plasmas **13**, 122509 (2006)]. Here, we extend this model by incorporating radial coupling. The model is applied to the study of the turbulence-shear flow interaction when the energy flux is low. Transition dynamics and their concomitant thresholds are examined within the context of this model. The effect of an external torque has also been considered. In particular, we analyze the damping rate of the shear flow once the external torque has been removed.

Keywords: Anomalous transport, Shear flow, Phase transition

1 Introduction

The importance of shear flows in magnetically confined plasmas is widely recognized. This in part due to the role that these flows play in improving confinement by turbulence suppression [1, 2]. A current problem in plasma physics is to understand how shear flows are created and how they interact with turbulence. This is a complex problem that can be approached at different levels, going from direct numerical simulations of the plasma to the development of simplified reduced models. In the present paper we follow the latter approach.

The spontaneous formation of shear flows with nontrivial radial structure is studied. Due to the lack of sufficiently high spatial and temporal resolution, it is difficult to formulate an experimental test that will definitively select the dominant mechanisms responsible for the transition. However recent TJ-II experimental results offer the possibility of improved diagnostics with increased radial resolution during and after the transition [3]. Motivated by this, we investigate in this paper the radial structure of the turbulence and poloidal flow in the context of phase transition models.

When the input power is low, we have a transition from L-mode to a different regime. In this regime, the fluctuation level decreases or increases at a slower rate than the input flux, and shear flow is spontaneously developed. We focus our attention on this transition in our starting model.

The model we use for our study is a modified version of the fluctuation-flow model with radial structure [6]. The fluctuation-flow model consists of three coupled partial differential equations of the reaction-diffusion type with nonlinear diffusivities for the averaged poloidal velocity shear, the envelope of the turbulence fluctuations level, and the pressure. We include the dependence of the coefficients on the pressure gradient [7]. We have derived an expression for the Reynolds stress term in the averaged poloidal flow equation which conserves angular momentum.

author's e-mail: lgarcia@fis.uc3m.es

2 Transport model

The model is formulated in terms of three fields: the averaged turbulence fluctuation level $E \equiv \left\langle (\tilde{n}/n_0)^2 \right\rangle^{1/2}$, where n_0 is the equilibrium plasma density and $\tilde{n}$ is the fluctuation density; the poloidal flow shear, $\sigma \equiv \partial \langle V_\theta \rangle / \partial r$, where $\langle V_\theta \rangle$ denotes poloidal and toroidal average over a magnetic flux surface; and the averaged pressure, p.

$$\begin{aligned}\frac{\partial E}{\partial t} =& N^{2/3} E - N^{-1/2} E^2 - N^{-1/3} \sigma^2 E \\ &+ \frac{\partial}{\partial x}\left[(D_1 E + D_0)\frac{\partial E}{\partial x}\right]\end{aligned} \tag{1}$$

$$\begin{aligned}\frac{\partial \sigma}{\partial t} =& -\sigma - \alpha_3 \frac{\partial^2}{\partial x^2}\left(N^{-4/3} E^2 \sigma\right) \\ &- \frac{\partial^2}{\partial x^2}\left[\left(D_2 N^{-5/3} E^2 + D_3\right)\frac{\partial^2 \sigma}{\partial x^2}\right]\end{aligned} \tag{2}$$

$$\frac{\partial p}{\partial t} = S + \frac{\partial}{\partial x}\left[(D_1 E + D_0)\frac{\partial p}{\partial x}\right], \tag{3}$$

where $N \equiv |\partial p/\partial x|$. This is a one-dimensional model in which quantities are assumed to depend only on a normalized radial coordinate, x. The equations are written in terms of dimensionless variables, and x goes from 0 to 1, which corresponds to the shear layer region at the plasma edge.

The first term in the equation for E represents a pressure driven, linear growth of the fluctuations. The second term on the right-hand side models the saturation of turbulence in absence of shear flow, and the third term models the turbulence suppression by shear flow. Here we assume low energy flux so we can neglect diamagnetic effects. The first term on the right-hand side of equation (2) models the poloidal flow shear damping due to magnetic pumping, while the other two terms are contributions from the Reynolds stress. The second term on the right-hand side of equation (2) is a negative viscosity term and represents the generation of poloidal flow by Reynolds stress, and the third term is a hyperdiffusivity and damps the poloidal flow.

We include the dependence of the coefficients on the pressure gradient as in Ref. [7]. Because of the bad magnetic field line curvature at the stellarator edge, we assume that the basic instability underlying the turbulence at the edge of TJ-II is the resistive interchange mode. From the dependence of the coefficients on the linear growth rate, γ, and mode width, W_k, we can derive the dependence of the coefficients on the pressure gradient. We assume that all other dependencies are weak and we take the coefficients to depend only on N. The expression for Reynolds stress contributions is derived by a quasi-linear calculation similar to he one proposed in Ref. [8] and has two terms. The one responsible for the generation of flow is a negative viscosity term and the other is a hyper-viscosity term. The Reynolds stress contributions to the poloidal shear flow equation conserve angular momentum.

The terms involving spatial derivatives are diffusion terms. In equations (1) and (3) these terms have the standard Fick's Law structure, with D_0 representing the collisional diffusion and $D_1 E$ representing a renormalized turbulent diffusion. The structure of the negative diffusion operator in equation (2) is due to the fact that is an equation for the shear, the derivative of the momentum. Hyper-diffusivity, with fourth order in the derivative of the shear, keeps a relation two in the orders of source/diffusion derivatives.

We assume that the energy source term $S(x)$ is zero in this layer and that the system is driven by an energy flux Γ_0 from the core, which determines the boundary condition at $x = 0$ according to:

$$\Gamma_0 = -(D_1 E + D_0) \left.\frac{\partial p}{\partial x}\right|_0, \quad p(1) = 0 \tag{4}$$

For the other equations we use zero derivative boundary conditions.

3 Analytic and numerical solutions

For stationary solutions, Eq. (3) is readily integrated, giving a relation between $E(x)$ and $N(x)$,

$$(D_1 E + D_0) N = \Gamma_0 \tag{5}$$

Apart from the trivial solution, $E = \sigma = 0$, Equations (1) and (2) have one fixed point solution with $\sigma = 0$, $E = E_0$, and $N = N_0$. From Eq. (1),

$$E_0 = N_0^{7/6} \tag{6}$$

By substitution of Eq. (6) in the relation (5), we obtain the (constant) density gradient for the fixed point solution,

$$D_1 N_0^{13/6} + D_0 N_0 - \Gamma_0 = 0. \tag{7}$$

For solutions close to the fixed point is possible to derive a simplified description of the system using a multiple scale perturbation analysis. As a first step, we introduce a small parameter δ representing the size of the perturbation, and consider the following expansion

$$\sigma = \delta\sigma_1, \quad E = E_0 + \delta^2 E_2, \quad N = N_0 + \delta^2 N_2 \tag{8}$$

By substituting the expansion in Eq. (2), and taking into account Eq. (6), we get at first order

$$\frac{\partial\sigma_1}{\partial t} = -\sigma_1 - \alpha_3 N_0 \frac{\partial^2\sigma_1}{\partial x^2} - \left(D_2 N_0^{2/3} + D_3\right)\frac{\partial^4\sigma_1}{\partial x^4} \tag{9}$$

We try as solutions modes like $\sigma_1 = \sigma_{10}\cos(k\pi x)$ which satisfy the boundary conditions. To study their stability properties, we consider a temporal and spatial dependence like

$$\sigma(x,t) = \delta\sigma_{10} e^{\gamma t}\cos(k\pi x) \tag{10}$$

Then, we get from Eq. (9),

$$\gamma = -1 + \alpha_3 N_0 (k\pi)^2 - \left(D_2 N_0^{2/3} + D_3\right)(k\pi)^4 \tag{11}$$

This means that the range of possible unstable modes is given by the relation

$$k_- < k < k_+, \tag{12}$$

where

$$(k_\pm \pi)^2 = \frac{\alpha_3 N_0 \pm \sqrt{(\alpha_3 N_0)^2 - 4\left(D_2 N_0^{2/3} + D_3\right)}}{2\left(D_2 N_0^{2/3} + D_3\right)} \tag{13}$$

To have instability, there should be an integer k between k_- and k_+. This gives us a critical value for N, N_c, and, consequently, a threshold value for the flux, Γ_c.

By applying Eq. (13) to different k-values, we can obtain the threshold for Γ_c. We have done a scan in D_2 with k going from 1 to 7 (Fig. 1), the rest of parameters being

$$D_0 = 10^{-3}, \quad D_1 = 10^{-2}, \quad D_3 = 10^{-6}, \quad \alpha_3 = 0.0175$$

We look now for stationary solutions with a given k-value, that is, with the poloidal flow shear at lowest order given by $\sigma(x) = \sigma_{10}\cos(k\pi x)$. From the stability properties of Eq. (2), the stationary solution is the fixed

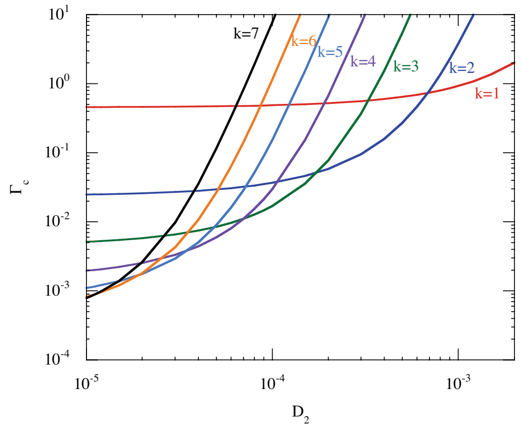

Fig. 1 Flux threshold vs. D_2 for different k-values. The rest of parameters are given in the text.

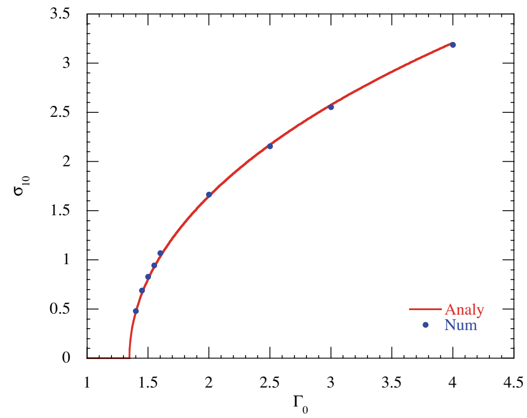

Fig. 2 Comparison of analytical (solid line) and numerical (dots) values of the shear flow for $D_2 = 1.5 \times 10^{-3}$ and $k = 1$.

point solution (7) for values of the flux below Γ_c. Since $\sigma^2 = \sigma_{10}^2[1 + \cos(2k\pi x)]/2$, we get from Eqs. (1) and (5) that at first order, $E(x) = E_s + E_{21}\cos(2k\pi x)$, and $N(x) = N_s + N_{21}\cos(2k\pi x)$ for values of the flux above Γ_c. By substituting these expansions in Eqs. (2) and (5), and taking into account that $D_0 \ll D_1 E$, and $D_3 \ll D_2 N^{-5/3} E^2$ for the parameters we are using, we get the following expressions,

$$E_s = E_c \left(\frac{\Gamma_0}{\Gamma_c}\right)^{\frac{2}{5}}, \tag{14}$$

$$N_s = \frac{\Gamma_c}{D_1 E_c}\left(\frac{\Gamma_0}{\Gamma_c}\right)^{\frac{3}{5}}, \tag{15}$$

$$\sigma_{10}^2 = 2\left[\frac{\Gamma_c}{D_1 E_c}\left(\frac{\Gamma_0}{\Gamma_c}\right)^{\frac{3}{5}} - E_c^{\frac{7}{6}}\left(\frac{\Gamma_c}{D_1}\right)^{-\frac{1}{6}}\left(\frac{\Gamma_0}{\Gamma_c}\right)^{\frac{3}{10}}\right] \tag{16}$$

where

$$E_c = (k\pi)^{-\frac{3}{5}}\left(\frac{\Gamma_c}{D_1}\right)^{\frac{2}{5}}\left[\alpha_3 - D_2\,(k\pi)^2\left(\frac{\Gamma_c}{D_1}\right)^{-\frac{2}{13}}\right]^{-\frac{3}{10}} \tag{17}$$

This gives a good approximation to the numerical results for Γ_0 close to the threshold. Since the experimental profiles of the shear flow and fluctuations close the shear layer have few oscillations, we will concentrate in values of the parameter space such as the most unstable modes are $k = 1$ or 2. In Fig. 2 we compare the analytical and numerical results for $D_2 = 1.5 \times 10^{-3}$ and $k = 1$. The flux threshold for these parameters is 1.358. The analytical results are obtained from Eq. (16), and the numerical results are obtained by advancing numerically Eqs. (1) to (3) until a stationary solution is reached.

4 External torque

To study the effect of an external torque, we add a term $\tau = \tau_0 \cos(k\pi x)$, to the r.h.s. of Eq. (2), so the Equation for the shear flow is now

$$\frac{\partial \sigma}{\partial t} = \tau_0 \cos(k\pi x) - \sigma - \alpha_3 \frac{\partial^2}{\partial x^2}\left(N^{-4/3}E^2\sigma\right) - \frac{\partial^2}{\partial x^2}\left[\left(D_2 N^{-5/3}E^2 + D_3\right)\frac{\partial^2 \sigma}{\partial x^2}\right] \tag{18}$$

In the rest of the calculations of this paper, we apply the torque during a time $t = 10$, and then we remove the torque to analyze the decay of the shear flow. The evolution of the integral of σ^2 for different values of τ_0 when $\Gamma_0 = 1$ is shown in Fig. 3. For this scan, $D_2 = 1.5 \times 10^{-3}$, and $k = 1$, so we are below the threshold flux in absence of external torque (subcritical regime). In most of the cases the shear flow has two decay scales and the change between them is more pronounced as τ_0 increases. The square root of the integral of σ^2 decays like $e^{\gamma_1 t}$ just after removing the external torque (first decay region), and like $e^{\gamma_2 t}$ at larger times (second decay region). The first decay rate is easily understood from Eq. (18). As we remove the torque, the instantaneous exponential decay rate will be $\gamma_1 = -\tau_0/\sigma_1$, where σ_1 corresponds to the stationary state with external torque τ_0. The second exponential decay rate is very similar for all the cases, with γ_2-values between -0.16 and -0.18.

The evolution of the integral of σ^2 when $\Gamma_0 = 1.35$ is shown in Fig. 4. This value of Γ_0 is very close to the critical value, $\Gamma_c = 1.35794$. For this scan, the evolution of the integral of σ^2 when we suppress the external torque is no longer exponential, and can be fitted to the algebraic expression $C/(1 + t/T)$, where C is a constant (value of the integral when we suppress the external torque), and we take as origin of t the time when we remove the external torque. This is due to the fact that we are approaching the critical point.

We have tried also scans in τ_0 with values of Γ_0 above the threshold (supercritical regime), in particular $\Gamma_0 = 1.37$ and 1.5. For these cases, the evolution of the integral of σ^2 when we suppress the external torque can be fitted to

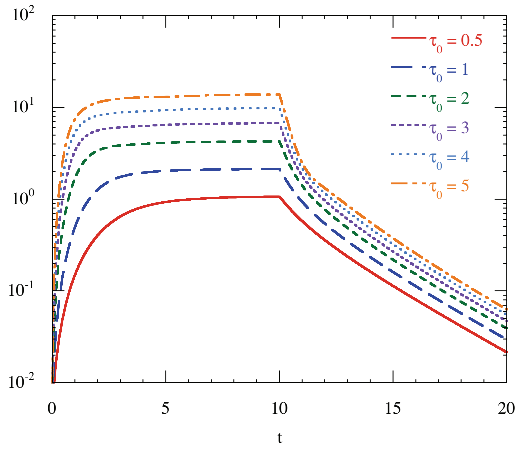

Fig. 3 Evolution of the integral of σ^2 for different values of τ_0 when $\Gamma_0 = 1$. The external torque is suppressed at $t = 10$.

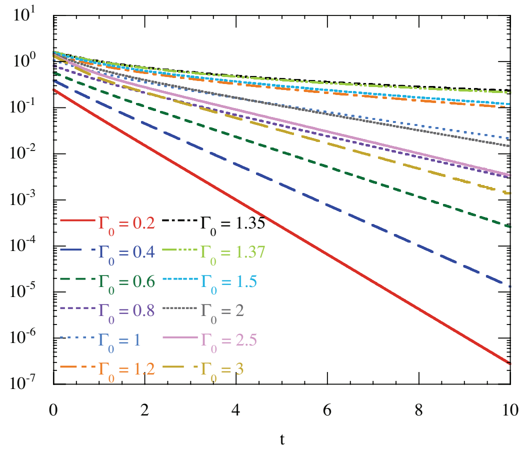

Fig. 5 Evolution of the integral of σ^2 for different values of Γ_0 when $\tau_0 = 0.5$. The origin of t is taken at the time that the external torque is suppressed.

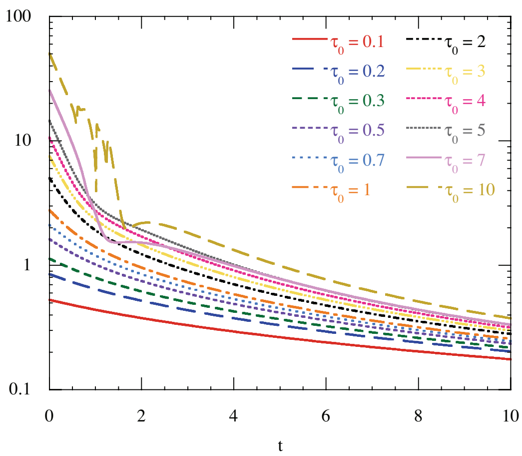

Fig. 4 Evolution of the integral of σ^2 for different values of τ_0 when $\Gamma_0 = 1.35$. The origin of t is taken at the time that the external torque is suppressed.

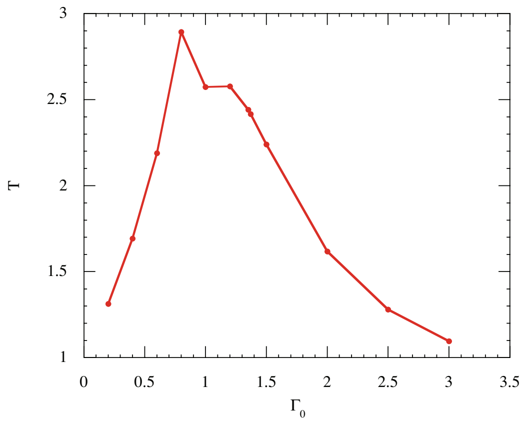

Fig. 6 Results of the exponential fit of the decay of the squared root of the integral of σ^2 for different values of Γ_0 when $\tau_0 = 2$.

$C/(1 + t/T) + C_0$, where C_0 is a constant with a value close to the integral of σ^2 for the stationary state in absence of external torque.

Finally, the results for a scan in Γ_0 are shown in Fig. 5. In the y-axis, we represent the integral of σ^2 when we suppress the external torque minus the value for the stationary state in absence of external torque. The slower decay corresponds to the flux value closer to Γ_c, $\Gamma_0 = 1.35$. The decay time tends to infinity as Γ_0 tends to Γ_c, which corresponds to the singularity of the transition point. The data of the evolution of the squared root of the integral of σ^2 for each Γ_0-value is fitted to $C \exp(-t/T) + C_0$, as it is done in biasing experiments in TJ-II [9]. The results for the decay time T are shown in Fig. 6. The slower decays correspond to flux values closer to Γ_c. The damping is close to the viscous damping (one in our units) only when the flux is far above the threshold. The results are similar when the value of the external torque is changed.

[1] K. H. Burrell, Phys. Plasmas **4**, 1499 (1997).
[2] P. W. Terry, Rev. Mod. Phys. **72**, 109 (2000).
[3] B. Gonçalves, C. Hidalgo, M. A. Pedrosa, R. O. Orozco, E. Sánchez and C. Silva, Phys. Rev. Lett. **96**, 145001 (2006).
[4] Y. Koide, M. Kikuchi, M. Mori et al., Phys. Rev. Lett. **72**, 3662 (1993).
[5] K. H. Burrell, M. E. Austin, D. P. Brennan et al., Phys. Plasmas **8**, 2153 (2001).
[6] D. del-Castillo-Negrete, B. A. Carreras. Physics of Plasmas **9**, 118 (2002).
[7] B. A. Carreras, L. Garcia, M. A. Pedrosa, C. Hidalgo. Physics of Plasmas **13**, 122509 (2006).
[8] P. H. Diamond, S.-I. Itoh, K. Itoh, T. S. Hahm, Plasma Phys. Controlled Fusion **47**, R35 (2005).
[9] M.A. Pedrosa et al., Plasma Phys. Controlled Fusion (2007).

Proceedings of ITC/ISHW2007

Self-similarly evolving, minimally dissipated, and dynamically stable self-organized states obtained by a universal theory

Y. Kondoh, A. Okada, N. Kobayashi, R. Nakajima, T. Takahashi and J. W. Van Dam[a]

Dept. of Electronic Engineering, Gunma University, Kiryu, Gunma 376-8515, Japan

[a] Institute for Fusion Studies, Univ. of Texas at Austin, Texas, USA

(Received: 15 Oct. 2007 / Accepted: 15 Oct. 2007)

With the use of a universal theory of self-organization, a novel set of simultaneous eigenvalue equations having dissipative terms are derived to find self-similarly evolving, minimally dissipated, and dynamically stable states of plasmas realized after relaxation and self-organization processes. Typical spatial profiles of plasma parameters, electric and magnetic fields and dissipative factors are presented, all of which are determined self-consistently with each other by physical laws and mutual relations among them, just as in experimental plasmas.

Keywords: self-organization, self-similarly evolving state, minimally dissipative state, dynamically stable, shear flow

1. Inroduction

By using model equations such as the Grad-Shafranov equation, stability of equilibrium configurations in a stationary state is analytically or numerically judged by using suitable stability criteria in the traditional algorithm to find stable states [1]. However, all dynamic quantities in any experimental systems are never stationary, but are continuously evolving along time. Reasonable judgment on experimentally stable states can be done only when the configurations have come into a phase of self-similarly evolving and dynamically stable states. A recent universal theory of self-organization for finding eigenvalue equations to obtain self-similarly evolving and dynamically stable states [2-7] has been shown to incorporate a previous theory [8] for obtaining the minimum dissipative state of magnetic energy, by means of which "the so-called Taylor state" [9] can be derived. The concept of selective decay together with that of helicity invariance in the traditional theories [9-11] is analytically proved in [4-6] to have theoretically unrelated with "relaxed states". The fusion plasma is known to be described for simulations by a set of charge, mass, momentum, and energy conservation laws, and Maxwell's equations to follow its dynamic evolution and to analyze relaxation processes and relaxed states. However, replacement of any element in the set by "the so-called helicity conservation law" [9-11] makes the dynamic evolution untraceable due to this nonphysical law. This fact also means that the all theoretical basis of the theories [9-11] has no theoretical and physical connection with simulation results [12] and experimental ones of relaxed plasmas [13, 14] observed and reported so far.

author's e-mail : kondohy@el.gunma-u.ac.jp

2. Theories and numerical results

Applying a principle of the minimum change rate of global auto-correlations for a generalized dissipative dynamic open or closed systems with N dynamical quantities of M dimensional variables and using the variational calculus to the second variation, we obtain the following N simultaneous eigenvalue equations, which is used as a universal theory to find self-similarly evolving and dynamically stable self-organized states and is applicable to various dynamical systems [3, 7, 15];

$$\partial q_i^{\,j\#}\left[\xi^k\right]\big/\partial\xi^j = D_i^{\,j\#}[\boldsymbol{U}] = \tau_{\mathrm{idf}}^{\;-1}\Lambda_{im}\boldsymbol{U}_{im}[\xi^k{}_{k\neq j}]. \quad (1)$$

Here, $D_i^{\,j}[\boldsymbol{q}]$ represents dissipative or non-dissipative, linear or nonlinear operators for the change of a dynamical quantity q_i by a variable ξ^j. Applying Eq.(1) directly to all equations of mass, momentum and energy conservation laws and Maxwell's equations with the displacement current neglected for the two-fluid model of fully ionized, compressible and dissipative fusion plasmas and using usual normalization, we obtain the following set of simultaneous eigenvalue equations;

$$\partial\bar{n}_{\mathrm{e}}/\partial t = -\bar{\nabla}\cdot(\bar{n}_{\mathrm{e}}\bar{\boldsymbol{u}}_{\mathrm{e}}) = \Lambda_{ne}\bar{n}_{\mathrm{e}}, \quad (2)$$

$$\partial\bar{n}_{\mathrm{i}}/\partial t = -\bar{\nabla}\cdot(\bar{n}_{\mathrm{i}}\bar{\boldsymbol{u}}_{\mathrm{i}}) = \Lambda_{ni}\bar{n}_{\mathrm{i}}, \quad (3)$$

$$\partial\bar{\boldsymbol{u}}_{\mathrm{e}}/\partial t = -(\bar{\boldsymbol{u}}_{\mathrm{e}}\cdot\bar{\nabla})\bar{\boldsymbol{u}}_{\mathrm{e}} - [\mathrm{f}_{\mathrm{me1}}\bar{\nabla}(\bar{n}_{\mathrm{e}}\bar{T}_{\mathrm{e}}) + \mathrm{f}_{\mathrm{me2}}\bar{\nabla}\cdot\bar{\boldsymbol{\Pi}}_{\mathrm{e}} + \mathrm{f}_{\mathrm{me3}}\bar{n}_{\mathrm{e}}(\bar{\boldsymbol{E}} + \bar{\boldsymbol{u}}_{\mathrm{e}}\times\bar{\boldsymbol{B}}) - \mathrm{f}_{\mathrm{me4}}(\bar{n}_{\mathrm{e}} + Z\bar{n}_{\mathrm{i}})(0.5\bar{\eta}_{\perp}\bar{\boldsymbol{j}}_{//} + \bar{\eta}_{\perp}\bar{\boldsymbol{j}}_{\perp})]/\bar{n}_{\mathrm{e}} = \Lambda_{ue}\bar{\boldsymbol{u}}, \quad (4)$$

$$\partial\bar{\boldsymbol{u}}_{\mathrm{i}}/\partial t = -(\bar{\boldsymbol{u}}_{\mathrm{i}}\cdot\bar{\nabla})\bar{\boldsymbol{u}}_{\mathrm{i}} - [\mathrm{f}_{\mathrm{mi1}}\bar{\nabla}(\bar{n}_{\mathrm{i}}\bar{T}_{\mathrm{i}}) + \mathrm{f}_{\mathrm{mi2}}\bar{\nabla}\cdot\bar{\boldsymbol{\Pi}}_{\mathrm{i}} - \mathrm{f}_{\mathrm{mi3}}\bar{n}_{\mathrm{i}}(\bar{\boldsymbol{E}} + \bar{\boldsymbol{u}}_{\mathrm{i}}\times\bar{\boldsymbol{B}}) + \mathrm{f}_{\mathrm{mi4}}(\bar{n}_{\mathrm{e}} + Z\bar{n}_{\mathrm{i}})(0.5\bar{\eta}_{\perp}\bar{\boldsymbol{j}}_{//} + \bar{\eta}_{\perp}\bar{\boldsymbol{j}}_{\perp})]/\bar{n}_{\mathrm{i}} = \Lambda_{ui}\bar{\boldsymbol{u}}_{\mathrm{i}}, \quad (5)$$

$$\partial\bar{T}_e/\partial t = (1-\gamma)\bar{T}_e\bar{\nabla}\cdot\bar{\boldsymbol{u}}_{\mathrm{e}} - \bar{\nabla}\bar{T}_e\cdot\bar{\boldsymbol{u}}_{\mathrm{e}} + \{\mathrm{f}_{\mathrm{ene1}}\sum_{,j}^{3}\bar{\boldsymbol{\Pi}}_{\mathrm{e}i,j}\,\partial\bar{u}_{\mathrm{e}i}/\partial\bar{x}_j + \mathrm{f}_{\mathrm{ene2}}[\kappa_{\mathrm{e}//0}\bar{\nabla}\cdot(\bar{\kappa}_{\mathrm{e}//}\bar{\nabla}_{//}\bar{T}_{\mathrm{e}}) + \kappa_{\mathrm{e}\perp 0}\bar{\nabla}\cdot(\bar{\kappa}_{\mathrm{e}\perp}\bar{\nabla}_{\perp}\bar{T}_{\mathrm{e}}) + \mathrm{f}_{\mathrm{ene3}}(Z\bar{\boldsymbol{u}}_{\mathrm{i}}/\bar{n}_{\mathrm{e}}$$

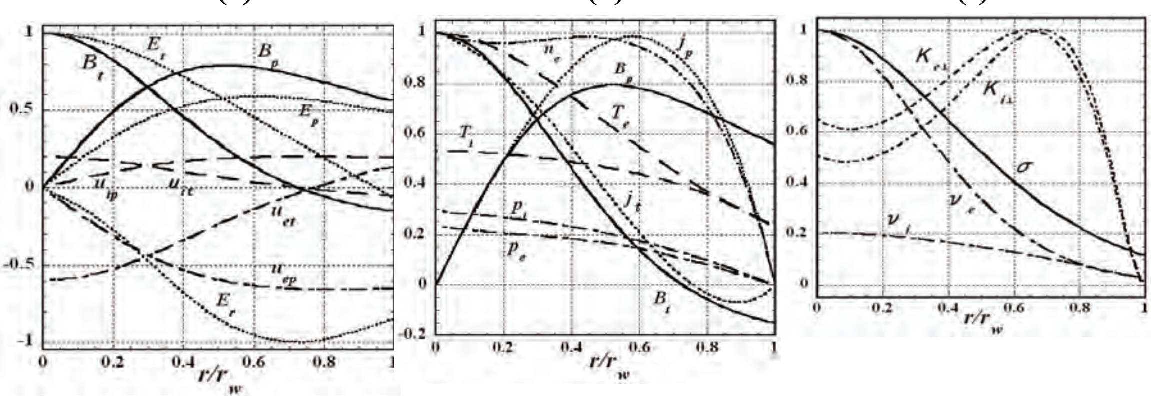

Fig.1 . Typical self-similarly evolving and dynamically stable self-organized configurations of the RFP in a simplified cylindrical.

$$+1)(\eta_{//}\bar{j}_{//}{}^2+\eta_\perp\bar{j}_\perp{}^2)-\mathrm{f}_{\mathrm{ene4}}(\overline{T}_\mathrm{e}-\overline{T}_\mathrm{i})/\tau^{\varepsilon}{}_{\mathrm{ei}}\}/\overline{n}_\mathrm{e}=\Lambda_{p\mathrm{e}}\overline{T}_\mathrm{e}, \qquad (6)$$

$$\partial\overline{T}_\mathrm{i}/\partial t=(1-\gamma)\overline{T}_\mathrm{i}\overline{\nabla}\cdot\bar{\boldsymbol{u}}_\mathrm{i}-\overline{\nabla}\,\overline{T}_\mathrm{i}\cdot\bar{\boldsymbol{u}}_\mathrm{i}+\{\mathrm{f}_{\mathrm{ene1}}\sum\nolimits_{,j}^{3}\overline{\boldsymbol{\Pi}}_{\mathrm{i}i,j}\,\partial\bar{u}_{\mathrm{i}i}/\partial\bar{x}_j$$
$$+\mathrm{f}_{\mathrm{ene2}}[\kappa_{\mathrm{i}//0}\overline{\nabla}\cdot(\bar{\kappa}_{\mathrm{i}//}\overline{\nabla}_{//}\overline{T}_\mathrm{i})+\kappa_{\mathrm{i}\perp 0}\overline{\nabla}\cdot(\bar{\kappa}_{\mathrm{i}\perp}\overline{\nabla}_\perp\overline{T}_\mathrm{i})$$
$$-\mathrm{f}_{\mathrm{ene4}}(\overline{T}_\mathrm{e}-\overline{T}_\mathrm{i})/\tau^{\varepsilon}{}_{\mathrm{ei}}\}/\overline{n}_\mathrm{i}=\Lambda_{p\mathrm{i}}\overline{T}_\mathrm{i}, \qquad (7)$$

$$\partial\boldsymbol{B}/\partial t=-\overline{\nabla}\times\overline{\boldsymbol{E}}=\Lambda_\mathrm{B}\overline{\boldsymbol{B}}, \qquad (8)$$

$$\overline{\nabla}\times\overline{\boldsymbol{B}}=\bar{\boldsymbol{j}}, \quad (9) \quad \overline{\nabla}\cdot\overline{\boldsymbol{E}}=\mathrm{f}_{\mathrm{ce}}(Z\overline{n}_\mathrm{i}-\overline{n}_\mathrm{e}), \quad (10) \quad \overline{\nabla}\cdot\overline{\boldsymbol{B}}=0, \quad (11)$$

$$\bar{\boldsymbol{j}}\equiv\mathrm{f}_{\mathrm{cj}}(Z\overline{n}_\mathrm{i}\bar{\boldsymbol{u}}_\mathrm{i}-\overline{n}_\mathrm{e}\bar{\boldsymbol{u}}_\mathrm{e})+\bar{\boldsymbol{j}}_{//\mathrm{bs}}, \qquad (12)$$

where $\mathbf{j}_{//\mathrm{bs}}$ is the bootstrap current, ($\mathrm{f}_{\mathrm{me1}}$, $\mathrm{f}_{\mathrm{me2}}$, $\mathrm{f}_{\mathrm{me3}}$, $\mathrm{f}_{\mathrm{me4}}$), ($\mathrm{f}_{\mathrm{mi1}}$, $\mathrm{f}_{\mathrm{mi2}}$, $\mathrm{f}_{\mathrm{mi3}}$, $\mathrm{f}_{\mathrm{mi4}}$) and ($\mathrm{f}_{\mathrm{ene1}}$, $\mathrm{f}_{\mathrm{ene2}}$, $\mathrm{f}_{\mathrm{ene3}}$, $\mathrm{f}_{\mathrm{ene4}}$), are factors by normalization for the conservation laws of electron and ion momentums and energy, respectively, and f_{ce} and f_{cj} are those for Eqs. (10) and (12), respectively. Using dominant terms in the limiting case of uniform conductivity σ and negligible viscosity ν and thermal conductivity κ, Eqs. (1) - (11) lead to the so-called Taylor state, just the same as in [7]. In general cases, however, these equations can be applicable to finite beta confinement systems of the Tokamak, the reversed field pinch (RFP), the field reversed configuration (FRC), and so on. Using the cylindrical model for simplicity and the 4 rank and 4th order Runge Kutta method under suitable boundary conditions on measurable quantities by referring to experimental data [14], we have numerically solved central terms = right-hand sides of Eqs. (1) - (11) to get self-similarly evolving and dynamically stable self-organized configurations of the RFP. A typical result is shown in Figs. 1(a), 1(b) and 1(c), where all physical quantities and dissipative factors are shown by their symbols. It is seen from the data profiles that all physical quantities are related self-consistently with each other, i.e. , $\kappa_{\mathrm{e}\perp}$ and $\kappa_{\mathrm{i}\perp}$ are determined by n_e, n_i, T_e, T_i, and B, and T_e and T_i are determined by $\kappa_{\mathrm{e}\perp}$, $\kappa_{\mathrm{i}\perp}$, σ , and j, and so on, to lead to negligibly small current density at the boundary wall like as in experimental plasmas. We also find from profiles of u_{ep}, u_{ip}, u_{et} and u_{it} in Fig. 1(a) that there exists the shear flow which depends on the profile of ν , i.e. , mainly on that of T_i, and would stabilize of the self-organized RFP plasma.

2. Concluding remarks

We have derived a novel set of simultaneous eigenvalue equations for finding self-similarly evolving, minimally dissipated and dynamically stable states realized after relaxation and self-organization processes [cf. Eqs.(1) - (12)]. The set of simultaneous equations is applicable to all type of magnetically confined fusion plasmas. Solving numerically the set of equations in the cylindrical model, we have shown typical self-similarly evolving and dynamically stable self-organized configurations of the RFP plasma including a lot of spatial information on related physical quantities useful for detailed experimental investigation. It should be emphasized that all physical quantities of interest are self-consistently determined by physical laws and mutual relations among them.

From the present universal theory of self-organization, we should recognize a clear fact that a paradigm shift from the traditional concept of stationary stability to more real concept of dynamical stability is definitely necessary for faster development of fusion science and technology in order to avoid near future energy crisis by shortening distance theories and experiments.

References

[1] Y. Kondoh, Nucl. Fusion **21**, 1607 (1981).
[2] Y. Kondoh, Phys. Rev. E **48**, 2975 (1993).
[3] Y. Kondoh, Phys. Rev. E **49**, 5546 (1994).
[4] Y. Kondoh, et. al., J. Plasma Fusion Res. SERIES, **5**, 598 (2002).
[5] Y. Kondoh, et. al., J. Plasma Fusion Res. SERIES **6**, 601 (2004).
[6] Y. Kondoh, et. al., J. Plasma Physics **72**, Part 6, 901 (2006).
[7] Y. Kondoh, et. al., Phys. Rev. E **70**, 066312-1 (2004).
[8] S. Chandrasekhar, et. al., Proc. Natl. Acad.Sci. **44**, 285 (1958).
[9] J. B. Taylor, Phys. Rev. Lett. **33**, (1974) 1139.
[10] L. C. Steinhauer and A. Ishida, Phys. Plasmas **4**, 2609 (1998).
[11] Z. Yoshida and S. M. Mahajan, Phys. Rev. Lett. **88**, 095001 (2002).
[12] R. Horiuchi and T. Sato, Phys. Rev. Lett. **55**, 211 (1851).
[13] Y. Kondoh, et. al., J. Phys. Soc. Jpn. **62**, 2038 (1993).
[14] Y.Yagi, et. al., Nuclear Fusion, **45**, 138 (2005).
[15] Y. Kondoh and J. W. Van Dam, Phys. Rev. E **52**, 1721 (1995).

A. S. Ware,[1] N. Daniels,[1] B. Fetscher,[1] D. E. Newman,[2] C. Hidalgo,[3] and M. A. Pedrosa[3]

[1] *University of Montana, Missoula MT 59812, USA*
[2] *University of Alaska - Fairbanks, Fairbanks, Alaska, USA*
[3] *CIEMAT, Madrid, Spain*

andrew.ware@umontana.edu

A one-dimensional transport model is used to study edge poloidal shear flow generation during gas puffing experiments and hysteresis effects in the generation of this flow. Gas puffing at the edge of the TJ-II stellarator has been used to control the development of an edge poloidal velocity shear layer [1] and study the threshold for flow generation [2]. The transport model couples together density, ion temperature, electron temperature, poloidal flow, toroidal flow, radial electric field, and a fluctuation envelope equation that includes a shear-suppression factor. All fields are integrated with a second-order modified Runge-Kutta method with adaptive time-stepping. Above a critical threshold the shear flow improves confinement by reducing turbulent transport. For subcritical flows (i.e., flows that do not trigger transition to a higher confinement regime), there is no true hysteresis in the flow [3]. An apparent lag may be observed if the rate of ramping the particle source is rapid relative to transport time scales. For critical flows, an edge transport barrier is formed and fluctuations are suppressed locally. Near the threshhold, the barrier location oscillates.

___________________ - Work supported by U.S. Department of Energy under Grant DE-FG02-03ER54699 at the University of Montana.

[1] C. Hidalgo, M. A. Pedrosa, L. Garcia, A. Ware, Phys. Rev. E , 067402 (2004).
[2] M. A. Pedrosa, C Hidalgo, E Calderon, T Estrada, A Fernandez, J Herranz, I Pastor and the TJ-II team, Plasma Phys. Control. Fusion , 777 (2005)
[3] A. S. Ware, N. Daniels, B. Fetscher, D. E. Newman, C. Hidalgo, and M. A. Pedrosa, 2007 European Physical Society Meeting, paper 4.042, Warsaw, Poland.

Density Collapse of Poloidally Rotating Plasma in TU-Heliac

Y. Tanaka, S. Kitajima, M. Sasao, H. Utoh, H. Aoyama, K. Iwazaki, H. Umetsu, K. Ishii, A. Okamoto, T. Kobuchi, S. Inagaki[b], Y. Suzuki[a], and H. Takahashi[a]

Department of Quantum Science and Energy Engineering, Tohoku University, Sendai 980-8579, Japan
[a]National Institute for Fusion Science, Toki 509-5292, Japan
[b]Research Institute for Applied Mechanics, Kyushu University, Kasuga 816-8580, Japan

The ohmic heated plasma in TU-Heliac was biased by a hot-cathode and the ***E***×***B*** poloidal rotation was driven. Coincident measurements of the line density and the ion saturation current revealed the existence of the density collapse accompanied by the fluctuation in the poloidally rotating plasma. The power spectra were calculated from the ion saturation current and the floating potential obtained by the high-speed triple probe. The density collapse frequency was 1~10 kHz. The fluctuation frequency was 100~1000 kHz. The density radial profile at the moment when the collapse occurred was estimated. The steep density gradient was vanished by the density collapse. The radial profile of the fluctuation frequency was compared to that of the ***E***×***B*** poloidal rotation frequency. Both profiles had the similar radial dependence. From this comparison, the poloidal mode number of the fluctuation was estimated to be m = 2 or 3. The collapse and the fluctuation localized in the core plasma region. This result suggested the existence of the cross-interaction between the density collapse and the fluctuation.

Keywords: heliac, stellarator, poloidal rotation, density collapse, fluctuation,

1. Introduction

H-mode was discovered in ASDEX Tokamak [1] and then the mechanism of the improvement has been studied for a long time. Recently it is considered that the plasma rotation suppresses the anomalous transport. It is also suggested that a turbulent flow can drive the poloidal rotation such as the zonal flow and that the poloidal shock is formed at a moment when the poloidal mach number exceeds unity [2]. Therefore, the understanding of the plasma rotation, especially in the super sonic regime, is important.

Spontaneous ***E***×***B*** rotation is formed in the improved plasma of the large device. An electrode biasing can drive the ***E***×***B*** rotation in the small device and the confinement improves. In Tohoku University Heliac (TU-Heliac), the negative biasing experiment has been carried out for the study of the transition phenomenon to the improved mode [3-11]. A hot-cathode made of LaB_6 was used for the electron injection to the plasma and the negative potential was formed. Typical behaviors of the improved mode were the threefold increase in the density and the formation of the radial electric field (2~4 kV/m). The ***E***×***B*** poloidal rotation frequency exceeded 100 kHz. At the same time, the density and the potential fluctuations were observed in the low frequency range (1~10 kHz) and the high frequency range (100 ~ 1000 kHz) [6, 9, 11]. The high frequency fluctuation burst and had the radial dependency. In this work, the characteristics of the poloidally rotating plasma are studied. Then the fluctuations are measured coincidently and the radial profile of the high frequency fluctuation is compared to that of the poloidal rotation.

2. Experimental Setup

TU-Heliac is a helical axis stellarator and has the bean shaped flux surface [3]. Top view of TU-Heliac is shown in Fig. 1. Major radius is 0.48 m and minor radius is 0.06 m. Toroidal period number is 4. The standard magnetic configuration was selected. The magnetic well depth at the last closed flux surface (LCFS), the rotational transform at the axis and the magnetic field were 2 %, 1.54 and 0.3 T, respectively. Working gas was He. A plasma was produced by the low frequency alternate ohmic heating. The frequency of the heating wave was 18.8 kHz. The plasma current, the loop voltage and the absorbed power to the plasma were 200 A, 200 V and 2 kW, respectively. A hot-cathode was used for the electron injection. The top position of the hot-cathode was R_{HC} = 86 mm. The origin of R_{HC} was the center of the center conductor coil. The hot-cathode was biased against the vacuum vessel. The bias voltage was -230 V and the electrode current was about 4 A. The fluctuation was one of the important plasma parameters and should be measured. In the

author's e-mail: yutaka.tanaka@ppl2.qse.tohoku.ac.jp

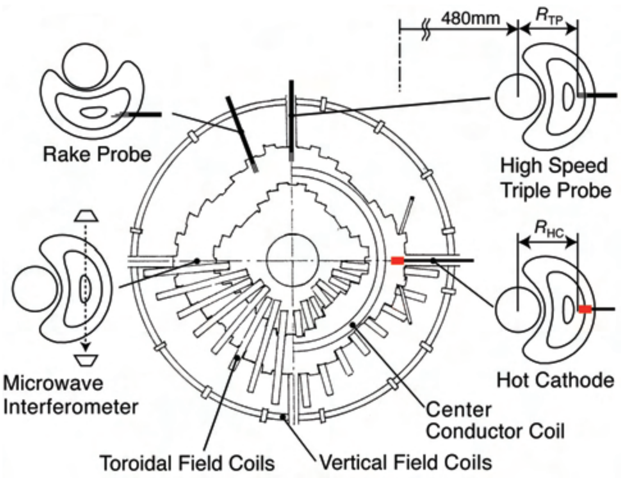

Fig. 1 Top view of TU-Heliac

hot-cathode biased plasma, the ***E***×***B*** poloidal rotation frequency exceeded 100 kHz. The fluctuation frequency reached 400 kHz by the poloidal rotation. Langmuir probe method had the advantage of spatial and time resolutions. Therefore, the high-speed triple probe system (cutoff frequency 1 MHz) was installed to TU-Heliac [11]. It was inserted from the low field side. Its position was defined by R_{TP} as shown in Fig. 1. The magnetic axis corresponded to R_{TP} = 79 mm and the LCFS corresponded to R_{TP} = 118 mm. The 50 GHz microwave interferometer and the rake probe were also used for the coincident measurement. The rake probe had 3 tips and its tips were set radially. The length between the top and bottom tips was 6.0 mm, which was small compared to the minor radius.

3. Density Collapse Accompanied by Fluctuation

The coincident measurements at the multi-position are important to understand the plasma physics. The positions of the triple probe and the rake probe were calibrated using the electron gun. These probes were set at ρ = 0.2 and the biasing experiments were carried out, where ρ was the normalized minor radius defined by $\rho = \langle r \rangle / a$, $\langle r \rangle$ was the average radius of the flux surface and a was the minor radius. ρ = 0.2 corresponded to R_{TP} = 87 mm. Figure 2 shows the typical time traces of the line density n_el and the ion saturation current I_s. The ion saturation current suddenly decreased on the time scale of 0.01 ms (ex. time = 8.50, 8.65 and 8.81 ms). After the sudden decrease, it slowly increased on the time scale of 0.1 ms. Simultaneously the line density, which was measured along the central chord as shown in Fig. 1, had the same tendency of increase and decrease, though it did not show the sudden decrease because it was the integrated parameter. Ion saturation current is proportional to density and root of electron temperature. Increase and decrease of the ion saturation current indicate that of the density. The

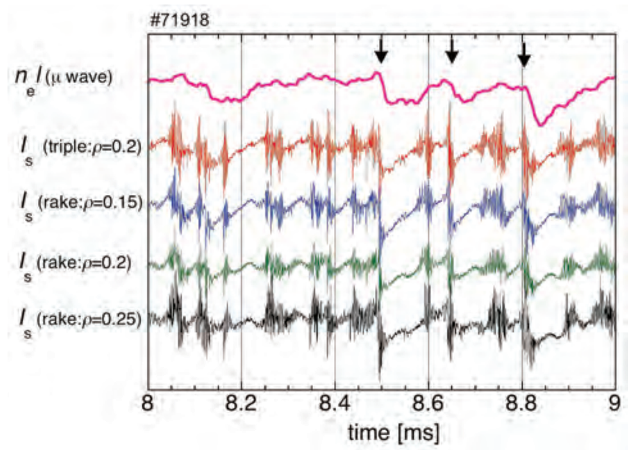

Fig. 2 Time traces of the line density n_el and the ion saturation current I_s. The positions of the triple probe and the rake probe were $\rho \sim 0.2$. The arrows indicate the time of the density collapse.

sudden decrease of the density was observed in different toroidal and radial positions. Therefore, this phenomenon is considered the density collapse. In the sawtooth of CHS, soft X-ray decreased at $\rho < 0.5$ and increased at $\rho > 0.5$ [12]. In the density collapse of TU-Heliac, the difference between the inside and the outside obtained by the rake probe was not observed. This reason is considered that the probe tips were close compared to the minor radius. Also the fluctuation was observed in the ion saturation current, though it was not observed in the line density because the microwave interferometer could not measure the local parameter. This fluctuation burst and had the simultaneous characteristic between all signals. It did not appear in the phase of the density increased after the density collapse (ex. time = 8.50~8.60 ms and 8.65~8.70ms). This result suggests that the growth rate of the fluctuation has the density or the density gradient dependence.

The power spectra were calculated from the ion saturation current I_s and the floating potential V_f measured by the triple probe as shown in Fig. 3. Fast Fourier Transform was used in the calculation in spite of the burst of the fluctuation. Both spectra had the similar power distribution. The density collapse frequency was 1~10 kHz. Floating potential is determined by electron temperature and space potential. The power of the floating potential indicates that the electron temperature or the space potential also collapsed with the density. The fluctuation frequency was 100~1000 kHz. The sharp peaks at 18 and 37 kHz were fundamental and second harmonic waves of the alternate ohmic heating. The peak at 3 MHz was the noise of the isolation amplifier.

The density radial profile at the moment when the collapse occurs is required for the understanding of the collapse, though it can not be measured by the present diagnostic system in TU-Heliac. The triple probe was

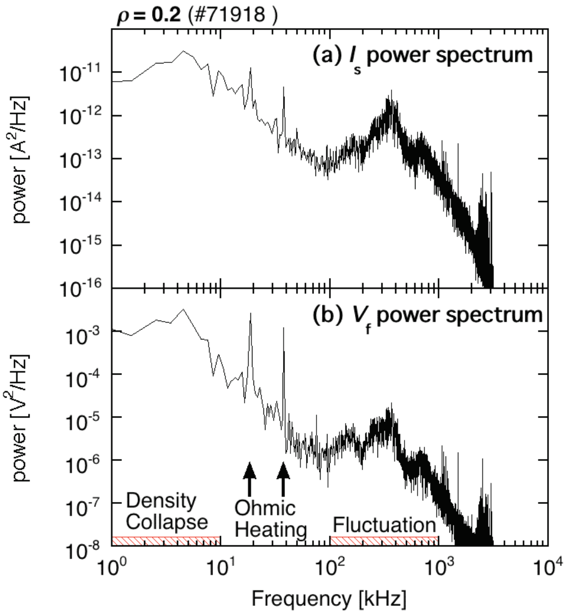

Fig. 3 Power spectra of (a) the ion saturation current I_s and (b) the floating potential V_f. Probe position was $\rho = 0.2$. The density collapse frequency was 1~10 kHz and the fluctuation frequency was 100~1000 kHz.

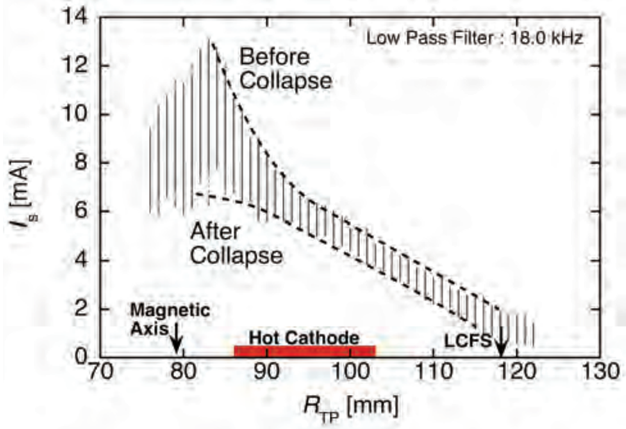

Fig. 4 Radial profile of the ion saturation current obtained by the triple probe. Low pass filter of 18.0 kHz was used to remove the 18.8 kHz ohmic heating wave. In R_{TP} = 76~87 mm, the ion saturation current decreased about 40 % after the collapse.

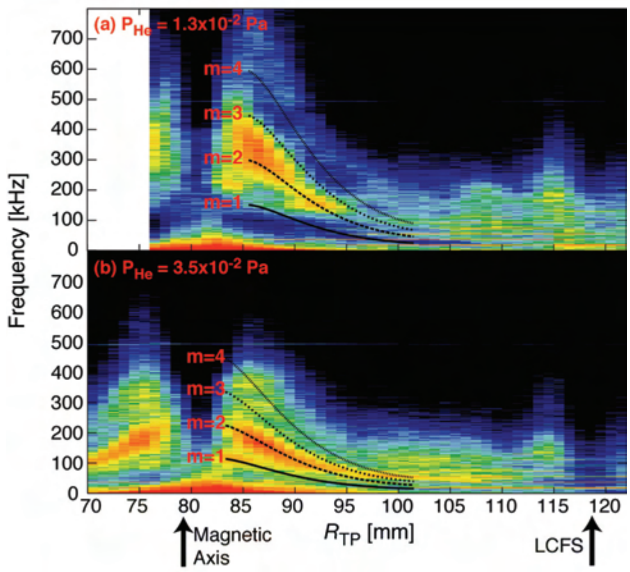

Fig. 5 Radial profile of the power spectra calculated from the ion saturation current at working gas pressure (a) p_{He}=1.3x10^{-2} Pa, (b) p_{He}=3.5x10^{-2} Pa. The lines show the poloidal rotation frequency calculated by Eq. (1). The arrows indicate the magnetic axis and LCFS.

moved its radial position shot by shot. The data of the ion saturation current was obtained moving its position every 1 mm. Digital low pass filter of 18.0 kHz was used to remove the 18.8 kHz ohmic heating wave and to pick up only the frequency corresponded to the collapse. The data obtained by 47 shots were plotted as shown in Fig. 4. The magnetic axis corresponded to R_{TP} = 79 mm and the LCFS corresponded to R_{TP} = 118 mm. The estimation of the density profile at the moment when the collapse occurred was possible from this figure. The maximum and the minimum in the ion saturation current indicated the density profiles before and after the collapse. The triple probe position in Fig. 2 was R_{TP} = 87mm. Before the collapse, steep gradient existed in R_{TP} = 83~90 mm. After the collapse, the ion saturation current decreased about 40 % in R_{TP} = 76~87 mm. The steep gradient was vanished by the collapse. This result suggests that the density gradient triggers the collapse.

The poloidal momentum balance between $\boldsymbol{J}_r\times\boldsymbol{B}$ driving force, ion viscosity and ion friction determines the poloidal rotation speed. We can control the friction term by filling the working gas because the friction results from charge exchange between ions and neutral particles. The radial profiles of the power spectra are shown in fig. 5. These were calculated from the ion saturation current obtained by the triple probe. Working gas pressure (a) 1.3x10^{-2} Pa, (b) 3.5x10^{-2} Pa were selected. Fig. 5 (a) lacks the high field side spectra. The triple probe was inserted from the low field side and the measurement of the high field side was restricted by the disturbance from the probe to the plasma. The fluctuation had the large power in R_{TP} = 85~95 mm in both pressure conditions and it had symmetry against the magnetic axis in the high-pressure condition. There was a hole on the magnetic axis, in which the fluctuation did not exist. The fluctuation had the radial dependence such as 1/r. The frequency in the low-pressure condition was 2 times higher than that in the high-pressure condition. The fluctuation frequency might be determined by the poloidal rotation frequency. Then the comparison between these frequencies is important. The $\boldsymbol{E}\times\boldsymbol{B}$ poloidal rotation frequency f_{EB} can be estimated from the radial profile of the floating potential and is written as

$$f_{EB} = \frac{dV_f / d\langle r \rangle}{2\pi \langle r \rangle B_\phi}, \qquad (1)$$

where B_ϕ is the toroidal magnetic field. Essentially the space potential should be used for the calculation of the rotation frequency though it has too large error near the magnetic axis and can not be used. This may be considered that the size of the triple probe (5 mm) is comparable to the radius of the flux surface. Eq. (1) approximately represents the correct rotation characteristic because it largely depends on $\langle r \rangle$ in the denominator. The frequency of mf_{EB} was also plotted in Fig. 5, where m was the positive integer. m = 1 line indicated the poloidal rotation frequency and it increased as it got close to the magnetic axis. It reached 150 kHz in the low-pressure condition. The fluctuations in both gas conditions had the similar radial dependence to m = 2~3 line. The physical meaning of m is the poloidal mode number. The fluctuation poloidal mode is estimated to be m = 2 or 3. It also showed the surprising result. The fluctuation burst simultaneously in the different radial positions as shown the rake probe in Fig. 2. On the other hand, the fluctuation frequency had the radial dependence.

4. Discussion

It was observed that the density profile was asymmetry against the magnetic axis as shown in Fig. 4. It may represent the plasma compressibility. To satisfy the continuity equation under the ***E***×***B*** poloidal rotation, the plasma is compressed at the certain poloidal angle. Ions try to remove the density anisotropy by the parallel thermal motion. Poloidal Mach number M_p is useful to estimate the plasma compressibility. M_p means the ratio of the parallel diffusion time by the ion thermal motion to the ***E***×***B*** poloidal rotation time. M_p is written as,

$$M_p = q\varepsilon^{-1} v_t^{-1} v_{EB}, \qquad (2)$$

where q is the safety factor, $\varepsilon = \langle r \rangle / R$ is the toroidal ripple, v_t is the ion thermal velocity and v_{EB} is the ***E***×***B*** poloidal velocity. Eq. (2) is rewritten to the convenient form as,

$$M_p = qRv_t^{-1}\omega_{EB} \ , \qquad (3)$$

where ω_{EB} is the ***E***×***B*** poloidal rotation frequency calculated by Eq. (1). Substituting ω_{EB} into Eq. (3), poloidal Mach number was calculated as $M_p \sim 10$. This result shows that the ion diffusion is not sufficient against the ion compression by the ***E***×***B*** poloidal rotation. Then the asymmetry of the ion saturation current suggests the compressibility of the plasma.

The density collapse and the fluctuation were observed in the core region of the plasma. The steep density profile was vanished by the density collapse. The fluctuation did not appear in the phase of the density increase after the collapse. These results suggest the existence of the cross-interaction between the density collapse and the fluctuation. The frequencies of the poloidal rotation and the fluctuation reached 15 % and 30~40 % of the ion cyclotron frequency. There is possibility of the electromagnetic wave such as Alfven wave. The magnetic fluctuation should be measured for the understanding of this phenomenon.

5. Summary

The hot-cathode biasing experiment was carried out in TU-Heliac. Coincident measurements of the line density and the ion saturation current revealed the existence of the density collapse accompanied by the fluctuation in the poloidally rotating plasma. The power spectra of the ion saturation current and the floating potential showed that the density collapse frequency was 1~10 kHz and that the fluctuation frequency was 100~1000 kHz. The steep density gradient was vanished by the density collapse. The radial profile of the fluctuation frequency was compared to that of the ***E***×***B*** poloidal rotation frequency. Both profiles had the similar radial dependence. From this comparison, the poloidal mode number of the fluctuation was estimated to be m = 2 or 3. The poloidal mach number reached 10 and suggested the plasma compressibility.

Acknowledgments

This work was supported by a Grant-in-Aid from the Ministry of Education, Science and Culture of Japan (No. 17360439).

References

[1] F. Wagner *et al.*, Phys. Rev. Lett. **49**, 1408 (1982).
[2] R. D. Hazeltine *et al.*, Phys. Fluids **14**, 361 (1971).
[3] S. Kitajima *et al.*, Nucl. Fusion, **46**, 200 (2006).
[4] H. Takahashi et al., Plasma Phys. Control. Fusion, **48**, 39 (2006).
[5] S. Kitajima et al., Plasma Phys. Control. Fusion, **48**, A259 (2006).
[6] Y. Tanaka *et al.*, Plasma Phys. Control. Fusion, **48**, A285 (2006).
[7] S. Kitajima *et al.*, Fusion Sci. Tech., **50**, 201 (2006).
[8] H. Takahashi *et al.*, Fusion Sci. Tech., **51**, 54 (2007).
[9] Y. Tanaka *et al.*, Trans. Fusion Sci. Tech., **51**, 265 (2007).
[10] M. Ogawa *et al.*, Trans. Fusion Sci. Tech., **51**, 268 (2007).
[11] Y. Tanaka *et al.*, Plasma Fusion Res., **2**, S1019 (2007).
[12] S. Takagi *et al.*, Rev. Sci. Instrum., **72**, 721 (2001).

Proceedings of ITC/ISHW2007

Low-frequency fluctuations of diverted plasma flow and their relation to edge fluctuations in the Uragan-3M torsatron

BELETSKII Aleksej A., GRIGOR'EVA Lyudmila I., SOROKOVOY Eduard L., CHECHKIN Viktor V., SOROKOVOY Yegor L., VOLKOV Yevgenij D., BURCHENKO Pavel Ya., KULAGA Anatolij Ye., TSYBENKO Sergej A., LOZIN Aleksej V., SLAVNYJ Aleksandr S.

Institute of Plasma Physics, National Science Center

"Kharkov Institute of Physics and Technology", Kharkov, Ukraine

Abstract. In the l=3/m=9 U-3M torsatron with a natural open helical divertor and a plasma produced and heated by RF fields, joint studies of low frequency (5-100 kHz) density (ion saturation current) fluctuations have been carried out at the plasma boundary (SOL) and in the diverted plasma flow (DPF). The knowledge of relation between fluctuation processes at the boundary and in the divertor region is important as the former are known to induce the anomalous transport, while the level of density fluctuations in some DPF can attain more than 20% of the equilibrium component. The spectral characteristics of DPF fluctuations are compared with those of the fluctuations in the SOL, and two characteristic frequency ranges are revealed. Modifications of spectral characteristics due to spontaneous transition to an improved confinement mode are investigated too.

Keywords: plasma confinement, H-transition, anomalous transport, fluctuations, divertor, power spectrum

1. Introduction

Low-frequency density and potential fluctuations in the edge plasma resulting in the anomalous transport are a subject of research in plasma confinement physics for a long period [1-3]. Changes in fluctuation behavior are a good indicator of transition to improved confinement modes. In particular, investigations of spontaneous transition to an improved confinement state (hereinafter, transition) in the U-3M torsatron reveal a distinct decrease of the fluctuation level and radial turbulent particle flux with transition near the plasma boundary [4,5]. Naturally, processes near the plasma boundary should be tightly related to processes in the diverted plasma flow (DPF). In particular, it is of interest to study these relations on the basis of joint measurements of fluctuation spectral characteristics at the edge and in the DPF.

2. Experimental conditions and measurement techniques

In the U-3M torsatron (l = 3, m = 9, R_o = 1m, $\bar{a} \approx$ 0.12 m, $\iota(\bar{a}) \approx 0.3$) the whole magnetic system is enclosed into a 5 m diameter vacuum chamber, so that an open natural helical divertor is realized. The toroidal magnetic field, B_ϕ = 0.7 T, is produced by the helical coils only, the ion toroidal drift $\boldsymbol{B}\times\nabla\boldsymbol{B}$ is directed upward (Fig. 1). A "currentless" plasma is produced and heated by RF fields ($\omega \approx \omega_{ci}$). The RF power irradiated by the antenna is $\lesssim$200 kW in the 30-50 ms pulse. The working gas (hydrogen) is admitted continuously into the vacuum chamber at the pressure of ~10^{-5} Torr.

To study low-frequency density (ion saturation current) fluctuations (hereinafter, fluctuations), plane Langmuir probe arrays in DPF [6] and a movable four-tip Langmuir probe array in SOL [4] are used. The dispositions of divertor probe (DP) arrays in two half field period-separated ($\Delta\phi$ = 20^0) symmetric poloidal cross-sections AA and DD and of the movable probe (MP) array in the cross-section VG ($\Delta\phi$ =52.5^0 from AA) are shown in Fig.1.1. As a recording facility, a 12 bit ADC with 1.6 μs sampling rate/channel was used.

To obtain spectral characteristics of the fluctuations, methods described in [7] were used.

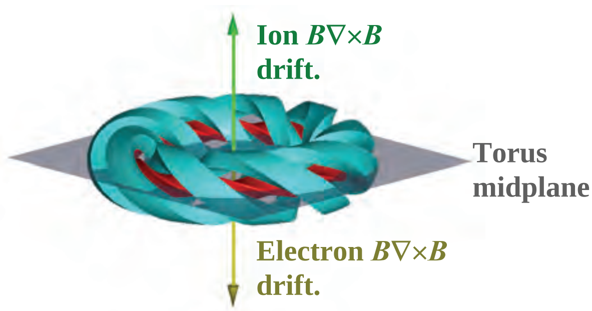

Fig.1. Electron and ion $\boldsymbol{B}\times\nabla\boldsymbol{B}$ drift directions.

Author's e-mail: beletskii@ipp.kharkov.ua

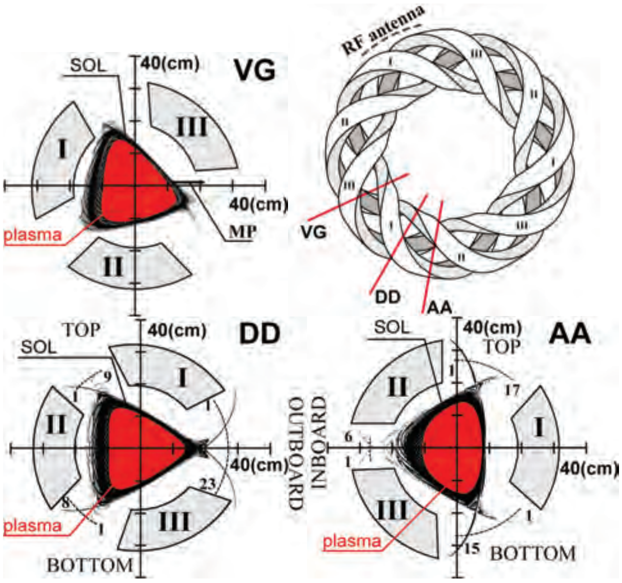

Fig.1.1. Disposition of divertor probe arrays 1-17, 1-15, etc. (cross-sections AA and DD) and movable probe array (cross-section VG, segment MP) relative to helical coils I,II,III and calculated edge structure of field lines. Positions of 4 MP tips are shown in the inset to VG.

3. Spectral characteristics of fluctuations in SOL and DPF

As an example, power spectra of fluctuations in the DPF maxima in two divertor magnetic channels (legs) symmetric about the torus midplane in the cross-section DD (top and bottom spacings) are presented in Fig. 2. The evolution of fluctuation power is traced within 4.8 ms, that is equal to 3000 ADC counts (Fig. 2a,b).

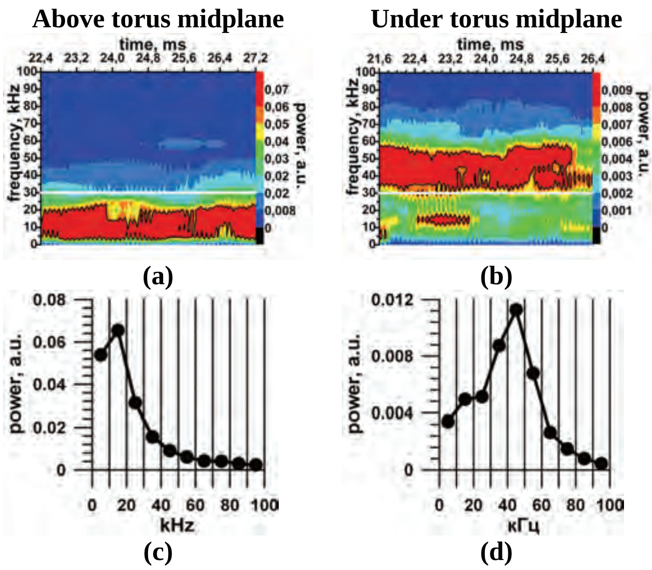

Fig.2. Time evolution of fluctuation power spectra (a,b) and corresponding time-averaged spectra (c,d) in the top (a,c) and bottom (b,d) spacings of the cross-section DD.

Corresponding power spectra averaged over this time period are shown in Fig. 2c,d. In combination with the data from the top and bottom spacings of the cross-section AA, a conclusion can be made, that there are two frequency ranges where the maximum fluctuation power is observed, namely, one with frequencies less than 30 kHz (over the torus midplane) and one with frequencies exceeding 30 kHz (under the midplane).

It is known [6] that the spatial DPF distributions in U-3M exhibit a strong vertical (up-down) asymmetry with the larger ambipolar flow and the non-ambipolar flow with an excess of ions always outflowing with the ion $\boldsymbol{B}\times\nabla\boldsymbol{B}$ drift (upward, in our case). At the same time, the electrons dominate in the non-ambipolar flow outflowing downward [6]. It is naturally to suppose that the observed vertical asymmetry in spectral characteristics of the fluctuations is in some way related to the DPF vertical asymmetry, and the fluctuations with frequencies < 30 kHz are connected with the fast ion loss that is responsible for the DPF asymmetry [6].

Studies of spectral characteristics of the fluctuations near LCMS depending on the radial distance also reveal two frequency ranges with maximum spectral power as in the DPF case. The results are shown in Fig. 3. With the MP moving toward a smaller radius, the maximal fluctuation power gradually shifts from a frequency range >30 kHz (Fig. 3b,d: r = 12.0 cm) to a range <30 kHz (Fig.3a,c: r=10.4 cm).

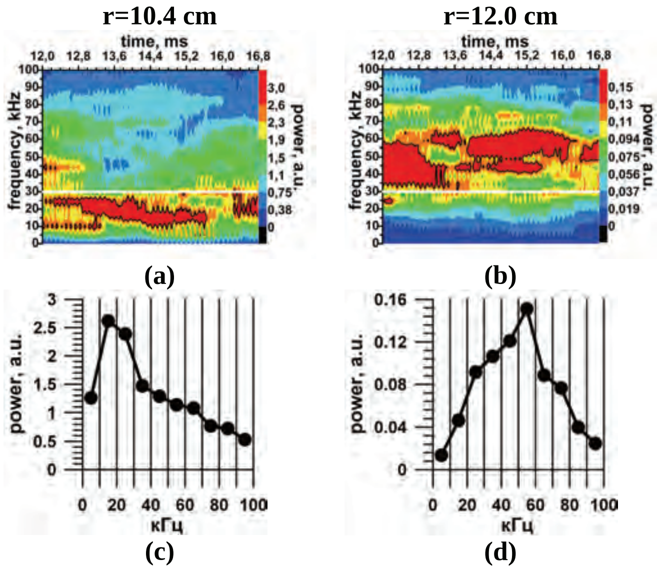

Fig.3. Time evolution of fluctuation power spectra (a,b) and corresponding time-averaged spectra (c,d) in close vicinity to LCMS, (a) and (c), MP position r=10.4 cm; and more distantly, (b) and (d), r=12,0 cm.

In addition to power spectra, cross-coherence spectra for fluctuations in SOL at different distances from the LCMS, on the one hand, and fluctuations in different

DPF, on the other hand, are also investigated. The coherence spectra between fluctuations detected in the bottom spacing of the DD cross-section in the DPF maximum (DP #1) and fluctuations in SOL for two MP positions, *r*=12.0 cm and *r*=10.6 cm, are shown in Fig. 4. In the case *r*=12.0 cm, the maximal coherence up to ~ 0.8 in the frequency range 40 – 60 kHz is observed. As it has been already shown above, the maximum fluctuation power, recorded in SOL (Fig. 3b,d) and in the DPF under the torus midplane (Fig. 2b,d) belongs to the same frequency range. The coherence gradually decreases with the MP displacing toward the LCMS.

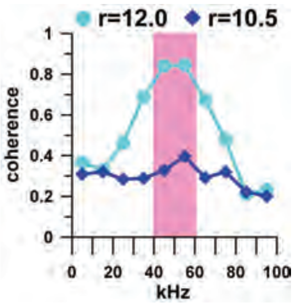

Fig.4. Cross-coherence spectra for fluctuations in the divertor region (DD, bottom, probe #1, see fig.1) and SOL (movable probe at *r*=12.0 cm and *r*=10.6 cm).

The large coherence apparently can be explained as follows. A bundle of magnetic field lines after crossing the MP tip at the radius *r*=12.0 cm due to the rotational transform enters the divertor region and falls on the DP #1 in the bottom spacing of the DD cross-section [8]. On the other hand, field lines located closer to the LCMS (e.g., *r*=10.6 cm) can make a many-fold pass round the torus before deviating to the divertor region. Therefore, fluctuations in these SOL layers should be less correlated with fluctuations in DPF.

The fact that the highest fluctuation power in the DPF on the electron $\boldsymbol{B}\times\nabla\boldsymbol{B}$ drift side and the maximum coherence are observed in the same frequency range is an evidence in favor of a common nature of the fluctuations in SOL at *r*=12 cm and in the DPF under the midplane.

Thus, two layers can be generally marked out in the SOL. More distantly from the LCMS, the development of fluctuation processes is connected with the electron loss – an electron escape to the divertor region on the electron $\boldsymbol{B}\times\nabla\boldsymbol{B}$ drift side, while in the layer closer to the LCMS the excitation of the fluctuations is related to the ion loss. It would be natural to relate the electron loss in the outer layer to a higher field line stochastization in this layer.

4. Changes in spectral characteristics with H-mode transition

Like some other plasma parameters, spectral characteristics of the fluctuations change during the transition. Typical fluctuation power spectra taken before and after the transition in DPF maxima in the top and bottom spacings of the AA and DD cross-sections and in the inboard spacing of the cross-section AA are shown in Fig. 5.

In the cross-section AA the fluctuation power decreases above the torus midplane and increases below

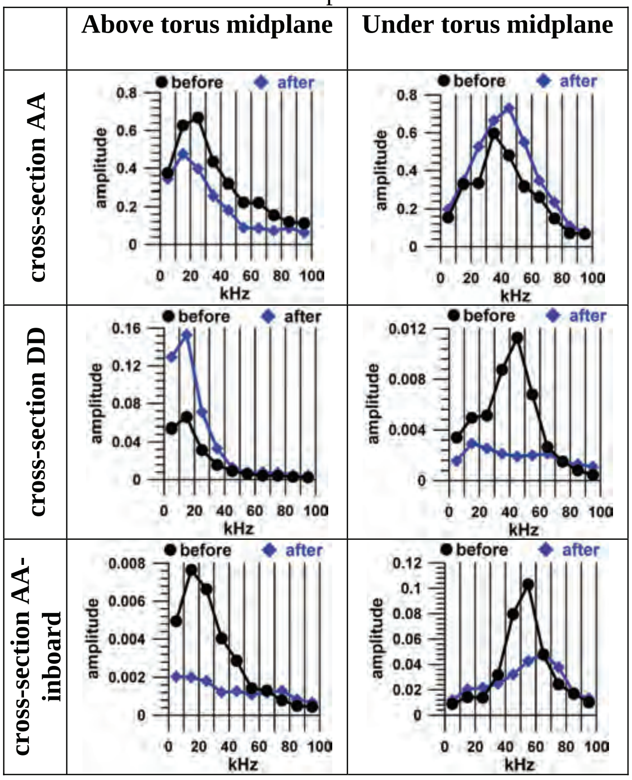

Fig.5. Power spectra before and after the H-mode transition in two symmetric poloidal cross-sections AA and DD.

the midplane after the transition. In the inboard spacing the fluctuation power decreases both above and below the midplane.

In the DD cross-section the power spectra change in the opposite way with transition: the fluctuation power increases above the torus midplane and decreases under it. The same tendency is also observed in the outboard spacing of the cross-section DD.

Taking into account that fluctuations with frequencies lower than 30 kHz (higher than 30 kHz) are presumably related to ion (electron) transport processes, the dynamics of particle loss during the transition could be described in the following way, basing on fluctuation spectral characteristics. In the cross-section AA an insignificant reduction of ion loss is observed (a slight decrease of ion outflow to the DPF above the midplane). At the same time, the electron loss insignificantly increases (a slight increase of electron outflow in the DPF under the midplane). In the inboard spacing of the AA cross-section, both the ion and electron loss are significantly reduced. In the cross-section DD a considerable reduction of electron loss (a sharp drop of electron outflow to the DPF under the torus midplane) and a considerable rise of ion loss (a sharp increase of ion outflow to the DPF) above the torus midplane occur with transition.

As a whole, these results are in a good agreement with those of studies of H-transition effects on equilibrium characteristics of DPF (in particular, on fast ion outflow to the DPF) in U-3M [9].

5. Summary

As a result of investigations of DPF fluctuations and comparison of their spectral characteristics in two symmetric poloidal cross-sections with those in SOL in the U-3M torsatron, the following conclusions can be made.

(i) A new manifestation of the DPF vertical asymmetry is observed, viz., a difference in the form of power and coherence spectra in symmetric divertor channels over and under the torus midplane.

(ii) As a result of search of correlation between fluctuations in SOL and DPF, their spectral characteristics and juxtaposing of these data with the distributions of non-ambipolar DPF [6], two layers of SOL are defined. The SOL layer with electron predominance is localized more distantly from the LCMS; the other layer with ion predominance is localized closer to the LCMS.

(iii) Basing on corresponding spectral characteristics, it is shown, that the DPF on the ion $\boldsymbol{B}\times\nabla\boldsymbol{B}$ drift side is formed predominantly by particles outflowing from the SOL layer nearest to the LCMS; on the electron drift side the DPF is formed predominantly by particles escaping from more distant layers of the SOL.

(iv) Changes occurring in spectral characteristics of the fluctuations during the H-mode transition confirm the character of electron and ion loss dynamics, associated with transition.

References

[1] M. Endler *et al.,* Journal of Nuclear Materials, 1999, **266-269**, 84-90 (1999).
[2] A. J. Wootton *et al*., Phys. Fluids B, **2**, 2879-2903 (1990).
[3] H. Y. Tsui *et al.*, Phys. Fluids B **5** 2491-2497 (1993).
[4] E. L. Sorokovoy *et al.*, Problems of Atomic Science and Technology, Series "Plasma Physics" No. 10, p. 21 (2005).
[5] V. V. Chechkin *et al*., Plasma Phys. Control. Fusion **48**, A 241 (2006).
[6] V. V. Chechkin *et al.* Nucl. Fusion **42** 192 (2002).
[7] E. J. Powers, Nucl. Fusion **14** 749 (1974).
[8] Sorokovoy *et al.* Problems of Atomic Science and Technology, Series: Plasma Physics No 1 p. 60 (1999).
[9] Chechkin V.V. *et al*., (2007) (This conference).

Proceedings of ITC/ISHW2007

On the link between flows, turbulence and electric fields in the edge of the TJ-II stellarator

J.A. Alonso, C. Hidalgo, M.A. Pedrosa, J.L. de Pablos and the TJ-II team

Laboratorio Nacional de Fusión, Asociación EURATOM-CIEMAT, Madrid, Spain

This paper presents a view of experimental results and progress in the investigation the role of Reynolds stresses in the self-organization of parallel/perpendicular flows in the edge region of the TJ-II stellarator. The structure of turbulence and flows has been investigated during the spontaneous development of edge ExB sheared flows[1] and the transition to biasing induced improved confinement regimes[2]. Edge turbulence was characterized by means of arrays of Langmuir probes and fast camera diagnostics. Edge radial electric fields and ExB shear increases and the level of edge fluctuations is significantly reduced during biasing-induced improved confinement regimes in TJ-II. In addition, parallel flows show changes in the order of $\Delta M_{\|} \approx 0.3$ in the edge plasma region.

In order to investigate the role of ExB sheared flows as a symmetry breaking mechanism[3] the cross correlation coefficient $\langle \tilde{v}_r \tilde{v}_{\|} \rangle / v_r^{rms} v_{\|}^{rms}$ was computed during the development of biasing induced ExB flows. Experimental results show that, although the level of turbulence decreases, the phase coherence increases and sustains gradients in the Reynolds component $\langle \tilde{v}_r \tilde{v}_{\|} \rangle$ that are found to be of same order of the change in the friction term $\mu \Delta M$. Significant turbulent parallel forces at plasma densities above the threshold value to trigger ExB sheared flows have also been found in the TJ-II stellarator[4].

These experiments can provide some light to critically test the importance of symmetry breaking mechanisms (via sheared electric fields) and convective turbulent transport on parallel momentum dynamics.

---

[1] M.A. Pedrosa, et al. 2005 Plasma Phys. Control. Fusion **46** 777
[2] C. Hidalgo, et al. 2004 Plasma Phys. Control. Fusion **46** 286
[3] O. Gurcan, et al. Phys. of Plasma (submitted)
[4] B. Gonçalves, et al. 2006 Phys. Rev. Lett. **96** 145001

Proceedings of ITC/ISHW2007

On the zonal flows identification in the plasma edge of the TJ-II stellarator

M.A. Pedrosa, C. Silva[1], C. Hidalgo, R.O. Orozco, D. Carralero and the TJ-II team

EURATOM-CIEMAT, Spain, [1]EURATOM-IST, Portugal

TJ-II has revealed to be an ideal laboratory to study the development of edge sheared flows that can be easily driven and damped at the plasma edge changing the plasma density or during biasing experiments. Cross-correlation between edge magnitudes (density and potential) simultaneously measured with Langmuir probes located at two different positions approximately 180º toroidally apart, has been obtained in TJ-II. Results show a long distance correlation between floating potential signals that increases when probes are approximately at the same radial location, whereas there is no correlation between ion saturation current signals. Cross-correlation shows a maximum value when plasma density is close to the threshold for the development of spontaneous edge sheared flows with cross-phase close to zero. Furthermore, correlation between potential signals increases in the presence of externally applied electric fields. These findings show for the first time that the development of fluctuating perpendicular flows (with zonal flow-like structure) is the first step in the transition to improved confinement regimes.

Keywords: Turbulence, zonal flows, plasma edge, correlation, electric fields, stellarators.

1. Introduction

It is well known and widely accepted the importance of turbulent transport effects on plasma confinement in fusion devices. In particular it is very important to develop techniques to improve plasma confinement. Recently, fusion community has focused its attention on turbulent toroidally and azimuthally symmetric sheared flows (zonal flows) and the role that they can play in the turbulence regulation. It has been theoretically assessed that zonal flows play a role in the dynamics of turbulence and its self-regulation [1, and references therein]. Experimental works in different magnetically confined plasmas have been carried out to prove the existence of these zonal flows and some fingerprints of their presence have been found in different fusion devices [2, 3, 4, 5, 6, 7]. Zonal flows have also been suggested as an important ingredient to explain the Low to High transition (L-H) in magnetic confinement devices [8].

Due to the recent development of two sets of Langmuir probes located at two different toroidal positions, TJ-II can be considered a good laboratory to study the presence of zonal flows in the plasma edge region. Moreover, it has been reported that sheared flows can be easily driven and damped at the plasma edge by changing the plasma density [9, 10] or during biasing experiments [11]. Toroidal cross-correlations between plasma edge magnitudes have been studied in TJ-II in extremely different plasma conditions and different magnetic configurations providing valuable experimental data.

author's e-mail: angeles.pedrosa@ciemat.es

2. Experimental set-up

Experiments were carried out in the TJ-II stellarator in Electron Cyclotron Resonance Heated plasmas ($P_{ECRH} \leq 400$ kW, $B_T = 1$ T, $\langle R \rangle = 1.5$ m, $\langle a \rangle \leq 0.22$ m, $\iota(a)/2\pi \approx 1.5 - 1.9$). Different edge plasma parameters were simultaneously characterized in two different toroidal positions approximately 180º apart using two similar multi-Langmuir probes, installed on fast reciprocating drives (approximately 1 m/s) [12]. One of the probes is in the low field side (LFS) and the other in the high field side (HFS) of the TJ-II as is schematically shown in figure 1.

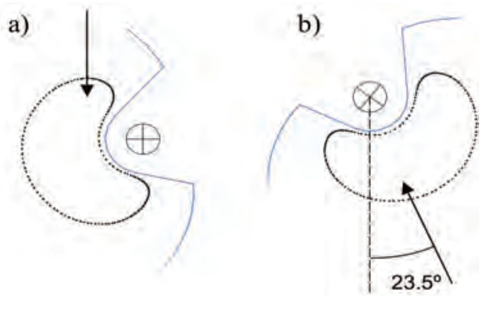

Fig 1 Schematic view of the location of the probes (arrows) at the high (a) and low (b) field sides in TJ-II.

3. Plasma edge measurements comparisons

Radial profiles of different plasma parameters have been measured at two far away toroidal locations simultaneously for the first time. Profiles were obtained both shot to shot and in a single shot with both probes and in different plasma configurations.

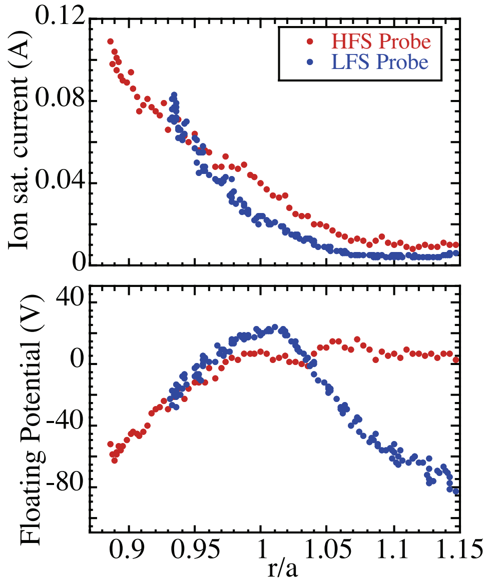

Fig. 2 Radial profiles of ion saturation current and floating potential measured simultaneously at two toroidal locations for plasma density above the threshold.

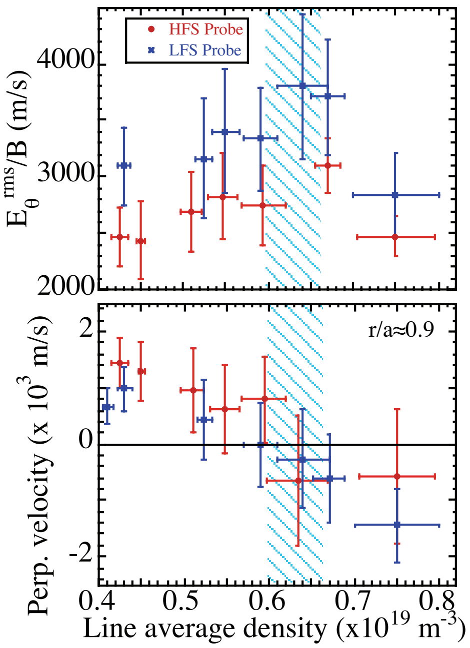

Fig. 3 Electric field fluctuations and perpendicular velocity measured at HFS and LFS positions as a function of plasma density at r/a≈0.9.

Figure 2 shows profiles of the ion saturation current and the floating potential measured simultaneously in the two mentioned toroidal positions in one shot. Profiles of the ion saturation current are slightly different in both probes: gradient is steeper at the LFS for all the plasma configurations studied up to now. Floating potential profiles are similar in both probes inside the last closed flux surface (LCFS) but they differ in the scrape-off layer (SOL) region probably due to the different particles losses rate at both positions.

The perpendicular electric field fluctuations and the phase velocity measured with both probes simultaneously and located both at r/a≈0.9 in different shots as a function of density are shown in figure 3. The behaviour of the velocity and fluctuations measured at the LFS is similar to the one reported at the HFS and the effect of the threshold density can be as well clearly seen [10, 13]. These results have been explained in TJ-II using a simple second order phase transition model [14].

4. Toroidal cross-correlations

Floating potential signals measured at both toroidal locations show a clear similarity mainly for low frequencies components, contrary to that observed with ion saturation current signals. Figure 4 shows the raw data of the floating potential and ion saturation current signals measured in both probes simultaneously at approximately the same radial position. The similarity in the floating potential signals is also observed in shorter time scales (lower than 1 ms), particularly in the fast events related to the shear flow development [13]. This means that the large amplitude floating potential fluctuations observed during the shear flow formation are toroidally symmetric.

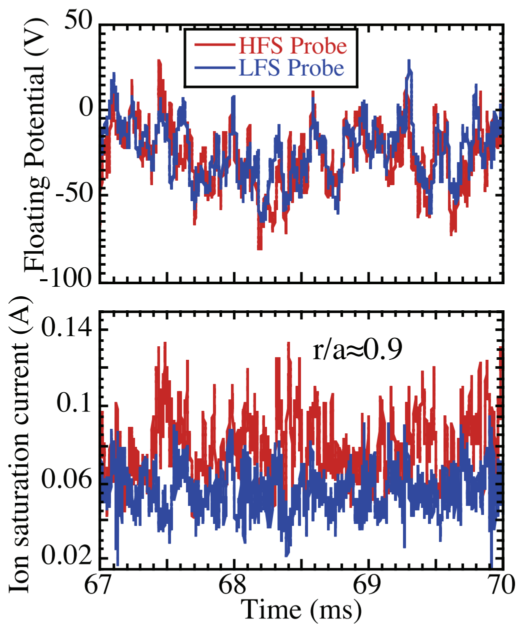

Fig. 4 Raw data of the floating potential and ion saturation current signals measured in both probes simultaneously.

To quantify the similarity between signals the toroidal cross-correlation has been computed in TJ-II in particular. The cross-correlation functions is defined as

$$\gamma_{xy}(\tau) = \frac{E\{[x(t+\tau)-\bar{x}][y(t)-\bar{y}]\}}{\sqrt{E\{[x(t)-\bar{x}]^2\}.E\{[y(t)-\bar{y}]^2\}}}$$

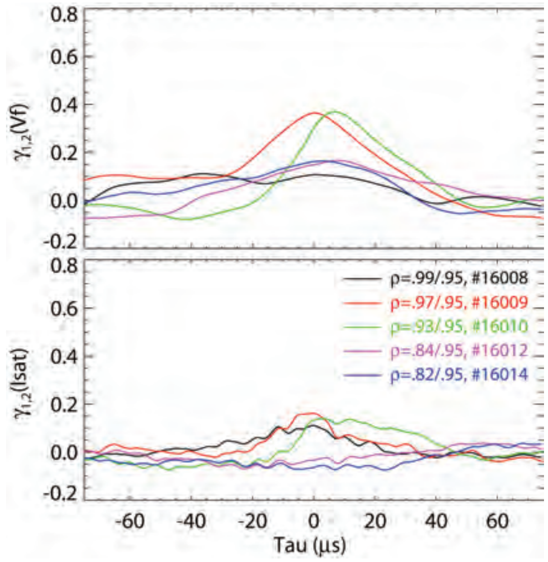

Fig. 5 Cross-correlation function for floating potential and ion saturation current signals measured at different radial positions of probe at the HFS and in ECRH plasmas without bias.

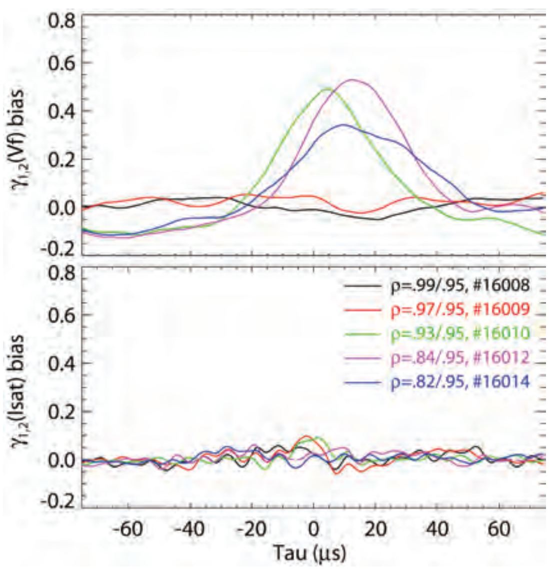

Fig. 6 Cross-correlation function for floating potential and ion saturation current signals measured at different radial positions of probe at the HFS and in ECRH plasmas with bias.

Cross-correlation of plasma edge magnitudes have been obtained from probe measurements, during experiments in TJ-II with and without electrode bias and for different plasma density values. As illustrated in figures 5 and 6, the ion saturation current signals correlation is significantly smaller than that of floating potential signals particularly during bias where the ion saturation current correlation is decreased and the floating potential correlation increased Bias makes also the cross-correlation more concentrated around τ=0. The maximum of the floating potential correlation (see figure 7) is observed when probes are approximately at the same radial location. The toroidal correlation shows a maximum in the region just inside the LCFS, being negligible in the SOL.

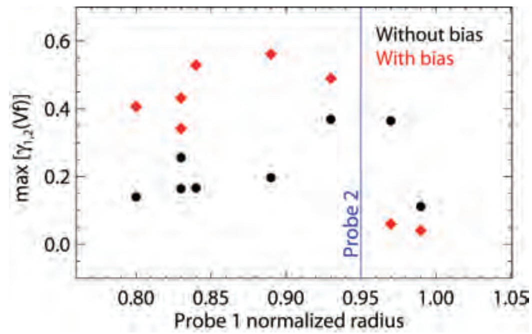

Fig. 7 Cross-correlation of floating potential signals measured as a function of the radial position of probe at the HFS in plasmas without and with bias. Vertical line indicates the position of the LFS probe.

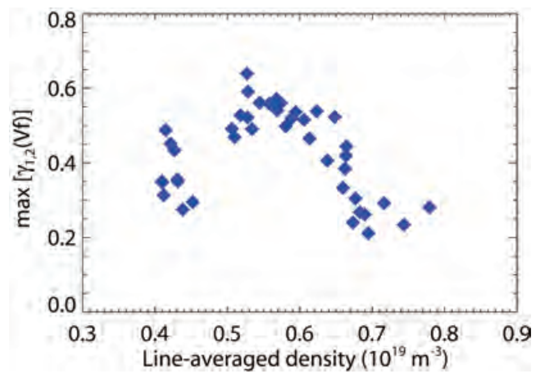

Fig. 8 Cross-correlation function of floating potential signals measured at approximately the same radial positions of both probes as a function of plasma density.

Figure 8 illustrates the dependence of the toroidal floating potential correlation on the line-averaged density (for the same pulses presented in figure 3). It is observed that correlation depends on the density, being larger for n ≈ (0. 5- 0.6)x10^{19} m^{-3}, which corresponds to the threshold density for shear flow development. Note that this correlation increase with density results mainly from the rise in the correlation at low frequencies (below 20 kHz).

Figure 9 shows the cross-power spectrum and the phase between the floating potential signals of the two probes. It is clear that the toroidal correlation is dominated by low frequencies (below 20 kHz) and that the phase between the two signals is close to zero for the whole frequency range. Electrode bias reduces the edge fluctuations and therefore the cross-power spectrum ($\left\langle \left| S_{xy}(f) \right| \right\rangle$) is also reduced. Note however that the coherence $\left\langle \dfrac{\left| S_{xy}(f) \right|}{\sqrt{\left| S_x(f) \right| \left| S_y(f) \right|}} \right\rangle$ increases during bias in agreement with the results presented in figures 5-7.

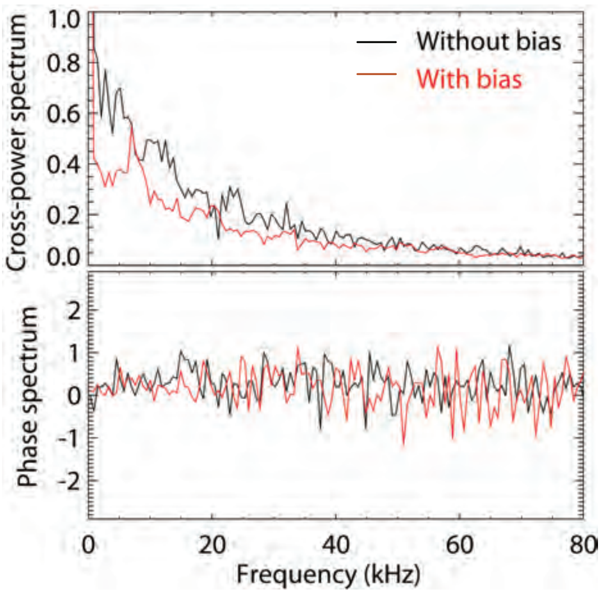

Fig. 9 Cross-correlation spectrum and cross-correlation phase spectrum between two floating potential signals toroidally apart.

Previous measurements of the parallel correlation in the SOL have shown an increase of correlation only when probes were located at the same field line [15, 16]. Other measurements have been performed more recently with the aim of identifying zonal flows [3, 4, 5, 6, 7], Measurements in TJ-II allows to compute the cross-correlation both in the SOL and in the edge plasma regions with the probes not located in the same field line being results compatible with those previously obtained [15, 16].

Experiments with fast visible cameras have investigated with 2-D resolution the development of edge sheared flows, showing a dithering phase at the threshold density with fluctuating perpendicular flows consistent poloidal symmetric structure.

5. Interpretation of the experimental results

The toroidal coupling of density and potential fluctuations has been investigated, for the first time, during the transition to improved confinement regimes in the TJ-II stellarator. It has been observed high cross-correlation at the plasma edge between floating potential signals measured approximately at the same radial location but toroidally apart. As the probes are not in the same filed line, this effect is compatible with the presence of zonal flows at the plasma edge. Moreover the phase between both signals is around zero indicating a toroidally symmetric structure, as is characteristic of the zonal flows. This fact is also demonstrated observing the similar waveforms of the raw data when probes are located radially closed. Besides that, the spectra are dominated by low frequency fluctuations as expected for zonal flows.

The observation of a maximum in the cross-correlation for a plasma density around the threshold value for shear flow development suggests a relationship between the generation of zonal flows and the improvement of confinement, being possible to consider the zonal flows generation as a trigger for plasma confinement improvement.

TJ-II experimental results are consistent with model for L-H transition based on the generation of zonal flows.

New experiments are going to be done in TJ-II looking for the presence of zonal flows and their relationship with confinement.

References

[1] P.H. Diamond et al., Plasma Phys. Control. Fusion **47** (2005) R35
[2] S. Coda et al., Phys. Rev Lett. **86** (2001) 4835
[3] M.G. Shats and W.M. Solomon, New Journal of Phys. **4** (2002) 30.1
[4] G.S. Xu et al., Phys. Rev Lett. **91** (2003) 125001
[5] G.D. Conway et al., 31st EPS Conference P-4.124 (2004)
[6] Y. Nagashima et al., Phys. Rev. Lett. **95** (2005) 095002
[7] A. Fujisawa et al., Phys. Rev Lett. **93** (2004) 165002
[8] P.N. Guzdar et al., Phys. REv. Lett. 87 (2001) 015001.
[9] C. Hidalgo et al., Phys. Rev. E, **70** (2004) 067402
[10] M.A. Pedrosa et al., Plasma Phys. Control. Fusion **47** (2005) 777
[11] C. Silva et al., Czech. J. Phys. **55** (2005) 1589
[12] M.A. Pedrosa, et al., Rev. Sci. Instrum. **70** (1999) 415.
[13] M.A. Pedrosa et al., 34th EPS Conference I2-020 (2007)
[14] B.A. Carreras et al., Phys. Plasmas **13** (2006) 122509
[15] Ch. P. Ritz et al., Rev. Sci. Instruí. **59** (1988) 1739
[16] H. Thomsen et al., Phys. Plasmas **9** (2002) 1233

Proceedings of ITC/ISHW2007

Neoclassical Transport Properties in High-Ion-Temperature Hydrogen Plasmas in the Large Helical Devise (LHD)

Seikichi MATSUOKA[1)], Masayuki YOKOYAMA[2)], Kenichi NAGAOKA[2)], Yasuhiko TAKEIRI[2)], Mikiro YOSHINUMA[2)], Katsumi IDA[2)], Tetsuo SEKI[2)], Hisayoshi FUNABA[2)], Sadayoshi MURAKAMI[1)], Atsushi FUKUYAMA[1)], Nobuyoshi OHYABU[2)], Osamu KANEKO[2)] and the LHD Experimental Group[2)]

[1)]*Department of Nuclear Engineering, Kyoto Univ., Kyoto 606-8501, Japan*
[2)]*National Institute for Fusion Science, Toki 509-5292, Japan*

High ion-temperature (Ti) hydrogen plasmas were successfully demonstrated in the experimental campaign (FY2006) in the LHD. The power increase of the perpendicular neutral beam injection has mainly contributed to make this realize. T_i exceeded 5 keV at the average plasma density (n_e) of 1.2 $\times 10^{19}$ m^{-3} and also achieved 3 keV at $n_e > 3 \times 10^{19}$ m^{-3}. The neoclassical (NC) analyses have been performed for such plasmas by utilizing GSRAKE code. We confirmed that even if T_i or the plasma density became higher for any shots, the NC transport is remained to a certain value due to the existence of the ambipolar radial electric field (E_r), which was roughly 2 orders of magnitude smaller for cases without considering the existence of ambipolar E_r.

Keywords: high-ion-temperature, neoclassical transport, radial electric field, GSRAKE code

1 Introduction

High ion-temperature (T_i) hydrogen plasmas were successfully demonstrated in the experimental campaign (FY2006) in the LHD. T_i exceeded 5 keV at the average plasma density (n_e) of 1.2 $\times 10^{19}$ m^{-3} and also achieved 3 keV at $n_e > 3 \times 10^{19}$ m^{-3} (See Fig. 1) [1]. In such high ion temperature palasmas, neoclassical transport ion thermal diffusivities ($\chi_{i,NC}$) are thought to be increased due to the ripple transport.

However, It has been considered that if radial electric field (E_r) exists in the plasma, neoclassical transport are reduced to the extent of the smaller electron diffusion which is determined by ambipolar condition, $\Gamma_e = \Gamma_\mathrm{i}$, where Γ_e and Γ_i are electron and ion particle flux respectively. And, by utilizing the electron or ion root of the radial electric field, reducing the neoclassical transport has been considered of great importance to improve the plasma confinement for non-axisymmetric helical systems. Thus, it is important to know how the neoclassical diffusivities of high-T_i plasmas are affected by the E_r quantitatively. For this purpose, the neoclassical transport analyses are conducted to some plasmas shown in Fig. 1 by utilizing GSRAKE code [2]. And systematic parameter-scan calculations with varying T_i and n_e have been performed based on these shots to see the parameter dependence of neoclassical ion diffusivity. It is clarified that the neoclassical thermal diffusivities are restrained due to ambipolar E_r. For many cases $E_r < 0$ is predicted, however, electron-root ($E_r > 0$) can appear for cases with low T_i. This indicates that neoclassical transport could be kept relatively small

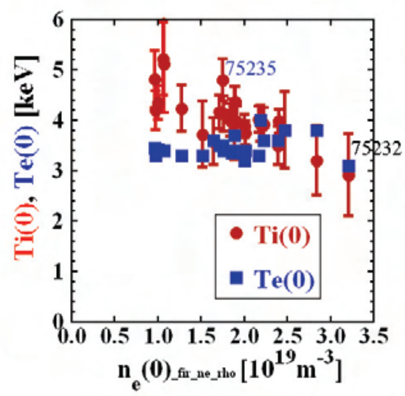

Fig. 1 The ion and electron temperature dependance on the density at the center of the plasma in the High-Ion-Temperature experiments in LHD

for even in higher T_i plasmas in LHD. In Sec.2, neoclassical transport analyses for LHD shot data are shown. And further neoclassical transport analyses for various plasmas in a parameter-sacn manner are described in Sec.3. Finally, summury is given in Sec.4.

2 Neoclassical transport analyses of LHD shot data

Neoclassical transport analyses were performed by utilizing GSRAKE code. GSRAKE code calculates particle and thermal fluxes for ions and electrons, and therefore, ambipolar E_r based on LHD magnetic field config-

author's e-mail: matsuoka.seikichi@LHD.nifs.ac.jp

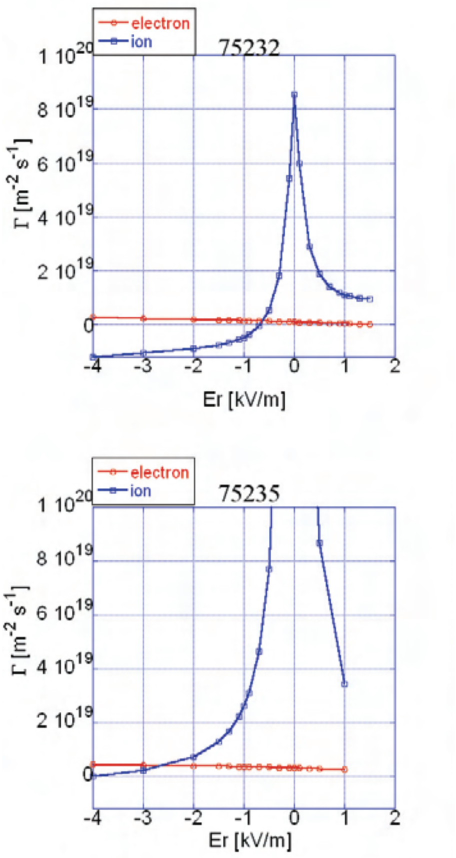

Fig. 2 E_r dependence of Γ_e and Γ_i at $\rho = 0.2$ of shots for 75232 (top) and 75235 (bottom). The intersection provides ambipolar E_r.

urations, using T_i and T_e (T_e is the electron temperature) and the plasma density profiles. At first, I chose the shot 75235 (at 1.35 sec) and 75232 (at 1.35 sec) from the high-ion-temperature experiments. While the ion temperature of 75235 is 4.8 keV at the density of $\sim 1.8 \times 10^{19}\mathrm{m}^{-3}$, that of 75232 is $\sim$ 3 keV at $\sim 3.2 \times 10^{19}\mathrm{m}^{-3}$. T_i of 75232 is comparable to T_e, T_i of 75235 is higher than T_e. Neoclassical transport calculations are carried out for these two shots. Γ_i and Γ_e at $\rho = 0.2$ for 75235 and 75232 are shown in Fig. 2. Here, ρ is normalized minor radius. Ambipolar E_r are shown in Fig. 3(a) for 75235 and 75232 respectively. Fig. 3(b) shows the ion-ion collisionalities $\nu_{i,p}$, normalized by the value at the platue-banana boundary. From Fig. 3(a) and (b), it is recognized that these plasmas are in $1/\nu$ regime in which neoclassical diffusion steeply increases in proportion to ν^{-1} when $E_r = 0$. In fact, as seen in Fig. 2, Γ_i becomes extremely large near $E_r = 0$. Then, ion thermal diffusivities devided by $T_i^{1.5}$ (Gyro-Bohm factor), $\chi_{i,NC}/T_i^{1.5}$, are shown in Fig. 3(c) where $\chi_{i,NC}/T_i^{1.5}$ at $E_r = 0$ is also shown for reference. The diffusivities are obviously reduced to almost the same magnitude (about 2-3 orders of magnitude smaller than that for $E_r = 0$), in spite of about 2 times higher T_i in 75235 than that in 75232. It is clearly indicates that ion diffusivity does not increase as T_i is increased due to the presence of predicted ambipolar E_r.

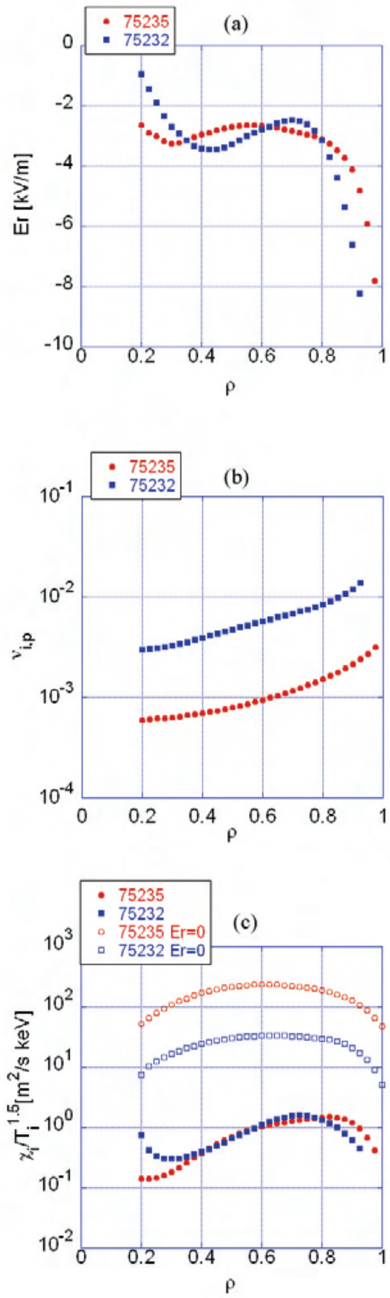

Fig. 3 Radial profiles of (a) ambipolar E_r, (b) ion collisionality with and (c) thermal diffusivities with or without E_r are shown for 75235 and 75232 respectively.

3 Temperature and density scan calculations

Then, in order to investigate the dependence of neoclassical transport on plasma parameters, such as T_i and *n*, have been performede based on 75235 and 75232. T_i and *n* of 75235 and 75232 are widely varied as shown in Fig. 4. $T_i(0)$ of 75235 ($\sim$ 4.8 keV) is multiplied by 0.3, 0.5 and 2, $n(0)$ of 75235 ($\sim 1.8 \times 10^{19}\mathrm{m}^{-3}$) is multiplied by 2, 5, 10, respectively. And then, $T_i(0)$ of 75232 ($\sim$ 3 keV) is multiplied by 0.5, 2, 4, *n* of 75232 ($\sim 3.2 \times 10^{19}\mathrm{m}^{-3}$) is multiplied by 0.5, 3, 5, respectively. In these calculations, I assumed that magnetic configuration equilibrium is fixed for simplicity, although T_i and *n* are varied.

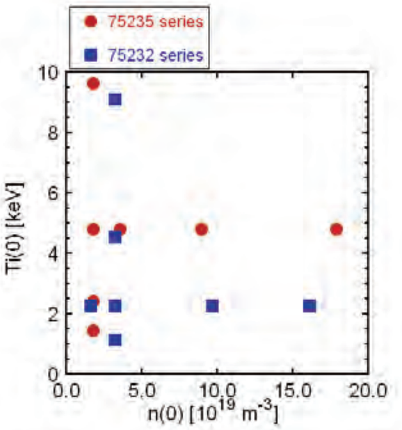

Fig. 4 Range of *n* and T_i scan calculations based on 75232 and 75235.

The results of parameter scan calculations are summurized in Fig. 5, where $\chi_i/T_i^{1.5}$ is shown for *n*-scan calculations and χ_i for T_i-scan calculations is shown. χ_i for T_i-scan and $\chi_i/T_i^{1.5}$ for *n*-scan are reduced to alomost the same extent in all cases. The collisionalities are all in $1/\nu$ regime. In Figs. 5(a) and (b) (*n*-scan), it is recognized that the neoclassical ion thermal diffusivity at $E_r = 0$ increses as n (thus collisionality) decreased. However, it reduces to almost the same lavel in the presence of ambipolar E_r regardless of the *n*-value. It is also the case for T_i-scan calculations. As expected, the incease of T_i (thus the decrease of collisionality) makes χ_i larger and lager for cases with $E_r = 0$ as shown in Figs. 5(c) and (d). However, it is reduced to almost the same level in the presence of ambipolar E_r. This fact indicates that the neoclassical χ_i will not increase even for higher-T_i (ranging of 10keV) cases in LHD, due to the presence of ambipolar E_r.

It is interesting to note that, in 75235-T_i scan, not only the ion root but also the electron root is predicted to exist at peripheral region of the plasmas when T_i is decreased (case of 0.3, 0.5 in Fig. 5(d)). It is considered that since the absolute value of electron root is larger than that of ion root, χ_i can be reduced more effectively. The electron root

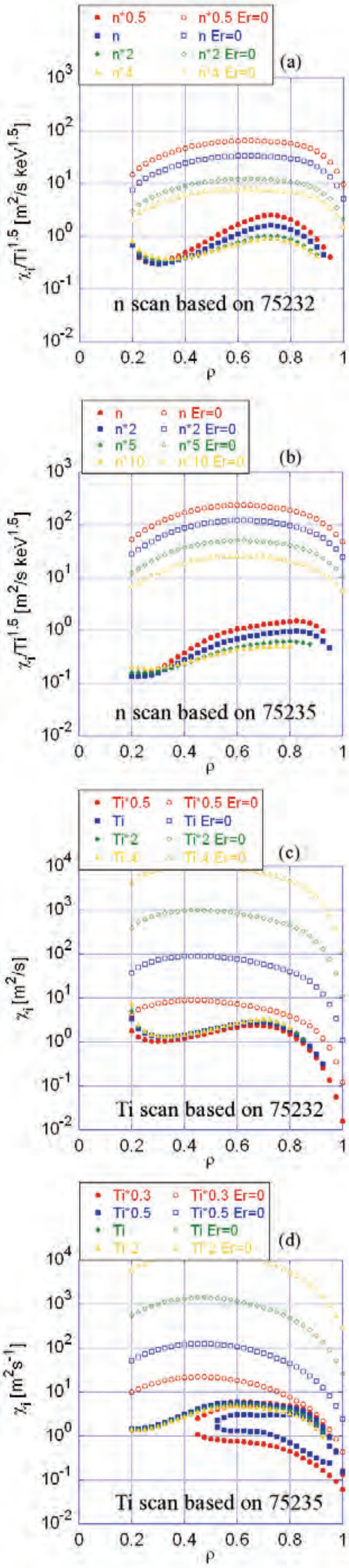

Fig. 5 neoclassical $\chi_i/T_i^{1.5}$ for *n* scan based on 75232 (a) and 75235 (b), and neoclassical χ_i for T_i scan based on 75232 (c) and 75235 (d) can appear for the case of 0.5 times $T_i(0)$ ($\sim$ 2.4 keV) of 75235 (Fig. 5(d)), but the case of 75232 (Fig. 5(c)), although T_i is almost the same. It should be noted here that T_e has been fixed (T_e is about 3.1 and 3.5 keV for 75232 and 75235, respectively, as shown in Fig. 1). Higher ratio of T_e/T_i for 75235 might help to make the electron root appear.

4 Summury

In this paper, neoclassical transport properties (especially for ions) are reported for high-T_i hydrogen plasmas achieved in LHD.

It is clearly demonstrated that ion thermal diffusivity avoids to be increased even with higher-T_i cases due to the predicted ambipolar E_r. It is also the case even for a range of $T_i \sim 10$ keV, which is clalified by parameter scan calculations. This is favorable fact for further increase of T_i in LHD by avoiding the ripple transport nature.

The possibility of the electron-root scenario for high-T_i plasmas is also pointed out by parameter scan calculations. This is interesting topic to be investigated.

[1] K.Nagaoka *et al*., in this conference, and M.Yokoyama *et al*., to be presented in the 49th APS-DPP Annual meeting, Nov. 2007

[2] C.D.Beidler *et al*., Plasma Phys. Control. Fusion. **37** 463 (1995).

Proceedings of ITC/ISHW2007

Parametric dependence of the perpendicular velocity shear layer formation in TJ-II plasmas

L. Guimarais[a], T. Estrada, E. Ascasíbar, M.E. Manso[a], L. Cupido[a], T. Happel, E. Blanco, R. Jiménez-Gómez, M.A. Pedrosa, C. Hidalgo, I. Pastor, A. López-Fraguas and the TJ-II Team

Laboratorio Nacional de Fusión. As. Euratom-CIEMAT, Madrid, Spain

[a] *As. Euratom-IST, CFN, Instituto Superior Técnico, Lisbon, Potugal*

In TJ-II plasmas, the perpendicular rotation velocity of the turbulence changes from positive to negative (from ion to electron diamagnetic direction) inside the LCMS when the line-averaged plasma density exceeds some critical value, this change being dominated by the inversion in the radial electric field. In this work we study the parameters that control the inversion in the perpendicular rotation. A parametric dependence of the critical density has been obtained studying plasmas confined in different magnetic configurations (different rotational transform and/or plasma volume) and heated with different ECH power levels. The studied data set shows positive exponential dependence on heating power and negative one on plasma radius, while the dependence on rotational transform has low statistical meaning. Besides, analysis of local plasma parameters points to plasma collisionality as the parameter that controls the inversion of the perpendicular rotation velocity of the turbulence.

Keywords: Stellarator, Reflectometry, Perpendicular Rotation, Collisionality

1. Introduction

In TJ-II ECH plasmas, a perpendicular velocity shear layer develops spontaneously at the plasma edge, above a certain line-averaged density [1]. The transition for the shear layer formation has been characterized using Langmuir probes [2], Ultra Fast Speed cameras [3] and microwave reflectometry [4]. Langmuir probe measurements indicate that below the critical density the perpendicular velocity of the turbulence is positive (in the ion diamagnetic direction) at both sides of the LCMS, while above this critical density, the perpendicular velocity remains positive outside the LCMS and it turns out to be negative inside. Besides, probe measurements show that there is a coupling between the development of the shear layer and an increase in the turbulence level at the plasma edge; the experimental results being consistent with the expectations of second-order transition models of turbulence-driven sheared flows [5]. In addition, HIBP measurements indicate that the radial electric field at the plasma edge reverses from positive to negative as the plasma density exceeds the critical value, while it remains positive in the plasma core [6]. These HIBP measurements indicate that the inversion in the perpendicular rotation velocity of the turbulence is dominated by the radial electric field.

In order to investigate the parameters that control the radial electric field, we have studied the dependence of the critical line-density on the ECH heating power and on the magnetic configuration: rotational transform and plasma volume. Besides, to further investigate the physics behind it, we have studied the behaviour of local plasma parameters: density, temperature and pressure and their radial gradients.

2. Experimental Results

The discharges used in this work correspond to ECH heated plasmas at 53 GHz, second harmonic and X-mode polarization. These discharges belong to six magnetic configurations, heated with three power levels: 200, 300 and 400 kW and with line-averaged densities from 0.3 to 1.2 10^{19} m^{-3}. The six magnetic configurations cover three rotational transform values (1.4, 1.8 and 2.2) and, for each rotational transform, two plasma volumes (0.65 and 1.0 m^3). The rotational transform profiles are shown in figure 1, while figure 2 shows the plasma volume as a function of the rotational transform at $\rho = 2/3$ for these configurations. Each magnetic configuration is labelled with three numbers that refer to the currents in the circular, helical and vertical coils of TJ-II; by changing these currents, the ι-profile and/or the plasma volume can be scanned. These magnetic configurations were

author's e-mail: guimas@cfn.ist.utl.pt

selected in order to have very low correlation between both configuration parameters: rotational transform and plasma radius. The electron and ion contributions to the plasma energy are calculated using the electron density and temperature profiles measured by the Thomson Scattering diagnostic and the ion temperature measured by the charge-exchange spectrometer. This data set (155 plasma discharges) reproduces the parametric dependence of the energy confinement time reported in [7]: the confinement improves with plasma density, plasma radius and rotational transform and degrades with heating power.

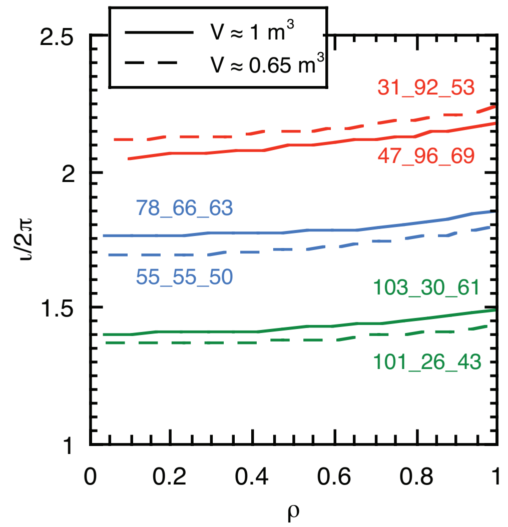

Figure 1: Rotational transform profiles for the six selected magnetic configurations.

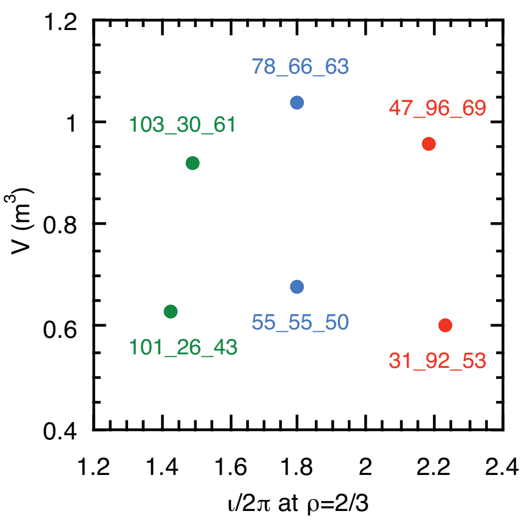

Figure 2: Plasma volume as a function of the rotational transform at ρ = 2/3 for the magnetic configurations shown in figure 1.

To monitor the inversion in the perpendicular rotation velocity we have used microwave reflectometry. The sign of the perpendicular rotation velocity of the turbulence can be resolved by the asymmetry of the turbulence spectra measured using the reflectometer [4, 8]. We have classified the discharges in three groups attending to the perpendicular rotation velocity in the plasma edge region (ρ ≥ 0.6). The first and second set of discharges includes plasmas with positive and negative perpendicular rotation velocity, respectively. The third set of discharges includes plasmas in which the inversion in the perpendicular rotation velocity is detected during the discharge; the corresponding critical line-density is obtained as the line-averaged density measured by the microwave interferometer at the inversion time. The obtained critical line-density values vary within a rather broad range, from 0.5 to 1 10^{19} m^{-3}, depending on magnetic configuration and ECH heating power. From this last set of discharges (44 discharges) we have extracted the parameter dependence of the critical line-density on ECH power, plasma radius and rotational transform, assuming a factorial dependence:

$$< n_{cr} > \propto P^{\alpha_P} a^{\alpha_a} \left(\iota / 2\pi\right)^{\alpha_\iota}$$

The best fit that results from the regression analysis is shown in figure 3 and is given by:

$$< n_{cr} > \propto P^{+0.34\pm0.03} a^{-1\pm0.1} \left(\iota / 2\pi\right)^{+0.09\pm0.05}$$

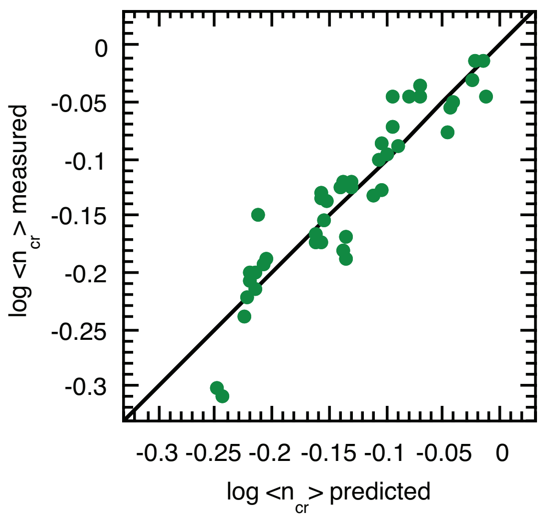

Figure 3: Critical line-density values obtained experimentally versus the best fit found in the regression analysis, represented in a log-log scale.

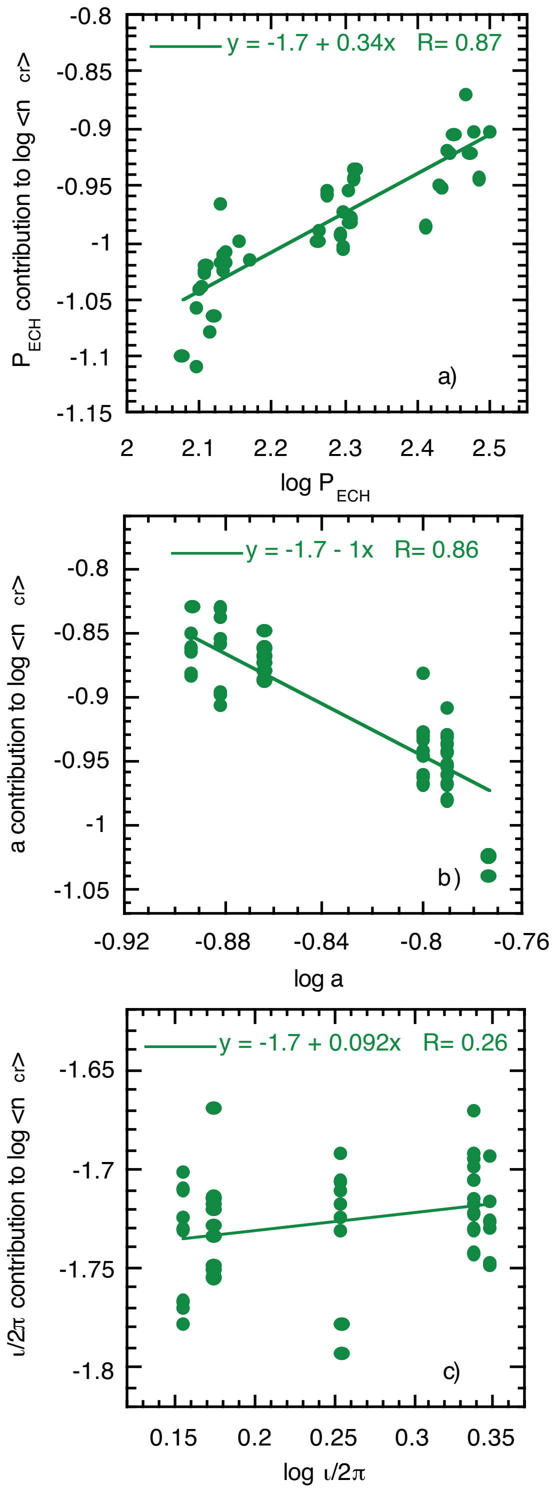

Figure 4: ECH power (a), plasma radius (b) and rotational transform (c) contribution to the critical line-density, represented in a log-log scale. The linear fits reproduce the regression coefficients.

The critical line-density shows opposite exponential dependences as compared with the energy confinement time: positive exponential dependence on the heating power and negative one on the plasma radius, while the dependence on the rotational transform has low statistical meaning. These dependences are shown in figures 4.a to 4.c. The contribution from each parameter to the critical line-density is obtained subtracting the contribution from the other parameters. These results partially confirm some preliminary results reported in [9]. The opposite exponential dependences as compared with the energy confinement time may reflect the influence of the radial electric field profile on the confinement. Moreover, particle transport analysis of TJ-II plasmas indicates that above the threshold density the particle confinement time improves considerably [10].

So far we have considered the line-density as the external knob to control the perpendicular rotation velocity; however, the large variation of the critical line-density with the ECH power and with the plasma volume indicates that line-density may not be the relevant parameter. To investigate the physics behind the radial electric field inversion we have studied the behaviour of local plasma parameters: electron density, temperature and pressure. These local values are obtained from the radial profiles measured using the Thomson scattering diagnostic in the three sets of discharges. Experimentally it is observed that, in a given magnetic configuration and at fixed ECH power, the inversion in the radial electric field (from positive to negative) takes place by increasing the plasma density; however, local values of plasma density or plasma pressure do not show any clear trend when data measured in plasmas with different ECH power and in different magnetic configurations are merged. The same result is found for the local values of density or pressure gradients. On the other hand, ECH power modulation experiments indicate that the inversion in the radial electric field (from positive to negative) occurs as the electron temperature decreases. These observations point to plasma collisionality as a likely candidate to control the sign of the radial electric field. In fact, experiments performed in LHD show that the sign of the radial electric field is controlled by the plasma collisionality [11]. This conclusion is supported by the plasma discharges analysed in this work. Local values of plasma collisionality measured in plasmas with different ECH power and in the six magnetic configurations are shown in figure 5. Plasma collisionality is calculated as the average of the local values measured within the radial range 0.5<ρ<0.7. Plasmas with negative radial electric field are found to have higher collisionality than those having positive radial electric field. The plasma collisionality measured at the inversion time is comparable to that measured for $E_r < 0$. This result explains the dependence of the critical line-density on the ECH power (shown in figure 4.a): as the ECH power is increased the electron temperature rises (the collisionality decreases) and a higher plasma density is required to increase the collisionality to the critical value that triggers the radial electric field inversion.

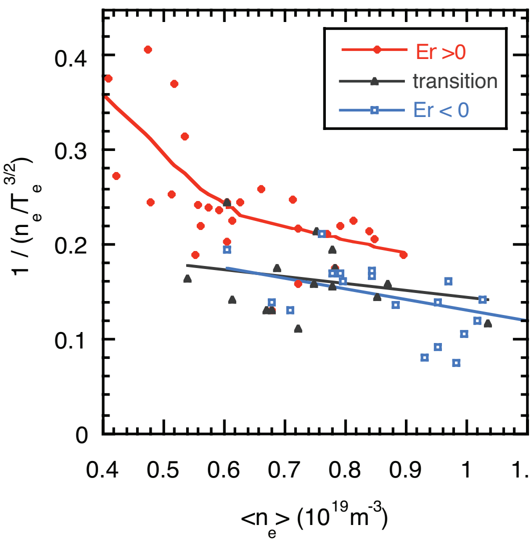

Figure 5: Plasma collisionality as a function of the line-density for plasmas heated with different ECH power and in the six different magnetic configurations. Plasmas with positive and negative radial electric field are represented in red and blue, respectively, while those in which the radial electric field transition is detected are shown in black.

The dependence of the critical density on the ECH heating power allows the study of the plasma response time during ECH power modulation experiments [12]. In these ECH power modulation experiments the temperature profile follows the power modulation frequency (360 Hz) while the density profile remains constant. The perpendicular velocity reverses following the ECH modulation in a time scale faster than 200 μs and in a wide plasma region, from the plasma edge up to ρ ≈ 0.6.

3. Conclusion

The behaviour of the perpendicular rotation velocity in the edge region of TJ-II plasmas has been studied in six different magnetic configurations, scanning both ECH power level and plasma density. The inversion in the perpendicular rotation velocity occurs when the line-averaged density reaches a certain critical value that depends on plasma conditions. The parametric dependence of the critical line-density on ECH power level and magnetic configuration characteristics shows a positive exponential dependence on EC heating power and a negative one on plasma radius; the dependence on rotational transform is weak and has low statistical meaning. Besides, analysis of local plasma parameters points to plasma collisionality as the parameter that controls the inversion of the perpendicular rotation velocity of the turbulence. This result explains the positive exponential dependence of the critical line-density on the ECH power. Further studies are needed to understand the dependence on the plasma radius.

[1] C. Hidalgo *et al*. Phys. Rev. E **70** (2004) 067402

[2] M.A. Pedrosa *et al.*, Plasma Phys. Control. Fusion **47** (2005) 777

[3] J.A. Alonso *et al.*, Plasma Phys. Control. Fusion **48** (2006) B465

[4] T. Estrada *et al.*, Nuclear Fusion **46** (2006) S792

[5] B.A. Carreras *et al.*, Phys. Plasmas **13** (2006) 122509

[6] A.V. Melnikov *et al.*, Fusion Sci. Tech. **51** (2007) 31

[7] E. Ascasíbar *et al.*, Nuclear Fusion **45** (2005) 276

[8] L. Cupido *et al.*, Rev. Sci. Instrum. **75** (2004) 3865

[9] M.A. Pedrosa *et al.*, Czech. J. Phys. **55** (2005) 1579

[10] V.I. Vargas *et al.*, 34th EPS Conference on Plasma Physics, Warsaw, Poland (2007)

[11] K. Ida *et al.*, Nuclear Fusion **45** (2005) 391

[12] T. Happel *et al.*, 8th International Reflectometry Workshop, St. Petersburg, Russia (2007)

Proceedings of ITC/ISHW2007

Time evolution of the rotational transform profile in current-carrying LHD plasmas

Yuji Nakamura, K. Y. Watanebe [a], Y. Narushima [a], K. Ida [a], M. Yoshinuma [a], S. Sakakibara [a], H. Funaba [a], K. Kawahata [a], M. Yokoyama [a], N. Nakajima [a], A. Fukuyama [b]

Graduate School of Energy Science, Kyoto University, Gokasho, Uji, Kyoto 611-0011, Japan
[a] National Institute for Fusion Science,322-6 Oroshi-cho, Toki 509-5292, Japan
[b] Graduate School of Engineering, Kyoto University, Yoshida, Kyoto, Kyoto 606-8501, Japan

nakamura@energy.kyoto-u.ac.jp

Though the net plasma current is not necessary for MHD equilibrium in helical plasmas, finite net toroidal currents have been observed in actual experiments. It is considered that the non-inductive current such as bootstrap current and beam driven current is the main component of the net plasma current. In the neutral beam (NB) heated LHD plasmas, non-inductive current driven by the NB injection to the co(counter)-direction increases (decreases) vacuum rotational transform. Both experimental results and numerical analyses show that the abrupt change of plasma current by the beam driven current is suppressed by the inductive component of the plasma current[1,2]. Because of the finite resistivity, total net current gets close to the non-inductive one with time, but it takes more than 4s to get the stationary state.

If the direction of NB injection is switched from the counter-direction to the co-direction in LHD experiments, the MSE measurement shows that the rotational transform is increased at the peripheral region as usual but it is decreased rapidly at the central region. Time duration for which the decreased central rotational transform is maintained seems to depend on the electron temperature. These experimental results indicate the importance of time evolution of the inductive current profile.

On the other hand, simulation studies for the rotational transform profile or net toroidal current profile in helical plasmas are performed[1,2] in association with the development of the integrated transport code for helical plasmas, TASK/3D code[3]. In these studies, time evolution of the rotational transform by the plasma resistivity in a non-axisymmetric plasma is obtained by solving the following equation;

$$\frac{\partial \iota}{\partial t} = \left(\frac{\phi_a}{s}\frac{\partial \phi_a}{\partial t}\right)\frac{\partial \iota}{\partial s} + \frac{1}{\phi_a^{\,2}}\left[\frac{\partial}{\partial s}\left\{\eta_{\parallel}\mathcal{V}'\frac{\langle B^2\rangle}{\mu_0^{\,2}}\frac{\partial}{\partial s}\left(S_{11}\iota + S_{12}\right)\right\} + \frac{\partial}{\partial s}\left\{\eta_{\parallel}\mathcal{V}'p'\left(S_{11}\iota + S_{12}\right) - \eta_{\parallel}\mathcal{V}'\langle \boldsymbol{J}_s\cdot\boldsymbol{B}\rangle\right\}\right]$$

where S_{11} and S_{12} are susceptance matrix elements[4] calculated by the metric tensors of three dimensional equilibrium, and $\langle \boldsymbol{J}_s \cdot \boldsymbol{B}\rangle$ represents the non-inductive current.

We will apply this simulation code to the LHD experiments in which the direction of NB injection is switched from the counter-direction to the co-direction, and clarify the role of inductive plasma current profile quantitatively.

[1] Yuji Nakamura, et al., Fusion Sci. and Technol. **50** (2006) 457-463.
[2] Yuji Nakamura, et al., Proc. of 21st IAEA Fusion Energy Conf. (Chengdu, China, 2006) IAEA-CN-149/TH/P7-1 (2006).
[3] M. Sato, et al., this conference.
[4] P. I. Strand and W. A. Houlberg, Phys. Plasma, **8** (2001) 2782.

Proceedings of ITC/ISHW2007

Development and application of the moments method transport analysis to plasma flows in 3D configurations

D. A. Spong*, J. H. Harris*, A. S. Ware+, S. P. Hirshman*, L. A. Berry*
**Oak Ridge National Laboratory, Oak Ridge, Tennessee 37831 U.S.A.*
+University of Montana-Missoula, Missoula, Montana 59812 U.S.A.

Shearing rates of neoclassical flows can attain levels that are relevant to turbulence suppression. Stellarators offer several options for the control and generation of such flows. First, configuration selection and profile control can lead to transport barrier formation, as has been demonstrated recently in the LHD (Large Helical device) experiment. Second, the nonlinear nature of the ambipolar electric field condition results in regimes where multiple roots can exist. Near points where these roots merge/bifurcate, weak changes in plasma parameters can result in large increases in $E \times B$ shearing rates. Such regimes have been found particularly in the case of the QPS compact quasi-poloidal stellarator and are analyzed here.

Keywords: moments method, $E \times B$ shear, sheared flow, neoclassical, ambipolar, momentum conservation. stellarator.

1. Introduction

A moments transport method has been developed for stellarators [1] that predicts the three-dimensional variation of the neoclassical plasma flow velocity over the plasma volume; in addition, the self-consistent ambipolar electric field, particle and energy fluxes are calculated. In previous applications of this model [2], we have examined the shearing rates of poloidal flow velocity components over a range of different stellarator devices, indicating a significant dependence on magnetic configuration. These velocity components include mixtures of perpendicular ($E \times B$) and parallel (neoclassical, Pfirsch-Schlüter) flows. While shearing of parallel velocities can be expected to have an impact on finite $k_{\|}$ turbulence and nonlinear MHD, drift wave turbulence suppression is thought to be most strongly influenced by shearing in the $E \times B$ flows. For this reason, in this paper, the moments analysis is extended to calculate $E \times B$ shearing rates and to search for regimes where this type of flow shearing can be enhanced.

2. Equations

A code (PENTA) has been developed that solves the moment equations derived in Ref. [3] for arbitrary stellarator configurations. The basic equations are the parallel momentum balance coupled with the perpendicular particle and energy transport equations.

$$\begin{bmatrix} \mathcal{M}_i + \Lambda_{ii} & \dfrac{\tau_{ii}}{m_i n_i}\Lambda_{ie} \\ \Lambda_{ei} & \mathcal{M}_e + \Lambda_{ee} \end{bmatrix} \begin{bmatrix} U_i \\ Q_i \\ U_e \\ Q_e \end{bmatrix} = -\begin{bmatrix} \mathcal{N}_i & 0 \\ 0 & \mathcal{N}_e \end{bmatrix} \begin{bmatrix} X_{i1} \\ X_{i2} \\ X_{e1} \\ X_{e2} \end{bmatrix} \qquad (1)$$

$$\begin{bmatrix} \Gamma_i \\ q_i / T_i \\ \Gamma_e \\ q_e / T_e \end{bmatrix} = \begin{bmatrix} \dfrac{n_i m_i}{\tau_{ii}\langle B^2 \rangle}\mathcal{N}_i & 0 \\ 0 & \dfrac{n_e m_e}{\tau_{ee}\langle B^2 \rangle}\mathcal{N}_e \end{bmatrix} \begin{bmatrix} U_i \\ Q_i \\ U_e \\ Q_e \end{bmatrix} + \begin{bmatrix} \mathcal{L}_i & 0 \\ 0 & \mathcal{L}_e \end{bmatrix} \begin{bmatrix} X_{i1} \\ X_{i2} \\ X_{e1} \\ X_{e2} \end{bmatrix} \qquad (2)$$

These are given in equations (1) and (2) where

$$U_a = \langle B u_{\|a} \rangle,\ Q_a = \frac{2}{5p_a}\langle B q_{\|a} \rangle,\ X_{a1} = -\frac{1}{n_a}\frac{dp_a}{ds} - e_a \frac{d\phi}{ds},\ X_{a2} = -\frac{dT_a}{ds}$$

$$\Lambda_{ii} = -\frac{\tau_{ii}}{n_i m_i}\begin{bmatrix} \ell_{11}^{ii} & -\ell_{12}^{ii} \\ -\ell_{21}^{ii} & \ell_{22}^{ii} \end{bmatrix} \simeq \begin{bmatrix} 0 & 0 \\ 0 & \sqrt{2} \end{bmatrix}; \quad \Lambda_{ee} = -\frac{Z\tau_{ee}}{n_e m_e}\begin{bmatrix} \ell_{11}^{ee} & -\ell_{12}^{ee} \\ -\ell_{21}^{ee} & \ell_{22}^{ee} \end{bmatrix} \simeq \begin{bmatrix} Z & -\frac{3}{2}Z \\ -\frac{3}{2}Z & \sqrt{2} + \frac{13}{4}Z \end{bmatrix}$$

$$\Lambda_{ei} = -\frac{Z n_i}{n_e}\frac{\tau_{ee}}{\tau_{ei}}\begin{bmatrix} 1 & 0 \\ -\frac{3}{2} & 0 \end{bmatrix}; \quad \Lambda_{ie} = -\frac{Z n_i m_e}{\tau_{ei}}\begin{bmatrix} 1 & -\frac{3}{2} \\ 0 & 0 \end{bmatrix};$$

and other quantities are as defined in Ref. [3]. The neoclassical transport coefficients/viscosities $\mathcal{M}_{i,e}$, $\mathcal{L}_{i,e}$, $\mathcal{N}_{i,e}$ have been expressed in terms of velocity integrals over mono-energetic coefficients that are computed by the DKES code [4]. In order to provide a database for these

author's e-mail: spongda@ornl.gov

calculations, DKES is run for a range of flux surfaces, collisionalities and electric field values.

3. High E × B shearing regime in QPS

The QPS is a compact (<R>/<a> = 2.7), low rotational transform (ι = 0.15 to 0.3) configuration with approximate quasi-poloidal symmetry and low effective ripple ($\varepsilon^{3/2} \sim 10^{-4}$ to 7×10^{-3}). This form of quasi-symmetry allows low effective levels of poloidal viscosity and higher poloidal flow velocities than other configurations. The combination of low transform and near poloidal symmetry results in better alignment between the ambiently-driven ⊥ flows (E × B and diamagnetic) and the direction of minimum gradients in |B|, leading to lowered magnetic pumping for such flows. This is reflected in smaller off-diagonal stress tensor components and less conversion of ⊥ flows to ∥ flows.

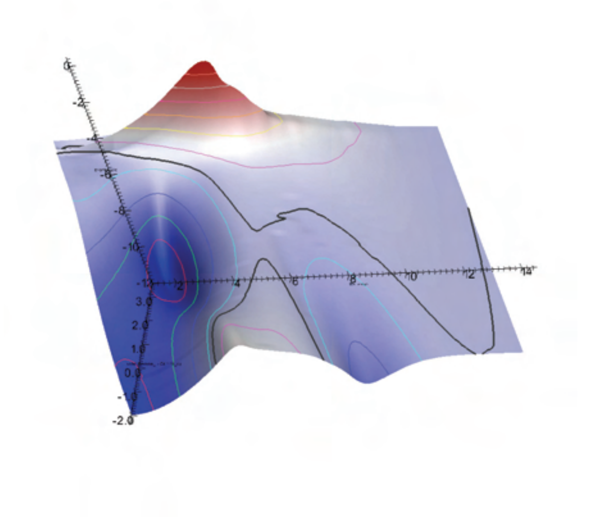

Fig 1(a) Elevation plot of Γ_{ion}-Γ_{elec} vs. e<a>E_r/kT_e and <r>/<a> for $n(0) = 7 \times 10^{19}$ m^{-3}.

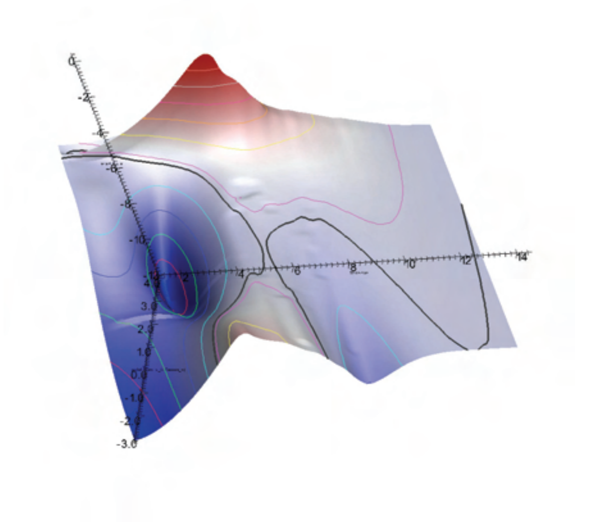

Fig 1(b) Elevation plot of Γ_{ion}-Γ_{elec} vs. e<a>E_r/kT_e and <r>/<a> for $n(0) = 10^{20}$ m^{-3} (solid black contour lines represent parameters for which Γ_{ion}-Γ_{elec} = 0.

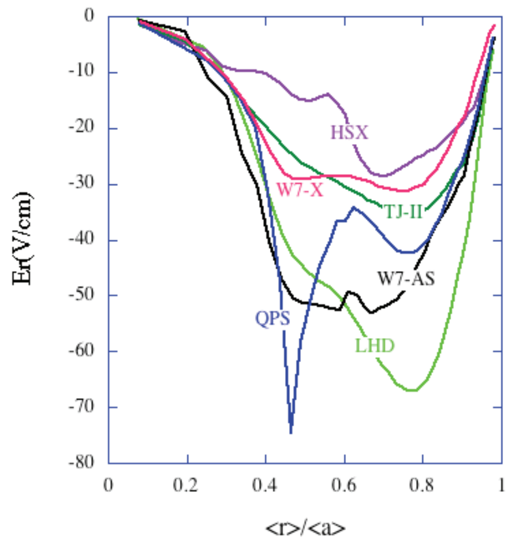

Fig. 2 Ambipolar electric field profiles for a range of configurations. All devices are scaled to <B> = 1 Tesla and <a> = 0.32 m.

From the perspective of the ambipolar transport condition (when properly coupled to neoclassical viscous effects) these characteristics can lead to the existence of additional ambipolar roots beyond the usual ion and electron solutions that are known for the case of transport models of simplified stellarators with limited helicities. An example of this characteristic is shown in Fig. 1.

As indicated, for these parameters and profiles [here $T_e(0) = T_i(0) = 0.6$ keV], the two ambipolar contours begin to merge/cross as the density is increased. This leads to a region of very high E × B shearing that could provide the basis for internal transport barrier formation.

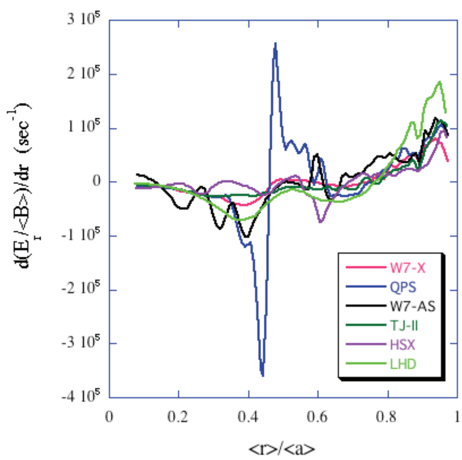

Fig. 3 E × B shearing rates for different configurations.

From limited surveys, such root merging, leading to high shearing rates has been found to be more prevalent in

QPS than other configurations. In Fig. 2, ambipolar electric field profiles are plotted for the same profiles and parameters for a range of devices. The associated $E \times B$ shearing rates are plotted in Fig. 3. In order to suppress drift turbulence, a simplified criterion is that such shearing levels need to be similar to drift wave growth rates. As analyzed in Ref. [5] for a variety of stellarators, typical growth rates range from 0.5 to 1.1×10^5 sec^{-1} for QPS (albeit based on different parameters and profiles than used here). The QPS shearing rates shown in Fig. 3 exceed these levels near the edge and <r>/<a> = 0.4 to 0.

4. E × B shearing in LHD SDC regime

A recent experimental achievement of substantial interest has been the generation of super dense core (SDC) plasmas in the LHD device [6] with low recycling and high density gradient internal diffusion barriers. This regime has been accessed by pellet injection and potentially offers extrapolation to high density/low temperature ignition scenarios. In a previous analysis of neoclassical flows in this regime, the moments model of this paper was applied to LHD, using an assumed sequence of increasingly peaked density profiles. This analysis has now been extended to examine a sequence of different equilibria with varying magnetic axis location and flux surface shaping. The highest levels of $E \times B$ shearing have been found either for equilibria with large axis shifts or those with oblate flux surface shapes at the $\zeta = 0$ plane. An example of shearing rates in the $E \times B$ velocity and contra-variant poloidal ion flow velocity are shown in Fig. 4. Results from a sequence of profiles are displayed here, starting with a broad density profile with $n(0) = 6 \times 10^{19}$ m^{-3} (red curve) and progressing to a very peaked density profile with $n(0) = 4.5 \times 10^{20}$ m^{-3} (magenta curve). While these shearing levels do not quite reach levels that might be expected to form transport barriers, they could provide a background level that could supplement self-regulating turbulence-generated zonal flows.

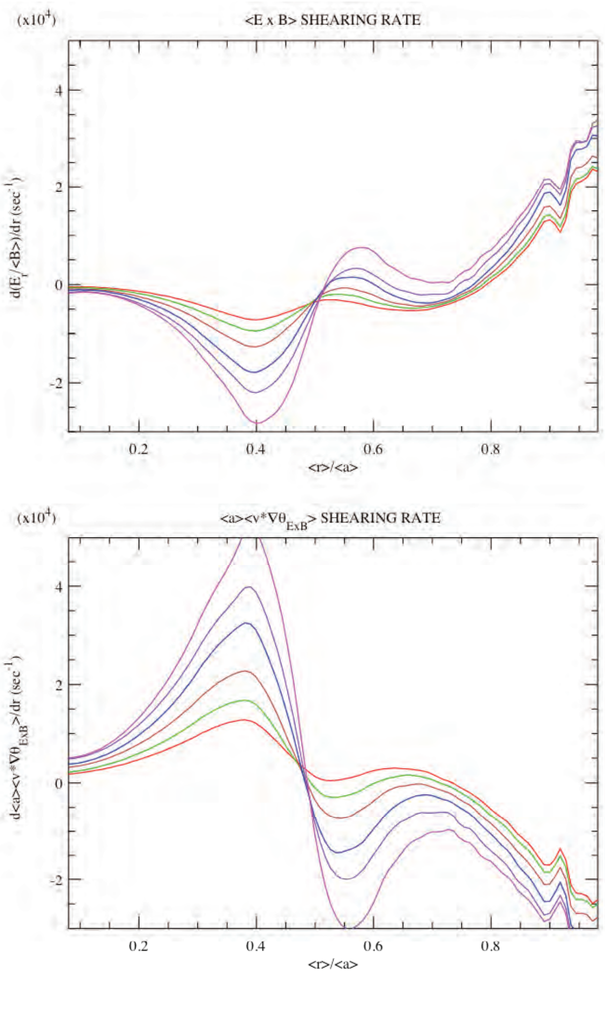

Fig. 4 $E \times B$ shearing rates and poloidal flow shearing rates for an outward shifted LHD equilibrium with $R_0 = 3.8$ m.

5. QPS flexibility at reduced magnetic field levels

If QPS is operated at reduced magnetic field levels in the range of <B> = 0.3 Tesla, the planar toroidal magnetic field coils have enough current capacity to introduce QP-symmetry breaking effects. These effects were analyzed previously in Ref. [2]. They have been re-analyzed with the current version of the PENTA code with respect to $E \times B$ shearing levels. As indicated in Fig. 5, variations in these coil currents can significantly modify the effective ripple [7] coefficient.

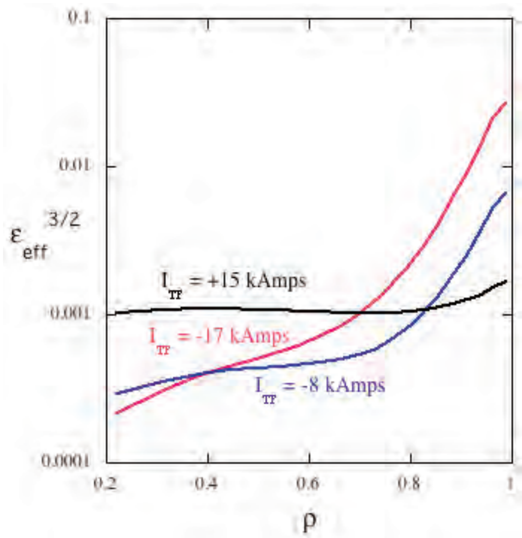

Fig. 5 – Effective ripple coefficient for low field QPS operation (<B> = 0.3 T) as a function of planar toroidal field current level.

Such variations in ripple levels lead to a range of different electric field levels, as are shown in Fig. 6. These lead to the differing $E \times B$ shearing levels that are shown in Fig. 7. As can be seen, in the <r>/<a> = 0.4 to 0.5 range, the cases with the higher effective ripple level tends to have lower shearing levels, while the cases with the lower effective ripple have higher shearing levels. This type of configuration change is thus expected to provide useful tests of the effects of different E × B shearing levels.

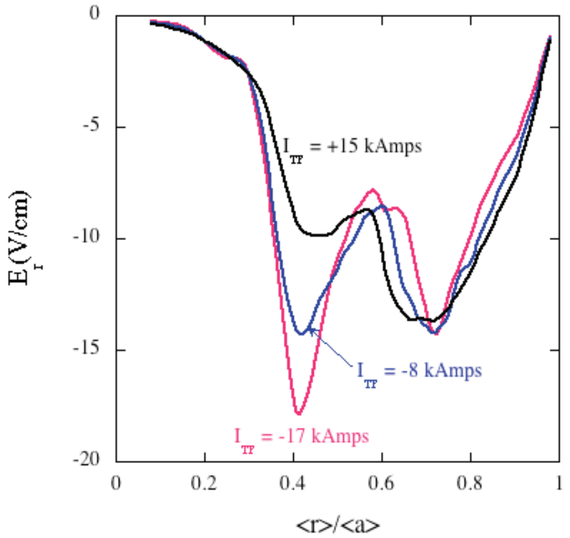

Fig. 6 Ambipolar electric field profiles vs. radius and toroidal planar coil current.

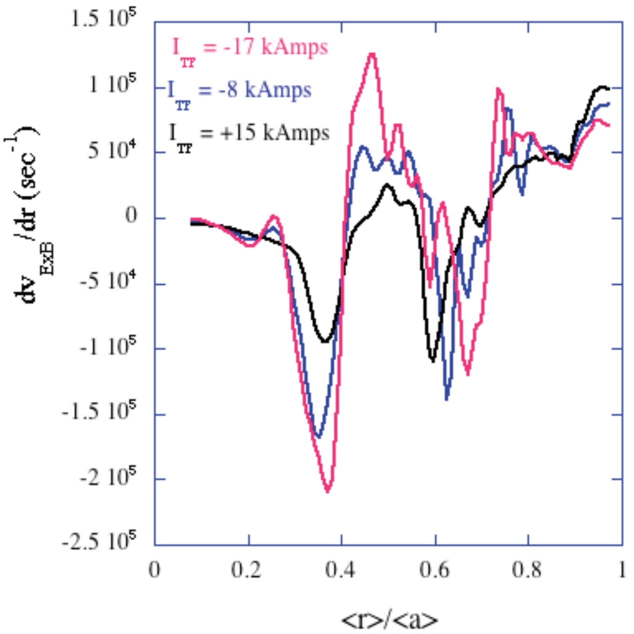

Fig. 7 E × B shearing levels vs. radius and toroidal planar coil current.

References

[1] D. Spong, Fusion Science and Tech. **50** (2006) 343.
[2] D. Spong, et al., Nuclear Fusion **47** (2007) 626.
[3] H. Sugama, S. Nishimura, Phys. of Plasmas 9 (2002) 4637.
[4] W. I. Van Rij, S. P. Hirshman, Phys. Fluids **B1** (1989) 563.
[5] G. Rewoldt, et al., Phys. of Plasmas **12** (2005) 1047.
[6] N. Ohyabu, et al., Phys. Rev. Lett. **97** (2006) 055002-1.
[7] V. V. Nemov, et al., Phys. of Plasmas 6 (1999) 4622.

author's e-mail: spongda@ornl.gov

Neoclassical viscosities in NCSX and QPS with few toroidal periods and low aspect ratios

S.Nishimura, D.R.Mikkelsen[a], D.A.Spong[b], S.P.Hirshman[b], L.P.Ku[a], H.E.Mynick[a], M.C.Zarnstorff[a]

National Institute for Fusion Science, 322-6 Oroshi-cho, Toki 509-5292, Japan
[a] Princeton Plasma Physics Laboratory, Princeton, New Jersey 08543-0451, USA
[b] Oak Ridge National Laboratory, Oak Ridge, Tennessee 37831-6169, USA

Previously reported benchmarking examples for the analytical formulas of neoclassical viscosities were made implicitly assuming applications in a future integrated simulation system for the LHD (Large Helical Device). Therefore the toroidal period numbers assumed there were mainly N=10. In this kind of calculation, however, an implicit (or sometimes explicit) assumption of ι/N<<1 is sometimes included. This assumption is included not only in simplified bounce averaged drift kinetic equations for ripple diffusions, but also in the equation before the averaging for non-bounce-averaged effects determining neoclassical parallel viscosity and the banana-plateau diffusions. To clarify the applicability of the analytical methods even for configurations with extremely low toroidal period numbers (required for low aspect ratios), we show here recent benchmarking examples in NCSX (National Compact Stellarator Experiment) with N=3 and QPS (Quasi-poloidal Stellarator) with N=2.

Keywords: neoclassical transport, neoclassical viscosity, moment equation approach, drift kinetic equation, non-symmetric toroidal plasmas, low-aspect ratio advanced stellarators

1. Inroduction

The moment equation approach for neoclassical transport [1,2] in non-symmetric toroidal plasmas had been developed mainly for neoclassical parallel flows and the associated parallel viscosity [3-6]. Even though it was shown in Ref.[7] that a consistent frame work including not only the flows but also radial diffusions (in other words, not only the parallel viscosity, but also poloidal and toroidal viscosities) can be constructed in this line of moment approach, methods to calculate all of required viscosity coefficients in general collisionality regimes in general toroidal configurations had not been shown. Motivated by design activities of advanced stellarators, a method to obtain the full neoclassical viscosity coefficients was developed in Ref.[8]. It was shown there that three mono-energetic viscosity coefficients M^*(parallel viscosity against flows), N^*(driving force for bootstrap currents), and L^*(radial diffusion) are required to describe the full neoclassical characteristics of general non-symmetric toroidal configurations. Since existing numerical methods such as variational methods and Monte Carlo methods for the drift kinetic equation described in the 3-D phase space (poloidal angle θ, toroidal angle ζ, pitch angle ξ) could be applicable [8], applications of the new theory were done for various types of advanced helical/stellarator configurations [9,10]. However, this step of the development of the moment approach was still in the "basic frame work". Even though there were many alternative methods for the L^* in the collisionless limit (aforementioned ripple diffusions), the other viscosity coefficients could be obtained only by the Drift Kinetic Equation Solver (DKES) code [8,9,10,11]. There are many demands for faster and easier estimation methods for the neoclassical quantities, in integrated simulation systems using iterative calculations of the equilibrium and the transport [12], in the configuration optimizations [9], and in experimental studies investigating dependences on configurations. Since the viscosities (or resulting neoclassical transport coefficients) are direct consequences of guiding center drift motions, evaluating them is an important part of understanding the characteristics of the designed magnetic configurations [9,10,13,14]. Even in tokamak experiments, neoclassical toroidal viscosity effects due to breaking the axisymmetry have recently been studied [15], and thus the framework of the moment approach for non-symmetric configurations and the methods to calculate the viscosity coefficients are now required for all studies of toroidal plasma confinements. In theories of axisymmetric tokamaks, simple analytical methods based on asymptotic expansions of the drift kinetic equations and connections of results of them are commonly used [1,16]. Since this approach using analytical methods will be required also in a future integrated simulation system for the LHD(Large Helical Device)[12], we had previously carried out derivations and benchmark tests of

author's e-mail: nishimura.shin@lhd.nifs.ac.jp

the analytical formulas for the three mono-energetic coefficients [17]. The previous benchmarking examples were made implicitly assuming applications in the LHD [a helical heliotron with major and minor radii of R_0=3.9m, a=0.6m, and magnetic field strength of $B_0 \leq 3$T]. Therefore the toroidal period numbers assumed there were mainly N=10, and the assumed $B_{mn}^{\rm (Boozer)}$ [$B=\Sigma B_{mn}\cos(m\theta - nN\zeta)$] spectra didn't include $n\neq 0,1$. One open issue remaining there is the ripple-trapped/untrapped boundary layer. Even though there are many alternative calculating methods for the bounce-averaged motion of the ripple-trapped particles, this boundary layer causes coupling effects between the bounce-averaged motion of ripple-trapped particles and the non-bounce-averaged motion of untrapped particles (collisional detrapping/entrapping). In Ref.[17], a previous boundary layer theory by Shaing and Callen for rippled tokamaks [18] was applied with an extension to multi-helicity stellarators. One effect of this coupling, which was investigated also in Ref.[17], is a difference of N^* (or $G^{\rm (BS)} \equiv -\langle B^2\rangle N^*/M^*$) in the $1/\nu$ regime ($E_s/v \approx 0$) from the collisionless detrapping ν regime ($E_s/v \neq 0$, $\nu/v \to 0$) value given by Refs.[3,4]. However, we had not shown any benchmarking examples for the $1/\nu^{1/2}$ diffusion, which is another important effect discussed in Ref.[18]. Even for the N^* in the $1/\nu$ regime, the numerical examples for more general cases had not been shown. To investigate these effects in configurations including B_{mn} of $n\neq 0,1$ and with extremely low toroidal period numbers (required for low aspect ratios) giving larger ι/N, we show in this paper recent calculation examples in NCSX (National Compact Stellarator Experiment)[10,13] and QPS (Quasi-poloidal Stellarator) [9,10,14].

2. Calculations in NCSX

The NCSX is a quasi-axisymmetric (QA) toroidal system with N=3, R_0=1.4m, a=0.32m, and $B_0 \leq 2$T. Here we consider the calculation on a flux surface with normalized toroidal flux of $(\psi/\psi_{\rm edge})^{1/2}$=0.51 (corresponding to $r \cong 0.165$m) in a standard configuration (NCSX-m50) with a finite beta of β=4% and a finite toroidal current of $I_{\rm p}$=178 kA as an example. The notations for the flux surface coordinates (mainly the Boozer coordinates) in Refs.[8,17] are followed and thus the radial derivatives of the poloidal and toroidal magnetic fluxes are χ' =0.1178T•m, ψ' =0.2513T•m, and covariant poloidal and toroidal components of the magnetic field are B_θ=0.0036T•m, B_ζ=2.3210T•m, respectively, on this flux surface. The $B_{mn}^{\rm (Boozer)}$ in a range of $0\leq m\leq 16$ and $|n|\leq 11$ are used. As described in Ref.[18], the boundary layer structure is determined by a drift kinetic equation $(V_{//} - C_a^{\rm PAS}) f_{a1} = 0$, where $V_{//} \equiv$ $\mathbf{b}\bullet\nabla_{(\mu={\rm const})}$ is the linearized orbit propagator and $C_a^{\rm PAS}$ is the pitch-angle-scattering operator with the collision frequency of $\nu_{\rm D}^a$[8]. Since $V_{//} f_{a1} \neq 0$ for the non-trivial solution of this equation, the existing bounce- or ripple-averaging methods assuming $V_{//} f_{a1}$=0 is not appropriate for this analysis. Therefore we should use the bounce- or ripple-averaging methods to obtain $\partial f_{a1}/\partial\mu$ in the ripple-trapped pitch-angle range, which gives the boundary condition for the boundary layer analysis [18], together with the analytical solution for the boundary layer as complimentary methods. For this analytical solution, a model expression of the magnetic field strength $B/B_0 = 1+\varepsilon_{\rm T}(\theta)+\varepsilon_{\rm H}(\theta)\cos\{L\theta - N\zeta - \gamma(\theta)\}$ is required. We use here $\varepsilon_{\rm H}(\theta) = \{B_{\max}(\theta) - B_{\min}(\theta)\}/(2B_0)$ for each poloidal angle θ to define $\varepsilon_{\rm H}(\theta)$. This is a truncation of the Fourier series used by Todoroki [20] who expanded not the amplitude but the phase of $B/B_0 - 1 - \varepsilon_{\rm T}(\theta)$.
Analogously, $1+\varepsilon_{\rm T}(\theta)$ is given by $1+\varepsilon_{\rm T}(\theta) = \{B_{\max}(\theta) + B_{\min}(\theta)\}/(2B_0)$. The residual ripple-well structure is distorted, or sometimes eliminated at $\theta \approx \pm\pi/2$, by finite rotational transform per toroidal period $(\chi'/\psi')/N$ in cases with small $\varepsilon_{\rm H}$. For this kind of situations, the effective ripple well depth $\delta_{\rm eff}$ and effective ripple well length correction α^* were introduced in the theory for rippled tokamaks [18]. We use also this technique with an extension to helical/stellarator configurations. The error of a well-known Shaing-Hokin formula [21] for the $1/\nu$ ripple diffusions in $\varepsilon_{\rm H} \to 0$ limits (for e.g., $\varepsilon_{\rm H} \leq 0.01$), which was pointed out in Ref.[8], is strongly reduced by introducing this method. By using these notations, an expression for the $1/\nu^{1/2}$ diffusion coefficient in Ref.[18], which is a contribution of ripple-trapped pitch-angle range $0\leq\kappa^2\leq 1$ for $\kappa^2 \equiv \{w - \mu B_0(1+\varepsilon_{\rm T} - \delta_{\rm eff})\}/(2\mu B_0 \delta_{\rm eff})$, can be extended to a form including more general non-symmetric configurations as

$$L^*_{(-1/2)} = 2.92\frac{2}{\pi^2}\left(\frac{v}{\nu_{\rm D}^a}\right)^{1/2}\frac{2^{3/4}}{(\psi')^2}\left(\frac{V'}{4\pi^2}\right)^{1/2}\times$$
$$\int_{-\pi}^{\pi}\frac{d\theta}{2\pi}\,\delta_{\rm eff}^{3/4}\left(B_0\frac{\pi - 2\sin^{-1}\alpha^*}{N\psi' - L\chi' - \chi'\partial\gamma/\partial\theta}\right)^{1/2}\times$$
$$\left\{\left(\frac{\partial\varepsilon_{\rm T}}{\partial\theta}\right)^2 - \sqrt{1-\alpha^{*2}}\,\frac{\partial\varepsilon_{\rm T}}{\partial\theta}\frac{\partial\varepsilon_{\rm H}}{\partial\theta} + \frac{2}{9}(1-\alpha^{*2})\left(\frac{\partial\varepsilon_{\rm H}}{\partial\theta}\right)^2\right\} \tag{1}$$

Here, for the aforementioned distribution function $\partial f_{a1}/\partial\mu$ in $0\leq\kappa^2\leq 1$ as the boundary condition, an analytical solution by Shaing and Hokin [21] is used to consider analytically the dependence on the magnetic configurations. From this form of $L^*_{(-1/2)} \propto \delta_{\rm eff}^{3/4} N^{-1/2}$, we can understand that this component of the diffusions can dominate over the $1/\nu$ diffusion of $L^*_{(-1)} \propto \delta_{\rm eff}^{3/2} N^0$

[21] only in configurations with small ripple amplitude $\delta_{\rm eff}$ and with small toroidal period numbers N, and therefore it will appear in QA configurations rather than the rippled tokamaks considered in Ref.[18]. In fact, previous numerical results in CHS-qa [23] with N=2 showed a clear $1/\nu^{1/2}$ dependence of L^* in a wide range of collisionality (ν/v).

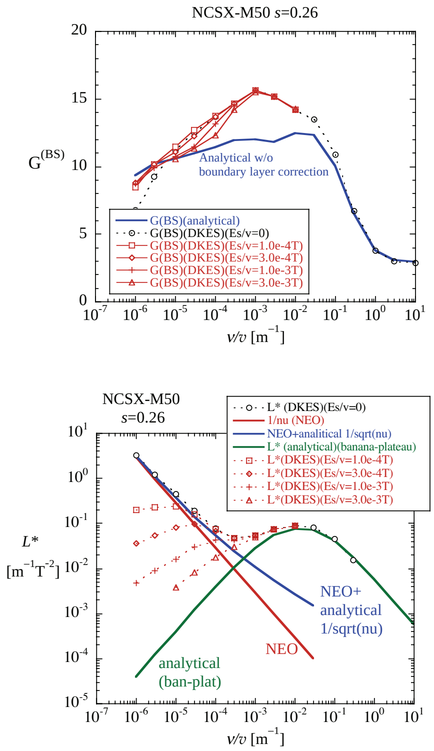

Fig.1 Mono-energetic viscosity coefficients in the NCSX given by the analytical methods (solid curves) and by the numerical method in the 3-D phase space (DKES) (open symbols). (a) the geometrical factor $G^{(BS)}\equiv-\langle B^2\rangle N^*/M^*$, (b) components of the diagonal diffusion L^*.

Figure 1(a) shows the mono-energetic viscosity coefficients N^* in the NCSX obtained by the analytical formulas [17] and those by the DKES [11] with the conversion formulas in Ref.[8]. The mono-energetic coefficient L^* ($E_s/v\approx0$) is analytically given by sum of three components: (1) $L^*_{(-1)}$ given by appropriate bounce-averaging codes with field line integral methods, (2) $L^*_{(-1/2)}$ given by Eq.(1), and (3) contributions of non-bounce-averaged drifts given by Eq.(16) in Ref.[17] ($L^*_{\rm (banana\text{-}plateau)}$). We used here the NEO code [22] for the $L^*_{(-1)}$ in the NCSX, and Figure 1(b) shows these components $L^*_{(-1)}$, $L^*_{(-1)}+L^*_{(-1/2)}$, $L^*_{\rm (banana\text{-}plateau)}$, and the DKES results. The sum $L^*_{(-1)}+L^*_{(-1/2)}$ approximately predicts a deviation of the DKES from a pure $\propto 1/\nu$ scaling given by the bounce-averaging codes at $\nu/v<10^{-3}{\rm m}^{-1}$. In these figures, we show also the dependences of the DKES results on the E×B drift parameter E_s/v. The N^* in NCSX is insensitive to E_s/v even in the range of $E_s/v\leq3\times10^{-3}$T since the $1/\nu$ diffusion of the ripple-trapped particles accompanying the boundary layer correction $N^*_{\rm (boundary)}$ in Eq.(14) in Ref.[17] is strongly reduced in this configuration. In spite of this reduction of $L^*_{(-1)}$ and accompanied $N^*_{\rm (boundary)}$, we can see another boundary layer effect in Fig.1(a). The N^* given by the DKES transiently becomes larger at $\nu/v\sim10^{-3}{\rm m}^{-1}$ compared with the analytical formula. This transient increase is peculiar to QA configurations where the $1/\nu^{1/2}$ component becomes comparable or dominates over the $1/\nu$ component in the radial diffusion, and thus was found also in CHS-qa [23]. Although this effect in the $1/\nu^{1/2}$ regime cannot be calculated by a method in Ref.[17] assuming a collisionless limit of the $1/\nu$ regime (This previous formula gives too small values for the QA configurations and thus is not included in Fig.1(a)), the transient increase, which is about 30% at most, will not be so important in the energy integrated coefficients.

3. Calculations in QPS

The QPS adopts a quasi-poloidal configuration reducing the radial drift of the trapped particles [19], with N=2, R_0=1m, a=0.3m, and $B_0\leq$1T. The parameters of the flux surface, where the calculation examples are made,

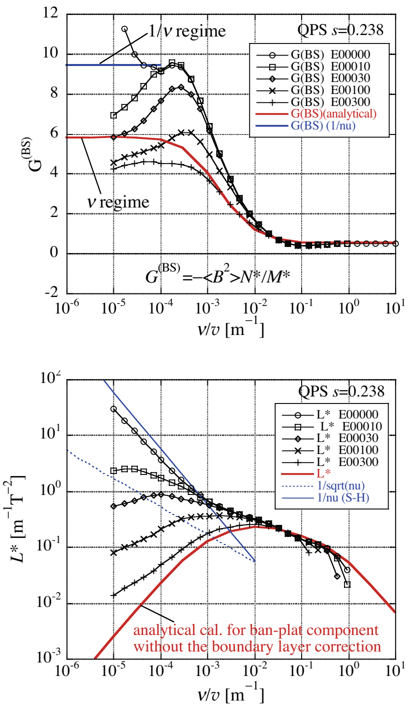

Fig.2 Mono-energetic viscosity coefficients in the QPS given by the analytical methods (solid curves) and by the DKES (lines with symbols). (a) the geometrical factor $G^{(BS)}\equiv-\langle B^2\rangle N^*/M^*$, (b) components of the diagonal diffusion L^*.

are $(\psi/\psi_{\rm edge})^{1/2}$=0.49 (corresponding to $r\cong$0.14m), χ' =0.0275T•m, ψ' =0.1423T•m, B_θ=0, and B_ζ=1.1403T•m. The $B_{mn}^{\rm (Boozer)}$ ranges are $0\le m\le 20$ and $|n|\le 20$. Results in the QPS are shown in Fig.2. In Fig.2(b), the $1/\nu$ diffusion coefficient $L^*_{(1/\nu)}$ given by the Shaing-Hokin formula [21] including the minor modifications of B expression in Sec.2 is shown to confirm a validity of following discussions on the boundary layer correction. Even for $L^*_{(-1)}\propto\delta_{\rm eff}^{3/2}$, the Shaing-Hokin theory still retains an accuracy of factor 2. Therefore we can investigate characteristics of the boundary layer correction on the parallel viscosity $N^*_{\rm (boundary)}$ with a weaker dependence on $\delta_{\rm eff}$ and $\varepsilon_{\rm H}$ by the analytical method. As confirmed in Ref.[17], we have to interpret a previous "$1/\nu$ regime" formula for the parallel viscosity derived by Shaing,et al.[3,4] and the N^* connection formulae including it (red solid curve in Fig.2(a)) as expressions for strong E_s/v limit (i.e., the ν regime or the $\nu^{1/2}$ regime discussed later). The correct $1/\nu$ regime ($E_s/v\approx 0$) value is given by adding a boundary layer correction term $N^*_{\rm (boundary)}$ which was neglected in Refs.[3,4]. Although the calculation of $N^*_{\rm (boundary)}$ in the QPS ($\partial\varepsilon_{\rm H}/\partial\theta\approx 1.5\partial\varepsilon_{\rm T}/\partial\theta$ and $\theta_{\rm M}$=±2.4rad) requires some minor modifications for Eq.(14) in Ref.[17], they will be reported in a separated article. In Fig.2(a), we showed the $1/\nu$ regime asymptotic value of N^* given by $N^{*\rm (sym)}+N^{*\rm (asym)}+N^*_{\rm (boundary)}$ [17]. It approximately predicts the numerical result for a weak radial electric ranges of $E_s/v<1\times 10^{-4}$T by the DKES.

4. Concluding remarks

The mono-energetic neoclassical viscosity coefficients are investigated in two low aspect stellarator configurations with contrasting design concepts. For M^*, $N^{*\rm (asym)}$, (σ_{Xa}, $G_{Xa}^{\rm (asym)}$) defined in Ref.[17] due to pure non-bounce-averaged motions [3,4], the validity of the analytically approximated formulas [8,17] has been confirmed even in the NCSX and in the QPS. In the two configurations, there are contrasting effects of the ripple-trapped/untrapped boundary layer at $\kappa^2\cong 1$ causing coupling effects between the bounce-averaged motion of ripple-trapped particles and the non-bounce-averaged motion of untrapped particles. The $1/\nu^{1/2}$ ripple diffusion $L^*_{(-1/2)}$ in the QA configurations is peculiar to the configurations with small ripples. In the ripple-trapped pitch angle range $0\le\kappa^2\le 1$ in these configurations, the $1/\nu^{1/2}$ component of the perturbed distribution function is not negligible compared with the small $1/\nu$ component. However, their effects on the ripple-untrapped pitch-angle range $\kappa^2>1$ is not important. In contrast to this, the boundary layer affects on this range $\kappa^2>1$ in configurations without quasi-axisymmetry and make other boundary layer corrections on the viscosity coefficients; $N^*_{\rm (boundary)}$ appearing in the $1/\nu$ regime ($E_s/v\approx 0$) and also $L^*_{\rm (boundary)}$ near the collisionality regime boundary between $1/\nu$ and plateau regimes. Even though the integration constant in $0\le\kappa^2\le 1$ is negligible compared with a large $1/\nu$ component, boundary layer effects as a driving force of $\propto(\delta_{\rm eff})^{1/2}$ for the flows in $\kappa^2>1$ is not negligible for the $\propto\nu^0$ component of the distribution function in these configurations without quasi-axisymmetry.

Acknowledgements

A main part of this work was done during one author (S.N.)'s visit to the Princeton Plasma Physics Laboratory (PPPL) and the Oak Ridge National Laboratory (ORNL) sponsored by the Graduate University for Advanced Studies (GUAS). A NIFS coordinated research program NIFS07KNXN103 also supports this work.

References

[1] S.P.Hirshman and D.J.Sigmar, Nucl.Fusion **21**, 1079 (1981)
[2] K.C.Shaing and J.D.Callen, Phys.Fluids **26**, 3315 (1983)
[3] K.C.Shaing, E.C.Crume,Jr.,et al., Phys.Fluids B **1**,148(1989)
[4] K.C.Shaing, B.A.Carreras et al., Phys.Fluids B**1**, 1663(1989)
[5] N.Nakajima and M.Okamoto, J.Phys.Soc.Jpn.**61**, 833 (1992)
[6] N.Nakajima, M.Okamoto, and M.Fujiwara. J.Plasma Fusion Res.**68**, 46 (1992)
[7] H.Sugama and W.Horton, Phys.Plasmas **3**, 304 (1996)
[8] H.Sugama and S.Nishimura, Phys.Plasmas **9**, 4637 (2002)
[9] D.J.Strickler, S.P.Hirshman, D.A.Spong, et al., Fusion Sci. Technol.**45**,15(2004)
[10] D.A.Spong, Phys.Plasmas **12**, 056114 (2005)
[11] W.I.van Rij and S.P.Hirshman, Phys.Fluids B **1**,563 (1989)
[12] Y.Nakamura, M.Yokoyama, N.Nakajima, et al., Fusion Sci.Technol. **50**, 457 (2006)
[13] D.R.Mikkelsen, H.Maassberg, M.C.Zarnstorff, et al., Fusion Sci.Technol. **51**,166 (2007)
[14] D.A.Spong, S.P.Hirshman, J.F.Lyon, et al., Nucl.Fusion **45**,918(2005)
[15] W.Zhu, S.A.Sabbagh, R.E.Bell, et al., Phys.Rev.Lett.**96**, 22002 (2006)
[16] W.A.Houlberg, K.C.Shaing, S.P.Hirshman, and M.C.Zarnstorff, Phys.Plasmas **4**, 3230 (1997)
[17] S.Nishimura, H.Sugama, and Y.Nakamura, Fusion Sci.Technol.**51**,61(2007)
[18] K.C.Shaing and J.D.Callen, Phys.Fluids **25**, 1012 (1982)
[19] H.E.Mynick, Phys.Fluids **26**, 1008 (1983)
[20] J.Todoroki, J.Phys.Soc.Jpn **8**, 2758 (1990)
[21] K.C.Shaing and S.A.Hokin, Phys.Fluids **26**, 2136 (1983)
[22] V.V.Nemov, S.V.Kasilov, W.Kernbichler, and M.F.Heyn, Phys.Plasmas **6**, 4622 (1999)
[23] S.Okamura, K.Matsuoka, S.Nishimura, et al., Nucl.Fusion **44**, 575 (2004)

Collisional transport of multi-ion-species plasmas in general non-symmetric toroidal configurations

S.Nishimura, H.Sugama, Y.Nakamura[a]

National Institute for Fusion Science, Oroshi-cho 322-6, Toki, 509-5292, Japan

[a] Graduate School of Energy Science, Kyoto University, Gokasho, Uji, 611-0011, Japan

A previous formulation of the neoclassical transport in helical/stellarator devices based on the moment equation approach is extended to allow the poloidal and toroidal variation of the densities and temperatures of $\delta n_a/n_a$, $\delta T_a/T_a < \delta B/B$. Since the transport of impurities with high collisionalities (so-called Pfirsch-Schlüter diffusions which are separated in our previous works) is determined by the local parallel force balance before the flux-surface averaging including these variations δn_a, δT_a an important purpose of this extension is to study radial profiles of the impurity density under the self-consistent ambipolar radial electric field E_r in plasmas containing electrons and main ions corresponding to the collisionless ($1/\nu$, ν, or banana) regimes or the plateau regime, and impurity ions in the Pfirsch-Schlüter regime. The Legendre-Laguerre expansion with orders of l=0,1 and j=0,1,2 is used for this local momentum balance to include the energy scattering collisions and the effect of the radial electric field in non-symmetric toroidal plasmas.

Keywords: neoclassical transport, multi-ion-species, impurity transport, moment equation approach, drift kinetic equation, non-symmetric toroidal plasmas

1. Introduction

Recently, various types of high-density operations are studied in helical/stellarator devices [1,2] and the neoclassical processes on the impurity transport in these high-density conditions also attract much attention [1,3]. Although codes based on the so-called moment equation approach [4] are used for this kind of studies in axisymmetric tokamaks, codes to handle multi-ion-species plasmas in the helical/stellarator devices are still under developments. Even though a method to obtain the neoclassical transport matrix in general multi-ion-species plasmas in general non-symmetric toroidal configurations had been shown [5], it handled only a part relating to the flux surface averaged part of the momentum balance $\langle \mathbf{B}\bullet\nabla\bullet\boldsymbol{\pi}_a\rangle - e_a\langle n_a\rangle\langle BE_{//}\rangle = \langle BF_{//a1}\rangle$. We had not shown any method to handle the poloidally and toroidally varying part (local structure) of the momentum balance and flows $n_a u_{//a}$, $q_{//a}$ before the flux-surface averaging. In this momentum balance, the densities n_a and temperatures T_a of each particle species (a = e^-, H^+, D^+, T^+, He^+, He^{2+}, …) are not flux surface quantities. Although the poloidal and toroidal variations of the potential are small because of a constraint by the total energy conservation to minimize the Joule loss $\mathbf{J}\bullet\mathbf{E}$, the density and temperature perturbations δn_a, δT_a are not limited by this constraint. Only the total pressure $\Sigma p_a = \Sigma n_a T_a$ can be the flux surface quantity in the MHD equilibrium. In a present study, we extend the stellarator moment equation approach [5] to allow the poloidal and toroidal variation of the densities and temperatures of $\delta n_a/n_a$, $\delta T_a/T_a < dB/B$. The theory for the "neoclassical transport of impurities"[6] in general toroidal plasmas including full parts of collisional diffusions and neoclassical parallel flows is completed by this extension. Since the parallel force balance including the variation δn_a, δT_a determines the transport of impurities with high collisionalities (so-called Pfirsch-Schlüter diffusions which are separated in our previous works), an important purpose of this extension is to study radial profiles of the impurity density (accumulation or shielded "hole") under the self-consistent ambipolar radial electric field E_r in plasmas containing electrons and main ions corresponding to the collisionless ($1/\nu$, ν, or banana) regimes or the plateau regime, and impurity ions in the Pfirsch-Schlüter(P-S) regime.

author's e-mail: nishimura.shin@lhd.nifs.ac.jp

2. Moment Equations

Although the moment equations for the poloidally and toroidally varying part must be derived from the Vlasov-Fokker-Planck equation [7], we will report details of this derivation in separated articles. Also on the flux surface averaged part of momentum balance, which is basically unchanged from Ref.[5] even in the extension of the theory except replacing $u_{//a}$ by $n_a u_{//a}/\langle n_a\rangle$, the details will not be described here. We show here only the essential part of the results on the poloidally and toroidally varying part. By taking the Legendre-Laguerre moments of the orders of l=0,1 and j=0,1,2 of a part of the linearized drift kinetic equation (LDKE) after separating σ_{Xa} as a source of the flux surface averaged part of the momentum balance [5], we obtain following equations. Hereafter, notations in Ref.[5] are followed. Furthermore we concentrate in this paper only in the local momentum balance in which the flux surface averaged components of flows and forces are subtracted. The particle and momentum conservation laws, which are the Legendre-Laguerre moments of the LDKE with orders of l=0 and j=0,1,2, are given by

$$\langle p_a\rangle \begin{bmatrix} 1 & 0 & 0 \\ 0 & \frac{5}{2} & 0 \\ 0 & 0 & \frac{35}{8} \end{bmatrix} \nabla\bullet \begin{bmatrix} n_a \mathbf{u}_{\| a}/\langle n_a\rangle \\ \frac{2\mathbf{q}_{\| a}}{5\langle p_a\rangle} \\ n_a \mathbf{u}_{\| a2}/\langle n_a\rangle \end{bmatrix}$$

$$+\langle n_a\rangle \begin{bmatrix} 1 & 0 & 0 \\ -1 & \frac{3}{2} & 0 \\ 1 & -\frac{3}{2} & \frac{15}{8} \end{bmatrix} \left[cE_s \frac{\nabla s\times\mathbf{B}}{\langle B^2\rangle} + u_{\|}^{(\mathrm{rigid})}\mathbf{b} \right]\bullet\nabla \begin{bmatrix} \frac{\langle T_a\rangle}{\langle n_a\rangle} n_{a1}^{(j=0)} \\ T_{a1}^{(j=1)} \\ \frac{\langle T_a\rangle}{\langle n_a\rangle} n_{a1}^{(j=2)} \end{bmatrix}.$$

$$-\sum_b \begin{bmatrix} 0 & 0 & 0 \\ 0 & e_{11}^{ab} & 0 \\ 0 & -e_{11}^{ab} & e_{22}^{ab} \end{bmatrix} \begin{bmatrix} n_{b1}^{(j=0)}\langle T_b\rangle/\langle n_b\rangle \\ T_{b1}^{(j=1)} \\ n_{b1}^{(j=2)}\langle T_b\rangle/\langle n_b\rangle \end{bmatrix}$$

$$= \frac{c}{e_a}\nabla s\times\mathbf{B}\bullet\nabla\frac{1}{B^2} \begin{bmatrix} \langle T_a\rangle\left(\partial\langle p_a\rangle/\partial s + e_a\langle n_a\rangle\partial\langle\Phi\rangle/\partial s\right) \\ \frac{5}{2}\langle p_a\rangle\partial\langle T_a\rangle/\partial s \\ 0 \end{bmatrix} \tag{1}$$

The parallel force balances, which are the Legendre-Laguerre moments of the LDKE with orders of l=0 and j=0,1,2, are given by

$$\langle n_a\rangle \begin{bmatrix} 1 & 1 & 0 \\ 0 & \frac{5}{2} & \frac{5}{2} \\ 0 & 0 & \frac{35}{8} \end{bmatrix} \mathbf{b}\bullet\nabla \begin{bmatrix} \frac{\langle T_a\rangle}{\langle n_a\rangle} n_{a1}^{(j=0)} \\ T_{a1}^{(j=1)} \\ \frac{\langle T_a\rangle}{\langle n_a\rangle} n_{a1}^{(j=2)} \end{bmatrix} . \tag{2}$$

$$= \begin{bmatrix} F_{\| a1} \\ F_{\| a2} \\ F_{\| a3} \end{bmatrix} \equiv \sum_b \begin{bmatrix} l_{11}^{ab} & -l_{12}^{ab} & l_{13}^{ab} \\ -l_{21}^{ab} & l_{22}^{ab} & -l_{23}^{ab} \\ l_{31}^{ab} & -l_{32}^{ab} & l_{33}^{ab} \end{bmatrix} \begin{bmatrix} n_b u_{\| b}/\langle n_b\rangle \\ \frac{2q_{\| b}}{5\langle p_b\rangle} \\ n_b u_{\| b2}/\langle n_b\rangle \end{bmatrix}$$

In Eqs.(1)-(2), the energy scattering coefficients e_{ij}^{ab} and the friction coefficients l_{ij}^{ab} are calculated by the coefficients $M_{ab}^{ij}, N_{ab}^{ij}, P_{ab}^{ij}$ and Q_{ab}^{ij} which are listed in Eqs.(4.8)-(4.17),(5.21),(5.22) and (6.6)-(6.12) in Ref.[6]. In contrast to the flux surface averaged part of the momentum balance in Ref [5] using the 13M approximation, we included the Laguerre order of j=2 following the tokamak P-S transport theory [6]. An important purpose of this approximation is to include the energy scattering collision effects [6] and also the E×B drift effect in Eq.(1), which is peculiar to non-symmetric toroidal configurations. These effects were not included previous formulations for the multi-ion-species plasmas in Refs.[8,9] based on the 13M approximation. Eq.(1) includes $u_{//}^{(\mathrm{rigid})}\mathbf{b}\bullet\nabla$ corresponding to the parallel velocity of the moving frame in which the adiabatic invariant $\mu\equiv m_a v_\perp^2/2B$ and parallel particle velocity $v_\| = \pm v(1-\mu B/w)^{1/2}$, where $w\equiv m_a v^2/2$, are defined [10,11]. In general non-symmetric toroidal plasmas this velocity is given by

$$u_\|^{(\mathrm{rigid})} \equiv \frac{BcE_s}{2\chi'\psi'}\left(\frac{\psi' B_\zeta - \chi' B_\theta}{\langle B^2\rangle} + \frac{V'}{4\pi^2}H_2 \right) . \tag{3}$$

Here, H_2 is a constant on the flux surface used in Ref.[12]. This term vanish in symmetric configurations as follows and thus the present theory automatically includes the rigid rotation of the symmetric plasmas [4,6]. In symmetric configurations, there are only Fourier modes (m,n) of B and distribution functions satisfying

$$\frac{\chi' m + \psi' n}{\chi' m - \psi' n} = \mathrm{const} \equiv \frac{\chi' L + \psi' N}{\chi' L - \psi' N} . \tag{4}$$

In these cases, H_2, $u_\|^{(\mathrm{rigid})}$, and ($u_\|^{(\mathrm{rigid})}\mathbf{b}$ +$cE_s\nabla s\times\mathbf{B}/\langle B^2\rangle$)•∇ become

$$H_2^{(\mathrm{symmetric})} = \frac{\chi' L + \psi' N}{\chi' L - \psi' N}, \qquad u_\|^{(\mathrm{rigid})} = \frac{BcE_s}{\langle B^2\rangle}\frac{B_\zeta L + B_\theta N}{\chi' L - \psi' N}$$

$$\left(u_\|^{(\mathrm{rigid})}\mathbf{b} + cE_s\frac{\nabla s\times\mathbf{B}}{\langle B^2\rangle} \right)\bullet\nabla = \frac{cE_s}{\langle B^2\rangle\sqrt{g}} \begin{bmatrix} \frac{B_\zeta L + B_\theta N}{\chi' L - \psi' N}\left(\chi'\frac{\partial}{\partial\theta} + \psi'\frac{\partial}{\partial\zeta} \right) \\ -\left(B_\zeta\frac{\partial}{\partial\theta} - B_\theta\frac{\partial}{\partial\zeta} \right) \end{bmatrix} \tag{5}$$

This operator vanishes for the "symmetric" Fourier components of ∝cos($m\theta-n\zeta$) and ∝sin($m\theta-n\zeta$) satisfying Eq.(4).

In Eq.(2), we do not include the poloidally and toroidally varying part of the parallel electric field determined by the charge neutrality [13]. A reason of it is that we cannot forbid an existence of l=0, j≥3 components in the electron distribution functions and in the electron force balance since we assume here cases with sufficiently high electron temperatures [1-3] giving long mean free paths of the electrons ($\tau_{ee}v_{Te}$>>L_c) even if the collisionality of the ions including the impurities may correspond to the P-S regime. When we allow the existence of l=0, j≥3 components in the electron distribution, the problem described by Eqs.(1)-(3) is not closed. In these cases with sufficiently electron temperatures, however, we can close this problem by the charge neutrality without the parallel electric field instead

author's e-mail: nishimura.shin@lhd.nifs.ac.jp

of including the higher order Laguerre terms. Although this procedure for the moment closure will be reported in a separated article, the conclusion of it is only replacing the friction coefficients $l^{\mathrm{ea}}_{3j} = l^{ae}_{j3}$ in Eq.(2) by other newly defined friction coefficients $\lambda^{\mathrm{e}a}_{3j} = \lambda^{a\mathrm{e}}_{j3}$. In Eq.(1), the resulting P-S current under this charge neutrality, which should be a function only of total pressure gradient, is independent of the density and temperature perturbations δn_a, δT_a of individual species. By the momentum conservation of the friction forces, the total pressure perturbation given by Eq.(2) satisfies $\sum_a p^{\mathrm{PS}}_{a1} = \sum_a \left[\langle T_a \rangle n^{(j=0)}_{a1} + \langle n_a \rangle T^{(j=1)}_{a1} \right] = 0$ (the total pressure is a flux surface quantity).

3. Numerical Examples

The problem described by Eqs.(1)-(3) including the replacement of $l^{\mathrm{ea}}_{3j} = l^{a\mathrm{e}}_{j3}$ by $\lambda^{\mathrm{e}a}_{3j} = \lambda^{a\mathrm{e}}_{j3}$ can be solved by a Fourier expansion method in the Boozer coordinates. In this section, we show a numerical example of the solution. By solving this problem, we can obtain the P-S diffusion coefficients defined by [5, 9],

$$\begin{bmatrix} \Gamma^{\mathrm{PS}}_a \\ q^{\mathrm{PS}}_a / T_a \end{bmatrix} = -\frac{c}{e_a} \begin{bmatrix} \langle \widetilde{U} F_{\parallel a1} \rangle \\ \langle \widetilde{U} F_{\parallel a2} \rangle \end{bmatrix} \equiv \sum_b \begin{bmatrix} (L^{\mathrm{PS}})^{ab}_{11} & (L^{\mathrm{PS}})^{ab}_{12} \\ (L^{\mathrm{PS}})^{ab}_{21} & (L^{\mathrm{PS}})^{ab}_{22} \end{bmatrix} \begin{bmatrix} X_{b1} \\ X_{b2} \end{bmatrix}. \quad (6)$$

The function $\widetilde{U}(\theta,\zeta)$ is defined in Appendix A in Ref.[5], and thermodynamic forces corresponding to radial gradients of the pressures and temperatures X_{a1}, X_{a2} also are defined in Eq.(10) in Ref.[5]. The Onsager symmetry $(L^{\mathrm{PS}})^{ba}_{ji} = (L^{\mathrm{PS}})^{ab}_{ij}$ is satisfied by the symmetric relations of the collision coefficients $e^{ba}_{ji} = e^{ab}_{ij}$ and $l^{ba}_{ji} = l^{ab}_{ij}$ [6], and the intrinsic ambipolar condition of Γ^{PS}_a also is satisfied by the momentum conservation of the friction. Because of the stellarator symmetry $B(-\theta,-\zeta)=B(\theta,\zeta)$, these coefficients are even functions of the radial electric field strength E_r. Figure.1 shows an example of the results. In this example, following Refs.[5,12], the magnetic field assumed there is that with $B=B_0[1-\varepsilon_t \cos\theta_B + \varepsilon_h \cos(L\theta_B - N\zeta_B)]$, $L=2$, $N=10$, $B_0=1$T, $\chi'=0.15$T·m, $\psi'=0.4$T·m, $B_\theta=0$, and $B_\zeta=4$T·m. The contained ion assumed here is a mixture of protons (H^+) and fully ionized neon (Ne^{10+}), which is used for the charge exchange spectroscopic measurements and the impurity transport studies in the Large Helical Device (LHD) [3], with an ion density ratio corresponding to $Z_{\mathrm{eff}}=5.74$, and the assumed temperatures are $T_e = T_i = 1$keV. With these assumptions, a dependence of the diffusion coefficients on the density in a range of $n_e \leq 5\times10^{20}\mathrm{cm}^{-3}$ (up to the "SDC" [2] density regime) is investigated here. The mean free path of electron-electron collision is $v_{\mathrm{Te}}\tau_{\mathrm{ee}}=28.3$m corresponding to the plateau regime even at $n_e=5\times10^{20}\mathrm{cm}^{-3}$.

author's e-mail: nishimura.shin@lhd.nifs.ac.jp

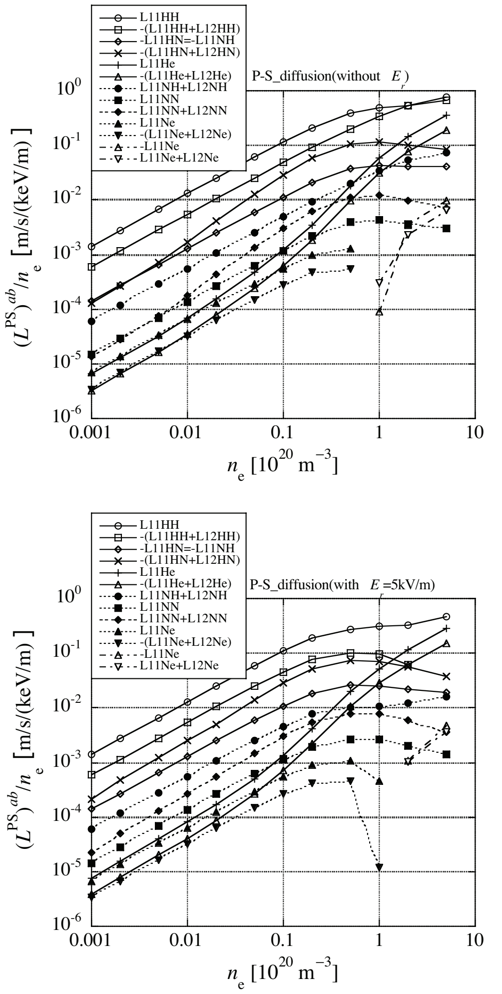

Fig.1 The impurity (Ne^{10+}) diffusion coefficients in (a) cases with energy scattering collision effects e^{ab}_{ij} and without the radial electric filed (E_r=0), (b) cases with both of the energy scattering collisions and a finite radial electric field of E_r =5kV/m.
The collisionless limit of $n_e=10^{17}\mathrm{m}^{-3}$ in (a) coincides with the 13M approximation [8,9] without both effects. The particle species are denoted by e ($a,b=e^-$), H ($a,b=H^+$), and N ($a,b=Ne^{10+}$) in these figures.

Since Eq.(6) includes full non-diagonal coupling terms between particles species, there are 21 P-S diffusion coefficients even in this simple 2-ion-species model. We show here only coefficients relating to ion particle diffusions (i.e., $a=H^+$, Ne^{10+} and $b=e^-$, H^+, Ne^{10+}), since a main application area of the P-S transport is the impurity transport studies in high-density operations. It is well known that neoclassical theory without the temperature gradient terms predicts a "pessimistic" impurity accumulation but the temperature gradient terms prevent it. Although the final goal of the impurity transport studies is determining the steady-state impurity density profile including not only Γ^{PS}_a but also the banana-plateau and ripple diffusion fluxes Γ^{bn}_a and the classical diffusion fluxes $\Gamma_a^{\rm cl}$, such a calculation is complicated. We show here only comparison of the density gradient terms $(L^{\rm PS})_{11}^{ab}$ and the temperature gradient terms $(L^{\rm PS})_{11}^{ab}+(L^{\rm PS})_{12}^{ab}$ in $\Gamma_a^{\rm PS}$ as the component tests. In Fig.1(a) without the radial electric field (E_r=0), we can see the effects of the energy scattering collisions by deviations from pure $\propto n_e$ scaling given by the 13M-moment approximation in Refs.[8,9]. It enlarges the negative value of (L11HN+L12HN) and positive value of (L11NH+L12NH). It also reduces the positive value of L11HH at $n_e>10^{20}{\rm m}^{-3}$. These are favorable tendencies in viewpoint of the impurity control. We can see also an increase and an invert of ion diffusions driven by electron temperature gradient in this high-density range, which indicate an importance of the electron temperature controls in for the impurity controls. The finite radial electric field effects with E_r=5keV/m on these diffusion coefficients are only changes of order of unity as in Fig.1 (b) since Eqs.(1)-(3) make the P-S current independent of Er. Because of this characteristic the relative flow velocities between particle species $u_{//a}-u_{//b}$ determining the friction forces $F_{//a1}$ are insensitive even when the absolute values of the flow velocities of individual species are largely changed by the E×B term in Eq.(1). Nevertheless, there are non-negligible effects in view point of impurity density profiles determined by balances of temperature gradient terms and the density gradient terms. The aforementioned increases of (L11HN+L12HN) and (L11NH+L12NH) are enhanced by a radial electric field effect at ne~10^17m-3. The radial electric field effect at $n_e>10^{20}{\rm m}^{-3}$ is complicated. These coefficients are reduced by the radial electric field at $n_e>10^{20}{\rm m}^{-3}$ and thus the ion temperature gradient is not effective for the impurity control in this high density limit with finite radial electric fields. In this condition, controls of density and temperature profiles of the electron will be more important.

4. Concluding Remarks

By adding this poloidally and toroidally varying part of the momentum equations to a previously formulation handling the flux-surface averaged part [5], the development of the “non-symmetric version of NCLASS” [12] based on the concept of “stellarator moment equation approach” toward a future integrated simulation system [14] is almost completed in viewpoint of the “basic framework”. (Although there are still many remaining technical problems on the viscosity coefficients in the flux-surface averaged part, this topic is discussed in another presentation in this conference P2-017). In non-symmetric configurations, a dependence of the P-S diffusions $\Gamma_a^{\rm PS}$, $q_a^{\rm PS}$ and the accompanied δn_a, δT_a on the E_r is predicted. Since a cause of this dependence on the E_r is the viscous damping of the “rigid rotation”, it also should be noted that the basic idea of this theory is applicable to tokamaks with the rotation damping due to the symmetry-breaking by MHD activities, and so on [15]. It also should be noted that the plasma rotation assumed in Eq.(3), resulting density perturbations in Eqs.(1)-(2), and the assumed electro-static potential being a flux surface quantity are consistent with previous experimental results.[16-17]

author’s e-mail: nishimura.shin@lhd.nifs.ac.jp

Acknowledgements

The authors thank Drs. Noriyoshi Nakajima, Kimitaka Itoh, Katsumi Ida, Mikirou Yoshinuma, Dave Mikkelsen, Mike Zarnstorff, Don Spong, Steve Hirshman, Masa Ono, Masayoshi Taguchi, and Rainer Burhenn for suggestions and discussions relating to this topic. The National Institute for Fusion Science (NIFS) coordinated research programs NIFS07KNXN103 and NIFS06KUHL007 also support this work.

References

[1] R.Burhenn, et al., Fusion Sci.Technol. **46**, 115 (2004)
[2] N.Ohyabu, T.Marisaki, S.Masuzaki, et al., Phys.Rev.Lett.**97**, 055002 (2006)
[3] Y.Nakamura, Y.Takeiri, R.Kumazawa, et al, Nucl.Fusion **43**, 219 (2003)
[4] W.A.Houlberg, K.C.Shaing, S.P.Hirshman, and M.C.Zarnstorff, Phys.Plasmas **4**, 3230 (1997)
[5] H.Sugama and S.Nishimura, Phys.Plasmas **9**, 4637 (2002)
[6] S.P.Hirshman and D.J.Sigmar, Nucl.Fusion **21**,1079 (1981)
[7] R.D.Hazeltine and J.D.Meiss, *Plasma Confinement* (Addison-Wesley, CA, 1992), p.196
[8] M.Taguchi, Phys.Fluids B **4**, 3638 (1992)
[9] H.Sugama and W.Horton, Phys.Plasmas **3**, 304 (1996)
[10] R.D.Hazeltine and A.A.Ware, Plasma Phys. **20**, 673(1978); R.D.Hazeltine and F.L.Hinton, Phys.Plasmas **12**, 102506 (2005)
[11] F.L.Hinton and S.K.Wong, Phys.Fluids **28**, 3082 (1985); H.Sugama and W.Horton, Phys.Plasmas **4**, 2215 (1997)
[12] S.Nishimura, H.Sugama, and Y.Nakamura, Fusion Sci.Technol.**51**, 61 (2007)
[13] R.D.Hazeltine and F.L.Hinton, Phys.Fluids **16**,1883 (1973)
[14] Y.Nakamura, M.Yokoyama, N.Nakajima, et al., Fusion Sci.Technol. **50**, 457 (2006)
[15] W.Zhu, S.A.Sabbagh, R.E.Bell, et al., Phys.Rev.Lett.**96**, 22002 (2006)
[16] K.Ida, T.Minami, et al., Phys.Rev.Lett. **86**, 3040 (2001); M.Yoshinuma, K.Ida, et al., in 16th International Stellarator Workshop (Toki, Japan, Oct.15-19, 2007)
[17] S.Nishimura, K.Ida, M.Osakabe, et al., Phys.Plasmas **7**, 437 (2000)
[18] K.Ida, A.Fujisawa, H.Iguchi, et al.,Phys.Plasmas **8**,1(2001)

Monte-Carlo Simulation of Neoclassical Transport in Magnetic Islands and Ergodic Region

Ryutaro KANNO[1,2], Masanori NUNAMI[3], Shinsuke SATAKE[1], Hisanori TAKAMARU[4], Yukihiro TOMITA[1,2], Keisuke NAKAJIMA[2], Masao OKAMOTO[4] and Nobuyoshi OHYABU[1,2]

[1]*National Institute for Fusion Science, Toki 509-5292, Japan*

[2]*Department of Fusion Science, Graduate University for Advanced Studies, Toki 509-5292, Japan*

[3]*Institute of Laser Engineering, Osaka University, Suita 565-0871, Japan*

[4]*Department of Computer Science, Chubu University, Kasugai 487-8501, Japan*

It is shown in Large Helical Device experiments that the transport modeling based only on the fluid description is not sufficient for expressing edge transport phenomena in a magnetic island. Existence of a bootstrap current around the island is strongly suggested. On the other hand, in recent tokamak experiments it is found that so-called stochastic diffusion theory based on the "field line diffusion" over estimates the radial energy transport in the collisionless edge plasma affected by resonant magnetic perturbations, though the perturbations induce a chaotic behavior in the field lines. These results imply that the conventional modeling of the edge transport should be reconsidered for a lower-collisionality case. In order to take a new look at the modeling of the edge transport, we investigate neoclassical effect on the transport in magnetic islands and ergodic region. By using a drift kinetic equation solver without an assumption of existence of nested flux surfaces (the KEATS code), it is possible for us to execute the investigation. The simulation results show that the radial energy flux of ions for a lower-collisionality case is quite small compared to the prediction of the stochastic diffusion theory, while the flux for a high-collisionality case is consistent with the prediction.

Keywords: neoclassical transport, edge plasma, magnetic island, ergodic region, Monte-Carlo simulation

1 Introduction

It is shown in Large Helical Device (LHD) experiments that the transport modeling based only on the fluid description is not sufficient for expressing edge transport phenomena in a magnetic island [1, 2, 3]. This result is given in the experiments of observing the healing of the $m/n = 1/1$ magnetic island in the edge, where m and n are the poloidal and toroidal mode numbers, respectively. A current depending on the pressure gradient (i.e. the bootstrap or Pfirsch-Schlüter current) is expected to explain the healing in the experiments. In results of a simulation study based on the fluid description [4], the healing phenomenon is not explained by the Pfirsch-Schlüter current only. The important role of a bootstrap current in the edge region is strongly suggested, and thus the kinetic modeling of the edge plasma is needed for understanding of the edge transport phenomena, where in the LHD experiments the temperature is $\gtrsim$500 eV and the plasma density $\sim 10^{19}$ m^{-3} in the island.

On the other hand, in recent tokamak experiments it is found that so-called stochastic diffusion theory based on the "field line diffusion" [5, 6] over estimates the radial energy transport in the edge region added resonant magnetic perturbations (RMPs) [7, 8]. This fact is discovered in the experiments of ELMs (edge localized modes) suppression by means of RMPs in collisionless tokamak plasmas [7, 8]. (Historically, the idea of suppressing the ELMs and controlling the edge transport by using RMPs has been proposed about 20 years ago [9].) When the RMPs induce a chaotic behavior in the field lines, the stochastic diffusion theory predicts that a thermal diffusivity is given as $\chi^a_{\mathrm{ql}} = \chi^a_{\parallel}|\delta B_{\mathrm{r}}/B_{\mathrm{t}}|^2$ or $v^a_{\mathrm{th}}\pi R_{\mathrm{ax}} q|\delta B_{\mathrm{r}}/B_{\mathrm{t}}|^2$ for the collisional or collisionless limit, where a is a particle species, $\chi^a_{\parallel} = 3.91 T_a \tau_a/m_a$ the parallel diffusivity, T_a the temperature, τ_a the collision time, m_a the particle mass, v^a_{th} the thermal velocity, R_{ax} the major radius of the magnetic axis, q the safety factor, δB_{r} the strength of RMPs, and B_{t} the toroidal component of the magnetic field. This prediction has been demonstrated in experiments on high-collisional tokamak plasmas [10]. However, in collisionless plasmas, the experimental thermal diffusivity χ_{ex} is inconsistent with the prediction of the stochastic diffusion theory, e.g. $\chi^{\mathrm{e}}_{\mathrm{ql}}/\chi^{\mathrm{e}}_{\mathrm{ex}} \gg 10$ for the electron thermal diffusivity [8]. Small RMPs cause the complete suppression of the ELM events, and have a negligible effect on the energy confinement.

The above experimental results in torus plasmas imply that the conventional modeling of the edge transport should be reconsidered for a lower-collisionality case. There is no established theory describing radial transport in magnetic islands and ergodic region. In order to take a new look at the modeling of the edge transport, we investigate

author's e-mail: kanno@nifs.ac.jp

neoclassical effect on the transport in magnetic islands and ergodic region. Here, even in the three dimensional field line structure disturbed by RMPs, the Coulomb collision causes the transition between a passing particle orbit and a trapped particle orbit in toroidal and helical ripples (localized and/or blocked particle orbits) [11]; in the present paper we call it the neoclassical effect on the edge transport phenomena. Recently, we develop a new transport simulation code without an assumption of existence of nested flux surfaces; the code is named "KEATS" [12, 13]. The code is programmed by expanding a well-known Monte-Carlo particle simulation scheme based on the δf method [14, 15]. By using the KEATS code, it is possible for us to execute the investigation. In this paper we show the simulation results, applying the code to a torus plasma having the ergodic region in the edge.

2 Simulation Model

We consider that a guiding center distribution function of plasma f is separated into an equilibrium-like background f_0 and a kinetic part δf of the distribution, $f = f_0 + \delta f$, where the kinetic part δf is considered as a small perturbation from f_0. The zeroth-order distribution function f_0 is given as a local Maxwellian distribution $f_0 = f_{\mathrm{M}}(\boldsymbol{x}, \xi, v) = n\{m/(2\pi T)\}^{3/2} \exp\{-mv^2/(2T)\}$, where $\xi = v_\parallel / v$ is the cosine of the pitch angle, $v_\parallel = \boldsymbol{v} \cdot \boldsymbol{b}$, $\boldsymbol{b} = \boldsymbol{B}/B$ the unit vector along a field line, $\boldsymbol{B}$ a magnetic field, $B = |\boldsymbol{B}|$, $v = |\boldsymbol{v}|$, $n = n(\boldsymbol{x})$ the density, m the particle mass, and $T = T(\boldsymbol{x})$ the temperature. Applying the decomposition $f = f_{\mathrm{M}} + \delta f$ to the drift kinetic equation, we have the following equation of the kinetic part δf:

$$\frac{\mathrm{D}}{\mathrm{D}t}\delta f = -\left\{\boldsymbol{v}_{\mathrm{d}} \cdot \nabla f_{\mathrm{M}} - C_{\mathrm{F}} f_{\mathrm{M}}\right\}, \tag{1}$$

where the operator $\mathrm{D}/\mathrm{D}t$ is defined as $\mathrm{D}/\mathrm{D}t := \partial/\partial t + (\boldsymbol{v}_\parallel + \boldsymbol{v}_{\mathrm{d}}) \cdot \nabla - C_{\mathrm{T}}$, $\boldsymbol{v}_\parallel = v_\parallel \boldsymbol{b}$ the parallel velocity, and $\boldsymbol{v}_{\mathrm{d}}$ the drift velocity of guiding center motion. The test particle collision operator C_{T} is given, for simplicity, as

$$C_{\mathrm{T}} = \frac{\nu_{\mathrm{def}}}{2} \frac{\partial}{\partial \xi} \left(1 - \xi^2\right) \frac{\partial}{\partial \xi}, \tag{2}$$

and it can be implemented numerically by random kicks in velocity space [16], which represents the Coulomb scattering process, where ν_{def} is the deflection frequency. Here, we should note statistical accuracy of the operator C_{T} expressed by the Monte-Carlo method [16], in particular, around $|\xi| \approx 1$. The operator C_{F} is the field particle collision term, which represents local momentum conservation (C_{F} is needed to treat accurately the parallel transport):

$$C_{\mathrm{F}} = \nu_{\mathrm{def}} \frac{m}{T} \boldsymbol{v} \cdot \boldsymbol{u}_0, \tag{3}$$

and $\boldsymbol{u}_0$ is given as

$$\boldsymbol{u}_0 = \int \mathrm{d}^3 v\, \nu_{\mathrm{def}}\, \boldsymbol{v}\, \delta f \Bigg/ \int \mathrm{d}^3 v\, \nu_{\mathrm{def}} \frac{mv^2}{3T} f_{\mathrm{M}}. \tag{4}$$

In general, effects of neutrals and an electric field are important in the edge transport, but in the present paper these effects are neglected for simplicity. (The modeling of a fluctuating field in the KEATS code is described in Refs. [13, 17].)

To solve Eq. (1) by Monte-Carlo techniques, we adopt the two-weight scheme of the δf formulation [14, 15]. In evolution of the δf part, the background f_{M} is assumed to be fixed because the background is in a quasi steady-state from the viewpoint of the δf part. The Monte-Carlo simulation code, KEATS, is programmed in an Eulerian coordinate system, i.e. so-called helical coordinates [4], thus the code does not need magnetic flux coordinates. Simulation results (e.g. estimation of particle and energy fluxes) of the KEATS code for a case of a simple tokamak field are agreed with ones of the "FORTEC-3D" code [15] which uses magnetic flux coordinates.

3 Simulation Results

For the investigation of neoclassical effect on the transport in the ergodic region, we use a magnetic configuration which is formed by adding RMPs into a simple tokamak field having concentric circular flux surfaces, where the major radius of the magnetic axis $R_{\mathrm{ax}} = 3.6$ m, the minor radius of the plasma $a = 1$ m, and the magnetic field strength on the axis $B_{\mathrm{ax}} = 4$ T. The Poincaré plots of the magnetic field lines on a poloidal cross section are shown in Fig.1. One can see the ergodic region in $r/a = 0.7 \sim 1$, where $r = \sqrt{(R - R_{\mathrm{ax}})^2 + Z^2}$. In the KEATS code, the number of test particles is $N_{\mathrm{TP}} = 16,000,000$.

To investigate effect of the existence of the ergodic region on the transport phenomena, we evaluate the ion energy flux $\boldsymbol{Q}_{\mathrm{i}}$ in two cases, i.e., in the configurations (a) having lower edge temperature $T_{\mathrm{edge}} \sim 200$ eV at a center of the ergodic region and (b) having higher edge temperature $T_{\mathrm{edge}} \sim 1$ keV. The temperature profile is given as $T_{\mathrm{i}} = T_{\mathrm{ax}}\{0.02 + 0.98 \exp[-4(r/a)^\alpha]\}$ with $T_{\mathrm{ax}} = 2$ keV and $\alpha = 2.5$ (case (a)) or 7.86 (case (b)), which neglects the existence of the ergodic region. The density profile is set homogeneous, $n_{\mathrm{i}} = \mathrm{const.} = 1 \times 10^{19}\ \mathrm{m}^{-3}$. The background f_{M} is fixed in the calculations. The radial profiles of the energy flux estimated from the KEATS computations for two cases (a) and (b) are shown in Figs.2a and b, respectively. For simplicity, the radial energy fluxes are given neglecting the existence of the ergodic region, because we have no magnetic coordinate system including several magnetic field structures as the core and ergodic regions. The energy flux $\boldsymbol{Q}_{\mathrm{i}}$ is averaged over concentric circular shell region in the whole toroidal angles as if there were nested flux surfaces. Here, in the KEATS computations the energy flux $\boldsymbol{Q}$ is given as

$$\boldsymbol{Q}(t, \boldsymbol{x}) = \overline{\int \mathrm{d}^3 v \frac{mv^2}{2} (\boldsymbol{v}_\parallel + \boldsymbol{v}_{\mathrm{d}}) \delta f}, \tag{5}$$

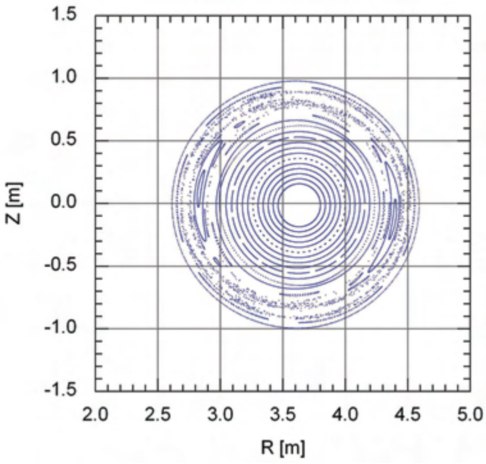

Fig. 1 Poincaré plots of magnetic field lines on a poloidal cross section.

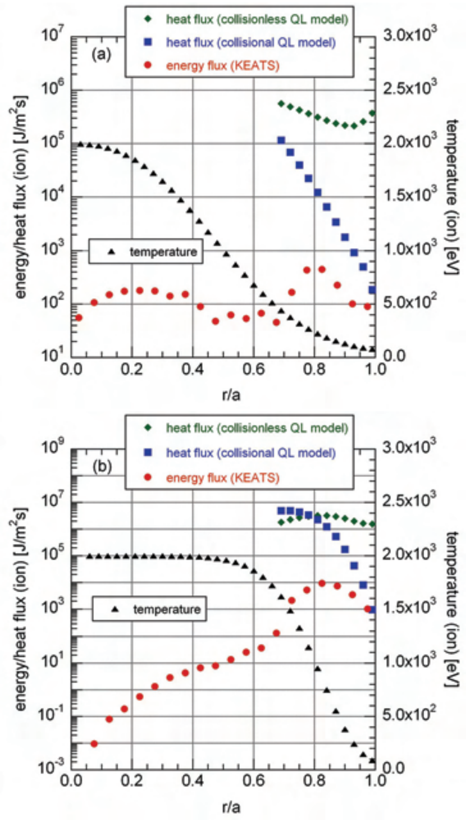

Fig. 2 Radial profiles of ion energy/heat flux for (a) lower and (b) higher edge temperatures, where $r = \sqrt{(R - R_{\rm ax})^2 + Z^2}$. The collisionless (or collisional) quasi-linear (QL) model means the prediction of the stochastic diffusion theory for the collisionless (or collisional) case.

where $\overline{\cdots}$ means the time-average, and the averaging time is longer than the typical time-scale of δf. The heat flux predicted by the stochastic diffusion theory is given as $\boldsymbol{q}_{\rm ql} = n\chi_{\rm ql}\nabla T$. From the results of the KEATS code, we find that the ion energy flux is affected by the RMPs, but the flux in the lower-collisionality region around $r/a \approx 0.8$ is quite small compared with the prediction of the stochastic diffusion theory, shown in both cases (a) and (b). On the other hand, in the high-collisionality region around $r/a \approx 1$, the flux is consistent with the prediction. These results can be explained theoretically, see Appendix.

4 Summary

We have been developing the neoclassical transport code, KEATS, to study the transport phenomena in the islands and ergodic region. We apply the code to the edge disturbed by resonant magnetic perturbations, and find that the ion energy flux estimated by the KEATS code for a lower-collisionality case is quite small compared to the prediction of the stochastic diffusion theory based on the "field line diffusion," while the flux for a high-collisionality case is consistent with the prediction.

Acknowledgements

This work was performed with the support and under the auspices of the NIFS Collaborative Research Program NIFS06KLDD007, NIFS06KTAT018 and NIFS07KTAD001, and was also supported by MEXT. HAITEKU(2004) and the 2006-2007 JIFT exchange program.

Appendix. Stochastic Analysis of Radial Transport in a Perturbed Field

A fluid equation in a steady-state corresponds to a stochastic differential equation described as $dX_t^i = \gamma U^i(\boldsymbol{X}_t)dt + c^i_j(\boldsymbol{X}_t)dW_t^j$ and $i, j = 1, 2, 3$ [18, 19], where γ is a constant (e.g. $\gamma = 5n/2$ for the heat balance equation if n = const.), $\boldsymbol{U} = (U^1, U^2, U^3)$ a flow in a steady-state, $D^{ij} = c^i_k g^{k\ell} c^j_\ell$ a diffusion coefficient, $g^{k\ell}$ a metric coefficient, $\boldsymbol{X}_t = (X_t^1, X_t^2, X_t^3)$ a diffusion process, and $\boldsymbol{W}_t = (W_t^1, W_t^2, W_t^3)$ a Brownian process. It is assumed that a fluid is exposed to noise caused by resonant magnetic perturbations (RMPs), and that a fluid particle motion is described by an Itô process $dY_t^i = \gamma\tilde{U}^i(t,\omega)dt + c^i_j(\boldsymbol{Y}_t)dW_t^j$ instead of the process $\boldsymbol{X}_t$, where the flow is represented as $\tilde{\boldsymbol{U}}(t,\omega) = \boldsymbol{U}(\boldsymbol{Y}_t)$ + "noise", ω is a label of a fluid particle, "noise" is a random function having zero mean and finite strength, and the definition of an Itô process is given in Ref. [20]. It is known that an Itô process $\boldsymbol{Y}_t$ coincides in law with a diffusion process $\boldsymbol{X}_t$ if and only if $\mathrm{E}^{\boldsymbol{x}_0}[\tilde{\boldsymbol{U}}(t,\omega)|\mathcal{P}_t^Y] = \boldsymbol{U}(\boldsymbol{Y}_t)$ [20], where $\boldsymbol{X}_0 = \boldsymbol{Y}_0 = \boldsymbol{x}_0$ is a starting point of a fluid particle at $t = 0$, $\mathcal{P}_t^Y$ is the σ-algebra generated by the set $\{\boldsymbol{Y}_s; 0 \le s \le t\}$, and $\mathrm{E}^{\boldsymbol{x}_0}[\cdots|\mathcal{P}_t^Y]$ denotes the conditional expectation with respect to $\mathcal{P}_t^Y$. This theorem means that the "noise" cannot cause the diffusion of fluid particles. We should reconsider the reason why the noise created by RMPs can affect the transport.

Let us take the following collision operator:

$$C(f) = \nu_{\rm col} \frac{\partial}{\partial \boldsymbol{u}} \cdot \left\{ \boldsymbol{u} f + v_{\rm th}^2 \frac{\partial f}{\partial \boldsymbol{u}} \right\}, \tag{A.1}$$

where $\nu_{\rm col} = \nu_{\rm col}(\boldsymbol{x})$ is the collision frequency, $v_{\rm th}$ the thermal velocity, and $\boldsymbol{v} = \boldsymbol{U}+\boldsymbol{u}$ the velocity of a guiding center, and $\boldsymbol{U} = \boldsymbol{U}(\boldsymbol{x})$ the mean velocity [21]. The operator (A.1) is simpler, but is used only to get a rough idea of collisional effects [22]. We consider the motion of a guiding center along a field line for estimation of radial spreading the guiding centers by their parallel motions in a perturbed magnetic field. The guiding center motion exposed to the collisions (A.1) is given as an Ornstein-Uhlenbeck process:

$$\mathrm{d}\boldsymbol{x} = \boldsymbol{v}\mathrm{d}t = (\boldsymbol{U} + \boldsymbol{u})\mathrm{d}t, \tag{A.2}$$

$$\mathrm{d}\boldsymbol{u} = -\nu_{\rm col}\boldsymbol{u}\mathrm{d}t + \sigma \mathrm{d}\boldsymbol{W}_{\|t}, \tag{A.3}$$

where $\boldsymbol{U} = U_\| \boldsymbol{b}$, $\boldsymbol{u} = u_\| \boldsymbol{b}$, $\sigma = v_{\rm th}\sqrt{\nu_{\rm col}}$, $\boldsymbol{W}_{\|t}$ a Brownian process for the parallel direction, i.e. $\mathrm{d}\boldsymbol{W}_{\|t} = \boldsymbol{b}\mathrm{d}W_t$, and $\boldsymbol{b} = \boldsymbol{B}/B$ the unit vector along a field line. Here, the effects of ripples are neglected for simplicity. The solutions of Eqs. (A.2) and (A.3) are described respectively as

$$\boldsymbol{x} = \boldsymbol{x}_0 + \int_0^t (\boldsymbol{U} + \boldsymbol{u})\mathrm{d}s, \tag{A.4}$$

$$\boldsymbol{u} = \mathrm{e}^{-\nu_{\rm col}t}\boldsymbol{u}_0 + \int_0^t \mathrm{e}^{-\nu_{\rm col}(t-s)}\sigma \mathrm{d}\boldsymbol{W}_{\|s}, \tag{A.5}$$

where $\boldsymbol{x}_0$ and $\boldsymbol{u}_0$ are the initial values at $t = 0$.

One may consider that effect of a perturbation field on the motion is interpreted as noise on the motion. If the effect is expressed by a linear operator $\tilde{\boldsymbol{v}} = \tilde{N}\boldsymbol{v}$, then

$$\mathrm{d}\boldsymbol{x} = (\boldsymbol{v} + \tilde{\boldsymbol{v}})\mathrm{d}t = (\boldsymbol{v} + \tilde{N}\boldsymbol{v})\mathrm{d}t. \tag{A.6}$$

The solution of Eq. (A.6) is given as

$$\begin{aligned}\boldsymbol{x} &= \boldsymbol{x}_0 + \int_0^t (1+\tilde{N})\{\boldsymbol{U} + \mathrm{e}^{-\nu_{\rm col}s}\boldsymbol{u}_0\}\,\mathrm{d}s \\ &\quad + \int_0^t \mathrm{d}s \int_0^s \mathrm{e}^{-\nu_{\rm col}(s-h)}\sigma(1+\tilde{N})\mathrm{d}\boldsymbol{W}_{\|h}. \end{aligned}\tag{A.7}$$

For the collisional limit $t \gg 1/\nu_{\rm col}$, the diffusion (caused by the perturbation field) in configuration space is derived from Eq. (A.7):

$$\mathrm{d}\boldsymbol{x} \approx (1+\tilde{N})\boldsymbol{U}\mathrm{d}t + \frac{v_{\rm th}}{\sqrt{\nu_{\rm col}}}(1+\tilde{N})\mathrm{d}\boldsymbol{W}_{\|t}, \tag{A.8}$$

i.e., for the collisional limit the diffusion in velocity space directly becomes the diffusion in configuration space. We should note that the diffusion in configuration space originates from the collisions in velocity space. When the RMPs are added to the original magnetic field having nested flux surfaces, the parallel motion of a guiding center may cause radial fluctuation in configuration space [5, 6]. If the noise $\tilde{\boldsymbol{v}} = (\tilde{v}^1, \tilde{v}^2, \tilde{v}^3)$ is given as

$$\tilde{v}^i = (\tilde{N}\boldsymbol{v})^i = \left|\frac{\delta B_{\rm r}}{B_{\rm t}}\right| \frac{\varepsilon^{ijk}}{\sqrt{g}}\hat{\theta}_j v_k\, \tilde{\phi}(t,i), \tag{A.9}$$

then the radial diffusivity $D_{\rm r} = D_\| |\delta B_{\rm r}/B_{\rm t}|^2$ is obtained in the fluid equations given from the drift kinetic equation having the collisions (A.1) for the collisional limit, where $\hat{\boldsymbol{\theta}}$ is the unit vector for the poloidal direction, $\delta B_{\rm r}$ the strength of the RMPs satisfying $|\delta B_{\rm r}/B_{\rm t}| \ll 1$, $B_{\rm t}$ the toroidal component of $\boldsymbol{B}$, $g = \det\left(g_{ij}\right)$ the square of Jacobian, ε^{ijk} the Levi-Civita symbol, $\tilde{\phi}(t,i)$ the ith component of a zero mean random vector having the mean square of $\mathrm{E}\left[\tilde{\phi}^2\right] = 1$ and being independent of $\mathrm{d}\boldsymbol{W}_{\|t}$, and $D_\| = v_{\rm th}^2/\nu_{\rm col}$ the parallel diffusivity. We should note that the noise term $\tilde{N}(\boldsymbol{U}+\boldsymbol{u}_0)$ cannot cause diffusion, as shown in the first paragraph in this section; see also Refs. [13, 17, 20].

The above discussion shows that for a high-collisional plasma (the characteristic time $t \gg 1/\nu_{\rm col}$), the guiding center motions become close to the prediction of the stochastic diffusion theory based on the "field line diffusion" [5, 6]. On the other hand, for a lower-collisionality plasma ($t \lesssim 1/\nu_{\rm col}$), the motions are not interpreted as the diffusion process predicted by the stochastic diffusion theory. These consequences are consistent with the results shown in Fig. 2 and also ones obtained in the test particle simulations [23].

[1] N. Ohyabu *et al.*, Phys. Rev. Lett. **88**, 055005 (2002).
[2] N. Ohyabu *et al.*, Plasma Phys. Control. Fusion **47**, 1431 (2005).
[3] Y. Nagayama *et al.*, Nucl. Fusion **45**, 888 (2005).
[4] R. Kanno *et al.*, Nucl. Fusion **45**, 588 (2005).
[5] A.B. Rechester and M.N. Rosenbluth, Phys. Rev. Lett. **40**, 38 (1978).
[6] B.B. Kadomtsev and O.P. Pogutse, in *Proc. 7th IAEA Int. Conf. on Plasma Physics and Controlled Nuclear Fusion Research* (IAEA, Vienna, 1979) Vol.1, pp.649.
[7] K.H. Burrell *et al.*, Plasma Phys. Control. Fusion **47**, B37 (2005).
[8] T.E. Evans *et al.*, Nature Phys. **2**, 419 (2006).
[9] N. Ohyabu *et al.*, Nucl. Fusion **27**, 2171 (1987).
[10] Ph. Ghendrih *et al.*, Plasma Phys. Control. Fusion **38**, 1653 (1996).
[11] S. Jimbo *et al.*, Nucl. Fusion **45**, 1534 (2005).
[12] M. Nunami *et al.*, Research Report NIFS Series No. NIFS-871 (2007).
[13] R. Kanno *et al.*, accepted for publication in Contributions to Plasma Physics.
[14] W.X. Wang *et al.*, Plasma Phys. Control. Fusion **41**, 1091 (1999).
[15] S. Satake *et al.*, Plasma Fusion Res. **1**, 002 (2006).
[16] A.H. Boozer and G. Kuo-Petravic, Phys. Fluids B **24**, 851 (1981).
[17] R. Kanno *et al.*, Plasma Fusion Res. **1**, 012 (2006).
[18] Y. Feng *et al.*, J. Nucl. Mater. **266-269**, 812 (1999).
[19] A. Runov *et al.*, Nucl. Fusion **44**, S74 (2004).
[20] B. Øksendal, *Stochastic Differential Equations* (Springer-Verlag, Berlin Heidelberg, 2003).
[21] P.C. Clemmow and J.P. Dougherty, *Electrodynamics of Particles and Plasmas* (Addison-Wesley, Reading, Mass., 1969).
[22] D.R. Nicholson, *Introduction to Plasma Theory* (John Wiley & Sons, New York, 1983).
[23] A. Maluckov *et al.*, Physica A **322**, 13 (2003).

Proceedings of ITC/ISHW2007

Computations of neoclassical transport in stellarators using a δf method with reduced variance *

Klaus ALLMAIER[1)], Sergei V. KASILOV[1,2)], Winfried KERNBICHLER[1)], Georg O. LEITOLD[1)], Viktor V. NEMOV[1,2)]

[1)] *Association EURATOM-ÖAW, Institut für Theoretische Physik - Computational Physics, TU Graz, Petersgasse 16, A–8010 Graz, Austria*

[2)] *Institute of Plasma Physics, National Science Center "Kharkov Institute of Physics and Technology", Akademicheskaya Str. 1, 61108 Kharkov, Ukraine*

An improved δf Monte Carlo method for the computation of neoclassical transport coefficients in stellarators is presented. Compared to the standard δf method without filtering, the computing time needed for the same statistical error decreases by a factor proportional to the mean free path to the power 3/2.

Keywords: bootstrap current, stellarator, δf Monte Carlo, variance reduction

A standard δf Monte Carlo method for the computation of neoclassical transport coefficients [1] assumes solution of the linearized drift-kinetic equation taking into account the source term in the equation for test particle weights which evolve with time. This method has a good convergence for tokamaks where the variance in all transport coefficients including bootstrap coefficient has no strong dependence on plasma collisionality. However, in stellarators, the variance in the bootstrap coefficient increases for this method as a square of the mean free path due to the accumulation of large random contributions to the test particle weights which occur in the phase space region occupied by trapped particles. In Ref. [2] a method has been presented which is a combination of the standard Monte Carlo method with a method employing constant particle weights and re-discretizations of the test particle distribution in phase space. There, this method has been tested in confinement regimes with negligible radial electric field. Below this method is described in more detail for general confinement regimes.

Mono-energetic transport coefficients are determined by the steady state solution of the linearized drift kinetic equation for the normalized perturbation of the distribution function $\hat{f}$ (marker)

$$\mathcal{L}_D \hat{f} \equiv \left(\frac{\partial}{\partial t} + \mathbf{V}_g \cdot \nabla - \mathcal{L}_C\right) \hat{f} = \dot{\psi} \equiv \mathbf{V}_g \cdot \nabla\psi, \quad (1)$$

where $\mathcal{L}_C$, $\mathbf{V}_g$, and $\dot{\psi}$ are Lorentz collision operator, drift velocity and its co-variant ψ-component, respectively, and velocity space variables are total energy and perpendicular adiabatic invariant. Here, ψ is a flux surface label, and a marker is defined through the local Maxwellian distribution function f_M and the total distribution function f via $f = f_M - \hat{f}\partial f_M/\partial\psi$. The mono-energetic radial diffusion coefficient and the normalized bootstrap coefficient, respectively, are given by

$$D_{\mathrm{mono}} = -\frac{1}{\langle|\nabla\psi|\rangle^2}\left\langle \frac{1}{2}\int_{-1}^{1} \mathrm{d}\lambda \hat{f}\dot{\psi}\right\rangle, \quad (2)$$

$$\lambda_{bb} = -\frac{3}{\rho_L B_0 \langle|\nabla\psi|\rangle}\left\langle \frac{1}{2}\int_{-1}^{1} \mathrm{d}\lambda \hat{f}\lambda B\right\rangle, \quad (3)$$

where $\lambda = v_{\parallel}/v$ is the pitch parameter, ρ_L is the Larmor radius in the reference magnetic field B_0, B is the magnetic field module and $\langle\ldots\rangle$ denotes the average over the volume between neighboring flux surfaces. The quantity λ_{bb} is linked to the equilibrium (bootstrap) current density $j_{\parallel}$ and gradient of the pressure p by $\lambda_{bb} = -\langle j_{\parallel}B\rangle (c\langle|\nabla\psi|\rangle \mathrm{d}p/\mathrm{d}\psi)^{-1}$. In the following D_{mono} is normalized by the plateau diffusion coefficient $D_{\mathrm{plateau}} = \pi v \rho_L^2 (8\sqrt{2}\iota R)^{-1}$ where ι and R are the rotational transform and major radius, respectively.

In order to introduce the Monte Carlo operator it is convenient to re-write (1) in the integral form using a Green's function G defined by

$$\mathcal{L}_D\, G(t, \mathbf{z}, \mathbf{z}_0) = 0 \quad (4)$$
$$G(0, \mathbf{z}, \mathbf{z}_0) = (g(\mathbf{z}_0))^{-1/2}\,\delta(\mathbf{z}-\mathbf{z}_0), \quad (5)$$

where $\mathbf{z} = (\vartheta, \varphi, \lambda)$ and g is a metric determinant of flux coordinates $(\psi, \vartheta, \varphi)$. This Green's function is normalized to 1,

$$\int \mathrm{d}^3 z\,(g(\mathbf{z}))^{1/2}\, G(t, \mathbf{z}, \mathbf{z}_0) = 1. \quad (6)$$

*This work, supported by the European Communities under the contract of Association between EURATOM and the Austrian Academy of Sciences, was carried out within the framework of the European Fusion Development Agreement. The views and opinions expressed herein do not necessarily reflect those of the European Commission. Additional funding is provided by the Austrian Science Foundation, FWF, under contract number P16797-N08.

author's e-mail: allmaier@itp.tugraz.at

Thus, a formal solution to Eq. (1) is

$$\hat{f}(t,\mathbf{z}) = \int \mathrm{d}^3 z_0 \, (g(\mathbf{z}_0))^{1/2} \Bigg(G(t-t_0,\mathbf{z},\mathbf{z}_0)\hat{f}(t_0,\mathbf{z}_0) \times \int_{t_0}^{t} \mathrm{d}t' G(t-t',\mathbf{z},\mathbf{z}_0)\dot{\psi}(\mathbf{z}_0) \quad (7)$$

If a steady state solution is looked for, $\hat{f}(t,\mathbf{z}) = \hat{f}(\mathbf{z})$, Eq. (7) becomes an integral equation for $F(\mathbf{z}) = (g(\mathbf{z}))^{1/2}\hat{f}(\mathbf{z})$ given below also in the operator form,

$$F(\mathbf{z}) = \int \mathrm{d}^3 z_0 K(\mathbf{z},\mathbf{z}_0)F(\mathbf{z}_0) + Q(\mathbf{z}) \equiv \mathcal{K}F + Q, \quad (8)$$

where $K(\mathbf{z},\mathbf{z}_0) = (g(\mathbf{z}))^{1/2} G(\Delta t,\mathbf{z},\mathbf{z}_0)$, Δt is the integration time step and

$$Q(\mathbf{z}) = \int \mathrm{d}^3 z_0 \, (g(\mathbf{z})g(\mathbf{z}_0))^{1/2} \int_0^{\Delta t} \mathrm{d}t' G(t',\mathbf{z},\mathbf{z}_0)\dot{\psi}(\mathbf{z}_0) \approx (g(\mathbf{z}))^{1/2}\dot{\psi}(\mathbf{z})\Delta t. \quad (9)$$

Introducing the Monte Carlo operator, $\mathbf{Z}(\Delta t,\mathbf{z}_0)$, being the random position of a test particle starting at $\mathbf{z}_0$ after a single time step modeled in a standard way [4] by the random change of λ in accordance with $\mathcal{L}_C$ and integration of particle drift equations, the kernel of the integral equation is given by an expectation value $K(\mathbf{z},\mathbf{z}_0) = \overline{\delta(\mathbf{z}-\mathbf{Z}(\Delta t,\mathbf{z}_0))}$.

The solution of (8) by direct iterations can be presented as an expectation value of an integral along the stochastic orbit,

$$F = \sum_{k=0}^{\infty} \mathcal{K}^k Q = C_0 \sum_{k=0}^{\infty} \overline{w_0\, \delta(\mathbf{z}-\mathbf{z}_k)}, \quad (10)$$
$$\mathbf{z}_k = \mathbf{Z}(\Delta t,\mathbf{z}_{k-1}), \qquad w_0 = \dot{\psi}(\mathbf{z}_0)\Delta t,$$

where $C_0 = \int \mathrm{d}^3 z \, (g(\mathbf{z}))^{1/2}$ and the random starting point $\mathbf{z}_0$ is chosen with the probability density $\overline{\delta(\mathbf{z}-\mathbf{z}_0)} = C_0^{-1}(g(\mathbf{z}))^{1/2}$. The averages (2) and (3) are given by expectation values as

$$D_{\text{mono}} = -\frac{1}{\langle|\nabla\psi|\rangle^2} \sum_{k=0}^{\infty} \overline{w_0\dot{\psi}(\mathbf{z}_k)}, \quad (11)$$

$$\lambda_{bb} = -\frac{3}{\rho_L B_0 \langle|\nabla\psi|\rangle} \sum_{k=0}^{\infty} \overline{w_0 \lambda_k B(\mathbf{z}_k)}. \quad (12)$$

When $k\Delta t$ exceeds a few collision times, the correlation between $\mathbf{z}_k$ and w_0 is lost and, therefore, such terms in (11) tend to zero, e.g. $\overline{w_0\dot{\psi}(\mathbf{z}_k)} \to \overline{w_0}\;\overline{\dot{\psi}(\mathbf{z}_k)} = 0$ because the expectation value $\overline{w_0} = C_0^{-1}\Delta t \int \mathrm{d}^3 z \, (g(\mathbf{z}))^{1/2}\dot{\psi}(\mathbf{z}) = 0$ due to Liouville's theorem. Thus, a finite sum over k is sufficient in (11). The method of constant test particle weights described by (11) and (12) has rather low variance in computations of D_{mono}, however, for λ_{bb} variance has a very unfavorable scaling with collisionality. Indeed, only the orbits originating in the boundary layer in velocity space of the width $\Delta\lambda \sim (L_c/l_c)^{1/2}$ where $L_c = 2\pi R/\iota$ and $l_c = v\tau_c$ are the connection length and mean free path, respectively, contribute to λ_{bb}. In addition, the contribution of a particle from the boundary layer is $\Delta\lambda$ times smaller than of a normal passing particle because of a higher trapping probability. Therefore, the variance in λ_{bb} scales for this method as $(l_c/L_c)^2$ in the long mean free path regime.

It should be noted that distribution of test particles after each step remains to be the equilibrium distribution, $\overline{\delta(\mathbf{z}-\mathbf{z}_k)} = C_0^{-1}(g(\mathbf{z}))^{1/2}$.

Therefore $\overline{w_0\lambda_{k-j}B(\mathbf{z}_{k-j})} = \overline{w_j\lambda_k B(\mathbf{z}_k)}$ where $w_j = \dot{\psi}(\mathbf{z}_j)\Delta t$, and

$$\sum_{k=0}^{\infty} \overline{w_0\lambda_k B(\mathbf{z}_k)} = \lim_{k\to\infty} \overline{W_k\lambda_k B(\mathbf{z}_k)} \quad (13)$$
$$= \lim_{K\to\infty} \frac{1}{K}\sum_{k=0}^{K} \overline{W_k\lambda_k B(\mathbf{z}_k)}, \quad (14)$$
$$W_k = \sum_{j=0}^{k} w_j. \quad (15)$$

The procedure in (13) corresponds to a standard δf method [1] where the test particle weight W_k is an integral of $\dot{\psi}$ along a stochastic orbit. In a tokamak, the variance in λ_{bb} does not scale with the collisionality, and the required CPU time for this method scales linearly with l_c/L_c. However, in stellarators variance in λ_{bb} again recovers the scaling $(l_c/L_c)^2$ because due to the non-zero bounce-averaged drift of trapped particles large contributions to W_k are acquired, which scale as $\dot{\psi}\tau_c$ and which become weakly correlated with the values of λ_k after detrapping of test particles. To overcome this problem, in Ref. [5] trapped particles with large W_k are replaced with particles with $W_k = 0$ (large weights are filtered out) which formally introduces some bias in the result.

For a formally "unbiased" method it is convenient to split the source in (8) into "passing" and "trapped" sources $Q_p = \chi Q$ and $Q_t = Q - Q_p$ using

$$\chi = \frac{1}{2}\Big(1 + \tanh\big((\lambda-\lambda_{t-p})/\Delta\lambda\big)\Big), \quad (16)$$

where λ_{t-p} is a trapped-passing boundary, and solve the problem with each source independently. Results for transport coefficients for these two sources are added up at the end. The problem with Q_p is solved with the standard method (13) because accumulation of large weights is avoided there. For the problem with Q_t the formal solution to (8) is presented as $F = F_M + \Delta F_M$ where F_M satisfies an equation which differs from (8) only by a source term,

$$F_M = \mathcal{K}F_M + Q_M, \quad (17)$$

where

$$Q_M = \frac{1}{M}\sum_{k=0}^{M-1} \mathcal{K}^k Q, \quad (18)$$

$$\Delta F_M = \sum_{k=0}^{M-1} \left(1 - \frac{k+1}{M}\right)\mathcal{K}^k Q. \quad (19)$$

In order to derive (17) the original equation (8) is presented as

$$F = \sum_{k=0}^{m-1} \mathcal{K}^k Q + \mathcal{K}^m F, \tag{20}$$

where m is an arbitrary natural number. Averaging the r.h.s. of (20) over $1 \le m \le M$ yields

$$F = \Delta F_M + \frac{1}{M}\left(\sum_{m=0}^{M-1} \mathcal{K}^m Q + \sum_{m=1}^{M} \mathcal{K}^m F\right) \tag{21}$$

Denoting the last term in (21) with F_M and substituting there F in the form of the series (10) one obtains

$$F_M \equiv \frac{1}{M}\left(\sum_{m=0}^{M-1} \mathcal{K}^m Q + \sum_{m=1}^{M} \mathcal{K}^m F\right) \tag{22}$$

$$= \sum_{k=0}^{\infty} \mathcal{K}^k Q_M, \tag{23}$$

which is a series solution to Eq. (17).

Equation (17) describes one iteration of the solution procedure. Given the source term Q such iteration provides Q_M which is used as a source term Q for the next iteration. Within an iteration, each of the test particles performs $M-1$ steps, and the quantity Q_M is computed by scoring weights on the 3D grid (except the first iteration). The contribution of the iteration to the distribution function, ΔF_M, is formally used in the averages (2) and (3) so that they are computed directly in analogy to (11) and (12). For the first iteration with Q being the original source (9) the algorithm with alternating weights (15) is used. After the first iteration these test particle weights are divided by M so that test particles represent the discretized distribution Q_M used as a source within the second iteration. Starting from this second iteration, an algorithm with fixed test particle weights (and scoring Q_M on the grid) is used. After the second iteration, the module of test particle weight is fixed. Due to annihilation of the weights on the grid and fixed module of the weight, the number of test particles needed for sampling the source term from the grid is decreasing with iterations and iterations are stopped when this number is below one, (see Fig. 1). The number of steps M for a single iteration is chosen to be much smaller than collision time and large enough in order to fill the grid using a limited number of test particles. Since source terms generated in this way are small in the passing and boundary region, particles are generated there with smaller weights and particles which enter the boundary layer from the trapped side are split in such a way that the number of test particles in the passing and trapped regions is of the same order. As a result, variance of this method is reduced to the scaling l_c/L_c. In addition, due to the decay of test particle number with iterations, the CPU time is also reduced and scales as $(l_c/L_c)^{3/2}$ for a given accuracy (see Fig. 2) which is much better than the scaling $(l_c/L_c)^3$ of the standard δf method without a filter. Results of testing of the method for a few toroidal devices stay in good agreement with results of NEO-2, a field line tracing code which computes transport coefficients in arbitrary collisionality regimes [3], as shown in Figs. 3-6. Benchmarking of the results from computations with finite radial electric fields with other methods has been started, first results can be found in Ref. [6].

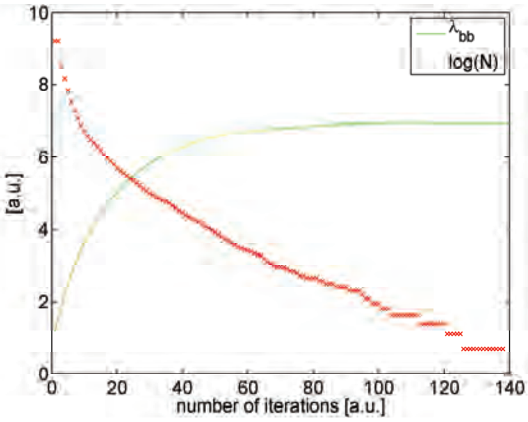

Fig. 1 Bootstrap coefficient λ_{bb} (green) and logarithm of the number of simulation particles (red) plotted over the number of iterations.

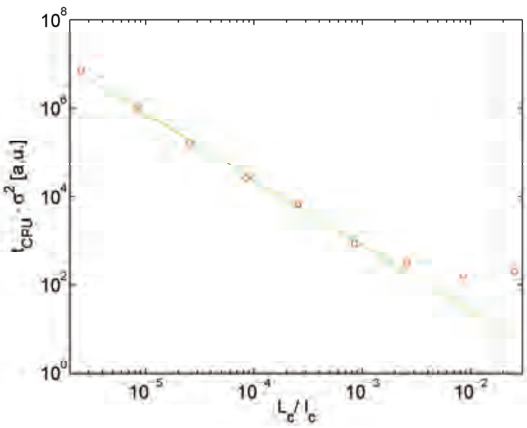

Fig. 2 CPU-time multiplied with the variance of the bootstrap coefficient σ^2 plotted over the collisionality parameter (red). The green line shows the scaling $(l_c/L_c)^{3/2}$.

[1] M. Sasinowski and A.H. Boozer, Phys. Plasmas **2**, 610 (1995).

[2] K. Allmaier, S. V. Kasilov, W. Kernbichler, G. O. Leitold and V. V. Nemov, *34th EPS Conference on Plasma Physics, Warsaw, 02–06 July 2007*, P-4.041, (2007).

[3] W. Kernbichler, S. V. Kasilov, G. O. Leitold, V. V. Nemov, and K. Allmaier, *33rd EPS Conference on Plasma Physics, Rome, 19–23 June 2006*, ECA Vol. **30I** P-2.189, (2006).

[4] A. H. Boozer and G. Kuo-Petravic, Phys. Fluids **24**, 851 (1981).

[5] M. Yu. Isaev, S. Brunner, W. A. Cooper, et al., Fusion Science & Technology **50**, 440 (2006).

[6] K. Allmaier, C.D. Beidler, M.Yu. Isaev, S.V. Kasilov, W. Kernbichler, H. Maassberg, S. Murakami, D.A. Spong, V. Tribaldos, *ICNTS - Benchmarking of Bootstrap Current Coefficients*, this workshop, (2007).

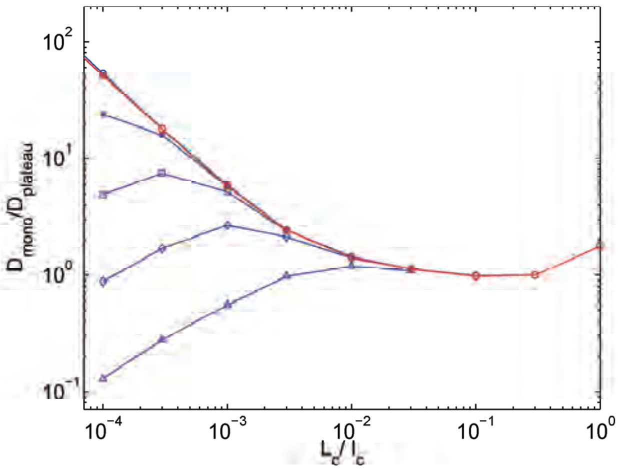

Fig. 3 Normalized diffusion coefficient $D_{\mathrm{mono}}/D_{\mathrm{plateau}}$ for LHD with R=375cm vs. collisionality parameter L_c/l_c at half plasma radius computed by NEO-MC (blue) and NEO-2 (red) for $E_r/v/B = 0$ (circles), $3 \cdot 10^{-5}$ (stars), $1 \cdot 10^{-4}$ (squares), $3 \cdot 10^{-4}$ (diamonds), $1 \cdot 10^{-3}$ (triangles)

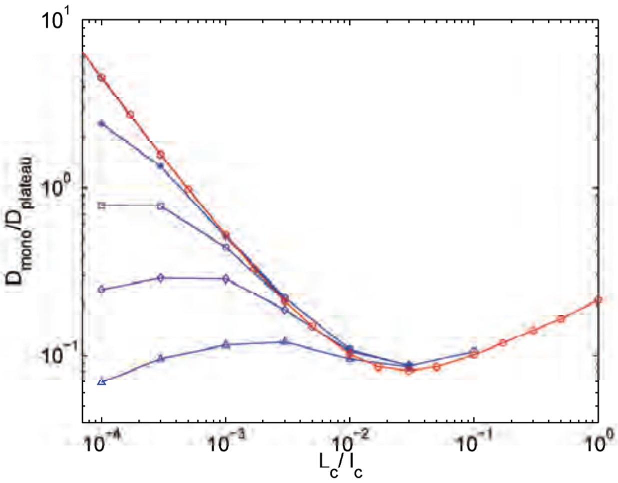

Fig. 5 Normalized diffusion coefficient $D_{\mathrm{mono}}/D_{\mathrm{plateau}}$ for W7-X standard configuration vs. collisionality parameter L_c/l_c at half plasma radius. Markers and colors are the same as in Fig. 3

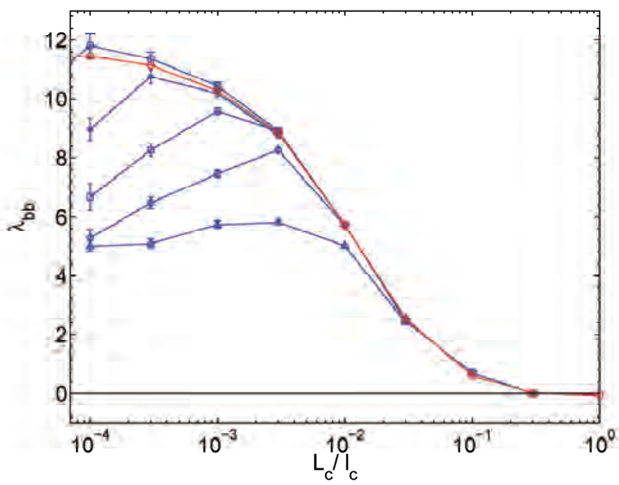

Fig. 4 Normalized bootstrap coefficient λ_{bb} for LHD with R=375cm vs. collisionality parameter L_c/l_c at half plasma radius. Markers and colors are the same as in Fig. 3

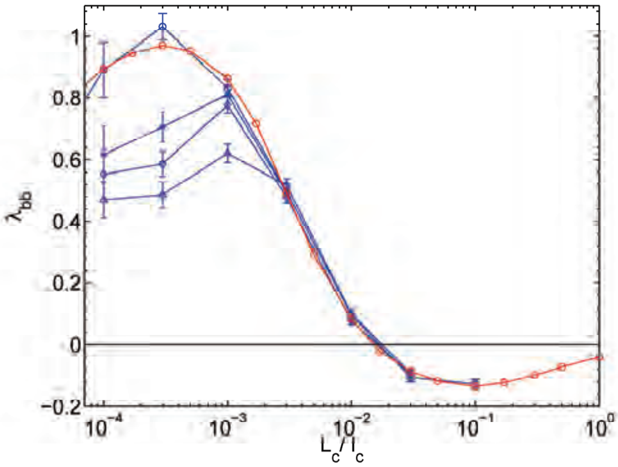

Fig. 6 Normalized bootstrap coefficient λ_{bb} for W7-X standard configuration vs. collisionality parameter L_c/l_c at half plasma radius. Markers and colors are the same as in Fig. 3

P2-022

Recent progress in NEO-2 - A code for neoclassical transport computations based on field line tracing*

Winfried KERNBICHLER[1)], Sergei V. KASILOV[1,2)], Georg O. LEITOLD[1)], Viktor V. NEMOV[1,2)] and Klaus ALLMAIER[1)]

[1)] *Association EURATOM-ÖAW, Institut für Theoretische Physik - Computational Physics, TU Graz, Petersgasse 16, A–8010 Graz, Austria*

[2)] *Institute of Plasma Physics, National Science Center "Kharkov Institute of Physics and Technology", Akademicheskaya Str. 1, 61108 Kharkov, Ukraine*

NEO-2 is a code for the computation of neoclassical transport coefficients and current drive efficiency in toroidal devices which is based on the field line integration technique. The possibility to use the complete linearized collision integral is realized in this code. In this report the results of comparison of the full matrix of transport coefficients in a tokamak with analytical models are presented. Effects of simplifications of the linearized collision model (e.g., reduction to a Lorentz model) are studied in order to provide a comparison with various momentum correction techniques used for the computation of transport coefficients in stellarators.

Keywords: neoclassical transport, linearized collison operator

Accurate computations of transport coefficients, bootstrap current and the generalized Spitzer function in tokamaks and stellarators is an important problem for stellarator optimization, generation of neoclassical data bases, and modeling of current drive. Based on the field line integration technique [1], the code NEO-2 has been developed for this purpose [2, 3]. This code solves the linearized drift kinetic equation in regimes where the effect of electric field on transport and bootstrap coefficients is negligible. Recently this code has been upgraded for computations of the full transport matrix and the possibility of treatment of magnetic fields in Boozer coordinates has been realized in addition to magnetic fields in real space coordinates. In the following, a comparison of NEO-2 results with results of analytical theory for tokamak are presented. Transport coefficients are computed here only for the electron component assuming the ions to be immobile.

Approximating the energy dependence of the perturbation of the distribution function by the expansion over a finite number of test functions,

$$\delta f(\psi,s,v,\lambda) \approx f_0(\psi,v)\sum_{m=0}^{M} f_m(\psi,s,\lambda)\varphi_m(v/v_T)\,, \quad (1)$$
$$\varphi_m(x) = \pi^{3/4}\sqrt{\frac{2\Gamma(m+1)}{\Gamma(m+5/2)}}\,L_m^{(3/2)}(x^2)\,,$$

where $f_0(\psi,v)$ is the Maxwellian and $L_m^{(3/2)}$ are associated Laguerre polynomials (Sonine polynomials) of the order 3/2, the linearized drift kinetic equation (DKE) is transformed to a set of coupled two dimensional differential equations,

$$\sigma\frac{\partial f_m^\sigma}{\partial s} - \kappa\sum_{m'=0}^{M}\left\{\nu_{mm'}\mathcal{L}f_{m'}^\sigma + \mathcal{K}_{mm'}f_{m'}^\sigma + \frac{1}{|\lambda|}D_{mm'}f_{m'}^\sigma\right\}$$
$$= \frac{\rho}{\langle|\nabla\psi|\rangle}\left(A_1 a_m^{(1)} + A_2 a_m^{(2)}\right)q_G^\sigma + A_3 a_m^{(3)} q_E^\sigma \quad (2)$$

with the pitch-angle scattering operator

$$\mathcal{L}f_{m'}^\sigma = \frac{1}{2|\lambda|}\frac{\partial}{\partial\lambda}(1-\lambda^2)\frac{\partial}{\partial\lambda}f_{m'}^\sigma(\psi,s,\lambda)$$
$$= 2\frac{\partial}{\partial\eta}\left(\frac{\eta|\lambda|}{\hat{B}}\right)\frac{\partial}{\partial\eta}f_{m'}^\sigma(\psi,s,\eta)\,, \quad (3)$$

and the integral part of the linearized collision operator

$$\mathcal{K}_{mm'}f_{m'}^\sigma = \frac{1}{|\lambda|}\sum_{\ell=0}^{L} I_{mm'}^\ell P_\ell(\lambda)\int_{-1}^{1}\mathrm{d}\lambda' P_\ell(\lambda')f_{m'}^\sigma(\psi,s,\lambda')\,, \quad (4)$$

where P_ℓ are Legendre polynomials. Here, ψ is a flux surface label, s is the distance counted along the m.f.l., $\lambda = v_\parallel/v$ is pitch, σ is the sign of $v_\parallel$, $\eta = (1-\lambda^2)/\hat{B}$ is the normalized perpendicular invariant (magnetic moment), $\hat{B} = B/B_0$ is the magnetic field module normalized to a reference magnetic field B_0 which is equal to (0, 0) harmonic of magnetic field expansion in Boozer coordinates, $B_0 = \langle B^3\rangle/\langle B^2\rangle$, $\kappa = 2/l_c$ with $l_c = v_T\tau_{ee}$ being the mean free path, $\rho = v_T/\omega_c$, $v_T = (2T_e/m_e)^{1/2}$, $\omega_c = eB_0/m_e c$ and $\tau_{ee} = 3m_e^2 v_T^3/\left(16\sqrt{\pi}n_e e^4\Lambda\right)$ are electron Larmor radius, thermal velocity, cyclotron frequency and collision time, respectively, and $\langle\ldots\rangle$ means the average over the volume between two neighboring magnetic surfaces (flux surface average). The quantities $\nu_{mm'}$, $I_{mm'}$, $D_{mm'}$ and $a_m^{(i)}$ are matrix elements independent of plasma parameters, whereas

*This work, supported by the European Communities under the contract of Association between EURATOM and the Austrian Academy of Sciences, was carried out within the framework of the European Fusion Development Agreement. The views and opinions expressed herein do not necessarily reflect those of the European Commission. Additional funding is provided by the Austrian Science Foundation, FWF, under contract number P16797-N08.

author's e-mail: winfried.kernbichler@TUGraz.at

the quantities A_i are the thermodynamic forces defined as,

$$A_1 = \left(\frac{1}{n}\frac{\partial n}{\partial\psi} - \frac{3}{2T}\frac{\partial T}{\partial\psi} + \frac{e}{T}\frac{\partial\Phi}{\partial\psi}\right)\langle|\nabla\psi|\rangle,$$
$$A_2 = \frac{1}{T}\frac{\partial T}{\partial\psi}\langle|\nabla\psi|\rangle, \qquad A_3 = \frac{e}{T}\frac{\langle E_\parallel\hat{B}\rangle}{\langle\hat{B}^2\rangle}. \tag{5}$$

The source terms q_G^σ and q_E^σ with drives by gradients and by parallel electric field, respectively, are defined as follows,

$$q_G^\sigma = \frac{\partial}{\partial\eta}\left(\frac{|\lambda|}{\hat{B}}\hat{V}_G\right), \qquad q_E^\sigma = \sigma\hat{B},$$
$$\hat{V}_G = \frac{1}{3}\left(\frac{4}{\hat{B}} - \eta\right)|\nabla\psi|k_G, \tag{6}$$

where k_G is the geodesic curvature.

Equations (2) are discretized over the η variable on an adaptive non-equidistant grid and the resulting set of coupled ordinary differential equations is solved with help of integration along the field lines. In particular, all necessary flux surface averages are computed during this integration as follows,

$$\frac{\langle\alpha\rangle}{\langle\beta\rangle} = \lim_{L_c\to\infty}\int_0^{L_c}\frac{ds}{B}\alpha \Big/ \int_0^{L_c}\frac{ds}{B}\beta\,. \tag{7}$$

As a result of computation, one obtains the matrix of transport coefficients L_{ij}^e defined through the thermodynamic forces A_j and thermodynamic fluxes I_i via

$$I_i = -\sum_{j=1}^{3} L_{ij}^e A_j\,, \tag{8}$$

where $I_1 = \Gamma_e$, $I_2 = Q_e/T_e$ and $I_3 = \langle j_\parallel\hat{B}\rangle/e$. Here Γ_e and Q_e are average particle and heat flux densities defined as total particle and heat fluxes divided by the flux surface area and $j_\parallel$ is parallel electron current density.

Symmetric matrix L_{ij}^e is conveniently expressed through dimensionless coefficients γ_{ij} which depend only on the device geometry, the mean free path l_c and effective charge number Z as follows, $L_{ij} = n_e\gamma_{ij}\beta_i\beta_j/\tau_{ee}$, where $\beta_1 = \beta_2 = \rho$ and $\beta_3 = l_c$. For this purpose solution to (2) is formally presented as a superposition of thermodynamic forces,

$$f_m^\sigma = \frac{\rho}{\langle|\nabla\psi|\rangle}\left(A_1\hat{f}_m^{\sigma,(1)} + A_2\hat{f}_m^{\sigma,(2)}\right) + A_3\hat{f}_m^{\sigma,(3)}. \tag{9}$$

Then γ_{ij} are determined by normalized solutions for single drive problems, $\hat{f}_m^{\sigma,(i)}$, as follows

$$\gamma_{ij} = \frac{\alpha_i\alpha_j}{l_c}\sum_m\sum_{\sigma=\pm1} b_m^{(i)}\left\langle\hat{B}\int_0^{1/B} d\eta \hat{f}_m^{\sigma,(j)} q_i^{-\sigma}\right\rangle \tag{10}$$

where $q_1^\sigma = q_2^\sigma = q_G^\sigma$, $q_3^\sigma = q_E^\sigma$, $\alpha_1 = \alpha_2 = l_c\langle|\nabla\psi|\rangle^{-1}$, $\alpha_3 = 1$ and numerical coefficients $b_m^{(i)}$ are, again, independent of problem parameters. With help of these coefficients the quantity λ_{bb} [3] is expressed as $\lambda_{bb} = 2\gamma_{31}$.

It should be noted that matrices L_{ij}^e and γ_{ij} correspond to the effective radius $r_{\rm eff}$ used as a radial variable where $dr_{\rm eff} = dV/S$, V is a volume limited by a flux surface and S is a flux surface area. In order to obtain these matrices for different definitions of plasma radius, e.g. for the radius defined via the toroidal flux, $r_\psi = (2\psi/B_{00})^{1/2}$, coefficients α_1 and α_2 should be multiplied with $dr_\psi/dr_{\rm eff}$.

For the large aspect ratio tokamak with circular flux surfaces coefficients γ_{ij} computed by NEO-2 are compared to the analytical results of Refs. [4, 5, 6]. In particular, dimensionless transport coefficients for the Hinton and Hazeltine model [4], $\gamma_{ij}^{\rm HH}$, are given by $\gamma_{ij}^{\rm HH} = K_{ij}q^2\epsilon_t^{-3/2}Z_{\rm eff}$ for $i,j = 1,2$, $\gamma_{ij}^{\rm HH} = K_{ij}q\epsilon_t^{-1/2}/2$ for $i = 1,2$ and $j = 3$ or $i = 3$ and $j = 1,2$,

$$\gamma_{33}^{\rm HH} = \frac{K_{33}\epsilon_t^{1/2} - 1}{2Z_{\rm eff}\left(0.29 + 0.46\,(1.08 + Z_{\rm eff})^{-1}\right)} \tag{11}$$

and matrix K_{ij} is defined by Eqs. (6.125) and (6.126) of Ref. [4]. Here q is safety factor and $\epsilon_t = r/R$ is the inverse aspect ratio. The results of the comparison are presented in Figs. 1 through 6 for $\iota = 1/q = 0.362$ and $\epsilon_t = 0.075$. The results of NEO-2 are computed with associated Laguerre polynomials up to forth order and Legendre polynomials up to third order. For all coefficients the dependence on collisionality as well as $Z_{\rm eff}$ is well reproduced. The main differences come from the finite toroidicity. Whereas NEO-2 does not assume smallness of the magnetic field modulation, theoretical approximations are based on the expansion over ϵ_t. It should be noted that in NEO-2 all nine transport coefficients are computed independently and Onsager symmetry of these coefficients is used for the control of the computation accuracy which improves with both, grid resolution and (mainly) number of Laguerre polynomials in modeling energy dependence. For the present computation violation of symmetries $\gamma_{13} = \gamma_{31}$ and $\gamma_{23} = \gamma_{32}$ is around 1% and violation of symmetry $\gamma_{12} = \gamma_{21}$ is around 10%.

Beside the full linearized collision operator, two different model operators are used in Figs. 7 through 9, namely, the mono-energetic collision model and mono-energetic collision model with momentum recovery. Last two models are obtained by putting in (2) $D_{mm'} = I_{mm'}^\ell = 0$ or only $D_{mm'} = 0$, respectively. In particular, the mono-energetic model here corresponds to the most common mono-energetic approach where transport coefficients are given by the convolution over energy of the results for the Lorentz model. It can be seen that mono-energetic model overestimates particle diffusion coefficient γ_{11} while mono-energetic model with momentum recovery underestimates this coefficient as compared to the full linearized collision model. The bootstrap coefficient γ_{31}, in turn, is underestimated by the mono-energetic model while the mono-energetic model with momentum recovery overestimates it. Finally, conductivity coefficient is well reproduced by the mono-energetic model while the mono-energetic model with momentum recovery significantly overestimates it. Differences between all three models are

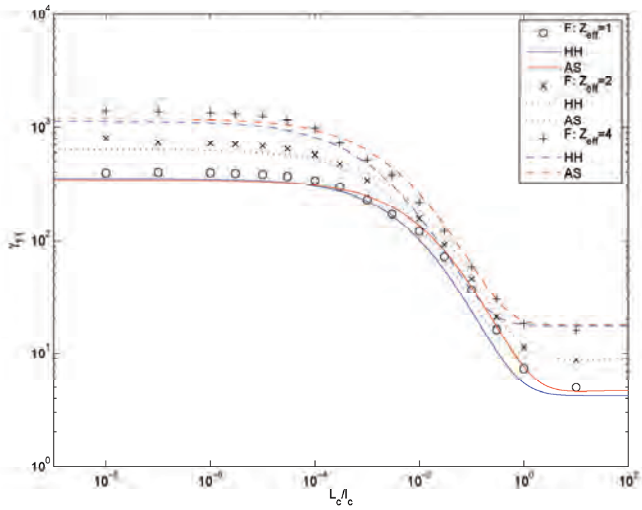

Fig. 1 Results of NEO-2 with full linearized collision operator (F) and analytical models of Ref. [4] (HH) and Refs. [5, 6] (AS) for the dimensionless diffusion coefficient γ_{11} at three values of the effective charge $Z_{\rm eff}$.

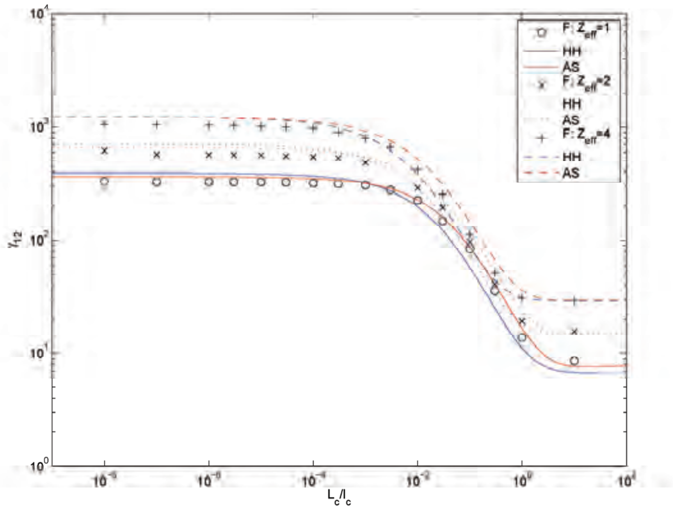

Fig. 2 The same as in Fig.1 for γ_{12}.

naturally reduced with higher $Z_{\rm eff}$. Currently NEO-2 has been and is being used for the benchmarking of various methods for the computation of mono-energetic transport coefficients and bootstrap coefficient [7,8] as well as momentum correction techniques [9].

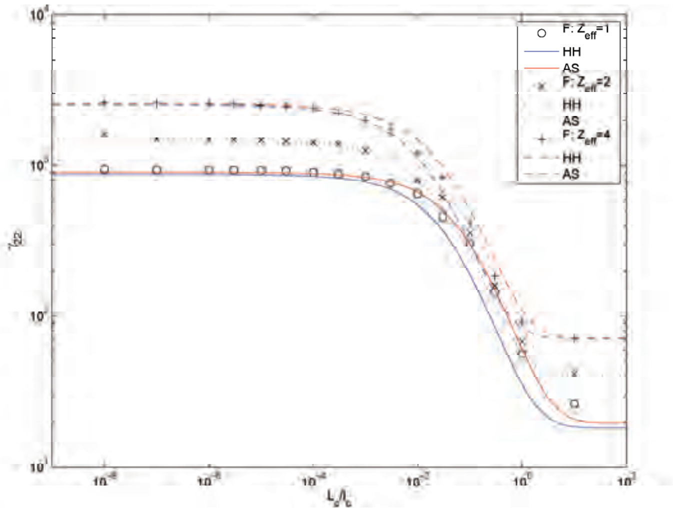

Fig. 3 The same as in Fig.1 for γ_{22}.

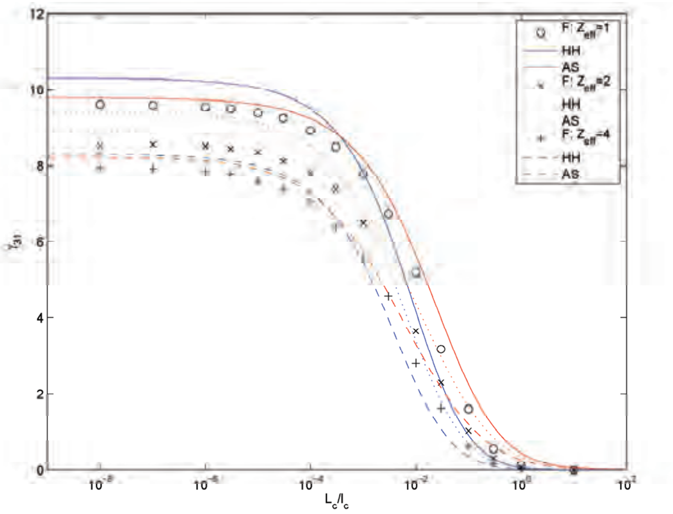

Fig. 4 The same as in Fig.1 for γ_{31}.

[1] V. V. Nemov, S. V. Kasilov, W. Kernbichler, and M.F. Heyn, Phys. Plasmas **6**, 4622 (1999).

[2] W. Kernbichler, S. V. Kasilov, G. O. Leitold, V. V. Nemov, and K. Allmaier, Computation of neoclassical transport in stellarators with finite collisionality, *Proc. of the 15th Int. Stellarator Workshop, Madrid, 3-7 October 2005*, P2-15 (2005).

[3] W. Kernbichler, S. V. Kasilov, G. O. Leitold, V. V. Nemov, and K. Allmaier, *33rd EPS Conference on Plasma Physics, Rome, 19–23 June 2006*, ECA Vol. **30I** P-2.189 (2006).

[4] F. L. Hinton and R. D. Hazeltine, Rev. Mod. Phys **48**, 239 (1976)

[5] O. Sauter, C. Angioni, and Y. R. Lin-Liu, Phys. Plasmas **6**, 2834 (1999).

[6] C. Angioni and O. Sauter, Phys. Plasmas **7**, 1224 (2000).

[7] K .Allmaier et al., *ICNTS - Benchmarking of Bootstrap Current Coefficients*, this conference (2007).

[8] K. Allmaier et al., *Computations of neoclassical transport in stellarators using a δf method with reduced variance*, this conference (2007).

[9] C. D. Beidler et al., *ICNTS - Benchmarking of Momentum Correction Techniques*, this conference (2007).

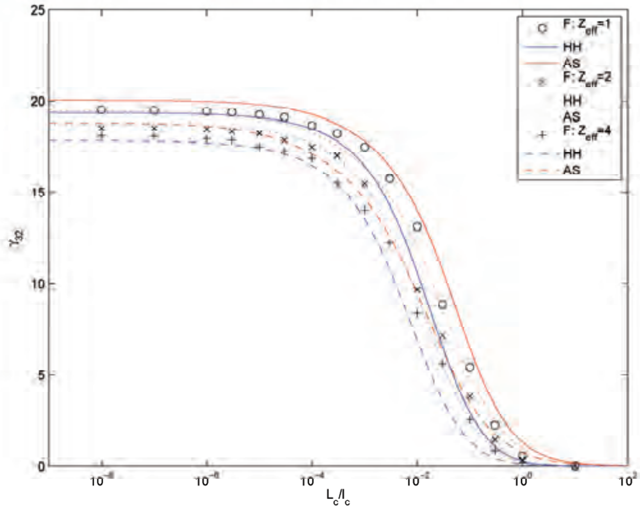

Fig. 5 The same as in Fig.1 for γ_{32}.

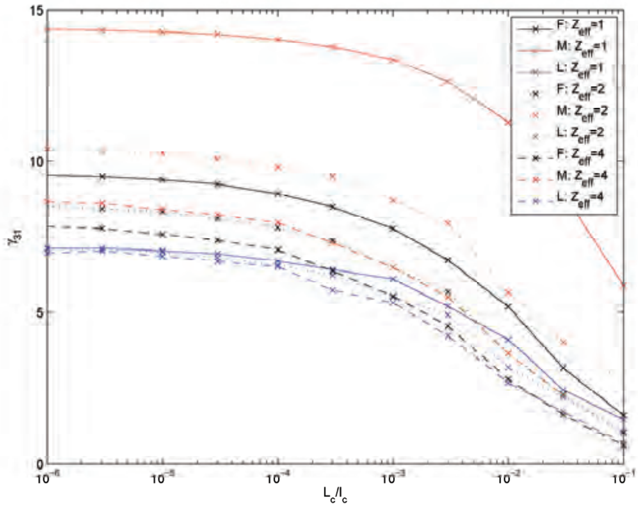

Fig. 8 The same as in Fig. 7 for the bootstrap coefficient γ_{31}

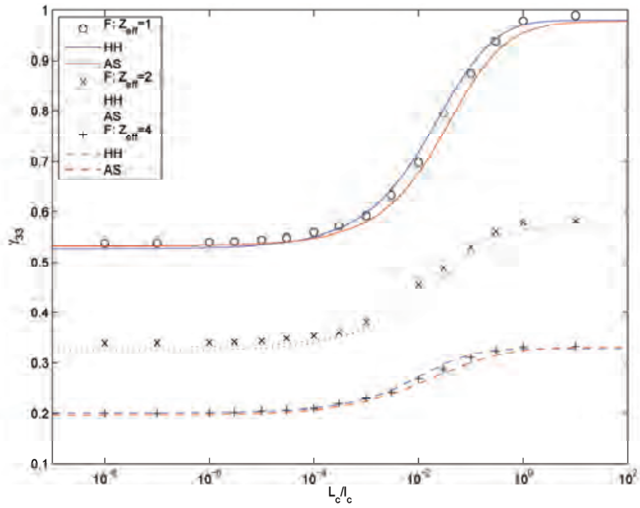

Fig. 6 The same as in Fig.1 for $-\gamma_{33}$.

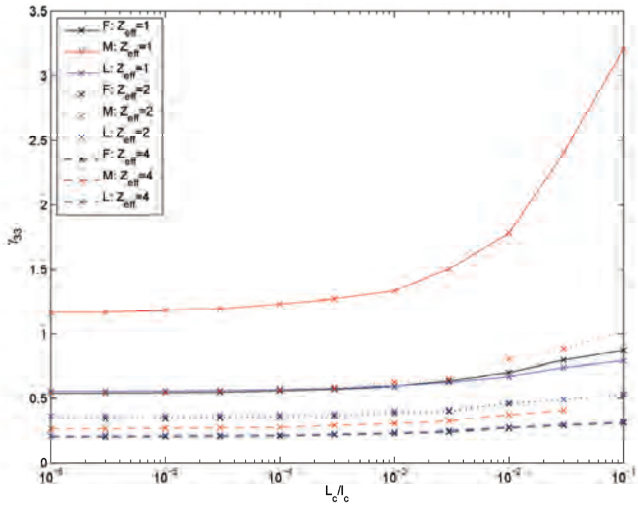

Fig. 9 The same as in Fig. 7 for the conductivity coefficient $-\gamma_{33}$

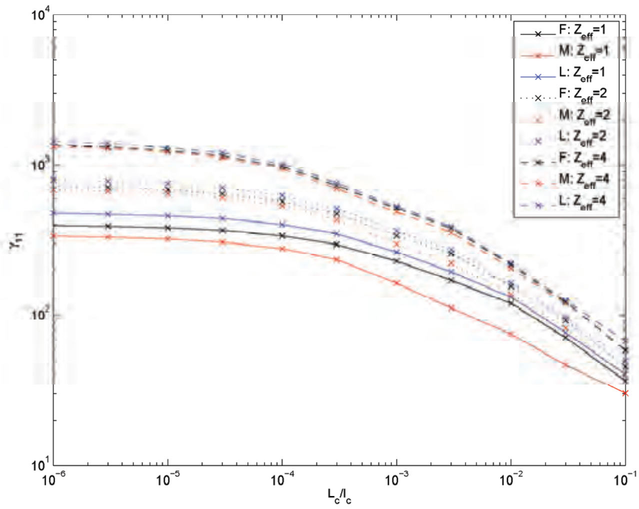

Fig. 7 Dimensionless particle diffusion coefficient γ_{11} for the full linearized collision operator (F), mono-energetic approach (L) and mono-energetic approach with momentum recovery (M).

Proceedings of ITC/ISHW2007

Development of non-local neoclassical transport code for helical configurations

Shinsuke Satake[1)], Ryutaro Kanno[1,2)] and Hideo Sugama[1,2)]

[1)] *National Institute for Fusion Science,322-6 Oroshi-cho, Toki 509-5292,, Japan*
[2)] *Department of Fusion Science, Graduate University for Advanced Studies, Toki 509-5292, Japan*

The progress in 3-dimensional, non-local neoclassical transport simulation code "FORTEC-3D" is described. The main purpose of the code is to solve the drift-kinetic equation in general 3-dimensional configuration using the δf Monte-Carlo method, and to calculate neoclassical fluxes and the time evolution of the ambipolar radial electric field simultaneously. In this article, we explain the new numerical schemes adopted for FORTEC-3D in order to overcome problems happened especially in the cases where the bifurcation of radial electric field occurs. Examples of test simulation for a LHD magnetic field configuration with bifurcated electric field are also shown. With improved numerical schemes, FORTEC-3D can calculate neoclassical fluxes and trace the time evolution stably as long as several ion collision times, which is long enough to observe GAM damping and transition of the ambipolar electric field.

Keywords: neoclassical transport, δf Monte-Carlo method, ambipolar radial electric field

1 Introduction

Detailed calculation of neoclassical transport in 3-dimensional configuration plasmas such as LHD is important for transport analysis, since in a 3-dimensional system the ambipolar condition $\Gamma_i(\rho,E) = \Gamma_e(\rho,E)$ determines the radial electric field profile $E(\rho)$, where Γ_i and Γ_e are ion and electron particle fluxes across the flux surface $\rho = const$. It is known that the ambipolar condition is mainly determined by neoclassical transport. If the ambipolar condition has multiple roots, bifurcation of radial electric field profile occurs.[1] In LHD plasmas, appearance of positive electric field, or the "electron root", is preferable since it reduces neoclassical transport compared with that in negative one, or the "ion root".[2] Moreover, strong sheared electric field profile at the bifurcation point is generally considered to be favorable from the viewpoint of suppression of anomalous transport.

Neoclassical transport theory for 3-dimensional helical configuration[3, 4] has been constructed under the assumption of local transport model where the typical orbit width in the minor-radius direction is assumed to be negligible compared with the background gradient scale lengths of a plasma. Recently non-local effects, or finite-orbit-width (FOW) effects, on neoclassical transport have attracted attention in the analysis of core transport in tokamaks, where particle orbits with large widths break the assumption of conventional neoclassical theory.[5, 6] In helical configurations, the deeply ripple-trapped and transition particles show large deviation in radial direction. The FOW effect of these orbits will be important in neoclassical transport analysis if the collisionality becomes quite low. The presence of strong-sheared electric field will also brings the non-local effect to neoclassical transport. However, the applicability of analytic neoclassical theory to these situations is questionable since it neglects the FOW effect from the beginning.

From the considerations above, we have been developing a simulation code to solve the drift-kinetic equation (DKE) including the FOW effect in 3-dimensional configuration. The simulation code, FORTEC-3D,[7, 8] uses the δf Monte-Carlo method[9, 10] which has been applied to some other transport codes both for tokamaks[11] and for helical configurations.[12, 13] The features of FORTEC-3D are : (1) It uses a conserved-form linearized Fokker-Planck collision operator. (2) It is a global simulation. The entire confinement region is solved at once. (3) Time evolution of radial electric field is solved simultaneously. The ambipolar electric field is then determined in consistency with neoclassical fluxes. (4) To reduce calculation time, only the ion transport is solved by the δf method, and electron transport is solved by GSRAKE code[14] which solves bounce-averaged DKE. Note that GSRAKE solution does not include the FOW effect, and then only the non-local effect for ions transport is treated in FORTEC-3D.

So far, FORTEC-3D has successfully applied for LHD configurations to solve the formation of ambipolar field for ion roots,[7] and to study the configuration dependence of GAM oscillation and damping[8]. However, from several test calculations we found that it was difficult to apply FORTEC-3D to the cases with electron roots, since bifurcated radial electric field profile became unphysical shape as shown later. We also found that numerical noise in particle flux and numerical error in collision operator were in-

author's e-mail: satake@nifs.ac.jp

tolerably large, which had not found in tokamak cases. We ascertained the cause of these problems were from inaccuracy in radial grids for evaluating flux and electric field, and from the emergence of huge-weight markers.

In this paper, improvements for numerical schemes in FORTEC-3D recently applied to overcome the problems above are explained. In section 2, basic equations for δf Monte-Carlo method are reviewed. In section 3, modification to collision operator is described. The new operator has good conservation property with less marker numbers. In section 4, improvement in the evaluation of flux and electric field are explained. Adoption of staggered-mesh in radial direction to evaluate these two quantities makes it possible to simulate the formation of bifurcated radial electric field profile stably. In section 5, new filtering scheme for marker weights to reduce numerical noise is introduced. By comparing several tests with varied strength of filters, it is shown that the filtering scheme does not affect the solutions. By these improvements, now FORTEC-3D is ready to solve neoclassical transport in helical plasmas in varied profiles and simulate evolution of electric field including bifurcations.

2 Basic equations of the δf method

In the δf method, time development of the perturbation of plasma distribution function from the local Maxwellian $\delta f = f - f_M$ is solved according to the DKE

$$\begin{aligned} \frac{D\delta f}{Dt} &\equiv \frac{\partial \delta f}{\partial t} + \left(\mathbf{v}_\parallel + \mathbf{v}_d\right) \cdot \nabla \delta f - C_{tp}(\delta f) \\ &= -\mathbf{v}_d \cdot \nabla f_M + \mathscr{P} f_M, \end{aligned} \quad (1)$$

where C_{tp} and $\mathscr{P}$ are test-particle and field-particle parts of linearized collision operator. The magnetic field is given in the Boozer coordinate system (ψ, θ, ζ)[15] as $\mathbf{B} = \nabla\psi \times \nabla\theta + \iota\nabla\zeta \times \nabla\psi$. Practically, we use ρ for a normalized radial coordinate defined from toroidal flux ψ as $\rho = \sqrt{\psi/\psi_{out}}$. A MHD equilibrium magnetic field is constructed from the VMEC code[16]. The time evolution of radial electric field $\mathbf{E} = -d\Phi/d\rho \nabla\rho = E_\rho \nabla\rho$ is solved from the following equation

$$\varepsilon_0 \varepsilon_\perp \frac{\partial E_\rho}{\partial t} = -e\left[z_i \Gamma_i - \Gamma_e\right], \quad (2)$$

where subscripts i and e describe particle species, and $\varepsilon_\perp \equiv [\langle|\nabla\rho|^2\rangle + \langle c^2|\nabla\rho|^2\rangle / v_A^2]$.

To solve eq. (1), two weights, w and p, are introduced which satisfy the relations $wg = \delta f$ and $pg = f_M$, respectively, where g is 5-dimensional simulation marker distribution function. Since the time evolution of marker distribution is given by $Dg/Dt = 0$, we obtain

$$\frac{dw}{dt} = \frac{p}{f_M}\left[-\mathbf{v}_d \cdot \nabla + \mathscr{P}\right] f_M, \quad (3a)$$

$$\frac{dp}{dt} = \frac{p}{f_M} \mathbf{v}_d \cdot \nabla f_M. \quad (3b)$$

The numerical procedures for the collision operator and for eq. (2) are described in the following sections.

3 Collision operator

The linearized Fokker-Planck operator in FORTEC-3D is made to satisfy the following relations.

$$\int d^3v \mathscr{M}\left(C_{tp}(\delta f) + \mathscr{P} f_M\right) = 0 \text{ for } \mathscr{M} = \{1, v_\parallel, v^2\}, \quad (4)$$

$$C_{tp}(\delta f) + \mathscr{P} f_M = 0 \text{ for } \delta f = (c_0 + \mathbf{c}_1 \cdot \mathbf{v} + c_2 v^2) f_M. \quad (5)$$

The test-particle operator C_{tp} is expressed by random scattering in the $(v_\parallel, v_\perp)$-space. The field-particle operator is given as follows

$$\begin{aligned} \mathscr{P} &= a\left[1 - 3\sqrt{\frac{\pi}{2}}(\phi - \phi')x^{-1/2}\right]\delta n \\ &+ b v_\parallel x^{-3/2} \phi \delta P + c x^{-1/2}(\phi - \phi')\delta E, \end{aligned} \quad (6)$$

where $x \equiv v^2/v_{th}^2$, $\phi(x)$ is the error function, and

$$\{\delta n, \delta P, \delta E\} = \int d^3v \left\{1, v_\parallel, v^2\right\} C_{tp}(\delta f) \quad (7)$$

are changes in constants-of-motions by C_{tp} only. Previously, the relation (3b) has been used to determine constants $(a, b, c) = (1/n, 2/nv_{th}, 2/3nv_{th})$. However, it was found that the numerical error in the conservation low (4) became larger as the numerical noise $f_M - pg$ became larger. The numerical error is significant in 3-D helical configuration cases compared with 2-D cases, because in 3-D cases it is difficult to keep enough marker population in a unit volume as in 2-D cases, and the marker distribution g is distorted in the velocity space in the presence of ripple-trapped particles. In the improved version, we do not use (3b) any more to make $\mathscr{P} f_M$, but the factors (a, b, c) are determined at every moment of collision so that the conservation low is strictly satisfied. In fig. 1, the residual relative error in momentum and energy arisen at one operation of $C_{tp} + \mathscr{P} f_M$ are compared between old and new $\mathscr{P} f_M$ for several tests with varied marker numbers. For previous operator, the numerical error is larger for fewer marker case. However, the error in new operator is just the rounding-error level even in the 1600-markers calculation. We have also confirmed the other property of collision operator (5) is also kept in the new operator.

4 Radial meshes

The relation between neoclassical fluxes and radial electric field (2) is solved on discrete meshes in the ρ-coordinate. Γ_i is evaluated by the volume averaged value between i-th and $i+1$-th meshes as follows

$$\begin{aligned} \Gamma_i(\rho_{i+\frac{1}{2}}) &= \frac{1}{\Delta V_{i+1/2}} \int_{\Delta V_{i+1/2}} d^3x \int d^3v \dot{\rho} \delta f \\ &= \frac{1}{\Delta V_{i+1/2}} \sum_{\{k|\rho_i \le \rho_k < \rho_{i+1}\}} w_k \dot{\rho}_k C(\rho_k, i), \end{aligned} \quad (8)$$

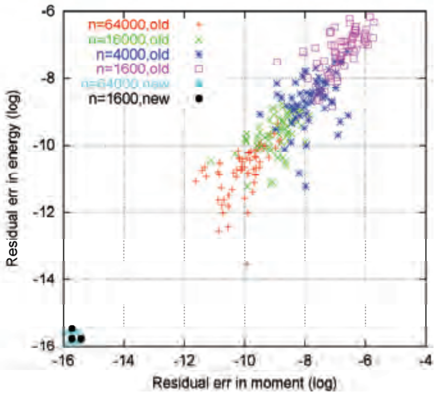

Fig. 1 Relative error in momentum and energy in one operation of $C_{Ip} + \mathscr{P} f_M$. The time interval for the operation is taken $\Delta t = 2\times 10^{-3}\tau_{ii}$.

where k is the marker index, and $C(\rho_k, i)$ is a shaping factor of a marker.[17] For electron flux GSRAKE solution is referred to : $\Gamma_e(\rho_{i+1/2}) = \Gamma_e(\rho_{i+1/2}, E_\rho(\rho_{i+1/2}, t))^{\mathrm{GSRAKE}}$. Previously, the electric field and fluxes were evaluated on the same points $\rho = \rho_{i+1/2}$ according to eq. (2). It is illustrated in Fig. 2. However, using this scheme, we found that the electric field profile fell into an unphysical shape as shown in Fig. 3, where multiple roots for ambipolar condition are expected from GSRAKE solutions. This is because all three values in eq. (2) were evaluated on the same position, that is, the evaluation was relied on a local information too much. Therefore, we adopted a new scheme which uses staggered-mesh for E_ρ and Γ_i, Γ_e as illustrated in Fig. 2. Fluxes are evaluated on half-grids $\rho = \rho_{i\pm 1/2}$ and time evolution of $E_\rho(\rho_i)$ is calculated as follows

$$\varepsilon_0\varepsilon_\perp \frac{\partial E_\rho(\rho_i)}{\partial t} = -e\left[z_i\bar{\Gamma}_i(\rho_i) - \bar{\Gamma}_e(\rho_i)\right], \qquad (9)$$

where $\bar{\Gamma}_i(\rho_i)$ and $\bar{\Gamma}_e(\rho_i)$ are averaged values of those which evaluated at $\rho = \rho_{i\pm 1/2}$. With this new scheme, FORTEC-3D can simulate continuous transition from ion-root to electron-root as shown in Fig. 3.

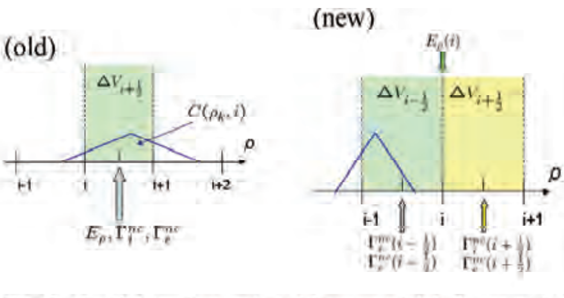

Fig. 2 Radial meshes and positions on which fluxes and electric field are evaluated in old and new schemes.

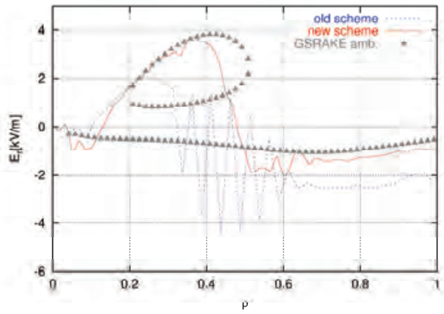

Fig. 3 Comparison of electric field profile between old and new schemes for flux and electric field. Squares are estimation of ambipolar field from GSRAKE.

5 Filtration

Reducing the numerical noise without relying on a massive number of markers is essential to any Monte-Carlo simulation. In the δf method, the origin of big noise is from markers which has huge weights w or p. If collisions and electric potential are neglected, the marker weights can be determined as

$$p_1 = p_0\frac{n_1}{n_0}\left(\frac{T_0}{T_1}\right)^{3/2} e^{\left[-\left(\frac{mv_1^2}{2T_1}\right)^2 + \left(\frac{mv_0^2}{2T_0}\right)^2\right]}, \qquad (10a)$$

$$w_1 = w_0 - (p_1 - p_0), \qquad (10b)$$

where subscript 0 and 1 represents initial and present values of them at marker position. From eq.(10), it is expected that markers which travels long distance in radial direction will have large marker weights. It is inevitable to appear such large-drift particles in low-collisionality helical plasmas, we need to set limits for weight values. In reality, we found only less than 0.1% of simulation markers have huge weights $p_1 \sim |w_1| \gg 10p_0$, and these markers makes the calculation very noisy and unstable. Therefore, we apply filters for markers by setting limits for p, $|w|/p$, and v/v_{th}. The second limiter is following from the assumption in δf method that $\delta f/f_M \ll 1$, and the third limiter is because fast ions tend to have large orbit widths. The markers which breaks the limits are filtrated out and redistributed around the magnetic axis, which contributes to keep marker population there.

To check the effect of filters, we have carried out several tests with varied strength of filters as shown in Table 1. Note here that the "old" simulation used old $\mathscr{P}$ operator and was not equipped with filters for p. In fig. 4, comparison of radial electric field at three different times with varied filters are shown. As is shown there, the time evolution of E_ρ and quasi-steady state profiles (at the last figure of three) are almost the same regardless of strength of filters. To check the time evolution in detail, we compare E_ρ and Γ_i on $\rho = 0.45$ for three filters in Fig. 5. Here, error-bars are evaluated from the variance between every 30 steps. It is found that the filters successfully suppress the numerical noise even in the weakest filter case, though the start timing of transition differs slightly among three simulations. It is also notable that the simulation marker number can be reduced if we adopt the filters.

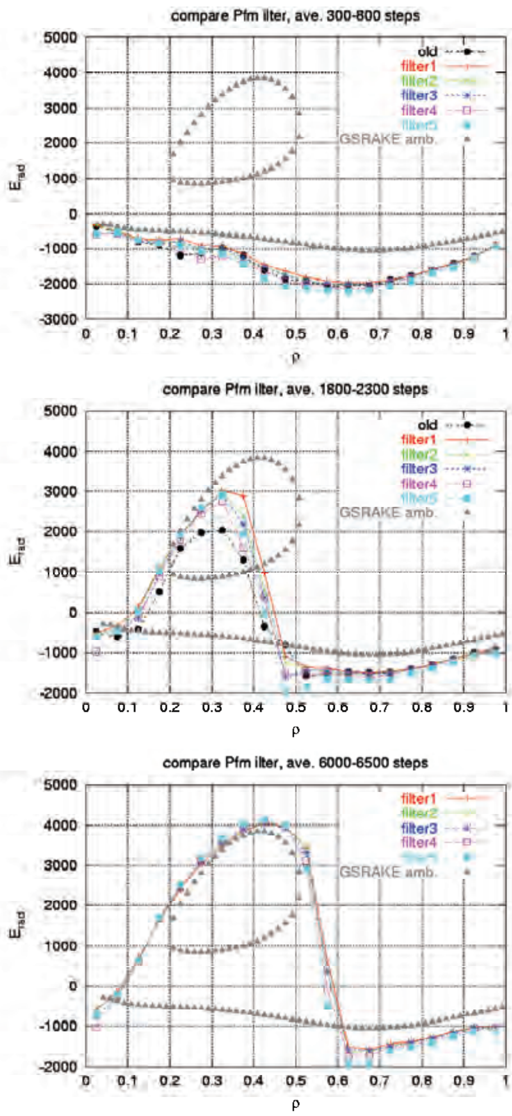

Fig. 4 Comparison of electric field profile between old and new schemes for different filters.

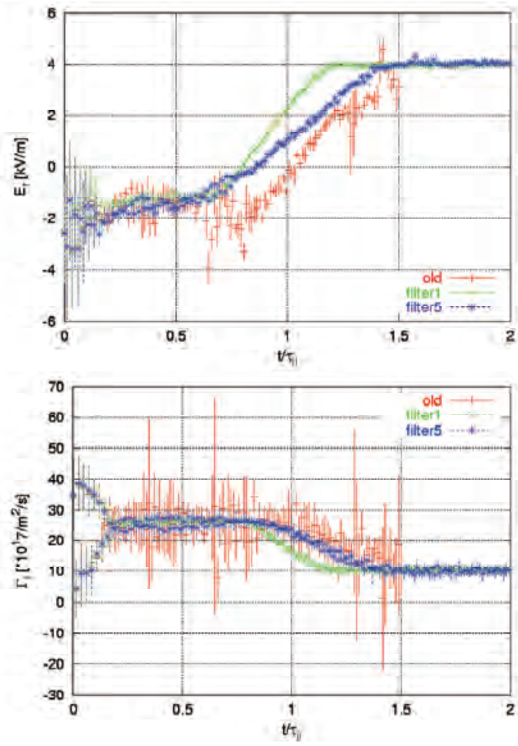

Fig. 5 Comparison of time evolution of E_r and Γ_i between old, filter 1 and filter 5 calculations on $\rho = 0.45$ surface. The oscillation at the beginning phase is GAM

Table 1 Filter strengths and marker numbers used in test-runs.

	p	$\|w\|/p$	v/v_{th}	marker num.
old	-	2.0	5.0	3.84×10^7
filter 1	5	2.0	4.5	3.84×10^7
filter 2	8	2.5	4.5	3.84×10^7
filter 3	10	2.5	4.5	1.28×10^7
filter 4	25	4.0	4.5	1.92×10^7
filter 5	10	10.0	4.5	1.92×10^7

6 Conclusion

The improvements for numerical schemes in FORTEC-3D were proved to reduce numerical errors and noises significantly with little changes in the observable values such as flux and electric field, etc. FORTEC-3D will be applied to study the FOW effects in helical plasmas, bifurcation phenomena, and so on. We are also planning to apply the δf method to solve electron transport and evaluate the bootstrap current in the presence of ambipolar electric field.

[1] D. E. Hastings *et al.*,Nuclear Fusion **25**, 445 (1985).
[2] R. Kanno *et al.*,*et al.*,Nuclear Fusion **37**, 1463 (1997).
[3] N. Nakajima *et al.*,J. Phys. Soc. Japan **61**, 833 (1992).
[4] M. Wakatani, *Stellarators and Heliotron Devices* (Oxford Univ. Press, 1998), Chap. 7.
[5] P. Helander, Physics of Plasmas **7**, 2878 (2000).
[6] S. Satake *et al.*,Physics of Plasmas **9**, 3946 (2002) .
[7] S. Satake *et al.*,Plasma Fusion Res. **1**, 002 (2006).
[8] S. Satake *et al.*,Nuclear Fusion **47**, 1258 (2007).
[9] W. X. Wang *et al.*,Plasma Phys. Control. Fusion **41** 1091 (1999).
[10] S. Brunner *et al.*,Physics of Plasmas **6**, 4504 (1999).
[11] W. X. Wang *et al.*,Physics of Plasmas **13** 082501 (2006).
[12] J. L. Lewandowski *et al.*,Physics of Plasmas **8**, 2849 (2001).
[13] M. Yu. Isaev *et al.*,Fusion Science and Technology **50**, 440 (2006).
[14] C. D. Beidler *et al.*,Plasma Phys. Control. Fusion **43**, 1131 (2001).
[15] A. H. Boozer, Phys. Fluids **23**, 904 (1980).
[16] S. P. Hirshman *et al.*,J. Comput. Phys. **96**, 99 (1991).
[17] C. K. Birdsall *et al.*,*Plasma Physics via Computer Simulation* (Inst. Phys. Pub., 1991), Chap. 4.

Proceedings of ITC/ISHW2007

Development of hierarchy-integrated simulation code for toroidal helical plasmas, TASK/3D

Masahiko SATO, Shinichiro TODA, Yuji NAKAMURA[1)], Kiyomasa WATANABE, Atsushi FUKUYAMA[2)], Sadayoshi MURAKAMI[2)], Masayuki YOKOYAMA, Hisamichi FUNABA, Hiroshi YAMADA and Noriyoshi NAKAJIMA

National Institute for Fusion Science, Toki 509-5292, Japan

[1)]*Graduate School of Energy Science, Kyoto University, Kyoto 611-0011, Japan*

[2)]*Graduate School of Engineering, Kyoto 606-8501, Japan*

The present status of the development of the hierarchy-integrated simulation code for troidal helical plasmas, TASK/3D, is reported. The TASK/3D is based on the integrated modeling code for tokamak plasmas, TASK. In order to extend the TASK for two dimensional configuration to the TASK/3D for three dimensional configuration, new modules for the radial electric field and rotaional transform for a general toroidal configuration have been developed. Numerical simulations for the time evolution of temperature and electric field are done for an LHD experiment by the combination of the diffusive transport module and the electric field module. Improvement of the rotational transform module is also reported.

Keywords: integrated simulation, helical plasma, radial electric field, plasma current

1 Introduction

In order to systematically clarify confinement physics in toroidal magnetic confinement systems, a hierarchy-renormalized simulation concept is being developed under domestic and international collaborations with universities and institutes. The hierarchy-renormalized simulation model in toroidal magnetic confinement systems consists of a hierarchy-integrated simulation approach and a hierarchy-extended simulation approach. The former approach, which is mainly based on a transport simulation combining various simplified models describing physical processes in different hierarchies, is suitable for investigating whole temporal behavior of experimentally observed macroscopic physics quantities, and the latter approach, which includes fluid core plasma description, kinetic core plasma description, and peripheral fluid/kinetic description, is focused on the description of mutual interaction among neighboring hierarchies in a more rigorous way. The hierarchy-integrated simulation code (TASK/3D) is based on the integrated modeling code for tokamak plasmas, TASK[1], developed in Kyoto University. In order to extend the TASK code developed for two dimensional configuration to three dimensional, the transport equations for the rotational transform and the radial electric field have been reformulated in a general toroidal configuration. With this new formulation, temporal evolution of the net current in LHD has been analyzed [2,3]. In this research, present status of the first-stage development of TASK/3D is reported.

This paper is organized as follows. In section 2, numerical model equations and module structure of TASK/3D are described. In section 3.1, we show numerical simulation results obtained by the combination of the diffusive transport module and the electric field module. where the profile of the radial electric field is determined by the ambipolar condition. In section 3.2, we show simulation results of time evolution of current profile by using rotational transform module. The improvement of the rotational transform module is also reported. Finally, section 4 is devoted to summary.

author's e-mail: masahiko@nifs.ac.jp

2 Numerical model in TASK/3D

In order to extension the TASK for two dimensional configuration to three dimensional, we are developing and adding new modules into TASK as indicated by red character in Fig.1. As a first step, we will carry out simulations by using the diffusive transport module TR, rotational transform module EI and electric field module ER. In TASK/3D, the TR module is used for solving the following particle transport equation and heat transport equation;

$$\begin{aligned}\frac{1}{V'}\frac{\partial}{\partial t}(n_sV') &= -\frac{\partial}{\partial \rho}\left(V'\langle|\nabla\rho|\rangle n_sV_s\right.\\ &\left.-V'\langle|\nabla\rho|^2\rangle D_s\frac{\partial n_s}{\partial\rho}\right)+S_s, \quad (1)\\ \frac{1}{V'5/3}\frac{\partial}{\partial t}\left(\frac{3}{2}n_sT_sV'^{5/3}\right) &= -\frac{1}{V'}\frac{\partial}{\partial\rho}\left(V'\langle|\nabla\rho|\rangle\frac{3}{2}n_sT_sV_{Es}\right.\\ &\left.-V'\langle|\nabla\rho|^2\rangle n_s\chi_s\frac{\partial T_s}{\partial\rho}+P_s\right), \quad (2)\end{aligned}$$

where n is density、T is temperature、ρ is normalized radial coordinate、V is volume enclosed by a magnetic surface, s expresses species of particles, and the prime denotes the derivative with respect to ρ. $\langle\rangle$ is average value on magnetic surface. The rotational transform module EI can be used for analyzing inductive plasma current, where the equation of the rotational transform is solved;

$$\begin{aligned}\frac{\partial\iota}{\partial t} =& \left(\frac{\partial\Phi_T}{\partial\rho}\right)^{-1}\frac{\partial\iota}{\partial\rho}\frac{\partial\Phi_T}{\partial t}\\ &+\left(\frac{\partial\Phi_T}{\partial\rho}\right)^{-1}\frac{\partial}{\partial\rho}\left\{\eta_\parallel\left(\frac{\partial\Phi_T}{\partial\rho}\right)^{-2}\frac{\partial V}{\partial\rho}\right.\\ &\left\{\langle B^2\rangle\frac{\partial}{\partial\rho}[(S_{11}\iota+S_{12})\Phi'_T]\right.\\ &\left.\left.+\frac{\partial\Phi_T}{\partial\rho}\frac{\partial P}{\partial\rho}(S_{11}\iota+S_{12})-\frac{\partial\Phi_T}{\partial\rho}\langle\mathbf{J}_s\cdot\mathbf{B}\rangle\right\}\right\},\end{aligned} \quad (3)$$

where Φ_T is toroidal magnetic flux, $\eta_\parallel$ is resistivity, $\mathbf{J}_s$ is noninductive current, $\mathbf{B}$ is magnetic field and P is plasma pressure. The elements of susceptance matrix, S_{11} and S_{12} are given by

$$S_{11} = \frac{V'}{4\pi^2}\left\langle\frac{g_{\theta\theta}}{g}\right\rangle \quad (4)$$

$$S_{12} = \frac{V'}{4\pi^2}\left\langle\frac{g_{\theta\zeta}}{g}\right\rangle. \quad (5)$$

In eq.(3) $\langle B^2\rangle$ and P' are entered instead of other elements of susceptance matrix, S_{21} and S_{22}, by using the MHD equilibrium condition. In helical plasmas, off diagonal element of susceptance matrix, S_{12} appears due to nonaxisymetry.

For electric field module ER, the equation of the electrostatic potential Φ_0 is solved;

$$\begin{aligned}\epsilon_0\epsilon_r\langle|\nabla\psi|^2\rangle\frac{\partial}{\partial t}\frac{d\Phi_0}{d\psi} =& \sum_{a=e,i}\langle\mathbf{B}_x\cdot\nabla\cdot\mathbf{\Pi}_{a1}\rangle\\ &-\sum_{a=e,i}\langle\mathbf{B}_x\cdot\mathbf{S}_{a1}\rangle\\ &+e_f\langle n_{f1}\mathbf{u}_{f1}\cdot\nabla\psi\rangle,\end{aligned} \quad (6)$$

where $\psi = \Phi_T/2\pi$. The second term and the third term of R.H.S. are source term and fast particle term due to NBI etc., respectivly. A relative permittivity ϵ_r is given by

$$\epsilon_r = 1+\frac{c^2}{\langle|\nabla\psi|^2\rangle}\left\{\left\langle\frac{|\nabla\psi|^2}{v_A^2}\right\rangle+\left\langle\frac{(g_2)^2}{v_A^2}\right\rangle-\frac{\langle g_2\rangle^2}{\langle v_A^2\rangle}\right\}, \quad (7)$$

where v_A is Alfvén velocity. g_2, which describes Pfirsch-Schluter current, is given by

$$\mathbf{B}\cdot\nabla\left(\frac{g_2}{B^2}\right) = \mathbf{B}\times\nabla\psi\cdot\nabla\left(\frac{1}{B^2}\right). \quad (8)$$

In the current stage of the development of the TASK/3D, the electric field module has been added to the TASK/3D, where the radial electric field is determined by ambipolar condition which is obtained by considering steady state of eq.(4). In the electric field module, replacing the ambipolar condition to the equation of time evolution for electric field is a future work. On the other hand, the rotational transform module EI has not been added to TASK/3D yet, although temporal evolution of the plasma current in LHD has been analyzed [3] by using the combination of the EI module, the VMEC MHD equilibrium module, and BSC/FIT module, where BSC/FIT modules are used for calculating non-inductive current. Adding the EI module into TASK/3D is underway.

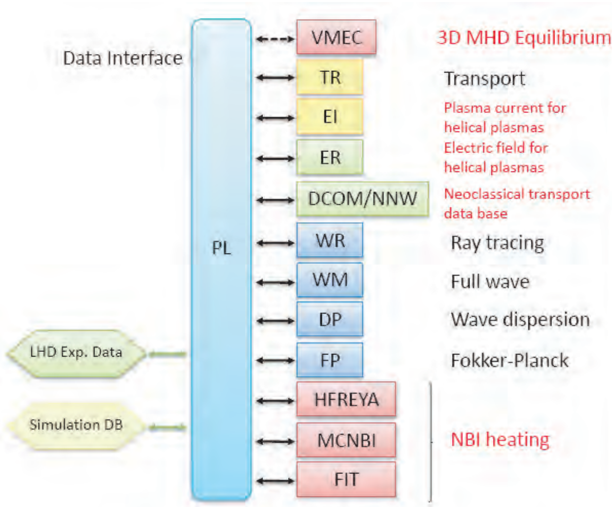

Fig. 1 Module structure of TASK/3D.

3 Numerical Results

3.1 Radial electric field module

In order to check the combination of TR module and electric field module, transport simulations are done for an LHD plasma, where the plasma is heated by NBI and the steady state is achieved. In the simulations, the time evolution of the temperature profile is calculated by using the heat transport equation (2) in the TR module and the radial electric field is determined by ambipolar condition in the ER module. The density and rotational transform profiles are fixed. For neoclassical transport model, the single helicity model proposed by Shaing[4] is used. We carried out simulations for two different anomalous transport models, a constant model and a parabolic model. Figure 2 shows time evolution of electron and ion temperatures obtained from the simulation, where the anomalous transport coefficient is chosen as $\chi_a = 1+\rho^2(m^2/s)$. In this simulation, the profiles of the density and rotational transform are fixed. The density profile is also plotted in Fig.2. The positive electric field initially appears around $\rho = 0.6$ in Fig.3. This is mainly due to the positive gradient of the density. As the electron temperature decreases, the positive electric field disappears. We also carried out the simulation for the constant anomalous model, where the anomalous coefficient is chosen as $\chi_a = 1(m^2/s)$. The behavior of teperature and electric field for $\chi_a = 1(m^2/s)$ is qualitatively same as the case for $\chi_a = 1 + \rho^2(m^2/s)$ The dependence of temporal evolution of profiles on the transport model is currently under investigation.

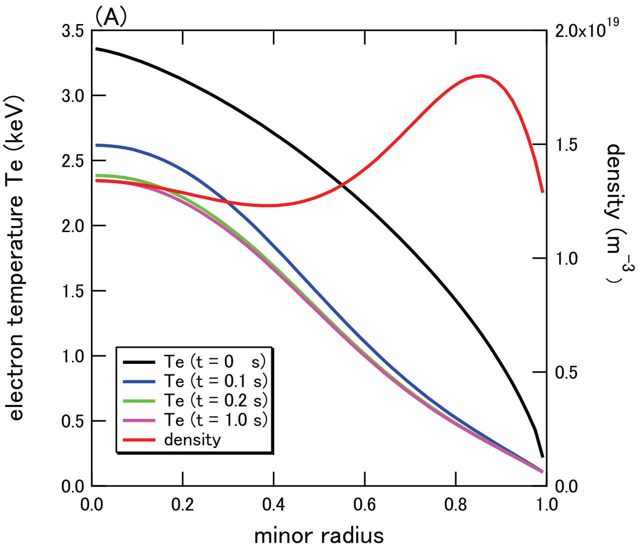

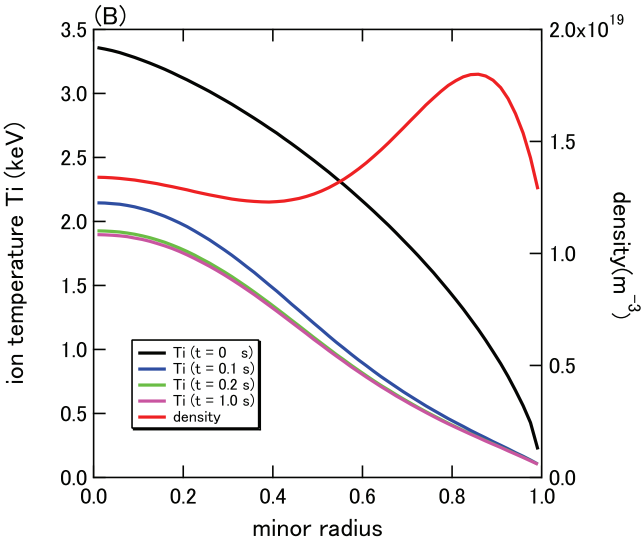

Fig. 2 Time evolution of radial profiles of (A) electron and (B) ion temprature calcurated by the combination of the diffusive transport module TR and the electric field module ER. The anomalous coefficent is chosen as $\chi_a = 1 + \rho^2(m^2/s)$. The profiles of the temperature and density observed in an LHD experiment are used for initial profiles in the simulation. In this simulation , the density profile indicated by red line is fixed.

3.2 Rotational transform module

The rotational transform module EI can be used for analyzing the plasma current in helical plasmas. As is shown in refs.[2] and [3], Fig.6 shows a waveform of the discharge

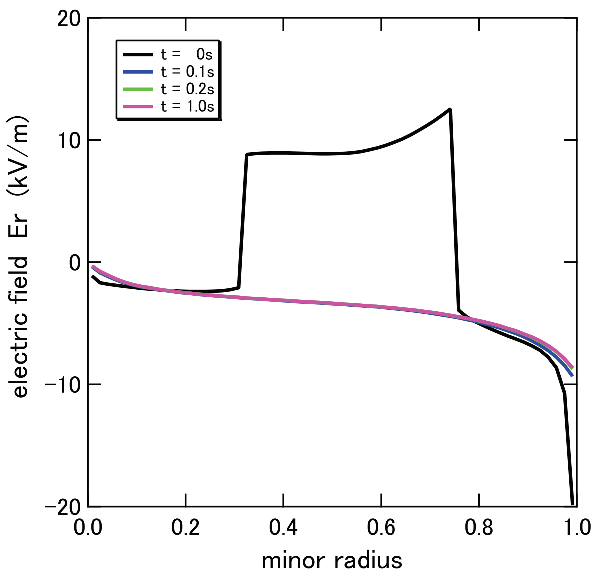

Fig. 3 Time evolution of radial profile of electric field corresponding to Fig.2.

with 2 neutral beam (NB) injection. The 1st NB is injected to the counter-direction from $t \sim 0.7s$ and the 2nd NB to the co direction from $t \sim 1.2s$. The blue line denotes the observed net toroidal current by Rogowski coils. Numerical simulations are done for the LHD neutral beam heated plasma shown in Fig.6. In this simulation, non-inductive current (bootstrap current and Ohkawa current) is calculated by BSC/FIT module. We use the time evolution of the plasma density and temperature profiles observed in the experiment. The equilibrium profile is calculated by the VMEC code at some time interval which is longer than the time interval for the EI module.

The earlier version of the EI module uses the square root of the normalized toroidal magnetic flux as radial coordinate ρ and the rotational transform is discretized at half mesh points. In this case, the calculated noninductive current becomes negative around $r = 0.9$ at t=4.5s as shown Fig.7(A). The problem is mainly due to the disagreement between the plasma boundary and the half mesh point. In order to solve this problem, the EI module has been updated. The new version of the EI module uses the normalized toroidal magnetic flux as radial coordinate s and the rotational transform is discretized at full mesh points. Figure 7(B) shows numerical results obtained by the updated EI module. In this case, the noninductive current does not become negative around $r = 0.9$ at t=4.5s.

It is important to decide appropriate time interval for recalculation of equilibrium profile by VMEC. We are investigating the dependence of numerical results on the time interval for recalculating equilibrium profile.

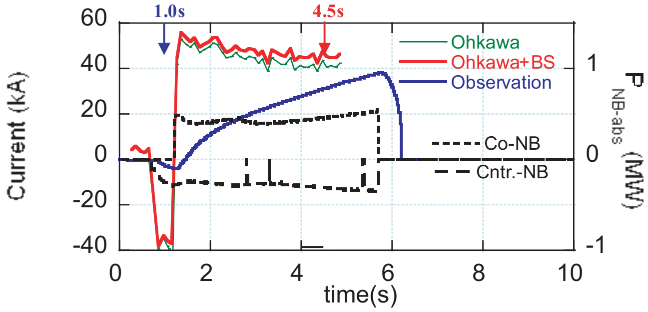

Fig. 4 Waveform of the discharge with 2 NB-injection. blue is observed current, red is calculated Ohkawa and bootstrap current , green is calculated Ohkawa current.Dotted line and dashed line are absorbed beam power.

4 Summary

The hierarchy-integrated simulation code for toroidal helical plasmas, TASK/3D, is being developed by based on TASK for two dimensional configuration. In the current stage, radial electric field module has been combined with the TR module, where the electric field is determined by the ambipolar condition and the single helicity model proposed by Shaing is chosen as neoclassical transport model. In order to check the electric field module ER, we carried out numerical simulations for an LHD experiment, assuming anomalous transport coefficient is a constant or a parabolic function. In the simulations, the density and rotational transform profiles are fixed.

For analyzing temporal evolution of the current profile in LHD, numerical simulations are done for an LHD experiment by using the combination of EI, VMEC, BSC/FIT modules, where experimental data is used for time evolution of the density and temperature profiles. By using full mesh points for discretization points, the updated EI module allows us to carry out reliable simulations.

In the next step, we will combine the EI module with the TASK/3D. Then, we can calculate temperature, density, radial electric field and rotational transform, simultaneously. Next, for neoclassical transport model, DCOM/NNW[5] will be added to TASK/3D, which is a neoclassical transport database for LHD plasmas constructed using the neural network method. Next, the ambipolar condition for determining electric field is replaced to the equation of time evolution of electric field, eq.(4). In this stage, nonlinearity of transport equations becomes stronger so that the present solver in TASK may not be suitable for solving such equations with strong nonlinearity. Hence, new stable and fast solver will be needed. For solving a set of nonlinear equations, Newton method is generally used. In the Newton iteration procedure, it is needed to solve large matrix problem, where the CPU time is consumed. We are trying to solve the problem by domain-decomposition method. After the stable and fast

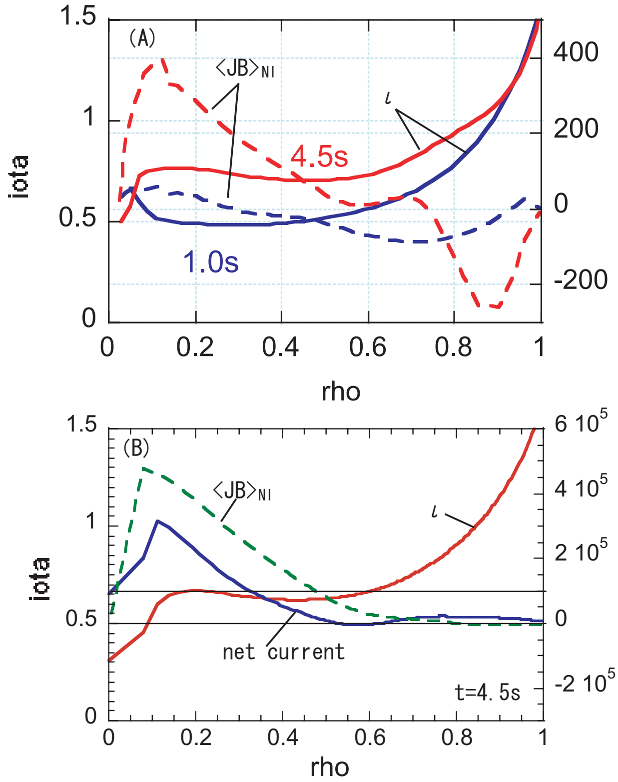

Fig. 5 Numerical results obtained from (A) earlier version of EI module and (B) updated version of EI module. In (A), solid lines are rotational transform profiles and dashed lines are non-inductive current profiles. The blue corresponds to result at $t = 1.0s$ and the red at $t = 4.5s$. In (B), the red solid line is rotational transform profile at $t = 4.5s$. The green dashed line and the blue solid line are non-inductive current profile and net current profile at $t = 4.5s$, respectively.

Newton solver is completed to develop, impurity module and heating modules will be added to TASK/3D in order to further develop the hierarchy-integrated simulation code for toroidal helical plasmas.

[1] A.Fukuyama et al., Proc. of 20th IAEA Fusion Energy Conf. (Villamoura, Portugal, 2004) IAEA-CSP-25/CD/TH/P2-3.
[2] Y. Nakamura et al., Fusion Sci. and Tech. 50 (2006) pp.457-463.
[3] Y. Nakamura et al., Proc. of 21th IAEA Fusion Energy Conf. (Chengdu, China, 2006) IAEA-CN-149/TH/P7-1.
[4] K. C. Shaing, Phys. Fluids 27 (1984) 1567.
[5] A. Wakasa et al., Jan. J. Appl. Phys. 46 (2007) 1157.

Proceedings of ITC/ISHW2007

Thermal Barrier Formation for Plasma Electrons and Ions in Kind of Connected Dip and Hump of Electrical Potential near ECR Points in Cylindrical Trap

Vasyl .I. Maslov[1], Ming Y. Yu[2]

[1]*NSC Kharkov Institute of Physics and Technology, Kharkov 61108, Ukraine*

[2]*Theoretical Physics I, Ruhr University, D-44780 Bochum, Germany*

(Received day month year / Accepted day month year should be centered 10-point type)

The experimentally observed formation of localized solitary barriers for plasma electrons and ions near the electron cyclotron resonance points near the ends of the cylindrical trap is investigated analytically. A new method of confinement of plasma particles in cylindrical traps is proposed.

Keywords: barrier, ECR point, cylindrical trap, solitary perturbation, evolution equation.

1. Inroduction

In [1] the formation of thermal barrier of plasma particles was observed near the location of electron cyclotron resonance (ECR). In this paper, such thermal barriers and their behavior in plasma are investigated theoretically. Mechanisms of thermal barrier formation in the plasma near the two butt-ends of cylindrical magnetic traps are considered. These barriers can enhance confinement of the plasma electrons and ions in cylindrical magnetic traps. We consider general case the plasma with negative ions.

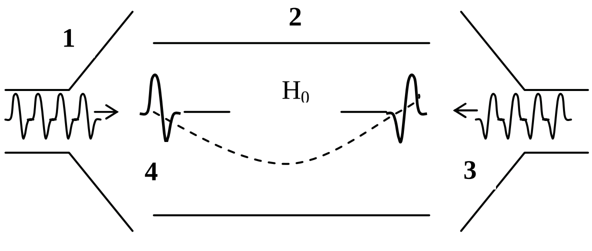

Fig. 1. Scheme of the thermal electrical barriers formation for plasma electrons and ions in ECR points on the edges of the magnetized cylindrical trap. Dotted line and symbol H(z) show the nonhomogeneous magnetic field. 1 is the qualitative scheme of the antenna for electromagnetic wave injection into the plasma trap; 2 is the cylindrical wall of the trap; 3 is the injected electromagnetic wave; 4 is the thermal barrier in kind of the dip and hump of the electric potential.

author's e-mail: vmaslov@kipt.kharkov.ua

2. Thermal barrier for plasma electrons

Consider two electromagnetic waves injected into a plasma trap through its butt-ends (see Fig. 1). Near the electron cyclotron resonance (ECR) points of the confining magnetic well, the energy of the waves are converted into that of the transverse motion of the electrons. We shall show that this energy conversion can be responsible for the observed [1] barriers of the plasma particles. A thermal barrier is a self-consistent structure consisting of a paired dip and hump of the electric potential (Fig. 1). The electron and ion phase spaces at the left barrier are shown in Figs. 2 and 3. The magnetic well H(z) has a minimum at the center of the trap, and it increases toward the edges of the trap. Near the ECR point the transverse electron velocity $V_\perp$ is increased up to $V_{\perp o}$ because of the resonant wave-particle interaction. The electrons are reflected by the magnetic mirror. Because of the inhomogeneous magnetic field H(z), the electron transverse velocity $V_\perp(z)=V_{\perp o}[H(z)/H_o]^{1/2}$, where H_o is the magnetic field at the ECR point, decreases in favor of its longitudinal velocity $V_\|(z)$ $V_\|(z)=V_{\perp o}(1-H(z)/H_o)^{1/2}$, which increases towards the center of the trap. This leads to an average electron flow towards the center, and thus an uncompensated increase of the electron density at the center of the trap.

The increase of the electron longitudinal velocity $V_\|$

with respect to that of the ions near the ECR point leads to a nonequilibrium state. The reflection of the electrons with nonequilibrium velocity distribution from the potential dip leads to a growth of the dip's amplitude. So these current-carrying electrons can excite the electric potential dip with amplitude φ_o on an ion mode with velocity V_c, close to zero, and are reflected from it.

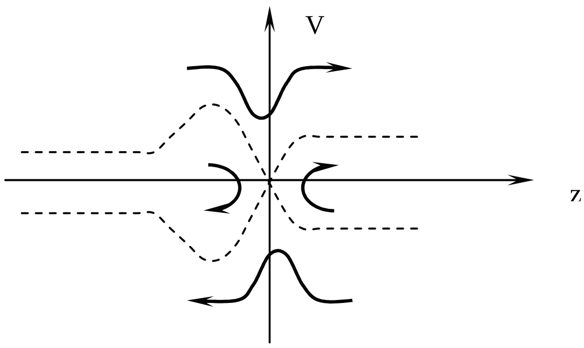

Fig. 2. Electron phase space. Dotted line is the separatrix, separating reflected and penetrated electrons. Arrows specify a direction of the electron movement.

From the electron Vlasov equation and ion hydrodynamic equations one can derive the evolution equation for the potential dip. In fact, we shall consider the slow evolution of the dip for its description. Taking into account that the resonant electrons are reflected from the dip, one can obtain from the Vlasov equation the expression for the steady state electron distribution function f_e

$$f_e=f_{oe}(-[V^2-2e(\varphi\pm\Delta\varphi)/m_e]^{1/2}\pm V_{||}), \qquad (1)$$

where f_{oe} is Maxwellian, $\Delta\varphi$ is the electric potential jump near the potential dip and has to be determined self-consistently. The plus and minus signs are for V greater and less than $A(\varphi)\mathrm{sign}(z)$, respectively. Here $A(\varphi)\equiv[2e(\varphi_o+\varphi)/m_e]^{1/2}$.

In the following we shall use the normalized quantities $\phi\equiv e\varphi/T_e$, $N_-\equiv n_{o-}/n_{o+}$, $N_e\equiv n_{oe}/n_{o+}$, $Q_\pm=q_\pm/e$, and $V_{s\pm}=(T_e/M_\pm)^{1/2}$. Furthermore, z is normalized by the electron Debye radius r_{de}, $V_{||}$ by the electron thermal velocity V_{the}, t by the inverse ion plasma frequency ω_{p+}^{-1}, and the speed V_c of the localized perturbation by the ion-acoustic velocity $(T_e/M_+)^{1/2}$. Here, T_e, is the temperature of electrons, n_{o-} and n_{o+} are the unperturbed densities of negative and positive ions, $q_\pm$ is the charge of positive and negative ions.

Integrating (1) on velocity, one can derive the electron density n_e in the first approximation on small $V_{||}$

$$n_e\approx n_{oe}\exp(\phi)[1-(2\Delta\phi/\sqrt{\pi})\beta_1-2V_{||}(2/\pi)^{1/2}\beta_2, \qquad (2)$$

$$\beta_1\equiv\int_o^\beta dx\,\exp(-x^2),\ \beta_2\equiv\int_o^\beta dx\,(x^2-\phi)^{1/2}\exp(-x^2)],$$

$$\beta\equiv(\phi_o+\phi)^{1/2}.$$

Far from the dip the plasma is quasineutral $n_e(z)\big|_{z\to\infty}=n_e(z)\big|_{z\to-\infty}=1-N_-$. Hence we derive, using (2), the expression for potential jump $\Delta\phi$ near the dip

$$\Delta\phi\approx V_{||}(2/\pi)^{1/2}(1-\exp(-\phi_o))/\beta_3, \qquad (3)$$

$$\beta_3\equiv[1-(2/\sqrt{\pi})\int_o^{\sqrt{\phi o}} dx\,\exp(-x^2)]$$

From hydrodynamic equations the expressions for densities of positive and negative ions can be obtained

$$n_{i\pm}=n_{\pm NL}+n_{\pm\tau},\ n_{\pm NL}=n_{o\pm}/[1-(\pm q_\pm)2\varphi/M_\pm V_c^2]^{1/2}, \qquad (4)$$

$$\partial n_{\pm\tau}/\partial z=\pm2(\partial\varphi/\partial t)(n_{o\pm}q_\pm/M_\pm V_c^3)\beta_4,$$

$$\beta_4\equiv[1-(\pm q_\pm)\varphi/M_\pm V_c^2]/[1-(\pm q_\pm)2\varphi/M_\pm V_c^2]^{3/2}$$

Substituting (2), (4) in Poisson's equation we can derive the nonlinear evolution equation

$$\partial^3{}_z\phi+\{\beta_5+\beta_6\}2\partial_t\phi/V_c^3+(\partial_z\phi/V_c^2)\{\beta_7+\beta_8\}-$$
$$-\{\exp(\phi)-\mathrm{sign}(z)V_{||}(2/\pi)^{1/2}\{\beta_9-$$
$$-\beta_{10}+(1-\exp(-\phi_o))\beta_{11}\beta_{12}/\sqrt{\pi}\}\}\partial_z\phi=0, \qquad (5)$$

$$\beta_5\equiv Q_+^2V^2_{s+}(1-2\phi Q_+V^2_{s+}/V_c^2)^{-3/2}(1-\phi Q_+V^2_{s+}/V_c^2),$$
$$\beta_6\equiv Q_-^2N_-V^2_{s-}(1+2\phi Q_-V^2_{s-}/V_c^2)^{-3/2}(1+\phi Q_-V^2_{s-}/V_c^2),$$
$$\beta_7\equiv Q_+^2V^2_{s+}(1-2\phi Q_+V^2_{s+}/V_c^2)^{-3/2},$$
$$\beta_8\equiv Q_-^2N_-V^2_{s-}(1+2\phi Q_-V^2_{s-}/V_c^2)^{-3/2},$$
$$\beta_9\equiv(\phi_o/(\phi_o+\phi))^{1/2}\exp(-\phi_o),$$
$$\beta_{10}\equiv\int_{\sqrt{-\phi}}^{\sqrt{\phi o}} dy(1-2y^2)\exp(-y^2)/(y^2+\phi)^{1/2},$$
$$\beta_{11}\equiv[1-(2/\sqrt{\pi})\int_o^{\sqrt{\phi o}} dx\exp(-x^2)]^{-1},$$
$$\beta_{12}\equiv[\exp(-\phi_o)/(\phi_o+\phi)^{1/2}+2(\phi_o+\phi)\exp(-\phi_o)+$$
$$+4\int_{\sqrt{-\phi}}^{\sqrt{\phi o}} dy\,y(y^2+\phi)^{1/2}\exp(-y^2)].$$

Here $\partial_z\equiv\partial/\partial z$, $\partial_t\equiv\partial/\partial t$. (5) has been derived in approximation of slow dip evolution, i.e. in approximation of the small growth rate of the dip amplitude γ_{nl} .

From the nonlinear equation (5) the dip is shown to propagate with a slow velocity $V_c\approx0$. From (5) the growth rate of the dip's small amplitude can also be obtained

$$\gamma_{nl}\approx\omega_{p+}(V_{||}/V_{the})^{3/2}(q_+/e)(n_+/n_e)^{1/2}\beta_{13}, \qquad (6)$$

$$\beta_{13}\equiv\{1+[1/3-(n_e/n_+)(e/q_+)](e\varphi_o/T_e)(\pi/2)^{1/2}(V_{the}/2V_{||})\}.$$

One can see that the dip is formed at ratio of electron current-carrying to thermal velocity $V_{||}/V_{the}$ larger than the threshold. The threshold decreases at decreasing of ratio of electron and positive ion densities n_e/n_+ and is equal to zero at $n_e/n_+<q_+/3e$. The threshold is maximum at $n_e/n_+=1$.

3. Barrier formation for plasma ions in kind of electric potential hump near the ECR point

As the electrons are reflected from the dip and the ion flow passes with velocity V_{o+} freely, the uncompensated volume charge of ions is formed after the dip, in the field of which the ions slow down and are reflected. This volume charge forms perturbation of the electric potential hump. The ion flow enhances this hump of the electric potential. At first we describe the quasi-stationary properties of the hump, neglecting the nonequilibrium condition. Then taking into account the nonequilibrium condition we can obtain the hump's excitation, in other words the growth of the hump's amplitude. Further we will show that the electric potential hump is almost fixed in space.

We consider general case, when flow of the positive ions passes with velocity V_{o+} in the plasma with electrons and also with negative and motionless positive ions of small densities.

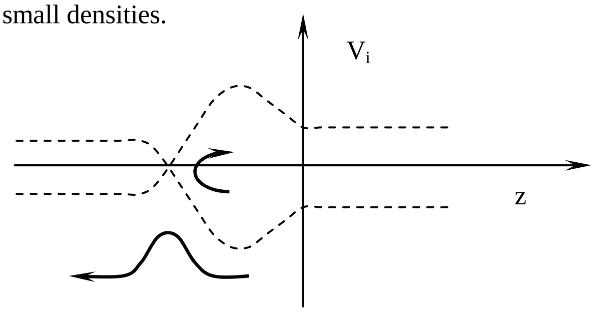

Fig. 3. Ion phase space. Dotted line is the separatrix, separating reflected and penetrated ions. Arrows specify a direction of the ion movement.

In linear approximation the perturbation excitation by the positive ion flow, propagating relative to negative and motionless positive ions of small densities, is described by the following dispersion ratio:

$$1+1/(kr_{de})^2-\omega^2_{p+}/(\omega-Kv_{o+})^2-\omega^2_{p-}/\omega^2-\omega^2_{pq}/\omega^2=0. \quad (7)$$

Here ω, k are the frequency and wave-vector of the perturbation; $\omega_{p\pm}$ are the plasma frequencies of the negative and the flow's positive ions; ω_{pq} is the plasma frequency of the positive motionless ions; r_{de} is the Debye radius of electrons; V_{o+} is the velocity of the positive ion flow.

From (7) we show that one can select the flow velocity such that following inequalities are correct

$$V_{ph}=\omega/k\approx(V_{o+}/2^{4/3})[(n_-m_+q_-^2/ n_+m_-q_+^2)+(n_{+q}q_{+q}^2/ n_+q_+^2)]^{1/3}<<V_{s+},$$
$$\lambda=2\pi/k=2\pi r_{de}/(V_{s+}^2n_+q_+^2/V_{o+}^2n_ee^2-1)^{1/2}>>r_{de} . \quad (8)$$

Hence the perturbation is almost motionless, that is $V_{ph}<<V_{s+}$. $V_{s+}=(T/m_+)^{1/2}$ is the ion-acoustic velocity of the flow positive ions. Here n_-, m_-, q_- (n_+, m_+, q_+) are the density, mass and charge of the negative (positive) ions.

From (7) we derive the growth rate of the perturbation excitation:

$$\gamma=(1.5)^{1/2}(V_{o+}/r_{de})[(n_-m_+q_-^2/n_+m_-q_+^2)+ +(n_{+q}q_{+q}^2/n_+q_+^2)]^{1/3}(V_{s+}^2q_+/V_{o+}^2e-1)^{1/2}. \quad (9)$$

On the non-linear stage of the instability development the electric potential perturbation φ represents the solitary hump of the finite amplitude φ_o.

The distribution function $f_e(v)$ of untrapped electrons, that are arranged outside the separatrix, looks like:

$$f_e(v)=[n_{oe}/V_{te}(2\pi)^{1/2}]\exp(e\varphi/T_e-m_ev^2/2T_e). \quad (10)$$

For trapped electrons, i.e. for electrons located inside the separatrix, the distribution function does not depend on energy because of an adiabaticity of the evolution.

Integrating the electron distribution function on velocity, we get following expression for electron density:

$$n_e=(n_o/(2\pi)^{1/2})(2/T)^{3/2}\int^{\infty}_{o}d\varepsilon(\varepsilon+e\varphi)^{1/2}\exp(-\varepsilon/T). \quad (11)$$

From the hydrodynamic equations for positive ions it is possible to get the following expression for their density:

$$n_+=n_{o+}/[1-2q_+\varphi/m_+(V_{o+}-V_h)^2]^{1/2}. \quad (12)$$

Here V_h is the velocity of the solitary perturbation.

As a result from (11), (12) and the Poisson's equation we have an equation for the spatial distribution of the electric potential ϕ of the perturbation of any amplitude:

$$\phi''=(2/\sqrt{\pi})\int^{\infty}_{o}da e^{-a}(a+\phi)^{1/2}-1/(1-2Q\phi/v_{oh}^2)^{1/2}. \quad (13)$$

$Q=q_+/e$, $\phi=e\varphi/T$, «’»$=\partial/\partial x$, $x=z/r_{de}$, $v_{oh}=(V_{o+}-V_h)/V_{s+}$.

From the apparent condition that the electric field of the electric potential hump is equal to zero for maximum potential $\phi'|_{\phi=\phi o}=0$ and from (13) we obtain the hump velocity, v_{oh}:

$$v_{oh}^2/Q=(A-2)^2/2(A-2-\phi_o),$$
$$A\equiv(8/3\sqrt{\pi})\int^{\infty}_{o}da e^{-a}(a+\phi_o)^{3/2}. \quad (14)$$

In the approximation of small amplitude from (13), (14) we obtain:

$$v_{oh}^2\approx Q, \quad L\approx[15\sqrt{\pi}/4(1-1/\sqrt{2})]^{1/2}\phi_o^{-1/4}. \quad (15)$$

If V_{o+} is close to $(q_+/e)^{1/2}V_{s+}$, the perturbation is approximately motionless.

Taking into account the small densities of negative and motionless positive ions, we derive from the Poisson equation the evolution equation:

$$2\omega^2_{p+}\partial^3\varphi/\partial t^3/(V_{o+}-V_h)^3=-(\omega^2_{p-}+\omega^2_{pq})\partial^3\varphi/\partial z^3. \quad (16)$$

From (16) the growth rate of the non-linear perturbation amplitude is derived:

$$\gamma_{NL}\approx \quad (17)$$

$$\approx\omega_{p+}(e\varphi_o/T)^{1/2}[(n_{o-}m_+q^2_-/n_{o+}m_+q^2_+)+(n_{oq}q^2_{+q}/n_{o+}q^2_+)]^{1/3}.$$

4. The electron mechanism of the barrier formation for plasma ions near the ECR point

Let us consider the mechanism of the electric potential hump formation by current-carrying (i.e. with $V_{||}\neq 0$) plasma electrons near the dip of the electric potential.

The potential jump $\Delta\phi$, formed near the dip, accelerates electrons to the first front of the dip. Further we assume that the current-carrying velocity $V_{||}$ of the electrons on the back front of the dip is close but smaller than the electron thermal velocity V_{th}. Hence on the first front of the electric potential dip the electron current-carrying velocity becomes more than electron thermal velocity due to the flow continuity law. Hence on the first front of the dip the Bunemann instability is developed [2]. Due to Bunemann mechanism interaction of electron flow with this region an electric potential hump is excited.

Let us describe the solitary perturbation in kind of electric potential hump. We will show that it represents a nonlinear perturbation on a slow electron-sound mode. As it is slow, resonant electrons can be trapped by such perturbation.

From Vlasov's equation the expression for the perturbation of the electron distribution function is derived. Integrating this expression on velocity in case of a small amplitude of the solitary perturbation φ_o we get the expression for the perturbation of electron density

$$\delta n'=\partial_t\varphi\beta_{14}+\varphi' R(y)+\varphi\varphi'\beta_{15}, \qquad (18)$$

$$\beta_{14}\equiv[y+(1-2y^2)(1-R(y))/y],\ \beta_{15}\equiv[1-y^2+(3/2-y^2)(R(y)-1)],$$

$$R(y)\equiv 1+(y/\sqrt{\pi})\int_{-\infty}^{\infty}dt\exp(-t^2)/(t-y),\ y\equiv(V_{||}-V_h)/V_{th}\sqrt{2}.$$

Here a point means derivative in time, and a prime is a spatial derivative. V_h, φ are the velocity and the potential of soliton. $\phi\equiv e\varphi/T_e$. T_e is the electron temperature. Substituting (18) in Poisson's equation, we derive in stationary approximation an equation, describing spatial distribution of potential:

$$(\phi')^2=\phi^2R(y)-[1+(2y^2-3)R(y)]\phi^3/6. \qquad (19)$$

The soliton width is followed from (19) to be approximately equal $\Delta z=(48T_e/\varphi_o)^{1/2}$. The soliton width decreases with amplitude growth.

One can show that $V_h\approx 0$ if $V_{||}\approx 1.32V_{th}$.

In case of large amplitudes, $e\varphi_o/T_e>1$, from Vlasov equation we have the expression for electron distribution function $f=f_o[(u^2-2e\varphi/m)^{1/2}+V_h\mathrm{sign}(u)]$ for $|u|=|V-V_h|>(2e\varphi/m)^{1/2}$. Here f_o is Maxwell distribution function. Thus we obtain the equation for the soliton shape

$$(\phi')^2=-\phi+(2/\sqrt{\pi})^{1/2}\int_{-\infty}^{\infty}dt(t-y)^2\exp(-t^2)\{[1+\phi/(y-t)^2]^{1/2}-1\} \qquad (20)$$

From (20) we derive the soliton width

$$\Delta z=[2e\varphi_o/T_e(\sqrt{2}-1)]^{1/2} \qquad (21)$$

From (21) we conclude that the soliton width grows with φ_o. Therefore, it is necessary to take into account the electrons, trapped by the soliton field. Assuming the distribution of their density as $n_{tr}(z)=n_2\exp[e\varphi(z)/T_{tr}]$, we derive similarly to (21), that width and velocity of the soliton grow with amplitude growth (in difference from the case of small amplitudes of the solitary perturbation) Here T_{tr} , n_2 are the trapped electron temperature and density.

Thus, neglecting the ion mobility, this solitary perturbation is stationary and an electron one. However at taking into account of the ion mobility it is necessary to expect occurrence of slow growth of the perturbation's amplitude, as a result of Bunemann instability development. In the following order of the theory of disturbances from (18) we derive the correction of the next order to a spatial derivative of electron density

$$n_{e1}'=\partial_t\varphi[y+(1-2y^2)(1-R(y))/y] \qquad (22)$$

This expression as follows from a spatial derivative from Poisson's equation must be equal to a spatial derivative from the ion density perturbation n_i'. It is possible to find n_i' in a linear approximation from ion hydrodynamic equations

$$\partial^2_t n_i=(m_e/m_i)\phi'' \qquad (23)$$

Equating the second time derivative from (22) and the first spatial derivative from (23), we obtain

$$\partial^3_t\phi=(6m_e/m_i)\phi''' \qquad (24)$$

The solution of (24) we search as

$$\phi(z,t)=\phi_o(t)\eta[z-\int_{-\infty}^{t}dt_1\delta v_o(\phi_o(t_1))]\ . \qquad (25)$$

$\eta(z)$ is quasistationary shape of the perturbation. We assume that $\partial_t\phi_o(t)=\gamma\phi_o(t)$. In (25) the change of soliton velocity with change of its amplitude is taken into account.

Substituting $\partial_t\phi$ for $\gamma\phi-\delta v_h\phi'$, we obtain from (24)

$$\gamma\approx(m_e/m_i)^{1/3}\phi_o^{1/2} \qquad (26)$$

In the case of the electron mechanism of the barrier formation for plasma ions the inverse spatial sequence of the hump and dip, comparing with that one shown in Fig. 1, is realized.

References

[1] T. Kaneko, R. Hatakeyama, N. Sato. IEEE Trans. on Plasma Science **28**, 1747 (2000).

[2] T. Sato, H. Takamaru and the Complexity Simulation Group. Phys. Plasmas **2**, 3609 (1995).

P2-026

Research of effective ripples in helical systems

O. Yamagishi

National Institute for Fusion Science,322-6 Oroshi-cho, Toki 509-5292, Japan

e-mail address: yamagisi@nifs.ac.jp

The ripple transport is one of problems that need to be overcome in the helical systems. Thus quasi-(toroidally, poroidally, helically) symmetric configurations have been designed in the world. On the other hand, it has been found in LHD [1] that the effective ripple, which is a measure of ripple transport, can be significantly reduced, without depending on the symmetry of the magnetic fields. This feature in asymmetric configurations like LHD seems to be important because it does not rely on the complicated coil geometry. However, the major radius at the magnetic axis in the vacuum is clearly inadequate to parameterize the effective ripple in general. One of attempts to explain the behavior of the effective ripple [2] is based on the combination of complicated magnetic field spectrum. In this work, it is tried to investigate how the effective ripple is related to B spectrum and other parameters. For example, since the ripples along a field line are affected by the rotational transform, it can be controlled simply if external currents can be controlled.

[1] S.Murakami et al., Nucl. Fusion **42**, L19 (2002)
[2] M.Yokoyama et al., Nucl. Fusion **42**, 1600 (2005)

Proceedings of ITC/ISHW2007

Tokamak Plasma Transport Simulation in the Presence of Neoclassical Tearing Modes

Y. Takahashi, K. Yamazaki, J. Garcia[a], H. Arimoto, T. Shoji

Nagoya University, Furo-cho, Chikusa-ku, Nagoya 464-8603, Japan

[a]Universitat Polite`cnica de Catalunya (UPC), Barcelona, Spain

For the prediction of the ITER plasmas, the effect of the neoclassical tearing mode (NTM) on the plasma confinement has been calculated using the 1.5-dimensional equilibrium and transport simulation code TOTAL. The time evolution of the NTM magnetic island has been analyzed using the modified Rutherford equation for a ITER normal shear plasma. The anomalous transport model used here is GLF23. The saturated magnetic island widths are w/a~0.048 at 3/2 mode and w/a~0.21 at 2/1 mode, and the reduction in fusion power output by NTM is 27% at the 3/2 mode, 82% at the 2/1 mode, and 89% at the 3/2 + 2/1 double mode. The stabilization effect of the electron cyclotron current drive (ECCD) with EC is also clarified. The threshold of ECCD power for the full stabilization is ~10[MW] against the 3/2 mode, and ~23[MW] against the 2/1 mode.

Keywords: ITER, tokamak, simulation, neoclassical tearing mode, electron cyclotron current drive, stabilization

1. Introduction

The neoclassical tearing mode (NTM) might limit the plasma pressure and would lead to a disruption in future tokamak reactors. The NTM makes the temperature profile flat inside magnetic island, and the central plasma temperature is reduced. Therefore, when the magnetic island is formed in the plasma, the fusion output power is decreased. The analysis and control of NTMs are one of the crucial issues in tokamak reactor [1]. The NTM is caused by a lack of the bootstrap current inside the magnetic island where the pressure profile is flattened [2]. The electron cyclotron current drive (ECCD) gives the NTM stabilization to replace the missing bootstrap current. The effect of NTM on the ITER plasma should be investigated, and the stabilization method of NTM should be clarified.

For the prediction of ITER plasmas, the time evolution of neoclassical tearing modes has been calculated by using the 1.5-dimensional (1.5-D) equilibrium and transport simulation code (toroidal transport linkage code TOTAL [3,4]). The magnetic island width is evaluated using the modified Rutherford equation [5,6]. In the simulation code, we used the GLF23 anomalous transport model that can simulate H-mode plasmas [7].

The purpose of this paper is to clarify the effect of the NTM magnetic island formation on the plasma confinement and to demonstrate its stabilization by the electron cyclotron current drive (ECCD) in ITER. In the next section, a numerical model is described. The details of modified Rutherford equation, the ECCD current profile and the current drive efficiency are also shown in this section. In section 3, simulation results are shown. The summary is given in section 4.

author's e-mail: takahashi-y@ees.nagoya-u.ac.jp

2. Numerical model

The time evolution of NTM has been calculated using 1.5-D equilibrium and transport code (toroidal transport linkage code TOTAL [3,4]). The plasma equilibrium is solved by the free-boundary Apollo code [8], and the plasma transport is evaluated including the impurity dynamics [9]. The anomalous transport model used here is the glf23 [7] that can simulate H-mode plasmas.

2.1 Modified Rutherford equation

The time evolution of a NTM island width, *W*, is calculated according to the modified Ruther ford equation. Here, *W* is the normalized magnetic island width with respect to the minor plasma radius, *a*.

$$\frac{dW}{dt} = \Gamma_{\Delta'} + \Gamma_{BS} + \Gamma_{GGJ} + \Gamma_{pol} + \Gamma_{EC} \quad (1)$$

$$\Gamma_{\Delta'} = k_1 \frac{\eta}{\mu_0} \Delta'(W) \left\langle |\nabla\rho|^2 \right\rangle \quad (2)$$

$$\Gamma_{BS} = k_2 \eta L_q j_{BS} \left\langle \frac{|\nabla\rho|}{B_p} \right\rangle \frac{W}{W^2 + W_d^2} \quad (3)$$

$$\Gamma_{GGJ} = -k_3 \frac{\eta}{\mu_0} \varepsilon_s^2 \beta_{ps} \frac{L_q^2}{\rho_s L_p} \left(1 - \frac{1}{q_s^2}\right) \left\langle |\nabla\rho|^2 \right\rangle \frac{1}{W} \quad (4)$$

$$\Gamma_{pol} = -k_4 \frac{\eta}{\mu_0} g(\varepsilon_s, \nu_i) \beta_{ps} \left(\frac{\rho_{pi} L_q^2}{L_p}\right)^2 \left\langle |\nabla\rho|^2 \right\rangle \frac{1}{W^3} \quad (5)$$

$$\Gamma_{EC} = -k_5 \eta \frac{L_q}{\rho_s} \left\langle \frac{|\nabla \rho|}{B_p} \right\rangle f \eta_{EC} \frac{I_{EC}}{a^2} \frac{1}{W^2} \qquad (6)$$

Here, $\Gamma_{\Delta'}$ is the classical stability index defined as the logarithmic jump of the radial magnetic field perturbation across the rational surface [10]. Γ_{BS}, Γ_{GGJ}, Γ_{pol} and Γ_{EC} are the perturbed bootstrap current, the stabilizing effect of the field line curvature [11], the ion polarization current and the EC current effect [12]. ρ is the coordinate of the normalized minor radius. η, ε_s, β_{ps}, ρ_{pi} and ρ_s are the neoclassical resistivity, the inverse aspect ratio, the local poloidal beta, the poloidal Larmor radius normalized by minor radius a and the rational surface position, respectively. The scale lengths, L_q and L_p, are defined as $L_q=(dq/d\rho)^{-1}$ and $L_p=-(dp/d\rho)^{-1}$.

2.2 Modified Rutherford equation

In this paper, the EC current profile is modelled by a Gaussian distribution as

$$j_{EC} = j_{EC0} \exp\left(-C \left(\frac{\rho - \rho_s}{W_{EC}} \right)^2 \right), \qquad (7)$$

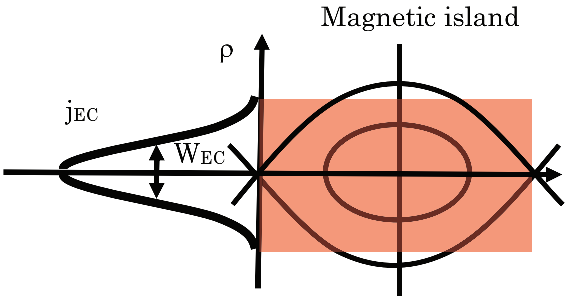

Figure 1. Model of EC current profile. The EC current density, j_{EC} is modelled by the Gaussian distribution.

where C=4ln2, j_{EC0} is calculated from the total EC current I_{EC}. The value ρ_s is the position of the current density peak. The efficiency of the EC current is given by [2]

$$\eta_{EC} = \frac{\int d\hat{\rho} \oint (d\alpha/2\pi) \cos(m\alpha) \langle\langle j_{EC} \rangle\rangle}{\int d\hat{\rho} \oint (d\alpha/2\pi) \langle\langle j_{EC} \rangle\rangle}, \qquad (8)$$

The value of I_{EC} is assumed to be proportional to the EC power, P_{EC}, as I_{EC} [kA]=4.35P_{EC}[MW] for the 3/2 mode and 4.15P_{EC}[MW] for the 2/1 mode [6].

3. Numerical result

Table 1 shows parameters of a typical ITER plasma analyzed in this paper. The local parameters at the rational surfaces of q=3/2 and 2/1 are shown table 2, where ρ_s,β_{ps} and j_{BS} are the normalized rational surface position, the local poloidal beta, and the local bootstrap current density, respectively. The coefficients of each term in the modified Rutherford equation used here are shown in table 3.

Table 1. Plasma parameters used here for ITER.

R_0 : major radius (m)	6.2
a : minor radius (m)	2.0
B_{t0} : toroidal field at R_0 (T)	5.3
I_P : plasma current (MA)	15
$\langle n_e \rangle$ (x 10^{20} m^{-3})	1.01
$\langle T_e \rangle$ (keV)	10.9
$\langle T_i \rangle$ (keV)	9.8
β	3.1

Table 2. Parameters relevant to the rational surface.

m/n	3/2	2/1
ρ_s	0.67	0.84
β_{ps}	0.65	0.46
J_{BS} (MA/m^2)	0.11	0.11

Table 3. Coefficients of each term in the modified Rutherford equation used here

k_1	1.0
k_2	10.0
k_3	1.0
k_4	1.0
k_5	5.0

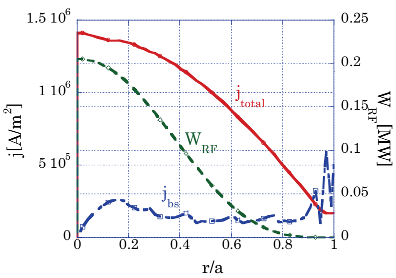

Figure 2. Plasma current density and input heating power profile as a function of normalized minor radius. The total input power is 40 MW, the average electron density is 1.0×10^{20} m^{-3} and the total current is 15 MA.

3.1 Reduction in plasma temperature and fusion power by NTM

In a ITER plasma the NTM magnetic islands are saturated around ten seconds after introducing the seed island. Figure 3 shows the electron temperature profile and the q profile when the magnetic island is saturated. The 3/2 mode island (q=1.5) exists at r/a=0.67, and the 2/1 mode island (q=2) exists at r/a=0.84. We assumed the transport coefficient is quite large inside the magnetic island. According to figure 3, the electron temperature at plasma center decreases due to the magnetic island formation. That is, the fusion power decreases too due to the NTM magnetic island. Table 4 shows the plasma parameters when the magnetic island exists in the plasma. Here, $T_e(0)$,

I_{BS}, I_{TOTAL} and Q are the central electron temperature, the total bootstrap current, the total current and the Q value, respectively. The Q value is defined by the ratio of the fusion output power to the input power. At 3/2 mode, the Q value decreases to 73% of no NTM case, at 2/1 mode, the Q value decreases to 18% of no NTM case, and at double tearing modes, the Q value decreases to 11% of no NTM. To reduce the magnetic island width is important in order to raise the fusion power output.

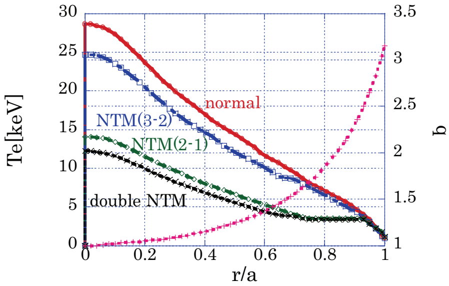

Figure 3. Electron temperature and safety factor q profile without and with 3/2, 2/1, and double neoclassical tearing modes.

Table 4. Central temperature, bootstrap current fraction and Q value in three cases

	Te(0)[keV]	I_{BS}/I_{total}(%)	Q
Normal	28.7	23.2	14.6
NTM(3/2)	24.9	20.3	10.7
NTM(2/1)	14.9	12.6	2.6
Double NTM	12.2	9.2	1.6

3.2 Time evolution and saturation of magnetic island width

The NTM magnetic island grows in time, and the island width is finally saturated. We assumes a seed island with w/a=0.05 introduced at time=30 [s]. Figure 4 shows the time evolution of the magnetic island width with 3/2, 2/1, and double modes. The 3/2 mode island width is saturated at w/a=0.048, and the 2/1 mode is saturated at w/a=0.21. As double mode, saturated each magnetic island width is nearly equal to single mode. The time constant for saturation is about 10 seconds. In 3/2 mode, the time for saturation of double mode is longer than single mode. In 2/1 mode, the time for saturation are same with single and double.

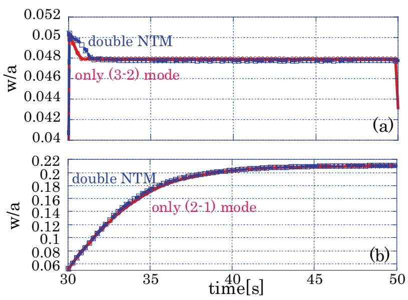

Figure 4. Time evolution of central temperature and magnetic island width of each modes (a) 3/2 mode, and (b) 2/1 mode.

Figure 5 shows the time evolution of every terms in the modified Rutherford equation as single mode. It should be noted that in equilibrium, the term $\Gamma_{\Delta'}$ changes from positive to negative.

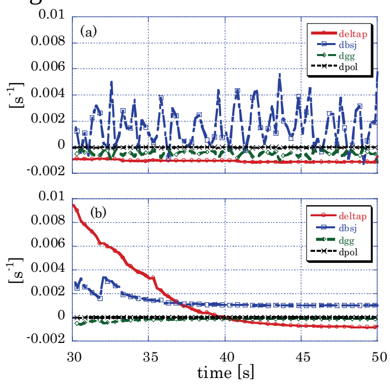

Figure 5. Total current and bootstrap current profile with (a) 3/2 and (b) 2/1 modes.

3.3 Time evolution and saturation of magnetic island width

We simulated the reduction in the magnetic island width by adding the electron cyclotron current drive (ECCD). Figure 6 shows the effect of the ECCD injected at 40[s] using the model described in section 3.2. The magnetic island width is fully erased by adding the large ECCD power. And, We simulated the different of reduction single and double mode. Figure 7 shows the reduction of magnetic island width in case of single and double. In 2/1 mode, their difference is very small. But in 3/2 mode, the effect of ECCD is big. Because, the temperature at 3/2 surface position in case of double is small in compare with single (Figure 3). The temperature at surface position 2/1 is same with double and single. We change the injection time of ECCD as shown in figure 8. Early injection of ECCD can easily reduce the magnetic island width. The value of the total EC current I_{EC} is assumed to be proportional to the EC power, P_{EC},

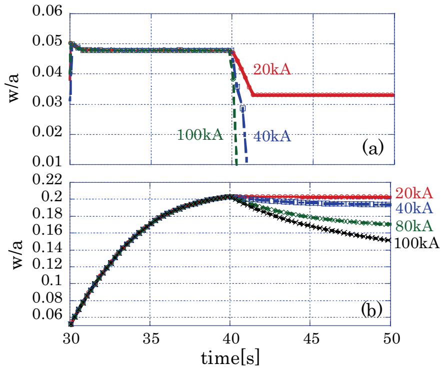

Figure 6. Time evolution of magnetic island width at (a) 3/2 mode and (b) 2/1 mode. Magnetic seed island with w/a=0.05 is introduced at time=30[s], and the EC current was injected from 40[s] with current width W_{EC}/a=0.04 and with EC total current of 20, 40, 100 and 200[kA].

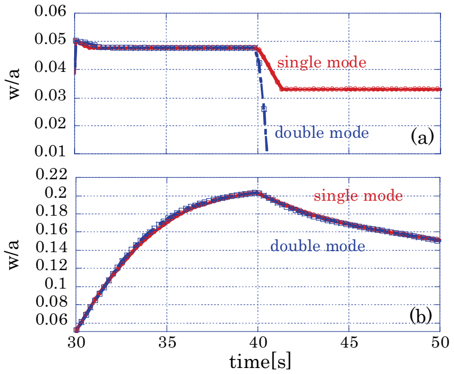

Figure 7. Time evolution of magnetic island of the seed island with w/a = 0.05 at time=30 [s] at (a) 3/2 mode injected current 20[kA], and (b) 2/1 mode injected current 100[kA]. The ECCD power is injected at time = 40 [s] in single (blue) and 3/2+2/1 double mode(red) case.

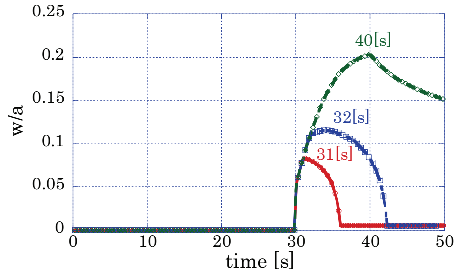

Figure 8. Time evolution of magnetic island of the seed island with w/a = 0.05 at time=30 [s]. The ECCD power of 100kA is injected at the time shown in the figure.

as I_{EC} [kA] = 4.35P_{EC}[MW] for the 3/2 mode and 4.15P_{EC}[MW] for the 2/1 mode. We need 10MW ECCD power for 2/1 mode stabilization, and 23MW for 3/2 mode stabilization, when the NTM is saturated.

4. Summary and discussions

The ITER plasma with the neoclassical tearing mode (NTM) is simulated using integrated transport code TOTAL. The anomalous transport model used here is GLF23, and the magnetic island width of NTM is calculated by the modified Rutherford equation. The magnetic island formation reduces the plasma temperature and the fusion output power. The decrease in the Q value due to NTM is estimated. The reduction in fusion output power by NTM is 27% at the 3/2 mode, 82% at the 2/1 mode, and 89% at the 3/2+2/1 double mode. The saturated magnetic island widths of each modes are w/a~0.048 at 3/2 mode and w/a~0.21 at 2/1 mode.

The Injection of ECCD is considered to stabilize the NTM and to recover the plasma confinement. We calculate the stabilization effect of ECCD with EC width w_{EC}/a=0.04. The threshold power for the NTM full stabilization by ECCD is ~10 MW against the 3/2 mode, and ~23 MW against the 2/1 mode.

For the reduction in ECCD power and the increase in the stabilization effects, the EC current width should be narrow. When the injection current width is half, the threshold power for the full stabilization is considered about half. The other method for ECCD power reduction is to modulate the EC current. The efficiency of ECCD can be raised by the current injection to the O point in magnetic island. The details of these analyses will be described somewhere in the future.

References

[1] ITER Physics Basis Editors *et al.*, Nucl. Fusion **39**, 2137 (1999).
[2] Hegna C C and Callen J D, Phys. Plasmas **4**, 2940 (1997).
[3] Yamazaki K and Amano T, Nucl. Fusion **32,** 633 (1992)
[4] Yamazaki K *et al.*, Fusion Engineering and Design **81**, 2743 (2006)
[5] Sauter O *et al*., Phys. Plasmas **4**, 1654 (1997)
[6] Hayashi N, Ozeki T, Hamamatsu K and Takizuka T, Nucl. Fusion **44**, 477 (2007)
[7] Waltz R E, Staebler G M, Dorland W, Hammett G W, Kotschenreuther M and Konings J A, Phys. Plasmas **4**, 2482 (1997)
[8] Yamazaki K, Amano T, Naitou H, Hamada Y and Azumi M, Nucl. Fusion **25**, 1543 (1985)
[9] Yamazaki K *et al.*, J. Plasma Fusion Res. SERIES **7,** 102 (2006)
[10] Furth H P, Rutherford P H and Selberg H, Phys. Fluids **16,** 1054 (1973)
[11] Kotschenreuther M, Hazeltine R D and Morrison P J, Phys. Fluids **28**, 899 (1985)
[12] Wilson H R *et al*., Phys. Plasmas **3**, 248 (1996)

Proceedings of ITC/ISHW2007

Axisymmetric equilibria with flow in reduced single-fluid models

Atsushi ITO[1)], Jesús J. RAMOS[2)] and Noriyoshi NAKAJIMA[1)]

[1)] *National Institute for Fusion Science, 322-6 Oroshi-cho, Toki 509-5292, Japan*

[2)] *Plasma Science and Fusion Center, Massachusetts Institute of Technology, Cambridge, Massachusetts, 02139-4307*

Reduced magnetohydrodynamic equations for axisymmetric toroidal equilibria of flowing high-β plasmas are derived with asymptotic expansions in terms of the inverse aspect ratio in order to construct models suitable for the extension to include hot ion effects that are obtained with asymptotic expansions. Depending on the flow velocity, different orderings are applied. Singular points at the poloidal flow velocity equal to poloidal sound and poloidal Alfvén velocity are reproduced. The poloidal sound singularity appears in the higher order equations.

Keywords: magnetohydrodynamics, equilibrium, flow

Plasma flows are suggested to lead transport barriers and pedestals that show steep profiles in the steady states of magnetic confinement. Flowing equilibria have been studied to describe these phenomena in the framework of magnetohydrodynamics (MHD)[1, 2]. However, for such steep plasma profile features, small-scale effects not included in the ideal MHD model should be significant. The small scale effects arising due to the Hall current have been studied with two-fluid or Hall MHD models [6, 7, 8, 9, 10, 11]. However, these models are consistent with kinetic theory only for cold ions. In order to include the hot ion effects that are relevant to fusion plasmas, an extension of the model is necessary. However, a consistent treatment of hot ions in a two-fluid framework must include the ion gyroviscosity and other finite ion Larmor radius effects. These effects are obtained by asymptotic expansions in terms of the small parameter δ that is the ratio between the ion Larmor radius and the macroscopic scale length, and are much simplified in the slow dynamics ordering $v \sim \delta v_{th}$ where v and v_{th} are the flow and thermal velocities respectively [12, 13]. In this study, we obtain reduced sets of equations for MHD equilibria with flow with asymptotic expansions in order to construct models suitable for the extension to include hot ion effects. We shall study two cases of the flow velocity in the orders of the poloidal sound and poloidal Alfvén velocities. These are the characteristic velocities that bring singularities in the equilibrium equations [2, 3, 4, 5].

The equilibrium equations for single-fluid MHD are

$$\nabla \cdot (\rho \mathbf{v}) = 0, \tag{1}$$

$$\nabla \times \mathbf{E} = 0, \tag{2}$$

$$\mathbf{E} = -\mathbf{v} \times \mathbf{B}, \tag{3}$$

$$\rho \mathbf{v} \cdot \nabla \mathbf{v} = \mathbf{j} \times \mathbf{B} - \nabla p, \tag{4}$$

$$\mu_0 \mathbf{j} = \nabla \times \mathbf{B} \tag{5}$$

$$\mathbf{v} \cdot \nabla p + \gamma p \nabla \cdot \mathbf{v} = 0, \tag{6}$$

where ρ is the mass density, $\mathbf{v}$ is the flow velocity, $\mathbf{E}$ and $\mathbf{B}$ are the electric and magnetic fields, $\mathbf{j}$ is the current density, and p is the pressure. Here we shall consider the corresponding toroidal axisymmetric equilibria, where the magnetic field $\mathbf{B}$ and the current density $\mathbf{j}$ can be written as

$$\mathbf{B} = \nabla \psi(R,Z) \times \nabla \varphi + I(R,Z) \nabla \varphi \tag{7}$$

$$\mu_0 \mathbf{j} = \nabla I \times \nabla \varphi - \Delta^* \psi \nabla \varphi, \tag{8}$$

where ψ is the poloidal magnetic flux and $\Delta^* \equiv R^2 \nabla \cdot [R^{-2} \nabla]$. The asymptotic expansion is defined in terms of the inverse aspect ratio $\varepsilon \equiv a/R_0 \ll 1$ where a and R_0 are the characteristic scale length of the minor and major radii respectively. The following high-β tokamak ordering is applied,

$$B_p \sim \varepsilon B_0, \quad p \sim \varepsilon \left(B_0^2/\mu_0\right). \tag{9}$$

The variables are expanded as

$$\begin{aligned}
\psi &= \psi_1 + \psi_2 + \psi_3 + \dots, \\
I &= I_0 + I_1 + I_2 + I_3 + \dots, \\
p &= p_1 + p_2 + p_3 + \dots, \\
\rho &= \rho_0 + \rho_1 + \dots, \\
R &= R_0 + x,
\end{aligned}$$

where $I_0 \equiv B_0 R_0$. The leading order of the force balance Eq. (4) yields

$$I_1 + \frac{\mu_0 R_0}{B_0} p_1 = \text{const.} \tag{10}$$

Here we consider the the flow velocity in the order of the poloidal sound speed,

$$v \sim (B_p/B_0) \sqrt{\gamma p/\rho} \sim \sqrt{\varepsilon} v_{Ap}, \tag{11}$$

where $v_{Ap} \equiv B_p/\sqrt{\mu_0 \rho}$ is the poloidal Alfvén velocity that is the order of the flow velocity for the usual reduced MHD (RMHD) [15]. Since

$$\rho v^2 \sim \varepsilon^2 p \sim \varepsilon^3 \left(B_0^2/\mu_0\right),$$

this requires the third-order accuracy of the total energy like the RMHD for finite aspect ratio tokamaks [15]. From

author's e-mail: atsushi@toki.theory.nifs.ac.jp

the requirements $\nabla\cdot\mathbf{v}\sim\varepsilon v/a$ to eliminate the fast magnetosonic wave and then $\mathbf{v}\cdot\nabla p\sim\varepsilon^2 v/a$, the flow velocity $\mathbf{v}$ can be written as [15]

$$\mathbf{v}\equiv\left(1+x/R_0\right)\nabla U\times\left(\mathbf{B}/B\right)+v_\parallel\left(\mathbf{B}/B\right)$$
$$\equiv\mathbf{v}_p+v_\varphi R\nabla\varphi, \tag{12}$$

$$\mathbf{v}_p\equiv\left[\frac{v_\parallel}{B}\nabla\psi+\left(1+\frac{x}{R_0}\right)\frac{I}{B}\nabla U\right]\times\nabla\varphi, \tag{13}$$

$$v_\varphi R\equiv\frac{Iv_\parallel}{B}-\left(1+\frac{x}{R_0}\right)\frac{\nabla\psi\cdot\nabla U}{B}. \tag{14}$$

The function U is expanded as

$$U=U_1+U_2+\dots$$

In the leading order, the poloidal flow is written in the standard stream function representation,

$$\mathbf{v}_p^{(0)}=R_0\nabla U_1\times\nabla\varphi, \tag{15}$$

and the toroidal flow velocity coicides with the parallel flow,

$$v_\varphi^{(0)}=v_\parallel. \tag{16}$$

The leading order of the φ-component of Ohm's law (3) yields

$$U_1=U_1\left(\psi_1\right), \tag{17}$$

and its next order is

$$R_0([U_2,\psi_1]+[U_1,\psi_2])=0, \tag{18}$$

which yields

$$U_2-U_1'\psi_2\equiv U_{2*}\left(\psi_1\right), \tag{19}$$

where $[a,b]\equiv(\nabla a\times\nabla b)\cdot\nabla\varphi$ is the Poisson bracket and the prime denotes the delivative of ψ_1. The first order of $\nabla\cdot\mathbf{v}$ is obtained from the projection of Faraday's law (2) along $\mathbf{B}$ as

$$(\nabla\cdot\mathbf{v})^{(1)}=\left[\frac{v_\parallel}{B_0}+2xU_1',\psi_1\right]. \tag{20}$$

The leading order of the pressure equation (6) yields

$$p_1=p_1[U_1(\psi_1)]=p_1(\psi_1), \tag{21}$$

and the next order is

$$R_0([p_2,U_1]+[p_1,U_2])=-\gamma p_1(\nabla\cdot\mathbf{v})^{(1)}. \tag{22}$$

Substituting Eq. (20) to Eq. (22), one obtains the equation for the second order pressure,

$$p_2-p_1'\psi_2+\gamma p_1\left(\frac{v_\parallel}{B_0R_0U_1'}+\frac{2x}{R_0}\right)\equiv p_{2*}\left(\psi_1\right). \tag{23}$$

Analogously, the continuity equation (1) gives the equations for the zeroth- and first-order density,

$$\rho_0=\rho_0[U_1(\psi_1)]=\rho_0(\psi_1), \tag{24}$$

$$\rho_1-\rho_0'\psi_2+\frac{\rho_0v_\parallel}{B_0R_0U_1'}+\frac{2x}{R_0}\rho_0\equiv\rho_*\left(\psi_1\right). \tag{25}$$

The projection of the force balance Eq. (4) along $\mathbf{B}$ is

$$\begin{aligned}&\mathbf{B}\cdot(\rho\mathbf{v}\cdot\nabla\mathbf{v}+\nabla p)\\&=-\frac{\rho I}{R^2}\left\{\nabla\left[\frac{Iv_\parallel}{B}-\left(1+\frac{x}{R_0}\right)\frac{\nabla\psi\cdot\nabla U}{B}\right]\times\nabla\varphi\right\}\\&\quad\cdot\left[\frac{v_\parallel}{B}\nabla\psi+\left(1+\frac{x}{R_0}\right)\frac{I}{B}\nabla U\right]\\&-\left(1+\frac{x}{R_0}\right)\frac{\rho I}{BR^2}\left\{\frac{v_\parallel}{B}\Delta^*\psi+\left(1+\frac{x}{R_0}\right)\frac{I}{B}\Delta^*U\right.\\&\quad\left.+\nabla\left(\frac{v_\parallel}{B}\right)\cdot\nabla\psi+\nabla\left[\left(1+\frac{x}{R_0}\right)\frac{I}{B}\right]\cdot\nabla U\right\}[U,\psi]\\&-\frac{\rho}{2R^2}\left[\left[\frac{Iv_\parallel}{B}-\left(1+\frac{x}{R_0}\right)\frac{\nabla\psi\cdot\nabla U}{B}\right]^2,\psi\right]\\&+\frac{\rho}{2}\left[v_\parallel^2+\left(1+\frac{x}{R_0}\right)^2\left[|\nabla U|^2-\left(\frac{\mathbf{B}}{B}\cdot\nabla U\right)^2\right],\psi\right]\\&+[p,\psi]=0.\end{aligned} \tag{26}$$

The first order of Eq. (26) is

$$[\rho_0B_0R_0v_\parallel,U_1]+[p_2,\psi_1]+[p_1,\psi_2]=0 \tag{27}$$

which yields the equation for $v_\parallel$,

$$B_0R_0\rho_0U_1'v_\parallel+p_2-p_1'\psi_2\equiv p_{3*}\left(\psi_1\right), \tag{28}$$

which is the Bernoulli law in the present system. Equations (23), (25) and (28) show the coupling of $v_\parallel$, p_2 and ρ_1 due to the slow magnetosonic (sound) wave, since these are decoupled in the cold ($p_1\to 0$) or incompressible ($\gamma\to\infty$) limits, and yield

$$v_\parallel=-\frac{(2x/R_0)\gamma p_1-(p_{2*}-p_{3*})}{(\beta_1-M_{Ap}^2)(B_0^2/\mu_0)}M_{Ap}v_A, \tag{29}$$

$$\begin{aligned}p_2=&p_1'\psi_2+\frac{(2x/R_0)M_{Ap}^2\gamma p_1}{\beta_1-M_{Ap}^2}\\&-\frac{M_{Ap}^2p_{2*}-\beta_1p_{3*}}{\beta_1-M_{Ap}^2},\end{aligned} \tag{30}$$

$$\begin{aligned}\rho_1=&\rho_0'\psi_2+\rho_*+\frac{(2x/R_0)M_{Ap}^2}{\beta_1-M_{Ap}^2}\rho_0\\&-\frac{p_{2*}-p_{3*}}{(\beta_1-M_{Ap}^2)(B_0^2/\mu_0)}\rho_0,\end{aligned} \tag{31}$$

where

$$\beta_1\left(\psi_1\right)\equiv\frac{\gamma p_1}{B_0^2/\mu_0}, \tag{32}$$

and $M_{Ap}^2(\psi_1) \equiv \mu_0 \rho_0 (R_0 U_1')^2$ is the poloidal Alfvén Mach number. The singularity is found for $\beta_1 = M_{Ap}^2$ where the poloidal flow velocity equals to the poloidal sound velocity. The projection of the force balance Eq. (4) along $\nabla\psi$ yields

$$|\nabla\psi|^2 \Delta^* \psi + I \nabla\psi \cdot \nabla I + \mu_0 R^2 \nabla\psi \cdot \nabla p + \mu_0 R^2 \nabla\psi \cdot (\rho \mathbf{v} \cdot \nabla \mathbf{v}) = 0. \quad (33)$$

The first and second orders of Eq. (33) are

$$|\nabla\psi_1|^2 \Delta_2 \psi_1 + 2\mu_0 R_0 x \nabla\psi_1 \cdot \nabla p_1 + I_1 \nabla\psi_1 \cdot \nabla I_1 + \mu_0 R_0^2 \nabla\psi_1 \cdot \nabla p_2 + B_0 R_0 \nabla\psi_1 \cdot \nabla I_2 = 0, \quad (34)$$

and

$$\begin{aligned} &|\nabla\psi_1|^2 \left(\Delta_2 \psi_2 - \frac{1}{R}\frac{\partial \psi_1}{\partial R}\right) + 2(\nabla\psi_1 \cdot \nabla\psi_2)\Delta_2\psi_1 \\ &+ \mu_0 x^2 \nabla\psi_1 \cdot \nabla p_1 + \nabla\psi_2 \cdot \nabla\left(I_1^2/2\right) \\ &+ 2\mu_0 R_0 x (\nabla\psi_2 \cdot \nabla p_1 + \nabla\psi_1 \cdot \nabla p_2) \\ &+ \nabla\psi_1 \cdot \nabla\left(\mu_0 R_0^2 p_3 + R_0 B_0 I_3 + I_1 I_2\right) \\ &- \mu_0 R_0^2 (\nabla\psi_1 \cdot \nabla U_1)\Delta_2 U_1 \\ &+ \mu_0 R_0^2 \nabla\psi_1 \cdot \nabla\left(|\nabla U_1|^2/2\right) = 0, \end{aligned} \quad (35)$$

where

$$\Delta_2 \equiv \left(\frac{\partial^2}{\partial R^2} + \frac{\partial^2}{\partial Z^2}\right)$$

The projection of the force balance Eq. (4) along $\nabla\varphi$ is

$$\begin{aligned} &\nabla\varphi \cdot \left[\rho \mathbf{v} \times (\nabla \times \mathbf{v}) + \mu_0^{-1} (\nabla \times \mathbf{B}) \times \mathbf{B}\right] \\ &= -\frac{\rho I}{R^2}\left\{\nabla\left[\frac{I v_\parallel}{B} - \left(1 + \frac{x}{R_0}\right)\frac{\nabla\psi \cdot \nabla U}{B}\right] \times \nabla\varphi\right\} \\ &\quad \cdot \left[\frac{v_\parallel}{B}\nabla\psi + \left(1 + \frac{x}{R_0}\right)\frac{I}{B}\nabla U\right] \\ &\quad - (I/\mu_0 R^2)[I, \psi] = 0. \end{aligned} \quad (36)$$

The difference between Eqs. (26) and (36) is given by

$$\begin{aligned} &[p, \psi] + (I/\mu_0 R^2)[I, \psi] \\ &- \left(1 + \frac{x}{R_0}\right)\frac{\rho I}{B R^2}\left\{\frac{v_\parallel}{B}\Delta^* \psi + \left(1 + \frac{x}{R_0}\right)\frac{I}{B}\Delta^* U \right. \\ &\quad \left. + \nabla\left(\frac{v_\parallel}{B}\right) \cdot \nabla\psi + \nabla\left[\left(1 + \frac{x}{R_0}\right)\frac{I}{B}\right] \cdot \nabla U\right\}[U, \psi] \\ &- \frac{\rho}{2R^2}\left[\left[\frac{I v_\parallel}{B} - \left(1 + \frac{x}{R_0}\right)\frac{\nabla\psi \cdot \nabla U}{B}\right]^2, \psi\right] \\ &+ \frac{\rho}{2}\left[v_\parallel^2 + (1 + \frac{x}{R_0})^2\left[|\nabla U|^2 - \left(\frac{\mathbf{B}}{B} \cdot \nabla U\right)^2\right], \psi\right] \\ &= 0. \end{aligned} \quad (37)$$

The first order of Eq. (37) yields

$$p_2 + \frac{B_0}{\mu_0 R_0} I_2 \equiv g_*(\psi_1), \quad (38)$$

and the second order is

$$\begin{aligned} &\left[p_3 + \frac{B_0}{\mu_0 R_0} I_3, \psi_1\right] + \frac{2x}{R_0}[p_2 - p_1' \psi_2, \psi_1] \\ &+ \frac{I_1}{\mu_0 R_0^2}[I_2 - I_1', \psi_1] - [g_*' \psi_2, \psi_1] \\ &+ \frac{\rho_0 U_1'^2}{R_0^2}\left[|\nabla\psi_2|^2/2, \psi_1\right] = 0 \end{aligned} \quad (39)$$

which yields

$$\begin{aligned} &p_3 + \frac{B_0 I_3}{\mu_0 R_0} + \frac{I_1}{\mu_0 R_0^2}\left(I_2 - I_1' \psi_2\right) + \frac{\rho_0 |\nabla U_1|^2}{2R_0^2} \\ &+ \left(\frac{x}{R_0}\right)^2 \frac{2M_{Ap}^2 \gamma p_1}{\beta_1 - M_{Ap}^2} - g_*' \psi_2 \equiv E_*(\psi_1). \end{aligned} \quad (40)$$

Substituting Eqs. (38) and (40) to Eqs. (34) and (35), we obtain the expanded Grad-Shafranov equation in the presence of poloidal-sonic flow,

$$\Delta_2 \psi_1 = -\mu_0 R_0^2 \left[\frac{2x}{R_0} p_1' + \left(\frac{\mu_0}{B_0^2}\frac{p_1^2}{2} + g_*\right)'\right], \quad (41)$$

$$\begin{aligned} &\Delta_2 \psi_2 + \mu_0 R_0^2 \left[\frac{2x}{R_0} p_1'' + \left(\frac{\mu_0}{B_0^2}\frac{p_1^2}{2} + g_*\right)''\right]\psi_2 \\ &= \frac{1}{R}\frac{\partial \psi_1}{\partial R} + M_{Ap}^2 \Delta_2 \psi_1 + \frac{|\nabla\psi_1|^2}{2}\left(M_{Ap}^2\right)' \\ &\quad - \mu_0 R_0^2 \left[E_*' + \left(\frac{x}{R_0}\right)^2 p_1' \right. \\ &\quad + \left(\frac{x}{R_0}\right)^2 \left(\frac{2M_{Ap}^2 \gamma p_1}{\beta_1 - M_{Ap}^2}\right)' \\ &\quad \left. - \frac{2x}{R_0}\left(\frac{M_{Ap}^2 p_{2*} - \beta_1 p_{3*}}{\beta_1 - M_{Ap}^2}\right)'\right]. \end{aligned} \quad (42)$$

The equation for ψ_1 (41) is same as for the static case while Eq. (42) for ψ_2 is modified by the flow and the singularity appears. In the cylindrical limit $x/R_0 \to 0$, the singularity can be removed when

$$p_{2*} = p_{3*} \equiv f_*(\psi_1)\gamma p_1(\psi_1),$$

$$\rho_*(\psi_1) \equiv f_*(\psi_1)\rho_0(\psi_1),$$

and

$$f_*(\psi_1) = f[U_1(\psi_1)] \quad \text{and} \quad f[U_1 = 0] = 0.$$

Then, the equations for $v_\parallel$, p_2, ρ_1 and ψ_2 are rewritten as

$$v_\parallel = -\left(\frac{2x}{R_0}\right)\frac{\beta_1 M_{Ap} v_A}{\beta_1 - M_{Ap}^2}, \quad (43)$$

$$p_2 = p_1' \psi_2 - \frac{\left(f_* - 2x/R_0\right) M_{Ap}^2 - f_* \beta_1}{\beta_1 - M_{Ap}^2}\gamma p_1, \quad (44)$$

$$\rho_1 = \rho_0' \psi_2 - \frac{(f_* - 2x/R_0) M_{Ap}^2 - f_* \beta_1}{\beta_1 - M_{Ap}^2} \rho_0, \tag{45}$$

$$\begin{aligned} &\Delta_2 \psi_2 + \mu_0 R_0^2 \left[\frac{2x}{R_0} p_1'' + \left(\frac{\mu_0}{B_0^2} \frac{p_1^2}{2} + g_* \right)'' \right] \psi_2 \\ &= \frac{1}{R} \frac{\partial \psi_1}{\partial R} + M_{Ap}^2 \Delta_2 \psi_1 + \frac{|\nabla \psi_1|^2}{2} \left(M_{Ap}^2 \right)' \\ &\quad - \mu_0 R_0^2 \left[E_*' + \left(\frac{x}{R_0} \right)^2 p_1' - \frac{2x}{R_0} (f_* \gamma p_1)' \right. \\ &\quad \left. + \left(\frac{x}{R_0} \right)^2 \left(\frac{2 M_{Ap}^2 \gamma p_1}{\beta_1 - M_{Ap}^2} \right)' \right]. \end{aligned} \tag{46}$$

In comparson with the analysis of the transonic flow for low-β tokamaks [5, 2], the singularity at the poloidal flow velocity equal to poloidal sound velocity in the density and pressure and its dependence on toroidicity has been reproduced as higher-order effects and the singularity in the higher order magnetic structure has been found in the present study. However, in order to reproduce the radial discontinuity of the density and pressure found in Ref. [2], a local analysis assuming $\beta_1 - M_{Ap}^2 \sim \varepsilon M_{Ap}^2$ will be necessary. Finally we note that the hyperbolic region between the cusp velocity and the poloidal velocity of the slow magnetosonic wave as pointed out in Ref. [4] may be degenerated because the difference between them goes to higher order in the present ordering.

Next we consider the case for the poloidal-Alfvénic flow $v \sim v_{Ap}$ where the usual RMHD ordering applies. The first order of Eq. (33) is

$$\begin{aligned} &|\nabla \psi_1|^2 \Delta_2 \psi_1 + 2\mu_0 R_0 x \nabla \psi_1 \cdot \nabla p_1 + I_1 \nabla \psi_1 \cdot \nabla I_1 \\ &+ \mu_0 R_0^2 \nabla \psi_1 \cdot \nabla p_2 + B_0 R_0 \nabla \psi_1 \cdot \nabla I_2 \\ &- M_{Ap}^2 [|\nabla \psi_1|^2 \Delta_2 \psi_1 - \nabla \psi_1 \cdot \nabla (|\nabla \psi_1|^2/2)] = 0. \end{aligned} \tag{47}$$

The first order of Eq. (37) yields

$$p_2 + \frac{B_0}{\mu_0 R_0} I_2 + \rho_0 (R_0 U_1')^2 |\nabla \psi_1|^2 / 2 \equiv g_*(\psi_1). \tag{48}$$

Substituting Eq. (48) to Eq. (47), we obtain the equation for ψ_1 in the following form,

$$\begin{aligned} &(1 - M_{Ap}^2) \Delta_2 \psi_1 - \frac{|\nabla \psi_1|^2}{2} \left(M_{Ap}^2 \right)' \\ &= -\mu_0 R_0^2 \left[\frac{2x}{R_0} p_1' + \left(\frac{\mu_0}{B_0^2} \frac{p_1^2}{2} + g_* \right)' \right]. \end{aligned} \tag{49}$$

The singularity at the poloidal flow velocity equal to poloidal Alfvén velocity arises in the first order of the magnetic structure. This singularity is independent of the toroidicity [16].

We have shown reduced sets of equations for MHD equilibria with flow with asymptotic expansions and reproduced the singular points at the poloidal flow velocity equal to poloidal sound and poloidal Alfvén velocity. They will be extended to include hot ion effects by setting $\delta \sim \varepsilon$ for the poloidal-sonic flow, and $\delta^2 \sim \varepsilon$, as usual reduced two-fluid models [17, 18], for the poloidal-Alfvénic flow.

This work was partially supported by the Ministry of Education, Culture, Sports and Technology of Japan, Grant-in-Aid for Young Scientists (B) No. 18740358 and the National Institutes of Natural Sciences, NIFS06NPRX001.

[1] K. C. Shaing, R. D. Hazeltine, and H. Sanuki, Phys. Fluids B **4**, 404 (1992).
[2] R. Betti and J. P. Freidberg, Phys. Plasmas **7**, 2439 (2000).
[3] H. P. Zehrfeld and B. J. Green, Nucl. Fusion **12**, 569 (1972).
[4] E. Hameiri, Phys. Fluids **26**, 230 (1983).
[5] E. K. Mashke and H. J. Perrin, Phys. Lett. A **102**, 106 (1984).
[6] K. G. McClements and A. Thyagaraja, Mon. Not. R. Astron. Soc. **323**, 733 (2001).
[7] Z. Yoshida, S. M. Mahajan, and S. Ohsaki, Phys. Plasmas **11**, 3660 (2004).
[8] J. Shiraishi, S. Ohsaki, and Z. Yoshida, Phys. Plasmas **12**, 092308 (2005).
[9] A. Ishida, C. O. Harahap, L. C. Steinhauer, and Y.-K. M. Peng, Phys. Plasmas **11**, 5297 (2004).
[10] J. P. Goedbloed, Phys. Plasmas **11**, L81 (2004).
[11] A. Ito, J. J. Ramos, and N. Nakajima, Phys. Plasmas **14**, 062501 (2007).
[12] J. J. Ramos, Phys. Plasmas **12**, 052102 (2005).
[13] J. J. Ramos, Phys. Plasmas **12**, 112301 (2005).
[14] H. R. Strauss, Phys. Fluids **20**, 1354 (1977).
[15] H. R. Strauss, Nucl. Fusion **23**, 649 (1983).
[16] G. N. Throumoulopoulos and G. Pantis, Plasma Phys. Control. Fusion **38**, 1817 (1996).
[17] R. D. Hazeltine, M. Kotschenreuther, and P. J. Morrison, Phys. Fluids **28**, 2466 (1985).
[18] J. J. Ramos, Phys. Plasmas **14**, 052506 (2007).

Proceedings of ITC/ISHW2007

ICNTS - Benchmarking of Bootstrap Current Coefficients

Klaus ALLMAIER[1)], Craig D. BEIDLER[2)], Maxim Yu. ISAEV[3)], Sergei V. KASILOV[1,4)], Winfried KERNBICHLER[1)], Henning MAASSBERG[2)], Sadayoshi MURAKAMI[5)], Victor V. NEMOV[1,4)], Donald A. SPONG[6)], Victor TRIBALDOS[7)]

[1)]*Insitut für Theoretische Physik, Association EURATOM-ÖAW, TU-Graz, Austria*
[2)]*Max-Planck Institut für Plasmaphysik, Association EURATOM, Greifswald, Germany*
[3)]*Russian Research Center "Kurchatov Institute", Moscow, Russia*
[4)]*Insitute of Plasma Physics, NSC-KhIPT, Kharkov, Ukraine*
[5)]*Department of Nuclear Engineering, Kyoto University, Kyoto, Japan*
[6)]*Oak Ridge National Laboratory, U.S. Department of Energy, USA*
[7)]*Laboratorio Nacional de Fusión, CIEMAT, Association EURATOM, Madrid, Spain*

October 11, 2007

The benchmarking of the mono-energetic particle transport coefficients for various stellarator configurations is completed, very good agreement was obtained by quite different codes (several Monte Carlo techniques, DKES, GSRAKE and NEO). Such an extensive benchmarking for the bootstrap current coefficient is still lacking. The bootstrap current is an off-diagonal term in the neoclassical transport matrix and standard δf-Monte Carlo techniques are well suited only for the diagonal transport terms in stellarator configurations. This benchmarking is based on four different codes.

Keywords: ICNTS, neoclassical transport, stellarators, bootstrap current coefficient

1. Introduction

The *International Collaboration on Neoclassical Transport in Stellarators* (ICNTS) was initiated in 2000 for solving the linearised mono-energetic drift-kinetic equations

$$V^1(f_1) - C^p(f_1) = -\dot{r}$$
$$V^1(g_1) - C^p(g_1) = p\,v\,b.$$

Here, V^1 is the Vlasov term acting only in the flux surface (the radius, r, and the absolute velocity, v, are only parameters), C^p is the pitch-angle collision term (Lorentz form), $p = v_{\|}/v$, $\dot{r}$ the radial component of the ∇B-drift velocity, and $b = B/B_0$ the normalised magnetic field strength. f_1 and g_1 are the *1st-order* distributions functions, i.e. the (small) deviation from the *0th-order* Maxwellian. The mono-energetic transport coefficients are defined by the following moments: $D_{11} = [\dot{r} f_1]$ is the particle diffusion coefficient, $D_{31} = v[pf_1]$ the boostrap current coefficient, $D_{13} = [\dot{r} g_1]$ the Ware pinch coefficent, and $D_{33} = v[pg_1]$ the electric conductivity coefficient. Here, $[A] = \int \langle A \rangle \, dp$ where $\langle ... \rangle$ denotes flux-surface averaging. Onsager symmetry leads to the relation $D_{31} = -D_{13}$. The 3×3 thermal transport matrix is obtained by energy convolution of the mono-energetic coefficients for different weights with respect to v.

The early ICNTS phase concentrated on the benchmarking of the D_{11} coefficient for the main stellarator configurations; see [1]. DKES (Drift-Kinetic Equation Solver) [2, 3] is based on a Fourier-Legendre expansion of both f_1 and g_1 in the 3D phase space and evaluates all mono-energetic diffusion coefficients depending on collisionality and radial electric field. MOCA [4] and DCOM [5] are full-f Monte Carlo codes evaluating D_{11} from the radial broadening of an ensemle of test particles in time following [6]. A δf MC technique [7] allows for a strictly local estimation of D_{11}, i.e. the radial drift velocity determines only the weight of the markers $w_f = \int \dot{r}\, dt$ for $r = const.$ This D_{11} benchmarking (also supported by other codes) is largely completed with very good agreement; the impact of the approximation of incompressible $E \times B$ flows for rather large radial electric fields, $E_r/vB > \iota r/R$, is analysed in [8].

Here, the scaling of the bootstrap current coefficient in the different collisionality regimes is briefly summarised: $D_{31} \propto 1/\nu^{*2}$ in the Pfirsch-schlüter regime, $D_{31} \propto 1/\nu^*$ in the plateau regime, and $D_{31} \rightarrow const.$ at very-low collisionalities, where $\nu^* = \nu R/v\iota$. This scaling holds both for stellarators and tokamaks.

2. The Numerical Tools

The bootstrap current coefficient evaluated by DKES could only be benchmarked with *standard* δf MC techniques either for an axisymmetric configuration or only for moderate collisionalities, so far. For estimating D_{11} and D_{33}, the marker equations $w_f = \int \dot{r}\, dt$ and $w_g = v \int p\, dt$ increase the weights of those markers which dominate the contribution to the corresponding coefficients at low collisionalities, i.e. ripple-trapped particles with large $\dot{r}$ to D_{11} and passing particles with large p to D_{33}. The ripple-

author's e-mail: Henning.Maassberg@ipp.mpg.de

trapped particle distribution function is nearly symmetric in p (allowing for a bounce-averaged treatment), but D_{31} is determined by the asymmetry in the passing particle distribution with rather small weights, w_f. Consequently, the large w_f of ripple-trapped particles leads to huge statistical problems for evaluating the D_{31} coefficient in stellarators at very-low collisionalities. This problem does not appear in axisymmetric configurations since $\dot{r}$ is a periodic function along the banana orbit, and the tokamak D_{31} can be evaluated directly with δf-MC techniques; see e.g. [9]. The situation is equivalent for evaluating the Ware pinch coefficient: D_{13} is mainly determined by the trapped particles with small p whereas the far passing particles dominate in the marker weights w_g. This equivalence was found in direct δf-MC simulations of D_{31} and D_{13}: rather similar convergence problems appeared at the same (intermediate) collisionalities.

One possibility to overcome this *artificial noise* problem in δf-MC simulations of the bootstrap current coefficient is a filtering technique used in the VENUS-δf code [10, 11]. The strongly weighted ripple-trapped particles, i.e. the markers with large $|w_f|$, are omitted for evaluating D_{31}, and only barely trapped particles and passing particles contribute. This filtering technique based on δf bounds is equivalent to a forced localisation in r: if the radial drift of ripple-trapped particles exceeds a maximum radial displacement, their contribution to D_{31} is simply ignored. The main disadvantage of this approach, however, is the somewhat *artificial* definition of the δf bounds: the sensitivity of D_{31} on these bounds must be controlled for each magnetic configuration depending on the degree of drift-optimisation and fraction of ripple-trapped particles. At very-low collisionalities, VENUS-δf calculations are very time expensive.

Another approach used in the NEO-MC code, is based on the iterative evaluation of the distribution function in those phase space regions (e.g. close to the trapped-passing boundary) mainly contributing to the bootstrap current coefficient. The standard δf-MC methods are based on the *0th-order* Maxwellian, and δf must describe the full deviation without any iteration. Iterative re-discretisations of the distribution function in the relevant phase-space region for evaluating D_{31} by using this information for the next step reduce significantly the *artificial noise* introduced by the ripple-trapped particles [12]. The convergence of this method is equivalent to $\delta f \to 0$ within the iteration. Furthermore, a constant marker weight scheme with decreasing number of test particles is used for trapped particles leading to an additional statistical improvement for a fixed number of starting test particles. The variance (*noise*) in this method scales with the mean free path (instead of mean free path squared as in the standard method) and finally the computing time needed in NEO-MC for the same statistical error decreases by a factor proportional to the mean free path to the power $3/2$.

In addition, NEO-2 calculations of the bootstrap current coefficient are included in the benchmarking. NEO-2 [13] integrates the linearised drift-kinetic equations along field lines for arbitray collisionalities, however, the poloidal $E \times B$ drift cannot be included. In NEO-2, the Green's function technique in combination with an adaptive (*3rd*-order) conservative finite-difference discretisation scheme with respect to the normalised magnetic moment is applied which allows for high accuracy at low collisionalities (where DKES and both MC techniques become very time consuming due to the high localisation of the *1st*-order distribution functions in the 3D-phase space). Furthermore, NEO-2 is extended to the full linearised collison operator [14] (instead of the simplified Lorentz form of the pitch-angle collision term).

Finally, the collisionless asymptotic value of D_{31} is used for the benchmarking. In particular the axisymmetric value in the large aspect ratio limit, $\epsilon = r/R \to 0$, is used for normalisation. In this limit, the collisionless asymptote is easily obtained from the mono-energetic flux-friction relation for an axisymmetric configuration:for this case, the relation $\mathbf{B} \cdot \nabla B = -\iota\epsilon (\mathbf{B} \times \nabla B) \cdot \mathbf{e}_r$ holds, where $\mathbf{e}_r$ is the radial unit vector, and all 3 mono-energetic transport coefficients are linked for small radial electric fields, E_r; see [15]. The parallel electric conductivity is given by

$$D_{33}(\nu^* \to 0) = D_{33}(\nu^* \to \infty) - \frac{2\nu}{3v} f_t$$

where f_t is the trapped particle fraction

$$f_t = 1 - \frac{3}{4} \langle b_{\max}^2 \rangle \int_0^1 \frac{\lambda \, d\lambda}{\langle \sqrt{1 - \lambda b_{\max}} \rangle}$$

with $b_{\max} = B/B_{\max}$. In the large aspect ratio limit, $f_t \simeq 1.46\sqrt{\epsilon}$ for a tokamak with circular cross section, and

$$D_{31}(\nu^* \to 0) = \frac{2}{3} \frac{f_t}{\iota\epsilon} \simeq \frac{0.9733}{\iota\sqrt{\epsilon}}, \qquad (1)$$

equivalent to the value given e.g. in [16] (here, the energy convolution with the Maxwellian leads to the factor 3/2). This $D_{31}(\nu^* \to 0)$ is used for the normalisation of all bootstrap current coefficients in this benchmarking. DKES and NEO-2 calculations for an axisymmetric configuration have shown, that the convergence to this collisionless asymptote is rather slow, $\propto \sqrt{\nu *}$, confirming the scaling of the size of the relevant boundary layer between trapped and passing particles; see e.g. [17]. Finally, D_{31} is independent of E_r in tokamaks as long as $E_r \ll \iota\epsilon B v$ holds.

In the stellarator *lmfp*-regime, D_{31} depends on E_r and ν^* in a rather complex manner. Nevertheless, for $\nu^* \to 0$, a purely geometrical factor, the Shaing-Callen limit [18, 19], is equivalent to the collisionless asymptote for axisymmetric configurations. However, the collisionalities in this benchmarking for stellarator configurations are in general too high to check the convergence of D_{31} to the collisionless Shaing-Callen limit. The convergence of

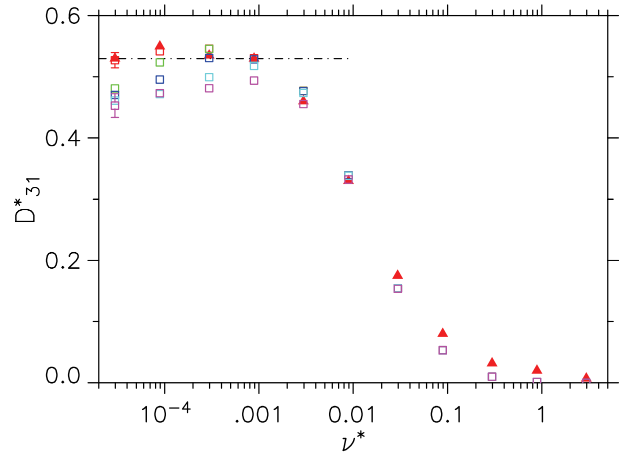

Fig. 1 Mono-energetic bootstrap current coefficients, D^*_{31} (normalised to the collisionless asymptote, eq.(1)), for NCSX vs. collisionality, ν^*. DKES (open squares) for $E_r/vB = 0$ (red), $1 \cdot 10^{-4}$ (green), $3 \cdot 10^{-4}$ (dark blue), $1 \cdot 10^{-3}$ (light blue), $3 \cdot 10^{-3}$ (magenta), and VENUS-δf (full triangles only for $E_r/vB = 0$). The Shaing-Callen value is given for reference (dot-dashed line).

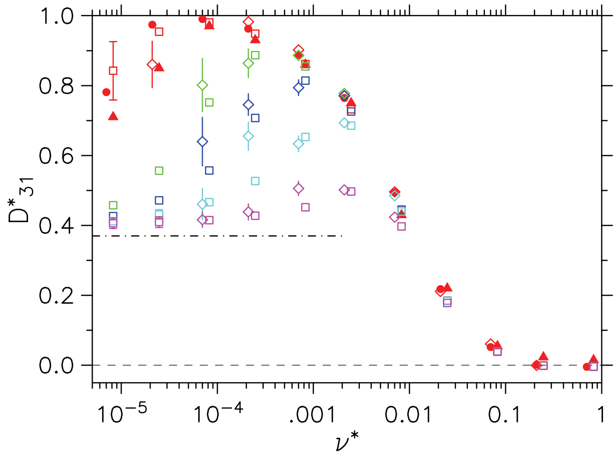

Fig. 2 Normalised mono-energetic bootstrap current coefficients, D^*_{31}, for LHD with $R = 3.75$ m vs. ν^*. DKES (open squares), VENUS-δf (full triangles), NEO-MC (open diamonds), and NEO-2 (full circles only for $E_r/vB = 0$) for $E_r/vB = 0$ (red), $3 \cdot 10^{-5}$ (green) $1 \cdot 10^{-4}$ (dark blue), $3 \cdot 10^{-4}$ (light blue), and $1 \cdot 10^{-3}$ (magenta); the Shaing-Callen value (dot-dashed line).

D_{31} calculations at extremely low collisionalities (down to $\nu^* \sim 10^{-8}$ is accessible for the tokamak case) is very poor and requires huge computing times. Consequntly, the Shaing-Callen limit is not seriously included in the D_{31}-benchmarking.

3. Benchmarking Results

Here, the benchmarking of the bootstrap current coefficient is discussed for 3 magnetic (vacuum) configurations at half the plasma radius: NCSX (*ncsx-2*), the "standard" LHD with $R = 3.75$ m (*lhd-375*), and the W7-X "standard" (*w7x-sc1*) configuration. NCSX is a quasi-axisymmetric configuration with high elongation [22], and the bootstrap current is expected to be rather similar to to the equivalent tokamak. This LHD configuration represents a *classical* stellarator configuration [20]. Finally, the W7-X configuration is strongly drift-optimised, and the bootstrap current is minimised [21].

Fig. 1 shows the benchmarking results for DKES and VENUS-δf for NCSX. The impact of E_r is rather small, i.e. this quasi-axisymmetric configuration is similar to a tokamak with respect to the bootstrap current coefficient (but the radial transport coefficient, D_{11}, is dominated by ripple-trapped particles on which E_r has a large effect [1]). The fairly high NCSX elongation leads to the reduced D^*_{31} at the low collisionalities (for the normalisation in eq. (1), an axisymmetric configuration without elongation was assumed).

For the LHD configuration, all 4 codes contribute to the benchmarking shown in Fig. 2 (for a 1st benchmarking of VENUS-δf and DKES, see Ref. [23]). As in the NCSX case, the agreement of the quite different codes is very good. With E_r, the D_{31} at very low ν^* are decreased to the Shaing-Callen value. This reduction of the D_{31} with increasing E_r starts at the same ν^* as the reduction of the D_{11} coefficient (from the $1/\nu$-regime). In the analytic theory [24], the coupling of the ripple-trapped particle distribution function and the passing particle distribution function changes in the transition from the $1/\nu$- to the $\sqrt{\nu}$-regime.

For this "standard" LHD configuration (without elongation), the D_{31} for $E_r = 0$ (except the very low ν^*) is rather similar to the equivalent tokamak (with circular cross section). An inward-shift of the magnetic axis leads to a drift-optimised stellarator configuration for $R = 3.60$ m [20] in the sense of σ-optimisation [25], and also the D_{31} for $E_r = 0$ at low ν^* are reduced by nearly a factor of 2, but the Shaing-Callen value is less affected. A stronger inward-shift (e.g. $R = 3.53$ m) further improves the *lmfp*-confinement (but violates the σ-optimisation), the bootstrap current coefficients are also reduced (found by DKES computations). Finally, an outward-shift of the magnetic axis results in negative D_{31} (reducing ι) in the plateau regime [23], the effect of the helical curvature terms in the B_{mn}-Fourier spectrum being increased.

The benchmarking for the W7-X "standard" configuration is shown in Fig. 3 with all 4 codes included. In this case, the D^*_{31} for only 3 E_r values are shown (more are available). Very time-expensive VENUS-δf computations at very low ν^* indicate the "convergence" of D_{31} to the Shaing-Callen value in the limit $\nu^* \to 0$ even for $E_r = 0$ (here, the statistical error of VENUS-δf is about 25%). At these low collisionalities, in particular DKES results have rather large errors (see Fig. 3), up to 2000 Fourier modes in the angle coordinates and 250 Legendre polynomials are used for the representation of the distri-

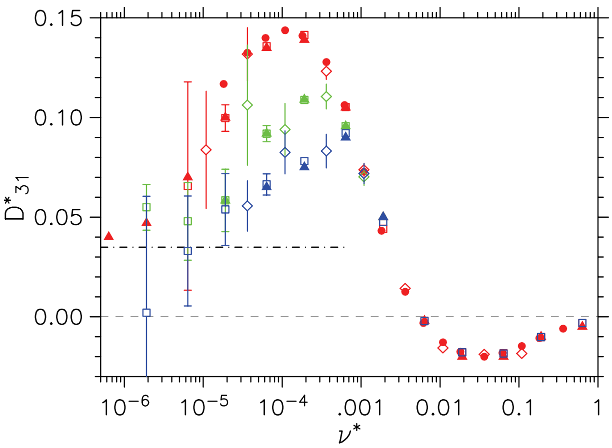

Fig. 3 Normalised mono-energetic bootstrap current coefficients D^*_{31}, for the W7-X "standard" configuration vs. ν^*. DKES (open squares), VENUS-δf (full triangles), NEO-MC (open diamonds), and NEO-2 (full circles) for $E_r/vB = 0$ (red), $1 \cdot 10^{-4}$ (green), and $1 \cdot 10^{-3}$ (dark blue); the Shaing-Callen value (dot-dashed line).

bution function), however, the D^*_{31} are fairly small (e.g. the relative errors are much smaller for the LHD configuration with large D^*_{31}). This W7-X example is similar to the LHD case where D_{31} is reduced with E_r (at larger E_r, however, D_{31} increases), however, the D_{31} are nearly one order of magnitude smaller than in the LHD case. These results confirm the W7-X optimisation criterium of minimised bootstrap current.

The variation of the toroidal mirror term in W7-X has a fairly strong impact on the bootstrap current coefficient; see [26]. The low-mirror configuration represents a *classical* highly-elongated stellarator configuration, and the D^*_{31} at low ν^* are increased by more than a factor of 2. On the other hand, the high-mirror configuration (with $B_{01}/B_{00} \simeq 0.1$) has the lowest D^*_{31}, but only at very small E_r. However, D_{31} increases with E_r to equivalent values as in the W7-X "standard" configuration, i.e. the high degree of bootstrap current minimisation in the high-mirror configuration is lost even for intermediate E_r.

4. Conclusions

For 3 quite different stellarator configurations, the benchmarking of the mono-energetic bootstrap current coefficient by 4 codes, i.e. DKES, VENUS-δf, NEO-MC and NEO-2, is performed and very good agreement was found. As a next step in the ICNTS activity, the impact of the violation of the momentum conservation in the simplified Lorentz form of the pitch-angle collision operator on the boostrap current will be analysed in detail; see [27].

Acknowledgements

One of the authors, M. Isaev, thanks W.A.Cooper and T.M.Tran for the help and the support of the VENUS-δf calculations. His work was supported by the CRPP-KIAM contract, by the MPG-grant, by Max-Planck Institut für Plasmaphysik, by NIFS/NINS under the Project of Formation of International Network of Scientific Collaboration (Japan), by the Fond National Suisse pour la Recherche Scientifique, and by the Departement of Atomic Science and Technology, RosAtom (Russia).

[1] C.D. Beidler *et al.*, *30th EPS Conf. Plasma Phys. Contr. Fus., St Petersburg 2003*, http://epsppd.epfl.ch/StPetersburg/pdf/P3_002.pdf (2003).
[2] S.P. Hirshman *et al.*, Phys. Fluids **29**, 2951 (1986).
[3] W.I. van Rij and S.P. Hirshman, Phys. Fluids **B1**, 563 (1989).
[4] V. Tribaldos, Phys. Plasmas **8**, 1229 (2001).
[5] S. Murakami *et al.*, Nucl. Fusion **42**, L19 (2002).
[6] A.H. Boozer and G. Kuo-Petravic, Phys. Fluids **24**, 851 (1981).
[7] M. Schmidt, *29th EPS Conf. Plasma Phys. Contr. Fus., Montreux 2002*, http://epsppd.epfl.ch/Montreux/pdf/P4_112.pdf (2002).
[8] C.D. Beidler *et al.*, *ICNTS - Impact of Incompressible $E \times B$ Flow in Estimating Mono-Energetic Transport Coefficients*, this workshop, (2007).
[9] M. Sasinowski and A.H. Boozer, Phys. Plasmas **2**, 610 (1995).
[10] O. Fischer *et al.*, Nucl. Fusion **42**, 817 (2002).
[11] M.Yu. Isaev *et al.*, Fusion Sci. Techn. **50**, 440 (2006).
[12] K. Allmaier *et al.*, *34th EPS Conf. Plasma Phys., Warsaw 2007*, P-4.041, (2007).
[13] W. Kernbichler *et al.*, *32nd EPS Conf. Plasma Phys., Tarragona 2005*, http://epsppd.epfl.ch/Tarragona/pdf/P1_111.pdf (2005).
[14] W. Kernbichler *et al.*, *33rd EPS Conf. Plasma Phys., Rome 2006*, http://epsppd.epfl.ch/Roma/pdf/P2_189.pdf (2006).
[15] H. Maaßberg and C.D. Beidler, *31st EPS Conf. Plasma Phys. Contr. Fus., London 2004*, http://epsppd.epfl.ch/London/pdf/P1_100.pdf (2004).
[16] A.H. Boozer and H.J. Gardner, Phys. Fluids **B2**, 2408 (1990).
[17] F.L. Hinton and M.N. Rosenbluth, Phys. Fluids **16**, 836 (1973).
[18] K.C. Shaing and J. Callen, Phys. Fluids **26**, 3315 (1983).
[19] J.L. Johnson *et al.*, Phys. Plasmas **6**, 2513 (1999).
[20] S. Murakami *et al.*, Nucl. Fusion **42**, L19 (2002).
[21] H. Maaßberg *et al.*, Phys. Fluids **B5**, 3728 (1993).
[22] G.H. Neilson *et al.*, Phys. Plasmas **7**, 1911 (2000).
[23] M.Yu. Isaev *et al.*, *submitted to* Plasma Fusion Res. (2007).
[24] C.D. Beidler and H. Maaßberg, Plasma Phys. Control. Fusion **43**, 1131 (2001).
[25] H.E. Mynick *et al.*, Phys. Rev. Lett. **48**, 322 (1982).
[26] N.B. Marushchenko *et al.*, *ECCD Scenarios for Different Configurations of the W7-X Stellarator*, this workshop, (2007).
[27] C.D. Beidler *et al.*, *ICNTS - Benchmarking of Momentum Correction Techniques*, this workshop, (2007).

Proceedings of ITC/ISHW2007

ICNTS - Benchmarking of Momentum Correction Techniques

Craig D. BEIDLER[1)], Maxim Yu. ISAEV[2)], Sergei V. KASILOV[3,4)], Winfried KERNBICHLER[4)], Georg O. LEITOLD[4)] Henning MAASSBERG[1)], Sadayoshi MURAKAMI[5)], Victor V. NEMOV[3,4)], Donald A. SPONG[6)], Victor TRIBALDOS[7)]

[1)] *Max-Planck Institut für Plasmaphysik, Association EURATOM, Greifswald, Germany*
[2)] *Russian Research Center "Kurchatov Institute", Moscow, Russia*
[3)] *Insitute of Plasma Physics, NSC-KhIPT, Kharkov, Ukraine*
[4)] *Insitut für Theoretische Physik, Association EURATOM-ÖAW, TU-Graz, Austria*
[5)] *Department of Nuclear Engineering, Kyoto University, Kyoto, Japan*
[6)] *Oak Ridge National Laboratory, Oak Ridge, Tennesee, USA*
[7)] *Laboratorio Nacional de Fusión, CIEMAT, Association EURATOM, Madrid, Spain*

October 11, 2007

In the traditional neoclassical ordering, mono-energetic transport coefficients are evaluated using the simplified Lorentz form of the pitch-angle collision operator which violates momentum conservation. In this paper, the parallel momentum balance with radial parallel momentum transport and viscosity terms is analysed, in particular with respect to the radial electric field. Next, the impact of momentum conservation in the stellarator *lmfp*-regime is estimated for the radial transport and the parallel electric conductivity. Finally, momentum correction techniques are described based on mono-energetic transport coefficients calulated e.g. by the DKES code, and preliminary results for the parallel electric conductivity and the bootstrap current are presented.

Keywords: ICNTS, neoclassical transport, stellarators, parallel momentum conservation

1. Introduction

The *International Collaboration on Neoclassical Transport in Stellarators* (ICNTS) was initiated in 2000. The starting point is the drift-kinetic equation (DKE) which is linearised with respect to the *1st-order* distribution function defined as the (small) deviation from the *0th-order* (unshifted) Maxwellian, F_M, with the density, electrostatic potential and temperature assumed to be constant on flux-surfaces. The *1st-order* DKE becomes inhomogeneous with a radial driving force, $-\dot{r}\, F_M'$ ($\dot{r}$ being the radial component of the ∇B-drift velocity and F_M' the radial derivative of the Maxwellian with total energy conserved), and with a parallel driving force, $\propto v_\| \, B\, F_M$. Splitting this DKE with respect to the driving forces leads to two *1st-order* distribution functions, f and g, where f is related to $-\dot{r}\, F_M'$ (symmetric in $v_\|$) and g to $v_\| \, B\, F_M$. The Vlasov operator couples symmetric and asymmetric terms; consequently, f (g) has also asymmetric (symmetric) contributions. With the linearised collision operator, $C^{\rm lin}$, the parallel momentum balances are given by

$$\frac{1}{V'}\frac{d}{dr}V'\left[\!\!\left[B\dot{r}v_\| \,\frac{f}{g}\right]\!\!\right] - \left[\!\!\left[\frac{\mathbf{B}\cdot\boldsymbol{\nabla}B}{B}\,(v_\|^2-\frac{1}{2}v_\perp^2)\,\frac{f}{g}\right]\!\!\right] - \left[\!\!\left[\frac{\mathbf{B}\times\boldsymbol{\nabla}\Phi}{\langle B^2\rangle}\cdot\boldsymbol{\nabla}B\,v_\|\,\frac{f}{g}\right]\!\!\right] - \left[\!\!\left[Bv_\| C^{\rm lin}\binom{f}{g}\right]\!\!\right] = \frac{0}{\frac{1}{2}v_{th}^2\langle B^2\rangle} \qquad (1)$$

where $[\![...]\!]$ means flux-surface averaging and velocity space integration and Φ the electrostatic potential. Here, the incompressible form of the $\mathbf{E}\times\mathbf{B}$ drift is used for consistency with e.g. DKES (Drift-Kinetic Equation Solver) [1, 2] and both momentum correction techniques [3, 4] described later. The important advantage of this approximation is the disappearance of the $(\mathbf{B}\times\boldsymbol{\nabla}\Phi)\cdot\boldsymbol{\nabla}B$ term in both acceleration terms, $\dot{p}$ and $\dot{v}$ ($p = v_\|/v$), in the conservative formulation; see [5]. Then, $\dot{p} \propto \mathbf{B}\cdot\boldsymbol{\nabla}B$, i.e. the mirror term, and $\dot{v} = 0$ allowing for a mono-energetic treatment of the *1st-order* DKE if the collision operator is replaced by the simple Lorentz form of the pitch-angle collision term which, however, violates momentum conservation. As shown in [5], the incompressibility approximation in the *1st-order* DKE is justified for radial electric fields, E_r, nearly up to the toroidal resonance value, $E_r^{\rm res} = \iota\epsilon vB$.

The 1st term in the parallel momentum balances (1) describes the radial transport of parallel momentum which, in general, is ignored in the traditional neoclassical theory (see e.g. the review [6]). In an axisymmetric configuration with $E_r = 0$, the $sin\theta$ part of f (symmetric in p) leads to the particle transport whereas the $cos\theta$ part (asymmetric in p) finally leads to the bootstrap current coefficient. This separation is broken at larger E_r: the $sin\theta$ component of f has also asymmetric contributions leading to radial transport of parallel momentum. The parallel momentum transport coefficients in mono-energetic form equivalent to eq.(1) are calculated with a new DKES ver-

author's e-mail: Henning.Maassberg@ipp.mpg.de

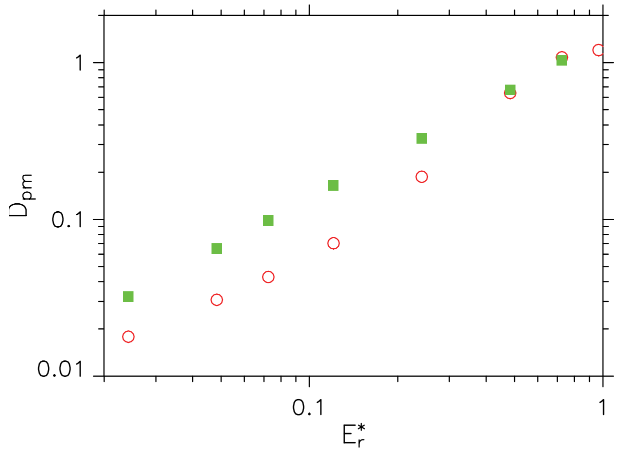

Fig. 1 Mono-energetic parallel momentum transport coefficients, D_{p1}/D_{11} (open circle) and D_{p3}/D_{13} (full square), vs. the normalised radial electric field, E_r^* for the LHD-360 configuration at $\nu^* = 7.2 \cdot 10^{-5}$.

sion. In Fig. 1, the mono-energetic $D_{p1} = [\dot{r}pf]$ (normalised to the particle transport coefficient $D_{11} = [\dot{r}f]$) and $D_{p3} = [\dot{r}pg]$ (normalised to the Ware pinch coefficient $D_{13} = [\dot{r}g] = -D_{31} = -[pf]$) are shown for rather large E_r (normalised to the toroidal resonance value, $E_r^* = E_r/E_r^{\rm res}$, for the LHD vacuum configuration with $R = 3.60$ m at half the plasma radius. (Here, [...] means integration over p and flux-surface averaging.) The value of the collisionality, $\nu^* = \nu R/\iota v$, places these results in the *lmfp*-regime. For an axisymmetric configuration where both D_{11} and D_{13} are independent of E_r (for $E_r^* \ll 1$), D_{p1}/D_{11} slightly exceeds D_{p3}/D_{13}, and both terms scale linearly in E_r^*. These results lead to a strong restriction for the radial electric field: only for $E_r^* \ll 1$, does the radial transport of parallel momentum become negligible. This restriction is stronger than the one related to validity of the incompressible $\mathbf{E} \times \mathbf{B}$ approximation; see [5]. Furthermore, also the 3rd term in eq.(1), the viscosity related to the $\mathbf{E} \times \mathbf{B}$ flow, can be ignored for $E_r^* \ll 1$.

The 2nd term in the parallel momentum balances (1) is the parallel viscosity describing the damping of parallel flows due to the magnetic field inhomogenity. In an asymptotic collisionless limit, the *1st-order* DKE for g (parallel driving force) can be directly integrated for sufficiently small E_r following Refs. [7, 8]. By flux-surface averaging, the 1st Legendre component of the DKE reduces to a 1D equation for the velocity dependence of the asymmetric part of g (here only for ions)

$$g^a = -\frac{\langle b^2 \rangle}{2\nu_{ii}(x)} \frac{1}{f_c} K(x) \int_0^1 \frac{\lambda \, d\lambda}{\langle \sqrt{1-\lambda b} \rangle}$$

and

$$C_{ii}^1(K) - \frac{f_t}{f_c} \nu_{ii}(x) K = \nu_{i0} x F_M,$$

with the thermal ion collision frequency, ν_{i0}, $x = v/v_{th}$, $b = B/B_{\max}$, and with the trapped particle fraction

$$f_t = 1 - f_c = 1 - \frac{3}{4} \langle b^2 \rangle \int_0^1 \frac{\lambda \, d\lambda}{\langle \sqrt{1-\lambda b} \rangle}.$$

$g^a(\lambda > 1) = 0$ for trapped particles. C_{ii}^1 is the 1st Legendre component of $C^{\rm lin}$, ion-electron collisions can be neglected. Impurities can act as an additional momentum sink (but are ignored here for simplicity). In this collisionless picture, the viscous damping of the parallel ion flow is equivalent to the friction of the passing with the trapped ions. In an equivalent approach [9], the collisionless electric conductivity is obtained.

2. Simple Pictures of Momentum Corrections

The computations of even mono-energetic transport coefficients (e.g. by DKES) are rather time expensive in the *lmfp*-regime. The treatment of the linearised collision operator with momentum conservation would require the solution of the DKE in the 4D-phase space instead of the 3D mono-energetic solution. Consequently, momentum correction techniques [3, 4] based on the mono-energetic transport coefficients become attractive. A rough estimation of the correction, however, can be obtained from eq.(1) with incompressible $E \times B$ flow for the different transport coefficients. The *1st-order* distribution functions are split: $f = f_1 + f_2$ and $g = g_1 + g_2$ where f_1 and g_1 are the solutions of the mono-energetic DKE with the Lorentz form of the pitch angle collision term, C^p, instead of $C^{\rm lin}$. Then, the corrections f_2 and g_2 are defined by

$$V \begin{pmatrix} f_2 \\ g_2 \end{pmatrix} - C^{\rm lin} \begin{pmatrix} f_2 \\ g_2 \end{pmatrix} = C^{\rm lin} \begin{pmatrix} f_1 \\ g_1 \end{pmatrix} - C^p \begin{pmatrix} f_1 \\ g_1 \end{pmatrix}$$

Neglecting parallel momentum transport and the $\mathbf{E} \times \mathbf{B}$-viscosity term for sufficiently small E_r leads to the balance equations for the 1st and 2nd Legendre components of the corrections, f_2 and g_2,

$$\left[\mathbf{B} \cdot \nabla B \, P_2(p) \frac{f_2}{g_2}\right] + \frac{3}{2} C^{\rm lin} \left(\left[B p \frac{f_2}{g_2} \right] \right) = \nu \frac{D_{31}}{D_{33}} - C^{\rm lin} \begin{pmatrix} D_{31} \\ D_{33} \end{pmatrix} \quad (2)$$

where $D_{31}(v) = [pf_1]$ and $D_{33}(v) = [pg_1]$ are the mono-energetic transport coefficients, calculated e.g. by DKES, and $P_2(p)$ is the 2nd Legendre polynomial.

In the *lmfp*-regime, the parallel viscosity evaluated for f_1 (by DKES) is proportional to $\nu*$, and only weakly dependent on E_r. Although this term is also determined by the symmetric component of f_1, the large $D_{11} = [\dot{r}f_1]$ has a quite different dependence on ν^* and E_r, e.g. in the $1/\nu$- and the $\sqrt{\nu}$-regimes. If any distribution function is split into a slow and a fast scale with respect to bounce-averaging, the slow part determines D_{11} [10], but does not contribute to the parallel viscosity. This can be shown by formulating the flux-surface averaging as bounce-averaging for the ripple-trapped particles, and the slow contribution vanishes due to the $\mathbf{B}\cdot\nabla B$ term (different to $\mathbf{B}\times\nabla B$ in $\dot{r}$). Consequently, the impact of momentum conservation on the radial transport in the stellarator *lmfp*-regime is negligible. For tokamaks, however, the situation is different. Here, the radial transport coefficients in the *lmfp*-regime (banana regime) are proportional to ν^* and corrections from the momentum conservation are not negligible. NEO-2 [11], based on the field-line integration technique, is generalised for a full linearised collision operator with momentum conservation. As shown in Ref. [12], the radial transport coefficients are reduced whereas the bootstrap current coefficient are increased with the full linearised collision operator compared to the Lorentz model.

The impact of momentum conservation for the parallel electric conductivity is of the order of 100%. The classical "Spitzer problem" in the collisional limit [13] can be analytically generalised to the collisionless limit [9]. The collisionless Spitzer function, $K(x)$, is defined by the 1D integro-differential equation in $x = v/v_{th}$

$$C_{ee}^1(K) - \left(\frac{f_t}{f_c}\,\nu_{ee}(x) + \frac{\nu_{e0}}{x^3} Z_{\text{eff}}\right) K = \nu_{e0} x F_M,$$

with the thermal electron-ion collision frequency, ν_{e0}, and the (energy-dependent) electron-electron collision frequency, $\nu_{ee}(x)$. C_{ee}^1 is the 1st Legendre moment of the linearised collision operator. The classical "Spitzer problem" corresponds to $f_t = 0$. In the mono-energetic approach, the normalised $D_{33}/\nu^* = 1$ in the collisional limit and is reduced to the passing (circulating) particle fraction, $D_{33}/\nu^* = f_c$, i.e. the trapped particles defined by f_t do not contribute. With momentum conservation, a stronger weighting of the trapped particles appears (defined by f_t/f_c) which reflects the passing-trapped electron fricton adding to the friction with ions and impurities (defined by the Z_{eff} term). Rather accurate approximations of both the collisional and collisionless Spitzer function, $K(x)$, have been developped; see [14] and [9], respectively. Momentum correction is important for the parallel electric conductivity for all collisionalities.

Fig. 2 shows the benchmarking for the parallel electric conductivity, σ^*, normalised to the collisional Spitzer-Härm value [6] for the W7-X high-mirror (*w7x-hm1*) and low-mirror (*w7x-lm1*) vacuum configurations at $r_a \simeq 1$ with $f_t = 0.5454$ and $f_t = 0.3536$, respectively. Instead of the Maxwellian, the collisional Spitzer function is used in the energy convolution of the mono-energetic DKES coefficients, D_{33} (solid lines). This approach was already used for the evaluation of the experimental current balance in W7-AS; see e.g. [15]. The first preliminary results (full circles) of the momentum correction technique developed by Taguchi [3] agree quite well with the simplified (collisional) correction technique implemented in the DKES energy convolution. (These data are normalised to the DKES data at the highest ν^*, so far). Furthermore, the asymptotic

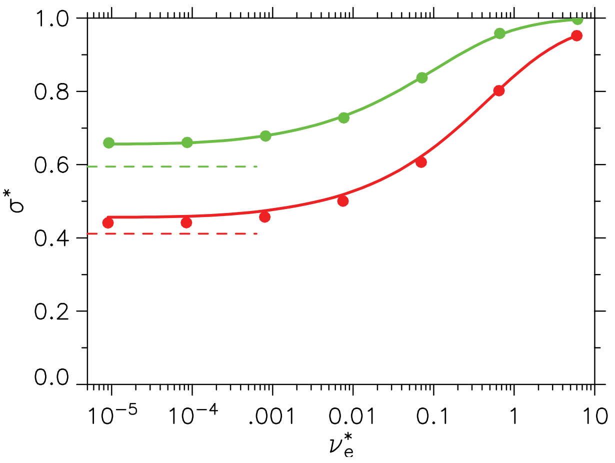

Fig. 2 Parallel electric conductivity, σ^*, normalised to the collisional Spitzer-Härm value vs. the electron collisionality for the high- and low-mirror W7-X configurations (lower and upper curves, respectively) at half the plasma radius for $Z_{\text{eff}} = 1$. σ^* based on the collisionless Spitzer function is given for reference (dashed lines).

limit $\nu^* \to 0$ based on the collisionless Spitzer function with all the trapped-particle effects included (completely kinetic modelling) is given for reference (dashed lines).

3. Momentum Correction Techniques

The momentum correction techniques [3, 4] are based on moment methods, i.e. a low-order expansion of the kinetic equation with the linearised collision operator both in Legendre (with respect to p) and in Sonine (with respect to x) polynomials. With flux-surface averaging, a linear system of equations is obtained which can be closed by using the 3 mono-energetic transport coefficients calculated numerically for different collisionalities and radial electric fields. In particular, the parallel particle and heat viscosities defined by the 2nd Legendere coefficients of f_2 and g_2 in eq.(2) are obtained. The expansion of the linearised collision operator couples the radial transport and parallel flows of all species, and, consequently, the *thermodynamic fluxes* are corrected and not the transport coefficients of each species. An exception is the parallel electric conductivity where ion effects can be neglected. As dicussed in the previous section, the radial transport in the stellarator *lmfp*-regime is nearly unaffected by the momentum correction.

Both momentum correction techniques have been implemented in the energy convolution based on databases of the 3 mono-energetic DKES transport coefficients. Results by using the [4] approach are given in [16, 17]. Recently, benchmarking was initiated, however, this activity is only in the preliminary phase (i.e. benchmarking the interfaces to the DKES data and the energy convolution algorithms). Rather preliminary results for the impact of the momentum conservation technique [3] for the bootstrap current density are shown in Fig. 3 both for the W7-X low- and high-mirror configuration (equivalent to Fig. 2). In these

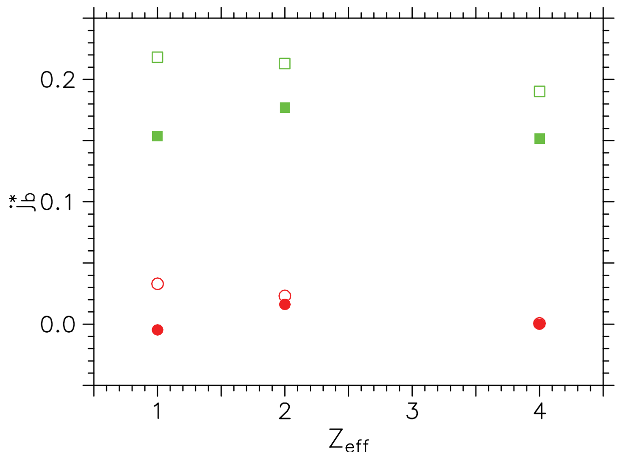

Fig. 3 Bootstrap current density, j_b^* (normalised to the equivalent tokamak value without momentum correction for $E_r = 0$), vs. $Z_{\rm eff}$ without (open symbols) and with momentum correction (full symbols) for the W7-X low-mirror (squares) and for the W7-X high-mirror configuration (circles) at half the plasma radius based on Taguchi's momentum correction technique [3].

calculations, an additional impurity species (fully ionised carbon) was introduced to describe the impact of $Z_{\rm eff}$ on the momentum balance. The radial electric field was calculated from the ambipolarity condition, and, additionally, the impurity density gradient from the condition of vanishing radial impurity flux. The inverse gradient lengths, n'/n and T'/T (with $T_e = T_i = T_C$) are the same for all scenarios. The plasma parameters correspond to low collisionalities, and an "ion-root" E_r is established. Since the electron transport coefficients in the $1/\nu$-regime are reduced with increasing $Z_{\rm eff}$ (and also the bulk ion density), this complex $Z_{\rm eff}$-dependence is eliminated by the normalisation of the bootstrap current density (sum over all species) to the equivalent tokamak value for the same $Z_{\rm eff}$ for $E_r = 0$, but without momentum conservation. With this normalisation, the impact of the momentum conservation on the bootstrap current is highlighted.

Momentum correction has only a moderate impact on the bootstrap current for both W7-X configurations; see Fig. 3. With this correction, the bootstrap current is reduced (a slight increase, however, was found in NEO-2 calculations for a tokamak case with $E_r = 0$). Momentum correction is largest at $Z_{\rm eff} = 1$ and becomes less important at higher $Z_{\rm eff}$, and the optimisation criterion of minimised bootstrap current is not affected which is realised in the W7x high-mirror configuration, at least for small E_r. Furthermore, the radial particle and energy fluxes are nearly identical with and without momentum correction as was analysed in Sec. 2.

Also the NEO-2 version with the momentum conserving collision operator [11] will be included in the benchmarking. NEO-2 expands the distribution function to higher orders in the Sonine polynomials compared to Refs. [3, 4] and solves for the full linearised collision operator. The distribution function is evaluated by the field-line integration technique which leads to the restriction $E_r = 0$. In the strict sence, NEO-2 is not a momentum correction technique since it is not based on the 3 mono-energetic transport coefficients. With the higher accuracy of the expansion, NEO-2 is an attractive tool for benchmarking with both momentum correction techniques described above.

4. Discussion/Conclusions

The benchmarking of momentum correction techniques has been initiated and preliminary results have been obtained. The particle and energy fluxes (and, consequently, the ambipolar radial electric field) in the stellarator *lmpf*-regime are only weakly affected by the violation of momentum conservation in the simplified pitch-angle collision operator used in evaluating the mono-energetic transport coefficients in all codes included in the ICNTS activity. The impact of momentum conservation on estimating the parallel electric conductivity is very well known, and the correction is rather large. Preliminary results for the bootstrap current indicate a moderate reduction with momentum conservation taken into account. Very good agreement is obtained in the benchmarking of mono-energetic bootstrap current coefficients [18]. Consequently, a detailed analysis of momentum conservation effects is a logical next step in the ICNTS.

[1] S.P. Hirshman *et al.*, Phys. Fluids **29**, 2951 (1986).
[2] W.I. van Rij and S.P. Hirshman, Phys. Fluids **B1**, 563 (1989).
[3] M. Taguchi, Phys. Fluids **B4**, 3638 (1992).
[4] H. Sugama and S. Nishimura Phys. Plasmas **9**, 4637 (2002).
[5] C.D. Beidler *et al.*, *ICNTS - Impact of Incompressible $E \times B$ Flow in Estimating Mono-Energetic Transport Coefficients*, this workshop, (2007).
[6] F.L. Hinton and R.D. Hazeltine, Rev. Mod. Physics **48**, 239 (1976).
[7] M. Taguchi, Plasma Phys. Control. Fusion **30**, 1897 (1988).
[8] M. Taguchi, Plasma Phys. Control. Fusion **31**, 241 (1989).
[9] M. Romé *et al.*, Plasma Phys. Control. Fusion **40**, 511 (1998).
[10] A.A. Galeev and R.Z. Sagdeev, Review of Plasma Physics **7**, 307 (1977).
[11] W. Kernbichler *et al.*, *32nd EPS Conf. Plasma Phys., Tarragona 2005*, http://epsppd.epfl.ch/Tarragona/pdf/P1_111.pdf (2005).
[12] W. Kernbichler *et al.*, *33rd EPS Conf. Plasma Phys., Rome 2006*, http://epsppd.epfl.ch/Roma/pdf/P2_189.pdf (2006).
[13] L. Spitzer and R. Härm, Phys. Rev. **89**, 977 (1953).
[14] S.P. Hirshman, Phys. Fluids **23**, 1238 (1980).
[15] H. Maaßberg *et al.*, Plasma Phys. Control. Fusion **47**, 1137 (2005).
[16] D.A. Spong, Phys. Plasmas **12**, 056114 (2005).
[17] D.A. Spong *et al.*, Nucl. Fusion **45**, 918 (2005).
[18] K. Allmaier *et al.*, *ICNTS - Benchmarking of Bootstrap Current Coefficients*, this workshop, (2007).

Proceedings of ITC/ISHW2007

ICNTS - Impact of Incompressible $\mathbf{E}\times\mathbf{B}$ Flow in Estimating Mono-Energetic Transport Coefficients

Craig D. BEIDLER[1)], Maxim Yu. ISAEV[1)], Sergei V. KASILOV[3,4)], Winfried KERNBICHLER[3)], Henning MAASSBERG[1)], Sadayoshi MURAKAMI[5)], Victor V. NEMOV[3,4)], Donald A. SPONG[6)] and Victor TRIBALDOS[7)]

[1)]*Max-Planck Institut für Plasmaphysik, Assoc. EURATOM, Greifswald, Germany*
[2)]*Russian Research Center "Kurchatov Institute", Moscow, Russia*
[3)]*Institut für Theoretische Physik, Assoc. EURATOM-ÖAW, TU-Graz, Austria*
[4)]*Institute of Plasma Physics, NSC-KhIPT, Kharkov, Ukraine*
[5)]*Department of Nuclear Engineering, Kyoto University, Kyoto, Japan*
[6)]*Oak Ridge National Laboratory, U.S. Department of Energy, USA*
[7)]*Laboratorio Nacional de Fusion, CIEMAT, Assoc. EURATOM-CIEMAT, Madrid, Spain*

October 11, 2007

In the neoclassical ordering, an incompressible $\mathbf{E}\times\mathbf{B}$ drift is assumed in the 1^{st} order drift-kinetic equation (i.e. the approximation $\mathbf{E}\times\mathbf{B}/\langle B^2\rangle$ is used). Then, the terms with $(\mathbf{E}\times\mathbf{B})\cdot\nabla B$ disappear in both equations for $\dot{p}$ and $\dot{v}$ allowing for a monoenergetic treatment (with a conservative formulation of the equations of motions), as it is used e.g. in DKES. As a consequence, the magnetic moment is not an invariant in this approximation. For large radial electric fields, however, this ordering scheme is violated since the $(\mathbf{E}\times\mathbf{B})\cdot\nabla B$ term in $\dot{p}$ becomes comparable with the mirror term ($\propto \mathbf{B}\cdot\nabla B$). The impact of this simplification is tested by strictly local δ-f Monte Carlo techniques (i.e. with $\dot{r}=0$ for the equation of motion in 1^{st} order) where the $\mathbf{E}\times\mathbf{B}$ drift is treated in compressible and incompressible form (both completely conservative) for large radial electric fields.

Keywords: ICNTS, neoclassical transport, stellarators, radial electric field

1 Introduction

The *International Collaboration on Neoclassical Transport in Stellarators* (ICNTS) was initiated in 2000. There is a subtle inconsistency in the way the effect of large radial electric fields are handled in obtaining neoclassical estimations of transport coefficients. Rather than being a limitation of the theory itself, the complication arises from some simplifying approximations used. The electric field enters the calculation through the $\mathbf{E}\times\mathbf{B}$ drift, $\mathbf{V}_E=\mathbf{E}\times\mathbf{B}/B^2$, and the *small gyroradius ordering* or *drift ordering* assumes that the ratio of this drift to the thermal speed of particles is of 1^{st} order, i.e. $V_E/v_{th}\sim\rho/L\sim\omega_{th}/\Omega=\delta<<1$, where ρ is the thermal gyroradius, L a characteristic plasma scale length and ω_{th} and Ω the transit frequency and gyrofrequency respectively. This approximation implies that the radial electric field is not so large as to distort gyration and varies slowly in time. The drift ordering is not very stringent, and is easily fulfilled even at the low-order electric field resonances (where the poloidal component of the drift speed vanishes) $E^{res}=\iota vBr/R$ since $V_{E^{res}}/v_{th}=\iota r/R$, where r/R is the inverse aspect ratio of the considered flux surface and ι its rotational transform.

In the drift ordering approximation particle motion is averaged over the the small gyro-scale and the resulting kinetic equation, now describing the distribution of guiding centers, is known as the *drift kinetic equation* (DKE) [1, 2]. Unfortunately, even with the drift ordering approximation solving the DKE is a daunting task. The inhomogeneity of the magnetic field along with the non-linearity of the collisional term makes the DKE a non-linear partial differential equation in a six dimensional space $f=f(\mathbf{r},v,p,t)$, $\mathbf{r}$ being the guiding center position in 3D space, v and $p=\mathbf{v}\cdot\mathbf{B}/v$ its speed and pitch angle in velocity-space, and t the time. The central point of neoclassical theory is solving this equation to obtain different flux-surface-averaged moments of its solution. To this end the distribution of guiding centers is linearized around a local Maxwellian distribution and several approximations are made in the drift motion of guiding centers. In the drift ordering approximation, the total energy conservation, $E=mv^2/2+q\Phi$ with $\mathbf{E}=-\nabla\Phi$, translates into an equation for the variation of the kinetic energy which is proportional to the divergence of the $\mathbf{E}\times\mathbf{B}$ drift, $\dot{v}=v(1+p^2)/4\,\nabla\cdot\mathbf{V}_E$ (notice that drift ordering precludes rapid variation of the magnetic and electric fields. Whenever the $\mathbf{E}\times\mathbf{B}$ drift is incompressible, $\nabla\cdot\mathbf{V}_E=0$, the total energy and the kinetic energy are conserved, which allows for quite some simplification in solving the DKE. Not only the speed of particles can be considered as a parameter, allowing for a mono-energetic treatment, but also the collision operator can be approximated by only its pitch

author's e-mail: V.Tribaldos@ciemat.es

angle scattering part. However, a direct calculation shows that $\nabla \cdot \mathbf{V}_E = -2V_E \nabla \ln B$ which in general is different from zero, thus to retain the benefits of incompressibility usually the exact drift $\mathbf{V}_E = \mathbf{E}\times\mathbf{B}/B^2$ is approximated by $\mathbf{V}_E = \mathbf{E}\times\mathbf{B}/\langle\mathbf{B}^2\rangle$. Since the magnetic field gradient is determined by the device's configuration the incompressible approximation restricts the usual neoclassical treatment to *small* radial electric fields.

The purpose of this work is to shed some light on the effect of the incompressible $\mathbf{E}\times\mathbf{B}$ flow for a wide range of radial electric fields and its impact on the determination of the mono-energetic particle diffusion coefficient, D^*. In Sec. 2 the basic equations of motion are discussed and a local δf Monte Carlo [3, 4] (MC) technique capable of dealing with compressible and incompressible flows (both completely conservative) is presented. Results of the comparison between the DKES (Drift Kinetic Equation Solver) [5, 6] and the new δf MC codes for different configurations will be shown is Sec. 3. Finally, Sec. 4 contains some discussion of the results.

2 Basics

The starting point of neoclassical transport theory is the DKE, that can be formally written as [2]

$$\frac{df}{dt} = \dot{\mathbf{r}}_D \cdot \nabla f + \dot{p}\frac{\partial f}{\partial p} + \dot{v}\frac{\partial f}{\partial v} = C(f,f) \qquad (1)$$

where $\dot{\mathbf{r}}_D = \mathbf{v}_D$, $\dot{p}$ and $\dot{v}$ are the drift speed and the time derivatives of the pitch (related to the conservation of the magnetic moment $\mu = mv_\perp^2/2B$) and the kinetic energy (derived from the conservation of the total energy $E = mv^2/2 + q\Phi$) given by:

$$\mathbf{v}_D = pv\frac{\mathbf{B}}{B} + \mathbf{V}_E + \frac{mv^2}{2qB^3}(1+p^2)\,\mathbf{B}\times\nabla B \qquad (2)$$

$$\dot{p} = -\frac{v}{2B^2}(1-p^2)\,\mathbf{B}\cdot\nabla B - \frac{p}{2B}(1-p^2)\,\mathbf{V}_E\cdot\nabla B \qquad (3)$$

$$\dot{v} = -\frac{v}{2B}(1+p^2)\,\mathbf{V}_E\cdot\nabla B \qquad (4)$$

and $C(f,f)$ is a collision operator.

Since $\mathbf{V}_E \cdot \nabla B = -B/2\,\nabla\cdot\mathbf{V}_E$ the second term in the r.h.s. in Eq.3 and Eq.4 depend explicitly on the compressibility of the $\mathbf{E}\times\mathbf{B}$ flow. The procedure used to solve the DKE consists of linearising the distribution of guiding centers, f, in Eq. 1 with respect to the drift ordering small parameter $\delta = \rho/L << 1$ as $f = f_0 - \delta f_1(\partial f_0/\partial r_r)$. For stationary conditions, i.e. neglecting the explicit time dependence, $\partial f/\partial t$, the solution to the zero order, δ^0, equation is identically satisfied by the local Maxwellian $f_0 = f_M$. Therefore, the goal is to find the solution, f_1, to the first order DKE:

$$\mathbf{v}_D^s \cdot \nabla_{\mathbf{r}_s} f_1 + \dot{p}\frac{\partial f_1}{\partial p} + \dot{v}\frac{\partial f_1}{\partial v} - C(f_M, f_1) = v_D^r \qquad (5)$$

Notice that the full first order distribution depends on the radial gradients of the zero order Maxwellian distribution, and that the inhomogeneous term is the radial drift of guiding centers v_D^r, thus the radial dependence enters the equation just like a parameter. Therefore, Eq. 5 describes a diffusion process in phase space rather than in real space. Different methods are usually applied to solve the Eq. 5, each with its strengths and drawbacks: i) analytical calculations [1]; ii) explicit spectral procedures, expanding f_1 in a base of eigenfunctions (like the DKES code [5, 6]) and iii) Monte Carlo techniques [7]. Analytical solutions are usually restricted to simplified magnetic fields and collisionality regimes, on the other hand explicit and MC numerical methods can deal with realistic configurations for broad collisionality ranges, but are extremely time consuming and sometimes not very accurate (e.g. non diagonal transport matrix elements in MC.

The usual approximation, as for example is done in DKES code, for computing the diffusion transport coefficients consists in neglecting $\nabla\cdot\mathbf{V}_E$ in equations 3 and 4, i.e. considering the $\mathbf{E}\times\mathbf{B}$ flow incompressible. Since $\dot{v} = 0$, the energy in Eq. 5 enters only as a parameter, once the collision operator is approximated by just its pitch-angle scattering part, and the coefficients are obtained by the convolution of mono-energetic solutions with the Maxwellian distribution. The price to pay in this approximation is that the radial electric field cannot be very large, and that the magnetic moment μ is not conserved (see Eq. 3). To check the approximation made by DKES for the mono-energetic diffusion coefficient for large radial electric fields it would be desirable to benchmark it against a MC type calculation with and without assuming $\nabla\cdot\mathbf{V}_E = 0$. In usual *full* f [7] MC calculations, based on fitting the slope of the time dependence of the radial broadening of a test particle ensemble (diffusion in real space), it is easy to include the full set of equations (conserving μ and E. However, when the radial electric field becomes *large* particles can win or lose kinetic energy as they move radially because of their drifts, thus making the calculation non-mono-energetic. The method proposed here to make such comparison is using the method of characteristic to solve partial differential equations like Eq. 5, which is at the base of the δf MC technique.

Formally, the solution to an equation of the type $a(x,y,...)\partial f/\partial x + b(x,y,...)\partial f/\partial y + ... = g(x,y,...,f)$ is a surface S such that at each point $(x,y,...)$ on S, the vector $\mathbf{V} = (a(x,y,..), b(x,y,...), ..., g(x,y,..,f))$ lies in the tangent plane. Such surface can be constructed by the union of curves C parametrized by s such that at each point on the curve, the vector $\mathbf{V}$ is tangent to the curve. In particular $C = \{(x(s), y(s), ..., g(s))\}$ will satisfy the following system of ordinary differential equations:$dx/ds = a(x,y,...); dy/ds = b(x,y,...); ...; du/ds = g(x,y,...,f)$, called characteristic curves, and the solution is $f(x,y,...) = u(x,y,...)$. Rephrasing this method for the collisionless

DKE means solving the system of equations:

$$\frac{d\mathbf{r}_D^s}{dt} = \mathbf{v}_D^s\,; \quad \frac{dp}{dt} = \dot{p}\,; \quad \frac{dv}{dt} = \dot{v}\,; \quad \frac{du}{dt} = v_D^r \quad (6)$$

$f_1 = u$ being its solution. Please notice that even though the system of equations 6 are the equations of motion of the guiding center, and the characteristic curves are the trajectories, thus clarifying the link with a MC particle simulation view, there is no equation for the radial drift r_D^r. Particles cannot escape the birth flux surface and no radial broadening calculation can be done. However, the solution $f_1 = u \sim \int v_D^r dt$ directly depends on the bounce-average of the radial drift speed along the parallel motion. The MC implementation is straightforward; the system of equations is integrated (taking care to retain the conservative nature of the motion) for an ensemble of markers (since no radial motion is included they cannot be regarded as particles anymore), all sharing the same energy and flux surface but with random toroidal and poloidal position and pitch. The effect of collisions in the DKE is simulated by applying a pitch angle collision operator [7].

3 Results

Three different magnetic configurations were studied with quite different B structures, namely: a tokamak with the same aspect ratio and rotational transform as the W7-AS stellarator, the LHD heliotron configuration with major radius $R_{axis} = 3.75$ m, and the W7-X standard configuration. The impact of the incompressibility of the $\mathbf{E}\times\mathbf{B}$ flow was studied by evaluating the diffusion coefficient for a wide range of radial electric fields. For each case two different collisionalities were chosen corresponding to the beginning of the ripple regime, $\nu/v = 10^{-3}\mathrm{m}^{-1}$, and one at the beginning of the *lmfp*, $\nu/v = 10^{-4}\mathrm{m}^{-1}$. The δf MC integrates 1024 markers for three collisional times divided in eight groups of 128 markers each. The error bar is obtained with the standard error from the eight estimations.

As was noted long ago, e.g. [8] Eq. 5 has a singularity when the poloidal component of the drift speed vanishes, which corresponds to resonant radial electric field values. In the following the radial electric field has been normalized to the first toroidal resonance $E_{res} = \iota v B r/R$.

In Fig. 1 the diffusion coefficient at half radius, $r/a = 0.5$, for an ideal tokamak configuration, with $B(r,\theta) = B_0(1 + r/R\cos\theta)$, $R = 2$m, $a = 0.2$m, and $\iota = 0.51$. This was selected because radial excursions from the flux surfaces are small and only one electric field resonance exists. There is a good agreement between DKES code results and the δf MC incompressible calculation; both displaying a peaked feature around the resonance followed by a strong decrease because of the disappearance of *banana* orbits. When compressible effects are included in the calculation the resonance is smoothed as well as the later sharp diffusion decrease flattened. The reason being the variation in the kinetic energy of the particles, $\dot{v}$ in Eq. 4, as can be seen in Fig. 2. The broadening of the kinetic energy spectra, due to $\dot{v}$, reduces the number of particles at the resonant field, $E_r/E_{res} = 1$ but also pushes some particles to energies that resonate at larger values of E_r/E_{res}. At very large radial electric fields there is a systematic difference between the DKES and MC results which is attributed to numerical diffusion. Nevertheless, please notice the rather small values of the diffusion coefficient.

The results for the other two devices (see Figs. 3 and 4) are similar to the tokamak result, apart from the different resonance structure due to their broader magnetic field spectra. The helical resonance peak at $E_{res} = (N_{periods} - m\iota)vBr/R$ can be clearly identified. As in the tokamak case the flattening is more pronounced at smaller collisionalities, pitch angle scattering is less efficient in moving particles out of the resonance. The incompressible approach is rather good for small E_r, but unexpectedly it is also working at large radial electric fields, provided that there is no resonance overlapping; see the almost mono-energetic structure of the PDF in Fig. 2 at $E_r/E_{res} = 4$. Finally, there is an inconsistency in comparing the mono-energetic diffusion coefficients of the DKES and incompressible δf codes with the compressible result since the latter, as has been shown, is not really mono-energetic. Moreover, considering only the pitch-angle part of the collision operator close to the resonance is not justified [8, 7].

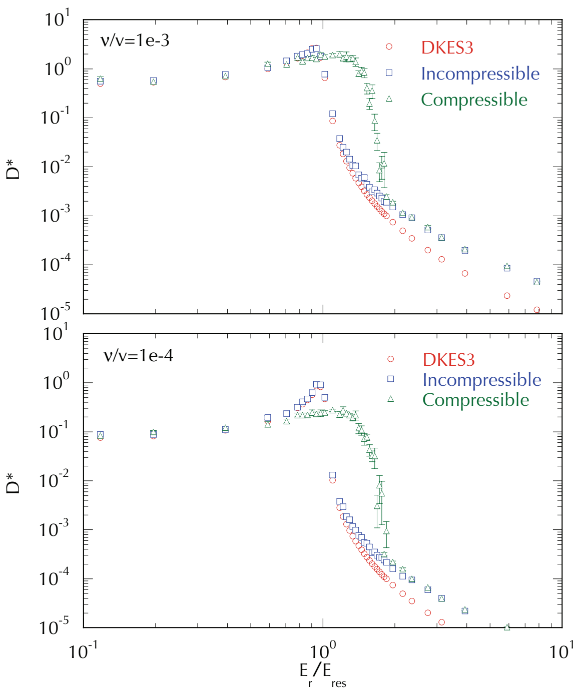

Fig. 1 Diffusion coefficient, normalized to the tokamak plateau, for the tokamak configuration versus the radial electric field, normalized to the first toroidal resonance E_{res}, for $\nu/v = 10^{-3}\mathrm{m}^{-1}$ (top) and $\nu/v = 10^{-4}\mathrm{m}^{-1}$ (bottom) obtained with the DKES code (circles) and the δf MC incompressible (squares) and compressible (triangles) approaches.

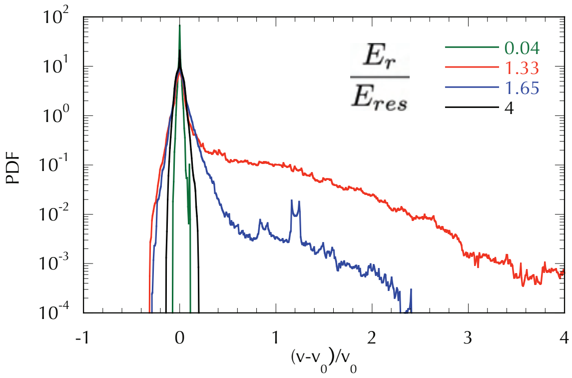

Fig. 2 Probability distribution function of velocities for $\nu/v = 10^{-3}\mathrm{m}^{-1}$ of Fig. 1 in the compressible approach.

4 Discussion

The aim of this work was to check the accuracy of local mono-energetic transport coefficient calculations for large radial electric fields. On the one hand DKES estimations are mono-energetic and local and transport is due to a pitch-angle diffusion process in phase space. But, the $\mathbf{E}\times\mathbf{B}$ term is treated as incompressible, $\nabla \cdot \mathbf{V}_E = 0$, to keep the kinetic energy constant. On the other hand, common full-f MC based calculations are not exactly local, because radial space broadening is used to describe the diffusion process. And, again their applicability is limited to consider small radial electric fields to keep particles' kinetic energy almost constant during their radial drifts. Here, a fully conservative δf MC code was introduced where local diffusion is computed in phase-space with particles (*markers*) remaining indefinitely on their birth flux surface (solving a general MC problem with particle losses).

The impact of the incompressible $\mathbf{E} \times \mathbf{B}$ flow approximation was tested comparing DKES results with the strictly local δf MC where the $\mathbf{E}\times\mathbf{B}$ drift is treated in compressible and incompressible form for large radial electric fields and several magnetic field configurations.

It was found that considering $\nabla \cdot \mathbf{V}_E = 0$ is indeed a good approximation for small radial electric fields, as expected, but also for large E_r far from the resonances. This also serves as a benchmark between DKES and the δf MC. The discrepancy between the results with and without $\nabla \cdot \mathbf{V}_E = 0$ close to the resonance is due to the variation of the kinetic energy. This results calls into question the *usual* mono-energetic calculations, which, to be safe, should be restricted to $E_r < 0.5 - 0.7\, E_{res}$.

[1] AA Galeev and RZ Sagdeev, Sov. Phys. JETP **26**, 233 (1968)
[2] RD Hazeltine, Phys. Fluids **15**, 77 (1973)
[3] M Sasinowsky and A Boozer, Phys. Plasmas **2**, 610 (1995)
[4] AM Dimits and WW Lee, J. Comput. Phys. **107**, 309 (1993)
[5] SP Hirshman *et al.*, Phys. Fluids **29**, 2951 (1986)
[6] WI van Rij and SP Hirshman, Phys. Fluids B **1**, 563 (1989)
[7] A Boozer and G Kuo Petravic, Phys. Fluids **24**, 851 (1981)
[8] EF Jaeger, CL Hedrik and DA Spong, Nuc. Fusion **19** Vol. 12, 1627 (1979)

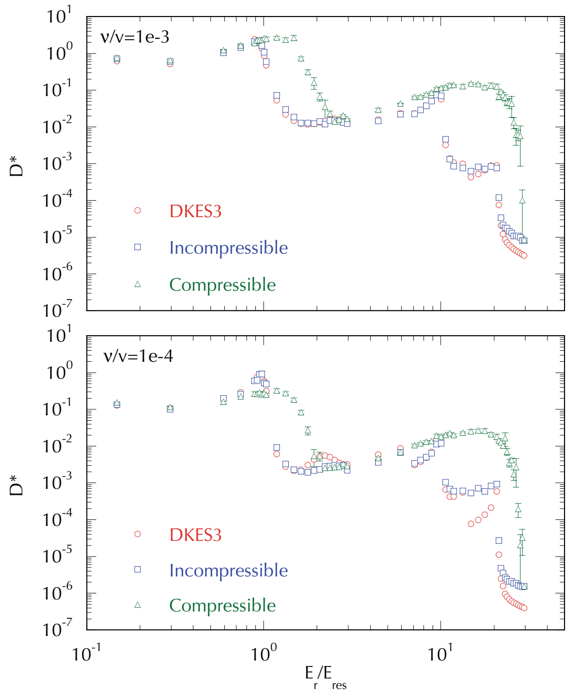

Fig. 3 Diffusion coefficient, normalized to the tokamak plateau, for LHD configuration with R_{axis} = 3.75 m versus the radial electric field, normalized to the first toroidal resonance , and $\nu/v = 10^{-3}\mathrm{m}^{-1}$ (top) and $10^{-4}\mathrm{m}^{-1}$ (bottom) for the DKES code (circles) and the δf MC incompressible (squares) and compressible (triangles) approaches.

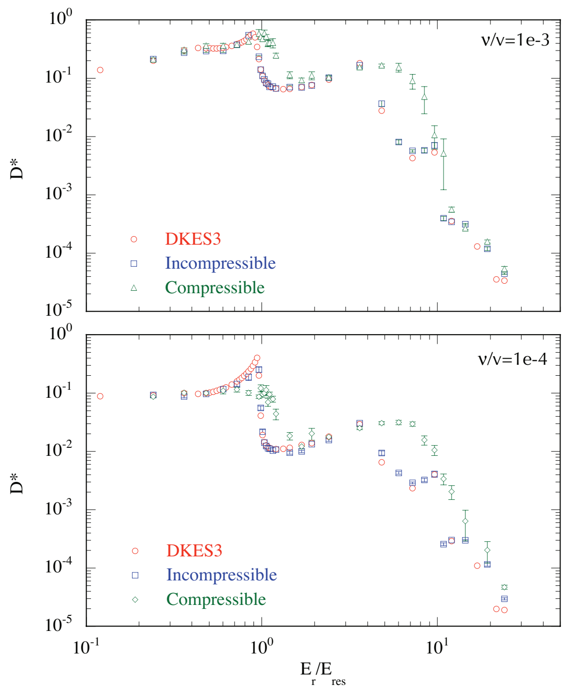

Fig. 4 Diffusion coefficient , normalized to the tokamak plateau, for W7-X standard configuration versus the radial electric field, normalized to the first toroidal resonance, and $\nu/v = 10^{-3}\mathrm{m}^{-1}$ (top) and $10^{-4}\mathrm{m}^{-1}$ (bottom) for the DKES code (circles) and the δf MC incompressible (squares) and compressible (triangles) approaches.

Observation of Internal structure of energetic particle driven MHD modes in the Large Helical Device

T. Tokuzawa, A. Ejiri[a], K. Kawahata, and LHD Experimental Group

National Institute for Fusion Science, Toki 509-5292, Japan

[a] Grad. School of Frontier Sciences, Tokyo Univ., Kashiwa 277-8561, Japan

(Received day month year / Accepted day month year should be centered 10-point type)

In the burning plasma the energetic alpha particles enhance MHD instabilities such as toroidal Alfvén eigenmodes and these modes affect the particle transport and the plasma confinement. The study of the energetic particle driven MHD mode is important as the preparation study of the future alpha particle transport. In the Large Helical Device three microwave reflectometer systems have been installed to measure the density fluctuation in the wide radial area with a high spatial resolution. These systems are used for knowing the internal structures of each MHD mode and these temporal behaviors. One of the results is the energetic particle mode driven by the injecting neutral beam is strongly localized at the plasma core region and it is agreement with the theoretical expectation.

Keywords: Alfvén eigenmode, MHD, Density Fluctuation, Microwave Reflectometer, Large Helical Device

1. Introduction

In the burning plasma energetic alpha particles enhance magneto hydrodynamics (MHD) modes such as toroidal Alfvén eigenmodes (TAEs). Also the study of the energetic particle transport is one of the important issues and it is found that the correlation between the temporal behavior of the instability and the lost particle is quite high. That is an MHD mode affects the alpha particle transport and changes plasma confinement. Therefore energetic particle driven MHD instability has been studying in several magnetic confinement devices [1-4]. Usually MHD phenomena are observed by magnetic probes and the excellent analytical technique is developed to know toroidal and poloidal mode number and travelling direction. Also theoretical analysis using three dimensional code has been developing [5]. For the comparison between the simulation code result and the experimental result, it is important to measure directly the internal radial distribution of these modes.

In Large Helical Device (LHD [6]) recently we have been applying three types of microwave reflectometer system for measuring the radial distribution of the fluctuation, because the microwave reflectometer has a potential of the localized measurement by using the cut-off effect in the plasma core region. The density perturbations δn associated with the displacement ξ of a shear Alfvén mode is described by [2],

$$\frac{\delta n}{n} = -\nabla \cdot \xi - \xi \cdot \frac{\nabla n}{n} \cong \left(\frac{-2\hat{R}}{R^2} + \frac{\hat{n}}{L_n} \right) \cdot \xi. \quad (1)$$

Here n is the plasma density, $\hat{n}$ is the density unit vector normal to the magnetic surface, R is the major radius, $\hat{R}$ is the unit vector along a major radius direction, and L_n is the density scale length. Therefore it was found that the reflectometer can measure the internal structure of MHD phenomena such as energetic particle mode and Alfvén eigenmodes.

At first we have applied a fixed frequency reflectometer system to measure the low frequency fluctuation such as an interchange mode, etc. One of the reasons is the limitation of the memory size of the data acquisition. Recently the real-time fast data acquisition system has been developed in LHD [7] and the sampling rate of up to 10 MSample/sec is available to use. It makes the high frequency fluctuation measurable during the whole plasma discharge. Also we make the frequency variable reflectometer systems, so called Hopping reflectometer. To measure the fluctuation profile in the wide range, a reflectometry needs a lot of frequency sources. If the plasma condition seems to be steady during the frequency changing period, the radial profile can be measured each sweep in one plasma discharge. In this paper we present these reflectometer systems and some experimental results.

author's e-mail: tokuzawa@nifs.ac.jp

2. Frequency Fixed *E*-band Reflectometer System

E-band fixed frequency heterodyne reflectometer system is utilized for the fluctuation measurement [8]. Currently the system has three channels of fixed frequencies of 78, 72, and 65 GHz. Power combined three microwaves travel to/from the LHD through the corrugated waveguide for avoiding the transmission loss. The extraordinary polarization wave is used. The simplified super heterodyne detection technique is used

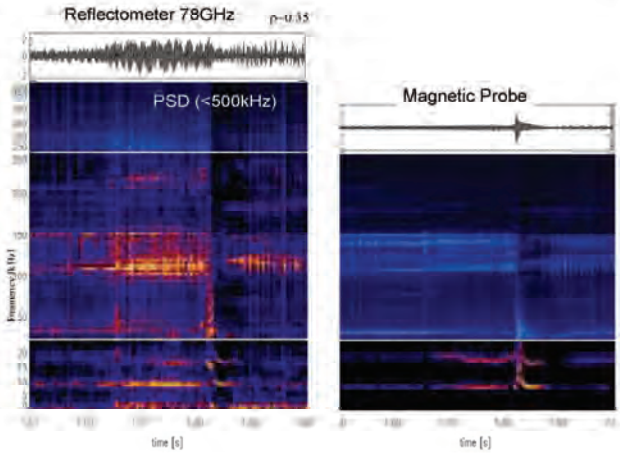

Fig.1 Time evolution of reflectometer signal and frequency spectrum (Left) and these of magnetic probe signal (right)

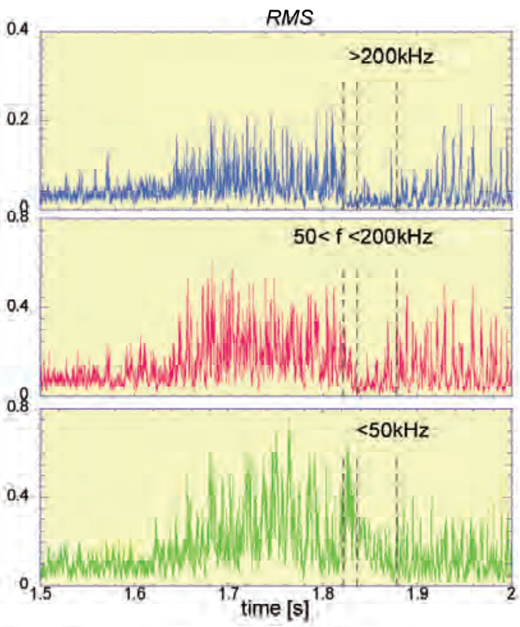

Fig.2 Time evolution of fluctuation power of reflectometer signal. Including each frequency component is higher than 200 kHz (top), higher than 50 kHz and less than 200 kHz (middle), and less than 50 kHz (bottom), respectively.

for the receiver system. In LHD the real-time data acquisition system has been able to be utilized and the sampling rate is up to 10 MSample/sec by using a compact PCI based digitizer. The system is very convenient to observe MHD phenomena such as energetic particle driven Alfvén eigenmodes. The example of the temporal behavior of the reflectometer signal of 78 GHz and magnetic probe signal and these frequency power spectra are shown in Fig. 1. In this plasma discharge some bursts are repeatedly and in this figure one of the bursts is presented. Coherent spectra of around 8 and 16 kHz are caused by low-*n* mode oscillation. In the range of 100~150 kHz there are a lot of coherent mode. These modes are identified the *n*=1 (*n*: toroidal mode number) TAE mode by the magnetic probe analysis. Also on the reflectometer signal it is observed higher mode around 230 kHz. Just after *t*=1.82s MHD-burst is occurred and at the same time TAE mode frequency components are rapidly disappeared shown in Fig. 2. Then passing 0.02s this mode is started to revive. This sudden disappearance may be caused that the distribution of high energy particle is changed by a MHD-burst. In this experiment the birth source of energetic particle is generated by the neutral beam. During this phenomenon is occurred, the injection power of neutral beam is kept constant. Therefore the TAE mode is re-exited quickly and then it keeps to a next burst.

2. Frequency Hopping *Ka*-band Reflectometer System

To know the radial distribution of fluctuation there are two methods in a reflectometry. One is the multi-channel system, and another is the wide band frequency source system. For the latter system, source frequency sweeps step by step in the whole frequency

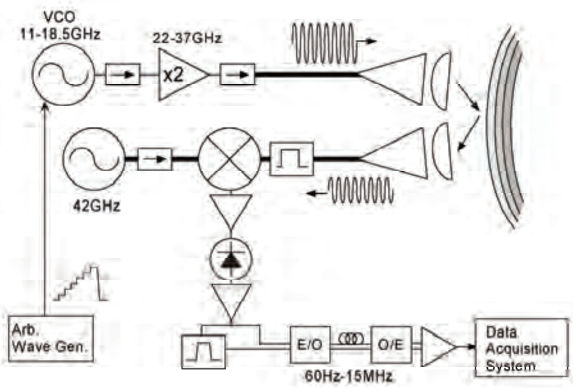

Fig.3 Schematic view of Frequency Hopping *Ka*-band Reflectometer system

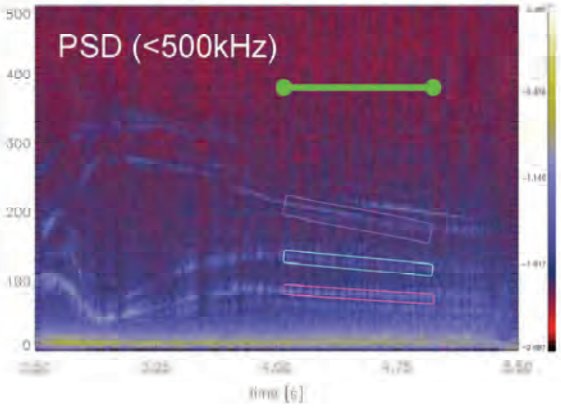

Fig.4 Frequency spectrum of interferometer mode CW Reflectometer

range. The step width is limited by the characteristic time of the measuring fluctuation frequency. Of course, during the frequency change, the plasma condition and the fluctuation level are assumed to be constant. The schematic of frequency hopping *Ka*-band reflectometer system is shown in Fig. 3. The system uses voltage controlled oscillator (VCO) as a source. The output frequency of this source is easily changed by the external controlled signal. The output wave is amplified and also this frequency is multiplied by two. The reflected wave is mixed with a local wave for the heterodyne detection and intermediate frequency (IF) signal is amplified and detected. Data acquisition system is the same as the previous *E*-band reflectometer system.

The experiment is carried out that the axial magnetic field strength is 1.0 T, the averaged electron density is under $0.5 \times 10^{19} m^{-3}$, and neutral beam is injected with constant. The source frequency is swept full range every 200 ms and the number of the frequency step is 20. Each time of the launching frequency is 10 ms and data sampling rate is 1 μs, then the data point is 10,000 and the frequency resolution is 100 Hz. It is enough to observe the MHD phenomena such as TAE. Figure 4 shows the frequency spectrum of the previous frequency fixed 78 GHz reflectometer signal. In this plasma condition there is no corresponding cut-off layer of 78 GHz wave and then this system is operated as an interferometer mode. We can see several continuous coherent frequency components. Figure 5 shows the radial profile of the fluctuation strength of the frequency hopping reflectometer signal during t=4.0-4.8s (4 sweep periods). It can be obtained that the frequency component around 200 kHz is large near at ρ=0.8 and the other component around 150 kHz is localized in the plasma centre. Here the meaning of the data points which are located under ρ=0 is that these frequency waves are not reflected from the plasma and they are

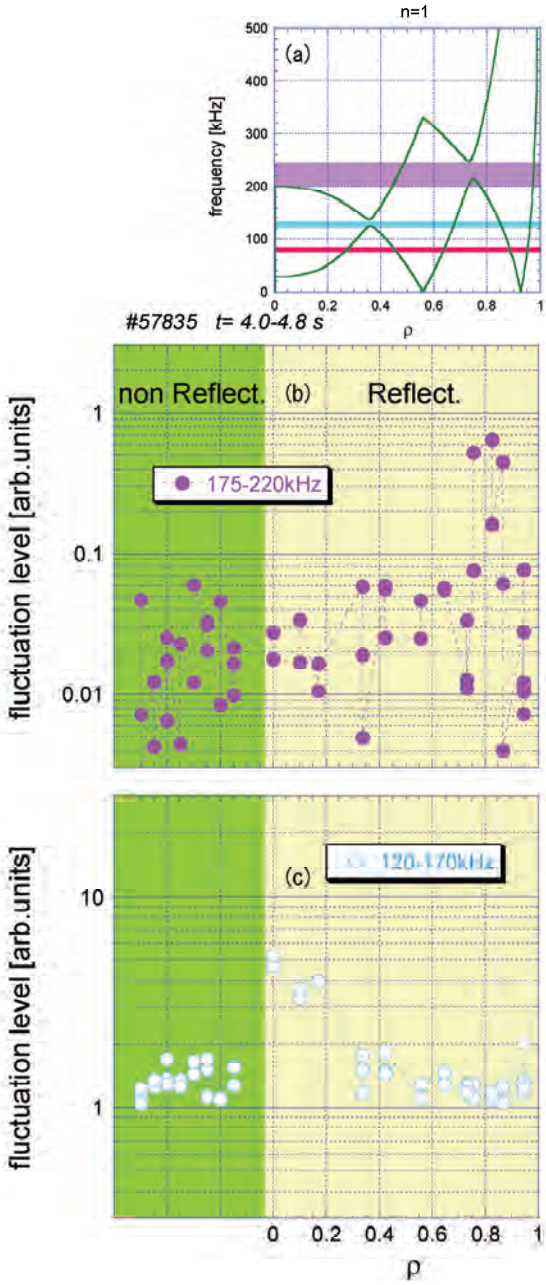

Fig.5 (a) Shear Alfvén spectra for n=1 and Radial profile of the fluctuation component of *Ka*-band Hopping reflectometer in the integrated frequency range that (b) 175-220 kHz and (c) 120-170 kHz

come back from the opposite wall. The calculated shear Alfvén spectra is shown in Fig.5(a). The frequency gap of around 200 kHz is located near at ρ=0.7. It is well agreement with the measured profile data. On the other hand, the coherent frequency mode of around 150 kHz is lower than the gap frequency and the temporal behavior is different with the 200 kHz frequency mode. It looks like the energetic particle mode (EPM). However, strictly speaking, this signal is not only the phase fluctuation of the reflected wave and it is not directly related to the density fluctuation. Therefore the direct phase measurement of reflected wave is necessary for the strict analysis of fluctuation.

2. Frequency Hopping *V*-band Reflectometer System

For more accurate fluctuation measurement we have developed a new system shown in Fig.6. Some components are added to the previous *Ka*-band system. Especially the single side band (SSB) frequency modulation is utilized for the direct phase measurement. Also the synthesizer is used as a source as a low phase noise source. The signal to noise ratio is up to 50 dB in the test of the system noise.

An example of this hopping system's measurement is shown in Fig.7. In this time window the launching frequency is changed from 52 GHz to 63 GHz and the step size is 1GHz with 50 ms duration. Some Alfvén eigenmodes can be observed in the whole launching frequency range. Disappointingly in this discharge the fluctuation is not kept constant and it can not be got the structure of the fluctuation mode. We plan to add more improvement in this system and will get the internal information of Alfvén eigenmodes in near future.

Summary

To study the internal structure of Alfvén eigenmodes, some reflectometer systems are installed on LHD. Both TAE and EPM modes can be observed with high resolution. Using frequency hopping technique the internal structure can be obtained. For the strictly analysis the direct phase measurement system has been applied. We will add more improvement in the system and study the Alfvén eigenmodes physics.

Acknowledgements

This work was partially supported by a Grand-in-Aid of the Japan Society for the Promotion of Science to one of the authors (TT) and also by NIFS07ULHH507 from the budget grant-in-aid of the National Institute for Fusion Science.

References

[1] S. E. Sharapov *et al.*, Phys. Rev. Lett. **93**, 165001 (2004)
[2] R. Najikian *et al.*, Phys. Rev. Lett. **91**, 125003 (2003)
[3] H. Kimura *et al.*, Nucl. Fusion **38**, 1303 (1998)
[4] S. Yamamoto *et al.*, Nucl. Fusion **45**, 326 (2005)
[5] C. Nührenberg, Phys. Plasmas **6** 137 (1999)
[6] O. Motojima *et al.*, Nucl. Fusion **43**, 1674 (2003)
[7] H. Nakanishi *et al.*, Fusinon Eng. Design **66-68** 827(2003).
[8] T. Tokuzawa *et al.*, 31st EPS Conf. P5-114 (2004)

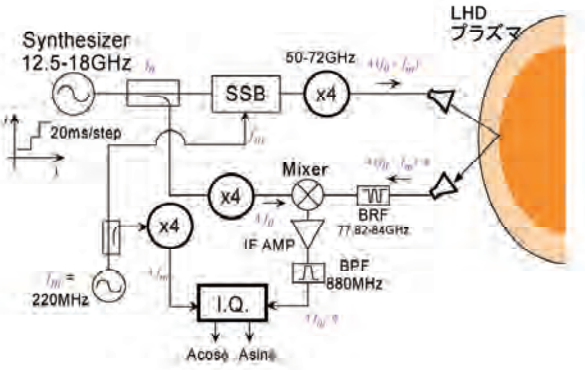

Fig.6 Schematic view of Frequency Hopping *V*-band Reflectometer system

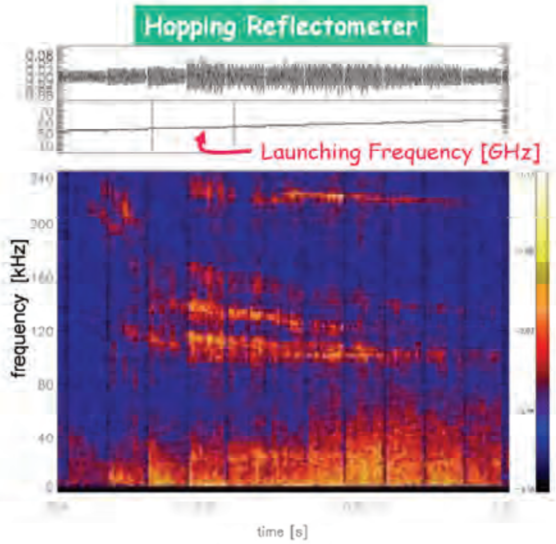

Fig.7 Temporal behavior of the Frequency Hopping *V*-band Reflectometer signal and its frequency spectra

Gyrokinetic Analysis of Alfv'en Eigenmode in Toroidal Plasmas with Non-Maxwellian Velocity Distribution Function

A. Fukuyama and H. Nuga

Department of Nuclear Engineering, Kyoto University,Kyoto 606-8501, Japan

fukuyama@nucleng.kyoto-u.ac.jp

Excitation of Alfv'en eigenmode by energetic ions has been attracted considerable attentions both experimentally and theoretically, since it may lead to loss of energetic ions, damage of first walls, and benefit as a tool for reconstructing the magnetic field structure. Numerous computational analyses of Alfv'en eigenmode have been carried out with various MHD models and gyrokinetic models to predict the mode frequency and the growth rate. Previous gyrokinetic analyses, however, assume Maxwellian or slowing-down velocity distribution functions for the energetic ions. In a plasma heated by ICRF waves, neutral beam injection (NBI), or alpha particles produced by fusion reaction, the velocity distribution function of energetic ions is far from the Maxwellian. Therefore quantitative analyses of Alfv'en eigenmodes require to include the effect of non-Maxwellian velocity distribution function.

In this article, we report gyrokinetic full-wave analyses of the Alfv'en eigenmodes with realistic velocity distribution functions. We employ the integrated modeling code TASK/3D [1] for tokamak plasmas and toroidal helical plasmas. The velocity distribution function of the energetic ion species is calculated by the Fokker-Planck module, TASK/FP. The gyrokinetic dielectric tensor is evaluated for arbitrary distribution function by the wave dispersion module, TASK/DP. The wave structure of the Alfv'en eigenmode is computed by the newly-updated full wave module, TASK/WM [2]. The TASK/WM module now uses the finite element method in the radial direction and calculate the wave electric field in the local orthogonal coordinates. Maxwell's equation with gyrokinetic dielectric tensor is solved in the magnetic surface coordinates and the fast Fourier transform in used in the poloidal and toroidal directions. We look for a complex eigen frequency which maximizes the volume integral of the square of the wave electric field amplitude for fixed excitation proportional to the electron density.

First we compare the mode frequency and damping rate of the toroidal Alfv'en eigenmode in a tokamak plasma with the Maxwellian without and with the effect of ion precession frequency. Next the effects of modified velocity distribution functions for ions heated by ICRF, NBI and alpha particles will be studied in the reversed magnetic shear configuration. Finally the toroidal and global Alfvén eigenmodes in LHD plasmas will be reported.

[1] A. Fukuyama et al., Proc. of 20th IAEA Fusion Energy Conf. (Villamoura, Portugal, 2004) IAEA-CSP-25/CD/TH/P2-3.

[2] A. Fukuyama et al., Proc. of 19th IAEA Fusion Energy Conf. (Lyon, France, 2002) IAEA-CN-94/TH/P3-14.

Proceedings of ITC/ISHW2007

Energetic ion driven MHD instabilities and their impact on ion transport in Heliotron J plasmas

Satoshi YAMAMOTO[1)], Gen MOTOJIMA[2)], Shinji KOBAYASHI[3)], Tohru MIZUUCHI[3)], Hiroyuki OKADA[3)], Kazunobu NAGASAKI[3)], Boyd BLACKWELL[4)], Katsumi KONDO[2)], Yuji NAKAMURA[2)], Noriyoshi NAKAJIMA[4)] and Fumimichi SANO[3)]

1) Kyoto University Pioneering Research Unit for Next Generation, Gokasho, Uji 611-0011, Japan

2) Graduate School of Energy Science, Kyoto University, Gokasho, Uji 611-0011, Japan

3) Institute of Advanced Energy, Kyoto University, Gokasho Uji 611-0011, Japan

4) Research School of Physical Science and Engineering, The Australian National University, Canberra, Australia

5) National Institute for Fusion Science, 322-6 Oroshi-cho, Toki, Japan

Energetic ion driven MHD instabilities such as global Alfvén eigenmode (GAE) are observed in NBI-heated Heliotron J plasmas. In order to investigate the configuration effect on GAEs, we changed the magnetic configuration with regard to iota profile due to the variation of plasma current and coil current. The characteristics of observed GAEs are related to the iota profile and magnetic shear. The GAEs are excited by the sideband excitation. The bursting GAE might be effect on energetic ion transport because the some plasma parameters are simultaneously modulated with bursting GAEs.

Keywords: MHD instability, advanced stellarator, low magnetic shear, Alfvén eigenmodes, energetic ion transport.

1. Introduction

To clarify the MHD instabilities destabilized by energetic ions is important for the Deuterium-Tritium (D-T) fusion plasmas because the MHD instabilities could lead to the loss of alpha particles from confinement region before their thermalization and the ejected alpha particles might cause significant damage of first wall of a fusion device. Therefore, MHD instabilities destabilized by the energetic ions such as Alfvén eigenmodes (AEs) and energetic particle modes (EPMs) are being extensively studied in many stellarators/heliotrons as well as tokamaks using the Alfvénic ions produced by neutral beam injection (NBI), ion cyclotron resonance heating (ICRH) and D-T reactions.

The characteristics including the existence and the damping mechanisms of AEs such as continuum damping mainly depend on the structure of magnetic field. Toroidicity-induced AEs (TAEs), which can exist in the TAE frequency gap formed by the poloidal mode coupling m and m+1 (m: poloidal mode number) of shear Alfvén continua, are observed and effect on the energetic ion transport in the CHS [1] and LHD [2] with high and/or moderate magnetic shear. In the low shear stellarator/heliotron W7-AS [3] and Heliotron J [4], Global AEs (GAEs), which can exist on just below of upper continuum and above of lower shear Alfvén continuum are typically observed. Moreover helicity-induced AEs (HAEs), which are observed in W7-AS and LHD [5], can exist in the HAE frequency gaps formed by both toroidal and poloidal mode coupling. It will be more important AEs as well as GAEs in advanced stellarators with low toroidal field period N_f (e.g. N_f = 2~5) because AEs having the frequency comparable with ion diamagnetic frequency could have large growth rate and the frequency of HAE is scaled with the number of toroidal field period [6]. Therefore, it is important and of interest to investigate the GAEs and HAEs in the Heliotron J plasmas for advanced stellarator type fusion reactor with low magnetic shear and toroidal field period.

2. Configuration effect on global AEs

Heliotron J [7] is the helical-axis heliotron device with major and effective mirror radii R=1.2 m and $<a_{eff}>$=0.15~0.22 m, simultaneously. The magnetic configuration of Heliotron J is characterized by the low magnetic shear for the avoidance of the rational surface with low mode number and the combination of local quasi-isodynamic and bumpy (mirror) magnetic field for the good particle confinement. The Heliotron J plasmas are produced by the second harmonic electron cyclotron heating (ECH) with 70GHz, and can be additionally

author's e-mail: syama@iae.kyoto-u.ac.jp

heated by the ECH, NBI and ICRF. We utilize the Alfvénic energetic ions produced by the tangentially co.- and counter-injected Hydrogen neutral beams with the energy of 24~27 keV for the destabilization of GAEs. The toroidal and poloidal magnetic probe array can determine the toroidal and poloidal mode number *n* and *m* of observed coherent MHD modes were installed on the vacuum vessel of Heliotron J.

In the NBI-heated Heliotron J plasmas, some GAEs with m=2/n=1 and m=4/n=2 are typically observed [4]. These modes propagate in the ion diamagnetic drift direction and of which frequency is correspond to that of discrete mode obtained from CAS3D3 [8] analysis where poloidal mode coupling are only taken into account. The magnetic fluctuation amplitudes of GAEs are in the order of $b_\theta/B_t \sim 10^{-6}$ at the position of the magnetic probes.

In order to investigate the configuration dependence on GAEs, we changed the magnetic configuration with regard to the differences of iota profiles. The plasma current and coil current can internally and externally vary the iota profile. In the plasma for AE excitation experiment, the plasma current consists of neutral beam driven current and bootstrap current. We changed the bumpy field in order to change the bootstrap current which is related to the confinement of trapped particle. The time evolution of amplitude of observed m=2/n=1 GAE and some plasma parameters are shown in Fig. 1, where the plasma beta obtained from diamagnetic loop, and line averaged electron density are almost same in the plasmas with different bumpy field. Both neutral beam driven and bootstrap currents flow in the co.-direction that increases the rotational transform. The differences of plasma current shown in Fig. 1 (d) are mainly resulted from the differences of bootstrap current. The amplitudes of observed m=2/n=1 GAEs are different in each magnetic configurations and is scaled with the amount of the plasma current.

In order to clarify the differences the amplitude of observed GAEs, We compared these observed frequencies at t = 0.26 s in each plasmas shown in Fig. 1 with shear Alfvén spectra that are calculated for equivalent two dimensional (2D) magnetic configuration

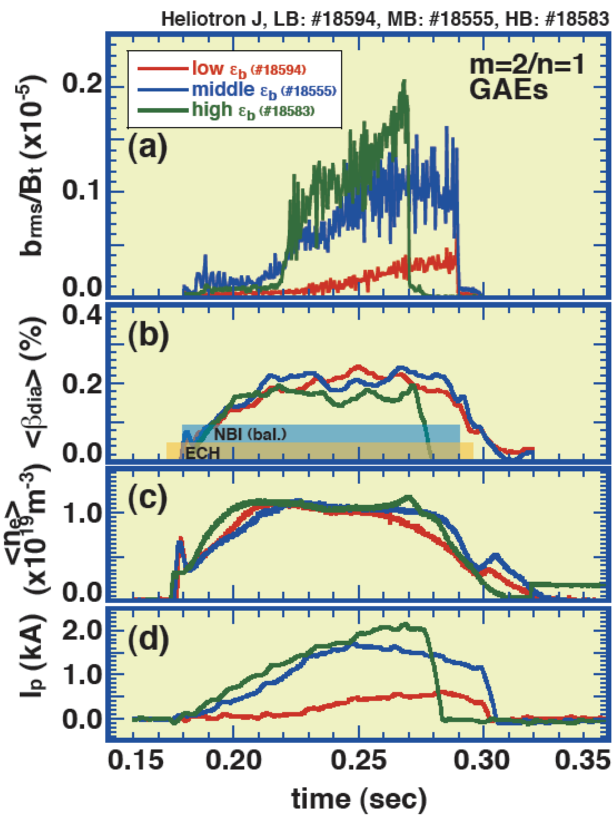

Fig. 1. Time evolution of (a) amplitude of observed m=2/n=1 GAEs, (b) plasma beta obtained from diamagnetic signals, (c) line averaged electron density and (d) plasma current.

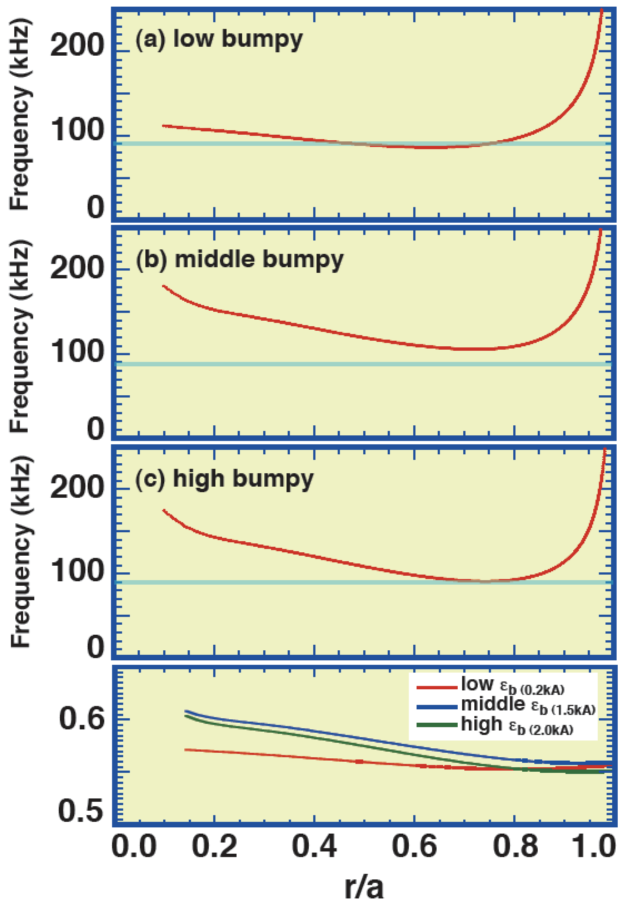

Fig. 2. Shear Alfvén spectra for n=1 for t = 0.26 s shown in Fig. 1 where poloidal mode coupling is taken into account. (a) Low bumpy case (b) middle bumpy case and (c) high bumpy case. (d) Profiles of rotational transform for each configuration.

where toroidal mode coupling is ignored. Shear Alfvén continua for $n = 1$ and profiles of rotational transform for the each configurations are shown in Fig. 2. In Fig. 2(a) ~ (c), red and blue lines denote the shear Alfvén continuum of $m = 2/n = 1$ and frequency of observed GAEs with $m = 2/n = 1$. As seen from Fig. 2, the observed mode frequencies lie just below the shear Alfvén continuum of $m = 2/n = 1$. The shear Alfvén spectra and rotational transform are almost same in each configurations in vacuum. The differences of shear Alfvén spectra shown in Fig. 2 (a) ~ (c) is caused by the plasma current including bootstrap current. The observed frequency does not clearly intersect the shear Alfvén continua, therefore, the GAEs would not be suffer from strong continuum damping. There are no differences in the electron and ion temperatures that indicates electron and ion Landau damping are same in each configuration. The bumpy field effects on the confinement of trapped particle, which cannot resonantly couple with the AEs. The reason of differences in observed GAEs amplitude might be explained by the differences of structure of GAEs. We need measurement of structure of observed GAEs and calculation of global mode analysis.

We also changed the iota profile due to the change of coil current shot by shot (named as iota scan experiment) and investigated the dependences of them on GAEs. In the iota scan experiments, we fixed the magnetic axis position and plasma volume and strength of bumpy field. The clear differences in amplitude of observed GAEs were not observed. The frequency of observed mode is related to the iota value.

3. Parametric studies of GAEs

AEs excited by the energetic ions will be destabilized when a certain threshold conditions are satisfied. The linear growth rate of AEs being proportional to the pressure gradient of energetic ions must be large enough to overcome the damping rate of the waves. Moreover, the velocity of energetic ions $v_{b//}$ is required to satisfy the resonance condition with the Alfvén wave. The GAE resonance condition for the fundamental excitation is $v_{b//}/v_A > 1$ and sideband excitation via the drift modulation of energetic ion orbit is $v_{b//}/v_A > k_{//(m,\ n)} / k_{//(m\pm1,\ n)} = [mi\text{-}n]/[(m\pm1)i\text{-}n]$. Here, $k_{//(m,\ n)}$ and $k_{//(m\pm1,\ n)}$ are the parallel wave number of waves, and i the rotational transform. The resonance condition for sideband excitation between $m = 2$ and $m = (2+1)/n = 1$ is $v_{b//}/v_A > 0.2$. We investigated the resonance condition with $v_{b//}/v_A$ changing the electron density $\langle n_e \rangle$. The $m \sim 2/n = 1$ GAEs are destabilized in the condition of $v_{b//}/v_A \geq 0.25$ as shown in Fig. 3. The linear growth rate of AEs is related to the velocity ratio $v_{b//}/v_A$ as well as energetic ion beta $\langle \beta_{b//} \rangle$ and has a peak at unity. The fluctuation amplitude of observed GAEs increased with an increase in $v_{b//}/v_A$. These results of parametric study for $v_{b//}/v_A$ agree with the linear theory of AEs.

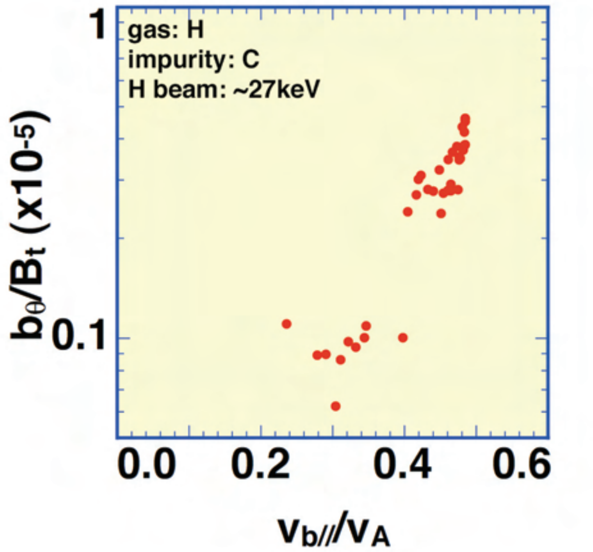

Fig. 3. The dependence of amplitude of observed m=2/n=1 GAEs against the ratio of energetic ion velocity and Alfvén velocity.

4. Energetic ion loss induced by the GAEs

In the plasma with magnetic configuration having the higher bumpy field, bursting GAEs ($m = 4/n = 2$), of which amplitude is two times larger than that of continuously observed GAEs are often observed, as shown in Fig. 4 (a)~(b). The frequency of bursting GAEs usually chirps down quickly. The time interval between each bursting GAEs increases with the increased in amplitude of bursting GAEs. This phenomenon can be explained by predator-prey model between energetic ion driven mode and energetic ions and might indicate the energetic ion transport induced by the energetic ion driven mode. The some plasma parameters such as H_α/D_α and, ion saturation current and plasma floating potential which are obtained from Langmuir probes located at outside last closed flux surface of plasma, are simultaneously increased with bursting GAEs, as shown in Fig. 4 (c)~(e). The increasing of ion saturation current is related to the increasing of amplitude of GAEs. Although the increasing in Langmuir probe signals cannot directly indicate the loss of energetic ion from the confinement region, the simultaneous increasing of the some plasma parameters indirectly indicates the energetic ion loss induced by the busting GAEs. The degradation of stored plasma energy induced by the bursting AEs observed in LHD and W7-AS were not observed in Heliotron J plasmas.

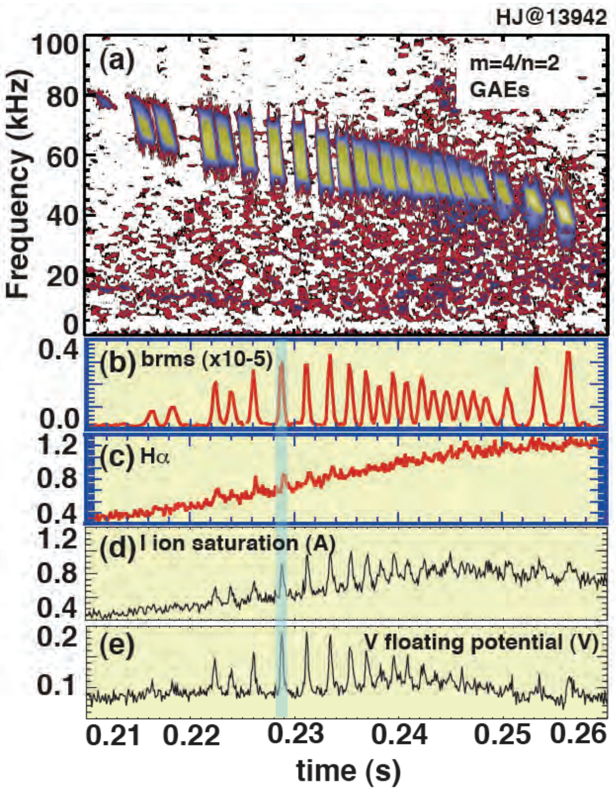

Fig. 4. Time evolution of (a) frequency spectrum and (b) amplitude of observed m=4/n=2 GAEs, (c) H_α/D_α signals, and (d) ion saturation current and floating potential obtained from Langmuir probes.

5. Conclusion

We investigated the dependence of magnetic configuration on GAEs using the variation of plasma current and coil current. In the high bumpy configuration, m=2/n=1 GAEs with the largest amplitude were observed. We compared with the observed frequencies and shear Alfvén spectra for n = 1. The differences of amplitude of observed GAEs in each configuration cannot be explained by the change of damping rate. GAEs were excited by the sideband excitation. The bursting GAEs with intense magnetic fluctuations might be affecting the energetic ion transport.

References

[1] K. Toi, et al., Nucl. Fusion **40**, 1349 (2000).

[2] S. Yamamoto, et al., Nucl. Fusion **45**, 326 (2005).

[3] A. Weller et al., Phys. Plasmas **8**, 931 (2001)

[4] S. Yamamoto, et al., Fusion Sci. Technol. **51**, 92 (2007).

[5] S. Yamamoto, et al., Phys. Rev. Lett. **91**, 245001 (2003).

[6] N. Nakajima, C.Z. Cheng and M. Okamoto, Phys. Fluids B **4**, 1115 (1992).

[7] T. Obiki, et al., Plasma Phys. Control. Fusion **42**, 1151 (2000).

[8] C. Nührenberg Phys. Plasmas **6**, 137 (1999).

P2-035

Resistive wall mode stability analysis including plasma rotation and error field

Masaru FURUKAWA[1)] and Linjin ZHENG[2)]

[1)] *Graduate School of Frontier Sciences, The University of Tokyo, Chiba 277-8561, Japan*
[2)] *Institute for Fusion Studies, University of Texas at Austin, Austin, TX 78712, USA*

(Received 15 October 2007 / Accepted 15 October 2007)

A theory for the formation of static magnetic islands induced by error fields is developed especially taking into account the Alfvén resonance effects due to the plasma rotation in cylindrical geometry. The Alfvén resonance effect totally changes the mode structure in the ideal magnetohydrodynamic (MHD) regions, which results in the significant change of the behavior of magnetic islands. It is found that the magnetic island becomes wider and the toroidal torque becomes larger when the resistive wall is located closer to the plasma and when the mode-rational surface is closer to the plasma edge.

Keywords: resistive wall mode, plasma rotation, magnetic island, error field, tokamak

DOI: 10.1585/pfr.1.001

1 Introduction

In recent tokamak experiments, stabilization of resistive-wall mode (RWM)[1, 2] is one of the central issues to sustain high-performance discharges. The stabilization of RWM by plasma rotation have been studied extensively, and it has been demonstrated that plasma rotation can stabilize RWM both experimentally[1, 3, 4] and theoretically[5, 6, 7, 8, 9, 10]. The critical rotation velocity for the stabilization of RWM had been considered as 1–2% of the Alfvén velocity at $q = 2$ surface[11] where q is the safety factor[2].

However, it was recently demonstrated experimentally that the critical rotation velocity can be greatly reduced if the error field resonant to the mode is carefully reduced[3, 4]. The resulting critical rotation velocity was about 0.3% of the Alfvén velocity, which is one-order smaller than the previous results. In DIII-D experiments, it was shown that the critical rotation velocity in the NBI torque reduction experiments is much smaller than that in the magnetic braking experiments in which the error field is increased to brake the plasma rotation[4]. Therefore, it is obvious that the error field plays a crucial role in this critical-rotation problem.

The formation of magnetic islands by an error field was studied in a rotating plasma theoretically[12]; the effect of the plasma rotation was included as the convection term in the nonlinear evolution equation of the magnetic island width, or so-called modified Rutherford equation[13]. However, the plasma rotation generates twin Alfvén resonances due to the Doppler shift at both sides of the mode-rational surface. When the plasma rotation is not so slow, the island region at the mode-resonance surface can be well separated from the Alfvén resonance positions. Therefore, we need to take into account the effect of Alfvén resonances in the ideal magnetohydrodynamic (MHD) region. Therefore, we developed a theory for this problem by including the Alfvén resonance effect[14]. It was found that the Alfvén resonance effect changes the tearing mode parameter Δ' significantly, which results in, most importantly, the complete rotation suppression of the magnetic islands. In the present paper, we study the effect of the position of the wall and the mode-rational surface on this problem.

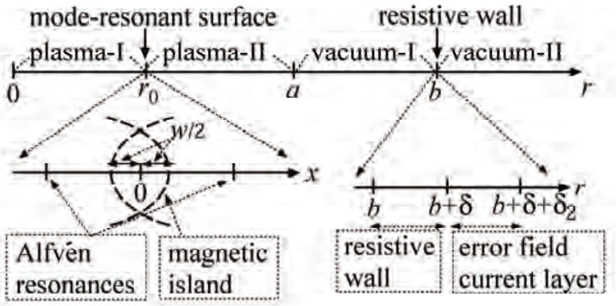

Fig. 1 Schematic picture of the geometry.

2 Matching of independent solutions

Here we consider a cylindrical plasma with a mode-resonant surface inside the plasma. Let us assume zero beta plasma, where beta is the ratio of the plasma pressure to the magnetic pressure. The plasma column is surrounded by a vacuum region, and a resistive wall is located in the vacuum region. Just outside the resistive wall, we assume a thin error field current layer. The schematic picture of the geometry is shown in Fig. 1

We apply the matching techniques: in almost whole

author's e-mail: furukawa@k.u-tokyo.ac.jp

region, non-dissipative and stationary equation is solved. Then, the solutions are connected across interfaces: the magnetic islands, the plasma-vacuum interface, the resistive wall and the error field current layer. The resistive wall and the error field current layer is assumed much thiner than the system size.

As for the time dependence, the characteristic growth rate of the mode seems to be much smaller than the plasma rotation frequency by the experimental observations[3, 4]. Therefore, in the following formulation, $\partial/\partial t + \mathbf{v}\cdot\nabla$ is approximated by $\mathbf{v}\cdot\nabla$, i.e., we consider a stationary state.

When the plasma is not rotating, we usually solve the Newcomb equation[15] in the plasma region except for the resistive layer. Then, we can calculate Δ'[16] which describes the tearing mode stability. The important difference of our study from the previous works is that we solve the following equation which includes the effect of equilibrium plasma rotation Ω_0 as[16]:

$$\frac{\mathrm{d}}{\mathrm{d}r}\left[(\rho n^2\Omega_0^2 - F^2) r\frac{\mathrm{d}}{\mathrm{d}r}(r\xi)\right] - \left[m^2(\rho n^2\Omega_0^2 - F^2) - r\frac{\mathrm{d}F^2}{\mathrm{d}r}\right]\xi = 0, \tag{1}$$

where ξ is the radial displacement of the plasma, ρ is the equilibrium mass density, F is defined as $F := \mathbf{k}\cdot\mathbf{B}$ where $\mathbf{k} := m\nabla\theta - (n/R_0)\nabla z$ is the wave-number vector, m and n are the poloidal and toroidal mode numbers, respectively, and R_0 is the plasma major radius. The cylindrical coordinate system (r, θ, z) is used. This equation has the singularity, i.e., the Alfvén resonances at two radial positions where $F^2 - \rho(n\Omega_0)^2 = 0$. It is noted that $F = 0$ at the mode-resonant surface, which is in between the twin Alfvén resonances. Since the $\rho(n\Omega_0)^2$ term is negligible in almost whole region except for the region near the Alfvén resonances, and since the separation of the Alfvén resonances from the mode-resonant surface is small, it is sufficient to assume constant Ω_0 at the mode-resonant surface in Eq. (1). The mass density ρ is also assumed constant for simplicity.

By integrating Eq. (1) in the plasma-I region (see Fig. 1) ranging from the magnetic axis $r = 0$ to the edge of the magnetic islands $r = r_0 - w/2$, we obtain an independent solution in the plasma-I region as $\xi^{\mathrm{pI}}(r)$. The suffix "pI" denotes "plasma-I". Similar notations will be used in the following. The boundary condition at $r = 0$ eliminates one of the two independent solutions; Eq. (1) has two independent solutions in principle. Similarly, by integrating Eq. (1) from the plasma edge $r = a$ to the other edge of the magnetic islands $r = r_0 + w/2$, we obtain two independent solutions $\xi_1^{\mathrm{pII}}(r)$ and $\xi_2^{\mathrm{pII}}(r)$, which are normalized so that $\xi_1^{\mathrm{pII}}(w/2) = \xi_2^{\mathrm{pII}}(w/2) = -\xi^{\mathrm{pI}}(-w/2)$ where the suffix denotes $x := r - r_0 = w/2$ or $-w/2$. The boundary conditions at $r = a$ will be mentioned below. Then, we obtain

$$\xi(r) = c^{\mathrm{pI}}\xi^{\mathrm{pI}}(r), \tag{2}$$

$$\xi(r) = c_1^{\mathrm{pII}}\xi_1^{\mathrm{pII}}(r) + c_2^{\mathrm{pII}}\xi_2^{\mathrm{pII}}(r), \tag{3}$$

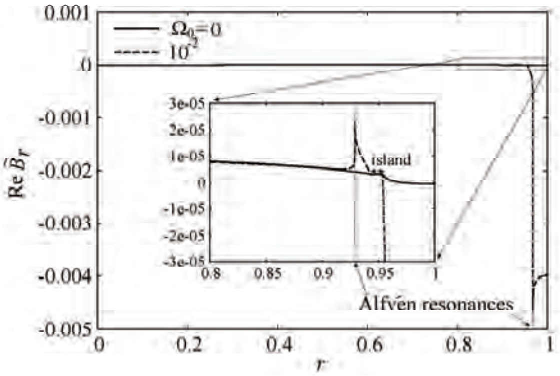

Fig. 2 Real part of the perturbed radial magnetic field.

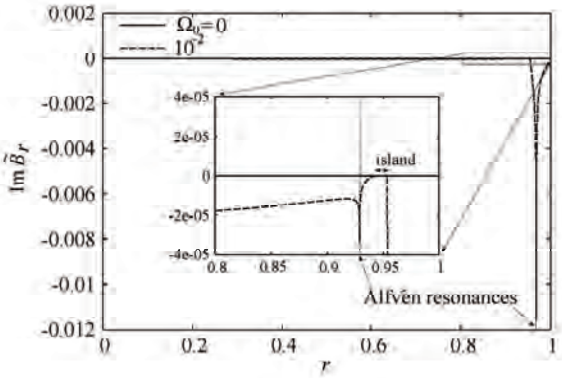

Fig. 3 Imaginary part of the perturbed radial magnetic field.

for the plasma-I and -II regions, respectively.

In integrating Eq. (1), we meet the singularity on the real r axis where $F^2 - \rho(n\Omega_0)^2 = 0$. This is resolved by adding a small artificial growth rate; this method was employed in Ref. [10]. We adopted the adaptive 4th-order Runge-Kutta method for the integration.

Here we show an example of the solution. Figures 2 and 3 shows the real and imaginary parts of the perturbed radial magnetic field, respectively. In the plasma region, it is expressed by $\tilde{B}_r = \mathbf{B}\cdot\nabla\xi = \mathrm{i}F\xi$. The wall position was chosen as $b = 1.1$ and the magnetic island width was $w = 0.01$. These length are normalized to the plasma minor radius $r = a$. For the finite rotation case, the plasma rotation frequency was chosen as $\Omega_0 = 10^{-2}$ normalized to the Alfvén time. We see the spiky behavior at the Alfvén resonances for the finite rotation case. Then it is easy to expect that Δ' is significantly changed from that without the Alfvén resonance effect. It is noted that $\tilde{B}_r$ is continuous across the resonance positions. The numerical solution of ξ was also benchmarked to the analytic solution of Eq. (1) near the Alfvén resonances[14].

In the vacuum region, the perturbed magnetic field is expressed as $\tilde{\mathbf{B}} = \nabla\psi$, where ψ also has a spatial dependence $e^{\mathrm{i}(m\theta-(n/R_0)z)}$. Then, ψ satisfies the Laplace equation $\nabla^2\psi = 0$. The independent solutions can be written as linear combinations of r^m and r^{-m}. Then, we have

$$\psi(r) = c_1^{\mathrm{vI}}\psi_1^{\mathrm{vI}}(r) + c_2^{\mathrm{vI}}\psi_2^{\mathrm{vI}}(r), \tag{4}$$

$$\psi(r) = c^{\mathrm{vII}}\psi^{\mathrm{vII}}(r), \tag{5}$$

in the vacuum-I and -II regions, respectively. Here, the independent solutions are chosen such that $\mathrm{d}\psi_1^{\mathrm{vI}}(b)/\mathrm{d}r = 0$ and $\psi_2^{\mathrm{vI}}(r) = \psi^{\mathrm{vII}}(r) \propto r^{-m}$. Thus ψ_1^{vI} is related to ideal wall solution, and $\psi_2^{\mathrm{vI}} = \psi^{\mathrm{vII}}$ is related to the no wall solution.

The boundary conditions at $r = a$ are the continuity of perturbed radial magnetic field and the total pressure. By using these conditions, we can set convenient boundary conditions such that $c_1^{\mathrm{pII}} = c_1^{\mathrm{vI}}$ and $c_2^{\mathrm{pII}} = c_2^{\mathrm{vI}}$.

Now, let us define Δ'_∞ and Δ'_b related to the no wall and ideal wall solutions, respectively; $\Delta'_\infty := (\partial\tilde{B}_r/\partial r)|_{-w/2}^{w/2}/\tilde{B}_r$ where $\tilde{B}_r$ and its jump are evaluated by using the no wall solution. Similarly, Δ'_b is defined by using the ideal wall (at $r = b$) solution. Then, the total Δ' can be written as[17]

$$\Delta' = \Delta'_\infty - \frac{c_1^{\mathrm{pII}}}{c^{\mathrm{pI}}}(\Delta'_\infty - \Delta'_b), \tag{6}$$

where c^{pI} is related to the magnetic island width[16] and c_1^{pII} is related to the error field.

The island equation can be written as[12]

$$-\mathrm{i}\, n\Omega_0 w = \frac{\eta}{\mu_0}\Delta', \tag{7}$$

where we seek the static islands instead of rotating ones. By giving the error field strength, Eq. (7) can be solved to determine the island width w and the phase of the error field. It is noted that this formulation has a limit that the island width must be much smaller than the separation between the twin Alfvén resonances.

At the resistive wall, we solve the diffusion equation of the perturbed magnetic field. By introducing the error field term just outside the resistive wall, we have the following relation,

$$c_1^{\mathrm{vI}}\psi_1^{\mathrm{vI}}(b) + \psi_{\mathrm{err}} = 0. \tag{8}$$

It is also used that the perturbed radial magnetic field is continuous across the wall and the current layer, thus we obtain $c_2^{\mathrm{vI}} = c^{\mathrm{vII}}$.

If the island width and the error field are obtained, we can calculate the perturbed magnetic field and therefore the toroidal torque[18, 19]. We calculated it on the error field current layer, which has the same magnitude and the opposite direction to the total torque on the plasma:

$$\tau_\phi = \mathrm{i}\,\pi^2 R_0^2 bk(\psi_{\mathrm{err}}\psi'^*(b) - \psi^*_{\mathrm{err}}\psi'(b)). \tag{9}$$

3 Effect of wall position on island width and torque

In the following, we will show numerical results based on the above formulation. The quantities shown below are normalized by using the minor radius a, toroidal magnetic field B_z, and the Alfvén time $\tau_{\mathrm{A}} := a/(B_z/\sqrt{\mu_0\rho})$. We adopted an equilibrium with toroidal current density profile as $j_t(r) = j_{t0}(1 - r^2)$. The edge safety factor was chosen as $q_a = 2.2$. For this current density profile, we have $q_0 = q_a/2 = 1.1$. The rational surface of $m/n = 2/1$ locates near the plasma edge, and the tearing mode is stable when an ideal wall is located at the plasma edge whereas unstable without the wall.

Figure 4 shows the magnetic island width w as a function of the plasma rotation frequency Ω_0. The magnitude of the error field was assumed to be $|\psi_{\mathrm{err}}| = 5 \times 10^{-3}$. The width w decreases as Ω_0 is increased. It is noted that we stopped the calculation when w exceeds one half of the separation of the twin Alfvén resonances because of the validity of Eq. (7). When Ω_0 is small, the separation of the Alfvén resonances is also small, and then the island width is also limited to small value. Thus no data is shown in the small Ω_0 and large w range. If we neglect the Alfvén resonance effect in Eq. (1), w is larger than the values in Fig. 4, and is proportional to $\Omega_0^{-1/3}$. In our case, w was found to be proportional to Ω_0^{-1} when w is relatively large[14]. Especially, it was found that the formation of magnetic islands can be completely suppressed by the plasma rotation when ψ_{err} is small [14]. It is seen that the curves for $b = 1.1$, 1.15 and 1.2 terminate around $\Omega_0 \gtrsim 0.015$. This is becomes of the complete suppression of the island formation. These are the consequences of the Alfvén resonance effect. It is found from Fig. 4 that w becomes larger if the wall position $r = b$ becomes closer to the plasma edge. This is naturally understood since the effect of the error field should be stronger when the wall is closer to the plasma.

Figure 5 shows the total torque on the plasma, which is denoted by $-\tau_\varphi$. The torque is in the direction to slow down the plasma rotation. It was found that the Alfvén resonance effect makes the torque larger by an order of magnitude, as well as changes the dependence on Ω_0; it increases as Ω_0 is increased[14]. If we neglect the Alfvén resonance effect in Eq. (1), the torque is proportional to $\Omega_0^{-2/3}$. From Fig. 5, we find that the torque becomes larger if the wall is located closer to the plasma. This is also naturally understood similarly to the island width case; bigger magnetic perturbation leads stronger torque.

4 Effect of edge safety factor on island width and torque

Finally, we show the effect of the edge safety factor on the magnetic island width and the torque. By increasing the edge safety factor q_a, the $m/n = 2/1$ mode-resonant surface moves inward in radius. Then, the effect of the error field is expected to become weaker. Figure 6 shows the magnetic island width w as a function of the plasma rotation frequency Ω_0 for the edge safety factor $q_a = 2.2$, 2.3, 2.4 and 2.5. The toroidal current density profile is

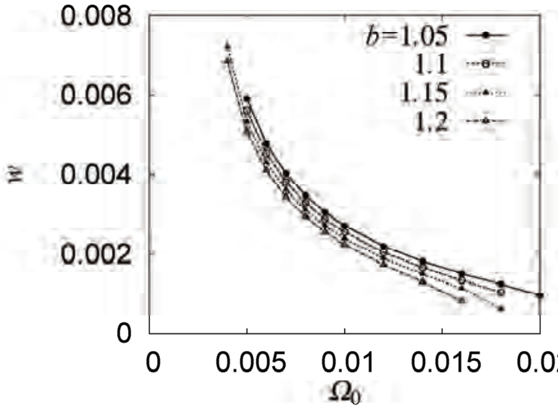

Fig. 4 Magnetic island width v.s. plasma rotation frequency for several wall positions.

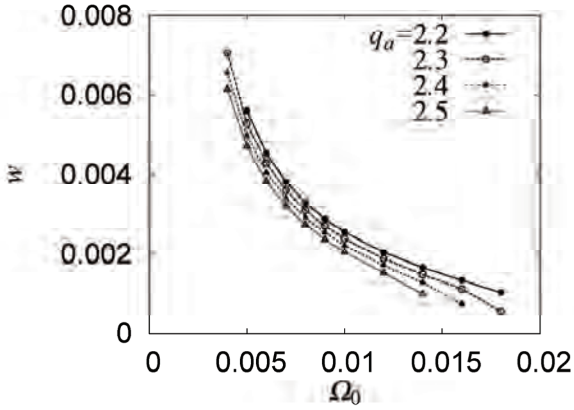

Fig. 6 Magnetic island width v.s. plasma rotation frequency for several edge safety factors.

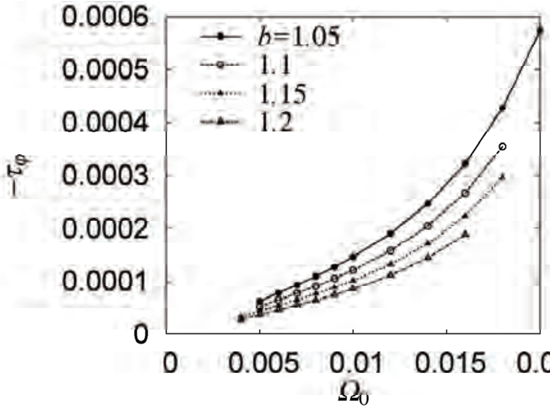

Fig. 5 Toroidal torque v.s. plasma rotation frequency for several wall positions.

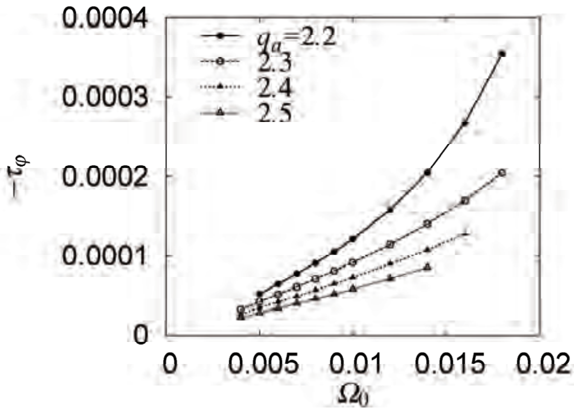

Fig. 7 Toroidal torque v.s. plasma rotation frequency for several wall positions.

fixed as $j(r) = j_{i0}(1 - r^2)$ and j_{i0} was changed. The error field and the wall position were chosen as $|\psi_{\rm err}| = 5 \times 10^{-3}$ and $b = 1.1$, respectively. It is found that w indeed becomes smaller for larger q_a. Figure 7 shows the toroidal torque. As naturally understood, we find the torque becomes smaller if q_a is increased.

5 Summary

We developed a theory for the formation of static magnetic islands induced by the error field for a rotating plasma in cylindrical geometry, especially taking into account the Alfvén resonance effect. The Alfvén resonance effect was shown to change the tearing mode parameter Δ' significantly, which results in reduction or even complete rotation suppression of the magnetic islands. In this paper, it was shown that the island width and the resulting toroidal torque increases if the resistive wall is closer to the plasma as well as if the mode-rational surface is closer to the plasma edge.

This work was supported by Joint Institute for Fusion Theory (JIFT) exchange program.

[1] Strait, E.J., *et al.*, Phys. Rev. Lett. **74**, 2483 (1995).
[2] Freidberg, J.P., "*Ideal Magnetohydrodynamics*" (Plenum Press, New York, 1987).
[3] Takechi, M., *et al.*, Phys. Rev. Lett. **98**, 055002 (2007).
[4] Reimerdes, H., *et al.*, Phys. Rev. Lett. **98**, 055001 (2007).
[5] Gimblett, C.G., Nucl. Fusion **26**, 617 (1986).
[6] Bondeson, A., Ward, D.J., Phys. Rev. Lett. **72**, 2709 (1994).
[7] Ward, D.J., Bondeson, A., Phys. Plasmas **2**, 1570 (1995).
[8] Betti, R., Freidberg, J.P., Phys. Rev. Lett. **74**, 2949 (1995).
[9] Finn, J.M., Phys. Plasmas **2**, 198 (1995).
[10] Zheng, L.-J., Kotschenreuther, M., Chu, M.S., Phys. Rev. Lett. **95**, 255003 (2005).
[11] La Haye, R.J., *et al.*, Nucl. Fusion **44**, 1197 (2004).
[12] R. Fitzpatrick, Phys. Plasmas **5**, 3325 (1998).
[13] P. H. Rutherford, Phys. Fluids **16**, 1903 (1973).
[14] M. Furukawa and L. -J. Zheng, submitted to Nucl. Fusion (2007).
[15] W. A. Newcomb, Ann. Phys. **10**, 2332 (1960).
[16] Wesson, J., "*Tokamaks*" (Clarendon Press, Oxford, 1997).
[17] M. F. F. Nave, J. A. Wesson, Nucl. Fusion **30**, 2575 (1990).
[18] Boozer, A.H., Phys. Plasmas **10**, 1458 (2003).
[19] Zheng, L.-J., Kotschenreuther, Phys. Rev. Lett. **97**, 165001 (2006).

P2-036

Measurement of the Pfirsch-Schlüter and Bootstrap Currents in HSX

J.C. Schmitt, J.N. Talmadge, P.H. Probert, D.T. Anderson

HSX Plasma Laboratory, Univ. of Wisconsin – Madison, WI USA

The Helically Symmetric Experiment is a quasi-helically symmetric axis stellarator that, to a good approximation, has no toroidal curvature. The helical axis of symmetry in |B| and lack of toroidal curvature results in a Pfirsch-Schlüter current that rotates as a function of toroidal angle. Also, the magnitude of this current is reduced by a factor of $1/|n-m\iota| \approx 1/3$ in HSX. Another consequence of the helical axis is that the bootstrap current flows in the direction opposite to that in a tokamak and acts to reduce the rotational transform. These currents are measured in HSX by an external Rogowski coil and an external dB/dt pickup coil array. A 10-chord Thomson scattering system measures the radial profiles of the electron temperature and density. Ion profiles are assumed. Two numerical codes, VMEC and BOOTSJ, calculate the equilibrium MHD current densities and bootstrap current densities in HSX. An additional code, V3FIT, calculates the magnetic field due to the main magnetic field and plasma currents. Comparisons of numerical estimates and recent measurements are presented for 1 Tesla QHS plasmas heated by 50 kW ECRH. The helical nature of the Pfirsch-Schlüter current is confirmed, and the bootstrap current, as calculated by BOOTSJ provides a good estimate of the toroidal current measured in HSX.

Keywords: boostrap current, Pfirsch-Schlüter current, HSX, VMEC, BOOTSJ, V3FIT

1. Introduction

The Helically Symmetric Experiment (HSX), is the world's first stellarator that has an axis of symmetry in |B| [1]. For HSX, $|B| = B_0[1-\varepsilon_h \cos((n-m\iota)\phi)]$, with n = 4, m = 1, $\iota \approx 1$ and the toroidal and poloidal angles, ϕ and θ, are related by $\theta = \iota\phi$ in a straight line coordinate system. In Boozer coordinates [2], this can be written as $|B| = B_0 \sum b_{nm} \cos(n\alpha_B - m\zeta_B)$, with toroidal angle, α_B, poloidal angle, ζ_B, toroidal and poloidal Fourier spectral numbers, n and m, and the amplitude of the spectral component, b_{nm}. For standard plasmas generated with the main field coil set of HSX, the vacuum magnetic field spectrum is dominated by the $(n,m) = \{(0,0),(4,1)\}$ terms, which are the mean background and dominant helical axis terms, and has almost no toroidal curvature, $b_{01} \approx 0$.

One consequence of the helical axis of symmetry is that the Pfirsch-Schlüter current rotates helically with |B| around the machine. Another consequence is a reduction in the magnitude of the Pfirsch-Schlüter current. Consider the following expression for the Pfirsch-Schlüter current [3].

$$J_{PS} = \frac{1}{B_0}\frac{dp}{d\psi} * \sum_{(n,m)\neq(0,0)} \frac{nI+mg}{n-m\iota}\delta_{nm}\cos(n\alpha_B - m\zeta_B) \qquad (1)$$

The magnitude of the dominant helical term is reduced by a factor of $n-m\iota \approx 3$.

Two significant differences in the bootstrap current exist in HSX compared to that in conventional toroidal fusion experiments. First, the direction of the bootstrap current is opposite to that in a tokamak. This leads to an effective decrease in the rotational transform. An expression for the bootstrap current for the case of one dominant Fourier component [4] also demonstrates the reduction of the dominant term by a factor of $n-m\iota \approx 3$.

$$J_{BS} \propto \frac{1}{B_0}\sqrt{b_{nm}}\frac{m}{n-m\iota}[gradients] \qquad (2)$$

2.1 Diagnostics

The radial profiles of the electron temperature and density of the plasma are measured by a 10-chord Thomson Scattering system. Figures 1 and 2 show several radial profiles of electron temperature and density that have been achieved in 1-Tesla QHS hydrogen plasmas, a standard operating regime for HSX.

Changes in the net toroidal plasma current in HSX are measured with a Rogowski coil which is mounted on the external side of the vacuum vessel. The vessel effectively filters magnetic fluctuations above 5 kHz, and the signal is further filtered at 3.1 kHz and amplified by 18.3 kV-sec/A.

author's e-mail: jcschmitt@wisc.edu

The signal is digitized at 200 kHz, digitally stored and numerically integrated. Figure 3 shows the measured time-evolution of the toroidal current

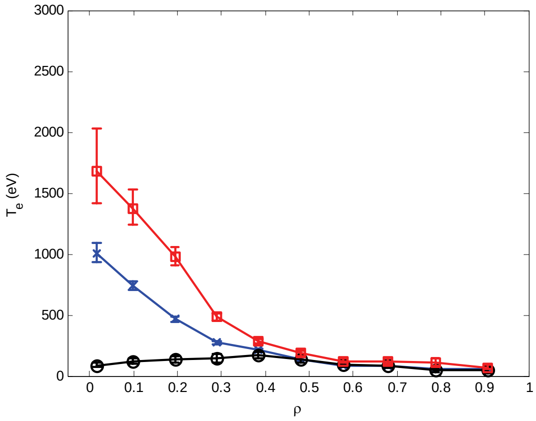

Fig. 1. Electron temperature radial profiles.
The various profiles are achieved by varying the electron-cyclotron resonance heating location. ECRH power ~ 44 kW (launched).

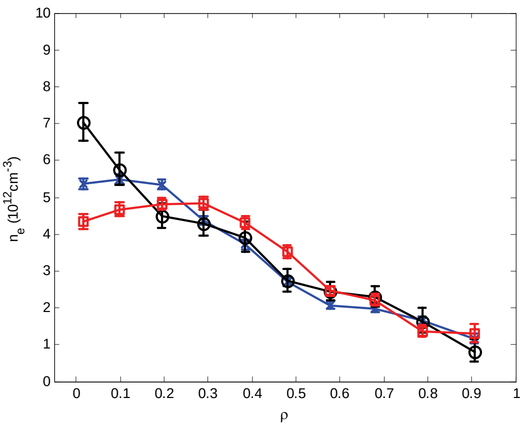

Fig. 2. Electron density profiles.
The line-averaged central density is $4.7 \pm 0.3 \times 10^{18}\ cm^{-3}$ in each case.

The toroidal current is seen to reach steady state only in cases where the electron temperature is low. This is shown in figure 3. The collisionality, $\nu_{*e} = (\nu_e/\varepsilon_h)/(\varepsilon_h^{1/2} v_{Te}/R q_{eff})$ and magnetic diffusivity, $\eta_{\parallel}/\mu_0$ are shown in figures 4 and 5. Most QHS plasmas are in the long mean free path regime, and the magnetic diffusivity varies greatly across the plasma.

In addition to the Rogowski coil, there is an array of 16 dB/dt triplets, which provide a measurement of the magnetic field vector due to both the main field coils and plasma currents. Measurements of similar plasma discharges have been performed with the array at two toroidal locations, approximately 1/3 field period apart.

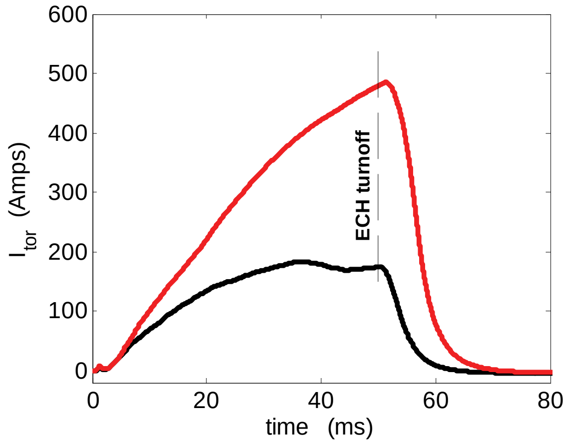

Fig. 3. Time evolution of the toroidal current.
Heating resonance: off-axis (black) , near-axis (red).

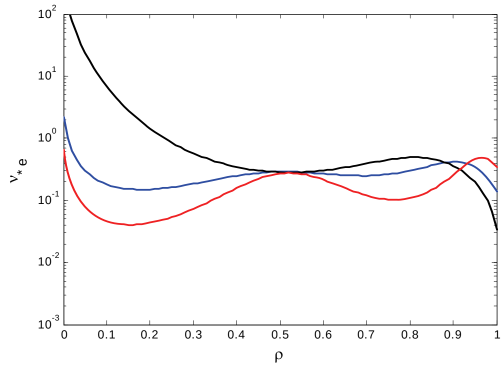

Fig. 4. Electron collisionality.

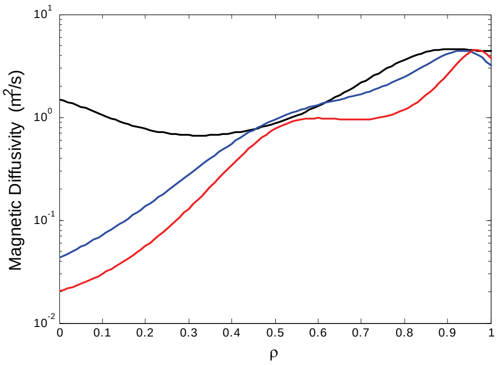

Fig. 5. Magnetic diffusivity.

2.2 Computational Modeling

The free-boundary MHD equilibrium solver, VMEC [5], is used to establish the equilibrium parameters. Measured profiles of electron temperature and density, along with assumed profiles of ion temperature and density $(T_i \le T_e/10 \quad Z_i = 1)$ are used to determine the pressure profile for VMEC. After VMEC calculates the equilibrium, the output is used in the BOOTSJ program to calculate the bootstrap current density [6]. VMEC is then re-run with the toroidal current density set equal to the density calculated by BOOTSJ. Further iterations of

BOOTSJ and VMEC could be performed, but the current densities have not been seen to vary much after a single iteration.

The output from VMEC is then fed into V3FIT, which calculates the magnetic response due to currents in the plasma and those due to the main field coils [7]. The response is calculated at the position of each dB/dt triplet.

3.1 Pfirsch-Schlüter Current

The Pfirsch-Schlüter current density in a typical QHS plasma discharge is shown in figure 6. Two toroidal positions are shown, corresponding to the approximate location of the 16 triplets.

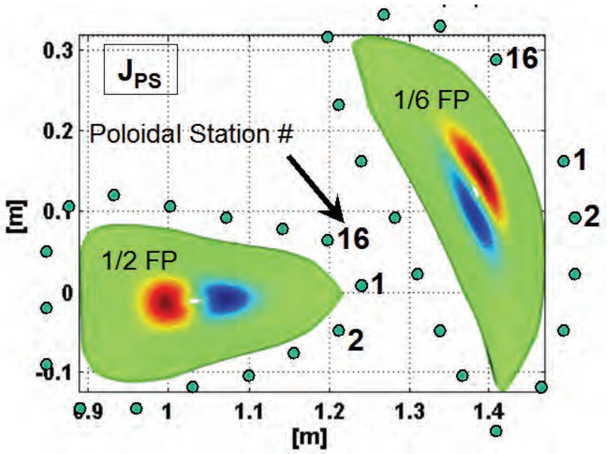

Fig. 6. Pfirsch-Schlüter current density at two toroidal locations and a sketch of the location of the dB/dt triplets.

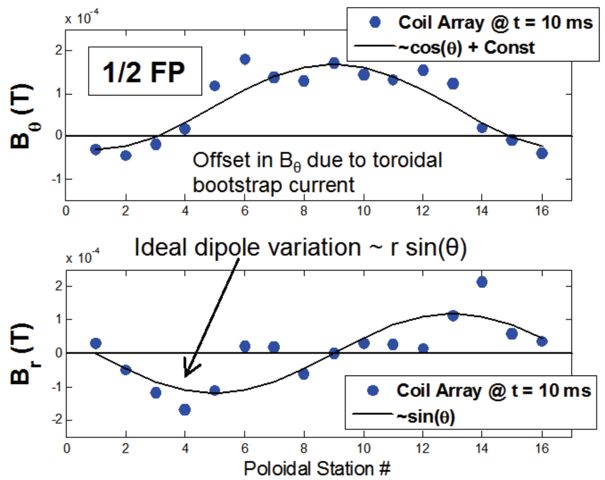

Fig. 7. Measured poloidal and radial magnetic fields at 16 poloidal stations.

The approximately 'poloidal' and 'radial' components of the measured magnetic at each triplet location for the 1/2 field period location is shown in figure 7. This is for a time of t = 10 ms into the plasma discharge, before the bootstrap current has risen to a large value. Two additional sinusoidal lines are sketched, representing the expected response from a cylindrical dipole current for a set of detectors at a constant radial distance from the plasma. The comparison agrees qualitatively, but there are significant differences, in particular for the poloidal stations nearest to (5, 6, 12, 13) and farthest from (9, 11) the plasma column. There is a slight offset in the poloidal comparison, due to the non-zero bootstrap current.

3.2 Bootstrap Current

The expected steady-state value of the bootstrap current for many profiles has been calculated by the use of VMEC and BOOTSJ. These values are then compared to the total toroidal current measured in HSX at the end of the plasma discharge, and a projected steady-state value, I_∞, which is determined by a best-fit of the measured current to the expression $I(t) = I_\infty\left(1 - e^{-t/\tau_{Tor}}\right)$. These two comparisons are shown in figure 8.

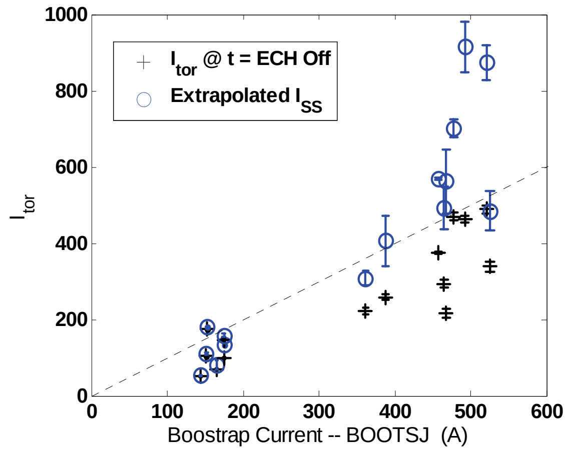

Fig. 8. Measured and projected values of total bootstrap current vs. estimated bootstrap current. Estimate is calculated by BOOTSJ.

The measurements of the toroidal current are consistent with numerical estimates of the bootstrap current. There are several cases where the toroidal current appears to be growing to a larger value than is expected from the calculation, but the discharge had ended before the steady-state had been reached. To date, the estimate of the bootstrap current provides an upper-limit to the measured toroidal current in 1-T QHS plasmas.

4. Temporal Evolution

The time-evolution of the toroidal current, stored energy and line-averaged central electron density are shown in figure 9. The electron pressure and density profiles are captured 0.5 ms before ECH turn-off, when the Thomson Scattering laser fired, and these profiles are shown in figures 1 and 2 as the highest central-T_e (red) line. The total steady-state bootstrap current is estimated by BOOTSJ to be 478 A. The measured toroidal current reaches 450 A at the end of the discharge, and is projected to be about 710 A in steady state.

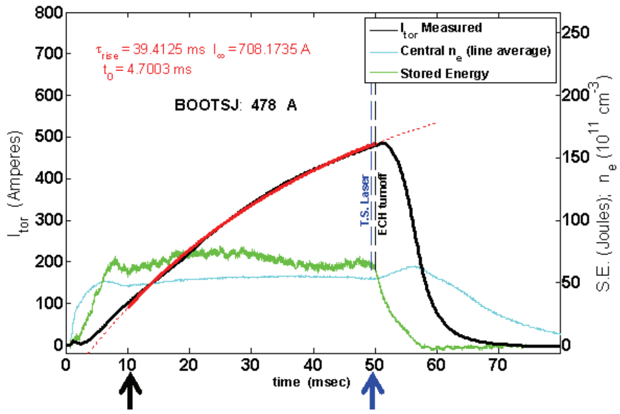

Fig. 9. Time evolution of toroidal current, stored energy, and line-averaged central n_e

The pressure and toroidal current density profiles (from BOOTSJ) used in VMEC are shown in figure 10. The pressure profile is centrally peaked and the bootstrap current is largest at the location of the steep pressure gradient. The rotational transform is altered from the vacuum case, approaching a value of $\iota \approx 1$ near s = 0.15.

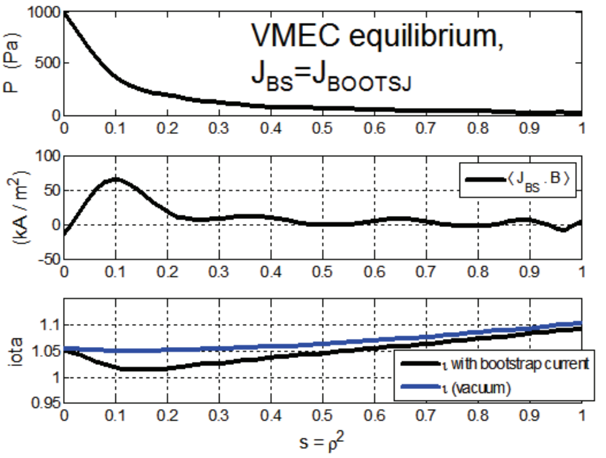

Fig. 10. Radial (VMEC 's') profiles of plasma pressure, bootstrap current and rotational transform. The vacuum transform is also shown.

The measured poloidal and radial magnetic fields due to the plasma current are shown for t = 10 ms and 50 ms for two different toroidal locations (figure 6) in figures 11 and 12. V3FIT was used to calculate the expected magnetic field for two cases: $I_{tor} = 0$ and $I_{tor} = I_{BS}$. These two cases roughly correspond to the situation early in the discharge (small bootstrap current) and late in the discharge (near-steady state current). The calculated magnetic field at the location of each triplet is shown in the figure.

There is considerable agreement between the measured and calculated magnetic fields due to the plasma current. Note that the toroidal current is still evolving, and no information is known about its true radial profile.

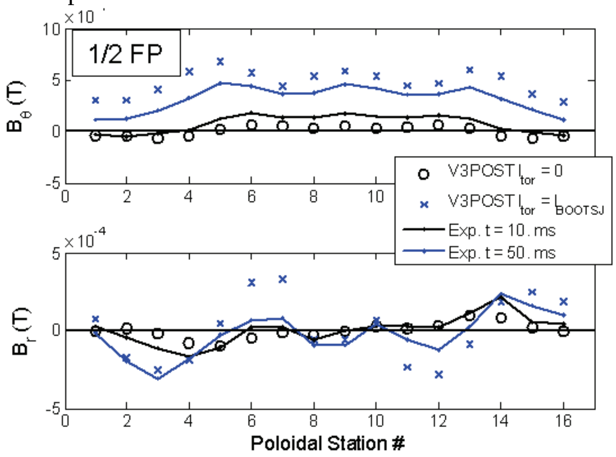

Fig. 11. Magnetic diagnostic responses, measured and calucated (V3FIT results marked as V3POST).
Toroidal location = 1/2 field period.

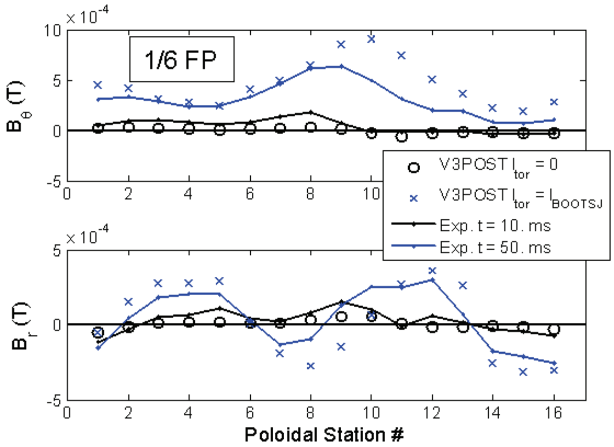

Fig. 12. Magnetic diagnostic responses at a toroidal location of 1/6 field period.

5. Special Thanks

The authors would like to thank the V3FIT team, and especially Steve Knowlton for invaluable contributions and for the V3FIT results that are shown here.

[1] F.S.B.Anderson, A.F.Almagri, D.T.Anderson, P.G. Mathews, J.N.Talmadge, and J.L.Shohet, Fusion Technol. **27**, 273 (1995).
[2] A.H. Boozer, Phys. Fluids **25**, 520, (1982).
[3] A.H. Boozer, Phys. Fluids **24**, 1999, (1981).
[4] A.H. Boozer and H.J. Gardner, Phys. Fluids B **2**, 2408, (1990).
[5] S.P. Hirshman, W.I. van Rij and P. Merkel, Comp. Physics Comm. **43**, 143 (1986).
[6] Shaing, et. al, Phys. Fluids B **1**, 148 (1989).
[7] S.P. Hirshman, et. al, Physics of Plasmas, **11**, 595 (2004).

Proceedings of ITC/ISHW2007

MHD Equilibrium and Stability of Low-Aspect Ratio RFP

R. Ikezoe, A. Sanpei, T. Onchi, K. Murata, K. Oki, H. Shimazu, T. Yamashita, H. Himura, S. Masamune

Kyoto Institute of Technology, Matsugasaki, Sakyo-ku, Kyoto 606-8585, Japan

ikezoe1t@nuclear.dj.kit.ac.jp

MHD equilibrium and stability properties of the RFP plasmas with aspect ratio (A) of as low as 2 have been studied in RELAX. Behavior of edge magnetic fluctuations of m=1 modes are mainly discussed together with q profile deduced from magnetic measurements in the outer region of the plasma (0.6<*r*/*a*<1) with the help of equilibrium reconstruction code (RELAXFIT). Spontaneous transition to transient quasi-single helicity (QSH) state, one of the characteristic behavior, has also been shown.

Keywords: reversed field pinch (RFP), low-aspect ratio, tearing mode, single helical state

1. Introduction

The reversed field pinch (RFP) is one of the magnetic confinement systems for nuclear fusion research. The equilibrium magnetic field profile in the RFP is self-sustained as a result of nonlinear MHD process. This self-generation and sustainment of the RFP configuration process is referred to as MHD relaxation and RFP dynamo, respectively. Thus, the RFP configuration is one of the typical examples of self-organized laboratory plasmas.

Recent progress in the RFP research has revealed the importance of the role of tearing modes in the RFP dynamics. It has been shown that the RFP configuration can bifurcate to either a (quasi-)single helicity ((Q)SH) state or to a multi-helicity (MH) state, depending upon the Hartmann number[1]. In the former configuration of QSH, internally resonant single helical (tearing) mode grows significantly larger than the others, and the associated large magnetic island is immersed in otherwise stochastic core region. Within the large magnetic island of the dominant mode, favorable confinement has been realized[2]. Furthermore, it has been pointed out that the QSH configuration might be sustained by the laminar dynamo mechanism, which does not accompany magnetic chaos. The QSH state is more or less like a helical equilibrium with toroidal field reversal.

In order to explore the MHD properties in low-A RFP configuration, we have constructed a low-aspect ratio (A) RFP machine "RELAX (REversed field pinch of Low Aspect ratio eXperiment) with aspect ratio of as low as 2 (A=*R*/*a*=0.51m/0.25m)"[3]. Since mode rational surfaces are less densely spaced in the core region in the low-A RFP, the width to which the dominant single island can grow without interacting the neighboring islands is larger than in conventional RFP. We may therefore be able to control bifurcation to QSH with the help of external helical field, which technique has been developed in our previous experiments[4]. Or, even in MH RFP state, we can expect different nonlinear characteristics of internally resonant tearing modes in low-A RFP configuration from that in medium- or high-A RFP.

We will describe characteristics of equilibrium configurations in RELAX with the help of an equilibrium reconstruction code RELAXFIT, which was modified from the MSTFIT code. Stability properties have been studied by edge magnetic fluctuation measurements and spectral analysis in RELAX. On the basis of these measurements, we will discuss the MHD equilibrium and stability properties in low-A RFP configurations.

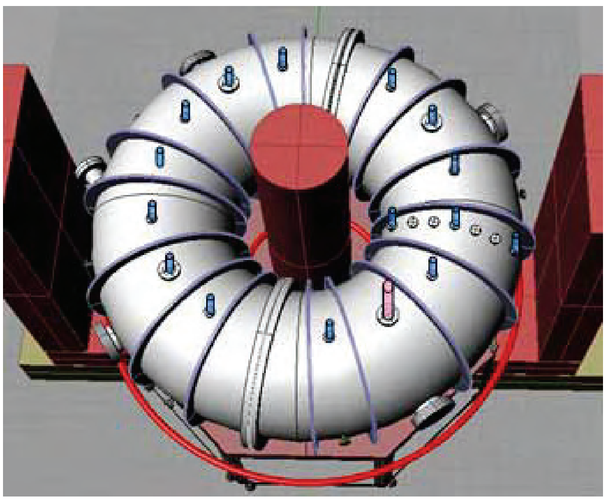

Fig.1: Magnetic diagnostics in RELAX.

author's e-mail: ikezoe1t@nuclear.dj.kit.ac.jp

2. Experimental arrangement

In the low-A RFP machine RELAX, he have used 4-mm thick SS vacuum vessel. The major radius *R* is 0.51m, and the minor radius *a*, 0.25m, with the aspect ratio of 2. The field penetration time of the vacuum vessel is about 2ms. RELAX is operated without outer conducting shell, and therefore, the vacuum vessel acts as a resistive shell.

Figure 1 shows the experimental arrangement. The RELAX experiment is equipped with two toroidal arrays of 14 toroidal and poloidal field pick-up coils inserted from top and bottom ports equally distributed toroidally (with toroidal separation angle of $\pi/8$) except at two poloidal gap locations. Subtracting (adding) the top and bottom signals provides the odd (even) components of the magnetic fields. A poloidal array consisting of 6 pick-up coils is located at a poloidal cross section. In addition, a radial array of pick-up coils is inserted from top to measure the radial profiles of *B*p and *B*t in the outer region (from edge to r/a=0.6).

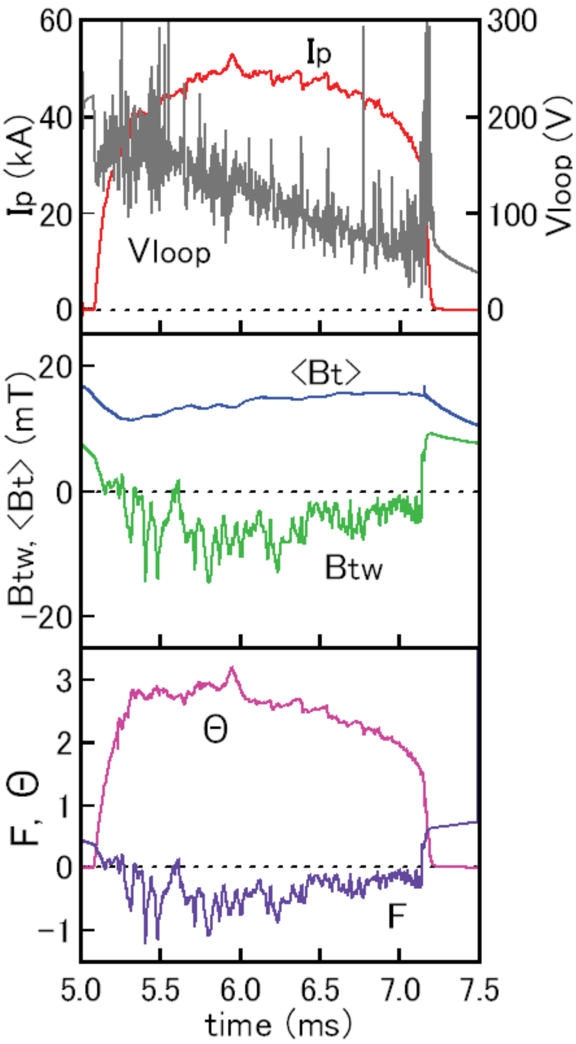

Fig.2: Typical waveforms of low-A RFP in RELAX.

The pick-up coils signals are sampled at a frequency of 2MHz and numerically integrated. The signals are then Fourier analyzed in space to get even and odd poloidal harmonics with a resolution in toroidal number up to n=8.

3. Equilibrium reconstruction with RELAXFIT

Equilibrium configurations in RELAX have been studied with the help of an equilibrium reconstruction code RELAXFIT, which was modified from the MSTFIT code[5] to extend the applicability of the code to low-A equilibrium regime. In RELAX, experimental constraints for the reconstruction are magnetic measurements in the outer region of the plasma ($0.6<r/a<1$) measured with the above-mentioned diagnostic system.

4. Experimental results

The Figure 2 shows typical waveforms of the plasma current *I*p, loop voltage *V*loop, toroidal field at the edge *B*tw, and cross sectional average toroidal field <*B*t>, together with time evolution of the pinch parameter Θ (=*B*pw/<*B*t>) and field reversal parameter *F* (*B*tw/<*B*t>), where *B*pw is the edge poloidal field. In the initial phase of RELAX experiment, attained plasma current is 40-60 kA, and the discharge duration is ~2ms with RFP configuration >1.5ms, in standard low-A RFP plasmas. Electron temperature estimated from a single-chord soft-X ray diagnostics with different absorbing filter is about 50eV. Details of the characterization of initial RELAX plasmas have been described elsewhere[6].

As shown in Fig.2, the edge magnetic fluctuation amplitude is higher in the initial current rise phase and current-top phase, accompanied by oscillatory change in plasma current, while it decreases gradually in the current decay phase (from 6.4 to 7.2 ms) with smoother change (decrease) in plasma current. Θ is around 2 and F is around –0.1, in this current decay phase.

Figure 3 shows time evolution of amplitudes of m=1 modes with toroidal mode number n from 0 to 8. As

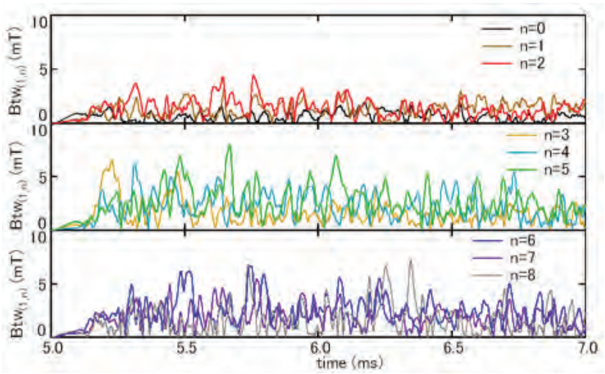

Fig.3: Time evolution of the amplitude of m=1 modes with toroidal mode numbers n from 0 to 8.

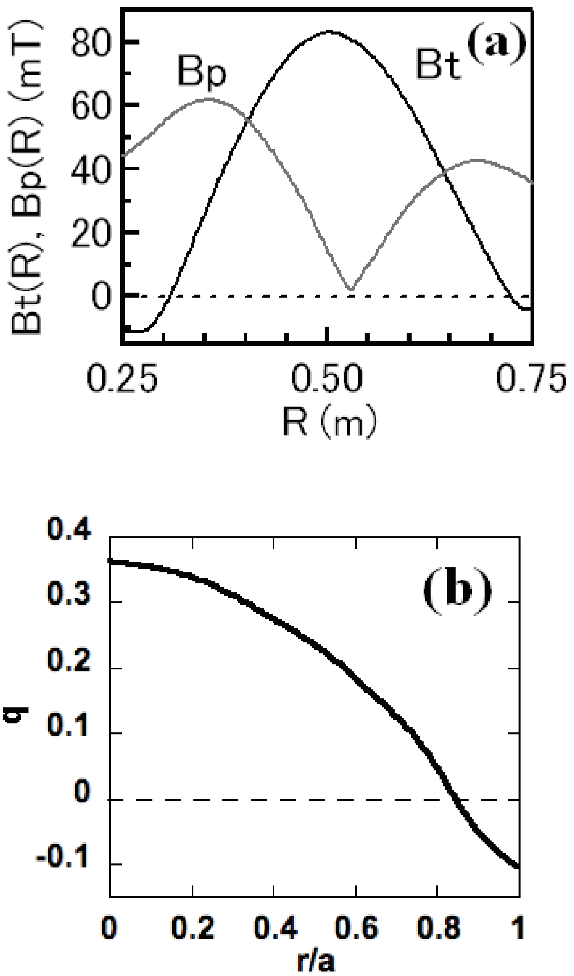

Fig.4: Reconstructed equilibrium profiles of poloidal and toroidal magnetic fields (a) and q profile (b) in the current decay phase with Θ=2 and *F*=-0.1.

discussed above, the amplitude of each mode is higher in the current rise and flat phases, while smoother evolution is observed in the current decay phase. We have applied the equilibrium reconstruction technique to the low-A RFP plasma in the current decay phase where m=1 mode amplitudes behave smoothly.

Figure 4 shows the results of equilibrium reconstruction in this current decay phase. The experimental radial profiles of *B*p and *B*t at 0.6<*a*/*r*<1.0 time averaged from 6.5 to 7.0 ms were used as one of the constraints for the equilibrium reconstruction. Figure 4(a) shows the reconstructed profiles of poloidal and toroidal magnetic fields as a function of radial coordinate on the equatorial plane, indicating that the shift of magnetic axis, or the Shafranov shift, is about 10 % of the minor radius. Figure 4(b) shows the radial profile of the safety factor *q* calculated from the reconstructed field profiles. The radial coordinate is the average radius of the corresponding magnetic surface in this case. The *q* profile shows that the innermost mode rational surface is *q*=1/3 at *r*/*a*=0.2, and the neighboring *q*=1/4 surface at 0.45. We could not avoid the innermost rational surface *q*=1/3 in this discharge.

Figure 5 shows the time-averaged toroidal mode spectrum of m=1 modes in the current decay phase from 6.5 to 7.0 ms. The m=1/n=5 mode has the maximum amplitude during this phase, and the fluctuation power distributes among internally resonant modes of m=1/n=3 to m=1/n=8 modes, where we can deduce the radial locations of the resonant surfaces of the corresponding modes from Fig.4(b). The mode spectrum looks like that of MH RFP state.

Toroidal mode spectrum of the m=1 modes in STE-2[4] whose aspect ratio was 4 (*R*/*a*=0.4m/0.1m) is shown in Fig.6 for reference. The m=1/n=8 core resonant mode has the maximum fluctuation power, and the power decreases gradually with increasing n, while the fluctuation power for the internally nonresonant modes is insignificant in this case. When we compare Figs.5 and 6, the effect of lowering the aspect ratio on the toroidal

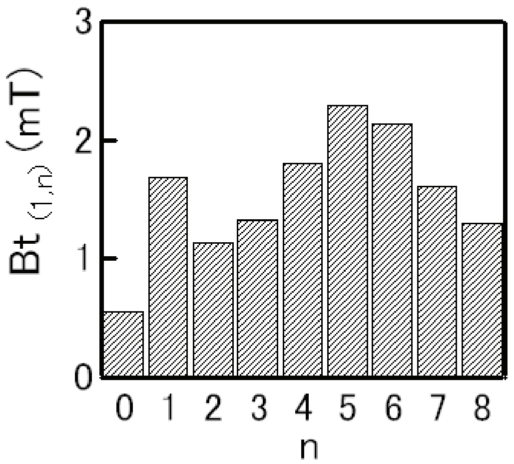

Fig.5: Toroidal mode spectrum of m=1 modes in the current decay phase.

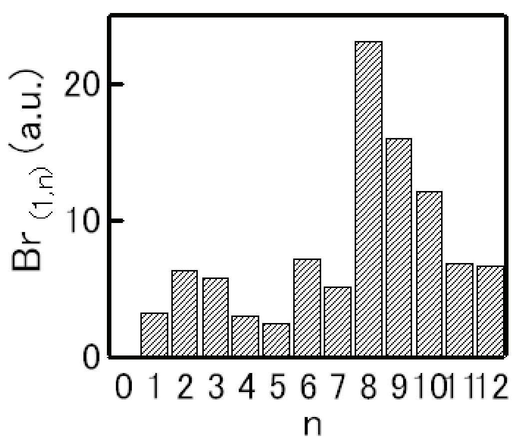

Fig.6 : Typical toroidal mode spectrum of m=1 modes in STE-2 with aspect ratio of 4 (*R*/*a*=0.4m/0.1m).

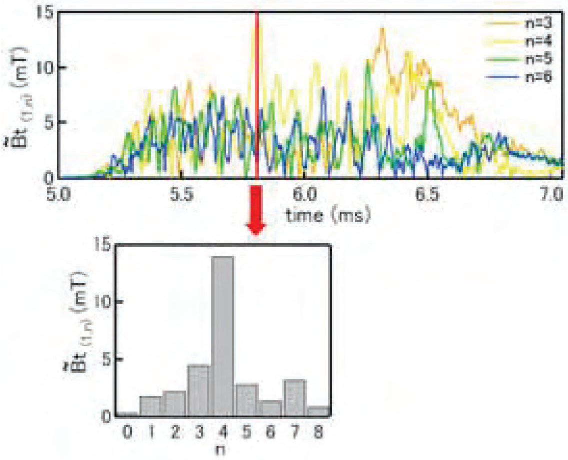

Fig.7: Quasi-single helicity state as transient phenomena with sequential occurrence in a single discharge. Toroidal mode spectrum of the m=1 modes is also shown.

mode spectrum of m=1 modes is evident. Significant portion of the fluctuation power is carried by core resonant modes, and the toroidal mode number of the corresponding modes change as a result of the change in q profile depending on the aspect ratio.

Look at the time evolution of m=1 mode amplitude in Fig.3 carefully, we may notice that there appears some phases where the fluctuation amplitude of a single mode becomes dominant over the other modes. The fluctuation amplitude concentrates to m=1/n=5 mode around 5.6 ms and 6.0-6.1 ms. When we make the toroidal mode spectrum during these short period of time, the resultant spectrum looks like that of quasi-single helicity state. Specifically, since the QSH-like spectrum persists for about 0.1 ms at 6.0-6.1 ms, we may be able to regard the phase as a transient QSH RFP state. The dominant mode in QSH state, m=1/n=5 mode in this case, depends on the discharge conditions.

Figure 7 shows another example of transient QSH RFP state with m=1/n=4 mode. The appearance of the QSH phase is more frequent and each QSH phase lasts longer than the case in Fig.3. This type of transient QSH appears under high-Theta discharge conditions. Detailed studies are required on the triggering mechanism to the QSH state. Active control with external helical field may have some influence on the transition and persistence of the QSH state.

5. Conclusion

MHD equilibrium and stability properties of the low-A RFP plasmas have been studied in RELAX. In the study of equilibrium, a reconstruction has been used to deduce the Shafranov shift of 10% of the minor radius. *q* profiles have also been deduced. Edge magnetic fluctuations have been analyzed and toroidal mode spectrum of m=1 modes are mainly discussed. The sustained RFP configuration is essentially the MH RFP state, with spontaneous transition to QSH state. In the MH state, toroidal mode spectrum of the m=1 modes agrees well with expectation from the q profile; fluctuation power distributes mainly among the core resonant modes. This is also the case with medium- to high-A RFP configurations. In most cases, toroidal mode number of the dominant modes are mainly twice of the aspect ratio. In the transient QSH state observed in RELAX, the dominant mode is either m=1/n=4 or m=1/n=5, depending on discharge conditions. The QSH state tends to persist for longer period in higher Θ and shallow F regime.

Acknowledgment

This work was supportd by a Grant in Aide for Scientific Research from Ministry of Education, Culture, Sports, Science and Technology No.17360441.

References

[1] S. Cappello and D. F. Escande, Phys. Rev. Lett. **85**, 3838 (2000).
[2] D. F. Escande *et al.*, Phys. Rev Lett. **85**, 1662 (2000).
[3] S. Masamune *et al*., Trans. Fusion Science and Technology, **51**, 197 (2007).
[4] S. Masamune and M. Iida, J. Plasma Fusion Res. SERIES **5**, 509 (2002).
[5] J. K. Anderson *et al.*, Nucl. Fusion **44**, 162 (2004).
[6] S. Masamune *et al.*, to be published in J. Phys. Soc. Jpn. **76** (No.12) 2007.

P2-038

Temporal evolution of the pressure profile and mode behavior during internal reconnection events in the MAST spherical tokamak

H. Tojo[1)], M. Gryaznevich[2)], A. Ejiri[1)], A. Sykes[2)], Y. Takase[1)]

[1)]*Graduate School of Frontier Sciences, The University of Tokyo Kashiwa 277-8561, Japan*
[2)]*EURATOM/UKAEA Fusion Association, Culham Science Centre, OX14 3DB, UK*

(Received 15 October 2007 / Accepted)

Mode behaviors including non-linear development and pressure profiles during internal reconnection events are clarified in the MAST spherical tokamak. In a $q_0 > 1$ discharge, tearing mode is a trigger but non-linearity of modes is not confirmed. On the other hand, in a $q_0 < 1$ discharge, harmonics of a $m/n = 4/1$ mode of ~22kHz are confirmed. Method for identification of poloidal mode in ST configuration is also given.

Keywords: IRE, spherical tokamak, bicoherence, poloidal mode, reconnection

DOI: 10.1585/pfr.1.001

1 Introduction

Internal Reconnection Events (IREs) have often been observed in spherical tokamaks (STs), limiting performance. IREs are MHD instabilities, which show mode growth of precursor and flatten pressure profile. They result in disruption in the worst case. Three-dimensional MHD simulations have shown that linear growth rate and mode number of pressure-driven modes depend on q_0 (safety factor at the magnetic axis) and β_t (toroidal beta), and that the non-linear coupling of linear modes leads to a large plasma deformation [1]. In this situation, magnetic reconnection occurs and core plasma energy is lost along the reconnected magnetic line. The relationship between the mode number (and its growth rate) and q_0 and β_t have not been clarified experimentally. Moreover non-linear coupling of modes just before IRE haven't been investigated in detail. In MAST [2], IREs appear in both $q_0 > 1$ and $q_0 < 1$ discharges and they often limit the achievable plasma beta in high-β regimes. Objectives of this study are to clarify mode number and its dependence on such parameters, and to confirm the existence of non-linear coupling.

2 Experimental setup

2.1 Mirnov coil array and identification of poloidal mode number

Mirnov coils (magnetic probes) are sensitive to external mode behavior and are employed to identify mode numbers. In MAST, magnetic coils are located along the toroidal direction (12ch at the most), and along the center column (40ch) and along the outboard (18ch at the most). In STs, the determination of poloidal mode numbers (m) is not easy because of the effects of non-circular magnetic flux surfaces and asymmetric magnetic field pitch angle. To overcome these problems we developed a method to evaluate the poloidal mode number and its intensity. Firstly, we assume helical filamentary currents, which generate magnetic fluctuations, on their resonant surface calculated from EFIT [3]. The poloidal positions of these filaments are decided by tracing a magnetic field line. The number of alternating positive and negative filament pairs coincides with the mode number. Figure 1 shows trajectories of magnetic lines at the surfaces $q = 1$, 1.5, 2, and 3. In this case, the initial poloidal angle ($\theta = 0$) is located at the outboard midplane. The poloidal location of each filament (i.e., marker filament) can be obtained from the intersection of the curve and an integer or a half integer toroidal turns (Fig. 1). The tangents of the lines become steep at $\theta \sim \pi$ because of the strong toroidal field at the inboard side. Therefore, poloidal distribution of the filaments is asymmetric, and most of them tend to locate at the high field side. Number of filaments (and their rational surface), current amplitude and the poloidal location of the initial filament were obtained from the best fit to the measured Mirnov coil signals. Performing fittings at each timing, we can derive poloidal rotation and amplitude growth of the mode. However in this report we used band-passed signals and assume single mode distortion located at a rational surface to study the role of the dominant mode. Note that this model is appropriate for localized rational modes, such as tearing modes.

2.2 Measurements of soft X-ray profile

Soft X-ray radiation (SXR) is useful to study MHD phenomena and it includes information on internal mode struc-

author's e-mail: tojo@fusion.k.u-tokyo.ac.jp

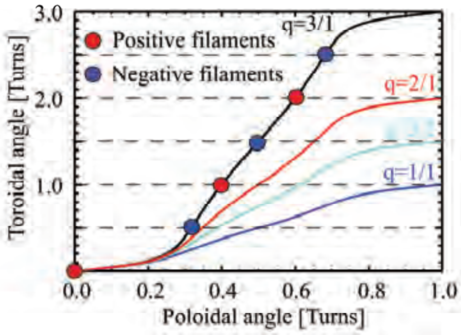

Fig. 1 Trajectory of the magnetic field lines at the rational surfaces q =1, 1.5, 2, 3. Poloidal angles of filaments are obtained from the intersections between the traces and horizontal lines with intervals of half integer turns.

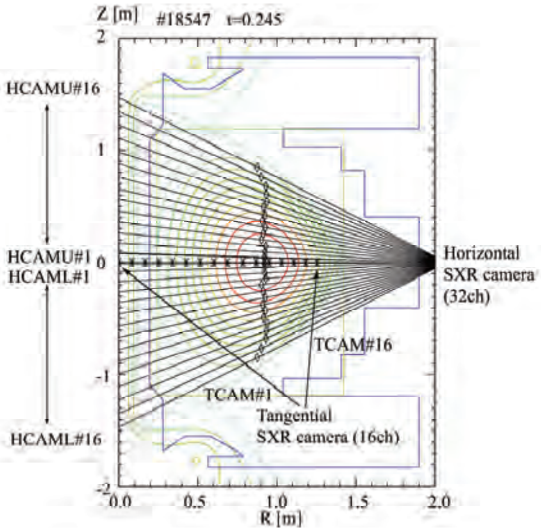

Fig. 2 Configuration of horizontal (sight lines) and tangential (asterisk) SXR cameras.

ture. Horizontal (32ch) and tangential (16ch) SXR cameras are employed and their sight lines are shown in Fig. 2. To compare behavior of SXR, q (calculated from EFIT) and (electron) pressure profile (measured by Thomson scattering), sight lines of each SXR channel are labeled by the minimum poloidal flux (ψ) obtained by the EFIT. In other words, along each sight line we determine the minimum of the ψ (symbols in Fig. 2) and corresponding radial position R.

2.3 Analysis using bispectrum to show non-linear coupling

To clarify non-linear development of the IRE precursors we performed bispectrum analysis which is a Fourier analysis for three wave interaction and used frequently in turbulence analysis [4] [5]. Generally, auto bispectrum is defined as

$$B(f_1, f_2) = \langle X(f_1)X(f_2)X^*(f_3)\rangle \quad (1)$$

where $f_3 = f_1 + f_2$ and $X(f)$ is a Fourier components of signal $x(t)$. To evaluate the degree of nonlinear coupling for each frequency component, following normalized auto bispectrum is commonly used as

$$b^2(f_1, f_2) = \frac{|B^2(f_1, f_2)|^2}{\langle|X(f_1)X(f_2)|^2\rangle\langle|X^*(f_3)|\rangle} \quad (2)$$

If there is a strong non-linear relation among f_1 and f_2, b^2 becomes large (nearly 1). We analyzed Mirnov coils data for understanding non-linear development in IRE precursor. To obtain accurate bicoherence, many ensembles should be averaged. In MAST, there are twelve (at the most) toroidal Mirnov coils around the center column at same poloidal position. We employed these coil data to perform the ensemble averaging. Total bicoherence is defined as

$$B^2_{tot} = \sum_{f_1, f_2} B^2(f_1, f_2) \quad (3)$$

which represents quantitative measure of the non-linear coupling.

3 IRE discharges

3.1 IRE with $q_0 > 1$

A typical discharge with $q_0 > 1$ and $\beta_t \sim 9\%$ is shown in Fig. 3. Increase of the plasma current (I_p) and drop of the electron density from interferometer were observed. The increase on the emission of D_α indicates interaction between the plasma and the vacuum vessel due to the loss of the plasma. One of unique characteristics of the events is that SXR radiation profile shows propagation of the drop starting from the area of fluctuations (precursor). This IRE has precursor not only in SXR radiation, but also in the Mirnov coil signals. The position of reconnection is close to HCAMU♯12 (R ~1.25) because HCAMU♯13-15 increase, while HCAMU♯3-11 decrease after t ~ 0.2545 (see arrows in Fig. 3). We executed the fitting code to determine the mode number. Here we applied band-pass (1-5kHz) filtering to the time integrated Mirnov signals. An example of the fitting is shown in Fig. 4. The squares represent the Mirnov coil data at t = 0.24720 and the line shows a fitted curve assuming only 2/1 mode (filaments) at the rational surface q = 2. They show good agreement. Figure 4 indicates time evolution of the calculated helical filament current (a), poloidal angle of a filament (b) and, fitting error (c). As described in 2.1, filament current reflects mode intensity and it can be used to derive the growth time. From t ~ 0.241 the filament current increases exponentially, indicating a linear growth. Time constant (τ_{fil}) of this growth is about 6 ms. The phase of the filament decreases continuously, showing a poloidal rotation of the filaments. The error of the fitting is represented by the normalized residual error χ^2. When χ^2 is less than 10, the quality of the fitting is acceptable in the present analysis. We preformed

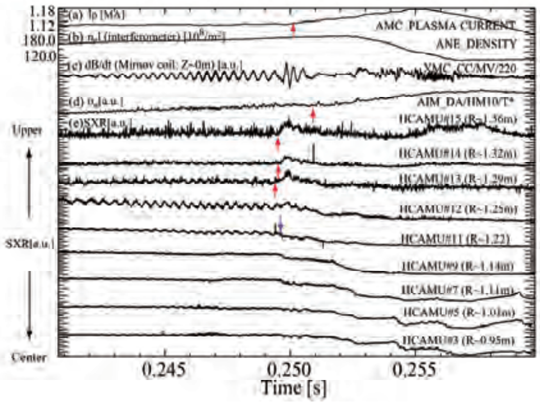

Fig. 3 IRE in discharge with $q_0 > 1$. (a): Plasma current [kA] (b): Line integrated electron density [$/m^2$] (c): dB/dt from Mirnov coil [a.u.] (d) Emission of D_α [a.u.] (e): SXR radiation [a.u.] on horizontal SXR camera from upper to center side of the plasma.

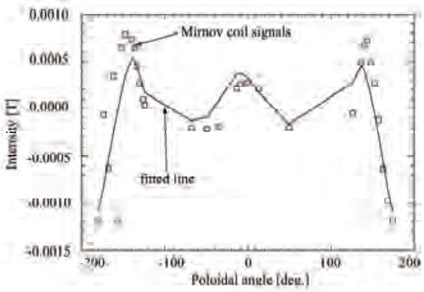

Fig. 4 Integrated Mirov coils signal (1-5kHz) and fitted curve of the model assuming only m/n =2/1 mode for ♯18547 at t = 0.24720s. The origin of poloidal angle is the magnetic axis determined by the EFIT.

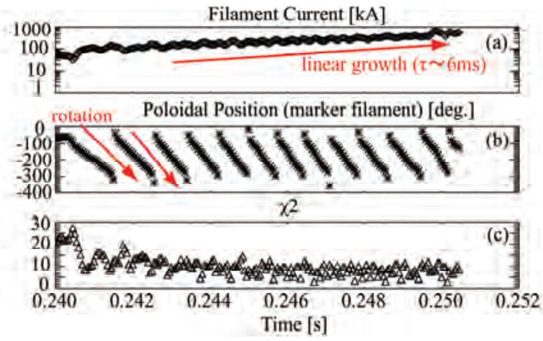

Fig. 5 Time evolution of the fitting parameters for ♯18547. (a): Filament current [kA] (b): Poloidal angle of the one chosen marker filament to understand poloidal rotation. (c): χ^2 (error of the fittings)

the bispectrum calculation on the toroidal Mirnov signals (ϕ = 10°, 50°, 70°, 110°, 130°, 170°, 230°, 290°) with 250kHz sampling rate in order to check non-linearity. The number of ensemble is 8 and data points per one ensemble is 750. There is strong bicoherence around (f_1, f_2) ~ (40kHz, 40kHz) indicating harmonic coupling with itself but these modes are localized near the centre of the plasma. Therefore the 2/1 mode was localized near the reconnection position and can be a candidate for the trigger of this IRE.

3.2 IRE with $q_0 < 1$

In the case of $q_0 < 1$, IRE should be distinguished from sawtooth oscillation, which is instability at q = 1 rational surface. In this study, IRE is defined as the instability with mode couplings and/or often accompanied by a collapse at a rational surface except for q = 1 surface. Figure 6 shows an IRE discharge with $q_0 < 1$. This IRE doesn't terminate the plasma but reduces β_t significantly. The position of the reconnection is around HCAMU♯14 (R ~1.45m). However, the area with strong oscillation is closed to HCAMU♯12(R ~1.2-1.3m) and the phase difference between HCAMU♯9 and 11 is significant. Therefore, this is tearing mode and the resonant surface is at R ~ 1.24 – 1.28m. The fitting code doesn't work well on this shot because the calculated position of the resonant surface (from EFIT) is presumably not good. However, as is indicated in section 2.1, the number of filaments (model of the mode) on outboard side is very few because of low aspect ratio configuration. Therefore the poloidal mode number can be estimated roughly by counting peaks along the centre stack and adding one for outboard filament. In this way m/n =2/1 is confirmed for this q_0 <1 discharge. Note that it is difficult to derive the growth time and rotation w/o the fitting. The width of 2/1 mode seems increasing, as shown by SXR radiation from outer side, for example, HCAMU♯14 from t ~ 0.392s. In addition, Mirnov coils show another high frequency mode (~22kHz). Unfortunately, there is no strong cross correlation between this high frequency mode and any of SXR channels, and the position of this mode is not clear from SXR signals. However, poloidal mode number (m) is presumably 4 and toroidal mode (n) is 1. These mode numbers are determined by the Mirnov coil arrays. Therefore, this mode is localizes at the edge. To clarify the relationship between these modes (i.e., 3kHz, and 22kHz), bicoherence spectrum is calculated. For t = 0.389 – 0.392 there is no significant coupling between the two modes. Instead of that, 4/1 mode (~22kHz) shows second and third harmonic mode (~45kHz, ~68kHz). Figure 7 shows the result in later period t = 0.392 – 0.395s. These frequency are localized on the frequency space and sharp coherence disappears, but broad bicoherence in the region $f_1 + f_2$ <50kHz appears, suggesting non-linear coupling among a lot of modes. This is consistent with the non-linear phase of the MHD simulation in the reference [1]. The total squared bispectrum (duration of ensemble is~3ms) at these two periods show a siginificant increase of about 50 times. However, we cannot decide which mode is a trigger of this IRE because the position of the high frequency mode has not been identified.

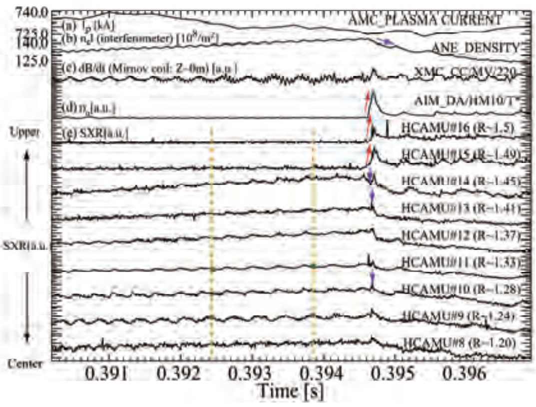

Fig. 6 IRE in a discharge with q_0 <1. (a): Plasma current [kA] (b): Line integrated electron density [$/m^2$] (c): dB/dt from Mirnov coil [a.u.] (d): Emission of D_α[a.u.] (e): SXR radiation [a.u.] on horizontal SXR camera from upper to center (SXR signals for midplane to upper chords.) side of the plasma.

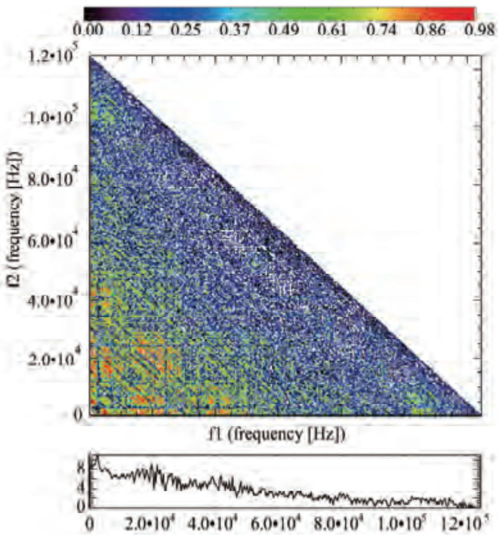

Fig. 7 ♯18501 Bicoherence spectrum (t = 0.392 – 0.395) of the toroidal Mirnov coils (top Fig.) and power spectrum on logarithmic scale (bottom Fig.).

4 IRE drive

To understand the drive of IRE is important for the prevention. For a comparison with the reference [1], which suggested pressure-driven mode as the source of the instabilities, we evaluated pressure gradient for some IRE discharges. Figure 8 shows time evolutions of a correlation between magnetic shear (S) and pressure gradient (dP/dr) for thirteen shots, where magnetic shear defined as $S = (r/q) \cdot dq/dr$. These two parameters are calculated by kEFIT which takes into account pressure profile from the Thomson scattering profile. Red circles represent the values just before each IRE. IRE occurs when pressure gradient exceed critical value, which becomes high at high shear. Note that although there are many shots showing increase of the gradient by the time of IRE, some shots don't show such behavior under the result from the kEFIT.

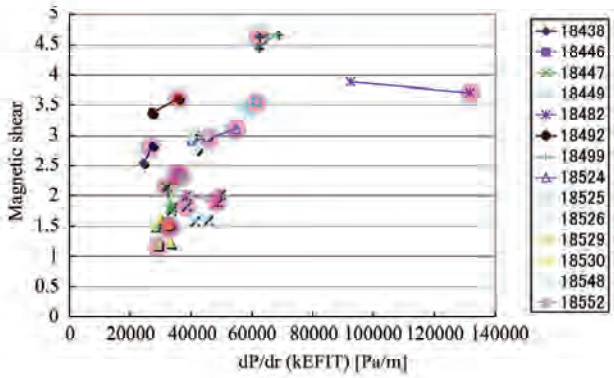

Fig. 8 Trace of magnetic shear (S) and pressure gradient from the kEFIT ressult at q = 2 rational surface before (0 ~ 21ms) IRE. Same symbol shows same shot. The red shaded circles indicate just before the IRE.

5 Summary and conclusion

In this paper, IREs in the MAST plasma are studied using a filament model, in which low aspect ratio effects are taken into account. In the case of $q_0 > 1$ no mode coupling concerning to IRE are observed but the growth of the 2/1 tearing mode with $\tau \sim 6ms$ is confirmed. The mode triggers a collapse. In the IRE with $q_0 < 1$, slow growth of the 2/1 tearing mode is observed and 2nd and 3rd harmonic from a 4/1 mode, (f_1, f_2) ~(22kHz, 22kHz) and (f_1, f_2) ~(22kHz, 44kHz), are confirmed in Mirnov coil signals. After that, these bicoherence peaks disappear and broad bicoherence on a range of $f_1 + f_2$ <50kHz is observed. This is consistent with the time evolution of each mode in [1]. Although we haven't found a clear evidence of non-linear development causing an IRE followed by collapse, the 2/1 mode may trigger the collapse. To find out the source of IRE traces of pressure gradient and magnetic shear. Critical pressure gradient at $q = 2$ increases with magnetic shear suggesting pressure-driven nature of IREs.

6 Acknowledgment

This work was supported by JSPF Grant-in-Aid for Scientific Research 16106013.

[1] N. Mizuguchi et al., Phys. Plasmas **7** (2000) 940.
[2] B. Lloyd et al., Nucl. Fusion **43** (2003) 1665.
[3] L. Lao et al., Nucl. Fusion **25** (1985) 1611.
[4] Y.C. Kim and E.J. Powers, Phys. Fluids **21** (1978) 1452.
[5] Y. Nagashima et al., Plasma Phys. Control. Fusion **49** (2007) 1611.

Proceedings of ITC/ISHW2007

Stabilization of the Vertical Mode in Tokamaks by Localized Nonaxisymmetric Fields

A. Reiman

Princeton Plasma Physics Laboratory, Princeton, NJ 08543, USA

reiman@pppl.gov

We find that vertical instability of tokamak plasmas can be controlled by nonaxisymmetric magnetic fields localized near the plasma edge at the bottom and top of the torus. The required magnetic fields can be produced by a relatively simple set of parallelogram-shaped coils (Fig. 1). By providing stable equilibria with more highly elongated cross-sections, the addition of these nonaxisymmetric fields can potentially lead to devices with improved confinement (empirically derived global confinement scaling laws for tokamaks find that confinement improves with increasing vertical elongation) and/or beta limits (the Troyon scaling law for plasma stability predicts an increase in the β limit for ballooning and kink modes with increasing elongation). There is evidence that the benefits of increasing elongation diminish and perhaps disappear altogether at sufficiently high elongation, but the elongation at which this occurs is well above that at which the largest present day tokamaks can routinely operate. Furth-Hartman coils [1] are calculated to have essentially the same vertical stabilization effect as the simple parallelogram-shaped coils described here, so that the vertical stabilization demonstrated experimentally by Furth-Hartman coils [2] supports the feasibility of stabilizing vertical modes by the simpler coil set. The analytical calculation assumes a large aspect ratio plasma that is well approximated by a cylinder, $\beta = 0$, and a uniform equilibrium current density. Stability is determined by a δW calculation, using the stellarator approximation [3] for both the equilibrium and stability calculations. The physical mechanism of the stabilization suggests that the stability properties do not depend on the precise shape of the coils, so that the coil winding surface can be curved to conform to the local shape of the plasma, if desired, or curvature of the coils can be introduced to optimize relative to other considerations.

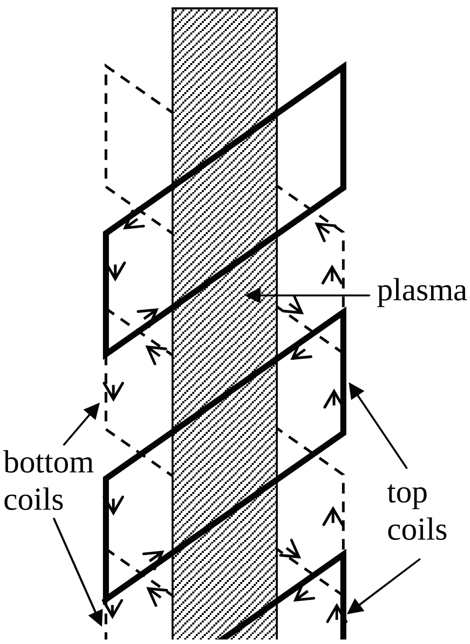

Fig. 1. View from above showing parallelogram-shaped coils above a length of cylindrical plasma, with portions of the coils below the plasma also visible (dashed lines). The arrows indicate the direction of current flow in the coils.

This work was supported by DOE contract DE-AC02-76CH03073.

[1] H. Furth and C. Hartman, Phys. Fluids **11**, 408 (1968).

[2] H. Ikezi, *et al.*, Phys. Fluids **22**, 2009 (1979); A. Janos, Ph.D. thesis, M.I.T., (1980).

[3] J. Greene and J. Johnson, Phys. Fluids **4**, 875 (1961); J. Johnson and J. Greene, Phys. Fluids **4**, 1417 (1961).

Proceedings of ITC/ISHW2007

Two-Fluid Flowing Equilibria of Helicity Injected Spherical Torus with Non-Uniform Density

Takashi KANKI, Loren C. STEINHAUER[1)] and Masayoshi NAGATA[2)]

Department of Maritime Science and Technology, Japan Coast Guard Academy, Kure, Hiroshima 737-8512, Japan

[1)]*University of Washington, Redmond Plasma Physics Laboratory, Redmond, Washington 98052, USA*

[2)]*Department of Electrical Engineering and Computer Sciences, University of Hyogo, Himeji, Hyogo 671-2201, Japan*

Two-dimensional two-fluid flowing equilibria of helicity-injected spherical torus with non-uniform density and both toroidal and poloidal flows for each species have been numerically determined by means of the nearby-fluids procedure. It is found from the numerical results that the equilibrium for the driven λ ($\equiv \mu_0 \boldsymbol{j} \cdot \boldsymbol{B} / B^2$) profile has a diamagnetic toroidal field, high-β (toroidal beta value, $\beta_t = 32\%$), hollow current profile, and centrally broad density. By contrast, the decaying equilibrium has a paramagnetic toroidal field, low-β ($\beta_t = 10\%$), centrally peaked current profile, and density with a steep gradient in the outer edge region. In the driven case, the toroidal ion and electron flows are in the same direction, and two-fluid effects are less important since the $\boldsymbol{E} \times \boldsymbol{B}$ drift is dominant. In the decaying case, the toroidal ion and electron flows are opposite in the outer edge region, and two-fluid effects are significant locally in the edge due to the ion diamagnetic drift.

Keywords: helicity injection, equilibrium, plasma flow, two-fluid effect, $\boldsymbol{E} \times \boldsymbol{B}$ drift, diamagnetic drift

1. Introduction

Many experiments on current drive of spherical torus using a coaxial helicity injection (CHI) have been performed to elucidate the current drive mechanism for CHI. In these experiments, $\boldsymbol{E} \times \boldsymbol{B}$ plasma toroidal rotation with an n=1 kink mode the during CHI has been observed. It is recognized that the effect of plasma flow is important in understanding the confinements and relaxed states of helicity-injected spherical torus (HI-ST) plasmas. Especially, in the Helicity Injected Torus-II (HIT-II) experiments, a rotating n=1 magnetic structure observed at the outer plasma edge is locked to the electron fluids and not to the ion fluids, suggesting a rotating magnetic field current drive [1]. Because of this behavior, the equilibrium computation of the HI-ST is required to take into account two-fluid effects [2,3]. The formalism for two-fluid flowing equilibria was developed [4], and two-dimensional equilibria in helicity-driven systems using the two-fluid model were previously computed, showing the existence of an ultra-low-q spherical torus configuration with diamagnetism and higher beta [5]. However, this computation assumed purely toroidal ion flow and uniform density. The purpose of this study is to apply the two-fluid model to the two-dimensional equilibria of HI-ST with non-uniform density and both toroidal and poloidal flows for each species by means of the nearby-fluids procedure [6], and to explore their properties. We focus our attention on the equilibria relevant to the Helicity Injected Spherical Torus (HIST) device, which are characterized by either driven or decaying λ ($\equiv \mu_0 \boldsymbol{j} \cdot \boldsymbol{B} / B^2$) profiles [7]. Here μ_0, $\boldsymbol{j}$, and $\boldsymbol{B}$ are the permeability of vacuum, current density, magnetic field. We have qualitatively reproduced the HIST equilibria in the driven or decaying λ profiles on the basis of the experimental data such as λ, $\boldsymbol{j}$, and $\boldsymbol{B}$ profiles.

2. Governing Equations

Let us assume axisymmetry about HIST geometric axis in cylindrical coordinates (r, θ, z). Hereafter all variables are dimensionless [6]. An axisymmetric two-fluid flowing equilibrium is described by a pair of generalized Grad-Shafranov equations for ion surface variable $\Upsilon(r, z)$ and electron surface variable $\psi(r, z)$ [6],

$$\overline{\psi}_i' r^2 \nabla \cdot \left(\frac{\overline{\psi}_i'}{n} \frac{\nabla \Upsilon}{r^2} \right) = \frac{r}{\varepsilon} \left(B_\theta \overline{\psi}_i' - n u_\theta \right) + n r^2 \left(H_i' - T_i S_i' \right), \quad (1)$$

$$r^2 \nabla \cdot \left(\frac{\nabla \psi}{r^2} \right) = \frac{r}{\varepsilon} \left(B_\theta \overline{\psi}_e' - n u_\theta \right) - n r^2 \left(H_e' - T_e S_e' \right), \quad (2)$$

and a generalized Bernoulli equations for the density n,

$$\frac{\gamma}{\gamma - 1} n^{\gamma - 1} \exp\left[(\gamma - 1) S_i \right] + \frac{u^2}{2} + \phi_E = H_i, \quad (3)$$

$$\frac{\gamma}{\gamma - 1} n^{\gamma - 1} \exp\left[(\gamma - 1) S_e \right] - \phi_E = H_e. \quad (4)$$

Here $\boldsymbol{u}$, T_α, ε, ϕ_E, and γ are the ion flow velocity, species (α=i, e) temperature, two-fluid parameter, electrostatic potential, and adiabatic constant, respectively. Note that ε value is 0.0625 in the HIST experiment, and that $\psi(r, z)$

author's e-mail: kanki@jcga.ac.jp

corresponds to the familiar poloidal flux function. The poloidal flow stream function $\overline{\psi}_\alpha$, total enthalpy function H_α and entropy function S_α are arbitrary surface functions of their respective surface variables. The three arbitrary functions $\Lambda_\alpha(\equiv \overline{\psi}'_\alpha)$, H_α, and S_α for each species can be assumed so as to reflect λ, $\boldsymbol{j}$, and $\boldsymbol{B}$ profiles on the basis of the experimental data by choosing appropriate function forms,

$$\Lambda_i(\mathrm{Y}) = \Lambda_{i0} + (\Lambda_{i1} - \Lambda_{i0})\left.\frac{df}{dx}\right|_{\mathrm{Y}-\Delta\mathrm{Y};\delta_{i1},\delta_{i2}}, \tag{5}$$

$$\Lambda_e(\psi) = \Lambda_{e0} + (\Lambda_{e1} - \Lambda_{e0})\left.\frac{df}{dx}\right|_{\psi-\Delta\psi;\delta_{e1},\delta_{e2}}, \tag{6}$$

$$f(x;\delta_1,\delta_2) = \frac{1}{\delta_1+\delta_2} \times \begin{Bmatrix} \delta_1^2 \exp[x/\delta_1]; \quad x<0 \\ \delta_1 x + \delta_2\sqrt{\delta_2^2 + x^2} - \delta_2^2 + \delta_1^2;\ x \ge 0 \end{Bmatrix}. \tag{7}$$

Here $\Lambda_{\alpha 0}$, $\Lambda_{\alpha 1}$, $\delta_{\alpha 0}$, $\delta_{\alpha 1}$, $\Delta\mathrm{Y}$, and $\Delta\psi$ are constant parameters. By adjusting these constant parameters, we can obtain the driven or decaying λ profiles. Other arbitrary functions H_α and S_α are the same function form as Λ_α.

Equations (1) and (2) have terms of order $1/\varepsilon$ on the right-hand side, and they cause singularities. We employ the nearby-fluids procedure to eliminate the singularities [6]. This procedure requires that two arbitrary functions Λ_i and Λ_e must differ only to $O(\varepsilon)$. We consider replacing these two arbitrary functions with a pair of arbitrary functions F and G expressed as follows:

$$\Lambda_e(\psi) = F(\psi), \quad \Lambda_i(\mathrm{Y}) = F(\mathrm{Y}) + \varepsilon G'(\mathrm{Y}). \tag{8}$$

Note that G and Λ_e correspond to the toroidal field function and the familiar Taylor $\lambda(\psi)$ function, respectively. Therefore, the toroidal field with $GG' > 0$ gives a paramagnetic profile, while that with $GG' < 0$ gives a diamagnetic one.

Next, we consider the boundary conditions for Eqs. (1)-(4). No magnetic flux penetrates the flux conserver (FC). Therefore, ψ is fixed at 0 at the FC wall. The bias flux is given by assigning fixed values of ψ to grid points corresponding to the entrance port of the FC. These values are calculated using the formula,

$$\psi_{\mathrm{bias}}(r) = \frac{4\psi_s}{(R_e - R_c)^2}(r - R_c)(R_e - r), \tag{9}$$

where R_c, R_e, and ψ_s are the radius of the central conductor, that of the entrance port, and the maximum value of the bias flux, respectively. A toroidal field coil current along the geometry axis inside the central conductor produces a vacuum toroidal field $B_{t.v}$. The effect of $B_{t.v}$ is inserted by G_0 in

$$G(\mathrm{Y}) = G_0 + \frac{1}{\varepsilon}\left[\int \Lambda_i(\mathrm{Y})d\mathrm{Y} - \int \Lambda_e(\psi)d\psi\right]. \tag{10}$$

Under the above assumptions and boundary conditions, the equilibrium is numerically determined by using a successive over-relaxation method for updating the poloidal flux function and a Newton-Raphson method for updating the density.

3. Numerical Results

We investigate the fundamental properties of the HIST equilibria in the driven or decaying λ profiles. The radial profiles of the magnetic structure at the midplane are shown in Fig. 1. In the driven λ profile, the toroidal field B_t has a diamagnetic profile due to the condition $GG' < 0$, and the toroidal beta value β_t is high (β_t = 32%). The condition means $\Lambda_e > \Lambda_i$ and then reflects that the absolute value of electron flow velocity is larger than that of ion flow velocity. The poloidal field B_z is much smaller than B_t and is almost flat in the core region. The toroidal current density j_t has a hollow profile and almost zero in the core region. In the decaying λ profile, B_t has a paramagnetic profile except for the inner edge region, and β_t is low (β_t = 10%). Also, j_t has a centrally peaked profile with a slightly outward shift.

The radial profiles of the plasma structure at the midplane are shown in Fig. 2. In the driven λ profile, the density n is a centrally broad profile. Both ion temperature T_i and electron temperature T_e have flat profiles, and their magnitudes are almost same. The electrostatic potential ϕ_E

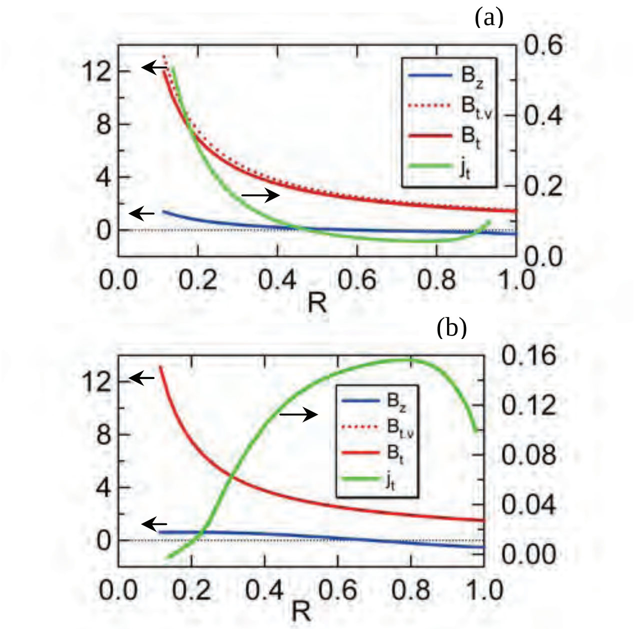

Fig.1 Radial profiles of the magnetic field and toroidal current density at the midplane; (a) driven λ profile and (b) decaying λ profile.

is peaked towards the periphery region, and reflects that the electric field is applied by the coaxial helicity source (CHS). In the decaying λ profile, n is a centrally peaked profile. Both T_i and T_e have similarly peaked profiles, and their magnitudes are almost same. Also, ϕ_E has almost flat profile which reflects that the electric field is hardly applied by the CHS.

The radial profiles of the flow structure at the midplane are shown in Fig. 3. In the driven λ profile, the electron toroidal flow velocity u_{et} is larger than the ion one u_{it}, and u_{it} and u_{et} are in the same direction. Both toroidal and poloidal electron flow velocities rise up sharply near the inner edge region and cause the hollow current profile. In the decaying λ profile, u_{it} is larger than u_{et} except for the inner edge region, and u_{it} and u_{et} are opposite in the outer edge region.

We investigate the generalized Ohm's law,

$$\begin{aligned} &\boldsymbol{E} + (1/\varepsilon)\boldsymbol{u}\times\boldsymbol{B} + \boldsymbol{F}_{2F} = 0, \\ &\boldsymbol{F}_{2F} = -\nabla p_i / n - \boldsymbol{u}\cdot\nabla\boldsymbol{u}. \end{aligned} \tag{11}$$

Here $\boldsymbol{E}$ and $\boldsymbol{F}_{2F}$ express the electric field and two-fluid effect, respectively. The terms $-\nabla p_i / n$ and $-\boldsymbol{u}\cdot\nabla\boldsymbol{u}$ cause the ion diamagnetic and inertial effects, respectively. The radial profiles of $\boldsymbol{E}$, $(1/\varepsilon)\boldsymbol{u}\times\boldsymbol{B}$, $\boldsymbol{F}_{2F}$, $-\nabla p_i / n$, and $-\boldsymbol{u}\cdot\nabla\boldsymbol{u}$ at the midplane are shown in Fig. 4. All components are radial. In the driven λ profile, the two-fluid effect is not so large except for both edge regions. The ion diamagnetic and inertial effects are relatively large both edge regions, but they are in the opposite direction. In the decaying λ profile, the two-fluid effect is dominant in the outer edge region due to the ion diamagnetic effect.

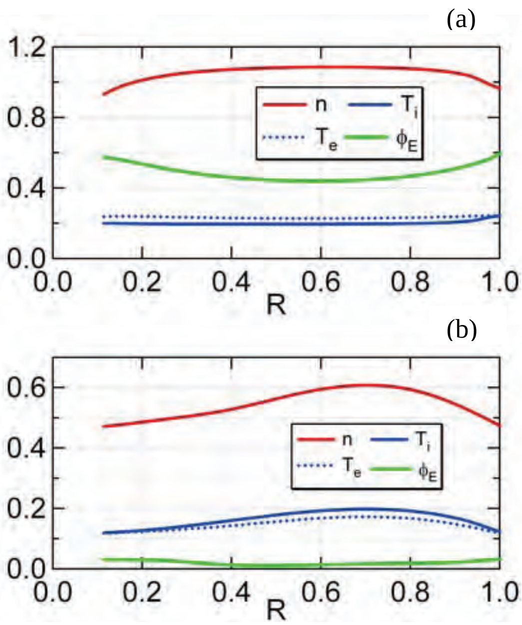

Fig.2 Radial profiles of the density, temperatures and electrostatic potential at the midplane; (a) driven λ profile and (b) decaying λ profile.

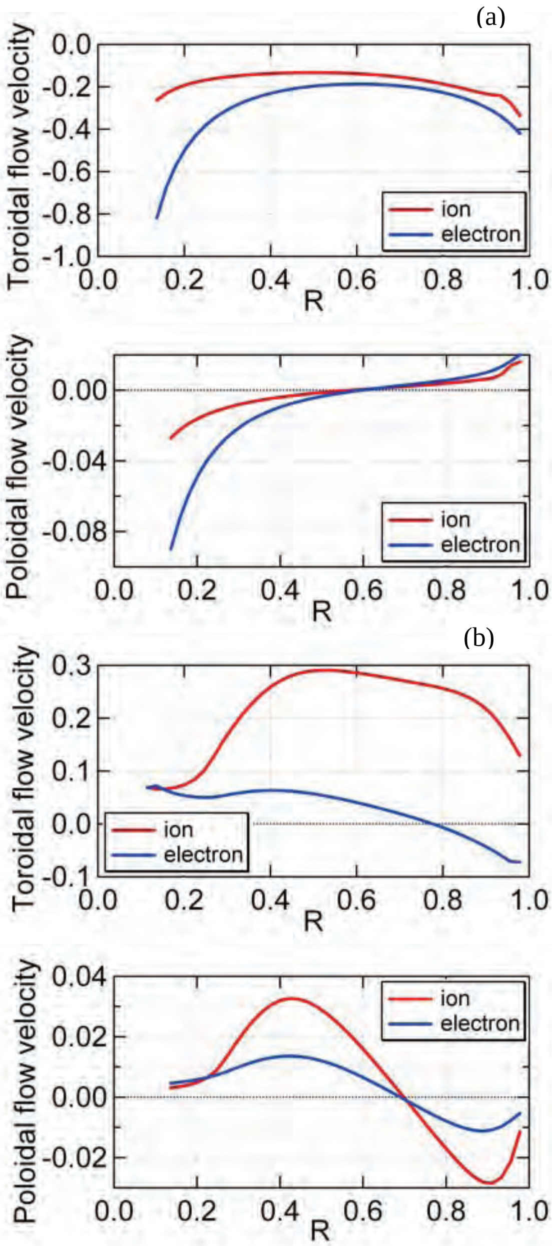

Fig.3 Radial profiles of the toroidal and poloidal flow velocities at the midplane; (a) driven λ profile and (b) decaying λ profile.

The radial profiles of the ion drift velocity at the midplane are shown in Fig. 5. In the driven λ profile, the $\boldsymbol{E}\times\boldsymbol{B}$ drift velocity is dominant. This velocity is the same direction as the toroidal ion flow one, but is the opposite direction to the toroidal current density. This result is consistent with the observation in the HIST and other CHI experiments. In the decaying λ profile, the ion diamagnetic drift velocity is dominant. This velocity is the same direction as the toroidal ion flow one, but is the opposite direction to the $\boldsymbol{E}\times\boldsymbol{B}$ one.

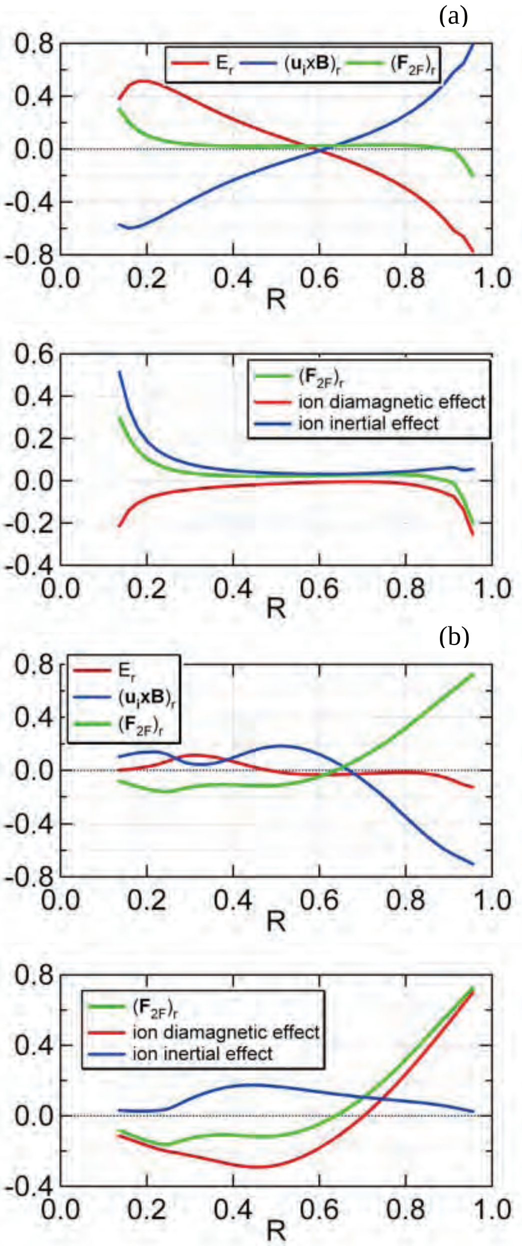

Fig.4 Radial profiles of $\boldsymbol{E}$, $(1/\varepsilon)\boldsymbol{u}\times\boldsymbol{B}$, $\boldsymbol{F}_{2F}$, $-\nabla p_i/n$, and $-\boldsymbol{u}\cdot\nabla\boldsymbol{u}$ at the midplane; (a) driven λ profile and (b) decaying λ profile. All components are radial.

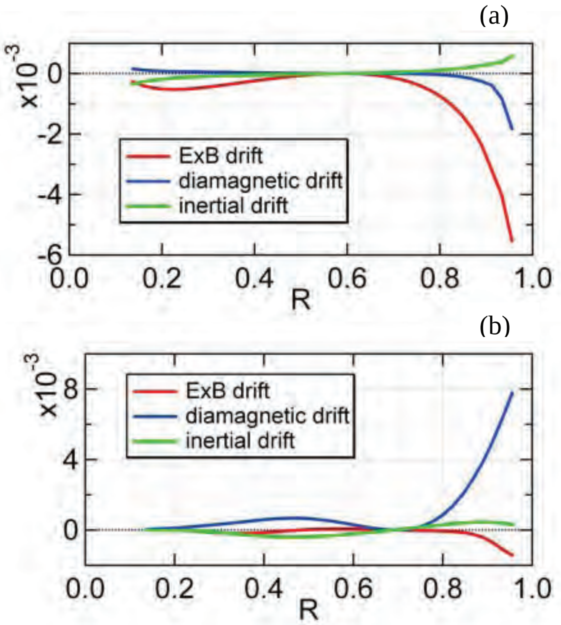

Fig.5 Radial profiles of the ion drift velocity at the midplane; (a) driven λ profile and (b) decaying λ profile. All components are toroidal.

3. Summary and Conclusions

We have computed the two-dimensional two-fluid flowing equilibria with non-constant density and the poloidal as well as toroidal flows for each species by using the nearby-fluids procedure. We focus our attention on the HI-ST equilibria relevant to the HIST device, which are characterized by either driven or decaying λ profiles, and explore their properties. Conclusions are summarized as follows. 1) In the driven λ profile, the equilibrium has the diamagnetic toroidal field, high-β (β_t=32%), hollow current profile, and centrally broad density. The toroidal ion and electron flows are in the same direction, and two-fluid effects are less important since the $\boldsymbol{E}\times\boldsymbol{B}$ drift is dominant. 2) In the decaying λ profile, the equilibrium has the paramagnetic toroidal field, low-β (β_t=10%), centrally peaked current profile, and density with the steep gradient in the outer edge region. The toroidal ion and electron flows are opposite in the outer edge region, and two-fluid effects are significantly locally in the edge due to the ion diamagnetic drift.

[1] K.J. McCollam and T.R. Jarboe, Plasma Phys. Control. Fusion **44**, 493 (2002).
[2] L.C. Steinhauer and A. Ishida, Phys. Rev. Lett. **79**, 3423 (1997).
[3] Z. Yoshida and S.M. Mahajan, Phys. Rev. Lett. **88**, 095001 (2002).
[4] L.C. Steinhauer, Phys. Plasmas **6**, 2734 (1999).
[5] T. Kanki and M. Nagata, Phys. Plasmas **13**, 072506 (2006).
[6] L.C. Steinhauer and A. Ishida, Phys. Plasmas **13**, 052513 (2006).
[7] M. Nagata, T. Kanki, N. Fukumoto and T. Uyama, Phys. Plasmas **10**, 2932 (2003).

Proceedings of ITC/ISHW2007

Intermittent dynamics of nonlinear resistive tearing modes at extremely high magnetic Reynolds number

Takahiro MIYOSHI[1)], Masahiro BECCHAKU[1)] and Kanya KUSANO[2)]

[1)]*Hiroshima University, Higashi-hiroshima 739-8526, Japan*

[2)]*The Earth Simulator Center, Japan Agency for Marine-Earth Science and Technology, Yokohama 236-0001, Japan*

(Received / Accepted)

Nonlinear dynamics of the resistive tearing instability in high magnetic Reynolds number (R_m) plasmas is studied by newly developing an accurate and robust resistive magnetohydrodynamic (MHD) scheme. The results show that reconnection processes strongly depend on R_m. Particularly, in a high R_m case, small-scale plasmoids induced by a secondary instability are intermittently generated and ejected accompanied by fast shocks. According to the intermittent processes, the reconnection rate increases intermittently at a later nonlinear stage.

Keywords: tearing instability, high magnetic Reynolds number, MHD, simulation, secondary instability

DOI: 10.1585/pfr.1.001

The tearing instability is one of the most basic and important mechanism of plasma dynamics both in fusion and astrophysical processes. Particularly, resistive tearing modes have been well investigated theoretically and numerically as the most basic modes of the tearing instability [1, 2, 3]. However, our understanding of the nonlinear dynamics of resistive tearing instability in case of magnetic Reynolds numbers, R_m, as high as the practical systems is still severely limited. A major reason of that is attributed to the fact that the numerical resolution of simulations is too strongly restricted to resolve a thin current sheet, which is believed to be formed in the realistic systems. Therefore, in this study, an accurate and robust resistive MHD scheme is developed, and nonlinear simulations at the highest-ever resolution are carried out in order to find a new dynamic regime of the resistive tearing instability.

First, we develop an accurate, efficient, and robust numerical solver for resistive compressible magnetohydrodynamics (MHD). The Harten-Lax-van Leer-Discontinuities (HLLD) approximate Riemann solver [4], which is one of the promissing shock capturing solver for ideal MHD from the viewpoint of its resolution, robustness, and efficiency, is applied to ideal terms of resistive MHD. Also, higher-order accuracy is achieved by the MUSCL method with limiters. As a divergence cleaning method, hyperbolic divergence cleaning method [5] is adopted. Resistive terms, on the other hand, are calculated by a classical centered finite difference method. In order to confirm the applicability of the present strategy to resistive MHD, severanl numerical tests are performed. As a first test, nonlinear simulations for the resistive tearing mode with a quite small apmplitude are compared with the linear theory [1]. When R_m is large enough (about more than 10^5), the results of both are almost corresponding. We also perform another test of which both the present scheme and the (fully) centered finite difference scheme apply the nonlinear simulation of the tearing instability for a linear force free magnetic field. The results of both are almost the same at an initial stage, while the centered finite difference scheme is brokendown at a later stage. Thus, it is concluded that the present scheme achieves a high degree of the numerical accuracy and robustness even for resistive MHD processes.

Subsequently, nonlinear simulations of resistive tearing modes are performed in a simple 2D slab geometry with uniform resistivity η ($\equiv R_m^{-1}$). The initial condition is given by the Harris equiribrium, $B_{0x} = \tanh(y/\delta)$, where the thickness of the initial current sheet δ is set to 0.5. The simulation box is such that $-12.8 \leq x \leq 12.8$ and $-6.4 \leq y \leq 6.4$. The periodic boundary condition is applied to x direction, while the symmetric condition is adopted for y boundary. In order to resolve the resistive layer sufficiently, non-uniform grid is adopted for y direction. The finest grid spacing is about 0.0102 for x direction and 0.0005 for y direction. In this paper, two cases of relatively low R_m, $R_m = 10^3$, and relatively high R_m, $R_m = 10^4$, are presented in particular. The nonlinear tearing mode at $R_m = 10^3$ steadily grows and is almost saturated as expected from the previous works. On the other hand, it is found that at a high R_m, $R_m = 10^4$, a new dynamics arises after the formation of a thin current sheet at the initial nonlinear stage. Fig. 1 show the current density and mass density distribution around the current sheet. We find that many secondary plasmoids are intermittently created in the thin current sheet and interacted with each other. Through the nonlinear interaction of the plasmoids, various fine structures associated with fast shocks are generated even in the uniform η model. Fig. 2 show the temporal evolution of the maximum electric field in the current sheet induced by the resistivity at both R_m cases. Though

author's e-mail: miyoshi@sci.hiroshima-u.ac.jp

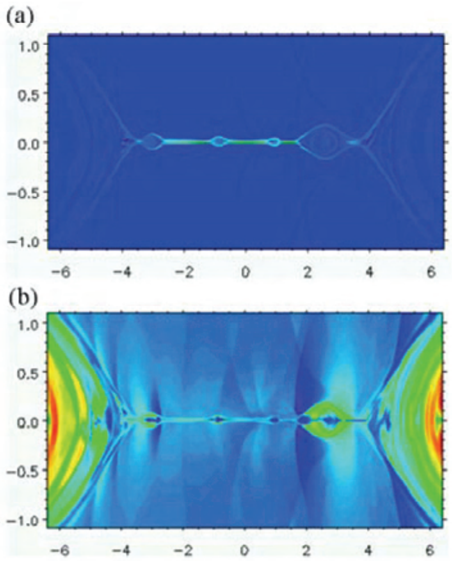

Fig. 1 Distributions of (a) the current density and (b) the density at $R_m = 10^4$

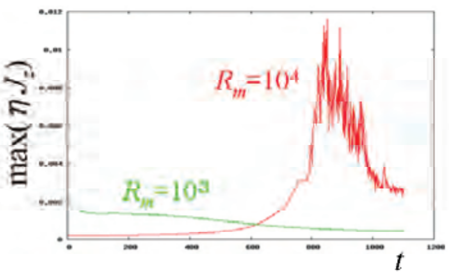

Fig. 2 Time evolution of the maximum resistive electric field in the current sheet at $R_m = 10^3$ (green line) and 10^4 (red line).

multiple X points are advected at $R_m = 10^4$, the resistive electric field is almost considered as the reconnection rate. It is found that the reconnection rate is much enhanced intermittently at $R_m = 10^4$ even though the linear growth rate of the resistive tearing instability is reduced with an increasing of R_m.

The results indicate that the nonlinear dynamics at a high R_m is much different from our conventional understanding based on the linear theory and the simulations at modest value of R_m. It strongly suggests that the realistic MHD dynamics at extremely high R_m (e.g., more than 10^{14} in the solar corona!) is still veiled, and it is likely that some hierarchical MHD dynamics is involved to connect macro-scale plasma evolution and micro-scale kinetic processes.

[1] H. P. Furth, J. Killeen. and M. N. Rosenbluth. Phys. Fluids **6**, 459 (1963).
[2] P. H. Rutherford, Phys. Fluids **16**, 1903 (1973).
[3] L.-N. Hau and S.-W. Chiou, J. Geophys. Res. **106**, 8371 (2001).
[4] T. Miyoshi and K. Kusano, J. Comput. Phys. **208**, 315 (2005).
[5] A. Dedner, F. Kemm, D. Kröner, C.-D. Munz

Stellarator Equilibrium Reconstruction: V3FIT

J. D. Hanson, J. Shields, S. P Hirshman[a], E. A. Lazarus[a], L. Lao[b], S. F. Knowlton

Physics Department, Auburn University, Auburn, AL 36849-5311, USA
[a]Oak Ridge National Laboratory, Oak Ridge, TN USA
[b]General Atomics, San Diego, CA USA

hanson@physics.auburn.edu

Equilibrium reconstruction is the process of inferring the radial profiles of an MHD equilibrium model by minimizing the mismatch between model-calculated and observed diagnostic signals. Axisymmetric equilibrium reconstruction, as exemplified by the EFIT code[1], has proven invaluable for the interpretation of tokamaks and RFPs. V3FIT is a non-axisymmetric equilibrium reconstruction code, based on the VMEC stellarator equilibrium code[2].

V3FIT (like most inverse problems) infers the parameters by minimizing a cost function that is quadratic in the signal misfits:

$$g^2(p) \equiv \sum_i w_i \left(\frac{S_i^o - S_i^m(p)}{\sigma_i} \right)^2$$

where p is a vector of parameters, $S^{o(m)}$ is an observed (model-computed) signal, σ is a normalizing factor, and w a weight. V3FIT currently minimizes g^2 by using Newton's algorithm to find the location in parameter space where the slope of g^2 is zero, using a Singular Value Decomposition of the finite-difference approximation to the Jacobian matrix

$$J_{ij} \equiv \frac{\partial S_i^m}{\partial p_j}.$$

An evaluation of model signals requires the convergence of the VMEC equilibrium code. The V3FIT reconstruction algorithm is tightly coupled to the VMEC convergence, since the small steps in parameter space are accomplished by changing the VMEC parameters for an already converged VMEC equilibrium, and further converging VMEC. Thus VMEC, after its first convergence, does not have to convergence very far as the reconstruction algorithm proceeds.

V3FIT results will be shown for reconstructions of stellarator equilibria with magnetic diagnostic signals and interferometer/polarimeter signals. The reconstruction results match closely the expected behavior when Gaussian noise is added to the simulated observed signals. Comparisons of V3FIT reconstructions with EFIT reconstructions will also be shown for experimental data from the DIII-D tokamak.

This work is supported in part by US DOE Grant DE-FG02-03ER54692B and a US DOE Postdoctoral Research Fellowship.

[1] L.L. Lao, H. St. John, R.D. Stambaugh, A. G. Kellman, and W. Pfeiffer, Nucl. Fus. **25**, 1611 (1985).
[2] S. P. Hirshman and J. C. Whitson, Phys. Fluids **26**, 3553 (1983).

P2-043

Effects of the stochasticity on transport properties in high-β LHD

Yasuhiro SUZUKI, Kiyomasa WATANABE, Hisamichi FUNABA, Satoru SAKAKIBARA, Noriyoshi NAKAJIMA, Nobuyoyshi OHYABU and LHD experiment group

National Institute for Fusion Science, Toki 509-5292, Japan

Effects of the stochasticity of magnetic field lines on transport properties are investigated. In a high-β LHD plasma, the structure of field lines in the edge region becomes stochastic by finite-β effects but the finite pressure gradient exists in the region. The radial diffusion coefficient and the Kolmogorov length of stochastic field lines are estimated. In the edge region, the radial diffusivity of stochastic field lines becomes large and the Kolmogorov length becomes short due to the increased β. In the region, the radial heat diffusivity becomes large due to the stochasticity of field lines.

Keywords: stochasticity, transport, radial heat diffusivity, HINT2

1. Introduction

Generating and keeping clear flux surfaces are an aim of magnetic confinement researches, because the stochasticity of magnetic field lines leads the degradation of the confinement connecting between core and edge region. There are some analytical works investigating the impact of the stochasticity of magnetic field lines on the radial transport property [1-4]. In those works, Rechester and Rosenbluth pointed out the radial heat diffusivity due to stochastic field lines relates to both the stochastic diffusion parallel and perpendicular to the magnetic field [1].

The stochasticity of field lines due to finite-β effects is an intrinsic property in stellarator/heliotron. Since the pressure-induced perturbed field breaks the symmetry of the field, the structure of magnetic field lines becomes stochastic, especially in the edge. In order to aim stellarator/heliotron reactors, the study of the transport due to stochastic field lines is critical and urgent issue.

The LHD is an L=2 heliotron device. A numerical code to calculate 3D MHD equilibrium without the assumption of nested flux surfaces predicts the field structure becomes stochastic due to the increased β [5,6]. In addition, in numerical simulations, the finite pressure gradient ∇p can exist in the stochastic region [5]. In the edge region of LHD plasmas, the connection length of stochastic field lines is still long compared to the parallel electron mean free path. That is, there is a possibility to keep the finite pressure on stochastic file lines. LHD experiments suggest the plasma pressure spread over the region expected stochastically [7]. This supports above speculation. However, that speculation does not include the effect of stochastic diffusion perpendicular to the field.

In this study, the radial heat diffusivity due to stochastic field lines is investigated in a high-β LHD equilibrium. In next section, the degradation of flux surface quality due to finite-β effects is studied in a LHD configuration. Then, the diffusive property of stochastic field lines is studied. Lastly, results are briefly summarized and shown future subjects.

2. Degradation of flux surface due to plasma β

Figure 1 shows Puncture maps of magnetic field lines for (a) the vacuum field and (b) a finite-β equilibrium on the horizontal cross section. The configuration is an inward shifted configuration (R_{ax}=3.6m, γ=1.254, B_Q=100%). The profile of the normalized plasma pressure p/p_0 is also plotted as the function of R on the equatorial plane. The finite-β field is calculated by HINT2, which is a 3D MHD equilibrium calculation code without the assumption of nested flux surfaces [5]. Since HINT2 uses the real coordinate system, it can treat the magnetic island and stochastic field. The diamagnetic beta $\langle\beta\rangle_{dia}$ is about 3%. For the finite-β, the region with closed flux surfaces decreases and field lines in the edge region becomes stochastic. Chains of small magnetic islands appear. The finite plasma pressure exists in spite of field lines becoming stochastic in the edge (see fig. 2(b)). Two arrows indicate the position of the vacuum last closed flux surface (LCFS) on the equatorial plane. The finite pressure spreads over the vacuum LCFS.

In fig.2, profiles of the electron temperature T_e (#46465, t=1.625), the distance along the magnetic field L_C started along R on the equatorial plane, contour lines with p=*const*. (Z<0) and puncture map of field lines (Z>0) for comparison are shown, respectively. The length of the calculation tracing field lines is limited to 2000m.

author's e-mail:ysuzuki@LHD.nifs.ac.jp

In figs, contour lines p=*const.* exists in the stochastic region with keeping the surface structure. HINT2 calculates converged pressure distribution in the finite-β field by

$$p^{i+1} = \bar{p} = \frac{\int_{-L_{in}}^{L_{in}} \mathcal{F} p^i \frac{dl}{B}}{\int_{-L_{in}}^{L_{in}} \frac{dl}{B}}, \qquad (1)$$

$$F = \begin{cases} 1: \text{for } L_C \geq L_{in} \\ 0: \text{for } L_C < L_{in} \end{cases},$$

where, i means a step number of iterations, L_C is the connection length of a magnetic field line starting each grid point (L_C is finite for open magnetic field lines), and L_{in} is prescribed as an input parameter to control the calculation. Equation 1 calculates the '*averaged*' plasma pressure on the flux tube. This corresponds to simulate the radial diffusion of field lines. In order to consider this effects, profiles of plasma pressure with different L_{in} (=30m and 300m) are shown in fig. 3. For L_{in}=300m, contour lines are different, especially in the stochastic region. If the distance along *B* is shorter than L_{in}, the averaged pressure $\bar{p}$ is set to zero. In fig. 2, since L_C is 10^1~10^2m, the distribution of $\bar{p}$ is sensitive to L_{in}. This study has an assumption that the electron temperature is low because of the consideration of high-β experiments (see fig. 2). Thus, we adopt L_{in} is 30m. As a result, contour lines of p/p_0 is consistent to the temperature profile.

(a) vacuum

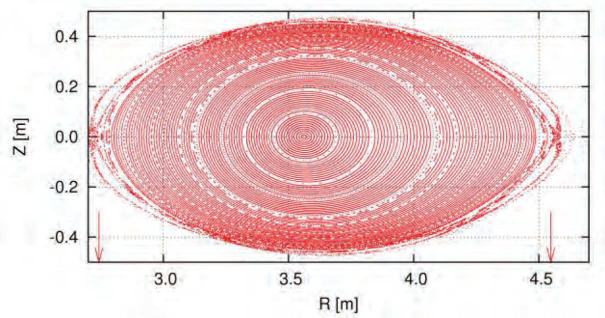

(b) $<\beta>_{dia}$~3%

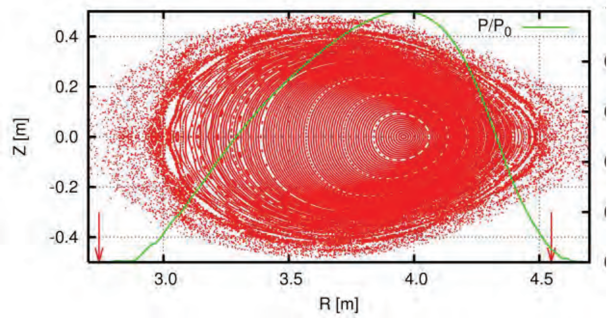

Fig.1 Puncture maps of magnetic field lines for the vacuum field and a finite-β equilibrium ($<\beta>_{dia}$~3%) are plotted at the horizontal cross section (ϕ=π/M). A green line indicates the normalize plasma pressure p/p_0 as the function of R on the equatorial plane. Two arrows in figs indicate the position of the vacuum LCFS on the equatorial plane.

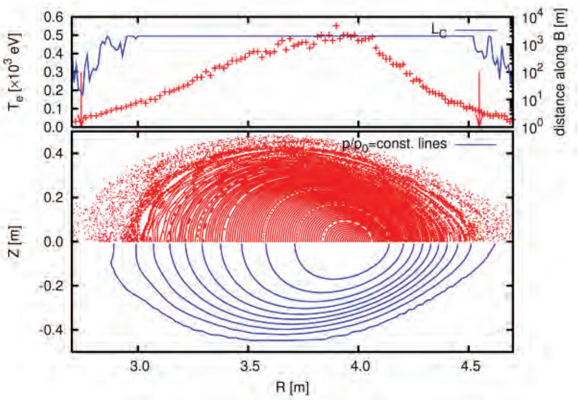

Fig.2 Profiles of the electron temperature T_e (#46465, t=1.625) and the distance along the magnetic field L_C on the plane corresponding to fig. 1(b) are plotted as the function of R. Contour lines with p=const. are also shown for the comparison.

In order to study the degradation of flux surfaces due to the increased β, the change of positions of the LCFS and magnetic axis is shown in fig. 4 as the function of $\langle\beta\rangle_{dia}$. At first, the change of the outward torus is noted. For low-β equilibria (< 1%), the LCFS slightly expands compared to the vacuum field. Then, increasing β (>1%), the LCFS still sustains near the vacuum LCFS. For high-β (>2%), the LCFS shrinks sharply. On the other hand, the inward region, the LCFS degrades monotonically due to the increased β. Thus, we guess the degradation of the transport is significantly important at high-β (>2%). The magnetic axis also monotonically changes due to the increased β. At a high-β ($\langle\beta\rangle_{dia}$~3%), the Shafranov shift Δ/a is about 0.5. However, the MHD equilibrium does not collapse and it is sustained.

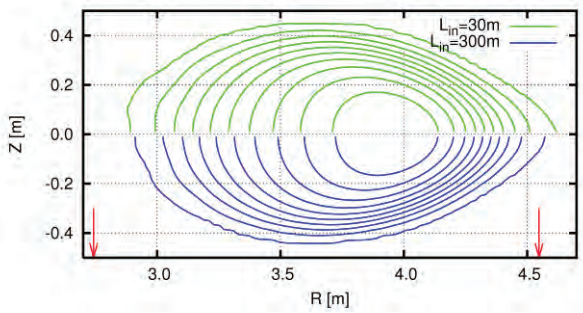

Fig.3 contour lines with different L_{in} (Z>0 and Z<0) are shown at the plane corresponding to fig. 1. Green lines indicate contour lines with L_{in}=30m and blue lines indicate L_{in}=300m. Lines in the edge are different.

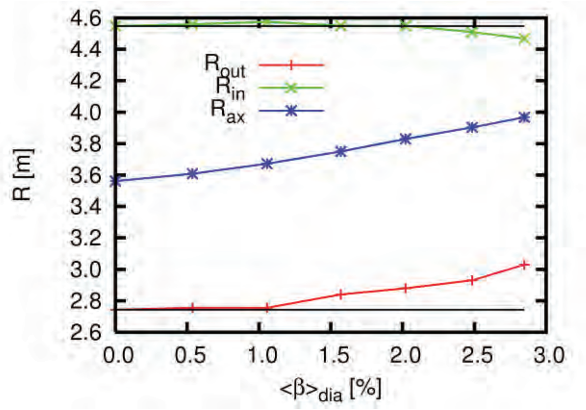

Fig.4 The change of positions of inward (red) and outward (green) LCFS on the plane corresponding to fig. 1is plotted as the function of $\langle\beta\rangle_{dia}$. The shift of the axis is also plotted for the reference (blue).

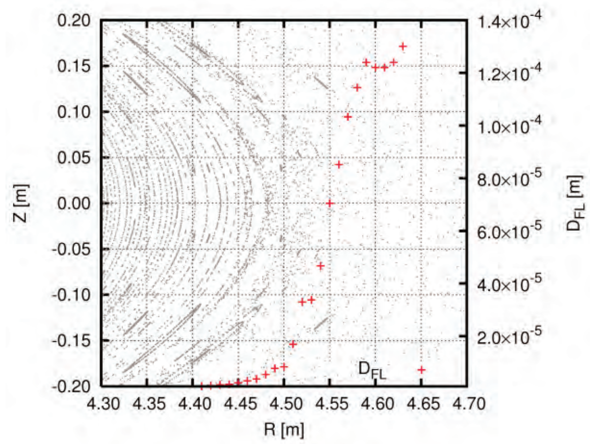

Fig.5 The radial profile of the diffusion coefficient D_{FL} is plotted as the function of R. The puncture map of field lines is also plotted as the reference.

3. Radial heat diffusivity due to stochastic field lines

The radial heat transport increases as it gains the stochasticity. In the collisionless plasma, where the electron mean free path λ_e is very long, the radial heat diffusivity χ_r due to '*only*' the stochasticity of magnetic field lines is given by

$$\chi_r = D_{FL} v_{th} \quad (2)$$

where v_{th} is the electron thermal velocity and D_{FL} is the diffusion coefficient of magnetic field lines and defined by

$$D_{FL} = \langle\Delta r^2\rangle / L_C \quad (3)$$

L_C is the correlation length to calculate the diffusion coefficient. Since χ_e is the contribution of only the stochasticity of magnetic field lines, the effective radial transport χ_{eff} is given by

$$\chi_{eff} = \chi_r + \chi_\perp. \quad (4)$$

On the other hand, in the collisional plasma, Krommes *et al*. identifies three different subregimes with decreasing collisionalty [4], which are fluid regime ($\tau_\perp < \tau_\parallel < \tau_k$), Kadomtsev-Ppgutse ($\tau_\parallel < \tau_\perp < \tau_k$) and Rechester-Rosenbluth ($\tau_\parallel < \tau_k < \tau_\perp$) regime. In typical parameters of LHD experiments, the collisionalty is Rechester-Rosenbluth (RR) regime in the region expected stochastically. The radial heat diffusivity due to the stochasticity of field lines is given by

$$\chi_r = D_{FL} \chi_\parallel / L_k \quad (5)$$

in the RR regime, where L_k is the Kolmogorov length. The Kolmogorov length L_k is a characteristic parameter to mesure the stochasticity [8]. Thus, equation 5 means the parallel contribution of the stochasticity is very important as well as the perpendicular contribution, because L_k plays the role of the correlation length along field lines.

In order to study χ_r, the diffusion coefficient D_{FL} is estimated at first. In fig. 5, the radial profile of the diffusion coefficient is plotted as the function of R. The puncture map of field lines is also plotted as the reference. The procedure to calculate the mean squared radial displacement $\langle\Delta r^2\rangle$ of field lines is following; (i) the distribution of the normalized toroidal flux $s = \Phi/\Phi_{edge}$ is given at first, where Φ is calculated by integrating inside contour lines at p=*const*. (ii) then, the normalized minor radius ρ is calculated and field lines are traced from distributed points on ρ=cont. plane. (iii) in the last, the mean squared displacement of $\langle\Delta\rho^2\rangle$ is calculated with tracing field lines and the distribution coefficient is given by

$$D_{FL} = {r_{eff}}^2 \langle\Delta\rho^2\rangle / L_C, \quad (6)$$

where r_{eff} is the effective minor radius. In fig. 5, D_{FL} is small in clear flux surfaces. However, in the stochastic region, the diffusion coefficient increases rapidly toward the outside of the torus. In the stochastic region, it is expected the perpendicular diffusion is very large.

The Kolmogorov length is also estimated to consider the parallel contribution of the stochasticity. In analyses of edge plasmas, especially the Dynamic Ergodic Divertor (DED), the Kolmogorov length is given by the quasi-linear form [4]. However, since the stochasticity in stellarator/heliotron is caused by pressure-induced perturbation, the number and amplitude of the mode of perturbations are unclear and the calculation of those values is difficult. Thus, we estimate the Kolmogorov length using a following definition,

$$d = d_0 \exp\left(\frac{l}{L_k}\right) \quad (7)$$

where, d is the circumference of small flux tube and l is the length of the flux tube. Using this definition, the impact finite-β effects on L_k is studied in vacuum configurations in LHD [7] and finite-β equilibria in Wendelstein 7-X [8]. In fig. 6, the profile of the inverse of the Kolmogorov

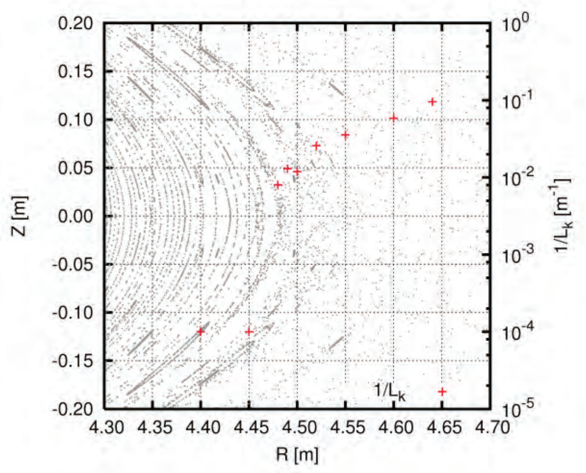

Fig.6 The radial profile of the inverse of the Kolmogorov length L_k is plotted as the function of R. The puncture map of field lines is also plotted as the reference.

length is plotted as the same plot corresponding to fig. 5. The inverse of the Kolmogorov length rapidly becomes long exponentially. This suggests the stochasticity of field lines increases with short length. In the outermost position to calculate L_k (R=4.64m), L_k is about 11m.

Finally, we estimate the radial heat diffusivity χ_r. At R=4.64m, D_{FL} and L_k are about 10^{-4} and 11, respectively. In fig. 2, the electron temperature is about 20~30eV. If T_e = 30eV and $n_e = 10^{19}$m^{-3}, χ_r ~25m^2/s. This is very large compared to χ_{eff} of the local transport analyses in the plasma core [9]. The comparison of the experiments and other estimation, which are obtained from the transport code for the edge plasma [10], is a future subject.

4. Summary

The stochasticity of magnetic field lines and effects on the transport properties due to finite-β effects are investigated. Flux surfaces keeps clear structure until the intermediate-β (<2%). However, for high-b, flux surfaces rapidly degrades due to the increased b. Characteristic properties, which are the diffusion coefficient of magnetic field lines and the Kolmogorov length are estimated. In a high-b equilibrium, stochastic properties appear in the edge. Using Rechester-Rosenbluth formulation, the radial heat diffusivity due to only the stochasticity of magnetic field lines. The estimated diffusivity is very large. It is necessary the comparison to the experiments and other estimation.

References

[1] A. B. Rechester and M. N. Rosenbluth, Phys. Rev. Lett. **40**, 38 (1978).

[2] T. H. Stix, Nucl. Fusion **18**, 353 (1978)

[3] B. B. Kadomtsev and O. P. Pogutse, in *Proceedings of the 7th International Conference, Insbruck 1978* (International Atomic Energy Agency, Vienna, 1979), Vol. 1, p.649

[4] J. A. Krommes, C. Oberman, and R. G. Kleva, J. Plasma Phys. **30**, 11 (1983).

[5] Y. Suzuki, N. Nakajima, K. Y. Watanabe, Y. Nakamura, and T. Hayashi, Nucl. Fusion **46**, L19 (2006)

[6] K. Y. Watanabe, Y. Suzuki *et al.*, Plasma Phys. Control. Fusion **49**, 605 (2007)

[7] T. Morisaki, *et al.*, J. Nucl. Matter. **313-316**, 548 (2003)

[8] E. Strumberger, Contrib. Plasma Phys. **38**, 106 (1998)

[9] H. Funaba, *et al.*, *in this conference*

[10] M. Kobayashi, *et al.*, *in this conference*

Proceedings of ITC/ISHW2007

Applications of HINT2 code to stellarator/heliotron

Yasuhiro Suzuki, N. Nakajima, J. Geiger[a], S. Yamamoto[b], K. Y. Watanabe, S. Sakakibara, A. Weller[a], A. Werner[a], M. Drevlak[a], Y. Nakamura[c], W. Kernbichler[d] V. V. Nemov[d] and J. Nührenberg[a]

National Institute for Fusion Science,322-6 Oroshi-cho, Toki 509-5292, Japan
[a] Max-Planck-Institut für Plasmaphysik, IPP-Euratom Assoc. Greifswald D-17491, Germany
[b] Kyoto University Pioneering Research Unit for Next Generation, Kyoto University, Gokasho Uji 611-0011, Japan
[c] Graduate School of Energy Science, Kyoto University, Gokasho, Uji 611-0011, Japan
[d] Association EURATOM-ÖAW, TU Graz, Graz 8010, Austria

To investigate the nature of three-dimensional (3D) MHD equilibrium and interpret the experiments, an equilibrium calculation code without the assumption of nested flux surfaces, HINT2 is developing. This code applied many stellarator/ heliotron devices and properties of MHD equilibrium were clarified. Some applications of HINT2 are shown and future plans are discussed.

Keywords: MHD, equilibrium, stochasticity, HINT2

1. Inroduction

The MHD equilibrium is the basis of both most theoretical considerations and physics interpretation of the experimental results. As a standard technique to calculate the 3D MHD equilibrium, inverse equilibrium solver VMEC [1], assuming the existence of perfect nested flux surfaces, is widely used. In such a technique, a flux coordinate system is directly constructed so as to satisfy the force balance or MHD equilibrium equation: $\vec{J} \times \vec{B} = \nabla p$. For the low-β equilibrium, if the vacuum magnetic field sustains clear flux surfaces, the standard technique is acceptable. However, by nature, the 3D MHD equilibrium may exhibit magnetic islands and stochastic regions in the plasma because of the absence of toroidal symmetry. For the high-β equilibrium, the degradation of flux surfaces by the finite β effect has to be determined, so that the standard technique based on the nested flux surfaces could not be directly applicable to them and other techniques are required such as HINT/HINT2 [2,3] and PIES [4] codes.

The HINT2 code is one of such solvers, where a relaxation method based on the dissipative MHD equations of the magnetic field. A special feature of HINT2 is the coordinates system, which uses a 'non-orthogonal rotating helical coordinate'. Since the helical coordinate system is Eulerian, HINT2 can treat magnetic islands and stochastic regions in plasmas.

The HINT2 code has been applied to the study of MHD equilibrium in many helical configurations, in order to clarify the properties inherent to 3D MHD equilibrium in various types of helical systems, which are LHD, W-7AS, W-7X, Heliotron-J. In this study, we show applications of HINT2 for high-β stellarator/heliotron researches.

author's e-mail: ysuzukil@LHD.nifs.ac.jp

2. Application of LHD

In order to understand how about HINT2 shows the finite-β MHD equilibrium, several quantities of a finite-β equilibrium with β~3.5% for an inward shifted (R_{ax}=3.6, γ=1.254, B_Q=100%) are shown in fig.1; (a) Puncture map of field lines, (b) rotational transform ι and distance along the magnetic field L_C, (c) a profile of the normalized plasma pressure p/p_0 (p_0 is the pressure at the magnetic axis), (d) contour lines of p/p_0, and (e) contour lines of square of the local residual force. Vertical lines in fig.1(a) and arrows in fig.1(b) and (c) indicate positions of the vacuum LCFS. In this finite β equilibrium, the initial pressure profile is set to $\mathrm{p} = \mathrm{p}_0(1-s)(1-s^4)$, where s is the normalized toroidal flux defined as $s = \Phi/\Phi_{edge}$. In fig.1(a), a region colored with blue corresponds to the region with clear flux surfaces and a region with red (green) corresponds to Puncture map of stochastic magnetic field lines started from 4.419 < R < 4.55 (R > 4.55). For β~3.5%, a considerable part in the plasma periphery is ergodized. The position of the LCFS is much inside the vacuum LCFS. However, from the comparison among fig.1(a), (c) and (d), it is understood that the plasma pressure spreads over the stochastic region and the pressure gradient $\nabla \mathrm{p}$ exists in the stochastic region.

This fact comes from the relaxation method of the pressure used in HINT2. The condition for a fixed $\boldsymbol{B}$ is written as

$$\mathrm{p}^{i+1} = \mathrm{p} = \frac{\int_{-L_{in}}^{L_{in}} \mathcal{F}\mathrm{p}^{i} \frac{dl}{B}}{\int_{-L_{in}}^{L_{in}} \frac{dl}{B}} \tag{1}$$

$$\mathrm{F} = \begin{cases} 1\text{:for } L_C \geq L_{in} \\ 0\text{:for } L_C < L_{in} \end{cases}$$

where i means a step number of iterations, L_C is the connection length of a magnetic field line starting each grid point (L_C is finite for open magnetic field lines), and L_{in} is the length along a magnetic field line followed from each grid point and prescribed as an input parameter. If the magnetic field line cannot be traced up to the prescribed value or the connection length L_C is shorter than L_{in} ($L_C < L_{in}$), the averaged plasma pressure is set to zero. That is, the distribution of relaxed plasma pressure depends on the relative magnitude between the connection length L_C and the parameter L_{in} prescribing the length of the field line trace. In other words, although HINT or HINT2 does not need the explicit boundary condition between plasma and the vacuum, the ratio of the connection length L_C to the length for pressure average L_{in} plays a role in controlling the distribution of the plasma pressure near the periphery. In fig.1, L_{in} is set to 30m, which corresponds to the length connecting the outside to the inside of the torus near the magnetic axis. It is seen from the comparison between fig.1(a) and (b) that the structure of magnetic field lines becomes stochastic outside the region with ι~1, because magnetic islands corresponding to some rational surfaces (i.e. n/m = 10/10, 10/9, 10/8, 10/7, 10/6, ...) overlap. Although these field lines are ergodized some magnetic field lines have long connection lengths L_C exceeding L_{in} as shown in fig.1(b), leading to the existence of the pressure and pressure gradient in the stochastic region. As mentioned above, in the case of HINT or HINT2 not assuming the existence of the nested flux surfaces, the relaxation method of the pressure profile mainly plays the role of determining the peripheral pressure profile instead of the plasma-vacuum boundary condition.

3. Application of Wendelstein 7-AS

The standard divertor configuration (SDC) for HDH-discharges has a boundary ι-value of the vacuum field of 5/9, where 9 natural islands form a clear separatrix. Additionally, correction coils located inside the vacuum vessel are used to increase the island size and keep a larger distance to the divertor plates. The corrugated separatrix boundary of such configurations can not be treated by free-boundary VMEC and thus

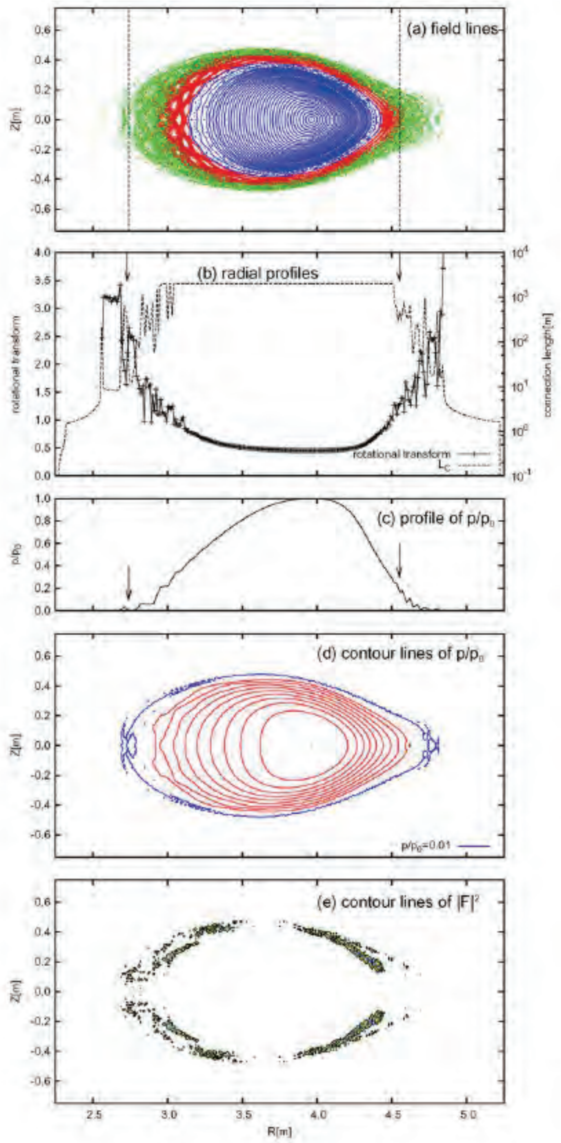

Fig.1 Various quantities of a finite-β equilibrium with β~3.5% on the horizontally elongated poloidal cross section in the inward-shifted LHD configuration: (a) Puncture map of magnetic field lines, (b) the rotational transform ι and the distance along the magnetic field L_C, (c) profile of the normalized plasma pressure, p/p_0, along the equatorial plane, (d) contour lines of p/p_0, and (e) contour lines of $|F|^2 = \left|\nabla p - \vec{J} \times \vec{B}\right|^2$.

equilibrium calculations were not available up to now. We compare the influence of different pressure profile forms on the configuration. The initial profiles used in this study are shown in Fig.2. They were choosen for variability and to have a zero pressure gradient at the boundary. Figure 3 shows how the initially flat ι-profile builds up shear by a central increase due to the Shafranov-shift. Thus, the 5/9-resonance appears in the ι-profile and islands develop whose position depends on the β and the underlying profile form. The broader profile (HDH-2) leads to larger islands closer to the boundary.

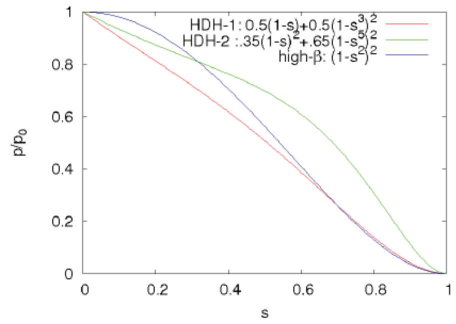

Fig2. Pressure profiles used in this study as the function of normalized toroidal flux *s*.

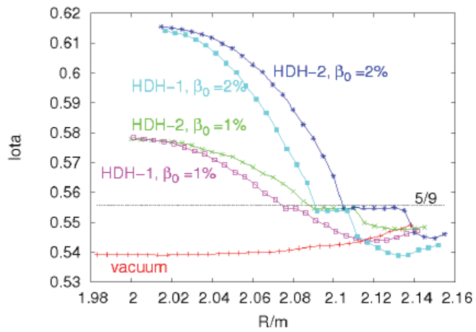

Fig.3 ι-profiles of the vacuum and finite-β calculations with different pressure profiles.

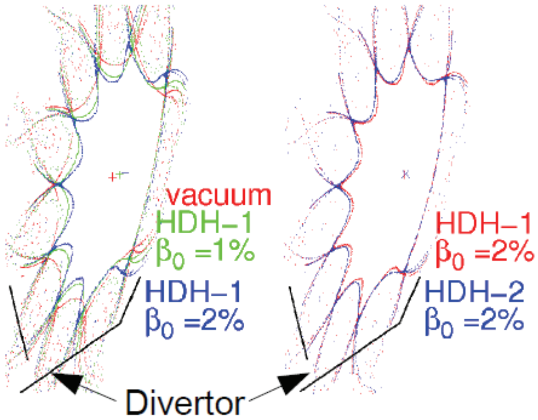

Fig.4 Axis position and separatrix depending on β (left) and pressure profiles (right).

The identations of the separatrix formed by the 5/9 boundary islands increase with β as seen in Fig.3. We also note that the x-points move poloidally which was already observed in the study performed with the old HINT-code [2]. Both effects are due to the poloidal expansion of the flux tubes due to the Shafranov-shift. Additionally, the island fans are moving radially on the target plates of the divertor which is also seen in the experiment. We note, that the separatrix structure seems not to depend strongly on the profile changes if the energy content is kept constant which is approximately fulfilled for the two profiles compared here.

4. Application of Wendelstein 7-X

Figure 4 shows the Large-Volume configuration for vacuum and for β~4.36%. Puncture plots of magnetic field lines are plotted at ϕ=0 plane. The profile of the rotational transform ι of this configuration has a low shear, clear flux surfaces in the core and clear 5/5 island structures in the edge region of the vacuum field. Thus, this configuration is sensitive to finite-β effects. The configuration had already been investigated with PIES [5]. Our study finds the following results; (i) the Shafranov shift and the change of ι is very small, (ii) the edge region is ergodized and the last closed flux surface (LCFS) retreats, that is, the plasma volume decreases.

In figs, green dots indicate the LCFS. The initial pressure distribution has been set to in this study, where *s* is the normalized toroidal flux Φ/Φ_{edge}.conforming to the profile used in Ref [5]. For b~4.36%, the edge region is ergodized and 5/5 islands evolve. Thus, the shape of the LCFS is changing according to the change of the edge region. However, clear flux surfaces are maintained inside 5/5 islands and other large resonances dot not appear.

We compare these results to those of PIES. In Ref [5], The LCFS of HINT2 is larger than the one of PIES. In both cases, 10/11 rational surfaces appear inside the LCFS. For PIES, the LCFS locates just outside 10/11 rational surface, whereas for HINT2, some more closed flux surfaces exist outside 10/11 rational surface. The LCFS of HINT2 locates outside 15/16 rational surface. In order to do a detailed comparison, the plasma volume inside the LCFS, V_{LCFS}, is studied. The volume V_{LCFS} for the vacuum is about 33.6m^3 (see Ref [5]). In the HINT2 calculation, V_{LCFS} is decreasing to ~ 31.6m^3, a volume reduction of ~ 6%. However, PIES sees a reduction of V_{LCFS} of ~ 21%, being much larger than the one of HINT2. This is a significant difference in the HINT2 and PIES results. There are some possibility explaining this difference. One is the numerical scheme of both codes. HINT2 is based on the relaxation method and calculations are done on a rectangular grid without the assumption of nested flux surfaces. On the other hand, PIES is an iterative solver on a quasi-flux coordinates system. This suggests differences in the effect of the finite pressure in the ergodic region. Another effect concerns the evolution of the pressure profile. Since HINT2 is based on the relaxation method, the pressure profile evolves during the relaxation process. The relaxed profile is almost the same as the initial profile but nevertheless slightly different. In order to confirm such effects more clearly, further studies and benchmarking are necessary.

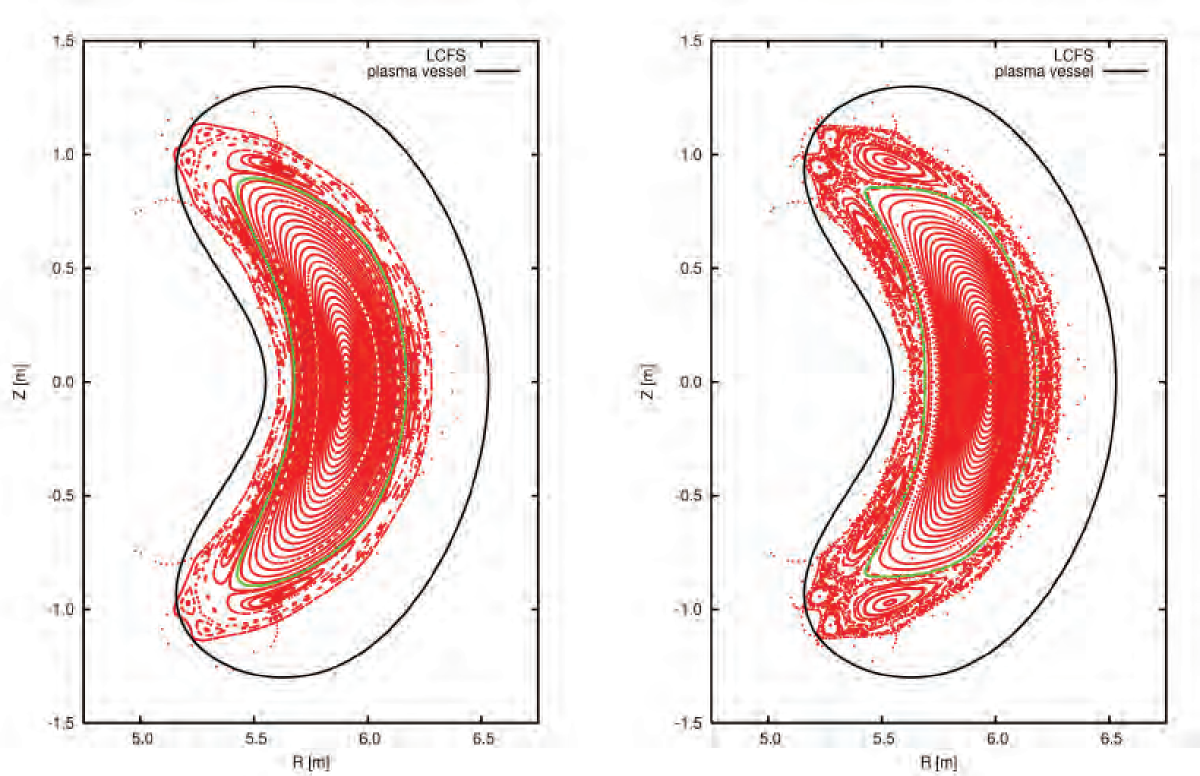

Fig.4 Puncture map of magnetic file lines for the vacuum field (left) and finite-β equilibrium (right).

5. Application of Heliotron J

Heliotron J device is an L=1/M=4 helical-axis heliotron with flat ι-profile and deep magnetic well for the vacuum field. Since the magnetic shear is low, the configuration is very sensitive to the pressure-induced perturbation and net toroidal currents. In experiments, the change of magnetic configuration due to the evolution of beam driven currents was observed and it is suggested the change of the magnetic configuration might be the trigger of a spontaneous transition [6]. In order to study effects of net toroidal currents to the configuration, the equilibrium including the net toroidal current is studied for the standard configuration. For the direction of toroidal currents is positive, the edge field structure is changed by appearing large magnetic islands. This affects the confinement through the plasma volume. However, for the negative direction, clear flux surfaces are kept by disappearing dangerous resonances.

6. Summary

HINT2 is useful and powerful tool to study 3D MHD equilibrium and it applies to many configurations.

Future plans of HINT2 are twofold. First direction is the further improvement of the code. One example is shown. A critical issue of stellarator/heliotron researches is the stochastic property of edge field lines due to the finite-β. Since HINT2 does not assume nested flux surfaces, the code can calculate the equilibrium with stochastic field. However, in the stochastic region, the plasma pressure is the flux surface quantity and the radial force is not balanced. In order to treat the plasma pressure in the stochastic region consistently, the anisotropic pressure is necessary. Second direction is the application to interpret the experiments.

References

[1] S. P. Hirshman, et al., Phys. Fluids **26** (1983) 3553
[2] K. Hatafuji, et al., J. Comput. Phys **81** (1989) 169
[3] Y. Suzuki, et al., Nucl. Fusion **46** (2006) L19
[4] A. Reiman, et al., Comput. Phys. Commun. **43** (1986) 157
[5] M. Drevlak, et al., Nucl. Fusion **45** (2005) 731
[6] T. Mizuuchi et al., Nucl. Fusion **47** (2007) 395

Proceedings of ITC/ISHW2007

The response of toroidal plasmas to error fields

Jong-kyu Park[1)], Allen H. Boozer[2)] and Jonathan E. Menard[1)]

[1)]*Princeton Plasma Physics Laboratory, Princeton, NJ 08543, U.S.A.*

[2)]*Department of Applied Physics and Applied Mathematics, Columbia University, NY 10027, U.S.A.*

October 14, 2007

The response of toroidal plasmas to three-dimensional magnetic error fields is studied by using Ideal Perturbed Equilibrium Code (IPEC). Since the toroidal plasmas are highly sensitive to small error fields, the perturbation theory is efficient and useful to describe the equilibrium $\nabla P = \boldsymbol{J} \times \boldsymbol{B}$ in the presence of error fields. The perturbed force balance equation in ideal MagnetoHydroDynamics (MHD) is solved by augmenting a stability code and by constructing the interface between plasma and external system. In an ideally perturbed equilibrium, a shielding current arises on a rational surface to prevent an island from opening. When error fields reach a critical magnitude, the shielding current will be dissipated and an island will open. This effect of error fields can be greatly mitigated by adjusting currents in auxiliary coils to reduce the shielding current, or equivalently the resonant field. From the coupling between the resonant field and error fields, the effects of various error fields on toroidal plasmas were studied. The most important external field is almost always localized on the outboard midplane, which gives an important implication to the study and control of the response of toroidal plasmas to error fields.

Keywords: toroidal plasma, MHD, perturbed equilibrium, error field, magnetic island

The magnetically confined toroidal plasmas, such as tokamaks and stellarators, are highly sensitive to externally driven magnetic perturbations. This sensitivity implies that the response of plasmas to small magnetic perturbations is a critical issue in design and control of equilibrium [1, 2, 3, 4, 5]. The small magnetic perturbations always exist in toroidal devices due to error fields, such as, imperfections of primary magnets and other conducting components. When an external perturbation occurs, plasma responds to it and relaxes to a new equilibrium state. Since the perturbations are in practice very small compared with the field of the original equilibrium, the perturbation theory is effective to describe the response of plasmas.

The perturbed force balance equation is given by

$$\boldsymbol{f}(\boldsymbol{\xi}) = -\nabla\delta P + \boldsymbol{J}\times\delta\boldsymbol{B} + \delta\boldsymbol{J}\times\boldsymbol{B} = \boldsymbol{0} \tag{1}$$

in ideal MagnetoHydroDynamics (MHD). Using Maxwell relations and adiabatic plasma response, $\delta\boldsymbol{J} = (\nabla\times\delta\boldsymbol{B})/\mu_0$, $\delta\boldsymbol{B} = \nabla\times(\boldsymbol{\xi}\times\boldsymbol{B})$ and $\delta P = -\boldsymbol{\xi}\cdot\nabla P - \gamma P(\nabla\cdot\boldsymbol{\xi})$, the force balance equation becomes a vector differential equation for the plasma displacement $\boldsymbol{\xi}$. Assuming that the plasma conserves its two independent profiles, rotational transform $\iota(\psi)$ and pressure $p(\psi)$, then the same equation can be derived from the theory of ideal, linear MHD stability. Through minimization of a perturbed potential energy $\delta W = -1/2\int dx^3\boldsymbol{\xi}\cdot\boldsymbol{f}(\boldsymbol{\xi})$, the exact same equation for $\boldsymbol{\xi}$ can be obtained. Therefore, an existing code in the stability analysis can be used to solve the problem of perturbed equilibria. Only the interface between plasma and external system is required to obtain an perturbed equilibrium given an external error field.

The Ideal Perturbed Equilibrium Code (IPEC) [6] modifies and augments the DCON ideal MHD stability code [7]. For a given axisymmetric equilibrium, the use of DCON gives a set of M plasma displacements $\boldsymbol{\xi}_i(\psi,\theta,\varphi)$, which is the set of M ideal MHD eigenmodes for a given toroidal harmonic number n, where $1 \le i \le M$ and M is the number of poloidal harmonics retained. Here (ψ,θ,φ) are magnetic coordinates which are straight on the field line. Each of these displacements $\boldsymbol{\xi}_i$ is associated with a certain deformation of the plasma boundary, $\boldsymbol{\xi}_i\cdot\boldsymbol{n}_b \equiv (\boldsymbol{\xi}_i\cdot\boldsymbol{n})(\psi_b,\theta,\varphi)$, where $\boldsymbol{\xi}_i$ is evaluated on the unperturbed plasma boundary at $\psi=\psi_b$ and $\boldsymbol{n}_b$ is the normal to the unperturbed plasma boundary. Each of these M displacements of the plasma boundary $\boldsymbol{\xi}_i\cdot\boldsymbol{n}_b$ defines a perturbed equilibrium if an external magnetic field produces a required force to support it. That is, the set of M ideal MHD eigenmodes found by DCON defines a set of M neighboring perturbed equilibria. Each of the neighboring equilibria is supported by an external magnetic field and has the same profiles of $\iota(\psi)$ and $p(\psi)$ as the unperturbed equilibrium; only the shape of the plasma has been changed.

A plasma displacement determines a magnetic perturbation $\delta\boldsymbol{B} = \nabla\times(\boldsymbol{\xi}\times\boldsymbol{B})$, so IPEC uses the displacement of the plasma boundary $\boldsymbol{\xi}\cdot\boldsymbol{n}_b$ to determine a part of the perturbed magnetic field that is normal to the unperturbed plasma boundary, $\delta\boldsymbol{B}\cdot\boldsymbol{n}_b$, and a part that is tangential to the plasma boundary, $\boldsymbol{n}_b\times\delta\boldsymbol{B}^{(p)}$. Since the normal field $\delta\boldsymbol{B}\cdot\boldsymbol{n}_b$ is continuous across the plasma boundary and the control surface, $\delta\boldsymbol{B}\cdot\boldsymbol{n}_b$ then gives a unique vacuum field

author's e-mail: jpark@pppl.gov

outside the plasma, $\delta \boldsymbol{B}^{(vo)}$, that vanishes at infinity. The difference between the tangential field infinitesimally outside the control surface $\boldsymbol{n}_b \times \delta \boldsymbol{B}^{(vo)}$ and the tangential field on the plasma side of the control surface $\boldsymbol{n}_b \times \delta \boldsymbol{B}^{(p)}$ determines an external surface current on the control surface, $\mu_0 \boldsymbol{K}^x = \boldsymbol{n}_b \times \delta \boldsymbol{B}^{(vo)} - \boldsymbol{n}_b \times \delta \boldsymbol{B}^{(p)}$. Once $\boldsymbol{K}^x$ is known, the externally produced normal magnetic field $\delta \boldsymbol{B}^x \cdot \boldsymbol{n}_b$ can be found by $\nabla \times \delta \boldsymbol{B}^x = \mu_0 \boldsymbol{J}^x$ in vacuum. Note that the *external* field $\delta \boldsymbol{B}^x$ designated by superscript x is a vacuum field without plasma response, compared with the *total field* $\delta \boldsymbol{B}$.

Each of the M neighboring equilibria calculated by DCON has a unique distribution of the external normal magnetic field $\delta \boldsymbol{B}_i^x \cdot \boldsymbol{n}_b$, where $1 \le i \le M$, that must be produced by currents outside the plasma to sustain that equilibrium. If an external magnetic perturbation, such as that due to a magnetic field error $\delta \boldsymbol{B}^x \cdot \boldsymbol{n}_b$, is specified on the unperturbed plasma boundary, this perturbation can be expanded as $\delta \boldsymbol{B}^x \cdot \boldsymbol{n}_b = \sum_{i=1}^{M} c_i \delta \boldsymbol{B}_i^x \cdot \boldsymbol{n}_b$, with expansion coefficients c_i. If this is done, the plasma displacement that gives the perturbed equilibrium produced by the field error is $\boldsymbol{\xi}(\psi, \theta, \varphi) = \sum_{i=1}^{M} c_i \boldsymbol{\xi}_i(\psi, \theta, \varphi)$. This is the method used by IPEC to find the perturbed equilibrium associated with a given magnetic field error [6].

The normal total magnetic fields of the M neighboring equilibria can be represented by

$$(\delta \boldsymbol{B} \cdot \boldsymbol{n}_b)(\theta, \varphi) = Re\left(\sum_m \Phi_m w(\theta) e^{i(m\theta - n\varphi)}\right), \tag{2}$$

in Fourier space, where the weight function $w(\theta) = 1/(\mathcal{J}(\theta)|\nabla\psi|(\theta))$ with the Jacobian $\mathcal{J}(\theta)$ is used for an orthogonal basis, by the definition of $\oint w f_m f_{m'} da = \delta_{mm'}$ on the boundary surface, with $f_m = e^{i(m\theta - n\varphi)}$.

The jump in the tangential field across the control surface just outside the plasma gives a surface current $\boldsymbol{J} = \boldsymbol{K}\delta(\psi - \psi_b)$. The surface current can also be expressed as $\boldsymbol{K} = \nabla\kappa(\theta, \varphi) \times \nabla\psi$ with a surface current potential $\kappa(\theta, \varphi)$. The potential $\kappa(\theta, \varphi)$ can be used for representing the surface current $\boldsymbol{K}$ by

$$\kappa(\theta, \varphi) = Re\left(\sum_m \mathcal{I}_m e^{i(m\theta - n\varphi)}\right) \tag{3}$$

with the vector $\mathcal{I}$ having units of current. Combining the total fluxes $\boldsymbol{\Phi}_i$ and external currents $\mathcal{I}_i^x$ of the M neighboring equilibria, one can obtain a plasma inductance matrix $\boldsymbol{\Lambda}$ on the Fourier space, where the M poloidal harmonics are retained. $\boldsymbol{\Lambda}$ gives the relation between an total flux and an external current by $\boldsymbol{\Phi} = \boldsymbol{\Lambda} \cdot \mathcal{I}^x$. Similarly, the external normal magnetic perturbation $\delta \boldsymbol{B}^x \cdot \boldsymbol{n}_b$ producing the surface current $\boldsymbol{K}^x$ can be expanded and related to the current by $\boldsymbol{\Phi}^x = \boldsymbol{L} \cdot \mathcal{I}^x$, where $\boldsymbol{L}$ is a surface inductance matrix since it depends only on the shape of the boundary surface.

The linear relation between an total flux $\boldsymbol{\Phi}$ and an external flux $\boldsymbol{\Phi}^x$ can then be written as

$$\boldsymbol{\Phi} = \boldsymbol{P} \cdot \boldsymbol{\Phi}^x \tag{4}$$

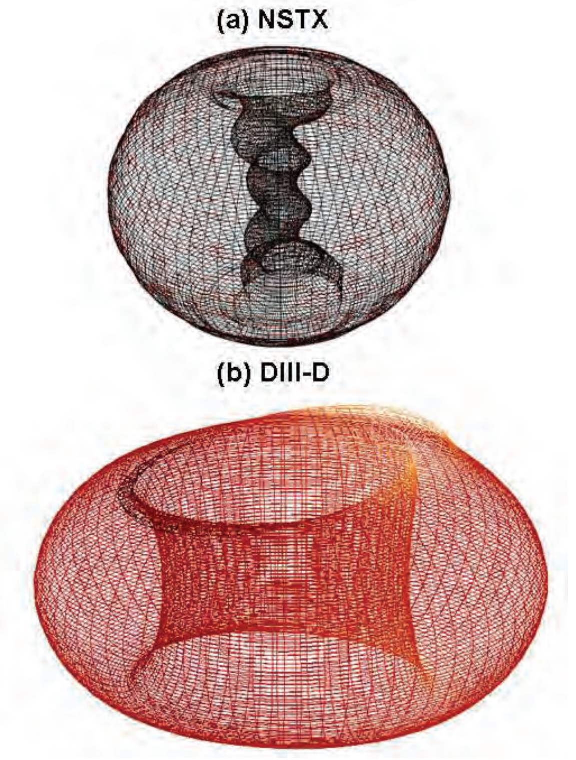

Fig. 1 The deformed plasma boundary of typical (a) NSTX (b) DIII-D tokamak plasmas due to each intrinsic error field. The scale is arbitrary.

with a permeability matrix $\boldsymbol{P} = \boldsymbol{\Lambda} \cdot \boldsymbol{L}^{-1}$. If a magnetic field error $\boldsymbol{\Phi}^x$ is specified on the boundary, one can expand it by $\boldsymbol{\Phi}^x = \sum_{i=1}^{M} c_i \boldsymbol{\Phi}_i^x = \sum_{i=1}^{M} c_i \boldsymbol{P}^{-1} \cdot \boldsymbol{\Phi}_i$, or equivalently by $\boldsymbol{\Phi} = \boldsymbol{P} \cdot \boldsymbol{\Phi}^x = \sum_{i=1}^{M} c_i \boldsymbol{\Phi}_i$ to obtain the perturbed equilibrium by $\boldsymbol{\xi}(\psi, \theta, \varphi) = \sum_{i=1}^{M} c_i \boldsymbol{\xi}_i(\psi, \theta, \varphi)$. Each actual flux $\boldsymbol{\Phi}_i$ is associated with a plasma displacement $\boldsymbol{\xi}_i$ through Eq. (2) and $\delta \boldsymbol{B} = \nabla \times (\boldsymbol{\xi} \times \boldsymbol{B})$. This is how IPEC constructs the interface and solve the perturbed equilibrium from a given error field [6]. Fig. 1 shows the computational examples, deformed plasma boundary of typical (a) NSTX [12] (b) DIII-D [13] plasmas due to each intrinsic error field.

An important consequence when plasma is ideally perturbed is a shielding current on a rational surface $\iota = n/m$ to prevent a magnetic island from opening. This indicates mathematically that the normal component of the resonant field has to be vanished on the rational surface, that is, $(\delta \boldsymbol{B} \cdot \boldsymbol{\nabla}\psi)_{mn} = 0$. This constraint in ideal MHD enforces inner boundary condition and discontinuous tangential field across the rational surface. The jump of tangential field is [8]

$$\Delta_{mn} \equiv \left[\frac{\partial}{\partial\psi} \frac{\delta \boldsymbol{B} \cdot \boldsymbol{\nabla}\psi}{\boldsymbol{B} \cdot \boldsymbol{\nabla}\varphi}\right]_{mn} \tag{5}$$

The shielding current $\boldsymbol{j}_s$ is related to the jump as

$$\boldsymbol{j}_s = \frac{\Delta_{mn} i e^{i(m\theta - n\varphi)}}{\mu_0 m (\oint dS\, B^2/|\boldsymbol{\nabla}\psi|^3)} \delta(\psi - \psi_{mn}) \boldsymbol{B}, \tag{6}$$

where ψ is a toroidal flux. A total resonant field driving magnetic islands, $(\delta\boldsymbol{B}\cdot\boldsymbol{n})_{mn}$, can be defined by the field produced by the shielding current, $\nabla\times\delta\boldsymbol{B}=\mu_0\boldsymbol{j}_s$. Note that $\boldsymbol{n}$ is normal to a magnetic surface at $\iota=n/m$, differently from $\boldsymbol{n}_b$ normal to the plasma boundary.

The sustainment of the shielding current is important to improve plasma performance since otherwise an island would open and destruct flux surfaces. This happens when error fields are larger than a critical magnitude. The importance of the shielding current, or equivalently the resonant field has been recently verified in tokamak experiments of locked modes [9]. The use of IPEC has shown that the external field driving the resonant field $(\delta\boldsymbol{B}\cdot\boldsymbol{n})_{mn}$ can be well described through perturbed equilibria.

A long standing supposition, which was supported by cylindrical theory [10, 11], is that the total resonant field driving islands, $(\delta\boldsymbol{B}\cdot\boldsymbol{n})_{mn}$, is proportional to the resonant component of the external field, namely, the external resonant field, $(\delta\boldsymbol{B}^x\cdot\boldsymbol{n})_{mn}$. When this supposition was applied to mode locking experiments in DIII-D and NSTX, the results were paradoxical. When the control coil currents were optimized empirically, the external resonant field was often increased–not decreased as the standard supposition required. However, the IPEC calculation has shown that the total resonant fields were indeed decreased consistently when the control coil currents were optimized.

The failure in the previous method is due to the strong coupling between the resonant field $(\delta\boldsymbol{B}\cdot\boldsymbol{n})_{mn}$ and the external field $(\delta\boldsymbol{B}^x\cdot\boldsymbol{n}_b)$ specified here on the plasma boundary. The poloidal harmonic coupling is very broad and shifted to higher poloidal harmonics than expected, as shown in Fig. 2 [6, 9].

The most important external field driving the total resonant field has to be defined through the coupling, that is, by the first singular vector when decomposing the coupling matrix $\boldsymbol{C}$ between the total resonant field $(\delta\boldsymbol{B}\cdot\boldsymbol{n})_{mn}$ and the external field on the boundary $(\delta\boldsymbol{B}^x\cdot\boldsymbol{n}_b)_{mn}$. If one defines $\mathcal{B}$ with the total resonant field on R rational surfaces, this is written as

$$\mathcal{B}=\boldsymbol{C}\cdot\boldsymbol{\Phi}^x. \qquad (7)$$

The i^{th} important mode can be also defined by the i^{th} singular mode in the SVD (Singular Value Decomposition) analysis of $\boldsymbol{C}$. Note again that each i^{th} important mode represents the external field on the plasma boundary, not the total field including plasma response.

A practical way to describe the important modes is to give the amplitude of the external field $(\delta\boldsymbol{B}^x\cdot\boldsymbol{n}_b)$ relative to the plasma boundary in real space. If the most important mode, or the first mode is highly dependent on equilibria when it is mapped in real space, the correction of the mode will be very difficult in practice. Fig. 3 shows the most important external field for $n=1$ in the (a) DIII-D and (b) NSTX. The three-dimensional field can be constructed as $(\delta\boldsymbol{B}^x\cdot\boldsymbol{n}_b)(\theta,\phi)=C(\theta)cos(n\phi)+S(\theta)sin(n\phi)$, where ϕ is the polar toroidal angle. This has to be distinguished from a magnetic toroidal angle, φ.

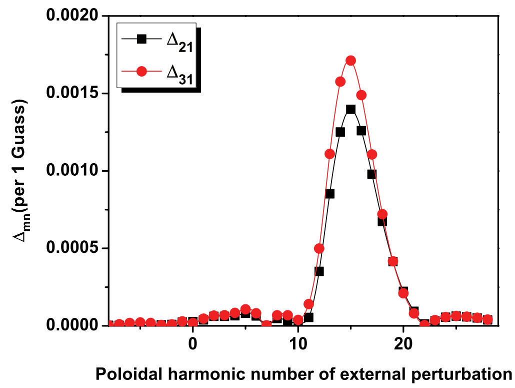

Fig. 2 (a) The typical poloidal harmonic coupling spectrum between the Fourier components of the external error field on the plasma boundary $(\delta\boldsymbol{B}^x\cdot\boldsymbol{n}_b)_{mn}$ and the total resonant field, which is here measured by Δ_{21} and Δ_{31}.

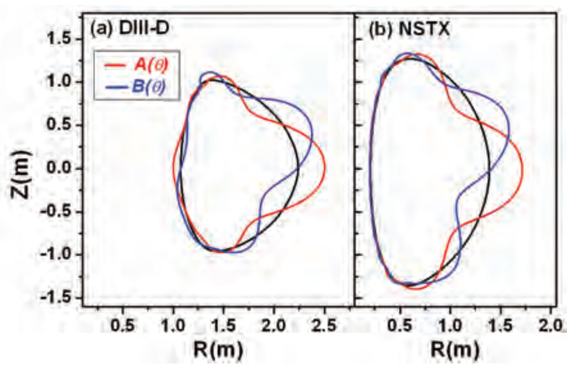

Fig. 3 The most important external field driving the total resonant field on rational surfaces, in the (a) DIII-D and (b) NSTX. The three dimensional distribution can be constructed by $\delta\boldsymbol{B}^x\cdot\boldsymbol{n}_b=A(\theta)cos(\phi)+B(\theta)sin(\phi)$ relative to the plasma boundary (black line).

An important implication is that the most important external field is localized on the outboard midplane. The localizations are very robust and almost regardless of various characteristics in equilibria [9]. For example, Fig. 4 (a) shows very little dependency of the localization on the plasma density, which is represented by the normalized beta, $\beta_n=\langle\beta_t\rangle I_p/aB_{t0}$, where β_t is the toroidal β, I_p is the plasma current, a is the minor radius and B_{t0} is the toroidal magnetic field at the magnetic axis. This explains well that the error-field control coils located on the outboard midplane could effectively mitigate the effect of error fields despite the limitation of poloidal harmonic controllability. The mitigation of error fields, therefore, can be optimized by developing the method to null the most important external field by designing proper control coils.

The detailed information of the coupling between the external field and the total resonant field can be used to many different purposes. For instance, one can find the external field only driving one magnetic island on a partic-

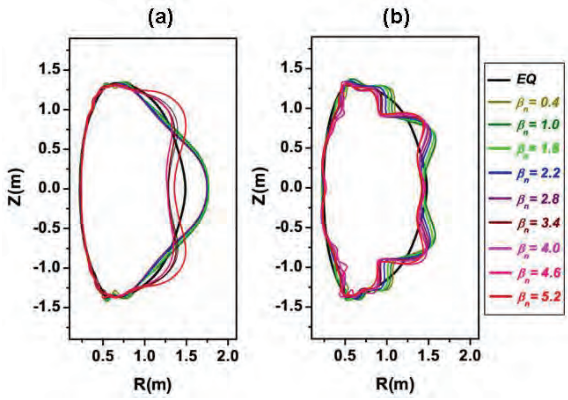

Fig. 4 (a) The most important $n = 1$ external field and (b) the $n = 1$ external field driving only $\iota = 1/2$ as a function of β_n in NSTX. The external fields are represented relatively to the plasma boundary as in Fig. 3.

ular rational surface, as shown in Fig. 4 (b). The external field beyond the most important part is typically not localized and may be too difficult to make relevant corrections in reality. Nonetheless, the specific pattern in the external field can be used to suppress islands in a particular region, for instance, the edge region. This is another important application of IPEC to the suppression of Edge Localized Mode (ELM), by applying intentional perturbations [14] in tokamaks.

[1] T. C. Hender and R. Fitzpatrick and A. W. Morris and P. G. Carolan and R. D. Durst and T. Eddlington and J. Ferreira and S. J. Fielding and P. S. Haynes and J. Hugill and I. J. Jenkins and R. J. La Haye and B. J. Parham and D. C. Robinson and T. N. Todd and M. Valovic and G. Vayakis, Nucl. Fusion, **32**, 2091 (1992)

[2] R. J. La Haye and R. Fitzpatrick and T. C. Hender and A. W. Morris and J. T. Scoville and T. N. Todd, Phys. Fluids B, **4**, 2098 (1992)

[3] R. J. Buttery and M. D. Benedetti and D. A. Gates and Y. Gribov and T. C. Hender and R. J. La Haye and P. Leahy and J. A. Leuer and A. W. Morris and A. Santagiustina and J. T. Scoville and B.J.D. Tubbing and JET Team and COMPASS-D Research Team and DIII-D Team, Nucl. Fusion, **39**, 1827(1999)

[4] J. T. Scoville and R. J. La Haye Nucl. Fusion, **43**, 250 (2003)

[5] A. H. Boozer, Rhys. Rev. Lett., **86**, 5059 (2001)

[6] J.-K. Park and A. H. Boozer and A. H. Glasser, Phys. Plasmas, **14**, 052110 (2007)

[7] A. H. Glasser and M. S. Chance, Bull. Am. Phys. Soc., **42**, 1848 (1997)

[8] A. H. Boozer and C. Nührenberg", Phys. plasmas, **13**, 102501 (2006)

[9] J.-K. Park and Michael J. Schaffer and Jonathan E. Menard and Allen H. Boozer, to be published in Phys. Rev. Lett. (2007)

[10] R. Fitzpatrick, Nucl. Fusion, **33**, 1049 (1993)

[11] R. Fitzpatrick, Phys. Plasmas, **5**, 3325 (1998)

[12] J. Spitzer and M. Ono and M. Peng and D. Bashore and T. Bigelow and A. Brooks and J. Chrzanowski and H. M. Fan and P. Heitzenroeder and T. Jarboe, Fusion Technology, **30**, 1337 (1996)

[13] J. L. Luxon and L. G. Davis, Fusion Technology, **8**, 441 (1985)

[14] T. E. Evans and R. A. Moyer and P. R. Thomas and J. G. Watkins and T. H. Osborne and J. A. Boedo and E. J. Doyle and M. E. Fenstermacher and K. H. Finken and R. J. Groebner and M. Groth and J. H. Harris and R. J. LaHaye and C. J. Lasnier and S. Masuzaki and N. Ohyabu and D. G. Pretty and T. L. Rhodes and H. Reimerdes and D. L. Rudakov and M. J. Schaffer and G. Wang and L. Zeng, Phys. Rev. Lett.,**92**, 235003 (2004)

Proceedings of ITC/ISHW2007

Study of toroidal current effect on rotational transform profile by MHD activity measurement in Heliotron J

G. Motojima, S. Yamamoto[a], H. Okada[b], S. Sakakibara[c], K. Y. Watanabe[c], K. Nagasaki[b], Y. Suzuki[c], T. Mizuuchi[b], S. Kobayashi[b], B. D. Blackwell[d], Y. Nakamura, K. Kondo, K. Hanatani[b], H. Arimoto, S. Watanabe and F. Sano[b]

Graduate School of Energy Science, Kyoto University, Gokasho, Uji 611-0011, Japan
[a]Kyoto University Pioneering Research Unit for Next Generation, Gokasho, Uji 611-0011, Japan
[b]Institute of Advanced Energy, Kyoto University, Gokasho, Uji 611-0011, Japan
[c]National Institute for Fusion Science, 322-6 Oroshi-cho, Toki 509-5292, Japan
[d]Plasma Research Laboratory, Research School of Physical Sciences and Engineering, The Australian National University, Canberra, Australia

Effect of toroidal current on rotational transform has been investigated in Heliotron J by measuring magnetohydrodynamic (MHD) activities at two configurations with rotational transform ($\iota/2\pi$) close to 0.5. The resonant mode has been observed in ECH + co-NBI plasma in the configuration with $\iota/2\pi = 0.48$ at $\rho = 0.7$. This result shows that the rotational transform is probably increased due to the toroidal current. The location of the rational surface is determined at $\rho = 0.8$-0.9 by soft X-ray (SX) fluctuations related to the MHD mode. Equilibrium calculation considering the toroidal current shows that the increase of the rotational transform by the toroidal current is consistent with experimental results. The resonant mode structure has been investigated also in ECH + counter-NBI plasma at $\iota/2\pi = 0.50$ configuration, and the location of the rational surface determined by SX signals is not significantly changed compared to vacuum condition, suggesting that the change in the rotational transform profile by the toroidal current is weak due to the balance between bootstrap current and counter-flowing NB current.

Keywords: Bootstrap current, NB current, MHD instability, magnetic fluctuation, Heliotron J

1. Introduction

Suppression of magnetohydrodynamic (MHD) instability is one of the key issues for realization of high performance plasma. In helical plasmas, stabilization of pressure-driven modes such as ideal and/or resistive interchange modes is a critical issue for high-β plasma. Heliotron J is a low magnetic shear helical-axis heliotron device with a magnetic well by which, it is considered that MHD instability is expected to be avoided or stabilized [1]. However, MHD instabilities have been experimentally observed in electron cyclotron heating (ECH) and/or neutral beam injection (NBI) heated plasmas of Heliotron J [2]. The m/n = 2/1 MHD instability exhibiting intense magnetic fluctuations and low frequency (f < 10 kHz) has been observed in the plasmas with the rotational transform close to 0.5, where m and n are the poloidal and toroidal mode numbers, respectively. The equilibrium configuration is changed by a toroidal current and a plasma pressure, and a low order resonant rational surface can appear in the plasma. Toroidal currents such as bootstrap current, electron cyclotron (EC) current and neutral beam (NB) current have been examined in Heliotron J [3,4]. They can modify MHD equilibrium and stability due to the change in rotational transform ($\iota/2\pi$) profile. The effects of the toroidal current on MHD modes have been investigated in CHS [5] and W7-AS [6]. Recent experiment also indicates that the modification of rotational transform by the toroidal current may induce a spontaneous transition in Heliotron J [7]. The objective of this paper is to study the effect of toroidal current on the rotational transform by measuring MHD activities in Heliotron J.

author's e-mail:gen@center.iae.kyoto-u.ac.jp

2. Experimental setup

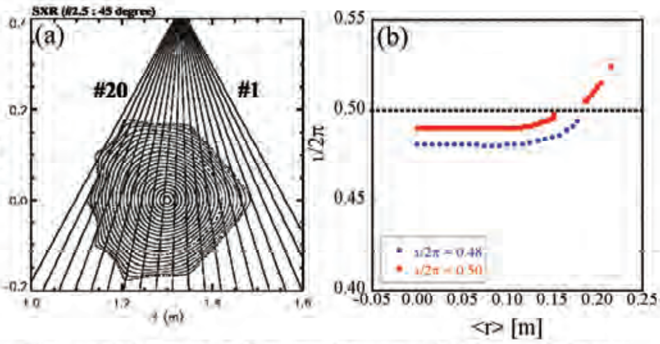

Fig. 1 (a) Magnetic flux surface and 20 lines of sight in SX array are shown. Radial profiles of rotational transform in vacuum condition are shown in (b).

Heliotron J is a medium-sized plasma experimental device. The device parameters are as follows; its plasma major radius R is 1.2 m, its averaged minor radius a is 0.1-0.2 m, its rotational transform $\iota/2\pi$ is 0.3-0.8, and its maximum magnetic field strength on the magnetic axis, B_0 is 1.5 T. The coil system is composed of an $L = 1$, $M = 4$ helical coil, two types of toroidal coils A and B, and three pairs of vertical coils. Here, L is the pole number of the helical coil and M is the pitch number of the field along the toroidal direction. A wide variety of magnetic configurations can be produced on the Heliotron J by varying the current ratios in various coils. In this study, two configurations with the rotational transform close to 0.5 were selected, namely, $\iota/2\pi = 0.48$ and 0.50 at $\rho = 0.7$ under vacuum condition while keeping magnetic field components almost constant. In Fig. 1(a), the poloidal cross-section for the $\iota/2\pi = 0.48$ configuration is shown. Figure 1(b) shows the rotational transform profiles in the vacuum condition. In this experimental condition, NB was injected to the ECH plasma (ECH+NBI plasma). Here, NB was injected to co-direction and counter-direction for negative (counter-clockwise) magnetic field and for positive (clockwise) magnetic field, respectively. The total toroidal current is measured by Rogowski coils wound on the inner wall of the poloidal cross-sections at two different toroidal angles. In order to determine the geometric structure of magnetic fluctuations accurately, 4 mirnov coils are installed in the toroidal direction and 14 mirnov coils are set poloidally on one poloidal cross section. The magnetic probes have the frequency response of up to 500 kHz. A soft X-ray (SX) diode has 20 vertical viewing chords. Figure 1(a) also shows lines of sight of the SX diode.

3. Experimental results

3.1 Separation of bootstrap current and NB current

In ECH + NBI plasmas, the toroidal current is composed of the bootstrap current and the NB current. These currents can be evaluated by comparing the experimental results obtained for positive and negative magnetic fields using the following equations, since the flow direction of the bootstrap current, which depends on **B**×∇B drift, is reversed by reversing the magnetic field, while that of the NB current associated with the injected direction is not. Under the experimental conditions discussed in this paper, the effect of the EC current is weak.

$$I_{BS} = \frac{I_p^{cw} - I_p^{ccw}}{2},$$

$$I_{NB} = \frac{I_p^{cw} + I_p^{ccw}}{2},$$

where I_p^{cw} and I_p^{ccw} are the toroidal currents in the positive and negative magnetic field experiments, respectively. Here, we have assumed that each toroidal current component of positive magnetic field is similar to that of negative magnetic field. We confirmed the stored energy between positive and negative magnetic field was almost identical. However, we should note that absorption rate of NB is affected by the direction of magnetic field due to the change in loss rate of high energy ions. Figure 2 shows the bootstrap current and the NB current roughly evaluated. The bootstrap current is 1.5 ± 0.2 kA at $\iota/2\pi = 0.48$ case and 1.8 ± 0.3 kA at $\iota/2\pi = 0.50$ case. While, the

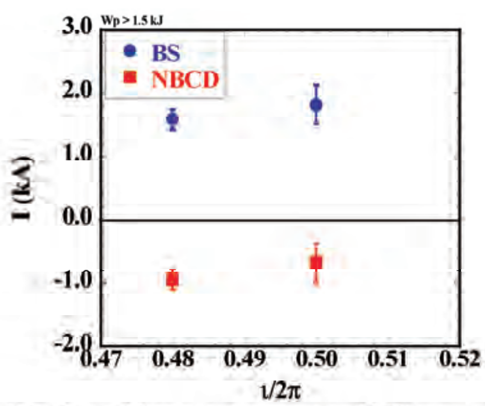

Fig. 2 Estimated bootstrap current and NB current.

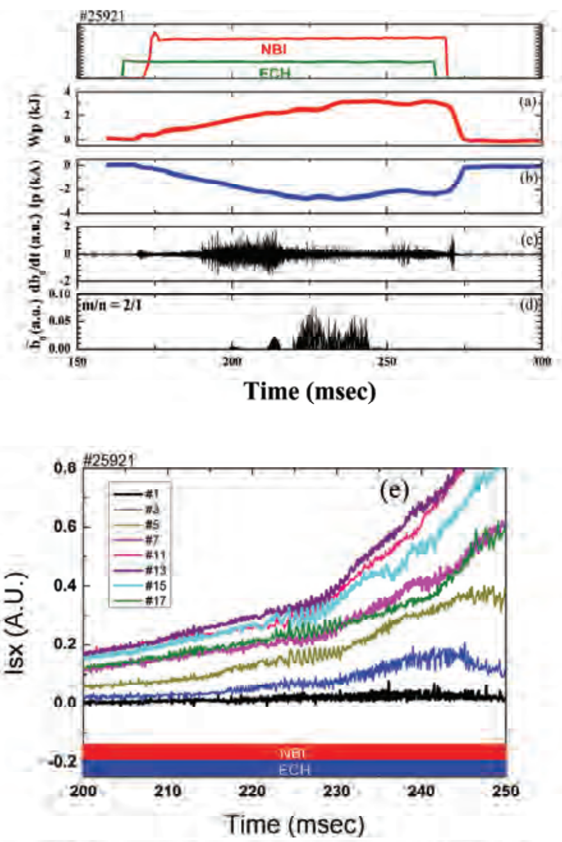

Fig. 3 Time evolution of an ECH + co- NBI plasma. The (a) stored energy, (b) toroidal current, (c) magnetic fluctuation, amplitude of (d) $m/n = 2/1$ and (e) extended view from 200 msec to 250 msec of SX signals.

NB current is -1.0 ± 0.2 kA at $\iota/2\pi$= 0.48 case and -0.8 ± 0.3 kA at $\iota/2\pi$ = 0.50 case.

3.2 ECH + co-NBI plasma

Figure 3 shows a discharge with ECH + co-NBI at $\iota/2\pi$ = 0.48 configuration. The ECH power of 208 kW is injected from 165 msec to 265 msec. The NB port-through power of 573 kW is injected in the co-direction from 175 msec to 265 msec into the target plasma. The net toroidal current is increased up to 2.5 kA. The m/n = 2/1 mode with low frequency (3 kHz) is observed from 225 msec to 245 msec. The m/n =2/1 mode rotates in the electron diamagnetic direction. The SX signal synchronizes with the magnetic fluctuations with the low frequency. Figure 4(a) shows the relative amplitude of the fluctuations observed in the SX signal. The peaks are observed at 5 ch (ρ = 0.90), 15ch (ρ = 0.45) and 18ch (ρ = 0.80). Figure 4(b) shows the phase difference among SX channels for the mode. The derived phase relation indicates the 'even' or 'odd' character of the m number, that is, the phase difference between the SX channels is ~ 2π (~π) for an even (odd) m number. The phases of 5ch and 18ch are almost same and it is consistent with the m = 2 determined using the magnetic probe arrays. Therefore, they correspond to the location of the resonant surface of the m/n =2/1 mode. In vacuum magnetic surface of $\iota/2\pi$ = 0.48 configuration, there is no rational surface of the m/n = 2/1, however, the rotational transform is affected by the plasma pressure and co-flowing toroidal current, resulting in crossing the rational surface of the m/n = 2/1. In order to clarify the effect of the toroidal current on the equilibrium, fixed boundary VMEC calculations considering toroidal current were carried out [10]. We assume that bootstrap current density is given by $j = j_0(s-s^2)$, and NB current is given by $j = j_0(1-s)^2$, where s denotes the normalized toroidal flux, and the relationship of $s = \rho^2$ holds. The total amount of these toroidal currents was chosen to be consistent with the experimental value evaluated in Fig. 2. The electron density is given by $n_e = 2\times10^{19}(1-s^3)$ m^{-3}, and electron and ion temperature are given by $T_e = 0.45\times(1-s)^2$ keV and $T_i = 0.15\times(1-s)^2$ keV. Figure 5 shows the radial profile of the rotational transform calculated by VMEC code with toroidal current. When the bootstrap current of 1.5 kA and NB current of 1 kA flow in co-direction, the rotational transform profile has the rational surface of the m/n =2/1 around ρ = 0.8. The location of the rational surface of the m/n =2/1 calculated is consistent with that obtained by SX signals. The m/n = 2/1 mode is not observed after 245 msec. The rational surface of the m/n =2/1 may disappear by the decrease of rotational transform due to the decrease of the toroidal current.

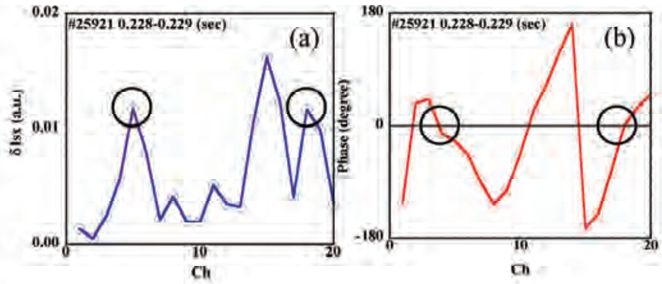

Fig. 4 Radial profile of (a) SX fluctuation amplitude and (b) phase difference among SX channels.

3.3 ECH + counter-NBI plasma

Figure 6 shows a discharge in ECH + counter-NBI with $\iota/2\pi$ = 0.50 configuration. The ECH pulse with the power of 312 kW is injected from 165 msec to 290 msec. The NB with the port-through power of 561 kW is injected in the counter-direction from 170 msec to 290 msec. The net toroidal current is increased up to 1 kA. The total toroidal current during counter-NBI injection is smaller than that during co-NBI injection, since the NB current flows in counter-direction against the bootstrap current. The m/n = 2/1 mode with low frequency (5 kHz) is observed from 165 msec to 280 msec. The mode rotates in electron diamagnetic direction. The SX signal synchronizing with the magnetic fluctuations of low frequency is observed. Figure 7 shows the relative amplitude of the fluctuations observed in the SX signal at 280 msec when the m/n = 2/1 mode is strongest. The peak

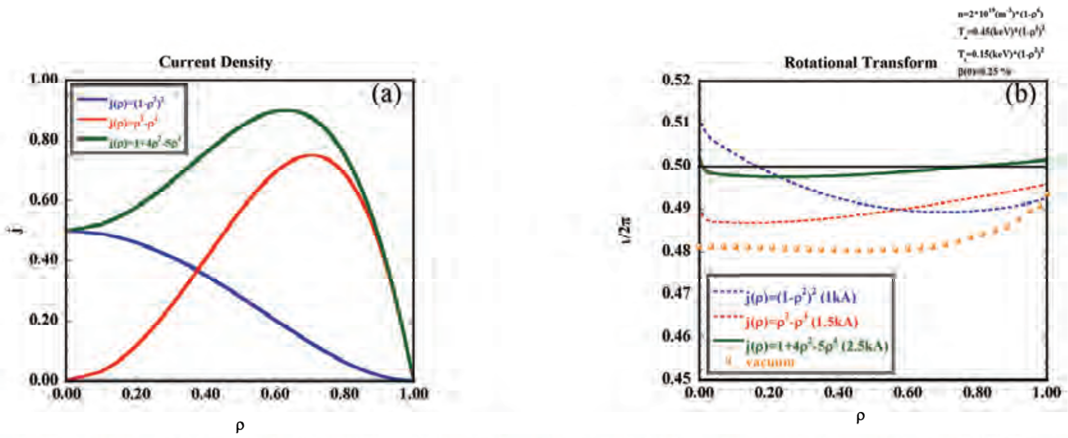

Fig. 5 (a) Toroidal current profile and (b) radial profile of rotational transform deduced from VMEC calculation with the effect of toroidal current and plasma pressure.

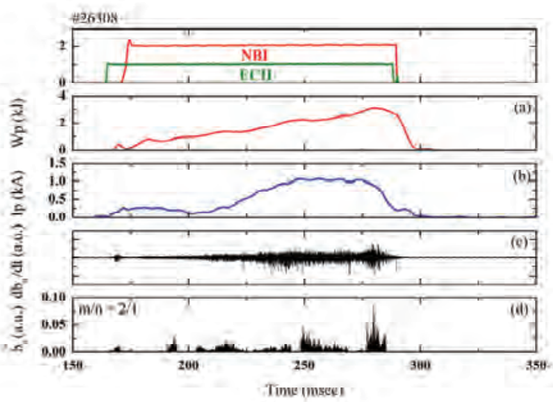

Fig. 6 Time evolution of an ECH + counter-NBI plasma. The (a) stored energy, (b) toroidal current, (c) magnetic fluctuation and amplitude of (d) $m/n = 2/1$.

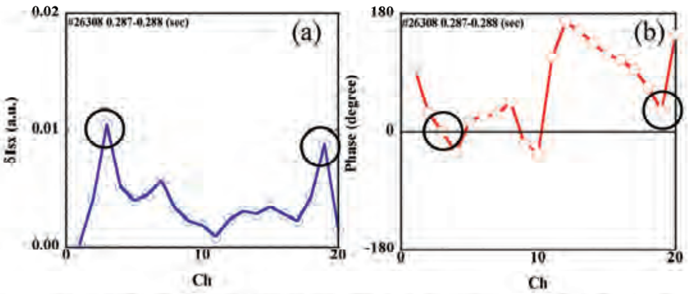

Fig. 7 Radial profile of (a) SX fluctuation amplitude and (b) phase difference among SX channels.

is observed at 3 ch and 19 ch. The phases of 3ch and 19ch are almost same and it is consistent with the $m = 2$ identified by magnetic probes. The positions are almost similar to the rational surface of 0.5 in vacuum condition. The VMEC calculations were performed in the same way as in the previous section. The profiles of toroidal currents and plasma pressure were similar to that of Sec 3.2. Figure 8 shows the calculated rotational transform profile with toroidal current. There is no significant difference between the rotational transform profile considering the toroidal currents and that of vacuum condition, compared with ECH + co-NBI plasma. These results suggest that the change in rotational transform profile by toroidal current is weak due to the balance between the bootstrap current and counter-flowing NB current.

4. Conclusion

The effect of toroidal current on the rotational transform has been studied in Heliotron J by measuring MHD activities. In ECH + co-NBI plasma with $\iota/2\pi = 0.48$ configuration, the $m/n = 2/1$ mode with low frequency was observed when the co-flowing toroidal current is increased up to 2.5 kA. The rotational transform is probably increased by the toroidal current, resulting in crossing the rational surface. Measurement of the mode structure using a 20 channel SX detector array showed that the rational surface was located around $\rho = 0.8$-0.9. The increase of the rotational transform by the toroidal current is consistent with the equilibrium calculation.

The $m/n = 2/1$ mode was observed also in ECH + counter-NBI plasma with $\iota/2\pi = 0.50$ configuration. By SX measurement, the rational surface was determined at the position which is not changed from that of vacuum condition. Equilibrium calculation also shows that there is no significant change in the rotational transform profile by the toroidal current. These results suggest that the change in the rotational transform profile by the toroidal current is weak in ECH + counter-NBI plasma due to the balance between bootstrap current and counter-flowing NB current.

References

[1] T. Obiki, et al., 2001 Nuclear Fusion **17** 611
[2] S. Yamamoto, et al., 2007 Fusion Sci. Technol. **51** 92
[3] G. Motojima, et al., 2007 Nuclear Fusion **47** 1045
[4] G. Motojima, et al., 2007 Fusion Sci. Technol. **51** 122
[5] S. Sakakibara, et al., 1995 Jpn. J. Appl. Phys. **34** L252
[6] E. Sallander, et al., 2000 Nuclear Fusion **40** 1499
[7] S. Kobayashi, et al., Proc. 34th EPS Conf. , Warsaw, Poland, 2007
[8] Hirshman S.P. and Betancourt O. 1991 J. Comput. Phys. **96**, 99

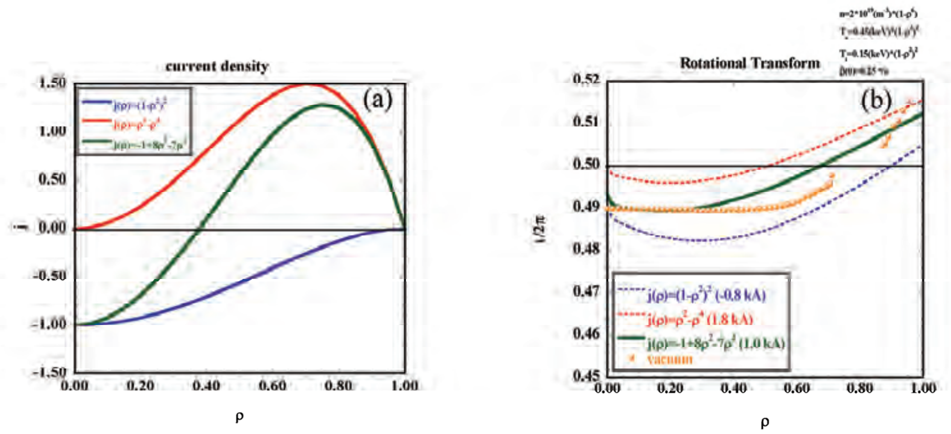

Fig. 8 (a) Toroidal current profile and (b) Radial profile of rotational transform deduced from VMEC calculation with the effect of toroidal current and plasma pressure.

Proceedings of ITC/ISHW2007

Transport analysis of dynamics for the plasma profiles in helical devices

Shinichiro TODA[1)] and Kimitaka ITOH[1)]

[1)]*National Institute for Fusion Science, Toki-shi, Gifu, 509-5292, Japan*

The plasma dynamics and structure are studied by use of the one-dimensional theoretical model for the anomalous transport diffusivities. In this analysis, the high collisional Pfirsch-Schlüter collisional regime is examined and the anomalous particle diffusivity is employed. The reduction of the anomalous particle diffusivity and the steep gradient in the density profile can be obtained. This prediction may be the theoretical explanation for the Internal Diffusion Barrier observed in Super Dense Core plasmas of Large Helical Device.

Keywords: helical toroidal plasmas, turbulent transport, transport barrier, improvement mode, radial electric field, particle confinement

1 Introduction

The turbulence-driven transport and transport barriers are the key issues in fusion research. Main efforts have been focused at the understanding of improved confinement modes (such as the H-mode). Among various improved confinement modes, two main kinds of transport barriers are observed in helical experimental results. At first, the transport barrier because of the radial transition of E_r and the improvement of the electron confinement ('electron internal transport barrier', e-ITB) were observed inside of the transition point for E_r. The transport analysis with the effect of zonal flows could predict an e-ITB in helical plasmas [1]. A comparison with the experimental results was made [2]. As the second kind of transport barriers, an internal diffusion barrier (IDB) is recently observed with the high gradient of the density in a super dense core (SDC) plasma in LHD when a series of pellets is injected [3]. In a core region, the obtained high density and the temperature are around $5\times10^{20}\mathrm{m}^{-3}$ and 0.85keV, respectively. A transport study of a SDC plasma is an urgent and critical issue in helical confinement plasmas. We solve the temporal transport equations for the density, the radial electric field and the temperature to study the dynamics of SDC plasmas in a cylindrical configuration. The additional source profile of the density which corresponds to that in the case of the pellet injection in LHD experiments is studied in the transport equations. The analytical form used here for the neoclassical particle and heat flux related with the helical ripple trapped particles in the high collisional regime is given in ref. [4]. The radial electric filed is assumed to be determined by the ambipolar condition which is constituted with the neoclassical particle flux. The profiles of the density and temperature are determined from the neoclassical and anomalous transport. A transport model for anomalous diffusivities is adapted to describe the turbulent plasma. A dynamics for a self-consistent solution for plasma profiles is examined and the barrier of the particle transport at the inner radial point in the density profile can be reproduced. That can explain a SDC plasma which is accompanied with an IDB in LHD. The profile of the thermal diffusivity is examined when a high-density plasma which corresponds to a SDC plasma is obtained as a calculation result.

author's e-mail: toda@nifs.ac.jp

2 Model Equations

The model equations used here are shown. The one-dimensional transport model is employed. The cylindrical coordinate is used and r-axis is taken in the radial cylindrical plasma in this article. The region $0 < \rho < 1$ is considered, where a is the minor radius and $\rho = r/a$. The expression for the radial neoclassical flux associated with helical-ripple trapped particles is given in [4] which covers the Pfirsch-Schlüter collisional regime, because the plasma state of a SDC corresponds to the high collisional regime. The total particle flux Γ^t is written as $\Gamma^t = \Gamma^{na} - D_a n'$, where Γ^{na} is the neoclassical flux associated with the helical-ripple trapped particles, and the prime denotes the radial derivative. Here, D_a is the turbulent (anomalous) particle diffusivity. The energy flux related with the neoclassical ripple transport, Q_j^{na} is obtained like the neoclassical particle flux. The total heat flux Q_j^t for the species j is written as $Q_j^t = Q_j^{na} - n\chi_a T_j' - 5D_a n' T_j/2$, where χ_a is the anomalous heat diffusivity and Q_j^{na} is the neoclassical contribution from the Pfirsch-Schlüter regime. A theoretical model for the anomalous heat conductivity χ_a is adopted and is explained later. The temporal equation for the density is

$$\frac{\partial n}{\partial t} = -\frac{1}{r}\frac{\partial}{\partial r}(r\Gamma^t) + S_n + S_p, \tag{1}$$

where the term S_n represents the particle source and the parameter S_p is the term to simulate the experimental procedure of the pellet injection. The detail about this term S_p will be explained later. The equation for the electron temperature is given as

$$\frac{3}{2}\frac{\partial}{\partial t}(nT_e) = -\frac{1}{r}\frac{\partial}{\partial r}(rQ_e^t) - \frac{m_e}{m_i}\frac{n}{\tau_e}(T_e - T_i) + P_{he}, (2)$$

where the term τ_e denotes the electron collision time. The term P_{he} represents the absorbed power due to the ECRH heating. The temporal equation for the ion temperature is

$$\frac{3}{2}\frac{\partial}{\partial t}(nT_i) = -\frac{1}{r}\frac{\partial}{\partial r}(rQ_i^t) + \frac{m_e}{m_i}\frac{n}{\tau_e}(T_e - T_i) + P_{hi}. (3)$$

The term P_{hi} represents the absorbed power of ions. The equation for the radial electric field in a nonaxisymmetric system is expressed by the ambipolar condition as

$$\sum_j Z_j \Gamma_j^{na} = 0. \qquad (4)$$

In this article, we examine the plasma which consists of the electron and the hydrogen ion. Therefore, the ambipolar condition, Eq. (4) can be rewritten as $\Gamma_i^{na} = \Gamma_e^{na}$. It is well known that the neoclassical transport is dominant when the radial electric field is formed in helical plasmas [5]. The analysis including the temporal equation of E_r [6] which includes the effect of the electric field diffusion is left for the future study. The source profiles are chosen here as follows. The particle source S_n is set to be $S_n = S_0 exp((r-a)/L_0)$, where L_0 is set to be $0.1m$. This profile represents the peaking at the plasma edge of the particle source due to the ionization effect. The intensity, S_0, governs the average density, and is taken as a control parameter to specify the density in this article. The radial profiles of the electron and ion heating terms, P_{he} and P_{hi}, are assumed to be proportional to $\exp(-(r/(0.5a)^2)$ for the sake of the analytic insight.

3 Model for Anomalous Transport Diffusivities and Boundary Conditions

We adopt the model for the turbulent heat diffusivity χ_a based on the theory of the self-sustained turbulence due to the ballooning mode and the interchange mode, both driven by the current diffusivity [7, 8]. The anomalous transport coefficient for the temperatures is given as $\chi_a = \chi_0/(1 + G\omega_{E1}^2)$ ($\chi_0 = F(s,\alpha)\alpha^{\frac{3}{2}}c^2 v_A/(\omega_{pe}^2 qR)$, where ω_{pe} is the electron plasma frequency. The factor $F(s,\alpha)$ is the function of the magnetic shear s and the normalized pressure gradient α, defined by $s = rq'/q$ and $\alpha = -q^2 R\beta'$. For the ballooning mode turbulence (in the system with a magnetic well), we employ the anomalous thermal conductivity $\chi_{a,BM}$. The details about the coefficients $F(s,\alpha)$, G and the factor ω_{E1}, which stands for the poloidal $E \times B$ rotation frequency, are given in [8] in the ballooning mode turbulence. In the case of the interchange mode turbulence for the system of the magnetic hill [7], we adopt the anomalous thermal conductivity $\chi_{a,IM}$. The details about the coefficients F, G and the factor ω_{E1} in the case of the interchange mode were given in [7]. The greater one of these two diffusivities is adopted as $\chi_a = max(\chi_{a,BM}, \chi_{a,IM})$. The value for the anomalous diffusivities of the particle is set as $D_a = \chi_a$ to examine the radial variation in the profile of the particle diffusivity D_a when the steep radial gradient in the density profile can be obtained as a calculation result.

The equations of density, temperature and electric field (1)-(4) are solved, with the prescribed source profiles, under the appropriate boundary conditions. We fix the boundary condition at the center of the plasma ($\rho = 0$) such that $n' = T_e' = T_i' = 0$. The boundary conditions at the edge ($\rho = 1$), with respect to the density and temperature, are given by specifying the gradient scale lengths. We employ these conditions, $-n/n' = 0.1$m, $-T_e/T_e' = -T_i/T_i' = 0.1$m in this article. The machine parameters which are similar to those of LHD are set to be $R = 3.6$m, $a = 0.6$m, $B = 3$T, $\ell = 2$ and $m = 10$. In this case, we set the safety factor and the helical ripple coefficient as $q = 1/(0.4 + 1.2\rho^2)$ and $\epsilon_h = 2\sqrt{1 - (2/(mq(0)) - 1}I_2(mr/R)$, respectively. Here, $q(0)$ is the value of the safety factor at $\rho = 0$ and I_2 is the second-order modified Bessel function.

4 Dynamical Response after Pellet Injection

Using these parameters and boundary conditions, the one-dimensional transport analysis for the LHD-like plasma has been performed and the profiles of n, T_e, T_i and E_r are solved using equations (1), (2), (3) and (4). We adapt a theoretical model for the anomalous transport diffusivities driven by the current diffusivity as a candidate. An example is taken from the plasma which is sustained by the ECRH. At first we obtain self-consistent steady profiles of n, T_e, T_i and E_r for the given source profile. In order to set the line-averaged density to be around $\bar{n} \simeq 1 \times 10^{20}\mathrm{m}^{-3}$, the line-averaged temperature of electrons to be around $\bar{T}_e \simeq 0.4$keV and the line-averaged temperature of ions to be around $\bar{T}_i \simeq 0.4$keV, the absorbed power of electrons is set to be 1MW and the coefficient S_0 is taken as $7 \times 10^{20}\mathrm{m}^{-3}\mathrm{s}^{-1}$, for the choice of the above mentioned anomalous transport coefficients, where the absorbed power of ions is taken as 0kW. The radial electric field takes the negative value in the entire radial region. Next, we use these obtained profiles of n, T_e, T_i and E_r as an initial condition, *i.e.*, we begin the new calculation from the profile of the density as $\bar{n} \simeq 1{\times}10^{20}\mathrm{m}^{-3}\mathrm{s}^{-1}$ and the negative E_r in the entire region. In this parameter region examined here, both typical energy and particle confinement times are about 1s. To simulate the experimental procedure of the pellet injection, we add the parameter S_p of the particle source in Eq. (1). This parameter S_p has a distribution as $S_p = S_{p0} exp(-(r/r_p)^2)$ and is set to have a value from the initial time $t = 0$ to 1ms. We set the half width of the profile S_p as $r_p = 0.2a$. In other words, we set as $S_{p0} = 1 \times 10^{23}\mathrm{m}^{-3}\mathrm{s}^{-1}$ for $0 < t \leq 1ms$ and $S_{p0} = 0\mathrm{m}^{-3}\mathrm{s}^{-1}$ for $t > 1$ms. We show the dynamics of the plasma radial profiles n (Fig. 1), T_e (Fig. 2), T_i (Fig. 3) and E_r (Fig. 4) at the times 0ms, 1ms and 10ms. The profiles labelled by

0ms represent the initial conditions used in the calculation in this article (with the dotted lines). As the time goes on, the density increases and the positive electric field appears. In Fig. 1, the rapid change of the gradient in the density profile at $t = 10$ms can be found at $\rho = \rho_T (\simeq 0.2)$. The parameter ρ_T represents the location of the transition from the positive E_r to the negative E_r at 10ms in Fig. 4. In Fig. 4, we can show the steep gradient of the radial electric field at the transition point ρ_T. (The profile of the radial electric field is determined by the ambipolar radial electric field and the single solution of the radial electric field for the ambipolar condition can be obtained at a radial point.) The gradient of the radial electric field is strong enough to suppress the anomalous transport: $|E_r'| \simeq 1 \times 10^5 \mathrm{Vm}^{-2}$ at $\rho = \rho_T$. Therefore, the improvement near the transition point can be obtained. In Figs. 2 and 3, the temperatures are found to decrease toward the plasma center when the value of the density rapidly increases. After the time 1ms, the density in the core region continues to increase because there is an inward neoclassical transport because the positive gradient of the temperature profiles. If the time passes over the confinement time, the plasma profiles takes initial ones. At $t = 10$ms, the clear barrier with respect to the particle transport in the density profile can be obtained in Fig. 1.

A profile in the region $\rho < 0.5$ of the anomalous transport diffusivity is shown in Fig. 5. In the region $\rho < \rho_T$, the reduction of the anomalous particle diffusivity can be found, because the value of the anomalous transport diffusivity is proportional to the square of the safety factor q and the temperatures of electrons and ions decrease toward the plasma center at 10ms. A clear reduction of the anomalous particle diffusivity is found at the transition point $\rho = \rho_T$ due to the strong gradient of E_r compared with the region $\rho > \rho_T$. In the region $\rho < 0.3$ at the time 10ms, the neoclassical particle diffusivity $D_{NEO}(= -\Gamma^{na}/n')$ is found to be much smaller than the absolute value of the effective anomalous particle diffusivity and is $|D_{NEO}| < 0.01 m^2 s^{-1}$ with the dotted line. In the core region, the slightly negative value for the effective neoclassical particle diffusivity D_{NEO} and the particle neoclassical pinch are obtained at the time 10ms. In Fig. 6, the dashed line shows the radial profile of the anomalous particle diffusivity D_a, the solid line shows the radial profile of the sum of neoclassical and anomalous particle diffusivity $D_{tot}(= D_{NEO} + D_a)$ at the time 10ms, respectively The clear reduction can be obtained in the sum of the neoclassical and anomalous transport. Therefore, we can obtain the clear barrier with respect to the particle transport in Fig. 1 (n profile at $t = 10$ms). It is emphasized that the barrier formation starts to occur after the end of the particle fuelling. It takes a few ms for the establishment of a barrier seen in Fig. 5. It is found that the anomalous particle transport has a much more important role on the improvement of the particle confinement in the plasma core region than the neoclassical particle transport in the parameter region examined here. If we set much smaller value for S_{p0}, $S_{p0} = 1 \times 10^{22} m^{-3} s^{-1}$ than that ($S_{p0} = 1 \times 10^{23} m^{-3} s^{-1}$) in this calculation, we can not find the steepening in the density gradient, because the gradient of E_r after the pellet fuelling (1ms) is not strong enough. It is shown that there is a threshold value for S_p to form the barrier with respect to the particle confinement in the density radial profile.

5 Summary and Discussions

We have studied the strong reduction of the particle transport when the dynamics and the radial structure of profiles of the density, the temperatures and the electric field are examined in toroidal helical plasmas. The analysis is performed by use of the one-dimensional transport equations. These transport equations includes the contributions from the neoclassical transport and the anomalous transport driven by the current diffusivity. The neoclassical theory for the particle and heat flux in the the Pfirsch-Schlüter regime is adapted. The radial profile of the electric field is determined by the ambipolar condition. The clear change of the gradient in the density profile and the reduction of the anomalous particle transport in the core region after the particle fuelling, if the value of the particle fuelling (the pellet size in the experiment) exceeds the threshold, can be shown when the temporal evolution of the plasma profiles are examined. This theoretical prediction may explain the Internal Diffusion Barrier (IDB) observed in LHD plasmas. It is predicted that the additional particle source S_p has a threshold value to obtain the reduction of the anomalous transport diffusivity. Furthermore, this threshold value of S_{p0} strongly depends on the shape of the distribution, e.g. the parameter r_p which determines the half-width length of the additional particle source. To study the threshold value of S_{p0} to obtain the clear barrier of the particle transport, the parameter survey of the calculations results is needed. These are left for future studies.

The authors would like to acknowledge Prof. A. Fukuyama for the helpful suggestions related with the numerical methods.

[1] S. Toda, K. Itoh, A. Fujisawa, S. -I. Itoh, M. Yagi, A. Fukuyama, P. H. Diamond and K. Ida, Nucl. Fusion **47** 914 (2007).

[2] K. Itoh, S. Toda, A. Fujisawa, S. -I. Itoh, M. Yagi, P. H. Diamond and K. Ida, Phys. Plasma **14** 020702 (2007).

[3] N. Ohyabu et al., Phys. Rev. Lett. **97** 055002 (2006).

[4] K. C. Shaing and J. D. Callen, Phys. Fluids **26** 3315 (1983).

[5] K. Ida, Plasma Phys. Control. Fusion **40** 1429 (1998).

[6] D. E. Hastings, Phys. Fluids **28** 334 (1985).

[7] K. Itoh, S. -I. Itoh, A. Fukuyama, H. Sanuki and M. Yagi, Plasma Phys. Control. Fusion **36** 123 (1994).

[8] K. Itoh, S. -I. Itoh, A. Fukuyama, M. Yagi and M. Azumi, Plasma Phys. Control. Fusion **36** 279 (1994).

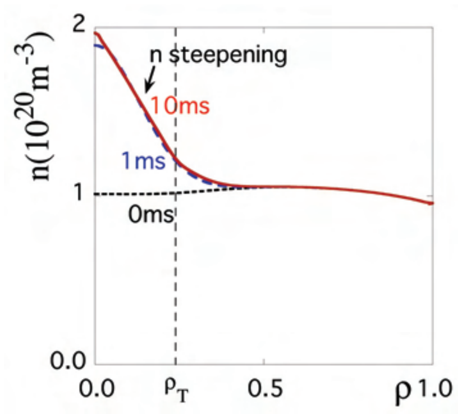

Fig. 1 The dynamics of the density radial profiles. The dotted line, the dashed line and the solid line show the states at the times 0ms, 1ms and 10ms, respectively.

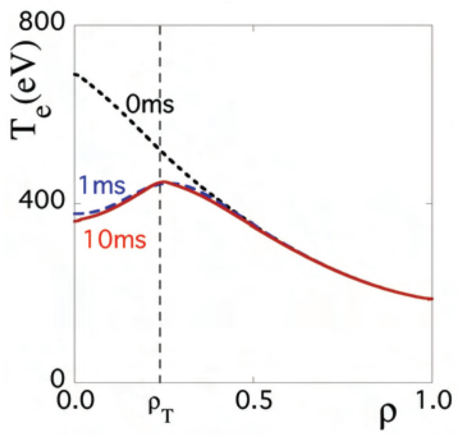

Fig. 2 The profiles of the electron temperature at the times 0ms, 1ms and 10ms. Because the density rapidly increases in the core region, the electron temperature is found to decrease in that region ($\rho < \rho_T$).

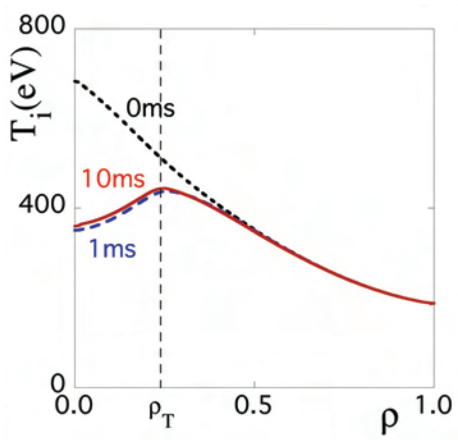

Fig. 3 The profiles of the ion temperature at the times 0ms, 1ms and 10ms.

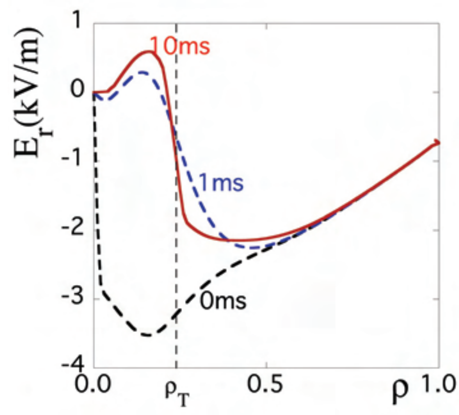

Fig. 4 The dynamics of the radial electric field. At the time 10ms, the radial transition of E_r from the positive value to the negative value can be obtained.

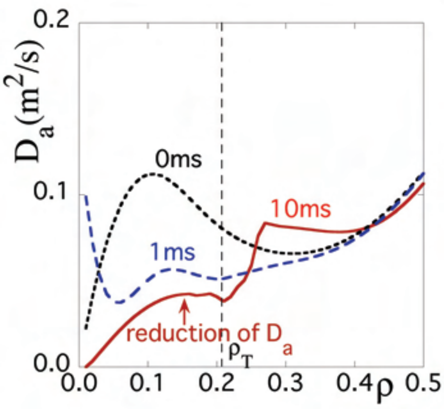

Fig. 5 The radial profiles of the anomalous particle diffusivity D_a in the region $0 < \rho < 0.5$ at the times 0ms (with the dotted line), 1ms (with the dashed line) and 10ms (with the solid line). We can show the clear reduction of the anomalous particle diffusivity at the time 10ms in the region $\rho < \rho_T$.

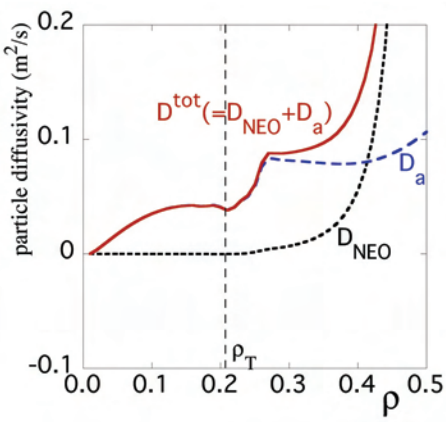

Fig. 6 The radial profiles of the particle diffusivity in the region $0 < \rho < 0.5$ at the times 10ms. We can show the strong reduction in the sum of the neoclassical particle diffusivity and the anomalous particle diffusivity at the time 10ms in the region $\rho < \rho_T$ with the solid line.

Proceedings of ITC/ISHW/2007

Frequency Spectra and Statistical Characteristics of Plasma Density Fluctuations Measured by Doppler Reflectometry in ECR Heated Plasma in the Presence of Induction Current in the L-2M Stellarator

Nina N. SKVORTSOVA[1)], Vyacheslav V. SAENKO[1)], Viktor Yu. KOROLEV[2)], German M. BATANOV [1)], Dmitrii V. MALAKHOV[1)], Anton A. PSHENICHNIKOV[1)], Aleksandr E. PETROV[1)], Karen A. SARKSYAN[1)], Nikolai K. KHARCHEV[1)]

[1)] *A.M. Prokhorov General Physics Institute, Moscow, 119991 Russia*

[2)] *Moscow State University, Moscow, 119899 Russia*

Data on the parameters of plasma density fluctuations in the edge plasma of the L-2M stellarator are presented. The density fluctuations were measured by Doppler reflectometry. Studies were made in the basic magnetic configuration of L-2M under ECRH conditions and in modified magnetic configurations where the rotational transform at $r/a \le 0.6$ (a being the radius of the last closed flux surface) was decreased to negative values by exciting induction current in the plasma. It is shown that induction current results in a shear of the poloidal plasma velocity at the edge of the plasma column. The probability density functions of plasma fluctuations are found to be different from normal (Gaussian) distributions and have heavy tails in both regimes. This type of turbulence is fairly described by shift-scale mixtures of 3 - 4 stochastic plasma processes, each with a normal probability density function. The induction current affects shift-scale mixtures, and components with high mean velocities (convective components) appear in some processes. The experiments showed that the characteristics of turbulent fluctuations in the edge plasma are sensitive to changes in the magnetic structure of the core plasma.

Keywords: plasma turbulence, non-Gaussian process, stellarator, Doppler reflectometry.

1. Inroduction

Experimental studies of low-frequency fluctuations of plasma density, plasma potential and particle flux in the L-2M stellarator have revealed the state of structural turbulence over all the volume of the plasma column [1]. The state of structural turbulence combines determinate-chaotic nature with the existence of ensembles of stochastic structures (vortices, solitons, wave packages) is superimposed on strong plasma turbulence [2].

The present paper reports on experimental studies of spectra and probability characteristics of structural turbulence in the edge plasma of the L-2M stellarator. Experiments were carried out under conditions that the "standard" magnetic configuration was modified by exciting an additional induction current. Plasma density fluctuations were studied with the use of a Doppler reflectometer [3].

2. Experimental conditions

The L-2M stellarator has two helical windings ($l = 2$), a major radius $R = 100$ cm, and a mean plasma radius $\langle a\rangle = 11.5$ cm [4]. The plasma was created and heated by one or two 75-GHz gyrotrons (at the 2nd harmonic of the electron gyrofrequency). The magnetic field at the center of the plasma was $B_t = 1.3$–1.4 T. The gyrotron power was $P_0 = 150$–300 kW, and the microwave pulse duration was up to 15 ms. Measurements were performed in a hydrogen plasma with mean density $\langle n\rangle = (0.8$–$2.0)\cdot 10^{13}$ cm^{-3} and central temperature $T_e = 0.6$–1.0 keV. In the edge plasma at radius $r/a = 0.9$, the density was at a level of $n(r) = (1$–$2)\ 10^{12}$ cm^{-3} and the electron temperature was $T_e(r) = 30$–40 eV. The duration of the steady-state phase of the discharge was 10 ms.

In the magnetic configuration of the L-2M stellarator, an induction current excited in the opposite direction to the toroidal magnetic field (hereafter referred to as a negative current) was used to change the value and sign of rotational transform and to increase the shear of magnetic lines. In [5], the radial profiles of rotational transform $i/2\pi$ were calculated for various values of the induction current. According calculations, the induction current of 10-15 kA may result in two large magnetic islands located in the central region, whereas at the plasma edge at $r/a = 0.8$, the magnetic structure changes only slightly.

The probing frequencies used in our experiment correspond to the peripheral regions where the electron density drops from $\sim 1.7\cdot 10^{13}$ cm^{-3} to $\sim 1.1\cdot 10^{13}$ cm^{-3}. The angles of incidence of the probing beam of the reflectometer are 4°, 8° and 12° with respect to the normal

author's e-mail: nina@fpl.gpi.ru

to the last closed magnetic surface According to the Bragg condition, the scattered signal corresponds to plasma fluctuations with poloidal wavenumber $k \approx 2$ cm^{-1}.

The stray signal from heating gyrotron radiation was suppressed with the help of a waveguide resonance filter, which provided 30-dB attenuation at a frequency of 75.3 GHz. The polarization of the probing radiation in the plasma corresponded to an ordinary wave. We used quadrature detection. Signals from two microwave diodes were amplified in wideband amplifiers with gain of 10 and were recorded by a 10-digit ADC operating at a sampling rate of 5 MHz. The time resolution of the diagnostic system was 200 ns.

A Doppler shift, which corresponds to the poloidal rotation velocity, was determined from the shift of the Fourier spectrum of a complex signal. In addition to complex Fourier spectra, we estimated and studied autocorrelation functions, probability density functions of fluctuation amplitudes and their increments for time samples recorded in one of two reflectometer channels.

3. Experimental results

As an illustration, Fig. 1 shows a time sample of the reflectometer signal in an ECRH discharge with an additional induction current.

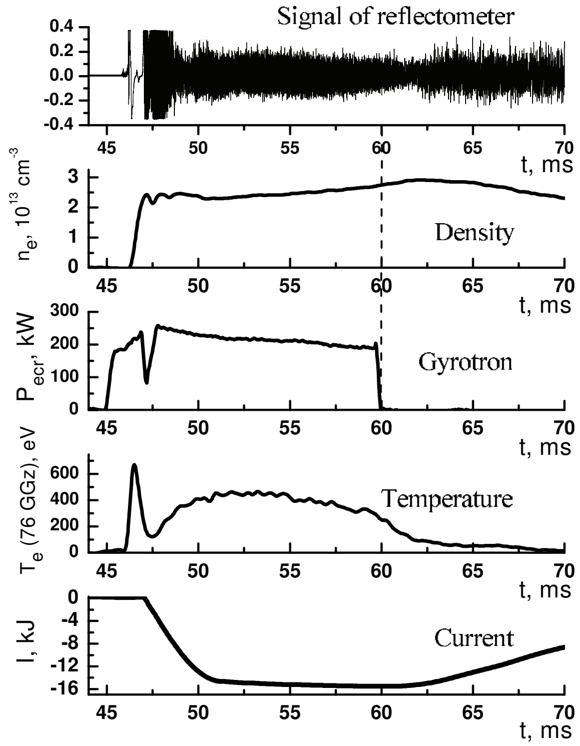

Fig.1. Time behavior of the refectometer signal, average plasma density, gyrotron power, central electron temperature, and plasma energy in a discharge with current I= –15 kA.

Also shown are time dependences of the average plasma density, gyrotron power, central electron temperature (ECE signal), and plasma energy. Note that the electron density is maintained during more than 10 ms after the gyrotron power is switched off. A similar behavior of the electron density and fluctuations is observed in discharges without induction current.

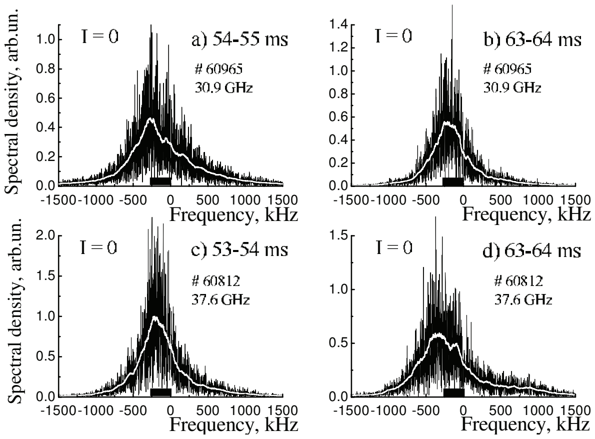

Fig.2. Spectra of the complex signals for two probing frequencies 30.9 GHz and 37.6 GHz for an ECRH discharge: (a, b) during and (b, d) after the gyrotron pulse. Black segments on the frequency axis show Doppler shifts.

Figure 2 shows spectra of the complex signals for two probing frequencies 30.9 GHz and 37.6 GHz for an ECRH discharge in the absence of induction current. Black segments on the frequency axis indicate Doppler shifts. The scattered spectra are continuous with feebly marked bands of width 50 kHz. It can be seen that the spectra are continuous with feebly marked bands of width 50 kHz. The peak of spectral intensity is shifted from the zero (probing) frequency by nearly 250 kHz into the red region. The spectrum is asymmetric: the spectral intensity falls sharply in the red wing, whereas it decreases smoothly in the blue wing of the spectrum. The shift of the peak intensity over frequency is usually interpreted as a Doppler shift.

Figure 2 shows spectra of the complex signals for two probing frequencies 30.9 GHz and 37.6 GHz for an ECRH discharge in the absence of induction current. Black segments on the frequency axis indicate Doppler shifts. The probing frequencies, it will be recalled, correspond to different plasma regions: the higher the frequency, the higher the plasma density. It can be seen from these spectra that the Doppler shift is the same for both probing frequencies during the heating pulse and in the plasma decay phase. The poloidal velocity corresponding to this shift is about 10^6 cm/s. In the absence of an induction current, the shape of the spectrum does not change during the ECR heating pulse and for 2-3 ms after its end. The Fourier spectra for probing frequencies 30.9 GHz and 37.6 GHz have the same values of the width and Doppler shift, which indicates that the poloidal plasma velocity is uniform a shear is absent in the edge plasma in the ECRH regime.

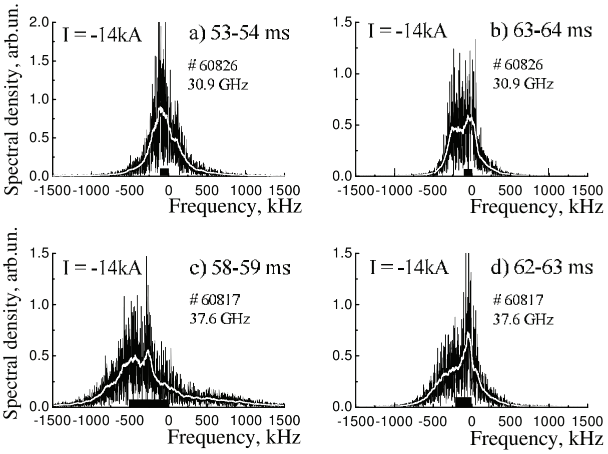

Fig.3. Spectra of the complex signals for two probing frequencies 30.9 GHz and 37.6 GHz for an ECRH discharge with additional induction current: (a, b) during and (b, d) after the gyrotron pulse. Black segments on the frequency axis show Doppler shifts.

Figure 3 shows spectra of the complex signals for two probing frequencies 30.9 GHz and 37.6 GHz for an ECRH discharge with additional induction current. Black segments on the frequency axis indicate Doppler shifts. The spectra in this regime change markedly, depending on the probing frequency. FWHM of the spectrum measured with a probing frequency of 30.9 GHz is smaller. At the same time, an intense spectral band (its intensity is nearly equal to the intensity of the continuous spectrum) appears in the frequency range 150-200 kHz. The red edge of the spectrum is shifts toward a lower frequency. In the scattered spectrum for a probing frequency of 37.6 GHz, the shift of the red edge increases from -500 kHz to -750 kHz. The scattered spectrum for a probing frequency of 34.8 GHz contains two intense bands in the range of -200 kHz and -400 kHz. Their intensity varies in time, but their positions are fixed.

Hence, the generation of a magnetic island structure in the inner region of the plasma column involves a change in behavior of the spectra measured in the narrow region near the last closed magnetic surface. The Doppler shifts of the spectra corresponding to different radii prove to be different, which is evidence for a radial shear of the poloidal plasma velocity.

As noted above, the reflectometer data were also used to study probability characteristics of plasma density fluctuations. Characteristically, the autocorrelation functions of fluctuation amplitudes demonstrated long-lived tails. Histograms showed that the probability density functions (PDFs) of fluctuation amplitudes and increments differ from Gaussian distributions by heavy tails. Previously, it was proposed to apply doubly stochastic Poison process to describing the PDFs of the increments of fluctuation amplitudes in structural plasma turbulence [6]. Taking this approach, we used the model of shift-scale mixtures of Gaussian distributions. A finite shift-scale mixture of Gaussian (normal) distributions is represented in the form

$$P\{X<x\}=\sum_{j=1}^{n} p_j \Phi\left(\frac{x-a_j}{\sigma_j}\right), \quad x \in \text{Ў}$$

where $\Phi(y)$ is the normal distribution function; p_j is the weight; n-number of component of mixtures, a_j and σ_j are the mathematical expectation and dispersion of the normal distribution, respectively.

Each component of the mixture is determined by a certain stochastic plasma process, such as the presence of an ensemble of stochastic plasma structures, the interaction between structures, etc. As applied to structural plasma turbulence, the concept of volatility as a multidimensional vector determining the behavior of fluctuations was considered in [7]. When processing the increments of fluctuations measured by the Doppler reflectometer, we calculated the volatility components, in which values of a_j and σ_j give information about the average rates and dispersion of rates of turbulence in each particular process and their total effect. Modeling the PDFs of fluctuation increments with the use of the Estimation Maximization algorithm [8] allowed us to determine the number and weight of such processes and to trace behavior of the components.

We studied how the mixture components and the PDF fluctuations alter in response to a change introduced in the magnetic configuration by the induction current.

It was found that the turbulent process in the edge plasma is fairly described by a mixture of 3 - 4 stochastic plasma processes for both the ECRH regime and the regime with an additional induction current. The velocity value deduced from the Doppler shift is a sum of two components: the poloidal rotation velocity and the phase velocity of the measured fluctuation. In our case, the latter component is a sum of phase velocities of particular processes:

$$u = u_{E\times B} + \sum_{k=1}^{n} u^{k}{}_{phase} \ ,$$

where k is the number of processes determined following the Estimation Maximization algorithm, and $u^{k}{}_{phase}$ are their phase velocities. For plasma density fluctuations measured in the regime with induction current, we observed the mixture components characterized by larger average velocities in comparison with similar components in the regime without induction current.

Figure 4 shows the results of numerical simulation of the PDF of increments of density fluctuations in the regime with additional induction current. Turbulence is described by a mixture of four processes of which one has a large average velocity characteristic of regimes with current. It is found that the characteristics of shift-scale mixtures of Gaussians change substantially in the presence of induction current.

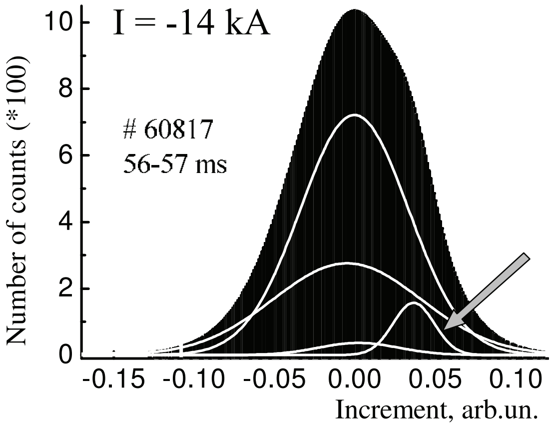

Fig.4. Modeling of the PDF of density fluctuation increments in the regime with additional induction current. An arrow indicates the process characterized by a large mathematical expectation.

The so-called "sliding separation of mixtures" [7] was used to trace the temporal evolution of the components of average velocity. In the ECRH regime, the average velocities of processes do not change during 3-5 ms after the heating pulse is switched off. In the regime with current, the average velocities in the mixture of processes drop by an order of magnitude with 0.1-0.2 ms after the ECRH pulse is switched off.

4. Conclusions

The spectra of turbulent fluctuations in ECR regime have nearly the same width and Doppler shift, which indicates that the poloidal plasma velocity is uniform over the region of observation. In the presence of the additional induction current, the characteristics of Fourier spectra of complex signals in the narrow near-separatrix region changed markedly and the Doppler shifts for three probing frequencies became different, which is evidence for a shear of the poloidal plasma velocity.

The processing the results of measurements by the Doppler reflectometer demonstrated efficiency of statistical methods of shift-scale mixtures of Gaussian distributions and the sliding separation of mixtures of Gaussian distributions. It is shown that, in structural plasma turbulence developing in the edge plasma of the L-2M stellarator, there exist 3-4 independent Gaussian processes, each having its particular propagation velocity. The algorithm of sliding separation of mixtures works and makes it possible to distinguish between the pure ECRH regime and the ECRH regime with additional induction current. A comparison between the pure ECRH regime and the ECRH regime with additional induction current shows that the behavior of subcomponents of volatility for these regimes is different and is an inherent characteristic of the regime.

As a result, it has been established that the frequency and probability characteristics of turbulent fluctuations in the edge plasma are sensitive to changes in the magnetic structure of the core plasma.

This work was supported by the Dynasty Foundation, the CRDF Program for Basic Research, and the RF Presidential Program "Support of Leading Scientific Schools" (project 5382.2006.2) and the Russian Foundation for Basic Research (project nos. 07-02-00455, 07-01-00517).

References

[1] G. M. Batanov, V. E. Bening, V. Yu. Korolev, et al., JETP Lett. **78**, 502 (2003).

[2] V. Yu. Korolev and N.N. Skvortsova. (Eds) “Stochastic Models of Structural Plasma Turbulence”. VSP, Leiden - Boston, The Netherlands. (2006).

[3] A. A. Pshenichnikov, L. V. Kolik, et al. Plasma Physics Reports. **31**, 554 (2005).

[4] V. V. Abrakov, D. K. Akulina, E. D. Andryukhina, et al., Nucl. Fusion **37**, (1997) 233.

[5] S.V.Shchepetov, D.K.Akulina, et al. 15 Stellarator Workshop. Madrid. **Or-2** (2006).

[6] N.N. Skvortsova, V.Yu. Korolev, G.M. Batanov et al Plasma Phys. Contr. Fusion. (2006). **48**. A393.

[7] V.Yu. Korolev, N.N. Skvortsova. A new method of the probabilistic and statistical analysis in case of plasma turbulence processes. In “The systems and means of informatics.” Ed. I.A. Sokolov. Moscow. The Institute of Informatics Problems (IPI RAN). 126, (2005). (In Russian).

[8] Skvortsova N. N., Batanov G. M. et al., New possibilities for the mathematical modeling of turbulent transport processes in plasma. in ”Stochastic Models of Structurial Plasma Turbulence” (V. Yu. Korolev and N. N. Skvortsova eds.) – Leiden, Boston: VSP, 87 (2006).

Proceedings of ITC/ISHW2007

Beta and Magnetic Configuration Dependence of Local Transport in the LHD Plasmas

Hisamichi FUNABA[1)], Kiyomasa WATANABE[1)], Satoru SAKAKIBARA[1)], Hiroshi YAMADA[1)], Masayuki YOKOYAMA[1)], Sadayoshi MURAKAMI[2)], Kazumichi NARIHARA[1)], Ichihiro YAMADA[1)], Kenji TANAKA[1)], Tokihiko TOKUZAWA[1)], Masaki OSAKABE[1)], Kazuo KAWAHATA[1)] and the LHD Experimental Group[1)]

[1)] *National Institute for Fusion Science, Toki, Japan*
[2)] *Department of Nuclear Engineering, Kyoto University, Kyoto, Japan*

In high beta plasmas on heliotron devices, the magnetic configuration changes as a result of the beta increment. Especially, the position of the magnetic axis is largely shifted outward. On the other hand, it is reported that the global confinement of low beta plasmas on LHD strongly depends on the magnetic configuration properties such as the magnetic axis position. In this paper, the influence of the change of the magnetic configuration on the local transport is studied in low beta plasmas at first. Next, the dependence of the local transport characteristics in high beta plasmas on the position of the magnetic flux surface are compared with those in the low beta plasmas. The local transport in the peripheral region of high beta plasmas is found to be more correlated with beta than the position of the magnetic flux surface, while the local transport in the core region has almost similar characteristics in the low beta plasmas. These results suggest that the local transport at the peripheral region in high beta plasmas on LHD is strongly affected by the anomalous transport caused by the increment in the magnitude or the gradient of beta.

Keywords: high beta, magnetic configuration, local transport, International Stellarator/Heliotron scaling

1. Introduction

The plasmas with the volume averaged beta, $\langle\beta\rangle$, value of close to 5% have been obtained on the Large Helical Device (LHD) [1]. Transport analysis of such high beta plasmas are made in this paper.

Transport study of helical plasmas has been mainly done for low beta plasmas up to now. The activity of the International Stellarator/Heliotron Scaling (ISHS) has intensively progressed. Scaling laws of the energy confinement time for helical plasmas have been proposed by this activity (ISS95 : International Stellarator Scaling 1995) [2], ISS04 : International Stellarator Scaling 2004) [3]). According to the ISS04 scaling, the global confinement property depends on the magnetic configurations as a factor. The factor is introduced as the renormalization factor. This renormalization factor strongly depends on the magnetic axis position in vacuum or the ellipticity of the outermost magnetic flux surface in the case of LHD, although the causes have not been clarified.

Recently, as the results of the transport analysis of high beta plasmas with more than 1% of $\langle\beta\rangle$, it is found that the transport property is degraded in high beta plasmas compared with the gyro-reduced Bohm (GRB) model or the ISS95 scaling. On the other hand, the magnetic flux surfaces are shifted outside with the increment in beta due to the Shafranov shift. The purpose of the analysis in this paper is to clarify that the confinement degradation with β increment observed on LHD is caused by the change of magnetic configuration by the increment in β or it is directly caused by the increment in β or $\nabla\beta$.

The energy confinement time by the ISS04 scaling, τ_E^{ISS04}, is expressed as follows:

$$\tau_E^{ISS04} = 0.134 \cdot a^{2.28} R^{0.64} P^{-0.61} \overline{n}_e^{\,0.54} B^{0.84} \iota_{2/3}^{0.41}, \quad (1)$$

where $a, R, P, \overline{n}_e, B$ and $\iota_{2/3}$ are the minor radius, the major radius, the absorbed power, the line average electron density, the volume averaged strength of the magnetic field, the rotational transform, $\iota = \iota/2\pi$ at the normalized average minor radius, $\rho = 2/3$, respectively. The advance from the previous ISS95 scaling to ISS04 is that the strong effect depending on the devices or the magnetic configurations is included although the dependence on the plasma parameters are similar. This effect is expressed as the renormalizaton factor, f_{ren}, which represents the dependence on the device or the magnetic configuration. In the case of LHD, this f_{ren} is strongly dependent on the position of the magnetic axis in vacuum, R_{ax}^{vac}, and the shape of the outermost magnetic flux surface. In ref. [3], the dependence of f_{ren} on the R_{ax}^{vac} is analyzed in detail and the derived f_{ren} values are shown in table 1. This f_{ren} is denoted as f_{ren}^{ISS04} hereafter. The f_{ren}^{ISS04} values are evaluated in the low beta discharges. For LHD, the beta values of the plasmas are in the range of $\langle\beta^{dia}\rangle \leq 1.5\%$.

The main purpose of this study is to distinguish the causes of the gradual confinement degradation with beta from following two effects: (1) the change of magnetic

author's e-mail: funaba@lhd.nifs.ac.jp

configuration by the increment in beta, (2) beta value or the gradient of beta. The global transport study is made taking the change of the magnetic configuration by the increment in beta into account. Then, analysis of the dependence of the local transport properties on magnetic configuration or the beta value is made.

Device	R_{ax}^{vac} [m]	$R_{geo}^{vac}(2/3)$ [m]	f_{ren}^{ISS04}
LHD	3.60	3.643	0.93 ± 0.15
LHD	3.75	3.740	0.67 ± 0.06
LHD	3.90	3.849	0.48 ± 0.05

Table 1. Relation among the positions of the magnetic axis in vacuum, R_{ax}^{vac}, the geometric center of the $\rho = 2/3$ magnetic surface in vacuum, $R_{geo}^{vac}(2/3)$ and f_{ren}^{ISS04} in the ISS04 scaling for three magnetic configurations on LHD [3] .

This paper consists of the following sections. In section 2, the method of transport analysis are described. The dependence of the local transport on the magnetic configuration in the low beta regime is investigated in Section 3. In Section 4, the relation between the local transport coefficients and the change of the geometric center position of the magnetic flux surface by increment in beta is shown. Then, its effect on the confinement degradation in the high beta region is discussed and a summary is provided in Section 5.

2. Experimental setup and the method of transport analysis

LHD is a heliotron type device with the poloidal period number $l = 2$ and the toroidal period number $m = 10$. The major radius position of the magnetic axis in vacuum, $R_{ax}^{vac} = 3.5 \sim 4.1$ m and the average minor radius $a \simeq 0.6$ m. The magnetic field strength at the toroidally averaged magnetic axis in vacuum, B_0, is up to almost 3 T.

The value of the volume average beta, $\langle\beta^{dia}\rangle$, is derived from the diamagnetic measurement [4]. The profiles of electron temperature, T_e, are measured by the Thomson scattering with YAG lasers. The power deposition profiles of NBI are calculated by a three-dimensional Monte Carlo simulation code [5]. These NBI deposition profiles, which are used in the local transport analysis, include the broadening from the birth profiles of NBI by the finite orbit effect. Here, the magnitude of the ionized power of NBI in the calculation is set to be equal to the experimentally estimated NBI absorbed power, which is the port through power minus the shine through power and contains about 10 % error [6] .

The thermal transport coefficients of electrons and ions, χ_e^{exp} and χ_i^{exp}, respectively are evaluated by using one-dimensional transport code for helical plasmas, PROCTR [7] . Here, $T_i = T_e$ and $n_i = fn_e$, are assumed, where f is determined by the following relation in order to make the kinetic stored energy become equal to the measured stored energy.

$$W_p^{dia} = \int \frac{3}{2}(1+f)\, n_e T_e dV, \tag{2}$$

where the integral is the volume integral. In this paper, the local transport is analyzed based on the measurements of T_e and n_e. By the assumption of $T_i = T_e$, the equipartition power between electrons and ions , $P_{ei} = 0$ is assumed. Therefore, behaviour of the effective transport coefficients which are evaluated by

$$\chi^{eff} = (\chi_e^{exp} + f\chi_i^{exp})/(1+f) \tag{3}$$

is studied.

3. Dependence of the local transport on the magnetic configuration in the low beta regime

In this section, the dependence of local transport on magnetic configurations is investigated in the low beta region first in order to clarify the causes of the degradation of the local transport property in the high beta region.

The dependence of the local transport coefficients on the magnetic configuration, which is represented by the geometric center of the magnetic flux surface in this paper, are investigated at some minor radius positions in the low beta plasmas. In order to evaluate this dependence, the renormalization factor for local transport coefficients, $g_{ren\chi}$, is introduced. And the reference local transport coefficient, χ^{ISS04}, based on the global confinement scaling of ISS04, is used in this analysis.

The energy confinement time by ISS04, τ_E^{ISS04}, is expressed as follows by using the non-dimensional parameters, such as the normalized Larmor radius (ρ^*), ν_b^*, β, A_p and $\iota_{2/3}$.

$$\tau_E^{ISS04} = C_\tau \cdot \tau_{Bohm} \cdot \rho^{*-0.79} \beta^{-0.19} \nu_b^{*0.00} A_p^{0.07} \iota_{2/3}^{1.06}, \tag{4}$$

where τ_{Bohm} is the global confinement time based on the Bohm type scaling and C_τ is a constant. Then, a modeled transport coefficient, χ^{ISS04}, which has the same non-dimensional parameter dependence as ISS04 is introduced in order to use as a reference for the local transport coefficient:

$$\chi^{ISS04} = C_\chi \cdot \chi^{Bohm} \cdot \rho^{*0.79} \beta^{0.19} \nu_b^{*0.00} A_p^{-0.07} \iota_{2/3}^{-1.06}. \tag{5}$$

Here, C_χ is determined to make the average of χ^{eff}/χ^{ISS04} become unity in the low beta region ($\langle\beta^{dia}\rangle < 1\%$) in the data set of $R_{ax}^{vac} = 3.60$ m (Table 2) .

ρ	C_χ
0.5	0.104
0.7	0.133
0.9	0.294

Table 2. The normalized average minor radius, ρ, and the coefficient in χ^{ISS04} expression, C_χ .

Therefore, the magnitude of χ^{eff}/χ^{ISS04} represents the ratio of the normalized transport coefficients to the value in the configuration of R_{ax}^{vac} = 3.6 m at each minor radius position. The ratio χ^{eff}/χ^{ISS04} increases as R_{ax}^{vac} moves torus-outward. This tendency of the local transport coefficients seems to agree qualitatively with the global confinement property. Then, the average value of the experimental results is defined as the renormalization factor for the local transport coefficients, $g_{ren\chi}$, at this local position. The factor $g_{ren\chi}$ is derived for various magnetic configurations and radial positions. The relation between $g_{ren\chi}$ and the geometric center position of each magnetic flux surface, $R_{geo}(\rho)$, in vacuum is shown in Fig. 1. The symbols ○, ◇ and △ correspond to the values at ρ = 0.9, 0.7 and 0.5, respectively. The data in $R_{geo}(\rho) = 3.6 \sim 3.7$ m, $R_{geo}(\rho) = 3.7 \sim 3.8$ m and $R_{geo}(\rho) = 3.8 \sim 3.9$ m are for the configurations of R_{ax}^{vac} = 3.60 m, R_{ax}^{vac} = 3.75 m and R_{ax}^{vac} = 3.90 m, respectively.

As the geometric center of the magnetic flux surface is shifted torus outward, $g_{ren\chi}$ increases at any minor radius positions. Moreover, it is found that the dependence of $g_{ren\chi}$ on the geometric center position of the magnetic surface is almost same at different minor radial positions.

The closed circles (●) in Fig. 1 represent the renormalization factor for transport coefficients which is derived from the global scaling ISS04, $g_{ren\chi}^{ISS04}$. This $g_{ren\chi}^{ISS04}$ is related with the global f_{ren} and it is compared with the renormalization factor for the local transport coefficients, $g_{ren\chi}$. The parameter $g_{ren\chi}^{ISS04}$ is is derived by normalizing $f_{ren}^{-1/(\alpha_P+1)}$ with the value at R_{ax}^{vac} = 3.60 m as the following,

$$g_{ren\chi}^{ISS04} \equiv f_{ren}^{-1/(\alpha_P+1)} / f_{ren}^{-1/(\alpha_P+1)}(R_{ax}^{vac} = 3.6\,\mathrm{m}), \qquad (6)$$

where α_P is one of the scaling coefficients when a global scaling law is expressed as

$$\tau_E = f_{ren} n^{\alpha_n} P^{\alpha_P} B^{\alpha_B} a^{\alpha_a} R^{\alpha_R}, \qquad (7)$$

where n is the density and $\alpha_n, \alpha_P, \alpha_B, \alpha_a$ and α_R are exponents for each parameter. In the case of ISS04, α_P = −0.61. The values of $g_{ren\chi}^{ISS04}$ at the R_{ax}^{vac} = 3.60, 3.75 and 3.90 m configurations are shown in Table 3.

R_{ax}^{vac} [m]	$R_{geo}^{vac}(2/3)$ [m]	f_{ren}^{ISS04}	$g_{ren\chi}^{ISS04}$
3.60	3.643	0.93	1.00
3.75	3.740	0.67	2.33
3.90	3.849	0.48	5.48

Table 3. f_{ren}^{ISS04} and $g_{ren\chi}^{ISS04}$ for three magnetic configurations on LHD.

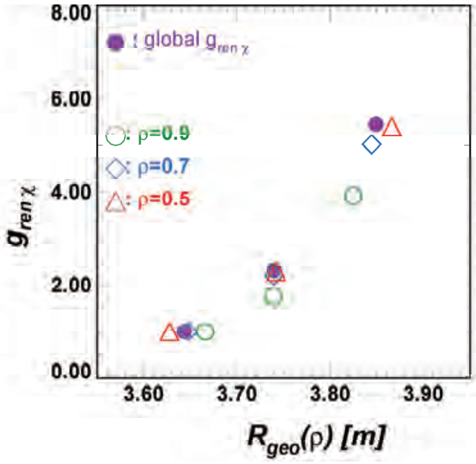

Fig. 1 Dependence of $g_{ren\chi}$ on the geometric center position of the vacuum magnetic flux surface, $R_{geo}(\rho)$. fren chi.

It should be noted that an assumed spatially uniform thermal transport coefficient, $\langle\chi\rangle$, in the R_{ax}^{vac} = 3.90 m configuration is about 5 times larger than that in the R_{ax}^{vac} = 3.60 m configuration when it is evaluated based on ISS04. The values of $g_{ren\chi}^{ISS04}$ almost agree with the values of $g_{ren\chi}$ which are evaluated from the local transport analysis from the results in Fig. 1. Here, as the flux surface corresponding to $g_{ren\chi}^{ISS04}$, the $\rho = 2/3$ surface is chosen because it is assumed that $R_{geo}(2/3)$ represents the property of a magnetic configuration.

4. Local transport property in the high beta regime and its dependence on the magnetic configuration

In Fig. 2, the dependence of χ^{eff}/χ^{ISS04} on $R_{geo}(\rho)$ in the high beta regime are compared with the dependence of χ^{eff}/χ^{ISS04} on $R_{geo}(\rho)$ in the low beta regime with various magnetic axis positions. Figs. 2, (a) (b) and (c) show the results for ρ = 0.5, 0.7 and 0.9, respectively. The closed circles (●) represent the relation between χ^{eff}/χ^{ISS04} and $R_{geo}(\rho)$. At the all positions of ρ = 0.5, 0.7 and 0.9, the magnitude of χ^{eff}/χ^{ISS04} increases with the torus outward shift of $R_{geo}(\rho)$ of the each magnetic flux. The dependence of increment in the ratio χ^{eff}/χ^{ISS04} on $R_{geo}(\rho)$ is steeper at the larger ρ position. One reason of this is that the magnitude of the shift of $R_{geo}(\rho)$ is smaller at larger ρ. At $\rho = 0.9$, an abrupt increment in χ^{eff}/χ^{ISS04} is found around $R_{geo}(\rho) \simeq 3.70$ m, where $\langle\beta^{dia}\rangle$ is about 1.0 ~ 2.5 %. The symbols of △, ◇ and ○ in Fig. 2, are the same as in Fig. 1, respectively. They represent the dependence of the normalized thermal transport coefficients on the geometric center position of the magnetic flux surfaces which is evaluated from the local transport analysis.

The degradation of the local transport with the increment in $\langle\beta^{dia}\rangle$ seems to be comparable with the degradation by the torus outward shift of the magnetic flux surface at $\rho = 0.7$. Moreover, The degradation at $\rho = 0.5$ seems to be comparable with or slightly smaller than the degradation by the torus outward shift. On the other hand, at the peripheral region of $\rho = 0.9$, it is observed that the degradation of the local transport is larger than that predicted from the torus outward shift of the magnetic flux surface. This results shows that some effects which are caused directly by the beta value or the gradient of beta may exist at the peripheral region.

5. Summary

The following results are obtained by comparing the dependence of the local transport coefficients on beta values and the geometric center positions of the magnetic flux surfaces with the above relations between the local transport coefficients and the geometric center positions of the magnetic flux surfaces in the low beta region . The degradation of the local transport with the increment in $\langle\beta\rangle$ seems to be comparable with or slightly smaller than the degradation by the torus outward shift of the magnetic flux surface at $\rho = 0.7$ or 0.5. On the other hand, at the peripheral region of $\rho = 0.9$, degradation of transport coefficients which is larger than those predicted from the torus outward shift is observed. It is considered that some effects which are directly caused by the beta value or the gradient of beta may exist.

[1] O. Motojima, *et al.*, Proc. of 21st IAEA Fusion Energy Conf., OV/2-1, (Chengdu, 2006).
[2] U. Stroth, M. Murakami *et al.*, Nucl. Fusion, **36** 1063 (1996).
[3] H. Yamada, *et al.*, Nucl. Fusion **45** 1684 (2005).
[4] K.Y.Watanabe *et al.*, Nucl. Fusion, **45** 1247 (2005).
[5] S. Murakami *et al.*, Trans. Fusion Technol.,**27**,256(1995).
[6] M.Osakabe, Y.Takeiri, *et.al.*, Rev. Sci. Instrum., **72**, 590(2001).
[7] H.C. Howe, ORNL/TM-11521 (1990).
[8] K.Y. Watanabe *et al.*, Plasma Phys. Control. Fusion, **49** 605 (2007).

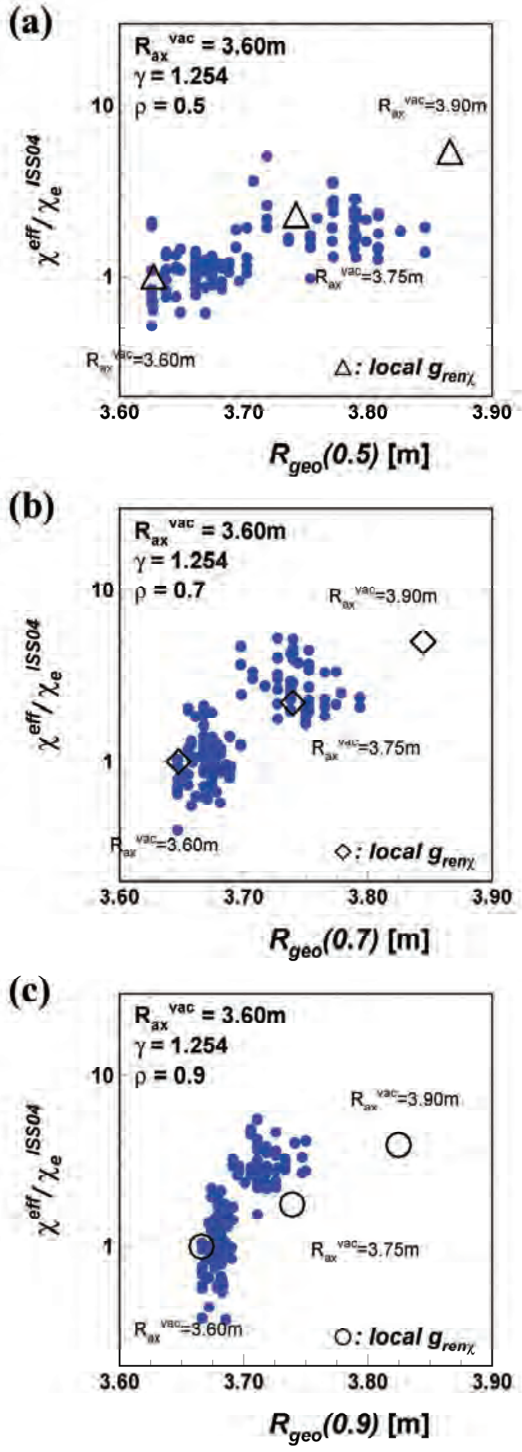

Fig. 2 Dependence of the local transport coefficients χ^{eff}/χ^{ISS04} on $R_{geo}(\rho)$. (a) $\rho = 0.5$, (b) $\rho = 0.7$ and (c) $\rho = 0.9$.

Particle transport and fluctuation characteristics around neoclassically optimized configurations in LHD

K. Tanaka, C. Michael, [a]L. N. Vyacheslavov, M. Yokoyama, [b]S. Murakami, [c]A. Wakasa, [d]H. Takenaga, [e]K. Muraoka, K. Kawahata, T. Tokuzawa, T. Akiyama, K. Ida, M. Yoshinuma, I. Yamada, K. Narihara, H. Yamada and the LHD Experimental group

National Institute for Fusion Science,322-6 Oroshi-cho, Toki 509-5292, Japan

[a]Budker Institute of Nuclear Physics, 630090 Nobosibirsk, Russia

[b]Department of Nuclear Engineering, Kyoto Univ., Kyoto 606-8501, Japan

[c]Graduate School of Engineering, Hokkaido Univ., Sapporo 060-8628, Japan

[d] Japan Atomic Energy Agency, 801-1, Mukoyama, Naka 311-0193, Japan

[e]School of Engineering, Chubu Univ., Kasugai 487-8501, Japan

Density profiles in LHD were measured and particle transport coefficients were estimated from density modulation experiments in LHD. The data set contains the wide region of discharge condition. The dataset of different magnetic axis, toroidal magnetic filed and heating power provided data set of widely scanned neoclassical transport. At minimized neoclassical transport configuration in the dataset (Rax=3.5m, Bt=2.8T) showed peaked density profile. Its peaking factor increased gradually with decrease of collisional frequency. This is a similar result observed in tokamak data base. At other configuration, peaking factor reduced with decrease of collsional frequency. Data set showed that larger contribution of neoclassical transport produced hollowed density profile. Comparison between neoclassical and experimental estimated particle diffusivity showed different minimum condition. This suggests neoclassical optimization is not same as anomalous optimization. Clear difference of spatial profile of turbulence was observed between hollowed and peaked density profiles. Major part of fluctuation existed in the unstable region of linear growth rate of ion temperature gradient mode.

Keywords: density profile, peaking factor, density modulation experiments, neoclassical transport, anomalous transport, diffusion coefficient, convection velocity, phase contrast imaging, turbulence

1. Introduction

Optimization of magnetic configuration for reducing energy and particle transports is an important issue for studies in stellarator/heliotron devices. In LHD, magnetic properties can be changed by scanning magnetic axis positions then systematic studies of the effects of magnetic configuration on transports are possible. Optimized configuration for reducing neoclassical transport was studied for R_{ax}=3.5~3.75m using the DCOM code and was found that the neoclassical transport was to be minimum at R_{ax}=3.5m in the plateau regime and at R_{ax}=3.53m in the 1/ν regime [1]. Then, it was experimentally observed that the effective helical ripple, which is an influential parameter of neoclassical transport in the 1/ν regime, played an important role on global energy confinement [2]. Inter machine studies show smaller effective helical ripple configuration showed higher enhancement of global energy confinements compared with international stellarator scaling 2005 [2]. This suggests that neoclassical optimization may also affect anomalous transport because transport in the data set of [2] was dominated by anomalous transport. In the previous work, systematic studies of particle transport and fluctuation properties were carried out at R_{ax}=3.6~3.9 m [3,4]. Particle diffusion was found to be anomalous and the smaller at the more inward shifted configuration. Simultaneously, the smaller fluctuation level was observed. Density profiles were hollow in many case of discharge, and became peaked ones at higher magnetic fields at higher collisionality. When density profiles were hollow, particle convection was comparable with that from the neoclassical prediction.

In this article, particle transports were studied at around optimized neoclassical configuration in order to investigate linkage between neoclassical and anomalous

author’s e-mail: ktanakal@nifs.ac.jp

transport.

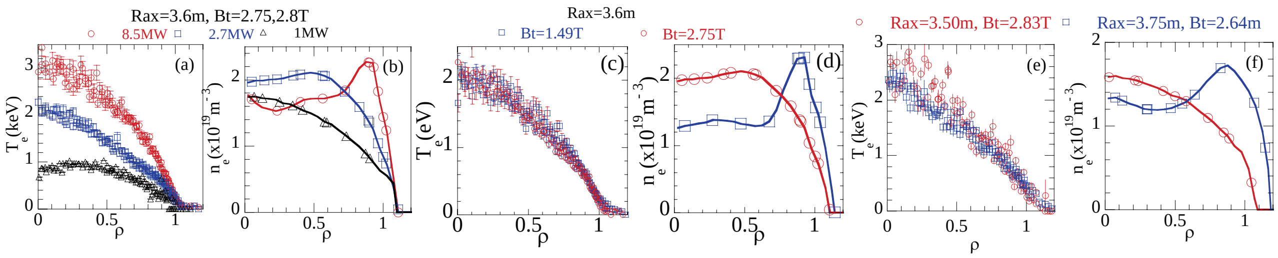

Fig.1 Comparison of (a), (c), (e) T_e and (b), (d), (f) n_e profiles under different condition. (a), (b) different NBI power, (c), (d) different magnetic field (e), (f) different magnetic configuration (Rax=3.5m and 3.75m is reduced and enhanced helical ripple configuration respectively

2. Experimental results

2.1 General character of density profile in LHD

Figure 1 shows electron temperature (T_e) and electron density (n_e) profiles under various conditions. The density profiles were measured by multi channel far-infrared interferometer [5] and electron temperature profiles were measured by YAG Thomson scattering [6]. The density profiles vary depending o the discharge condition. This is clear contrast to tokamak density profiles, which are peaked in the most of the case [7, 8]. Density profile changes from peaked one to hollow one with increasing of heating power as shown in Fig. 1 (b). With higher heating power, steeper T_e gradient was formed. This higher Te gradient can cause outward convective flux [3]. Figure 1 (c) and (d) show T_e and n_e profiles under different toroidal magnetic field (Bt) with almost identical T_e profiles. The toroidal magnetic field is also can affects the density profile. The density profiles became more hollow at lower magnetic field. The magnetic configuration can affect density profile as well. As shown in Fig.1 (f), at more outward configuration, density profiles tend to be hollow. Magnetic axis position were also influential parameter on density porofile.

Figure 2 shows parameter dependence of density peaking factor. The density peaking factor was defined as the ratio between the density at ρ (normalized radius) =0.2 and volume averaged density. The volume averaged density was calculated within the last closed flux surface. Figure 2 (a) shows comparison of dependence on ν_b^*, which is normalized by the collisional frequency at plateau and banana regime and defined by the following equation.

$$\nu^*_b = \nu_{ei}/(\varepsilon_t^{3/2} v_T/qR) \qquad (1)$$

where ε_t is an inverse aspect ratio, v_T is an electron thermal velocity, q is a safety factor and R is a major radius. In the single helicity stellarator, the boundary of plateau and banana region can be defined [9]. LHD is multiple helicity configuration, however, for the comparison with JT60U elmy H mode data, ν_b^* was used. In JT60U, the peaking factor increases with decrease of ν_b^*. This is widely observed in tokamak [7,8]. In LHD, density peaking gradually increased with decrease of ν_b^* at Rax=3.5m, Bt=2.8T only. At other configuration (Rax=3.6m in Bt=2.75,2.8T, Rax=3.75m in Bt=2.64T and Rax=3.9m, Bt=2.54T), the density peaking factor reduced with decrease of ν_b^*. This is an opposite tendency to tokamak.

The data in Fig.2 are from NBI heated plasma, however, particle fueling from the NBI did not affect density peaking in both JT60U and LHD [3,4,7]. The variations of density profiles are not due to the difference of particle fueling but due to the difference of transport. Figure 2(a) suggests there is a common physics mechanism to determine density profile in JT60U and Rax=3.5m, Bt=2.8T in LHD, but there are different mechanism in other configuration of LHD.

Figure 2 (b) and (c) show dependence on normalized collision frequency (νh*) of the stellarator/helical configurations, which is defined as following equation.

$$\nu^*_h = \nu_{ei}/(\varepsilon_{eff}^{3/2} v_T/qR) \qquad (2)$$

where ε_{eff} is an effective helical ripple, which represents multiple helicity and is defined as [10],

$$\varepsilon_{eff} = \left(\frac{9\sqrt{2}}{16} \frac{\nu}{v_d^2} D \right)^{2/3} \qquad (3)$$

where ν, v_d and D are the collision frequency, the drift velocity and the particle diffusivity in the enhanced helical ripple trapped region (the 1/ν region), respectively. At the upper boundary of the 1/ν region, ν^*_h becomes around unity.

As shown in Fig.2 (b), (c), the density peaking factor reduced with decrease of ν^*_h. Also, configuration dependence on ν^*_h became clear compared with Fig.2 (a).

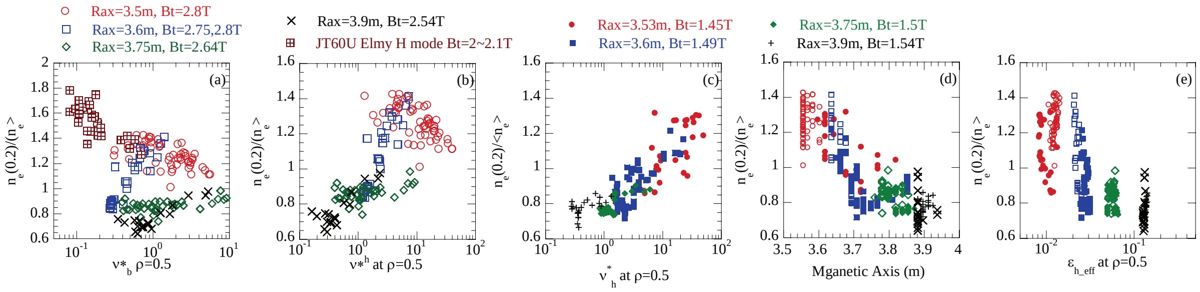

Fig.2 Parameter dependence of density peaking factor (a) comparison between LHD and JT60U, comparison between four configuration of LHD at (b) high filed and (c) low filed, dependence on (d) shifted magnetic axis position and (e) effective helical ripple

Data set of four configurations (Rax=3.5, 3.6, 3.75 and 3.9m) contained different ν^*_h and corresponding different peaking factor. At both high field (Fig.2 (b)) and low field (Fig.2 (c)), the density peaking factor was higher at more inward shifted configuration, where neoclassical transport was smaller. At the lower magnetic filed, density peaking factor was smaller and peaking factor depends more clearly on ν^*_h. As shown in Fig. 1 (d), density profile becomes more hollow at lower field. And the hollow density profile can be due to neoclassical outward convection [3]. One possible interpretation is, at lower field, the contribution of neoclassical can became larger.

Figure 2 (d) shows peaking factor dependence on shifted magnetic axis. The appropriate magnetic flux surface was selected for the Abel inversion and mapping for Thomson scattering. The axis position is at the vertical cross section. One important thing is the data of Fig.2 (d) included both low and high filed. The peaking factor of shifted data of Rax=3.53m at 1.45T was close to the peaking factor of Rax=3.75m at 2.64T. This indicates that the shifted inward configuration is equivalent to the outward shifted configuration without Shavranov shift.

Figure 2 (e) shows dependence on effective helical ripple (eq.(2)). The effective helical ripple was calculated taking into account for the finite beta effects [11]. Most of the data of LHD in Fig.2 are in plateau regime, where ν^*_h is larger than unity. Although the effective helical ripple is representative ripple in 1/ν regime, the effective helical ripple played a role on density profile as well as global energy confinement [2]. However, as shown in Fig.2 (e), the density peaking varies at almost same ε_{eff}. Other hidden parameter should exist to determine density profile.

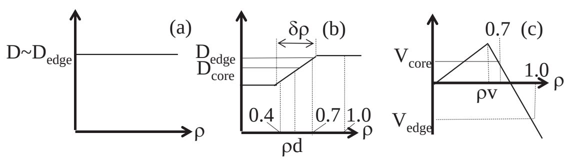

Fig.3 Assumed profile of D and V. (a) spatially constant D for localized modulation amplitude (b) two variable D for core sensitive case and (c) two variable V for all cases

2.2 Parameter dependence of particle transports

Particle transport in LHD was studied from density modulation experiments [3,4]. The diffusion coefficient (D) and convection velocity (V) were determined to fit modulation amplitude, phase and background density profiles [3,4]. Figure 3 shows the model used for the fitting. When modulation frequency is high or diffusion coefficient low, model of spatially constant D was used as shown in Fig.3 (a). When modulation penetrated deeper to core, two diffusion coefficient model was used as shown in Fig.3 (b).

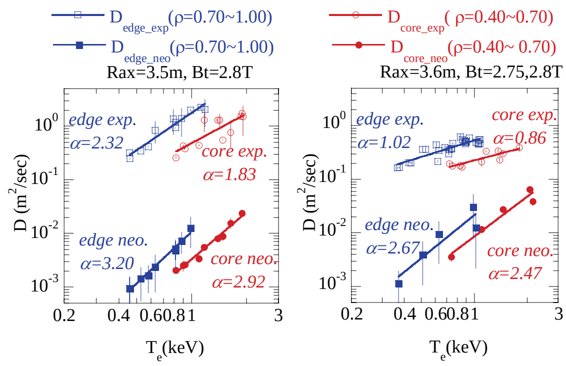

Fig. 4 Electron temperature dependence of diffusion coefficient (a) Rax=3.5m, Bt=2.8T and (b) Rax=3.6m ,Bt=2.75,2.8T. Dcore_exp, Dedge_exp are experimentally estimated core and edge diffusion coefficient. Dcore_neo, Dedge_neo are neoclassical values calculated by DCOM. Error bar of experimental values are fitting error, error bar of neoclassical values are standard deviations at ρ=0.4~0.7 for core value, and at ρ=0.7~1-.0 for edge value. T_e is also averaged at ρ=0.4~0.7 for core value, and at ρ=0.7~1-.0 for edge value.

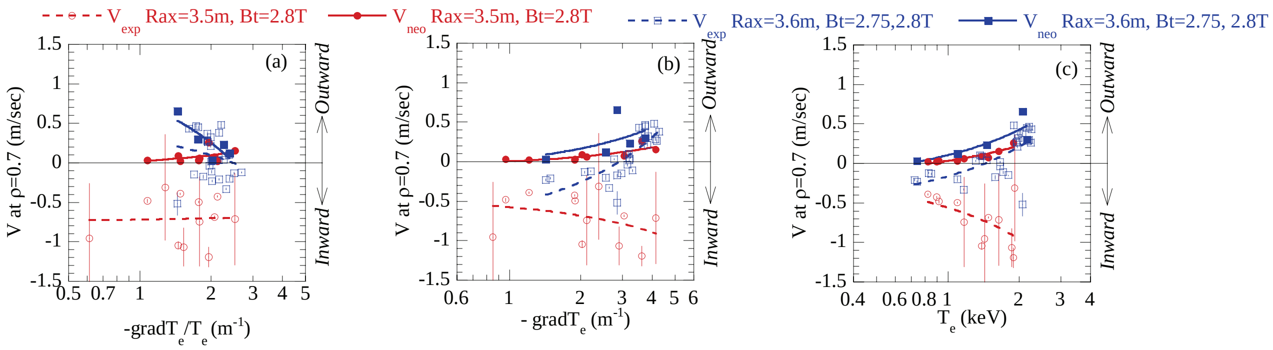

Fig.5 Dependence of Vcore (at ρ=0.7) on (a) normalized T_e gradient, (b) T_e gradient and (c) T_e. normalized T_e gradient, T_e gradient and T_e are averaged value at ρ =0.4~0.7.

In the model of Fig.3 (b), the diffusion coefficient transit at ρ=ρd with transition with δρ. The convection velocity was assumed to be zero at plasma center and to increase linearly and change slope at ρ=ρv. The value of ρd was fixed to be 0.7 for all cases. For Rax=3.5m, Bt=2.8T, δρ was fixed to 0.6 and , ρv was fixed to be 0.5. For other configuration, when modulation penetrated deeper to core, δρ was fixed to 0.3 and ρv was fixed to be 0.5. In order to compare with previous results [3,4], D_{edge} was D_{core}, V_{edge} and V_{core} was defined as follows. The spatial constant D was used as a D_{edge}, since the modulation amplitude was localized in the edge region. D_{core} and D_{edge} were defined the averaged value between ρ =0.4 and 0.7 and between ρ =0.7 and 1.0 respectively for the two values model of D. V_{core} and V_{edge} was defined as the value at ρ=0.7 and ρ=1.0 respectively.

Figure 4 shows the T_e dependence of D_{core} and D_{edge}. Neoclassical values calculated by DCOM[1] are also shown. The fitted lines are $A \times T_e^{\alpha}$, where A is a proportional factor and α is an exponent. Neoclassical values are smaller at Rax=3.5m than at Rax=3.6m at same T_e. However, experimental estimated D_{core} and D_{edge} were larger at Rax=3.5m than at 3.6m. Clear difference of T_e dependence of both neoclassical and anomalous D was also observed. The exponent of both neoclassical and experimental D_{core} and D_{edge} were larger at Rax=3.5m than at Rax=3.6m. At Rax=3.5m, the exponent of D_{core_neo} were factor 1.6 larger than at D_{core_exp} and exponent of D_{eddge_neo} were factor 1.4 larger than D_{core_exp}. At Rax=3.6m, the exponent of D_{core_neo} were factor 2.6 larger than at D_{core_exp} and exponent of D_{eddge_neo} were factor 2.6 larger than D_{core_exp}. At Rax=3.6m, large difference of the exponent between neoclassical and anomalous D were observed. This suggests the neoclassical D will be close to experimental D at higher T_e at Rax=3.6m .

Figure 5 shows comparison of parameter dependence of V_{core} of neoclassical and experimental values. The neoclassical particle flux is given by the following equation [12].

$$\Gamma_{e\_neo} = -nD_1 \left\{ \frac{\nabla n_e}{n_e} + \frac{eE_r}{T_e} + \left(\frac{D_2}{D_1} - \frac{3}{2} \right) \frac{\nabla T_e}{T_e} \right\} \quad (4)$$

The off diagonal term of the eq.(4) is convective flux, then , neoclassical convection velocity was defined by the following equation.

$$V_{e\_neo} = -D_1 \left\{ \frac{eE_r}{T_e} + \left(\frac{D_2}{D_1} - \frac{3}{2} \right) \frac{\nabla T_e}{T_e} \right\} \quad (5)$$

The data set used in this article was in the transition region or ion root region. In equation (4), the contribution of radial electric field on convection velocity was small and neoclassical convection was dominated by thermo diffusion term, which is the second term of eq.(5). As shown in Fig. 5, at Rax=3.6m, when convection velocity was outward directed and density profile was hollow, experimental convection velocity was comparable with neoclassical convection. This is same as the case of Rax=3.75, and 3.9m [3]. The clear T_e dependence of V_{core} was observed as shown in Fig.5 (c). So, the electron temperature is likely to be determine V_{core} as well as D

2.3 Configuration dependence of neoclassical and anomalous particle transport coefficient

There is an expectation that neoclassical optimization minimize anomalous transport simultaneously [2]. This is supported by theoretical work. In the single helicity heliotron configuration, smaller helical ripple configuration can generate larger zonal flow and can stabilize turbulence effectively [13]. The configuration dependence of particle transport coefficients are shown in Fig. (6) about high field case, and in Fig.7 about low field case.

Since both diffusion coefficients and convection velocity depends on T_e as described in the previous section, for the comparisons between different configurations, the values at the same Te were connected. As shown in Fig. 6 (a) and (b), at high field, the minimum of neoclassical D is

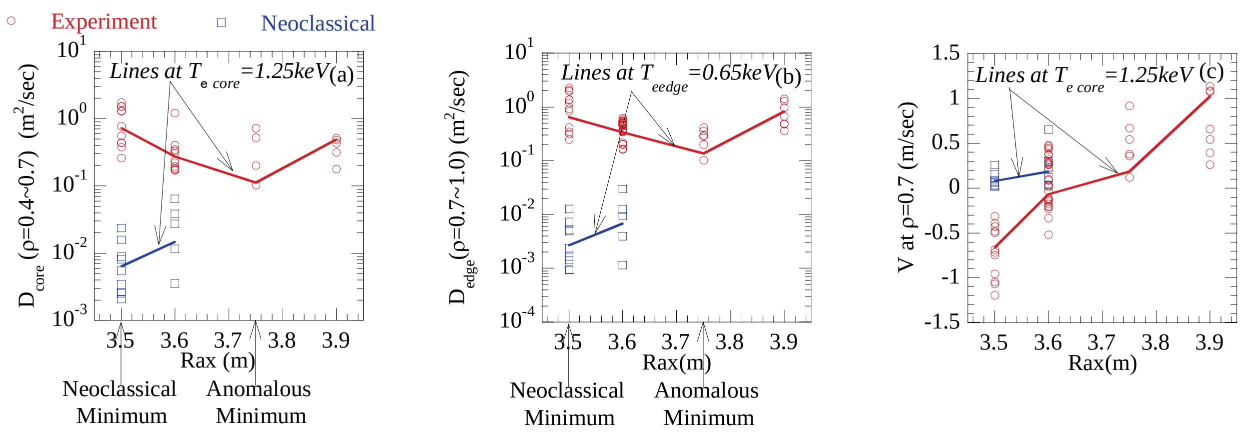

Fig.6 Comparison between neoclassical and anomalous transport coefficients at high field (a) Dcore, (b) Dedge and (c) Vcore at high filed (Bt=2.8T for Rax=3.5m,Bt=2.75, 2.8T for Rax=3.6m, Bt=2.64T for Rax=3.75m, Bt=2.54T for Rax=3.9m) Red and blue lines indicate the values at the same temperature. Neoclassical values were calculated by DCOM code[1]

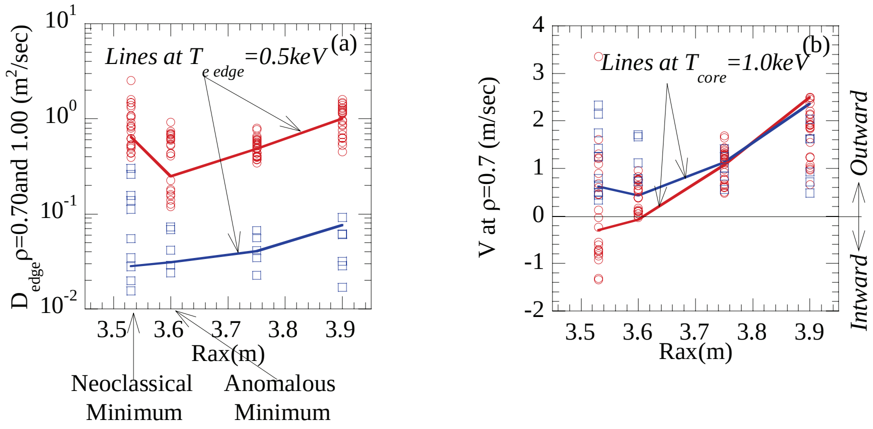

Fig.7 Comparison between neoclassical and anomalous transport coefficients at high field (a) Dedge and (c) Vcore at low filed (Bt=1.45T for Rax=3.53m,Bt=1.49T for Rax=3.6m, Bt=1.5T for Rax=3.75m, Bt=1.54T for Rax=3.9m) Red and blue lines indicate the values at the same temperature. Neoclassical values were calculated by GSRAKE code[14]

at Rax=3.5m, however experimental D was minimum at Rax=3.75m. On the other hand as shown in Fig.7 (a), at low field, neoclassical D_{edge} was minimum at Rax=3.53m, but experimental D_{edge} was minimum at Rax=3.6m. There are difference of the minimum configuration between neoclassical and anomalous particle diffusivity. The core convection both at high field and at low field became smaller at more inward shifted configuration. However, inward directed convection cannot be explained by neoclassical calculation.

2.3 Possible role of turbulence on density profile

The inward directed pinch in tokamak was widely observed and cannot be explained by ware pinch when collisional frequency becomes smaller [8,15]. The role of ITG/TEM turbulence was suggested [8,16]. In heliotron configuration, recently, theoretical work was done to investigate role of ITG/TEM turbulence[17]. In ref. 17, the direction of the quasi linear particle flux was estimated for the peaked and hollow density profile for the magnetic configuration of LHD. When density profile was hollow quasi linear particle flux was directed inward, then, as density profile becomes peaked, the direction of fluctuation driven particle flux reversed to outward. Since, particle source was negligible in the core region, particle flux should be zero. Possible interpretation of the role of fluctuation is as follows.

When density profile was hollow, particle flux driven by ITG/TEM turbulence was inward directed. This inward directed particle flux can be balanced with outward directed neoclassical convection to satisfy the particle balance. This is consistent with the results that diffusion was anomalous and outward convection was comparable with neoclassical when density profile was hollow [3].

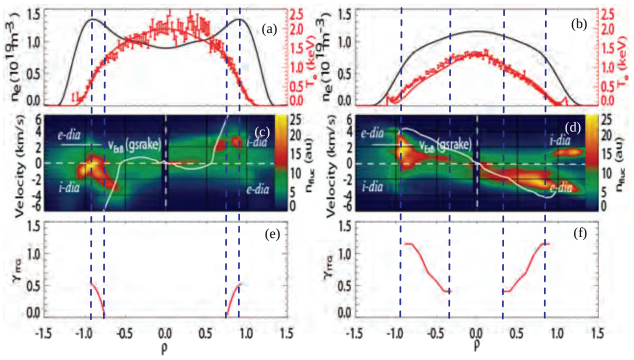

Fig.8 Comparison of (a), (b) n_e and T_e profile and (c), (d) fluctuation amplitude profile (k=0.1~0.6mm^{-1}) and (e), (f) ITG/TEM linear growth rate calculated by GOBLIN code [17]

When density profiles are peaked, particle flux can be driven by turbulence only. This is also consistent both diffusion and inward convection was anomalous for peaked density profiles.

Turbulence was measured by two dimensional phase contrast imaging [18,19] for hollow and peaked density profile. As shown in Fig.8, clear difference of fluctuation amplitude was observed. The linear growth rate of ITG/TEM turbulence was calculated by the GOBLIN code [17]. As shown in Fig.8 (c), (d), dominant part of turbulence existed at the location where linear growth rate was positive as shown in Fig. 8 (e), (f). Figure 8 (c) and (d) showed fluctuation amplitude only. The turbulence driven particle flux cannot be measured by using phase contrast imaging. However, observed fluctuation can possibly drive inward directed particle flux at hollow density profile and zero flux for peaked density profile.

3. Summary

The parameter dependence of density profile and particle transport was studied in the wide range of operational regime of LHD. Two different dependence on ν^*_b of density peaking factor was found. One is the gradual increase of peaking factor with reduction of ν^*_b at Rax=3.5m, 2.8T, where neoclassical transport minimum in the dataset. This is similar with tokamak behavior. The other is decrease of peaking factor with decrease of ν^*_b. This is observed in the other configuration and is particular in LHD. Smaller neoclassical may result in tokmak like behavior. The electron temperature dependences of D and V were investigated at around optimum neoclassical configuration at Rax=3.5m, 2.8T, and Rax=3.6m, 2.75,2.8T. The diffusion coefficient was one order magnitude larger than neoclassical value at both configurations, however, T_e dependence was different. At Rax=3.5m, 2.8T, T_e dependence was stronger than ones at Rax=3.6m, 2.75, 2.8T. At neoclassical minimum configuration (Rax=3.5m, 2.8T), the convection velocity at $\rho = 0.7$ was inward direction, which was not predicted by neoclassical theory. On the other hands, at Rax=3.6m, 2.75,2.8T, the convection velocity at $\rho = 0.7$ was inward directed at lower T_e and reverse to outward direction at higher T_e. When the convection velocity was outward directed, it was comparable with neoclassical value. These indicates, at neoclassical minimum configuration (Rax=3.5m, 2.8T), both diffusion and convection was determined by the anomalous process, but at Rax=3.6m, 2.75,2.8T, diffusion process was determined by the anomalous process, however convection was determined by neoclassical process at higher T_e. The present results shows neoclassical minimum is not same as anomalous minimum. The difference of the spatial profile of turbulence was observed, which suggested role of ITG/TEM turbulence on density profile

Acknowledgements

This work was supported by the National Institute for Fusion Science budget NIFS05ULHH511.

References

[1] S. Murakami et al Nucl. Fusion **42** (2002) L19–L22
[2] H.Yamada et al. Nucl. Fusion, **45**, 1684 (2005)
[3] K. Tanaka et al, FUSION SCIENCE AND TECHNOLOGY **51** 97 JAN. (2007)
[4] K. Tanaka *et al*., Nucl. Fusion **46** (2006) 110.
[5] K. Tanaka *et al*., to be submitted to PFR.
[6] K. Narihara *et al*., Rev. Sci. Instrum. **72** (2001) 1122.
[7] H. Takenaga, K. Tanaka, K. Muraoka et al., to be submitted Nucl. Fusion
[8] Angioni *et al*., Phys. Plasmas **10** (2003) 3225
[9] K. Miyamoto published by Iwanami Book Service Centre, Tokyo 1997 Fundamentals of Plasma Physics and Controlled Fusion.
[10] C. D. Beidler and W.N.G. Hitchon, Plasma Phys. Control. Fusion **36** (1994) 317.
[11] M.Yokoyama at al., *Journal of Plasma and Fusion Research*, **81**,83, (2005)
[12] V.Tribaldos,, *Phys. Plsama **8**, 1229, (2001)*
[13] H.Sugama, T-H. Watanabe, *Phys. Plasmas* **13**, 012501, (2006)
[14] C.D. Beidler and W.D. D'haeseleer, *Plasma Phys. Control. Fusion* **37** 463 (1995)
[15] Hoang G.T. *et al* 2003 *Phys. Rev. Lett.* **90** 155002-1
[16] Hoang G.T. *et al* 2004 *Phys. Rev. Lett.* **93** 135003-
[17] O. Yamagishi *et al.*, Phys. Plasmas **14** (2007) 012505.
[18] C. Michael et al., Rev. Sci. Instrum. **77**, 10E923-1(2006)
[19] C. Michael et al.,to be published, Journal of Plasma and Fusion Research

Proceedings of ITC/ISHW2007

Quantifying profile stiffness

B.Ph. VAN MILLIGEN[1)], R. SÁNCHEZ[2)], V. TRIBALDOS[1)], and V.I. VARGAS[1)]

[1)] *Asociación EURATOM-CIEMAT para Fusión, Avda. Complutense 22, 28040 Madrid, Spain*

[2)] *Fusion Energy Division, Oak Ridge National Laboratory, P.O. Box 2001, Oak Ridge, TN 37831-2001, USA*

October 10, 2007

Profile stiffness is quantified using a simple technique. The approach is tested on a paradigmatic numerical stiff transport model for one field (particles). The stiffness is found to exhibit radial structure and to depend on collisionality, which might help explaining the observed lack of stiffness in stellarators, as compared to tokamaks. The extension of the approach to heat transport requires some care. A proposal for a stiffness quantifier for heat transport is made, and it is tested on data from the TJ-II stellarator.

Keywords: profile stiffness, anomalous transport, critical gradient, tokamak-stellarator comparison

DOI: 10.1585/pfr.1.001

Profile stiffness (also known as profile consistency or resilience) is the striking phenomenon that temperature or pressure profiles tend to adopt the same shape, regardless of the applied drive, at least in a certain parameter range. The phenomenon is well-established for tokamaks, but elusive in stellarators [1]. This is slightly enigmatic, since (a) power degradation is a universal phenomenon in stellarators, with a similar power dependence as in tokamaks [2] and (b) it is believed that threshold-triggered instabilities (leading to enhanced transport) should be operative both in tokamaks and stellarators. This leads to the expectation that profile stiffness should also be present in stellarators, if to a less degree (and less obviously) than in tokamaks.

The detection of profile stiffness based on the direct comparison of profiles does not allow a quantification of the degree of stiffness, while the full 1-D modelling of transport requires making assumptions not related to the stiffness issue. Therefore, a stiffness quantifier is needed to resolve this issue. In the present work we apply a standard quantifier for profile stiffness to a paradigmatic stiff particle transport model. We then discuss the possible (non-standard) extension of the method to heat transport and present first results for the TJ-II stellarator.

Profile stiffness can be understood as the sub-linear response of profile amplitudes to a (small) change in drive. Pure diffusive transport models with fixed parameters produce a proportional response of profiles to changes in fuelling or heating, since the diffusion equation is linear in the profile amplitude and the source strength. Thus, the search for profile stiffness is closely related to the study of the dependence of transport coefficients on (gradients of) the transported quantity, since such a dependence would break the linearity of the diffusion equation.

Such studies have been undertaken before [3], in the framework of the analysis of perturbative transport. In the cited reference, a distinction was made between the steady state (or "power balance") transport coefficient $D^{\rm pb} = -\Gamma/\nabla n$ (here, Γ is the particle flux and ∇n the density gradient), and the perturbation response value $D^{\rm inc} = -\partial\Gamma/\partial\nabla n$, dubbed the "incremental" transport coefficient. If $D^{\rm inc} > D^{\rm pb}$, the profiles will respond sub-linearly to changes in the source term, thus producing stiffness. Accordingly, a "stiffness factor" can been defined (by analogy to [4]):

$$C = \frac{D^{\rm inc}}{D^{\rm pb}} = \frac{\nabla n}{\Gamma}\frac{\partial\Gamma}{\partial\nabla n}, \tag{1}$$

so that $C > 1$ would indicate some degree of stiffness.

The evaluation of $D^{\rm inc}$ requires a (small) perturbation of the source term and profiles, either spontaneous or induced externally. However, the relevant variables of systems near a critical steady state tend to fluctuate spontaneously around a mean value. This property can be exploited to obtain another, equivalent estimate of the stiffness that does not require perturbing the system. Interpreting the mean amplitude of the fluctuations around the steady state values (i.e. their standard deviation) as the small change symbolised by ∂ symbol in Eq. (1) [5]:

$$D^{\rm fluct} = RMS(\Gamma)/RMS(\nabla n) \tag{2}$$

where $RMS(f) = \left\langle (f - \langle f \rangle)^2 \right\rangle^{1/2}$, and the angular brackets refer to a time average. In steady state, and assuming that the system response to perturbations is linear to first approximation, we expect $D^{\rm fluct} \simeq D^{\rm inc}$.

In the following, we study the stiffness parameter C using a simplified transport model, considered paradigmatic for transport controlled by a critical gradient. The model is described in considerable detail elsewhere [6]. The simplified model is Markovian in nature and the time evolution of the single field $n(x,t)$, which may be interpreted as a (particle) density, obeys, in one dimension, a Generalized Master Equation:

$$\frac{\partial n(x,t)}{\partial t} = S(x,t) + \frac{1}{\tau_D}\int_0^1 dx' p(x-x';x',t)n(x',t) - \frac{n(x,t)}{\tau_D}, \tag{3}$$

author's e-mail: boudewijn.vanmilligen@ciemat.es

The domain of the system is $0 \leq x \leq 1$, implying a normalisation of the spatial scales of the system to the system size. τ_D is a waiting time and specifies the mean time a particle remains at a given location before taking a step. We set $\tau_D = 1$, implying a normalisation of the time scales of the system to the mean waiting time. $S(x,t)$ is an external particle source, and compensates edge losses due to the absorbing boundary conditions imposed at $x = 0, 1$. The function p is a "particle step distribution". When p is Gaussian, $p(x - x', x', t) = \exp\left[-(x - x')^2/4\sigma^2\right]/2\sigma\sqrt{\pi}$, standard diffusion is recovered in the limit of small step sizes σ (and assuming a smooth density profile [7]):

$$\frac{\partial n}{\partial t} = \frac{\partial^2}{\partial x^2}\left[\frac{\sigma^2}{\tau_D} n\right] + S. \tag{4}$$

Thus, the model is closely related to standard transport models in common use.

The step distribution p is chosen as follows to produce the required critical gradient mechanism:

$$p = \begin{cases} p_0: & |\nabla n| < [\nabla n]_{\text{crit}} \quad (\text{sub} - \text{critical}) \\ p_1: & |\nabla n| \geq [\nabla n]_{\text{crit}} \quad (\text{super} - \text{critical}) \end{cases} \tag{5}$$

When the local gradient is below the critical value (sub-critical), transport is governed by the p_0 step distribution, and when it is above (super-critical), it is governed by the p_1 step distribution. Here, p_0 and p_1 are fixed and symmetric stable probability distributions (of the Lévy type, of which the Gaussian is a special case). Transport at any given location x will therefore be sub- or super-critical as a function of the local value of the density gradient. This introduces a mechanism for self-regulation into the model.

In this work, p_0 is always chosen to be a Gaussian (with width σ_0), while p_1 can either be a Gaussian (with width σ_1) or a Cauchy distribution $p_1(x - x', x', t) = \sigma_1/\pi(\sigma_1^2 + (x - x')^2)$. While a Gaussian distribution models 'normal' diffusive transport, a Cauchy distribution (with a 'long tail') is used to model processes with long-range correlations, typically called 'avalanches' or 'streamers' in the plasma transport context, and representative of turbulent or 'anomalous' transport.

To compute D^{inc}, we will be comparing steady state profiles at slightly different values of the amplitude of the source S. For simplicity, the steady state flux Γ is computed as $\Gamma(x) = \int_{0.5}^{x} dx' S(x')$. The lower limit of the integral corresponds to the system centre at $x = 0.5$. This calculation is sufficiently accurate for the purpose of evaluating D^{inc}. However, for the calculation of D^{fluct} we will use a different estimate of the flux that includes fluctuating contributions (see below).

The numerical calculations are performed in the domain $0 \leq x \leq 1$, on a grid with either $N = 2000$ (high resolution) or $N = 200$ (low resolution) grid points, using standard integration techniques for stiff differential equations to advance Eq. (3) in time. In all cases, the source $S(x,t) = S_0$ is taken constant. We first performed a scan of the source rate at high resolution (13 cases), and after

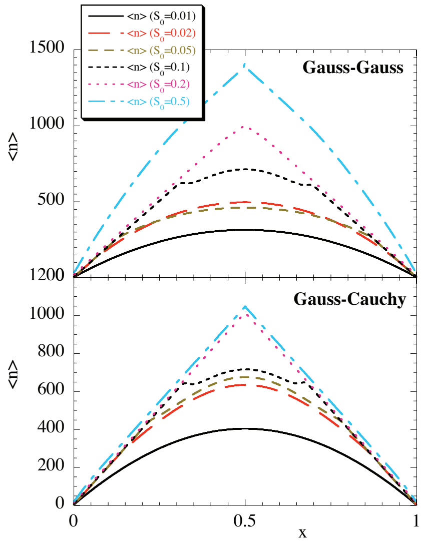

Fig. 1 Profiles vs. S_0: Gauss-Gauss (top) and Gauss-Cauchy (bottom).

checking that the results at lower resolution were equivalent, we performed a bi-dimensional parameter scan of both the source rate and the sub-critical diffusion coefficient, the latter being proportional to σ_0^2 (130 cases).

Source scan: More details on the high-resolution calculations discussed here can be found in Ref. [8]. We set $\sigma_0 = 0.002$, while p_1 is Gaussian with $\sigma_1 = 0.008$ for the cases labelled Gauss-Gauss or "GG" (both transport channels are Gaussian), or p_1 is Cauchy with $\sigma_1 = 0.004$ for the cases labelled Gauss-Cauchy or "GC". The critical gradient is chosen $[\nabla n]_{\text{crit}} = 2000$.

For both series (GG and GC), a scan of the source rate was performed, choosing $S_0 \in \{0.01, 0.02, 0.05, 0.1, 0.2, 0.5, 10\}$. The parameter D^{inc} was computed by comparing the profiles corresponding to two subsequent values of S_0.

Steady state profiles are shown in Fig. 1. The GG and GC profiles are very similar, except for the highest fuelling rate ($S_0 = 0.5$): whereas the GC profile remains critical across the system, the GG profile "bulges", i.e. becomes super-critical. This difference can be ascribed to the larger transport capacity of the super-critical transport channel in the GC case.

In order to quantify the stiffness, we computed the stiffness factor C. Fig. 2 shows the radial profiles of the stiffness factor C for the GC case. The spikes in the figure occur when the local values of the gradient $\nabla n(x)$ corresponding to the two subsequent values of S_0 being analysed are equal. Such points should be ignored, since their statistical error is large, and thus we will base the analysis on the global traces while ignoring the spikes. The figure shows that the critical region (where $C \gg 1$) grows from the edge inward as the source is increased. Next, a super-critical region (with $C \simeq 1$) starts to grow from the edge inward. The super-critical state covers almost the whole sys-

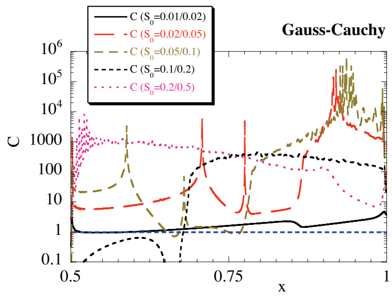

Fig. 2 Case Gauss-Cauchy: profiles of C for different combinations of the fuelling S_0.

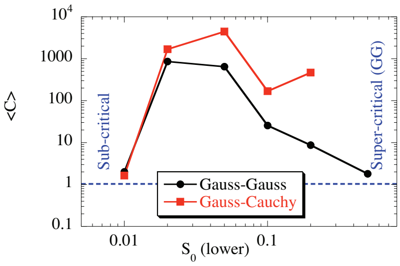

Fig. 3 Source scan, $\langle C \rangle$ vs. S_0.

tem in the GG case at highest fuelling (not shown), while it only affects a narrow boundary layer for the highest fuelling GC case.

Fig. 3 shows $\langle C \rangle$, the radial average of C. The points in the figure are labelled by the *lower* of the two S_0 values used. In comparison to the GG cases, the GC cases do not only yield (slightly) larger values of C, but the range of values of S_0 where $C \gg 1$ exceeds the corresponding range for the GG cases.

Bi-dimensional parameter scan (source rate and diffusivity). Here we scan the source amplitude S_0 and σ_0. The latter can be interpreted as a scan of the sub-critical diffusivity (or "collisionality"). As in Ref. [6], we set $\tau_D = 1$, $S(x) = S_0$, and $[\partial n/\partial x]_{\text{crit}} = 50$. To compute C, the same runs were repeated with $S(x) = 1.1 \cdot S_0$.

Fig. 4 shows $\langle C \rangle$ for the GG cases with $\sigma_1 = 0.08$, and for GC with $\sigma_1 = 0.04$. For GG, the largest possible value of σ_0 is σ_1. For GC, no such limit exists on σ_0. It is observed that $\langle C \rangle$ is a sensitive diagnostic for criticality.

In all series studied, $\langle C \rangle$ is seen to increase gradually with increasing σ_0, reach a maximum value and then drop somewhat abruptly and make a sharp transition to its sub-critical expectation value ($C = 1$) at a precise value of σ_0. For the GC cases, the point where the system transits from a fully sub-critical state to a critical state has been computed in previous work [6]. This critical power threshold is given by: $S_c = 2\sigma_0^2/\tau_D [\nabla n]_{\text{crit}}$, or $\sigma_0 = \sqrt{S_c}/10$ with our choice of parameters. This matches the results exactly.

Stiffness from fluctuations. In the case of our numerical model, it is straight-forward to compute the fluctuating gradient, while the flux can be evaluated from particle conservation ($\partial n/\partial t = -\partial\Gamma/\partial x + S$) in combination with Eq. (3). Thus:

$$\Gamma(x,t) = \int_0^1 dx' K(x-x',x',t)\frac{n(x',t)}{\tau_D(x')}, \tag{6}$$

where $K(x-x',x',t) = \Theta(x-x') - P(x-x',x',t)$, $\Theta(x)$ is the Heaviside function and $P(\Delta,x',t) = \int_{-\infty}^{\Delta} dxp(x,x',t)$ is the cumulative step probability distribution.

Fig. 5 shows the calculation of $\left\langle C^{\text{fluct}} \right\rangle$. Compare these results to Fig. 4. Although the maximum numerical value of $\left\langle C^{\text{fluct}} \right\rangle$ is somewhat lower than that of $\langle C \rangle$, the global trend is the same. The deviation between C and C^{fluct} at points with large stiffness is to be expected, as the system response will be strongly non-linear at such points. The calculation of C^{fluct} is not possible when the system is locally static, which explains why these figures have less data points than Fig. 4.

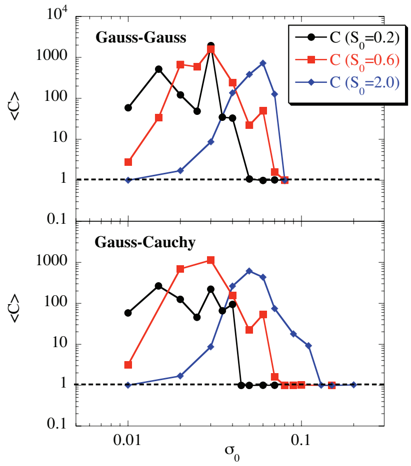

Fig. 4 $\langle C \rangle$ vs. σ_0 for various values of S_0, cases Gauss-Gauss (top) and Gauss-Cauchy (bottom).

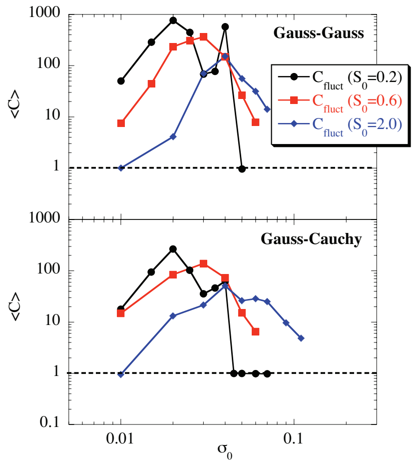

Fig. 5 $\left\langle C^{\text{fluct}} \right\rangle$ vs. σ_0 and S_0, cases Gauss-Gauss (top) and Gauss-Cauchy (bottom).

Heat transport. The preceding analysis was simplified by the fact that the thermodynamic force and the critical parameter were both equal to ∇n. For heat transport, these two quantities do not coincide and the definition of a stiffness quantifier is less obvious. The traditional proposal, $C = \chi^{\rm inc}/\chi^{\rm pb} = -\partial q/\partial(n\nabla T)/\chi$ [4], where χ is the heat diffusivity, will respond only weakly when the system criticality is not determined by $n\nabla T \simeq$ const. In general, a stiffness quantifier C that responds sharply to a given critical condition should be proportional to the inverse of the change in that critical condition, as might indeed be deduced from the modelling efforts in, e.g., [9]. Since we expect Electron Temperature Gradient modes to play a role in the stiffness (if any) of the temperature profile, we believe that the critical parameter must be $\nabla T/T$ [10], so that we define the stiffness of the temperature profile by

$$C^{\rm LTe} = \frac{1}{\chi}\frac{\partial(\chi\nabla\ln T)}{\partial(\nabla\ln T)}. \tag{7}$$

This unorthodox proposal is designed to detect the dependence of the heat diffusivity, χ, on the expected critical parameter for the ETG instability, $\nabla T/T$. Note that many alternative definitions are possible.

Application to the TJ-II Stellarator. Here we report on the first attempt to estimate the stiffness of the temperature profile in the stellarator TJ-II. Profiles at TJ-II are obtained using the single-pulse high-resolution Thomson Scattering diagnostic [11], yielding around 200 data points for the electron temperature T and density n along a chord spanning most of the plasma cross section, with a spatial resolution of 2.25 mm.

The goal of the present analysis is to determine the global transport response to a change in heating. Therefore, we fit the profiles to simple functional forms, thus ignoring any detailed radial structure. This improves the robustness of the calculation of radial derivatives needed to compute $C^{\rm LTe}$. The temperature profile is fit to the sum of two Gaussians, while the density profile is fit to a Gaussian multiplied by a second-order polynomial in ρ^2 (for symmetry). $\rho = \sqrt{\psi}$ is a radial coordinate, where ψ is the normalised poloidal magnetic flux, obtained from the theoretical calculation of the magnetic flux surfaces in vacuum. Finite pressure effects can safely be ignored. The discharges studied here are those reported in Ref. [12].

The error in the profile reconstruction, evaluated using the Jacobian of the fit matrix, is of the order of 10%, lower in the centre but increasing towards the edge. While the temperature profile reconstruction is reliable (i.e. with an error less than 10%) out to about $\rho = 0.7$, the density profile reconstruction is reliable only out to about $\rho = 0.4$. The calculation of $C^{\rm LTe}$ is not very sensitive to the details of the density profile.

To compute χ and $C^{\rm LTe}$, an estimate of the heat flux q is required. The heating source is assumed to have a Gaussian deposition profile, centred at $\rho = 0$, with a fixed width of $\Delta\rho = 0.2$. The heating efficiency is estimated to be

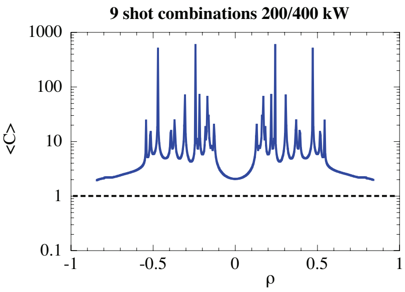

Fig. 6 Stiffness estimate for TJ-II.

60%. Radiation and other losses are ignored. The heat flux is obtained by integrating the net deposited power. In any case, the stiffness factor $C^{\rm LTe}$ is not very sensitive to the details of this calculation. Fig. 6 shows the mean stiffness factor, averaged over 9 equivalent discharge combinations with similar densities and different heating levels. Ignoring the spikes, one observes that a certain profile stiffness exists ($\langle C^{\rm LTe}\rangle > 1$) in the radial range $0.15 \le \rho \le 0.55$, roughly coincident with the T gradient region.

Discussion. The quantification of profile stiffness is directly related to the detection of the dependence of the transport coefficient on the profile gradient. In accordance with this idea and with literature, we make use of a stiffness quantifier C, and show that it provides a useful quantification of stiffness in a paradigmatic transport model. It appears that stiffness has a radial structure and a dependence on system parameters (such as the source or drive, and the collisionality), which could possibly shed some light on the observed differences between tokamaks and stellarators.

The extension of these results to heat transport requires some care. We have suggested a definition and applied it to TJ-II data.

[1] U. Stroth, Plasma Phys. Control. Fusion **40**, 9 (1998).
[2] B. Carreras, IEEE Trans. Plasma Sc. **25**, 1281 (1997).
[3] N.J. Lopes Cardozo, Plasma Phys. Control. Fusion **37**, 799 (1995).
[4] F. Ryter, F. Leuterer, G. Pereverzev, *et al.*, Phys. Rev. Lett. **86**, 2325 (2001).
[5] B.A. Carreras, V.E. Lynch, P.H. Diamond and M. Medvedev, Phys. Plasmas **5**, 1206 (1998).
[6] B.Ph. van Milligen, R. Sánchez, and B.A. Carreras, Phys. Plasmas **11**, 2272 (2004) and *ibid.*, **11**, 3787 (2004).
[7] R. Sánchez, B.Ph. van Milligen, and B.A. Carreras, Phys. Plasmas **12**. 056105 (2005).
[8] B.Ph. van Milligen, B.A. Carreras, V.E. Lynch, and R. Sánchez, Nucl. Fusion **47**, 189 (2007).
[9] F. Imbeaux, F. Ryter, and X. Garbet, Plasma Phys. Control. Fusion **43**, 1503 (2001).
[10] X. Garbet, N. Dubuit, E. Asp, *et al.*, Phys. Plasmas **12**, 082511 (2005).
[11] C.J. Barth, F.J. Pijper, H.J. van der Meiden, *et el.*, Rev. Sci. Instrum. **70**, 763 (1999).
[12] V.I. Vargas, D. López-Bruna, J. Herranz, F. Castejón, and TJ-II Team, Nucl. Fusion, **47**, 1367 (2007).

Proceedings of ITC/ISHW2007

Measurements of micro-turbulence in high beta and high density regimes of LHD and comparison with resistive g-mode scaling

Clive MICHAEL[1)], Kenji TANAKA[1)], Leonid VYACHESLAVOV[2)], Andrei SANIN[2)], Tsuyoshi AKIYAMA[1)], Yoshiro NARUSHIMA[1)], Kiyomasa WATANABE[1)], Hisamichi FUNABA[1)], Sadayoshi MURAKAMI[3)] Katsumi IDA[1)], Mikiro YOSHINUMA[1)], Ryuichi SAKAMOTO[1)], Kazuo KAWAHATA[1)], and Shigeki OKAJIMA[4)]

[1)]*National Institute of Fusion Science, Toki 509-0293, Japan* [2)] *Budker Institute for Nuclear Physics, Novisibirsk, Russia* [3)] *Department of Nuclear Engineering, Kyoto Univ., Kyoto 606-8501, Japan* [4)] *Chubu University, Kasugai, Japan*

November 26, 2007

Density fluctuations are analyzed in high volume average beta and high core density discharges in the Large Helical Device (LHD) using a 2D phase contrast imaging system and far infra-red interferometer. Though both these regimes share similarly high beta gradients, the physical origin of the fluctuations appears to be different. In high volume average beta plasmas, both large and ion-gyro scale density fluctuation levels are compared with the growth rate of resistive interchange modes and a clear correlation is found most particularly in the edge as expected due to having the strongest magnetic hill in this region. In high core density plasmas with internal diffusion barrier, resistive interchange is not a candidate for fluctuations near the barrier because magnetic well exists there. However, fluctuations near the core have a bursty character in time and are destabilized when the temperature profile is transiently hollow immediately after pellet injection and are quiescent and much reduced when it becomes peaked, consistent with a slab ion temperature gradient mode. In configurations with outward shifted magnetic axis, where core plasma pressure and density are greater, fluctuation bursts occur less frequently suggesting anomalous transport is lower.

Keywords: high beta, density fluctuation, phase contrast imaging, MHD, resistive interchange, super dense core regime, ion temperature gradient turbulence

1 Introduction

The Large Helical Device (LHD) has set many impressive results with respect to high performance plasma operation, including operation at low field ($B \sim 0.425$T), high volume average beta (up to 5%) [1], as well as at high field ($B > 2$T), high central beta with high central density produced through an internal diffusion barrier (IDB) [2]. Such high performance regimes are invaluable for fusion reactor operation; high volume average beta for reduction of magnetic field requirement, and high central density operation for production of another possible route to fusion through low temperature, high density operation. It is essential to gain an understanding of limiting factors influencing the performance of these plasmas for a route to a fusion reactor, in particular energy transport, which degrades the performance (such as beta gradient, density gradient, etc) either in a soft manner (gradually increasing with performance) or a hard manner (increasing suddenly above a performance threshold). Transport studies have been carried out on these regimes [3], it is mostly found that transport exceeds the neoclassical level significantly and that it is dominated by fluctuation-driven processes. Moreover, high density operation is not well studied yet. Therefore this study focuses on fluctuation behavior in high performance discharges from measurements based on 2D CO2 laser phase contrast imaging and FIR interferometer, and the role that these fluctuations play on transport.

These two regimes are studied separately, and some attempt is made to unify the results of these regimes, given that they both share high beta (pressure) gradients, which are free energy sources for fluctuations. However, the important processes in each regime appear to be different. In high volume average beta, the main confinement degradation comes from the edge where resistive interchange (or g mode) turbulence appears to be excited as a result of the magnetic hill common to Stellarators and RFPs. In the high core density discharges [4], resistive g is not a candidate for turbulence around the internal diffusion barrier because magnetic well exists in the inner region. In this case it appears that the opposite sign of density and temperature profiles, produced transiently after pellet injection, appears to strongly drive unstable modes in a burst like fashion characteristic of a very hard critical threshold. This is characteristic of a slab ITG mode instability; though other MHD effects such as a ballooning mode may play a role. It appears that outward shifted configurations have less hollow temperature profiles resulting in lower fluctuation level therefore achieving higher central pressure.

This paper is organized as follows. The density fluctuation diagnostic systems are first discussed in Sec 2; in-

author's e-mail: clive@nifs.ac.jp

cluding the technique for spatial localization from line-integrated measurements. In Sec. 3, we introduce measurements in high volume average beta discharges, including theory, experiments and results of dependence of fluctuation (of both large scale and ion gyro-scale) level and position on beta, as well as a comparison of fluctuation characteristics with thermal conductivity obtained from power balance. In Sec. 4, we present the dynamical evolution of core turbulence level in dense core discharges for plasmas in configurations with vacuum magnetic axis position $R_{ax} = 3.65\text{m}, 3.75\text{m}$, and compare with differences of pressure rise. Finally, in Sec. 5, we summarize and compare these regimes.

2 Density fluctuation measurements with CO2 laser phase contrast imaging and FIR interferometer

For density fluctuation measurements we use the CO2 laser 2D phase contrast imaging diagnostic for diagnosis of ion gyro-scale fluctuations (with $1 < k < 10\text{cm}^{-1}$), and the FIR interferometer [5] for diagnostic large scale fluctuations (with $k < 1\text{cm}^{-1}$). Phase counters of the FIR have sufficient precision (1/60 fringe) and bandwidth ($f < 50\text{kHz}$) to diagnose fluctuations at high beta, though at low beta, the fluctuation level is comparable to the noise. Note that the PCI diagnostic does not admit $k = 0$ components because of its optical arrangement, while the FIR interferometer does. Both the PCI and FIR systems only directly measure the line integrated density fluctuation amplitude, rather than the local value. However, with the 2D PCI diagnostic, some moderate spatial resolution is possible as described below. Routinely the fluctuation components near the edge are much stronger than any core components, so for diagnosis of edge resistive g modes, line-integral values are sufficient, but for detailed analysis, and for analysis of turbulence near the core of high core density discharges, a proper analysis to resolve fluctuations along the line of sight is necessary to analyze changes in core fluctuations as distinct from edge fluctuations.

The 2D phase contrast imaging diagnostic system on LHD employs a 2D imaging principle to split the line-integrated fluctuation signal into contributions from different layers along the line of sight, according to the "magnetic shear" principle [6, 7, 8]. The sightline is vertical passing at $R = 3.603\text{m}$, so penetrates from the edge to the core, depending on the magnetic axis position of the plasma (R_{ax}), implying core and edge fluctuation components (from both top and bottom) can be separated. The system cannot, however, fundamentally recover the local fluctuation amplitude because of line-integration effects unless the spectrum is isotropic, which it generally is not [?]. The line-integrated $\tilde{N}$ signal is split into contributions along the line of sight and is related to the local amplitude $\tilde{n}$ according to $\tilde{N}^2(\rho) = \tilde{n}^2(\rho) l_z l_{res}$, where l_z represents the ratio of fluctuation power propagating exactly perpendicular to the probing beam to the total fluctuation power, and l_{res} is an instrumental resolution which is increases with measured fluctuation wavelength. For typically measurements, the peak wavelength is such that the instrumental width is around half a radius, or less near the edge because the average wavelength is generally smaller than in the core.

3 High volume average beta

For high volume average beta plasmas, turbulent transport induced by resistive interchange modes excited, driven by beta gradient in the magnetic hill region in the edge is expected to be a limiting mechanism on the attainable plasma beta in helical devices. In LHD, these modes have been shown to have a "soft" character since their occurrence does not produce a catastrophic effect on plasma operation and since plasma operation has been extended well beyond the Mercier instability boundaries [9]. This is in contrast to pressure (beta) driven instabilites in the edge of Tokamak devices, such as ELMS, which grow very quickly beyond the instability threshold producing a sudden crash. Though the physical mechanism is different, such as a peeling-balooing modes, since the Tokamak does not have magnetic hill because the toroidal current is internal to the plasma. Low order mode numbers are routinely identified and have been compared successfully to predictions of resistive interchange modes [10]. However, theoretically, resistive interchange can be excited up to high order mode numbers, up to the dissipative gyro-scale. Non-adiabatic response due to resistive effects produces an anomalous flux. This is in contrast to a turbulent transport induced by drift wave type instabilities (such as ion temperature gradient (ITG) and trapped electron mode (TEM)) whose drive mechanisms do not depend so directly on beta, rather on functions of normalized density (L_n^{-1}) and temperature (L_T^{-1}) gradients such as $\eta = L_T^{-1}/L_n^{-1}$ (although they are known to be stabilized at higher beta [11]). Because drift and resistive interchange instabilities coexist in the same spatial scale, distinction between them becomes difficult. However, they can be distinguished possibly in (1) coherence with magnetic fluctuations, since ITG/TEM are electro-static, while resistive-g has a magnetic component. In reality, however this may be difficult to detect for ion gyro-scale fluctuations, since magnetic probes external to the plasma are most sensitive to large scale fluctuations and the non-locality of magnetic probe measurements would tend to reduce the coherence of small scale fluctuations, and (2) phase velocity; drift waves propagate poloidally at around the drift velocity plus ExB velocity while resistive interchange turbulence propagates at only the ExB velocity [12].

Previous work on LHD [13] has looked at the role of resistive interchange turbulence and its relationship to the electron heat transport coefficient, and it was shown that at high beta, a transport increases more strongly with beta than predicted by a simple gyro-Bohm type model (incorporating drift wave instabilities); and that a model describing resistive interchange turbulence accurately reproduced the beta tendency of electron heat conductivity. This established (1) the role of high beta/ resistive g on energy transport. Here, however, we plan to show the other possible links, (2) role of high beta on fluctuations and (3) role of fluctuations on energy transport. This is the first such work of a comparison of density fluctuations and energy transport; previously particle transport coefficients were compared with the fluctuation level in low beta high field discharges [14].

3.1 Theory of resistive interchange turbulence

A simple analytic theory verified by numerical simulation was developed by [15, 16, 17]. The growth rate is given as:

$$\gamma = S^{-1/3}\left(\nabla\beta\frac{R_0^2\kappa_n}{2}m\frac{2\pi d\rho}{d\iota}\right)^{2/3}\tau_{hp}^{-1} \tag{1}$$

where, the magnetic Reynolds number $S = \tau_R/\tau_{hp} \propto T^{3/2}n^{-1/2}$, the resistive skin time $\tau_R = r^2\mu_0/\eta$, and the poloidal Alfvén time $\tau_{hp} = R_0\sqrt{\mu_0 m_i n}/B$, with $\eta \propto T^{3/2}n^0$ being the Spitzer resistivity. Therefore, the scaling of the growth rate is not simply given by $\beta = n_e T_e/B^2$, it is given by:

$$\gamma \propto n_e^{1/6}(n_e T_e)^{1/6}B^{-2/3}\kappa_n^{2/3}L_p^{-2/3} \tag{2}$$

Under this theory, the thermal conductivity is:

$$\chi = \gamma W^2, \tag{3}$$

where W is the radial width of the mode [16]. This theory does not clearly guide which is quantity is relevant to compare with density fluctuation level. On one hand, Eq. (3) is derived from mixing length theory, for which $\tilde{n}/n = \lambda/L_n$ where λ is the wavelength of the fluctuation and L_n is the density scale length, therefore being independent of growth rate γ. The γ dependence in Eq. (3) comes from the associated velocity fluctuation amplitude. There are many criticisms to the use of linear growth rates for assessing fluctuation level when another physical process is important for saturation. However, in one study, non-linear and linear simulations have been shown to agree [18]. Therefore, for this case, we compare fluctuation levels $\tilde{n}/n$ with γ, however the obtained increasing trend goes against simple mixing length theory.

3.2 Fluctuation measurements and consistency with resistive g

For this study, density, temperature and magnetic field strength were systematically varied in a series of discharges. At certain times during the flat-top of each discharge when the plasma was at equilibrium, fluctuation and parameter profiles were stored in a small database to be analyzed. The range of central densities and electron temperatures, and magnetic field strengths spanned are shown in Fig. (1), together with lines of constant β, ν_{ei} (related to magnetic Reynolds number S), and gyro-radius. It can be seen that the temperature does not change strongly with density. The volume average β_{vol} reached only up to 3% in these discharges as the helical pitch configuration parameter was $\gamma = 1.25$ rather than $\gamma \sim 1.20$ at which the recent very high beta shots were obtained [1]. The value β_{vol} was calculated from measured density and electron temperature values, applying a single correction factor for all discharges to match the average diamagnetic β.

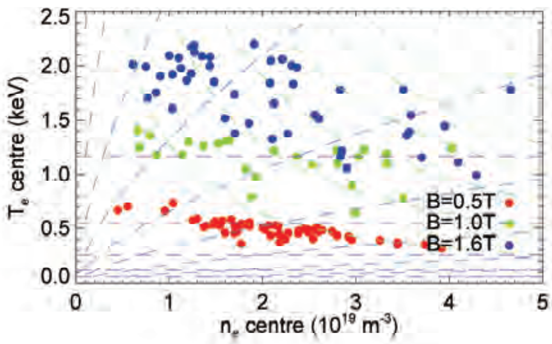

Fig. 1 Density, temperature and magnetic field strengths covered over in the parameter scans, together with contours of β, ν_{ei} and Larmor radius.

The β_{vol} dependence of the line integrated fluctuation levels from the FIR and PCI systems as described in Sec. (2) are plotted in Fig. (2). It is clear that for both systems, there is a strong increasing trend of fluctuation level with β. The increase with β_{vol} appears to be most significant for $\beta_{\text{vol}} > 1\%$, consistent with the findings that $\chi_{exp}/\chi_{gmod} = 1$ for $\beta_{\text{vol}} > 1\%$ in [13], where χ_{exp} is the experimentally derived thermal conductivity and χ_{gmod} is the resistive g mode growth conductivity as in Eq. (3). For the 2D PCI (with $k > 1\text{cm}^{-1}$), the fluctuation level appears to double roughly as beta goes from $\sim 0.3\%$ to 3%, while for the FIR, which measures $k < 1\text{cm}^{-1}$, the increase is much larger. This may be attributed to the fact that resistive interchange turbulence can drive both large scale and ion gyro-scale fluctuations, and has a strong beta dependence, while the level of electrostatic drift wave turbulence (ITG/TEM), which does not depend so explicitly on beta, is strong at the ion gyro-scale but non-existent at large scales. In both diagnostics there also appears to be a large scatter at high β. This may be due to (1) the loss of detail due to line-integration effects, and (2) the resistive g mode growth rate has additional dependence than simply β_{vol}. The motivates us to look more in detail at the comparison of the fluctuation level with the resistive g mode growth rate scaling formula as written in Eq. (2).

A local analysis is performed on one shot from the

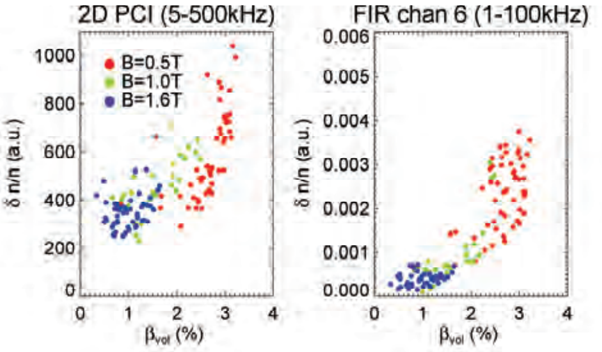

Fig. 2 $\beta_{\rm vol}$ dependence of line integrated fluctuation level for both (a) ion gyro scale structures with $k > 1{\rm cm}^{-1}$ from 2D PCI, and (b) large scale structures with $k < 1{\rm cm}^{-1}$ from the FIR interferometer.

database at $\beta_{\rm vol} = 2.5\%$ considering profiles of density, temperature and pressure, density fluctuation amplitude and normal curvature κ_n, as plotted in Fig. (3). Profiles of fluctuation amplitude both above and below the mid-plane are shown, considering the Shafranov shift as determined from Thomson scattering. The mismatch of these two profiles may be attributable to either (1) because different directional wave-vector components are measured on the top compared with the bottom, or because (2) fluctuation structure is not symmetric on a flux surface, possibly due to ballooning structure. The spatial resolution is around $\Delta\rho = 0.2$ at the edge and around $\Delta\rho = 0.5$ towards $\rho = 0.3$, because the average k is higher towards the edge and since $\Delta\rho \propto 1/k$. The strongest peak appears around $\rho = 1.05$, and appears to correspond to a peak in the pressure gradient profile, plotted in Fig. (3c), demonstrating that pressure gradient may be the free energy source at the edge. However, the normal curvature is positive only outside $\rho = 0.75$ so the the fluctuation power inside this radius must be driven by a different mechanism other than resistive interchange.

Taking the component at $\rho = 0.9$, we compare the local $\tilde{n}/n$ with the local g-mode growth rate in Fig (4). It can be seen that there is a much clearer relationship than in Fig. (2), particularly at higher γ. The cause of this better agreement is the increased density dependence arising from the S dependence in Eq. (2). This density dependence is highlighted in Fig. (5), where line integrated $\tilde{N}/N$ is compared with both $\langle nT\rangle/B^2 \sim \beta_{\rm vol}$ and $\langle n(nT)\rangle/B^2$ (where $\langle\rangle$ denotes volume averaging). The χ^2 residual of points conforming to a smooth curve is a factor of two better in the case of the stronger density dependence (b). (Note, however that the g-mode growth rate γ_g^6 from Eq. (2) has a B^{-4} scaling as compared with the B^{-2} dependence here.)

The increased density dependence is also highlighted by comparing 2 discharges with similar $\beta_{\rm vol}$, but significantly different density. The profiles of fluctuation level $\tilde{n}/n$, n, T and are compared in Fig. (6). It is clear that

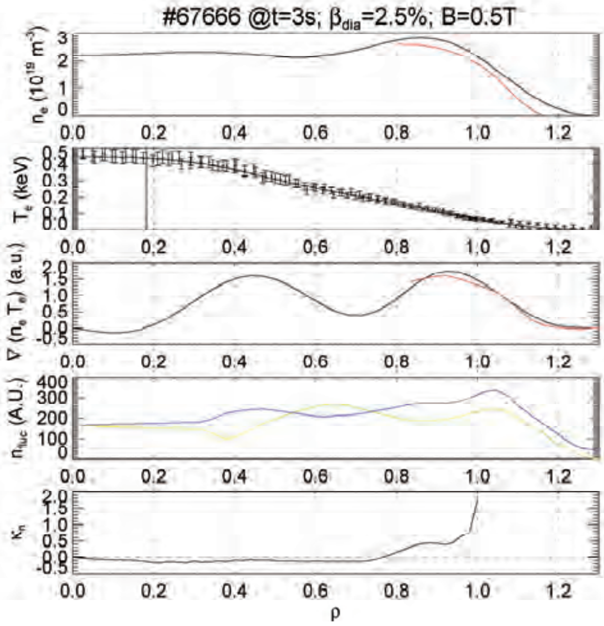

Fig. 3 Comparison of profiles (a) density, (b) temperature, (c) pressure gradient, (d) fluctuation amplitude, and (e) normal curvature κ_n for a shot with $\beta_{\rm vol} = 2.5\%$.

the higher density discharge has about twice the fluctuation level, and is largest between $\rho = 0.8 - 1.0$ where resistive g is located. The scaling of fluctuation level here is clearly attributable to stronger density, despite having similar $\beta_{\rm vol}$.

The position of the strongest fluctuation peak as a function of $\beta_{\rm vol}$ is plotted in Fig. (7), separated out into parts above and below the mid-plane, as discussed before. As $\beta_{\rm vol}$ is increased, the region of magnetic well extends towards the edge, as indicted by the shaded region, meaning that the resistive g peaks must be localized further towards the edge at higher beta. This seems to be consistent with the measured positions, indicated by dots, more particularly for components on the bottom. For components on the top, there appears to be a concentration of peaks

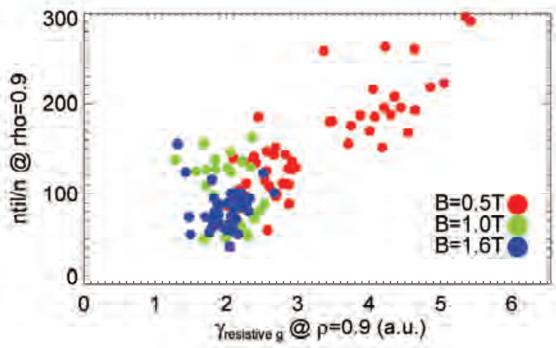

Fig. 4 Comparison of local fluctuation amplitude $\tilde{n}/n$ at $\rho = 0.9$ and resistive g driving growth rate γ_g at the same ρ.

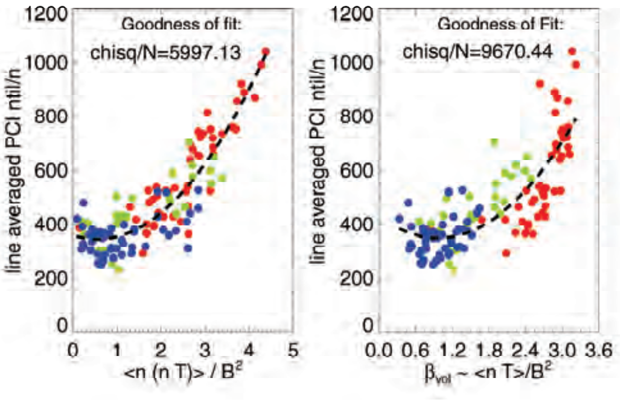

Fig. 5 Dependence of Line integrated fluctuation level from PCI on (a) $\langle n(nT)\rangle/B^2$, and (b) $\beta_{\rm vol}$.

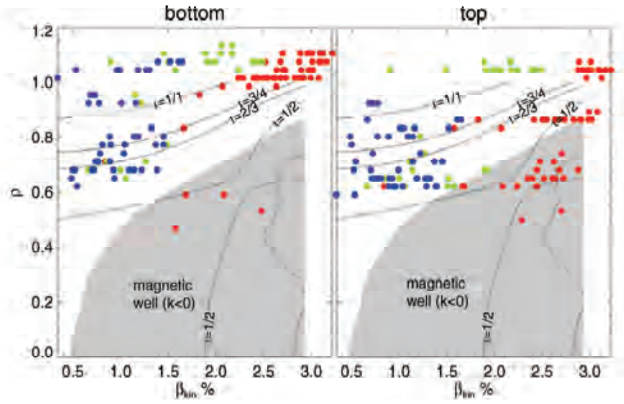

Fig. 7 Position ρ of strongest peak of $\tilde{n}(\rho)$ on (a) bottom and (b) top sides of the midplane, as a function of $\beta_{\rm vol}$, compared with changes in the magnetic structure including well/hill boundary and rational surfaces

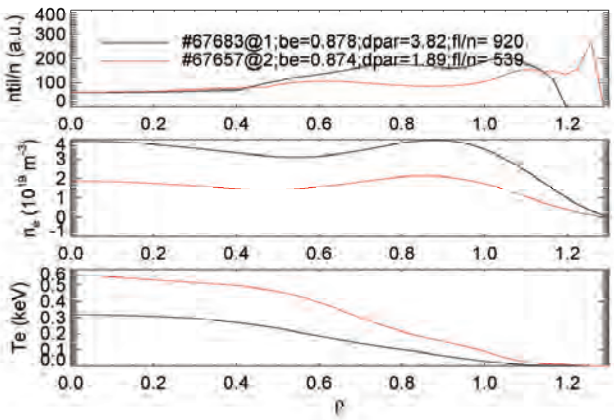

Fig. 6 For shots with similar $\beta_{\rm vol}$, but significantly different density, comparison of profiles of (a) fluctuation level $\tilde{n}/n$, (b) density, (c) temperature.

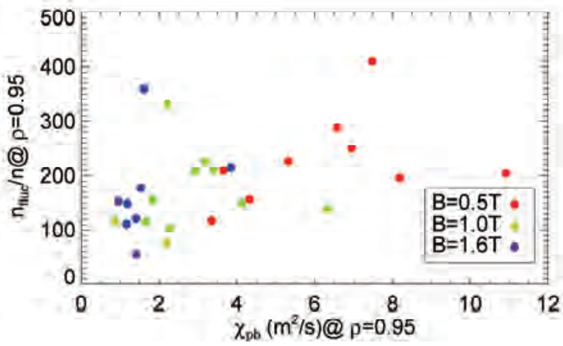

Fig. 8 Comparison of χ with $\tilde{n}/n$ from 2D PCI at $\rho = 0.95$.

around the $\iota = 1/2$ rational surface, approximately where the magnetic shear is close to zero. This type of MHD activity close to rational surfaces has also recently been reported in [19].

In summary, all these results appear to demonstrate the consistency between measured fluctuation amplitudes and positions and the expectation with resistive g mode. The largest discrepancies are from the existence of fluctuations inside the region of magnetic well which may be some drift wave component. Hybridization of resistive g and drift-waves is also possible [17]. This distinction could be more rigourously made on the basis of the difference between the poloidal phase velocity and to the ExB velocity, or the coherence between density and magnetic fluctuations.

3.3 Comparison of fluctuation amplitude with power balance χ at high β

The role of fluctuations on confinement itself is very important to confirm the original assertion that transport is dominated by anomalous processes; and to check that the measured fluctuations are important for confinement, even regardless of the role of what is the driving mechanism of the fluctuations (resistive g or drift wave). For the set of discharges analyzed above, power balance analysis was carried out to determine the "effective" thermal conductivity $\chi = (\chi_e + \chi_i)/2$ as per the procedure described in [13], based on the FIT code [20] which computes the power deposition from NBI by calculating fast particle orbits and their interactions with bulk plasma. The PROCTR code [21] is then used to analyze the diffusivity. For the comparison we choose to compare the edge local fluctuation level with the edge χ ($\rho = 0.95$). The results, for a selected subset of shots in the previous section are plotted in Fig. (8). It is clear that there is is an increasing trend of fluctuation level and conductivity. However, there are significant outliers; these may be due to the fact that turbulence saturates to a level depending on the power input, rather than on the conductivity itself (dependent on gradient), because the gradient steepens to a value such that the heat flux balances the input power in steady state. [*** put this figure in too***].

4 High core density

Recently, pellet-fueled high density plasmas were achieved with central density approaching $10^{21}\mathrm{m}^{-3}$ [2, 4]. These plasmas are characterized by having a high density core with a "diffusion barrier" around mid radius, correlating with the position of zero magnetic shear. Though these plasmas are made at high field ($B > 2$T), the central beta approaches that of the high volume average beta plasmas, and so the beta gradients in the diffusion barrier region are very high; therefore they may have some similar characteristics to high volume average beta plasmas. However, the diffusion barrier is always in the region of magnetic well, meaning that resistive interchange turbulence is not a candidate to explain turbulence.

It has recently been shown [4] that the maximum attainable central density and stored energy increases as the magnetic configuration is changed to move the magnetic axis further outward. For formation of the diffusion barrier, and improved performance at outward shifted configurations, turbulent transport play a significant role. In a separate study [22], the temporal evolution of turbulence (from 2D PCI) and particle particle transport studied after multiple pellet injection with in the configuration with vacuum R_{ax} = 3.6m. In this analysis, fluctuation and plasma properties are compared between R_{ax} = 3.65m and R_{ax} = 3.75m, to confirm whether fluctuation properties are reduced in line with improved confinement. Because the 2D PCI sightline passes around R = 3.603m, as the magnetic axis moves outwards, the system is no longer sensitive to core fluctuation properties. In particular, for the highest performance around R_{ax} = 3.9m, fluctuations around the diffusion barrier cannot be measured; however, they can be measured sufficiently up to R_{ax} = 3.75m for which the sightline penetrates down to $\rho = 0.4$.

The time evolution of the central pressure, computed from Thomson scattering, and fluctuation level $\tilde{n}/n$ at ρ = 0.4 are compared for both configurations in Fig. (9). After pellet injection, the temperature is reduced considerably, and the density falls, while the temperature rise so that the pressure rises. It can be seen that at R_{ax} = 3.75m, the pressure has risen more quickly and to a higher value than in the case of R_{ax} = 3.65m. The fluctuation behavior changes strongly in time after pellet injection. In both configurations, there appears to be strong bursts in time, up to a time when the bursts no longer occur and the fluctuation level is dramatically reduced. However, it is easy to notice that in the R_{ax} = 3.75m case, bursts persist over a shorter period of time, and there appears to be a "quiet" period between the bursts meaning that the time average fluctuation level, and hence induced transport, should be smaller. This correlates with the stored energy being higher in this case, so it demonstrates that the reason for the higher pressure may be due to reduced fluctuation level despite stronger density/pressure gradient.

One possible reason for the reduced fluctuation level

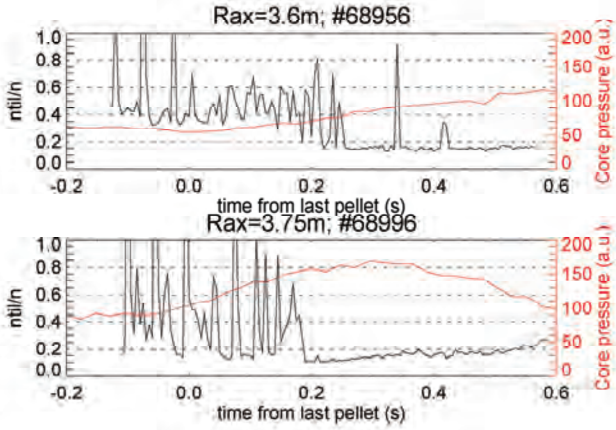

Fig. 9 Comparison of the time evolution of the central pressure, computed from Thomson scattering, and fluctuation level $\tilde{n}/n$ at ρ = 0.4 for configurations with (a) R_{ax} = 3.65m and (b) R_{ax} = 3.75m

when the pressure is higher is due to the difference of the hollowness of the temperature profile, which is produced transiently after pellet injection. Contour plots of the electron temperature profile evolution are shown for both cases in Fig. (10). The temperature profile is more hollow immediately after pellet injection in the inward shifted case (R_{ax} = 3.65). For R_{ax} = 3.65m, the temperature profile switches from hollow to peaked At $t - t_0$ = 0.25s, around about the same time as the bursts of fluctuations disappear. The same is true for R_{ax} = 3.75m, where the profile switches from hollow to peaked and fluctuations disappear at around $t - t_0$ = 0.18s. This indicates that the opposite sign of temperature and density gradient is unstable. Such an instability threshold is characteristic of a slab ITG mode but this does not discount other possible drive mechanisms such as ballooning modes. Because the case of R_{ax} = 3.75m has a less hollow temperature profile, it is closer to marginal stability and so fluctuation bursts do not occur so frequently.

The burst-like nature of fluctuations observed in dense core plasmas is similar in nature to ELM activity in the edge of Tokamak devices. In both cases, these occur when the pressure gradient is very high, but in the case here, it seems that pressure gradient does not drive the mode, rather some simple ITG-like mode. The bursts may be due to the profiles being near a marginal stability threshold, and that the instability has a very distinct hard threshold. Such ITG instability thresholds have been demonstrated in Tokamak transport before.

[1] K. Y. Watanabe. Confinement study on the reactor relevant high beta lhd plasmas. In *these proceedings*. (2007).
[2] N. Ohyabu *et al.* Phys Rev Lett **97**, 055002/1 (2006)
[3] K Tanaka *et al.* Nucl Fusion **46**, 110 (2006)
[4] R. Sakamoto these proceedings (2007)
[5] K. Kawahata *et al.* Fusion Eng & Des **34-35**, 393 (1997)
[6] A.L. Sanin *et al.* Rev Sci Instrum **75**, 3439 (2004)

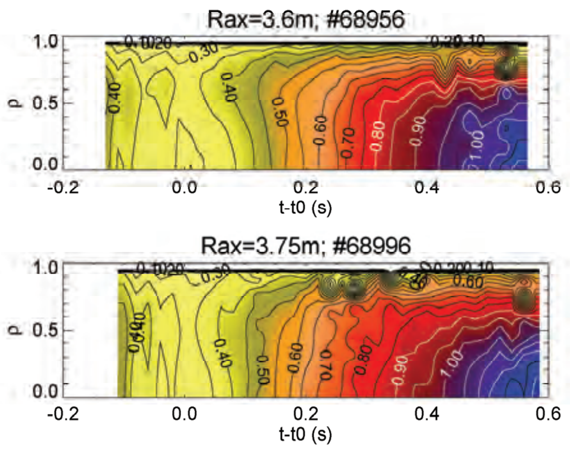

Fig. 10 Contour plots of temporal/spatio evolution of temperature profiles from Thomson scattering (fitted with a polynomial) after pellet injection for configurations with (a) R_{ax} = 3.65m and (b) R_{ax} = 3.75m.

[7] L.N. Vyacheslavov IEEE transactions on plasma science **33**, 464 (2005)
[8] CA Michael *et al.* Rev Sci Instrum **77**, 10E923 (2006)
[9] K. Y. Watanabe *et al.* Nucl Fusion **45**, 1247 (2005)
[10] A. Komori *et al.* Phys Plasmas **12**, 56122 (2005)
[11] P Snyder. Phd thesis, Princeton, (1999).
[12] K. Tanaka *et al.* J Phys Soc JPN **62**, 3092 (1993)
[13] H. Funaba *et al.* Fusion Sci Technol **51**, 129 (2007)
[14] K. Tanaka *et al.* Fusion Sci Technol **51**, 97 (2007)
[15] B. A. Carreras *et al.* Phys Fluids **30**, 1388 (1987)
[16] B. A. Carreras and P. H. Diamond Phys Fluids B **1**, 1011 (1989)
[17] M. Wakatani AIP Conf Proc pages 141 (1997)
[18] T. Dannert and F. Jenko Phys Plasmas **12**, 72309 (2005)
[19] K. Ida *et al.* Phys Rev Lett page submitted (2007)
[20] S. Murakami *et al.* Fusion Technology **27**, 256 (1995)
[21] H Howe ORNL/TM-11521 (1990)
[22] K Tanaka. In *H mode Workshop*, Tsukuba, Japan, (2007).

Proceedings of ITC/ISHW2007

Investigation of the fluctuation properties of the ion saturation current in the edge and divertor plasmas in LHD

S. Masuzaki, N. Ohno [a], V.P. Budaev [b], S. Sakakibara, T. Morisaki, M. Kobayashi, N. Ohyabu, A. Komori and the LHD Experimental Group

National Institute for Fusion Science,322-6 Oroshi-cho, Toki 509-5292, Japan
[a] Eco Topia Science Institute, Nagoya University, Nagoya 464-8603, Japan
[b] Nuclear Fusion Institute, RRC Kurchatov Institute, 123182, Kurchatov Sq.1, Moscow, Russia

(Received day month year / Accepted day month year should be centered 10-point type)

Fluctuation properties of the ion saturation current measured by using Langmuir probes in the edge and divertor plasmas were investigated based on probability distribution function (PDF) analysis in the Large Helical Device (LHD). In the edge plasma region, both positive and negatively skewed PDFs were observed. Unlike tokamak cases, negatively skewed PDFs were found at divertor legs. On a divertor plate, sign of skewness of I_{sat} PDF inverts from positive to negative value during a discharge.

Keywords: Large Helical Device (LHD), edge plasma, divertor plasma, ion saturation current, fluctuation, intermittent events, probability distribution function (PDF)

1. Introduction

In magnetic fusion devices, energy and particle fluxes crossing the last closed flux surface (LCFS) are transported to plasma facing components conductively and convectively in scrape-off layer (SOL). The distributions of heat and particle loads on plasma facing components are very important parameters for designing devices, and are determined by the balance between the parallel and perpendicular transports. The perpendicular transport coefficients, such as diffusion coefficient are anomalous, and fluctuation phenomena are believed to strongly relate to the transport [1].

In tokamaks, it is widely observed that SOL consists of the near- and far-SOL [2]. The difference between these regions is the density decay length. In the near-SOL, just outside LCFS, the density profiles are usually exponential with short (a few cm) decay length. On the other hand, the decay length is long, and the profiles are nearly flat in the far-SOL. Therefore plasma with substantial density exists in front of main chamber first wall, and the particle load on first wall cannot be ignored. The transport in the far-SOL is believed to be not diffusive but convective associated with intermittent events, so called ‘blob’, and the probability distribution function (PDF) of the density fluctuations in the far-SOL has non-Gaussian tail.

In the Large Helical Device (LHD), the world largest superconducting helical device with heliotron-type magnetic configuration, there is a unique edge magnetic field lines structure. There exist an intrinsic stochastic layer just outside of LCFS, residual islands embedded in the stochastic layer, the edge surface layers and the intrinsic divertor structure (helical divertor), this magnetic structure is one of the characteristics of the heliotron-type configuration [3]. Figure 1 (a) shows a Poincare plot of magnetic field lines in a horizontally elongated cross-section in LHD. Blue and red points outside LCFS indicate open field lines striking divertor plates. Yellow lines are contours of magnetic field strength, and they show that the gradient of magnetic field strength largely changed in a poloidal cross-section. For the difference of magnetic structure in the edge plasma region, comparison the fluctuation properties in the edge and divertor plasmas between tokamaks and helical devices could make it possible to understand the physics of cross-field transport.

It was reported that the intermittent properties of I_{sat} measured by a Langmuir probe on a divertor plate is similar to that observed in tokamaks SOL and linear divertor simulator [4]. It was observed that large positive and negative bursty signals dominates the time-evolutions of I_{sat} measured at lower field side and striking point of the divertor leg, respectively, and this is consistent with theoretical prediction of blob transport [5]. In this paper, the fluctuation properties of the ion saturation current, I_{sat}, measured by Langmuir probes in the edge and divertor

author’s e-mail: masuzaki@LHD.nifs.ac.jp

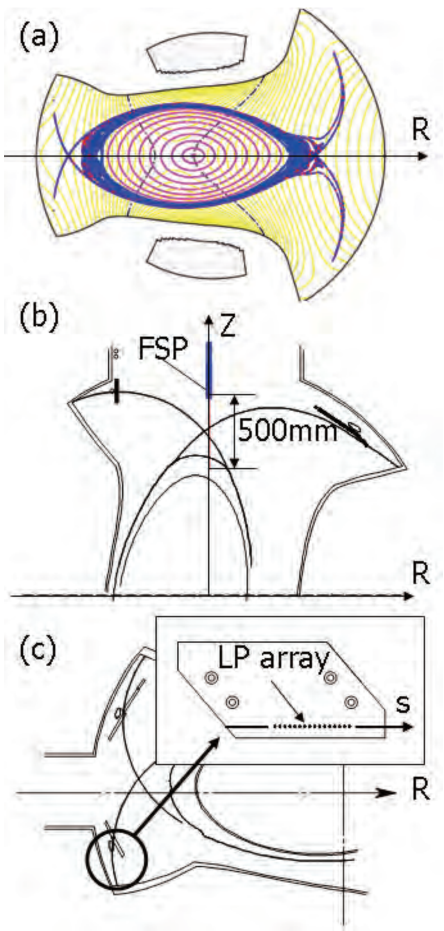

Fig. 1 (a) Poincare plot of magnetic field lines in a horizontally elongated cross-section in LHD. Blue and red points outside LCFS indicates open field lines striking divertor plates. Yellow lines are contours of magnetic field strength. Poloidal cross-sections of LHD plasma and vacuum vessel at the positions of (b) FSP (fast scanning Langmuir probe) and of (c) the divertor plate in which LP array is installed, respectively.

plasmas in the unique edge magnetic structure are investigated based on PDF analysis.

2. Experimental set-up

Hydrogen plasmas heated and sustained by neutral beam injection (NBI) are investigated in this study. Figure 1 (b) and (c) show positions of the Langmuir probes. Fast scanning Langmuir probe (FSP) moves 500 mm vertically from the top wall along Z-axis as shown in Fig. 1(b) using a pneumatic cylinder. The position of first wall is Z~1.6 m. The maximum velocity of FSP is about 1 m/s. One electrode made of graphite, dome-type with 2 mm of diameter, was provided for this study, and I_{sat} profiles along Z-axis were measured. On the divertor plate which locates torus inboard-side in the horizontally elongated cross-section, there is a Langmuir probe array (LP array) consisting of 16 dome-type electrodes with a 2 mm of diameter as shown in Fig. 1(c). The distance between electrodes is 6 mm, and I_{sat} profiles along S-axis were obtained. S-axis is along the edge of the divertor plate, and the direction is almost toroidal. Sampling frequencies and dynamic ranges of the LP array and FSP for their data acquisition are 500 kHz and 1 MHz, respectively.

3. Results and discussions

The fluctuation properties of I_{sat} signals measured by Langmuir probes were analyzed based on PDF analysis. For fully random signal, PDF has a Gaussian distribution. The deviation of PDF from Gaussian distribution function can be characterized by skewness, $S = \langle x^3\rangle/\langle x^2\rangle^{3/2}$, and flatness, $F = \langle x^4\rangle/\langle x^2\rangle^2$. Skewness and flatness are measures of asymmetry and of the tail's weight with respect to core of PDF, respectively, and $S = 0$, $F = 3$ for Gaussian distribution.

3.1 Result of the edge plasma measurement

I_{sat} profiles in the edge plasma were measured by FSP during discharges with a magnetic configuration of R_{ax} = 3.60 m, where R_{ax} is major radius of magnetic axis. Figures 2(a) and (b) show an I_{sat} profile during a discharge with 2×10^{19} m^{-3} of line averaged electron density and 3 MW of NBI heating power and field lines connection length, L_c, profile along Z-axis calculated with field lines tracing code, respectively. Smaller Z is closer to LCFS. Field lines trace

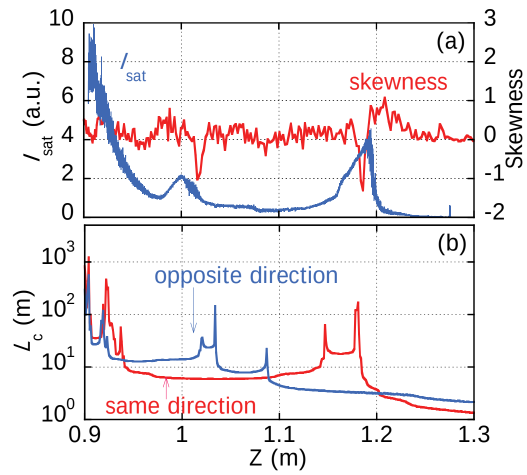

Fig. 2 (a) I_{sat} profile along Z axis measured by using FSP and skewness profile estimated using every 1000 data points. (b) Profiles of connection length of magnetic field lines (L_c) along Z axis calculated with field lines tracing code. Red and blue lines show L_c profiles calculated for same and opposite directions of magnetic field direction, respectively.

was conducted for two directions. One is the same direction as magnetic field, and another one is the opposite direction. Two I_{sat} peaks appear at Z = 1.0 m and 1.2 m, and they correspond to long L_c groups positions in Fig. 2 (b). The difference of positions between I_{sat} peaks and L_c peaks is considered to be caused by the alignment error of FSP. These long field lines approach the vicinity of LCFS, and they are main channel of particle and energy flow from LCFS to divertor. On the other hand, field lines less than 100 m do not approach LCFS [6].

Skewness profile is also plotted in Fig. 2(a). Skewness was estimated after removing DC component from raw I_{sat} signal using high-pass digital filter (>100Hz), and using 1000 data points (1 ms). Therefore the spatial resolution of this analysis is about 1 mm. In tokamaks, negative skewness has been observed near or inside LCFS, and skewness is positive and becomes larger with increase the distance from LCFS [7]. In LHD R_{ax}=3.60 m configuration case, there are two negative peaks at the vicinity of I_{sat} peaks (Z ~ 1.02 m and ~ 1.18 m) , that is the vicinity of L_c peaks as shown in Fig. 2. This result indicates that negative bursts corresponding to density drops are dominant in this region. Fig. 2(b) shows that these field lines at the L_c peak positions connect to divertor plates less than 10 m, and that means these peaks are divertor legs. Relatively large positive skewness appears beside negative peaks of skewness as shown in Fig. 2(a). This observation is consistent with previous observation in divertor plasma [5]. From Z ~ 1.20 m to 1.28 m, skewness decreases from 1 to 0 with decay length of 2 cm, and I_{sat} becomes noise level at Z > 1.28 m. It suggests that transport becomes diffusive in the outermost region. Assuming the positive spikes in I_{sat} at Z > 1.21 m region are blobs, a possible explanation of determining the decay length of skewness is lifetime of blobs. Lifetime of blob is roughly estimated as L_c/C_s, where C_s is ion sound speed. In the case of around Z = 1.21 m, L_c ~ 10 m and C_s ~ 3×10^4 m/s (assuming T_e = 10eV), and the lifetime is ~ 0.3 ms. Assuming blob speed to be 100 - 1000 m/s, the propagation length is 3 - 30 cm.

3.2 Temporal change of PDF property in divertor plasma

Temporal change of PDF property of I_{sat} measured by Langmuir probe array on a torus-outboard divertor plate (see Fig. 1(c)) was observed during discharges with R_{ax} = 3.60 m and P_{NBI} = 5.9 MW. Typical waveforms of plasma parameters in such a discharge are shown in Figs. 3(a)-(c). Normalized I_{sat} profiles on the Langmuir probe array at t = 1.3 s and 1.8 s are depicted in Fig. 3(d). In Fig. 3(c), time-evolution of skewness and flatness of I_{sat} signal at the peak of the I_{sat} profile are depicted. Skewness increases in the early phase of neutral beam injection, and it has peak at t ~ 1.4 s. Then it decreases gradually, and it becomes

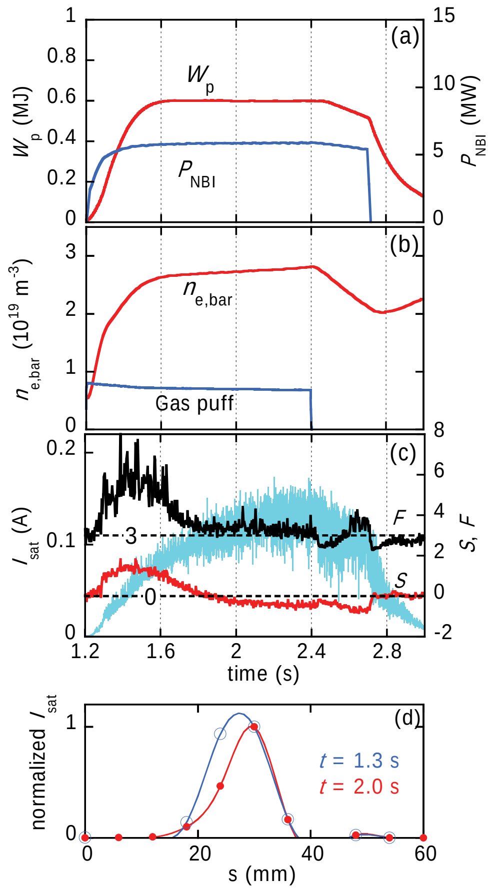

Fig. 3 Typical time evolutions of (a) stored energy, W_p, and neutral beam deposition power, P_{NBI}, (b) line averaged density, $n_{e,bar}$, and gas-puff, (c) I_{sat}, skewness (S) and flatness (F) during a discharge with magnetic configuration of R_{ax} = 3.60 m. (d) I_{sat} profile on the Langmuir probe array during same dischage. Horizontal axis is probe position (see Fig. 1(c)). Blue and red lines are fitting results.

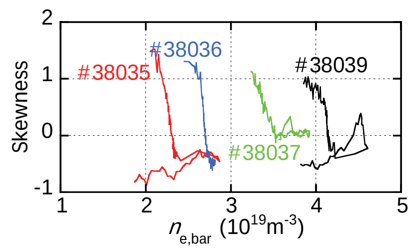

Fig. 4 Skewness of I_{sat} as a function of line averaged density.

negative after t ~ 1.8 s. The negative sign of skewness is kept until the NBI termination, and then skewness and flatness become 0 and 3, respectively. To reveal the key parameters of changing sign of skewness, electron density and temperature dependences of skewness were investigated. A series of discharges with different densities ($n_{e,bar}$ = 2 - 4×10^{19}m^{-3}) were conducted. In Fig. 4,

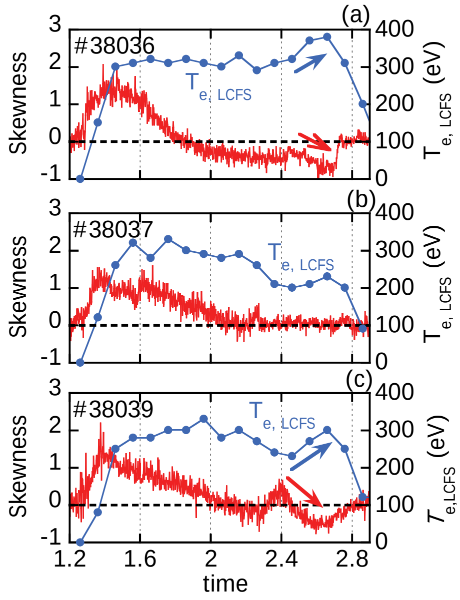

Fig. 5 Time-evolutions of skewness of I_{sat} and electron temperature at LCFS, $T_{e,LCFS}$, during the same series of discharge as Fig. 4.

skewness of I_{sat} in each discharge is plotted as a function of line averaged density, and the figure suggests that inversion of skewness sign does not depend on electron density. Figure 5 shows time-evolutions of skewness of I_{sat} and electron temperature at LCFS in the same series of discharges as Fig. 4. Skewness increases during electron temperature increase, and then decreases during electron temperature is almost constant. It seems that skewness does not depend on $T_{e,LCFS}$ in the later phase. In Fig. 5(a), sign of skewness becomes negative after t ~ 1.8 s. On the other hand, in Fig. 5(b), skewness becomes 0 at t ~ 2.1 s, and it is kept until t = 2.9 s. The difference between Figs. 5(a) and (b) is electron temperature at LCFS. In the former case, $T_{e,LCFS}$ ~ 300 eV and ~ 200eV in the latter case. This result suggests that skewness depend on $T_{e,LCFS}$, and its sign does not become negative when $T_{e.LCFS}$ is around 200 eV. In Fig. 5(c), skewness increases at t ~ 2.3 s with decrease of $T_{e.LCFS}$, and decreases from t ~ 2.4 s with increase of $T_{e.LCFS}$. This result also suggests that skewness depends on $T_{e,LCFS}$.

In Fig. 4(d), two I_{sat} profiles are shown. They are in positive (t = 1.3 s) and negative (t = 2.0 s) skewness phases, respectively. From the fitting results, the peak of I_{sat} profile shifts about 3 mm, and this shift is considered to be caused by modification of magnetic field lines structure. Modification of magnetic field lines structure could be a cause of the inversion of skewness sign. As described in section 3.1, it was observed that the negative skewness region in divertor leg is narrow, and at the vicinity of that, there is positive skewness rergion. Therefore, a small movement of magnetic structure on the divertor plate due to some reason such as a small change of rotational transform caused by toroidal plasma current could change the sign of skewness.

4. Summary

Fluctuation properties of I_{sat} in the edge and divertor plasmas in LHD were investigated based on PDF analysis.

In the LHD edge plasma region, skewness of PDF of I_{sat} has both positive and negative values, and negative region is relatively narrow. Negative peaks of skewness appear at the positions of divertor legs. In the outermost region of the edge plasma, skewness decrease from ~1 to 0 with the decay length of a few cm. This decay length is comparable to the blob propagation length roughly estimated from the lifetime of blob.

On a torus-outboard divertor plate, it was observed that the sign of skewness inverts from positive to negative at a probe channel during a discharge. Electron density does not affect this behavior but electron temperature and/or modicication of magnetic field lines structure at the divertor plate caused by toroidal plasma current could affect it.

Acknowledgements

This work was supported by the NIFS budget NIFS06ULPP511.

References

[1] B.A. Carreras, J. Nucl. Mater. **337-339**, 315 (2005).
[2] B. Lipschultz et al., Nucl. Fusion **47**, 1189 (2007).
[3] N. Ohyabu *et al*., Nucl. Fusion **34**, 387 (1994).
[4] V.P. Budaev *et al*., Plasma Fusion Res. **1**, 001 (2006).
[5] N. Ohno *et al*., Contrib. Plasma Phys. **46**, 692 (2006).
[6] S. Masuzaki *et al*, Nucl. Fusion **42**, 750 (2002).
[7] J.A. Boedo *et al*, Phys. Plasma **10**, 1670 (2003).

Proceedings of ITC/ISHW2007

Analysis of neutrals in helical-axis Heliotron J plasmas using the DEGAS Monte-Carlo code

Yousuke Nakashima, Yuta Higashizono, Shinji Kobayashi[a], Hisashi Yabutani[b], Tohru Mizuuchi[a], Nobuhiro Nishino[c], Mamoru Shoji[d], Kazunobu Nagasaki[a], Hiroyuki Okada[a], Fumimichi Sano[a], Katsumi Kondo[b], Kensuke Murai[b], Hirokazu Kawano and Teruji Cho

Plasma Research Center, University of Tsukuba, Tsukuba, Ibaraki 305-8577, Japan

[a] Institute of Advanced Energy, Kyoto University, Gokasho, Uji 611-0011, Japan

[b] Graduate School of Energy Science, Kyoto University, Gokasho, Uji 611-0011, Japan

[c] Graduate school of Engineering, Hiroshima University, Hiroshima, 739-8527, Japan

[d] National Institute for Fusion Science, 322-6 Oroshi-cho, Toki 509-5292, Japan

(Received / Accepted)

Analysis of neutral particle behavior in Heliotron J device with non-axisymmetric configuration is described based on the results of neutral transport simulation. DEGAS three-dimensional (3-D) Monte-Carlo code was applied to Heliotron J in order to investigate precisely the spatial distribution of neutral particle density in the device. A detailed three-dimensional mesh structure for the simulation has been designed in complicated helical axis plasma geometry as well as the whole volume of Heliotron J vacuum chamber. In this mesh model, a carbon target is also modeled for the simulation of the plasma-material interaction experiments. Plasma parameter dependence on neutral diffusion was investigated and a significant effect of helical geometry was clarified. Simulation results were also compared with the two-dimensional image captured with a CCD camera viewing the carbon target and the plasma-material interaction under non-axisymmetric configuration was discussed.

Keywords: neutral transport, three-dimensional Monte-Carlo simulation, DEGAS, helical system, Heliotron J, carbon target

1. Introduction

Analysis of neutral transport is an important issue for the investigation of edge plasma behavior and plasma-wall interactions. Especially in non-axisymmetric plasma confining systems, the neutral transport analysis becomes much complicated, since the structure of plasma and the vacuum vessel wall become a three-dimensional structure, which prevent us to assume a simple toroidal symmetry, such as tokamaks. In order to investigate the neutral transport in non-axisymmetric systems, three-dimensional (3-D) Monte-Carlo simulation is a powerful method. So far DEGAS Monte-Carlo code [1,2] has been applied to the GAMMA 10 tandem mirror device and the helical device LHD for neutral transport simulation in three-dimensional geometry [3-5]. Recently 3-D simulation study by using this code has started in Heliotron J device [6]. In this study, a distinctive behavior of neutrals in helically structured plasmas with localized neutral particle source is analyzed under the 3-D mesh model using the DEGAS ver.63 code. In this paper, the detailed results of 3-D Monte-Carlo simulation in order to investigate behavior of neutrals in non-axisymmetric Heliotron J plasmas are described. The effect of interactions between the limiter and the non-axisymmetric plasmas is also discussed from the viewpoint of particle source with localized in the complicated 3-D geometry.

2. Heliotron J and the simulation model

2.1 Mesh structure of Heliotron J

Heliotron J is the helical axis heliotron device with a helical winding coil of L/M = 1/4, where L and M are the pole number of the helical coil and the helical pitch, respectively [7,8]. In a standard magnetic field configuration, the average major and minor radii of the plasma are 1.2 m and 0.17 m, respectively. Figure 1(a) shows the poloidal cross-section of Heliotron J together with the line of sight in the Dα line-emission detector array and fast cameras. As shown in the figure, the line of sight is located to cover the entire surface of the carbon

author's e-mail: nakashma@prc.tsukuba.ac.jp

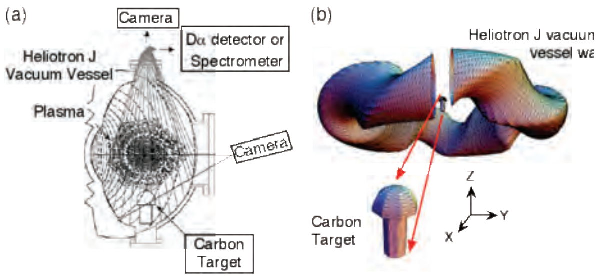

Fig.1 (a) Poloidal cross-section of the plasma and layout of the fast camera and Dα diagnostic system. (b) Mesh model of the Heliotron J vacuum vessel, plasma and carbon target for the DEGAS simulation.

target by using the multi-channel Dα array detector system [9]. In Heliotron J, two fast cameras are installed to observe the plasma and the carbon target and one is located at the top of the vacuum chamber and is looking down both the plasma and the target vertically. Another camera is set horizontally viewing the plasma and the top of the target [10].

The 3-D mesh model covering the whole area of Heliotron J for the DEGAS simulation is shown in Fig. 1(b). In this simulation, 3-D modeling of the carbon target is carried out in addition to the plasma and vacuum vessel wall in order to study the neutral particle behavior near the target. The mesh is divided into radially 15 segments and 28 segments in the poloidal cross-section, respectively. The toroidal segmentation is taken into 512 to investigate the toroidal variation of neutral density in detail especially near the target. The target head is hemispheric shape with 4 cm in radius made of carbon and a set of probes is installed on the tip. The mesh model of the target is divided into 40 segments in azimuthal direction and vertically divided into 34 segments.

2.2 Modeling of plasma parameter

Figure 2 shows the radial profiles of plasma parameters used in the DEGAS simulation. As input data for the DEGAS code, plasma parameters (N_e, T_e and T_i) are determined from the measured results with a microwave interferometer, a soft X-ray detector and a neutral particle energy analyzer, respectively. Since the obtained plasma parameters from the experiments are practically insufficient for the 3-D simulation, an appropriate assumption is required for making up an input dataset of the simulation code. A toroidal symmetry in the plasma parameters is assumed for this reason. Edge plasma parameters are determined from Langmuir probe measurements. In this simulation electron density and temperature in the SOL region are given to be 1×10^{12} cm^{-3} and 10 eV, respectively.

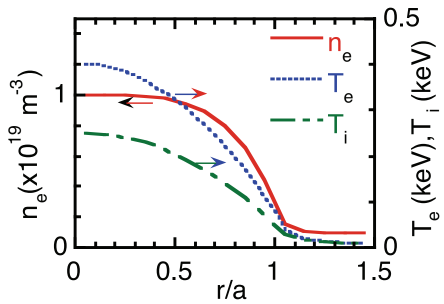

Fig.2 Radial plasma parameter profiles used in the DEGAS simulation.

3. Simulation results and Discussion

3.1 Neutral penetration and diffusion from the carbon target

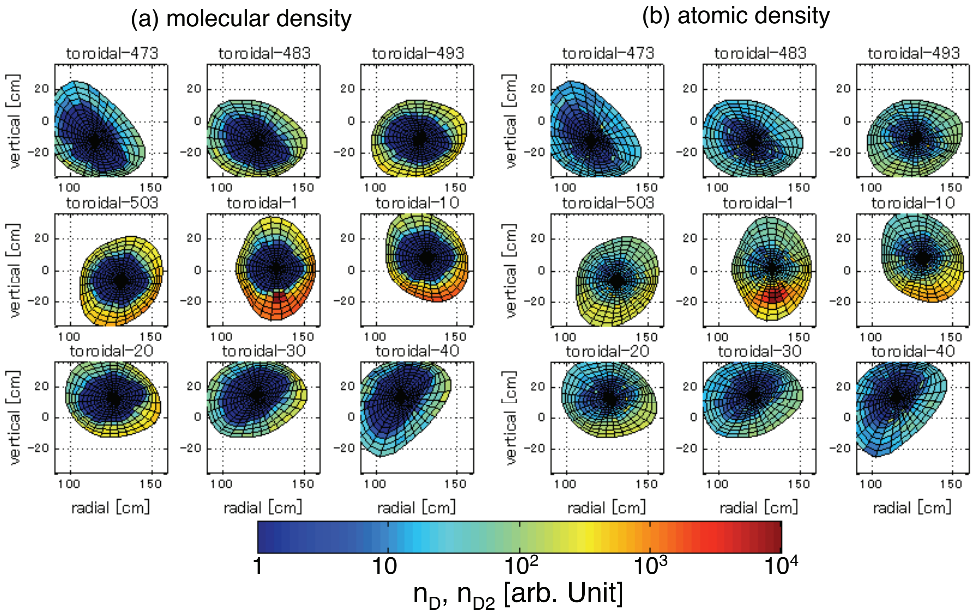

Fig. 3 3-D simulation result of deuterium neutral density profile with a point source on the target tip.

For the purpose of understanding the neutral behavior in the plasma and the vacuum chamber with helical structure, 3-D simulation was performed in the case with a point particle source on the carbon target. Figure 3 shows the simulation result of deuterium neutral density profile with a point source on the target tip. In Fig. 3(a), poloidal cross-section views of the deuterium molecule density are aligned in the toroidal direction at intervals of about 15 cm. At the location close to the poloidal plane "toroidal-1" the carbon target is installed and the test particles are launched at 10 mm inside the LCFS from the bottom of the vacuum vessel. In the simulation, deuterium molecules are injected toward the plasma center from the top of the target according to cosine distribution. As shown in the figure, deuterium molecules cannot penetrate radially toward the plasma core. Near the target position, they poloidally diffuse through the SOL region decreasing by less than two order of magnitude up to the opposite side. In the toroidal direction, on the other hand, deuterium molecules decreases by almost three order of magnitude about 60 cm distance from the target and the poloidal non-uniformity due to the local recycling induced by the target disappears. Deuterium atoms have longer penetration length toward the plasma core as shown in the Fig. 3(b). However, a strong non-uniformity in the atomic density near the target is observed compared with the molecular density.

Figure 4 shows the bird's-eye view of the Dα emission profiles determined from the simulation results. Each poloidal cross-section is toroidally aligned at intervals of about 22 cm. Compared with the atomic/molecular density profiles, the emission region is more deeply penetrated to the plasma core. From this figure it is found that in the case of the point particle source, such as the carbon target, the Dα line-emission region is localized within a quarter of the whole toroidal circumference.

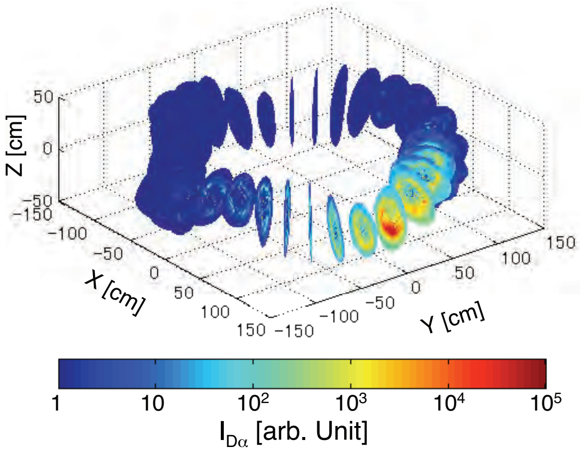

Fig. 4 Bird's-eye view of the Dα emission profiles determined from the simulation results.

3.2 Density dependence on neutral transport

In order to investigate the density dependence on the neutral transport, neutral density profile in the different density condition is calculated. Figure 5 shows the simulation result of deuterium neutral density profile in the case that the plasma density is reduced by one fourth ($N_e(0)$ = 2×10^{12} cm^{-3}) under the same condition of the other parameter as in Fig. 4. As shown in Fig. 5(a), azimuthal localization of molecules due to recycling on

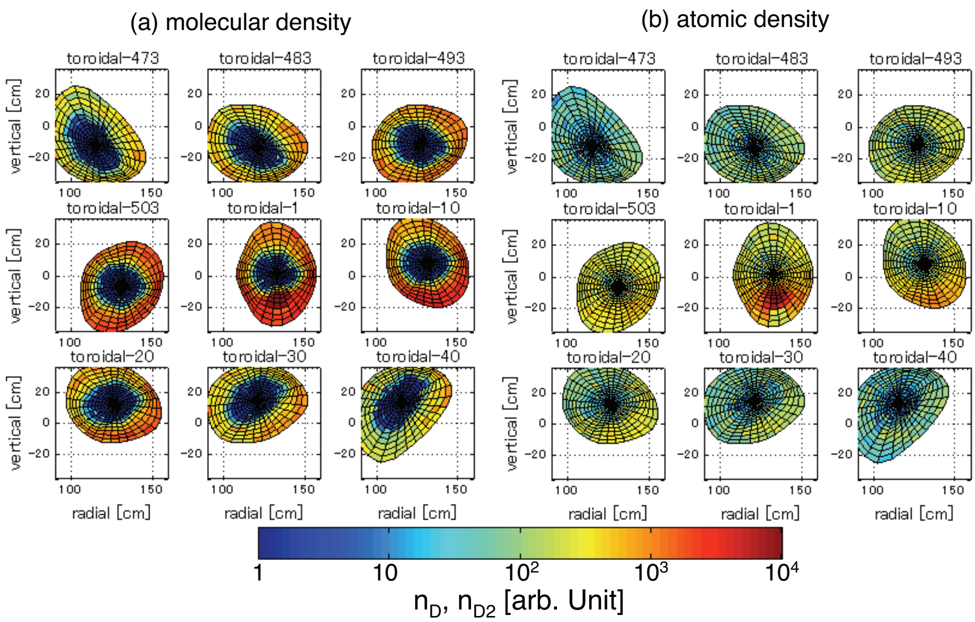

Fig. 5 The simulation result of deuterium neutral density profile in the case that the plasma density is reduced by one fourth under the same condition of the other parameter as in Fig. 4

the target is clearly reduced, which indicates that the molecules can easily diffuse through the SOL region with reduced density. On the contrary, the poloidal non-uniformity by more than one order of magnitude remains in atomic density shown in Fig. 5(b). The mechanism to explain these phenomena is not clarified. However it may affect the atomic deuterium transport that the interaction with the helically bending wall surface.

3.3 Comparison with the 2-D camera view

In order to verify the reliability of the simulation, a simulation result was compared with experimental data. Figure 6(a) shows a typical side view image of the carbon target captured with the horizontally viewing CCD camera. A strong light emission is observed on the target surface and it is found that the emission region is slightly shifted to the left side on the surface. Furthermore it is recognized that the emission cloud has a structure which is expanding along the magnetic field line.

Figure 6(b) shows the simulation results near the carbon target. In this simulation, a particle source on the top of the carbon limiter is given based on the 2-D image of Dα line intensity on the surface measured with the vertically viewing camera [11]. In the present computational circumstances, the limitation of the segmentation number in the toroidal mesh makes it difficult to perform more detailed simulation along the toroidal direction. However, the calculated 2-D image of Dα intensity also has a similar structure to the experimental results. This result indicates the validity of this analysis method applied to the helical system.

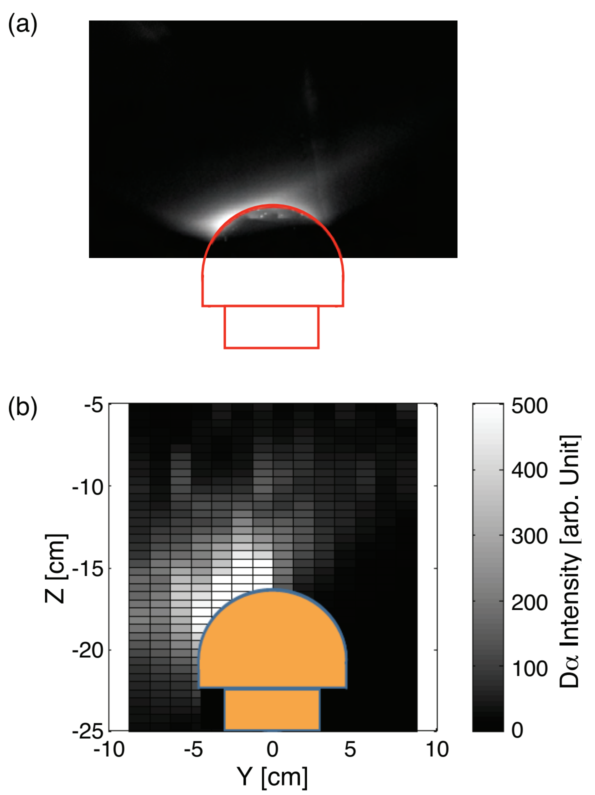

Fig.6 Comparison between 3D-DEGAS simulation and experiment. (a) 2-D image of the side view of the carbon target. (b) Predicted 2-D image of the Dα intensity near the carbon target.

4. Summary

Using three-dimensional Monte-Carlo code DEGAS ver.63, neutral transport simulation was successfully performed in the Heliotron J with helical-axis heliotron magnetic configuration, and the behavior of neutrals this region was investigation in detail based on the simulation results. A mesh model of the carbon target was installed into the 3-D mesh structure modeling the Heliotron J vacuum vessel and plasma with non-axisymmetric configuration. The 3-D simulation with assuming a particle source due to recycling on the target showed that the shapes of the wall and plasma in the helical structure significantly influence the neutral transport. The simulation with the particle source determined from the vertically viewing Dα image of the target well reproduced the 2-D image by the horizontally viewing CCD camera. From above these results, this analysis method using 3-D simulation is demonstrated in its validity and provides the important information for understanding of the plasma transport and confinement in helical fusion devices.

Acknowledgement

The authors would like to acknowledge the members of the Heliotron J supporting group in the experiment. This work was performed with the support by the bidirectional collaboration research program (NIFS06KUHL010).

References

[1] D. Heifetz *et al.*, J. Comput. Phys. **46**, 309 (1982).
[2] D. P. Stotler *et al.*, Phys. Plasmas **3**, 4084 (1996).
[3] Y. Nakashima *et al.*, J. Plasma Fusion Res. SERIES **6**, 546 (2004).
[4] Y. Nakashima *et al.*, J. Nucl. Mater. **337-339**, 466 (2005).
[5] M. Shoji, *et al.*, J. Nucl. Mater. **337-339**, 186 (2005).
[6] S. Kobayashi, *et al.*, Proc 31th EPS conf. Plasma Phys. (London, 2004). **28G**, P-5.097.
[7] F. Sano *et al.* Nucl. Fusion. **45**, 1557 (2005).
[8] T. Mizuuchi *et al.*, Nucl. Fusion **47**, 395 (2007).
[9] S. Kobayashi *et al.*, Rev. Sci. Instrum. **77**, 10E527 (2006).
[10] N. Nishino *et al.*, J. Nucl. Mater. **337-339**, 1073 (2005).
[11] Y. Nakashima *et al.*, to be published in Contrib. Plasma Phys. (2007).

Proceedings of ITC/ISHW2007

Global gyrokinetic simulations for stellarators

R.Kleiber

Max-Planck-Institut für Plasmaphysik, Wendelsteinstrasse 1, 17491 Greifswald, Germany

ralf.kleiber@ipp.mpg.de

The code EUTERPE solves the electrostatic gyrokinetic equation globally for fully three-dimensional equilibria using a particle-in-cell method.
Results from simulations of linear ITG instabilities with adiabatic electrons are presented for the two configurations Wendelstein 7-X and LHD as examples of structurally different equilibria. Using a constant density profile the mode structure and driving mechanism for ITG modes found in these equilibria for different plasma β are discussed.
Since stellarators naturally possess a strongly sheared neoclassical radial electric field it is important to assess its influence on ITG instabilities. In order to do this, a simple model of the radial electric field has been included in the simulations. This model assumes that (for constant density) the electric field is determined by its balance with the pressure gradient. In the framework of this model the influence of a neoclassical electric field on growthrate and structure of ITG instabilities is investigated for the two stellarator configurations.
In order to carry out nonlinear simulations the field equation has to be modified such that it contains the flux surface average of the electrostatic perturbation. Since especially for three-dimensional configurations the corresponding matrix is no longer a sparse one, a scheme is presented which uses a matrix-free approach for the averaging operator.

Proceedings of ITC/ISHW2007

Elimination of small magnetic wells in gyrokinetic stability calculations for a quasi-symmetric configuration

D. R. Mikkelsen, G. W. Hammett, M. Zarnstorff, W. Dorland[a], M. A. Barnes[a]

Princeton Plasma Physics Laboratory, Princeton, NJ 08543, USA
[a] University of Maryland, College Park, MD, USA

mikk@pppl.gov

The existence of local ripple wells in stellarators complicates the calculation of microinstability properties [1]. This is particularly true for quasi-symmetric configurations (e.g., HSX, NCSX, QPS), which have much more complex Boozer spectra than other types of stellarators and which consequently have many small local ripple wells [1, 2]. Resolving these configurational details is a heavy computational burden: high spatial resolution is required to capture the small scale of the wells, and high velocity-space resolution is required to include the narrow trapped regions.

Physical intuition suggests that in a distribution of ripple wells of diminishing extent and depth, only the larger wells play an important role in determining the microinstability properties. This should particularly be true for quasi-axisymmetric configurations such as NCSX, because they are designed to have one very large magnetic well per poloidal circuit and the ‘bad curvature’ region is well aligned with it. Nevertheless, a method of simplifying the configuration and the criteria for identifying ‘small’ ripple wells requires justification through convergence tests. A ‘brute force’ smoothing of |B| vs distance along the field line that ignores all 'small' wiggles can be easily implemented, but this would not be consistent with other elements of the configuration description. An alternative that is more self-consistent, would be to remove some Boozer components (small Bmn, or small n*Bmn, ...) and then calculate all drifts and geometric quantities from the reduced Boozer spectrum, but this reduced Boozer spectrum will not represent a true MHD equilibrium. We will determine whether these faults can be tolerated in the context of linear stability calculations.

We will examine several strategies for simplifying the NCSX configuration description, and evaluate how these simplifications affect the growth rates and frequencies of 'pure' ITG microinstabilities (i.e., adiabatic electrons). The characteristics of a successful simplification scheme may depend on the collisionality and the relative importance of ITG and TEM drive, so we will eventually examine TEM and ITG/TEM-hybrid modes and include scans in collisionality.

[1] G. Rewoldt, L.-P. Ku, W. M. Tang, Phys. Plasmas **12** (2005) 102512.
[2] G. Rewoldt, L.-P. Ku, W. M. Tang, W. A. Cooper, Phys. Plasmas **6** (1999) 4705.

Proceedings of ITC/ISHW2007

A flute mode turbulence and a related transport in the divertor of a mirror

Isao KATANUMA[1)], Hiroshi SAIMARU[1)], Yoshinari MIZOGUCHI[1)], Katsuya YASHIRO[1)], Teruji CHO[1)] and Vladimir P. PASTUKHOV[2)]

[1)]*Plasma Research Center, University of Tsukuba, Tsukuba 305-8577, Japan*
[2)]*RRC "Kurchatov Institute", Kurchatov Square, 1, 123182 Moscow, Russia*

We investigate a flute mode turbulence and its related radial transport in a magnetic divertor. The computer code was made to simulate flute modes. This code can be applied to a magnetic shearless confinement system as well as a tandem mirror. Computer simulation carried out in a modeled magnetic divertor shows that the flute modes enhance the radial transport during its growing phase.

Keywords: divertor, flute, interchange, simulation, mirror

1. Introduction

A magnetic divertor is an application of the stable dipole magnetic configuration on a planet. And the magnetic divertor configuration has an equilibrium up to $\beta \simeq 1$, where β is the ratio of plasma pressure to the vacuum magnetic field on axis. The open magnetic confinement system such as GAMMA10 has the possibility of a fully axisymmetric system with MHD stable state by containing a magnetic divertor region.[1)]

A typical divertor magnetic field is shown in Fig.1, where the axial length $L = 200$ and a magnetic null point locates at $(r, z) = (65, 0)$. This axisymmetric mirror plasma is found to be stabilized by the plasma compressibility rather than by the ion finite Larmor radius effects around the magnetic null for the fatter radial density profiles.[2)] That is, $\partial pU^\gamma/\partial\psi > 0$ is the stability condition of plasma in Fig.1, where p is plasma pressure, $U \equiv \int \frac{d\ell}{B}$ is the specific volume of a magnetic field line, γ is the heat index and $2\pi\psi$ is the magnetic flux surrounded by the surface $\psi = const$.

The flute modes are one of the most dangerous instabilities in the magnetic shearless confinement system, so the stability analysis of the flute modes usually has a priority over other modes.[3)] However the transport process resulting from the flute instabilities has not been studied so much to the authors' knowledge. So the purpose of this paper is to investigate the flute instability and related plasma radial transport in a magnetic divertor shown in Fig.1.

As mentioned above in this paper, the flute modes are stabilized by mainly plasma compressibility in a divertor mirror cell. So that the fluid approximation can be applied to the flute mode analysis here. In the marginally stable state the plasma pressure radial profile is assumed to satisfy the relation of $pU^\gamma = const$. Ions passing near the magnetic null region do not conserve its magnetic moment μ, which can disturb the marginally stable state, i.e. $\partial pU^\gamma/\partial\psi \lesssim 0$, where the flute modes become unstable. In the following we consider the slightly unstable state to the flute modes.

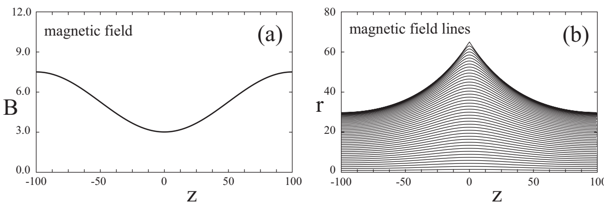

Fig. 1 Modeled magnetic divertor. (a) is axial profile of magnetic field and (b) plots magnetic field lines.

2. Basic equation

The freedom of compressible Alfvén modes and shear Alfvén modes and acoustic modes is unnecessary to calculate the flute instability, because those modes are more stable than the flute modes and that those modes usually have high frequency oscillations. One of authors (Pastukhov)[4)] has proposed a method how to remove the Alfvén modes and acoustic modes from the MHD equations, the equation of motion of which is given as

$$\frac{\partial\hat{w}}{\partial t} + [\![\Phi, \hat{w}]\!] - [\![\hat{\rho}, \langle\frac{v_\alpha^2}{2}\rangle]\!] + \frac{1}{U^\gamma}\frac{\partial U}{\partial\psi}\frac{\partial(\hat{\rho}_0\tilde{T} + \hat{T}_0\tilde{\rho})}{\partial\varphi} = UQ_w^*$$
$$+ \frac{3X_M}{20}\left(\frac{T_i + T_e}{2T_i}\right)\left\{\frac{\partial}{\partial\psi}\left(\hat{\rho}\langle r^2\rangle\frac{\partial}{\partial\psi}\left(\frac{1}{U^{2/3}\sqrt{\hat{T}_0}}\frac{a^2}{\langle r^2\rangle}\hat{w}\right)\right)\right.$$
$$\left. + \frac{a^2}{\langle r^2\rangle}\left\langle\frac{1}{r^2B^2} + \lambda^2B^2\right\rangle\frac{\hat{\rho}}{U^{2/3}\sqrt{\hat{T}_0}}\frac{\partial^2\hat{w}}{\partial\varphi^2}\right\} \tag{1}$$

Here $a^2 = \langle r^4\rangle/\langle r^2\rangle$ and $\hat{w}$ has the following form.

$$\hat{w} = \frac{\partial}{\partial\psi}\left(\hat{\rho}\langle r^2\rangle\frac{\partial\Phi}{\partial\psi}\right) + \frac{\partial}{\partial\varphi}\left(\hat{\rho}\left\langle\frac{1}{r^2B^2} + \lambda^2B^2\right\rangle\frac{\partial\Phi}{\partial\varphi}\right) \tag{2}$$

where $\Phi \equiv c\phi$, c light speed, ϕ electrostatic potential, w is related to the specific volume averaged vorticity $\nabla\times(\rho c\boldsymbol{B}\times\nabla\phi/B^2)$ due to plasma $\boldsymbol{E}\times\boldsymbol{B}$ drift flux, and v_α^2 is the square of plasma fluid velocity. Poisson bracket is defined as

$$[\![\Phi, \hat{w}]\!] \equiv \frac{\partial\Phi}{\partial\psi}\frac{\partial\hat{w}}{\partial\varphi} - \frac{\partial\Phi}{\partial\varphi}\frac{\partial\hat{w}}{\partial\psi} \tag{3}$$

author's e-mail: katanuma@prc.tsukuba.ac.jp

The second term in the right hand side in eq.(1) represents the viscosity of fluid and the third term contains the effects that the vorticity can move along a magnetic null.

The transport equations of mass density and heat are given in the following on the assumption of the adiabatic index $\gamma = 5/3$.

$$\frac{\partial \hat{\rho}_0}{\partial t} - \frac{\partial}{\partial \psi}\left(\overline{\tilde{\rho}\frac{\partial \Phi}{\partial \varphi}}\right) = 4\pi d_M \frac{\partial}{\partial \psi}\left[\frac{\hat{\rho}_0 \langle r^2\rangle U}{\hat{T}_0^{3/2}} \frac{\partial}{\partial \psi}\left(\frac{\hat{\rho}_0 \hat{T}_0}{U^{5/3}}\right)\right] + \overline{\tilde{Q}}{}^*_\rho U \quad (4)$$

$$\frac{\partial \tilde{\rho}}{\partial t} + [\![\Phi, \tilde{\rho}]\!] + \frac{\partial}{\partial \psi}\left(\widetilde{\tilde{\rho}\frac{\partial \Phi}{\partial \varphi}}\right) - \frac{\partial \Phi}{\partial \varphi}\frac{\partial \hat{\rho}_0}{\partial \psi} = \tilde{Q}^*_\rho U + 4\pi d_M \times \left\{\frac{\partial}{\partial \psi}\left[\frac{\hat{\rho}_0 \langle r^2\rangle U}{\hat{T}_0^{3/2}} \frac{\partial}{\partial \psi}\left(\frac{\tilde{\rho} \hat{T}_0}{U^{5/3}}\right)\right] + \left[\frac{\hat{\rho}_0}{\hat{T}_0^{1/2} U^{2/3}} \left\langle \frac{1}{r^2 B^2}\right\rangle \frac{\partial^2 \tilde{\rho}}{\partial \varphi^2}\right]\right\} \quad (5)$$

$$\frac{\partial \hat{T}_0}{\partial t} - \frac{\partial}{\partial \psi}\left(\overline{\tilde{T}\frac{\partial \Phi}{\partial \varphi}}\right) = X_M \frac{2U^{2/3}}{3\hat{\rho}_0} \frac{\partial}{\partial \psi}\left(\frac{\hat{\rho}_0^2 \langle r^2\rangle}{U} \frac{\partial}{\partial \psi}\left(\frac{\sqrt{\hat{T}_0}}{U^{1/3}}\right)\right) + \frac{8\pi d_M}{3\sqrt{\hat{T}_0}} \frac{\partial}{\partial \psi}\left(\langle r^2\rangle U \frac{\partial}{\partial \psi}\left(\frac{\hat{\rho}_0 \hat{T}_0}{U^{5/3}}\right)\right) + \frac{U^{5/3}}{\hat{\rho}} \overline{\tilde{Q}}{}^*_T \quad (6)$$

$$\frac{\partial \tilde{T}}{\partial t} + [\![\Phi, \tilde{T}]\!] + \frac{\partial}{\partial \psi}\left(\widetilde{\tilde{T}\frac{\partial \Phi}{\partial \varphi}}\right) - \frac{\partial \Phi}{\partial \varphi}\frac{\partial \hat{T}_0}{\partial \psi} = \frac{U^{5/3}}{\hat{\rho}}\tilde{Q}^*_T + X_M \frac{U^{2/3}}{3\hat{\rho}_0} \times \frac{\partial}{\partial \psi}\left(\frac{\hat{\rho}_0^2 \langle r^2\rangle}{U} \frac{\partial}{\partial \psi}\left(\frac{\tilde{T}}{U^{1/3}\sqrt{\hat{T}_0}}\right)\right) + \frac{X_M \hat{\rho}_0}{3U^{2/3}\sqrt{\hat{T}_0}} \left\langle \frac{1}{r^2 B^2}\right\rangle \frac{\partial^2 \tilde{T}}{\partial \varphi^2} \quad (7)$$

Here $\rho \equiv M_i n_i + M_e n_e = \langle \rho \rangle \equiv \hat{\rho}/U$ is mass density. The slow time variable equilibrium component $\hat{\rho}_0(\epsilon^3 t, \psi)$ and fast variable fluctuating components $\tilde{\rho}(\epsilon t, \psi, \varphi)$ are defined, where the equilibrium quantity is represented by the hat with subscript $\hat{}_0$ and fluctuating quantity is by the tilde $\tilde{}$, i.e. and $\hat{\rho} = \hat{\rho}_0 + \tilde{\rho}$. The quantity $\hat{T}$ is related to the temperature defined by $\hat{T} \equiv pU^\gamma/\hat{\rho} = (T_i + T_e)U^{\gamma-1}/M_i$. The symbol $\overline{A}$ means the average of A over φ, $\hat{A}$ means the quantity of A integrated in the specific volume of a magnetic field line, and the symbol $\langle A \rangle$ means the integration of A along a magnetic field lines,

$$\overline{A} \equiv \frac{1}{2\pi}\int_0^{2\pi} A \mathrm{d}\varphi\,, \quad \hat{A} \equiv \int \frac{A \,\mathrm{d}\zeta}{J(\psi, \varphi, \zeta)}\,, \quad \langle A \rangle \equiv \frac{\hat{A}}{U} \quad (8)$$

where $J(\psi, \varphi, \zeta) \equiv \nabla\psi \times \nabla\varphi \cdot \nabla\zeta$ is Jacobian. The magnetic field line curvatures are included in the coefficients U, $\langle r^2 \rangle$, $\langle \frac{1}{r^2 B^2} \rangle$ in the eqs.(1)-(7), and the definition of U is

$$U \equiv \int \frac{\mathrm{d}\zeta}{J(\psi, \varphi, \zeta)} \quad (9)$$

The coordinates (ψ, φ, ζ) adopted here are the flux coordinates, where magnetic field is represented as $\boldsymbol{B} = \nabla\psi \times \nabla\varphi$. Here $2\pi\psi$ gives the magnetic flux inside the surface of $\psi = const$, and φ corresponds to an angle coordinate. The remaining coordinate ζ is usually taken as z-axis or along magnetic field line.

The classical diffusions included in eqs.(1)-(7) are defined by

$$X_M = \chi_\perp \frac{B^2}{\rho}\left(\frac{4T_i}{T_i + T_e}\right)\left(\frac{p}{\rho}\right)^{1/2}$$
$$d_M = \frac{m_e^{1/2}(T_i + T_e)T_i^{1/2}}{\sqrt{2} m_i^{1/2} T_e^{3/2}} \left(\frac{B^2}{4\pi\rho}\left(\frac{p}{\rho}\right)^{1/2} \chi_\perp\right) \quad (10)$$

$$\chi_\perp = \frac{T_i}{m_i \omega_{ci}^2 \tau_i}\,, \qquad \epsilon^3 \equiv \frac{\chi_\perp}{b c_s}\left(\frac{2T_i}{T_i + T_e}\right) \quad (11)$$

Here τ_i is the classical ion-ion coulomb collision time[5], $c_s \equiv \sqrt{\gamma p/\rho}$ is the ion sound speed , and b is a distance defined by $b \equiv \sqrt{\psi_b/B_M}$, where the subscript $_M$ means some axial position on axis. The quantities related to classical transport X_M and d_M in eq.(10) are the dimensionless quantities which are constant along a magnetic field line. The mass density ρ and other plasma quantities T_e, T_i are assumed to be constant along a magnetic field line through this paper. The parameter ϵ defined in eq.(11) is a small expansion parameter, where we assume $\epsilon^2 = 10^{-2}$ in the numerical calculation of next section in this paper.

The basic equations in this section contain the interchange modes (similar to the Rayleigh-Taylor instabilities) and the modes associated with the presence of nonuniform plasma flows (similar to the Kelvin-Helmholtz instabilities) as well as the electrostatically incompressible stable plasma flows. So this close set of equations describe the nonlinear low-frequency MHD plasma convection and resulting transport processes in weakly dissipative plasmas in axisymmetric shearless systems.

3. Numerical results

Numerical calculation by using the basic equations (1)-(7) is carried out in the magnetic divertor shown in Fig.1 for the purpose of investigating the effects of flute mode fluctuations on the plasma radial transport.

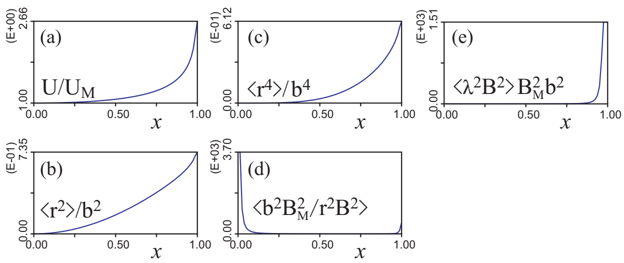

Fig. 2 Basic parameters of magnetic divertor.

The geometrical parameters of the magnetic divertor in Fig.1 are plotted in Fig.2, where the specific volume $u \equiv U/U_M$ in (a), $\langle r^2 \rangle/b^2$ in (b), $\langle r^4 \rangle/b^4$ in (c), $\langle \frac{1}{r^2 B^2} \rangle B_M^2 b^2$ in (d), and $\langle \lambda^2 B^2 \rangle B_M^2 b^2$ as a function of $x \equiv \sqrt{\psi/\psi_b}$. The classical diffusion coefficients of quasi-equilibrium ($m = 0$) density and temperature are proportional to $\langle r^2 \rangle$ in eqs.(4) and (6), which have maximum values at $x = 1$ in Fig.2(b). The classical diffusion coefficients of the perturbed components ($m \neq 0$) of vorticity and temperature in the φ direction are proportional to $\langle r^4 \rangle \langle \frac{1}{r^2 B^2} + \lambda^2 B^2 \rangle / \langle r^2 \rangle^2$ and $\langle \frac{1}{r^2 B^2} \rangle$ in eqs.(1) and (7), which diverge at the axis in Fig.2(d). The effects that fluid can flow freely in the azimuthal direction along a magnetic null line are included through $\langle \lambda^2 B^2 \rangle$ in eqs.(1) and (2). The potential Φ is determined by eq.(2). A dimensionless parameter ϵ in eq.(11) contains the magnitude of the classical diffusion.

The equations (1)-(7) have the steady state solutions if the classical diffusion is neglected, i.e. $\epsilon = 0$, that is

$$\hat{\rho}_0(\psi) = const.\,, \quad \hat{T}_0(\psi) = const.\,, \quad \hat{w}_0(\psi) = const. \quad (12)$$

The field line integrated vorticity $w_0 = -1$ gives a plasma azimuthal rigid rotation so that there is no shear flow in this initial condition. As long as eq.(12) is satisfied any fluctuations do not generate in eqs.(1)-(7). So we add a small fluctuation $\tilde{T}$ to the initial condition eq.(12), i.e. $\hat{\rho}_0 = 1$, $\hat{T}_0 = 1$, $\hat{w}_0 = -1$, in the following numerical calculation, where the initial perturbation $\tilde{T}$ added to equilibrium temperature $\hat{T}_0$ is plotted in Fig.3(b).

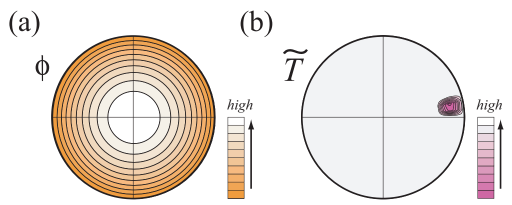

Fig. 3 Initial condition of ϕ and $\tilde{T}$.

Henceforth, the normalized time τ defined as $\tau = \frac{\epsilon c_{sM}}{b} t$ is introduced. The specific volume averaged perturbed quantity $\widetilde{A}$ is plotted in place of $\tilde{A}$ in the following figures. The initial condition $\hat{w}_0 = -1$ gives the axisymmetric potential profile shown in Fig.3(a), where the plasma rotates clockwise rigidly around axis at the amount of 2π during $\tau \simeq 4$. This initial condition is unstable to the flute modes.

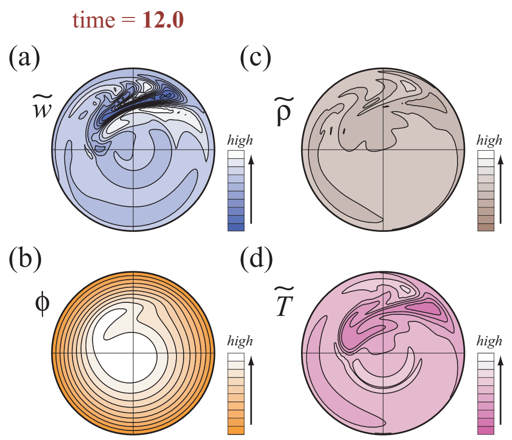

Fig. 4 The potential and the perturbed quantities at $\tau = 12$.

The flute modes grow in a linear phase with the rotation of plasma around axis by $\boldsymbol{E}\times\boldsymbol{B}$-drift, and then the first big flute instability appears at $\tau = 12$ in Fig.4. A typical parasol shaped equi-contour surfaces to Rayleigh-Taylor instabilities of $\widetilde{T} \equiv \tilde{T}/U^{2/3}$ can be seen in Fig.4(d)

The radial profiles and radial fluxes Γ_ρ of mass density and Γ_T of temperature are plotted at $\tau = 12$ in Fig.5. Initial flux volume integrated mass density $\hat{\rho}_0 = \rho_0 U$ and temperature $\hat{T}_0 = T_0 U^{2/3}$ profiles are close to the initial profiles except for the region $x \simeq 1$ where the classical radial flux dominates in Figs.5(e) and (f). In the region where flute instability occurs, the anomalous radial fluxes are much larger than the classical ones in Figs.5(e) and (f). The plasma rotates clockwise in whole region as seen in Figs.5(b) where the potential has a monotonously decreas-

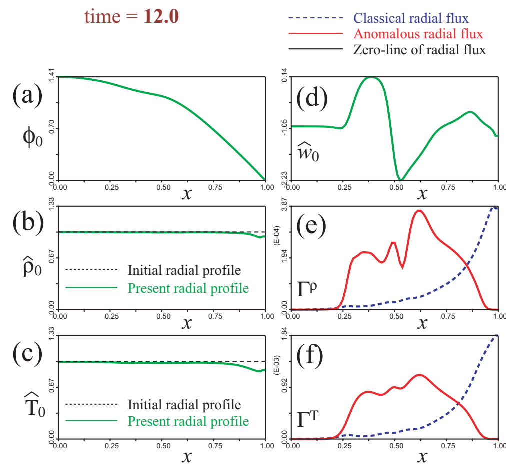

Fig. 5 Radial profiles of ϕ_0, $\hat{\rho}_0$, $\hat{T}_0$, $\hat{w}_0$ and radial fluxes of mass density Γ_ρ and temperature Γ_T at $\tau = 12$.

ing radial profile. In the region $x \lesssim 0.25$, where the flute modes do not reach yet, classical transport dominates and plasma rotates rigidly in the azimuthal direction. The parasol shaped low temperature region generated by the flute instability in Fig.4 continues in $\tau \simeq 10$ and then disappears.

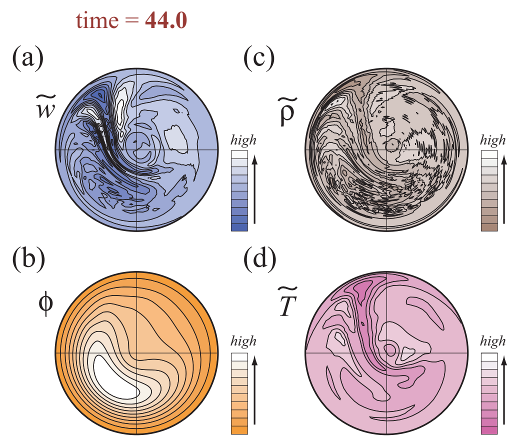

Fig. 6 The potential and the perturbed quantities at $t = 44$.

The flute instabilities appear and disappear repeatedly in time with enhancing radial transport during the existence of the instabilities. Figure 6 plots the profiles of perturbation quantities at $\tau = 44$. The potential has a peak off axis at that time in Fig.6(b). The low temperature region penetrates at axis in Fig.6(d) which is accompanied by the penetration of the low density region in Fig.6(c). Many short wave length perturbations are seen in mass density $\widetilde{\rho}$ than that in temperature $\widetilde{T}$ because the modes associated with the presence of nonuniform plasma flows (similar to the Kelvin-Helmholtz instabilities) grows in mass density where the classical diffusion coefficient of mass density in eq.(5) is much smaller than that of the temperature in eq.(7).

The radial profile of potential ϕ_0 has a maximum at

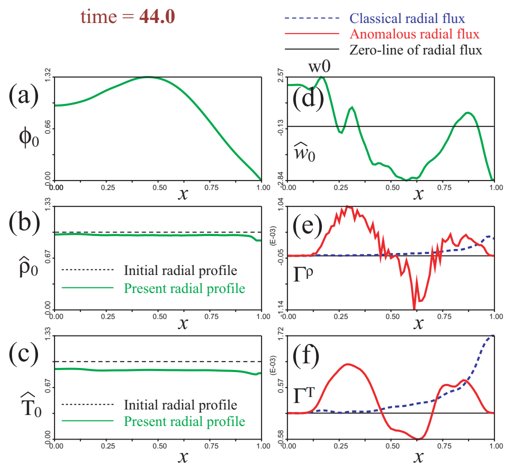

Fig. 7 Radial profiles of ϕ_0, $\hat{\rho}_0$, $\hat{T}_0$, $\hat{w}_0$ and radial fluxes of mass density Γ_ρ and temperature Γ_T at $\tau = 44$.

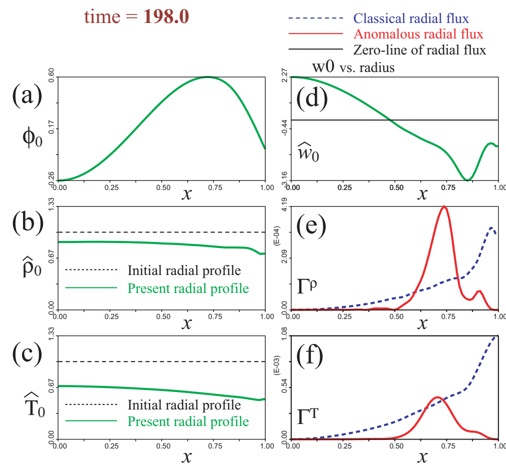

Fig. 9 Radial profiles of ϕ_0, $\hat{\rho}_0$, $\hat{T}_0$, $\hat{w}_0$ and radial fluxes of mass density Γ_ρ and temperature Γ_T at $\tau = 198$.

$x \simeq 0.45$ at $\tau = 44$ in Fig.7(a). That is, two counter flows exist at this time. Fig.7(d) plots the radial profile of w_0, maximum and minimum values of which are 2.57 and -2.87, respectively. These magnitudes are larger than the initial magnitude of w_0. Because the total vorticity is conserved in this simulation, there is inward transport of angular momentum. In the region $0.1 < x < 0.8$ the enhanced radial transport exists and the plasma shakes forward and backward radially as shown in Figs.7(e) and (f).

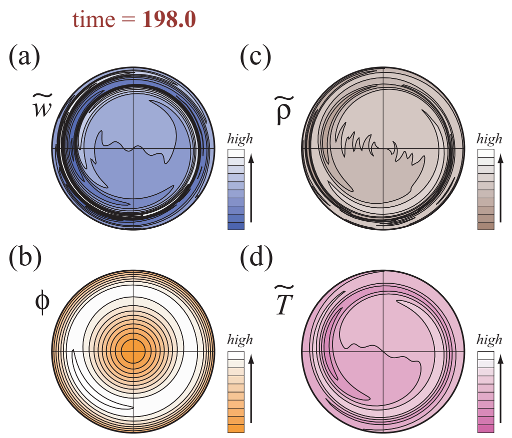

Fig. 8 The potential and the perturbed quantities at $t = 198$.

The system comes to a quasi-steady state after the long run as shown in Fig.8, in the meaning that the structures do not change so much in time. In this state any perturbations are not observed in the region $x \lesssim 0.6$ in Fig.8. Although the potential in Fig.8(b) has almost axisymmetric profile, its radial profile is not constant shown in Fig.9(a). The radial profile w_0 is also not constant radially, which means that there are shear flows (not rigid rotation).

In the region $x \gtrsim 0.6$ in Fig.8 the vortex structures of $\widetilde{w}, \widetilde{\rho}, \widetilde{T}$ are seen, where the anomalous radial transports are enhanced in ρ_0 and T_0 in Fig.9(e) and (f). The equilibrium quantities of $\hat{\rho}_0$ and $\hat{T}_0$ shown in Fig.9(b) and (c) has a flatter slope in the region $x \lesssim 0.5$ than those in $x \gtrsim 0.5$, which reminds us of the transport barrier observed in toroidal confinement systems. However, these radial profiles decreases radially so that the system is unstable to the flute modes when without counter shear flows. That is, Figs.8 and 9 show that the counter shear flows prevent the flute modes from being unstable.

5. Summary

We made a computer code using the basic equations obtained in Ref.4. These equations exclude the shear Alfvén modes and compressional modes from MHD equations in order to follow the flute modes and the instability driven by nonuniform plasma flows (similar to the Kelvin-Helmholtz instabilities). We carried out the computer simulation in a modeled divertor mirror cell in the initial condition with finite rigid rotation but no shear flows.

Initial small temperature dip around the outer boundary causes the flute instabilities. The flute instabilities are accompanied by the large enhanced radial transport of mass density and temperature. At the end of the computer simulation, the counter shear flow appears which suppresses the anomalous radial transport as something like transport barrier formation. The equilibrium mass density and temperature have profiles decreasing radially, which should be unstable to flute modes, continue to be stable under the existence of counter shear flows.

[1] I.Katanuma, Y.Sasagawa, Y.Tatematsu, Y.Nakashima, T.Cho, V.P.Pastukhov, Nucl. Fusion, **46**, 608 (2006).
[2] Y.Sasagawa, I.Katanuma, Y.Mizoguchi, T.Cho, V.P.Pastukhov, Phys. Plasmas, **13**, 122506 (2006).
[3] I.Katanuma, Y.Tatematsu, K.Ishii, T.Tamano, K.Yatsu, J. Phys. Soc. Jpn., **69**, 3244(2000).
[4] P.V.Pastukhov 2005 Plasma Phys. Rep. **31**, 577.
[5] S.I.Braginskiin *Reviews of Plasma Physics*, ed. A.M.A.Leontovich (Consultants Bureau, New York, 1965) Vol. 1.

Proceedings of ITC/ISHW2007

A model of interaction between magnetic island and drift wave turbulence

Akihiro ISHIZAWA[1)], Patrick H. DIAMOND[2)] and Noriyoshi NAKAJIMA[1)]

[1)]*National Institute for Fusion Science, Toki 509-5292, Japan*

[2)]*University of California San Diego, La Jolla, California 92093-0424, USA*

October 15, 2007

A modified Rutherford equation of magnetic island is introduced. The island equation includes multi-scale interaction with drift wave turbulence and is coupled with turbulent wave energy equation. In this model, drift wave turbulence is prey and magnetic island corresponds to predator. The magnetic island suppresses the growth of turbulence by flattening temperature gradient because of the violation of magnetic surfaces. On the other hand, the turbulence affects perturbed neoclassical bootstrap current in the Rutherford equation through anomalous transport. In these interactions heat flux is fixed, and thus perpendicular thermal diffusion coefficient depends on the turbulence energy and the island width. A stabilizing effect of the turbulence on magnetic island growth is found and new critical island width of neo-classical tearing mode excitation is obtained.

Keywords: magnetic island, drift wave turbulence, multi-scale, NTM

DOI:

1 Introduction

Recently, multi-scale interaction between micro-turbulence and macro-scale magnetohydrodynamic (MHD) instability has been studied extensively [1, 2, 3]. The interaction would play crucial role in the analysis of neoclassical tearing mode (NTM), which limits the beta of tokamak plasmas[4, 5]. The NTM is driven by perturbed neoclassical bootstrap current density inside the separatrix of magnetic island, and it is unstable in high beta tokamak plasma, even if the current density profile is linearly stable against tearing mode. Thus, NTM is a nonlinear instability and it starts to grow when the width of island caused by an external perturbation exceeds a threshold.

The excitation mechanism of NTM is an open problem that is divided into two parts: the threshold and the trigger. The threshold which is called critical island width is evaluated as follows. When magnetic island appears the pressure gradient is reduced inside the island because of strong heat conductivity along magnetic field. This flattening of pressure gradient reduces neoclassical bootstrap current inside the magnetic island and destabilizes the magnetic island. When the island width is very small the flattening is not completed because it is not able to overcome perpendicular transport. Hence, competition between parallel and perpendicular heat transport determines critical island width [6]. The critical island width is also affected by the polarization current [7, 8]. On the other hand, the trigger problem is the process of producing the seed magnetic island caused by external phenomena. Once the width of seed island exceeds the critical island width, then the island grows as NTM. The external phenomena can be MHD modes of different helicities such as sawteeth and edge localized modes and induce the seed island through toroidal mode coupling [9, 10]. The external phenomena can also be micro-turbulence because the turbulence is able to produce seed island through nonlinear mode coupling [11].

The anomalous perpendicular transport due to drift wave turbulence should play crucial role in evaluating critical island width. In addition, magnetic island affects the turbulence simultaneously. We need a model which describes these mutual interaction between them. In this paper, we propose a simple model of interaction between drift wave turbulence and magnetic island. The point of our model is that we fix heat flux instead of thermal diffusivity coefficient when we evaluate temperature gradient. Then we introduce effects of drift wave turbulence on thermal diffusivity and introduce effect of magnetic island which reduces the growth of turbulence by flattening temperature gradient inside the island.

We present our model of interaction between magnetic island and the turbulence in Sec. 2. In Sec. 3 we evaluate critical island width by using the model. Finally we summarize results in Sec. 4.

author's e-mail: ishizawa@nifs.ac.jp

2 Model of interaction between magnetic island and drift wave turbulence

We present magnetic island equation which couples with drift wave turbulence energy equation. The modified

Rutherford equation of magnetic island evolution is [4]

$$\frac{\tau_R}{r_s}\frac{dw}{dt} = r_s\Delta' + \frac{L_s r_s}{B_0 w}\delta J_{BS}, \tag{1}$$

where w, r_s, B_0, τ_R, and L_s are island width, minor radius of resonant surface, uniform toroidal magnetic field, resistive diffusion time, and magnetic shear length, respectively. In this equation Δ' is the stability parameter of tearing mode and is negative so that it is stable against tearing mode. We remark that the island width is related to perturbed magnetic field as $\delta B = k_\theta B_0 w^2/L_s$. Here we assume that density profile is uniform n_0, then the perturbed bootstrap current is

$$\delta J_{BS} = \frac{\epsilon^{1/2} n_0}{B_\theta}\delta\left(\frac{dT_e}{dr}\right), \tag{2}$$

where ϵ, T_e, and B_θ are aspect ratio, electron temperature, and poloidal magnetic field, respectively. When we calculate temperature gradient

$$\frac{dT_e}{dr} = -\frac{Q_e}{\chi_\perp}, \tag{3}$$

we fix heat flux Q_e, and thus perpendicular heat diffusivity $\chi_\perp$ is variable. The heat diffusivity coefficient consists of diffusion due to perturbed magnetic field in the presence of magnetic island $\chi_{\perp island}$, anomalous transport by drift wave turbulence $\chi_{\perp turb}$, and neoclassical transport $\chi_{\perp neo}$ as,

$$\chi_\perp = \chi_{\perp turb} + \chi_{\perp island} + \chi_{neo}, \tag{4}$$

$$\chi_{\perp turb} = \chi_{\perp turb}(\varepsilon) = \chi_0\varepsilon(w), \tag{5}$$

$$\chi_{\perp island} = \chi_\parallel\left(\frac{\delta B}{B_0}\right)^2 = \chi_\parallel\left(\frac{k_\theta}{L_s}w^2\right)^2, \tag{6}$$

where $\chi_{\perp turb}$ is assumed to be proportional to turbulence energy ε, $\chi_\parallel$ is parallel thermal diffusivity, and k_θ is poloidal wave number. Then Eq. (3) is rewritten as,

$$\frac{dT_e}{dr} = \frac{-Q_e}{\chi_0\varepsilon(w) + \chi_\parallel(w^2 k_\theta/L_s)^2 + \chi_{neo}}. \tag{7}$$

By using Eqs. (7) and (2) the island equation (1) is written as,

$$\begin{aligned}\frac{d\hat{w}}{d\hat{t}} &= \hat{\Delta}' + \\ &\frac{\hat{\beta}_e}{\hat{w}}\hat{Q}_e\left(\frac{1}{\varepsilon(0)+\hat{\chi}_{neo}} - \frac{1}{\varepsilon(\hat{w}) + \hat{w}^4/\hat{w}_d^4 + \hat{\chi}_{neo}}\right) \quad (8)\\ &= \hat{\Delta}' + \\ &\frac{\hat{\beta}_e}{\hat{w}}\frac{\hat{Q}_e}{\varepsilon(0)+\hat{\chi}_{neo}}\left(1 - \frac{\hat{w}_d^4(\varepsilon(0)+\hat{\chi}_{neo})}{\hat{w}^4 + \hat{w}_d^4(\varepsilon(\hat{w})+\hat{\chi}_{neo})}\right), \quad (9)\end{aligned}$$

where $\hat{\chi}_\perp(\varepsilon(\hat{w})) = \varepsilon(\hat{w})$. Normalizations are $\hat{w} = w/r_s$, $\hat{t} = t/\tau_R$, $\hat{\chi}_\parallel = \chi_\parallel/\chi_0$, $\hat{\chi}_{neo} = \chi_{neo}/\chi_0$, $\hat{k}_\perp = k_\theta r_s^2/L_s$, $\hat{L}_s = L_s/L_{T0}$, $\hat{B}_\theta = B_\theta/B_0$, $\hat{Q}_e = Q_e L_{T0}/T_e\chi_0$, $\hat{\beta}_e = \beta_e\epsilon^{1/2}\hat{L}_s/\hat{B}_\theta$, $\hat{w}_d = (\hat{\chi}_\parallel\hat{k}_\perp^2)^{-1/4}$.

In order to close interaction loop between magnetic island and the turbulence we need equation of turbulence wave energy[12]

$$\frac{d\varepsilon}{dt} = \gamma(\varepsilon, w)\varepsilon - \beta\varepsilon^2, \tag{10}$$

where

$$\gamma(\varepsilon, w) = \gamma_0 L_{T0}\left(\frac{1}{L_T(\varepsilon, w)} - \frac{1}{L_{Tcr}}\right)_{>0}, \tag{11}$$

where $(f)_{>0}$ is zero if f is negative. In this equation we include feedback from magnetic island to the turbulence. The strong parallel thermal diffusion flattens pressure gradient inside the separatrix of the island. This reduces growth rate γ by increasing length scale of temperature gradient

$$\frac{1}{L_T(\varepsilon, w)} = \frac{-1}{T_e}\frac{dT_e}{dr} \tag{12}$$

$$= \frac{1}{L_{T0}}\frac{\hat{Q}_e}{\hat{w}^4 + \hat{w}_d^4(\varepsilon(\hat{w}) + \hat{\chi}_{neo})}. \tag{13}$$

When we calculate the temperature gradient we fix heat flux again. By substituting this equation to Eq. (11) we have equation of turbulence energy including the effect of magnetic island as,

$$\frac{1}{\tau_R\gamma_0}\frac{d\varepsilon}{d\hat{t}} = \left(\frac{\hat{Q}_e}{\hat{w}^4 + \hat{w}_d^4(\varepsilon(\hat{w}) + \hat{\chi}_{neo})} - \frac{1}{\hat{L}_{Tcr}}\right)_{>0}\varepsilon - \hat{\beta}\varepsilon^2, \tag{14}$$

where $\hat{L}_{Tcr} = L_{Tcr}/L_{T0}$ and $\hat{\beta} = \beta/\gamma_0$. Hence, we have obtained a closed set of equations of magnetic island and the turbulence Eqs. (9) and (14).

3 Critical island width of NTM

We have established a model which is able to evaluate critical island width of NTM. We consider a situation that the turbulence saturates because drift frequency time, which is characteristic time scale of drift wave turbulence, is much faster than the resistive diffusion time $\tau_R\gamma_0 >> 1$, where $\gamma_0 \approx \omega_*$. Thus, we neglect left hand side of Eq. (14) and have the equation of turbulence energy as,

$$\varepsilon(w) = \frac{-1}{\hat{\beta}\hat{L}_{cr}} + \frac{1}{2}\left(-F(\hat{w}) + \sqrt{F(\hat{w})^2 + 4\hat{Q}_e/\hat{\beta}}\right), \tag{15}$$

where $F(\hat{w}) = \hat{w}^4/\hat{w}_d^4 + \hat{\chi}_{neo} - \frac{1}{\hat{\beta}\hat{L}_{cr}}$. Substituting this $\varepsilon(w)$ into Eq. (9) we have the island equation of our model.

We show curves of island growth $d\hat{w}/d\hat{t}$ calculated by our model and by the standard model

$$\frac{d\hat{w}}{d\hat{t}} = \hat{\Delta}' + \frac{\hat{\beta}_e}{\hat{w}}\frac{\hat{w}^2}{\hat{w}^2 + \hat{w}_d^2} \tag{16}$$

in Fig. 1. Here we set parameters $\hat{\Delta}' = -1$, $\hat{\beta}_e = 0.2$, $\hat{\chi}_{neo} = 0.1$, $\hat{Q}_e = 2$, $\hat{\chi}_\parallel\hat{k}_\perp^2 = 10^9$, $\hat{\beta} = 0.6$, and $\hat{L}_{Tcr} = 0.5$. The critical island width $w_{critical}/r_s$ is given by $d\hat{w}/d\hat{t} = 0$. The critical island width of our model is larger than the standard model. Thus, the turbulence has a stabilizing effect on the excitation of NTM. Notice that we cannot apply our model to evaluate saturated island width because a large magnetic island strongly reduces turbulence energy and makes it negative in our model. For the above parameter set the turbulence energy ε is positive when $w/r_s < 0.00548$. Figure 2 shows curves of parallel diffusion coefficient $\chi_\parallel$ as a function of critical island width. Our model implies $w_{critical}/r_s \propto \hat{\chi}_\parallel^{-1/3}$, while the standard model implies $w_{critical}/r_s \propto \hat{\chi}_\parallel^{-1/2}$. Figure 3 shows curves of plasma beta β_e as a function of critical island width. Our model implies $w_{critical}/r_s \propto \hat{\beta}_e^{-1/3}$, while the standard model implies $w_{critical}/r_s \propto \hat{\beta}_e^{-1}$, and thus our model suggests weak dependence of $w_{critical}$ on β_e compared to the standard model.

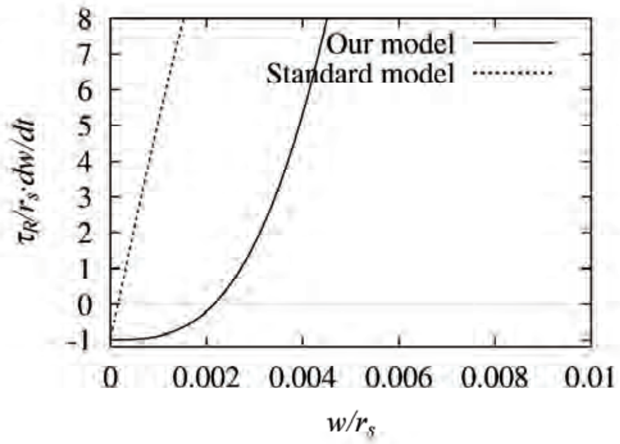

Fig. 1 Curves of island growth $d\hat{w}/d\hat{t}$ as a function of island width w/r_s. Solid curve indicates our model and dashed curve indicates standard model.

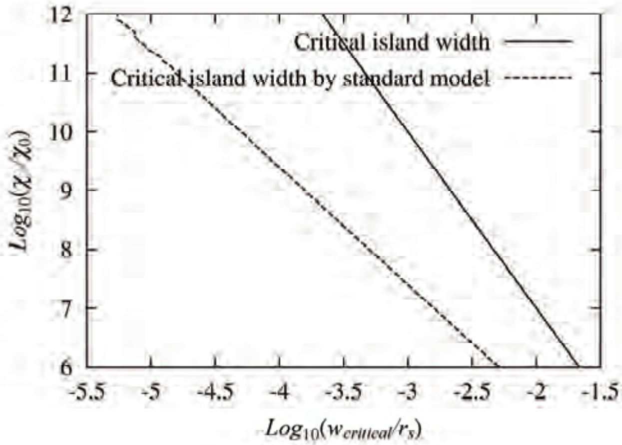

Fig. 2 Curves of parallel diffusion coefficient $\chi_\parallel$ as a function of critical island width. Solid curve indicates our model and dashed curve indicates standard model.

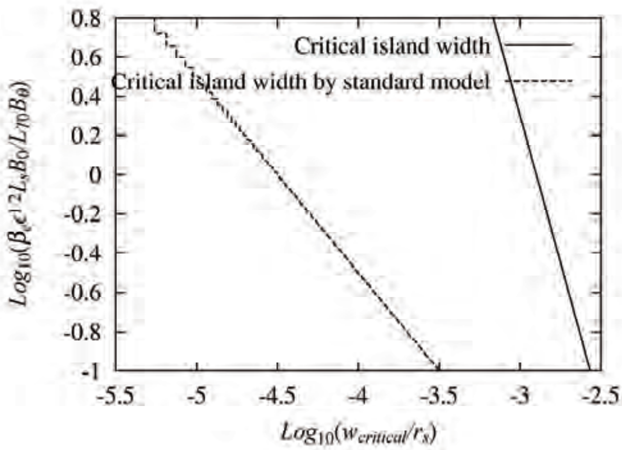

Fig. 3 Curves of plasma beta β_e as a function of critical island width. Solid curve indicates our model and dashed curve indicates standard model.

4 Summary and discussion

We have obtained a predator-prey model of interaction between magnetic island and drift wave turbulence. The turbulence affects perturbed bootstrap current in the island equation of NTM through anomalous perpendicular transport. When we evaluate bootstrap current we fix heat flux and make heat diffusivity depend on the turbulence and the island width. In order to close interaction loop between the magnetic island and the turbulence we introduce turbulence wave energy equation including effect of magnetic island. The magnetic island makes temperature gradient flatten inside it and reduces growth rate of the turbulence.

Our model predicts larger critical island width than the one by standard model. This implies that the drift wave turbulence has stabilizing effect on magnetic island excitation of NTM. In addition we found new β_e scaling of the critical island width of NTM $w_{critical}/r_s \propto \hat{\beta}_e^{-1/3}$. In order to compare our model with experimental observation we would include the polarization current effect in our future work.

[1] C. J. McDevitt and P. H. Diamond, Phys. Plasmas **13**, 032302 (2006).
[2] M. Yagi, S. Yoshida, S.-I. Itoh, H. Naitou, H. Nagahara, J.-N. Leboeuf, K. Itoh, T. Matsumoto, S. Tokuda and M. Azumi, Nucl. Fusion **45**, 900 (2005).
[3] A. Ishizawa and N. Nakajima, Phys. Plasmas **14**, 040702 (2007).
[4] R. J. La Haye, Phys. Plasmas **13**, 055501 (2006).
[5] C. C. Hegna, Phys. Plasmas **5**, 1767 (1998).
[6] R. Fitzpatrick, Phys. Plasmas **2**, 825 (1995).
[7] J. W. Connor, F. L. Waelbroeck, and H. R. Wilson, Phys. Plasmas **8**, 2835 (2001).
[8] R. Fitzpatrick and F. L. Waelbroeck, Phys. Plasmas **12**, 022307 (2005).
[9] R. J. La Haye and O. Sauter, Nucl. Fusion **38**, 987 (1998).
[10] C. C. Hegna, et al, Phys. Plasmas **6**, 130 (1999).
[11] S.-I. Itoh, K. Itoh, and M. Yagi, Phys. Rev. Lett. **91**, 045003 (2003).
[12] P. H. Diamond, S.-I. Itoh, K. Itoh, and T. S. Hahm, Plasma Phys. Controlled Fusion **47**, R35 (2005).

Proceedings of ITC/ISHW2007

Onset of Turbulence in a Drift Wave–Zonal Flow System

Ryusuke NUMATA[1)], Rowena BALL[1,2)], Robert L. DEWAR[1)] and Linda. STALS[2)]

[1)]*Department of Theoretical Physics, Research School of Physical Sciences & Engineering, The Australian National University, Canberra, ACT 0200, Australia*

[2)]*Mathematical Sciences Institute, The Australian National University, Canberra, ACT 0200, Australia*

Numerical analyses of bifurcation phenomena in the Hasegawa-Wakatani model are presented, that provide new insights into the interactions between turbulence and zonal flows in the tokamak plasma edge region. The simulation results show a regime where, after an initial transient, drift wave turbulence is suppressed through zonal flow generation. As a parameter controlling the strength of the turbulence is tuned, this zonal-flow-dominated state is rapidly destroyed and a turbulence-dominated state re-emerges. The transition is explained in terms of the Kelvin-Helmholtz stability of zonal flows. This is the first observation of an upshift of turbulence onset in the resistive drift wave system, which is analogous to the well-known Dimits shift in turbulence driven by ion temperature gradients.

Keywords: bifurcation, transition, drift wave, turbulence, zonal flow

1 Introduction

Fusion plasmas and other turbulent flows in quasi-two-dimensional (2D) geometry can undergo spontaneous transitions to a turbulence-suppressed regime. Known as *L–H* (low-to-high confinement) transitions in plasmas, they are studied intensively because confinement enhancement may supervene through the concomitant abatement of anomalous or turbulent particle and heat fluxes. In tokamak edge plasmas *L–H* transitions are associated with nonlinearly self-generated poloidal $\boldsymbol{E}\times\boldsymbol{B}$ shear or zonal flows, which absorb energy from drift waves and consume the small scale eddies that mediate turbulent transport. It is now widely accepted that control of emergent zonal flows is crucial to achieving and sustaining improved confinement [1].

In this paper we present the results of analytic and numerical investigations of transitions between turbulence-dominated and zonal-flow-dominated regimes, using the Hasegawa–Wakatani (HW) model [2, 3] for electrostatic resistive drift wave turbulence in 2D slab geometry. We find that bifurcations in the model correspond to the onset of drift wave driven turbulence, generation of zonal flows, and re-emergence of drift wave turbulence as the zonal flows become unstable. This latter phenomenon is analogous to the Dimits shift [4] described for turbulence driven by ion temperature gradients (ITG).

2 Hasegawa–Wakatani model

The physical setting of the HW model may be considered as the edge region of a tokamak plasma of nonuniform density $n_0 = n_0(x)$ and in a constant equilibrium magnetic field $\boldsymbol{B} = B_0\nabla z$. Following the drift wave ordering [5], the ion vorticity $\zeta \equiv \nabla^2\varphi$ (φ is the electrostatic potential, $\nabla^2 = \partial^2/\partial x^2 + \partial^2/\partial y^2$ is the 2D Laplacian) and the density fluctuations n are governed by the equations

$$\frac{\partial}{\partial t}\zeta + \{\varphi,\zeta\} = \alpha(\varphi - n) - D\nabla^4\zeta, \tag{1}$$

$$\frac{\partial}{\partial t}n + \{\varphi,n\} = \alpha(\varphi - n) - \kappa\frac{\partial\varphi}{\partial y} - D\nabla^4 n, \tag{2}$$

where $\{a,b\} \equiv (\partial a/\partial x)(\partial b/\partial y) - (\partial a/\partial y)(\partial b/\partial x)$ is the Poisson bracket, D is the dissipation coefficient. The background density is assumed to have an unchanging exponential profile: $\kappa \equiv (\partial/\partial x)\ln n_0$. Electron parallel motion is determined by Ohm's law with electron pressure $p_e = nT_e$,

$$j_z = -env_{e,z} = -\frac{1}{\eta}\frac{\partial}{\partial z}\left(\varphi - \frac{T_e}{e}\ln n\right), \tag{3}$$

assuming electron temperature T_e to be constant (isothermal electron fluid). This relation gives the coupling between ζ and n through the adiabaticity operator $\alpha \equiv -T_e/(\eta n_0\omega_{ci}e^2)\partial^2/\partial z^2$ appearing in Eqs. (1) and (2). In our 2D setting α becomes a constant coefficient when acting on the drift wave components of φ and n by the replacement $\partial/\partial z \to \mathrm{i}k_z$, where $2\pi/k_z = L_\parallel \gg L_y$ is a length characteristic of the drift waves' phase variation along the field lines. However, since zonal components of fluctuations ($k_y = k_z = 0$ modes) do not contribute to the parallel current, this resistive coupling term must be modified with care [6]. Recalling that turbulence in the tokamak edge region, where there is strong magnetic shear, is considered here, $k_y = 0$ should always coincide with $k_z = 0$ because any potential fluctuation on the flux surface is neutralized by parallel electron motion. Let us define zonal and non-zonal components of a variable f as

$$\text{zonal: } \langle f\rangle = \frac{1}{L_y}\int f\,\mathrm{d}y, \quad \text{non-zonal: } \tilde{f} = f - \langle f\rangle,$$

author's e-mail: ryusuke.numata@anu.edu.au

where L_y is the periodic length in y, and remove the contribution by the zonal components in the resistive coupling term in Eqs. (1) and (2). Subtraction of the zonal components from the resistive coupling term $\alpha(\varphi - n) \to \alpha(\tilde{\varphi} - \tilde{n})$ yields the modified HW (MHW) equations,

$$\frac{\partial}{\partial t}\zeta + \{\varphi, \zeta\} = \alpha(\tilde{\varphi} - \tilde{n}) - D\nabla^4\zeta, \qquad (4)$$

$$\frac{\partial}{\partial t}n + \{\varphi, n\} = \alpha(\tilde{\varphi} - \tilde{n}) - \kappa\frac{\partial\varphi}{\partial y} - D\nabla^4 n. \qquad (5)$$

The variables in Eqs. (4) and (5) have been normalized by

$$x/\rho_s \to x,\ \ \omega_{ci}t \to t,\ \ e\varphi/T_e \to \varphi,\ \ n_1/n_0 \to n,$$

where $\rho_s \equiv \sqrt{T_e/m}\omega_{ci}^{-1}$ is the ion sound Larmor radius ($v_{si} \equiv \sqrt{T_e/m}$ is the ion sound velocity in the cold ion limit), n_1 is the fluctuating part of the density.

Wakatani and Hasegawa found [3] that excitations of waves having k_z that maximizes the linear growth rate (for given k_x and k_y) are most likely to occur, since the plasma can choose any parallel wavenumber (k_z). Using the parallel wave number of the maximum growth rate, α is given by $\alpha = 4k^2k_y\kappa/(1 + k^2)^2$. This also gives $\alpha = 0$ for the zonal mode.

The MHW model spans two limits with respect to the adiabaticity parameter α. In the adiabatic limit $\alpha \to \infty$ (collisionless plasma), the non-zonal component of electron density obeys the Boltzmann relation $\tilde{n} = n_0(x)\exp(\tilde{\varphi})$, and the equations are reduced to the Hasegawa–Mima equation [5]. In the hydrodynamic limit $\alpha \to 0$, the equations are decoupled. The vorticity is determined by the 2D Navier-Stokes equation, and the density becomes a passive scalar. The advantage of our choice of α as a free parameter is the capability for treating the limits in a unified manner.

In the adiabatic, ideal limit ($\alpha \to \infty$, $D \to 0$) the MHW system has two dynamical invariants, the energy E and the potential enstrophy W,

$$E = \frac{1}{2}\int(n^2 + |\nabla\varphi|^2)\mathrm{d}\boldsymbol{x},\quad W = \frac{1}{2}\int(n - \zeta)^2\mathrm{d}\boldsymbol{x}, \quad (6)$$

where $\mathrm{d}\boldsymbol{x} = \mathrm{d}x\mathrm{d}y$, which constrain the fluid motion. Conservation laws are given by

$$\frac{\mathrm{d}E}{\mathrm{d}t} = \Gamma_n - D_\alpha - D_E,\quad \frac{\mathrm{d}W}{\mathrm{d}t} = \Gamma_n - D_W, \qquad (7)$$

where fluxes and dissipations are given by

$$\Gamma_n = -\kappa\int\tilde{n}\frac{\partial\tilde{\varphi}}{\partial y}\mathrm{d}\boldsymbol{x},$$

$$D_\alpha = \alpha\int(\tilde{n} - \tilde{\varphi})^2\mathrm{d}\boldsymbol{x},$$

$$D_E = D\int((\nabla^2 n)^2 + |\nabla\zeta|^2)\mathrm{d}\boldsymbol{x},$$

$$D_W = D\int(\nabla^2 n - \nabla^2\zeta)^2\mathrm{d}\boldsymbol{x}.$$

Unlike the Hasegawa–Mima model which is an energy-conserving system, the MHW model has an energy source Γ_n. Due to the parallel resistivity, $\tilde{n}$ and $\tilde{\varphi}$ can fluctuate out of phase which produces non-zero Γ_n. The system can absorb free energy contained in the background density profile through the resistive drift wave instability.

3 Simulation Results

The MHW equations are solved in a doubly periodic square slab domain with box size $L = 2\pi/\Delta k$ where the lowest wavenumber $\Delta k = 0.15$ ($L \sim 42$). The equations are discretized on 256×256 grid points by the finite difference method. We examine the effects of the parameters κ and α on the nonlinearly saturated state, and fix $D = 10^{-4}$ throughout this paper.

We start simulations by imposing small amplitude random perturbations. The perturbations grow linearly in the initial phase and generate drift waves, then the drift waves undergo secondary instabilities which excite zonal flows until nonlinear saturation occurs. In the saturated state, we observe that $\Gamma_n \simeq D_\alpha \gg D_E, D_W$. The spatial structure of the saturated electrostatic potential is shown in Fig. 1. We observe that zonally elongated structures of the electrostatic potential are generated in the MHW model because the modification removes the unphysical resistive dissipation of the zonal modes. The zonal flows carry nearly all the kinetic energy in the final state — they have absorbed nearly all the energy from the drift waves. The build-up of the zonal flow and resulting transport suppression highlight the importance of the modification of the model in the nonlinear regime [7].

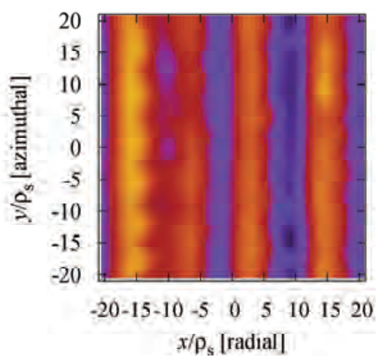

Fig. 1 Contour plot of φ in the saturated state. Zonally elongated structure of the electrostatic potential is clearly visible in the MHW model.

Let us show how the parameters affect the saturated state in the MHW model. In Fig. 2, we plot the ratio of the kinetic energy of the zonal flow ($F \equiv 1/2\int(\partial\langle\varphi\rangle/\partial x)^2\mathrm{d}\boldsymbol{x}$)

P2-059

to the total kinetic energy ($E^k \equiv 1/2 \int |\nabla\varphi|^2 d\boldsymbol{x}$) against α. It is clearly seen that there are two types of saturated states: one where zonal flows prevail and the other dominated by isotropic turbulence. Conversion from one state to the other occurs over a narrow range of the parameter space. We can see that zonal flows are generated in the adiabatic regime ($\alpha \gg 1$) while isotropic flows are generated in the hydrodynamic regime ($\alpha \ll 1$). Transition to the turbulent state also occurs if the drift wave instability is driven strongly by increasing the density gradient parameter κ.

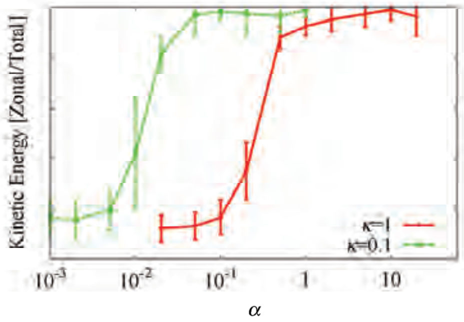

Fig. 2 Parameter dependence of the zonal kinetic energy normalized by the total kinetic energy. Transitions from a zonal-flow-dominated state to a turbulence-dominated state occur.

4 Stability of Zonal Flow

We examine the stability of the zonal flows obtained from the numerical simulations, and compare the stability threshold and the transition point in this section. We consider the perturbation around the zonal flow background. The electrostatic potential and the density are decomposed as $\varphi = \varphi_0(x) + \hat{\varphi}(x)\exp i(k_y y - \omega t)$, and $n = \hat{n}(x)\exp i(k_y y - \omega t)$ where $d\varphi_0/dx = V$ gives the background flow in the y direction. By linearizing the MHW equations, we obtain an eigenvalue equation containing the effect of κ and α,

$$\left[\frac{d^2}{dx^2} - k_y^2 + \frac{k_y V''}{\omega - k_y V}\right]\hat{\varphi} - \frac{i\alpha}{\omega - k_y V + i\alpha}\left(1 - \frac{k_y \kappa}{\omega - k_y V}\right)\hat{\varphi} = 0. \quad (8)$$

We neglect the viscosity. The generated zonal flows in the y direction are assumed to have a sinusoidal profile, $V = V_0 \sin(\lambda x)$. The amplitude V_0 and wavenumber $\lambda = n_\lambda \pi/L$ are determined from the simulation results as $V_0 \propto \kappa^2$, and $\lambda \approx 0.3$. We solve the eigenvalue equation by the standard shooting method in the domain $\mathcal{D} = \{x| - L/2 \le x \le L/2\}$. The boundary is assumed to be rigid $\hat{\varphi}(\pm L/2) = 0$ for simplicity.

In two limits ($\alpha \to 0$ and $\alpha \to \infty$), some conditions for stability are known (see [8] and references therein), and the eigenvalue problem is rather simple because it is not necessary to consider the continuous spectra on the real ω axis. If we find the eigenvalue ω and the corresponding eigenfunction $\hat{\varphi}$, the complex conjugate of ω is also an eigenvalue and the corresponding eigenfunction is given by the complex conjugate of $\hat{\varphi}$. Thus, we can always restrict our quest for eigenvalues in the upper half plane of the complex ω plane, and can neglect interactions between the point spectra and the continuous spectrum.

For the case of finite α the complex conjugate of an eigenvalue is not a eigenvalue, therefore we must solve for negative ω_i too. Moreover, there exist two continuous spectra in this case:

$$\omega = k_y V,\ k_y V - i\alpha \quad \text{where } |V| \le V_0. \quad (9)$$

Both represent convective transport due to the background flow. One of them is damped by the resistivity. These continua may interact with the point spectrum. Thus the situation is much more complicated in the intermediate α case compared with the adiabatic and hydrodynamic limits.

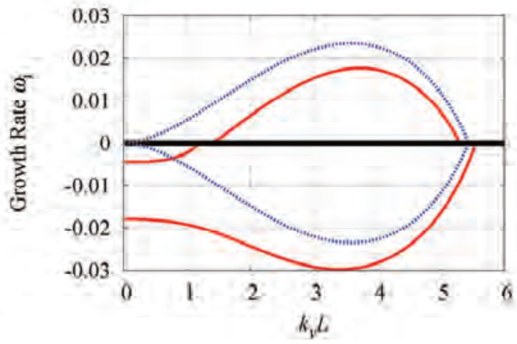

Fig. 3 Growth rates for HW case. Solid curves show the grawth rates for $\alpha = 0.0001$, and thick lines near the real ω axis denote two continuous spectra. Two branches from the $\alpha \to 0$ case (dotted line) are also shown for reference.

We first show the effect of α and neglect effect of κ. We consider $n_\lambda = 2$ for simplicity. Figure 3 shows the imaginary parts of the eigenvalues for $\alpha = 0.0001$. Two branches from the $\alpha \to 0$ case (dotted line) are also shown for reference, so that it is seen that ω_i is slightly shifted downwards for finite α. For increasing α, we observe the positive eigenvalues disappearing at $\alpha \approx 0.000417$.

Next, we consider the effect of κ in addition to α. Since κ always appears in the form of $\kappa\alpha$ and α is small in the vicinity of the threshold, the effect of κ is rather minor. κ does not significantly affect the behavior of the eigenvalues except that κ controls the amplitude of flow ($V_0 \propto \kappa^2$).

We summarize the stability of zonal flows by showing the bifurcation diagram in α-κ plane together with the numerically obtained results. The only excitable mode that can be resolved in the numerical simulation is the $k_y = 0.15$

mode, which is the first unstable mode of the primary instability (resistive drift wave instability). In Fig. 4, we show the stability threshold of $k_y = 0.15$ mode for the primary instability and the tertiary instability (KH instability). Each mark in the figure denotes a numerically obtained saturated state: ▲, ■, • represent respectively the zonal-flow-dominated, transitional, and turbulence-dominated states. In these states zonal flows contain more than 90%, 20-90%, and less than 20% of the total kinetic energy, respectively. The qualitative tendency of the thresholds in the bifurcation diagram shows agreement between the numerical simulations and the KH analysis, i.e. increasing α (κ) is stabilizing (destabilizing). Zonal-flow-dominated states are observed in between the primary and the tertiary instability thresholds. The emergence of a turbulent state is shifted from the primary threshold to the tertiary threshold due to the turbulence suppression effect of the zonal flow, which is analogous to the Dimits shift observed in ITG turbulence.

The reasons for the quantitative discrepancy between the boundary of the zonal and the turbulent states may be because of the simplification made in the KH analysis; the simplified flow profile, the boundary condition and viscosity may also affect the results.

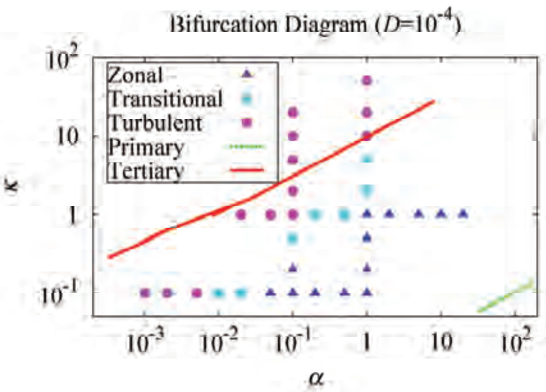

Fig. 4 Bifurcation diagram showing the correlation between the linearized stability estimates described in the text and the regimes observed in our turbulence simulations.

5 Conclusion

In summary, we have analyzed bifurcation phenomena in two-dimensional resistive drift wave turbulence. First, we have performed numerical simulations of the modified HW model to study bifurcation structures in a two-parameter (α-κ) space. We have shown that, in the MHW model, zonal flows are self-organized and suppress turbulence and turbulent transport over a range of parameters beyond the linear stability threshold for resistive drift waves. By performing a systematic parameter survey, we have found that such zonal-flow-dominated states suddenly disappear as a threshold is crossed, being replaced by a turbulence-dominated state.

The threshold of the onset of turbulence has been compared with the linear stability threshold of an assumed laminar zonal flow profile. Numerical analysis of the eigenvalue problem determining the stability of the assumed zonal flow profile in the HW model confirms the following trend: κ determines the amplitude of the zonal flows, thus, large κ destabilizes the zonal flows. On the other hand, the adiabatic response of parallel electrons given by α stabilizes them. The constructed bifurcation diagram in the α-κ plane for the HW model confirms the scenario of the onset of turbulence in the drift wave/zonal flow system being due to the disruption of zonal flows by KH instability.

Acknowledgments

The authors would like to acknowledge B. D. Scott for providing the simulation code used in this work. We thank P. N. Guzdar, W. Dorland, C. Tebaldi, and J. A. Krommes for useful discussions. This work is supported by the Australian Research Council.

[1] P. H. Diamond, S.-I. Itoh, K. Itoh, and T. S. Hahm, Plasma Phys. Control. Fusion **47**, R35 (2005).

[2] A. Hasegawa and M. Wakatani, Phys. Rev. Lett. **50**, 682 (1983).

[3] M. Wakatani and A. Hasegawa, Phys. Fluids **27**, 611 (1984).

[4] A. M. Dimits, G. Bateman, M. A. Beer, B. I. Cohen, W. Dorland *et al.*, Phys. Plasmas **7**, 969 (2000).

[5] A. Hasegawa and K. Mima, Phys. Rev. Lett. **39**, 205 (1977).

[6] W. Dorland and G. W. Hammett, Phys. Fluids B **5**, 812 (1993).

[7] R. Numata, R. Ball, and R. L. Dewar, in *Frontiers in Turbulence and Coherent Structures*, eds. J. P. Denier and J. S. Frederiksen (World Scientific, Singapore, 2007), vol. 6 of *World Scientific Lecture Notes in Complex Systems*, pp. 431–442, Proceedings of the COSNet/CSIRO Workshop on Turbulence and Coherent Structures in Fluids, Plasmas and Nonlinear Media, Canberra, Australia, 10-13 January 2006.

[8] R. Numata, R. Ball, and R. L. Dewar, accepted for publication in Phys. Plasmas (2007).

P2-060

Algebraic analysis approach for multibody problems

Shun-ichi OIKAWA and Hideo FUNASAKA

Graduate School of Engineering, Hokkaido University, N-13, W-8, Sapporo 060-8628, Japan

Here we propose an algebraic analysis approach for multibody Coulomb interaction. The momentum transfer cross section using the algebraic approximation is close to the exact one. The CPU time for the algebraic approximation is only around 20 minutes on a PC, while the exact analysis needs 15 hours to integrate the whole set of multibody equations of motion, in which all the field particles are at rest.

Keywords: anomalous diffusion, multibody problems, algebraic analysis

Since it is difficult to rigorously deal with multibody Coulomb collisions, the current classical theory considers them as a series of temporally-isolated binary Coulomb collisions. Let us first breafly review a binary collision between ions. In the center of mass coordinate (r, θ) in the collision plane, the test particle with a reduced mass of μ moves along a hyperbola as

$$\boldsymbol{r}(\theta) = \frac{b \sin\theta_0}{\cos\theta - \cos\theta_0}\begin{bmatrix} \cos\theta \\ \sin\theta \end{bmatrix} \tag{1}$$

with a velocity of

$$\boldsymbol{g}(\theta) = \frac{g_0}{\sin\theta_0}\begin{bmatrix} \cos\theta_0 \sin\theta \\ 1-\cos\theta_0\cos\theta \end{bmatrix}, \tag{2}$$

with which the velocity change is given by $\Delta\boldsymbol{g} = 2g_0\cos\theta_0\boldsymbol{e}_x$. As shown in Fig. 1 its scattering angle, $\chi \equiv \pi - 2\theta_0$, is given by $b = b_0\tan\theta_0$, where b is the impact parameter, $b_0 \equiv e^2/4\pi\varepsilon_0\mu g_0^2$ corresponds to $\chi = \pi/2$ scattering, and g_0 the initial relative speed at $r = \infty$ and $\theta = -\theta_0$.

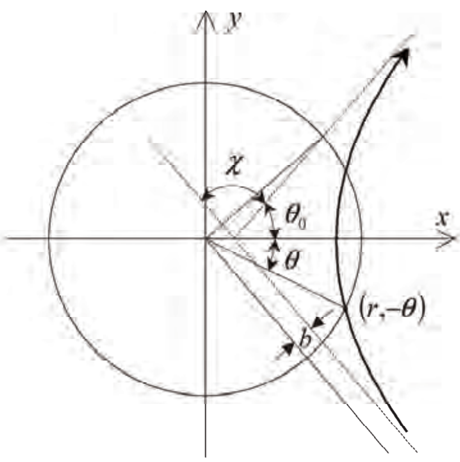

Fig. 1 Unperturbed trajectory $r = r(\theta)$ in an orbital plane. The scattering center is at the origin. An impact parameter is $b = b_0\tan\theta_0$. Interaction region is inside the circle with a radius $r_\ell = \Delta\ell/2$.

The angular component of the equation motion gives the well-known invariance of

$$r^2\frac{\mathrm{d}\theta}{\mathrm{d}t} = \mathrm{const} = bg_0, \tag{3}$$

and the radial component is given by

$$\frac{\mathrm{d}g_r}{\mathrm{d}t} = \frac{g_0^2 b_0}{r^2}\left(1+\frac{b_0}{r}\tan^2\theta_0\right), \tag{4}$$

where $g_r \equiv \dot{r}$ denotes the radial velocity. The first term on the right hand side of Eq. (4) stands for the Coulomb force, and is much smaller for small angle scatterings, i.e. $\chi \ll 1$, than the second term which results from the conservation of angular momentum Eq.(3), since, at the closest point $r = r_{\min}$, we have

$$\frac{b_0\tan^2\theta_0}{r_{\min}} \simeq \frac{2}{\chi} \gg 1.$$

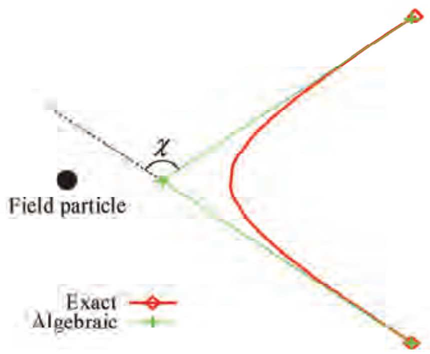

Fig. 2 Algebraic trajectory (broken line) and exact trajectory (curved line). A Field particle is on the left.

Thus the main force on the particle is not a Coulomb force, but the one due to the conservation of angular momentum. As a consequence, the exact hyperbolic trajetory Eq. (1) for the particle can be approximated as a broken line with an impulse force of

$$\mu\Delta\boldsymbol{g} = 2\mu g_0\cos\theta_0\boldsymbol{e}_x$$

author's e-mail: oikawa@qe.eng.hokudai.ac.jp

at the closest point $r = r_{\min}$. With this in mind, we have approximated a multibody problem to a series of binary deflections at their closest point as shown in Fig. 2, in which a test particle starts at the lower-right point, and its final point is at the upper-right point due to the interaction with a field particle.

In the following we assume that all the filed particles are at rest and their spatial distribution is almost uniform with a spacing of the average inter particle separation, $\Delta\ell \equiv n^{-1/3}$, where n stands for the number density as shown in Fig. 3.

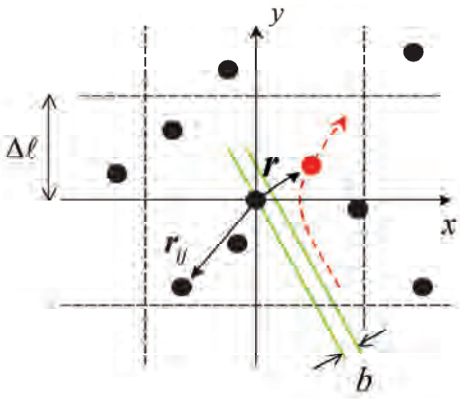

Fig. 3 A gray circle (or red in color) is a test particle at $\boldsymbol{r}$, and almost-uniformly-distributed black circles are field particles at $\boldsymbol{r}_{ij} = (i\Delta\ell + \delta x)\,\boldsymbol{e}_x + (j\Delta\ell + \delta y)\,\boldsymbol{e}_y, -N \le i, j \le N$.

First we seek for a field particle that gives the test particle an impulse force at the earliest time. The test particle moves along a strait line with a velocity of $(0, g)$ in the (ξ, η) coordinate system, in which η-axis is in the direction of the velocity vector $\boldsymbol{g}$ of the test particle. It is the field particle with $\eta = \eta_{\min}$, the minimum $|\eta|$, that we need. When the test particle moves to the position of $(0, \eta_{\min})$,

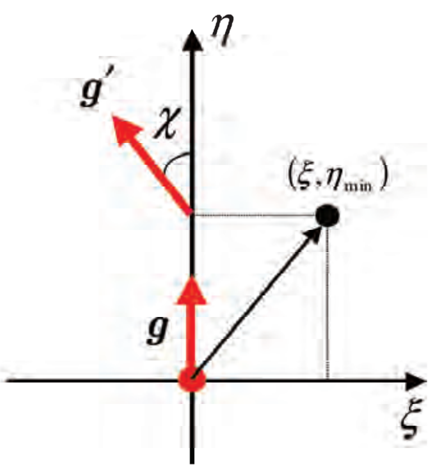

Fig. 4 Coordinates transform.

it changes the velocity $\boldsymbol{g}$ by $\Delta\boldsymbol{g}$ as shown in Fig. 4. This procedure will be repeated until the test particle leaves the prescribed interaction region, i.e. $r < \Delta\ell/2$ as depicted in Fig. 1.

The *exact* calculation hereafter refers to that obtained by solving the following equation of motion for the test particle:

$$\frac{d\boldsymbol{r}}{dt} = \boldsymbol{g} \tag{5}$$

$$\mu\frac{d\boldsymbol{g}}{dt} = \frac{e^2}{4\pi\varepsilon_0}\sum_{i=-N}^{N}\sum_{j=-N}^{N}\frac{\boldsymbol{r}-\boldsymbol{r}_{ij}}{|\boldsymbol{r}-\boldsymbol{r}_{ij}|^3}, \tag{6}$$

where the field particles positions $\boldsymbol{r}_{ij}$

$$\boldsymbol{r}_{ij} = (i\Delta\ell + \delta x)\,\boldsymbol{e}_x + (j\Delta\ell + \delta y)\,\boldsymbol{e}_y \quad (-N \le i, j \le N)$$

using the 5-th order Runge-Kutta-Fehlberg method known as the RKF56.

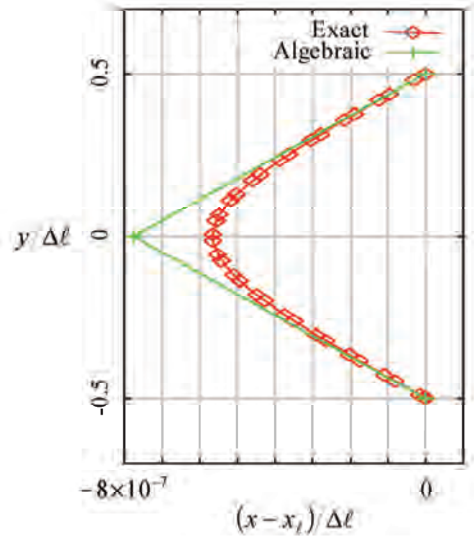

Fig. 5 Comparison of algebraic trajectory and exact trajectory in the case of binary Coulomb collision ($N = 0$) with an impact parameter $b = 0.2\Delta\ell$.

Figure 5 compares trajectories of the algebraic approximation and the exact hyperbola in the case of the pure binary Coulomb interaction, i.e. $N = 0$ in Eq. (6), with an impact parameter $b = 0.2\Delta\ell$. The only one field particle is at the origin in this case; $\boldsymbol{r}_{00} = \boldsymbol{0}$. The test particle starts at the lower right point goes through the closest point and ends at the upper right point in the figure. In the case of multiple field particles, we have assumed that there are nearly uniformly distributed 21×21 field particles at rest. In the algebraic approximation to multiboby problems ($N > 1$), as explained earlier, after a coordinate tranformation $(x, y) \to (\xi, \eta)$, where

$$\eta_{ij} = \frac{(\boldsymbol{r}_{ij} - \boldsymbol{r})\cdot\boldsymbol{g}}{g}, \tag{7}$$

we find the field particle with minmum $|\eta_{ij}|$.

Figures 6, 7, and 8 are three examples out of 10^5 Monte Carlo calculations for an impact parameter b =

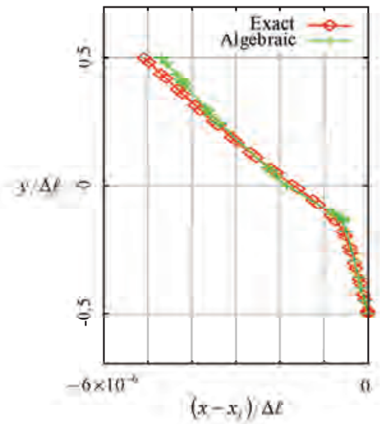

Fig. 6 Comparison of algebraic trajectory and exact trajectory in the case of multibody Coulomb collisions with an impact parameter $b = 0.2\Delta\ell$. This is an example of small angle scatterings.

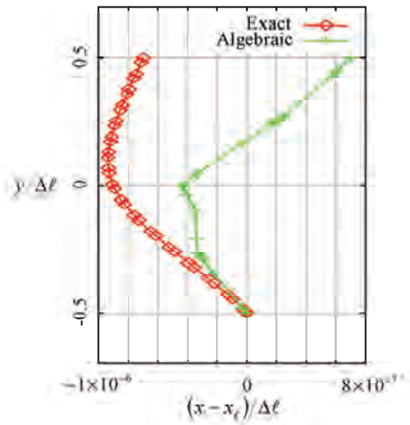

Fig. 8 Comparison of algebraic trajectory and exact trajectory in the case of multibody Coulomb collisions with an impact parameter $b = 0.2\Delta\ell$. The discrepancy is as small as 10^{-13} meter in typical fusion plasmas.

$0.2\Delta\ell$, and compare trajectories of the algebraic and the exact trajectories in the case of the multiple Coulomb interaction, i.e. $N = 10$ [1] in Eq. (6). The indivisual approximation is good in most cases as shown in Figs. 6 and 7, while 8 is one of few example which the approximation is bad. The algebraic trajectory in Fig. 7 seems to deviate from the exact one, however, the deviation is as small as $\Delta\ell \times 10^{-6} \sim 10^{-13}$ meter in typical fusion plasmas.

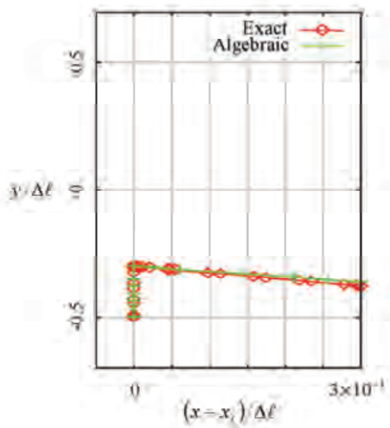

Fig. 7 Comparison of algebraic trajectory and exact trajectory in the case of multibody Coulomb collisions with an impact parameter $b = 0.2\Delta\ell$. This is an example of large angle scatterings.

Finally we conducted the above calcution for different impact parameters $0 < b < r_\ell$. Figure 9 shows the accumulated variance of velocity change, $\left\langle (\Delta g)^2 \right\rangle$, which is in proportion to the conventional momentum transfer cross section, $\sigma_{\rm m}$, as

$$\sigma_{\rm m} = 4\pi b_0^2 \ln \frac{b_{\rm max}}{b_0} \tag{8}$$

The error in $\sigma_{\rm m}$ due to the algebraic calculation is seen to be quite small for both the binary ($N = 0$) and multibody ($N = 10$) cases, where there is only one field particle and there are 21×21 field particles, respectively. It should be noted that in the binary interactions the cross section $\sigma_{\rm m}$ is converged at $b \ll \Delta\ell$ which is far less than the Debye length $\lambda_{\rm D}$. The CPU time for the algebraic approximation is only around 20 minutes on a PC, while the exact analysis needs 15 hours to integrate the whole set of multibody equations of motion.

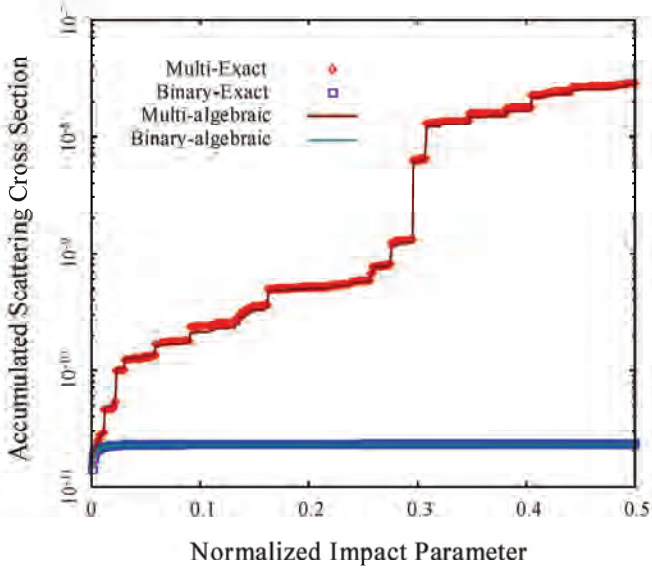

Fig. 9 Accumulated scattering cross section $\sigma_{\rm m} = \sigma_{\rm m}(\bar{b})$ vs normalized impact parameter $\bar{b} = b/\Delta\ell$.

In the future, we apply this method to three dimensional multibody collision.

[1] H. Funasaka, Master thesis, Graduate School of Engineering, Hokkaido University (2007).

Proceedings of ITC/ISHW2007

Effects of multi-helicity confinement fields on zonal flows and ion temperature gradient turbulence

Tomo-Hiko WATANABE[1,2)], Sergi FERRANDO-MARGALET[1)], and Hideo SUGAMA[1,2)]

[1)]*National Institute for Fusion Science, Toki 509-5292, Japan*

[2)]*The Graduate University for Advanced Studies (Sokendai), Toki 509-5292, Japan*

October 17, 2007

Effects of multi-helicity confinement magnetic fields on zonal flows and ion temperature gradient (ITG) turbulence are investigated by means of the gyrokinetic-Vlasov simulation code (GKV code). Detailed magnetic field parameters for the standard and inward-shifted configurations of the Large Helical Device (LHD) experiments are introduced in the simulation model. By the linear GKV simulations, it has been shown that, in the inward-shifted configuration, the maximum ITG mode growth rate slightly increases while the zonal flow is maintained for a longer time [S. Ferrando-Margalet, H. Sugama, and T.-H. Watanabe, "*Zonal flows and ion temperature gradient instabilities in multiple-helicity magnetic fields*" Phys. Plasmas (2007) in press]. Correspondingly, the nonlinear GKV simulations of the ITG turbulence in simple model configurations are extended to the more elaborate ones in the present study. The obtained results show effective regulation of the ITG turbulence by the zonal flows in the inward-shifted case. The zonal flows generated with three-times larger averaged amplitudes than those in the standard configuration lead to a lower ion heat transport level. The obtained results confirm the theoretical prediction that the neoclassical optimization of helical systems contributes to reduction of the anomalous transport by enhancing the zonal-flow level.

Keywords: zonal flow, ITG turbulence, gyrokinetic simulation, helical system, LHD

1 Introduction

Sheared $\boldsymbol{E} \times \boldsymbol{B}$ plasma flows with toroidal and poloidal symmetries, namely the zonal flows, have widely been believed as one of key ingredients for regulating the turbulent transport in magnetic confinement fusion [1]. In toroidal systems, the zonal flow is coupled to the geodesic acoustic mode (GAM) oscillation [2]. A linear response of the zonal flow driven by the ion temperature gradient (ITG) turbulence in a tokamak was derived from the gyrokinetic theory by Rosenbluth and Hinton [3]. It is considered that the residual zonal flow remaining constant after Landau damping of the GAM plays an important role in reduction of the tokamak ITG turbulent transport.

The gyrokinetic theory of the zonal flow has been extended to helical systems [4, 5], and the idea of the zonal flow optimization for effective reduction of the turbulent transport has come out [4, 5, 6]. The zonal flow was first identified in the Compact Helical System (CHS) experiments [7], and is recognized as a mutual important subject in the anomalous transport studies for tokamak and helical systems.

The role of zonal flows in regulating the turbulence is, thus, investigated for understanding the transport property observed in the Large Helical Device (LHD) [8] experiments. From the LHD experiments it is found that not only the neoclassical but also the anomalous transport is reduced in the inward-shifted configuration [9]. Here, it is noteworthy that the radial drift motion of helical-ripple-trapped particles is decreased by shifting the magnetic axis inward while the unfavorable magnetic curvature destabilizing the ballooning-type modes such as the toroidal ITG mode is increased. The gyrokinetic theory of zonal flows in helical systems has shown that the slower decay of the zonal flow expected in the inward-shifted LHD configuration lead to lower turbulent transport than that in the standard one [4, 5]. The theoretical estimate of the linear response of the zonal flow is verified by the gyrokinetic-Vlasov simulations [4, 5, 10, 11] by means of the GKV code [12]. The nonlinear GKV simulations for the simplified models of the LHD have demonstrated that the ITG turbulent transport in the inward-shifted configuration, which has 60% larger growth rates of the ITG stability, is regulated by the stronger zonal flows to a level comparable to the standard case [10].

In the present study, realistic parameter sets for the LHD experimental conditions are employed in the GKV simulations of the ITG turbulence, where differences in the linear stability between the standard and inward-shifted cases become smaller [11, 13] while slower decay of the zonal flow in the inward-shifted case. Then, it is expected that the lower anomalous transport will be found in the inward-shifted case, as actually observed in the LHD experiments. This paper is organized as follows. After a brief introduction of our simulation model in section 2, the GKV simulation results of the ITG turbulence and zonal flows are shown in section 3. A conclusion is given in section 4.

author's e-mail: watanabe.tomohiko@nifs.ac.jp

P2-061

Table 1 Parameters used in GKV simulations of ITG turbulence and zonal flows in LHD model configurations.

	Standard	Inward-shifted
r/R_0	0.099	0.114
q_0	1.9	1.7
$\hat{s}$	-0.85	-0.96
ϵ_t	0.087	0.082
ϵ_L/ϵ_t	0.91	1.20
$\epsilon_{L-1}/\epsilon_t$	-0.28	-0.74
$\epsilon_{L+1}/\epsilon_t$	0	-0.24
$(r/\epsilon_t)\epsilon'_{00}$	0.22	0.71
$(r/\epsilon_t)\epsilon'_t$	1.02	1.00
$(r/\epsilon_t)\epsilon'_L$	1.96	2.44
$(r/\epsilon_t)\epsilon'_{L-1}$	-0.63	-0.36
$(r/\epsilon_t)\epsilon'_{L+1}$	0	-0.61

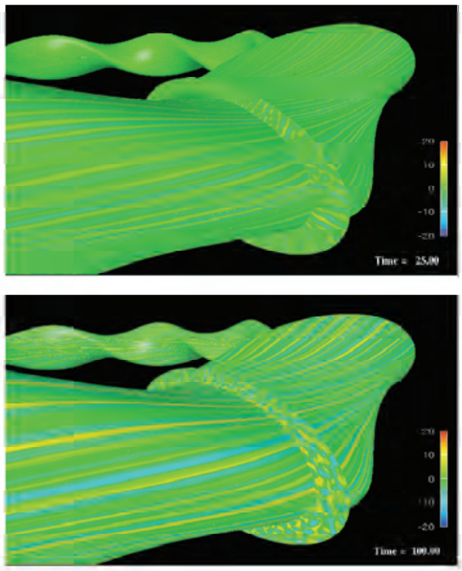

Fig. 1 Color contours of the electrostatic potential of the zonal flow and the ITG turbulence obtained by the GKV simulation for the standard model configurations at $t = 25$ (upper) and $t = 100 L_n/v_{ti}$ (lower).

2 Simulation Model

The nonlinear gyrokinetic equation [14] for the perturbed ion gyrocenter distribution function, δf, in the low-β electrostatic limit is numerically solved by the GKV code [12] as a partial differential equation defined on the five-dimensional phase-space. We introduce a model collision term given by the gyrophase average of the Lenard-Bernstein collision operator [15]. The quasi-neutrality condition with the adiabatic electron response (for $T_e = T_i$) is used for calculation of the electrostatic potential, ϕ_{k_x,k_y}. In the GKV code, we employ the toroidal flux tube model [16] with the field-aligned coordinates, and also assume constant volume-averaged density and temperature gradients with scale-lengths of L_n and L_T as well as the constant magnetic shear parameter, $\hat{s} = (r_0/q_0)dq/dr$. Here, $q(r)$ stands for the safety factor, and $q_0 = q(r_0)$. See Ref. [12] for more details.

In the helical version of the GKV code, the averaged minor radius, r_0, is defined by $\Psi_t = \pi B_0 r_0^2$ where Ψ_t means the toroidal flux. The toroidal and helical effects of the confinement field are introduced by the change of magnetic field strength,

$$B = B_0 \{1 - \epsilon_{00}(r) - \epsilon_t(r)\cos z - \sum_{l=L-1}^{l=L+1} \epsilon_l(r)\cos[(l - Mq_0)z - M\alpha]\}, \quad (1)$$

where L and M denote the poloidal and toroidal periodicities of the main component of the helical field. For the LHD, $L = 2$ and $M = 10$. The main helical field is represented by ϵ_L. The side-band components and the averaged normal curvature are also given by ϵ_{L-1}, ϵ_{L+1}, and $\epsilon'_{00} = d\epsilon_{00}/dr$, respectively. We also set the field-line label α to be constant ($\alpha = 0$) because of weak α-dependence of the linear ITG instability. For the ITG turbulence simulations shown below, we employ a huge number of grid points over 50 billions [that is, $128 \times 128 \times 512 \times 128 \times 48$ in the fluxtube coordinates of $(x, y, z, v_\parallel, \mu)$ of the five-dimensional phase-space]. Further details of the GKV simulation model for helical systems are found in Ref. [10].

3 Gyrokinetic Simulation of ITG Turbulence and Zonal Flows

Nonlinear gyrokinetic simulations of the ITG turbulence and zonal flows for helical systems [10] are extended so as to incorporate the realistic parameter sets for the LHD experiments as has been done in the linear GKV simulations of the ITG instability and zonal flows [11]. Differences in the linear growth rates of the ITG instability between the standard and inward-shifted model configurations, which were about 60% in Ref. [10], are largely decreased by using the new parameter sets [11]. Moreover, the collisionless decay of the zonal flow in the realistic model for the inward-shifted configuration takes longer time than those for the standard and the previous cases [11]. These results support the scenario derived from the theoretical analysis of the zonal flow response in helical systems [4, 5], such that the stronger zonal flow driven by the ITG turbulence in the inward-shifted case may lead to a lower level of the turbulent transport than that in the standard configuration.

The GKV code employs the toroidal flux tube domain with the same local plasma parameters of $\eta_i \equiv L_n/L_{Ti} = 3$, $L_n/R_0 = 0.3$, $T_e/T_i = 1$, and $\alpha = 0$ for the standard and inward-shifted cases. Other parameters are summarized in Table 1. We set the toroidal periodicity of the simulation domain $N_\alpha = 6$, and the half-widths of the ra-

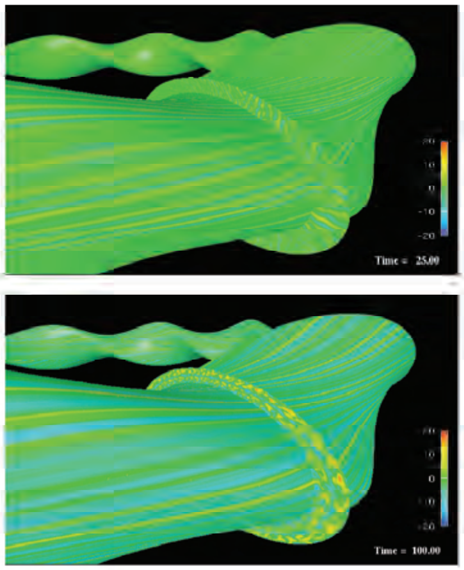

Fig. 2 Color contours of the electrostatic potential of the zonal flow and the ITG turbulence obtained by the GKV simulation for inward-shifted model configurations at t = 25 (upper) and $t = 100L_n/v_{ti}$ (lower).

dial and toroidal (field-line-label) box size are given by $r_0\Delta q/q_0\hat{s}$ and $\pi r_0/q_0 N_\alpha$, where the change of the safety factor $\Delta q = -1/6$.

Color contours of the electrostatic potential ϕ obtained from the GKV simulations of the ITG turbulence are shown in Figs. 1 and 2 for the standard and inward-shifted model configurations, respectively. Here, the potential fluctuations are mapped on the innermost flux surface and the elliptic poloidal cross-section. Radially-elongated eddy patterns of potential (streamers) are first driven by the toroidal ITG instability, and propagate in the direction of the ion diamagnetic drift. The ballooning-type mode structures are clearly found in the linear growth phase of the instability. The growth of the ITG instability is saturated by the self-generated $\boldsymbol{E}\times\boldsymbol{B}$ zonal flows, and the streamers are destroyed into small eddies in the later turbulent state.

Power spectra of the potential fluctuations of the ITG turbulence are shown in Fig. 3, where the data is time-averaged from $t = 60$ to $100L_n/v_{ti}$. We see the same peak amplitude of the spectrum, $\sum_{k_x}\langle|\phi_{k_x,k_y}|^2\rangle/\Delta k_y$ between the inward-shifted and standard cases, while the spectrum in the former broadens into the low-k_y side.

It is expected from the linear GKV simulations of the ITG mode [11] that, because of the higher maximum growth rate, ion thermal diffusivity, χ_i, grows faster for the inward-shifted configuration than for the standard one. In the nonlinear simulations, we have observed that the peak value of $\chi_i \simeq 3.8\rho_{ti}^2 v_{ti}/L_n$ for the former case is about 50% larger than that of $\chi_i \simeq 2.6\rho_{ti}^2 v_{ti}/L_n$ for the latter case. In the statistically steady states of the turbulent transport, however, χ_i averaged from $t = 60$ to $t = 250L_n/v_{ti}$ for the inward-shifted case is about 20%

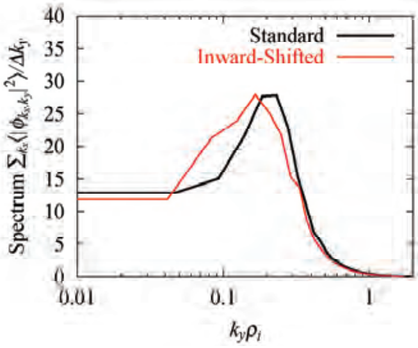

Fig. 3 Power spectra of potential fluctuations of the ITG turbulence obtained from the GKV simulations for the standard (black) and the inward-shifted (red) model configurations. The spectrum is time-averaged from t = 60 to $100L_n/v_{ti}$.

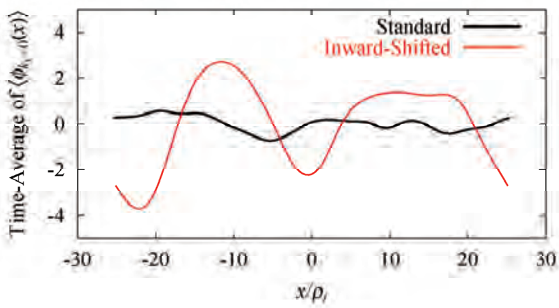

Fig. 4 Radial profiles of the zonal flow potential averaged from t = 60 to $250L_n/v_{ti}$. Black and red curves represent the results obtained from the standard and inward-shifted cases, respectively.

smaller than that from the result for the standard configurations, that is, $\chi_i \sim 1.45\rho_{ti}^2 v_{ti}/L_n$ for the former case and $\chi_i \sim 1.78\rho_{ti}^2 v_{ti}/L_n$ for the latter one. See also Ref. [17].

The lower ion heat transport found in the inward-shifted case is attributed to a larger amplitude of the zonal flows generated by turbulence. Radial profiles of the zonal flow potential are shown in Fig. 4, where the flux-surface average of the k_y = 0 components of the potential, $\langle\phi_{k_y=0}(x)\rangle$, are time-averaged from t = 60 to $t = 250L_n/v_{ti}$. The zonal-flow potential spectrum also shows about a three-times larger amplitude in the inward-shifted case than that in the standard configuration [17]. It should be noted that the stronger zonal-flow generation in the inward-shifted model configuration is consistent with larger values of the zonal-flow response function as discussed in our previous works [4, 5, 10, 11].

The transport reduction associated with the zonal-flow generation is also found in Lissajous plots of time-histories of the simulation data in Fig. 5, where the vertical axis measures the squared potential of the zonal flow, $\sum\langle|\phi_{k_x,0}|^2\rangle$. The horizontal axes in upper and lower panels

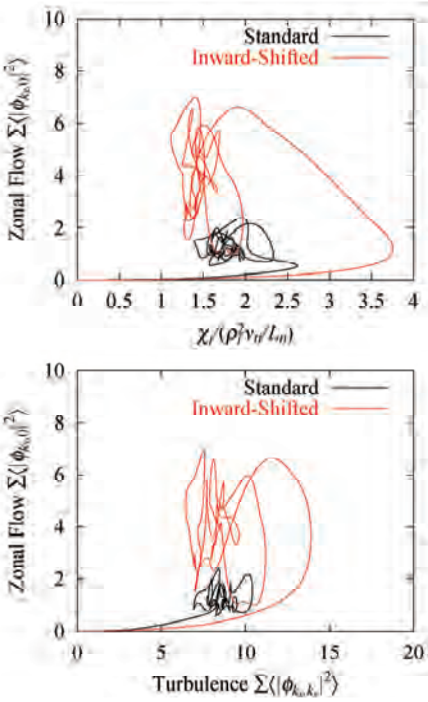

Fig. 5 Lissajous plots of the simulation results shown in the space of χ_i-$\Sigma\langle|\phi_{k_x,0}|^2\rangle$ (upper) and $\Sigma\langle|\phi_{k_x,k_y}|^2\rangle$- $\Sigma\langle|\phi_{k_x,0}|^2\rangle$ (lower). Black and red curves represent the results obtained from the standard and inward-shifted cases, respectively.

of Fig. 5 stand for the transport coefficient, $\chi_i/(\rho_{ti}^2 v_{ti}/L_n)$, and the turbulent fluctuations, $\Sigma\langle|\phi_{k_x,k_y}|^2\rangle$, respectively. In the upper panel, starting from the initial condition near the origin of $(0,0)$, the data point moves along the horizontal axis as the instability grows. One can see that χ_i is greatly reduced when the zonal flow is excited, where the orbit of the data point turns to the upper left corner of the figure. In the nonlinear saturation stage of the instability ($t > 60L_n/v_{ti}$), the data points for the two configurations fluctuate only inside two different regions, namely, the region with high transport and weak zonal flows for the standard configuration and the region with low transport and strong zonal flows for the inward-shifted configuration. Contrarily, the data points in the lower panel move around in a common horizontal range with a similar turbulent fluctuation level, but with different zonal flow amplitudes.

4 Conclusion

The nonlinear gyrokinetic-Vlasov simulations present the results that the ion thermal diffusivity χ_i driven by the ion temperature gradient turbulence for the inward-shifted LHD plasma takes a lower time-averaged value in the steady turbulent state because of the stronger zonal-flow generation. The obtained results confirm the theoretical prediction derived from the gyrokinetic analysis of the zonal flow response in helical systems, that is, the neoclassical optimization results in reduction of the anomalous transport through enhancement of the zonal flow. This provides ones a physical understanding on a possible mechanism of the confinement improvement found in the inward-shifted configurations of the LHD experiments.

Acknowledgments

This work is supported in part by grants-in-aid of the Ministry of Education, Culture, Sports, Science and Technology (No. 16560727, 17360445, and 17·05373), and in part by the National Institute for Fusion Science (NIFS) Collaborative Research Program (NIFS05KKMT001, NIFS06KTAT038, NIFS06KDAD006, and NIFS06KNXN060). Numerical simulations are carried out by use of the Earth Simulator under the support by Japan Agency for Marine-Earth Science and Technology, and by use of the Plasma Simulator and the LHD numerical analysis system at National Institute for Fusion Science.

[1] P.H. Diamond, S.-I. Itoh, K. Itoh, T.S. Hahm, Plasma Phys. Control. Fusion **47**, R35 (2005).

[2] N. Winsor, J.L. Johnson, J.J. Dawson, Phys. Plasmas **11**, 2448 (1968).

[3] R.M. Rosenbluth, F.L. Hinton, Phys. Rev. Lett. **80**, 724 (1998).

[4] H. Sugama and T.-H. Watanabe, Phys. Rev. Lett. **94**, 115001 (2005).

[5] H. Sugama and T.-H. Watanabe, Phys. Plasmas **13**, 012501 (2006).

[6] H.E. Mynick, Phys. Plasmas **13**, 058102 (2006).

[7] A. Fujisawa, et al., Phys. Rev. Lett. **93**, 165002 (2004).

[8] O. Motojima, et al., Nucl. Fusion **43**, 1674 (2003).

[9] H. Yamada, *et al.*, Plasma Phys. Controlled Fusion **43**, A55 (2001).

[10] T.-H. Watanabe, H. Sugama, and S. Ferrando-Margalet, Nucl. Fusion **47**, 1383 (2007).

[11] S. Ferrando-Margalet, H. Sugama, and T.-H. Watanabe, "*Zonal flows and ion temperature gradient instabilities in multiple-helicity magnetic fields*" Phys. Plasmas (2007) in press.

[12] T.-H. Watanabe, H. Sugama, Nucl. Fusion **46**, 24 (2006).

[13] O. Yamagishi, et al., Phys. Plasmas **14**, 012505 (2007).

[14] E.A. Frieman, L. Chen, Phys. Fluids **25**, 502 (1982).

[15] P.C. Clemmow, J.P. Dougherty, *Electrodynamics of Particles and Plasmas* (Addison-Wesley, Redwood City, 1969).

[16] M.A. Beer, S.C. Cowley, G.W. Hammett, Phys. Plasmas **2**, 2687 (1995).

[17] H. Sugama, T.-H. Watanabe, and S. Ferrando-Margalet, *Joint Conference of 17th International Toki Conference on Physics of Flows and Turbulence in Plasmas and 16th International Stellarator/Heliotron Workshop 2007* (Toki, Japan, 2007), I-08.

Proceedings of ITC/ISHW2007

Simulation study of energetic ion transport due to Alfvén eigenmodes in an LHD plasma

Y. Todo, N. Nakajima, M. Osakabe, S. Yamamoto [a], and D. A. Spong [b]

National Institute for Fusion Science,322-6 Oroshi-cho, Toki 509-5292, Japan
[a] Kyoto University Pioneering Research Unit for Next Generation, Gokasho, Uji 611-0011, Japan
[b] Oak Ridge National Laboratory, Oak Ridge, Tennessee 37831, USA

The creation of hole and clump in energetic ion energy spectrum associated with the Alfvén eigenmodes was observed with the neutral particle analyzer (NPA) on LHD shot #47645. The difference in slowing-down time between the hole and clump suggests that the energetic ions were transported for 10% of the plasma minor radius. The spatial profile and frequency of the Alfvén eigenmodes was analyzed with the AE3D code. The phase space structures of the energetic ions on the NPA line-of-sight were investigated in an axisymmetric equilibrium comparable to the LHD equilibrium with the Poincaré plots where one oscillating Alfvén eigenmode for each plot is employed. The phase space regions trapped by the Alfvén eigenmodes appear as islands in the Poincaré plots. The radial width of the islands corresponds to the transport distance of energetic ions. The island width depends on the Alfvén eigenmode amplitude. It was found that the Alfvén eigenmodes with amplitude $\delta B_r / B \sim 10^{-3}$ transport energetic ions for 10% of the minor radius.

Keywords: energetic ion transport, Alfvén eigenmode, Poincaré plot, LHD, neutral particle analyzer

1. Inroduction

The creation of hole and clump in energetic ion energy spectrum associated with the Alfvén eigenmodes was observed with the neutral particle analyzer (NPA) on LHD shot #47645 [1]. The frequencies of the Alfvén eigenmodes are roughly 55 kHz and 68 kHz, respectively. Both the Alfvén eigenmodes have toroidal mode number n=1. The hole and clump are created around energy 150 keV. The difference in slowing-down time between the hole and clump suggests that the energetic ions were transported for 10% of the plasma minor radius.

In this paper, we try to find the candidates of the Alfvén eigenmodes using the AE3D code [2]. We also investigate the Alfvén eigenmode amplitude consistent with the energetic-ion transport suggested by the NPA data. The Poincaré plots were made to investigate the phase space structures of the energetic ions on the NPA line-of sight. The phase space regions trapped by the Alfvén eigenmodes appear as the islands in the Poincaré plots. The radial width of the islands corresponds to the transport distance of energetic ions. As island width depends on Alfvén eigenmode amplitude, we can discuss the amplitude consistent with the NPA observation.

2. Analysis of Alfvén eigenmodes

The Alfvén eigenmodes with toroidal monde number n=1 in the LHD shot #47645 were analyzed with the

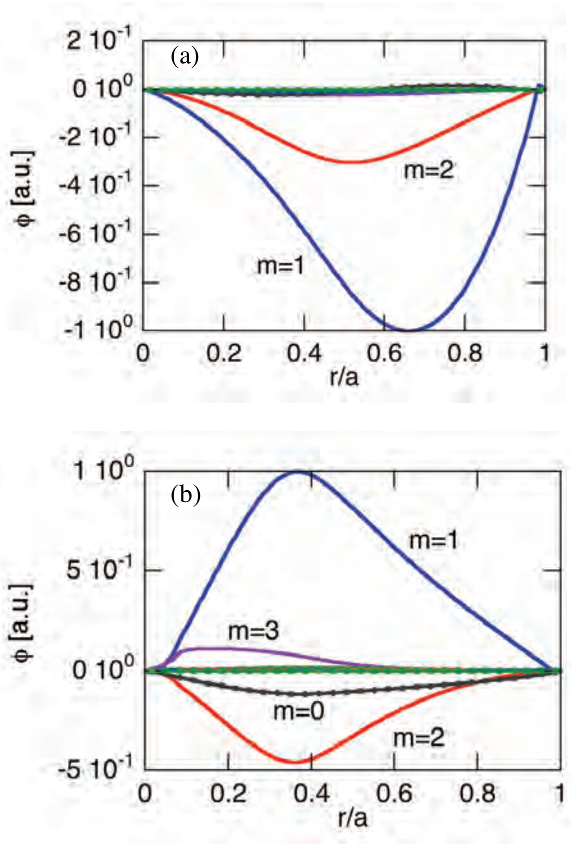

Fig.1 Spatial profiles of the n=1 toroidal Alfvén eigenmodes analyzed with the AE3D code for the LHD shot #47645. The frequencies are (a) 42.7 kHz and (b) 79.1 kHz, respectively.

author's e-mail: todo@nifs.ac.jp

AE3D code where the Galerkin method is used in the Boozer coordinates. An MHD equilibrium was constructed in the Boozer coordinates. Two toroidal Alfvén eigenmodes (TAE modes) were found with The eigen-frequencies 42.7 kHz and 79.1 kHz. The eigen-frequencies are comparable to the Alfvén eigenmode frequencies observed at the experiment. The spatial profiles of electrostatic potential are shown in Fig. 1. The primary poloidal harmonics of both the two TAE modes are m=1 and m=2. The primary poloidal harmonics have the same sign for the TAE mode with frequency 42.7 kHz, while they have the opposite sign to each other for the mode with frequency 79.1 kHz.

3. Analysis of energetic-ion orbit

The energetic-ion orbits were calculated with different starting points on the NPA line-of sight. The orbits were calculated in an MHD equilibrium constructed in the HINT coordinates [3]. The energetic-ion energy is 150 keV with which the hole and clump creation in energy spectrum was observed with the NPA. The pitch angle is determined by the direction of the NPA line-of-sight. The poloidal orbit-frequency is defined by $\omega_\theta = 2\pi / T_\theta$ where T_θ is the poloidal circulation time. The toroidal orbit-frequency is defined by $\omega_\varphi = \Delta\varphi / T_\theta$ where $\Delta\varphi$ is the toroidal angle which the energetic ion proceeds in T_θ.

The orbit frequency of the energetic ions is defined by

$$f_{m/n} = \left(n\omega_\varphi - m\omega_\theta\right)/2\pi,$$

where n and m are toroidal and poloidal mode nubers. We take n=1 and m=1 which are identical to the primary poloidal harmonic of the TAE modes shown in Fig. 1. In Fig. 2, the orbit frequency is shown versus the major radius of the starting point on the NPA line-of-sight. We see that there exist energetic ions with the same orbit frequency as the Alfvén eigenmode frequencies observed at the LHD experiment. These energetic ions resonate with the Alfvén eigenmodes.

4. Phase space structure of energetic ions

In axisymmetric systems, $E' = E - \omega P_\varphi / n$ is conserved in the wave-particle interaction. Here, E and P_φ are respectively the total energy and the canonical toroidal momentum of the particle. This enables to utilize Poincaré plots where the particles with the same $E'$are employed. The phase space structure associated with finite-frequency waves can be analyzed with the Poincaré plots. Furthermore, as the harmonics of the two TAE modes other than n=1 are negligibly small, we expect some similarities in phase space structure between the LHD equilibrium and axisymmetric systems.

Then, we investigate an axisymmetric equilibrium

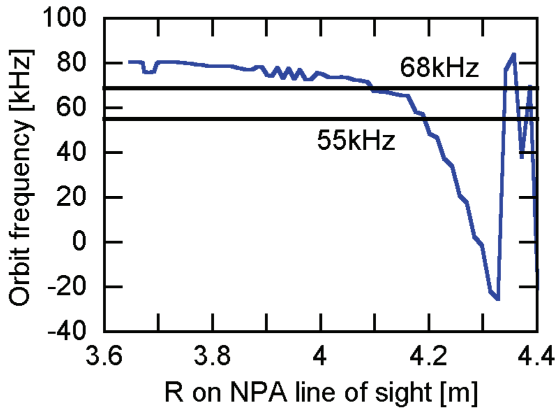

Fig.2 Blue curve represents energetic-ion orbit frequency with m/n=1/1 as a function of the starting point major radius on the NPA line-of-sight. Black lines denote Alfvén eigenmode frequencies observed in the LHD experiment.

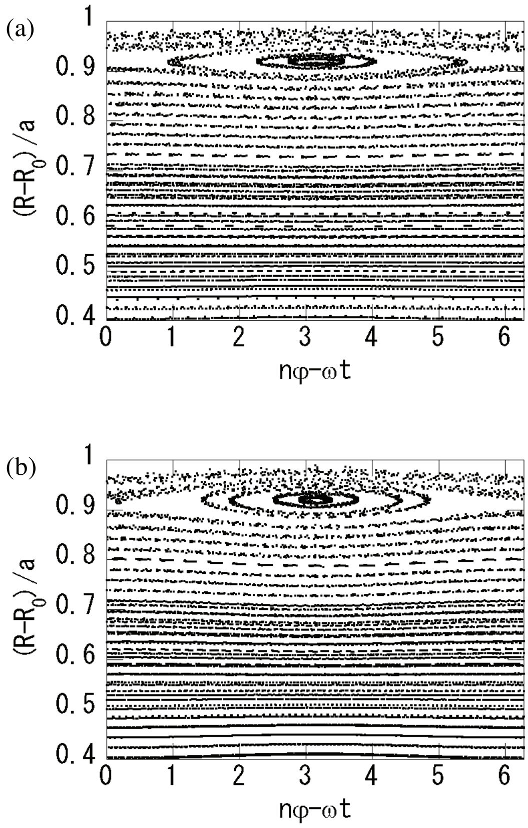

Fig.3 Poincaré plots for the lower frequency TAE with amplitude (a) $\delta B_r / B = 10^{-3}$ and (b) $\delta B_r / B = 2\times 10^{-3}$.

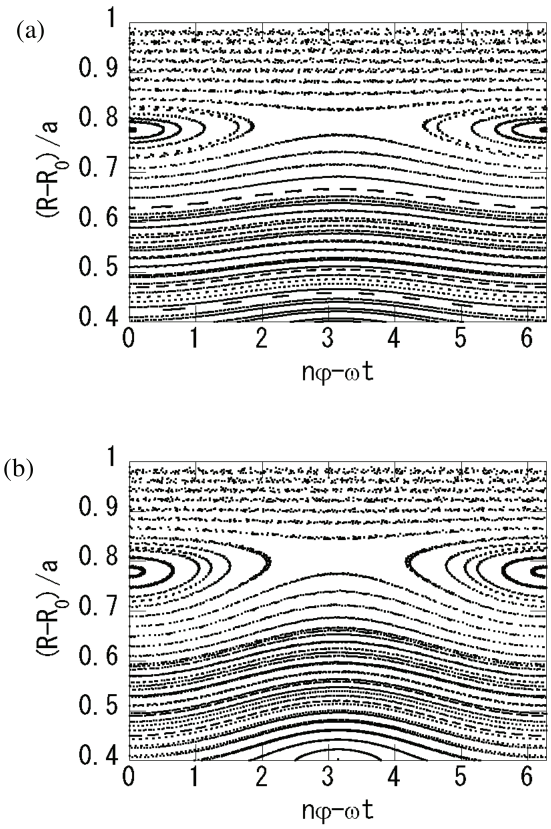

Fig.4 Poincaré plots for the higher frequency TAE with amplitude (a) $\delta B_r / B = 10^{-3}$ and (b) $\delta B_r / B = 2 \times 10^{-3}$.

comparable to the LHD plasma #47645. The parameters of the axisymmetric equilibrium are major radius 3.67m, minor radius 0.54m, toroidal magnetic field 0.5T, and safety factor profile $q(r) = 2.11 - 1.23(r/a)^2$. The value of E' is that of a particle with energy 150keV at $r = 0.7a$. The two TAE modes are mapped to the axisymmetric equilibrium. The frequencies are renormalized to the experimental values 55kHz for the lower frequency TAE shown in Fig. 1(a) and 68kHz for the higher frequency TAE shown in Fig. 1(b).

The Poincaré plots for the lower frequency TAE are shown in Fig. 3. The phase space regions trapped by the Alfvén eigenmodes appear as the islands in the Poincaré plots. The radial width of the islands corresponds to the transport distance of energetic ions. The island width depends on the Alfvén eigenmode amplitude. The lower frequency TAE with amplitude $\delta B_r / B = 2 \times 10^{-3}$ transports energetic ions for 10% of the minor radius. The phase space structures with the higher frequency TAE is analyzed in Fig. 4. Comparing Fig. 4(a) and (b), we see that the higher frequency TAE with amplitude $\delta B_r / B = 10^{-3}$ transports energetic ions for 10% of the minor radius.

4. Summary

The spatial profile and frequency of the Alfvén eigenmodes in the LHD shot #47645, where the creation of hole and clump in energetic ion energy spectrum associated with the Alfvén eigenmodes was observed, was analyzed with the AE3D code. The difference in slowing-down time between the hole and clump observed at the experiment suggests that the energetic ions were transported for 10% of the plasma minor radius. The phase space structures of the energetic ions on the NPA line-of-sight were investigated investigated in an axisymmetric equilibrium comparable to the LHD equilibrium with the Poincaré plots where an oscillating Alfvén eigenmode for each plot is employed. The phase space regions trapped by the Alfvén eigenmodes appear as the islands in the Poincaré plots. The radial width of the islands corresponds to the transport distance of energetic ions. The island width depends on the Alfvén eigenmode amplitude. It was found that the Alfvén eigenmodes with amplitude $\delta B_r / B \sim 10^{-3}$ transport energetic ions for 10% of the minor radius.

References

[1] M. Osakabe *et al.*, Nucl. Fusion **46**, S911 (2006).

[2] D. A. Spong and Y. Todo, “Shear Alfvén spectrum and mode structures for 3D configurations”, 49th Annual Meeting of the Division of Plasma Physics (12-16 November 2007, Orlando), PP8.00098.

[3] K. Harafuji, T. Hayashi, and T. Sato, J. Comput. Phys. **81**, 169 (1989).

Proceedings of ITC/ISHW2007

Modification of α-particle emission spectrum and its effect on plasma heating characteristics in non-Maxwellian deuterium-tritium plasmas

Hideaki Matsuura and Yasuyuki Nakao

Department of Applied Quantum Physics and Nuclear Engineering,

Kyushu University, Motooka 744, Fukuoka 819-0395, Japan

The α-particle emission spectrum in a tail-created (non-Maxwellian) deuterium-tritium (DT) burning plasma is examined by solving the Boltzmann-Fokker-Planck (BFP) equations for deuteron, triton and α-particle simultaneously. It is shown that owing to the existence of energetic component in fuel-ion energy distribution functions due to neutral-beam injection (NBI) and/or nuclear elastic scattering (NES), the generation rate of the high-energy (>3.52MeV) α-particle increases significantly compared with the case of Gaussian distribution. The influence of the broadened energy spectrum on the α-heating characteristics is discussed.

Keywords: neutral beam injection heating, knock-on tail formation, α-particle emission spectrum, nuclear elastic scattering, Boltzmann-Fokker-Planck equation

1. Inroduction

Energetic ions in burning plasma have important roles in various stages of fusion-reactor operations. The energetic deuterons produced by neutral-beam-injection (NBI) heating and/or ion-cyclotron resonance frequency (ICRF) heating[1,2] create a non-Maxwellian tail in deuteron and triton velocity distribution functions. The nuclear elastic scattering[3,4] (NES) of injected-beam and/or energetic α-particle by thermal ion also causes a knock-on tail formation in fuel-ion distribution functions[5-8]. In magnetically-confined deuterium-tritium (DT) plasmas, the resulting modification of the neutron emission spectrum was computed, and its application to the plasma diagnostics was proposed[9]. By observing the deviation of the neutron emission spectrum from Gaussian distribution, the knock-on tail formation in fuel-ion velocity distribution functions was experimentally ascertained[10,11]. A similar modification of the emission spectrum would also be observed for fusion-produced α-particle. This modification may influence the plasma confinement condition via α-heating power, the fractional energy deposition to ions and turbulent transport process of energetic α-particle, and/or α-particle diagnostics. It is hence important to grasp accurately the modification of α-particle spectrum in reactor plasmas.

In this paper, we consider a DT plasma accompanied with injection of a mono-energetic deuterium beam. On the basis of the Boltzmann-Fokker-Planck (BFP) model[12,13], the modification of the α-particle emission spectrum is evaluated simultaneously considering the distortion of deuteron, triton and α-particle distribution functions. It is shown that the modification is significantly influenced by the tail formations in both deuteron and triton distribution functions due to beam injection and NES. The effect of the modification on plasma heating characteristics (fractional energy deposition to ions) is discussed.

author's e-mail:mat@nucl.kyushu-u.ac.jp

2. Analysis Model

2.1 Boltzmann-Fokker-Planck model

The BFP equation for ion species a (a= D, T and α-particle) is written as

$$\sum_j \left(\frac{\partial f_a}{\partial t}\right)^{\mathrm{C}} + \sum_i \left(\frac{\partial f_a}{\partial t}\right)_i^{\mathrm{NES}} + \frac{1}{v^2}\frac{\partial}{\partial v}\left(\frac{v^3 f_a}{2\tau_c^*(v)}\right) + S_a(v) - L_a(v) = 0\,, \qquad (1)$$

where $f_a(v)$ is the velocity distribution function of the species a. The first term in the left-hand side of Eq.(1) represents the effect of the Coulomb collision[14]. The summation is taken over all background species, i.e. j= D, T, α-particle and electron. The collision term is hence non-linear, retaining collisions between ions of the same species. The second term accounts for the NES of species a by background ions. We consider NES between 1) α-particle and D and 2) α and T, i.e., (a,i) = (D,α), (T,α), (α,D) and (α,T) . The NES cross-sections are taken from the work of Cullen and Perkins[4].

The third term in the left-hand side of Eq.(1) represents the diffusion in velocity space due to thermal conduction. To incorporate the unknown loss mechanism of energetic ions into the analysis, we simulate the velocity-dependence of the energy-loss due to thermal conduction and the particle-loss time (see Ref.5-7).

The source ($S_a(\upsilon)$) and loss ($L_a(\upsilon)$) terms take different form for every ion species. For deuteron, the source and loss terms are described so that the fueling, beam-injection, transport loss and the loss due to T(d,n)^{4}He reaction are balancing [5-7];

$$S_D(\upsilon) - L_D(\upsilon) = \frac{S_{\mathrm{D}}}{4\pi\upsilon^2}\delta(\upsilon - \upsilon_D^{fueling}) + \frac{S_{\mathrm{NBI}}}{4\pi\upsilon^2}\delta(\upsilon - \upsilon_D^{NBI}) - \varsigma_D f_D - \frac{f_D(\upsilon)}{\tau_p^*(\upsilon)} \quad . \tag{2}$$

Here $\upsilon_D^{fueling}$ indicates the speed of the fueled deuteron, which is much smaller than the thermal speed, i.e. nearly equal to zero. The fueling rate S_D is determined so that the deuteron density is kept constant, i.e. $S_D = n_D/\tau_p + n_D n_T\langle\sigma\upsilon\rangle_{DT} - S_{NBI}$. The S_{NBI} is the NBI rate per unit volume and υ_D^{NBI} is the speed corresponding to injected beam energy E_{NBI}. We express the injection rate S_{NBI} using the beam energy E_{NBI} and injection power P_{NBI}, i.e. $S_{NBI} = P_{NBI}/(E_{NBI}V)$. Here V represents the plasma volume. Referring to the design parameter for ITER[15], we assume $V = 800\mathrm{m}^3$. The T(d,n)^{4}He reaction rate coefficient is written as

$$\langle\sigma\upsilon\rangle_{\mathrm{DT}} = \frac{4\pi}{n_D n_T}\int \upsilon_{D(T)}^2 \varsigma_{D(T)}(\upsilon_{D(T)}) \times f_{D(T)}(\upsilon_{D(T)})d\upsilon_{D(T)} \quad , \tag{3}$$

with

$$\varsigma_{\mathrm{D(T)}} = \frac{2\pi}{\upsilon_{D(T)}}\int \upsilon_{\mathrm{T(D)}} f_{T(D)}(\upsilon_{\mathrm{T(D)}}) \times \left[\int_{|\upsilon_{\mathrm{D}}-\upsilon_{\mathrm{T}}|}^{\upsilon_{\mathrm{D}}+\upsilon_{\mathrm{T}}} d\upsilon_r \upsilon_r^2 \sigma_{DT}(\upsilon_r)\right] d\upsilon_{\mathrm{T(D)}} \quad . \tag{4}$$

The T(d,n)^{4}He fusion cross has been taken from the work of Bosch[16].

For triton the NBI injection term has not been included in Eq.(2), and the source and loss terms are described so that the fueling rate, transport loss and the loss due to T(d,n)^{4}He reaction are balancing [5-7].

For α-particle, the source and loss terms are written as

$$S_\alpha(\upsilon) - L_\alpha(\upsilon) = S_\alpha(\upsilon) - \frac{f_\alpha(\upsilon)}{\tau_p^*(\upsilon)} \quad , \tag{5}$$

where NBI and fueling rate in Eq.(2) are replaced by the α-particle generation rate due to T(d,n)^{4}He reaction,

$$S_\alpha(\upsilon) = \frac{(dE/d\upsilon)}{4\pi\upsilon^2}\frac{dN_\alpha}{dE} \quad , \tag{6}$$

where $N_\alpha(E)$ represents the α-particle generation rate, which is described in the next section.

2.2 neutron and α-particle emission spectrums

The α-particle (neutron) emission energy spectrums are written as

$$\frac{dN_{\alpha(n)}}{dE}(E) = \iiint f_D(\vec{\upsilon}_D) f_T(\vec{\upsilon}_T) \times \frac{d\sigma}{d\Omega}\delta(E - E_{\alpha(n)})\upsilon_r d\vec{\upsilon}_D d\vec{\upsilon}_D d\Omega \quad , \tag{7}$$

where $E_{\alpha(n)}$ is the α-particle (neutron) energy in the laboratory system;

$$E_{\alpha(n)} = \frac{1}{2}m_{n(\alpha)}V^2 + \frac{m_{\alpha(n)}}{m_\alpha + m_n}(Q+K) + V\cos\varphi\sqrt{\frac{2m_n m_\alpha}{m_n + m_\alpha}(Q+K)} \, , \tag{8}$$

where $m_{\alpha(n)}$ is the α-particle (neutron) mass, V is the centre-of-mass velocity of the colliding particles, φ is the angle between the centre-of-mass velocity and the α-particle (neutron) velocity in the centre-of-mass frame and K represents the relative energy given by

$$K = \frac{1}{2}\frac{m_n m_\alpha}{m_n + m_\alpha}\left|\vec{\upsilon}_D - \vec{\upsilon}_T\right|^2 . \tag{9}$$

Using the α-particle emission spectrum, the source term of BFP equation for α-particle, i.e. Eq.(6), is determined. By means of the computational iterative method, both the energy spectrum and the deuteron, triton and α-particle velocity distribution functions are consistently obtained. The differential cross sections of the T(d,n)^{4}He reaction are taken from the work of Drosg [17].

3. Results and Discussion

In Figure 1 we first show the (a) deuteron and (b) triton distribution functions as a function of deuteron or triton energy when 10, 40 and 100 MW NBI heating are made. In the calculations, the ion and electron densities $n_e = 2n_D = 2n_T = 4\times10^{19}\mathrm{m}^{-3}$, electron temperature $T_e = 20\mathrm{keV}$, energy and particle confinement times $\tau_E = (1/2)\tau_p = 3\mathrm{sec}$ and beam-injection energy $E_{NBI} = 1\mathrm{MeV}$ are assumed. The dotted lines in both

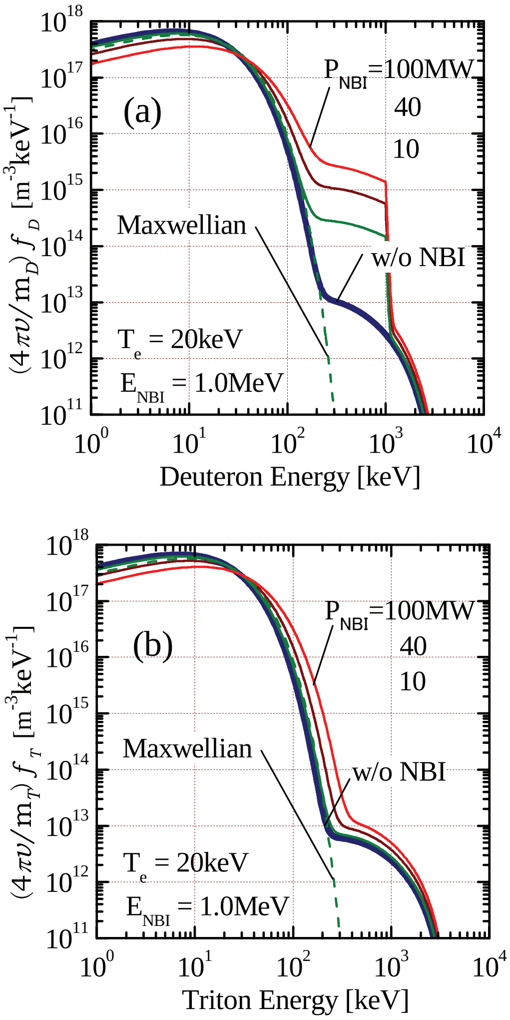

Fig.1 (a) Deuteron and (b) triton distribution functions when 10, 40 and 100 MW NBI heatings are made. The dotted lines denote Maxwellian when no NBI heating is made.

deuteron and triton distribution functions denote Maxwellian at 20keV temperature. The bold lines represent the distribution functions when no NBI heating is made. It is found that the non-Maxwellian tails due to NBI are formed less than 1-MeV energy range in the deuteron distribution function. The relative intensity of the tail is increased by NBI with increasing beam-injection powers. The knock-on tails due to NES of injected beam and α-particle are also observed in the triton distribution function and in the energy range above 1-MeV in the deuteron distribution function. We also find that the bulk temperature increases due to large NBI powers.

In Figure 2 the normalized neutron emission spectrum in deuterium-tritium plasmas is exhibited as a function of neutron energy in the laboratory system. The calculation conditions are the same as the ones in Fig.1. The bold line expresses the neutron spectrum when no NBI heating is applied, which is well agreed with the previous calculation[9] and experiment[11]. The dotted line denotes a Gaussian distribution corresponding to the case when no NBI heating is made. It is found that the neutron emission spectrum is broadened toward both low and high energy directions, and fraction of the neutron with both more and less than 14MeV energy increases with increasing NBI powers. We next show the normalized α-particle emission spectrum in Fig.3 as a function of the α-particle energy. The calculation conditions are the same as the ones in Fig.1 and 2. As was seen in Fig.2, the broadness of the α-particle emission spectrum also tends to be conspicuous for large NBI heating powers. For example, when 40-MW NBI heating is made, the fraction of the generation rate of α-particle with 5-MeV birth energy is almost 50 times larger than the case when no NBI injection is made and is almost 10^4 times larger than the value for Gaussian distribution.

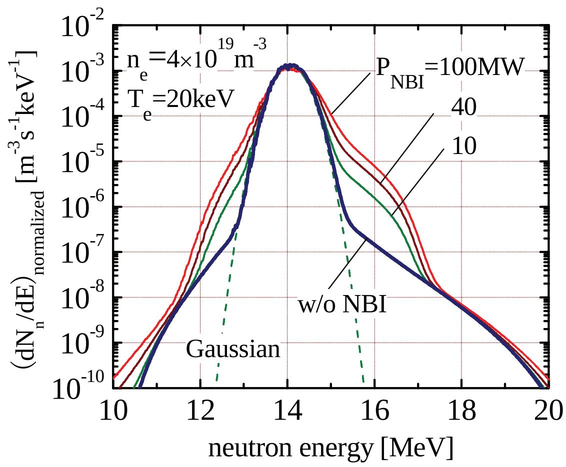

Fig.2 The neutron emission spectrum as a function of neutron energy in the laboratory system.

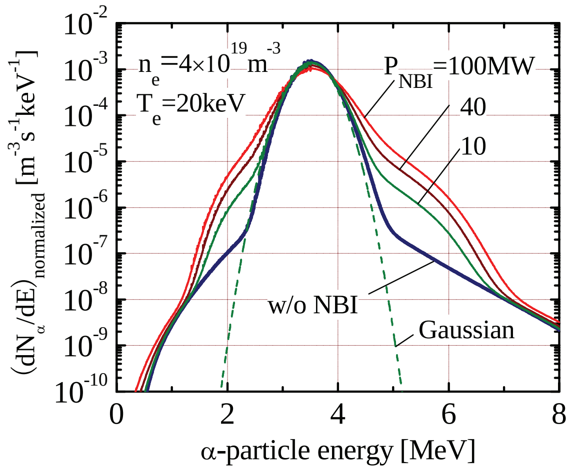

Fig.3 The α-particle emission spectrum as a function of α-particle energy in the laboratory system.

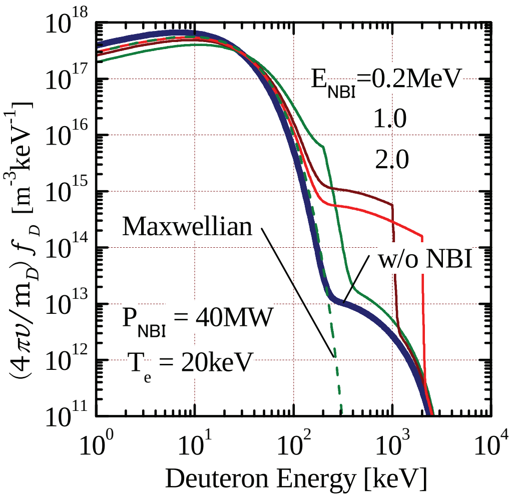

Fig.4 The deuteron distribution function when NBI heating is made with 0.2, 1.0 and 2.0-MeV beam-injection energies.

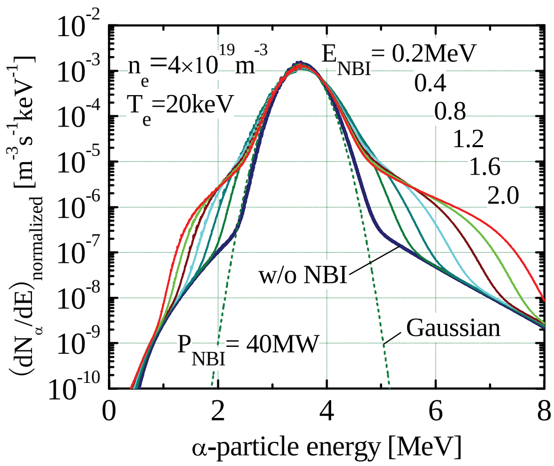

Fig.5 The α-particle emission spectrum as a function of α-particle energy in the laboratory system.

In Fig.4 we next show the deuteron distribution function for 0.2, 1.0 and 2.0 MeV beam-injection energies. In this case, the NBI heating power is taken as 40MW, and other plasma parameters are the same as the ones in Fig.1-3. It is shown that the fraction of the energetic deuteron increases with increasing beam-injection energy. In Fig.5 the normalized α-particle emission spectrum is shown. The calculation conditions are the same as the ones in Fig.4. As a result of the increment in the energetic component of deuteron distribution function (as shown in Fig.4), the fraction of the energetic (>4MeV) α-particle to total generation rate also increases.

The α-particle emission spectrum in the presence of NBI heating has been evaluated. When electron densities $n_e = 4\times10^{19}\,\mathrm{m}^{-3}$, electron temperature $T_e = 20\mathrm{keV}$, NBI power $P_{NBI} = 40(60)\mathrm{MW}$ and energy $E_{NBI} = 1\mathrm{MeV}$ are assumed, the fraction of the power carried by α-particle with energy above 4MeV to total α-heating power almost reaches to 13.3 (15.2)%, which is roughly 1.5 times larger than the value when Gaussian distribution is assumed for the spectrum, i.e. 8.7 (10.0) %.

The transport processes of α-particle in the fusion devices, e.g. ripple and orbit losses[18,19], tend to be influenced by α-particle's energy. The increment in the fraction of the energetic (≥3.5MeV) α-particle may cause the enhancement of the α-particle loss[18]. On the contrary, the initial kinetic energy of fuel ions (before the T(d,n)^{4}He reaction occurs) must be transformed into a part of the emitted α-particle and neutron energies. Thus if the correct α-particle spectrum is not adopted into a calculation, we may underestimate the α-heating power to some extent.

In the fusion devices, the α-particle diagnostics using γ-ray generating nuclear reaction, e.g. ^{9}Be(α,nγ)^{12}C reaction, has been developed[20]. The influence of the broadened emission spectrum on the diagnostics method should be examined. Further detailed investigation for the correlation between the α-particle spectrum and burning plasma characteristics would be required.

References

[1] T.Mutoh, et al., Nucl. Fusion, **47** (2007) 1250.
[2] S.Murakami, et al., Nucl. Fusion, **46** (2006) S425.
[3] J.J.Devany and M.L.Stein, Nucl. Sci. Eng. **46**, 323 (1971).
[4] S.T.Perkins and D.E.Cullen, Nucl. Sci. Eng., **20**, 77 (1981).
[5] H.Matsuura, Y.Nakao, Phys. Plasmas, **13**, 062507 (2006).
[6] H.Matsuura, Y.Nakao, Phys. Plasmas, **14**, 054504 (2007).
[7] M.Nakamura, Y.Nakao, V.T.Voronchev, K.Hegi, H.Matsuura, O.Mitarai, J. Phys. Soc. Jpn. **75**, 024801 (2006).
[8] H.Matsuura, Y.Nakao, K.Kudo, Nucl. Fusion, **39**, 145 (1999).
[9] L.Ballabio, et al., Phys. Rev. E, **55**, 3358 (1997).
[10] A.A.Korotkov, et al., Phys. Plasmas, **7**, 957 (2000).
[11] J.Källne, et al., Phys. Rev. Let, **85**, 1246 (2000).
[12] H.Matsuura, Y.Nakao, K.Hirose, K.Kai, K.Kudo, M.Ohta, Proceedings, 7th International Conference on Emerging Nuclear Energy Systems, Chiba, 1993, edited by H.Yasuda (World Scientific, Singapore, 1994) p.266.
[13] Y.Nakao, K.Kai, H.Matsuura, K.Kudo, Fusion Technol., **27** (1995) 555.
[14] M. N. Rosenbluth, W. M. MacDonald, D. L. Judd, Phys. Rev. **107**, 1 (1957).
[15] R. Aymar, Fusion Eng. Des., **55**, 107 (2001).
[16] H.-S. Bosch and G. Hale, Nucl. Fusion **32**, 611 (1992).
[17] M. Drosg, O. Schwerer, Handbook of Nuclear Activation Data, IAEA, Vienna, **1,** 111 (1987).
[18] B.C. Stratton, et al., Nucl. Fusion **39**, 1309 (1999).
[19] C.Estrada-Mila, J.Candy, R.E.Waltz, Phys. Plasmas, **13**, 112303 (2006).
[20] V.G.Kipitily, et al., Plasma Phys. Contr. Fusion, **48**, R59 (2006).

Proceedings of ITC/ISHW2007

Electron cyclotron heating of plasma with density above 10^{20}m^{-3} in W7-X

Yuriy TURKIN, Craig D. BEIDLER, Volker ERCKMANN, Joachim GEIGER, Heinrich P. LAQUA, Henning MAAßBERG, Nikolai B. MARUSHCHENKO, and W7-X Team

Max-Planck-Institut für Plasmaphysik, EURATOM-Association, Greifswald, Germany

12 October 2007

Electron cyclotron resonance heating (ECRH) of plasma in the Wendelstein 7-X (W7-X) stellarator at high densities is investigated by means of predictive simulations using coupled 1-D transport and ray-tracing codes. The heating efficiency and level of non-absorbed radiation are examined for various heating and plasma parameters. The transport modeling with the assumption of neoclassical core confinement has shown that high-β plasmas up to 5.5% are achievable at a magnetic field of 2.5T for the multi-pass O2-mode heating with overall absorption efficiency of 95%. The finite β-effects that can deteriorate power absorption efficiency are discussed.

Keywords: ECRH, W7-X, stellarator, plasma heating, O2-heating, steady-state operation, neoclassical transport
DOI: 10.1585

The W7-X stellarator being built at IPP-Greifswald will be equipped with a flexible ECRH system designed for 30 minutes operation with total power 10 MW generated by 10 gyrotrons [1]. The ECRH system will be the main heating source during the initial stage of W7-X operation. At low to moderate densities, heating is with the 2nd harmonic of the extraordinary mode (X2 at 140GHz and B=2.5T) with low-field-side launch in a bean-shaped plane. High-density and high-β regimes above the X2-cut-off density, i.e. from 1.2×10^{20}m^{-3} to $2\text{-}2.1\times10^{20}$m^{-3}, are accessible using the 2nd harmonic of the ordinary mode (O2).

In the present work the high performance O2-heating scenarios for W7-X are investigated by means of predictive simulations using a new 1-D transport code [2]. Neoclassical core confinement with empirical anomalous transport at the plasma edge is assumed [3]. The anomalous diffusivity scales inversely with plasma density in the region of high density gradient and exponentially decays towards the plasma axis. The radial electric field, electron and ion temperatures are advanced self-consistently with a calculation of the power deposition profiles by the ray-tracing code TRAVIS [4]. The shape of the density profile with a gradient region of about 10cm is fixed. The modeling is performed for the *standard magnetic configuration*, which is optimized for maximum confinement. More details about approaches used in simulations presented here can be found in reference [5].

Geometry of the ECRH heating system used in simulations is shown in Fig. 1. To prevent overheating of the vessel and in-vessel components by the shine-through radiation a reflecting mirror is foreseen opposite to the ECRH launchers, thus allowing the second pass absorption of the microwave beam and thereby significantly reducing the focused non-absorbed ECRH power.

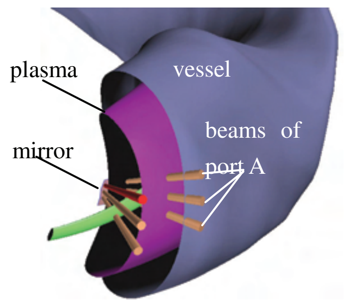

Fig. 1 Geometry of the ECRH beams; only six beams from 12 (10 plus 2 spare) [1] are shown: three beams (right) launched through port A and three beams (left) launched through port E; the other six beams are located symmetrically in the next module; the reflecting stainless-steel liners between ports are not shown. The beam in red is the spare beam.

Preliminary calculations [1] have shown that single-pass absorption of the power decreases from 80% to 50% when the density increases from 10^{20}m^{-3} to 2.1×10^{20}m^{-3} due to unfavorable temperature dependence and even after two passes of the microwave beam the non-absorbed ECRH power can be high. To increase absorption, the third pass of beams is provided by the reflecting stainless-steel liner installed on the outer side of the vessel between the ECRH ports.

author's e-mail: yuriy.turkin@ipp.mpg.de

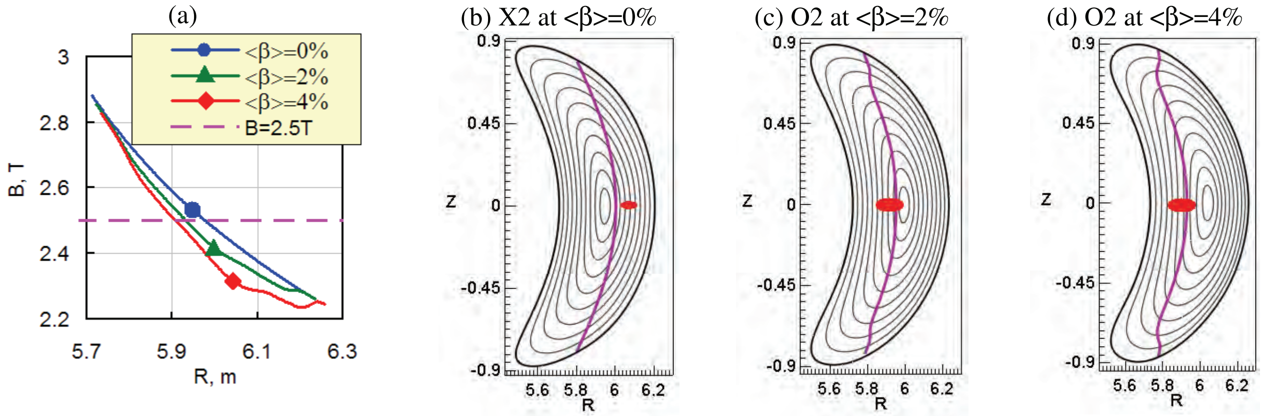

Fig. 2 Effect of high-β on the W7-X standard magnetic configuration: (a) magnetic field along major radius in bean-shape plane for different volume averaged β and the same coil currents; the magnetic axis positions are shown by markers; (b, c, d) ECRH deposition zones (red ellipses) projected onto bean-shape plane for X2/O2 heating scenarios and different magnetic configurations. The dashed line in (a) and magenta lines in (b, c, d) are the cold resonance positions (B=2.5T).

In the simulations described below all beams are aimed to the reflecting mirrors and the ray tracing code simulates three-pass absorption. The creation and sustaining of hot dense plasma by ECRH strongly depends on the magnetic field. And at the same time the high-β plasma changes the magnetic configuration. In Fig. 2a the magnetic field strength dependence on volume averaged plasma β is shown. With increasing <β> the magnetic field at the axis is reduced from 2.56T to 2.35T due to the Shafranov shift and plasma diamagnetism. Fig. 2bcd show schematically the power deposition zones which are painted by mapping of deposition profiles to the corresponding flux surfaces for the beam arrangement shown in Fig. 1. It is seen that the ECRH resonance region moves to the high field side. In this case the O2 absorption can degrade due to the decrease of the electron temperature in the resonance zone.

The ECRH power scans for the standard magnetic configuration have been performed for densities of 0.8-2.1×10^{20}m^{-3} and O2-mode (140GHz at B=2.5T) heating from 1MW to 10MW taking into account the β-effects mentioned above. The value of magnetic field has been chosen to have the central O2-mode ECRH deposition for the <β>=2% configuration, see Fig. 2c. The simulations have been started from low density at given power using off-axis X2-heating (100% single-pass absorption) and vacuum magnetic configuration (Fig. 2b) with simultaneous ramp-up of the density. Then below the X2-cut-off density at 0.8×10^{20}m^{-3}, the magnetic configuration has been changed to the <β>=2% configuration and the polarization has been switched to O2-mode. The calculations have been continued with increasing density till O2-cut-off. To model the moving of the absorption zone from central deposition to off-axis deposition and thus absorption degradation due to the β-effects, the <β>=4% configuration (Fig. 2d) has been used for higher densities and powers; see gray areas in Fig. 3. The results of scans are depicted in Fig. 3. It is seen that nearly full absorption is achieved for a wide range of density and input power; see region below 95% curve (cyan) in Fig. 3a; the single-pass absorption for these conditions is about 70%; see Fig. 3b. The discontinuities in Fig. 3 are related to the absorption degradation for far off-axis power deposition and to the modeling procedure in which precalculated equilibriums are used instead of self-consistent recalculation of them. However the main results remain valid. In order to prevent confinement degradation, the coil currents must be raised within the range of 5% along with the β increase to compensate magnetic field decrease at the axis. The heating efficiency of the O2-mode depends on plasma parameters, especially on electron temperature, because the optical thickness is proportional to T_e^2. The electron temperature in turn decreases with density increase as predicted by scaling laws [3] leading to absorption degradation and finally to thermal collapse; see solid red lines in Fig. 3.

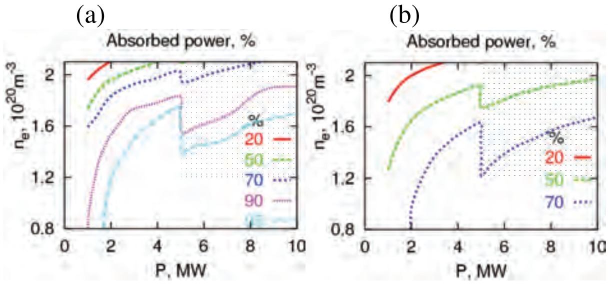

Fig. 3 Percentage of absorbed power for the three-pass scheme of O2-mode heating as a function of input power and plasma density: (a) after three passes; (b) after the first pass. Calculations in grayed area have been performed with <β>=4% equilibrium for standard magnetic configuration, for the other (n_e, P) the 2% equilibrium has been used.

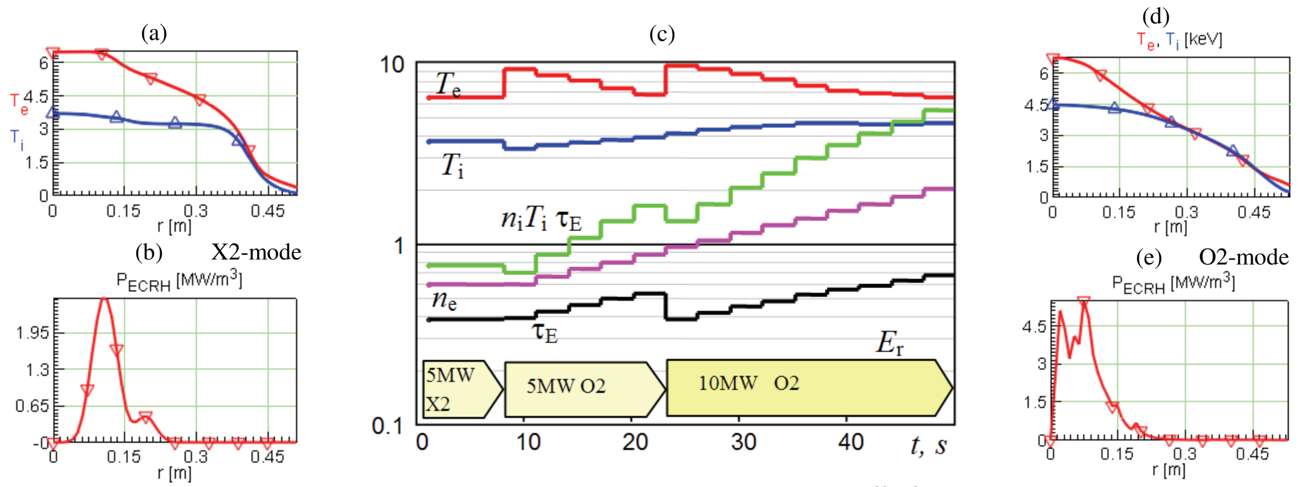

Fig. 4 (a) initial temperature and (b) low-field-side power deposition profiles at $n_e=0.6\times10^{20}m^{-3}$; (c) time evolution of the main plasma parameters: central T_e, T_i, triple product $n_iT_i\tau_E$ in $10^{20}m^{-3}$ keV·s, central n_e, energy confinement time τ_E; (d,e) final temperatures and ECRH profile at $n_e=2\times10^{20}m^{-3}$ and high-field-side deposition.

The time traces of the plasma parameters for the 10MW O2-mode scenario are shown in Fig. 4. Initially the $0.6\times10^{20}m^{-3}$ plasma is heated by 5MW X2-mode with low-field-side deposition as in Fig. 2b. Then the heating is switched to O2-mode with the same input power, but with the central deposition and $\langle\beta\rangle=2\%$ magnetic configuration (Fig. 2c). The central power deposition increases the electron temperatures leading to temperature decoupling in the center. The simulation is continued by ramping-up the density (magenta curve in Fig. 4c) towards the target density $2\times10^{20}m^{-3}$. At the density $10^{20}m^{-3}$ the heating is increased to 10MW and the $\langle\beta\rangle=4\%$ configuration with 5%-increase of the coil currents (that corresponds to the magnetic field increment of 0.12Tesla) to retain central power deposition is loaded. More heating increases the electron temperature; the ion temperature also goes up due to the strong collisional coupling at high densities. The final temperatures are shown in Fig. 4d, for the density profile see Fig. 6a. The following plasma parameters are reached: $n_iT_i\tau_E=5.5\times10^{20}m^{-3}$ keV·s, $\tau_E=0.67$s, and volume averaged $\langle\beta\rangle=5.5\%$ with power absorption efficiency of 95%.

In Fig. 5 the projections of the beams to the poloidal and equatorial planes are shown. The intensity of red spots on the rays are proportional to the absorption rate, most of the ECRH power (>70%) is absorbed at the first pass. The beams propagate at angles optimized with respect to the absorption efficiency for O2 or X3-mode operations and refraction effects are quite small even at high density.

Finally, for comparison with O2 ECRH plasmas, we have simulated the plasma heated by "positive" NBI (p-NBI, 60 keV H^+); see Fig.6. In the p-NBI case, the main power is absorbed at outer radii, especially the low energy components of the beam. This leads to confinement degradation, whereas for the O2 case the more central

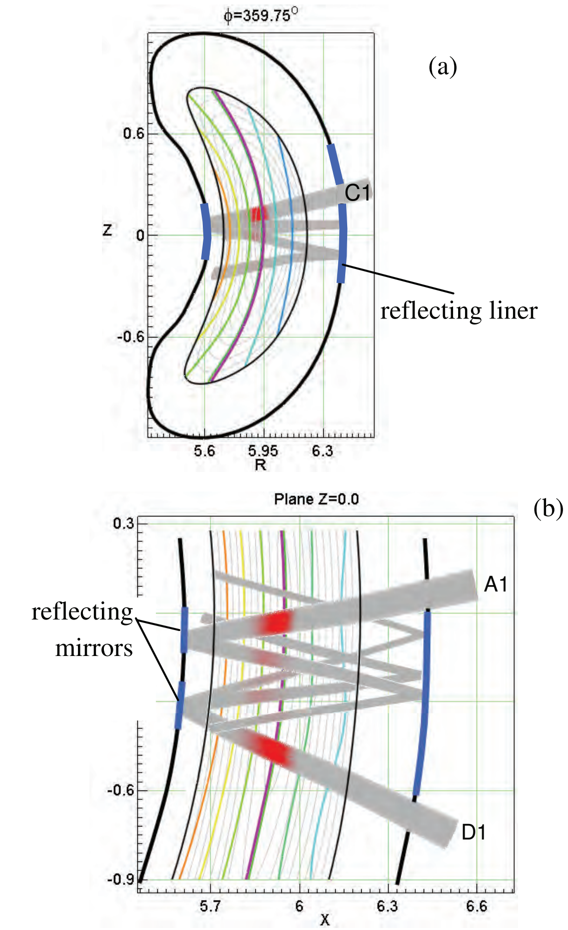

Fig. 5 Trajectories of ECRH beams: (a) poloidal plane with only one beam shown, (b) equatorial plane with the two beams going from mirror A1 of port E and mirror D1 of port A; magenta lines are the cold resonance positions; color lines in figures are the lines of constant magnetic field.

deposition allows for higher temperatures and improved confinement times. Indeed for these heating parameters, τ_E=0.46s at <β>=4.2% and τ_E=0.67s at <β>=5.5% are obtained for p-NBI and O2 ECRH, respectively.

Summary

The O2-ECR heating efficiency is analyzed for various plasma parameters and heating conditions using ray tracing modeling coupled with a 1D-transport code. The transport modeling with the assumption of neoclassical core confinement has shown that high-β plasmas up to 5.5% are achievable at a magnetic field of 2.5T for the multi-pass O2-mode heating with overall absorption efficiency of 95%. The O2-mode heating scenarios look promising for high-density-operation regimes of W7-X with high separatrix density that is the most favorable condition for operation of the divertor. It is worth noting that the neoclassical predictions give an upper limit of plasma performance in W7-X. Further predictive transport simulations will be considered for high-β plasmas for which the moving of the resonance zone due to the Shafranov shift and the diamagnetic current can decrease absorption efficiency.

[1] V. Erckmann, P. Brand et al. Electron cyclotron heating for W7-X: Physics and Technology**.** *Fusion science and technology***,** 52, 291(2007)

[2] Yu. Turkin, H. Maaßberg et al. *Fusion Science and Technology*, **50**, 387(2006)

[3] Yu. Turkin, C. D. Beidler et al. Transport Simulations for W7-X. *33rd EPS Conference on Plasma Phys.* Rome, 19 - 23 June 2006 ECA Vol.30I, P-2.113 (2006)

[4] N. B. Marushchenko et al. in *Proc. of the 16th Toki Conf.*, Japan, December 2006, http://itc.nifs.ac.jp/index.html

[5] C. D. Beidler, J. Geiger et al. Transport Modeling for W7-X on the Basis of W7-AS Experimental Results. Paper I-21 in *Proc. of the 17th Toki Conf.*, Japan, October 2007

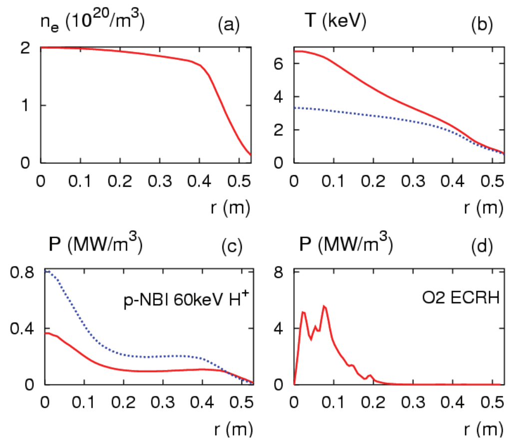

Fig. 6 (a) and (b): Plasma profiles for a 10MW heating simulation of W7-X. The solid line in figure (b) refers to O2 ECRH power depositions in plot (d). The dotted line in (b) refers to NBI power depositions shown in plot (c). The dotted line in (c) corresponds to the power deposited to ions.

Effect of nuclear elastic scattering on slowing down of ICRF resonated ions and plasma heating characteristics

Atsushi Fujimaru, Hideaki Matsuura, Yasuyuki Nakao
Department of Applied Quantum Physics and Nuclear Engineering, Kyushu University, 744 Motooka, Fukuoka 819-0395, Japan

In scattering collisions between light nuclei, effect of nuclear force becomes appreciable when the colliding particle energy is higher than ~ several 100keV. A deuterium-tritium (DT) plasma accompanied with ion-cyclotron range of frequencies (ICRF) heating at the second harmonic of deuteron is considered, and the nuclear elastic scattering (NES) effect on the energy deposition of resonated deuteron is examined on the basis of the two-dimensional Boltzmann-Fokker-Planck (BFP) equation for a resonated deuteron. It is shown that the fraction of resonated deuteron energy deposited to ions increases by about 10 % owing to the NES effect.

Keyword: nuclear elastic scattering, the fraction of resonated deuteron energy deposited to ions, DT plasma, ICRF heating

1. Inroduction

In scattering collisions between light ions, main interaction is Coulomb scattering. When the colliding particle energy is higher than ~ several 100keV, however, the effect of nuclear force on scattering process of light ion becomes appreciable. The cross section obtained by subtracting purely Coulomic component from the measured scattering cross section is defined as nuclear elastic scattering (NES) cross section [1,2]. It is necessary to evaluate the NES effect on slowing down process of high energy ions for comprehension of a characteristic of nuclear burn plasma.

In recent ICRF heating experiments on Large Helical Device (LHD), highly-energetic trapped ions (≥~1MeV) were observed [3]. In the presence of neutral beam injection (NBI) heating, it was found that the fraction of beam-ion energy deposited to ions increases owing to the effect of NES [4,5]. The NES effect can appear also in plasma under ICRF heating because the highly-energetic resonated ion loses its energy via collisional process. It is important to grasp the NES effect on ICRF plasma heating.

In this paper, we consider a deuterium-tritium (DT) plasma accompanied with ICRF heating at the second harmonic of deuteron, and examine the NES effect on the energy deposition of resonated deuteron. The two-dimensional Boltzmann-Fokker-Planck (BFP) equation is solved to obtain the velocity distribution function of resonated deuteron. Using the obtained distribution function, the fraction of resonated deuteron energy deposited to bulk ions is evaluated.

author's e-mail:fujisin @nucl.kyushu-u.ac.jp

2. Analysis Model

In this paper to facilitate the analysis triton- and electron-distribution functions are assumed to be Maxwellian at the same temperature. We solve the following BFP equation [4-8] for deuteron:

$$\sum_j \left(\frac{\partial f_D}{\partial t}\right)_j^{Col} + \sum_i \left(\frac{\partial f_D}{\partial t}\right)_i^{NES} + \left(\frac{\partial f_D}{\partial t}\right)^{RF} - \frac{1}{v^2}\frac{\partial}{\partial v}\left\{\frac{v^3}{2\tau_C^*(v)} f_D\right\} - \frac{f_D}{\tau_P^*(v)} - \left(\frac{\partial f_D}{\partial t}\right)_R^{loss} + S(v) = 0, \quad (1)$$

where $f_D(v, \mu)$ is the velocity distribution function of deuteron (μ is the direction cosine between the velocity of deuteron and the external magnetic field). The $\tau_C^*(v)$ and $\tau_P^*(v)$ stand for the typical energy-loss time due to thermal conduction and particle-loss time due to particle transport respectively [5]. It is assumed that they are followed Bittoni's treatment [9].

The first term in Eq. (1) represents the effect of the Coulomb collisions with bulk charged particles, i.e., j = D, T, α-particle and electron [10,11].

The second term accounts for the NES with bulk deuteron and triton, i.e., i= D, T [4-8]. In this paper, the NES cross sections are taken from Cullen and Perkins [2].

The third term in Eq. (1) represents the effect of RF diffusion. The quasi-linear diffusion in velocity space owing to ICRF injection [12] can be written as

$$\left(\frac{\partial f_D}{\partial t}\right)^{RF} = \frac{1}{v_\perp}\frac{\partial}{\partial v_\perp}\left(v_\perp D \frac{\partial f_D}{\partial v_\perp}\right). \tag{2}$$

Here $v_\perp$ represents vertical velocity component to the external magnetic field and, D represents diffusion coefficient due to ICRF second harmonics [12-15], and can be written as

$$D = \frac{C_D}{v_{th}^2}\left| J_1\left(\frac{k_\perp v_\perp}{\omega_{cD}}\right) + \frac{E_-}{E_+} J_3\left(\frac{k_\perp v_\perp}{\omega_{cD}}\right)\right|^2. \tag{3}$$

Here E_-/E_+ can be shown as following form [11].

$$\frac{E_-}{E_+} \approx -\frac{L}{R}. \tag{4}$$

From the equation of dispersion relation of cold plasmas, the parameter of Bessel function can be written as

$$\frac{k_\perp v_\perp}{\omega_{cD}} = \frac{\sqrt{2}}{c}\left[\frac{RL}{R+L}\right]^{1/2} v\sqrt{1-\mu^2}, \tag{5}$$

where c represents the speed of light, and ω_{cD} denotes the cyclotron frequency of deuteron. The coefficient C_D is determined from the ICRF absorbed power, P_{ICRF}, which is described as

$$P_{ICRF} = -2\pi m_D \iint D v_{th}^2 v \left[v^2\left(1-\mu^2\right)\frac{\partial f_D}{\partial v} - v\mu \frac{\partial f_D}{\partial \mu}\right] dv d\mu. \tag{6}$$

The forth and fifth term in Eq. (1) represent the diffusion in velocity space due to thermal conduction and particle transport respectively.

The sixth term in Eq. (1) denotes the effect of particle loss due to $T(d,n)^4He$ reaction.

$$\left(\frac{\partial f_D}{\partial t}\right)_R^{loss} = \frac{n_T f_D}{\sqrt{2\pi}}\left(\frac{2m_T}{m_D}\right)^{3/2}$$

$$\times \frac{1}{v}\int_0^\infty dv_T v_T \exp\left(-\frac{m_T}{m_D}v_T^2\right)$$

$$\times \int_{|v-v_T|}^{v+v_T} dv_r v_r^2 \sigma_{DT}(v_r). \tag{7}$$

Here v_T and v_r represent the velocity of triton and the relative velocity between deuteron and triton respectively. In addition, $\sigma_{DT}(v_r)$ denotes the cross section of $T(d,n)^4He$ reaction, and is provided by Duane [16].

The seventh term in Eq. (1) represents particle source. The particle losses due to fusion reaction and particle transport are compensated by some appropriate fueling method. The source term $S(v)$ can be written as following form.

$$S(v) = \frac{S_0}{4\pi v^2}\delta(v - v_{fuel}), \tag{8}$$

where, S_0 can be written as

$$S_0 = n_D n_T < \sigma v >_{DT} + \frac{n_D}{\tau_P}, \tag{9}$$

and v_{fuel} is the speed of the fueled particle, which is much smaller than the thermal velocity (nearly zero).

3. Results and Discussion

In Fig. 1(a) the velocity distribution function of deuteron, and (b) the Maxwellian at the same temperature

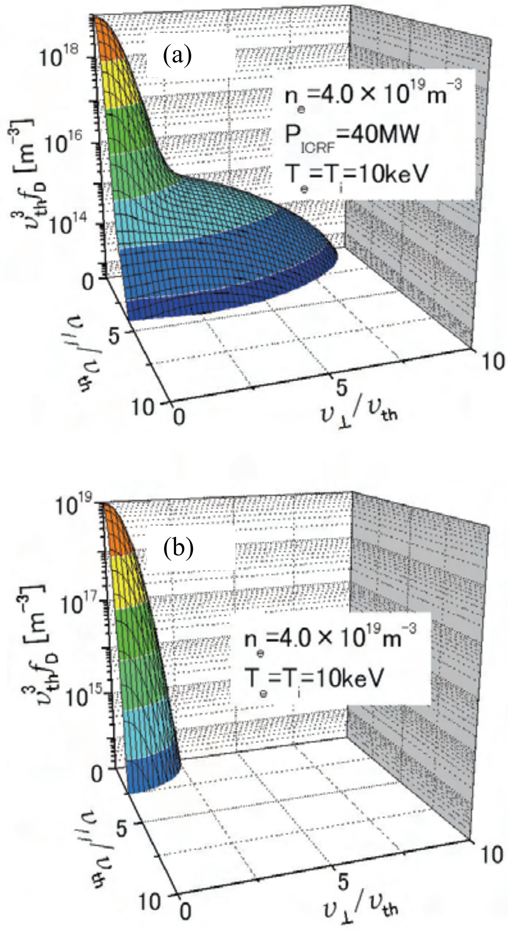

Fig. 1(a) The velocity distribution function of deuteron, and (b) Maxwellian.

are shown. In this calculation the bulk temperature T_i=T_e=10keV, ion and electron densities n_e = $2n_D$=$2n_T$=4×10^{19}m^{-3}, energy and particle confinement time τ_E=(1/2)τ_P=3sec , and ICRF power absorbed by deuteron 40MW are assumed. Here v_{th} represents the thermal velocity of deuteron, and $v_\perp$ ($v_{//}$) denotes the vertical (parallel) velocity component to the external magnetic field. As a result of the ICRF heating, a non-Maxwellian tail is formed in high energy region, because of the vertical velocity component increased due to the ion-cyclotron resonance. From the obtained deuteron distribution function, the transferred energy from high-energy resonated deuteron to bulk ions via NES is estimated as

$$P_{D\to i}^{NES} = -\sum_{i=D,T} \int \frac{1}{2} m_D v^2 \left(\frac{\partial f_D}{\partial t}\right)_i^{NES} d\mathbf{v} \times V_p. \qquad (10)$$

Where V_p represents plasma volume, and throughout the calculations V_p =800m^3 is assumed.

The integrand in Eq. (10) is shown in Fig. 2. In this case the bulk temperature T_i=T_e=10keV, ion and electron

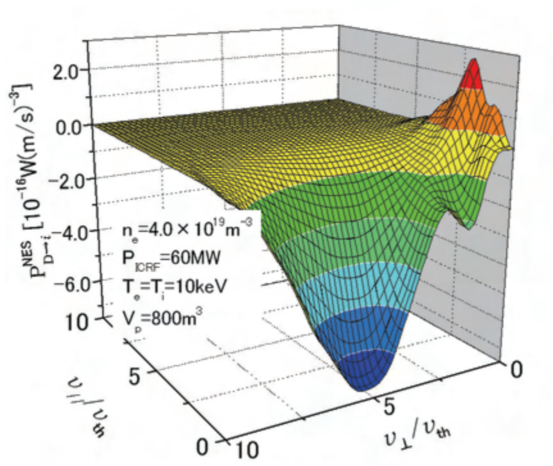

Fig. 2 The deposited energy to bulk ions via NES.

densities n_e = $2n_D$=$2n_T$=4×10^{19}m^{-3}, energy and particle confinement time τ_E=(1/2) τ_P =3sec , and ICRF power absorbed by deuteron 40MW are assumed. It is found that deuterons which have the large vertical velocity component lose their energy due to NES. In consequence, the deposited energy from high energy resonated deuteron to bulk ions increases relatively compared with the case that only Coulomb scattering is considered.

In Table. 1 the transferred powers from deuteron (a) to bulk ions and electrons via Coulomb scattering, and (b) to bulk ions via NES, the loss powers from plasma due to (c) T(d,n)^{4}He reaction, and (d) Transport and Conduction, (e) the ICRF absorbed power, (f) the transferred power from alpha particle to deuteron via Coulomb scattering are shown. In this case the bulk temperature T_i=T_e=10keV, ion and electron densities n_e=$2n_D$=$2n_T$=4×10^{19}m^{-3}, energy and particle confinement time τ_E=(1/2) τ_P =3sec , and ICRF power absorbed by deuteron 40MW are assumed. About 70% of resonated deuteron energy is deposited to plasma, and about 30% is lost from plasma. Besides, it is found that the transferred power to bulk ions via NES is smaller than that via Coulomb scattering relatively. By using the plasma heating powers due to Coulomb scattering and NES, the fraction of plasma heating power deposited to ions is calculated. The plasma heating power due to Coulomb scattering and NES are written respectively as $P_{D\to j}^{C}$ (i.e., j= D, T, e) and $P_{D\to i}^{NES}$(i.e., i= D, T), the fractional power deposition to ions can be written as

$$F_{ion}^{Coulomb+NES} = \frac{\sum_{i=D,T} P_{D\to i}^{NES} + \sum_{i=D,T} P_{D\to i}^{C}}{\sum_{i=D,T} P_{D\to i}^{NES} + \sum_{j=D,T,e} P_{D\to j}^{C}}. \qquad (11)$$

If NES is not included, the fraction is written as

$$F_{ion}^{Coulomb} = \frac{\sum_{i=D,T} P_{D\to i}^{C}}{\sum_{j=D,T,e} P_{D\to j}^{C}}. \qquad (12)$$

To express numerically the NES effect on the fractional power deposition to ions, we introduce the following enhancement parameters:

$$\xi = \left(\frac{F_{ion}^{Coulomb+NES}}{F_{ion}^{Coulomb}} - 1\right) \times 100[\%]. \qquad (13)$$

By using this parameter, the NES effect on the fractional power deposition to ions is evaluated. In the case shown in Table. 1, for example, the fractional power deposition to ions is calculated from Eq. (11) and (12) as $F_{ion}^{Coulomb+NES} = 0.30$, and $F_{ion}^{Coulomb} = 0.29$, so, the enhancement parameter ξ is estimated as $\xi = 3.4[\%]$.

In Fig. 3 the ξ value is plotted as a function of plasma temperature. In this case the ion and electron densities n_e=$2n_D$=$2n_T$=4×10^{19}m^{-3}, energy and particle confinement time τ_E=(1/2) τ_P =3sec, and ICRF power absorbed by deuteron 40MW (solid line), and 60MW (dotted line) are assumed. For T=15keV temperature, the ξ value reaches 12% and 5% for ICRF power absorbed by deuteron 60, 40 MW, respectively. It is found that the enhancement parameter ξ increases with increasing P_{ICRF}. This is because the high-energy component in deuteron distribution function becomes relatively large

Table. 1 The transferred, heat and loss power.

(τ_E=3.0sec、T_e=T_i=10keV、n_e=$2n_{D(T)}$=4.0×10^{19}m^{-3}、B=5.0T、V_p=800m^3)

(a)			(b)		(c)	(d)
D→D	D→T	D→e	D→D	D→T	0.36	12.3
5.7	2.9	21.0	0.43	0.08		

(e)	(f)
40.0	2.3

(e)+(f)	(a)+(b)+(c)+(d)	error
42.3	42.9	1.4%

[MW]

and the transferred energy from resonated deuteron to bulk ions via NES increases for high P_{ICRF}. It should be noted that the ξ value decreases at the low- and high-temperature range. The reason would be that in low-temperature plasmas the slowing down of energetic ions due to Coulomb scattering (mainly) by electrons is intensified; thus the high-energy component in deuterium velocity distribution function becomes relatively small, which causes a reduction in the transferred power from resonated deuteron to ions via NES. On the other hand at the high-temperature range, relative velocity between energetic resonated deuteron and bulk ions becomes small, and the contribution of NES is reduced compared with that of Coulomb scattering.

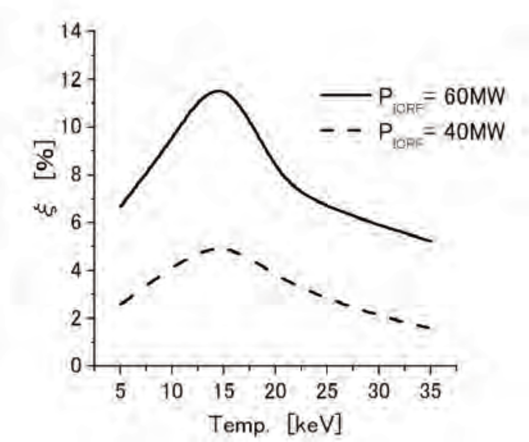

Fig. 3 The ξ value as a function of plasma temperature

4. Conclusion

It is revealed that the fraction of ICRF heating power deposited to bulk ions increases owing to the NES effect. In the case of the bulk temperature T_i=T_e=15keV, ion and electron densities n_e=2n_D=2n_T=4×10^{19}m^{-3}, energy and particle confinement time τ_E=(1/2)τ_P =3sec, and ICRF power absorbed by deuteron 60MW (40MW), the enhancement parameter ξ reaches almost 12% (5%).

References

[1] J.J.Devaney, M.L.Stein, Nucl. Sci. Eng. **43** 323 (1971).
[2] D.E.Cullen, S.T.Perkins, Nucl. Sci. Eng. **81** 75 (1982).
[3] T.Mutoh, *et al*,. Nucl. Fusion. **47** 1250 (2007).
[4] H.Matsuura, Y.Nakao, Nucl. Fusion. **39** 145 (1999).
[5] H.Matsuura, Y.Nakao, Phys. Plasmas. **13** 062507 (2006).
[6] H.Matsuura, Y.Nakao, Phys. Plasmas. **14** 054504 (2007).
[7] Y.Nakao, K.Kai, H.Matsuura, K.Kudo, Fusion Technol., **27** 555 (1995).
[8] H.Matsuura, Y.Nakao, K.Hirose, K.Kai, K.Kudo, M.Ohta, *Proceedings, 7th International Conference on Emerging Nuclear Energy Systems*, Chiba, 1993, edited by H.Yasuda (World Scientific, Singapore, 1994) p.266.
[9] E.Bittoni, J.G.Cordey, and M.Cox, Nucl. Fusion. **20** 931 (1980)
[10] M.M.Rosenbluth, W.M.Macdonald, and D.L.Judd, Phys. Rev. **107** 1 (1957).
[11] J.Killeen, G.D.Kerbel, M.G.McCoy, and A.A.Mirin, " Computational Methods for Kinetic Models of Magnetically Confined Plasmas " (Springer-Verlag, New York, 1985).
[12] T.H.Stix, *Wave in Plasma* (Yoshioka Publisher, Kyoto, (1996).
[13] T.H.Stix, Nucl. Fusion, **15** 737 (1975).
[14] D.Anderson, *et al*., Nucl. Fusion, **27** 911 (1987).
[15] L.G.Eriksson, *et al*., Nucl. Fusion, **33** 1037 (1993).
[16] B.H.Duane, *Rep. BNWL-1685, Battelle Pacific North west Lab.,* Richmond, WA (1972)

Proceedings of ITC/ISHW2007

Simulation study of ICRF wave propagation and absorption in 3-D magnetic configurations

T. Yamamoto[1)], S. Murakami[1)] and A. Fukuyama[1)]

[1)]Department of Nuclear Engineering, Kyoto University, Kyoto 606-8501, Japan

(Received 15 October 2007)

ICRF wave propagation and absorption are investigated by TASK/WM, in which Maxwell's equation for RF wave electric field with complex frequency is solved as a boundary value problem in 3D magnetic configurations. Magnetic flux coordinates based on the MHD equilibrium by VMEC code are considered. The wave propagation is solved in the tokamak configuration (JT-60U) and also in the helical configuration (LHD) in the minority ion heating regime. Characteristics of the ICRF wave propagation and absorbed in the 3D magnetic configurations are shown.

Keywords: Simulation, ICRF heating, wave propagation, helical configuration

1 Introduction

The ICRF heating has been successfully studied and the efficiency of this heating method has been shown in LHD. The numerical analysis of ICRF heating has been carryed out by GNET[1] and also have shown the efficiency and detail information about the energetic tail ion distribution generated by ICRF heating. However, a detail analysis of the wave propagation and absorption process has not been carryed out enough in 3D magnetic configurations.

In this paper we study the ICRF wave propagation and absorption by TASK/WM[2, 3], in which Maxwell's equation for RF wave electric field with complex frequency is solved as a boundary value problem in 3D magnetic configurations. We consider VMEC coordinate as the magnetic coordinate obtained from MHD equilibrium. We first solve the wave propagation in the tokamak configuration (JT-60U) and , then, the propagation in the helical configuration (LHD), where the minority ion heating regime is assumed.

2 Simulation model

TASK/WM solves Maxwell's equation for the electric field $\mathbf{E}$ with complex frequency ω as a boundary value problem in 3D magnetic configurations.

$$\nabla\times\nabla\times\mathbf{E} = \frac{\omega^2}{c^2}\overleftrightarrow{\epsilon}\cdot\mathbf{E} + i\omega\mu_0\mathbf{j}_{\rm ext} \tag{1}$$

Here, the external current $\mathbf{j}_{\rm ext}$ represents the antenna current in ICRF heating. Assuming cold plasma and collisional dumping, the dielectric tensor is

$$\overleftrightarrow{\epsilon} = \begin{pmatrix} S & -iD & 0 \\ iD & S & 0 \\ 0 & 0 & P \end{pmatrix},$$

$$S = 1 - \frac{1}{\epsilon_0}\sum_s \frac{\omega_{ps}^2}{\omega}\frac{\omega + i\nu_s}{(\omega+i\nu_s)^2 - \Omega_s^2},$$

$$D = \frac{1}{\epsilon_0}\sum_s \frac{\omega_{ps}^2}{\omega}\frac{\Omega_s}{(\omega+i\nu_s)^2 - \Omega_s^2},$$

$$P = 1 - \sum_s \frac{\omega_{ps}^2}{\omega}\frac{1}{\omega + i\nu_s}, \tag{2}$$

where particle species s, the dielectric constant in vacuum ϵ_0, the collisionality ν, the plasma frequency ω_p and the cyclotron frequency Ω.

We rewrite the Maxwell's equation (1) in a magnetic coordinates (ψ, θ, φ). LHS of (1) is written as

$$\begin{aligned}(\nabla\times\nabla\times\mathbf{E})^p \\ = \frac{1}{J}\Big[\frac{\partial}{\partial x^q}\Big\{\frac{g_{rp}}{J}\left(\frac{\partial E_r}{\partial x^q} - \frac{\partial E_q}{\partial x^r}\right) + \frac{g_{rq}}{J}\left(\frac{\partial E_p}{\partial x^r} - \frac{\partial E_r}{\partial x^p}\right) \\ + \frac{g_{rr}}{J}\left(\frac{\partial E_q}{\partial x^p} - \frac{\partial E_p}{\partial x^q}\right)\Big\} - \frac{\partial}{\partial x^r}\Big\{\frac{g_{qp}}{J}\left(\frac{\partial E_r}{\partial x^q} - \frac{\partial E_q}{\partial x^r}\right) \\ + \frac{g_{qq}}{J}\left(\frac{\partial E_p}{\partial x^r} - \frac{\partial E_r}{\partial x^p}\right) + \frac{g_{qr}}{J}\left(\frac{\partial E_q}{\partial x^p} - \frac{\partial E_p}{\partial x^q}\right)\Big\}\Big],\end{aligned} \tag{3}$$

where the metric coefficient $g_{ij} = \mathbf{e}_i\cdot\mathbf{e}_j$, $\mathbf{e}_i = \partial\mathbf{r}/\partial\mathbf{x}^\mathbf{i}$, Jacobian J, $(x^1, x^2, x^3) = (\psi, \theta, \varphi)$. The indexes (p, q, r) are $(1, 2, 3), (2, 3, 1), (3, 1, 2)$.

The dielectric tensor is written as

$$\tilde{\epsilon}_{ij} = \overleftrightarrow{g}_{ij}^{-1}\cdot\overleftrightarrow{\mu}_{ij}\cdot\overleftrightarrow{\epsilon}_{ij}\cdot\overleftrightarrow{\mu}_{ij}^{-1}, \tag{4}$$

author's e-mail: yamamoto@p-grp.nucleng.kyoto-u.ac.jp

where the rotation transform tensor $\overleftrightarrow{\mu}$ is

$$\mu_{11} = \frac{1}{\sqrt{g^{11}}},$$
$$\mu_{12} = \frac{1}{J\sqrt{g^{11}}}\left\{\frac{B^\theta}{B}(g_{23}g_{12} - g_{22}g_{31}) + \frac{B^\varphi}{B}(g_{33}g_{12} - g_{23}g_{31})\right\},$$
$$\mu_{13} = \frac{B^\theta}{B}g_{12} + \frac{B^\varphi}{B}g_{13}, \quad \mu_{21} = 0,$$
$$\mu_{22} = \frac{B^\varphi}{B}J\sqrt{g^{11}}, \quad \mu_{23} = \frac{B^\theta}{B}g_{22} + \frac{B^\varphi}{B}g_{23},$$
$$\mu_{31} = 0, \quad \mu_{32} = -\frac{B^\theta}{B}J\sqrt{g^{11}},$$
$$\mu_{33} = \frac{B^\theta}{B}g_{32} + \frac{B^\varphi}{B}g_{33}. \tag{5}$$

The electric field $\mathbf{E}$ and metric coefficient g_{ij} are evaluated at grid points ψ_l in radial direction and expanded to Fourier series in poloidal and toroidal direction.

$$\mathbf{E}(\psi_k, \theta, \varphi) = \sum_{mn} \mathbf{E}_{mn}(\psi_k)e^{i(m\theta+n\varphi)},$$
$$g_{ij}(\psi_k, \theta, \varphi) = \sum_{m'n'} (g_{ij})_{m'n'}(\psi_k)e^{i(m'\theta+n'N_h\varphi)}, \tag{6}$$

where N_h is rotation number of helical coil in φ. The antenna current $\mathbf{j}_{\rm ext}$ is given as

$$j^1 = (j^1)_{mn}e^{i(m\theta+n\varphi)}\Theta(\psi_d - \psi),$$
$$j^{2,3} = (j^{2,3})_{mn}e^{i(m\theta+n\varphi)}\delta(\psi - \psi_d), \tag{7}$$

where step function $\Theta(x)$, delta function $\delta(x)$, and the radial antenna position ψ_d. These equations satisfy $\nabla \cdot \mathbf{j}_{\rm ext} = 0$.

We assume that the plasma is surrounded by a perfect conductor and that there is a vacuum layer between the plasma surface and the perfect conductor wall. Then, the tangential electric field at the wall is set zero as the boundary condition;

$$E_\theta^{mn} = 0, \quad E_\varphi^{mn} = 0. \tag{8}$$

The poloidal electric field at the magnetic axis $\psi = 0$ is zero. The toroidal electric fields of the modes $m \neq 0$ are zero. That of mode $m = 0$ is finite and the radial derivation is zero. These are boundary condition on the magnetic axis $\psi = 0$;

$$\begin{cases} m = 0 & \frac{\partial E_\varphi^{0n}}{\partial \psi} = 0 \\ m \neq 0 & E_\varphi^{mn} = 0. \end{cases} \tag{9}$$

The Maxwell's equations (3)-(7) are solved under the boundary conditions (8) and (9) on the 3D configuration given by numerical equilibrium data of the magnetic flux coordinates.

3 Simulation results

3.1 Tokamak configuration (JT-60U)

We first study the ICRF minority heating in the tokamak configuration, taking JT-60U plasma as example. The assumed configuration parameters are as follows; plasma major radius $R_0 = 3.5$m, plasma minor radius $a = 0.98$m, plasma shape elongation $\kappa = 1.3$, plasma shape triangularity $\delta = 0.31$, magnetic field at magnetic axis $B_0 = 3.3$T.

The obtained results for the minority ion heating regime is showen in Fig.1. The assumed plasma parameters are as follows; temperature at magnetic axis T_0 = 3.0keV, temperature on plasma boundary T_s = 0.3keV, density at magnetic axis $n_0 = 1.0 \times 10^{20}/\mathrm{m}^3$, density on plasma boundary $n_s = 0.1 \times 10^{20}/\mathrm{m}^3$, minor ion ratio 5%, ration of collision frequency to wave frequency $\nu_s = 0.003$. The temperature and density profiles are given by $T(r/a) = (T_0 - T_s)(1-(r/a)^2) + T_s$, $n(r/a) = (n_0 - n_s)(1-(r/a)^2)^{1/2} + n_s$ respectively. Also, the used antenna parameters are antenna current density $j_{\rm ext} = 1.0$A/m, wave frequency f_{RF} = 45.0MHz. The upper side figures in Fig.1 assumes the wave frequency f_{RF} = 45.0MHz and the lower side figures is f_{RF} = 48.0MHz.

Three lines drawn in Fig.1 (b), (f) represent ion cyclotron layer (a green line), two-ion-hybrid cut-off (a blue line) and resonance (a red line) layers from the outside. It is observed that the absorption region of minority ion locates near the minority ion cyclotron layer in Fig.1 (b), (f). The coherent waves are observed (c), (d), (g), (h). The E_+ component (right-circularly polarized component) of the electric field is absorbed and the amplitude of coherent waves is damped near the minority ion cyclotron layer (c), (g). While, the damping of amplitude of the E_- component (left-circularly polarized component) not observed near the minority ion cyclotron layer. The reason is that the E_- component of the electric field do not provide the minority ion at the minority ion cyclotron layer under the assumption of cold plasma. The absorption increases at the two-ion-hybrid resonance and cut-off layers near the minority ion cyclotron layer near $z = 0$ (a), (b). Since the width between resonance and cut-off is narrow, the wave is reflected or transmitted at the cut-off layers. The reflected waves is superposed incoming waves and the amplitude of E_+ component is enhanced (c). The amplitude of the transmitted wave is enhanced at the resonance layer (c). These are the reasons for increasement of the absorption.

The lower in Fig.1 are results for the same parameters as those of upper except f_{RF} = 48MHz. Since the wave frequency increases from 45.0MHz to 48.0MHz, the ion cyclotron layer and the two-ion-hybrid cut-off and resonance layer shift toward the higher magnetic field side. Therefore, the absorption region moves from 4.0m (b) to 3.75m (f).

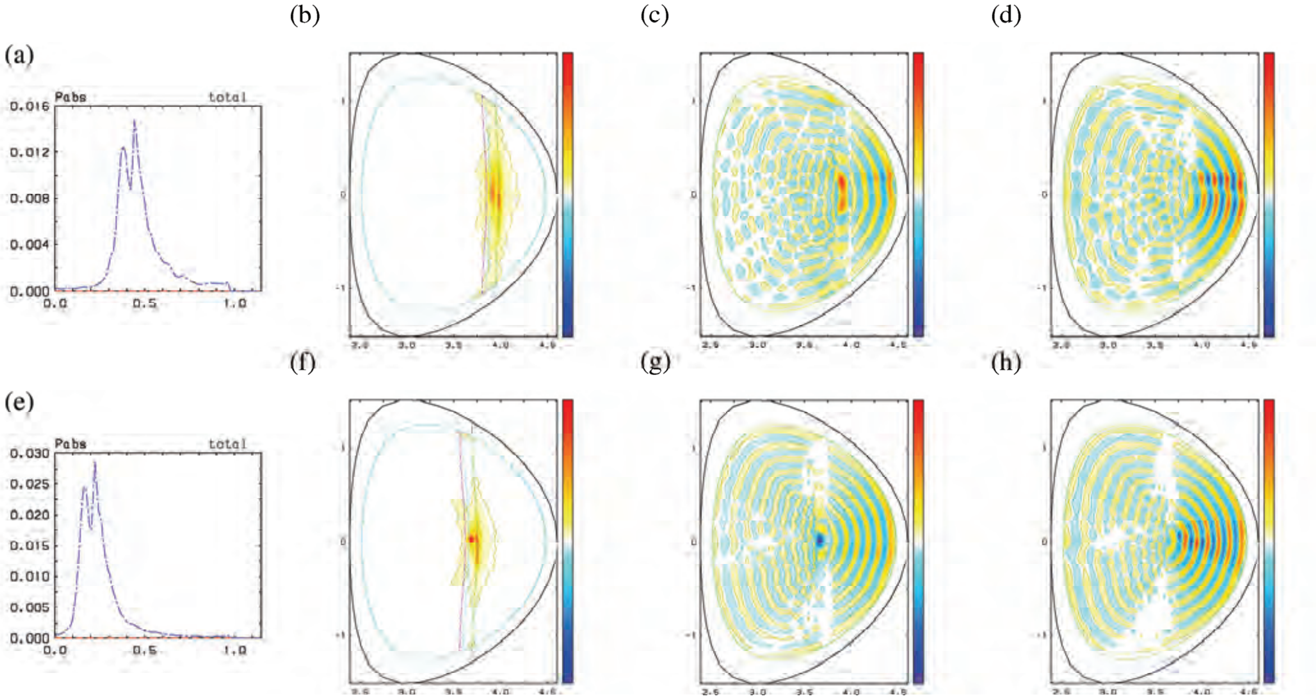

Fig. 1 Radial H absorption distributions (a), (e), contour plots of H absorption (b), (f) and E_+ component (c), (g) and E_- component (d), (h) of the electric field on the poloidal cross section; upper (f_{RF} = 45.0MHz), lower (f_{RF} = 48.0MHz); JT-60U

3.2 Helical configuration (LHD)

We study the ICRF minority heating in the Helical configuration, taking the LHD plasma as an example. The configuration parameters of LHD are as follows; plasma major radius $R_0 = 3.6$m, plasma minor radius $a = 0.58$m, magnetic field at magnetic axis $B_0 = 2.75$T.

The magnetic surface structure obtained by VMEC code is shown in Fig.2, where a vertically elongated cross section is plotted.

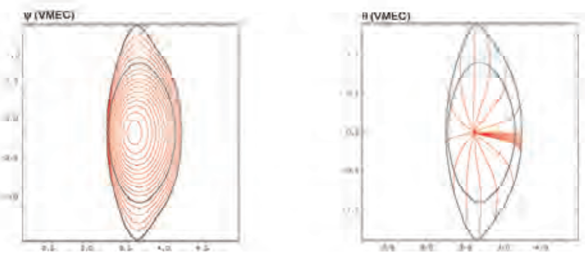

Fig. 2 Conter plots of a magnetic surface structure, ψ (left fig.), θ (right fig.)

The obtained results for the minority ion heating regime in the LHD plasma is showed in Fig.4. Upper side figures in Fig.4 are results with following plasma parameters; temperature at magnetic axis T_0 = 2.0keV, temperature on plasma boundary T_s = 0.2keV, density at magnetic axis $n_0 = 0.1 \times 10^{20}/\mathrm{m}^3$, density on plasma boundary $n_s = 0.01 \times 10^{20}/\mathrm{m}^3$, minority ion ratio 5%, ration of collision frequency to wave frequency $\nu_s = 0.003$. The used antenna parameters is antenna current density $j_{\rm ext} = 1.0\mathrm{A/m}$, wave frequency f_{RF} = 38.5MHz. Also, the temperature and density profile are given $T(r/a) = (T_0 - T_s)(1-(r/a)^2) + T_s$, $n(r/a) = (n_0 - n_s)(1-(r/a)^8) + n_s$ respectively. These parameters is used in an experiment on LHD.

The lower in Fig.4 are results used the same parameters as those of upper except $n_0 = 0.7 \times 10^{20}/\mathrm{m}^3$, f_{RF} = 36.0MHz, the center mode number of the toroidal wave mode number $nph0 = 0$; $n = nph0 + n''N_h$, where n'' = integer (n in Eq.6), is the toroidal mode number of the waves exited by antenna current. The toroidal mode number dependency is showed in 3. It shows that $nph0 = 0$ is the leading mode number. Therefore, the lower in Fig.4 was analyzed with $nph0 = 0$.

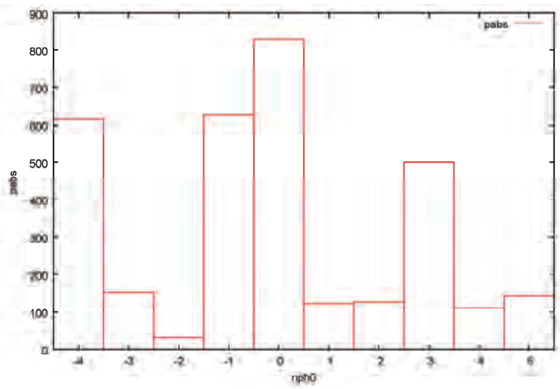

Fig. 3 Toroidal mode dependency

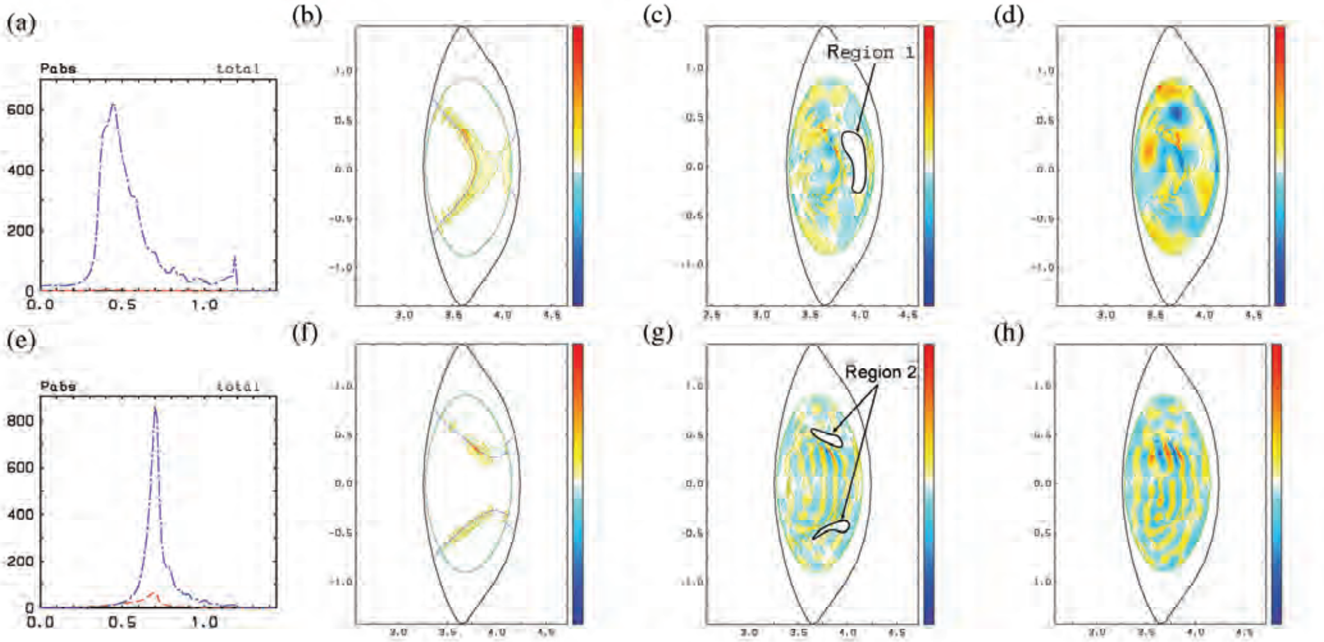

Fig. 4 Radial H absorption distributions (a), (e), contour plots of H absorption (b), (f), E_+ component (c), (g) and E_- component (d), (h) of the electric field on the poloidal cross section; LHD

Three lines drawn in Fig.4 (b), (f) represent ion cyclotron layer (a green line), two-ion-hybrid cut-off (a blue line) and resonance (a red line) layers from the outside. It is observed that the absorption region of minority ion locates near the minority ion cyclotron layer in Fig.4 (b), (f). These are the same tendency as that of tokamak plasma. But, it is not clear whether coherent waves are observed in the contour plots of the electric field on upper Fig.4 (c), (d). While, coherent waves is observed in lower Fig.4 (g), (h). In upper figures, the wave length is comparable to the plasma width. In lower figures,the wave length is shorter than the plasma width, because plasma dencity is higher. This is the reason for coherent waves observed. We observe that E_+ component of electric field is damped at region 1 and 2 in Fig.4 (c), (g) respectively. Region 1 and 2 locates at ion cyclotron layers. Region 1 is larger than ion cyclotron layer, because wave length is conparable to the plasma width.

4 Conclusions

We have studied the ICRF wave propagation and absorption in a 3D magnetic configuration using TASK/WM, in which Maxwell's equation for RF wave electric field is solved as a boundary value problem. The magnetic flux coordinates based on MHD equilibrium by VMEC code is considered. We have solved the wave propagation in the tokamak configuration (JT-60U) and in the helical configuration (LHD) in the minority ion heating regime.

The obtained results shows that ICRF wave is absorbed the region near the ion cyclotron layer and the two-ion-hybrid cut-off and resonance layer.

These analyses were carryed out under assumption of cold plasma. Not only the basic harmonics but also the second and higher harmonics are important. Therefore, we need to analyze including finite larmor effects. Furthermore, we need to analyze time evolution of velocity distribution function using GNET code.

[1] S. Murakami *et al* Nucl. Fusion 46 (2006) S425-S432.
[2] A. Fukuyama *et al Proc. 18th Int. Conf. Fusion Energy 2000* THP2-26.
[3] A. Fukuyama and T. Akutsu *Proc. 19th Int. Conf. on Fusion Energy 2002* THP3-14.

P2-067

Electron Bernstein Waves Simulation in Helical Systems

Sergi FERRANDO-MARGALET[1)], Yasuo YOSHIMURA[1)], Kazunobu NAGASAKI[2)], Chihiro SUZUKI[1)], Shinji KOBAYASHI[2)], Yasuhiro SUZUKI[1)], Kazuo TOI[1)], Shin KUBO[1)], Ryosuke IKEDA[1)] and Hiroe IGAMI[1)]

[1)]*National Institute for Fusion Science, 322-6 Oroshi-cho, Toki 509-5292, Japan*
[2)]*Institute of Advanced Energy, Kyoto University, Gokashou, Uji, Kyoto 611-0011, Japan*

Following experimental results obtained in the CHS and the Heliotron-J devices concerning mode conversion into and heating with Electron Bernstein Waves (EBWs), numerical simulations have been carried out involving the ray-tracing, mode conversion and power deposition of EBWs for models of these experimental scenarios. EBWs-based heating has been confirmed for all the cases studied so far as measured by the experiment. Further investigation is being done to extend the range of the simulations and confirm more detailed issues like the power deposition location.

Keywords: ray tracing, electron Bernstein waves, mode conversion, ECRH, numerical simulations.

1 Introduction

Due to their electrostatic nature, Electron Bernstein Waves (EBWs) do not experience any density limit. This makes them particularly useful to interact with over-dense plasmas. However, the 'over-dense' condition is not only reached due to a very high plasma density. Propagation cutoffs depend also on the frequency of the wave and the local magnetic field, therefore they can occur also in low density-low field conditions. This makes EBWs a popular subject both in the tokamak and helical communities for their ability to overcome the density limits and deposit power in otherwise inaccessible regions of the plasma. The study of EBWs and their applications is a matter of particular interest in Japanese helical devices. Experimental campaigns involving research on EBWs have been carried out in the LHD and CHS experiments in NIFS as well as in the Heliotron-J in Kyoto University. In order to contrast these experimental results with the theory and to devise new experiments, numerical simulations of ray tracing, mode conversion and power deposition of EBWs are carried out with the aid of the ART ray-tracing code [1] and the bundle of codes COBE [2].

2 CHS - OXB

An increase of the plasma stored energy when ECH is switched on is observed in CHS for a comparatively over-dense plasma [3]. The core parameters are: n0 = 9.6 $10^{19} m^{-3}$, T0 = 0.4 keV, f0 = 54.5GHz, B_0 = $1.9T$. The density for this shot would block propagation of the launched O-mode waves: cutoff density (f0 = 54.5GHz) = 3.8 $10^{19} m^{-3}$. The increase of stored energy is thought to be due to the absorption of EBW mode-converted from the launched O-mode wave (OXB) [see Fig. 1].

author's e-mail: ferrando@nifs.ac.jp

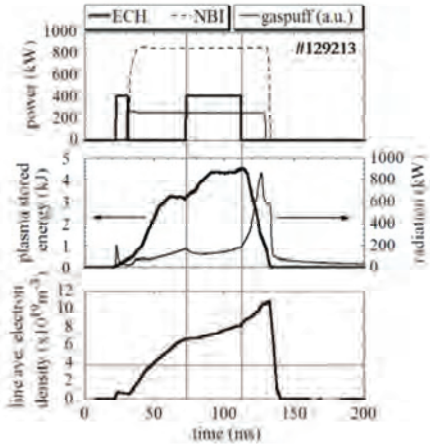

Fig. 1 Experimental data from the shot 129213. It can be seen an increase of the stored energy during the second ECRH injection.

An estimated profile of the neutral beam driven current has been used to calculate the VMEC equilibrium with the total measured current of -2.8kA. The evolution of the O-mode wave was simulated with the ART code. The numerical simulation show a clear OXB conversion in the evolution of the ray path. The power is absorbed between $s = 0.6 - 0.7$ beyond the O-cutoff ($s \sim 0.8$).

The OXB conversion can be identified from the evolution of the perpendicular refractive index and the CMA diagram. The O-mode wave propagates towards the core of the plasma. Near the O-cutoff region, it converts to X-mode ($N_\perp$ goes to 0). The X-mode wave propagates back until it reaches the Upper Hybrid Layer (UHL). In the UHL the X-mode is transformed to EBW (the $N_\perp$ increases drastically in a vertical line). Finally the B-mode wave propagates through the O-cutoff where it is finally fully absorbed (see Fig. 2).

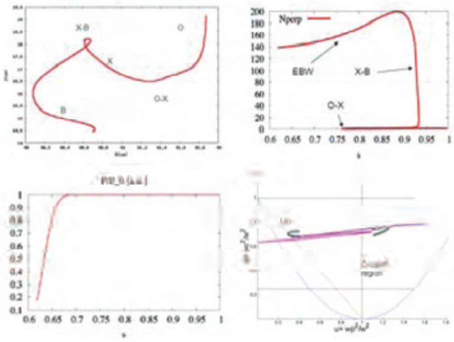

Fig. 2 Numerical results of the OXB simulation for CHS shot 129213. Ray path in R-Z coordinates (top left), $N_\perp$(top right), normalised power deposition profile (bottom left) and CMA diagram of the ray evolution (bottom right). profile

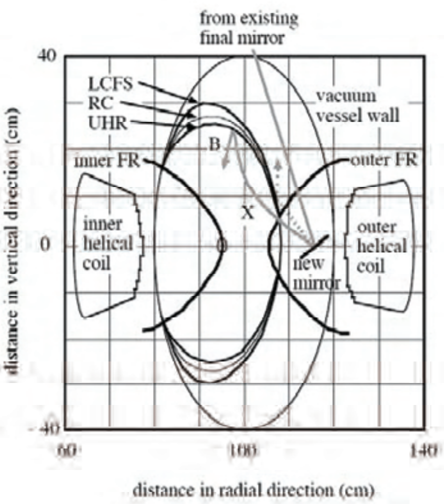

Fig. 3 CHS XB experiment launching scheme. The mirror is aimed at the region where the fundamental harmonic on the last flux surface.

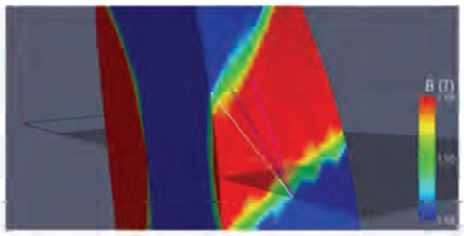

Fig. 4 CHS launching position and angles for the XB heating experiment. The scale of the magnetic field strength has been reduced in order to highlight the fundamental resonance stripe on the las magnetic surface.

3 CHS - XB

An X-mode wave is launched from the top window and directed with a steerable mirror in the outer part of the torus (see Fig.3) [4]. The relevant parameters for the simulation are as follows: ECH power = 275kW, ECH frequency = 54.5GHz, polarisations = X-mode, NBI power = 845kW, Rax = 0.949m, Bax = 1.95T, plasma current = -11kA , β = 0.2. The magnetic geometry of CHS is such that the fundamental resonance reaches the magnetic axis but also appears in the outer region of the torus near the mirror. The rays were launched with a fixed vertical angle aiming at the fundamental resonance stripe (see Fig.4). A horizontal angle scan was carried out detecting an increase of the core electron temperature.

The simulations show that conversion is achieved when the wave is launched at towards the fundamental resonance region. However, the power is mainly absorbed away from the core of the plasma. Nevertheless, deposition nearer to the axis region is obtained for high horizontal and vertical angles. More simulations are on the way to simulate the ray's behaviour at wider horizontal angles > 20 *Deg*. The power deposition regions with respect to horizontal and vertical toroidal angles are displayed in Fig.5.

4 Heliotron J - XB

The plasma conditions in Heliotron-J provide a low single-pass absorption, therefore reflexion in the vacuum vessel is expected. The necessary conditions for an XB conversion are achieved if waves are launched in such a way that the reflexion takes place in the inner part of the torus' corner section [5]. The rays reflected in the vacuum vessel are modelled imposing the launching point in the inner part of the torus and launching towards the outer region. Horizontal and vertical scans have been carried out to investigate the XB conversion and the core deposition of Bernstein waves. Figure 6 shows the ray-path of three sample rays directed respectively to clockwise, counter-clockwise and downwards launching conditions, all with satisfactory XB conversion. In Fig.7, the deposition location of the Bernstein-transformed waves is shown with respect to the horizontal launching angle. It is clear in this case that deposition takes place in the core region of the plasma as expected from the experimental results.

5 Conclusions

Helical devices with their complicated geometry offer a wide range of possibilities for mode conversion and power deposition. Ray tracing simulations for different mode-conversion scenarios leading to Bernstein wave heating in helical systems have been performed by means of the ART code.

OXB and XB simulations in CHS have been shown to be in agreement with experimental results. The OXB ray tracing calculations show a clear OXB conversion that justified the power deposition beyond the O-mode cutoff point. The XB simulations, show successful conversion

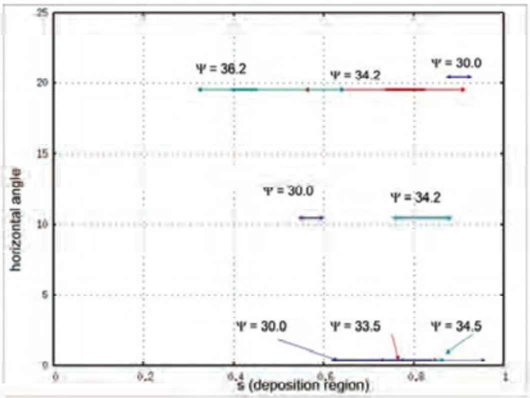

Fig. 5 Table indicating the power deposition region with respect to horizontal launching angle. The vertical angle of each simulation is also indicated. The thin lines represent partial X-mode absorption and the thick lines indicated Bernstein wave absorption.

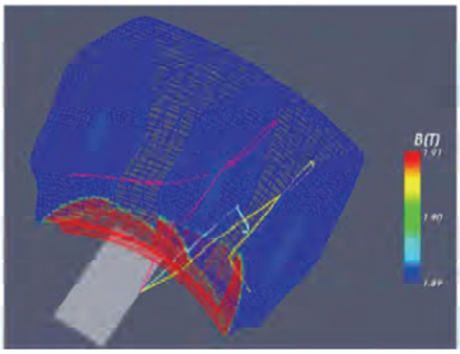

Fig. 6 Sample rays experiencing XB conversion when launched from the inner side of the torus simulating evolution after reflection in the inner wall. They represent reflections towards the clockwise, counter-clockwise and downwards directions. The scale of the magnetic field strength has been chosen to highlight the fundamental resonance region.

when the ray is directed towards the fundamental resonance stripe on the outer boundary and show that the power deposition region tends to towards the core as the horizontal angle is widened. In this last case more calculations are on the way for greater horizontal and vertical angles to better model the experimental results shown in [4].

In the Heliotron-J case, in order to model the trajectory of rays reflected on the vacuum vessel in the inner part of the torus after being injected from the outer region port, the launching point for the simulation has been imposed a few centimetres inwards from the inner boundary of the plasma in the corner region. Vertical and horizontal angular scans have been carried out with the ART code obtaining XB conversion in many cases. The deposition profiles show that the energy absorbed from these rays is deposited mainly in the core region in agreement with experimental measurements.

More simulations of EBW heating in Japanese helical

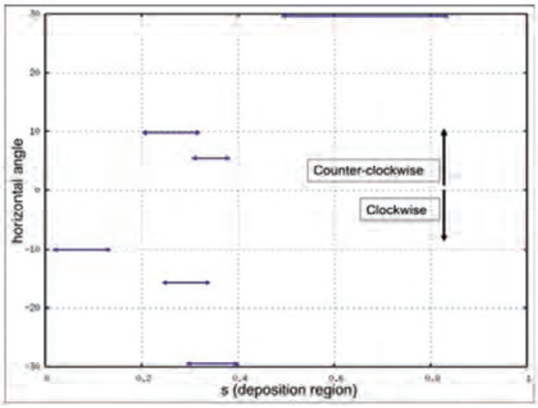

Fig. 7 Table indicating the power deposition region with respect to horizontal launching angle for the Heliotron-J XB conversion experiment.

systems are presently being performed.

[1] F. Volpe, PhD Thesis, Max Planck Institute fuer Plasmaphysik, Greifswald, Germany (2003).

[2] S. Ferrando i Magalet, PhD Thesis, École Polytechnique Fédéral de Lausanne, Lausanne, Switzerland (2006).

[3] Y. Yoshimura *et al*, Fusion Science and Technology **52**, 216 (2007).

[4] Y. Yoshimura *et al* "Experimental conditions for electron Bernstein heating by use of EC waves injected from the high-field side in CHS", in these proceedings.

[5] K. Nagasaki *et al* "Electron Bernstein Wave Heating in Heliotron Systems", Proc. 12th Joint Workshop on ECE & ECH, Aix-en-Provence, France, 2002, p. 317-322.

Proceedings of ITC/ISHW2007

ECCD scenarios for different configurations of the W7-X Stellarator

N.B. MARUSHCHENKO, C.D. BEIDLER, V. ERCKMANN, H. MAASSBERG and Yu. TURKIN

Max-Plank-Institut für Plasmaphysik, IPP-EURATOM-Association, 17491 Greifswald, Germany

October 15, 2007

In order to avoid significant change of the edge value of the rotational transform in the W7-X stellarator, electron cyclotron current drive (ECCD) will be used for compensating the bootstrap current (an ohmic transformer is absent). Since ECCD efficiency is quite sensitive not only to the plasma parameters, but also to the magnetic configuration, it is an important task to estimate properly the range of ECCD values taking into account all features of the magnetic configuration, and to assess its ability to counteract the residual bootstrap current. In this work we analyze the requisite ECCD for scenarios with the different magnetic configurations with help of the ray-tracing code TRAVIS, coupled self-consistently with the 1D transport code. The neoclassical transport modeling is based on the DKES database of mono-energetic transport coefficients.

Keywords: stellarator, bootstrap current, electron cyclotron heating, current drive

1. Introduction

The W7-X stellarator (under construction in Greifswald, Germany) is a large-scale device with average major radius $R_0 \simeq 5.5$ m and plasma radius $a \simeq 0.53$ m, equipped with superconducting coils, with a low-shear configuration of the Helias (Helical Advanced Stellarator) type [1] with five field periods. The toroidal mirror ratio $B_{\max}/B_{\min}$ on axis can be varied significantly, from 1.004 to 1.22 for the "low-mirror" and the "high-mirror" configurations, respectively (for the "standard" configuration $B_{\max}/B_{\min} = 1.09$). The corresponding trapped-particle fractions on axis are varied due to ripples from $f_{\rm tr} \simeq 0.02$ for "low-mirror" up to $f_{\rm tr} \simeq 0.45$ for 'high-mirror", while $f_{\rm tr} \simeq 0.3$ for the "standard" configuration. Through its dependence on the toroidal mirror ratio value, mono-energetic bootstrap current coefficients are largest for the "low-mirror" configuration. In particular, the bootstrap current is minimized for the "high-mirror" configuration, whereas the neoclassical confinement is optimum in the "standard" configuration. The total plasma current affects the edge value of the rotational transform, which may fall outside the required range for proper island divertor operation without external field compensation. Due to the absence of an ohmic transformer, electron cyclotron current drive (ECCD) will be used for compensating the bootstrap current. Since the ECCD efficiency is quite sensitive not only to the plasma parameters, but also to the magnetic configuration, it is an important task to estimate properly the range of ECCD values taking into account all features of the magnetic configuration, and to check its ability to counteract the residual bootstrap current. It is necessary to take special care for high densities where the ECCD efficiency is reduced. Additionally, the effects of finite plasma pressure ($\beta > 0$) may play a significant role, especially in the high-density scenarios, changing the deposition and current drive profiles. Since the task of self-consistent simulation of this case is still too complex, the effects of finite β will be only briefly discussed (when it is possible), just to indicate the tendency.

2. W7-X ECRH system and ECCD scenarios

The ECRH system in W7-X is designed for continuous operation with a total injected power up to 10 MW at 140 GHz [2] (the resonance magnetic field is $B_0 = 2.5$ T). The ports for launching the RF power are situated symmetrically around two "bean-shaped" planes, i.e. near the maximums of B (the ports E10 and A51 near the cross-sections $\phi = 0$ and $\phi = 72°$, respectively). In order to prevent an overheating of the chamber by the shine-through power and to control its reflection, mirrors are installed at the inner wall and all beams planned for O2 operation must be directed to these mirrors. Because of symmetrical location of the mirrors about the launch ports, only five beams out of ten can be launched in the same direction, and operation with maximal counter-ECCD is possible with a total power up to only 5 MW. While the X2 (extra-ordinary mode at the 2nd harmonic) scenario is applicable in the density range $n_e < 1.2 \times 10^{20}$ m^{-3}, for higher densities, up to 2.2×10^{20} m^{-3}, the O2 (ordinary mode at the 2nd harmonic) scenario will be applied. Note, that for densities near the O2 cut-off, $n_e \simeq 2.4 \times 10^{20}$ m^{-3}, single-pass absorption of the O2-mode is strongly reduced together with increasing refraction effects, the upper density limit for operation is about $n_e \simeq 2.2 \times 10^{20}$ m^{-3} (or even less, depending on the specific case). Due to the high optical thickness of the plasma for the X2-mode, there are no strict launch conditions for this scenario, and this freedom can be used for tailoring a desired deposition and current drive profile

author's e-mail: nikolai.marushchenko@ipp.mpg.de

[3]. For the O2-mode, the plasma is optically "gray", and this scenario is more limited for the expected range of parameters. Since the optical depth for the O2-mode scales as $\tau_{O2} \propto T_e^2$, the most attractive path to the O2 scenario is to preheat the plasma by the X2-mode, then change the polarization from X- to O-mode by means of rotation of the corrugated mirrors, and finally to increase the density to the requested value [4, 5].

Below we consider in detail both ECCD scenarios, with the X2-mode for the moderate density range, $n_e < 10^{20}$ m^{-3}, and with the O2-mode for the higher densities. To simplify comparison of the X2 and O2 scenarios, the launch conditions for the X2-mode are taken identical to those required for the O2-mode.

3. Numerical tools

The numerical models for calculating the ECCD efficiency developed to date (both the Fokker-Planck [6] calculations and the adjoint approach [7] in ray-tracing calculations) do not cover completely the range of collisional regimes for the electrons involved in the current drive, especially in stellarators. Only two opposite limits are in use, with and without taking into account the trapped particles. The first one, called the collisional limit, is formulated under the condition $\nu_e \gg \tau_b^{-1}$, where ν_e and τ_b are the electron collision frequency and the bounce-time, respectively. This limit, being, in fact, the straight magnetic field line approach, overestimates the ECCD efficiency. The second limit, called the collisionless one, is based on the opposite assumption, $\nu_e \ll \tau_b^{-1}$, i.e. takes into account the trapped particles. This limit may lead to underestimating of the ECCD efficiency. Nevertheless, the collisionless limit is more reasonable for the W7-X conditions, especially for the regimes with moderate densities and high temperatures. In this work we analyze the requisite ECCD scenarios for operating with the different magnetic configurations with help of the ray-tracing code TRAVIS [8, 9]. The (adjoint) Green's function applied for the ECCD calculations is formulated with momentum conservation taken into account [4]; this is especially important and even critical for those scenarios, where the number of trapped particles is quite small, $f_{\rm tr} \ll 1$, and/or mainly bulk electrons are responsible for absorption of the RF power (e.g. when the obliqueness of launch is not high and $N_\| \ll 1$).

The plasma profiles and bootstrap current were calculated by the 1D transport code [5] (for details, see also [10]) coupled self-consistently with the ray-tracing code TRAVIS [8, 9]. The transport modeling is based on the DKES database of mono-energetic transport coefficients, and thermal transport coefficients are obtained by energy convolution with a local Maxwellian. The DKES code [11] uses as collision operator the Lorentz pitch-angle scattering term without momentum conservation, leading to an overestimate of the bootstrap current depending on $Z_{\rm eff}$ (in present the calculations, $Z_{\rm eff} = 1.5$ is assumed).

4. Simulation results

The calculations were done for five different beams launched from the ports E10 and A51 with 1 MW power for each beam. Both X2 and O2 scenarios are modeled for the same fixed launch conditions for three different magnetic configurations. While the RF-beams in O2 scenarios must be directed onto the corresponding mirrors at the inner wall, the chosen direction is not optimal for ECCD efficiency in X2-mode. Since the single-pass absorption of the O2-mode is less than 100%, four passes are taken into account in the calculations. If after two passes through the plasma less than 90% of the power was absorbed, this scenario was excluded from consideration.

Keeping in mind the general scenario which requires switching from the X2 to the O2 scenario, let us consider first the moderate density range, $n_e \lesssim 10^{20}$ m^{-3}, where both scenarios can work. For the present conditions, the choice $B = 2.562$ T seems as optimum for both X2 and O2 scenarios. For the X2 scenario, an off-axis absorption does not lead to the "electron-root" feature and collisional decoupling of electrons and ions. For the O2 scenario, due to the shift of the resonance in the low-field-side direction, absorption appears in the region of increasing (along the ray) T_e, prolonging the area of effective cyclotron interaction and, consequently, increasing the single-pass absorption.

In Fig.1 (top), the X2 ECCD profiles, $j_{cd}(\rho)$, which summarize the contributions from all beams, are shown (the corresponding deposition profiles have a very similar shape). Negative ECCD is chosen since the bootstrap current is positive for these simulations. Due to very high optical thickness, the location of the deposition profile (ECCD as well) for the X2-mode is almost completely defined by the resonance location, and the Doppler broadening is mainly responsible for the width of $j_{cd}(\rho)$ profile. For each configuration, the temperature dependence during the density scan is not strongly pronounced due to an absence of its strong variation: for the "standard" configuration with n_e increased from 0.4×10^{20} m^{-3} to 1.1×10^{20} m^{-3}, T_e is varied from 5.7 keV to 4.4 keV, respectively. Since the "standard" configuration is optimized for neoclassical confinement, the steady-state temperature obtained by transport simulation is highest in comparison with the "low-" and "high-mirror" configurations. On the other hand, due to the reduced trapped particle fraction, the longitudinal conductivity is higher in the "low-mirror" configuration, which leads to an increase of ECCD. Nevertheless, due to the reduced confinement the temperature in the "low-mirror" configuration is for the same heating conditions also lower, and the decrease of $f_{\rm tr}$ is masked by a decrease of T_e. In the case of the "high-mirror" configuration, an increase of $f_{\rm tr}$ and a decrease of T_e have the same effect, and the ECCD efficiency is significantly reduced. For comparison, the case of the "standard" configuration with $\langle\beta\rangle = 0.02$ is shown (see Fig.1, dashed red). One can see, that the finite pressure effects may lead to a very strong effect. Due to the

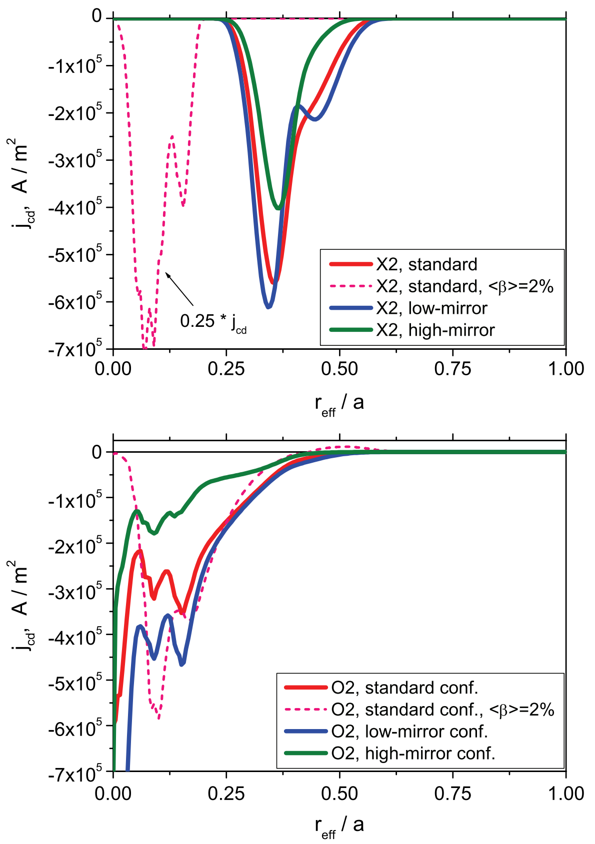

Fig. 1 Summarized ECCD profiles (5 beams 1 MW each) for the different configurations: "standard" (red), "low-mirrors" (blue), and "high-mirrors" (green). Additionally, the case of $\langle\beta\rangle = 0.02$ for the "standard" configuration is shown (pink dashed). Top - X2 scenario, bottom - O2 scenario. For all cases, the density is the same, $n_e = 0.8 \times 10^{20}$ m^{-3}.

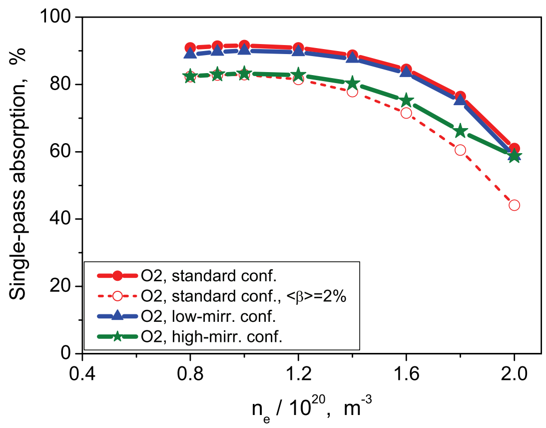

Fig. 2 Single-pass absorption of the O2-mode summarized for all beams: the same as in Fig.1.

Shafranov shift combined with the diamagnetic effect, the deposition profile (ECCD as well) moves into the axial region, making an appearance of the "electron-root" almost unavoidable.

The O2 scenario is more sophisticated. First of all, the plasma is optically "gray" and a significant part (up to 20% or even more) of the power is absorbed during the second pass (third and fourth passes are of minor importance). Direct consequence of it is involving in cyclotron interaction the electrons with $k_\| v_\| < 0$ ("anomalous" Doppler effect), which create the current contribution of opposite sign, reducing $j_{cd}(\rho)$ in this point [7]. Interesting, that for the "standard" configuration with $\langle\beta\rangle = 0.02$ this effect is most pronounced, and even negative values of $j_{cd}(\rho)$ appear (see Fig.1, bottom, red dashed). Important to mention also, that despite of launching the RF beams near the maximum of B ("bean-shaped" plane) the trapped particles are quite well involved in the cyclotron interaction, absorbing up to 10% of the power and significantly reducing the ECCD. The absorption of the O2-mode, being proportional to T_e^2, is very sensitive to the shape of T_e profile (n_e profile is almost flat in the present simulations). On the other hand, the T_e profile is defined mainly by the deposition profile. Due to this feedback, the resulting deposition profiles (as well as ECCD) for the scenarios with the resonance shifted to the low-field-side are rather independent of density, and its shape is quite similar to those shown in Fig.1 (bottom) for quite broad range of densities (with only change of $j_{cd}(\rho)$ magnitude, which scales roughly as $1/n_e$).

In the Fig.2, the single-pass absorption for the O2 scenario as a function of density is shown. The values obtained (summation over five beams) are quite high for all tested magnetic configurations, i.e. are about 80 - 90% for $n_e < 1.8 \times 10^{20}$ m^{-3}. Important to mention here, that the single-pass absorption in the "standard" magnetic configuration with $\langle\beta\rangle = 0.02$ is significantly reduced in comparison with the vacuum configuration (compare the red solid and pink dashed lines). As was mentioned above, this effect is due to a combination of the Shafranov shift and of the diamagnetic effect, which leads, in fact, to shifting of the deposition profile into the high-field-side direction, reducing the optical depth.

In Fig.3, the results of the density scan for the three magnetic configurations are shown. Following the standard theoretical predictions, the current drive for both X2- and O2-mode scales roughly as $1/n_e$. As expected, the current driven by X2-mode is larger than that of the O2-mode for all tested configurations. There are three main factors which lead to this jump of ECCD efficiency (from red circles to red triangles). First, the single-pass absorption of the O2-mode is less than 90%, and the rest of the power is absorbed in the plasma periphery, where the temperature is low. Second, since the deposition profile is quite broad, both the "anomalous" Doppler effect and the participation of the trapped particles in the cyclotron interaction reduce the ECCD efficiency.

The bootstrap current can be compensated by X2-ECCD for the "high-mirror" and "low-mirror" configurations (in the last case, the uncompensated residual current appears acceptable). For the "standard" configuration (apart from the lower densities), this compensation can be

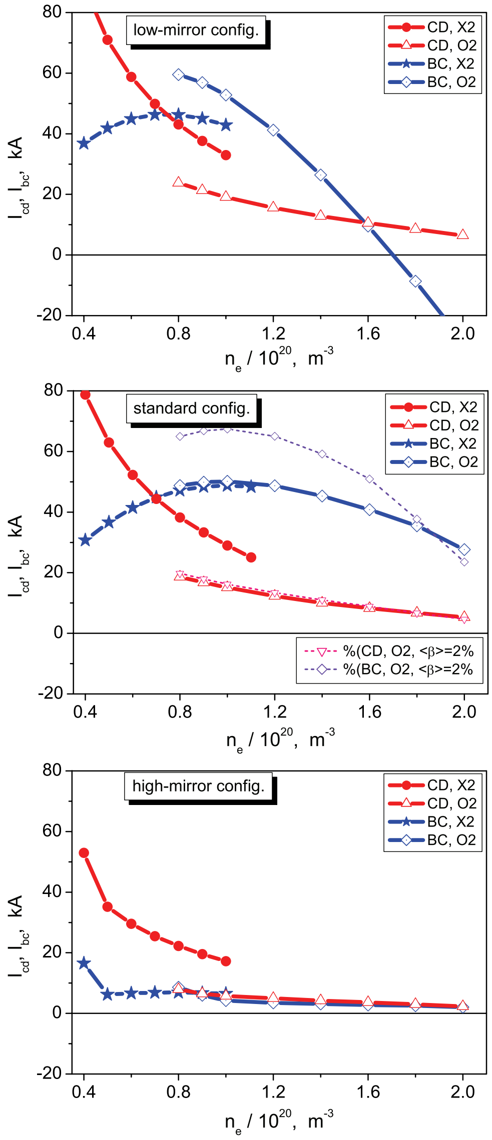

Fig. 3 Density scan for different magnetic configurations. Both I_{cd} (red color, circles for X2 and triangles for O2 scenarios) and I_{bc} (blue color, stars for X2 and rectangles for O2 scenarios, respectively) are shown.

done by further optimization of the launch conditions (in the present study, all beams are directed onto the mirrors, although this is not necessary). Full current control at high density (in operation with O2-mode) is only obtained for the "high-mirror" configuration. Note, that for the "standard" configuration with $\langle\beta\rangle = 0.02$, the bootstrap current is significantly increased, while the ECCD is almost unchanged. This problem requires additional study.

5. Discussion

In the present paper, the results of numerical simulations of different ECCD scenarios for W7-X are presented, the X2 scenario, which is applicable for the low and moderate density range, $n_e < 1.2 \times 10^{20}$ m^{-3}, and the O2 scenario for higher densities up to $n_e < 2.2 \times 10^{20}$ m^{-3}. Three different magnetic configurations have been tested, with the trapped particle fraction varied from 1.004 to 1.22. The aim of this study was to estimate the ability of the ECRH system of W7-X for compensating the residual bootstrap current and to control the edge value of the rotational transform.

In high-density operation at low ECRH power, the bootstrap current might exceed the maximum ECCD both for the X2- and the O2-scenarios. Only the "high-mirror" configuration was shown to have rather small bootstrap currents thus confirming the corresponding W7-X optimization criterion. For the "standard" configuration with improved neoclassical confinement, however, ECCD control of the bootstrap current is only possible in X2-mode at lower density. With full current control by ECCD, only a few skin-times (i.e. less than 10 sec) are necessary to obtain stationary conditions for optimum divertor operation.

High density scenarios are also important for the W7-X island divertor operation since fairly high separatrix densities (about 0.4×10^{20} m^{-3}) are required. Consequently, the O2-scenarios are expected to be very important for longer discharges. For these conditions, however, only the "high mirror" configuration allows for bootstrap current control by ECCD. In particular for the "standard" configuration, another discharge scenario must be chosen to obtain stationary conditions. Here, the edge value of the rotational transform in the vacuum configuration must be reduced by the amount which is generated by the bootstrap current in the final steady state. The discharge is operated at low density and rather low heating power with strong co-ECCD (in X2-mode) up to roughly stationary plasma current, i.e. the desired island divertor configuration is reached. In this scenario, however, the evolution of the plasma current scales on the L/R-time (i.e. several 10 sec). Then, the density as well as the heating power can be ramped up and the co-ECCD is reduced with the increasing bootstrap current, i.e. the total current is controlled. The internal current densities and the ι-profile become stationary again on the skin time. Such a discharge scenario, however, is much more complex compared to the case of full ECCD control of the bootstrap current.

[1] J. Nührenberg and R. Zille, Phys. Letters **114A** (1986) 129
[2] V. Erckmann *et al.*, Fusion Sci. and Technol. **52** (2007)
[3] H. Maassberg *et al.*, Plasma Phys. Control. Fusion **47** (2005) 1137
[4] M. Romé *et al.*, Plasma Phys. Control. Fusion **40** (1998) 511
[5] Yu. Turkin *et al.*, Fusion Sci. and Technol. **50** (2007) 387
[6] C.F.F. Karney, Comp. Phys. Reports **4** (1986) 183
[7] M. Taguchi, Plasma Phys. Control. Fusion **31** (1989) 241
[8] N.B. Marushchenko *et al*, 2006 Proc. of 14th Joint Workshop Electron Cyclotron Emission and Electron Cyclotron Heating, Santorini, Greece, May 9-12, 2006, http://www.hellasfusion.gr/ec14/papers/26.pdf
[9] N.B. Marushchenko *et al* 2006 Proc. of 16th Toki Conference, Toki, Japan, December 5-8, 2006, http://itc.nifs.ac.jp/index.html
[10] Yu. Turkin *et al.*, this conference, P2-064
[11] W.I. van Rij and S.P. Hirshman, Phys. Fluids B1 (1989) 563

Proceedings of ITC/ISHW2007

Experimental conditions for electron Bernstein wave heating by use of EC waves injected from high-field side in CHS

Y. Yoshimura, K. Nagasaki[a], S. Ferrando-Margalet, T. Akiyama, M. Isobe, A. Shimizu, C. Suzuki, C. Takahashi, K. Nagaoka, S. Nishimura, T. Minami, K. Matsuoka, S. Okamura, CHS group, S. Kubo, T. Shimozuma, H. Igami, H. Takahashi, and T. Mutoh

National Institute for Fusion Science,322-6 Oroshi-cho, Toki 509-5292, Japan

[a] Institute of Advanced Energy, Kyoto University, Uji 611-0011, Japan

In the Compact Helical System (CHS), electron heating by electron Bernstein waves was experimentally investigated to study a technique for the high-density plasma heating over cutoff. The EBWs are excited through mode conversion process from X-mode waves injected to plasmas from the high-field side. In the experiment, within a range of oblique EC wave beam injection angle, evident heating effect was observed. Dependences of the heating effect on the wave's polarization and the toroidal injection angle show that the absorption of the mode-converted EBWs should be the cause of the plasma heating effect.

Keywords: electron Bernstein wave, EBW, slow X-B, high-density plasma heating, high-field side injection, ECH, CHS

1. Inroduction

Electromagnetic (EM) plasma waves such as ordinary (O) or extraordinary (X) mode waves suffer cutoff in high-density plasmas, and the EM plasma waves cannot contribute to electron heating over the cutoff density. Electron Bernstein (B) waves, on the other hand, have the advantages of an absence of density limit and a strong absorption even in low-temperature plasmas. Since the B-waves are a kind of electrostatic wave in plasmas, they have to be excited by means of mode conversion processes from injected EM-waves. Three types of mode conversion process are considered: the so-called fast X-B, slow X-B, and O-X-B. Among them, the O-X-B mode conversion technique [1] has been considered the most promising way to heat overdense plasmas because ECH systems including steerable beam injection antennas from the low-field side are technically available on existing tokamaks and helical systems [2-6].

Compared to the O-X-B process, the slow X-B process can more simply and easily realize mode conversion to B-waves, since the difficulty of achieving high O-X mode conversion efficiency does not exist. When injected through a fundamental resonance layer from the high-field side (so called the X-B access window), the X-mode EC-waves propagate into the plasmas and are mode converted into the B-waves at the upper hybrid resonance (UHR) layer. The B-waves are absorbed at the Doppler-shifted electron cyclotron resonance, resulting in plasma heating. When injected away from the X-B access window, the X-mode EC-waves suffer right-hand cutoff and cannot heat the plasmas effectively.

So far in the WT-3 tokamak, using an O-X polarization twister installed at the high-field side, B-wave heating was performed by injecting O-mode EC-waves to avoid the right-hand cutoff of X-mode waves [7]. Also in the COMPASS-D tokamak, electron heating and current drive by the high-field side X-mode injection were demonstrated [8]. However, generally speaking, EC wave injection from the high-field side (that is, from the inner side of the torus) is accompanied with difficulties due to insufficient available space for installing an EC-wave injection antenna system or a reflection mirror.

The Compact Helical System [9] provides a good opportunity to investigate the slow X-B heating scenario experimentally, since due to its two helical coils generating plasma confining magnetic field, it has two X-B access windows in the poloidal cross section. In the vertically elongated poloidal cross section, one window is at the inner side of the torus in a position similar to tokamaks, while the other is at the outer side where a wider space is available for installing an elaborate structure such as the movable mirror for beam direction scan, as seen in Fig. 1. Installing a mirror inside the CHS vacuum vessel, the slow X-B experiments were performed [10]. In this paper, the dependences of the slow X-B heating effect on the wave's polarization and the beam direction are presented as follows. The experimental setup such as CHS and the EC wave injection system are described in Sec. 2. The slow X-B experimental results are presented in Sec. 3. Then Sec. 4

author's e-mail: yoshimura.yasuo@LHD.nifs.ac.jp

summarizes the contents of this paper.

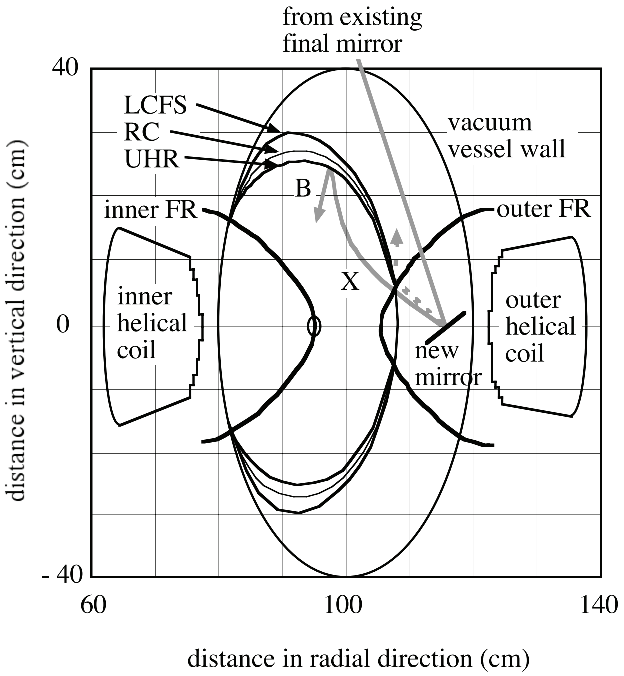

Fig. 1 Experimental configuration for slow X-B experiment.

2. Experimental Setup

The CHS is a helical device with the toroidal period number m = 8 and the polarity l = 2. The magnetic field structure with the rotational transform for plasma confinement is generated totally by the external coils such as a couple of helical coils and three pairs of poloidal coils. The major radius of CHS plasma is about 1.0 m and the averaged minor radius is 0.2 m, so that the aspect ratio is 5. The magnetic field at the plasma axis can be set up to about 2.0 T.

The ECH system on CHS furnishes two gyrotrons. The operating frequency of one of them is 54.5 GHz and that of another one is 106.4 GHz. The slow X-B experiments described in this paper were performed with the 54.5 GHz one. The transmission line for the 54.5 GHz waves was constructed as a quasi-optical Gaussian beam transmission system using 12 mirrors, three of them inside the CHS vacuum vessel and two of them l/4 and l/8 grating polarizers. The three inner-vessel mirrors are installed on the top port and the final plane mirror can be tilted 2-dimensionally so that the injected EC-wave beam direction can be scanned in both the poloidal and toroidal directions. The beam injections from the top port result in the injections from the low-field side. The injected EC-wave beams are circularly focused having the beam size (1/e radius of the electric field amplitude) of 22 mm at the equatorial plane. Using the two polarizers, the polarization of EC-wave beams can be varied arbitrarily. The total length between the gyrotron output window and the CHS plasma center is about 17 m. The maximum injection power and pulse length of the 54.5 GHz waves to the CHS vacuum vessel are 415 kW and 100 ms, respectively.

In addition to the existing EC-wave power injection system described above, a new plane mirror was installed inside the vacuum vessel between plasma and an outer helical coil. By directing the EC-wave beam from the existing antenna system at the top port to the new mirror, an injection of 54.5 GHz EC-wave from the high-field side becomes possible. The beam is reflected 39 degrees upward and can be steered in the toroidal direction by tilting this new mirror toroidally. The experimental configuration is schematically drawn in Fig. 1.

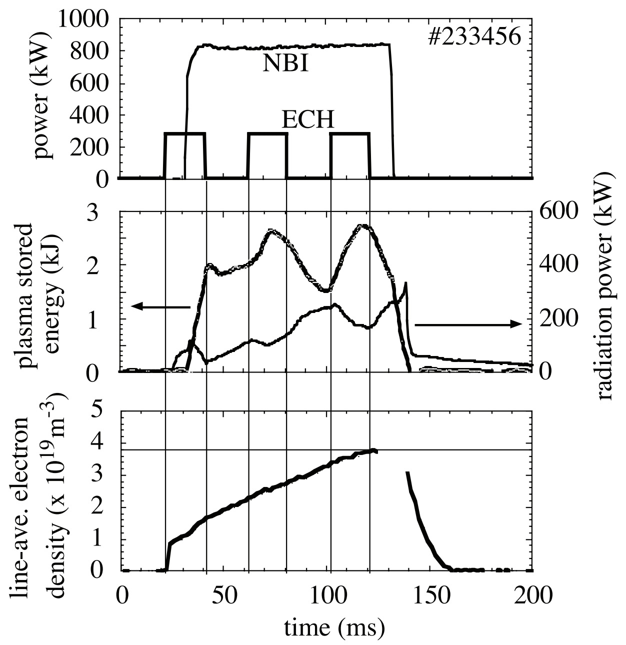

Fig. 2 Waveforms in the slow X-B discharge.

3. Dependences of heating effect on the EC-wave beam direction and the polarization

Figure 2 shows a typical time evolution of a discharge of the slow X-B heating. An EC-wave power of 275 kW was obliquely injected in three pulses during the discharge at incidence angles of 20 degrees counterclockwise in the toroidal direction and 39 degrees upward. The wave polarization was set at nearly the X-mode. The first pulse was for plasma generation, and the second and the third ones were applied to the plasmas sustained with 845 kW neutral beam injection (NBI). The plasma stored energy significantly increased with the second and the third injections of ECH power. The central electron temperature increased from about 1.0 to 1.5 keV by the second injection and from about 0.6 to 1.2 keV by the third injection, while the line-average electron density linearly increased during the plasma duration. The increases in the plasma stored energy were then caused by increases in the electron temperature. The electron temperature profiles measured using Thomson scattering measurement during and just before the third ECH power injection are plotted in Fig. 3. It can be clearly seen that the electron heating occurred at the plasma core region, not at the peripheral region where the outer fundamental resonance layer exists. The heating effect is considered to be a result of the B-wave heating, and the resultant improvement in NBI heating efficiency and reduction in radiation power from the plasma.

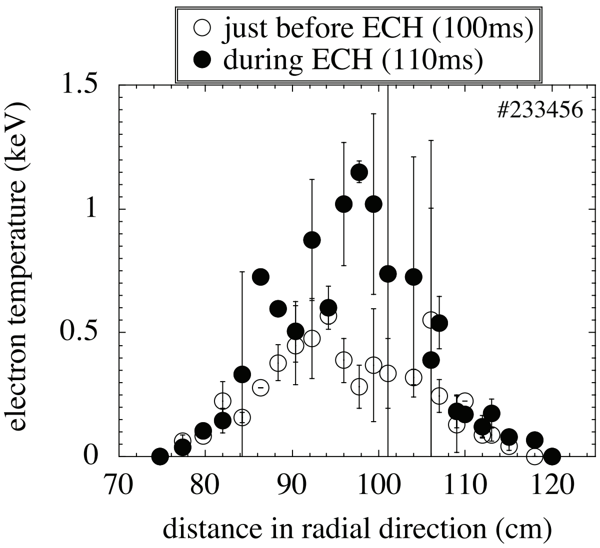

Fig. 3 Electron temperature profiles just before EC-wave injection and during injection measured using Thomson scattering measurement.

At the third injection timing of this discharge, the line-average electron density reached close to the O-mode cutoff density of 3.8×10^{19} m^{-3} for the 54.5 GHz EC-waves. In other discharges, the heating effect was also observed for plasmas even with the density over the O-mode cutoff. The magnetic field on the plasma axis was set at 1.95 T, that is, the fundamental resonance magnetic field of the 54.5 GHz EC-waves. Here, an essential point regarding the magnetic field setting is not the on-axis resonance condition but the presence of another fundamental resonance layer in the plasmas (X-B access window) in front of the new mirror as seen in Fig. 1.

In the toroidal scan of the EC-wave beam direction, effective plasma generation and significant plasma heating occurred only at the counterclockwise injection. Otherwise, the plasmas could not overcome the radiation barrier. This dependence can be understood as follows. Due to the rather upward (39 deg) beam reflection from the new mirror, the beam path is beyond the range of the X-B access window when the beams are injected with a toroidal incidence angle of around 0 degrees or clockwise. However, because the helical coil winding of the CHS is left-handed, that is, the vertically elongated poloidal cross section rotates counterclockwise around the magnetic axis with the toroidal angle, the X-B access window moves upward and “opens” for beams injected counterclockwise.

In the polarization scan of the injected EC-waves, it was confirmed that the heating effect degraded when the polarization was set at nearly O-mode. Figure 4 shows the variation of the direction of the magnetic field along an EC-wave beam path which aims at the magnetic axis and is injected perpendicularly to the flux surfaces. The beam path is on the equatorial plane. The definition of the angle is as follows. Looking from outside of the torus, the toroidal direction in the right side is 0 deg, and the angle increases counterclockwise. At the LCFS, the direction is -13 deg. In the perpendicular injection case, the O-mode injection is realized by setting the linear polarization with the electric field oscillation in the direction of -13 deg, and the X-mode in the 77 deg.

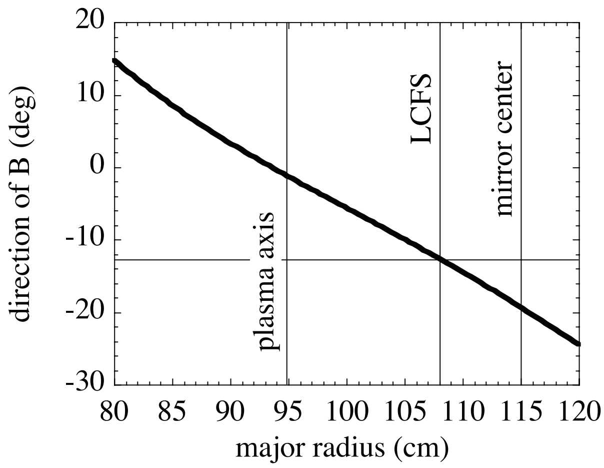

Fig. 4 Variation of the magnetic field direction along a beam path perpendicular to the flux surfaces.

The dependence of the heating effect on the linear polarization direction is plotted in Fig. 5. The heating effect is evaluated with the value of the plasma stored energy during EC-wave injection divided by that just before injection. Only at the polarization direction of -10 deg, the heating effect vanished. In the slow X-B experiment the EC-waves were injected obliquely, then the linear polarization with the direction of -13 deg does not mean the pure O-mode but the O-mode purity is considered high. This plot shows that the X-mode component is important for the heating, and that the mode conversion to the B-wave would be the key for the plasma heating. Setting pure O- and X-mode polarization by the elliptical polarization would make the dependence clearer.

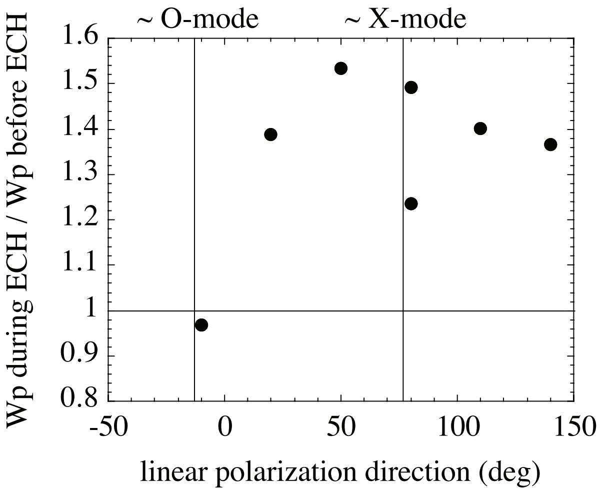

Fig. 5 Dependence of the heating effect on the polarization of the EC-waves.

The numerical calculations to confirm the realization of slow X-B heating in the experimental configuration are under investigation. Some of the results can be seen in this conference [11].

4. Conclusions

In CHS, the slow X-B heating technique was investigated by using an inner-vessel mirror which enables the EC-wave beam injection to plasmas from the high-field side through the fundamental resonance layer. As a result of the beam direction scanning, the increases of the plasma stored energy and the electron temperature were performed only when the EC-wave beams were injected through the X-B access window. The polarization scanning experiment showed that nearly O-mode polarization had no heating effect. Those results and dependences show that the slow X-B heating was realized in CHS.

Acknowledgements

The authors would like to express their thanks to the CHS staff for performing the CHS experiments. This work was carried out under the framework of bidirectional collaborative research program between Kyoto University (Heliotron-J group) and NIFS (Code number: NIFS04KUHL005).

References

[1] J. Preinhaelter and V. Kopecky, J. Plasma Phys. **10**, 1 (1973).
[2] H. P. Laqua *et al.*, Phys. Rev. Lett. **78**, 3467 (1997).
[3] H. P. Laqua *et al.*, Nucl. Fusion **43**, 1324 (2003).
[4] A. Mueck *et al.*, proc. 32th EPS conf. ECA**29C**, P-4.110 (2005).
[5] Y. Yoshimura *et al.*, Plasma Fusion Res. **1**, 029 (2006).
[6] H. Igami *et al.*, to be published in Rev. Sci. Inst.
[7] T. Maekawa *et al.*, Phys. Rev. Lett. **86**, 3783 (2001).
[8] V. Shevchenko *et al.*, Phys. Rev. Lett. **89**, 265005 (2002).
[9] K. Matsuoka *et al.*, Plasma Phys. Control. Fusion **42**, 1145 (2000).
[10] Y. Yoshimura *et al.*, Plasma Fusion Res., **1**, 053 (2006).
[11] S. Ferrando-Margalet *et al.*, in this conference, P2-067

Proceedings of ITC/ISHW2007

Observation of Ion Tail in ECH/ECCD Plasmas in Helical Devices

Shinji KOBAYASHI, Mitsutaka ISOBE[a], Masaki OSAKABE[a], Hiroyuki MATSUSHITA[a], Masashi KANEKO[a], Tetsuo OZAKI[a], Pavel GONCHAROV[a], Kazunobu NAGASAKI, Yasuo YOSHIMURA[a], Hiroe IGAMI[a], Shin KUBO[a], Takashi SHIMOZUMA[a], Satoshi YAMAMOTO[b], Kazuo TOI[a], Yoshihiko NAGASHIMA[c], Kenji SAITO[a], Hiroshi KASAHARA[a], Katsumi IDA[a], Mikiro YOSHINUMA[a], Sadatsugu MUTO[a], Tohru MIZUUCHI, Hiroyuki OKADA, Katsumi KONDO[d], Kiyoshi HANATANI, Fumimichi SANO and Shoichi OKAMURA[a]

Institute of Advanced Energy, Kyoto University, Gokasho, Uji, 611-0011, Japan
[a]National Institute for Fusion Science, Oroshi-cho, Toki-shi 509-5292, Japan
[b]Kyoto University Pioneering Research Unit for Next Generation, Kyoto University, Gokasho Uji 611-0011, Japan
[c]RIAM, Kyushu University, Kasuga 816-8580, Japan
[d]Graduate School of Energy Science, Kyoto University, Gokasho, Uji, 611-0011, Japan

The high energy ion tail, having the energy more than five times higher than the bulk temperature, has been observed in the electron cyclotron heating (ECH) and electron cyclotron current drive (ECCD) plasmas of Heliotron J and CHS. The tail temperature of ion increases with decreasing the density and increasing the ECH power. The ion tails appear under the condition of high tail temperature of electrons measured by the soft X-ray charge-coupled-device system. The comparison of the fraction of the ion tail density between CHS and Heliotron J shows that the tail ions are accelerated selectively in the parallel direction to the magnetic field. The high energy electron is a key factor of the formation of the ion tail.

Keywords: Electron cyclotron heating, ion tail, electron tail, anomalous heating, neutral particle analysis

1. Introduction

The formation of the ion tail has been observed in the electron heated plasmas, i.e. electron cyclotron heating (ECH) or electron cyclotron current drive (ECCD) plasmas, in several torus devices [1-4]. The rise and decay times of the ion tail have been much shorter than the collisional energy relaxation time between electrons and ions. This phenomenon has been considered to be due to (1) the acceleration by the strong Landau damping of lower-hybrid (LH) waves excited by the parametric three-wave decay process [1] or (2) the anomalous electron-ion coupling because of the slide-away regime of the electron energy distribution [5]. The high energy charge exchange flux was observed experimentally in the X-mode launch from high magnetic field side in the W7-A stellarator [1]. The low-frequency decay wave corresponding to the LH range of frequency was measured with probe, which might be the cause of the ion acceleration. In the TCV tokamak, it was found that the high energy CX flux increased with the current drive efficiency by ECCD [4]. The numerical calculation shows the TCV experiments were in the slide-away regime. An excitation of waves satisfying the dispersion relation of $\boldsymbol{k}\cdot\boldsymbol{v}_i = \omega = k_{\parallel}v_e$ has been expected due to the slide-away of the electron energy distribution function in Ref. [5].

author's e-mail:kobayashi@iae.kyoto-u.ac.jp

In a low magnetic shear helical device, Heliotron J [6], high energy CX flux has been measured in the 70 GHz 2nd harmonic ECH plasmas [7], even the reflection of the launched EC waves has not been controlled. In this paper, we describe the result on the ion tail measurements in the ECH/ECCD plasmas in Heliotron J and Compact Helical System (CHS) [8]. The rise time of the ion tail formation is examined in Heliotron J. The dependence of the tail temperature on the electron density is studied in Heliotron J and CHS. The density of ion tail is investigated from the viewpoint of the normalized ECH power. The mechanism of the formation of the ion tail is discussed by the experimental results obtained in Heliotron J and CHS.

2. Experimental results

2.1 Heliotron J

The 70 GHz ECH system has been installed in Heliotron J, medium sized (R_0/a = 1.2m/0.17m) helical-axis heliotron device with L/M =1/4 helical coil, where L and M are the pole number of the helical coil and helical pitch respectively [6]. The 2nd harmonic ECH experiments have been carried out using two injection methods; corner section and straight section launch [9]. In the case of the corner section launch, the focused EC

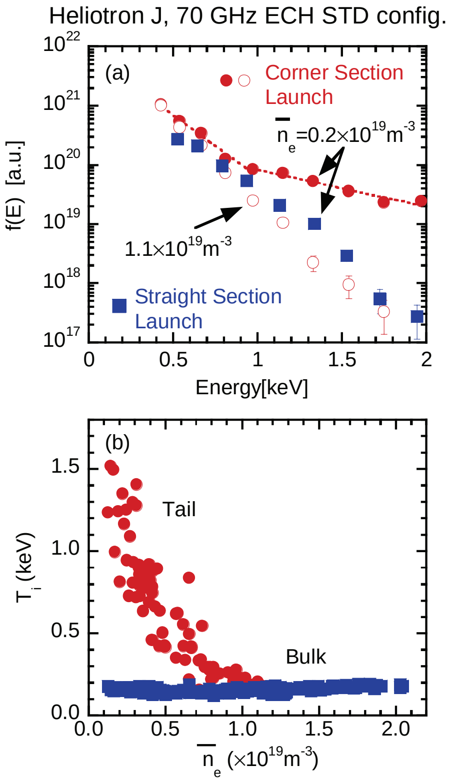

Fig.1 (a) Energy spectra of charge exchange flux obtained in 70 GHz ECH plasmas of Heliotron J and (b) tail and bulk temperature of ion as a function of line-averaged electron density.

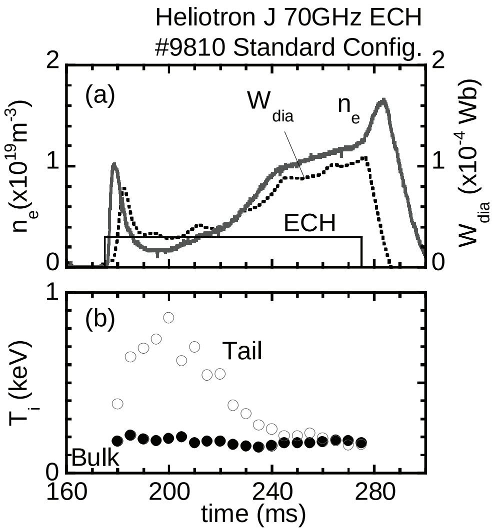

Fig.2 Time evolution of plasma parameters in ECH plasmas of Heliotron J, (a) line-averaged density and stored energy and (b) tail and bulk temperature of ion.

waves using mirror system were launched from the outer torus side of the corner section, where the tokamak-like magnetic field was formed. The non-focused EC waves were launched at the straight section. The gradient of the magnetic field strength at the straight section is small owing to the formation of the quasi-omnigenous magnetic field.

Figure 1(a) shows the CX energy spectrum measured by the CX neutral particle analyzer (CX-NPA) [10] obtained in the standard configuration of Heliotron J. The CX-NPA is E//B type one, whose energy range is from 0.4 to 80 keV for hydrogen and from 0.2 to 40 keV for deuterium, respectively. CX-NPA detected the ions with the pitch angle of 110 degree to the magnetic field in the standard configuration of Heliotron J. In the experiments of the corner section launch under the low density condition at the line-averaged electron density n_e of 0.2×10^{19} m^{-3}, the high energy ion flux was found in the energy range more than five times higher than the bulk ion temperature. The bulk temperature estimated to be 210 eV from the slope of the CX spectrum in the energy range from 0 to 1 keV. A folded spectrum more than 1 keV shows the tail temperature is 710 eV. In the higher density at $n_e = 1.1 \times 10^{19}$ m^{-3}, no clear tail was observed, which shows the tail formation depends on the electron density. The ray tracing calculation of the EC waves shows the absorption profile in the corner section launch is localized at the resonance layer [11]. In the straight section launch, on the contrary, ion tail has not been measured clearly even in the low density condition at $n_e = 0.2 \times 10^{19}$ m^{-3}. A relatively long-path absorption profile was expected by the ray tracing calculation in the straight section launch [9]. It was also found that the tail temperature depended on the injection power of ECH (P_{ECH}) in the case of the corner section launch, that is, the tail temperature was 840 eV at the electron density of 0.4×10^{19} m^{-3} with P_{ECH} of 310 kW, while that at P_{ECH} = 240 kW was 250 eV. These results indicate the focused strong EC waves are favorable to the formation of the ion tail.

Figure 1(b) shows the dependence of the bulk and tail temperatures on the line-averaged electron density. These data were obtained in the ECH injection power of 310 kW in the corner section launch. The tail component was observed in the case that the density was lower than 1.0×10^{19} m^{-3}. The tail temperature increased up to 1.5 keV with decreasing the density. The bulk ion temperature, on the other hand, was not so sensitive to the density in the density range below than 2×10^{19}m^{-3}.

Figure 2 (a) and (b) show the time evolution of the line-averaged density, stored energy and tail and bulk ion temperatures measured by the CX-NPA system. The tail temperature increased up to 640 eV by 10 ms at the beginning of the discharge. The decay of the tail temperature was very quick according to the change in the electron density. The electron temperature measured by the SX absorber foil method was about 1 keV. The energy exchange time from electron to ion was about 0.3 sec

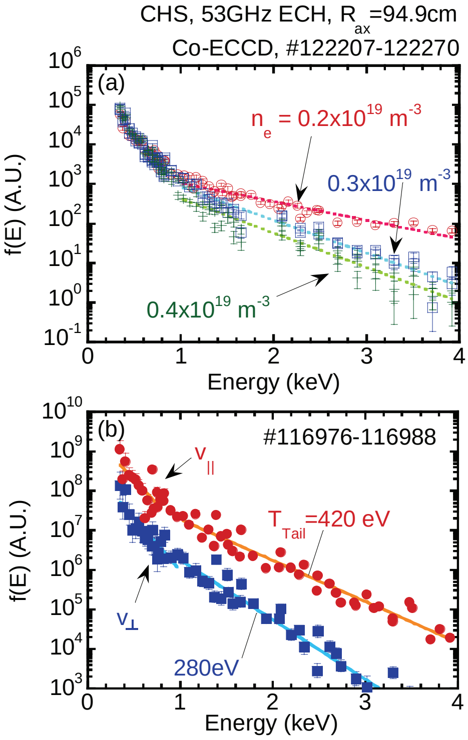

Fig.3 (a) CX energy spectra in 54 GHz ECH plasmas of CHS in n_e = 0.2, 0.3 and 0.4 × 10^{19} m^{-3} and (b) comparison of CX energy spectra between parallel and perpendicular velocity .

under the condition, which shows that the formation of ion tail cannot be explained by the classical collision process.

2.2. Compact Helical System

CHS is a planner axis helical device (R_0/a = 1.0m/0.2m) with L/N=2/10 helical coil, where N is the toroidal period number [8]. The 53 GHz ECH system in CHS has three steerable mirrors and polarizer to control the injection angle of the EC waves in both toroidal and poloidal directions and the polarity [12]. In CHS, the effect of the X-mode launch from high field side is negligible. The ECCD experiment using the 53 GHz ECH system in CHS is described in Ref. [13].

The CX energy spectrum measured with fast neutral analysis diagnostics (FNA) [14] is shown in Fig. 3 (a) obtained in the ECH plasmas at the line-averaged electron density of 0.2, 0.3 and 0.4 × 10^{19} m^{-3}, respectively. The ECH injection angle was oblique one and the toroidal current due mainly to ECCD was about 3 kA in the Co-direction under the experimental conditions, which increased the rotational transform. The folded spectra were observed in the energy range more than 0.8 keV. The tail temperature increased with decreasing the density. The density dependence will be discussed later by comparing with the results obtained in Heliotron J.

To examine the velocity distribution of tail ions, the parallel and perpendicular velocity components of CX flux to the magnetic field were measured by changing the toroidal angle of FNA. Figure 3 (b) shows the comparison of the CX energy spectra between the parallel and perpendicular directions. These data were obtained in the Co-ECCD plasmas at the electron density of 0.2 × 10^{19} m^{-3}. The CX flux in the parallel velocity direction was higher than that of the perpendicular one. The bulk and tail temperatures in the parallel direction were 170 and 420 eV, respectively, while those for the perpendicular direction are 160 and 290 eV, respectively. The fraction of ion tail density is defined by the following formula,

$$\int_{Ec}^{5\times Ec} f_{Tail}(E)\,dE \Big/ \left(\int_{0}^{Ec} f_{Bulk}(E)\,dE + \int_{Ec}^{5\times Ec} f_{Tail}(E)\,dE \right) \quad (1)$$

where $f_{Bulk}(E)$, $f_{Tail}(E)$ and E_c are the energy spectra of the bulk and tail ions and the critical tail energy, respectively. When E_c is given by 1 keV, the tail density fraction is 1.3 % for the parallel direction, while that in the perpendicular case is 0.7 %. These results suggest the tail ions are accelerated selectively to the parallel direction. When the injection angle of ECH was varied from Co- to counter direction in CHS, no clear difference was seen in the ion tail flux on the ECH injection angle.

Figure 4 shows the electron energy distribution measured using the pulse height analysis technique with the soft X-ray charge-coupled device (SX-CCD) system in CHS. [15]. An existence of the high energy electron more than 2 keV was confirmed in the low density ECH plasmas. The slope of the electron tail becomes flat when the ion tails are formed, that is, the ion tails appear under the condition that the tail temperature of electron is higher than 4 keV. Thus the high energy electron has a key factor for the formation of the ion tail.

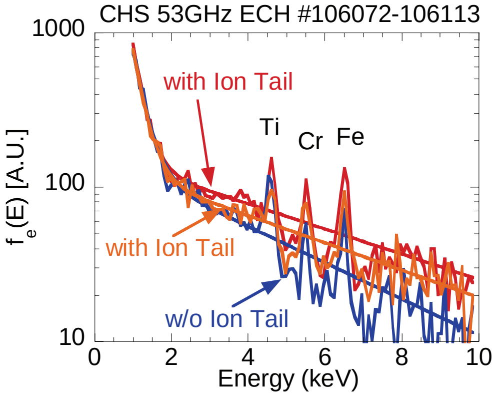

Fig.4 Energy spectrum of electron measured by the SX-CCD system obtained in ECH plasmas of CHS.

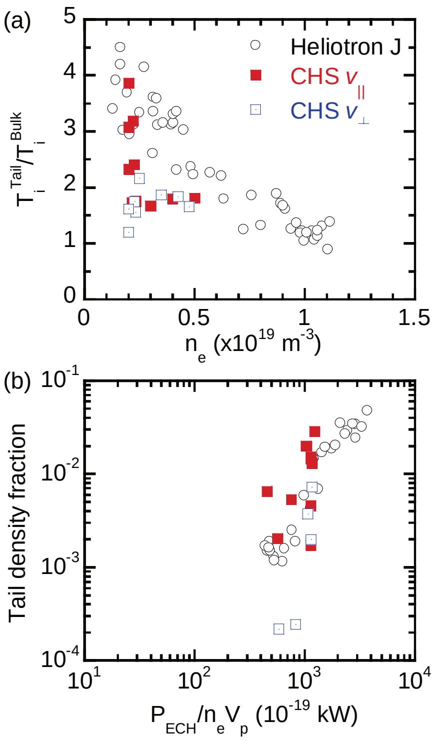

Fig.5 (a) Temperature ratio of tail and bulk ions as a function of electron density and (b) dependence of fraction of ion tail density on the normalized ECH power obtained in Heliotron J and CHS.

3. Discussions

In this section, we compare the measurement results of ion tail in Heliotron J and CHS. Figure 5 (a) shows the temperature ratio of tail to bulk ions in Heliotron J and CHS as a function of the electron density. The closed and open squares show the temperature ratios determined by the CX spectra with parallel and perpendicular velocity components in CHS, respectively. In Heliotron J, the CX-NPA has set almost perpendicularly. The temperature ratios in Heliotron J and in the parallel component in CHS increase with decreasing the density. The temperature ratio in the case of the perpendicular component of CHS is lower than the Heliotron J results. This is attributed to the difference in the injection power of ECH between CHS and Heliotron J.

Figure 5 (b) shows the fraction of ion tail density as a function of the ECH injection power normalized by the total electron numbers (electron density times plasma volume V_p). The tail density fraction in CHS and Heliotron J increases with the normalized power. A slightly higher fraction of the tail density is obtained at the parallel component in CHS than the others. The perpendicular component in CHS, on the other hand, is in the same order of Heliotron J results.

In order to clarify the effects of the LH-decay wave heating on the ion tail formation, we are planning a X-mode launch from high field side using the ECH system of Large Helical Device [16].

4. Summary

We confirmed the formation of the ion tail under the low electron density conditions in ECH plasmas of Heliotron J and CHS. The ion tail formed under the condition that the high energy electron was produced by the focused EC wave. The LH decay wave heating is not considered as the main source of the ion acceleration in Heliotron J and CHS because the effect of the X-mode launch from high field side can be neglected. Although the physical mechanism of the selective acceleration of ions to the parallel direction is still unknown, the high energy electron produced by the focused strong ECH is key factor for the ion tail formation.

Acknowledgement

One of the authors (S.K.) wishes to thank the experimental members of Heliotron J, CHS and LHD groups. This work is partly supported by the NIFS Collaborative Research Program. (NIFS04KUHL003, NIFS05KUHL007 and NIFS05KLBB003)

References

[1] V. Erckmann and U. Gasparino, Plasma Phys. Control. Fusion **36**, 1869 (2001).
[2] P. G. Bulyginsky et al, *Control. Fusion Plasma Phys (Proc XI Europ. Conf., Aachen)* **part I** 457, (1983).
[3] Z. A. Pietrzyk et al, Nucl. Fusion **33** 197 (1993)
[4] A.N.Karpushov et al., (*Proc. 30th EPS Conf. Contr. Fusion Plasma.Phys., St. Petersburg 2003*), **27A** p3-123. (2003).
[5] B.Coppi et al., Nucl. Fusion **16** 309 (1976)
[6] F. Sano, et al., Nucl. Fusion **45**, 1557 (2005)
[7] M. Kaneko, et al., *(Proc. 30th EPS Conf Contr. Fusion Plasma Phys., St. Petersburg, 2003)* **27A**, P-3.28 (2003)
[8] S. Okamura et al., Nucl. Fusion **45** 863 (2006)
[9] K. Nagasaki, et al., Nucl. Fusion **45** 13 (2005)
[10] S. Kobayashi et al., (*Proc. 20th IAEA Fusion Energy Conf. Vilamoura, Portugal 2004*) EX/P4-41.
[11] H. Shidara, et al., Fusion Science and Technology, **45** 41 (2004)
[12] Y. Yoshimura et al., Fusion Sci. Tech. **52**, 216 (2007)
[13] K. Nagasaki et al., in this conference
[14] K. Ida, et al., Nucl. Fusion **39** 1649 (1999)
M. Isobe, et al., Nucl. Fusion **41** 1273 (2001)
[15] Y. Liang, et al., Rev. Sci. Instru **71** 3711 (2000)
Y. Liang, et al, Rev. Sci. Instru. **72**, 717 (2001)
[16] Y. Shimozuma et al., Plasma Phys. Control. Fusion **45** 1183 (2003)

Proceedings of ITC/ISHW2007

Demonstration of Plasma Current Control by Using High Power Millimeter-Waves

Takashi NOTAKE[1)], Takashi SHIMOZUMA[2)], Shin KUBO[2)], Hiroshi IDEI[3)], Katsumi IDA[2)], Mikirou YOSHINUMA[2)], Takashi KOBUCHI[4)], Kiyomasa WATANABE[2)], Shigeru INAGAKI[3)], Tokihiko TOKUZAWA[2)], Yasuo YOSHIMURA[2)], Hiroe IGAMI[2)], Tetsuo SEKI[2)], Kazunobu NAGASAKI[5)], Hitoshi TANAKA[5)], Teruo SAITO[1)] and Yoshinori TATEMATSU[1)]

[1)] Research Center for Development of Far-Infrared Region, University of Fukui, Fukui 910-8507, Japan

[2)] National Institute for Fusion Science, Toki, 509-5292, Japan

[3)] Research Institute for Applied Mechanics, Kyushu University, Fukuoka, 816-8580, Japan

[4)] Faculty of engineering, Tohoku University, Sendai, 980-8579, Japan

[5)] Graduate school of Energy Science, Kyoto University, Kyoto, 606-8501, Japan

Active current drive is one of promising tools to improve plasma quality even in the helical devices through the control of the rotational transform or magnetic shear profiles and suppression of some magnetohydrodynamics activities. The current drive by electron cyclotron waves is the most suitable actuator for these purposes in terms of controllability of driven current with high density. Optimum conditions for efficient electron cyclotron current drive (ECCD) in large helical device (LHD) are explored using 3-dimensional ray-tracing code which can treat electron cyclotron waves with large parallel refractive index. In the experiment, inversion of plasma currents corresponding to injected ECCD modes is first demonstrated and the result can be elucidated by the Fisch-Boozer theory. Displacements of rotational transform are also verified by use of the motional stark effect polarimetry.

Keywords: electron cyclotron resonance heating, electron cyclotron current drive, plasma current control, magnetic shear control, rotational transform control, gyrotron.

1. Introduction

The current drive to form the poloidal magnetic field is vital in the Tokamak devices. There is no necessity to drive plasma current externally in the helical devices because the magnetic fields to confine plasmas can be yielded by only external coils. However, the plasma currents driven by plasma pressure gradients or powerful neutral beam injection change the magnetic field structure such as rotational transform and magnetic shear. Plasma performances will degrade according to these changes. Therefore, the study of controlling the plasma current is significant even in the helical devices.

Electron cyclotron current drive (ECCD) is the most prospective tool to control plasma current profile because the power transitions from electron cyclotron waves to resonant electrons are take placed very locally which lead to locality of plasma current with high density [1-2]. Besides, we can select the location of driven plasma current almost arbitrarily by adjusting some parameters such as magnetic field strength, wave-frequency, parallel refractive index and so on.

This paper consists of following sections. The section 2 describes inspection for effective ECCD in LHD configurations. The section 3 is devoted to explanation of experimental results. The plasma current control by ECCD is firstly demonstrated and shift of rotational transformation is observed. Finally, our research is summarized in the section 4.

2. Scrutiny for ECCD in LHD

In an inward shifted configuration of large helical device (LHD), improvements of not only neoclassical transport but also anomalous one are observed experimentally. According to a linear MHD theory, on the one hand, it is predicted that some MHD instabilities affect plasma confinement in such inward shifted configurations due to the magnetic-hill structure. As one of the reasons for present fine confinement capability in the configuration, some non-linear effects are pointed out. They may prevent MHD activities from growing further. However in order to extend an operation parameter range of LHD, MHD activities should be suppressed by some kind of ways because they must cause severe degradation to plasma confinement in high β plasmas. ECCD has possibility that it can improve MHD properties only by local current control without degradations both of

author's e-mail: notake@fir.fukui-u.ac.jp

neoclassical and anomalous transports even in the inward shifted configurations.

To improve plasma confinement capability by ECCD in LHD, two schemes can be conceivable. One of them is ECCD to co-direction (Co-ECCD) which raises rotational transform and result in exclusion of low-order rational surfaces at plasma core region where magnetic shear is very weak. The other is ECCD to counter-direction (Ctr-ECCD) which can enhance negative magnetic shear locally. Therefore, driving plasma current to arbitrary directions is desirable as current drive actuator.

The mechanism of ECCD is based on asymmetric modification of electron resistivity in the momentum space formed by selective electron cyclotron resonance. Electron cyclotron waves are absorbed by electrons that have velocity component satisfying the following condition taking Doppler up-shift and relativistic down-shift into consideration [3-5].

$$\frac{\omega^2N_\parallel^2+l^2\Omega^2}{\omega^2N_\parallel^2+l^2\Omega^2-\omega^2}\left(\frac{v_\perp}{c}\right)^2+\frac{\omega^4N_\parallel^4+2\omega^2N_\parallel^2l^2\Omega^2+l^4\Omega^4}{\omega^2N_\parallel^2l^2\Omega^2+l^4\Omega^4-\omega^2l^2\Omega^2}\left(\frac{v_\parallel}{c}-\frac{\omega^2N_\parallel}{\omega^2N_\parallel^2+l^2\Omega^2}\right)^2=1$$

Where $N_\parallel$, l, Ω, ω, $v_\perp$, $v_\parallel$ and c mean parallel refractive index, harmonic number of cyclotron resonance, electron cyclotron frequency, wave frequency, perpendicular thermal velocity, parallel thermal velocity and light velocity, respectively. For $N_\parallel$<1, this equation describes an ellipse, and resonant interaction is only possible for

$$l\Omega/\omega > (1-N_\parallel^2)^{0.5}$$

which excludes anomalous cyclotron resonance. On the other hands, for $N_\parallel$>1, it represents a hyperbolic curve in the velocity space. As for an example, the calculated resonant curves in the momentum space under the certain parameters are shown in Fig.1. In the case of large $N_\parallel$ injection, the resonant curves move toward high parallel velocity regions in velocity space due to strong up-shift of cyclotron resonance frequency. And the resonance begins to arise even in the lower magnetic field side than 3 Tesla corresponding to fundamental resonance condition of usual ECRH for 84GHz-waves. These findings indicate that electron cyclotron waves with large $N_\parallel$ tend to interact with electrons having higher parallel velocity component. Therefore, injecting electron cyclotron waves with large $N_\parallel$ must be effective in terms of collisionality to achieve high ECCD efficiency

The effect of electron trapping is another critical issue. Trapped electrons reduce the ECCD efficiency or may reverse the direction of the driven current since the diffusions in velocity space involved with electron cyclotron damping is mainly to perpendicular directions [6]. Especially, LHD has not only toroidicity but also helicity and the fraction of them strongly depends on magnetic configurations. In order to avoid such trouble, depositing the wave power at magnetic ripple top region is ideal. Fig.2 shows contour plots of magnetic ripples for the two magnetic configurations of LHD. Upper column corresponds to the case of magnetic axis is set at 3.5m which is one of the inward shifted configurations. This configuration has fine confinement performance and suitable for effective ECRH. On the other hand, lower column shows magnetic ripples when the magnetic axis set at 3.75m which is standard magnetic configuration of LHD. This configuration may be more suitable from the viewpoint of the ECCD efficiency because it hardly has magnetic ripple near the magnetic axis. So, the improvement of the efficiency degradation due to trapped electrons can be expected. However, only 84GHz gyrotoron is available in this configuration by the limit of achievable magnetic field strength. As shown in the Fig.2, magnetic ripples are more enhanced in the peripheral regions. Unfortunately, it is not compatible that to inject electron cyclotron waves with large $N_\parallel$ component and to deposit it near the magnetic axis where magnetic ripples are weak since strong Doppler up-shift is induced. To inspect more rigorously, we have to solve the Fokker-Planck equation under the 3-dimensional LHD configuration.

To try higher power ECCD experiments, the survey of optimum condition under the inward shifted configuration is considered in this paper.

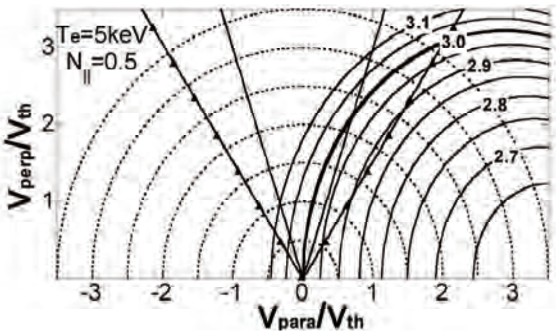

Fig.1. Resonance curves in the velocity space. Here, electron temperature, parallel refractive index, harmonic number and wave frequency are set to 5keV, 0.5, 1 and 84GHz respectively. Numerics on the lines indicate magnetic field strength.

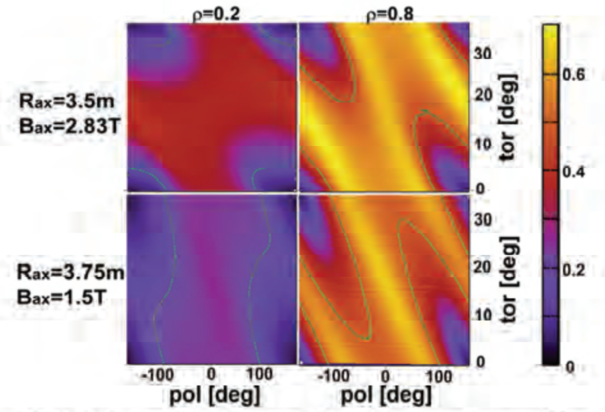

Fig.2. The profiles of magnetic field strength normalized by the maximum value on the each flux surfaces. Zero of toroidal and poloidal angles correspond to vertically elongated cross section and inside of equatorial plane respectively.

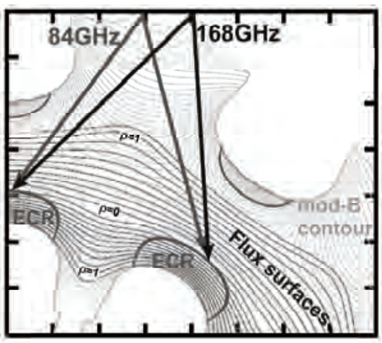

Fig.3. The ECCD configuration by using 2O-port antenna. Two gyrotrons whose frequencies are 84 and 168GHz are connected to the port.

To investigate optimum incident angle for ECCD, a ray-tracing calculation is carried out. Ray-tracing is a sophisticated technique, providing quite a little insights on wave-propagation and absorption in dispersant fusion plasmas. Its condition of validity called WKB approximation is the following.

jrkj ü k²

Electron cyclotron waves in the wavelength range of millimeters are sufficiently adequate for existing fusion research machines. Ray-tracing code had developed for ECRH in the 3-dimensional magnetic field structure of LHD, but by that code quasi-perpendicularly propagating waves with respect to magnetic field lines in weakly relativistic thermal plasma can only be treated [7]. Therefore existing ray-tracing code is extended in order to deal with obliquely propagating waves. Under the propagation angles satisfying following condition,

Njcosòj > j1 à lÒ=!j; vₜ=c;

the relativistic down shift of the cyclotron frequency can be neglected because Doppler effect become dominant. Where θ and v_t mean propagation angle with respect to magnetic field lines and electron thermal velocity, respectively. So, we can use absorption coefficients obtained from the non-relativistic dielectric tensor for a hot Maxwellian plasma [8]. In this frame, power absorption line is decided using the conventional Fried-Conte function described by

Z(ð) = i P 2 exp(à ð²) K ⌈ 2ið à1 exp(à t²=2)dt

which can be calculated numerically. Here, an argument ð is defined as follows.

ð ñ c(! à !c)=(⌈ 2 vₜ!Ncosò)

The 2O-port antenna installed the horizontally elongated cross section of LHD is suitable for ECCD because it can swing the beam to toroidal directions widely. From this port, we aim a beam at magnetic axis of neighbor vertically elongated cross sections as shown in Fig.3. According to the Fisch-Boozer theory, plasma currents by ECCD are supposed to be driven to clockwise/counterclockwise directions corresponding to the beam injection to counterclockwise/clockwise directions respectively.

Fig.4 shows parameter changes along the central ray obtained from multi ray-tracing calculation applied to 84GHz beam from 2O-port antenna [9]. Here, the magnetic axis of 3.5m and average magnetic field strength of 2.829T is employed and beam is aimed at magnetic axis of vertically elongated cross section. In this configuration, on-axis ECCD will be possible because the power of electron cyclotron waves almost absorbed within the ρ=0.2.

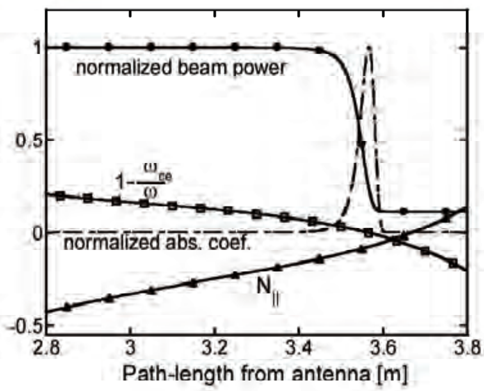

Fig.4. Ray-tracing result for the fundamental O–mode ECCD obliquely injected from 2O-port antenna.

3. Experimental results and discussion

In LHD, ECCD is tried using 2O port antenna at the magnetic configuration of Rax=3.5m. Magnetic field strength, injection angle and wave polarization [7-8] are optimized based on oblique ray-tracing code as mentioned above. Target plasma is sustained by only ECRH to omit NBCD effects and ECCD is superposed to the target plasma from 0.25s to 0.75s. Fig. 5 shows comparison of temporal evolutions of total plasma currents measured with Rogowski coil. Bootstrap current is contained in the total plasma currents, but that contribution is weak judging by balanced ECCD discharge. For Co- and Ctr-ECCD discharges, directions of driven plasma current are consistent with linear theory. Therefore authentic plasma current control by ECCD is demonstrated successfully. However, absolute values of plasma currents are still very low because of high electron temperature which leads to huge L/R time compared with ECCD duration. So some extent of the driven current may be cancelled by the induced back electromotive force. However, certain shifts of polarization angle which reflect changes of rotational transform are observed by the motional Stark effect polarimetry [10] as shown in the Fig.6. This result very encourages us to control magnetic field structure and then improve confinement capability of LHD plasma. However, further experiments are needed with higher power and longer pulse duration time to impact drastically the plasma performance through the modification of plasma current profile and magnetic field structures.

4. Summary

With a view to control of plasma current and magnetic field structure in LHD, the application of ECCD is considered in detail and actually tested. The inversion of directions of plasma currents is clearly observed. So plasma current control by ECCD is successfully demonstrated for the first time in LHD because this inversion is consistent with conceptual prospect. ECCD will be expected as an indispensable tool in order to improve plasma performance.

Acknowledgment

I would like to express my gratitude to the many colleagues, especially, Dr. Takahiro Suzuki of JAEA and Prof. Testuo Watari of NIFS who gave me valuable comments. This work was supported by the NIFS under the grant code numbers NIFS06ULRR501,502 and 503.

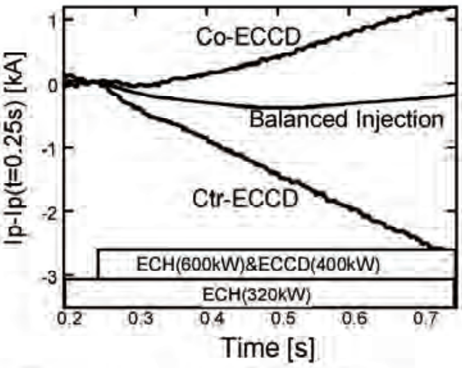

Fig.5. Temporal evolution of the total plasma currents. Plasma currents are normalized by the values at the ECCD is injected (t=0.25s.)

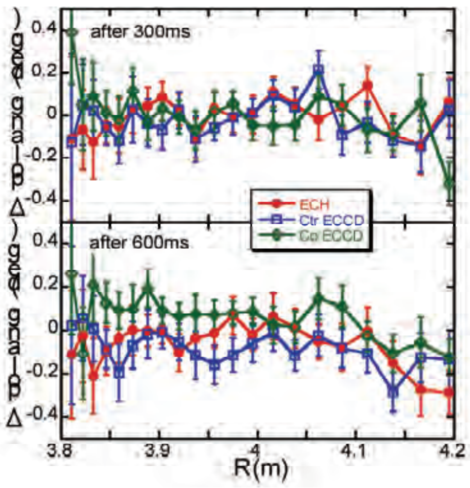

Fig.6. Change of polarization angle during ECCD diagnosed by MSE polarimetry measurement.

References

1) R.Prater, Physics of Plasmas, vol.**11** (2004) p.2349
2) V.erckmann and U.Gasparino, vol.**36**, PPCF (1994)
3) P.U.Lamalle, et.al., Fusion Science and technology, vol.**45** (2004) p.153
4) E.Westerhof, Fusion science and Technology, vol.**99** (1996) p.99
5) NJ.Fisch and A.H.Boozer Physical Review Letters, vol.45, (1980)
6) T.Ohkawa, G.A.Report GA-A13847 (1976)
7) S.Kubo, T.Shimozuma, H.Idei et. al., Journal of Fusion Research Series, vol.5 (2002)
8) M.Bornatciti, Nuclear Fusion, vol.**23** (1983)
9) T.Notake, S.Ito, S.Kubo, et. al., Transaction of Fusion Science and Technology, vol.**51**, (2007)
10) K.Ida, et.al., Rev. of Sci. Instrum. **76**, 053505 (2005)

Proceedings of ITC/ISHW2007

ECE and Reflectometry on the Helically Symmetric Experiment

Konstantin M. LIKIN[1)], Carsten LECHTE[2)], Huijuan LU[1)], F. Simon B. ANDERSON[1)]

[1)]*The HSX Plasma Laboratory, University of Wisconsin, Madison, WI 53706, USA*

[2)]*University of Stuttgart, Stuttgart, Germany*

For plasma heating in the Helically Symmetric Experiment (HSX) with on-axis magnetic field of 0.5 Tesla, the extraordinary wave at the second harmonic is used, while the ordinary wave at the fundamental resonance is efficient in operation at 1 Tesla. A non-Maxwellian distribution function is detected in HSX plasmas by various diagnostics. The electron cyclotron emission (ECE) spectra are measured with an eight channel radiometer. By switching the narrow band filters, measurements have been made across the plasma column within +/- 0.6 of its effective radius. To model the ECE spectra we use (1) a Bi-Maxwellian distribution function and (2) results from the CQL3D Fokker-Planck code. Results of measurements and modeling are reported in this paper. Plasma fluctuations can be responsible for enhanced heat transport from the plasma. Fourier spectra of ECE signals, as well those from the nine-chord interferometer, Langmuir probes, and magnetic coils show the presence of a coherent mode in the plasma core. To study the density fluctuations, a new reflectometer has been installed and tested on HSX. We present ECE data and the first reflectometer results on density fluctuations in 0.5 Tesla HSX plasmas. As do the other diagnostics, the reflectometer detects the coherent mode in the 50 – 250 kHz frequency range of plasma fluctuations. A wavelet technique is applied to get the time evolution and the radial localization of this mode.

Keywords: Stellarator, plasma heating, electron distribution function, electron cyclotron emission, plasma density fluctuations, reflectometer, wavelet analysis.

1. Inroduction

In plasma heating experiments on fusion machines the particles may have a non-thermal distribution function in momentum space, i.e. there are more particles with high energy as compared to the thermal equilibrium state. Even a small number of high energy particles leads to enhanced emission at the cyclotron harmonics and makes a comparison between experiment and theory, which deals with Maxwellian plasmas, more difficult. Moreover the presence of a non-thermal component obscures a bulk plasma response on small perturbations, such as cold gas injection and/or heating pulse modulation, and as a result in such cases the perturbation method is impractical for measuring the electron thermal conductivity of bulk plasma from ECE signals. Also an excessive number of runaway particles may absorb a significant part of the heating power resulting in uncertainty in determining the power absorbed by the thermal particles based on ECE and/or the diamagnetic loop data.

On the HSX stellarator we use the extraordinary wave at the second harmonic to make plasmas at 0.5 T. HSX also operates at the full designed magnetic field of 1 Tesla, in this case the wave polarization corresponds to the ordinary wave. Available launched power is up to 100 kW and is focused on the plasma axis into a beam spot of 4 cm in diameter. Based on ray tracing calculations [1] the absorbed power density in the HSX plasma is high enough (up to 5 W/cm^3) to produce a tail of high energy electrons, in particularly, in 0.5 T operation when the plasma density is low. For instance, an electron can get up to 10 keV in one pass through the beam at such power density. To make a correct interpretation of measured ECE spectra, we solve the radiative transport equation (1) in bi-Maxwellian plasma [2,3] and (2) with the electron distribution function from the Fokker-Planck code [4].

The ECE radiometer can measure plasma density fluctuations if the plasma isn't simply a black body. It is our case for the plasma parameters at 0.5 T. The calculated optical depth is less than 1. We have found a coherent mode in the frequency spectrum of ECE signals in QHS plasmas. The mode was first detected by the interferometer [5] and then by a set of Mirnov coils. We have estimated the relative amplitude of this mode based on ECE fluctuations.

Recently we installed the reflectometer on HSX. The reflectometer can operate with an extraordinary polarized probing beam in 0.5 T operation and/or the ordinary wave at 1 T. The frequency of the probing beam can (1) be fixed during the plasma discharge and/or (2) be swept to measure a radial profile of fluctuations. We intensively use the wavelet analysis on reflectometer data and make a comparison with Fourier spectra from the Mirnov coils. The wavelet method allows us to see the fast time change

e-mail: kmlikin@.wisc.edu

(on scale of tens of microseconds) in the plasma fluctuation spectrum. Numerical modeling helps us to estimate the amplitude of measured fluctuations.

The standard magnetic configuration in our stellarator is quasi-helical symmetric (QHS) when the symmetric spectral component dominates along the field line. In the configuration with broken symmetry the mirror term is added to the magnetic field spectrum and we name this configuration Mirror. The gross magnetic properties are the same in both configurations but they differ in amplitude of magnetic field ripples (QHS has less ε_{eff} at r/a_p = 2/3 by an order of magnitude). In this paper we present the results. obtained at 0.5 T with 50 kW of launched power at (1.4 - 1.6)$\cdot 10^{12}$ cm^{-3} of the line averaged plasma density (Fig. 1).

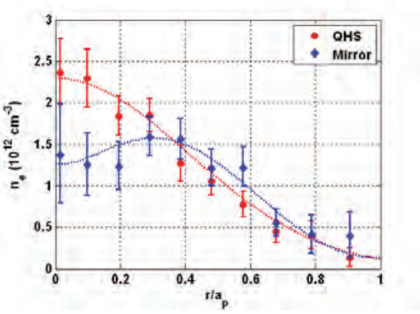

Fig.1 Plasma density profile in QHS and 10% Mirror

2. ECE Measurements and Modeling

The HSX radiometer has eight narrow band filters. By switching the filters we can get the ECE spectrum over the entire plasma. In this paper we report the results obtained with two sets of intermediate frequency (IF) filters. One set allows us to measure the emission from the high magnetic field (HF) side while the other one from the low magnetic field (LF). As we use the extraordinary wave at the second harmonic for heating and ECE measurements the emission cannot be detected from the heating resonance layer. At the plasma periphery the plasma optical depth is too low (τ < 0.1) to get a decent emission. Thus, we configure the ECE channels between 0.2 and 0.7 of the effective plasma radius.

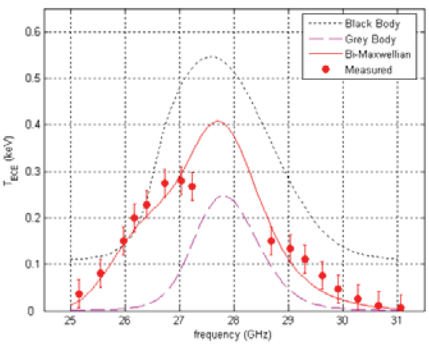

Fig.2 Measured ECE spectrum and the fit based on Bi-Maxwellian plasma model

The ECE radiometer has been calibrated against the Thomson scattering (TS) in plasmas with off-axis heating when the plasma stored energy measured by the diamagnetic loop and integrated from TS profiles is in agreement. For the HF set of IF filters the resonance is shifted outboard at r=+0.3$\cdot a_p$ and for the LF set we use inboard resonance at r=-0.2$\cdot a_p$, in both cases the TS profiles are identical. Then we took data in on-axis resonance with the two sets of filters. The measured ECE spectrum is shown in Fig. 2. It is clearly seen that the spectrum is non-symmetric (28 GHz corresponds to the plasma axis) due to the presence of supra-thermal electrons.

To find the population and the temperature of the high energy electrons the Bi-Maxwellian plasma model is applied. We use TS profiles ($T_e(0)$ = 0.6 keV, $n_e(0)$ = 2.6$\cdot 10^{12}$ cm^{-3}) to calculate the optical depth of the bulk plasma. The results of modeling are shown in Fig. 2. The higher emission at the HF side compared to the level of grey plasma is mostly due to the broad population of supra-thermal electrons, and the tail temperature is responsible for enhanced signals at the LF side (Fig. 3). The best fit to the measured spectrum is for T_{tail} = 4.5 keV, n_{tail} = 0.6$\cdot 10^{11}$ cm^{-3}. The calculations made with the CQL3D Fokker-Planck code support the simple Bi-Maxwellian model (Figs. 4,5). In Fig. 5 the results at 1 T are also shown. At 50 kW of launched power the plasma stays thermal at a high density (> 6$\cdot 10^{12}$ cm^{-3}). The central

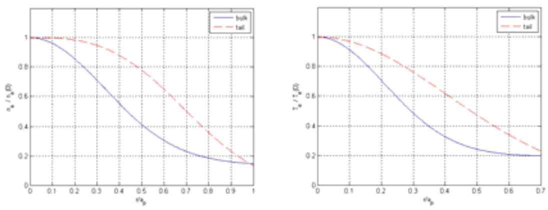

Fig.3 Normalized N_e and T_e profiles for bulk and tail plasmas

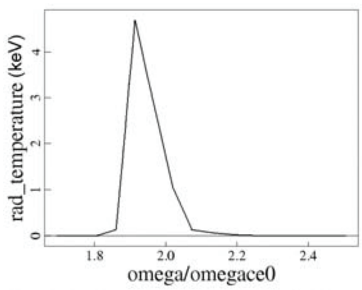

Fig.4 Black body spectrum from CQL3D code

electron temperature is 1.2 keV at 50 kW and 2 keV at 100 kW corresponding to the experimental data.

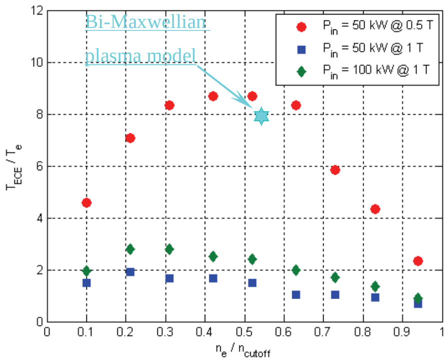

Fig.5 Normalized T_{ECE} calculated by CQL3D

In the QHS configuration the ECE radiometer is able to detect the coherent plasma density fluctuations in the narrow frequency band (38 - 44 kHz). The amplitude of the mode is defined as follows.

$$rms \equiv \sqrt{\int_{\Delta f} pdf} \Big/ A_{DC} \qquad (1)$$

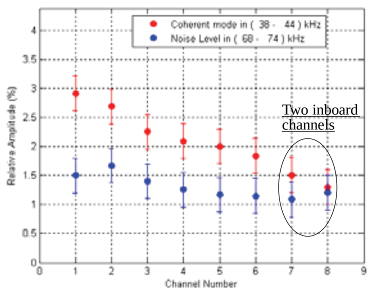

Fig.6 Amplitude of plasma density fluctuations measured by ECE radiometer

The channels (1 – 6) correspond to the LF side and channels 7 and 8 are on the HF side. For the thermal plasma channel #1 receives emission at r = 0.2·a_p, channel #6 – at r = 0.6·a_p, #7 and #8 – at -0.5·a_p and -0.6·a_p, respectively (Fig.6). The mode is well pronounced in the plasma core (r < 0.7·a_p) in the QHS configuration. According to Dr. C.Deng, the mode is driven by high energy electrons. The frequency of the mode is equal to the precision frequency of trapped particles circulating around the machine.

3. Reflectometer on HSX

Reflectometry is a well known method for measuring the plasma density [6]. We use a heterodyne detection with double frequency conversion so that the output signal frequency band is broad enough to detect plasma density fluctuations up to 10 MHz. To get reflections from low and high density plasmas two overlapping microwave sources are used. A fast pin switch (switch time ~ 10 nsec) is used to connect the appropriate source to the output channel. An extraordinary wave is used in 0.5 T operation. The polarization can be easily changed for 1 T plasmas by rotating the horn antenna. The probing beam is focused inside the vacuum vessel into a small spot (~ 10 cm in diameter). To protect the sources and the mixer diodes narrow band-stop filters at 28 GHz are used.

In this paper we present the first results on plasma density fluctuations measured with the new reflectometer on HSX. The frequency spectra are measured in QHS and Mirror configurations. In Fig. 7 the spectra at fixed probing beam frequency (f_o = 19 GHz), which corresponds to the plasma density gradient region, are shown. The Mirror spectrum is much broader than the QHS one. To estimate

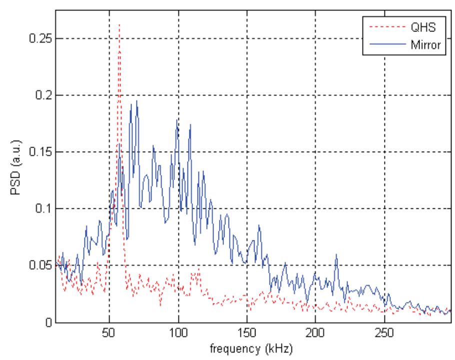

Fig.7 FFT of the reflectometer signals in QHS and 10% Mirror

the amplitude of fluctuations we need to apply 2-D modeling for the wave propagation in the HSX plasma.

In the QHS configuration the reflectometer detects the coherent mode as well. The frequency of the probing beam can be swept. We use a step function for a single sweep in order to localize the mode. The single sweep (Fig. 8) is chosen to be 10 msec so that there are up to 5 full sweeps in the 50 msec plasma discharge. The X-wave

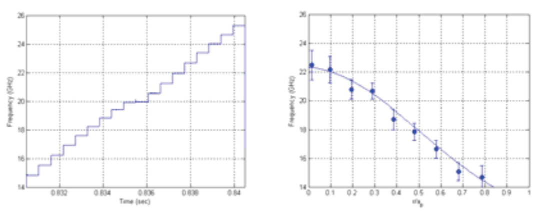

Fig.8 Probing beam frequency sweep and X-wave cut-off frequency in HSX plasma

cut-off frequency is calculated based on TS profile (see Fig.1) and Biot-Savart code (Fig. 8). We use wavelet analysis to get good temporal resolution. The Mironov coil is monitoring the presence of the mode in the time window of this full sweep. Based on time evolution of the wavelet

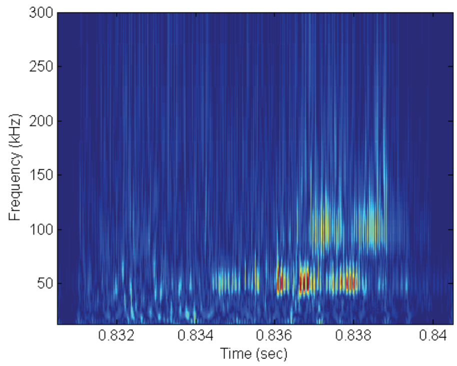

Fig.9 Wavelet coefficients in QHS (one full sweep of the reflectometer)

coefficients (Fig. 9) and the calculated cut-off frequency we easily see that the mode is localized within the plasma core ($r < 0.4 \cdot a_p$).

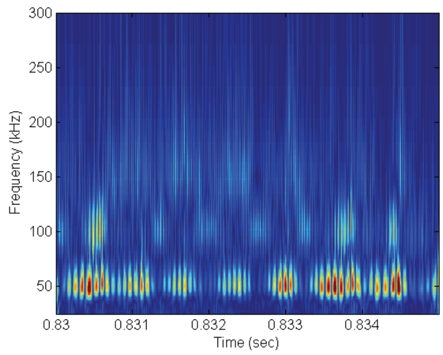

Fig.10 Time evolution of the coherent mode (5 msec time window)

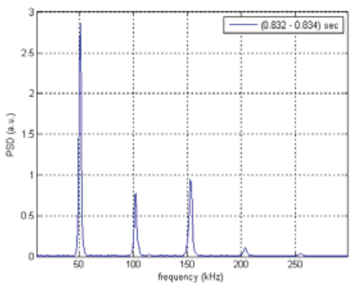

Fig.11 FFT of reflectometer signal in time interval of (0.832 – 0.834) sec

We looked at the evolution of the mode in a short time interval at fixed frequencies. Deep in the plasma core, at the probing beam frequency greater than 23 GHz, the harmonics of the main mode (50 kHz) are found (Fig. 10). At this moment we do not know why the mode has harmonics. Another feature of the mode is its bursty character. The fast changes are on the order of the electron-electron collision time (100 μsec). The FFT technique has a better frequency resolution than the wavelet analysis. The Fourier spectrum in a 2 msec time window shows a very narrow frequency band where the mode exists (Fig. 11).

4. Summary

ECE spectra in HSX plasma have been measured at 0.5 T. The Bi-Maxwellian model and CQL3D Fokker-Planck code show the presence of 5 keV tail of electrons in the distribution function. The ECE radiometer detects the coherent mode in QHS plasma as do the interferometer, Mirnov coils and Langmuir probes. This mode is thought to be driven by high energy trapped particles circulating around the machine.

First results on plasma density fluctuations have been obtained with the new reflectometer. The frequency spectrum in 10% Mirror configuration is much broader than in QHS. The reflectometer data show that the coherent mode in QHS plasmas is localized in plasma core and its amplitude gradually reduces with the mirror percentage (at 8% of mirror term the mode vanishes). The wavelet analysis helps us to see the bursty behavior of the coherent mode and its harmonics. The fast changes are on the order of electron-electron collision time.

Acknowledgments

The authors are thankful to Dr. C.Deng for his help in preparing the experiments on reflectometry and fruitful discussions of the results. This work could not be done without the help of the HSX team and the authors thank everyone.

This work is supported by DOE grant # DE-FG02-93ER54222.

References

[1] K.M. Likin *et.al*, *Electron cyclotron emission and electron cyclotron heating* (ed. A.G. Litvak, Nizhny Novgorod: Institute of Applied Physics, 2005), p.204

[2] E.V. Suvorov and A.A. Fraiman, *High-frequency plasma heating* (ed. A.G. Litvak, New York: American Institute of Physics, 1992)

[3] M.Bornatici, F.Engelmann, Phys.Plasmas, 1994, **1** , p.189

[4] R.W.Harvey, F.W.Perkins, Nucl. Fusion, 1997, **37**, p.69

[5] C.Deng *et al*., APS Bulletin, 2005, **50** , 8, p.166

[6] C.Laviron *et.al.*, Plasma Phys. Contr. Fusion, 1996, **38**, p.905

Proceedings of ITC/ISHW2007

Operation Characteristics of Microwave Sources Based on Slow-Wave Interaction in Rectangular Corrugation

Y. Takamura, Y. Kazahari, H. Oe, K. Ogura, A. Sugawara, M. Hirata[a]

Graduate School of Science and Technology, Niigata University, Niigata 950-2181, Japan
[a] Plasma Research Center, University of Tsukuba, Tsukuba 305-8577, Japan
(Received 15 October 2007 / Accepted 3 August 2007)

Studies of slow-wave device with a novel disk cathode and two types of rectangular corrugation are reported. The beam voltage is weakly relativistic, less than 100kV. A disk cathode can generate a uniformly distributed annular beam in the weakly relative region. Rectangular corrugation having the ratio of corrugation width to periodic length of 50% or 20% is used. By using the first one, output powers of about 200kW are obtained around 100kV. For the other, the effect of slow cyclotron resonance is observed in the low energy region around 30kV. Output powers are in the range of a few W. For the slow cyclotron maser, the operation mode between axisymmetric and nonaxisymmetric modes can be controlled by changing the end condition of rectangular corrugation.

Keywords: slow-wave device, weakly relativistic, disk cathode, annular electron beam, rectangular corrugation

1. Introduction

Slow-wave high-power microwave devices such as backward wave oscillator (BWO) can be driven by an axially injected electron beam without initial perpendicular velocity and has been studied extensively as a candidate for high or moderate power microwave sources. In the slow-wave devices, slow-wave structure (SWS) is used to reduce the phase velocity of electromagnetic wave to the beam velocity. In order to increase the power handling capability and/or the operating frequency, oversized SWSs have been used successfully. The term “oversized” means that the diameter D of SWS is larger than free-space wavelength λ of output electromagnetic wave by several times or more.

In Refs. [1] and [2], K-band and Q-band oversized BWO operating in the weakly relativistic region less than 100kV are reported. Output power in the range of hundreds of KW is obtained by using a sinusoidally corrugated SWS. However, for moderate power level of MW or less, the rectangular corrugation may be better than the sinusoidal corrugation. We propose to use a novel disk cathode made of metal only [2]. It can generate a uniformly distributed annular beam in the weakly relativistic region and is used in our slow-wave device. In this work, we use two types of rectangularly corrugated SWSs for which the ratio of corrugation width to periodic length differs. Upper cut-off frequency is about 25GHz for the both SWSs. We examine operation characteristics of the slow-wave devices based on each SWS, in high (around 100 kV) and low (around 30kV) beam energy region.

author’s e-mail: f06e090g@mail.cc.niigata-u.ac.jp

2. Cold Cathode

We use a cold cathode to obtain a beam with high current density. It is very difficult to generate a uniformly distributed annular beam by the cold cathode, especially in the weakly relativistic region less than 100kV. In the past, we have used a hollow cathode with velvet on the axsymmetric emitting edge in order to obtain an annular electron beam [1]. By controlling velvet, fairly uniform annular beams have been obtained as shown in Fig. 1. The beam shape is observed by the burn pattern on thermally sensitive paper. The average radius of the annulus is nearly the same as the cathode diameter.

Recently, the uniformity of the beam is improved much more by using a novel disk cathode. The idea of disk cathode was presented by Loza *et al* [3], and used in the relativistic region [4]. In this paper, the disk cathode is tested in the weakly relativistic region. The burn pattern is shown in Fig.1. The annular beam by the disk cathode distributed more uniformly compared with the hollow cathode with velvet. Moreover, any coating on the disk cathode surface is not required. The disk cathode is suitable for the weakly relativistic case.

Fig.1 The burn patterns of annular electron beam. Left-side is the pattern of 5-shot overlay for the hollow cathode with velvet at about 90kV. Right-side is the pattern of 1-shot for the disk cathode without velvet at about 80kV.

3. Rectangular SWS

Cylindrical SWS is periodically corrugated as shown in Fig.2. Dispersion characteristics of SWS are determined by average radius R_0, corrugation amplitude h, corrugation width d and periodic length z_0. The corrugation wave number is given by $k_0=2\pi/z_0$. The dispersion characteristics of structure are controlled by changing R_0, h, d and z_0.

Dispersion characteristics of rectangular SWS are obtained by a numerical method based on a mathematical formula in Ref. [5]. Figure 3 shows the each dispersion characteristic of axisymmetric transverse magnetic (TM_{01}) mode for type A and B, whose parameters are listed in table 1. The slow space charge mode and the slow cyclotron mode coupling to fundamental TM_{01} mode may lead to the Cherenkov and slow cyclotron instability. For type A SWS in Fig.3 (a), slow-wave device operate as BWO based on Cherenkov instability. The interacting point of beam is around the upper cut off at π-point. For type B SWS in Fig.3 (b), dispersion curve around upper cut-off at π-point becomes flat, compared with type A. And the interaction point between beam line of slow space charge mode and TM_{01} mode shifts toward traveling wave region at 80keV. Decreasing beam energy to 30keV, the interaction point moves to backward wave region.

In this work, each rectangular SWS of type A and B is used. We examine operation characteristics of the slow-wave device using each SWS in high (around 100 kV) and low (around 30 kV) energy region.

Table 1 Parameters of rectangular SWS

	R_0 [mm]	h [mm]	z_0 [mm]	d/z_0 [%]
Type A	15.1	1.1	3	50
Type B	15.38	1.38	2.2	20

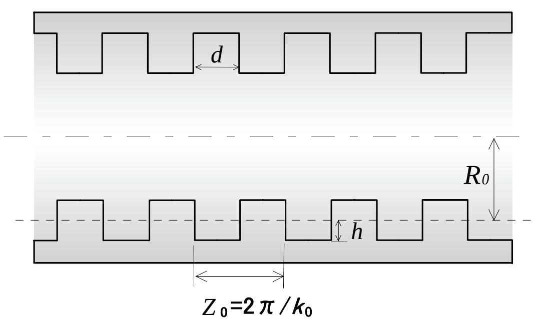

Fig.2 Periodically corrugated cylindrical SWS.

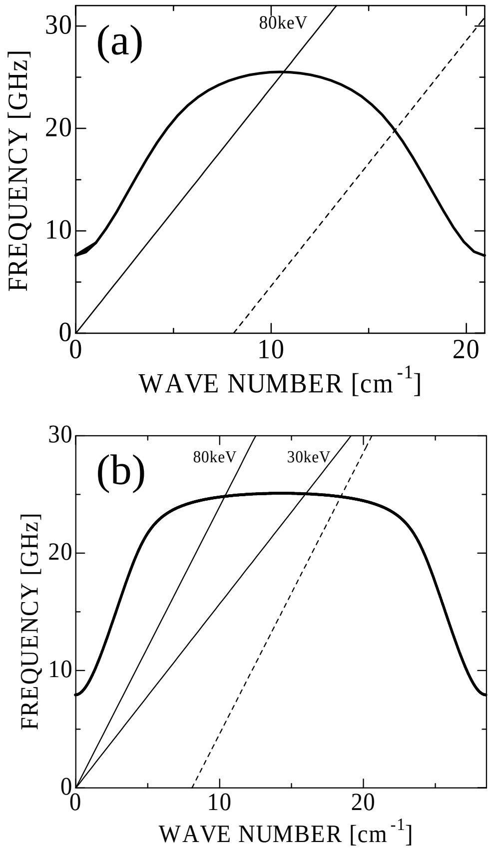

Fig.3 Dispersion characteristics of TM_{01} for rectangular SWS. (a) is for type A. (b) is type B. Solid and dashed lines are the beam line of slow space charge mode and slow cyclotron mode at 0.8T, respectively.

4. Experiment with rectangular SWS

The experimental setup is schematically shown in Fig.4. Output voltage up to 100 kV from the pulse forming line is applied to the cold cathode. A disk cathode is used as a cold cathode. A uniform axial magnetic field B_0 for the beam propagation is provided by ten solenoid coils. The value of B_0 can be changed from 0T to 0.9T. The microwave output is picked up by a rectangular horn antenna typically located 600 mm away from the output window.

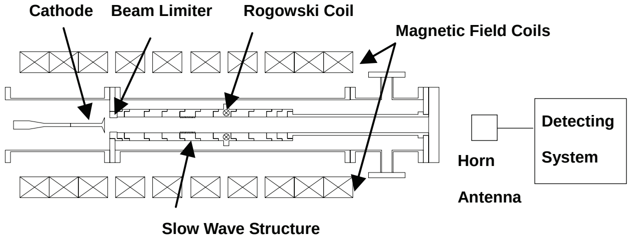

Fig.4 Schematic diagram of the experimental setup.

Figure 5 shows an example of detected signals. The beam voltage and current are about 100kV and 300A, at the microwave peak time. The operation frequency estimated from delay time is about 26GHz.

Figure 6 shows the dependence of the microwave power on the cathode voltage with type A SWS. The oscillation starting voltage is about 60kV. Output powers increase by increasing the cathode voltage. For type A SWS, the estimated maximum power is about 200kW at 100kV. For type B SWS, the microwave output can not be obtained in the high energy region from 60kV to 100kV. However, the microwave power in the range of a few W is obtained in the low energy region around 30kV, less than the oscillation starting voltage. In Fig. 7, the power dependence on the magnetic field for type B SWS is shown. The microwave outputs resonantly increase around 0.65T. This might be caused by slow cyclotron resonance as discussed later. For type A SWS, such an effect of slow cyclotron resonance cannot be observed in the low energy region, less than the oscillation starting voltage.

In our slow-wave device, both axisymmetric TM_{01} mode and nonaxisymmetric hybrid HE_{11} mode exist as a candidate of the operation mode. To examine the mode, the radiation patterns are measured by shifting the receiving horn antenna in an equatorial plane around a pivot at the center of output window. The electric fields component of E_θ and E_ϕ is measured by the horn antenna. E_θ (E_ϕ) is horizontal (vertical) component of the electric field in the equatorial plane. Figure 8 show the radiation patterns with type B SWS. The beam voltage is about 30kV. The magnetic field is 0.6T, around peaks of output in Fig.7. The operation mode changes by the straight cylinder length before SWS in Fig.4. For the straight cylinder of 34mm, the operation mode is TM_{01} mode as Fig.8 (a). By changing the straight length to 68mm, the radiation pattern changes to the pattern HE_{11} mode as Fig.8 (b). The axisymmetric and nonaxisymmetric mode can be controlled by the axial condition of SWS.

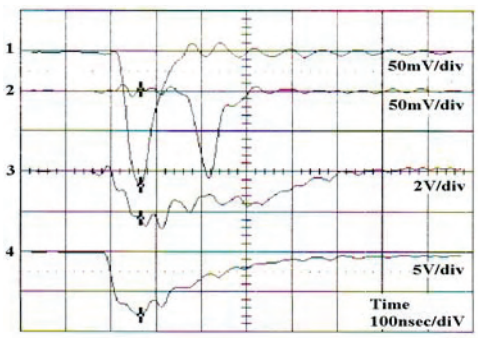

Fig.5 Waveform of measured signals: 1 prompt signal, 2 delayed signal, 3 beam current signal and 4 beam voltage.

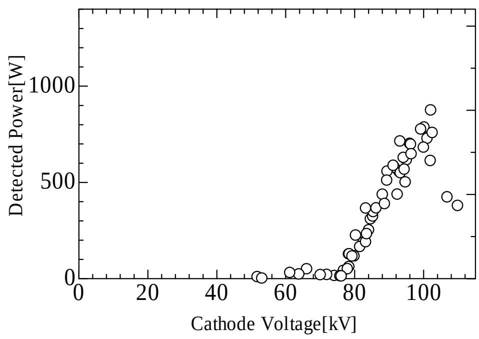

Fig.6 Output powers versus the cathode voltage for a 10-period type A SWS.

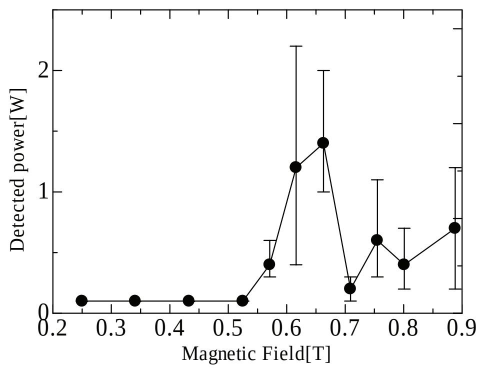

Fig.7 Output powers versus the magnetic field for a 10-period type B SWS. The beam voltage is around 30kV.

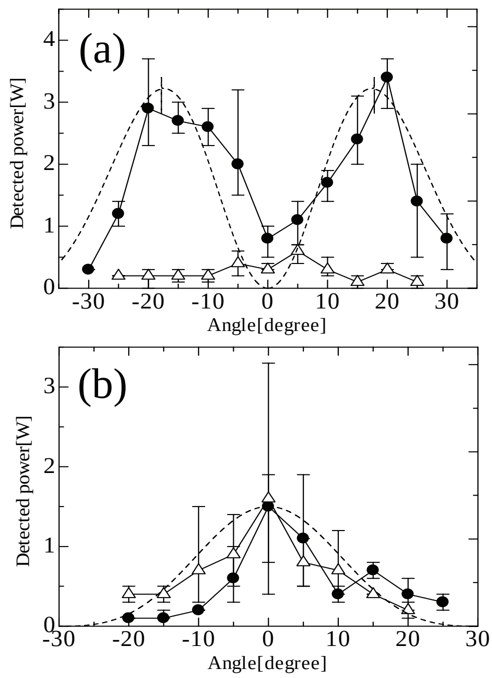

Fig.8 Radiation patterns with the straight cylinder of (a) 34mm and (b) 68mm for type B SWS. (●) and (△) are respectively E_θ and E_ϕ components. Dashed curves are theoretical curves of (a) TM_{01} and (b) HE_{11} mode, respectively.

5. Discussion and Conclusion

We study slow-wave device with a disk cathode and two types of rectangular SWS. The beam voltage is weakly relativistic, less than 100kV. We propose a novel cold cathode, which is a disk type cathode made of metal only. It can generate a uniformly distributed annular beam in the weakly relativistic region.

The estimated output power of about 200kW is obtained by using type A SWS at about 100kV. However, the microwave can not oscillate for type B SWS, because the interacting point of beam shifts to traveling wave region in high energy region around 100kV. Around about 30kV less than the oscillation starting voltage, radiations in the range of a few W is obtained. The dispersion characteristic of TM_{01} mode for type B is shown in Fig.9. Beam interactions are taken into account, based on a field theory developed in Ref. [6] for cylindrical SWS driven by an annular beam. The slow cyclotron mode depends on the axial magnetic field B_0. By increasing B_0, the beam line of slow cyclotron mode shifts to the right in Fig.9. The Cherenkov interaction resonantly synchronizes with slow cyclotron interaction at the fundamental frequency with 1.35T. This is a slow cyclotron maser operation reported in Refs. [7] and [8]. In our experiments, the resonance occurs around 0.65T and might be a combined operation of the Cherenkov and the second harmonic slow cyclotron interactions. For the slow cyclotron maser, it is demonstrated that the axisymmetric and nonaxisymmetric mode can be controlled by changing the end condition of SWS.

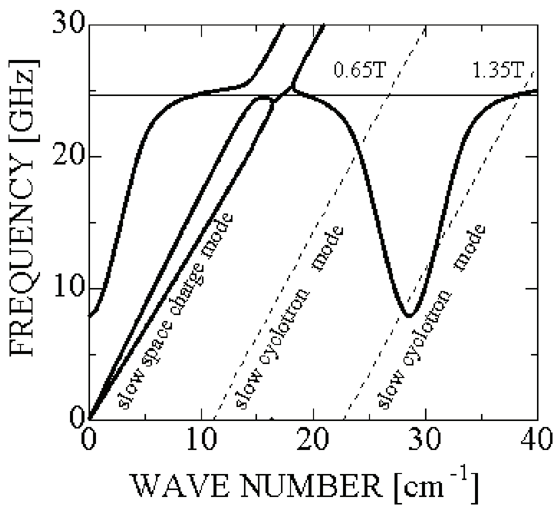

Fig.9 Dispersion curves of fundamental TM_{01} for type B SWS. The beam energy is 30keV.

Acknowledgments

This work was partially supported by a Grant-in-Aid for Scientific Research from Ministry of Education, Science, Sports and Culture of Japan, and partially performed under the Collaborative Research Program between NIFS and University of Tsukuba in cooperation with Japanese universities.

References

[1] K. Ogura et al., IEEJ Trans. FM, **125**, 733(2005).
[2] S. Aoyama et al., Trans. Fusion Sci. Tech. **51**, 325(2007).
[3] O. T. Loza and P. E. Ivanov, *Proc. 13th Int. Conf. High-Power Particle Beams*, Nagaoka, Japan, pp.603-606 (2000).
[4] Kelly Han et al., *IEEE Trans. Plasma Sci*., 30, No.3, June 2002.
[5] P. J. Clarricoats and A. D Olver, *Corrugated Horns for Microwave Antenna* (Peter Peregrinus, London, 1984).
[6] K. Ogura,et at., J. Plasma Phys., 72, 905 (2006).
[7] K. Ogura,et at., Phys. Rev. E, 53, 2726 (1996).
[8] K. Ogura,et at., J. Phys. Soc. Jpn., 67, 3462 (1998).

Study of poloidal electric field generation by ECH in a helical plasma

I.Higashi, S.Murakami

Department of Engineering, Kyoto University, Kyoto 6060-8501, Japan

Poloidal electric field generated by ECH is investigated in a helical plasma. A linearized Fokker-Planck equation is solved by the adjoint method assuming a helically symmetic configuration for simplicity. It is found that the generated electric potential in the helical plasma is about 20% larger than that in the tokamak plasma. This indicates that about two times greater poloidal electic field is generated in a l=2 helical plasma.

Keywords: poloidal electric field, ECH, helical plasma

1 Introduction

Electron cyclotron heating (ECH) accelerates electrons perpendicularly and generates trapped particles, which tend to localize at the resonance region. Those resonant trapped particles would enhance a inhomogeneous electrostatic potential on a flux surface and generate a poloidal electric field resulting in the large radial transport due to the radial drift by $\boldsymbol{E}\times\boldsymbol{B}$drift.

M.Taguchi(1992)[1] evaluated the poloidal electric field generated by ECH in a tokamak plasma by solving an adjoint equation to the linearized Fokker-Planck equation with a quasi-linear diffusion term. Because of the deeper magnetic ripple by the helical coils the larger poloidal electric field would be generated in helical plasma than that in tokamaks.

In this paper, the poloidal electric field generated by ECH is investigated in a helical plasma in the collisionless regime. Applying the same method by Taguchi, the poloidal electric field is calculated assuming helically symmetric configuration and compared with one in a tokamak plasma.

2 Basic equation

We consider a toroidal plasma, where the magnetic field is expressed in the Booer coordinates (ψ, θ, ζ), where ψ, θ, ζ are the toroidal flux, the poloidal angle and the torodial angle, respectively. When the RF power is assumed to be weak, the gyrophase-averaged distribution function for the electrons is slightly distorted from the Maxwell distribution function $f_{e0} = n_{e0}(m_e/2\pi T_e)^{3/2}\exp(-m_e v^2/2T_e)$, where m_e and T_e are the electron rest mass and electron temperature. The distorted part f_{e1} is determined by the lineraized drift kinetic equation:

$$v_{\parallel}\boldsymbol{b}\cdot\nabla f_{e1} - C_e(f_{e1}) = ev_{\parallel}\boldsymbol{E}\cdot\boldsymbol{b}\frac{\partial f_{e0}}{\partial W} + Q_{\mathrm{rf}}(f_{e0}) - \frac{\partial f_{e0}}{\partial t} \qquad (1)$$

where the energy $W = \frac{1}{2}mv^2$, the magnetic moment $\mu = v_{\perp}^2/2B$ and $\sigma = v_{\parallel}/|v_{\parallel}|$ as independent variables in velocity space. $\boldsymbol{b} = \boldsymbol{B}/B$,$v_{\parallel} = \boldsymbol{v}\cdot\boldsymbol{b}$, $v_{\perp} = (v^2 - v_{\parallel}^2)^{1/2}$, C_e is the linearized Fokker-Plack collision operator, and Q_{rf} and $\boldsymbol{E} = -\nabla\phi$ are the velocity-space diffusion and the poloidal electric field due to ECH, respectively. To calculate the electrostatic potential ϕ we introduce the adjoint equation

$$v_{\parallel}\boldsymbol{b}\cdot\nabla\tilde{f}_{m,n} + C_e(\tilde{f}_{m,n}) = -\frac{\nu_{ee}f_{e0}\mathrm{e}^{\mathrm{i}(m\theta+n\zeta)}}{\sqrt{g}} \qquad (2)$$

where $\nu_{ee} = (4\pi n_{e0}e^4\ln\Lambda)/m_e^2 v_e^3, v_e = (2T_e/m_e)^{1/2}$, $\ln\Lambda$ is the Coulomb logarithm, θ is the poloidal angle and $1/\sqrt{g}$ is Jacobian. We multiply (2) by f_{e1}/f_{e0}, integrating over velocity space and averaging over the flux surface. Then, the electrostatic potential ϕ can be expressed as

$$\frac{n_{e0}e}{T_e}\left\langle\frac{1}{\sqrt{g}}\mathrm{e}^{\mathrm{i}(m\theta+n\zeta)}\phi\right\rangle = -\frac{1}{\nu_{ee}}\left\langle\int\frac{\tilde{f}_{m,n}}{f_{e0}}\left[Q_{\mathrm{rf}}(f_{e0}) - \frac{\partial f_{e0}}{\partial t}\right]dv\right\rangle + \left\langle\frac{n_{e1}}{\sqrt{g}}\mathrm{e}^{\mathrm{i}(m\theta+n\zeta)}\right\rangle \qquad (3)$$

where

$$n_{e1} \equiv \int f_{e1}dv \qquad (4)$$

Here, $\langle A\rangle$ is the flux surface average of a quantity A:

$$\langle A\rangle = \oint\frac{d\theta d\zeta}{\sqrt{g}}A/\oint\frac{d\theta d\zeta}{\sqrt{g}}$$

author's e-mail: higashi@p-grp.nucleng.kyoto-u.ac.jp

And we have used the relation

$$\left\langle \int f v_\parallel \boldsymbol{b} \cdot \nabla g dv \right\rangle = -\left\langle \int g v_\parallel \boldsymbol{b} \cdot \nabla f dv \right\rangle$$

and the adjoint property of the collision operator,

$$\int \frac{f_{e1}}{f_{e0}} C_e(\tilde{f}_{m,n}) dv = \int \frac{\tilde{f}_{m,n}}{f_{e0}} C_e(f_{e1}) dv$$

A similar relation can also be derived for ions. It becomes

$$\frac{n_{i0} e Z_i}{T_i} \left\langle \frac{1}{\sqrt{g}} e^{i(m\theta+n\zeta)} \right\rangle = -\left\langle \frac{n_{i1}}{\sqrt{g}} e^{i(m\theta+n\zeta)} \right\rangle \quad (5)$$

Z_i is the charge number of ion and T_i is the ion temperature.

We expand the electrostatic potential in a Fourier series:

$$\phi = \sum_{m,n=-\infty}^{\infty} \phi_{m,n} e^{-i(m\theta+n\zeta)} \quad (6)$$

The left hand side of (3) becomes

$$\begin{aligned} LHS &= \frac{n_{e0} e}{T_e} \left\langle \frac{1}{\sqrt{g}} \phi_{m,n} \right\rangle \\ &= \frac{n_{e0} e}{T_e} \frac{2\pi}{\oint \sqrt{g} d\theta d\zeta} \phi_{m,n} \end{aligned} \quad (7)$$

Using charge neutrality, the second term in the right hand side of (3) becomes

$$\begin{aligned} \left\langle \frac{n_{e1}}{\sqrt{g}} e^{i(m\theta+n\zeta)} \right\rangle &= \left\langle \frac{Z_i n_{i1}}{\sqrt{g}} e^{i(m\theta+n\zeta)} \right\rangle \\ &= -Z_i \frac{n_{i0} e Z_i}{T_i} \left\langle \frac{1}{\sqrt{g}} e^{i(m\theta+n\zeta)} \phi \right\rangle \\ &= -\frac{n_{e0} e Z_i}{T_i} \frac{2\pi}{\oint \sqrt{g} d\theta d\zeta} \phi_{m,n} \end{aligned} \quad (8)$$

Transposing the second term in the right hand side and arranging the equation give us

$$\frac{e\phi_{m,n}}{T_e} = -\frac{\nu_{\rm rf}}{\nu_{ee}} \frac{F_{m,n}}{1 + Z_i T_e / T_i} \quad (9)$$

$$F_{m,n} = \frac{\left\langle \int \frac{f_{m,n}}{f_{e0}} \left[Q_{\rm rf}(f_{e0}) - \frac{\partial f_{e0}}{\partial t} \right] dv \right\rangle}{\left\langle \int \frac{W}{T_e} Q_{\rm rf} dv \right\rangle} \frac{\oint \sqrt{g} d\theta d\zeta}{2\pi} \quad (10)$$

where

$$\nu_{\rm rf} \equiv \frac{1}{n_{e0} T_e} \left\langle \int W Q_{\rm rf} dv \right\rangle \quad (11)$$

3 Solution of the adjoint equation

In the collisionless regime we expand $\tilde{f}_{m,n}$ as $\tilde{f}_{m,n} = \tilde{f}^{(0)}_{m,n} + \tilde{f}^{(1)}_{m,n} + \cdots$. Then the distribution functions $\tilde{f}^{(0)}_{m,n}$ and $\tilde{f}^{(1)}_{m,n}$ satisfy the equations

$$v_\parallel \boldsymbol{b} \cdot \nabla \tilde{f}^{(0)}_{m,n} = 0 \quad (12)$$

$$v_\parallel \boldsymbol{b} \cdot \tilde{f}^{(1)}_{m,n} + C_e(\tilde{f}^{(0)}_{m,n}) = -\frac{\nu_{ee} f_{e0}}{\sqrt{g}} e^{i(m\theta+n\zeta)} \quad (13)$$

This function $\tilde{f}^{(0)}_{m,n}$ is determined by the solubility condition for (13). The linearized Fokker-Planck collision operation C_e is approximated well for $v > (2-3)v_3$ by

$$C_e(f) \approx (1+Z_i) \frac{\nu_{ee}}{x^3} \frac{v_\parallel}{B} \frac{\partial}{\partial \mu} \left(\mu v_\parallel \frac{\partial f}{\partial \mu} \right) - f_{e0} \frac{\nu_{ee}}{x^2} \frac{\partial}{\partial x} \left(\frac{f}{f_{e0}} \right) \quad (14)$$

where $x = v/v_e$. For simplicity we use this approximate collision term here. Then the solubility condition can be written as

$$\begin{aligned} &2(1+Z_i) \frac{1}{x^3} \frac{\partial}{\partial \lambda} \left[\lambda \left\langle (1-\lambda B)^{1/2} \right\rangle_b \frac{\partial \tilde{f}^{(0)}_{m,n}}{\partial \lambda} \right] \\ &\quad - \left\langle \frac{B}{(1-\lambda B)^{1/2}} \right\rangle_b \frac{f_{e0}}{x^2} \frac{\partial}{\partial x} \left(\frac{\tilde{f}^{(0)}_{m,n}}{f_{e0}} \right) \\ &= -\left\langle \frac{B}{(1-\lambda B)^{1/2}} \frac{1}{\sqrt{g}} e^{i(m\theta+n\zeta)} \right\rangle_b f_{e0} \end{aligned} \quad (15)$$

$\lambda = 2\mu/v^2$. Here the bounce average $\langle A \rangle_b$ is defined by

$$\langle A \rangle_b = \begin{cases} \langle A \rangle & (0 \le \lambda < \lambda_c) \\ \iint \sqrt{g} d\theta d\zeta A / \oint \sqrt{g} d\theta d\zeta & (\lambda_c < \lambda \le \lambda_{\max}) \end{cases}$$

where $\lambda_c = 1/B_{\max} \lambda_{\max} = 1/B_{\min}$. In order to solve (15), we consider the following eigenvalue equation:

$$\begin{aligned} &\frac{d}{d\lambda} \left[\lambda \left\langle (1-\lambda B)^{1/2} \right\rangle_b \frac{dG}{d\lambda} \right] \\ &\quad + \frac{1}{2} \left\langle \frac{B}{(1-\lambda B)^{1/2}} \right\rangle_b \kappa G = 0 \end{aligned} \quad (16)$$

$$(0 \le \lambda < \lambda_c,\ \lambda_c < \lambda \le \lambda_{\max})$$

subject to the boundary conditions

$$G(\lambda_c - 0) = G(\lambda_c + 0)$$

$$\frac{dG(\lambda_c - 0)}{d\lambda} = \frac{dG(\lambda_c + 0)}{d\lambda}$$

$$G(0) = 1, \quad \frac{dG(\lambda_{\max})}{d\lambda} \textit{ is finite}$$

The eigenfunctions G_n with eigenvalues κ_n satisfy the orthogonality condition

$$\int_0^{\lambda_{\max}} \left\langle \frac{B}{(1-\lambda B)^{\frac{1}{2}}} \right\rangle_b G_n G_m d\lambda = 0 \quad (\kappa_n \neq \kappa_m)$$

Using this, we can express the solution of (16) in the form

$$f_{m,n}^{(0)} = \sum_{n=1}^{\infty} \frac{x^3}{(1+Z_i)\kappa_n + 3} G_n(\lambda) S_n f_{e0} \qquad (17)$$

where $\kappa_0 (= 0) < \kappa_1 < \kappa_2 < \cdots$ and

$$S_n = \frac{\int_0^{\lambda_{\max}} G_n \left\langle \frac{B}{(1-\lambda B)^{\frac{1}{2}}} \frac{1}{\sqrt{g}} e^{i(m\theta + n\zeta)} \right\rangle_b d\lambda}{\int_0^{\lambda_{\max}} G_n^2 \left\langle \frac{B}{(1-\lambda B)^{\frac{1}{2}}} \right\rangle_b d\lambda}$$

Note that the eigenfunction $G_0 = 1$, so that $S_0 = 0$. Substituting the solution (17) into (9), we obtain

$$F_{m,n} = \frac{\oint \sqrt{g} d\theta d\zeta}{2\pi} \frac{1}{\left\langle \int \frac{W}{T_e} Q_{\rm rf} dv \right\rangle} \times \sum_{n=1}^{\infty} \frac{S_n}{(1+Z_i)\kappa_n + 3} \left\langle \int x^3 G_n Q_{\rm rf} dv \right\rangle \qquad (18)$$

since

$$\left\langle \int x^3 G_n \frac{\partial f_{e0}}{\partial t} dv \right\rangle \propto \int_0^{\lambda_{\max}} \left\langle \frac{B}{(1-\lambda B)^{\frac{1}{2}}} \right\rangle_b G_n G_0 d\lambda = 0 \quad (n \geq 1) \qquad (19)$$

4 Evaluation of $\phi_{m,n}$

The quasi-linear diffusion term $Q_{\rm rf}$ for electron-cyclotron damping is written as

$$Q_{\rm RF} = \frac{1}{v_\perp} \frac{\partial}{\partial v_\perp} \left[D v_\perp \left(\frac{v_\perp}{v_e} \right)^{2(l-1)} \times \delta \left(\omega - \frac{l\omega_c}{\gamma} - k_\parallel v_\parallel \right) \frac{\partial f_{e0}}{\partial v_\perp} \right] \qquad (20)$$

where $\gamma = [a - (v/c)^2]^{-\frac{1}{2}}$, c is the speed of light in vacuum and l is the harmonic number; ω and ω_c are the frequency of the injected wave and the non-relativistic electron-cyclotron frequency respectively. Throughout this paper we consider only the X-mode wave. Then D is taken to be independent of the velocity. Moreover, for simplicity, we approximate the relativistic resonance condition as

$$\omega - \frac{l\omega_c}{\gamma} - k_\parallel v_\parallel \approx \omega - l\omega_c \left(1 - \frac{v^2}{2c^2} \right) - k_\parallel v_\parallel = 0 \qquad (21)$$

This resonance condition becomes a semicircle in velocity space

$$\left(\frac{v_\parallel}{v_e} - \frac{1}{2S} \right)^2 + \left(\frac{v_\perp}{v_e} \right)^2 = \frac{1 - 4u_0 S}{(2S)^2} \qquad (22)$$

where $u_0 = (\omega - l\omega_c)/k_\parallel v_e$ is the normalized parallel velocity of the resonant electrons and $S = l\omega_c v_e / k_\parallel c^2$ relates the strength of the relativistic correction.

4.1 Helical symmetric configuration

We assume a helical symmetric plasma with magnetic configuration $B = B_h(1 - \epsilon_h \cos\theta')$ ($\theta' = M(\theta + \frac{N}{M}\zeta)$). Using $x = \lambda B_h(1 - \epsilon_h)$ we rewrite (16) and boundary condition .

$$x\alpha \frac{d^2}{dx^2} G + \left(x \frac{d\alpha}{dx} + \alpha \right) \frac{d}{dx} G + \frac{1}{2} \beta \kappa G = 0 \quad (23)$$

$$\alpha = \int_{\theta_1'}^{\theta_2'} \frac{1}{(1 - \epsilon_h \cos\theta')} \left(1 - \frac{1 - \epsilon_h \cos\theta'}{1 - \epsilon_h} x \right)^{1/2} d\theta' \qquad (24)$$

$$\beta = \int_{\theta_1'}^{\theta_2'} \frac{1}{(1 - \epsilon_h)} \left(1 - \frac{1 - \epsilon_h \cos\theta'}{1 - \epsilon_h} x \right)^{-1/2} d\theta' \qquad (25)$$

$$\frac{d\alpha}{dx} = -\frac{1}{2} \int_{\theta_1'}^{\theta_2'} \frac{1}{(1 - \epsilon_h)} \left(1 - \frac{1 - \epsilon_h \cos\theta'}{1 - \epsilon_h} x \right)^{-1/2} d\theta' \qquad (26)$$

$$G \to {\rm const} \times [1 - \frac{1}{2}\kappa(1 - x)] \qquad x \to 1 \quad (27)$$

$$G \to 1 - \frac{1}{2}\kappa x \qquad x \to 0 \qquad (28)$$

We evaluate the eigenfunctions G_n and eigenvalues κ_n by a relaxation method. The eigenvalues κ_n are given in table 1.

$\epsilon \backslash n$	1	2	3	4	5
0.1	2.886	8.400	15417	26.643	40.196
0.3	2.377	4.983	12.837	20.314	31.568

Table 1 eigenvaluesκ_n

4.2 Results

We evaluated the poloidal electric field in a helical symmetric plasma and the results are compared with tokamak ones by Taguchi[1]. The poloidal electric field is represented as Eq.(9) and is analayzed in a helical plasma.

Figure 1 shows F_m values in a tokamak and a helical plasma changing the magnetic field ripple ϵ; 0.1, 0.3 and the normalized parallel velocity; 0, 0.5, -1.0. We can see that the F_m increases as the ϵ becomes larger in both helical and tokamak plasma cases. And the differences of F_m is larger in the larger ϵ cases. The value of $\phi_1^h/\phi_1^t \sim 1.25 - 2$ in the case of F_m with $\epsilon = 0.3$. The values of F_m with various ϵ of a helical plasma are shown in figure 2.

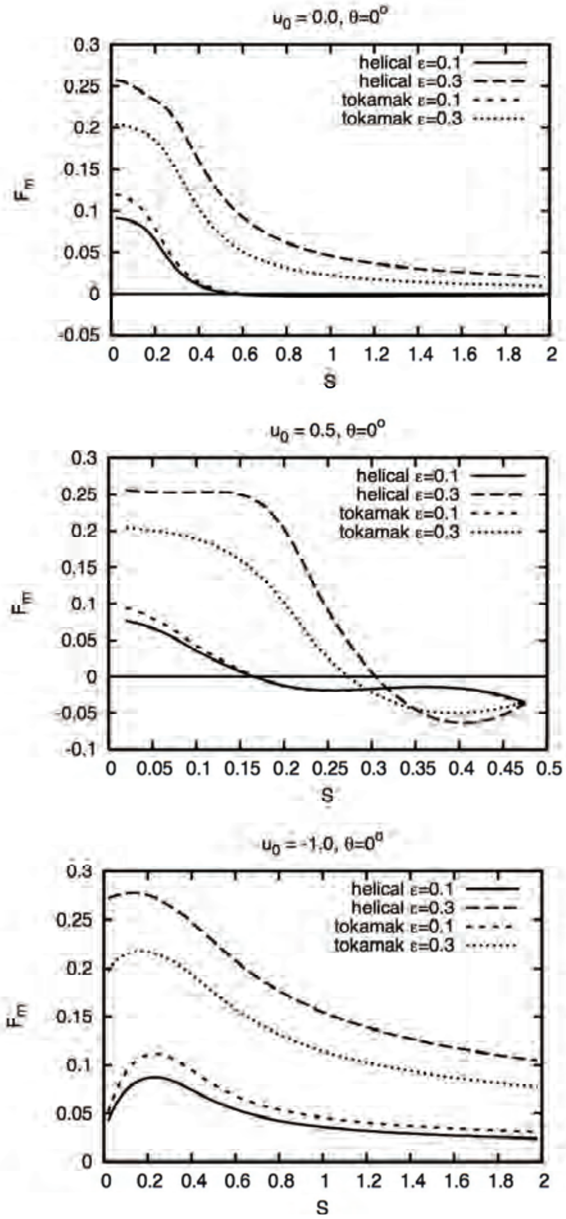

Fig. 1 Comparisons of F_m in the tokamak and helical plasma

5 Conclusion

We have studied the poloidal electric field generated by ECH in a helical plasma. The linearized Fokker-Planck equation has been solved by the adjoint method assuming a helically symmetic configuration for simplicity. We have found that the generated electric potential of the helical plasma is about 20% larger than that of the tokamak configuration. This indicates that the two times greater poloidal electic field is generated in a l=2 helical plasma.

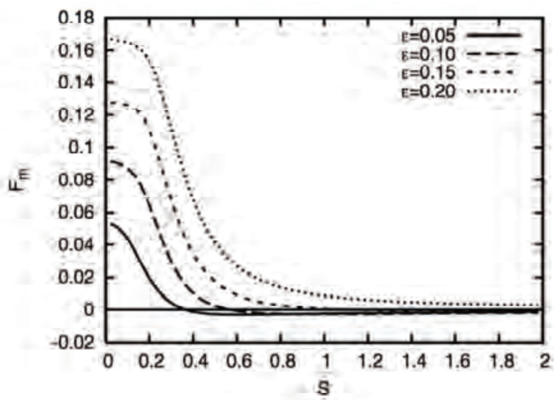

Fig. 2 Plots of F_m for helical plasma with ϵ = 0.05, 0.1, 0.15, 0.2

[1] M.Taguchi, J.Plasma Physics. **47**(1992), part 2, 261
[2] S.Murakami, et al, Nucl. Fusion **40**(2000) 693

Proceedings of ITC/ISHW2007

Efficient Heating at the Third Harmonic Electron Cyclotron Resonance in Large Helical Device

Takashi SHIMOZUMA[1)], Shin KUBO[1)], Hiroe IGAMI[1)], Yasuo YOSHIMURA[1)], Takashi NOTAKE[2)], Nikolai B. MARUSHCHENKO[3)], Yurij. TURKIN[3)], Takashi MUTOH[1)] and LHD Experimental Group[1)]

[1)]*National Institute for Fusion Science, 322-6 Oroshi-cho, Toki 509-5292 Japan*
[2)]*University of Fukui, Research Center for Development of Far-Infrared Region, 3-9-1 Bunkyo, Fukui 910-8507 Japan*
[3)]*Max-Plank-Institut für Plasmaphysik, EURATOM-Association, Greifswald, Germany*

(Received / Accepted)

Efficient heating at the third harmonic electron cyclotron resonance was attained by injection of millimeter-wave power with 84 GHz frequency range at the magnetic field strength of 1 T in LHD. The plasma center clearly increased and the increment of the temperature reached 0.2 – 0.3 keV. Dependence of the power absorption rate on the antenna focal position was experimentally investigated, showing that the optimum position located in the slightly high-field side of the resonance layer. Ray-tracing calculation was performed in the realistic three-dimensional magnetic configuration. The results are compared with the experimental results.

Keywords: electron cyclotron resonance heating, gyrotron, harmonic resonance, quasi optical antenna, ray tracing

DOI: 10.1585/pfr.1.001

1. Introduction

High harmonic heating of the electron cyclotron resonance (ECR) is an attractive method to extend a heating regime of plasma parameters by alleviating the density limitation due to some cutoffs of the EC wave propagation. In the LHD launching geometry, the magnetic field strength is almost constant along the ray paths launched from upper- and lower-port antennas which cross near the magnetic axis. Under this condition, the ray can keep resonant with the plasma over a considerable length. So good absorption is predicted over a wide density range even for the 3rd harmonic heating by the linear theory [1].

Experimentally the 3rd harmonic heating was tried in Heliotron DR and effective heating was observed [2]. In TCV tokamak, 3rd harmonic heating was carried out with the 2nd harmonic heating by using two different frequency gyrotrons such as 82.7 GHz for the 2nd harmonic and 118 GHz for the 3rd harmonic resonance. Hundred percent absorption was attained on existence of high energy electrons produced by the 2nd harmonic resonance heating [3, 4]. After that, the sophisticated feedback control of antenna focal position realized 100 % absorption by only 3rd harmonic resonance heating [5]. In W7-X, the 3rd harmonic heating is planned as a candidate of a normal heating scenario in the high density regime ($0.6 – 2.0 \times 10^{20}$ m^{-3}) by using 140 GHz, 10 MW ECH system [6].

Effective 3rd harmonic heating has been already achieved on the 2 T LHD plasma by injection of 168 GHz millimeter wave power from upper-port antennas. In the experiments of the 3rd harmonic resonance heating, obvious heating of the bulk plasma (ΔT_e=0.2 keV) around the plasma center by 340 kW power injection was observed [7].

Because ECH power of 84 GHz range has been upgraded up to 1.3 MW recently, we have tried the 3rd harmonic extraordinary(X)-mode heating by injection of 84 GHz range power at the magnetic field strength of 1 T with the magnetic axis of 3.75 m. When the same frequency is used, a cutoff density for the 3rd harmonic X-mode heating at 1 T becomes 4/3 higher than that for 2nd harmonic X-mode heating at 1.5 T. It is about 6×10^{19}m^{-3}.

2. Experimental setup and results

The ECH system consists of 84 GHz range and 168 GHz gyrotrons, high voltage power supplies, long distance transmission lines, and in-vessel quasi-optical antennas. It has been improved step by step. At the last campaign(2006) of LHD experiments five 84 GHz range and three 168 GHz gyrotrons are operated and ECH power could be injected from six antennas in the vertically elongated cross section (upper-port and lower-port antennas) and two antennas in the horizontally elongated cross section(outer-port antennas).

Two kinds of antenna systems for ECH are installed in the LHD vacuum vessel. The vertical injection antenna system consists of four or two millimeter-wave focusing and steering mirrors. High power measurement of this system shows a good agreement with the designed beam-waist size of 15 mm in radial and 50 mm in toroidal direction for the upper-port antennas and of 30 mm for the lower-port

author's e-mail: shimozuma.takashi@LHD.nifs.ac.jp

antennas. The direction of the beam can be steered radially and toroidally. The injected millimeter-wave beams from these antennas consequently have a grazing incidence angle to the cyclotron resonance and continues to interact along a long ray-path. For horizontal injection, the antenna system consists of 2 mirrors, one is fixed and another is steerable. Movable range covers the whole plasma cross section for perpendicular injection and can change about ±30 degrees toroidally. In this case, the injected beams perpendicularly pass through the ECR layer with the shortest gradient length.

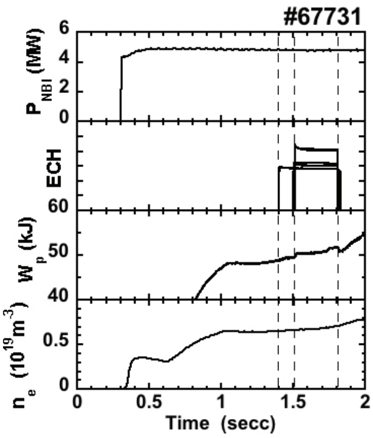

Fig. 1 Wave form of NBI power, ECH timing, stored energy W_p and line-averaged density from top to bottom.

A magnetic configuration was chosen such that the 3rd harmonic electron cyclotron resonance located on the magnetic axis for both in the vertically and horizontally elongated cross sections, because microwave beams from all antennas could access almost perpendicularly to the magnetic field line of force. So the magnetic field strength of 1 T on the magnetic axis placed on R_{ax} = 3.75 m was adopted.

In the experiments, target plasmas were produced and sustained by only NBI power. The electron temperature of a target plasma was about 1 keV and the line-averaged density was $0.6 \times 10^{19}\mathrm{m}^{-3}$ at the center. ECH power (1.3 MW) was injected from t=1.4 sec and 1.5 sec stair-likely as shown in Fig. 1. The ECH pulse which has a longer pulse width corresponds to 84 GHz power from the outer-port antenna. The ECH pulse with a shorter pulse width is 82.7 GHz from top-antennas and 84 GHz from bottom-antennas. The absorption rate for the different way of resonance can be discriminated independently and effectively by the stair-like injection. Obvious increase of the stored energy was observed during both the first and second ECH pulses, while there was no change in the density.

Figure 2 shows electron temperature profiles just before (t=1.37 sec) and during (t=1.57sec) ECH power injection. The plasma center was efficiently heated, and the increment of the temperature reached 0.2 – 0.3 keV.

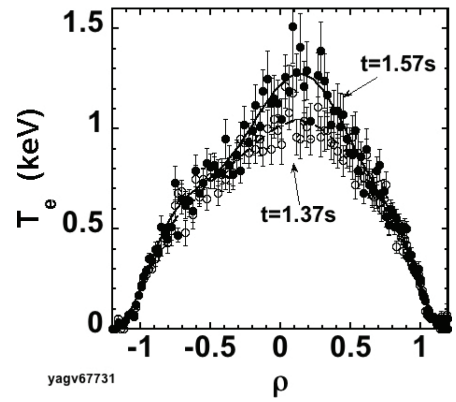

Fig. 2 Electron temperature profiles just before (t=1.37sec) and during (t=1.57sec) ECH. ρ is the normalized minor radius.

Absorbed power was estimated by the increment of the plasma stored energy $\mathrm{d}W_p/\mathrm{d}t$ before and after ECH on-timing, assuming that the other plasma parameters did not change so much. The dependence on the focal point R_{foc} of the upper-port antennas (82.7 GHz) was examined in special(Fig. 3). The maximum absorption rate was obtained on the antenna focal position R_{foc}=3.7m, which was slightly smaller than the 3rd harmonic ECR layer (3.75m). The absorption rate, however, is rather low, because the temperature and density of the target plasma was fairly low. The absorption rate for the other antennas were estimated to be about 8 %.

Detailed calculations by ray-tracing in the LHD magnetic configuration is required to discuss the absorption rate and its dependence on the antenna focal point.

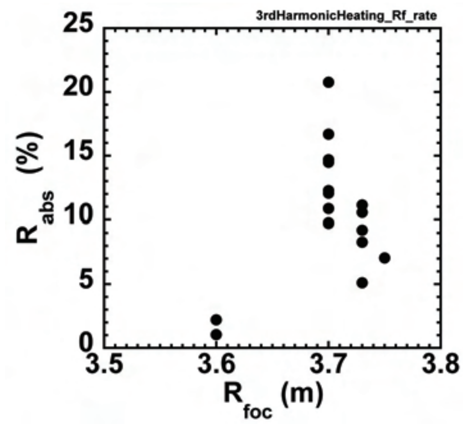

Fig. 3 Efficiency of absorbed power for 82.7GHz antenna was estimated by change of $\mathrm{d}W_p/\mathrm{d}t$ at ECH on-timing. Antenna focal point on the equatorial plane R_{foc} dependence is shown.

3. Preliminary ray-trace calculation in LHD magnetic configuration

In order to estimate the absorption rate, ray trace calculation was carried out for a given electron temperature and density profiles in the LHD magnetic field configuration.

The ray-tracing code, "TRAVIS (IPP)", has been developed for ECH/ECCD and ECE studies in an arbitrary three-dimensional magnetic configuration [8, 9]. The basic ray-tracing equations include weakly relativistic formulation for Hamiltonian with taking into account possible anomalous dispersion effects. Gaussian power distribution of an injected beam is assumed and the beam cross-section is discretized by the arbitrary number of radial and azimuthal points. The wave absorption can be calculated in fully relativistic formulation. The power deposition is decomposed for passing and trapped electrons contributions.

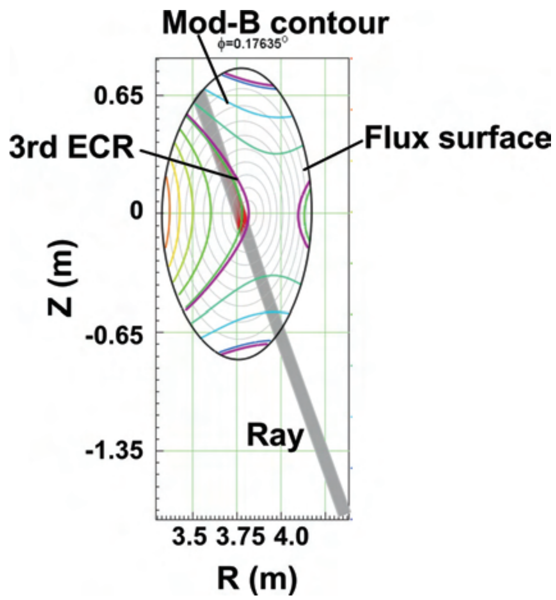

Fig. 4 Ray trace calculation together with mod-B contours and flux surfaces.

An X-mode is assumed to be perpendicularly injected from the lower-port antenna focused on the magnetic axis. In Fig. 4, the configuration of calculation is illustrated with mod-B counters, flux surfaces and wave rays. The 3rd harmonic electron cyclotron resonance is also depicted. Calculated rays from the lower-port antenna are typically shown. The profile of the electron temperature is assumed $(T_{e0} - T_{ea}) \times (1 - \rho^3)^{1.5} + T_{ea}$ with T_{e0}=1.3 keV, where $\rho = r/a$ is a normalized minor radius, and T_{e0} and T_{ea} are the electron temperature at the plasma center and the edge, respectively. The central electron density n_{e0} is assumed to be $1 \times 10^{19}\mathrm{m}^{-3}$. The profile of the electron density was assumed the same as the electron temperature.

The power absorption is localized near the 3rd harmonic resonance ($B = 1$ T) and the deposition is almost limited within $\rho \sim 0.2$, which is shown in Fig. 5 (a). Most part of the power is absorbed by the passing electrons near the magnetic axis. A small fraction is absorbed by the trapped electrons within $\rho \sim 0.2$ and around $\rho \sim 0.4 - 0.5$. The integrated absorbed power is shown in Fig. 5 (b). Total amount of the absorption power reaches 0.6 MW for 1.3 MW injection. Maximum absorption rate is about 50 %.

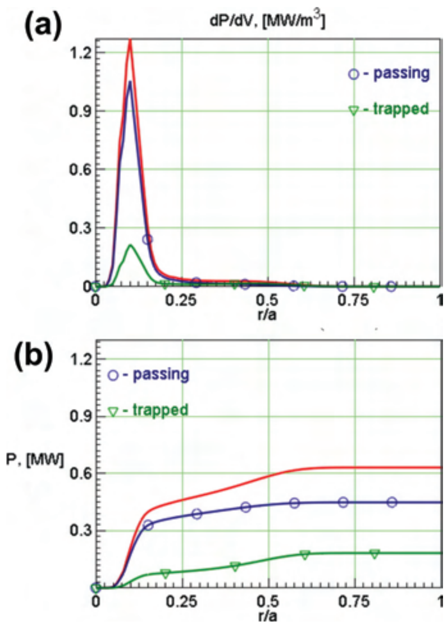

Fig. 5 Power deposition. (a) Deposited power density is plotted as a function of normalized minor radius and (b) integral value of absorbed power along the ray path. Total amount is decomposed into each component absorbed by passing and trapped electrons.

4. Discussion and summary

The experimental results show the efficient heating at the 3rd harmonic resonance even in the fairly low electron temperature ($\sim$ 1 keV) and low electron density ($\sim 0.6 \times 10^{19}\mathrm{m}^{-3}$). However experimentally obtained absorption rate of about 20 % is lower than that expected by the ray-tracing calculation, which was carried out in the realistic three-dimensional magnetic configuration of LHD. One possible reason of the discrepancy seems to be the differences of values and profiles of the temperature and density for between the actual plasma and the modeled one. Because the optical thickness scales as $\tau \sim n_e \cdot T_e^2$, a little temperature change possibly leads to fairly large difference of the absorption rate. Figure 6 shows a contour-plot of the single-pass absorption rate in the electron temperature and density space for the injection from the upper-port antenna with $R_{foc} = 3.7$ m. In these calculations the dispersion relation of a cold plasma was assumed for ray calculation and the weekly relativistic effect were included for the absorption [10]. The profiles of the electron temperature and density are assumed to have the same ones such as $(1-\rho^2)^2$.

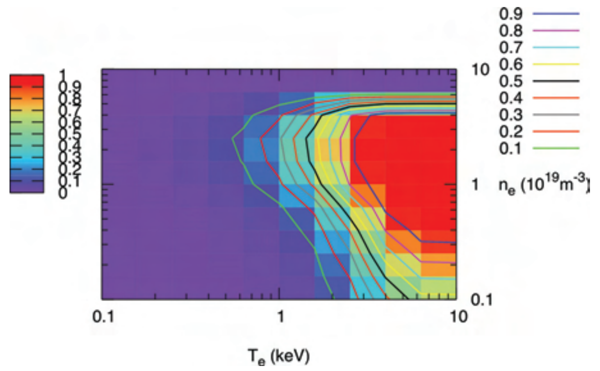

Fig. 6 Single-pass absorption rate for the injection from upper-port antenna is contour-plotted in the electron temperature and density space.

The values of temperature, T_e, and density, n_e, in the figure represent the values in the center. The figure clearly shows almost 100 % absorption is expected in the high temperature ($\gtrsim$ 3 keV) and high density ($1-4\times10^{19}\text{m}^{-3}$) region up to the right-hand cut-off density. However in the low temperature ($\lesssim$1 keV) and low density ($\lesssim 1\times10^{19}\text{m}^{-3}$), the absorption rate can change from several percent to several tens percent according to the small change of plasma parameters.

Another possible reason is the production of supra-thermal electrons by the 3rd harmonic ECR, which could be drifting out from a plasma quickly before thermalization and do not contribute to the increment of diamagnetic energy of the plasma. These facts can partly explain the discrepancy between the values of the single-pass absorption calculated by the ray-tracing and the absorption rate evaluated from the temporal change of dW_p/dt.

In summary, the 3rd harmonic electron cyclotron resonance heating experiments were performed. Especially, because of the upgrade of 84 GHz gyrotrons and transmission line, the efficient heating results were obtained even for the 3rd harmonic resonance. During the ECH pulse of 0.4 sec. stored energy of the plasma increased several percents. The central electron temperature raised about 0.2 – 0.3 keV. Dependence of the absorption rate on the antenna focal position shows the maximum at a slightly higher-field side of the resonance position. Preliminary calculation using ray-tracing code "TRAVIS", which has been developed in IPP Greifswald (Germany), was successfully carried out in the three-dimensional magnetic configuration of LHD.

In order to discuss a detailed quantitative comparison is required between experimental and calculated results for the optimization of the heating efficiency in view of injection configuration. These works are under way.

Acknowledgment

The authors gratefully acknowledge the LHD technical group for their sophisticated operation of LHD, and the heating and diagnostic devices. They also thank Professors A. Komori, S. Sudo and O. Motojima for their continuous guidance and encouragement. This work has been supported by NIFS under NIFS06ULRR501,502,503.

[1] U. Gasparino, H. Idei, S. Kubo, et al., Nuclear Fusion, 38(1998)pp223-235.
[2] N. Yanagi, S. Morimoto, M. Sato et al., Nuclear Fusion, 31(1991)261-271.
[3] S. Alberti, T. P. Goodman, M.A. Henderson, et al., Nuclear Fusion 42(2002)pp42-45
[4] G. Arnoux et al, Plasma Phys. Control. Fusion 47(2005)295-314
[5] S. Alberti et al, Nucl. Fusion 45(2005)1224-1231
[6] H. P. Laqua, V. Erckmann, R. Brakel, et al., 15th International Stellarator Workshop, Madrid,3-7, October 2005, IT-20.
[7] T. Shimozuma, H. Idei, et al., 27th European Physical Society Conference on Controlled Fusion and Plasma Physics, Budapest, Hungary, June 12-16, 2000, P4.019
[8] N. B. Marushchenko, V. Erckmann, H. Maaßberg, Yu. Turkin, 34th European Physical Society Conference on Plasma Physics, Warsaw, Poland, July 2-6, 2007, P5.129.
[9] N. B. Marushchenko et al., to be published in Plasma and Fusion Research, 2007.
[10] S. Kubo, T. Shimozuma et al., Plasma Phys. Control. Fusion 47(2005)A81-A90.

Proceedings of ITC/ISHW2007

Study of energetic ion confinement during combined NBI and ICRF heating in LHD

S. Murakami, K. Saito[1], T. Seki[1], T. Mutoh[1], R. Kumazawa[1], M. Isobe[1], M. Nishiura[1], T. Ozaki[1], M. Osakabe[1], T. Tokuzawa[1], M. Sasao[2], A. Fukuyama, S.V. Kasilov[3], and LHD Experimental Group

Department of Nuclear Engineering, Kyoto University, Kyoto 606-8501, Japan
[1]National Institute for Fusion Science, Oroshi, Toki, Gifu 509-5292, Japan
[2]Graduate School of Engineering, Tohoku University, Sendai 980-8579, Japan
[3]Institute of Plasma Physics, National Science Center, KIPT, Kharkov, Ukraine

Email: murakami@nucleng.kyoto-u.ac.jp

In the LHD, significant performances of ICRF heating (fundamental, minority heating regime) have been demonstrated and up to 1MeV of energetic tail ions have been observed by fast neutral particle analysis (NPA). These obtained results indicate a good property of energetic ion confinement in helical systems. Recently the perpendicular NBI heating system (P<6MW) has been installed in LHD and a strong coupling between the perpendicularly injected beam ions and the higher harmonics ICRF heating is expected.

In this paper the energetic ion confinement during combined NBI and 2nd harmonics ICRF heating is studied in LHD. We perform the 2nd harmonics ICRF heating experiment in LHD with the perpendicular and tangential injection NBI heating. Energetic ion distributions are measured by several types of NPAs. The differences of the energetic ion distributions are investigated changing the heating conditions.

The energetic ion distribution is also investigated by GNET code[1-3], in which a linearized drift kinetic equation for energetic ions is solved including complicated behaviour of trapped particles in 5-D phase space. The energetic ion distributions are evaluated with NBI and ICRF heating assuming experimentally obtained plasma parameters. As a result, the simulated NPA count number using the GNET results show relatively good agreements with the experimental results.

These results indicate an effective energetic particle generation in the 2nd harmonics ICRF heating in LHD.

[1] MURAKAMI, S., et al., Nuclear Fusion **40** (2000) 693.
[2] MURAKAMI, S., et al., Fusion Sci. Technol. **46** (2004) 241.
[3] MURAKAMI, S., et al., Nuclear Fusion **46** (2006) S425.

Time-Dependent NBI-Heating Simulation of LHD Plasmas with TOTAL (Toroidal Transport Analysis Linkage) Code

T. Ohnishi[1)], K. Yamazaki[1)], H. Funaba[2)], H. Arimoto[1)], T. Shoji[1)]

[1)]*Nagoya University, Furo-cho, Chikusa-ku, Nagoya 464-8603, Japan*

[2)] National Institute for Fusion Science,322-6 Oroshi-cho, Toki 509-5292, Japan

Abstract. The time-dependent simulation of neutral-beam-heated LHD plasmas has been carried out using a simulation code TOTAL (Toroidal Transport Analysis Linkage) focusing on the time evolutions of beam energy and kinetic energy. This code consists of 3-dimensional equilibrium VMEC with bootstrap currents and a 1-dimensional transport HTRANS with neoclassical loss determined by ambipolar radial electric field as well as anomalous transport. The neutral beam deposition is calculated by the Monte Carlo code HFREYA, and the slowing down process was calculated by the Fast Ion Fokker-Plank code FIFPC. The simulated time evolution of total energy including beam energy roughly agrees with the time evolution of the experimentally measured energy. The temporal change in the beam velocity distribution is also clarified.

Keywords: NBI-heating, LHD, Fokker-Plank equation, velocity distribution function, neoclassical transport, anomalous transport

1. Introduction

In order to get high temperature plasmas, neutral beam injection (NBI) heating plays an important role. Since plasma is heated due to collision with fast particle injected by neutral beam injection device, NBI scheme heats both plasma ion and electron efficiently in the future fusion reactors.

Up to now, the simulation of NBI heating in LHD experiments usually has been done in steady-state manner, and the time-dependent heating process has not been clarified in details. In this paper, we focused on the time-dependent simulation of neutral-beam-heated LHD plasma; especially, on the time evolution of kinetic energy and beam energy. In the next section, the simulation model is described. The simulation results are shown in Section 3, and the summary is given in the final section.

2. Simulation Model

In order to analyze LHD plasma heated by negative-NBI heating scheme, we have used Fast Ion Fokker-Planck Code (FIFPC) [1], which solves the slowing down process of fast ions, HFREYA code, which computes the deposition of injected neutral particle in helical plasma, and Toroidal Transport Analysis Linkage (TOTAL)[2, 3] code, which consists of 3-dimensional (3-D) equilibrium/ 1-D transport equations with both neoclassical transport and anomalous transport.

e-mail: t-ohnishi@ees.nagoya-u.ac.jp

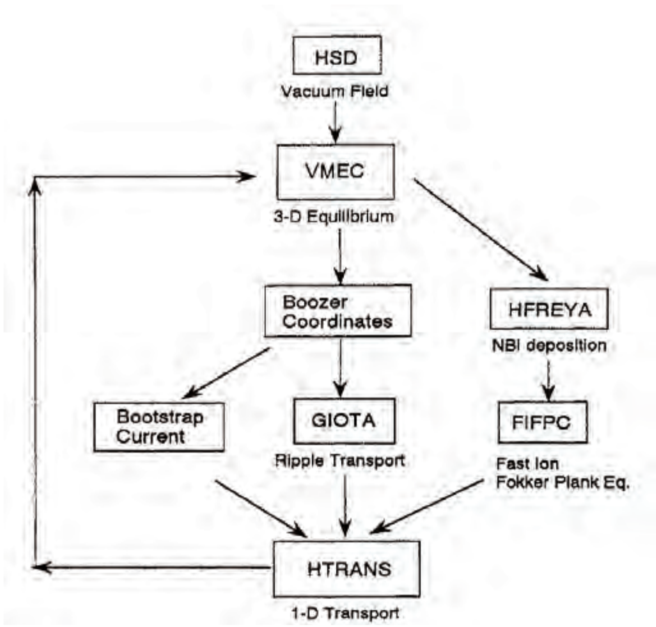

Fig.1 Schematic flow chart of the TOTAL code.

For the analysis of the LHD transport, a 2.0-D equilibrium-transport code has been developed in which the 3-D equilibrium code VMEC [4] and the 1-D transport code HTRANS are used. The NBI deposition is calculated by the HFREYA code, which is a helical modification of FREYA [5], and the slowing down calculation is done with the Fokker-Planck code

FIFPC[1]. The anomalous transport is assumed fitted to the global experimental scaling laws ISS95 scaling law [6] with some confinement improvement factor. The schematic flow chart of this simulation code is shown in Fig. 1.

2.1.Equilibrium analysis

The initial vacuum magnetic surface is calculated by the magnetic tracing code HSD [7] with carefully arranged multi-filament currents. In the paper, the free boundary version of VMEC is used. The FCT and Boot-strap currents can be included; these currents are estimated to be not large enough to affect the present transport analysis done in this paper. The 3-D magnetic field obtained by the finite beta equilibrium of VMEC is used to evaluate the NBI heat deposition and the multi-helicity neoclassical ripple transport coefficients.

2.2. Fokker-Planck equation

To analyze this simulation, we have used FIFPC to solve the Fokker-Planck equation that describes the slowing down process of fast ions. The FIFPC may be used alone for treating neutral beam injection problems, or in combination with transport codes which describe the evolution of helical core plasma. The code is designed to calculate the fast ion distribution function in polar coordinates in velocity space at time t. The Fokker-Planck equation which yields the velocity space fast ion distribution function f(x, θ, t) is

$$\begin{aligned}\tau_s\frac{\partial f}{\partial t} &= -\frac{\tau_s}{\tau_{cx}(x)}f+\frac{1}{x^2}\frac{\partial}{\partial x}\left[\left(x^3-2Bx+x_c^3+\frac{C}{x^2}\right)f\right]\\ &+\frac{1}{x^2}\frac{\partial^2}{\partial x^2}\left[\left(Bx^2+\frac{C}{x}\right)f\right]+\frac{D}{x^3}\left(1-\frac{D_1}{x^2}+D_2x\right)\\ &\times\frac{1}{\sin\theta}\frac{\partial}{\partial\theta}\left(\sin\theta\frac{\partial f}{\partial\theta}\right)+E\left(-\cos\theta\frac{\partial f}{\partial x}+\frac{\sin\theta}{x}\frac{\partial f}{\partial\theta}\right)\\ &-\tau_s\frac{\dot{R}(t)}{R(t)}\left[-(1-\frac{1}{2}\sin^2\theta)x\frac{\partial f}{\partial x}+\frac{1}{2}\sin\theta\cos\theta\frac{\partial f}{\partial\theta}\right]\\ &+\tau_s\sum_l \dot{n}_{f_l}S_l(x,\theta)\,, \end{aligned} \tag{1}$$

where the terms on the right-hand side are due to charge exchange, drag, speed diffusion, angular scattering, the electric field, compression, and the source of injected fast ions, respectively. The plasma major radius, R(t), is time-dependent due to adiabatic compression which is not used here. The Spitzer slowing down time τ_s and the charge-exchange lifetime $\tau_{cx}(v)$ are given by

$$\tau_s = 120\frac{(T_e/1keV)^{3/2}}{(n_e/10^{13}cm^{-3})Z_f^2}\frac{m_f}{m_H}ms, \tag{2}$$

and

$$\tau_{cx}(v) = \frac{6.6[1+1.1\times10^{-15}(0.5m_Hv^2)^{3.3}]}{(n_o/10^8cm^{-3})(1-0.155\log0.5m_Hv^2)^2}\times\sqrt{(\frac{25000eV}{0.5m_Hv^2})}ms, \tag{3}$$

where m_f and m_H are the fast ion mass and the mass of hydrogen. B, C, D, D_1, D_2 and E are constant coefficients given in Ref.[1].

3. Simulation Results

We adopt a typical LHD discharge of the shot number 24512 [8](inward shifted configuration with magnetic axis radius R_{ax} = 3.6m;, magnetic filed strength B_0 = 1.5T) to investigate the NBI-heating process. A tangent injection beam ion energy, E_b, and beam power P_b are 142.9 keV and 4.72 MW, respectively. We have used input value of average electron density $<n_e>_{sim}$ as shown in Fig.2. This figure also shows the experimental value $<n_e>_{exp}$ and NBI power.

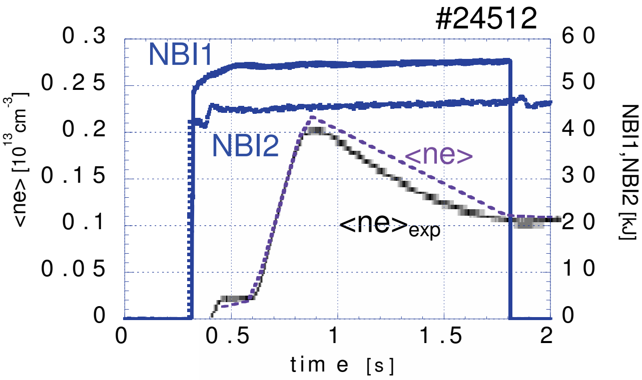

Fig.2 Experimental value of average electron density $<ne>_{exp}$ and NBI power $NBI_{1,2}$ and input value of <ne>.

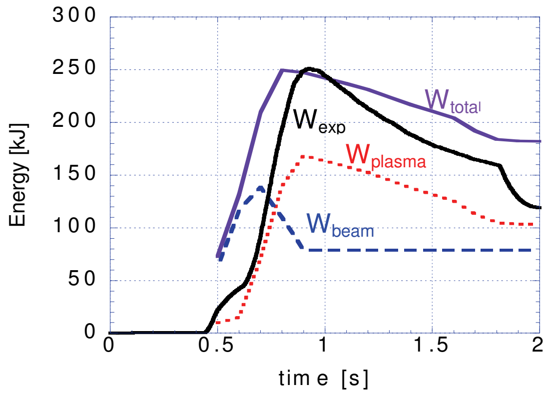

Fig.3 Time evolution of experimental and simulated beam/plasma energy in LHD.

The simulation results and typical experimental plasma energy data observed by diamagnetic coil measurement are shown in Fig. 3. In the figure, W_{total} is the summation of the simulated kinetic plasma energy, $W_{plasma} = 3nk(Te + Ti)/2$, and the beam energy, W_{beam}. In order to compare W_{exp} and W_{total} , we should define $W_{total} = W_{plasma} + fW_{beam}$, where f ~ 1/5 - 1/3. The profiles of W_{exp} and W_{total} roughly agree with each other

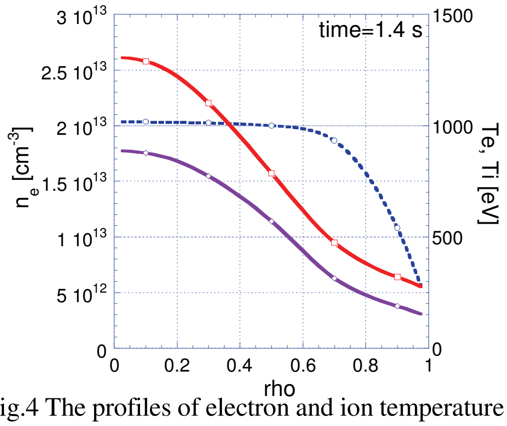

Fig.4 The profiles of electron and ion temperature and electron density at 1.4 s obtained in simulation.

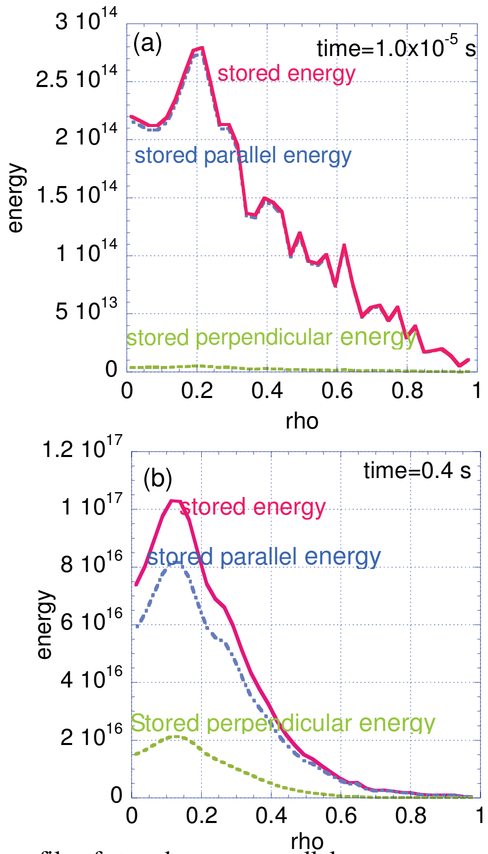

Fig.5 profile of stored energy, parallel energy component and perpendicular energy component in plasma: (a) 1.0×10^{-5} s; (b) 0.4 s.

The Fig.4 shows electron density, n_e, and electron and ion temperature, Te and Ti, at 1.4 s. The density profile in the core is flat up to ρ=0.6. The electron temperature in plasma core is 1.4 keV, and the ion temperature is 0.9 keV.

The Fig.5 shows stored beam energy in the plasma at (a) 1.0×10^{-5} s and (b) 0.4 s. The parallel component and perpendicular component of stored energy is also plotted in Fig.5. At 1.0×10^{-5} s, the stored energy is almost parallel component energy. The perpendicular component is very low energy. At 0.4 s, the perpendicular energy increases to about a quarter of parallel energy. The beam energy is gradually transferred to various angles by diffusion and scattering process. So we investigated the distribution function in velocity space in order to analyze the details of energy transfer.

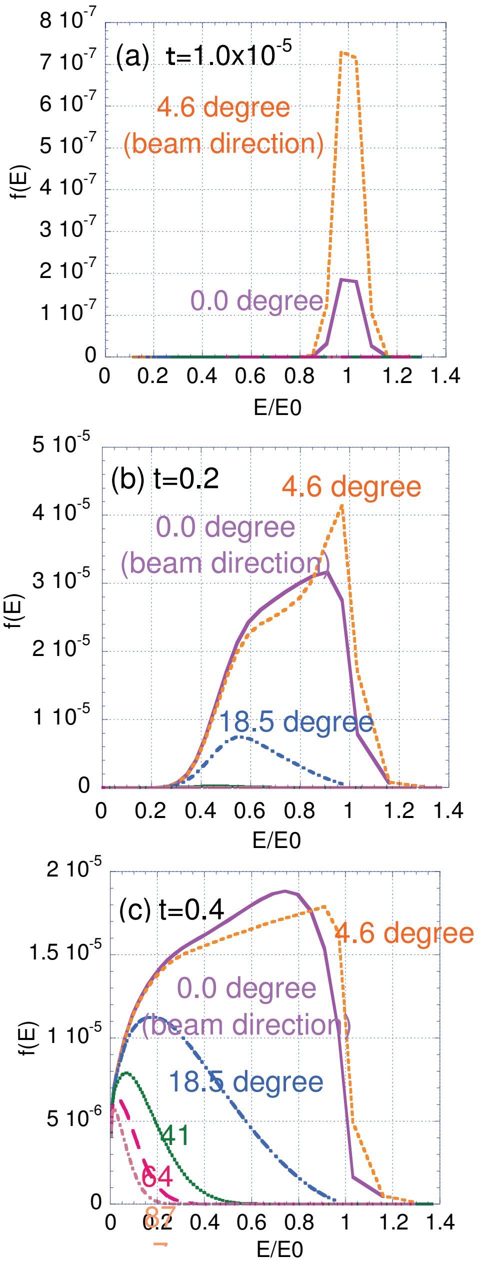

Fig.6 The distribution function of the beam ions calculated by Fast Ion Fokker-Planck Code (FIFPC); (a) 1.0×10^{-5} s, (b) 0.2 s, (c) 0.4

The Fig.6 shows the distribution function in velocity space at ρ = 0.47. The figures (a), (b) and (c) are profiles of the distribution function at 1.0x10^{-5} s, 0.2 s and 0.4 s respectively. At 1.0x10^{-5} s, there are many ions of high energy at E/E_0=1. The beam energy is gradually transferred to high angles.

We can see from Figs. 5 and 6 that the beam consists only from the well circulating particles, and the most energetic ions are located in the plasma core.

In the code, particle orbit effects can be included by bounce average orbit in the heating process, however, this effect is not evaluated in the present simulation, because the present discharge analyzed here is the medium field, low beta operation. In the lower magnetic field and higher beta plasma case, this effect should be included.

4. Summary

We analyzed NBI-heating time-dependent process with TOTAL code. The stored energy is almost parallel component directly after injection. Later, the energy is gradually transferred to perpendicular component by diffusion and scattering process. In order to analyze the velocity distribution in detail, we used Fast Ion Fokker-Planck Code (FIFPC), which solves the Fokker-Planck equation. Directly after injection, there are many ions of high energy at E/E_0=1. Later, the high energy ion is gradually transferred to plasma core direction.

We can conclude from here that (i) the beam consists only from the well circulating particles, and (ii) the most energetic ions are located in the plasma core; there, the beam can hardly lead to edge-localized instabilities.

In summary, the time evolution of simulated total energy including beam energy roughly agrees with that of the experimentally measured energy. The temporal change in the beam velocity distribution is also clarified.

References

[1] R.H.FOWLER, et al., Computer Physics Communications **13** (1978) 323

[2] K. Yamazaki, T. Amano, Nuclear Fusion **32** (1992)

[3] K. Yamazaki, et al., Fusion Engineering & Design **81** (2006) 2743-2748

[4] HIRSHMAN, S.P., Van RIJ, W.I. MERKEL, P., Comput. Phys. Commun. **43** (1986) 143.

[5] LISTER, G.G., POST, D.E., GOLDSTON, R., in Plasma Heating in Toroidal Devices (Proc. 3rd Symp. Varenna, 1976), Editrice Compositori, Bologna (1976) 303.

[6] U. Stroth, M. Murakami, R.A. Dory, H. Yamada, et al., Energy confinement scaling from the international stellarator database, Nucl. Fusion **36** (1996) 1063-1077.

[7] K.Yamazaki, et al., M., Fusion Technol. **21** (1992) 147.

[8] Ya. I. Kolesnichenko et al., Phys. Plasmas **Vol.11**, No.1 (2004) 158-170

P2-079

Development of radial neutral beam injection system on LHD

M.Osakabe, K. Nagaoka, K.Tsumori, Y.Takeiri , K.Ikeda, Y.Oka,M.Sato, T.Kondo, M.Shibuya, E.Asano, S.Komada, O.Kaneko and LHD experimental group

National Institute for Fusion Science,322-6 Oroshi-cho, Toki 509-5292, Japan

A radial Neutral Beam Injector (NBI) is newly installed on the Large Helical Device (LHD). The aims of the NBI are its usage as a diagnostic NB for charge exchange recombination spectroscopic measurement and using the NB as a heating source for ions in plasmas. A new positive-ion source was developed for this NBI at NIFS. The structure of the cusp field of the source was determined by the numerical code and its performances were verified by experiments. The performances of the developed source fulfill its specification. Especially, the maximum beam current of 102[A] exceeds the requirement of 75[A] about 33[%].

Keywords: NBI, large positive ion sources, radial beam injection

1. Introduction

A positive-ion based Neutral Beam Injector (NBI) is newly installed on the Large Helical Device (LHD). The major purposes of installing this NB on LHD are; (1) to provide a tool for ion temperature profile measurement and for electric field profile measurement by using this NB as a diagnostic beam for Charge eXchange Recombination Spectroscopic (CXRS) measurement, (2) to achieve the high ion temperature regime on LHD by producing peaked density profiles with central beam fueling and by an intensive ion heating with low energy and high power beam, and (3) to use this NB as a probe beam for investigating the confinement property of perpendicular fast ions on LHD.

In this article, we will show our research and development results for the new positive ion-source for the radial NBI. In designing the ion-source, the thickness of a plasma-electrode, which is an electrode facing to the ion-source plasma, was the most important issue since it significantly affects the optics of extracted ion-beam. Considering the beam-optics, the thickness of the electrode is preferred to be as thin as possible. But, in the actual case, the electrode needs to have finite, i.e., non-zero, thickness so that it can have enough strength to avoid the distortion by the gravity and by thermal heat loads. The required thickness depends on the heat loads onto the electrode, and also on the material and cooling structure of it.

The arc-efficiency is also an important parameter of ion-sources, where the efficiency is defined by the ratio of extracted beam current to the required arc-power in sustaining ions-source plasmas. Since the heat load onto a plasma electrode can be considered to be proportional to the arc-power, the increase of the arc-efficiency will reduce the heat load onto the electrode. Thus, achievement of high arc-efficiency will help to reduce the thickness of a plasma electrode.

The specification of the radial-NBI on LHD and its ion-sources are briefly discussed in Sec.2. The design of cusp-field configuration for the ion-source is shown in Sec.3. The determination of its plasma-electrode thickness is shown in Sec.4. The operation of the source at the NBI are shown in Sec.5. The section 6 is a summary.

2. Specification of the radial-NBI and its ion-sources

Figure 1 shows the schematic drawing of the radial-NBI on LHD. Its specifications are shown in Table 1. As shown in this table, the required performances on the ion-source is almost comparable to those of the giant positive ion sources for NBI [1-3].

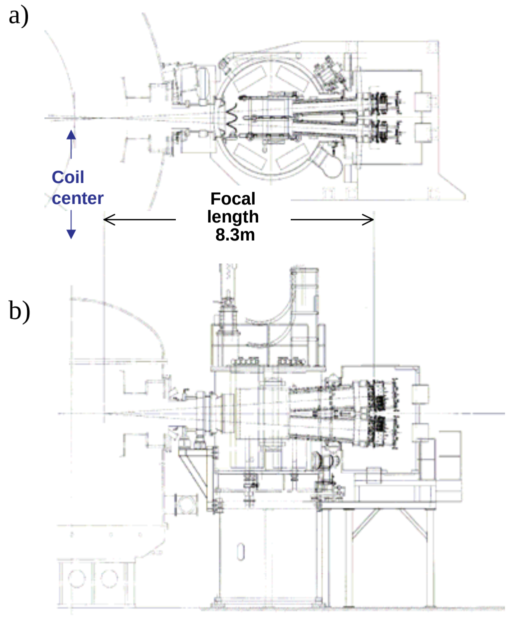

Fig.1 Schematic drawing of the radial-NBI on LHD. (a) Top-view and (b) side –view.

author's e-mail:osakabe.masaki@lhd.nifs.ac.jp

Table 1 Specification of LHD radial-NBI

Beam species	Hydrogen
Injection energy	40 [keV]
Total Injection power	6 [MW]
Beam pulse duration	10 [s]
Injection port-size	ϕ 0.8[m]
Size of NB-protection armor at the injection counter wall	(W)1[m] x (H)1 [m]
Focal length and pivot length of ion-sources	8.3[m]
Type of ion source	Positive ion-source
Electrode system	Accele-decel-ground electrodes system.
Number of ion sources	4
Beam current required for single ion source	75[A]
Beam extraction area	(W)0.21[m] x (H)0.5 [m]
Transparency of the electrode	35[%]

The injection energy was chosen to be 40-keV with Hydrogen beam ion species. This energy was determined by the requirement of CXRS measurement. To have enough penetration of NB into the core-region of LHD plasmas, the beam was injected radially to the LHD torus, thus the injected fast ions has its kinetic energy mostly on the perpendicular direction to the magnetic-field lines.

One of the largest limitations in designing a radial-NB injector on LHD is the small-protection area of its injection counter wall and the limitation on the size of injection-port. The former limitation comes from the fact that there is no enough space left in the inboard side of LHD vacuum vessel to install protection armor tiles

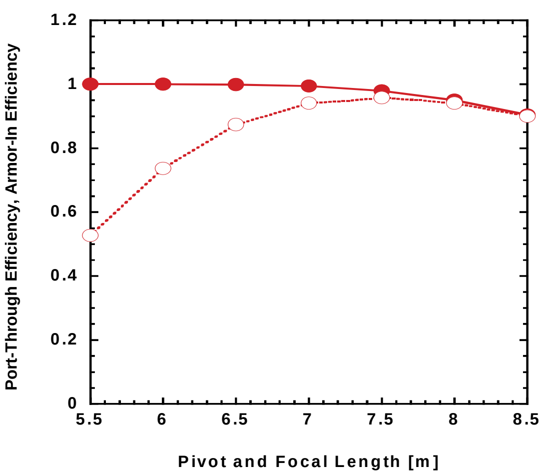

Fig.2 Calculated port-through efficiency (solid lines with closed circles) and armor-in efficiency (dashed lines with open circles)of the radial-NB.

with cooling structures at the toroidal section where plasmas are vertically elongated. At this location, the vacuum vessel walls, which cover the helical coils, significantly project to the LHD-plasma. Therefore, it is very important to consider the injectors's configuration which maximize the armor-in efficiency as well as port-through efficiency. Here, armor-in efficiency is defined by the ratio of the beam power which goes into the inside of the protection armor plates to the total neutral beam power. The pivot-length and focal-length of the ion-sources were determined to maximize the armor-in efficiencies and to minimize the difference of these two efficiencies, simultaneously. It was found that the focal length is better to be equal to the pivot length of the ion-sources to maximize the armor-in efficiency. From Fig.2, the pivot and focal length of 8[m] is determined to be the best, but they were set to 8.3[m] at the final design to avoid the interference with the diagnostic ports for CXRS-measurements.

3. Design of an arc-chamber of the ion-source for the radial-NBI

Several structures of cusp magnetic-field were surveyed for the ion-source of the radial-NBI using a code developed by Tsumori. *et.al.*[4,5]. Among them, two of the configurations were chosen as candidates for the ion-source. The calculated distributions of cusp field lines and those of primary electrons from filaments are shown in Fig.3. The calculation shows that type-A configuration has better confinement than type-B, i.e., the 63% of electrons launched from filament locations are confined for type-A, while only 15% are confined for type-B. On the other hand, type-B configuration has more electrons in the region close to the plasma electrode and better uniformity in this region than type-A as shown in Fig.3(c) and (d).

A series of experiments to compare the arc-efficiencies of these two configurations was performed at NIFS-NBI test-stand since it was very difficult to determine which cusp configurations are better in the efficiency just from the simple orbit calculations. The arc-efficiency of 0.44[A/kW] were obtained for type-A configuration, while that of 0.35[A/kW] are for type-B as shown in Fig.4. We must note that the half of the plasma-electrode was masked to limit the beam current in these experiments since the acceleration power supply at the test-stand can only handle the beam current of 40[A]. Thus, the arc-efficiencies in the test-stand experiment became about a half of those for non-masked configuration. No significant differences were observed on beam-profiles between the two cusp configurations. It was confirmed by experiments that the confinement of primary electrons was more important than the uniformity and the numbers

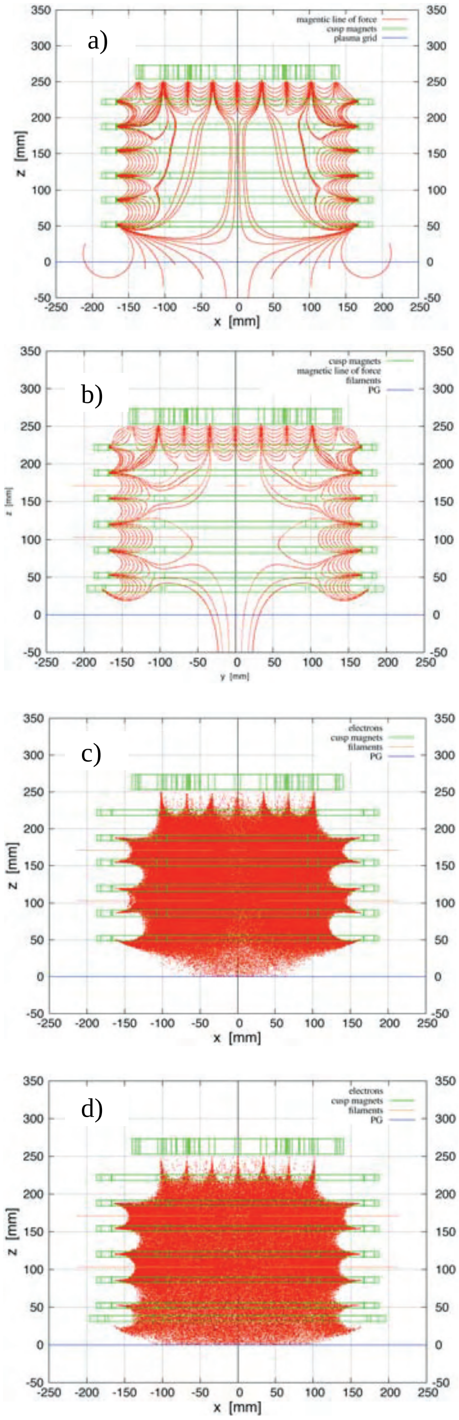

Fig. 3 Calculated magnetic filed lines for (a)type-A and (b)type-B cusp configurations. Magnetic field lines are shown by red lines and the location of permanent magnets are by green lines in these figures. Primary electron distribution are shown by red-dots in (c)type-A and (d)type-B. The z=0 lines show the location of plasma electrode.

of them in the region near plasma electrode by the experiment. Thus, the type-A configuration is adopted as the cusp configuration of the ion sources for the radial NBI.

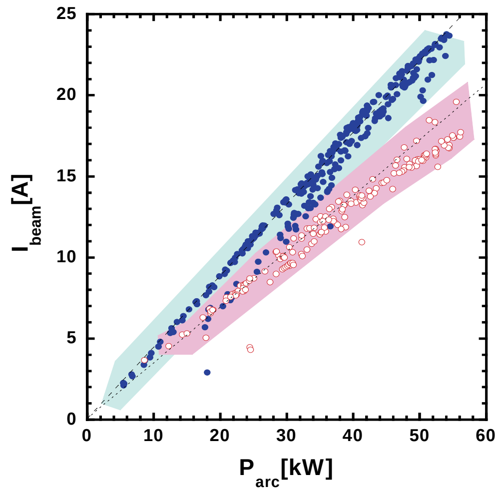

Fig.4 The comparison of arc-efficiency for type-A (closed-blue-circles) and type-B (open-red-circles) cusp configurations.

4. Determination of plasma electrode thickness of the ion-source for the radial-NBI

As a plasma electrode of the ion-source, we have adopted a oxygen-free copper electrode with water-cooling channels which is placed to each raw of beam extraction holes. The thickness of the electrode is required to be greater than 4-mm from the view point of mechanical strength and heat load handling, while this is to be less than 3.3-mm from the view point of beam-optics. To overcome the conflict, experiments of beam extraction using electrodes of both thicknesses were also performed at the NBI test-stand. For these two electrodes, the perveances, which express the beam currents normalized by acceleration voltages according to

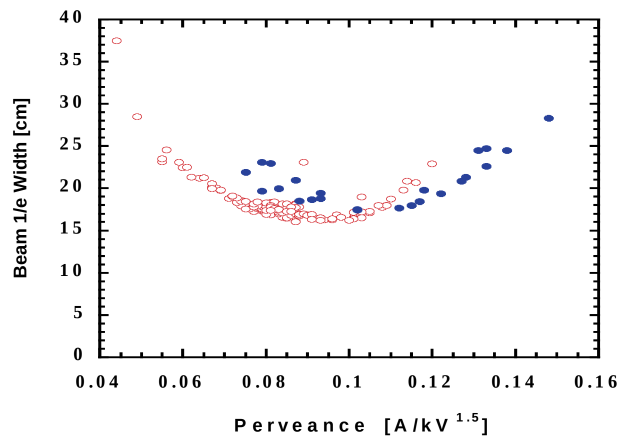

Fig.5 Perveance dependence of beam profile width. The beam widths for a 4-mm thick plasma-electrode are shown by the open-red-circles, while those for a 3.3-mm thick electrode are by closed-blue-circles.

the Child-Langmuir law, were scanned to find their optimum value where the beam widths have their minimum in the experiments (Fig.5). The distance of the gap between a plasma-electrode and a decel-electrode was 6.5[mm] at the experiments for the 3.3[mm] thick electrode, and was 6[mm] at those for 4[mm] thick one. As shown in Fig.5, the optimum perveance for the electrode of 3.3[mm] thickness is larger than that for the 4[mm] thickness. Thus, the electrode of 3.3[mm] thickness has preferable feature, as is expected. Taking the gap(d_{gap}) dependence of the Child-Langmuir law, where the beam current is proportional to d_{gap}^{-2}, into an account, this tendency becomes more significant.

The distortion of plasma-electrode by the heat loads can be evaluated by the change of beam profile with the heat loads. The dependence of beam widths on the heat loads of the plasma electrode are shown for the 3.3[mm] thick electrode in Fig.6. The heat loads were measured by a water calorie-metric method using the cooling water of the electrode. Scan of the heat loads are done by changing the duration time of arc-discharges preceding with the beam extraction. These heat loads in the figure correspond to the beam duration time of 0.3[s] to 4[s]. To minimize the dependence of beam widths on perveances, beams are extracted at around the optimum perveance condition. As shown in Fig.6, the dependence of beam widths on the heat loads are almost negligible. Therefore, it was concluded from these experiments that the 3.3[mm] is thick enough as a plasma-electrode of the ion-source.

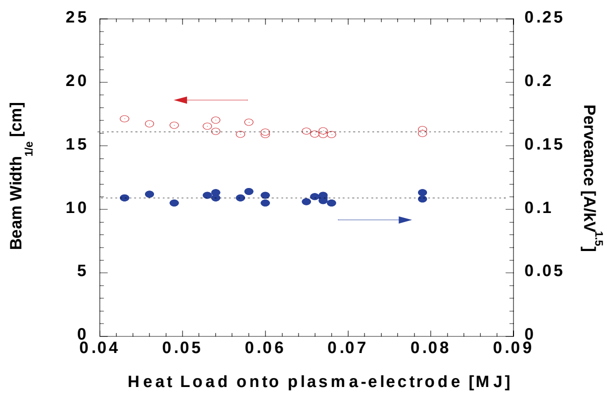

Fig.6 Dependence of beam widths on the heat loads of plasma-electrode. The beam widths are shown by open-red-circles, the perveances of the beam are also shown by closed-blue-circles.

5. Operation of ion-source at the radial-NBI

The acceleration power supply of the radial-NBI is designed to operate two ion-sources with single power supply. With the operatin of single ion-source with this power supply, the maximum beam current can be evaluated (Fig.7). The arc-efficiency of the source was 0.78[A/kW] in thses experiments. The maximum beam current of 102[A] was achieved at the acceleration voltage of 40[kV]. The averaged current density exceeds 250[mA/cm^2] with this maximum beam current. The maximum of the current was limited by the operational limit of arc-discharge, i.e., arc-discharges of the ion-source became unstable when the arc-power exceeded 120[kW]. The optimum perveance was examined using the calorie-meter array in the injector. It was 0.28[A/kV$^{1.5}$] when the gap distance (d_{gap}) was set to 5.5[mm]. The total injection power of 7.2[MW] was achieved with simultaneous four ion-sources operation.

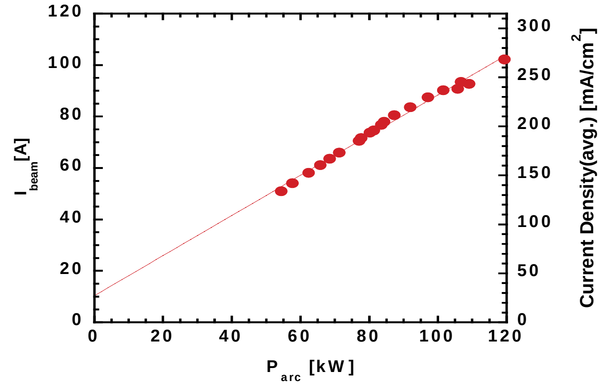

Fig.7 Arc-discharge power dependence of extracted beam current of the source at the radial-NBI.

6. Summary

A radial-NBI using positive ion-sources was installed and is successfully operated on LHD. To fulfill the specifications of the NBI, a giant positive ion source was newly developed at NIFS. The performances of the developed source fulfill its specification. Especially, the maximum beam current of 102[A] exceeds the requirement of 75[A] about 33[%].

Acknowledgement

Authors wish to thank the continuous encouragement by the Director general (Prof. Motojima) and the project leader of LHD (Prof. Komori). This work is supported by the NIFS05ULBB501.

References

[1] M.C.Vella, *et.al.*, Rev. Sci. Instrum. **59**,2357 (1988)

[2] T.S.Green, *et.al.*, Proceedings of the 10th International Conference on Plasama Physics and Controlled Nuclear Fusion Research, London,1984 (IAEA Vienna, 1985), Vol.3, p.319

[3] S.Tanaka,*et.al.*, Rev. Sci. Instrum. **57**, 145(1986)

[4] K.Tsumori, Ph.D Thesis, “Improvement on Large Scaled Hydrogen Negative Ion Sources for Neutral Beam Injector “ (in Japanese), Nagoya university, 2007

[5] O.Kaneko, *et. al.* Nucl. Fusion, **46,** 692 (2003)

Proceedings of ITC/ISHW2007

Beamlet monitoring on the beam accelerator with multi-slot grounded grid for LHD-NBI

K. Tsumori, K. Nagaoka, M. Osakabe, K. Ikeda, Y. Takeiri, Y. Oka, O. Kaneko, M. Shibuya, E. Asano, T. Kondo, M. Sato and S. Komada.

National Institute for Fusion Science,322-6 Oroshi-cho, Toki 509-5292, Japan

tsumori@nifs.ac.jp

In order to obtain the better beam injection power, the investigation on beam characteristics is one of the important issues for the neutral beam injectors (NBI). The beam accelerator consists of the multi-electrode grids with multi-apertures, and the accelerator has following three functions to gather the multi-beamlets. The first is the beam focusing which is determined by a ratio of the electrostatic potentials supplied to the grids. The second is the beam concentration by gathering the multi-beamlets at a point near the beam injection port. The last is the correction of the beamlet trajectories deflected by the magnetic field prepared to sweep the co-extracted electrons with H^- ions in the negative ion sources. The whole beam is a superposition of the multi-beamlet, and the observation of the beamlet characteristics is necessary to separate the errors of the beamlet-handling functions described above. A new type of beam accelerator is installed in one of the LHD-NBI beamlines. The accelerator consists of a hybrid configuration of the grids with multi-apertures and multi-slots, and the configuration has the different beam characteristics comparing to the conventional accelerators [1,2]. In order to investigate the beamlet characteristics, we installed a beamlet monitoring system with a graphite plate and infrared camera. The beamlet profiles are observed as a temperature images on the graphite plate, and the images are recorded with the infrared camera. Using the monitoring system, we found that the minimum beamlet divergent angles in the directions parallel to the slot long and short sides are 4 and 6 mrad, respectively. Some errors in the beamlet steering angles, which is applied to multi-beamlets concentration are observed. The errors are corrected in the accelerator for the LHD experiment.

[1] K. Tsumori, K. Nagaoka, M. Osakabe et. al, Rev. of Sci. Instrum, **75** (2004) 1847.
[2] K. Tsumori et al, proceedings of the 20th IAEA conference FT/1-2b, Vilamoura (2004).

Proceedings of ITC/ISHW2007

Unstable Slower Branch of Fast Cyclotron Waves in Gyrotrons and BWOs

Kazuo MINAMI
Faculty of Engineering, Tokyo Denki University, Chiyoda-Ku, Tokyo, 101-8457 Japan

kminami@msa.biglobe.ne.jp

Common existence of an unstable slower branch of fast cyclotron waves in gyrotrons and backward wave oscillators (BWOs) is analyzed numerically within the scope of linear treatment of beam-plasma systems. The dispersion relation including space charge mode and fast electron cyclotron mode for large orbit annular beam neutralized by ions in a BWO is calculated for various values of amplitude *h* of corrugation in the slow wave structure (SWS). It is shown that, as *h* tends to zero, conventional Cherenkov instability in the axial direction in the space charge mode vanishes, whereas Cherenkov instability in the azimuthal direction (CIAD) [1, 2] in the fast cyclotron mode survives to be unstable. This fact has not been known in plasma physics and gyrotron engineering. The CIAD can be another principle of cyclotron emission in addition to cyclotron resonance maser (CRM) instability in gyrotrons, when high-density neutralized beams are working.

Gyrotrons and BWOs are typical examples for high-power microwave sources. The former and the latter belong to the categories of fast and slow wave devices, respectively. Both devices have been developed independently, and they are considered to have no particular relationship with each other. However, they have a common similarity in structure: Both are operated in the passage of an electron beam streaming through a metal waveguide immersed in an axial magnetic field. The model of analysis for BWOs becomes identical to that for gyrotrons when the amplitude *h* of corrugation of the SWS in BWOs tends to zero. The electron beam in BWOs generally has more or less a small transverse velocity and resultant cyclotron motion, because the beam is conventionally produced by magnetically insulated diode in vacuum. Experimentally, cyclotron motions in the beam have existed in BWOs. Previously, sufficiently large axial magnetic field B_0 was assumed in the analyses on BWOs, and no effects of cyclotron resonance was taken into account, analytically. In recent years, however, analyses of BWOs with finite strength B_0 have been developed considerably [3]. Inclusion of finite B_0 has made analytical models of fast and slow devices borderless. In other words, the distinction between gyrotrons and BWOs became ambiguous near cyclotron resonance. Theoretical treatment of a combined Cherenkov-cyclotron resonance interaction is becoming possible in recent years, accordingly. In this paper, the author shows numerical examples of common existence of unstable slower branch of fast cyclotron wave in slow and fast wave devices.

[1] Y. Choyal, T. Watanabe and K. Minami, *IEEE Trans. Plasma Sci.* **32(**2004)1298.
[2] K. Minami, Y. Choyal and T. Watanabe, J. Plasma Phys. **73**(2007)523.
[3] K. Minami, M. Saito, Y. Choyal, K. P. Maheshwari and V. L. Granatstein: *IEEE Trans. Plasma Sci*. **30(**2002)1134.

Proceedings of ITC/ISHW2007

Non-Bethe's Theory and its Experimental Verification of Two Coupled Microwave Cavities

K. MINAMI and M. SUGITO[a]

Tokyo Denki University, Chiyoda-Ku, Tokyo, 101-8457 Japan
[a] *National Institute for Fusion Science, 322-6 Oroshi-cho Toki 509-5292 Japan*

kminami@msa.biglobe.ne.jp

Theory on two coupled microwave cavities different from that given by Bethe [1] is formulated and verified experimentally. Recent development of microwave communication including movable phones has changed human life significantly. Nevertheless, we do not necessarily understand basic electromagnetic field for communication among metal structure with a small hole or aperture, for example. In 1944, Bethe analyzed such problems in detail and elucidated how incomplete existed solutions were and how complicated corrected ones were. At the end of the paper, he discussed the field patterns in two coupled microwave cavities separated by a metal screen with a small circular hole. In the cavities, co-phase $(\phi = 0)$ and anti-phase $(\phi = \pm\pi)$ oscillations were distinguished, where ϕ is the phase difference. The fields in both sides of the hole in the former oscillate in phase, as if there is no effects of the screen at both sides of the hole and oscillate as a whole cavity, whereas in the latter the fields are 180 degree out of phase with each other, as if two cavities oscillate nearly independently.

In order to verify his theory experimentally, we try to detect microwave transmission through cylindrical coupled cavities for frequency range 2-4 GHz. Inner wall of the fabricated cavities is silver with inner radius 77 mm and length 160-200 mm changed by movable disks. Coupled cavities with Q factors on the order of 10^4 have an identical axis and separated by a copper circular disk with a hole of various sizes and locations. Two loop antennas are inserted in the radial direction. One of them is to feed microwave less than 50 mW with 0.4 % frequency modulation to excite TE or TM modes to the first cavity, and the other detects the transmission coefficient $|T|^2$ from the second cavity that is displayed on the digital oscilloscope TDS2024B (Tektronix) through 40 dB amplifier Model-APA0204 (ALC microwave Ltd). Somewhat surprisingly, no predicted modes by Bethe are observed until now. Instead, it has been found that the observed modes of resonance as a function of frequency are explained by an assumption of $\phi = \pm\pi/2$, namely, the coupling hole is a reactive (inductive or capacitive) element for microwaves propagating in positive and negative directions inside the cavities. The coupled cavities are successfully analyzed by using the scattering matrix theory for microwave circuits [2]. Our limited experiments do not invalidate the Bethe's theory.

[1] H. Bethe, Phys. Rev. Second Series **66**(1944)163.
[2] J. L. Altman, Microwave Circuits, New York: van Nostrand, p. 202(1964).

Proceedings of ITC/ISHW2007

Automatic Analysis of Multichannel Time Series Data Applied to MHD Fluctuations

D. G. Pretty[1)], B. D. Blackwell[1)], F. Detering[1)], M. Hegland[3)], J. Howard[1)], D. Oliver[1)], M. J. Hole[2)] and J. H. Harris[4)]

[1)]*Plasma Research Laboratory, and*
[2)]*Department of Theoretical Physics, Research School of Physical Sciences and Engineering, and*
[3)] *Mathematical Sciences Institute, all of the Australian National University, ACT, 0200, AUSTRALIA*
[4)] *Oak Ridge National Laboratory, Tn, USA*

We present a data mining technique for the analysis of multichannel oscillatory timeseries data and show an application using poloidal arrays of magnetic sensors installed in the H-1 heliac. The procedure is highly automated, and scales well to large datasets. In a preprocessing step, the timeseries data is split into short time segments to provide time resolution, and each segment is represented by a singular value decomposition (SVD). By comparing power spectra of the temporal singular vectors, singular values are grouped into subsets which define fluctuation structures.

Thresholds for the normalised energy of the fluctuation structure and the normalised entropy of the SVD are used to filter the dataset. We assume that distinct classes of fluctuations are localised in the space of phase differences (n, n+1) between each pair of nearest neighbour channels. An expectation maximisation (EM) clustering algorithm is used to locate the distinct classes of fluctuations, and a cluster tree mapping is used to visualise the results. Different classes of fluctuations in H-1 distinguished by this procedure are shown to be associated with MHD activity around separate resonant surfaces, with corresponding toroidal and poloidal mode numbers. Equally interesting are some clusters that don't exhibit this behaviour.

Keywords: Data mining, plasma physics, Mirnov oscillations, magnetic fluctuations

1 Motivation

Rotational transform parameter scans have been undertaken in the H-1NF heliac [1, 2, 3]. Using 28 Mirnov coils over 92 discharges, with each shot incrementally changing the magnetic geometry, a large set of timeseries data was produced.

The motivation for the present work has been to find an algorithm which, with minimal human interaction, can group together all similar fluctuations over a large number of shots. Here we present our method, showing that it can be used to discover interesting spectral features and to map classes of fluctuations to any known parameter of the dataset, e.g.: magnetic geometry.

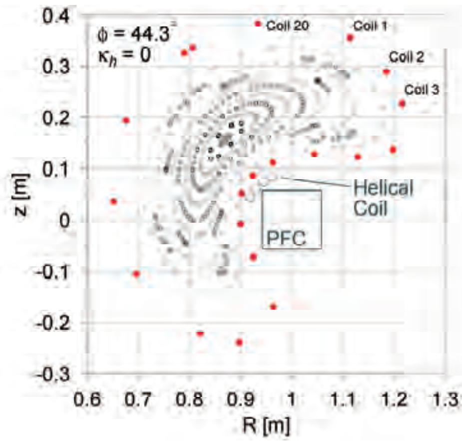

Fig. 1 One of two poloidal Mirnov coil arrays installed in the H-1 heliac

2 Data

Two toroidally-separated poloidal Mirnov coil arrays were used in the experimental campaign described here, one array is shown in figure 1. An additional linear array of 5 coils is also installed. In all, 28 Mirnov coils are used in this dataset.

The experimental parameter scanned is κ_h, the ratio of current in the helical winding coil to that in the toroidal and poloidal field coils. To a good approximation, κ_h scales linearly with rotational transform on axis (ι_0). Due to the precisely controllable coil power supplies, very reproducible plasmas can be formed with an accuracy in vacuum field rotational transform of 1 part in 1000. The range of configurations used here is shown in figure 2, from a monotonic profile with $\iota_0 = 1.12, \iota_a = 1.28$ ($\kappa_h = 0$) to a reverse-shear profile with $\iota_0 = 1.45, \iota_a = 1.46, \iota_{\min} = 1.41$ ($\kappa_h = 1.07$).

The time evolution of Mirnov spectra and line-averaged electron density for shot typical of this dataset are shown in figure 3. The RF power is essentially constant at 60 kW, producing peak density of $\bar{n}_e = 10^{18}\mathrm{m}^{-3}$. The

author's e-mail: david.pretty@anu.edu.au

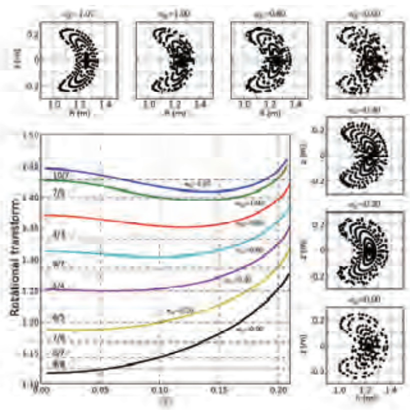

Fig. 2 Rotational transform profiles used in this campaign. Poincaré plots shown for the various magnetic configurations.

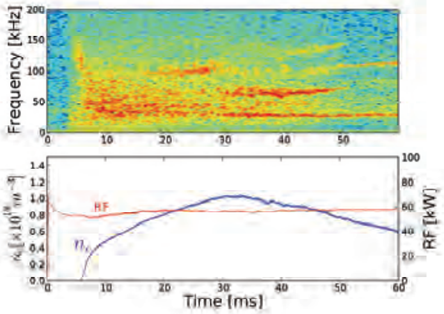

Fig. 3 Typical shot for this campaign (at κ_h = 1.0), showing Mirnov spectra in the top panel and line-averaged electron density in the lower panel. Heating power (60 kW RF) is essentially constant throughout the discharge.

Mirnov spectra shows multiple co-existing modes, with the higher frequency features (f > 50 kHz) showing Alfvénic density scaling ($f \propto n_e^{-1/2}$).

3 Data Pre-processing

Data mining procedures generally have 3 stages: firstly the data needs to be pre-processed into a format suitable for the main algorithm; secondly the main algorithm (neural network, clustering, association rules, etc) is applied to the data, finally the results are visualised and interpreted. The pre-processing used here involves separating out different mode components from the timeseries data and mapping them to a phase space in which the main clustering algorithm is used to distinguish different classes of fluctuation.

For each shot, we split the timeseries data into short time segments, in this case we use Δt = 1 ms. For each short time segment, we take the singular value decomposition (SVD) [4] of all Mirnov channels. Noise is filtered out of the system by placing a threshold on the normalised energy of a singular value ($p_k = a_k^2/E$, $E = \sum_{k=1}^{N_{\mathrm{Ch}}} a_k$ for s.v. a_k and $N_{\mathrm{Ch}} < N_s$ where N_{Ch} is the number of channels and N_s is the number of samples in Δt). Noisy short time segments can be filtered with a threshold value of normalised entropy ($H = -\sum_k p_k \log p_k / \log N_{\mathrm{Ch}}$).

A mode can be be described by several singular values, for example a rotating mode will have two orthogonal bases (i.e. sine and cosine topos (spatial basis vector) with chronos (temporal basis vector) also with $\pi/2$ phase difference). We assume that singular vectors whose chronos have similar power spectra belong to the same mode, grouping together sets of singular values with normalised cross-power above a threshold value γ:

$$\gamma_{a,b} = \frac{G(a,b)^2}{G(a,a)G(b,b)}, \; G(a,b) = \langle |\mathcal{F}(a)\mathcal{F}^*(b)| \rangle, \quad (1)$$

where $\mathcal{F}$ is the Fourier transform, and $\langle \ldots \rangle$ represents the spectral average. An examination of a randomly selected subset of SVDs showed that a threshold of $\gamma = 0.7$ is suitable for the present dataset. Each group of singular values defines a *fluctuation structure*.

For each fluctuation structure, we take the inverse SVD using only the allocated subset of singular values (others are set to zero) to return timeseries data for each coil representing the given fluctuation. From these timeseries we take the phase differences between nearest neighbour coils to produce coordinates in N_{Ch}-dimensional phase space ("$\Delta\phi$-space") in which the clustering algorithm operates.

4 Clustering

We aim to discover any underlying lower-dimensional model of the dataset, i.e.: to group data points into classes or modes which can then be mapped back to other properties, such as magnetic geometry. We assume that distinct modes of fluctuation will be localised in the $\Delta\phi$-space defined by the nearest neighbour phase-differences. This $\Delta\phi$-space localisation can be easily understood in the simplified case of poloidally equispaced Mirnov arrays in cylindrical geometry – here a mode with poloidal mode number m will be localised in the region of $\Delta\phi(i, i+1) = 2\pi m/N_M$, where N_M is the number of Mirnov coils in the array. Clearly the heliac geometry is not so simple, however the clustering algorithm can find arbitrary phase structures and there is no need to interpret the phase structure before clustering.

We use the expectation maximisation (EM) clustering algorithm which finds the most likely values of latent variables in a probabilistic model [6]. Here we model the data by N_{Cl} N_{Ch}-dimensional Gaussian distributions in $\Delta\phi$-space, with mean and standard deviation for each cluster as the set of latent variables. To ensure the results are not biased by the assumption of Gaussian cluster shape, we compare the EM clustering results with results from an ag-

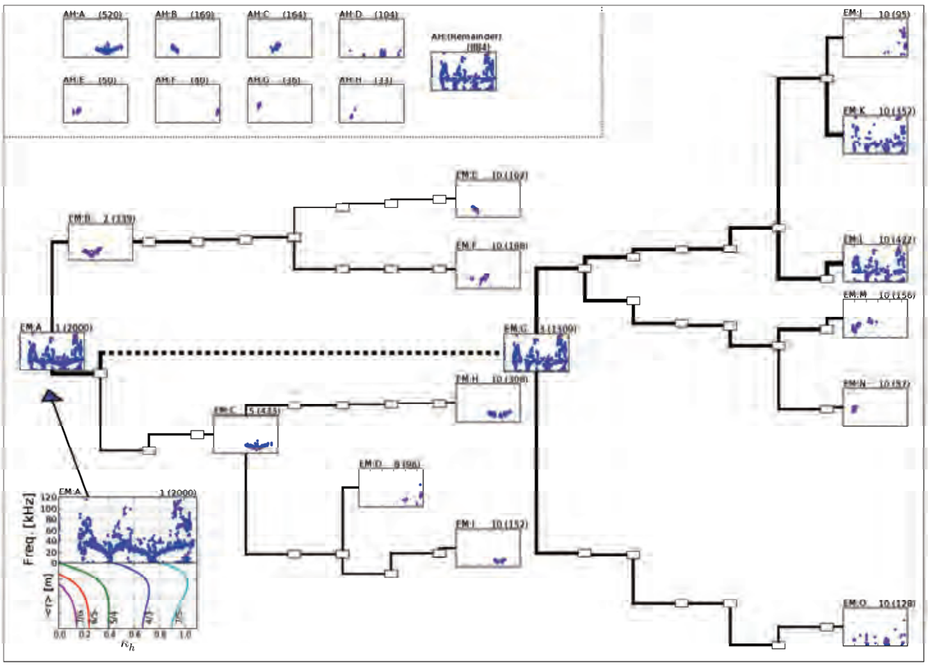

Fig. 4 A Cluster tree representation of the κ_h scan data. The figure in the bottom left corner contains the whole dataset; its upper panel shows the fluctuation structures mapped to f and κ_h, the numbers 1 (2000) at the top right are the tree level, N_{Cl} , and cluster population respectively. The lower panel shows the contours of low-order rational surface within the plasma minor radius (y-axis) for the configurations. For clarity, only a subset of clusters within the tree have their contents displayed and EM:G has been displaced to prevent overlap. Vertical parent-child distance is proportional to the distance between cluster means, while line thickness is inversely proportional to the Gaussian width of the cluster. Several AH clusters are also shown for comparison.

glomerative hierarchical (AH) clustering algorithm. Good agreement is found between results from both methods.

5 Results

Shown in figure 4 is a cluster tree graph with plots showing frequency vs. κ_h of selected clusters, each point plotted in a graph corresponds to a fluctuation structure. The root of the tree (left side) has the trivial case of $N_{Cl} = 1$, such that the whole dataset is contained in a single cluster. The highest level branch shown here (right side) has $N_{Cl} = 10$. The localisation of the clusters in the $f - \kappa_h$ projection shown here is due to the relation of the phase structure to the magnetic configuration – neither frequency nor κ_h are included in the clustering metric.

Vertical displacement at a node in the tree is proportional to the distance in phase space between the parent and child clusters. Results from AH clustering are also shown for comparison. The AH clusters show good agreement with EM clusters at the $N_{Cl} = 10$ end of the tree.

Near the root of the tree we find well defined clusters which have resonant structure in the $f - \kappa_h$ projection. For the EM:B cluster, the frequency minimum occurs at $\kappa_h = 0.4$, corresponding to the $\iota = 5/4$ rational surface in the low-shear region of the plasma. The EM:C cluster has frequency minimum at $\kappa_h \simeq 0.72$, where the $\iota = 4/3$ surface is located in the region of zero-shear. Both modes show $f \sim |\iota - n/m|$ resonant behavior, as do other clusters for higher order rational surface configurations. Analysis of the phase structure of these modes has shown that the dominant Fourier components are those expected for the relevant rational surface, i.e.: $(n, m) = (4, 3)$ for the $\iota = 4/3$ mode [7].

Cluster EM:O has very well defined $(n, m) = (0, 0)$ structure and also exists in configurations where low order rational surfaces exist in low-shear regions. Cluster EM:J appears to be a helical Alfvén eigenmode (HAE) coupled between the (7, 5) and (10, 7) resonance, this $\delta_n = 3$, $\delta_m = 2$ is consistent with the relatively large $(n, m) = (3, 2)$ Fourier component of the heliac magnetic geometry.

6 Discussion

The clustering occurs only in $\Delta\phi$-space, and is unbiased by the κ_h and frequency coordinates plotted in cluster tree figure 4. The clusters can also be mapped to any other known plasma properties.

Complications arise in the case of H-1 configuration scans due to the changing shape of magnetic field with κ_h. The coil coordinates have been mapped to κ_h-averaged magnetic angles to account for this.

The process has been kept general enough for it to be applicable to any set of geometrically ordered timeseries data. While the simple phase difference clustering metric works fine in this case, an alternative metric may be required if timeseries from other diagnostics are included.

The scalability depends on the clustering algorithm used. The EM method scales well with the number of datapoints N_{dp} ($N_{dp} \times N_{\mathrm{Cl}}$), while the AH method scales poorly (N_{dp}^2). Variations to the EM clustering algorithm and alternative ways to quantify the results are areas of ongoing investigation.

Data mining methods apart from the clustering analysis described here are also being investigated. "Association rule mining" is one such approach. It is designed to discover temporal patterns in the entire spectrograms such as shown in figure 3. In this context we search for rules (frequent patterns) in the form of "if a strong mode at $f \simeq 10\,\mathrm{kHz}$ occurs from 10-20ms then a mode at $f \simeq 20\,\mathrm{kHz}$ from 40-50ms will occur (with e.g.: 50% probability)".

7 Acknowledgements

The authors thank the H-1 team for continued support of experimental operations. This work was performed on the H-1NF National Plasma Fusion Research Facility established by the Australian Government, and operated by the Australian National University, with support from the Australian Research Council Grant DP0344361 and DP0451960.

References

[1] S. M. Hamberger, B. D. Blackwell, L. E. Sharp and D. B. Shenton, H-1 design and construction. Fusion Technol. 17 (1990) 123–130

[2] J. H. Harris et al, Fluctuations and stability of plasmas in the H-1NF heliac. Nucl. Fusion 44 (2004) 279–286

[3] B. D. Blackwell, Results from helical axis stellarators, Phys. Plasmas 8 (2001) 2238–2244

[4] T. Dudok de Wit, A.-L. Pecquet, J.-C. Vallet and R. Lima, The biorthogonal decomposition as a tool for investigating fluctuations in plasmas. Phys. Plasmas. 1 (1994) 3288–3300

[5] A. Dempster, N. Laird and D. Rubin, Maximum likelihood from incomplete data via the EM algorithm. J. Royal Stat. Soc. 39 (1977) 1–38

[6] W. H. E. Day and H. Edelsbrunner, Efficient Algorithms for Agglomerative Hierarchical Clustering Methods, J. Classification 1 (1984) 7–24

[7] D. G. Pretty, PhD Thesis, Australian National University (2007)

Proceedings of ITC/ISHW2007

Design Study of Lost Fast-Ion Probe on the Large Helical Device

K. OGAWA, [1]M. ISOBE, [1]K. TOI

Department of Energy Science and Engineering, Nagoya University, Nagoya 464-8603, Japan
[1]National Institute for Fusion Science,322-6 Oroshi-cho, Toki 509-5292, Japan

(Received ****** / Accepted ******)

A lost fast-ion probe (LIP) with a scintillator screen was designed for measurements of energetic ion loss flux caused by energetic-ion-driven MHD instabilities as well as magnetic field ripple in the Large Helical Device (LHD). The optimum position for the installation of the probe was determined by searching for energetic ion trajectories along which energetic ions launched from the probe can reach the region inside the last closed flux surface, without intersecting with any in-vessel components of the LHD vacuum chamber. The LIP is installed at the outboard side of a horizontally elongated poloidal cross section. It can be moved in the horizontal direction by 750 mm per 1.5 minutes with a pneumatic motor. The aperture of LIP was arranged to measure losses of co-going energetic ions, whose detectable ranges of the pitch angle and gyroradius are 35-50 degrees and 1.5-15 cm, respectively. The scintillator P46 was adopted, being taken into account its high sensitivity and short decay time even at high temperature. The light emitted from the scintillator by energetic ion bombardment is detected by a photomultiplier array with high-time-resolution (up to 200 kHz) and an image intensified CCD camera (up to 2 kHz). Accordingly, thus designed LIP is expected to detect fast loss events of energetic ions induced by MHD instabilities such as Alfvén eigenmodes.

Keywords: lost-ion probe, energetic ion, scintillator, orbit calclation, Alfven eigenmodes

1. Introduction

Good confinement of energetic particles such as alpha particles is crucial for realization of a nuclear fusion reactor. Large amount of loss of energetic ions caused by energetic-ion-driven magneto hydrodynamic (MHD) instabilities should be avoided, because it would quench fusion burn, leading to localized serious damages of the first wall. In the Large Helical Device (LHD), energetic-ion-driven MHD instabilities such as toroidicity-induced Alfvén eigenmodes (TAE) and energetic-particle mode (EPM) are excited in neutral beam (NB)-heated plasmas [1, 2], and induce anomalous transport of energetic ions [3]. We should measure distribution of pitch angle (χ=arccos($v_{//}/v$)) and energy of lost-fast ions due to energetic-ion-driven MHD instabilities, in order to understand detailed loss mechanisms and minimize it. A most powerful diagnostic tool to detect fast-ion loss flux is a lost fast-ion probe (LIP) with scintillator screen [4]. The LIP has been successfully applied to helical/stellarator plasmas [5, 6] as well as tokamaks [7-9]. For this reason, we have designed the LIP which will be installed at the outboard side of a horizontally elongated poloidal cross section in LHD.

The LHD is a helical device with toroidal field periods of 10 and poloidal periods of 2. It has a plasma major radius R is ~3.6 m and an average minor radius $<a>$ is ~0.6m. The toroidal magnetic field strength B_t can be increased up to 2.9 T.

Figure 1 shows a top view of the LHD, NBI injectors, and location of the head part of LIP. The LHD has four NB injectors, three of which (BL-1~3) inject hydrogen neutral beams tangentially (co- or counter-direction) into the plasma, having energies up to 180 keV, and another one (BL-4) injects beam perpendicularly at energy of 40 keV.

2. Positioning Study

In order to detect lost energetic ions effectively, the probe should be placed close to the plasma. On the other hand, the damages of the probe such as melting by lost energetic ion flux should be avoided. From this point of view, a scanning range of the probe in the horizontal direction was carefully determined as explained below.

The procedure of positioning study is as follows : 1) An energetic ion is launched from the possible candidate position of LIP head, having various initial velocities and pitch angles expected in LHD plasma

Author's e-mail: ogawa.kunihiro@LHD.nifs.ac.jp

conditions, 2) The Lorentz force equation for charged particle's motion ($m\frac{dv}{dt}=q(v\times b)$) is solved backwardly in time in the LHD magnetic field in the Cartesian coordinates, 3) If the fast ion launched from the LIP head enters inside the last closed flux surface of an LHD plasma, we judge that a trajectory of lost ion is found.

Figure 2 show typical orbits of energetic ions reaching the LIP. One has initial energy E_i of 150 keV and pitch angle χ of 108.7 degrees (Fig.2a) and the other has E_i of 150 keV and χ of 41.8 degrees (Fig.2b). B_t and the magnetic axis position of the vacuum field R_{ax} are 0.75 T and 3.6 m, respectively in this case. In this calculation, the trajectories of energetic ions are followed in the static magnetic field without any field perturbations and the radial electric field is assumed to be zero ($\boldsymbol{E}$=0). In the case shown in Fig.2(a), a launched ion doesn't go back into the plasma region and hits the first wall surface immediately. It means that such ion does not reach the probe from the plasma confinement region, that is, will not be detected by the probe actually. On the other hand, in the case shown in Fig. 2 (b), the ion goes back into the plasma and it means that it is detectable by the probe. As can be seen, this is co-going transit energetic ion whose orbit deviates substantially from magnetic flux surfaces.

We have tried to find energetic ions which have small χ, because such ions would easily interact with Alfvén eigenmodes (AE). We have evaluated the numbers of such lost trajectories, by changing the radial position of the probe head in the horizontal direction. Figure 3 shows the counts of lost ions as a function of the radial position in the horizontal direction, where 750 particles are launched from the LIP head, having various energies and pitch angles. We evaluated the counts of lost ions found using above calculation, retracting the position of the LIP head outward in the accessible range of LIP (from R=4.46 m to R=4.6 m) by every 20 mm step. This calculation was carried out for the reference configuration of R_{ax}=3.6 m in two different B_t of 0.75 T and 1 T.

3. Diagnostic Setup

Figure 4 shows a schematic view of the designed LIP installed in the horizontally elongated poloidal cross section of LHD. The probe head is attached to a stainless steel shaft of 3 m long. The LIP head can be inserted in the horizontal plane shifted upward by 80 mm for the equatorial plane of the LHD device, to the inner most position (R=4.46 m) by a pneumatic motor, as shown in Fig. 4a. The LIP passes through a diverter leg to the innermost position. A stainless steel shaft is partially covered with a graphite sleeve of 380 mm long and 5 mm thick, to protect the LIP against high heat flux flowing from a main plasma along divertor leg. The scintillator box of LIP is made of stainless steel and covered with molybdenum plates. Lost energetic ions pass thorough a front- and rear- aperture, and then hit a scintillator surface of which strike point gives information of both gyroradius and pitch angle of the lost ion. (Fig.5) Once a size of aperture, scintillator position and magnetic field strength at the scintillator position are specified, a pattern of scintillator light is uniquely decided.

Two dimensional image of scintillation light due to impact of lost-fast ions has to be transferred outside of the vacuum vessel. In our probe, because the plane of scintillator surface is parallel to the axis of the probe shaft, the scintillation pattern appeared on the screen is first reflected 90 degrees by means of a polished stainless steel mirror mounted inside the probe head box. After this reflection, two dimensional light image is transferred by a series of relay lens mounted inside the probe shaft and is measured with an image-intensified CCD camera and/or photomultiplier tubes. (Fig4b) Form the analysis of light pattern appeared on the scintillator surface, gyroradius and pitch angle of lost-ion flux can be derived.

4. Details of the LIP Head

The position that the LIP is installed to LHD is shown in Fig.1. When the direction of B_t is clock wise (CW) as seen from the top, the ion grad-B and curvature drifts are upward and ions tend to drift toward the probe. The LIP designed in this study can work only in this operation. The LIP will not be able to detect any lost-ion flux when B_t is directed to be counter-clock-wise because of following primary two reasons. One is that ions tend to go away from the LIP because the ion grad-B drift is downward. Another is that gyromotion of energetic ions becomes opposite compared with the CW-B_t case. Even if lost-energetic ions reach the LIP and enter the detector box, they can not hit the scintillator surface. Detail of the LIP head is shown in Fig.6. The size of LIP head is 58 mm (width) × 52 mm (length) × 66 (height), but has defective part near the aperture. The angle between the side surface of the LIP and the aperture is selected to be 21 degrees, so that lost ions having wide range of gyroradius and pitch angle would pass through the aperture effectively. The front aperture has 3 mm wide and 1 mm high whereas the rear aperture has 24.1 mm wide and 1 mm high. The size of aperture was determined so as to obtain optimum energy and pitch angle resolution and signal intensity from calculation. The distance between the two apertures is 10 mm. The normal vector of the aperture is 113 degrees with respect to the local magnetic field direction, to guide energetic ions with 35 to 50 degrees (co-going particle).

Also, in Fig. 5, calculated hit point area of lost ions having the range of 1.5 to 15 cm in gyroradius and 35 to 50 degrees in pitch angle is shown on the scintillator screen. It should be noted that the gyroradius is defined with $\rho=|v|/\omega_c$ where ρ, v, and ω_c indicate gyroradius, velocity of ion, and cyclotron frequency of ion at the position of probe. That is, the gyroradius and pitch angle are not equal to those in a plasma. As a scintillator material, YAG:Ce (P46) is used, because it has high sensitivity and short decay time even at high temperature. P46 is deposited on a quartz plate coated with aluminum, and emits green light. The light emitted from the scintillator is detected by an array of photomultiplier with high-time-resolution (up to 200 kHz).

5 Conclusion

A lost fast ion probe with scintillator (LIP) installed on LHD was designed by finding trajectories of energetic ions which connect from the probe to the plasma confinement region. It is concluded that when the LIP is placed in the range of R=4.46 m to 4.6 m in a planned port position of LHD, energetic lost ion flux due to AEs would be detected. This LIP will be a powerful tool to study interaction between energetic ions and energetic ion driven instabilities.

[1] K. Toi *et al.*, Plasma Phys. Control. Fusion **46**, S1(2004).
[2] S. Yamamoto *et al*., Nucl. Fusion **45**, 326 (2005)
[3] M. Osakabe *et al*., Nucl. Fusion **46**, S911 (2006)
[4] D.S. Darrow *et al.*, Rev. Sci. Instrum. **66** ,476 (1995)
[5] M. Isobe *et al.*, Nucl. Fusion **46,** S918 (2006)
[6] A. Werner *et a.l.* Rev. Sci. Instrum. **72**, 1 (2001)
[7] D.S. Darrow *et al*., Nucl. Fusion **36**, 1 (1996)
[8] D.S. Darrow *et al*., Rev. Sci. Instrum. **77**, 10E701 (2006)
[9] M. García-Muñoz *et al*., Nucl. Fusion **47**, L10 (2007)

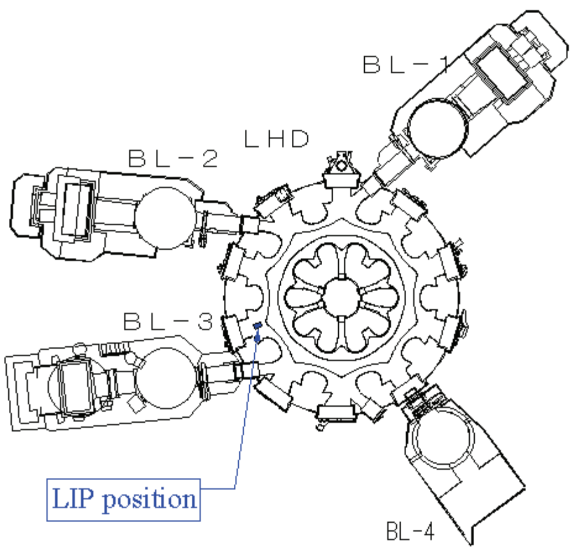

Fig.1 Top view of LHD where NB injectors and a newly designed LIP are arranged. Both BL-1(180keV) and BL-3(180keV) are in operation to be co or counter injection simultaneously. On the other hand, BL-2 (180keV) is in operation to the opposite direction against BL-1 and BL-3. BL-4 is used for perpendicular NBI. The position of LIP is marked near BL-3.

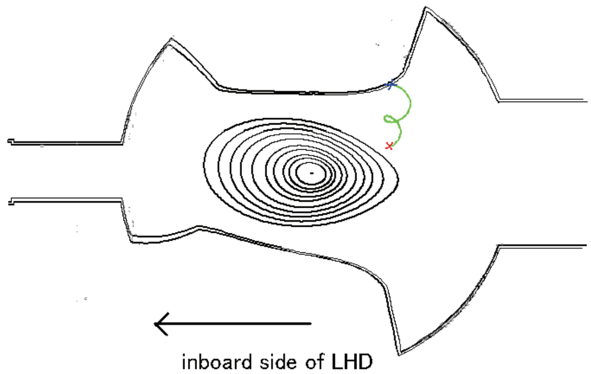

(a)

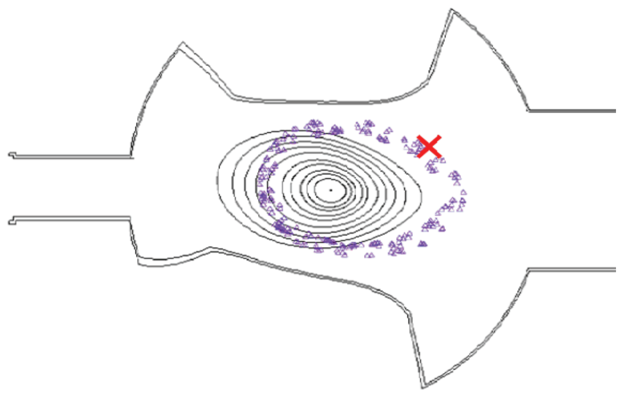

(b)

Fig.2 Examples of calculated trajectory. Red X mark indicates the initial position of orbit (equal to position of probe head). Blue X mark indicates the hit poison of the ion at the vessel surface. The condition is Bt=0.75 T, Rax = 3.6 m, E=0, B=0. (a) Poloidal projection of a calculated orbit trajectory in LHD, where the initial condition is Ei=150 keV, χ=108.7 degrees. In this case, the probe can't detect this lost energetic ion. (b) Poincare plot of a calculated orbit trajectory in LHD. Initial condition is Ei=150 keV, χ=41.8 degrees. In this case, the probe can detect them.

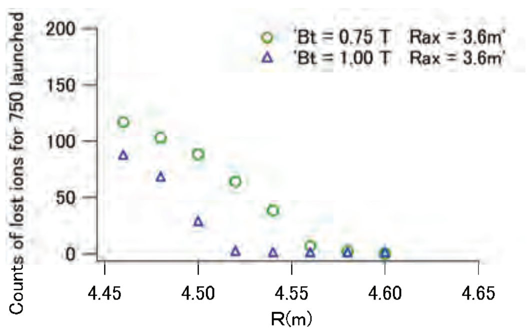

Fig.3 Counts of energetic ions that are lost from the plasma core region and reach to the LIP, where 750 particles are launched from the probe, having various energies and pitch angles. In the configuration of Rax=3.6m. The results at *Bt* = 0.75 T and 1 T are shown by circles and triangles, respectively.

a)

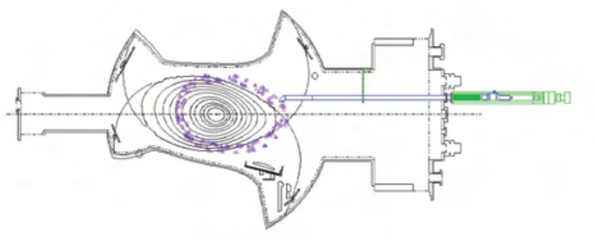

b)

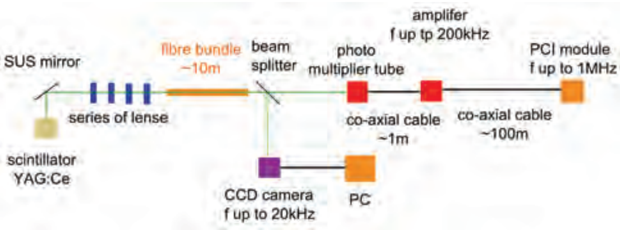

Fig.4 a) Schematic view of LIP placed at the innermost position in the horizontally elongated section of LHD. An example of Poincare plots of the trajectorie of lost ion with 150keV energy and 35.0 degrees pitch angle. It can be moved in the horizontal direction by 750 mm per 1.5 min with a pneumatic motor. A stainless pipe supports probe head is covered by a graphite sleeve of 380 mm length and 5 mm thickness, to protect from high heat flux along divertor leg
b) The route of signal transfer system and data acquisition system of LIP.

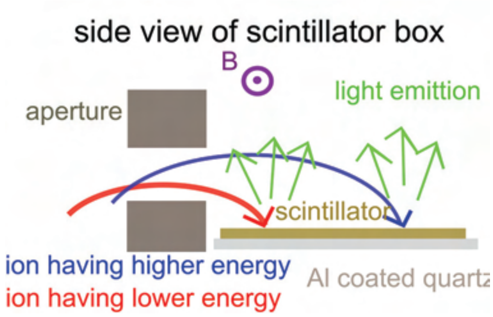

Fig.5 The side view of scintillator box. Lost energetic ions pass through apertures, and then hit a scintillator surface. Strike point gives information of both gyroradius and pitch angle of the lost ion.

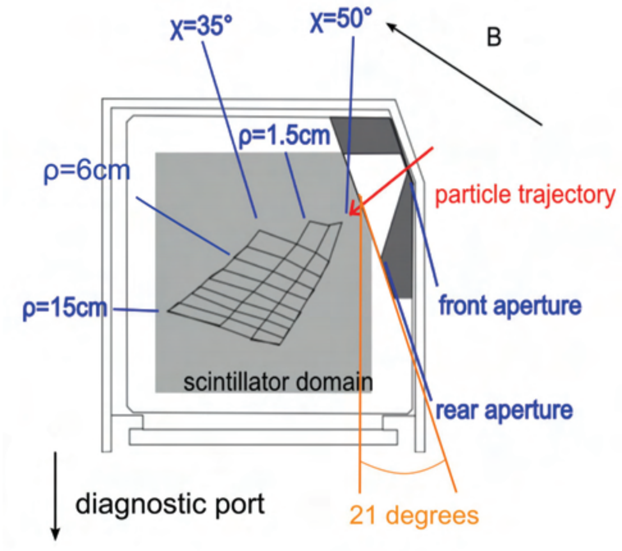

Fig.6 Schematic view of the probe head and expected arrival area of energetic ion. Expected hit point area of lost ions having the range of 1.5 to 15 cm for gyroradius and 35 to 50 degrees. The normal vector of the aperture is 113 degrees with respect to the local magnetic field direction. The size of a front aperture is 3 mm (width) × 1 mm (height) and the size of a rear aperture is 24 mm (width) × 1 mm (height). The distance between two apertures is 10 mm.

Proceedings of ITC/ISHW2007

A Method for Ion Distribution Function Evaluation Using Escaping Neutral Atom Kinetic Energy Samples

P.R. Goncharov, T. Ozaki, E.A. Veshchev, S. Sudo

National Institute for Fusion Science, 322-6 Oroshi-cho, Toki, 509-5292, Japan

A reliable method to evaluate the probability density function for escaping atom kinetic energies is required for the analysis of neutral particle diagnostic data used to study the fast ion distribution function in fusion plasmas. Digital processing of solid state detector signals is proposed in this paper as an improvement of the simple histogram approach. Probability density function for kinetic energies of neutral particles escaping from the plasma has been derived in a general form taking into account the plasma ion energy distribution, electron capture and loss rates, superposition along the diagnostic sight line and the magnetic surface geometry. A pseudorandom number generator has been realized that enables a sample of escaping neutral particle energies to be simulated for given plasma parameters and experimental conditions. Empirical probability density estimation code has been developed and tested to reconstruct the probability density function from simulated samples assuming Maxwellian and classical slowing down plasma ion energy distribution shapes for different temperatures and different slowing down times. The application of the developed probability density estimation code to the analysis of experimental data obtained by the novel Angular-Resolved Multi-Sightline Neutral Particle Analyzer has been studied to obtain the suprathermal particle distributions. The optimum bandwidth parameter selection algorithm has also been realized.

Keywords: neutral particle analysis, ion distribution, statistical data processing, empirical probability density, kernel bandwidth selection

1. Introduction

Measurements of kinetic energy distributions of neutral atoms escaping from magnetically confined plasma are used in controlled fusion experiments as a method to investigate the ion component distribution function and its evolution due to the application of various plasma heating schemes. The ion distribution function reflects the kinetic effects, the single particle confinement properties depending on the particular magnetic configuration, the finite β effects such as MHD induced fast ion losses, radial electric field effects, etc. The nuclear fusion reaction rate is determined by the ion distribution and thus its studies at suprathermal energies near the rate coefficient curve maximum are of primary importance. Advanced neutral particle diagnostics based on solid state detectors with high energy resolution, e.g. [1], are used to study the suprathermal ion distribution function. Statistical data processing is required to obtain a smooth normalized probability density function for particle energies using the measured random samples [2].

2. Escaping Neutral Particle Energy Distribution

The probability density function (PDF) *f(E)* for kinetic energies of neutral H^0 particles escaping from the plasma of a magnetic confinement fusion device in a general form is given by

$$f(E) = A e^{\int_{\rho_{\min}}^{1} Q^-(\tilde\rho)\lambda_{mfp}^{-1}(E,\tilde\rho)d\tilde\rho} \int_{\rho_{\min}}^{1} g(E,\rho)\times \left[Q^+(\rho) e^{-\int_{\rho_{\min}}^{\rho} Q^+(\tilde\rho)\lambda_{mfp}^{-1}(E,\tilde\rho)d\tilde\rho} - Q^-(\rho) e^{-\int_{\rho_{\min}}^{\rho} Q^-(\tilde\rho)\lambda_{mfp}^{-1}(E,\tilde\rho)d\tilde\rho} \right] d\rho \qquad (1)$$

where *A* is the normalization constant. The source function for H^0 atoms of energy *E* within the plasma

$$g(E,\rho) = n_i(\rho) f_i(E,\rho) \sum_l n^{(l)}(\rho) \langle \sigma v \rangle^{(l)} \qquad (2)$$

is expressed via the local plasma proton distribution $n_i(\rho) f_i(E,\rho)$ and the sum of rates over all targets for the electron capture process. The derivatives $Q^+(\rho) = d\Lambda/d\rho > 0$ and $Q^-(\rho) = d\Lambda/d\rho < 0$ of the sight line distance Λ along the two intervals between $\rho = 1$ and $\rho = \rho_{\min}$ are obtained from the known structure of magnetic surfaces $\rho = const$. The neutral flux attenuation enters in the form of Poisson exponents, where $\lambda_{mfp}(E, \rho)$ is the H^0 mean free path with respect to all electron loss reactions.

author's e-mail: pavel@nifs.ac.jp

3. Numerical Experiment

Ideally, the passive diagnostic data is an array (E_1, …, E_N) of energies of escaped neutral particles measured along a certain observation direction, and N is the total number of particles collected during a certain time interval. This array is a sample of realizations of the random variable E distributed according to the law (1). Such form of data is achievable with solid state detectors by using pulse height analysis techniques, while the other analyzers, e.g. $\vec{E} \parallel \vec{B}$ ones, intrinsically form a histogram of the incoming particle energies over a certain number of subintervals called energy channels. Technical details may be found in [1]. The formulation of the problem considered here is to obtain an estimate $f^{(*)}(E)$ of the unknown exact probability density function $f(E)$ of neutral particle energies from the experimental data. The sought function preferably should satisfy a specified precision criterion. The obtained PDF estimate is then to be used to reconstruct the ion distribution for further analysis.

Assuming a predefined theoretical PDF $f(E)$ one can carry out a numerical experiment by generating a sample of escaped atom energies for given plasma parameters and experimental conditions. We apply the inverse cumulative distribution function (CDF) approach. First, a sample of pseudorandom numbers (u_1, …, u_N) uniformly distributed within the $[0,1)$ interval is generated using an algorithm from [3]. Then, the energy values are calculated as solutions of the equation

$$F(E_j) = u_j, \tag{3}$$

where $$F(E) = \int_0^E f(\tilde{E})d\tilde{E} \tag{4}$$

is the CDF. These simulation results can be supplied as input data for the PDF estimation procedure to test its performance, since the original exact $f(E)$ used in the simulation is known.

Two typical ion energy distribution laws have been used in the numerical simulation, namely, (a) Maxwellian distribution with ion temperature T_i

$$f_i(E) = \frac{2}{\sqrt{\pi}} \frac{1}{T_i} \sqrt{\frac{E}{T_i}} \exp(-E/T_i), \tag{5}$$

$$F_i(E) = \frac{2}{\sqrt{\pi}} \gamma\left(\frac{3}{2}, \frac{E}{T_i}\right), \tag{6}$$

where $\gamma(\alpha, x) = \int_0^x t^{\alpha-1} e^{-t} dt$ is the lower incomplete gamma-function; and (b) the classical slowing down distribution for a delta-like fast ion source function

$$S(v - v_0) = \frac{S_0}{4\pi v^2} \frac{e^{-\frac{(v-v_0)^2}{\epsilon^2}}}{\epsilon\sqrt{\pi}} \tag{7}$$

$$f_i(v) = \frac{S_0}{8\pi} \frac{\tau_s}{v^3 + v_c^3} \left(erf\left(\frac{v^*(v,t) - v_0}{\epsilon}\right) - erf\left(\frac{v - v_0}{\epsilon}\right)\right) \tag{8}$$

where the slowing down time $\tau_s = \dfrac{3m_p T_e^{3/2}}{4\sqrt{2\pi} n_e e^4 \Lambda m_e^{1/2}}$, the critical velocity $v_c^3 = \dfrac{3\sqrt{2\pi} T_e^{3/2}}{2m_p m_e^{1/2}}$, Λ is the Coulomb logarithm, and $v^*(v,t) = \left(\left(v^3 + v_c^3\right)e^{3t/\tau_s} - v_c^3\right)^{1/3}$ [4]. The ion velocity $v = \sqrt{2E/m_p}$, v_0 is the injection velocity, S_0 and ϵ determine the source rate and width, and t is the time. Fig. 1 (a) shows the Maxwellian PDF for two different T_i values and Fig 1 (b) shows the classical slowing down PDF at t = 0.8 s for injection energy E_0 = 150 keV and two different pairs of the target plasma n_e and T_e values. Histograms of the corresponding pseudorandom number samples governed by these PDFs are shown in Fig. 1 (c) and (d).

4. Data Processing Method

As an improvement of the neutral particle diagnostic data analysis, we have applied the probability density estimation using kernel smoothing techniques, e.g., [5, 6]. The kernel PDF estimate

$$f^{(K)}(E) = \frac{1}{Nh} \sum_{j=1}^{N} K\left(\frac{E - E_j}{h}\right), \quad h > 0 \tag{9}$$

is determined by the kernel function $K(z)$ and the kernel bandwidth h. The performance criterion of this method is the value of the mean integrated squared error

$$MISE\left(f^{(K)}, f\right) = \left\langle \int_0^{+\infty} \left[f^{(K)}(E) - f(E)\right]^2 dE \right\rangle, \tag{10}$$

where averaging is over different samples of N realizations (E_1, …, E_N), and its "asymptote" for $N >> 1$ (large sample approximation)

$$AMISE\left(f^{(k)}, f\right) = \frac{c_1}{Nh} + \frac{c_2 c_3^2 h^4}{4}, \tag{11}$$

where $c_1 = \int K^2(z)dz$, $c_2 = \int \left(f''(z)\right)^2 dz$ and $c_3 = \int z^2 K(z)dz$. The optimum kernel derived in [7] is $K(z) = \frac{3}{4}\left(1 - z^2\right) I_{(-1,\,1)}(z)$, where $I_{(-1,\,1)}(z)$ equals unity within (-1, 1) and equals nought outside. However, it is emphasized [5, 6] that the choice of the kernel function shape has a small influence on the method performance, while the bandwidth parameter choice is more important. Therefore, Gaussian kernel

$$K(z) = \frac{1}{\sqrt{2\pi}} e^{-z^2/2} \tag{12}$$

has been used, since it has continuous derivative.

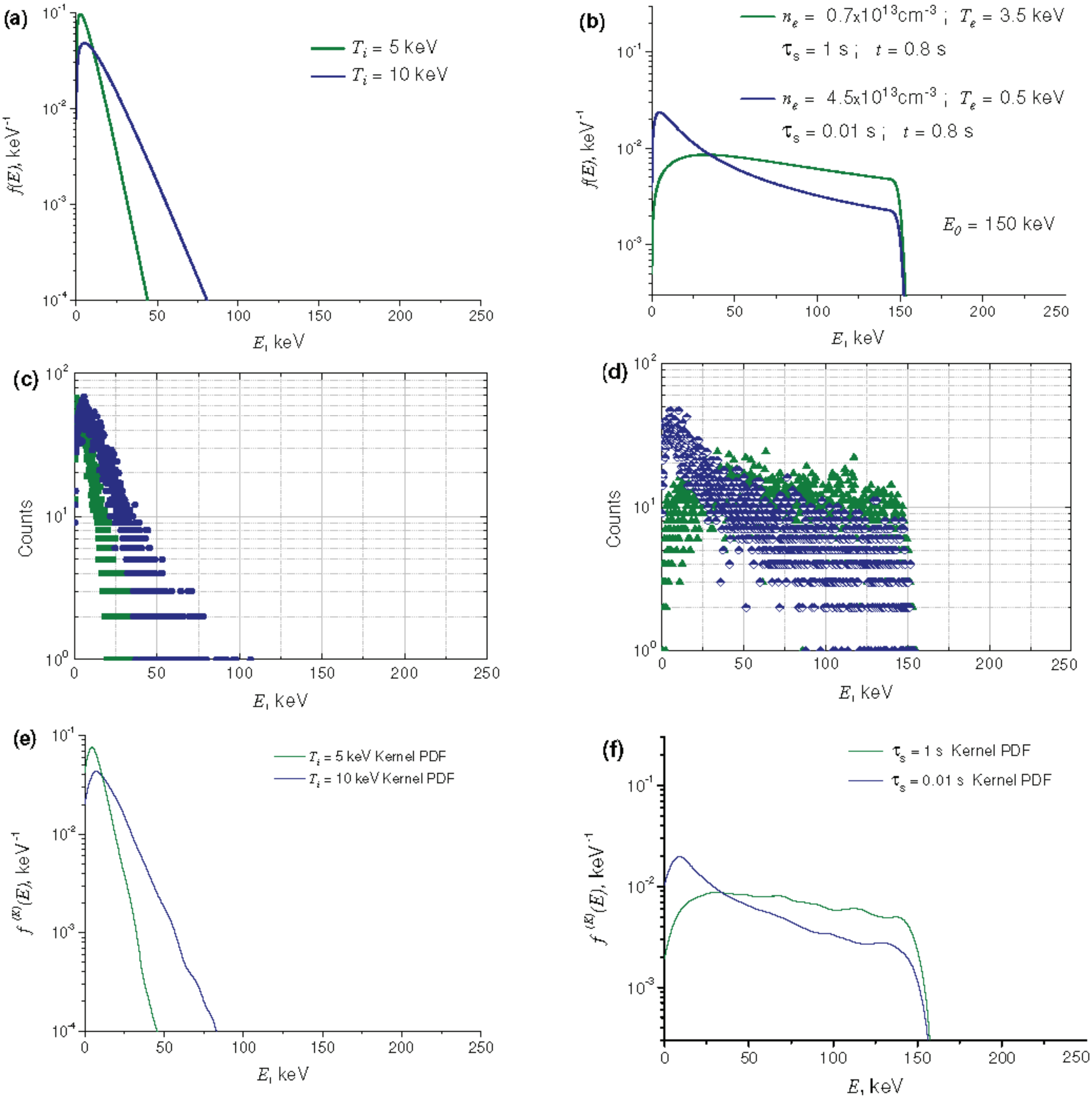

Fig. 1. (a) Maxwellian PDF for $T_i = 5$ keV (green) and $T_i = 10$ keV (blue); (b) classical slowing down PDF for $\tau_s = 1$ s (green) and $\tau_s = 0.01$ s (blue); (c) histograms of pseudorandom number samples distributed according to the laws shown in (a); (d) histograms of pseudorandom number samples distributed according to the laws shown in (b); (e) kernel PDFs calculated from Maxwellian law pseudorandom number samples shown in (c); (f) kernel PDFs calculated from slowing down distribution law pseudorandom number samples shown in (d).

A reliable practical method for optimum h selection was proposed in [8] and revisited recently in [9]. The bandwidth is sought by solving the equation

$$h = \left(\frac{1}{2\sqrt{\pi} N \phi_4(\eta(h))} \right)^{1/5}, \qquad (13)$$

where the function ϕ_r is expressed via kernel derivative

$$K^{(r)}(z) = (-1)^r He_r(z) K(z) \qquad (14)$$

as follows

$$\phi_r(h) = \frac{1}{N(N-1)h^{(r+1)}} \sum_{i=1}^{N} \sum_{j=1}^{N} K^{(r)}\left(\frac{E_i - E_j}{h} \right). \qquad (15)$$

The function

$$\eta(h) = \left(\frac{-6\sqrt{2}\phi_4(a)}{\phi_6(b)} \right)^{1/7} h^{5/7} \qquad (16)$$

depends on the values

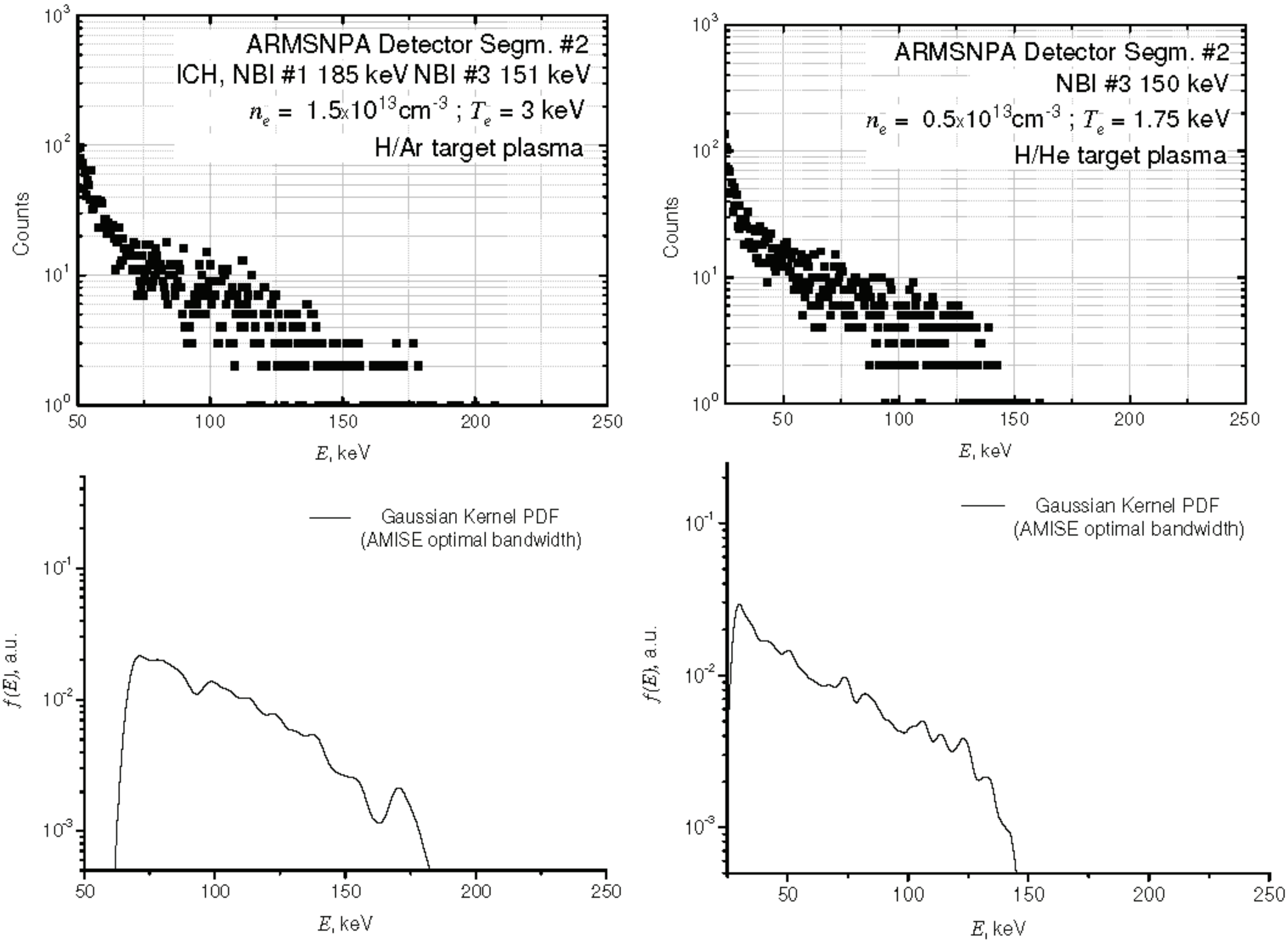

Fig. 2. Experimental H^0 energy spectra (upper) and PDF estimates (lower) for two different ion heating schemes.

$$a = \left(\frac{16\sqrt{2}}{5N}\right)^{1/7} \hat{\sigma} \quad \text{and} \quad b = \left(\frac{480\sqrt{2}}{105N}\right)^{1/9} \hat{\sigma}, \quad (17)$$

where $\hat{\sigma} = \sqrt{\dfrac{1}{N-1}\displaystyle\sum_{i=1}^{N}\left(E_i - \bar{E}\right)^2}$, $\bar{E} = \dfrac{1}{N}\displaystyle\sum_{i=1}^{N} E_i$. (18)

Direct implementation of formula (15) is slow. An approximate fast calculation technique is given in [9].

5. Application to Experimental Data

These methods have been tested by reconstructing the probability density function from the generated pseudorandom number samples assuming Maxwellian and classical slowing down plasma ion energy distribution shapes for different temperatures and different slowing down times. The test results are shown in Fig. 1 (e) and (f). The analysis of passive chord-integrated experimental data obtained with the Angular-Resolved Multi-Sightline Neutral Particle Analyzer [1] on Large Helical Device is illustrated in Fig. 2. Kernel smoothing methods require a certain choice of the bandwidth parameter. An automatic choice described in Section 4 is preferable for routine data processing.

References

[1] E.A. Veshchev, T. Ozaki, et al., Rev. Sci. Instrum., **77**, 10F129 (2006).

[2] P.R. Goncharov, T. Ozaki, et al., Proc. 34th EPS Conf. Plasma Phys., P5.081 (Warsaw, 2007).

[3] S.K. Park, K.W. Miller, Comm. ACM, **31**, 1192 (1988).

[4] J.G. Cordey, M.J. Houghton, Nucl. Fusion, **13**, 215 (1973).

[5] A.W. Bowman, A. Azzalini, *Applied smoothing techniques for data analysis*, Clarendon (1997).

[6] M.P. Wand, M.C. Jones, *Kernel Smoothing*, Chapman and Hall, London (1995).

[7] V.A. Epanechnikov, Theory Probab. Appl., **14**, 153 (1969).

[8] S.J. Sheather, M.C. Jones, J. R. Statist. Soc. B, **53**, 683 (1991).

[9] V.C. Raykar, R. Duraiswami, *Very fast optimal bandwidth selection for univariate kernel density estimation*, University of Maryland, CS-TR-4774/UMIACS-TR-2005-73 (2006).

Proceedings of ITC/ISHW2007

Helium ion observation during 3rd harmonic ion cyclotron heating in Large Helical Device

Tetsuo Ozaki, Pavel R. Goncharov, Evgeny A. Veshchev[1)], Shigeru Sudo, Tetsuo Seki, Hirofumi Kasahara, Yuichi Takase[2)], Takuya Ohsako[2)], High-Energy Particle Group and LHD Experimental Group

National Institute for Fusion Science, 322-6, Oroshi, Toki, Gifu 509-5292, Japan

1) *Graduate University for Advanced Studies, Hayama, Kanagawa, 240-0193, Japan*

2) *Department of Complexity Science and Engineering, Graduate School of Frontier Sciences, The University of Tokyo, Kashiwa, Chiba, 277-8561, Japan*

(Received / Accepted)

In the higher harmonic ion cyclotron resonance heating (ICH) using the fast wave, the resonance layer of helium appears near the plasma core. It is very important to measure the helium ion in order to investigate the confinement of α particle, which is produced by the nuclear reaction in ITER or fusion reactor. In the Large Helical Device (LHD), we try to observe the charge exchange helium particle by using the Compact Neutral Particle Analyzer (CNPA). The helium acceleration at lower than 5 keV, can be confirmed by comparing the signal ratio in adjusted plate voltages of CNPA to helium and hydrogen. The successful helium measurement in LHD leads to the development of the α particle measurement.

Keywords: ICH, 3rd harmonics, helium, α particle, CNPA, LHD, plate voltage, resonance

1. Introduction

It is very important to investigate α particle heating mechanism in future fusion reactor because α particle has a main role to heat the fusion plasma. High-energy particles including α particle are emitted not only by the charge exchange but also by the MHD instabilities in the fusion reactor [1]. Their particles give damage to the plasma wall addition to create a poor plasma confinement. Decelerated α particle (or a helium ion) with the energy over 1 keV makes bubbles and gives a serious damage on the wall surface unlike hydrogen. In LHD [2], we find the helium flux over 10^{19} m^{-2}*s, whose energy is over 1.2 keV by using the microscopic measurement of the irradiated material [3]. Therefore the suitable method for measuring helium ion distribution should be established immediately.

It is very difficult to use spectroscopic methods or the passive charge exchange neutral particle method for helium ion. Helium ions are almost fully ionized except near peripheral region. A few helium atoms are escaped from plasmas by the double charge exchange reaction between the background helium neutral and the fully ionized helium ion, whose cross section is too small. Therefore the helium ion has not been observed until now by the particle measurement. Here we describe that we succeed the observation of helium in higher harmonic ion cyclotron resonance heating (ICH) [4].

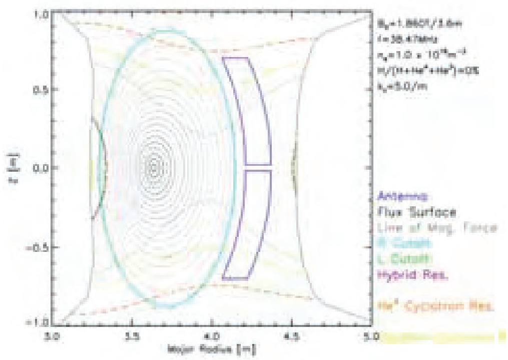

Fig.1. Magnetic surface, ICH antenna and resonance layers.

2. Higher Harmonic Ion Cyclotron Resonance Heating

It is one of most suitable method to use ICH in LHD in order to obtain the accelerated helium ion. We have tried ICH in He^3/He^4 mixture plasma. However the effective heating has not been obtained probably due to the

author's e-mail: ozaki@nifs.ac.jp

contaminated hydrogen acceleration rather than helium acceleration. Here we propose the higher harmonic ICH without the hydrogen resonance. This technique is utilized in the electron heating using Landau damping [5]. To this purpose, the ICH should not provide its power to the hydrogen ion. If the ions are accelerated, they cannot be confined and their energy cannot be deposited due to the low confinement magnetic field in high beta plasma. We choose the suitable combination between the magnetic field and the frequency of ICH so as there is no ion cyclotron resonance for the hydrogen in the plasma core region. One of their combinations has the resonance for the He^4 around plasma core region. Therefore the hydrogen gas should be used at this combination of the magnetic field and the frequency in order to obtain high electron heating efficiency. If we are interested in the helium acceleration, the helium gas should be chosen in the same combination.

If we detect the helium ion by using the charge exchange neutral particle measurement, the hydrogen ion always behaves as a noise because their masses and charges are too close each other. Fortunately there is a possibility of the helium observation because there is no acceleration of the hydrogen in this combination. Figure 1 shows the resonance layers at the magnetic field of 1.86 T and the ICH frequency of 38.47 MHz, drawn on the vertical cross section of LHD magnetic surfaces [6]. The plasma and the ICH antenna are also shown. The He^4 resonance appears at ρ=1/3 in the 3rd harmonics of the ICH frequency. Therefore the high efficient helium acceleration can be expected. On the other hand, there are the hydrogen resonance layers only at the peripheral region of the plasma. Unfortunately there are the electron cyclotron resonance layers near the plasma edge in the configuration. The electron heating efficiency is not high and is expected to be strongly depended on the power deposition to helium ion.

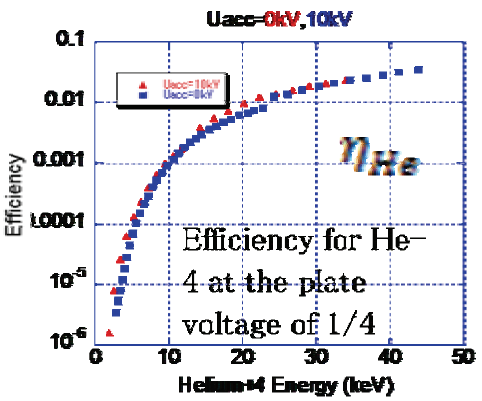

Fig.2(a). Efficiency for He-4 at the plate voltage of 1/4.

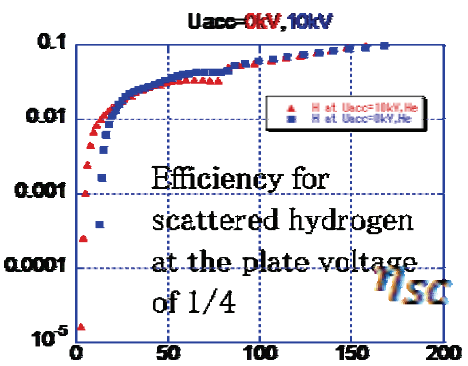

Fig.2(b) Efficiency for scattered hydrogen at the plate voltage of 1/4.

3. Compact Neutral Particle Analyzer

The compact neutral particle analyzer (CNPA) [7] for measurement of the charge neutral exchanged particle is installed perpendicular direction against LHD plasma almost at the mid-plane. CNPA is a traditional E//B particle analyzer with a diamond-like carbon film as a stripping foil, the permanent magnet for the energy analysis of the particle and condenser plates for the particle mass separation. To precise detection in low energy region, there is a particle acceleration tube of 10 keV. Therefore the hydrogen with the energy range from 0.8 to 168 keV can be observed by 40 rectangular-shape channeltrons, which is set on the position for the hydrogen measurement.

The spatial resolution is determined to be 5 cm by the several apertures in the neutral particle flight. Time resolution is set to be 0.1 ms, which can cover the whole plasma duration within the buffer memory with the CAMAC ADC. Data acquisition, data pre-process and analyzing data display are routinely completed within 3 minutes discharge cycle.

If the condenser plate voltage is changed, the different mass as helium can be observed in principle. According to simple orbit calculation in CNPA, the beam spot of the helium is different from the channeltron array, which is adjusted to the hydrogen even if the plate voltage is tuned [8]. Here we assume the single ionized helium ion after translation of the carbon film of helium. The spot size is assumed to be determined by the aperture size (2 mmϕ) and the geometric configuration of the plasma and the detector. In low energy region, the spot size may be enlarged due to the scattering in the foil.

The helium beam spots do not correspond to the detector array in higher energy channels when the plate voltage is adjusted to a low energy channel because the detector array position is adjusted to the proton. Now we continue accurate calculation for obtaining the detector efficiency of helium. The helium energy spectrum can be obtained because we are interested in lower energy helium spectra in LHD experiments.

The calibration procedures are as follows;

(1) Compare the simulation model [9] including accurate orbit calculation and the experimentally calibrated value in hydrogen.

(2) (1) is almost agreed. Therefore we believe the simulation model and calculate the efficiency in helium and the scattered hydrogen when the plate voltage is set to be 1/4 for the hydrogen.

(3) The calculated efficiencies for the helium and the scattered hydrogen are shown in Figs. 2(a) and (b).

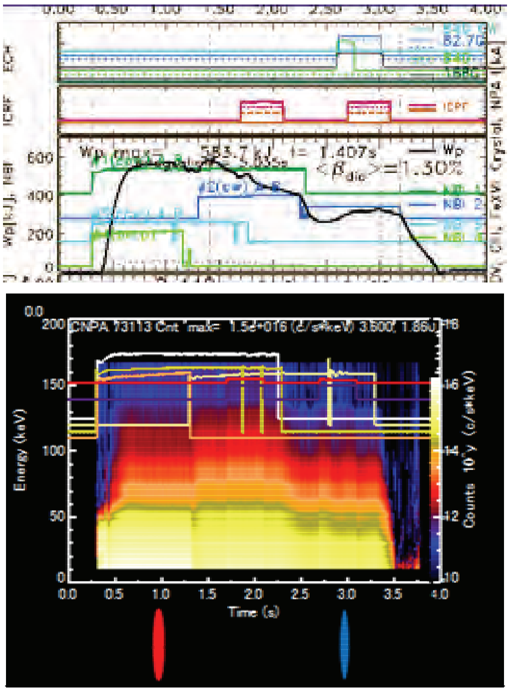

Fig.3(a). The time histories of the plasma parameters and the neutral particle energy spectrum in the voltage setting of hydrogen.

4. Experimental Results

LHD has a toroidal mode number of m=10, helical mode number of l=2. The major radius and minor radius are 3.9 m, 0.6 m, respectively. The helical ripple is 0.25 and a magnetic field is a maximum of 3 T. Although the standard magnetic axis is 3.75 m, it can be changed from 3.4 m to 4.1 m by applying a vertical magnetic field. There are three different heating systems of the electron cyclotron resonance heating (ECH, 2 MW), the neutral beam injection heating (NBI, 15 MW) and ICH (3MW). As for electron temperature, a maximum of 10 keV is observed by using a Thomson scattering and an electron cyclotron emission. Electron density can be changed from 0.1 to 4×10^{19} m^{-3}. The density profile is measured with a multi-channel interferometer.

In order to obtain the high electron temperature plasma, NBI#1, #2 and #3 are injected during 0.4 seconds at the beginning of the discharge [10]. After that, the plasma is maintained by the NBI#2. During this phase, the power of NBI#2 keeps low as the effect of ICH application can be clearly seen. The line averaged plasma density of 2×10^{19} m^{-3}, the central plasma temperature of 2 keV can be observed. ICH pulses are applied at two different timings. The ECH is overlapped at the second ICH pulse in order to obtain high electron heating at the high electron temperature. However the high electron temperature is not enough because the electron resonance region at this combination between the 2nd harmonic frequency of ECH and the magnetic field, is off-axis. Typical stored energy increment due to the ICH application of 1.55 MW, is 50 kJ at Wp=300kJ. Temperature rising is small in hydrogen plasma. Main contribution of Wp increment may come from the density rising at the plasma edge.

We change the gas from the hydrogen to the helium in order to study the electron heating reduction due to the

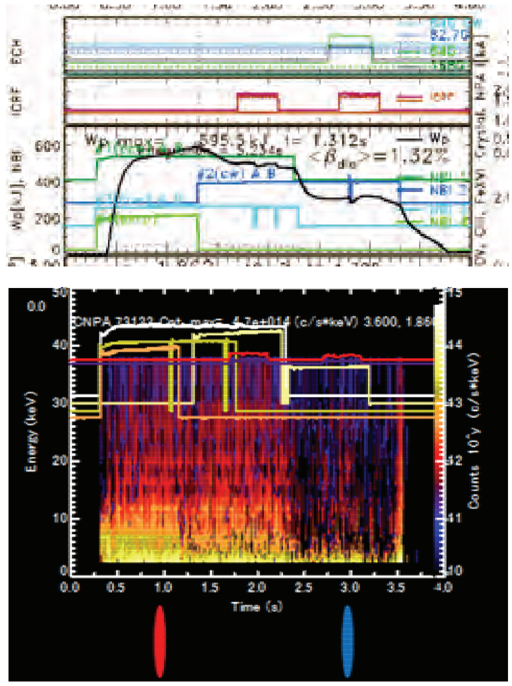

Fig.3(b), The time histories of the plasma parameters and the neutral particle energy spectrum in the voltage setting of helium.

power absorption by the helium ion. The helium resonance layer is around ρ=1/3 at the 3rd harmonics of ICH. As the result, the Wp is obviously reduced by the helium gas puffing. The reduction rate is depended on the amount of the puffing. Therefore the absorption to the electron may be reduced because the injection power of ICH is partially absorbed by the helium ion. The increasing rate of Wp is large at the high electron temperature. This means that effective electron heating by ICH can be obtained in the high temperature, especially at hydrogen plasma. On the contrary, in helium plasma, the temperature dependence of the increasing rate of Wp is not significant. In hydrogen plasma, the ICH power is easily absorbed to plasma electron because there is no resonance region against hydrogen. However, in helium plasma, the power deposition of ICH to the electron is not enough due to the existence of the helium ion resonance layer.

To confirm the helium acceleration, we compare the spectra of the helium and hydrogen by using CNPA with different plate voltages. Figures 3(a) and (b) show the ratio between the signal of He and H in two similar shots. We must remember that most signals are hydrogen even if we set the plate voltage for helium. Therefore the ratio means the ratio between the scattered hydrogen plus helium and the real hydrogen. The large ratios at low and high energy regions are due to the large scattering at the foil and the close trajectory of the hydrogen beams, respectively. The ICH is applied at 3.0 seconds, but not applied at 1.0 second. He/H ratio lower than the helium energy of 5 keV at 3.0 seconds is obviously larger than at 1.0 second. This means the low energy helium ion is accelerated by the higher harmonic ICH.

Higher harmonics heating provides the α particle simulation experiment although it is not effective for the electron heating. There is another candidate of the helium acceleration as He^3/He^4, but it is too difficult due to the hydrogen contamination. By tuning the magnetic field and frequency of ICH, higher acceleration energy of the helium ion over 5 keV can be expected.

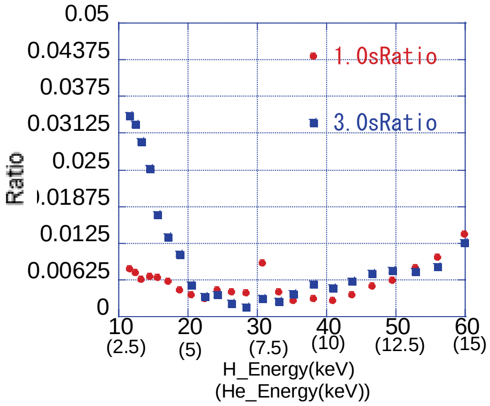

Fig.4. Energy dependence of He/He ratio.

5. Summary

The helium acceleration experiment to study the future α particle measurement has been done. It is very important to establish the α measurement because the helium/ α makes a bubble and gives a serious damage on the wall surface. The higher harmonic ICH without the hydrogen resonance is utilized in the electron heating using Landau damping. There is the helium resonance layer at ρ=1/3. In LHD, we can find the helium particle using the charge exchange neutral particle method at this experiment. By the helium acceleration, the electron heating efficiency is reduced. This fact suggests the way of efficient heating. At the same time, we can obtain the useful tool to develop the α particle measurement.

Acknowledgements

This work was performed under NIFS-ULBB509, the grants aid of No. 17540475 and 18035013.

References

[1] L. Chen, Phys. Plasmas, 1 (1994) 1519-1522.
[2] O. Motojima et al, Fusion Eng. Des., 20 (1993) 3-14.
[3] Y. Kubota, et al., , J. Nucl. Mater., 313-316 (2003) 239-244.
[4] T. Mutoh, et al., Phys. Rev. Lett., 85 (2000) 4530-4533.
[5] H.Kasahara, et al.,5th Asia Plasma Fusion Association, Jeju, Korea, Aug.,(2005).
[6] T. Seki, private communication.
[7] T. Ozaki, et al., Rev. Sci. Instrum. 77, 10E917 (2006)
[8] T. Ozaki, et al., JPFR Series, (to be published).
[9] T. Ozaki, et al., proc. of Burning Plasma Diagnostics in Varenna (2007) (to be published).
[10] Y. Takase, private communication.

Proceedings of ITC/ISHW2007

Improvement of the Accuracy of the Imaging Bolometer Foil Laser Calibration

H. ParchamyAraghy, B.J. Peterson, N. Ashikawa, H. Hayashi, H. Kawashima[1], and S. Konoshima[1]

National Institute for Fusion Science,322-6 Oroshi-cho, Toki 509-5292, Japan

[1] Japan Atomic Energy Agency, Naka-shi, Ibaraki-Ken, 311-0193, Japan

An imaging bolometer with a single graphite-coated metal foil is a diagnostic tool for diagnosing plasma radiation from magnetic fusion plasmas. We could obtain the local foil properties (the thermal diffusivity, κ, and the product of the thermal conductivity, k, and the thickness, t_f) of the metal imaging bolometer foil by analyzing the calibration data. For improving the IRVB a Tantalum (Ta) foil is offered due to strength, low neutron cross-section, and high sensitivity, however there is a large discrepancy between the value of the foil thickness from the experimental value and the nominal value. For calibrating of the foil the He-Ne laser beam is focused on 63 various locations which are determined by using the marks on the frame. The parameters of the foil are determined by comparing the measured thermal radiation data from an IR camera (FLIR/SC500) (60 Hz, 320 × 240 pixels, 7.5-13 μm) with the corresponding results of a finite element model.

Keywords: Accuracy, calibration, He-Ne laser beam, improve, imaging, bolometer
.

1. Introduction

The infrared imaging video (IRVB) bolometer with a single graphite-coated metal foil is a diagnostic tool that can act as a broadband absorber of radiation from nearly all spectral regions from of the foil plasma and convert its energy into a measurable temperature rise [1].

The calibration technique of the infrared imaging bolometer foil gives confidence in the measured values of the total radiation power from the plasma, and compensates for non-uniformities in the foil [2, 3]. The local foil properties of the foil such as the thermal diffusivity, κ, and the product of the thermal conductivity, k, and the thickness, t_f, are obtained by the foil calibration for one part on the foil when the foil is heated by the laser power [2]. Tantalum (Ta) is offered for improved sensitivity, foil strength, and lower neutron cross-section compared to the previously used gold foil of the imaging bolometer for the JT-60U tokamak [4].

Here, the improvement of the accuracy of the laser calibration of the imaging bolometer foil is considered.

2. The single graphite-coated metal(Ta and Au)foil

For improving the accuracy of the foil calibration of the imaging bolometer foil a new calibration setup in laboratory (low noise environment) has been designed and set up [4].

A single graphite-coated gold foil with an effective area of 9 × 7 cm^2 and a nominal thickness of 2.5 μm for use in the IRVB of LHD and a single graphite-coated tantalum foil with an effective area of 9 × 7 cm^2 and a nominal thickness of 5 μm for use in the IRVB of JT-60U is used on the calibration setup. Both sides of the foils are blackened with graphite. The blackened sides are heated by a 500 W heat lamp for drying the foils after spraying. The foils that are supported by a copper frame are shown in Fig. 1.

Calibration of the foil was made using a He-Ne laser as a known radiation source to heat the foil. The laser beam (~27 mW) is directed by three mirrors that are positioned by z and x-axis stages, to propagate through a CaF2 window in a chamber that is evacuated by a turbomolecular pump below 10^{-3} Torr and is focused on the foil. The blackbody radiation power from the foil that is heated by the laser beam is detected by an IR camera through a ZnSe window.

The IR camera (FLIR/SC500) with a frame rate of 60 Hz and pixel number of 320 × 240 is a microbolometer detector type that is sensitive to the far infrared wavelength range (7.5-13.0). The IR camera is moved by using a lab-jack (in z direction) and x-axis-stage (in x direction) for providing the thermal images of the foil which is heated by the He-Ne laser beam. In Fig.1, two contour thermal images from the laser spot after focusing on the foil (the center and the edge) resulting from the blackbody radiation from the foil are shown.

author's e-mail: journal@jspf.or.jp

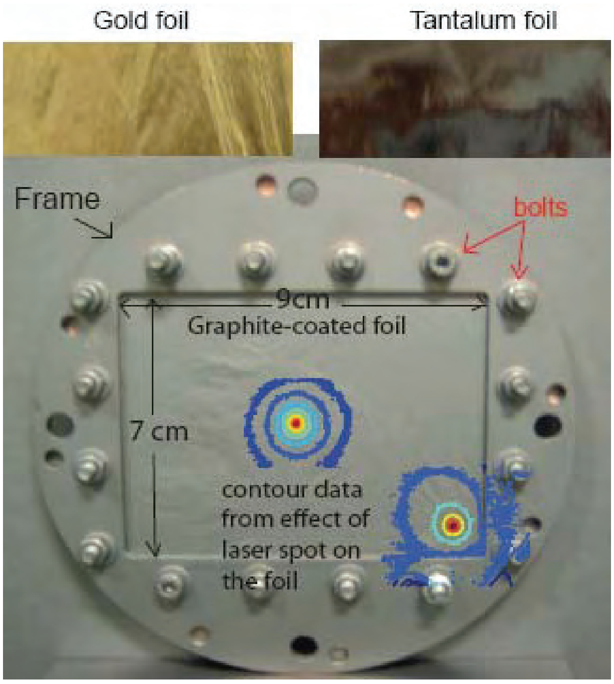

Fig.1 The single graphite-coated (one for Ta and one for Au separately) foil that is supported by a copper frame and temperature contour images from the laser spot after focusing on the foil (center and edge).

3. Improvement of Foil Calibration

The accuracy of the calibration of imaging bolometer foil is improved by using a new calibration setup and a FLIR/SC500 IR camera with a close-up lens at laboratory (low noise environment). This combination provides a spatial resolution of ~ 0.09 mm which is ~ 7 times better than the previous in situ calibration using a different Indigo/Omega IR camera where the spatial resolution of this camera is ~ 0.648 mm. The laser beam is focused on various locations which are determined by using the marks on the frame. Calibration data were taken at 63 (7 × 9) points on the foil. For the foil calibration using a HeNe laser, the laser power is necessary for solving the heat diffusion equation in two dimensions analytically by using the finite element model (FEM). A new model is made by finite element modeling according to the resolution of the FLIR/SC500 camera and the laser beam diameter.

The foil temperature rise was taken from the peak of a 2D Gaussian fitted to the temperature profile from the IR camera. The IR thermal data are averaged over 200 time frames of the steady state data. The FEM is used for solving of the two-dimensional heat diffusion equation with a constant thickness and thermal parameters of the foil and approximately 2000 spatial points assuming a constant temperature at the foil boundary. The FEM used the measured beam profile, fit to a 2-D Gaussian, as the heat source term.

A second order polynominal is fitted to the kt_f (the thermal conductivity is assumed to be constant at the nominal value) and ΔT data from the FEM to find the effective value of the t_f of the foil from the experimental value of ΔT. The variation of t_f from two locations (center and edge) of the gold foil (with nominal value of the foil thickness, t_f = 2.5 μm), and the tantalum foil (with a nominal value of the foil thickness, t_f= 5 μm), is shown in Fig.2.

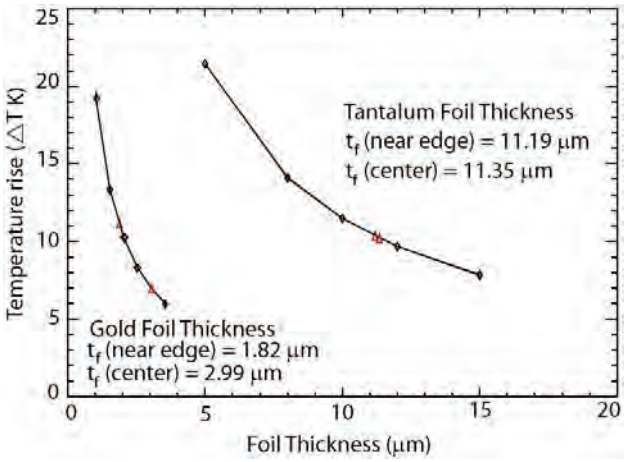

Fig.2 The appropriate value of the product of the kt_f of the (Au and Ta) foil from the experimental value of the ΔT is found from fitting a second order polynominal to the kt_f and the ΔT data from the FEM.

Acknowledgment

The authors are grateful to the support given by the MEXT Grant-in-Aid # 16082207.

References

[1] B. J. Peterson, A. Yu. Kostrioukov, N. Ashikawa, M. Osakabe, and S. Sudo, Rev. Sci. Instrum., vol. 74, 2003 , pp. 2040.

[2] H. Parchamy, B. J. Peterson, et al., Rev. Sci. Instrum. 77, 515 (2006)

[3] H. Parchamy, B. J. Peterson, et al., Plasma Fusion Res. 2, (2007) (in press).

[4] B. J. Peterson, et al., Plasma Fusion Res. 2, (2007) (in press)

[5] H. Parchamy, B. J. Peterson, H. Hayashi, S. Konoshima, N. Ashikawa, and the LHD team, Submitted for publish to IEEE TPS

Proceedings of ITC/ISHW2007

Development of Imaging Bolometers for 3-D Tomography of Radiation from LHD

Byron J. Peterson[1], Masahiro Kobayashi[1], Artem Yu. Kostryukov[2], Homaira Parchamy Araghy[1], Naoko. Ashikawa[1], Yi Liu[3], Naofumi Iwama[4], Masahiko Emoto[1], Hisato Kawashima[5], Shigeru Konoshima[5], Yuehe Feng[6], Hiromi Hayashi[1], Shinji Yoshimura[1], and DongCheol. Seo[7]

[1]*National Institute for Fusion Science, Toki-shi, Gifu-ken 509-5292, Japan*
[2]*St. Petersburg State Technical University, St. Petersburg 195251 Russia*
[3]*Southwestern Institute of Physics, Chengdu, 610041 China*
[4]*Daido Institute of Technology, Nagoya-shi, Aichi-ken, 457-8530 Japan*
[5]*Japan Atomic Energy Agency Naka-machi, Ibaraki-ken 311-0193 Japan*
[6]*Max-Planck Institute for Plasma Physics, Greifswald, D-17491 Germany*
[7]*National Fusion Research Center, Daejeon 305-806 Rep. of Korea*

Imaging bolometers are a powerful tool for diagnosing plasma radiation in a reactor relevant environment. In a tokamak, an imaging bolometer with a tangential view has demonstrated the ability to provide two-dimensional poloidal profiles of radiation through tomographic inversion under the assumption of toroidal symmetry. In helical devices the imaging bolometers have shown their usefulness in the interpretation of 3-dimensionl radiation structures. In the Large Helical Device, modeling of transport in the stochasitic edge region predicts a very three-dimensional structure in the flow velocities and in the associated accumulation of carbon impurity ions. In this paper we make a proposal for the diagnosis of these three-dimensional radiation structures. This is to be done through the measurement of the radiation using multiple imaging bolometers and the tomographic inversion of their signals to produce a three-dimensional image of the plasma radiation for comparison with the three-dimensional structure of the carbon radiation from the transport model. We present and discuss the recent results of this ongoing research including imaging bolometer development, possible symmetry assumptions and prospective research targets.

Keywords: bolometer, imaging, three dimensional, tomography, helical, infrared

1. Inroduction

Bolometers play an important role in fusion devices in the diagnosis of radiative losses from the plasma [1]. The conventional bolometer detector is a gold or platinum resistive bolometer which consists of a thin radiation absorbing foil backed by an insulating layer of either kapton or mica which is in turn backed by a resistive grid of the same material as the absorbing layer [2]. The change in temperature of the foil due to the absorption of radiation is sensed by the change in the resistance of the grid as it heats up.

These resistive bolometers have several drawbacks, especially regarding application to a radiation rich, steady state fusion reactor including: signal drift, restrictions on absorber thickness, the risk of numerous wire vacuum feedthroughs, radiation induced electronic noise and the lack of neutron resistant materials. Therefore, research and development has been carried out on an alternative detector known as the InfraRed imaging Video Bolometer (IRVB) which addresses these concerns through the application of infrared technology to measure the temperature of a thin absorber foil [3,4].

The use of infrared imaging of the absorber foil advances bolometer diagnostics from the conventional one dimensional arrays of resistive bolometers to two dimensional images of the plasma radiation from imaging bolometers. These imaging bolometers have been used in LHD to investigate radiative phenomena [5] and a single imaging bolometer on the JT-60U tokamak has provided two-dimensional radiation profiles through tomographic inversion under the assumption of toroidal symmetry [6].

Helical devices differ from tokamaks in their three dimensional nature, compared to the two dimensional

author's e-mail:peterson@LHD.nifs.ac.jp

nature of tokamaks resulting from their toroidal symmetry. Therefore, while a single imaging bolometer can provide the two dimensional (minor radial and poloidal) radiation profiles needed to fully diagnose the radiation from a tokamak plasma, in helical devices multiple imaging bolometers can be used to perform the three dimensional tomography necessary to fully diagnose the radiation. This is analagous to multiple one dimensional arrays of resistive bolometers being used to perform two-dimensional tomography in a tokamak. In this paper we discuss preparations for such three dimensional tomography of radiation on the Large Helical Device (LHD), including imaging bolometer development on LHD, symmetry assumptions and prospective subjects of research.

2. Imaging bolometer development on LHD

In addition to IR camera development by industry, imaging bolometer detectors are advancing through our research into absorbing foil materials, suitable IR optics, camera shielding materials and calibration techniques. This work has been summarized recently [7,8]. A typical IRVB system consists of a foil mounted in a frame in a pinhole camera in the vacuum vessel, a vacuum IR window an IR optical system consisting of lenses and mirrors and the IR camera. In LHD two types of cameras are currently being used. The first is an FLIR SC500 long wave (7.5 - 13 μm) camera with 320 x 240 pixels and a frame rate of 60 Hz. The second is an Indigo Phoenix mid wave (3 - 5 μm) camera with 320 x 256 pixels and a frame rate of 345 Hz. Foils have been installed at four locations in LHD as shown in Figure 1. Currently an SC500 camera is operating at the 6.5-U port IRVB and a Phoenix camera is operating on the 6-T port IRVB. We plan to install another SC500 camera at port 1-O in the next year. In the future we plan to move another Phoenix camera from JT-60U to LHD port 6.5-L in time for the DD experiments planned for LHD. This system includes a neutron/gamma/magnetic shield, a 3.7 meter IR periscope with 4 CaF_2 lenses, an Al mirror and a sapphire vacuum window with a 5 micron thick Ta foil and is shown in Figure 2. The other foils installed on LHD are 1 micron Au or Al. Other possible IRVB installations would include moving the SC500 camera from 6.5-U port to the 8-O port and replacing it with an Omega IR camera with a periscope. Another possible installation would be with a second Omega IR camera at the 8-I port. This would give a total of 6 IRVBs with over 1000 channels. Except for the IRVB moved from JT-60U to Port 6.5-L, all the other IR cameras would need to have shielding against neutrons and gammas added before the first DD campaign on LHD.

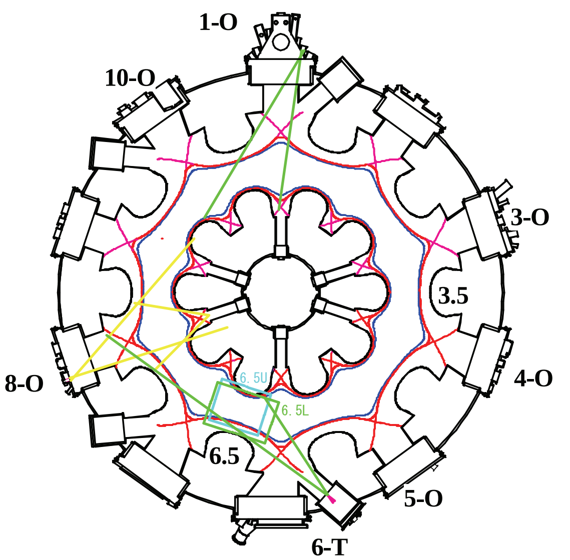

Fig.1 Top view of LHD vacuum vessel (black) showing existing (cyan and green) and prospective (yellow) IRVB foils.

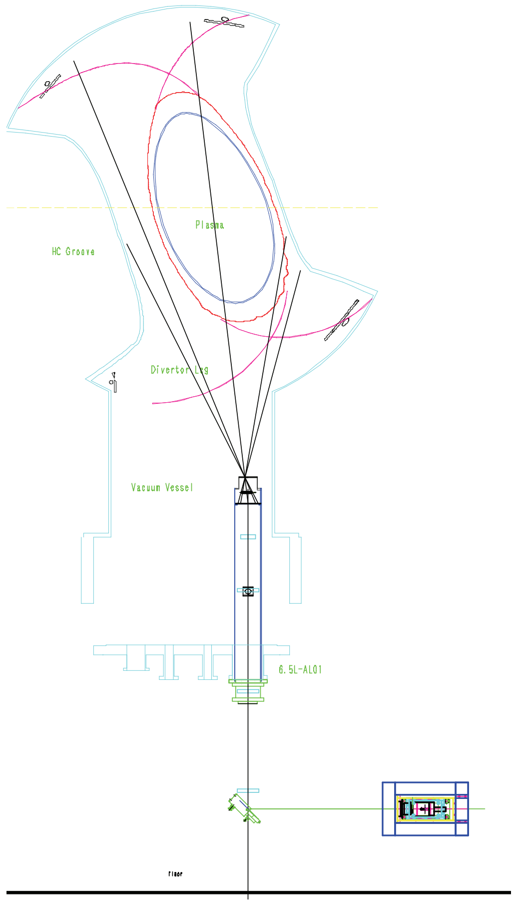

Fig.2 Side view of LHD Port 6.5-L showing position of foil, lenses, vacuum window, mirror, and IR camera in shield.

3. Plans for three dimensional tomography on LHD

In general, in order to carry out computed tomography the target volume is divided into cells with the centers of each cell representing the points at which one would like to know the measured quantity. The number and spacing of the cells determine the spatial resolution. In general for a well defined solution to the tomographic inversion the number of cells should not exceed the number of channels and each cell should be viewed by as many detectors from as many angles as possible. In order to reduce the number of unique cells and/or improve the spatial resolution certain assumptions regarding symmetry can be invoked. For instance in a tokamak by assuming toroidal symmetry, one of three spatial dimensions can be ignored greatly simplifying the problem.

In the same way in a helical device several different assumptions may be made to reduce the number of unique cells and simplify the tomographic inversion. For example let us start by dividing each half field period (18 degrees toroidally) into 10 radial sectors (8 inside the last closed flux surface (LCFS) and 2 in the ergodic region), 6 toroidal sectors and 8 poloidal sectors for a total of 480 cells/ half field period or 9600 cells throughout the entire toroidal volume. Since we do not have enough IRVBs to see every part of the plasma, we must make symmetry assumptions to reduce this number of cells.

The first assumption that can be made is what is called helical symmetry. If zero toroidal angle is defined to be at either the horizontally or the vertically elongated crossection, then this can be expressed as $S(r, \theta, \phi) = S(r, -\theta, -\phi)$ in toroidal coordinates minor radius, r, poloidal angle, θ, and toroidal angle, ϕ, where S is the local plasma emissivity. This essentially means that the plasma reproduces itself every half field period or 18 degrees toroidally in LHD. This reduces the number of unique cells to 480 in the previously given example.

Another assumption which is less strict is called toroidally periodic symmetry. This can be expressed as $S(r, \theta, \phi) = S(r, \theta, \phi+2\pi/m)$, where m is the number of toroidal field periods, or 10 in the case of LHD. This means that the plasma reproduces itself every field period or 36 degrees toroidally in LHD. This would result in 960 unique cells in our example.

Another much more simplifying assumption is called flux surface symmetry which requires that the radiation is constant on the flux surface. In the region of well formed flux surfaces inside the LCFS this removes the two coordinates of poloidal and toroidal angle from consideration, leaving only the minor radius. In our example this would reduce the number of cells inside the LCFS to 8 from 384, while the ergodic region where such symmetry can usually not be assumed would be divided into 96 or 192 depending on if helical symmetry or toroidally periodic symmetry where chosen, respectively. The choice of which of these symmetries to assume depends on the characteristics of the phenomena to be studied as is discussed next.

4. Physical targets of three dimensional tomography in LHD

Several phenomena which have appeared in LHD present excellent subjects for the application of three-dimensional tomography. The first of these is asymmetric radiative collapse, which occurs at the radiative density limit in LHD [9]. This has been observed by two IRVBs and diode arrays at two toroidal locations to be roughly toroidally symmetric. With three-dimensional tomography the degree of toroidal symmetry could be evaluated and the evolution of this phenomena's three-dimensional structure could be studied in detail. In this case toroidally periodic symmetry would be the appropriate assumption since the toroidal symmetry breaks the helical symmetry and the asymmetry is observed inside the LCFS.

A second interesting phenomena is the change in radiation structure predicted by the EMC3/EIRENE edge transport code in the ergodic region as the density increases. In the horizontally elongated cross-sections shown in Figure 3, the carbon radiation is localized polodally and radially at the inboard x-point at low density and moves inward towards the LCFS as density increases. With three-dimensional tomography this structure and its density dependence could be experimentally confirmed. The appropriate symmetry assumption for this study would be helical symmetry in the ergodic edge and flux surface symmetry inside the LCFS.

A third phenomenon of interest might be the serpens mode that has been observed under partially detached plasmas in LHD. This phenomenon has been described as a rotating belt of cold dense radiating plasma beneath the LCFS [10]. Since it rotates poloidally and toroidally none of the assumptions above may be applicable, but by observation with the multiple imaging bolometers this rotation could be observed in detail and confirmed.

4. Summary

Developemnt of imaging bolometers for LHD has been reviewed with a view towards the development of three-dimensional tomography of radiation. The present status of imaging bolometers on LHD and future plans have been presented. Possible simplifying symmetry assumptions have been reviewed and explained. Prospective subjects of study for three-dimensioanal tomography have been presented from phenomena previously observed on LHD. However, much work remains in order to realize this plan.

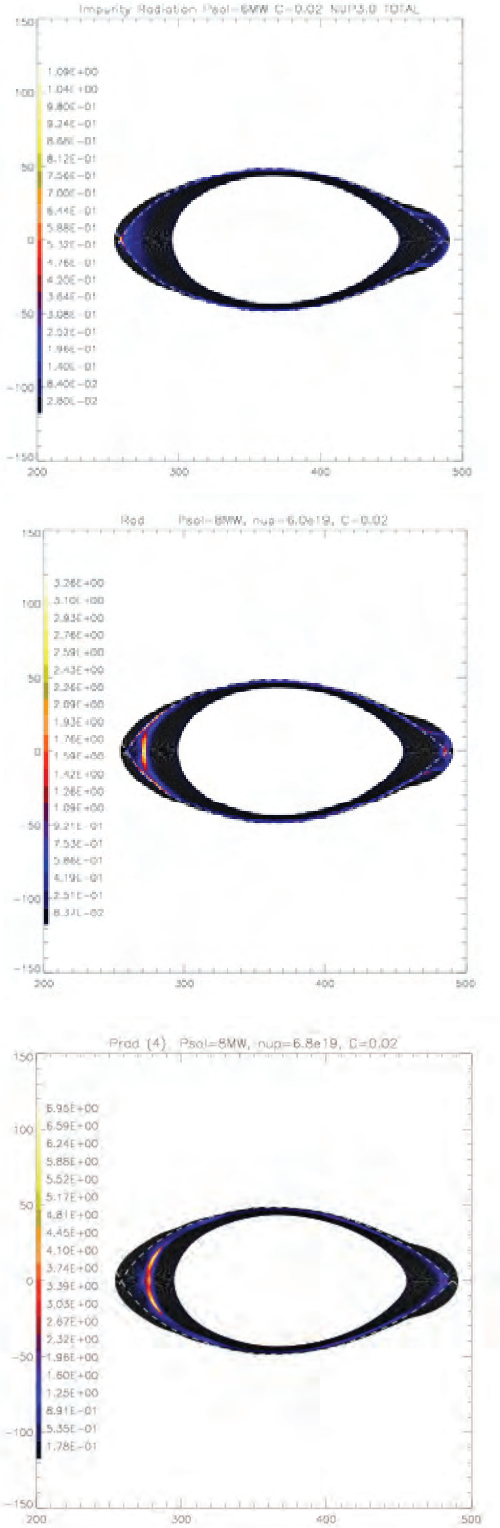

Fig.3 Two-dimesional profiles of carbon radiation intensity from the ergoic edge of LHD calculated by the EMC3/EIRENE code for n_{LCFS} = (a) 3 x $10^{19}/m^3$, (b) 6 x $10^{19}/m^3$ and (c) 6.8 x $10^{19}/m^3$.

References

[1] A.W. Leonard, *et al.*, Rev. Sci. Instrum. **66**, 1201 (1995).
[2] K.F. Mast, *et al.*, Rev. Sci. Instrum., **62**, 744 (1991).
[3] B.J. Peterson, Rev. Sci. Instrum. **71,** 3696 (2000).
[4] B.J. Peterson et al., Rev. Sci. Instrum. **74,** 2040 (2003).
[5] B.J. Peterson et al., Plasma Phys. Contr. Fusion **45,** 1167 (2003).
[6] Y. Liu et al., to be published in Plasma Fusion Res. (2007).
[7] B. Peterson et al., to be published in Plasma Fusion Res. (2007).
[8] H. Parchamy et al., to be published in Plasma Fusion Res. (2007).
[9] B. J. Peterson, et al., Plasma Fusion Res. **1,** 45 (2006).
[10] J. Miyazawa et al., J. Plasma Fusion Res. **81**, 331 (2005)

Proceedings of ITC/ISHW2007

Optimization of 48, 57μm poloidal interferometer / polarimeter for ITER

Rostyslav PAVLICHENKO[1], Kazuo KAWAHATA[1], Tsuyoshi AKIYAMA[1] and Shigeki OKAJIMA[2]

[1] *National Institute for Fusion Science , Toki-shi, 509-5292, Japan*
[2] *Chubu University, Kasugai-shi, Aichi 487-8501, Japan*

The determination of the profile of the toroidal plasma current (safety factor) has been considered as essential diagnostic for ITER. In absence of neutral beam, the only reliable diagnostics which can provide the information on the q-profile is polarimetry. About ten viewing chords could cover significant part of the poloidal cross section of the plasma in a fan-like arrangement at the equatorial port. The probing beams enter the vacuum vessel through a penetration in the blanket modules at the low-field side. The four additional quasi-vertical viewing chords are inserted through the upper port. Retroreflectors at the high field side mirror the laser beams back towards the initial penetrations and allowed to measure Faraday rotation and phase shift. The present work considered the combined interferometer / polarimeter configuration for laser wavelength of about 50 μm. At this wavelength the ellipticity is small but has to be taken for account. Thus, the promising Cotton-Mouton effect, which is considered as an alternative for plasma density measurements, will be difficult to implement. The initial optimization of the viewing chords arrangement for several ITER plasma scenarios (sensitivity to the toroidal current profiles) has been done. The additional issue of delivering laser radiation to the plasma will be addressed. The advantages of the waveguide approach for beam focusing in the long (more than 50 m) optical path are shown.

1. Introduction

Control of the current density profile becomes a paramount issue for the future tokamak experiments. Polarimetry can provide information on the density and magnetic field from which current profile could be reconstructed. Previous system [1] was design to operate at λ =118.8 μm CH_3OH oscillation line. It is well known that there are two main approaches to build the polarimetry system. To obtained information about magnetic field one have to measure the value of Faraday rotation angle α_F, which is proportional to poloidal magnetic field $B_{p\|}$ and electron density n_e.

$$\alpha_{\mathrm{F}} = 2.62\times10^{-13}\lambda^2\int_Z n_e(z)B_{p\|}(z)\,dz \qquad (1)$$

From α_F values profile of the poloidal component of the magnetic field could be calculated. It became obvious that the electron density along same beam line have to be known. For this purpose along beam chord a phase measurements by interferometer or measurements of the ellipticity angle α_{CM} (Cotton-Mouton effect (CM)) have to be performed.

$$\alpha_{\mathrm{CM}} = 2.62\times10^{-11}\lambda^3\int_Z n_e(z)B_t^2(z)\,dz \qquad (2)$$

2. System description

Maximum number of twelve probing beams comes into the plasma through the diagnostic plug at the low-field side (LFS). At the high field side (HFS) of the blanket shield module (BSM) small (∅37 mm) corner retroreflectors (CRR) are placed to reflect backwards the laser beams. Recently for ITER-scale experiments and for the plasma experiments on Large Helical Device (LHD) we have been developing short wavelength FIR laser. These research activities are carried out to overcome the common ‘fringe jumps’ phenomena which occurs because of electron density increasing during pellet injection experiments. On LHD 13-channels 119 μm laser interferometer has routinely operated to provide information on the electron density profile.

The wavelengths of the new two-color interferometer are 57.2 μm (1.6 W) and 47.6 μm (0.8 W) in a twin optically pumped CH_3OD laser [2].

For ITER experiments we advocate the classical dual interferometer / polarimeter approach for its considerable simplicity to reconstruct experimental data. We consider the propagation of polarimeter beams through a thin layer of plasma (thickness z_0) in the presence of a magnetic field. This calculation takes into account both the Faraday rotation and the Cotton-Mouton effect.

author’s e-mail: pavlichenko.rostyslav@LHD.nifs.ac.jp

P2-089

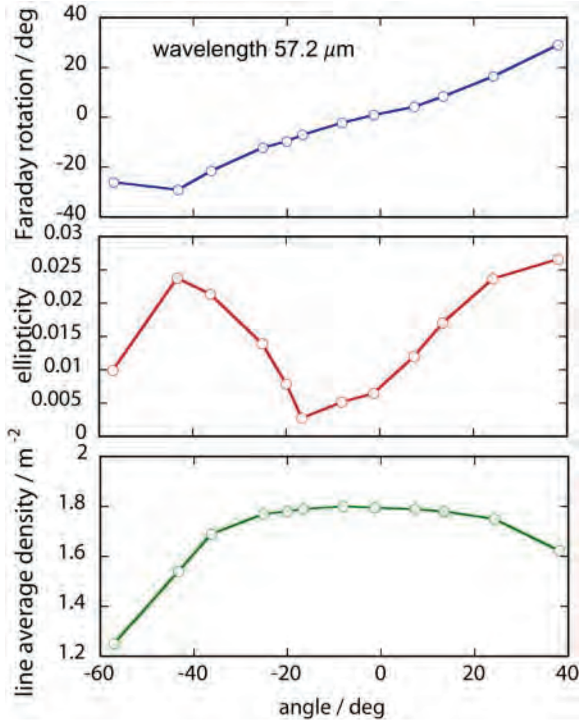

Fig. 1: Calculated Faraday rotation (top) and ellipticity (center), line density (bottom) 57 μm.

3. Alternated transmission line and numerical simulation of the expected values of the rotation angle and ellipticity

The calculation of the expected values of Faraday rotation angle and ellipticity for chosen ITER 'plasma burn' scenario #2 (plasma current I_p=15.0197 MA, q_0 = 0.99, 'flat' electron density profiles are shown at the Fig. 1. One can see that for the chosen wavelength of 57.2 μm Faraday rotation angle is about 25−30°, which is still large enough.

Recently for ITER-scale experiments and for the plasma experiments on Large Helical Device (LHD) we have been developing short wavelength FIR laser. These research activities are carried out to overcome the common 'fringe jumps' phenomena because of rapid raise of the plasma electron density, which occurs during pellet injection experiments. On LHD 13-channel 118.8 μm CH3OH laser interferometer has routinely operated to provide information on the electron density profile. The wavelengths of the new two-color interferometer are 57.2 μm (power 1.6 W) and 47.6 μm (power 0.8 W) in a twin optically pumped CH_3OD.

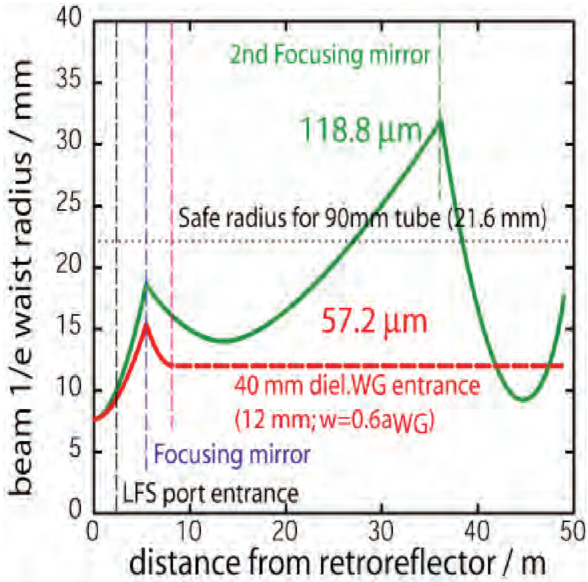

Figure 2: Calculated Gaussian beam radius (waist of 1/e intensity value) for wavelength 118 and 57 μm.

Since 47.6 μm and 57.2 μm have different polarization a Martin-Puplett diplexer is placed in front of the laser output. One of the most important issues is the developing of high quality heterodyne detection system with fast and sensitive characteristics. One of the main differences from 118.8 μm system is that instead of using quasi-optical transmission line (evacuated tubes of 90-120 mm in diameter) 40 mm dielectric waveguides become an attractive candidate. Those waveguides were made from Pyrex® borosilicate glass (with relative dielectric constant ε_r = 4.6−5.0) or acrylic resin (ε_r = 2.7−6.0)). From the other hand an oversized waveguides offer an attractive practical solution to transport light through the complicated geometry surrounding the fusion reactor.

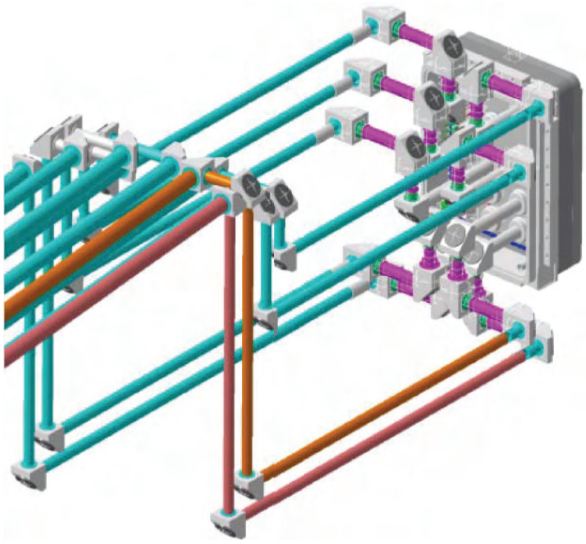

Figure 3: Poloidal polarimetry transmission lines and port plug to tokamak.

However, they can suffer from serious radiation-induced optical absorption and radioluminescence. Special fabrication and glass hardening techniques must be developed before suitable radiation -resistance dielectric waveguides can be used in ITER. By switching from pure quasi-optical (QO) beam free space propagation to 'waveguide ideology' for the transmission line that lies outside port plug (transmission line that correspond to the straight line at the Fig. 2) we can resolve several obstacles such as: mode matching / mode conversion, misalignment in the 'middle part' of the polarimeter optical path, which will be very difficult to maintain.

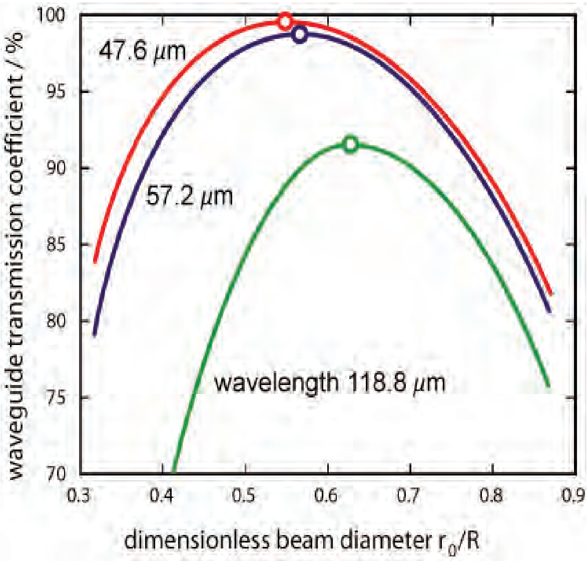

Figure 4: Coupling of Gaussian beam at the entrance of the dielectric waveguide. The inside diameter of the waveguide is 40 mm

From other hand waveguide system has precise mode matching (Fig. 2) (defined by waveguide diameter), easy alignment and more robust to mechanical vibrations. To deliver radiation from / to plasma each laser beam line is equipped with up to 8 miter-bends, with small conversion losses (Fig. 3). To avoid beam power dissipation Gaussian beam must enter the waveguide hawing optimized diameter. The calculation of waveguide transmission coefficient have been done for λ=48, 57, 118.8 μm

$$T = \left(1 - \exp\left(-F\frac{R^2}{r_0^2}\right)\right)F^{-1} \qquad (3)$$

where $F = 1 + \frac{\varepsilon_r + 1}{\sqrt{\varepsilon_r - 1}}\frac{L}{R}\frac{1}{k^2 r_0^2}$ and R, L - waveguide radius and length, $k = 2\pi/\lambda$ - laser beam wavelength, r_0-radius of the 1/e beam intensity level at the waveguide entrance, ε_r-waveguide material (relative dielectric constant) was chosen such as: $\sqrt{\varepsilon_r} = 2.1$. The calculation (refer to Fig. 4) shows that transmission coefficient values for 47.6 and 57.2 coupling into 40 mm diameter waveguide are about 99.6−98.42%, which is 7−8% higher than that for 118.8 μm.

The beam propagation inside the oversized dielectric waveguide have the same efficiency as for the free space, thus, preserves its polarization (99.6%). It was already confirmed by the long-term operation of FIR interferometer at LHD [5] (acrylic resin waveguide, length about 40m) and from several reports on JET polarimeter diagnostic (Pyrex® glass waveguide, length about 30m) that polarization of the laser beam in the waveguide remains almost constant. It was already shown [1, 3] by other research groups mechanical and optical properties of the corner retroreflectors became ultimately 'Achilles heel' of the system. The positions of the retroreflectors are limited by mechanical design of blanket shield modules on HFS inner wall (see Fig. 5). It was found that for wavelength 118.8 μm previously, which CRR can cope with misalignment up to 15 - 20 mm in poloidal plane without any serious effect on the reflectivity. For the shorter wavelength those values become twice smaller: up to 7.5 mm (see Fig. 6).

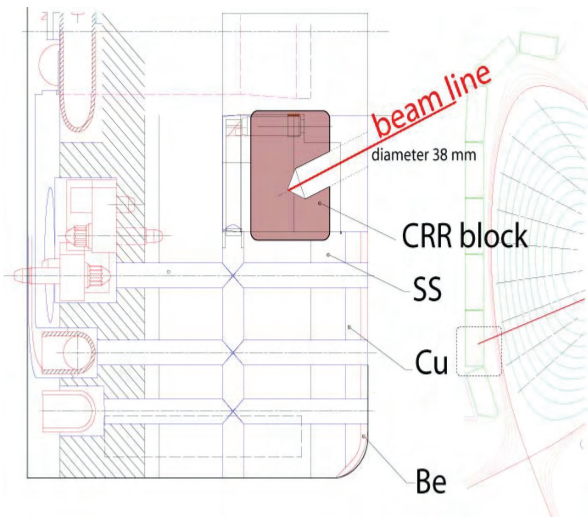

Figure 5: Outline of the retroreflector block incorporated into the blanket shield module. Without the plasma the beam is aimed at the center of the retroreflector.

This gives us much more freedom to cope with beam displacement caused by mechanical vibrations and due to refraction in plasma. Present level of CRR manufacturing could deal with 'ideal' sharp corner to sustain desirable sharpness which is about 5% from the laser beam width.

4. Final remarks

Recently proposed poloidal high power polarimeter will operate at 47.6 μm, 57.2 μm infrared oscillation. The output power of 57.2 μm laser is estimated to be over 1.6W and that of 47.6 μm is about 0.8W. Two color beat signals are simultaneously detected by a Ge:Ga detector with success. It was shown that preferable polarimeter-interferometer configuration will unveil some extra advantages in respect of 'full-polarimetric' system. Shorter wavelength laser will significantly improve (diminish) refraction problems. For present chord alignments and beam wavelength caused considerably small Cotton-Mouton effect. Alternated waveguide transmission line (with miter bends included) showed better focusing and tuning as well as much simple further maintenance, the Cotton-Mouton polarimeter becomes clear only in the case when the viewing chords are orientated in the equatorial plane, where the poloidal component of the magnetic field B_p is zero (pure toroidal polarimetry). Under some plasma condition there is a possibility of coupling Faraday and Cotton-Mouton effects.

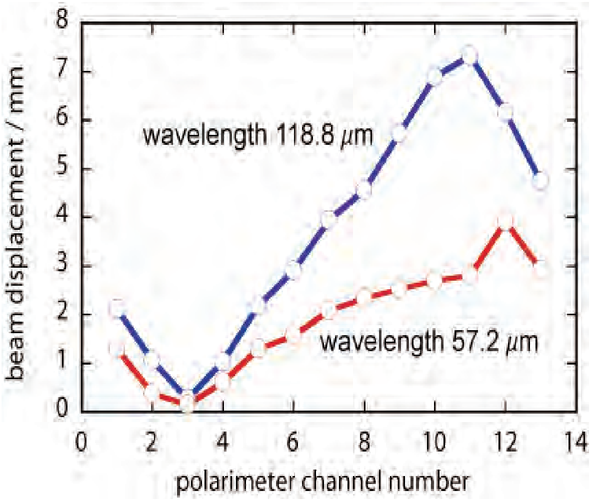

Figure 6: Beam displacement characteristics for the vertical fan of the chords at the position of the center of the correspondent corner retroreflectors.

Small Faraday rotation angle along some central chords suggests that placing additional beam lines must be done to improve spatial resolution of the system. Promotion of the dielectric waveguide addresses the issue of the radiation effect on those components. The appropriate additional 'shielding' of the waveguides studies now under the consideration. Further research is needed to define the most adapted materials for dielectric waveguides for FIR polarimetry.

References

[1] A. J. H. Donné, et.al, Rev. Sci. Instrum., **75**, (2004) 4701.

[2] K. Kawahata, et.al, Rev. Sci. Instrum., **77**, (2006) 10F132.

[3] V. S. Voitsenya, et.al, Rev. Sci. Instrum., **76**, (2005) 083502.

[4] H. Soltwich, Plasma Phys. Control. Fusion, **35**, (1993) 1777.

[5] K. Kawahata, et.al, Rev. Sci. Instrum., **71**, (1999) 707.

Proceedings of ITC/ISHW2007

Study on Analytical Method of Energy Resolved Soft X-ray Imaging with Beryllium Filters in LHD Plasmas

Chihiro SUZUKI[1)], Katsumi IDA[1)], Takashi KOBUCHI[2)], Mikirou YOSHINUMA[1)] and LHD Experimental Group[1)]

[1)]*National Institute for Fusion Science, 322-6 Oroshi-cho, Toki 509-5292, Japan*
[2)]*Tohoku University, 6-6 Aoba, Aramaki, Aoba-ku, Sendai 980-8579, Japan*

In the energy resolved soft X-ray imaging carried out in LHD, two dimensional images for different photon energy ranges have been obtained by taking differences between two images measured with adjacent filter thicknesses. For the initial analysis, the dependence of the measured signal intensity on the energy range was compared with the calculated one for continuum radiation. The effects of possible errors in this analytical method have been examined in this study. The effects of the small fraction of impurities in the filter material on the signal intensity are estimated to be ignorable, while the errors of the calculated intensity due to the tolerance of the filter thickness (±10%) are expected to be larger than the other errors. Actual dispersion of the filter thickness should be precisely measured in the future. In addition, the effects of K_α lines from titanium, chromium and iron in higher energy range should be evaluated by another CCD system prepared for photon counting mode.

Keywords: soft X-ray imaging, CCD camera, beryllium filter, thickness tolerance, filter transmittance, detection efficiency, LHD

1. Introduction

Soft X-ray imaging technique using a CCD (Charge Coupled Device) camera has ever been applied to the diagnostics of magnetically confined high temperature plasmas [1, 2]. The energy resolved soft X-ray imaging has recently been carried out by changing the thickness of beryllium (Be) filter during a long pulse discharge of the Large Helical Device (LHD) [3]. This diagnostic method can possibly be applied in the future for the detection of the difference in two dimensional (2D) soft X-ray profile caused by local non-Maxwellian component of electron energy distribution function.

For the initial analysis of this experimental result, the following procedure has been applied. Firstly, 2D images for specific photon energy ranges have been obtained by taking the intensity differences between two images measured with filter pairs of adjacent thicknesses. On the other hand, the expected dependence of the signal intensity on the photon energy range has been calculated from the theoretical power spectra of continuum radiation for various electron temperatures. Finally, the dependence of the measured signal intensity on the photon energy range has been compared with the calculated ones in order to check the validity of the results, which results in rough estimation of effective (line-integrated) electron temperature.

There are several possible causes of errors in the analytical method mentioned above. According to the specification of the Be filters used in this study, small fractions of impurities are included in the filter material, and actual filter thickness may not exactly agree with the specified value (within some tolerance). The magnitude and shape of the filter transmission curve (i.e. detection efficiency curve) may be changed by these effects, which results in errors in the calculation. In addition, the slow change in the impurity radiation could occur during a long pulse discharge even if the plasma density and temperature are under steady state. Finally, the effects of line radiations which are ignored in the calculation should be considered.

In this study, the results of the energy resolved soft X-ray imaging diagnostic is discussed from the viewpoints described above. The study mainly focuses on errors in the signal intensity and the effective electron temperature evaluated from the filter specification. Though reliability of the quantum efficiency curve of the CCD chip (provided by the manufacturer) should also be considered, it is not discussed here because the measurement of the quantum efficiency curve is difficult.

2. Experiment

Since the detail of the experimental setup has already been described elsewhere [3], only a brief explanation is given here. A schematic diagram of the diagnostic system installed in a tangential viewport of LHD is shown in Fig. 1. The system consists of a soft X-ray CCD camera (Andor Technology, DO435-BV) together with a pinhole, a pneumatic mechanical shutter, and a remotely rotatable filter disk which mounts 8 beryllium (Be) filters (99.8% purity). The selectable filter thicknesses are 50–1650 μm, including a common 50 μm Be window.

Figure 2 illustrates an example of the contour of the

author's e-mail: csuzuki@lhd.nifs.ac.jp

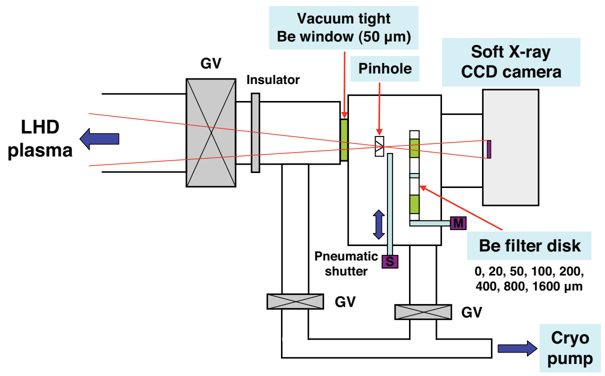

Fig. 1 Schematic diagram of the experimental setup.

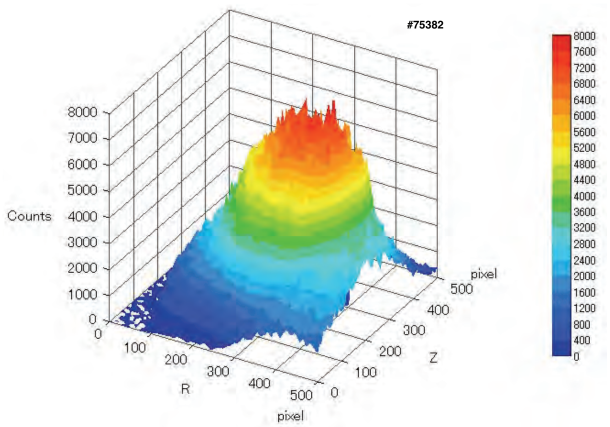

Fig. 2 Contour of the 2D image of the signal difference between the two images measured with 70 and 100 μm beryllium filters.

2D image obtained from the signal differences between the images measured with 70 and 100 μm filter thicknesses, which were obtained in a long pulse discharge sustained by ion cyclotron resonance heating (ICRH) [4]. The plasma was under quasi steady state, and the central electron temperature measured by the Thomson scattering diagnostic was about 1.3 keV at 8.9 s from the beginning of the discharge. The frame period and the exposure time of the CCD were adjusted to 10 and 5 seconds, respectively. The diameter of the pinhole was set at 0.1 mm. The hardware binning of 2×2 CCD pixels results in 512×512 superpixels in major radius (R) and vertical (Z) directions. In addition, 8×8 superpixels are averaged when the contour is drawn.

3. Detection Efficiency

The curve of overall detection efficiency versus photon energy for the signal intensity difference between the images measured with a pair of the adjacent Be filter (like Fig. 2) can be calculated from the product of the filter transmission and quantum efficiency of the CCD chip. Hence the origins of the errors in these curves may possibly affect the analytical procedure mentioned in section 1. The quantum efficiency curve of the CCD is not discussed in this article because of the reason described in section 1.

In this study, ultra-high purity beryllium foils (Grade IF-1) are used as the filters. According to the specification, the Be purity of this grade is 99.8 % (minimum), and thickness tolerance is within ±10%. The impurities of iron, beryllium oxide, aluminum, etc. are listed in the table of the small fraction of impurities in the filter material. Transmission of a filter composed of multiple materials are calculated by the formula

$$T = \exp\left(-d\rho \sum_i f_i \mu_i\right), \tag{1}$$

where d and ρ are the thickness and the mass density of the filter, and f_i and μ_i are the fraction of material mass and the mass absorption coefficient due to element i in the filter, respectively. After the detection efficiency curve of the 99.8% Be filter was calculated by including all of the impurities listed, the maximum deviation due to the thickness tolerance was estimated for the efficiency curve.

The effects of these filter specification on the overall detection efficiency curves are shown in Fig. 3, for the two combinations of the filter thicknesses (50-70 μm and 850-1650 μm). In Fig. 3(a), the curves for pure and 99.8% Be filters are plotted by broken and solid lines, respectively. As shown, the effect of the impurities becomes larger in high energy region. Slight shift of the peak of the efficiency curve is observed for higher energy range which results in the error of the peak energy of the transmittance. The effects of the purity on the magnitude of the detection efficiency are relatively small. The most influential impurities to the transmittance are iron and nickel whose fractions are 300 and 200 ppm, respectively. The structure of the absorption edges for these materials can be observed in the curve of 850-1650 μm filter combination.

On the other hand, the deviations of the transmission curves due to the tolerance of the filter thickness are drawn in Fig. 3 (b), where solid lines correspond to the exact thickness for the 99.8% Be filter and broken lines the maximum positive and negative deviations for ±10% tolerance. The effects of thickness tolerance on the magnitude of the detection efficiency are very large (≃50%) because of taking differences of the efficiency curves. The shape of the efficiency curve does not change.

4. Comparison with Calculation

Since power spectra of continuum radiations (bremsstrahlung and bound-free transitions) have dependence on photon energy (E) expressed by a factor $E\exp(-E/T_e)$, where T_e is an electron temperature, the dependence of signal intensity on filter combination for a given T_e can be calculated by integrating the product of a power spectrum and a detection efficiency curve shown in Fig. 3. As an initial step of the analyses, we

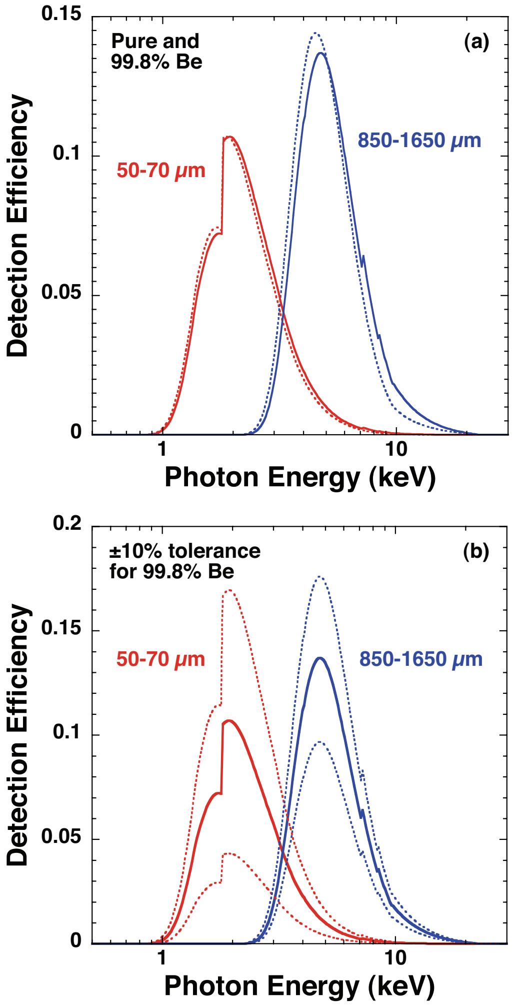

Fig. 3 Deviations of the detection efficiency curves due to (a) impurities in the filter material and (b) the thickness tolerance (±10%).

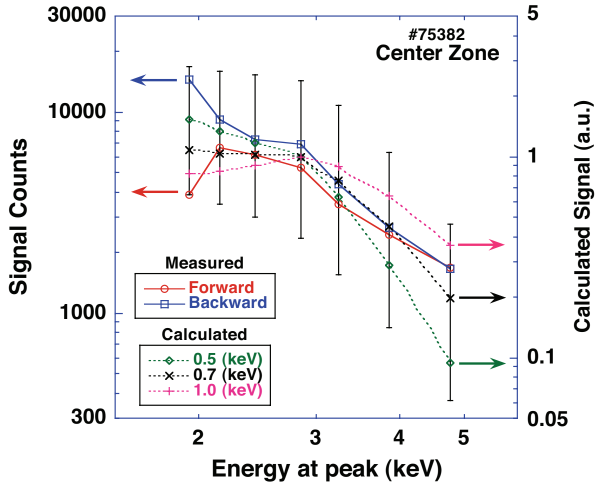

Fig. 4 The dependence of the signal intensity in the central zone (near the magnetic axis) on the photon energy range (solid lines). The horizontal axis is represented by the photon energy at the maximum efficiency for each filter combination. The calculated intensities for the electron temperatures of 0.5, 0.7 and 1.0 keV are also plotted by broken lines with the error bars due to the thickness tolerance for the case of 0.7 keV.

have compared the dependences of the measured signal intensities on filter combinations (i.e. on photon energy range) with those of the calculated ones.

The 7 images for the differences between the adjacent filters measured in the same discharge as Fig. 2 are divided into 16×16 zones by averaging in 32×32 superpixels. As for the central zone (near the magnetic axis), The measured and calculated intensities against the photon energy at the maximum efficiency for each filter combination are summarized in Fig. 4 plotted by solid and broken lines, respectively. The circle (red) and square (blue) symbols denote the experimental data in the central zone obtained by the forward and backward rotations of the filter disk, respectively, during the same shot. Therefore the disagreement between the forward and backward rotation is attributable to the slow change in the soft X-ray emission intensity from impurity ions during the discharge. The calculated intensities for the electron temperatures of 0.5, 0.7 and 1.0 keV are plotted by broken lines with the error bars due to the thickness tolerance for the case of 0.7 keV. Among the calculated intensities for the three electron temperatures, the most similar one to the experimental data is the one for 0.7 keV as plotted by times symbols (black) in Fig. 4. However, the error bars due to the thickness tolerance of the filter described above are very large. The effect of line radiations are not included in the calculation, which will be discussed in the next section.

5. Discussion

As shown in Fig. 4, inherent error in filter thickness may lead to large errors in final results due to deviation of transmission curve by taking the difference of the signals. If the vertical error bars in Fig. 4 are ignored, the effective (line-integrated) electron temperature for the central zone seems to be roughly 0.7 keV. However, the large magnitude of the error bars made it difficult to determine the temperature if the dispersion of the filter thickness would be actually ±10 %. This indicates that actual dispersion of the filter thickness, which may be smaller than 10 %, should be precisely measured (by a thickness tester) in the future for comparisons between the experimental results and the calculations. Smaller dispersions would minimize the vertical error bars.

Even if the error bars are minimized, the effects of line radiations should be discussed especially in higher energy range. Previous measurements of soft X-ray energy spectra in the Compact Helical System (CHS) by a CCD camera for photon counting mode show that K_α lines from titanium (4.8 keV), chromium (5.7 keV) and iron (6.6 keV) are significant [5]. In addition, large peaks of these three K_α lines are observed also in a similar discharge of LHD by X-ray pulse height analyzer (PHA) measurement [6]. Therefore these line radiations would influence the observed signal intensity especially in higher energy range. Another CCD camera used for the photon counting mode will also be installed in LHD in the near future as an alternative way to measure the effects of the soft X-ray line spectra.

6. Summary

We have developed a diagnostic system for the energy resolved soft X-ray imaging in a long pulse LHD discharge by using a CCD camera and Be filters with different thicknesses. Two dimensional images of soft X-ray intensity for different photon energy ranges have been obtained by taking differences between two images measured with adjacent filter thicknesses. The dependences of the measured signal intensities on the energy range were compared with the calculations for the continuum radiation. The effects of possible errors in this analytical method have been studied.

The errors due to the small fraction of impurities in the filter material are estimated to be ignorable, while the errors due to the tolerance of the filter thickness ($\pm10\%$) are too large for the comparisons, which are even larger than the error due to the discharge steadiness. Actual dispersion of the filter thickness should be precisely measured for further study. In addition, the effects of K_α lines from titanium, chromium and iron in higher energy range should be studied by another soft X-ray CCD system mainly used for the photon counting mode in the near future.

Acknowledgments

This work was partly supported by a grant-in-aid for scientific research from MEXT, and the JSPS-CAS Core-University Program in the field of "Plasma and Nuclear Fusion". This work was carried out under budget code NIFS06ULBB510.

[1] Y. Liang *et al.*, Plasma Phys. Control. Fusion **44**, 1383 (2002).
[2] T. Kobuchi *et al.*, Plasma Phys. Control. Fusion **48**, 789 (2006).
[3] C. Suzuki *et al.*, *Proc. 34th EPS Conf. on Plasma Phys.*, Warsaw, 2-6 July 2007 ECA (2007) P2.139.
[4] R. Kumazawa *et al.*, Nucl. Fusion, **46**, S13 (2006).
[5] Y. Liang *et al.*, Rev. Sci. Instrum. **71**, 3711 (2000).
[6] S. Muto, S. Morita, and LHD Experimental Group, Rev. Sci. Instrum. **72**, 1206 (2001).

Proceedings of ITC/ISHW2007

Measurement of radiation profile at density ramp-up phase by using AXUV photodiode arrays in Heliotron J

S. Watanabe, K. Nagasaki[a], H. Matsuoka, H. Arimoto, T. Mizuuchi[a], H. Okada[a], S. Kobayashi[a], K. Kondo, S. Yamamoto[a], N. Tamura[b], C. Suzuki[b], G. Motojima, K. Murai, F. Hamagami, H. Yasuda, K. Mukai, A. Nakajima, D. Katayama, H. Takahashi and F. Sano[a]

Graduate School of Energy Science, Kyoto University, Gokasho, Uji, Kyoto 611-0011, Japan

[a] *Institute of Advanced Energy, Kyoto University, Gokasho, Uji, Kyoto 611-0011, Japan*

[b] *National Institute for Fusion Science,322-6 Oroshi-cho, Toki 509-5292, Japan*

(Received day month year / Accepted day month year should be centered 10-point type)

Measurement of radiation profiles has been made in electron cyclotron resonance heated (ECRH) plasmas on Heliotron J by using AXUV photodiode arrays. The measured radiation in low density is attributed to the effect of low energy photon below about 10eV at edge region, and the profile in the chord-integrated signal is found to be broad. The radiation collapse at density ramp-up is also investigated. The radiation starts to decrease from the edge side at the collapse, and then the reduction in the radiation gradually shifts to the core plasma during the collapse event. The plasma starts to collapse when the edge radiation intensity reaches a certain value, independent of the density.

Keywords: Heliotron J, radiation profile, AXUV, soft x-ray profile, radiation collapse

1. Introduction

Radiation from plasmas plays an important role in confinement and transport in toroidal devices. The radiative process is related to the impurity transport, radiation collapse, and MARFE phenomenon. The energy loss from the radiation is a key issue for high density plasma confinement in stellarators which reach higher densities than tokamaks. The physics of density limit have been investigated by several scenarios, which involve the increase in radiated power with density [1]. The observation in W7-AS and LHD suggests that the density limit is determined by the power balance between the input power and the radiative power [2, 3].

Absolute extreme ultraviolet photodiodes (AXUVD) are widely used for plasma diagnostic to understand the radiation process. The AXUVD is capable of measuring the radiation with high time resolution with energy sensitivity from visible to soft-x ray region. Some of the applications are , for example, a total radiation power monitor from visible to soft-x region with unfiltered AXUVD, a fast measurement of vacuum ultraviolet (VUV) and soft-x emission with filtered AXUVD, and a fast spectroscopic measurement of plasma impurities with AXUVD using multilayer filters [4-6]. In this paper, we present measurement results on radiation profiles by using the AXUVD for ECRH plasmas in Heliotron J. The radiation profile in low density is shown, and the radiation collapse event at density ramp-up phase is also reported.

2. Experimental setup

Heliotron J is a medium sized helical-axis heliotron device with a low magnetic shear ($<R_0>$=1.2 m, a=0.1-0.2 m, B_0<1.5T). The coil system consists of an l/m=1/4 continuous helical coil, two sets of toroidal coils and three pairs of vertical field coil. The combination of these coil sets produces flexible helical-axis heliotron fields. The two sets of toroidal coils controls the bumpiness component of the magnetic field in Boozer coordinates, ε_b=B(m/n=0/4)/B(m/n=0/0), which is an important component in the helical-axis heliotron configuration because of its contribution to neoclassical transport and improved particle confinement. For plasma heating, second-harmonic X-mode ECRH (70GHz 0.4 MW) is applied. The details of Heliotron J are described in Ref. 7.

Two AXUVD arrays (AXUV 16ELO/G, IRD) have been installed in Heliotron J in order to measure radiation profiles. One array views over the whole poloidal cross section with an optical filter system, and the other views from the plasma center to the SOL in the inboard side of torus without optical filter. The AXUVD has a high time resolution with the rise time of 0.5 μs. The filter system at one photodiode array is composed of aluminum foils with

e-mail: w.shinya@center.iae.kyoto-u.ac.jp

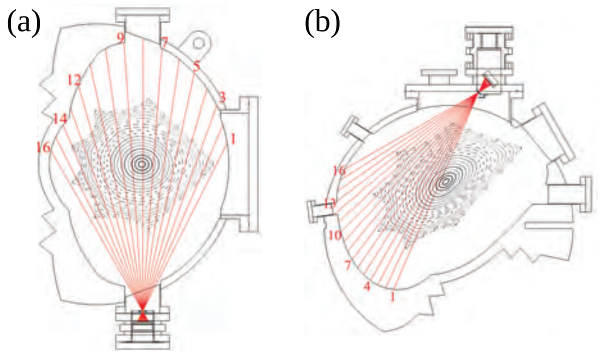

FIG. 1 Magnetic flux surface and lines of sight of AXUVD arrays (a) viewed over the whole poloidal cross section and (b) viewed from the plasma center to the SOL in the inboard side of torus

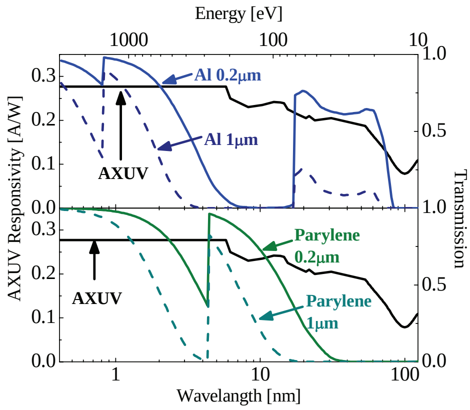

FIG. 2 AXUVD responsivity and transmission of aluminum and parylene filters

1.0 μm and 0.2 μm thicknesses, parylene foils of 1.0 μm and 0.2 μm thicknesses, and a bandpass filter for 155 nm (FWHM 26.6 nm, FN155-N-.5D-MTD-SP, ACTON). The transmission characteristics in these filters and the spectral responsivity in AXUVD are shown in Fig. 2. The aluminum foil eliminates the effect of the low energy photon and transmits the high energy photon. On the other hand, the parylene foil eliminates the photon energy from UV to VUV regions. The transmission curves in the foils are also shown in Fig. 2. The radiation in soft-X and VUV region is estimated by using combination of the aluminum and parylene foils.

3. Measurement of radiation profile

3.1 Measurement with optical filter system

The radiation profiles have been measured in low density ($\overline{n_e}$ ~0.7×10^{19} m^{-3}) ECRH plasmas by using the AXUVD array to view over the whole poloidal cross section. Shown in Fig. 3 are the radiation profiles of the chord-integrated signals without the optical filter and with 0.2 μm aluminum and 0.2 μm parylene filters, where 8ch signal corresponds to the magnetic axis. Note that the 9 and 16ch signals are not used due to a trouble in the AXUVD array system. The radiation profile in the integrated signals without filter is rather asymmetric

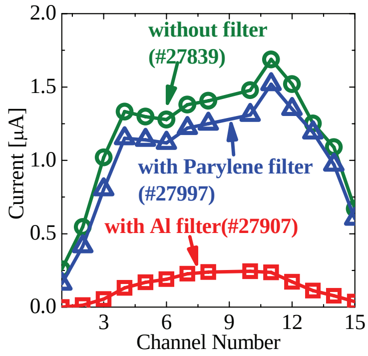

FIG. 3 Radiation profiles without the optical filter and by using 0.2 μm aluminum and 0.2 μm parylene filters

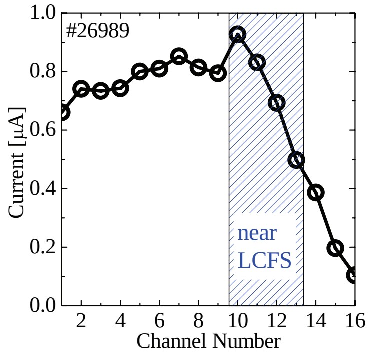

FIG. 4 Radiation profile by using AXUVD in Fig. 1(b)

which have a peak at 11ch at the inside of the torus, and resembles in shape with the parylene filter. The parylene filter of 0.2 μm thickness eliminates the energy photon below about 50 eV, but has the transmission characteristics in visible light. On the other hands, the radiation profile by using the 0.2 μm aluminum filter, which eliminates the effect of energy photon from about 80 to 200 eV and below 10 eV, is centrally peaked, and the intensity at the edge region is low. The radiation intensity with the aluminum filter is about 20% as low as without the filter. The result indicates that the radiation from low energy photons below about 10 eV dominates and causes the asymmetry in the measured radiation without filter. Shown in Fig. 4 is the radiation profile in the integrated signals without the filter by using the AXUVD illustrated in Fig. 1(b). The profile is hollow which have a peak at 10ch near the last closed flux surface (LCFS). The radiation intensity with the aluminum filter near LCFS (2, 14ch) in Fig. 1(a) is much lower than without filter. The effect of low energy photon below 10 eV should be dominant near the edge region.

3.2 Radiation profile during collapse event

In this section, the radiation profile at density ramp-up in ECRH plasmas is studied by using two AXUVD arrays. The measurement has been carried out in the plasma at more than 2 × 10^{19} m^{-3} in electron density. The typical time evolution of plasma discharge is shown in Fig. 5. The

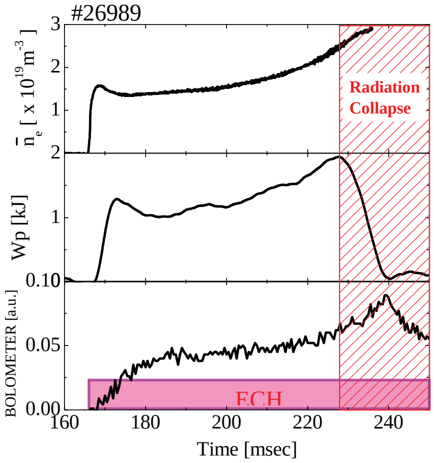

FIG. 5 Typical wave forms of a radiative collapse discharge for ECR heating plasma (shot #26989)

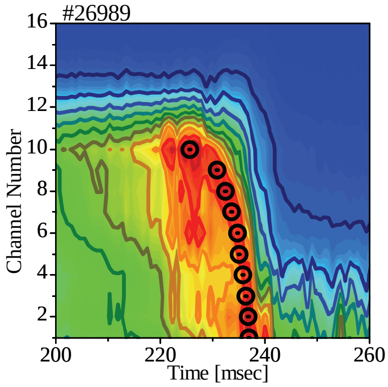

FIG. 6 Radiation profile evolution in the chord-integrated signal with radiation collapse event. The open circles indicate the maximum intensity of the signal at each channel inside 10ch during the collapse event.

bolometer signal is measured by a metal resistor type bolometer without metal foil filter [8]. The signal includes the effect of the neutral particle because no filter is applied to block off the particle. As the radiation collapse arises after 227 ms in this discharge, the stored energy decreases and the bolometer signal increases. Figure 6 shows the radiation profile in the chord-integrated signal measured by the AXUVD array in Fig. 1(b). The 10ch signal viewing near the last closed flux surface is largest and increases with density. The signal decreases suddenly with the stored energy at the collapse event. As the radiation collapse proceeds, the peak of the profile moves toward the central region. The open circles in Fig. 6 indicate the maximum intensity of the signal at each channel inside 10ch during the collapse event. The peak of the radiation profile shifts gradually from edge to core plasma after near the time for the maximum stored energy. Since no significant changes in the signals at core region (1-5ch) are observed at t~227 ms, it can be seen that the collapse emerges from the edge region. The collapse phenomena often occurred in wall conditioning discharges in early FY2007 campaign in

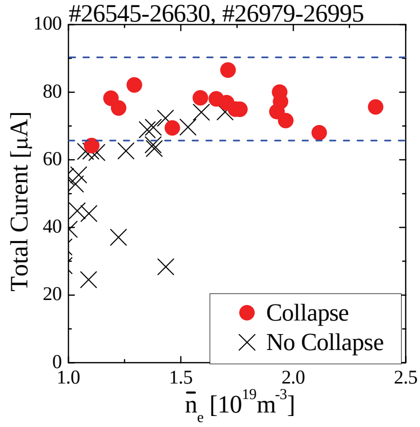

FIG. 7 Total radiation intensity just before the collapse event (collapse case) and at time for the maximum stored energy (non-collapse case) in the early experimental campaign

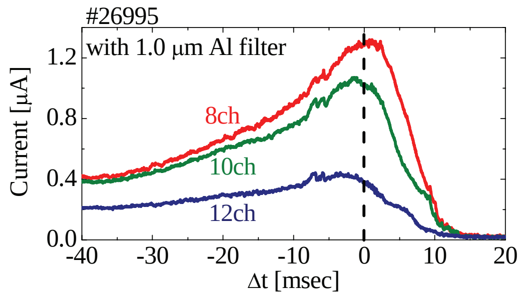

FIG. 8 Time series of radiation intensities at the collapse event by using AXUVD with 1.0 μm aluminum filter. The dashed line indicates the time for the maximum stored energy and Δt is time interval from the timing.

Heliotron J. Figure 7 shows the density dependence of the total radiation intensity. Here the total radiation is estimated by summing the intensities in all the channels at the time for the maximum stored energy. The radiation collapse occurs when the total signal current reaches between about 65 and 90 μA, independent of the electron density. Since the density is lower than the ECRH cut-off density, the collapse should be triggered by radiation loss above certain radiation intensity.

The change in radiation during the collapse event was also measured by the AXUVD array with the optical filter system shown in the Fig. 1(a). Similarly as Fig. 6, the radiation intensity without filter firstly decreases from the edge side and then the reduction region shifts to the core region at same time scale as Fig. 6. On the other hands, the measurement by the array with 1μm aluminum filter was carry out in order to eliminate the energy photon below about 400 eV in the discharge with the collapse as shown in Fig. 8, where Δt is time interval from timing in the maximum stored energy. No clear shift of reduction region of radiation intensity by using the aluminum filter is observed during the collapse event. Figure 9 shows the time in peak (over 95% of maximum) of radiation intensity at each channel. The time in shift of

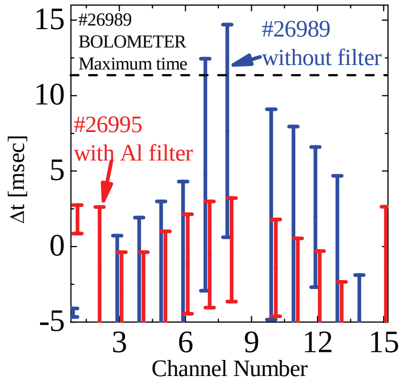

FIG. 9 Time region in the peak (over 95% of maximum) of the radiation intensity at each channel in AXUVD array

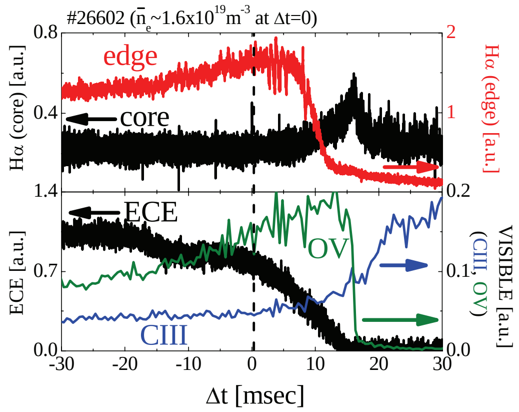

FIG. 10 Time series of the signals from Hα, OV, CIII and ECE at the collapse event

the reduction region exceeds 10 ms in non-filter case, but a few ms in the aluminum filter case. The timing at reduction of the central channel (8ch) signal in the radiation profile without filter is later than with the filter. The change in radiation profile during the collapse event should be the effect of shift of emission region from energy photon below about 400 eV. The signals of Hα at edge and core region, OV and CIII viewed whole poloidal cross section are shown in Fig. 10. Similarly in the signals of AXUVD, the timing at reduction in Hα signal at the core is later than at the edge, and the signal at the core is kept increasing to near Δt=15 ms. On the other hands, the OV and CIII signals increase at the collapse event, and the OV signal drops at Δt~15 ms. The electron cyclotron emission (ECE) signal, shown in Fig. 10, decreases after Δt=0 ms. Since the density is lower than the ECRH cut-off density, it suggests that the electron temperature decrease during the collapse event. As the ionization potential of CIII and OV are respectively 47.9 and 114 eV, the signal drop in OV is due to cooling of the plasma. As a result of energy loss in the radiation collapse, the radiation from the energy photon below 400 eV should be dominant, and increases by reduction in the electron temperature.

4. Summary

Measurement of radiation profiles was carried out for ECRH plasmas in Heliotron J by using two AXUVD arrays. The radiation profile in the line-integrated signals is rather asymmetric, which has a peak in inside of the torus in low density plasma of $\overline{n_e}$ ~0.7×10^{19} m^{-3}. Comparison between the radiation profiles with and without the filter showed that the radiation from low energy photons below about 10eV dominated and caused the asymmetry. The radiation intensity near LCFS is high, and the radiation from the low energy photon was found strong at the edge region.

The radiation collapse at density ramp-up ($\overline{n_e}$>2×10^{19} m^{-3}) was also investigated. The peak of radiation moves from the edge side during the collapse event. No significant changes in the radiation at the core region are observed just after the collapse event, and the collapse emerges from the edge region. The radiation collapse occurs when the emission intensity reaches a threshold, independent of the electron density, suggesting that the collapse should be triggered by radiation-loss above certain radiation intensity. The radiation intensity with 1 μm aluminum filter decreases at each channel near timing of maximum in the stored energy. The reduction timing for radiation without filter is later than that with the filter. The ECE signal decreases with increasing the density, and the signals from Hα at the core, OV and CIII signals increase during the collapse. These measurement results suggest that the electron temperature decreases from the edge region, and the low temperature region spreads into the core region.

Acknowledgements

The authors are grateful to the Heliotron J team for their excellent arrangement of the experiments.

References

[1] Greenwald M, Plasma Phys. Cont. Fusion **44** R27-80 (2002)
[2] Giannone L et al., Plasma Phys. Cont. Fusion **42** 603 (2000)
[3] Peterson BJ et al., Plasma Fusion Res. **1** 045 (2006)
[4] Suzuki C et al., Rev. Sci. Insutrum. **75** 4142 (2004)
[5] Xiao Q et al., Rev. Sci. Insutrum. **67** 3334 (1996)
[6] Lanier NE et al., Rev. Sci. Insutrum. **72** 1188 (2001)
[7] Obiki T. et al., *Nucl. Fusion.* **41** 833 (1999)
[8] Besshou S et al., Jpn. J. Appl. Phys. **23** L839 (1984)

Proceedings of ITC/ISHW2007

Direct Measurement of an Electron Bernstein Wave on the Internal Coil Device Mini-RT

E. Yatsuka, D. Sakata, K. Kinjo, J. Morikawa[a)], Y. Ogawa[a)]

Graduate School of Frontier Sciences, Univ. Tokyo, 5-1-5 Kashiwa-no-ha, Kashiwa-shi, Chiba 277-8561, Japan

[a)]High Temperature Plasma Center, Univ. Tokyo, 5-1-5 Kashiwa-no-ha, Kashiwa-shi, Chiba 277-8568, Japan

(Received 15 October 2007)

Measurements of electron cyclotron range of frequencies (ECRF) electric fields by using small (5 mm) antenna have been carried out in the Mini-RT device, and signals having two characteristics of electron Bernstein wave (EBW) have been detected. One of them is short wavelength (~2 cm). The order of corresponding refractive index is 10, while calculation predicts several 10 to 100. The other characteristic is backward wave, i.e. group velocity is opposite to phase velocity. In the Mini-RT device, plasma production is achieved by using ECH, therefore we can expect the existence of high-energy electrons. High-energy electrons can affect dispersion relation, and waves having relatively long wavelength can propagate around upper hybrid resonance (UHR).

Keywords: electron Bernstein wave, mode conversion, electrostatic mode, backward wave, overdense plasma, density gradient, cyclotron harmonic resonance, upper hybrid resonance, interferometry, antenna

Electron Bernstein Wave (EBW) is one of the most promising methods for high beta plasma heating. This wave can propagate across magnetic surfaces without density limit and strongly be damped due to cyclotron harmonic damping. However, EBW is an electrostatic mode and its wavelength is comparable to electron Lamor radius [1], thus it is hard to launch EBW directly into plasma except for the special case as slender plasma, e.g. glow discharge positive column plasma [2]. In Ref. [2], the first observation of EBW radiation, i.e. inverse process of absorption, was discussed.

Excitation of EBW in plasma via mode conversion process [3] is needed to achieve EBW heating for thick plasma, e.g. fusion plasma. In linear device, electron cyclotron range of frequency (ECRF) electric field in plasma was investigated by using wire antenna [4]. As a result, mode-converted EBW was observed with so-called fast X-B method. Recently, mode conversion efficiencies have been evaluated by using electron cyclotron emission (ECE) via mode conversion from EBW to electromagnetic waves [5,6]. This method is suitable for studying EBW heating without disturbance, but it is hardly applicable for devices that have steep magnetic field gradient such as internal coil device.

Internal coil devices have been constructed to investigate high beta plasma confinement [7,8], which is based on the theory of self-organized states in flowing plasma [9]. The objective of this research is production of highly overdense plasma by using EBW heating.

author's e-mail: yatsuka@ppl.k.u-tokyo.ac.jp

This Letter reports the preliminary results of ECRF electric field measurements in the internal coil device Mini-RT (Miniature Ring Trap). We produce plasma by injecting an X-mode microwave (2.45 GHz, 2.5 kW c.w.). High Temperature Superconductiong (HTS) Coil, that is called Floating Coil (F-Coil), produces poloidal magnetic field, which is similar to that of a planet. Typical strength of magnetic field is 0.01-0.1 T. Figure 1 shows two magnetic configurations in Mini-RT, i.e. (a) Dipole configuration and (b) Separatrix configuration. Solid (Dotted) lines denote magnetic surfaces (magnetic field strengths). Figure 2 shows typical radial profiles of electron density; (i) Dipole configuration, (ii) Separatrix configuration. By applying Levitation Coil (L-Coil)

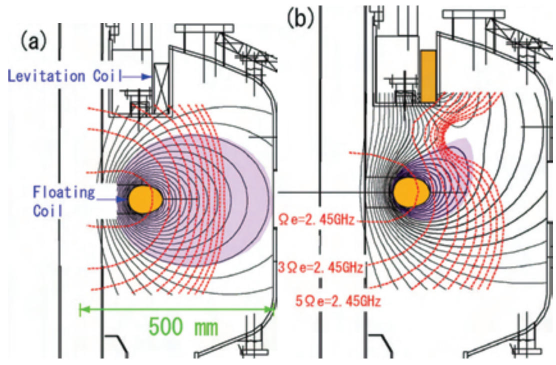

Fig.1 Cross section of the Mini-RT device. (a) Dipole configuration (L-Coil current is not applied) (b) Separatrix configuration

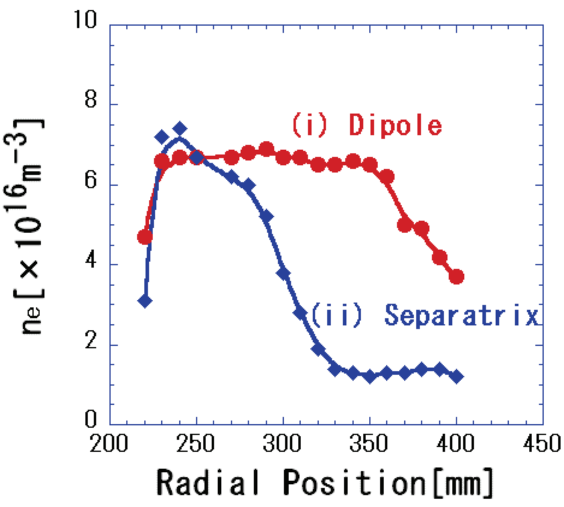

Fig.2 Radial profiles of electron density n_e. (i) Dipole configuration, (ii) Separatrix configuration.

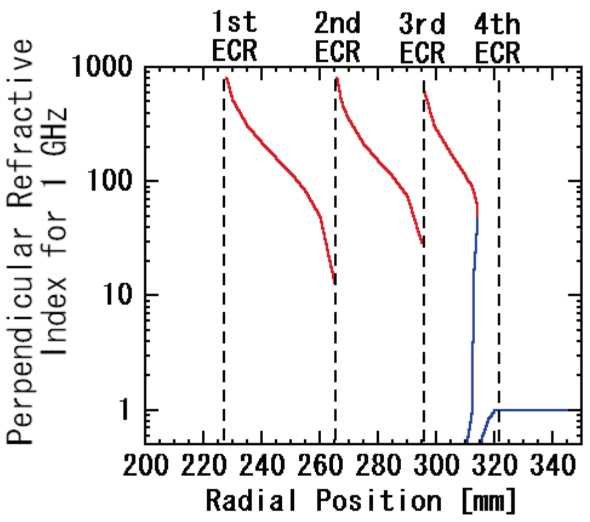

Fig.3 Perpendicular refractive index of hot wave with typical density profile of Mini-RT.

current, we can produce separatrix, and plasma is confined in closed flux surfaces. We can also create steep density gradient region (L_n ~ 5 cm) around separatrix [10,11]. Peak density is around cut-off density of 2.45GHz, O-Mode microwave, i.e. 7.6×10^{16} m^{-3}.

Dispersion relation predicts that typical value of perpendicular refractive index of EBW is several 10 to 100. Figure 3 shows calculated radial profile of refractive index on mid-plane for 1.0 GHz. We assumed trapezoidal density profile, which is similar to Fig. 2 (ii); and electron temperature is uniformly 10 eV, which is typical value of Langmuir probe measurements [11]. We calculated dispersion relation of hot wave [12] propagating

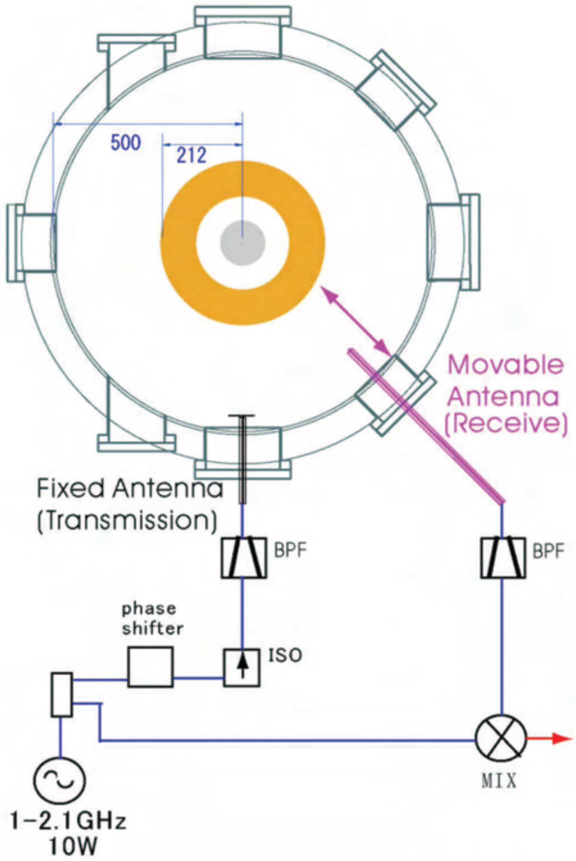

Fig.4 Top view of Mini-RT and block diagram of circuit.

perpendicular to magnetic field. We assumed perpendicular injection of X-Mode from low field side, which is one of the most appropriate for mode conversion to EBW. Injected X-Mode electromagnetic wave tunnels evanescent region which lies between right hand cut-off (R-Cutoff) and upper hybrid resonance (UHR), i.e. 310 < R < 315 mm. Energy of X-wave transfers into EBW around UHR.

Mode conversion efficiency C have been evaluated by

$$C = 4e^{-\pi\eta}\left(1-e^{-\pi\eta}\right)\cos^2\left(\phi/2+\theta\right), \tag{1a}$$

$$\eta = \frac{\Omega_e L_n}{c}\frac{\alpha}{\sqrt{\alpha^2+2L_n/L_B}}\left[\frac{\sqrt{1+\alpha^2}-1}{\alpha^2+(L_n/L_B)\sqrt{1+\alpha^2}}\right]^{1/2}, \tag{1b}$$

$$\alpha = \left.\frac{\omega_{pe}}{\Omega_e}\right|_{UHR}, \tag{1c}$$

where c, Ω_e, ω_{pe}, L_n and L_B are light speed, electron cyclotron frequency, electron plasma frequency,

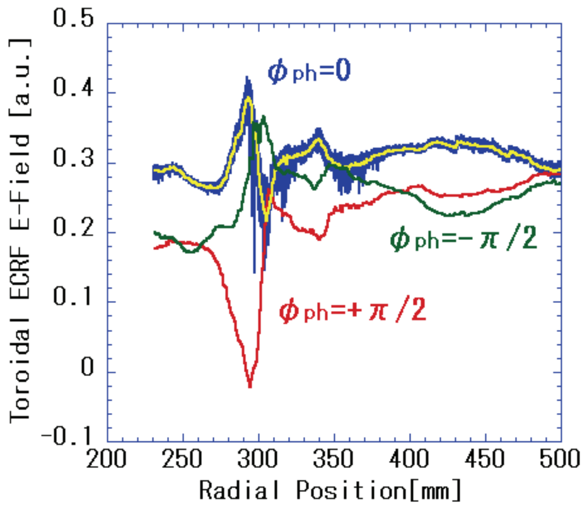

Fig.5 Interferometer traces for $\phi_{ph} = \pm\pi/2$, 0. Frequency of a launched wave was 1.0 GHz. We can obtain fluctuated data, and signals are averaged over each millimeter to determine amplitude and phase of an ECRF electric field.

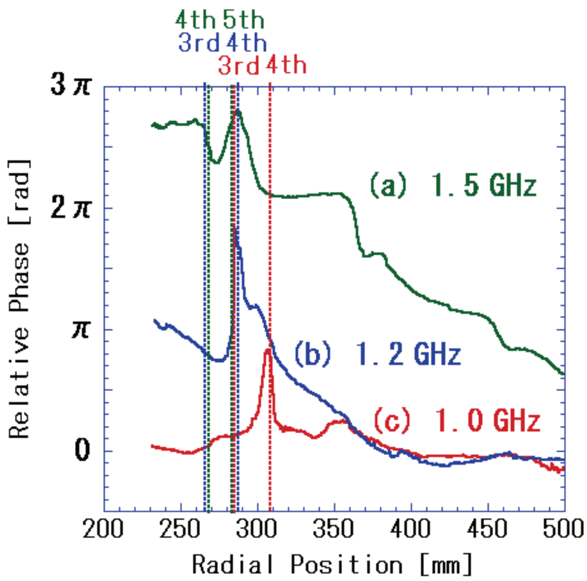

Fig.6 Radial profiles of phase of ECRF electric field with (a) 1.0 GHz, (b) 1.2 GHz, (c) 1.5GHz

characteristic length of density and that of magnetic field, respectively [13,14]; and ϕ is the phase difference between X-Mode propagating toward L-Cutoff and reflected component propagating toward the UHR; and θ is the phase of $\Gamma(i\eta/2)$. By using expression (1a) without considering phase effect, i.e. term of cosine is unity, we obtain 70~90 % mode conversion efficiency with separatrix configuration in Mini-RT.

To investigate mode conversion process in plasma directly, we launch X-Mode microwave by using ceramic-coated dipole antenna (element length is 100 mm). Frequency and power of diagnostic microwave are 1-2.1 GHz, 10 W, respectively. By using lower frequencies than plasma heating, i.e. 2.45 GHz, we can investigate waves in overdense plasma even where underdense region of heating microwave. To avoid penetration of high power of microwave with 2.45GHz, we set band pass filter (BPF, -44.5 dB @2.45 GHz). Figure 4 shows the block diagram of ECRF electric field measurements. We can obtain DC voltage signal

$$E_0(\vec{r}) + E_1(\vec{r})\cos[\phi(\vec{r}) + \phi_{ph}], \qquad (2)$$

where $E_0(\vec{r})$, $E_1(\vec{r})$, $\phi(\vec{r})$ represent offset, amplitude of ECRF electric field and phase of that, respectively. We can control an external phase shift ϕ_{ph} to determine the parameters $E_0(\vec{r})$, $E_1(\vec{r})$ and $\phi(\vec{r})$. Spatial profiles of ECRF electric fields are detected by using coax-fed monopole (element length is 5mm, direction is toroidal) antenna movable radially.

Figure 5 shows toroidal component of an ECRF electric field on the mid-plane with separatrix configuration. We can see a characteristic of short wavelength related with the EBW around major radius *R*=300 mm in Fig. 5. Roughly evaluated wavelength of that is 2 cm, while 30cm in vacuum. Therefore the order of refractive index of EBW is 10. Location of the Last Closed Field Surface (LCFS) was major radius *R*~300mm. The EBW was detected at steep density gradient region.

Radial profiles of phase of ECRF electric field with several frequencies are shown in Fig. 6. We used data for three external phase shifts that were averaged over each millimeter. The characteristic of phase reversal has been seen for each frequency. Dotted lines in Fig. 6 denote the location of cyclotron harmonic resonance layers on mid-plane. Phase reversal phenomena occur between 3rd and 4th harmonic ECR for 1.0 and 1.2 GHz, 4th and 5th harmonic ECR for 1.5 GHz. And the location of it coincides with short wavelength region.

We can consider the direction of group velocity, i.e. energy flux, is inward of the device. While positive (negative) gradient of relative phase with respect to major radius means phase velocity is outward (inward) of the device. Thus phase reversal region suggests the direction of phase velocity v_{ph} is opposite to group velocity v_g. From the dispersion relation, we can find that the EBW has the characteristic of backward wave, i.e. group velocity v_g is negative [15]. Therefore Fig. 6 also suggests the direct detection of EBWs between cyclotron harmonic resonance surfaces, e.g. 3rd and 4th ECR for 1.0 GHz injection.

As well known, ECH enables to produce high- energy

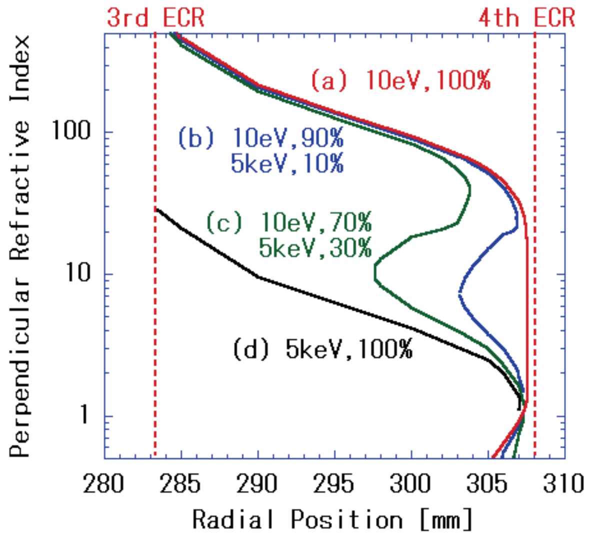

Fig.7 Radial profile of perpendicular refractive indices, for 1 GHz, of hot waves with (a) all electrons has temperature of 10 eV, (b ,c ,d) 10%, 30%, 100% high-energy electrons has that of 5 keV. Dotted lines denote the location of harmonic ECR on mid-plane.

electrons due to quasi-linear diffusion of resonant electrons [16]. In the Mini-RT device, plasma is produced by ECH, thus we have prospects of production of high-energy electrons. We estimate effective temperature of high-energy electron is 5 keV by using scaling law of Ref. [17].

$$\rho / L = 5 - 6 \times 10^{-2}, \tag{3}$$

where ρ and L are high-energy electron Lamor radius and magnetic scale length, respectively. We have estimated $L \sim 4$ cm and $B = 0.0875$ T.

We have assumed electron distribution function is two components isotropic Maxwellian, i.e. summation of bulk electrons (10 eV) and high-energy electrons (5 keV), for simplicity. We have calculated for four cases, i.e. (a) no high-energy electrons, (b) 10% of them exist, (c) 30% of them exist and (d) hot electrons. We have also assumed F-Coil current I_F is 30 kA and L-Coil current I_L is 15 kA, which are equal conditions for Figs. 5 and 6. In this configuration, mode conversion occurs between 3rd and 4th harmonics of ECR. Dispersion relation of hot waves propagating perpendicular to magnetic field is written as

$$\varepsilon_{xx}(\varepsilon_{yy} - n^2) - \varepsilon_{xy}\varepsilon_{yx} = 0, \tag{4}$$

where n and ε are refractive index and specific dielectric tensor of hot waves [12], respectively.

High-energy electrons affect dispersion relation of hot wave especially around the UHR. If there is no high-energy electron, i.e. in the case of (a), refractive index dramatically rises around UHR. Refractive indices have relatively long wavelength region (refractive index is small) with increasing of high-energy electrons. The reason why refractive indices, for (b) and (c), are so complex is due to assumption of two components Maxwellian distribution function. Finite Lamor radius (FLR) effect from high-energy electrons around UHR enables propagation with long wavelength.

On the other hand, refractive indices show identical characteristics around 3rd harmonic ECR, for the case with (a), (b) and (c) of Fig. 7. Around resonance region, wavelength is comparable to Lamor radius, therefore sufficient FLR effect from bulk electrons can be expected.

In summary, ECRF electric field measurements by using antenna have been carried out in the Mini-RT device. And signals having two characteristics of EBW, i.e. short wavelength (~ 2 cm) and backward wave, have been detected. Dispersion relation predicts that typical value of refractive index of EBW in Mini-RT is several 10 to 100. However roughly evaluated refractive index is 10 experimentally. Plasma production in Mini-RT is achieved by ECH, therefore we can expect the existence of high-energy electrons. We evaluated the effects of high-energy electrons to dispersion relation, and obtained relatively long wavelength region around UHR.

The authors would like to acknowledge Dr. T. Kaneko for his technical advices for measurements. The authors also thank to Prof. T. Mito and Dr. N. Yanagi for discussion about cooling superconducting magnet and excitation of it.

[1] I. B. Bernstein, Phys. Rev. **109**, 10 (1958).
[2] K. Mitani and H. Kubo, J. Phys. Soc. Jpn. **19**, 211 (1964).
[3] T. H. Stix, Phys. Rev. Lett. **23**, 878 (1965).
[4] H. Sugai, Phys. Rev. Lett. **47**, 1899 (1981).
[5] G. Taylor *et al.*, Phys. Plasmas **9**, 167 (2002).
[6] B. Jones *et al.*, Phys. Rev. Lett. **90**, 165001 (2003).
[7] Y. Ogawa *et al.*, J. Plasma Fusion Res. **79**, 643 (2003).
[8] Z. Yoshida *et al.*, Plasma Fusion Res. **1**, 008 (2006).
[9] S. M. Mahajan and Z. Yoshida, Phys. Rev. Lett. **81**, 4863 (1998).
[10] T. Goto *et al.*, Jpn. J. Apl. Phys. **45**, 5197 (2006).
[11] E. Yatsuka *et al.*, Trans. Fusion Sci. Tech. **51**, 310 (2007).
[12] T. H. Stix, *Waves in Plasmas* (American Institute of Physics, 1992) p. 257-262.
[13] A. K. Ram and S. D. Schultz, Phys. Plasmas **7**, 4084 (2000).
[14] A. K. Ram *et al.*, Phys. Plasmas **3**, 1976 (1996).
[15] F. W. Crawford *et al.*, J. Geophys. Res. **72**, 57 (1967).
[16] C. F. Kennel and F. Engelmann, Phys. Fluids **9**, 2377 (1966).
[17] N. A. Uckan, Phys. Fluids **25**, 2381 (1982).

Proceedings of ITC/ISHW2007

Physical data assessment for energy confinement scaling laws

Heiko DREIER[1)], Roland PREUSS[1)], Andreas DINKLAGE[1)] and Volker DOSE[2)]

[1)] *Max–Planck-Institut für Plasmaphysik, EURATOM Association, Teilinstitut Greifswald, D-17489 Greifswald*
[2)] *Max–Planck-Institut für Plasmaphysik, EURATOM Association, D-85784 Garching*

The principle of *data adaptive planning* (DAP) is applied to estimate the information gained by a single datum from a given set of data about the parameters of interest. The information gain is thereby quantified by an information measure. By using DAP one is capable to express the importance of a single datum. A W7-AS confinement data set was analysed with respect to different energy confinement scaling laws, the importance of the data points is assessed with respect to the respective scaling law. The physical question (i.e. the scaling law constraints) thereby shows significant impact on the expected information gain of single data points.

Keywords: energy confinement, scaling laws, Connor-Taylor model, Bayesian experimental design, data adaptive planning

1 Introduction

Fusion experiments like stellarators today are complex and also expensive devices. To gain a maximum of output by acceptable effort and costs a purposive design and planning of such experiments is necessary. For this, it is also important to assess the available data from previous measurements with respect to the experimental goals.

During the past years, data bases like the International Stellarator Confinement Data Base (ISCDB) [1] containing the experimental results of different fusion machines have grown and are widely used as reference and for inter-machine comparison (see, e.g., [2, 3]). Current work also includes the assignment of specific physical models to the data (or sets of data), using model comparison techniques [4, 5].

Given a set of measured data, it is useful to estimate the information gain of a single data point, e.g., to identify the most informative datum, with respect to a certain physical model describing the experimental situation. It seems reasonable that in this case the underlying model should have a significant influence on that evaluation. Also, the impact of the other data has to be taken into account. A possible method for the validation of a given data set, basing on the concept of Bayesian experimental design, is presented in this paper. With this method, the assessment of data from fusion experiments with respect to different physical models is possible.

author's e-mail: heiko.dreier@ipp.mpg.de

1.1 Scaling laws

Because the detailed dependencies between plasma parameters (electron density n, heating power P), machine parameters (minor radius a, magnetic field strength B) and quantities describing the energy confinement (confined energy W, energy confinement time τ_E) are not completely known, semi-empirical scaling laws are used for comparison of different experiments. Also, the design of future experiments is possible by extrapolation of the scaling relation.

A typical approach is given by a power scaling law, e.g. the International Stellarator Scaling 2004 (ISS04 [3]), which was found by studies of data from different stellarator experiments:

$$\begin{aligned}\tau_E^{ISS04} &= 0.134 \cdot a^{2.28} \cdot R^{0.64} \\ &\quad \cdot P_{tot}^{-0.61} \cdot n^{0.54} \cdot B^{0.84} \cdot \iota_{2/3}^{0.41}.\end{aligned}$$

A different approach was introduced by Connor and Taylor [6]: Here, the basic assumption is that scaling invariance properties of the particular plasma model lead to constraints of scaling exponents. Plasma models are assumed to be derived from some basic equations like:

- the Fokker-Planck equation describing collisions,
- the Maxwell equations describing the influence of β,
- and the continuity equation, momentum equation and the energy equation for the MHD description of the plasma.

Following this ansatz, the Connor-Taylor scaling model for the confined energy can be rephrased for volume averaged quantities:

$$\frac{W}{na^4B^2} \propto \left(\frac{P}{na^4B^3}\right)^{\alpha_1} \left(\frac{a^3B^4}{n}\right)^{\alpha_2} \left(\frac{1}{na^2}\right)^{\alpha_3} \tag{1}$$

Here, the α_i are the scaling parameters. Depending on the physical plasma model, these parameters may be dependent of each other, or even zero. E.g., for the case of a collisional low-β plasma one obtains $\alpha_3 = 0$, whereas α_1 and α_2 have to be estimated.

The scaling laws can be linearised by taking the logarithm. Then the linearised power law reads

$$\ln W = \alpha_c + \alpha_a \ln a + \alpha_P \ln P + \alpha_n \ln n + \alpha_B \ln B.$$

1.2 Data adaptive planning

The approach of Bayesian experimental design (BED) offers a mathematically consistent way for the optimisation of diagnostics as well as for the design of experiments and experimental campaigns using a physical question, expressed by a set of parameters of interest, as the design criterion. It bases on the maximisation of a utility function, namely the Kullback-Leibler distance, which is a measure for the information gain by a measurement. The method was proposed by Lindley [7], a review on different applications can be found in [8], the design of plasma diagnostics is studied in [9, 10].

The BED approach can also be utilised for the assessment of a data point. For this, the expected information gain for this particular measurement is calculated with respect to

- the physical question of interest,
- the experimental configuration,
- the measurement error and error statistics and
- other data available.

If existing data sets are implemented, the Kullback-Leibler distance as the utility function for the assessment reads:

$$\begin{aligned} U_{KL}(D, \boldsymbol{d}, \boldsymbol{\xi}) &= \int \mathrm{d}\boldsymbol{\alpha}\, p(\boldsymbol{\alpha}|\, D, \boldsymbol{d}, \boldsymbol{\xi}) \\ &\quad \cdot \ln \left[\frac{p(\boldsymbol{\alpha}|\, D, \boldsymbol{d}, \boldsymbol{\xi})}{p(\boldsymbol{\alpha}|\, \boldsymbol{d})}\right] \end{aligned}$$

This expression is an measure for the information gained by the new datum D about the parameters of interest, $\boldsymbol{\alpha}$. It is given in *bit* if the base-2 logarithm is used. The probability density function (PDF) $p(\boldsymbol{\alpha}|\, D, \boldsymbol{d}, \boldsymbol{\xi})$ is called "posterior distribution", describing the knowledge about $\boldsymbol{\alpha}$ given the new datum D, the experimental configuration $\boldsymbol{\xi}$ of the new measurement, and the old data $\boldsymbol{d}$. The prior function $p(\boldsymbol{\alpha}|\, \boldsymbol{d})$, on the other hand, shows the knowledge about $\boldsymbol{\alpha}$ before the new measurement (given only the old data).

For Bayesian experimental design, the information measure has to be averaged over the expected values for D, described by the PDF $p(D|\boldsymbol{\xi}, \boldsymbol{d}) = \int \mathrm{d}\widetilde{\boldsymbol{\alpha}}\, p(\widetilde{\boldsymbol{\alpha}}|\, \boldsymbol{d})\, p(D|\, \widetilde{\boldsymbol{\alpha}}, \boldsymbol{\xi})$, to cover all possible outcome of the future experiment. Here, $\widetilde{\boldsymbol{\alpha}}$ is the result for the parameters of interest given only the old measurements $\boldsymbol{d}$. This leads to the Expected Utility (EU) function

$$\begin{aligned} EU(\boldsymbol{\xi}, \boldsymbol{d}) &= \int \mathrm{d}D\, p(D|\, \boldsymbol{d}, \boldsymbol{\xi}) \cdot U(D, \boldsymbol{d}, \boldsymbol{\xi}) \\ &= \int \mathrm{d}\widetilde{\boldsymbol{\alpha}}\, p(\widetilde{\boldsymbol{\alpha}}|\, \boldsymbol{d}) \int \mathrm{d}D\, p(D|\, \widetilde{\boldsymbol{\alpha}}, \boldsymbol{\xi}) \\ &\quad \int \mathrm{d}\boldsymbol{\alpha}\, p(\boldsymbol{\alpha}|\, D, \boldsymbol{d}, \boldsymbol{\xi}) \\ &\quad \cdot \ln \left[\frac{p(\boldsymbol{\alpha}|\, D, \boldsymbol{d}, \boldsymbol{\xi})}{p(\boldsymbol{\alpha}|\, \boldsymbol{d})}\right]. \end{aligned}$$

For a linear physical problem $\boldsymbol{d} = \boldsymbol{X} \cdot \boldsymbol{\alpha}$ and $D = \boldsymbol{\xi}^T \cdot \boldsymbol{\alpha}$ (matrix $\boldsymbol{X}$ contains the experimental configurations of the old data) and assuming a Gaussian error statistics, the EU can be calculated analytically after some algebra:

$$EU(\boldsymbol{d}, \boldsymbol{\xi}) = \frac{1}{2} \left[\log(1+G) - \frac{G}{(1+G)^2}\right], \tag{2}$$

with

$$G = \frac{\boldsymbol{\xi}^T \left(\boldsymbol{X}^T \boldsymbol{C}\, \boldsymbol{X}\right)^{-1} \boldsymbol{\xi}}{\sigma^2}; \quad C_{ii} = 1/s_i^2. \tag{3}$$

The measurement error of the new datum is thereby given with σ, the error of the old data are encoded with $\boldsymbol{s}$.

2 Results

For the study presented here, the Expected Utility of every datum from a given set was calculated according to linearised scaling laws. For this, the respective datum was removed from the data set and treated as "new datum". The experimental configuration (n, P, a and B) of this measurement then corresponds to $\boldsymbol{\xi}$, $\boldsymbol{X}$ and $\boldsymbol{d}$ are the configuration and the data outcome from the other data points in the set (see eqs. (2) and (3)).

The data set itself consists of 153 $\iota = 1/3$ data of W7-AS taken from ISDB. In this data base, the values for the configuration parameters n, P, a and B as well as for the measured confined energy are listed. Furthermore, the measurement errors for all quantities are given. For the data analysed here the collisional low-β model was identified to be the most probable one [5]; therefore, $\alpha_3 = 0$ was used in the Connor-Taylor scaling law. As a second model, a linearised power law was applied.

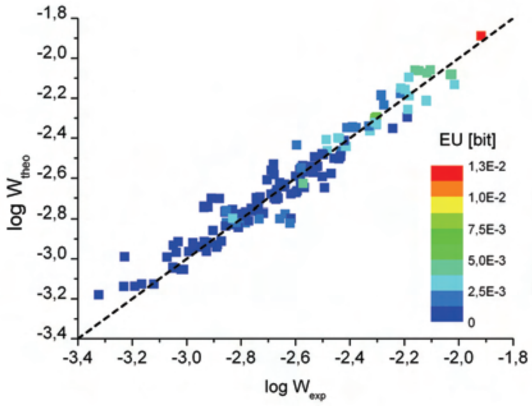

(a)

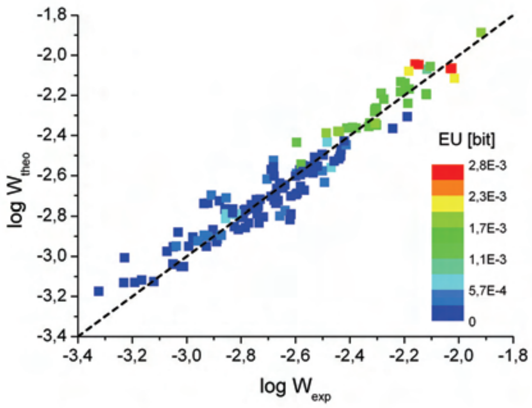

(b)

Fig. 1 Data set plotted against experimental and theoretical value of the confined energy. The theoretical value was calculated by a power scaling law (a) and the Connor-Taylor model for collisional low-β plasmas (b). The EU of the respective datum is color-coded.

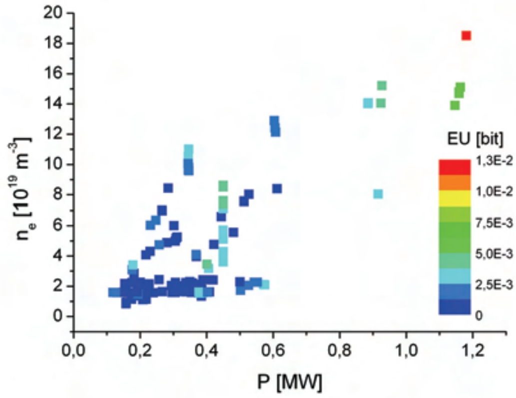

(a)

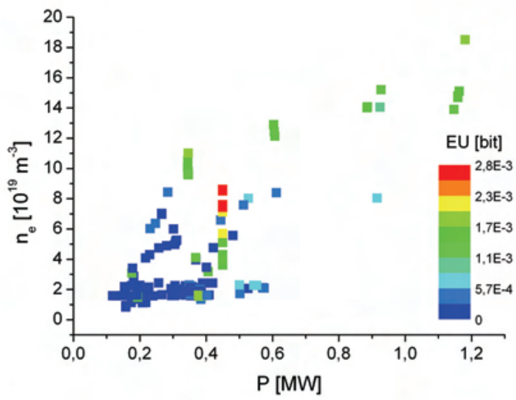

(b)

Fig. 2 Expected Utilities of the data set with respect to the experimental configuration parameters P and n, (a) for the power law model, (b) for the low-β model.

Figure 1 shows the data set plotted against the experimental value of the confined energy, W_{exp} and the theoretical value W_{theo} calculated by the respective scaling law. The EU is given as color scheme.

For both analysed scaling laws the data points with the highest expected information gain are found at high values of W. As a difference, the most informative point with respect to the low-β model is not the one at maximum W, which is the case for the power law model.

The absolute scales for the EU are different for both scaling laws. This results from the fact that two different physical questions are analysed here. The set of parameters of interest, the scaling exponents, are not identical. Therefore, the absolute values of the expected information gain for the different problems cannot be compared directly.

The behavior of the Expected Utility was then analysed with respect to the experimental configuration parameters a, n, B and P. To study the influence of these parameters, the data set is plotted in the n-P plane next (fig. 2). This plane is of interest because density and heating power can be varied. Again, one finds similarities between the different scaling laws: In both cases, data points in regions with a low sample rate (high n and P), far away from the most of the data, are very informative. In case of the power scaling law, the highest EU is given for the datum with maximum n and P. In contrast, this is not the case for the low-β scaling.

In order to study the impact of the further control parameters, the data set is plotted with respect to the minor radius a and the magnetic field B (fig. 3): In the case of the power law high values of the EU occur in all regions of a and B, for the Connor-Taylor model the highest values of the EU are found only at the

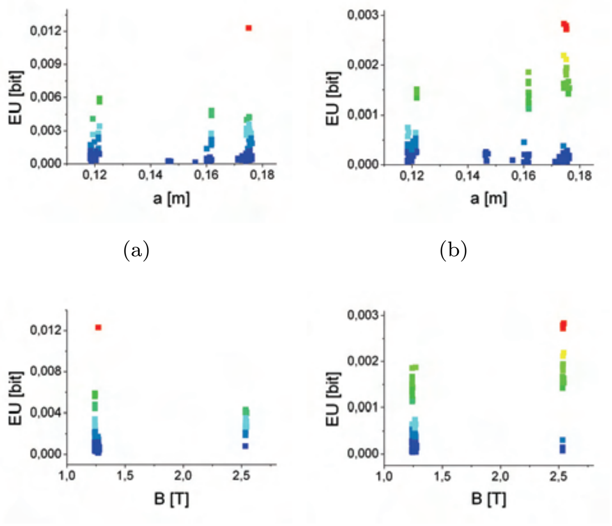

(a) (b) (c) (d)

Fig. 3 Expected Utilities of the data set with respect to the minor radius a (upper row) and the magnetic field strength B (lower row), for the power law model (left column) and for the low-β model (right column), respectively.

highest values of a and B.

These findings can be explained by taking into account the dependency on a and B in the low-β model: Both parameters are related to the α_1 and α_2 terms with high exponents (a^4, B^3, see eq. (1)), so high values of a and B will have a strong influence on the outcome of the model. In contrast, the parameters n and P enter the model only to the power of 1. Therefore, data points with high a and/or B will lead to higher information gain in case of the low-β model. This indicates that measurements at high a and B are more important for the validation of this model.

3 Conclusion

In this work, data adaptive planning was used to calculate the expected information gain of a datum with respect to a set of 153 $\iota = 1/3$ data from W7-AS. The capability of DAP to implement a physical question as an assessment criterion in a mathematical consistent way was demonstrated by applying the method to two different energy confinement scaling laws: a power law similar to the International Stellarator Scaling, and the Connor-Taylor scaling for collisional low-β plasmas. The expected information gain from the single data points turned out to be different for both models: Whereas for the power law the information gain of data points with values of low a and B are on a par data with values of high a and B, for the low-β model the data in the range of high a and B turn out to be more valuable. This can be explained by the dependence of the Connor-Taylor terms on high powers of a ($\propto a^4$) and B ($\propto B^3$). The Connor-Taylor terms are therefore dominated by these parameters at high values.

These results show the influence of the physical question on the Expected Utility: Different physical models will lead to different values of the information gain from a certain datum. DAP is a tool to quantify these differences and to estimate the contribution of individual data to the overall result. It is a new quality for the assessment of data going beyond qualitative arguments.

For future work, further analysis of the parameters influencing the value of the expected information gain have to be made. In particular, the measurement error and the error statistics may have significant impact (see [10]).

In addition, the DAP formalism can be used for the systematic planning of future experiments and experimental campaigns: The calculation of the expected information gain for a possible future measurement offers the possibility to estimate the most informative experimental condition for the next experiment.

[1] http://www.ipp.mpg.de/ISS; http://iscdb.nifs.ac.jp
[2] U. Stroth et al., Nucl. Fusion **36**, 1063-1077 (1996)
[3] H. Yamada et al., Nucl. Fusion **45**, 1684-1693 (2005)
[4] A. Dinklage et al., Nucl. Fusion **47**, 12651273 (2007)
[5] R. Preuss et al., Proceedings of the 34th European Physical Society Conference on Plasma Physics, Warsaw (2007)
[6] J. Connor, J. Taylor, Nucl. Fusion **17**, 1047-1055 (1977)
[7] Lindley, D. V., Bayesian Statistics - A Review, SIAM, Philadelphia (1972)
[8] K. Chaloner, I. Verdinelli, Stat. Sci. **10**, 273-304 (1995)
[9] R. Fischer, in Bayesian Inference and Maximum Entropy Methods in Science and Engineering, AIP Conference Proc. 735 (2004), 76-83
[10] H. Dreier et al., Fusion Sci. Technol. **50**, 262-267 (2006)

Proceedings of ITC/ISHW2007

Integrated Analysis of Spectroscopic Data

Dirk Dodt[1), Andreas Dinklage[1), Rainer Fischer[2), Klaus Bartschat[3) and Oleg Zatsarinny[3)

Max-Planck-Institut für Plasmaphysik, EURATOM Association

[1)Wendelsteinstraße 1, 17489 Greifswald, Germany

[2)Boltzmanntraße 2, 85748 Garching, Germany

[3)Department of Physics and Astronomy, Drake University, Des Moines, IA 50311, USA

Spectroscopic data are analysed by fitting a collisional-radiative model to the emission spectrum of a low-temperature plasma in the wavelength range of visible light. The inference procedure employs Bayesian probability theory and accounts for all measurement and model uncertainties. This allows for the validation of model parameters, such as atomic data obtained in recent close-coupling calculations, which are ore only partly or not at all accessible by beam-type experiments. Initial results indicate that the spectroscopic data contain significant information about some Einstein coefficients for spontaneous emission of less prominent spectral lines.

Keywords: Integrated Data Analysis, Optical Emission Spectroscopy, Neon, Edge Plasma, Atomic Data

1 Introduction

The line radiation emitted by excited neutrals in a plasma can be used to obtain information about characteristic plasma parameters. More specifically, properties of the plasma species causing the excitation can be assessed. The energy dependence of the elementary processes allows, to detect deviations from thermal energy distribution functions. In the case of low-temperature plasmas, the main excitation channel is electron impact excitation, and thus the spectrum carries information about the electronic component of the plasma.

An established technique is to analyse the relative magnitude of line intensities measured, for example, in neutral-beam plasma diagnostics to infer the electron density n_e and the temperature T_e [1]. The approach presented here uses a collisional-radiative model (CRM) to reconstruct electron energy distribution functions from a whole range of the spectrum of a cylindrical neon discharge plasma. The population of different atomic levels is described by a set of balance equations. With these level populations, the light emission along a line of sight can be modelled. Hence, starting from the electron energy distribution function (EEDF), these steps lead to a full forward model of the spectroscopic data, incorporating the intensities of 87 emission lines. The approach described in [2] is extended by a description of the full spectral data. The basic idea is to calculate the probability of fitting the forward model to a full spectrum. The inference is done in the framework of Bayesian probability theory.

For the data analysis approach in Bayesian probability theory, it is necessary to describe all uncertainties involved. In addition to error statistics of the data, the uncertainties of model parameters are incorporated in the analysis. For the interpretation of spectroscopic data, Einstein coefficients and excitation cross sections are such model parameters. The provision of a complete and validated data set is a persistent issue in the interpretation of any spectroscopic measurement. The incorporation of the uncertainties of the extensive sets of atomic data is a challenging issue, because it can involve the probabilistic description of a great number of parameters. Since resolving this issue is a prerequisite for any uncertainty assessment in the interpretation of such spectroscopic data, the validity of the employed atomic dataset with respect to the spectroscopic results is addressed below.

A particular benefit of the approach presented in this paper results from the use of a full collisional-radiative model, which accounts for all correlations in the data, i.e., how the line intensities are affected by all transitions relevant to the observed spectrum. This enables using the spectral lines to assess the validity of the atomic data used for the collisional-radiative modelling.

The spectroscopic data to be analysed are obtained from a cylindrical neon discharge, a well-investigated system with various published results (e.g. [6, 7]) that can be used for validation. The full set of atomic data being employed was calculated by a *B*-spline Breit-Pauli *R*-matrix (close-coupling) model, as described in detail in refs. [3, 4].

2 Data descriptive model of the spectroscopic measurement

The forward model maps the quantity of interest, the EEDF $f_e(E)$ onto a simulation of the measured data $\vec{D}$ (spectrometer pixels). It consists of a chain of different elements described below. More details about the data model can be found in [5]. Schematically, we have

author's e-mail: dirk.dodt@ipp.mpg.de

$$\underbrace{\underbrace{f_e(E)}_{\text{kinetic theory}} \rightarrow n_i}_{\text{collisional radiative model}} \rightarrow I_{ij} \rightarrow \underbrace{\int_{\text{l.o.s.}} I_{ij}dV \rightarrow L(\lambda)}_{\text{radiation transport}} \underbrace{\rightarrow \vec{D}}_{\text{measurement}} .$$

Different parameterisations of the energy distribution are employed to determine electron collision rates for the collisional-radiative model (CRM). Here, the data are well described with a Druyvestein distribution. EEDFs derived from hybrid modelling of neon discharges accounting for a kinetic treatment of the electrons [6, 7] are used to validate the obtained result. The CRM consists of a set of balance equations for the population densities n_i of 31 excited states of neutral neon, taking into account populating and depopulating elementary processes.

The *locally emitted power* $I_{ij}\left[\mathrm{W/(m^3 \cdot sr)}\right]$ can be readily obtained by multiplication with the inverse lifetime of the excited states and the photon energy, and division by the full solid angle (4π).

The radiation has to pass through the plasma before it leaves the discharge device. The apparent lifetime of the excited states is affected by the transport of photons if the plasma is optically thick, i.e., for transitions to the ground or metastable states of the atom [8]. The description of this opacity, together with the integration along the line of sight (l.o.s.) of the spectrometer, yields the *effective spectral radiance* $L(\lambda)$ as a function of the wavelength λ.

The modelling of the actual measurement comprises the translation of $L(\lambda)$ into the detected signals and the mapping of wavelengths to pixel numbers. This requires details on the detector response, which were measured with a standard light source (sensitivity calibration). The wavelength mapping is fitted to the data within the reconstruction.

Figure 1 shows the result of the forward model together with the measurement. The parameters giving the best fit are obtained by maximising the probability distribution function (PDF) for the parameter vector $\vec{\Theta}$, which is called the *posterior* $P(\vec{\Theta}|\vec{D}, I)$. It describes the probability of a certain parameter set to be true, given the measurement $\vec{D}$. The posterior is set up according to Bayes' rule:

$$P(\vec{\Theta}|\vec{D}, I) = P(\vec{D}|\vec{\Theta}, I) \cdot \frac{P(\vec{\Theta})}{P(\vec{D})} \tag{1}$$

It contains the *likelihood* $P(\vec{D}|\vec{\Theta}, I)$ and the *prior* $P(\vec{\Theta})$. The *evidence* $P(\vec{D})$ is not taken into account, since it does not affect the position maximum of the posterior and can be deduced from the normalisation constraint. The likelihood corresponds to quantifying the probability of a certain outcome of the measurement, given the true and unknown state of the system $\vec{\Theta}$. For a Gaussian distribution of the error statistic of the spectrometer pixels, it is given by

$$P(\vec{D}|\vec{\Theta}, I) = \frac{1}{\prod_i \sigma_i (2\pi)^{n}} \exp\left\{-\frac{1}{2}\sum_i \cdot \frac{(D_i - D_{\text{sim},i})^2}{\sigma_i^2}\right\} \tag{2}$$

The prior is describing the knowledge about the model parameters which is not contained in the data, but originates from independent sources. For example, atomic data that are subject to uncertainty may be described by means of a parameter with a prior distribution reflecting the known confidence region.

The marginalisation theorem for probability distributions describes how to integrate out parameters $\vec{\eta}$ we are not interested in:

$$P(\vec{D}|\vec{\Theta}, I) = \int P(\vec{D}|\vec{\Theta}, \vec{\eta}, I) d\vec{\eta}. \tag{3}$$

In the data model there is no formal distinction between the so-called *nuisance parameters* $\vec{\eta}$ and the *parameters of interest* $\vec{\Theta}$. The result of the projection down to the dimensions of the parameters of interest is a broadened PDF compared to a posterior not taking into account additional parameters from the beginning. The parameters of interest in this analysis are either the EEDF or Einstein coefficients we are interested in for validation purposes. A table with all relevant nuisance parameters can be found in [9].

3 Atomic Data for Collisional-Radiative Models

In the forward model a consistent set of atomic data, obtained from a *B*-spline Breit-Pauli *R*-matrix (BSRM) model for the treatment of e–Ne collisions [3], was taken as the starting point. The BSRM approach is based on the close-coupling approach. In contrast to all other commonly used perturbative or non-perturbative methods to generate such atomic data, the use of non-orthogonal, term-dependent sets of atomic orbitals makes it possible to obtain fairly accurate descriptions of both the energy levels and the oscillator strengths with comparatively small configuration-interaction expansions. In traditional methods with orthogonal sets of one-electron orbitals, a similar accuracy can, in principle, be achieved by very large expansions using so-called pseudo-orbitals [3].

The major advantage of using this dataset is the full provision of all required data for the collisional-radiative model, which goes far beyond the availability in standard databases such as [10]. Furthermore, the wavefunctions for the basic states are derived consistently from common structure calculations. This means that all derived atomic data, such as oscillator strengths and cross sections, depend on the same set of wavefunctions. From a detailed analysis of the calculations, critical matrix elements can

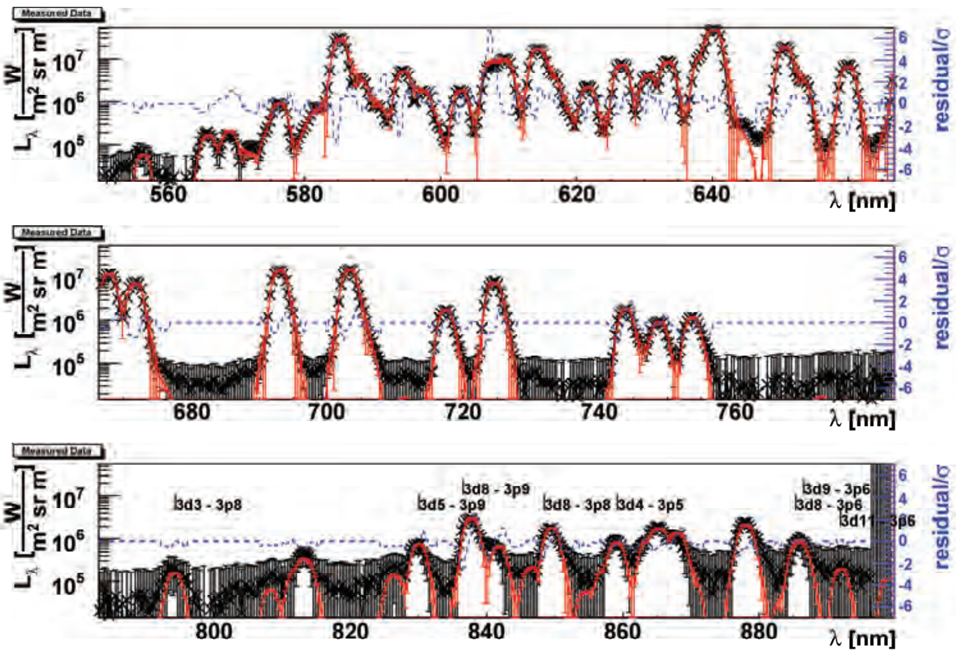

Fig. 1 Result of the forward model. The red line depicts the modelled spectrum, black crosses show the measurement and its uncertainties, and the dashed line is the difference between the two in units of standard deviations. The labels in the lower part of the spectrum mark lines whose Einstein coefficients are extracted from the spectrum.

be identified and, if appropriate, a larger uncertainty may be assigned to these transitions.

4 Validation of Einstein Coefficients

Some Einstein coefficients entering the model are not available in the literature. An independent, experimentally based validation of the result of the structure calculations mentioned above is desirable and also needed before the data are included in databases like [10].

For the analysis of the EEDF, the Einstein coefficients are treated as nuisance parameters. Prior PDFs are assigned to them accounting for the uncertainty stated in [10] or specified according to a discussion of the BSRM results. The chosen uncertainty contributes to the uncertainty of the reconstructed EEDF and is accounted for by the probabilistic approach providing a non-Gaussian error propagation.

Figure 2 shows the result of the reconstructed EEDF from the spectroscopic data displayed in fig. 1, where the inferred EEDF is capable to describe all spectral features. The reconstructed EEDF agrees within the error margin with an EEDF derived from hybrid modelling of neon discharges [6, 7] up to energies of about 20 eV. The disagreement for higher energies was found to depend on the chosen parameterisation of the EEDF. This issue requires further studies, but the rate coefficients of the CRM that depend on the energy integral are barely affected by these deviations. Given this consistent result of the data reconstruction, i.e., within the relevant error margins, the emission spectrum is expected to contain also information on the atomic data.

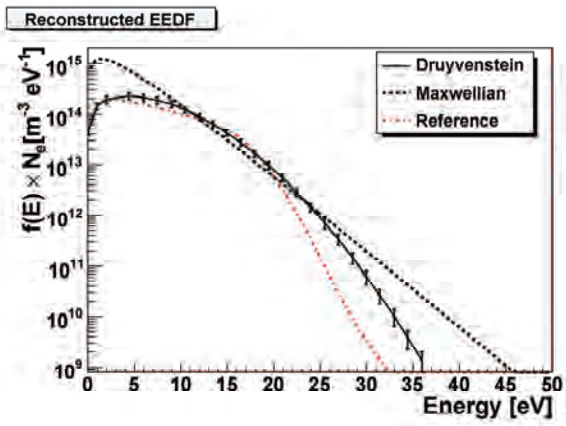

Fig. 2 Result for the reconstructed EEDF. On the ordinate axis the EEDF, multiplied with the reconstructed electron density, is plotted. The Maxwellian distribution shown for comparison is not able to reproduce the reference distribution from hybrid modelling [6].

For the validation of the Einstein coefficients they are assigned a scale invariant prior probability distribution (Jeffrey's prior [11]). This means the results of the BSRM calculations are not included for these parameters and the width of the posterior distribution purely reflects the significance of the spectroscopic data for the considered coefficients.

The result of the analysis for the full set of available Einstein coefficients is shown in fig. 3 Displayed are the probabilities of the respective Einstein coefficients derived

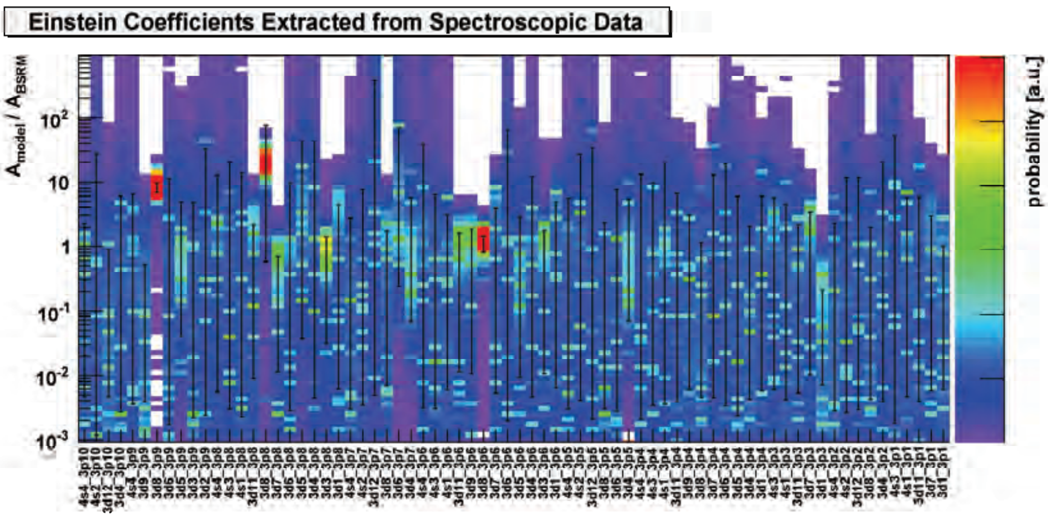

Fig. 3 The marginal distributions of various Einstein coefficients. The value of the coefficient is divided by the result of the BSRM calculations, with a value of 1.0 corresponding to full agreement (vertical left axis). The probability for a certain value of the coefficient to be true, given the measured data and model assumptions, is color-coded on the right, with violet/blue indicating a low and orange/red indicating a high probablity. The respective transition is given on the horizontal axis. The intervals depicted with the black lines show the root-mean-square variance of the distributions.

from the spectroscopic measurement and normalised to the BSRM results. There are a few lines that can be determined rather well, i.e., a narrow marginal posterior distribution is obtained. For example, a result consistent with the BSRM predictions is found for the $3d_8 \rightarrow 3p_6$ transition, whereas the value for $3d_8 \rightarrow 3p_8$ extracted from the spectroscopic data deviates significantly from the BSRM result. Further studies are needed to clarify whether this can be attributed to shortcomings in the spectroscopic analysis or problems with the BSRM calculations.

Figure 3 also reflects that the spectrum is not informative for many transitions, as indicated by a broad probability distribution for the respective transitions. Note that some transitions with a wavelength outside the measured spectrum are also included in the fit. They influence the spectrum through their effect on the collisional radiative model. However, as one might expect, these transitions have a particularly broad posterior distribution.

5 Conclusions

A full forward model for an emission spectroscopic measurement of a low-temperature plasma was used in a Bayesian data analysis. The electron energy distribution of the plasma was inferred and its error band resulting from uncertainties in the underlying atomic data was described. The extensive data set of excitation cross section obtained by recent close-coupling calculations allowed for the validation of Einstein coefficients for spontaneous emission, which have not been measured to date.

6 Acknowledgements

This work was funded by Deutsche Forschungsgemeinschaft through Sonderforschungsbereich Trans Regio 24 (Fundamentals of Complex Plasmas). KB and OZ were supported by the United States National Science Foundation under grants PHY-0244470 and PHY-0555226.

7 References

[1] B. Schweer, G. Mank, A. Pospieszczyk, B. Brosda, and B. Pohlmeyer, J. Nucl. Mat. **196**, 174 (1992).

[2] R. Fischer and V. Dose, Plasma Phys. Control. Fusion **41** 1109 (1999)

[3] O. Zatsarinny and K. Bartschat, J. Phys. B: At. Mol. Opt. Phys. **37**, 2173 (2004)

[4] O. Zatsarinny, Comp. Phys. Commun. **174**, 273 (2006).

[5] D. Dodt, A. Dinklage, R. Fischer, and D. Loffhagen, AIP CP **872** 264 (2006)

[6] D. Uhrlandt and S. Franke, J. Phys. D: Appl. Phys. **35**, 680 (2002)

[7] S. Franke, diploma thesis *Bilanzgleichungen zur Modellierung der Dynamik einer Neon-Glimmentladung*, Greifswald 1996

[8] J.E. Lawler and J.J. Curry, J. Phys. D: Appl. Phys. **31**, 3235 (1998)

[9] D. Dodt, A. Dinklage, and R. Fischer, to be published in AIP CP (2007)

[10] Yu Ralchenko, F.-C. Jou, D.E. Kelleher, A.E. Kramida, A. Musgrove, J. Reader, W.L. Wiese, and K. Olsen (2007). *NIST Atomic Spectra Database* (version 3.1.3). [Online]. Available: http://physics.nist.gov/asd3 [2007, October 11]. National Institute of Standards and Technology, Gaithersburg, MD, USA.

[11] D.S. Sivia: *Data Analysis: A Bayesian Tutorial, 2nd ed.* (Oxford University Press, USA, 2006)

Proceedings of ITC/ISHW2007

Status of the QPS Project

J. F. Lyon, B. E. Nelson, J. H. Harris, D. A. Spong, R. D. Benson[a], M. J. Cole, P. J. Fogarty[b], K. D. Freudenberg, P. Goranson[b], A. Lumsdaine[a], M. Madhukar[a], T. E. Shannon[a], G. H. Neilson[c], P. Heitzenroeder[c]

Oak Ridge National Lab., Fusion Energy Division, Oak Ridge, TN, USA
[a] The University of Tennessee, Magnet Development Laboratory, Knoxville, TN, USA
[b] DevTech, Clinton TN, USA
[c] Princeton Plasma Physics Laboratory, Princeton NJ, USA

lyonjf@ornl.gov

The Quasi-Poloidal Stellarator (QPS) is being developed to test key stellarator physics issues at plasma aspect ratios 1/2-1/4 that of other stellarators. QPS has a quasi-poloidal (linked-mirror-like) rather than quasi-toroidal (tokamak-like) magnetic configuration, which allows poloidal flow and poloidal flow shear a factor of ~10 larger than in any other toroidal confinement system, and very low effective ripple to reduce neoclassical transport. It is the only toroidal device stable to drift wave turbulence over a range of temperature and density gradients, which should reduce anomalous transport even in absence of flow shearing. The magnetic field structure leads to a large fraction of trapped particles in regions of low/favorable field line curvature, which strongly reduces the drive for a class of trapped-particle instabilities. All other toroidal devices have a significant fraction of the trapped particles in regions with bad curvature. QPS also allows extending the stellarator data base to very low aspect ratio ($R/a > 2.3$), similar to the ST extending the tokamak data base to very low R/a.

The complex 3-D design requirements (large plasma radius at very low aspect ratio, a plasma cross section that varies toroidally from bean-shaped to D-shaped, and five types of toroidally-elongated non-planar coils) and the need for reduced cost and risk in fabrication drive the design. There are 2 field periods with 10 coils per period, 3 sets of poloidal field coils and 12 toroidal field coils. Independent controls on these coil currents permit varying key physics features by factor 10–30: the degree of quasi-poloidal symmetry, poloidal flow damping, neoclassical transport, stellarator/tokamak shear and trapped particle fraction.

The QPS design consists of complex, highly accurate, stainless steel modular coil winding forms that are cast and machined; conductor wound directly onto the winding forms; a vacuum-tight cover welded over each coil pack; coils vacuum pressure impregnated; and the winding forms bolted together to form a structural shell inside the vacuum vessel. The largest and most complex of the winding forms has been cast using a patternless process and is being precision machined. An internally cooled, compacted cable conductor that can be wound into complex 3-D shapes has been developed. High-temperature cyanate ester resin is used for vacuum pressure impregnation of the coils because it has several important advantages over the usual epoxy, including higher operating temperature, lower water absorption, and better handling characteristics during vacuum impregnation. Winding clamps were designed and fabricated with an open design that allows conductors to be placed and positioned in both the lateral and vertical directions automatically, without the need for additional geometric measurements or calibrated clamping pressure.

Proceedings of ITC/ISHW2007

Particle kinetic-energy measurement in compact toroid injection into a gas neutralizer

Dazhi Liu, Yoshiyuki Ito, Naoyuki Fukumoto, Tsuguhisa Sekioka, Yusuke Kikuchi and Masayoshi Nagata

University of Hyogo, 2167 Shosha, Himeji, Hyogo 671-2280, Japan

Particle kinetic-energy measurement in the experiments of compact toroid (CT) injection into a hydrogen gas neutralizer is presented. The typical injected CT parameters are: (1 ~ 4) $\times 10^{21}$ m^{-3} in electron density and 30 ~ 70 $km \cdot s^{-1}$ in velocity. By using microchannel plate detectors, kinetic-energy of ions and neutrals after CT passing the neutralizer has been measured with an electrostatic ion energy analyzer and evaluated by time-of-flight method, respectively. The pressure in the neutralizer was scanned. At the pressure $\approx 6 \times 10^{-3}$ torr, charge exchange between CT plasma and the neutral particles with high energy has been identified, which is characterized by significant decay of CT plasma density and magnetic field profile. The velocity of the produced neutral particle flow is close to the ion velocity of the CT plasma.

Keywords: compact toroid injection, charge exchange, neutralization, microchannel plate detector.

1. Introduction

A compact toroid (CT) is a dense, well confined plasma configuration with embedded, comparable toroidal and poloidal magnetic field. Normally, CTs are formed by using a coaxial plasma gun through gas discharge between inner and outer electrodes. Once formed, a CT can be accelerated to high velocity by **J×B** force, where **J** is the radial current density and **B** the azimuthal magnetic field associated with **J**. Typical parameters of a CT are: several hundreds of $km \cdot s^{-1}$ in velocity and $10^{21} m^{-3}$ in electron density. CT injection was proposed as a promising fueling technique for reactor-grade tokamak by Perkins and Parks in 1988[1, 2]. An accelerated CT is able to penetrate into the center of a tokamak provided that the kinetic energy density of the CT exceeds magnetic field energy density of the tokamak. This can be described as: $\rho_{CT}V^2/2 > B^2/2\mu_0$, where ρ_{CT} is the CT mass density, V is the CT velocity and B is the field strength at the tokamak center. In addition, recent experiments on injection of supersonic gas jets as a new fueling approach have been successfully conducted on some tokamak facilities [3-5]. However, the ability to penetrate into tokamak plasmas needs to be enhanced for larger fueling efficiency. Thus a new technique for acceleration of plasma jet has been proposed by Rozhansky et al. [6]. The jet was accelerated to 100 $km \cdot s^{-1}$ by using a plasma gun, leading to deep penetration into plasmas in Globus-M.

In the present paper, we report a new approach to produce neutral gas jets with high velocity using a CT injector. The CT will be injected to a neutralization region filled with high pressure hydrogen gas (up to 10^{-2} torr). It is conjectured that charge-exchange collision will occur between high velocity ions and the neutral H atoms and H_2 molecules leading to the production of a high velocity neutral flow. Therefore, kinetic energy measurements of the neutrals and ions after the neutralization are crucial to clarify the charge exchange process.

author's e-mail:d-liu@eng.u-hyogo.ac.jp

2. Experimental setup

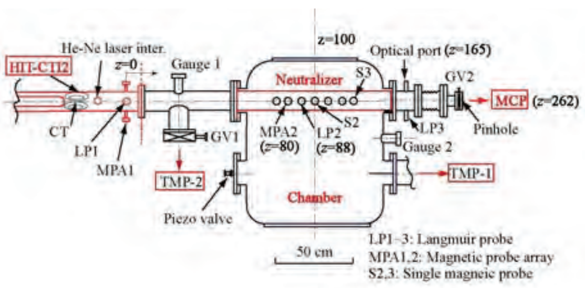

Fig. 1 Experimental setup.

The experimental setup is shown in Fig.1. A single-stage, coaxial plasma gun (HIT-CTI2) was employed to form CTs [7]. The power supply for the injector was a bank of capacitor of 10 kV/0.6 mF. Hydrogen was the working gas. The diameters of the inner and outer electrodes are 60 mm and 134 mm, respectively. A segment of stainless steel tube (length = 109 cm) was attached to the exit of the CT injector as the CT neutralizer. A set of seven holes (dia. = 42 mm) were located in the neutralizer along CT trajectory for Langmuir and magnetic probes. The neutralizer was located inside a stainless steel chamber. The pressure in the CT neutralization tube was controlled by a pulsed Piezo gas valve (PV-5020) with maximum gas output of 100 Pa·m^{3}s^{-1} for hydrogen. The inline gas pressure was 1.8 ~ 2.5 atmosphere.

The vacuum of the system was attained by using a 500 l·s^{-1} turbo-molecular pump (TMP-1). The base pressure was 1×10^{-6} torr, typically. During the experiments another turbo-molecular pump (TMP-2) with effective pumping speed 50 l·s^{-1} was used to minimize the loss of hydrogen gas.

A He-Ne laser interferometer (λ = 633 nm) and a magnetic probe array were routinely installed in the HIT-CTI2 for CT density (line-averaged) and magnetic field measurements. A monochromator was used to monitor H_β emission (λ = 486.1 nm) at the exit of the neutralization tube (z = 165 cm). Three Langmuir probes (LP1~3) were located at z = 0, 88, 165 cm to measure plasma density. Magnetic probes (MPA1, MPA2, S2 and S3) were used to measure CT magnetic field and its profile.

Microchannel plate detectors (MCP) were used to detect particles after CT passing the neutralizer. For neutral detection, a deflection coil was used to remove the charged particles in the flow; for ion detection, an electrostatic ion energy analyzer (IEA), which consists of an ion energy selection part and a MCP detector, was employed. High vacuum (< 2×10^{-6} torr) should be maintained in the MCP chamber for proper operation. To fulfill this requirement a pinhole (dia. = 0.8 mm and hole length = 3 mm) was used for differential pumping by using a dedicated turbo molecular pump connected to the MCP chamber. At the maximum pressure in the CT neutralizer, P_N = 10^{-2} torr, the pressure in the MCP chamber was 1.5×10^{-6} torr.

3. Experimental results and discussion

3.1 Observation of charge exchange process

The injection experiments were performed with the following CT parameters at the exit of the injector (z = 0): 2.5 kG in CT magnetic field, (1 ~ 4) ×10^{21} m^{-3} in electron density and 30 ~70 km·s^{-1} in velocity. The CT velocity was controlled by gun discharge voltage (V_{gun}). For instance, when V_{gun}= 6 kV, the CT velocity was about 40 km·s^{-1}.

Fig.2 shows typical discharge waveforms when charge exchange occurred, from top: H_β emission, MCP intensity and the plasma density measured by Langmuir probes at z = 0, 88, 165 cm. When P_N < 6×10^{-3} torr, no charge exchange phenomena was observed. The plasma density at z =165 cm (LP3) is about 6% of that at the z = 88 cm (LP2). The peak of H_β coincides with the onset of LP3 signal.

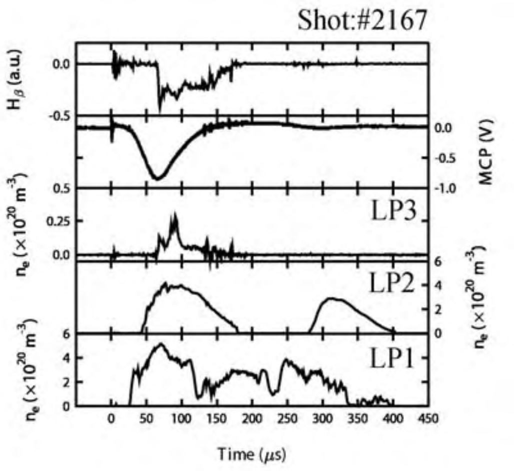

Fig.2 Typical discharge waveforms when charge exchange occurred. V_{gun}= 6 kV, P_N = 6×10^{-3} torr.

The CT magnetic filed profile in the same shot is shown in Fig.3. It clearly demonstrates that the CT still kept its integrity and field profile at this location. However, the CT-shaped profile vanished at the S3 location (z = 128 cm).

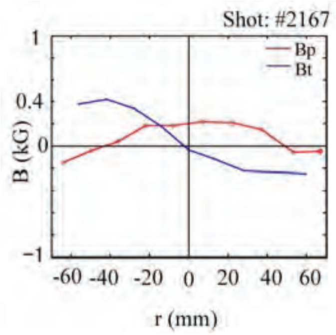

Fig. 3 Magnetic field profile of the CT at z = 80 cm.

At V_{gun}= 6 kV, a comparison of plasma density was made at different neutralizer pressure P_N, from 10^{-6} to 10^{-2} torr, see Fig. 4. At $P_N \geq$ 6×10^{-3} torr the charge exchange (CX) occurred and the electron density decreased by one order of magnitude compared with those shots without occurrence of charge exchange. Meanwhile, the CT magnetic field also demonstrated the same trend. In Fig. 5, the field strength decays significantly, about 50%, compared with those shots in which no CX occurred. The square marker shows the value of natural decay of CT magnetic field according to Fukumoto *et al.* with magnetic field decay time τ_d = 24 μs [7].

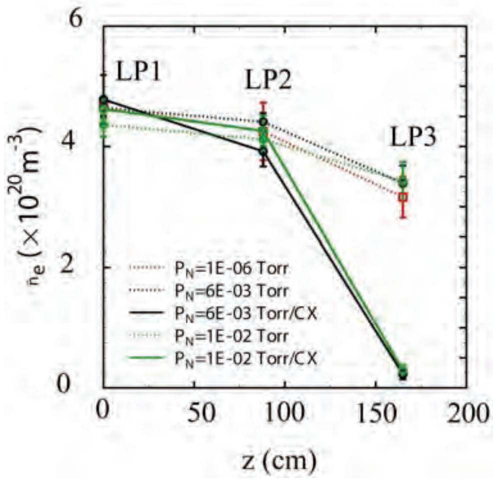

Fig. 4 Comparison of plasma density at different P_N and w/ and w/o CX occurred. V_{gun} = 6 kV.

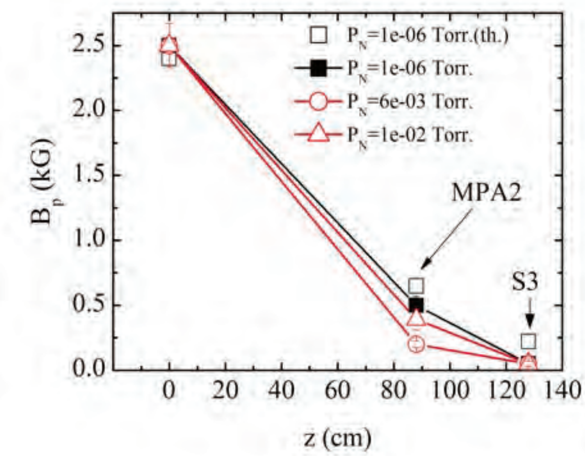

Fig.5 Comparison of CT magnetic field decay at different P_N and w/ and w/o CX occurred. Red lines are with CX. V_{gun} = 6 kV.

3.2 Particle kinetic energy measurement

Fig. 6 shows typical raw MCP signals in the neutral kinetic energy measurement. The difference in these two signals (red curve) is attributed to more production of neutrals when CX occurred. Correspondingly, the velocity of neutrals can be determined by the time of flight (TOF) method, $V_H \approx 262/68.2 = 38$ km·s^{-1}, which is close to the injection velocity of H$^+$ in the CT plasma at V_{gun}= 6 kV. This result also verified our observation of CX occurred in the high P_N shots.

The kinetic energy of ions was measured with IEA. Fig.7 shows the energy spectrum of ions at different P_N. V_{gun} was fixed at 6 kV in the measurement. The amplitude of the signals of high energy ions (> 200 eV) decreases with increasing P_N. This is because the charge exchange collision between the ions and neural atoms and molecules is the dominant ion momentum loss channel at high ion energy. It can be justified by the atomic cross-section data: for E_p= 200 eV, σ_m = 5×10^{-19} m^{-2} and σ_{cx} = 4×10^{-19} m^{-2}, where σ_m is the momentum transfer cross section and σ_{cx} is the charge exchange cross section for P+H collision [8].

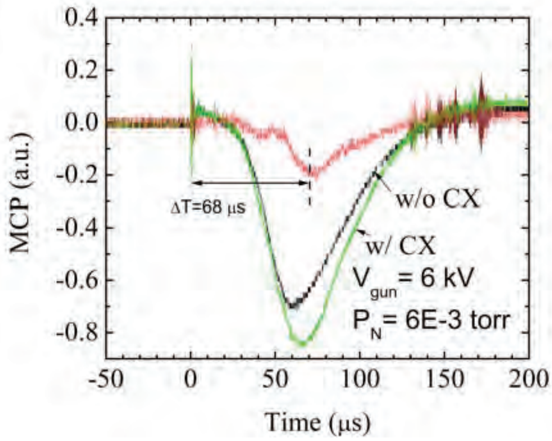

Fig.6 MCP signals for neutral kinetic energy measurement w/ and w/o CX occurred.

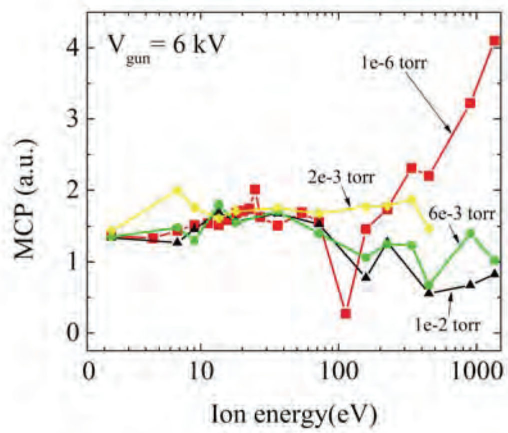

Fig.7 Ion kinetic energy spectrum at different P_N.

4. Conclusions

We have performed the injection of compact toroid into a hydrogen gas neutralizer filled with variable gas pressure. At pressure ≈ 6 × 10^{-3} torr, charge exchange process between ions in the CT plasma and the neutral particles has been identified, which is characterized by significant decay of CT plasma density and magnetic field profile.

By using microchannel plate detector, the velocity of neutral particle flow produced in the charge exchange process, has been measured. It is close to the ion directional velocity in the CT plasma prior to CX. The fraction of ions with high kinetic energy (>200 eV) decreases with increasing neutralizer pressure because of ion momentum loss mainly caused by the charge exchange process.

Acknowledgements

The author, Dazhi Liu, thanks the Japan Society for the Promotion of Science (JSPS) postdoctoral fellowship for financial support.

References

[1] Perkins L.J., Ho S.K. and Hammer J.H., Nucl. Fusion **28**, 1365 (1988).
[2] Parks P.B., Phys. Rev. Lett. **61**, 1364 (1988).
[3] J. Bucalossi *et al*., Proc. 29th EPS Conf. On Control. Fusion, Montreaux, 2002, **26B**, O-2.07 (2002).
[4] J. Li *et al.*, Plasma Phys. Control. Fusion **42,** 135 (2000).
[5] L. Yao *et al.*, Nucl. Fusion **44**, 420 (2004).
[6] V. Rozhansky *et al.*, Proc. 33rd EPS Conf. On Plasma Phys., Roma, 2006, **30I**, P-4.107 (2006).
[7] N. Fukumoto, *et al*., Nucl. Fusion **44**, 982 (2004).
[8] P.S. Kristic *et al*., Atomic and Plasma-Material Data Tables **76**, 1 (2000).

Proceedings of ITC/ISHW2007

Dynamic evolution of near-UV emission spectrum observed in the microwave plasma-surface interaction

A. Matsubara[1], S. Takayama[2], K. Nakayama[1], T. Kanaba[1], M. Tomimoto[1], R. Akiyama[2], S. Okajima[1], and M. Sato[2]

[1]*Chubu University, 1200, Matsumoto, Kasugai, Aichi, 487-8501, Japan*

[2]*National Institute for Fusion Science, 322-6 Oroshi, Toki, Gifu, 509-5292, Japan*

The material heating during the carbothermic reduction of magnetite in a 2.45 GHz microwave multimode furnace has been investigated with multipoint spectroscopic measurements. The heating mode shifts from volumetric heating to plasma heating after sudden rise in temperature of the material from ~700 °C to ~1000 °C accompanied by the light emission of plasma. Then, the emission spectrum in the near-UV range (240 nm - 310 nm) changes drastically from a continuous spectrum to a discrete line spectrum with increasing temperature of material, representing progress of reduction process of iron oxide. The position dependency of the spectral evolution indicates the importance of the plasma-surface interaction in the large-scale surface structure on the material.

Keywords: plasma surface interaction, microwave iron making, reduction process, spectroscopy, near-UV emission, continuous spectrum, cathodoluminescence, surface structure.

1. Introduction

Plasma-surface interaction that is one of crucial issues in fusion research as well as plasma processing has been studied in some cases in field of the microwave material processing also. The microwave processing is based on the heating of material under the microwave irradiation. The microwave energy absorbed into the material transfers consequently to the thermal energy of the material. The main advantage of that method enables volumetric heating of materials since the absorption length is comparable or larger than the scale length of most electrically insulating materials such as ceramics, polymers, and certain composite materials, even metal if it is powdered state, as a rule, leading significant energy savings and reduction in process time. Sometimes electric discharge occurs on the surface of the material, which has been believed to be helped by the presence of vapours of various substances and thermal electrons emerging from hot spots on the surface. The occurrence of the discharge has been routinely to be avoided, because the volumetric heating is lost; the part of microwave energy is absorbed as the kinetic energy of the plasma electron. However a few applications utilize such plasma in order to modify the surface condition or boost specific chemical reaction. One of the applications is microwave ironmaking presented here.

High-purity pig irons have been produced successfully in a multimode microwave test reactor from powdered iron ores (magnetite) with carbon as a reducing agent in a nitrogen atmospheric pressure environment [1]. The method has the potential advantage that the CO_2 emission can be reduced by tens of percent in conventional blast furnaces, if the electric power for the microwave is generated by renewable energy, such as solar, hydro and nuclear power [2]. A feature of the microwave method is the sudden rise in temperature of the material from ~700 °C to ~1000 °C accompanied by light emission of plasma, called the temperature jump [3]. The nature of the temperature jump is emergence of an additional energy flow to the material through the plasma.

The in-situ visible emission spectroscopy has been introduced to demonstrate the characteristics of the heating mechanism including volumetric and/or plasma surface heating [4]. The light emission after the temperature jump during the microwave ironmaking consists of strong atomic/molecular lines that can be assigned as those listed in the spectrum database based on the spark and arc discharge, indicating the presence of plasma electrons with several electron volts in the electron temperature. It was found that the structure of emission spectrum near-UV range (240 nm-310 nm) changes drastically from the continuous spectrum to discrete line spectra of iron with increasing surface temperature [3]. The continuous spectrum was assigned as a cathode luminescence due to the impingement of a plasma electron onto the sample surface of magnetite. It was also stated that the evolution from continuous spectrum to lines spectrum was the first observation to capture the progress of reduction process of ion oxide via in-situ spectroscopic method.

In those series of experiments, the multi-points spectroscopic and pyrometric measurements were

author's e-mail:Matsubara.Akihiro@sti.chubu.ac.jp

conducted. The purpose of this article, therefore, is to present the results obtained those multipoint systems. These results not only supplement the prior statement associated to the spectral evolution, but also demonstrate importance of the plasma surface heating in the reduction of iron ore after the temperature jump. Especially, the position dependency of the evolution of emission spectrum promotes deeper understanding of the plasma-surface interaction such as the reaction cycle being in the complex surface structure on the material.

2. Experimental setup

The multimode test furnace at the National Institute for Fusion Science is shown in Fig. 1. According to the concepts developed in Germany in order to improve the homogeneity of the electromagnetic field, the applicator shape is hexagonal [5]. The furnace is equipped with five magnetrons. The microwave power of one magnetron is 2.5 kW at a frequency of 2.455 ± 0.030 GHz. Two mode stirrers scatter the standing waves. Before starting the process, the chamber was evacuated by the rotary pump and refilled with nitrogen gas. During processing, a continuous nitrogen gas flow of about one litter/minute was used with a pressure a little higher than ambient pressure.

A multi-point emission spectroscopic diagnostic was conducted through the viewing port on the furnace. Ten sightlines with a distance of 2.2 mm and a spot diameter of 1.0 mm were provided by means of the fiber bundle and magnifying lens located above the furnace. Figure 2 shows the schematic of the sight lines for the spectroscopic measurement, as well as for the pyrometry. Seven sightlines, labeled as f1, f2… f7, are directed to the sample surface through the hole of the insulator board as the top-cover, and the remaining three (f8 - f10) are terminated by the surface of that insulator. The spectrometer was a Czerny-Tuner imaging polychromator with a focal length of 250 mm. The exposure time was 2 s and the cycle time for capturing was 5 s [3].

InGaAs pyrometers (labeled as IR's in Figs.1 and 2) were taken for the temperature measurement. IR1, IR2, and IR3 were directed to the sample surface, the crucible outer surface and the crucible bottom, respectively. The detection wavelength range for IR1 and IR3 was 1.95 μm - 2.5 μm, that for IR2 was 0.8 μm - 1.6 μm. The spot size was 10 mm for IR1, 4 mm for IR2, and 3 mm for IR3. As shown in Fig.2, IR1 and f1 (mentioned before) were adjusted in such a way that they cross each other at the point at 15 mm above the bottom of the crucible along its central axis. It is noted that the position of the observation spot (i.e., intersection of the sight lines and surface of material) slides on the surface with increasing the surface temperature, since the powdered material shrinks and melts as shown schematically in Fig.2; the height of the powdered material

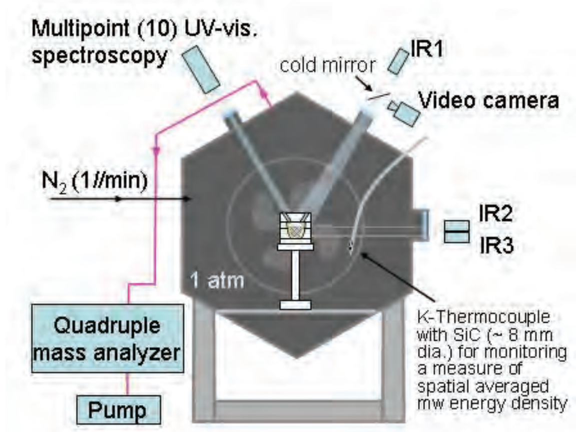

Fig.1 Schematic diagram of the multi-mode test furnace and diagnostics system. The opposite side distance of hexagonal cross-section is 1.1 m.

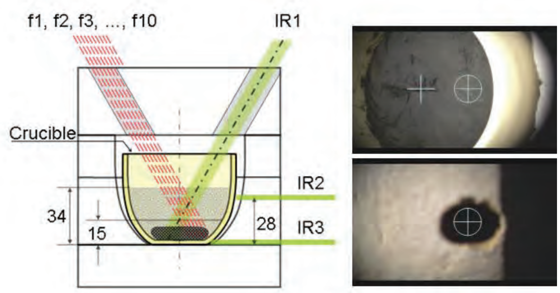

Fig.2 Sight lines for multipoint spectroscopic observation and configuration of material, crucible and insulator (left). Video camera pictures of the sample surface without top insulator (upper right) and with top insulator with the sighthole (lower right).

was set before the heating at 34 mm (light-shaded area), and this height changed to around 10 mm after the heating (dark-shaded area). The photograph at upper right in Fig.2 shows the surface of the material captured before heating by video camera located above the furnace (See also Fig.1). The central point of the cross-mark with circle of 10 mm in actual diameter indicates the sight axis of the IR1, and the left cross-mark is the observation spot of f1 for the initial height of the material.

The purified reagent of Fe_3O_4 with graphite was prepared according to the preparation performed in the prior experiment [3]. The mix ratio was $M_{Fe3O4} : M_C = 90 : 10$ (= 54.0 g : 6.0 g) by weight. Corresponding mol ratio was $n_{Fe3O4} : n_C = 1.0 : 2.0$. The crucible was thermally insulated by alumina-silica fiberboards as illustrated in Figs. 1 and 2.

3. Results and Discussion

3.1 Heating characteristics

Fig. 3(h) shows temperature traces obtained for IR1, IR2, and IR3. The heating mode is volumetric heating initially, but changes in plasma surface heating after the temperature jump at 740 s -.840 s. The series of the picture at the lower of Fig. 3 depicts the surface condition captured by the video camera of which the field of view is indicated in Fig. 2. During the volumetric heating the bright crack structure on the surface as shown in the second picture labeled as $t = 185$ s continues, but the micro-scale discharge spark often occurs along the crack. After $t = 700$ s, the size of spark grows approximately each time it appears (see third picture labeled $t = 743$ s), and finally it triggers the large-scale emission like flame covering whole top surface (see fourth picture labeled $t = 840$ s). At the same time, the increase in temperatures by IR1 and IR2 becomes rapid, and the intense emission spectrum begins to be observed, which shows typical phenomena of the temperature jump. There is no jumping behavior in the temperature trace obtained by IR3, indicating the heating is mainly due to the plasma generated on the top surface of the material. In Fig.3(h) the dashed-dotted line by the label of SiC-TC, which means the temperature trace for the thermocouple tip covered with the silicon-carbide powder (see Fig. 1), represents the relative change in the measure of the spatial averaged microwave energy density. The temperature of the SiC-TC decreases at the temperature jump, implying the emergence of the plasma being the microwave absorber.

3.2 Evolution of the spectrum

Figures 3(a)–3(g) show the time evolution of the emission spectrum as a contour map for various position of the sight line of f1 - f7. It is found that the drastic transition from continuous spectrum to discrete spectrum is seen in every sight line. The temperature range for the transition is approximately 1050 °C -1250 °C that is consistent with that stated in prior report [3]. This range is coincident with the temperature range of high reduction rate for magnetite and wustite [1]; therefore, the decay of the continuous spectrum suggests the significant progress of the reduction process of magnetite.

Typical continuous and discrete spectrums appearing in the evolution are shown in Fig. 4. Almost all the discrete spectra are well assigned to the spectra of iron atom observed in arc and spark discharges, and the origin of the continuous spectrum has been considered to be cathodoluminescence of magnetite [3]. It should be noted that the spectral intensity of the continuous spectrum is at least three orders of magnitude larger than that of black body emission for present surface temperature around 1000 °C. The wavelength range of the continuous spectrum of the present results coincides with that of cathodoluminescence [6] and absorption spectrums [7] of magnetite. Therefore, the transition from continuous spectrum to discrete spectrum can represent the progress of reduction process from magnetite to iron.

From Figs. 3(a)–3(g), it is also noticed that the decay of the continuous spectrum begins earlier for larger number

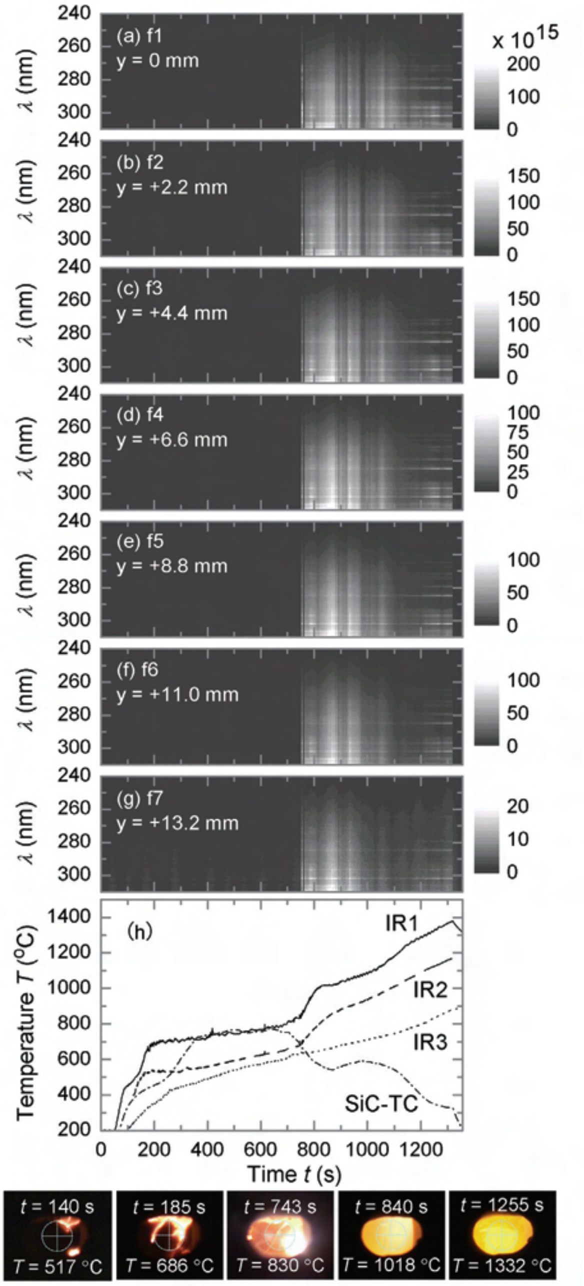

Fig.3 Time evolution of the emission spectrum for various sight lines (a)-(g). Temperature traces obtained for IR1, IR2, and IR3 (h). The temperature of SiC-TC (see text) is also included in (h). A series of the picture of the appearance of the surface (see also Fig.2).

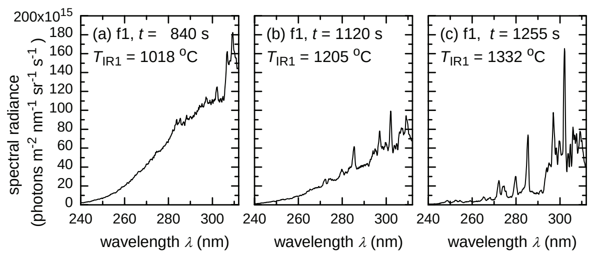

Fig.4 Emission spectrums appearing in the evolution . The peaks around 308 nm in (a) are OH spectrum. Almost all the peaks in (b) and (c) are spectra of iron neutral.

of the sight line. Figures 5(a) and 5(b) depict the time evolution of the spectral intensities, I_{SR}, at the wavelength of λ = 289 nm and λ = 302 nm. The former and latter wavelengths are associated to the continuous spectrum and the iron spectrum, respectively. In the intensity of the iron spectrum, the component of the continuous spectrum is already subtracted. It can be seen that the steady decrease in I_{SR} of the continuous spectrum (λ = 289 nm) is earlier for f5 than f1. The beginning time of the decreasing is t~950 s for f5, but t~1050 s for f1. On the other hand, the value of I_{SR} of iron spectrum (λ = 302 nm) for f1 increases moderately, but that of f5 decreases briefly at t~1100 s, and then increases rapidly. These behaviors depending on the position vary smoothly spatially, which can be recognized by Fig. 5(c) for the continuous spectrum and by Fig. 5(d) for iron spectrum.

The possible interpretation for the position dependence is presented as follows. First, it is assumed that after the temperature jump the position of the observation spot for each sight line slides immediately for the edge of the material (toward the right hand side of Fig.2), because the material should shrink rapidly and its height drops substantially. This assumption has been based on the observation that the emission band spectrum of CN decays rapidly just after the temperature jump, implying the consumption of the space in the powdered material. Fundamental process on the surface is likely that when a part of the surface layer melts resulting from the reduction of iron oxide induced by the plasma bombardment, it clumps together and drops for the bottom. Then, in the central part of the material (near the axis of the crucible), the new surface layer of the powder material of iron oxide comes to the surface. The reaction cycle, such as reduction, clumping, and dropping, completes faster for nearer the edge of material, because the reaction cycle can also progress from the side surface of the material. This is reason why the continuous spectrum decays faster for nearer edge. The brief drop and the significant increases in the iron spectrum in the final stage of the heating can be related to the growth and decay of the large-scale crack structure that is found for the present case. The cracks grow via erosion with the reaction cycle, but they decay via melt meaning the end-state of the reaction. In present case the brief drop can be due to escaping of material from the observation spot with growing the crack, and significant increase can be due to returning of the material to the observation spot with spreading the melt region.

4. Summary

We presented the experimental results obtained by the multipoint spectroscopic and pyrometric measurements during the microwave ironmaking. Both results demonstrate the importance of the plasma surface heating in the reduction of iron ore after the temperature jump. Especially, the position dependencies of the evolution of continuous spectrum and iron spectrum make us address the reaction cycle on the large-scale surface structure in the material.

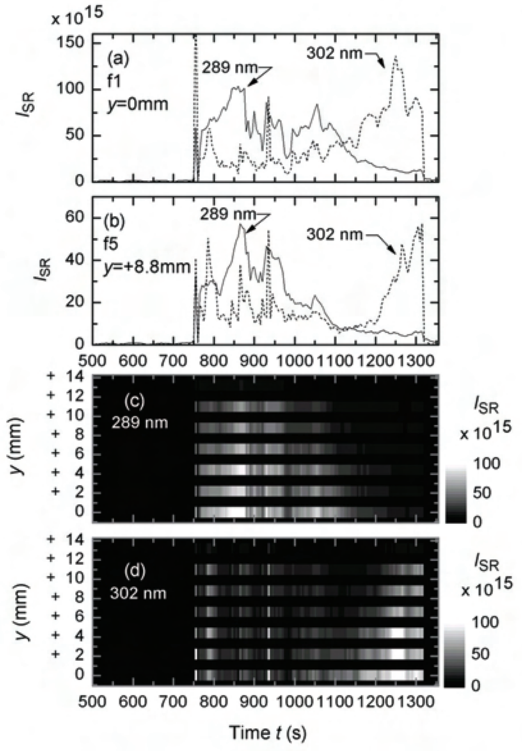

Fig.5 The time evolution of the spectral intensity, I_{SR}, (spectral radiance in the unit [photons m^{-2} s^{-1} sr^{-1} nm^{-1}]) at the wavelength of λ = 289 nm and λ = 302 nm for the sight line of f1 (y = 0 mm) in (a) and f5 (y = 8.8 mm) in (b), and for various position of the sight line as the contour map in (c) for λ = 289 nm and (d) for λ = 302 nm, respectively.

Acknowledgement

This research is supported in part by a Grant-in-Aid for Scientific Research on Priority Areas (465) of the Ministry of Education, Culture, Sports, Science and Technology in Japan.

References

[1] K. Ishizaki, et al., ISIJ, **46**, 1403 (2006).
[2] K. Nagata, et al., *Proc.11th International Conference on Microwave and High Frequency Heating*, (3-6 Sep 2007, Oradea, Romania) pp. 87-90.
[3] A. Matsubara, et al., submitted to JMPEE.
[4] M. Sato, et al., *Proc.10th International Conference on Microwave and High Frequency Heating*, (11-15 Sep 2005, Modena, Italy) p.p. 272-275.
[5] L. Feher, et al., DE-PS 19633245C1 (27.11.1997);
L. Feher, et al., DE-PS 10329411 (31.1.2005).
[6] I. Balberg, et al., Phys. Rev. Lett. **27**, 1371 (1971).
[7] P.A. Milies, et al., Rev. Mod. Phys. **29**, 279 (1957).

Proceedings of ITC/ISHW2007

Radial Profile of K_α line energy shift from Metallic Impurities measured with X-Ray Pulse Height Analyzer in LHD

Sadatsugu MUTO, Shigeru MORITA, and LHD Experimental Group

National Institute for Fusion Science, Toki 509-5292, Gifu, Japan

Radial profiles of metallic impurity have been successfully obtained in Large Helical Device, using an assembly equipped with conventional semiconductor detectors and soft x-ray pulse-height analyzers. Long pulse discharges have enabled the radial scanning of the assembly to measure the radial profiles of K_α lines of metallic impurities. The assembly of soft x-ray pulse-height analyzer makes it possible to obtain the concentrations of the impurities in connection with a cord calculation.

Keywords: Pulse Height Analyzer, Iron, chromium, titanium, Large Helical Device.

1. Introduction

Measurement of x-ray energy spectrum is important to investigate fundamental properties of magnetically confined high temperature plasma, since the spectrum reflects information on electron temperature, impurity, and non thermal electron. [1] Recently, it is intended to rise up the spectral, special and temporal resolution in the x-ray diagnostics to obtain significant information such as the shift of magnetic axis, electron temperature profile, and especially impurity transport. [2] However, in an x-ray region it is fundamentally difficult to get simultaneously the energy and another resolution mentioned above. Recent technology has not yield any applications which can fully resolve the problem.

An assembly of pulse height analyzer (PHA) has been constructed in Large Helical Device (LHD). The assembly is equipped with a utility called a radial scanning system which modulates and identifies the sight line of PHA along the major radius direction of LHD. The scanning range of the system fully covers the plasma in the major radial direction. With the system the radial profile of x-ray spectrum is obtained. Accordingly, Abel inversion of x-ray spectrum is available, although signals obtained with an x-ray detector are line integrated along the sight line of the detector,

It is the most important advantage of the PHA that the energy resolution is enough to distinguish each K_α line of impurity and the absolute number of photons can be obtained. Especially, K_α lines of impurities heavier than argon have been observed in LHD. [2]

The radial profiles of K_α lines emitted from metallic impurities such as titanium, chromium, and iron have been successfully observed with the assembly. The energy shift of K_α line is also observed. In addition to the experiment the intensity profile of K_α line emitted from respective charge state of metallic impurity is calculated as a function of electron temperature and density profiles. As a result absolute density has been estimated in comparison with the experimental results and the calculation.

In this article experimental results in LHD are presented on the radial profiles of K_α line observed with the assembly. Furthermore, the analysis on the density of the respective charge state is also reported.

2. Assembly for x-ray measurement

The profiles of K_α lines have been carried out in LHD using the assembly. The performance of the assembly has been reported with observed K_α lines of metallic impurities and continuum in a reference [3]. It must be mentioned here that the energy resolution of the PHA is 160 eV at 3.2 keV and the maximum counting rate is 10 kcps in the present experiment. The sight line of the detector is modulated along the major radial direction of LHD in a few hundred milliseconds. Next scanning starts in a time interval of a few seconds. Then, scanning is available approximately four times in ten seconds. It is also the advantage of the assembly to permits adjustable acceptance of the sight line and scanning time. As a result, the spatial resolution is approximately 20 millimeters on the central cord.

The observed x-ray spectrum must be inverted to a local emissivity profile. The x-ray intensity obtained with the assembly is line integrated. The calculation process of the inversion is qualitatively reported with the arrangement of the assembly. [2]

3. Experimental results

Examples of x-ray spectra obtained in the present experiment are shown in Fig.1. Taking into account the transmission rate of a beryllium filter with a thickness of

author's e-mail: journal@jspf.or.jp

1 mm, the spectrum has to be modified. Then, the real intensity is stronger in the energy range below 4.0 keV. The spectra consist of emissions from two different origins. One is the continuum emission from electrons as bremssstrahlung. The other is the K_α lines emitted from metallic impurities. The radiation loss due to metallic impurities is comparable with that of the continuum in the energy range above 4.0 keV as is shown in the figure. Accordingly, the intensity of the K_α lines must be estimated by subtracting the continuum. The intensities of the spectra are strongly dependent on the electron temperature. Particularly, it is available to estimate the electron temperature from the continuum. In addition to the continuum it is also confirmed that K_α line emitted from iron at a radius of $\rho = 0.5$ shifts toward lower energy side than that of $\rho = 0.2$. This fact is one of significant results in order to obtain the density profile of respective charge state of metallic impurity, since lower charge state of ion emits lower energy photon.

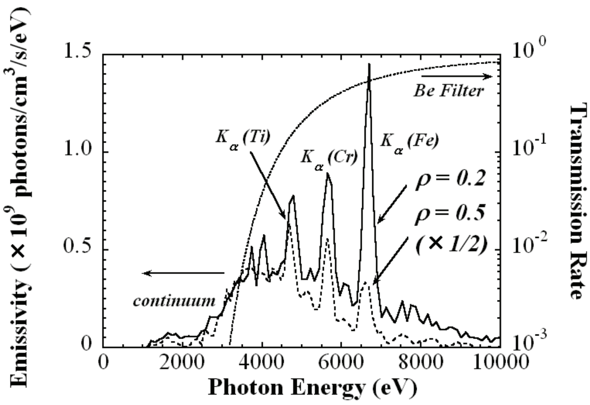

Fig.1 Typical x-ray energy spectra inverted from the radial profile of the spectrum which has been observed with the assembly in a single discharge. Solid and broken lines represent the spectra locally emitted from the radius of $\rho = 0.2$ and $\rho = 0.5$, respectively. The measurement has been carried out in hydrogen and helium discharges heated by NBI. K_α emissions from titanium, chromium and iron appear at 4.7 keV, 5.6 keV and 6.6 keV, respectively. The dotted line represents the transmission rate of the beryllium filter. The sign of 'ρ' represents the normalized radius of the LHD plasma.

Figure 2 shows typical profiles observed with the assembly. The radial profile of electron temperature estimated from continuum is also indicated. At present the flat top duration of the discharge is approximately 8 sec. Especially, the electron temperature, density, and the intensity of x-ray have been maintained to be constant during the accumulation time of the PHA. Consequently, the intensities of K_α lines reflect only the amount of the impurities.

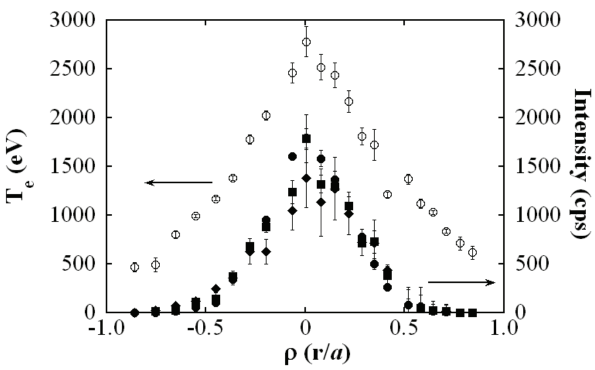

Fig.2 Typical radial profiles of K_α line emitted from metallic impurities of titanium, chromium, and iron, respectively. The intensities are line integrated along the sight line of the detector. Filled circles, filled rectangular, and filled diamond represent the line intensity of iron, chromium, and titanium, respectively. Solid lines are fitting functions for the observed profiles. Each function is a single Gaussian. Open circles with error bars represent electron temperature estimated from continuum. The accumulation time of x-ray for each point is 240 milliseconds.

4. Results of analysis and discussions

Figure 3 shows the intensity of the iron K_α lines emitted from two different positions in LHD plasma. In the figure results from a cord calculation is also indicated as vertical lines. The energy of line is depending on charge state as is indicated in the figure. Accordingly, the K_α line spectrum reflects the amount of respective charge state. In addition it is shown in the figure that the emission is mainly contributed from helium, lithium, beryllium, and boron like ions. In the present experiment the electron temperature is approximately 2 keV at the plasma center. Then, it is suggested from the calculation and the experimental results that there is much lower contribution from hydrogen like ion than helium like ion. In the calculation the diffusion coefficient is assumed to be 0.2 m^2/s. This assumption is consistent with the result from an argon transport experiment in LHD. [2]

It is obtained with the assembly that the intensity of the K_α line shifts toward lower energy side as the normalized minor radius increases as is shown in Fig.3. This fact qualitatively reflects that K_α lines from lower charge states increase at higher radius, since the electron temperature decreases. The shift is able to be qualitatively explained using Fig.4. In the figure the most intense line is emitted from lithium like ion in the region within $\rho =$ 0.6. However, the intensity of lower charge state than lithium like ion rapidly increase in the region higher than $\rho = 0.5$. On the contrary, helium like ion decreases.

Consequently, it is qualitatively consistent with the experimental result shown in Fig.3 that the cord calculation predicts the spectrum to shift toward lower energy side.

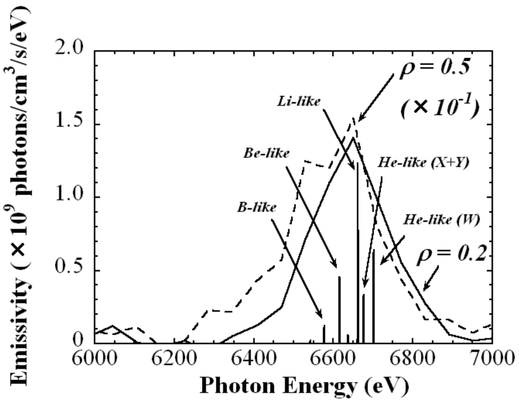

Fig.3 Energy shift of iron K_α line. The spectra are obtained from the inversion process of the experimental result and the subtraction of continuum. The spectra are also modified in consideration with the reduction of the beryllium filter. The solid line and the gray line represent the spectra emitted from the radius of ρ = 0.2 and the radius of ρ = 0.5, respectively. The solid vertical line means the result from the cord calculation.

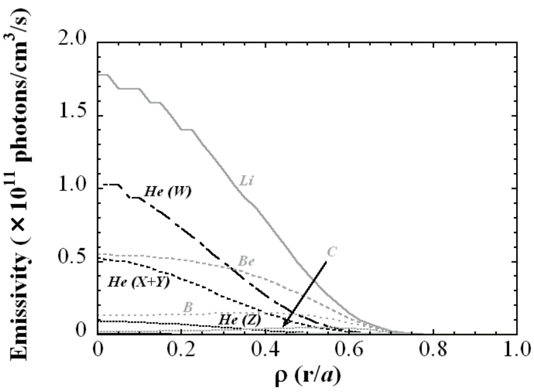

Fig.4 The radial profiles of iron K_α line derived from the cord calculation. Each line represents the emission from respective charge state. The lines emitted from lower charge state than carbon is too low to indicate.

The present experimental result on the energy shift gives rise to important information concerning the density profile of respective charge state of the metallic impurity. It is also the important advantage of the assembly to measure the photon number in addition to the energy resolution. Especially, the assembly makes it possible that the local intensity of the spectrum is obtained from the line integrated spectrum by the inversion process. Accordingly the absolute density profile of respective charge state is able to be quantitatively investigated to fit the spectrum by the cord calculation. Figure 5 shows the observed line spectra fitted by calculated functions in the case of ρ = 0.2. The calculation is consistent with the observed K_α lines emitted from iron, chromium, and titanium.

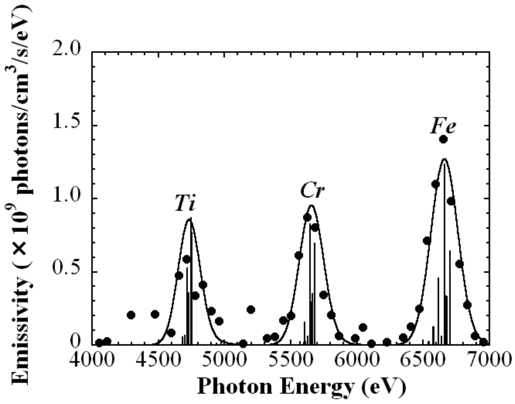

Fig.5 Typical K_α line spectrum obtained from the inversion process and the subtraction of the continuum at the radius of ρ = 0.2. The reduction of the intensity due to the filter is also taken into account. Filled circles and solid line represent the observed spectrum and fitting functions obtained by the cord calculation in consideration with the energy resolution of the PHA. The vertical lines also mean the results of the cord calculation without the energy resolution.

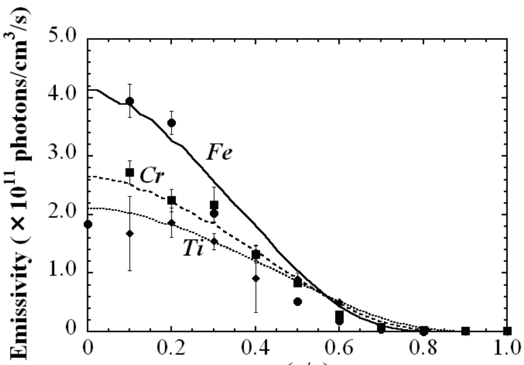

Fig.6 The radial profiles of K_α lines emitted from titanium, chromium, and iron. Filled circles, filled rectangular, and filled diamond represent the line intensity of iron, chromium, and titanium, respectively. Solid line, broken line, and dotted line are fitting functions for the observed profiles of iron, chromium, and titanium, respectively.

In the case of chromium and titanium the intensity profile of the K_α line is different from that of iron. The intensity of K_α line emitted from higher charge state increases and that from lower charge state decreases as the atomic number decreases. Particularly, the intensity of

K_α line emitted from beryllium like ion is much lower than that from lithium and helium like ion in the case of titanium. The spectrum of titanium consists of only the emission from lithium and helium like ion as is indicated by vertical lines in Fig.5. Although the energy difference of the emission from respective charge state is much smaller than the energy resolution of the PHA, the line width of the observed spectrum becomes gradually wider as the atomic number increases.

Radial profiles of K_α lines are also fitted. Figure 6 shows the observed radial profile of K_α lines and calculated functions. The intensity is obtained from the line spectrum by energy integration. In the case of chromium and titanium, the fitting is consistent within error bars. However, the observed intensity of iron decreases more rapidly than the result on the calculation in the region higher than ρ = 0.3. The assumption of temperature profile in the cord calculation seems to be slightly different from the actual profile. The intensity is sensitively depending on the profile of the electron temperature.

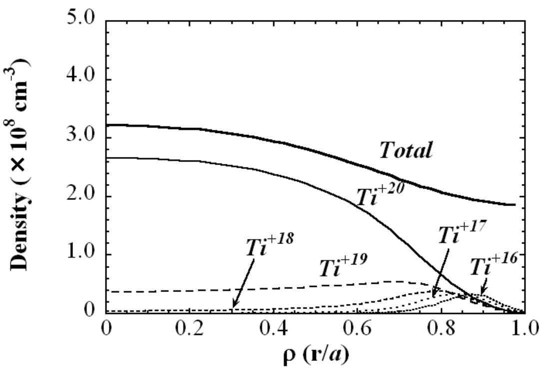

Fig.7 The radial density profile of respective charge state of titanium. Only the charge states mainly contributing to the spectrum are shown.

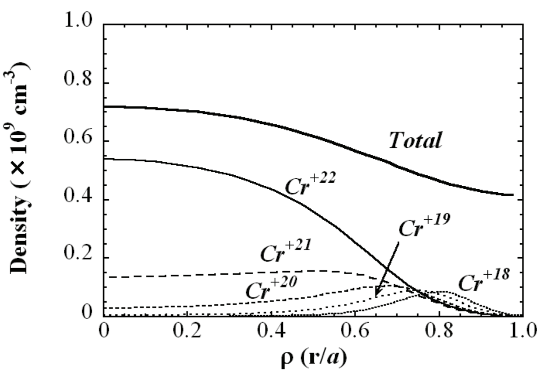

Fig.8 The radial density profile of respective charge state of chromium.

Figure 7 shows the density profile of titanium which is estimated by the fittings of spectrum and intensity profile. In the present experiment the amounts of bear and hydrogen like ion are much lower than helium like ion, although the atomic number of titanium is lowest in the observed impurities. It is commonly shown in Fig.7-9 that the helium like ion is dominant around the plasma center.

The concentrations of titanium, chromium, and iron are estimated to be 9.7×10^{-4} %, 2.1×10^{-3} %, and 5.9×10^{-3} % at the plasma center, while the electron density is 3.6×10^{13} cm^{-3}. Then, the densities of the metallic impurities are much lower than that of the electron. It is due to the difference of the x-ray photo-emission efficiency between the bremssstrahlung and the K_α lines that the intensities are comparable in the range higher than 4.0 keV. The efficiency of the K_α line is approximately four orders higher than that of the electron in x-ray region.

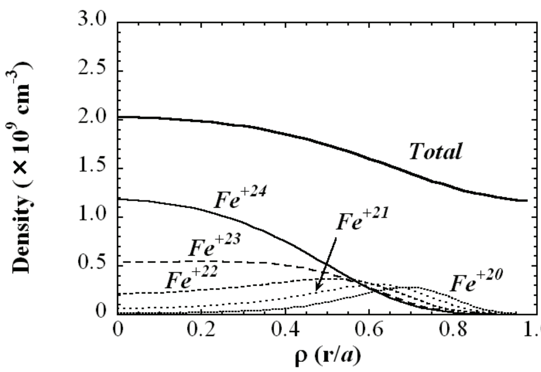

Fig.9 The radial density profile of respective charge state of iron.

5. Summary

Development of an assembly equipped with a radial scanning system attained a remarkable progress on measuring radial profile of x-ray spectrum in connection with conventional utilization of PHA. The line spectra have been successfully observed with good resolution enough to analyze the energy shift of the K_α line. From the analysis the radial density profile of respective charge state is estimated in the case of titanium, chromium, and iron, respectively.

References

[1] S.Muto *et al.*, Rev.Sci.Instrum. **74**, 1993(2003).
[2] S.Muto *et al.*,J.Plasma Fus.Res.SERIES**,** to be published.
[3] S.Muto *et al.*, Rev.Sci.Instrum. **72**, 1206 (2001).

Proceedings of ITC/ISHW2007

Analysis of Temporal Evolution of Dynamic and Diffusive Components in Drift Particle Fluxes in the Edge Plasma of the L-2M Stellarator Operated in Different Confinement Regimes

Nina N. SKVORTSOVA [1)], German M. BATANOV[1)], Nikolay K. KHARCHEV[1)], Yuryi V. KHOL'NOV[1)], Dmitryi V. MALAKHOV[1)], Alexander E. PETROV[1)], Vyacheslav V. SAENKO[1)], Karen A. SARKSYAN[1)], Dmitryi G. VASILKOV[1)], Victor Yu. KOROLEV[2)], Yuryi V. ZHUKOV[2)]

[1)] *A.M. Prokhorov General Physics Institute, Moscow, 119991 Russia*

[2)] *Moscow State University, Moscow, 119899 Russia*

The article presents an analysis of dynamic and diffusive components in turbulent fluxes measured in the edge plasma of the L-2M stellarator. It is shown that a shift-scale mixture of several (three-four processes, depending on macroscopic characteristics of the plasma) normal processes adequately describes the measured particle fluxes. The Estimation Maximization algorithm is applied to probability densities of flux increments in order to determine the number of mixture components and the weight of each component in the mixture. The method of sliding separation of mixtures is applied to separate between the dynamic and diffusive components of volatility and to trace their temporal evolution. Some characteristic L-2M regimes are examined. It is shown that turbulent particle transport in the edge plasma occurs by both the ballistic and diffusive mechanisms, and their contributions are of the same order of magnitude.

Keywords: turbulence, turbulent flux, stellarator, non-Gaussian statistics, volatility, diffusion.

1. Introduction

Strong structural low-frequency turbulence in magnetoactive plasma is frequently observed in the course of investigations of low-frequency fluctuations in toroidal magnetic confinement systems [1]. A characteristic feature of strong structural low-frequency turbulence is the presence of ensembles of stochastic plasma structures and probability density functions (PDF) for all plasma variables differ from the normal distributions. In particular, PDFs of turbulent particle fluxes are leptokurtic and have heavy-tailed distributions.

The approach based on inhomogeneous random walks allows the PDF of increments of amplitudes of turbulent particle fluxes to be represented in the form of shift-scale mixtures of normal distributions. In this case, it is possible to separate dynamic (convective) and diffusive components in turbulent particle fluxes. This approach was applied to analyzing turbulent fluxes in the FT-2 tokamak and L-2M stellarator [2].

The article presents an analysis of dynamic and diffusive components in turbulent fluxes measured in the edge plasma of the L-2M stellarator. For analysis we use a wide database of experiments under diversified operating conditions (in the basic and modified magnetic configurations, the use of boronization of the chamber wall surface to suppress impurity fluxes from the wall).

2. Estimation of turbulent processes in plasma in terms of volatility

Turbulent processes in the edge plasma of the L-2M stellarator were estimated in terms of volatility. Volatility, as applied to turbulent fluxes, means "the degree of unpredictable change over time of edge turbulent fluxes". The probabilistic concept of volatility has long been in use in financial statistics; however, to our knowledge, this characteristic has never been employed in papers devoted to plasma turbulence. Volatility of a random process is determined by at least two types of factors. The first type can be characterized as a dynamic (convective) factor. The influence of the dynamic factor makes itself evident in the fact that the process varies because of the presence of a certain trend or a combination and, hence, interaction of trends that indicates the presence of structures in a plasma. The dynamic component corresponds to a drift (which can occur by a variety of processes), for example, to ballistic transport. The second type of factors is termed stochastic or diffusive. With the use of special mathematical statistical procedures, the diffusive component can be represented as a sum of subcomponents, each being related to a particular type of stochastic structures, their interaction,

author's e-mail: nina@fpl.gpi.ru

etc. In the basic model of nonhomogeneous random walk described by a subordinate Cox process, volatility is naturally represented as a sum of the dynamic and diffusive components [3].

In previous studies of low-frequency turbulence, it was shown that processes of turbulent particle transport are described by subordinate Cox processes and is described, to a high degree of accuracy, by shift-scale mixtures of normal distributions [4]. If X is an increment of a random process under consideration, then its distribution is a shift-scale mixture of normal distributions if

$$P(X<x)=\iint \Phi(\frac{x-v}{u})dP(U<u,V<v)= \mathrm{E}\Phi(\frac{x-V}{U}), \quad x\in\Re, \tag{1}$$

where $U\geq 0$ and V are finite random variables. In this case, volatility is characterized by a vector containing components of three types: a weight (positive numbers, which add up 1), drift factors (averages), and diffusion coefficients (standard deviations) of the corresponding components. Each of these mixture components corresponds to a particular mechanism and a particular structure in plasma turbulence, which is characterized by parameters α_j и σ_j, whereas the weight p_j defines the proportion of structures of the *j*th type in the whole process of plasma turbulence.

In [5], it is shown that a finite shift-scale mixture of normal distributions (1) is represented in the form

$$\sum_{j=1}^{k} p_j\Phi(\frac{x-a_j}{\sigma_j})=\mathrm{E}\Phi(\frac{x-V}{U}), \tag{2}$$

where the pair of random variables U and V has a discrete distribution

$P((U,V)=(\sigma_j,a_j))$, j = 1,..., k, so that

$$DV=\sum_{j=1}^{k} p_j(a_j-\bar{a})^2, \tag{3}$$

$$\mathrm{E}U^2=\sum_{j=1}^{k} p_j\sigma_j^2, \quad \bar{a}=\sum_{j=1}^{k} p_j a_j. \tag{4}$$

Expression (3) defines that volatility component which is associated with the presence of local trends; it will be referred below as a "dynamic component" of volatility. Expression (4) defines a "diffusive component" of volatility. Total (multidimensional) volatility of the process is the square root of the sum of two components, one of which represents a spread of local trends, whereas the other characterizes diffusion.

3. Analysis of dynamic and diffusive components of turbulent fluxes

The L-2M stellarator has two helical windings (l= 2), a major radius R = 100, and a mean plasma radius <a> = 11.5 cm [6]. The plasma was created and heated by one or two 75-GHz gyrotrons under conditions of electron cyclotron resonance heating (ECRH) at the second harmonic of the electron gyrofrequency. The magnetic field at the plasma center was B_t = 1.3–1.4 T. The gyrotron power was P_0 = 150–300 kW, and the microwave pulse duration was up to 15 ms. Measurements were carried out in a hydrogen plasma with an average density of <n> = $(0.8–2.0)\cdot 10^{13}$ cm^{-3} and central temperature of T_e = 0.6–1.0 keV. Turbulent flux was measured in the edge plasma at a radius r/a = 0.9, the density was at a level of n(r) = $(1–2)\cdot 10^{12}$ cm^{-3} and the electron temperature was $T_e(r)$ = 30–40 eV.

The local fluctuating particle flux as defined as $\tilde{\Gamma}=(\delta n_e\cdot\delta v_r)$ [4], where δn_e denotes the plasma density fluctuations, and $\delta v_r=\delta E_\Theta/B$ expressed through the fluctuation of the poloidal electric field $\delta\mathrm{E}_\Theta=(\delta\varphi_1-\delta\varphi_2)/r\Delta\Theta$, where $\delta\varphi$ is the floating-potential fluctuation in the plasma, and Θ is the poloidal angular coordinate, r is the middle radius. Local turbulent particle fluxes were measured in the edge plasma of L-2M by probe systems consisting of three single cylindrical probes. The flux was measured at different distances of the last closed flux surface (LCFS).

Time samples of local fluxes in L-2M are not homogeneous and independent. The PDFs of local fluxes in L-2M stellarator are leptokurtic and have heavier tails as compared to a Gaussian distribution Statistical analysis of characteristics of fluctuating particle flux is carried out with time samples of flux increments, which are homogeneous and independent.

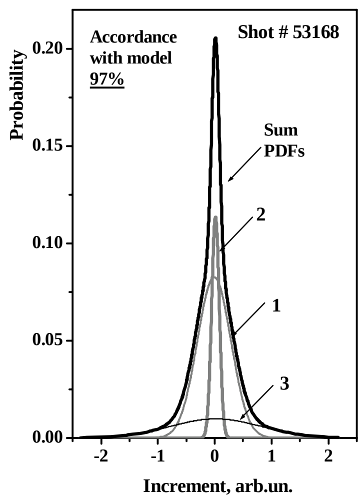

Fig.1. Modeling of PDF of increments of the turbulent flux measured in L-2M stellarator.

The finite mixtures of several (three or four, depending on macroscopic characteristics of the plasma) normal distributions adequately describe The PDFs of flux increments [5]. As an illustration, Fig. 1 shows the histogram of a time sample of the flux increments along with the result of processing. The Estimation Maximization (EM) algorithm was applied to probability densities of flux increments in order to determine the number of mixture components and the weight of each component in the mixture. In this particular case, the PDF of flux increments is a scale mixture of three normal distributions that correspond to three stochastic plasma processes. This particular experiment was conducted in the basic magnetic configuration (rotational transform at the magnetic axis is 0.175, mean plasma radius is 11.5 cm), with preliminary boronization.

The method of sliding separation of mixtures was used to separate between the dynamic and diffusive components of volatility and to trace their temporal evolution. Time variations in the components of the sums (3) and (4) were calculated using a time window "sliding" over a time sample of flux increments. This technique for analyzing the structural plasma turbulence is described in more detail in the review [3].

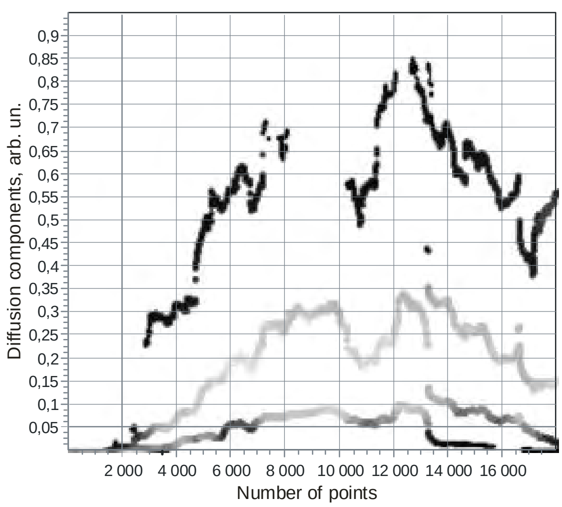

Fig.2. Time behavior of three subcomponents of the diffusive component of flux for shot No. 55623.

Figure 2 shows the time behavior of three diffusive subcomponents of volatility (i.e., summands in (3)) for the experiment conducted in the modified configuration of magnetic field (rotational transform 0.082, mean plasma radius 12.5 cm, the LCFS contacts with the chamber wall).

Note that the number of subcomponents remains unchanged, but their intensity varies with time. Hence, each of the components reflects a temporally continuous process, and the contribution from this process to the sum varies with time.

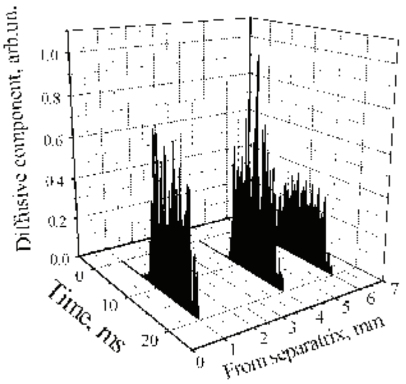

Fig.3. Time behavior of the diffusive component of volatility turbulent fluxes measured at different radial distances from LCFS in three shots.

Figure 3 and 4 show how the diffusive (4) and dynamic (3) components vary with time in the radial turbulent flux measured at different distances from LCFS. Measurements were performed from a shot to shot under identical experimental conditions. Characteristically, the dynamic component (which is associated with convection) is more volatile than the diffusive component.

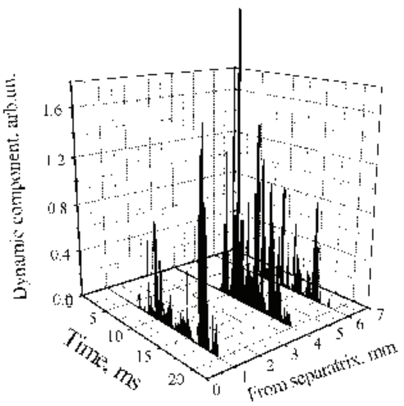

Fig.4. Time behavior of dynamic component of turbulent fluxes measured at different radial distances from LCFS in three shots.

Figure 5 shows the time behavior of the diffusive and dynamic components of volatility during the steady-state phase of the discharge. The flux radial turbulent was measured at a distance of 6 mm from LCFS. The experiment was conducted in the modified configuration of magnetic field (rotational transform 0.082, mean plasma radius 12.5 cm, the LCFS contacts with the wall).

From the curves in Fig. 5 it will be noticed the dynamic component compares with the diffusive component This is a typical example of discharges excited in the modified magnetic configuration, where the LCFS contacts with the chamber wall, and is also observed when the quality of the chamber wall surface is insufficient, when the effect of chamber wall boronization ceases.

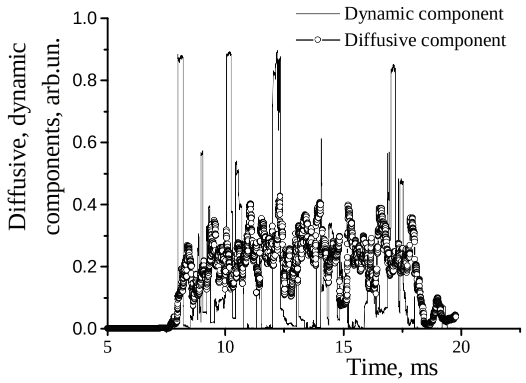

Fig.5. Time behavior of the dynamic and diffusive components for shot No. 55623.

Figure 6 shows the results of measurements of the local turbulent flux (a) before and (b) after boronization. The positive and negative values in the figure correspond to an outward and an inward flux, respectively. After boronization, the radial turbulent particle flux near the LCFS changes drastically and is preferentially directed outward.

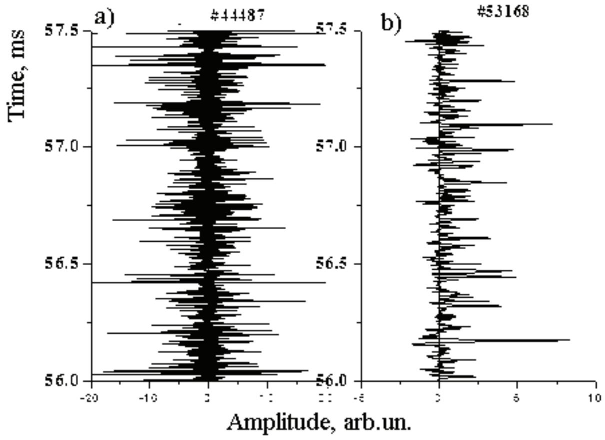

Fig.6. Comparison of the local turbulent flux (a) before and (b) after boronization, shot No.53163.

The time behavior of the dynamic and diffusive components for this case is shown in Fig. 7. Note that the component involved three turbulent processes in this case too. It can be seen that the diffusive component is dominant while the dynamic component is suppressed. Recall that the dynamic component is associated with convective transport, whereas the diffusive component characterizes the stochastic component of volatility.

The effect may be explained as follows. After boronization, the flux of carbon and oxygen from the chamber wall decreases; accordingly, radiative losses at the edge also decrease. As a result, the electron temperature at the plasma periphery increased to ~ 100 eV and a jump in T_e forms near the LCFS in a narrow r/a = 0.05) layer, with a very large temperature gradient [7]. The temperature gradient increases a shear of the electric field, which suppresses convection.

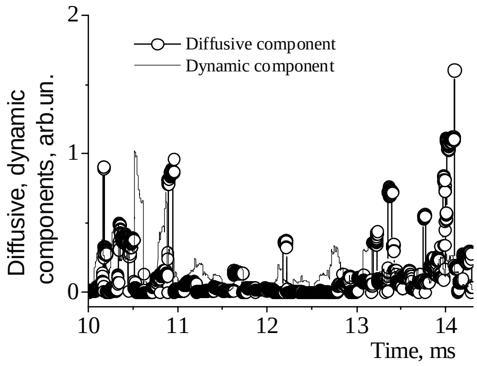

Fig.7. Time behavior of the dynamic and diffusive components for shot No. 53163.

4. Conclusions

A new approach, based on the analysis of time samples of the increments of turbulent particle fluxes, is used to estimate the dynamic and diffusive components in the edge turbulent flux of the L-2M stellarator. It is shown that a shift-scale mixture of several (three-four processes, depending on macroscopic characteristics of the plasma) normal processes adequately describes the PDFs of flux increments. The number of mixture components and the weight of each component are determined using the EM algorithm The method of sliding separation of mixtures is applied to separate between the dynamic and diffusive components of volatility and to trace their temporal evolution. With the above methods of analysis, some characteristic L-2M regimes have been examined. It is shown that turbulent particle transport in the edge plasma occurs by both the ballistic and diffusive mechanisms, and their contributions are roughly estimated.

This work was supported by the Dynasty Foundation, and the Russian Foundation for Basic Research (project nos. 07-02-00455).

References

[1] G. M. Batanov, V. E. Bening, V. Yu. Korolev, et al., JETP Lett. **78** (2003). 502.

[2] V.Yu. Korolev and N.N. Skvortsova. Eds) “Stochastic Models of Structural Plasma Turbulence”.VSP, Leiden - Boston, The Netherlands. 2006.

[3] V.Yu. Korolev, N.N. Skvortsova. In “The systems and means of informatics.” Ed. I.A. Sokolov. IPI RAN. (2005) 126 (In Russian).

[4] N.N. Skvortsova, V.Yu. Korolev, et al. Plasma Physics Reports. **31** (2005) 57.

[5] N.N. Skvortsova, V.Yu. Korolev, G.M. Batanov et al Plasma Phys. Contr. Fusion. **48** (2006) A393.

[6] V.V. Abrakov, D. K. Akulina, E. D. Andryukhina, et al., Nucl. Fusion **37** 1997. 233.

[7] G.S. Voronov, E.V. Voronova, D.K. Akulina et al. Plasma Phys. Contr. Fusion. **48** (2006) A303.

AUTHOR INDEX

Vol. (I) page 1 - 438　Vol. (II) page 439 - 861